PROCEEDINGS OF THE ELEVENTH INTERNATIONAL SYMPOSIUM ON ARTIFICIAL LIFE AND ROBOTICS

(AROB 11th'06)

Jan.23-25, 2006
B-Con Plaza, Beppu, Oita, JAPAN
Supported by Commemorative Organization for the Japan World Exposition ('70)

Editors: Masanori Sugisaka and Hiroshi Tanaka
ISBN 4-9902880-0-9

The Eleventh International Symposium on Artificial Life and Robotics 2006(AROB 11th ’06),
B-Con Plaza, Beppu, Oita, Japan, January 23-25, 2006

Program of The Eleventh International Symposium on

ARTIFICIAL LIFE AND ROBOTICS

(AROB 11th '06)

January 23-25, 2006
B-Con plaza, Beppu, Oita, Japan

Editors: Masanori Sugisaka and Hiroshi Tanaka

THE ELEVENTH INTERNATIONAL SYMPOSIUM ON ARTIFICIAL LIFE AND ROBOTICS

(AROB 11th '06)

ORGANIZED BY

Organizing Committee of International Symposium on Artificial Life and Robotics (Department of Electrical and Electronic Engineering, Oita University, Japan)

OPERATED BY

Santa Fe Institute (SFI, USA)
The Society of Instrument and Control Engineers (SICE, Japan)
The Robotics Society of Japan (RSJ, Japan)
The Institute of Electrical Engineers of Japan (IEEJ, Japan)
Institute of Control, Automation and Systems Engineers (ICASE, Korea)
Chinese Association for Artificial Intelligence (CAAI, China)

CO-OPERATED BY

The Institute of Systems, Control and Information Engineers (ISCIE)
The Institute of Electronics, Information and Communication Engineers (IEICE)
The Institute of Electrical and Electronics Engineers, Inc.(IEEE Japan Council)
Japan Robot Association (JARA)

SPONSORED BY

The Commemorative Organization for the Japan World Exposition('70)
Mitsubishi Electric Corporation Advanced Technology R&D Center
Oita Gas Co., Ltd.
ME System Co., Ltd.
Sanwa Shurui Co., Ltd.
Yatsushika Brewery Co., Ltd.
Yanai Denki

SUPPORTED BY

Kyushu Bureau of Economy, Trade and Industry, Ministry of Economy, Trade and Industry
Oita Prefecture
Oita City
Beppu City
The Federation of the Chamber of Commerce and Industry in Oita Prefecture
The Oita Prefectural Organization of the Industrial Groups
Kyodo News
JIJI Press
Oita Godo Shimbunsya
The Asahi shimbun Co.
The Mainichi Newspapers Co.
THE YOMIURI SHIMBUN
The Nishinippon Newspaper Co.
The NIKKAN KOGYO SHIMBUM. LTD.

Nihon Keizai Shimbun, Inc.
NHK Oita Station
Oita Broadcasting System
Television Oita System
Oita Asahi Broadcasting Co., Ltd.
Oita System Control Research Society

ADVISORY COMMITTE CHAIRMAN

F. Harashima (Tokyo Denki University, Japan)

GENERAL CHAIRMAN

M. Sugisaka (Oita University, Japan)

PROGRAM CHAIRMAN

H. Tanaka (Tokyo Medical & Dental University, Japan)

VICE-CHAIRMAN

J.J. Lee (KAIST, Korea)
J.L. Casti (Technical University of Vienna, Austria)
Y.G. Zhang (Academia Sinica, China)

ADVISORY COMMITTEE

T. Fukuda (Nagoya University, Japan)
F. Harashima (Tokyo Denki University, Japan)
H. Kimura (The University of Tokyo, Japan)
M. Tomizuka(University of California Berkeley, USA)
S.Ueno (Kyoto University, Japan)

INTERNATIONAL ORGANIZING COMMITTEE

K. Aihara (The University of Tokyo, Japan)
C. Barrett (Los Alamos National Laboratory, USA)
M. Bedau (Reed College, USA)
Z. Bubnicki (Wroclaw University of Technology, Poland)
J.L. Casti (Technical University of Vienna,Austria)
J.M. Epstein (The Brookings Institution, USA)
T. Fukuda (Nagoya University, Japan)
H. Hashimoto (The University of Tokyo, Japan)
D. J. G. James (Coventry University, UK)
K.Kyuma(Mitsubishi Electric Corporation, Advanced Technology R&D Center, Japan)
C.G. Langton (Santa Fe Institute, USA)
M.H. Lee (Pusan National University, Korea)
J.J. Lee (KAIST, Korea)
S. Rasmussen (Santa Fe Institute, USA)
T.S. Ray (University of Oklahoma, USA)
M. Sugisaka (Oita University, Japan) (Chairman)
C. Taylor (University of California-Los Angeles, USA)

W.R. Wells (University of Nevada-Las Vegas, USA)
Y.G. Zhang (Academia Sinica, China)

INTERNATIONAL PROGRAM COMMITTEE

K. Abe (Nihon University, Japan)
K. Aihara (The University of Tokyo, Japan) (Co-chairman)
T. Arita (Nagoya University, Japan)
M. Bedau (Reed College, USA)
R. Belew (University of California-San Diego, USA)
Z. Bubnicki (Wroclaw University of Technology, Poland)
A. Buller (ATR Network-Informatics Laboratories, Japan)
S-M. Chen (National Taiwan University of Science and Technology, Taiwan)
Y.Y. Fan (University of California-Davis, USA)
S. H. Han (Kyungnam University, Korea)
I. Harvey (University of Sussex, UK)
H. Hashimoto (The University of Tokyo, Japan)(Co-chairman)
N. Homma (Tohoku University, Japan)
H. Inooka (Tohoku University, Japan)
S. Ishikawa (Kyushu Institute of Technology, Japan)
T. Ishimatsu (Nagasaki University, Japan)
T. Iwamoto (Mitsubishi Electric Corporation, Advanced
Technology R&D Center, Japan)
J. Johnson (The Open University, UK)
M. Kaneko (Hiroshima University, Japan)
O. Katai (Kyoto University, Japan)
M. Kono (University of Miyazaki, Japan)
H. Kawamura (Hokkaido University, Japan)
S. Kawata (Tokyo Metropolitan University, Japan)
S. Kitamura (Kobe University, Japan)
S. Kumagai (Osaka University, Japan)
J. M. Lee (Pusan National University, Korea)
H.H. Lund (University of Southern Denmark, Denmark)
M. Minami (Fukui University, Japan)
H. Miyagi (The University of Ryukyus, Japan)
T. Nagashima (Muroran Institute of Technology, Japan)
M. Nakamura (Saga University, Japan)
K. Nakano (The University of Electro-Communications, Japan)
R. Nakatsu (Kwansei Gakuin University, Japan)
J. Nishii (Yamaguchi University, Japan)
W. Nistico (University of Dortmund, Germany)
S. Omatu (Osaka Prefecture University, Japan)
K. Onishi (Niigata University, Japan)
M. Okamoto (Kyushu University, Japan)
M. Osano (Aizu University, Japan)
M. Oswald (Vienna University of Technology, Austria)
R. Pfeifer (University of Zurich-Irchel, Switzerland)
T. S. Ray (University of Oklahoma, USA) (Co-chairman)
S. Sagara (Kyushu Institute of Technology, Japan)
P. Sapaty (National Academy of Sciences of Ukraine, Ukraine)
T. Sawaragi (Kyoto University, Japan)
T. Shibata (AIST, Japan)
K. Shimohara (ATR, Japan)
K-B. Sim (Chung-Ang University, Korea)

K. Sugawara (Tohoku Gakuin University, Japan)
M. Sugisaka (Oita University, Japan)
H. Suzuki (The University of Tokyo, Japan)
H. Tanaka (Tokyo Medical & Dental University, Japan) (Chairman)
M. Tanaka-Yamawaki (Tottori University, Japan)
K. Tsuchiya (Kyoto University, Japan)
K. Uosaki (Osaka University, Japan)
H. Umeo (Osaka Electro-Communication University, Japan)
K. Watanabe (Saga University, Japan)
T. Yamamoto (University of Ryukyus, Japan)
H. Yanagimoto (Osaka Prefecture University, Japan)
M. Yano (Tohoku University, Japan)
Y. Yin (The Beijing University of Science and Technology, China)
M. Yokota (Fukuoka Institute of Technology, Japan)

LOCAL ARRANGEMENT COMMITTEE

X. Feng (National University of Singapore, Singapore)
S. Sagara (Kyushu Institute of Technology, Japan)
A. Loukianov (Baical State University of Economy & Law, Russia)
M. Rizon (Northern Malaysia University College of Engineering, Malaysia)
X. Fan (Oita University, Japan)
M. Sugisaka (Oita University, Japan) (Chairman)
J. Wang (Oita University, Japan)
X. Wang (Niihama National College of Technology Japan)
F. Dai (Matsue National College of Technology, Japan)
M. Ito (Konan University, Japan)
R. Mamat (Terengganu Advanced Technical Institute, Malaysia)

HISTORY

This symposium was founded in 1996 by the support of Science and International Affairs Bureau, Ministry of Education, Culture, Sports Science and Technology, Japanese Government. Since then, this symposium has been held every year at B-Con Plaza, Beppu, Oita, Japan except in Oita, Japan (AROB 5th ’00) and in Tokyo, Japan (AROB 6th ’01). The eleventh symposium will be held on 23-25 January, 2006, at B-Con Plaza, Beppu, Oita, Japan. This symposium invites you all to discuss development of new technologies concerning Artificial Life and Robotics based on simulation and hardware in the twenty first century.

OBJECTIVE

The objective of this symposium is the development of new technologies for artificial life and robotics which have been recently born in Japan and are expected to be applied in various fields. This symposium will discuss new results in the field of artificial life and robotics.

TOPICS

Artificial brain research
Artificial intelligence
Artificial life
Artificial living
Artificial mind research
Bioinformatics chaos

Brain science
Cognitive science evolutionary computations
Complexity
Computer graphics
DNA computing
Fuzzy control
Genetic algorithms
Human-machine cooperative systems
Human-welfare robotics
Innovative computations
Intelligent control and modeling
Micromachines
Micro-robot world cup soccer tournament
Mobile vehicles
Molecular biology
Multi-agent systems
Nano-biology
Nano-robotics
Neural networks
Neurocomputers
Neurocomputing technologies and its application for hardware
Pattern recognition
Robotics
Robust virtual engineering
Virtual reality
Others

COPYRIGHTS

Accepted papers will be published in the proceeding of AROB and some of high quality papers in the proceeding will be requested to re-submit their papers for the consideration of publication in an international journal ARTIFICIAL LIFE AND ROBOTICS (Springer) and APPLIED MATHEMATICS AND COMPUTATION (North-Holland). All correspondence related to the symposium should be addressed to AROB Secretariat.

Dept. of Electrical and Electronic Engineering,
Oita University
700 Dannoharu, Oita 870-1192, JAPAN
TEL：+81-97-554-7841, FAX：+81-97-554-7818
E-MAIL arobsecr@cc.oita-u.ac.jp
Home Page http://arob.cc.oita-u.ac.jp/

MESSAGES

Masanori Sugisaka
General Chairman
(Professor, Oita University)

Masanori Sugisaka
General Chairman of AROB

It is my great honor to invite you all to the Eleventh International Symposium on Artificial Life and Robotics (AROB 11th '06).

The symposiums from the first (February 18-20, 1996) to the tenth (February 4-6, 2005) were organized by Oita University under the sponsorship of the Science and Technology Policy Bureau, the Ministry of Education, Science, Sports, and Culture (Monkasho), Japanese Government and Air Force Office of Scientific Research, Asian Office of Aerospace Research and Development (AFOSR/AOARD), USA and co-operated by Santa Fe Institute (USA), SICE, RSJ, IEEJ, ICASE, CAAI, ISCIE, IEICE, IEEE (Japan Council), and JARA.

I would like to express my sincere thanks to Monkasho, The Commemorative Organization for the Japan World Exposition('70) and scientific societies for their repeated support.

This Eleventh symposium is sponsored by The Commemorative Organization for the Japan World Exposition('70) and Japanese companies (Mitsubishi Electric Corporation Advanced Technology R&D Center, Oita Gas Co. Ltd., ME System Co.Ltd., Sanwa Shurui Co. Ltd., Yatsushika Brewery Co. Ltd. And others. I would like to express special thanks for The Commemorative Organization for the Japan World Exposition('70) and the companies stated above.

The symposium invites you to discuss the development of new technologies in the 21st century concerning Artificial Life and Robotics, based on simulation and hardware.

We hope that AROB 11th '06 will facilitate the establishment of an international joint research institute on Artificial Life and Robotics in future. I hope that you will obtain fruitful results from exchange of ideas between researchers during the symposium.

Hiroshi Tanaka
Program Chairman
(Professor, Tokyo Medical and Dental University)

Hiroshi Tanaka
Program Chairman of AROB

On behalf of the program committee, it is my great pleasure and honor to invite you all to the Eleventh International Symposium on Artificial Life and Robotics (AROB 11th ’06). This symposium is made possible owing to the cooperation of Oita University and Santa Fe Institute. We are also debt to Japanese academic associations such as SICE, RSJ, and several private companies. I would like to express my sincere thanks to all of those who make this symposium possible.

As is needless to say, the Alife and biologically-inspired Robotics approach now attracts wide interests as a new paradigm of science and engineering. Take an example in the field of bioscience, the accomplishment of HGP (Human Genome Project) and subsequent post-genomic comprehensive “Omics data” such as transcriptome, proteome and metabolome, bring about vast amount of bio-information. However, as a plenty of omics data becomes available, it becomes sincerely recognized that the framework by which these omics data can be understood to make a whole picture of life is critically necessary, thus, in the post-genomic era, Alife approach is expected to give one of new alternative ideas to integrate this vast amount of bio-data.

This example shows the Alife approach is very promising and becomes widely accepted as a paradigm of next generation of life science. We hope this symposium becomes a forum for exchange of the ideas of the attendants from various fields who are interested in the future possibility of complex systems approach.

I am looking forward to meeting you in Beppu, Oita.

Y. G. Zhang
Vice Chairman
(Professor, Academia Sinica)

Y. G. Zhang
Vice Chairman of AROB

Dear all friends and all participants,

Here I would like to show my warm welcome to you all attending the Eleventh International Symposium on Artificial Life and Robotics (AROB'06). As you know, this annual symposium was founded in 1996 by the support of Science and International Affairs Bureau, Ministry of Education, Science, Sports, and Culture (presently, Ministry of Education, Culture, Sports, Science and Technology) of Japan. Since then AROB is gradually become worldwide famous international symposium. Now AROB is already not an "academic baby", but "academic teenage", and AROB also owns an international journal, named the "Journal of Artificial Life and Robotics" published by Springer in last eight years.

The objective of AROB is aimed to develop new technologies for Artificial Life and Robotics which have been born recently. The important devotion of AROB is not only pay attention to the development of theory on Artificial Life, but also expected to apply the principle to various fields, especially, the combination of both the Artificial Life and Robotics together. So far there are only few international symposiums or conference on artificial life, however, AROB is the only one that to explore the new generation of Robotics in far-sight with artificial life principle. This is a very great and difficult career, and need continuous and consistent efforts of more and more scientists and engineers. All participants to AROB are the part of team and we are devoting to the same target.

Beppu, the place of held most AROB symposium, is very charming city in Japan, she has variety of hot spring (jijaoku), spa, beautiful bay and colorful mountains. Her phantasmagoric visual change in various season attract many tourists. I hope all of you enjoy and appreciate her.

Finally, I would like to show my great thanks to all people who are working for this AROB'06, including all staffs of AROB Lab, secretariat, and students, the successful holding of AROB symposium is dependent on the contributions of you all.

Ju-Jang Lee
Vice Chairman
(Professor, KAIST)

Ju-Jang Lee
ViceChairman of AROB

The 11th International Symposium on Artificial Life and Robotics (AROB) will be held in Beppu, Oita, JAPAN from Jan. 23rd to 25th, 2006. This year's Symposium will be held amidst the high expectations of the increasingly important role of the new interdisciplinary paradigm of science and engineering represented by the field of artificial life and robotics that is continuously attracts wide interests among scientist, researchers, and engineers around the globe.

Since the time of the very first AROB meeting in 1996, each year, distinguished researchers and technologists from around the world are looking forward to attend and to meet at AROB. AROB is becoming the annual excellent forum that represents a unique opportunity for the academic and industrial communities to meet and assess the latest developments in this fast growing artificial life and robotics field. AROB enables them to address new challenges and share solutions, discuss research directions for the future, exchange views and ideas, view the results of applied research, present and discuss the latest development of new technologies and the relevant applications. In addition, AROB offers offer the opportunity of hearing the opinions of well known leading experts in the field through the keynote sessions, provides the bases for regional and international collaborative research, and enables to foresee the future evolution of new scientific paradigms and theories contributed by the field of artificial life and robotics and associated research area. The twenty-first century will become the century of artificial life and intelligent machines in support of humankind and AROB is contributing through wide technical topics of interest that support this direction.

It is a great for me as the Vice Chairman of the 11th AROB 2006 to welcome everyone to this important event. Also, I would like to extend my special thanks is owed to all the authors and speakers for contributing their research works, the participants, and to forget the organizing team of the 11th AROB.
Looking forward to meet you at the 11th AROB in Beppu-Oita and wish you all the best.

Plenary talker:

Prof. ToshioFukuda

PT1 Multi-locomotion robots -PDAC for intelligent control-

T. Fukuda,
Masahiro Doi, Hideki Kajima, Yoshihiko Asano, Takayuki Matsuno
(Nagoya University, Japan)
Yasuhisa Hasegawa (Tsukuba University, Japan),

In this paper, we introduce the novel control method for multi-locomotion robot named Passive Dynamic Autonomous Control (PDAC). PDAC assumes two following premises: 1) point-contact 2) interlocking. The second premise means that the angles of robot joints are connected with the angle around contact point. The approach of PDAC is to describe the robot dynamics as a 1-DOF autonomous system, which is the dynamics around contact point. This approach makes it possible to generate natural motion. The effectiveness of proposed method is confirmed by experiments using multi-locomotion robot.

Prof. Hideki Hashimoto

PT2 Present State and Future of Intelligent Space Discussion on Implementation of RT in our Environments

Hideki Hashimoto
Institute of Industrial Science
University of Tokyo, Japan
http://dfs.iis.u-tokyo.ac.jp

"Intelligent Space" is a platform which we can implement advanced technologies easily to realize smart services to human. We have developed and reported the vision system based on color information, the handover scheme networking multi cameras, the human following mobile robot systems, the path generator based on human watching, etc. In this talk, I will summarize the present state of Intelligent Space and try to describe a future from a viewpoint of system integration. Also we are now introducing RT(Robot Technology) to develop the Intelligent Space as an actual standard platform which could be approved by Robotics Community.

Prof. Ju-Jang Lee

PT3 Development of Future Intelligent Sweet Home for the Disabled

Ju-Jang Lee
Korea Advanced Institute of Science and Technology
Korea

This presentation introduces a new smart house, *Intelligent Sweet Home*, developed at HWRS-ERC center of KAIST, Korea for testing advanced concepts on independent living of the elderly and people with disabilities. The work focuses on technical solutions for human-friendly motion/mobility assistance and advanced human-machine interfaces that provide easy control of both assistive robotic systems and home-installed applications. To improve the inhabitant comfort, an intelligent bed, intelligent wheelchair and transferring system between bed and wheelchair have been developed and tasted. The solutions applied to their design comply with most of the user's requirements and suggestions collected by a special questionnaire survey among people with disabilities. The intelligent sweet home behaves in accordance with the user commands and/or the recognized intentions of the user. Various interfaces based on hand gesture, voice, body movement and posture have been studied and tested. The presentation shows the overall structures of the system and explains the design and functionality of main system components. I hope that this plenary talk will provide not only speech on the progress of new technologies but also the future vision of a better life for the disabled and elderly.

The Eleventh International Symposium on ARTIFICIAL LIFE AND ROBOTICS (AROB 11th '06)

January 23 (Monday)

Room E: 10:40-11:00

Opening Ceremony

Chair: H.H. Lund (University of Southern Denmark, Denmark)

Welcome Addresses

1. General Chairman of AROB	M. Sugisaka (Oita University, RIKEN, Japan)
2. Program Chairman of AROB	H. Tanaka (Tokyo Medical& Dental University, Japan)
3. Vice Chairman of AROB	Y. G. Zhang (Academia Sinica, China)
4. Vice Chairman of AROB	J. J. Lee (Korea Institute of Science and Technology, Korea)

January 24 (Tuesday)

Hotel Shiragiku: 18:20-20:20

AROB Award Ceremony

Chair: K. Watanabe (Saga University, Japan)

Banquet

Chair: S. Sagara (Kyushu Institute of Technology, Japan)

Welcome Addresses

T. Hano (President of Oita University, Japan)

H.H. Lund (University of Southern Denmark, Denmark)

TIME TABLE

	RoomA	RoomB	RoomC	RoomD	RoomE
1/22 (Sun) 13:00–17:00	Registration (Registration Desk)				
	Welcome Party (at Beppu Kamenoi Hotel 3th Floor)				
1/23 (Mon) 8:00	Registration (Registration Desk)				
8:40	GS2(4) Chair D. Ai will end at 10:00	OS13(5) Chair J .J. Lee	GS21(5) Chair S. Sagara	GS12(5) Chair S. Ishikawa	
10:20	Coffee Break				
10:40					Ceremony Plenary Talk PT1 T. Fukuda Chair J .J. Lee
11:40	Lunch				
12:40	GS3(4) Chair X. Wang	OS10(4) Chair T.Yamamoto	GS22(4) Chair N. Homma	GS11(4) Chair J-Q. Liu	
14:00	Coffee Break				
14:10	OS1(7) Chair F. Dai	OS4(7) Chair J. M. Lee	GS20(7) Chair C-Y. Lee	GS4(7) Chair Z. Shi	
16:30–17:50	OS2(4) Chair S. Omatu	GS7(5) Chair M. Eaton will end at 18:10	GS6(4) Chair K. Ikeda		

GS: General Session OS: Organized Session

GS1 Artificial Brain Research
GS2 Artificial Intelligence-Ⅰ
GS3 Artificial Intelligence-Ⅱ
GS4 Artificial Life
GS5 Computer Graphics
GS6 Complexity
GS7 Cooperative Systems
GS8 Evolutionary Computations
GS9 Genetic Algorithms-I
GS10 Genetic Algorithms−Ⅱ
GS11 Human-Machine
GS12 Image Processing
GS13 Intelligent Control and Modeling-I & Cognitive Science
GS14 Intelligent Control and Modeling-Ⅱ
GS15 Innovative Computations-I
GS16 Innovative Computations-Ⅱ
GS17 Mobile Vehicles & Human-Welfare Robotics
GS18 Molecular Biology
GS19 Neural Networks
GS20 Robotics-I
GS21 Robotics-Ⅱ
GS22 Robotics-Ⅲ
GS23 Others
OS1 Student's Session-Recognition and Control for Robot
OS2 Intelligent Systems
OS3 Biomimetic Machines and Robots
OS4 Ubiquitous Automated Systems
OS5 Bio-inspired Approach and Application
OS6 Cognitive Robotics
OS7 Intelligent Systems and Learning
OS8 Vision, Automata and Neural Network
OS9 Robotics, Automata and Control
OS10 Soft Robotics and Information
OS11 Dynamics and Control for Complex Systems
OS12 Analysis and Implementation of Neural Systems
OS13 Intelligent Sensor and Algorithm
OS14 Robot Control and Application

Date	Time	RoomA	RoomB	RoomC	RoomE
1/24	8:00	Registration (Registration Desk)			
(Tue)	8:40	GS9(5) Chair A. Nakamura will end at 10:20	GS17(5) Chair P. Sapaty will end at 10:20	OS7(6) Chair K. Abe	
	10:40	Coffee Break			
	10:50				Plenary Talk PT2 H. Hashimoto Chair: K-B. Sim
	11:30	Lunch			
	12:30	GS10(4) Chair H. Yamamoto will end at 13:50	GS8(5) Chair M. Oswald	GS13(5) Chair J. S. Yang	
	14:10	Coffee Break			
	14:30	OS11(5) Chair H. Suzuki	GS15(4) Chair T. Arita will end at 15:50	GS14(3) Chair T. Nakashima will end at 15:30	
			GS16(4) Chair Y. Ishida will end at 17:10	GS19(6) Chair Y. Kinouchi will end at 17:30	
	16:10	OS12(5) Chair T. Kohno will end at 17:50	GS5(3) Chair A. Niimi will end at 18:10		
	18:20	AROB Award Ceremony (Chair K. Watanabe) Banquet -Hotel Shiragiku- (Chair S. Sagara)...... Welcome Address T. Hano / H. H. Lund			
	20:20				

GS: General Session OS: Organized Session

GS1 Artificial Brain Research
GS2 Artificial Intelligence-Ⅰ
GS3 Artificial Intelligence-Ⅱ
GS4 Artificial Life
GS5 Computer Graphics
GS6 Complexity
GS7 Cooperative Systems
GS8 Evolutionary Computations
GS9 Genetic Algorithms-I
GS10 Genetic Algorithms−Ⅱ
GS11 Human-Machine
GS12 Image Processing
GS13 Intelligent Control and Modeling-I & Cognitive Science
GS14 Intelligent Control and Modeling-Ⅱ
GS15 Innovative Computations-I
GS16 Innovative Computations-Ⅱ
GS17 Mobile Vehicles & Human-Welfare Robotics
GS18 Molecular Biology
GS19 Neural Networks
GS20 Robotics-I
GS21 Robotics-Ⅱ
GS22 Robotics-Ⅲ
GS23 Others
OS1 Student's Session-Recognition and Control for Robot
OS2 Intelligent Systems
OS3 Biomimetic Machines and Robots
OS4 Ubiquitous Automated Systems
OS5 Bio-inspired Approach and Application
OS6 Cognitive Robotics
OS7 Intelligent Systems and Learning
OS8 Vision, Automata and Neural Network
OS9 Robotics, Automata and Control
OS10 Soft Robotics and Information
OS11 Dynamics and Control for Complex Systems
OS12 Analysis and Implementation of Neural Systems
OS13 Intelligent Sensor and Algorithm
OS14 Robot Control and Application

	RoomA	RoomB	RoomC	RoomE
1/25 8:00	Registration (Registration Desk)			
(Wed) 8:40	OS14(6) Chair S. H. Han	OS6(6) Chair M. Yokota	OS5(6) Chair I. Yoshihara	
10:40	Coffee Break			
11:00				Plenary Talk PT3 J.J.Lee Chair J. Du
11:40	Lunch			
12:40	GS1(5) Chair Y. G. Zhang	OS3(6) Chair K. Watanabe will end at 14:40	OS8(5) Chair Y. Yoshitomi	
14:20	GS18(4) Chair K. Ohnishi will end at 15:40	GS23(11) Chair M. Rizon	OS9(6) Chair M. Kono	
16:20	Farewell Party (Room A)			
17:00				

GS: General Session OS: Organized Session

GS1 Artificial Brain Research
GS2 Artificial Intelligence- Ⅰ
GS3 Artificial Intelligence-Ⅱ
GS4 Artificial Life
GS5 Computer Graphics
GS6 Complexity
GS7 Cooperative Systems
GS8 Evolutionary Computations
GS9 Genetic Algorithms-I
GS10 Genetic Algorithms−Ⅱ
GS11 Human-Machine
GS12 Image Processing
GS13 Intelligent Control and Modeling-I & Cognitive Science
GS14 Intelligent Control and Modeling-Ⅱ
GS15 Innovative Computations-I
GS16 Innovative Computations-Ⅱ
GS17 Mobile Vehicles & Human-Welfare Robotics
GS18 Molecular Biology
GS19 Neural Networks
GS20 Robotics-I
GS21 Robotics-Ⅱ
GS22 Robotics-Ⅲ
GS23 Others
OS1 Student’s Session-Recognition and Control for Robot
OS2 Intelligent Systems
OS3 Biomimetic Machines and Robots
OS4 Ubiquitous Automated Systems
OS5 Bio-inspired Approach and Application
OS6 Cognitive Robotics
OS7 Intelligent Systems and Learning
OS8 Vision, Automata and Neural Network
OS9 Robotics, Automata and Control
OS10 Soft Robotics and Information
OS11 Dynamics and Control for Complex Systems
OS12 Analysis and Implementation of Neural Systems
OS13 Intelligent Sensor and Algorithm
OS14 Robot Control and Application

TECHNICAL PAPER INDEX

January 23 (Monday)

Room E

11:00~11:40 Plenary Talk
Chair J. J. Lee（Korea Institute of Science and Technology, Korea）

PT-1 *Multi-locomotion robots -PDAC for intelligent control-*
T. Fukuda (Nagoya University, Japan)

January 24 (Tuesday)

Room E

10:50~11:30 Plenary Talk
Chair K-B. Sim（Chung-Ang University, Korea）

PT-2 *Present state and future of intelligent space –discussion on implementation of RT in our environments*
H. Hashimoto(University of Tokyo, Japan)

January 25 (Wednesday)

Room E

11:00~11:40 Plenary Talk
Chair J. Du (Beijing Technology and Business University, China)

PT-3 *Development of future intelligent sweet home for the disabled*
J. J. Lee (Korea Institute of Science and Technology, Korea)

January 23 (Monday)

8:00~Registration

Room A

8:40~10:00 GS2 Artificial Intelligence-Ⅰ
Chair: D. Ai (University of Science and Technology Beijing, China)

GS2-1 *Locating static targets by matching image frames*
X. Wang(Niihama National College of Technology, Oita University, Japan)
M. Sugisaka (Oita University, Japan)
J. Wang (Hebei University of Science and Technology, China)

GS2-2 *Perceptual and introspective learning for developmental robot*
Z. Shi, Q. Li (Chinese Academy of Sciences, China)

GS2-3 *A robot control method using evolutive binary decision diagrams*
M. Kanoh (Chukyo University, Japan)
H. Itoh (Nagoya Institute of Technology, Japan)

GS2-4 *Waste incinerator emission prediction using probabilistically optimal ensemble of multi-agents and neural networks*
D. Yamaguchi, M. Takahashi, E. Tazaki (Toin University of Yokohama, Japan)
K. J. Mackin (Tokyo University of Information Sciences, Japan)

12:40~14:00 GS3 Artificial Intelligence-Ⅱ
Chair: X. Wang (Niihama National College of Technology, Japan)

GS3-1 *Model-based reinforcement learning for large-scale multi-agent games with sampling-based state estimation*
H. Fujita, S. Ishii (Nara Institute of Science and Technology, Japan)

GS3-2 *Analyzing robustness in multi-agent reinforcement learning -A comparison between profit sharing and Q-learning*
T. Nehashi, K. Takadama(Tokyo Institute of Technology, Japan)
K. Miyazaki (National institution for Academic Degrees and University Evaluation, Japan)

GS3-3 *Natural policy gradient reinforcement learning method for a looper-like robot*
Y. Nakamura, T. Mori, S. Ishii(Nara Institute of Science and Technology (NAIST), Japan)

GS3-4 *Vector control of induction motor using advanced hybrid system based on GA and Bacteria Foraging*
D-H. Kim (Hanbat National University, Korea)

14:10~16:30 OS1 Student's Session-Recognition and Control for Robot
Chair: F. Dai (Matsue National College of Technology, Japan)

Co-Chair: J. Hayashida (Matsue National College of Technology, Japan)

OS1-1 *Remote Control of robot using wireless LAN*
N. Kawasaki, F. Dai, Y. Fujihara (Matsue National College of Technology, Japan)

OS1-2 *Research on face recognition system by genetic algorithm*
F. Dai, T. Kodani, Y. Fujihara (Matsue National College of Technology, Japan)

OS1-3 *Research on autonomous mobile robot for visually handicapped humans*
T. Nakamura, F. Dai, Y. Fujihara (Matsue National College of Technology, Japan)

OS1-4 *Walking orbit of biped robot by using the simulation*
K. Umezaki, M. Sugisaka (Oita University, Japan)

OS1-5 *Motion trace through head control*
E. Goubaru, M. Sugisaka (Oita University, Japan)

OS1-6 *Characteristic measurement of artificial muscle*
S. Ichikawa, M. Sugisaka (Oita University, Japan)

OS1-7 *Motion control of biped robot*
K. Kabata, M. Sugisaka (Oita University, Japan)

16:30~17:50 OS2 Intelligent Systems
Chair: S. Omatu (Osaka Prefecture University, Japan)
Co-Chair: H. Ido (Niihama National College of Technology, Japan)

OS2-1 *Intelligent classification of bill money*
S. Omatu (Osaka Prefecture University, Japan)
T. Kosaka(Glory TD Himeji, Japan)
M. Teranisi (Nara University of Education, Japan)

OS2-2 *Intelligent smell classification by neural networks*
S. Omatu,T. Fujinaka, S. Okazaki(Osaka Prefecture University, Japan)
T. Sumiya, M. Ono (Funai Electric Advanced Applied Technology, Research Institute Inc., Japan)

OS2-3 *Graph construction with maximum number of trees by continuous edge addition*
H. Ido, Y. Ohama, T. Takahashi (Niihama National College of Technology, Japan)

OS2-4 *Graph Extension with Constant Connectivity*
H. Ido (Niihama National College of Technology, Japan)
S. Omatu (Osaka Prefecture University, Japan)

Room B

8:40~10:20 OS13 Intelligent Sensor and Algorithm
Chair: J. J. Lee(Korea Advanced Institute of Science and Technology, Korea)
Co-Chair: M. Habib (Korea Advanced Institute of Science and Technology, Korea)

OS13-1 *Design and fabrication of tactile sensor system of FBG optical fiber sensors*
J. S. Heo, J.J. Lee (Korea Advanced Institute of Science and Technology, Korea)

OS13-2 *Implementation of an intelligent personalized digital library system based on improved negotiation mobile multi agents,*
Y. I. Cho (Suwon University, Korea)

OS13-3 *Crowd simulation with virtual force model*
C.Y. Lee (Kyungpook National University, Korea)
S. Baek (ETRI, Korea)

OS13-4 *Driver fatigue detection using genetic algorithm*
S. Jin, S-Y. Park. J. J. Lee(Korea Advanced Institute of Science and Technology, Korea)

OS13-5 *Virtual planes and active vision for fast 3D real time obstacle detection and avoidance*
M. K. Habib, J. J. Lee(Korea Advanced Institute of Science and Technology, Korea)

12:40~14:00 OS10 Soft Robotics and Information
Chair: T. Yamamoto (University of the Ryukyus, Japan)
Co-Chair: H. Kinjo (University of the Ryukyus, Japan)

OS10-1 *Identification using dynamical neural network with modified BP method*
K. Nakazono, H. Kinjo (University of the Ryukyus, Japan)
K. Ohnishi (Keio University, Japan)

OS10-2 *Nonholonomic system control using neurocontroller evolved by genetic algorithm*
N. Ogino, H. Kinjo, K. Nakazono, T. Yamamoto(University of the Ryukyus, Japan)

OS10-3 *Searching performance of real-coded genetic algorithm using biased probability distribution functions and mutation*
H. Nakanishi, H. Kinjo, N. Oshiro, T. Yamamoto (University of the Ryukyus, Japan)

OS10-4 *A self-organizing model of place cells with periodically distributed receptive fields*
N. Oshiro, K. Kurata, T. Yamamoto(University of the Ryukyus, Japan)

14:10~16:30 OS4 Ubiquitous Automated Systems
Chair: J. M. Lee (Pusan National University, Korea)
Co-Chair: S-C. Kim (Pusan National University, Korea)

OS4-1 *On-line prognostics health maintenance for induction motors based on time-series data mining*
J. Park, Y. Kim, Y-I. Kim, H. Bae, S. Kim (Pusan National University, Korea)

OS4-2 *The curvature detect system of the lane using image*
J-w. Kim, S-k. Ha, S-b. Cho, K-r. Baek (Pusan National University, Korea)

OS4-3 *Implementation mass flow controller for adaptive PID*
B. Cho, K. Baek (Pusan National University, Korea)

OS4-4 *A force reflection electronic joystick using single hall sensor*
S.K. Cho, S. S. Han, J.M. Lee (Pusan National University, Korea)

OS4-5 *An self-localization of mobile robot in an RFID sensor space*
B. S. Choi, H. S. Choi, J. M. Lee (Pusan National University, Korea)

OS4-6 *Fuzzy posture control for biped walking robot based on force sensor for ZMP*
K.C. Choi, M.C. Lee, J. M. Lee (Pusan National University, Korea)

OS4-7 *Bluetooth network for distributed autonomous robotic system*
S-H. Whang, I-H. Jang, K-B. Sim (Chung-Ang University, Korea)

16:30~18:10 GS7 Cooperative Systems
Chair: M. Eaton (University of Limerick, Ireland)

GS7-1 *Mapping children and playgrounds into multi-agent systems*
A. Derakhshan, F. Hammer, H. H. Lund (University of Southern Denmark, Denmark)
Y. Demazeau (CNRS, Laboratoire LEIBNIZ, Institut IMAG, France)

GS7-2 *Reference-position detection using fan beam laser for cooperative localization of multiple mobile robots*
H. Takai, J.Mitsuoka (Hiroshima City University, Japan)
K. Tachibana(Osaka Gakuin University, Japan）

GS7-3 *Learning method of cooperative team play using the immune system*
N. Kogawa, K. Kobayashi, M. Obayashi, T. Kuremoto (Yamaguchi University, Japan)

GS7-4 *A study on stability analysis of cooperative AGV systems using decentralized control algorithm*
J. H. Suh, K. S. Lee(Dong-A University, Korea)
Y. B. Kim(Pukyong National University, Korea)

GS7-5 *Development of learning support system for piano-keying*
-Relationship between the activity of finger muscles and key release velocities of an expert-
T. Tamei, T. Shibata, S. Ishii(Nara Institute of Science and Technology, Japan)

Room C

8:40~10:20 GS21 Robotics-Ⅱ
Chair: S. Sagara (Kyushu Institute of Technology, Japan)

GS21-1 *Implementation of infrared wireless communication system for multi-mobile robots' team operations*
H. Takai, T. Ninomiya (Hiroshima City University, Japan)
K. Tachibana (Osaka Gakuin University, Japan)

GS21-2 *The development of robot palletizing simulator using pallet pattern algorithm and trajectory optimization*
S-n. Yu, S-j. Lim, H-k.Yoon, C-s.Han (Han Yang University, Korea)

GS21-3 *Redundant arm positioning control by linear visual servoing based on linear approximation of forward kinematics*
S. Mukai, N. Maru (Wakayama University, Japan)

GS21-4 *A study of an autonomous mobile robot for sewer inspection system*
A. Ahrary, A. Nassiraei (FAIS-Robotics Research Institute, Kyushu Institute of Technology, Japan)
M. Ishikawa (Kyushu Institute of Technology, Japan)

GS21-5 *Detection of face pose with neural networks*
Y-Z. Chang, G-T. Hung (Chang Gung University, Taiwan)

12:40~14:00 GS22 Robotics-Ⅲ
Chair: N. Homma (Tohoku University, Japan)

GS22-1 *A study on the development of actively controlled anti-seasickness bed*
Y. B. Kim (Pukyong National University, Korea)
J. H. Suh, K. S. Lee (Dong-A University, Korea)

GS22-2 *A modeling and position control based on two –mass system for machine stand vibration system*
S. Watanabe, F. Ohkawa, R. Oguro, J. Kobayashi (Kyushu Institute of Technology, Japan)

GS22-3 *Reinforcement learning of switching multiple controllers to control a real robot*
Y. Tokita, Y. Nakamura, S. Ishii (NARA Institute of Science and Technology, Japan)
J. Yoshimoto (Okinawa Institute of Science and Technology Promotion Corporation, Japan)

GS22-4 *Real time control of humanoid-robot cooperative motion using a genetic algorithm and neural network*
K-J. Choi, Y-K. Hwang, D. S. Hong (Changwon National University, Korea)

14:10~16:30 GS20 Robotics- Ⅰ
Chair: C-Y. Lee (Kyungpook National University, Korea)

GS20-1 *Navigation system for an autonomous robot using an ocellus camera in indoor environment*
T. Umeno, E. Hayashi (Kyushu Institute of Technology, Japan)

GS20-2 *RAC for underwater vehicle-manipulator systems using dynamic equation*
T. Yatoh, S. Sagara, M. Tamura (Kyushu Institute of Technology, Japan)

GS20-3 *Digital tracking control of space robots using transpose of Generalized Jacobian Matrix*
S. Sagara (Kyushu Institute of Technology, Japan)
Y. Taira (National Fisheries University, Japan)

GS20-4 *Optimal parameter tuning in proportional control for the unicycle mobile robot :An experimental study*

D. Hazry, M. Sugisaka (Oita University, Japan)

GS20-5 *Development of an autonomous personal robot "System of recognition for work"*
H. Mizoguchi, Y. Matsumoto, E. Hayashi (Kyushu Institute of Technology, Japan)

GS20-6 *A model of Mckibben muscle actuator based on experiment*
H. Zhao (University of Science and Technology Beijing, China / Oita University, Japan)
M. Sugisaka (Oita University, Japan)
D. Yu (University of Science and Technology Beijing, China)

GS20-7 *Offensive strategy of a billiard robot*
J-S. Yang, J-T. Li (Tamkang University, Taiwan)
C.Y. Yang (Northern Taiwan Institute of Science and Technology, Taiwan)

16:30~17:50 GS6 Complexity
Chair: K. Ikeda (Kyoto University, Japan)

GS6-1 *VeriSync:A verification system for firing squad synchronization protocols on one-dimensional cellular automata*
K. Matsumoto, H. Umeo (University of Osaka Electro-Communication, Japan)

GS6-2 *State-efficient synchronization protocols for communication-restricted cellular automata*
T. Yanagihara, M. Kanazawa, H. Umeo (University of Osaka Electro-Communication, Japan)

GS6-3 *Analysis and simulation of group dynamics based on interaction between decision making and Heider's POX systems*
T. Nomura (Ryukoku University, Japan)

GS6-4 *Cut off of Zipfs power law in US cities*
K. Yamasaki, M. Ohshiro, K.J. Mackin, E. Nunohiro (Tokyo University of information Sciences, Japan)

Room D

8:40~10:20 GS12 Image Processing
Chair: S. Ishikawa (Kyushu Institute of Technology, Japan)

GS12-1 *Visualization of an invisible space based on the MR technique*
S. Hashimoto, J. K. Tan, S. Ishikawa (Kyushu Institute of Technology, Japan)

GS12-2 *Face emotion recognition-a survey*
M. Karthigayan, M. Rizon , S. Yaacob, R. Nagarajan（Northern Malaysia University College of Engineering, Malaysia)

GS12-3 *Moments in IC chip classification*
M. Karthigayan, R.Nagarajan, S. Yaacob, P. Pandian, M. Rizon (Northern Malaysia University College of Engineering, Malaysia)

M. Rozailan (Terengganu Advanced Technical Institute(TATI), Malaysia)

GS12-4 *Dimensions reduction for face recognition using principal component analysis*
M. F. Hashim, M. Rizon ,P. Saad, M. Karthigayan S. Yaakob, H. Yazid (Kolej Kejuruteraan Utara Malaysia (KUKUM), Malaysia)
M. R. Mamat (Terengganu Advanced Technical Institute (TATI), Malaysia)

GS12-5 *Automatic motion detection for surveillance*
N. Mokhtar, M. Sugisaka (Oita University, Japan)

12:40~14:00 GS11 Human-Machine
Chair: J-Q. Liu (ATR Network Informatics Labs., Japan)

GS11-1 *Surface based spatial awareness for mobile robots*
K. Kanev (The University of Aizu, Japan)
S. Kimura (Kanazawa University, Japan)

GS11-2 *Interactive musical editing system to support human errors and offer personal preferences for an automatic piano- A system of inferring phrase expression-*
Y. Hikisaka, E.Hayashi (Kyushu Institute of Technology, Japan)

GS11-3 *Minimal design of "in situ" communication agents*
N. Matsumoto, H. Fujii, M. Okada (ATR Network Informatics Laboratories, Japan)

GS11-4 *A novel human-environment interface for conceptualizing spatial information in non-speech audio*
S. Nomura, M. Tsuchinaga, Y. Nojima, T. Shiose, H. Kawakami, O. Katai (Kyoto University, Japan)
K. Yamanaka (Federal University of Uberlandia, Brasil)

14:10~16:30 GS4 Artificial Life
Chair: H.H Lund (University of Southern Denmark, Denmark)

GS4-1 *Emerging cell array based on reaction-diffusion*
S. Miyashita (University of Zurich, Switzerland)
S. Murata (Tokyo Institute of Technology, Japan)

GS4-2 *Biomimetic control of mobile robots based on the information processing model of Paramecium*
A. Hirano, T. Tsuji, N. Takiguchi (Hiroshima University, Japan)
H. Ohtake (Osaka University, Japan)

GS4-3 *Evolutionary simulation of an agent based mobility system using indirect communication*
F. Zanlungo (University of Bologna, Italy)
T. Arita (Nagoya University, Japan)

GS4-4 *Evolution, development and learning in the prisoner's dilemma game*
Y. Ogawa, T. Arita (Nagoya University, Japan)

GS4-5 *Describing metabolic pathways using an artificial chemistry based on pattern matching*

and recombination
Y. Suzuki, K. Tominaga (Tokyo University of Technology, Japan)

GS4-6 *Morphogenesis of 3D sheets exploiting a spatial condition*
S. Miyashita (University of Zurich, Switzerland)

GS4-7 *Sexual reproduction in digital organisms*
D. Ai, X. Ban. Y. Yin, X. Tu (University of Science and Technology Beijing, China)

<u>January 24 (Tuesday)</u>

8:00~ Registration

Room A

8:40~10:20 GS9 Genetic Algorithms-Ⅰ
Chair: A. Nakamura (National Institute of Advanced Science and Technology (AIST), Japan)

GS9-1 *Development of NC tool path generation system by absolute and incremental type individual*
H. Yamamoto, R.B. Ramli (Gifu University, Japan)

GS9-2 *A study of selecting optimal parameters for genetic algorithm*
S.Y. Park, S. Jin, J.J. Lee (Korea Advanced Institute of Science and Technology(KAIST), Korea.)

GS9-3 *The new DFM approach based on genetic algorithm*
M. Yoshikawa, H. Terai (Ritsumeikan University, Japan)

GS9-4 *Design of an augmented automatic choosing control with constrained input by extremizing a combination of Hamiltonian and Lyapunov functions*
T. Nawata (Kumamoto National College of Technology, Japan)
H. Takata (Kagoshima University, Japan)

GS9-5 *Colour quantisation using simulated annealing*
G. Schaefer, L. Nolle (Nottingham Trent University, United Kingdom)
T. Nakashima(Osaka Prefecture University, Japan)

12:30~13:50 GS10 Genetic Algorithms-Ⅱ
Chair: H. Yamamoto (Gifu University, Japan)

GS10-1 *Applying genetic algorithm to a programming training support system*
E. Nunohiro, K. J. Mackin, M. Ohshiro, K. Yamasaki(Tokyo University of Information Sciences, Japan)

GS10-2 *Automatic generation of B-spline curve using the evolution technique*
M. Saito, S. Serikawa (Kyushu Institute of Technology, Japan)

GS10-3 *A genetic approach to the design of autonomous agents for futures trading*

H. Kitano, T. Nakashima, H. Ishibuchi (Osaka Prefecture University, Japan)

GS10-4 *Comparison between self-organization with sampling and genetic algorithms in multi-modal function*
T. Higo, K. Takadama (Tokyo Institute of Technology, Japan)
M. Katuhara, T. Majima (National Maritime Research Institute , Japan)

14:30~16:10 OS11 Dynamics and Control for Complex Systems
Chair: H. Suzuki(The University of Tokyo, Japan)
Co-Chair: S. Horai (The University of Tokyo, Japan)

OS11-1 *A simple model of evolving ecosystems*
T. Shimada, K. Aihara (Aihara Complexity Modelling Project, ERATO, JST, The University of Tokyo, Japan)
Y. Murase, S. Yukawa, N. Ito(The University of Tokyo, Japan)

OS11-2 *The behavioral adaptation and the diversification in ecosystem*
Y. Murase, S.Yukawa, N. Ito (The University of Tokyo, Japan)
T. Shimada (Aihara Complexity Modelling Project, ERATO, JST, Japan)

OS11-3 *Stability of equilibrium state of multi-type SIS model on network with certain property*
N. Sugimine (Aihara Complexity Modelling Project, ERATO, JST, Japan)
K. Aihara (Aihara Complexity Modelling Project, ERATO, JST, The University of Tokyo, Japan)

OS11-4 *On chaos suppression by resonant parametric perturbation*
M. Sekikawa (Aihara Complexity Modelling Project, ERATO, JST, Japan)
N. Inaba (Utsunomiya University, Japan)
K. Aihara (The University of Tokyo, Japan)

OS11-5 *State estimation with finite data rates and information pattern*
H. Shimokawa (Aihara Complexity Modelling Project, ERATO, JST, Japan)
K. Aihara (The University of Tokyo, Aihara Complexity Modelling Project, ERATO, JST, Japan)

16:10~17:50 OS12 Analysis and Implementation of Neural Systems
Chair : T. Kohno(The University of Tokyo, Japan)
Co-Chair: Y. Hirata (The University of Tokyo)

OS12-1 *Modeling of birdsong learning with chaotic Elman network*
M. Funabashi (The University of Tokyo, Japan)
K. Aihara (The University of Tokyo, Japan)

OS12-2 *Classification of the spike sequences by discriminating their sources of time correlation*
K. Fujiwara (The University of Tokyo, Japan)
K. Aihara(The University of Tokyo, and ERATO, JST, Japan)

OS12-3 *Spike train surrogates and dual coding*
Y. Hirata, H. Suzuki (The University of Tokyo, Japan)

K. Aihara (The University of Tokyo, Aihara Complexity Modelling Project, ERATO, JST, Japan)

OS12-4 *Dynamic switching of neural coding schemes in a network with gap junctions*
Y. Katori, K. Aihara (Aihara Complexity Modelling Project, ERATO, JST, Japan)
N. Masuda (Aihara Complexity Modelling Project, ERATO, JST, RIKEN Brain Science Institute, Japan)

OS12-5 *MOSFET implementation of two-dimensional neuron model*
T. Takemoto (The University of Tokyo, Japan)
T. Kohno, S. Tsuji (Aihara Complexity Modelling Project, ERATO, JST, Japan)
K. Aihara (Aihara Complexity Modelling Project, ERATO, JST, The University of Tokyo, Japan)

Room B

8:40~10:20 GS17 Mobile Vehicles & Human-Welfare Robotics
Chair: P. Sapaty (National Academy of Sciences, Ukraine)

GS17-1 *A stepping motor control for electric vehicle*
M. Sugisaka, K. Ahmad (Oita University, Japan)

GS17-2 *Reinforcement learning with self-instruction by using dual Q-tables*
O. Nishimura, H. Matsui, C. Hioki, Y. Nomura (Mie University, Japan)
C. Hioki (Toyota Communication Systems Co., Ltd., Japan)

GS17-3 *Position estimation of a mobile robot using U-SAT (Ultrasonic Satellites)*
S.Y. Kim, C. S. Kim, S. M. Kim , M. H. Lee(Pusan National University, Korea)

GS17-4 *Robotics safety issues for human welfare in an automated manufacturing system*
B. Rajamony, M. Rizon (Northern Malaysia University College of Engineering, Malaysia)

GS17-5 *Asymmetry analysis of human motions for examining rehabilitation training*
K. Noda, J.K. Tan, S. Ishikawa (Kyushu Institute of Technology, Japan)
N. Kito, K. Okumura (Kawashima Orthopedic Hospital, Japan)

12:30~14:10 GS8 Evolutionary Computations
Chair: M. Oswald (Vienna University of Technology, Austria)

GS8-1 *Optimization of coordinated control parameters of traffic signals using ACO*
M. Shinohara, K. Shoji, F. Toyama, J. Miyauchi (Utsunomiya University, Japan)

GS8-2 *Evolution strategies based gaussian sum particle filter for state estimation of nonlinear stochastic systems*
K. Uosaki, T. Hatanaka (Osaka University, Japan)

GS8-3 *A new algorithm for obtaining molecular information based on TaqMan real time PCR*
Z. Ibrahim (Universiti Teknologi Malaysia, Malaysia / Meiji University, Japan)
Y. Tuboi, S. Sasaki, T. Yamaguchi, O. Ono (Meiji University, Japan)

GS8-4 *Automatic evolution of bipedal locomotion in a simulated humanoid robot with many degrees of freedom*
M. Eaton, T.J.Davitt (University of Limerick, Ireland)

GS8-5 *Interpretability-accuracy tradeoff by multiobjective genetics-based machine learning for pattern classification problems*
Y. Nojima, H. Ishibuchi (Osaka Prefecture University, Japan)

14:30~15:50 GS15 Innovative Computations- Ⅰ
Chair: T. Arita (Nagoya University, Japan)

GS15-1 *Recovering the network through mutual recognition and copying*
Y. Ishida, Y. Sugawara (Toyohashi University of Technology, Japan)

GS15-2 *Dynamics of spatial strategies in regulating copying strategies in a self-repair network*
Y. Ishida, M. Oohashi (Toyohashi University of Technology, Japan)

GS15-3 *Sensor data mining system with multiagent approach for metrological data and pachinko system*
A. Niimi (Future University-Hakodate, Japan)

GS15-4 *Application of graduated PCR in concentration-controlled direct-proportional length-based DNA computing*
Z. Ibrahim (Universiti Teknologi Malaysia, Malaysia / Meiji University, Japan)
Y. Tsuboi, O. Ono (Meiji University, Japan)

15:50~17:10 GS16 Innovative Computations-Ⅱ
Chair: Y. Ishida (Toyohashi University of Technology, Japan)

GS16-1 *Molecular computing approach for constraint assignment problem*
Z. Ibrahim(Universiti Teknologi Malaysia, Malaysia / Meiji University, Japan)
Y. Tsuboi, O. Ono (Meiji University, Japan)

GS16-2 *Matrix multiplication by DNA computing*
N. Kasai,Y. Tsuboi, O.Ono(Meiji University, Japan)
Z. Ibrahim (Meiji University, Japan / Universiti Teknologi Malaysia, Malaysia)

GS16-3 *Independent agents in a globalized world modelled by tissue P systems*
M. Oswald (Vienna University of Technology, Austria)

GS16-4 *A bioinformatics method for signaling pathways in cells*
J-Q. Liu, K. Shimohara (ATR Network Informatics Laboratories, Japan)

17:10~18:10 GS5 Computer Graphics
Chair: A. Niimi (Future University-Hakodate, Japan)

GS5-1 *3-D Modeling of remote dynamic situations using mobile stereo cameras*
I. Yamaguchi, J. K. Tan, S. Ishikawa (Kyushu Institute of Technology, Japan)

GS5-2 *Tracking an object using an update type two-dimensional histogram*
H. Uemura, J. K Tan, S. Ishikawa (Kyushu Institute of Technology, Japan)

GS5-3 *Detecting method of coconuts location using circular hough transform*
M. Rizon, H.Yazid, P.Saad, A.Y. M. Shakaff, A.R.Saad, S. Yaacob, M.Karthigayan,
M. F. Hashim (Northern Malaysia University College of Engineering, Malaysia)
M. Sugisaka (Waseda University, Oita University, Japan)
M. R. Mamat (Terengganu Advanced Technical Institute (TATI), Malaysia)

Room C

8:40~10:40 OS7 Intelligent Systems and Learning
Chair: K. Abe (Nihon University, Japan)
Co-Chair: N. Homma(Tohoku University, Japan)

OS7-1 *Brain regions related to odor learning and memory in terrestrial slug, Inciralia fruhstorferi:Two lobes of the cerebral ganglion show different spatio-temporal activities*
Y. Makino, H. Makinae, T. Obara, M. Yano (Tohoku University, Japan)

OS7-2 *Natural intelligence: Noise-resistance of neural spike communication*
N. Homma, M. Sakai (Tohoku University, Japan)
K. Fuchigami (Toshiba Med. Sys. Corp., Japan)
K. Abe (Nihon University, Japan)

OS7-3 *Acquisition of deterministic exploration behavior by reinforcement learning*
K. Shibata (Oita University, Japan)

OS7-4 *Hierarchical Q-learning in POMDP environments*
H. Kamaya (Hachinohe National College of Technology, Japan)
K. Abe (Nihon University, Japan)

OS7-5 *Improvement of finishing quality on blow mold's constriction parts by using an intelligent finishing robot*
F. Nagata (Fukuoka Industrial Technology Center, Japan)
T. Hase, M. Omoto, Z. Haga (Meiho Co.Ltd., Japan)
K. Watanabe(Saga University, Japan)

OS7-6 *Self-organizing neural networks for incremental category learning*
M. Sakai, K. Takei, N. Homma (Tohoku University, Japan)
Y. Koyanaka (FANUC LTD, Japan)
K. Abe (Nihon University, Japan)

12:30~14:10 GS13 Intelligent Control and Modeling-Ⅰ& Cognitive Science
Chair: J. S. Yang (Tamkang University, Taiwan)

GS13-1 *Simplified geometric models in skill-based manipulation for practical use*
A. Nakamura, K. Kitagaki, T. Suehiro (National Institute of Advanced Industrial Science and Technology (AIST), Japan)

GS13-2 *Constructing technique of state space with low dependence on sensor configurations for autonomous mobile robots*
T. Shibuya, T. Hamagami(Yokohama National University, Japan)

GS13-3 *Emergent Societies :An advanced IT support of crisis relief missions*
P. Sapaty (National Academy of Sciences, Ukraine)
M. Sugisaka(Oita University, Japan)
R. Finkelstein(Robotic Technology Inc., USA)
J. Delgado-Frias (Washington State University, USA)
N. Mirenkov (University of Aizu, Japan)

GS13-4 *Cognitive contour detection for negative filtering*
Z. Petres, B. Resko (The University of Tokyo, Japan / Hungarian Academy of Sciences, Hungary)
H. Hashimoto (The University of Tokyo, Japan)

GS13-5 *Multistable perception model by multilayered bidirectional associative memory*
K. Kitamura, T. Isokawa. H. Nishimura, N. Kamiura, N. Matsui (University of Hyogo, Japan)

14:30~15:30 GS14 Intelligent Control and Modeling - Ⅱ
Chair: T. Nakashima (Osaka Prefecture University, Japan)

GS14-1 *Comparative study on fuzzy and non-fuzzy cost-sensitive classification systems*
T. Nakashima, Y. Yokota, H. Ishibuchi (Osaka Prefecture University, Japan)
G. Schaefer (Nottingham Trent University, United Kingdom)

GS14-2 *Emergent design of a control system for cooperation between robots*
K. Nakayama, K. Shimohara (ATR Network Informatics Lab., Japan)
H. Matsui (Mie University, Japan)

GS14-3 *A design of mass estimated adaptive friction compensator for position control of linear motor system*
J. W. Lee, J. H. Suh, K.S. Lee (Dong-A University, Korea)

15:30 ~17:30 GS19 Neural Networks
Chair: Y. Kinouchi(Tokyo University of Information Sciences, Japan)

GS19-1 *Implicit principle discovery in tourism geography information based on data mining*
D. Junping (Beijing Technology and Business University, China)
G. Wensheng (University of Science and Technology, China)

GS19-2 *Development of neural network based pattern classification system for cDNA micro array*
D-W. Kim, C-H. Park, H-C.Yang, K-B. Sim (Chung-Ang University, Korea)

GS19-3 *Remarks on tracking method of neural network weight change for adaptive type neural network direct controller*
T. Yamada (Ibaraki University, Japan)

GS19-4 *Situation recognition mechanism based on the fuzzy ART for a communication robot*
K. Iwatsubo, Y. Hoshi, B. T. Nohara (Musashi Institute of Technology, Japan)
Y. Haga (Bandai Co.,Ltd., Japan)

GS19-5 *Multi-module neural network system with concept formation and primitive consciousness*
Y. Kinouchi, K. Masuda (Tokyo University of Information Sciences, Japan)
S. Inabayashi (Pacific Technos Corp., Japan)

GS19-6 *A bayesian approach to blind source separation with variable number of sources*
J. Hirayama. S. Maeda, S. Ishii (Nara Institute of Science and Technology, Japan)

January 25 (Wednesday)

8:00~ Registration

Room A

8:40~10:40 OS14 Robot Control and Application
Chair: S. H. Han (Kyungnam University, Korea)

OS14-1 *A controller design for a motion generator based on dual linear motors*
D. H. Lee, S.Y. Seo, W. S. Choi, S-H. Lee, H. S. Kim (Kyungnam University, Korea)

OS14-2 *Stiffness analysis of a limited-DOF parallel manipulator including the compliance of both joints and links*
H. S. Kim, C-R. Shin, J-W. Kim, S-H. Lee (Kyungnam University, Korea)

OS14-3 *A robust adaptive control of robot manipulator based-on DSPs*
S. H. Han, U. Z. Na, W. S. Lee, H. B. Shin, Y. K. Kim (Kyungnam University, Korea)

OS14-4 *A Study on image based visual feedback control of robot system*
S. H. Han, U. Z. Na, H. R. Kim, Y. K. Kim, C. R. Shin(Kyungnam University, Korea)

OS14-5 *Lateral-shearing interferometer for optical testing of DVD pick-up lenses*
B. C. Kim, S.H.Kim. Y. K. Kwon, W. I. Kim (Kyungnam University, Korea)

OS14-6 *Permanent magnet biased magnetic bearings and robotic applications*
T. H. Son, U.J. Na (Kyungnam University, Korea)

12:40~14:20 GS1 Artificial Brain Research
Chair: Y.G. Zhang (Academia Sinica, China)

GS1-1 *A free-scale model of knowledge growth*
Y. G. Zhang, L. Tang (Academia Sinica, China)
M. Sugisaka (Oita University, Japan)

GS1-2 *Fundamental study of dielectric elastomer as artificial muscle*
J. Hayashida, F. Dai, Y. Fujihara (Matsue National College of Technology, Japan)

GS1-3 *A state space filter for reinforcement learning*
M. Nagayoshi (Kobe University, Hyogo Assistive Technology Research and Design Institute, Japan)
H. Murao, H. Tamaki (Kobe University, Japan)

GS1-4 *Prediction of the aperiodic time series of a visual target by humans*
M. Shikauchi, S. Ishii, T. Shibata (Nara Institute of Science and Technology, Japan)

GS1-5 *Robotic emotion generation using dynamics-based information processing*
M. Hashimoto (Shinshu University, Japan)
Y. Katoh (Harmonic Drive Systems Inc, Japan)

14:20~15:40 GS18 Molecular Biology & Bio-inspired Approach
Chair: K. Ohnishi (Niigata University, Japan)

GS18-1 *Data manipulation of DNA relational database*
Y. Kita, S. Kashiwamura (Hokkaido University, Japan)
A. Kameda (CREST, Japan Science and Technology Agency (JST), Japan)
M. Yamamoto, A. Ohuchi(Hokkaido University, CREST, Japan Science and Technology Agency(JST), Japan)

GS18-2 *Stability evaluation method of DNA tile structure*
N. Iimura, F. Tanaka (Hokkaido University, Japan)
M. Yamamoto, A. Ohuchi(Hokkaido University, CREST, Japan Science and Technology Agency(JST), Japan)
A. Kameda (CREST, Japan Science and Technology Agency (JST), Japan)

GS18-3 *Evolutionary emergence of the 16S/18S-ribosomal RNA from a poly-tRNA structure containing a"(5')tRNA(Gly)-spacer-tRNA(Cys)-spacer-tRNA(Leu)(3')"region*
K. Ohnishi, S. Hokari (Niigata Univeresity, Japan)

GS18-4 *Stochastic analysis of schema distribution in multiplicative landscape*
H. Furutani, S. Katayama , M.Sakamoto(University of Miyazaki, Japan)
T. Ito (Ube National College of Technology, Japan)

Room B

8:40~10:40 OS6 Cognitive Robotics
Chair: M. Yokota (Fukuoka Institute of Technology, Japan)
Co-Chair: G. Capi (Fukuoka Institute of Technology, Japan)

OS6-1 *Integrated multimedia understanding based on mental image directed semantic theory*
M. Yokota, G. Capi (Fukuoka Institute of Technology, Japan)

OS6-2 *Associative learning method in hyper-column model*
A. Shimada, R. Taniguchi (Kyushu University, Japan)
N. Tsuruta (Fukuoka University, Japan)

OS6-3 *Incremental acquisition of behavioral concepts through social interactions with a*

caregiver
T. Taniguchi, T. Sawaragi (Kyoto University, Japan)

OS6-4 *A step towards artificial 'Kansei'*
K. Sugita, G. Capi, M. Yokota(Fukuoka Institute of Technology, Japan)

OS6-5 *A spoken language interface to a mobile robot*
J. Bos (Universita di Roma "La Sapienza", Italy)
T. Oka (Fukuoka Institute of Technology, Japan)

OS6-6 *Performance evaluation of evolutionary multiobjective optimization*
G. Capi, M. Yokota (Fukuoka Institute of Technology, Japan)
K. Bode (Polytechnic University of Tirana, Albania)

12:40~14:40 OS3 Biomimetic Machines and Robots
Chair: K. Watanabe (Saga University, Japan)
Co-Chairman: K. Izumi (Saga University, Japan)

OS3-1 *Mobile robot navigation by visual perception with vision decision agent in an unstructured environment*
C. D. Pathiranage, K. Watanabe, K. Izumi(Saga University, Japan)

OS3-2 *Guiding mobile robots in ubiquitous environment using binocular vision system and intelligent decision making*
J. C. Balasuriya, K. Watanabe, K. Izumi (Saga University, Japan)

OS3-3 *Kansei and human experience analysis for mobile robot navigation in ubiquitous environment*
J. C. Balasuriya, K. Watanabe, K. Izumi (Saga University, Japan)
C. A. Marasinghe(University of Aizu, Japan)

OS3-4 *A natural language based human friendly network robotic system*
C. Jayawardena, K. Watanabe, K. Izumi (Saga University, Japan)

OS3-5 *Some properties of coupled Van del Pol Oscillators with Inhibitory or excitory connections*
K. Izumi, A. Tajima, G. L. Liu, K. Watanabe (Saga University, Japan)

OS3-6 *Optimal design method for region setting in fuzzy energy switching control of underactuated manipulators*
K. Ichida, K. Izumi, K. Watanabe, N. Uchida (Saga University, Japan)

14:40~16:20 GS23 Others
Chair: M.Rizon (Northern Malaysia University College of Engineering, Malaysia)

GS23-1 *Design and implementation of a novel part-feeding fixture mechanism for a stationary robot*
T. C. Manjunath (Indian Institute of Technology Bombay, India)

GS23-2 *Remarks on texture synthesis and texture segmentation with the aid of multi-level logistic model of Markov Random Field*
T. Kubik (Wroclaw University of Technology, Poland)

M. Sugisaka (Oita University, Japan)

GS23-3 *Tension-based movement corrections of the artificial agent*
B. Matosiuk, B. Grzyb (Maria Curie-Sklodowska University, Poland)

GS23-4 *Development of a mobile robot for video and thermal monitoring of railway tunnels*
N. M. Bykova, S. V. Yeliseev, A. A. Loukianov, A. P. Khomenko (Irkutsk State University of Railway Transport, Russia)

GS23-5 *A unique design and implementation of a mobile octagon*
D. Trivedi, A. Joshi, S. A. Patekar, T. C. Manjunath (Indian Institute of Technology Bombay, India)

GS23-6 *Design of an home/office automation for the physically handicapped using mobile robots*
T. C. Manjunath (Indian Institute of Technology Bombay, India)

GS23-7 *An efficient path planning mechanism for a micro-robot*
T. C. Manjunath(Indian Institute of Technology Bombay, India)

GS23-8 *Design of a intelligent sensing interface for a flexible manufacturing system*
T. C. Manjunath(Indian Institute of Technology Bombay, India)

GS23-9 *Application of uncertain variables to knowledge-based decision making in complex systems with uncertain and random parameters*
Z. Bubnicki (Wroclaw University of Technology, Poland)

GS23-10 *Firing Cell: An artificial neuron with a simulation of long-term-potentiation-related memory*
J. Bialowas (Medical University of Gdansk, Poland)
B. Grzyb (Maria Curie- Sklodowska University, Poland)
P. Poszumski (Institute of Oceanology Polish Academy of Science, Poland)

GS23-11 *Land-cover/land-use mapping based on color feature extraction*
T. Kubik, W. Paluszynski (Wroklaw University of Technology, Poland)
A. Iwaniak, P. Tymkow(Agricultural University of Wroklaw , Poland)

Room C

8:40~10:40 OS5 Bio-inspired Approach and Application
Chair: I. Yoshihara (University of Miyazaki, Japan)
Co-Chair: M. Yasunaga (University of Tsukuba, Japan)

OS5-1 *A functional motif scanning algorithm for invertebrate EST analysis*
M. Ohkubo, F. Aranishi (University of Miyazaki, Japan)

OS5-2 *Molecular clocks in aquatic invertebrates*
F. Aranishi, T. Okimoto (University of Miyazaki, Japan)

OS5-3 *Self-organizing map of species using ribosomal protein DNA sequences*
Y. Higashi, M. Yoshihara, I. Yoshihara, K. Yamamori, N. Kenmochi

(University of Miyazaki, Japan)

OS5-4 *Non-transcriptional region analysis of dictyostelium discoideum using 1/f noise*
M. Sato, I. Yoshihara, K. Yamamori (University of Miyazaki, Japan)
M. Yasunaga (University of Tsukuba, Japan)

OS5-5 *A bio-inspired tracking-camera system*
K. Hayashi, N. Aibe, Y. Yamaguchi (University of Tsukuba, Japan)
Y. Yamamoto (Yamamoto System Design Inc., Japan)
I. Yoshihara (University of Miyazaki, Japan)

OS5-6 *A robot semantic recognition using support vector machine*
H-C. Lai, C-T. Chou, S- J. Horng ,G-C. Chao (National Taiwan University of Science and Technology, Taiwan)

12:40~14:20 OS8 Vision, Automata and Neural Network
Chair: Y. Yoshitomi (Kyoto Prefectural University, Japan)
Co-Chair: A. Date (University of Miyazaki, Japan)

OS8-1 *Flowering analysis based on image segmentation*
H. Kamikokuryo, M. Yokomichi (University of Miyazaki, Japan)

OS8-2 *Recognition of word expressed by sign language using thermal image processing*
Y. Yamaguchi (KKC Information System Corp., Japan)
Y. Yoshitomi (Kyoto Prefectural University, Japan)
H. Fushimi (NTT DATA SANYO SYSTEM Corp., Japan)

OS8-3 *Hierarchies based on the number of counters or the space allowed by four-dimensional multicounter automata*
M. Saito, M. Sakamoto, K. Iihoshi, T. Ito, H. Furutani, M. Kono (University of Miyazaki, Japan)
K.Inoue (Yamaguchi University, Japan)

OS8-4 *Iterative use of a pair of the self –organizing maps looking at data in two different ways*
A. Date (University of Miyazaki, Japan)
K. Kurata (University of the Ryukyus, Japan)

OS8-5 *Orbit control for the KEK 12GeV PS-MR by using NN algorithm*
Y. Hitaka (Kitakyushu National College of Technology, Japan)
M. Shirakata, H. Sato (Proton Synchrotron Accelerator Division, KEK, Japan)
M. Yokomichi, M. Kono (University of Miyazaki, Japan)

14:20~16:20 OS9 Robotics, Automata and Control
Chair: M. Kono (University of Miyazaki, Japan)
Co-Chair: M. Yokomichi (University of Miyazaki, Japan)

OS9-1 *Trajectory for saving energy of direct-drive manipulator in throwing motion*
A. Sato (Miyakonojo National College of Technology, Japan)
O. Sato, N Takahashi, M. Kono (University of Miyazaki, Japan)

OS9-2 *Underwater moving object tracking and grasping with telerobotic system*

P. Zhang, E. Shimizu, M.I to (Tokyo University of Marine Science and Technology, Japan)

OS9-3 A *designing method research of the control system for autonomous underwater vehicle (AUV) using linear matrix inequalities(LMIs)*
Y. Nasuno, E. Shimizu, M. Ito (Tokyo University of Marine Science and Technology, Japan)
T. Aoki, I. Yamamoto, S. Tsukioka, H. Yoshida, T. Hyakudome, S. Ishibashi (Japan Agency for Marine-Earth Science and Technology (JAMSTEC), Japan)

OS9-4 *Three-dimensional synchronized alternating turing machines*
T. Ito, M. Sakamoto, M. Saito, K. Iihoshi, H. Furutani, M. Kono(University of Miyazaki, Japan)
K. Inoue(Yamaguchi University, Japan)

OS9-5 *Leaf-size bounded computation for four-dimensional alternating turing machines*
K. Iihoshi, M. Sakamoto, T. Ito, M. Saito, H. Furutani, M.Kono(University of Miyazaki, Japan)
K. Inoue(Yamaguchi University, Japan)

OS9-6 *Existence and comparison for solutions in stochastic algebraic Riccati equation*
N. Takahashi, M. Kono(University of Miyazaki, Japan)
M. Nakai (YASKAWA Electric Corp., Japan)
M. Ishitobi (Kumamoto University, Japan)

The Eleventh International Symposium on Artificial Life and Robotics 2006 (AROB 11th'06),
B-con Plaza, Beppu, Oita, Japan, January 23-25, 2006

Multi-Locomotion Robot
- PDAC for Intelligent Control -

Toshio Fukuda†, Masahiro Doi†, Hideki Kajima†,
Yoshihiko Asano†, Takayuki Matsuno† and Yasuhisa Hasegawa‡

† Department of Micro-Nano Systems Engineering, Nagoya University
Furo-cho 1, Chikusa-ku, Nagoya, 464-8603, JAPAN
‡ Institute of Engineering Mechanics and Systems, University of Tsukuba
Tennodai 1-1-1, Tsukuba, Ibaraki, 305-8573, JAPAN

1 Introduction

In recent years there have been many successful researches that focus on dynamic and skillful motions inspired by animal dexterity[1]-[5]. However, in general, they were mainly focused on a single type of motion, such as biped or quadruped of locomotion. On the other hand, many animals, such as primates, use a primary form of locomotion but switch to other types depending on their surroundings, situation and purpose. For instance, a gorilla has high mobility in a forest by selecting a bipedal walking in a narrow space, a quadrupedal walking on rough terrain and a brachiation in the forest canopy. Inspired by these high mobility of an animal, we have developed a anthropoid-like "Multi-locomotion robot" that can perform several types of locomotion and choose the proper one on an as-need basis(Fig. 1)[6]. A development of a bio-inspired robot which has multiple types of locomotion for high mobility is one of challenging issues, because other problems arise in addition to research topics on humanoid robot study. One is a comprehensive control architecture that is capable to achieve multiple types of locomotion. A common control architecture should be designed when the robot achieves a seamless transient motion connecting one locomotion to another such as a transient from trot to gallop, because a transient motion between typical types of locomotion can not be realized by fusing control signals from the corresponding controllers. Based on this notion, we have proposed a novel method named Passive Dynamic Autonomous Control(PDAC) [7, 8] that achieve not only a bipedal walk but also a quadrupedal walk. This paper focuses on the PDAC algorithm and control method for the bipedal walk.

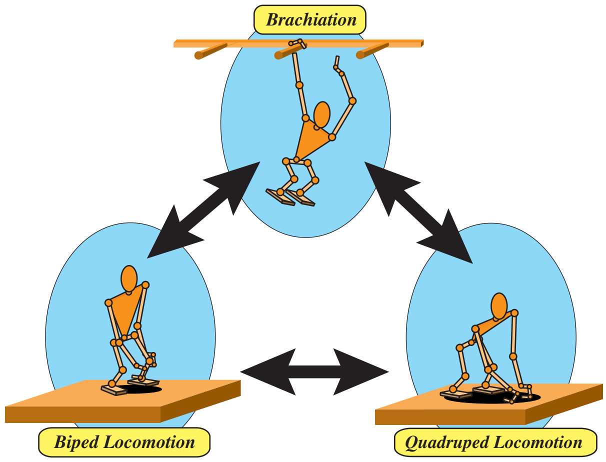

Figure 1: Concept of the multi-locomotion robot

A lot of researches of ZMP-based control[9] have been presented[10, 11]. However, ZMP-based control could not realize an efficient locomotion since it does not take advantage of the robot inherent dynamics. To solve this problem, it is necessary to develop the dynamics-based method. Some researchers proposed the method to use the robot dynamics directly by making the point-contact between a robot and the ground[1, 12, 13, 14]. Miura and Shimoyama[15] presented stilt-like biped and control method to stabilize the gaits by changing the robot posture at foot-contact. Kajita *et al.*[16] proposed the control method based on the conserved quantity introduced due to a horizontal COG (Center Of Gravity) trajectory. Goswami *et al.*[17, 18] reported the method to realize quasi-passive walking on the horizontal ground. Grizzle and Westervelt *et al.*[19, 20, 21] proposed the control method of the underactuated planar robot with a trunk and proved its stability. Although some of these point-contact methods actually realized smooth dynamic walking, their walking was 2-dimensional or that of a robot without trunk. Thus, the main goal of a biped walk is to propose the new control method based on the point-contact and realize 3-dimensional dynamic walking of a multiple link robot with a trunk.

In this paper, we introduce the novel control method named Passive Dynamic Autonomous Control (PDAC). PDAC assumes two following premises: 1) point-contact 2) interlocking. The second premise means that the angles of robot joints are connected with the angle around contact point. Although this concept was proposed first by Grizzle *et al.*[19], we propose another new method to control the robot dynamics by means of PDAC. The approach of PDAC is to describe the robot dynamics as a 1-DOF autonomous system, which is the dynamics around contact point. This approach makes it possible to calculate the period from foot-contact to next foot-contact (we term this foot-contact period hereinafter), hence the foot-contact period of the lateral motion and that of the sagittal one can be made identical. Each motion is designed by means of PDAC based on the assumption that the sagittal and lateral motions can be separated. After that, by keeping the conservative quantity of the autonomous system, the walking motion is stabilized. In addition, we propose coupling method of each motion to make the each foot-contact period identical. Finally, by means of the proposed method, 3-dimensional natural dynamic walking based on the robot inherent dynamics is achieved.

In following section, the multi-locomotion robot is introduced and then PDAC is explained in detail in section 3. The 3-dimensional walking is designed by means of PDAC in section 4. Section 5 describes the experimental results. Finally, section 6 is conclusion.

2 Multi–Locomotion Robot

The dimensions of the multi-locomotion robot we developed is designed based on those of a gorilla, and therefore the robot is called "Gorilla Robot III". Figure 2 shows the overview of Gorilla Robot III and its link structure. This robot is about 1.0[m] tall, weighs about 22.0[kg], and consists of 25 links and 26 AC motors including two grippers. The real-time operating system VxWorks (Wind River Systems Inc) runs on a Pentium III PC for processing sensory data and generating its behaviors. The rate gyroscope and force sensor attached at each wrist measures the angular velocity around the grasping bar to calculate the pendulum angle during the brachiation, and reaction forces from grasping bars in order to judge whether the robot successfully grasps the bar or not, respectively. Some photo sensors are attached on the sole in order to perceive foot-contact.

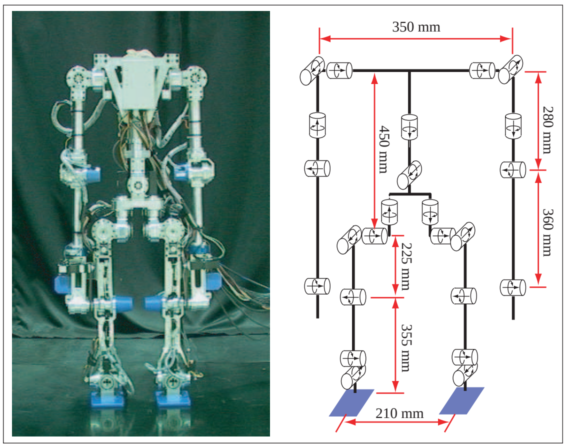

Figure 2: Gorilla Robot III

This robot has been designed to perform biped locomotion, quadruped locomotion and brachiation. We also consider the intermediate motion between a bipedal and quadrupedal walk in order to realize seamless transfer from a bipedal walk to a quadrupedal walk and from a quadrupedal walk to a bipedal walk without pause. As the first step, we designed the controller for both locomotion using the same algorithm "PDAC". The snapshot of the quadrupedal walk is shown in Fig.3, and a bipedal walk is shown in section 5. Brachiation is an interesting form of locomotion performed by long-armed apes by using their arms to swing from branch to branch. This motion is a dynamic and dexterous action routinely performed by some kinds of apes[22, 23]. Fukuda *et al.* developed a six-link brachiation robot[24] as a pioneering research analyzing dynamics of brachiation, "Brachiator II"[25]-[29] that is 2-link underactuated system like "Acrobot" [2, 30], and "Brachiator III"[31, 32] that achieves three-dimensional brachiation with redundant mechanisms.

Based on these study, we designed over-hand and side-hand motions of "Gorilla Robot II"[6], using a motion learning algorithm, and "Gorilla Robot III" achieves a continuous brachiation shown in Fig. 4 by implicitly using PDAC method in locomotion action control.

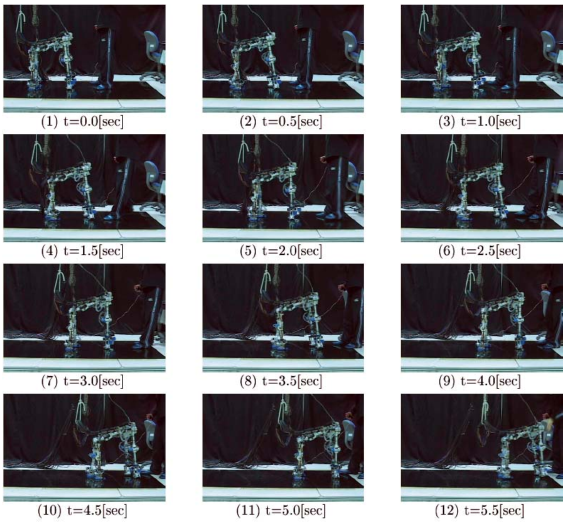

Figure 3: Snapshots of the quadrupedal walking of PDAC. The step length is about 0.09[m] and velocity is about 0.176[m/s]

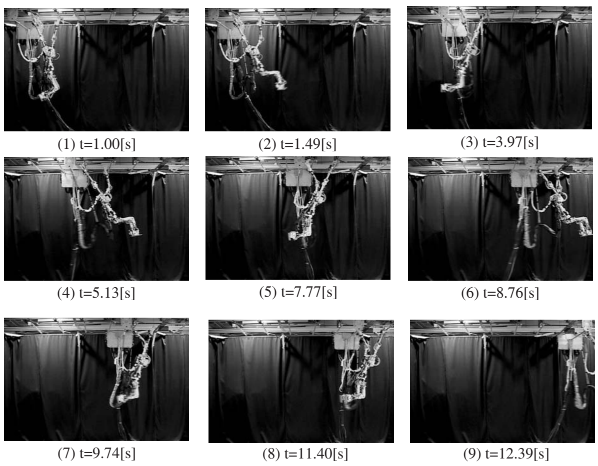

Figure 4: Snapshots of continuous brachiation. All bars are set at regular intervals of 0.4 m and at the same height of 2.7 m

3 Passive Dynamic Autonomous Control

3.1 Target Dynamics

The concept of PDAC is the same as that Grizzle *et al.*[19] proposed before. We begin with the two following premises. First, the contact state between a robot and the ground is point-contact. Second, robot joints are interlocked with the angle around the contact point. The first premise means that the first joint of a robot, i.e. the ankle joint of the stance leg, is passive. The second means that the angles of active joints are described as the function of the angle around the contact point. Assuming that PDAC is applied to the serial n-link rigid robot shown in Fig. 5, these two premises are expressed as follows:

$$\tau_1 = 0 \tag{1}$$

$$\begin{aligned}\Theta &= [\theta_1, \theta_2, \cdots, \theta_n]^T \\ &= [f_1(\theta), f_2(\theta), \cdots, f_n(\theta)]^T = f(\theta),\end{aligned} \tag{2}$$

where θ is the angle around the contact point in the absolute coodinate system. Since it has no effect on the robot dynamics due to point-contact, the level ground is assumed, therefore $\theta_1 = f_1(\theta) = \theta$.

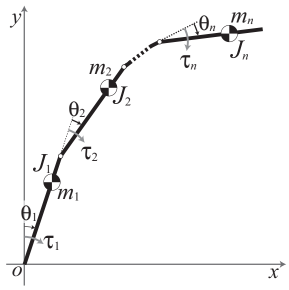

Figure 5: Mechanical model of the serial n-link rigid robot. θ_i and τ_i are the angle and the torque of ith joint respectively. m_i and J_i are the mass and the moment of inertia of ith link respectively.

The dynamic equations of this model are given by

$$\frac{d}{dt}\left(\boldsymbol{M}(\Theta)\dot{\Theta}\right) - \frac{1}{2}\frac{\partial}{\partial\Theta}\left(\dot{\Theta}^T\boldsymbol{M}(\Theta)\dot{\Theta}\right) - \boldsymbol{G}(\Theta) = \boldsymbol{\tau}, \tag{3}$$

where $M(\Theta) = [M_1(\Theta), M_2(\Theta), \cdots, M_n(\Theta)]^T$, $\Theta = [\theta_1, \theta_2, \cdots, \theta_n]^T$, $G(\Theta) = [G_1(\Theta), G_2(\Theta), \cdots, G_n(\Theta)]^T$, $\tau = [\tau_1, \tau_2, \cdots, \tau_n]^T$, $\frac{\partial}{\partial\Theta} = [\frac{\partial}{\partial\theta_1}, \frac{\partial}{\partial\theta_2}, \cdots, \frac{\partial}{\partial\theta_n}]^T$. Since in this model the dynamic equation around the contact point has no term of the Coriolis force, it is given as

$$\frac{d}{dt}\left(\boldsymbol{M_1}(\Theta)\dot{\Theta}\right) - \boldsymbol{G_1}(\Theta) = \boldsymbol{\tau_1}. \tag{4}$$

By differentiating Eq. (2) with respect to time, the following equation is acquired,

$$\begin{aligned}\dot{\Theta} &= \frac{\partial f(\theta)}{\partial\theta}\dot{\theta} \\ &= \left[\frac{\partial f_1(\theta)}{\partial\theta}, \frac{\partial f_2(\theta)}{\partial\theta}, \ldots, \frac{\partial f_n(\theta)}{\partial\theta}\right]^T \dot{\theta}.\end{aligned} \tag{5}$$

Substituting Eq. (1), (2) and (5) into Eq. (3) yields the following dynamic equation,

$$\frac{d}{dt}\Big(M(\theta)\dot{\theta}\Big) = G(\theta), \tag{6}$$

where

$$M(\theta) := M_1\Big(f(\theta)\Big)\frac{df(\theta)}{d\theta} \tag{7}$$

$$G(\theta) := G_1\Big(f(\theta)\Big). \tag{8}$$

By multiplying both sides of Eq. (6) by $M(\theta)\dot{\theta}$ and integrating with respect to time, the dynamics around the contact point is obtained as follows:

$$\int \Big(M(\theta)\dot{\theta}\Big)\frac{d}{dt}\Big(M(\theta)\dot{\theta}\Big)\,dt = \int M(\theta)G(\theta)\dot{\theta}\ dt$$

$$\Longleftrightarrow \dot{\theta} = \frac{1}{M(\theta)}\sqrt{\int 2G(\theta)M(\theta)\ d\theta}. \tag{9}$$

Assuming that the integration in right side of Eq. (9) is calculated as $\int G(\theta)M(\theta)\ d\theta = D(\theta)+C$, Eq. (9) is described as the following 1-DOF autonomous system,

$$\dot{\theta} = \frac{1}{M(\theta)}\sqrt{2\big(D(\theta)+C\big)} \tag{10}$$

$$:= F(\theta). \tag{11}$$

In this paper, we term Eqs. (10) and (11) target dynamics.

3.2 Dynamics Interlocking

As mentioned previously, PDAC is based on the two premises: passivityindexpassivity and interlocking. These premises make it possible to describe the whole robot dynamics as the 1-DOF autonomous system, owing to which the simple and valid controller based on the robot dynamics can be composed. However, interlocking of joint angles has possibility to bring about the problem that the robot vibrates and the controller loses its stability during locomotion, especially at foot-contact, since if the passive joint vibrates, all of other active joints also do. In order to solve this problem, all of robot joints are controlled according to the desired dynamics of each joint derived from the interlocking function Eq. (2) and the target dynamics Eq. (11) as follows:

$$\dot{\theta}_i = \frac{\partial f_i}{\partial \theta}F\big(f_i^{-1}(\theta_i)\big) \qquad (i = 1, 2, 3, \cdots). \tag{12}$$

These desired dynamics are independent from each other, thus it is necessary to connect the desired dynamics of active joints with the target dynamics in order to prevent the whole walking motion being broken in case of the error between the target dynamics and the actual dynamics of θ. Hence, we define the connection between the target dynamics and the active joints. The controller decides the desired angular velocities of each joint as described below,

$$\dot{\theta}_1^d = F\big(f_1^{-1}(\theta_1)\big) \tag{13}$$

$$\dot{\theta}_i^d = \frac{\partial f_i}{\partial \theta}F\big(f_i^{-1}(\theta_i)\big) + k_i\big(f_i(\theta) - \theta_i\big) \quad (i = 2, \cdots)$$

$$\Longleftrightarrow \dot{\Theta}^d := F(\Theta), \tag{14}$$

where k_i is the strength of connection determined experimentally since its value has little effect on the robot dynamics. As for humanoid robots, the ground slope at the contact point is deduced from the angle of the ankle joint of the swing leg at foot-contact, and θ is calculated from θ_1 and the ground slope. The remarkable point is that if there is no error such as the model error or disturbance, the second term of Eq. (14) is constantly zero and the actual dynamics of θ is identical with the target dynamics definitely.

Figure 6 shows the block diagram of PDAC of bipedal locomotion. The control loop including a robot (enclosed by the dotted line in Fig. 6) have no input, thus it can be considered that the control system is autonomous. This autonomy makes it possible to realize the natural dynamic motion based on the inherent dynamics of a robot. The loop described by the broken line is executed only at the moment of foot-contact. In this loop, the target dynamics of next step is determined according to both the desired parameters such as walking velocity and the robot status, then F is updated. Since this updating compensates the error between the previous target dynamics and the actual ones around the contact point, it is possible to realize stable walking.

3.3 PDAC Constant

Since as mentioned previously, the target dynamics is autonomous, in addition, independent of time, it is considered as a kind of conservative system. Therefore, it is conceivable that the target dynamics has a conserved quantity. As for PDAC, it is the constant of integration in right side of Eq. (9). That is, C in Eq. (10) is the conserved quantity of the target dynamics, which is named PDAC Constant. It is clear that PDAC Constant is decided in accordance with initial condition and that the robot motion is generated as it is kept constant. In order to stabilize walking, the controller updates the target dynamics according to

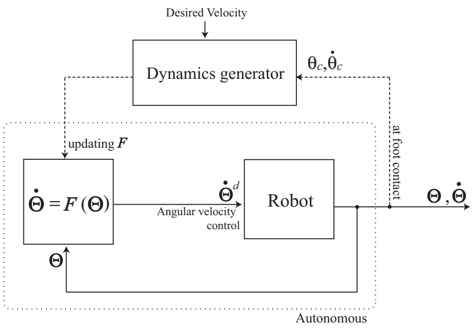

Figure 6: Block diagram of PDAC of bipedal locomotion. θ_c and $\dot{\theta}_c$ are the angle and the angular velocity of θ_1 at foot-contact respectively.

PDAC Constant. This method to update is presented later.

4 Bipedal Walking Control

In this paper, it is assumed that lateral motion and sagittal one can be separated and controlled independently since lateral side-to-side rocking motion is quite small and step-length in the sagittal plane is relatively short. Although both motions are composed independently, the period from foot-contact to next foot-contact (foot-contact period) in the both plane are necessary to be identical. We design each motion by means of PDAC by giving both the desired step-length, λ^d, and desired foot-contact period, T^d, and propose the coupling method of both motions. In addition, the landing position control is designed based on PDAC. At first the sagittal motion control is presented that is followed by the lateral motion control satisfying the condition of the foot-contact period is explained.

4.1 Sagittal motion control

4.1.1 3-link model

For the sake of simplicity, the 3-link model as shown in Fig. 7 is used, i.e. upper body of robot is not moved.

4.1.2 Interlocking of sagittal joints

Grizzle *et al.*[19] used the following interlocking in their previous paper: to maintain the angle of the torso at some constant value and to command the swing leg to behave as the mirror image of the stance leg. In

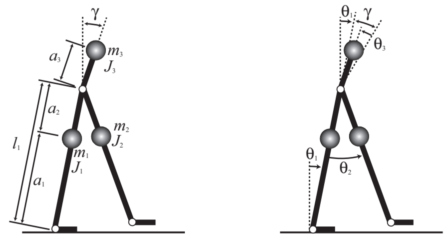

Figure 7: 3-link model in the sagittal plane. m_i, J_i, l_i and a_i are the mass, the moment of inertia, the length of link and the distance from the joint to the link COG of link i respectively. γ is the angle of the forward tilting. In the right figure, θ_1, θ_2 and θ_3 are the ankle angle of the stance leg, the angle from the stance leg to the the swing leg, the angle to swing the trunk up respectively.

this paper, we use the same interlocking, that is,

$$\theta_1 = f_1(\theta) = \theta - \beta \tag{15}$$
$$\theta_2 = f_2(\theta) = 2\theta \tag{16}$$
$$\theta_3 = f_3(\theta) = \theta, \tag{17}$$

where β is the ground slope at the contact point (ascent is positive). From Eqs. (15)-(17) and (1), Eq. (6) is

$$\begin{aligned} M_s(\theta) &= J_1 - J_2 + m_1 a_1^2 + m_2 l_1^2 - m_2 a_2^2 + m_3 l_1^2 \\ &\quad + m_3 a_3 l_1 \cos(\gamma - \theta) \qquad (18) \\ &:= E_1 + E_2 \cos(\gamma - \theta) \qquad (19) \\ G_s(\theta) &= (m_1 a_1 + m_2 l_1 + m_2 a_2 + m_3 l_1) g \sin\theta \\ &\quad + m_3 g a_3 \sin\gamma \qquad (20) \\ &:= E_3 + E_4 \sin\theta. \qquad (21) \end{aligned}$$

Thus,

$$\begin{aligned} &\int M_s(\theta) G_s(\theta) d\theta \\ =& \int \big(E_1 + E_2\cos(\gamma - \theta)\big)\big(E_3 + E_4 \sin\theta\big) d\theta \qquad (22) \\ =& E_2 E_4 \left(\frac{\sin(\gamma\theta)}{2} - \frac{\cos(2\theta - \gamma)}{4}\right) \\ +& E_2 E_3 \sin(\theta - \gamma) - E_1 E_4 \cos\theta \\ +& E_1 E_3 \theta + C_s \qquad (23) \\ :=& D_s(\theta) + C_s \qquad (24) \end{aligned}$$

where C_s is the integral constant, which is PDAC Constant of the sagittal motion. From Eq. (10), the target dynamics in the sagittal plane is

$$\dot{\theta} = \frac{1}{M_s(\theta)} \sqrt{2\big(D_s(\theta) + C_s\big)} \tag{25}$$

$$:= \quad F_s(\theta). \tag{26}$$

From Eqs. (15)-(17), $f_1^{-1}(\theta_1) = \theta_1 + \beta$, $f_2^{-1}(\theta_2) = \frac{1}{2}\theta_2$, $f_3^{-1}(\theta_3) = \theta_3$ are obtained, thus the desired angular velocity of sagittal joints are described as follows:

$$\dot{\theta}_1^d = F_s(\theta_1 + \beta) \tag{27}$$

$$\dot{\theta}_2^d = 2F_s\left(\frac{\theta_2}{2}\right) + k_2(2\theta - \theta_2) \tag{28}$$

$$\dot{\theta}_3^d = F_s(\theta_3) + k_3(\theta - \theta_3). \tag{29}$$

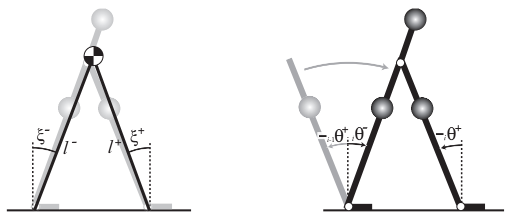

Figure 8: Parameters at foot-contact. l^- and ξ^- are the length and inclination of the inverted pendulum which connects the supporting foot and the COG of the whole robot before impact, while l^+ and ξ^+ are those after impact. ${}_i\theta^-$ and ${}_i\theta^+$ are the angles around the contact point before and after impact of the ith step.

4.1.3 Foot contact model

In this paper, it is assumed that foot-contact is occurred for a moment and the angular momentum around the contact point is valied instantly. The angular momentum is described as

$$P = M_s(\theta)\dot{\theta}. \tag{30}$$

Figure 8 depicts some parameters at foot-contact. Assuming that the translational velocity along the pendulum at foot-contact is zero since it is quite small, the angular velocity around the contact point is acquired as follows:

$$l^+P^+ = l^-P^- \cos(\xi^- + \xi^+) \tag{31}$$

$$\Longleftrightarrow \quad {}_i\dot{\theta}^+ = \frac{l^- M_s({}_i\theta^-)^-}{l^+ M_s({}_i\theta^+)^+}\cos(\xi^- + \xi^+)\ {}_i\dot{\theta}^- \tag{32}$$

$$\Longleftrightarrow \quad {}_i\dot{\theta}^+ := H_s\, {}_i\dot{\theta}^- \tag{33}$$

From this value, PDAC Constant at the ith step, ${}_iC_s$, is obtained as below,

$${}_iC_s = \frac{1}{2}\Big(M_s\left({}_i\theta^+\right) {}_i\dot{\theta}^+\Big)^2 - D_s\left({}_i\theta^+\right). \tag{34}$$

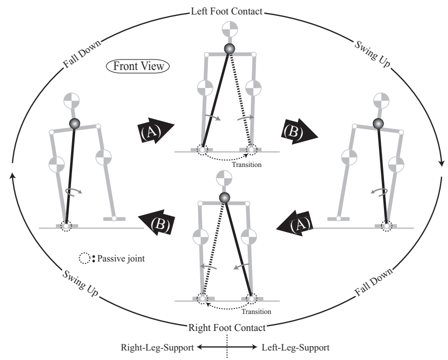

Figure 9: The lateral motion of lateral-based walk (front view). The inverted pendulum falls off in phase(A) and swing up in phase(B)

4.2 Lateral motion control

4.2.1 Lateral motion

Many reserchers investigated and proposed the lateral motion control[12, 33, 34]. In this paper, we design the lateral motion by means of PDAC as depicted in Fig. 9. In order to continue the side-to-side rocking motion, a robot lifts its pelvis in phase(A) and (B). The inverted pendulum whose length is variable is used as the model of the lateral plane since the motion to lift pelvis is quite small, in additon, a robot posture is valied little thus the motion to lift pelvis can be considered that to lengthen the pendulum. The lateral motion can be continued in spite of the loss of angular momentum at foot-contact by changing the pendulum length at impact.

4.2.2 Collision Inverted Pendulum Model

The following model shown in Fig. 10 is used as the model of the lateral motion: two inverted pendulums which are opposite each other continue to rock, iterating the collision between them, which is named Collision Inverted Pendulum Model (CIPM). This CIPM is intuitively like that the Newton's Pendulum is inverted. Figure 11 shows the trajectory of COG and two coordinate systems Σ^R and Σ^L that correspond to right- and left-leg-support period respectively, and Fig. 11(b) depicts the phase portraits of ϕ^R and ϕ^L. These two phase portrait's coalescing yields the phase portrait of CIPM (see Fig. 11(c)). In the phase portrait of CIPM, there is the area in which has the circular nature between the coordinate systems Σ^R and Σ^L. In this area, the periodic motion can be realized due to the circular nature.

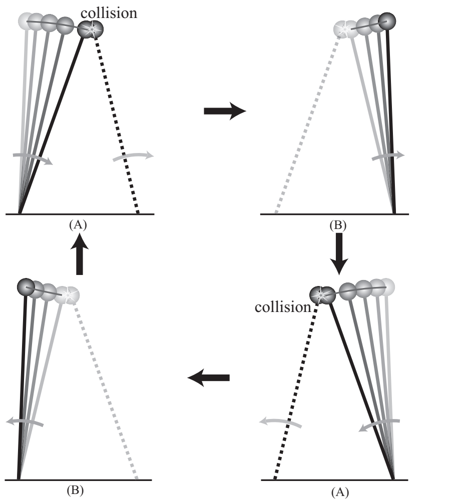

Figure 10: Motion of CIPM. The collision between the foot and the ground is regarded as that between two pendulums. (A) and (B) correspond to those in Fig. 9.

4.2.3 Coupling with the sagittal motion

As mentioned previously, it is necessary that the foot-contact period of the sagittal motion and that of the lateral motion are made identical. In case of the adjustment of step-length, the sagittal foot-contact period differs from the desired foot-contact period, thus the lateral motion needs to be valied according to the period of sagittal motion .

In order to control the lateral foot-contact period, the foot width is adjusted as shown in Fig. 12. $l - \Delta l + \delta l$ and $\phi_2 + \delta\phi_2$ are acquired from ϵ geometrically. It is assumed that this adjustment is so small that its effect on the target dynamics in phase (A) can be neglected. By the adjustment, the parameters of the target dynamics in phase (B) is valied as follows:

$$a_2 = \frac{1}{\left(\phi_3 - (\phi_2 + \delta\phi_2)\right)^2}(\Delta l - \delta l) \quad (35)$$

$$b_2 = -\frac{2\phi_2}{\left(\phi_3 - (\phi_2 + \delta\phi_2)\right)^2}(\Delta l - \delta l) \quad (36)$$

$$c_2 = l_0 - \frac{\phi_3^2 - 2(\phi_2 + \delta\phi_2)\phi_3}{\left(\phi_3 - (\phi_2 + \delta\phi_2)\right)^2}(\Delta l - \delta l). \quad (37)$$

The condition that the pendulum paused at the end of phase (B) is $F_{l_B}(\phi_3) = 0$, hence

$$D_{l_B}(\phi_3) - D_{l_B}(\phi_2 + \delta\phi_2) + \Big(M(\phi_2 + \delta\phi_2)\dot{\phi}_2\Big)^2 = 0. \quad (38)$$

In addition, the condition of the foot-contact period is necessary to be satisfied, namely,

$$\int_{\phi_2+\delta\phi_2}^{\phi_3} \frac{1}{F_{l_B}(\phi)} d\phi + \int_{\phi_3}^{\phi_1} \frac{1}{F_{l_A}(\phi)} d\phi = T_s. \quad (39)$$

The first term of the left side in Eq. (39) is the period of phase (B) and the second term is that of subsequent phase (A). Two conditions of Eq. (38) and (39) have two unknowns, i.e. the adjustment value, ϵ, and

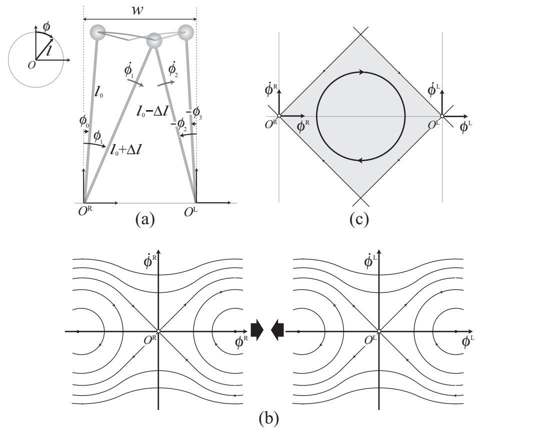

Figure 11: (a) Trajectory of COG and polar coordinate systems Σ^R, Σ^L. l and ϕ denote the length and the angle of an inverted pendulum. (l_0, ϕ_0) and $(l_0 + \Delta l, \phi_1)$ are the coordinates in Σ^R at the beginning and ending of phase (A), $(l_0 - \Delta l, \phi_2)$ and (l_0, ϕ_3) is that of Σ^L of phase (B) respectively. $\dot{\phi}_1$, $\dot{\phi}_2$ denotes the angular velocity at the end of phase (A) and at the beginning of phase (B). (b) Phase portraits of ϕ^R and ϕ^L (c) Phase portrait of CIPM. The gray tetragon surrounded by the pair of separatrixes is named CIP-Area.

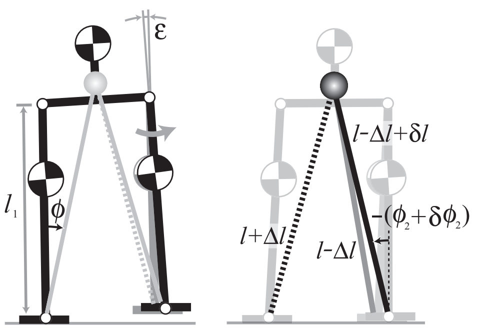

Figure 12: Adjustment of foot width. ϵ is the angle to open the swing leg to adjust the foot width. $l - \Delta l + \delta l$ and $\phi_2 + \delta\phi_2$ are the pendulum length and angle at the beginning of phase (B) after adjustment.

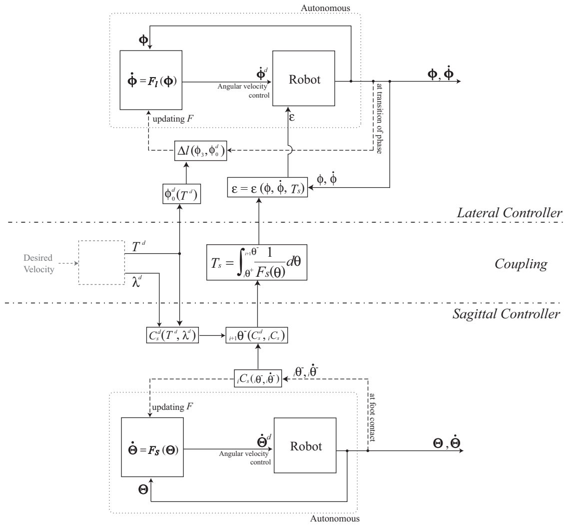

Figure 13: Block diagram of the coupling between the sagittal and lateral motions

the pendulum angle at the end of phase (B), ϕ_3. By solving these two conditions by means of linear approximation of ϵ and two dimensional approximation of ϕ_3, the adjustment value, ϵ, can be calculated

$$\epsilon = \epsilon(\phi, \dot{\phi}, T_s). \tag{40}$$

Figure 13 depicts the block diagram of the algorithm described in previous sections. At foot-contact, the sagittal controller decides the step-length, i.e. the value of θ at next foot-contact in order to stabilize the sagittal motion. Next, the foot-contact period of the sagittal motion is calculated by integration. Finally, the lateral controller determines the adjustment value of foot width according to both the sagittal foot-contact period and the present status in the lateral plane. This series of controls can be considered as the landing position control of three dimensional walking since the step-length is adjusted in the sagittal plane and the foot width is adjusted in the lateral plane.

The box enclosed by gray dashed line is the algorithm to decide the desired foot-contact period and step-length so that the energy consumption is minimized. However, this has not been solved and it's the future work, hence we give the desired foot-contact period and step-length to the controller directly in this paper.

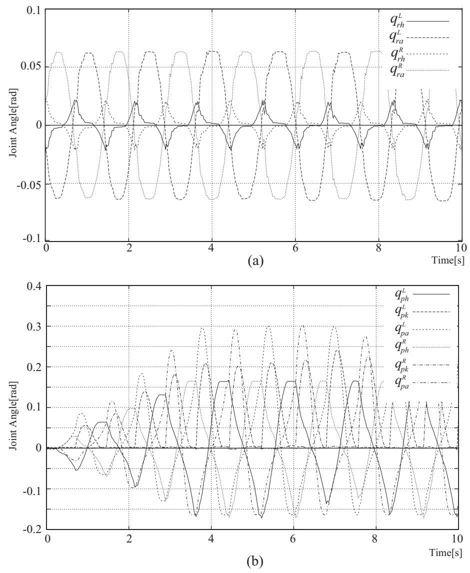

Figure 15: Angle of the joints (a) in the lateral plane (b) in the sagittal plnae

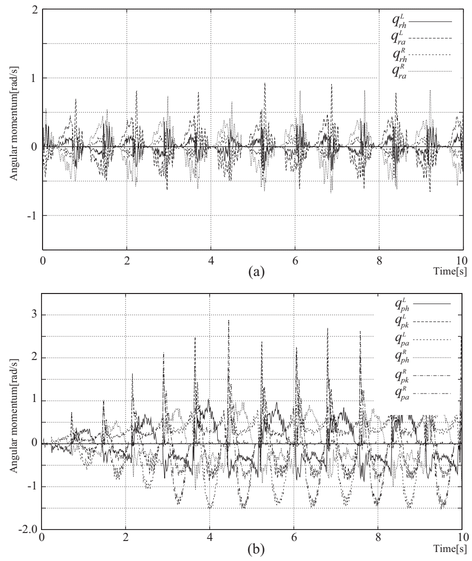

Figure 16: Angular Velocity of the joints (a) in the lateral plane (b) in the sagittal plnae

5 Experiment

The experiment of the walking proposed in the previous section on the flat and level ground was conducted. Since, in order to start the walking, the robot needs the potential energy, we lifted up the lateral pendulum to the position at the beginning of phase

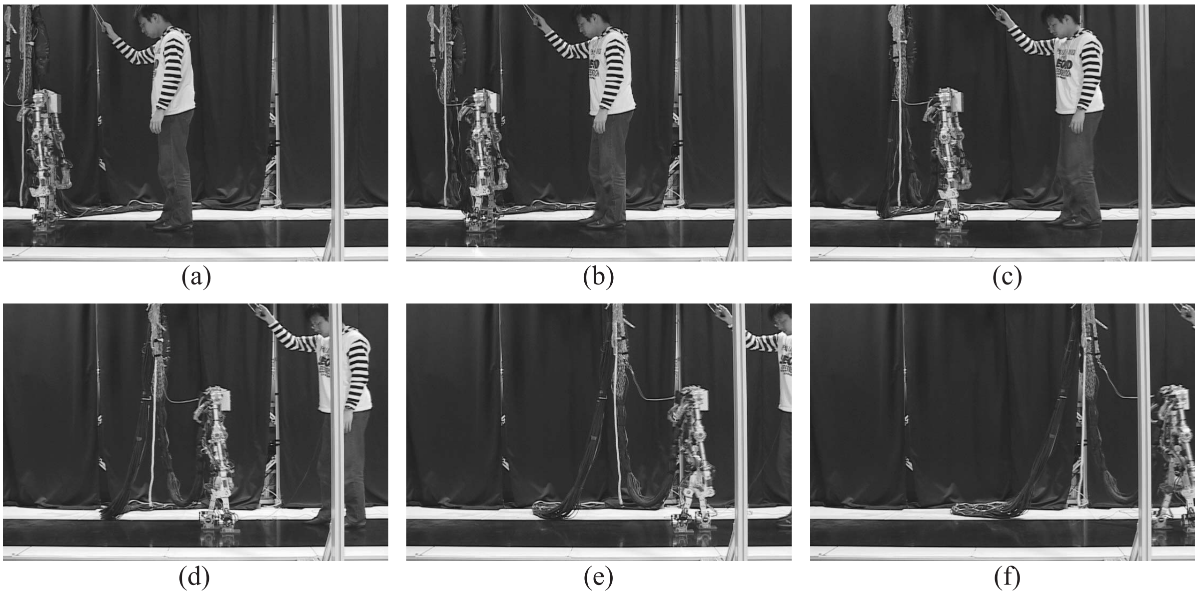

Figure 14: Snapshots of the walking of PDAC. Each figure shows the snapshots at (a)1st (b)7th (c)12th (d)16th (e)19th (f)22th step.

(A) and released. In experiment, the robot bends its knee joint of the swing leg so as to prevent the foot being in friction with the ground immediately after foot-contact on the assumption that the effect of knee bending on the robot dynamics can be neglected. The foot of the swing leg is actuated so as to be kept parallel to the ground.

The desired step-length is given to be gradually increased within initial 5 steps up to 0.15[m] and the desired foot-contact period is given at 0.7[s]. In consequence, the dynamic and natural walking is realized over 25 steps. The step-length is about 0.15[m] and the walking velocity is about 0.23[m/s]. Fig. 14 shows the snapshots of the PDAC walking at 1st, 7th, 12th, 16th, 19th, 22th step respectively. The angle and angular velocity of the lower body joints are depicted in Fig. 15 and Fig. 16. As shown in these figures, the smooth dynamics motion is realized periodically.

6 Conclusion

This paper introduced multi-locomotion robot with high mobility at first and then proposed Passive Dynamic Autonomous Control (PDAC) for the comprehensive control method of multiple types of locomotion. PDAC is the method to take advantage of the robot inherent dynamics and realize natural dynamic motion. We applied PDAC to the biped walk control. On the assumption that the sagittal and lateral motion can be separated and controlled individually, each motion was designed based on the given desired step-length and period. In order to stabilize walking, the landing position control according to the status was designed. In addition, the coupling method between these motions, which makes the period of each motion identical, was proposed. Finally, the 3-dimensional dynamic walking whose step-length is about 0.15[m] and velocity is about 0.23[m/s] was realized.

References

[1] M. H. Raibert, *Legged Robots that Balance.* MIT Press, Cambridge, MA (1986).

[2] M. Spong, "The swing up control problem for the acrobot," *IEEE Control Syst. Mag.***15**(1),49-55 (1995).

[3] T. McGeer, Passive dynamic walking, *The Int. Journal of Robotics Research*, **9**(2),62-82 (1990).

[4] Qinghua Li, Atsuo Takanishi, Ichiro Kato, "Learning control of compensative trunk motion for biped walking robot based on ZMP," in *Proc. IEEE/RSJ Int. Conf. on Intelligent Robots*

and Systems, North Carolina, USA, pp. 597-603 (1992).

[5] S.Kajita, T. Yamaura, A. Kobayashi, "Dynamic Walking Control of a Biped Robot Along a Potential Energy Conserving Orbit," in *IEEE Transaction on Robotics and Automation*, **8** (4), 431-438 (1992).

[6] H. Kajima, Y. Hasegawa and T. Fukuda, "Study on brachiation controller -adjustment method of strength and timing parameters-," in *Proc. IEEE/RSJ Int. Conf. on Intelligent Robots and Systems*, EPFL, Switzerland, pp.2497-2502 (2002).

[7] M. Doi, Y. Hasegawa, and T. Fukuda, "Passive Trajectory Control of the Lateral Motion in Bipedal Walking," *IEEE International Conference on Robotics and Automation*, 2004, pp. 3049-3054.

[8] M. Doi, Y. Hasegawa, and T. Fukuda, "Passive Dynamic Control of Bipedal Walking," *Proc. of IEEE-RAS/RSJ International Conference on Humanoid Robots*, 2004.

[9] M. Vukobratovic, B. Brovac, D. Surla and D. Stokic, "Biped Locomotion:dynamics, stability, control, and application", Springer-Verlag, 1990.

[10] A. Takanishi, M. Ishida, Y. Yamazaki and I. Kato, "The Realization of Dynamic Walking Robot WL-10RD", The proceeding of Int. Conf. Advanced Robotics, 1985, pp. 459-466.

[11] K. Nishiwaki, S. Kagami, Y. Kuniyoshi, M. Inaba and H. Inoue, "Online Generation of Humanoid Walking Motion based on a Fast Generation Method of Motion Pattern that Follows Desired ZMP" The proceeding of the Int. Conf. Intelligent Robots and Systems, 2002, pp. 2684-2689.

[12] A. D. Kuo, "Stabilization of Lateral Motion in Passive Dynamic Walking", The International Journal of Robotics Research, Vol. 18, No. 9, September 1999, pp. 917-930.

[13] A. A. Grishin, A. M. Formal'sky, A. V. Lensky and S. V. Zhitomirsky "Dynamic Walking of a Vehicle With Two Telescopic Legs Controlled by Two Drives", The International Journal of Robotics Research, Vol. 13, No. 2, 1994, pp. 137-147.

[14] M. Yamada, J. Furusho and A. Sano, "Dynamic control of walking robot with kick-action", The proceeding of the ICAR, 1985, pp. 405-412.

[15] H. Miura and I. Shimoyama, "Dynamic Walking of a biped", The International Journal of Robotics Research, Vol. 3, No. 2, 1984, pp. 60-74.

[16] S. Kajita, T. Yamaura and A. Kobayashi, "Dynamic walking control of a biped robot along a potential conserving orbit", IEEE Transactions on Robotics Automation, Vol. 8, No. 4, 1992, pp431-438.

[17] A. Goswami, B. Espiau and A. Keramane, "Limit cycles in a passive compass gait baiped and passivity-mimicking control laws", Autonomous Robots 4, 1997, pp.274-286, Kluwer Academic Publishers.

[18] B. Thuilot, A. Goswami and B. Espiau, "Bifurcation and Chaos in a Simple Passive Bipedal Gait", The proceeding of Int. Conf. Robotics and Automation, 1997, pp. 792-798.

[19] J. W. Grizzle, G. Abba and F. Plestan, "Asymptotically Stable Walking for Biped Robots: Analysis via Systems with Impulse Effects", IEEE Transaction on Automatic Control, Vol. 46, No. 1, 2001, pp. 56-64.

[20] F. Plestan, J. W. Grizzle, E. R. Westervelt and G. Abba, "Stable Walking of a 7-DOF Biped Robot", IEEE Transactions on Robotics and Automation, Vol. 19, No. 4, August 2003, pp. 653-668.

[21] E. R. Westervelt, G. Buche and J. W. Grizzle, "Inducing Dynamically Stable Walking in an Underactuated Prototype Planar Biped", The proceeding of Int. Conf. Robotics and Automation, 2004, pp. 4234-4239.

[22] E.L. Simons, *Primate Evolution:An Introduction to Man's Place in Nature*, Macmillan (1972).

[23] James R. Usherwood and John E. A. Bertram, Understanding brachiation: insight from a collisional perspective, *The Journal of Experimental Biology* **206**, 1631-1642 (2003).

[24] T. Fukuda, H. Hosokai and Y. Kondo, "Brachiation type of mobile robot,"in *Proc. IEEE Int. Conf. Advanced Robotics*, Pisa, Italy, pp.915-920 (1991).

[25] T. Fukuda, F. Saito and F. Arai, "A study on the brachiation type of mobile robot(heuristic creation of driving input and control using CMAC)," in *Proc. IEEE/RSJ Int. Conf. on Intelligent Robots and Systems*, Osaka, Japan, pp. 478-483 (1991).

[26] F. Saito, T. Fukuda, F. Arai, "Swing and locomotion control for two-link brachiation robot," in *Proc. IEEE Int. Conf. on Robotics and Automation*, Atlanta, Georgia, USA, pp.719-724 (1993).

[27] F. Saito, T. Fukuda, F. Arai, "Swing and locomotion control for a two-link brachiation robot," *IEEE Control Syst. Mag.* **14**(1), 5-12 (1994).

[28] Y. Hasegawa,T. Fukuda,K. Shimojima, "Self-scaling reinforcement learning for fuzzy logic controller - applications to motion control of two-link brachiation robot," *IEEE Trans. Ind Electron*, **46**,1123-1131 (1999).

[29] J. Nakanishi, T. Fukuda and D.E. Koditschek, "A brachiating robot controller," *IEEE Transactions on Robotics and Automation* **16**(2),109-123 (2000).

[30] Matthew D. Berkemeier and Ronald S. Fearing, "Tracking Fast Inverted Trajectories of the Underactuated Acrobot," in *IEEE Transaction on Robotics and Automation*, **15** (4), 740-750 (1999).

[31] F. Saito and T. Fukuda, "A First Result of The Brachiator III - A New Brachiation Robot Modeled on a Siamang," *Artificial Life V*, pp.354-361, MIT Press, 1997.

[32] Y. Hasegawa, Y. Ito and T. Fukuda, "Behavior coordination and its modification on brachiation-type mobile robot," in *Proc. IEEE Int. Conf. on Robotics and Automation*, San Francisco, California, USA, pp.3984-3989 (2000).

[33] A. Sano and J. Furusho, "Realization of Dynamic Quadruped Locomotion in Pace Gait by Controlling Walking Cycle", International Symposium on Experimental Robotics, 1991, pp. 491-502.

[34] H. Hemami and B. F. Wyman, "Modeling and Control of Constrained Dynamic Systems with Application to Biped Locomotion in the Flontal Plane", IEEE Transactions on Automatic Control, Vol. AC-24, No. 4, August 1979, pp. 526-535.

The Eleventh International Symposium on Artificial Life and Robotics 2006 (AROB 11th'06),
B-con Plaza, Beppu, Oita, Japan, January 23-25, 2006

Present State and Future of Intelligent Space Discussion on Implementation of RT in our Environment

Hideki HASHIMOTO

Institute of Industrial Science, University of Tokyo
4-6-1 Komaba, Meguro-ku, Tokyo 153-8505 JAPAN
http://dfs.iis.u-tokyo.ac.jp

Abstract

Latest advances in network sensor technology and state of the art of mobile robot, and artificial intelligence research can be employed to develop autonomous and distributed monitoring systems.

"Intelligent Space" is a platform which we can implement advanced technologies easily to realize smart services to human. We have developed and reported the vision system based on color information, the handover scheme networking multi cameras, the human following mobile robot systems, the path generator based on human watching, etc. In this talk I will summarize the present state of Intelligent Space and try to describe a future from a viewpoint of system integration. Also we are now introducing RT(Robot Technology) to develop the Intelligent Space as an actual standard platform which could be approved by Robotics Community. I will discuss how to use RT in our Intelligent Space and show our new results.

Keywords: Intelligent space, spatial memory, vision, tracking, mobile robot

1. Introduction

'Intelligent Space(iSpace)' has been proposed by Hashimoto lab. in university of Tokyo [1]. Intelligent Space is an environmental system, which is able to support human in informative and physical ways. Most of intelligent system interacts with human in a passive space, but in Intelligent Space, a space, which contains human and artificial systems, is an intelligent system itself. Human and artificial systems become clients of Intelligent Space and simultaneously the artificial systems become agents of Intelligent Space. Since the whole space is an intelligent system, Intelligent Space, a spatial system, is able to monitor and to provide services to clients easily. Specific tasks, which cannot be achieved only by Intelligent Space, are accomplished by utilizing its clients. For examples, Intelligent Space utilizes computer monitors to provide information to the human, and robots are utilized to provide physical services to the human as physical agents. Robot as well as human is supported by Intelligent Space if it is necessary. When a robot is lacking of sensors to navigate around in Intelligent Space, the robot is treated as a client of Intelligent Space and lacking information is provided to the robot by Intelligent Space.

The ultimate goal of Intelligent Space project is to accomplish an environment that comprehends human's intentions and satisfies them. It seems that such a system is hardly achieved, since a huge number of functions should be prepared and human-like intelligence is required. Even though such a complete system cannot be achieved immediately, it is convinced that a useful system can be achieved with current technology by proper system integration.

This paper is organized as follows. Section II introduces the basic concepts and achievements of the iSpace. Section III introduces the present state of iSpace as the artificial spatial memory, real time vision and feature tracking, which have been developed for active human support. Section IV explains the DIND data fusion with Covariance Intersection(CI) that is ongoing research in iSpace. Section V introduces the robot technology for human-iSpace interaction. Finally, the directions for future work and conclusions are described in Section VI and Section VII, respectively.

2. Concepts and Achievements of iSpace

The iSpace is a space (room, corridor or street), which has ubiquitous distributed sensory intelligence (various sensors, such as cameras and microphones with intelligence) actuators (TV projectors, speakers, and mobile agent) to manipulate the space, as shown in Fig. 1. The iSpace propagates mobile robots in the space, which act in the space in order to change the state of the space. These mobile robots are called mobile agents. Mobile Agents cooperating with each other and with the core of the iSpace to realize intelligent services to inhabitants. Mobile robots become more intelligent through interaction with the iSpace. Moreover, robots can understand the requests (e.g. gestures) from people, so that the robots and the space can support people effectively.

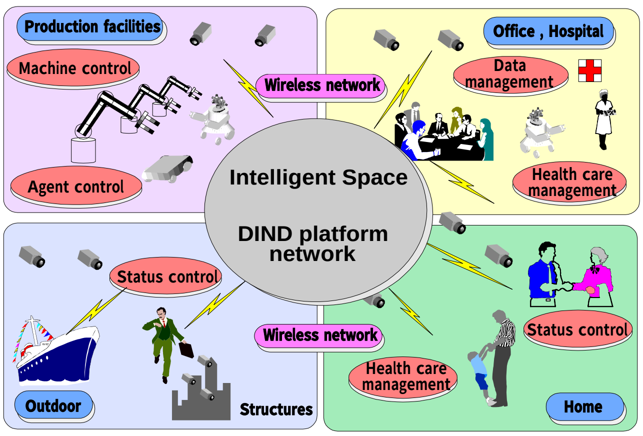

Fig. 1. Vision of Intelligent Space, as a human support system for more comfortable life.

The Intelligent Space can physically and mentally support people using robot and VR technologies; thereby providing satisfaction for people. These functions will be an indispensable technology in the coming intelligence consumption society. Inhabitants in the iSpace are producing intelligent reactions against instantaneous situation. The iSpace evaluates situations (actions-reactions) from sensed information. The ranges of the services of the mobile agents are from guiding in the exhibition area to delivering parcels in a train station. For both type of services, the mobile robots have to navigate in a human shared environment, which is very dynamic, because the inhabitants changes its position quite often.

These intelligent devices have sensing, processing and networking functions, and are named distributed intelligent networked devices (DINDs) [2]. These devices observe the positions and behaviour of both humans and robots coexisting in the iSpace. The information acquired by each DIND is shared among the DINDs through the network communication system. Based on the accumulated information, the environment as a system is able to understand the intention of humans. For supporting humans, the environment/system utilizes machines including computers and robots.

3. Present State of Intelligent Space

3.1 New Intelligent Space Scheme

The Intelligent Space is constructed as shown in Fig. 2. Figure 3 shows the present configuration of the Intelligent Space in the Hashimoto Lab. Our laboratory room, which is about 5 m in both width and depth, is used for the iSpace. The present configuration involves eight pan-tilt-zoom CCD cameras, handled by 4 sensing nodes (PCs), an ultrasound positioning system and two mobile robots. Moreover, the iSpace has a large size screen and speakers for presenting information to the users of the space. All the modules are connected through the local area network. Also, for achieving appropriate conditions for the operation of cameras, the lighting in the space can be easily adjusted.

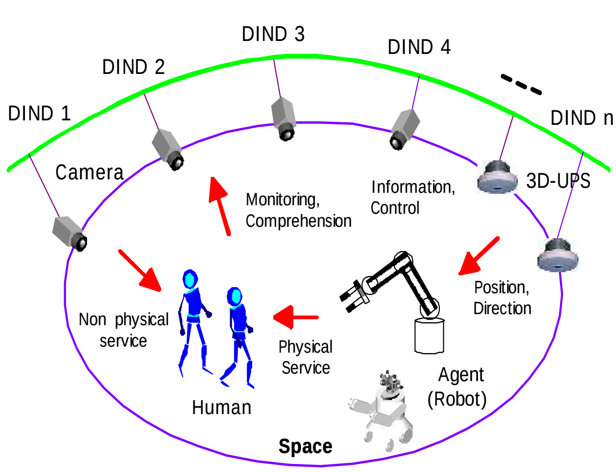

Fig. 2. Structure of Intelligent Space(iSpace).

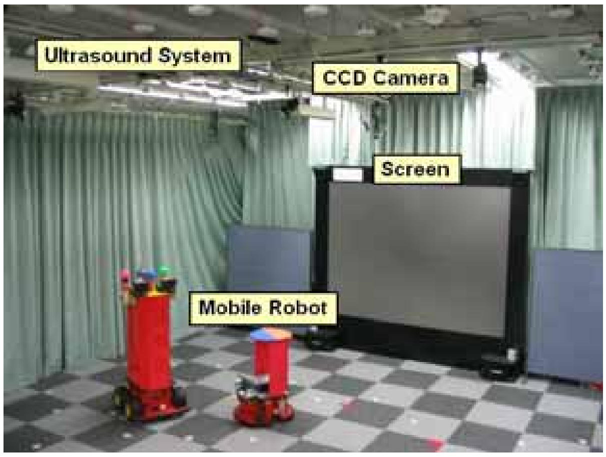

Fig. 3. Experiment environment.

Camera system

In the iSpace, CCD cameras are adopted as sensors for tracking the objects in the space. The cameras are placed so that the whole area of the room is covered. The placement of the cameras can also be optimized to expand the viewable area of the cameras, which was a subject of our previous research [3].

In our currently used system, the human and robot tracking is done by background subtraction and using color information [4]. Skin color is used for human tracking. The robot tracking makes use of color markers positioned on top of the robot. Using the information from all cameras the position of both the humans and robots can be reconstructed. The tracking software also provides a GUI for easy operation.

Ultrasound positioning system

The ultrasound positioning system in the iSpace is used to obtain the 3D position of objects in the space. In consists of small size transmitters and 96 receivers positioned on the ceiling and connected to the control unit. The transmitters send an ultrasound signal, which is detected by the receivers from which the position of the transmitter can be calculated. In order to obtain the information form the positioning system the nodes on the network access a network server connected with the system.

Mobile robots in the iSpace

In the iSpace we currently use two mobile robots. One is a Pioneer 2-DX robot and the other a Pioneer 2-AT mobile robot, both produced by ActivMedia Robotics (www.activrobots.com). A PC is mounted on each mobile robot in order to provide processing of date from the sensors mounted on robots and for communication with the iSpace via wireless LAN.

For the detection of the robot position data fusion of information from cameras, ultrasound system and robot wheel encoders are implemented. Based on the obtained position, tracking and position control of the robot are performed. The observations from both cameras and the ultrasound positioning system are also used to detect the humans and obstacles in the space, which is in turn used for planning the path of the robots.

3.2 Spatial Memory

The spatial memory as an aid system for human activity utilizing knowledge in iSpace has been proposed, as shown in Fig. 4. It is expected as a new interface between human and iSpace. The spatial memory was designed in order to utilize information in the form of documents, images, web pages, commands, etc. instantaneously and intuitively. The spatial memory regards three-dimensional space like mass storage of computers, i.e. three- dimensional point is treated as an address of stored memory such as various data and commands for machines. Consequently, we can access a stored memory by indicating the point using our own arms, which we named “human indicator”. We implemented a prototype of the spatial memory system which was supposed to be utilized for a desk work in iSpace.

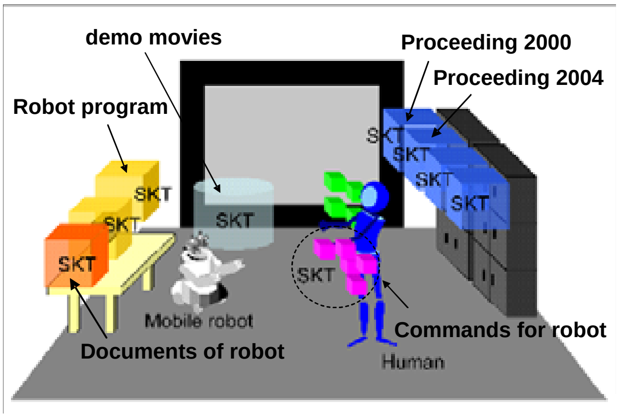

Fig. 4. Illustration of the spatial memory.

The implemented system was evaluated through two types of experiments. First, the usability of the spatial memory was investigated from the viewpoints of accessibility and effectiveness of memorizing [5]. The results of the usability investigations showed that almost all subjects could complete the access to all SKTs without additional learning, in a time as short as in the second performance in all subsequent performances. These results confirmed that the accessibility was improved and the spatial memory improved memorizing the stored knowledge once it was learned. Second, the performance efficiency using the spatial memory was evaluated from the viewpoint of time required for completion of the task [6]. The efficiencies in two experiments performed by using the spatial memory and by not using it were compared. The results confirmed that the time required for the processes of both access and saving data is reduced by using the spatial memory. Applying the t-test under the 5% level of significance, significant difference of the input efficiency in the two performances was confirmed.

3.3 Real Time Image Processing & Feature Extraction

The main source of information in Intelligent Space is the image information of the distributed camera system. Therefore, it is crucial for the robust and efficient operation to adapt fast and accurate image processing methods. Already color information based tracking algorithm [7] is operating in our environment which requires a special marker object to enable tracking. However, color based segmentation can only be used in controlled environment (e.g. in random environment any object can have the same color as the marker that confuses the existing system).

That is why Hashimoto Lab has endowed the existing system with a shape recognition ability, which combined with the color based segmentation yields more reliable results in less laboratory environments. The shape recognition ability is based on an intelligent contouring method which was inspired by cognitive functions of biological vision systems. For, both shape recognition and intelligent contouring is performed using vast parallel computational architecture. The proposed architecture is built up by numerous, simple computational elements that can perform only primitive functions such as addition, subtraction. These computational elements are connected to each other like the neurons in the brain. This architecture can be much more efficient in certain tasks than the complex, classical algorithms as in spite of the fact that thousands of simple operations are done, due to its special architecture, they can be performed in a fully parallel manner that can offer real time operation.

In contrast with conventional image processing algorithms, the proposed model performs a pixel-to-object transformation on the input image. The output data consists of recognized line segments of certain properties that can be mapped to predefined features of the object being tracked [8]. In the Fig. 5, the recognized line segments of a certain property are together with sought colors. If the same color occurs in the neighbourhood of line segments of different characteristics, it will not be mistaken for the sought object.

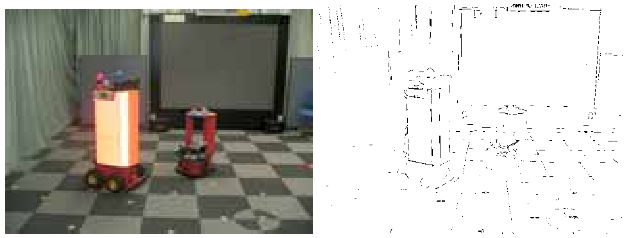

Fig. 5. The input image and the line object recognized by the proposed model.

3.4 Features Tracking

The schema that involves the use of a space doted by intelligence requires an environment capable of recognize its own controllable components as mobile robots. The process of gain knowledge about its own interaction layer and the rest of the events in the space is a crucial task in the intelligent space objectives. The use of camera sensors as a DIND in the proposed framework gives the Intelligent Space a rich and huge amount of information. In the past simple object recognition was achieved by means of artificial beaconing or simple image descriptors [1, 2]. However, potential level of interpretation using visual information and the recent achievements in computer vision allows the intelligent space to reach a new level of perception capabilities.

The inclusion of modern techniques of structure recovery from multiples images [9] to the classical definition and the successful use of modern probabilistic approaches already used in other applications [10] allows a new problem statement for robot localization in Intelligent Space [11].

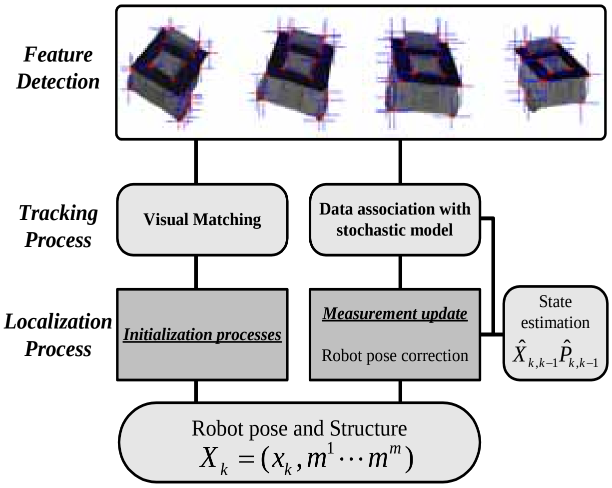

Fig. 6. Scheme of localization.

Problem statement is defined as follows:

- Any robot should be recognized by the environment not because of complex structure recognition, instead it will be recognized as an individual agent because of its properties of be controlled. The only requirement of the system should be this controllability of robotic agents against the environment.
- No prior robot model is necessary and unknown metric landmarks are available on it.
- The system obtains structural information of each robot at the same time the localization process is running.

To achieve the goals proposed is of absolute importance the definition of a robust feature extraction and tracking. The problem to address is to obtain an enough amount of features that belong to robot structure. This requirement is translated into two main conditions. Both should define by construction what should be considered a feasible landmark.

- A projection model of the feature is required, so it should be related to a three dimensional concept through its image detection
- Such a feature should be capable of being tracked during robot motion with unequivocal matching between frames.

Natural landmark tracking is extensively used in many essential tasks such as optical flow, camera calibration or pose computation. Depending on the prior information available, two kind of algorithms used to obtain features from robot structure are possible, as shown in Fig. 6.

- *Matching based on visual information*: Landmark extraction and tracking methods when there is no additional information available apart from the sequence of images captured during object motion. A complete tracker based only in image interpretation is defined. The tracker starts using a classic approach borrowed from spare stereo matching approaches [12]. It should be modified to fit the specific conditions which it should be exposed to such as hard cluttering and high projective changes during robot motion.
- *Data association with stochastic model*: Using a stochastic representation of all parameters in the system the development of data association uses a probabilistic estimation for each landmark. The estimation is modelled as a random process, so it is possible to design a 'Mahalanobis' test to look for the closest candidate in consecutive frames [13].

4. DIND Data Fusion with Covariance Intersection(CI)

4.1 Distributed Data Fusion Network

One of the most important areas of research in the field of control and estimation is distributed data fusion. The motivation for decentralization is that it can provide a degree of scalability and robustness that cannot be achieved with traditional centralized architectures. In industrial applications, decentralization offers the possibility of producing plug-and-play systems in which sensors can be slotted in and out to optimize a trade off between price and performance. This has significant implications for intelligent space with network sensors as well because it can dramatically reduce the time required to incorporate new computational and sensing components into fighter aircraft, ships, and other types of platforms.

The benefits of decentralization are not limited to sensor fusion onboard a single platform; decentralization also can allow a network of platforms to exchange information and coordinate activities in a flexible and scalable fashion that would be impractical or impossible to achieve with a single, monolithic platform. Interplatform information propagation and fusion form the crux of the distributed intelligent network devices (DIND) for the intelligent space. The goal of DIND is to equip all intelligent space entities - car, ships, and even individual mobile agents - with communication and computing capabilities to allow each to represent a node in a vast decentralized command and control network. The idea is that each entity can dynamically establish a communications link with any other entity to obtain the information it needs to perform its multi-tasking role.

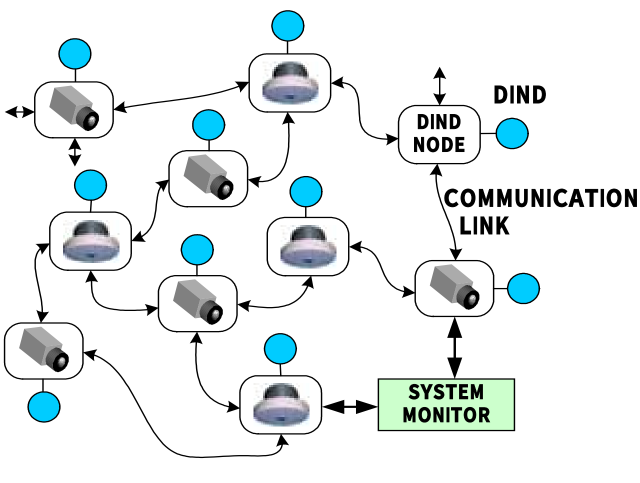

Fig. 7. A distributed data fusion network. Each box represents a fusion node. Each node possesses 0 or more sensors and is connected to its neighbouring nodes through a set of communication links.

A distributed data fusion system is a collection of processing nodes, connected by communication links, as shown in Fig. 7, in which none of the nodes has knowledge about the overall network topology. Each node performs a specific computing task using information from nodes with which it is linked, but no "central" node exists that controls the network. There are many attractive properties of such decentralized systems [16, 17], including:

- Distributed systems are reliable in the sense that the loss of a subset of nodes and/or links does not necessarily prevent the rest of the system from functioning. In a centralized system, however, the failure of a common communication manager or a centralized controller can result in immediate catastrophic failure of the system.
- Distributed systems are flexible in the sense that nodes can be added or deleted by making only local changes to the network. For example, the addition of a node simply involves the establishment of links to one or more nodes in the network. In a centralized system, however, the addition of a new node can change the topology in such a way as to require massive changes to the overall control and communications structure.

4.2 Using Covariance Intersection for Distributed Data Fusion

The network consists of *N* DIND nodes whose connection topology is completely arbitrary (i.e., it might include loops and cycles) and can change dynamically. Each node has information only about its local connection topology (e.g., the number of nodes with which it directly communicates and the type of data sent across each communication link).

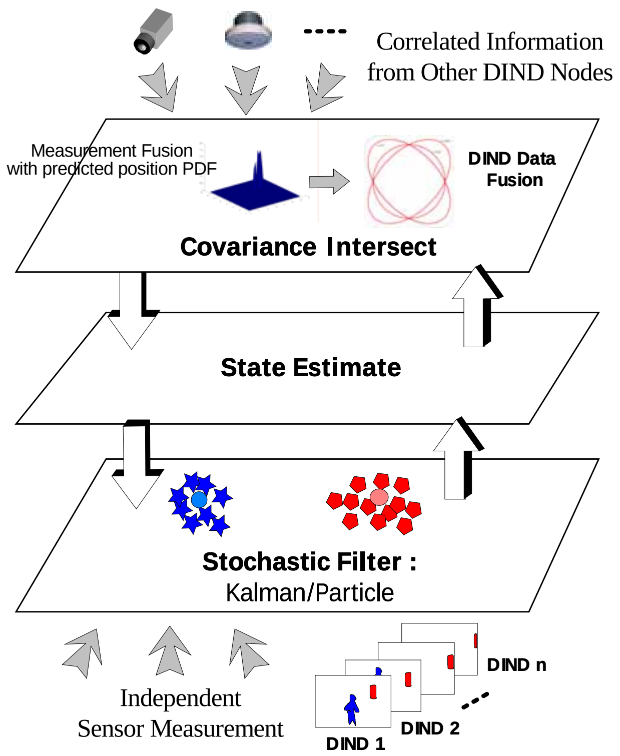

Fig. 8. A canonical node in a general data fusion network that constructs its local state estimate using CI to combine information received from other nodes and a stochastic filter to incorporate independent sensor measurements.

Assuming that the process and observation noises are independent, the only source of unmodeled correlations is the distributed data fusion system itself. CI can be used to develop a distributed data fusion algorithm which directly exploits this structure. The basic idea is illustrated in Fig. 8. Estimates that are propagated from other nodes are correlated to an unknown degree and must be fused with the state estimate using CI. Measurements taken locally are known to be independent and can be fused using the Kalman filter equations.

5. Implementation of RT in Intelligent Space

We have introduced state-of-the-arts in our intelligent space project which is motivated to be adapted to a real environment to give more services to human. However, conventional robot system development has difficulty in integrating these advanced robotics technologies which are remained in laboratory level. One of the reasons of it is originated from the lack of standard platform which should be using the same protocol to integrate individual technologies.

RT-middleware(AIST, Japan) [14] is the one of several solutions in this moment and being supported by Japanese government comparing with other middleware platforms which are more to industrial applications. Therefore, we've been working on implementing our intelligent space on the RT-Middleware network platform [15]. Firstly, we introduce preliminary approach on implementing tele-micromanipulation system with RT-Middleware to collect the knowledge which is inevitable for prospective intelligent space system implementation issue. We have proved flexibility which is required for building complex system such as intelligent space using RT-Middleware

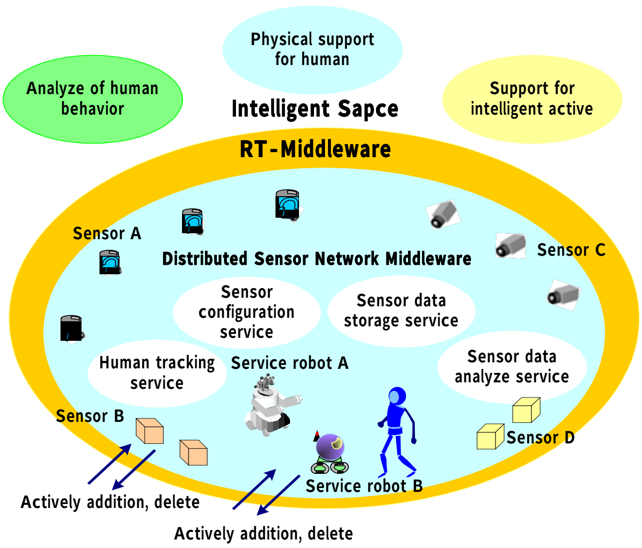

Fig. 9. Implementation of RT in Intelligent Space

We also started to make RT-component of human detecting sensor to be distributed to the intelligent space.

The necessary features are currently being organized. Sensors (ultrasonic, vision), actuators (mobile robot) are to be implemented to RT-component in the first stage. Then, the ongoing algorithm development of spatial memory, feature tracking, real-time vision should be implemented on RT-Middleware network infrastructure to improve the intelligent space. Figure 9 shows the implementation of RT in iSpace.

6. Future of Intelligent Space

The current level of Intelligent Space technology enables the control of the robot motion. The future development of iSpace technology will however enable us to control the robot manipulators as well. This fact will beside a vast increase in possible applications have a large positive feedback impact on the iSpace itself. When manipulator control is possible within iSpace, sensors will namely be mounted on manipulators as well. As a result a more accurate input data will be available.

An interesting topic within iSpace research is the interface between human beings and iSpace. Improved interface would enable humans to control object within IS with voice or hand movement (depending on the type of sensors used). As a result iSpace would be ideal tool for the development of systems capable of helping disabled people. Robots would namely be able to guide blind people or offer help to people in the wheelchair (bring a book from a shelf for example).

Another important area of iSpace research deals with the prospect of its usage outside closed buildings, which represent a well-defined boundary. If there is no such boundary, iSpace systems sensors are subjected to noise from different sources. Therefore there are currently no known applications of iSpace outside buildings. When the development goes beyond this obstacle many new applications will be feasible. iSpace together with its robots could be used in areas which are dangerous for human beings because of different reasons (poisonous gases and extreme temperatures in fire fighting when large fires break out for example).

7. Conclusion

This paper introduced the current research result on Intelligent Space Project. The Intelligent Space involves a ubiquitous distributed sensory network, which can track human and other object is the space; mobile robots, what gives guiding support to the humans, and utilizes the observed information of the sensory network; and artificial spatial memory for human-iSpace interaction. At the present state, the distributed sensory network can track several humans even the case of occlusion with other object or with each other, based on observation from several direction and global color model of the observed object. The artificial spatial memory is an efficient technology to handle the information exchange between human and iSpace, and gives robust gesture recognition of human hand. And we discussed the extremely important problem of data fusion in iSpace. It described a data fusion/update technique that makes no assumptions about the independence of the estimates to be combined. Also, we introduced robot localization based on natural landmark tracking and RT(Robot Technology) to develop the Intelligent Space as an actual standard platform which could be approved by Robotics Community.

References

[1] J.H. Lee, G. Appenzeller, and H. Hashimoto, “An agent for intelligent spaces: Functions and roles of mobile robots in sensored, networked, thinking spaces,” in Proc. IEEE Conf. Intelligent Transportation Systems, Boston, MA, pp. 983–988, 1997.
[2] J.H. Lee and H. Hashimoto, “Intelligent space -concept and contents,” Adv. Robot., vol. 16, no. 3, pp. 265–280, 2002.
[3] T. Akiyama, J.-H. Lee, and H. Hashimoto, “Evaluation of CCD camera arrangement for positioning system in intelligent space,” in Proc. of Seventh Int. Symp. Artificial Life and Robotics (AROB’02), pp. 310-315, 2002.
[4] K. Morioka, H. Hashimoto, “Appearance based object identification for distributed vision sensors in Intelligent Space”, in Proc. of 2004 IEEE/RSJ Int. Conf. On Intelligent Robots and Systems (IROS’04), pp. 199-204, 2004.
[5] M.Niitsuma, H.Hashimoto and H.Hashimoto, “An Evaluation of Spatial Memory Based on Human Performance”, Proc. of the 31st Annual Conf. of the IEEE Industrial Electronics Society, pp.406-411, 2005.
[6] M.Niitsuma, H.Hashimoto and H.Hashimoto, “Efficiency Evaluation of Human Performance Using Spatial Memory”, Proc. of the 36th Int. Symp. on Robotics, 2005.
[7] K. Morioka, J. H. Lee, and H. Hashimoto. Human-following mobile robot in a distributed intelligent sensor network. IEEE Transaction on Industrial Electronics, 51(1), 2004.
[8] Zoltán Petres, Barna Reskó, Péter Baranyi, and Hideki Hashimoto. Cognitive Psychology Inspired Distributed Intelligent Network Devices. In Proceedings of SICE Annual Conference 2005 (SICE 2005), Okayama, Japan, pp. 3299–3304, 2005
[9] O.D. Faugeras and Q.-T. Luong, The Geometry of Multiple Images. MIT Press, 2001.
[10] A.J. Davison, “Real-Time Simultaneous Localization and Mapping with a Single Camera”, In Proc. International Conference on Computer Vision, Nice, 2003.
[11] D. Pizarro, E.Santiso and M. Mazo, “Simultaneous Localization and Structure Reconstruction of Mobile Robots with External Cameras”, In International Symposium on Industrial Electronics ISIE05, June 2005.
[12] Shi and C. Tomasi, “Good Features to Track”, In Proceedings of the IEEE Conference on Computer Vision and Pattern Recognition, pp. 593--600, 1994.
[13] J. Ñeira and J.D. Tardos. “Data association in stochastic mapping using the joint compatibility test” , In IEEE Trans. on Robotics and Automation, 2001.
[14] Noriaki ANDO, Takashi SUEHIRO, Kosei KITAGAKI, Tetsuo KOTOKU, Woo-Keun Yoon, “RT-Middleware: Distributed Component Middleware for RT(Robot Technology)”, 2005 IEEE/RSJ Intl. Conf. On Intelligent Robots and Systems(IROS2005), pp.3555-3560, 2005.
[15] Noriaki ANDO, Mihoko Niitsuma, Yoshihisa TOSHIMA,”System Design of Intelligent Space by RT-Middleware”, RSJ2005, 2005(Japanese).
[16] Nicholson, D. and Deaves, R., Decentralized track fusion in dynamic networks, in Proc. 2000 SPIE Aerosense Conf., 2000.
[17] J Black, T J Ellis, Multi Camera Image Tracking, Technical Report no MVG99/1 Dept. EEIE, City University, London, 1999.

Development of Future Intelligent Sweet Home for the Disabled

Ju-Jang Lee

Department of Electrical Engineering and Computer Science
Korea Advanced Institute of Science and Technology
373-1, Guseong-dong, Yuseong-gu, Daejeon, 305-701, Korea
(Tel.: +82-42-869-3432, Fax.: +82-42-869-3410, E-mail: jjlee@ee.kaist.ac.kr)

Abstract

This presentation introduces a new smart house, *Intelligent Sweet Home*, developed at HWRS-ERC center of KAIST, Korea for testing advanced concepts on independent living of the elderly and people with disabilities. The work focuses on technical solutions for human-friendly motion/mobility assistance and advanced human-machine interfaces that provide easy control of both assistive robotic systems and home-installed applications. To improve the inhabitant comfort, an intelligent bed, intelligent wheelchair and transferring system between bed and wheelchair have been developed and tested. The solutions applied to their design comply with most of the user's requirements and suggestions collected by a special questionnaire survey among people with disabilities. The intelligent sweet home behaves in accordance with the user commands and/or the recognized intentions of the user. Various interfaces based on hand gesture, voice, body movement and posture have been studied and tested. The presentation shows the overall structures of the system and explains the design and functionality of main system components. I hope that this plenary talk will provide not only speech on the progress of new technologies but also the future vision of a better life for the disabled and elderly.

1. Introduction

As the number of the elderly is drastically increasing along with the number of the handicapped caused by a variety of accidents in the complicated and diversified society, the demand for the benefits and support of ever-progressing scientific technology is also increasing to lead more safe and comfortable lives as means of care-giving aids and to live well independently and conveniently along with people without disabilities with the blessed feeling of equality. In particular, the elderly or the handicapped has serious problems in doing a certain work with their own effort in daily life so that some assistive devices or systems will be very helpful if it can assist or do the work instead of human beings endowing as much independence as possible so as to improve their quality of life.

If our ultimate goal is the realization of such a welfare state, a smart house for assisting the elderly and the handicapped can be an alternative to solve daily living problems in individual activities since it integrates systems for movement assistance of the inhabitants carrying out necessary tasks, devices for continuously monitoring of their health status, and interfaces for controlling home-installed devices in a human-friendly manner. Such a solution also has strong positive emotional impact on the inhabitants improving their quality of life, giving them privacy and feeling that they live in an ordinary house, not in a hospital, and reducing significantly the medical care costs per person.

Our work is distinguished in the sense of fully supporting indispensable daily tasks with various functionalities to comply with the needs of the users from the statistical and questionnaire survey, and is based on the idea that the technologies and solutions for such smart house should be human-friendly, i.e. smart houses should possess high level of intelligence in their control, actions and interactions with the users, offering them high level of comfort and functionality. The effect of smart house toward its inhabitants is strongly dependable on the list of the devices that build the home environment and the efficiency of the automatic system that synchronizes their operation. The way of interaction of the inhabitant with the home-installed devices is also a significant aspect of smart house design. As a solution, *Intelligent Sweet Home* consists of several assistive systems and human-friendly interfaces. Intelligent bed, intelligent wheelchair and transferring system were designed and developed for the movement assistance and active services since the people with movement limitations usually spend most of time on bed or wheelchair. The conventional way for control of home-installed devices by switches and remote controllers is not suitable for some categories of people with movement disabilities. In order to offer an alternative for such people, accessible interfaces using hand gesture, voice, body movement and health condition were developed based an intention reading technique. The information exchange between subsystems is performed by the home network using wired and wireless communications.

2. The KAIST's Intelligent Sweet Home

2.1. History

The smart house idea started at KAIST in 1996 with the design of a prototype robotic arm, KARES I, mounted on a wheelchair. Various control modes and human-robot interaction were tested during the same project. The smart house development continued with the KARES II project. In the new project, a novel, very flexible, and small robot was made. In parallel to that research, various new interface systems were developed and tested in other research projects of the HWRS-ERC. The next project stage emphasized refining the smart house concept, developing a common strategy for control and information exchange, and designing new advanced robotic modules. An experimental smart house, called *Intelligent Sweet Home*, was arranged at

KAIST for practical testing of the new design solutions and concepts.

2.2. Survey

To develop a strategy that offers a beneficial response to some specific preferences and needs of the potential Korean users, the research team was greatly influenced by the results from a special questionnaire survey that we conducted among patients of the National Rehabilitation Center, district hospitals, and nursing homes. We involved 70 people between the ages of 18 and 75 who have lower-limb dysfunctions or are elderly (who form the main portion of the Korean people with movement impairment). We sought to gather users' opinions regarding the effectiveness of the assistive systems that they use, the importance they assign to various everyday activities, a list of important tasks that cannot be supported by existing assistive systems, the difficulties experienced by these users when they perform certain tasks with assistive devices, the activities for which they currently need assistance from an external helper, and directions for further improvement of assistive devices. We also asked the reasons that make existing assistive devices non-applicable or inefficient in a range of tasks (such as too big, too small, too heavy, too noisy, requiring too much external power, too complicated, and difficult to control, etc). The survey results helped us to define the outlines and target tasks of our smart house design. It was found that people interviewed gave very high priority to activities such as independence in going outdoors, assistance in meal preparation, eating, drinking, and control of home appliances from the bed or wheelchair, and bringing/removing objects while they are in the bed. The survey results revealed that most of the people interviewed consider it very important to feel themselves comfortable in the bed and wheelchair where they spend most of their time. The majority of those surveyed noted that they are in difficulties when they need to change their body posture or want to transfer between the bed and wheelchair.

2.3. The Intelligent Sweet Home Concept

From a functional point of view, the smart house can be considered a large-scale robot capable of interaction with its inhabitant(s) in a way that provides gentle assistance, health monitoring of vital parameters, living comfort (appropriate humidity, temperature, lighting), and monitoring of home security. The smart house can respond to situation changes or a user's demands by activating one or more different agents (hoist, robotic arm, bed, etc). Multiple assistive systems in the smart house can cooperate in the execution of a single task using synchronized actions and information sharing. Depending on the sensory information, each agent can act autonomously in certain tasks and situations. Cooperation between the systems may increase the list of tasks in which the user can be assisted. Given tasks may also become more efficient and more precisely executed.

We based our smart house design concept on the following main considerations:

1) USER-ORIENTED CONTROL: The algorithm for processing task requests should prioritize the user's commands associated with urgent needs and sensor signals that indicate worsening of the user's state of health or safety risks.
2) FLEXIBILITY: The smart house organization should consider the nature of the disabilities of the user. Customization, based on a modular approach and common communication protocol, can make the design process much faster, easier, and more cost effective.
3) EFFICIENCY IN ASSISTANCE AND HUMAN-MACHINE INTERACTION: Home-installed technology should support users efficiently, allowing them to perform important everyday activities independently. Human-machine interaction should require minimal cognitive load, offering at the same time high speed of information transfer.
4) HUMAN-FRIENDLY DESIGN: Human-machine interaction should be human friendly. The smart house should possess a high level of intelligence for control, actions, and interactions. The machine response should consider the user's health/emotional state, offering them a simple and natural means of interaction. The smart house environment should include recognition of the direct user's commands as well as detection and proper interpretation of the user's intentions.
5) COMFORTABLE POSTURE AND MOBILITY: Smart house technology should allow simple body posture change, either on the user's command or automatically, by timing-based algorithms and information of the pressure distribution history. The design should also consider technology for smooth transportation to most places within the home and wheelchair control manners that require simple user's instructions and automatic steering. The smart house design should also consider devices for effortless transfer of the user between the bed and wheelchair.

2.4. System Architecture

Our smart house design includes several robotic modules to assist motion and mobility, devices for human-machine interaction, sensors, and health-monitoring building blocks. A general block diagram of the *Intelligent Sweet Home* is shown in Fig. 1. All home-installed components are integrated via a central control unit. Referring to the sensory information and the user's commands, the central unit generates a set of actions for each agent and the sequence in which these actions will be executed. Most of the assistive modules developed (intelligent wheelchair, robotic arm, etc) have been designed to perform their inherent functions as well as to cooperate in tasks with other related systems. This approach has several advantages: such modules can be used as stand-alone devices, and their control can be based on high level commands when linked to another system. The cooperation among home-installed systems leads to very efficient and precise execution of given tasks and increases the list of everyday tasks in which the inhabitant can be assisted. When a new module is added to the initial architecture, the management system modifies the earlier control strategy to allow more flexible and efficient use of each module. All systems in the proposed smart house are connected via a home network that includes both wired and wireless communication modules.

The project exploits various ideas of human-machine interfaces (HMI), emphasizing solutions that do not require attachment of intermediate sensors to the user and that reduce the user's cognitive load in task planning, command setting, and receival of feedback information from home-installed devices. For this purpose, we explored interface concepts based on hand gestures, voice, body movements, and an intention-reading technique. The same HMI is used to control various agents, for example, the gesture-based soft remote control system can be used to control the TV, air conditioner, position of the mobile robot, etc.

Our smart house architecture contains two types of robotic modules: robots that help in manipulation, and robots for assistance in posture and mobility. The set of robots for assisting in manipulation includes a bed-mounted robot, a wheelchair-mounted robot, and a mobile robot for object delivery. The bed-mounted robot is responsible for tasks related to serving the user while they are in the bed (bringing objects, covering the user with the quilt, etc). In our prototype, a MANUS robotic arm was adopted and used as a bed-mounted robot. In certain tasks, this robot is assisted by a small mobile robot that transports objects to or from the bed. The wheelchair-mounted robot (developed in the KARES II project) is intended to assist the user in handling various objects, opening doors, etc, while they are in the wheelchair. A detailed description of the design and functionality of the robots for object handling can be found in some of our previous papers. The robots for manipulation assistance may be excluded from the smart house structure when the user has reasonable motion, adequate muscle strength in the upper limbs, and adequate hand dexterity.

The intelligent bed has been designed to provide maximum posture comfort. The bed can change its configuration automatically or upon command. The bed also provides physical support for the user when changing posture via special force-sensitive bar mechanism. The robotic hoist is a special autonomous robot to transfer the user from the bed to the wheelchair and vice versa. The intelligent wheelchair provides easy user access to various places indoors and out. The sensor-based wheelchair facilitates user control by automatic obstacle avoidance maneuvers. The robots for assistance in posture and mobility are described in greater detail in the next section.

An original ceiling-mounted navigation system, called *Artificial Stars*, has been developed to provide information about the positions and orientations of the installed mobile robotic systems. Originally, it was applied to the robotic hoist navigation. Later, the same navigation information will be used for planning the path of the intelligent wheelchair and mobile robot for object delivery (links are shown in Fig. 1 with dashed lines). The pressure sensor system detects the user's posture in the bed. The pressure information is used to control the bed configuration.

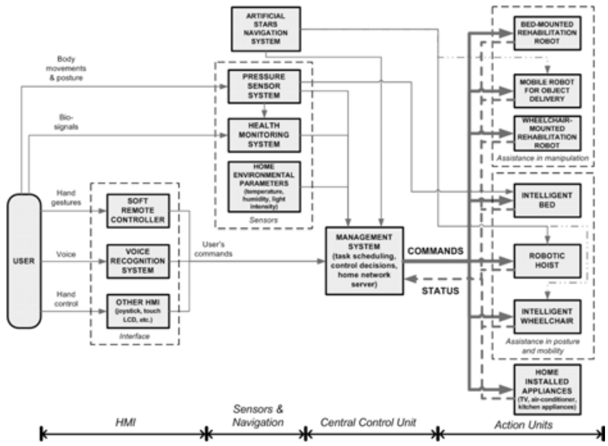

Fig. 1. Block diagram of the *Intelligent Sweet Home*

3. Intelligent Bed Robot System

Usually, one third or a quarter of life is spent for being in bed. Especially, peoples who need care usually spend the whole day for being in bed. If their movements are measured and evaluated quantitatively, not only robots can assist humans properly, but also theses data can be used for a health monitoring and an evaluation of rehabilitation progress.

Body movements are very important for humans to live. Moving the body makes humans take adaptive behaviour to the outside world. It is said that physical conditions and mental conditions are buried in the body movements, because humans often move their bodies when they are in good health, but move rarely their bodies when they are in bad health. Therefore, it is thought that physical and mental conditions can be estimated by measuring the body movements.

A measuring system which has sensors attached to a human body directly is usually for the body movement or posture estimation. There is the system that can recognize postures using accelerometers [2]. Although this system can measure the body movement or posture accurately, many sensors must be attached to the body to measure accurate movements. Since attaching many sensors to the body produces mental burdens and restricts person's activities, it is difficult to measure unaffected body movements. In order to measure unaffected body motions, sensors need to be attached not to the body but to an environmental side as a bed.

Many researches are performed for body motion tracking by using video camera [3], [4], [5]. However, it is difficult for these systems using video camera to extract motion features because the body is lost of sight in a quilt. Static charge sensitive bed is famous for monitoring the body movements in bed. It can measure respiration, a heart rate and twitch movements [6]. Temperature sensors distribution bed can measure gross movements such as body turns [7]. Pressure sensor distribution bed is applied in many researches [8]. Harada et al. has applied Pressure sensor distribution bed to estimate the body posture. His approach was based on the body model. This approach estimated the subtle posture and motion between main lying postures (supine and lateral posture). Since the body model had lots of model parameter determined, it takes lots of calculation time to determining the posture.

In our system, the control of manipulator is performed from the result of patient's posture and

motion estimation. Therefore, short calculation time is required to control the manipulator based on posture estimation. In the previous paper, the system description of IBRS, which is capable of estimating the patient's posture and motion on bed in real-time and supporting the patient using manipulator, was introduced [1]. In this paper, the control scheme of robot arm is focused on.
Section 4 briefly introduces the research background for designing IBRS and the proposed system. In Section 5, control and measurement algorithm for the system is described. Experimental results and conclusion are followed in Section 6 and 7.

4. System Description

Most previous researches have a focus on the system which can monitors the patient's posture and motion on bed. In this paper, we will propose the robotic system which can actively help the patient using robotic manipulator. While there exists the patient on the bed, the pressure sensors monitor his posture and motions. When he moves on the bed, the robotic manipulator can support his body.
Before we design an intelligent bed robot system, we conducted a survey of patients' opinion on IBRS at a rehabilitation center and hospitals in Korea. At the survey, we made a questionnaire focused on activities in bed, the functionality of IBRS, and difficulties in doing something without assistant. The survey said that people with motor difficulties in their legs need assistant in doing body movement for posture change or taking a ride on a wheel-chair. They also answered a robot system supporting the stability of body posture during movement would be helpful.

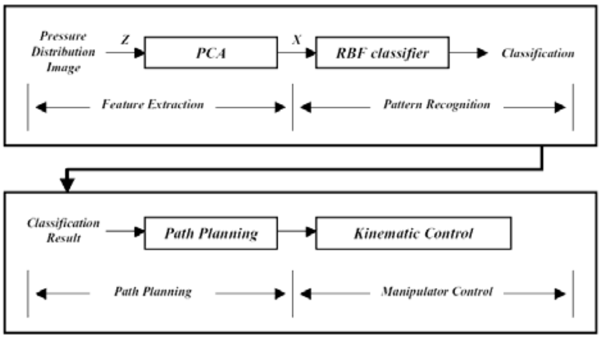

Fig. 2 System architecture for IBRS.

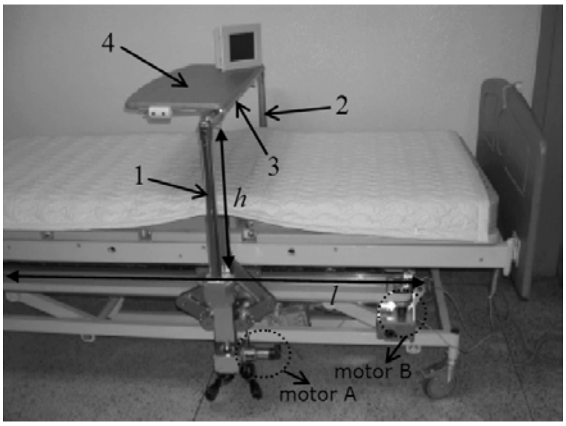

Fig. 3. Intelligent Bed Robot System

To assist user's movement while one is on the bed and allow gentle active support of the user when he/she changes body posture, we attached a bar-type robotic arm as shown in Fig. 3. The same robotic arm can also be used to deliver some objects on the tray mounted to it.
The robotic arm is shaped as a frame that is composed by two supporting bars (1 and 2) connected by horizontal bar (3). A tray (4) is attached to the bar 3. The height of the supporting bars (denoted as h in Fig. 3) can be actively controlled by 50W DC motor (A). The frame is mounted to a mobile platform that allows the robotic arm to reach and serve the whole area on the bed by moving it along the bed (this motion is noted with l in Fig. 3). Two 50W DC motors (B) on both sides of the bed drive the moving platform. Two torque sensors mounted to each supporting bar measure the 2-dimensional forces applied to the horizontal bar 3 as shown in Fig. 4. If the force, applied to the bar contains only a horizontal component (f_x), the torques τ_A and τ_B measured by each torque sensor have the same directions, while application of vertical force component f_y causes torques with opposite directions. When the user needs to change his/her posture on the bed, at first the user roughly positions the horizontal bar of the robotic arm near his/her chest by using voice command. The horizontal bar comes close to the user according to the position and the posture of the user as shown in Fig. 5. Then, the user grasps the horizontal bar and adjusts the position/height of the bar by pushing or pulling it. The forces coming from the user are sensed by the torque sensors and cause movement of each supporting bars. This "follow" mode of robotic arm can be change to "support" mode by voice command. In "support" mode, the supporting bars are fixed, and the user can slightly change his/her position and posture leaning over the horizontal bar.
To position the horizontal bar near the user's chest by voice command and achieve automatic bending of the bed according to the intention of the user, we applied posture recognition and analysis of the history of user's motion on the bed. To this end, we distributed an array of pressure sensors over the bed surface as shown in Fig. 6. Force Sensing Resistors (FSRs) are used to measure the pressure in the contact points. The FSR is a thin film sensor made from piezoresistive polymer which resistance decreases in proportion to the force applied on its active surface. We used pressure sensors that can measure forces up to $10 kg/cm^2$. Sensors were uniformly distributed with 70mm and 50mm spatial interval in vertical and horizontal direction respectively. The dimensions of the pressure sensitive mat are $1900mm \times 800mm \times 12mm$. Since the mat covers a bed which shape is changeable, the mat is divided into 3 parts, which dimensions coincide to the bed segments to provide easy bending of the mat correspond to bending of the bed. To get the pressure values, the control box scans the pressure sensors one by one using multiplexers, reads the pressure value of the selected sensor, and transmits the data to the main computer as a pressure distribution image. Sampling frequency of the image is $10 Hz$ and the resolution is 10 bit. Analyzing the pressure data, the program recognizes both user's posture and motion.

5. Control and Measurement

5.1. Measurement of patient intension using pressure sensor mattress

The mass of the body and the force produced by the muscle generate the pressure on the FSR sensors attached on the mattress. Normally, RBF neural networks are widely used for function approximation and pattern recognition wherein the pattern dimension in this application is usually small. But, the pressure distribution image in our system has a high dimensional property. The pressure distribution image has 336 features (equal to the number of FSR sensors). Due to the high redundancy present in the pressure distribution image vector, principal component analysis (PCA) was used to reduce the dimensionality of data. The detail algorithm was introduced in the previous paper [1].

5.2. Control of supporting manipulator

The robot arm has two kinds of operation mode. One is "support" and the other is "follow". In the "support" mode, the robot arm is operated based on kinematic control. After the bed system estimates the position of patient, it controls the robot arm with the predefined path. Otherwise, in the "follow" mode, two torque sensors measure the intension of patient on the supporting manipulator.

5.2.1. Kinematic Control

In robotic motion planning and control, the solutions to the kinematics problems are essential to achieve the goals of a robotic operation. The forward kinematics problem in robotics is concerned with the transformation of position and orientation information in a joint space to a Cartesian space described by a forward kinematics equation

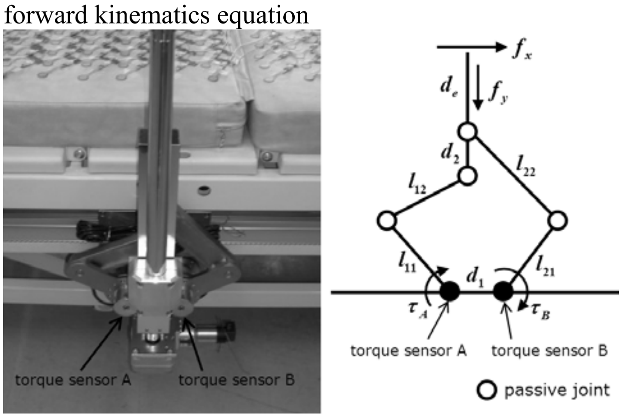

Fig. 4. Structure of supporting bar

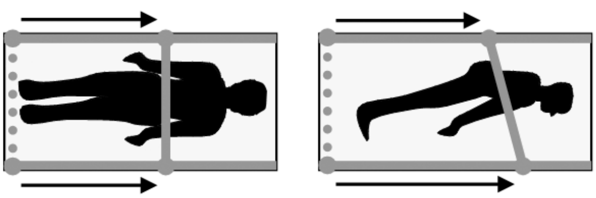
Fig. 5. Various positioning of the horizontal bar


Fig. 6. Pressure sensors-laid bed

$$r(t) = f(q(t)) \tag{1}$$

where $q(t) \in R^m$ is joint variables, $r(t) \in R^n$ is Cartesian variables, and f(.) is a continuous nonlinear function whose structure and parameters are known for a given manipulator. The inverse kinematics problem is to find the joint variables given the desired positions and orientation of the end-effector through the inverse mapping of the forward kinematics equation (1)

$$q(t) = f^{-1}(r(t)) \tag{2}$$

The inverse kinematics problem involves the existence and uniqueness of a solution, and effectiveness and efficiency of solution methods. The inverse kinematics problem is thus much more difficult to solve than the forward kinematics problem for serial manipulator. The difficulties are compounded by the requirement of real-time solution in sensor-based robotic operations. The most direct way to solve (2) is to derive a closed-form solution from (1). Unfortunately, obtaining a closed-form solution is difficult for most manipulators due to their nonlinearity of f(.).

The two robot arms of the developed bed robot system are linked with the supporting bar. Although this supporting could change its length, the maximum length is defined. So, in the control procedure, this limitation should be considered.

5.2.2. User intention analysis using torque sensors

In the "follow" mode, the patient can control the robot arm. When he/she pull or push the supporting bar, robot arm measures the variation of torque sensors, then controls motor A and motor B. As shown in figure 4, two torque sensors are equipped for estimating user intention. Desired position of user is calculated from the combination of torque sensors.

The relation between torque sensors and user intension can be expected intuitively. But, the structure of robot arm system is not easy to explain mathematically. Therefore, the fuzzy network was designed to infer the human intention. The rule table for fuzzy network is introduced in Table 1. The motor A and B is controlled based on rule table.

Table 1. Fuzzy rule table to infer the patient's intension from two torque sensors.

Motor A		τ_B				
		PL	PS	ZO	NS	NL
τ_A	PL	ZO	ZO	PS	PL	PL
	PS	ZO	ZO	PS	PS	PL
	ZO	NS	NS	ZO	PS	PS
	NS	NL	NS	NS	ZO	ZO
	NL	NL	NL	NS	ZO	ZO

Motor B		τ_B				
		PL	PS	ZO	NS	NL
τ_A	PL	PL	PL	PS	ZO	ZO
	PS	PL	PS	PS	ZO	ZO
	ZO	PS	PS	ZO	NS	NS
	NS	ZO	ZO	NS	NS	NL
	NL	ZO	ZO	NS	NL	NL

* P: positive, N: negative, L: large, S: small, ZO: zero

6. Experimental Results

Mainly four kinds of postures on the bed (supine, right lateral, left lateral, and sitting posture) are considered in this paper. These postures were used for body posture estimation process. In our system, discrimination that the current patient's posture belongs to the posture class is more important than the fact such as opening degree of legs. The patient's motion and intension are estimated from changes between the posture classes. The proposed algorithm was applied to estimate pose and motion.

Figure 7 shows the postures to be estimated. The patient in a sleep takes main four postures.

Table 2 describes the processing time according to the number of principal components (PC). The processing time for estimating the posture increases in proportion to the increasing number of PC.

In order to finish the measurement and estimation at the processing rate 10Hz, the process should be fast and exact. As shown in table 2, proposed algorithm (PCA+RBFNN) with 20 PCs hits highest performance. Though structure with higher PCs has higher accuracy, the calculation cost is much higher.

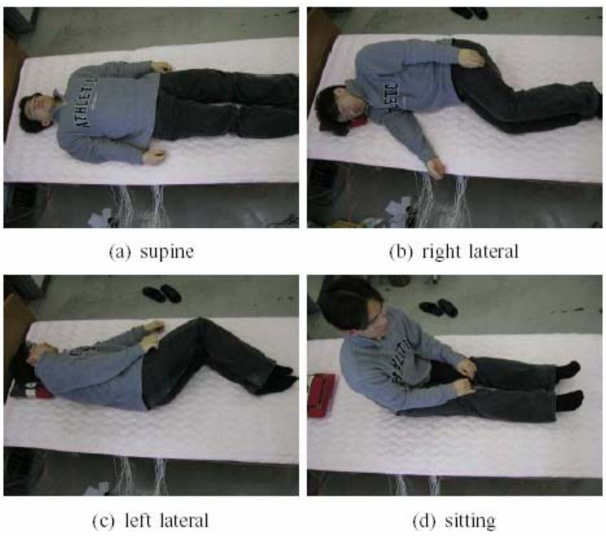

Fig. 7 Postures to be estimated.

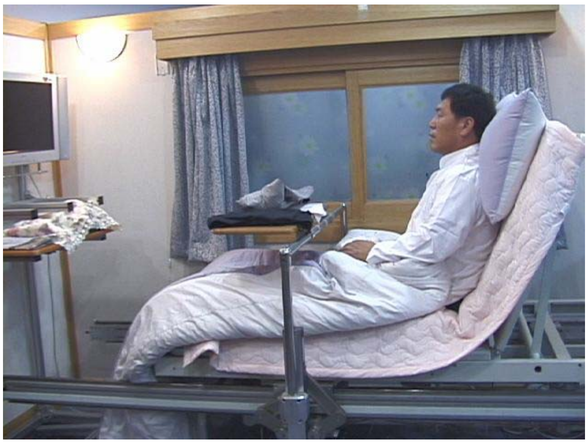

Fig. 8. Demonstration of Intelligent Bed Robot System

Table 2. Processing time and Recognition accuracy according to the number of PC.

Structure	Number of PC	Processing time (ms)	Recognition accuracy
PCA	5	13	85.1
	10	18	87.2
	20	22	91.6
	30	29	91.8
	50	57	90.9
PCA+RBFNN	5	21	87.9
	10	30	90.8
	20	44	93.6
	30	63	93.7
	50	82	93.4

The overall demonstration was performed as shown in figure 8. The developed bed robot system serves the patient with bar-type supporting robot arm and foldable mattress based on the sensor data which is obtained from pressure sensor distributed mattress.

7. Conclusion

In this paper, the unrestraint human pose and motion estimation system using the pressure sensor distribution bed was described. This system is thought to be used for analyzing the body pose and motion, assisting the patient with robotic manipulator. Furthermore, it can be used for a health monitoring and evaluation of rehabilitation progress and so on.

Acknowledgment

This paper was partially supported by HWRS-ERC (Human-Friendly Welfare Robot System Engineering Research Center), Republic of Korea.

References

[1] Kap-Ho Seo, Changmok Oh, and Ju-Jang Lee, "User Pose Estimation Using Sensor Distribution Bed", IECON2004, pp. 598 – 602, November, 2004

[2] A. K. Nakahara, D. L. Jaffe, and E. E. Sabelman, "Development of a Second Generation Wearable Accelerometric Motion Analysis System," *Proc. 2nd National Rehabilitation Research and*

Development Service Meeing, 2000.

[3] J. O'Rourke and N. I. Badler, “Model-Based Image Analysis of Human Motion Using Constraint Propagation,” *IEEE Trans. Pattern Analysis and Machine Intelligence*, vol. 2, no. 6, pp. 522-536, 1980.

[4] J. Rehg and T. Kanade, “Visual Tracking of High DOF Articulated Structures: An Application to Human Hand Tracking,” *Proc. 3rd European Conf. Computer Vision*, pp. 35-46, 1994.

[5] C. R. Wren, B. P. Clarkson, and A. P. Pentland, “Understanding Purposeful Human Motion,” *IEEE Int'l Conf. Automatic Face and Gesture Recognition*, 2000.

[6] J. Alihanka, K. Vaahtoranta, and I. Saarikivi, “A New Long-term Monitoring of Ballistocardiogram, Heart Rate, and Respiration,” *AM. J. Physiol.*, vol. 240, pp. 384-392, 1981.

[7] T. Tamura, J. Jhou, H. Mizukami, and T. Togawa, “A System for Monitoring Temperature Distribution in Bed and Its Application to The Assessment of Body Movement,” *Physil. Meas.*, vol. 14, pp. 33-41, 1993.

[8] T. Harada, T. Sato, and T. Mori, “Estimation of Bed-Ridden Human's Gross and slight Movement Based on Pressure Sensors Distribution Bed,” *IEEE Int'l Conf. Robotics and Automation*, pp. 3795-3800, 2002.

The Eleventh International Symposium on Artificial Life and Robotics 2006 (AROB 11th'06),
B-con Plaza, Beppu, Oita, Japan, January 23-25, 2006

Locating Static Targets by Matching Image Frames

Xin Wang[1,2] **Masanori Sugisaka**[2] **Jin Wang**[3]

[1]Department of Electrical and Information, Niihama National College of Technology, Japan
[2]Department of Electrical and Electronic Engineering, Oita University, Japan
[3]College of Textile & Garments, Hebei University of Science and Technology, China

Abstract

We present a new algorithm to locate targets by matching image frames taken from a moving platform. We have noticed that an image point is environment sensitive, but those energy changes of grouped points have their own statistical similarities in two image frames within limited time interval. This approach analyzes correspondence of energy points around every feature points between inter-frames in image sequence in order to decide those feature points. Successful results are given for a vide frames.

1. Introduction

Motion detection is made difficult as both the observer and some elements of the scene may be moving. But detecting objects from a moving platform is one of the key issues to the successful applications of mobile system, for example, mobile robot system [2][3]. A common motion analysis problem is to obtain comprehensive information about moving and static targets presented in a scene. Prior knowledge, which includes information about the camera motion, mobile or static, and information about the time interval between consecutive images for example man-aid initial selection or varies information base, can also help to decrease the complexity of analysis [1][4][5]. One of important differences between motion in moving camera or moving platform and static camera is that all is moving in the former case and only object are moving in the later.

Generally, from the practical point of view, there are three groups of motion-related problems: motion detection, object detection and location, and derivation of 3D object properties. Our problem belongs to the second group, i.e. tracking a static target from a moving platform [6][8]. Our method is to match corresponding feature points (FP), and to locate them. The presented method is based on calculating the local minimum energy points around a feature point, analyzing the image tensor, and then deciding the corresponding relations between frame intervals. We discuss the case of a camera on a moving platform and the target is static on the assumptions that motion is with maximum frame velocity constraint, which a target is scanned at discussing frame time intervals, and with target mutual correspondence, which the target exhibits some stable points and not all but part of these points correspond to exactly some points in the next image frame. In the presented approach, we build a contour model of a target to get some low-energy feature points. In order to get the corresponding relation on the feature points between frames, it is necessary to select relevant key areas around these points, to find some interest points in these areas, and then to get the optimal correspondences or possible solutions. In the next section, our algorithm to select the feature points are introduced; Section 3 gives the principle about the statistical analysis in order to locate static targets. Experimental results and discusions are in Section 4.

We denote $I(\mathbf{x})$, $\{\mathbf{x}=(\mathrm{x},\ \mathrm{y}):\ \mathbf{x}\in \mathcal{R}^2\}$, as a frame in an image sequence, the i_{th} frame as $I_i(\mathbf{x})$, and the j_{th} as $I_j(\mathbf{x})$, $(i, j = 1, 2, \dots, n | i < j, i \neq n, j \neq 1)$. Two target frames $I_i(\mathbf{x})$, $I_j(\mathbf{x})$, in which the targets are, are sampled by their appeared orders in image sequence. The input frame is $I_i(\mathbf{x})$, output is $I_j(\mathbf{x})$.

2. Active Contour

The traditional active contour model, also named snake, is defined as an energy minimizing spline–the snake energy depends on its shape and location within an image. The main idea of snake model is to estimate an initialized curve, and use this curve to initialize the conventional snake equations in order to get solutions about its Euler-Lagrange equation. It is recomputed to eliminate high-energy segments and renew the low-energy contours until constrains are satisfied. The energy functional is a weighted combination of internal and external forces. The internal forces emanate from the shape of the snake, while the external forces come from the image and/or from higher-level image understanding processes. The snake is defined parametrically as $\mathbf{v}=v(s)=[x(s),\ y(s)]$, where x(s), y(s) are x, y co-ordinates along the contour and $s\in[0,\ 1]$, $v(s)$ can be approximated as a B-spline. The energy functional to be minimized may be written as:

$$E_s^* = \int_0^1 E_{sna}(\mathbf{v})ds \tag{1}$$

$$= \int_0^1 (E_{int}(\mathbf{v}) + E_{ext}(\mathbf{v}))ds \tag{2}$$

where $E_{int}(\mathbf{v})$ represents the internal energy of the spline due to bending. External energy $E_{ext}(\mathbf{v})$ includes image forces $E_{im}(\mathbf{v})$ and external constraint forces $E_{cst}(\mathbf{v})$:

$$E_{ext}(\mathbf{v}) = E_{im}(\mathbf{v}) + E_{cst}(\mathbf{v}) \tag{3}$$

$E_{im}(\mathbf{v})$ is derived from the image data over which the snake lies. $E_{cst}(\mathbf{v})$ come from external constraints imposed either by a user or some other higher-level process which may force the snake toward or away from particular features. We just select $E_{cst}(\mathbf{v}) = 0$.

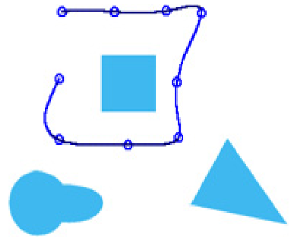

Fig. 1: Initial control points on a rectangle.

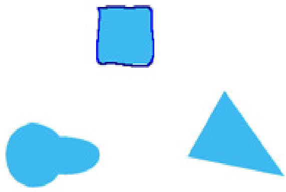

Fig. 2: Converged contour after 25 iterations.

From (2), the functional to be minimized is (1). Then from the calculus of variations, the Euler-Lagrange condition states that the spline curve $v(s)$ which minimizes $E_{sna}(\mathbf{v})$ must satisfy

$$\frac{d}{ds}E_{v_s} - E_{\mathbf{v}} = 0 \tag{4}$$

where E_{v_s} is the partial derivative if $E(\mathbf{v})$ with respect to $dv(s)/ds$ and $E_{\mathbf{V}}$ is the partial derivative of $E_{sna}(\mathbf{v})$ with respect to $\mathbf{v}$. Then the Euler-Lagrange equation reduces to

$$\frac{\partial v(s,t)}{\partial t} - \frac{\partial}{\partial s}[\alpha(s)\frac{\partial v(s,t)}{\partial s}] + \frac{\partial^2}{\partial s^2}[\beta(s)\frac{\partial^2 v(s,t)}{\partial s^2}] - \nabla E_{ext}[v(s,t)] = 0 \tag{5}$$

where $\alpha(s)$, $\beta(s)$ specify the elasticity and stiffness of the snake, which control the internal spline energy.

The process and one of our results by the described model are shown in the figures [1][6]. Fig. 1 shows an initial contour with nine control points. The results after 25 iterations are given in Fig. 2. In Fig. 3, nine feature points about the rectangle target are made, which is from the converged contour shown in Fig. 2.

3. Statistical Similarity Analysis

Feature points represent specific places in an image that carry distinctive features of the object being studied. Assume that there be two local windows $A'_m \subset I(\mathbf{x})$ and $A'_n \subset I(\mathbf{x}+\Delta\mathbf{x})$. Pay attention to the image energy distribution around a feature point, two tracking windows with different scales in input space $A'_m \subset I_i(\mathbf{x})$ and output space $A'_n \subset I_j(\mathbf{x})$ are selected. Let the elements in the tracking windows be the ones around every feature point. If more than two of elements of A'_m in A'_n are decided, the corresponding position of the $\mathbf{x}$ in $I_j(\mathbf{x})$ can be estimated. If some corresponding points of $\mathbf{x}$ are found in A'_n, we can also estimate the target in this new

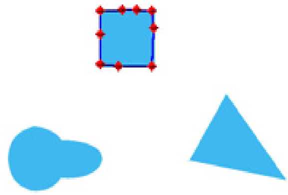

Fig. 3: Feature points from the converged contour.

frame by parts of its feature points. Corresponding elements in A'_m and A'_n are recognized by simple directive *chain codes* [6] with their neighborhoods. This process are illustrated in Section . More details can be found in [14].

Let A_m={$\mathbf{x}_m$} be the set of all energy points in the first starting image that is input state space, and $A_n = \{\mathbf{y}_n\}$ the energy points in the second image that is output state space. Let $\mathbf{c}_{mn}$ be a vector connecting points $\mathbf{x}_m$ and $\mathbf{y}_n$ (thus $\mathbf{y}_n$=$\mathbf{x}_m$+$\mathbf{c}_{mn}$). Let the probability of correspondences of two points $\mathbf{x}_m$ and $\mathbf{y}_n$ be Γ_{mn}. Two points $\mathbf{x}_m$ and $\mathbf{y}_n$ can be considered potentially corresponding if their distance satisfies the assumption of maximum velocity

$$|\mathbf{c}_{mn}| \leq \gamma_{max} \tag{6}$$

where γ_{max} is the maximum distance which a point may move in the time interval between two consecutive images. Two correspondences of points $\mathbf{x}_m\mathbf{y}_n$ and $\mathbf{x}_k\mathbf{y}_l$ are termed consistent of

$$|\mathbf{c}_{mn} - \mathbf{c}_{kl}| \leq \Delta \tag{7}$$

where Δ is a pixel distance deviation. Consistency of corresponding point pairs will increases the probability that a correspondence pair is correct. We determine the sets of energy points $A_m \subset A'_m \subset I_i(\mathbf{x})$, $A_n \subset A'_n \subset I_j(\mathbf{x})$, and construct a data structure as follows:

$$[\mathbf{x}_m, (\mathbf{c}_{m_1}, \Gamma_{m_1}), (\mathbf{c}_{m_2}, \Gamma_{m_2}), \ldots, (EPC, EPP)]$$

where EPC, and EPV are special symbols indicating that no potential correspondence was found. We iteratively calculate the probability of correspondence of a point $\mathbf{x}_m$ with all potential points $\mathbf{y}_n$ as a weighted sum of probabilities of correspondence of all consistent pairs $\mathbf{x}_k\mathbf{y}_l$, $\mathbf{x}_k$ are neighbors of $\mathbf{x}_m$ and the consistency of $\mathbf{x}_k\mathbf{y}_l$ is evaluated by $\mathbf{x}_m$ and $\mathbf{y}_n$. To a function F [14]:

$$\Gamma_{mn}^{(s)} = \mathcal{F}(\Gamma_{mn}^{(s-1)}, \Gamma_{kl}^{(s-1)}) \tag{8}$$

Those points that hold high probabilities that obviously differ from those energy points without correspondences.

Intuitively, we give N local approximate locations in $I_i(\mathbf{x})$ by coarse hand initialization. After executing the algorithm, an active contour model is formed first and then the contour converges to N low-energy positions. There are N FPs in the state space $\breve{A}_m$. An input state space A_m, A_m={$\mathbf{x}_m$}, is constructed around a *kernel* in $\breve{A}_m$. A'_m gives a *tracking window* in $I_i(\mathbf{x})$. We can compute the possible energy points around every FP in the

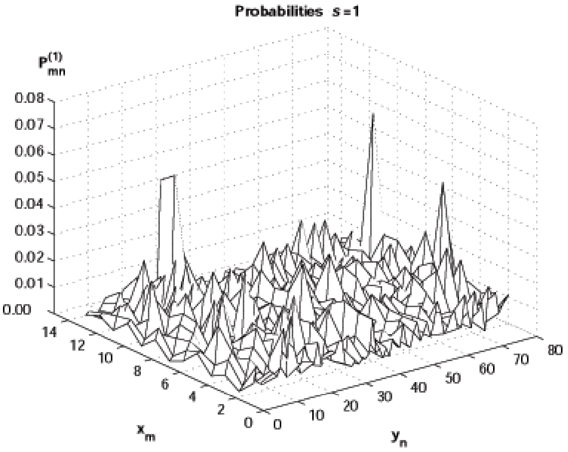

Fig. 4: Initial energy distribution.

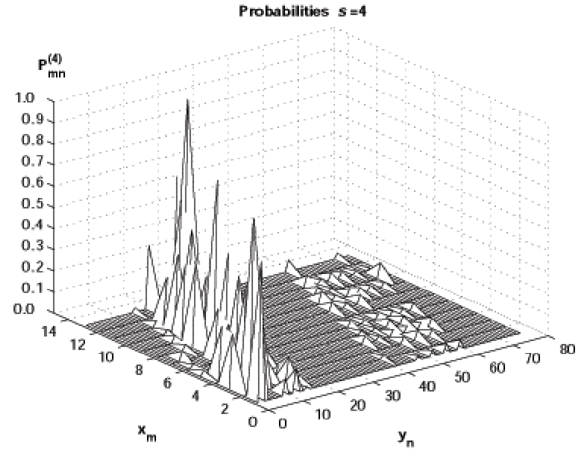

Fig. 6: The energy distribution after 4 iterations.

tracking window, and build another *tracking window* A'_n including a corresponding output state space $A_n=\{\mathbf{y}_n\}$ in $I_j(\mathbf{x})$. In this paper, we give the results of one FP between frames to illustrate our method. This principle is also suitable for more ones. The area of A'_n is up to the maximum distance γ_{max} in (6). Finally the corresponding relations are established by application of the algorithm presented. We get a new FP in the frame A'_n including $A_n=\{\mathbf{y}_n\}$. More FPs, which are to form a new input space state, can also be calculated by repeating the same process. The target is matched by tracking its these kernels in consecutive image frames. This process is illustrated in (9).

$$\begin{aligned} \breve{A}_m^{(t)} &\Rightarrow A_m^{(t_1)}, A_n^{(t_1)} \Rightarrow \breve{A}_m^{(t_1)} \Rightarrow A_m^{(t_2)}, A_n^{(t_2)} \\ \ldots &\Rightarrow \breve{A}_m^{(t_n)} \Rightarrow A_m^{(t_{n+1})}, A_n^{(t_{n+1})} \ldots \qquad (9) \end{aligned}$$

where t_k, $k = 1, 2, \ldots$, denotes sampling time at k. The interval is up to the velocity of the moving platform.

4. Experiments and Discussions

In this section, some experimental results based on the presented method are illustrated. We use the same video image [7] to execute our experiments. In Fig. 5, (a) is the original input image frame 2; (b) is the output images frame 9; (c) gives the active contour model based on the algorithm described in Section 2. The feature points and an area of A'_m are shown in (d). $A'_m \subset R^2$, there are 24×24 (unit: 5 pixels) elements in it. (d) gives the 21 original energy points after the first detection. 13 of the 21 energy points are then kept after excluding the points on the edge; (g) shows the energy points in A'_n, $A'_n \subset R^2$, there are 100×50 elements in it. A_m and A_n are detected from A'_m and A'_n respectively, $A_m \subset A'_m$, $A_n \subset A'_n$. A_n is in a larger area so there are more elements i.e. energy points in it. The reason why a larger A'_n in (g) is selected is that the size of A'_n up to the velocity constraints of D_{max} in (6) resulted from the moving camera. The larger the size is the more energy points are detected, but also accompanied with much time cost. (e) and (h) give the detected results by using the algorithm described in Section 3. The FP's position is also marked by black-white "+" where is the center of mass in A'_n. $\mathbf{x}_m$ and $\mathbf{y}_n$ are located by "+" symbols with white circle background in (e) or (h). All 13 pairs of elements are decided between A_m and A_n. (e) and (h) show that even if we selected a smaller local area around a FP, it is still possible to catch some corresponding elements in A_n since FPs locate on the low energy positions. To show these results more clearly, (f) and (i) focus on the detected corresponding part in (e) and (h), and give their amplified effects. The results have given very good corresponding relations. The whole process is shown in Fig. 5(c) to Fig. 5(i) where the values of $\mathbf{x}_m$ and $\mathbf{y}_n$ are their indexes in A_m and A_n in their storage spaces.

The correspondence points are decided with errors less than 5 pixels because our calculating unit is 5 pixels.

5. Conclusions

We proposed a new approach starting from some converged points by the snake principle. We depict the attributes of a target by its significant energy points. Our idea to understand a target is from its points of this target to its lines, from its points to its lines and areas. This is related to manipulate our knowledge database in our further works. The proposed energy point detection approach also gives very satisfied results.

In this work, we proposed three processes to track a static target from a moving platform where an camera is moving and an target is static: active contour model, which are used to estimate kernel points at the final converged contour position; the points detection, which is in a area around a feature point, along with measures of image energy, as the system input measurement; and a statistical similarity analysis method, which uses correspondence pairs detection, as the former system output and the next system input. This approach takes us another advantage to occlusion problems, because the target/object can be estimated by parts of their features.

Acknowledgements

This research was also done while Xin Wang was a staff at School of Engineering, the University of Tokushima.

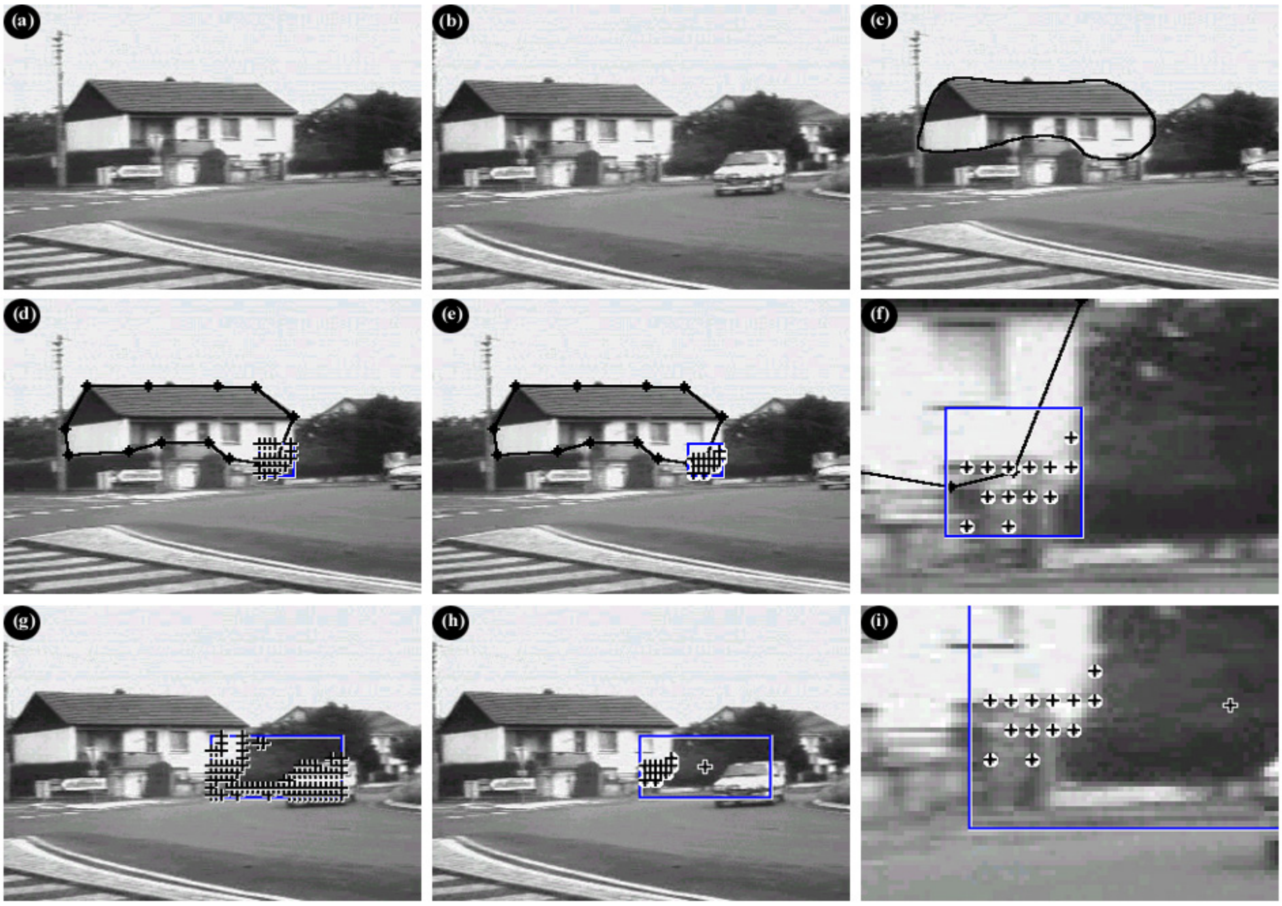

Fig. 5: Tracking a static target, a house corner, in image sequence from a moving platform.

References

[1] X. Wang, M. Sugisaka, W. Xu, "Model based recognition for artificial brain," *Proc. of the 9th Int. Symposium on Artificial Life and Robotics,* Vol, 2, pp. 605-609, 2004.

[2] A. Kumar, A. Tannenbaum, and G. Balas, "Optical flow: a curve evolution approach," *IEEE Trans. Image Processing*, vol.5, no.5, pp. 598-610, 1996.

[3] L. Robert, and O. Faugeras, "Curve-based stereo: Figural continuity and curvature," *Proc. CVPR'91*, pp. 57-62, 1991.

[4] S. B., Pollard, J. Mayhew, and J. P. Frisby, "Implementation details of the PMF stereo algorithm," *3D Model Recognition from Stereoscopic Cues, MIT Press, Cambridge*, MA, pp. 33-41, 1991.

[5] R. Green, D. Gray, and J. Powers, *Artificial Vision*, Academic Press, London, 1997.

[6] D. A. Forsyth, J. Ponce, *Computer Vision*, Prentice Hill, USA, 2003.

[7] X. Wang, M. Sugisaka, W. Xu, "Active contour model based tracking analysis" *Proc. of the 12th Int. Conference of Systems Engineering, UK,* Vol, 3, pp. 347-352, 2003.

[8] M. Brown, D. Terzopoulos, *Real time computer vision*, Cambridge University Press, 1994.

[9] B. Jähne, *Image processing for scientific applications*, CRC Press, New York, 1997.

[10] D. Scharstien, "Stereo Matching with Nonlinear Diffusion," *International Journal of Computer Vision*, vol.28, no.2, pp. 155-174, 1998.

[11] H. Zhang, S. Roth, it Camera aided robot calibration, CRC Press, Boca Raton, 1996.

[12] L. Torresani, C. Bregler, "Space-time tracking," *Computer Vision - ECCV 2002, Part I*, pp. 801-812, 2002.

[13] W. Kropatsch, R. Klette, F. Solina, and R. Albrecht, *Theoretical foundations of computer vision*, Springer Wien, New York, 1996.

[14] X. Wang, M. Sugisaka, W. Xu, "Recognizing static target in video frames taken from moving platform" *Proc. of the Int. Conference on Control, Automation, and System,* Korea, pp. 223-227, 2003.

[15] X. Wang, M. Sugisaka, W. Xu, "Image energy pilot, FA soil-salt recognition Approach," *The 4th Int. Conference on Advanced Mechatronics Toward Evolutionary Fusion of IT and Mechatronics*, pp. 373-376, 2004.

[16] W. Yu, K. Daniilidis, and G. Sommer, "Approximate orientation steer ability based on angular Gaussians," *IEEE Trans. Image Processing*, vol. 10, no. 2, pp. 193-205, 2001.

The Eleventh International Symposium on Artificial Life and Robotics 2006 (AROB 11th'06),
B-con Plaza, Beppu, Oita, Japan, January 23-25, 2006

Perceptual and Introspective Learning for Developmental Robot

Zhongzhi Shi　Qingyong Li

Key Laboratory of Intelligent Information Processing, Institute of Computing Technology,
Chinese Academy of Sciences, Beijing 100080, China
shizz@ics.ict.ac.cn

Abstract For the development robot learning strategies play very important role. Through learning the system performance will be improved. A learning model which contains observation learning and introspective learning will be proposed in this paper. Perceptual learning should be considered as an active process that embeds particular abstraction, reformulation and approximation within the Abstraction framework. Introspective learning is an inside learning of brain, which means without input information from outside environment. Perceptual learning and Introspective learning methods will be described respectively.

Key words: developmental robot, learning model perceptual learning, introspective learning

1. Introduction

By a developmental robot means that the robot generates its "brain" through online, real time interactions with its environment[14]. For robots, the developmental program starts to run at the ``birth" time of the robotics, which enables the robot to develop its cognitive and behavioral skills through direct interactions with its environment using its sensors and effectors. The basic nature of developmental learning plays a central role in enabling a human being to incrementally scale his or her level of intelligence from ground up. In order to scale up the robot's capability to understand what happens around it, the learning mechanism embedded in a developmental program must perform systematic self-organization, according to what it sensed, what it did, action imposed by the human when necessary, the reward it received from the humans, and the context. As a fundamental requirement of scaling up, the robot must develop a value system.

Learning is the basic cognitive activity and accumulation procedure of experience and knowledge. Through learning the system performance will be improved. A general learning model has been proposed as Fig 1.

In general machine learning focuses on observation learning, that is inductive learning, analogical learning, case-based learning, explanation learning, evolutional learning, connectionist learning and so on. A lot of statistical learning methods and algorithms have been proposed and used in existing data mining system. Introspective learning is also play very important role for human learning. The general learning model could show the both learning activities.

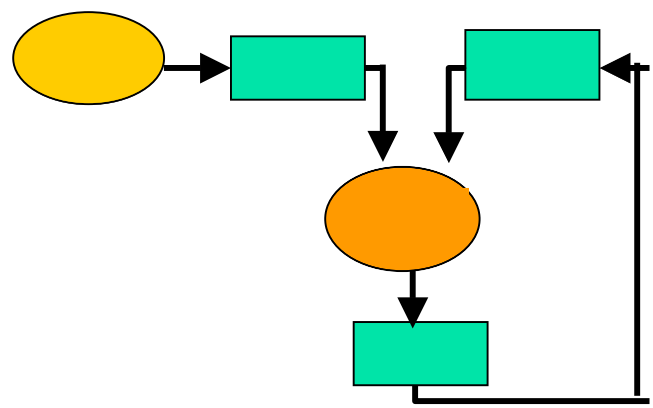

Fig 1　Learning model

Perceptual learning should be considered as an active process that embeds particular abstraction, reformulation and approximation within the Abstraction framework. The active process refers to the fact that the search for a correct data representation is performed through several steps. A key point is that perceptual learning focuses on low-level abstraction mechanism instead of trying to rely on more complex algorithm. In fact, from the machine learning viewpoint, Perceptual learning can be seen as a particular abstraction that may help to simplify complex problem thanks to a computable representation. Indeed, the baseline of Abstraction, i.e. choosing the relevant data to ease the learning task, is that many problems in machine learning cannot be solve because of the complexity of the representation and is not related to the learning algorithm, which is referred to as the phase transition problem. Within the Abstraction framework, we use the term perceptual learning to refer to specific learning task that rely on iterative representation changes and that deals with real-world data which human can perceive.

In this paper Section 2 will discuss perceptual learning. Introspective learning is described in Section 3. The conclusions will be given the final section.

2. Perceptual Learning

After Hubel and Wiesel[5;6] first showed that neurals in mammalian primary visual cotex (V1) were optimally stimulated by bars and edges, a large part of experimental, computational, and theoretical studies have been concerned with exploring the response characteristics of neurons in V1 and in higher visual areas.

Aiming to reveal underlying relationships between the environmental information and internal representation of the visual cortex, Olshausen and Field introduced a learning algorithm for sparse coding[11]. It was shown that, by seeking sparse code for natural images, the network could develop a set of receptive fields similar to those simple cells found in the striate cortex (V1). Though such network successfully captures sparse nature of the input data, it is a feedforward model and it ignores one primary constraint on the visual system: *perception task*. The tasks faced by the organism are likely to be an even more important constraint. That is to say, sparse coding states only that information must be represented sparsely, it does not say anything about what information should be represented.

In the classical feed-forward, modular view of visual processing, the early visual areas (LGN, V1 and V2) are modules that serve to extract local features, while higher extrastriate areas are responsible for shape inference, object recognition and so on. However, recent findings in primate early visual systems reveal that the computations in the early visual cortex are rather complex and dynamic, as well as interactive and plastic, subject to influence from global context, higher order perceptual inference, task requirement and behavioral experience. The evidence argues that the early visual cortex does not merely participate in the first stage of visual processing, but is involved in many levels of visual computation[7;8]. The idea that various levels in cognitive and sensory systems have to work together interactively and concurrently had been proposed in more general computational terms, particular by McClelland and Rumelhart in terms of interactive activation neural networks [10], by Grossberg in terms of adaptive resonance theory[3], and Dayan et al in terms of the Helmholtz machine[2]. Hinton proposed a graphical model and learning algorithms for perceptual system[4].

An important question in the study of visual processing is how to identify the features used by human subjects to classify visual stimuli: which features of an image are extracted and represented by the visual cortex? It has previously been proposed that complex objects are represented in the visual cortex in terms of sparse structures such as sparse coding or Gabor basis functions[11]. These 'building blocks' are universal in the sense that they are equally applicable to all natural images. Alternatively, we investigate a new supervised model, called here classification-oriented sparse coding (briefly as COSC) model, which encodes sparse and class-specific features. Based on Olshausen's sparse coding scheme[12], COSC model incorporates an additional constraint, named *discriminability*, to learn the sparse and informative image features which are specifically selected to support visual classification— one of the basic tasks of visual perception. COSC models probes into what information should be represented under feedback of visual classification tasks and provides a way of extracting sparse and informative features from natural images though linear Hebbian learning.

The consideration of granularity is motivated by the practical needs for simplification, clarity, low cost, approximation, and tolerance of uncertainty. As an emerging field of study, granular computing attempts to formally investigate and model the family of granule-oriented problem solving methods and information processing paradigms.

2.1 Linear image synthesis model

The starting point is from Olshausen[11]. A perceptual system is exposed to a series of small image patches, drawn from one or more large images, just like the CRF of neurons. Imagine that each image patch, represented by the vector I (numbered row-wise), has been formed by the linear combination of N basis functions. The basis functions form the columns of a fixed matrix, **A**. The weighting of this linear combination is given by a vector, s. Each component of this vector has its own associated basis function, and represents a response value of a neuron in vision system. The linear synthesis model is therefore given by:

$$I(x,y) = As = \sum_{i=1}^{n} s_i * a_i(x,y) \qquad (1)$$

In a cortical interpretation, the s model the responses of (signed) simple cells, and the column of matrix A closely related to their CRF's.

This model can be represented by a simple neural network, where x is an n-dimensional vector denoting the input to the network, s_i denotes the activity of the i-th neuron, and a_i (the i-th column of the A) is an n-dimensional vector composed of the connection weights between the i-th neuron and the input.

The goal of sparse coding is to find a set of a_i that forms a complete code (that is, spans the image space) and results in the coefficient values being as statistically independent as possible over an ensemble of natural images. The reason for statistical independence have been elaborated else where [1], but it can be summarized briefly as providing a strategy for extracting the intrinsic structure in visual signal.

2.2 Sparse coding model

In an influential paper, Olshausen and Field applied two criteria to seek the optimal basis vector and the coefficients [11]. One of the criteria is how well the code describes the input. It can be measured by the squared error between the input and its reconstruction by the network:

$$\text{Error}(s, A) = \sum_{x,y} \left[\mathrm{I}(x, y) - \sum_i s_i a_i (x, y) \right]^2 \tag{2}$$

As an additional criteria for sparse coding, Olshausen and Field proposed the 'sparseness' cost for seeking sparse codes. The sparseness cost function is given by

$$\text{Sparseness}(s, A) = \sum_i S\left(\frac{s_i}{\sigma_i}\right) \tag{3}$$

where S(x) is a nonlinear function such as |x|, $\exp(-x^2)$, and $\log(1+x^2)$. The cost sparseness favors the codes which consist of minimal number of non-zero coefficients. As a result, the network seeks the coefficients which are statistically independent each other over an ensemble of input data. In the case that the data contains some forms of higher-order statistical structure as found in natural images, it can be captured by using this sparseness cost function.

So the search for a sparse code can be formulated as an optimization problem by constructing the following cost function to be minimized:

$$\mathrm{E}(s, A) = \sum_{x,y} \left[\mathrm{I}(x, y) - \sum s_i a_i (x, y) \right]^2 + \lambda_s \sum_i S\left(\frac{s_i}{\sigma_i}\right) \tag{4}$$

For the visual classification purposes we must seek a reasonable transform method which maximizes the distance between the classes while minimizing the distance within each classes in coefficient state-space. So the code coefficients (or features) are efficient for discrimination, unlike the sparse code that seeks the space efficient for representation.

2.3 Classification-oriented sparse model

A. Discriminability constraint

In order to code the sensory visual information supervised by the visual classification task, it is necessary to incorporate a constraint for the classification task. Intuitively, it is very important for the coded coefficients to be good for classification, so the coefficients (or neuron responses) produced by the sparse coding model can be easily utilized by the higher neurons which process such task. Linear discriminant analysis, using within-class scatter and between-class scatter to choose coordinate for transformation, is broadly used for pattern classification. We investigate a somewhat similar approach, and incorporate the '*discriminability*' cost function which constrains the neuron activities to be more valuable for classification.

Supposed that $X_1 = \{I_1{}^1,\ I_2{}^1,\ ...,\ I_{N1}{}^1\}$ and $X_2 = \{I_1{}^2,\ I_2{}^2,\ ...,\ I_{N2}{}^2\}$ represent the pattern sets, here we only consider the two-class classification, and $\mathrm{I}_i{}^j = [s_1,\ s_2, ..., s_n]$, where $s_k, 1 \le k \le n$ is the coefficient produced by sparse coding model. N_1 and N_2 are the number of patterns in class X_1 and X_2.

The sparse coding model transforms the input stimuli into code coefficient vectors, I. We define the distance between two coefficient vectors as below:

$$\mathrm{D}(I_1, I_2) = \sqrt{\sum_{i=1}^{n} (s_i{}^1 - s_i{}^2)^2} \tag{5}$$

Within-class distance measures the distance between a coefficient vector and the center of class which includes the vector. The formula is

$$\mathrm{D}_w = D(I_i{}^j,\ \tilde{m}_j) \tag{6}$$

where $\tilde{m}_j$ is the center of the class j. On the contrary, between-class distance measures the distance between a coefficient vector and the center of class which excludes the vector. The equation is

$$\mathrm{D}_B = D(I_i{}^j,\ \tilde{m}_{\hat{j}}) \tag{7}$$

where $\tilde{m}_{\hat{j}}$ represent the center of the excluding class.

In order to make the patterns be correctly classified, we expect: 1) the within-class distance is smaller, so the class is more compact in the N-dimensional coefficient space; 2) the between-class distance is greater, thus the interval between the class 1 and class 2 is bigger. That is to say, we should maximize the between-class distance in the same time minimize the within-class distance. So we make a tradeoff to optimize a ratio. The ratio is given by

$$DR = \frac{D_W}{D_B} \tag{8}$$

When we look into the Eq.(8) we can find that its derivative for coefficient s is too complex to optimize. So we smartly transform the magnitude of the ratio by logarithm. The transformed ratio is as below:

$$Dis(s) = \ln(DR^2) = \ln\left(\sum_{i=1}^{n}(s_i^{j} - \tilde{m}_j)^2\right) - \ln\left(\sum_{i=1}^{n}(s_i^{j} - \tilde{m}_{\bar{j}})^2\right) \tag{9}$$

As a result, the model produces an N-dimensional coefficient space in which the coefficients in the same class tightly locate in a subspace and are apart from the other class.

B. Learning

Learning is accomplished by minimizing the total cost function:

$$E(s, A) = Error(s, A) + \lambda_s Sparseness(s, A) + \lambda_d Dis(s) \tag{10}$$

where λ_s and λ_d are positive weights. The function to be minimized, $E(s, A)$, is the sum of three terms: the first term computes the reconstruction error, which forces the basis functions, A, to span the input space; the second term incurs a penalty on the coefficient activities, which encourages sparse representation; and the third term calculates the discriminability which drives the coefficients to be more efficient for pattern classification.

The process for minimizing $E(s, A)$ can be divided into two nested stages. In the inner stage, E is minimized with respect to the s_i for a batch of pattern, holding the A fixed. In the outer stage (i.e, on a long timescale, over many image presentations), E is minimized with respect to the A. The inner stage minimization over the s_i can be performed by conjugate gradient method, so the s_i are determined by the differential equation:

$$\frac{dE}{ds_i} = -2b_i + \frac{\lambda_s}{\sigma} S'\left(\frac{s_i}{\sigma}\right) + \lambda_d\left(\frac{2*(s_i^{j} - \tilde{m}_j)}{\sum_{i=1}^{n}(s_i^{j} - \tilde{m}_j)^2} - \frac{2*(s_i^{j} - \tilde{m}_{\bar{j}})}{\sum_{i=1}^{n}(s_i^{j} - \tilde{m}_{\bar{j}})^2}\right) \tag{11}$$

where

$$b_i = \sum_{x,y}\left(I(x,y) - \sum_j s_j a_j(x,y)\right)a_i(x,y).$$

According to Eq.(11), the s_i are drived by a sum of three terms. The first term takes a spatially weighted sum of the current residual image using the basis function $a_i(x, y)$ and the weights. The second term applies the derivative of sparseness. Especially, the third term incurs a movement which makes the s_i near the center of the included class and apart from the excluded class.

The outer stage minimization over the A may be finished by simple gradient descent method. The learning rule for it is given by

$$\Delta a_i(x,y) = \eta\left\langle s_i\left[I(x,y) - \sum_j s_j a_j(x,y)\right]\right\rangle \tag{12}$$

where η is the learning rate. In the neural network view, a_i are updated by Hebbian learing between the outputs coefficients, s_j, and the resulting residual image.

Because there is no closed-form solution for the s_i in terms of the input I(x, y), so s_i is calculated by recurrent computation similar to an *analysis/synthesis* loop. An intuitive interpretation for this algorithm is that in the inner stage, the gradient of 'sparseness' sparsifies the distribution of s by differentially reducing the value of small coefficients more than great coefficient, at the same time, the gradient of 'discriminability' makes the coefficient near to homogeneous center and apart from the unhomogeneous center. Then, the a_i learn on the error induced by the sparseness criteria and discriminability criteria, resulting in a basis function set which can tolerate sparseness and discriminability in the condition of minimizing mean square reconstruction error.

2.4 Selective attention model based on response saliency

Response saliency is the response extent for a neuron compared with a group of neurons which respond to the same stimulus. The purpose of the response saliency is to represent the conspicuity for every neuron in the same perception level for a stimulus and to guide the selection of attended neuron, based on the value of response saliency[9]. The neuron response that has great response saliency value will be chosen to further process. On the contrary, the neuron that has small value will be omitted.

In the framework of sparse coding, the simple cells in the primary visual cortex (V1) produce sparse code for the input stimuli. That is say, simple cell takes very small (absolute) values or very large values often; to compensate, it takes values in between relatively more rarely. The sparse code focuses on the possibility distribution of response. Intuitively, the response value itself provides very useful information: the response value is bigger, the information represented by the neuron is more important; otherwise, the information is less important. Obviously, the response value gives a foundation for the attention mechanism. Supposed here that A_i represents simple cell i, and R_i represents the simple cell's response.

Every simple cell (corresponding to the column of A in equation 1) carries a specific pattern. Furthermore, every such pattern is selective for location, orientation and frequency. Based on Gestalt similarity perception principle and Hebb rule, we can get that the neurons with similar selectivity increase the response values; on the contrary, the neurons with different selectivity decrease the response values. So we can suppose that the response saliency value of a neuron, which has great discrepancy among a group of neurons responding to the same stimulus, will decrease; and the value for a neuron which has small discrepancy will increase relatively. The neuron set responding to the same stimulus assumes as S, $S=\{A_1,\ A_2,\ \ldots,\ A_m\}$; the discrepancy between A_i and A_j is represented as $D(A_i,\ A_j)$, and the value for $D(A_i,\ A_j)$ is a function of simple cell's selective characteristics: location (L), orientation (O) and frequency (F). The equation as below:

$$\mathrm{D}(A_i, A_j) = W_1 * \mathrm{N}\left(\sqrt{(L_{ix}-L_{jx})^2+(L_{iy}-L_{jy})^2}\right) + W_2 * \mathrm{N}\left(\left|O_i - O_j\right|\right) + W_3 * \mathrm{N}\left(\left|F_i - F_j\right|\right) \quad (13)$$

$$Diff\,(A_i, S) = \sum_{A_j \in S} (1 - D(i,j) * R_j) / \mathrm{Count}(S) \quad (14)$$

Here, operation **N**(.) represents the normalization operator which makes the values between 0 and 1, and $0 \le W_1, W_2, W_3 \le 1$ represents the weights, $W_1+W_2+W_3=1$.

Then, the response saliency (RS) value is the weighted sum of norm response value and neuron discrepancy as following:

$$\mathrm{RS}(A_i) = \mathrm{N}(|R_i|) + \lambda * Diff\,(A_i, S) \quad (15)$$

Here λ is a weight which determinates the importance of each components

3. Introspective Learning

Introspective learning is an inside learning of brain, which means without input information from outside environment [13]. Introspective learning process involves three steps: blame assignment, Explain failure, and Repair failure. Blame assignment, the system first makes definite and limited expectation of reasoning process, then compares the expectation with the actual reasoning to find out the difference. The difference between anticipant action and actual action is called as expectation failure. The confirmation of failure means that there are definite expectation values at the present position of reasoning in the system. Supervise expectation failure during reasoning, the system compares results with corresponding expectation at every step of reasoning to find out failure. Explain failure, the system looks for the explanation for failure according to the criteria of expectation failure and the trace of reasoning, then puts forward a relevant advice to update the reasoning based on the reason found out for avoiding latter same failure. Repair failure, the measures of repairing reasoning are attached to specific expectation, thus the accessional measures can be put forward when an expectation failure occurs. The description of the measure cannot specify how and what to repair, so the system should involve the mechanism of making repair measure. The repair module makes actual repair measures and repair according to the description of failure and the method advised to repair.

The figure 2 is the general model of introspective learning. Besides the three process mentioned above, it includes knowledge base, trace of reasoning, expectation model of reasoning and supervised protocol and so on. The supervised protocol regulates how and where to supervise the system's reasoning and the switch of the system's control power. The knowledge base involves the relevant knowledge of reasoning, it is not only the base of reasoning but also blame assignment and explain failure. The expectation model of reasoning is a perfect model, it offers the criteria of reasoning expectation and becomes the central basis of blame assignment. The introspective learning units of intelligent knowledge system use existing knowledge about background, the expectation and the trace of reasoning to look over if expectation failure occurs at present state according to supervised protocol. Expectation failure occurs at two situations that one is when an expectation of perfect state is not accordance with the present actual reasoning and the other is when a catastrophic failure takes place in the system. If the reasoning unit does not find out the expectation failure, it means that all expectations are in accordance with actual situation and the system will be informed normal and regain the control power. If a failure is found, the reasoning unit will make use of the background knowledge, the trace of reasoning and the perfect expectation model to look for the preliminary reasons for the failure and explain the failure. When a failure is found, the available information is probably not sufficient for diagnosing and repairing. So, the introspective learning unit may pause its explanation and repairing, permit the system to continue working until ample information acquired. If necessary information is attained, the task of explanation and repair will restart from the position of pause. The explanation of failure can offer clues to the introspective reasoning unit for repairing failure. The learning aim of repair failure is made after explain failure, the repair failure module will make the repair measures according to the learning aim and update the reasoning. When the repair finishes or when the repair is found impossible, the system will acquire the control power.

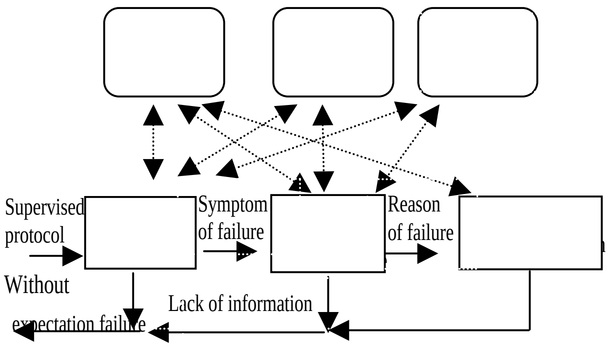

Fig. 2 Introspective learning model

4. Conclusions

For the developmental robot two learning strategies have been proposed in the paper. One is perceptual learning. We have put forward a novel sparse coding model, called classification-oriented sparse coding (COSC) model, for learning sparse and discriminable structures in the natural images which is valuable for the higher perception task: visual classification. Vision attention mechanism is an active strategy in information processing procedure of brain, which has many interesting characteristics, such as selectivity, competition. Attention is everywhere in the visual pathway. A typical scene within the neuron's classic receptive field (CRF) contains many different patterns which compete for neural representation because of the limited processing capacity of neurons in the visual system. In this paper, we also proposed an attention model, that is saliency-based data-driven module, in the framework of efficient coding hypothesis.

Another learning strategy is introspective learning. We proposed a introspective learning process involves three parts that are blame assignment, explain failure and repair failure. In the future we are continue working on learning methods and algorithms for autonomous mental development which enables robots to incrementally scale its level of intelligence.

Acknowledgement

The research work in this paper is supported by the National Basic Research Priorities Programme (No.2003CB317004), the 863 Project (2003AA115220) and National Natural Science Foundation of China (No. 60435010).

References

[1] Atick, J.J., Redlich, A.N. (1990). Towards a theory of early visual processing. Neural Computation, 2:308-320.

[2] Dayan, P., Hinton, G.E., Neal, R.M, Zemel, R.S. (1995). The Helmholtz machine. Neural Comput 7(5):889–904.

[3] Grossberg, S. (1987). Competitive learning: from interactive activation to adaptive resonance. Cogn Sci 11:23–63.

[4] Hinton, G.E. (2005). What kind of a graphical model is the brain? IJCAI2005, Award lecture.

[5] Hubel D, Wiesel T (1962): "Receptive fields, binocular interaction and functional architecture in the cat's visual cortex." J.Physiology (Lond) 160:106-154

[6] Hubel D. H. and Wiesel, T. N. (1968). Receptive fields and functional architecture of monkey striate cortex. *J Physiol.* Mar;195(1):215-43.

[7] Lee T S, Mumford D, Romero R, Lamme VA. (1998). The role of the primary visual cortex in higher level vision. Vision Res 38:2429-2454.

[8] Lee T S. 2003. Computations in the early visual cortex. Journal of Physiology 97:121–139.

[9] Qingyong Li, Jun Shi, Zhongzhi Shi. (2005). A model of Attention-Guided Visual Sparse Coding. ICCI 2005: 120-125

[10] McClelland JL, Rumelhart DE. (1981). An interactive activation model of context effects in letter perception. Part I: an account of basic findings. Psychol Rev 88:375–407.

[11] Olshausen B A and Field D J. (1996). Emergence of simple-cell receptive field properties by learning a sparse code for natural images. Nature 381:607-609.

[12] Olshausen B.A, Field D.J. (2004). Sparse coding of sensory inputs. Current Opinion in Neurobiology 14: 481-487.

[13] Zhongzhi Shi, Sulan Zhang, Case-based Introspective Learning, IEEE ICCI 2005, 43-48.

[14] Juyang Weng. Developmental Robotics: Theory and Experiments. *International Journal of Humanoid Robotics*, 1(2): 199-236, 2004.

The Eleventh International Symposium on Artificial Life and Robotics 2006 (AROB 11th'06),
B-con Plaza, Beppu, Oita, Japan, January 23-25, 2006

A Robot Control Method Using Evolutive Binary Decision Diagrams

Masayoshi Kanoh† and Hidenori Itoh‡
†School of Life System Science and Technology, Chukyo University
101 Tokodachi, Kaizu-cho, Toyota 470-0393, Japan.
‡Graduate School of Engineering, Nagoya Institute of Technology
Gokiso-cho, Showa-ku, Nagoya 466-8555, Japan.

Abstract

In this paper, we propose a learning-based method for controlling robots using evolutive binary decision diagrams (BDDs). BDDs are a ways of to represent a logic function using a directed graph which consists of binary switches having one input and two outputs, and are mainly used to design LSI. Moriwaki et al. proposed n-output BDDs (n-BDDs) which can evolve BDDs, and they applied n-BDDs to food chain simulation of evolutional agents. In the evolution method, variable ordering of n-BDDs is fixed, but they showed that n-BDDs provided good performance for deciding best output on some inputs. In this paper, we introduce a new genetic manipulation for avoiding the problem of variable ordering to n-BDDs, and apply the new n-BDDs to learn motion control of robots. We demonstrate that our method is capable of providing good performance in this paper.

1 Introduction

Demand for robots is shifting from their use in industrial applications to their use in domestic situations. Such robots require sophisticated body designs and interfaces to do this. Humanoid robots which have multi-degree-of-freedom have been developed, capable of working with humans using a body design similar to humans. However, it is very difficult to control intricately robots with human generated, preprogrammed, learned behavior. Learned behavior should be obtained by the robots themselves in a human-like way, not programmed manually.

Moriwaki et al. proposed n-BDDs which can evolve multi-terminal BDDs (MTBDDs) [1], and they applied n-BDDs to food chain simulation of evolutional agents. In the evolution method, variable ordering of n-BDDs is fixed, but they showed that n-BDDs provided good performance for deciding best output on some inputs. We introduce n-BDDs to learn motion control of robots in this paper. We consider that a controller which is learned by a robot using n-BDDs can be used for a controller of other similar robots.

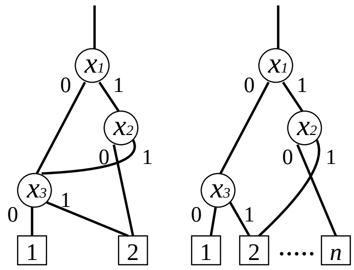

(a) BDD (b) MTBDD

Figure 1: Examples of BDD and MTBDD.

However, learning of robot's motion control involves very large state space, so that it is difficult to provide variable ordering for n-BDDs manually. In this paper, we introduce a new genetic manipulation for avoiding the problem of variable ordering to n-BDDs. To confirm the effectiveness of our method, we used action learning of a mobile robot, LEGO Mindstorms. Moreover, as learning of high-dimensional state spaces, our method was applied to motion control of a humanoid robot, HOAP1 (Humanoid Open Architecture Platform). We demonstrate that our method is capable of providing good performance.

2 What are BDDs?

A binary decision diagram (BDD) is a data structure that is used to represent a Boolean function [2, 3]. Figure 1 shows examples of BDDs. The Boolean function is represented in a BDD as a rooted, directed, acyclic graph where each nonterminal vertex is labeled by a variable x_i and has two directed edges connecting to child nodes. The left edge represents a variables assignment to zero (0-edge), and the right edge represents an assignment to one (1-edge). A "1" or "2" labels all terminal vertexes. MTBDDs are an extension of BDDs, and the difference is that MTBDDs have multiple outputs. For example, the MTBDD in Figure 1 has n outputs. Moriwaki et al. introduced to evolve

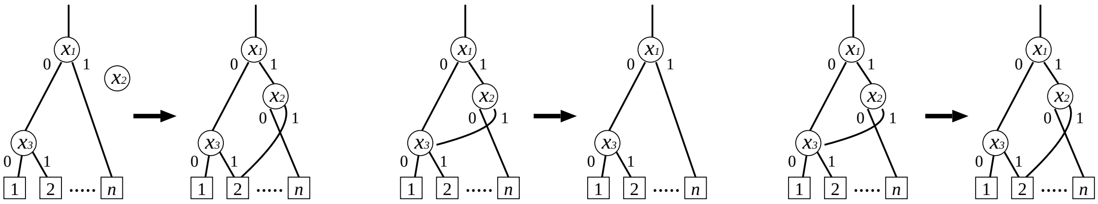

(a) insertion (b) deletion (c) mutation

Figure 2: Genetic operations of n-BDDs.

MTBDDs by using genetic operations, and they called them n-BDDs [1].

3 N-BDDs for controlling robots

3.1 N-BDDs

Figure 2 shows genetic operations of n-BDDs [1]. Genetic operations, insertion, deletion and mutation are defined to operate an n-BDD as a gene.

Insertion inserts a new nonterminal vertex on an edge selected at random. Either of 0-edge or 1-edge of the new vertex must connect to the vertex which was connected before. The other edge connects to a subordinate vertex at random.

Deletion deletes a nonterminal vertex selected at random. The edge connected to the deleted vertex must connect to one of the vertexes which was connected by the deleted vertex before.

Mutation changes the direction of one of the edge of a nonterminal vertex selected at random. The note connected by the edge must be a subordinate vertex of the mutated vertex. This restriction avoids the loop and cycle of edges.

3.2 New Genetic Manipulation for Controlling robot

To avoid the problem of variable ordering in n-BDDs, we introduce a new genetic manipulation for insertion. Figure 3 shows the new insertion method.

Moreover, we consider the placement of n-BDDs. Generally, the state space for controlling robots is to be high-dimensional state spaces, because robots have many motors. Only if we use an n-BDD for a robot, the number of their output increases. Therefore, we propose to place n-BDDs at each motor. Figure 4 is an example placement of n-BDDs. Using this placement, we can introduce crossover to evolution of n-BDDs. Concretely, it is done by changing n-BDDs placed at each motor between two robots. We consider that various individuals are carried out to next generation by the crossover method.

Insert vertex
Input S: a set of already used variables in n-BDD.

```
1.  begin
2.     R := φ;
3.     create a new nonterminal vertex V
                          which variable is x_V;
4.     if x_V is used as the root node
5.     then go to 3.;
6.     if x_V ∈ S
7.     then begin
8.        if there are edges e that can insert x_V
9.        then add all candidates e to R as elements;
10.       else go to 3.;
11.    end;
12.    if R = φ
13.    then insert V on an edge selected at random;
14.    else begin
15.       select an edge e from R at random;
16.       insert V on e;
17.    end;
18. end.
```

Figure 3: New insertion operation.

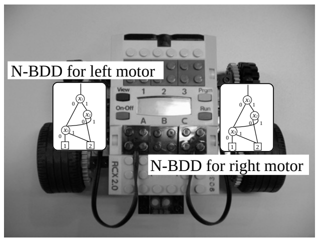

Figure 4: N-BDDs placement.

4 Experiments

In order to confirm the effectiveness of our method, we did two experiments: learning a line-tracing robot and controlling a humanoid robot.

4.1 Learning Line-Tracing Robot

Consider a course shown in Figure 5. This environment has a track with black line. The learning robot

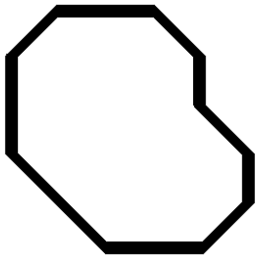

Figure 5: Course.

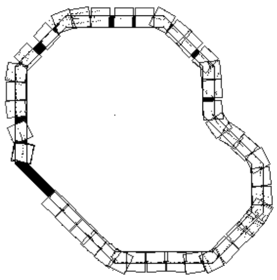

Figure 6: Result.

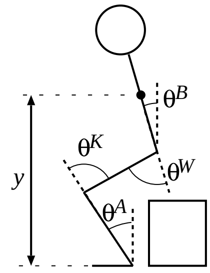

Figure 7: Learning motion.

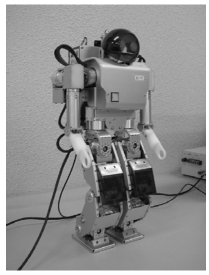

Figure 8: HOAP1.

Table 1: Sensed color and variable value.

Sensed color	(x_0, x_1)
black	$(0, 1)$
gray	$(0, 0)$
white	$(1, 0)$

Table 2: Actions for Mindstorms.

Terminal vertex	Motor output
a_0	-2 (backward)
a_1	0
a_2	2 (forward)

can sense floor color using a light sensor, and takes action. Table 1 and 2 show floor colors sensed by the robot and actions of the robot, respectively. In Table 1, gray is sensed on the border between black and white floors. The robot learn to trace gray color.

To simulate learning, we used the GURS [4] which is a LEGO Mindstorms simulator. Fitness increases if robot is on gray floor and its both motor does not stop. We used 30 individuals in each generation. For crossover, insertion, mutation and deletion rates, we used the value of 0.5, 0.3, 0.15 and 0.05, respectively. In the evolution, one individual is carried out to next generation (elite strategy), and the other 29 individuals are selected by roulette strategy.

Figure 6 shows a result of evolution with n-BDD at 50th generation. You can see that the robot can trace the border between black and white well.

4.2 Controlling a Humanoid Robot

In this section, as learning of high-dimensional state spaces, n-BDD is applied to a humanoid robot learning to stand up from a chair (Figure 7). The learning was simulated using the virtual body of HOAP1. Figure 8 shows HOAP1. The robot is 48 centimeters tall, weighs 6 kilograms, has 20 DOFs, and has 4 pressure sensors each on the soles of its feet. To simulate learning, we used the Open Dynamics Engine [5].

Table 3: Sensed degree and variable value.

Sensed degree	(x_0, x_1)
$\frac{3}{4}(\theta_{\max} - \theta_{\min}) \leq \theta < \theta_{\max}$	$(1, 1)$
$\frac{1}{2}(\theta_{\max} - \theta_{\min}) \leq \theta < \frac{3}{4}(\theta_{\max} - \theta_{\min})$	$(1, 0)$
$\frac{1}{4}(\theta_{\max} - \theta_{\min}) \leq \theta < \frac{1}{2}(\theta_{\max} - \theta_{\min})$	$(0, 1)$
$\theta_{\min} \leq \theta < \frac{1}{4}(\theta_{\max} - \theta_{\min})$	$(0, 0)$

Table 4: Actions for HOAP1.

Terminal vertex	Motor output
a_0	-20.0 [deg/sec](backward)
a_1	0
a_2	20.0 [deg/sec](forward)

The robot's state is sensed by the following variable vector $\boldsymbol{x}(t)$:

$$\boldsymbol{x}(t) = (x_0^W, x_1^W, x_0^K, x_1^K, x_0^A, x_1^A, x_0^B, x_1^B). \qquad (1)$$

where x_i^W, x_i^K and x_i^A are variables for waist, knee and ankle angles respectively, and x_i^B is for the pitch of its body (Figure 7). Outputs of these variables are determined by current degree θ of joint (see Table 3). Here, the values in the table are $\theta_{\min}^W = -80.0$ [deg], $\theta_{\max}^W = 70.0$ [deg], $\theta_{\min}^K = 0.0$ [deg], $\theta_{\max}^K = 120.0$ [deg], $\theta_{\min}^A = -60.0$ [deg], $\theta_{\max}^A = 60.0$ [deg], $\theta_{\min}^B = -60.0$ [deg], $\theta_{\max}^B = 60.0$ [deg]. Actions of the robot are determined as Table 4.

One generation terminates when the robot fell down or time passed over $t_{total} = 10$ [sec]. Fitness is determined by height y [cm] of the robot's breast (see Figure 7). We used 30 individuals in each generation. For crossover, insertion, mutation and deletion rates, we used the value of 0.75, 0.15, 0.075 and 0.025, respectively. In the evolution, we used the same strategy as section 4.1.

Figure 9 shows an evolution result at 1000th generation. You can see that the robot stood up while main-

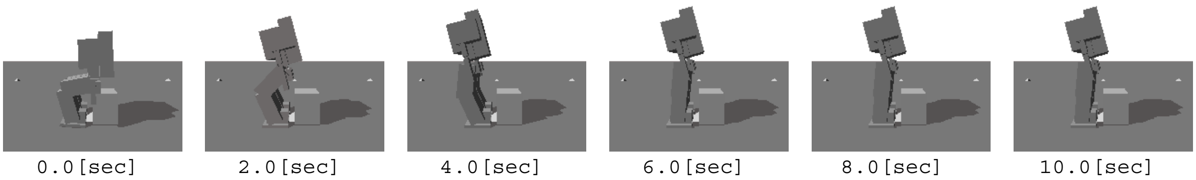

Figure 9: Result at 1000th generation.

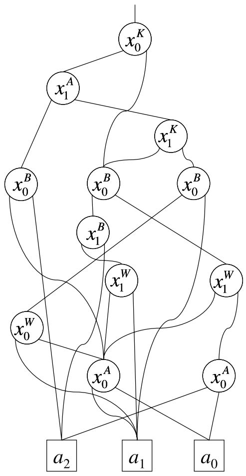

Figure 11: N-BDD of waist.

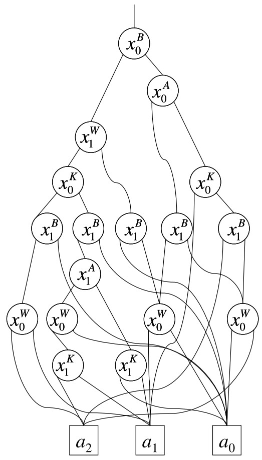

Figure 12: N-BDD of knee.

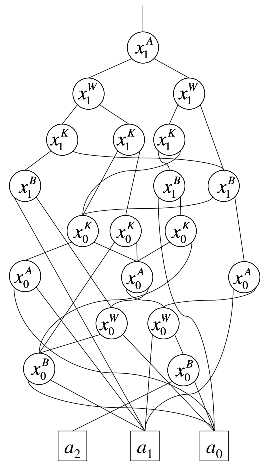

Figure 13: N-BDD of ankle.

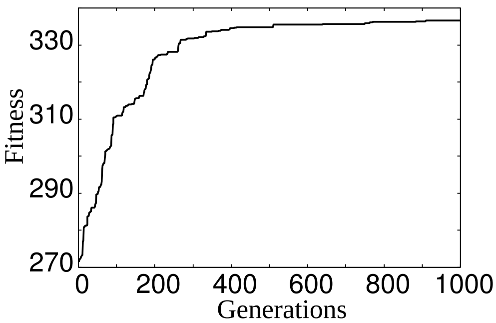

Figure 10: Fitness.

taining its balance. Figure 10 shows the fitness per generation with n-BDD. The results shown in the figure are averaged over 10 repetitions of the experiment. In all experiments, the robot obtained the stand-up motion. Figure 11, 12 and 13 show n-BDDs at each joint in a successful experiment. You can see that variable ordering of each joint differs from the others.

5 Conclusions

In this paper, we proposed a learning-based method for controlling robots using new manipulations for n-BDDs. We did two experiments, and verified the effectiveness of our method. The future work of this study is verification of effectiveness of crossover of n-BDDs, and is other motion generation, for example, walking.

Acknowledgements

This work was supported in part by the Chukyo University Research Fund.

References

[1] K. Moriwaki et al., "A genetic method for evolutionary agents in a competitive environment," *Soft Computing in Engineering Design and Manufacturing*, pp. 153–162, 1997.

[2] S. B. Akers, "Binary decision diagrams," *IEEE Trans. on Comp.*, vol. C-27, no. 6, pp. 509–516, 1968.

[3] R. E. Bryant, "Graph-based algorithms for boolean function manipulation," *IEEE Trans. on Comp.*, vol. C-35, no. 8, pp. 677–691, 1986.

[4] J. Rasmussen, "The general unified robot simulator (gurs)," http://www.daimi.au.dk/%7Erepsej/ thesis.html.

[5] R. Smith, "Open dynamics engine (ode)," http:// opende.sourceforge.net/ode.html.

The Eleventh International Symposium on Artificial Life and Robotics 2006 (AROB 11th'06),
B-con Plaza, Beppu, Oita, Japan, January 23-25, 2006

Waste Incinerator Emission Prediction using Probabilistically Optimal Ensemble of Multi-Agents and Neural networks

Daisuke Yamaguchi[1]
Kenneth J. Mackin[2] , Muneo Takahashi[1] and Eiichiro Tazaki[1]
[1] Department of Electronics and Information Engineering Toin University of Yokohama
Aoba-ku, Yokohama , 225-8502 JAPAN
[2] Department of Information Systems Tokyo University of Information Sciences
Wakaba-ku, Chiba , 265-8501 JAPAN

Abstract

Dioxin emission from waste incinerator plants is one of the hottest ecological problems today. In waste incinerator plants, the chemical reactions in the incinerator occur under a very dynamic environment, making its control a very complex task, and current state-of-the-art incinerator facilities have not succeeded in completely removing the dioxin emission. In this paper, we propose applying a probabilistically optimal ensemble technique, based on fault masking among individual classifier for N-version programming. Our purpose is to research the validity of using a training based classifier method for emission prediction, compared against the results of previous statistical methods and fuzzy decision methods. One agent locates it with one member in optimization in the multi agent. We create an optimal ensemble of trained neural networks and use the majority voting result to predict waste incinerator emission. In a probabilistically optimal ensemble, the members of the ensemble are chosen so that the members are correctly independent of each other. We show that an optimal ensemble of multi agent greatly improves the prediction error rate of emission of dioxins.

Keyword : Multi-agent, Neural Network, Emergence, Control Dioxin Emission, Incinerator Control, Optimal Ensemble

1 introduction

The emission of dioxins from waste incinerators is one of the most important environmental problems today. It is known that optimization of waste incinerator controllers is a very difficult problem due to the complex nature of the dynamic environment within the incinerator. There has been past research in intelligent estimation of dioxin emission from waste incinerators. Fujiyoshi et al. [1] has proposed applying fuzzy control to incinerator control to decrease the dioxin emission. Ichihashi et al. [2] has applied statistical analysis to calculate the correlation of various input signals with dioxin emissions. Fukushima [3] has proposed applying fractal fuzzy control in order to estimate and control dioxin emission. For this research, we investigate the validity of applying neural network trained multi-agents for the prediction of dioxin emission to be used for the combustion control in order to decrease the dioxin emission. Neural networks, as with other training based classifiers, inherently have a risk that when classifying an untrained data set, the classifying error rate may be much worse than the training result. In order to overcome this risk, we applied a probabilistically optimal ensemble technique proposed by Imamura et al. [4] to N-version programming of software agents. Our purpose is to research the validity of using a training based classifier method for emission prediction, compared against the results of previous statistical methods and fuzzy decision methods. We plan to continue this approach and apply the proposed method to actual incinerator plant controllers to test the validity of the method.

2 Incinerator control using multi-agent system

For each of the different types of incinerator sensor data, there is an apparent correlation just described, but direct correlation between the sensor data and carbon monoxide concentration is not very strong. This is because the environment in the incinerator is a complex dynamic environment in which the different items are dependent on each other, and is not a simple dependency relationship.

Artificial neural networks (ANN) can be character-

The Eleventh International Symposium on Artificial Life and Robotics 2006 (AROB 11th'06),
B-con Plaza, Beppu, Oita, Japan, January 23-25, 2006

ized by its "black box" approach to learn and classify complex data patterns. For this research, we propose applying 3 layer network structure (1 input layer, 1 hidden layer, 1 output layer) for the training of an incinerator emission prediction agent, using the neural network to learn the complex relationship between incinerator sensor data.

The proposed multi-agent system for incinerator emission prediction is part of a larger incinerator controller system plan. The incinerator controller system will consist of two separate multi-agent systems, the dioxin prediction section and the combustion controller section. Each section will use a separate, independently trained multi-agent system. The dioxin prediction multi agent-system uses incinerator sensor input and predicts the carbon monoxide (hence dioxin) emission rate before the actual emission occurs. The combustion controller multi-agent system uses the output from the dioxin prediction system as a trigger, as well as incinerator sensors for input, and outputs changes in incinerator control values in order to decrease the predicted carbon monoxide emission.

For this paper, we will propose methods applying N-version programming using software agents to construct the dioxin prediction section. We will discuss the combustion controller system in future works.

3 Dioxin prediction with software agent

First we describe the basic software agent for dioxin prediction. We considered the 3 layer artificial neural network (1 input layer, 1 hidden layer, 1 output layer) as the basic training classifier in the agent. We use a sigmoid function for the synapse function of the neuron, with back propagation (BP) training of the incinerator data. The number of hidden neurons was decided by results of preliminary experiments of the neural network.

As a preliminary experiment, we tested a neural network which took all of the sensor data except carbon monoxide concentration values for input, and the single output of the network was used to predict the correct carbon monoxide concentration. Time delay of input data was not considered here.

For the network training we used the database of collected incinerator sensor data, and applied BP training based on the difference between predicted carbon monoxide concentration and the actual carbon monoxide concentration recorded for the same time frame.

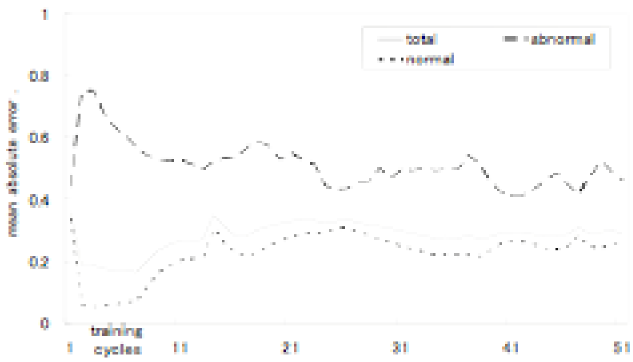

Figure 1: **Preliminary experiment results of prediction error for untrained data**

Figure 1 shows the training results of the preliminary experiment which predicted the carbon monoxide values directly using the neural network. From the results of the preliminary experiment, we found that the prediction accuracy is completely different between normal range carbon monoxide values, and high carbon monoxide values. The network learned to accurately predict normal range carbon monoxide values fairly quickly, but the same network failed to learn abnormal (high) range carbon monoxide values during the same training period. When network training was continued in order to increase the abnormal range carbon monoxide prediction, this time the accuracy of normal range carbon monoxide prediction deteriorated. This finding confirmed our initial estimate that it would be difficult to train the neural network due to the complexity of the correlation between carbon monoxide concentration and each of the other sensor values.

For this reason, we decided to focus on detection of abnormally high carbon monoxide emission ($100ppm$) as the preliminary goal of the dioxin prediction network. The network output was changed from direct carbon monoxide concentration prediction value, to binary output where 1 predicts high carbon monoxide concentration ($100ppm$) and 0 predicts normal carbon monoxide concentration ($100ppm$).

As for the neural network input, we considered the possibility that the large number of input nodes increases the problem domain and complicates the classification, causing an adverse affect on the network training efficiency. With this assumption, we decided to minimize the number of input nodes in order to first achieve a workable learning curve and prediction accuracy.

It can be assumed that there must be some relationship between oxygen concentration, flapper angle and carbon monoxide concentration, from the similar changes seen in time-series data as in Figure 1. Based on this assumption, for the initial model we use only flapper angle and oxygen concentration data as neural network input. Further, we can see that flapper angle, oxygen concentration and carbon monoxide concentration each show a particular time delay in their relationship. For this reason, in order to predict the carbon monoxide value for a given instance, time delay for the flapper angle and oxygen values must be taken into account. Data at some fixed time frame previous to the given output instance should be used as the input data. Recurrent network structures could be used to automatically treat such time sequence data effectively, but for the initial model, we map sequential data of flapper angle and oxygen concentration of specified time delay to individual input nodes to the network. Specifically, we used 60 second delay for flapper angle (60) and 30 second delay for oxygen data (30), to predict the emission for time t.

4 Experiment results of single agent in Neural network

We trained the software agent with the above described neural network using BP and evaluated the prediction accuracy. A standard sigmoid function was used as the neuron's base synapse function. The number of neurons used in each layer was 3 input neurons (1 flapper input, 1 oxygen input and 1 fixed input), 6 hidden layer neurons, and 1 output neuron.

For the training data, 100 cases of normal range carbon monoxide data and 100 cases of abnormal (100*ppm*) carbon monoxide data, for a total of 200 cases were randomly selected from the incinerator sensor database. For the untrained data used to plot the training curve of network accuracy, 100 cases of normal range carbon monoxide data and 100 cases of abnormal range (100*ppm*) carbon monoxide data, for a total of 200 cases were randomly selected from the incinerator sensor database.

Figure 2 shows the change in output error for the untrained dataset of the proposed neural network. The absolute output error for normal range carbon monoxide values, absolute output error for abnormal range (100*ppm*) carbon monoxide values, and absolute output error for all values is graphed.

The absolute output error for a single neural network shown in Figure 2 was 0.18 for all values, 0.23 for

Figure 2: **Prediction error of untrained data using single neural network**

normal range carbon monoxide values, and 0.13 for abnormal range carbon monoxide values. As was seen in the preliminary experiment, as the network trained to decrease the abnormal range output error, the normal range output error in turn became higher.

5 Pobabilistically optimal ensemble of multi-agents

Neural networks, as with other training based classifiers, inherently have a risk that when classifying an untrained data set, the classifying error rate may be much larger than the training result. In order to overcome this risk, we applied a probabilistically optimal ensemble technique proposed by Imamura et al. [4] to N-version programming of software agents.

Fault masking in N-version programming assumes that the individual members give completely independent results. If certain members give similar output, then correct fault masking will not occur. In a probabilistically optimal ensemble, the members of the ensemble are chosen so that the members are correctly independent of each other. This is realized by selecting members so that the measures error rate of the ensemble comes closest to the expected error rate of the ensemble. If the members are correctly independent of each other, then proper fault masking should allow the measured error rate to become very close to the expected error rate.

The expected *bi omab* failure rate f of the probabilistically optimal ensemble can be calculated by the equation [4]

$$f = \sum_{k=m}^{n} \binom{}{k}(1 \quad p)^{n-k}p^k \tag{1}$$

where p is the failure rate of each individual, n is the size of the ensemble, m is the minimum number of faulty outputs for an ensemble to fail. We assume the same failure rate p for individuals for simplicity.

In the case where the ensemble has 3 members, majority vote (2 votes) for output, and $p = 0\ 19$, then $f = 0\ 086$.

For our research we trained 6 neural network agents using different initial weights, and the same training set. Using the same training set, we compared the measured ensemble failure rate for ensemble size 3, for all combinations of agents. Using individual failure rate p = 0.19 , the expected ensemble error rate was $f = 0\ 086$.

Table 1 shows the results of the measured ensemble failure rate. The ensemble with the closest ensemble failure rate (0.085) was selected as the optimal ensemble.

The selected optimal ensemble was evaluated using untrained data. The resulting ensemble error rate was $f = 0\ 087$, indeed very close the training ensemble error rate, and vastly improved over the error rate 0.19 for the single neural network agent.

Table 1: Measured ensemble failure rate

ANN no.	ensemble failure rate
0,1,2	0.11
0,1,3	0.115
0,1,4	0.095
0,1,5	0.085
0,2,3	0.115
0,2,4	0.12
0,2,5	0.1
0,3,4	0.13
0,3,5	0.12
0,4,5	0.115
1,2,3	0.13
1,2,4	0.135
1,2,5	0.115
1,3,4	0.14
1,3,5	0.13
1,4,5	0.115
2,3,4	0.145
2,3,5	0.135
2,4,5	0.125
3,4,5	0.125

6 Conclusion

In this research we applied a probabilistically optimal ensemble technique [4] to create an N-version programming classifier system using software agents trained by 3-layer neural networks to predict incinerator emission. We were able to confirm that by using an optimal ensemble of independent software agents, the classification error rate can be greatly reduced.

For future works, we will consider methods to improve prediction accuracy of the individual neural network, including the increase in the types of sensor input data, reevaluation of neural network structure, combining fuzzy rules to treat input data, as well as effect of using different base synapse functions for neurons.

References

[1] Makoto Fujiyoshi, Ryutaro Fukushima, Mitiharu Masuya, Intelligent Control System for Fluidized Bed Incinerator, Proceedings of 18th Fuzzy System Symposium , Japan, pp.25-28, 2002

[2] H. Ichihashi, et. al, Fuzzy Bi-plot of Correlation Analysis for Waste Incinerator, Proceedings of 19th Fuzzy System Symposium , Japan, 2003

[3] R. Fukushima, Fractal Fuzzy Intelligent Control System, Proceedings of 20th Fuzzy System Symposium , Japan, 2004

[4] Kosuke Imamura, Kris Smith, A Probabilistically Optimal Ensemble Technique for Training Based Classifiers, Proceedings of Joint 2nd International Conference on Soft Computing and Intelligent Systems and 5th International Symposium on Advanced Intelligent Systems , Japan, 2004

The Eleventh International Symposium on Artificial Life and Robotics 2006 (AROB 11th'06),
B-con Plaza, Beppu, Oita, Japan, January 23-25, 2006

Model-based Reinforcement Learning for Large-scale Multi-agent Games with Sampling-based State Estimation

Hajime Fujita and Shin Ishii
Graduate School of Information Science
Nara Institute of Science and Technology
8916-5 Takayama, Ikoma, 630-0192 JAPAN

Abstract

We present a model-based reinforcement learning (RL) scheme for large-scale multi-agent problems with partial observability, and apply it to the card game "Hearts", which is a well-defined example of an imperfect information game. To reduce the computational cost, we use a sampling technique based on Markov chain Monte Carlo (MCMC) in which the heavy integration required for the estimation and prediction can be approximated by a plausible number of samples. Computer simulation results show that our RL agent can perform learning of an appropriate strategy and exhibit a comparable performance to an expert-level human player in this partially-observable multi-agent problem.

1 Introduction

Reinforcement learning (RL) [12] has been devoted much attention as an effective framework for strategic decision processes in multi-agent systems [9]. An optimal control problem in multi-agent environments, however, has a high degree of difficulty due to interactions among agents. These may make the Markov property of the state space fail because the changing behaviors of other agents provide dynamic nature. Although several RL researches based on the game theory have attained some remarkable results in a reasonably sized state space [1, 6], it is difficult to deal with real-world applications due to their serious complexity.

In addition, the environments often have partial observability; the agents cannot directly access internal states of the environment, but can get only observations which contain partial information about the state. Decision-making problems in such a situation can be formulated as partially observable Markov decision processes (POMDPs) [5]. When introducing this framework to realistic problems, however, serious difficulties arise because not only the estimation process for a large number of unobservable states, but also computing the optimal policy depending on the estimation require too heavy computation. To deal with large-scale multi-agent problems with partial observability, an estimation method with an effective approximation and explicit learning of the environmental model to follow its dynamics are necessary.

In this article, we present an automatic strategy-acquisition scheme for large-scale multi-agent problems with partial observability, and deal in particular with the card game "Hearts". To estimate unobservable states, we use a sampling technique [13] based on Markov chain Monte Carlo (MCMC) [2] for estimating the unobservable variables with a plausible number of samples. To predict the unknown environmental behaviors, we use a model-based approach [11] in which the learning agent based on our RL method has multiple action predictors for acquireing policies of the opponent agents. These ideas provide us with an effective solution for large-scale partially observable problems and ability to apply for various multi-agent settings; this is shown by computer simulations using expert-level rule-based agents. These results suggest that our method is effective in solving realistic multi-agent problems with partial observability.

2 Preliminary

A POMDP [5] is a framework to make an agent learn and act in a partially observable environment, and consists of (1) a set of real states $\mathcal{S} = \{s_1, s_2, \ldots, s_{|\mathcal{S}|}\}$, (2) a set of observation states $\mathcal{O} = \{o_1, o_2, \ldots, o_{|\mathcal{O}|}\}$, (3) a set of actions $\mathcal{A} = \{a_1, a_2, \ldots, a_{|\mathcal{A}|}\}$, and (4) a reward function $R : \mathcal{S} \times \mathcal{A} \to \mathcal{R}$. The dynamics of the model is represented as transition probability $P(s_{t+1}|s_t, a_t)$ and observation probability $P(o_t|s_t, a_t)$. The objective of each agent is to acquire the policy which maximizes an expected future reward in the partially observable world, in which the state s_t is not observable for each agent; only the observation o_t, which contains partial information about the state, is available.

The targets of this study are partially observable and multi-agent problems; there are multiple agents in a common environment with partial observability. In this article, we then use the following notations. indicates an action turn of the learning agent. The variables (state, observation and action) for agent i ($i = 0, \ldots, M$) are denoted by s_t^i, o_t^i and a_t^i, where M is the number of opponent agents and $i = 0$ signifies the learning agent; s_t, o_t and a_t are the same as s_t^0, o_t^0 and a_t^0, respectively. A strategy of an agent i is denoted by ϕ^i. Note that we make an assumption that there is only one learning agent in the environment, and the other agents' strategies ϕ^i $(i = 1 \quad M)$ are fixed, for the time being. This assumption will be loosened later. An action sequence of the opponent agents is denoted by $u_t = \ a_t^1 \quad a_t^M$ and a history for the learning agent at its -th action turn is given by $H_t \cdot \quad (o_t \quad) \ (o_{t-1}\ a_{t-1}\ u_{t-1}) \quad (o_1\ a_1\ u_1)$.

3 Model

In our RL method, an action is selected according to the greedy policy: $\pi(H_t) =$ argmax $_{a_t} U(H_t\ a_t)$, where $U(H_t\ a_t)$ is the utility function at a time step , defined by

$$U(H_t\ a_t) = \sum_{s_t \in \mathcal{S}_t} P(s_t\ H_t)$$
$$\sum_{s_{t+1} \in \mathcal{S}_{t+1}} P(s_{t+1}\ s_t\ a_t) \left[R(s_t\ a_t) + V(s_{t+1})\right] \quad (1)$$

where $R(s_t\ a_t)$ denotes an immediate reward at the time step $+ 1$, and $V(s_{t+1})$ denotes the state value function of the next state s_{t+1}. In our application, the card game Hearts, the reward is defined as $R(s_t\ a_t) =$ when the agent gets penalty points (may be 0) after the -th play. The value function V is approximated by a normalized Gaussian network (NGnet) [8] with a feature extraction technique to its 52-dimensional input; by considering the game property, a state s_t is converted to a 36-dimensional input p_t before the value function is updated so as to approximate the relationship between the input p_t and the scalar output $\sum_{i=t}^{13} R(s_i\ a_i)$ according to the Monte Carlo RL method [12].

In large-scale problems, it is difficult to learn the value function over the belief space [3]. We then use a completely observable approximation [7]; the agent maintains the state value function so that the self-consistency equation holds on the underlying MDP, and calculates the state-action utility value $U(s_t\ a_t)$ by a one-step-ahead prediction. After that, it calculates the history-action utility value $U(H_t\ a_t)$ as an expectation of the state-action utility with respect to the belief state under the knowledge that the optimal value function for the belief space can be approximated well by a piecewise-linear and convex function [10]. The calculation of the utility function, however, includes three difficulties: (a) the computation for constructing the belief state $P(s_t\ H_t)$ over possible current states is intractable due to the large state space and high dimensionality; (b) the prediction to possible next states is difficult because the environmental model $P(s_{t+1}\ s_t\ a_t)$ is unknown for the agent and may be changed in a multi-agent setting; and (c) the summation in equation (1) over possible current states and next states has computational intractability because there are so many candidates in a realistic problem. Some effective approximations, therefore, are required for avoiding the above difficulties.

To avoid difficulty (a), we do not deal with the whole history H_t but do a one-step history $h_t = (o_t \quad) \ (o_{t-1}\ a_{t-1}\ u_{t-1})$, which leads us to make an assumption (A): the belief state represents a simple one-step prior knowledge about states, but does not carry the complete likelihood information. The history H_t contains two kinds of information. The first is about impossible states at the -th turn; for example, in the game Hearts, if an agent played 9 after a leading card | 3 in a past trick, the agent no longer has any club cards at the -th turn and any state in which this agent holds club cards is impossible. The second is about likelihood, considering the characteristics of the opponent agents; for example, in the same situation as above, it is unlikely for the agent to have any heart card higher than 9. Although the belief state $P(s_t\ H_t)$, which is the sufficient statistic for the history H_t, should involve these two kinds of information, we partly ignore the latter kind by replacing the whole history H_t with a one-step history h_t; namely, the belief state $P(s_t\ H_t)$ is approximated by the partial belief state $P(s_t\ h_t)$ in this study. No impossible state, on the other hand, is considered in light of the former type of information, but each possible state has a one-step likelihood between the (1)-th and -th time steps. Although the maintenance of likelihood over possible states requires heavy computation and a large amount of memory in realistic problems, this assumption enables us to estimate internal states easily at each time step.

To solve problem (b), the agent uses action predictors. Since the state transition of usual multi-agent games depends on the other players' actions, the transition probability $P(s_{t+1}\ s_t\ a_t)$ in equation (1) is calculated by the product of action selection probabilities for M opponent agents, that is,

$$P(s_{t+1}\ s_t\ a_t) \quad P(s_{t+1}\ s_t\ a_t\ \hat{\Phi})$$
$$= \prod_{i=1}^{M} \frac{\exp(F^i(o_t^i\ a_t^i)/T^i)}{\sum_{\mathcal{A}^i} \exp(F^i(o_t^i\ a_t^i)/T^i)} \quad (2)$$

where $\hat{\Phi} = \ \hat{\phi}^1 \quad \hat{\phi}^M$. Note that $\hat{\phi}^i$ is not a real policy ϕ^i but a policy approximated by the action predictor. The learning agent maintains M action predictors corresponding to the M opponent agents. Note that the opponent agent's observation o_t^i is not observable to the agent, but it can be determined from the estimated current state $\hat{s}_t$ without any ambiguity in usual games whose observation process is deterministic. $F^i(o_t^i\ a_t^i)$ denotes the utility of action a_t^i for a given observation o_t^i of the i-th agent, which is an output of the action predictor. $\mathcal{A}^i$ denotes the set of possible actions for agent i, and T^i is a constant which denotes the assumed randomness of the agent i's policy. Equation (2) represents the behavior model of the environment. The action predictors thus approximate the environmental dynamics for the learning agent. Each predictor is implemented as Multi-Layered Perceptron (MLP), and its input and output are reduced to reasonably sized vectors by a feature extraction technique which is the same as our previous study [4].

To avoid the computational intractability problem (c), we use sampling-based approximation; the agent obtains independent and identically distributed (i.i.d.) random samples, $\hat{s}_t$ and $\hat{s}_{t+1}$, whose probabilities are proportional to the partial belief state $P(s_t\ h_t)$ and acquired environmental model $P(s_{t+1}\ s_t\ a_t\ \hat{\Phi})$, respectively. By considering the two approximations described above, the utility function in equation (1) can be calculated as

$$U(H_t\ a_t)$$
$$\frac{1}{K}\sum_{i=1}^{N} P(\hat{s}_t^{(i)}\ h_t)\sum_{j=1}^{K}\left[R(\hat{s}_{t+1}^{(j)}\ a_t)+V(\hat{s}_{t+1}^{(j)})\right] \quad (3)$$

Samples of current states $\hat{s}_t$ are obtained by the Metropolis-Hastings (MH) algorithm, the most popular Markov chain Monte Carlo (MCMC) technique [2], in the following three steps: the first step is to sample a previous state $\hat{s}_{t-1}^*$ so as not to violate the whole history H_t, no impossible state being sampled (according to the former type of information described above); the second step is to calculate a one-step likelihood $P(\hat{s}_t^*\ \hat{s}_{t-1}^*\ a_t)$ by using the action predictors according to equation (2); and the last step is to replace $\hat{s}_t^*$ with $\hat{s}_t^{(i+1)}$ according to the probability $p = \min\ 1\ P(\hat{s}_t^*\ \hat{s}_{t-1}^*\ a_t)/P(\hat{s}_t^{(i)}\ \hat{s}_{t-1}^{(i)}\ a_t)$ and otherwise $\hat{s}_t^{(i)}$ remains. Note that a Markov chain is uniform according to assumption (A). These three steps are iterated times, and the agent obtains estimated current states $\hat{s}_t^{(i)}\ i = 1$. Samples of next states $\hat{s}_{t+1}$ are obtained by a simple sampling technique, according to equation (2) given an estimated current state $\hat{s}_t^{(i)}$, an action a_t and an action sequence $\hat{u}_t = \hat{a}_t^1 \quad \hat{a}_t^M$ by the available fact that $\hat{s}_{t+1}^{(j)}$ can be determined without any ambiguity in usual games due to the deterministic nature of $P(s_{t+1}\ s_t\ a_t\ u_t)$. This is iterated K times for each of current states, and the agent obtains predicted next states $\hat{s}_{t+1}^{(j)}\ j = 1 \quad K$ with the learned model. Two summations in equation (1) are simultaneously approximated by using K samples in equation (3). The three approximations described above (the partial belief state, action predictor and sampling) enable us to solve large-scale and

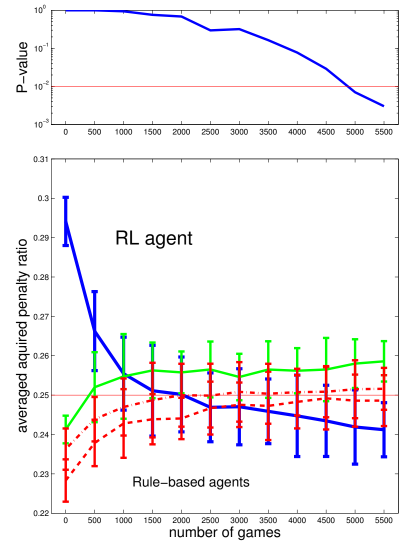

Figure 1: Computer simulation result in an environment where there are one learning agent trained by our RL method and three rule-based agents.

partially observable problems. In particular, they provide an effective solution to multi-agent problems whose underlying state space is discrete, including various multi-agent games.

4 Computer simulations

We applied our RL method to the card game Hearts, which is a well-defined example of large-scale and multi-agent problems with partial observability. To evaluate our method, we carried out computer simulations where an agent trained by our RL method played against rule-based agents which have more than 65 general rules for playing cards from their hands. The performance of an agent can be evaluated by the acquired penalty ratio, which is the ratio of the penalty points acquired by the agent to the total penalty points of the four agents. If the four agents have equal strength, their penalty ratio averages 0.25. The rule-based agent used in this study is much stronger than the previous one [4], due to the improvement in the rules, so to have almost the same strength as an expert-level human Hearts player. The learning agent based on our previous RL method then remained much weaker than this rule-based agent even after 100,000 training games. Since the outcome of this game tends to depend on the initial card distribution (for example, an expert player with a bad initial hand may be defeated by an unskilled player), we prepared a fixed data set for the evaluation; the data set is a collection of initial card distributions for 100 games, each of which was generated randomly in advance. In the evaluation games, the initial cards were distributed according to this data set. Since performance is influenced by seat position (that is, an agent may have an advantage/disadvantage based on its seat position if the agents have different strengths), we rotated the agents' positions for each initial hand to eliminate this bias; each of the 100 evaluation games was repeated four times with the four types of seating position. The performance of each agent, therefore, is evaluated by the 400 fixed and unbiased games. Note that learning of the agent was suspended during the evaluation games. Each learning run comprised several sets of 500 games, in which initial cards were distributed to the four agents at random and seat positions of the agents were determined randomly. In an experiment, accordingly, 400 evaluation games and 500 learning games were alternated.

Figure 1 shows the result. The abscissa of the lower panel denotes the number of training games and the ordinate denotes the penalty ratio acquired by each agent. Each point and error bar represents an average and standard deviation of the penalty ratio, respectively, for the 400 evaluation games over 17 learning runs, each consisting of 5,500 training games. The upper panel represents P-values of the -test where the null hypothesis is "the RL agent has the same strength as the rule-based agents" and the alternative hypothesis is "the RL agent is stronger than the rule-based agents". The test was done independently at each point on the abscissa. The horizontal line denotes the significance level of 1%. The constant T^i in equation (2) was $1\ 0$, and the numbers of samples in equation (3) were $= 80$ and $K = 20$. The penalty ratio of the RL agent decreased with the learning process, and after about 5,000 training games, the agent became significantly stronger than the rule-based agents. Since the agent showed a better performance than the expert-level rule-based agents after only several thousand training games, the new RL method based on a sampling method is a salient improvement over the previous one, both in learning speed and in strength.

Figure 2 shows the result when two RL agents and two rule-based agents played against each other. We executed 16 learning runs, each consisting of 4,000 training games. The abscissa and the ordinate of the lower panel denote the same as in Fig.1. The parameter values, other experimental setups and the representation of the upper panel are also the same. The penalty ratios of both RL agents came to acquire a smaller penalty ratio than the rule-based agents after about 5,000 training games. In the previous experiment, our method was based on the POMDP approximation; it was assumed that there is only one learning agent in the environment. In this experiment, our method was applied directly to multi-agent environments, in which there are multiple learning and hence dynamic environment, and the new RL method showed good performance even in this

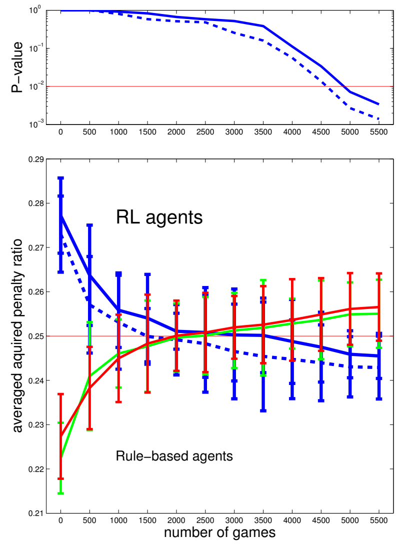

Figure 2: Computer simulation result in an environment where there are two learning agents trained by our RL method and two rule-based agents.

complex setting. This ability is attributed to the fast learning owing to using three action predictors.

References

[1] Crites, R. H. and Barto, A. G., Advances in Neural Information Processing Systems, Vol. 8, pp.1017–1023, 1996.
[2] Gilks, W. R., Richardson, S. and Spiegelhalter, D. J., Chapman and Hall, 1996.
[3] Hauskrecht, M., Journal of Artificial Intelligence Research, Vol. 13, pp. 33–94, 2000.
[4] Ishii, S., Fujita, H, Mitsutake, M., Yamazaki, T., Matsuda, J. and Matsuno, Y., Machine Learning, Vol. 59, pp. 31–54, 2005.
[5] Kaelbling, L. P., Littman, M. L. and Cassandra, A. R., Artificial Intelligence, Vol. 101, pp. 99–134, 1998.
[6] Littman, M. L., Proceedings of the Eleventh International Conference on Machine Learning, pp. 157–163, 1994.
[7] Littman, M. L., Cassandra, A. R. and Kaelbling, L. P., Proceedings of the Twelfth International Conference on Machine Learning, pp. 362–370, 1995.
[8] Sato, M. and Ishii, S, Neural Computation, Vol. 12, pp. 407–432, 2000.
[9] Shoham, Y., Powers, R. and Grenager, T., Proceedings of AAAI Fall Symp. on Artificial Multiagent Learning, pp. 1–13, 2004.
[10] Smallwood, R. D. and Sondik, E. J., Operations Research, Vol. 21, pp. 1071–1088, 1973.
[11] Sutton, R. S., Proceedings of the Seventh International Conference on Machine Learning, pp. 216–224, 1990.
[12] Sutton, R. S. and Barto, A. G., MIT Press, 1998.
[13] Thrun, S., Advances in Neural Information Processing Systems, Vol. 12, pp. 1064–1070, 2000.

Analyzing Robustness in Multi-Agent Reinforcement Learning
- A comparison between Profit Sharing and Q-Learning -

Tuyoshi Nehashi
Tokyo Institute of Technology,
4259 Nagatsuta-cho,
Midori-ku, Yokohama
226-8503 JAPAN
nehashi@cas.dis.titech.ac.jp

Keiki Takadama
Tokyo Institute of Technology,
4259 Nagatsuta-cho,
Midori-ku, Yokohama
226-8503 JAPAN
keiki@dis.titech.ac.jp

Kazuteru Miyazaki
National institution for Academic Degrees and University Evaluation,
1-29-1 Gakuennishimachi,
Kodaira-city, Tokyo
187-8587 JAPAN
teru@niad.ac.jp

Abstract

This paper focuses on uncertainty of multi-agent reinforcement learning and analyzes the robustness against the uncertainty caused by state transitions of other agents that prevents agents from appropriate learning. In this paper, we categorize the uncertainty by analyzing what kind of factors cause the uncertainty through a comparison of Q-learning and Profit Sharing in simple environment. Through intensive simulations, the following implications have been revealed: (1) a combination of a noise added to in environments and indirect interaction among agents causes the uncertainty; (2) random initial positions do not cause the uncertainty; (3) our simulations derives inverse implications obtained by [Arai 98], that is, the accumulated-based Profit Sharing is inferior to Q-learning in terms of the average acquisition rewards. This indicates that accumulating Q value does not cause the uncertainty of state transitions.

Key words: multi-agent reinforcement learning, profit sharing, Q-learning, uncertainty, state transition.

1. Introduction

Research on multi-agent reinforcement learning has been investigated in the context of multi-agent systems [Weiss, 1999]. As a typical research, [Arai 98] compared Q-Learning and Profit Sharing in the multi-agent reinforcement learning environments (pursuit problem) and reported the robustness of Profit Sharing in such environments. The point of her paper is that an uncertainty is caused by (1) the state transitions of other agents that prevent agents from appropriate learning, (2) perceptual aliasing by restricting an input and (3) both influence. This claim shows a main difficulty of multi-agent reinforcement learning.

However, the uncertainty claimed here is not described in detail, and thus it is not clear what kinds of factors cause the uncertainty. From this background, this paper aims at categorizing causes of the uncertainty of state transitions and analyzing reasons why cooperative behaviors of a multi-agent system becomes difficult.

This paper is organized as follows. Section 2 starts by categorizing the uncertainty of state transitions. Details of simulations are given in Section 3. Section 4 describes a simulation result and Section 5 discusses comparisons of the simulation results of PS and Q-learning. Finally, our conclusions are given in Section 6.

2. Uncertainty

2.1 The uncertainty of state transitions

The uncertainty is caused by an environment based on a non-Markov decision process as shown in the following figure. This figure shows a state transitions of three agents A, B and C. S0 indicates the current state and S1~S4 indicate the next state. After taking the action a0 by agent A in S0, the next state becomes either of S1 to S4 by the action b0 or b1 of the agent B and c0 or c1 of agent C. Here, if each agent has not yet learned, the state transitions probability from S0 to S1 ~ S4 may change dynamically and a next state may also change further.

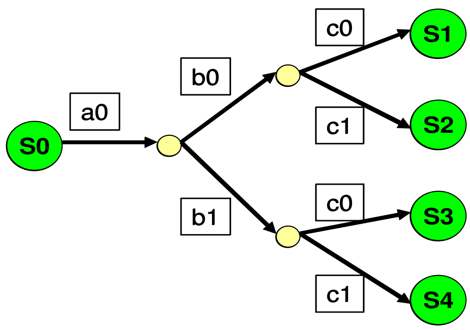

Figure 1: The uncertainty of state transitions by existence of other agents

2.2 Categorization

To clarify factors that cause the uncertainty, we propose the following categorization.

(1) **An environmental noise:**

- (1-1) Transportation (*def.*, If an agent goes into a specific place, it moves at the moment by a certain probability.)
- (1-2) Random initial position (*def.*, An initial position changes at random when an agent starts.)
- (1-3) Random goal position (*def.*, The area of the goal moves or changes at random.)

(2) **Ability of agents:**
- (2-1) Restriction of action (*e.g.*, An agent cannot move to the right by a certain failure.)
- (2-2) Restriction of percept (*def.*, A sensing input is limited. e.g. perceptual aliasing)

(3) **Interaction:**
- (3-1) Indirect interaction (*def.*, A cooperative behavior which is restricted by other agents to achieve common goals.)
- (3-2) Direct interaction (*e.g.*, A competitive behavior in addition to cooperative.)

What should be noticed here is that the issues of the goal random, restriction of percept, and direct interaction are investigated in [Arai 98].

3. Problem description

Experiment environment is composed of 2x8 masses, where the upper 1x8 masses are used for an agent A, while the lower 1x8 masses are for an agent B. Each agents can move to the right and left, and cannot stop. The 6th is the initial position. Reward 10 will be given when both agents are located at the 1st or 2nd position. After reward is given, agents start from the initial position. One step is counted when moving one mass, and one episode is a sequence of steps until agents get rewards.

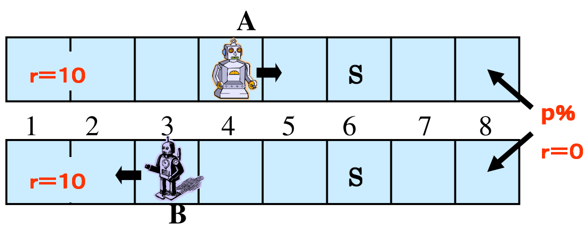

Figure 2: Image of experiment environment. S: initial positions, r: rewards.

In this paper, we investigate the other factors listed in the above items. (*i.e.* transportation, random initial position and indirect interaction.) Regarding transportation factors transportation, if either of agents is located at the 8th position, reward 0 is given by p% probability. In this simulation, we set p=80. For random initial position, agents are set random positions expect goal. Indirect interaction is finally implemented by torus environment where the 1st position is connected the 8th position. In this environment, moving left does not make sense because it cannot make agents step at the 1st position, and thus agents have to acquire their actions that move to goal at the same time.

4. Simulation

4.1 Simulation cases

We divide simulations as the following four cases:

(Case1) The predetermined initial position without torus environment
(Case2) The predetermined initial position with torus environment
(Case3) Random initial position without torus environment
(Case4) Random initial position with torus environment

In each case, we compare among Q-learning [Watkins 92], the estimated-based PS (Profit Sharing) [Grefenstette 88], and the accumulated-based PS [Miyazaki 94].

Q-learning updates Q values the following equation (1) in every step.

$$Q(s,a) \leftarrow Q(s,a) + \alpha(r + \gamma \max_{a' \in A(s')} Q(s',a') - Q(s,a)) \quad (1)$$

In equation (1), s, s', a, a' and $Q(s,a)$ indicate the current state, the next state where an agent will actually move, the current action, the next action taken at the next state, and Q value, respectively. r is the reward that an agent acquires. The parameter α ($0<\alpha\leq1$) is the learning rate which changes the learning speed, while the parameter γ ($0<\gamma\leq1$) is the discount rate which decides the propagation rate of the reward. $A(s')$ is the set of actions which is able to be selected at the next state s'.

Profit Sharing (the estimated-based and accumulated-based PSs) updates Q values according to the following equation (2) and (3).

- Estimated-based PS

$$Q(s_t,a_t) \leftarrow Q(s_t,a_t) + C_{bid}[r(t) - Q(s_t,a_t)] \quad (2)$$

- Accumulated-based PS

$$Q(s_t,a_t) \leftarrow Q(s_t,a_t) + r(t) \quad (3)$$

In equations (2) and (3), t, C_{bid} ($0<C_{bid}\leq1$), and $r(t)$ indicate a step, the parameter correspond to α in the Q-learning, and reinforcement function, respectively. The rewards are added to Q value according to the reinforcement function when acquiring rewards. In this simulation, we used geometric increasing function $(r(t) = (1/2)^{t-1} \times reward)$ introduced by [Miyazaki 94]. What is the essential difference from Q-learning is to update all Q value in the episode when rewards are given. In this simulation, we set α=0.1, γ=0.9, and C_{bid}=0.1.

All of three learning mechanisms employ Boltzmann distribution as action selection. The parameter of the inverse temperature is 0.1.

4.2 Simulation results

Figure 3 shows the simulation results on the acquired rewards per one step averaged in every 10 episodes until 10000 episodes, which are also averaged from 10 times of different random seeds.

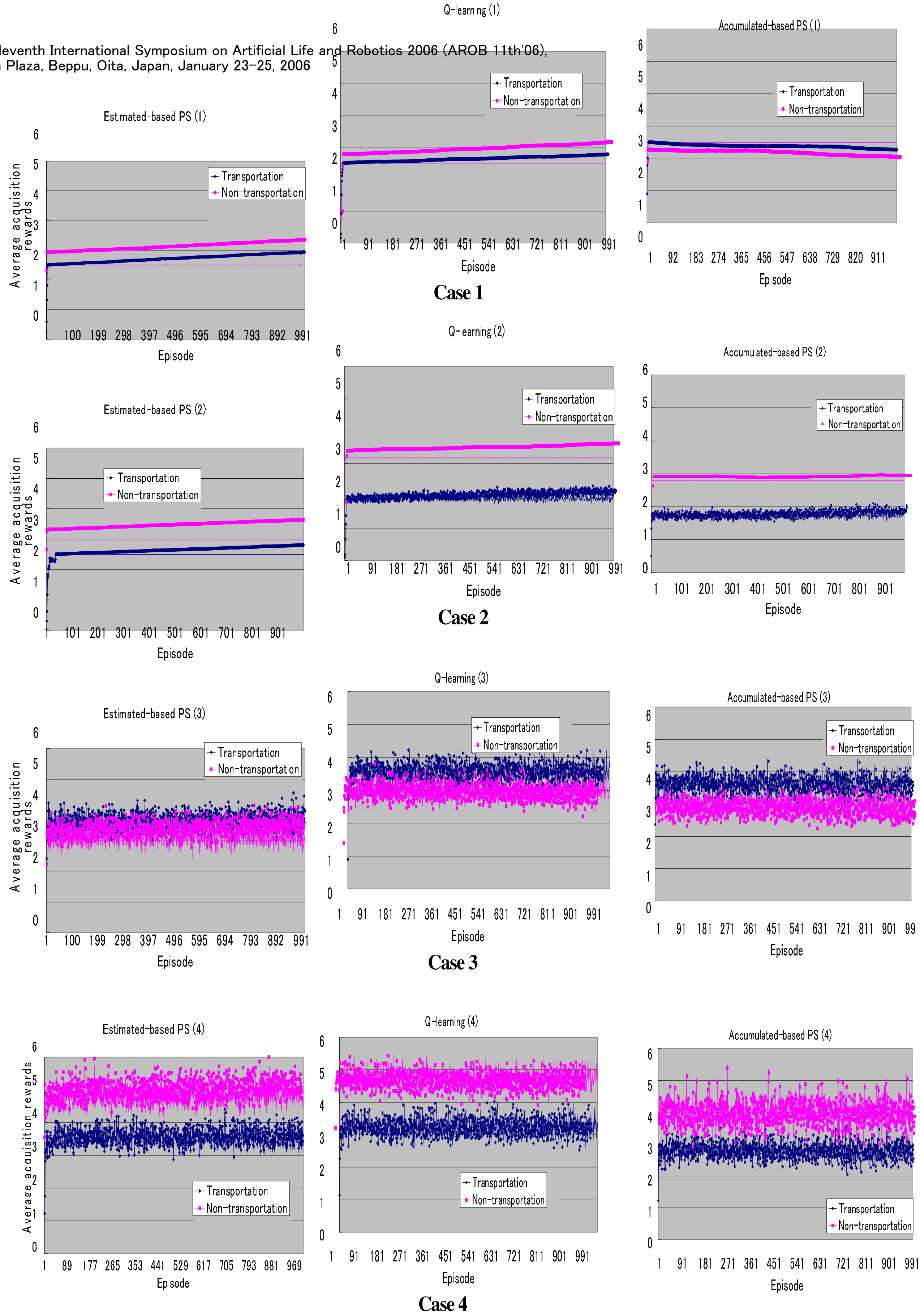

Figure 3: Simulation results

The vertical axis indicates the average acquired rewards per each one step, and the horizontal axis indicates the episodes. The gray and blue lines indicate the results of transportation and non-transportation environments, respectively. From these results, we find the following implications. (1) In the non-transportation environment, a big difference is not seen in comparison of the estimated-based PS and Q-learning. (2) However, in the transportation environment, the difference is appeared in cases (2) and (4).

5. Discussions

5-1 Comparison of Profit Sharing and Q-learning

・ **The transportation and indirect interaction**

Simulation result shows that the estimated-based PS is superior to Q-learning in terms of the average acquisition rewards in cases (2) and (4), while the estimated-based PS approximately equals to Q-learning in cases (1) and (3). This suggests that indirect interaction caused by torus with transportation in multi-agent learning gives a big influence to Q-learning rather than Profit Sharing. That is, since Q-learning updates Q values in order to identify environment, Q-learning cannot always find the optimal solution even if it finds the optimal solution at once and a convergence value is far from the optimal solution. In contrast, since Profit Sharing updates Q values of experimented situations, Profit Sharing has a chance to reinforce episodes without going to the transportation point. Therefore, Q-learning agents go to the transportation position many time compared with Profit Sharing agents, which derives that the convergence value of Q-learning is worse than Profit Sharing.

・ **Random initial position**

Simulation result shows that the estimated-based PS approximately equals to Q-learning in terms of the average acquisition rewards in cases (1) and (3) regardless of whether transportation position is included or not in an environment. This suggests that the factor of random initial position does not derive the difference of Q-learning and Profit Sharing in this environment. This is because Q values in all states are estimated through learning, which enables agent's select correct action in any random initial position.

5-2 Comparison of the estimated-based and accumulated-based PSs

・ **The robustness of Profit Sharing**

Simulation result shows that the accumulated-based PS is inferior to the estimated-based PS in terms of the average acquisition rewards in cases (2) and (4). [Arai 98] claimed that the accumulated-based PS is robust to the uncertainty of state transitions, because accumulated rewards in Q values are not sensitive in comparison of Q-learning. However from these results, we claim the robustness is caused by mechanism of Profit Sharing, in particular estimating Q value at each updating. It is necessary to analyze this in the near future.

6. Conclusions

This paper presented our first attempt that analyzes the robustness in multi-agent reinforcement learning. Towards this goal, we investigated the uncertainty of state transitions introduced by [Arai 98] as one of the causes that make multi-agent reinforcement learning complicated, and categorized the uncertainty in more detail. Through intensive simulations, the following implications were revealed: (1) a combination of transportation and indirect interaction is one of the causes of the uncertainty of state transitions, (2) a random initial position dose not cause the uncertainty of state transitions, and (3) the robustness of Profit Sharing in multi-agent environment is supported by its mechanism.

The following issues should be pursued in the near future, (1) detailed analyses of the difference between the estimated-based and the accumulated-based PSs in terms of influence to multi-agent learning; (2) investigations of other factors that may cause the uncertainty of state transitions; (3) improvements of categorizing the uncertainty of state transitions; and (4) experiments on other examples.

Acknowledgements

The research reported here was supported in part by a Grant-in-Aid for Scientific Research (B, No. 17360424) from the Ministry of Education, Culture, Sports, Science and Technology (MEXT).

References

[1] Arai, S., Miyazaki, K. and Kobayashi, S.: "Methodology in Multi Agent Reinforcement Learning -Approaches by Q-Learning and Profit Sharing-", *Transactions of the Japanese Society for Artificial Intelligence,* Vol.13, No.5, pp.609-618 (1998). (In Japanese).

[2] Grefenstette, J.J.: "Credit Assignment in Rule Discovery Systems Based on Genetic Algorithms," *Machine Learning*, Vol.3, pp. 225-245 (1988).

[3] Miyazaki, K., Yamamura, M. and Kobayashi, S.: "A Theory of Profit Sharing in Reinforcement Learning", *Transactions of the Japanese Society for Artificial Intelligence*, Vol.9, No.4, pp.580-587 (1994). (In Japanese).

[4] Watkins, C.J.C.H. and Dayan, P.: "Technical Note: Q-learning", *Machine Learning*, Vol.8, pp. 55-68 (1992).

[5] Weiβ,G.: *Multi-agent Systems -Modern Approach to Distributed Artificial Intelligence-*, The MIT Press (1999).

The Eleventh International Symposium on Artificial Life and Robotics 2006 (AROB 11th'06),
B-con Plaza, Beppu, Oita, Japan, January 23-25, 2006

Natural policy gradient reinforcement learning method for a looper-like robot

Yutaka Nakamura Takeshi Mori Shin Ishii
Graduate School of Information Science
Nara Institute of Science and Technology (NAIST)
8916-5 Takayama-cho, Ikoma, Nara 630-0192, Japan

Abstract

To develop a mobile robot which has the adaptability to various environments, we configured a looper-like robot simulator and a CPG controller for this robot, and applied a reinforcement learning (RL) method to the automatic acquisition problem of 'vermicular' motions by this robot. Computer simulation shows a good CPG controller for the looper-like robot can be obtained by our proposed method.

1 Introduction

To realize a mobile robot that acts in a real environment, adaptability to changes in the environment due to its dynamic nature and disturbances is necessary. RL is a framework for autonomous acquisition of control rules and has been successfully applied to various automatic control problems, such as balancing a cart-pole [1], swinging up an acrobot [2]. Because real robots often have a large number of degrees of freedom, RL methods to control them require some devices to avoid the "curse of dimensionality".

Motivated by the animal's control mechanism for rhythmic locomotion, which is induced by neural circuits in the spinal cord of vertebrates called central pattern generators (CPGs), robot control schemes using a CPG controller have been studied mainly in the field of robotics [3][4]. In those studies, a CPG controller is implemented as a kind of recurrent neural network which generates rhythmic outputs, and the character of the CPG controller is determined by connection weights in the network. Because the parameter of the CPG controller is designed to such that the CPG controller and the robot interact with each other and are eventually entrained into a stable limit-cycle attractor, a robot controlled by a CPG controller is robust against possible disturbances from the environment.

Although there have been some studies of designing a CPG controller, the determination of CPG parameters is still difficult, since parameters of the CPG controller must be tuned depending on both the target physical system (robot) and the environment. Therefore, autonomous learning framework for a CPG controller is necessary to realize the adaptability to dynamic environments. We formerly proposed an RL framework called a CPG-actor-critic model for designing a CPG controller [5]. Since control signals are restricted to be rhythmic in favor of the CPG, this RL method would be able to avoid "curse of dimensionality". In this method, the parameter of the CPG controller is updated according to the gradient of the performance indicator, the average reward per step for example, with respect to the parameter (policy gradient) and this gradient can be obtained by interaction with the environment. After learning, the CPG controller becomes to generate stable locomotion suited to the environment surrounding the robot.

In the current study, we configure a looper-like robot simulator and its CPG controller. Because a looper has an ability to move by simple and rhythmic telescopic motions, a looper-like robot would have an ability to behave in various environments. We apply our proposed method to the automatic acquisition task of 'vermicular' locomotion of the looper-like robot. Computer simulations show that a good CPG controller for the looper-like robot can be obtained by our proposed method. This adaptability is important to develop a mobile robot which is able to overcome unexpected circumstances to go through various rough terrains.

2 Control scheme

Looper-like robot The looper-like robot comprises two links each possessing a wheel, as depicted in Figure 1. The two links are connected to each other by a linear slider joint. This robot is controlled by three signals: the force that expands or contracts the linear slider, the brake for the head link's (front) wheel, and

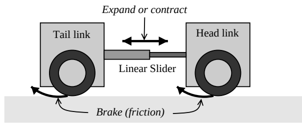

Figure 1: Looper-like robot simulator

that for the tail link's (rear) wheel. The robot moves in the forward direction, if the expansion of the linear slider and braking of the rear wheel occur simultaneously, and subsequently the contraction of the linear slider and braking of the front wheel occur simultaneously.

In the simulation, the friction coefficient between the link and the ground was assumed to be controlled directly, instead of modelling the braking control of the two wheels. We also assumed that there is a spring in the linear slider to keep the joint length within a specific range. Then, the link movements are defined as

$$\begin{aligned} m\ddot{x}_1 &= \tau_1 - k_s(l - x_1 + x_2) - \tau_2\dot{x}_1 \\ m\ddot{x}_2 &= -\tau_1 + k_s(l - x_1 + x_2) - \tau_3\dot{x}_2 \end{aligned}, \qquad (1)$$

where x_1 and x_2 denote the position of the head link and that of the tail link, respectively. Here, m, l and k_s denote the mass of the link, the length of the spring and the spring constant, respectively, while τ_1, τ_2 and τ_3 are control signals which correspond to the force of the linear slider, the friction coefficient of the head link and that of the tail link, respectively. Constants m, l, and k_s were set to 0.1, 0.2, and 2.0, respectively.

CPG controller The CPG controller comprises three neural oscillators, and each of them consists of two neurons. The $(2i-1)$-th and the $2i$-th neurons' dynamics are defined as

$$\begin{aligned} \frac{1}{c}\dot{y}_{2i-1} &= -y_{2i-1} + \tanh\left(W^{\mathrm{S}}y_{2i-1} + W^{\mathrm{I}}y_{2i} + u_i\right) \\ \frac{1}{c}\dot{y}_{2i} &= -y_{2i} + \tanh\left(-W^{\mathrm{I}}y_{2i-1} + W^{\mathrm{S}}y_{2i}\right) \end{aligned}, \qquad (2)$$

where y_{2i-1} and y_{2i} denote the $(2i-1)$-th and the $2i$-th neurons' states, respectively. W^{S}, W^{I} and c are the self-excitatory connection weight, the mutual-inhibitory connection weight and the time constant, respectively. Also, u_i is an input to the i-th neural oscillator and calculated from the robot's state $\mathbf{x}$ and the CPG controller's state $\mathbf{y}$. W^{S}, W^{I}, and c were fixed at 1.1, 0.7, and 0.1, respectively. These parameters were determined so that the frequency of the neural oscillator's output was similar to that of the looper-like robot's intrinsic movements, which are physically determined by the spring constant and the link's mass, as $2\pi\sqrt{m/k_s}$. Figure 2 shows the behavior of the first neural oscillator: phase portrait between y_1 and y_2 (a) and their time series (b).

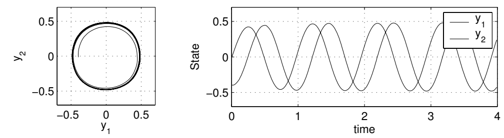

(a) (b)

Figure 2: Behavior of the first neural oscillator

Control scheme Figure 3 shows the control scheme using a CPG controller. The CPG controller observes the robot's state $\mathbf{x}$ and outputs control signal $\boldsymbol{\tau}$. The control signal $\boldsymbol{\tau}$ is calculated as

$$\begin{aligned} \tau_1 &= -0.3y_1 \\ \tau_2 &= \exp(y_3)/(1 + \exp(y_3)) \\ \tau_3 &= \exp(y_5)/(1 + \exp(y_5)), \end{aligned}$$

where the sigmoid function is employed to prevent the friction coefficient from becoming negative.

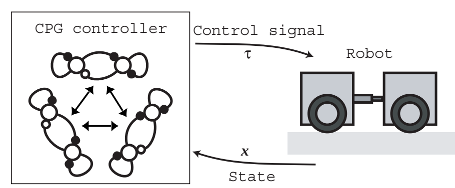

Figure 3: Control scheme using a CPG controller

3 Learning method

In this section, we describe an RL algorithm for the CPG controller, which we formerly proposed and called the CPG-actor-critic model. In a naive application of usual RL to training of a CPG controller, the CPG controller is regarded as an actor. In this case, the control signal depends not only on the state of the target system, but also its own state, because the CPG controller has its own dynamics. This is problematic because most RL algorithms assume the target policy is stationary (time-independent), and furthermore, heavy computation would be required for training recurrent neural networks like the naive CPG controller.

In order to overcome these difficulties, the CPG controller is divided into two parts, the basic CPG and

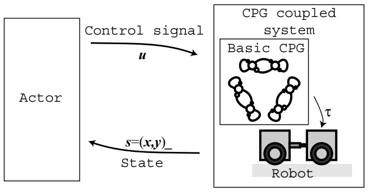

Figure 4: CPG-actor-critic model

the actor, as depicted in Figure 4 [5]. The basic CPG is a part of the CPG controller with fixed connection parameters, and its intrinsic properties, for example frequency and amplitude of its basic oscillatory behaviors, is determined by these fixed parameters, i.e., W^I, W^S, and c. We treat the physical system and the basic CPG as a single dynamical system, and we call this system the CPG-coupled system.

The actor is the controller for the CPG-coupled system. Since the actor turns out to be a feed-forward neural network which has no its own dynamics, we can easily apply usual RL algorithms to the training of the actor. The control signal $\mathbf{u}$ for the CPG-coupled system is conceptually represented as

$$\mathbf{u} \sim \pi(\mathbf{u}, \mathbf{s}), \tag{3}$$

where π denotes the control policy of the actor and $\mathbf{s} \equiv (\mathbf{x}, \mathbf{y})$ is a state of the CPG-coupled system.

Natural policy gradient method For the sake of simplicity, we assume that Eqs. (1) and (2) are discretized in time by an appropriate method, and the learning system receives an immediate reward $r(\mathbf{s}(t), \mathbf{u}(t))$ at a discrete time step t. The policy $\pi_{\boldsymbol{\theta}}(\mathbf{s}, \mathbf{u})$ is defined by a parametric stochastic policy, i.e., the probability of a control signal $\mathbf{u}$ at a state $\mathbf{s}$: $p(\mathbf{u}|\mathbf{s}; \boldsymbol{\theta})$, where $\boldsymbol{\theta}$ is a parameter vector of the policy. We assume that $\pi_{\boldsymbol{\theta}}$ is differentiable with respect to each parameter component θ_i, and there exists a stationary invariant distribution of states under any stochastic policy $\pi_{\boldsymbol{\theta}}$.

The objective of RL here is to obtain the policy parameter that maximizes the expected reward accumulation defined by $\rho(\boldsymbol{\theta}) \equiv \mathrm{E}_{\boldsymbol{\theta}}\left[\sum_t \gamma^{t-1} r(\mathbf{s}(t), \mathbf{u}(t))\right]$, where $\gamma \in (0, 1]$ is a discount factor. The partial differential of $\rho(\boldsymbol{\theta})$ with respect to the policy parameter θ_i is calculated [6][7] by

$$\frac{\partial \rho(\boldsymbol{\theta})}{\partial \theta_i} = \left\langle \psi_i(\mathbf{s}, \mathbf{u}) Q_\theta(\mathbf{s}, \mathbf{u}) \right\rangle, \tag{4}$$

where $\psi_i(\mathbf{s}, \mathbf{u}) \equiv \frac{\partial}{\partial \theta_i} \ln \pi_{\boldsymbol{\theta}}(\mathbf{u}|\mathbf{s})$ and $Q_{\boldsymbol{\theta}}(\mathbf{s}, \mathbf{u})$ denotes the action-value function (Q-function). $\langle \cdot \rangle$ stands for the expectation with respect to the stationary distribution of the state-action pair $(\mathbf{s}, \mathbf{u})$. When the Q-function is approximated by a weighted sum of bases $\boldsymbol{\psi}$: $Q^w_{\boldsymbol{\theta}}(\mathbf{s}, \mathbf{u}) \equiv \sum_i w_i \psi_i(\mathbf{s}, \mathbf{u})$, where $\mathbf{w}$ is the weight vector of the approximate Q-function, the optimal weight in the least square sense, $\tilde{\mathbf{w}} = \arg\min_{\mathbf{w}} \left\langle \left(Q_{\boldsymbol{\theta}}(\mathbf{s}, \mathbf{u}) - Q^w_{\boldsymbol{\theta}}(\mathbf{s}, \mathbf{u})\right)^2 \right\rangle$, provides the natural policy gradient with no estimation bias for the gradient, so that the policy parameter can be updated [8][1] as

$$\theta_i := \theta_i + \eta \tilde{w}_i, \tag{5}$$

where η is the learning rate. Then, it is sufficient to obtain the optimal weight $\tilde{\mathbf{w}}$ instead of to well approximate the Q-function itself which may be a high-dimensional function.

When we introduce an approximate state-value function $\hat{V}_{\boldsymbol{\theta}}(\mathbf{s}) \equiv \sum_j v_j \phi_j(\mathbf{s})$, where ϕ_i for $i = 1, \ldots, M$ are arbitrary basis functions of state $\mathbf{s}$, and $\mathbf{v}$ is the weight vector, the weight vectors, $\mathbf{w}$ and $\mathbf{v}$, are estimated together based on the least square method:

$$\mathbf{W} = \left\langle r \boldsymbol{\varphi}^T \right\rangle \left\langle \boldsymbol{\varphi} \boldsymbol{\varphi}^T \right\rangle^{-1}, \tag{6}$$

where $\boldsymbol{\varphi}(t) = \begin{pmatrix} \boldsymbol{\psi}(\mathbf{s}(t), \mathbf{u}(t)) \\ \boldsymbol{\phi}(\mathbf{s}(t)) - \gamma \boldsymbol{\phi}(\mathbf{s}(t+1)) \end{pmatrix}$ and $\mathbf{W} \equiv \begin{pmatrix} \mathbf{w} \\ \mathbf{v} \end{pmatrix}$ [9][5][1]. Note that $\mathbf{W}$ is the parameter of the value function (critic).

4 Experiment

The aim of this experiment is to obtain a control rule which allows the looper-like robot to move in the forward direction. For this purpose, an immediate reward $r(\mathbf{s}(t))$ was given by

$$r(\mathbf{s}(t)) = 5(\dot{x}_1 + \dot{x}_2).$$

We assumed the control signal was generated as

$$\begin{aligned} u_1 &= \theta_1 X_1 + \theta_2 X_2 + \epsilon_1 \\ u_2 &= \theta_3 y_1 + \theta_4 y_2 + \epsilon_2 \\ u_3 &= \theta_5 y_1 + \theta_6 y_2 + \epsilon_3 \end{aligned} \quad , \tag{7}$$

where $\mathbf{X} = \{x_1 - x_2 - l, \dot{x}_1 - \dot{x}_2\}$, and ϵ_i $(i = 1, 2, 3)$ is a small random noise obeying a normal distribution. The policy parameter $\boldsymbol{\theta}$ determines phase relations among the robot and the neural oscillators and is trained by RL.

Basis functions of the state-value function Figure 2 showed the phase portrait between two neurons which compose a neural oscillator. Because the phase portrait presents a circle whose center is the origin, the angle $\omega_1 = \arctan(y_2/y_1)$ carries essential information of the state of the first neural oscillator. Similarly, $\omega_2 = \arctan(y_4/y_3)$ and $\omega_3 = \arctan(y_6/y_5)$ are useful features of the second and the third neural oscillators, respectively. Furthermore, when the looper-like robot repeats expansion and contraction, $\omega_4 = \arctan((x_4 - x_3)/(x_2 - x_1))$ is also an important feature of the robot's movements. Because the phase difference seemed to be more important than the phase in this experiment, we employed 49 basis functions for the approximate state-value function: $\phi_{16(i-2)+j}(\mathbf{s}) = \exp\left(-3(\cos(\omega_i - \omega_1 + \pi/16j) - 1)\right)$ for $i = 2, 3, 4$ and $j = 1, 2, \ldots, 16$ and $\phi_{49} = 1$.

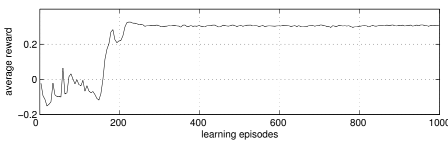

Figure 5: Learning curve

The horizontal axis denotes the number of learning episodes, and the vertical axis denotes the average reward in one episode. This figure shows the moving average in 5 episodes.

At the beginning of an episode, the robot was initialized to a motionless state, and was controlled by the current actor for 10 sec. Figure 5 shows the learning curve, indicating that after about 200 episodes the robot was able to move forward. Figure 6(a) shows the movements of the looper-like robot before learning and after learning. Before learning the robot accidentally moved backward, but after learning the robot was able to move forward quickly. Figure 6(b) shows changes of the phase difference between ω_i $(i = 2, 3, 4)$ and ω_1. These results suggest that the robot came to move fast by enabling the neural oscillator composing the CPG controller to possess an appropriate phase relation.

5 Conclusion

In this study, we configured a CPG-based control architecture for a looper-like robot, and applied RL to obtain a control rule for the robot simulator to move in the forward direction. Computer simulation showed that a good CPG controller for this robot can be obtained by our RL method. To apply our RL method to the autonomous control problem of a real looper-like robot and to develop a robust mobile robot are our future work.

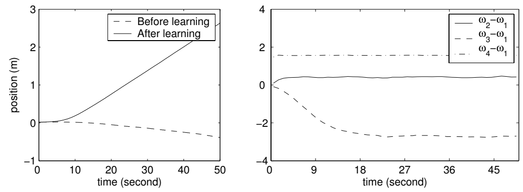

(a) (b)

Figure 6: Control result

The position of the looper-like robot's center (a) and phase differences of the feature variables from the first neural oscillator ω_1.

References

[1] J. Peters, S. Vijayakumar and S. Schaal: "Reinforcement learning for humanoid robotics", Third IEEE International Conference on Humanoid Robotics 2003, Germany (2003).

[2] J. Yoshimoto, S. Ishii and M. Sato: "On-line em reinforcement learning", IEEE-INNS-ENNS international Joint Conference on Neural Networks(IJCNN 2000), Vol. 3, pp. 163–168 (2000).

[3] G. Taga, Y. Yamaguchi and H. Shimizu: "Self-organized control of bipedal locomotion by neural oscillators in unpredictable environment", Biological Cybernetics, **65**, pp. 147–159 (1991).

[4] Y. Fukuoka, H. Kimura and A. H. Cohen: "Adaptive dynamic walking of a quadruped robot on irregular terrain based on biological concepts", International Journal of Robotics Research, **22**, 3–4, pp. 187–202 (2003).

[5] Y. Nakamura, T. Mori and S. Ishii: International conference on parallel problem solving from nature (PPSN VIII), pp. 972–981 (2004).

[6] V. R. Konda and J. N. Tsitsiklis: "Actor-critic algorithms", SIAM Journal on Control and Optimization, **42**, 4, pp. 1143–1146 (2003).

[7] R. S. Sutton, D. McAllester, S. Singh and Y. Manour: "Policy gradient method for reinforcement learning with function approximation", Advances in Neural Information Processing Systems, Vol. 12, pp. 1057–1063 (2000).

[8] S. Kakade: "A natural policy gradient", In Advances in Neural Information Processing Systems, **14**, pp. 1531–1538 (2001).

[9] S. J. Bradtke and A. G. Barto: "Linear least-squares algorithms for temporal difference learning", Machine Learning, **22**, pp. 33–57 (1996).

The Eleventh International Symposium on Artificial Life and Robotics 2006 (AROB 11th'06),
B-con Plaza, Beppu, Oita, Japan, January 23-25, 2006

Vector Control of Induction Motor Using advanced Hybrid System based on GA and Bacteria Foraging

Dong Hwa Kim
Dept. of Instrumentation and Control Eng., Hanbat National University,
16-1 San Duckmyong-Dong Yuseong-Gu, Daejon City, Korea, 305-719.
E-mail: kimdh@hanbat.ac.kr, Hompage: aialab.net
Tel: +82-42-821-1170, Fax: +82-821-1164

Abstract

This paper is dealing with hybrid system (GA-BF) using the conventional GA (Genetic Algorithm) and BF (Bacterial Foraging) which is social foraging behavior of bacteria. To illustrate characteristics of the proposed hybrid system, a variety of test function is introduced and simulated to illustrate characteristics by mutation of GA-BF, crossover of GA-BF, performance by variation of step size. variation of chemotactic step of GA-BF, and variation of life time of GA-BF. This approach provides us with novel models of their foraging behavior and with new methods for distributed nongradient optimization, and also provides a connection between evolutionary forces in social foraging and distributed nongradient optimization algorithm design for global optimization over noisy surfaces. On the other hand, PID controllers have been widely used in industrial systems such as chemical process, biomedical process, and the main steam temperature control system of the thermal power plant. Very often, it is difficult to achieve an optimal PID gain with no prior expert knowledge, since the gain of the PID controller has to be manually tuned by a trial and error approach. This paper proposes a hybrid approach by combining a Euclidian data distance (EU) based Genetic Algorithm (GA) and bacterial foraging based Optimization (PSO) method for tuning the PID controller of an Automatic Voltage Regulator (AVR). Using the hybrid EU-GA-PSO approach, global and local solutions could be simultaneously found for optimal tuning of the controller parameters.

1. Introduction

In the last decade, evolutionary computation based approaches have received increased attention from the engineers dealing with problems which could not be solved using conventional problem solving techniques [1]. A typical task of a GA in this context is to find the best values of a predefined set of free parameters associated with either a process model or a control vector. One of the active areas of research in GA is system identification [2]. A recent survey of evolutionary algorithms for the evaluation of improved learning algorithm and control system engineering can be found in [3]. The general problem of evolutionary algorithm based engineering system design has been tackled in various ways. GA has also been used to optimize nonlinear system strategies. On the other hand, since natural selection of bacterial foraging tends to eliminate animals with poor foraging strategies for locating, handling, and ingesting food, optimization models can be provided for social foraging where groups of parameters communicate to cooperatively forage in engineering. This paper focuses on dealing with an enhanced optimal solution using a hybrid approach consisting of BA (Bacterial Foraging) and GA (Genetic Algorithm).

This paper provides optimal vector control method by viewing the relevant research in foraging theory, foraging by communicating organisms (social foraging) which sometimes operate in swarms, and the relevance of these areas to optimization.

2. Novel Hybrid System Using GA and Bacteria Foraging

1.1 Overview of Bacterial Foraging

This paper considers the foraging behavior of E. coli, which is a common type of bacteria as in the previous comment [4]. Its behavior to move comes from a set of up to six rigid 100–200 rps spinning flagella, each driven as a biological motor. An E. coli bacterium alternates between running and tumbling. Running speed is 10–20 $\mu m/\sec$, but they cannot swim straight. When we can summarize the chemotactic actions of bacteria as the following description:

- If in neutral medium, alternate tumbles and runs, its action is having search.
- If swimming up a nutrient gradient (or out of noxious substances), swim longer (climb up nutrient gradient or down noxious gradient), its behavior seeks increasingly favorable environments.
- If swimming down a nutrient gradient (or up noxious substance gradient), then search action is avoiding unfavorable environments.

So, it can climb up nutrient hills and at the same time avoid noxious substances. The sensors it needs for optimal resolution are receptor proteins which are very sensitive and high gain. That is, a small change in the concentration of nutrients can cause a significant change in behavior. This is probably the best-understood sensory and decision-making system in biology.

Mutations in E. coli affect the reproductive efficiency at different temperatures, and occur at a rate of about 10^{-7} per gene and per generation. E. coli occasionally engages in a conjugation that affects the characteristics of a population of bacteria. Since there are many types of taxes that are used by bacteria such as, aerotaxis (it are attracted to oxygen), light (phototaxis), temperature (thermotaxis), magnetotaxis (it can be affected by magnetic lines of flux. Some bacteria can change their shape and number of flagella which is based on the medium to reconfigure in order to ensure efficient foraging in a variety of media. Bacteria can form intricate stable spatio-temporal patterns in certain semisolid nutrient substances. They can eat radially their way through a medium if placed together initially at its center. Moreover, under certain conditions, they will secrete cell-to-cell attractant signals so that they will group and protect each other. These bacteria can swarm.

2.2 Optimization by Bacterial Swarm Foraging

The main goal based on bacterial foraging is to apply in order to find the minimum of $P(\phi), \phi \in R^n$, not in the gradient $\nabla P(\phi)$. Here, when ϕ is the position of a bacterium, and $J(\phi)$ is an attractant-repellant profile. That is, it means where nutrients and noxious substances are located, so *P<0, P=0, P>0* represent the presence of nutrients. A neutral medium, and the presence of noxious substances, respectively can be defined by

$$H(j,k,l) = \{\phi^i(j,k,l) \big| i = 1,2,...,N\}. \tag{1}$$

Equation represents the positions of each member in the population of the N bacteria at the jth chemotactic step, kth reproduction step, and lth elimination-dispersal event. Let $P(i, j, k, l)$ denote the cost at the location of the ith bacterium $\phi^i(j,k,l) \in R^n$, and

$$\phi^i = (j+1,k,l) = \phi^i(j,k,l) + C((i)\varphi(j), \tag{2}$$

so that $C(i)>0$ is the size of the step taken in the random direction specified by the tumble. If at $\phi^i(j+1,k,l)$ the cost $J(i, j+1, k, l)$ is better (lower) than at $\phi^i(j,k,l)$, then another chemotactic step of size $C(i)$ in this same direction will be taken and repeated up to a maximum number of steps N_s. N_s is the length of the lifetime of the bacteria measured by the number of chemotactic steps. Functions $P_c^i(\phi)$, i=1, 2, . . . , S, to model the cell-to-cell signaling via an attractant and a repellant is represented by [5]

$$\begin{aligned} P_c(\phi) &= \sum_{i=1}^{N} P_{cc}^i \\ &= \sum_{i=1}^{N}\left[-L_{attract}\exp\left(-\delta_{attract}\sum_{j=1}^{n}(\phi_j-\phi_j^i)^2\right)\right] \\ &\quad+\sum_{i=1}^{N}\left[-K_{repellant}\exp\left(-\delta_{attract}\sum_{j=1}^{n}(\phi_j-\phi_j^i)^2\right)\right], \end{aligned} \tag{3}$$

When we where $\phi = [\phi_{1,...,}\phi_p]^T$ is a point on the optimization domain, $L_{attract}$ is the depth of the attractant released by the cell and $\delta_{attract}$ is a measure of the width of the attractant signal. $K_{repellant} = L_{attract}$ is the height of the repellant effect magnitude), and $\delta_{attract}$ is a measure of the width of the repellant. The expression of $P_c(\phi)$ means that its value does not depend on the nutrient concentration at position ϕ. That is, a bacterium with high nutrient concentration secrets stronger attractant than one with low nutrient concentration. Model use the function $P_{ar}(\phi)$ to represent the environment-dependent cell-to-cell signaling as

$$P_{ar}(\phi) = \exp(T - P(\phi))P_c(\phi) \tag{4}$$

where T is a tunable parameter. Model consider minimization of $P(i, j, k, l) + P_{ar}\left(\phi^i(j,k,l)\right)$, so that the cells will try to find nutrients, avoid noxious substances, and at the same time try to move toward other cells, but not too close to them. The function $P_{ar}\left(\phi^i(j,k,l)\right)$ implies that, with M being constant, the smaller $P(\phi)$, the larger $P_{ar}(\phi)$ and thus the stronger attraction, which is intuitively reasonable. In tuning the parameter M, it is normally found that, when M is very large, $P_{ar}(\phi)$ is much larger than $J(\phi)$, and thus the profile of the search space is dominated by the chemical attractant secreted by E. coli. On the other hand, if T is very small, then $P_{ar}(\phi)$ is much smaller than $P(\phi)$, and it is the effect of the nutrients that dominates. In $P_{ar}(\phi)$, the scaling factor of $P_c(\phi)$ is given as in exponential form.

This paper describes the method in the form of an algorithm to search optimal value of parameters.

[step 1] Initialize parameters *n, N,* N_C, N_S, N_{re}, N_{ed}, P_{ed}, *C(i)(i=1,2,…,N),* ϕ^i.

Where, n: Dimension of the search space, N: The number of bacteria in the population, N_C : chemotactic steps, N_{re} : The number of reproduction steps, N_{ed} : the number of elimination-dispersal events, P_{ed} : elimination-dispersal with probability, C(i): the size of the step taken in the random direction specified by the tumble.

[step 2] Elimination-dispersal loop: $l=l+1$

[step 3] Reproduction loop: $k=k+1$

[step 4] Chemotaxis loop: $j=j+1$

[substep a] For i =1,2,…,N, take a chemotactic step for bacterium i as follows.

[substep b] Compute fitness function, ITSE (i ,j, k, l).

[substep c] Let ITSE_{last}=ITSE (i,j,k,l) to save this value since we may find a better cost via a run.

[substep d] Tumble: generate a random vector $\Delta(i) \in R^n$ with each element $\Delta_m(i), m = 1,2,..., p$, a random number on [-1, 1].

[substep e] Move: Let

$$\phi^i(j+1,k,l)=\phi^i(j,k,l)+C(i)\frac{\Delta(i)}{\sqrt{\Delta^T(i)\Delta(i)}}$$

This results in a step of size $C(i)$ in the direction of the tumble for bacterium *i*.

[substep f] Compute ITSE $(i, j+1,k,l)$.

[substep g] Swim

i) Let m=0 (counter for swim length).

ii) While m< N_s (if have not climbed down too long).

- Let m=m+1.
- If ITSE $(i, j+1,k,l)$ < ITSE_{last} (if doing better), let ITSE_{last}=ITSE $(i, j+1,k,l)$ and let

$$\phi^i(j+1,k,l)=\phi^i(j+1,k,l)+C(i)\frac{\Delta(i)}{\sqrt{\Delta^T(i)\Delta(i)}}$$

and use this $\phi^i(j+1,k,l)$ to compute the new ITSE $(i, j+1,k,l)$ as we did in [substep f]

- Else, let m= N_s . This is the end of the while statement.

[substep h] Go to next bacterium (*i*, 1) if $i \neq N$ (i.e., go to [substep b] to process the next bacterium).

[step 5] If $j < N_C$, go to step 3. In this case, continue chemotaxis, since the life of the bacteria is not over.

[step 6] Reproduction:

[substep a] For the given *k* and *l*, and for each $i=1,2,...,N,$ let

$$ITSE^i_{health}=\sum_{j=1}^{N_c+1} ITSE(i,j,k,l)$$

be the health of bacterium *i* (a measure of how many nutrients it got over its lifetime and how successful it was at avoiding noxious substances). Sort bacteria and chemotactic parameters $C(i)$ in order of ascending cost $ITSE_{health}$ (higher cost means lowerhealth).

[substep b] The S_r bacteria with the highest $ITSE_{health}$ values die and the other S_r bacteria with the best values split (and the copies that are made are placed at the same location as their parent).

[step 7] If $k < N_{re}$, go to [step 3]. In this case, we have not reached the number of specified reproduction steps, so we start the next generation in the chemotactic loop.

[step 8] Elimination-dispersal: For $i=1,2...,N,$ with probability P_{ed} , eliminate and disperse each bacterium (this keeps the number of bacteria in the population constant).

To do this, if you eliminate a bacterium, simply disperse one to a random location on the optimization domain. If $l < N_{ed}$, then go to [step 2]; otherwise end.

3. Vector Control of Induction Motor

The direct torque and flux control for induction machine drives has been developed as direct torque control (DTC) and as direct self control (DSC). The technique was generalized to all ac drives, as torque vector control (TVC), and it was recognized as a viable alternative to field-oriented control (FOC). Industrial drives with DTC are present on the market today. DTC abandons the stator current control philosophy, characteristic of FOC and achieves bang-bang torque and flux control by directly modifying the stator voltage in accordance with the torque and flux errors. DTC is characterized by fast dynamic response, structural simplicity, and strong robustness in the face of parameter uncertainties and perturbations. It does not employ current controllers and pulsewidth modulation (PWM), and it is well suited for sensorless drives. Classic DTC has still several drawbacks: It exhibits large torque, flux, and current ripple, produces annoying acoustical noise, operates with nonzero steady-state torque error, has difficulties in controlling the flux at low speeds, and the switching frequency is variable and lower than the sampling frequency [6]-[9].

4. Simulation of Vector Control By GA-BF

In this paper, Test function $F_1(x)=\sum_{i=1}^{3}x_i^2$ is introduced for comparing the characteristic of chemotactic step in hybrid GA-BF (Genetic Algorithms- Bacteria Foraging). This paper illustrates characteristics between the proposed GA-BF and SGA (Simple Genetic Algorithm) using test function, De Jong [6]. Fig. 1 is showing characteristic GA-BF between objective function and generation (Generations: 1-70) to variation of life time of bacteria Ns. Table I is function value to chemotactic step.

Table 1
Function value to chemotactic step

Chemotactic step	x1	x2	X3	Optimal objective function	Average objective function
100	-9.32E-08	3.78E-07	-8.57E-09	1.52E-13	1.59E-13
500	2.97E-08	1.92E-08	2.32E-08	1.79E-15	3.26E-15
1000	-1.70E-08	-1.44E-08	-2.31E-09	5.01E-16	1.43E-15

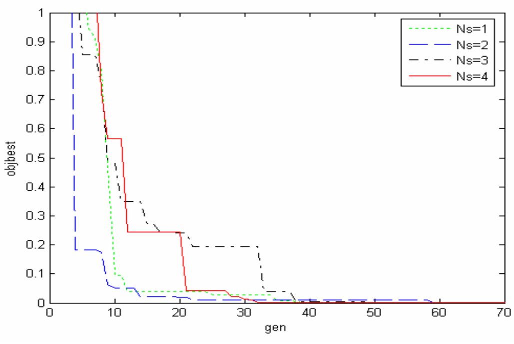

Fig. 1. Characteristic GA-BF to variation of Ns. (Generations: 1-70)

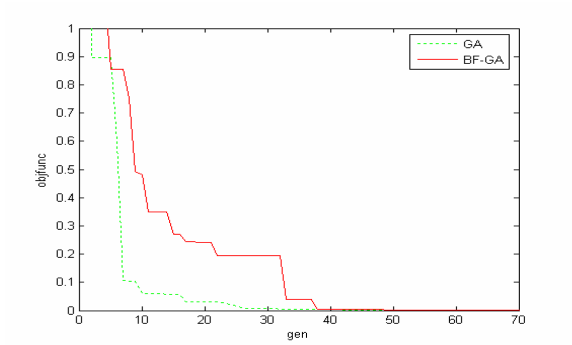

Fig. 2. Characteristics of GA and GA-BF by test function. (Generations: 1-70)

Fig. 2 illustrates characteristics of GA and GA-BF by test function between objective function and generation (Generations: 1-70). If performance of test generations Ns is a satisfactory result, the characteristic of BF (Bacteria Foraging) moves forward, and otherwise, BF searches new direction to obtain optimal result from generations after lifetime Ns. Fig. 3 is process of optimal search in GA and GA-BF.

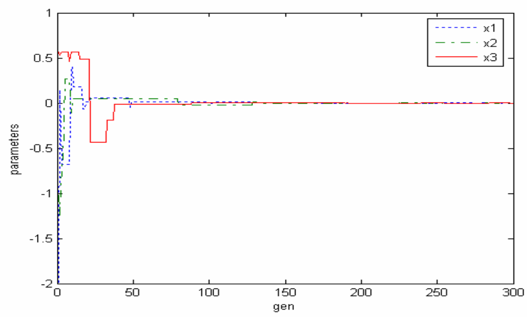

Fig. 3. Process of optimal search in GA-BF.

Table 2 shows initial condition and resulting parameter simulated for test function. The value of Table III is simulated results based on range (searching range), chemotactic step, total number of chemotactic reaction of bacteria, step size, basic unit for movement of bacteria Ns, the number of critical reaction S, the number of bacteria N, generations G, mutation Mu, crossover Cr.

Table 2
Comparison by test function $F_1(x)$.

Chemotatic step	x1	x2	X3	Optimal objective function	Average objective function
GA	7.22E-08	5.07E-08	-9.43E-09	7.87E-15	8.03E-15
GA-BF	-1.70E-08	-1.44E-08	-2.31E-09	5.01E-16	1.43E-15

5. Conclusion

Recent many approaches of evolutionary algorithms for the evaluation of improved learning algorithm and control system engineering have been studying. The general problem of evolutionary algorithm based engineering system design has been tackled in various ways because of learning time and local or suboptimal solution. This paper suggested the hybrid system consisting of GA (Genetic Algorithm) and BF (Bacterial Foraging) and proved the characteristic of that system using test functions and vector control of induction motor.

This approach proposed in this has the potential to be useful in practical optimization problems (e.g., engineering design, online distributed optimization in distributed computing and cooperative control) as models of social foraging are also distributed nongradient optimization methods. Moreover, it remains to be seen how practically useful the optimization algorithms are for engineering optimization problems, because they depend on the theoretical properties of the algorithm, theoretical and empirical comparisons to other methods, and extensive evaluation on many benchmark problems and real-world problems.

Reference

[1] B. Maione, D. Naso, and B. Turchiano, "GARA: A genetic algorithm with resolution adaptation for solving system identification problems," in Proc. Eur. Control Conf., Porto, Portugal, Sept. 4–7, 2001, pp. 3570–3575.

[2] C. M. Fonseca and P. J. Fleming, "Multiobjective optimization and multiple constraint handling with evolutionary algorithms-Part I: A unified formulation;" "-Part II: Application example," IEEE Trans. System, Man, Cybern. A: Systems and Humans, vol. 28, no. 1, pp. 26–47, Jan. 1998.

[3] PASSINO, K. M., "Biomimicry of Bacterial foraging for Distributed Optimization," University Press, Princeton, New Jersey, 2001.

[4] Dong Hwa Kim, Jae Hoon Cho, "Adaptive Tuning of PID Controller For Multivariable System Using Bacterial Foraging Based Optimization," Lecture Notes in Computer Science Proceeding of Springer (SCI), June 12-15, 2005, Poland.

[5] Dong Hwa Kim, Jae Hoon Cho, "Intelligent Control of AVR System Using GA-BF," Lecture Notes in Computer Science Proceeding of Springer (SCI), June 12-15, 2005, KES 2005, Melbourne, Australia.

[6] A. Benchaib, A. Rachid, E. Audrezet, and M. Tadjine, "Real-time sliding-mode observer and control of an induction motor," IEEE Trans. Ind. Electron., vol. 46, pp. 128–137, Feb. 1999.

[7] J.-O. Krah and J. Holtz, "High performance current regulation and efficient PWM implementation for low-inductance servo motors," IEEE Trans. Ind. App., vol. 35, pp. 1039–1049, Sept./Oct. 1999.

[8] Ion Bolden, S.A. Nasar, "Electric Drives," CRC Press, 1999.

[9] Andrzej M., Trzynadlowski, "Control of Induction Motors," ACADEMIC Press, 2001.

Remote Control of Robot using Wireless LAN

Nobuya KAWASAKI, Fengzhi DAI, Yutaka FUJIHARA
Department of Control Engineering
Matsue National College of Technology

Abstract

Wireless LAN becomes rapidly widespread and its communication speed is made extensive improvements.

In the conventional case of a remote control to the robot with the radio controller, the signal to control the robot is only transmitted unidirectional from the radio controller and the data of sensors and images etc captured by the robot can't be returned to the host computer for controlling the robot. But, it becomes easy to send directly the data from the robot by using wireless LAN instead of radio controller.

Therefore, two-way communication can be done between the host computer and remote controlled robot, and robots can be controlled by feed back control.

However, when PC of the desktop type or the note type is slotted into the robot to use wireless LAN, it becomes difficult to downsize the robot and to reduce the cost. At present, the network connection became possible in the field of the built-in microcomputer board, and Ethernet can be easily and cheaply used.

In this research, the microcomputer board is installed in the robot to control wireless LAN and the Ad hoc mode is utilized that can communicate directly among wireless LAN devices; it also follows IEEE802.11b of the long distance communication standard.

The communication is mainly controlled by the firmware of the AVR microcomputer, and the wireless LAN device uses the 16bit PC Card interface of 5V power supply system. And the operation of transmitting the signal from host computer is mainly checked.

1. Introduction

In the conventional case of a remote control to the robot with the radio controller, the signal to control the robot is only transmitted unidirectional from the radio controller and the data of sensors and images etc captured by the robot can't be returned to the host computer for controlling the robot. But, it becomes easy to send directly the data from the robot by using wireless LAN instead of radio controller.

Therefore, two-way communication can be done between the host computer and remote controlled robot, and robots can be controlled by feed back control. Furthermore, the host computer can control the robot to work at the various situations by using the voices and images from the robot.

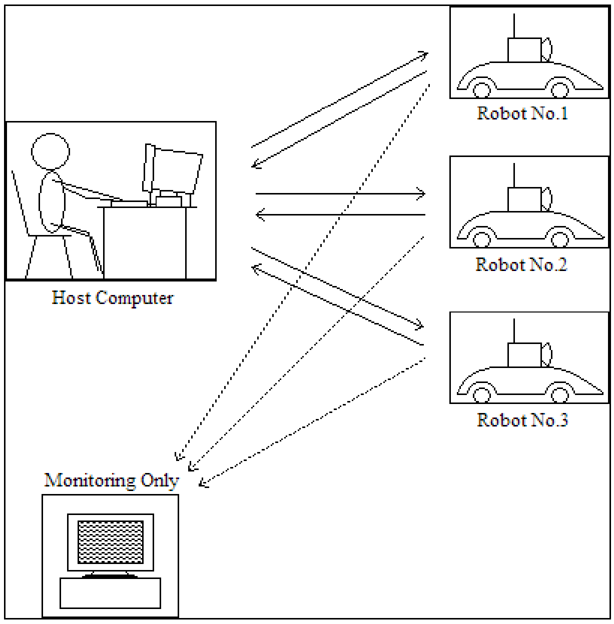

Fig.1 Concept of system

In this paper, we propose a method to install wireless LAN to microcomputer of robot as the basic study to achieve network robot system. Fig.1 shows the concept of system.

2. Microcomputer on which mounted Wireless LAN

When a robot has a large size, it is possible that the desktop type personal computer (PC) is installed into the robot to control wireless LAN. But, it becomes difficult that a PC is installed in connection with a robot becomes a miniature.

Moreover, if PC is being included into every robot one unit, the efficiency of the cost is bad.

A network connection has recently become possible by the microcomputer board of embedded type and we can handle Ethernet easily and cheaply.

Therefore, we propose a method to control wireless LAN by microcomputer board embedded in the small size robot as a network robot through Ethernet.

2.1 Outline of Control

There are several communication protocols and correspondence procedures in wireless LAN. In this study, using Ad hoc mode, we directly hold correspondence between the wireless LAN devices according to IEEE802.11b that is a protocol of long-distance communication.

We use an available 16bit PC Card interface of 5V power supply for the wireless LAN device, and an AVR microcomputer is used for the control of wireless LAN and for the control of I/O by firmware.

2.2 AVR Microcomputer

An AVR microcomputer is the CMOS 8bit RISC architecture microcomputer developed by Atmel Corporation.

AVR microcomputer exhibits better performance than PIC and H8 microcomputer. Because AVR microcomputer has many kind of command and can execute for about 90% of all commands within one clock. And also its processing speed is about 1MIPS/MHz.

Moreover, the commands of AVR microcomputer are easy to handle, and AVR microcomputer has many registers and SRAM. Also it has a development environment in which can handle an assembler, C++ and Basic can be programmed freely. And as usage of programmer, these languages are divided into some systems. So, programmer can easily handle these languages.

But, there are hardly materials and reference books written in Japanese because this microcomputer is the minor handling in Japan compared with PIC and H8 microcomputer.

In order to handle PC Card as an outside memory, we select the model number ATmega162 [1] among AVR microcomputer for movement control.

ATmega162 is belonging to the 4414 or 8515 group of AVR microcomputer. These groups are superior to handle the outside memory and commands of I/O are especially abundant. The pin arrangement of this microcomputer is shown in Fig.2 and basic movement specifications are shown in Table.1.

Table.1 Specification of AVR microcomputer

SRAM	1KB
EEPROM	512B
Flash Memory	16KB
External Memory	64KB
Clock	16MHz
I/O	35ch

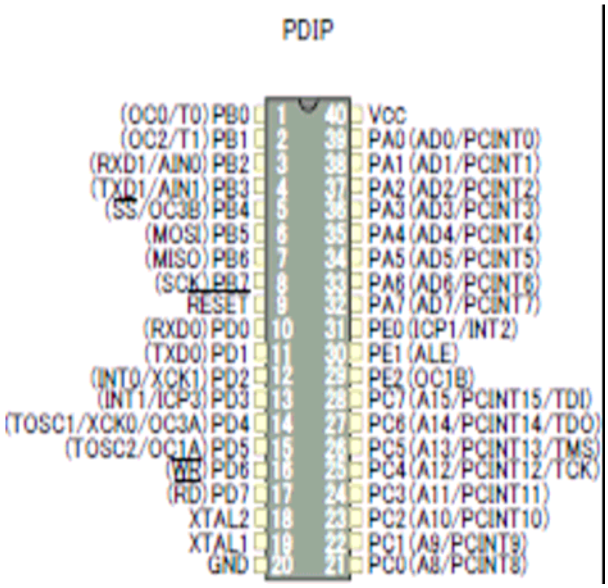

Fig.2 Pin arrangement of AVR microcomputer

2.3 16bit PC Card

A 16bit PC Card interface of PCMCIA interface is used in this time. It is divided into "memory card" and "I/O + memory card" in this interface, and wireless LAN card is being sorted by the latter. And, in the PC Card, there are three access spaces that consist of the common memory space, the attribute memory space and the I/O space.

Common memory is the usual memory space that can access freely from the host CPU, and the attribute memory is the special memory space used only for a configuration. Wireless LAN includes “I/O + memory card”, therefore it is not necessary to mount a common memory in the wireless LAN card. Therefore, a wireless LAN card does the reading and writing of the data with alternately changing the attribute memory space and the I/O space [2].

In this study, it is possible that the PC Card can be controlled by the data access of 8bit. Therefore, an extra addition circuit is unnecessary so that the microcomputer control the PC Card. Because the control of the PC Card by the microcomputer becomes possible by connecting directly each address port and the data port of the PC Card to the microcomputer respectively, and fixing the signal of other I/O ports of the PC Card constantly.

2.4 Wireless LAN

The correspondence procedures of wireless LAN consist of an Infrastructure mode and an Ad hoc mode. The former is the system that communication is done through the access point, and the access point does all the control of communication. Because it is suitable for the exchange between more than one wireless LAN devices, this system is used to control such as the autonomous robot.

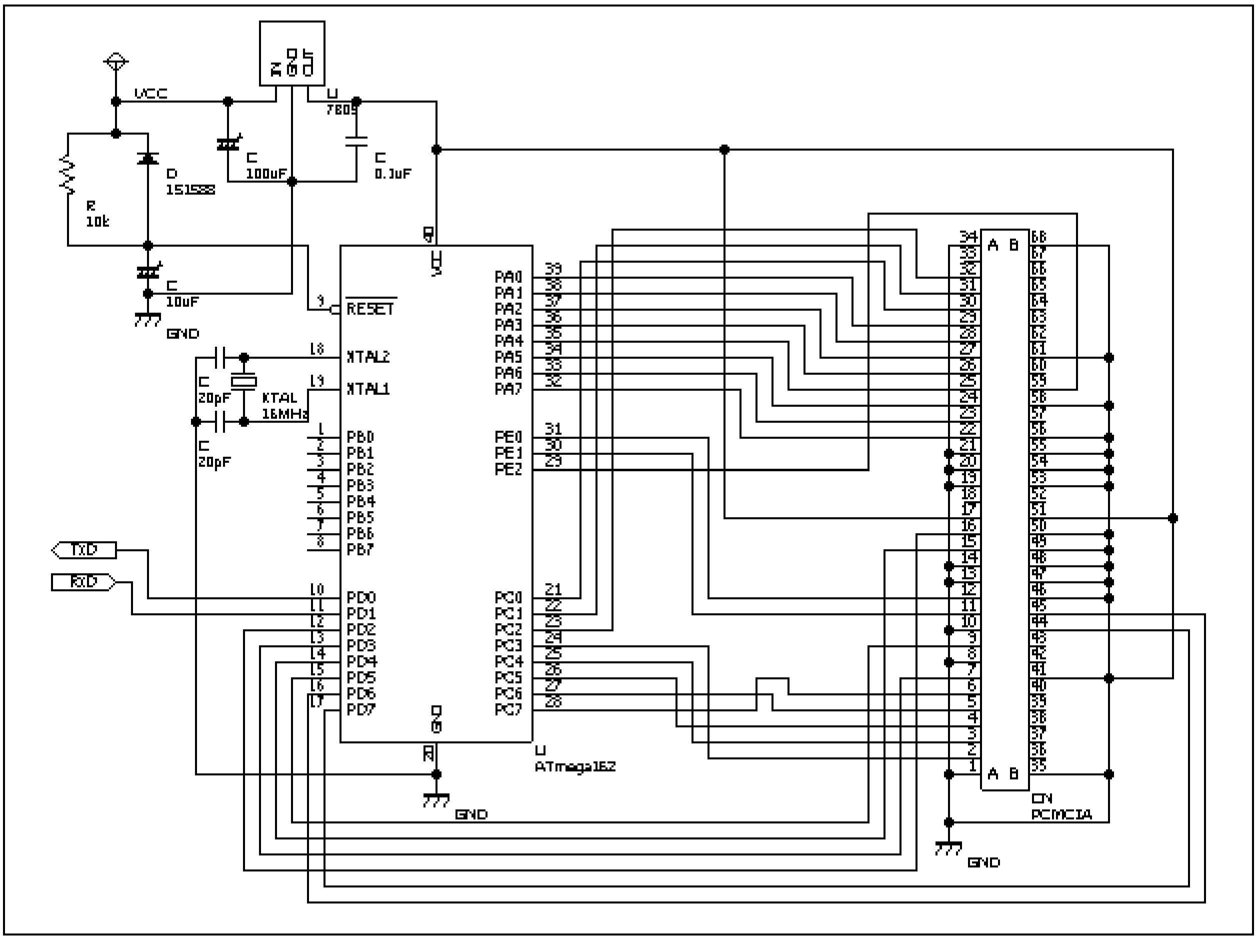

Fig.3 Circuit Diagram

The latter is the form that communication is done with the wireless LAN devices, and we have to manage the communication by ourselves. And also, this form is suitable for controlling a robot directly because of the communication of one to one [3].

In this study, because our object is a movement verification of one to one communication, we decided to adopt the Ad hoc mode.

And, also we used IEEE802.11b from the two reasons. One reason is that it is prohibited by Japanese laws to use the electric wave of the 5.2GHz band out of doors, and the other is that the processing speed of the microcomputer is low. Characteristics of IEEE802.11b are shown in Table 2.

Table.2 Specification of Wireless LAN

	802.11a	802.11g	802.11b
Speed	54Mbps		11Mbps
Bandwidth	5.2GHz	2.4GHz	
Method	OFDM	DSSS	OFDM
Obstacle	△	◎	

3. Method of control

First, each signal line of the PC Card is handled as follows. A circuit diagram to satisfy this condition is shown in Fig.3 and signals of the PC Card are shown in Table.3.

Next, the control of the PC Card is done by using I/O by the firmware of AVR microcomputer. Therefore, we describe how to handle the Ad hoc mode referring to the source program of the general-purpose wireless LAN driver of Linux [4]. We use UDP (User Datagram Protocol) as Internet protocol for realizing the real time communication to directly control the robot. And we process data of serial communication by using USART (Universal Synchronous Asynchronous Receiver Transmitter) function of AVR microcomputer for I/O of the outside.

4. Summary

In this study, we formulated and proposed a plan of the main part to control the mobile robot by wireless LAN. In future, we must plan to mount both communication forms of wireless LAN and also adjust a serial communication to USB1.1 standard for increasing the communication speed.

Furthermore, we should aim to improve this system by mounting TCP (Transmission Control Protocol) of Internet protocol; the reason is UDP is deficient in reliability.

Table.3 Signals of PC Card

Signal (Pin No.)	Control
A0-A9 (29-22,12,11)	CPU Control
D0-D7 (30-32,2-6)	
CE1# (7)	
OE# (9)	
WE# (15)	
IORD# (44)	
IOWR# (45)	
IREQ# (16)	
WAIT# (59)	
CE2# (42)	Hi Level
RESET (58)	Low Level
A10-A25 (8,10,21,13,14,20,19,46-50,53-56)	
REG# (61)	
D8-D15 (64-66,37-41)	Non Connect
CD1# (36)	
CD2# (67)	
IOIS16# (33)	
SPKR# (62)	
STSCHG# (63)	
INPACK# (60)	
VS1# (43)	
VS2# (57)	
Vcc (17,51)	
Vpp1 (18)	
Vpp2 (52)	
GND (34,68)	

References

[1] Atmel Corporation: ATmega162 Application Notes; http://www.atmel.com/dyn/products/product_card.asp?part_id=2023
[2] Hitoshi MIYAZAKI: Chapter1-9 PC Card; Transistor Technology SPECIAL No.63 - All in interface around personal computer, CQ Publisher, (1998/07/01)
[3] Yukio MITSUIWA: Chapter4-8 802.11b Experiment on Microcomputer Board for Wireless LAN; Hardware Selection - Hardware control by LAN, CQ Publisher, (2005/05/15)
[4] Kyousuke ISIKAWA: Wireless LAN PC Card Control of Microcomputer; http://www.asahi-net.or.jp/~qx5k-iskw/robot/wave.html

The Eleventh International Symposium on Artificial Life and Robotics 2006 (AROB 11th'06),
B-con Plaza, Beppu, Oita, Japan, January 23-25, 2006

Research on Face Recognition System by Genetic Algorithm

Fengzhi DAI, Tatsuya KODANI, Yutaka FUJIHARA
Department of Control Engineering,
Matsue National College of Technology,
daifz (fujihara)@matsue-ct.jp

Abstract

Computer vision and recognition plays more important role on modern intelligent control. Object detection is the first and the most important step for the object recognition. Traditionally, special object can be recognized by the template matching method. But the recognizing speed has always trouble. In this paper, the improvement of the general genetic algorithm-based face recognition system is proposed. Genetic algorithm (GA) has been considered as robust and global searching method. In this paper, the chromosomes generated by GA contain the information of the facial model, by which can we recognize it from an image. The purpose of the paper is to propose a practical method for face detection and recognition. Finally, the experimental results, the comparison to the traditional template matching method and some considerations are also given.

Keywords: face detection, face recognition, genetic algorithm, image processing, template matching

1. Introduction

If we search on the web or a conference proceeding about intelligent control, lots of papers and applications are presented. Among them, image processing and recognition occupy very large percentage. The higher the degree of intelligence is, the more important the image detection and recognition technology are.

For an intelligent control system, it is necessary to automatically acquire the information of the external world by sensors, to recognize its position and the surrounding situation. Camera is one of the most important sensors for computer vision.

For controlling an intelligent system (autonomous mobile vehicle, robot, etc), the most important part is the control strategy. But before automatically controlling it to move, image recognition is needed. That is to say, the robot endeavors to find out what is in an image (environment of the robot) taken by the camera: traffic signs, obstacles or guidelines, etc.

Object detection is an important step in the object recognition. Its reliability and time-response have a major influence on the performance and usability of the whole object recognition system [1]. The template matching method is a practicable and reasonable way used to the object detection [2]. And this paper gives the improvement of the general template matching method.

Also, to search an image, lots of data need to be processed. GA has been considered as robust and global searching method (although it is said that GA is not used for finding the global optimization) [3]. In this paper, the chromosomes generated by GA contain the information of the image data, and the genetic and evolution operations are used to obtain the best match in an image to the template. Searching the best match is the goal of the paper.

This thought emerged from the features of GA and the need of easily and quickly recognizing the face of people by an intelligent system. The single concept and feature of image processing and GA will not be introduced in the paper, for lots of books and papers have been written about them.

In this paper, section 2 introduces the general method of pattern recognition. The theory and GA encoding, experimental setting in this paper will be given. In section 3, the experiment and the analysis are addressed. Conclusions will be given in section 4.

2. Theory and experimental setting

For an image recognition system, first, the interested part that has special features has to be detected from the original image. This is called object detection. And after that, this part will be compared to the template to see if it resembles to the template or not, which is called object recognition. For example, if we want to find a special person in an image, first, we have to detect people in the image, and then recognize him/her whether is the interested person or not. The whole procedure is shown in Fig.1.

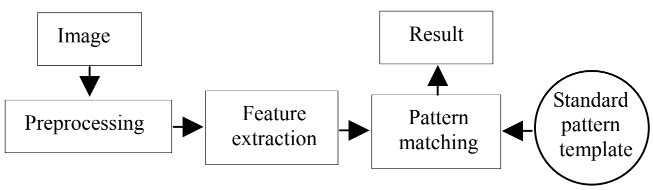

Fig.1 Object recognition system

One of the oldest techniques of pattern recognition is matching filtering [4], which allows the computation of a measure of the similarity between an image $f(x, y)$ and a template $h(x, y)$. Define the mean-squared distance

$$d_{fh}^2 = \iint \{f(x,y) - h(x,y)\}^2 \, dxdy \qquad (1)$$

and $R_{fh} = \iint f(x,y)h(x,y)dxdy$, if the image and template are normalized by

$$\iint f^2(x,y)dxdy = \iint h^2(x,y)dxdy \tag{2}$$

then

$$\begin{aligned} d_{fh}^2 &= \iint \{f(x,y) - h(x,y)\}^2 dxdy \\ &= \iint \{f^2(x,y) - 2f(x,y)h(x,y) + h^2(x,y)\}dxdy \quad (3) \\ &= 2\iint f^2(x,y)dxdy - 2R_{fh} \end{aligned}$$

In the right hand of above equation, the first term is constant, thus R_{fh} can measure the least-squared similarity between the image and template [5]. If R_{fh} is a large value, then the image is judged to match the template. If R_{fh} is less than a pre-selected threshold, either rejecting this recognition or creating a new class, which means the similarity between the image and the current template is not satisfied.

Statistical object recognition involves locating and isolating the targets from an image, and then identifying them by statistical decision theory. The comparable experiment of template matching method is given in section 3.

2.1 Genetic encoding

As introduced above, the chromosomes generated by GA contain the information of image data, so the first step is to encode the image data into a binary string [6]. The parameters of the center of face (x, y), the rate of scale to satisfy eqn.(2), and the rotating angle θ are encoded into the elements of gene. Some important parameters of GA used in this paper are given in Table 1 and the searching field is in Table 2.

Table 1 Some GA parameters

Source	Files of the image and template
Fields	$x, y, rate, \ \theta$
Generations	Max = 300 (the stopping criterion)
Population Size	200
Reproduction (selection)	P_r of the best individuals will be selected to survive. The remained (1-P_r) will be treated by the genetic operators (crossover and mutation)
Crossover	Offspring is produced from parents by exchanging their genes at the crossover point, the ratio is P_c
Mutation	Produce spontaneous random changes in various chroms. General random change method at the rate of P_m

Table 2 Settings for the experiment

x	8 bits
y	8 bits
$rate$	8 bits
θ	8 bits
P_r	0.6
P_c	0.5
P_m	0.01

As shown in Table 2, one chromosome contains 4 bytes: the coordinate (x, y) of the center of the template, the rate of scale and the angle θ of rotation.

2.2 Experimental setting

The experiment is done by firstly given two files, the original image file and the template file. By searching the image file, GA is used to find whether in the image there is the object of template or not. If the answer is YES, then in the original image the result gives the coordinate of it, the rate of scale and the rotating angle to the template.

And for comparison, the general template matching method is also presented [7]. The executive time shows the effectiveness of the GA-based recognition method.

Fig.2 and Fig.3 are the original images and the templates for the experiment. The values are the width× height pixels of the image.

In Fig.2, three images are presented, the content and the size of which are different. Fig.2(a) has two faces, Fig.2(b) gives the face that has the angle to the perpendicular. The person in Fig.2(c) wears the hat, and the background is more complicate than (a) and (b).

(a) 238×170 (b) 185×196 (c) 275×225

Fig.2 Three original images

(a) template-1 62×62 (b) template-2 60×64

Fig.3 Templates for matching

The two templates in Fig.3 are not extracted from only one image. For the common use, the template should be extracted as the average of several feature images. In Fig.4, the template (a)-0 is generated from (a)-1, (a)-2 and (a)-3, which is the average value of the gray levels from those three models. The same is also for (b)-0.

(a)-1 (a)-2 (a)-3 → (a)-0

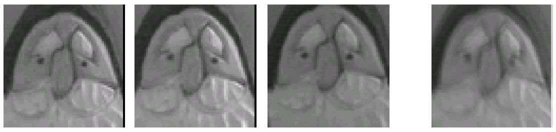

(b)-1 (b)-2 (b)-3 → (b)-0

Fig.4 Generation of template

3. Experiment and comparison

The genetic operations and GA parameters are presented in Table 1 and Table 2. The fitness is defined in eqn(4).

$$fitness = \sum_{(x,y)\in R} \left| f(x, y, rate, \theta) - template(x, y) \right| \tag{4}$$

In eqn(4), *template*(*x*, *y*) is the gray level of the coordinate (x, y) in the template image file. *f*(*x*, *y*, *rate*, *θ*) is the gray level in the original image file, the coordinate of which is calculated from (x, y) by translation, change of scale and rotation of the template file. The field *R* is the whole region of the template.

The maximum generation is made 300, and the threshold of the matching rate is set to 0.9 [6]. That is to say, if within 300 generations the matching rate can reach 0.9, then it is said that the template is found in the original image (the template is matched to the original image within the threshold). Otherwise the result gives the best match until the GA is trained to 300 generations.

The results of the GA-based face recognition are given in Fig.5 and Table 3. Fig.5(a), (c) and (d) are searched to match to the template of Fig.3(a), while Fig.5(b) is matched to Fig.3(b).

In Fig.5, (a) and (b) reach the matching rate 0.9 within 300 generations, while (c) and (d) cannot reach the matching rate 0.9 within 300 generations, but the best match is given in Table 3.

In the images (a), (b) and (c) of Fig.5, we obtain that the result can match the template well. The coordinate (x, y), the rate of scale and the angle of rotation can be calculated correctly. But for Fig.5(d), the result is not satisfied.

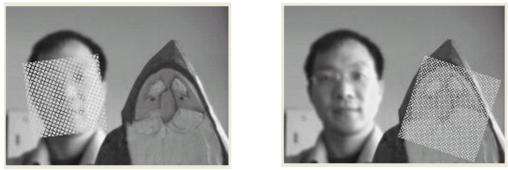

(a) (b)

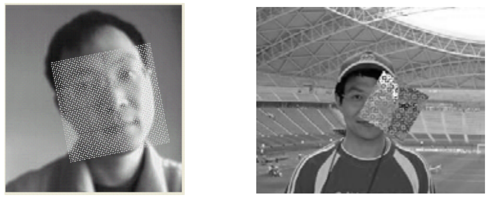

(c) (d)

Fig.5 Result of searching by GA

Table 3 Results of searching by GA

Image in Fig.4	Explanation
(a)	Original image is Fig.2(a), template is Fig.3(a).
	The 18th generation gives the result, fitness = 0.916591, time = 2second. (x, y) = (64, 97), rate = 1.31, θ = 353°
(b)	Original image is Fig.2(a), template is Fig.3(b).
	The 2nd generation gives the result, fitness = 0.901470, time = 0second. (x, y) = (179, 112), rate = 1.45, θ = 18°
(c)	Original image is Fig.2(b), template is Fig.3(a).
	The 300th generation gives the result, fitness = 0.889581, time = 39second. (x, y) = (111, 103), rate = 1.72, θ = 349°
(d)	Original image is Fig.2(c), template is Fig.3(a).
	The 300th generation gives the result, fitness = 0.832722, time = 39second. (x, y) = (165, 120), rate = 1.00, θ = 30°

The reasons is that (i) the template Fig.3(a) cannot represent the recognized face commonly. That is to say, although the person to be recognized is the same, the template cannot give all the features for this person at all time, in all conditions (the generation of template is shown in Fig.4). (ii) is that the algorithm itself has some problems. For example, by using GA-based recognition method, the settings of the searching field (*x*, *y*, *rate*, *θ*), the determination of the genetic operations, the selection and optimization of the fitness function are all important to the recognizing result.

For the purpose to compare the effect of the GA-based algorithm, the result of the general matching method [7] is also presented. From Fig.6, we see that although both the original image (the left-top image) and the template (the right-top image) are simplified by either decreasing or binarizing the image, the matching time is 1 minute and 22 seconds, cannot within several seconds. The recognized result is the left-bottom image in Fig.6.

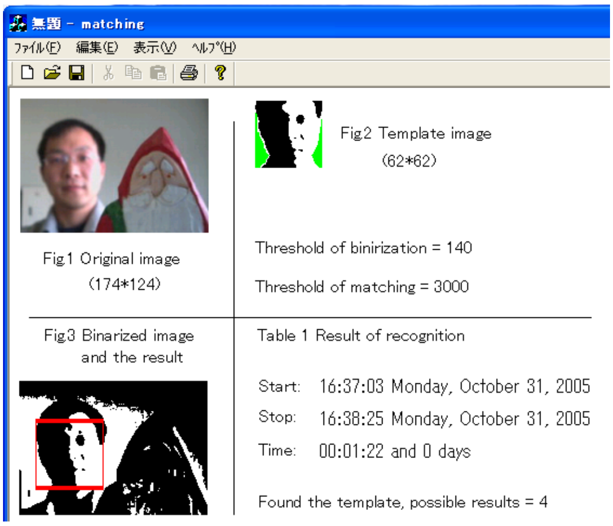

Fig.6 Result by the general matching method

4. Conclusions

In this paper, the GA-based image recognition method is tested and the comparison with the general matching method is presented.

As we know, GA starts with an initial set of random solutions called population. Each individual in the population is called chromosome, representing a solution to the problem. By stochastic search techniques based on the mechanism of nature selection and natural genetics, genetic operations (crossover and mutation) and evolution operation (selecting or rejecting) are used to search the best solution [8].

In this paper, the chromosomes generated by GA contain the information of the image, and we use the genetic operators to obtain the best match between the original image and the template. The parameters are the coordinate (x, y) of the center of the template, the rate of scale and the angle θ of rotation.

In fact, translation, scale and rotation are three main invariant moments in the field of pattern recognition [9]. But for the face recognition, the facial features are difficult to be extracted and calculated by the general pattern recognition theory and method [10]. Even these three main invariant moments will not be invariant because the facial expression is changed.

Thus the recognized result only gives the best matching one upper the predetermined threshold. Both the GA-based and the general template matching method are presented in the paper, and the comparison with the traditional pattern matching method shows that the recognizing is satisfied, although under some conditions the result is not very good (Fig.5(d)).

Based on the results of experiments in the paper, further work will be major emphasized to (i) optimizing the fields of GA chromosomes, (ii) improving the fitness function by adding some terms to it. These works are important and necessary to improve the GA-based face recognition system.

References

[1] M. Sugisaka, X. Fan: Development of a face recognition system for the liferobot, Proc. of the Seventh Int. Symp. on Artificial Life and Robotics, vol. 2, pp. 538-541, Oita, Japan (2002)

[2] K. R. Castleman: Digital image processing, Original edition published by Prentice Hall, Inc., a Simon & Schuster Company, Press of Tsinghua University, China (1998)

[3] H. Iba: Foundation of genetic algorithm – solution of mystic GA, Omu Press (1994) (in Japanese)

[4] K. Deguchi, I. Takahashi: Image-based simultaneous control of robot and target object motion by direct-image-interpretation, Proc. the 1999 IEEE/RSJ International Conf. of Intelligent Robot and System, vol. 1, pp. 375-380, Kyongju, Korea (1999)

[5] B. Jaehne: Digital image processing - concepts, algorithms, and scientific applications, The Third Edition, Springer-Verlag (1995)

[6] T. Agui, T. Nagao: Introduction to image processing using programming language C, Shoko-do press (2000) (in Japanese)

[7] Ishibashi's Studying Room of C++ (in Japanese). http://homepage3.nifty.com/ishidate/vcpp.htm

[8] M. Gen, R. Cheng: Genetic algorithms and engineering design, A wiley-Interscience Publication (1997)

[9] T. Agui, T. Nagao: Image processing and recognition, Syokoudou Press (1992) (in Japanese)

[10] H. Takimoto, Tasue Mitsukura, M. Fukumi, N. Akamatsu: A design of face detection system based on the feature extraction method, Proc. of 12th Symp. on Fazzy, Artificial Intelligence, Neural Networks and Computational Intelligence, pp.409-410, Saga, Japan (2002)

Research on Autonomous Mobile Robot for Visually Handicapped Humans

Takahiro NAKAMURA, Fengzhi DAI, Yutaka FUJIHARA
Department of Control Engineering,
Matsue National College of Technology

Abstract

In this paper, we propose the autonomous mobile robot by improving the electric wheelchair for elderly people. The research aims at automatically moving the robot to the destination by GPS and image processing. Beforehand, the robot gets the information of the destination by GPS, it automatically moves to the destination by comparing the information of place where it is now, with that of the destination. But the robot cannot automatically move safely in this case.

The self-position recognition is a very important function for the autonomous mobile robot. Under the indoor environment, the robot can easily detect the walls or the pillars to recognize the self-position with simple sensors. On the other hand, because in the outdoor environment there are fewer steady objects for recognizing the position of the robot, it is difficult for the robot to recognize the self-position and automatically move.

Thus we propose that the robot uses the braille blocks that were laid on the sidewalk. The braille blocks are equipment to lead visually handicapped humans to walk, and it is laid widely in urban area. The robot can automatically move safely on the sidewalk by driving along the braille blocks.

So the autonomous mobile robot uses not only the information of GPS but also the braille blocks that were laid on the sidewalk. The images of the braille blocks are processed by Hough transformation, and based on the data, the robot can arrive at the destination by fuzzy control. Furthermore, we will set up the base station to monitor the autonomous mobile robot with wireless LAN for safety drive. We will assist the robot from the base station to ensure the driver against danger.

1. Introduction

The visually handicapped humans can come and go freely in the place where they usually visit, but they cannot go to other place alone. Typically, the helpers are needed to help them. But such situations are big burden for both helpers and handicapped persons. In particular, it is said that mental burden of handicapped persons is larger. So we develop the autonomous mobile robot that is improved from the electric wheelchair for the elderly people [1][2][3].

The object of this study is to automatically navigate the robot to the destination by GPS and image processing. The robot previously gets the information of destination by GPS and automatically moves to the destination by comparing the information of the current place with that of the destination. But in the case of the urban area where the route of the autonomous mobile robot is limited, the robot cannot be navigated safely only by GPS data.

So the braille blocks that are laid widely in urban area are utilized to navigate the robot safely. The images of the braille blocks are processed by Hough transformation, and based on the data, the robot can arrive at the destination by fuzzy control. Furthermore, in order to assist the robot from the base station to ensure the driver against danger, the communication between the base station and the mobile robot by using the wireless LAN is also proposed in this paper.

2. Present state

2.1 The walking of the visually handicapped humans individually

Now, the visually handicapped persons can individually go out to walk by the helping of the care person, the white walking stick, the guide dog and the auxiliary device.

Walking with the care person gives the big burden to both the helpers and the handicapped persons themselves, especially for their mental burden. The visually handicapped persons must train themselves to walk safely with the white walking stick. However, the white walking sticks are mostly used to get the information of the road surface. But they are not enough to sense the conditions of the direction of movement. For example, when the visually handicapped persons use the white walking stick, they often bang against the car that is parked in the sidewalk of the road.

The guide dog is satisfied for the safety of a walk of the visually handicapped persons. But if the visually handicapped person says, "I want to go to the library", the guide dog cannot lead them to the destination [4].

2.2 The braille blocks

The braille blocks are the emblem to lead the visually handicapped humans to the destination and they are installed consecutively in the sidewalk.

The braille blocks consist of the inductive blocks and the admonitory blocks (in Fig.1). The inductive blocks are marshaled salient of long square. The admonitory blocks are marshaled salient of small circular form.

Their colors are yellow, and can be easily recognized by the amblyopic persons.

The inductive blocks are consecutively installed and show the route that the visually handicapped humans can walk on them. The admonitory blocks are installed at the branch point and the dead end of the inductive blocks, or the entrance of a building and so on.

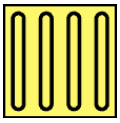

(a) The inductive blocks

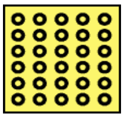

(b) The admonitory block

Fig.1 The braille blocks

3. The system of the autonomous mobile robot

3.1 Introduction of the mobile robot

The electric wheelchair that is developed by the SUZUKI company (Fig.2 (a)) is converted to the mobile robot by installing GPS, computer, CCD camera for image processing and other sensors for safety drive (Fig.2 (b)). By the Japanese traffic law, the electric wheelchair is treated as wheelchairs for the physically handicapped and is rated as walkers. Navigators do not need to have the driver's license. Therefore, anyone can drive it [5]. The specification of the electric wheelchair is as follows.

- Dimensions: 1170×660×1060[mm]
- Weight: 79kg
- Forward speed: 2～6km/h
- Reverse speed: 2km/h
- Drive system: Direct drive system with rear-wheel drive
- Braking system: Electromagnetic brake that uses motor dynamic braking
- Control system: Microcomputer variable speed electronic control unit for accelerator lever

(a) Before conversion

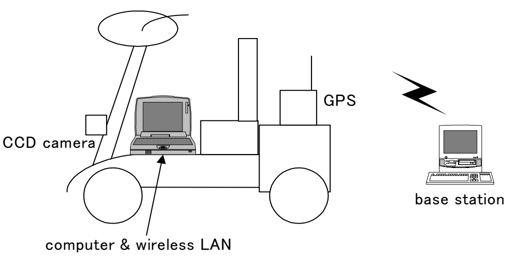

(b) After conversion

Fig.2 The electric wheelchair and improved mobile robot

3.2 Structure of the system

The structure of the mobile robot system developed in our study is showed in Fig.3.

The robot previously gets the information of destination by GPS and then automatically moves to the destination by comparing the information of the current place with that of the destination. At the same time, the images of the direction of robot movement taken from the CCD camera are processed by the computer mounted on the robot and the braille blocks can be recognized for navigation. In the image processing, the binarization, the thinning, the elimination of the isolated point and the edge detection are performed. After these procedures, the straight line of the forward direction is recognized by Hough translation.

The autonomous mobile robot can decide the controlled variable of both the speed regulation and the steering angle by the results of the recognition of the straight line using Hough translation. The speed is adjusted by the distance to the next moving point. The steering division uses the fuzzy rules to decide the controlled variables. When the DC motor moves, it detects the angle by a variable resistor and the value of the angle is fed back to the controller.

Furthermore, the wireless LAN is used by the robot in order to increase security and communicate to the base station for monitoring the mobile robot. If the person at the base station judges that there are some dangers to the robot from the monitoring image, he can directly control the robot via LAN to avoid the danger state of the robot.

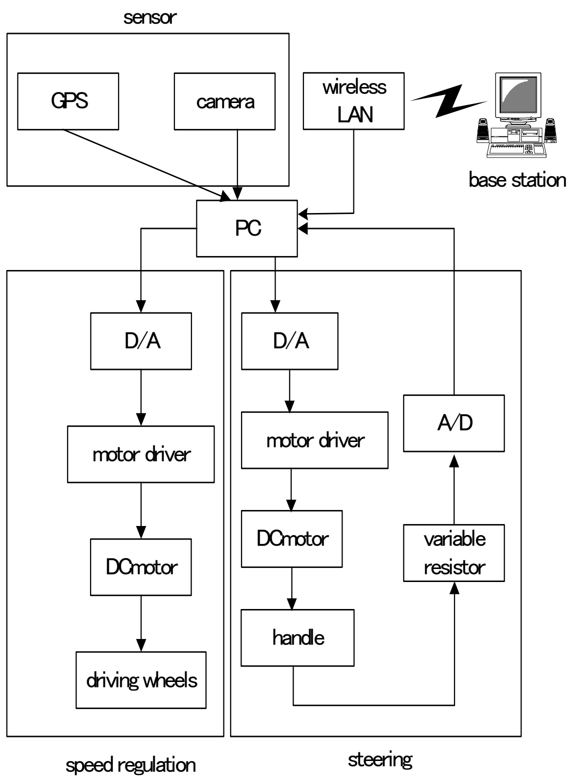

Fig.3 Structure of the system

3.3 Image processing

The flowchart of image processing is shown in Fig.4. First, the camera that is mounted on the autonomous mobile robot gets the image of the braille blocks on sidewalks. The image is processed by binarization and only yellow color is left to be recognized. The input image is shown in Fig.5 (a), and the binarized image is in Fig.5 (b).

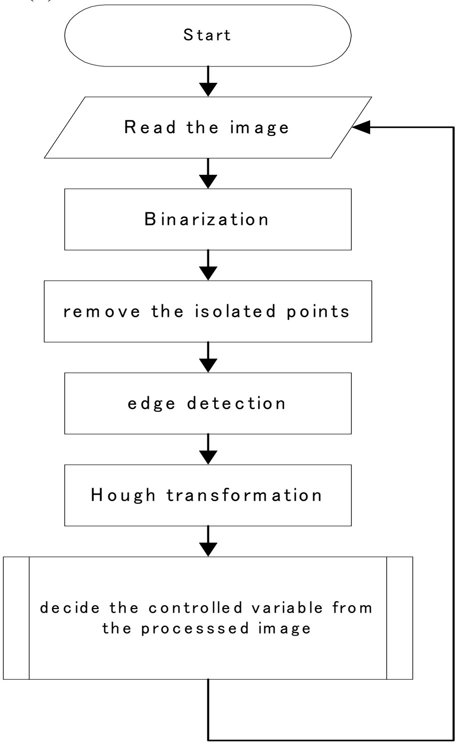

Fig.4 Flowchart of the image processing

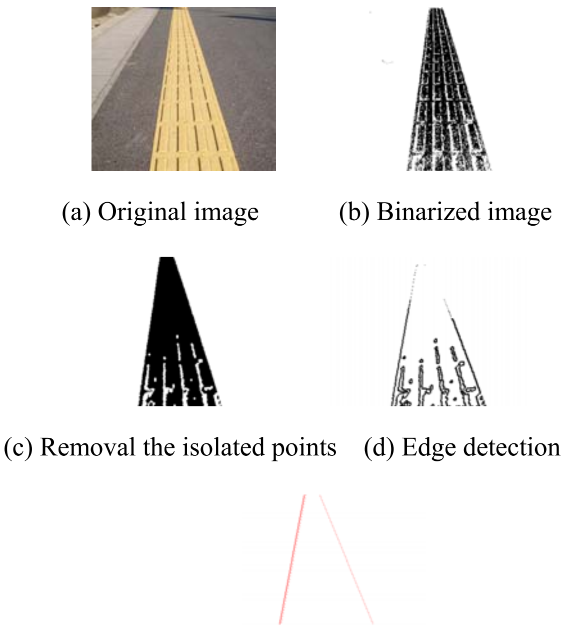

(a) Original image (b) Binarized image

(c) Removal the isolated points (d) Edge detection

(e) Hough transformation

Fig.5 Image processing

But only by this process, the isolated points remain in the image, which must be removed. The result is shown in Fig.5(c). After the removal, the edge should be detected, which is given by Fig.5 (d). This result is then processed by Hough transformation, and the outline of braille blocks is shown as two straight lines clearly, the result of which is given by Fig.5 (e).

3.4 Hough transformation

Hough transformation transforms the orthogonal coordinate of each pixel of the object into the polar coordinate system to recognize the input image.

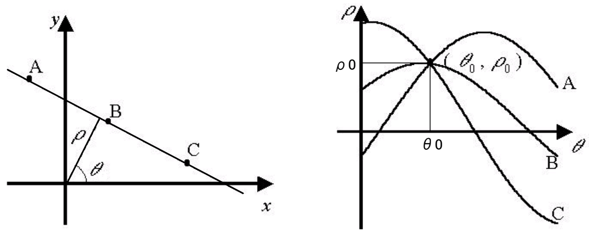

(a) XY-plane (b) ρ - θ plane

Fig.6 recognition of a straight line by Hough transformation

A straight line in the XY-plane shown in Fig. 6(a) is expressed by the equation (1) in polar coordinate.

$$\rho = x\cos\theta + y\sin\theta \tag{1}$$

Where,
ρ : The length from the origin to the straight line.
θ : The angle between the perpendicular line and the x axis.

When the point (x, y) of the orthogonal coordinates transforms to the polar coordinate, the point on the orthogonal coordinates correspond to the curve on ρ - θ plane. If a lot of points on orthogonal coordinates are translated , a lot of curves are drawn in the ρ - θ plane. The common point that the curves intersect can represent a straight line in the original x-y plane. The straight line can be expressed by the equations (2), (3) [6].

$$x = -\frac{\sin\theta}{\cos\theta}y + \frac{\rho}{\cos\theta} \tag{2}$$

$$y = -\frac{\cos\theta}{\sin\theta}x + \frac{\rho}{\sin\theta} \tag{3}$$

3.5 The decision of controlled variable for steering angle

Only by the straight line obtained from Hough transformation, it is still difficult for the robot to navigate accurately in every situation. For example, the robot is controlled to move according to the centerline of the braille blocks, but it often deviates from the centerline at the place of sharp curve or crossing point of a series of the braille blocks. Therefore, the calculation of the objective vector, or the target vector to move from the obtained features of the image is necessary to navigate the robot autonomously.

Several parameters such as the radius of curve, the velocity of the robot and so on are necessary to calculate the angle of the target vector. So we propose the navigation method that use the center of gravity of a straight line introduced by Hough transformation. The center of gravity can be easily obtained [7].

3.6 Derivation of angle of target vector

In Fig.7, the coordinate of target from the center of gravity of (x_1, y_1), (x_2, y_2) of two straight lines is calculated from the equation (4).

$$x_0 = (x_1 + x_2)/2, y_0 = (y_1 + y_2)/2 \qquad (4)$$

Then, the steering angle θ is calculated by the equation (5).

$$\theta = Tan^{-1}(YL - y_0)/(2x_0 - XL) \qquad (5)$$

By using some membership functions from these computational results, fuzzy rules can be applied to autonomously control the robot.

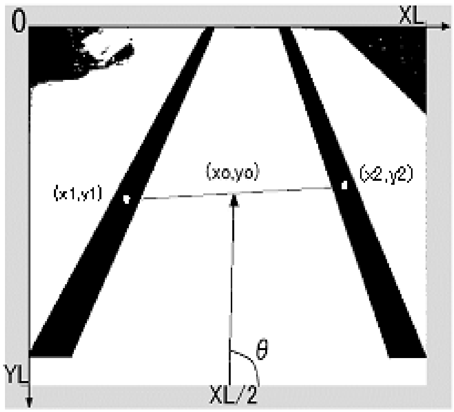

Fig.7 Derivation of angle of target vector

4. Fuzzy control

Fuzzy control to navigate the robot is used in this paper. Even if accurate mathematical models of system cannot be obtained and sensor data is uncertain or imprecise, the controlled variable can be decided with the knowledge that is accumulated from the past experience. We define the desirability function by the fuzzy rules of the form, IF A_i THEN B_i, where A_i denotes a fuzzy logic formula from fuzzy predicates, and B_i is a fuzzy set of controls. For example, when a car is driven through the hard curve, the fuzzy rule is expressed by "if curve is hard then speed down".

In this research, the steering angle of target vector that is decided from the braille blocks is obtained by the membership function that has five triangular peaks shown in Fig.8 [8][9].

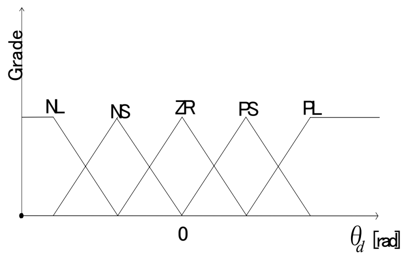

Fig.8 The membership function

5. Conclusions

In this paper, we propose the system of autonomous mobile robot for welfare with image processing and GPS. Now we are in the process of developing the robot. The structure of the whole system and the procedure of image processing are well explained and we have the plan to check that the robot can autonomously move to destination with safety and accuracy on the sidewalk of the urban area by the presented fuzzy rules.

References

[1] Tomoaki Yoshida, Akihiro Ohya, Shin'ichi Yuta: Autonomous Mobile Robot Navigation Using Braille Blocks in Outdoor Environment, The Robotics Society of Japan, Vol.22, No.4, pp.469-477, 2004

[2] Ikuko Yairi, Kentaro Kayama, Seiji Igi: Robotic Communication Terminals as a Mobility Support System for Elderly and Disabled People – Our Recent Research Progress and Plan for Practical Use, The 18th Annual Conference of the Japanese Society for Artificial Intelligence, 2004

[3] Koji Tokuda, Masanori Sugisaka, Mbaitiga Zacharie: Automatic Control of an Electric Vehicle using Visual Information, Proceeding of the Tenth International Symposium on Artificial Life and Robotics, Session of Mobile Vehicles - Ⅰ, 2005

[4] http://www.e-switch.jp/cats/nakai2.htm

[5] SUZUKI ET4E manual, Suzuki Motor Co

[6] Shinichi Murakami: Image Processing Engineering, University Press of Tokyo Denki university, 1996

[7] Takumi Kamioka, Yutaka Fujihara: Development of Tele-operational and Autonomous Rescue Robots, Proceedings of The 6th China – Japan International Conference on Industrial Management, pp.73-78, 2002

[8]Yutaka Fujihara, Takumi Kamioka, Nobuo Takahashi, Manabu Takao, Kazuhiro Uchimura, Fengzhi Dai, Hiroyuki Uchida: Development of the Autonomous Airship by Fuzzy Control, Proceedings of the Seventh International Conference on Industrial Management , pp. 183-190, 2004

[9] Fengzhi Dai, Yutaka Fujihara: Competitive Learning Algorithm for Fuzzy Rule Optimizing to a Mobile Vehicle, Proceedings of the Seventh International Conference on Industrial Management, pp. 172-176, 2004

The Eleventh International Symposium on Artificial Life and Robotics 2006 (AROB 11th'06),
B-con Plaza, Beppu, Oita, Japan, January 23-25, 2006

Walking orbit of biped robot by using the simulation

Koji UMEZAKI, Masanori SUGISAKA
Department of Electrical and Electronic Engineering, Oita University
700 Dannoharu, Oaza, Oita 870-1192 Japan
E-mail: msugi@cc.oita-u.ac.jp

Abstract

The movement robot is researched and developed by a lot of enterprises and research laboratories. Those robots are expected to cooperate with human and work in a dangerous place in blast furnace and all that of atomic is enumerated as a reason. The biped robot is expected for the reason of excellent mobility and to be possible to act even in the small space.

Then this research, the obit where the biped robot walks used and demands the simulation. This time, we consider transmission of position of ZMP and correcting value in forward walking.

1. Introduction

The multilegged movement robot is researched and developed by many enterprises and research laboratories. As the reason, as for the mulitilegged, it is raised that mobility in not flat ground is excellent compared with the wheeled movement robot. Those robots, it is expected to work cooperatively with work and human in a dangerous place such as in atomic blast furnaces.

Before, we generated operation by the biped robot with a servo motor But, those were problems the environment that can be operated by the difference of the influence of the friction of the back of the foot of the biped robot and the floor must be limited, else that position and those movement transitions of center of gravity and ZMP were not able to be understood.

Then, in this research, the position and movement transition of center of gravity and ZMP depict by using the simulation. Then, we examined the result.

2. Metaphysic

・ZMP(Zero Moment Point) [1]

It is a point of application when it substitute acting on one point with a normal element of the ground reaction that distributes the overall sole of feet. It is a point that the inertia force caused by gravity and the walking motion and the reaction force from ground equiponderates dynamically.

・Target ZMP [1]

Target ZMP is a point that put over effort force f acting on center of gravity, and cross the floor. If target ZMP has observed ZMP there, a target point is without the occurrence of overturning moment.

・Supporting leg polygon [1]

Supporting leg polygon is shown in Fig.1. This is the one that the parts that the foot grounded was close round so as not to become concave. As for ZMP, the area that can be operated because of the feature is limited within the area of the supporting leg polygon.]It

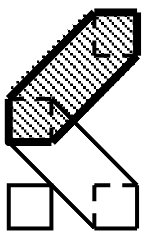

Fig.1 supporting leg polygon

is impossible to come off the motion when target ZMP is not in the supporting leg polygon. Observed ZMP is out of synchronization when target ZMP is outside of the supporting leg polygon. It's contemplated that biped robot topples down by generating the overturning moment.

・**Equation of model** [2][3]

The balance of axis of x element circumjacent based on center of gravity is shown in equation (1) and equation (2).

$$N_y = m(x_{cg} - x_{ZMP})(\ddot{z}_{cg} + g) - m(z_{cg} - z_{gnd})\ddot{x}_{cg} \quad (1)$$
$$N_x = m(y_{cg} - y_{ZMP})(\ddot{z}_{cg} + g) + m(z_{cg} - z_{gnd})\ddot{y}_{cg} \quad (2)$$

Here, we hypothecate the height of center of gravity to be constant. $\ddot{z}_{cg} = 0$

Therefore, there become equation (3) and equation (4).

$$\tilde{N}_y = mg(x_{cg} - x_{ZMP}) - m(z_{cg} - z_{gnd})\ddot{x}_{cg} \quad (3)$$
$$\tilde{N}_x = mg(y_{cg} - y_{ZMP}) + m(z_{cg} - z_{gnd})\ddot{y}_{cg} \quad (4)$$

$[N_x, N_y, N_z]^T$: Moment that acts on center of gravity circumjacent

$[x_{cg}, y_{cg}, z_{cg}]^T$: Position of center of gravity

$[x_{ZMP}, y_{ZMP}, z_{ZMP}]^T$: Position of ZMP

・**Planned obit** [2][3]

The orbit generation run in the way hereinafter prescribed.

1. We plan the landing position of sole of foot and timing.
2. We settle on No.1 as required to comply with position of center of gravity.
3. We settle on No.2 in accordance with position of the whole body.

The planned orbit of center of gravity is shown in Fig.2. The orbit of target ZMP is shown in Fig.3.

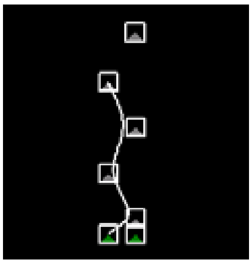

Fig.2 the planned orbit of center of gravity

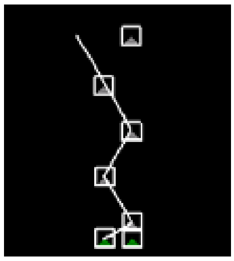

Fig.3 the planned orbit of target ZMP

We take notice to the position of center of gravity, it moves smoothly. We take notice to the position of ZMP, it moves when center of gravity reaches on the supporting leg. Moreover, the planned orbit of center of gravity stops on the supporting leg. However, the orbit of target ZMP has come off from the area of the supporting leg polygon. The purpose of this is to assume that the sole of foot of the model has adsorbed the floor when we calculated target ZMP by the simulation.

3. Setting of simulation

Application programming language

: Borland C++ Builder5

Model : weigh 3.0[kg]

length of leg 0.29[m]

length of thigh 0.145[m]

length of shin 0.155[m]

Degree of freedom : Hip joint 3DOF

Knee joint 1DOF

Ankle joint 2DOF

Option

Necessary time for one step 0.5[s]

Rate of double support phase in one step 0.2

The maximum acceleration 0.5[m/s^2]

Distance from target orbit to landing position of foot 0.03[m]

4. Result of simulation

The change in target ZMP, observed ZMP and correcting value when forward walking is shown from Fig.4 in Fig.9. The x element is shown from Fig.4 in Fig.6 (Back and forth movement). The y element is shown from Fig.7 in Fig.9 (Right and left movement).

The comprising item of motion is shown. First, start up a program. Next, it is state of rest for tow seconds. Afterward, to do the forward walking, we keep pushing the keyboard of five seconds. We release the keyboard. We stop the program in three seconds later. The model shifts from the state of both feet earth to the one feet earth with the left leg as for a reason that was state of rest for two seconds in the start immediately after beginning. Therefore, the correction is done. Then, it is because it was considered that this correcting value become 0. The reason where the keyboard is separated and done the state of rest of the program in three seconds is moreover that it decelerates gradually in no rest after motion separate the keyboard soon, and it enters the state of rest.

We think about correcting value. Correcting value Ux of x element is generated with start and finish of motion. In these, the inertia force caused when the state of rest one is moved and when do the state of rest the moving one is causes. Correcting value Uy of y element is generated with start of motion. In this, the inertia force when shifting from the state of rest in the state of motion is a cause as well as the case of x element. Moreover, the similar amount of correction shape of waves has been repeatedly generated while both x element and y element are walking. A constant speed can be said that will repeat by these while walking thought is done the correction.

We think from Fig.4 and Fig.7 about observed ZMP. The amount of the correcting value is extremely small

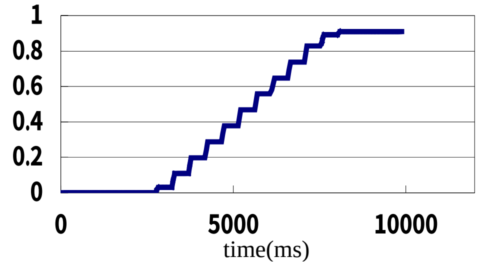

Fig.4 target ZMP (x element)

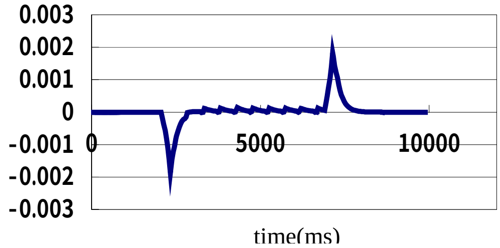

Fig.5 correcting value (x element)

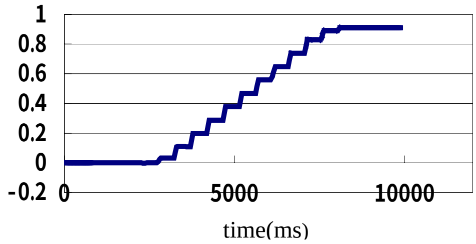

Fig.6 observed ZMP (x element)

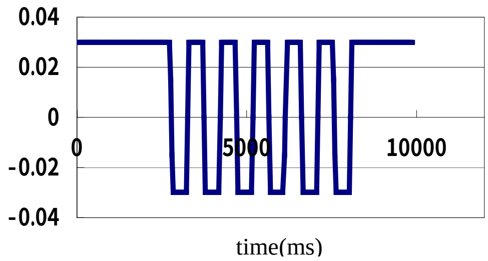

Fig.7 target ZMP (y element)

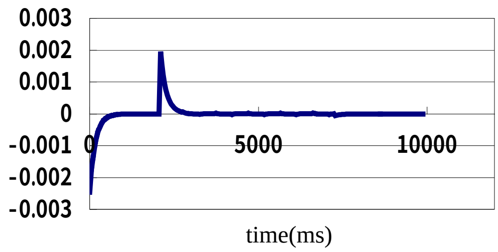

Fig.8 correcting value (y element)

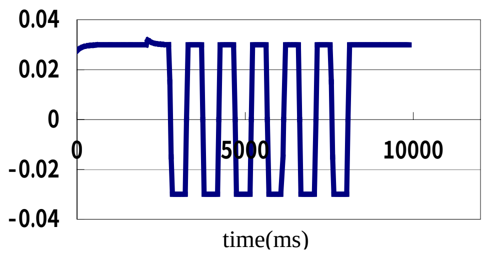

Fig.9 observed ZMP (y element)

compared with the amount of the change of ZMP and it is not influenced in x element. It understands influenced in y element thought it is a little at the beginning of motion.

5. Discussion

This time, we described the orbit of ZMP in the forward walking. The correction by inertia force is done to start and finish of motion in x element as understood from the simulation result. In y element, the correction is done by inertia force at the beginning of motion. These correcting values don't become 0. However, we think that secure walking motion can be done by less correcting value.

Reference

[1] http://www.ops.dit.ne.jp/~manava/robot
[2] http://rogiken.org/newmanoid/index.html
[3] T.Shinohara, "Real-time orbit generation of biped robot", 2001

Motion trace through head control

Eiji GOUBARU Masanori SUGISAKA
Department of Electrical and Electric Engineering, Oita University
700 Dannoharu Oita 870-1192 Japan.
E-mail: msugi@cc.oita-u.ac.jp

Abstract

Recent years, researches about motion trace moving object is extensively studied. If we can motion trace-moving object, we can apply the skills of automotive control and so on.

For example, if obstacle avoidance of moving object instead of obstacle avoidance of the static object becomes possible, the control becomes possible as for a more complex situation.

Facial recognition was researched in my laboratory, but, this research is weak of change in light, so that my main research improve that and to motion trace through head control of mobile robot.

1. Introduction

Recent years, the introduction of robot was bean considered in various fields. Various functions were bean required and the robot use was expanded. One of the functions requires environmental recognition and avoidance of an obstacle. In order to develop such robot, this laboratory, for some time, has mainly respond to the field of welfare and nursing. A mobile recognition robot has been researched and developed [1][2][3].

Researches about motion trace moving object is extensively studied. In this research, we used our laboratory robot. Image import from CCD camera, we compute feature point and center point to track moving object, and implement motion control of the head.

2. Experiment System

The robot which is being used in this research was manufactured by incorporated company DENKEN in 2000.The figure is shown in Fig.1.It consists of 2 drive 2 caster (2DC2W) systems.

The mobile robot is equipped on the right and left with the driving wheel, auxiliary caster rings at the front and back, a driving wheel on either side rotates by DC motor. Equipped with the rotary encoder of resolution 80 (Pulse Per Resolution) beside the driving wheel, and counting the number of pulses, the right-and-left independence can be achieved and a wheel can be controlled.

The difference in the rotation speed of a right-and-left driving wheel performs a steering function. The CCD camera (EVI-G20: Sony) is carried by the height of about 130 [mm] at 55 degrees of perpendicular directions at the head. The picture obtained from the camera is taken in by the memory on an image-processing board (FDM-PCI3: FOTORON).

Fig. 1 View of The Mobile robot

3. Image Processing

3.1 Pixel Skipping

When the size of image is 300 by 300 [pixel], it is difficult to implement in real time processing, when the size of picture is small, moving object will be not detected.

In order to make realize real time processing, image processing time must be shortened. Therefore, by setting the area of pixel which to be removed and to be taken the image is processing again by re-sizing and showing only the taken pixel area. In this research, re-sizing of image is 30 by 30. Fig. 2 shows that gray color is taken pixel area.

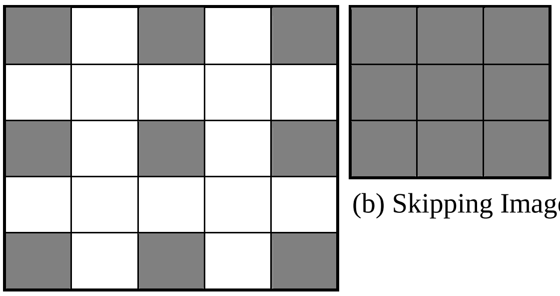

(a) Original Image (b) Skipping Image

Fig. 2 Pixel Skipping

3.2 Conversion From RGB To HSI

The image is taken in from a CCD camera; it is a picture expressed with a total of 24 bits of 8 bits each of RGB.

Then, in order to treat the feature from a picture independently as much as possible, the following equation performs HSI conversion of the hue, saturation and intensity. Each of R, G and B is standardized to take values between 0 and 1, with a maximum total intensity of 1.

$$I=(R + G + B)/3 \quad (1)$$

$$S=1-\min\{R,G,B\}/I \quad (2)$$

$$H=\arccos\{(P - W)*(R - W) /[|P - W||R - W|] \quad (3)$$

Let P be the point as shown in Fig. 3.

Fig.3 shows the triangle of points(r,g,b) =(R/(R+G+B),G/(R+G+B),B/(R+G+B)) that satisfy r + g + b = 1. The center point W has coordinates (1/3,1/3,1/3). We can find the angle H = for any point P on the triangle by the geometry of the triangle. Hue is a value between 0 and 360 [4].

In order to improve the threshold value, HSI value is corrected from the HSI image, then conversion from RGB to HSI is performed. After the conversion is performed. The threshold value of HSI value is finalized.

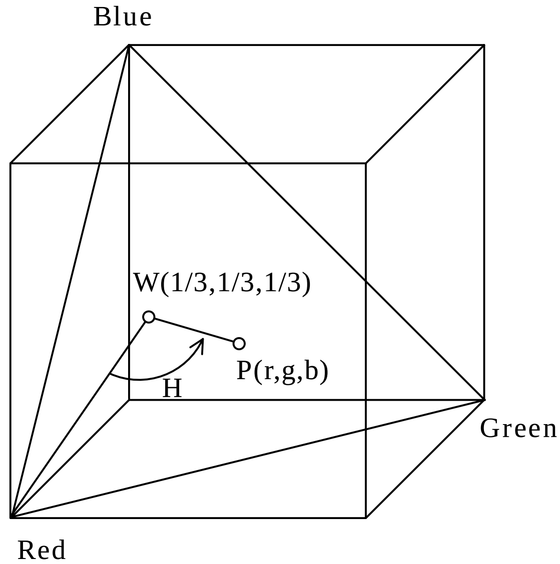

Fig. 3 A slice of the color cube

However, if HSI value is not threshold area, the camera will not recognize the object. As the first step, we change the hue value to make RGB relational expression.

3.3 Labeling Technique

The label represents number. The number, which represents value from 0 to 255, is boundary value. The processed image is labeled separate boundary value. Labeling-propagation processing by using raster scanning is shown in Fig. 4. Fig. 4 shows that the label represents by using alphabet value. As a result, characteristics of the moving object are calculated.

	A				1	
	1				1	
	1				1	
	1				1	
	1	1	1	1	1	
		1	1	1		

(a) Labeling Start

	A				A	
	A				A	
	A				A	
	A				A	
	A	A	A	A	A	
		B	B	B		

(b) Labeling End

Fig. 4 labeling-propagation processing by using raster scanning

4. Motion Detect Experiment

Motion detect experiment was actual conducted in the environment. Tracking moving object motion trace using red circle mark is carried out. After the red circle mark is detected, the head of the robot will move following the direction of the red circle mark movement. As the first step of processing is pixel skipping, second step is conversion from RGB to HSI and third step is labeling. The green point of the image (c) is shown in Fig. 5 is center of circle.

(a) Original Image

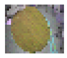

(b) Skipping Image

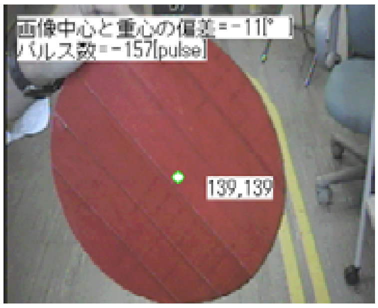

(c) Result Image

Fig. 5 Motion Detect Process

Since the image (c) is shown in Fig. 5, center of the circle is calculated. Therefore, head of the robot rotate to center of the circle. However, moving object is difficult to detect in strong light. When moving object and other object are similar saturation, other object is detected, too.

5. Conclusions

In this research, we are able to improve threshold in light. However, moving object is difficult to detect in strong light. When moving object and other object are similar saturation, other object is detected, too. Therefore, we would like to improve than this research in strong light and weak light, and we would like to consider about occlusion.

References

[1]Syuiti Otsu, Masanori Sugisaka : Research on the environmental recognition in a mobile robot , Oita University Graduate School Master Paper(2003)

[2]Syohei Kuriyama, Masanori Sugisaka : Development of the mobile robot run system using dead reckoning and vision information , Oita University Graduate School Master Paper(2003)

[3]Toshio Maeyama , Masanori Sugisaka : The

obstacle avoidance run in the mobile robot using the CCD camera, Oita University Graduate School Master Paper(2002)
[4] http://www.cse.unr.edu/~looney/cs674/ch6html.htm Chapter 6. Processing Color Images

The Eleventh International Symposium on Artificial Life and Robotics 2006 (AROB 11th'06),
B-con Plaza, Beppu, Oita, Japan, January 23-25, 2006

Characteristic measurement of artificial muscle

Satoshi ICHIKAWA Masanori SUGISAKA

Department of Electrical and Electric Engineering, Oita University

700 Dannoharu Oita 870-1192 Japan.

E-mail: msugi@cc.oita-u.ac.jp

Abstract

Recent years, artificial muscle is researched as a wearable actuator that a user can use in comfort. Therefore, we research the support equipment by using the artificial muscle. In this research, we made an artificial muscular robot. And, we measured the characteristic of each artificial muscle. As a result, we were able to obtain the expansion and contraction characteristic of the artificial muscle.

1. Introduction

Various commodities that support the senior physically and psychologically appear by the coming of the aged society. Many of them are equipped directly by the user. As for such equipment, physical safety and a psychological sense of security are requested.

To secure physical safety and a psychological sense of security, the following are needed.

（１）Even if controlling becomes impossible, it doesn't become a trouble.

（２）It is small and light. (The senior citizen can easily carry possession.)

（３） It flexibly fits the human body.

（４） No operation sound.

Recently, the artificial muscle is paid to attention as a wearable actuator that can be equipped the senior being relieved.

Therefore, we research the support equipment by using the artificial muscle.

In this research, we made an artificial muscular robot. And, we measured the characteristic of each artificial muscle.

２． Artificial muscle

There are various kinds of artificial muscles. They are shown in the following.

・Actuator that used polymeric material

・Actuator that used shape-memory material

・Actuator using electrostatic power

・Actuator that used air pressure

In this research, the air actuator use as a suitable actuator for the support equipment that the user equips, the balance of the generative force and the contraction percentage is good (It is possible to adjust it by the design concerning the air pressure) and, the viscoelasticity characteristic is similar to the muscle.

The McKibben type artificial muscle used by this research has structure that wrapped the rubber tube by a mesh of a net plastic fiber, and fixed both ends.

Pattern diagrams are shown in Fig.1. It expands radically when pressurizing it in an inside rubber tube as shown in Fig.2, and power to constrict axially is generated. If the state before pressurizing air pressure at artificial muscles is set to 100, after the maximum pressurization will be set to 70.

The artificial muscle used from this by this research has the expansion and contraction rate of 30%.

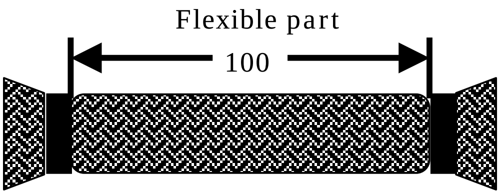

Fig.1 Pattern diagrams before artificial muscle is pressurized

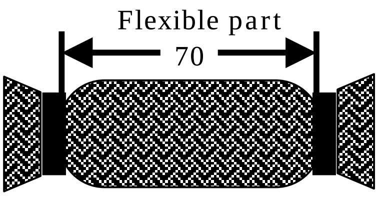

Fig.2 Pattern diagrams after artificial muscle is pressurized

3. artificial muscular robot

The model chart of an artificial muscular robot is shown in Fig.3.

The frame of the robot is wooden, and it has articulatio coxae, the articulatio genus, and the ankle joint. Articulatio coxae and the ankle joint are made from the articulatio spheroidea. The articulatio genus is made from the hinge joint. The number of Fig.3 expresses arrangement of artificial muscles. Each artificial muscle does the same role as person's muscle.

①：long peroneal muscle, short peroneal muscle （125mm）

②：anterior tibial muscle, posterior tibial muscle （125mm）

③：tibialis anterior（245mm）

④：musculus triceps surae（400mm）

⑤：musculus quadriceps femoris（330mm）

⑥：hamstrings（330mm）

⑦：gluteus maximus（305mm）

⑧：musculus iliopsoas（305mm）

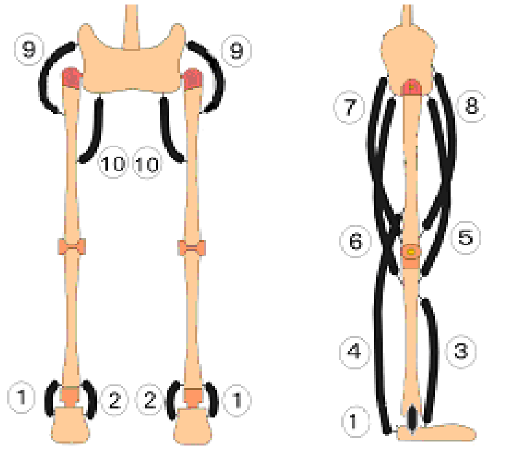

（1） elevational view （2） left side view

Fig.3 Pattern diagrams of artificial muscular robot

4. experimental apparatus

The outline chart of the apparatus used by this research is shown in Fig.4.The air tube of the artificial muscle and the compress air supply tubes from the air compressor are connected with the air pressure controller. The control signal from the computer is given to the air pressure controller, and the artificial muscle can be expanded and contracted freely.

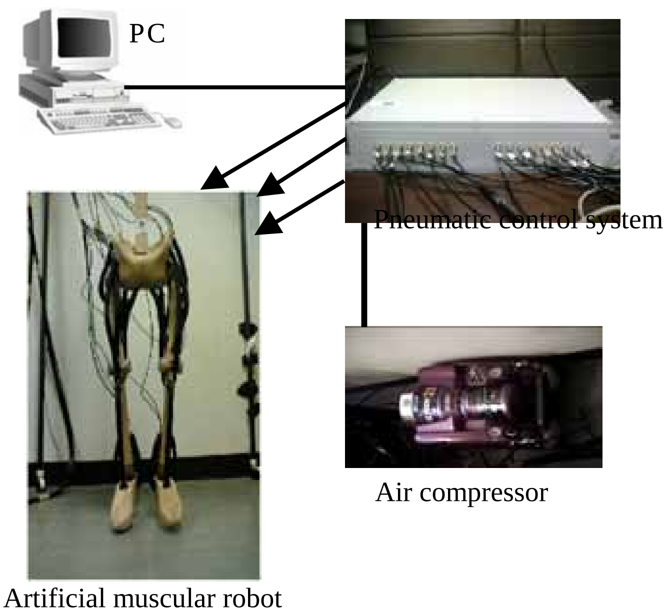

Fig.4 Experiment device outline chart

5. Expansion and contraction characteristic measurement

The artificial muscle with different two lengths is used (225mm, 450mm). First of all, the load is not put on the artificial muscle and constant air pressure is injected. The measurement result is shown in Fig.5 and Fig.6.

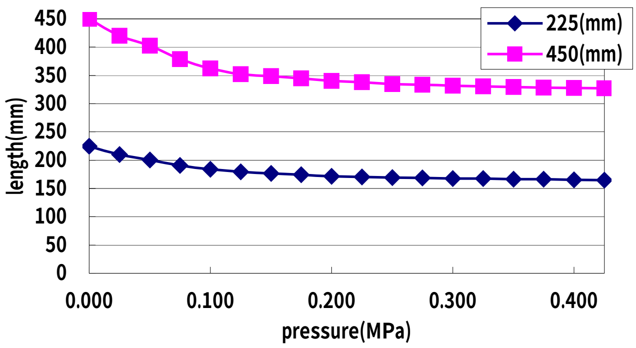

Fig.5 pressure(Mpa)—length(mm)

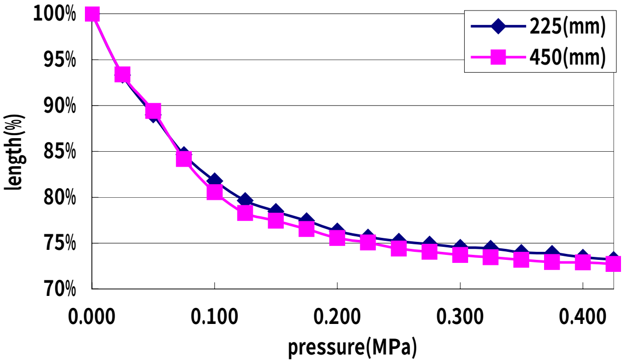

Fig.6 pressure(Mpa)—length(%)

Next, the load is not put on two artificial muscles and constant air pressure is exhausted. The measurement result is shown in Fig.7 and Fig.8.

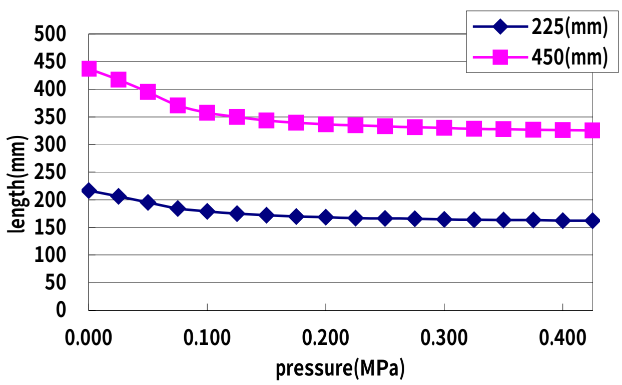

Fig.7 pressure (MPa)—length (mm)

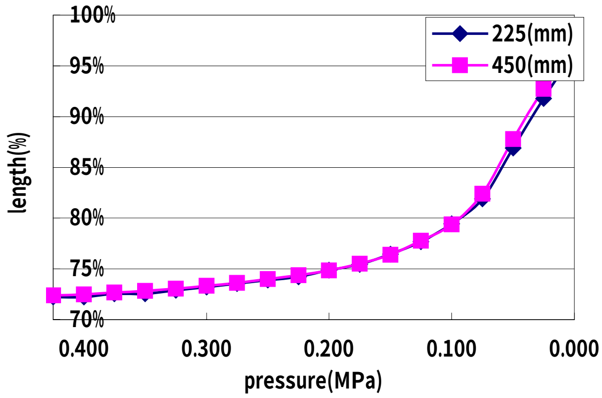

Fig.8 pressure (MPa)—length (%)

These are collectively shown in Fig.9.

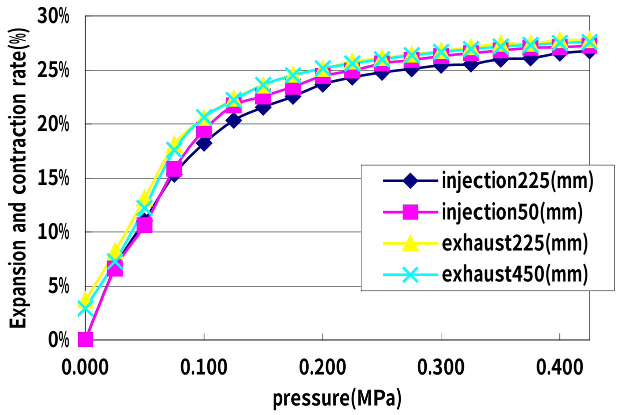

Fig.9 Expansion and contraction characteristic chart of no load

Injection and exhaust in the same length showed the characteristic with a different each curve (Fig.9).

As this cause, it was thought that elastic modification of the rubber tube that is the material of artificial muscles had influenced.

To this verification, 500g loads were hung on artificial muscles, and the expansion and contraction characteristic was measured. The result is shown in Fig.10.

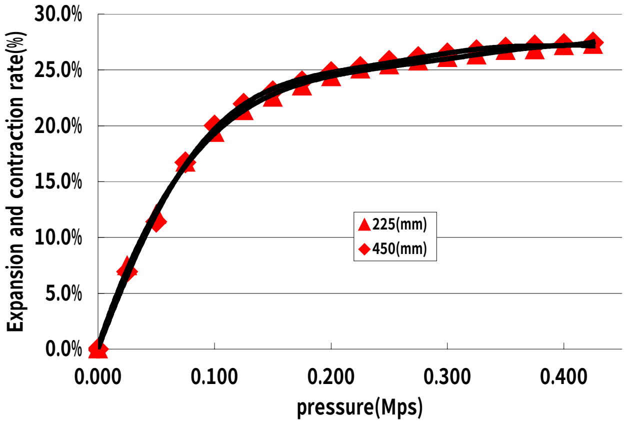

Fig.10 Expansion and contraction characteristic chart of load 500g

From Fig.10, if a certain amount of load was hung on artificial muscles, the influence of hysteresis is improvable.

６． Conclusion

In this research, an artificial muscular robot's creation and expansion and contraction characteristic measurement of artificial muscles were performed. However, there are many things that should still be measured, such as the expansion and contraction characteristic when hanging load. Therefore, other characteristics will be measured in the future. And, we move it to an artificial muscular robot by using the result.

References

[1] S.Douno,A.Saitou,R.Kuwata
“ Knit Structure SMA Actuator for Wearable Artificial Muscle Systems ”

[2]http://f-kawaraban.cside.com/find/kinoukaibou/muscles.htm

The Eleventh International Symposium on Artificial Life and Robotics 2006 (AROB 11th'06),
B-con Plaza, Beppu, Oita, Japan, January 23-25, 2006

Motion control of biped robot

Kensaku KABATA Masanori SUGISAKA
Department of Electrical and Electric Engineering, Oita University
700 Dannoharu Oita 870-1192 Japan.
E-mail: msugi@cc.oita-u.ac.jp

Abstract

Recent years, researches about biped robot are extensively studied. The vertical projection area of biped robot on the floor side is small, therefore, biped robot can move crooked road and narrow road.

So we think it is best system on life space that has many irregular ground.

In this paper, we made the robot with servomotor, and generate walking motion by application software.

1. Introduction

Recent years, researches about biped robot are extensively studied at the enterprise and the university. The purpose is human assistance, but it aims entertainment now.

Modern society is created for human to live easily. Therefore, to assist human, we need robot that is suitable for life space.

In the past research, wheel type robot was a mainstream. As a reason, the major factor is easy and steady to control. But, the fault is not able to move at irregular ground. The vertical projection area of biped robot on the floor side is small, therefore, biped robot can move crooked road and narrow road. So we think it is best system on life space that has many irregular ground.

In this research, we made the robot with servomotor, and generate walking operation by application software.

2. Specific of biped robot

Specific of biped robot are shown in Fig.1 and Table 1.

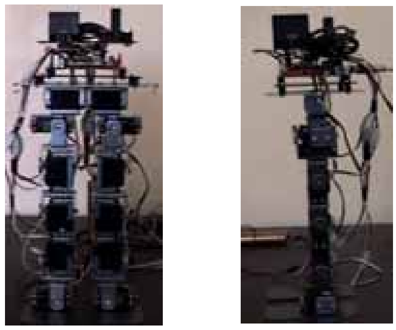

Fig.1 Photograph of biped robot

Table 1 Specific of biped robot

Actuator	Servomotor
Computer	Intel Pentium Ⅲ 487MHz
Mother board	HSWB-01
Application software	HSWB-01C
Size	Height 449[mm] × Width 200[mm] × Length 120[mm]
Degree of Freedom	Hip joint 3×2 Knee joint 1×2 Ankle joint 2×2

3. Experiment

3.1 The method of motion creation

We use HSWB-01C to control the biped robot. This application software is to control servomotor equipped in the biped robot.

First of all, we set home position to create motion of the biped robot. Next, we create the position of servomotor by the hour.

We can create various motions by the position of the servomotor. We set position by the trial and error.

In this paper, we use this method shown in Fig.2 to move biped robot.

STEP 1. Set home position.

STEP 2. Create the position of servomotor by the hour.

STEP 3. Transmit it to the robot.

STEP 4. Motion

Fig.2 Method of motion creation

3.2 Walking motion

Figure of biped robot's joints are shown in Fig.3.

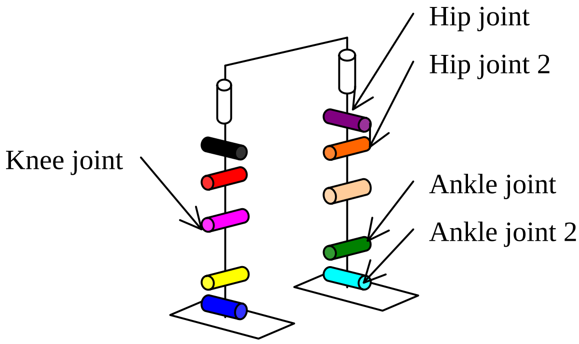

Fig.3 Figure of biped robot's joints

Angle change graph of Right-and-Left (Hip joint, Ankle joint 2) and Angle change graph of Backward-and-Forward (Hip joint 2, Knee joint, Ankle joint) are shown in Fig.4.

Position of servomotor (Fig.3) and the color of graph (Fig.4) are corresponding.

Fig.4 (a) shows the change in Right-and-Left. Fig.4 (b) shows the change in Backward-and -Forward.

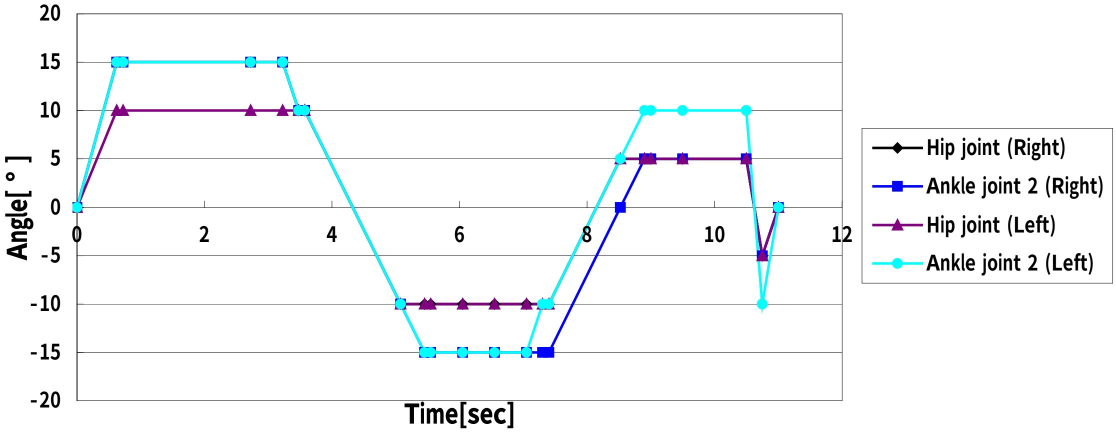

(a) Right-and-Left

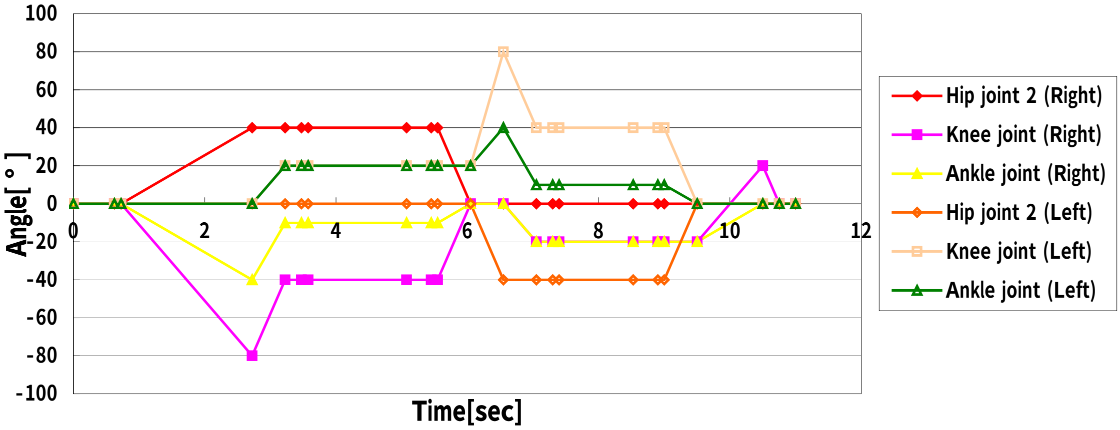

(b) Backward-and-Forward

Fig.4 Angle change graph

3.3 Comparing with human walking motion and robot walking motion

The rate of double stance phase and single stance phase in biped robot's walking motion are shown in Table 2. Double stance phase is a period standing with both legs, and switches axopodium. Single stance phase is a period standing with one leg, and goes ahead.

Table 2 Robot's walking cycle

Double stance phase	Single stance phase
41%	59%

The ratio of double stance phase and single stance phase in human's static walking is shown in Table 3.

The ratio of double stance phase and single stance phase in human's dynamic walking is shown in Table 4.

The result of this experiment is similar to the ratio of double stance phase and single stance phase in human's static walking.

Table 3 Human's walking cycle (static)

Double stance phase	Single stance phase
40%	60%

Table 4 Human's walking cycle (dynamic)

Double stance phase	Single stance phase
20%	80%

4. Conclusion

In this paper, we researched about biped robot's walking motion. We transmit instruction value to the robot, and generate walking motion by application software.

Comparing with human walking motion and robot walking motion, the ratio of this result is similar to the ratio of double stance phase and single stance phase in human's static walking.

But, we do not calculate ZMP (Zero Moment Point), so the walking motion is not proven steady. In the future, we make the simulation that uses ZMP.

Reference

[1] Nikkei mechanical・Nikkei design joint compilation, "Robolution", Nikkei BP Co. , P.40~41, 2001

[2] Ryuichi Nakamura, Hiroshi Saito, "Basic Kinematics", Ishiyaku publication Co.Ltd, P.334~342, 2002

The Eleventh International Symposium on Artificial Life and Robotics 2006 (AROB 11th'06),
B-con Plaza, Beppu, Oita, Japan, January 23-25, 2006

Intelligent Classification of Bill Money

Sigeru Omatu+ Toshihisa Kosaka++, and Masaru Teranisi+++
+Osaka Prefecture University, Sakai, Osaka 599-8531, Japan
omatu@cs.osakafu-u.ac.jp
++ Glory TD Himeji, Hyougo 670-8567 Japan
+++ Nara University of Education, Nara, 630-8528, Japan

Abstract

For the pattern classification problems the neuro-pattern recognition which is the pattern recognition based on the neural network approach has been paid an attention since it can classify various patterns like human beings. In this paper, we adopt the learning vector quantization (LVQ) method to classify the various money. The reasons to use the LVQ are that it can process the unsupervised classification and treat many input data with small computational burdens. We will construct the LVQ network to classify the Italian Liras. Compared with a conventional pattern matching technique, which has been adopted as a classification method, the proposed method has shown excellent classification results.

1. Introduction

Bill money classification by transaction machines has been important to make progress the office automation [1]. Since sizes of bills are different according to kinds of bills, the measurement data of bills include various variations. Human being can classify the bills correctly even if they are suffered from those variations such as rotation and shift. But usual pattern recognition using a conventional transaction machine cannot give us the correct classification result under such cases since the basic method is a pattern matching principle. Furthermore, the conventional pattern matching method requires many template patterns for many kinds of bills, which takes much time and needs much experience [1].

Recently, neural networks which are based on the biological mechanism of human brain have been focussed since they have intelligent pattern recognition ability [2]. In this paper, we will apply the neural network approach to classify the bill money under various conditions by using transaction machines. The learning vector quatization (LVQ) has been used to classify the bills since it can treat high dimensional input and has simple learning structure [3]. The LVQ network adopted here has 64x15 units in the input layer and many units at the output layer. The bills are Italian Liras of 8 kinds, 1,000, 2,000, 5,000, 10,000, 50,000 (new), 50,000 (old), 100,000 (new), 100,000 (old) Liras with four directions A,B,C, and D where A and B mean the normal direction and the upside down direction and C and D mean the reverse version of A and B. The simulation results show that the proposed method can produce the excellent classification results.

2. Competitive Neural Networks

We will explain the competitive neural networks that are used to classify the bill money. The structure of a LVQ competitive network is shown in Fig. 1. The input for the LVQ is bill money data where an original image consists of 128x64 pixels and the input data to the network is compressed as 64x15 pixels to decrease the computational load. The output of the network consists of the Italian Liras of 8 kinds, 1,000, 2,000, 5,000, 10,000, 50,000 (new), 50,000 (old), 100,000 (new), 100,000 (old) Liras with four directions A,B,C, and D where A and B mean the normal direction and the upside down direction and C and D mean the reverse version of A and B.

In the input layer the original bill money data are applied and all the units at the input layer are connected to all the neurons at the output layer with connection weight W_{ij}. W_{ij} denotes the connection weight from the unit j in the input layer to unit i in the output layer. The output layer will output only one neuron which is called winner neuron. The winner neuron is selected as the neuron with the minimum distance between an input vector and its connection weight vector. The connection weights W_{ij} are set by the random number at the beginning. Here, we set the mean vector of the cluster plus small random number. Then the following learning algorithm of the connection weight vector is used.

LVQ algorithm

Step 1. Find the unit c at the output layer which has the minimum distance from the input data $\mathbf{x}$ (t)

$$\|\mathbf{x}(t) - \mathbf{W}_c\| = \min_i \|\mathbf{x}(t) - \mathbf{W}_i\|$$

where ‖ ‖ denotes the Euclidean norm and t denotes the iteration time.

Step 2. If the input **x** (t) belongs to Category c, then

$$\mathbf{w}_c(t+1) = \mathbf{w}_c(t) + \alpha(t)(\mathbf{x}(t) - \mathbf{w}_c(t))$$

$$\mathbf{w}_i(t+1) = \mathbf{w}_i(t)\ , \quad i \neq c$$

and if the input **x** (t) belongs to the other Category j (j ≠ c), then

$$\mathbf{w}_c(t+1) = \mathbf{w}_c(t) - \alpha(t)(\mathbf{x}(t) - \mathbf{w}_c(t))$$

$$\mathbf{w}_i(t+1) = \mathbf{w}_i(t)\ , \quad i \neq c$$

where $\alpha(t)$ is a positive function and denotes learning rate.

In the usual LVQ $\alpha(t)$ is given by

$$\alpha(t) = \alpha_0(1 - \frac{t}{T})$$

where (0< α_0 <1) is a positive and T is a total number of learning iterations.

The above algorithm for selection of new weight vector $W_c(t+1)$ can be explained graphically as shown in Fig. 2 .

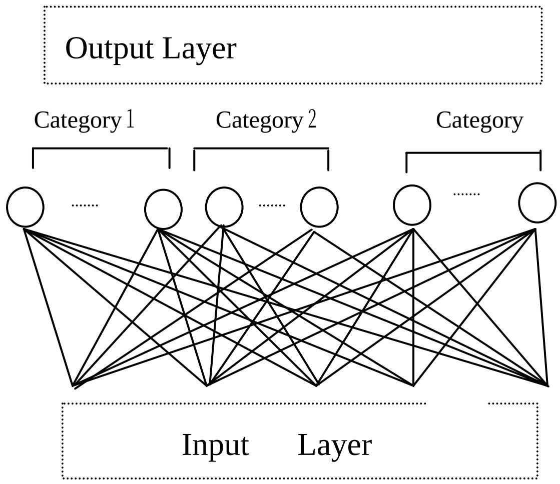

Fig. 1. Structure of the LVQ networks.

In the above LVQ algorithm, the learning rate $\alpha(t)$ plays an important role for convergence. To adjust the parameter, Kohonen has proposed an optimization method without proof as follows:

$$\alpha_c(t) = \frac{\alpha_c(t-1)}{1 + s(t-1)\alpha_c(t-1)}$$

where s(t) =1 if **x**(t) belongs to the same Category c and s(t)=-1 if **x**(t) does not belong to the same Category c. Here, $\alpha_c(t)$ denotes the learning rate for the pattern of Category C. In what follows, we will prove the above relation. From the learning rule of the LVQ, we have

$$\mathbf{w}_c(t+1) = \mathbf{w}_c(t) + s(t)\alpha_c(t)(\mathbf{x}(t) - \mathbf{w}_c(t))$$
$$= (1 - s(t))\alpha_c(t)\mathbf{w}_c(t) + s(t)\alpha_c(t)\mathbf{x}(t)$$

and

$$\mathbf{w}_c(t) = \mathbf{w}_c(t-1) + s(t-1)\alpha_c(t-1)$$
$$(\mathbf{x}(t-1) - \mathbf{w}_c(t-1))$$
$$= (1 - s(t-1))\alpha_c(t-1)\mathbf{w}_c(t-1)$$
$$+ s(t-1)\alpha_c(t-1)\mathbf{x}(t-1)$$

Substituting the latter equation the former one, we have

$$\mathbf{w}_c(t+1) = (1 - s(t)\alpha_c(t))(1 - s(t-1)\alpha_c(t-1))\mathbf{w}_c(t-1)$$
$$+ s(t)\alpha_c(t)\mathbf{x}(t) + s(t-1)\alpha_c(t-1)(1 - s(t)\alpha_c(t))\mathbf{x}(t-1).$$

We assume that the optimal rate adjusts the effect of x(t) and x(t-1) equally within the absolute value, that is,

$$\alpha_c(t) = (1 - s(t)\alpha_c(t))\alpha_c(t-1)\ .$$

Then we have

$$\alpha_c(t) = \frac{\alpha_c(t-1)}{1 + s(t-1)\alpha_c(t-1)}\ .$$

From the above equation, we can see that the value of $\alpha_c(t)$ become larger than 1 when s(t-1)= - 1, which may make the learning algorithm unstable. Thus, we must fix the $\alpha_c(t)$ to a boundary value α_0 when it becomes larger than 1.

$$\alpha_c(t+1) = \alpha_0 \quad \text{if} \quad \alpha_c(t+1) > 1\ .$$

Using the above OLVQ1 algorithm, we will classify the Italian bills in the following section.

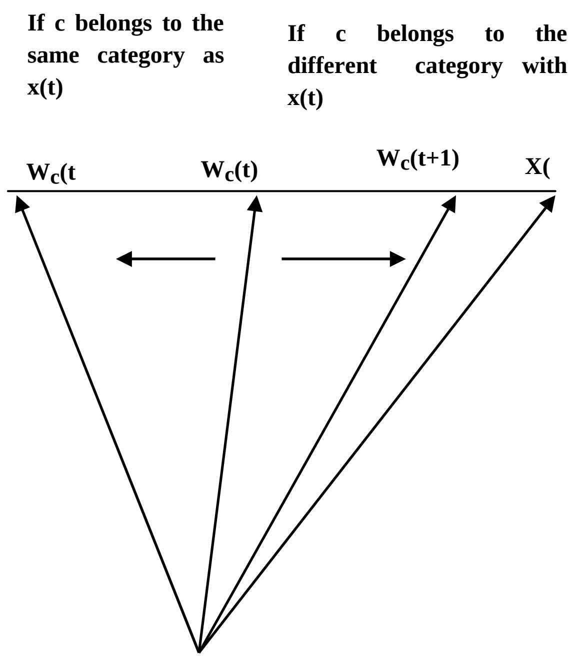

Fig.2. Principle of the LVQ algorithm where the right hand side shows the same category case of **x**(t) and Category c and the left hand side denotes the different category case.

3. Preprocessing Algorithm

The images obtained by transaction machine, there are variations such as rotation or shift. Therefore, we must adjust the images such that the variations may be reduced as much as possible by using the preprocessing. The flow char of the preprocessing procedure is illustrated in Figure 3. In this figure, the original image with 128x64 pixels are observed at the transaction machine in which rotation and shit are included. After correction of these effects, we select a suitable aria which show the bill image and compressed as the image with 64x15 pixels to the neural networks. Although the neural network of the LVQ type could process any order of the dimension of the input data, the small size is better to achieve the fast convergence result. Thus, we have selected the above size of the image.

4. Italian Lira Classification

The bills used here are Italian liras, which have 8 kinds such as 1,000 Liras, 2,000 Liras, 5,000 Liras, 10,000 Liras, new 50,000 Liras, old 50,000 Liras, new 100,000 Liras, and old 100,000 liras. Those Lira bills are used at the input of the transaction machine where four directions such as A, B, C, and D appear since normal direction, reverse direction, and their upside down directions occur at the input as shown in Fig.4. Thus, thirty-two bill images are one set of the classification pattern of the experiment.

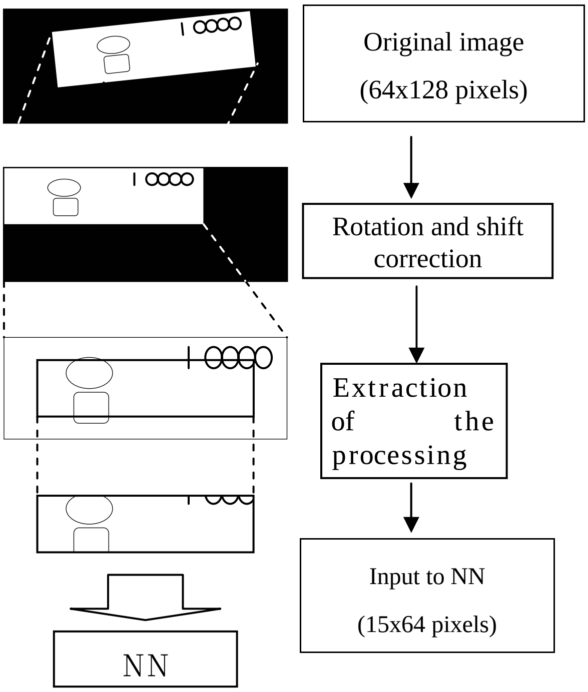

Fig. 3. Preprocessing algorithm.

Total number of data sets is 30 and 10 data sets are

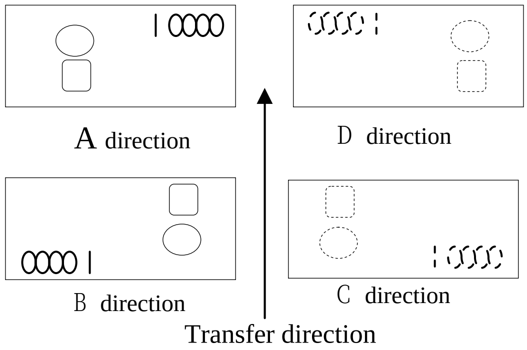

Fig. 4. Four directions of bill money.

used for training of the network and the remaining 20 data sets are used to test the network. In order to reduce the misclassification, we have set the threshold value d_θ such that if $d_c > d_\theta$, unit c is not fired. This means that if the minimum distance is not less than d_θ, the input data is not classified. The parameters of the neural network used here are as follows:

Number of units in the input layer=960

Number of units in the output layer in the initial state=32 where every 50 iterations the number has been adjusted.

Total learning time T=150, $\alpha_i(0) = 0.5$, $i = 1, \cdots M$

Initial values of the weight vectors=mean vectors for training patterns $d_\theta = \min_c (m_c + 4.5\sigma_c)$

After training the neural network, 20 data sets are tested how well the LVQ network could work. Tables 1 and 2 show those values at t=160. We can see the improvement by learning. Table 5 shows the number of the neuron units at t=160 which are determined by increasing them.

Table 1. Recognition rate (%) at t=160.

		Directions			
		A	B	C	D
Italian Liras	1,000	100	100	100	100
	2,000	100	100	100	100
	5,000	100	100	100	100
	10,000	100	100	100	100
	50,000(new)	100	100	100	100
	50,000(old)	100	100	95	95
	100,000(new)	100	100	90	100
	100,000(old)	100	100	95	90

From the original image data we can see that the difference between 50,000 Lira old and new is slight and the difference between old and new100, 000 Liras as shown in Figs. 5 and 6. Therefore, it is rather difficult to recognize them so perfectly. But in this case the misclassification like old and new bills within the same values is not serious. Thus, we have regarded this misclassification as the correct one. Furthermore, we have introduced the threshold value to prevent from making the misclassification. Thus, even if the minimum distance criterion results in the correct classification, we have decided these bells are unknown. Without threshold constraints, we could obtain 100% classification rate.

Table 2. Not fired rate (%) at t=160.

		Directions			
		A	B	C	D
Italian Liras	1,000	5	0	5	0
	2,000	0	10	25	25
	5,000	15	20	5	0
	10,000	10	0	0	5
	50,000(new)	5	0	0	0
	50,000(old)	0	5	0	0
	100,000(new)	0	0	0	0
	100,000(old)	0	5	0	0

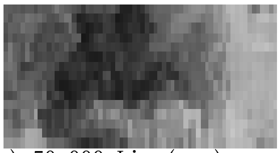

(a) 50,000 Lira(new)
A direction

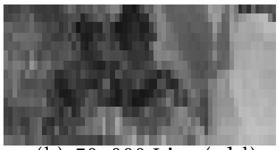

(b) 50,000 Lira(old)
A direction

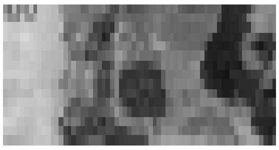

(c) 50,000 Lira(new)
D direction

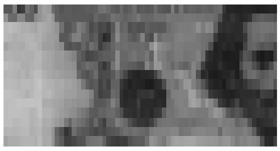

(d) 50,000 Lira(old)
D direction

Fig. 5. New and old 50,000 Liras.

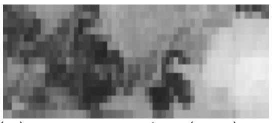

(e) 100,000 Lira(new)
A direction

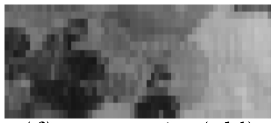

(f)100,000 Lira(old)
A direction

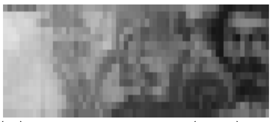

(g) 100,000 Lira(new)
D direction

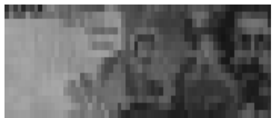

(h) 100,000 Lira(old)
D direction

Fig.6. New and old 100,000 Liras.

Table 3. Number of units after learning.

		Directions			
		A	B	C	D
Italian Liras	1,000	2	2	2	2
	2,000	2	1	1	1
	5,000	1	1	1	1
	10,000	1	2	2	1
	50,000(new)	2	1	1	1
	50,000(old)	2	1	3	1
	100,000(new)	1	1	1	1
	100,000(old)	1	1	1	1

5. Conclusions

We have proposed a new classification method of Italian Liras by using the OLVQ1 algorithm. The experimental results show the effectiveness of the proposed algorithm compared with the conventional pattern matching method.

References

[1] S. Fukuda, T. Kosaka, and S. Omatu: Bill Money Classification of Japanese Yen Using Time Series Data, Trans. Of IEE of Japan, Vol.115-C, No.3, pp.354-360, 9995(in Japanese).
[2] J. Dayhoff: Neural Network Architectures: An Introduction, International Thompson Computer Press, New York, 1990.
[3] T. Kohonen: Self-Organizing Maps, Springer, Berlin, 1997.

The Eleventh International Symposium on Artificial Life and Robotics 2006 (AROB 11th'06),
B-con Plaza, Beppu, Oita, Japan, January 23-25, 2006

Intelligent Smell Classification by Neural Networks

Sigeru Omatu[+], Toru Fujinaka[+], Seiji Okazaki[+], Toru Sumiya[++], and Masatoshi Ono[++]
[+]Osaka Prefecture University, Sakai, Osaka 599-8531, Japan
: omatu@cs.osakafu-u.ac.jp
[++] Funai Electric Advanced Applied Technology, Research Institute Inc.,
Kawasaki, Kanagawa 210-0855, Japan

Abastract

In this paper, a reliable electronic nose (EN) system designed from the combination of various metal oxide gas sensors (MOGS) is applied to detect the early stage of fire from various sources. The time series signals of the same source of fire in every repetition data are highly correlated and each source of fire has a unique pattern of time series data. Therefore, the error back propagation (BP) method can classify the tested smell with 99.6% of correct classification by using only a single training data from each source of fire. The results of the k-means algorithms can be achieved 98.3% of correct classification which also show the high ability of the EN to detect the early stage of fire from various sources accurately.

1. Introduction

Every year the damage from the household fire disaster brings about not only severe loss to property assets, but also physical and psychological injuries of the people. Although most of the residences have installed the fire detectors system such as smoke detectors, those devices cannot detect the early stage of fire since their warning signals are triggered by the high smoke density or the high air temperature. In this paper, the reliability of a new electronic nose (EN) system developed from various metal oxide gas sensors (MOGSs) to specify the smell from various sources of fire is presented.

Jame A. Milke [1] has proved that two kinds of MOGSs have the ability to classify several sources of fire more precisely than conventional smoke detector. However, his results can be achieved only 85% of correct classification. In this paper, a new EN that has been successfully applied to classify not only the same smell from different brands, but also the same smell at different concentration levels [2] is applied to measure smells from various sources of fire such as household burning materials, cooking smells, the leakage from the liquid petroleum gas (LPG). The time series signals of the MOGSs from the beginning to the time until the MOGSs are fully absorbed the smell from each source of fire are recorded and analyzed by the error back propagation (BP) neural networks and the k-means algorithms. The average classification rate of 99.6% can be achieved by using the BP method with only a single training data from each source of fire. The results from the k-means algorithm can be achieved 98.3% of correct classification that also confirms the reliability of this new device to be able to detect various sources of fire in the early stage much better than the results of Jame A. Mike [1].

2. Metal Oxide Gas Sensors for EN

A commercial MOGS has been developed widely for more than thirty years.

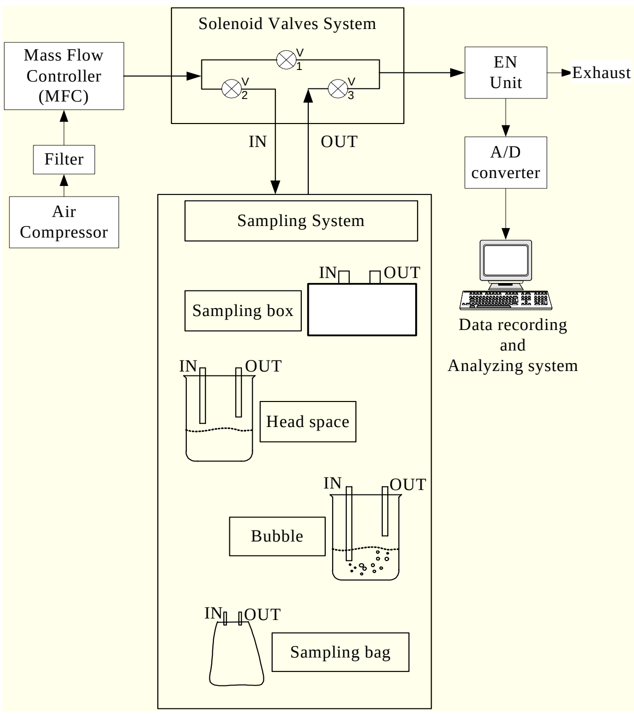

Fig. 1 Schematic diagram of the electronic nose system.

Generally, it is designed to detect some specific smell in electrical appliances such as an air purifier, a breath alcohol checker, and so on. Each type of MOGS has its own characteristics to response to different gases. When combining many MOGSs together, the ability to detect the smell is increased. An EN system shown in Fig. 1 has been developed based on the concept of human olfactory system by using the combination of MOGSs from FIS Inc. listed in Table I as the olfactory receptors in the human nose. The MOGSs unit is combined with the air flow system to flow the air and the tested smell into the MOGSs unit. The data logger converts the analog signals to digital signals and stores them in the data recording system before being analyzed by multivariate analytical methods, such as the BP method and the k-means algorithms.

The main part of the MOGS is the metal oxide element on the surface of the sensor. When this element is heated at a certain high temperature, the oxygen is absorbed on the crystal surface with the negative charge. The reaction between the negative charge of the metal oxide surface and deoxidizing gas makes the resistance of the sensor vary as the partial pressure of oxygen changes [3]. Based on this characteristic, we can measure the total voltage changes during the sensors absorbing the tested odor.

Table I List of MOGSs from the FIS Inc.

Sensor Model	Main Detection Gas
SP-53	Ammonia, Ethanol
SP-MW0	Alcohol, Hydrogen
SP-32	Alcohol
SP-42A	Freon
SP-31	Hydrocarbon
SP-19	Hydrogen
SP-11	Methane, Hydrocarbon
SP-MW1	Cooking vapor

Since the MOGS is sensitive to the temperature and the humidity, the MOGSs unit is put in a small chamber that has a heating system to increase the air temperature during winter season. The heating unit can also decrease the air humidity in the chamber. The clean water is manually sprayed into the chamber when the humidity drops lower than the control level. In this experiment the temperature in the chamber is kept between 20-30°C and the humidity is kept between 30-40%RH. The tested smell is sucked to mix with the fresh air before passing to the MOGSs unit. The distance from the tested smell to the MOGSs unit is approximately 1.5 m.

3. Experimental Data Collection

The smell from twelve sources of fire listed in Table II are measured by the EN system explained in previous section. Each source of fire has been tested with forty repetition data measured in different days in order to check the repeatability response of the MOGSs to the same smell.

For each data, the voltage signal of the normal air is measured every second for one minute and its average value, $\bar{v}_{air}$, is used as an air reference point. After that, the voltage signals of the sensors when absorbing tested smell, $v_{smell,t}$, are collected every two minutes for each smell sample. Finally, the total change in signals at each period, $V_{smell,t}$, is calculated by

$$V_{smell,t} = v_{smell,t} - \bar{v}_{air}$$

where t is the time from 1 to 120s.

After testing one smell the MOGSs need to be cleaned by removing the tested smell and supplying only the fresh air until the MOGSs return to stable point before testing the new sample. This process is just like the human nose which need to breath the fresh air before able to recognize the new smell accurately. Some time series data from the experiment in Fig.2 show that all smells approach the saturation stages within the measuring periods. The signals from the same source of fire in every repetition data are similar in most data sources. The results using the BP method and the k-means algorithm to analyze the time series data from each source of fire every two seconds and the average signals during the saturation stages(time 100-120s) are discussed in Section V.

Table II List of Burning Materials in the Experiment

Sources of fire	Abbreviation
Steam from boiling water	Steam
Burning joss stick	Joss
Burning mosquito coil	Mos
Aroma oil	Aroma
Aroma candle	Candle
Flame from liquid petroleum gas(LPG)	Flame
Leakage of LPG	LPG
Steam from Japanese soup called "oden"	Oden
Boiling vegetable oil	Oil
Toasted bread	Toast
Burning paper	Paper
Burning wood	Wood

4 Correlation of the Experimental Data

Before classifying each source of data, the correlation of each data source is investigated by using the similarity index (SI) and the principal components analysis (PCA).

4.1. similarity index

In the statistical application, the correlation value developed mainly by Karl Pearson is widely used to find the relationship between two random variables. In this paper, we call the correlation value as a similarity index

(SI). The SI value varies from -1 to 1. Two random variables with a SI of either 1 or 1 are highly correlated because knowledge of one provides precise knowledge of the other. However, the SI provides information only about linear relationships between random variables. Random variables could have a nonlinear relationship but still have a SI close to 0 [4]. Therefore, we make an assumption on this application that each data pattern has nearly linear relationship to the other data patterns. The SI value between two data is calculated by

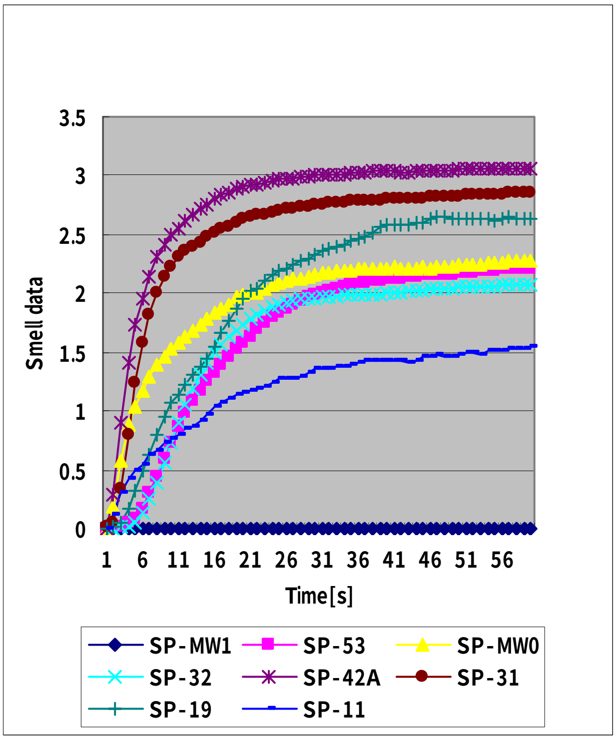

Fig.2 Time series data from some sources of fire in the experiment.

$$r_{xy} = \frac{\sum_{i=1}^{n} x_i y_i - n\overline{xy}}{\sqrt{(\sum_{i=1}^{n} x_i^2 - \overline{x}^2)(\sum_{i=1}^{n} y_i^2 - \overline{y}^2)}}$$

where r_{xy} is the SI value, x and y are the comparing data, $\overline{x} = \frac{1}{n}\sum_{i=1}^{n} x_i$, $\overline{y} = \frac{1}{n}\sum_{i=1}^{n} y_i$, and n is the size of each data which equals 480 (60 periodsx8 sensors).

By using the SI to find the relationship between the repetition data of each data source, we found that all data sources except the paper and the wood have high average SI values above 0.99. During the experiment, the paper and the wood have inconsistent burning rates, therefore the signals from the repetition data of these sources are more fluctuated than the other sources that have better consistent burning rate.

4.2 principal components analysis

In this paper, the well known PCA is applied to analyze two cases of the experimental data. The full time series data case uses the data signals every two seconds, but the saturation stage data case uses only the average data from time 100 to 120s for analyzing.

The plots of two main components are shown in Fig.3. The distribution of the paper and the wood burning smell are more scattered than the other kinds of smells especially in the case of saturation stage data. Most of the tested data are separated into their own clusters with some overlap zones between different data source.

5. Experimental Results and Discussion

5.1 experimental result

Two case of data are analyzed by the BP method and k-means algorithm. The full time series data (TSD) case uses the data from all MOGSs every two seconds as the input data. The saturation stage data (SSD) case uses only the average value from time 100 to120s of all sensors as the input data.

The BP structure contains three layers. The input layer of the TSD case, and the SSD case consists of four hundred eighty nodes (8 sensors x 60 periods), and eight nodes(average signal from 8 sensors), respectively. For the hidden layer, we have tried with several values and the size that gives a good accuracy and a reasonable training time for both data cases is forty nodes. The output layer contains twelve nodes, each node represents one data source. The learning rate, the momentum rate, and the minimum mean square error (MSE) during the training period are set by trial and error method to 0.1, 0.001, and 0.0003, respectively.

Based on the information during investigating the correlation of the data, most data sources are highly correlated to their repetition data with high SI values. Therefore, only one data that has the highest average SI value to the other repetition data from each sources of fire are used as the training data for the BP and the rest of the data are used as the test data. We assume that a pattern is classified correctly if (output $\leq$ 0.7 and target=1) or (output $\leq$ 0.3 and target =0). For the k-means algorithm, the training data of the BP method are used as the initialize data and then assigns the data patterns to the nearest cluster center by calculating the Euclidean distance. After that, the new cluster center is recalculated. The process continues until the position of the cluster center is not changed. The final results of this experiment are shown in Table III.

The results using the TSD from both the BP method and the k-means algorithm are sufficiently effective. The data signals from the MOGSs are affected by many factors, such as the sampling condition, the inconsistency burning rate, the fluctuation from the standard air, and so on. Therefore, the saturation stages of the data are varied by those factors. By including the signal before approaching the saturation stage, the accuracy to classify all smell is increased.

5.2 Discussion

Although the distribution of PCA shown in Fig. 3 cannot clearly separate similar smell such as the aroma oil and the aroma candle, the BP method and the k-means algorithms are able to classify them perfectly as shown in Table III. The results of TSD using the BP method have only two incorrect classified data. These two data are not misclassified as the other smells. Only the output values of their paper node are not high enough to classify them as the paper. The output values of these two data on the paper node are only 0.4951, and 0.4799, respectively and the output of the others output nodes are nearly 0. The results are much better than the results from [1] which used two kinds of MOGSs to classify several sources of fire into three fire condition levels, flaming, smoldering, and nuisance, with only 85% of correct classification. The smoke density of the tested data is not high enough to trigger the alarm of the smoke detector. In case of unusual burning smells in the residences such as the wood burning, flaming from the LPG, or the leakage LPG, it is necessary to have a proper device to detect these sources before unable to stop the fire. We can conclude that the new EN system shown in this paper is a proper device for this application.

6. Conclusions

We have proposed a new EN system designed from various kinds of MOGSs. The EN has the ability to identify various sources of fire in the early stage with more than 99% of accuracy by using only a single training data in the BP case. The results from the k-means algorithm are also able to predict the sources of fire with more than 98% of accuracy. It can be concluded that the EN is suitable for detecting the early stage of fire.

References

[1] Jame A.Mike, "Applicaiton of Neural Networks for Discriminating Fire Detectors", International Conference on Automatic Fire Detection, AUBE'95, 10th, Duisburg, Germany, pp.213-222, April 4-6, 1995.

[2] Bancha Charumporn, Michifumi Yoshioka, Toru Fujinaka, and SigeruOmatu, "An Electronic Nose System Using Back Propagation Neural Networks with a Centroid Training Data Set", proceeding of the Eight International Symposium on Artificial Life and Robotics, Japan, pp.605-608, January 24-26, 2003

[3] General Information for TGS sensors, Figaro Engineering, available at www.figarosensor.com/products/general.pdf. M. Tanaka, "Modeling of Mixtures of Principal Component Analysis Model with Genetic Algorithm," Proc. 31st Int'l Symposium on Stochastic Systems Theory and Its Applications, pp. 157-162, Yokohama, Japan, 1999.

[4] William L. Carlson and Betty Thorne, Applied Statistical Methods, Prentice Hall International, 1997

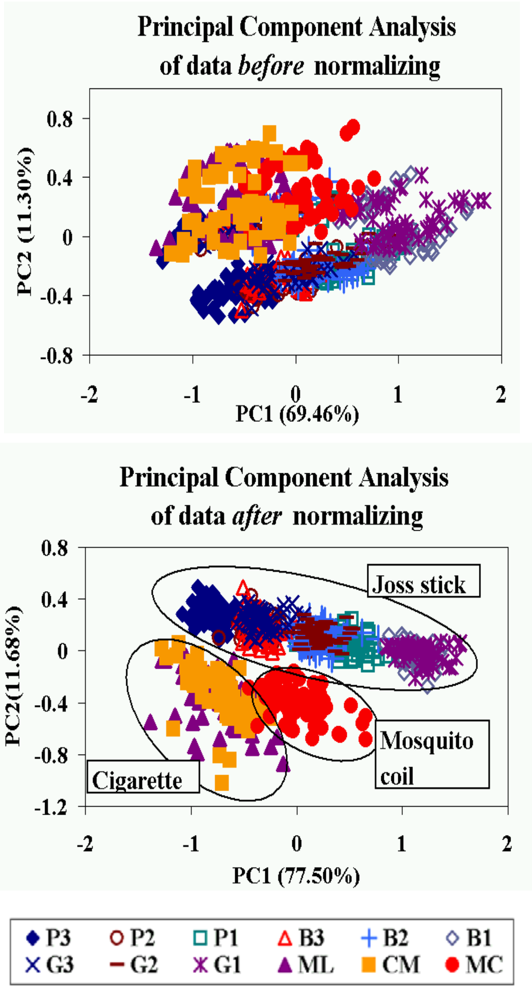

Fig.3. Two main components of the experimental data using the PCA.

Table III Experimental Results

Sources	TSD				SSD			
	BP		k-means					
	True	%	True	%	True	%	True	%
Steam	39/39	100	40/40	100	38/39	97	39/40	98
Joss	39/39	100	40/40	100	39/39	100	40/40	100
Mos	39/39	100	40/40	100	39/39	100	40/40	100
Aroma	39/39	100	40/40	100	39/39	100	40/40	100
Candle	39/39	100	40/40	100	39/39	100	40/40	100
Flame	39/39	100	40/40	100	39/39	100	40/40	100
LPG	39/39	100	40/40	100	39/39	100	40/40	100
Oden	39/39	100	40/40	100	39/39	100	40/40	100
Oil	39/39	100	40/40	100	38/39	97	37/40	93
Toast	39/39	100	40/40	100	38/39	97	40/40	100
Paper	38/39	95	35/40	88	31/39	80	28/40	70
Wood	39/39	100	37/40	93	32/39	82	28/40	70
Average		99		98		96		94

The Eleventh International Symposium on Artificial Life and Robotics 2006 (AROB 11th'06),
B-con Plaza, Beppu, Oita, Japan, January 23-25, 2006

Ggraph Construction with Maximum Number of Trees by Continuous Edge Addition

Hideshi Ido+, Yosuke Ohama++, and Tomoki Takahashi++
+ Electrical Engineering and Information Science, ++Electrical Engineering
Niihama National College of Technology,
7-1,Yagumo-cho, Niihama, 792-8580, Ehime, Japan
+ ido@ele.niihama-nct.ac.jp

Abstract

The simple computational algorithm is presented to construct the graph with maximum number of trees by adding edges one by one. The number of trees of a graph would become an index to estimate the overall reliability of probabilistic communication networks with same link probabilities. Our procedure Max-trees selects one edge which gives the maximum number of trees among edges not included in the original graph. And this process is continuously repeated in each step of adding edge, we get the sequence of new edges to be added. As examples of execution results, the edge sequence and the maximum number of trees are shown for each starting graph of two types which are a tree of series edges and a star-shaped tree for nodes n=7 and 8.

To see how many trees these graphs have, the minimum numbers of trees for graphs with the same number of edges are similarly calculated by the minimum version algorithm Min-trees. An edge sequence of Max-trees makes long cycles, and Min-trees makes 3-cycles. And, the ratio of the maximum number of trees to the minimum of those is about from 1 to 6 within these examples.

Keywords: Continuous edge addition, Maximum and Minimum number of trees, Node determinant, Clique

1 Introduction

The number of trees of a graph would be an index to estimate the reliability of probabilistic communication networks with either high or low link probabilities when those probabilities are independent and same [1].

Some analytical methods have been reported for the number of trees of graphs obtained from the complete graph by deleting several types of subgraphs[2],[3]. Other ones are to maximize the number of graphs when some edges or subgraphs are deleted from the complete graph[4],[5]. Another one is to get the expressions of the trees of a graph which is obtained by connecting graphs of special structures[6].

These analytical methods are based on obtaining the expressions derived from a node determinant of the target graphs. And the graphs need to have any special structures. Therefore simple expressions haven't been known for arbitrary graphs with no structural conditions so far.

On the other hand, it is well known that the numerical calculation of the number of trees can be performed by the node determinant for any graph. So, we have tried to computationally construct graphs with the maximum number of trees by adding new edges continuously to the original graph. Also we constructed graphs with the minimum number of trees on the similar way. And the ratio of the maximum number of trees to the minimum of those is about from 1 to 6 for two types of starting graphs which are a tree of series edges and a star-shaped tree for nodes n=7 and 8.

In the subsequent chapters, we show the algorithm for graph construction and results about the ratio of the maximum number of trees to the minimum for these examples.

2 Algorithm of the Maximum Number of Trees

First we introduce some graph theoretical terms. A graph denoted by $G(V,E)$ is composed with a node set V and an edge set E. Each edge denoted by (i,j) connects a pair of nodes i and j. A graph is said to be simple if it has no parallel edges, no self-loops and no directed edges. In this paper, we treat only simple graphs as shown in Fig.1 (a). A tree is a subgraph which connects all nodes of G and includes no closed circuits, as shown in Fig.1 (b).

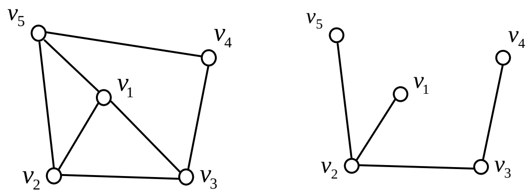

(a) (b)

Fig.1.(a)Simple Graph, (b)Tree

The complete graph of n nodes has one edge (i,j) between every node pair i, j, and includes $\frac{1}{2}n(n-1)$ edges. The node determinant T of a graph G with n nodes is a determinant of the matrix $A=(a_{ij})$, where for $1 \le i, j \le n-1$, each diagonal element a_{ii} is the number of edges incident to node i, and each non-diagonal element a_{ij} is –1 if there is an edge between two nodes i and j, otherwise 0. Then, T represents the number of trees of the graph G. Since the value of T is always an integer for any graph, the determinant T must be computed by using double precision floating point number for matrix A .And usual Gaussian elimination is available for this purpose.

Algorithm: *Max-trees*

step1. Find the set $\overline{P}$ of position (i, j) where there isn't an edge (i, j) in the given original graph $G(V, E)$. Now, set $G_0 \leftarrow G(V, E)$ and $k \leftarrow 0$.

Step2. Calculate the number of trees T^* of each graph obtained by adding an edge (i, j) to the graph G_k, for each position $(i, j) \subset \overline{P}$, respectively.

Step3. Find the edge (i, j) that gives the maximum number of trees among T^*'s in step2. And replace $G_{k+1} \leftarrow G_k +$ edge (i, j), $\overline{P} \leftarrow \overline{P}$ - position (i, j), and $k \leftarrow k+1$.

Step4. If the set $\overline{P}$ is empty, then terminate, otherwise go to step2.

In this algorithm, step2 and step 3 will be repeated until G_k reaches to the complete graph.

To compare the maximum number of trees with the minimum number of trees on the same number of edges, we make the minimum version algorithm Min-trees derived from Max-trees algorithm. Namely, in the minimum version, "the maximum number of trees among T^*'s" is replaced by "the minimum number of trees among T^*'s" in step3. Then we call the maximum version algorithm as Max-trees, and the minimum version algorithm as Min-trees, respectively.

3 Examples and Results

Two algorithms described above can be adapted to relatively small simple graphs with nodes $n \leq 20$. These algorithms are programmed in C and run on sx5 computer.

When the algorithm starts, it usually needs the initial graph although it works to make a star shaped tree as an initial graph. Therefore, we examined two types of trees, one is a series edge and the other is star shaped as shown in Fig.2.

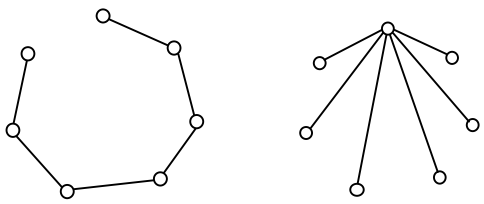

(a) Series-edge tree. (b) Star-shaped tree.

Fig.2. Two types of trees as initial graphs.

Results of edge sequences are represented by numbers near dotted lines as shown in Figs.3-Fig.6 for Max-trees and Min-trees, series edge and star-shaped of nodes n=7. And the numbers of trees are shown in Table 1 and 2 comparing Max-trees with Min-trees according to edge sequences for nodes $n = 7$ and 8, respectively.

3.1 Characteristics of Edge Sequence

Edge sequences shown in Fig.3 and Fig.5 obtained by

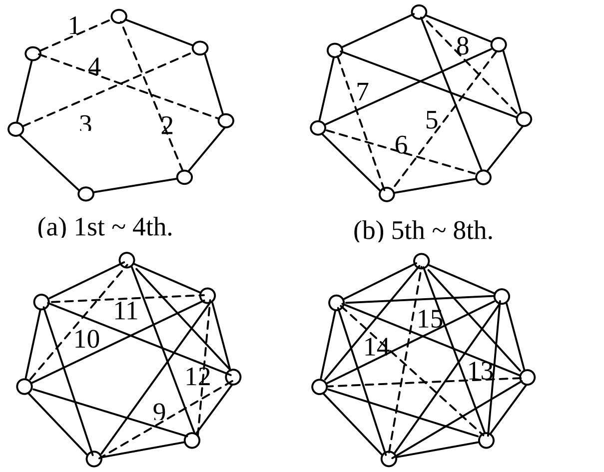

(a) 1st ~ 4th. (b) 5th ~ 8th. (c) 9th ~ 12th. (d) 13th ~ 15th.

Fig.3. Edge sequence by Max-trees for Series-edge tree of n=7.

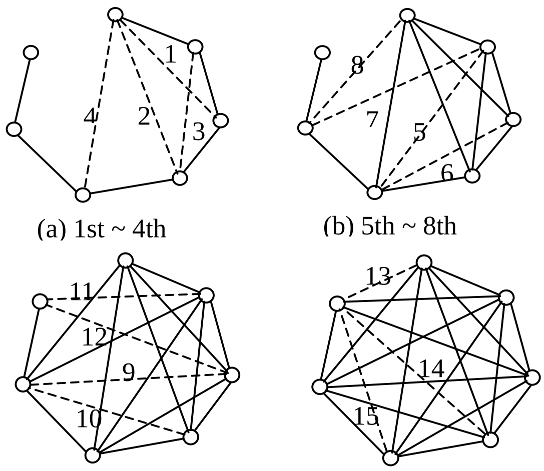

(a) 1st ~ 4th (b) 5th ~ 8th (c) 9th ~ 12th. (d) 13th ~ 15th.

Fig.4. Edge sequence by Min-trees for Series-edge tree of n=7.

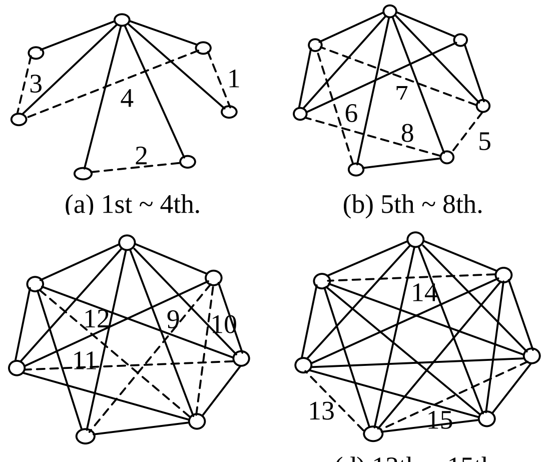

(a) 1st ~ 4th. (b) 5th ~ 8th. (c) 9th ~ 12th. (d) 13th ~ 15th.

Fig.5. Edge sequence by Max-trees for Star-shaped tree of n=7.

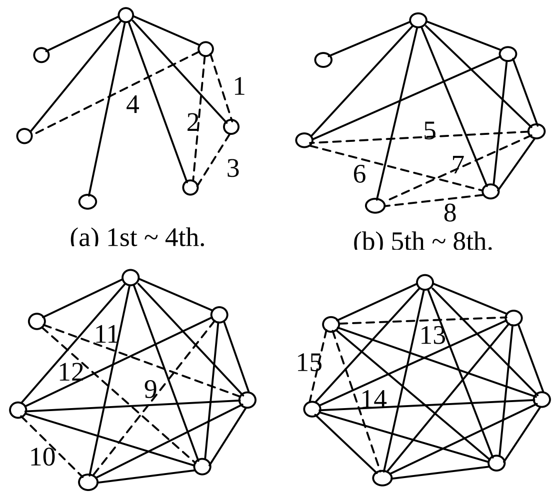

(a) 1st ~ 4th. (b) 5th ~ 8th.

(c) 9th ~ 12th. (d) 13th ~ 15th.

Fig.6. Edge sequence by Min-trees for Star-shaped tree of n=7.

Max-trees mean that it is effective to make long cycles as many as possible for getting more trees. Similarly, edge sequences shown in Fig.4 and Fig.6 obtained by Min-trees mean that it is effective to make 3-cycles as many as possible for getting less trees. Namely, these characteristics can be clearly observed at the early part of each edge sequence. Particularly Min-trees is enlarging a size of a clique(a complete subgraph) by added edges.

3.2 Characteristics of the Number of Trees

Numbers of trees for each edge sequence obtained by Min-trees in both Table 1 and 2 are the same values. The reason for this phenomenon is that, as mentioned above, Min-trees make a clique of the same number of edges and the other edges are remained as parts of the original tree.

Table 1. Comparison of Trees for $n = 7$.

Initial tree	Series-edge		Star-shaped	
Added edges	Max-trees	Min-trees	Max-trees	Min-trees
1	7	3	3	3
2	19	8	9	8
3	51	16	27	16
4	117	40	63	40
5	231	75	144	75
6	408	125	320	125
7	720	300	576	300
8	1,200	540	1,024	540
9	1,840	864	1,792	864
10	2,800	1,296	2,688	1,296
11	4,200	3,024	4,032	3,024
12	6,125	5,292	5,880	5,292
13	8,575	8,232	8,575	8,232
14	12,005	12,005	12,005	12,005
15	16,807	16,807	16,807	16,807

Table 2. Comparison of Trees for $n = 8$.

Initial tree	Series-edge		Star-shaped	
Added edges	Max-trees	Min-trees	Max-trees	Min-trees
1	3	3	3	3
2	9	8	9	8
3	27	16	27	16
4	72	40	72	40
5	168	75	168	75
6	377	125	377	125
7	841	300	841	300
8	1,537	540	1,537	540
9	2,800	864	2,800	864
10	4,928	1,296	4,928	1,296
11	8,056	3,024	8,056	3,024
12	12,440	5,292	12,440	5,292
13	19,200	8,232	19,200	8,232
14	28,800	12,005	28,800	12,005
15	40,800	16,807	40,800	16,807
16	57,600	38,416	57,600	38,416
17	80,640	65,856	80,640	65,856
18	110,592	100,352	110,592	100,352
19	147,456	143,360	147,456	143,360
20	196,608	196,608	196,608	196,608
21	262,144	262,144	262,144	262,144

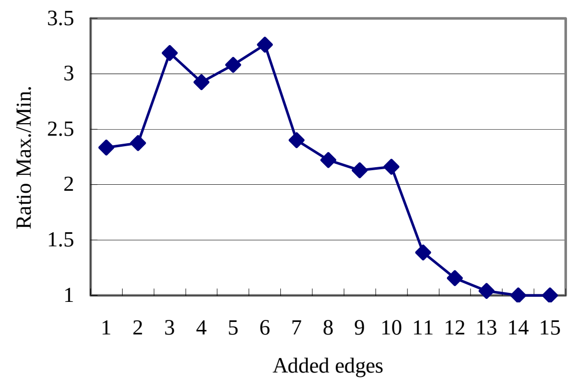

(a) Series-edge of n=7.

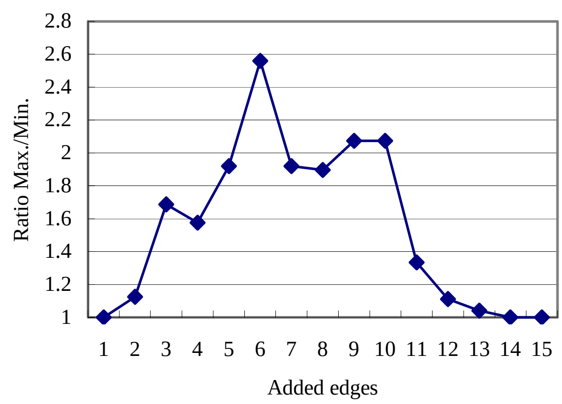

(b) Star-shaped of n=7.

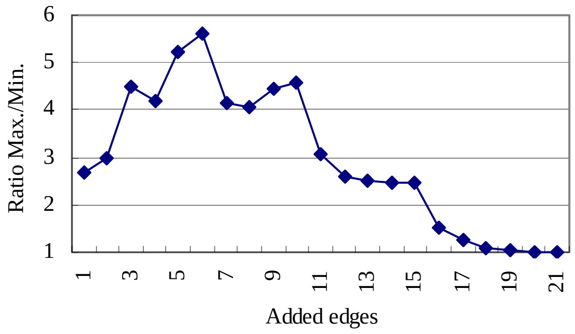

(c) Series-edge of n=8.

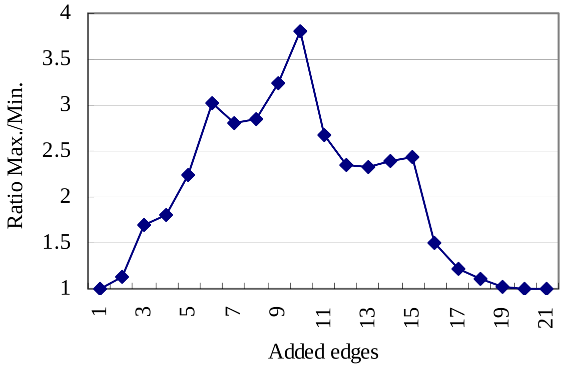

(d) Star-shaped of n=8.

Fig.7. Ratio of Max-trees/Min-trees.

Therefore, if we start Min-trees from any different trees, this phenomenon always happens and the number of trees depends upon the number of edges, apart from the number of nodes. Then, Min-trees of this case will give the global minimum edge sequences.

Fig.7 shows the ratio of Max-trees to Min-trees according to the number of added edges. These figures (a)-(d) show that if we want to strengthen the networks by adding edges continuously, the over all reliability varies in a wide range according to an edge sequence.

3.3 Additional Considerations

The same maximum numbers and the same minimum numbers of trees have often happened at more than one node-pair in the process of algorithm. Then, it may be the case of isomorphic graphs. If those are not isomorphic, we will select one with the maximum after additional calculation steps for a next edge.

4. Conclusion

We presented the simple algorithm Max-trees that gives the maximum number of trees by adding edges to the original graph one by one. The number of trees becomes an index to estimate the network reliability.

Edge sequences obtained by Max-trees for examples indicate that long cycles are needed for more trees. And also, the minimum version algorithm Min-trees gives edge sequences which make a clique. And these edge sequences get the same minimum numbers of trees for any original trees.

References

[1] Leggett J.D.,Bedrosian S.D., “Synthesis of Reliable Networks”,IEEE Trans. Circuit Theory, Vol.CT-16, No.8, pp.384-385, 1969.

[2] Kasai T.,Kusaka H.,Yoneda S. and Taki I., “Total Number of Trees in Four Kinds of Incomplete Graphs Derived from a Complete Graph (in Japanese) ”,Jour. Inst. Elect. Comm. Engrs. Japan.Vol.49, No.1,pp.69-77, 1966.

[3] Ishikawa H., Ido H.,and Sasaki T., “Number of Trees in a Certain Incomplete Graph (in Japanese)”, Trans. IEICE, Vol.57-A,No.5, pp.423-424, 1974.

[4] Shier D.R., “Maximizing the Number of Spanning Trees in a Graph With n Nodes and m Edges”,Jour. Res. of Nat. Bur. of Stds.-B. Math. Sci.,Vol.78B, No.4, pp.193-196, 1974.

[5] Ido H., Ishikawa H., and Sasaki T., “Number of Trees in a Specified Incomplete Graph and its Min-Max Problem(in Japanese)”, Trans. IEICE, Vol.58-A,No.1, pp.81-82, 1975.

[6] Hatakeyama M.,Sato K., “Construction Method for Connection Graph of Cycles from General Graph(in Japanese)”, Proc.2003 IEICE Gen.Conf.,A-1-6,2003.

The Eleventh International Symposium on Artificial Life and Robotics 2006 (AROB 11th'06),
B-con Plaza, Beppu, Oita, Japan, January 23-25, 2006

Graph Extension with Constant Connectivity

Hideshi Ido+, Sigeru Omatu++

+Electrical Engineering and Information Science, Niihama National College of Technology,
7-1,Yagumo-cho, Niihama, 792-8580, Ehime, Japan
ido@ele.niihama-nct.ac.jp

++Computer and Systems Sciences, Graduate School of Engineering,
Osaka Prefecture University, 1-1 Gakuen-cho, Sakai City, 599-8531
omatu@sig.cs.osakafu-u.ac.jp

Abstract

According to scaling up the communication networks, numbers of communication stations(nodes) and the corresponding communication links(edges) are rapidly increasing. Then the reliability of the networks has become important. To keep the reliability of the networks, the connectivity(invulnerability) of the networks should be increased. In this paper, a method of extending the connectivity of a graph with constant connectivity has been proposed and some examples have been shown to realize the networks.

Keywords: Network Reliability, Connectivity, Graph Extension.

1 Introduction

Communication networks have been extended year after year to speed up the information transmission and grade up the quality of information. Then the reliability of communication networks has become more important to make the network system more robust. Since the communication networks could be represented as a graph, the graph theory could be applied to analysis of the reliability.

We have considered the robustness of the networks from viewpoint of connectivity of the graph and proposed an extension method of a network with a constant connectivity when the nodes of the network have been increased by one more node[1].

In this paper, we extend the result when the communication network has been extended by more than one nodes with the same connectivity based on the concept of the maximum connectivity of the graph theory.

First, we will introduce some concepts of graph theory and summarize the results on the graph with maximum connectivity. Then we will state the results to construct the extended graph with constant connectivity for the communication network with more nodes. Finally, some examples are shown to show the effectiveness of the present extension method.

2 Definition of the Graph Connectivity [2]

We regard the stations and the links of communication networks as a set of nodes and a set of edges of a graph, respectively. Let the sets of nodes and edges of the graph be denoted as V and E, respectively and let the communication network be a simple graph denoted by $G(V,E)$. The connectivity of the graph $G(V,E)$ is shown as $\omega(G)$ and the edge between nodes s,t is denoted by (s,t). To open the edge is called as remove of the edge and we define the degree of node by the number of edges which have been connected to the node.

The minimal graph is the graph with $\lceil (nk+1)/2 \rceil$ edges where n is the number of nodes and $k(2 \le k < n)$ is the connectivity and $\lceil\ \rceil$ denotes the Gaussian notation.

3 Preliminary Results

For the construction method of the graph with pre-assigned connectivity $k(2 \le k < n)$ and node n, Hakimi's report is the first one[3]. Tutte has proposed a method[4] to extend the nodes n for the 3-connected graph under some constraint on the edges. We have proposed a method to enlarge k step by step[5] and a method to extend the nodes n with a connectivity k.

We have proposed the following construction algorithm of new graph which preserve the connectivity when we add a new node. Note that only when n and k are both odd, only one node has the degree $k+1$ and the remaining ones have the degrees of k.

Then we have use the following construction algorithm to extend the nodes n of the network by one.

<u>Construction algorithm</u>

Step1. Set the removable p edges $(v_i, v_j) : v_i, v_j \in W$ such that the degree of node $v_i \ge k-1$, for each $v_i \in W$ where $W = \{v_1, v_2, ..., v_h\}$ for different h nodes of the graph $G(V,E)$. Let $G_1(V,E_1)$ be the graph which was deleted p edges from $G(V,E)$.

Step2. Let $A = \{v_1, v_2, \cdots, v_h, \cdots, v_l\}$ be different l $(h \le k \le l)$ nodes of the graph $G_1(V,E_1)$ such as $W \subset A \subset V$. Add to $G_1(V,E_1)$ a new node $u \notin V$ and l edges (u, v_i): $v_i \in A, 1 \le i \le l$ and set the new graph as $G^*(V^*, E^*)$.

For the above construction algorithm, the following Lemmas have been proved in [4] which show that the connectivity by the above construction method is k.

[Lemma 1] For a graph with connectivity $k \ge 2$ if we apply the construction algorithm to the extension of the network and the graph $G_1(V, E_1)$ satisfies $\omega(G_1) \geq k-1$, then $\omega(G^*) \geq k$ holds for the graph $G^*(V^*, E^*)$.

[Lemma 2] For the minimal graph $G(V,E)$ with n nodes and the connectivity $k\,(k \geq 2)$, we assume that $h = l = k$ and the construction algorithm is adopted for the extension under the following conditions

(a) $p = (k+1)/2$ when n and k are both odd

(b) $p = \lceil k/2 \rceil$ when n or k is even.

Then if $\omega(G_1) = k-1$, then the graph $G^*(V^*, E^*)$ is the minimal graph with number of nodes $(n+1)$ and $\omega(G^*) = k$.

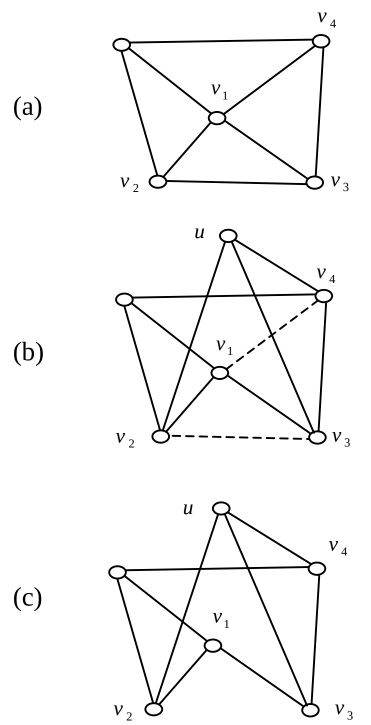

Fig.1. Construction of minimal graph where (a) is original graph with three cycle, (b) added graph by a new node u and three edges, (c) the 3-connected minimal graph.

To see the meaning of these Lemmas, we consider the case of $k = 3$, $n = 5$ as shown in Fig.1(a). If we add the new node u and we select three cycle $\{v_1, v_2, v_3\}$ at the node v_1 with the node degree 4 as shown in Fig.1(b), we can remove two redundant edges (v_1, v_4) and (v_2, v_3) denoted by the dotted lines[6]. Thus, we obtain the minimal graph with the connectivity 3 by adding the new edges $(u, v_i), i = 2,3,4$ as shown in Fig.1(c).

4 More General Extension Theorems

For more general extension of the original graph including plural nodes we propose two theorems. Let $G_1(V_1, E_1)$ and $G_2(V_2, E_2)$ be the simple graphs with connectivity $k_1 = \omega(G_1)$ and $k_2 = \omega(G_2)$ respectively, where $k_1 > k_2$ and $|V_1| \geq (k_1 - k_2) + |V_2|$ are assumed.

[Theorem 1] As shown in Fig.2, for each node u_i of G_2, select the distinct set V_{di} of $(k_1 - k_2)$ nodes of G_1. And add new $(k_1 - k_2)$ edges between these $(k_1 - k_2)$ nodes of each distinct set V_{di} and the node u_i of G_2 respectively. Then we have got the resultant graph G^* of connectivity $\omega(G^*) = k_1$.

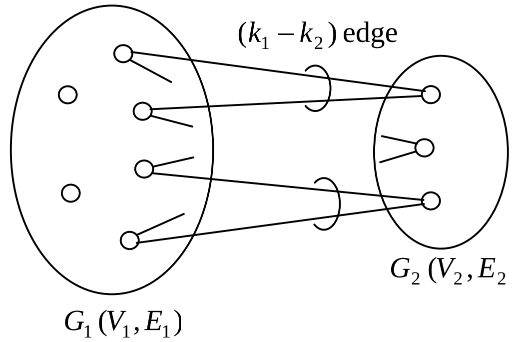

Fig.2. More general extension of the graph G_1 including G_2.

(Proof) We want to show that all remaining nodes of G^* are connected after removing any set of $(k_1 - 1)$ nodes. Let A be the set of $(k_1 - 1)$ nodes to be removed from G^*.

(1) Case of $A \subset V_1$. Since new edges added between G_1 and G_2 are incident to at least $(k_1 - k_2) + k_2 = k_1$ nodes of G_1, then even if $(k_1 - 1)$ nodes of A are removed from G^*, the remaining graph is connected.

(2) Case of $A \subset V_2$. All of the remaining nodes of G_2 are connected to the connected graph G_1.

(3) Case of $A \subset V_1 \bigcup V_2$ except (1) and (2). The remaining subgraph of G_1 is connected, and all the remaining nodes of G_2 are connected to G_1. (Q.E.D)

This Theorem 1 gives a sufficient condition so that the resultant graph G^* keeps connectivity k_1. Therefore G^* may have some redundant edges for connectivity k_1. This will be shown in some examples below.

The next theorem establishes the extension method connecting two graphs with same connectivity k.

[Theorem 2] When two graphs G_1 and G_2 have the same connectivity $k_1 = k_2 = k$, select each set V_d and U_d of distinct k nodes from G_1 and G_2 respectively and connect by new k edges between a node of V_d and one of U_d on 1-1 correspondence. Then the resultant graph G^* has connectivity $\omega(G^*) = k$.

Fig.3 shows the location of k edges by theorem 2. The proof for this theorem is clear and omitted.

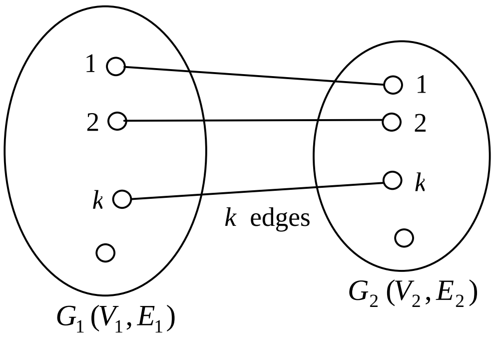

Fig.3. Connection by k edges for G_1 and G_2 of same connectivity k.

It will be easily observed that theorem 2 takes the similar edge location as theorem 1 in case of $(k_1 - k_2) = 1$.

5 Examples

Some examples are shown in Fig.4 ~ Fig.10 to see previous two theorems. For simplicity G_1 and G_2 are restricted to smaller graphs with $|V_1| = 4$, $k_1 = 2$ and 3, $|V_2| = 3$, $k_2 = 0,1,2,$ and 3,respectively.

[Example 1] Fig.4 shows the case of $k_1 = 2$ and $k_2 = 0$. 6 new edges are added, then the connectivity of the resultant graph G^* is $k_1 = 2$ (Theorem 1).

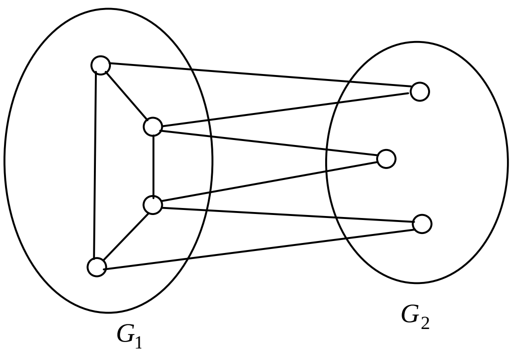

Fig.4. $k_1 = 2$ and $k_2 = 0$.

[Example 2] Fig.5 shows the case of $k_1 = 2$ and $k_2 = 1$. 3 new edges are added between G_1 and G_2, then the connectivity of the resultant graph G^* is $k_1 = 2$ by Theorem 1. And G^* has a redundant edge among 3 new edges.

[Example 3] Fig.6 shows the case of $k_1 = 2$ and $k_2 = 2$. 2 new edges are added between G_1 and G_2, then the connectivity of the resultant graph G^* is $k_1 = 2$ by Theorem 2.

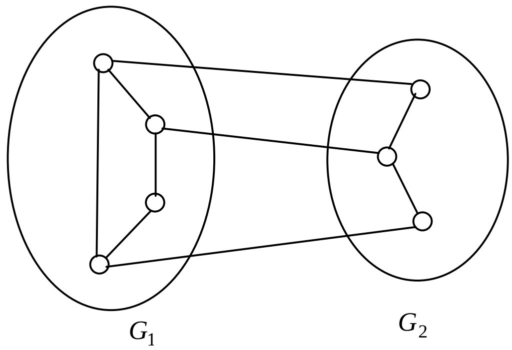

Fig.5. $k_1 = 2$ and $k_2 = 1$.

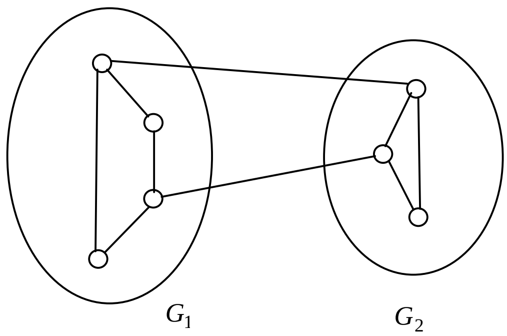

Fig.6. $k_1 = 2$ and $k_2 = 2$.

[Example 4] Fig.7 shows the case of $k_1 = 3$ and $k_2 = 0$. 9 new edges are added between G_1 and G_2, then the connectivity of the resultant graph G^* is $k_1 = 3$ by Theorem 1.

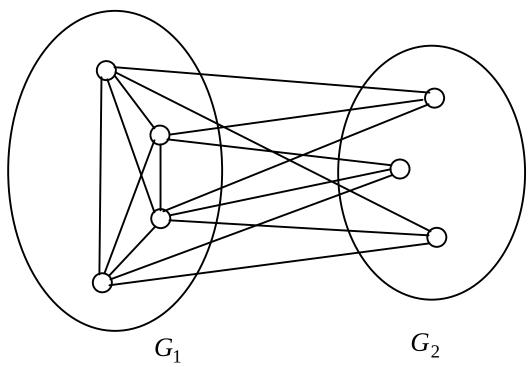

Fig.7. $k_1 = 3$ and $k_2 = 0$.

[Example 5] Fig.8 shows the case of $k_1 = 3$ and $k_2 = 1$. 6 new edges are added between G_1 and G_2, then the connectivity of the resultant graph G^* is $k_1 = 3$ by Theorem 1. And G^* has a redundant edge among 6 new edges.

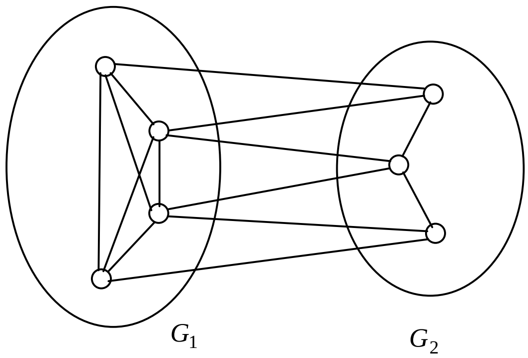

Fig.8. $k_1 = 3$ and $k_2 = 1$.

[Example 6] Fig.9 shows the case of $k_1 = 3$ and $k_2 = 2$. 3 new edges are added between G_1 and G_2, then the connectivity of the resultant graph G^* is $k_1 = 3$ by Theorem 1.

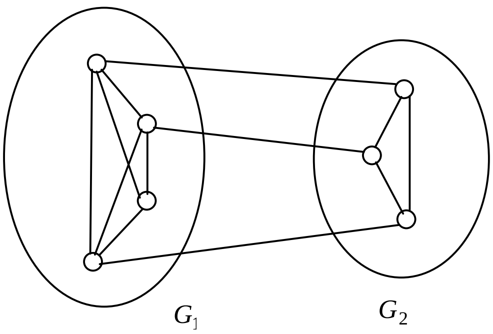

Fig.9. $k_1 = 3$ and $k_2 = 2$.

[Example 7] Fig.10 shows the case of three graphs G_1, G_2 and G_3 with $k_1 = 3$, $k_2 = 2$ and $k_3 = 2$, respectively. First, 3 new edges are placed between G_1 and G_2, then another 3 edges of dotted lines are added between G_2 and G_3. The connectivity of the resultant graph G^* is $k_1 = 3$ by Theorem 1.

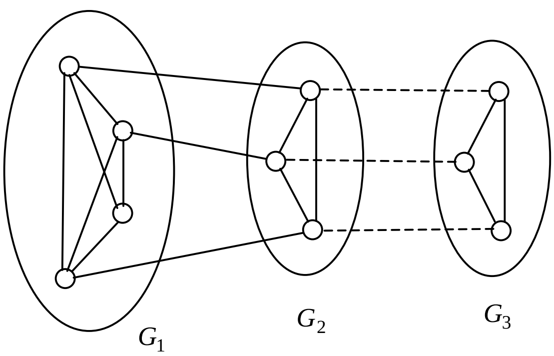

Fig.10. $k_1 = 3$, $k_2 = 2$ and $k_3 = 2$.

6 Further Considerations

About the extension of the graph keeping its connectivity, we first added edges between G_1 and G_2. But, there may be another procedure that first increase the connectivity of G_2 from k_2 up to k_1, then next add edges between G_1 and G_2. According to the latter, the example 6 shown in Fig.9 needs only 6 new edges, although the example 4 shown in Fig.7 need 9 new edges.

When we are going to connect 3 or more graphs, it may be useful to apply repeatedly theorems described above. In this case, the order which graphs are to be connected becomes an important problem to be determined

Related to the total number of edges, the minimal graph with minimum edges for nodes n and connectivity k is important. as described at Introduction. When G_1 and G_2 are both minimal graphs, then the resultant graph may become minimal, if the process of detecting and removing redundant edges succeeds. So, it needs to establish the reliable procedure to distinguish the set of necessary edges and the set of redundant edges.

Another problem is to extent these theorems to the network with link capacities or link directions.

7 Conclusions

The simple procedure for graph extension is proposed. It becomes useful when the network is required to enlarge its communication stations or to connect with an another network. This method has the advantage to be able to apply repeatedly, so we can make the large network starting from small ones.

The problems to detect redundant edges and to get the minimal graph are left for further considerations.

References

[1] Ido H., "An Extension of Networks with a Constant Connectivity"(in Japanese), IEICE Trans. Vol. J71-A, No.10, pp.1983-1984, 1988.

[2] Harary F., "Graph Theory", Addison-Wesley, 1972.

[3] Hakimi S.H.: "An Algorithm for Construction of the Least Vulnerable Communication Network or the Graph with the Maximum Connectivity", IEEE Trans. On Circuit Theory, CT-16, No.5, pp.229-230, 1969.

[4]. Tutte W. T., "A Theory of 3-connected Graphs", Indagations MATHEMATICS, Vol.23, pp.441-455, 1961.

[5] Ido H., Sasaki T., "On the Construction of Systems with the Minimal Structure" (in Japanese), IEICE Trans. Vol. 63-A, No.6, pp.398-405, 1980.

[6] Halin R., "A Theorem on n-connected Graphs", Journal of Combinatorial Theory, Vol.7, pp.150-154, 1969.

The Eleventh International Symposium on Artificial Life and Robotics 2006 (AROB 11th'06),
B-con Plaza, Beppu, Oita, Japan, January 23-25, 2006

Design and Fabrication of Tactile Sensor System of FBG Optical Fiber Sensors

Jin-Seok Heo
Dept. of Mechanical Engineering
Korea Advanced Institute of Science and Technology,
Daejon, Korea 305-701
dandyheo3070@kaist.ac.kr

Jung-Ju Lee
Dept. of Mechanical Engineering
Korea Advanced Institute of Science and Technology,
Daejon, Korea 305-701
leejungju@mail.kaist.ac.kr

Abstract

This paper describes the flexible 3x3 array force sensors using fiber Bragg grating (FBG) and silicone rubber for the tactile sensor to detect the distributed normal force. This sensor has the simple principle. Once, the external force is applied to the transducer which is made of flexible silicone rubber, the reflective wavelength of the fiber Bragg grating which is embedded to the transducer is changed. Then the change of reflective wavelength, so called, Bragg wavelength indicates external force change. The chirping effect and the light loss for micro bending must be considered to design this flexible transducer. The performance of this transducer can be simulated using finite element method (FEM). The prototype is fabricated and the performance of prototype is evaluated. The temperature compensation is applied to this prototype for more precise measuring. And this array sensor is attached to the silicone rubber which is similar to the human skin to check the applicable possibility of the intelligent robot system.

1. Introduction

Sensory information of human skin for feeling some materials and determining many of their physical properties is provided by sensors in the skin. This tactile information is a kind of sense of touch that is one of the five senses including the sense of sight, hearing, smell and taste. Nowadays, many researchers try to apply the five senses to the intelligent robot system. Especially, many kinds of the tactile sensor combined small force sensors are introduced for intelligent robots, teleoperational manipulators and haptic interfaces. These tactile sensors which are able to detect the contact force, the vibration, the texture and the temperature can be recognized as the next generation information collection system.

Some tactile sensors using the MEMS(Micro Electric-Mechanical System) technology have been introduced[1-4]. Although these sensors have a good spatial resolution, they remain some problems to apply the practical system: they are not enough flexible to attach the curved surface and the more elements of sensor connect, the more wires they need. Therefore, in this paper, we will show the flexible 3x3 array force sensor using flexible optical fiber sensor and newly designed small transducer that can be easily applied to the curved surface minimizing the wiring.

2. The Structure of the Flexible FBG Sensor

2.1 The Principle of the FBG sensor

Fiber Bragg grating (FBG) sensors based on wavelength-division multiplexing (WDM) technology are attracting considerable research interest and appear to be ideally suitable for structural health monitoring of smart structure[5]. FBG sensors are easily multiplexed and have many advantages such as linear response and absolute measurement. As the spectral response of the FBG sensor signal renders the measurement free from intensity fluctuations, it guarantees reproducible measurements despite optical losses due to bending or connectors. The basic principle of a fiber Bragg grating (FBG)-based sensor system lies in the monitoring of the wavelength shift of the returned Bragg-signal, as a function of the measurand (e.g. strain, temperature and force). The Bragg wavelength is related to the refractive index of the material and the grating pitch. Sensor systems involving such gratings usually work by injecting light from a spectrally broadband source into the fiber, with the result that the grating reflects a narrow spectral component at the Bragg wavelength, or in transmission this component is missing from the observed spectrum. Fig.1 shows this simply and schematically. The intensity of the reflected optical signal is a function of the Bragg grating wavelength that relates to the applied strain on the fiber Bragg grating. Therefore, the dynamic strain can be derived from the intensity change measurement as function of the wavelength of the reflected optical signal. The operation of a FBG is based on a periodic, refractive index change that is produced in the core of an optical fiber by exposure to an intense UV interference pattern. This grating structure results in the reflection of the light at a specific narrow band wavelength, called Bragg wavelength. The Bragg condition is given by

$$\lambda_B = 2n_e\Lambda \quad (1)$$

where λ_B is the Bragg wavelength of the FBG, n_e is the effective index of the fiber core, and Λ is the grating period. The shift of the Bragg wavelength due to strain and temperature can be expressed as

$$\Delta\lambda_B = \lambda_B\left[\left(\alpha_f + \xi_f\right)\Delta T + \left(1 - p_e\right)\Delta\varepsilon\right] \quad (2)$$

$$p_e = \left(\frac{n^2}{2}\right)\left[p_{12} - \nu\left(p_{11} - p_{12}\right)\right] \quad (3)$$

where α_f is the coefficient of the thermal expansion (CTE), ξ_f is the thermo-optical coefficient, and p_e is the strain-optical coefficient of the optical fiber. The value of p_e =0.22[7] was measured experimentally and used for this study. If there is no temperature change, we can measure the strain from the wavelength shift as

$$\varepsilon = \frac{1}{\left(1 - p_e\right)} \frac{\Delta\lambda_B}{\lambda_B} \quad (4)$$

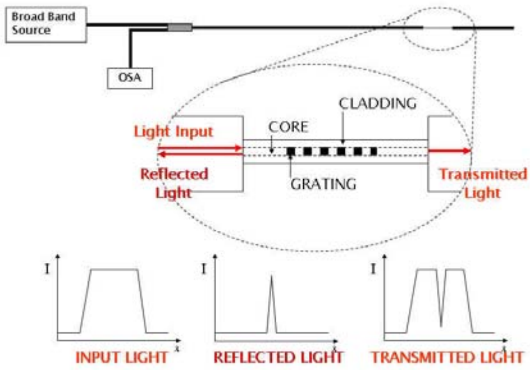

Fig.1 FBG sensor encoding operation

2.2 The Structure of Flexible FBG Force Sensors

In general case of small force sensor, the diaphragm type transducer which can be easily deflected by the applied force is mostly used. But, this diaphragm type transducer can be occurred the chirping which is caused by the non-uniform strain distribution and the loss of reflected light by micro bending of the optical fiber. These two effects have influence on the performance of sensor. Therefore, the minimizing these two effects must be considered when the small sensor is designed.

First of all, the light loss caused by micro bending is much significant than that by the macro bending of optical fiber when the smaller sensor is fabricated. As the sensor size is minimized, the possibility that the local deflection of optical fiber is appeared is increased. As shown in Fig. 2, if the micro bending is occurred in the optical fiber, the intensity of the reflected light is remarkably decreased. Then, the proper Bragg wavelength can not be detected. Therefore, the transducer must be designed to minimize this micro bending effect.

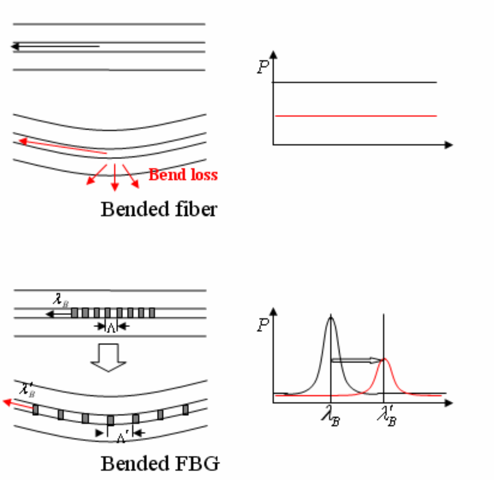

Fig. 2 Micro bending effect of Bragg wavelength

In the case of using fiber Bragg grating sensor, FBG is frequently experienced non-uniform strain distribution. This non-uniform strain distribution makes the distorted Bragg wavelength, so called, chirping (Fig. 3) which interferes to find the exact Bragg wavelength. Therefore, the transducer must be designed to avoid this chirping effect.

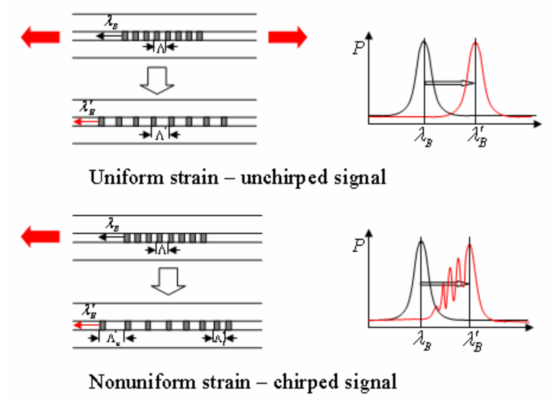

Fig. 3 The chirping effect of FBG

To avoid these drawbacks, the transducer is designed as shown in Fig. 4. The transducer which looks like the bridge can be extended symmetrically to the optical fiber direction when the external normal force is applied to the top of that. This extension of the transducer makes the uniform elongation of the Bragg grating which is attached under the transducer. As this structure can be extended to only the fiber direction, there is no micro bending. Then, the Bragg wavelength shift occurs without the chirping and the light loss of Bragg wavelength.

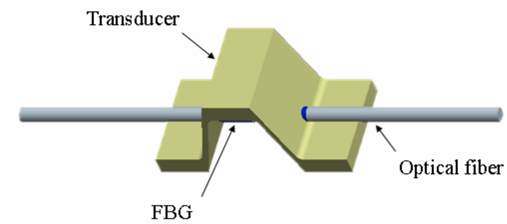

Fig 4. Newly designed transducer using fiber Bragg grating sensor

3. Design of the Transducer using FEM

First of all, the capacity of flexible force sensor must be decided. As this sensor will be applied to the tactile sensor system, maximum force range of 10N that is similar to the capacity of human skin is accepted. The length of FBG which is used in this sensor is 2mm. The shorter FBG can be used, the shorter spatial resolution can be realized when this force sensor can be utilized as the tactile sensor. Some researches introduce the dozens of μm FBG length [6]. Therefore, the spatial resolution of this array sensor can be improved more and more keeping pace with the development of minimized grating length. The 5mm spatial resolution of this array sensor is designed considering the size of transducer. Fig. 5 shows the designed dimension of transducer. And the transducer is made of beryllium copper (BeCu) which is often used as the spring material. As the extension to the optical fiber direction must be increased, the thickness of side rims is minimized as possible as we fabricate. And the diameter of holes which are on the center of the each rim is 0.3mm. That is suitable size to insert the optical fiber sensor which has 250μm diameter.

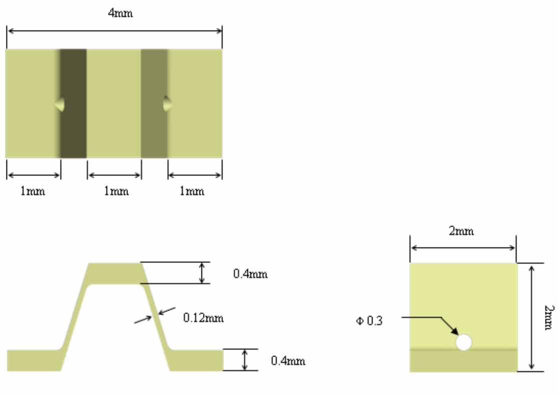

Fig. 5 The dimension of the transducer

If the extension of the transducer where the fiber Bragg grating sensor is attached can be simulated, the shift of the Bragg wavelength can be also estimated by using the equation (4). Using the finite element method, the extension of the transducer can be calculated like Fig. 6-(a). As the structure of transducer is symmetric, the half geometric model is used and 2-dimensional element model is applied. And Fig. 6-(b) shows the estimated extension of the transducer and the shift of Bragg wavelength by the applied external normal force.

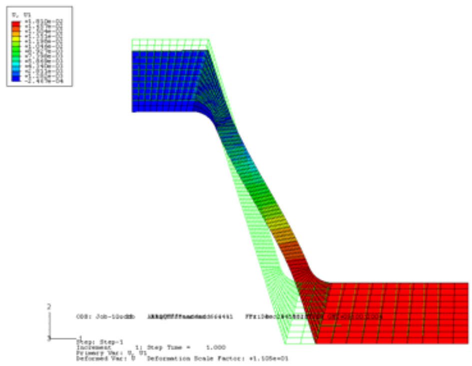

(a)

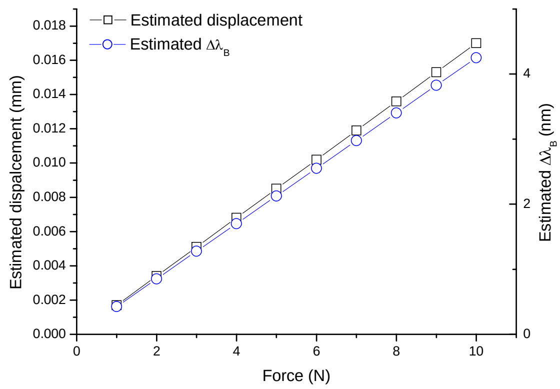

(b)

Fig. 6 Finite element analysis of the transducer: (a) FEM model, (b) Estimated extension and Bragg wavelength shift by the external normal force

4. Fabrication and evaluation of the taxel

As shown in Fig. 7, the alignment system using the microscope and the precision stage is made use of in fabricating the taxel (the element of the tactile sensor) to avoid the fracture of the optical fiber sensor. Aligned fiber Bragg grating sensor is fixed by the epoxy.

Fig. 7 Fabrication of the taxel

The fabricated prototype taxel is calibrated by the verified uniaxial loadcell as show in Fig. 8. The broadband light source having the 1527~1602nm wavelength is incident in the optical fiber and the light is separated by the 2 by 1 coupler. The isolator cannot transfer the reflected light to the broadband light source source. The separated light is transmitted in the Bragg grating. And the reflected light is experienced the applied load is sent the tunable Fabry-Perot filter (TFPF) which can detect the Bragg wavelength. The prototype sensor is set on the z-stage and is aligned to the loadcell. As the z-stage moves up, the mesa of the prototype sensor is pressed by the loadcell. That is, the same force is applied to the loadcell and the prototype sensor and then the prototype sensor can be calibrated by comparing with the data of verified loadcell.

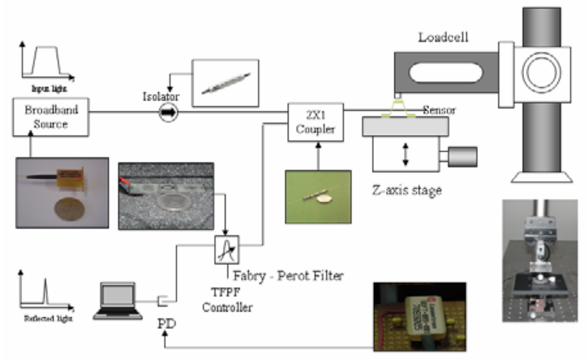

Fig. 8 Calibration system of prototype taxel

Fig. 9 shows the Bragg wavelength change by the applied force. There is linear relation between the Bragg wavelength change and the force. But some difference between the estimated and the experimental shift of the Bragg wavelength comes out. This difference results from the exclusion of the optical fiber in the FEM model. Using this relation, we can find the exact force detecting the Bragg wavelength. The accuracy of the prototype sensor is 99.9% and the resolution is 0.01N. The resolution of this optical force sensor depends on that of the tunable Fabry-Perot filter which detects the Bragg wavelength (0.02nm). Namely, if the resolution of the TFPF will be improved, that of the force sensor will be enhanced.

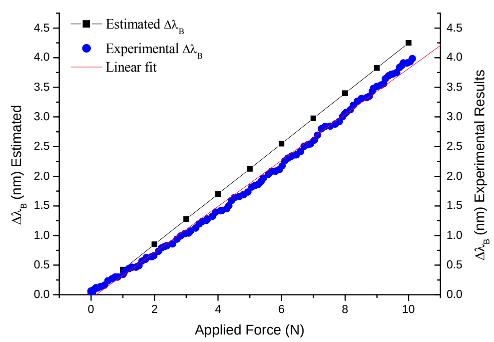

Fig. 9 Estimated and Experimental Bragg wavelength shift vs loadcell signal

5. Conclusion

In this paper, the force sensor using fiber Bragg grating for the tactile sensor is newly designed and experimentally verified. The size of sensor is 5mm and the used length of FBG is 2mm. If shorter FBG is used, then smaller size of the flexible force sensor will be made. Especially, to avoid the chirping and light loss by micro bending effect, the transducer of taxel is newly designed. Using the FEM, the Bragg wavelength shift is estimated and this estimated result is well matched to the experimental results. There is linear relation between the applied force and the Bragg wavelength shift in each taxel. The resolution of the taxel is about 0.002N. The fiber Bragg grating sensors are multiplexed using wavelength division multiplexing method.

Acknowledgement

This research (paper) was performed for the Intelligent Robotics Development Program, one of the 21st Century Frontier R&D Programs funded by the Ministry of Commerce, Industry and Energy of Korea.

Reference

[1] T. Mei, W. J. Li, Y. Ge, Y. Chen, L. Ni and M. H. Chan, "An integrated MEMS three dimensional tactile sensor with large force range", Sensors and Actuators (A), Vol. 80, pp155-162, 2000

[2] M. J. Yoon, K. H. Yu, G. Y. Jeong, S. C. Lee and T. G. Kwon, "Development of a Distributed Flexible Tactile Sensor System", J. of KSPE, Vol. 19, No. 1, pp. 212~218, 2002

[3] N. Futai, N, Futai, K. Matsumoto and I. Shimoyama, "A flexible micromachined planar spiral inductor for use as an artificial tactile mechanoreceptor", Sensors and Actuators (A), vol. 111, pp293~303, 2004

[4] U. Paschen, M. Leineweber, J. Amelung, M. Schmidt and G. Zimmer, "A novel tactile sensor system for heavy-load applications based on an integrated capacitive pressure sensor", Sensors and Actuators (A), vol. 68, pp294~298, 1998

[5] C. Y. Ryu, C. S. Hong, C. G. Kim, S. B. Lee, and S. S. Choi, "Strain measurement of the laminated composite using attached fiber Bragg grating sensor", Proceeding of the 3rd optoelectronics and communications conference, pp272~273, 1998

[6] Meng-Chou Wu, R. S. Rogowski, and K. K. Tedjojuwono, "Fabrication of extremely short length fiber Bragg grating for sensor application", Sensors, Proceeding of IEEE, vol. 1, pp 49~55, 2002

The Eleventh International Symposium on Artificial Life and Robotics 2006 (AROB 11th'06),
B-con Plaza, Beppu, Oita, Japan, January 23-25, 2006

Implementation of an Intelligent Personalized Digital Library System based on Improved Negotiation Mobile Multi Agents,

Young Im Cho
Dept. of Computer Science, Suwon University
Wauri 2-2, Bongdap-up, Hwaseong, Kyeongki-do, KOREA
e-mail : ycho@suwon.ac.kr

Abstract

There are several problems in the searching of database of the existing digital library. To overcome some problems, I proposed a new platform of mobile multi agents for a personal digital library. For developing a new platform, I proposed DMMAF agent

For the higher relationship among searched documents from mobile servers, an unsupervised neural network is applied. For the user's preference, some modular clients are applied to a neural network. A multi agent platform and a mobile agent platform are combined to develop a new mobile multi agent platform so as to decrease a network burden. Also, a new negotiation algorithm and a scheduling algorithm are activated for the effectiveness of PDLS.

PDLS is more intelligent system capable of establishing database in his computer by learning interests of users. We tried to set up the theoretical structure of the multi mobile agents and develop an algorithm of the modified intelligent negotiation agent for inducing interaction among multi agents.

I. Introduction

Recent developments of the internet and network technologies evoke the technical change of the data processing from a conventional centralized and local processing system to the distributed processing system. The research about this network and the various approaches have been studied in order to efficiently manage mutual operations in such a network environment.

Many studies have been actively carried out in a distributed processing environment by using agent systems for efficient network management. An agent system has the following characteristics: multi agents in the distributed environments promote efficiency by solving one problem through any cooperation. Each agent manages the problem by dividing a common work into the number of agents, or each agent manages it independently, and then they solve the problems by analyzing the results. In addition, it has some advantages such that intelligent agents reflecting the tendency of users make no limitation of movement in a network, and it remarkably decreases the network traffic [1].

There are so many application areas of agents in the real world. One of these areas is a digital library system. The digital library is called an *electronic library* or a *virtual library*. This is a library developed to replace the conventional library, in order to serve information from databases on the web to users, according to the development of computers and the related fields.

However, there are several problems in the searching of data of the existing digital libraries. First, as the searching method is one dimensional and distinguishes the existence of the searching keyword from the database, the result is very simple. Secondly, the results may contain unnecessary information under a condition that was not given the prior information about the user. Thirdly, whenever a client connects to the servers, he has to receive the certification and be under the dominant power of the influence of network.

To overcome such problems, I proposed a new platform of mobile multi agents for a personal digital library in this paper. For developing a new platform, I combined the existing DECAF (Distributed Environment Centered Agent Framework) multi agent framework [2] with Voyager which is a mobile ORB (Object Request Broker). Also a new negotiation algorithm and a scheduling algorithm are proposed, so that I developed a PDLS (***P***ersonal ***D***igital ***L***ibrary ***S***ystem) using this new platform. Although the partial studies for a personal digital library have been carried out, there has been none about the integrated and systemized personal digital library.

For the higher relationship among searched documents from mobile servers, an unsupervised neural network is applied. For the user's preference, some modular clients are applied to a neural network. A multi agent platform and a mobile agent platform are combined to develop a new mobile multi agent platform so as to decrease a network burden. Also, a new negotiation algorithm and a scheduling algorithm are activated for the effectiveness of PDLS.

PDLS is different from the electronic paper service system which is supplied only to members. It is a more intelligent system that is capable of establishing a database in users' computer by learning the interests of those individuals. In this paper, I tried to set up the theoretical structure of the multi mobile agents and develop an algorithm of the modified intelligent negotiation agent for inducing interaction among multi agents.

This paper is composed of five chapters. Multi agents and DECAF framework is explained in chapter 2. PDLS based on a new mobile multi agent platform is explained in chapter 3. The simulation results of PDLS are explained in chapter 4, and finally the conclusions are in chapter 5.

2. Multi Agent System

2.1 DECAF framework and Voyager

DECAF (Distributed Environment-Centered Agent Framework) is a conventional framework to design a lot of intelligent agents [2]. DECAF is a kind of operating system including agent communication, planning, scheduling, monitoring, coordination, diagnosis, and learning among agents. DECAF makes a socket program by itself, and presents some building blocks which makes messages and communicates between agents. Therefore, users or programmers can produce agents without having some knowledge about API approaches. Also, users or programmers do not need to make the communication codes directly to communicate among agents. DECAF produces a KQML protocol automatically which sends messages and searches other agents and interacts between agents. Agent systems have been developed using various languages and platforms, and they are classified into so many types by purpose. In DECAF, many agents' tasks are divided by both GPGP (Generalized Partial Global Planning) and TAEMS (Task Analysis Environment Modeling and Simulation) algorithms.

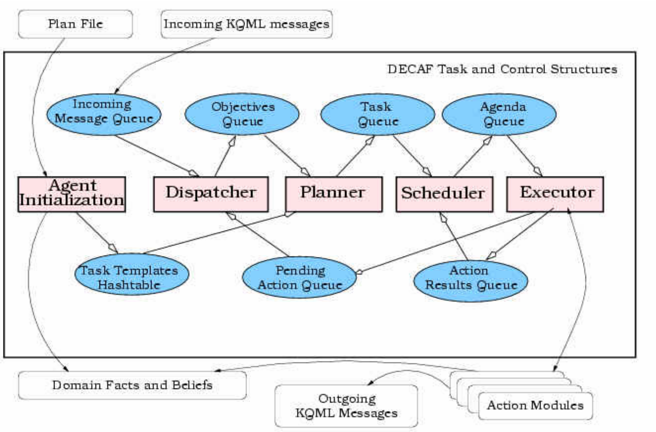

Figure 1. DECAF

GPGP is for improving of PGP which acts as a coordination algorithm of multi agents [3]. The first advantage of GPGP is that it reduces the system overhead which occurs by overlapping interaction among agents. And the second advantage of GPGP is that it is independent from some specific domain areas. Therefore, GPGP can make heterogeneous multi agents system having different functions. User's requirements can be decomposed by GPGP, and be structured by TAEMS [4]. User's requirements can be decomposed by GPGP, and be structured by TAEMS(Task Analysis Environment Modeling and Simulation)[4]. The root task can be decomposed into subtasks, and the subtasks can be decomposed into methods. The leaf node acts as a method which means actually acted elements.

Voyager [5] is a distributed mobile agent's framework for developing agent's applications, whereas DECAF is a non-mobile agent's framework. Voyager is an interactive framework with Java programming. Also, Voyager can activate any Java class in remote sites, and it makes use of network bandwidths effectively.

2.2 The Concept of Agent based Digital Library

A digital library serves a lot of information on-line [6,7]. The advantages of digital libraries are user friendly, on-site service and accessibility. However, in case of not having standardized platform, the search of heterogeneous information from digital libraries may be hard, as well as impossible. If it does not have or learn about the user's information, unnecessary or useless information will appear in the searched results from the digital library.

Each agent can access DBMS and search documents according to the user profile. And then each agent categorization of the searched results.

3. Personal Digital Library System based on a DMMAF Agent Platform

3.1 System Structure

The proposed system, in Figure 2, is a Personalized Digital Library System (PDLS) based on a new multi mobile agent platform. The system combines a mobile system and a distributed processing system to make an optimization of behaviors in a distributed environment. To establish a distributed environment, DECAF is used, and to activate a mobile framework, Voyager is used here.

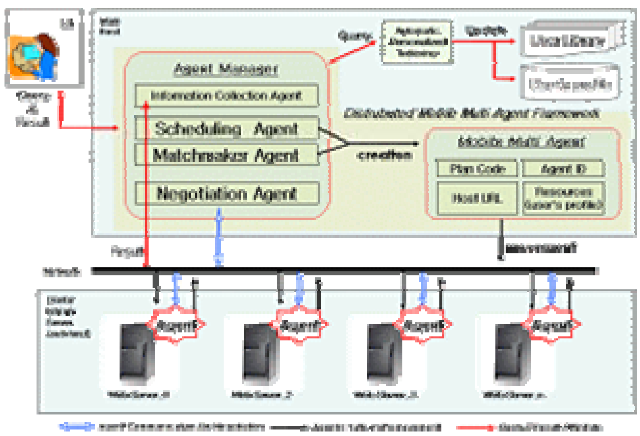

Figure 2. PDLS Structure
b

The PDLS is composed of two parts: client group and server group. The client group is composed of three modules. First, a user interface module lets users make use and control the library. Second, a user profile control module learns the user's preferences by neural network (SOM [8]), and makes databases accordingly. Third, a PLA (Personal Library Agent) module makes multi agents in real time, and searches information from the library according to the user's profile, and stores the searched results into a database. The interactions among detailed modules in PDLS are explained in Figure 3(b).

As shown in Figure 2, PLA has two modules and two databases. The monitoring agent module is composed of Voyager and DECAF, and it monitors the agents' movements and controls their executions. When the user's requirements are transferred to the PLA, the monitoring agent module checks whether the servers are available or not. After that, it makes some agents, and passes them to the servers. The searched results are saved in a temporary repository. They are filtered by negotiation agents, and the final results are saved in the result repository.

```
/* improved negotiation algorithm of multiagents */

Switch(one of 5 relations) { /* relation_name(sender, receiver) */
  case 1: Add_R(Ai_Mi, Aj_Mj)
        /* (i≠j), Ai=agent, Mi=method */
      while(Aj_Mj is finished)
          no-operation (Ai-Mi); break;
  case 2: Compensate_R(Ai_Mi, Aj_Mj)
      Ai_Mi and Aj_Mj are operated in real situation
      by call(inference) function;
      Inference() is from user profiles or user information
       repository;
      break;
  case 3: Replace_R(Ai_Mi, Aj_Mj)
      Aj_Mj=Ai_Mi;
      break;
  case 4: Contradict_R(Ai_Mi, Aj_Mj)
      Aj_Mj=Aj_Mj;
      break;
  case 5: Activate_R(Ai_Mi, Aj_Mj)
      if wait(Aj_Mj) then awake(Aj_Mj) and restart;
      break;
  default:
}
```

Figure 3. Negotiation Algorithm among Multi Agents

In the proposed platform, the relationship among multi agents in negotiation agent module is in Figure 3. Agent_Task Group generates Task_1, Task_2 and Task_3 according to Agent 1, Agent 2, and Agent 3. Tasks are automatically decomposed into methods and do their assigned tasks. Each method has five types of methods' relationships. *Add_R* is to add the results of actions to the results of the other methods. *Activate_R* is to let the running method run continuously, *Compensate_R* is the relationship that the results among methods need to be compensated. *Replace_R* is to replace the results of receiving methods with the results of sending methods. *Contradict_R* is to disregard the results of receiving methods. Also, there are lots of relationships between methods and tasks and between methods and resources, such as *Enable, Facilitate, Produce, Consume, Limits* and so on. In the negotiation algorithm, if the agents in the same levels do the different actions, then *max* operation is operated to produce the output of the agents, and if the agents in the lower levels do the different actions, then *min* operation is operated.

3.3. The Construction of User's Profile

The construction of the initial user's profile is constructed by the user's first input information. According to the user's searched results, PDLS endows the user's keywords to weight values, and updates user's profile information by SOM (self organizing map) network in real time [7].

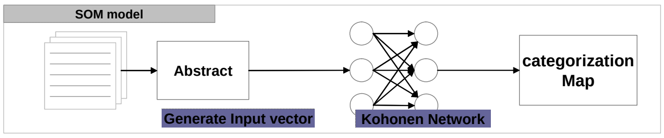

Figure 4. SOM network

SOM is an unsupervised neural network, In this paper, 2-layered SOM network is used here.

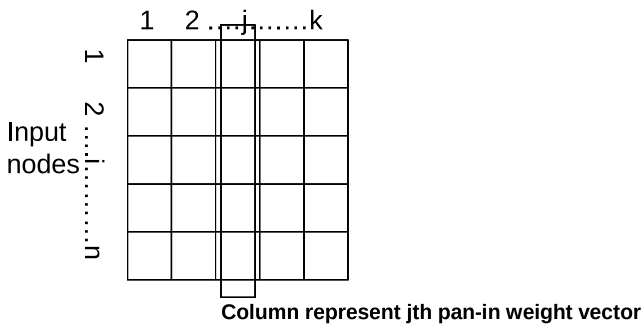

Figure 5. Weight Vector in SOM

In Figure 5, *wij* means a weight vector from node *i* to node *j* in SOM network. In SOM, a weight vector having the nearest Euclidian distance is categorized when searching documents.

The user interface of PDLS is composed of four windows. The user's window is for entering the user's information and for recalling the user's profile from databases. The monitoring window is for checking agent's activities. The remote window shows the final results, and finally the local window shows the constructed hard disk information of the user's computer by PDLS.

4. Simulation Results

The user interface is composed of four panes, and each pane is interconnected. The login window and query window is for user login. The user pane is for checking the agents' activation states including monitoring. The remote pane is for representing the information of remote servers and searched results. The local pane is for representing the building states of a local library. The scenario for PDLS simulation is in Figure 6.

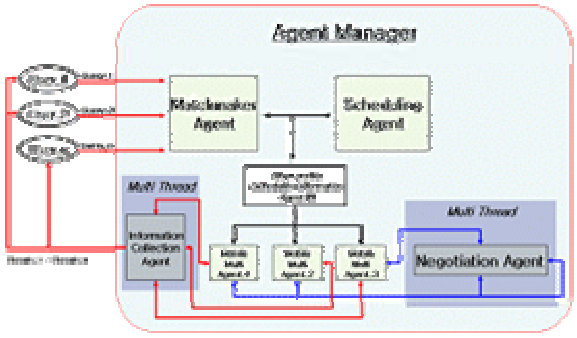

(a) Module Relations

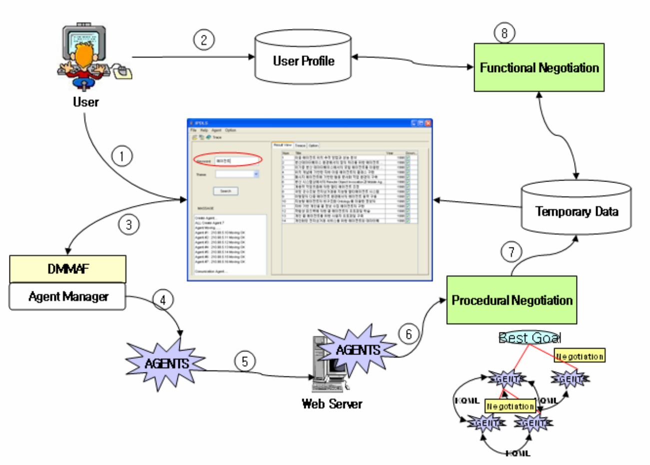

(b) PDLS Simulation Scenario

Figure 6. PDLS Interface and Simulation Scenario

① User login by user interface
② The monitoring agent(MA) is activated, and MA check the current connected remote digital library. At the same time, a user profile is read from database.
③ The queries according to users are sent to PLA.
④ MA makes a search agent 1and registers it in ANS.
⑤ The search agent 1 is sent to the remote library.
⑥ The agent 1 is activated by receive the parameters from PLA.
⑦ The results from the agent 1 with information such as name and index and abstract of the remote library are sent to PLA. And then they are sent to the negotiation agent(NA) for negotiation. At the same time, they inform to the MA and ANS.
⑧ A is clustered using SOM network according to the received results
⑨ The results by the user profile can be shown in the remote plane.
⑩ user can move to his local library after receiving his necessary results.
⑪ The user profile's update is activated.

Table 1. Keyword based Categorized Results

Category	Agent System	Neural Network	Digital Library
1	framework	learning	virtual
2	mobile	neural	library
3	java	architecture	indexing
4	multi	network	structure
5	personalized	simulation	distributed
6	distributed	layer	agent
7	environment	agent	retrieval
8	neural	artificial	autonomous
9	architecture	associative	neural
10	autonomous	algorithm	multi

Table I shows the categorized simulation results. As a results, there are 3 categorization by PDLS: agent system, neural network, digital library. 10 keywords in each categorization is classified by SOM network. For example, if the words such as framework, mobile, jave are found in any documents, the documents are classified "Agent System" group in PDLS.

All

36	1			7
11	50	4	29	
		32		
25	60	1	4	
10	16			8

Agent System

				7
	10	4	26	
	6	15		
	24		2	
1				5

Neural Network

21	1			
7	36		3	
		15		
			2	
9	6			

Digital Library

15				
4	4			
		2		
25	36	1		
	10			3

Figure 7. SOM Categorization Results

Figure 7 shows the simulation results according to the random documents in servers. The parameters used in SOM are like the followings. 2 dimensional array for output display and radius 2 for classification are used here. Also, the learning times and learning rate are 500 times and 0.05, respectively. The computer specification is CPU 1.8 GHZ(RAM 1024MB), and window NT based Mysql are used for simulation.

In Figure 7, the numbers in matrix mean the number of the classified documents. If the sum of the numbers in each category, the total will be 100, as we simulated using 100 documents.

The searching times between the proposed PDLS and the traditional client-server model are shown in Figure95. As time passed, PDLS showed a faster search time as well as a much safer search than the client-server model. The result showed that as the numbers of servers were increased, the searching time was decreased in PDLS.

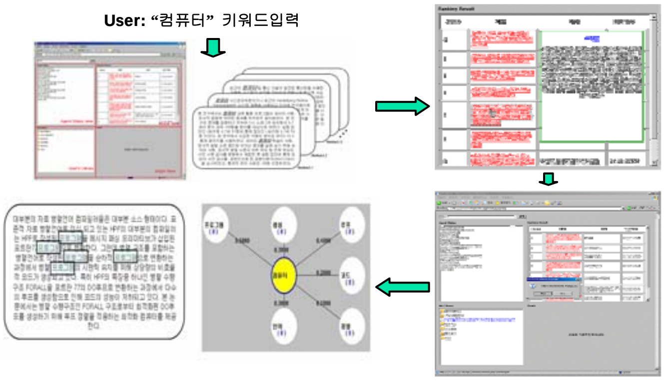

(a) Actual Results

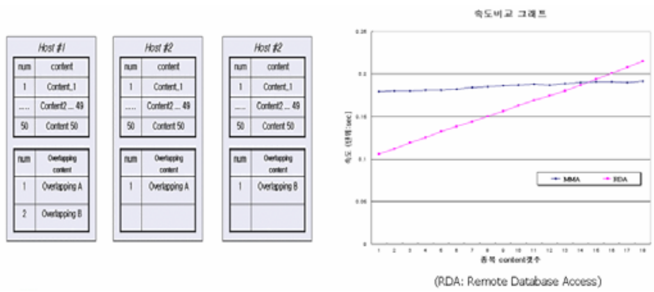

(b) Comparison of Simulation Results

Figure 8. Simulation Results

5. Conclusions

In this paper, I proposed a Personal Digital Library System. PDLS is designed based on a new mobile multi agent platform using Voyager and DECAF agent framework. The new platform is a hybrid system of a mobile and a distributed system in order to achieve an optimality in distributed Environments, and to make it operate effectively by the propose of a new negotiation algorithm and a new scheduling algorithm. From the simulation results of PDLS, the performance and the user's satisfaction of this system is higher than any other information search systems as of now. Also, as the numbers of servers and agents are increased, the searched time of PDLS is lowered. And the degree of the user's satisfaction is increased four times than the conventional client-server model. In the future, PDLS needs to be compensated in order to be activated in the real world.

Acknowledgements

This paper is carried out by supporting of KOSEF(KOrea Science and Engineering Foundation) during 2003 to 2005 as an Eminent Wonan Science Program.

References

[1] David C., Colin H., Aaron Kershenbaum, Mobile Agents: Are They a Good Idea?, 1995

[2] John R. Graham, Keith S. Decker, Towards Distributed, Environment Centered Agent Framework. Appearing in *Intelligent Agents IV, Agent Theories, Architectures, and Languages* Springer-Verlag, 2000, Nicholas Jennings, Yves Lesperance, Editors

[3] Keith S. Decker, Victor R. Lessor Generalizing the partial global algorithm. Intelligent Cooperative Information Systems, 1(2), pp.319~346. 1992

[4] Keith S. Decker, Task Environment Centered Simulation, 1996

[5] ObjectSpace, Voyager Core Technology 2.0 User Guide, ObjectSpace, 1998

[6] Sánchez, AGS: Introducing Agents as Services Provided by Digital Libraries, 1997

[7] Jonas Holmstrom, A framework for Personalized Library Services, October 2002

[8] Kohonen, Self Organizing Feature Map, 1995

Crowd simulation with virtual force model

Choon-Young Lee
School of Mechanical Engineering
Kyungpook National University
Daegu, 701-702, Korea
cylee@knu.ac.kr

Seongmin Baek
Digital Actor Research Team
ETRI
Daejeon, Korea
baeksm@etri.re.kr

Abstract

This paper presents a method of creating crowd scene by simulation with a virtual force model. The simulation results can be converted to a realistic crowd scene by incorporating motion capture data. Virtual force is used to generate a specific motion of character agent. Model of virtual force is based on the Helbing's particle model and reflection force of the proposed method can be controlled by a set of parameters. Our experiments show that the generation of somewhat exaggerated crowd scene in movie can be easily done.

1. Introduction

These days, the techniques for creating human-crowd scene have been studied actively because the demand of a large-scale crowd scene increases in the film industry. Previous researches focused on collision detection using particle or bounding volume, human-behavior, and using motion capture data. However, these methods are somewhat insufficient to human crowd. For example, the trajectory that generated by the simulation of particle is natural but it is very difficult problem to convert the simulation result into human motion. In other problem, it has disadvantage that the performing actions are limited when applying to the crowd.

This paper presents a method for simulating crowd scene by virtual force model. The result of this simulation can be converted into natural human locomotion by multi-layer posture.

Virtual force generates various interactive situations between agents. These interactions give more vivid motions of agents. Posture database stores important information for using these postures easily and efficiently in assigning motion capture data to a n agent. Our method takes advantage of the fact that it can create variable motions using a few motions and generate a natural human-crowd scene. Experimental results show various situations can be generated with the proposed force model.

The organization of this paper is as follows. In section 2, we explain related works for crowd simulation. Virtual force based simulation scheme is described in section 3. The experimental results are shown in section 4. We summarize future direction in section 5.

2. Related Works

There has been a great deal of past research in a number of crowd simulations, especially, collision detection that is known by bottleneck in computer simulation. I-Collide[2] is adopted a tow-level approach to control complex and the number of objects in a large scale environments. Hubbard[3] proposed progressive refinement method to guarantee accuracy while maintaining steady and high frame rate. Kim[4] presented an efficient collision detection algorithm among spheres moving with unknown trajectory. Reynolds[13][14], Xiaoyuan[18], Niederberger[9] solved a collision detection about non-human creature and focused on the behaviours of creature.

In Improv[11], it is suggested a method that control the interactive actors by interpolation after defining the range of joint angle using script language. Improv consists of two subsystems, an animation engine and a behaviour engine. The combined system provided an integrated set of tools for authoring the minds and bodies of interactive actors. Lee *et al*.[6] presented that a connected set of a human-like character is able to be created from non-linear sequences of motion, automatically organized for search, and used real-time control of an avatar using three interface techniques: selecting from a set of available choices, sketching a path, and acting out a desired motion in front of a camera. Kovar *et al*.[5] constructed a directed graph called a motion graph that includes connections among the database for creating realistic, controllable motion. The motion graph consists of original motions and automatically generated transitions. Li *et al*.[7] described motion texture that consists of LDS(linear dynamic system) for synthesizing complex human character that is statistically similar to the original motion captured data. Pullen *et al*.[12] discussed a method for creating animations by setting a small number of key-frames and used motion capture data to enhance the animation. Arikan *et al*.[1] created the new motion performs the specified actions at specified times by assembling the motion capture data from motion database and sketch on the timeline with annotations.

Motion blending method produces new motions from example motions according to time-varying weights. Park *et al.*[10] suggested a motion transition graph to solve on-line motion blending and transition simultaneously. Rose *at el.*[15] presented technique for interpolating between example motions. They used *verb*, parameterized motions, and *verb graph* with smooth transition between motions.

Thalmann[16] and Ulicny[17] presented the method that control the crowd by real time in virtual environment. Musse *et al.*[8] described a model for simulation of human crowd by a hierarchy composed of virtual crowds, groups and individuals in real time.

3. Virtual Force Model

The social force model by Helbing [19] was a foundation of the proposed virtual force model. For a crowd consisting of N agents, the force acting on the i-th agent is denoted by

$$f_i = f_i^{\,S} + \sum_{\substack{j=1 \\ i \neq j}}^{N} f_{ij}^{\,I} + \sum_{k=1}^{M} f_{ik}^{\,O} \tag{1}$$

where $f_i^{\,S}$ denotes the self-driven force which forces the agent toward desired location with desired speed, $f_{ij}^{\,I}$ denotes the interaction force on agent i with agent j, and $f_{ik}^{\,O}$ denotes the obstacle avoidance force due to the k-th object.

Here, we focused on the modeling of interaction force $f_{ij}^{\,I}$. Commonly, this force is modeled by exponentially decaying function with distance in radial direction. Oval like shape is used as equi-force line for interaction force and the shape is controlled by three independent parameters.

$$f_{ij}^{\,I} = A\exp(-g(d_{ij})/B)n_{ij} \tag{2}$$

where $g(d_{ij})$ represents effective distance conversion for calculating interaction force. Helbing used $g(d_{ij}) = d_{ij}$ so that the resulting interaction force reduces according to the Euclidean distance.

4. Simulation Results

We conducted three kinds of experiment using the proposed virtual force model. The first case is to get together at the specified position for all agents (Fig. 1). The second case is to move randomly and the shape of virtual force is controlled interactively with the user during simulation (Fig. 2). The final case is to crack a group of ranks by a virtual force model (Fig. 3). Fig. 4 shows a crowd scene generated by the virtual force model.

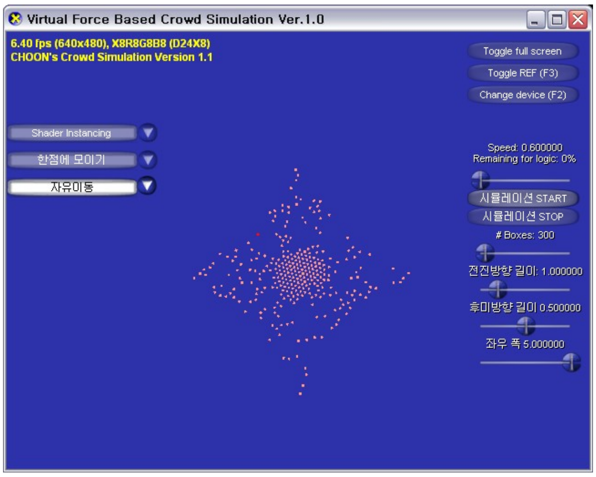

Fig. 1. All agents get together at some position

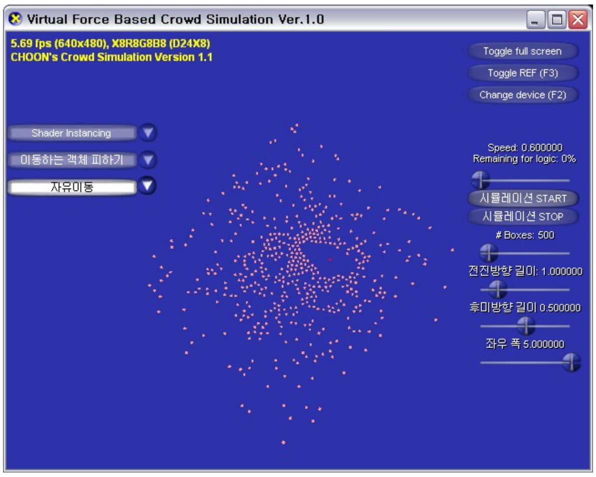

Fig. 2. Random Movement

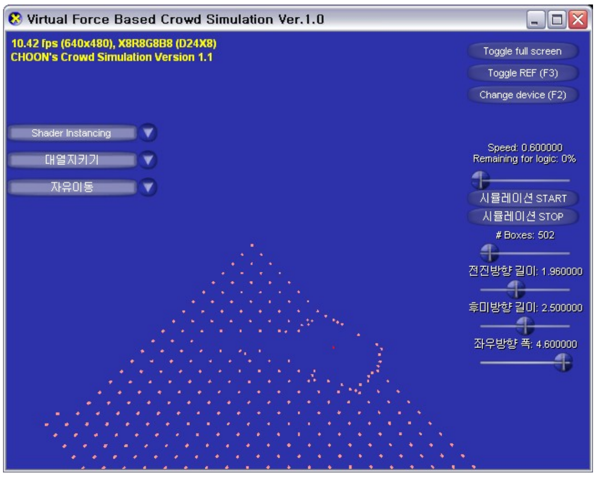

Fig. 3. Virtual Force for a group of ranks

Fig. 4. A crowd scene made by the proposed method

5. Conclusions

To create a human crowd scene in a movie, an easy and efficient method is needed. The crowd motions should be looked like those of real humans and conformed to the scenario continuity. In this paper, simulation result by a virtual force can be mapped to the human motions and a few experiments for crowd scenes were conducted.

The general formulation of virtual force by using spline curve will be our further research topics.

Acknowledgements

This work was supported by ETRI Research Fund, 2005.

References

[1] ARIKAN, O., FORSYTH, D. A., AND O'BRIEN, J. F. 2003. Motion Synthesis from Annotations. In Proceedings of ACM SIGGRAPH 2003.

[2] J. D. Cohen, M. C. Lin, D. Manocha, and M. K. Ponamgi, I-COLLIDE: An Interactive and Exact Collision Detection System for Large-Scale Environments. In Proc. of Symposium on Interactive 3D Graphics: pp189-196, 1995.

[3] P. M. Hubbard. Collision Detection for Interactive graphics applications. IEEE Transactions on Visualization and Computer Graphics, 1(3): pp218-230, 1995.

[4] H. K. Kim, L. J. Guibas, and S. Y. Shin, Efficient Collision Detection among Moving Spheres with Unknown Trajectories, CS-TR-2000-159, 2000.

[5] Kovar, L., Gleicher, M., and Pighin, F. 2002. Motion Graphs. In Proceedings of ACM SIGGRAPH 2002, pp473-482, 2002.

[6] J. Lee, J. Chai, Reitsma, P.S.A., HODGINS, J. K., AND POLLARD, N.S. 2002. Interactive control of avatars animated with human motion data. In Proceedings of ACM SIGGRAPH 2002, pp491-500, 2002.

[7] LI, Y., WANG, T., AND SHUM, H. Y. 2002. Motion Texture: A Two-Level Statistical Model for Character Motion Synthesis. In Proceedings of ACM SIGGRAPH 2002, pp465-472, 2002.

[8] S.R. Musse, D. Thalmann. Hierarchical Model for Real Time Simulation of Virtual Human Crowds. IEEE Transactions on Visualization and Computer Graphics 7(2), pp152-164, 2001.

[9] C. Niederberger and M. Gross. Hierarchical and Heterogeneous Reactive Agents for Real-Time Applications. Computer Graphics Forum 22(3), 2003.

[10] Park, S. I., Shin, H. J., and Shin S. Y. year. On-line Locomotion Generation Based on Motion Blending. In Proceedings of the 2002 ACM SIGGRAPH/Eurographics symposium on Computer animation, pp 105-111, 2002.

[11] Perlin, K., and Goldberg, A. 1996. Improve: A System for Scripting Interactive Actors In Virtual Worlds. In Proceedings of ACM SIGGRAPH 1996, pp205-216, 1996.

[12] Pullen, K. and Bregler, C., "Motion Capture assisted animation: Texturing and synthesis", In Proceedings of SIGGRAPH 02, 2002, pp. 501-508

[13] C. W. Reynolds. Flocks, herds, and schools: A distributed behavioral model, In Proc. of SIGGRAPH 97, pp25-34, 1987.

[14] C. W. Reynolds. Steering Behaviors for Autonomuos Characters. In Conference Proceedings of the 1999 Game Developers Conference, pp763-782, 1999.

[15] Rose C, Cohen MF, Bodenheimer B. Verbs and adverbs:mulidimensional motion interpolation. IEEE Computer Graphics and Applications 1998; 18(5): 32–40.

[16] D. Thalmman, S. R. Muss, F. Garat. Guiding and Interacting with Virtual Crowds. In Proc. of EUROGRAPHICS Workshop on Animation and Simulation, pp22-34, 1999.

[17] B. Ulicny and D. Thalmman. Towards Interactive Real-Time Crowd Behavior Simulation. Computer Graphics Forum 21(4), pp767-773, 2002.

[18] Tu, Xiaoyuan, and D. Terzopoulos, Artificial Fishes: Physics, Locomotion, Perception, Behavior. In Proc. of SIGGRAPH 94, pp43-50, 1994.

[19] D. Helbing, I. farkas, and T. Vicsek, "Simulating dynamical features of escape panic," Nature, Voll. 407, pp. 487-490, 2000.

The Eleventh International Symposium on Artificial Life and Robotics 2006 (AROB 11th'06),
B-con Plaza, Beppu, Oita, Japan, January 23-25, 2006

Driver Fatigue Detection using Genetic Algorithm

Shanshan Jin and So-Youn Park and Ju-Jang Lee
Electrical Engineering and Computer Science
Korea Advanced Institute of Science and Technology(KAIST)
373-1, Guseong-dong, Yuseong-gu, Daejeon, 305-701, Korea
shanshan@odyssey.kaist.ac.kr, arashi@odyssey.kaist.ac.kr, jjlee@ee.kaist.ac.kr

Abstract

Nowadays, a lot of traffic accidents occurred due to driver fatigue. Driver fatigue detection based on computer vision is one of the most prospective applications of image recognition technology. There are several kinds of factors that reflect driver's fatigue. Many efforts have been done on developing fatigue monitoring, but most of them focus on only a single behavior, feature of eye, or head motion, or mouth motion, etc. When the fatigue monitoring is implemented on a real model, it is difficult to predict the driver fatigue accurately or reliably only based on driver's single behavior. Additionally, The changes of driver's performance are more complicated and not reliable. In this paper, we represent a model that simulates a space in a real car. A web camera as a vision sensor is located to acquire video images of the driver. Three typical characteristics of driver fatigue are concerned, pupil shape, eye blinking frequency, and yawn frequency. As the influences of these characteristics to the driver fatigue are quite different from each other, we propose a genetic algorithm(GA) based neural network(NN) system to make fusion of these 3 parameters. We use GA to determine the structure of neural network system. Finally, Simulation results show the proposed fatigue monitoring system detects driver fatigue probability more exactly and robustly.

Keywords *: Driver Fatigue, Genetic Algorithm, Neural Network.*

1 Introduction

Nowadays, a lot of traffic accidents occurred due to driver fatigue. Developing systems for actively detecting driver's fatigue and warning the tired driver is rather necessary[1]. Driver fatigue detection based on vision is one of the most prospective applications of image recognition technology. There are several kinds of factors that reflect driver's fatigue[2]. Driver fatigue

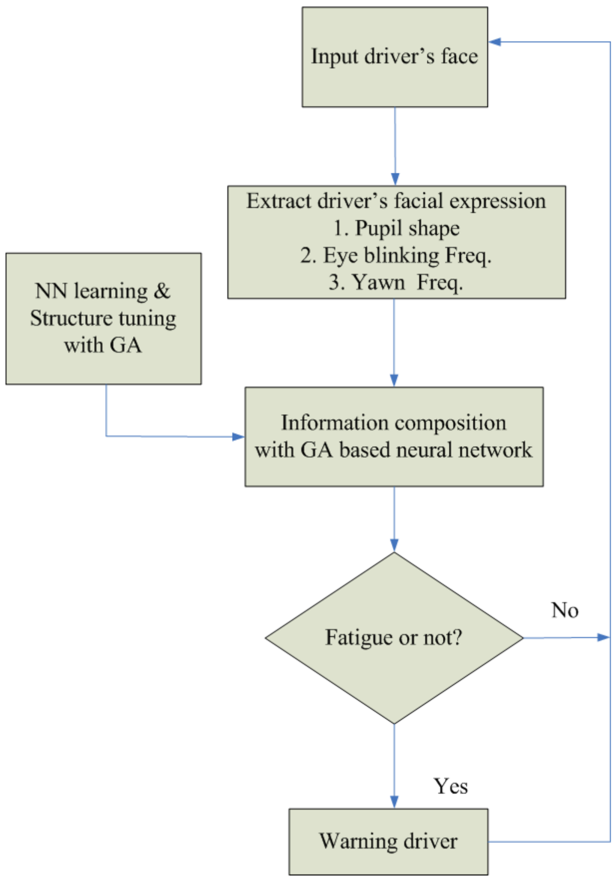

Figure 1: Driver fatigue detection system

detection heavily relies on facial expression recognition and tracking. Much research has been done on facial recognition technology, but most of them focus on only a single behavior of facial expression, such as feature of eye, or head motion, or mouth motion, etc[3]. When the fatigue monitoring is implemented on a real model, it is difficult to predict the driver fatigue accurately or reliably only based on singular elements of driver's behavior. The system relying on a single behavior may encounter difficultly when the detection of one facial expression cannot be acquired accurately or reliably due to the uncertainty of real model. In order to make the fatigue monitoring system more stable and reliable, the 3 main characteristics of driver's facial expression are used. Pupil shape, eye blinking frequency, and yawn frequency are detected, but the influence of these 3 elements on driver fatigue is quite different and nonlinear. Using these 3 kinds of driver's facial information, we propose the GA based neural network system to achieve the fatigue warning system. In this paper, we use back propagation learning algorithm to train weight value and apply genetic algorithm to optimize the structure of neural network. The driver fatigue detecting system is shown as Fig.1.

The rest of paper is organized as follows: Section 2 outlines the facial expression extraction for fatigue detection and section 3 describes the driver fatigue detection system using neural network and genetic algorithm. Simulation results for driver fatigue monitoring are given in section 4. Finally, conclusion is presented in section 5.

2 Facial Expression Extraction

In order to detect fatigue probability, we should extract the facial expression parameters first. As fatigue level can be properly characterized by eye and mouth movement, a vision sensor is needed to recognize and track eye and mouth. We can use a common video camera as a vision sensor on the premise that environment is bright enough. In this paper, pupil shape, eye blinking frequency, and yawn frequency can be measured using a Logitech web camera (QuickCam Pro 3000).

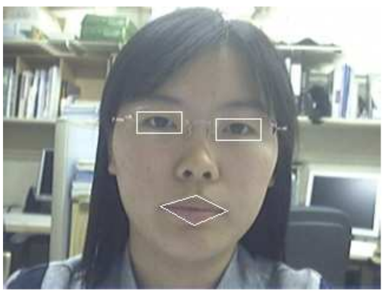

Figure 2: Eye and mouth regions from input image

Kalman filtering is widely used for object tracking. It can impose a smoothing constraint on the face motion. For the trajectory of each facial feature, this constraint removes random jumping due to the uncertainty in the image. Combining the Kalman filtering with the pupil motion can predict the current location of each feature [4]. The Gabor wavelet based method is used to identify each feature in the tracking initialization. Linear and nonlinear filters have been used for eye detection: oriented Gabor wavelets form an approximation of the eye gray level images; non linear filters are applied to color image[3]. Based on the above algorithms, we can detect the facial expression and obtain the data of each motion. Fig.2 shows the eye and mouth field regions; the facial feature in these regions is highly considered. The parameters needed in this paper for fatigue detection is as follows:

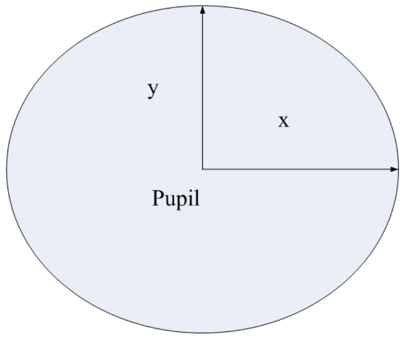

Figure 3: Pupil shape

- Pupil Shape
  The degree of eye opening can be detected by the shape of pupil. When the pupil gets occluded by the eyelids, their shapes get more elliptical. So we can test the ratio of pupil ellipse axes to characterize degree of eye opening. We use parameter X1 which is defined as (1) to describe pupil elliptical degree. Pupil shape is described in Fig.3.

$$X1 = y/x \tag{1}$$

- Eye Blinking Frequency
  When people concentrate on specified work, eye blinking frequency is much lower than they are not tired. Eye blinking frequency(per minute) as one parameter is detected to compute the fatigue probability.

- Yawn Frequency
  Besides pupil shape and eye blinking, another parameter that can potentially capture one's fatigue probability is frequent Yawning. We can focus on monitoring mouth movement to detect yawning. Another parameter of yawn frequency is the

occurrence frequency of yawning over time(per minute).

3 Driver Fatigue Detection System Configuration

As the diver environment and fatigue generation are quite complicated, it is difficult to determine driver's fatigue probability only by one performance or by simple combination of several performances. Moreover, the degree of each eye and mouth movement to express fatigue is so different and uncertain. Due to the above reason, here, we propose a neural network system to monitor driver's fatigue. In addition, we use genetic algorithm for selecting the optimal structure of neural network system.

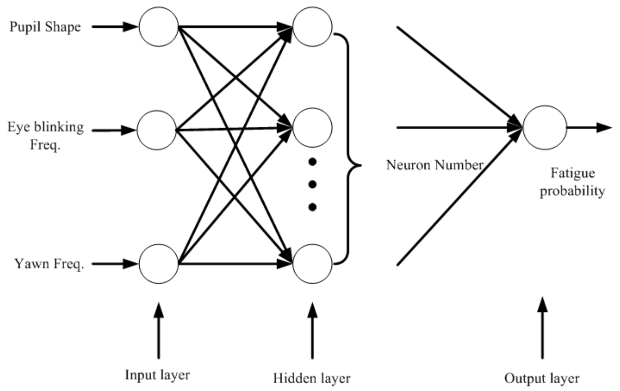

Figure 4: Neural Network System

3.1 Neural Network System

Neural network can simply solve the nonlinear complicated problem and results in quite accurate approximation of unknown system. Here, we use feedforward neural network with backpropagation learning algorithm. It is illustrated as Fig.4.

3.2 Neural Network Structure Tuning with Genetic Algorithm

As GA is stochastic and less likely to get trapped in local minima, it is an appropriate optimization algorithm to identify both structure and parameter of neural networks[5]. The Hidden layer number and neuron number of each hidden layer can be optimized by GA. The fitness function is neural network performance. Individuals of GA represent the layer and neuron number. GA process in detail is given in Fig.5.

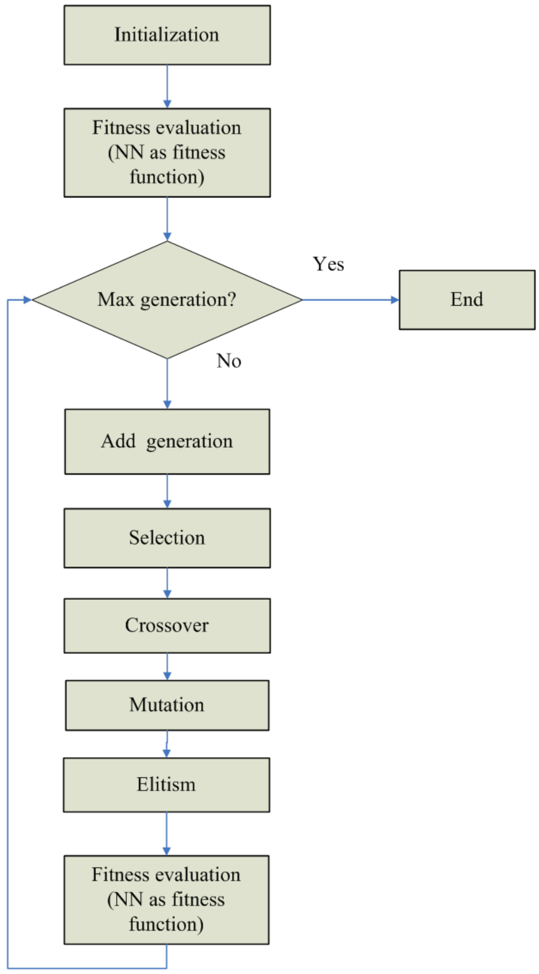

Figure 5: Genetic Algorithm Process

4 Simulation

In order to simulate the GA based NN fatigue detection system discussed above, we collected 60 data set of different people's pupil shape, eye blinking frequency, and yawn frequency for training the system. Furthermore, 50 set of extra data is used as the performance detection data. The initial weight of neural network is randomly generated, and the signal function of hidden layer is sigmoidal function. Here we use one hidden layer for simulation. The specified parameter value is given in Table1.

Driver fatigue probability is detected by the given system. Probability above 0.5 means the driver is very tired and should be warned. Fig.6 represents the detected fatigue probability compared with the desired value of performance data set. It clearly shows that the system totally detects the driver fatigue probability very well. From the simulation results, we know

Table 1: Simulation parameters

Parameter	Value
Input nodes	3
Output nodes	1
Hidden layer	1
Neuron number range	1∼ 30
Epoch number	500
Population size	20
Generation	20

that the best individual of neuron number is 4, and actually there are no obvious changes between distinct generations. As the data set we considered is not as complicated as the real situation, the fatigue system may be learned rather easily. If we consider more difficult and uncertain circumstance, the fatigue detection must be more relied on the increasing of generation.

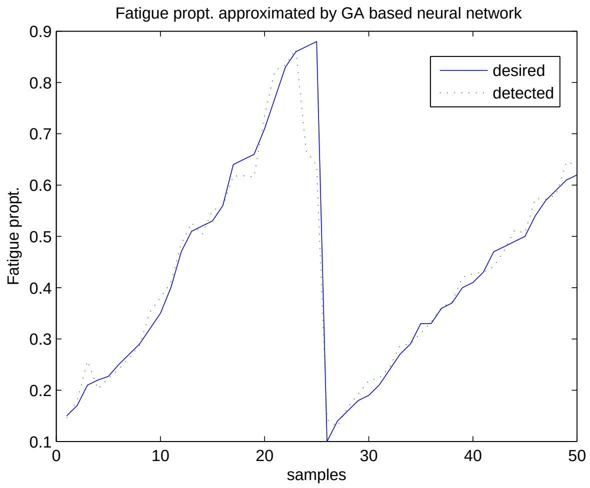

Figure 6: Fatigue Probability approximated by NN and GA

5 Conclusion

In this paper, we configured a driver fatigue detection system with genetic algorithm. The system was displayed as a neural network, and the optimal structure of the neural network was tuned by genetic algorithm. First, the facial expression of the driver was extracted by a video camera, so 3 main parameters: driver's pupil shape, eye blinking frequency, and yawn frequency can be obtained. Second, Neural network system based on the input of these 3 parameters was combined with genetic algorithm.

With the proposed system, we did the simulation using samples of different people's facial expression parameters. The results showed that our driver fatigue monitoring system just detected the driver fatigue quite exactly. Due to the intricate and uncertain real car environment, we should learn more information about the driver fatigue, and then our system may detect the fatigue level more correctly and appropriately.

References

[1] Wang Rong-ben, Guo Ke-you, Shi Shu-ming and Chu Jiang-wei, "A monitoring method of driver fatigue behavior based on machine vision," *Proc. IEEE Intelligent Vehicles Symposium*, 9-11 June 2003, pp. 110-113.

[2] Haisong Gu, Qiang Ji and Zhiwei Zhu, "Active facial tracking for fatigue detection," *Proc. Applications of Computer Vision, Sixth IEEE Workshop*, 3-4 Dec. 2002, pp. 137-142.

[3] T.D'Orazio, M.Leo, P.Spagnolo and C.Guaragnella, "A neural system for eye detection in a driver vigilance application," *Proc. Intelligent Transportation Systems, 7th International IEEE Conference*, 3-6 Oct. 2004 pp. 320-325.

[4] Zhiwei Zhu and Qiang Ji, "Real time and non-intrusive driver fatigue monitoring," *Proc. Intelligent Transportation Systems, 7th International IEEE Conference*, 3-6 Oct. 2004 pp. 657-662.

[5] Muhammad Firdaus Hashim, Puteh Saad, Mohd Rizon Mohamed Juhari and Shahrul Nizam Yaakkob, "A face recognition system using template matching and neural network classifier," *1st International Workshop on Artificial Life and Robotics.*, 14-15 May 2005, pp. 1-6.

The Eleventh International Symposium on Artificial Life and Robotics 2006 (AROB 11th'06),
B-con Plaza, Beppu, Oita, Japan, January 23-25, 2006

irtual Planes and Active ision for Fast 3D Real Time Obstacle Detection and Avoidance

aki K. abib and Ju-Jang ee

Department of Electrical Engineering and Computer Science
Korean Advanced Institute of Science and Technology (KAIST),
373-1, Guseong-dong, Yuseong-Gu, Daejeon, 305-701,
Republic of Korea
maki ieee.org

Abstract

This paper presents the development of a fast 3D virtual planes and active vision based concept that can support real time obstacle detection and avoidance in a dynamic environment. This work enables an autonomous mobile robot to detect and avoid moving and static objects that may appear in front of the robot while navigating in real time. The developed approach encodes the space coarsely by using small number of 2D laser spots projected through fiber grating based active vision on the scene in front of an autonomous mobile robot to locate, track and avoid any object that may appear along the course of the robot movement. Efficient algorithm is developed to represent the detectable depth in front of the sensor system with dynamic resolution and decompose spatially the space along that depth into a number of parallel virtual planes that are perpendicular to the line of the robot movement. To facilitate the real time tracking of dynamic objects, each virtual plane is divided into five zones and the laser spots within each zone are used as a base for the tracking. The distance between the virtual planes represents the spatial decomposition of spot's movement space, i.e., spot's moving path on the image plane. The detection of a spot at a certain virtual plane indicates the availability of an obstacle or object at the range of that plane with respect the robot. The longer a spot moves along its path the closer virtual plane to the robot activated. Accordingly, the virtual plane closer to the robot has a higher priority in the detection and tracking process than the others. The laser posts, depth dynamic resolution, space spatial decomposition into virtual planes and the zones within each virtual plane have the advantage of reducing significantly the computation time of 3D information that is required for real time detecting, avoiding and tracking objects in dynamic environment. The paper discusses and illustrates the developed concept along with results analysis.

1 Introduction

Autonomous mobile robots are useful for many applications in indoor and outdoor environments and in environments that are characteristically more unstructured and unpredictable. These applications range from surveillance of buildings and supervision of plants, transport patients and delivery items, cleaning houses and guiding people, maintenance and repair in dangerous and inaccessible places, undersea operations, space exploration, mining operations, to hazardous-waste disposal. The use of autonomous mobile robots in such application allows humans to remain in a safe environment while acting in a supervisory capacity. In door mobile robots may need to carry out in populated and natural human habitat environments.

Autonomous mobile robots are designed with aim to govern themselves, manage its resources including power, find paths between any two random point within its environment, avoid obstacles while navigation these paths, collect information about the environment, adjust strategies and adapt to changes based on the surrounding or in itself, learn or gain new capabilities, and make decisions without outside assistance. It is necessary to achieve these activities efficiently and safely. Autonomous mobile robots must rely upon on-line sensory information to take actions and be able to react appropriately to unforeseen changes in the environment or to unpredictable objects blocking their trajectories. This requires having significant sensing capabilities, to reason about sensing data, and be flexible. They must be able to detect and track moving and non-moving targets as a function of time, to report their status and approach a proper decision to avoid or track them as necessary. Therefore, it is necessary to have an efficient sensor system that can fulfill these tasks properly and in real time. A common property shared by all types of sensors is their noisy responses. This sensor uncertainty, together with the inaccuracy of the robot's actuators and the unpredictability of real environments, make the design of mobile robot controllers a difficult task.

Some robot navigation systems may rely on global maps for global path planning and navigation. Other navigation systems use maps locally, to plan collision-free paths, to avoid obstacles, or to identify environment features for localization. Local navigation techniques are the ones

The Eleventh International Symposium on Artificial Life and Robotics 2006 (AROB 11th'06),
B-con Plaza, Beppu, Oita, Japan, January 23-25, 2006

responsible to achieve these reactive issues. These techniques are sensory-based approaches, using only local sensory information, or an additional small fraction of the world model. Humans and other animals have a remarkable ability to coordinate their actions with complex, changing environments. With little conscious effort, we routinely reach or walk through cluttered scenes, avoiding obstacles, reaching goals, and intercepting moving targets safely and effectively. The change in the state of the robot action is a function of its current state and collected information about the environment. Behavior arises from interactions between the components of this mutually coupled system and reflects the constraints of both components. There are many successful navigation algorithms for various types of mobile agents and for various situations. The challenge thus becomes one of identifying behavioral variables relevant to the situations and the task goals that evoke the desired behavior in the system to shape the appropriate behavioral dynamics [1, 4]. Important approached for local navigation and reactive collision avoidance methods have been studied. This includes: the dynamical steering method, the artificial potential field, the vector field histogram, the curvature-velocity method, the dynamic window approach, and the global dynamic window approach [1-3, 7, 10, 11].

Among the popular sensors that have been actively studied actively many fields including robotics research include: laser range finders, sonar sensors, infrared sensors and vision sensors. Vision sensor has numerous advantages for achieving such a task. Nevertheless, they have their own drawbacks. Vision systems are costly and very computationally challenging given the complexity of most of the algorithms developed by researchers. One of the traditional approaches in mobile robot research has been the use of stereovision systems to extract range information from pairs of images. Applying such approach time real time navigation in a dynamic environment faces the difficulty of the intrinsic computational expense of extracting three-dimensional 3D information from stereo pairs of images and this leads to limits the number of points that can be tracked. These limitations initiate the work in this paper to explore the use of an alternative sensor that could deliver 3D range information directly and facilitate real time detection and avoidance of obstacles.

2 F ased Active ision Sensor

When a fiber-grating projector constitutes two-overlaid fiber sheets arranged at a right angle and irradiated by laser light, a sphere-like lens formed at each intersection of two fiber gratings. Spherical waves interfere with one another and generate a tetragonal 2D array of laser spots. Then, the generated 2D laser spots array is projected onto a plane ahead of the sensor system as shown in Figure 1. For the purpose of this work, the author selected a fiber of 20 mm in diameter and 10 mm in length [5, 8].

The developed sensor hardware is based on this principles and it consists of a fiber grating based vision sensor, a frame memory, an image processing and decision making board, laser driving circuit, alarm indicators, and interfacing capabilities with a higher-level controller along with a user friendly interface when it is used as an independent module. The fiber grating based vision sensor consists of a bright laser-spots array projector and a CCD camera. The laser-spots array projector consists of a semiconductor laser light source that is compact and lightweight in design (laser diode of 830 nm wavelength, and 30 mW output power) and a fiber grating. Typically, the wavelength generated by the solid-state device in the range 750 850 nm. The laser diode, the collimating lenses, and the FG are integrated and mounted into one unit.

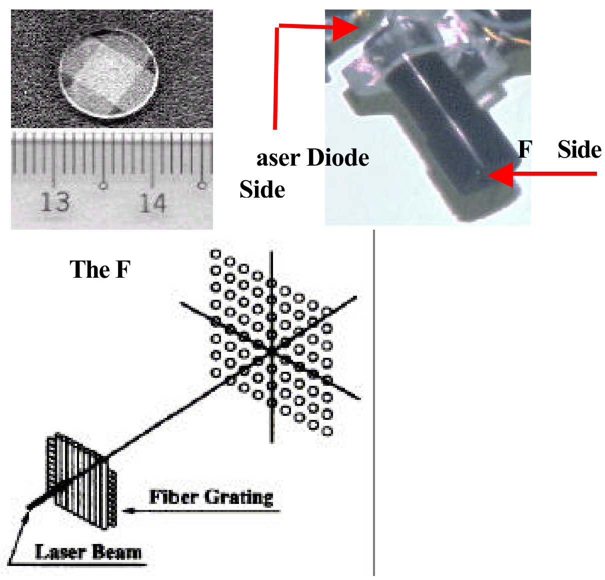

Fig. 1 2D laser spot pattern generated through two overlaid F sheets irradiated by a laser beam

3 Optical Arrangement and orking Principles

Fig. 2 shows the layout of the optical arrangement for the FG vision sensor. The coordinate system is based on the lens of the CCD camera and the U-V coordinate is based on the image plane. The spot array projector is located parallel to the CCD camera at (0, $-d$, 0), and the image plane is located at (0, 0, l). With this arrangement, the FG vision sensor treated as one unit, positioned and oriented as required with respect to the plane of projection [6, 7, 9].

With reference to Fig. 2, a 3D coordinate system is defined and the physical coordinates of any disturbed spot

The Eleventh International Symposium on Artificial Life and Robotics 2006 (AROB 11th'06),
B-con Plaza, Beppu, Oita, Japan, January 23-25, 2006

on an object can be expressed by (s, s, s), s for spot. It is possible to clarify the measurement space of a detectable object height or range in relation with the optical arrangement as follows: When projecting a bright spot on a person or on an object, the position of the projected spot translates from its original reference in a particular direction on the image plane from $(u,\ )$ to $(u,\ +d)$. The number of pixels that represent spot's translation (shift in position) due to the presence of an object is determined from the $(u,\ )$ coordinate values on the image plane and is used to calculate the 3D location (s, s, s) of a reflected spot at which the beam was projected:

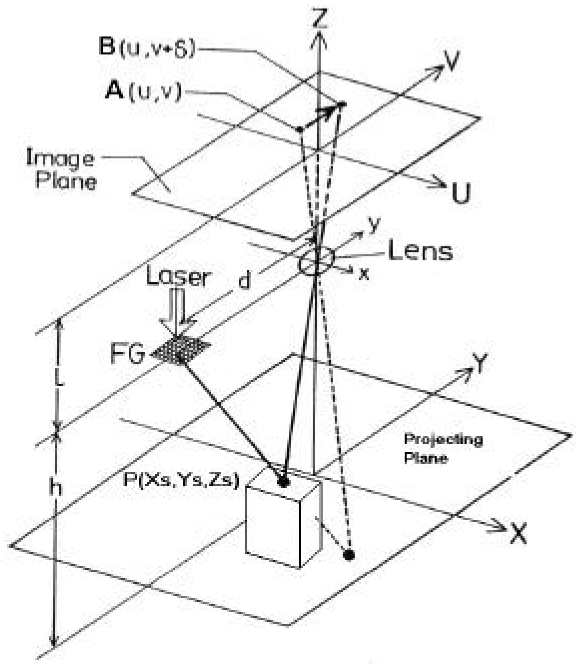

Fig. 2 F vision sensor optical arrangement

The physical location (s, s, s) of a reflected spot at which the beam was projected can be calculated using the following equations,

$$s \quad \frac{{}^{2}d}{dl+\ d} \qquad (1)$$

$$s = \frac{u}{l}(\quad s) \qquad (2)$$

$$s = \frac{+d}{l}(\quad s) \qquad (3)$$

Where: is the depth of the center of the CCD camera lens from the surface of the virtual reference plane. d is the shift quantity in pixels that describe the translation in spot position on the image plane. l is the distance from the lens to the image plane; d is the center distance from the laser-spot generator to the lens of the CCD camera; u and are the reference image plane coordinates of a spot (i.e., the original coordinates of a spot before moving).

Each spot has a certain path to move along it, and this path is represented by a certain number of pixels. The number of pixels is in a spot is moving is proportional to the depth calculated from the virtual reference plane. Table 1 shows the experimental data that compares a spot's movement limit in pixels for different type lenses.

Table 1

ens Focal ength mm	ovement imit of Spot s Path with F rotating by an Angle f Pixels
4.8	3
.5	4
8.	54

4 The eneration of the irtual Planes

For the purpose to help an autonomous mobile robot detects and avoids in real time dynamic or static obstacles such as human or objects while navigating, the developed optical sensor was integrated with the robot. Before deciding the number of virtual planes and the distance between them, it is important to analyze the relation between the detectable depth of an object in front of the robot and the distance (d) between the laser spot projector and the CCD camera. Fig, 3 illustrate this relation. As the distance d increases the maximum detectable object depth will decrease (calculated from a selected reference plane in front of the robot), i.e., the undetectable depth from the robot will increase and this is valid for all types of lenses. Also, as the distance (d), the resolution of the FG based sensor will improve.

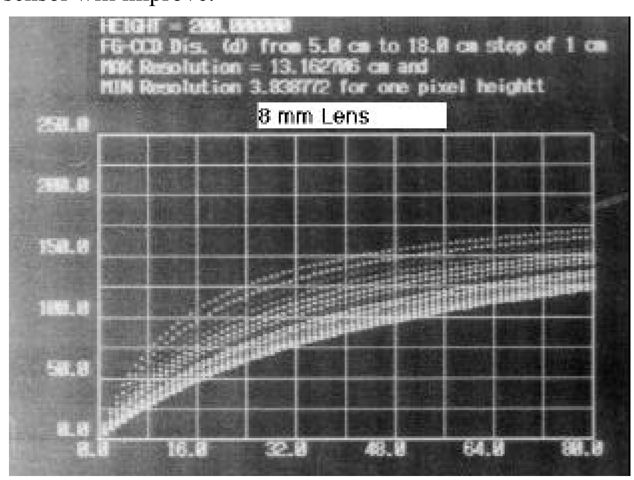

Fig. 3 the relation between the maximum detectable depth, the F -CCD Distance and the sensor resolution.

Therefore, for detecting and avoiding obstacles in real time the author selected following parameters:

a. Lens with 8.0 mm focal length attached to the CCD camera.
b. 12 mm distance (d) for proper pixel resolution related to the application, and
c. 200 cm depth from the robot ( ) between the reference virtual plane surface in front of the robot and the sensor on the robot.

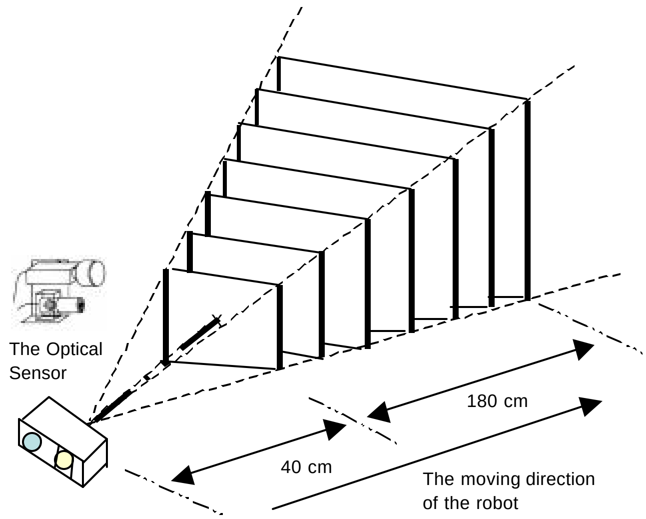

a

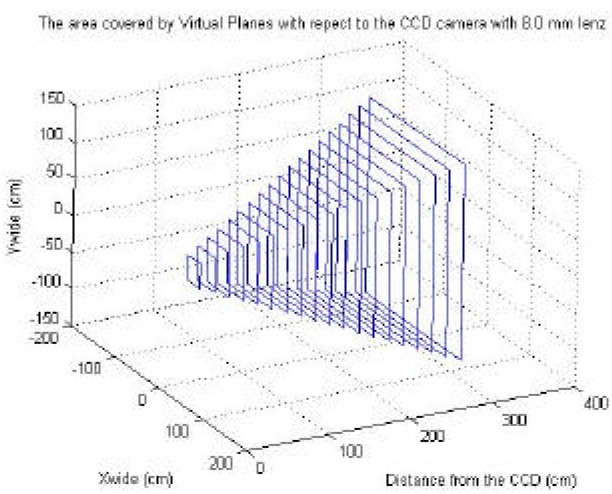

b

Fig. 4 a, b and c shows the concept and the alignment of virtual planes

The sensor is fixed on the robot and aligned in a way that can achieve a horizontal projection of the laser spots a head of the robot while selecting a reference virtual plane in front of the robot at the maximum detectable depth between the sensor on the robot as and the reference plane. The space in between is divided in to several virtual planes as shown in Fig. 4-a. As mentioned earlier, the targeted reference virtual plane is selected at 200 cm from the sensor on the robot and the space between this reference and the robot has been divided into 9 virtual planes with distance of 20 cm between each of them to cover a depth between 40 cm to 200 cm from the robot. The first virtual plane starts at a distance of 40 cm from the sensor edge on the robot. The dimension of the area covered by each of the virtual planes is inversely proportional with the focal length of the lens attached to the CCD camera and it is directly proportional with its distance from the CCD camera. This leads to the necessity to adjust the positions of the virtual planes and recalculate the area covered by them when having any of the following circumstances:

i. Change the lens attached to the CCD camera with a lens of different focal length and,
ii. Reconfigure the distances between the virtual planes and with respect to the CCD camera and the change in the number of the virtual planes.

Fig. 4-b and c illustrates the generated virtual planes and their covered areas with different projection for lens with 8.0 mm focal length.

5 Operational Software Development

The developed system software consists of the following main parts:

i. For the purpose to enhance spot's area, reject background noise, minimize is effect, and optimize searching for and deciding a spot, an efficient dynamic floating threshold algorithm has been developed.

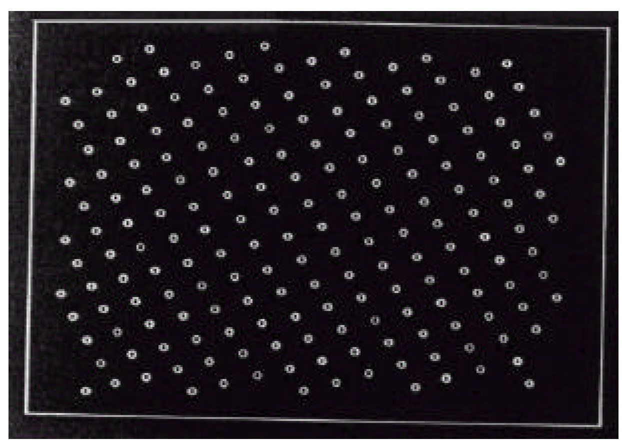

Fig. 5 The identified laser spots as seen on the reference plane.

ii. The generation of a reference spot frame. The aim of this part is to identify all possible laser spots and to calculate the position in image coordinates and its brightness for each of the identified spot. Since the area of each spot is not uniform, the position of a spot $(u_{ref},\ _{ref})$ is calculated by determining the center of gravity for the extracted spot's area (See Fig. 5).

iii. During the calculation of spot's reference frame, the relevant laser spots on each virtual plane and their translated movements in pixels are experimentally determined and tabled. The laser spots associated with the first virtual plane (the one closer to the robot) demonstrate largest translation in spot position than other planes to reflect the closeness of an obstacle with respect to the robot, i.e., the obstacle is within 40 cm from the robot. While the laser spots associated with the last virtual plane (the one at the far end from the robot), demonstrate the smallest translation in spot position than other virtual planes. This reflects the detection of an obstacle at the far end of the marked depth distance, i.e., between 180-200 cm. The laser spots and the associated spots' translation on the other virtual planes reflect the detection of an obstacle at a depth distance between the mentioned two ends. It is clear from the alignment in Fig. 4-a that,

   a. The virtual plane at the far end from the sensor on the robot has more laser spots associated with it than the virtual plane at the near end from while their spot's translation in pixels is smaller. This is true when the area covered by the virtual plane at the near end can't accommodate all of the projected laser spots.
   b. The laser spots associated with a virtual plane closer to the robot is a subset of the laser spots associated with a virtual plane just before it in the sequence toward the far end.

iii. Real time detection, avoiding, tracking, communicating and reporting alarms to a different level of control.

To facilitate the detection and the directional movement of any obstacle or object in front of the robot during the navigation task, each of the virtual planes is divided into 10 zones as shown in Fig. 6. These zones are: Upper-Right 1, Upper-Right 2, Upper Center, Upper-Left 2, Upper-Left 1, Lower-Left 1, Lower-Left 2, Lower Center, Lower-Right 2 and Lower-Right 1. The partitions into zones and the width of each zone are decided to facilitate fast detection and tracking of an obstacle. Also, the number of zones and their widths can be changed according to the need and requirements of the task at hand. To save time and have a quick decision, the searching process for any moved spot starts from the lower zones. Also, the author used state based events to contract the transitions that will lead to conclude the current status for the space in front of the robot in relation to the appearance of an object.

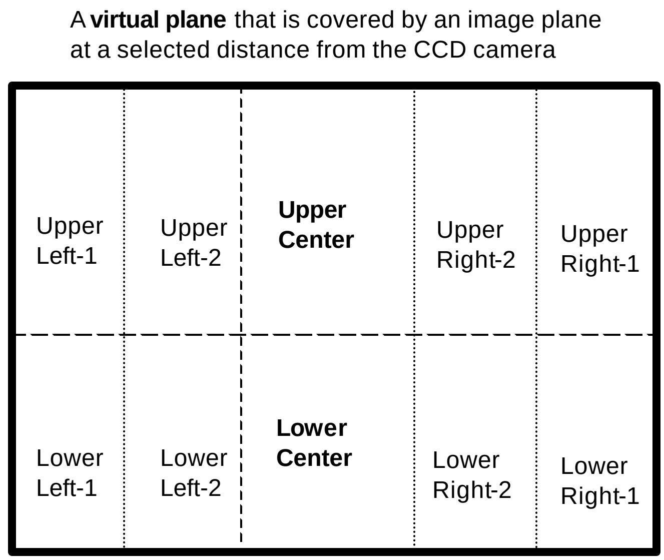

Fig. the available ones within each virtual pane.

Conclusion

In this paper, a 3D fiber grating based vision sensor to detect and track static and moving objects (human of obstacles) in indoor environment has been presented. The main feature of the introduces work is the use of virtual planes with FG based active vision to decompose the space in front of the robot into multiple layers and the partitioning of each virtual plane into zones. This helped to detect and extract in real time 3D information about any object that may appear within the active view of the sensor. The same concept can be applied to track and monitor human behavior in a realistic environment. The author is considering to apply computational intelligence techniques to conclude the targeted details about the obstacles location and movement directions

References

[1] B.R., Fajen and W.H., Warren, "A Dynamical Model of Visually-Guided Steering, Obstacle Avoidance, and Route Selection", International Journal of Computer Vision, Vol. 54, 3, 2003, pp. 13 34.

[2] C.R., Weisbin, G., De Saussure, J.R., Einstein, F.G., Pin, and E., Heer," Autonomous mobile robot navigation and learning , IEEE Computer, Volume 22, Issue 6, 1989, pp. 29 35.

[3] O. Khatib, "Real-time obstacle avoidance for manipulators and mobile robots", International Journal of Robotics Research, Vol. 5, No. 1, 1986, pp. 90 98.

[4] S., Suzuki, M. K., Habib, J., Iijima, and S., Yuta," How to Describe the Mobile Robot's Sensor-Based

Behavior", Robotics and Autonomous Systems, 7, 1991, pp. 227-237.

[5] H., Machida, J., Nitta, A., Seko, and H., Kobayashi," High Efficiency Fiber Grating for Producing Multiple Beams of Uniform Intensity", Applied Optics, Vol. 23, No. 2, 1984, pp. 330-332.

[6] K., Nakazawa, S., M., Nakajima,, and H., Kobayashi, " Development of 3D shape measurement system using Fiber Grating", Trans. IEICE, Vol. j69-D, No. 12, 1986, pp. 1929-1935.

[7] J. Borenstein and Y. Koren, The vector field histogram: fast obstacle avoidance for mobile robots , IEEE Transactions on Robotics and Automation, Vol. 7. No. 3, 1991, pp. 278-288.

[8] Machida Endoscope Co. Ltd., Tokyo, Japan, 1996.

[9] J. Yamaguchi, H. Gou, and M. Nakajima, "Finding Intruders System using Hologram Disk", Technical Digest of the 8th Sensor Symposium, 1989, pp. 83-86.

[10] D. Fox, W. Burgard. and S. Thrun, "The Dynamic Window Approach to Collision Avoidance", IEEE Robotics and Automation Magazine, Vol. 4, No. 1, 1997, pp.23-33.

[11] O. Brock and O. Khatib, "High-Speed Navigation Using the Global Window Approach", in IEEE Intl. Conf. on Robotics and Automation ICRA'99, Detroid, Michigan, 1999, pp.341-346.

The Eleventh International Symposium on Artificial Life and Robotics 2006 (AROB 11th'06),
B-con Plaza, Beppu, Oita, Japan, January 23-25, 2006

Identification Using Dynamical Neural Network with Modified BP Method

Kunihiko Nakazono
University of the Ryukyus
Senbaru 1, Nishihara, Okinawa. 903–0213
nakazono@tec.u-ryukyu.ac.jp

Kouhei Ohnishi
Keio University
Hiyoshi 3–14–1, Yokohama. 222–8522
ohnishi@sd.keio.ac.jp

Hiroshi Kinjo
University of the Ryukyus
Senbaru 1, Nishihara, Okinawa. 903–0213
kinjo@tec.u-ryukyu.ac.jp

Abstract

In the present paper, we propose a dynamical neural network (DNN) with the characteristics of inertia, viscosity, and stiffness and a training algorithm based on the backpropagation (BP) method. In a previous study, we proposed a modified training algorithm for the DNN based on the error BP method. However, in the previous method it was necessary to determine the values of the DNN parameters by trial and error. So, in the proposed DNN, the BP method is designed to train not only the connecting weights but also the property parameters of the DNN. Simulation results show that the DNN with characteristics of inertia, viscosity, and stiffness trained by the modified BP method obtains good training performances for time series signals generated from an unknown system. In the present paper, we compare the DNN with a conventional neural network in order to verify the validity of the DNN.

1 Introduction

Recently, recurrent neural networks and spiking neural networks have attracted more research interest than layered neural networks having static mapping capability [1, 2, 3, 4]. The recurrent neural network is a possible candidate for improving the system dynamics because it incorporates a feedback structure in the neuron unit and takes time delayed inputs into consideration. Research on spiking neural networks is also ongoing. Spiking neural networks treat spike trains and process the signals based on spike pulses. However, the network structure in recurrent neural networks and spiking neural networks is complex compared to that in layered neural networks with a training algorithm.

Here, we propose a dynamical neural network (DNN) that realizes a dynamical property and has a network structure with the properties of inertia, viscosity, and stiffness without time delayed input elements. In a previous study, the proposed DNN was constructed with a training algorithm that used error backpropagation (BP) method [5]. However, the BP method modified only the connecting weights, and the property parameters for the DNN had to be determined by trial and error. We therefore designed a GA-based training method [6] to train both the connecting weights and the parameters of the DNN [7, 8]. But the GA-based training method took the executing time of computer program that evolved in GA simulation.

The validity of the proposed DNN was verified by identifying periodic functions such as a simple one-period sine waveform and several periodic sine waveforms [7], and time series signals [8]. In the present paper, it is verified by identifying the time series signals of an unknown system with strong nonlinearity. Simulation results show that the proposed DNN provides higher performance than the conventional neural network.

2 Structure of DNN

In the present paper, we propose a DNN using a neuron having the properties of inertia, viscosity, and stiffness. In this neuron model, we assume that the image output from the neuron possesses the properties of inertia, viscosity, and stiffness, and that the output is propagated in the next neuron. The proposed DNN is composed of three hierarchy layers, and the proposed neuron adopts only in a hidden layer. The structure of the DNN is shown in Figure 1.

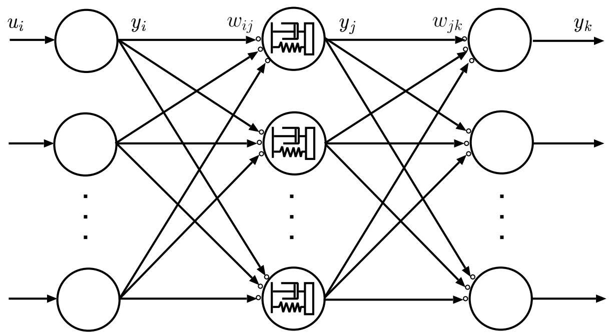

Fig. 1 Structure of DNN

The equations for the DNN are expressed as follows:

$$y_i = u_i, \quad (i = 1, 2, \cdots, N_I) \tag{1}$$

$$y_j = K_j f_j(net_j) + D_j \dot{f}_j(net_j) + M_j \ddot{f}_j(net_j) \tag{2}$$

$$net_j = \sum_{i=1}^{N_I} w_{ij} y_i, \quad (j = 1, 2, \cdots, N_J) \tag{3}$$

$$y_k = f_k(net_k) \tag{4}$$

$$net_k = \sum_{j=1}^{N_J} w_{jk} y_j, \quad (k = 1, 2, \cdots, N_K) \tag{5}$$

where u_i is the input value to the DNN, and y_i, y_j, and y_k are the output values in the input, hidden, and output layers, respectively. The connecting weight from unit i in the input layer to unit j in the hidden layer is denoted by w_{ij}. Similarly, w_{jk} is a connecting weight from unit j in the hidden layer to unit k in the output layer. The total sum of the products of the connecting weight w_{ij} and w_{jk} and the output value is denoted by net_j and net_k, respectively. M_j, D_j, and K_j are the property parameters of inertia, viscosity, and stiffness, respectively, and N_I, N_J, and N_K are the number of neurons in the input, hidden, and output layers, respectively. The activation function $f_j(x)$ in the hidden layer uses a sigmoid function in the the range of $[0, 1]$. Also the activation function $f_k(x)$ in the output layer is a linear function.

3 Training algorithm based on modified BP method

First, we derive a minimizing sequence of the measurement of error function E:

$$E = \frac{1}{2}\sum_{k=1}^{N_K} e_k^2 = \frac{1}{2}\sum_{k=1}^{N_K}(d_k - y_k)^2 \tag{6}$$

where d_k is the desired signal. In order to minimize the measurement of the error function E of equation (6), both of the connecting weights and the property parameters of the DNN are modified.

The derivation of the BP method is shown in this section. The connecting weights and the propery parameters of the DNN are updated sequentially based on the steepest descent method.

$$w^{(\mathrm{new})} = w^{(\mathrm{old})} - \eta \frac{\partial E}{\partial w} \tag{7}$$

$$K_j^{(\mathrm{new})} = K_j^{(\mathrm{old})} - \eta \frac{\partial E}{\partial K_j} \tag{8}$$

$$D_j^{(\mathrm{new})} = D_j^{(\mathrm{old})} - \eta \frac{\partial E}{\partial D_j} \tag{9}$$

$$M_j^{(\mathrm{new})} = M_j^{(\mathrm{old})} - \eta \frac{\partial E}{\partial M_j} \tag{10}$$

η is the training rate ($\eta > 0$).

The derivations of $\partial E/\partial w_{jk}$ and $\partial E/\partial w_{ij}$ are described as follows.

$$\frac{\partial E}{\partial w_{jk}} = \frac{\partial E}{\partial net_k} \cdot \frac{\partial net_k}{\partial w_{jk}} = \frac{\partial E}{\partial net_k} \cdot y_j \tag{11}$$

$$\frac{\partial E}{\partial w_{ij}} = \frac{\partial E}{\partial net_j} \cdot \frac{\partial net_j}{\partial w_{ij}} = \frac{\partial E}{\partial net_j} \cdot y_i \tag{12}$$

In the upper expression, the derivations are defined as

$$\delta_k = \frac{\partial E}{\partial net_k} \tag{13}$$

$$\delta_j = \frac{\partial E}{\partial net_j} \tag{14}$$

and δ_k and δ_j are calculated, respectively. First, δ_k is expanded as

$$\begin{aligned} \delta_k &= \frac{\partial E}{\partial net_k} = \frac{\partial E}{\partial e_k} \cdot \frac{\partial e_k}{\partial y_k} \cdot \frac{\partial y_k}{\partial net_k} \\ &= e_k \cdot (-1) \cdot \frac{df_k(net_k)}{dnet_k} \\ &= -e_k f_k'(net_k) \end{aligned} \tag{15}$$

δ_k finally becomes equation (15).

When δ_j is calculated in the same way, it becomes Equation (16).

$$\begin{aligned}\delta_j &= \frac{\partial E}{\partial net_j} \\ &= \sum_{k=1}^{N_K}\left(\frac{\partial E}{\partial e_k}\cdot\frac{\partial e_k}{\partial y_k}\cdot\frac{\partial y_k}{\partial net_k}\right)\cdot\frac{\partial net_k}{\partial y_j}\cdot\frac{\partial y_j}{\partial net_j} \\ &= \sum_{k=1}^{N_K}\delta_k\cdot w_{jk}\cdot\frac{\partial y_j}{\partial net_j} \qquad (16)\end{aligned}$$

$\partial y_j/\partial net_j$ is expressed as equations (17)–(20).

$$\begin{aligned}&\frac{\partial y_j}{\partial net_j} \\ &= K_j\frac{\partial f_j(net_j)}{\partial net_j} + D_j\frac{\partial \dot{f}_j(net_j)}{\partial net_j} + M_j\frac{\partial \ddot{f}_j(net_j)}{\partial net_j} \qquad (17)\end{aligned}$$

$$\begin{aligned}\frac{\partial f_j(net_j)}{\partial net_j} &= f'_j(net_j) \qquad (18)\\ \frac{\partial \dot{f}_j(net_j)}{\partial net_j} &= f''_j(net_j)\cdot\dot{net}_j \qquad (19)\\ \frac{\partial \ddot{f}_j(net_j)}{\partial net_j} &= f'''_j(net_j)\cdot\dot{net}_j^2 + f''_j(net_j)\cdot\ddot{net}_j \qquad (20)\end{aligned}$$

Next, the derivation of $\partial E/\partial K_j$ is described as follows.

$$\begin{aligned}\frac{\partial E}{\partial K_j} &= \sum_{k=1}^{N_K}\frac{\partial E}{\partial net_k}\cdot\frac{\partial net_k}{\partial y_j}\cdot\frac{\partial y_j}{\partial K_j} \\ &= f_j(net_j)\cdot\sum_{k=1}^{N_K}w_{jk}\delta_k \qquad (21)\end{aligned}$$

When the property parameters D_j and M_j for the error function E are calculated in the same way, it becomes Equations (22) and (23).

$$\begin{aligned}\frac{\partial E}{\partial D_j} &= \sum_{k=1}^{N_K}\frac{\partial E}{\partial net_k}\cdot\frac{\partial net_k}{\partial y_j}\cdot\frac{\partial y_j}{\partial D_j} \\ &= \dot{f}_j(net_j)\cdot\sum_{k=1}^{N_K}w_{jk}\delta_k \qquad (22)\\ \frac{\partial E}{\partial M_j} &= \sum_{k=1}^{N_K}\frac{\partial E}{\partial net_k}\cdot\frac{\partial net_k}{\partial y_j}\cdot\frac{\partial y_j}{\partial M_j} \\ &= \ddot{f}_j(net_j)\cdot\sum_{k=1}^{N_K}w_{jk}\delta_k \qquad (23)\end{aligned}$$

In this way, the connecting weights and property parameters of the DNN are updated based on the concept of the modified BP method.

4 Numerical simulation

4.1 System identification

The effectiveness of the proposed DNN is verified by numerical simulation in order to identify a time series signal. The method by which a time series signal from an unknown system is identified is shown in Figure 2. The DNN is structured to have two input ($u(t)$ and $d(t-1)$) and single output. The input signal $u(t)$ both of the DNN and the unknown system is a periodic signals expressed in Equation (24).

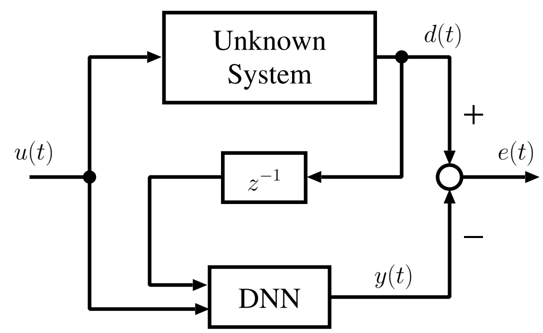

Fig. 2 System identification

$$u(t) = 0.1\sin(2\pi f t),\quad f = 0.01, 0.05, 0.1 \qquad (24)$$

The periodic input signal which has three frequencies $f = 0.01, 0.05, 0.1$ is inputted every five cycles sequentially.

The desired signal, namely the training data $d(t)$, is the output signal of the unknown system. In numerical simulation, the validity of the proposed DNN is verified by identifying the unknown system, for example, as a nolinear system, expressed in Equation (25).

$$d(t) = 0.5\sin(2d(t-1)) + 0.1\sin(2d(t-2)) + u(t) \qquad (25)$$

4.2 Simulation results

At this time, the number of neurons N_J in the hidden layer is 5 units and the training rate is set to $\eta = 0.1$. The training involved 10,000 iterations. The result of the error function E is shown in Figure 3.

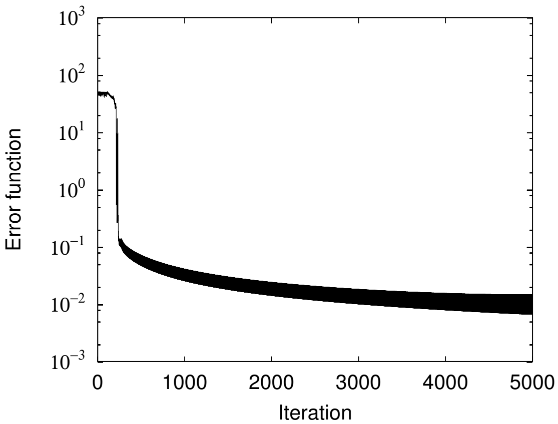

Fig. 3 Error function

The figure shows the result of the error function in the range of $[0, 5000]$. The result of the simulation shows that the DNN provides good performance. The error function E decreases gradually and E almost converge about 0.01.

The result of regenerating the signal utilizing the trained DNN is shown in Figure 4. The output $y(t)$ of

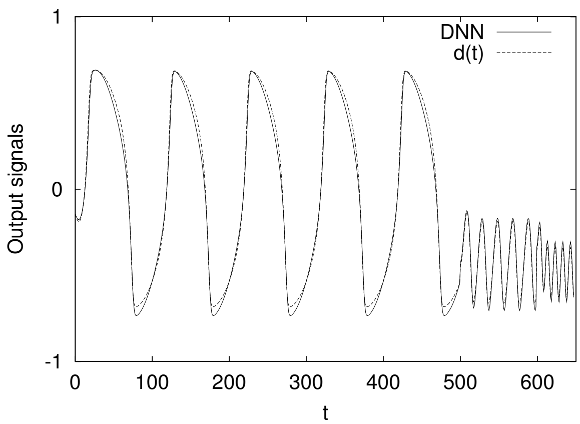

Fig. 4 Regenerated signal

the trained DNN negligibly deviates from the desired signal $d(t)$. The DNN trained by the modified BP mothod obtained good training performance for the time series signal generated from the output of the nonlinear system.

5 Conclusion

In the present paper, the proposed DNN, exhibiting the effectiveness of dynamical neuron with properties of inertia, viscosity, and stiffness, was configured. The training algorithm adopt the modified BP method. We designed a modified BP method to train both the connecting weights and the parameters of the DNN. Simulation results showed that the DNN trained by the BP method realized good training performance for time series signals generated from the unknown system with strong nonlinearity.

References

1 D. E. Rumelhart, J. L. McClelland, and PDP Research Group (1989), Parallel distributed processing, MIT Press.

2 R. J. Williams and D. Zipser (1989), A Learning algorithm for continually running fully recurrent neural networks, Neural Computation, 1, No.2, pp.270–280.

3 H. Kinjo, K. Nakazono, and T. Yamamoto (1997), Pattern Recognition for time series signals using recurrent neural networks by genetic algorithms (in Japanese), Trans. of ISCIE, Vol. 10, No. 6, pp.304–314.

4 W. Mass and C. M. Bishop (1999), Pulsed neural networks, pp. 16-53, MIT Press.

5 K. Nakazono, K. Ohnishi, H. Kinjo, and T. Yamamoto (2003), Identification of periodic function using dynamical neural network, AROB 8th '03, Vol.2, pp. 633–636.

6 Edited by L. Davis (1991), Handbook of genetic algorithms, Van Nostrand Reinhold, New York.

7 K. Nakazono, K. Ohnishi, and H. Kinjo (2004), System identification using dynamical neural network withn GA-based training, AROB 9th '04, Vol.1, pp. 75–78.

8 K. Nakazono, K. Ohnishi, and H. Kinjo (2005), Identification of time series signals using dynamical neural network with GA-based training , AROB 10th '05, CD-ROM, pp. 25–28.

The Eleventh International Symposium on Artificial Life and Robotics 2006 (AROB 11th'06),
B-con Plaza, Beppu, Oita, Japan, January 23-25, 2006

Nonholonomic System Control Using Neurocontroller Evolved by Genetic Algorithm

Norikazu Ogino, Hiroshi Kinjo, Kunihiko Nakazono
and Tetsuhiko Yamamoto
ogino,kinjo,yamamoto@mibai.tec.u-ryukyu.ac.jp
Faculty of Engineering, University of the Ryukyus
Nishihara, Okinawa 903-0213, Japan

Abstract

In this paper, we propose a design method of tracking control using a neurocontroller for a two-wheel vehicle optimized using genetic algorithm(GA). The two-wheel vehicle is a class of nonholonomic system. For nonholonomic systems, there are many control methods that utilize a chained form by applying stability theories. In this paper, we propose a design method for a nonholonomic system controller without chained form conversions. The controller is a neural network controller (NC). The training method of the NC utilize a genetic algorithm. In this paper, we use NC for tracking control. Simulation shows that the NC trained using the GA has a good control performance for the two-wheel vehicle.

Keywords: nonholonomic system, tracking control, genetic algorithm, neurocontroller, two-wheel vehicle

1 Introduction

The control system design of a nonholonomic system is difficult and complex. It is impossible to stabilize the system using a static consecutive feedback loop. It is necessary to construct uncontinuous or time-varying feedback system. Recently, many control methods for control system design have been proposed [1]-[5]. One of the solutions to the problematic control system design of the nonholonomic system is to utilize a chained form conversion of the control objects. However, the chained form conversion has some limitations of the controllable ranges in the state variables.

We propose a neurocontroller for the nonholonomic system. The neurocontroller is a controller using a neural network (NN). The neural network can obtain a solution close to the most suitable solution by learning. The most populare learning methd for NN is back propagation (BP). However, the BP cannot be used when the solution is traped in the local optimum. The training performance of the BP depends on the sequence of training patterns. We use a genetic algorithm (GA) for the NN training. GA training is easier than BP from the viewpoint of mathematics.

In this study we use a two-wheel vehicle, which is the simplest nonholonomic system, as a control object. We construct a tracking system of the two-wheel vehicle using a neural network controller (NC) with GA training.

2 Two-wheel vehicle

2.1 Nonhoronomic restraint of two-wheel vehicle

The two-wheel vehicle that is used in this study is shown in Figure 1. (x, y) denotes the coordinates of the middle point P between both wheels of the vehicle, and θ denotes the angle between the horizontal axis and traveling direction of the vehicle. η denotes the direction of the vehicle. R_l and R_r are the radii of the right and left wheels, respectively. The distance between the wheels is assumed to be $2W$.

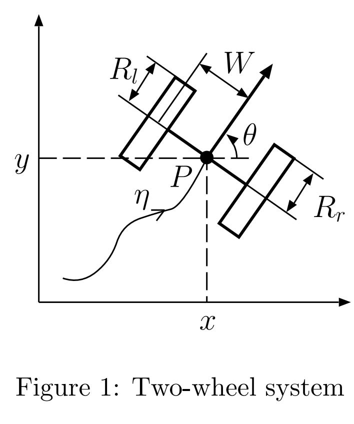

Figure 1: Two-wheel system

The relationships between speed $d\eta/dt$ and speed dx/dt in the direction of x, and speed dy/dt in the direction of y are described by the following equations.

$$\frac{dx}{dt} = \frac{d\eta}{dt}\cos\theta, \quad \frac{dy}{dt} = \frac{d\eta}{dt}\sin\theta \tag{1}$$

The speeds dx/dt and dy/dt have the folowing relation.

$$\frac{dy}{dt} = \frac{dx}{dt}\tan\theta. \tag{2}$$

This is a geometrical restraint shown at the position and speed of two-wheel vehicle.

2.2 System equation of two-wheel vehicle

Let u_1 and u_2 be the control inputs. u_1 is the speed of the vehicle $d\eta/dt$ and u_2 is the angular speed $d\theta/dt$ of the wheel, respectively. It can be shown that the inputs are

$$u_1 = \frac{d\eta}{dt} = \frac{R_l\omega_l + R_r\omega_r}{2} \tag{3}$$

$$u_2 = \frac{d\theta}{dt} = \frac{-R_l\omega_l + R_r\omega_r}{2W}, \tag{4}$$

where ω_l and ω_r are the angular speeds of the left and right wheels, respectively.

The state equation of the two-wheel vehicle is described by

$$\frac{d}{dt}\begin{pmatrix} x \\ y \\ \theta \end{pmatrix} = \begin{pmatrix} \cos\theta \\ \sin\theta \\ 0 \end{pmatrix} u_1 + \begin{pmatrix} 0 \\ 0 \\ 1 \end{pmatrix} u_2. \tag{5}$$

This formula is called the driftless system.

3 Control system

3.1 Constitution of a controller

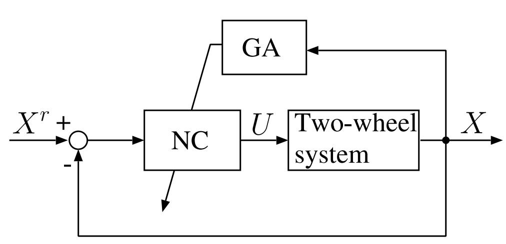

Figure 2: Control system

Figure 2 shows the control system. $U = [u_1, u_2]^T$ is the input to the two-wheel vehicle. The output of the vehicle system is $X = [x, y, \theta]^T$. The input to the NC is $(X^r - X)$ and the output is U. Here, X^r is the desired value. The NC is trained using the GA. We use a real-coded GA to modify the connecting weights of the NC.

3.2 Construction of NC

We use a three-layered NN as controller. The numbers of neurons are 3 for the input layer, 5 for the hidden layer, 2 for the output layer. For the activity function of NC, the input and output layers use a linear function, and the hidden layer uses a sigmoid function.

3.3 Learning method

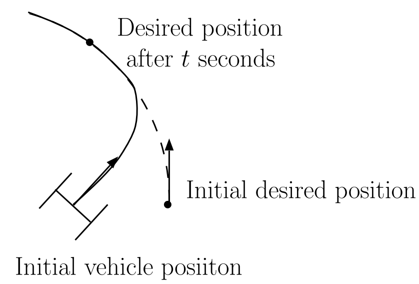

Figure 3: Tracking method

Figure 3 shows the tracking method. In Fig. 3, vehicle is set to the initial state and the bullet denotes the desired state and the dotted line the desired trajectory.

We consider the problem that the vehicle traces the desired trajectory after t[s]

$$t = \frac{\sqrt{(x - x^r)^2 + (y - y^r)^2}}{0.2} + \frac{|\theta - \theta^r|}{0.1} \tag{6}$$

Here, x, y and θ are the current states. In this study, t is limited to $0.01 \leq t \leq 0.1$.

We train the NC to control the vehicle to trace the desired trajectroy using the GA. The fitness function used in the GA is defined by

$$f = \frac{1}{E}, \tag{7}$$

where E is an error function described the following equation.

$$E^{(t)} = (x^{(t)} - x^{r(t)})^2 + (y^{(t)} - y^{r(t)})^2, \tag{8}$$

where $x^{(t)}$ and $y^{(t)}$ express states after t seconds. Likewise, $x^{r(t)}$ and $y^{r(t)}$ express the state of the desired value after t seconds.

Before moving the vehicel, NC is tarined based on the error function $E^{(t)}$. If $E^{(t)} < 10^{-5}$ then finish the training and control the vehicle at step 1. Aftere moving the vehicle, we check the vehicle state and perform the NC training. We iterate the NC training and vehicle moving until the end of the control time.

4 Simulation of tracking control

4.1 Method of simulation

The plant that is described by the continuous time model is calculated by the Runge-Kutta method with a time step of 0.01[s] and zero-order hold control. The desired position (x^r, y^r) is assumed to turn counterclockwise along the circumference of a circle with a radius of 0.25[m] centered on (x, y)=(0,0). The circumferential velocity is set to 0.2[m/s]. The desired angle θ^r is the angular difference between the direction of the desired position and the horizontal axis. The initial state of the desired value is set to x=0.25[m], y=0.0[m] and $\theta=\frac{\pi}{2}$[rad].

Table 1 shows the parameters of the GA training.

Table 1: GA parameters

Population	50
Parents	15
Range parameter of α	0.6
Generations	1000

4.2 Simulation 1

Figures 4-8 show the control results from the initial state x=0[m], y=0[m] and $\theta=\frac{\pi}{2}$[rad] of the vehicle. Figure 4 shows the control trajectory. Figure 5 shows the error between the desired and control trajectories. Figure 6 shows training iteraton. Figure 7 shows the system states. Figure 8 shows the control inputs.

From Figure 4, it can be seen that the vehicle traces the same line as that desired. From Figure 5, it is observed that there are very small errors after 0.5 seconds. From Figure 6, it can be seen that there are many learning iterations when the error is large (refer to Figure 5). From Figure 8, we can see that the control inputs u_1 and u_2 be come approximately constant after 0.5[s], that is, $u_1 = 0.2$[m/s] and $u_2 = 0.8$[rad/s]. u_1 and u_2 in stady state are alomst the same as the speed of the desired values.

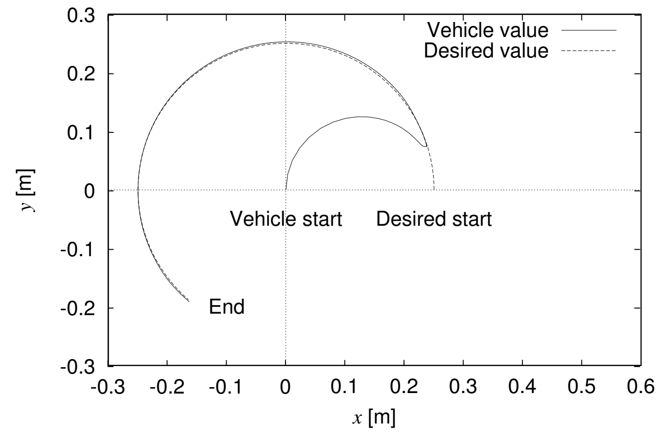

Figure 4: Tracking result

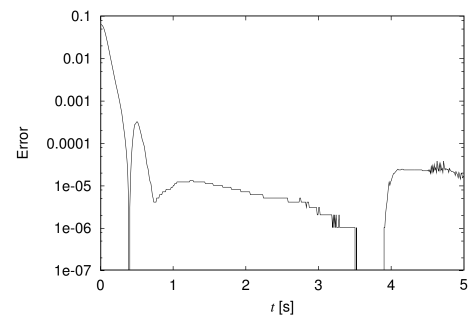

Figure 5: Error

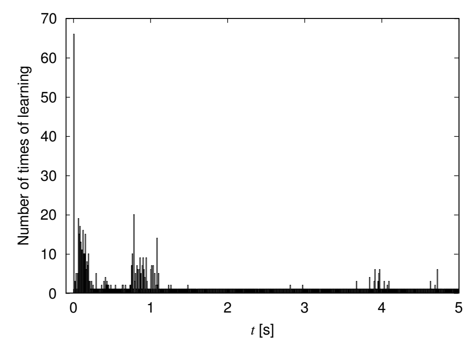

Figure 6: Learning situationn

4.3 Simulation 2

Figure 9 shows the control result from the initial state x=0.5[m], y=0.5[m] and $\theta=\frac{\pi}{2}$[rad] of the vehicle. It can be seen that tracking control is well performed.

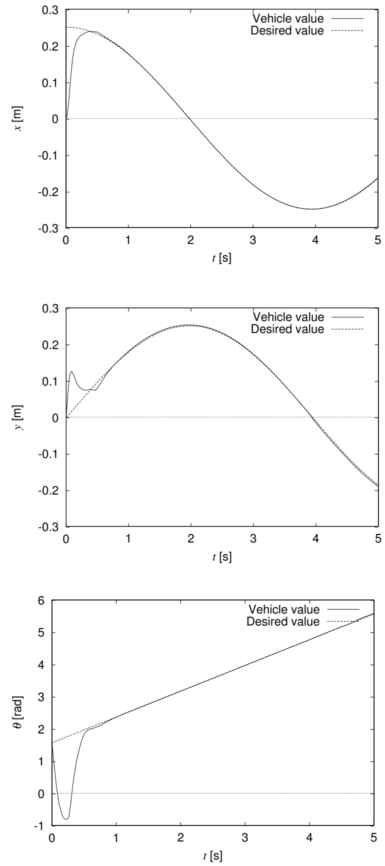

Figure 7: System stats

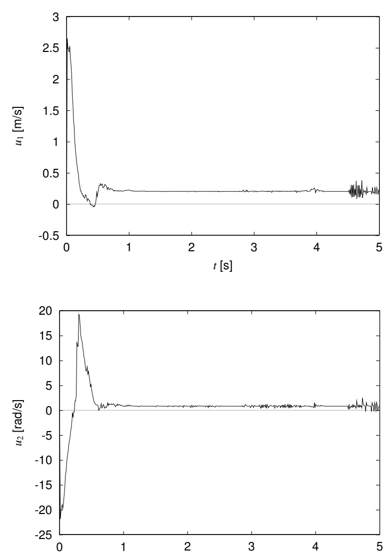

Figure 8: Control inputs

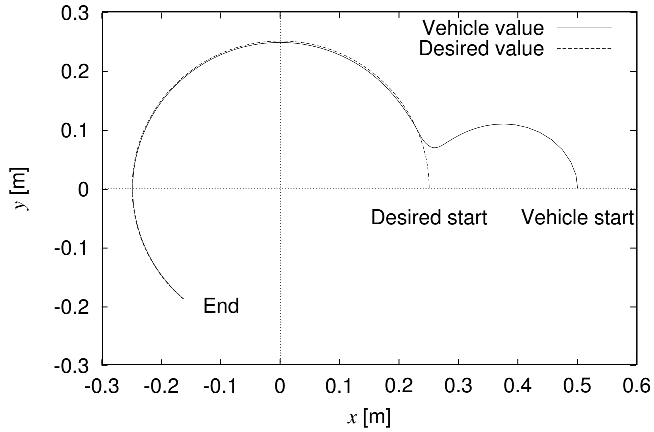

Figure 9: Tracking result

5 Summary

By this study, we proposed a tracking control method for a nonholonomic system using a neurocontroller evolved using a GA. As a result of simulation, we succeeded in the tracking control of the nonholonomic system. There is no limitation in the controlable ranges because this method does not use chained form conversion in the control objects. It is shown that the neurocontroller has suficient performance in the control of the nonholonomic system. the application of this neurocontroller to a more complicated object is the subject of future work.

References

[1] M. Sanpei (1997), Feedback Control of Nonholonomic Systems (in japanese), *Journal of SICE*, Vol. 36, No. 6: 396-403

[2] Y. Nakamura (1997), Perspective of Nonholonomic System Control (in japanese), *Journal of SICE*, Vol. 36, No. 6: 291-296

[3] C. Samson (1995), Control of Chained Systems Application to Path Following and Time-Varying Point-Stabilization of Mobile Robots, *IEEE Trans. Automatic Control*, Vol. 40, No. 1: 64-77

[4] Z. Jiang and H. Nijmeijer (1999), A Recursive Technique for Tracking Control of Nonholonomic Systems in Chaind Form, *IEEE Trans. Automatic Control*, Vol. 44, No. 2: 265-279

[5] M. Yamada, S. Ohta, Y. Syumiya and Y. Funahashi (2002), Multirate Sampled Data Control Form Based on Periodic Switching, *Trans. of SICE*, Vol. 38, No. 4: 369-378

The Eleventh International Symposium on Artificial Life and Robotics 2006 (AROB 11th'06),
B-con Plaza, Beppu, Oita, Japan, January 23-25, 2006

Searching Performance of Real-Coded Genetic Algorithm Using Biased Probability Distribution Functions and Mutation

Hiroki Nakanishi, Hiroshi Kinjo, Naoki Oshiro, Tetsuhiko Yamamoto
hiroki,kinjo,yamamoto@mibai.tec.u-ryukyu.ac.jp
Faculty of Engineering, University of the Ryukyus
Nishihara, Okinawa 903-0213, Japan

Abstract

One of the crossover methods for the real-coded genetic algorithm (RGA) is the unimodal normal distribution crossover method (UNDX). The UNDX is superior to the blend crossover method (BLX). However, the UNDX does not have a higher performance than the BLX in terms of searching speed and conversion stagnation. In this paper, we present a method of improving the searching performance of the RGA. We propose the use of biased probability distribution functions (BPDFs) in the crossover process. The crossover with BPDFs frequently produces offspring that are close to the best individuals in the current generation and it is highly likely that these offspring will offer the best solution to the problem. Furthermore, we propose a mutation that has a constant and extended range that is wider than that of the UNDX. Simulations show the efficiency of the proposed method.

Keywords: Real-coded GA, crossover method, unimodal normal distribution crossover (UNDX), biased probability distribution function, optimization problems.

1 Introduction

Recently, the real-code genetic algorithm (RGA) has been well used for solving problems. A well-known crossover method of the RGA is the blend crossover method (BLX). The BLX uses a uniform distribution function for breeding offspring. An excellent crossover method is the unimodal normal distribution crossover method (UNDX). The UNDX uses a Gaussian distribution function. Generally, GA solution searching takes a long time. Sometimes, using a GA results in evolution stagnation. In this paper, we present an improvement in GA solution searching performance. We present the first algorithm for solution searching that uses a variable distribution for breeding offspring. The proposed method involves the use of biased probability distribution functions (BPDFs) in a crossover process. The crossover with BPDFs frequently produces offspring that are close to the best individuals in the current generation and it is highly likely that these offspring will offer the best solution to the problem. Furthermore, we propose a mutation that has a constant and extended range that is wider than that of the UNDX. The cause of the evolutionary stagnation is that the search area becomes smaller with the progress of the generation. The mutation maintains the search area constant.

In a simulation study, we apply the proposed method to the optimization problems of three test functions: the Sphere function, Rastrigin function, and Rosenbrock function. The results show that the proposed method has a good searching performance for the test functions.

2 Unimodal normal distribution crossover

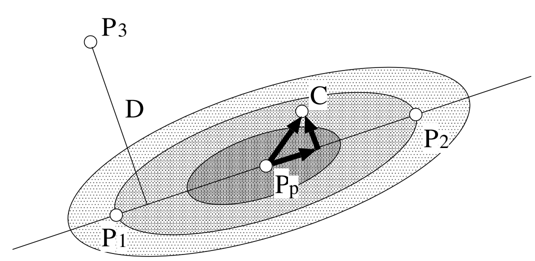

Fig.1 Unimodal Normal Distribution Crossover, UNDX

Figure 1 shows the original UNDX. The mechanism of breeding offspring in the UNDX is described by

$$c = p_p + \xi d + D \sum_{i=1}^{n-1} \eta_i e_i, \tag{1}$$

$$\xi \sim N(0, \sigma_\xi^2), \quad \eta_i \sim N(0, \sigma_\eta^2)$$

where c is the offspring individual, P_p is the center between the individual parents p_1 and p_2, d is the subtraction vector between the individual parents. e_i is the orthonormal basis vector, n is the dimensions of search space and D is the distance between the parent p_3 and main searching line. ξ and η_i are the normal distribution functions with the mean zero deviations σ_ξ^2 and σ_η^2, respectively. The UNDX uses two normal distribution functions in the offspring production process. The first and second terms denote the main search ingredient. The third term is the subsearch ingredient.

3 Biased probability distribution functions and mutation

3.1 Crossover method with BPDF

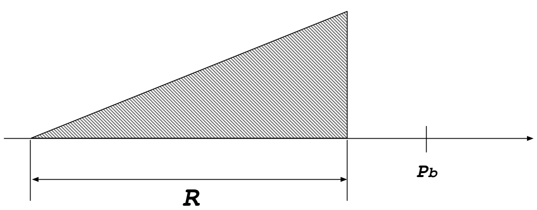

(a) p_b is outside of range R

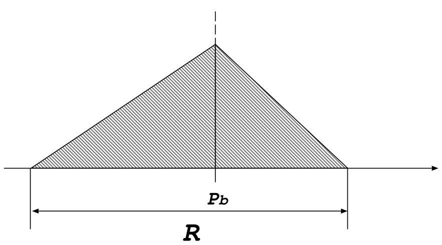

(b) p_b is inside of range R

Fig.2 Crossover using biased probability density functions (BPDFs) ($n = 1$)

Figure 2 shows the crossover with BPDFs. The crossover with BPDFs produces offspring biased to the individual p_b based on a triangle distribution function. Figure 2 (a) shows the case when p_b is outside of the range R. Figure 2 (b) shows the case when p_b is inside of the range R. R is an offspring production range determined using the same process as the UNDX. The p_b is the best individual in the generation field. The crossover with BPDFs produces offspring that are close to the best individuals in the current generation and it is highly likely that these offspring will offer the best solution to the problem.

3.2 Mutation

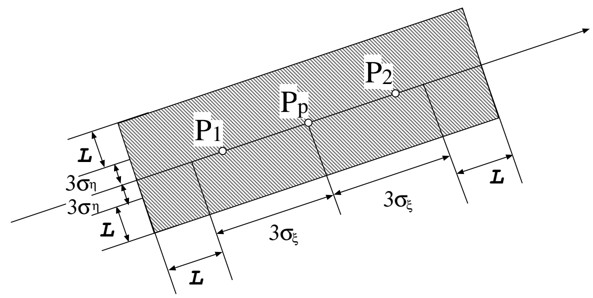

Fig.3 Mutation

Figure 3 shows the mutation method. L is a constant that widens the offspring generation range. Generally, the search area R in the generation field decreases with progress of the evolution. Sometimes, R is very small. The reduced field causes the evolution stagnation. In this mutation method, the search field is guaranteed to any constant width because there is the constant range L in the crossover field.

4 Performance test

4.1 Test functions

In this section we investigate the searching performance of the proposed method for optimization problems for three two-variable functions: the Sphere function, Rastrigin function, and Rosenbrock function.

The searching performance is measured using successful evolution rates obtained from the minimum values of the following three functions: the Sphere function, Rastrigin function, and Rosenbrock function.

The Sphere function is described by

$$f_1(x, y) = x^2 + y^2. \tag{2}$$

The minimum value of this function is 0.0 and occurs when $(x, y) = (0, 0)$. The sphere function is the simplest case.

The Rastrigin function is described by

$$f_2(x, y) = 20 + \{x^2 - 10\cos(2\pi x)\} + \{y^2 - 10\cos(2\pi y)\}. \tag{3}$$

The minimum value of this function is 0.0 and occurs when $(x, y) = (0, 0)$. The Rastrigin function has many peaks. There are many suboptimum solutions. The function has multimodal characteristics. The function is of the separation type without a dependence relation between variables.

The Rosenbrock function is described by

$$f_3(x, y) = 100(x - y^2)^2 + (y - 1)^2. \tag{4}$$

The minimum value of this function is 0.0 and occurs when $(x, y) = (1, 1)$. The Rosenbrock function has a single-peak shape. The solution of the function is a deep valley in a bend. The function has an interdependence relation between variables and has strong nonseparation characteristics.

4.2 Experiment parameter

Parent individuals are chosen by roulette selection using a fitness function based on the function f. The fitness function F is defined in the next expression.

$$F = C_f - f(x, y) \tag{5}$$

Here, C_f is a constant. We set $C_f = 100$ for functions f_1 and f_2 and $C_f = 500$ for function f_3. The population numbers are set to 20 for functions f_1 and f_2 and 50 for function f_3.

We use the crossover method with BPDF with the probability of $\alpha = 20\%$. The mutation rate is set to $\beta = 10\%$.

In this experiment, we compare the evolutionary performances of four methods: the original UNDX, the addition of the BPDF with rate α, the addition of the mutation with rate β, and the addition of both the BPDF and mutation with rates α and β. We call the latter three methods methods A, B, and C, respectively.

4.3 Results

Figure 4 shows the evolution performance for the Sphere function. Figure 4(a) shows the case of the range of the initial parent individuals $[-5, 5]$. Figure 4(b) shows the case of the range of the initial parent individuals $[-5, -4]$. The range of the initial parent individuals shown in Fig. 4 (a) includes the solution to the problem. The range of the initial parent individuals in Fig. 4 (b) does not include the solution to the problem. The horizontal axis denotes generation. The vertical axis S denotes the success rate. The condition for successful evolution is $f_1 < 0.001$. The lines show the mean of 100 evolution trial iterations. In Fig. 4 (a), there is no difference between the four methods. In Fig. 4 (b), we can observe that the proposed methods are faster than the original UNDX.

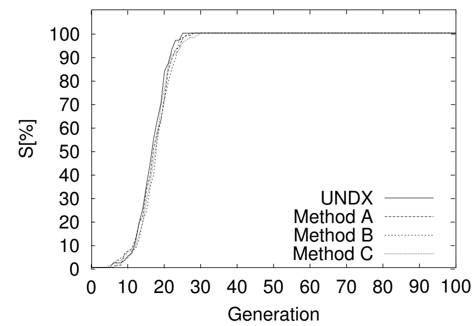

(a) Range of initial values is $[-5.0, 5.0]$

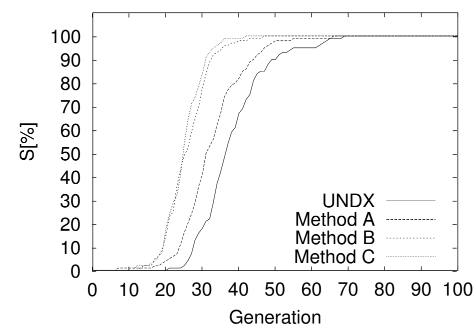

(b) Range of initial values is $[-5.0, -4.0]$

Fig.4 Evolution performance for Sphere function

Figure 5 shows the evolution performance for the Rastrigin function. The range of the initial parent individuals in Fig. 5 (a) includes the solution to the problem. The range of the initial parent individuals in Fig. 5 (b) does not include the solution to the problem. The lines show the mean of 1000 evolution trial iterations . From Fig. 5 (a), the success rate of method A is higher than that of the original UNDX during early generation. In late generation, there is no difference in success rate between method A and the original UNDX. In this test, methods B and C, i.e., those used with mutation, increase searching performance. From Fig. 5 (b), the success rates of three proposed methods are higher than that of the original UNDX. Both the original UNDX and method A converge to a local optimum. Methods B and C have higher performances than the original UNDX and method A. We can observe that the mutation has an important role in the search solution for the multimodal function.

Figure 6 shows evolution performance for the Rosenbrock function. The range of the initial parent individuals in Fig. 6 (a) includes the solution to the problem. The range of the initial parent individ-

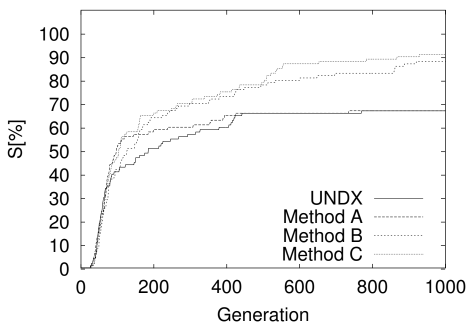

(a) Range of initial values is $[-5, 5]$

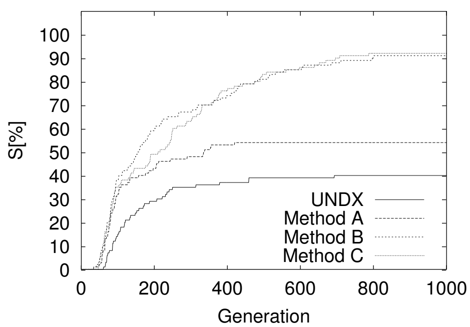

(b) Range of initial values is $[-5, -4]$

Fig.5 Evolution performance for Rastrigin function

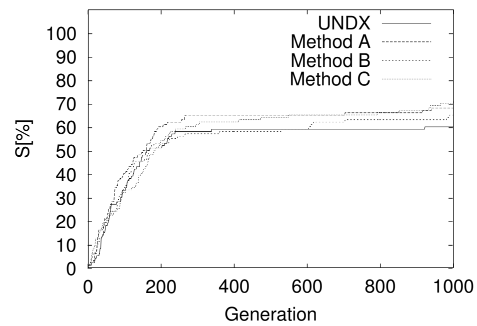

(a) Range of initial values is $[-0.25, 1.5]$

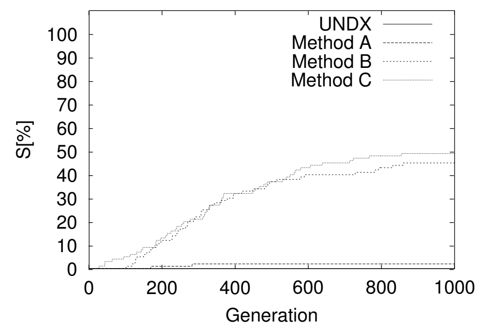

(b) Range of initial values is $[-0.5, 0.5]$

Fig.6 Evolution performance for Rosenbrock function

uals in Fig. 6 (b) does not include the solution to the problem. The lines depicting the success rate S are calculated for the mean of 1000 trials. From Fig. 6, in the case that the range of the initial parent individuals includes the solution, it can be seen that the four methods obtain the solution. In the case that the range of the initial parent individuals does not include the solution, it can be seen that only methods B and C obtain the solution.

5 Summary

In this paper, we propose the crossover method of the real-coded GA to speed up solution searching in the UNDX. The method uses biased probability distribution functions (BPDFs) in the crossover. Furthermore, we proposed a mutation that avoids stacking in a local optimum and evolutionary stagnation. In the simulation study, we apply the method to the optimization problems of the Sphere function, Rastrigin function, and Rosenbrock function. The results show that the proposed method has a good searching performance for the test functions.

References

[1] L. Davis (1991), Hand Book of Genetic Algorithms, Van Nostrand Reinhold

[2] L. J. Eshelman and J. D. Schaffer (1993), "Real-Coded Genetic Algorithms and Interval-Schemata", Foundations of Genetic Algorithms 2, Edited by L. Darrell Whitley, Morgan Kaufmann Publishers

[3] H. Kita, I. Ono and S. Kobayashi (2000), Multi-Parental Extension of the Unimodal Normal Distribution Crossover for Real-Coded Genetic Algorithms (in Japanese), *Transactions of the SICE*, Vol. 36, No. 10, pp. 875-883

[4] D. E. Goldberg (1989), Genetic Algorithms in Search, Optimization & Machine Learning, Addison-Wesley

[5] H. Okamura, K. Kitasuka and T. Dohi (2002), Perfomance Evolution of Genetic Algorithms Based on Markovian Analysis (in Japanese), *Transaction of ISCIE*, Vol. 16, No. 7, pp. 303-312

The Eleventh International Symposium on Artificial Life and Robotics 2006 (AROB 11th'06),
B-con Plaza, Beppu, Oita, Japan, January 23-25, 2006

A self-organizing model of place cells with periodically distributed receptive fields

Naoki Oshiro, Koji Kurata and Tetsuhiko Yamamoto
Faculty of Engineering, University of the Ryukyus,
1 Senbaru, Nishihara, Okinawa. 903–0213
oshiro@mibai.tec.u-ryukyu.ac.jp

Abstract

In this paper, we proposed new information separation method with inhibitory self-organizing map (SOM). SOM has topological structure and dimension, and inhibitory-connected SOMs are able to extract hierarchical structure of inputs has same dimension of map structure. We realized learning mechanism using this composition of SOM similar to some results of recent study that spatial inputs caused periodic distribution of receptive field in entorhinal cortex.

1 Introduction

Self-Organizing Map (SOM) can extract major informations from multi-dimensional information [1, 2]. We studied a model consisting of two SOMs connected via anti-Hebbian connections, and showed that it can extract two different information components on the two SOMs each [3]. The model was applied to extract position and rotation from visual information acquired by a camera on a mobile robot in a room surrounded by walls of different colors. In this application, one of the two SOMs consists of two-dimensional array of cells so that it can represent two-dimensional positional information, and the other SOM consisting of one-dimensional array of cells is assigned for one-dimensional information of direction of the robot. Numerical simulations showed that position-sensitive and direction-insensitive cells are formed on the two-dimensional SOM, and direction-sensitive and position-insensitive cells are formed on the one-dimensional SOM.

Such cells are found in real animal brains. In recent study of cortical micro circuits, it was found that spatial information are represented by 'grid cell' in the dorsocaudal medial entorhinal cortex (dMEC) [4]. Grid cells are a kind of position cells but their 'receptive field' shows periodic grid structure in the area within which rats are allowed to walk around. A receptive field of a position cell is a set consisting of positions at which the cell fires. It is striking that the receptive field of a position cell in dMEC was not connected but distributed periodically in hexagonal lattice, for in most of the self-organizing models receptive fields of the cells tend to be connected. Also in our preceding paper [2], the place cells had connected receptive field.

In this paper, we show that SOMs connected via anti-Hebbian synapses form this grid-structured receptive field. This new representation of position may contribute to more precise robot navigation.

2 Kohonen's SOM algorithm

The self-organizing map (SOM) was proposed by Kohonen [1, 5] as a model of the cerebral cortex and its self-organization. It was successful at reproducing a functional map of the visual cortex [6, 7], and was applied to many kinds of data as a statistical tool of nonlinear auto-regression [5].

A SOM usually consists of a two-dimensional array of neuron-like units, each of which has an *reference vector* $\boldsymbol{m}_i$, which is n-dimensional, as well as input vectors $\boldsymbol{x}$.

The SOM algorithm is as follows:

(SOM1) Assign random values for the reference vectors.

(SOM2) Choose or generate an input vector $\boldsymbol{x}$ in some random manner.

(SOM3) Find the unit whose reference vector is the closest to the input vector $\boldsymbol{x}$ in the sense of n-dimensional Euclidean distance. The unit is called the *winner*.

(SOM4) Apply the following learning rule for the reference vectors:

$$\boldsymbol{m}_i := \boldsymbol{m}_i + h_{ci}(\boldsymbol{x} - \boldsymbol{m}_i), \tag{1}$$

$$h_{ci} = \alpha \exp\left(-\frac{\|\boldsymbol{r}_c - \boldsymbol{r}_i\|^2}{2\sigma^2}\right), \tag{2}$$

where $\boldsymbol{r}_i$ is the two-dimensional position of the unit i on the unit array, and c is the index assigned to the winner unit.

(SOM5) Return to (SOM2) and repeat (SOM2) - (SOM4) many times.

This is called *neighborhood learning*, because a modification of the reference vectors takes place mainly in the neighborhood of the winner, as is represented by h_{ci}, which is called the *neighborhood function*. As a result of this learning rule, the reference vectors are scattered all over the input signal region and neighboring units tend to grow similar reference vectors, which means a topological map of the input signal region is *self-organized* on the unit array.

3 Layer composition of connected SOMs

We prepare two layers, the superior and inferior layers, for representing spatial information. Each layer consists of cells arranged in two-dimensional hexagonal array. We assume each of the cells in the inferior layer receive inputs from all of the cells in the superior layer via anti-Hebbian synapses.

All the cells on both layers receive a same locational information $\boldsymbol{x} = (x, y)$ (Figure 1). The superior layer receives no inputs from the inferior, so it works just as usual SOM for the two-dimensional positional information. On the other hand, the learning process of the inferior layer is influenced by the superior through the anti-Hebbian synapses.

The robot moves randomly within a room, and its position is represented by two-dimensional vector $\boldsymbol{x}$ and supplied as input to the model.

The learning rule is detailed as follows:

(SOMAH1) Assign random values for all reference vectors in the both layers $\boldsymbol{m}_i^{(1)}, \boldsymbol{m}_j^{(2)}$, where $i = 1, ..., N^{(1)}$, $j = 1, ..., N^{(2)}$, and superscript $^{(1)}$ stands for the superior layer and $^{(2)}$ for the inferior layer. Initialize inhibitory connections $s_{j,i}$ to zero. As iterative learning proceeds, the learning parameters α and β are updated as follows:

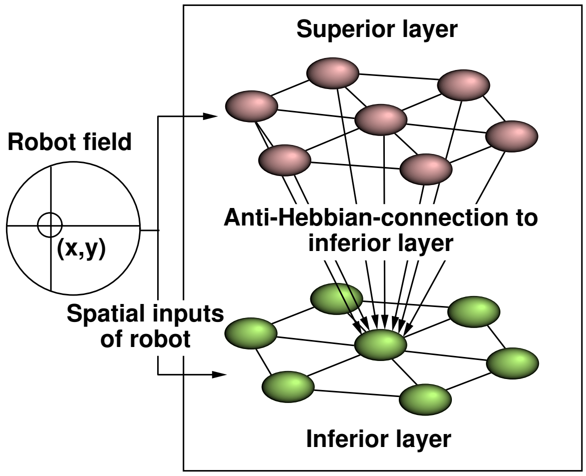

Figure 1: Structure of the proposed model. Layers are designed for formation of grid structure of spatial information. Each layer consists of hexagonal layout of cells and one-directional suppression. Locational information of robot $\boldsymbol{x} = (x, y)$ given to both layers.

$$\alpha := \alpha_0(1 - t^{(1)}/t^{(1)}_{\max}), \beta := \beta_0(1 - t^{(2)}/t^{(2)}_{\max}). \tag{3}$$

where α_0, β_0 are initial value of α, β, and $t^{(l)}$, $t^{(l)}_{\max}$ $(l = 1, 2)$ are iterative learning times and maximum of iterative learning times respectively. This update equation leads stability of learning.

(SOMAH2) Set the position $\boldsymbol{x} = (x, y)$ of the robot randomly.

(SOMAH3) Find the winner, $c^{(1)}$ in the superior layer for the input $\boldsymbol{x}$.

$$c^{(1)} = \underset{i}{\operatorname{argmin}} \left\| \boldsymbol{m}_i^{(1)} - \boldsymbol{x} \right\|. \tag{4}$$

Then find the winner $c^{(2)}$ in the inferior layer for the input, considering the inhibitory input $s_{j,c^{(1)}}$ from the winner in the superior layer.

$$c^{(2)} = \underset{j}{\operatorname{argmin}} \left\{ \left\| \boldsymbol{m}_j^{(2)} - \boldsymbol{x} \right\|^2 + s_{j,c^{(1)}} \right\}. \tag{5}$$

(SOMAH4) Update the reference vectors of all the units in both layers,

$$\boldsymbol{m}_i^{(l)} := \boldsymbol{m}_i^{(l)} + h_{c^{(l)}i}\left(\boldsymbol{x} - \boldsymbol{m}_i^{(l)}\right), \tag{6}$$
$$(l = 1, 2).$$

(SOMAH5) Update the inhibitory connections,

$$s_{j,i} := s_{j,i} + \Delta s_{j,i}, \tag{7}$$

$$\Delta s_{j,i} = \beta \left(y_i^{(1)} y_j^{(2)} - \frac{1}{N^{(1)} N^{(2)}} \right). \tag{8}$$

where β is learning parameter of inhibitory connections, and

$$y_i^{(l)} = \begin{cases} 1, & i = c^{(l)}, \\ 0, & \text{otherwise}, \end{cases} \tag{9}$$

$$(l = 1, 2). \tag{10}$$

(SOMAH6) Return to (SOMAH2) and repeat (SOMAH2) $\sim$ (SOMAH5) many times.

We can naturally let the both layers self-organize simultaneously as described above, but the learning process of the superior layer is independent of the inferior. We, therefore, simulate only the learning process of the superior layer first until it reaches the equilibrium, and then the learning process of the superior is stopped or all the reference vectors $\boldsymbol{m}_i^{(1)}$ are fixed, and the learning process of the inferior layer and the anti-Hebbian connections is started using the output of the superior layer.

4 Simulation results

In the equilibrium of the learning process the learning rules (9) and (10) assure that the distribution of the two winners on the two layers should be statistically independent of each other or the joint probability of the two winners should be uniform. If the two SOM layers were one-dimensional array, the two-dimensional input would be decomposed into two one-dimensional components and mapped on each of the two SOMs. In this case, however, the two SOM layers are two-dimensional as well. So, the superior layer is sufficient to represent all of the input information, and nothing seems to be left for the inferior layer.

4.1 One-dimensional example

Before showing our main results, we will elucidate the our model's property by more simple situation, where we selected one-dimensional input and set the dimension of the two SOM arrays two as well. Each SOM has same number of cells $N^{(1)} = N^{(2)} = 5$, and learning parameters are $\alpha^{(1)} = 0.1$, $\sigma^{(1)} = 0.6$, $t_{\max}^{(1)} = 20,000$ for superior layer, $\alpha^{(2)} = 0.001$, $\beta^{(2)} = 0.005$,

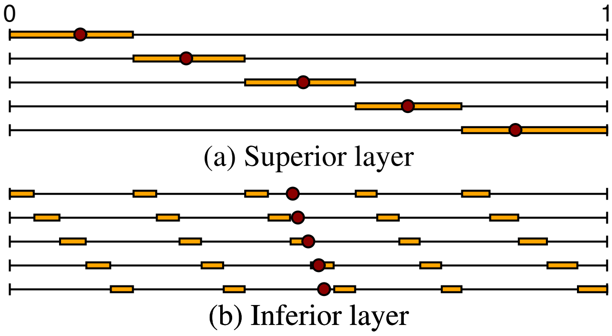

Figure 2: Learning results with one-dimensional input for two one-dimensional SOMs. (a) Superior layer: Reference vectors (filled circle) and receptive fields (rectangular mark) of cells distributed widely in the inputs range. (b) Inferior layer: Receptive fields are not connected but consist of five small segments.

$\sigma^{(2)} = 1.5$, $t_{\max}^{(2)} = 480,000$ for inferior layer. Range of input $\boldsymbol{x} = x$ is $[0, 1]$.

In Figure 2, the receptive fields and the reference vectors of the five cells in each layer are shown. Because the superior layer is a usual SOM, the receptive field of each cell is a connected segment around the reference vector, which are nicely ordered on the input range $[0, 1]$. As for the inferior layer the receptive field of a cell is not connected but consists of five small segments, each of which is contained in one of the receptive fields of the cells in the superior layer. Thus, the receptive field of a cell in the superior layer is divided into five small segments, each of which are contained in the receptive field of each cell in the inferior layer. The reference vectors of the inferior layer show little correspondence to the receptive fields. This means the anti-Hebbian connections from the superior layer play an important role in realizing these unusual receptive fields. We can easily see that the distribution of the two winners are statistically independent in this result. This representation is equivalent to two-digit "pental" number system.

4.2 Two-dimensional positional inputs

We used two SOM layers each of which consists of 19 cells arranged in a hexagonal array ($N^{(1)} = N^{(2)} = 19$). Learning parameters of this experiment are $\alpha^{(1)} = 0.02$, $\sigma^{(1)} = \{0.8\ (0 \le t^{(1)} \le 15,000),\ 0.2\ (15,000 < t^{(1)} \le t_{\max}^{(1)})\}$ and $\alpha^{(2)} = 0.0001$, $\beta^{(2)} = 0.005$, $\sigma^{(2)} = 1.2$. Also, $t_{\max}^{(1)} = 40,000$, $t_{\max}^{(2)} = 260,000$. Input vector $\boldsymbol{x} = (x, y)$ is generated

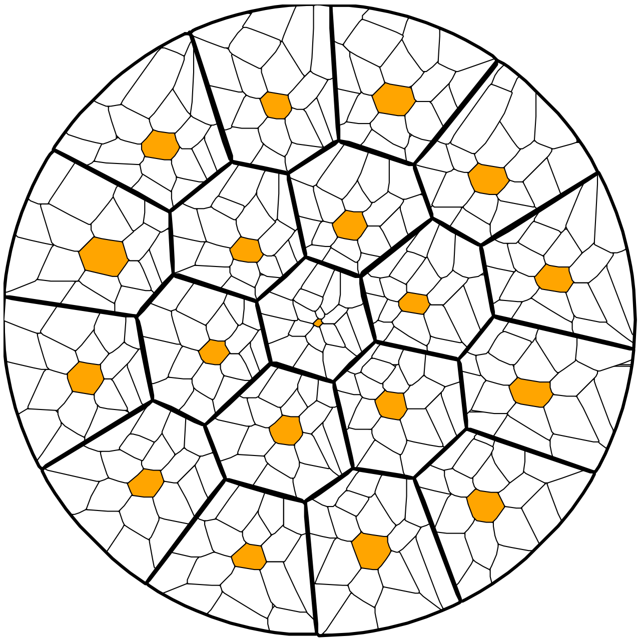

Figure 3: Receptive fields of the cells in both layers for spatial inputs. The whole input area is divided into the receptive fields of the cells in the superior layer (bold line), each of which is subdivided into smaller area (thin line), which constituting the receptive fields of inferior layer. The receptive field of the 9-th cell in the inferior layer is shaded. We can see it is disconnected and periodically arranged.

randomly with uniform distribution within a circle of radius 1.

Learning results are shown in Figure 3. As in one-dimensional simulation, the receptive fields of the superior layer are connected and cover the whole input area altogether. Each of the receptive fields of the inferior layer is not connected but consists of many small areas, each of which are contained in one of the receptive fields of the superior layer. The small areas constituting the receptive field of the inferior layer show very regular periodic arrangement, which is very similar to that observed for the 'grid cell' in dMEC of rats.

5 Conclusion

We showed that two SOM layers connected via anti-Hebbian synapses can form an expression similar to 'multi-ary' number system, and when two-dimensional position vector is supplied to the model, the inferior layer forms disconnected receptive fields showing a periodic grid structure, which is very similar to what was observed in dMEC of rats by Hafting et al. [4]. According to our model, there must be some other position cells with wider and connected receptive fields in somewhere in rats' brain.

We have to compare our results with Hafting's observation in more details. Multi-ary representation obtained in our model has advantage of higher resolution with fewer cells, which would be nice for robots as well as rats.

Acknowledgment

The authors thank Dr. Akira Date for drawing our attention to Hafting's works.

References

[1] T. Kohonen, "Self-Organized Formation of Topologically Correct Feature Map", *Biological Cybernetics*, **43**, pp.59-69, 1982.

[2] K. Kurata, N. Oshiro, "Separating visual information into position and direction by SOM", *Artificial Life and Robotics*, **8** (1), pp.5–8, 2004.

[3] N. Oshiro, K. Kurata, "Separating visual information into position and direction by two inhibitory-connected SOMs", *Artificial Life and Robotics*, **9** (2), pp.86–89, 2005.

[4] T. Hafting, M. Fyhn, S. Molden, M. Moser and E. Moser, "Microstructure of a spatial map in the entorhinal cortex", *Nature*, **436**, pp.801–806, 2005.

[5] T. Kohonen, *Self-Organizing Maps*, Springer-Verlag, Berlin, 1994.

[6] E. Erwin, K. Obermayer and K. Schulten, "Models of Orientation and Ocular Dominance Columns in the Visual Cortex: A Critical Comparison", *Neural Computation*, **7**, pp.425-468, 1995.

[7] H. Shouno, K. Kurata, "Formation of a Direction Map using Kohonen's Self-Organization Map by Projection Learning" , *Biological Cybernetics*, **85**, pp.241-246, 2001.

The Eleventh International Symposium on Artificial Life and Robotics 2006 (AROB 11th'06),
B-con Plaza, Beppu, Oita, Japan, January 23-25, 2006

On-Line Prognostics Health Maintenance for Induction Motors Based on Time-Series Data Mining

Jinsu Park, Yountae Kim, Young-In Kim, Hyeon Bae, Sungshin Kim

School of Electrical and Computer Engineering, Pusan National University, Busan, Korea

Pusan National University 30 Changjeon-dong, Keumjeong-ku, Busan 609-735, Korea
E-mail: soblessed@dreamwiz.com, dream0561@pusan.ac.kr, kyi97@pusan.ac.kr, Baehyeon@pusan.ac.kr, sskim@pusan.ac.kr

Abstract – The motor is an essential part in manufacturing systems. The issues of preventive and condition-based maintenance, online monitoring, system fault detection, diagnosis, and prognosis are of increasing importance. This paper introduces an on-line prognostics health maintenance (OPHM) for induction motors. The proposed OPHM algorithm is bases upon stator currents from induction motors. The stator currents are measured by the current meters and stored in the time series data. Preprocessing methods are applied to treat the signals, because the intact time series data is not suitable to represent the current signals. After preprocessing of the signals, the features have to be extracted by the time series data mining methods that include synchronization and wavelet analysis. The discovered features are constructed to the motor faults templates for the template matching method. The test results for based on real data show that the proposed approach is very useful and powerful method to detect the features in the signals.

Keywords: fault detection, feature extraction, time-series data mining

1. Introduction

The most popular way of converting electrical energy to mechanical energy is an induction motor. This motor plays an important role in modern industrial plants. The risk of motor failure can be greatly reduced routine maintenance is completed, such as scheduling motor replacement or repairs and warnings of impeding failure can be recognized. In recent years fault diagnosis has become a challenging topic for many electric machine researchers and we introduce a real-time diagnosis algorithm for motors called on-line prognostics health maintenance (OPHM).

The major faults of electrical machines can broadly be classified as follows [1]:

- Abnormal connection of the stator windings
- Broken rotor bar or cracked rotor end-rings
- Static and/or dynamic air-gap irregularities
- Bent shaft (akin to dynamic eccentricity)
- Shorted rotor field winding
- Bearing and gearbox failure

Faults in electric machines produce one of more of the following symptoms:

- Unbalanced air-gap voltages and line currents
- Increase torque pulsations
- Decreased average torque
- Increase losses and reduction in efficiency
- Excessive heating

The diagnostic methods to identify the above faults may involve several different types of fields of science and technology [1], [2]. Several methods are applied to detect the faults in induction motors as the following:

- Electromagnetic field monitoring
- Temperature measurements
- Infrared recognition
- Radio frequency (RF) emissions monitoring
- Noise and vibration monitoring
- Chemical analysis
- Acoustic noise measurements
- Motor current signature analysis (MCSA)
- Model, AI and NN based techniques

In this research, we use several time-series data mining techniques for fault diagnosis. First, we introduce a synchronizing method, which is a very important issue in digitalized time-series measurement equipment. Wavelet transform is a method for time varying or non-stationary signal analysis, and uses a new description of spectral decomposition via the scaling concept. Wavelet theory provides a unified framework for a number of techniques, which have been developed for various signals processing applications. One of its features is multi-resolution signal analysis with a vigorous function of both time and frequency localization. This method is effective for stationary signal processing as well as non-stationary signal processing. Mallat's pyramidal algorithm based on convolutions with quadratic mirror filters is a fast method similar to FFT for decomposing the original signal in an orthonormal wavelet basis or decomposing of the signal in a set of independent frequency bands. The independence is due to the orthogonality of the wavelet function [3]. However, performance changes according to the mother wavelet. Unfortunately, selecting a suitable mother wavelet is very difficult. To overcome this problem, we developed a non-supervising method, which supports the selection of the most suitable mother wavelet for fault diagnosis.

2. Synchronization with Hilbert Transform

2.1 Hilbert Transform

The Hilbert transform of the signal, *x(t)*, is defined to be the signal whose frequency components are all phase shifted by $-\pi/2$ radians.

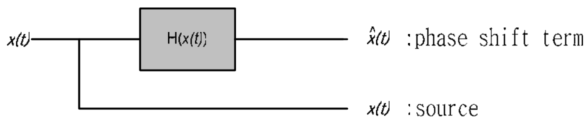

Fig. 1 Hilbert transform.

The resulting signal is denoted by

$$\hat{x}(t) = H\{x(t)\} \tag{1}$$

$\hat{x}(t)$ is produced by passing *x(t)* through a filter with a transfer function.

$$H(f) = -j\,\mathrm{sgn}(f) \tag{2}$$

The magnitude and phase of *H(f)* are given by

$$|H(f)| = 1 \tag{3}$$

$$\angle H(f) = -\frac{\pi}{2}\mathrm{sgn}(f) \tag{4}$$

This phase shift is very useful for synchronizing each measured signal.

2.2 Synchronization

We use the Hilbert transform to align the phases of each measured signal. The phase of the original signal can be established by using the arctangent from the created phase shift term that results from the Hilbert transform and the original signal. Each signal is aligned to zero degrees, as shown in Fig. 2.

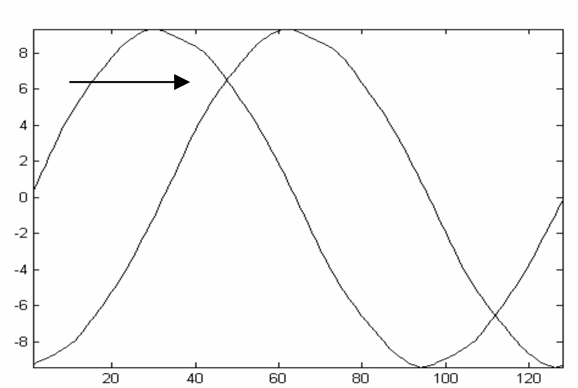

Fig. 2 Synchronization of signal.

3. Wavelet Transformation

A wavelet is a function ψ belonging to $L^2(R)$ with a zero average. It is normalized and centered in the in the neighborhood of t=0. A family of time-frequency atoms is obtained by scaling ψ by a^j and translating is by b:

$$\psi_{a,b} = |a|^{\frac{-j}{2}}\psi\left(\frac{t-b}{a^j}\right) \tag{5}$$

These atoms also remain normalized. The wavelet transform of f belonging to $L^2(R)$ at the time b and scale a^j is:

$$Wf(b,a^j) = \left\langle f, \varphi_{b,a^j}\right\rangle = \int_{-\infty}^{+\infty} f(t)\frac{1}{\sqrt{a^j}}\varphi^*\left(\frac{t-b}{a^j}\right)dt \tag{6}$$

A real wavelet transform is complete and maintains an energy conservation as long as the wavelet satisfies a weak admissibility condition which is:

$$\int_0^{+\infty}\frac{|\Psi(w)|^2}{|w|}dw = \int_{-\infty}^{0}\frac{|\Psi(w)|^2}{|w|}dw = C_\psi < +\infty \tag{7}$$

When $Wf(b, a^j)$ is known only for $a<a_0$ to recover f we need a complement of information corresponding to $Wf(b, a^j)$ for $a<a_0$. This is obtained by introducing a *scaling function* ϕ that is an aggregation of wavelet at scales larger than 1. $\hat{\psi}(w)$ and $\hat{\varphi}(w)$ are Fourier transforms of $\psi(t)$ and $\varphi(t)$ respectively. $\psi(t)$ is a band pass filter, and $\varphi(t)$ is a low-pass filter. Taking positive frequency into account $\hat{\varphi}(w)$ has information in $[0, \pi]$ and $\hat{\psi}(w)$ in $[\pi, 2\pi]$. Therefore they both have complete signal information without any redundancy. Decomposition of the signal in $[0, \pi]$ using Mallat's algorithm gives:

$$\begin{aligned} h(n) &= \left\langle 2^{-j}\varphi(2^{-1}t)\varphi(t-n)\right\rangle \\ g(n) &= \left\langle 2^{-j}\psi(2^{-1}t)\varphi(t-n)\right\rangle \end{aligned} \qquad j = 0,1,2,\ldots \tag{8}$$

Wavelet decomposition does not involve the signal in $[\pi, 2\pi]$. In order to decompose the signal in whole frequency band, wavelet packet can be used for this purpose. After decomposition for l times, we will get 2^l frequency bands each with the same bandwidth. That is:

$$\left[\frac{(i-1)f_n}{2}, \frac{if_n}{2}\right] \qquad i = 1,2,\ldots,2^j \tag{9}$$

where f_n is the Nyquist Frequency, in the i^{th} frequency band. Wavelet packet de-composes the signal into one low-pass filter $h(n)$ and 2^l-1 band-pass filters $g(n)$, provides diagnosis information in 2^l frequency bands.

Functions $h(n)$ and $g(n)$ can be obtained by inner product of $\psi(t)$ and $\varphi(t)$.

$$\begin{aligned} h(n) &= \left\langle 2^{-j}\varphi(2^{-1}t)\varphi(t-n)\right\rangle \\ g(n) &= \left\langle 2^{-j}\psi(2^{-1}t)\varphi(t-n)\right\rangle \end{aligned} \qquad t \in R, n \in Z \tag{10}$$

$$\begin{aligned} A_j(n) &= \textstyle\sum_k h(k-2n)A_{j-1} \\ D_j(n) &= \textstyle\sum_g g(k-2n)A_{j-1} \end{aligned} \qquad n = 1,2,3,\ldots \tag{11}$$

where $A_0(k)$ is the original signal and A_j is the low frequency approximation at the resolution j. D_j is called high frequency detail signal. After de-composition of j time, we can obtain one approximation signal A_j and D_1, D_2, …, D_j detail signals.

Wavelet packet decomposition is:

$$x_{2n}(t) - \sqrt{2}\sum_k h(k)x_n(2t-k)$$
$$x_{2n+1}(t) - \sqrt{2}\sum_k g(k)x_n(2t-k) \tag{12}$$

where $x_1(t)$ is the original signal. Comparing (12) with (10), we can find that A_j in (10) is decomposed but also D_j in (10) is decomposed in (12).

Wavelet and wavelet packet decompose the original signal that is non-stationary or stationary into independent frequency bands with multi-resolution.

4. Experimental Results

4.1 Current Signals and Data Preprocessing

The motor rating used in this paper depended on the electricity conditions. The rated voltage, speed, and horsepower were 220V, 3450RPM, and 5kw, respectively. Motor specifications include the number of slots, the number of poles, slip, and other factors. The actual motor specifications used were 34 slots, 4 poles, and 24 rotor bars. Slip is determined by calculating the actual motor speed and the rated speed. The input current signal was sampled 16,384 tines, had a maximum frequency 3kHz, and measurement internal of 2.1333. The faults that were studied were a broken rotor, faulty bearing, a bowed rotor, unbalance, and static and dynamic eccentricity.

If the wavelet decomposition is used to detect faults in induction motors, the unsynchronized current phase problem should significantly influence the results. If target signals are not synchronized as shown in Fig. 3, unexpected results will appear in the wavelet decomposition.

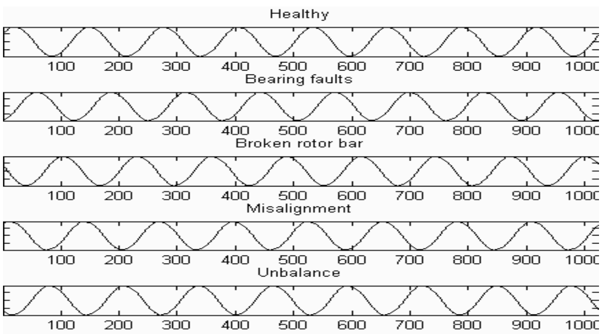

Fig. 3 Original current signals.

Therefore the signals were re-sampled by synchronizing the signals using phase 0 by using Hilbert transform. The average value divided by one cycle signal was calculated in order to reduce the noise of the original signals as shown in Fig. 4.

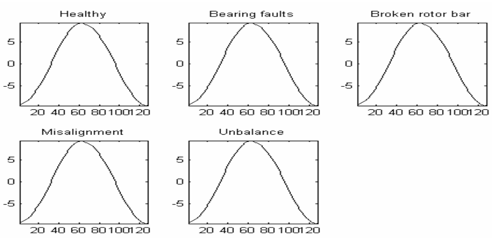

Fig. 4 Data synchronizing and filtering.

Last, four fault templates were made consisting of a broken rotor bar, bearing fault, misalignment, and unbalance. The fault templates were based on 40 test sets. Figure 5 shows that the template was produced by finding the difference between the averaged fault signal and healthy signal.

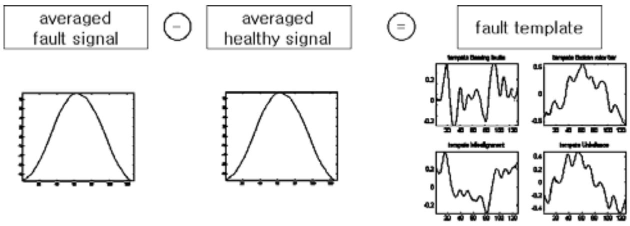

Fig. 5 Fault templates.

These produced templates have high frequency terms related to the characteristics of each fault. For this reason, wavelet decomposition was used to extract the detail terms. It thought that this improved performance and is introduced in the next section.

4.2. Applying wavelet decomposition and finding a suitable mother wavelet for diagnosis

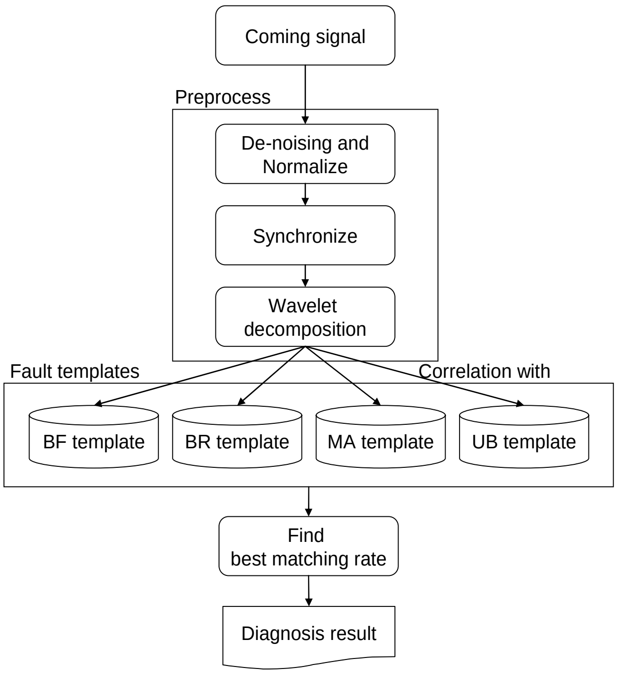

Fig. 6 Flow chart of diagnosis processes.

The wavelet decomposition was applied to the produced templates. We use a produced-detail coefficient in the first step of decomposition. Figure 7 shows the characteristics of discrete wavelet transform. The detail coefficient produces a high frequency source signal.

These become new fault templates and are used in a template matching method. A correlation is used to determine the matching rate. The flow chart in Figure 6 shows the entry process of our proposed diagnosis. First, an unknown signal preprocessed. The results are mathematically correlated with the four templates. But, before this process, we need to find most suitable mother wavelet for the motor diagnosis. The most suitable mother wavelet is taken from the various wavelet sets in Table 1.

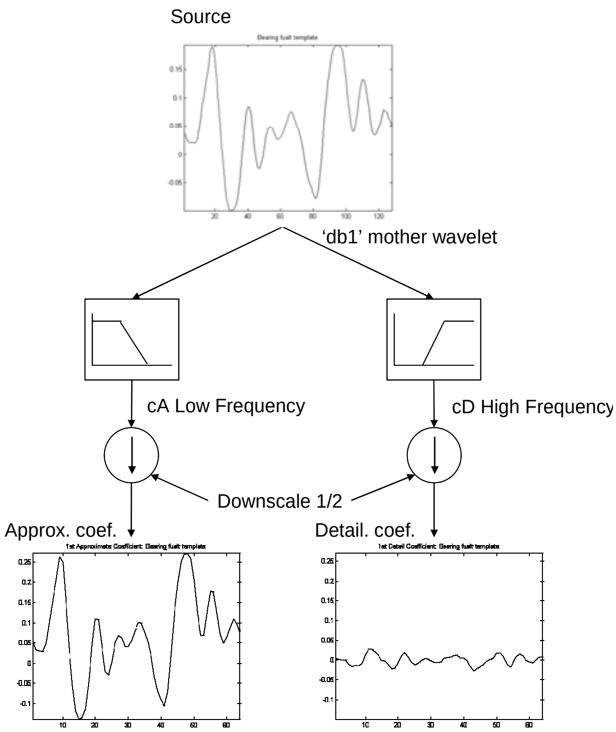

Fig. 7 Characteristics of DWT.

Table 1 Mother wavelets for DWT

Wavelets	Window size
Daubechies	1-15
Symlets	2~15
Coiflets	1~5
Meyer	.

Each mother wavelet is used to match the signal to a wavelet to times. The number of hits is used to evaluate the diagnosis. Table 2 shows that the Daubeches wavelet of window size 1 (Harr wavelet) is the most suitable mother wavelet for diagnosis. The Daubeches wavelet has an accuracy rate of about 97.5%. Diagnosis misalignment and unbalance was especially accurate at 100%

Table 2 A list of results of diagnosis test sets in best 4 mother wavelets (Each 40 times).

Wavelets	Faults				Total
	BF	BR	MA	UB	
'db1'	37	39	40	40	156
'coif1'	31	38	20	33	122
'db2'	28	38	19	34	119
'sym13'	25	31	5	18	79

5. Conclusion

The proposed OPHM algorithm is based upon several time-series data mining techniques. The stator current is measured by a current meter and stored in the time series data. Preprocessing methods are applied to the signals, because the intact time series data is not suitable for representing current signals. After preprocessing the signals, the features have to be extracted by the time series data mining methods which include synchronization and wavelet analysis. The resulting features are matched to the motor faults templates. Wavelet analysis is a possible method for detecting faults in induction motors, but it depends on locating the most suitable mother wavelet. We have established that the Daubeches wavelet is the most suitable mother wavelet for diagnosis of motor. It can produce a diagnostic accuracy rate of about 97.5%. In future work, we will develop the OPHM based stand-alone hardware for diagnosing inductive motors and try to design the optimal mother wavelet for diagnosis.

ACKNOWLEDGEMENT

This work was supported by the Regional Research Centers Program(Research Center for Logistics Information Technology), granted by the Korean Ministry of Education & Human Resources Development.

References

[1] P. Vas, Parameter Estimation, Condition Monitoring, and Diagnosis of Electrical Machines, Clarendron Press, Oxford, 1993.

[2] G. B. Kliman and J. Stein, "Induction motor fault detection via passive current monitoring," International Conference in Electrical Machines, Cambridge, MA, pp. 13-17, August 1990.

[3] K. Abbaszadeh, J. Milimonfared, M. Haji, and H. A. Toliyat, "Broken Bar Detection In Induction Motor via Wavelet Transformation," IECON'01: The 27^{th} Annual Conference of the IEEE Industrial Electronics Society, pp. 95-99, 2001.

[4] Masoud Haji and Hamid A. Toliyat, "Pattern Recognition-A Technique for Induction Machines Rotor Fault Detection Eccentricity and Broken Bar Fault," Conference Record of the 2001 IEEE Industry Applications Conference, vol. 3, pp. 1572-1578, 30 Sept.-4 Oct. 2001.

[5] S. Nandi, H. A. Toliyat, "Condition Monitoring and Fault Diagnosis of Electrical Machines – A Review," IEEE Industry Applications Conference, vol. 1, pp. 197-204, 1999.

[6] B. Yazici, G. B. Kliman, "An Adaptive Statistical Time-Frequency Method for Detection of Broken Bars and Bearing Faults in Motors Using Stator Current," IEEE Trans. On Industry Appl., vol. 35, no. 2, pp. 442-452, March/April 1999.

The curvature detect system of the lane using image

Kim Jun-won
Dep. of EE.
Pusan National University.
Busan, Republic of Korea.
nonfast@pusan.ac.kr

Ha Sung-kil
Dep. of EE.
Pusan National University.
Busan, Republic of Korea.
skha@pusan.ac.kr

Cho Seog-bin
Dep. of EE.
Pusan National University.
Busan, Republic of Korea.
chosb@pusan.ac.kr

Baek Kwang-ryul
Dep. of EE
Pusan National University
Busan, Republic of Korea
krbaek@pusan.ac.kr

Abstract

In this paper, we research real-time algorithm for the extraction of lane information. The algorithm in this paper based on EDF(edge distribution function), that give priority to lane direction and curvature information detect which are toughness and reliable. And it composes a system optimization for the efficient conduct of lane curvature information detect algorithm base on EDF. At first, this paper converts image using IPM(inverse perspective mapping) for reliable lane-information detect algorithm. In order to search the direction and a curvature of the lane from the image where the IPM is applied it divided an image equally with y direction, against each part histogram of the edge-magnitude which relates in the direction angle of the edge, an edge distribution function defined. It becomes to extracted lane information and scatter diagram using edge-pixel that agrees with peak value of the EDF for gets lane information from divided image.

Keywords image, transformation, curvature, detect, lane, EDF

1 Introduction

Recently, automation equipment is developed that substitutes the human. The AGV(automatic guided vehicle) is one example, it is used at harbor of the world-wide various nations. Also small-sized automation equipments are tendency which increase in industry.
There is to control of automation equipments that it is important that acquires information of the location and progress direction. Various techniques is used in order to get these information, there are technique using magnet tape and technique using RF & laser beacon. However, there are fault difficult of the foundation and modification, moreover it is expensive. So image processing technique is increased. It is useful in current environment and need not additional equipment. In that one is the location and direction detect using image. It is many difficult in data processing because the image data is many too much at the past. Also the efficiency of the camera cannot be good, it did not use well. But now the operation speed of the processor comes to be quick and various applications includes the resolution of camera image getting better very, the method using image is receiving footlights.
In this paper, it added from the image processor in equipment of existing and the algorithm it will be able to acquire information in traveling and moving easily it proposed. It proposed the algorithm which minimizes the operation which is whole algorithm and it guaranteed a real-time characteristic.

2 The Pretreatment Algorithm for an Image

2.1 Camera calibration

Camera calibration entails solving for a large number of calibration parameters, it requires large scale nonlinear search. For example, focal distance from lens until CCD camera, vision angle of lens, the lens distortion.[1] In addition errors appear when mapping from 3D to 2D is nonlinear, the error appear when it acquire image data. In this paper, camera calibration use DLT(direct linear transformation) equation by M. Bretozzi and A. Broggi.[2]

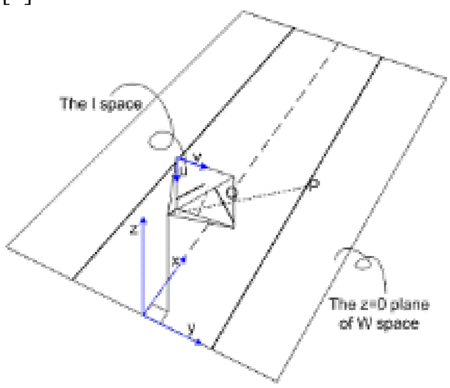

Fig. 1. Relationship between the two coordinate systems

The parameter acquires data using coordinates and direction angle of the camera, vision angle and resolution of the lens. This method the calculation is simple for data acquisition; it has the advantage of real-time. W-image and I-image are shown in Fig. 1.

2.2 Image conversion algorithm

It does pretreatment that convert the images from the camera into top-view for lane detect. It applies mathematics algorithm and it is calculated and there is a possibility of making the vector table where in actual location it corresponds. The data which is converted it is acquired information about a traveling direction and a curvature. It use Sobel mask for a traveling direction and a curvature, it use accumulation distribution function and image division for a curvature.

2.2.1 Interrelation of image coordinate and actual location [3]

Two Euclidean spaces are defined for convert I-image into W-image in Fig. 1.

$$\begin{aligned}&\bullet W=\{(x,y,z)\}\in E^3\text{, representing the 3-D world space}\\&\quad(\text{world-coordinate})\text{, where the real world is defined.}\\&\bullet I=\{(u,v)\}\quad\in E^2\text{, representing the 2-D image space}\\&\quad(\text{screen-coordinate})\text{, where the 3-D scene is projected.}\end{aligned}\tag{1}$$

2.2.2 Convert top-view image

The image which it is having actually from two space I-image and the W-image is the I-image.

$$\begin{aligned}&\text{viewpoint : camera position is } C=(l,d,h)\in W\\&\text{viewing Direction : optical axis } \hat{o} \text{ is determined by}\\&\qquad\qquad\text{the following angles}\\&\quad\bar{\gamma}:\ \text{the angle formed by the projection (defined by versor } \hat{\eta})\\&\qquad\text{of the optical axis } \hat{o} \text{ on the plane z=0 and the } x \text{ axis}\\&\quad\bar{\theta}:\ \text{the angle formed by the optical axis } \hat{o} \text{ and versor } \hat{\eta}\\&\text{Aperture : camera angular aperture is } 2\alpha\\&\text{Resolution : camera resolution is } n\times n\end{aligned}\tag{2}$$

And when it applies the equation for a conversion with follow equation it is same and when it applies this, it show in Fig. 2.

$$\begin{aligned}x(u,v)&=h\times\frac{\cos\left[(\bar{\theta}-\alpha)+u\dfrac{2\alpha}{n-1}\right]}{\tan\left[(\bar{\gamma}-\alpha)+v\dfrac{2\alpha}{n-1}\right]}+l\\y(u,v)&=h\times\frac{\sin\left[(\bar{\theta}-\alpha)+u\dfrac{2\alpha}{n-1}\right]}{\tan\left[(\bar{\gamma}-\alpha)+v\dfrac{2\alpha}{n-1}\right]}+d\\z&=0\qquad u,v=0,2,\cdots,n-1\end{aligned}\tag{3}$$

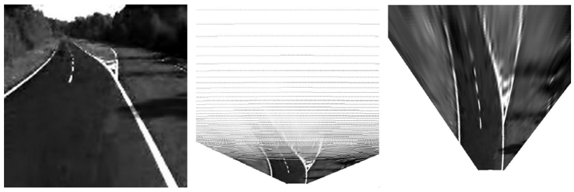

(a) (b) (c)

Fig. 2. (a)Original image (b) Remapped image (c) Remapped image using inverse transform

Fig. 2(a) is I-image and Fig. 2(b) is a image by the mapping W-image from I-image. Namely, it must interpolation for original W-image reconstruct. Fig. 2(c) is remapped image using inverse transform that it used the method which summons the coordinate of the $W(u,v,z=0)$ from the $I(x,y)$. Show equation (4a) and (4b).

$$u(x,y,0)=\frac{\arctan\left[\dfrac{h\times\sin\gamma(x,y,0)}{y-d}\right]-(\bar{\theta}-\alpha)}{\dfrac{2\alpha}{n-1}}\tag{4a}$$

$$v(x,y,0)=\frac{\arctan\left[\dfrac{y-d}{x-l}\right]-(\bar{\gamma}-\alpha)}{\dfrac{2\alpha}{n-1}}\tag{4b}$$

The value of the tangent becomes infinite from the angle which is parallel with the surface in $z=0$. This point is a disappearance point. When it mapping from lower region of disappearance point, the image become top-view image with the Fig. 2(c) it is same.

3 Lane Information Detection Algorithm

3.1 The edge detect algorithm [4]

The edge is defined slope of the change which image brightness. The 1st differential from location of image, namely slope vector it is equation (5).

$$\Delta f=\begin{bmatrix}G_x\\G_y\end{bmatrix}=\begin{bmatrix}\dfrac{\partial f}{\partial x}\\\dfrac{\partial f}{\partial y}\end{bmatrix}\tag{5}$$

Here, slope vector ∇f in point (x,y) is maximum variable direction of $f(x,y)$, amplitude and direction are equation (6a), (6b).

$$\Delta f(x,y)=\sqrt{G_x^2+G_y^2}\tag{6a}$$

$$\alpha(x,y)=\tan^{-1}\left(\frac{G_y}{G_x}\right)\tag{6b}$$

This paper used Sobel mask for algorithm.

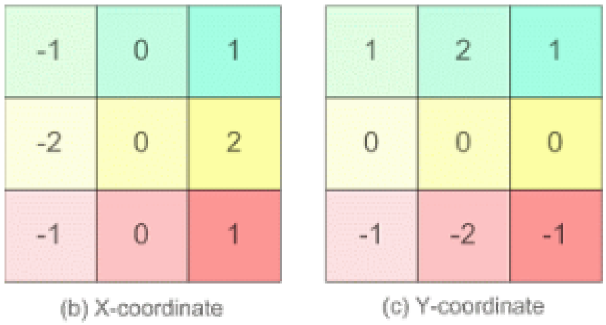

Fig. 3. Sobel mask

$$f_G(x,y)=\begin{cases} f(x,y), & if \quad f(x,y)>TH \\ 0, & if \quad f(x,y)\le TH \end{cases} \qquad (7)$$

$TH: Threshold$

After X-coordinate and Y-coordinate masking, it store data $\alpha(x,y)$ by threshold. Finally, it applies with the data about a slope.

3.2 Convert one-loop algorithm

It is repeated two loops when it applied Eq. (4), (5). So, it make vector table because image information is unchanged. The process receives 9 data which corresponds to the location of the I-image from the buffer it shows Fig. 4.

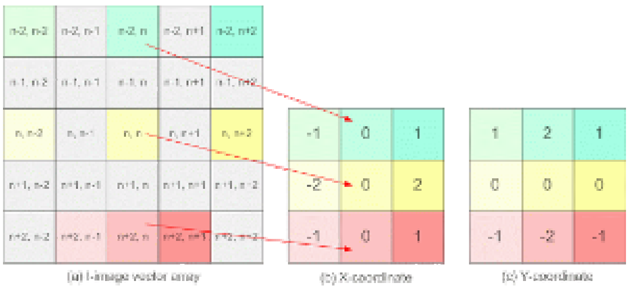

Fig. 4. Sobel mask using vector array

And then it store final operation value (vector location, $\alpha(x,y)$).

3.3 Cumulative distribution function [5]

Suggest CDF(cumulative distribution function) for edge direction of lane. it show follow equation.

$$F(d)=\sum_{n(d)}\Delta f(x,y)\theta \qquad (8)$$

Here, $n(d)$ means number of pixel that edge direction is $\alpha(x,y)=d$, range of angle d is $d\in(0^\circ,180^\circ)$.
And it use gaussian filter for remove noise, then become Fig. 5.

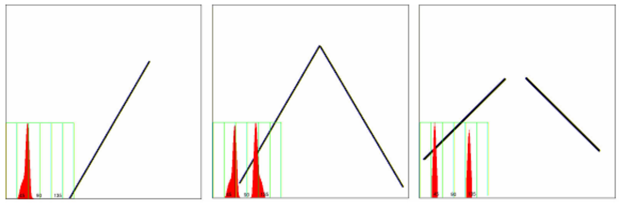

(a) 60° (b) 60° and 120° (c) 45° and 135°

Fig. 5. CDF of the edge direction for lane image

3.3.1 Direction angle detect using CDF

There is a possibility of getting LMP(local maximum point) using CDF. This is made by the pixels where the edge direction is from the converted image.

$$\Gamma=\{(x,y)|\alpha(x,y)=\theta\} \qquad (9)$$

Here, $\alpha(x,y)$ is edge direction from (x,y). There is getting Fig. 6. by gathering the data which gets near to the LMP.

$$\Gamma=\{(x,y)|LMP-\delta\le\alpha(x,y)\le LMP+\delta=\theta\} \qquad (10)$$

δ is constant value, when the value becomes larger and the noise comes to be large, when the value becomes lover and the information comes to be lack.

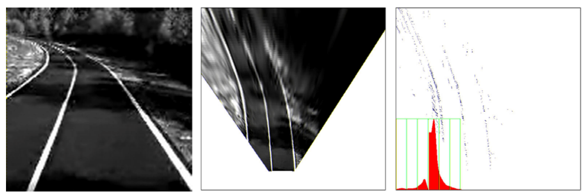

(a) (b) (c)

Fig. 6. (a) Original image (b) Remapped image (c) Edge direction of the lane boundary

3.3.2 Curvature information acquisition of the lane

This paper used PABLF(principal axis-based line fitting) for acquisition of slope information in image. This method must assume which lane is a straight line.

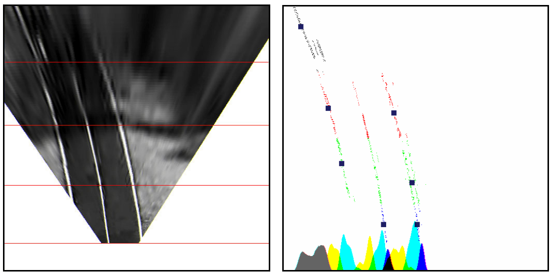

Fig. 7. Image division

It detect gravity center using (p+q) difference moment for detect region of each part.

$$m_{pq} = \sum_{(x,y)\in\Gamma} x^p y^q f(x,y) \tag{11}$$

m_{pq} is (p+q) difference moment, Γ is pixel of $f(x,y)$. So, gravity center with follow it is same.

$$\bar{x} = \frac{m_{10}}{m_{00}}, \quad \bar{y} = \frac{m_{01}}{m_{00}} \tag{12}$$

Follow equation is slope of principal axis by center moment.

$$\mu = \sum_{(x,y)\in\Gamma} (x-\bar{x})^p (y-\bar{y})^q f(x,y) \tag{13a}$$

$$\Phi = \frac{1}{2}\tan^{-1}\left(\frac{2\mu_{11}}{\mu_{20}-\mu_{02}}\right) \tag{13b}$$

The next is the equation using PABLF method.

$$y = \tan\Phi(x-\bar{x})+\bar{y} \tag{14}$$

Finally, it is bought the slope of each region. It searches the slope change quantity of each region then it is known the change the slope from the whole image.

4 Conclusion

This paper describes an image processing algorithm capable of extracting lain-related information (curvature, direction) using an edge distribution function (EDF), which is designed for the model function of the road lane. When image transformation is processed, Sobel masking is processed at the same time. So, performance of the system is improved. And without the change of external circumstance, the algorithm can apply to the driven system for gathering road information.

But, it cannot be applied when lane is damaged. And it needs improvement because there is an error in uphill and downhill road.

Acknowledge

This work was supported by "Research Center for Logistics Information Technology (LIT)" hosted by the Ministry of Education & Human Resources Development in Korea.

5 Reference

[1] Roger Y. Tsai, "A Versatile Camera Calibration Technique for High-Accuracy 3D Machine Vision Metrology Using Off-the-Shelf TV Cameras and Lenses" IEEE journal of robotics and automation, vol. RA-3, NO.4, August 1987.

[2]-[3] Massimo Bertozzi, Alberto Broggi, "GOLD: A Parallel Real-Time Stereo Vision System for Generic Obstacle and Lane Detection", IEEE Transactions on image processing, Vol. 7, NO. 1, January 1998.

[4] J. W. Lee, U.K. Yi, and K.R. Baek, "A cumulative distribution function of edge direction for road-lane detection", IEICETRANS. INF. & SYST., Vol.E84-D, No.9 September 2001.

[5] A.D. Bimbo, L. Landi, and S.Santini, "Determination of road directions using feedback neural nets", Signal process., Vol32, pp.147-160, 1993

Implementation mass flow controller for adaptive PID

Bongsu Cho
Dept. of Electronics Engineering in Pusan Natl' University
BUSAN, KOREA, IP : 609-735
e-mail : mscho97@pusan.ac.kr

Kwangryul Baek
Dept. of Electronics Engineering in Pusan Natl' University
BUSAN, KOREA, IP : 609-735
e-mail : krbaek@pusan.ac.kr

Abstract

MFC(Mass Flow Controller) is a equipment that measures and controls flow rates of fluid. The MFC control problem includes the operating pressure and the physical parameters of fluid when the MFC system operates. Also, commonly, the piezo valve makes use of the control valve. The piezo valve controls a detailed displacement and is not sensitive for a temperature and a pressure. But, when the piezo valve assembles the MFC system, a distance error generates. Though this distance error is very small distance, a large error of flow rates generate.

In this paper, we implement MFC system and propose adaptive PID controller with self tuning. It makes use of adaptive PID controller with self tuning in order to compensate these problems of the MFC system. The adaptive PID control algorithm makes use of a method to estimate the parameters of a MFC system. This paper implements MFC system using iegler Nichols's method and the proposal adaptive PID. And, it makes a comparative analysis of the proposal adaptive PID and the traditional PID.

Keywords: MFC(mass flow controller), adaptive PID, self tuning

1. Introduction

Recently, it is important to measure and control flow rates of fluid in many industries. The mass flow control is an important factor for a decision of the quality of product in many industries. Therefore, the high speed and highly accurate control of mass flow controller have demanded on the industry.

Most of MFC are still using the PID algorithm. The PID controller shows superior performance on the MFC system. But the PID controller in the MFC system has a few problems. The flow rates of fluid are related to a pressure drop and a cross-sectional area of pipe, when a fluid flows through a pipe. Also the flow rates are related to physical parameters of fluid [2].

$$P = P_1 - P_2 = \frac{128ul}{\pi d^4}Q \tag{1.1}$$

$$Q_m = \rho Q \tag{1.2}$$

where P_1 = pressure at inlet of pipe, pascal
P_2 = pressure at outlet of pipe, pascal
P = pressure drop flrom inlet to outlet, pascal
u = absolute viscosity of fluid,pascal second
l = length of the pipe, meter
d = inside diameter of the pipe, meter
Q_m = mass flow rate, kilogram/second
Q = volume flow rate, cubic meter/second
ρ = fluid density, kilogram/cubic meter

Due to this reasons, the parameters of MFC system are changing according to the operating condition of the MFC system. When the MFC system control, a operating pressure and a kind of fluid become important variables.

Also, the piezo valve has the characteristic of nonlinearity that includes a hysteresis characteristic. The maximum stroke of the piezo valve is 50 um, actually, 20um distance is enough in the flow control. But, when the piezo valve assembles the MFC system, a distance error generates. This distance error is about 5 20um. Though this distance error is very small, the operating point of piezo valve is enough to change. A change of operating point has a effect on the system characteristic, because piezo valve has hysteresis characteristic.

It is very difficult to find out the value of parameters of the MFC system. When the MFC system implements using the PID algorithm, a man of ripe experience must be repeatedly tune the different PID coefficient about each of the MFC system.

In this paper, we implement MFC system and propose adaptive PID controller with self tuning. The mass flow measurement makes use of the heated bypass capillary thermal mass flow meter, and the mass flow control make use of piezo valve in the MFC system [4,5]. It makes use of adaptive PID control algorithm with self tuning in order to compensate these problems of the MFC system. The adaptive PID algorithm estimates the parameters of MFC system. And parameters of PID controller are updated by this estimated MFC system parameters [1,3]. The adaptive PID algorithm compensates the operating condition due to using the estimated parameters for operating MFC system. And this paper implement MFC system using iegler Nichols's method as traditional PID controller and proposal adaptive PID. And, it makes a comparative analysis of the traditional PID and the proposal adaptive PID.

2. Design adaptive PID controller

2.1 Design PID controller

The MFC system assumes that it approximates a second system. A transfer function of the MFC system is given by Eq (2.1), and a transfer function of PID controller is given by Eq (2.2). If express Parameters for PID controller as Eq (2.3), A transfer function of close loop become Eq (2.4). Therefore, if it gets a parameters of the MFC system, the close loop system become first system with a gain 1 and time constant τ.

$$G_p(s) = \frac{K}{(p_1 s+1)(p_2 s+1)} \tag{2.1}$$

$$G_c(s) = k_p\left(1+\frac{1}{T_i s}+T_d s\right) \tag{2.2}$$

$$T_d = \frac{p_1 p_2}{p_1+p_2},\ T_i = p_1+p_2,\ k_p = \frac{T_i}{K\tau} \tag{2.3}$$

$$G_{close-loop}(s) = \frac{G(s)}{1+G(s)} = \frac{1}{\tau s+1} \tag{2.4}$$

2.2 Structure of adaptive PID controller

Parameters of the MFC system change according to operating pressure, a kind of fluid and assembly error of piezo valve. When operating conditions of the MFC system changes, the new parameters are estimated and parameters of PID controller are redesigned. This paper proposes adaptive PID controller system that parameters of the MFC system estimate from operating data of the MFC system using the method of least mean squares, and parameters of PID controller are readjusted using these estimated parameters.

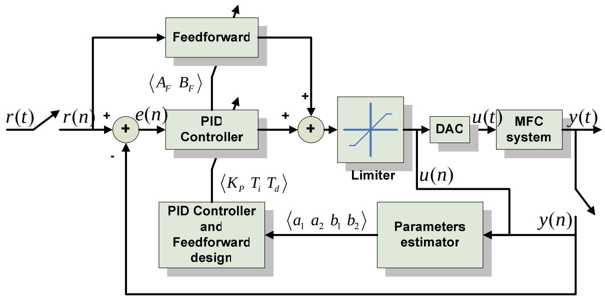

Figure 2.1 Adaptive PID controller system

2.3 Estimation of MFC system

If continuous equation of MFC system that express Eq (2.1) convert discrete equation with sampling time T, discrete equation express Eq (2.5).

$$y[n]=a_1 y[n-1]+a_2 y[n-2]+b_1 u[n-1]+b_2 u[n-2] \tag{2.5}$$

where, $a_1 = e^{-\frac{T}{p_1}}+e^{-\frac{T}{p_2}},\quad a_2 = -e^{-(\frac{1}{p_1}+\frac{1}{p_2})T},$

$$c = \frac{p_2 e^{-\frac{T}{p_1}} - p_1 e^{-\frac{T}{p_2}}}{p_1 - p_2},$$

$$b_1 = K(-a_1+c+1),\quad b_2 = K(-a_2-c)$$

In this paper, I propose method as follow. It expresses relation between input and output of MFC system as Eq (2.5). The parameters are estimated by input and output data. The parameters are defined a vector as Eq (2.6). And the input and output data y[k-1], y[k-2], , y[k-n], u[k-1], u[k-2], , u[k-n] are defined a vector as Eq (2.7). Using the method of least mean square, the estimated parameters calculate Eq (2.8).

$$\boldsymbol{\theta} = [a_1\ \ a_2\ \ \cdots\ \ a_n\ \ b_1\ \ b_2\ \ \cdots b_n]^T \tag{2.6}$$

$$\mathbf{f}^T[k]=\left[y[k-1]\ y[k-2]\cdots y[k-n]\ u[k-1]\ u[k-2]\cdots u[k-n]\right] \tag{2.7}$$

$$\boldsymbol{\theta} = \left[\mathbf{F}(N)^T \mathbf{F}(N)\right]^{-1} \mathbf{F}^T(N)\mathbf{y}(N) \qquad (2.8)$$

where, $\mathbf{F}(N) = [\mathbf{f}^T(n)\ \mathbf{f}^T(n+1) \cdots \mathbf{f}^T(N)]^T$

Because Eq (2.8) includes inverse matrix, estimating new parameters need many calculations. So we use recursive least mean square method. It expresses recursive equation as Eq (2.9)　(2.12)[1,3].

$$\mathbf{P}(N) = \left[\mathbf{F}(N)^T \mathbf{F}(N)\right]^{-1} \qquad (2.9)$$

$$\mathbf{L}(N+1) = \mathbf{P}(N)\mathbf{f}(N+1)\left[1+\mathbf{f}^T(N+1)\mathbf{P}(N)\mathbf{f}(N+1)\right]^{-1} \qquad (2.10)$$

$$\boldsymbol{\theta}(N+1) = \boldsymbol{\theta}(N) + \mathbf{L}(N+1)\left[y(N+1) - \mathbf{f}^T(N+1)\boldsymbol{\theta}(N)\right] \qquad (2.11)$$

$$\mathbf{P}(N+1) = \mathbf{P}(N) - \mathbf{L}(N+1)\mathbf{f}^T(N+1)\mathbf{P}(N) \qquad (2.12)$$

Using this method, parameters of MFC system become Eq (2.13)

$$p_1 = -\frac{T}{\ln r_1},\quad p_2 = -\frac{T}{\ln r_2},\quad K = \frac{b_1 + b_2}{1 - a_1 - a_2} \qquad (2.13)$$

here, $r_1, r_2 = \dfrac{a_1 \pm \sqrt{a_1^2 + 4a_2}}{2}$

3. Actual experiment

3.1 MFC system

The MFC system consists of a measurement part, a control valve part and control and signal processing part. Figure 3.1 is the block of MFC system.

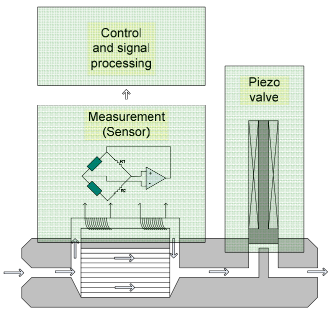

Figure 3.1 : block of MFC system

3.1.1 Measurement part

The measurement part consists of the constant temperature control thermal mass flow meter. And the sensor for the mass flow measurement makes use of coiled platinum wire around bypass capillary. Advantages of this thermal mass flow meter are to measure mass flow of gases and liquids regardless of a temperature and a pressure, and have lower sensitivity related a surrounding thermal changing, high response and superior stability.

3.1.2 Control valve

A control valve uses a piezo valve. The piezo valve controls a precision displacement regardless of a temperature and a pressure. And a response speed is less below 1ms.

3.1.3 Control and signal processing

The control and signal processing part consist of a microprocessor and a peripheral device in order to control the MFC system. And it includes an analog circuit for sensing signal.

3.2 Design using Ziegler & Nichols's method

As design PID controller using　iegler　Nichols's method as traditional PID controller, PID parameters are $K_P = 0.24,\ K_I = 0.001073,\ K_D = 13.41$ and step response is Figure 3.2.

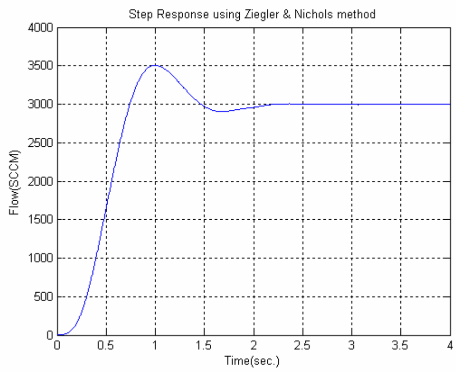

Figure 3.2　iegler　Nichols's step response

If operating conditions of the MFC system change, PID controller is redesigned. Without redesign, the step response becomes to change according to operating pressure, a kind of fluid and assembly error of piezo valve. This response is Figure 3.3.

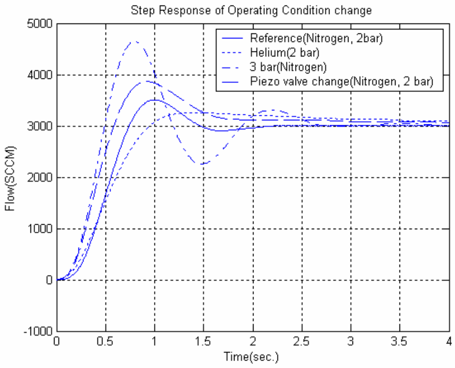

Figure 3.3 Operating condition change

3.3 Design adaptive PID controller

As proposed adaptive PID controller design, step response is Figure 3.4. Because proposal adaptive PID controller includes feedforward, it shows fast step response and improved transient response. As operating conditions of the MFC system change, step response is not a little change. Figure 3.5 is step response that operating conditions are changing.

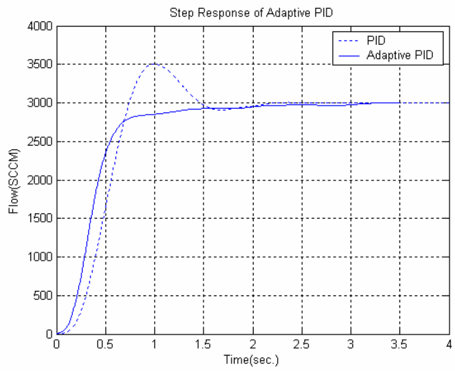

Figure 3.4 : Adaptive PID controller's step response

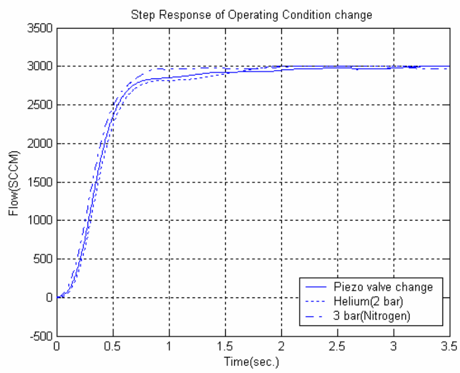

Figure 3.5 : Operating condition change in adaptive PID

4. Conclusions

This paper implements the MFC system using thermal mass flow meter and piezo valve. Control algorithm use proposed adaptive PID algorithm instead of iegler Nichols's method. Proposed algorithm is that parameters of the MFC system are estimated from operating data of the MFC system using the method of least mean squares. Parameters of PID controller are readjusted using these estimated parameters. As result of the algorithm it shows more superior response than iegler Nichols's method as traditional PID. In proposed algorithm, when operating conditions of the MFC system change(operating pressure, a kind of fluid and assembly error of piezo valve), system step responses show similar step response.

Acknowledgment

This work was supported by Research Center for Logistics Information Technology (LIT) hosted by the Ministry of Education Human Resources Development in Korea.

References

[1] Charles L. Phillips, H. Troy Nagle (1995), *Digital Control System Analysis and Design*. pp 404 413

[2] Robert N. Bateson (1996), *Introduction to control system technology*. pp 118 140

[3] Simon Haykin (2002), *Adaptive filter theory*. pp 610 635

[4] Kaoru H, Masayoshi E (2002), "Stainless steel-based integrated mass-flow controller for reactive and corrosive gases.", Sensors and Actuators, pp 33 38

[5] J. Schuurmans, T. Jones (2002), "Control of mass flow in a hot strip mill using model predictive control.", Proc. of the 2002 IEEE int. Conf. on Control Applications, pp 18 20

A Force Reflection Electronic Joystick Using Single Hall Sensor

SeungKeun Cho
Dep. of EE.
Pusan National University.
Busan, Republic of Korea.
skcho04@pusan.ac.kr

SunSin Han
Dep. of EE.
Pusan National University.
Busan, Republic of Korea.
ranger112@pusan.ac.kr

JangMyung Lee
Dep. of EE.
Pusan National University.
Busan, Republic of Korea.
jmlee@pusan.ac.kr

Abstract

A force feedback electronic joystick for the efficient remote control of a mobile robot is proposed and implemented in this paper. There are several limitations in controlling a mobile robot in tele-operation mode based on CCD vision, which is a very popular method for the tele-operation of a mobile robot. For examples, shadows and curved areas cannot be viewed by the narrow view-angle camera, especially in bad weather conditions like snows or rains. To overcome this problem, a virtual force is generated according to the distance between the obstacle and the robot and a collision vector estimated from the ultrasonic sensor data. Therefore, the operator can control the position and speed of the mobile robot smoothly using both visual and haptic information. The sixteen ring – structure ultrasonic sensors are attached onto a mobile robot that was manufactured for this experiment, and two small-size DC motors are attached at each axis of the joystick. Although potentiometers have generally been used to measure the motion of the joystick bar, a non - contact electronic joystick was used so that a hall sensor would resolve the degradation problem caused by track-wear. Finally, the addition of the force feedback mode has been shown to be very helpful for experimentally avoiding obstacle.

Keywords Force Feedback, Collision Vector, Tele-operation, Hall sensor, Potentiometer

1 Introduction

The robotics industry has changed because of the development of the micro processor and sensor. The robotics ability to do dangerous or simple tasks instead of human being in industry has been greatly improved. However, recently developed robots are limited in their ability to recognize all dangerous situations and unexpected incidents unlike human beings. Tele-operation allows used human beings to operate robots for tasks that require the judgment and selection. The service robot, which is used in a hospital or hotel, and the AGV, which is used in the Autonomous Port or factory, are based on an autonomous driving, but they can also be tele-operated when emergency situations occur. The latest teleoperation systems use a bilateral control method which transfer information from a slave site to a master site as we transfer information from the master site to the slave site. It is used to control the contact force, position, or velocity of the teleoperated robot, and it is commonly called teleoperation with force reflection. The general method of implementing tele-operation systems is to provide visual information of the remote environment to the human operator. This method can provide the visual information needed to perform simple task, but can not ensure safe operation where visual information is limited be camera's narrow viewing angle, bad weather or surrounding obstacle

Therefore, the operator can robustly control in any circumstance if the physical information about the working environment is supplied to the operator along with vision information. [1]

In this paper, we studied bilateral control that used both a teleoperated mobile robot and a joystick with two degrees of freedom, In addition to the Virtual Mass-Spring-Damper Model was used. The relationship between the mobile robot and the objects in the remote environment were modeled to get collision vector. [2]

Specially, A Hall sensor was used in the electronic joystick instead of a potentiometer. The use of a non-contact electronic joystick solves the performance degradation problem due to a track wear, the non-linear problem, and complexity of the mechanism structure.

Chapter 2 describes the composition of the entire system especially master joystick, Chapter 3 describes the method that provides the operator with virtual force using suggested collision vectors. Chapter 4 describes the results from the experiment using the mobile robot, And chapter 5 concludes the paper..

2 Composition of the Tele-operation

In this study, the entire system is composed of the human operator, master joystick, slave mobile robot and communication block. The schematic diagram is shown in figure 1. If a human operator give force to the electronic joystick, displacement occurs as Force, This displacement is then read by the Hall sensor and transferred to the control part. The control part then perform on A/D conversion and finally the speed order, which is calculated by the control part, is given to the mobile robot. The mobile robot moves giving PWM which corresponds to that speed. The repulsive force, which corresponds to the distance between robot and obstacles is detected by ultra sonic sensor and transferred to the motor drive. The human operator can use the repulsive force. Finally, the mobile robot follows reference point given by the human operator while supplying information about obstacles. The human operator uses feedback concerning the force, which corresponds to the distance and approach velocity between a teleoperated mobile robot and obstacles in the remote environment, so a telepresence is realized.

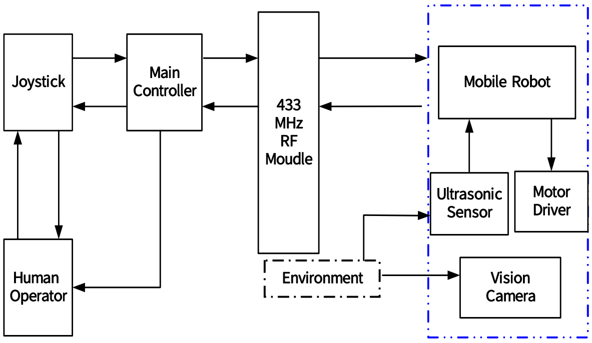

Fig. 1. The Total System architecture.

2.1 Electronic joystick

In this paper, a non – contact electronic joystick with single hall sensor is used to tele-operate a mobile robot. The performance of the existing contact electronic joystick using a potentiometer deteriorated due to track wear. To solve this problem a non-contact joystick was developed using a hall sensor. It has better accuracy and durability[4]. The Fig 2 shows a model of the non-contact joystick.

As can be seen in Fig 2, direction of the magnetic flux is indicated at the rotational center of the joystick.

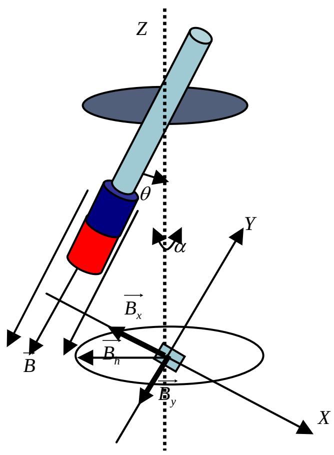

Fig. 2. The Mechanism of the Joystick.

When a permanent magnet is inclined at an angle of θ degrees, the horizontal vector B_h of magnetic flux density B is detected by the hall sensor, and B_x, B_y is determined from X,Y –axis direction. The hall sensor generates a voltage signal corresponding to B_x, B_y which has a phase difference is 90°. The relationship between B and B_h is expressed in Eq. (1)

$$B_h = \lambda(\theta) B \sin(\theta) \tag{1}$$

Because of the distribution feature of the magnetic flux of the permanent magnet, a non-linear element exists as $\lambda(\theta)$. If the direction of the flux is parallel with the direction of the joystick bar, $\lambda(\theta) = 1$. Due to the increasing rotation angle, θ, the horizontal vector B_h does not consistently increasing, but decreases when a specific rotational angle is exceeded. So a non-linear element, $\lambda(\theta)$, is defined as a decreasing function about the rotational angle θ^2.

$$\lambda(\theta) = \frac{1}{1 + k\theta^2} \tag{2}$$

Where, k is a constant value corresponding to the geometrical features of the permanent magnet and joystick mechanism, and the magnetic flux density.

The output voltage of the hall sensor has a linear relationship with a horizontal vector of magnetic flux density, so the output voltage satisfies Eq. (3). Where, C is a ratio constant value.

$$\begin{aligned} V_x &= CB_h \cos(\alpha) = C\lambda(\theta) B \sin(\theta) \cos(\alpha) \\ V_y &= CB_h \sin(\alpha) = C\lambda(\theta) B \sin(\theta) \sin(\alpha) \end{aligned} \tag{3}$$

The output voltage of the hall sensor is processed through an A/D converter in the Micro Processor, so Eq. (3) can become follow Eq.(4). [5].

$$\begin{aligned} AD_x &= \varsigma \times \frac{\sin(\theta)}{1 + k\theta^2} \times \cos(\alpha) \\ AD_y &= \varsigma \times \frac{\sin(\theta)}{1 + k\theta^2} \times \sin(\alpha) \end{aligned} \tag{4}$$

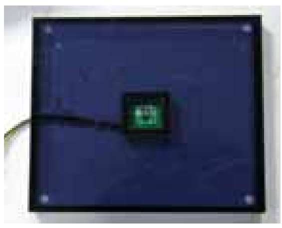

(a) Electronic control part

(b) Hall sensor module

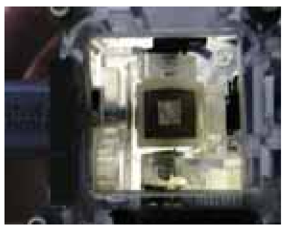

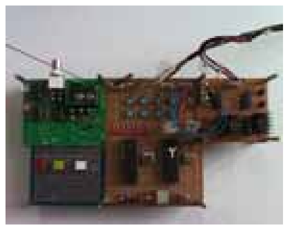

(c) Joystick mechanism part

Fig. 3. Joystick System.

Where, ς is a constant value corresponding to the amplifier value of a signal conversion circuit with sensor output. In Eq. (2) and (4), the constant values k and ς are essential features of the joystick system. Both k and ς change when the mechanism specifications change.

The mechanism and controller of the joystick is shown at Fig. 3.

The permanent magnet is made of alnico and is 1800~2000 Gauss.

The perpendicular distance between the permanent magnet and the Hall sensor is 13mm. The length of the total joystick bar including permanent magnet is 31mm.

Fig. 4 is a block diagram of joystick system. A potentiometer is used to verify the usefulness of the Hall sensor. The joystick controller is designed using PIC Micro-Controllers. This repulsive the force at the joystick based on the force values, F_x, F_y, which are sent from the controller to the operator. For this purpose, it drives two DC motors by sending out PWM (Pulse Width Modulation) output corresponding to F_x and F_y. The L6203 DC Motor drives are used to amplify the power.

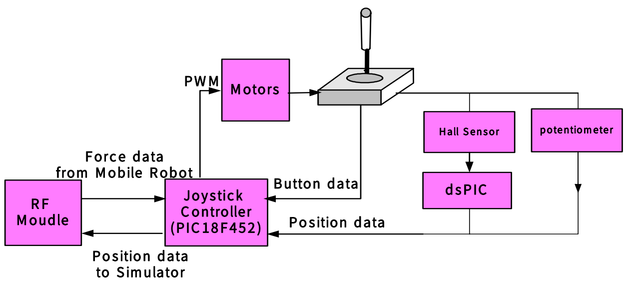

Fig. 4. The Joystick System block Diagram.

3 Virtual Force Feedback

3.1 Order value Acquisition of human operator

When the operator gives a force, F_h, to the joystick, the position coordinates of the joystick are changed to the degree of displacement, X_m, using Eq. (5) and (6) as shown in Fig. 5. The displacement, X_m, generates the desired velocity V_d by the following equation.

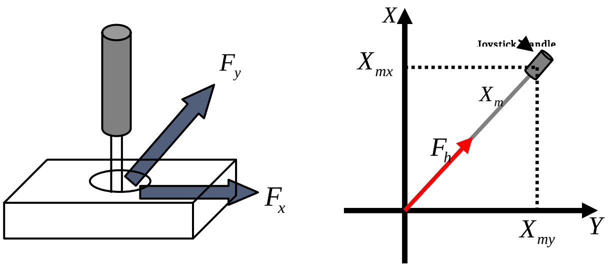

Fig. 5. Joystick axis and coordinates

$$V_d(s) = K_m \cdot X_m(s) \tag{5}$$

$$X_d(s) = K_v \cdot V_d(s) \cdot ds \tag{6}$$

where, K_m and K_v are constant scaling values, and ds is a control period, and X_m and V_d are the position and velocity of next reference point.

3.2 Virtual Force Feedback

The virtual force, F_b, which feedbacks to the operator can be derived from the next equation:

$$F_b = \{\sum_{i_{od}=0}^{n_{od}} F_{od}(s) + \sum_{i_{os}=0}^{n_{os}} F_{os}(s)\} \tag{7}$$

where, F_{od} and F_{os} are derived from next equation:

$$F_{od,s}(s) = K\ (X\ (s)) + D\ (\dot{X}(s))$$
$$= \begin{cases} \sum\{K\ (\rho\ - \|\vec{C}\|)\vec{C}_{unit} - D\ (\Delta\|\vec{C}\|)\vec{C}_{unit}\}, & when\ \|\vec{C}\| < \rho_0 \\ 0 & ,\quad otherwise. \end{cases}$$
(8)

As can be seen in Eq. (8), the virtual impedance method is a form of generating virtual force using distance and velocity, the modeling robot and a reference point, and the relationship between the robot and the obstacles as a spring and d damper. This method differs from the general impedance method[6,7,8]. We suggest a new virtual impedance method which uses a discrete value (approaching velocity) as damper:

where, ρ_o is the measurable range of the ultrasonic sensor.

The method for deriving C (collision vector) is introduced in chapter 3.3.

In Eq. (9), F_b, which is generated from a mobile robot at a remote site, is transferred to the operator in the master site.

$$\tau_b(s) = sat(K_b \cdot F_b(s)) \tag{9}$$

$$sat(x) = \begin{cases} x & ,\quad if\ |x| \le x_{\max} \\ \mathrm{sgn}(x) \cdot x_{\max} & ,\quad otherwise \end{cases} \tag{10}$$

where, K_b is the constant of force feedback gain.

In spite of limited visual information due to transmission delays, limited bandwidth, or camera trouble, the operator has the distance between the moving robot and the obstacles not seen on the visual display according to the force, τ_b, felt from the joystick.

3.3 collision vector detection for obstacle

The ultra sonic sensor (SRF 04) consist of 16 ring structures place at 22.5° intervals on the robot. A decoder and multiplexor are used to reduce interference among the ultra sonic sensors. In this paper, the collision vector ($\vec{C}$) which is oriented toward the mobile robot's center, and is vertical to a tangent line of obstacle, is suggested in order to derive the virtual repulsive force using the suggested virtual impedance method.

Three situations exist when an obstacle is recognized using the ultrasonic sensor.

First a small cylindrical obstacle or human is detected by a single ultrasonic sensor.

Second, a bigger obstacle is detected by two ultrasonic sensors. And third, an obstacle is detected by three ultrasonic sensors, in which case this may be a wall.

1. The collision vector for the obstacle in the first situation is simply the distance to from the detecting sensor:

$$\vec{C} = \vec{L} \tag{11}$$

2. For the second case, when there are two vectors, L_1 and L_2, which were detected by two neighboring ultrasonic sensors, the collision vector can be obtained by finding a perpendicular line from the center of robot to the line of obstacle location, $\overline{P_1P_2}$.

The second case is illustrated in Fig. 6.

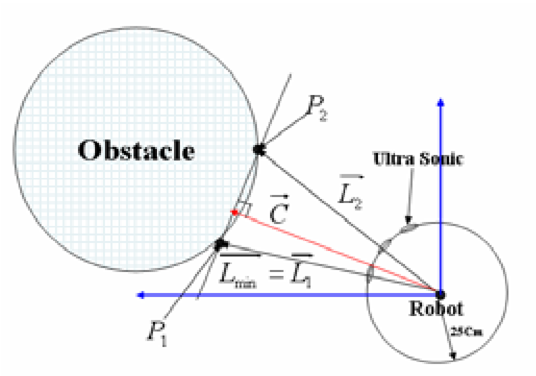

Fig. 6. The get collision vector of an obstacle

3. The collision vector for the third situation can be derived using the same method as the second situation.

4 Experiments and Results

The mobile robot used in this experimental is equipped with CCD camera, encoders, ultra sonic sensors and two DC motors. Each wheel of the mobile robot is operated by two DC motors. The motor specs are 24V, 35W, 0.8A, 20rpm(10 : 1 Reduction gear), 30kgf-cm torque. The figure of robot is shown at Fig. 7.

The mobile robot was tele – operated in the hallway of the special building in Pusan National UNIV. The remote site had dark lighting and limited sight so that distances could not be ascertained using the camera.

The experiment was performed to demonstrate the usefulness of the suggested virtual impedance control with collision vector using force reflection joystick.

Fig. 7. The Mobile Robot Figure

Fig. 8 (a) and (b) show the results of the tele-operation. Fig.8 (a) is the result from using only the camera, Fig. 8 (b) is the result from using the force reflection joystick with the camera.

The results show that tele-operation of the robot using force reflection is more efficient and stable than when using only the camera.

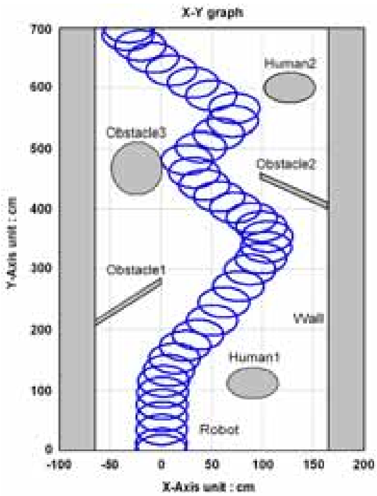

(a) Without Force Reflection

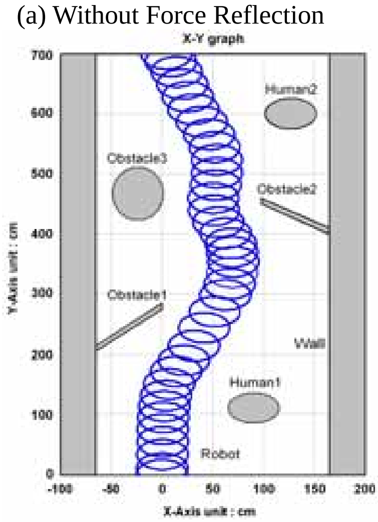

(b) With Force Reflection

Fig. 8. The Experimental results

Three operators worked the robot during the experiment will similar results from all three. When the camera alone was used, there were 1 to 2 collisions with obstacles. When the force reflection joystick and the camera were used, there were no collisions and the time needed to navigate to the goal was reduced by 13~14 seconds.

Fig. 9 shows the trajectory of the joystick bar in order to compare the performance of the dual potentiometer and the single Hall sensor. Because the output of the Hall sensor and the movement of joystick bar has non – linear characteristics, the motion of the joystick bar con not correctly represented.

The result of the trajectory is almost circular when using a single Hall sensor.

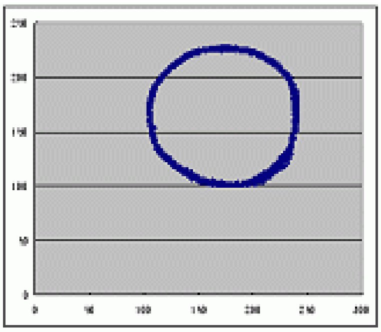

(a) Using Hall Sensor

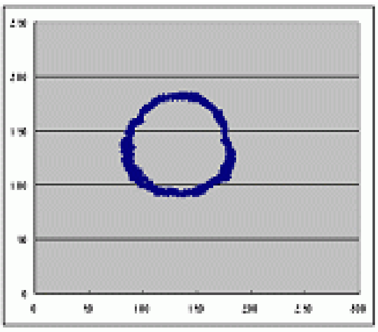

(b)Using Dual Potentiometer

Fig. 9. Compassion of the performance of the Hall sensor and Dual Potentiometer

5 Conclusion

In this paper, the efficiency of tele-operation using the force reflection joystick is established through an experiment. When the mobile robot is being driven, information about obstacle is measured using ultra sonic sensor.

This information is communicated to the operator as feelings in the joystick. This method can improve the stability and controllability of robot through information acquired through repulsive force. This method is different than the existing method which uses only vision information. Also, using the single Hall sensor instead of dual structure potentiometer that has a non-linear section the displacement of the stick, can accurately be measured. The performance of the joystick was improved and can be widely used in fields that require remote control mobile robot or precision work.

If information is acquired using a hybrid method which mixes various sensor types with ultra sonic sensors, although a mobile robot is located at a remote site, it can be accurately tele-operated by a human operator.

Acknowledge

This work was supported by "Research Center for Logistics Information Technology (LIT)" hosted by the Ministry of Education & Human Resources Development in Korea.

References

[1] S. S. Lee and J. M. Lee, "Haptic interface design for the tele-surgery", *Proc. of the CIDAM Workshop on Service Automation and Robotics*, Hong Kong, pp. 81-91, June 19-20, 2000.

[2] S. K. An, S. J. Han, H. R. Hur, and J. M. Lee, "Implementation of a Remote Peg-in-Hole Operation Using a Two Degrees of Freedom Force-Reflective Joystick," *J. of Electrical Engineering and Information Science*, vol. 4, no. 3, pp. 315-322, Jun.. 1999.

[3] "Angular Position Sensing Measurement with Sentron Hall ASIC" *Sentron Application Note.* No 17, 2001.

[4] H. C. Kim, D. H. Kang, J. M. Lee, "Development of a Non-contact electronic Joystick using Single Hall Sensor", *KACC* 2005. pp. 68-73, 2005.

[5] Jay L. Devore, "Probability and Statistics for Engineering and the Science" Publication by Duxbury, pp. 247-271, 1995.

[6] T. Arai, H. Ogata, and T. Suzuki, "Collision Avoidance Among Multiple Robots Using Virtual Impedance", *Proc. of IEEE/RSJ Int. Workshop on Intelligent Robots and Systems*, pp.479-485, Sept. 1989.

[7] J. Ota, T. Arai, E. Yoshida, D. Kurabayashi, and T. Mori, "Real Time Planning Method for Multiple Mobile Robots", *Proc. of IEEE Int. Symposium on, Assembly and Task Planning*, pp. 406-411, 1995.

[8] Ming ouhyung, Wu-Nan Tasi, Ming -Chang Tsai, "A Low-Cost Force Feedback Joystick and its use in pc video games", *IEEE Transactions on Consumer Electronics*, Vol.41.No.3. August 1995

The Eleventh International Symposium on Artificial Life and Robotics 2006 (AROB 11th'06),
B-con Plaza, Beppu, Oita, Japan, January 23-25, 2006

An Self-Localization of Mobile Robot in an RFID Sensor Space

ByoungSuck Choi
Dep. of EE.
Pusan National University.
Busan, Republic of Korea.
woodc@pusan.ac.kr

HyoSik Choi
Dep. of EE.
Pusan National University.
Busan, Republic of Korea.
chs3040@pusan.ac.kr

JangMyung Lee
Dep. of EE.
Pusan National University.
Busan, Republic of Korea.
jmlee@pusan.ac.kr

Abstract

This paper presents an efficient localization scheme for an indoor mobile robot using RFID tags on the floor. The mobile robot carries an RFID reader at the bottom of the chassis, which reads the RFID tags on the floor to localize the mobile robot. Each RFID tag stores its own absolute position which is used to calculate the position and velocity of the mobile robot. Locating the RFID tags, which constitutes an intelligent sensor space, may require several factors: economics, feasibility, and accuracy. In this paper, the optimal allocation scheme of the RFID tags on the floor to satisfy the accuracy constraint has been proposed and verified by the experiments. Based on reading the RFID tags, the mobile robot navigation has been successfully demonstrated to avoid obstacles and to reach the goal within a pre-specified time.

Keywords RFID system, tag, mobile robot, allocation

1 Introduction

Recently robots have been developing rapidly with the strong support from the constitutional technologies such as integrated circuits, sensors, artificial intelligence, image processing, computers and microprocessors. As a result, intelligent robots, which recognize the environment, and ubiquitous robots, which are connected to the network environment, are receiving attention instead of industrial robots, which perform repetitive labor[1]. Mobile robots, which are completely different from the manipulators, have expanded the fields that they can be applied to their mobility. Several applications of the mobile robot can be easily found: a vacuum robot which frees housekeepers, a service robot which guides visitors and explains articles in a museum, or a surveillance robot which performs dangerous tasks.

For successful task execution and autonomous navigation, the position and orientation of the mobile robot itself must always be quickly and precisely recognized within the environment[2]. With a precise estimate of its position/orientation, the mobile robot can plan a trajectory to its goal. To estimate the position of the mobile robot, encoders and gyroscope sensors have been used to calculate its position based on its known initial position[3][4]. This method is effective when the initial position information is precisely given and displacement is small. However, when wheel slippage occurs during travel, errors in estimation increase and they aggregate so that the position is not precisely calculated[5]. To remove the problem of accumulative errors, ultrasonic sensors, IR sensors, vision sensors, and GPS have been recommended to establish the absolute position of the mobile robot based on the measured position and visual information[6]. However, there are also several problems with these systems. For example, the GPS-based positioning system is not effective after the mobile robot enters a building and the ultrasonic-sensor based positioning system suffers from the interference of neighboring sensors. Also, a vision sensor is so sensitive to illumination and color that it is very expensive to maintain a suitable sensing environment. Another severe shortcoming of vision sensor is that the amount of computations required increases requires a heavy computational burden with the increase of resolution and number of cameras increases. To resolve all of these problems, a new concept of an 'intelligent space' or 'sensor network space' has been introduced [7][8]. In the sensor network space, the robot recognizes its position not by sensors attached its body but by the sensors that exist in the network space.

In this paper, a new sensor network space is proposed. This space is formed by RFID tags and readers. Several RFID tags are attached to the floor, which are read by the RFID reader attached to the bottom of the mobile robot. Since each tag provides its position information, the robot's position can be established. Usually the RFID tags have formed located a square pattern on the floor. However, in this paper, we propose a triangular pattern which provides better accuracy than the square pattern with the same number of tags in the same space. In section 2, the constitution of the RFID sensor space has been illustrated, and section 3 describes the position estimation scheme in the sensor space and the allocation pattern of the RFID tags. In section 4, the robot position has been estimated by simulation and experiments and section 5 concludes and summarizes the main contributions of this paper.

2 RFID Sensor Space

In this section, an RFID sensor space is illustrated to estimate position of a mobile robot.

2.1 Position estimation system of robot

In the conventional approaches, several different kinds of sensors are attached to the mobile robot to recognize its location as shown in fig. 1-(a). To efficiently estimate position, a variety of sensors are needed, which implies that the robot must process all of the resulting data in to locate. Generally it is not guaranteed to utilize the same position estimation system for each robot. That is, the position estimation system should be matched to each robot's localization capability when there are multiple robots working together.

On the contrary, the position estimation of each robot in the sensor space can be accomplished through the distributed sensors in the space as shown in fig. 1-(b).

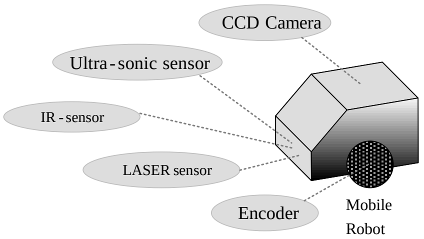

(a) A conventional position estimation system.

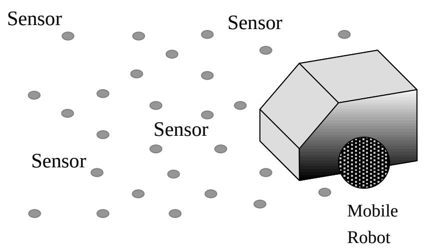

(b) A position estimation system in a sensor space.

Fig. 1. Types of position estimation systems.

Each mobile robot establishes its position coordinates when it detects and uses a sensor's position information. Since each mobile robot does not need to carry sensors, but only a reader, other robots operating in the sensor space cannot interfere with its position estimation. That is, each robot can be free from other robots in recognizing its own location. Even though there are obstacles in the space, the position estimation process can be continued without any degradation.

2.2 RFID sensor network system

Figure 2 illustrates the RFID sensor space proposed for the localization of a mobile robot in this paper. The RFID tags are regularly allocated on a two-dimensional X-Y plate on which a mobile robot with an RFID reader moves on. To form a wireless communication channel between an RFID reader and the tags, a suitable antenna pattern is engraved in each reader and tag. When the communication channel is connected, that is, the distance between the reader and tags becomes small enough for electric induction, the RFID reader provides electric power by RF to the tag and receives the position information that has been pre-stored in the tags. The computer system installed on the mobile robot processes the position information from the tags to estimate the position of the mobile robot. Figure 3 illustrates the composition of an RFID system for the localization of a mobile robot.

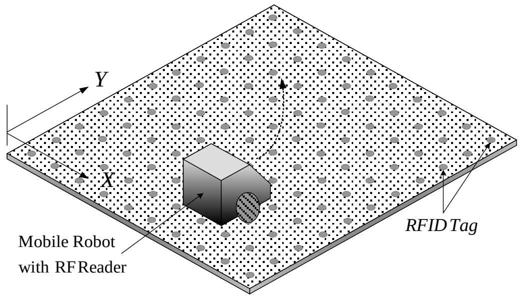

Fig. 2. An RFID sensor space.

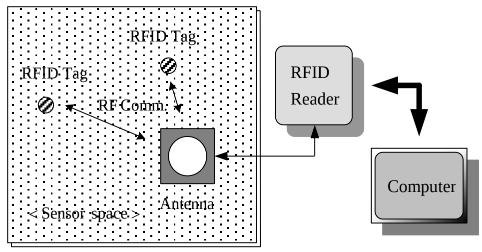

Fig. 3. Composition of an RFID system.

3 Position Estimation of a Mobile Robot

3.1 Position of a mobile robot

The center coordinates of a mobile robot can be represented in a two dimensional X-Y plane as follows[9] :

$$P = \begin{bmatrix} x_R & y_R & \theta_R \end{bmatrix}^T \quad (1)$$

where θ_R represents the orientation of the robot.

In Fig. 4, the position and velocity of a mobile robot moving on a two dimensional space have been illustrated. When the mobile robot is moving along a curved path with a constant curvature, the position and velocity of the robot can be derived from the mobile robot kinematics. When a mobile robot is moving from location A to B, where location A is denoted as (x_R, y_R, θ_R) at time = t, and location B is demoted as (x'_R, y'_R, θ'_R) at time $= t + \delta t$, the following interesting relationships in the circular motion of the mobile robot occur:

$$v_L : v_R = R - \frac{l}{2} : R + \frac{l}{2} \quad (2)$$

$$R = \frac{l}{2}\left(\frac{v_R + v_L}{v_R - v_L}\right) \quad (3)$$

Where v_L and v_R represent the velocity of the left and right wheels, respectively, R is the rotation radius with respect to ICC(Inertial Center of Circle), and represents the distance between the two wheels.

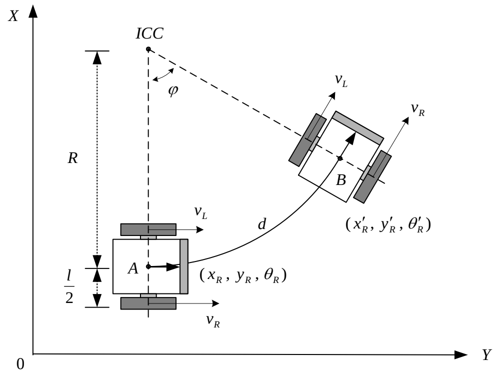

Fig. 4. Position and velocity of a mobile robot.

Also the coordinated of ICC, the travel distance and angle, d and φ, can be obtained as follows:

$$ICC = [\, x_R - R\sin(\theta_R),\quad y_R + R\cos(\theta_R)\,] \tag{4}$$

$$d = \int_t^{t+\delta t} \frac{v_L + v_R}{2} dt \tag{5}$$

$$\varphi = \frac{d}{R} = \frac{\int_t^{t+\delta t} (v_L + v_R)\, dt}{l(v_L + v_R)} (v_R - v_L) \tag{6}$$

Using the rotation radius, travel distance and angle from the equations of (4)~(6), the linear and angular velocities of the mobile robot in the circular motion also can be obtained[10].

3.2 Position estimation in RFID sensor space

The RFID sensor space for estimating the position of a mobile robot was observed in the previous chapter. If the tags are arranged at regular intervals and the distance between them does not exceed the range of reader, then the reader's recognition area for the tags would be similar to that in figure 5.

The position of the mobile robot (x_{est}, y_{est}) that has a reader antenna at its bottom, can be obtained through the tags that are located within the reader's recognition area.

$$x_{est} = \frac{\max\{x_1, \cdots, x_N\} + \min\{x_1, \cdots, x_N\}}{2} \tag{7}$$

$$y_{est} = \frac{\max\{y_1, \cdots, y_N\} + \min\{y_1, \cdots, y_N\}}{2}, \tag{8}$$

where N represents the number of tags detected by the reader and $x_1, x_2, x_3, y_1, y_2, \cdots$ represents the coordinate information of the tags.

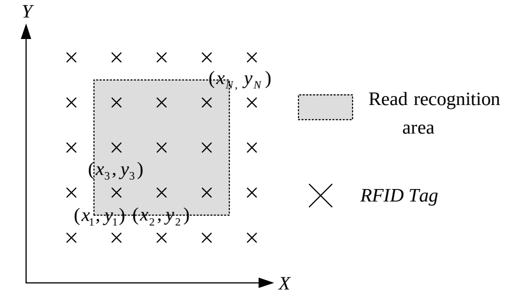

Fig. 5. RFID reader's recognition area.

When the position of the mobile robot is estimated as shown in fig. 5, fig. 6 illustrates position estimation error.

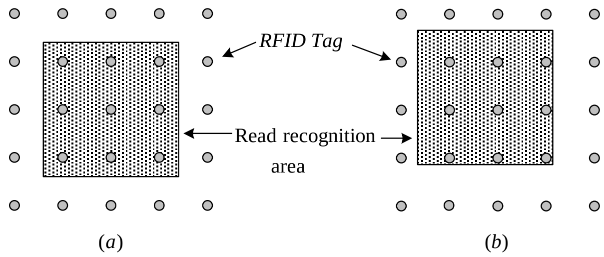

Fig. 6. Estimation error in RFID sensor space.

In fig 6. the position of reader-coordinates of the mobile robot-is estimated to be the same position in figs. 6-(a) and 6-(b), because the tags have the same coordinate data.

However, the real position of mobile robot is not same. The estimation error occurred between the real position of robot and estimated position. Recovery of the estimation error is related to the gap between the RFID tags. Figure 7 illustrates the relationships between the estimation error and gap between the RFID tags.

If the X-dimension only is considered for the tags, then it is assumed that the each tags from left to right has coordinates, $a_1, a_2, a_3, \cdots, a_{n-1}, a_n, a_{n+1}$, and the gap between the tags is d_{tag}.

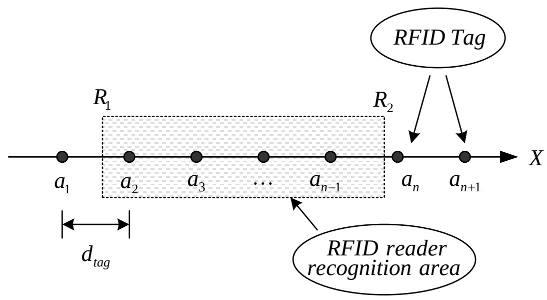

Fig. 7. Estimation error and gap of tag.

Also, the left boundary of the reader's recognition area is R_1, the right is R_2. That is, the RFID reader can detect tags located between R_1 and R_2.

The estimation coordinate, R_{est}, and the real center position of the reader R_{real}, illustrated in fig. 9, are represented as follows:

$$R_{est} = \frac{a_2 + a_{n-1}}{2} \tag{9}$$

$$R_{real} = \frac{R_1 + R_2}{2} \tag{10}$$

The Estimation error, e_{est}, is defined as follows:

$$e_{est} = \left| R_{est} - R_{real} \right| = \left| \frac{R_1 + R_2}{2} - \frac{a_2 + a_{n-1}}{2} \right| \tag{11}$$

where the coordinates of R_1 and R_2 are represented as follows:

$$\begin{cases} a_1 < R_1 < a_2 \\ -d_{tag} < R_1 - a_2 < 0 \end{cases} \tag{12-a}$$

$$\begin{cases} a_{n-1} < R_2 < a_n \\ 0 < R_2 - a_{n-1} < d_{tag} \end{cases} \tag{12-b}$$

From (11) and (12), the estimation error can be represented as follows:

$$e_{est} = \left| \frac{(R_1 - a_2) + (R_2 - a_{n-1})}{2} \right| \le \frac{1}{2} \left| d_{tag} \right| \tag{13}$$

Equation. (13) shows that the estimation error is proportional to the gap between the tags and maximum value is half of the gap.

Therefore, if the gap between the tags is reduced, then the accuracy of the estimation is improved. This solution increases costs because it increases the number of tags. The optimal allocation of the RFID tags in the sensor space proposed in this paper aims to improve the accuracy of the position estimation without increasing the number of tags. Traditionally tags have been allocated in a square pattern (fig. 5), but a triangular pattern (fig. 8) decreases the estimation error without increasing the number of tags.

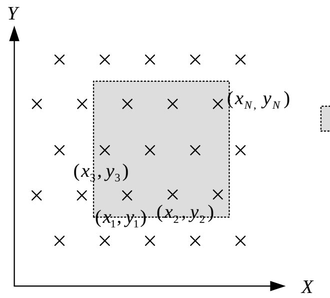

Fig. 8. RFID tag allocation and reader's recognition area in triangular pattern.

Figure 9 illustrates the decrease in estimation error in the triangular pattern space. The coordinates of R_1 and R_2 are represented in fig. 9 as follows:

$$\begin{cases} b_1 < R_1 < a_2 \\ -\frac{d_{tag}}{2} < R_1 - a_2 < 0 \end{cases} \tag{14-a}$$

$$\begin{cases} b_{n-1} < R_2 < a_n \\ 0 < R_2 - b_{n-1} < \frac{d_{tag}}{2} \end{cases} \tag{!4-b}$$

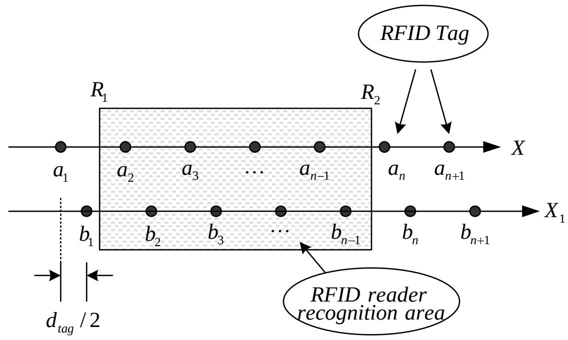

Fig. 9. Estimation error decrease in triangular pattern.

As shown in fig. 9, the estimation error in x-direction decreases as follows:

$$e_{est} = \left| \frac{(R_1 - a_2) + (R_2 - b_{n-1})}{2} \right| \le \frac{1}{4} \left| d_{tag} \right| \tag{15}$$

4 Experiments and Results

Before conducting a real experiment with a mobile robot, the position estimation accuracy of the two tag allocation patterns are simulated and compared. It is assumed that the mobile robot precisely follow the prescribed path. As can be seen in fig. 10, the position of the mobile robot is estimated every 0.1 seconds along a constant curvature Path-1 and Path-2. To compare the estimation accuracy, the RFID tags are allocated in two different patterns, square (fig. 10-(a)) and triangular (fig. 6-(b)). The RFID reader's recognition area was set as 2.5 m * 2.5 m

4.1 Simulation

For the simulation experiments, two different path are set as Path-1 and Path-2 as shown in fig. 10. For the given path, the velocity and position of the mobile robot can be estimated using equations (2)~(4), and the path characteristics are summarized in Table 1.

As illustrated in fig. 6, the two allocation patterns of RFID tags are tested under the same conditions, and the results are summarized in Table 2 for Path-1 and in Table 3 for the Path-2. Through the close observation of the estimation accuracy of the two pat-terns in Tables 2 and 3, it can be concluded that the triangular pattern provides better accuracy, especially in the x-coordinate estimation.

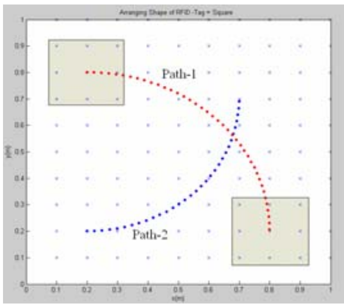

(a) Motion trajectory in square pattern.

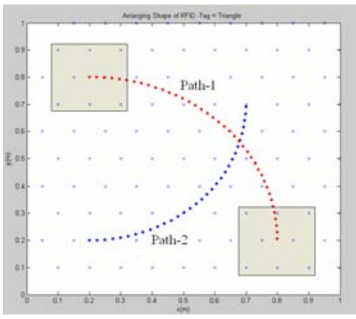

(b) Motion trajectory in triangular pattern

Fig. 10. Allocation of RFID tags and the recognition area of reader.

Table 1. Characteristics of Path-1 and Path-2

	Path-1	Path-2
Starting Point	(0.2, 0.8)	(0.2, 0.2)
Ending Point	(0.8, 0.2)	(0.7, 0.7)
Rotation Radius	0.6 m	0.5 m
Velocity	$v_L = 0.28m/s$ $v_R = 0.2m/s$	$v_L = 0.2m/s$ $v_R = 0.3m/s$
ICC	(0.2, 0.2)	(0.2, 0.7)

Table 2. Position estimation data of Path-1 (simulation)

Position		Square pattern		Triangular pattern	
X(m)	Y(m)	X(m)	Y(m)	X(m)	Y(m)
0.2	0.8	0.2	0.8	0.2	0.8
0.27	0.8	0.3	0.8	0.28	0.8
0.34	0.78	0.3	0.8	0.33	0.8
0.4	0.76	0.4	0.8	0.4	0.8
0.48	0.73	0.5	0.7	0.5	0.7
0.56	0.68	0.6	0.7	0.6	0.7
0.61	0.63	0.6	0.65	0.63	0.6
0.66	0.58	0.65	0.6	0.65	0.6
0.7	0.52	0.7	0.5	0.7	0.5
0.74	0.46	0.75	0.45	0.75	0.45
0.76	0.42	0.8	0.4	0.75	0.4
0.78	0.37	0.8	0.4	0.8	0.4
0.79	0.31	0.8	0.3	0.8	0.3
0.8	0.2	0.8	0.2	0.8	0.2

Table 3. Position estimation data of Path-2 (simulation)

Position		Square pattern		Triangular pattern	
X(m)	Y(m)	X(m)	Y(m)	X(m)	Y(m)
0.2	0.2	0.2	0.2	0.2	0.2
0.27	0.21	0.3	0.2	0.28	0.2
0.35	0.22	0.3	0.25	0.33	0.25
0.42	0.25	0.4	0.2	0.43	0.2
0.48	0.29	0.5	0.25	0.5	0.25
0.52	0.32	0.55	0.3	0.5	0.3
0.58	0.37	0.6	0.4	0.58	0.4
0.60	0.41	0.6	0.4	0.6	0.4
0.63	0.45	0.6	0.4	0.63	0.4
0.67	0.54	0.7	0.5	0.68	0.5
0.70	0.62	0.7	0.6	0.7	0.6
0.70	0.69	0.7	0.7	0.7	0.7

4.2 Real experiments

The simulation results were verified through the real experiments. A mobile robot was utilized to carry an RFID reader at the bottom of the chassis, which reads the positions of the mobile robot when-ever the reader passes a tag.

Figure 11 shows the RFID reader and a tag used for the real experiments. The main frequency of the RFID system was 13.56Mhz, the position coordinates of the tags were pre-stored, and the tags were regularly allocated at specific locations following a designed pattern. To show the superiority of the triangular pattern, the tags are allocated every 0.1m in a row for both of the square and triangular patterns. Figure 12 shows the mobile robot and RFID sensor space for the experiments. To allow a comparison with the simulation, the mobile robot followed the Path-1 and Path-2 while the RFID reader recognized and read the position data from the tags.

(a) RFID Reader (b) RFID Tag

Fig. 11. RFID reader and tag for the experiments.

The estimation error is represented through graphs in figure 13. As can be seen by comparing the error values, error for the triangular pattern has a lot smaller error than the square pattern for both of the Path-1 and Path-2.

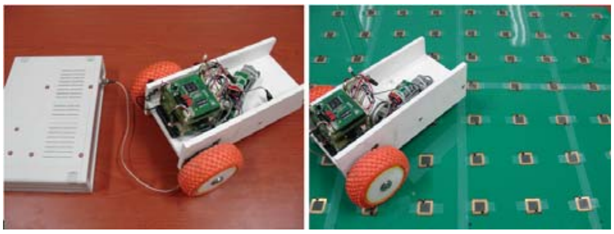

(a) Mobile Robot (b) Sensor Space

Fig. 12. Mobile robot and sensor space for the experiments.

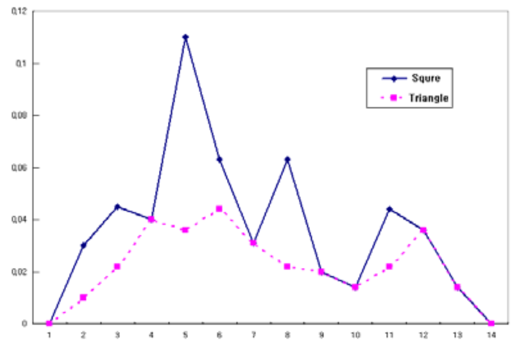

(a) Estimation error in path-1

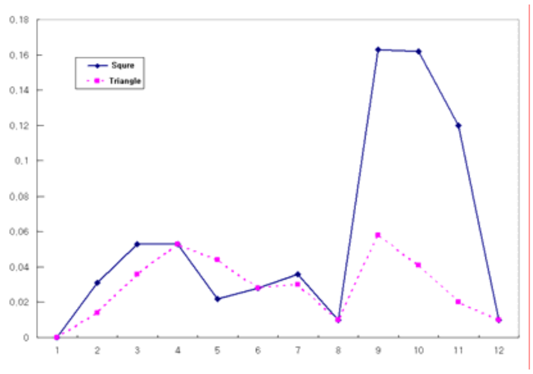

(b) Estimation error in path-2

Fig. 13. Estimation error of the each pattern.

5 Conclusion

This paper proposes a new pattern of RFID tag allocation for the efficient and accurate estimation of the mobile robot position in an RFID based sensor space. This pattern overcomes the shortcomings of the conventional absolute position estimation schemes and improves its efficiency and accuracy. The importers are demonstrated by a simulation of a moving object over an RFID-based sensor space. To illustrate the improved accuracy and economics of the position estimation scheme, the square and triangular tag patterns have been surveyed. The triangular pattern is shown to be the square pattern for position estimation of a mobile robot. Note that based on the approach described in an RFID sensor space, the absolute position of a mobile robot can be estimated precisely without any interference from environments. Therefore, this scheme is very effective for estimating the position of any object in the sensor space and it could be a good tool to form an ubiquitous environment.

Acknowledge

This work was supported by "Research Center for Logistics Information Technology (LIT)" hosted by the Ministry of Education & Human Resources Development in Korea.

References

[1] Ren C, Luo, Kuo L. Su, Shen H. Shen and Kuo H. Tsai, “Networked Intelligent Robots Through the Internet: Issues and Opportunities,” P*roceedings of the IEEE*, Vol. 91, Issue 3, pp. 371-382, March 2003.

[2] San Mok Lee, “Using Vision Sensor and Sonar Sensor of Mobile Robot Localization,” *Chungnam National University*, 2001.

[3] Komoriya, K., Oyama, E., “Position estimation of a mobile robot using optical fiber gyroscope,” *Intelligent Robots and Systems IROS ’94. Proceedings of the IEEE/RSJ/GI International Conference on*,, Vol. 1, pp. 143-149, 12-16 Sep. 1994.

[4] Sooyong Lee, Jae-Bok Song, “Robust mobile robot localization using optical flow sensors and encoders,” *Robotics and Automation, 2004. Proceedings. ICRA '04. 2004 IEEE International Conference on* Vol. 1, No. 26, pp. 1039-1044, April 2004.

[5] Young Shick Ro, Kyung Sup Park, “A study of Optimal Position Estimation for Mobile Robots,” *Journal of Engineering Research*, Vol. 26, No. 1, pp. 243-257, 1995.

[6] Ohno, K.., Tsubouchi, T., Shigematsu, B.., Maeyama, S., Yuta, S, “Outdoor navigation of a mobile robot between buildings based on DGPS and odometry data fusion,” *Robotics and Automation, 2003. Proceedings of ICRA '03. IEEE International Conference on*, pp. 1978-1984, Sept. 2003.

[7] Joo-Ho Lee, Hideki Hashimoto, “Controlling Mobile Robots in Distributed Intelligent Sensor Network,” *IEEE Transaction on Industrial Electronics*, Vol. 50, No. 5, Oct. 2003.

[8] Kazuyuki Morioka, Joo-Ho Lee, Hideki Hashimoto, “Human-Following Mobile Robot in a Distributed Intelligent Sensor Network,” *IEEE Transaction on Industrial Electronics*, Vol. 51, No. 1, Feb. 2003.

[9] W. E. Dixon, D. M. Dawson, E. Zergeroglu and A. Behal, Nonlinear Control of Wheeled Mobile Robots, *Springer*, 2003, pp. 1-4.

[10] G. Dudek and M. Jenkin, Computational Principles of Mobile Robotics, *Cambridge university press*, 2000, pp. 15-22.

The Eleventh International Symposium on Artificial Life and Robotics 2006 (AROB 11th'06),
B-con Plaza, Beppu, Oita, Japan, January 23-25, 2006

Fuzzy Posture Control for Biped Walking Robot Based on Force Sensor for ZMP

K. C. Choi
Department of Mechanical and Intelligent systems Engineering, Pusan National University, Korea

M. C. Lee
School of Mechanical Engineering, Pusan National University, Korea

J. M. Lee
Department of Electronics Engineering, Pusan National University, Korea

Abstract

In these days, biped walking robots are concentrated on a service robot. Biped walking robots are suitable in a human life work such as walking up and down stairs and acrossing a threshold because they have two leg mechanism like a human. However, it is very difficult subject that robot maintains valance in walking. One way to solve this problem is using an accurate dynamic model of biped robot in 2-Dimension and 3-Dimension. Another method to solve this problem is modeling biped robot simply and controlling the robot with an adaptive control, intelligent control and robust control algorithm and so on. ZMP(zero moment point) concept was invented in this field.

In this paper, ZMP trajectory following for biped walking robot based on force sensors and posture control using fuzzy algorithm are studied. The posture control of the biped robot is performed by ZMP information in static standing. In this paper, posture of biped walking robot is controlled by fuzzy algorithm referring to the obtained ZMP trajectory information. The result of this study is confirmed by experiment applied fuzzy posture control to against disturbance and keep valance on a slope in static standing

Keywords: Biped robot, ZMP, Force sensor, Fuzzy, Posture control

1. INTRODUCTION

A biped robot has a structure similar to human's leg and has higher mobility than conventional wheeled robots. However stability of a biped walking robot is not yet solved completely and has to be solved to use advantage of a biped walking robot[1]. The biped walking robot is a multi-body system and has complex dynamics and many non-linear factors. Therefore it is very difficult to move a biped robot stably.

Concept of ZMP has been introduced as important criterion for the stability of a biped walking robot[2]. If ZMP is measured only by using force sensors, we don't need consider complicate dynamic analysis of a biped walking robot. The measured ZMP gives advantage that can directly recognize state of surface of land without the other sensors such as acceleration sensor and gyro-sensor[3]. The robot can recognize own posture by using ZMP by ground reaction force. In this paper, ZMP is measured to judge stability of a biped robot by using force sensor attached on a sole of a foot. A posture control algorithm using fuzzy logic controls posture of the robot as using the obtained ZMP information.

The section 2 describes system configuration and kinematics of the biped walking robot which is manufactured for this research. Section 3 introduces analytic ZMP acquisition problem and then explains method obtaining ZMP based on the force sensors. Section 4 introduces posture control algorithm by fuzzy logic, and Sections 5 and 6 show experiment result and conclusions.

2. SYSTEM CONFIGURATION AND KINEMATICS ANALYSIS

2-1. System configuration

The developed biped walking robot is shown in Fig. 1. It's height and weight are 28㎝ and 3.2kg, respectively. The biped robot is composed of 12 degrees of freedom. Fig. 2 shows coordinates of the developed biped robot.

The system can be divided into a control unit, a sensor module, and a motor module. The main control system is a Pentium Ⅳ computer and has trajectory compensation algorithm of the biped walking robot and send command to control motor module of each joint.

The sensor module consists of a ATMEGA 128 that has 4-channel of A/D converter. Force data is acquired by using FSR(force sensor resistor) sensors. ZMP is calculated using force data and sent to control unit. The RS485 communication is used between the PC and the motor and the sensor module.

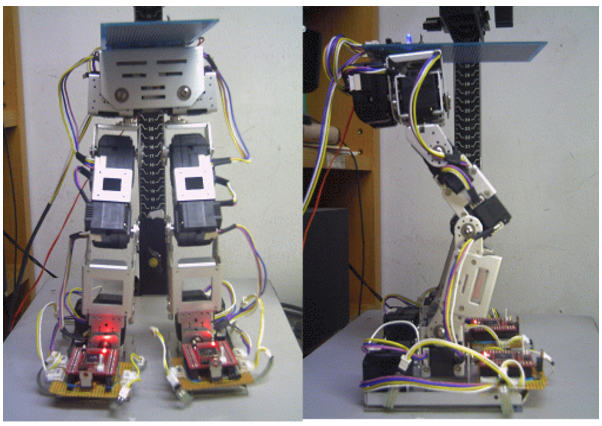

Fig. 1 The developed biped robot

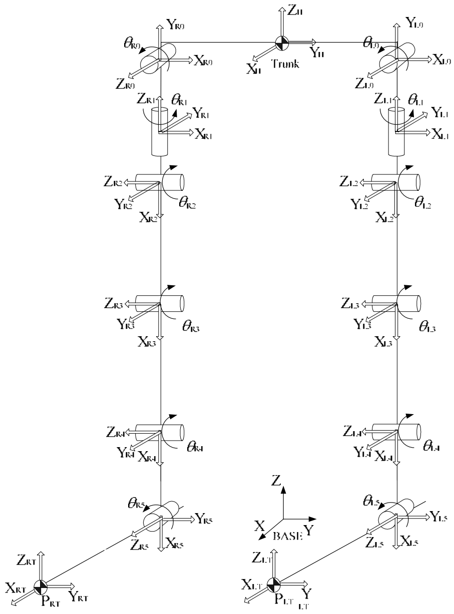

Fig. 2 The coordinates of the biped robot

2-2. Kinematics

In trajectory generation of the biped robot, forward and inverse kinematics equation are used to calculate a posture of the robot and angle of each joint.

Kinematics analysis is based on Denavit-Hartenberg's kinematics notation. The biped robot has 12 degrees of freedom. Coordinate system of the biped robot is shown in Fig. 2. The base coordinates "BASE" is located on a ground surface in the middle point of the feet. The trunk coordinates "Trunk" is located on the middle point of waist directly above "BASE". The left "P_{LT}" and right "R_{LT}" coordinates are located on the tip of the foot.

3. ZMP MEASUREMENT BASED ON SENSOR

3-1. Problem of Analytic ZMP

The biped robot is supposed that robot is doing accurate action for analytic ZMP acquisition. That is, position or angular velocity, angular acceleration of each joint should be controlled correctly and each link must be a perfect rigid body. However control error of a biped walking robot exists clearly and a biped walking robot is not a perfect rigid body.

Specially, because each link of the biped walking robot is connected, the error due to connection affects stability of a biped robot. If we use actuator with the high torque and high accuracy or manufacture the robot using a rigid-body, this error can be reduce. But when the biped robot is standing on the sloped bottom, the robot may falls down because obtaining analytic ZMP in real time is so difficult.

3-2. ZMP measurement based on force sensor

If we use the attached force sensor on a sole of a foot of the biped walking robot, position of the ZMP is found by simple calculation.

Fig. 3 shows the force sensors attached on a sole of a foot of the designed biped robot. The force sensors measure ground reaction force from the sole. ZMP of the actual biped walking robot is calculated by using the detected force from force sensors. The sensors consist of 8 force sensors attatched on each sole of a foot corner. Formula for acquiring ZMP is as

$$ZMP = \frac{\sum_{i=1}^{8} f_i \times r_i}{\sum_{i=1}^{8} f_i} \qquad (1)$$

Because force sensor has some measurement noise, 3rd Chebyshev lowpass filter is used to acquire ZMP. The cutoff frequency and sampling frequency are set as 2Hz and 100Hz, respectively.

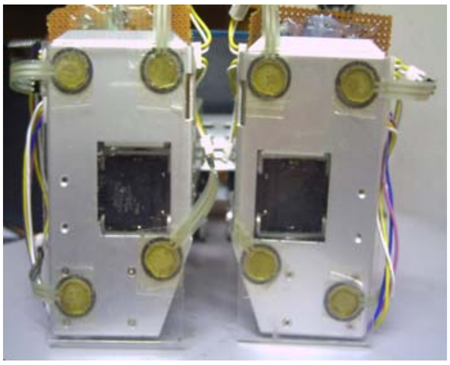

Fig. 3 The force sensors attached on a robot sole

4. POSTURE CONTROL OF ROBOT

4-1. Fuzzy Posture algorithm

This study is to keep stability of biped robot without changing walking trajectory. So a proposed algorithm is carried out by compensator which changes the coordinate of "Trunk" without coordinate change of other joints.

Posture of a biped robot is stable when ZMP exists in 'Desired area' which is assumed as the most stable area according to ZMP. If ZMP does not exist in 'Desired area', robot has to move a ZMP to the 'Desired area'. Fuzzy algorithm compensates coordinate of "Trunk" to move the measured ZMP to the desired ZMP, which calls ZMP compensator. Robot has a new reference angle of each motor, which is obtained to analyze inverse kinematics for stability of robot by ZMP compensator. ZMP compensation is accomplished by driving motor of each joint. Coordinate of "Trunk" is compensated for acumulative error. Fig. 4 is schematic diagram for posture control using ZMP compensation by fuzzy algorithm based on force sensor.

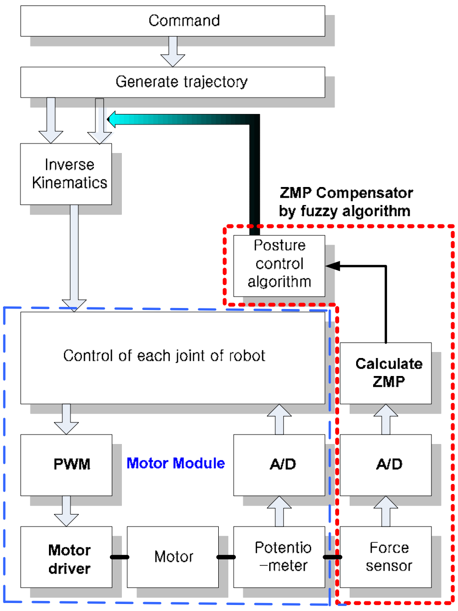

Fig. 4 The schematic diagram for posture control using ZMP by fuzzy algorithm

4-2. Fuzzy rule for compensating coordinate of "Trunk"

Three membership functions are constructed for x1 and x2, where x1 is error between measured ZMP and desired ZMP and x2 is error between measured ZMP variation and desired ZMP variation. Each of the input variables has three fuzzy sets: N, Z, P. Membership functions consist of overlapped isosceles triangles as shown in Fig. 5. All membership functions have equal base length. The universe of discourse is assumed as $-a \leq x1 \leq a$(cm) and $-b \leq x2 \leq b$(cm/sample time) for the two variables, which the universe of discourse is decided by displacement of robot "Trunk" for x1 and by moving velocity of robot for x2. Output value of fuzzy logic, which is to compensate coordinate of "Trunk", is constructed in five membership function for u_com as shown in Fig 6.

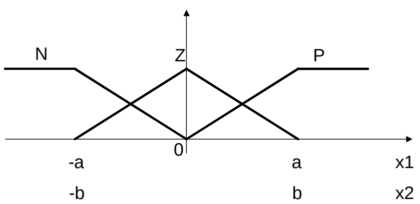

Fig. 5 Fuzzy membership functions of input variables

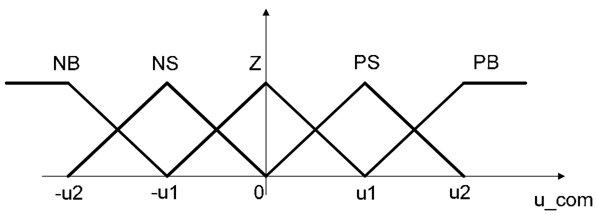

Fig. 6 Fuzzy membership functions of output variables

Nine rules are constructed in a 3x3 fuzzy table, which involves x1 and x2 in order to stabilize the biped walking robot by ZMP compensation. If x1 is P and x2 is N, posture of robot incline forward and move backward to reference ZMP. Therefore, posture of robot can keep the 'Desired area' of ZMP for stability without ZMP compensation. The membership function for the coordinate of "Trunk" compensation is defuzzified by the centroid method. The defuzzified output values are compensated by reference coordinate of "Trunk" for inverse kinematics.

Table 1 The rule base to trail the desired ZMP

x1 \ x2	P	Z	N
P	NB	NS	Z
Z	NS	Z	PS
N	Z	PS	PB

5. EXPERIMENTS

An experiment is carried out in single support phase and in static standing. A comparison of stability is carried out between posture control with ZMP compensation algorithm and without it against disturbance. Experiment is also carried out in single support phase on a slope. Desired ZMP is fixed on a zero position which is center of sole.

First, when the robot received disturbance forward and backward, the obtained ZMP trajectory is shown in Fig. 7 and Fig 8. We can see that x_{zmp} decreases and increases when disturbance is given backward and forward. If disturbance is given backward, "Trunk" moves forward to move desired ZMP under backward disturbance until ZMP is compensated. When disturbance is removed, ZMP trajectory is shown in the forward area because "Trunk" has moved forward to compensate for incremental error as shown Fig. 8. If ZMP is not compensated by fuzzy algorithm under backward disturbance, although disturbance is suddenly removed, ZMP trajectory is not shown in forward area as shown Fig. 7.

We experiment to evaluate the stability of the robot on a slope(incline is a direction to clime a slope, decline is a opposite slope). First, when the proposed posture control algorithm using only position sensor is applied, ZMP trajectory is shown proportionally according to angle of decline and incline as shown in Fig. 9. If an angle of inclination is more increased, robot is fallen down because ZMP is not compensated.

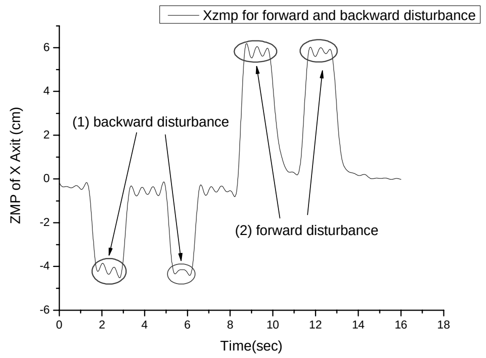

Fig. 7. The ZMP trajectory for disturbance (without fuzzy posture algorithm)

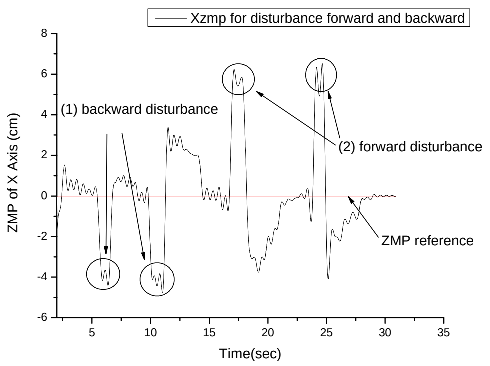

Fig. 8 The ZMP trajectory for disturbance (with fuzzy posture algorithm)

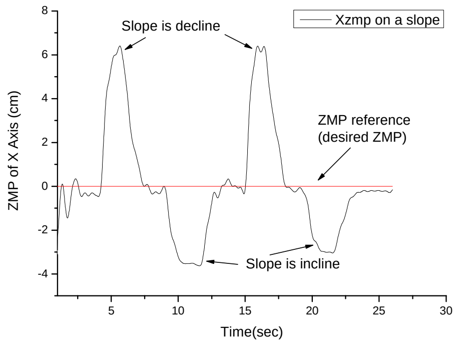

Fig. 9 The ZMP trajectory on a slope without fuzzy posture control

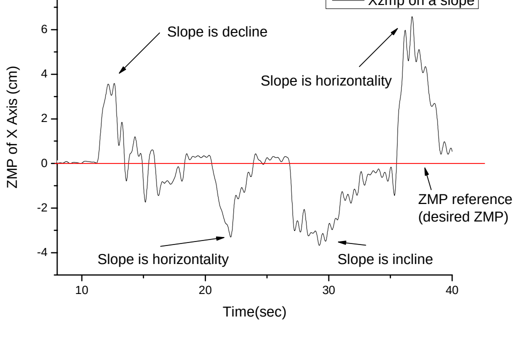

Fig. 10 The ZMP trajectory on a slope with fuzzy posture control

Fig. 10 shows the result of experiment by fuzzy posture algorithm using ZMP information according to incline and decline. It is more stable than posture control algorithm without ZMP information. If slope is declined, ZMP trajectory is moved to the desired ZMP because ZMP compensator compensates coordinate of "Trunk". After then, as slope is moving to horizontal direction, ZMP trajectory is shown in the backward area temporary because posture of robot can not be completely compensated due to time delay by lowpass filter, a slow sampling time. And fuzzy membership function is not yet optimal. After then robot again move to compensate to the desired ZMP on a horizontal land.

6. CONCLUSIONS

The fuzzy posture control algorithm using ZMP information was introduced. The ground reaction force and the ZMP information was acquired as using force sensors. And we could find position of center of gravity of the biped walking robot as using the acquired ZMP and could control in real time so that ZMP always exists within 'Desired area' by fuzzy posture algorithm. The fuzzy posture algorithm using ZMP is able to control the posture suitably even if the bottom of road has a slope. Further works on the proposed 'fuzzy posture algorithm using ZMP information' improve posture stability by choosing the optimal fuzzy membership function and decrease time delay. So, robot has stability on a dynamic environment in walking

Acknowledgment

This work was supported (in part) by the Ministry of information & Communications, Korea, under the Information Technology Research Center(ITRC) Support Program.

References

[1] J. Furusho and M. Masubuchi (1986). "Control of a Dynamical Biped Locomotion System for Steady Walking", Journal Dynamic Systems, Measurement and Control, vol. 108, pp. 111-118.

[2] C. Zhu and A. Kawamura (2003). "Walking Principle Analysis for Biped Robot with ZMP Concept, Friction constraint, and Inverted Pendulum Model," Proc. of IEEE/RSJ International Conf. on Intelligent Robots and Systems, pp. 364-369.

[3] J. Furusho and A. Sano (1990) "Sensor-Based Control of a Nine-Link Biped," Journal of Robotics Research, vol. 2, no. 2, pp. 83-98.

The Eleventh International Symposium on Artificial Life and Robotics 2006 (AROB 11th'06),
B-con Plaza, Beppu, Oita, Japan, January 23-25, 2006

Bluetooth Network for Distributed Autonomous Robotic System

Se-Hee Whang In-Hun Jang Kwee-Bo Sim
School of Electrical and Electronics Engineering
Chung-Ang University
221 Heukseok-Dong, Dongjak-Gu, Seoul 156-756, Korea

Abstract

Distributed Autonomous Robotic System (DARS) is a system that independent autonomous robots in the restricted environments infer their status from pre-assigned conditions and operate their jobs through the cooperation with each other. In the DARS, a robot contains sensor part to percept the situation around themselves, communication part to exchange information, and actuator part to do a work. Especially, in order to cooperate with other robots, communicating with other robots is one of the essential elements. Because Bluetooth has many advantages such as low power consumption, small size module package, and various standard protocols, Bluetooth is rated as one of the efficient communicating technologies which can apply to small-sized robot system. In this paper, we will develop Bluetooth communicating system for autonomous robots. For the purpose, the communication system must have several features – separated module, flexible interface. We will discuss how to construct and what kind of procedure to develop the communicating system.

1 Introduction

In the Distributed Autonomous Robotic System (DARS) [1] [2], each independent individual robot understands its situation through the surroundings, and then operates its jobs through cooperation with each others. For these cooperative works, the ex-change of the information between the robots should be essential and communication module is an important element to construct a distributed autonomous robot.

Bluetooth is a kind of short distance wireless communication methods and is developed for a portable device. Because of its features, Bluetooth is regarded as the most suitable wireless technology for build up the small-sized robots. In this paper, we will introduce Bluetooth network for distributed autonomous robotic system. First of all, the Bluetooth network has the ability of independent operations. We will design the system to organize a network scheme and to maintain the network scheme in the small sized communication module. In addition to these features, the network module should serve a kind of standard interface which commonly used by the most people. If the Bluetooth network is developed in this way, development convenience will be increased because of independent operation of each part in the robots and this Bluetooth network will be applicable to other embedded systems easily. Except the previous hardware features, many considerable view points are remained – about network scheme, constructing sequence, and routing problem. We should deliberate on how to organize the network system, what kind of network form to be constructed, and what sequence to be used.

The features of Bluetooth are briefly demonstrated in the chapter 2. The constitutions of network module are described in the chapter 3. The problems related to network formation are investigated in the chapter 4. The conclusions and future works about the Bluetooth network system are denoted in the final chapter.

2 Bluetooth

2.1 Features

Bluetooth is designed for portable devices using the power of a battery, so it satisfies the conditions – low cost, low power, and compact size. With these reason, Bluetooth is recognized as suitable wireless communication technology for applying to robotics. Besides, this technology commonly supports various standard protocols. Basically most of Bluetooth modules serve HCI level interface and higher protocol stacks are implemented by software. Sometimes, the rest serve RF-COMM level interface – higher protocol than HCI – in the Bluetooth module. The following figures show com-positions of Bluetooth Stack in the typical system using Bluetooth.

2.2 Network Support

Fundamentally, Bluetooth is developed to support master and slave structure. One master should have up to 7 slaves. Master and slave role can be operated in a module. There are two kind of network concept in Bluetooth. The first, a piconet is made up of only one master and several slaves. The next, a scatternet, which consists of piconets, is larger than the piconet.

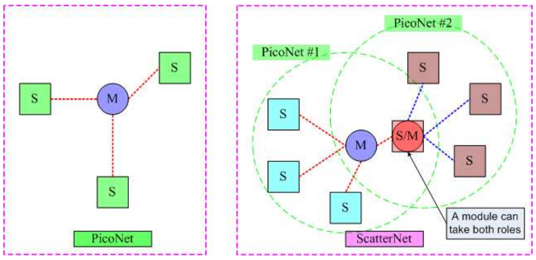

Figure 1: Bluetooth networks (Piconet/Scatternet)

3 Network Module

Bluetooth communication system consists of Bluetooth network modules – define as a hardware module in this paper – and each module operates independently of the embedded system connected to it. In a word, Bluetooth network module takes charge of constructing wireless networks. Since only Bluetooth module cant construct and maintain networks, Additional circuital elements are required. Moreover when this network system is applied for other system, standard interfaces are necessary for serving more convenience to developers.

3.1 Hardware

Bluetooth network module is basically composed of a Bluetooth module and a net-work controller to organize a network system with the Bluetooth modules. We use the Bluetooth module which contains CSR Bluetooth chipset and use ATmega128 as a network controller. This Bluetooth chip-set supports UART interface and is the most commonly used. An ATmega128 contains about 128KB memory and supports 2 UART interfaces and is widely used in the world. The network controller communicates only HCI commands with the Bluetooth module. Interfacing with network controller and Bluetooth module, logic voltage difference problem may occur. However, it is easily solved by a level shifter device. If external UART use the same voltage of Bluetooth module, exchanging ATmega128 for ATmega128L can solve the interfacing voltage problem.

3.2 Adaptation to Robots

In our lab, we are developing an agent robot for DARS. In this agent robot, Bluetooth network module takes a role of communication part and uses UART as an interface with other parts. Fig. 2 Shows the construction of the agent robot.

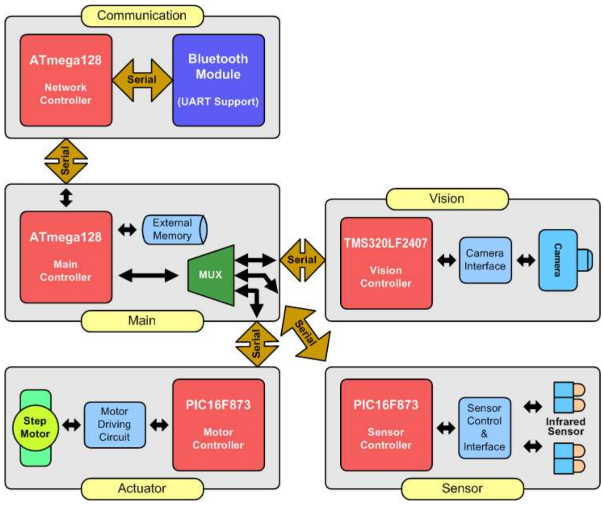

Figure 2: Adaptation of Bluetooth Network Module

3.3 Development & Test

Bluetooth module which we use supports several kinds of interfaces such as UART, USB, and SPI. In order to test Bluetooth network system in the same environments that robot operates, we had better directly program to the robot. However, if only the operation of Bluetooth module is inspected, the result would be similar to that of direct programming. So we recommend the following procedures.

1. The operation procedures of every Bluetooth module should be designed in order of time sequence.

2. After that, to test the designed procedures is executed. In this stage, we recommend test with serial dongles, because HCI level command is standard and HCI level test program is offered.

3. If thus much is correctly performed, network controller may be programmed. After the programming, test of each Bluetooth network module and entire Bluetooth network system should be examined. Passing the test, the Bluetooth network system would be operated well.

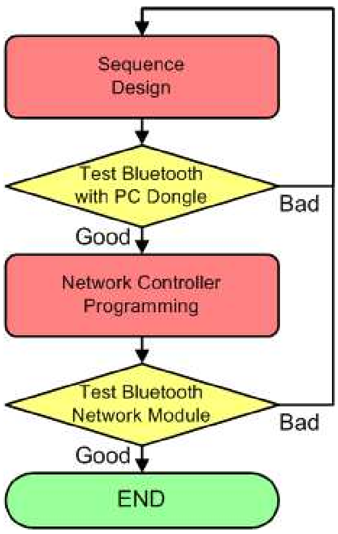

Figure 3: Bluetooth Development and Test

4 Bluetooth Network

In this paper, we use the tree structure of the network formation, because tree formation is easy and light to adapt for small embedded system. Besides, in order to implement self-organized Bluetooth networks, self-organizing algorithm is essential and usually has four procedures – discovery, organization, maintenance, and re-organization [8] [9].

4.1 Researches in Scatternet

There are three major parts about researches in scatternet – scatternet structure formation algorithm, routing algorithm, and scheduling in the bridge node. Routing and Role scheduling is dependent on the network structure, so these three parts of scatternet researches are organically associated with each others.

There are three kinds of representative formation algorithm by the shape of the scatternet structure – tree, star, and ring. Representative tree structure researches are MIT-TSF [3], MIT-BSFA [4] [5], and Bluetrees [6]. This structure has high extensibility but also has potentiality of bottleneck at the root of the tree. In the star structure, BlueStar [7] is the representative algorithm. Star structure is connected to a number of piconets through the bridge node. In the ring structure two kinds of algorithms exist by whether the basic unit is node or piconet. Nevertheless, the connected form of basic units is a ring.

4.2 Formation of Bluetooth Network

In this paper, we use the tree structure of the network formation, because tree formation is easy and light to adapt for small embedded system. Besides, in order to implement self-organized Bluetooth networks, self-organizing algorithm is essential and usually has four procedures – discovery, organization, maintenance, and re-organization.

1. Discovery phase
   : All of Bluetooth modules are initialized and receive unique module name from network controller. After initializing, each module sends inquiry command to detect neighbor modules and stores information about neighbor modules.

2. Organization phase
   : Using stored information about neighbor modules, Bluetooth network structure would be constructed. At this time, efficiency of the structure is affected by which is the root of the tree. To estimate the efficiency thorough the tree root candidate, we define simple fitness function. The Bluetooth module, which has the largest Fitness function value, becomes the root of the tree.

   (a) initialize variables : $sum = 0, f_{candidate} = 0$

   (b) number of neighbors around candidate module :
   $sum+ = n_{neighbor}, f_{candidate}+ = sum$

   (c) candidate is replaced with neighbors during the origin candidates neighbors and operates the followings.

   - initialize variables : $sum = 0$
   - fitness function adds multiplied sum by coefficient of neighbor order :
     $f_{candidate}+ = (1/2)^{order} \cdot sum$

   (d) Unless the neighbor module does not exist, repeat the 3 procedure

3. Maintenance phase
   : Each module updates the information about neighbor module through periodic inquiry command.

4. Re-organization phase
   : Through the updated information, recalculate the simple fitness function value of every Bluetooth module. If necessary, change the structure of the tree.

4.3 Routing of Bluetooth Network

Bluetooth transmit rate is up to 1MBPS in Bluetooth core specification 1.1. Hence, transmission of the massive packet – such as image data – could lead any problems. Also, because of the structural problems, the larger numbers of modules exist, the heavier transmission load is concentrated at the root of the tree. As these reasons, we should use the pre-processed and light-weight packet data.

Except these problems, data packet usually hops a number of steps. Accordingly, we must design the tunneling packet structure and related algorithm.

5 Conclusion and Future Works

In this paper, we develop the Bluetooth network system for distributed autonomous robotic system. In this system, we use Bluetooth modules, because of its advantages – low power consumption, cheap price, small size, and various standard protocols. To guarantee the applicability and flexibility of the hardware module, we design Bluetooth network module with a microcontroller and additional circuits. Also To build simple and light weight structure, we select tree-shaped network scheme and define a simple construction algorithm. Nevertheless, this Bluetooth module has several problems. After understanding about this modules features, we could use the Bluetooth network system.

This Bluetooth System has numerous rooms for performance improvements in the circuit, network formation algorithm, and routings. We should try to increase the performance in various ways – hardware improvement and other network structure formation algorithm.

For hardware improvements, there are several possibilities. We can replace the Bluetooth module with another module which has more high speed transmission rate. Also circuital modification is needed for convenience of usage. If the higher profile stack and application program interface (API) are contained in the network controller, it is certain that easier and more flexible than that of the old system.

In the network scheme, we should compare a tree formation algorithm with the other network formation algorithm. We should examine what kind of algorithm is really suitable for the Bluetooth network system.

Acknowledgements

This research was supported by the Brain Neuroinformatics Research Program by Ministry of Commerce, Industry, and Energy.

6 References

References

[1] H. Asama, T. Fukuda, T. Arai, and I. Endo, *Distributed Autonomous Robotic Systems*, Springer Verlag, 1994.

[2] H. Asama, T. Fukuda, T. Arai, and I. Endo, *Distributed Autonomous Robotic Systems 2*, Springer Verlag, 1996.

[3] G. Tan, A. Miu, J. Guttag and H. Balakrishnan, "Forming Scatternets from Bluetooth Personal Area Networks," In MIT Technical Report MIT_LCS-TR-826, 2001.

[4] C. Lay and K.Y. Siu, "A Bluetooth Scatternet Formation Algorithm," Proc. of the Conf. on Global Telecommunications, Vol. 5, pp. 2864-2869, 2001.

[5] C. Law, A.K. Mehta and K.Y. Siu, "Performance of a New Bluetooth Scatternet Formation Protocol," Proc. Of ACM Symp. on Mobile Ad Hoc Networking and Computing, pp. 182-192, 2001.

[6] G. Zaruba and S. Basagni, "Bluetrees-Scatternet Formation to Enable Bluetooth-Based Ad Hoc Networks," Proc. of the IEEE International Conf. on Communications, Vol. 1, pp. 273-277, 2001.

[7] Petrioli, S. Basagni and I. Chlamtac, "Configuring BlueStars: Multihop Scatternet Formation for Bluetooth Networks," Proc. of the IEEE Trans. on Computers, Vol. 52, Issue 6, pp. 779-790, 2003.

[8] C. Chevallay, R.E. Van Dyck, T. A. Hall, "Self-organization Protocols for Wireless Sensor Networks," Conf. on Information Sciences and Systems, 2002.

[9] G. J. Pottie. "Wireless Sensor Networks," in IEEE Information Theory Workshop, June, 1998, pp. 139-140.

The Eleventh International Symposium on Artificial Life and Robotics 2006 (AROB 11th'06),
B-con Plaza, Beppu, Oita, Japan, January 23-25, 2006

Mapping Children and Playgrounds into Multi-Agent Systems

Alireza Derakhshan*, Frodi Hammer*, Henrik Hautop Lund*, Yves Demazeau†

*The Maersk Mc-Kinney Moller Institute for Production Technology
University of Southern Denmark, Campusvej 55, DK-5230 Odense M, Denmark
†CNRS, Laboratoire LEIBNIZ, Institut IMAG
46, avenue Félix Viallet, F-38031 Grenoble Cédex, France

kianosh@mip.sdu.dk frodi@mip.sdu.dk hhl@mip.sdu.dk yves.demazeau@imag.fr

Abstract

We present how to adapt a playground using multi-agent systems based upon live human agents. The playground consist of tiles having sensing capabilities and abilities to communicate with their four neighbours. We propose a mapping of the children playing on the playground to a multi-agent system inhabited by BDI agents, which use an artificial neural network to learn the children's desires and intentions and identify these within seven categories; thus, enabling the playground to adapt accordingly. The playground has been developed, implemented and tested on a group of children. Based on a 6×6 environment we show that it is possible to learn and recognise childrens desires and intentions based on the behaviour they exhibited on the playground.

1 Introduction

In the western society there exists increasing problems related to obesity in the population. These problems cannot only be confronted by being increasingly aware of proper diet, but also physical activity needs to be taken into consideration. One attempt is to introduce IT known from robotics, artificial intelligence and multimedia on playgrounds in order to increase children's interest in these and thereby increasing their physical activity [1, 2]. For instance, could some of the techniques known from today's computer games be taken into consideration on the playgrounds; computer games are dynamic universes versus the static nature of playgrounds. These dynamic elements could be introduced on the playground, by transforming them into a physical form which are capable of physical interactions. This would indeed help keeping the children's interest in the playground and therefore proportionally increase the physical activity level of the children.

By introducing this form of dynamic behaviour onto the playground, the playground should have the possibility to adapt in favour of each individual child playing on it making it as interesting as possible as a whole. These adaptations could be as small as changing the colour of a LED to a child's favourite colour, or to larger adaptations which change the morphology of the elements on the playground according to e.g. the child's build. This would essentially allow for equal play on the playground along its users irrespective to age, weight, speed, etc.

1.1 Playground Prototype

To allow dynamic behaviours on the playground a new playground prototype has been developed. This prototype consists of several building blocks or tiles (see fig. 1). These tiles allow a high degree of freedom for children to create their own game depending on e.g. the assembling of the tile, thereby making the games depend on the playgrounds morphology. The assembled playground then contributes to the play (here by sound and/or visual interaction) allowing an interesting and even dynamic storyline to emerge with which the children can e.g. merge with their own imaginary stories. Additionally, by embedding ambient intelligence into the tiles the playground gets the characteristics of being personalizing, adaptive and anticipatory according to the interactions exhibited by the children.

The tile prototype's dimensions are $21cm \times 21cm \times 6cm$ (width, height, depth) and it consists of a rubber-like shell, a sandwich plastic case, a PCB and a force sensor as illustrated in fig. 2. The rubber-like shell

Fig. 1. An example of four tiles assembled into a playground.

has a "bump" indicating the location of the force sensor and a Plexiglas mark for light output. The PCB uses an Atmel ATmega 128 microcontroller; a general purpose microcontroller supporting 128kB of self-programmable flash memory which runs up to 16MHz. A 4-way communication bus is interfaced to the serial USART on the microcontroller via a Quad UART chip (TL16C754BPN). The Quad UART is furthermore interfaced to a multi-channel line driver/receiver (MAX211) in order to support RS-232 level connections between the tiles. Four bright Light Emitting Diodes, capable of showing red, green and blue colours at different intensities are connected to the microcontroller. A Force Sensitive Resistor (FSR) sensor (FlexiForce A201) is interfaced of the A/D converter on the microcontroller which supports up to a 10-bit resolution measurement of the sensor value.

1.2 Related Work

As the work presented here is being both novel and interdisciplinary, the area of related work is limited to some technical and conceptual aspects.

The Smart Floor [3] was developed for transparent user identification and tracking. The Smart Floor measures the force exerted on a tile in order to identify the person according to the footstep's force signature. The system assumes that the footstep signatures can be uniquely recognized among a small "enough" group (approximately 15 people), but gets error prone when the number of people becomes large. Before any identification can take place, each user must put their footstep signature into the system database – new users cannot be seamlessly integrated.

The KidsRoom [4] is a perceptually-based, multi-person, fully automated, interactive, narrative play space where children are taken on a fantasy journey

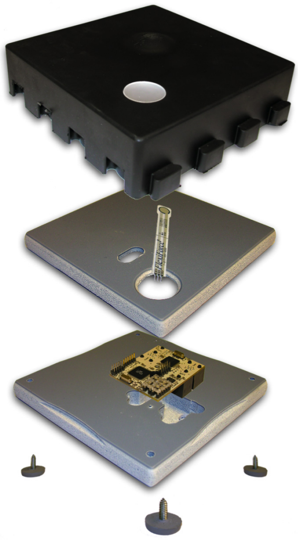

Fig. 2. The tile consist of a rubber-like shell, a FSR sensor, a plastic case, a PCB and some tightening screws.

through different worlds. The KidsRoom is based on a 24×18 ft. room modelled as a real child's bedroom. In addition the room has monitoring capabilities that can track and analyse the behaviour of the children; thus, by using sound, images, animations and music, the room can communicate with the children. In addition the child or children can be part of the story narrators, making them able to change the journey's course by their own behaviour and interaction with the room.

The relating part of the KidsRoom to the playground is the amount of freedom the child is given and the unawareness the child has of the room's capabilities. Therefore the child does not have to push certain buttons or do anything extraordinary for the storyline to proceed. In a sense, the room triggers a game and the child then decides how he or she wants to play this game and the room adjusts its behaviour (storyline) by analysing (by using computer vision) the child's behaviour.

The vessel berthing system [5] uses a multi-agent system to enhance the efficiency of a container terminal operation. The essence is that the intelligent agent can dynamically adapt to the changing environment. For example one agent (schedule agent) must assign limited number of berths and resources (Cranes, Trucks, etc.) in a terminal to a number of vessels. One of the interesting aspects is that the agents are modelled with a generic BDI architecture extended with an intelligent entity making them capable of learning and adapting; hence, making the agent a better decision maker. This intelligent entity is a mixture of an artificial neural network and fuzzy logic, named "Adaptive Neuro Fuzzy Interface System" (ANFIS) [6].

2 Children, Playgrounds and Multi-Agent Systems

One way of optimizing the activity level of the children playing on the playground is to increase or maintain the level of fun over time. In order to do this it is necessary to have knowledge about each child's playing behaviour. This could be knowledge of favourite moving patterns, such as jumping, running, doing somersaults etc. It could be imagined that these moving patterns could be mapped to specific games that favours these behaviours. E.g. in the "smash game"[7] a location is indicated to the user that the user have to "smash" e.g. by jumping on this location. In this type of game, if a child favours running instead of jumping, the locations to smash should be located farther apart increasing the running in the game and thus also increasing/maintaining the fun for that child.

Since all children are different their individual interest in the game are also more or less different. Hence, in order to increase/maintain a child's interest in the game, the playground should be able to adapt accordingly. This implies that it must be possible to recognise and/or predict the behaviour of a child playing at the playground. However, when several children are playing together on the playground, the playground needs to be adapted in order to maintain several interests; thus, also the collective behaviour of the children needs to be recognised and/or predicted.

We state that a playground can be viewed from a multi-agent system (MAS) perspective. In general MAS are considered consisting of agents, environments, interactions and organizations [8]. This could be mapped into the playground as shown in fig. 3 where the children are considered as being agents, the playground being the environment, the interactions are those between the children and the playground or other children respectively and finally the organizations – if any – are due to the formations of the children. We now need to consider how the environment and the agents can be modelled in the MAS.

2.1 Modelling the Environment

The playground defines the environment. Since the playground consists of several tiles, the possible interactions with the environment are defined by the tiles.

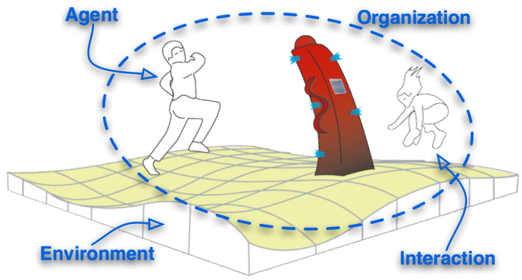

Fig. 3. Mapping the children and playground into a MAS.

The possible input sources of the tiles are the FSR sensor and the communication lines; hence pressure can be measured and movements can be calculated. Pressure can be read directly from the FSR sensor on each tile, and by using the communication lines, two successive pressure points can be used to calculate the distance travelled and the time the movement took. Of course, the distance can only be calculated as long as some *a priori* knowledge about the topology of the tiles is known. These three physical units are illustrated in fig. 4.

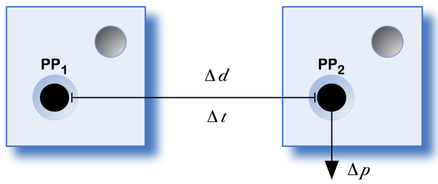

Fig. 4. The three physical units that can be measured in the environment. PP_1 and PP_2 are the pressure points.

Combining the pressure, the distance and the time several interactions with the environment can be defined. For simplicity we have reduced the numerical span of the physical units from infinite to two leaving us with the following:

Time (t) is either slow or fast.

Pressure (p) is either soft or hard.

Distance (d) is either near or far.

With these three units eight interactions can be composed as listed in tab. 1. The definitions of p, t and d are all relative and can thereby be specified according to any appropriate threshold function.

2.2 Modelling the Agents

When modelling human or cognitive behaviour, the BDI agent architecture is the most commonly used in

Interaction	Δt	Δp	Δd
Walk	slow	soft	near
Touch	fast	soft	near
Step	slow	hard	near
Tug	fast	hard	near
Stretch	slow	soft	far
Stroke	fast	soft	far
Jump	slow	hard	far
Run	fast	hard	far

Tab. 1. The interactions defined according to the parameters time (t), pressure (p) and distance (d).

the literature. BDI is an abbreviation for belief-desire-intention and the agent model was first proposed by Bratmann [9] and can be illustrated as in fig. 5.

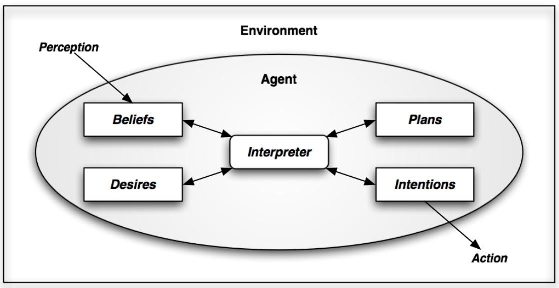

Fig. 5. The BDI agent architecture [10].

The beliefs correspond to the information the agent has perceived from the environment which can be incomplete or even incorrect. The desires hold information about the objectives the agents has to accomplish and their priority – the desires are often referred to as the motivational attribute of the agent. Intentions represent the deliberative component of the agent (i.e. which are the desires that the agent has committed to achieve). When an agent has committed to some desire, it tries to achieve this intention until it beliefs that the intention is satisfied or until it beliefs that the intention no longer is achievable. The plans consist of a library of plans that specify courses of action which achieve a specific intention. The interpreter is responsible for the execution cycle of the agent. It updates the beliefs according to new perceptions from the environment, generate new desires according to new beliefs, select which of the current active desires should act as intentions, and finally selects an action to perform according to the agent's current intentions and plan library.

When several agents, i.e. several children playing together on the playground, a collective behaviour emerges from the organisation of the agents; that is, the organisation defines which interaction patterns comply in between the agents. This agent–agent interaction, which defines the group behaviour, originate from the desires and intentions of the individual agents. Thus, from having individual desires and intentions, the agents also have joint desire and intentions.

The agent–environment interactions (or agent actions) listed in tab. 1 define the basic entities of the possible behaviours on the playground. A sequence of actions corresponds to a plan being, which when being executed complies with the desires and intentions of the child playing by exhibiting these actions. So, by *recognising* or *learning* this plan, the desires and intentions of the child playing could be identified. This would allow for an agent only observing the agent–environment (children–playground) interactions to learn to recognize and/or identify the child's desires and intentions in order to adapt the playground to serve these.

In order to design an agent architecture that allows for this, we follow Shoham et al's "AI agenda" [11] and look for an optimal (or at least effective) agent design for the environment amongst the agents inhabiting it – that is the children. Thus, we propose an agent architecture where the desires and intentions of the child can be learned by an artificial neural network (ANN). The input to the ANN then corresponds to the child's belief set which can be decomposed into a plan (that is, a sequence of actions) and the perceived environment (some limitation of the surrounding environment). Having this action/perception correlation also indicates the effect of a given action performed in the environment to the agent.

3 Observing Childrens Play

In order to collect data a playground consisting of 36 tiles arranged in a 6×6 grid was used. A play called "Bug Smasher" inspired from the "Smash" game [7] was implemented. The play shows three bugs (indicated by green LEDs) moving around randomly keeping a certain distance to the child. The child then must try to squeeze the bugs by stepping on them. Several responses according to the actions in tab. 1 were implemented.

To observe the children playing, two types of test were performed; an *individual* test which settles the childrens individual desires and intentions, and a *group* test which settles the joint intentions of two children playing together.

The individual test was performed with 23 children aged 5-6 years. In general two major behaviours were observed. A "Playing" behaviour was defined according to children whos behaviour was under influence by the environment. A "Not Playing" behaviour was defined according to children who were not under influence by the environment (i.e. playing their own imaginary play). In the test, 10 of the children were generally "Playing" while the remaining 13 were generally "Not Playing".

Eight of the children also participated in the group test. All of them had a general "Playing" behaviour. However, the playing behaviour varied from being cooperative initially to becoming occasionally competitive, e.g. some of the children pushed each other trying to squeeze a bug (see fig. 6).

Fig. 6. Two children are competing to squeeze the bugs in the group test. Each test lasted 5 minutes and was performed in a neutral environment (here a kindergarten).

4 Learning desires and intentions

In order to adapt the playground three main disciplines must be considered, namely; observation, classification and finally adaptation (see fig. 7). An agent being able to observe the child's interactions with the environment can learn the child's desires and intentions and use these in order to increase/maintain the child's physical activity by adapting the playground accordingly.

From the tests, behaviours complying with the seven desires and intentions were defined analytically as shown in fig. 8. A sequences of 36 actions in the collected data was selected as defining the behaviours in the training set of the agents ANN as unambiguously as possible[1]. In verifying the trained agent, a test set including the rest of the collected data was all correctly classified (see fig. 9). However, as can be seen

[1]Only 5 of the analytically 7 behaviours existed in the collected data.

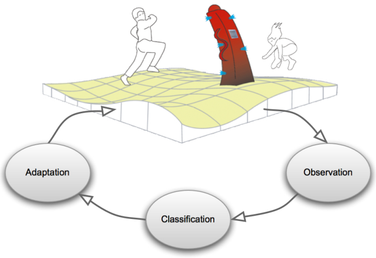

Fig. 7. The cycle of adaptation on the playground.

in fig. 9 the percentages by which the classifications are given are not as unambiguous as desirable – an example is Silje; indications are that the children change behaviours during the play. By producing a graphical representation of how the agent classifies epochs of 36 actions, we see that Silje is indeed switching different behaviours as expected (see fig. 10). Also notice, that the individual behaviours can be distinguished from group behaviours by the agent; meaning that the agent also is capable of recognizing joint intentions that is agent–agent interaction, by observing the agent–environment interaction.

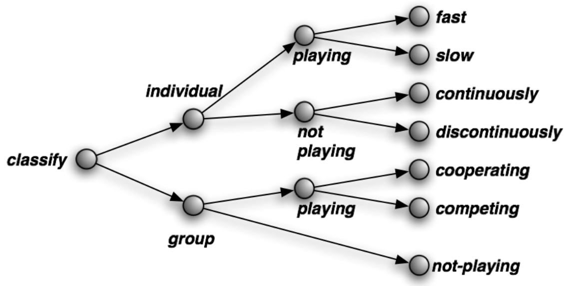

Fig. 8. The seven classifications of the ANN corresponding to different criteria. The continuously and discontinuously complies with the behaviour being predictable or not.

5 Conclusion & Future Work

We have presented an approach to adapt playground inspired from multi-agent systems; modelling children as agents, the playground as the environment, allowing children– playground (agent–environment) and children–children (agent–agent) interactions and for the children as being organised. This approach enabled the children as being view upon as BDI agents where their actions are determined by their desires and intentions.

	Name	Classification in percentage						
		I. Playing Fast	I. Playing Slow	I. Not-Playing Cont.	I. Not-Playing Disc.	G. Playing Cooperating	G. Playing Competing	G. Not-Playing
Individual	Anna	0.0	6.5	10.3	**79.9**	0.0	0.4	0.0
	Emilie P.	0.0	1.2	**69.0**	29.0	0.0	0.0	0.0
	Silje	0.0	1.3	**49.0**	41.3	0.3	2.8	0.0
	Søren	0.0	**41.7**	8.0	34.6	2.8	2.8	0.0
	Clara	0.0	2.5	**78.8**	7.1	10.3	0.3	0.0
	Frederik	0.0	**86.3**	0.7	3.3	0.4	0.0	0.0
Group	Clara & Silje	0.0	13.5	1.4	1.0	**45.4**	31.0	0.0
	Emilie & Emilie P.	0.0	15.2	1.6	0.7	**34.8**	33.7	0.0
	Mads & Frederik	0.0	10.0	1.3	1.9	**59.7**	24.8	0.0
	Oliver & Victor	0.0	5.9	3.3	2.4	**40.5**	37.7	0.0

Fig. 9. Selected agent classifications of the test set. Bold indicates the classification, while underline indicates the target.

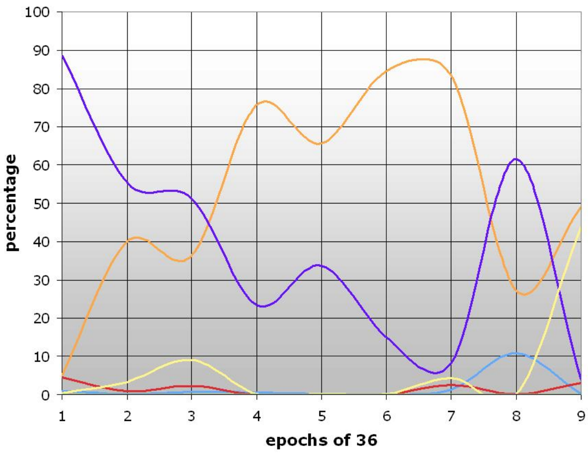

Fig. 10. Classifications of Silje's behaviour by the trained agent. The orange curve shows "I. Not-Playing Cont." while the purple shows "I. Not-Playing Disc.". The yellow is "I. Playing Slow".

Seven desires and intentions of the children were defined by their behaviour, from a combination of how many children were playing and of how much they were under influence by the environment. A training set consisting of selected examples from the collected data representing each of the defined behaviours was constructed and an ANN capable of classifying the behaviours was trained.

Having the first two phases of fig. 7 the last phase is to use this knowledge about the children to adapt the playground in their favour, an aspect which we present in another paper.

Acknowledgements

The hardware platform was partially developed by T. Klitbo. The design of the tiles was made by C. Isaksen from Isaksen Design. KOMPAN A/S participated in the development of the tiles. C. Balslev Nielsen created some of the contacts with the children from without the results would not have been possible.

References

[1] H. H. Lund and C. Jessen. Playware – intelligent technology for children's play. Technical Report TR-2005-1, Maersk Institute, University of Southern Denmark, June 2005.

[2] H. H. Lund, T. Klitbo, and C. Jessen. Playware technology for physically activating play. *To appear in Artificial Life and Robotics Journal*, 9, 2005.

[3] Robert J. Orr and Gregory D. Abowd. The smart floor: a mechanism for natural user identification and tracking. In *CHI '00: CHI '00 extended abstracts on Human factors in computing systems*, pages 275–276, New York, NY, USA, 2000. ACM Press.

[4] A. Bobick, S. Intille, J. Davis, F. Baird, C. Pinhanez, L. Campbell, Y. Ivanov, A. Schutte, and A. Wilson. The KidsRoom: A Perceptually-Based Interactive and Immersive Story Environment. Technical Report 398, E15, 20 Ames Street, Cambridge, MA 02139, December 1996.

[5] P. Lokuge and D. Alahakoon. Enhancing efficiency of container terminal operations: Using intelligent bdi agents with adaptive neuro fuzzy inference systems. In *Proceedings of the* 23^{st} *National IT Conference*, pages 34–43, Colombo, Sri Lanka, 2004. AAMAS.

[6] Jyh-Sing Roger Jang. ANFIS: Adaptive-Network-Based Fuzzy Inference System. *IEEE Transactions on Systems, Man, and Cybernetics*, 23:665–684, 1993.

[7] Robert Headon and Rupert Curwen. Ubiquitous Game Control. In *Ubicomp Workshop on Designing Ubiquitous Computing Games*, 30 September 2001.

[8] Yves Demazeau. From interactions to collective behaviour in agent-based systems. In *Proceedings of the First European conference on cognitive science*, pages 117–132, Saint Malo, France, 1995.

[9] M. E. Bratman, D. J. Israel, and M. E. Pollack. Plans and resource-bounded practical reasoning. *Computational Intelligence*, 4:349–355, 1988.

[10] Michael Wooldridge. Practical reasoning with procedural knowledge. In *FAPR*, pages 663–678, 1996.

[11] Yoav Shoham, Rob Powers, and Trond Grenager. Multi-agent reinforcement learning: A critical survey. Technical report, Stanford University, 2003.

The Eleventh International Symposium on Artificial Life and Robotics 2006 (AROB 11th'06),
B-con Plaza, Beppu, Oita, Japan, January 23-25, 2006

Reference-position detection using fan beam laser for cooperative localization of multiple mobile robots

Hiroyuki Takai*, Jun Mitsuoka* and Keihachiro Tachibana**

*Graduate School of Information Sciences, Hiroshima City University
3-4-1 Ozuka-Higashi, Asa-Minami, Hiroshima 731-3194 JAPAN

** Graduate School of Computer Science, Osaka Gakuin University
2-36-1 Kishibe-Minami, Suita, Osaka 564-5811 JAPAN

Abstract

In recent years, mobile robot systems that perform team operations such as repairing industrial equipment have been researched. However, since a number of robots have to work in a small indoor workspace for cooperation, they are prone to collisions and sensor signal interference. We formed a hypothesis that their collisions were caused by the ambiguity of their positional information.

Since each robot has its own coordinate axis, they cannot compare their positional information. In order that each robot can detect the same position in the same coordinate axis correctly, they need to decide reference positions in their workspace. We considered detecting "corners / edges" which were formed by walls and pillars that are in most buildings as indoor reference positions.

In order to detect direction of "corners / edges" clearly, we propose to use the fan beam laser that can create a visual representation of the object's geometrical features. Since image sensors can capture the image of "the corner / edge", the direction of "the tip of the corner / edge" can be detected using image processing algorithms. Because more than two robots can capture the image of "the same corner / edge" illuminated by the fan beam laser simultaneously, they can detect direction of "the tip of the corner / edge" as the direction of the reference position.

The direction detection method using a fan beam laser was proven and successful results were obtained. Each robot can acquire accurate positional information using triangulation based on detected reference position's direction and mutual localization among teammate robots.

1. Introduction

Recently, multiple autonomous mobile robots that can perform team operations have been developed. These robots are used for maintenance of nuclear reactors, repairing industrial equipment, and so on.

When the number of robots increases in the workspace for cooperative operation, they will often suffer from collisions or signal interference. One of the proposed collision avoidance methods of mobile robot teams is the exchange of their action programs through inter-robot communication. Communication signal interference known in wireless communication as "the hidden terminal problem" or "the exposed terminal problem" occurs when these robots transmit omni-directional signals simultaneously. Occurrences of these robots' collisions or signal interference depend on their mutual location. Inaccurate positional information is one of the causes of mobile robots' collisions or signal interference.

Accurate outdoor positional information can commonly be detected using GPS (Global Positioning System). However, indoor mobile robots cannot use GPS because they cannot receive signals from GPS satellites. In addition, since artificial landmarks also are hard to prepare for in advance in unknown workspace, accurate detection of positional information on global coordinate axis in indoor workspace is quite difficult. Therefore, we studied how to acquire the global coordinate axis among teammate robots in their workspace.

One of the proposed mutual localization methods uses teammate robots as landmarks, if these robots can detect direction and measure distance between each other. We have developed an infrared wireless communication system that can detect the angle of arrival (AOA) of communication signals from the communicating partner. Normally, an image sensor and ultrasonic sonar also have been attached to remote controlled mobile robots as embedded sensors. These robots can measure the distance to the partner based on the time difference of arrival (TDOA) of infrared communication signals and ultrasonic waves provided the communication system is used with ultrasonic sonar simultaneously. Consequently, each robot can compute it's relative location between each other by triangulation ranging based on detected direction and measured distance.

However, in order to avoid collisions with fixed obstacles and to form smooth action programs, these robots need to acquire their absolute positions in their workspace. These robots need to find out stationary reference positions used as the basis that determines their coordinate axis in their workspace to acquire their absolute positions. We considered detecting "corners / edges" which were formed by walls and pillars that are in most buildings as indoor reference positions.

Since more than two robots have to detect direction of "the same corner / edge" in order to share its positional information, we propose to use the fan beam laser that can create a visual representation of the object's geometrical features. Image sensors can capture the image of "the corner / edge" created by fan beam laser and can detects its direction as a reference position using image processing algorithms. The reference position can be calculated by triangulation ranging based on its detected direction, since each robot has computed its relative location mutually using the inter-robot communication system. These robots can exchange calculated positional information of reference positions through their inter-robot communication network. A map of their workspace also can be created from shared positional information of reference positions.

In this paper, the method of multi-robot mutual relative localization using the infrared inter-robot wireless communication system and the method of reference position detection using the fan beam laser are described.

2. Multi-robot mutual localization using inter-robot communication system

When the number of robots increases to accomplish complicated tasks in a small indoor workspace, they are prone to collisions and sensor signal interference. Occurrences of their collisions or signal interference depend on their mutual location and can be decreased by inter-robot communication using directional communication medium such as infrared rays or millimeter waves. We have designed an infrared wireless communication system for inter-robot communication.

When these robots move or rotate, usual infrared wireless communication often loses communication links owing to the directivity of infrared rays. In the system that we designed, in order to maintain communication links, several infrared transceivers are put on the circumference of the robot body and faced outwards. Figure 1 shows the arrangement of transceivers.

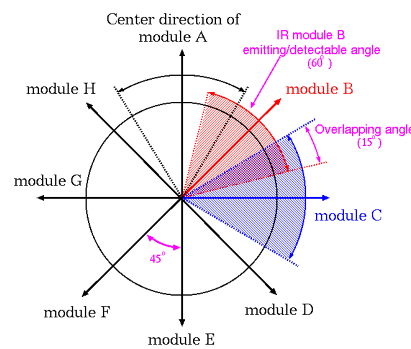

Fig.1 Arrangement of transceivers

In order to maintain a communication link by tracking the communicating partner, each transceiver receives a communication signal and the transceiver detects the AOA of the communication signal simultaneously. These transceivers are also switched to adjacent transceivers that face communicating partners when these robots move or rotate.

This communication system is able to communicate in parallel with different partners in different directions by using different transceivers simultaneously. As a result, space-division communication can take place. These robots create a communication network by relaying information among them. The created communication network is called ad hoc network, since each robot is independently mobile and may change position depending on their tasks. Figure 2 shows an inter-robot communication network.

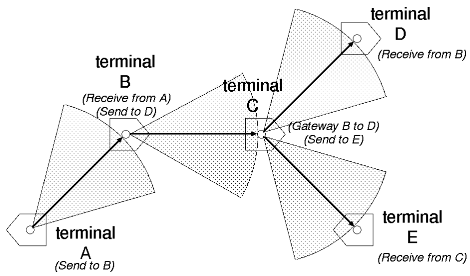

Fig.2 An inter-robot communication network

These robots can detect direction of partner robots using this infrared communication system and can also measure distance between partners using ultrasonic sonar with support of the communication system. Consequently, these robots can compute their mutual location by triangulation using information about their direction and distance.

The computation method of mutual location requires three known partners' location in the workspace. These partners' locations are arranged on coordinates from $P_1(x_1,y_1)$ to $P_3(x_3,y_3)$, and P_2 is the origin. When, the coordinate of the robot is $P(x,y)$ and the movement direction of the robot is θ, these parameters are computed from equation 1.

$$\left.\begin{aligned} x &= \overline{p_2 p}\cos\phi \\ y &= \overline{p_2 p}\sin\phi \\ \theta &= \phi - \theta_{01} - \theta_{12} + \pi \end{aligned}\right\} \quad (1)$$

Parameters are computed as follows.

$$\phi = \tan^{-1}\frac{\overline{p_1 p_2}\sin(\theta_{12}+\alpha)\sin\theta_{23} - \overline{p_2 p_3}\sin\theta_{12}\sin\theta_{23}}{\overline{p_1 p_2}\cos(\theta_{12}+\alpha)\sin\theta_{23} + \overline{p_2 p_3}\sin\theta_{12}\cos\theta_{23}}$$

$$\overline{p_2 p} = \frac{\sin\theta_{23}\cos\phi + \cos\theta_{23}\sin\phi}{\sin\theta_{23}}\overline{p_2 p_3}$$

$$\alpha = \tan^{-1}\frac{y_1}{x_1}$$

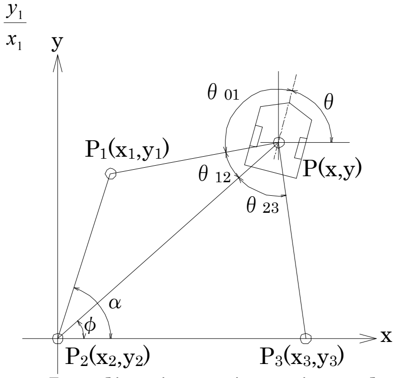

Fig 3. Localization using triangulation

Figure 3 shows mutual localization using triangulation based on the AOA of communication signals. The robot detects AOA (θ_{01}, θ_{12}, θ_{23}) of communication signals and computes coordinate $P(x,y)$ by triangulation.

We tested this mutual localization method using PSD (Position Sensitive Device) PIN photo diode (Hamamatsu S6560) that can detect incidence angle of infrared rays as the reception devices. In an experiment of AOA detection, angle detection error is approximate 0.5 degrees and this result is able to detect an AOA precisely. The accuracy of mutual localization is approximately 90% with the true value based on the detected AOA.

3. Reference position detection using fan beam laser

Although mutual location information is extremely useful for local mutual cooperation among adjacent robots, it is not suitable for the use that needs to point to appointed positions such as stationary obstacles in their workspace. In order to point to appointed positions, these robots have to decide a global coordinate axis based on several reference positions in their workspace.

"Corners / edges" which were formed by walls and pillars can be used as indoor reference positions in most buildings, since artificial landmarks are hard to prepare for in advance in unknown workspace. The fan beam laser that can create a visual representation of the object's geometrical features is suitable for detection of "corners / edges". Figure 4 shows a model of "corner / edge" detection using fan beam laser.

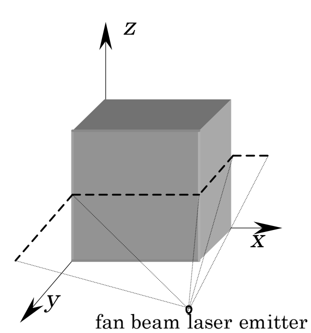

Fig 4. A model of "corner / edge" detection

We probed the feasibility of the "corners / edges" detection method using fan beam laser with experiments. The laser emitter (Coherent, LVM3 Laser-line micro 670nm 2.5mW 60deg) and the image sensor (RF system Lab, PRO-5 2CCD color wireless TV camera with lens) were used in experiments. The laser emitter and the image sensor were attached to a motorized turntable (SIGMA KOKI, SGSP-160YAW) horizontally at a 10cm interval vertically. The image sensor can capture 320 (horizontally)×480(vertically) pixel images and its horizontal view angle is approximately 23 degrees. We also measured angle detection error of this image sensor using a captured image. The angle detection error is approximately 1.5 degrees.

We also examined the positional detection method based on the "corners / edges" detection. A motorized X-Y axis linear stage pair (SIGMA KOKI, SGSP46-500(X) and SGSP65-1200(X)) was used for a simulation of a mobile robot that moves around an obstacle of cuboid set on the flat floor. The turntable in which the laser emitter and the image sensor were attached was put on the X-Y axis linear stage pair. The robot moved from $P_1(x_1,y_1)$ to $P_6(x_6,y_6)$ and the position of the cuboid's edge $P_a(x_a,y_a)$, $P_b(x_b,y_b)$ and $P_c(x_c,y_c)$ were measured. Figure 5 shows experiment environment with an obstacle. Table 1 shows results of this experiment. In the table 1, "x" and "y" are arrangement coordinates. Detected angle θ and ϕ are shown in "angle", "x'" and "y'" are results of triangulation. The detection errors are less than 3% in this experiment.

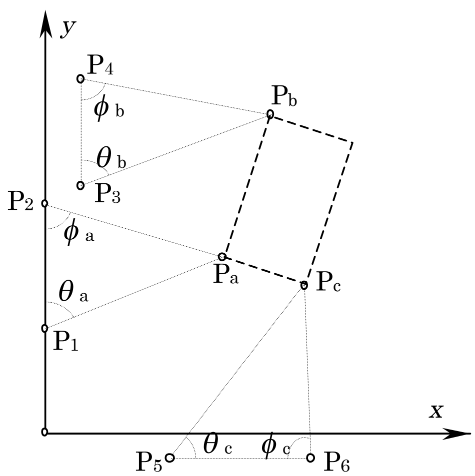

Fig. 5 Experiment environment

Table 1 Results of triangulation

	x	y	angle	x'	y'	reference
P_a	50	50				
P_1	0	30	68.8	49.8	51.0	
P_2	0	65	73.4	49.8	51.0	
P_b	63.5	90				
P_3	10	70	70.4	63.3	89.0	
P_4	10	100	78.3	63.3	89.0	
P_c	72	43				
P_5	35	-7.5	54.8	71.5	44.2	
P_6	75	-7.5	86.1	71.5	44.2	

Length: cm, Angle: deg

Conclusion

We proposed cooperative localization methods using inter-robot communication and fan beam laser. Also we examined the positioning method and successful results were obtained. In this method, accurate reference positions were detected.

If this method is used effectively, the global coordinate axis of the robots' workspace will be acquired.

Acknowledgements

This work is supported in part by Japan Society for the Promotion of Science Grant-in-Aid for Scientific Research (C) (No. 17500118).

References

1. ASAMA H., et al (Eds.) (1994) "Distributed Autonomous Robotic Systems" (DARS), Springer, Tokyo

2. TAKITA Y, et al (1995) "Navigation and Recognition of the Unknown Space Using Infra-red-Following Servo System for Moving Robots", Transactions of the Japan Society of Mechanical Engineers, vol.61, no. 590, series C, pp.209-216

3. TAKAI H., et al. (2005) "A Space-Division Wireless Communication System for Ad Hoc Networking and Cooperative Localization of Multiple Mobile Robots". 16th IFAC World Congress 2005. IFAC, ID:05004

4. TAKAI H. et al (2002) "A Geometric Arbiter Selection Algorithm on Infrared Wireless Inter-robot Communication", Distributed Autonomous Robotic Systems 5 (DARS 5), Springer, Tokyo, pp.61-70

The Eleventh International Symposium on Artificial Life and Robotics 2006 (AROB 11th'06),
B-con Plaza, Beppu, Oita, Japan, January 23-25, 2006

Learning method of cooperative team play using the immune system

Nagahisa Kogawa †

Masanao Obayashi ‡

Kunikazu Kobayashi ‡

Takashi Kuremoto ‡

†Graduate School of Science and Engineering
Yamaguchi University
2-16-1 Tokiwadai Ube , Yamaguchi
755-8611 Japan

‡Faculty of Engineering
Yamaguchi University
2-16-1 Tokiwadai Ube , Yamaguchi
755-8611 Japan

Abstract

In recent years, the immune system came to be well known with the latest development of medicine and physiological research. It is a large-scale system equipped with the complicated biological defense function. It has the function of memorizing and learning.

In this paper, we focus on the immune system described above. And a learning method of a multi-agent system that has features of the immune system is proposed. A soccer problem is considered as a standard problem of the multi-agent system. Therefore we treat this problem, because an environment of agent is dynamical, it is highly complex.

We propose a system that copes well with the problem that when, how and in what situation agent takes an appropriate action for team using reinforcement learning and a method based on immunity such as immune algorithm. It is verified that agents select optimal and cooperative actions in a dynamic environment using the RoboCup Soccer Simulator.

1 Introduction

Information systems that imitate a biological information processing mechanism have been actively researched. The biological information processing mechanism is roughly divided into four parts; a brain nerve system, a genetic system, an internal secretion system and an immune system. From the engineering point of view, the brain nerve system and the genetic system are modeled as neural networks and genetic algorithms, respectively and they have been used in many fields. On the other hand, although both the internal secretion system and the immune system have an advanced information processing mechanism, there are few examples applied in engineering. Especially, the immune system came to be well known with the latest development of medicine and physiological research.

The immune system is a large-scale system equipped with the complicated biological defense function and has the function of memorizing and learning using the interaction between cells such as stimulation and suppression. And the immune system means a system that uses features of the immune information processing mechanism in a broad sense. This system is equal to artificial neural network that consists of neurons corresponding to immune cells which have the ability to adapt and learn. And the system implements a task in alliance with each immune cell using a dynamical network, maintains diversity by recombining genes and has a strategy that controls these characteristic and diversity.

In this paper, we focus on the immune system described above. And a learning method of a multi-agent system that has features of the immune system is proposed

Recently the multi-agent system has attracted attention of many researchers as an important research object of complex systems. An unexpected aspect appears as the whole system as a result of interaction among agents. It is called emergence in the multi-agent system. The emergence cannot be throughly understood by analyzing only composite elements. It is important to analyze emergence in the multi-agent system research. The assignment roles as the whole system emerge with the result that multiple autonomous agents effectively implement a task. It is one of phenomenon of emergence. It is generally said that researches on complex system refer to solve phenomenon like this.

A soccer problem is considered as a standard problem of the multi-agent system. Therefore, we treat this problem. This problem is dynamical. An environment of agent is highly complex. A performance of the whole system can be clearly evaluated based on an explicit criterion, such as the number of goals. However it is difficult to determine when, how and in what situation agent takes an appropriate action for team from peformance evaluation point of view and also from action selection point of view. Therefore the soccer problem is standard one in multi-agent system. We study how to realize a cooperative behavior by soccer players. And it is expected that various knowledge acquired in construction of effective agent group is applicable to general multi-agent systems [1].

A lot of researches using the RoboCup Soccer Simulator have been conducted for many purposes. For example, Murata et al. proposed a method of dynamically arranging soccer agent using genetic algorithms [2]. Irie et al. presented a method that action value function of various local goal is designed [3]. Kumada et al. showed a soccer agent with ability to predict other agents [4]. Ishiguro et al. proposed a method of arbitrating among mobile robots using immune network as a research of robustness by adaptability and diversity of immune type system [5].

In this paper, a new agent's model that has feature of the immune system is constructed to correspond to a dynamical environment of soccer problem. And the way to learn and emerge cooperative behavior between agents is studied. The proposed system copes well with the problem that when, how and in what situation agent takes an appropriate action for team using reinforcement learning and a method based on immunity such as immune algorism. It is verified that agents select optimal and cooperative actions in a dynamic environment using the RoboCup Soccer Simulator.

2 Proposed system

A concept of the immune system that is applied to soccer problem is proposed. First, an antigen has an environmental information which each agent obtains. And an antibody has an antigen's information and agent's action against the antigen. Next, soccer team is regarded as one living body. Each agent gets environmental information obtained from real-time simulator and select an action against the antigen. Then this environmental information and this action are added to a group of antibodies as an antibody. It is impossible to prepare antibodies corresponding to all situations in advance. Therefore antibodies are created and added.

Each agent belongs to a team selects an antibody corresponding to an antigen from the team's group of antibodies. That is, each agent creates a new antibody and implements action of antibody or selects an antibody from the group of antibodies and implements action of antibody.

Next, a history of selected antibodies is memorized in each agent. Reinforcement learning is implemented with these histories. And antibodies are evaluated. An optimization using the immune system such as selection, crossover, mutation and memorization is performed against evaluated antibodies. It is expected that certain strategy arises from above processes.

2.1 Definition of antigen

Circumference of an agent is divided into totally 24 areas; eight directions and three distances, as shown in Figure 2. Each agent gets positions of objects from information obtained from the simulator. And each agent calculates which area each object exists in. Then whichever object exists in, it is represented as binary digit.

Totally 63 bits is assigned to an antigen. The three 5-bits are assigned to information on a ball, goals of partners and opponents. Each 5-bits presents an area where each object exists in. The two 24-bits are assigned to information on partners and opponents. Each 24-bits presents whether object exists in each area or not. It is possible that circumference of an agent is simply presented using the above way.

The structure of an antigen is shown in Figure 1.

Antigen

Ball	Our goal	Opponent goal	Partners	Opponents

Figure 1: Structure of an antigen

2.2 Perceptive area of agent

The perceptive area of an agent represents circumference of the agent. Environmental information has only frontal information of the agent from simulator per step. And thus the agent gets environmental information to search around during certain times in order to get the information on circumference.

The perceptive area of an agent is shown in Figure 2.

2.3 Definition of antibody

An antibody consists of an antigen's information and an action part corresponding to the antigen. The action part is constructed from a basic action and an action parameter. The basic action is three kinds; kick, move and wait. The action parameter presents direction and elapsed time of basic action. Antibody is also represented as binary digit. Totally 70 bits is

The Eleventh International Symposium on Artificial Life and Robotics 2006 (AROB 11th'06),
B-con Plaza, Beppu, Oita, Japan, January 23-25, 2006

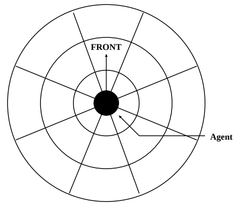

Figure 2: Perceptive area of an agent

assigned to an antibody. The 63 bits are assigned to an antigen. Totally seven bits is assigned to an action part. The two bits and five bits are assigned to a basic action and an action parameter respectively. The basic action presents a series of actions. For example in case of kick a series of actions means that the agent approaches to a ball and kicks to a certain direction during certain period.

It is expected that phenomenon of pass arises from wait as basic action. And an antibody has a value that is evaluation of the antibody. The value is used to select an antibody against an antigen and is updated by reinforcement learning.

The structure of an antibody is shown in Figure 3.

Antibody			
Antigen	Action	Direction and Time	Evaluation

Figure 3: Structure of an antibody

2.4 Definition of action

Actions of agent are designed in advance. The kick and move are defined by eight directions and three distances, namely the kick or move correspond to each perceptive area. The wait is designated to waiting time in three levels corresponding to distance of perceptive area. Actions of kick and move are shown in Figure 4.

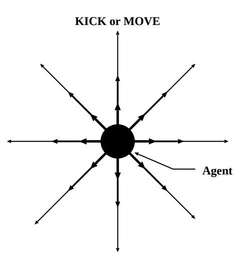

Figure 4: Action of agent of the proposed system

2.5 Selection of antibody

In the proposed system, each agent selects antibodies corresponding to an antigen from the group of antibodies. Moreover, each agent selects an antibody by softmax method with boltzmann distribution using evaluation of antibodies. And also each agent creates a new antibody for searching when no antibody corresponds to the antigen. In this way, one antibody is chosen from group of antibodies and action is determined.

2.6 Learning method

2.6.1 Evaluation of antibody

It is difficult to determine when, how and in what situation agent takes an appropriate action for team from performance evaluation point of view and also from action selection point of view. The evaluation of the antibody is determined using reinforcement learning. In the proposed system, profit sharing is used. It has following features. The evaluation value is immediately reinforced with experience. And profit sharing can be adapted to multi-agent system.

2.6.2 Optimization of group of antibodies

The optimization using the immune system such as selection, crossover and mutation is implemented after evaluation of antibodies is determined using reinforcement learning. In case of using only reinforcement learning, it is supposed that efficient search to the environment cannot be conducted. It is expected that useful knowledge is obtained by reinforcement learning to an inexperienced environment.

In selection part, if antibodies have negative evaluation value, these are eliminated. In crossover part, new antibodies are produced from antibodies that have high evaluation value by one-point crossover. In memorization part, if antibodies have sufficiently high evaluation value, these are memorized. Then the agent doesn't search anyone when antigens corresponding to these antibodies are selected. Therefore it is supposed that learning speed of other antibodies is accelerated. Finally, it is expected to get optimal group of antibodies.

3 Computer simulation

A team is constituted of three agents. An opponent team is constituted of three agents that have a fixed simple strategy. That is, the agent kicks a ball if it exists near the agent. All soccer games are played on the RoboCup soccer simulator. It is verified that a performance of the proposed system to solve a soccer problem that a few player learns action of pass on local soccer filed.

Figure 5 and 6 show the number of reward acquisitions against pass per 1,000 episodes. Figure 5 shows results of the proposed system and a conventional method. Profit sharing is adopted as the conventional method.

Figure 6 shows a result of the proposed system with a priori knowledge. The knowledge is generally common sense for soccer. That is, (1) An agent can select the kick action only if the ball is near to the agent. (2) An agent can kick the ball only toward only the areas where partners exist in. (3) An agent can move only toward the areas where other agents don't exist in except for the area where the ball exists in.

The number of reward acquisitions against pass using the proposed method is increasing from about 11,000 episodes. On the other hand, that using the conventional method is increasing from about 21,000 episodes. Therefore the proposed method has higher ability to explorer than the conventional method. Moreover the proposed system with a priori knowledge has higher ability than them. It is effective to use the knowledge about common sense for soccer in this problem so that the state space of the problem is too large.

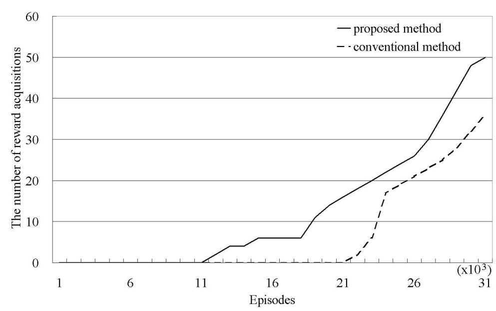

Figure 5: Result of the proposed and conventional methods

4 Summary

We propose a system that copes well with the problem that when, how and in what situation agent takes an appropriate action for team using reinforcement learning and a method based on immunity such as immune algorithm. The performance of the proposed system is evaluated using soccer problem that a few player learn action of pass on local soccer filed. It is sure that the proposed method is better than the conventional method. But it is necessary to improve the proposed method, because its convergence speed is slow. In this research, the problem that is to pass at the back of opponents is treated. The action of pass is evaluated clearly. But it is important to analyze phenomenon of emergence in multi-agent system. A future subject is to emerge action of pass to devise architectures of individual agent without evaluating immediate action of pass.

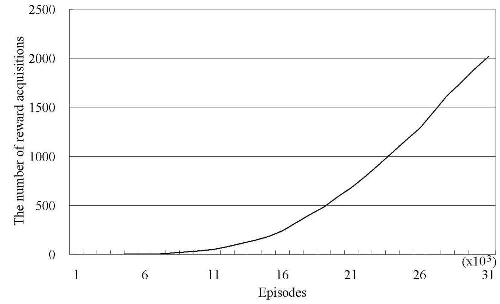

Figure 6: Result of the proposed method with a priori knowledge

It is difficult to determine when, how and in what situation agent takes an appropriate action for team from performance evaluation point of view and also from action selection point of view. Moreover there are many problems; the state explosion problem, the problem caused by asynchronous system. More excellent learning method is necessary to adapt these problems.

Acknowledgements

We thank the reviewers for their comments and suggestions to improve this paper.

References

[1] A. Ohuchi, M. Yamamoto, H. Kawamura, *Theory and Application of Multi-agent Systems -Computing Paradigm from Complex Systems Engineering-*, Corona Publishing, 2002 (in Japanese)

[2] T. Murata, K. Suzuki, A. Ohuchi, "Dynamic Position Arrangements of Soccer Agents with Genetic Algorithms", *Journal of the Japanese Society for Artificial Intelligence*, Vol.14 No.3, pp. 446-454, 1999 (in Japanese)

[3] T. Irie, N. Inui, Y. Kotani, "Design of an Action Value Function of various Local Goal in RoboCup Soccer", *Research of Information Processing Society of Japan Game Informatics*, Vol.4 No.8, pp. 47-54, 2000 (in Japanese)

[4] Y. Kumada, K. Ueda, "Emergence of Cooperative Tactics by Soccer Agents with Ability of Prediction and Learning", *Lecture Notes in Computer Science*, Vol.2159, pp. 539-542, 2001

[5] T. Kondo, A. Ishiguro, Y. Watanabe at el., "Evolutionary Construction of an Immune Network-Based Behavior Arbitration Mechanism for Autonomous Mobile Robots", *Electrical Engineering in Japan*, Vol.123 No.3, pp.1-10, 1998

The Eleventh International Symposium on Artificial Life and Robotics 2006 (AROB 11th'06),
B-con Plaza, Beppu, Oita, Japan, January 23-25, 2006

A Study on Stability Analysis of Cooperative AGV Systems using Decentralized Control Algorithm

Jin Ho Suh
Dept. of Electrical Engineering
Dong-A University
840, Hadan-dong, Saha-gu, Busan, Korea
suhgang@donga.ac.kr

Young Bok Kim
Dept. of Control and Mechanical Engineering
Pukyong National University
San 100, Yongho-dong, Nam-gu, Busan, Korea
kpjiwoo@pnku.ac.kr

Kwon Soon Lee
Dept. of Electrical Engineering
Dong-A University
840, Hadan-dong, Saha-gu, Busan, Korea
kslee@dau.ac.kr

Keywords: Automatic guided vehicle (AGV), Passive velocity field control (PVFC), Decentralized control

Abstract

In this paper, we propose the stability analysis to apply decentralized control to cooperative AGV systems whose subsystems are under nonholonomic constraints and convey a common rigid object in a horizontal plain. Moreover, it is shown that multiple AGV systems ensure stability and the velocities of augmented systems converge to a scaled multiple of each desired velocity field for cooperative mobile robot systems. Finally, the application of proposed virtual passivity-based decentralized algorithm via system augmentation is applied to trace a circle.

1. Introduction

A wheeled mobile robot named automatic guided vehicle (AGV) is an important element to convey work in the present flexible material handling system of factory automation and robots with the various kinds of payloads are developed. Therefore, we take a great interest in the cooperative object-transportation system by multiple vehicles.

However, the passive velocity field control (PVFC) algorithm applied to a single manipulator could not extend to multiple AGV systems [2]. Especially, multiple robotic systems can execute various tasks which could not be done by a single manipulator such as the handling of a heavy object, for example, transportation of port containers using cooperative AGV systems. Therefore, many control algorithms have been proposed for the coordinated motion control of multiple robot systems. Moreover, various decentralized control algorithms have been proposed to overcome some problems of the centralized control algorithm in which each robot system is controlled by its own controller without explicit communication among cooperative systems.

2. The proposed decentralized control algorithm for cooperative AGV systems

2.1. Cooperative AGV systems

We consider a case where two AGVs convey a rod for simplicity, however, the similar discussion can be applied for cases where AGVs arre carrying a general planer rigid object. In this section, we describe the configuration of cooperative AGVs as shown in Fig. 1. In considered systems, an object denoted by a rod is connected to each mobile robot by a free joint without friction and the length of an object is 2L.

From the kinematic constraints by the passive joints, the holonomic constraints between the generalized coordinates are defined as follows:

$$\begin{pmatrix}\bar{x}_1\\ \bar{y}_2\end{pmatrix}=\begin{pmatrix}x_1-h\sin\theta_1\\ y_1+h\cos\theta_1\end{pmatrix}=\begin{pmatrix}x_c-L\cos\varphi\\ y_c+L\sin\varphi\end{pmatrix} \tag{1}$$

$$\begin{pmatrix}\bar{x}_2\\ \bar{y}_2\end{pmatrix}=\begin{pmatrix}x_2-h\sin\theta_2\\ y_2+h\cos\theta_2\end{pmatrix}=\begin{pmatrix}x_c+L\cos\varphi\\ y_c-L\sin\varphi\end{pmatrix} \tag{2}$$

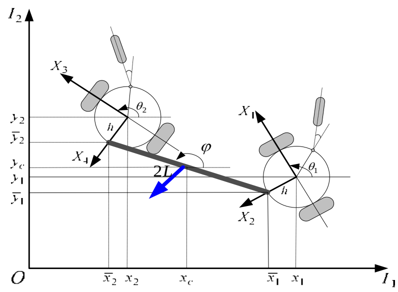

Fig. 1 Configuration of 3-wheeled AGV systems for moving a rigid object

If we define the constraint force, the actual dynamic equation of whole system can be decomposed into the following equations

$$H_i(\beta_i)\dot{\eta}(t)+f_i(\beta_i,\eta_i)=G_i(\beta_i)\tau_{mi}-J_i^T\lambda_i \tag{3}$$

$$M_o\ddot{x}_o=-J_o^T\lambda\ ,\quad I_o\ddot{\varphi}=-J_\varphi^T\lambda \tag{4}$$

Then, we can define a local control input given by

$$\tau_{mi}=G_i^{-1}(H_i v_i+f_i+J_i^T\lambda_i)-G_i^{-1}H_iJ_i^T\lambda_i \tag{5}$$

where v_i $(i=1,2)$ is new input. If we inject new control input v_i into cooperative mobile robots. Therefore, the actual dynamic equation of whole system is represented by

$$\overline{M}_w\ddot{x}_w=\overline{G}_w v(t)-J_w^T\lambda \tag{6}$$

2.2. Decentralized control algorithm

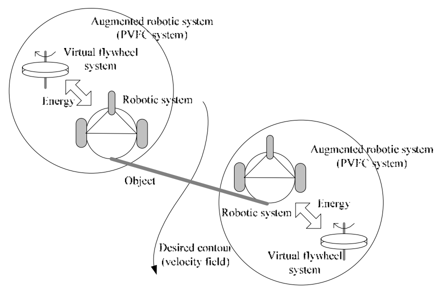

Fig. 2 Configuration of cooperative AGV systems with virtual-based flywheel system

The proposed scheme is shown in Fig. 2. Also, if the actual control input is defined as

$$v_1=v_1'-\begin{pmatrix}I_{2\times 2} & 0_{2\times 2}\end{pmatrix}\left(J_\varphi\ddot{\varphi}+\dot{J}_\varphi\dot{\varphi}\right) \tag{7}$$

$$\nu_2 = \nu_2' - \begin{pmatrix} 0_{2\times2} & I_{2\times2} \end{pmatrix}(J_\varphi \ddot{\varphi} + \dot{J}_\varphi \dot{\varphi}) \quad (8)$$

Adding the dynamic equation of x_o, we can describe the motion equation of an object as follows:

$$(I_{2\times2} + M_o + I_{2\times2})\ddot{x}_o = \nu_1' + \nu_2' \quad (9)$$

First of all, the procedure in order to apply an individual PVFC algorithm can be designed that the motion equation in Eq. (9) is separated as the following virtual dynamic equation

$$\overline{M}_i'\ddot{x}_o = \nu_i' \quad (i=1,2) \quad (10)$$

where $\rho_i\ (i=1,2)$ is load sharing coefficient and it is satisfied with $\rho_1 + \rho_2 = 1$.

Also, the dynamics of the virtual flywheel is given by

$$M_{fwi}\ddot{x}_{fwi} = \nu_{fwi} \quad (i=1,2) \quad (11)$$

where ν_{fwi} is the coupling control input to the flywheel. Thus, the dynamics of the augmented system are composed as follows:

$$\overline{M}_{ai}'\ddot{X}_{ai} = \nu_{ai}' \quad (i=1,2) \quad (12)$$

where $\dot{X}_{ai} = \begin{pmatrix} \dot{x}_o & \dot{x}_{fwi} \end{pmatrix}^T$ is the velocity of the augmented system, ν_{ai}' is the augmented control input, and $\overline{M}_{ai}'$ is the augmented inertia matrix and is defined by

$$\overline{M}_{ai}' = \begin{pmatrix} \overline{M}_i' & 0 \\ 0 & M_{fwi} \end{pmatrix} \quad (13)$$

For each X_{ai}, we can define the kinetic energy of the augmented dynamic system, $\overline{H}_a'$ which is expressed in local coordinate by

$$\overline{H}_a' = \sum_{i=1}^{2} \frac{1}{2}\dot{X}_{ai}^T \overline{M}_{ai}' \dot{X}_{ai} \quad (14)$$

Theorem 1: *Consider the decentralized PVFC as shown in Fig. 2 where the motion equation is given by Eq. (10), and the individual PVFC control law consists of the virtual dynamic augmentation Eq. (11) and coupling control law Equation. Furthermore if the control input about control internal force is defined by*

$$\nu_{Ii}' = (1 + k_f)\begin{pmatrix} F_{di} \\ 0 \end{pmatrix} \quad (15)$$

and an actual control input about given system ν_i' *is also defined by*

$$\nu_i' = \nu_{ai}' + \nu_{Ii}' \quad (i=1,2) \quad (16)$$

where ν_{Ii}' *is desired internal force and satisfies* $\nu_{I1}' + \nu_{I2}' = 0$. *Then the passivity and convergence properties of decentralized PVFC are summarized as follows:*

(1) The augmented feedback system is passive with respect to the supply rate defined by

$$s(F, \dot{x}) = \langle F, \dot{x} \rangle = F^T \dot{x} \quad (17)$$

where F *and* $\dot{x}$ *are input and output.*

(2) For the augmented α_i*-velocity error* $e_{\alpha i}$*, the velocity of an object* $\dot{X}_{ai}$ *is a Lyapunov stable solution in the absence of environment forces.*

Proof of (1): The derivation of kinetic energy defined by

$$\overline{H}_{ai}' = \sum_{i=1}^{2} \frac{1}{2}\dot{X}_{ai}^T \overline{M}_{ai}' \dot{X}_{ai} = \overline{E}_i > 0 \quad (18)$$

Then,

$$\begin{aligned} \frac{d}{dt}\overline{H}_{ai}' &= \sum_{i=1}^{2}(\dot{X}_{ai}^T \overline{M}_{ai}' \ddot{X}_{ai} + \frac{1}{2}\dot{X}_{ai}^T \dot{\overline{M}}_{ai}' \dot{X}_{ai}) \\ &= \sum_{i=1}^{2}(\dot{x}_o^T \overline{M}_i' \ddot{x}_o + \dot{x}_{fwi}\underbrace{M_{fwi}\ddot{x}_{fwi}}_{=\nu_{fwi}}) + \frac{1}{2}\sum_{i=1}^{2}\underbrace{\dot{X}_{ai}^T \dot{\overline{M}}_{ai}' \dot{X}_{ai}}_{=0} \\ &= \sum_{i=1}^{2}\underbrace{\dot{X}_{ai}^T \overline{G}_{ai}' \dot{X}_{ai}}_{=0} + \underbrace{\dot{X}_{ai}^T \overline{R}_{ai}' \dot{X}_{ai}}_{=0} = 0 \end{aligned} \quad (19)$$

Therefore, upon integration of Eq. (19), we can obtain

$$\int_0^t \dot{\overline{H}}_{ai}'(t)dt = \overline{H}_a'(t) - \overline{H}_a'(0) = 0 > -\overline{H}_a'(0) \quad (20)$$

Since $\overline{H}_a'(0) \geq 0$, the system is passive with respect to the supply rate.

Proof of (2): Given $\alpha \in \Re$, let's define the positive definite storage function $\overline{W}_\alpha$ as follows:

$$\overline{W}_\alpha = \frac{1}{2}\sum_{i=1}^{2} e_{\alpha i}^T \overline{M}_{ai}' e_{\alpha i} \quad (21)$$

Differentiating Eq. (21) and the fact that $\dot{\overline{M}}_{ai}' + 2\overline{G}_{ai}'$ is skew symmetric, we obtain

$$\begin{aligned} \frac{d}{dt}\overline{W}_\alpha &= \frac{1}{2}\sum_{i=1}^{2}(\dot{e}_{\alpha i}^T \overline{M}_{ai}' e_{\alpha i} + \underbrace{e_{\alpha i}^T \dot{\overline{M}}_{ai}' \dot{e}_{\alpha i}}_{=0} + e_{\alpha i}^T \overline{M}_{ai}' \dot{e}_{\alpha i}) \\ &= -\sum_{i=1}^{2}\alpha_i \gamma_i (4\overline{H}_{ai}' \overline{E}_i - \langle\langle V_{ai}, \dot{X}_{ai} \rangle\rangle_{ai}^2) \leq 0 \end{aligned} \quad (22)$$

Since $\overline{W}_\alpha$ is a positive definite function of α_i-velocity error $e_{\alpha i}$, we know that the augmented α_i-velocity error $e_{\alpha i} = 0$ is Lyapunove stable of the error dynamics using Barlalet's lemma [3] ■

3. Conclusions

In this paper, we propose a new control methodology for cooperative AGV systems systems convey a rigid object, and the proposed decentralized control algorithm is also analyzed using passive velocity field control algorithm. Especially, the closed-loop input/output systems for multiple AGV systems are passive with the environment force as inputs, the system velocities as outputs, and the environment mechanical powers as supply rates as if it is similar to an original passive velocity field contorl.

Acknowledgement

This work was supported by grant No. R01-2005-000-10418-0 from Korea Science and Engineering Foundation in Ministry of Science & Technology.

References

[1] G. Campion, G. Bastin, and B. D'Andrea-Novel, "Structural properties and classification of kinematic and dynamic models of wheeled mobile robots," *IEEE Trans. on Robotics and Automation*, Vol.12, No.1, pp. 47-62, 1996.

[2] P. Y. Li and R. Horowitz, "Passive velocity field control (PVFC) Part I –Geometry and Robustness-," *IEEE Trans. on Automatic Control*, Vol.46, No.9, pp. 1346-1359, 2001.

[3] J. J. Slotine and W. Li, *Applied Nonlinear Control.* Prentice-Hall, New Jersey, 1991.

[4] J. H. Suh, et. al., "Decentralized control of cooperative 3-wheeled mobile robots using passive velocity field control," *In Proc. of Int. Sym. on AROB*, pp. 433-436, 2004.

The Eleventh International Symposium on Artificial Life and Robotics 2006 (AROB 11th'06),
B-con Plaza, Beppu, Oita, Japan, January 23-25, 2006

Development of learning support system for piano-keying - Relationship between the activity of finger muscles and key release velocities of an expert -

Tomoya Tamei Tomohiro Shibata Shin Ishii
Graduate School of Information Science, Nara Institute of Science and Technology
8916-5, Takayama, Ikoma, Nara, 630-0192 Japan
tomo-tam@is.naist.jp

Abstract

This study aims at comparing behaviors of an expert piano player between two contrasting piano-keying cases: when a player applies significant force to keys (case A) and when the same player relaxes their muscles as much as possible (case B). For this, we developed a simultaneous measurement system for the motions of an index finger and a key, and for Electromyographic (EMG) signals of the index finger. The results acquired in a pilot experiment show the clear difference in the key motion and the EMG signals between the two cases. Additionally, we found the strong correlation between extensor muscle activities and the key-release velocities. The results suggest that the developed measurement system has a possibility to evaluate the proficiency of pianists in particular for relaxed keying motions.

1 introduction

Observing and imitating the motions of an expert of, for example, sports and playing an instrument are a good starting point for amateurs. It is, however, necessary to know the time course of appropriate force for each muscle movement, because it is generally thought that the motor program of experts is optimized to achieve highest accuracy with a minimum effort, whereas amateurs often give much amount of force, which hinders appropriate learning. Furthermore, trainers often refer to the importance of relaxation of muscles because uneconomic use of force hinders learning, and may incur injuries. To our knowledge, there are very few motor learning support systems which is not only for learning motions of experts but also for learning appropriate time course of force to be suitable to learner's muscles.

The arguments above are applicable to piano-playing. It is often said that the relaxation of player's muscles is important to achieve deft and fine finger movements or rich expression by producing sweet sound. How to relax muscles during the play is hard to learn even for students who have studied piano-playing for a long time.

Therefore, we confine our interest to the simple piano-keying with an index finger, and investigate the difference in skill of piano-keying between beginners and experts, and search for indices for muscle relaxation of players during piano-playing.

There are some previous studies related to this study. Parlitz et al. measured keying force from expert and amateur pianists at 'tied finger exercise' by means of a pressure sensor sheet placed beneath keys [1]. Their results indicated that amateur pianists often take much amount of force to achieve the same tempo and volume as those of experts. They also found that experts strike keys with less effort than amateurs. Their study, however, did directly focused on relaxed playing, nor measure player's muscle activities. Oshima et al. investigated the relationship between key-release velocity and sound proficiency with a note of the importance of the relaxation in player's muscles [2]. They, however, did not measure muscle activities and henceforce were not concerned the relationship between the muscle activities and key key-release velocities.

This article first presents our simultaneous measurement system for joint angles, displacements of keys, and Electromyographic (EMG) signals of a player's index finger to make their concern clear. We then show the results of recording behaviors of an expert piano player using this apparatus. We show our system successfully captures salient and direct features of an expert, indicating the relationship between the key-release velocity and muscle relaxation.

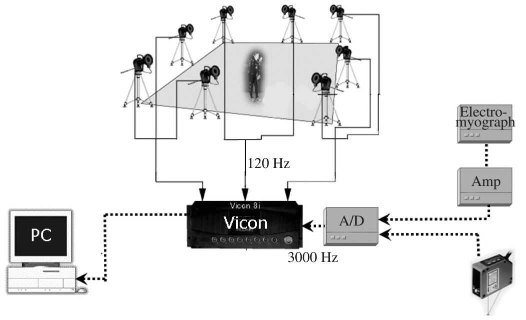

Figure 1: System configuration

Figure 2: Marker locations

Figure 3: Electrode locations

2 Methods

2.1 System configuration

Figure 1 shows our developed system for measuring simultaneously motion, EMG and the displacement of a key. We used an optical motion capture system Vicon512 (Oxford Metrics) for measurement of motions at a sampling frequency of 120 Hz.

EMG signals were measured by an electromyograph BA1104m (DEGITEX LABORATORY) with active-type electrodes. The displacement of a key was measured with a laser displacement sensor CD3-250 (SICK OPTEX). The outputs of them were input to an A/D converter of Vicon512, which enabled synchronized recording of motion data and other data. The sampling frequency was 3000 Hz for recording of the EMG and the displacement, while 120 Hz for motion as described above. The postprocessing of EMG signals will be described below.

2.2 Measured joints and finger muscles

In this study, MP, PIP and DIP joints of the right index finger were measured. We attached infrared reflection markers for motion capturing to five points: fingertip, DIP, PIP and MP joints and the back of the subject's right hand as shown in Figure 2. We measured EMG signals of external muscles of the index finger at four points as shown in Figure 3. Two of them were flexor muscles: flexor digitorum superficialis (FDS) and flexor digitorum profundus (FDP), and the other two were extensor muscles: extensor digitorum (ED) and extensor indicis (EI).

2.3 Procedure

We conducted experiments where a subject was requested to strike a piano key repetitively with an index finger of the right hand by moving the three finger joints.

The subject was a healthy adult woman who majored at a music college in piano-playing and was a piano instructor with years of experience. She understood our research aim.

She sat on a chair and placed from her elbow to ahead of wrist (locality of carpus) of the right arm on the armrest in order to use only three joints of an index finger without using other joints such as a shoulder, elbow and wrist as much as possible. She was instructed to be relaxed as possible as she was able to do, (Figure 3).

The subject was instructed to let the key down synchronized with a metronome under four conditions as follows:

- ARCH1: let a key down every one meter in time with the tempo of M.M.=50 with a natural form (arched) of fingers.
- ARCH2: let a key down every two meters in time with the tempo of M.M.=50 with natural form (arched) of fingers.
- EXTE1: let a key down every one meter in time with the tempo of M.M.=50 with the PIP and DIP joints being extended, but by moving mainly the MP joint.
- EXTE2: let a key down every two meters in time with the tempo of M.M.=50 with the PIP and DIP joints being extended, but by moving mainly the MP joint.

Each task consisted of keyings of 10 times for each of the two cases: the subject was instructed to apply significant force to a key (case A), or was instructed to relax her muscles as possible as she can during keying (case B).

2.4 Data processing

The motion data of an index finger were used to calculate the joint angles of MP, PIP and DIP based on the acquired three-dimensional information of the 5 markers. The joint angle data were smoothed by a second-order Butterworse filter at a cuttoff frequency of 3 Hz.

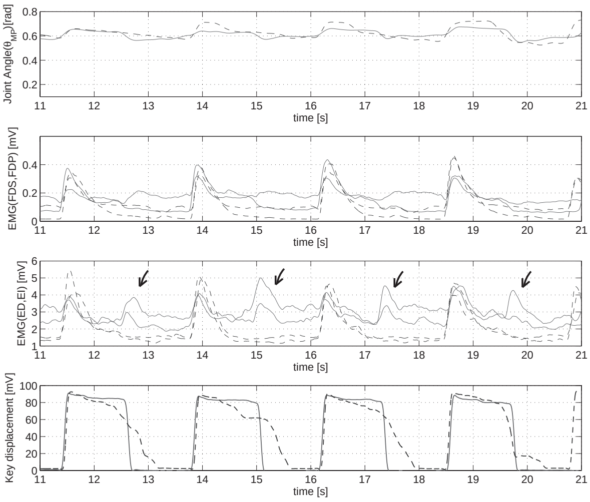

Figure 4: Sample time course of joint angles, EMGs, and key displacements during condition ARCH2

The EMG signals were down-sampled by taking the average of every 25 points after full-wave rectification. The sampling rate of the EMG signals henceforce became 120 Hz which was the same as the sampling rate of motion capturing. Additionally, we performed smoothing by taking the moving average over five points:

$$EMG_{ma}(t) = \frac{1}{5} \sum_{i=-2}^{2} EMG_{ave}(t-i). \quad (1)$$

Next, the data were filtered by a second-order low-pass filter proposed by Akazawa [3] which is known to be effective in approximating the tension in a muscle. The impulse response function of the Akazawa filter is:

$$h(t) = 6.44 \times \left(e^{-10.80t} - e^{16.52}\right). \quad (2)$$

Both the key displacement and motion data were smoothed by a second-order Butterworse filter at a cuttoff frequency of 10 Hz.

3 Results

A sample result acquired in condition ARCH2 is shown in Figure 4. The top, the second, the third and the bottom panels present time course of the MP joint angles, flexor muscles (FDS and FDP), extensor muscles (ED and EI) and the key displacement, respectively. In the bottom panel, higher displacement corresponds to keying down. For all panels, solid lines and dashed lines denote the results of case A and case B, respectively.

As shown in Figure 4, EMG signals in case A are generally higher than in case B. In both of the cases, the flexor and extensor muscles were activated when

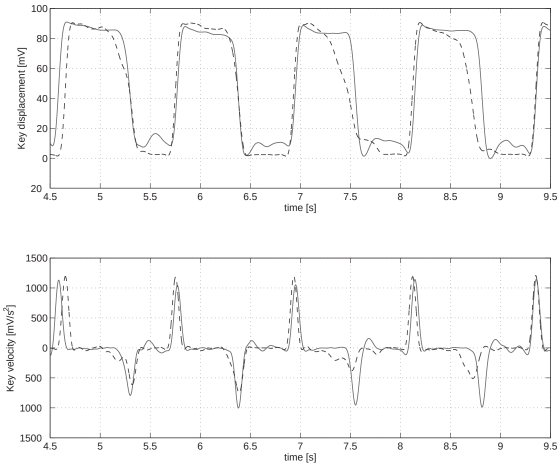

Figure 5: Key-touch and key-release velocities during condition ARCH1

the key was pressed. The extensor muscles, however, were not activated in case B during key-release whereas they were activated in case A (indicated by arrow in the third panel of Figure 4).

It appears less difference between the two cases when the subject stroke a key, while the difference during key-release is clearly shown; the displacement of the key changed more gently in case B. We calculated the key velocities by taking the difference of adjacent key displacements to investigate if there was difference in key-touch velocity or key-release velocity between the two cases. An example result of ARCH1 is shown in Figure 5. The top panel shows the time course of key displacements, and the bottom panel presents the corresponding key velocities. The solid lines denote the results in case A and the dashed lines case B. In the bottom panel, positive peaks correspond to key-touch timings, while the negative peaks correspond to key-release timings.

We found that there is seemingly a strong relationship between extensor muscle activities and key-release velocities at a key-release period in both cases. Figure 6 actually depicts that there is a strong correlation between the extensor muscle (ED) activities and the key-release velocities. This figure shows normalized maximum key-release velocity at the peak EMG of ED during the key-release period, acquired in every task. Each line presents a regression line over data points in each task. Moreover, in order to examine the difference in key-release velocity in the case B over different experimental conditions, i.e., the finger form and the number of keying meters, we performed two-way analysis of variance (ANOVA), and found:

- the finger form: no significant difference (p-value: 0.665),

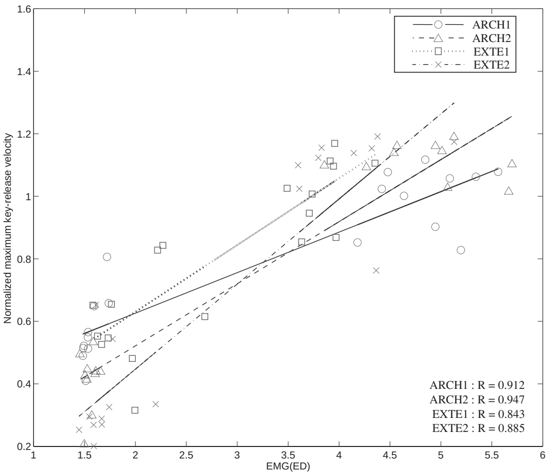

Figure 6: Correlations between extensor muscle activities and maximum key-release velocities

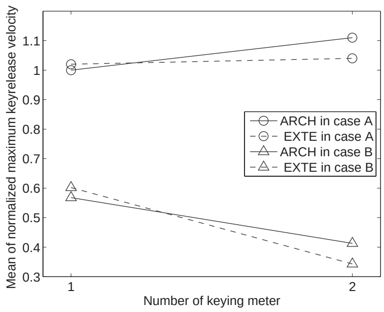

Figure 7: The averaged normalized maximum key-release velocity

- the number of keying meters: a significant difference (p-value: 0.000),
- interaction: no significant difference (p-value: 0.212).

These results indicate that the velocity difference was due to the number of keying meters, but not to the other factors. The averaged normalized maximum key-release velocity for each experimental condition is shown in Figure 7.

4 Discussion

In this study, the most salient difference in activation patterns between flexor and extensor muscles were observed during the key-release period in case A.

As shown in the third panel of Figure 3, the extensor muscles activated not only during key-touching periods but also during key-releasing periods indicated by arrows in the figure in case A (cf. solid lines), but not in case B (cf. dashed lines), while such secondary activations are not observed for the flexor muscles as presented in the second panel of this figure. These results would support a common belief among pianists that a certain sweet sound on a key can be generated by feeling the force to the finger applied by the key during releasing.

As contrasted to the key-release period, there were no such difference in the activation pattern between the flexor muscles and the extensor muscles during the key-touching period. Both muscles were simultaneously activated in both case A and B, while the activity of the flexor muscles were higher than that of the extensor muscles, which simply means the stiffness of joints were higher in case A than in case B.

Key-release velocities in case B were slower than in case A in either task, as clearly shown in Figure 7. We further found that there is a strong correlation between the extensor muscle activities and the key-release velocities as shown in Figure 6. As a consequence, measuring extensor muscles during the key-release period gives a useful index of key-release velocity involving in generating certain sweet sound (cf. [2]).

In addition, the subject reported a difficulty in ARCH1 and EXTE1 tasks in which the subject were required to let a key down every one meter; letting down a key every one meter requires higher key-release velocity compared to the tasks to do the same thing every two meters. Figure 7 actually reflects what she mentioned.

Integrating sound recording and analysis into our system is necessary because we need to define a certain goal to be achieved as a sound.

Acknowledgement

We thank Dr. Oshima at ATR Media Information Science Laboratories, for giving us a lot of useful comments.

References

[1] D.Parlitz, T.Peschel, and E.Altenmular. Assessment of dynamic finger forces in pianists: Effects of training and expertise. *J Biomechanics*, 31:1063–1067, 1998.

[2] C.Oshima, K.Nishimoto, and M.Suzuki. Effects of key-release velocity in piano performance -basic analyses on features of low key-release velocity points-. 2004-MUS-056:15–20, 2004.

[3] Y.Koike and M.Kawato. Estimation of dynamic joint torques and trajectory formation from surface electromyography signals using a neural network model. *Biological Cyberbetics*, 73:291–300, 1995.

Implementation of infrared wireless communication system for multi-mobile robots' team operations

Hiroyuki Takai*, Toshio Ninomiya* and Keihachiro Tachibana**

*Graduate School of Information Sciences, Hiroshima City University
3-4-1 Ozuka-Higashi, Asa-Minami, Hiroshima 731-3194 JAPAN

**Graduate School of Computer Science, Osaka Gakuin University
2-36-1 Kishibe-Minami, Suita, Osaka 564-5811 JAPAN

Abstract

Recently, mobile robots' team operation has been proposed as one of the effective solutions that enable the execution of complicated tasks [1]. These robots that join team operations need to communicate mutually for smooth task execution. Although radio waves are usually used for mobile robot's remote control or communication of mobile computer terminals, one drawback is that they spread out signals omni-directionally that can cause communication interference.

We have proposed an infrared wireless communication system that can detect angle of arrival (AOA) of infrared signals from communicating partners for mobile robots' team operations. Infrared rays have strong directivity and limited beam width. They are advantageous to communicate between adjacent robots, since they can decrease communication interference. Signal intensity decreases with the square of the communicating distance. Also the reception capability is in inverse proportion to the data transmission rate. Transmission efficiency and reception capability are also restricted by the performance of the circuit elements such as infrared LEDs and photo diodes.

A position sensitive device (PSD) PIN photo diode (HAMAMATSU S6560) that can detect incidence angle of infrared rays is used as the reception device of this infrared wireless communication system. This PSD has 2 current output electrodes and these ratios show the incidence angle. We implemented communication signal amplifiers and threshold decision mechanisms that can restore digital pulse signals from received analog signals. These electronic circuits were tested and successful results were obtained.

1. Introduction

In recent years, multiple mobile robots that can perform team operations have been developed. These robots are used for SAR (search and rescue) operation, surveillance, patrol and so on. When the number of robots increases in the same workspace to accomplish their tasks, they will often collide or interfere with adjacent robots. Therefore, they need to communicate to decrease their collisions in order to achieve their tasks smoothly. Radio waves or infrared rays are used as carriers in inter-robot communication.

Usually, radio waves are used for mobile robots' remote control or communication of mobile computer terminals. However, radio waves spread out signals omni-directionally and cause communication interference that is known in wireless communication as "the hidden terminal problem" or "the exposed terminal problem". This signal interference can be decreased using directional communication mediums such as infrared rays or millimeter waves.

Infrared rays have strong directivity and limited beam width. Moreover, infrared rays can be used in circuits easier than millimeter waves. However, infrared wireless communication often loses communication links when mobile robots move or rotate. In order to execute tasks smoothly, we have designed an infrared wireless communication system that can maintain their communication links by tracking the partner robot. This communication system communicates with partner robots and simultaneously detects an incidence angle of infrared rays that points to the partner's direction using PSDs in order to track the partner.

In this system, several transceivers used PSDs as reception devices are put on the circumference of the robot body and faced outwards. These transceivers detect angle of arrival (AOA) of the communication signals in order to maintain communication links by switching to adjacent transceivers that face communicating partners.

Infrared signal intensity decreases with the square of the distance between the communicating partners. Also the reception capability is in inverse proportion to the data transmission rate. We designed amplifiers and threshold decision mechanisms that can restore digital pulse signals from received infrared signals.

This paper describes the design and implementation of the infrared wireless inter-robot communication system.

2. Basic design of the infrared wireless inter-robot communication system

Infrared rays have strong directivity and limited beam width. Although it can eliminate communication interference, usual infrared wireless communication often loses communication links when mobile robots move or rotate. We have designed an infrared wireless communication system that can maintain communication links. The communication system is formed by several infrared transceivers that are put on the circumference of the robot body and faced outwards. Figure 1 shows the arrangement of the transceivers.

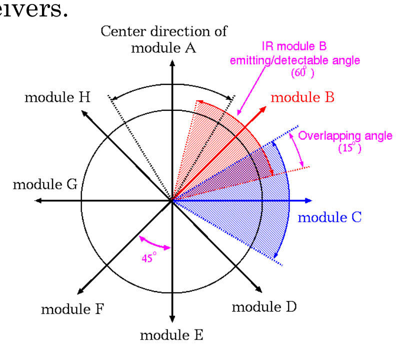

Fig. 1 Arrangement of transceivers

In this system, these transceivers used PSD photo diodes that can detect incidence angle of infrared rays as reception devices. The incidence angle of infrared rays is used in order to find the partner's direction.

The PSD photo diodes (HAMAMATSU S6560) that are reception devices have 2 current output electrodes and these ratios show the incidence angle. Figure 2 shows a schematic view of this PSD.

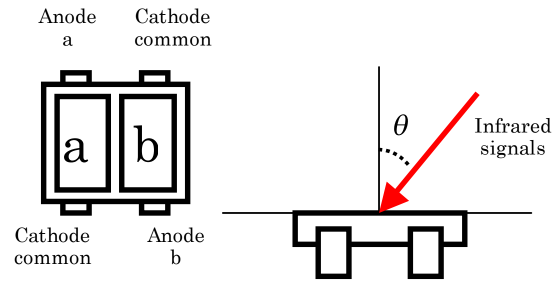

Fig.2 A schematic view of the PSD

The electric current output 'a' and 'b' of the PSD has the relations of the equation 1 with the incidence angle of the infrared signals θ.

$$\theta = (a - b) / (a + b) \tag{1}$$

The electric current output 'a' and 'b' of the PSD are feeble analog signals that need amplification. Figure 3 shows a block diagram of a signal processing amplifier. In figure 3, the signal processing amplifier outputs not only a digitized incidence angle but also serial data of communication signals.

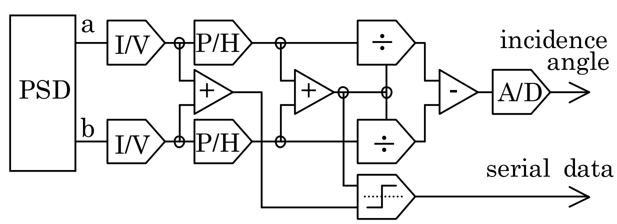

Fig. 3 Block diagram of amplifier

The detected incidence angle also encoded to the 2bit direction code in order to select transceivers that are facing to communicating partners. Figure 4 shows the direction code in an infrared transceiver.

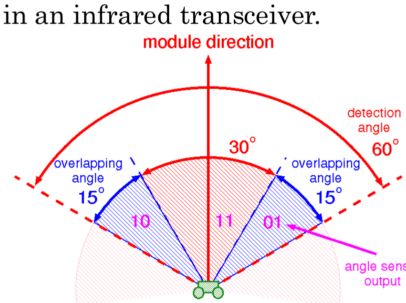

Fig. 4 The direction code and detected angle

When a partner is in the left, center, and right view of a transceiver, the partner's direction is encoded to the direction code '10', '11', and '01', respectively. When a partner moves or rotates, these transceivers detect the partner's direction in order to switch to an adjacent transceiver that is facing the partner. The direction code is used in order to maintain the communication link by switching these transceivers. Figure 5 shows transceiver exchange circuit. In figure 5, the serial data that is received by each transceiver is on the left side, and the direction code that is outputted from each transceiver is below. Since the serial data can be received from selected transceivers continuously, the infrared communication system can maintain their communication links.

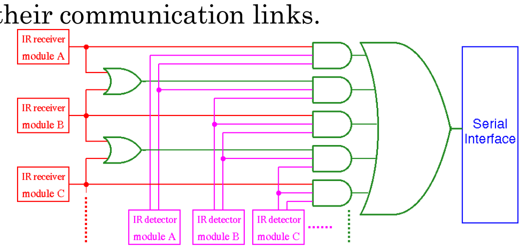

Fig. 5 Transceiver exchange circuit.

Since infrared rays have strong directivity and limited beam width, infrared communication suffers from hardly any interference, if partners are in different directions. This communication system can communicate with different partners in different directions by using different transceivers simultaneously. As a result, space-division communication can take place. When each robot relays information between different partners, a communication network is created in their workspace. It is an ad hoc communication network because each robot is independently mobile and may change position depending on their task. Figure 6 shows an inter-robot communication network.

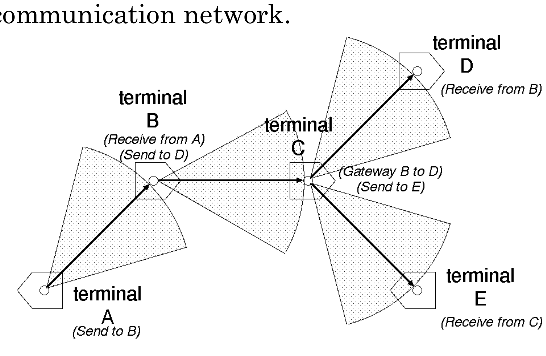

Fig. 6 An inter-robot communication network

3. Feasibility study of the infrared wireless communication system

As previously mentioned, the infrared wireless communication system is able to adapt for the inter-robot communication, if its mechanism is designed appropriately. However, infrared signal intensity decreases with the square of the distance from the transmitter to the receiver. Also the communication capability is in inverse proportion to the data transmission rate. We studied the performance of the inter-robot communication system.

In order to operate multiple mobile robots that perform team operations such as SAR operation or surveillance by remote control smoothly, the inter-robot communication system needs high-speed data transmission. The communication system has to send not only its positional information but also gathered information such as compressed video images, direction of thermal sources, gas concentration data and so on. We determined 384 kbps as a data transmission speed of the communication system in order to design the circuit, because it is similar to the speed used for the uplink from mobile phone terminals of walking users that transmit compressed QVGA video images.

We implemented an infrared transmitter, two types of infrared receivers and two types of threshold decision circuits for feasibility study of this communication system. The infrared transmitter uses two infrared-LEDs (STANLEY DNF324U, 850nm) driven by 2SA1300 transistor. One of the infrared receivers uses a PSD (HAMAMATSU S6560, 960nm) that can detect an incidence angle of infrared rays. Another one uses a photo diode (TOSHIBA TPS703, 960nm) that has similar capabilities to the S6560 (except its angle detection) in order to test the design of amplifiers.

Two threshold decision circuits that restore serial data from received infrared pulse signals were tested. Figure 7 shows the threshold decision circuits. In figure 7, the circuit (A) calculates the median value of high side peak and low side peak as threshold voltage. Also in the circuit (B), the difference between high side peak and low side peak is divided into three in order to give hysteresis effects.

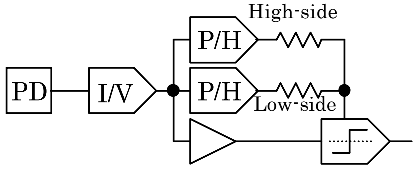

(A) a median value threshold

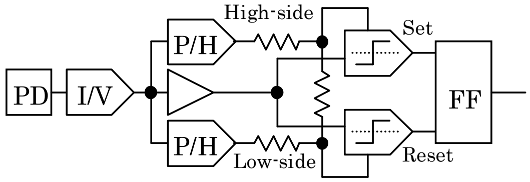

(B) a hysteresis threshold

Fig. 7 Threshold decision mechanisms

The infrared receiver that uses TPS703 photo diode and is connected to MOSFET (2SK241) amplifiers was used for the test. In the test, the receiver detected infrared signals of 460kbps from the infrared transmitter in 1m distances and outputted 400mVpp approximately.

In this test, the threshold decision circuits were possible to recover to digital pulse from the received signal voltage of 100mVpp, and it was also possible to receive signals up to 460kbps. However, when the outputted signals of the infrared receiver were less than 400mVpp, the wrong serial data was received because errors were included in the digital pulse sequence. At a slow transmission speed, these circuits were impossible to recover to the correct digital signals, because the threshold value is changed by the electric discharge of peak-hold capacitors.

Conclusion

We proposed and designed an infrared wireless communication system that is suitable for multiple mobile robots. We also implemented an infrared transmitter, two types of infrared receivers and two types of threshold decision circuits in order to study the feasibility of the communication system.

The infrared receivers were able to detect infrared signals of 460kbps from 1m distances and outputted 400mVpp approximately in this experiment. The threshold decision circuits were able to operate in the signal of 100mVpp 460kbps. However, when the outputted signals of the infrared receiver were less than 400mVpp, wrong serial data was received.

The photo-diode used for infrared reception detects both an infrared signal and background noise. In addition, the duty ratio of received signals influences the nonlinear character of the photo-diode, and makes amplification of signals unstable. The design of the amplifier circuit that suited the character of the photo-diode will be needed for high-speed long-distance infrared wireless communication.

Acknowledgements

This work is supported in part by Japan Society for the Promotion of Science Grant-in-Aid for Scientific Research (C) (No. 17500118).

References

1. ASAMA H., et al (Eds.) (1994) “Distributed Autonomous Robotic Systems” (DARS), Springer, Tokyo

2. YOSHIDA E, et al (2000) “Performance Analysis of Local Communication by Cooperating Mobile Robots”, IEICE Transactions of Communication, series EB, vol. E83-B, no. 5, pp.1048-1059

3. TAKAI H., et al. (2001) “A Space-Division Optical Wireless Communication System for Fully Distributed Multiple Autonomous Mobile Robots”. In: K.SCHILLING, H.ROTH (Eds.). Telematics Applications in Automation and Robotics 2001 (TA2001). PERGAMON press, pp.333-338

4. TAKAI H. et al (2002) “A Geometric Arbiter Selection Algorithm on Infrared Wireless Inter-robot Communication”, In: ASAMA H., ARAI T., FUKUDA T., HASEGAWA T (Eds.). Distributed Autonomous Robotic Systems 5 (DARS 5), Springer, Tokyo, pp.61-70

5. TAKAI H, et al (2002) “Development of a Space-Division Infrared Receiver for Fully Distributed Inter-robot Communication Network”, 2002 IEEE International Conference of System, Man and Cybernetics, IEEE, ID:WA1E3

6. TAKAI H, et al (2003) “Function Integration for Team Operations of Mobile Robots: Inter-robot Communication and Mutual Localization”, Proceedings of the 11th International Conference of Advanced Robotics (ICAR 2003), IEEE, pp.1431-1436

7. TAKAI H, et al (2005) “A Space-Division Wireless Communication System for Ad Hoc Networking and Cooperative Localization of Multiple Mobile Robots”, Preprints of the 16th IFAC World Congress, ID:05004

The Eleventh International Symposium on Artificial Life and Robotics 2006 (AROB 11th'06),
B-con Plaza, Beppu, Oita, Japan, January 23-25, 2006

The Development of Robot Palletizing Simulator using Pallet Pattern Algorithm and Trajectory Optimization

Seungnam Yu, Sungjin Lim
Dep. Precision Mech. eng.
Han Yang University
Seoul, 133791, Korea

Heukwon Yoon
Dep. Indus. Eng.
Han Yang University
Seoul, 133791, Korea

Changsoo Han
Dep. Mechanical Eng.
Han Yang University
Seoul, 133791, Korea

Abstract

Palletizing task is necessary to promote efficiency of keeping and shipping task. This is, however one of the most monotonous and heavy laborious work in the factory. So, many types of Robot palletizing system have been developed. But many robot motion commands is still depends on the teach pendent. That is, the operator input the motion command line one by one. It is very troublesome and most of all, user must know how to type the code. So we propose the new GUI Interface of Palletizing System that can be used more conveniently. To do this, we use the algorithm of PLP, "Fast Algorithm" and realize the 3D Auto-Patterning Visualization.
The usages of 3D pattern are following. First, an operator can identify the result of own task and edit it. Second, pass the position of object to a robot simulator. Using that position, palletizing operation can be simulated. We use the "Hyundai HHI series" and analyze the kinematics and dynamics to realize into a robot simulator. In this paper we propose the 3D patterning algorithm and 3d robot palletizing simulator. Future work is optimal path generation of robot manipulator and connecting this simulator to a real robot controller.

- PLP(Pallet Loading Problem)
- Fast Algorithm
- Pallet loading Pattern
- Robot Simulator
- Trajectory Optimization

1 Introduction

This paper will focus on palletizing, which is a form of unitizing. Palletizing refers to a uniform load stacked on a wooden pallet, using a pre-determined case pattern sequence and given number of layers. The process of palletizing typically involves the stacking of boxes, trays, bundles, bags, pails or drums in a predetermined pattern configuration. This paper will focus on the use of boxes only, as they make up the vast majority of palletizing application. Actually, the number of case patterns that can be programmed into a fully automatic palletizer is virtually limitless; however, when a pattern is programmed into a palletizer, it is not simply a software change in the controller itself. One of the biggest problems of manufactures is building loads to customer's specifications.

We propose the off-line robot palletizing simulator to combine Fast algorithm and 3D robot simulator. Fig.1 shows basic schematic of the simulator.

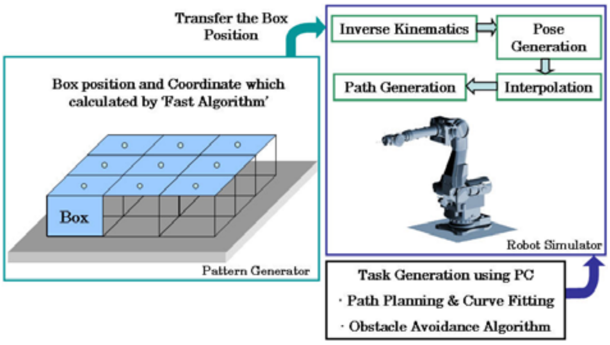

Fig. 1 Proposed schematic of Palletizing simulator

2. Fast Algorithm

2.1 Steudel's Heuristic Algorithm

The objective of the pallet loading problem (PLP) is to maximize the number of products loaded onto a pallet that is used for the transportation and storage of products. We can reduce the distribution and storage costs of pro duct by increasing pallet utilization.

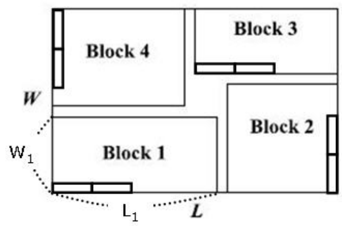

Fig. 2 Steudel's Heuristic Algorithm

Fast Algorithm proposed in this study is basically, improved algorithm compare with the 4-block pattern heuristic algorithm which proposed Steudel. Typical pattern of Stuedel's heuristic algorithm represented Fig.2. This heuristic finds the 4-block pattern where each block is a homogeneous pattern with the same box orientation [1]. This heuristics consist of two phases. First, an initial solution is made with the combination of L_i and W_i that maximizes the utilization of all four pallet edges. Dynamic programming was applied to find the combination and the initial solution has one of the four patterns shown in Fig.3. An initial solution that has a central hole sufficiently large to load more than one box in the case of P1 and P3, or an infeasible pattern, such as P2 and P4, due to the overlapped area,

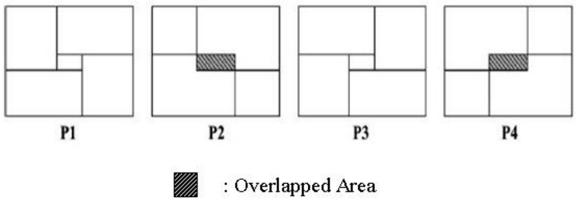

Fig. 3 Four patterns of the initial solution

this will involve the second phase. In the second phase, Treatment 1 is Fixing (L3, W3) and (L4, W4), resize L1 and L2 and Treatment 2 is Fixing (L1, W1) and (L4, W4), resize W2 and W3. We can choose the better solution to compare the first and second method.

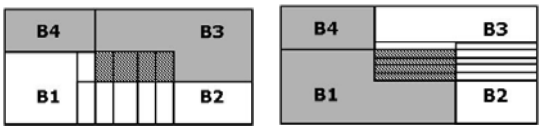

(a) (B)

Fig. 4 Treatment of Steudel's Algorithm
Treatment 1, (b) Treatment 2

2.2 The Fast Algorithm

2.2.1 Definition

The Fast Algorithm which we proposed has similar process to generate the initial solution of 4 patterns. And additionally, we adapt our Treatment 3 to apply the heuristic recursively to the central hole in the following three methods to remove the overlapped area. (Fig.5)

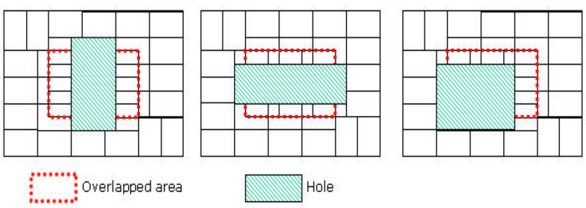

Fig. 5 Treatment of the Fast Algorithm

- In the first method: the boxes that are cut by the two horizontal edges of the overlapped area.
- In the second method: the boxes that are cut by the two vertical edges.
- In the third method: the boxes that are cut by the left vertical edge and the lower horizontal edge.

2.2.2 Schematic of Fast Algorithm

We do not consider the all size of blocks; therefore this algorithm has more rapid calculation time. First phase's initial solutions find the combination rather than using DP and define the 4 parameters. (Fig.6)

$\bar{a}$: When maximize the length of block and dispose the boxes lengthwise, maximal possible number of box = $5l$

$\underline{a}$: When maximize the length of block and dispose the boxes lengthwise, minimal possible number of box = $2l$

$\bar{b}$: When maximize the width of block and dispose the boxes lengthwise, maximal possible number of box = $8w$

$\underline{b}$: When maximize the width of block and dispose the boxes lengthwise, minimal possible number of box = $2w$

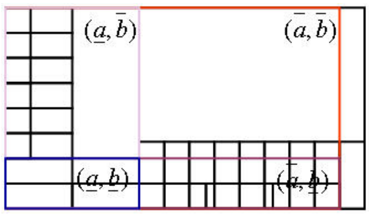

Fig. 6 A parameters of Fast Algorithm

In the first phase, make combinations of (L1, W1) such as $(\bar{a},\bar{b})$, $(\bar{a},\underline{b})$, $(\underline{a},\bar{b})$ and $(\underline{a},\underline{b})$ and given (L_1, W_1) is the width and length of the other blocks can be determined.

$$(L_2,W_2)=(L_4,W_4)=\left(\left[\frac{L-L_1}{w}\right]w,\left[\frac{W-W_1}{l}\right]l\right)$$

$$(L_3,W_3)=(L_1,W_1)$$

After making the four initial solutions in the first phase, redefine these solutions by applying the three treatments in the second phase

2.2.3 Computational Experience

We implemented the algorithm in Visual C++ 6.0 and compiled it with the maximized-speed option.

Table 1 The test result problem of small size

(L,W,l,w)	Amount of box loaded
(1000,1000,205,159)	30
(1000,1000,200,150)	33
(22,16,5,3)	23
(30,22,7,4)	23
(14,10,3,2)	23
(53,51,9,7)	42
(34,23,5,4)	38
(57,44,12,5)	41
(87,47,7,6)	97
(1200,800,176,135)	38

(L: Length of Pallet, W: Width of Pallet
l: Length of Box, w: Width of Box)

Upper result acquired from a computer of K6-350MHz CPU and 64Mbyte RAM. All problems were calculated within 1 second and resulted in optimal solutions. [1] This algorithm test is about two dimensional pattern generation of boxes and its calculation speed. To use this algorithm, however, consider the three dimensional space and physical constraint of box loading. To realize this, we consider the three constraint condition of palletizing, which is approach direction of robot hand to the pallet, multiple box gripping and weight center of palletized boxes. More information about this condition is referred to [2].

To use this algorithm to the industrial robot system, we developed GUI interface for a pallet loading problem using Fast Algorithm (Fig.7), and Fig.8 shows the calculated target position of each box.

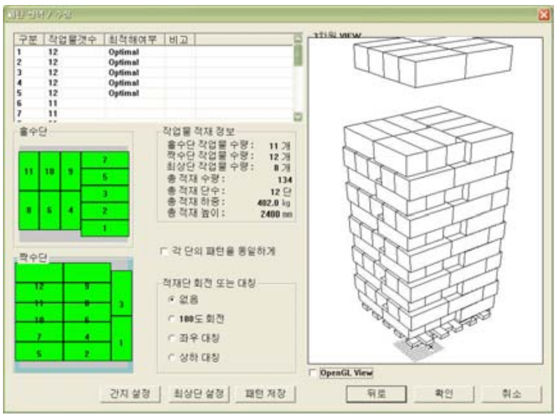

Fig. 7 Pallet Pattern Generation Software

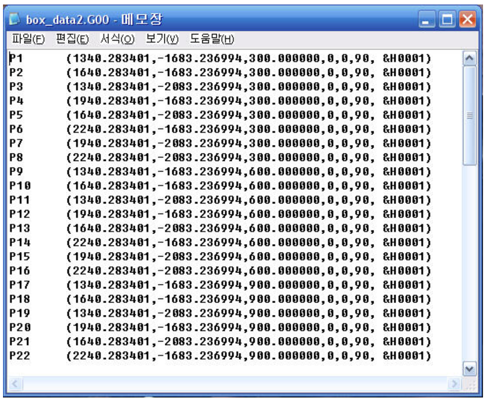

Fig. 8 Box target position (Robot Coordinates)

3. The Development of 3D Robot Simulator

3.1 Overview

For an industrial robot, to generate the palletizing task, several methods had been introduced and used. First one is On-line teaching the robot using teach pendent or mimic and memorize the worker's motion. Second one is Off-line method which is to generate task data using computer and download it to the robot controller. Especially, we focus to the Off-line task generation and simulation using robot simulator. In this phase, we represent three dimensional robot simulator based on the dimension data of our real target machine, HX300 which is a 6-axis industrial robot of Hyundai Heavy Industrial Co. This robot model is realized by commercial CAD modeler, and GUI interface is developed using OpenGL® and MFC of Microsoft Visual C++®.

To solve and analyze the forward and inverse kinematics equation, we use D-H table and Lagrangian Dynamic Equation. And this simulator is possible to compute and display the joint torque, angle, angular acceleration simultaneously.

3.2 Computation and Development of Robotic system

We solve the transformation matrix of each joint space and derive the inverse kinematical equation. And we compute the energy equation of potential and kinetic energy of system using Lagrangian equation; finally we acquire the following equations (More detail equations are referred to [3])

$$U_{ij} = \frac{\partial T_i}{\partial q_j} = \frac{\partial (A_1 A_1 \cdots A_j \cdots A_i)}{\partial q_j}$$

$$K_i = \int dK_I$$
$$= \frac{1}{2} Trace\left[\sum_{p=1}^{i}\sum_{r=1}^{i} U_{ip}\left(\int r_i r_i^{T} dm_i\right)\cdot U_{ir}^{T}\dot{q}_p\dot{q}_r\right]$$

(A_i : transformation matrix of ith joint space

q_i : ith joint angle)

$$L = K + P = \frac{1}{2}\sum_{i=1}^{6}\sum_{p=1}^{i}\sum_{r=1}^{i} Trace(U_{ip}J_iU_{ir}^{T})\dot{q}_p\dot{q}_r$$
$$+\frac{1}{2}\sum_{i=1}^{6} I_{i(act)}\dot{q}_i^{2} - \sum_{i=1}^{6}[-m_i q^{T}\cdot({}^{0}T_i\bar{r}_i)]$$

(J_i : Pseudo inverse matrix to express '$\int r_i r_i^{T} dm_i$' term)

To build the dynamic equation, we differentiate each term and we derive the following equations.

$$T_i = \sum_{j=1}^{6} D_{ij}\ddot{q}_j + I_{i(act)}q_i^{6} + \sum\sum D_{ijk}\dot{q}_j\dot{q}_k$$

$$D_{ij} = \sum_{p=\max(i,j)}^{6} Trace(U_{pj}J_pU_{pi}^{T})$$

$$D_{ijk} = \sum_{p=\max(i,j,k)}^{6} Trace(U_{pjk}J_pU_{pi}^{T})$$

$$D_i = \sum_{p=i}^{6} - m_p q^{T} U_{pi}\bar{r}_p$$

T_i is angular acceleration inertia, D_{ij} is inertia of actuator, D_{ijk} is Coriolis term and Centrifugal force and D_i is gravity term. Using these equations, we realize the three dimension robot simulator as Fig.9.

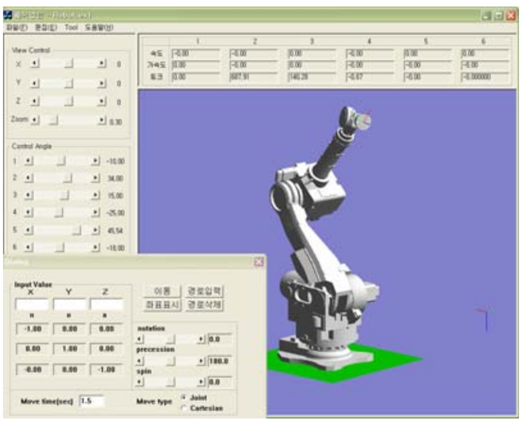

Fig. 9 Robot Simulator for Palletizing Task

The performance test of upper simulator combined with Fast algorithm is explained to [2].

4. Conclusion and Future work

In this paper, we proposed Fast Algorithm for PLP, 3D robot simulator and schematic of combination of two systems. To develop total Off-line palletizing simulator, however, the function of Trajectory generation and optimization of task are required. Fig.10 shows current status of our research. As a future work, we study the trajectory generation algorithm using path planning and obstacle avoidance. Especially, two topics will be considered. First issue is Cartesian Curve Fitting for a path defined by user and second one is Collision-Free Path Planning (CFPP) for automatic path generation.

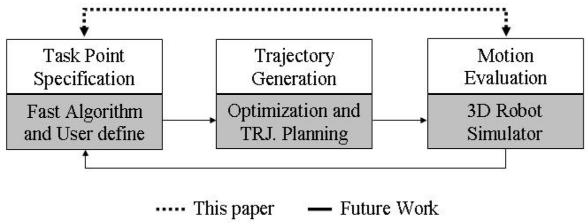

Fig. 10 Development Process

References

[1] Young-Gun G, Maing-Kyu Kang, 2000, "A fast algorithm for two-dimensional pallet loading problems of large size", European Journal of Operational Research 2001, pp.193-202

[2] Seung-Nam Yu, Heu-Kwon Yoon, Sung-Jin Lim, Young-Hoon Song and Chang-Soo Han, "The development of Robot Palletizing S/W using "Fast Algorithm and 3D Robot Simulator", KSME 2005, pp.1663-1668

[3] Sung-Jin Lim, 2004, "A Study on analyzing inverse kinematics and inverse dynamics of 6 DOF articulated robot", Hankuk Aviation University

[4] John J. Craig, 1989 "Introduction to Robotics, Mechanics and Control Second Edition", Addison Wesley, pp230~246

[5] Naak-hyung Lee, 1998, "A Design Experience on PC-Based Open Control for Robot Systems", Han yang University

[6] T. Lozano-Perez, "A Simple Motion Planning Algorithm for General Robot Manipulators", IEEE Journal of Robotics and Automation 1987, Vol. RA-3, No.3,

[7] C.W Warren, J.C. Danos, and B.W. Mooring, "An Approach to Manipulator Path Planning", The International Journal of Robotics Research, Vol.8, No.5, pp.87-95

The Eleventh International Symposium on Artificial Life and Robotics 2006 (AROB 11th'06),
B-con Plaza, Beppu, Oita, Japan, January 23-25, 2006

Redundant arm positioning control by linear visual servoing based on linear approximation of forward kinematics

Satoshi Mukai
Department of Opto-Mechatronics
Wakayama University
930 Sakaedani, Wakayama 640-8510, Japan

Noriaki Maru
Department of Opto-Mechatronics
Wakayama University
930 Sakaedani, Wakayama 640-8510, Japan

Abstract

We proposed a simple visual servoing scheme called linear visual servoing (indicated as LVS). It is based on the linearity of the transformation from binocular visual space to joint space of the arm of the humanoid robot which has a similar kinetic structure as a human being. LVS is very robust to calibration errors, especially to camera angle errors, because it uses constant Jacobian matrix with neither camera angles nor joint angles to calculate feedback command. Furthermore, the amount of calculation is very small compared to conventional visual servoing schemes. Hence, it is especially suitable for humanoid robots which use active stereo vision. But conventional LVS can not deal with redundant arm, because it is based on linear approximation of inverse kinematics. In this paper, we propose a redundant arm positioning control method by linear visual servoing based on linear approximation of forward kinematics. Simulation results are presented to demonstrate the effectiveness of the proposed method.

1 introduction

Vision based control is indispensable for Humanoid Robots that perform specified tasks in an uncertain and changing environment. Various kind of mechanism of visual feedback have been proposed. One is look and move and the other is visual servoing. Visual servoing is more robust to calibration errors than look and move. But conventional visual servoing schemes are not so robust to calibration errors, especially to camera angles, because they use non-linear Jacobian matrix with camera angles and joint angles. Furthermore, complex non-linear calculation is required to obtain Jacobian matrix. We proposed a simple visual servoing scheme called linear visual servoing (indicated as LVS). It is based on the linearity of the transformation from binocular visual space to joint space of the arm of the humanoid robot which has a similar kinetic structure as a human being. Binocular visual space is defined by vergence angle and horizontal and vertical viewing directions. LVS is very robust to calibration errors, especially to camera angle errors, because it uses constant Jacobian matrix with neither camera angles nor joint angles to calculate feedback command. Furthermore, the amount of calculation is very small compared to conventional visual servoing schemes. Hence, it is especially suitable for humanoid robots which use active stereo vision. But conventional LVS can not deal with redundant arm, because it is based on linear approximation of inverse kinematics. In this paper, we propose a redundant arm positioning control method by linear visual servoing based on linear approximation of forward kinematics. We linearize the forward kinematics which is the transformation from joint space to binocular visual space. Then we use the pesudo inverse matrix of the linear approximation matrix to produce feedback command. Although the conventional redundant arm control methods based on pesudo inverse matrix need joint angle, the proposed method does not need it. Simulation results are presented to demonstrate the effectiveness of the proposed method.

2 LVS based on Linear Approximation of Forward Kinematics

2.1 Model of the Humanoid Robot

Fig.1 shows the hand-eye coordination of the Humanoid Robot which has a similar kinematic structure as a human being. The arm consists of two links and four joints. The elbow joint has 1 d.o.f. and the shoulder joint has 3 d.o.f. The shoulder joint is located at the origin of arm coordinate Σ_A. The two cameras are mounted on pan-tilt heads, and the heads are mounted on a base frame which turns horizontally and vertically round the neck joints. We show the parameters of the hand-eye coordination of the Humanoid robot in **Table 1**. These parameters are defined to be proportional to those of a human being. They are the most suitable values for the approximation of the transformation from binocular visual space to joint space as a linear mapping[6].

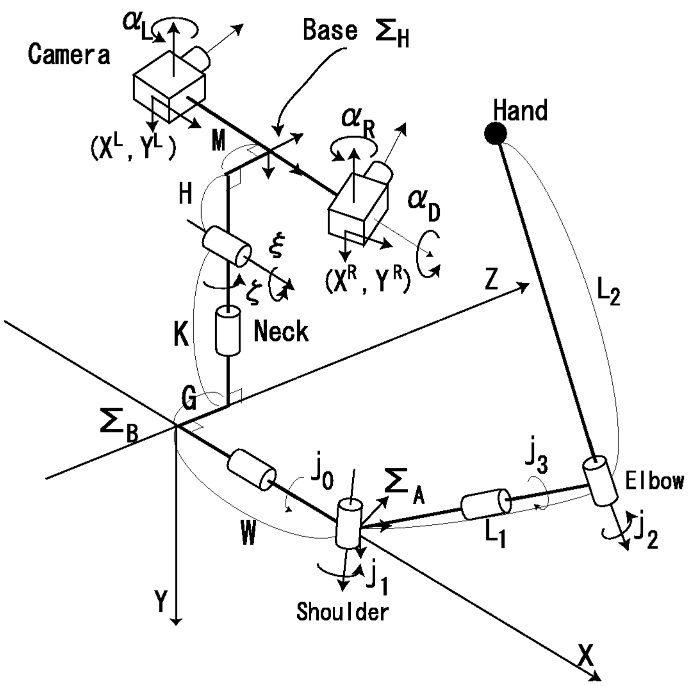

Fig. 1: Model of the hand-eye coordination of the humanoid robot

Table 1: Parameters of the model

Link Length	$L_1 = 450$, $L_2 = 710$
Camera Position	W=365, K=345, G=0
Baseline Length/2	E=50
Neck Length	H=165, M=60
Focal Length	f=4.5 (unit : mm)

2.2 Binocular Visual Space

The binocular visual space is defined by the vergence angle γ and the horizontal and vertical viewing directions θ, δ(see **Fig.2**). This space has been employed by psychologists and physiologists as a model of binocularly-perceived space. The binocular visual coordinate of a fixation point is described as

$$\mathbf{V} = \begin{bmatrix} \gamma \\ \theta \\ \delta \end{bmatrix} = \begin{bmatrix} \alpha_L - \alpha_R \\ (\alpha_L + \alpha_R)/2 \\ \alpha_D \end{bmatrix}, \qquad (1)$$

where α_L, α_R and α_D are the camera angles.

The binocular visual space has a close relation to the camera image. We show the stereo camera geometry in **Fig.3**.

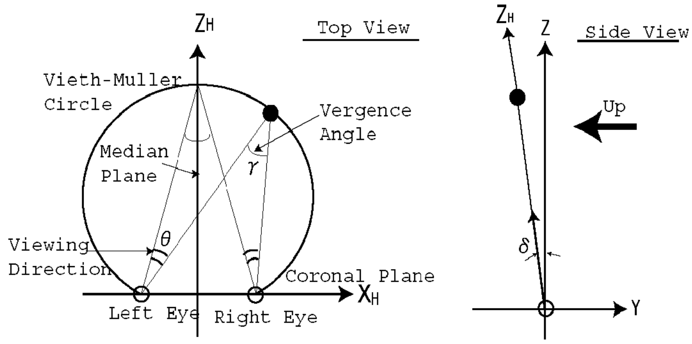

Fig. 2: Binocular visual space

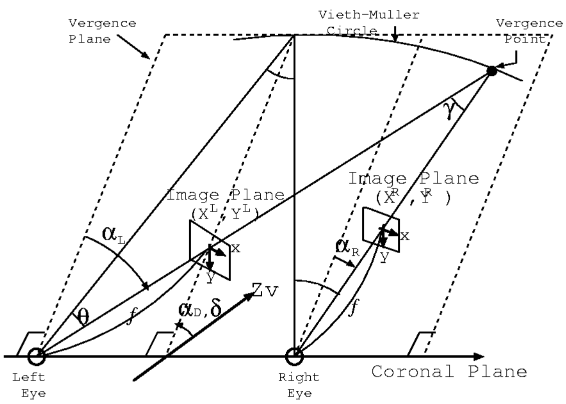

Fig. 3: Model of the active stereo cameras

The coordinates of a feature point projected on the camera image planes are transformed into binocular visual coordinates by

$$\mathbf{V} = \begin{bmatrix} \alpha_L - \alpha_R \\ (\alpha_L + \alpha_R)/2 \\ \alpha_D \end{bmatrix} + \begin{bmatrix} (X^L - X^R)/f \\ (X^L + X^R)/2f \\ (Y^L + Y^R)/2f \end{bmatrix}, \quad (2)$$

where (X^L, Y^L) and (X^R, Y^R) are the coordinates of a feature point in the left and right image respectively. Note that we use the approximation such as $\tan^{-1}(X^{L,R}/f) \simeq X^{L,R}/f$. This approximation is available around the fixation point. Camera angles and image data are transformed into binocular visual coordinates.

2.3 Linear Approximation of Forward Kinematics

We linearize the transformation from joint space to binocular visual space using the least-squares approximation using the nodal point in every 10[deg] in the region shown in **Table 2**. **Fig.4** shows the result of linear approximation.

Table 2: Approximation region

$-20[\text{deg}] \leq j_0 \leq 20[\text{deg}]$
$30[\text{deg}] \leq j_1 \leq 60[\text{deg}]$
$60[\text{deg}] \leq j_2 \leq 100[\text{deg}]$
$-10[\text{deg}] \leq j_3 \leq 40[\text{deg}]$

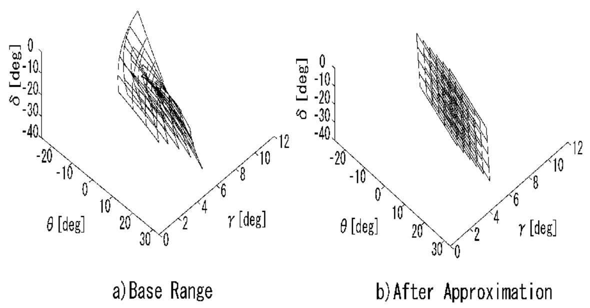

Fig. 4: Result of Approximation(Binocular Visual Space)

Then the transformation from joint space to binocular visual space is given by

$$\boldsymbol{V} = \boldsymbol{R}\boldsymbol{j} + \boldsymbol{C}, \tag{3}$$

where $\boldsymbol{V} = (\gamma, \theta, \delta)^T$ and $\boldsymbol{j} = (j_0, j_1, j_2, j_3)^T, \mathbf{R} : matrix(3X4), \mathbf{C} : vector(3X1)$.

2.4 LVS using Pesudo Inverse Matrix

The linear visual servoing using pesudo inverse matrix is given by

$$\begin{aligned}
\boldsymbol{u} &= -\lambda \boldsymbol{R}^{+}(\boldsymbol{V} - \boldsymbol{V_d}), \\
&= -\lambda \boldsymbol{R}^{+} \begin{bmatrix} \{(X^L - X^R) - (X_d^L - X_d^R)\}/f \\ \{(X^L + X^R) - (X_d^L + X_d^R)\}/2f \\ \{(Y^L + Y^R) - (Y_d^L + Y_d^R)\}/2f \end{bmatrix}, \\
&= -\lambda \boldsymbol{R}^{+}\boldsymbol{T}(\boldsymbol{I} - \boldsymbol{I_d}), \qquad (4) \\
\boldsymbol{T} &= \begin{pmatrix} 1/f & -1/f & 0 & 0 \\ 1/2f & 1/2f & 0 & 0 \\ 0 & 0 & 1/2f & 1/2f \end{pmatrix}, \\
\boldsymbol{I} &= (X^L, X^R, Y^L, Y^R)^T, \\
\boldsymbol{I_d} &= (X_d^L, X_d^R, Y_d^L, Y_d^R)^T,
\end{aligned}$$

where $\boldsymbol{u}$ are control signals to joint velocity controllers, $\boldsymbol{V}$ is the binocular visual coordinates of the end tip of the leg, $\boldsymbol{V_d}$ is the binocular visual coordinates of a target and λ is a scalar gain, $\boldsymbol{R}^{+}(= \boldsymbol{R}^{T}(\boldsymbol{R}\boldsymbol{R}^{T})^{-1})$ is the pesudo inverse matrix of linear approximation matrix of the forward kinematics obtained in the previous section. Although the conventional redundant arm control methods based on pesudo inverse matrix need joint angle, the proposed method does not need it.

Linear visual servoing is very robust to calibration error, especially to camera angle errors and joint angle errors, because the control law includes neither camera angles nor joint angles. Furthermore, the amount of the calculation is very small compared to the conventional visual servoing schemes.

3 Simulation

We have conducted simulation to demonstrate the effectiveness of the proposed method. **Fig.5** and **Fig.6** shows the simulation result. From these figures, we can see that the proposed method is effetive to control redundant arm using LVS.

4 Conclusion

In this paper, we have proposed a redundant arm positioning control method by LVS based on linear approximation of forward kinematics. It uses pesudo inverse matrix of linear approximation matrix. We have shown the effectiveness of the proposed method by simulation. In this paper, we did not shown how to utilize redundancy to realize dexterity. We will study about that.

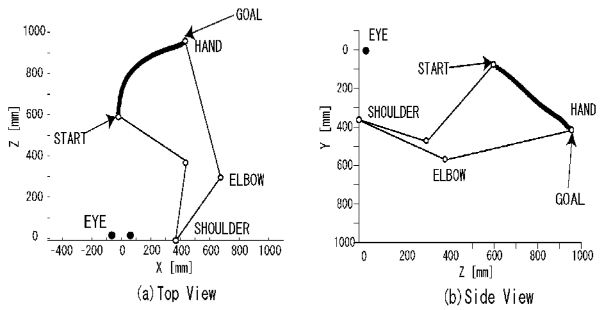

Fig. 5: Trajectory of the hand

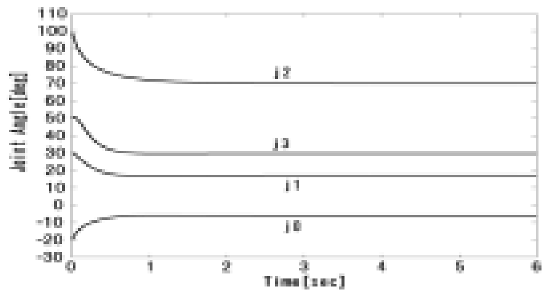

Fig. 6: Trajectories of the joint angles

References

[1] L.E.Weiss, A.C.Sanderson and C.P.Neuman, "Dynamic sensor-based control of robots with visual feedback", *IEEE J.Robotics Automation*, vol.RA-3, No.5, pp.404–417, 1987.

[2] B.Espiau, F.Chaumette and P.Rives, "A new approach to visual servoing in robotics", *IEEE Trans. Robotics Automation*, vol.8, no.3, pp.313–326, 1992.

[3] K.Hashimoto, T.Ebine and H.Kimura, "Visual Servoing with Hand-Eye manipulator - Optimal Control Approach", *IEEE Trans. Robotics Automation*, vol.12, no.5, pp.766–774, 1996.

[4] N.Maru, H.Kase, S.Yamada and F.Miyazaki "Manipulator control by visual servoing with the stereo vision", *Proc. IEEE/RSJ Int. Conf. on IROS*, vol.3, pp.1865–1870, 1993.

[5] T. Mitsuda, N.Maru, K.Fujikawa, F.Miyazaki: "Visal Servoing based on Linear Approximation of the Inverser Kinematics", Journal of the Robotics Society of Japan, vol.14, no.5, pp.743-750, 1996. (in Japanese)

[6] T. Mitsuda, N.Maru, K.Fujikawa, F.Miyazaki :" Linear Approximation of the Inverser Kinematics by using a Binocular Visual Space", Journal of the Robotics Society of Japan, vol.14, no.8, pp.1145-1151, 1996. (in Japanese)

[7] T.Mitsuda, N.Maru and F.Miyazaki, "Binocular visual servoing based on linear time-invariant mapping", *Advanced Robotics*, Vol.11, No.5, pp.429–443, 1997.

[8] T.Mitsuda, N.Maru and F.Miyazaki, "Visual servoing based on the constant linear mapping", *Proc. of the 2nd ACC*, pp.22–25, 1997.

[9] Kyota Namba and N.Maru, "3-D positioning control by linear visual servoing", *Proc. of AROB*, 2002.(CD-ROM)

[10] Y.Yamamura and N.Maru, "Leg Positioning control of the Humanoid Robot by linear visual servoing", *Proc. of WAC2000*, 2004.(in press)

[11] J.Aloimonos, I.Weiss and A.Aandyopadhyay "Active Vision", *Proc. of First ICCV*, pp.552–573, 1987

[12] D.H.Ballard, C.M.Brown, "Principles of Animate Vision", *CVGIP:Image Understanding*, Vol. 56, No. 1, pp.3–21, 1992

The Eleventh International Symposium on Artificial Life and Robotics 2006 (AROB 11th'06),
B-con Plaza, Beppu, Oita, Japan, January 23-25, 2006

A Study of an Autonomous Mobile Robot for Sewer Inspection System

[1,2]Alireza Ahrary, [1,2]Amir Nassiraei, [2]Masumi Ishikawa
[1]FAIS-Robotics Research Institute
Collaboration Center 4F, 2-1 Hibikino, Wakamatsu-ku, Kitakyushu City, 808-0135, JAPAN
[2]Kyushu Institute of Technology
2-4 Hibikino, Wakamatsu-ku, Kitakyushu City, 808-0196, JAPAN
ali@ksrp.or.jp, amir@ksrp.or.jp, ishikawa@brain.kyutech.ac.jp

Abstract

This paper describes KANTARO, a prototype autonomous mobile robot designed for inspecting sewer pipes. It is able to move autonomously in 200-300 mm diameter sewer pipes. KANTARO can also carry various sensors such as a camera for detecting faults and a 2D laser scanner for recording the pipe features.

Keywords: Autonomous mobile robot, Sewer inspection, Sewer system, Navigation, Fault detection system.

1 Introduction

Pipe walls in sewer systems are prone to be damaged due to aging, traffic and chemical reactions, through which inflow such as rainwater and groundwater seeps into the pipe systems. Regional city government reports [1] state that this inflow amounts to approximately 30% of the total flow. In addition to the inflow of groundwater into the sewer pipes, outflow from damaged systems also occurs, contaminating the surrounding environment [2]-[4].

The current state of the pipe maintains is carried out using a cable-tethered robot with an onboard video camera system. These platforms are connected to the outside world by a cable that gets used for energy supply, for transmission of commands from the human operator to the device, for data transmission back to the operator, as a life-line in case the device gets stuck in the pipe, and as a measuring line for the distance traveled. By this video-supported visual inspection, any notable damages or abnormalities are recorded in the video stream. The reliability of this system depends on the experience of an operator. The system is also prone to human error. Consequently, effective autonomous robot with online techniques to identify and extract objects of interest such as cracks from sensory signals is of immediate concern.

There are some approaches on optimizing the design, handling and sensors abilities of these cable-tethered robots. An example related to this area is KARO [5]. The monolithic KARO robot prototype resembles much a standard non-autonomous sewer inspection robot, and it is tethered via a cable to a surveillance unit. Using inclinometers and an on-board control program, KARO is able to automatically correct for tilt in its pose and wheel slippage when driving inside a sewer pipe, thus freeing the human operator from this crucial control task. The main innovation of KARO is its wide range of novel inspection and navigation sensors, namely a microwave sensor and a 3D optical sensor, complementing the standard video camera and some ultrasound transducers.

A step forward in completely autonomous sewer inspection robot is a semi-autonomous tethered sewer inspection robot. Piper [6] is good example close to this area. Piper's operating range is limited by the mandatory cable, having a length of about 45 meters. Two user-programmable microcontrollers provide for controlling locomotion and for automatically adjusting pan and tilt of the video camera head to the robot's locomotion speed. The video images can be either taped or captured on a computer. Its dimensions (9 inches width and 13.5 inches height) prohibit its application in smaller pipes.

KURT [7] is a six wheeled autonomous robot of approximate dimensions 30x45x30 cm. With its pivoted ultrasound sensor, KURT1 is able to classify the type of a pipe junction, i.e. whether it is L-shaped, X-shaped, or T-shaped. A special innovative method for navigation under uncertainty enables KURT1 to detect and correct errors due to false classification or due to errors while performing turns at pipe junctions.

MAKRO [8] is the prototype of a fully autonomous, self-steering articulated robot platform. It is designed for autonomous navigation in roughly cleaned, non-man-entry sewer pipes within a diameter range of 300 to 600 millimeters at dry weather conditions.

MAKRO is consisting of six segments connected by five motor-driven active joints, allows for simultaneously climbing a step and turning, e.g. at a junction consisting of a 600 millimeter pipe and a branching 300 millimeter pipe with equal top levels. MAKRO carries all the needed resources on-board. Standard NiCd batteries provide the power for its 21 motors, the sensors, and the electronics, including an industry standard PC/104+ computer system and seven microcontrollers.

The work we report here is an autonomous mobile sewer inspection robot, KANTARO. KANTARO differs from above conventional robot in two aspects: First it is smaller than others and able to allowing for an autonomous uptime of about nine hours. Second, it is able to detect various types of faults automatically.

KANTARO is able to move autonomously in 200-300 mm diameter sewer pipes and it can also carry various sensors such as a camera for detecting faults and a 2D laser scanner for recording the pipe features.

The paper is organized as follows. First, we describe the KANTARO's hardware design in Section 2. Then we sketch an outline related to the task of navigating and detecting the faults autonomously through the sewer system in Section 3. We conclude this paper in the last section.

2 KANTARO's hardware design

The sewer system is no easy place for such a robot to work. It is narrow, slippery, dirty and wet. The system must be constructed such that it is able to drive through long pipe sections quickly and with a minimum of energy consumption. Turning at narrow and slippery junctions must be possible with a minimum of mechanical wear out.

2.1 Mechanism

With regard to current sewer inspection technology, all commercial robots are capable to move in straight pipes but not any kind of pipe-bends such as "curves", "joints" and "T-junctions". However, because of the high range of pipe-bends in the sewer pipe system, pipe-bends pose a main problem for sewer inspection robots. Design a robot that can move into the straight pipes and pass pipe-bends will be a great industrial progress in sewer inspection industry.

We designed a compact and a novel moving mechanism for the sewer pipe inspection robots. The design is based on the concept of passive adaptation of robot wheels to the bends in the pipe. This is accomplished by proper wheel orientation and passive damping of springs. A single robot, include of this new moving mechanism, can carry the controller, electronics, motors and sensors and it is able to pass any kind of the pipe bends, moves in different size of pipe, goes step down and passes the obstacles with no intelligent control and sensor reading.

To achieve to wiring less and easy to assemble and disassemble robot, we designed the robot as a module system. As it showed in Fig. 1 robot consists of two main parts, upper box and bottom box that can connect to each other by a main connector.

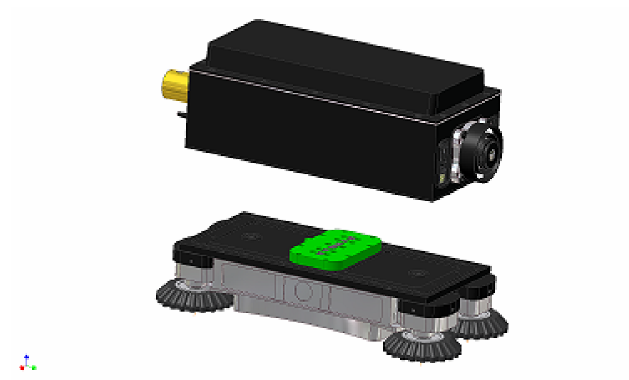

Figure 1: The KANTARO mechanism.

2.2 Sensors

Basically, if some sensor redundancy is desired, the benefit of having more sensor information must be weighed against the computer power required for exploiting it.

In our case, one should use few sensors and implement domain dependent and cheap, yet robust algorithms instead, which compensate for any uncertainty in the sensor interpretation and the resulting incompleteness of the internal representation.

2.2.1 Camera

In many computer vision applications including robot navigation, a camera with extremely wide-angle view is required. The conventional camera, however, has a limited angle of view. Therefore "fish-eye" lens is employed in this paper. Omni-directional view has recently become popular in mobile robots.

Here in our robot, we use a fish-eye lens CCD camera located in center with surrounded by circle type white LED light system. Fig. 2 shows the KANTARO camera and the lighting system.

The environment in the pipe is less affected by changes of external light. The lighting condition is controlled by a white LED array around the camera to acquire the best quality image.

Figure 2: The KANTARO vision system.

2.2.2 Laser scanner

2D and 3D laser scanners are excellent distance sensors, because they can recognize the shape of a detected object accurately. Since conventional scanners are large and heavy, it is difficult to install them in KANTARO that moves through pipes with diameter of 200-300 mm. Because of this, we develop a special 2D laser scanner that can measure the distance in sewer pipes and the angle of rotation and can be installed in KANTARO. The 2D laser scanner can locate features such as manholes and junction points. Fig. 3 shows the external view of the 2D laser scanner.

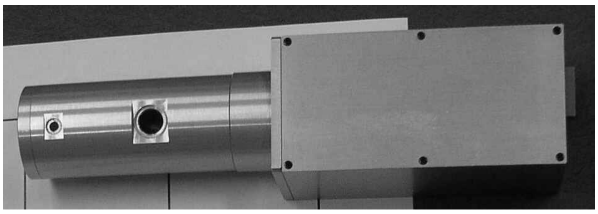

Figure 3: 2D laser scanner.

The triangulation method is used to measure the distance inside of pipes by the semiconductor 2D laser scanner using rotary scanning. It receives the reflected light by a light detecting element located at the axis of rotation, and measures the distance and the angle of rotation using a lens installed at the axis of rotation. Data is transmitted to a computer with the sampling speed of 10 KHz. The network is connected with the transmission rate of 1Mbps. The distance error is ±1mm or less.

3 Navigation

One of the central issues in developing an autonomous sewer robot is its navigation with the following problems. First, computing the current position based on distinetivation local features such as manholes and pipe joints, and finds a path. Second, follow this path in the real sewer pipe system.

Existing map of the sewer pipe system specify pipes, manholes and other local features is helpful to solve this overcoming problems. The high slip in sewer pipes caused unreliable odometry for an autonomous sewer robot. Furthermore, the metric information from the sewer pipe system map is not applicable in navigation for an autonomous sewer robot. Note that data from Global Positioning System (GPS) is inaccessible in underground sewer pipe system. Consequently, an autonomous robot has to compute the current position based on local features.

In our previous works [9]-[11], various methods were proposed for the detection of local features and computing the current position. We conducted experiments for sewer robot navigation in a dry sewer test field at RRI, Kitakyushu. They succeeded in detecting local features by use sensors information. We use a fast and accurate method to compute the distance data between local features and robot. Finally, the refined current distance can be used for autonomous sewer robot navigation.

In other works, we presented the detection of local features in sewer pipes based on fusion of laser scanner data and image data [12]. We still have to perform further experiments with different pipe material, different diameters and test these methods in real sewer pipe system.

4 Automated fault detection system

By current video-supported visual inspection system, any notable damages or abnormalities are recorded in the video stream. The reliability of this system depends on the experience of an operator. The system is also prone to human error. Consequently, effective autonomous online techniques to identify and extract objects of interest such as cracks from sensory signals are of immediate concern.

In our previous works, we described a method for detecting faulty areas in a sewer pipe system based on images acquired by KANTARO [13] [14]. The proposed method is able to detect various types of faults automatically and can be implemented in a real time system. The proposed approach demonstrates high performance of detection and it is able to detect even faint faults in small areas.

Graphic user interface (GUI) for the fault detection is illustrated in Fig. 4. Some additional information such as edge image and correlation variation is displayed to help experts doing data analysis.

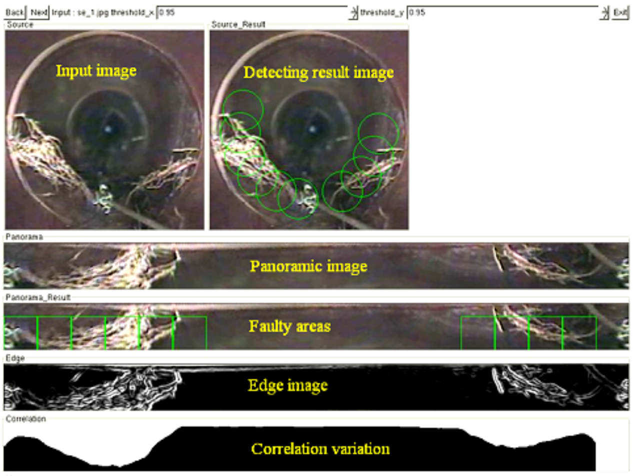

Figure 4: The GUI for fault detection.

5 Conclusions

The RRI dry sewer test field is definitely real world, but it is not an operational sewerage system. Although we have made clear that we have respected many constraints in our test scenario that are present in the real application area, it is obvious that it is simplified in a number of aspects and this simplification was deliberate. In consequence, we do not claim to have a fully operational autonomous sewer system robot.

Future work should aim to develop our robot much easier to use in the real world. Finally we hope that KANTARO use into the city sewer system in near future.

Acknowledgements

This research was supported by the FAIS-Robotics Research Institute, funded by the Organization for Small & Medium Enterprises and Regional Innovation, JAPAN (SMRJ).

References

[1] Material provided by Sewer System Administration Dept., City of Kitakyushu, Japan.

[2] Durbeck, W., "Stand der Eigenkontrollverordnung in den Landern der Bundesrepublik Deutschland aus der Sicht der Industrie", *Dokumentation 4. Int. Kongress Leitungsbau*, Hamburg, Germany, pp. 153-166, Oct. 1994.

[3] Keding, M. Riesen, S. van Esch, "Der Zustand der offentlichen Kanalisation in der Bundesrepublik Deutschland. Ergebnisse der ATVUmfrage 1990", *Korrespondenz Abwasser*, Nr. 10, pp. 1148-1153, 1990.

[4] Rudolph, U., Wellnitz, J., "Zustand und Sanierungsbedarf der Abwasserkanale in den neuen Bundeslandern", Korrespondenz Abwasser, 38 Nr. 12, pp. 1625-1630, 1991.

[5] http://www.iitb.fhg.de/servlet/is/1604/

[6] http://www.angelusresearch.com/piper.htm

[7] http://www.kurt2.de/

[8] http://www.ais.fhg.de/projects/Makro/makro.html

[9] A. Ahrary, L. Tian, S. Kamata, M. Ishikawa, "An autonomous sewer robots navigation based on stereo camera information," *Proc. of the 17th IEEE Int. Conf. on Tools with Artificial Intelligence*, Hong Kong, 2005.

[10] A. Ahrary, M. Ishikawa, "Detecting pipe feature points for sewer pipe system based on image information," *Proc. of the 10th Int. Conf. on Mechatronics and Information Technology,* Chongqing, China, 2005.

[11] A. Ahrary, L. Tian, S. Kamata, M. Ishikawa, "A cooperative stereo matching algorithm for sewer inspection robots," *Proc. of the IASTED Int. Conf. on Robotics and Applications,* Cambridge, USA, 2005.

[12] A. Ahrary, M. Ishikawa, "Fusion of laser scanner and image information data for landmark detection in sewer pipe system," *Proc. of the 9th Int.Conf. on Mechatronics Technology,* Kuala Lumpur, Malaysia, 2005.

[13] A. Ahrary, M. Ishikawa, "Visual fault detection for autonomous sewer robots," *Proc. ITC-CSCC 2005*, vol.1, pp.201-202, Jeju, Korea, 2005.

[14] A. Ahrary, M. Ishikawa, "An automated fault detection system for sewer inspection robots," *Proc. of the 36th Int. Symposium on Robotics,* Tokyo, Japan, 2005.

The Eleventh International Symposium on Artificial Life and Robotics 2006 (AROB 11th'06),
B-con Plaza, Beppu, Oita, Japan, January 23-25, 2006

Detection of Face Pose with eural etworks

Yau- en Chang and Gau-Tin Hung,
Medical Augmented Reality Research and Development center,
Department of Mechanical Engineering,
Chang Gung University, Tao-Yuan 33302, Taiwan

Abstract

In this paper, we propose a strategy to detect the position of a face and estimate its pose using two neural networks. At the first stage of the arrangement, the color information was adopted to extract skin regions from grabbed images and the potential face regions are cropped according to vertical and horizontal projection of the segmented image. From this cropped image, we implement two neural networks to arbitrate the existence of face region and the position of features in consecutive operations. The first neural network is used to classify critical regions of the cropped image into three categories, i.e. eyes, mouths and non-of-them. The second neural network is then implemented to arbitrate the most possible composition of two eyes and one mouth. After the feature positions are found, we can derive the pose of the face by the geometric relationship between eyes and mouth. Experimental results show that the proposed method can successfully and robustly detect the existence and inclination of a face from images.

Keyword Face Detection, Artificial Neural Network.

1. Introduction

Face detection from complex and arbitrary backgrounds has been under intensive study in image processing and computer vision. Early efforts in face detection can be traced as early as the beginning of the 1970s. Due to constant progress in computing power, the amount of research into face detection has grown in recent years.

A survey of face detection is reported in [5], where the techniques are roughly divided into two categories: feature-based and image-based. The feature-based methods consider the nature characteristics of human face, and the image-based methods directly investigate or learn those known/given images.

In [6], an image-based face detection approach is proposed to detect upright and frontal views of human face using neural networks. In [1], a detection method is proposed by searching for elliptical contour and considering color distribution within the region enclosing the contour. [2] proposed a method to detect critical features, i.e. eyes, by the morphology techniques of image processing. In [3], triangles are used to model the relation between eyes and mouth, cooperated with the color information nearby the vertices of them. [4] adopted YCrCb color space to detect the human face in order to reduce the effects of illumination. As these works detect human face with skin color information and the outline of the face, they are classified as feature-based methods accordingly.

In this work, face pose, in addition to its position, is to be estimated. This task is vital in an active display system, surveillance system or a robot with intelligent interface, etc. We will resort to both feature-based and image-based methods to solve this tough task.

Considering its tremendous power in modeling the mapping between two sets of data, artificial neural networks (ANN) are used. Two neural networks are used to arbitrate the existence of face region and the position of features in consecutive operations. The first neural network is adopted to classify the connected region of the rest pixels into three categories, i.e. eyes, mouths and others. The second neural network is then implemented to arbitrate the most possible composition of two eyes and one mouth. After the feature positions are found, the pose of the face can be derived by the geometric relationship between them.

2. Face Pose Detection

The developed system of face pose detection consists of three parts: skin color segmentation, feature localization, and estimation of face pose. In the following sections, we will introduce our approach in detail.

Yau- en Chang is with the Mechanical Engineering Department ,Chang Gung University, Tao-Yuan 33302, TAIWAN (corresponding author to provide phone: 886-3-211-8800; fax: 886-3-211-8050; e-mail: zen@mail.cgu.edu.tw).

Gau-Tin Hung is with the Mechanical Engineering Department, Chang Gung University, Tao-Yuan 33302, TAIWAN (e-mail: d9322006@stmail.cgu.edu.tw).

2.1 Segmentation of Skin Color

In this research, the color information was adopted to extract skin regions from grabbed images. As the RGB color space is sensitive to illumination, the segmentation is based on pixels represented in the CIE Lab color space. Table 1 shows the color values classified as skin. The potential face regions are cropped according to vertical and horizontal projection of the segmented image. Fig.1 shows the results of skin color segmentation and its projection. At this stage, the system finds potential regions where human face might appear.

2.2 ocali ation of the Face Features

For scenarios with complex background, potential face regions should be verified firstly. We implement two neural networks to arbitrate from this cropped image the existence of face region and the position of features in consecutive operations. Fig.1 demonstrates typical results of skin color segmentation and its projection. At this stage, the system finds out the region which human face might appear.

At the first stage, we eliminate the skin color pixels from the cropped image to exaggerate important features. In order to discriminate rest pixels for feature regions, we search and label all of the connected regions [7] within the eliminated image. Fig.2 shows the results of the elimination and labeling of the connected regions.

The first neural network is employed to classify the connected feature regions into three categories: eyes, mouths and others. We randomly selected 528 images of eyes and 636 images of mouths, each of 15 by 8 pixels, from the MIT-CBCL face recognition database [8] and our own database to train the network. Some of the training data are shown as Fig.3.

The network is of the two-layered Multi-layered Perceptron (MLP) architecture with 15 neurons in the first hidden layer and 8 neurons in the second hidden layer. Three output neurons were used to classify the input images into eye, mouth, and others. A standard back-propagation algorithm [9] was used to train this 120-15-8-3 network for 2000 cycles.

However, due to limited training data, the classification performance of the ANN is not stable. As shown in Fig.4, similar images may result in different categories. In this figure, squares represent the vertices of the mouth region, and the diamonds stand for eyes, respectively. To solve this problem, we design the second ANN to improve the correctness in feature detection.

The second neural network is then implemented to arbitrate the most possible composition of two eyes and one mouth. In order to clearly verify the combination of selected 3 candidate features, 9 attributes were selected, including the relative distances of them, and relative coordinates in the images. The first 3 attributes are defined as:

$$\begin{cases} {}_{in}^{1} = \overline{P_{eye1}P_{eye2}} \big/ sum\left(\overline{P_{eye1}P_{eye2}} + \overline{P_{eye2}P_{mout}} + \overline{P_{eye1}P_{mout}}\right) \\ {}_{in}^{2} = \overline{P_{eye2}P_{mout}} \big/ sum\left(\overline{P_{eye1}P_{eye2}} + \overline{P_{eye2}P_{mout}} + \overline{P_{eye1}P_{mout}}\right) \\ {}_{in}^{3} = \overline{P_{eye1}P_{mout}} \big/ sum\left(\overline{P_{eye1}P_{eye2}} + \overline{P_{eye2}P_{mout}} + \overline{P_{eye1}P_{mout}}\right) \end{cases}$$

where $\overline{P_{eye1}P_{eye2}}$, $\overline{P_{eye1}P_{mout}}$ and $\overline{P_{eye2}P_{mout}}$ stand for the distances between those three critical features. The rest 6 attributes are defined as:

$$\begin{cases} {}_{in}^{4} = P_{eye1}^{x} / S_x \\ {}_{in}^{5} = P_{eye1}^{y} / S_y \\ {}_{in}^{6} = P_{eye2}^{x} / S_x \\ {}_{in}^{7} = P_{eye2}^{y} / S_y \\ {}_{in}^{8} = P_{mout}^{x} / S_x \\ {}_{in}^{9} = P_{mout}^{y} / S_y \end{cases}, \left[S_x, S_y\right] = si\ eof\left(\text{Cropped Image}\right)$$

where S_x and S_y denotes the size of the cropped image. Two output neurons were used to indicate whether a candidate combination is a correct configuration of two eyes and one mouth, and they are in reasonable relative positions.

In this work, we randomly selected 430 sets of proper combination and 325 sets with wrong combination. Typical combinations of the marked features are shown in Fig.5. Also, the back-propagation algorithm was used to train this 9-8-5-2 network for 2000 cycles.

Fig.6 shows an experimental result that demonstrates the effectiveness of the second ANN to detect critical features and to estimate face pose.

3. Conclusion

We propose a novel strategy using ANN to reliably detect the position of human face and estimate the face pose at the same time. The first neural network is used to classify the connected region of the rest pixels into three categories, i.e. eyes, mouths and nothing. The second neural network is then implemented to arbitrate the most possible composition of two eyes and one mouth.

After the feature positions are found, we can derive the pose of the face by the geometric relationship between eyes and mouth. Experimental results show that the proposed method can successfully and robustly detect the existence and inclination of a face from images with a frame rate of 30 frame/sec.

Acknowledgements

This study is supported by Technology Development Program for Academia (TDPA) of the Ministry of Economic Affairs, Taiwan, R.O.C., under contract no. 94-EC-17-A-19-S1-035.

References

[1] S. Birchfield, "Elliptical head tracking using intensity gradients and color histograms," *Proceedings of t e IEEE Computer Society Conference on Computer Vision and Pattern Recognition*, pp.232-237, 1998.

[2] C.C. Han, H.Y. Liao, G.J. Yu, and L.H. Chen, "Fast face detection via morphology-based pre-processing," *Pattern Recognition*, Vol.33, pp. 1701-1712, 2000.

[3] C.H. Lin and K.C. Fan, "Triangle -based approach to the detection of human face," *Pattern Recognition*, Vol.34, pp.1271-1284, 2001.

[4] R.L. Hsu, "Face detection in color images," *IEEE Transaction on Pattern nalysis and Mac ine Intelligence*, Vol.24, pp.696-706, 2002.

[5] Erik Hjelmas and Boon Kee Low, "Face Detection: A Survey," *Computer Vision and Image nderstanding*, 83, 236-274, 2001.

[6] Henry A. Rowley, Shumeet Baluja, and Takeo Kanade, "Neural Network-Based Face Detection," *IEEE Trans. Image on Pattern nalysis and Mac ine Intelligence*, vol. 20, issue 1, pp. 23-38, 1998.

[7] Rafael C. Gonzalez and Richard E. Woods, *igital Image processing*, 2nd edition, Prentice-Hall, 2001.

[8] http://cbcl.mit.edu/software-datasets/heisele/facerecognition-database.html

[9] Fredric M. Ham, Ivica Kostanic, *Principles of Neurocomputing for Science Engineering*, McGraw-Hill, 2001.

Table 1. Values of the skin color in CIE Lab space

		a	b
Set 1	142.56	140.44	125.56
Set 2	168.33	142.78	136.44
Set 3	156.67	138.11	132.78
Set 4	143.56	143.22	125
Set 5	134.33	139.44	123.33

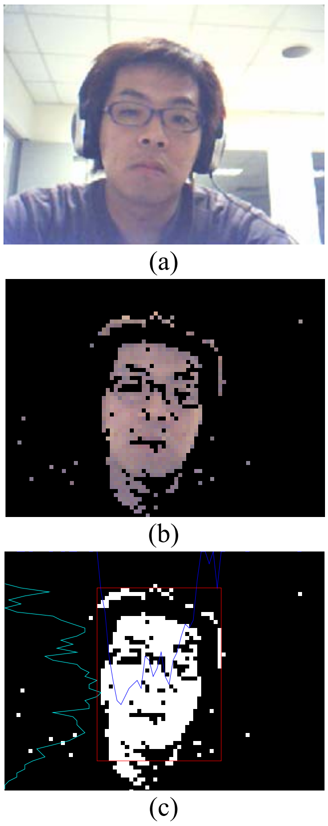

Fig.1 (a) Original image (b) results of color segmentation and (c) its projection

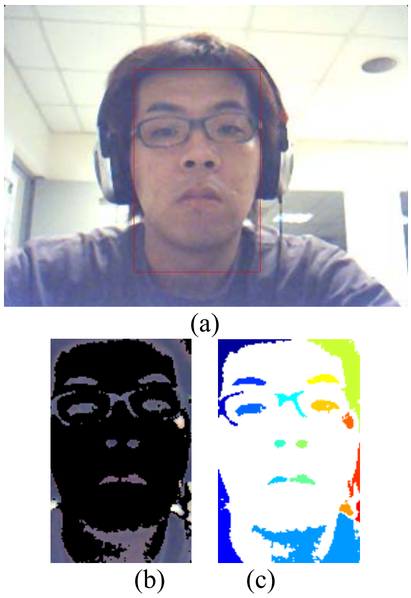

Fig.2 (a) Elimination of the skin color in a cropped image (b) labeling of the connected region by different colors

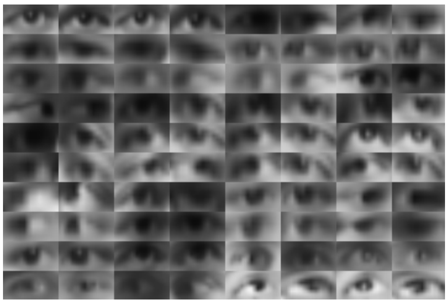

(a) Images of various eyes

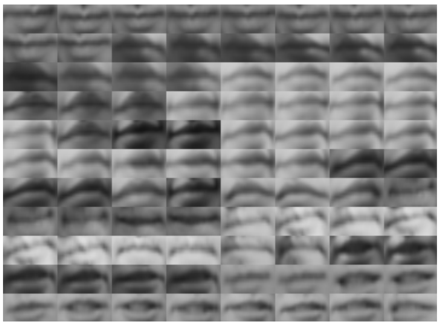

(b) Images of various mouths

(c) Images of objects other than eyes and mouths

Fig.3 Training data of ANN corresponding to the regions of eyes, mouth and others

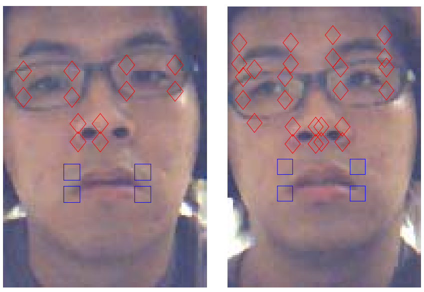

Fig.4 The results of ANN classification. Similar images may result in different categories

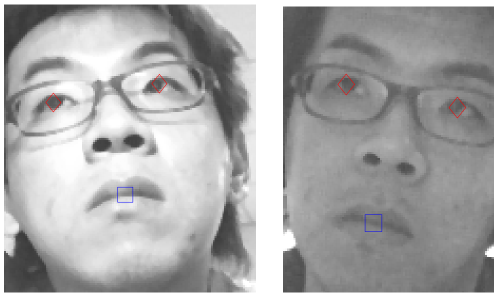

(a)

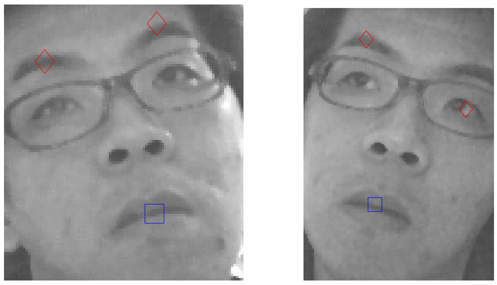

(b)

Fig.5 (a) Correct and (b) incorrect combination of critical features

Fig.6 Detection of the face and estimation of its pose in a cluttered environment

The Eleventh International Symposium on Artificial Life and Robotics 2006 (AROB 11th'06),
B-con Plaza, Beppu, Oita, Japan, January 23-25, 2006

A Study on the Development of Actively Controlled Anti-Seasickness Bed

Young Bok Kim
Faculty of Mechanical Engineering
Pukyong National University
San100, Yongdang-Dong
Nam-Gu, Busan 608-739, Korea
kpjiwoo@pknu.ac.kr

Jin Ho Suh
Department of Electrical Engineering
Dong-A University
840-1, Hadan-Dong, Saha-Gu,
Busan 604-714, Korea
suhgang@hanmail.net

Kwon Soon Lee
Division of Electrical, Electronics & Computer Engineering
Dong-A University
840-1, Hadan-Dong, Saha-Gu,
Busan 604-714, Korea
kslee@daunet.donga.ac.kr

Abstract

In ship operation the consequence of roll and pitching motion can seriously degrade the performance of mechanical and personnel effectiveness. So many studies for the roll stabilization and trimming control system design have been performed and good results have been achieved where the stabilizing fins, tanks, rudders and flaps are used.[1-7]

However the ultimate objective of such approach must be focused on improving the boarding sensitivity. But there exist many weak points, for examples, increasing of navigation resistance, ship control performance degradation and increasing of system complexity. And, the achieved control performance could not give us enough comfortable boarding sensitivity. The residual rolling and pitching motion are main drawbacks.

To get rid of these disadvantages, the main hull control system design approach has been considered using semiactive absorber.[8] In this system, dampers, spring, dynamic dampers and control system with sensors are incorporated.

In our system considered in this study, just two motors and control system with sensors are used for the bed. In other word, the control system can be installed on each bed. So, we can control every bed on the specified control objectives respectively. Above all, the good advantages of this system are the facts followed from simple idea and usefulness. Of course the structural modifications are needed. Considering actual sea states, a new apparatus for our objectives is necessary, such that we design a control system and verify the usefulness of developed system from the experimental study.

I. Introduction

New developments in naval architecture have been focused on fast ships for passenger and freight transportation. During 1970-1990 most new passenger ferries were built with speeds in the range 35-40kn and were considered to be fast. Since 1990, the speed of newly developed fast ferries has been increased about 70kn. Further more, several container vessels will be able to cross the Atlantic between North America and Europe with 40kn ship speed. New technologies are being developed to achieve the necessary performances in the several points of view.[9]

In ship operation and etc, wave, wind and other facts induce undesirable ship motions. For examples, roll, pitching motion and heaving are included in this category. These motions cause seasickness and degrade the performance of mechanical and personnel effectives.

In the many articles [1-7], excellent solutions have been introduced where fins, tanks, rudders and flaps are used to reduce and suppress rolling and pitching. These strategies are mainly focused on improving the ship stability. In other word, the ship herself is the plant considered. Therefore the physical points for human are not considered in a sense.

In the paper [8], a vibration reduction skill for main hulls is introduced using semiactive absorbers. In this article, the considered fact is the motion(vibration) oscillated by repeated excitations from the propellers, main engine and wave load. Because, the high-pitch propeller and long-stroke diesel engine have been more widely used, widespread problems relating to main hull require attention. Furthermore such vibrations affect the comfort of passengers and crew, damage the structure and impair the fighting efficiency of war ships.[8]

In this paper, we do focus on the very specialized category or equipment which will bring the riding comport to the human. This is extended idea appeared in reference [10]. Especially, we design a bed to cope with unpredictable environment like winds and waves etc. The designed system is composed of sensors and several electric equipments. Comparing with hull control system, it is very simple and there exists easy application properties. If we consider the characteristics of the ocean vehicle, we can see that a fact of easy application to the real system is absolutely necessary condition. So, we introduce and verify the system properties of proposed system from experimental study.

II. Problem Statement

In this paper, we consider the main aspects of the problem, namely seasickness, sea states and ship motions. Studies on seasickness published in reference [11], it concludes that seasickness is a cumulative effect related to vertical eleration at certain frequencies. There is frequency band around 1[rad/s]. In this area, the seasickness is most inducable. In the related studies, a mathmatical model of motion sickness incidence (MSI), an index defined as the percentage of the subjects who became ill after two hours dew to motion, is given as follws:

$$\mathrm{MSI} = 100\left[0.5 \pm \mathrm{erf}\left(\frac{\pm\log_{10}(|a_v|/g) \mp \mu_{\mathrm{MSI}}}{0.4}\right)\right] \qquad (1)$$

where **erf** is the error function; $|a_v|$ is the vertical acceleration, averaged over a half-motion cycle, in a chosen place; and

$$\mu_{\mathrm{MSI}} = -0.819 + 2.32(\log_{10}\varpi_e)^2$$

where ϖ_e is the dominant frequency[rad/s] of the vertical acceleration.

Ocean waves are generated by winds and those are described by terms of wave energy spectra. In The World Meteorological Organization(WMO), the sea states are distingushed by ten grades.

In this paper, our research intrest is focused on oscillated vibration induced by roll and pitch motion of ship regardless of the classified sea states. Ultimately, we supress this type of vibration and get the riding comfort.

III. Considered System and System Description

Here let us describe the considered system(plant) which is illustrated in Fig. 1.

As shown Fig. 1, the bed is controlled by two motors for suppressing the roll and pitch motion respectively. Especially, the motor installed on the left side of bed is only controlled to suppressing pitch motion or heave motion. Based on this idea, some desirable riding comfort and performance can be achieved, because the heave motion is mainly related to seasickness.

Let us explain the system properties in operational point. If the undesirable motions(pitching, rolling and heaving) are oscillated and measured by sensors, then the motor(for roll) is controlled to suppress the motion oscillated by ship rolling and the motor(for pitch) is controlled to suppress the motion induced by ship pitching or heaving.

Let us describe the controlled system :

a. Roll dynamics of the bed
b. Pitch dynamics of the bed

For the convenience, we express the each dynamics with 2nd order system as following :

$$I_x\ddot{\theta}_x + D_x\dot{\theta}_x + K_x\theta_x = T_{xd} + T_x \qquad (2)$$

$$I_y\ddot{\theta}_y + D_y\dot{\theta}_y + K_y\theta_y = T_{yd} + T_y \qquad (3)$$

where, equation (1) denotes the roll dynamics and (2) is pitch dynamics.

And,

θ_x, θ_y : angle for each dynamics

I_x, I_y : inertia moments

D_x, D_y : damping coefficients

K_x, K_y : spring coefficients

T_{xd}, T_{yd} : disturbances

T_x, T_y : control forces

The parameters are calculated or estimated by simulation and experiment.

It is assumed that there does not exist any coupling terms in the system description.

IV. Controller Design and Experiment

As illustrated in the previous illustrations, it is assumed that there is no coupling term. Then the controller is designed for each system dynamics as shown in Fig. 2.

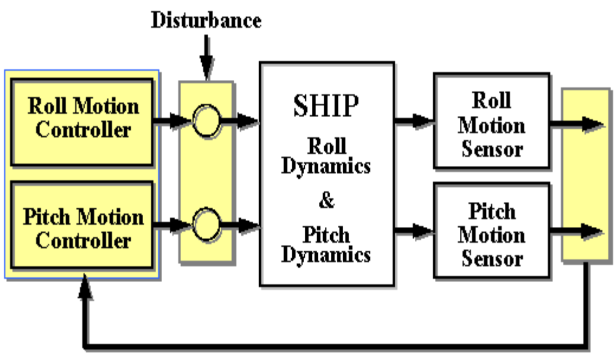

Fig. 2 Block diagram for system control

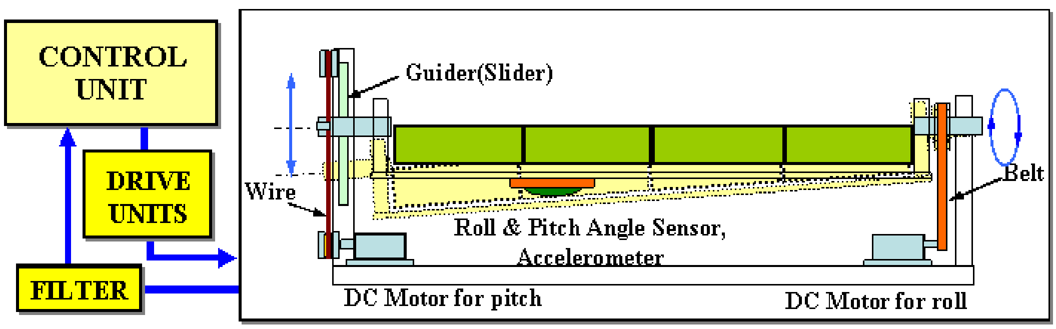

convenience, we

design two controllers based on the PID control scheme.

In the results, the controllers :

$$C_i(t) = K_{Pi}e(t) + K_{Ii}\int e(t)dt + K_{Di}\frac{d}{dt}e(t)$$
$$i = 1, 2.$$

where,

$C_1(t)$: roll motion controller,
$C_2(t)$: pitch motion controller

and

$K_{P1} = 2,\ K_{P2} = 1,$

$K_{I1} = 0.01,\ K_{I2} = 0.01$

$K_{D1} = 0.03,\ K_{D2} = 0.005.$

Let us introduce the experimental results with the designed controllers.

Where the frequency range of the disturbance input is specified in 3[Hz] because of the constraint on the sensor specification used in this study.

In Fig. 3, the uncontrolled case is shown where (a) denotes roll motion and (b) is pitch motion when the plant is exposed to oscillated vibration induced by disturbances. As shown in this figure, the bed is strongly exposed to and affected by disturbance. So, any desirable riding comfort can not be expected.

Fig. 4 shows the controlled case when the disturbance exists. In this case, based on the proposed system design scheme, the effect of oscillated vibration is actively suppressed and good riding comfort is achieved. To compare the controlled case with the uncontrolled case, we show the results in Fig. 5.

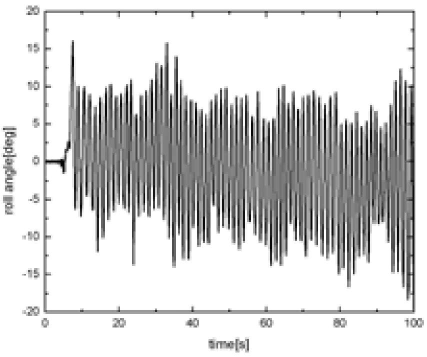

(a)roll motion

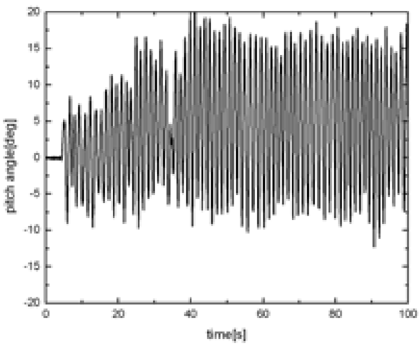

(b)pitch motion

Fig. 3 Uncontrolled case, when oscillated vibration exits

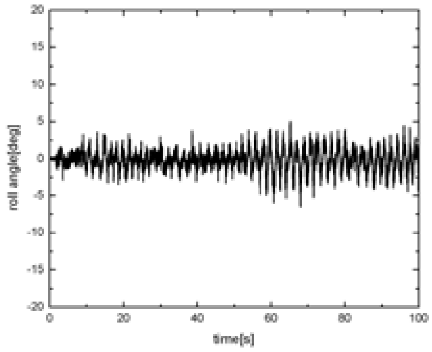

(a)roll motion

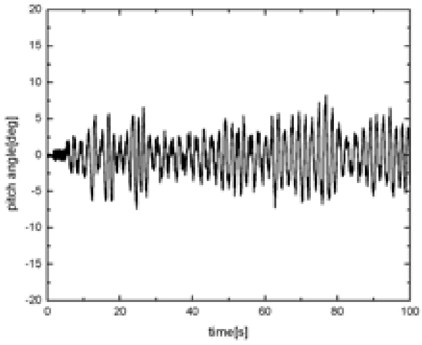

(b)pitch motion

Fig. 4 Controlled case, when oscillated vibration exits

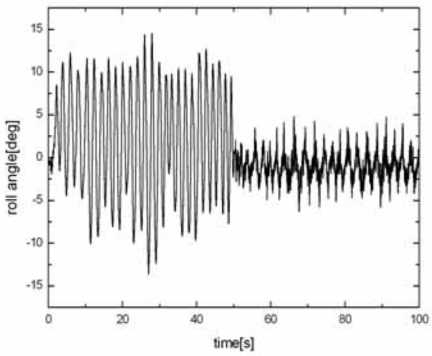

(a)roll motion

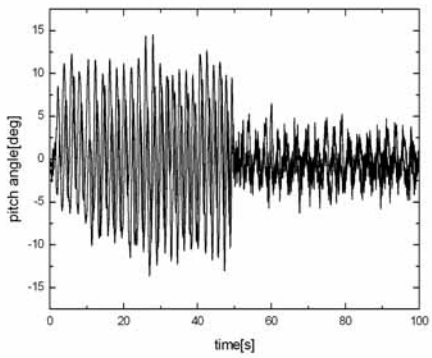

(b)pitch motion

Fig. 5 Experimental results for comparison, when the disturbances exist

V. Conclusions

In this paper, we proposed and introduced an anti-seasickness bed to achieve good riding comfort of the ship. In many researchs, the authors have proposed effective control strategies. As introduced in the previous section, fin-stabilizer, anti-rolling tanks and etc are used for suppressing roll and pitch motions. These apparatus are useful for obtaing ship stability and riding comfort in a sense. But ultimate performance evaluation may not be achieved. So, in this article we tried to get more clarified and specified control performance. However we expect that the proposed apparatus may be useful for evaluating the unsolved problems in previous apparatus and skills. In the experimental results, we identified those possibilities.

Acknowledgement

This work was supported by grant No. R01-2005-000 -10418-0 from Korea Science & Engineering Foundation in Ministry of Science & Technology.

References

[1] Y. Koike, “Study and at-sea experiment on actively controlled anti-rolling system”, Journal of the SNAJ, Vol. 174, pp. 137-143, 1994

[2] Y. Koike, “Application of hybrid anti-rolling system to actual ship”, Technical Review of IHI, Vol. 35, No. 6, pp. 395-399, 1995

[3] K. Mibasi, “Vibration absorber for marine machinery”, Mitsui Zosen Giho, No. 138, pp. 33-40 , 1989

[4] K. Otaka, “The research trends of ship vibration”, Techno Marine, No. 764, pp. 127-130, 1993

[5] S. Yamaguchi and A. Shinkai, “On activating and optimizing procedures of a fluid tank system for ship stabilization”, Journal of the SNAJ, No. 171, pp. 125-131, 1991

[6] K. Tanida, “Active vibration absorber”, Techno Marine, No. 707, pp. 283-290, 1988

[7] K. Tanida, “The applications of the active vibration control for the super structure”, Techno Marine, No. 777, pp. 62-67, 1994

[8] W. J. Hsueh, “Vibration reduction of main hulls using semiactive absorbers”, J. of Marine Science and Technology, No. 3, pp. 50-60, 1998

[9] J. M. De la Cruz, J. Arandra, J. M. Giron-Sierra, F. Velasco, S. Esteban, J. M. Diaz and B. de Andres-Toro, “Improving the comfort of a fast ferry”, IEEE Control System Magazine, Vol. 24, No. 2, pp. 47-60, 2004

[10] T. Ono and H. Inooka, “Development of a rotation-type actively-controlled bed for an ambulance; Control system design based on the principle of matching”, Vol. 41, No. 3, pp. 202-209, 2005

[11] J. F. O'Hanlon and M. E. MacCawley, “Motion seasickness incidence as a function of frequency and acceleration of vertical sinusoidal motion”, Aerospace Med., Apr., 1974

The Eleventh International Symposium on Artificial Life and Robotics 2006 (AROB 11th'06),
B-con Plaza, Beppu, Oita, Japan, January 23-25, 2006

A Modeling and Position Control based on Two-Mass system for Machine Stand Vibration System

Sou Watanabe, Fujio Ohkawa, Ryuichi Oguro and Jun Kobayashi

Graduate School of Computer Science and Systems Engineering, Kyushu Institute of Technology
680-4 Kawazu, Iizuka, Fukuoka, 820-8502, JAPAN
E-mail : sou@maple.ces.kyutech.ac.jp

Keywords : Machine Stand Vibration, Two-Mass System, Position Control, Modeling

Abstract

This paper describes a modeling and position control for a linear slider with Machine Stand Vibration. We focus on the similarity between the Machine Stand Vibration System (MSVS) model and the Two-Mass System(2MS) model. Then the MSVS model was transformed into the 2MS model. By this means, the conventional position control methods for the 2MS are available for the MSV. It is shown that a position control method of the MSVS is realized by using the controller based on 2MS by simulations.

1 Introduction

Recently, machining center requires high-speed positioning of a linear slider system to improve productivity. Most conventional linear slider systems consist of a ball screw slider. The ball screw slider has a motor, slider, ball screw, coupling and so on. When a length of the ball screw slider becomes longer and/or a mass of a work mounted on the slider becomes heavier, an elasticity of the ball screw slider (ex. a coupling, ball nuts and so on) cannot be ignored to control the system. Namely, a vibration phenomenon may be occured, and it exerts a harmful influence on high-speed and high-accurate positioning of the slider. The other side, a direct drive system with a linear motor has a little elasticity factor such as the ball screw slider. However, in the direct drive system, a reaction force influences the machine stand directly because there is no gear element in the linear motor slider. Recently, the rigidity of the machine stand becomes lower because a weight of the machine stand reduces. Therefore, a quick motion of direct drive system by a linear motor makes vibration phenomenon in machine stand due to its elasticity. This phenomenon is called the machine stand vibration, and the system which has this phenomenon is called MSVS[1]. The Machine Stand Vibration greatly influences high-accurate positioning of the slider. To overcome this problem, many control methods have been proposed[2, 3]. That most methods are based on a system model, which consisted of masses, springs and dampers[4]. The sliders are expressed the mass and the dynamics of the machine stand is expressed the mass, the springs and the dampers. Therefore, control systems of MSVS become complicated especially in comparison with one for 2MS. A 2MS model is a famous general one composed of masses, springs and dampers. Many position control methods of the 2MS have been proposed since the 80's and are employed as one of benchmark problems of the robust control. If the dynamics of the MSVS can be expressed with a 2MS, control methods for the 2MS can be applied to MSVS. It can expect that the control system becomes much more easy in that case.

In this paper, we propose the modeling and position control method for the MSVS. The methods are derived by the similarity between the MSVS and the 2MS. First; we analyze a dynamics of the MSVS and 2MS, and obtained the common mathematical model of these systems in chapter 2 and 3. Then, a transfer function of the MSVS into the transfer function of the 2MS is obtained in chapter 4. We realize the position control of the MSVS with the control system based on the 2MS model. The effectiveness of the proposed method is validated by simulations. The control method used here is the most general one based on PD control with a disturbance observer (chapter 5). Chapter 6 shows the conclusion of this paper.

2 General Model of MSVS

In this section, we describe a general model of MSVS. Figure1 shows a physical model of a linear slider system of MSV. Table1 shows physical parameters of the system shown in Figure1. Eq(1) is a differential equation that descrebes the motion of the linear slider system. A transfer function between f to x_1 is derived from Eq.(1). This transfer function is being used in many papers. Therefore, the Eq.(2) is defined as a transfer function of MSVS based on the general model.

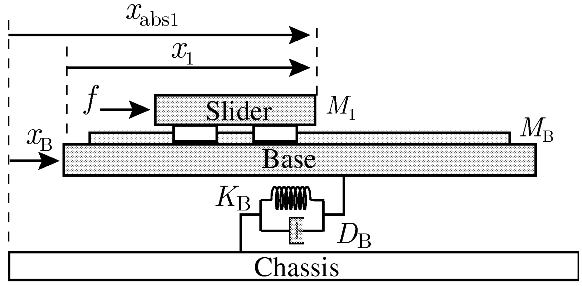

Figure 1: General model of the MSVS

Table 1: Parameters of Figure1

Symbol	Meaning of the Symbols	Unit
x_1	Relative Position of Slider to Base	m
x_{abs1}	Absolute Position of Slider	m
M_1	Mass of Slider	kg
M_B	Mass of Base	kg
f	Force Reference for Slider	N
K_B	Spring Constant	N/m
D_B	Damper Constant	kg/s

$$\begin{cases} M_1\ddot{x}_1 + M_1\ddot{x}_\mathrm{B} = f \\ M_1\ddot{x}_1 + (M_1 + M_\mathrm{B})\,\ddot{x}_\mathrm{B} + D_\mathrm{B}\dot{x}_\mathrm{B} + K_\mathrm{B}x_\mathrm{B} = 0 \end{cases} \tag{1}$$

$$\frac{X_1(s)}{F(s)} = \frac{1}{M_1 s^2} + \frac{1}{M_\mathrm{B}s^2 + D_\mathrm{B}s + K_\mathrm{B}} \tag{2}$$

3 General Model of 2MS

In this section, we describe a general model of 2MS. Figure2 shows a general model of 2MS. The side of the mass which can give it direct input is called 1st side, and the other side is called 2nd side. Parameters in Figure2 are shown in Table2.

A transfer function between f_ref to x_M is derived as shown in Eq.(3). This equation is defined as a transfer function of 2MS based on general model.

$$\frac{X_\mathrm{M}(s)}{F_\mathrm{ref}(s)} = \frac{1}{M_\mathrm{M}} \frac{s^2 + \dfrac{(D_\mathrm{C}s + K_\mathrm{C})}{M_\mathrm{L}}}{s^2\left(s^2 + \dfrac{(D_\mathrm{C}s + K_\mathrm{C})}{M_\mathrm{M}} + \dfrac{(D_\mathrm{C}s + K_\mathrm{C})}{M_\mathrm{L}}\right)} \tag{3}$$

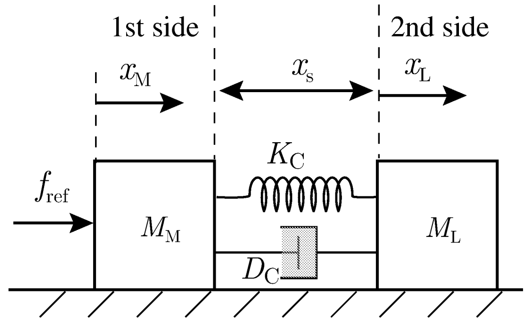

Figure 2: General model of 2MS

Table 2: Parameters of Figure2

Symbol	Meaning of the Symbols	Unit
x_M	Position of 1st side	m
x_L	Position of 2nd side	m
x_s	difference between x_M and x_L	m
M_M	Mass of 1st side	kg
M_L	Mass of 2nd side	kg
f_ref	Force Reference for 1st side	N
K_C	Spring Constant between 1st side and 2nd side	N/m
D_C	Damper Constant between 1st side and 2nd side	kg/s

4 Relationship between the MSVS and the 2MS

Next, we propose a method to transform the MSVS into the 2MS. The method applies the similarity between the MSVS and the 2MS. Eq.(4) can be obtained from Eq.(2).

$$\frac{X_1(s)}{F(s)} = \frac{M_1 + M_\mathrm{B}}{M_1 M_\mathrm{B}} \left\{ \frac{s^2 + \dfrac{D_\mathrm{B}}{M_1 + M_\mathrm{B}}s + \dfrac{K_\mathrm{B}}{M_1 + M_\mathrm{B}}}{s^2\left(s^2 + \dfrac{D_\mathrm{B}}{M_\mathrm{B}}s + \dfrac{K_\mathrm{B}}{M_\mathrm{B}}\right)} \right\} \tag{4}$$

Moreover, new parameters are defined as follows.

$$\begin{cases} M_\mathrm{p} = \dfrac{(M_1 + M_\mathrm{B})\,M_\mathrm{B}}{M_1} \\ M_\mathrm{t} = M_1 + M_\mathrm{B} \\ \alpha = \dfrac{M_1 + M_\mathrm{B}}{M_1} \end{cases} \tag{5}$$

It can be expressed with Eq.(6) when Eq.(4) is collected by using these parameters.

$$\frac{X_1(s)}{F(s)} = \frac{1}{M_\mathrm{p}} \frac{s^2 + \dfrac{(D_\mathrm{B}s + K_\mathrm{B})}{M_\mathrm{t}}}{s^2\left(s^2 + \dfrac{(D_\mathrm{B}s+K_\mathrm{B})}{M_\mathrm{p}} + \dfrac{(D_\mathrm{B}s+K_\mathrm{B})}{M_\mathrm{t}}\right)}\alpha^2 \quad (6)$$

The Eq.(6) is the same form as the Eq.(3) considering that M_p is a mass of 1st side, M_t is a mass of 2nd side and the Eq.(3) is multiplied by constant value. Figure3 shows a block diagram of Eq.(6). Then, x_m and x_l are positions of 1st side and 2nd side respectively, K_c and D_c are spring and damping constant between 1st side and 2nd side in Figure3. Table3 shows a relationship between the MSVS(variables : x_1, x_B, f, parameters : K_B, D_B) and the 2MS(variables : x_m, x_s, f_1, parameters : K_c, D_c). Consequently, the dynamics of the MSVS can be expressed with a 2MS, control methods for the 2MS can be applied to the MSVS. It can be expected that designing the control system becomes easy in that case.

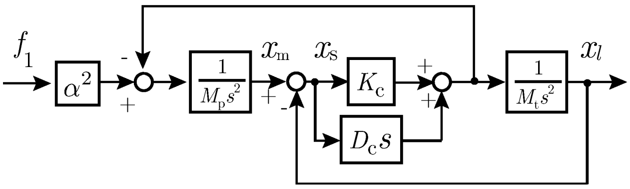

Figure 3: Block diagram of MSVS based on 2MS

Table 3: Relationship between MSVS and 2MS

MSV	2MS	Conversion Coefficient
x_1	x_m	1
x_B	x_s	$\frac{M_1+M_\mathrm{B}}{M_1}$
f	f_1	$\frac{1}{\alpha^2}$
K_B	K_c	1
D_B	D_c	1

5 Simulations

We realize the position control of the MSVS with the control system based on the 2MS model by simulation. Many position control methods of the 2MS have been proposed. The control method used in this paper is the most general one based on PD control with a disturbance observer[5]. Figure4 shows a block diagram of this controller.

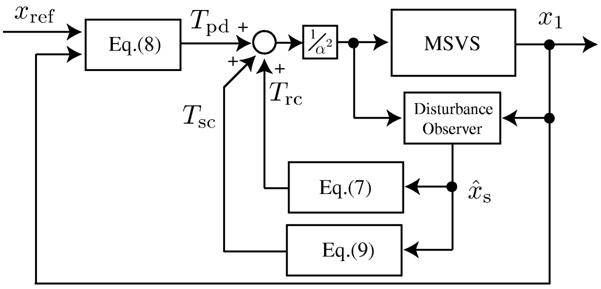

Figure 4: Block diagram of the controller based on 2MS

The purpose of this controller is to transform characteristic equations of 1st side and 2nd side. The characteristic equations after transforming is shown in Eq.(7). This equations of 1st and 2nd side are same form after transforming.

$$\left(s^2 + \beta s + \frac{K_\mathrm{c}}{M_\mathrm{t}}\right)\left(s^2 + K_\mathrm{v}s + K_\mathrm{v}K_\mathrm{p}\right) \quad (7)$$

A torque reference to realize this transform is Eq.(8). F_rc is used for the cancellation of reaction force for 1st side, F_pd is used for position control for 1st side and F_sc is suppression control for 2nd side.

Torque reference

$$F_\mathrm{ref} = \frac{1}{\alpha^2}\left(F_\mathrm{rc} + F_\mathrm{pd} + F_\mathrm{sc}\right) \quad (8)$$

- Cancellation of reaction for 1st side

$$F_\mathrm{rc} = K_\mathrm{c}x_\mathrm{s} \quad (9)$$

- Position control for 1st side (PD feedback)

$$F_\mathrm{pd} = M_\mathrm{p}K_\mathrm{v}\left\{K_\mathrm{p}\left(x_\mathrm{ref} - x_\mathrm{m}\right) - \dot{x}_\mathrm{m}\right\} \quad (10)$$

- Suppression control for 2nd side

$$F_\mathrm{sc} = -\beta\frac{M_\mathrm{p}}{K_\mathrm{c}}(K_\mathrm{c}\dot{x}_\mathrm{s} + K_\mathrm{v}K_\mathrm{c}x_\mathrm{s} + K_\mathrm{v}K_\mathrm{p}\int K_\mathrm{c}x_\mathrm{s}dt) \quad (11)$$

The parameters used for the simulations are shown in the Table4. The parameters shown in Table4 are transformed in the relations of Eq.(5). Figure5 shows simulation result of PD feedback control as conventional method. Figure6 shows simulation results of position control and vibration suppression based on

Table 4: Parameters for simulations

Symbol	Value	Unit
M_1	3.22	kg
M_{B}	42.0	kg
K_{B}	505324	N/m
D_{B}	0.0	kg/s
K_{p}	40	1/s
K_{v}	160	1/s
β	1	

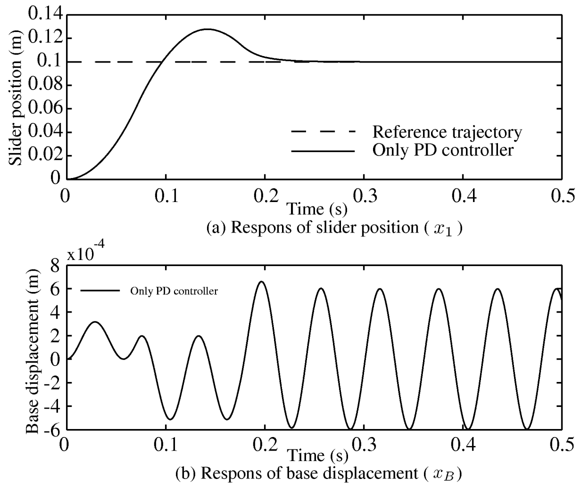

Figure 5: Simulation results of slider position control and vibration suppression based on conventional PD control

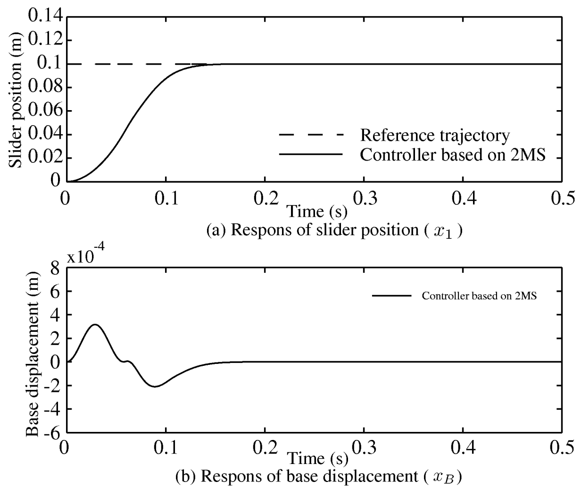

Figure 6: Simulation results of slider position control and vibration suppression based on 2MS

2MS. In Figure5, the slider position has overshoot phenomenon for reference trajectory. Additionally, the base has vibration phenomenon in 15Hz as the character of the spring. By this influence, accurate positioning of the slider cannot be realized. In Figure6, the slider position have no overshoot phenomenon for reference trajectory. Moreover, the base vibration is suppressed by the controller based on 2MS. It is considered that the position control and vibration suppression can be realized using the controller based on 2MS.

6 Conclusion

This paper describes a modeling and position control for a linear slider with Machine Stand Vibration. The methods are derived by the similarity between the MSVS and the 2MS. It is shown that control methods using in 2MS can be applied to MSVS by simulations. Almost all cases of 2MS, the mass of 1st side is smaller than the mass of 2nd side. However, the method discussed here, the mass of 1st side becomes bigger than the other one. The investigation of this point is now in progress.

References

[1] H.Honda, et al, "A Position Control for Serial Twin Sliders with Linear Motor Drive", *IEEJ*, Vol. 124, No. 9 pp. 901-908, 2004. (in Japanese)

[2] H.Zidan, et al, "Feedforward Control Design for Vibration of Machine Stand",*IEEJ*, Vol. 120, No. 3 pp. 404-409, 2000. (in Japanese)

[3] K.Sato, et al, "Adaptive PI Control Method for Positioning Control using Linear Slider - Feedforward Control Approach-", *Proceedings of the IEEE International Conference on Control Applications*, pp.588–593, 2002.

[4] K.Ito, et al, "GA-Based Autonomous Design of Robust Fast and Precise Positioning Considering Machine Stand Vibration Suppression", *IEEJ*, Vol. 124, No. 6 pp. 607-615, 2004. (in Japanese)

[5] H.Tsurumori, et al, "The Vibration control of 2 inertia which made PD control a base", *Proceedings of the 22nd SICE Kyushu Branch Annual Conference*, pp.101–104, 2004. (in Japanese)

The Eleventh International Symposium on Artificial Life and Robotics 2006 (AROB 11th'06),
B-con Plaza, Beppu, Oita, Japan, January 23-25, 2006

Reinforcement learning of switching multiple controllers to control a real robot

Yoichi Tokita† Yutaka Nakamura† Junichiro Yoshimoto‡ Shin Ishii†
† Graduate School of Information Science
Nara Institute of Science and Technology (NAIST)
8916-5 Takayama-cho, Ikoma, Nara 630-0192, Japan
‡ Initial Research Project, Okinawa Institute of Science and Technology
Promotion Corporation

Abstract

Reinforcement learning (RL) for automatic control of real robots is a challenging issue, because they usually have non-linear dynamics with a large number of degrees of freedom. In this study, we propose an RL method that switches controllers which have been developed in the eld of control theory. We apply our method to an automatic control problem of an acrobot simulator. The results show that our method is able to obtain a good controller autonomously and that the robustness against the error in system identi cation is improved.

1 Introduction

Reinforcement learning (RL) methods have been successfully applied to automatic control problems of various dynamical systems, such as balancing control of a cart-pole [1]. In RL, a control rule can be obtained autonomously without any knowledge of the target system. Since most real robots have non-linear dynamics with a large number of degrees of freedom, and the action space would also be large, however, to develop an RL method to deal with such situations is a challenging issue. This di culty is called "curse of dimensionality" in the context of RL, and we formerly proposed an RL method to overcome the di culty, in which the action space was restricted by utilizing the knowledge about the robot and incorporating in part the existing control theory.

In this study, we in particular focus on the control of an acrobot, one of the simplest under-actuated robots, as an instance of dynamical systems. In the eld of control theory, swinging-up and stabilizing this robot can be realized by combining multiple controllers, each of which tries to achieve a local subtask making up the global control task [2] (we call such a local controller an "incomplete controller"). Since the criterion to switch incomplete controllers optimally is theoretically unsolved, however, a human designer must tune the switching way based on trials and errors. Furthermore, precise system parameters, such as the friction coe cient of each joint and the inertia moment of each link, must be known to design the incomplete controllers.

In our previous work [3], the parameters of the target system were estimated by a system identi cation method, and then incomplete controllers were designed based on the identi ed system. We also devised a framework to adaptively switch the incomplete controllers based on RL, then succeeded in desirable control of a real acrobot. However, its successful rate was not so high and the robustness was not su cient. This degeneration of the performance might be due to the inaccurate system identi cation. Since each incomplete controller was designed based on the approximated system, it could be incompatible with the control of the real robot, if the approximation error was not negligible. In this study, therefore, we propose a learning method for improving each incomplete controller by RL, to enhance the compatibility with the real robot system.

2 Acrobot control by switching controller

2.1 Acrobot

The acrobot is an under-actuated robot consisting of two links and two joints, as shown in Fig. 1. This robot is regarded as a simple model of a gymnast swinging on a high bar. The torque can be applied to the second joint (corresponding to the gymnast's waist), but not to the rst joint (corresponding to the gymnast's hand on the bar). A state of the acrobot is represented by a four-dimensional vector: angles of

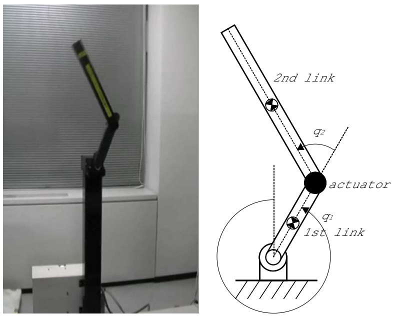

(a) (b)

Figure 1: Acrobot

the two joints (denoted by q_1 and q_2 in Fig. 1), and their angular velocities. The objective of the control task is to swing up and balance the acrobot at the upright position $(q_1, q_2, \dot{q}_1, \dot{q}_2) = (0, 0, 0, 0)$ from the hanging position $(q_1, q_2, \dot{q}_1, \dot{q}_2) = (-\pi, 0, 0, 0)$.

2.2 Switching control

Spong realized swinging-up and stabilizing control of the acrobot by designing several incomplete controllers and a rule to switch them [2], where each incomplete controller is a controller for a local subtask (e.g., stabilizing at the upright position or swinging up) and used in a particular situation. In this control scheme, the global controller (GC) is composed of a switching controller (SC) and a set of incomplete controllers (ICs), in which the SC observes the state of the robot and selects a single IC, and then the selected IC generates a control torque.

Although the dynamics of the acrobot are essential for designing ICs, it is difficult to directly make use of it in an actual situation. Therefore, it is often required to perform system identification by operating the robot reasonably. Then, ICs are designed based on the identified system equation. In our study's case, we employ the following five ICs: an LQR controller for stabilizing at the upright position, Σ_1 and Σ_2 controllers for swinging-up the acrobot from the hanging position, a brake controller for avoiding large angular velocities, and a τ_0 controller for yielding no torque (See [2][3]).

By appropriately switching these ICs, the swinging-up and stabilizing control of the acrobot can be realized [2] but the way to design the optimal SC theoretically has been unknown. We formerly proposed an RL method to obtain an appropriate SC to combine and switch ICs being based on the identified system. The switching rule was then modified to be suited to the real robot, but ICs, which were suited to the identified system, were not trained by using the real robot. This may cause the performance degeneration of the obtained controller.

3 Method

In our previous work [3], the global control rule (GC) for the real acrobot was obtained by the following procedure.

1. System identification
2. Design of ICs based on the identified system
3. Acquisition of SC by RL using the computer simulation
4. Tuning of SC by additional RL using the real robot

As a result, we obtained a GC that realizes swinging-up and stabilizing the real robot, but the successful rate remained around 50%.

Because the estimation of system equation from observed trajectories of the target system has instability due to the sampling bias, the identified system may be different from the true one. Therefore, ICs, designed for such an identified system, may not necessarily suit to the target system. To overcome this problem, in this study, ICs are designed to have internal parameters so that they are adjusted by RL. Because the internal parameters are trained through interactions with the target system, ICs are expected to become a suitable one to the target system. The learning of the switching rule (SC) and that of IC parameters are alternately performed in our new method. Our method can be applied, especially when the accuracy of system identification is not sufficient.

3.1 Training of SC

The output of the SC is an index of ICs, denoted by a, and the action is selected according to action-value function:

$$a(t) = \arg\max_a Q(\mathbf{x}(t), a). \quad (1)$$

The action-value function $Q(\mathbf{x}, a)$ indicates the utility, expected future rewards, if the robot is controlled by an IC a at a robot's state $\mathbf{x}$, and is trained based on the SARSA(λ) algorithm [5].

3.2 Training of IC

In this learning phase, we assume that action a is deterministically selected by the SC. Under this assumption, the control torque u can be speci ed for the robot's state as

$$u = f(\mathbf{x}; \mathbf{W}), \tag{2}$$

where $\mathbf{W}$ denotes a set of parameters of ICs, and is updated by RL . We employ a policy gradient method [4] for the training of this parameter vector, and we assume that the control torque is generated by equation (2) plus white Gaussian noise; the distribution of control torques follows a normal distribution whose mean is given by equation (2).

3.3 Learning procedure

Our learning procedure is summarized as follows.

1. System identi cation
   (a) Observe time-series of states and control signals by operating the real robot
   (b) Design ICs for the identi ed system
2. Learning on the identi ed system
   (a) Learning of the SC
3. Additional learning on the target system
   (a) Learning of the ICs
   (b) Learning of the SC

4 Experiment

First, we performed the system identi cation. Two datasets X_1 and X_2 were obtained from system trajectories by operating the real robot, and two system parameters $\hat{\Theta}_1$ and $\hat{\Theta}_2$ were calculated from the two datasets. Since these datasets were di erent from each other due to the sampling bias, system parameters $\hat{\Theta}_1$ and $\hat{\Theta}_2$ were not necessarily the same. We then denote the di erently identi ed systems by Ψ_1 and Ψ_2, respectively. It is not guaranteed whether a good controller for system Ψ_1 works well for system Ψ_2 as well.

In this experiment, we assumed that system Ψ_2 was the real target system while system Ψ_1 was the identi ed and hence approximated system. We rst designed ICs for system Ψ_1 (parameter of these ICs was denoted by $\mathbf{W_1}$) and then performed RL of SC on system Ψ_1. After a good SC was obtained, we performed additional learning of ICs on system Ψ_2 and subsequently RL of SC on system Ψ_2.

The GC observes the acrobot's state with a xed time interval of 0.01 sec, and outputs a control torque according to the IC selected at the state. The control torque was limited within the range between $-4.5(Nm)$ and $4.5(Nm)$. At each time step, the GC (and SC) receives an immediate reward de ned as

$$R(x) = 0.1 \exp(-16 \|\mathbf{x}\|), \tag{3}$$

where $\|\cdot\|$ denotes the Euclidean norm. This reward becomes the largest at the goal state $\mathbf{x} = (0, 0, 0, 0)$; the return is expected to be maximum when the robot is stabilized at the upright position. At the beginning of each episode, the robot was set to an initial state, and each episode was terminated after 60 sec elapsed.

We employed a CMAC to approximate the action-value function [6] for the SC, which consisted of 20 maps with di erent o sets. In the learning phase of ICs, we employed a radial basis function (RBF) network to approximate the state-value function used by the policy gradient method. The center of each RBF was located at a lattice point in the state space.

Learning of SC for system Ψ_1 Fig. 2 shows the learning curve in the SC learning phase performed on system Ψ_1. In this case, the parameters of ICs were xed at $\mathbf{W_1}$. After about 10,000 learning episodes, a good controller that can stabilize the robot at the upright position was obtained. Let $Q_1(\mathbf{x}, a)$ be the action-value function obtained in this phase.

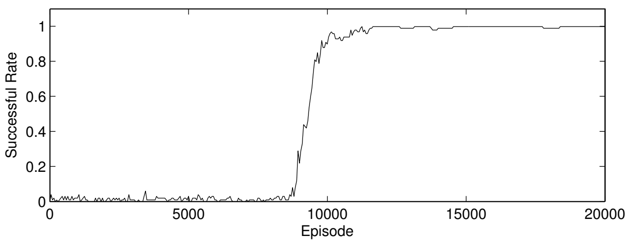

Figure 2: E ectiveness of SC-learning on Ψ_1

Learning of ICs for system Ψ_2 RL of ICs was performed on system Ψ_2. In this phase, the action-value function of SC was xed at $Q_1(\mathbf{x}, a)$. Fig. 3 shows the learning curve. Although the controller might be incompatible with this control task, the controller grew to achieve the task with the success rate of about 50%

after 5,000 learning episodes. Let $\mathbf{W_2}$ be the parameters of ICs obtained in this phase.

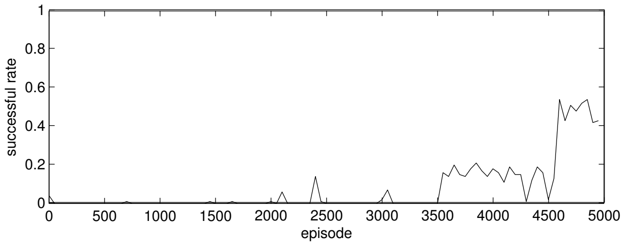

Figure 3: E ectiveness of ICs-learning on Ψ_2

Learning of SC on Ψ_2 In this phase, RL was performed to train the SC by using system Ψ_2, while the parameters of ICs were xed at $\mathbf{W_2}$. Fig. 4 shows the learning curve. After 2,000 learning episodes, a good controller was obtained. Let $Q_2(\mathbf{x}, a)$ be the action-value function obtained in this phase. Fig. 5 shows a typical control sequence using the control rule ($\mathbf{W}_2$ and $Q_2(\mathbf{x}, a)$) after this learning phase.

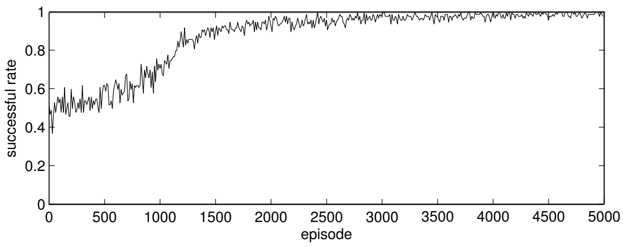

Figure 4: E ectiveness of SC-learning on Ψ_2

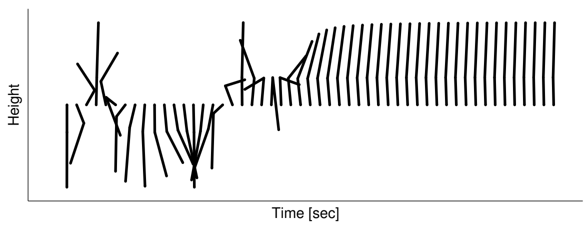

Figure 5: Example of controlling system Ψ_2

Discussion For comparison, we also performed an additional RL of the SC on system Ψ_2 where the parameters of ICs were xed at $\mathbf{W_1}$, but no good controller was obtained in this case. This result showed that ICs should be trained at least in our experimental setting. Recently, system identi cation techniques have been improved but it is still di cult to be applied to real robots, because there are many factors to be considered, for example, sensor noise and time-delay of signals. Although our proposed method is based on the control theory and the system identi cation, it can be applied to situations where the system identi cation is not very reliable.

5 Conclusion

In this study, we proposed an RL method for training of a controller consisting of several incomplete controllers, where not only the switching controller but also incomplete controllers were trained. We applied our method to the swinging-up and stabilization control problem of the acrobot simulator, and the results showed that a good controller can be obtained by our RL method.

On the other hand, a large number of training episodes was necessary for obtaining a good controller. This is a critical issue in implementing our scheme on a real robot, because the real robot would be broken by iterating a large number of episodes. To improve the learning speed is our urgent future work.

References

[1] K. Doya, "Reinforcement learning in continuous time and space," Neural Computation, 12, pp.219-245, 2000.

[2] M. W. Spong, "The swing up control problem for the acrobot," IEEE Control System Magazine, 15, pp.49-55, 1995.

[3] M. Nishimura, J. Yoshimoto, Y. Tokita, Y. Nakamura and S. Ishii, "Control of real acrobot by learning the switching rule of multiple controllers," The IEICE Transaction on Fundamentals of Electronics and Computer Science (JAPANESE EDITION), J88-A(5), pp.646-657, 2005.

[4] H. Kimura and S. Kobayashi, "An analysis of actor/critic algorithms using eligibility traces: reinforcement learning with imperfect value function," 15th International Conference on Machine Learning, pp.278-286, 1998.

[5] R. S. Sutton, "Learning to predict by the methods of temporal differences," Machine Learning, 3, pp.9-44, 1988.

[6] R. S. Sutton, "Generalization in reinforcement learning: Successful examples using sparse coarse coding," Advance in Neural Information Processing Systems, 8, pp.1038-1034, 1996.

Real Time Control of Humanoid-Robot Cooperative Motion Using a Genetic Algorithm and Neural Network

Kook-Jin Choi
Dept. of Mechanical Design and Manufacturing
Changwon National University
Changwon, Gyeongnam, 641-773, Korea
choi@changwon.ac.kr

Yoon-Kwon Hwang
Dept. of Mechanical Design and Manufacturing
Changwon National University
Changwon, Gyeongnam, 641-773, Korea
ykhwang @sarim.changwon.ac.kr

Dae Sun Hong
Dept. of Mechanical Design and Manufacturing
Changwon National University
Changwon, Gyeongnam, 641-773, Korea
dshong @changwon.ac.kr

Abstract

This study proposes a method to achieve real time posture control of humanoid robots using a neural network and genetic algorithm. Here, a humanoid-robot motion pushing an object is considered. When the robot takes a motion to push an object, the palm and the sole are assumed to be fixed at the object and the ground, respectively, and sense the reaction force from the object and the ground. The reaction force results in change of torques of the joints. This study finds an optimized posture using a genetic algorithm such that torques are evenly distributed over the all joints. Then, a number of different optimized postures are generated from varying the reaction forces at the palm and the sole. The data is to be used as training patterns of MLP(Multi-Layer Perceptron) neural network with BP(Back Propagation) learning algorithm. Using the trained neural network, humanoid robot can find the optimal posture at different reaction forces in real time. To verify the effectiveness of the proposed method, a number of simulations are carried out. The simulation result shows that the proposed method can be used for real time posture control of humanoid robots.

Keywords : Humanoid Robot, Optimization, Genetic Algorithm, Neural Network, Cooperative motion.

1. Introduction

A number of research works on the motion control of humanoid robots have been reported on the basis of accurate kinematics and dynamic analysis. However, it has been known that human being takes a motion or posture by learning and experience. Also, human involuntarily takes a stable motion or posture against the inside or outside environment. This study proposes a method to achieve real time posture control of humanoid robots using a neural network and genetic algorithm.

Humanoid robots have a number of joints, essential components for robots' motion, and each joint usually consists of pair of an actuator and a reducer. When a humanoid robot performs additional work as well as walking, torques of the joint actuators along its motion need to be adequately controlled, i.e. optimized, so as to increase working capabilities such as enlargement of working space and increase of overall working force.

Until now, a number of research works on optimization of humanoid-robot motion have been reported: optimization of postures for generation large force using nonlinear equations[1][2], optimization of joint torque ratio using a steepest descent method[3], generating large Cartesian force with manipulator combination[4], and optimization of the locomotion trajectory and velocity using genetic algorithms[5][6]. The nonlinear-equation-based method and the steepest descent method can find analytic solutions. However, they not only might not find a valid solution but also takes too much time to find solutions when the degree of freedom of motion becomes larger or the robot motion becomes more complex. The works on optimization of trajectory and velocity[5][6] are restricted to used for stabilizing robot locomotion under no external force. Thus, when humanoid robots are required to work with external environment, new efficient approaches to optimization of robot motion in consideration of external forces are required.

For such purpose, this paper proposes a method of optimization of humanoid-robot cooperative motion with respect to external force using a genetic algorithm and neural network. This study adopts an eighteen degree-of-freedom humanoid robot, and a motion pushing an object is considered. When the robot takes a motion to push an object, the palm and the sole are assumed to be fixed at the object and the ground, respectively, and sense the reaction force from the object and the ground. The reaction force results in change of torques of the joints. This study finds an optimized posture using a genetic algorithm such that torques are evenly distributed over the all joints. Then, a number of different optimized postures are generated from varying the reaction forces at the palm and the sole. The data is to be used as training patterns of MLP neural network with BP learning algorithm. Using the trained neural network, humanoid robot can find the optimal posture at different reaction forces in real time. To verify the effectiveness of the proposed method, a number of simulations are carried out. The simulation result shows that the proposed method can be used for real time posture control of humanoid robots.

2. Modeling and analysis of humanoid robot

2.1 Degree of freedom and coordinate system

This study considers a humanoid robot with eighteen degrees of motion: two legs each of which having six degrees and two arms each of which having three degrees of freedom. Fig. 1 shows the degree of freedom of motion and the coordinate system. Usually, coordinate system for robots follows D-H parameter system. However, this study takes a point fixed to ground as the origin, and follows a joint coordinate system for clarity.

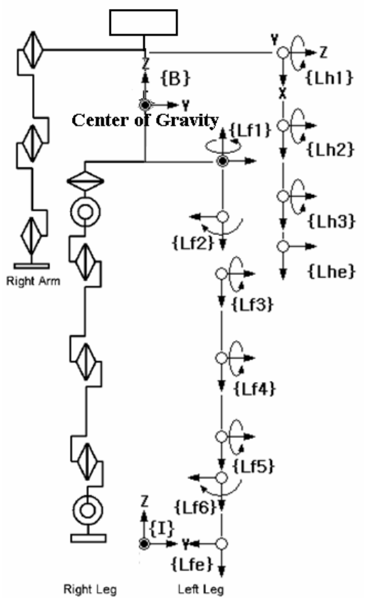

Fig. 1. Degree of freedom and coordinate system.

2.2 Jacobian analysis and torque

Forward kinematics of a robot manipulator expresses the relation of the joint rotation and the end-effector displacement. Based upon the forward kinematics, the end-effector velocity is determined from the angular velocity of joint and the Jacobian. That is, the Jacobian $\boldsymbol{J}$ plays a role of transforming the angular velocities ($\dot{\boldsymbol{\theta}}_i$) the joints to the velocities of the end effector (${}^0_n\dot{\boldsymbol{d}}$) in Cartesian space, the relation is expressed by

$$\dot{X} = J\dot{\theta} \qquad (1)$$

where $\boldsymbol{\theta}$ is a vector consisting of the joint angles, while $\boldsymbol{X}$ is a vector consisting of the displacements of the end effector. The Jacobian matrix is expressed by a 6×n (n: the number of joints) matrix: upper three rows for linear velocity and lower three rows for angular velocity. The Jacobian matrix deriving from the forward kinematics is express by the following equations:

$${}^0_6J_{Leg} = \begin{bmatrix} {}^0_6J_{vLeg} \\ {}^0_6J_{\varpi Leg} \end{bmatrix} = \begin{bmatrix} {}^0_1\boldsymbol{R\kappa}\times({}^0_e\boldsymbol{P}-{}^0_1\boldsymbol{P}) & \cdots & {}^0_6\boldsymbol{R\kappa}\times({}^0_e\boldsymbol{P}-{}^0_6\boldsymbol{P}) \\ {}^0_1\boldsymbol{R\kappa} & \cdots & {}^0_6\boldsymbol{R\kappa} \end{bmatrix} \qquad (2)$$

$${}^0_3J_{Arm} = \begin{bmatrix} {}^0_3J_{vArm} \\ {}^0_3J_{\varpi Arm} \end{bmatrix} = \begin{bmatrix} {}^0_1\boldsymbol{R\kappa}\times({}^0_e\boldsymbol{P}-{}^0_1\boldsymbol{P}) & \cdots & {}^0_3\boldsymbol{R\kappa}\times({}^0_e\boldsymbol{P}-{}^0_3\boldsymbol{P}) \\ {}^0_1\boldsymbol{R\kappa} & \cdots & {}^0_3\boldsymbol{R\kappa} \end{bmatrix} \qquad (3)$$

The torques can be found from the Jacobian matrix. Since a work can be represented by the inner product of a force vector and a displacement vector, the torques are derived by the following equations:

$$\begin{aligned} \boldsymbol{F}^T \cdot \delta x &= \tau^T \cdot \delta\boldsymbol{\Theta} \\ \delta x &= \boldsymbol{J} \cdot \delta\boldsymbol{\Theta} \\ \boldsymbol{F}^T \cdot \boldsymbol{J} \cdot \delta\boldsymbol{\Theta} &= \boldsymbol{\tau}^T \cdot \delta\boldsymbol{\Theta} \\ \boldsymbol{F}^T \cdot \boldsymbol{J} &= \boldsymbol{\tau}^T \\ \boldsymbol{\tau} &= \boldsymbol{J}^T \cdot \boldsymbol{F} \end{aligned} \qquad (4)$$

The initial posture considered in this study is shown in Fig. 2. The figure shows that palms of both hands are ready to push an object while the left leg takes a step forward. Under such initial posture, forces applied to the palms of hands and the soles of feet are assumed to be constant, then the torques are calculated from the constant forces.

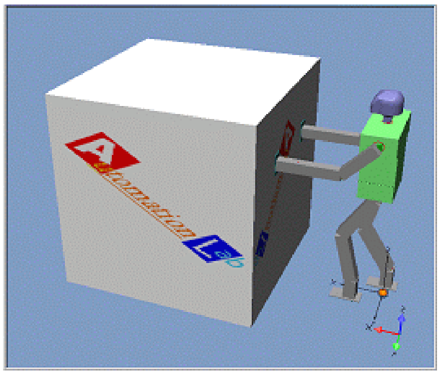

Fig. 2. Initial posture of the humanoid robot.

The maximum torque of the leg is generated at joint 9 corresponding to the left knee, while the maximum one of the hand is at joint 13 and 16 corresponding to the shoulder joints.

3. Optimization using a Genetic Algorithm

3.1 Parameters and objective functions

Genetic algorithm is a search algorithm which simulates evolution process of survival of the fittest with crossover and mutation in ecology system, and can be applied to find solution in various complex optimization problems. This study adopts a genetic algorithm with roulette wheel selection, simple crossover and mutation. In addition, elitist strategy, the strongest individual will be survived in the next generation, is used for enhancing performance of the algorithm. Table 1 shows parameters used in this algorithm.

Table 1. Parameters of the genetic algorithm.

Parameters	Value
Maximum Generation	300
Population Size	100
Number of Variables	3
Probability of Crossover, Pc	0.8
Probability of Mutation, Pm	0.01
Range of Px (COG of robot)	$0 \leq$ Px ≤ 0.15 (m)
Range of Pz (COG of robot)	$0.6 \leq$ Pz ≤ 0.8 (m)
Range of Ry (COG of robot)	$-15 \leq$ Ry ≤ 15 (°)

In this study, two kinds of objective functions are considered, as shown in Table 2. In the table, Case1 aims to maximize the overall surplus torque ratio for increasing overall acting force, while Case2 aims to maximize the surplus torque of the actuator having the smallest one.

Table 2. Objective functions for optimization.

No	Name	Objective function	Purpose
1	Case1	$F(x) = \sum_{i=\text{`}}^{n} \left(1 - \left\| \frac{\tau_i}{\tau_{\max i}} \right\|^2 \right)$	Maximize the surplus torque ratio
2	Case2	$F(x) = \wedge(\tau_{\max i} - \tau_i)$	Maximize the minimum surplus torque

3.2 Simulation and results

Based upon the objective functions in Table 2, a series of simulations are carried out, and the results are shown in Fig. 3 and Fig. 4.

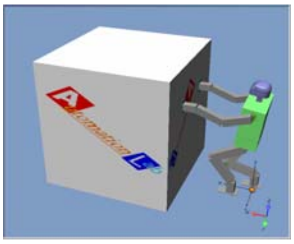

Fig. 3. Result for Case1.

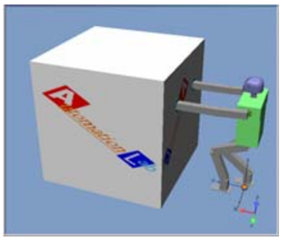

Fig. 4. Result for Case2.

Fig. 3 shows the simulation results for Case1. Sum of the torque ratios is reduced by 25.56%: 101.75 at the initial posture to 75.22 at the final posture. This result means that the acting force can be increased as much as the torque ratio has been reduced. Fig. 3 shows that the robot posture is rotated by -8° around the Y-axis. The apparent posture seems to be different from that of normal human. This result comes from the fact that the humanoid robot does not have the backbone that human being has. The torque ratio at the hip joints has been greatly reduced, while the ratio at the right knee joint has been increased. As a result, the sum of torque ratios for all joints has been reduced. Fig. 4 shows the results for Case2. Sum of generating torque ratios is reduced by 29.95%: 101.05 at the initial posture to 71.10 at the final posture. It should be noted that the arms have been moved near the singular point for minimizing the torque of the arms; This result is coincide with the objective of Case2. The arm motion seems to be identical to human action that he stretches out his hand when he feels strong force at the palms. Also Fig. 4 shows that the surplus torque of the arm joint at the final posture is 57.47Nm. Actually, the maximum torque of the motor is known to be 57.8Nm, thus the generating torque is shown to be only 0.33Nm. It can be seen from this result that the toque ratio at the arm joint is remarkably reduced, but torque ratios at both the hip joints and the right knee joint are slightly changed.

The simulation results show that surplus torque has been increased for both cases, that is, acting force has been increased at the final posture. Thus, it is concluded that the proposed method can be extended to the control of torques for humanoid robots cooperative with external environment.

4. Neural network for real time control

4.1 Multi-layer perceptron

To achieve real time control of humanoid-robot cooperative motion, a neural network with MLP(Multi-Layer Perceptron) is used in this study. Fig. 5 shows MLP for real time control which is composed of three layers: input, hidden and output layer. Here, BP(Back Propagation) learning algorithm is used for training.

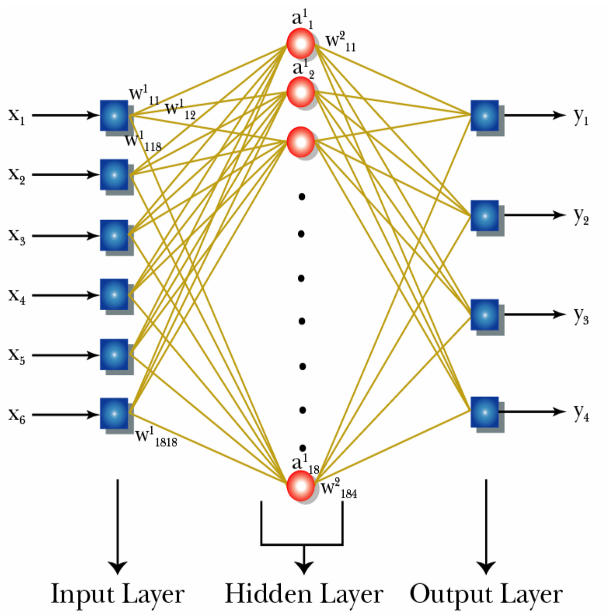

Fig. 5. MLP structure for real time control.

Reaction forces at the palm and sole are used as inputs, and the output is optimal posture.

Table 3. Parameters of the neural network.

Parameters	Value
Number of total node	28
Learning rate	0.1
Momentum rate	0.9
Training step	500,000

A number of different optimized postures obtained from the above GA algorithm are used as training pattern of MLP. Table 3 shows the parameters used in this study.

4.2 Result of real time control

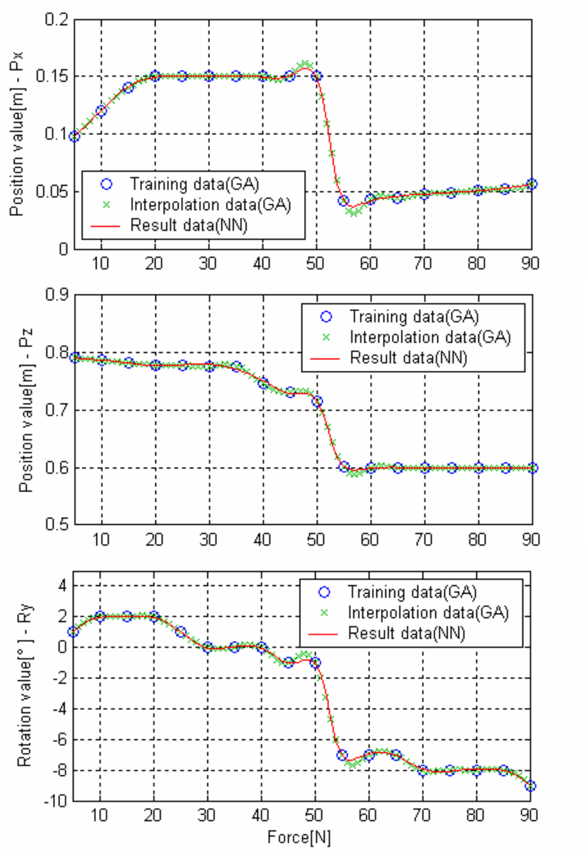

Fig. 6. Result from the neural network.

In Fig. 6, blue circles are training data, green cross marks are interpolated training data, and red line is the output from the trained neural network. It can be seen from the graphs that the neural network outputs are successfully generalized to the result of the GA. It means, trained neural network can

5. Conclusion

This paper proposed a method of real time control for humanoid-robots using a genetic algorithm and neural network. An eighteen degree-of-freedom humanoid robot is adopted, and a motion pushing an object is considered. Then, an optimized posture is found by a genetic algorithm such that torques are evenly distributed over the all joints. To achieve real time control for humanoid robots, this study adopts an MLP neural network with BP learning algorithm in which optimized postures obtained from the above GA algorithm and used as the training patterns. To verify the effectiveness of the proposed method, a number of simulations were carried out by the trained neural network. The result shows that humanoid robot can find optimal postures at different reaction forces in real time. It can be seen that the proposed method can be used for real time posture control of humanoid robots. In further research, more complex and various tasks are considered to improve the proposed method.

Acknowledgment

This work was supported by the Korea Science and Engineering Foundation (KOSEF) through the Machine Tool Research Center at Changwon National University.

References

[1] H. Yoshida, K. Inoue, T. Arai, and T. Mae, "Mobile Manipulation of Humanoid Robots Optimal Posture for Generating Large Force Based on Statics" International Conference on Robotics & Automation, pp. 2271-2276, Washington D.C., May, 2002.

[2] Y. Yokokohji, S. Nomoto, and T. Yoshikawa, "Static Evaluation of Humanoid Robot Postures Constrained to the Surrounding Environment through their Limbs" International Conference on Robotics & Automation, pp. 1856-1863, Washington D.C., May, 2002.

[3] C.B. Kim and H.S. Cho, "A Study on the Trajectory Optimization Planning of Biped Walking Machine" (in Korean) Journal of the Korean Society of Precision Engineering Vol. 15, No. 3, pp. 157-167, March, 1998.

[4] Y.F. Zheng, and Q. Yin, "Coordinating multilimbed robots for generating large Cartesian force" Proceedings 1990 IEEE International Conference on Robotics and Automation, vol.3, pp.1653-8, 1990.

[5] L. Rodrigues, M. Prado, P. Tavares, K. Da Silva, and A. Rosa, "simulation and control of biped locomotion ga optimization" Proceedings of 1996 IEEE International Conference on Evolutionary Computation, pp.390-5, 1996

[6] J.S. Gong, K.S. Han and J.G. Kim, "A Study on Genetic Algorithm-based Biped Robot System"(in Korean) Journal of the Korean Society of Precision Engineering Vol. 20, No, 8, pp. 135-143, August, 2003.

The Eleventh International Symposium on Artificial Life and Robotics 2006 (AROB 11th'06),
B-con Plaza, Beppu, Oita, Japan, January 23-25, 2006

Navigation system for an autonomous robot using an ocellus camera in indoor environment

Takuma Umeno **Eiji Hayashi**
Department of Mechanical Information Science and Technology
Faculty of Computer Science and Systems Engineering, Kyushu Institute of Technology
680-4, Kawazu, Iizuka-City, Fukuoka Prefecture, Japan

Key Words: Personal robot, Autonomous driving, Ocellus camera

Abstract

We are attempting to develop an autonomous personal robot that has the ability to perform practical tasks in a human living environment by using information derived from sensors and a knowledge database. When a robot is made to adjust to a human environment, the issue of safety must be considered in regard to its autonomous movement. Thus, robots absolutely require systems that can recognize the external world and perform correct driving control. We have thus developed a navigation system for an autonomous robot. The system requires only image data captured by an ocellus CCD camera. This navigation system has two functions: One is to determine whether or not the robot is driving itself accurately down a corridor. The other is to allow the robot to search for obstacles present on the floor. We applied this system to a robot in an indoor environment and in a discussion of our experimental results considered the system's advantages and problems.

1. Introduction

Currently, autonomous self-driving robots are expected to provide various services within humans' living environments. Such robotic technology is already seeing practical use in industry. But so far the robots for industry simply follow a given motion by humans. Therefore, we are developing an autonomous personal robot with the ability to perform practical tasks in a human living environment by using information derived from sensors and a knowledge database.

Our robot has a drive mechanism consisting of two front wheels and one back wheel. The front wheels are attached to a motor that operates the wheels on either side independently while the back wheel is a passive castor wheel. This method has the advantage that a far smaller turn can be negotiated than, for instance, that using a steering system that steers the wheel of a passenger car. DC servo motors are used for the robot's drive mechanism, and position control and speed control are achieved by the drive mechanism's control system. The robot also has two arms and hands and sensors; these devices enable the robot to respond to various demands. An installed wireless LAN can provide a remote control for humans. All devices are controlled by a PC, and lead batteries supply electric power.

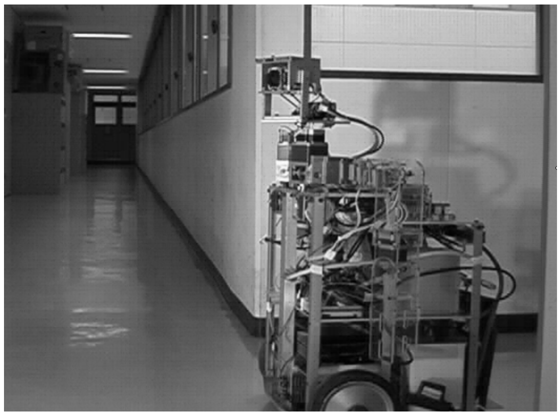

Fig. 1 Robot appearance

The navigation system uses only an ocellus CCD camera and processes the image information displayed by that camera. In order to detect the robot's distance errors in a corridor, the system uses the sides of the corridor as feature parameters and extracts them using the Hough transformation algorism. Thus, this system allows the robot to advance in a straight line without distance errors, because the changing amounts of feature elements extracted from actual images are compared with the ones calculated from the knowledge database. In order to detect obstacles, the system extracts the pixel group whose pixel groups are much different from the main background pixels and interprets them as obstacles. The system can predict the distances to the obstacles and also the obstacle's height and width by using the extracted information and attached drive encoders.

2. Visual feedback system for autonomous driving

2.1 Outline

We developed a visual feedback system for robots that can detect distance errors using image information captured by an ocelus CCD camera. First of all, as an initial step in developing the overall system, we have started to develop a system that enables the robot to advance in a straight line in corridors. This visual feedback system detects the errors in distance calculation from the accurate driving course when the robot is advancing.

2.2 Method for estimating distance error

We have considered that the most significant feature elements in an image are the lines on the sides of a corridor. We applied the Hough transformation algorism to the system for image processing in order to extract lines on an image as feature elements. The processing flow is as follows.

Ⅰ. Image Acquisition

The image obtained by the CCD camera is read into a PC in the robot. This visual processing system uses only an 8-bit gray-scale image.

Ⅱ. Edge processing

The system uses Sobel edge enhancement.

.

Ⅲ. Segmentation processing

To limit the extracted data that are required for form extraction, the system performs Segmentation processing.

Ⅳ. Thinning processing

The edge extracted by the edge processing has line width. In order to decrease the amount of calculation necessary and to stabilize the Hough transformation, the system performs thinning processing.

Ⅴ. Hough transformation and Characteristic point

The Hough transformation can extract the straight lines contained in an image.

For detecting the robot's distance errors, the system should evaluate the extracted straight lines. So, the system uses the pattern database. This database can show the predicted straight lines changed by advancement situation of robot. Figure 2 shows the pattern database. The system compares the extracted straight lines in an image with the lines given by the pattern database. As a result, the system can estimate the distance errors.

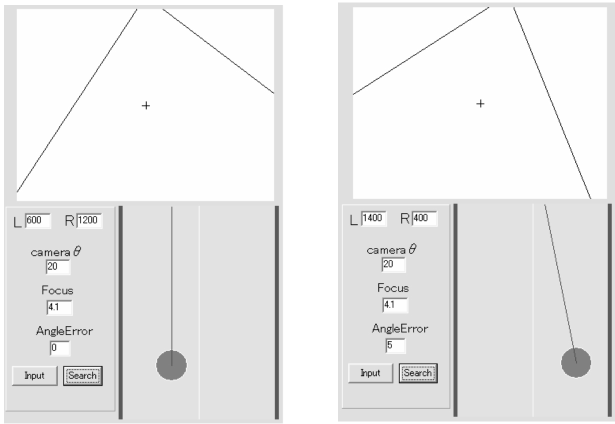

Fig2. Patterns of straight lines based on robot's position

2.3 Experiment

We let the system work continuously while the robot was advancing down a corridor. We evaluate the availability of system by considering whether or not the system can estimate the distance error accurately. Figure 3 shows the straight lines extracted by the system in the case of that the robot advances straight. Figure 4 shows that the robot experiences a distance error to left. The results of the experiment show that the system was able to detect distance errors at an accuracy of +-5cm.

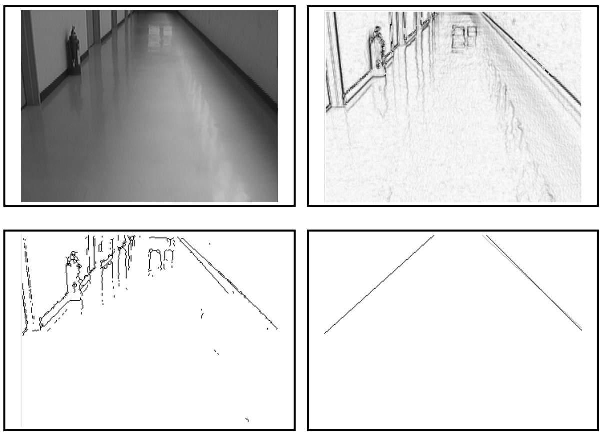

Fig3. A result when the robot drives itself correctly

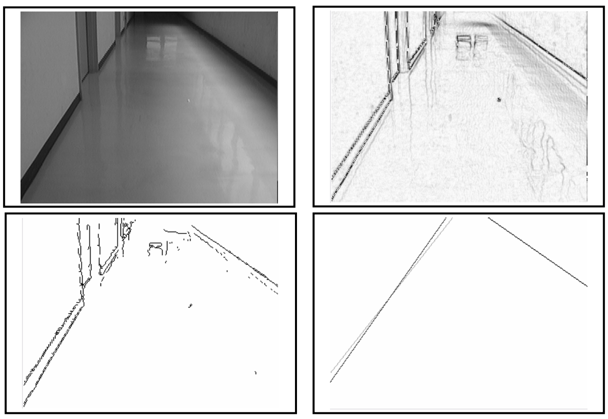

Fig4. A result when the robot generates a driving error

3. The visual processing system

3.1 Outline of the system

In order to ensure that the robot can drive safely in an indoor environment, the system must detect obstacles. Thus, data for avoiding obstacles is needed. We have developed a system of recognizing obstacle that uses only image data captured by an ocellus CCD camera. The purpose of this system is to enable the robot to detect obstacles and roughly recognize an obstacle's size and position.

3.2 Method of extracting obstacles

First of all, the system converts 24bit RGB image data into HSV data. The system samples a group of image pixels in a rectangular region at the bottom center of an image. The system uses the group of image data inside this region as its sample image data. The system uses the deflection calculated by the sample data. The system extracts the floor region in terms of the difference of all pixels in the image.
Figure 5 shows an extracted obstacle.

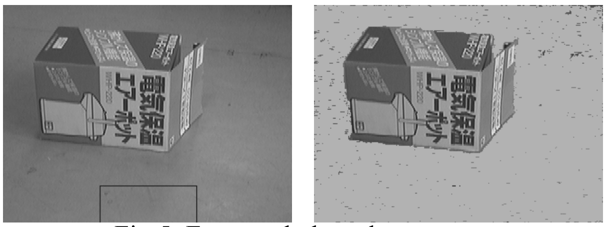

Fig.5 Extracted obstacle.

The conditions of a real environment shift due to changes in light and shadows. Therefore, it is considered that this system is a source of some errors. We added the edge enhancement processing to the system so that the system can extract objects more accurately.

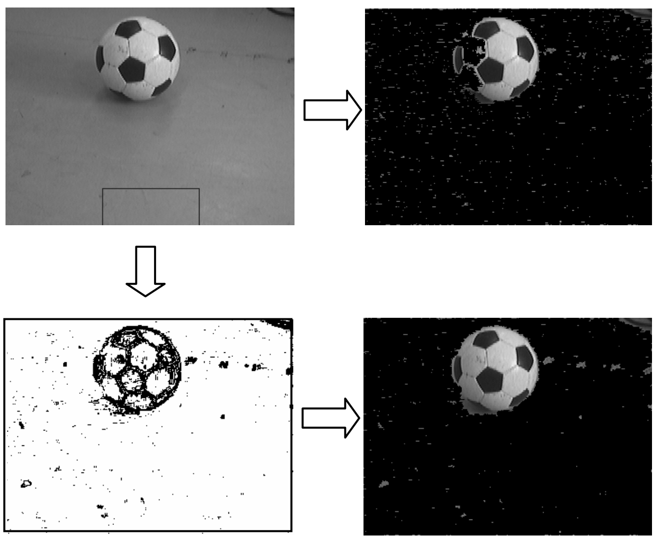

Fig.6 Obstacle extracted using edge data.

The chain code is used to make one set of each group of image pixels extracted from image. The group of image pixels that leads to the detection of an obstacle is distinguished by this process.

Fig.7 Chain code.

Next, the system analyzes the object that has been determined to be an obstacle. We define the lower side of a group of image pixels as the distance to the object, and the system presumes the width of the obstacle based on the width of a group of image pixels. In addition, we defined the uppermost part of a group of image pixels as the height or a depth of the object. The robot runs on the floor side, and presumes the height of the obstacle based on the position of the change in the image pixel group, the camera position, and the angle between the two images.

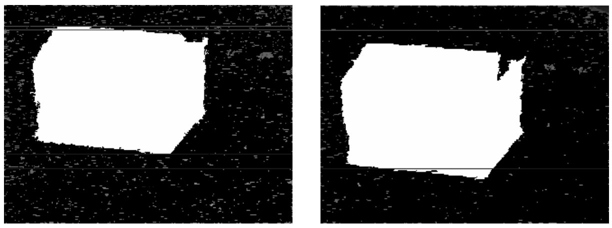

Fig.8 Estimation about obstacle's data

The data identified by the system as an obstacle is reflected in the decision processing part of the robot. As a result, the robot can roughly recognize the obstacle. Figure 9 presents an image showing the obstacle in the system's virtual space.

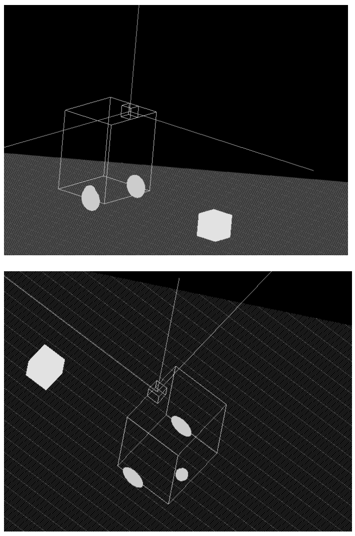

Fig.9 Obstacle in virtual space

The entire flow of the obstacle extraction process is shown below.

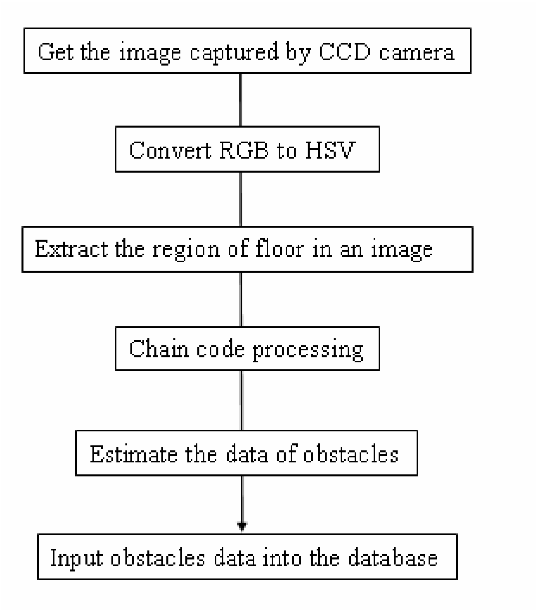

Fig.10 System flow.

4. Conclusions

We have proposed a system that enables an autonomous robot to navigate an indoor environment using only an ocellus camera.

The developed system could produce visual feedback and successfully recognize objects when the robot drives down a corridor. The system could also obtain available information necessary for the robot's safety using a visual approach.

Our next subject of study is to develop a system for action planning.

References

[1] Funakubo, Process and recognition of the vision pattern, Keigakusyuppan, 1990.

[2] Shinoda, Self-driven robot on the grand, Journal of the Robotics Society of Japan, Vol. 18, No.7, pp.928-932. 2000.

[3] Toru Azuma, Yoshihiro Takenaga, Eiji Hayashi, Development of a self-driven personal robot、Artificial Life and Robotics(AROB 8th '03)、pp.1-3、Oita, Japan, 2003

[4] Eiji Hayashi, Keisuke Ikeda, Development of a system for self-driving by an autonomous robot, proceeding of 10th international symposium on artificial life and robotics, Vol.10th, pp.4, Beppu, Oita, Japan, 2005

[5] Takuma Umeno, Eiji Hayashi, Development of an autonomous personal robot "The visual processing system for autonomous driving", proceedings of the 10th international symposium on artificial life and robotics、Vol.10th, pp.44, Beppu, Oita, Japan, 2005

RAC for Underwater Vehicle-Manipulator Systems Using Dynamic Equation

Takashi Yatoh Shinichi Sagara Masakazu Tamura

Department of Control Engineering, Kyushu Institute of Technology
Tobata, Kitakyushu 804-8550, Japan
E-mail: sagara@cntl.kyutech.ac.jp

Abstract

We have proposed continuous-time and discrete-time resolved acceleration control methods for underwater vehicle-manipulator systems and the effectiveness of the control methods have been shown by experiments. In this paper, we propose a new RAC method for UVMS using kinematic and dynamic equations. Experimental result shows the effectiveness of the proposed method.

1 Introduction

Underwater Vehicle-Manipulator Systems (UVMSs) are expected to make important roles in ocean exploration. Many studies about dynamics and control of UVMS have been reported [1–3], however the experimental studies are only a few.

We have proposed continuous-time and discrete-time Resolved Acceleration Control (RAC) methods for UVMS [4–8], and the effectiveness of the RAC methods are demonstrated by using a floationg underwater robot with vertical planar 2-link manipulator shown in Fig. 1. Here, in the case of singular configuration of manipulators the control input cannot be generally calculated, so we have proposed a discrete-time RAC method considering singular configulation of manipulator [8].

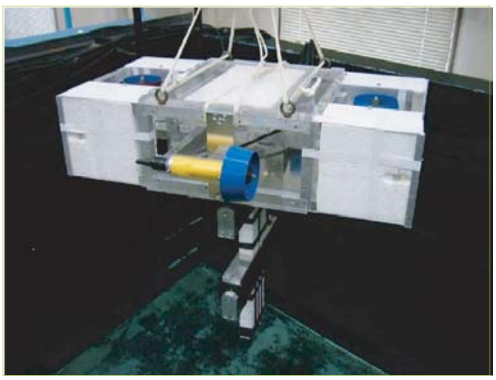

Fig. 1 Floating 2-link underwater robot

Our proposed methods described above are based on the time derivatives of kinematic and momentum equations. Since the coefficient matrix and vector of the dynamic equation include the coefficient matrix and vector of the time derivative of momentum equation. Then in this paper, we propose a new RAC method for UVMS using kinematic and dynamic equations. The effectivenes of the proposed method is shown by experiment.

2 Modeling [4]

The underwater robot model used in this paper is shown in Fig. 2. It has a robot base (vehicle) and 2-DOF manipulator which can move in a vertical plane. Thrusters are mounted on the base to provide propulsion for position and attitude control of the vehicle.

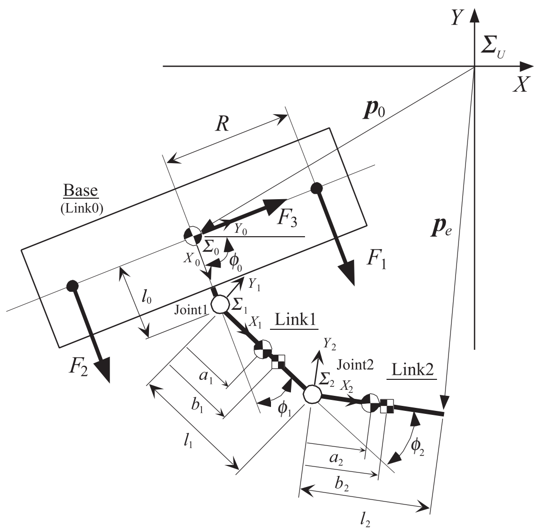

Fig. 2 2-link underwater robot model

Symbols used in this paper are defined as follows:

Σ_U : inertial coordinate frame
Σ_i : ith link coordinate frame ($i = 0,\ 1,\ 2$; link 0 means base)
l_i : length of link i
ϕ_i : relative joint angle
$\boldsymbol{p}_0$: position vector of origin of Σ_0 with respect to Σ_U
$\boldsymbol{p}_e$: position vector of end-tip of manipulator with respect to Σ_U
$\boldsymbol{a}_i$: position vector from joint i to center of gravity of link i with respect to Σ_U
$\boldsymbol{b}_i$: position vector from joint i to center of buoyancy of link i with respect to Σ_U
F_j : thruster force ($j = 1,\ 2,\ 3$)
R : length form origin of Σ_0 to thruster

First, from Fig. 2 a time derivative of $\boldsymbol{p}_e$ is

$$\dot{\boldsymbol{p}}_e = \boldsymbol{A}\dot{\boldsymbol{x}}_0 + \boldsymbol{B}\dot{\boldsymbol{\phi}} \tag{1}$$

where $\boldsymbol{x}_0 = [\boldsymbol{p}_0^T,\ \phi_0]^T$ and $\boldsymbol{\phi} = [\phi_1,\ \phi_2]^T$, $\boldsymbol{A} \in R^{2\times 3}$ and $\boldsymbol{B} \in R^{2\times 2}$ are matrices consisting of attitude angle of base and joint angles.

Next, let $\boldsymbol{\eta}$ and $\boldsymbol{\mu}$ be a linear and an angular momentum of the robot including hydrodynamic added mass tensor $\boldsymbol{M}_{a_i}$ and added inertia tensor $\boldsymbol{I}_{a_i}$ of link i. Then

$$\boldsymbol{\eta} = [\eta_1,\ \eta_2,\ 0]^T = \sum_{i=0}^{n} \boldsymbol{M}_{T_i}\dot{\boldsymbol{r}}_i, \tag{2}$$

$$\boldsymbol{\mu} = [0,\ 0,\ \mu_3]^T \sum_{i=0}^{n} \boldsymbol{I}_{T_i}\boldsymbol{\omega}_i + \tilde{\boldsymbol{r}}_i\boldsymbol{M}_{T_i}\dot{\boldsymbol{r}}_i \tag{3}$$

where

$$\boldsymbol{M}_{T_i} = m_i\boldsymbol{E} + {}^U\boldsymbol{R}_i\boldsymbol{M}_{a_i}{}^i\boldsymbol{R}_U,$$
$$\boldsymbol{I}_{T_i} = {}^U\boldsymbol{R}_i(\boldsymbol{I}_i + \boldsymbol{I}_{a_i})^i\boldsymbol{R}_U,$$

and m_i is the mass of link i, ${}^U\boldsymbol{R}_i$ is the coordinate transformation matrix from Σ_i to Σ_U, $\boldsymbol{E}$ is the unit matrix, $\boldsymbol{r}_i$ is the position vector of the gravity center of the link i with respect to Σ_U, $\boldsymbol{\omega}_i$ is the angular velocity vector of joint i with respect to Σ_U.

From Eqs. (2) and (3) the following equation can be obtained:

$$\boldsymbol{s} = [\eta_1,\ \eta_2,\ \mu_3]^T = \boldsymbol{C}\dot{\boldsymbol{x}}_0 + \boldsymbol{D}\dot{\boldsymbol{\phi}} \tag{4}$$

where $\boldsymbol{C} \in R^{3\times 3}$ and $\boldsymbol{D} \in R^{3\times 2}$ are matrices including the added mass $\boldsymbol{M}_{a_i}$ and the added inertia $\boldsymbol{I}_{a_i}$.

In the meanwhile, the drag force and moment of joint i can be generally represented as follows [9,10]:

$$\boldsymbol{f}_{d_i} = \frac{\rho}{2}C_{D_i}D_i{}^U\boldsymbol{R}_i\int_0^{l_i} ||\boldsymbol{w}_i||\boldsymbol{w}_i dx_i, \tag{5}$$

$$t_{d_i} = \frac{\rho}{2}C_{D_i}D_i{}^U\boldsymbol{R}_i\int_0^{l_i} \hat{\boldsymbol{x}}_i \times ||\boldsymbol{w}_i||\boldsymbol{w}_i dx_i \tag{6}$$

where

$$\boldsymbol{w}_i = \begin{bmatrix} 0 & \boldsymbol{0} \\ \boldsymbol{0} & \boldsymbol{E} \end{bmatrix} {}^i\boldsymbol{R}_U\left(\dot{\boldsymbol{r}}_i + \boldsymbol{\omega}_i \times \hat{\boldsymbol{x}}_i\right),$$

and $\hat{\boldsymbol{x}}_i = [x_i,\ 0,\ 0]^T$, ρ is the fluid density, C_{D_i} is the drag coefficient, D_i is the width of link i.

Furthermore, the gravitational and buoyant forces acting link i are described as follows:

$$\boldsymbol{f}_{g_i} = (\rho V_i - m_i)\boldsymbol{g}, \tag{7}$$
$$\boldsymbol{t}_{g_i} = \boldsymbol{b}_i \times \rho V_i\boldsymbol{g} - \boldsymbol{a}_i \times m_i\boldsymbol{g} \tag{8}$$

where V_i is the volume of link i and $\boldsymbol{g}$ is the gravitational acceleration vector.

3 Resolved Acceleration Control

In the section, we propose a new RAC method for UVMS using kinematic and dynamic equations. First, we summarize the kinematic and momentum equations of a robot with manipulator, and our basic RAC law. Next, using the dynamic equation the RAC law is modified.

Differentiating Eqs. (1) and (4) with respect to time, the following equation can be obtained:

$$\boldsymbol{H}\ddot{\boldsymbol{x}}_0 + \boldsymbol{D}\ddot{\boldsymbol{\phi}} = \ddot{\boldsymbol{x}}_0 + \dot{\boldsymbol{s}} - (\dot{\boldsymbol{C}}\dot{\boldsymbol{x}}_0 + \dot{\boldsymbol{D}}\dot{\boldsymbol{\phi}}), \tag{9}$$
$$\boldsymbol{A}\ddot{\boldsymbol{x}}_0 + \boldsymbol{B}\ddot{\boldsymbol{\phi}} = \dot{\boldsymbol{p}}_e - (\dot{\boldsymbol{A}}\dot{\boldsymbol{x}}_0 + \dot{\boldsymbol{B}}\dot{\boldsymbol{\phi}}) \tag{10}$$

where $\boldsymbol{H} = \boldsymbol{C} + \boldsymbol{E}$, From Eqs. (9) and (10) the following equation can be obtained.

$$\begin{bmatrix} \ddot{\boldsymbol{x}}_0 \\ \ddot{\boldsymbol{\phi}} \end{bmatrix} = \begin{bmatrix} \boldsymbol{H} & \boldsymbol{D} \\ \boldsymbol{A} & \boldsymbol{B} \end{bmatrix}^{-1} \begin{bmatrix} \ddot{\boldsymbol{x}}_0 + \dot{\boldsymbol{s}} - (\dot{\boldsymbol{C}}\dot{\boldsymbol{x}}_0 + \dot{\boldsymbol{D}}\dot{\boldsymbol{\phi}}) \\ \ddot{\boldsymbol{p}}_e - (\dot{\boldsymbol{A}}\dot{\boldsymbol{x}}_0 + \dot{\boldsymbol{B}}\dot{\boldsymbol{\phi}}) \end{bmatrix} \tag{11}$$

If the values of the external forces are exact, using Eq. (11) and the desired values of the base position and attitude $\boldsymbol{x}_d$ and the end-tip position $\boldsymbol{p}_d$, the desired acceleration values of the base $\ddot{\boldsymbol{x}}_d$ and joint $\ddot{\boldsymbol{\phi}}_d$ can be obtained. However, the complete hydrodynamic model cannot be obtained. Furthermore, we assume that the added mass and inertia are constant. Therefore, instead of $\ddot{\boldsymbol{x}}_d$ and $\ddot{\boldsymbol{p}}_d$ the following modified desired values of the base $\ddot{\boldsymbol{x}}_d^*$ and the end-tip $\ddot{\boldsymbol{p}}_d^*$ are utilized:

$$\begin{bmatrix} \ddot{\boldsymbol{x}}_d^* \\ \ddot{\boldsymbol{p}}_d^* \end{bmatrix} = \begin{bmatrix} \ddot{\boldsymbol{x}}_d \\ \ddot{\boldsymbol{p}}_d \end{bmatrix} + \boldsymbol{K}_v \begin{bmatrix} \dot{\boldsymbol{x}}_d - \dot{\boldsymbol{x}}_0 \\ \dot{\boldsymbol{p}}_d - \dot{\boldsymbol{p}}_e \end{bmatrix} + \boldsymbol{K}_p \begin{bmatrix} \boldsymbol{x}_d - \boldsymbol{x}_0 \\ \boldsymbol{p}_d - \boldsymbol{p}_e \end{bmatrix} \tag{12}$$

where $\boldsymbol{x}_d$ and $\boldsymbol{p}_d$ are the desired values of the base and end-tip, and $\boldsymbol{K}_v$ and $\boldsymbol{K}_p$ are velocity and position feedback gain matrices, respectively.

Substituting $\ddot{\boldsymbol{x}}_d^*$, $\ddot{\boldsymbol{p}}_d^*$ for $\ddot{\boldsymbol{x}}_0$, $\ddot{\boldsymbol{p}}_e$ on the right side of Eq. (11), the acceleration $[\ddot{\boldsymbol{x}}_0,\ \ddot{\boldsymbol{\phi}}]^T$ that should be provided with the robot are calculated.

The underwater robot has thrusters and joint actuators. Since the joint actuators are driven by velocity type sevo controller, the control input of the joints are directly utilized. On the other hand, to drive the thrusters we obtain the control input force and torque by using the following dynamic equation.

$$\boldsymbol{M}_B(\boldsymbol{q})\ddot{\boldsymbol{q}} + \boldsymbol{b}_B(\boldsymbol{q}, \dot{\boldsymbol{q}}) + \boldsymbol{f}_{DG} = \boldsymbol{f}_T \tag{13}$$

where $\boldsymbol{M}_B(\boldsymbol{q})$ is the inertia matrix, $\boldsymbol{b}_B(\boldsymbol{q}, \dot{\boldsymbol{q}})$ is the vector of Coliolis and centrifubal forces, $\boldsymbol{f}_{DG}$ is the vector consisting of the drag, gravitational and buoyant forces, and $\boldsymbol{f}_T$ is the force and torque vector.

Now, $\boldsymbol{C}$, $\boldsymbol{D}$, $\dot{\boldsymbol{C}}$ and $\dot{\boldsymbol{D}}$ are from Eq. (4) we have

$$\dot{\boldsymbol{s}} = \boldsymbol{C}\ddot{\boldsymbol{x}}_0 + \boldsymbol{D}\ddot{\boldsymbol{\phi}} + \dot{\boldsymbol{C}}\dot{\boldsymbol{x}}_0 + \dot{\boldsymbol{D}}\dot{\boldsymbol{\phi}} \tag{14}$$

where, $\dot{\boldsymbol{s}}$ is the external force including hydrodynamic force and thrust of the thruster which act on the robot. That is

$$\dot{\boldsymbol{s}} = \boldsymbol{f}_T - \boldsymbol{f}_D - \boldsymbol{f}_G \tag{15}$$

where, $\boldsymbol{f}_T$ is thruster force, $\boldsymbol{f}_D$ is hydorodynamic force, $\boldsymbol{f}_G$ is gravity and a buoyancy force.

From Eqs. (14) and (15) the following equation, that is the dynamic equation, can be obtained:

$$\begin{bmatrix}\boldsymbol{C} & \boldsymbol{D}\end{bmatrix}\begin{bmatrix}\ddot{\boldsymbol{x}}_0 \\ \ddot{\boldsymbol{\phi}}\end{bmatrix} + \begin{bmatrix}\dot{\boldsymbol{C}} & \dot{\boldsymbol{D}}\end{bmatrix}\begin{bmatrix}\dot{\boldsymbol{x}}_0 \\ \dot{\boldsymbol{\phi}}\end{bmatrix} + \boldsymbol{f}_D + \boldsymbol{f}_G = \boldsymbol{f}_T \tag{16}$$

We have the following relations from Eqs. (13) and (16):

$$\begin{bmatrix}\boldsymbol{C} & \boldsymbol{D}\end{bmatrix} = \boldsymbol{M}_B(\boldsymbol{q}), \tag{17}$$

$$\dot{\boldsymbol{C}}\dot{\boldsymbol{x}}_0 + \dot{\boldsymbol{D}}\dot{\boldsymbol{\phi}} = \boldsymbol{b}_B(\boldsymbol{q}, \dot{\boldsymbol{q}}) \tag{18}$$

Therefore, from Eqs. (15), (17) and (18) the elements of Eq. (11) can be obtained without direct calculation of the $\boldsymbol{C}$, $\boldsymbol{D}$, $\dot{\boldsymbol{C}}$, $\dot{\boldsymbol{D}}$ and $\dot{\boldsymbol{s}}$.

4 Experiment

In this section, to verify the effectiveness of the proposed control method, the experiment is done.

Fig. 3 shows a configuration of experimental system. Physical parameters of the underwater robot are

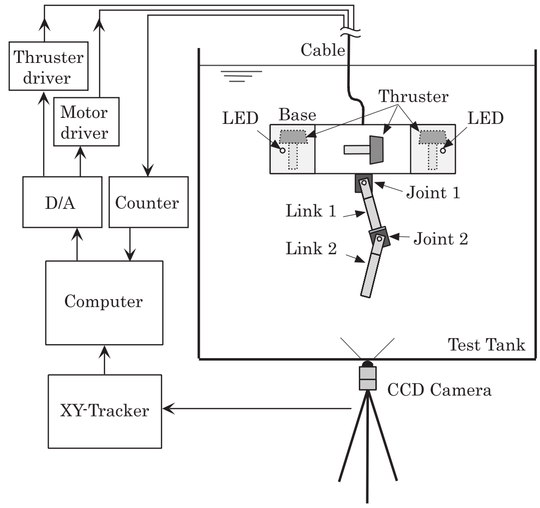

Fig. 3 Configuration of underwater robot system

Table 1 Physical parameters of underwater robot

	Base	Link 1	Link 2
Mass [kg]	26.04	4.25	1.23
Moment of inertia [kg m^2]	1.33	0.19	0.012
Link length (x axis) [m]	0.2	0.25	0.25
Link length (y axis) [m]	0.81	0.04	0.04
Link width [m]	0.42	0.12	0.12
Added mass(x) [kg]	72.7	1.31	0.1
Added mass(y) [kg]	6.28	3.57	2.83
Added moment of inertia [kg m^2]	1.05	0.11	0.06
Drag coefficient(x)	1.2	0	0
Drag coefficient(y)	1.2	1.2	1.2

shown in Table 1. The details of the system, the dynamic equation of robot and thruster characteristics are shown in [4].

The experiment was carried out under the following condition. The desired end-tip and base position were set up along a straight path from the initial position to the target. On the other hand, the basic desired attitude of vehicle was set up the initial values. The sampling period was T=1/60[s] and the feedback gains were $\boldsymbol{K}_v$ = diag{100, 100, 10, 20, 20} and $\boldsymbol{K}_p$ = diag{600, 600, 140, 100, 100}. Furthermore, the initial relative angles of the robot were $\phi_0 = -\pi/2$[rad], $\phi_1 = \pi/3$[rad] and $\phi_2 = -5\pi/18$[rad].

The typical experimental result is shown in Fig. 4. From Fig. 4 it can be seen that the end-tip of manipulator and base follow the reference trajectories in spite of the influence of the hydrodynamic forces and the tracking errors are very small. The experimental result shows that the control performance can be improved by using the proposed method.

5 Conclusion

In this paper, an analog RAC system for UVMS using dynamic equation was proposed. The experimental result showed the effectiveness of the proposed method.

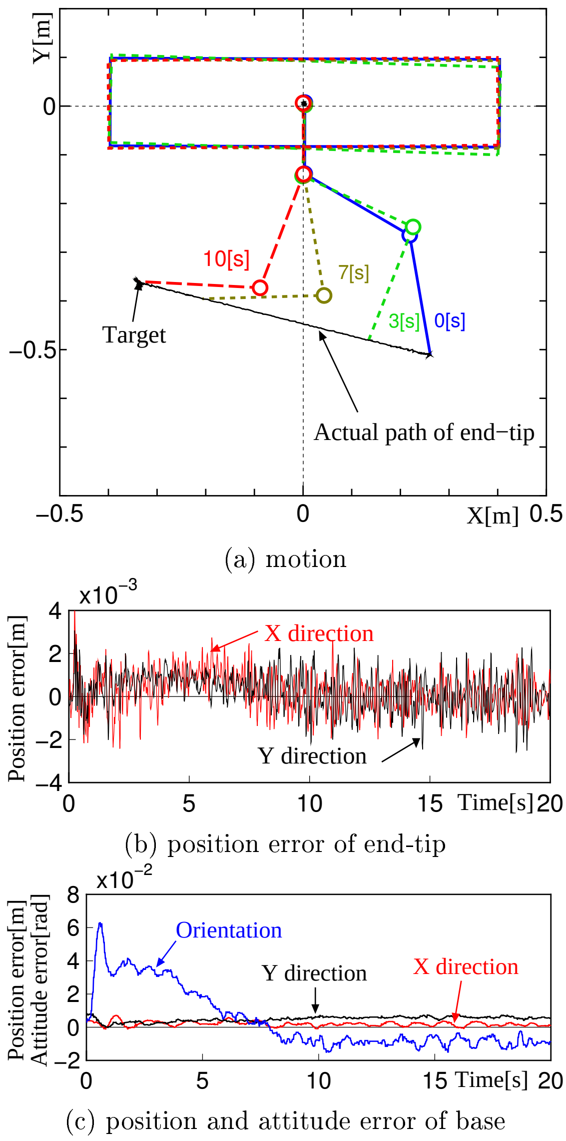

(a) motion

(b) position error of end-tip

(c) position and attitude error of base

Fig. 4 Experimental result

References

[1] T. W. McLain *et al.*, "Experiments in the Coordinated Control of an Underwater Arm/Vehicle System", *Autonomous Robots 3*, Kluwer Academic Publishers, pp. 213 – 232, 1996.

[2] G. Antonelli *et al.*, "Tracking Control for Underwater Vehicle-Manipulator Systems with Velocity Estimation", *IEEE J. Oceanic Eng.*, Vol. 25, No. 3, pp. 399 – 413, 2000.

[3] N. Sarkar and T. K. Podder, "Coordinated Montion Planning and Control of Autonomous Underwater Vehicle-Manipulator Systems Subject to Drag Optimization", *IEEE J. Oceanic Eng.*, Vol. 26, No. 2, pp. 228 – 239, 2001.

[4] S. Yamada and S. Sagara, "Resolved Motion Rate Control of an Underwater Robot with Vertical Planar 2-Link Manipulator", *Proc. of AROB 7th*, pp. 230 – 233, 2002.

[5] S. Sagara, "Digital Control of an Underwater Robot with vertical Planar 2-Link Manipulator", *Proc. of AROB 8th*, pp. 524 – 527, 2003.

[6] S. Sagara, K. Shibuya and M. Tamura, "Experiment of Digital RAC for an Underwater Robot with vertical Planar 2-Link Manipulator", *Proc. of AROB 9th*, pp. 337 – 340, 2004.

[7] S. Sagara, K. Shibuya and M. Tamura, "Digital Resolved Acceleration Control of Underwater Vehicle-Manipulator Systems", *Proc. Int. Symp. Bio-inspired Systems*, Part V: Robotics and Motion Control, pp. 21 – 26, 2004.

[8] S. Sagara, M. Tamura T. Yatoh and K. Shibuya, "Digital RAC for Underwater Vehicle-Manipulator Systems Considering Singular Configuration", *Proc. of AROB 10th*, pp. 671 – 674, 2005.

[9] B. Lévesque and M. J. Richard, "Dynamic Analysis of a Manipulator in a Fluid Environment", *Int. J. Robot. Res.*, Vol. 13, No. 3, pp. 221 – 231, 1994.

[10] S. McMillan *et al.*, "Efficient Dynamic Simulation of an Underwater Vehicle with a Robotic Manipulator", *IEEE Trans. Syst., Man, Cybern.*, Vol. 25, No. 8, pp. 1194 – 1206, 1995.

The Eleventh International Symposium on Artificial Life and Robotics 2006 (AROB 11th'06),
B-con Plaza, Beppu, Oita, Japan, January 23-25, 2006

Digital Tracking Control of Space Robots Using Transpose of Generalized Jacobian Matrix

Shinichi Sagara† Yuichiro Taira‡

† Department of Control Engineering, Kyushu Institute of Technology
Tobata, Kitakyushu 804-8550, Japan
E-mail: sagara@cntl.kyutech.ac.jp

‡ Department of Ocean Mechanical Engineering, National Fisheries University
Nagata-Honmachi, Shimonoseki 759-6595, Japan
E-mail: taira@fish-u.ac.jp

Abstract

For free floating space robots having manipulators, we have proposed a discrete time control methods using the transpose of Generalized Jacobian Matrix (GJM) and computer simulations have shown the effectiveness of the proposed methods. The control methods belong to a class of constant value control. In this paper we propose a digital trajectory tracking control method using the transpose of GJM.

1 Introduction

Since space robots having manipulators are expected to work in future space missions, many control methods of space robot manipulators have been proposed [1]. Most of them, however, use the inverse of Generalized Jacobian Matrix (GJM) which is a coefficient matrix between the end-effector's velocity and the joint velocity of the manipulator. Therefore, if the robot system becomes in a singular configuration, the manipulator is out of control because the inverse of GJM does not exist.

For the singular configuration, a different approach, which uses the transpose of GJM, is considered. Masutani et al. [2] have proposed a sensory feedback control of space robot manipulators using the transpose of GJM. The method, however, has been developed in continuous time domain. Here, in practical systems digital computers are utilized for controllers. So, we have proposed a discrete time control methods using the transpose of GJM [3, 4]. The proposed methods guarantee the stability of the control system in discrete time domain by using Lyapunov's direct method for difference equations. Furthermore, computer simulations have shown the effectiveness of the proposed methods.

The control methods using the transpose of GJM use position and orientation errors between the desired and actual values of the end-tip of the manipulator. Namely, the control methods belong to a class of constant value control such as PID control. Therefore, the value of errors depends on the desired linear and angular velocity of the end-tip based on the desired trajectory.

In this paper based on the reference [4] we propose a digital trajectory tracking control method using the transpose of GJM. Computer simulations are performed to confirm the validity of the proposed method.

2 Modeling [5]

2.1 Robot model

In this paper, we consider a free-floating space robot manipulator as shown in Fig. 1. It has an uncontrolled base and n-DOF manipulator with revolute

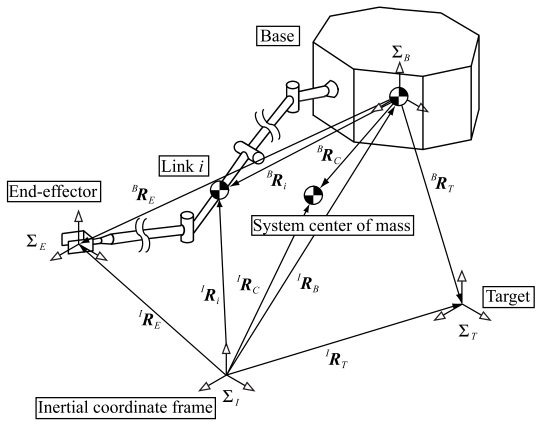

Fig. 1 Space robot model

joints. The target of the end-effector of the manipulator is stationary in an inertial coordinate frame. Symbols used in this paper are defined as follows:

Σ_I : inertial coordinate frame
Σ_B : base coordinate frame
Σ_E : end-effector coordinate frame
Σ_T : target coordinate frame
${}^*\boldsymbol{r}_E$: position vector of origin of Σ_E with respect to Σ_*
${}^*\boldsymbol{r}_T$: position vector of origin of Σ_T with respect to Σ_*
${}^*\boldsymbol{v}_E$: linear velocity vector of origin of Σ_E with respect to Σ_*
${}^*\boldsymbol{\omega}_E$: angular velocity vector of origin of Σ_E with respect to Σ_*
$\boldsymbol{q}$: joint angle vector
$\boldsymbol{\phi}_*$: angle vector representing the orientation of Σ_* with respect to Σ_I
${}^{**}\boldsymbol{A}_*$: rotation matrix from Σ_* to Σ_{**}
$\boldsymbol{U}$: identity matrix
$\tilde{\boldsymbol{r}}$: skew-symmetric matrix defined as

$$\tilde{\boldsymbol{r}} = \begin{bmatrix} 0 & -z & y \\ z & 0 & -x \\ -y & x & 0 \end{bmatrix}, \quad \boldsymbol{r} = [x,\ y,\ z]^T$$

2.2 Kinematic model

A discrete-time differential kinematic model is given by the following equations [3,4]:

$$ {}^I\boldsymbol{v}_E(k) = {}^I\boldsymbol{J}_L^*(\boldsymbol{\phi}_B(k),\ \boldsymbol{q}(k))\dot{\boldsymbol{q}}(k), \tag{1}$$

$$ {}^I\boldsymbol{\omega}_E(k) = {}^I\boldsymbol{J}_A^*(\boldsymbol{\phi}_B(k),\ \boldsymbol{q}(k))\dot{\boldsymbol{q}}(k) \tag{2}$$

where ${}^I\boldsymbol{J}_L^*$ and ${}^I\boldsymbol{J}_A^*$ are called the GJMs of the linear and angular velocities, respectively.

The difference equation of the position error $\boldsymbol{e}_{PI}$ is given by the equation [3,4]

$$\boldsymbol{e}_{PI}(k) = \boldsymbol{e}_{PI}(k-1) - T\,{}^I\boldsymbol{J}_L^*\dot{\boldsymbol{q}}(k) \tag{3}$$

where T is a sampling period and

$$\boldsymbol{e}_{PI}(k) = {}^I\boldsymbol{r}_T - {}^I\boldsymbol{r}_E(k) \tag{4}$$

And the difference equation of the orientation error $\boldsymbol{E}_{OI}$ can be expressed as

$$\boldsymbol{E}_{OI}(k) = \boldsymbol{E}_{OI}(k-1) - T\boldsymbol{E}_X(k)\,{}^I\boldsymbol{J}_A^*\dot{\boldsymbol{q}}(k) \tag{5}$$

where

$$\boldsymbol{E}_{OI} = \begin{bmatrix} {}^I\boldsymbol{n}_T - {}^I\boldsymbol{n}_E(k) \\ {}^I\boldsymbol{s}_T - {}^I\boldsymbol{s}_E(k) \\ {}^I\boldsymbol{a}_T - {}^I\boldsymbol{a}_E(k) \end{bmatrix} \tag{6}$$

$$\boldsymbol{E}_X(k) = \begin{bmatrix} {}^I\tilde{\boldsymbol{n}}_E(k) \\ {}^I\tilde{\boldsymbol{s}}_E(k) \\ {}^I\tilde{\boldsymbol{a}}_E(k) \end{bmatrix}$$

$${}^I\boldsymbol{A}_E(\boldsymbol{\phi}_E(k)) = \left[{}^I\boldsymbol{n}_E(k)\ {}^I\boldsymbol{s}_E(k)\ {}^I\boldsymbol{a}_E(k)\right]$$

$${}^I\boldsymbol{A}_T(\boldsymbol{\phi}_T) = \left[{}^I\boldsymbol{n}_T\ {}^I\boldsymbol{s}_T\ {}^I\boldsymbol{a}_T\right]$$

The vectors ${}^I\boldsymbol{n}_*$, ${}^I\boldsymbol{s}_*$ and ${}^I\boldsymbol{a}_*$ are unit vectors along the axes of Σ_* with respect to Σ_I. Since it may be difficult to use the orientation error in Eq. (8) for the stability analysis as a feedback orientation error for the control law, the orientation error used in the control law is defined as

$$\boldsymbol{e}_{OI}(k) = -\frac{1}{2}\boldsymbol{E}_X^T(k)\boldsymbol{E}_{OI}(k). \tag{7}$$

If the condition [2]

$${}^I\boldsymbol{n}_E^T(k)\,{}^I\boldsymbol{n}_T + {}^I\boldsymbol{s}_E^T(k)\,{}^I\boldsymbol{s}_T + {}^I\boldsymbol{a}_E^T(k)\,{}^I\boldsymbol{a}_T > -1$$

holds, the equation that $\boldsymbol{E}_{OI} = \boldsymbol{0}$ is equivalent to the equation that $\boldsymbol{e}_{OI} = \boldsymbol{0}$.

3 Digital Control

In this section, the basic control law is summarized and based on the control law we proposed a tracking control method.

For free-floating space robot manipulators we have proposed the following control law [4]:

$$\begin{aligned}\boldsymbol{x}_d(k) = {}&{}^I\boldsymbol{J}_L^*(k)\left[k_p\boldsymbol{e}_{PI}(k) - \boldsymbol{K}_{LV}\,{}^I\boldsymbol{v}_E(k)\right] \\ &+ {}^I\boldsymbol{J}_A^*(k)\left[k_o\boldsymbol{e}_{OI}(k) - \boldsymbol{K}_{AV}\,{}^I\boldsymbol{\omega}_E(k)\right]\end{aligned} \tag{8}$$

where k_p and k_o are positive scalar gains for position and orientation, respectively, and $\boldsymbol{K}_{LV}$ and $\boldsymbol{K}_{AV}$ are symmetric and positive definite gain matrices for linear and angular velocities of an end-effector. Furthermore, $\boldsymbol{x}_d$ is a control input vector of joint actuators, and torque and velocity are both applicable for the control input. In this paper, we use the control law (8) for the torque input type.

To apply the control law (8) to a tracking control, the following equations are utilized instead of Eqs. (4) and (7):

$$\hat{e}_{PI}(k) = {}^I\boldsymbol{r}_T(k) - {}^I\boldsymbol{r}_E(k), \tag{9}$$

$$\hat{e}_{OI}(k) = -\frac{1}{2}\boldsymbol{E}_X^T(k)\hat{\boldsymbol{E}}_{OI}(k) \tag{10}$$

Table 1 Physical parameters

	Length m	Mass kg	Moment of inertia $kg \cdot m^2$
Base	3.5	2000	3587.9
Link 1	2.5	50	26.2
Link 2	2.5	50	26.2
Link 3	0.5	5	0.23
Object	4.0	100	200.0

where

$$\hat{\boldsymbol{E}}_{OI}(k) = \begin{bmatrix} {}^I\boldsymbol{n}_T(k) - {}^I\boldsymbol{n}_E(k) \\ {}^I\boldsymbol{s}_T(k) - {}^I\boldsymbol{s}_E(k) \\ {}^I\boldsymbol{a}_T(k) - {}^I\boldsymbol{a}_E(k) \end{bmatrix}.$$

To examine the performance of the tracking control using Eq. (8), three types of simulations are performed using a horizontal planar 3-DOF robot with object.

Physical parameters of the robot and object are shown in Table 1. Simulations are carried out under the following condition. A point of interest of the object moves along a straight path from the initial position to the target position and the object angle is set up to the initial value. The sampling period is $T = 0.01$s. The feedback gains are set to the following cases.

Case 1 : This is the basic case. The feedback gains are $k_p = k_o = 50000$, $\boldsymbol{K}_{LV} = \mathrm{diag}\{5000,\ 5000\}$ and $\boldsymbol{K}_{AV} = 5000$.

Case 2 : Position and orientation feedback gains, k_p and k_o, are set to large values than the values of Case 1. The gains are $k_p = k_o = 100000$, $\boldsymbol{K}_{LV} = \mathrm{diag}\{5000,\ 5000\}$ and $\boldsymbol{K}_{AV} = 5000$.

Case 3 : Linear and angular velocity feedback gains, $\boldsymbol{K}_{LV}$ and $\boldsymbol{K}_{AV}$, are set to small values than the values of Case 1. The gains are $k_p = k_o = 50000$, $\boldsymbol{K}_{LV} = \mathrm{diag}\{3000,\ 3000\}$ and $\boldsymbol{K}_{AV} = 3000$.

Fig. 2 shows the motion of the robot of the Case 1. From Fig. 2 it can be seen that the tracking control using the control law (8) is valid. Fig. 3 shows the simulation results of all cases. From this figure, the tracking errors of Case 2 and 3 are smaller than the errors of Case 1 while the desired velocity is transitional, however the convergent performance of the target becomes slightly worse.

So, to get the good control performance we propose

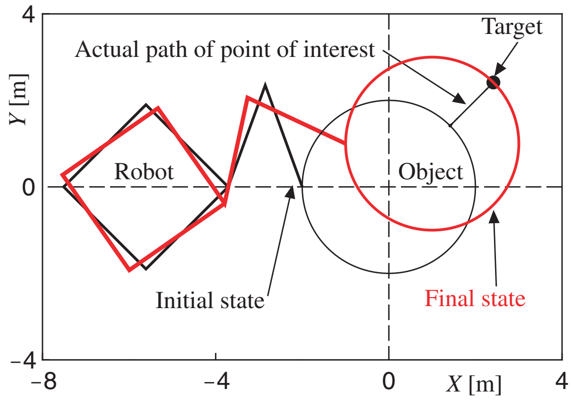

Fig. 2 Motoin of the robot (Case 1)

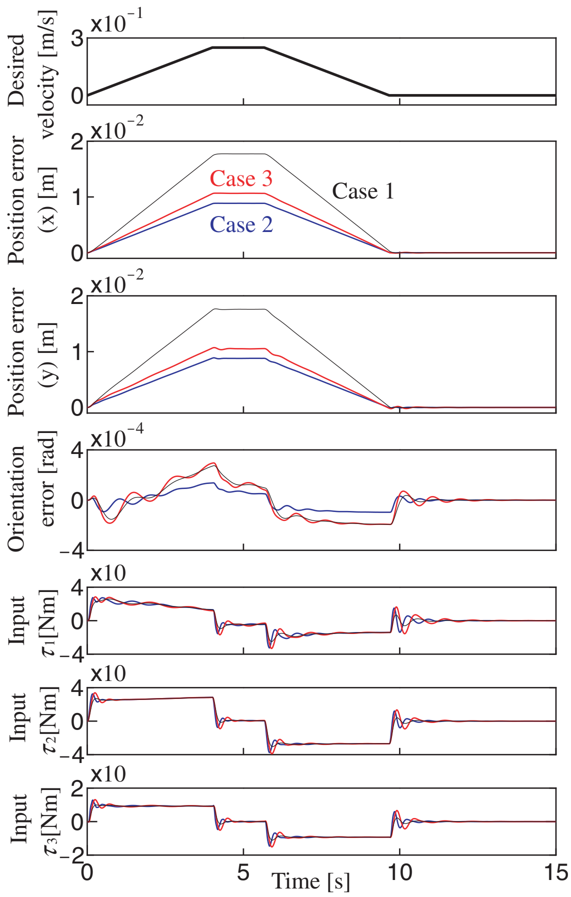

Fig. 3 Simulation result (Case1, 2 and 3)

the modified control law:

$$\begin{aligned}\boldsymbol{\tau}_d(k) &= {}^I\boldsymbol{J}_L^*(k)\left[\hat{k}_p(k)\hat{\boldsymbol{e}}_{PI}(k) - \hat{\boldsymbol{K}}_{LV}(k)^I\boldsymbol{v}_E(k)\right] \\ &+ {}^I\boldsymbol{J}_A^*(k)\left[\hat{k}_o(k)\hat{\boldsymbol{e}}_{OI}(k) - \hat{\boldsymbol{K}}_{AV}(k)^I\boldsymbol{\omega}_E(k)\right]\end{aligned} \tag{11}$$

where

$$\hat{k}_p(k) = k_p\{1+\alpha_L\nu_L(k)\},$$
$$\hat{k}_o(k) = k_o\{1+\alpha_A\nu_A(k)\},$$
$$\hat{\boldsymbol{K}}_{LV}(k) = \boldsymbol{K}_{LV}\{1-\beta_L\nu_L(k)\},$$
$$\hat{\boldsymbol{K}}_{AV}(k) = \boldsymbol{K}_{AV}\{1-\beta_A\nu_A(k)\},$$
$$\nu_L(k) = \frac{||\boldsymbol{v}_{E_d}(k)||}{v_{d_{\max}}}, \qquad \nu_A(k) = \frac{||\boldsymbol{\omega}_{E_d}(k)||}{\omega_{d_{\max}}}$$

and $\boldsymbol{v}_{E_d}(k)$ and $\boldsymbol{\omega}_{E_d}(k)$ are the desired velocities of $\boldsymbol{v}_E(k)$ and $\boldsymbol{\omega}_E(k)$, respectively, $v_{d_{\max}}$ and $\omega_{d_{\max}}$ are the maximum values of the norm of $\boldsymbol{v}_{E_d}(k)$ and $\boldsymbol{\omega}_{E_d}(k)$, α_i $(\alpha_i \geq 0)$ and β_i $(0 \leq \beta_i \leq 1)$ $(* = L,\ A)$ are setting parameters.

To verify the validity of the proposed control law (11), simulation is performed. Fig. 4 and 5 show the motion of the robot using the control law (11) and the time history, respectively. The values of the feedback gains, k_p, k_o, $\boldsymbol{K}_{LV}$ and $\boldsymbol{K}_{AV}$, for this simulation and Case 1 are the same. The setting parameters are $\alpha_A = \alpha_L = 0.8$ and $\beta_A = \beta_L = 0.3$. From Fig. 4 and 5, good control performance can be achieved using the proposed control law.

4 Conclusion

In this paper, a digital tracking control method for space robot manipulators was proposed. The simulation result showed the effectiveness of the proposed method.

References

[1] Y. Xu and T. Kanade (eds), *Space Robotics: Dynamics and Control*, Kluwer Academic Publishers, 1993.

[2] Y. Masutani, F. Miyazaki and S. Arimoto, "Modeling and Sensory Feedback Control for Space Manipulators", *Proc. 1989 NASA Conf. Space Telerobotics*, pp. 287 – 296, 1989.

[3] Y. Taira, S. Sagara and R. Katoh, "Digital Control of a Space Robot Using the Transpose of the Generalized Jacobian Matrix," (in Japanese), *Trans. JSME Series C*, Vol. 67, No. 654, pp. 436 – 442, 2001.

[4] Y. Taira, S. Sagara and R. Katoh, "Digital Control of a Space Robot Using the Transpose of the Generalized Jacobian Matrix (2nd Report, A Unified Approach for Torque and Velocity Type Control Laws)," (in Japanese), *Trans. JSME Series C*, Vol. 67, No. 663, pp. 3540 – 3547, 2001.

[5] Y. Taira and S. Sagara, "A Design of Digital Adaptive Control Systems for Space Robot Manipulators Using a Transpose of the Generalized Jacobian Matrix", *Int. J. AROB*, Vol. 9, pp. 41 – 45, 2005.

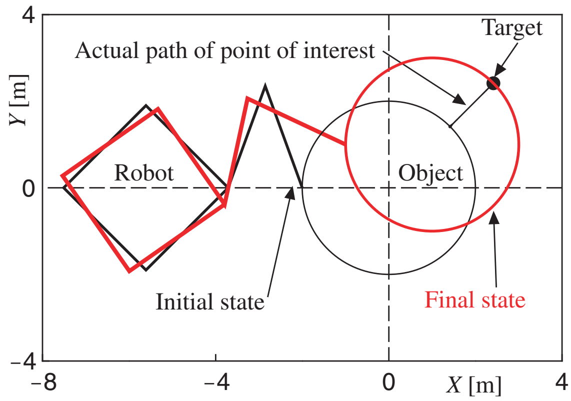

Fig. 4 Motoin of the robot (Proposed method)

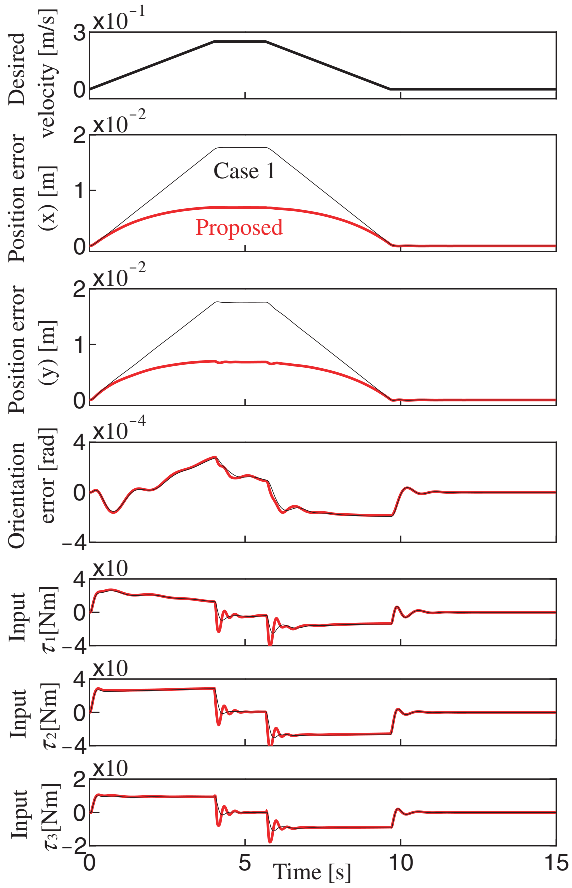

Fig. 5 Simulation result (Proposed method)

Optimal Parameter Tuning in Proportional Control for the Unicycle Mobile Robot: An Experimental Study

Desa Hazry[1] and Masanori Sugisaka[2]

[1]Graduate School of Engineering, Department of Electrical and Electronics Engineering

[2]Department of Electrical and Electronic Engineering

The University of Oita, 700 Oaza Dannoharu, Oita, 970-1192, Japan

Tel: +81-97-554-7831, Fax: +81-97-554-7841

E-mail: hazry@cc.oita-u.ac.jp msugi@cc.oita-u.ac.jp

Abstract

Proportional-integral-derivative (PID) control is a control strategy that has been successfully used over many years. Simplicity, robustness, a wide range of applicability and near-optimal performance are some of the reasons that have made PID control are so popular in the academic and industry sectors. This paper introduces a method for parameter estimation in mobile robot as a first step of the research in realization of the autonomous unicycle mobile robot. Motion is achieved by using two independent DC electric motors that drive one wheel each. Differential drive is used to steer the robot. Two caster wheels are used to keep the robot horizontally. The velocity of each wheel is controlled indirectly by applying voltages to the motors. Experiment condition is stated as mobile robot on the floor and running with a constant velocity. The desired velocity is 80 (pulse/sec) in order to carry out a wheel rotation as one revolution in one second. We use proportional controller in order to get the constant and stabilized speed-movement of mobile robot. Coefficient parameter for each wheel is decided by confirmation of the minimal means square error of deviations wheel rotation of each wheel.

Key words: PID controller, optimal parameter tuning, mobile robot.

1 Introduction

At the moment, there exist many different methods to find suitable controller parameters [1]. The methods differ in complexity, flexibility, and in the amount of process knowledge used. Depending on the application, there is a need to have several types of tuning method. There are simple, easy to use methods which require little information, e.g. the method described in [2] as well as more sophisticated methods which require more information and more computations. In previous research [3], [4], [5] we use the proportional controller but the confirmation is done by computer simulation. In order to provide consistent, reliable and stabilized movement during running course, the experiment was performed in the real environment. This paper introduces the mean square root for parameter estimation. In addition, the mean square root forms have the added benefit of numerical stability and guaranteed positive semi-definiteness of the state covariance. This finding will assist in executing a more accurate testing in future experiments.

The paper is organized as follows. Section 2 explains the overview of the mobile robot. In section 3, operations of DC motor controlled by pulse-width modulation are introduced. Section 4, proportional control rules are discussed. In section 5, tuning method for the optimal coefficient parameter is presented and finally, conclusions are drawn in the section 6.

2 Overview of the Robot Model

It is assumed that the plane of each wheel is perpendicular to the ground. The contact between the wheels and the ground is pure rolling and non-slipping. The velocity of the center of the mass of the robot is orthogonal to the wheel axis. The mobile robot has two independent motors, thus providing both drive and steering (differential steering system). At the back and rear, two passive castors are provided for support. The passive support does not considered in obtaining the kinematics and dynamics model. The encoder is used to measure rotation with accuracy of 4.5 degree with equal to 80 intervals per revolution. The robot uses 10cm diameter wheel.

3 Pulse-Width-Modulation (PWM) DC Motor Wheel Operations

PWM DC motor controls the wheel motor speed by driving the motor with short pulses. These pulses vary in duration to change the speed of the motor. Pulse-width modulation control works by switching the power supplied to the motor on and off very rapidly. The longer the pulses, the faster the motor turns, and vice versa. The DC voltage is converted to a square-wave signal, alternating between fully on and zero, giving the motor a series of power. DC motors are controlled by relays which switch the power on/off and change the polarity to give forward/reverse of wheel rotation. These relays are switched by bits zero to three of output port 0x281. The speed of the motors at any time is set by a byte. The right wheel speed byte is the output of port 0x282 and the left wheel speed byte is the output of port 0x283. A byte value of 0 will run a motor at full speed, while a byte value of 255 will stop the motor (see **Table 1**). The actual speed of the wheel rotation DC motor may be estimated by counting the encoder pulse in a fixed 0.1 seconds of period time. The counter card can be configured to automatically count the pulse received in a periodic interval.

Table 1: Byte-speed setting control wheel rotation number

HEX	Byte (Speed)	Rotation Number (Pulse/s)
FF	255	0
C0	192	40
80	128	90
40	64	140
0	0	170

4 Proportional Control

At this stage, we run the mobile robot only by proportional control because by computer simulation in previous research [3], [4], [5] we found that the numbers of wheel rotations reach to the target value in proportional control. We control the speed of the mobile robot by proportional control using the number of pulse obtained from the encoders. The control rules are given by the following equation:

$$\begin{aligned} r\_ope &= r\_ope + c(t) \\ l\_ope &= l\_ope + c(t) \end{aligned} \tag{1}$$

where,

$$c(t) = Kp_{r,l} \ \text{x} \ e(t) \tag{2}$$

$r \,\&\, l\_ope$ is the right and left wheel desired wheel rotation pulse number. $c(t)$ is the correction factor to be applied to the system. $Kp_{r,l}$ is the adjustment coefficient parameter right and left wheel for the observed error. $e(t)$ is the error function or error of the wheel rotation number, where $e(t)$ is equal to the differences between desired rotation pulse number and current rotation pulse number.

5 Experimental Results

In order to prove the effectiveness of the proposed control method in a practical application, a laboratory experimental setup has been employed. Experiment condition is stated as the mobile robot on the floor with straight running. The desired pulse rotation number for each wheel is 80(pulse/sec) in order to carry out a wheel rotation as one revolution in one second. The minimum mean squares error of wheel rotation deviation from target rotation is taken as a coefficient control parameter.

5.1 The mean square error (MSE)

MSE is an old, proven measure of control and quality [6]. MSE equals the mean of the squares of the deviations from the target, i.e.,

$$\text{MSE} = \frac{1}{m}\sum_{i=1}^{m}(x_i - T)^2 \tag{3}$$

where,

x_i = ith value of a group of m values,
T = Target of intended values.

MSE should be zero. Usually, the model is not perfect. The smaller MSE, the better performance of the model.

5.2 Determining proportional control parameter

Preliminary experimental has been conducted with the proportional parameter value between the ranges of 0.1 to 1.8 for the right and left wheel. The result is shown as below:

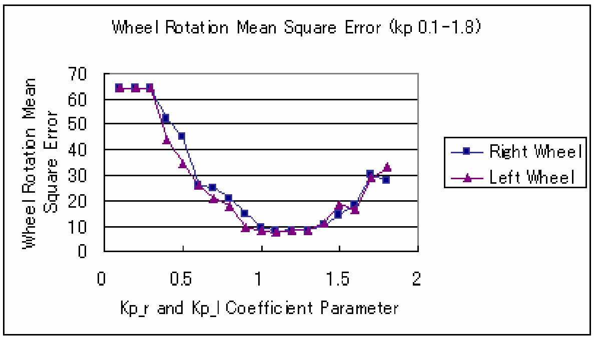

Fig. 1: Preliminary experiment to confirm Kp parameter

The lowest mean square error of the wheel rotation number is the best coefficient parameter. From the result we found that the lowest Kp coefficient parameter for right and left wheel is 1.1. From this result, we use to perform the fine tuning experiment. In fine tuning the test has been perform in the range of 1.0 to 1.2. The results are shown in **Fig. 2** and **Fig. 3**.

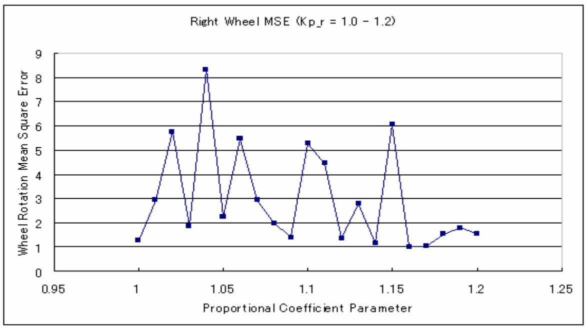

Fig. 2: Right wheel mean square error- fine tuning

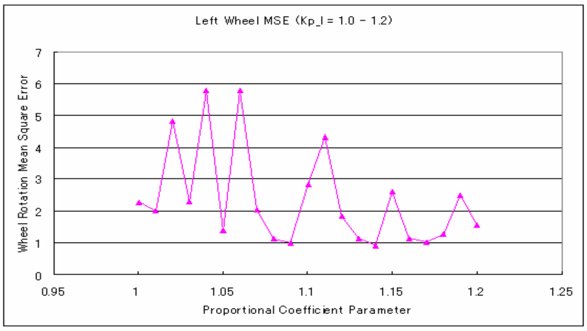

Fig. 3: Left wheel mean square error – fine tuning

From **Fig. 2** and **Fig. 3**, the minimal wheel rotation square error selected to be the Kp coefficient parameter for the right and left wheel. The selected coefficient parameter is 1.14 for the left wheel and 1.16 for the right wheel.

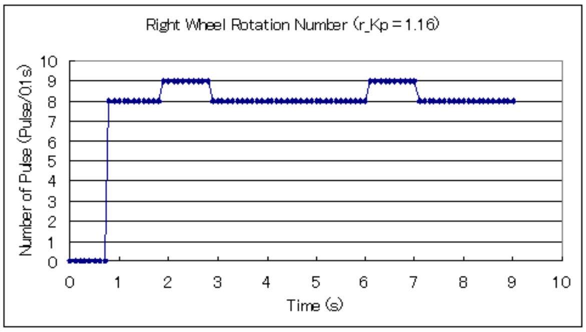

Fig. 4: Right wheel rotation number

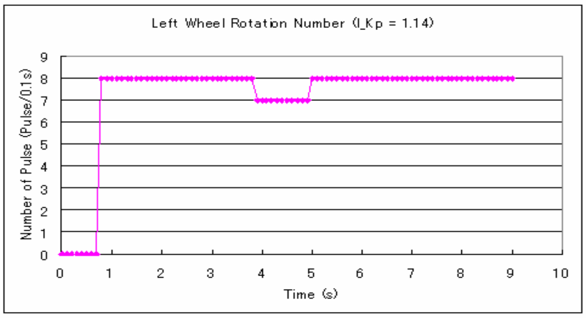

Fig. 5: Left wheel rotation number

From the result shown above (**Fig. 4** and **Fig. 5)**, we found the target number of wheel rotation is stabilized but there is some amplitude are slightly out. We assume that, this is because of odometry non-systematic errors which may be cause by wheel-slippage or irregularities of the floor. We also found that the robot will reach target speed approximately after 0.7sec after the command is send due to load of mobile robot and resistance of the wheel.

6 Conclusions

In previous research [3], [4], [5] the movement of mobile robot is stabilized with the proportional controller but their confirmation of coefficient proportional parameter is done by computer simulation. The purpose of this study is to find out the best parameter for the proportional controller for each left and right wheel on real environment which is actual running on the laboratory floor. We found that the mobile robot is stabilized, means rotation of each wheel reached at the desired value and adhere to that value by using coefficient parameter of Kp=1.14 for the left wheel and Kp=1.16 for the right wheel. To make wheel rotation reach at the desire value of wheel rotation we use pulse-width modulation. Pulse-width modulation can be use to control the speed of mobile robot by switching ON nd OFF very quickly the power supply (voltage) to the DC motor in order to make a variation of speed. This finding will assist in executing a more accurate testing in future experiments.

The authors are currently working, in making stable-target tracking research. The coefficient parameter with the proportional controller in this paper and other several controllers will be used. Experiment data will be collected in order to verify the result presented in this paper.

References

[1] K. Z. Tang, S. N. Huang K. K. Tan and T. H. Lee, "Combined PID and Adaptive Nonlinear Control for Servo Mechanical Systems," *Article of Elsevier Mechatronics*, Vol.14, Issue 6, pp. 701- 714, 2004.

[2] Ziegler, J. G and Nicholas, N. B, "Optimum Settings for Automatics Controllers," *Trans. ASME*, pp.759-768, 1942.

[3] M. Sugisaka and T. Hashizume, "Run Control of The Mobile Robot Using Visual Information," *Proc. of The Int. Symposium on Artificial Life and Robotics*, pp. 667-670, 2005.

[4] Toshio Maeyama and Masanori Sugisaka, "The obstacle Avoidance Run in The Mobile Robot using The CCD Camera", *Thesis of Master Studies, Faculty of Engineering, Oita University Graduate School*, 2002.

[5] Masanori Sugisaka and Toshio Maeyama, "Obstacle Avoidance in the Mobile Robot Using the CCD Camera", *Proc. of The Int. Symposium on Artificial Life and Robotics*, pp.238-241, 2002.

[6] G. J. Battaglia, "Mean Square Error", *AMP Journal of Technology*, Vol. 5, pp.31-36, June 1996.

The Eleventh International Symposium on Artificial Life and Robotics 2006 (AROB 11th'06),
B-con Plaza, Beppu, Oita, Japan, January 23-25, 2006

Development of an autonomous personal robot "System of recognition for work"

Hiroshi Mizoguchi, Yuki Matsumoto, and Eiji Hayashi
Department of Mechanical Information Science and Technology
Faculty of Computer Science and Systems Engineering, Kyushu Institute of Technology
680-4, Kawazu, Iizuka-City, Fukuoka Prefecture, Japan
E-mail: haya@mse.kyutech.ac.jp

***Key Words*:** Robot, Recognition, autonomous, Roots, Map

Abstract

Due to the profusion of research in robotics in recent years, new kinds of robots, including domestic robots and rescue robots, have been developed. However, regardless of these advances, the development of a robot to replace human health workers in the home and in the hospital has proved problematic. Despite the challenges inherent in this area, our laboratory is developing an autonomous personal robot that can work in the above settings and is easy to command.

In the performance of its tasks, the robot moves to the position of a work object shown on a map. As a result, it is possible to move to the approximate area in front of the work object. But because of external factors such as the margin of movement error and so on, when the robot moves, the positions of the robot and the work object can vary. This system identifies an object by searching for the object's image in the robot's database and comparing it to a CCD camera image based on pixel information.

1. Introduction

Recently, the chances of seeing a working robot in our surroundings have increased. Robots with various functions have been developed based on recent technological advances. However, a robot capable of helping us autonomously has not yet appeared. Thus, our laboratory is developing an autonomous personal robot that can work in the home and the hospital while being easy to command.

In order to allow the robot to work autonomously, it is necessary to create a program for the robot that allows it various actions.

In this paper we explain an algorithm of route searching and a method of image processing used with a recognition system. In addition, we describe the results of an experiment to evaluate the work search system, and discuss its results.

2. Composition of robot

The robot developed based on this research is composed of a recognition system that understands peripheral information and a decision system that determines the robot's actions. Figure 1 shows the system and the processing composition.

2.1. Recognition system

This system acquires peripheral information from various sensors and uses it to develop the robot's understanding of its surroundings.

2.2. Movement determination system

This system determines the robot's direction of movement and speed and so on based on a feed-forward input from the finite space map and feedback input from the recognition system.

The robot decides its next action based on input from the recognition system and the decision system, and then sends instructions to the drive control system.

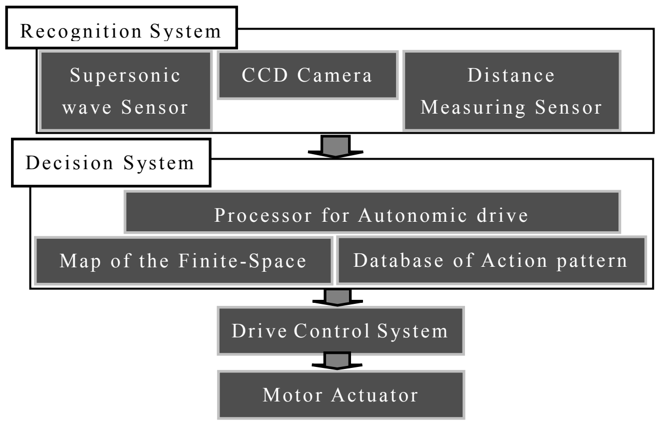

Fig.1 processing system for personal robot

3. Finite space map

The robot assumes a limited space exists within the home, office, sickroom, etc. Thus, the robot's range of action is defined by the limited space on each floor.

It is necessary to calculate the necessary corrections and process the image data in order to detect and evade obstacles, as well as to maintain a sufficient error margin. It can be said it is inefficient when the obstacle is detected in every case when moving to the same space many times.

Therefore, the robot is constructed to be capable of processing information efficiently using a "finite space map" which contains information regarding the object's various aspects.

3.1. Concept of finite space map

The limited space map is given to the robot as two- dimensional information. Information in this map includes the size of the object, the position of the object, and the size of the room. This arranged object is assumed to be within the limited range of a rectangle or quadrangle. When the robot moves based on this information, feed-forward operation is achieved.

This map shows the robot's initial coordinates on the map grid, as well as the position of the target and the arrangement of objects in the room. Figure 2 shows this limited space map.

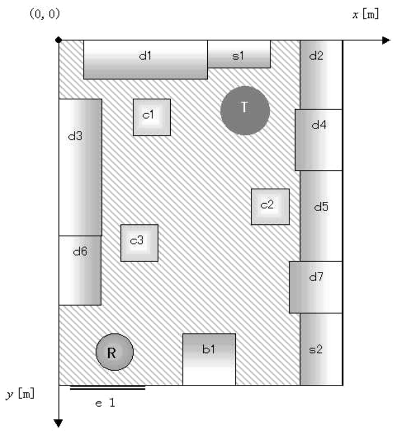

Fig.2 Finite space map

3.2. System for route searching

When the robot's initial route is interrupted by an unknown object, the robot should make an evasive movement. The robot is able to detect and evade unknown objects, but is also able to determine a more efficient alternate route.

Therefore, when establishing a route to the target point, two or more routes can be determined.

The robot derives the route from the limited space map, and decides the one with the shortest distance from two or more routes in the beginning. This flow chart is shown in Fig3.

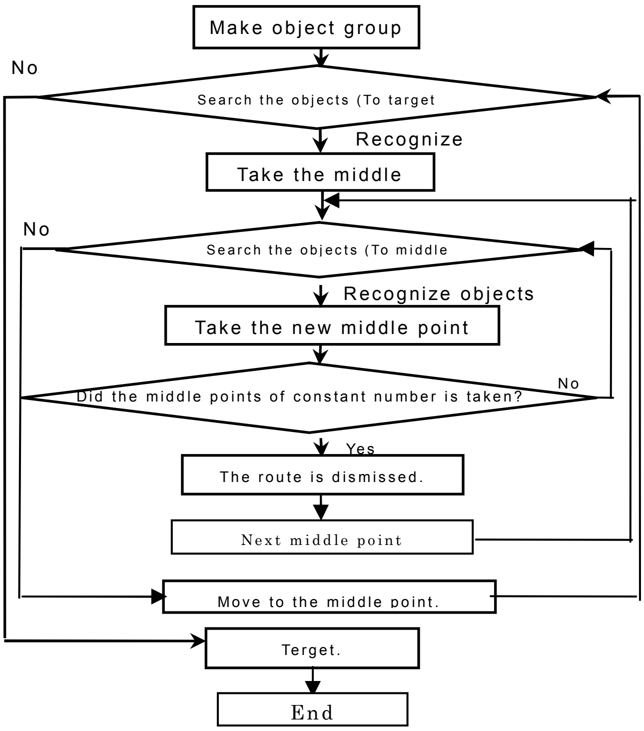

Fig.3 Flowchart

Next, it is explained how a middle point is determined. When the arrangement of objects is assumed as shown in Figure 4a, the presence of an obstacle is determined.

To evade the obstacle, the candidate in the middle point is taken away in a point left from the corner of the obstacle at a diagonal of 45 degrees and a length of 50cm.

A middle point that can actually be reached is chosen from among the candidates in the middle area (Fig.4b). In this case, four middle points P1, P2, P3, and P4 can be obtained.

When the robot takes two middle points P3 and P4, the robot judges object from P3 or P4. Then it judges the same object. When the candidate in the middle point is taken away, the system takes this point. These are the last middle points.

A comparison of the length of the P0-P1 route with the length of the P0-P3-P1 route shows that the latter is obviously longer. Therefore, P1 is excluded from the middle point P3. P2 and P4 are excluded for the reasons same as P1.

Then, all the routes are deleted from P3. This route is dismissed because it becomes a route as shown in d and it is not capable of reaching the target point. It is similar in the case of P4.

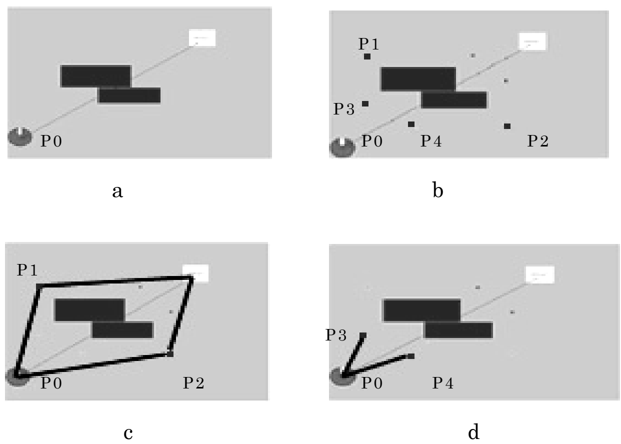

Fig.4 Method of taking the middle point

4. System of recognition for work

4.1. Purpose of system

When the robot works, it moves toward the approximate front of the work object shown in the map. But because of external factors, including the movement error margin and so on, when the robot moves, the positions of the robot and the work object are not constant.

Thus, the recognition system discovers the work object from among the images obtained by the CCD camera, and establishes the position of the work object.

Moreover, the position of the robot and the object specified in this system is used also for the robot's self-positional correction. For example, when an object in a certain fixed place, such as elevator buttons and light switches in a room, is discovered, the robot's position and those of the fixed objects can be confirmed. As a result, the error margin between the robot's position within the limited space map and the robot's position in real space during repeated movements can be corrected. Figure 5 shows the flow of the system.

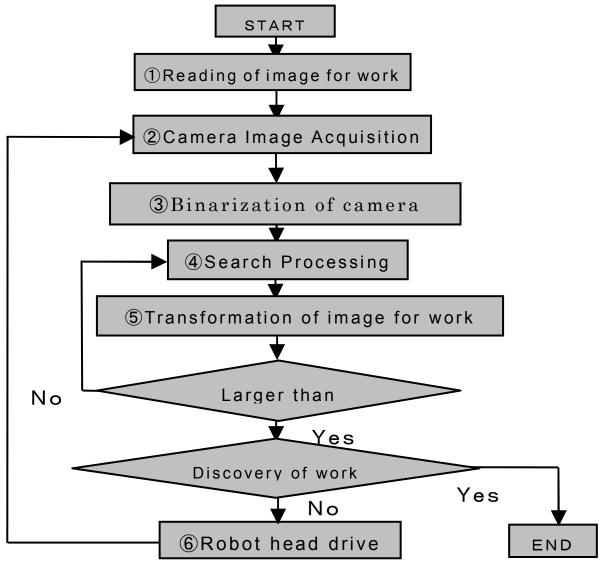

Fig.5 System flow

4.2. System processing

We explain the processing of the system flow shown in Figure 5. First, data regarding the work object is read. This data is taken from the robot's knowledge data base. The data regarding the object contains various information such as object image, the size, the position, etc.

Next, the CCD camera image is acquired. In addition, the object's shape are extracted by processing the edge extraction to the acquisition image. The acquired image is converted into binary data. This transforms the image data into monochrome data, and thus pixel information can be simplified.

Search processing seeks the object's image from among the acquired images. The object is searched for by seeking pixel information shared by the acquired image and the object image.

The object image changes according to the distance between the camera and the object or the angle via which the camera sees the object. Then, the object's distance and the angle to it is processed by the geometric transformation calculation and the projection conversion. The distance and the angle of the image when the work object is discovered become the results of a positional decision of the work object of the system.

A CCD camera is positioned in the robot's head which rotates as the robot searches for the object. The rotational range facing forward is 60 degrees

5. Experiment

An experimental evaluation of the system was performed. In this experiment the robot moves to the front of the room to face the elevator and searches for the elevator button.

The experiment involved the robot searching for the elevator button from various distances and angles, and determining the correct position for pushing the button. Tables 1-4 show the results regarding distance and angle.

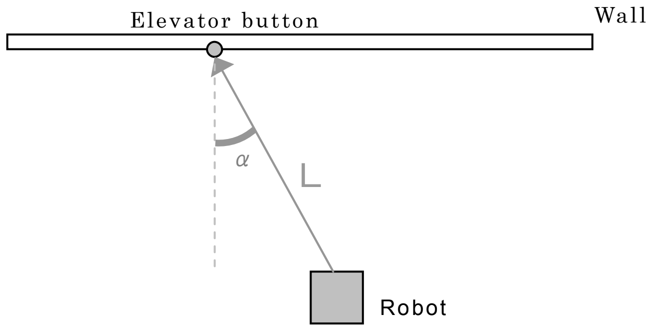

Fig.6. Situation of experiment

Table 1. Result of experiment （Case1 L=300mm）

Angle α[°]	Result of distance[ｍｍ]	Result of angle[°]
0	３００	１１
１５	３００	１５
３０	３００	２７

Table 2. Result of experiment （Case2 L=400mm）

Angle α[°]	Result of distance[ｍｍ]	Result of angle[°]
0	４００	9
１５	３８０	２０
３０	３８０	２６

Table 3. Result of experiment （Case3 L=500mm）

Angle α[°]	Result of distance[ｍｍ]	Result of angle[°]
0	４９０	2
１５	４７０	２０
３０	４４０	３０

Table 4. Result of experiment （Case4 L=600mm）

Angle α[°]	Result of distance[ｍｍ]	Result of angle[°]
0	６００	5
１５	５３０	２６
３０	５５０	１９

6. Consideration

We can say as follows considerations from this experiment result.

First, an object the size of an elevator button can be discovered when the distance between the robot and the object is 300 to 600mm. However, the object's shape could not be easily obtained when the robot was too close to the object. Moreover, the button could not be discovered when the distance between the robot and the object was too great. We can say that the shorter the distance between the robot and the object, the more accurate is distance estimation. The shorter the distance to the object, the larger the image received by the camera, and thus more details of the object's shape can be captured.

We can say that the determination of the angle between the robot and the object is difficult only in the pixel match. We consider that this system should adopt only the determination of distance by the pixel match, and analyze the angle based on the perspective that appears in the camera image.

7. Conclusion

In this study, a system designed to search for an object was designed, and experimental results show that the object could be discovered with a high degree of probability.

Moreover, the distance to the object could be estimated with great accuracy. However, estimation of the angle remains problematic, and the robot has not come to work for object.

Improvement of the accuracy of position estimation is also needed. Estimation of the angle to the object is not a transformation condition of the object image, and should analyze the entire camera image as for consideration as described.

REFERENCES

[1]Takuma Umeno, Eiji Hayashi, Development of an autonomous personal robot "The visual processing system for autonomous driving", proceedings of the 10th international symposium on artificial life and robotics, Vol.10th, pp.4, Beppu, Oita, Japan, 2005.

[2]Eiji Hayashi, Keisuke Ikeda, Development of an system for self-driving by autonomous robot, proceedings of the 10th international symposium on artificial life and robotics, Vol.10th, pp.44, Beppu, Oita, Japan, 2005.

[3]Toru Azuma, Yoshihiro Takenaga, Eiji, Hayashi, Development of a self-driven personal robot, Artifical Life and Robotics(AROB 8th'03), pp.1-3, Oita, Japan, 2003.

A Model of Mckibben Muscle Actuator Based on Experiment

Huailin Zhao*,** (zhao_huailin@yahoo.com) Masanori Sugisaka** Datai Yu*
* School of Information Engineering, University of Science and Technology Beijing
** Department of Electrical and Electronic Engineering, Oita University, Japan

Abstract: Mckibben muscles are a kind of pneumatic artificial muscles. It can be used as actuators to actuate robots. Aiming at the force-length model, the paper compared the ideal model with experiments and revised the ideal model. Then it analyzed the reason leading to the hysteresis phenomena, and established the hysteresis model. The experiments showed that the hysteresis model was consistent and robust to different length Mckibben muscle actuators.

Keyword: Mckibben muscle actuator, force-length model, hysteresis model

1. Introduction

There has been some ink used for Mckibben muscles [1-3]. It is a kind of pneumatic artificial muscles. It can generate enough force and maintain proper compliance at the same time-a little like real muscles. So it can be used as an actuator to actuate the robot. A robot actuated by Mckibben muscles probably will behave like an animal. But it is not easy to find a model in literatures. And different Mckibben muscle products are different. So we have to establish the special model of the kind used in our project. What we are interested about the model is its force characteristic, because it is used as an actuator.

2. The ideal static model

Mckibben muscles used in our project are like Fig.1. It has a double-layer structure like Fig.1 (b). It consists of a rubber tube covered in tough braided fiber mesh, which shortens in length when inflated with compressed gas. Gas can be input in from its one end, and the other end is closed. L and D are the nominal length and the nominal diameter. Another important structure parameter is θ -the mesh weave angle. L and D will change when θ changes. So L and D must have close relationships with θ.

If the actuator is supposed as a regular cylinder, a geometry model can be established (see Fig.2). Except L, D and θ, there are structure parameters n-the number of tunes that the fiber winds and b-the length of the fiber. θ will increase and L will decrease when compressed gas is input. But b will keep constant. Based on the assumption that the actuator is a conservative system, an ideal static model can be gotten as [2]

$$F=P_g b^2(3L^2/b^2-1)/(4\pi n^2) \quad (1)$$

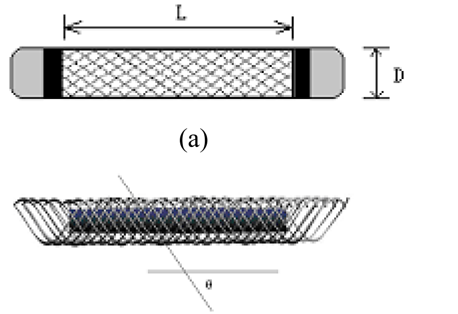

(a)

(b)

Fig.1 Structure of Mckibben muscles

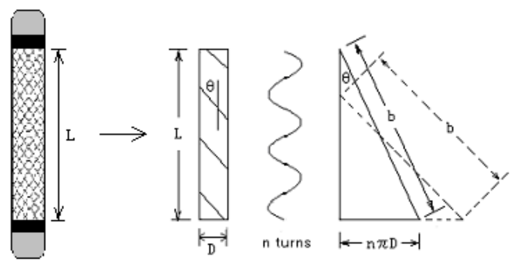

Fig.2 Geometry model

In which, F is the pulling force generated by the actuator, P_g is the relative gas pressure between the outer environment and the inner rubber, which can be read from the pressure gage. L is the current length. b and n are the structure parameters.

Based on the ideal model (1), the force output is related with the gage pressure, current length, and the structure parameters. Fig.3 is the simulation of force-length characteristic for a Mckibben muscle actuator that its free length is 450mm. It is easy to be seen that the maximal contraction ratios for different gage pressures are same based on this model.

3. Revising of the force-length model

Analyzing the ideal model and observing the simulation figure, we can easily find something that is not consistent with the fact. First, it is not real that the maximal contraction ratios are same to different gage pressures (see Fig.3). Basic experiments have shown that the maximal contraction ratios are related with the pressures very much. The contraction ratio will be different if the gage pressure changes. Second, from Fig.3, the maximal contraction ratio can be calculated: (450-300)/450*%=33.3%. Based on the experiments, the maximal contraction ratio of the actuators used in our project is less than 30%. Any way, the force-length model must be revised.

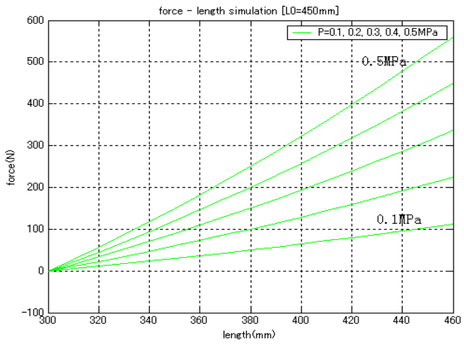

Fig.3 Simulation of force-length model (450mm)

Now let's do some experiments to measure the related data. Fig.4 is the experiment system. The experiment data is about the force–length relationship. In the experiment, to every gage pressure (0.1Mpa, 0.2Mpa, 0.3Mpa, 0.4Mpa, 0.5Mpa), the length is changed from L_0 (free length) to the minimal length and then returned to the free length again. Doing the experiment this way is because Mckibben muscle actuator has hysteresis characteristic [4]. Here the gage pressure is limited within [0.1, 0.5]Mpa. Fig.5 is the experiment data.

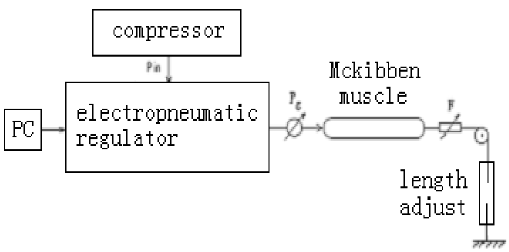

Fig.4 Experiment system

Comparing the ideal model and the experiment (see Fig.6), it is found there are some differences as the following:

- To the same current length and the same pressure, the model force is larger than that of the experiment.
- The maximal contraction ratios related with different pressures are different in the experiment.
- And all the contraction ratios in experiment are less than the corresponding ones of the model.

What's the reason leading to those differences? After analyzing, we know that the ideal model is based on some suppositions [2]. One of the suppositions is that all the absorbed energy can be output, in another word - no energy loss. But actually this is not possible. Another supposition is that Mckibben muscle actuator is thought as an ideal cylinder and the inner rubber is very thin and contacts the mesh very closely. But this is not the fact too.

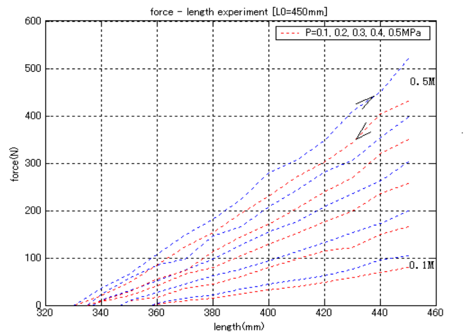

Fig.5 Experiment data (450mm)

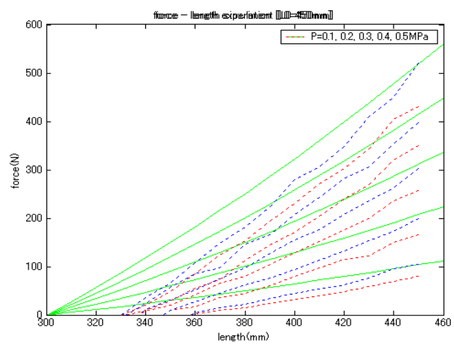

Fig.6 Comparison between the experiment and the model (450mm)

Now let's revise the model. Based on the above comparison, the following should be done:

- Reduce the force.
- Revise the contraction ratio and make it has relationship with the gage pressure.
- Reduce the contraction ratio.

Synthesizing the above three points, we revise the model into:

$$F = c_1 b^2/(4\pi n^2)\, P_g\{3[(1-c_2R_c)L/b]^2-1\}$$

In which, R_c is the definition of the contraction ratio ($R_c=(L_0-L)/L_0$)). Parameter $c_1<1$, is used to reduce the force output. c_2 is related with the gage pressure. So c_2R_c is related with gage pressure too and used to change the contraction ratio. c_2R_c can be called the new contraction ratio. Be sure that $(1-c_2R_c)<1$.

Based on the experiment data and the new model, c_1 and c_2 can be got as the following:

$$c_1 = 0.90$$

$$c_2 = 1.11e^{-9Pg}+0.34$$

So the revised model is

$$F=0.9b^2/(4\pi n^2)\, P_g\{3[(1-(1.11e^{-9Pg}+0.34)R_c)L/b]^2-1\} \quad (2)$$

Comparing the revised model with the experiment, we got Fig.7. Now the model and the experiment are consistent with each other.

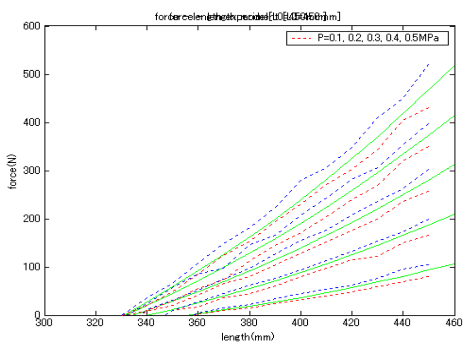

Fig.7 Comparison between the revised model and the experiment (450mm)

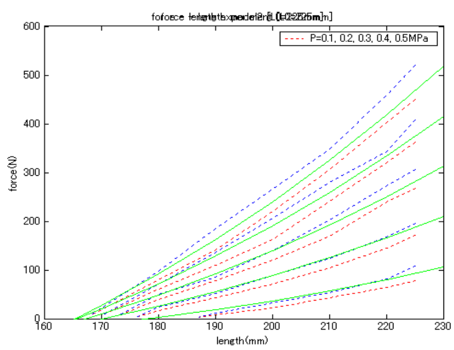

Fig.8 Comparison between the revised model and the experiment (225mm)

The revised model is based on the data with free length 450mm. Does the model fit to actuators with different lengths? In another word, is the model robust to length? Now let's do the same experiment with another Mckibben muscle that its length is 225mm, right just half of the former one and compare with the revised model (see Fig.8).

From Fig.8, it is found that there is difference between the revised model and the experiment data. But the difference is not large. So we can conclude that the revised model is somewhat robust to the length.

4. The hysteresis model

From the above experiments, we find that the hysteresis characteristic is clear and can't be ignored. The difference is large between the force outputs when the pressure increasing and that when the pressure decreasing (see Fig.7 and Fig.8). So the hysteresis model must be established too.

Analyzing the hysteresis phenomenon, we think it is mainly due to the frictions between the inner rubber and the outer mesh as well as between the fibers in the mesh. They should be Coulomb friction generated by the relative movements when Mckibben muscle contracts. Any way it is not easy to calculate it, because the relative movements between the two layers and between the fibers are very complicated (see Fig.9).

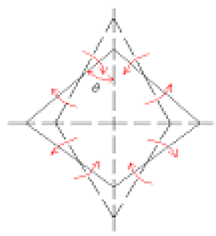

Fig.9 The relative movement of the fibers when contracting

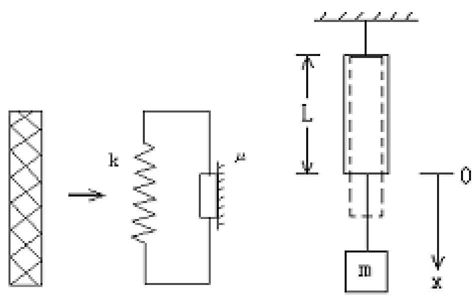

(a) (b)

Fig.10 Friction model

Based on the analyzing, force output can be divided into two parts as the following:

$$F=F_s \pm F_d$$

In which, F_s is the basic static force and can be calculate by (2), and F_d is the friction force and can be expressed as

$$F_d = \mathrm{sgn}(dx/dt)\,\mu\,F_N$$

In which, μ is the symphetical friction coefficient and F_N is the corresponding positive pressure. We will establish F_d by experiments because it is not easy to value μ and F_N.

From the experiment data, it is easy to find that F_d is related with the gage pressure and the contraction ratio. Based on the experiment, a linear model of F_d can be got as following:

$$F_d = 2F_{dm}(L - L_{min})/(L_0 - L_{min}) \qquad (3)$$

In which,

$$F_{dm} = 33.91P_g + 2.13$$

$$L_{min} = \{-1 + c_2 + [(1-c_2)^2 + 4bc_2/(3^{1/2}L_0)]^{1/2}\}L_0/(2c_2)$$

$$(c_2 = 1.11e^{-9P_g} + 0.34)$$

So we can denote the hysteresis model as following:

$$F = F_s \pm F_d$$

In which, F_s is calculated by (2) and F_d calculated by (3). Fig.11 is the comparison between experiment and the model for a 450mm actuator. They are consistent with each other.

Now there is a similar question: is the hysteresis model robust to other actuators with different lengths? By the similar way, model F_d for 225mm can be got, and the comparison can be done too. The comparison shows that there is some difference. But the difference is not large. There is data showing that the maximal difference of their F_d is less than 1N.

Now let's rewrite the hysteresis model again as following:

$$F = F_s \pm F_d$$

$$= 0.9b^2/(4\pi n^2)\,P_g\{3[(1-(1.11e^{-9P_g}+0.34)R_c)L/b]^2 - 1\}$$

$$\pm 2F_{dm}(L - L_{min})/(L_0 - L_{min})$$

In which,

$$F_{dm} = 32.291P_g + 2.83$$

$$L_{min} = \{-1 + c_2 + [(1-c_2)^2 + 4bc_2/(3^{1/2}L_0)]^{1/2}\}L_0/(2c_2)$$

$$(c_2 = 1.11e^{-9P_g} + 0.34)$$

And note:

$$L_{min} \le L \le L_0$$

$$0.1\mathrm{Mpa} \le P_g \le 0.5\mathrm{Mpa}$$

5. Conclusion

Mckibben muscles are a special kind of actuators. The robot actuated by it will behave a little like animals. Based on the ideal force-length model and the experiments, an actual model is established. At last a hysteresis model is designed too. All the comparisons show that the models are consistent with the experiments and are robust to other ones with different lengths.

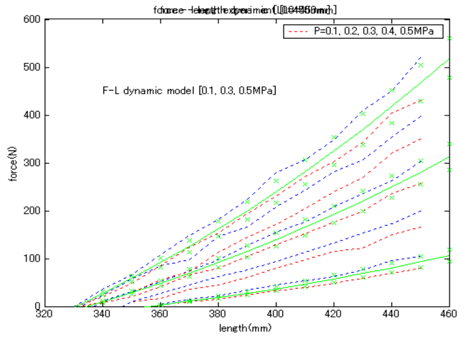

(a) P_g=0.1Mpa,0.3Mpa,0.5Mpa

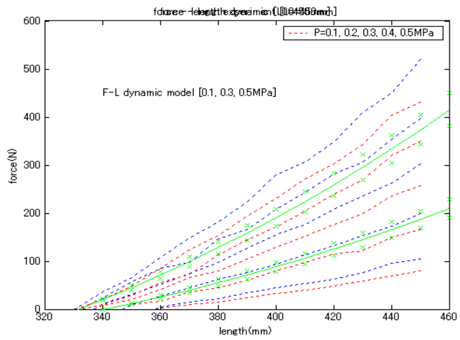

(b) P_g=0.2Mpa,0.4Mpa

Fig.11 Comparison between the experiment and the model (450mm)

Reference

[1] Masanori Sugisaka, Huailin Zhao, Norrima Mokhtar, The artificial muscle and its application in robot, Proceeding of 9th international artificial life and robotics symposium, Jan.2003, Japan

[2] Huailin Zhao, Masanori Sugisaka, Modeling of Pneumatic Artificial Muscle Actuator, Proceeding of 10th international artificial life and robotics symposium, Feb.2004, Japan

[3] John Iovine, "Artificial pneumatic muscle", Poptronics, Nov.2000, p49-65;

[4] Frank Daerden, Dirk Lefeber, Pneumatic Artificial Muscles: actuators for robotics and automation, European Journal of Mechanical and Environmental Engineering,47(1):10-21,2002

The Eleventh International Symposium on Artificial Life and Robotics 2006 (AROB 11th'06),
B-con Plaza, Beppu, Oita, Japan, January 23-25, 2006

Offensive Strategy of a Billiard Robot

Jr-Syu Yang
(corresponding author)
Department of Mechanical and Electro-Mechanical Engineering
Tamkang University
No.151, Yingzhuan Rd., Danshui Town, Taipei County 251, Taiwan, R.O.C
096034@mail.tku.edu.tw

Je-Ting Li
Department of Mechanical and Electro-Mechanical Engineering
Tamkang University
No.151, Yingzhuan Rd., Danshui Town, Taipei County 251, Taiwan, R.O.C

Chan-Yun Yang
Department of Mechanical Engineering
Northern Taiwan Institute of Science and Technology
No. 2, Xue Yuan Rd., Peitou, Taipei Country 112, Taiwan, R.O.C

Abstract

Billiard is one of the most complex game to play for human beings in the real world. The objective of this paper is to develop an offensive strategy to make a position play for a billiard robot in a nine ball game. The robot is composed of a machine vision, decision-making, control and actuating subsystems in a miniature pool table. The experimental results indicate that the robot is able to make a position play to pocket the object balls from number one to four sequentially and successfully.

Keywords： billiard robot, position play, decision- making

1 Introduction

The billiard robot is designed to imitate the learning ability of human beings to play billiard. The billiard is one of the amusing activities for years. The game of billiard is played on a rectangular table (billiard table). One ball (cue ball) is struck with the end of a cue stick, causing it to bounce into other balls and reflect off the side of the table. A player needs to have capability of the geometrical concept and offensive strategy to win the game. A good billiard player needs to visualize the geometrical relations between cue ball, object balls and pockets, and to control the strength of shot to strike the object balls into designate pockets one by one sequentially.

There are several related researches that simulate the billiard game in virtual environments. Koo applied the concept of fuzzy logic to develop the decision algorithm on computer generated pool environments [1]. Koo demonstrated the balls identification and calibration for a pool robot by the image processing technique [2]. Nakama developed a shooting mechanism for a billiard robot by a precise position mechanism [3]. A wearable computer and augmented reality were demonstrated to help players to enhance the game of billiards [4]. All of them are lack of the integration both of strategy part and mechronics part. Yang demonstrated a shooting angle compensator for a billiard robot by the neural and fuzzy theory [5]. He also developed a pocket selection algorithm for the billiard robot by the grey theory [6].

2 Experimental setup

(1) Machine vision subsystem：

There are a CCD camera with an image capture card and a PC in this subsystem. The CCD is installed on the position of 2.7 meters high above the pool table (Fig. 1). First, the images of balls and pockets are captured to identify locations of the cue ball, each numbers of object balls (color balls), and pockets. Then, the centers of these balls and pockets are calculated by the developed image processing software in a PC. The geometrical data of this specific case will be sent to the decision-making subsystem for the further calculation (Fig. 2).

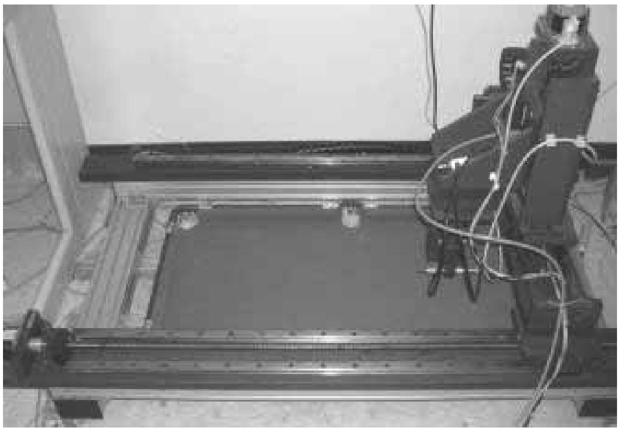

Fig. 1. The billiard robot

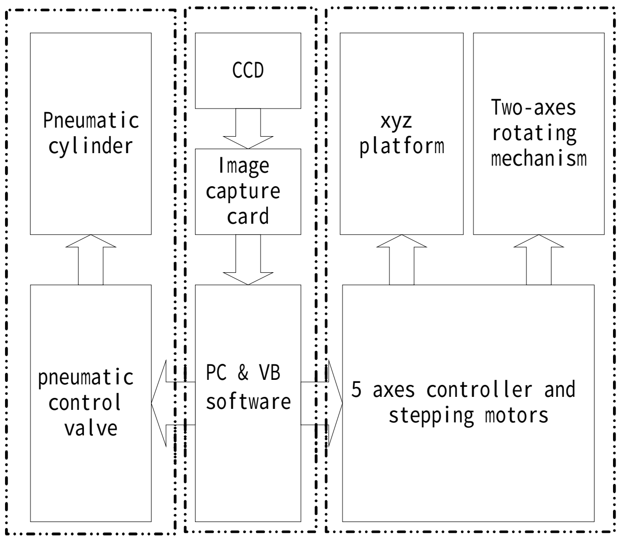

Fig. 2. Flow chart of the experimental setup

(2) Decision-making subsystem：

The decision-making algorithm is developed by the following four factors of the extension theory [7]. The factors are (i) the shooting angle (θ), (ii) the distance (d_1) between the centers of the object ball and the corresponding pocket (Fig. 3), (iii) distance (d_2) between the centers of the cue ball and object ball, and (iv) the perpendicular distance (d_b) from the center of block ball to the line (Y) (Fig. 4). The offensive strategy is developed based on these four factors. It will make up the shooting priority step by step automatically.

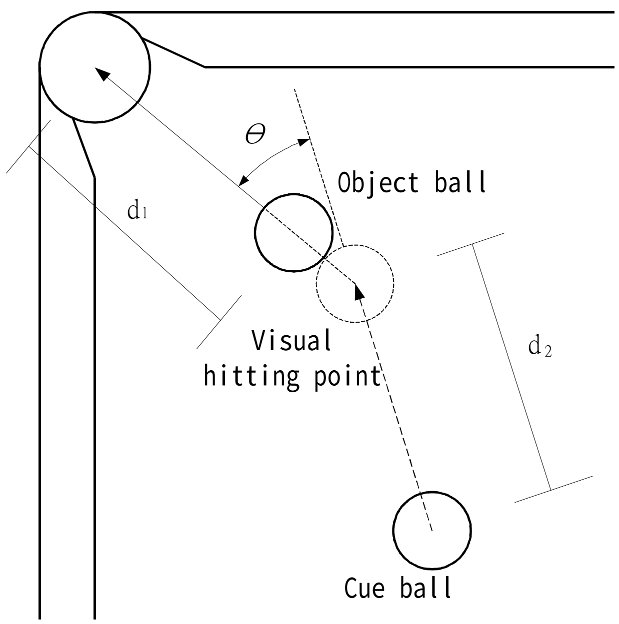

Fig. 3. The positions of cue ball, object ball and pocket

(3) Mechanical position subsystem:

There are a x-y-z position platform and a two-axes rotating mechanism to align the actuating mechanism for the robot. The motion commands are determined by the center controller (PC) and sent to the corresponding motor controllers to drive the pneumatic cylinder to the desired position to strike the cue ball.

(4) Actuating mechanism subsystem:

There are a pneumatic pressure control valve and a cylinder in this subsystem. The first one is applied to control the strength of shot of this billiard robot. The second one is used to strike the cue ball to imitate the shooting behavior of human beings to play billiard with a cue stick.

3 Offensive strategy

The objective of the developed offensive strategy of the billiard robot is to win the nine ball game. The nine ball game is played with nine object balls numbered one through nine and a cue ball. On each shot, the first ball that the cue ball contacts must be the lowest number of object balls on the table. But, the balls need not be pocketed in order. If a player pockets any ball on a legal shot, he/she remains at the table for another shot and continues until he misses, fouls, or wins the game by pocketing the nine ball [8]. In the research, it is arranged to have a cue ball and 4 object balls (number one to four) on the table for simplification.

The offensive strategy is determined by the above four factors of the extension theory [7]. The matter element is assigned as

$$R=(N,C,V)=\begin{bmatrix} N & C_1 & V_1 \\ & C_2 & V_2 \\ & C_3 & V_3 \\ & C_4 & V_4 \end{bmatrix}=\begin{bmatrix} \begin{matrix} selection \\ factor \end{matrix} & \theta & \langle 0°,90° \rangle \\ & d_1 & \langle 0,300 \rangle \\ & d_2 & \langle 85,215 \rangle \\ & d_b & \langle -1,1 \rangle \end{bmatrix}$$

The relational function can be assigned as

$$K_1(\theta)=\begin{cases} -1 \ , & |\theta|>90 \\ \dfrac{90-|\theta|}{90} \ , & |\theta|<90 \end{cases} \qquad (1)$$

$$K_2(d_1)=\begin{cases} \dfrac{d_1+300}{300} \ , & d_1\le 0 \\ \dfrac{300-d_1}{300} \ , & d_1\ge 0 \end{cases} \qquad (2)$$

$$K_3(d_2) = \begin{cases} \dfrac{|d_2 - 150| - 65}{|d_2 - 165| - |d_2 - 150| - 70}, & d_2 \notin, < 85,215 > \\ 65 - |d_2 - 150|, & d_2 \in < 82,215 > \end{cases} \quad (3)$$

$$K_4(d_b) = \begin{cases} -1, & 0 \le d_b \le 32 \\ 1, & d_b > 32 \end{cases} \quad (4)$$

The shoot angle (θ) between the direction of the cue ball to the hitting point and the direction of the hitting point to the pocket is a very important factor to let the object ball run into the pocket after collision (Fig. 3). If the angle (θ) is equal to zero, that means the cue ball, object ball, and the pocket are on the straight line. It is the easiest way to pocket the object ball. If the absolute value of angle (θ) is getting larger ($\theta \ge 90°$, on either right or left side), it is more difficult to pocket the object ball successfully (eqn. (1)). If the distance d_1 is small, that means the object ball is close to the pocket. It is easier to pocket the object ball. The half length of the pool table is 300 pixel (1 cm = 8 pixel) (eqn. 2). The distance d_2 is between 85 and 215 pixel from many striking experiments for pocketing the object ball into designed pocket successfully (eqn. (3)). The diameter of the ball is 4 cm (32 pixel). If the distance d_b is small than 32 pixel, there is a block ball on the moving direction from the cue ball to the object ball (Fig. 4). It will cause a foul during the game. In this case, the value of $k_4(d_b)$ is equal to –1. By contrast with this block ball, the value of $k_4(d_b)$ is equal to 1 (eqn. (4)).

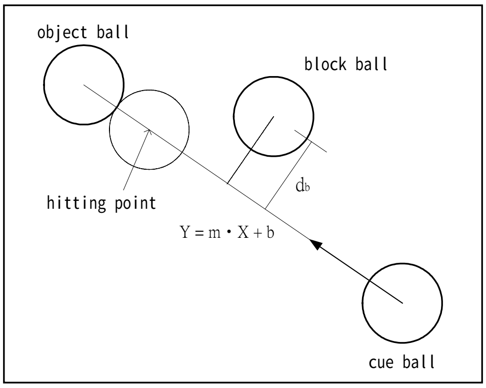

Fig. 4. The position of block ball

In the ball game, it is necessary to make a position play for the next shot. The predicted position of the cue ball and other object balls after collision are calculated to make a position play in this offensive strategy in order to win the ball game. For example, the white ball is the cue ball (Fig. 5). First, the ball 1 is pocketed into pocket 4 and the cue ball is controlled to stop at the position $P_{1,2}$ for the next shot. And the ball 2 is pocketed into pocket 2 and the cue ball is controlled to stop at the position $P_{2,3}$ for the next shot. Then, the ball 3 is pocketed into pocket 1 and the cue ball is controlled to stop at the position $P_{3,4}$ for the next shot. Finally, the ball 4 is pocketed into pocket 4.

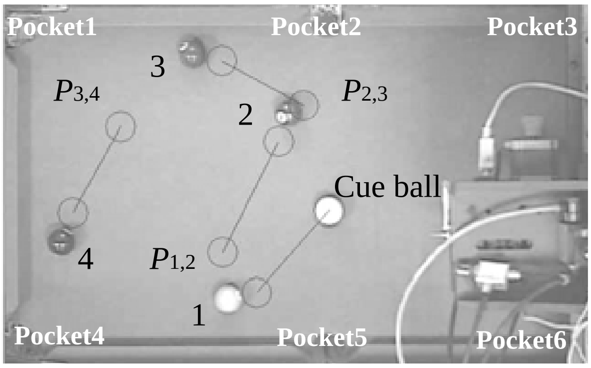

Fig. 5. Specific example of a position play

4 Result

Figure 6 shows the experimental results of a cue ball and 4 object balls on the table in 9 pictures taken by a digital camera continuously. The picture (1) shows that the actuating mechanism is in the stand by situation before a shot. Picture (2) shows that the cue ball is striking and running into the object ball 1. Then, the object ball 1 one is moved and pocketed into the right bottom pocket (picture (3)). And the cue ball is bounded and stop at a good position for the next shot (picture (4)). After that, the object ball 2 is pocketed into the left side pocket (picture (5)). And the cue ball is bounded and controlled to stop on a good position for the ball 3 (picture (6)). Similarly, the object ball 3 and 4 are pocketed into the left bottom pocket and right bottom pocket respectively (picture (7)~(9)). The experimental results, indicate that the robot is able to make a position play to pocket the object balls from number 1 to 4 sequentially and successfully.

5 Conclusion

In this paper, we presents an intelligent billiard robot with the offensive strategy to strike object balls sequentially. The robot shows its ability to “read” the table and make its own decision to sink the object balls into the pockets in the nine ball game automatically and successfully.

Acknowledgements

The National Science Council of Taiwan, ROC, is gratefully acknowledged for financial support under grant of NSC91-2213-E-032-006.

References

[1] S. C. Chua, E. K. Wong, Alan W. C. Tan, and V. C. Koo, 2002, “Decision Algorithm for Pool Using Fuzzy System, ” Proceedings of the International Conference on Artificial Intelligence in Engineering & Technology (ICAIET2002), 17-18 June 2002 Kota Kinabalu, Malaysia, pp. 370-375.

[2] S. C. Chua, E. K. Wong and V. C. Koo, 2003, "Pool Balls Identification and Calibration for a Pool Robot," Proceedings of the International Conference on Robotics, Vision, Information and Signal Processing (ROVISP 2003), January 2003, Penang, Malaysia, pp. 312-315.

[3] H. Nakama, I. Takaesu and H. Tokashiki, 2001, "Basic Study on Development of Shooting Mechanism for Billiard Robot", JSME, Robotic Workshop, 1A1F8.

[4] T. Jebara, C. Eyster, J. Weaver, T. Starner and A. Pentland, 1997 "Stochastics: Augmenting the Billiard Experience with Probabilistic Vision and Wearable Computers," In Proceedings of the International Symposium on Wearable Computers, Cambridge, Massachusetts. pp. 138-145.

[5] B. R. Cheng and J. S. Yang, 2004, "Design of The Neural-Fuzzy Compensator for a Billiard Robot," IEEE International Conference on Networking, Sensing and Control (ICNSC'04), March, 21-23, 2004, Taipei, Taiwan, CD-R.

[6] J. S. Yang, Z. M. Lin and C. Y. Yang, 2004, "Grey Decision-Making for a Billiard Robot," IEEE International Conference on Systems, Man & Cybernetics (SMC'04), Oct, 10-13, 2004, Hague, Netherland, CD-R.

[7] W.Cai, 1983, "The Extension Set and Incompatible Problem," J. of Scientific Exploration, 1, p.81-93.

[8] Billiard : The official rules & records book, Billiard Congracess of America, 1990.

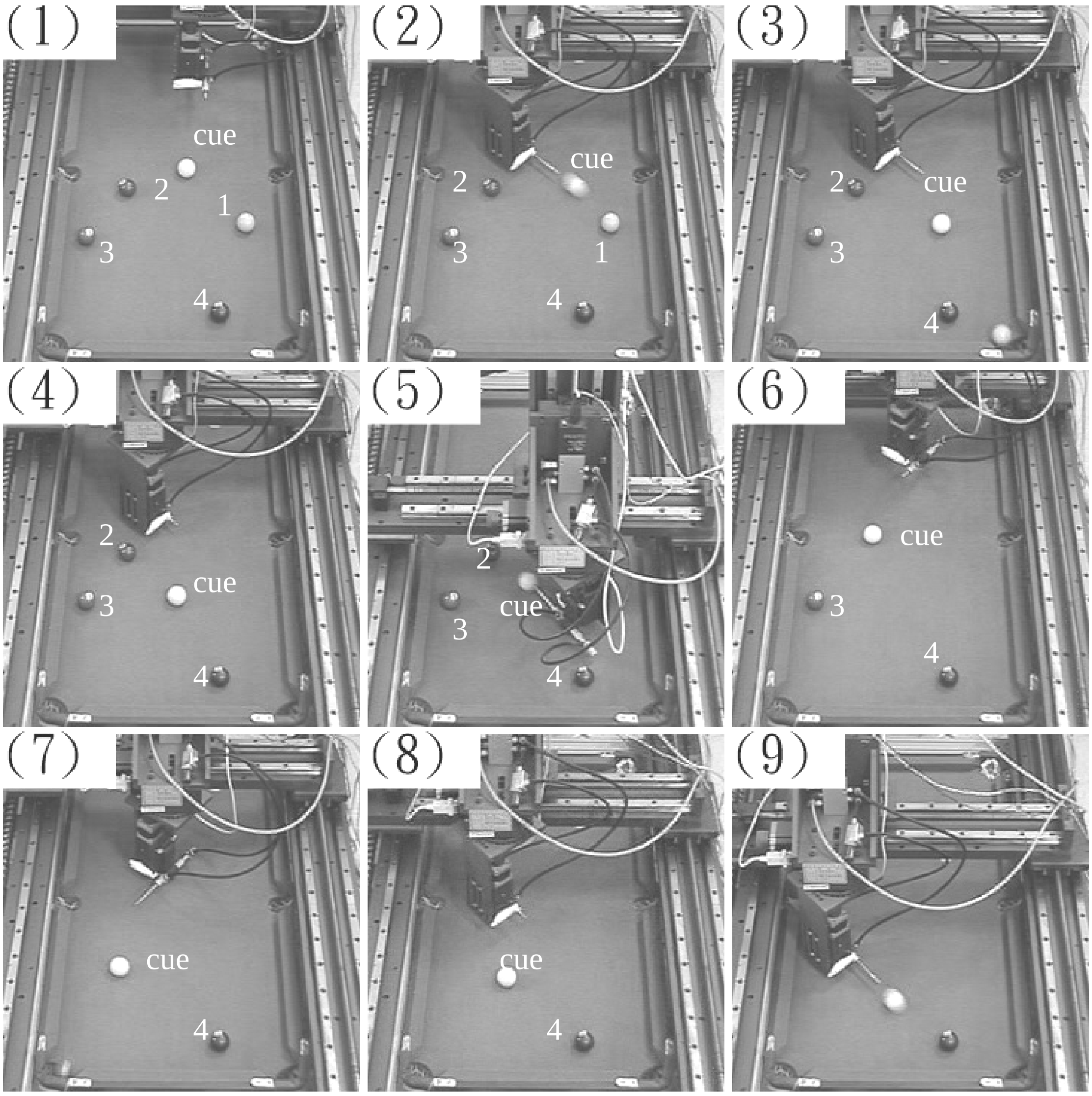

Fig. 6. Experimental result

The Eleventh International Symposium on Artificial Life and Robotics 2006 (AROB 11th'06),
B-con Plaza, Beppu, Oita, Japan, January 23-25, 2006

VeriSync: A Verification System for Firing Squad Synchronization Protocols on One-Dimensional Cellular Automata

Kouhei Matsumoto and Hiroshi Umeo
Univ. of Osaka Electro-Communication
Neyagawa-shi, Hatsu-cho 18-8, Osaka, 572-8530, Japan

Abstract

In this paper, we develop a verification system *VeriSync* that enables us to verify the correctness of the synchronization protocols, focusing on the class of optimum-time two-sided firing squad synchronization algorithms. We give a genealogy from Waksman's algorithms [7] to Balzer [1], ending with Gerken [2]. A formal design technique is also proposed that can ensure the correctness of synchronization processes.

1 Introduction

Cellular automata are considered to be a simple model for complex systems in which an infinite one-dimensional array of finite state machines (cells) updates itself in a synchronous manner according to a uniform local rule. Synchronizing a large scale of cellular automata has been known as the firing squad synchronization problem since its development, and the problem was originally proposed by J. Myhill in order to synchronize all parts of self-reproducing cellular automata [4]. The firing squad synchronization problem has been studied extensively for more than forty years [1-7].

Since the problem was defined by Myhill in 1957, a rich verity of synchronization protocols have been developed. A class of optimum-time two-sided firing squad synchronization algorithms is interesting from mathematical point of view and important in the design of other class of synchronization protocols. Waksman [7] presented a 16-state optimum-time synchronization algorithm. Afterward, Balzer [1] and Gerken [2] developed an eight-state and a seven-state synchronization algorithm, respectively, thus decreasing the number of states required for the synchronization. All of the algorithms are referred to as optimum-time two-sided firing squad synchronization algorithms. Global synchronization is a fundamental computing primitives in parallel and distributed systems, thus the correctness of the synchronization protocols is very important from practical applications, however, verification techniques for local rules of cellular automata are very few. We develop a verification system *VeriSync* that enables us to verify the correctness of the synchronization protocols, focusing on the class of optimum-time two-sided firing squad synchronization algorithms. We give a genealogy from Waksmann's algorithms [7] to Balzer [1], ending with Gerken [2]. A formal design technique is also proposed that can ensure the correctness of synchronization processes.

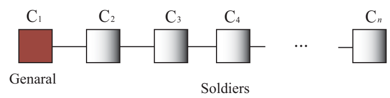

Figure 1: One-dimensional cellular automaton.

2 Two-Sided Firing Squad Synchronization Algorithm

The firing squad synchronization problem is formalized in terms of the model of cellular automata. Figure 1 shows a finite one-dimensional cellular array consisting of n cells, denoted by C_i, where $1 \leq i \leq n$. All cells (except the end cells) are identical finite state automata. The array operates in lock-step mode such that the next state of each cell (except the end cells) is determined by both its own present state and the present states of its right and left neighbors. All cells (*soldiers*), except the left end cell, are initially in the *quiescent* state at time $t = 0$ and have the property whereby the next state of a quiescent cell having quiescent neighbors is the quiescent state. At time $t = 0$ the left end cell (*general*) is in the *fire-when-ready* state, which is an initiation signal to the array. The firing squad synchronization problem is stated as follows.

Given an array of n identical cellular automata, including a *general* on the left end which is activated at time $t = 0$, we want to give the description (state set and next-state function) of the automata so that, *at some future time*, all of the cells will *simultaneously* and, *for the first time*, enter a special *firing* state. The set of states must be independent of n. Without loss of generality, we assume $n \geq 2$. The tricky part of the problem is that the same kind of soldier having a fixed number of states must be synchronized, regardless of the length n of the array.

Firing squad synchronization algorithms have been designed on the basis of parallel divide-and-conquer strategy that calls itself recursively in parallel. Those recursive calls are implemented by generating many *Generals* that are responsible for synchronizing divided small areas in the cellular space. Initially a *General* G_0 located at the left end is responsible for synchronizing the whole cellular space consisting of n cells. In Fig. 2 (left), the *General* G_i, $i = 2, 3, ...$, is responsible for synchronizing the cellular space between G_i and G_{i-1}, respectively. G_1 synchronizes the subspace between G_1 and the right end of the array. Thus, all of the *Generals* generated by G_0 are located at the left end of the divided cellular spaces to be synchronized by them independently. On the other hand, in Fig. 2 (right), the *General* G_0 generates *General* G_i, $i = 1, 2, 3, ...,$. Each G_i, $i = 1, 2, 3, ...$, synchronizes the divided space between G_i and G_{i+1}, respectively. In addition, G_i, $i = 2, 3, ...$, does the same operations as G_0. Thus, in Fig. 2 (right), we find *Generals* located at either end of the subspace for which they are responsible.

If all of the recursive calls for the synchronization are issued by *Generals* located at *one* (both *two*) end(s) of partitioned cellular spaces for which the *General* is responsible, the synchronization algorithm is said to have *one-sided* (*two-sided*) recursive property. We call the synchronization algorithm with one-sided (two-sided) recursive property as one-sided (two-sided) recursive synchronization algorithm. Figure 2 illustrates a time-space diagram for one-sided (Fig. 2 (left)) and two-sided (Fig. 2 (right)) recursive synchronization algorithms both operating in optimum $2n-2$ steps.

It is noted that optimum-time synchronization algorithms developed by Balzer [1], Gerken [2] and Waksman [7] are two-sided ones and an algorithm proposed by Mazoyer [3] is an only synchronization algorithm with the one-sided recursive property.

[Observation 1] Optimum-time synchronization algorithms developed by Balzer [1], Gerken [2] and Waksman [7] are two-sided ones. The algorithm proposed by Mazoyer [3] is a one-sided one.

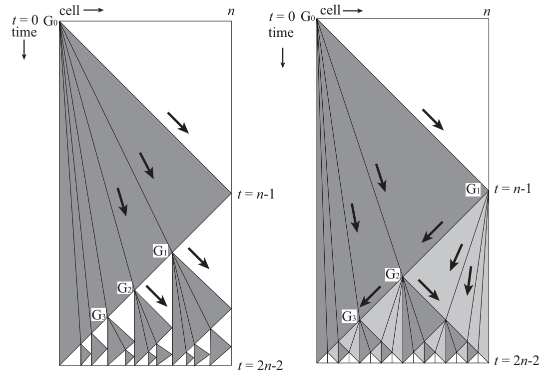

Figure 2: Optimum-time one-sided (left) and two-sided (right) firing squad synchronization scheme.

3 *VeriSync*: Overview of Verification System

3.1 Optimization and Numbering

Gerken [2] reduced the number of states realizing Balzer's algorithm and constructed a seven-state, 118-rule synchronization protocol. In our computer examination, no errors were found, however, 13 rules were found to be redundant. In Table 1, we give a list of the transition rules for Gerken's algorithm. The symbols ">", "/", "..." and "#" represent the general, quiescent, firing and boundary states, respectively. The system *VeriSync* optimizes a transition rule set by *synchronization-test* on n cells where $2 \leq n \leq 10000$. The transition rule set which was designed by Gerken [2] can be optimized resulting in 105 rules from 118 onrs. Table 1 shows a complete list of transition rules in which each rule consists of a unique rule number, left-state, center-state, right-state and next-state.

[Theorem 1] The transition Table 1 can synchronize any n cells in optimum $2n-2$ steps.

3.2 Rule Classification

The system *VeriSync* classifies synchronization rules to verify the correctness of the rule set. We focus our attention to the subset of Gerken's [2] transition rules which can synchronize any n cells such that $n = 2^k (k \geq 1)$. In our verification process, the rule set is mainly divided into two categories in which α- or β-areas in Figure 3.

Stage 1, it makes the transition rule set used in α-area has 39 rules denoted by $\mathcal{R}_1$ (See Table 2). Stage 2, it makes the transition rule set used in β-area has 38 rules denoted by $\mathcal{R}_2$ which includes the part of $\mathcal{R}_1$ (See Table 3). And Stage 3, it creates the transition

Table 1: Gerken's 7-state synchronization protocol $\mathcal{R}$ consisting of 105 rules.

No.	LS	CS	RS	NS
1	/	/	/	→ /
2	/	/	ˆ	→ /
3	/	/	<	→ /
4	/	/	[	→ /
5	/	/	♯	→ /
6	>	/	/	→]
7	>	/	ˆ	→]
8	>	/	[	→]
9	>	/	♯	→ <
10	]	/	/	→ >
11	]	/	ˆ	→ >
12	]	/	<	→ >
13	]	/	♯	→ [
14	ˆ	/	/	→ ˆ
15	ˆ	/	>	→ ˆ
16	ˆ	/	ˆ	→ ˆ
17	ˆ	/	<	→ [
18	ˆ	/	[	→ <
19	<	/	/	→ /
20	<	/	ˆ	→ /
21	<	/	<	→ /
22	[	/	/	→ /
23	[	/	[	→ /
24	/	>	/	→ ˆ
25	/	>	]	→ ˆ
26	/	>	ˆ	→ >
27	/	>	<	→ [
28	]	>	/	→ ˆ
29	]	>	]	→ ˆ
30	]	>	ˆ	→ >
31	]	>	<	→ [
32	ˆ	>	]	→ ˆ
33	ˆ	>	ˆ	→ >
34	ˆ	>	<	→ [
35	<	>	/	→ >
36	<	>	]	→ >
37	<	>	<	→ ...
38	<	>	♯	→ ...
39	♯	>	/	→ >
40	♯	>	]	→ >
41	♯	>	<	→ ...
42	>	]	/	→]
43	>	]	>	→]
44	>	]	ˆ	→]
45	>	]	[	→ <
46	ˆ	]	/	→ /
47	ˆ	]	>	→ /
48	ˆ	]	ˆ	→]
49	ˆ	]	[	→ <
50	[	]	/	→]
51	[	]	>	→]
52	[	]	ˆ	→]
53	[	]	[	→ <
54	/	ˆ	/	→ /
55	/	ˆ	>	→ ˆ
56	/	ˆ	ˆ	→ ˆ
57	/	ˆ	<	→ [
58	/	ˆ	[	→ <
59	>	ˆ	/	→]
60	>	ˆ	>	→ ˆ
61	>	ˆ	ˆ	→ ˆ
62	>	ˆ	[	→ <
63	]	ˆ	/	→ >
64	]	ˆ	]	→ ˆ
65	]	ˆ	ˆ	→ ˆ
66	]	ˆ	<	→ [
67	ˆ	ˆ	/	→ /
68	ˆ	ˆ	>	→ ˆ
69	ˆ	ˆ	]	→ ˆ
70	ˆ	ˆ	ˆ	→ ˆ
71	ˆ	ˆ	<	→ [
72	ˆ	ˆ	[	→ <
73	<	ˆ	/	→ /
74	/	<	/	→ <
75	/	<	ˆ	→ <
76	/	<	[	→ <
77	>	<	/	→]
78	>	<	>	→ ...
79	>	<	ˆ	→]
80	>	<	[	→]
81	>	<	♯	→ ...
82	ˆ	<	>	→ <
83	ˆ	<	ˆ	→ /
84	ˆ	<	[	→ /
85	ˆ	<	♯	→ <
86	[	<	/	→ /
87	[	<	>	→ <
88	[	<	ˆ	→ /
89	[	<	[	→ /
90	[	<	♯	→ <
91	/	[	/	→ [
92	/	[	]	→ [
93	/	[	<	→ [
94	/	[	♯	→ [
95	]	[	/	→ >
96	]	[	]	→ >
97	]	[	<	→ >
98	]	[	♯	→ >
99	ˆ	[	/	→ ˆ
100	ˆ	[	]	→ [
101	ˆ	[	<	→ [
102	<	[	/	→ ˆ
103	<	[	]	→ [
104	<	[	<	→ [
105	<	[	♯	→ [

rule set has 8 rules denoted by $\mathcal{R}_3$ which generates a new general state in the boundary of α-area and β-area and keeps a general state (See Table 4). Figure 4 shows that it synchronizes by including $\mathcal{R}_1$, $\mathcal{R}_2$ for optimum-time two-sided synchronization algorithm on cells $n = 2^k$.

We show verification of optimum-time two-sided synchronization algorithm developed by Gerken. G_i is generated with collision point where 1/1-wave and $1/2^i-1$-wave. So, the generation position of G_i can be formulated for the synchronization algorithm. Figure 5 illustrates a general generation position P, a general generation time T in α-area. And, the generated G_i can be synchronize cellular-space below. The transition rule set $\mathcal{R}_3$ is necessary to generates G_i and to stay it in the place.

$$\mathrm{P}_\alpha(n,i) = n/2^i + 1 \tag{1}$$

$$\mathrm{T}_\alpha(n,i) = n - 1 + \sum_{j=1}^{i} n/2^j \tag{2}$$

[Theorem 2] $\mathcal{R}_1 \cup \mathcal{R}_2 \cup \mathcal{R}_3$ is necessary to synchronize cells, where $n = 2^k (k \geq 1)$ for optimum-time two-sided synchronization algorithm developed by Gerken.

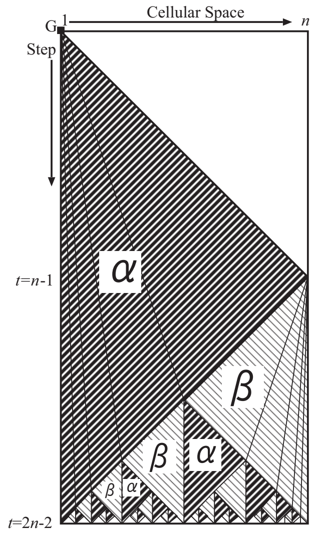

Figure 3: Computation for α- and β-area in the time-space diagram.

Table 2: State transition table $\mathcal{R}_1$ consisting of 39 rules for 7-state optimum-time synchronization algorithm.

1	/	/	/	→ /
5	/	/	♯	→ /
6	>	/	/	→]
9	>	/	♯	→ <
10	]	/	/	→ >
15	ˆ	/	>	→ ˆ
16	ˆ	/	ˆ	→ ˆ
24	/	>	/	→ ˆ
26	/	>	ˆ	→ >
28	]	>	/	→ ˆ
29	]	>	]	→ ˆ
30	]	>	ˆ	→ >
32	ˆ	>	]	→ ˆ
33	ˆ	>	ˆ	→ >
39	♯	>	/	→ >
40	♯	>	]	→ >
42	>	]	/	→]
43	>	]	>	→]
44	>	]	ˆ	→]
45	>	]	[	→ <
46	ˆ	]	/	→ /
47	ˆ	]	>	→ /
48	ˆ	]	ˆ	→]
49	ˆ	]	[	→ <
55	/	ˆ	>	→ ˆ
56	/	ˆ	ˆ	→ ˆ
59	>	ˆ	/	→]
60	>	ˆ	>	→ ˆ
61	>	ˆ	ˆ	→ ˆ
63	]	ˆ	/	→ >
64	]	ˆ	]	→ ˆ
65	]	ˆ	ˆ	→ ˆ
66	]	ˆ	<	→ [
67	ˆ	ˆ	/	→ /
68	ˆ	ˆ	>	→ ˆ
69	ˆ	ˆ	]	→ ˆ
70	ˆ	ˆ	ˆ	→ ˆ
71	ˆ	ˆ	<	→ [
72	ˆ	ˆ	[	→ <

4 Conclusions

We have developed a verification system for optimum-time two-sided synchronization firing squad synchronization protocols. Also, I verified the algorithm developed by Gerken [2]. We must proceed with the proof of the firing squad synchronization algorithm more.

Table 3: State transition table $\mathcal{R}_2$ consisting of 38 rules for 7-state optimum-time synchronization algorithm.

1	/	/	/	→	/	72	ˆ	ˆ	[	→	<
2	/	/	ˆ	→	/	73	<	ˆ	/	→	/
3	/	/	<	→	/	74	/	<	/	→	<
4	/	/	[	→	/	75	/	<	ˆ	→	<
6	>	/	/	→	]	76	/	<	[	→	<
8	>	/	[	→	]	83	ˆ	<	ˆ	→	/
9	>	/	♯	→	<	84	ˆ	<	[	→	/
10	]	/	/	→	>	85	ˆ	<	♯	→	<
14	ˆ	/	/	→	ˆ	86	[	<	/	→	/
17	ˆ	/	<	→	[	89	[	<	[	→	/
18	ˆ	/	[	→	<	90	[	<	♯	→	<
19	<	/	/	→	/	91	/	[	/	→	[
20	<	/	ˆ	→	/	93	/	[	<	→	[
21	<	/	<	→	/	95	]	[	/	→	>
22	[	/	/	→	/	97	]	[	<	→	>
23	[	/	[	→	/	99	ˆ	[	/	→	ˆ
54	/	ˆ	/	→	/	101	ˆ	[	<	→	[
66	]	ˆ	<	→	[	102	<	[	/	→	ˆ
71	ˆ	ˆ	<	→	[	104	<	[	<	→	[

Table 4: State transition table $\mathcal{R}_3$ consisting of 8 rules for 7-state optimum-time synchronization algorithm.

35	<	>	/	→	>	78	>	<	>	→	...
36	<	>	]	→	>	81	>	<	♯	→	...
37	<	>	<	→	...	82	ˆ	<	>	→	<
41	♯	>	<	→	...	87	[	<	>	→	<

References

[1] R. Balzer: An 8-state minimal time solution to the firing squad synchronization problem, *Information and Control*, 10, pp.22-42, (1967).

[2] Hans-D., Gerken: Über Synchronisations-Probleme bei Zellularautomaten. Diplomarbeit, Institut fur Theoretische Informatik, Technische Universitat Braunschweig, pp. 50 (1987).

[3] J. Mazoyer: A six-state minimal time solution to the firing squad synchronization problem, *Theoretical Computer Science*, 50, pp.183-238, (1987).

[4] E. F. Moore. (1964): The firing squad synchronization problem. in *Sequential Machines, Selected Papers* (E. F. Moore, ed.), Addison-Wesley, Reading MA., pp. 213-214.

[5] H. Umeo, T. Sogabe and Y. Nomura: Correction, optimization and verification of transition rule set for Waksman's firing squad synchronization algorithm. *Proc. of the Fourth Intern. Conference on Cellular Automata for Research and Industry*, Springer, pp. 152-160 (2000).

[6] H. Umeo, M. Hisaoka and T. Sogabe: A Survey on Optimum-Time Firing Squad Synchronization Algorithms for One-Dimensional Cellular Automata. *Intern. J. of Unconventional Computing*, Vol. 1, pp. 403-426 (2005).

[7] A. Waksman: An optimum solution to the firing squad synchronization problem. *Information and Control*, vol. 9, pp. 66-78 (1966).

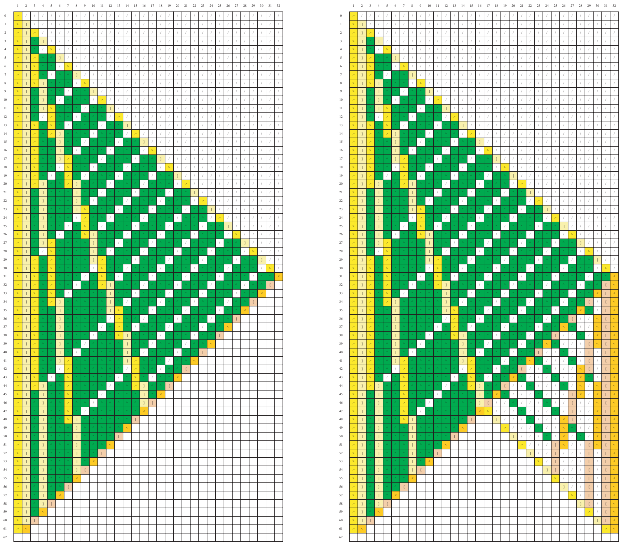

Figure 4: Configurations of $\mathcal{R}_1$ (left) and $\mathcal{R}_1 \cup \mathcal{R}_2$ (right) implementation of optimum-time two-sided synchronization algorithm on cells $n = 2^k (k \geq 1)$.

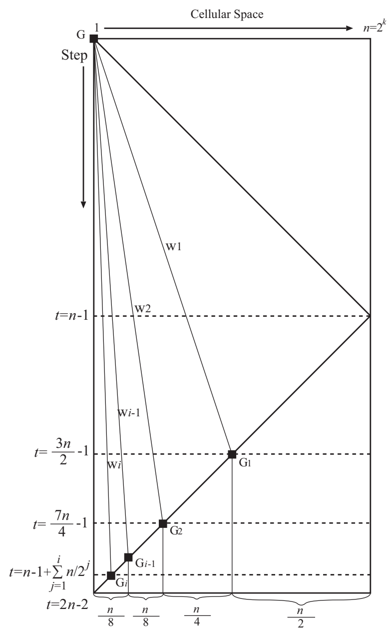

Figure 5: Time-space diagram for α-space on n cells, where $n = 2^k (k \geq 1)$.

State-Efficient Synchronization Protocols for Communication-restricted Cellular Automata

Takashi Yanagihara, Masaru Kanazawa and Hiroshi Umeo

Univ. of Osaka Electro-Communication, Graduate School of Engineering,
Faculty of Information Science and Technology, Department of Informatics,
Neyagawa-shi, Hatsu-cho, 18-8, 572-8530, Osaka, Japan

Abstract

In this paper, we propose several state-efficient bit-transfer-based synchronization protocols for one-dimensional cellular automata. It is shown that there exists a 1-state $\mathrm{CA}_{5-\mathrm{bit}}$ that can synchronize any n cells in $2n-2$ optimum-step. The result is interesting, since we know that there exists no 4-state synchronization algorithm on *conventional* cellular automata with transition functions such that $\delta : Q^3 \rightarrow Q$, where Q is a set of internal states.

1 Introduction

Cellular automata (CA) are considered to be a good model of complex systems in which an infinite one-dimensional array of finite state machines (cells) updates itself in a synchronous manner according to a uniform local rule. In the long history of the study of CA, generally speaking, the number of internal states of each cell is finite and the local state transition rule is defined in a such way that the state of each cell depends on the previous states of itself and its neighboring cells. Thus, in the finite state description of the CA, the number of communication bits exchanged in one step between neighboring cells is assumed to be O(1) bits. However, such inter-cell bit-information is hidden under the definition of the conventional automata-theoretic finite state description.

In the present paper, we study a firing squad synchronization problem on a very restricted model of cellular automata, $\mathrm{CA}_{k-\mathrm{bit}}$, for which inter-cell communication at one step is restricted to k-bit, where k is any positive integer such that $k \geq 1$. We hereinafter refer to the model as k-bit CA. The number of internal states of $\mathrm{CA}_{k-\mathrm{bit}}$ is assumed to be finite in the usual sense. The next state of each cell is determined by the present state of the cell and two binary k-bit inputs from its left- and right-neighbor cells. A 1-bit CA model, where $k = 1$, can be thought of as being one of the simplest CAs to have a low computational complexity. On the k-bit CA we consider the firing squad synchronization problem that has been studied extensively on the conventional CA model and propose several time-optimum firing squad synchronization protocols together with its implementation on a computer. Although many researchers have examined various aspects of the conventional cellular automata [1-5, 7, 8, 11-14, 20-23], studies focusing on the amount of bit-information exchanged in inter-cell communications are few. Mazoyer [6] first studied this model under the name of CAs with *channels* and proposed a time-optimum firing squad synchronization algorithm in which only one-bit information is exchanged. Umeo [15] and Umeo et al. [17, 19] have studied algorithmic design techniques for sequence generation and connectivity recognition problems on $\mathrm{CA}_{1-\mathrm{bit}}$. In addition, Umeo and Kamikawa [16, 18] showed that infinite non-regular sequences such as $\{2^n \mid n = 1, 2, 3, ..\}$, $\{n^2 \mid n = 1, 2, 3, ..\}$, Fibonacci and the prime sequences can be generated in real-time by $\mathrm{CA}_{1-\mathrm{bit}}$. Worsch [24] established a computational hierarchy between one-way 1-bit CAs.

First, in Section 2, we introduce a class of bit-communication-restricted cellular automaton having k-bit inter-cell communication ($\mathrm{CA}_{k-\mathrm{bit}}$) and define

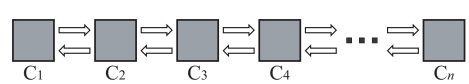

Figure 1: One-dimensional cellular automaton having k-bit inter-cell communication links.

the firing squad synchronization problem on $\mathrm{CA}_{k-\mathrm{bit}}$. In Section 3, we propose several state-efficient bit-transfer-based synchronization protocols for $\mathrm{CA}_{k-\mathrm{bit}}$. Due to space constraints, we do not present the detailed proofs of the theorems discussed herein.

2 Cellular automaton having k-bit inter-cell communication

A one-dimensional k-bit inter-cell communication cellular automaton consists of an infinite array of identical finite state automata, each located at a positive integer point (See Fig. 1). Each automaton is referred to as a cell. A cell at point i is denoted by C_i, where $i \geq 1$. Each C_i, except for C_1, is connected to its left- and right-neighbor cells via a left or right one-way communication link. These communication links are indicated by right- and left-pointing arrows in Fig. 1, respectively. Each one-way communication link can transmit k bits at each step in each direction. A cellular automaton with k-bit inter-cell communication (abbreviated by $\mathrm{CA}_{k-\mathrm{bit}}$) consists of an infinite array of finite state automata $A = (Q, \delta)$, where

1. Q is a finite set of internal states.
2. δ is a function, defining the next state of any cell and its binary outputs to its left- and right-neighbor cells, such that δ: $Q \times \{0,1\}^k \times \{0,1\}^k \rightarrow Q \times \{0,1\}^k \times \{0,1\}^k$, where $\delta(p, x_1, x_2, ..., x_k, y_1, y_2, ..., y_k) = (q, x'_1, x'_2, ..., x'_k, y'_1, y'_2, ..., y'_k)$, $p, q \in Q$, $x_i, x'_i, y_i, y'_i \in \{0,1\}, 1 \leq i \leq k$, has the following meaning. We assume that at step t the cell C_i is in state p and is receiving k binary inputs x_i and $y_i, 1 \leq i \leq k$, from its left and right communication links, respectively. Then, at the next step, $t+1$, C_i assumes state q and outputs x'_i and $y'_i, 1 \leq i \leq k$, to its left and right communication links, respectively. Note that k binary inputs to C_i at step t are also outputs of C_{i-1} and C_{i+1} at step t. A quiescent state $q \in Q$ has a property such that $\delta(q, \overbrace{0,0,...,0}^{k}, \overbrace{0,0,...,0}^{k}) = (q, \overbrace{0,0,...,0}^{k}, \overbrace{0,0,...,0}^{k})$.

Thus, the $\mathrm{CA}_{k-\mathrm{bit}}$ is a special subclass of *normal* (i.e., *conventional*) cellular automata. Let N be any normal cellular automaton having a set of states Q eand a transition function $\delta : Q^3 \rightarrow Q$. The state of each cell on N depends on the previous states of the cell and its nearest neighbor cells. This means that the total information exchanged per one step between neighboring cells consists of $O(1)$ bits. By encoding each state in Q with a binary sequence of length $\lceil \log_2 |Q| \rceil$, sending the sequences sequentially bit by bit in each direction via each one-way communication link, receiving the sequences bit-by-bit again, and then decoding the sequences into their corresponding states in Q, the $\mathrm{CA}_{1-\mathrm{bit}}$ can simulate one step of N in $\lceil \log_2 |Q| \rceil$ steps. This observation yields the following computational relation between the normal CA and $\mathrm{CA}_{1-\mathrm{bit}}$.

[Lemma 1] Let N be any *normal* cellular automaton having time complexity $T(n)$. Then, there exists a $\mathrm{CA}_{1-\mathrm{bit}}$ which can simulate N in $kT(n)$ steps, where k is a positive constant integer such that $k = \lceil \log_2 |Q| \rceil$ and Q is the set of internal states of N.

In addition, the next lemma can be stated in the case where each cell can transfer k-bits at each step.
[Lemma 2] Let N be any s-state *normal* cellular automaton. Then, there exists an s-state $\mathrm{CA}_{k-\mathrm{bit}}$ which can simulate N in *real time*, where k is a positive integer such that $k = \lceil \log_2 s \rceil$.

3 Firing Squad Synchronization Problem on $\mathrm{CA}_{k-\mathrm{bit}}$

In this section, we study a famous firing squad synchronization problem on the newly introduced $\mathrm{CA}_{k-\mathrm{bit}}$ model for which solution gives a finite-state protocol for synchronizing a large scale of cellular automata. The problem was originally proposed by J. Myhill to synchronize all parts of self-reproducing cellular automata [8]. The firing squad synchronization problem has been studied extensively in more than 40 years [1-14, 17, 19-23].

The firing squad synchronization problem is formalized in terms of the model of cellular automata. All cells (*soldiers*), except the left end cell, are initially in the *quiescent* state at time $t = 0$ and have the property whereby the next state of a quiescent cell having quiescent neighbors is the quiescent state. At time $t = 0$ the left end cell (*general*) is in the *fire-when-ready* state, which is an initiation signal to the array. The firing squad synchronization problem is stated as follows. Given an array of n identical cellular automata, including a *general* on the left end which is activated at time $t = 0$, we want to give the description (state set and next-state function) of the automata so that,

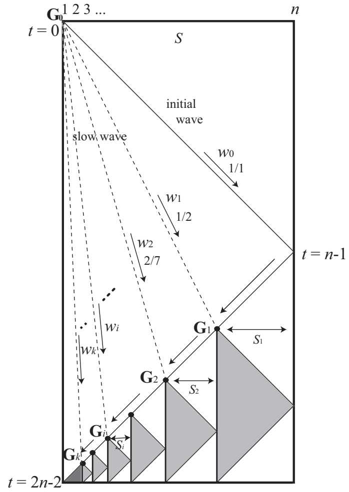

Figure 2: A time-space diagram for Mazoyer's optimum-time synchronization scheme.

at some future time, all of the cells will *simultaneously* and, *for the first time*, enter a special *firing* state. The set of states must be independent of n. Without loss of generality, we assume $n \geq 2$. The difficult part of the problem is that the same types of soldier having a fixed number of states must be synchronized, regardless of the length n of the array.

All of the implementations given below are based on Mazoyer's 6-state synchronization scheme shown in Fig. 2.

[Theorem 1][5] There exists a 6-state normal cellular automaton that can synchronize any n cells in $2n-2$ optimum steps.

[Theorem 2] There exists a 54-state $\mathrm{CA}_{1-\mathrm{bit}}$ that can synchronize any n cells in $2n-1$ steps.

Figure 3 (below) illustrates the snapshots of our 54-state $(2n-1)$-step synchronization protocol on $\mathrm{CA}_{1-\mathrm{bit}}$. The small black triangles ▶ and ◀ indicate a 1-bit signal transfer in the right or left direction, respectively, between neighboring cells. A symbol in a cell shows internal state of the cell. For ease of understanding of the synchronization processes and for the reference, we provide snapshots of the Mazoyer's 6-state synchronization processes of the same size on conventional cellular automata. See Fig. 3.

[Theorem 3] There exists a 6-state $\mathrm{CA}_{2-\mathrm{bit}}$ that can synchronize any n cells in $2n-2$ optimum-step.

[Theorem 4] [1,2,11] There is no four-state CA that can synchronize any n cells.

The question that remains is: "What is the minimum number of states for an optimum-time solution of

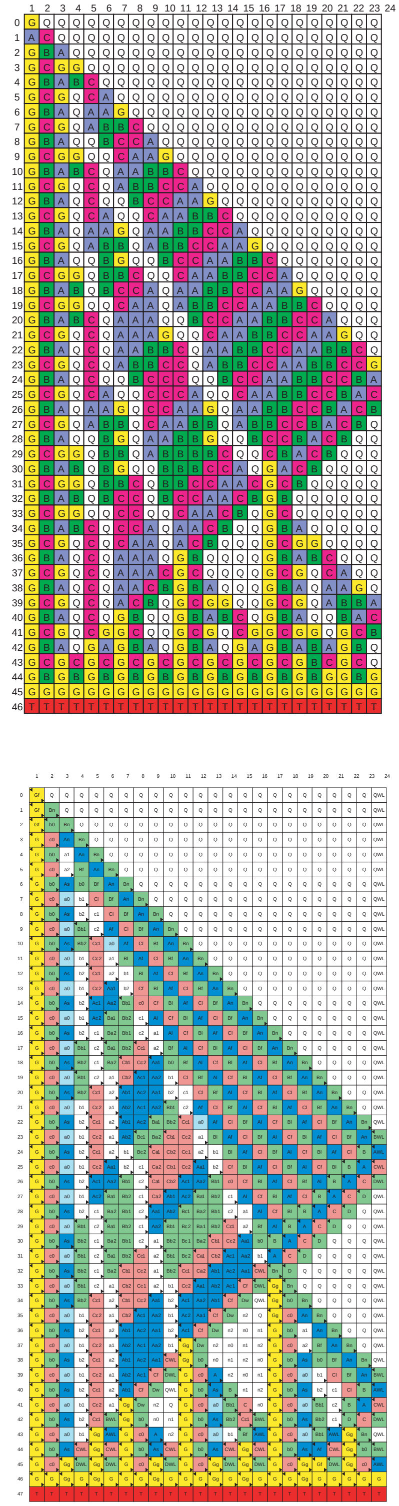

Figure 3: Snapshots for Mazoyer's synchronization processes (above) and those for our 54-state $(2n-1)$-step protocol (below) on 24 cells.

the problem?". At present, that number is *five or six*. On the $\mathrm{CA}_{3-\mathrm{bit}}$ model, we can establish the following theorem.

[Theorem 5] There exists a 4-state $\mathrm{CA}_{3-\mathrm{bit}}$ that can synchronize any n cells in $2n-2$ optimum-step.

[Theorem 6] There exists a 3-state $\mathrm{CA}_{4-\mathrm{bit}}$ that can synchronize any n cells in $2n-2$ optimum-step.

[Theorem 7] There exists a 2-state $\mathrm{CA}_{4-\mathrm{bit}}$ that can synchronize any n cells in $2n-2$ optimum-step.

[Theorem 8] There exists a 1-state $\mathrm{CA}_{5-\mathrm{bit}}$ that can synchronize any n cells in $2n-2$ optimum-step.

4 Conclusions

We have made an investigation into a trade-off between internal states and communication bits in firing squad synchronization protocols for communication-restricted cellular automata and proposed several time-optimum state-efficient bit-transfer-based synchronization protocols. It has been shown that there exists a 1-state $\mathrm{CA}_{5-\mathrm{bit}}$ that can synchronize any n cells in $2n-2$ optimum-step. The result is interesting, since we know that there exists no 4-state synchronization algorithm on conventional O(1)-bit communication cellular automata. The $\mathrm{CA}_{k-\mathrm{bit}}$ is confirmed to be an interesting computational subclass of CAs that merits further study. We conclude with the following question for further investigations.

- What is the minimum number of states for protocols on each $\mathrm{CA}_{k-\mathrm{bit}}$, $k = 1, 2, 3, 4, 5, ..?$

References

[1] R. Balzer: An 8-state minimal time solution to the firing squad synchronization problem. *Information and Control*, vol. 10 (1967), pp. 22-42.

[2] A. Berthiaume, T. Bittner, L. Perković, A. Settle and J. Simon. (2004): Bounding the firing synchronization problem on a ring. *Theoretical Computer Science*, 320, pp. 213-228.

[3] Hans-D., Gerken. (1987): Über Synchronisations - Probleme bei Zellularautomaten. *Diplomarbeit*, Institut für Theoretische Informatik, Technische Universität Braunschweig, pp. 50.

[4] E. Goto: A minimal time solution of the firing squad problem. Dittoed course notes for Applied Mathematics 298, Harvard University, (1962), pp. 52-59.

[5] J. Mazoyer: A six-state minimal time solution to the firing squad synchronization problem. *Theoretical Computer Science*, vol. 50 (1987), pp. 183-238.

[6] J. Mazoyer: On optimal solutions to the firing squad synchronization problem. *Theoretical Computer Science*, vol. 168(1996), pp. 367-404.

[7] M. Minsky: *Computation: Finite and infinite machines.* Prentice Hall, (1967), pp. 28-29.

[8] E. F. Moore: The firing squad synchronization problem. in *Sequential Machines, Selected Papers* (E. F. Moore ed.), Addison-Wesley, Reading MA., (1964), pp. 213-214.

[9] J. Nishimura, T. Sogabe and H. Umeo. (2003): A design of optimum-time firing squad synchronization algorithm on 1-bit cellular automaton. *Proc. of the 8th International Symposium on Artificial Life and Robotics*, Vol.2, pp. 381-386.

[10] J. Nishimura and H. Umeo: An Optimum-Time Synchronization Protocol for 1-Bit-Communication Cellular Automata. *Proc. of The 9th World Multi-Conference on Systemics, Cybernetics and Informatics*, (2005).

[11] P. Sanders. (1994): Massively parallel search for transition-tables of polyautomata. In *Proc. of the VI International Workshop on Parallel Processing by Cellular Automata and Arrays*, (C. Jesshope, V. Jossifov and W. Wilhelmi (editors)), Akademie, 99-108.

[12] A. Settle and J. Simon. (1998): Improved bounds for the firing synchronization problem. In *SIROCCO 5: Proc. of the 5th International Colloquium on Structural Information and Communication Complexity*, Carleton Scientific, 66-81.

[13] A. Settle and J. Simon. (2002): Smaller solutions for the firing squad. *Theoretical Computer Science*, 276, 83-109.

[14] S. L. Torre, M. Napoli and M. Parente: A compositional approach to synchronize two dimensional networks of processors. *Theoretical Informatics and Applications*, 34 (2000) pp. 549-564.

[15] H. Umeo: Linear-time recognition of connectivity of binary images on 1-bit inter-cell communication cellular automaton. *Parallel Computing*, 27, pp. 587-599, (2001).

[16] H. Umeo and N. Kamikawa: A design of real-time non-regular sequence generation algorithms and their implementations on cellular automata with 1-bit inter-cell communications. *Fundamenta Informaticae*, 52 (2002) 255-275.

[17] H. Umeo, K. Michisaka and N. Kamikawa: A synchronization problem on 1-bit-communication cellular automata. Proc. of International Conference on Computational Science-ICCS2003, LNCS 2657, pp.492-500, (2003).

[18] H. Umeo and N. Kamikawa: Real-time Generation of Primes by a 1-Bit-Communication Cellular Automaton. *Fundamenta Informaticae*, 58(2003) 421-435.

[19] H. Umeo, M. Kanazawa, K. Michisaka and N. Kamikawa: State-Efficient 1-Bit-Communication Solutions for Some Classical Cellular Automata Problems. Proc. of the International Workshop on Tilings and Cellular Automata (Ed. M. Margenstern), pp.1-12, (2004).

[20] H. Umeo, M. Hisaoka and T. Sogabe: A Survey on Firing Squad Synchronization Algorithms for One-Dimensional Cellular Automata. International Journal of Unconventional Computing, Vol.1, pp.403-426, (2005).

[21] R. Vollmar. (1981): On Cellular Automata with a Finite Number of State Change. *Computing, Supplementum*, vol. 3(1981), pp. 181-191.

[22] R. Vollmar. (1982): Some remarks about the "Efficiency" of polyautomata. *International Journal of Theoretical Physics*, vol. 21, no. 12, pp. 1007-1015.

[23] A. Waksman: An optimum solution to the firing squad synchronization problem. *Information and Control*, vol. 9 (1966), pp. 66-78.

[24] T. Worsch: Linear time language recognition on cellular automata with restricted communication, *Proc. of LATIN 2000:Theoretical Informatics* (Eds. G. H. Gonnet, D. Panario and A. Viola), LNCS 1776, pp.417-426, (2000).

The Eleventh International Symposium on Artificial Life and Robotics 2006 (AROB 11th'06),
B-con Plaza, Beppu, Oita, Japan, January 23-25, 2006

Analysis and Simulation of Group Dynamics based on Interaction between Decision Making and Heider's POX Systems

Tatsuya Nomura
Department of Media Informatics
Ryukoku University
1–5, Yokotani, Seta–ohe–cho, Otsu, Shiga 520–2194, Japan

Abstract

Heider's balance theory is one of theories on micro characteristics of triad relations in social psychology. However, it has not sufficiently been discussed what relations there are between group dynamics, this micro characteristic, and other psychological processes. This paper proposes a model of interaction between the social network dynamics based on POX systems and decision making process under the human network, while comparing the proposed model with the previous group dynamics model based on only POX systems.

1 Introduction

As one of theories on micro characteristics of individuals in social psychology, balance theory proposed by F. Heider [1] states a psychological stability of an individual included in a triad relation. In this theory, a person (P), another person (O), an object or the third person (X), and relations from P to O, from O to X, and from P to X construct a system (called POX system). These relations have either + or − value corresponding to the fact that the person likes or dislikes the object respectively. Heider's theory argues that a POX system is balanced if and only if the product of the signs on these three relations is +, and if the system is not balanced P changes one of the relations to O and X so that the POX system becomes balanced. As shown in Figure 1, if the system is not balanced, then P inverts either the sign of $P \rightarrow O$ or that of $P \rightarrow O$ to balance the POX system.

Although the original balance theory is limited to triad relations, its extension to groups consisting of more than three persons have been proposed [2, 3, 4]. These studies of balance in social networks focus on network structures of balanced situations based on graph theory.

However, it has not sufficiently discussed what structures actually appear in large groups as a macro structure of group dynamics based on micro behaviors of the original POX systems in individual persons. As an approach to this problem in the field of artificial societies, Wang and Thonegate [5] proposed a simulation model of group dynamics based on POX systems, consisting of full connected graphs. However, this study focuses on non–digraphs, that is, cases where all the dyad relations are symmetric. We proposed a formalization of group dynamics based on POX systems as a finite Markov chain with a state space consisting of signs on all the edges in digraphs, characterized the concept of balance as absorbing states of this Markov chain, and executed computer simulations of the group dynamics based on the Markov chain [6].

However, the model by Wang and Thonegate and our model focus on group dynamics only based on POX systems, and they lack interaction between POX systems and other psychological processes. To construct more realistic models of group dynamics, this paper proposes a model of interaction between the social network dynamics based on POX systems and decision making process under the human network.

2 Group Dynamics as a Finite Markov Chain

In the same way as the previous work [6], we assume that there are N persons and relations between them are represented as a fully connected digraph in which these relations have + or − value, where + and − mean that the person likes and dislikes the other person, respectively. In addition, it is assumed that these individuals make decisions for a subject by agreement (+) or disagreement (-).

This social network can be represented as a signed digraph $G = (P, A)$, $P = \{p_1, p_2, \ldots, p_N, s\}$, $A = \{(a_{12}, s_{12}), (a_{13}, s_{13}), \ldots, (a_{21}, s_{21}), (a_{23}, s_{23}), \ldots, (a_1, s_1), \ldots, (a_N, s_N)\}$. P is the set of $(N+1)$ vertices

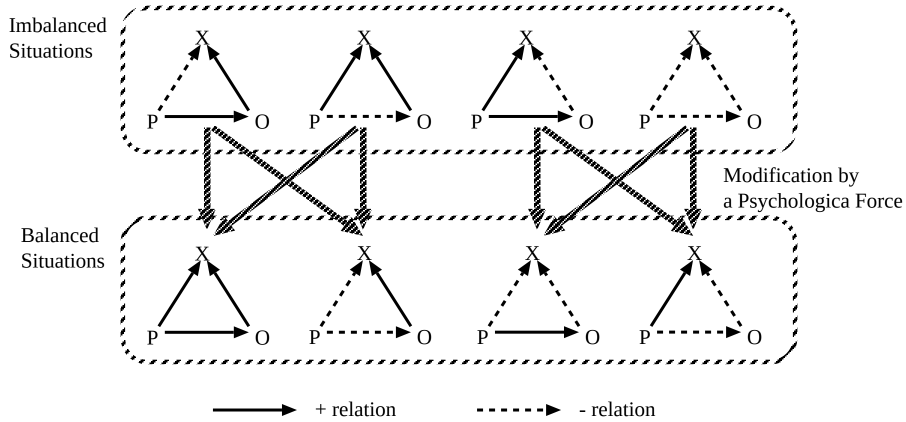

Figure 1: Balanced and Imbalanced Situations of POX Systems in Heider's Balance Theory.

in the digraph, corresponding to the N persons and the subject s, and A is the set of pairs of edges a_{ij} from the i–th person to the j–th person and signs on them s_{ij}, and pairs of edges a_i from the i–th person to the subject s and signs on them s_i.

In this model, each individual synchronously does the following actions:

1. It selects one of the POX systems including itself (these POX systems include the triads consisting of the edge to the subject). If the selected POX system is imbalanced, it balances the POX system by randomly selecting any of the edges toward the others and reversing the sign on the selected edge (if the selected POX system includes the subject, the sign of the edge toward the other is changed and that toward the subject is not changed).

2. Among the POX systems including the subject, if the number of the imbalanced ones is larger than that of the balanced ones, the sign of the edge toward the subject is reversed.

The above procedure 1 represents balance of the POX systems in each individual. The above procedure 2 represents decision making of the individual based on subordination to a majority and balance of POX systems. The number of the balanced POX systems including the subject is the sum of the total of the number of the others having the same opinion as the individuals and liked by the individual, and the number of the others having the opposite opinions to the individual and disliked by the individual. Moreover, the number of the imbalanced POX systems including the subject is the sum of the total of the number of the others having the opposite opinion to the individuals and liked by the individual, and the number of the others having the same opinions to the individual and disliked by the individual. Thus, reversion of the sign toward the subjects means reversion of these numbers, and the procedure represents decision making for the subject based on minimization of the imbalanced POX systems including the subject.

The change of signs from individuals to others in the above procedure 1 is stochastic and dependent only on the current signs, although the change of signs of individuals toward the subject is deterministic. Thus, group dynamics based on these procedures equals to a finite Markov chain with the state space $S = \{(s_{12}, s_{13}, \ldots, s_{21}, s_{23}, \ldots, s_1, \ldots, s_N)\}$, in which the total number of states is 2^{N^2}. Figure 2 shows an example of this finite Markov chain with 3 persons.

Relations between Absorbing States and Balanced Situations

Absorbing states in the above finite Markov chain as group dynamics are situations where all the POX systems are balanced. It is shown that these situations coincide with the following situations of the group: (1) the group is partitioned into two subgroups (including the case that one of the subgroups is empty), (2) all the relations between individuals in the same subgroup are positive, (3) all the relations between individuals in the different subgroups are negative, (4) the individuals in the same subgroup have the same attitude toward the subject, and those in the different subgroup have the opposite attitude.

It is trivial that in the situations satisfying the above four conditions all the POX systems are balanced. The converse is proved as follows.

First, all the POX systems consisting of N–persons are balanced. In the previous work [6], it was proved that this condition is a necessary and sufficient con-

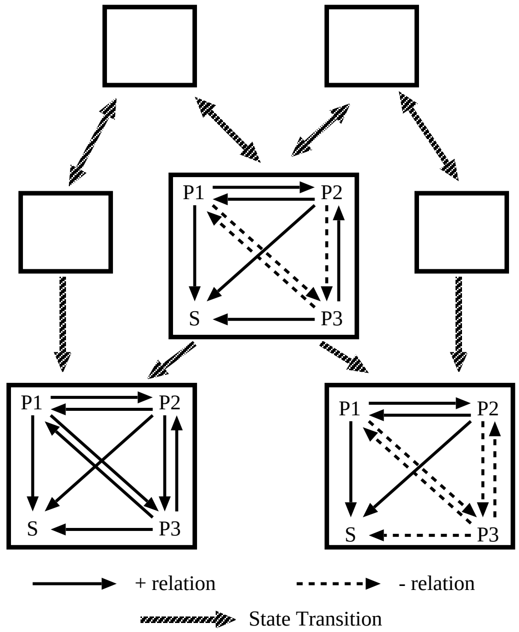

Figure 2: An Example of the Finite Markov Chain of the Group Dynamics (3 Persons)

dition for the above conditions (1)–(3). In fact, when all the POX systems consisting of N–persons are balanced, it is proved that the relation between persons $p_i \sim p_j \stackrel{\text{def}}{=} \{p_i = p_j$ or the edge $p_i \to p_j$ is $+\}$ is an equivalence relation. For this equivalence relation $\sim$, persons in the same equivalence class are connected each other by edges with $+$ and vertices in the different classes are connected each other by edges with $-$. Since balance of all the POX systems does not permit the existence of more than three classes, this situation equals to the above conditions 1–3.

Then, if persons in the same subgroup have the different attitudes toward the subject, the POX systems consisting of these persons and the subject are imbalanced since the relations between these persons are positive. Moreover, if persons in the different subgroups have the same attitude toward the subject, the POX systems consisting of these persons and the subject are imbalanced since the relations between these persons are negative. Thus, the above condition (4) must be satisfied.

3 Simulation

As shown in the previous section, the group dynamics based on individual POX systems and decision making is represented as a finite Markov chain having absorbing states corresponding to situations where the group is polarized into two subgroups. However, this analysis does not clarify whether this finite Markov chain has cyclic states. In other words, there is a possibility of the existence of cyclic states where modification of some POX systems and that of other POX systems are repeated one another.

In order to investigate the above problem, we executed some computer simulations. The simulations were executed for configurations of $N = 4$–8. For each configuration, 300 trials with different random seeds were executed. For each trial, the probability of selection of each POX system in the procedure 1 mentioned in section 2 were fixed as follows: $\frac{1}{2(N-1)(N-2)}$ for the POX system not including the subject, and $\frac{1}{2(N-1)}$ for the POX systems including the subject (note that the total number of POX systems including the subject and that not including it for a person are $N-1$ and $(N-1)(N-2)$ respectively).

Table 1 shows types of grouping in absorbing states and the numbers of the corresponding states, the numbers of trials that converged to the corresponding states, and mean number of iteration for convergence to each grouping. The state converged to one of absorbing states shown in the previous section in all the trials for all the configurations, and any cyclic state was not observed. Moreover, no trend existed that there is a specific absorbing state to which convergence is faster than the other states.

Comparison with the Previous Model

In the previous work [6], we proposed the group dynamics model based on only POX systems, without the decision making process. This previous model showed the analysis and simulation results similar to the model proposed in section 2. However, there are some phenomena different between the previous and proposed model.

The absorbing states of the previous model are also situations where the group is polarized into two subgroups, including the case that one of them is empty, and the simulation results showed that the state converged to one of absorbing states in all the trials. However, the speed of convergence to the absorbing states in the proposed model was much faster than that in the previous model. Figure 3 shows means of iteration numbers spent until convergence for each N in the proposed and previous models. For increase of the number of persons, the convergence speed of the proposed model increased linearly, although that of the previous model increased exponentially.

Furthermore, there was a bias on which absorbing state the group converged to, although this bias was

Table 1: Results of Simulations

N	4			5			6			
Types of Grouping (#. Corresponding States)	4 : 0 (1)	3 : 1 (4)	2 : 2 (3)	5 : 0 (1)	4 : 1 (5)	3 : 2 (10)	6 : 0 (1)	5 : 1 (6)	4 : 2 (15)	3 : 3 (20)
#. Convergence	82	149	69	57	116	127	43	92	110	55
Mean #. Iteration	14.2	12.8	13.7	37.6	29.4	24.2	41.3	54.2	47.5	46.1
N	7				8					
Types of Grouping (#. Corresponding States)	0 : 7 (1)	1 : 6 (7)	2 : 5 (21)	3 : 4 (35)	0 : 8 (1)	1 : 7 (8)	2 : 6 (28)	3 : 5 (56)	4 : 4 (35)	
#. Convergence	18	67	112	103	17	61	114	71	37	
Mean #. Iteration	81.7	65.5	63.1	63.1	111.9	123.7	102.8	98.0	97.1	

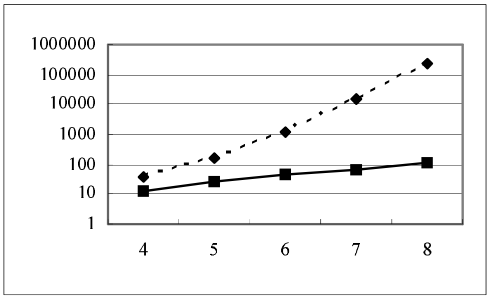

Figure 3: Means of Iteration Numbers Spent Until Convergence (Solid Line: The Proposed Model, Dashed Line: The Previous Model without Decision Making Process)

not observed in the previous model. For example in $N = 4$, the situation where all the persons like each other appeared 82 times among 300 trials, although the polarized group situations appeared about 20–40 times in average. In the same simulations of the previous model, the situation where all the persons like each other appeared 29, 16, 7, 5, 2 times among 300 trials for $N = 4, 5, 6, 7, 8$ respectively. For each N, a χ^2–test revealed that there was a statistically significant difference with 0.001 or 0.01 level on these numbers of convergence between the proposed model and previous model.

The above facts suggest that the decision making process has an effect of acceleration and bias in convergence of the group dynamics based on micro behaviors of POX systems.

4 Summary

This paper proposed a model of interaction between the social network dynamics based on POX systems and decision making process under the human network, while comparing the proposed model with the previous group dynamics model based on only POX systems.

As future problems, we should investigate a cause of observed acceleration and bias in convergence of the proposed model in comparison with the previous model while exploring the corresponding psychological phenomena. In addition, we need to extend the full–connected graph structure of the model to general graphs including 2–D cellular structures.

Acknowledgments

This study was supported by the Japan Society for the Promotion of Science, Grants–in–Aid for Scientific Research No. 15330133.

References

[1] Heider, F. (1958), *The Psychology of Interpersonal Relations*. John Wiley & Sons. (Japanese Edition: M. Ohashi, Seishin, 1978).

[2] Cartwright, D., Harary, F. (1956), Structural balance: A generalization of Heider's theory. *Psychological Review*, 63: 277–293.

[3] Harary, F., Norman, R. Z., Cartwright, D. (1965), *Structural Models: An Introduction to the Theory of Directed Graphs*. John Wiley & Sons.

[4] Flament, C. (1963), *Applications of Graph Theory to Group Structure*, Printice–Hall. (Japanese edition: K. Yamamoto, Kinokuniya, 1974).

[5] Wang, Z., Thorngate, W. (2003), Sentiment and social mitosis: Implications of Heider's balance theory. *Journal of Artificial Societies and Social Simulations*, 6(3). (electric publication: `http://jasss.soc.surrey.ac.uk/6/3/2.html`).

[6] Nomura, T. (2004), Analysis and simulation of group dynamics based on Heider's balance theory and a finite Markov chain. In *Proc. 2nd International Conference of the European Social Simulation Association*. (CD–ROM Proceedings).

Cut off of Zipfs Power Law in US Cities

The Eleventh International Symposium on Artificial Life and Robotics 2006 (AROB 11th'06),
B-con Plaza, Beppu, Oita, Japan, January 23-25, 2006

Kazuko Yamasaki[1],Masanori Ohshiro[1],Kenneth J. Mackin[1],Eiji Nunohiro[1]
[1] *Tokyo University of Information Sciences, Chiba city 265-8501 Japan.*

Sometimes power law has upper cut-off. We show this is not result from limitation of size but from non linearity between two variables like number of cities (classes) and population (total number of units), through both data analysis and analytical model.

A. introduction

The main differences of economical or social system from physical system in a laboratory about it's size are (1)Up to now, many system sizes are growing. (2)System size does not always have limits. Power law often has upper cut-off because of finite size effect. We introduce other type of cut-off of Zipfs power law [1]in growing systems.
Populations of the cities is well known to show Zipfs power law Fig.1[3]. But looking at the populations of cities in each state, we found sometimes upper cut-off of power law like words in a book, the number of products produced by a firm [5],[6],[7] and the number of alliances of a firm (the number of one directional edges of a node in a directed network). This cut-off is caused by the common fact that, at the first stage of evolution, the growth of the number of the cities, the number of kinds of words and the growth of the number of firms or nodes, which we call as the classes, are dominant , while ,in the latter stage, the population ,the growth of the number of words, products and edges ,which we call as the units, in a class are dominant. We show two types of states whose population has almost power law distribution and power law with cut-off.
And we also show theoretical analysis based on preferencial attachment. There are many studies and models to explain Zipfs law. The preferencial attachment can be thought as semi macroscopic model being described by a few parameters, which is widely applicable and can coexist with microscopic models. For example, random text is defined originally by microscopic multi-nomial stochastic process in itself, but we can see attachment is proportional to the number of words of a kind. Firms have their own reason to produce a new product and cities have their own reason to change the population and there must be a lot of correlations between them. But data analysis shows the plausibility of preferencial attachment to them. It has universal feature.
Simon introduced Yule distribution,which was used to get power law exponents analytically. In his model, constant growth of the number of classes was supposed. And he also showed that the distribution function is exponential when the number of classes is constant. A lot of studies have succeeded to him about power law distribution of various systems. Recently preferencial attachment has gotten the focus again in the development of networks theory. Barabasi[2] also explained construction of scale free networks by preferential attachment. They defined the steady state distribution for describing the growing system, by superposition of distribution functions which start at different initial times.
We formulated a preferencial attaching and detaching model which can describe new cut-off mentioned above. In this model, one side of a edge(a unit) is always unattached by a node(a class) because of morphological difference between our model and networks. The solvability of analytical equation also depends on Yule distribution.

B. data analysis

In preferencial attachment model, the growth of number of units and the growth of number of classes are supposed to be linear. Fig1(b) shows historical growth of number of cities vs. the total population of US from the beginning of the evolution. Right side figures in Fig2 show historical growth of number of cities vs. the total population of states. These lines are almost linear and the cumulative distribution holds power law (Ziphs law) almost whole range.
Contrary to these figures, Right side figures in Fig**??** show historical growth of number of cities vs. the total population of states. These lines are not linear during the first stage of evolution. Left side figures in Fig**??** show the cumulative distribution function of the population in a city, that has power law (Zipfs law) with smooth curved tail, which can be regarded as exponential decay approximately.
That suggests rapid non linear growth of the number of cities at first stage may cause exponential decay tail because larger units tend to be created earlier under preferencial attachment.

C. model

The approximation ,such as initial finite number of classes and successive liner growth, make the model easy. Consider a system of a classes and units.

1. At time $t = 0$ we start with a fixed number, N, of class, each of them containing a unit.

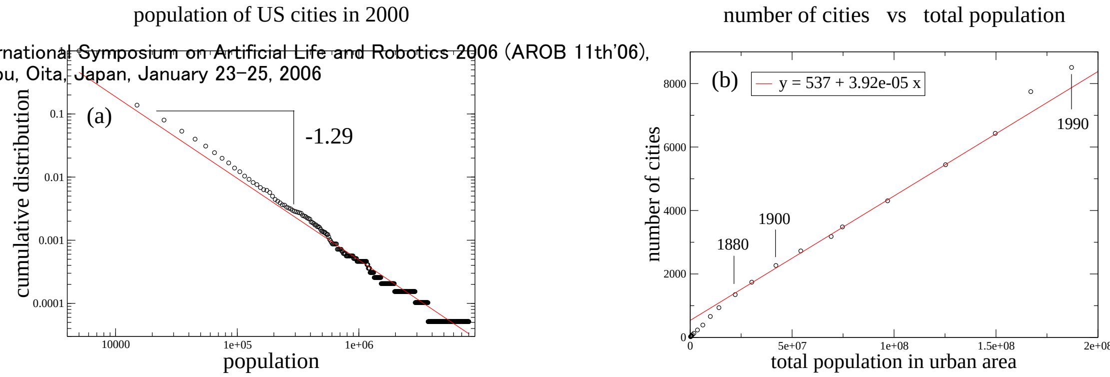

FIG. 1: (a) shows the cumulative distribution of population in a city in US. Power law is kept almost whole range. In (b), x axis is the total population of urban area in US and y axis is the number of cities.

2. At every time step of growth
   - "a class with a single unit" is born with a probability b $(0 \leq b \leq 1)$.
   - we choose a class with probability proportional to the number of units it already has and add a new unit to it with a probability of λ $(0 < \lambda \leq 1)$.
   - we choose a class with probability proportional to the number of units it already has and subtract a new unit from it with a probability of μ $(0 \leq \mu < 1$, $\mu < \lambda)$.

Corresponding master equation of $p(k, t_i, t)$ which is the probability at time t, for a class i introduced at time t_i, to have k number of units. t can be thought of as a time scale proportional to the total number of units.

$$\frac{\partial p(k,t_i,t)}{\partial t} = \lambda \frac{(k-1)}{g(t)} p(k-1,t_i,t) + \mu \frac{(k+1)}{g(t)} p(k+1,t_i,t) - (\lambda+\mu) \frac{k}{g(t)} p(k,t_i,t) \tag{1}$$

where $p(1, t_i, t_i) = 1$. At any time t the total number of classes are $\int_0^t dt_i b(t_i) = \int_0^t dt_i (N\delta(t_i) + b)$ and the total number of units are $g(t) = \sum_{n=1}^{N} k_n = (\lambda - \mu)t + \int_0^t dt_i b(t_i)$ where, k_n is number of units in a class n. In this equation,$g(t)$ describes a kind of competition in our society. The solution of this master equation is given as fallows. See apenndix in detail.

$$p(k,t) = I_0 + I_1 \tag{2}$$

$$I_1 \propto e^{-\gamma k} \tag{3}$$

with $\gamma = -\log \eta_{0,t}$

and $\eta_{t_i,t} = \dfrac{1 - \varepsilon_{t_i,t}}{1 - \frac{\mu}{\lambda}\varepsilon_{t_i,t}}$

$$\varepsilon_{t_i,t} \equiv \left(\frac{t_i + N(\lambda-\mu)^{-1}(1+\bar{b})^{-1}}{t + N(\lambda-\mu)^{-1}(1+\bar{b})^{-1}} \right)^{\frac{1}{(1+\bar{b})}} \tag{4}$$

where $\bar{b} \equiv \dfrac{b}{\lambda - \mu}$

We observe that as t increases $I_1(k)$ has a slower decay which is the effect of decrease of $\eta_{0,t}$ with time. The small ε and large k (i.e., $\varepsilon_{0,t} << 1$, $\varepsilon_{0,t} k \sim o(1)$) limit of Eq. 3 can be given as

$$I_1 \propto t^{-1} \varepsilon_{0,t} e^{-\varepsilon_{0,t} k} + o(t^{-1}\varepsilon_{0,t}^2) \tag{5}$$

$$I_2 \propto k^{-(2+\bar{b})} + o(k^{-(3+\bar{b})}) + o(\varepsilon_{0,t}^{2+\bar{b}}) \tag{6}$$

$$p(k,t) \propto t^{-1} \varepsilon_{0,t} e^{-\varepsilon_{0,t} k} + k^{-(2+\bar{b})} \tag{7}$$

We observe that the first two terms of Eq. 7 are of the same order in the range $t \sim k^{(1+\bar{b})}$, $t >> 1$, $k >> 1$.

D. conclution

One of the features of economical or social systems, contrary to the physical systems, is that they sometimes have not reached limitation of sizes so far. And it sometimes happens that dominance of the growth shift from the number of classes (firms or cities) at the first stage of evolution to the number of units (productions or persons). And we show that this causes the smooth cut-off of power law, through both data analysis and analytical model.

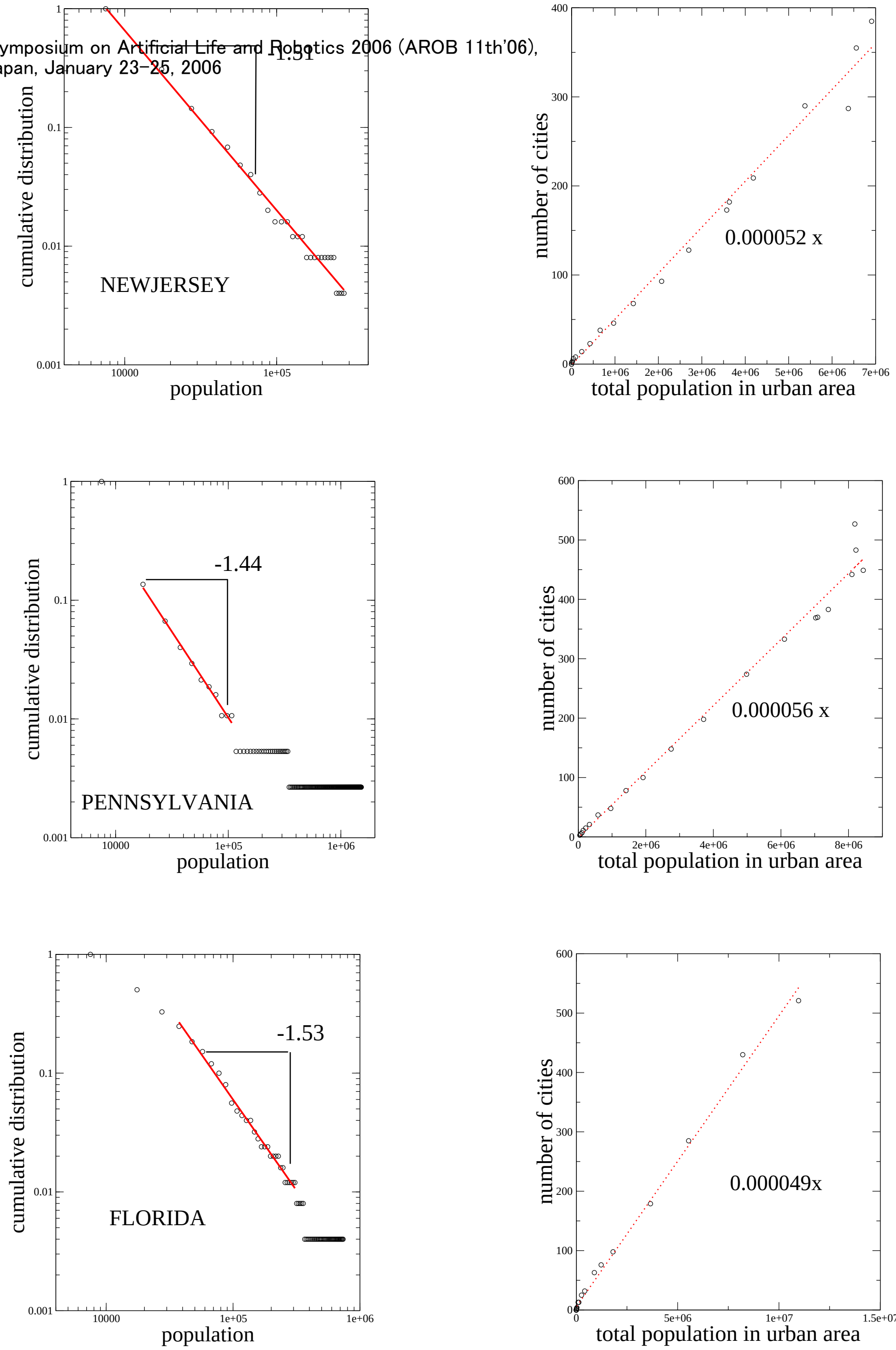

FIG. 2: Left side figure shows the cumulative distribution of population in a city in various states. Power law is kept almost whole range. In right side figure, x axis is the total population of urban area in corresponding states and y axis is the number of cities.

---

[1] G. Zipf, Cambridge,MA: Addison-Wesley (1949).
[2] Jeong H, Tombor B, Albert R, et al. *Nature* 407, 651-654 (2000)
[3] "Incorporated Place Population Estimates in 2000 http:www.census.govepcdwwwplaces.htm"
[4] Y. Ijiri and H.A. Simon, (North-Holland, Amsterdam, 1997)
[5] G. De Fabritiis, F. Pammolli and M. Riccaboni "on size

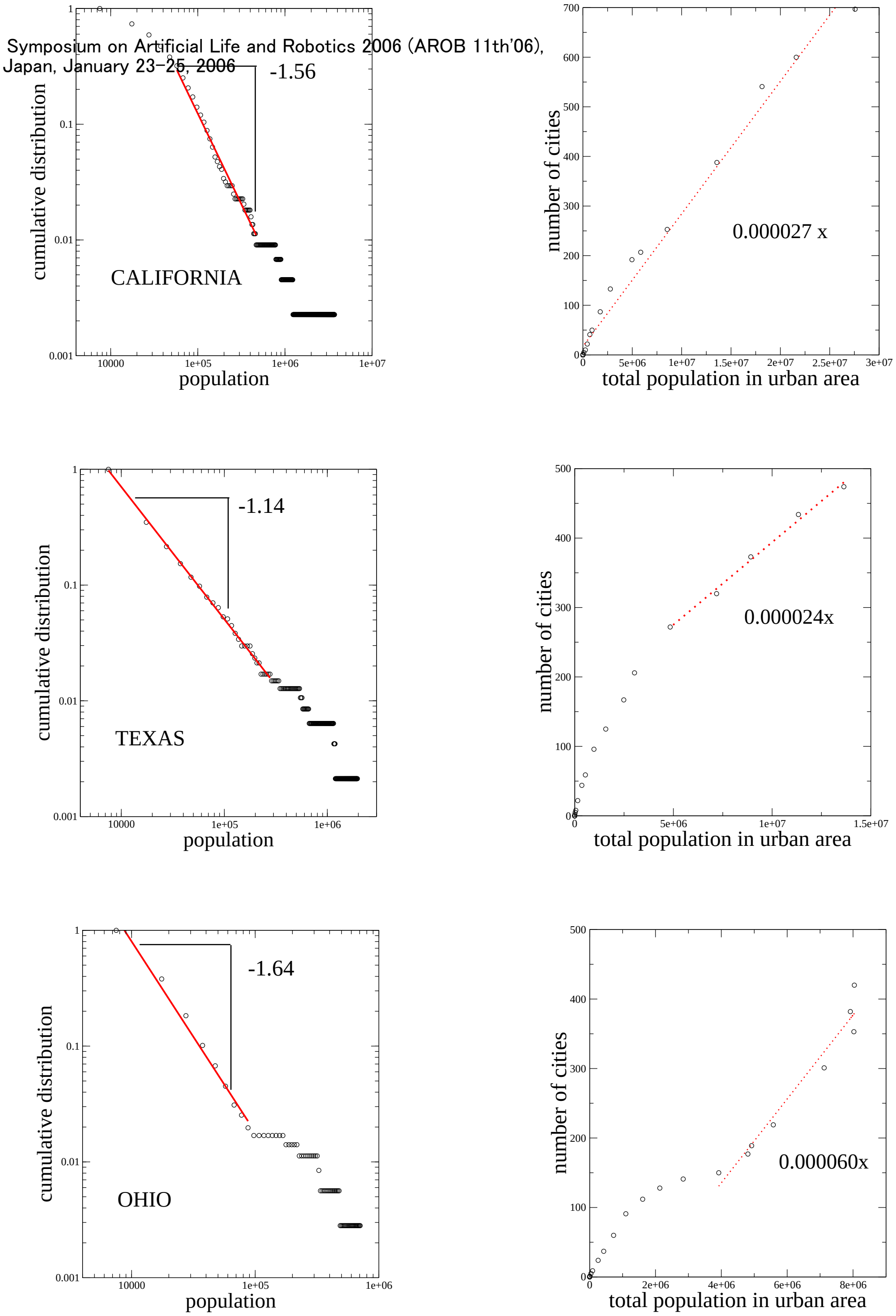

FIG. 3: Left side figures shows the cumulative distribution of population in a city in various states. Power laws are cut off exponentially. In right side figures, x axis is the total population of urban area in corresponding states and y axis is the number of cities. The appearance of new cities is slowing down as the total population grows.

and growth of business firms" PHYSICA A **324**, 38 (2003)

[6] K. Yamasaki, K. Matia, D. Fu, S. V. Buldyrev, F. Pammolli, M. Riccaboni and H. E. Stanley, Preferential Attachment and Growth Dynamics in Cpmplex Systems, submitted to PRL.

[7] Dongfeng Fu, F. Pammolli,S. V. Buldyrev, M. Riccaboni,K. Matia, K. Yamasaki, H.E. Stanley The Growth of Business Firms:Theoretical Framework and Empirical Evidence, Proc. of National Academy of Sciences in press

Visualization of an Invisible Space Based on the MR Technique

Sunao Hashimoto Joo Kooi Tan Seiji Ishikawa
Department of Mechanical & Control Engineering
Kyushu Institute of Technology
Sensuicho 1-1, Tobata, Kitakyushu 804-8550, Japan
hasimoto@ss10.cntl.kyutech.ac.jp, {etheltan, ishikawa}@cntl.kyutech.ac.jp

Abstract

This paper describes a novel technique for realizing a transparent space employing a mixed reality technique and a three-dimensional (3-D) modeling technique. Accidents often happen when a person, a car, etc., comes out suddenly from a blind corner. If the visibility of such a blind corner is improved, many of the accidents will not occur. The idea of this study is to devise a technique for achieving better visibility at various places of bad visibility by use of a mixed reality technique. Mixed reality was born from virtual reality study. It provides a technique for superposing virtual objects in a real space.

As the initial step of realizing the above idea, in the present paper, a technique is described for giving a 3-D view of a space beyond a thick wall employing a computer vision technique and a see-through vision. The technique provides an observer with a view of a 3-D dynamic scene of the adjacent space partitioned by a wall in real-time without going into it.

Future application of the preset technique may include its installation to various corners in the building and in the intersections on the road with bad visibility. This will surely contribute to reducing traffic accidents in future.

Keywords: 3-D recovery, mixed reality, virtual reality.

1 Introduction

Mixed reality is a technique for unifying virtual entities and a real world using some instruments for see-through vision. Many applications of the mixed reality studies have already been reported [1].

Employing the mixed reality technique, useful information can be added to a real world. This can be regarded as visualization of invisible information. An example of the invisible information in our daily life is blind or occluded spots. Many traffic accidents happen when a person, a motorcycle, a car, etc., suddenly come out of a blind corner. If the corner has good visibility, most of the accidents may not occur. The idea of this study is to devise a technique for achieving better visibility at various places of bad visibility by use of a mixed reality technique.

There are some researches [2,3] with respect to making transparent objects, but the former cannot realize real-time operation, whereas the latter doesn't give exact views when an observer changes his/her viewing direction.

In this paper, we propose a method of making an invisible space visible by the employment of mixed reality technique and a simple 3-D recovery technique. By the employment of the simple 3-D recovery, the proposed technique realizes real-time operation. Moreover the technique offers exact views to an observer, irrespective of his/her viewing point, since it makes a 3-D virtual model of the real world observed. Overview of the proposed method is given followed by the description of computational strategies for realizing a transparent environment. Experimental results are shown with discussion.

2 Overview of the system

Configuration of the proposed system is shown in **Fig.1**. A camera is set in the space that is separated by a wall or a partition and invisible from an observer. The space is denoted as an invisible region. The scene in the invisible region is taken images by the camera. The taken scene recovers in a 3-D way and is described in the virtual space simulating the invisible region. An observer puts on a see-through type head mounted display (HMD), which is equipped with a position and orientation sensor. Employing the information from the sensor, the PC computes the view of the invisible space that could be seen from the observer and displays it on the HMD. Then the observer sees the wall superposed by the computed view of the invisible space, thus realizing a transparent view of an invisible space.

3 Computational strategies

In order to create a 3-D virtual space, which is a model of an invisible space, camera calibration is performed in the first place. The camera parameters are then calculated and finally 2-D projective transformation is defined between the floor in the 3-D space and the image plane of the camera.

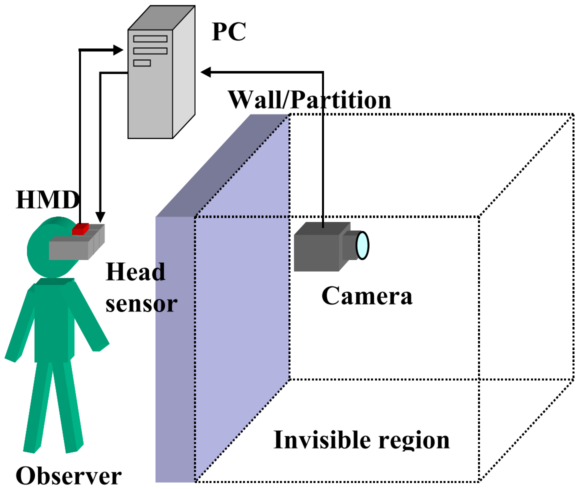

Fig. 1 Configuration of the system.

3.1 Acquiring the depth information

In the proposed technique, a single camera is used to observe an invisible region. The depth information is acquired by the employment of 2-D projective transformation between the floor, the XY plane of the world coordinate system, and the image plane. Let us denote the object's position on the *XY* plane in the world coordinate system by $(X_g,Y_g,0)$ and its projection on the image plane by (x_g,y_g). Then the 2-D projective transformation between the planes are given by

$$\begin{pmatrix} X_g \\ Y_g \\ 1 \end{pmatrix} = \begin{pmatrix} h_0 & h_1 & h_2 \\ h_3 & h_4 & h_5 \\ h_6 & h_7 & 1 \end{pmatrix} \begin{pmatrix} x_g \\ y_g \\ 1 \end{pmatrix} \tag{1}$$

4 Flow of the procedure

The proposed system takes images of an invisible region every moment and performs background subtraction. If some newly appeared objects are found in a certain frame, after some noise reduction procedures, it separates each object by labeling, calculates their feet's position, and computes their locations in the world coordinate system employing Eq.(1). Once the coordinates $(X_g,Y_g,0)$ is obtained with the detected object, a perpendicular line is drawn from the point $(X_g,Y_g,0)$ to the optical axis, whose foot is the point $P(X_c,Y_c,Z_c)$ discussed in the former section. Then the plane passing through $(X_g,Y_g,0)$ and perpendicular to the optical axis is specified. This plane is referred to as a layer on which the object is projected.

In **Fig.2**, two objects located at $(X_{g1},Y_{g1},0)$ and $(X_{g2},Y_{g2},0)$ define the layers 1 and 2 that are perpendicular to the optical axis of the camera. The objects are projected on the respective layers in the virtual space.

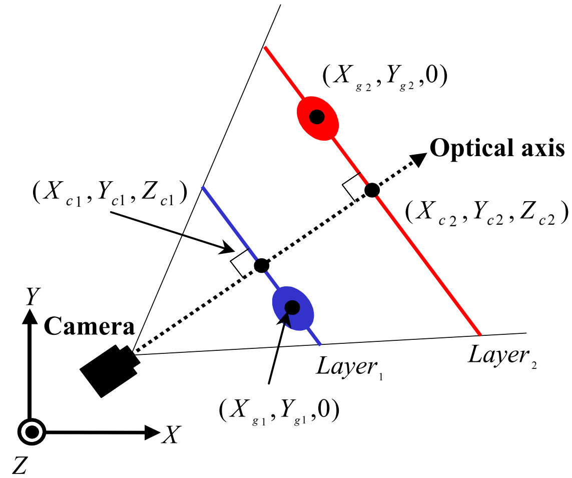

Fig. 2 Location of objects and layers.

5 Experimental results

5.1 Produced 3-D virtual space

The first experiment was conducted to create a virtual space from the images of two persons walking around in a room. The environment of the experiment is shown in **Fig.3a** where two persons are taken images of their walking motions by the settled camera. Figure.3b illustrates the input images. The created virtual space is shown in Fig.3c, in which two persons' images are correctly arranged in the 3-D virtual space. These images move around according to the two persons' movement in the real room.

5.2 Produced transparent space

In the second experiment, transparent space is realized and demonstrated. In **Fig.4a**, the experimental environment includes a walking person as Human, an observer as User, and a partition as Wall that separates the Human and the User. The User cannot see the Human directly as the Wall obstructs the User's sight, the situation of which is given in Fig.4b. The transparent space is realized in Fig.4c, where the Human's model in the 3-D virtual space is superposed onto the real image of the Wall. The human model walks around the same place where the real person walks. Therefore, if the wall is removed as shown in Fig,4d, the Human model and the real person are situated at the same place. All of the performance is realized almost real-time.

6 Discussion and conclusions

In this paper, we have proposed a novel idea of making an invisible place visible by the employment of a mixed reality technique. We have shown a system for taking images of a dynamical scene of a space hidden by a partition, creating a 3-D virtual space describing the dynamical scene, and displaying the virtual space along with the real space to an observer. In the performed experiment, an observer could watch a person or two persons walking around in a space hidden by an opaque partition through the partition.

The performance was satisfactory. In fact, the system achieved almost real-time processing for displaying the scene beyond the opaque partition. The displacement between the displayed virtual person and the real person was small enough to judge his location exactly. It is noted that the created virtual space is a 3-D space. Although we have employed a single camera for observing the invisible space, we assume that the persons walk on the floor and objects are placed on the floor. In this way, we obtain depth information of the objects. If a person jumps up in the air, the system looses his depth information. But when he lands on the floor again, the system well recognizes his exact location.

As was mentioned above, the created virtual space is a 3-D space. This allows an observer change his/her observing position. His/her view is computed every time he/she changes his/her observing location and orientation. The sensor mounted on the HMD detects the information. However the appearance of the virtual human becomes not very natural, if the observer's position change becomes larger. We need more number of cameras to realize a natural virtual human model.

The proposed technique may have various application fields. Especially it can be employed for a variety of safety purposes including children or aged people watching, pedestrians, motorcycles, or cars sensing at blind corners, and it would be very nice if the system could give alarm to those people nearby.

References

[1] Y. Ohta, H. Tamura (1999), Mixed Reality, Ohmsha

[2] J. Hoshino (2001), See-Through Representation of Video, *Proceedings of ISMR 2001*, pp.155-156

[3] M. Inami, N. Kawakami, D. Sekiguchi, Y. Yanagida, T. Maeda and S. Tachi (2000), Visuo-Haptic Display Using Head-Mounted Projector, *Proceedings of IEEE Virtual Reality 2000*, pp.233-240

(a)

(b)

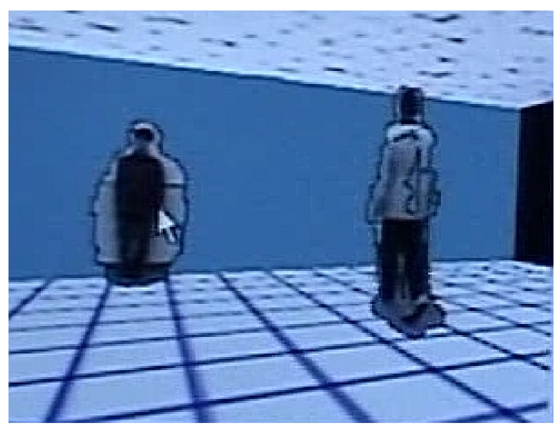

(c)

Fig. 3 Experiment 1: Producing a 3-D virtual space. (a) Environment; (b) Input images; (c) A 3-D virtual space containing two appropriately arranged persons.

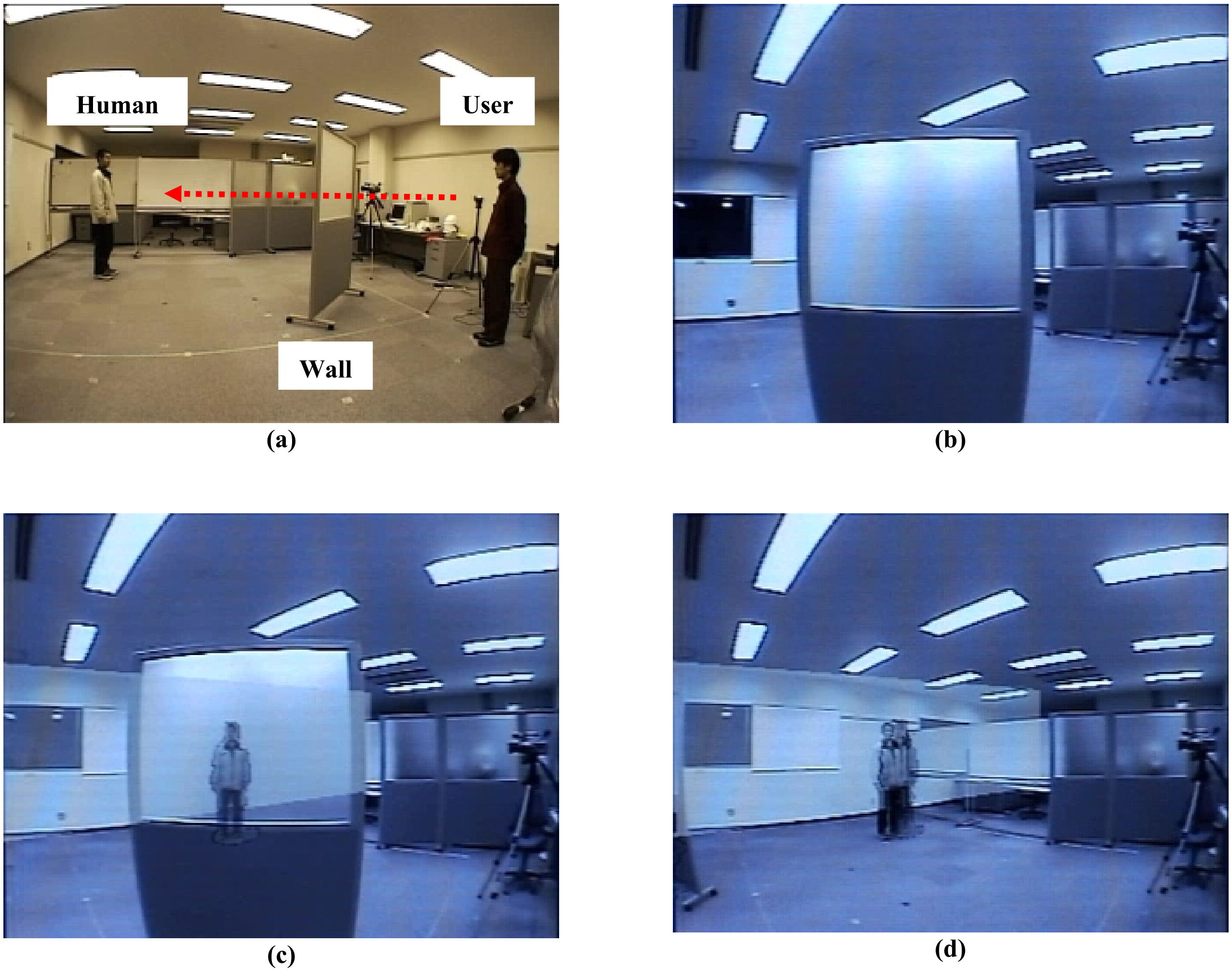

Fig. 4 Experiment 2: Producing a transparent space.
(a) Environment; (b) User's observing scene;
(c) Transparent space; (d) Removal of the wall.

FACE EMOTION RECOGNITION – A SURVEY

M. Karthigayan **Mohd Rizon** **Sazali Yaacob** **R.Nagarajan**
School of Mechatronics
Northern Malaysia University College of Engineering
01000 Kangar, Perlis, Malaysia.
Email:karthigayan@ieee.org

ABSTRACT
The facial emotion is playing a vital role in visual communication system. The vision system is being integrated to the robot to recognize the facial gestures or emotion. The integration of the vision system and EMG sensors enables designing advanced emotion recognition package. The main objective of the paper is to discuss the various types of feature extraction and recognition system for face emotion and its application.

INTRODUCTION
In recent years, there has been a growing interest in improving all aspects of interaction between humans and computers especially in the area of human emotion recognition by observing facial expression. Ekman and Friesen developed the most comprehensive system for synthesizing facial expression based on what they call as action units [1]. In the early 1990's the engineering community started to use these results to construct automatic methods of recognizing emotion from facial expression in still or video [2]. Human being possesses an ability of communication through emotion in day to day interactions with others. Some emotions attracted most of the interest in human computer interaction environments. The categories of emotion, as applied in human computer interaction are: Sadness, Anger, Joy, Fear, Disgust or Dislike and Surprise. In this paper, a survey on face emotion recognition from the last decade is presented. Image acquisition, feature extraction and classification are also discussed as connected areas of face recognition.

FACE EMOTION
Face emotion presents an abstract means of description of facial expressions by utilizing concepts included in the MPEG-4 standard. It has been used in online-gaming [3]. Facial animation is a great means of improving HCI applications and especially in computer games, since it provides a powerful and universal means of expression and interaction. A simple method of synthesizing realistic facial expressions using lightweight representations has been realized. The recognition of emotions has been applied in various applications. Human face may acts as visual interface to interact with a computer for communication and recognizing emotions. An human arm motion model is recreated by a CRT display and by an industry robot [4]. Another effort is to build a human computer facial gesture and expression for use in robot application. It has the ability to track facial features in real time (30Hz). Kalman filter has been used in this recognition of facial gestures [5].

Both audio and video information are combined to get better recognition of emotions. These methods can classify the six basic emotions. The statistical technique and hidden markov model were applied in this process of recognition [6, 7]. The correlation dimensions for the electroencephalogram (EEG) in positive and negative emotional states are estimated. The results show that the correlation exponent for the emotional state is higher than that for the rest state even if the variation between subjects is considered. Discrimination is created between yes and no for communication via EEG, particularly for severely disabled persons [8]. Welfare support system is also developed by robot vision. Robot vision is constructed using a model of a knowledge, emotion and intention, from which welfare oriented active vision is realized [9, 10, 11]. Human interface of an eating assist robot has been developed for helping the disabled patients. A spoon and CCD camera are fixed on the tip of the robotic arm. Here, A Galvanic Skin Reflex (GSR) sensor is also implemented to evaluate the emotion. Such a spoon-feeding robot assisting a disabled patient with cervical vertebrae damage has been successfully demonstrated [12]. Physiological signals are used for emotion recognition. A support vector machine was introduced as the physiological signal pattern classifier. The support vector machine overcomes the difficulty of large overlap among clusters and large variance within cluster. The advantage of this system is that it requires shorter signal monitoring time than pervious ones, and thus better suited for practical use [13].

Welfare robot has been developed to support the lives of senior citizen. The general measurement of emotion for basic research is still being carried out. Rule of emotion measurement has been discussed and new rules for emotion measurement have been derived and applied. The results have been found to be satisfactory [14]. The face emotion can be also classified based EMG, vision system and speech. The recognition of emotions has been applied in various applications. The applications of emotions can be robot, web, online gaming, biometric security system etc [15, 16]. A robot, named as IFBOL, understands a partner's feeling [17]. IFBOL, a Sensibility Technology Communication Robot, can detect emotion, recognize conversation, go by affection of conversation partner and speak with sentiment. Mental health is very important to lead a safe and secured life. This IFBOL robot is able to communicate with people upon their feeling and stress. This robot expresses one's feelings with eyelid and eye, besides learning the habit and personality of the conversing partner, so as to respond to the partner. Robot-Assisted Activity (RAA) to provide physical and mental support and the emotion driven model for RAA have been proposed [18]. Japan community feels that robots can give more support for senior citizens. More researchers are concentrating on welfare robot for aged people in many countries. The robot has been proposed for the aged people to feel their emotion and to support them. The construction of robot model uses hierarchical knowledge. The robot can perform complex actions based on the robot's internal and external environmental information. Many robots are involved to support physically and mentally for the senior citizens. These robots work on the basis of face emotion control. Many previous works were carried out on six universal facial expressions or emotions. They are happy, sad, fear, angry, surprise and disgust. Instead of universal facial expressions, many people show 'personalized' or 'individualized' facial expressions typically. A method has been proposed to construct a personalized classifier based on novel selection method [19]. Robust facial expression recognition system using the result of face detection by a convolution neural network and rule based processing has been described [20]. The algorithm which has been proposed to demonstrate the ability to discriminate smiling from talking is based on the saliency score. The sensitive system that incorporates "affects recognition" into computer based learning has been discussed [21]. Some problems of artificial emotions in mental therapy had been discussed from the perspectives of sociology of emotions, clinical sociology and the sociology of health and illness [22]. The physiological data of skin conductance and EMG interpret the emotion and the user's affective states in the form of empathic feedback. Facial EMG has been proposed to measure user's emotional state continuously [23]. Double structured neural network has been applied in the methods of face detection and emotional extraction. In this two methods are proposed and carried out; they are lip detection neural network and skin distinction neural network [24]. Jaw muscle mediation plays a vital role in the recognition of emotion. In this, the results of a wavelet analysis performed on electro-myography signals are recorded from the cat masseter (jaw) muscle during hypothalamic stimulation [25]. The effects of facial color on virtual facial image synthesis for dynamic facial color and expression of smile by using an average facial image of 68 females are analyzed [26]. An autonomous robot is equipped with emotion recognition to evaluate the changes of both the environment and its internal state. Fuzzy emotion model has been created for the autonomous robot [27]. Several autonomous robots are controlled based on emotions. Facial expression was measured using convergent measures, including facial EMG, automatic feature-point tracking and manual Facial Action Coding System (FACS). FACS unit conveys the information that can inform interpretation of psychological states [28, 29]. This finding indicates that dysphoric persons have impaired interpersonal reactivity that is specific to happy facial displays. Empathic Companion, an animated interface agent that accompanies the user in the setting of a virtual job interview is explained. A character based interface that uses physiological signals of the user in real-time and address user emotions derived from those signals are also described [30]. A novel method of a spatio-temporal approach has been proposed to classify 6 universal expressions from visual data and use them to derive the level of interest using psychological evidences. The average recognition rate of the proposed facial expression classifier is 90.9% without classifier fusion and 91.2% with fusion using a five fold cross validation scheme on a database of 488 video sequence that include 97 subjects [31]. Temporal template method has been proposed to detect automatic face action recognition. In this classifier, the first stage consists of a general K-nearest neighbor (KNN) classification scheme and the second stage uses domain specific knowledge in a rule-based system. It has reached a recognition rate of 70.6% for lower face automatic recognition and recognition rate of 81.8% for upper face automatic recognition [32]. Visual data also play a vital role in recognition of emotion of audio-visual model. A triple hidden markov model is introduced to perform recognition. This is the first time emotion recognition is carried out from both visual and audio from video clips [33, 34]. Two studies are carried out for this emotion measures; they are first and second study with 16 and 15 participants respectively. Support vector machines are applied to recognize emotion from multi-modal bio–potential signals. It shows 41.7% and 66.7% recognition rate for 5 and 3 emotions respectively from the experiments results. The 5 emotions are joy, anger, sadness, happiness and relax. The 3 emotions are joy, anger and relax [35]. In the study of Affective Computing for Behavior- Based UI Adaption, the video-cameras and EMG sensors are employed for monitoring emotions [36]. The ongoing emotional state of the computer users is measured. To provide feedback in the software design process on the emotional state, the facial EMG is measured for both verbal and performance (Joey and Richard Hazlett, 2005).

CONCLUSION

In this paper, a brief survey of face emotion recognition has been presented. The features of eye, lips, cheeks, eye brows, mouth and skin contraction are extracted to classify the face emotion. The feature extraction methods such as wavelet transform, eigenface, projection profile and gabor transformation have been considered by researchers. If IFBOL and RAA are implemented as face emotion recognition system to understand human feelings. Several application of robotics on the basis of face emotion has been recorded. A real-time face emotion change from one category of emotion to another has not been mentioned in any research. Emotion recognition can also be achieved be measuring brain wave, vision, heart rate, EMG, speech and pulse. However, vision and EMG were utilized in several papers. Several changes in blood sugar content, blood pressure, temperature and Ph value can occur with respect to emotion. These are yet to be incorporated in emotion recognition system.

REFERENCE

1) Haibo Li, “Computer Recognition of Human Emotion”, *Proceedings of International Symposium on Intelligent Multimedia, Video and Speech Processing*, Hong Kong, pp. 490-493, 2-4 May 2001.
2) Nicu Sebe, Michael S. Lew, Ira Cohen, Ashutosh Garg and Thomas S. Huang, “Emotion Recognition Using a Cauchy Naïve Bayes Classifier”, *Proc. of Sixteenth International Conference on Pattern Recognition*, vol. 1 pp. 17-20, 11-15 August 2002.
3) Raouzaiou A, Karpouzis K and Kollias S, “Emotion Representation for online Gaming”, *Proceedings of International Conference on Multimedia and Expo. ICME '03*,vol.1, pp. I 417-420, 6-9 July 2003.
4) Shibata S, Ohba K and Inooka H, “Emotional Evaluation of Human Arm Motion Models”, *Proc. of the Second IEEE International Workshop on Robot and Human Communication*, pp. 346-351, 3-5 November 1993.
5) Alexander Zelinsky and Jochen Heinzmann, “Real-Time Visual Recognition of Facial Gestures for Human-Computer Interaction”, *Proc. of the Second International Conference on Automatic Face and Gesture Recognition*, pp. 351-356, 14-16 October 1996.
6) Liyanage C. De Silva and Pei Chi Hg, “Bimodal Emotion Recognition”, *Proc. of the fourth IEEE International Conference on Automatic Face and Gesture Recognition*, pp. 332-335, 28-30 March 2000.
7) Liyanage C. De Silva, Tsutomu Miyasato and Ryohei Nakatsu, “Facial Emotion Recognition Using Multi-Modal Information” *Proc. of International Conference on Information, Communication and Signal Processing (ICICS’97)*, vol 1, pp. 397-401, 9-12 September 1997.
8) Chang Su Ryu, Seunghwan Kim and Seon Hee Park, “An Estimation of the Correlation Dimension for the EEG in Emotional States”, *Proc. of the IEEE International Conference on Engineering in Medicine and Biology Society*, vol. 4, pp. 1547-1550, 30 October – 2 November 1997.
9) Tomomi Hashimoto, “Proposal of Emotion Model in Robot-Assisted-Activity”, *Proc. of the Twenty sixth Annual Conference of the IEEE on Industrial Electronics society (IECON2000)*, vol. 1, pp. 527-529, 22-28 October 2000.
10) Tomomi Hashimoto and Toru Yamaguchi, “Model of Knowledge, Emotion and Awareness”, *Proc. of the Sixth IEEE International Workshop on Robot and Human Communication (ROMAN97)*, pp. 326-331, 29 September – 1 October 1997.
11) Toru Yamaguchi, Shinya Mizuno, Takuya Yoshida and Tomomi Hashimoto, “Cooperative Works for Agent Robot and Human Using Robot Vision Based on the Model of Knowledge, Emotion and Intention”, *Proc. of the IEEE International Conference on Systems, Man and Cybernetics*, vol. 2, pp. 987-992, 12-15 October 1999.
12) Yoshihiko Takahashi, Naoya Hasegawa, Katsumi Takahashi and Takuro Hatakeyama, “Human Interface Using PC Display with Head Pointing Device for Eating Assist Robot and Emotional Evaluation by GSR Sensor”, *Proc. of the 2001 IEEE International Conference on Robotics and Automation*, pp. 3674-3679, 21-26 May 2001.
13) Kyung Hwan Kim, Seok Won Bang and Sang Ryong Kim, “Development of Person-Independent Emotion Recognition System Based on Multiple Physiological Signals”, *Proc. of the Second Joint EMBS/BMES International Conference of Biomedical Engineering Society*, pp 50-51, 23-26 October 2002.
14) Fuji Ren, Matsumoto k, Mitsuyoshi S, Kuroiwa S and Gai Lin, “Researches on the Emotion Measurement System” *IEEE International Conference on Systems, Man and Cybernetics*, vol. 2, pp.1666 – 1672, 5-8 Oct 2003.
15) Thomas Mc Kenna “Video Surveillance and Human Activity Recognition for Anti Terrorism and Force Protection”, *Proceedings of the IEEE conference on Advance Video and Signal based Surveillance*, pp. 2, 21-22 July 2003.
16) Ka Leung Lee and Yangsheng Yu, “Real-Time Estimation of facial Expression Intensity”, *Proceedings of the IEEE International conference on Robotics and Automation*, Taiwan. pp. 2567-2572, 14-19 Sept 2003.
17) Kenji Tamural, Shohei kat, Takanori Yamakita, Kenji Kimurad and Hidenori Itoh. A System of Dialogical Mental Health Care with Sensibility Technology Communication Robot. International Symposium on Micromechatronics and Human Science, pp. 67-71, 2003.
18) Tomomi Hashimoto, Toshimitsu Hamada and Toshiko Alolzawa. “Proposal of Emotion-driven Control Model for Robot-Assisted Activity”, *Proceedings of IEEE International Symposium on Computational Intelligence in Robotics and Automation*, Kobe, pp. 125-129, July 16-20 2003.
19) Dae-Jin Kim, Zeungnam Bien and Kwang-Hyun Park, “Fuzzy Neural Network (FNN) – Based Approach for Personalized facial Expression Recognition with Novel Feature selection Method.”, *The 12th IEEE International Conference on Fuzzy Systems*, vol.2, pp. 908 – 913, 25-28 May 2003.
20) Matsugu M, Mori K, Mitari Y, Keneda Y, “Facial Expression Recognition Combined with Robust Face Detection in a Convolution”, *Proceedings of the International Joint Conference on Neural Network*, Vol3, pp. 2243 – 2246, 20-24 July 2003.
21) Newman K.B., “Sensitive systems – incorporating affect recognition into computer based learning”, *Proc. of the Sixth International Conference on Computer Based Learning in Science (CBLIS)*, pp. 37-46, 5-10 July 2003.
22) Tatsuya Nomura, “Problems of Artificial Emotions in Mental Therapy”, *Proc. of the IEEE International Symposium on Computational Intelligence in*

Robotics and Automation, pp. 567-570, 16-20 July 2003.

23) Richard L. Hazlett, "Measurement of User Frustration: A biological Approach", CHI 2003: New Horizons, pp. 734-735, 5-10 April 2003.
24) Hironori Takimoto, Yasue Mitsukura, Minoru Fukumi and Norio Akamatsu, "Face Detection and Emotional Extraction System Using Double Structure Neural Network", *Proc. of the International Joint Conference on Neural Networks*, vol. 2, pp. 1253-1257, 20-24 July 2003.
25) Petrock A and Reisman S, "Wavelet Analysis of Masseter Muscle EMG during Emotional Provocation", *Proc. of the Twenty Ninth IEEE Annual Conference on Bioengineering*, pp. 132-133, 22-23 March 2003.
26) Takashi Yamada and Tumio Watanabe, "Effects of facial Color on Virtual Facial Image Synthesis for Dynamic Facial Color and Expression under Laughing Emotion", *Proc. of the 2004 IEEE International Workshop on Robot and Human Interactive Communication(ROMAN2004)*, pp. 341-346, 20-22 September 2004.
27) Changsheng Yu and Li Xu, " An Emotion-Based Approach to Decision Making and Self Learning in Autonomous Robot Control", *Proc. of fifth World Congress on Intelligent Control and Automation*, pp. 2386-2390, 15-19 June 2004.
28) Jeffrey F. Cohn, Karen Schmidt, Ralph Gross and Paul Ekman, "Individual Differences in Facial Expression: Stability over Time, Relation to Self-Reported Emotion and Ability to Inform Person Identification", *Proc. of the Fourth IEEE International Conference on Multimodal Interfaces (ICMI'02)*, pp. 491-496, 14-16 October 2002.
29) Lou Benedict P. Ang, Erwin F. Belen, Ramon A. Bernardo. Jr, Eleazar. Boongaling, Grace H. briones and Jonathan B. Coronel, "Facial Expression Recognition through Pattern Analysis of Facial Muscle Movements Utilizing Electromyogram Sensors", *Proceeding of IEEE TENCON 2004*, Thailand, pp. 600-603, 21-24 Nov 2004.
30) Prendinger H, Dohi H, Wang H., S. Mayer and M. Ishizuka, "Empathic Embodied Interfaces: Addressing User's Affective State", 2004: http://research.nii.ac.jp/~prendinger/papers/helmut-ADS-04.pdf.
31) Yeasin M, Bullot B and Sharma R, "From Facial Expression to Level of Interest: A Spatio-Temporal Approach", *Proceedings of the 2004 IEEE Computer Society Conference on Computer Vision and Pattern Recognition (CVPR'04)*, vol. 2, pp. II99- II927, 2004.
32) Michel Valstar, Ioannis Patras and Maja Pantic, "Facial Action Unit Recognition Using Temporal Templates", *Proc. of Thirteenth International Workshop on Robot and Human Interactive Communication*, pp. 253-258, 20-22 September 2004.
33) Mingli Song, Chun Chen and Mingyu You, "Audio-Visual Based Emotion Recognition Using Tripled Hidden Markov Model", *Proc. of IEEE International Conference on Acoustic, Speech and Signal Processing*, vol. 5, pp. 877-880, 17-21 May 2004.
34) Mingli Song, Jiajun Bu, Chun Chen and Nan Li, "Audio-Visual Based Emotion Recognition – A New Approach", *Proc. of the 2004 IEEE Computer Society Conference on Computer Vision and Pattern Recognition (CVPR'04)*, vol. 2, pp. II-1020-II-1025, 27 June – 2 July 2004.
35) Kazuhiko Takahashi, "Remarks on SVM-Based Emotion Recognition from Multi-Modal Bio-Potential Signals", *Proc. of the 2004 IEEE International Workshop on Robot and Human Interactive Communication (ROMAN2004)*, pp. 95-100, 20-22 September 2004.
36) Pedro Branco and Miguel Encarnacao L, "Affective Computing for Behavior-Based UI Adaptation", IUI/CADUI Conference Workshop on behavior – based User Interface Customization – Intelligent User Interface 2004, 13 January 2004: www.research.ibm.com/iui-workshop/papers/brancoencarnacao.pdf.
37) Joey Benedek and Richard L. Hazlett, "Incorporating Facial EMG Emotion Measures as Feedback in the Software Design Process", 2005: www-2.cs.cmu.edu/~cga/behaviour/benedek.pdf

The Eleventh International Symposium on Artificial Life and Robotics 2006 (AROB 11th'06),
B-con Plaza, Beppu, Oita, Japan, January 23-25, 2006

MOMENTS IN IC CHIP CLASSIFICATION

M.Karthigayan R.Nagarajan Sazali Yaacob Paulraj Pandian Mohd Rizon Mohd Rozailan[+]

School of Mechatronics, Northern Malaysia University College of Engineering, 02600 Jejawi, Perlis, Malaysia
[+]Terengganu Advanced Technical Institute (TATI), Jalan Panchor, Teluk Kalong, 24000 Kemaman, Terengganu, Malaysia
Email: karthigayan@ieee.org

Abstract

In this paper, an Industrial machine vision system incorporating Optical Character Recognition (OCR) is employed to inspect the marking on the Integrated Circuit (IC) Chips. This inspection is carried out while the ICs are coming out from the manufacturing line. A TSSOP-DGG type of IC package from Texas Instrument is used in the investigation. The IC chips are laser printed. This inspection system ensures whether the laser printed marking on IC chips are proper. One of the artificial intelligence components the neural network, is used for this inspection. The inspections are carried out to find the print errors such as illegible character, missing characters and up side down printing. The vision inspection of the printed markings on the IC chip are carried out in three phases namely image preprocessing, feature extraction and classification. MATLAB platform and its toolboxes are used for designing the inspection processing technique. Neural network is used as a classifier to detect the defectively marked IC chips coming from the manufacturing line. Moments are used as feature for this inspection.

Keywords
machine vision, moments, backpropagation.

1. Introduction

Since 1950, Optical Character Recognition *(*OCR) has been very active in the application of automatic pattern recognition; now it is used to read the printed characters at high speed [1, 2]. OCR is widely used in recognition of hand written characters and printed characters using Artificial intelligence techniques [1-4]. The OCR is applied for business card recognition [5] where the manual input is optional; however, by scanning, the OCR is able to create an easier database. The document reading and analysis have reached an important position in certain markets. The application of OCR in the postal automation has followed into the banks and industrial inspection processes [6, 7].

IC chips play a vital role in electronic industries. Mass production of IC chips have brought down the price of the electronic products. Texas Instrument is one of the well-established IC chips manufacturing companies in the world market. In the Texas group, Texas Instrument, Malaysia TI(M), is one of the leading producers of IC chips in. The IC chips undergo many inspections and verifications to ensure a guaranteed quality. Quality control of IC is performed by inspecting the placement of die, inspecting lead dimension, inspecting packaging and inspecting marking of symbols (IC number, year of manufacture and batch code etc). In this research work OCR is employed to check the markings of the IC chips especially, the marking on the *Thin Shrink Small Outline Packages (TSSOP-DGG*) using neural network. Figure 1 illustrates various marking errors that can occur during production where as Figure 2 shows the error free marking.

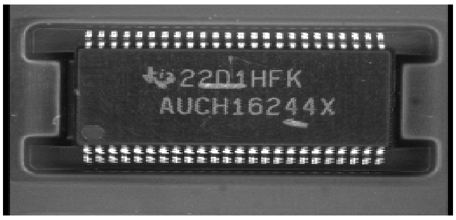

(a)Illegible

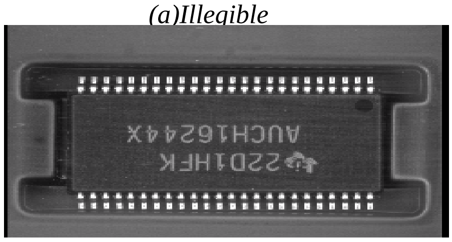

(b) Upside down print

(c) Missing character

Fig. 1: IC chip marking errors

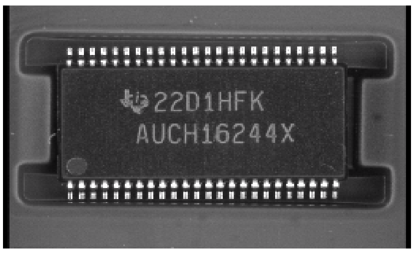

Fig. 2: An error free IC chip

2. Industrial setup

A digital video camera is used to capture the IC marking images of chips coming out of manufacturing line one by one. These images are zoomed about 20 to 30 times in size. Figure 3 shows the dimensions of IC chip. The zooming index depends on the size of the IC chip. Inspection module of the earlier commercially available industrial version checks about 7300 to 7500 IC chips per hour. IC chips undergo on fly inspection as shown in Figure 4 where OCR checks any defects in the markings on the ICs. If there is any defect in the IC chip marking, the marking inspection will check and inform the production inspector the classification of defect; the production inspector then inspects the IC chip manually for taking further decision. A monitor displays the current image of the IC chip.

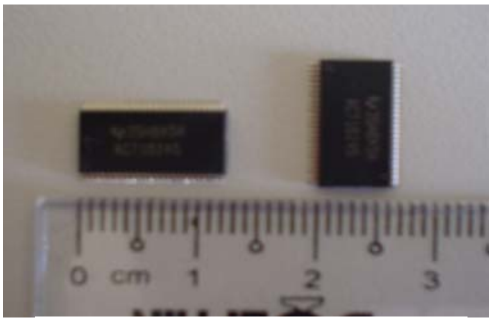

Fig. 3: Dimension of IC chips

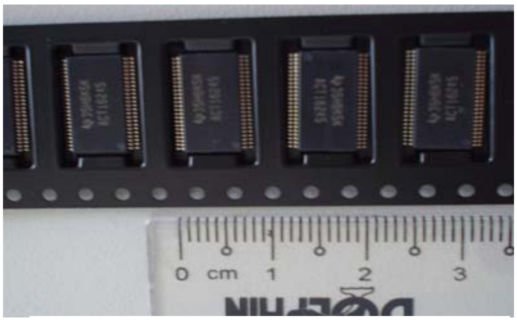

Fig. 4: IC chips in the conveyor

3. Marking Inspection Process

After final packaging, the IC chips are lined up in a conveyor for marking inspection. The marking on the IC chips are captured as a movie clip by a Charged Couple Device (CCD) non-standard camera. Images of the IC chips are extracted from the Moving Picture Expert Group (MPEG) format. The extracted images undergo certain image processing techniques namely preprocessing [1, 6, 7], feature extraction [7,8] and classification using AI technique [9-12] These processing stages are shown in Figure 5.

3.1 Preprocessing

The inspection begins with the extraction of single image from the moving picture. The extracted color image is converted into a 256 gray scale image. Then, the gray scale image is binarized with a threshold value. The binarization converts the image pixels into '0' (black) and '1' (white). The threshold value differentiates the foreground and background of the given image. Region of Interest (ROI) as specified by the production inspector is extracted for feature extraction. If the ROI is not specified, a search for the ROI from the extracted full image has to be made but it is time consuming.

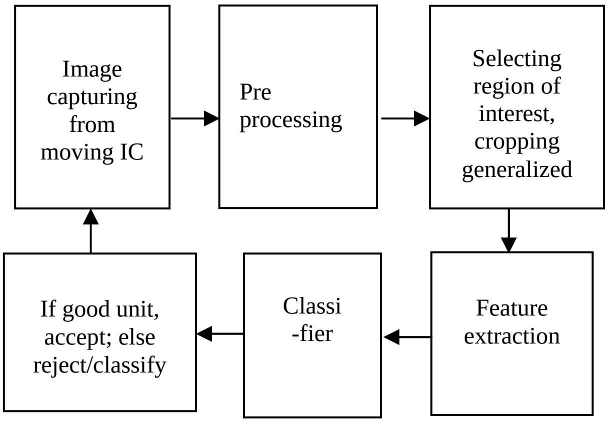

Fig. 5: Image processing sequence

3.2 Moments Feature Extraction

Feature extraction is carried out to the processed and cropped image. Feature extraction processing time for moments is 0.2610 -0.2710 sec. This has been found by experimental results. Moments have been used in recognizing the printed and hand written characters and are also widely used in pattern recognition. There are different types of moments used for recognition of characters; here Central moments of binary image for each column of the image orders are obtained. The image orders can be 2 or 3. In the order 1, moments values are zero. On the other hand, orders more than 3 produces smaller and smaller moments values that cannot be generally used for feature extraction.

Let f(x,y) be an image. Then, the 2D continuous function of

the moment of order (p+q), M_{pq}, is defined as [6].

$$M_{pq} = \int_{-\infty}^{\infty}\int_{-\infty}^{\infty} x^p y^q f(x,y)\,dxdy \tag{1}$$

The central moment , μ_{pq}, of f(x,y) is defined as is [6].

$$\mu_{pq} = \int_{-\infty}^{\infty}\int_{-\infty}^{\infty} (x-\bar{x})^p (y-\bar{y})^q f(x,y)\,dxdy \tag{2}$$

where $\bar{x} = \frac{M_{10}}{M_{00}}$ and $\bar{y} = \frac{M_{01}}{M_{00}}$.

If f(x,y) is a digital image then equation (2) becomes

$$\mu_{pq} = \sum_x \sum_y (x-\bar{x})^p (y-\bar{y})^q f(x,y) \tag{3}$$

where p and q are nonnegative integer values.

The moment values are considered for extracting the feature. This method takes the central moments value of each column of the binary image. D_i, i =1,..,k is the central moment value of each column from 0 to k of the marking. D_i can be computed using Equation (3). In this work k is taken as 25.

4. Marking Classification Using Neural Network

Recently there has been a high level of interest in applying artificial neural network architecture for solving many problems [9-12]. The application of neural network gives easier solution to complex problems such as character recognition. Here, neural network is employed to classify the character by the extracted features (moments). A feed forward neural network is proposed to identify the various types of illegible marking of symbols is shown in Figure 6**.** The moments value for two different orders such order 2 and order 3 are considered for training. The extracted features are taken as input to the network model.

The Training is carried out for 10 times for moments. Table 1 and Table 2 indicate duration of convergence in seconds. The networks with each of the above mentioned data are trained using a backpropagation training algorithm. The learning parameters for moments are chosen as given in Table 1 and Table 2: The cumulative errors versus epoch characteristics of the training for moments (order2 and order 3) are shown in Figure and Figure 8. The time and epoch details for moments is given in Table1 and Table 2.

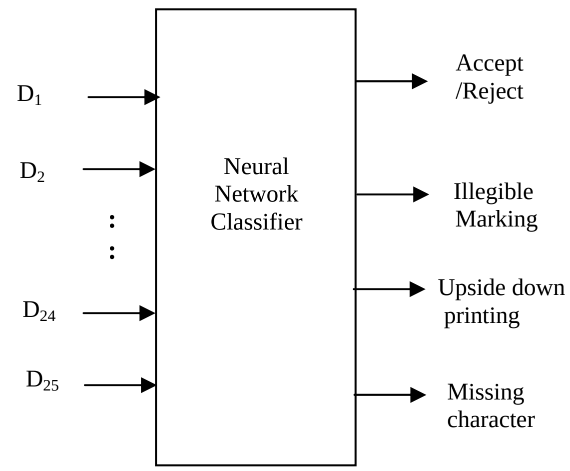

Fig. 6: Neural network model for moments

Conclusıon

AI techniques such as neural network are applied to marking inspection of IC chips. The preprocessing and feature extraction method have been suggested for this inspection. A feed forward neural network has been developed for training and testing the samples of marking. Trainings are carried out for moments order 2 and moments order 3 using backpropagation algorithm. Comparing moments order 2 and order 3, order 3 is faster for training.

Acknowledgement

The authors wish to acknowledge the funding of UMS IRPA grant No: 04-02-10-0024-PR0001 through UTM in carrying out this research.

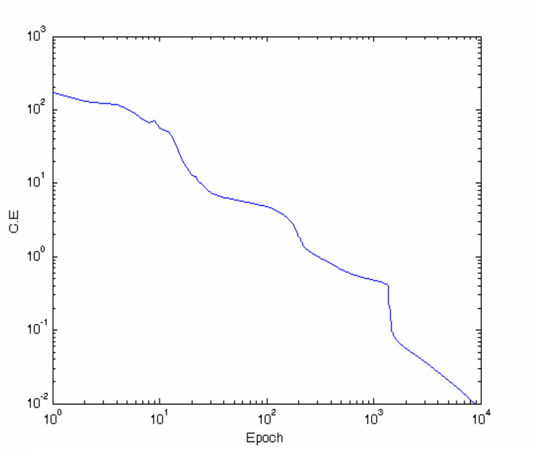

Fig. 7: Cumulative error versus epoch plot for moments second order

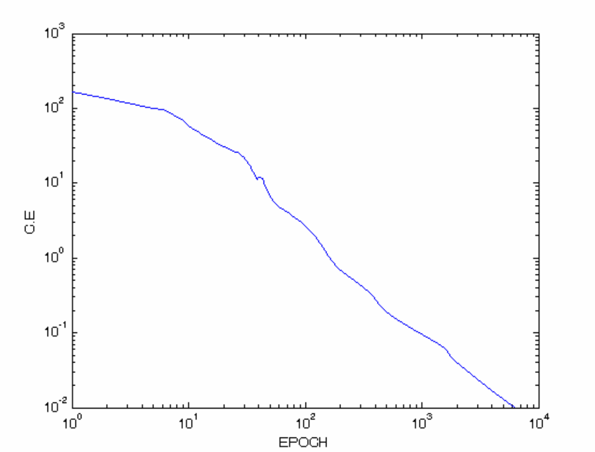

Fig. 8: Cumulative error versus epoch plot for moments third order

References

1) Mantas J (1986), An Overview of Character Recognition Methodologies, Pattern Recognition, V0l19(6), pp.425-430.
2) Shunji Mori, Ching Y Suen and Kazuhiko Yamamoto (1992), Historical Review of OCR Research and Development, Proceedings of the IEEE, vol80 (7).
3) Adnan Amin, Humoud Al-Sadoun and Stephen Fischer (1996), Hand-Printed Arabic Character Recognition System Using An Neural Network, Pattern Recognition, vol.29(4), pp.663-675.
4) Nagarajan, R., Sazali Yaacob, Paulraj Pandian, Karthigayan, M. Shamsudin Hj Amin and Marzuki Khalid (2003), A Neural Network Application for Inspecting the Marking of Symbols on Integrated Circuit Chips. The 7th Triennial AEESEAP Conference Enhancing Engineering Education and Training, Malaysia, 8-9 August 2003.
5) Wumo Pan, Jianming Jin, Guangshun Shi and Wang, Q.R (2001), A System for Automatic Chinese Business Card Recognition. Proceedings of the Sixth International on Document Analysis and recognition, IEEE Computer society, pp. 577 – 581.

Table 1. Data Trained for Second Order of Moments for Neural Network

$q_h = q_0 = 1.0$ Input neuron: 25 Output neurons: 6 Hidden neurons: 20 Activation function: $(1/(1+e^{-x}))$ Momentum factor: 0.87 Learning rate: 0.20 No. of samples: 664 No. of trained samples: 400 Training tolerance: 0.01 Maximum no. of epoch: 19000 Testing tolerance: 0.05			
No.	Epoch	Time in sec	% Misclassification
1	11251	423	0
2	16567	624	0
3	8832	334	0
4	9390	352	0
5	10010	382	0
6	9320	373	0
7	8597	345	0
8	8473	340	0
9	8414	316	0
10	11000	420	0

Table 2 Data Trained for Third order of Moments for Neural Network

$q_h = q_0 = 1.0$ Input neuron: 25 Output neurons: 6 Hidden neurons: 20 Activation function: $(1/(1+e^{-x}))$ Learning rate: 0.2 Momentum factor: 0.87 No. of samples: 664 No. of trained samples: 400 Training tolerance: 0.01 Maximum no. of epoch: 14000 Testing tolerance: 0.05			
No.	Epoch	Time in sec	% Misclassification
1	7144	286	0
2	7874	315	0
3	7560	294	0
4	9649	376	0
5	9683	389	0
6	9086	364	0
7	10038	403	0
8	6787	272	0
9	9114	355	0
10	6325	246	0

6) Rafael C Gonzalez and Richard E Woods (1993),. Digital Image processing. Addison-Wesley Longman, Inc.

7) Mauritius Seeger and Christopher Dance (2001), Binarising Camera Images for OCR, Proceedings of Sixth International Conference on Document Analysis and Recognition, pp.54 – 58.

8) Oivind Due Trier , Anil K.Jain and Torfinn Taxt (1996), Feature Extraction Methods for Character Recognition- a Survey", Pattern Recognition, Vol.29(4), pp.641-662.

9) Sivanandam, S.N, and Paulraj, M (2003), Introduction to Artificial Neural Network. Vikas Publishing House.

10) Laurene Fausett (1994), Fundamentals of Neural Networks. Prentice Hall Publishing..

11) Clifford Lau (1992), Neural Networks-Theoretical Foundation and analysis, IEEE press, New York, 1992.

12) Bernard Widrow and Michael, A Lehr (1990), 30 years of Adaptive Neural Network Preceptron, Madeline and Backpropagation, Proceedings of IEEE, pp.1415-1442.

The Eleventh International Symposium on Artificial Life and Robotics 2006 (AROB 11th'06),
B-con Plaza, Beppu, Oita, Japan, January 23-25, 2006

DIMENSIONS REDUCTION FOR FACE RECOGNITION USING PRINCIPAL COMPONENT ANALYSIS

Muhammad Firdaus Hashim[1], Mohamed Rizon[2], Puteh Saad[1], M. Rozailan Mamat[3], M.Karthigayan[2], Shahrul Yaakob[1] and Haniza Yazid[1]

[1]*Artificial Intelligence and Software Engineering Research Lab*
School of Computer and Communication Engineering, Kolej Kejuruteraan Utara Malaysia (KUKUM),
Blok A, Kompleks Pusat Pengajian KUKUM, Jalan Kangar- Arau, 02600 Jejawi Perlis.
[2] *School of Mechatronic Engineering, Kolej Kejuruteraan Utara Malaysia (KUKUM),*
Blok A, Kompleks Pusat Pengajian KUKUM, Jalan Kangar- Arau, 02600 Jejawi Perlis.
[3]*Terengganu Advanced Technical Institute (TATI)*
Jalan Panchor, Teluk Kalong, 24000 Kemaman, Terengganu, Malaysia
E-mail:rizon@kukum.edu.my

Abstract

In this paper, a technique has been developed to identify the face of an unknown person's by applying eigenfaces and neural network. The original image has been extracted and the face segmentation is implemented to detect irises location of both eyes. The face segment has been considered in this work because the processing time is faster instead of going for the whole image. Eigenfaces has been applied to extract relevant information and reduced some dimension from the face segment (grayscale). The eigenfaces values are considered as an input to the neural network. The backpropagation neural network is applied for face recognition. The database for this investigation consists of eight people with various 68 face images had been used for the learning. PCA including implemented Jacobi's method for eigenvalues and eigenvectors has been performed.

Keywords*:* Face Recognition, Feature Extraction, Neural Network, Principal Component Analysis.

1 Introduction

Machine recognition of human faces is a challenging problem due to the changes in the face identity and variation between images of the same face due to illumination and viewing direction. The issues are how the features are adopted to represent a face under environmental changes and how the classification has been done to a new face image based on the chosen representation.

Automatic face recognition systems have been applied in many applications such as security system, mug shot matching and model-based video coding. T.Phiasai [1] integrates PCA and moment invariant for varied-pose face recognition. They implement PCA for global feature extraction to determine the error. M.A. Turk and Alex P.Pentland [2] developed the eigenfaces further to recognize human faces and obtained some particular advantages over previous work. The advantages of this approach are that, it is easy to implement using neural network architecture.

The extraction of face segmentation from an intensity image of human frontal face is to represent new data set instead using the whole image. The irises detection proposed by Kawaguchi et. al. [3] is applied to face segmentation.

PCA is applied to find important aspects of face segment. Furthermore, the representation the face segment with less data as input for recognition phase. The dimensions of eigenfaces have been reduced to synchronize the neural network inputs.

The recognition process begins with neural network. It has been used to determine the unknown face through learning classification of data calculated by PCA. Figure 1 shows the block diagram of face recognition system.

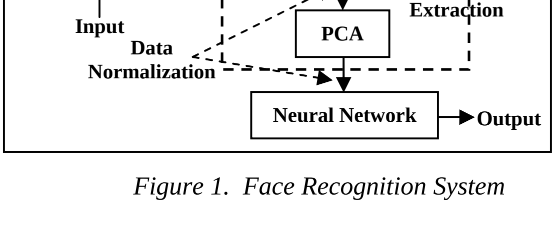

Figure 1. Face Recognition System

The Eleventh International Symposium on Artificial Life and Robotics 2006 (AROB 11th'06),
B-con Plaza, Beppu, Oita, Japan, January 23-25, 2006

2 Preprocessing

In the preprocessing step the algorithm of [3, 4] is used to detect the irises of both eyes from a human face in an intensity images. Here, it has reduce space used intensity variation to select potential area of irises location. Next, each pair of prospect area computed a cost using separability filter and Hough Transform to measure the fit of the pair of circles to the image. The proposed algorithm select a pair of circles with smallest cost as the eye location of both eyes. The implementation of the method take the center of the both irises (radius, r) and expands the coordinate to extract the face segment as shown in Figure 2.

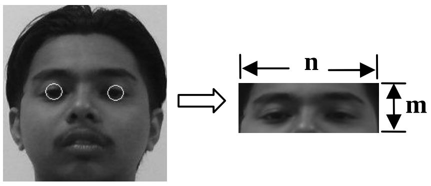

Figure 2. Face Segmentation

3 Principal Component Analysis (PCA)

PCA has been reviewed from the computational aspects in [5, 7 and 8] including the identification of eigenvalues and eigenvectors using Jacobi's method.

Given the image with $m \times n$. m be the dimension and n the variables for each dimension. The original size of $m \times n$ changed to $m \times m$ by firstly subtracted each variables, n with the mean from each of the data dimensions, m where the new data set mean is zero [5].

The next step to create the square matrix is applied the covariance matrix. It measured between two dimensions by

$$\text{cov}(x, y) = \frac{\sum_{i=1}^{n} (x_i - \bar{x})(y_i - \bar{y})}{n-1} \tag{1}$$

Thus, if the dimensions, $m = x_1, x_2, \ldots, x_m$, the covariance matrix with $m \times m$:

$$C = \begin{pmatrix} \text{cov}(x_1, x_1) & \text{cov}(x_1, x_2) \ldots \text{cov}(x_1, x_m) \\ \text{cov}(x_2, x_1) & \text{cov}(x_2, x_2) \ldots \text{cov}(x_2, x_m) \\ \text{cov}(x_3, x_1) & \text{cov}(x_3, x_2) \ldots \text{cov}(x_3, x_m) \\ \vdots & \vdots \quad \vdots \quad \vdots \\ \text{cov}(x_m, x_1) & \text{cov}(x_m, x_2) \ldots \text{cov}(x_m, x_m) \end{pmatrix} \tag{2}$$

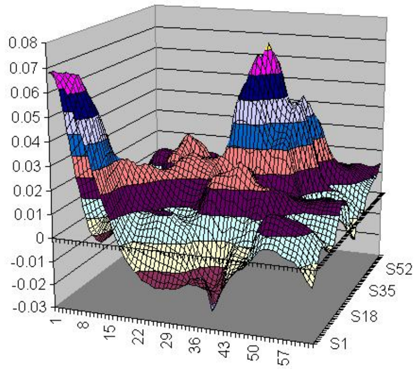

Figure 3. Covariance matrix

Figure 3 shows the covariance matrix where the $\text{cov}(a,b) = \text{cov}(b,a)$, the matrix is symmetrical about the main diagonal and square, $m \times m$. The covariance matrix is then used to calculate the eigenvalues and eigenvectors [6, 7, 8 and 9].

3.1 Eigenvectors Selection

The eigenvectors determined useful features for the image ordered by highest eigenvalues. The asset of the eigenvectors is the eigenvalues where each of them associated with it. The extracted eigenvectors represent the combinations of the set of facial image, which capture most of the variability in the image and can be viewed as creating a lower dimensional subspace of regular image space [10].

From figure 3, the eigenvalues decreases quickly as their number increases. The eigenvectors with higher eigenvalues provide more information. The all-off diagonals are zero except main diagonal that stored eigenvalues. Furthermore, the eigenvectors with lower eigenvalues or specific eigenvectors can be reduced because it only creates noise in the image [10, 11].

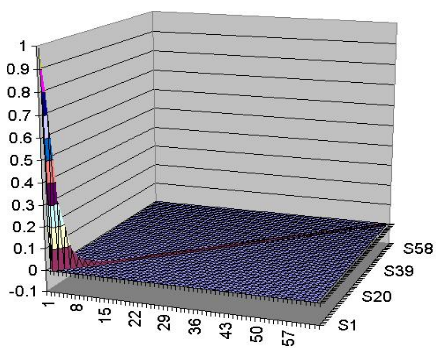

Figure 4: Eigenvalues matrix

The last eigenvectors with lower eigenvalues by the amount of variance found between images can be reduced. Here, three variations has been proposed to choose eigenvectors [10]. Firstly, the last 40% of the eigenvectors have been removed [11]. Then, the second variation (equation 3) uses the minimum number of eigenvectors to guarantee that energy e is greater than threshold (typically 0.9). It is ratio of the sum of all eigenvalues up to and including i over the sum of all eigenvalues:

$$e_i = \frac{\sum_{j=1}^{i} \lambda_j}{\sum_{j=1}^{k} \lambda_j} \tag{3}$$

The last variation (equation 4) depends upon the stretching dimension. The stretch, s_i for the i^{th} eigenvectors is the ratio of that eigenvalues over the largest eigenvalue (λ_1):

$$s_i = \frac{\lambda_i}{\lambda_1} \tag{4}$$

All eigenvectors with s_i greater than a threshold (0.01) are retained.

4. Face Recognition

The backpropagation neural network is used to achieve our objectives to identify unknown person's face [12]. The strength of the classifier depends on the data that it receives during training. A large number of training patterns would make the network stronger. However, need be careful not to include all patterns in the training set [13].

PCA value has been given as an input to the neural network. There are two groups (database) of images that are tested by neural network. They are trained data and untrained data. Here, three neurons has been used at output layer for eight persons, thus it has been set the target for this approach made the number of weight between hidden and output (w_{kj}) less.

5. Experimental Result

PCA and neural network have been used for feature extraction and recognition respectively. These features have been tested with 68 different impressions from eight persons. Every image is an intensity image with plain background, the eyes of both eyes appear in the image and the head region about y axis is approximately within the interval $(30,-30)$. The eigenvalues and eigenvectors play a major role in PCA. The code for eigenvalues and eigenvectors has been developed using VC++. MATLAB has been used for verification purpose. The PCA also tested with two dimensions data in [5].

The experiment defined that the energy, e selected about 93% of eigenvalues and highest eigenvalues have been removed. However the stretch, s only choose about 13% started from highest eigenvalues and the lowest have been removed. It is possible that the first eigenvectors encode information that is not relevant to identify image, such as lighting [11].

The image size is about 360×480 and the image size has been reduced. Irises detection has been used for face segmentation. Each face segment has 120 pixels of column and the rows between 60 to 70 pixels of rows. However, only 20 eigenvectors are selected to reduce input series and synchronized the whole pattern. Thus, each pattern has 20×120 of pixels.

Table 1: Recognition Result

Face	Actual Output	Network Output
1	0 0 0	0.000011 0.000011 0.000011
2	0 0 1	0.000194 0.000194 0.998024
3	0 1 0	0.000194 0.998024 0.000194
4	0 1 1	0.000000 0.999970 0.999970
5	1 0 0	0.998024 0.000194 0.000194
6	1 0 1	0.999850 0.000000 0.999850
7	1 1 0	0.999700 0.999700 0.000000
8	1 1 1	0.999800 0.999800 0.999800

In the recognition step, if mean squared error of network output less than error (0.0001) than the nodes trained are complete. 10 neurons have been used in hidden layer in the network. Table 1 shows the recognition result through the network.

6. Conclusion

In this paper, the PCA feature extraction method and neural network for recognition has been proposed. The Jacobi's method has been performed to calculate the eigenvalues and eigenvectors. This method is easy and reliable however the computation speeds is slow that restricts its usefulness to special situations when the speed is the priority. Feature extraction and feature selection are significant in image analysis applications. PCA has proven itself to have the capability to select the most important features amongst the set of features extracted.

Acknowledgments

The authors would like to acknowledge KUKUM for supporting this research work.

References

[1] T.Phiasai, S.Arunrungrusmi and K.Chamnongthai, Face Recognition System with PCA and Moment Invariant Method, *In Proc. IEEE Int. Symposium Circuits Systems*, vol. II, 2001, pp. 65 – 68.

[2] M.A. Turk, A.L.Pentland, "Face recognition using Eigenfaces", *Proceeding of IEEE Computer Society Conference on Computer Vision and Pattern Recognition*, 1991, pp. 586-591.

[3] T.Kawaguchi, D.Hidaka, M.Rizon,"Robust Extraction of Eyes from Face", *Proceeding of IEEE on Pattern Recognition 5th International Conference*, 2000, pp. 1109-1114.

[4] M. Firdaus et al, "A face recognition system using template matching and neural network classifier", *Proceeding of the 1st International workshop on artificial life and robotics"*, pp. 1-6, 2005.

[5] Lindsay I Smith, *A Tutorial on Principal Components*, 2002.

[6] J.H.Matheew, *Eigen Values and Eigen Vectors*, pp. 612-621, 2003.

[7] M. Firdaus et al, "An approach of feature extraction for face recognition", *sub'd to conference on intelligent systems and robotics (iCISAR2005)*, December 2005.

[8] M. Firdaus et al, "Face recognition using neural network", *sub'd to international conference on intelligent systems (ICIS)*, December 2005.

[9] M.T Health, Scientific Computing: An Introductory Survey, McGraw-Hill, 2002, pp. 191-200.

[10] W. S. Yambor, B. A. Draper, and J. R. Beveridge, "Analyzing PCA-based face recognition algorithms: eigenvectors selection and distance measure", *In Empirical Evaluation Techniques in Computer Vision*, 2000.

[11] H. Moon and J. Phillips, "Computational and performance aspects of PCA-based face-recognition algorithm", *Perceptions*, vol 30, pp. 303-321, 2001.

[12] Marzuki Khalid, *Multilayer Neural Network and Backpropagation Algorithm.* Citing internet sources URL www.cairo.utm.my

[13] S.C. Debipersad, A.D. Broadhurst, Face Recognition Using Neural Network, *Proceeding of IEEE on Communication and Signal Processing (COMSIG)*, 1997, pp. 33-36.

Automatic Motion Detection for Surveillance

Mokhtar Norrima , Sugisaka Masanori
Dept. of Electrical and Electronic Engineering,
Oita University, 700 Dannoharu,
Oita 870-1192, JAPAN
TEL +81-97-554-7841 FAX +81-97-554-7818
E-MAIL: norrima@miosh.net, msugi@cc.oita-u.ac.jp

Abstract

Automatic motion detection features is able to enhance surveillance efficiency and quality. The aim of this research is to automatically recognize and detect motion around the robot's environment in order to equip the mobile robot with surveillance task or ability. The required information exactly based on the input obtained from the CCD (Charge Coupled Device) camera mounted on the mobile robot. As the first step of achieving the goal, the dynamic nature of the robot and world setup for this research is stationary mobile robot and moving objects. Experiments on different setup environment such as different motions, size of moving objects and lighting conditions have been conducted. The 'adjacent pixels comparison' is the proposed method to detect motion in this experiment. The results have verified the motion detection experiments operating as expected.

1. Intoroduction

Recent years, many researches have been carried out in order to increase robots tasks and capabilities. Application on various fields such manufacturing, surveillance, services, medical and even entertainment have contributed to high demand on robotics researches. Since surveillance has become important to ensure security and safety, the research on automatic motion detection has been conducted in order to equip our mobile robot with surveillance capability.

The input to a dynamic scene analysis system used in this experiment is a sequence of image frames taken from a changing environment. The CCD camera mounted on the mobile robot is used to acquire the image. Basically, the changes in a scene are considered when moving objects presents or lighting condition changes. There are four possibilities for the dynamic nature of the mobile robot and world setup:

1. Stationary mobile robot, stationary objects.
2. Stationary mobile robot, moving objects.
3. Moving mobile robot, stationary objects.
4. Moving mobile robot, moving objects.

However, in this experiment, only stationary mobile robot, stationary objects and stationary mobile robot, moving objects setup have been conducted. The dynamic nature of 3 and 4 will be the next step in this research.

2. Mobile robot system description

The mobile robot used by in this experiment was manufactured by DENKEN company in 2000. The robot is 130cm high, 45 cm width and 50 cm depth. The whole figure is shown in Fig.1. It is consists of 2 drive 2 caster (2DC2W) systems. Driving wheel is equipped on right and left while the auxiliary caster wheel support for forward and backward movement. The driving wheel on either side is using DC motor and being equipped with the rotary encoder (80 Pulses Per Resolution). By counting the number of pulses, right and left independence driving wheel can be controlled. The difference of the rotation speed of right and left driving wheel performs steering function. The CCD cameras (EVI-G20 : Sony) is mounted on top of the mobile robot at 55 degrees of perpendicular head directions. However, in this research we only use the left CCD camera. The image size used in the experiment is 120 X 120 pixels. The image size is made small to speed up image processing time. Then, the image obtained from the CCD camera is kept by the image-processing board (FDM-PCI3: FOTORON).

Figure 1: Mobile robot

3. Methodology

The method used is to detect changes between two frames by directly compare the corresponding pixels of two frames to determine whether they are the same. This may be the simplest or very low level of image processing but from the conducted experiments, the present of moving objects and no moving objects manage to be recognized within 1 second response.

In the simplest form, difference picture $DP_{jk}(x,y)$ between frames $F(x,y,j)$ and $F(x,y,k)$ is obtained by :

$$DP_{jk}(x,y) = \begin{cases} 1 \text{ if } |F(x,y,j) - F(x,y,k)| > \tau \\ 0 \text{ otherwise} \end{cases} \quad (1)$$

where τ is a threshold. In a difference picture or frame, pixels which have value 1 may be considered to be the result of object motion or illumination changes. Picture or frame with value 0 indicates no moving objects in the current scene. By this assumption the frames are properly registered.

4. Image Processing

The image taken from CCD camera is an image with a total of 24 bits of 8 bits each of RGB. Then, the image is converted to monochrome image in order to ease image processing in the next step. Next, the edge filter and equation 1 is used to extract the line in order to use 'adjacent pixel comparison' to recognize moving objects and no moving objects situation in front of the mobile robot.

The 'adjacent pixels comparison' is the proposed method in this research. By this method, adjacent pixels value in the frame is checked whether their values are within the same range. Then, if the pixel values are within the same range, it will mask the area in the frame to check whether all adjacent pixels have the value within the range. If the number of adjacent pixel is less than the threshold value it will be considered as noise. However, if the number of adjacent pixel is greater than the threshold value it will be considered as moving objects present in front of the mobile robot. Illustration is shown on figure 1 and figure 2 for easy understanding.

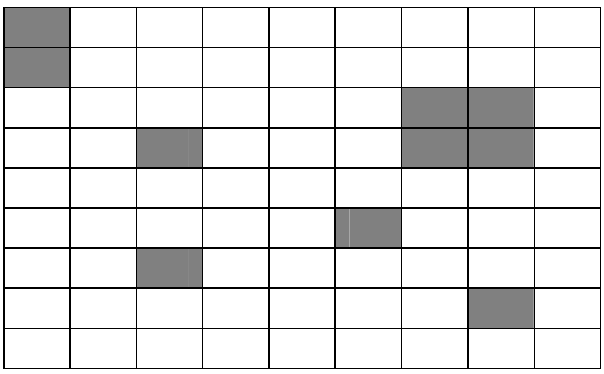

Figure 2: No moving objects scene frame

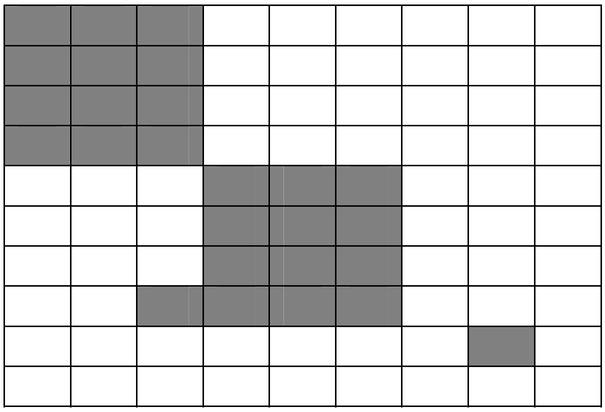

Figure 3: Moving objects scene frame

5. Experimental Method and Results.

The experiment was conducted on various situations such as following:

- No moving object
- Different size of moving objects
- Light is switch on (during day and night time)
- Light is switch off (during day time)

The results of experiment are shown in figure 4, 5, 6, 7, 8, 9, 10, 11, 12, 13, 14, and 15.

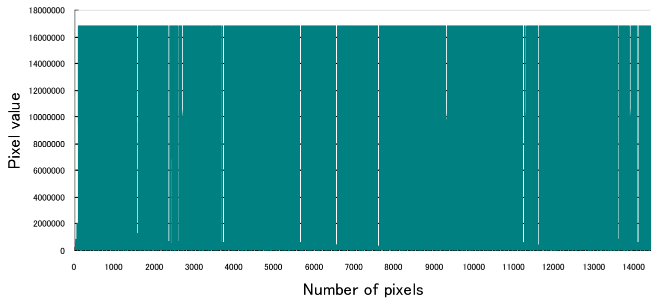

Figure 4: No moving object scene

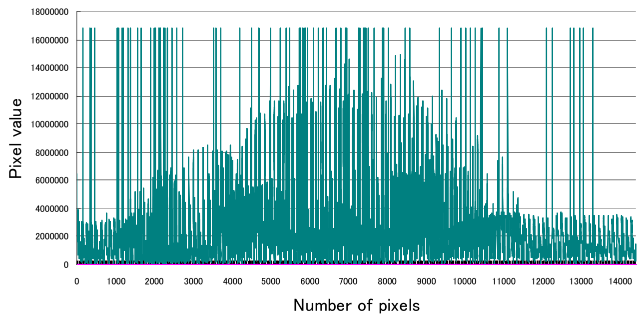

Figure 5: Moving object scene, in the present of human body movement

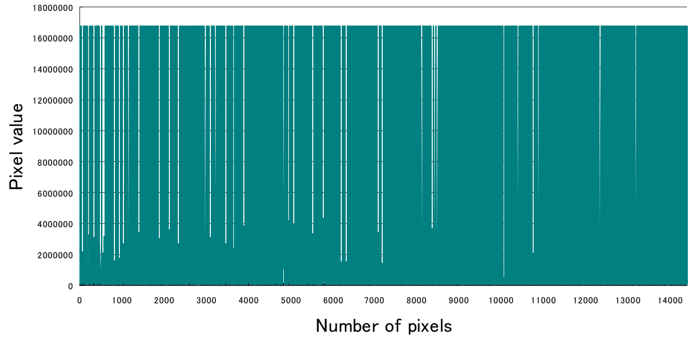

Figure 6: Moving object scene, with arm movement

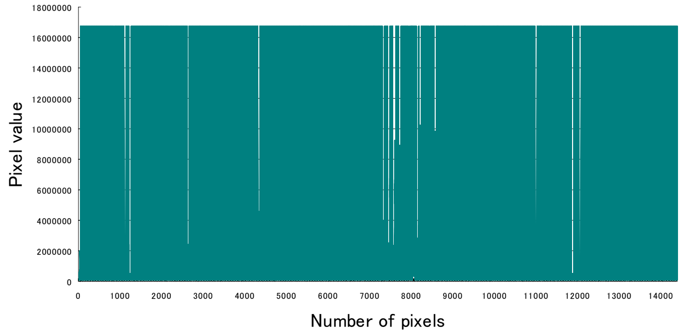

Figure 7: Moving object scene, with object as small as handphone size.

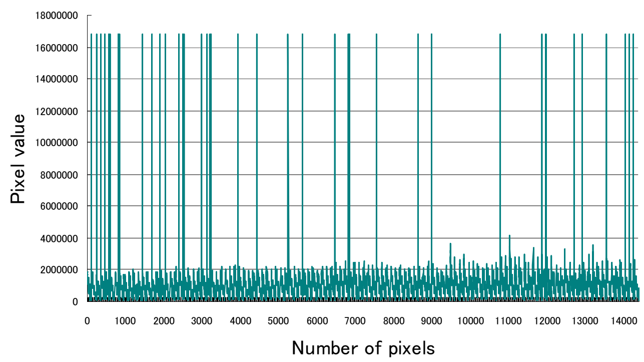

Figure 8: No moving object scene, with light off.

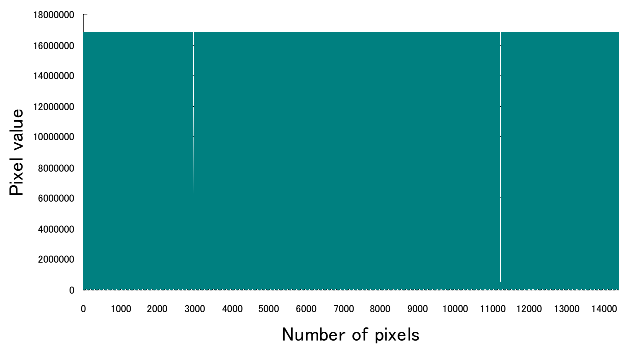

Figure 9: No moving object scene, with light is on.

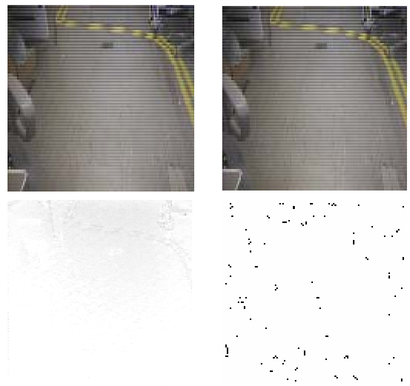

Figure 10: No moving object images.

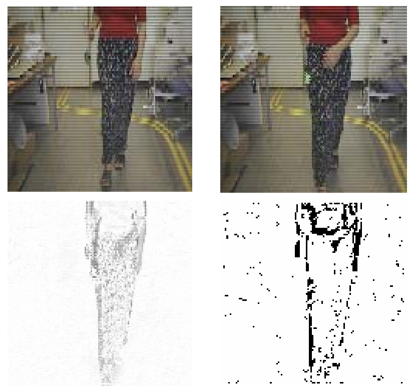

Figure 11: Moving human body images.

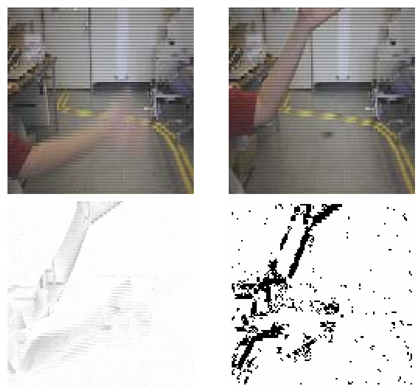

Figure 12: Moving arm images.

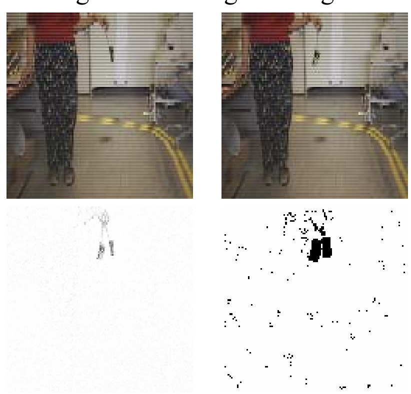

Figure 13: Moving handphone images

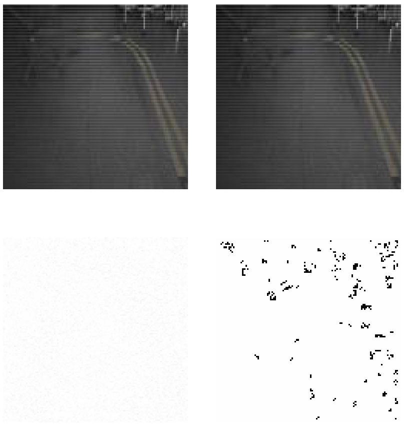

Figure 14: No moving object with light off images

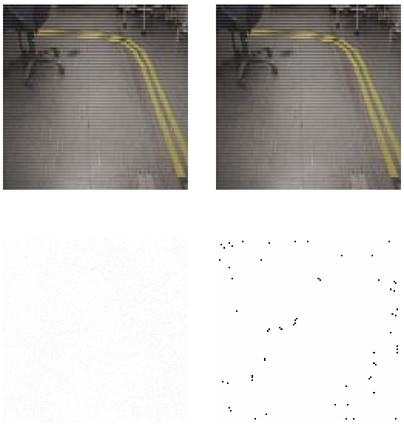

Figure 15: No moving object with light on images

6. Discussions

The technique was tested with various conditions as stated before. From the graph shown in figure 4, it is understood that when there is no moving object present, the pixel value rarely changing. Graph shown in figure 5 indicates large moving objects (human body) as the pixel value is changing rapidly. Graph shown in figure 6, indicates small changes as only medium size of objects, in this case human arm movement. While graph shown in figure 7, indicates only small changes as very small objects which is mobile phone movement.

In addition, lighting condition is also considered which have no effect on the adjacent pixel comparison technique because no significant change is detected. However the different between pixel values is bigger because in the present of light, the pixel value is higher while when the light is off the pixel value is low. This can be clearly seen by comparing graphs shown in figures 7 and 8.

7. Conclusions

Significant progress has been made toward the goal of automatically detecting moving objects. The demonstrated results show that the ability to determine that a scene change can be detected by different size of moving objects and independent of lighting condition. Therefore, the goal to increase our mobile robot functionality manages to become reality.

In addition, this technique can be used not only by mobile robot but static CCD cameras or CCTVs in any security systems. In this experiment, the frame is captured twice to detect the changes. However, in a systems where multiple CCD cameras or CCTVs, it can be controlled by using master server in order to check on every check points of CCD cameras and CCTVs. By using this technique, surveillance can be done in more efficient way, by only focusing objects movements rather than monitoring all CCD cameras or CCTVs. From my point on view, this can save a lot of time, promote smart staff management and at the same efficient surveillance can be done. Nonetheless, the results to date already offer potential benefits in today's remote monitoring and surveillance. Besides that, the technique used, can reduce false alarm rate.

References

[1]Syohei Kuriyama , Masanori Sugisaka: Development of the mobile robot run system using dead reckoning and vision information, Oita University Graduate School Master Paper (2003)

[2] John S.Boreczky and Lynn D.Wilcox: A Hidden Markov Model Framework for Video Segmentation Using Audio and Image Features , Proceedings of the International Conference on Acoustics, Speech, and Signal Processing , pp.3741-3744 (1998).

[3] S. Uchihashi and J. Foote: Summarizing video using ashot importance measure and frame-packing algorithm, Proceedings of ICASSP'99, pp. 3041-3044.

[4]Sofia Tsekeridou,Stellios Krinidis, Ioannis Pites: Scene change detection based on Audio-visual analysis and interaction(1998).

[5] A. Hanjalic: Shot-boundary detection: Unraveled and resolved?, IEEE Transactions on Circuits and Systems fo Video Technology, vol. 12, no. 2, pp. 90–105 (February 2002)

[6]Chris Stauffer and W.E.L. Grimson.: Adaptive background mixture models for realtime tracking, *CVPR99*, Fort Colins, CO, (June 1999).

[7] http://www.reindeergraphics.com/

[8] http://homepage3.nifty.com/ishidate/vcpp.htm

[9]http://www.cs.rochester.edu/u/nelson/research/motion/motion.html

[10] http://www.ee.washington.edu/research/isl/mingye/boeing/node15.html

[11]http://www.opengl.org/resources/tutorials/advanced/advanced97/notes/node123.html

Surface Based Spatial Awareness for Mobile Robots

Kamen Kanev
Department of Computer Software, The University of Aizu, Aizu-Wakamatsu 965-8580, Japan
kanev@u-aizu.ac.jp

Shigeo Kimura
Department of Mechanical Systems Engineering, Kanazawa University, Kanazawa 920-1192, Japan
skimura@t.kanazawa-u.ac.jp

Abstract

Human awareness of the spatial environment and the way humans fit into it is a well-known phenomenon, which is still beyond the reach of current mobile robots and related technologies. Global position and orientation data, however helpful it might be, does not bring to a direct solution of the spatial awareness problem [1]. Indeed humans do not need and in most cases do not rely on global positioning data to place themselves and to become aware of the surrounding environment. Instead clues derived from the sizes, shapes, colors, textures and other properties of surrounding objects and their visible surfaces seem to play quite a significant role. Many advances in robotic vision have been achieved following similar approaches but good practical implementations are still to be seen.

In this work we discuss a method for enhancing physical objects and their surfaces with digital data layers that are barely visible to the naked human eye but could be reliably read and decoded by mobile robot vision optics. In such a way an easily accessible spatial data is directly encoded and blended into the mobile robot environment. Based on it, links to object properties and other parameters are established and could be used for developing spatial awareness models for mobile robots.

Our method can be applied to automated storage facilities and assembly line environments where robots and mobile carts are commonly used for dispatch of materials. The method is also suitable for educational purposes, where robot models can be enhanced with precise positioning capabilities by a simple wireless camera and a digitally encoded tabletop surface.

Concluding the work, a few possible applications in connection with robotics, human-machine interface and pseudo-artificial intelligence to assist the human life will be briefly discussed in order to demonstrate the ample capabilities of the proposed method. One such example is a positioning method for mobile security robots and automated floor cleaning robots in large office buildings or hospitals. Another example is a human assisting method based on cell phone cameras that helps people locate themselves in large shopping complexes and underground. Reasonable position awareness can be achieved using only local data, stored on a portable device, with additional context related information downloadable from the Internet. Such a system may prove to be vital in saving human lives by showing emergency exits and providing other essential guidance in the case of large-scale earthquake, fires, violent terrorist attacks and other disasters.

1. Introduction

Nowadays GPS technologies are the method of choice for securing reliable position and orientation data for moving vehicles on a continuous basis. However, when GPS satellite signals are not readily accessible or if a higher precision and context awareness is required other methods must be considered [1]. In this work we will focus on local methods that take advantage of the close surroundings in order to derive position and orientation data. Such methods are well applicable to moving platforms and robotized equipment in buildings and underground where GPS is not generally available. A typical example is the system by Makino et al [2], which uses a local position tracking system based on 1D barcodes painted on the corridor walls. An intelligent wheelchair with a video camera and a laptop computer can read these barcodes and extract wheelchair position data.

When equipment is scaled down for experiments, modeling or education, local methods are usually preferred for their precision and independence. A good practical solution however may need specialized even custom designed tracking equipment. For example Rosenfeld et al [3] have designed a special table with position sensitive detectors to investigate bi-directional user interfaces. Two-wheeled moving platforms are placed on the tabletop and their positions are tracked based on the modulated LED signals that are emitted.

A quick comparison between the wheelchair [2] and the tabletop [3] systems outlined above shows that the wheelchair system is self contained and uses only static information from the surrounding environment. In contrast the tabletop system is based on active exchange of information between the moving platforms and the tabletop.

The methods that we will discuss in more detail here will be close to the first example, it terms that we will use only static information embedded in the surrounding environment. However our approach will be equally good for both medium scale motion devices such as wheelchairs or robotized platforms as well as for downsized applications on a tabletop.

2. Surface encoding

The idea of painting barcodes on walls and using them for guidance [2] has evolved rather significantly. Large QR-codes [4] that can be read and decoded by common mobile phones are already posted in many places in Japan (Fig.1).

Fig.1. Large QR-codes posted on buildings in Ginza and in Tokyo subway.

While one can get an instant access to a link or some other information source through such a QR-code for guidance, this is clearly not sufficient for precise position and orientation. In fact providing position and orientation feedback based on 1D and 2D barcodes has some important limitations that are discussed in more detail in [5]. More specialized methods and in particular the cluster pattern method invented and patented by the authors seem to be more appropriate for surface encoding.

Fig.2. A model car with a small wireless camera facing downwards.

First let us consider a simple experimental setup consisting of a tabletop and a mobile car model placed on. Our objective will be to track the position and the orientation of the car as it moves. A sample construction of a model car with compact wireless camera placed in the front right seat and facing down is shown in Fig.2. When the model car moves, partial images of the tabletop under the camera can be obtained and sent over a wireless link to a PC for processing.

An experimental setup of a map with an embedded cluster pattern and an enlarged view of the model car placed on the map are shown in Fig.3. Car position and orientation in respect to the map is calculated by decoding the digital cluster pattern layer embedded in the map.

Fig.3. A map with an embedded cluster pattern and a detail of a model car with a wireless camera on the map.

With a continuous video stream we have no control over what will be seen by the camera at the moment a specific frame is taken. Therefore if the tabletop were covered with barcodes, there would be no guarantee that a complete barcode could be seen unless a rather large and thus inefficient camera view was used. When clusters of graphical objects are used however, large components such as complete barcodes become unnecessary and camera views can be kept as narrow as possible. In Fig.4 a sample cluster pattern is shown and the camera view, with a fully decodable set of graphical objects is denoted by a solid line rectangle.

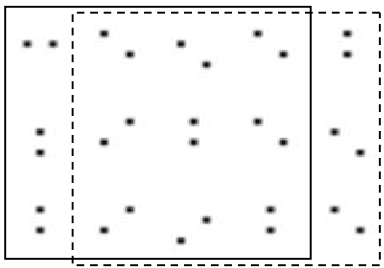

Fig.4. A sample cluster pattern with camera views enclosed in sold and dashed rectangles.

Now suppose the camera view moves slightly to the right as denoted by the dashed rectangle. The column of clusters on the left of the dashed rectangle go out of the view while the column of clusters on the right of the solid rectangle go into the view. Accordingly the clusters that fall within the overlapping area of the solid and the dashed rectangles stay in view. For efficient decoding such type of cluster carpet has to provide for:

$$Decode_x(view1) = x_1$$
$$Decode_x(view2) = x_1 + \Delta x$$

where Δx denotes the minimum, digitally encoded displacement in x direction.

Purely for illustration purposes let us assume that the binary values 0,0,0,0,1 are assigned to the columns in Fig.4 from left to right. Then we will have:

$$Decode_x(view1) = 0000_2 = 0$$
$$Decode_x(view2) = 0001_2 = 1$$

and the displacement Δx is 1.

Our cluster pattern encoding scheme is based on the above illustrated idea and handles two dimensional encoding simultaneously in X and Y directions [6,7]. In contrast to barcodes, our cluster-based approach requires no markers and no physical blocks but instead virtual blocks can be formed and used whenever necessary.

The cluster pattern approach ensures uniform area coverage with no artifacts and visually disturbing components. This feature is quite important when the digitally encoded layer has to be integrated with the current environment. In our tabletop example, the cluster pattern carpet can be combined with a map as in Fig.3 or even differently printed covers can be prepared for different experiments.

It is important to minimize the area ink coverage when printing the digitally encoded carpet. Our cluster pattern method works well with less than 1% area ink coverage and can be printed on transparent media. In such a case one transparent cluster pattern encoded sheet can be prepared and used with table covers that have different printed content.

3. Feedback and links

Tracking information consisting of position and orientation feedback can be enhanced with additional references. For example in our tabletop setup the cluster pattern enabled map carpet can be linked to voice, image and even video content. Voice guidance may consist of standard announcements similar to those given by car navigation systems and when the car model approaches a street crossing, pictures of the real crossing taken from the drivers seat can be shown. Further enhancements can be achieved by playing video clips or using augmented reality techniques.

A simple, self-contained working model consisting of a notebook computer, USB image capture device and the cluster pattern enhanced map from Fig.3 has been implemented as a proof of concept. Our model is based on driver software that installs in the task tray and monitors the input image stream. First, incoming image frames are analyzed and individual graphical objects are identified, then clusters of graphical objects are formed and virtual blocks of clusters are constructed, and finally position and orientation data is derived (Fig.5).

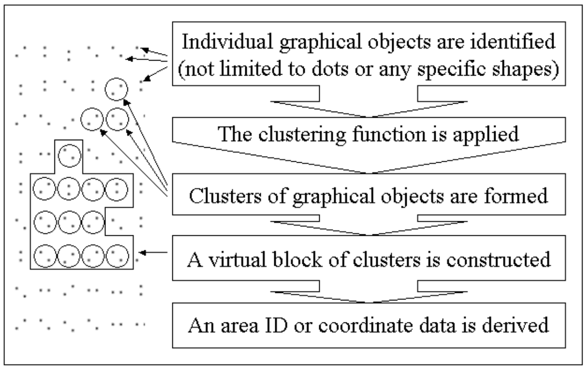

Fig.5. The cluster pattern processing sequence.

Obtained position and orientation data is directed to the standard output (Fig.6) and thus can be easily piped to other applications.

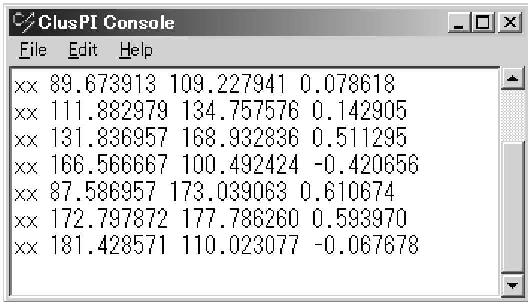

Fig.6. Cluster pattern processing results as they appear on the standard output.

For our test implementation we have prepared some code that takes a line of three real values: the x-coordinate, the y-coordinate and the rotation angle, and searches in a reference table for a match. The reference table itself consists of area definitions and angle ranges with associated links. An example of a square area, defined by its center, width and height and for angle ranges pointing in up, left, down and right directions with their respective links is shown in Fig.7. Line descriptions are included in the area definition as

C-style comments. Areas of other shapes and with different parameterization can also be represented in a similar way.

```
define_rectangle {
  /*x y dx dy dummy*/
  241.8410 351.7782 13.3891 10.0592 0
  {
    /*begin_angle end_angle function parameter(s)*/
    {45 135 to_browser 1-Up.JPG}
    {135 225 to_browser 1-Right.JPG}
    {225 315 to_browser 1-Down.JPG}
    {315 45 to_browser 1-Left.JPG}
  }
}
```

Fig.7. A rectangular surface area definition example.

4. Application areas

The tabletop example as described in the previous chapter is fully functional and can be used for practical applications. Systems as the one described in [3] could be almost directly implemented using our tabletop approach. Our method however offers a distinct advantage when a larger tabletop is needed. In our case this will amount only to printing a new, larger tabletop cover or may be just printing and adding some patches. In contrast the physical size of the system in [3] is predetermined by the hardware specifications. More concrete tabletop applications in education will be explored in the future.

Implementations for larger scale systems such as wheelchairs are also almost direct. Instead of having barcodes painted on walls as in [2] we can have the cluster pattern painted instead. Given the special properties of the cluster pattern that make it nearly invisible for the human eye and allow for smooth blending with other printed content entire walls can be covered with it. May be the most convenient way would be to have the cluster pattern code embedded in the wallpaper. Since there will be no individual physical units such as barcodes the system can achieve higher granularity, better positioning and will be generally more reliable. Automated floor cleaning and security robots can also be included in this line.

There are special circumstances where humans may greatly benefit from direct position and orientation feedback. In normal conditions humans can relatively easy derive the necessary position related clues from the surrounding environment. Usually there are well seen inscriptions on the walls like room names and numbers, signs indicating the entrances and exits, floor maps etc. In case of emergency such as fire or an earthquake however, smoke or fallen objects may obscure those signs. In such cases the ability to get directions based only on local information becomes vital and may be even life saving. Our suggestion is to use the cluster pattern encoding already applied to the walls or embedded in the wallpaper for position and orientation recognition. Java enabled mobile phones with built-in cameras are very good candidates for such an application.

5. Conclusion

We have experimented with image capture devices that connect to an USB port of a PC directly or through RF channels. In both cases all real-time image processing, cluster pattern recognition and coordinate decoding have been done on a Windows PC. Our code has been developed entirely in C and is in process of modification for other platforms.

We are also considering porting our code to an integral device consisting of a CMOS image sensor and a DSP for local image processing and decoding. Such a device would directly generate a data stream similar to the one shown in Fig.6 and could be connected through a simple serial protocol to cell phones, PDAs, audio and video players and other equipment.

References

1. Gellersen H., Schmidt A., Beigl M., Multi-Sensor Context-Awareness in Mobile Devices and Smart Artifacts, Mobile Networks and Applications 7, 341-351, Kluwer Academic Publishers, 2002.
2. 尾形利文，牧野秀夫，石井郁夫，中静真：非可視型バーコードを用いた視覚障害者用位置案内装置の研究．電子情報通信学会論文誌 D-II, J80-D-II，11，pp.3101-3107 (1997)
3. Rosenfeld D., Zawadzki M., Sudol J., Perlin K., Physical Objects as Bidirectional User Interface Elements, *IEEE Computer Graphics and Applications*, January/February 2004, pp. 2-7.
4. Hara M. et al., *Optically Readable Two-dimensional Code and Method and Apparatus Using the Same*, US patent 5,726,435, Patent and Trademark Office, Washington, D.C., 1998.
5. K. Kanev, and S. Kimura, “Print Based Interfaces with Direct Point and Click Functionality,” In *Proceedings of the Eighth Int. Conf. on Human and Computers HC’05*, Aizu-Wakamatsu, Aug. 31-Sept. 2, 2005, pp. 128-135.
6. カネフカメン，木村繁男：デジタル情報坦体，特許登録第３６３５３７４号，日本国特許庁（ＪＰ）
7. Kanev K., Kimura S., Digital Information Carrier, WO 2005/055129, International Patent Application Published under PCT, WIPO.

Interactive musical editing system to support human errors and offer personal preferences for an automatic piano
- A system of inferring phrase expression -

Yuta Hikisaka

Graduate School of Computer Science and System Engineering
Kyushu Institute of Technology
680-4, Iizuka City, Fukuoka, Japan, 820-8502
hiki@mmcs.mse.kyutech.ac.jp

Eiji Hayashi

Department of Mechanical Information Science and Technology
Kyushu Institute of Technology
680-4, Iizuka City, Fukuoka, Japan, 820-8502
haya@mse.kyutech.ac.jp

Abstract

We have developed an automatic piano that can accurately control the motion of both the keys and the pedal based on performance data that a user has elaborated for a particular piece of music. However, this system cannot sight-read a new piece of music, as in the simulation of a human being's expressive performance. Therefore, we have developed a program that can memorize and use knowledge databases and user preferences concerning the interpretation of a piece of music.

We analyzed performance data of performances of highly skilled pianists in order to observe performance tendencies, and found that phrases of similar patterns existing in the same composition were performed with similar expression by the same pianist. Moreover, it was found that the pattern of notes in the score sometimes influence how the expression comes out.

Therefore, we developed a system of inferring phrase expression to infer the expression from the patterns of the note. We evaluated the system by comparing performance information inferred from the databases with the pianist's actual performance.

Key words: *automatic piano, knowledge database, music interface, user's preference, computer music, inference system*

1. Introduction

We have developed a performance system for an automatic piano. In this system, 90 actuators are installed in the 88 keys and 2 pedals of a grand piano. Those actuators operate key strokes and pedaling to be executed on the piano. (See Figure 1)

Reproducing music with the piano is similar in some ways to reproducing music on the computer. Essentially, variations in tempo, dynamics, and so on are needed to arrange the respective tones in the desired way. However, in the case of piano music, there are 1000 or more notes in a score of even a short piece of music, and the editor must spent enormous amounts of time working with the arrangement in order to simulate the expressions of an actual performance.

Even for the skilled computer user, it becomes prohibitively burdensome to reproduce a score and add expression simultaneously using the automatic piano and a computer music system. That is because the musical data cannot be rewritten all at once. By contrast, highly skilled pianists can sight-read an unfamiliar piece of music, even if the performance is not completely in accord with a specific musical interpretation. The computer system cannot sight-read a new piece of music; it cannot simulate a human pianist's expressive performance.

Therefore, in this research, we have developed an interactive musical editing system to edit music more efficiently[1]~[4].

This time we devised a method for inferring a performance from information on the score and a particular user's editing characteristic for similar phrases. We evaluated the system by comparing performance information inferred from individualized databases with the pianist's actual performance.

In this paper, we describe the method of inference based on analytical results and its result in an actual simulated performance.

Figure1. View of the automatic piano

2. Musical Editing Support System

2.1 System Architecture

The structure of the system is shown in Figure 2. The user edits music via the user's interface on the computer display. Also, the user can access a database that has musical grammar, the user's preferences, and so on. As a result, editorial work is reduced and efficient editing becomes possible.

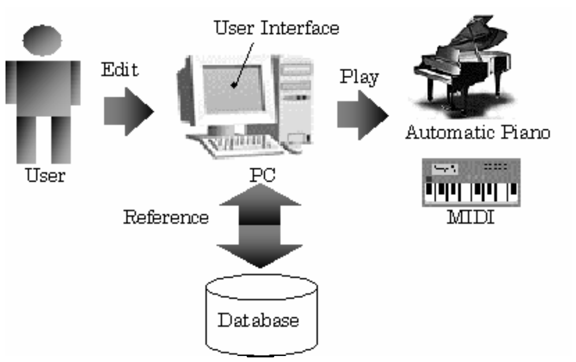

Figure 2 Structure of the editing system

2.2 Format of Performance Information

The parameters of performance information are shown in Tables 1 and 2.

The automatic piano that we have developed uses a music data structure that is similar to MIDI. We defined performance information, dividing it into two categories, the notes and the pedals.

The note information is comprised of six parameters involved in producing a tone: "Key (note)", "Velo (velocity)", "Gate", "Step", "Bar", and "Time". "Velo" is dynamics, given by the value of 1～127. "Gate" is the duration of the note in milliseconds. "Step" is the interval of time until the next note, and it also exhibits tempo. "Bar" is the vertical line placed on the staff to divide the music into measures.

The pedal information is comprised of four parameters: "Key (indicating the kind of pedal, "Damper" or "Shifting")", "Velo (the pedaling quantity)", "Time (the duration of applying the pedal)", and "Bar".

Table 1. The parameters of note information

Parameter	Key	Velo	Gate	Step	Time	Bar
Unit	-	-	m sec	m sec	m sec	-
Reference	21～108	1～127	-	-	-	-

Table 2. The parameters of pedal information

Parameter	Key	Velo	Time	Bar
Unit	-	-	m sec	
Reference	Damper or Shift	0～127	-	-

2.3 Editing Support Process with Database

The procedure of the editing by the system is shown in Figure 3.

Temporary music data (TMD) is the data of a piece of music without expression. Because expression has not been added, the necessary editing of the TMD is extensive.

Therefore, if the user chooses, the TMD is automatically translated by the system into original music data (OMD), similar in structure to TMD; after that, the user can start to edit it. The automatic translation program uses a Score Database, Musical Rules Database, and Preference Database, the details of which are described later in the paper. The user adds editing to the OMD and makes slight adjustments. When editing, the system watches over the data the user enters and music knowledge is provided. Concurrently, phrases in the music are discovered. When a phrase with the same pattern as one already edited occurs in the music, it is automatically translated. After editing, the system extracts the expressions and the preferences that are peculiar to the user from the OMD. These expressions are stored in the Preference Database, which is then used when editing other music, resulting in improved editorial efficiency.

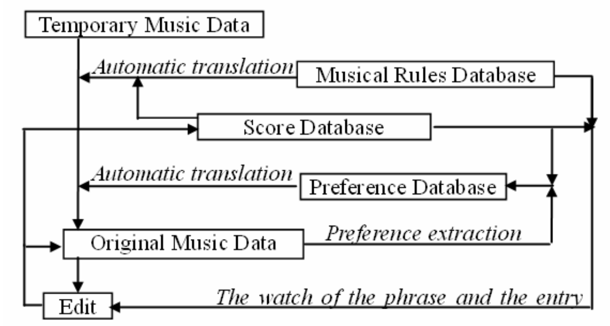

Figure3. Structure of the editing system

2.4 Details of the Databases

2.4.1 Score Database

This database has symbols including notes and time signature rests and so on in standard musical notation. Symbols were pulled together in order of bars, and bar symbols are arranged in time series.

This database is composed of three tables, the "Element table" (showing the position of the note and the composition of the chord), the "Symbol table" (showing the position of the music symbol) and the "Same table" (showing the position of the repetition of the phrase).

2.4.2 Musical Rules Database

This database has the architecture of musical grammar necessary to interpret symbols in musical notation. This database is composed of five tables containing "Dynamics marks", "Articulation marks", "Symbol of Changing Dynamics or Changing Tempo (Symbol that affects the speed of a note or the increase or decrease of the volume)", "Time signature", and "Tempo marks".

Analyzing a music symbol according to its usage allows efficient information processing by the system.

2.4.3 Preference Database

This database contains the expressions of the user's characteristic performance. The expressions show the relationship between tempo and dynamic.

The "Edit" selection in the user's interface gives the user access to the parameters for expression. A user can edit his or her parameters, and the respective databases will automatically change at least one of their parameters.

3. System of Inferring phrase expression

As a result of the analysis, it has been found that the phrase in this pattern that exists in the same tune becomes a performance of a similar expression mutually by our research. Thus, we were able to develop a system of inferring phrase expression to infer the expression from the patterns of the notes.

In the following paragraph, we describe an analytical result.

3.1 Analytical Result

We analyzed a pianist's performance data in to clarify his editorial tendency. Figure 4 shows the score of bars 1 to 7 of Beethoven's Moonlight Sonata. The graphs of the analysis results are shown in Figure 5. The horizontal axis of each graph is time (in milliseconds), and the vertical axis is velocity (1 to 127). As a result, we found that similar phrases like that of the third and the fourth bars create highly similar expressions as shown in Figure 5. In the following paragraph, we describe the method of inference design based on an analytical result.

Figure4. Bars 1～7 of "Moonlight Sonata"

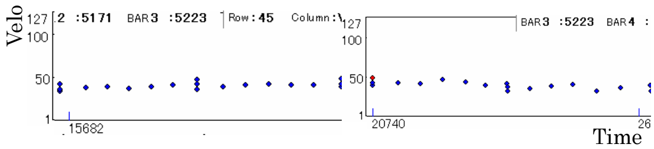

Figure5. The result of analysis

3.2 Phrase Feature Database

In Figure 5, it is found that the pattern of "Velo" exists in each beat. To express such a detailed performance feature, we constructed a Phrase Feature Database. Tables 3 to 5 show the composition of the database.

Table 3. Phrase Feature Database; Tuplet Data Table

Parameter	Summary
Index	Primary Key
BarNum	Number of bars
BeatNum	Number of beats
Tuplet	Number of notes included in tuplet
Rhythm	The number in which RhythmPtn is identified
Pattern	The number in which HighLowPtn is identified
TimeSig	The number of rhythm sign in Musical Rules Database
Tempo	The number of tempo mark in Musical Rules Database

Table 4. Phrase Feature Database; Tuplet Pattern Table

Parameter	Summary
Index	Primary Key
Tuplet	Number of notes included in tuplet
Rhythm	The number in which RhythmPtn is identified
RhythmPtn	Composition of notes in tuplet
HighLow	The number in which HighLowPtn is identified
HighLowPtn	Composition of "Key" in tuplet

Table 5. Phrase Feature Database; Tuplet Rate Table

Parameter	Summary
Index	Primary Key
Tuplet	Number of notes included in tuplet
Velo	"Velo" of first note in tuplet
VeloRate1	The rate of "Velo" of second note to "Velo" of first note.
VeloRate2	The rate of "Velo" of third note to "Velo" of first note.
Step	"Step" of first note in tuplet
StepRate1	The rate of "Step" of second note to "Step" of first note.
StepRate2	The rate of "Step" of third note to "Step" of first note.

3.3 Method of Inferring phrase expression

First, the vector is calculated at every beat in the original phrase of the inference, and the ratio of the sizes of the vectors at other beats to the vector at the first beat is calculated. The components of the vector are Velo and Step. (See Figure 6) Next, the expression of every beat in the phrase is inferred. The user sets Velo and Step of the first beat of the phrase. Velo and Step of other beats are calculated using the ratio of the vector of the first beat. However, only Velo and Step of each beat can be calculated with this method. Then, the expression of the remainder of the phrase is inferred using the Phrase Feature Database.

4. Inference Result

The phrase of the fourth bar was inferred from the first bar of Beethoven's Moonlight Sonata, which Gerhard Oppitz performed. And the phrase feature data base used for the inference was made based on the performance of Gerhard Oppitz. Figure 7 shows the performance by Oppitz.

Figure 8 shows the performance of the fourth bar inferred by the system. Figure 9 is an actual performance of the fourth bar by Oppitz. When Figure 8 and Figure 9 are compared, their expression is shown to be very similar. Therefore, it is thought that this system inferred effectively.

5. Conclusion

We developed a system of inferring phrase expression to infer the phrase expression from information on the score and user's performance characteristics. Then, the system was evaluated by comparing inferred phrase expression to the actual performance of the pianist.

Moreover, a "Phrase Feature Database" that stores the performance features of each pattern of tuplets was constructed. As a result, it became possible to express the features of a detailed phrase.

In the future, it will be necessary to improve the system so that it can infer a phrase even if the Preference Database and Phrase Feature Database are made from performances of other tunes.

$$Size = \sqrt{Velo^{2} + Step^{2}}$$

$$Angle = Tan^{-1}\left(\frac{Velo}{Step}\right)$$

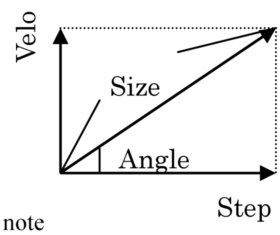

Figure6. Vector of a note

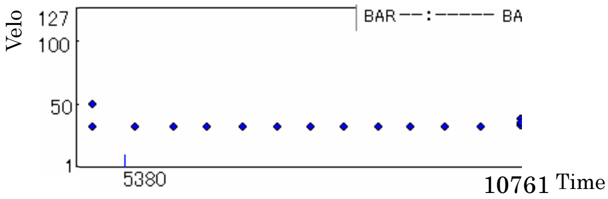

Figure7. Bar 1 of "Moonlight Sonata" by Gerhard Oppitz

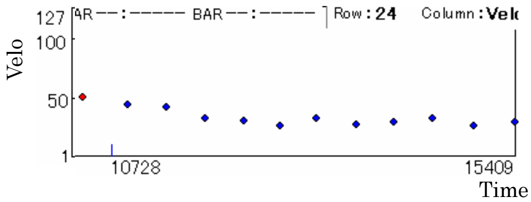

Figure8. Bar 4 of "Moonlight Sonata" inferred by our system

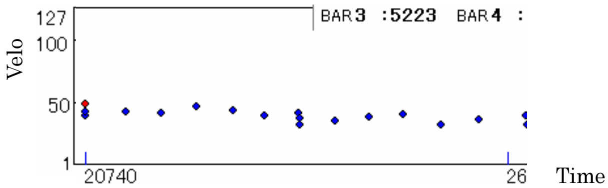

Figure9. Bar 4 of "Moonlight Sonata" by Gerhard Oppitz

References

[1] Hayashi, E. et al, "Behavior of piano-action in a grand piano.I", Journal of acoustical Society of America, Vol.105, pp.3534-3544, 1999.

[2] Hayashi, E et al, "Interactive musical editing system for supporting human errors and offering personal preferences for an automatic piano", Proc. of the 7th International Symposium on Artificial Life and Robotics, Vol.2, pp 513-516, 2002.

[3] Takamatsu, Y., Hayashi, E., et al, "Study on the Performance Information Edit Support System for an Automatic Piano", Technical Report of Information Processing Society of Japan, MUS-52, pp.111-118, 2003. (*in Japanese*)

[4] Takamatsu, Y., Hayashi, E., et al, "Interactive musical editing system for supporting human error and offering personal preferences for an automatic piano -Preference database for crescendo and decrescendo-", Proc. of the 10th International Symposium on Artificial Life and Robotics, pp 309-312, 2005.

Minimal design of *"in situ"* communication agents

Nobuyoshi MATSUMOTO, Hiroyuki FUJII, Michio OKADA
Department of Ecological Communications,
ATR Network Informatics Laboratories
2-2-2 Hikaridai, "Keihanna Science City,"
Kyoto, 619-0288
JAPAN.
nobu@atr.jp

Abstract

Communication involves exchanging incomplete information with others. Communication robots to date have been constructed to deal with problems of how to resolve the incomplete nature of information. Communication is not enriched by gaining large quantities of information but by clarifying intentions or messages that contain insufficient information. Communication design should reflect this fact. It is difficult to simulate communication, since there is so much background information needed to realize communication that cannot be controlled through engineering [1,2,3].

In this paper, we discuss a standardized method of designing robots capable of long-term communication, which we call "minimal design." It is unlike other industrial robot design methods. We have already produced such communication robots, and here we give explanations of them.

Furthermore, we discuss the importance of "in situ" robot design. The Latin "in situ" is a technical term used in biological research. It means "in the place where it occurs." In minimal design, a robot is designed in accordance with a particular situation and the user's preference: communication depends on the situation. From this viewpoint, we discuss our recent communication agents.

Finally, we illustrate by example a new concept for designing robot faces that is very different from conventional methods: it is based on a projected face that can be easily produced by using computer graphics. Some actuators and a spring-action equalizing device are also used in our proposed system. This combination of light projection, conventional actuators, and equalizing device is based on recent the advances made in robotics and screen agents.

Keywords: communication robot, minimal design, quasi-interpersonal behavior, *in situ,* robotness, multi-bodies agents

1. Introduction

A communication robot does, however, need an independent design methodology that fulfills its communication role, and this methodology should be simple. We named this type of robot design methodology the "minimal design.”   In this paper, we define a communication robot as one that does not necessarily communicate as a human does. Nor does it need to assume a human appearance. After discussing current design of a robot, we explain our innovative approach to designing communication robots. The most important feature for communication is possessing a physical appearance that bonds a robot to a human. In this regard, physical appearance is the essential characteristic of a communication robot rather than elaborate internal mechanisms. Furthermore, we stress the importance of “**robotness**” as the essence of a non-human object that has agency and life-likeness.

A robot that can anticipate cooperative work with a human must be designed from the perspective of communication ability. Human-robot communication is a **quasi-interpersonal behavior,** and we believe that a communication robot need not imitate humans. Instead, a minimally designed robot should articulate messages needed for human-robot communication. Many researchers tend to develop all-round communication robots that look much like mechanical humans, but such robots do not bring much satisfaction. As a result, they need to concentrate more on the ability to inspire the human imagination.

While we are still a long way from developing perfect all-purpose communication robots, we can solve problems in human-robot communication in other ways. Communication can be performed by minimal role-sharing robots, but the biggest problem in human-robot communication is the sustainability of long-term communication. Maintaining long-term communication is therefore an immediate problem for researchers working in the field of communication robots. In this paper, we discuss solutions to such problems and show examples of our research. We also give our perspective for the future.

2. Quasi-interpersonal nature of communication

When we consider the design of a robot, we focus attention on the quasi-interpersonal nature of communication. Humans generally realize that a robot is not a living creature. Through our field observations, we have noticed that children also communicate with our communication robots differently from their communications with living organisms. Nowadays, many humanoid robots appear on TV programs and in newspapers and exhibitions, and many people expect humanoids to become supreme communication robots. However, almost all humanoids are built to move as humans do, not to communicate. In our opinion, a humanoid is not an ideal embodiment of a communicating agent. While body motion is an important part of communication, robots' movements do not interact with people but with physical environments, whereas a human can even communicate with things that are certainly not alive.

This type of quasi-interpersonal communication can be found everywhere in the daily lives of ordinary people, but such communication does not continue for long. Designing good relationships among humans and artifacts is also an important consideration when designing communication robots. Although most robots are designed as independent machines, we however emphasize the importance of relationships.

Our proposed communication robots are role-sharing and multi-bodied. The robots described below increase the transparency of the referent-agent relationship. When a robot acts like a human, a human must search for the communication key from many communication channels. A communication robot developed with the minimal design approach is a realization of well-adapted information design. It seems more rational to use simple role-sharing robots in research on human-robot communication than using a single complex robot. Unfortunately, human interest in communication robots ended a long time ago. Robot researchers now need to return to developing methods of continuous communication between robots and humans.

At this point, we would like to focus on the original character of a robot. We confirmed the importance of characterizing a robot through our field observations of child-robot interaction. A robot's character strongly influences communication, and our distinctively designed robots have the property of attracting children. However, we must also point out the key observation that a fixed character on a robot limits opportunities for continuous communication. The stereotypes arising from mapping a robot's static character have the effect of restricting possible interpretations by subjects. Therefore, we need a robot as an embodied medium that can deal with various communication tasks.

3. Robotness

We have recognized the importance of **"robotness"** for a communication robot: Robots need not be substitutes for carrying out human roles. They must support humans, or no one would accept robots as neighbors of humans in the near future. "Robotness" has greater importance in robot design than designing mechanical human copies. In our sense, a robot must behave like a robot, nor a human. Our goal of communication robots is an equivalence of communicative roles with humans rather than an equivalence of motion with humans. Eventually, a robot must exist and perform as a robot.

Communication robots represent one concept of a tangible form or realization of active media. In existing mainstream robots, various functions of representations are recognized as important. However, we stress the importance of embodied media attracting the action of others. For example, most humanoid robots do not prompt human touch although physical contact is a good way to communication needless to say, on-screen agents are not capable of this. Furthermore, most of these robots are covered with cold plastic skins, which do not invite touch. Furthermore, What we call communication robots do not appeal to the five human senses, except for vision and hearing. The other three senses are not dealt with when engineers design a communication robot. But vision and hearing can be handle with on-screen communication agents. In developing an embodied communication robot more attention should be given to the other three senses in order to maximize its potential advantages over on-screen agents.

A good communication robot cannot be designed by the present method of only enriching the functions of a robot. By applying such a method, the problem of lost "life-likeness" mentioned above cannot be overcome. In order to realize interaction with people over a long period, it is also an important condition that a robot's appearance be attractive to humans. Norman, who presented various practical difficulties in his book "The Psychology of Everyday Things[4]," classified the elements of design into instinctive design, behavioral design, and introspective design in his recent work "Emotional Design[5,6]." The ease of use discussed in Norman's previous work was intended only for behavioral design. Norman stressed the importance of balance among instinctive design in connection with appearance, introspective design in connection with the meaning of appearance, and action design. Moreover, he claimed that not only ease of use but also the attractive features of a design could satisfy people. For a design method of communication, it should be remembered that attractive things are better than high-performance things.

In this paper, we describe our efforts to design a continuous-communication robot that is different from the products of conventional robot research. Toward this goal, we stress the importance of subtraction design and minimal design, in which subtraction is systematically performed based on a certain intention. Minimal design should not only minimize elements but also clarify the interface in communication, that is, the design should be completed after identifying what is essential. Furthermore, we propose a minimal design that can also clarify aspects of the interfaces in communication, such as the type of action or the situational.

3.1. Differences between a robot and a computer

According to the "Media Equation," even a non-living thing like a computer express a kind of life-likeness[7]. However, there are differences between a computer and a robot. First, an embodied robot has strong agency that reminds one of a living thing, while a computer has a minute-scale sense of agency. On the other hand, a computer stands for absolute accuracy and correctness in operation. Comparatively speaking, a communication robot often makes mistakes. This makes people realize that a robot is not always right and thus not perfect.

In fact, well engineered computer systems do not make an errors in their own procedures. Almost all errors and faults are caused in such systems through human intervention, such as using wrong programs or trying to input unacceptable types of data. A computer system is a symbol of infallible judgment, but a robot makes many errors and slip-ups just as a human does. The boundary line between a robot and its environment has much more complicated elements than an ordinary computer systems has. Consequently, the decisions that a robot makes sometimes fail. These faults do not necessarily indicate defects of the robot. Moreover, faults often compose the character of a robot. Accordingly, the character of a robot is often determined by human subject and not by system designers.

3.2. Differences between a robot and a machine (without agency)

A machine that does not have agency is well-suited to many aspects of daily life. Humans feel the eyes of a robot, as if they are observed by the robot. In such cases, people feel put into a fishbowl without privacy. But a machine without agency does not project the impression of someone watching them. Humans need not respond or give feedback to a system without agency.

4. Design Methodology

4.1. Design by addition

To illustrate by contrast the subtractive design proposed in this paper, we call the main guiding principle of conventional robot design "additional design" here. In the design of a conventional communication robot, transfer equipment and a structure for voice dialog are added to a fixed-position, industrial-type factory robot. Although there are still robots that use wheels as a simple method of transferring equipment, bipedal robots have also received much research attention in recent years. Communication robot designers naturally assume that the summation of efforts toward improved robot performance results in good communication. Communication ability does not complete the design of a robot: When we design a communicative agent, we also need to take into account the relationship between humans and robots..

4.2. Design by subtraction

A design based on function curtailment could be called "subtraction design," as opposed to the methodology of function addition. As a robot designed by functional addition becomes more like a living thing that actually exists, ironically the difference between the robot and the living organism becomes even clearer. Such a problem could be avoided by adopting a design peculiar to the robot, not by copying the figure of a living thing. A clear policy is needed to determine how far a design should be reduced.

5. Minimal Design

We discussed design by subtraction in the preceding section. In this section, we discuss minimal design, which is what we call the directional simplification of subtraction design. In order to emphasize the main point of communication, it is better to omit non-essential design elements. The decision of which design elements to omit is determined by goal setting. An airplane has wings but it doesn't beat the air with its wings. Accordingly, a rational idea does not always copy living things. As mentioned above, a minimally designed robot is not complete in itself. It is designed for communication with others and for initiating human interest in communication with it. A minimal design targets the principle design goals of communication.

Ludwig Mies van der Rohe, an exemplar of modern architecture design, said "Less is more," which means a good design requires chip off non-essential qualities. For our purposes, no one can fully pre-design right answers for all communication. Every new result of successful communication is simply put into a set of "right" answers. Moreover, "right" answers depend on situations and circumstances. Incomplete design evokes human interest, and, fundamentally, a robot should do the things that only robots can do. Consequently, the unpredictable nature of the robot's expressions in human-robot communication conveys a sense of subjectivity. All subjective understandings that are accepted by a person can be "right" answers. In this way the answers are generated and shared among a person and robots. Minimal design is intended to facilitate a ***"tabula rasa"*** that can evoke human imagination. Sometimes unsatisfactory situations arise from reading unwritten meanings that could hardly be expressed by robots, and this effect is similar to optical illusions. You can see what we do not draw.

5.1. Multi-bodies agents

Through our field observations, to deal with the absence of an absolute communication robots, we propose that human-robot communication should be conducted by two or more robots at the same time. In this way, each robot would have a different character. Moreover, such a robot would reminds people of a unique robot. Such a robot would form an attachment to a particular person. As a result, the robot could maintain long-term communication with humans.

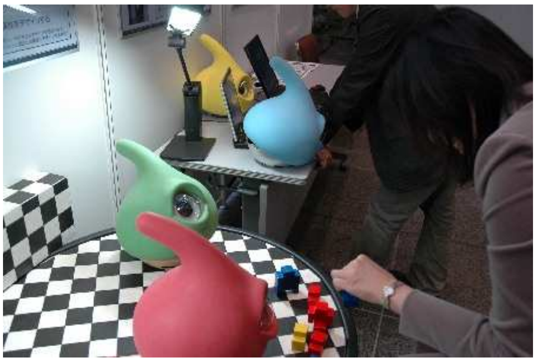

Figure 1. Multi-bodies agents Muu

Figure 2. Example of human-multi-bodies agents interaction

6. *"in situ"* design

In minimal design, a robot is designed in accordance with a situation and the user's preference: communication depends on the situation. The Latin ***"in situ"*** is a technical term used in biological research. It means "in the place where it occurs." We stress the importance of incorporating "in situ" robot design in minimal design. A message can have various meanings in a given situation; non-verbal expressions also affect communication. However, even if communication is successful the first time in a controlled environment, such as an experimental laboratory, there is no guarantee that the second time will be successful.

A robot must be designed not to fit into various environments but to tune in to the relationship between itself and a particular user. Fitness to the circumstance or the environment has an influence on the duration of human-robot communication. We need to establish a fundamental theory of adequate performance for a given circumstance, which we call in situ robot design. The shapes of living things are adapted to their circumstances.

The "bodyplan" of living things is highly suggestive for in situ robot design. Thompson (1973) wrote interesting ideas on the concept of bodyplan[8]. He suggested the similarity of geometric coordinate transformation on fins. According to his idea, a globefish and a rockfish can be interpreted through a geometric coordinate transformation process. We divide the bodyplan of living things into static and dynamic aspects of living things. "In situ" design implies use of artificial and mechanical homologous organs for minimally designed robots.

7. Proposed Design of a Communication Robot

A robot with physical actuators has the disadvantage of slow response time in comparison to CG screen agents. Also, in robots with moving parts, the weight of those parts limits response time. At the same time, the power-to-weight ratio of robots also limits their communication ability. Furthermore, unlike living creatures, a robot cannot change its facial expressions without changing prepared parts, which is certainly a "non-life-like" process. Moreover, living organisms are affected by both the genetic and epigenetic environments. These two problems can be solved in our proposed design by using a spherical screen and an LCD projector. A face image forms the center of recognition of "life-likeness," which can be seen in children's drawings[9,10]. Facial expressions remain the greatest unsolved problem of communication robots. Software processing limits the responses of a robot, but it is also necessary to redesign facial parts that incorporate sensor inputs and data through networks.

We also plan to combine the projected face described above with actuators used in conventional robots. Furthermore, we plan to incorporate the spring-action equalizing device implemented in our previous communication robot Muu. This type of hybrid robot doubles as a screen agent and a conventional robot. Therefore, the above two problems can be solved by using our proposed method. Blinking is a facile action that requires the least cost in term of bodily motion. It can express acceptance with eye contact to a subject. Unfortunately, our recent communication robot Muu was unable to blink. When our robots reveal emotions without saying any words, they need to move the entire body to reveal emotions. Also, blinking movements can be bound as symbols to short messages in communication. In contrast, our newly designed robots reveal emotions without difficulty by blinking.

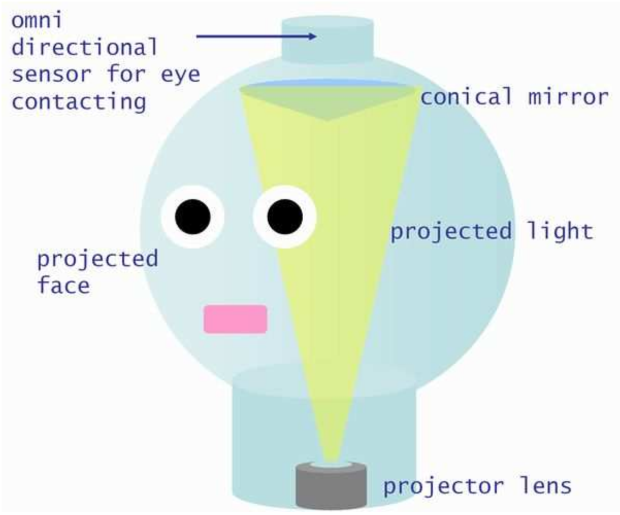

Figure 3. Projected face of a robot

Summary

Until recent times, robots have merely been tools for production. Now, however, people have certain expectations of robots as partners in communication, and recently many communication robots have been developed. Many of these robots are designed on the same principle as factory robots: the approach of design by addition. Furthermore, many robots have been created to imitate the shape, motion, and characteristics of living things, as mechanical animals. Although such robots do resemble living things at first glance, the differences soon clearly stand out. In this paper, we proposed a technique called "minimal design," the primary aim of which is to maintain communication. Based on this method, we stress the importance of the "**quasi-interpersonal**" nature and "**robotness**" in the design of communication robots. Also, we showed the significance of designing a robot based on the relationship between the user and the situation. In minimal design, non-essential elements are omitted to emphasize the essential design elements. Different needs demand different types of robots.

To clarify the design task, we presented the strategy of minimal design as well as communication robots based on minimal design. Although minimally designed communication robots are dissimilar to animals or humans, they still remind us of animal characteristics in some ways; however, since they are not physically similar to animals, users do not expect too much. In addition, we suggested a useful method for robots to express feelings in a similar way how to characters express themselves in cartoons and children's drawings. Such robots are well-suited to long-term communication because of the uncertainty arising from their not giving a single prefixed answer in human robot communication.

Minimal design does not imply a sharp departure from exploiting the improvements made in the elemental technology of robotics. On the contrary, technology can be used to make superior communication robots in a minimally designed way. Through minimal design, it is possible to develop a communication robot that never bores its users. In addition, we introduced a methodology named "in situ design" to match the robots with particular used and circumstances. We will continue investigating robot identity and the integration of robots in roles involving long-term communication.

Acknowledgements

The research reported here was supported in part by a contract with the National Institute of Information and Communications Technology entitled, 'Research on Human Communication'.

References

[1] N. Matsumoto, H. Fujii, M. Goan and M. Okada, "Minimal communication design of embodied interface," Proceedings of the 2005 International Conference on Active Media Technology(AMT2005), pp225-230, May 2005.
[2] N. Matsumoto, H. Fujii, and M. Okada, Minimal design for human-agent communication, Proceedings of 10th International Symposium on Artificial Life and Robotics(AROB 10th), pp214-217, 2005.
[3] N Matsumoto, H Fujii, M Goan and M Okada, Minimal Design Strategy for Embodied Communication Agents, IEEE International Workshop on Robots and Human Interactive Communication; RO-MAN 2005(Aug. 2005), 335-340.
[4] Norman D. , "The Psychology of Everyday Things", Basic Book, New York, 2004.
[5] Norman D. "Emotional Design", Basic Book, New York, 2004.
[6] Norman D., Emotion and design: Attractive things work better. ACM Interactions July-August:36-42, 2002.
[7] B. Reeves and C. Nass, "The Media Equation," CSLI Publications, Leland Stanford Junior University, 1998.
[8] Thompson D. W., On Growth and Form("Seibutsu no Katachi" Japanese Translated Version), Tokyo Daigaku Shuppan, 1973.
[9] P. Ekman and W.V.Friesen, "Unmasking the Face," Prentice-hall, 1975.
[10] M. V. Cox, "Children's Drawing by," Penguin books, 1992.

The Eleventh International Symposium on Artificial Life and Robotics 2006 (AROB 11th'06),
B-con Plaza, Beppu, Oita, Japan, January 23-25, 2006

A Novel Human-Environment Interface for Conceptualizing Spatial Information in Non-Speech Audio

Shigueo Nomura, Masayoshi Tsuchinaga, Yaichi Nojima,
Takayuki Shiose, Hiroshi Kawakami, Osamu Katai,
Dept. of Systems Science
Kyoto University
Kyoto, 606-8501, Japan

Keiji Yamanaka
Faculty of Elect. Engrg.
Federal University of Uberlândia
Uberlândia, 38400-902, Brasil

Abstract

We propose a novel concept toward interfaces that can provide visually impaired persons with the chance to recover the freedom to conceptualize their environment without depending on such conventional voice synthesizer systems. Fourteen subjects participated in ten experiments to provide results for evaluating their performances to conceptualize spatial information based on cues in "artificial-sounding" ("AS") and "natural-sounding" ("NS") tones. The source of "AS" tones was the digitized sound used by vOICe Learning Edition, and the source of "NS" tones was a fan noise with analogs in everyday world. Experimental results revealed that the use of "NS" tones was essential to improve conceptualization performances of subjects as eventual users of novel human-environment interfaces.

1 Introduction

Recently, interest and necessity have grown in using sounds more complex than ubiquitous interrupting beeps to provide information to computer users. An actual example of interface is the evaluated vOICe Learning Edition [1] that translates arbitrary video images produced by an ordinary camera into sounds. However, like vOICe, the problem is that dimensions (pitch, loudness, and duration) of sound themselves have been used to represent the characteristics of the data. This leads to the use of "artificial-sounding tones" with no analogs in the everyday world and requires extensive trials before actually using the interface. We propose to break away from such typical use of artificial-sounding tones by designing novel interfaces based on "natural-sounding tones" that utilize the same user skills employed in everyday tasks such as crossing the street. An example of such a skill is our "built-up association" of reverberation with empty space. All other things being equal, the more reverberance in a room, the more space there is. So, this built-up association provides a natural conceptualization of spatial information based on user experience and familiarization with everyday sounds, that is, provides friendly information for users without the necessity of hard cross-modal training.

The main purpose is a novel concept of interface to support visually impaired persons and to provide them with the chance to recover the freedom to conceptualize and interact with their environment without depending on such concepts as artificial pattern recognition or voice synthesizer systems. As an essential work background to achieve this main purpose, we utilized our already conceived "sound visualization" [2] function and our already developed virtual 3D acoustic environment for training the "perception of crossability [3]."

Section 2 presents apparatus and procedure for experiments. Experimental results are presented in Section 3. In Section 4, conceptualization performance of subjects hearing different tones is discussed. Section 5 presents a conclusion of this work.

2 Method

2.1 Apparatus

To generate "artificial-sounding" ("AS") and "natural-sounding" ("NS") tones for investigating conceptualization performances by subjects hearing these tones, we used the virtual 3D acoustic environment system based on sound space processors as shown in Fig. 1.

The source of "AS" tones is the digitized sound used by vOICe Learning Edition with no analogs in the everyday world. On the other hand, the source of "NS" tones is the real sound of a fan noise that was saved by a precise microphone.

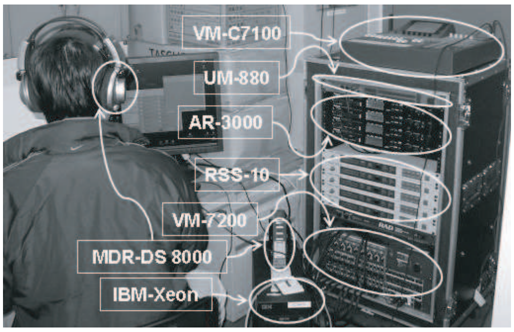

Figure 1: A front view of devices for generating non-speech audio.

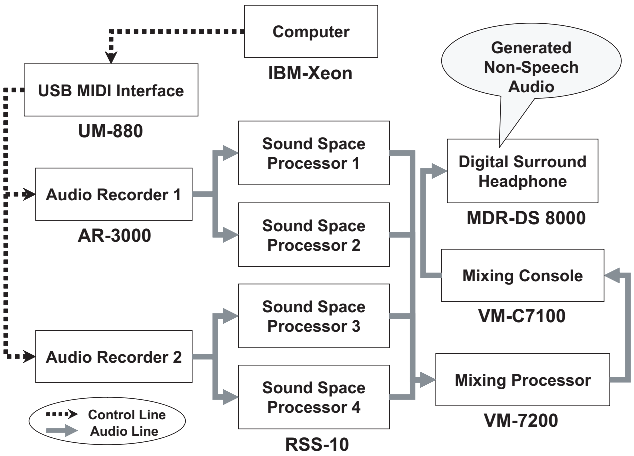

Figure 2: A schematic overview of apparatus for experiments.

Figure 2 shows a schematic overview of the apparatus used in our experiments. Each device identification is followed by its model number.

2.2 Procedure

Figure 3 shows the upper view of a course virtually created by using the 3D acoustic environment system. During experiments, subjects travel across the course and must perceive changes in "aural surface" using their auditory system. Based on our previous work [3], appropriate reverberation and reflection levels are adopted as $-30dB$ in this virtual environment.

In Fig. 3, we have the following conditions for experiments:

1. A set of four generated sounds ("AS" or "NS" tones) constitutes a piece of wall that represents "aural surface" of the virtual course.

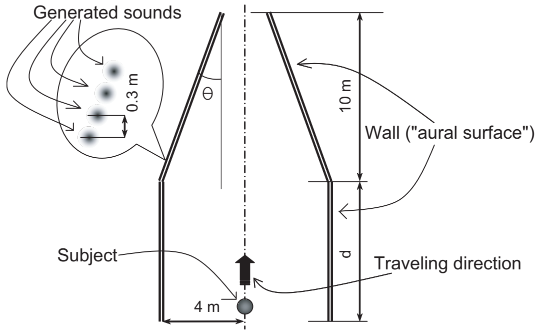

Figure 3: The upper view of a virtual course for experiments.

2. The distance d is calculated as $d = v.t$, where v can be $4km/h$ or $12km/h$, and $t \in \{3.0, 3.5, 4.0, \ldots, 6.0\}s$.

3. According to the value of angle θ, we set up the following geometric shapes of virtual courses:

   - Convergent for $\theta \in \{3^o, 5^o, 30^o\}$. The change in "aural surface" is to become the course narrow after traveling the distance d.
   - Straight for $\theta = 0$. There is no change in "aural surface" for the entire course.
   - Divergent for $\theta \in \{-3^o, -5^o, -30^o\}$. The change in "aural surface" is to become the course wide after traveling the distance d.

Fourteen subjects participated in ten experiments for evaluating two different tones ("AS" and "NS") used to perceive changes in "aural surface" of these virtual courses. All subjects had no audition problems. No visual information was used in experiments.

Instructions for each subject before starting experiments are as follows:

1. During a duration of time from $3s$ to $6s$ (each duration is randomly defined) corresponding to the distance d in Fig. 3, the subject travels across a straight course in the virtual acoustic environment.

2. After spending the above duration of time, a clock starts to measure the time interval until pressing a key that represents a perception response of the subject. Each pressed key by the subject represents the following decisions:

   - The key "←" must be pressed when the subject perceives that the traveled course is converging as shown in Fig. 4a.

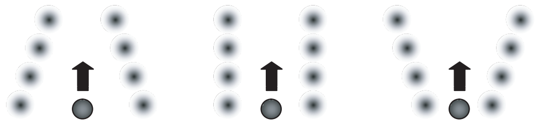

Figure 4: Types of changes in virtual courses.

- The key "↓" must be pressed when the subject perceives that there is no change on the traveled course as shown in Fig. 4b.
- The key "→" must be pressed when the subject perceives that the traveled course is diverging as shown in Fig. 4c.

3. Each decision for pressing any key must be taken as soon as possible but with belief.

Subjects performed tasks of the following two experimental stages during experiments:

- Training: Two steps were performed in this stage. First step was to provide familiarization with existence of three types of virtual courses as shown in Fig. 4; these courses were presented to subjects as converged by 30^o, diverged by -30^o, and unchanged; the traveling speed was set at $12km/h$; three courses for each type of tone ("AS" and "NS") were virtually created. Second step was to acquire abilities for capturing necessary cues in each type of tone and classifying the virtual course where the subject is traveling; in this step, subjects were asked to press the key corresponding to the type of course in which they thought; after each response, the correct answer was informed.
- Testing: In this stage, each subject achieved ten experiments (5 ones for each type of tone) to provide results for analysis of conceptualization performance based on different tones. We have two types of experiments. In the first experiment, the subject hears "AS" tone and travels across the virtual course with speed at $4km/h$ or $12km/h$; the values of angle θ as shown in Fig. 3 can be -30^o, -5^o, -3^o, 0^o, 3^o, 5^o, or 30^o; for each speed we have seven different virtual courses where the subject travels across to classify them; a total of fourteen different virtual acoustic courses based on cues in "AS" tone must be classified by conceptualizing spatial information; the order of these courses is randomly arranged to avoid the influence of learning process by subjects on performance evaluation. In the second experiment, the unique difference in relation to the first one is that the subject hears "NS" tone instead of "AS".

Subjects were divided into two groups with seven ones: (X) composed by $SX1, SX2, \ldots, SX7$, and (Y) composed by $SY1, SY2, \ldots, SY7$ that performed different sequences of experiments in each group.

Table 1: Conceptualization performances of all subjects, where $v_1 = 4km/h$ and $v_2 = 12km/h$.

	"AS" tone		*"NS" tone*	
Change	v_1	v_2	v_1	v_2
-30^o	81%	83%	93%	90%
-5^o	53%	70%	36%	80%
-3^o	34%	60%	26%	53%
0^o	49%	47%	53%	50%
3^o	37%	30%	39%	51%
5^o	53%	31%	61%	71%
30^o	84%	87%	97%	93%

Table 2: Performance of subjects traveling at $12km/h$; * indicates subjects with the best performances.

	"AS"	*"NS"*		*"AS"*	*"NS"*
$SX1$	54%	69%	$SY1$	57%	60%
$SX2$	$\boxed{51\%}$	$\boxed{40\%}$	$SY2^*$	60%	86%
$SX3$	51%	63%	$SY3$	49%	60%
$SX4^*$	69%	89%	$SY4$	49%	77%
$SX5$	51%	69%	$SY5$	60%	77%
$SX6$	$\boxed{46\%}$	$\boxed{43\%}$	$SY6$	71%	80%
$SX7$	77%	86%	$SY7$	71%	80%

3 Experimental Results

Results from the testing stages are presented in Tables 1, 2, and 3 as follows:

- Table 1 presents results of conceptualization process by all subjects. The average results are categorized by type of tone ("AS" or "NS"), course change (θ), and traveling speed (v_1 or v_2).

Table 3: Best conceptualization performance from each group of subjects.

	Subject SX4		*Subject SY2*	
Change	*"AS"*	*"NS"*	*"AS"*	*"NS"*
-30^o	80%	100%	40%	100%
-5^o	80%	100%	80%	100%
-3^o	100%	100%	100%	60%
0^o	40%	20%	20%	60%
3^o	20%	100%	20%	80%
5^o	60%	100%	60%	100%
30^o	100%	100%	100%	100%

- Table 2 presents performances of subjects traveling at $12km/h$. This traveling speed was selected by considering results in Table 1. Each rate is the average of results corresponding to all changes in "aural surface."

- Table 3 presents detailed results for subjects $SX4$ and $SY2$ that reached the best performances in their respective groups.

After the testing stages, we asked subjects about the tone that they thought more preferable for conceptualizing spatial information. Among others, only subjects $SX2, SX7$, and $SY3$ chose "AS" tone. And, we can verify that only the choice by subject $SX2$ matched performance result as shown in Table 2.

4 Discussion

In Table 1, we verify that conceptualization performance by using "NS" tone was better than performance by using "AS" tone in the most of virtual courses. An exception occurred for virtual course diverged by -3^o in which conceptualization performance reached 60% using "AS" tone and setting the traveling speed at $12km/h$. Also, we can notice a considerable improvement on performance results corresponding to changes at $-5^o, -3^o, 3^o$, and 5^o when the traveling speed was set at $12km/h$ using "NS" tone.

In Table 2, only subjects $SX2$ and $SX6$ suffered decrease (respectively, 51% to 40%, and 46% to 43%) in their performances when they heard "NS" tones.

In Table 3, we can notice that both subjects improved their performances mainly in the case of virtual courses converged by 3^o and 5^o when they heard "NS" tone instead of "AS" one. The performance of subject $SX4$ was improved from 20% to 100% using "NS" tone in virtual course converged by 3^o and from 60% to 100% in the case of 5^o. Similar improvement was reached by the subject $SY2$ too.

5 Conclusion

We evaluated "artificial-sounding" ("AS") and "natural-sounding" ("NS") tones as non-speech audio means for eventual interface users to capture cues and perform natural conceptualization of spatial information.

Experimental results showed that "NS" tones were more appropriate than "AS" ones to classify different types of virtual courses by subjects traveling across these courses and hearing those tones.

Furthermore, improved performances were verified in tasks to perceive too small changes in "aural surface" when subjects heard "NS" tones even at high traveling speed.

Finally, we concluded that the use of "NS" tones with similar conditions to everyday world such as reverberation and reflection is an essential requirement for designing novel friendly human-environment interfaces.

Acknowledgements

We are very grateful to Prof. Kiyohide Ito from Future University in Hakodate for his valuable contribution to this work supplying us with a fan noise sound source data used in our experiments.

References

[1] W. D. Jones, "Sight for Sore Ears," *IEEE Spectrum*, Vol. 41(2), pp. 13–14, 2004.

[2] S. Nomura, T. Shiose, H. Kawakami, O. Katai, and K. Yamanaka, "A Novel "Sound Visualization" Process in Virtual 3D Space: the Human Auditory Perception Analysis by Ecological Psychology Approach," *Proc. of* 8^{th} *Asia Pacific Symposium on Intelligent and Evolutionary Systems*, pp. 137–149, Cairns, Dec. 2004.

[3] T. Shiose, K. Ito, and K. Mamada, "The Development of Virtual 3D Acoustic Environment for Training 'Perception of Crossability'," *Proc. of the* 9^{th} *International Conference on Computers Helping People with Special Needs*, pp. 476–483, Paris, Jul. 2004.

The Eleventh International Symposium on Artificial Life and Robotics 2006 (AROB 11th'06),
B-con Plaza, Beppu, Oita, Japan, January 23-25, 2006

Emerging Cell Array based on Reaction-Diffusion

Shuhei Miyashita
Department of Informatics
University of Zurich
Andreasstrasse 15
CH8050 Zurich, Switzerland

Satoshi Murata

Tokyo Institute of Technology
4259 Nagatsuta, Midori
Yokohama, 226–8502 Japan

Abstract

This paper demonstrates self-replication and self-organization phenomenon based on reaction-diffusion mechanism by computer simulation. The simulation model consists of one dimensional cell array. Each cell contains two kinds of chemical substances - activator u and inhibitor v - that can generate reaction-diffusion wave, which is a spatial concentration pattern. The cells are supposed to be divided or be deleted depending on its concentrations of chemical substances. As we tried several kinds of diffusion coefficients to the model, in some simulations, self-replication process and generating cell array with metabolic process were observed. By applying division rule and apoptosis rule, cell arrays duplicate itself oscillating two states, that is, self-replication process were observed. And by applying division rule and annihilation rule, a cell array that has stable length is generated changing its cell components, that is, generating cell array with metabolic process were observed. Surprisingly, these two phenomena are realized independently of the initial number of cells.

1 Introduction

Self-replication and self-organization abilities of multicellular organisms are one of the most fundamental characteristics that discriminate creatures from non-creatures. As each cell contains the same genome, this feat is realized in a distributed and autonomous way with the absence of centralized control. However, no matter how big progress has been made in molecular biology over the past few decades, overall picture of principles behind the spatiotemporal dynamics of these processes is still lacking.

In 1952, A.M.Turing advocated a reaction-diffusion mechanism and suggested that the reaction-diffusion mechanism, which is a kind of spatial concentration pattern, plays a key role in forming a periodic shape on a small creature called hydra [1]. L.Wolpert suggested a concept of positional information when he thought that all identical cells should recognize their own position in order for the cells that had identical gene [2]. C.G.Langton built a cellular automata model of self-replication (SRloops) on a two dimensional cell array [3]. As the model consists of discrete internal state with finite state automata, it is not easy to relate this models to the biological cell. K.Tomita et al. created graph automata, which enable description of dynamic topological change of cell network, [4]. They extended the concept of cellular automata to certain graphs of cells. This model is able to describe morphological change such as cell division or cell death. But little attention has been given to a relation between morphogenetic process and reaction-diffusion mechanism.

2 Model

2.1 Reaction-diffusion

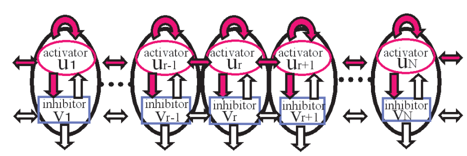

Figure 1: One dimensional cell array.

In this research, one dimensional cell array model was chosen for simplification. Fig.1 is a schema of the model. These nodes represent cells containing two kinds of chemical substances - activator u and inhibitor v - that can generate reaction-diffusion wave. These two chemicals react each other and diffuse to neighboring cells according to its concentration gradient.

$$\begin{aligned} du_r/dt &= +5u_r(t) - 6v_r(t) + 1 \\ &\quad + D_u\{u_{r-1}(t) + u_{r+1}(t) - 2u_r(t)\} \quad (1) \\ dv_r/dt &= +6u_r(t) - 7v_r + 1 \\ &\quad + D_v\{v_{r-1}(t) + v_{r+1}(t) - 2v_r(t)\} \quad (2) \end{aligned}$$

The reaction-diffusion model that we use is the same as Turing's, which is expressed as partial differential equations (1), (2). Where, u_r and v_r represents the concentration of activator and inhibitor, respectively with subscript r as an identification number. D_u and D_v represent diffusion constants of activator and inhibitor, respectively ($D_u = 0.7, D_v = 1.2$). To the system, Dirichlet boundary conditions were applied, which set the chemical concentration at the boundary to zero. The initial concentrations are set as equilibrium point $(u, v) = (1.0, 1.0)$.

2.2 Cell cycle and cell differenciation

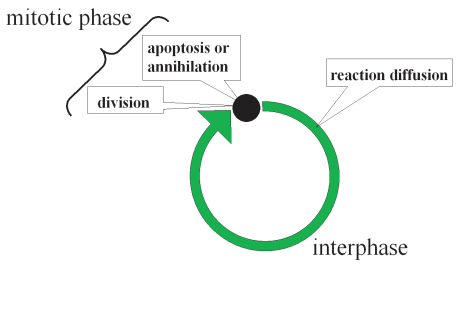

Figure 2: Cell cycle.

Since cell cycle is determined by various factors, in this paper, cell cycle is supposed to be generated synchronously. Fig.2 represents the cell cycle of the model. Every cell has interphase and mitotic phase in the cell cycle. In mitotic phase, reaction and diffusion of the chemical substances take place. In interphase, cells are differentiated depending on the concentrations (see below).

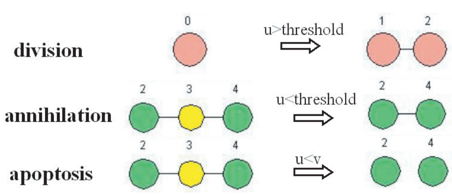

Figure 3: Cell differenciation.

Fig.3 shows cell differentiation rules. Cell division (top) is took place when the concentration of activator becomes larger than specific threshold (division threshold set as 1.5) in mitotic phase. The cell is divided into two cells, and the concentration of each chemical substance right before division is applied to the concentration of the cell divided. Contrary, annihilation rule (middle) is activated when the concentration of activator becomes smaller than another specific threshold (annihilation threshold set as 1.0) in mitotic phase. In this rule, the cell is deleted but the cell connections of both sides are kept connected. Apoptosis rule (bottom) is similar to the annihilation rule, which is activated when the concentration of activator becomes smaller than that of inhibitor in the same phase. The system is divided into two separate groups by the cell deletion. Every differential equation is integrated by the Runge-Kutta method ($\delta t = 0.01$, 1step=$100\delta t$, 1 interphase corresponds to 150 steps).

3 Simulations and Results

In the computer simulations, equations (1), (2) and cell differentiation rules are simulated synchronously according to the cell cycle.

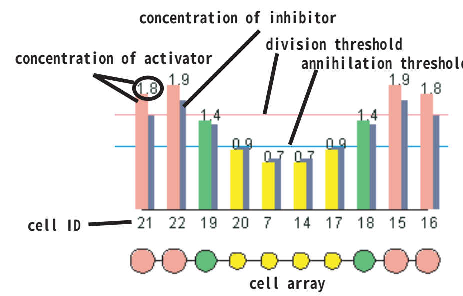

Figure 4: Simulation model.

Figure 4 shows the simulation model. Bars above each cell represent the concentrations of activator and inhibitor. The concentrations of activator is displayed front and that of inhibitor is displayed behind. Values of the concentrations of activator is presented on each shoulder of bar. division threshold, annihilation threshold and identification numbers of cells are also listed.

3.1 Self-replication process

In this model, division rule and apoptosis rule are applied in mitotic phase. Fig.5 shows self-replication process when we settled one cell as an initial condition. In the first stage, cell divisions are repeated two times in mitotic phase and the initial cell grows into 8 (#1 - #4). Then apoptosis rule is activated and four cells positioned at the center (cell 8,13 at #4) are deleted and four cells at the side (cell 9,10,11,12 at #4) are divided. Consequently, the system duplicates itself oscillating between state #5 and #6.

Fig.6 shows the case that the number of initial cells is larger than the oscillating number 10 (#7). The phenomenon that final state converges to the state #5 and #6 are observed.

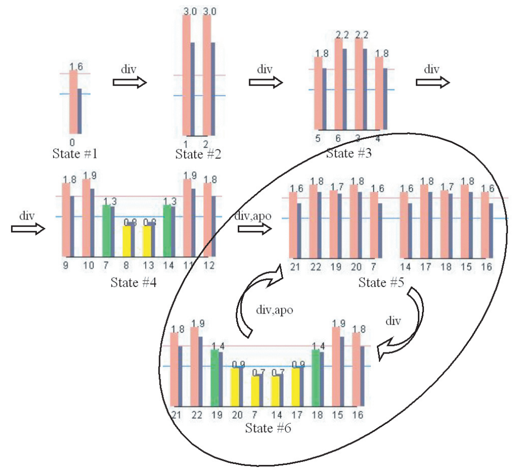

Figure 5: A self-replication process from one cell.

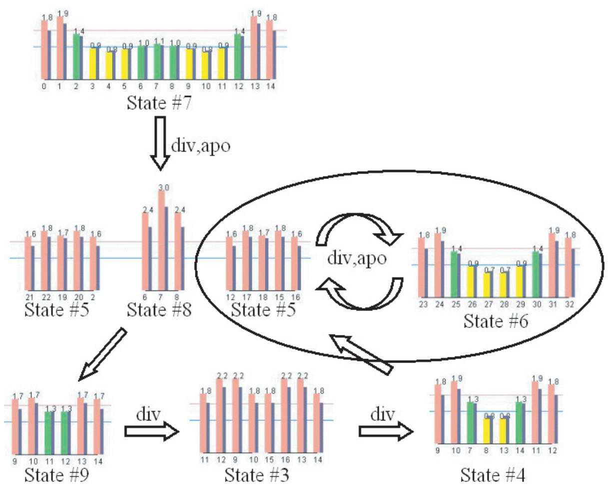

Figure 6: A self-replication process from 15 cells.

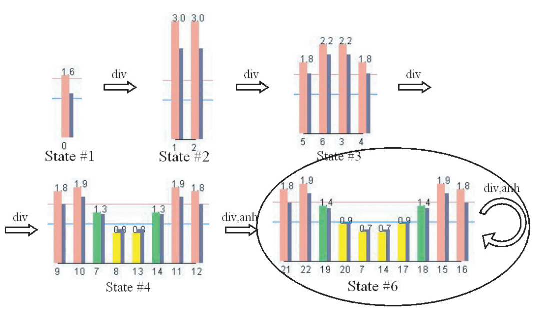

Figure 7: A generating cell array with metabolic process from one cell.

3.2 Generating cell array with Metabolic process

Division rule and annihilation rule are applied in mitotic phase. Fig.7 shows that the number of cells increases and the number finally becomes to 10 according to the cell division rule. In the mitotic phase at state #6, four cells positioning at the center (cell 20,7,14,17 at #6) are annihilated. And other four cells (21,22,15,16) at the sides are divided. At the end, the number of cells is kept stable to the fixed number, 10. The system perpetually produces new cells replacing some old cells.

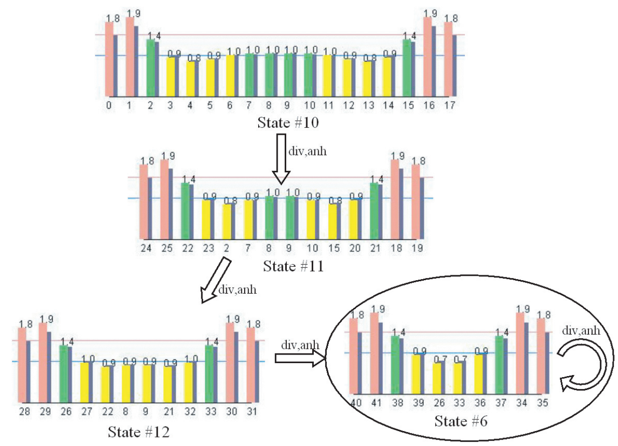

Figure 8: Generating cell array from 18 cells.

In order to investigate stability of the process, 18 cells are set for a initial state. Fig.8 shows the number of cells finally converges to the same pattern (#6).

4 Discussions

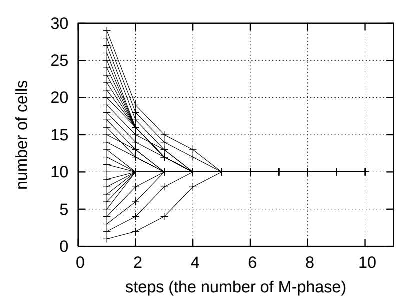

Figure 9: The number of cells transition graph.

In addition to the simulation 3.2, we settled different number of cells as a initial condition and showed the results in Fig.9. The X-axis represents the number of passed mitotic phases and Y-axis represents the number of cells. The figure shows that the length of all cell arrays which start from 1 cell to 30 cells finally converge to 10. This suggests not only that we can settle variable numbers of cells for a initial condition (at least 1 to 30) but also we can cut any cell connections as we want which leads to generate two cell arrays consisting of same size, 10.

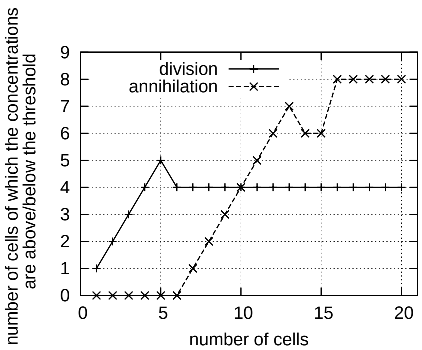

Figure 10: Exceed threshold graph.

Since patterns of reaction-diffusion waves are seem to be unique to the length of cell arrays especially the length is short, we counted the number of cells which exceed division threshold and which are below annihilation threshold in the first mitotic phase. The X-axis in Fig.10 represents the number of cells, and Y-axis represents the number of cells of which the concentrations are above (or below) the threshold. As the figure indicates, When the number of cells is less than 9, the number of cells that the concentration exceed division threshold is larger than that the concentration are below annihilation threshold. That is, the length becomes short in the next mitotic phase. And when we settle the number of cells more than 11, the other way round. This figure clearly shows that the length of the system converges to 10.

Fig.11 represents the number of cells when mitotic phase passed ten times in different diffusion coefficients. Initial number of cells were settled from 1 to 30 for each parameter sets. X and Y axis represent diffusion coefficients Du and Dv, respectively and Z axis represents the number of cells. As it can be seen, the system doesn't always converge to one state and though the system shows its robustness for external disturbances in adequate diffusion coefficients, the ranges of these parameters are narrow.

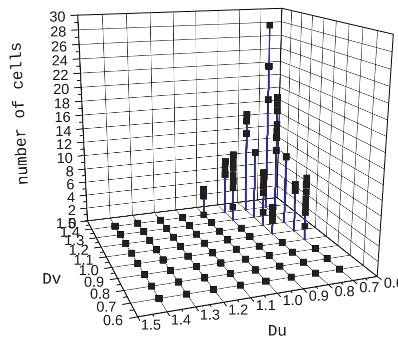

Figure 11: The number of cells in each parameter sets.

5 Conclusion

In conclusion, two fundamental organic behaviors, that is, self-replication process and generating cell array with metabolic process were observed by applying reaction-diffusion mechanism on distributed space. In self-replicaion process, a phenomenon that cell arrays duplicate itself oscillating two states were observed. And in generating cell array with metabolic process, a phenomenon that a cell array which has stable length is generated changing its cell components were observed. This research shows posibilities that reaction-diffusion system plays some roles in controlling these vital activities of living things.

Acknowledgment Many thanks to Peter Eggenberger Hotz for helpful suggestions. This research is supported by the Swiss National Science Foundation, project #200021-105634/1.

References

[1] A.M.Turing: A reaction-diffusion model for development, The chemical basis of morphogenesis, Phil Trans. Roy. Soc. of London, Series B; Biological Sciences, **237**, 5,PP.37-72 (1952)

[2] L.Wolpert Positional Information and the Spatial Pattern of Cellular Differentiation, J. Theoret. Biol., **25**, PP.1-47 (1969)

[3] C.G.Langton: Self-reproduction in cellular automata, Physica D: Nonlinear Phenomena, **10**, Issues 1-2, PP.135-144 (1984)

[4] K.Tomita, H.Kurokawa, S. Murata: Graph Automata: Natural Expression of Self-reproduction, Physica D: Nonlinear Phenomena, **171** No.4, PP.197-210 (2002).

The Eleventh International Symposium on Artificial Life and Robotics 2006 (AROB 11th'06),
B-con Plaza, Beppu, Oita, Japan, January 23-25, 2006

Biomimetic Control of Mobile Robots based on the Information Processing Model of *Paramecium*

Akira Hirano†, Toshio Tsuji†, Noboru Takiguchi††, and Hisao Ohtake†††

†Graduate School of Engineering, Hiroshima Univ., Hiroshima 739-8527, Japan

††Graduate School of Advanced Sciences of Matter, Hiroshima Univ., Hiroshima 739-8530, Japan

†††Graduate School of Engineering, Osaka Univ., Osaka 565-0871, Japan

Abstract

In order to survive in complex natural environments, living organisms have been genetically acquiring various algorithms. Protozoans, for example, respond to various stimuli to search for a hospitable environment. Recently, the concept of *Software Biology* has been proposed, in which the algorithms of living organisms are considered as a kind of software that could be utilized for robot control.

Thus far, we have focused on the information processing algorithm of *Paramecium*, and proposed its computer model, *Virtual Paramecium*, based on biological knowledge. *Virtual Paramecium* can approximately realize the chemotactic behavior of the actual *Pramecium* based on the information processing model. In this paper, we report the results obtained when a mobile robot is controlled using *Virtual Paramecium*, and confirm the effectiveness of the biomimetic control based on the information processing algorithm of living organisms.

1 Introduction

In order to survive in complex natural environments, the genome of living organisms undergoes various changes, thereby forming various algorithms for survival. Recently, the concept of *Software Biology* has been proposed; this concept proposes the use of algorithms of living organisms for control of machines, that can adapt to environmental changes [1]. In the research field of adaptive control, neural networks have been introduced to control robots, and their effects have already been demonstrated. However, there is a possibility that the mechanism occurring in an actual living organism is not reflected in robot control because the cellular characteristics that comprise the neural network are very simple in comparison with a living cell. Hence, developing a computational model of unicellular organism is considered one of the effective approach for achieving robot control.

Some models that focus on the internal processing system of living organisms have been proposed. The model called E-CELL [4] has been developed by Tomita et al. to simulate the behavior of the entire cell based on the chemical reaction, and another model has been developed by Bray and Lay [2] and Hauri and Ross [3] to simulate part of the internal processing of E. coli bacteria. Our research group has also developed the *E. coli* model based on the chemical equation of the internal processing system, and has applied it to mobile robot control [5, 6, 7].

At present, we are constructing a computational model of *Paramecium* [8, 9], *Virtual Paramecium*, because its internal processing system is more advanced than that of *E. coli*. Further, we have confirmed that *Virtual Paramecium* can reproduce the chemotactic response of a living *Paramecium* [9]. In this paper, we report the results of our study on the control of a mobile robot by using *Virtual Paramecium*; in addition, we confirm the effectiveness of the biomimetic control that is based on the information-processing algorithm of living organisms.

2 *Paramecium*

Paramecium can be assumed to be a discoid shape measuring approximately 250 μm in length and 50 μm in width; it has a uniform cilia layer on the cell surface. The direction of ciliary beat is modified by the stimuli from the environment. For instance, *Paramecium* accelerates their motion toward areas of low K^+ concentration by increasing their ciliary beat frequency. On the other hand, *Paramecium* exhibits an escape reaction from areas of high K^+ concentration, thereby accumulating in the areas of low K^+ concentration. This response behavior with regard to the chemical environment is called chemotaxis.

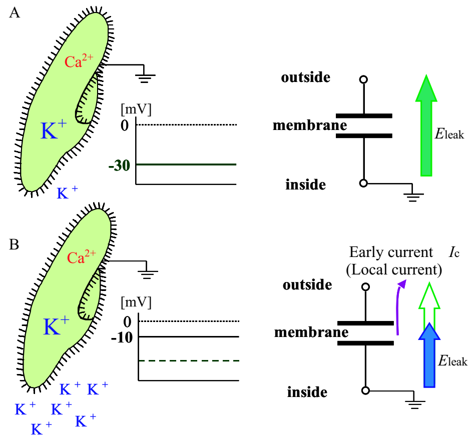

Figure 1: Membrane potential change of *Paramecium*.

Paramecium processes information by electrophysiological phenomena. Ion channels and ion pumps reside in the membrane, these proteins play an important role in maintaining the ionic connection between the interior and the exterior of the cell. In the cell, the Ca^{2+} concentration is maintained at a level lower than that of the external environment, while the K^+ concentration is maintained at a higher level. In a standard salt solution, the membrane potential is maintained at approximately 30 mV lower than that of the external environment when *Paramecium* does not receive the stimuli from the environment. When *Paramecium* receives a stimulus, the ion channels open and ionic flow occurs between the interior and the exterior of the cell. The membrane potential is then depolarized or hyperpolarized by the ionic flow. We consider that the depolarization of membrane potential occurs when *Paramecium* senses danger in the new environment; on the other hand, the hyperpolarization of membrane potential can be considered to occur when *Paramecium* senses that the new environment is safe. The ciliary movement is determined based on the information processed by the cell.

3 *Virtual Paramecium*

Virtual Paramecium comprises three units, namely, the sensory unit, information processing unit, and motor control unit. In this section, we describe the overview of each unit.

3.1 Sensory unit [9]

Figure 1 illustrates the relationship between the change in membrane potential and environmental changes. It can be considered that a compulsory electrical change in membrane potential, similar to that in the voltage-clamp experiments [10], is generated when the ionic composition of the environment changes (see Figure 1). For instance, the resting membrane potential rises when the K^+ concentration in the environment increases, and then the potential difference generated between the environment and the interior of the cell decreases (see Fig. 1 A → B). An early current is generated as shown in Fig. 1B, when the cell of *Paramecium* is considered as a capacitor. Then, the sensory unit determines the probability of the aperture rate of ion channels that are opened by changed in the environmental conditions.

First, in the sensory unit, the resting membrane potential E_{leak}, which depends on $[\text{Ca}^{2+}]_\text{o}$ and $[\text{K}^+]_\text{o}$, is calculated by using the Goldman-Hodgkin-Katz equation [10]:

$$E_{\text{leak}} = \frac{\alpha_{\text{Ca}} E_{\text{Ca}} + \alpha_{\text{K}} E_{\text{K}}}{\alpha_{\text{Ca}} + \alpha_{\text{K}}}, \tag{1}$$

where α_{Ca} and α_{K} are the existence ratios of the Ca^{2+} and K^+ channels, respectively. Also, E_{Ca} and E_{K} are the equilibrium potentials which are generated by the difference in the concentration of ions inside and outside the cell. These are calculated using the following eqution:

$$E_{ion} = \frac{RT}{cF} \ln \frac{[ion]_\text{o}}{[ion]_\text{i}} \quad (ion \in \{\text{Ca}^{2+}, \text{K}^+\}), \tag{2}$$

where c is the ionic valency, F the Faraday constant, R the gas constant, and T the absolute temperature. Also, $[ion]_\text{o}$ is the ionic concentration of the environment, and $[ion]_\text{i}$ the intracellular ionic concentration.

Then, the early current $I_\text{c}(t)$ is calculated by:

$$I_\text{c}(t) = \frac{1}{R_m}(E_{\text{leak}}(t) - V(t)), \tag{3}$$

where R_m is the input resistance of the membrane in *Paramecium*, and $V(t)$ the membrane potential. A positive value of $I_\text{c}(t)$ means outflow of current. In this study, it is assumed that the early aperture rate of each ion channel is proportional to the size of $I_\text{c}(t)$. The early aperture ratios of the Ca^{2+} channel and the K^+ channel are calculated as follows:

$$O_{\text{Ca}} = \begin{cases} b_{\text{Ca}} I_\text{c} & (I_\text{c} \geq \text{Th}_1) \\ 0 & (I_\text{c} < \text{Th}_1), \end{cases} \tag{4}$$

$$O_{\text{K}} = \begin{cases} 0 & (I_\text{c} > \text{Th}_2) \\ -b_{\text{K}} I_\text{c} & (I_\text{c} \leq \text{Th}_2), \end{cases} \tag{5}$$

where b_{Ca}, b_{K}, Th_1, and Th_2 are constants. The early aperture rate O_{Ca} of the Ca^{2+} channel increases when the early current is larger than the threshold Th_1 and flows outwards ($I_c \geq \mathrm{Th}_1 > 0$). Conversely, the early aperture rate O_K of the K^+ channel increases when the early current is smaller than the threshold Th_2 and flows inwards ($I_c \leq \mathrm{Th}_2 < 0$). Thus, the early aperture rate of each ion channel is determined corresponding to the change in the environmental conditions.

3.2 Infomation processing unit [8]

In this unit, the change in membrane potential and the Ca^{2+} concentration in cilia are calculated using the inputs of the sensory unit.

First, the changes in the membrane potential of *Paramecium* are modeled as follows:

$$\dot{V}(t)=\frac{1}{C_m}[I_c(t)-I_{Ca}(t,V)-I_K(t,V)-I_{leak}(t,V), \quad (6)$$

where $V(t)$ is the membrane potential, $I_c(t)$ is the early current, and C_m is the membrane capacity. The Ca^{2+} current $I_{Ca}(t,V)$, the K^+ current $I_K(t,V)$, and the leakage current $I_{leak}(t,V)$ are given by the following equations [8]:

$$\begin{aligned} I_{Ca}(t,V) &= \bar{g}_{Ca} m^5\{1-(1-h)^5\}(V(t)-E_{Ca}), && (7)\\ I_K(t,V) &= \bar{g}_K n(V(t)-E_K), && (8)\\ I_{leak}(t,V) &= g_{leak}(V(t)-E_{leak}), && (9)\end{aligned}$$

where $\bar{g}_{Ca}$, $\bar{g}_K$, and g_{leak} are the maximum values of the ion conductance for Ca^{2+}, K^+, and leakage ion channels, respectively. Equilibrium potentials for Ca^{2+}, K^+, and leakage ions are expressed as E_{Ca}, E_K, and E_{leak}, respectively. Also, m, h, and n are the activation probabilities of each ion channel. Activation probabilities, $x \in \{m,h,n\}$, of each channel are calculated based on the Hodgkin-Huxley equations [11] as follows:

$$\begin{aligned} \dot{m}(t,V,O_{Ca}) &= \alpha_m(V,O_{Ca})\cdot(1-m(t,V,O_{Ca}))\\ &\quad -\beta_m(V)\cdot m(t,V,O_{Ca}), && (10)\\ \dot{h}(t,V,O_{Ca}) &= \alpha_h(V,O_{Ca})\cdot(1-h(t,V,O_{Ca}))\\ &\quad -\beta_h(V)\cdot h(t,V,O_{Ca}), && (11)\\ \dot{n}(t,V,O_K) &= \alpha_n(V,O_K)\cdot(1-n(t,V,O_K))\\ &\quad -\beta_n(V)\cdot n(t,V,O_K). && (12)\end{aligned}$$

O_{Ca} and O_K are the early open ratios of the Ca^{2+} channel and the K^+ channel that are calculated by the sensory unit. The complicated changes in depolarization are realized by the above mechanism.

Next, the Ca^{2+} concentration in cilia is calculated. Deciliated *Paramecium* whose cilia are removed by chemical treatment is utilized in order to formulate the electrical characteristics of only the cell body. The changes in the membrane potential are given as:

$$\begin{aligned}\dot{V}(t)=&\frac{1}{C_m}[I_c(t)-I_{Ca(cell)}(t,V)\\ &-I_K(t,V)-I_{leak}(t,V)], \quad (13)\end{aligned}$$

where $I_{Ca(cell)}$ is the current in the cell of the deciliated *Paramecium*, and is defined by the following equation:

$$\begin{aligned}I_{Ca(cell)} = \bar{g}_{Ca(cell)} m^5_{(cell)}\{1-(1-h_{(cell)})^5\}\\ (V(t)-E_{Ca}), \quad (14)\end{aligned}$$

where $\bar{g}_{Ca(cell)}$ is the maximum value of the ion conductance for the Ca^{2+} channel in the cell, and $x_{(cell)}(x \in \{m,h\})$ is the activation probability in only the cell body defined by:

$$\begin{aligned}\dot{x}_{(cell)}(t,V,O_{Ca}) =&\alpha_{x(cell)}(V,O_{Ca})\\ &\cdot(1-x_{(cell)}(t,V,O_{Ca}))\\ &-\beta_{x(cell)}(V)\cdot x_{(cell)}(t,V,O_{Ca}). \quad (15)\end{aligned}$$

By using both $I_{Ca(cell)}$ and the Ca^{2+} current I_{Ca} in the whole *Paramecium*, the Ca^{2+} current in cilia $I_{Ca(cilia)}$ is expressed as:

$$I_{Ca(cilia)} = I_{Ca} - I_{Ca(cell)}. \quad (16)$$

Thus, the ionic flow of Ca^{2+} in the cell body and that in cilia can be separated. Finally, the Ca^{2+} concentration in cilia is calculated as follows :

$$\begin{aligned}\frac{d\left[Ca^{2+}\right]_{in}}{dt} &= -\frac{1}{2F}\left[I_{Ca(cilia)}+(I_p)_{Ca}\right], && (17)\\ (I_p)_{Ca} &= 2F\frac{(\bar{J}_p)_{Ca}}{1+\left(\frac{K_m}{\left[Ca^{2+}\right]_{in}}\right)^3}, && (18)\end{aligned}$$

where $[Ca^{2+}]_{in}$ is the Ca^{2+} concentration in cilia, F the Faraday constant, $(\bar{J}_p)_{Ca}$ the maximum active Ca^{2+} extrusion, and K_m the $[Ca^{2+}]_{in}$ at which the active Ca^{2+} extrusion is at half its maximum value. Also, $(I_p)_{Ca}$ is the current produced by the Ca^{2+} pump which discharges Ca^{2+} to the exterior of the cell, and it is assumed that $(I_p)_{Ca}$ is included in I_{leak} calculated by Eqs. (6) and (13) for simplicity.

3.3 Motor control unit

During its movements through water, *Paramecium* follows a spiral path while rotating around its long axis [12]. This is one of the effective mechanisms that can be employed to escape from the dangerous elements in an environment. The proposed *Virtual Paramecium*

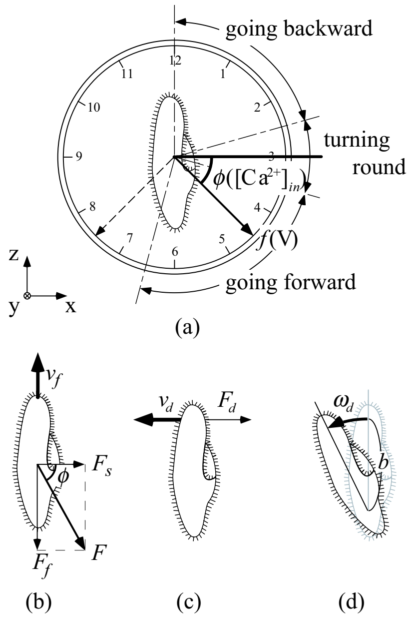

Figure 2: Driving forces generated by ciliary movements.

[9] reproduces the behavior of an actual *Paramecium*. Here, we describe the motor control unit and the planar movements of *Virtual Paramecium* in order to apply it to control of mobile robots.

The swimming condition of *Paramecium* depends on the frequency and direction of the ciliary beat. It is easy to understand the direction of the ciliary beat of *Paramecium* by considering the front of *Paramecium* as the direction corresponding to 12 o'clock on an analog clock, as shown in Figure 2(a) [10]. As *Paramecium* senses stimuli, the direction of the ciliary beat changes between half past six and 12 o'clock, while it is half past four in the normal condition (see Figure 2(a)). The swimming velocity increases when the ciliary beat direction approaches 6 o'clock. Also, *Paramecium* moves backward as the ciliary beat direction approaches 12 o'clock. The driving force F can be resolved into the driving power F_d and the rotational power F_s (see Figure 2(b)). In addition, it is possible to determine the spiral movement in combination with F_d, which is generated by the movement of peculiar cilia around the peristome [12].

The ciliary beat direction is regulated by the Ca^{2+} concentration in cilia [10, 13]. First, the ciliary beat direction $\phi([\mathrm{Ca}^{2+}]_{in})$ is modeled as the following functions of $[\mathrm{Ca}^{2+}]_{in}$:

$$\phi([\mathrm{Ca}^{2+}]_{in}) = \pi\left(\frac{1}{A_\phi \log_{10}([\mathrm{Ca}^{2+}]_{in})} - 0.5\right)$$

$$\left(A_\phi = A_{\phi 1} \quad ([\mathrm{Ca}^{2+}]_{in} < C_\phi)\right)$$
$$\left(A_\phi = A_{\phi 2} \quad ([\mathrm{Ca}^{2+}]_{in} \geq C_\phi)\right), \qquad (19)$$

where $A_{\phi 1}$ and $A_{\phi 2}$ are constants that determine the direction of the ciliary beat, and C_ϕ is the concentration value of $[\mathrm{Ca}^{2+}]_{in}$ when the direction of the ciliary beat approaches 3 o'clock.

The ciliary beat frequency is regulated by the membrane potential [14]. Although the steady-state frequency of the ciliary beat is 10 – 20 Hz, it is increased to approximately 50 Hz corresponding to the change in the membrane potential. In addition, the ciliary beat frequency decreases when the Ca^{2+} concentration increases to more than 10^2 μM. Therefore, the ciliary beat frequency, $f(V, [\mathrm{Ca}^{2+}]_{in})$, is modeled as the following equations of the membrane potential:

$$f(V, [\mathrm{Ca}^{2+}]_{in}) = f(V) - f([\mathrm{Ca}^{2+}]_{in}), \qquad (20)$$

$$f(V) = f_0 + A_{f1}(|A_{freq} - V(t)|)^{A_{f2}}, \qquad (21)$$

$$f([\mathrm{Ca}^{2+}]_{in}) = \left(\frac{f_{max}}{1 + \exp(A_{f3} \log_{10}(A_{f4}[\mathrm{Ca}^{2+}]_{in})}\right), (22)$$

where A_{fi} (i = 1, 2, 3, 4) are constants, f_0 the steady-state value of ciliary beat frequency, f_{max} the maximal value, and A_{freq} the membrane potential value during the resting beat frequency. The driving force F is calculated as follows:

$$F = a_0 f(V, [\mathrm{Ca}^{2+}]_{in}), \qquad (23)$$

where a_0 is the coefficient which transforms the ciliary beat frequency into the driving force F in *Paramecium*.

By using Eqs. (19), (20), $\cdots$, (23), the movements of *Paramecium* in two-dimensional space can be calculated. The velocity of *Paramecium* is calculated by:

$$v_f = -a_1 F sin(\phi), \qquad (24)$$

where v_f is the velocity in the longitudinal direction of body, and a_1 is the coefficient which transforms the driving force into v_f (see Figure 2(b)). The velocity v_d, which is perpendicular to the longitudinal axis, and the turning angle velocity ω_d by v_d are given by the following equations:

$$v_d = -a_2 f_d, \qquad (25)$$

$$\omega_d = \frac{v_d}{b}, \qquad (26)$$

where a_2 is a coefficient that transforms f_d into v_d and b is the distance between the fulcrum of rotation and

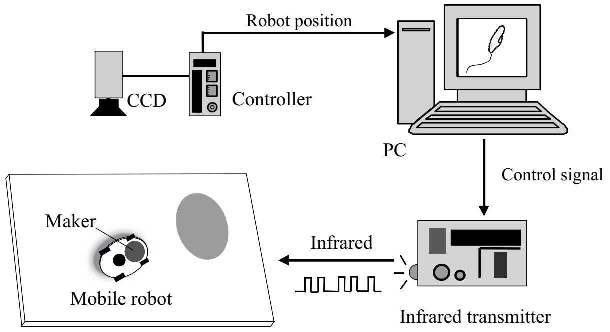

Figure 3: Mobile robot control system.

the point of application of f_d (see Figure 2(c), (d)). The orbital period of spiral movement in *Paramecium* is defined as T_f, and the sign of F_d is inverted from positive to negative, or vice versa, in every $T_f/2$ period. Thus, it is possible to reproduce the serpentine movement that the spiral movement of *Paramecium* is projected on the two-dimensional plane.

4 Biomimetic control experiments

4.1 Control system configuration

Figure 3 illustrates the control system for a mobile robot. The biomimetic control experiments of a mobile robot were carried out according to the following procedure. DQ-04 (TAKARA), whose length is approximately 5 cm, was adopted as the mobile robot. This robot has four wheels in the front and rear, and only two rear wheels on the right and left can be controlled independently. In these experiments, an image processing system was adopted for environmental measurement because it was difficult to mount any sensors on the robots. The measurement area was square (2.5 m × 2.5 m), and the two-dimensional position of a marker on the head of the robot was measured using a CCD camera suspended from the ceiling. The virtual chemical environment was set as a function of the position in the horizontal plane beforehand. The chemical concentration was input to the sensory unit of *Virtual Paramecium* every 40 millisecond. *Virtual Paramecium* processes the input information and determines the control input to the robot. Then, the control signal was sent to the robot to realize the comparable behavior to the actual organisms calculated by *Virtual Paramecium*.

4.2 Cruise control of the mobile robot

The relationship between the rotation speed of the two rear wheels in the mobile robot and its movement can be given by the following equation:

$$\begin{bmatrix} v \\ \omega \end{bmatrix} = \begin{bmatrix} \frac{1}{2} & \frac{1}{2} \\ \frac{1}{2c_r} & -\frac{1}{2c_r} \end{bmatrix} \begin{bmatrix} v_L \\ v_R \end{bmatrix}, \tag{27}$$

where $2c_r$ is the length of the axle; and v_L and v_R are the speeds of the rear wheels. In these experiments, each rear wheel was controlled according to the following equation:

$$\begin{bmatrix} v_L \\ v_R \end{bmatrix} = \gamma \begin{bmatrix} \frac{1}{2} & \frac{1}{2} \\ \frac{1}{2c_r} & -\frac{1}{2c_r} \end{bmatrix}^{-1} \begin{bmatrix} v_f \\ \omega_d \end{bmatrix}, \tag{28}$$

where γ is a coefficient that transforms the movement velocity of *Virtual Paramecium* into the mobile robot, in consideration of each size. The values of v_f and ω_d are calculated using the motor control model (24) and (26).

4.3 Experimental results

The biomimetic control of a mobile robot was executed using *Virtual Paramecium*. The parameters included in *Virtual Paramecium* were determined based on previous studies [9, 10].

In this paper, reactions of the mobile robot toward the area where the K^+ concentration was different form that of the standard salt solution were examined. The results obtained when the K^+ concentrations of the stimulation solution were set to 16 mM and 0.25 mM are shown in Figure 4(a) and (b), respectively. The left side of Figure 4 shows the trajectories of the mobile robot, while the right side shows the time course of the swimming velocities of *Virtual Paramecium*, which the negative velocity implies backward movement.

Figure 4(a) shows the escape reaction of the mobile robot from the area where the K^+ concentration is higher than that of the standard salt solution. Further, the mobile robot exhibited accelerated movement toward the area where the K^+ concentration was lower than the standard salt solution (see Figure 4(b)). Additionally, in Figure 4(b), the escape reaction to the area of standard salt solution is shown after cruising in the environment with low K^+ concentration for a short duration. On the basis of above results, we confirmed the effectiveness of the biomimetic control that was based on the information processing algorithm of living organisms.

5 Summary

In this paper, the results of our study on the control of a mobile robot by using *Virtual Paramecium* have

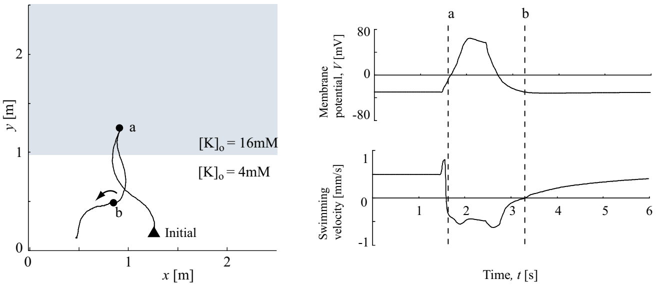

(a) Response to the area of $[K^+]_o = 16$mM

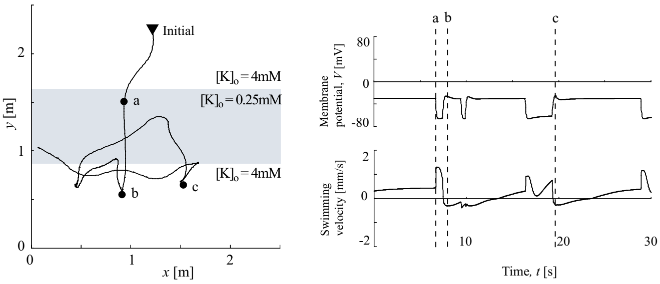

(b) Response to the area of $[K^+]_o = 0.25$mM

Figure 4: Responses of a mobile robot to the virtual chemical environments.

been reported. We confirmed that the escape reaction increased in the area where the K^+ concentration was higher than that of the standard salt solution, and the mobile robot attempts to continue to reside in the area with a low concentration of K^+. On the basis of above results, we confirmed the effectiveness of the biomimetic control that was based on the information processing algorithm of living organisms.

In future research, our experimental results will be compared to the control results by using the information processing algorithm of *E. coli* bacteria [7].

Acknowledgements

This work is partially supported by the 21st Century COE Program of JSPS (Japan Society for the Promotion of Science) on *Hyper Human Technology toward the 21st Century Industrial Revolution.*

References

[1] H. Ohtake (1998) : "Software of living organisms," KYORITSU SHUPPAN CO., LTD.. (in Japanese)

[2] D.Bray, and S.Lay (1994) : "Computer Simulated Evolution of a Network of Cell-Signaling Molecules", Biophysical Journal, Vol. 66, pp. 972–977.

[3] D. C. Hauri and J. Ross (1995) : "A Model of Excitation and Adaptation in Bacterial Chemotaxis", Biophysical Journal, Vol. 68, pp. 708–722.

[4] M. Tomita, K. Hashimoto, K. Takahashi, T. S. Shimizu, Y. Matsuzaki, F. Miyoshi, K. Saito, S. Tanida, K. Yugi, J. C. Venter, C. A. Hutchison III (1999) : "E-CELL: software environment for whole-cell simulation," Bioinfomatics, Vol. 15, No. 1, pp. 72–84.

[5] T. Morohoshi, T. Tsuji, H. Ohtake (1998) : "A Model of Bacterial Motor Control and Computer Simulation of the Chemotaxis," Journal of the Society of Instrument and Control Engineers, Vol. 34, No. 11, pp. 1731–1738. (in Japanese)

[6] T. Tsuji, K. Hashigami, M Kaneko, H. Ohtake (2002) : "Emerging chemotaxis of virtual bacteria using genetic algorithum," Transaction of IEE of Japan, Vol. 122-C, pp. 201–207. (in Japanese)

[7] T. Tsuji, A. Sakane, O. Fukuda, M. Kaneko, H. Ohtake (2002) : "Bio-mimetic control of mobile robots based on a model of bacterial chemotaxis", Trans. of the Japan Society of Mechanical Engineers, Vol. 68, No. 673, pp. 171–178. (in Japanese)

[8] A. Hirano, T. Tsuji, N. Takiguchi, H. Ohtake (2005) : "Modeling of the Membrane Potential Change of *Paramecium* for Mechanical Stimuli", SICE Symposium on Decentralized Autonomous Systems, Vol. 41, No. 4, pp.351–357. (in Japanese)

[9] A. Hirano (2005) : "A Model of Chemotactic Response of Paramecium Based on Electrophysiology," Dissertation for the degree of Master of Engineering, Graduate School of Engineering, Hiroshima University.

[10] Y. Naitoh (1990) : "Behavior of unicellular animals," University of Tokyo Press. (in Japanese)

[11] A.L.Hodgkin and A.F.Huxley (1952) : "A Quantitative Description of Current and Its Application to Conduction and Excitation in Nerve," The Journal of Physiology, Vol. 117, pp. 500–544.

[12] K. Sugino and Y. Naitoh (1988) : "The method for measuring a helical trajectory of Paramecium ," Medical science, Igaku-Shoin Ltd., Vol. 39, No. 5, pp.485–490. (in Japanese)

[13] Y. Naitoh and H. Kaneko (1972) : "Reactivated Triton-Extracted Models of Paramecium: Modification of Ciliary Movement by Calcium Ions," Science, Vol. 176, pp. 523–524.

[14] P. Brehm and R. Echkert (1978) : "AN ELECTROPHYSIOLOGICAL STUDY OF THE REGULATION OF CILIARY BEATING FREQUENCY IN *PARAMECIUM*," *J. Physiol.*, 283, pp. 557–568.

The Eleventh International Symposium on Artificial Life and Robotics 2006 (AROB 11th'06),
B-con Plaza, Beppu, Oita, Japan, January 23-25, 2006

Evolutionary simulation of an agent based mobility system using indirect communication

Francesco Zanlungo
Department of Physics
University of Bologna
Bologna, via Irnerio 46 40126

Takaya Arita
Graduate School of Information Science
Nagoya University
Chikusa-ku, Nagoya, Aichi, 464-8601 Japan

Abstract

We study the evolutionary dynamics of a mobility system in which agents are able to explore the environment and to communicate between them in order to increase the efficiency of the system, i.e. to minimize the average time needed to reach their goal, choosing the quickest path and avoiding the formation of traffic jams. The agents use an evolvable pheromone-like indirect communication system, of which we also give an interpretation as the average of different kinds of direct communication.

Key words: Indirect communication, evolution of neural networks, mobility systems, multi-agent system

1 Introduction

A town is a complex system in constant evolution. Both the environment (the structure of the town, its dimensions, the road and public transportation system, the location of the places of interest) and the behaviour of the inhabitants are constantly changing, and influencing each other. Focusing only on the mobility system, new roads, railways and subway lines are built according to the needs of the citizens, but the presence of these new structures modifies the behaviour and habits of the citizens, and so on.

In this paper we propose a simple system of agents whose behaviour is regulated by evolving neural networks. These agents move on a 2D manhattan grid that represents a town's road system, with the connected traffic problems. The knowledge of the structure of this road system is obtained through the exploration of the system by the agents, and communicated to other agents through a "pheromone-like" field.

It is our opinion that the model that we propose can be a fruitful environment to study the evolutionary dynamics of a system of different interacting agents regulated by a simple behavioural mechanism, and eventually the emergence of some kind of "global behaviour". In particular, we are interested in studying the emergence and evolution of an indirect communication system. This model could also be useful to get some insight about the evolution of actual mobility and urban systems.

It can also be seen as an attempt to understand if some kind of pheromone-like communication could be used to improve the efficiency of a real mobility system and avoid the formation of traffic jams.

2 The model

2.1 The mobility system

The agents are located on the nodes of a manhattan 2D network ("a town"). At each time step they have a probability $p \leq 1$ to perform just one of five possible actions, i.e. to move to one of the four neighbour sites (at manhattan distance $d = 1$, where the distance between the points P_1 and P_2 is defined by $d(P_1, P_2) \equiv |x_1 - x_2| + |y_1 - y_2|$) or to rest on the site they are located in. We want our town to have wider roads, in which higher speed is possible, and narrower roads. We also want to have a traffic problem, i.e. agents should be slowed down when a great number of them is located in the same site (when we talk about the agent's speed, we are actually talking about its probability p to perform an action). To achieve this we define, identifying a site with its discrete coordinates (i, j) and the number of agents on that site with $n(i, j)$, the probability to act as

$$p((i,j), n(i,j)) = w(i,j)t_{(i,j)}(n(i,j)) \qquad (1)$$

where $0 \leq w(i,j) \leq 1$ is the wideness of the site and $t_{(i,j)}$ is a (eventually) site dependent "traffic jam function", which we ask to be (not necessarily strictly) decreasing and to have $t_{(i,j)}(1) = 1\ \forall (i,j)$. In particular, we are going to use $t(n) = (1/n)^{\gamma}$, with $\gamma \geq 0$.

Even if we talk about "wide and narrow road" it is clear from the definition that the wideness is related to the site, and not to the roads, since no road is actually present in this model. We order the wide sites in rows inside the grid (see figure 1 for the basic structure of the town) to simulate the presence of a road, but p has no dependence on the direction of the motion so there is no difference between an agent that is following a "road" and an agent that is just crossing it.

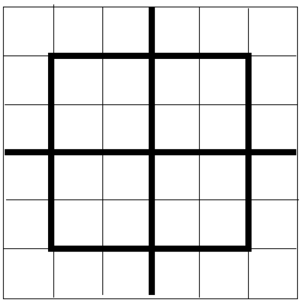

Figure 1: Basic structure of the town's road system. Thick means wide.

This is a very simple and abstract model that is, according to our opinion, feasible to study the general features of the interaction of a group of agents in a mobility system. Nevertheless in building the model we were inspired by the actual car traffic systems. A node in the network represents a crossroad (plus some portions of the roads leading to it). If a large number of cars is located in the same crossroad, a traffic jam occurs. w stands for the maximum speed that the car can have on that (cross)road, while t is the "tendency" of the crossroad to the formation of traffic jams.

We can also think of this model as a system of pedestrians, in which the wide roads correspond to public transportation, and t is the waiting time to use it.

2.2 Communication

The way the citizens of a town learn to use its mobility system is obviously quite complicated and differentiated (past experience, communication with other agents, centralized communication like news from the radio, etc.). In our model we wanted to introduce some kind of mechanism that could represent an average of all these processes, that could be regulated by the agents themselves and that could be utilized just through a local observation of the environment (to avoid a too complex sensory system or the introduction of memory).

We decided to use pheromone based communication which has shown to be an efficient way to evolve communities of collaborating agents [1].

We introduce a pheromone field $P(i,j)$, generated by the same agents which drop an amount q of pheromone every time that they cannot perform an action, i.e. every time that "they have to wait" because they are located in a narrow road or they are stuck in a traffic jam. This means that if the indirect communication system emerges, pheromone should be interpreted as "repulsive" and used to inform the other agents about "bad places". Pheromone evaporates according to a coefficient c_e and turns into evaporated pheromone $P_e(i,j)$ that diffuses with coefficient c_d [1]. Agents are able to perceive the gradient of this field, i.e. the difference with the neighbouring sites $P_e(i,j) - P_e(neigh)$.

We could interpret this pheromone field as a "rumor" that stands for the "collective knowledge" of the urban structure, and spreads between agents. Actually in our model the rumor is spreading on the urban structure, but we can think that in this model are present immobile and mobile agents, and the rumor is spreading between the (not explicitly represented) first ones. Adopting this point of view, the medium that mobile agents are using to communicate are the immobile agents.

2.3 The decision mechanism and its evolution

The evolution of neural networks through genetic algorithms has shown to be an efficient way to develop agents and robots able to move in complex environments [2].

We use a fully connected neural network with 6 inputs (the distance from the goal in x and y coordinates $(g_x - x)$ and $(g_y - y)$ plus the 4 "pheromone gradients"), a layer with h hidden neurons and 5 outputs corresponding to the 5 possible actions. The action with the highest output value is performed. The connections of the networks are kept fixed during the whole generation, i.e. there is no learning, just evolution of connection weights and of the number of the hidden neurons (h).

We define the fitness function in the following way. Each agent is created in a randomly selected starting point (s_x, s_y). If τ is the time to reach its randomly selected goal point (g_x, g_y) (a minimum distance between start and goal is imposed), the ratio $r = (|g_x - s_x| + |g_y - s_y|)/\tau$ is measured. If the agent does not reach the goal in a maximum time T, r is set to zero. The operation is repeated R times and the average value of the ratio is the agent's fitness $f = \bar{r}$.

Since we did not know the value of h that could solve our problem, we used the following evolution strategy, (inspired by [3, 4]) to optimize also this parameter. We start using different networks divided in N_s species, according to their structure (i.e. to the value of h), each one with an equal number of members (in each experiment we have networks with different structure and weights interacting and competing at the same time on the urban structure). Tournament selection is performed inside a single species for g_s generations, then the dimension (number of agents) of the species is changed according to its fitness. The size of the tournament is changed according to the species's new size, and evolution is performed again for g_s generations inside the species's boundary, and so on. Mutation of the connection weights was performed adding, with probability $p_m = 0.05$, a gaussian noise with mean zero .

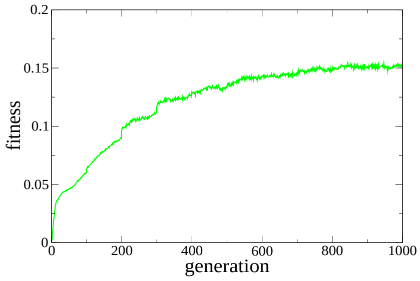

Figure 2: Evolution of the average fitness value through generations in the case of no traffic jams.

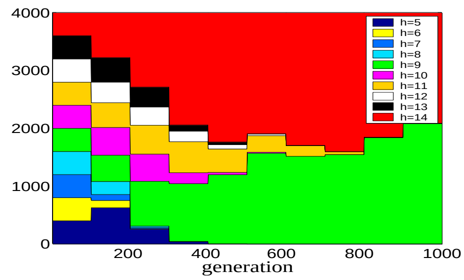

Figure 3: Evolution of the h species' size for the same simulation shown in figure 2. Initially 10 species (corresponding to values of h between 5 and 14) are present, then $h = 9$ (green) and $h = 14$ (red) invade the population.

3 Experiments

We used 4000 agents and a 50x50 grid, averaging over $R = 20$ runs. Wide roads were defined to have $w = W = 1$ and narrow ones to have $w = N = 0.05$. The values of the pheromone parameters were $q = 0.1$, $c_e = 0.1$, $c_d = 0.1$ (we reserve for future works the task of optimizing these parameters through evolution, and eventually also of evolving the pheromone dropping mechanism).

3.1 No traffic jams

In a first class of experiments we used $\gamma = 0$ (i.e. $t(n) = 1\ \forall n$) on the whole grid. In this case no traffic jam can be generated, and the only problem is to find the quickest path to the goal. We first fixed $w(i, j) = N$ $\forall(i, j)$ and checked that we were able to evolve networks with the maximum possible fitness $f = 0.05$. Then, without introducing pheromone, we used a structure of wide roads according to figure 1. The networks evolved to $f = 0.064$ which we assumed to be the maximum fitness in absence of further information (the fitness attained by agents going straight to the goal). We will consider pheromone communication to be successful if it is able to improve this value.

The agents that dropped pheromone evolved to reach a fitness roughly 3 times higher ($f = 0.202$), i.e., indirect communication had emerged. In this experiment, pheromone communication is used to mark the narrow roads (wide roads correspond to the minima of the pheromone field). The agents developed an ability to reach the wide roads following the decreasing pheromone gradient when they were distant from their goal, to move on the the minima (follow the wide road) in order to approximate the goal, and then to leave the minima (despite the positive pheromone gradient) in order to reach the goal when they were near to it. The results of this experiment are shown in figures 2 and 3.

3.2 Traffic jams in a uniform grid

We then fixed $w = W$ on the whole grid and used $\gamma > 0$, i.e. the agents did not have to find any "best path" but just to avoid traffic jams.

Using $\gamma = 1$ agents going straight to the goal performed with an average fitness $f = 0.292$, while the pheromone dropping agents had an higher fitness ($f = 0.377$). We tested the performance of these agents without allowing them to drop pheromone and we unexpectedly found that their fitness did not change at all. Actually the genetic algorithm had developed a network that reached the goal moving always clockwise (in the specific case). Due to the nature of the manhattan metric this allowed them to reach the goal on a minimal distance path, reducing strongly the probability of a collision (through the introduction of a "circulation rule", i.e. of some kind of collective behaviour, as clock-wise or counter clock-wise circulation, see figure 4). The emergence of this rule has no relationship with communication, since it was based only on the "distance to the goal" inputs. Actually, for this low value of γ, the circulation rule was enough effective to avoid the formation of traffic jams, and it prevented the emergence of communication.

In the case of $\gamma = 2$ the agents going straight to the goal without using a circulation rule performed with $f = 0.024$, while the pheromone dropping agents reached a (4 times higher) value of $f = 0.098$. If we made them run without pheromone, i.e. without communication, they performed with $f = 0.030$. This value is quite lower than the one they had when we allowed them to communicate, but higher than the one attained by agents going straight to the goal. This shows that both communication and a circulation rule had emerged.

We tested on this experiment also the pheromone dropping agents that we had evolved in the previous experiment without traffic jams. Despite the completely

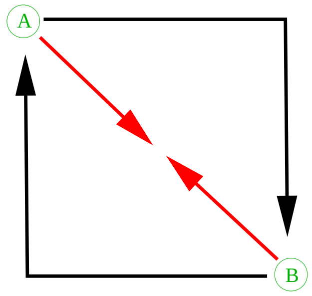

Figure 4: An agent has to reach point B from A, and another A from B. Black corresponds to a circulation rule that avoids collision, while red corresponds to go straightly to the goal. Notice that the two paths cover the same distance in manhattan metric.

different nature of this experiment, they were able to double the fitness of the agents going straight to the goal ($f = 0.051$). This happens because the agents, trained in the first experiment to follow the wide roads as minima of the pheromone field, result also able to avoid the traffic jams (maxima of the pheromone field) in this experiment.

3.3 Complete model

In real mobility systems, the greatest traffic problems occur when one of the main communication routes is blocked due to a traffic jam (often caused by a traffic accident). To simulate this problem on our simple geometry we used the basic structure of figure 1 with a traffic function that used $\gamma = 1.75$ for the sites with $w = W$ and $\gamma = 0$ where $w = N$ (this can be interpreted as a rule that says that accidents, and thus traffic jams, are easier to occur where the speed is high). In this way we created a dilemma about the use of wide roads.

In this environment, the agents going straightly to the goal performed with values that changed strongly according to different repetitions of the experiment, but that where always smaller than 0.05 (between 0.035 and 0.048 in the experiments that we have performed). The crucial point is that these values are lower than 0.05, i.e. the introduction of wide roads on which traffic jams are easy to occur is harmful if they are not used in a "intelligent" way.

We then tested with these conditions the network evolved dropping pheromone in absence of traffic jams, which performed with $f = 0.063$ (almost the same value on each test), i.e. it was able to use the wide roads in a way good enough to improve over the value of 0.05. Furthermore, if we added to the road system a further "ring" of wide roads, the fitness of the agents going straightly to the goal decreased again (0.033-0.037), while the one of agents using pheromone increased to 0.067.

We finally tried to evolve explicitly a network for this problem. The maximum reached average fitness was 0.092, but this fitness dropped to 0.060 when we tried to extract a "best" uniform population.

4 Conclusions

We have shown that simple neural networks are able to evolve a (pheromone based) indirect communication system that is effective in solving both the problem of finding a "good path" and to avoid "traffic jams" in a simple mobility system.

We have found that a network evolved in a time-constant environment (no traffic jams) could be effective also in the other two experiments without further evolution, showing the effectiveness of the pheromone communication in both the tasks of avoiding problems (pheromone maxima) and following good paths (minima). The cases with traffic jams (i.e. the environment is constantly changing according to the behaviour of the agents) showed the emergence of global behaviours ("circulation rules") and the presence of a not trivial evolutionary dynamics (the presence of differentiated neural networks, different in connection weights and structure, seems to cause an higher value of the fitness), which should be further investigated in future works.

References

[1] Y. Nakamichi and T. Arita, "Effectiveness of Emerged Pheromone Communication in an Ant Foraging Model", Proceedings of the Tenth International Symposium on Artificial Life and Robotics, 324-327, 2005.

[2] S. Nolfi and D. Floreano, "Evolutionary Robotics", MIT Press, 2000.

[3] K. O . Stanley and R. Miikkulainen, "Evolving Neural Networks through Augmenting Topologies", Evolutionary Computation 10(2), 99-127, 2002.

[4] F. Gomez and R. Miikkulainen, "Solving Non-Markovian Control Tasks with Neuroevolution", Proceedings of the Sixteenth International Joint Conference on Artificial Intelligence, pages 1356-1361, Morgan Kaufmann, San Francisco, California, 1999.

The Eleventh International Symposium on Artificial Life and Robotics 2006 (AROB 11th'06),
B-con Plaza, Beppu, Oita, Japan, January 23-25, 2006

Evolution, Development and Learning in the Prisoner's Dilemma Game

Yukimasa Ogawa   Takaya Arita
Graduate School of Information Science, Nagoya University
Furo-cho, Chikusa-ku, Nagoya 464-8601, Japan
E-mail: ogawa@create.human.nagoya-u.ac.jp, arita@nagoya-u.jp

Abstract

Evolution, learning and development are the three main adaptive processes that enable living systems to adapt to environments on different time scales. The purpose of our study is to investigate the relationships among evolution, learning and development, especially in dynamic environments where there is no explicit optimal solution through generations, and the fitness of an individual depends on the interactions in a population. To do this, we construct a computational model using the iterated Prisoner's Dilemma game as dynamic environments. In the model, evolution and learning are achieved by a genetic algorithm and a Meta-Pavlov learning, respectively. Development is handled by two alternative computation-universal mechanisms: a tag system and a Turing machine. The results showed that almost all experiments we conducted finally established cooperation through evolution, learning and development, while there were various scenarios in which cooperative relationships were established, corresponding to the flexibility in the respective roles of them.

Keywords: development, genetic algorithm, trilateral adptation, the iterated prisoner's dilemma, artificial life.

1 Introduction

Evolution, learning and development are the three main adaptive processes that enable living systems to adapt to environments on different time scales. These processes do not occur in isolation, and interactions among them are very complex and not clearly understood in both biology and engineering. Combinations of them have a long history in the fields of artificial life, evolutionary computation, and engineering. Also, recently, interactions between evolution and development, so-called "evo-devo" have attracted researchers in both biology and artificial life. However, very few models combine all these three adaptive processes, among which Downing introduced a developmental process into Hinton and Nowlan's very simple model in which environment was static and the optimal solution was fixed, and focused on the evolution of developmental process by analyzing the feature of the genomes arising in the process of the Baldwin effect [1].

The purpose of our study is to investigate the relationships among evolution, learning and development, especially in dynamic environments where there is no explicit optimal solution through generations, and the fitness of an individual depends on the interactions in a population. To do this, we have adopt a synthetic approach and construct a computational model using the Iterated Prisoner's Dilemma (IPD) game as dynamic environments. In the model, evolution is achieved by a genetic algorithm and learning is achieved by a simple improvement algorithm termed Meta-Pavlov. Development is a kind of mapping process from genotype to phenotype, and is the least understood one of the three. We focus on two computation-universal mechanisms for development: a tag system and a Turing machine, and compare them with the results of the experiments.

2 Model

We construct a computational model in which three processes (evolution, learning and development) create the strategies for the Iterated Prisoner's Dilemma (IPD) game (Figure 1). The IPD game is a simple 2-player non-zero-sum game, in each round of which each player independently chooses an action from cooperate (C) or defect (D) without knowing the other's choice, and obtains the score according to the payoff matrix (Table 1). We adopt the framework proposed by Downing [1], while we incorporate a tag system [4] as an alternative mechanism for development, and interpret the developed phenotypes as strategies for the IPD game. The genotype encodes both a mechanism performing a developmental process, which is either a tag system or a Turing machine, and an initial tape on which the mechanism runs. The final developed tape as a phenotype is interpreted as a deterministic strat-

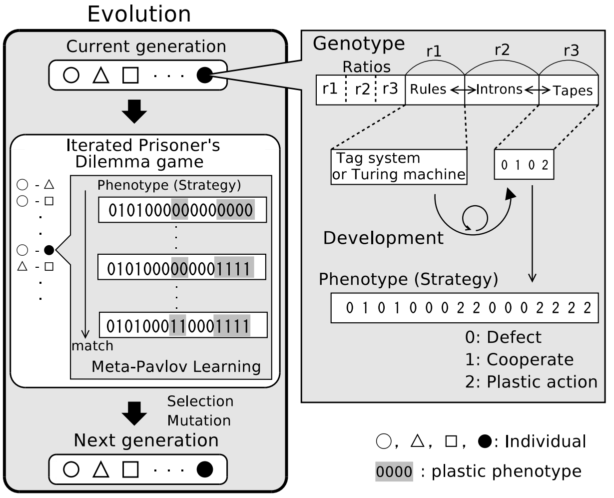

Figure 1: Evolution, development and learning in the model.

Table 1: Payoff matrix for the Prisoner's Dilemma game.

player \ opponent	cooperate	defect
cooperate	(3, 3)	(0, 5)
defect	(5, 0)	(1, 1)

(player's score, opponent's score)

egy of the IPD game. The action of the plastic phenotype is changed via a simple improvement algorithm termed "Meta-Pavlov" [3] during a game. The average score of each individual is regarded as a fitness value, new population is generated by the roulette wheel selection according to the scores, and then mutation is performed on a bit-by-bit basis.

The essential point of the model is that the developmental process can determine not only the strategies but also the possible amount of improvement by learning during game play, and at the same time the evolutionary process can determine this developmental process (Figure 2). Individuals evolved in the model are characterized in the space shown in this figure, of which the horizontal axis represents the possible amount of improvement by learning and the vertical axis represents the level of the degree of dependence on development. For example, evolution can generate the individual (at the coordinate origin) that never undergoes a developmental process, which means the genotype-phenotype mapping is 1 to 1, and has no learning ability, which means the phenotype has no plasticity.

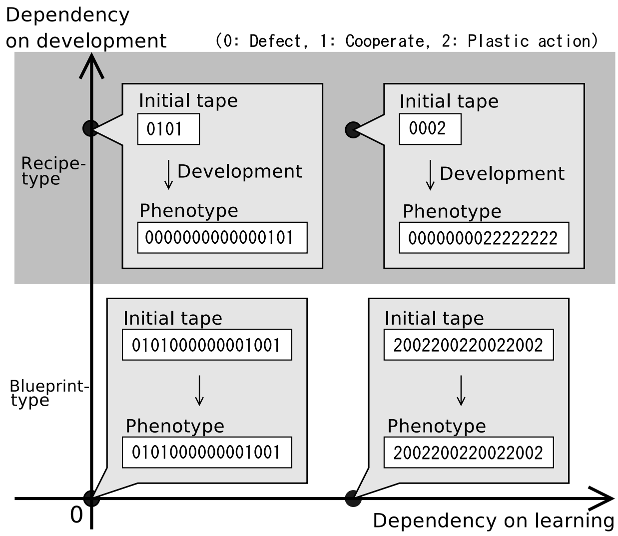

Figure 2: Individuals in the space of learnability and developability.

2.1 Genotype

Each genotype has *genotype-length* bits, and is composed of four fields: ratio, rule, intron, and tape. The ratio field have 3 bits, which encodes three integers: r_1, r_2 and r_3, each representing the ratio in length of the rules, the introns and the tapes, respectively. The intron field just separates the rule and the tape field, and is not used at all in subsequent development and learning. The tape field is used as an initial tape on which the developmental process runs.

In case of a tag system, the rule field encodes the transition rules, each of which specifies the elements to be removed from the beginning of a tape, and the elements to be appended onto the end of the tape. Each transition rule requires $(P_{ts}+Q_{ts})$ $_{ts}$ bits, where P_{ts} and Q_{ts} are the numbers of removed and appended elements, respectively, and $_{ts}$ is the number of bits used to encode these elements. The tape symbol encodes an integer between 0 and $2^{n_{ts}}$ 1. These integers are converted to 0, 1 or 2 with nearly equal probability.

In case of a Turing machine, the rule field encodes transition rules as 5-tuples of the form $(s \quad s^* \quad ^* \ a)$, in which s is the current state, is the tape symbol being read, s^* is the next state, * is the next symbol, and a is the action, that is either overwriting with *, or inserting * to the immediate right of on the tape. Each transition rule requires $2m_{tm} + 2 \ _{tm} + 1$ bits, where $_{tm}$ and m_{tm} are the numbers of bits used to encode a tape symbol and a state, respectively. Each

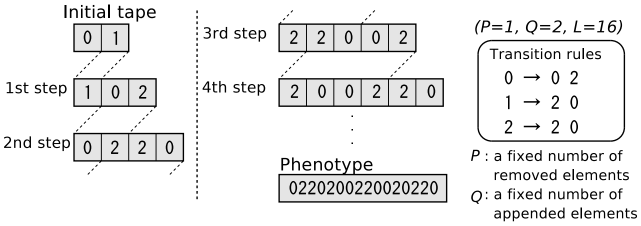

Figure 3: An example of development in case of a tag system.

element is expressed with 0, 1 or 2 as in the case of a tag system.

2.2 Development

The phenotype is generated from both the transition rules for a tag system or a Turing system and an initial tape into which developmental process decodes the genotype.

Figure 3 shows an example of development in case of a tag system. In general, the transition rules for a tag system specify that a fixed number of elements should be removed from the beginning of the sequence, and depending on these elements, several number of elements should be appended onto the end of the sequence. In the current model, both the number of the elements removed and the number of the elements appended are fixed, and are 1 and 2 respectively. In the example shown in Figure 3, first, 0 is removed from the beginning of the tape, and then the rule corresponding to 0 is retrieved from the transition rules. Since 0 02 is included in the transition rules, 02 is appended onto the end of the tape in this case. This type of replacement process continues until the tape size reaches L.

Figure 4 shows an example of development in case of a Turing machine, which is the same as the one adopted in [1]. The head always begins the developmental process in state 0 at the left edge of the cell on the tape. In this figure, the current state and the tape symbol are s_0 and 0, respectively, and then the rule corresponding to (s_0 0) is retrieved from the transition rules. As (s_0 0) (s_0 2 *Insert*) is included in the transition rules, 2 is inserted to the immediate right of 0 on the tape, and the head moves right one cell. If the head reaches the right edge of the cell on the tape, it is again set to the left edge of the cell on the tape. This type of movement and replacement process continues until either the tape size reaches L or the number of the steps reaches $max\text{-}devp\text{-}steps_{tm}$.

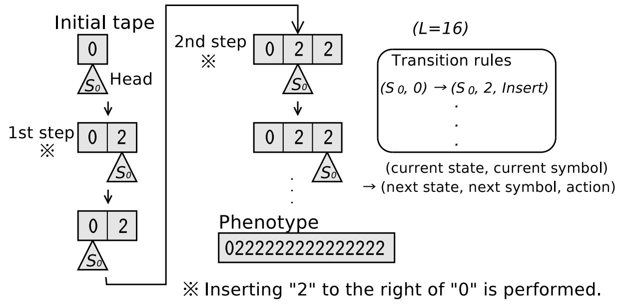

Figure 4: An example of development in case of a Turing machine.

2.3 Phenotype

The final developed tape as a phenotype is interpreted as a deterministic strategy for the IPD game, and it defines the next action according to the history of actions of both players, which is the same as in Lindgren's model [2] but is introduced plasticity as in Suzuki 's model [3]. Each strategy is represented as a string of 0's (defect), 1's (cooperate) and 2's (plastic action). "x" is used to express this plastic phenotype in this paper.

A strategy of memory m has an action history h_m which is a m_length binary strings as follows:

$$h_m = (a_{m-1} \qquad a_1 \ a_0)_2 \tag{1}$$

where a_0 is the opponent's previous action (0 and 1), a_1 is the previous player's action. a_2 is the opponent's next to previous action, and so on. S for a strategy of memory m can be expressed by associating an action A_k (0, 1 or 2) with each history k as follows:

$$S = [A_0 A_1 \quad A_{n-1}] \ (\quad = 2^m) \tag{2}$$

2.4 Learning and Evolution

A plastic phenotype can be changed by learning based on Meta-Pavlov during a game. Each agent changes its phenotypes according to the result of each round by referring to the Meta-Pavlov learning matrix (Table 2). It does not express a strategy but the way to change its own strategy (phenotype) according to the result of the current round, though this matrix is the same as that of the Pavlov strategy. The learning process is described as follows: At the beginning of the game, the plastic phenotype is set randomly to either 0 or 1. If the phenotype used in the round is plastic, the phenotype is changed to the corresponding value in this matrix based on the result of the round. The

Table 2: Strategy matrix for Meta-Pavlov learning.

player \ opponent	cooperate	defect
cooperate	C	D
defect	D	C

agent uses the new strategy specified by the changed phenotype from the next round on.

We shall consider a population of N individuals interacting according to the IPD. Each bit of gene is set randomly in the initial population. The round robin tournament is conducted among strategies under the condition in which the performed actions could be changed by noise with probability p_n. Each plastic phenotype is set randomly at the beginning of games. Rounds are repeated with the probability p_f, which is decided at the end of each round. The tournament is "ecological": The average score of each individual is regarded as a fitness value, a new population of individuals is generated by the roulette wheel selection according to the scores, and mutation is performed on a bit-by-bit basis with the probability p_m.

3 Evolutionary Experiments

We conducted 20 trials for 10000 generations in each of the experiment with the tag system and that with the Turing machine, focusing on the strategies of memory 4 ($m = 4$). The other parameters were as follows: *genotype-length* = 300, $N = 1000$, $p_m = 1/5000$, $p_n = 1/25$, $p_f = 0\ 995$, $= 5$, $P_{ts} = 1$, $Q_{ts} = 2$, $_{ts} = 5$, $L = 16$, $m_{tm} = 3$, $_{tm} = 5$, $max\text{-}devp\text{-}step_{tm} = 100$.

First of all, we have found that cooperation was finally established through evolution, learning and development in most of the trials we conducted, while there were various scenarios in which cooperative relationships were established, corresponding to the flexibility in the respective roles of them. The last generation in each trial was classified into the following five types: XX, XL, DX, DL and US as shown in Table 3, in which D represents strong dependency on development, L represents strong dependency on learning, X represents weak dependency and US represents the gray type owing to instability in the boundary areas. For example, XX represents that the average individual depended neither on development nor on learning, and DL represents that the average individual depended both on development and on learning. Dependency on development (D-dependent) was decided in case that the average times of rule application in development was more than 5, and dependency on learning

Table 3: Classification of the results by dependence on development or learning.

Classification				Tag system	Turing machine
stable	D-independent	L-independent	XX	0	3
		L-dependent	XL	1	7
	D-dependent	L-independent	DX	2	9
		L-dependent	DL	15	1
unstable			US	2	0

(L-dependent) was decided in case that the average ratio of plastic phenotypes chosen during game play was more than 0.5, in the last generation. The average score was kept around 2.4 in the last generation in almost all trials in L-dependent case (XL and DL), while DX trials varied in the score from trial to trial, and achieved the highest score, 2.6.

From this table, we see that 15 trials of 20 trials were DL in case of the tag system. This means that the tag system tended to work efficiently to help evolution explore the cooperative roles of learning and development in dynamic environments, in other words, three adaptive processes evolved the individuals depending on both learning and development, which could result in the smooth establishment of cooperative relationships.

Figure 5 shows an evolutionary transition of the average score, dependency on learning and dependency on development in a typical trial of DL. Dependency on learning and dependency on development were calculated as the average ratio of "2"s in all of the developed expressions (which is different from the definition of L-dependent) and the number of times of applying rules (in development) divided by 50, respectively. The dashed line shows the threshold that separates D-dependent and D-independent. The evolutionary scenario in this figure is summarized as follows: Defect strategy spread until around the 50th generation, which decreased the score (which is difficult to see from this figure). Simultaneously, partially plastic strategies (e.g. [0xxx0x0x0x0x010x]) spread in the population. Then, fully plastic strategies (e.g. [xxxxxx0xxxxxxxxx]) occupied the population, which increased the plasticity and the average score. Around the 1300th generation, some strategies (e.g. [xx0x000x0x0000xx]) spread, which decreased the plasticity, but around the 1600th generation, the plasticity increased again. Finally, some robust strategies (e.g. [x00x000x000x000x]) occupied the population. The number of times of applying developmental rules was around 8 throughout the generations.

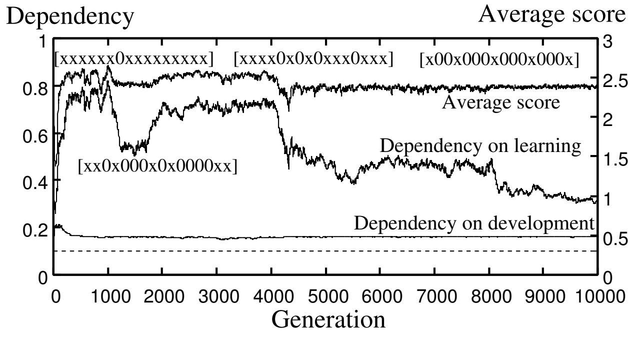

Figure 5: An experimental result (tag system).

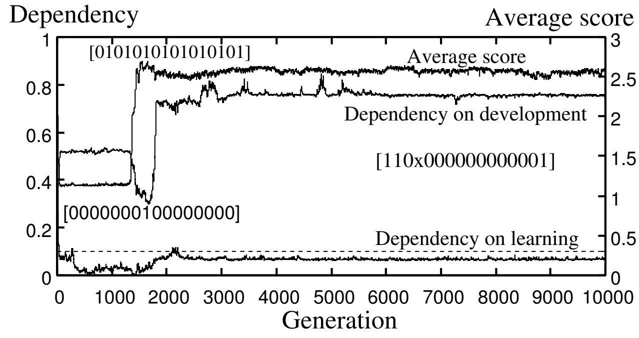

Figure 6: An experimental result (Turing machine).

11 trials of 15 DL trials showed the similar evolutionary scenario to the above described one, while 4 trials had other scenarios like the one, for example, in which dependency on learning did not reach such a high value and some robust strategies like [x00x0xx00xx0x00x] evolved to occupy the population while keeping the average score high.

As for the cases of the Turing machine, we see from this table that 16 trials of 20 trials were classified into XL or DX, which means that either learning or development tended to work exclusively to build cooperative relationships. The possible cause of this is the flexibility in the complementary roles of learning and development in evolution of cooperation. Just 2 trials of the 9 DX were the special case in which cooperative relationships could not be established since defect-oriented strategies continued to occupy the population.

A typical case of XL is summarized as follows: D-dependent defect strategies spread in the population in initial phase. However, dependency on learning did not increase and the strategies like [x00x00x00x00001x] finally evolved with the average score converging to about 2.4 and with dependency on learning hovering around 0.4. Figure 6 shows a transition in a typical trial of DX. Firstly, D-dependent defect strategies (e.g. [0000000100000000]) grew in the population, which decreased the average score until around the 1300th generation. But then, "Tit-for-Tat"-like non-plastic strategies (e.g. [0101010101010101]) spread in the population, which increased the average score sharply. Finally, some cooperative strategies without plasticity (e.g. [110x000000000001]) occupied the population, so that average score converged to about 2.6.

4 Conclusion

We have constructed a computational model using the iterated Prisoner's Dilemma game as dynamic environments in order to investigate the relationships among evolution, learning and development. Development is handled by two alternative computation-universal mechanisms: a tag system and a Turing machine in the model. The evolutionary experiments have shown that when adopting a tag system, each individual tended to depend on both learning and development, which often resulted in the smooth establishment of cooperative relationships. While, when adopting a Turing machine, either development or learning worked exclusively and built cooperative relationships. These results show the flexibility in the roles of learning and development in establishment of cooperation. Differences between the results of the two developmental mechanisms could possibly be due to the fact that the tag system could work more efficiently to help evolution explore cooperative roles of learning and development in dynamic environments.

References

[1] Downing, K. L.: Development and the Baldwin Effect, *Artificial Life*, Vol. 10, No. 1, pp. 39–63, 2004.

[2] Lindgren, K.: Evolutionary Phenomena in Simple Dynamics, *Artificial Life II*, pp. 295–311, 1991.

[3] Suzuki, R. and Arita, T.: Interactions between Learning and Evolution: The Outstanding Strategy Generated by the Baldwin Effect, *Biosystems*, Vol. 77, Issues 1–3, pp. 57-71, 2004.

[4] Wolfram, S.: *A New Kind of Science*, Wolfram Media, pp. 93–96, 894–895, 2002.

The Eleventh International Symposium on Artificial Life and Robotics 2006 (AROB 11th'06),
B-con Plaza, Beppu, Oita, Japan, January 23-25, 2006

Describing Metabolic Pathways Using an Artificial Chemistry Based on Pattern Matching and Recombination

Yoshikazu Suzuki Kazuto Tominaga
School of Computer Science
Tokyo University of Technology
Katakura, Hachioji 192–0982 Japan

Abstract

In this paper, we apply our artificial chemistry to describing a real chemical system. The subject of description is a metabolic pathway: the oxidation of fatty acids. We modelled the pathway using straightforward design of molecules and reaction rules in the artificial chemistry. The description was executed by a simulator and correct behavior was observed. The qualitative modelling and simulation are a promising application of artificial chemistries.

Keywords: artificial chemistry, metabolic pathways, qualitative modelling, qualitative simulation.

1 Introduction

Artificial chemistry is becoming one of the most active research areas in artificial life field, and various artificial chemistry systems have been built [1]. An artificial chemistry is an abstract chemical model. It is usually used to construct virtual systems in order to study behavior of various living systems and/or necessary conditions for virtual systems to show such behavior. We proposed an artificial chemistry based on string pattern matching and recombination [2] and have constructed several virtual systems including an imaginary cell with cell cycle [3].

Recently, artificial chemistries are becoming applied to natural chemical systems. For example, Benkö et al. used an artificial chemistry based on graphs to produce chemically expected reaction pathways [4]. We applied our artificial chemistry to modelling DNA computing [5]. The capability of modelling natural chemical or biochemical systems will be a good property for artificial chemistries to broaden their applicable area.

Although DNA computing uses natural molecules (i.e., DNA) and their properties, modelling it does not contribute directly to understanding living systems, for it is performed in test tubes in laboratory. In this paper, we attempt to model a system in natural organisms — the metabolic pathway of the oxidation of fatty acids — to explore possibilities of using the artificial chemistry as a tool to model such a system.

2 An Artificial Chemistry Based on Pattern Matching and Recombination

This section briefly explains a simple artificial chemistry based on pattern matching and recombination of stacks of strings [2], which we are going to use in the following discussion.

2.1 Elements and Objects

An *element* is denoted by an upper-case character, or a capitalized sequence of alphabetical characters. For example, `A`, `B` and `Coa` are elements. An element corresponds to an atom or a group of atoms in nature.

An *object* (corresponds to a molecule or a compound of molecules) is a character string or a stack of strings, such as those depicted below.

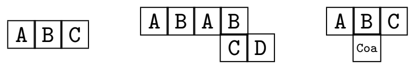

These objects are denoted by the string notations `0#ABC/`, `0#ABAB/3#CD/`, `0#ABC/1#Coa/` respectively; the numbers represent displacements of the line (in numbers of elements) relative to the first line. A displacement can be positive, zero or negative.

2.2 Patterns

A *pattern* matches (or does not match) an object, and it can utilize two kinds of *wildcards*. An *element wildcard*, which is denoted by a number such as `1`, matches any element. A *sequence wildcard*, denoted by a number and an asterisk such as `2*` and `*2`, matches any sequence of zero or more elements; the position of an asterisk represents the direction in which the sequence can extend.

A pattern is denoted in a similar way to an object. For example, the pattern `0#A1C/` matches the object `0#ABC/`; the pattern `0#*1AB/1#CD/` matches the object `0#ABAB/3#CD/`. Note that the displacements are meaningful and that the length of a sequence wildcard is treated as zero in the notation for patterns.

2.3 Recombination Rules

A *recombination rule* transforms a group of objects into a group of objects, conserving elements just like a chemical reaction does. It is expressed in a manner similar to chemical formulae, but in terms of patterns. An example rule is

$$\texttt{0\#*1AB/1\#CD/} + \texttt{0\#AB2*/} \rightarrow \texttt{0\#*1ABAB2*/1\#CD/}$$

which is illustrated as follows.

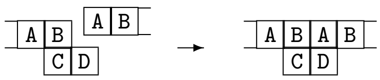

If this rule is applied to the objects `0#ABAB/3#CD/` and `0#ABC/`, the object `0#ABABABC/3#CD/` is produced and the reactants disappear.

2.4 Sources and Drains

Objects are kept in the *working multiset*. A *source* is defined as an object, and it supplies objects of the specified form to the multiset one at a time without limit. A *drain* is defined as a pattern, and it eliminates objects matched by the pattern, one at a time, from the multiset.

2.5 Dynamics

A *system* is a construct $\langle \Sigma\ S\ D\ R\ P_0 \rangle$ where Σ is a set of elements, S is a multiset of sources, D is a multiset of drains, R is a set of recombination rules, and P_0 is the *initial working multiset*, which specifies objects in the working multiset at the initial state. The system is interpreted nondeterministically as follows.

1. Initialize the working multiset to be P_0.
2. Do one of the following operations.
   - † Apply one recombination rule to a collection of objects.
   - † Operate one source.
   - † Operate one drain.
3. Go to Step 2.

3 Modelling a metabolic pathway

In this section, we are going to describe a metabolic pathway in natural organisms using the artificial chemistry explained in the previous section. The pathway to describe is the oxidation of fatty acids. Fat provides energy for organisms that do not perform photosynthesis. Fat is decomposed to glycerol and fatty acids, and fatty acids are degraded to acetyl CoA in mitochondria [6, Chapter 2].

3.1 The oxidation of fatty acyl CoA

The oxidation pathway of fatty acids to acetyl CoA is depicted in Figure 1 [6, Chapter 2]. Shown at the top of the figure is a molecule of fatty acyl CoA, which is activated form of fatty acid. It has a long hydrocarbon chain; R in the figure stands for the tail of it.

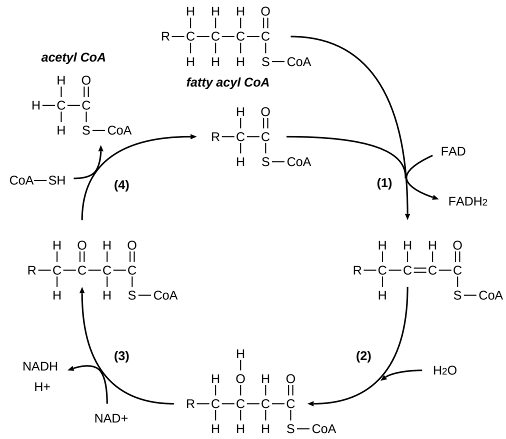

Figure 1: The oxidation cycle of fatty acids.

The pathway is cyclic. One cycle oxidizes the fatty acyl CoA and produces one molecule of acetyl CoA (at the top left of the figure). The acyl CoA loses two carbon atoms from its chain in one cycle and finally it becomes acetyl CoA itself.

The cycle comprises four steps of reactions ((1) to (4) in the figure); let us look at each step.

- † Step 1: Acyl CoA reacts with FAD (flavin adenine dinucleotide; activated carrier). FAD gets two hydrogen atoms from the acyl CoA and becomes $FADH_2$.
- † Step 2: Hydration. The product of Step 1 is hydrated.
- † Step 3: Dehydrogenation. NAD^+ (nicotinamide adenine dinucleotide; activated carrier) removes two hydrogen atoms from the product of the previous step, making NADH and a proton (H^+).

† Step 4: Thiolysis. The product of Step 3 reacts with CoA-SH and becomes acyl CoA with shorter chain, producing one acetyl CoA. If no tail is left (i.e., R is H), two acetyl CoA are produced in this step, and the oxidation completes.

3.2 Atoms and Molecules

We design elements in our artificial chemistry as follows. For the atoms C, H, O and S, we provide corresponding elements `C`, `H`, `O` and `S`. The activated carriers CoA, FAD and NAD are represented by the elements `Coa`, `Fad` and `Nad`, respectively. Using these elements, NADH is represented by an object `0#NadH/`, for example. We use the element `Po` to denote positive charge so that NAD^+ and H^+ are expressed as `0#NadPo/` and `0#HPo/`. Furthermore, we introduce a dummy element, `X`, to represent vacancy.

Depicted below are example objects: fatty acyl CoA CH_3-CH_2-CH_2-CO-S-CoA (left) and a product of Step 1 CH_3-CH=CH-CO-S-CoA (right) assuming R is H in Figure 1. Because the latter has a double bond, two hydrogen atoms are missing compared to the former. The vacancies are denoted by the element `X`.

3.3 Recombination rules

The designed recombination rules are shown in Figure 2. The numbers given to the rules correspond to the numbers of steps in Figure 1.

The hydrocarbon chain of the acyl CoA changes its length during the process. In the rules, this part is represented by wildcards so that they can match a chain of any length.

Because we introduced the dummy element `X` to represent a vacancy, the rules do not conserve elements in the artificial chemistry (i.e., we relaxed a restriction imposed by the definition of our artificial chemistry given in Section 2.3); however, they are designed to conserve atoms in real reactions.

The oxidation cycle described in terms of our artificial chemistry is shown in Figure 3.

3.4 Initial working multiset

We give the following objects in the initial working multiset. A number in brackets is the number of objects of the form, determined empirically so that the simulator (discussed in the next section) effectively shows the process.

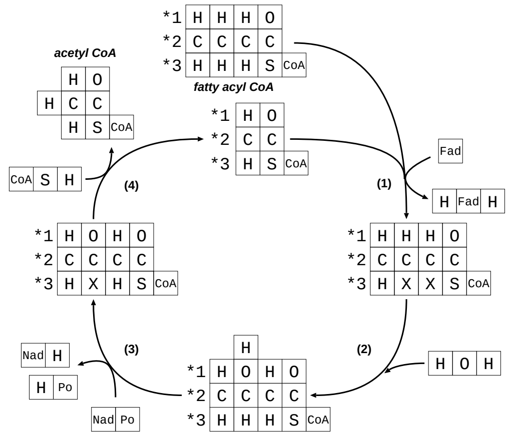

Figure 3: The oxidation cycle described by the artificial chemistry.

- † Fatty acyl CoA [10]: below is an example object: `0#HHHHHHHHHO/-1#HCCCCCCCCCC/0#HHHHHHHHHSCoa/`
- † FAD [100]: objects of the form `0#Fad/`.
- † NAD^+ [100]: objects `0#NadPo/`.
- † CoA-SH [100]: objects `0:#CoaSH/`.
- † H_2O [100]: objects `0#HOH/`.

4 Execution

We developed a simulator for our artificial chemistry. The current simulator is implemented in Objective-C and runs on the Cocoa framework of Mac OS X. Figure 4 shows the window of the simulator running the description given in the previous section. The table shows molecular species and their numbers, and the molecule window (bottom right) shows the form of specified species (by mouse click). In this figure, the product of the oxidation cycle, acetyl CoA, is shown. The execution of the above description consumed all the given acyl CoA molecules and produced acetyl CoA molecules, which is the correct behavior.

5 Discussion

As Figures 1 and 3 show, this artificial chemistry modelled the pathway in a straightforward manner. The elements correspond atoms and molecules naturally, and the recombination rules can be designed intuitively from the chemical formulae and the pathway graph. Describing chemical pathways using the artificial chemistry has significant benefits. First, a pathway is expressed as a mathematical system, so there is

$$\texttt{0\#*1HHHO/0\#*2CCCC/0\#*3HHHSCoa/} + \texttt{0\#Fad/} \rightarrow \texttt{0\#*1HHHO/0\#*2CCCC/0\#*3HXXSCoa/} + \texttt{0\#HFadH/} \tag{1}$$

$$\texttt{0\#*1HHHO/0\#*2CCCC/0\#*3HXXSCoa/} + \texttt{0\#HOH/} \rightarrow \texttt{0\#H/-1\#*1HOHO/-1\#*2CCCC/-1\#*3HHHSCoa/} \tag{2}$$

$$\texttt{0\#H/-1\#*1HOHO/-1\#*2CCCC/-1\#*3HHHSCoa/} + \texttt{0\#NadPo/} \rightarrow \texttt{0\#*1HOHO/0\#*2CCCC/0\#*3HXHSCoa/} + \texttt{0\#NadH/} + \texttt{0\#HPo/} \tag{3}$$

$$\texttt{0\#*1HOHO/0\#*2CCCC/0\#*3HXHSCoa/} + \texttt{0\#CoaSH/} \rightarrow \texttt{0\#HO/-1\#HCC/0\#HSCoa/} + \texttt{0\#*1HO/0\#*2CC/0\#*3HSCoa/} \tag{4}$$

Figure 2: Recombination rules for the oxidation pathway.

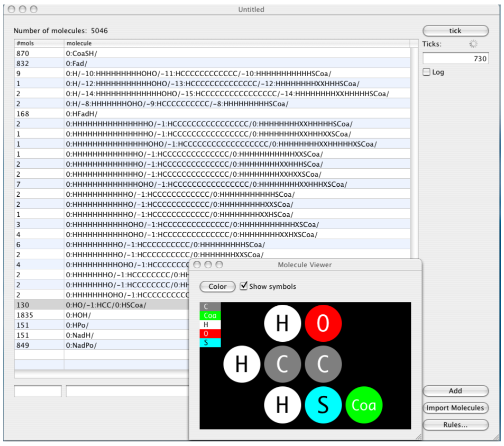

Figure 4: The simulator window.

no ambiguity. Second, it is executable on a simulator. Although the current simulator does not deal with concentrations or energy, it still can perform qualitative simulation. Furthermore, one can choose an arbitrary level of abstraction: for example, CoA can be represented by an element `Coa` like in the description given in this paper, or can be treated as composed of many atoms of `C`, `H`, `O`, etc.; the designer of the system can choose any level.

Other than the oxidation of fatty acids, we have described the following metabolisms: glycolysis, the citric acid cycle, the catabolism of amino acids, and the urea cycle. One more useful property of the artificial chemistry is that when the union of all the systems above (i.e., the union of the initial working multisets and the recombination rules) is given to the simulator, the execution shows the behavior of the composite system.

6 Concluding remarks

In this paper, we presented a description of a metabolic pathway described in terms of an artificial chemistry, and thereby showed possibility for the artificial chemistry to be applied to qualitative modelling and simulation of chemical pathways. While there is room for improvement in the expressive power of the artificial chemistry, we think this is a promising application of artificial chemistries in general.

References

[1] Peter Dittrich, Jens Ziegler, and Wolfgang Banzhaf. Artificial chemistries — a review. *Artificial Life*, 7:225–275, 2001.

[2] Kazuto Tominaga. A formal model based on affinity among elements for describing behavior of complex systems. Technical Report UIUCDCS-R-2004-2413, Department of Computer Science, University of Illinois at Urbana-Champaign, March 2004.

[3] Kazuto Tominaga. Describing protein synthesis and a cell cycle of an imaginary cell using a simple artificial chemistry. In *Proceedings of the Workshop on Artificial Chemistry and Its Applications, part of the 8th European Conference on Artificial Life (ECAL) 2005*, 2005.

[4] Gil Benkö, Christoph Flamm, and Peter F. Stadler. Explicit collision simulation of chemical reactions in a graph based artificial chemistry. In *Advances in Artificial Life: Proceedings of the 8th European Conference on Artificial Life (ECAL) 2005*, pages 725–733. Springer, 2005.

[5] Kazuto Tominaga. Modelling DNA computation by an artificial chemistry based on pattern matching and recombination. In *Proceedings of the Workshop on Artificial Chemistry and Its Applications, part of the 9th International Conference on the Simulation and Synthesis of Living Systems (ALIFE9)*, 2004.

[6] Bruce Alberts, Alexander Johnson, Julian Lewis, Martin Raff, Keith Roberts, and Peter Walter. *Molecular Biology of the Cell*. Garland Science, New York, NY, 4th edition, 2002.

The Eleventh International Symposium on Artificial Life and Robotics 2006 (AROB 11th'06),
B-con Plaza, Beppu, Oita, Japan, January 23-25, 2006

Morphogenesis of 3D Sheets Exploiting a Spatial Condition

Shuhei Miyashita
Artificial Intelligence Laboratory
Department of Informatics, University of Zurich
Andreasstrasse 15, CH8050 Zurich, Switzerland

Abstract

This paper reports on the morphogenesis of three-dimensional folding sheets in computer simulation. In order to exploit the topology of these cellular sheets, we introduced cell connection map, which can prescript cell connections regardless of changing the number of cells. We show that morphogenetic patterns such as exponential growth, self-replication process and annihilation process can be easily realized just by observing the number of neighbors of each cell. That means this feat is achieved in a distributed and autonomous way.

1 Introduction

Multicellular organisms usually consist of large numbers of cells, which are able to shape an organism by an intricate web of cell-cell interactions, a process called morphogenesis. As each cell contains the same genome, morphogenesis relies on autonomous and distributed processes with no centralized control. Although the elucidation of the molecular details of morphogenesis has made big progress in biology, an overall picture is still lacking. We hypothesize that morphogenesis depends on the following two conditions:

1. Morphogenesis is an autonomous, distributed process without any centralized control for all cells.
2. In essence, morphogenesis of living things is basically understood as expanding and folding sheets.

We used these two conditions as guidelines to screen the existing literature of morphogenetic models. Alan Turing's reaction-diffusion model [1] uses two chemical substances that are able to produce spatial patterns in space. The point of this mechanism is that in essence, reaction-diffusion mechanisms are means of breaking the symmetry among homogeneous cells in autonomous and distributed way. Focusing on the form of gastrointestinal tract, H.Honda advocates that in general the form of multi cellular system is realized as two-dimensional sheets rather than three-dimensional solids [3]. There exist many approaches for morphogenesis that can be divided into several types: Lindenmayer grammars [4], cellular automata [5], [9], concentration gradient[2], mechanical approaches [6], recurrent diagram networks to express the bodies of simulated creatures [7], and extended grid space into graph model [8]. However, little attention has been given to the characteristics of form - the topology of the cellular network.

2 Model

In our model, we choose the cell as the level of abstraction. System consists of cells connecting each other.

Cells differentiate depending on the number of neighbors.

Cells divide and die (cell differentiation) depending on the number of neighbors. This is according to the fact that one of the possible biological mechanism assumed to code the behavior of morphogenesis would be the concentration of chemical substances that diffuse into neighboring cells through channels. In other words, its concentration could reflect the number of neighbors.

Differentiation rules are applied synchronously.

These cell behavior rules are applied synchronously in specific order. After specific time passes (100 steps), all cells count its neighbors and take actions. (The definition of step is prescripted below.) Once cell division is took place, the cell is divided into four cells. This is in order to sustain the symmetry of the cell network. In cell deletion, the cell is deleted by cutting connection to its neighbors.

Cell-cell mechanical interaction

Cells are expressed as mass points. Links between them are represented as mechanical connections. The mechanical interactions are expressed as spring and damper model. Although it takes time to converge to the form, the form of cell network topology is unique to each sequence. We show the parameters of the system in Table.1. The equation of motion for the cell i is expressed in eq.1. Where subscript i, j is an identification number of the cell.

Table 1: Sets of parameters.

Symbol	Definition	Value
k	spring coefficient	50
l	spring natural length	50
m	mass	10
c	damper coefficient	30
g	gravity	50
a	cross product	2000

$$m\ddot{\mathbf{q}}_\mathbf{i} + c\sum_j(\dot{\mathbf{q}}_\mathbf{i} - \dot{\mathbf{q}}_\mathbf{j}) + k\sum_j\left(1 - \frac{l}{|\mathbf{q}_\mathbf{i} - \mathbf{q}_\mathbf{j}|}\right)(\mathbf{q}_\mathbf{i} - \mathbf{q}_\mathbf{j}) + a\frac{\sum_j\left((\mathbf{q}_\mathbf{j} - \mathbf{q}_\mathbf{i}) \times (\mathbf{q}_\mathbf{j+1} - \mathbf{q}_\mathbf{i})\right)}{|\sum_j\left((\mathbf{q}_\mathbf{j} - \mathbf{q}_\mathbf{i}) \times (\mathbf{q}_\mathbf{j+1} - \mathbf{q}_\mathbf{i})\right)|} + g\mathbf{q}_\mathbf{i} = 0 \quad (1)$$

The position of the cell q_i is defined as a vector. The cell that exists in neighbor of cell i is denoted as j. Gravity is added to the system for z-axis direction and cross-product force is also added in order to swell the form of the sheet. The differential equation is integrated by the Euler method ($\delta t = 0.01$, 1step=$30\delta t$).

Cell connection map is introduced to constrain the form in "a sheet"

Since cell reconnection after cell division sustaining adequate topology is tricky, we introduced cell connection map, which prescripts relation of cell connection. Fig.1 shows the example of cell connection map. When cell is divided, the square corresponding to the cell is also divided into four small squares. ("a)" and "c)" corresponds to "d)" and "e)", respectively). Links are connected if squares touches other squares through the edge. As we are interested in how the two-dimensional sheets expand, the most external cells, which exist at edge of the connection map, are fixed in the same position. Due to this settling, the system grows like an expanding balloon. Although many parameters are decided arbitrarily, the most important thing here is that once the feature of the model is decided, the form converges to unique form.

Form can be evaluated using cell connection map

Form of living things always relates to its function, and it plays an important role in the evolutionary process. But evaluating form is quite difficult and sometimes tends to be arbitrary. However, if we evaluate the form by analyzing cell connection map, the whole cell relations can be detected and estimated easily. We

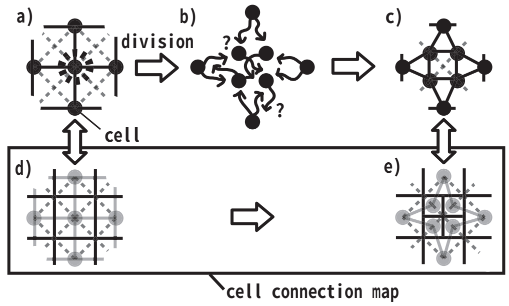

Figure 1: Cell reconnection.

introduced fitness value (F), -kind of entropy- which is prescribed as the follow equation (2), where S_i denotes the area of each cell in cell connection map with subscript i as an identification number of the cell.

$$F = -\frac{1}{N}\sum_i log\frac{S_i}{S_T} \quad (2)$$

We set the area of the whole map 1.0. S_T represents sum of all areas of the cell. We generalized the value by dividing a number of cells, N. The characteristics of this fitness value is as follows:

1. The fitness value gets larger when the distribution of area sizes gets larger.
2. If the sum of areas are same, the larger the number of cells is, the bigger the value becomes.
3. If cell distribution is same, it doesn't depend on its scale. That means that the value doesn't depend on order of morphogenesis.

3 Simulations and Results

By applying several parameter sets, some fundamental morphogenetic process were observed.

Exponential growth

Figure 2 shows the examples of exponential growth of the system. X-Z side view, X-Y top view, Cell connection map in left to right order. (The magnifier is changed in each view.) In the left model(seq.A), we set rule that if the number of neighbor cells is 0,2,4,6, or 8, the cell is divided, and if the number is more than 10, the cell is deleted. And these rules are applied one after the other starting with division rule. The figure shows by only counting the neighbors, the system can generate bended "two dimensional" morphological form from one single cell. In the right model(seq.B), if the number of neighbor cells is 0,2,4,6, or 8, the cell is divided, and if the number is 1,3,5,7, or 9, the cell is deleted. This time division rule is applied twice then cell deletion rule is applied once starting with division rule. Judging from the X-Y and X-Z view, the form generated by the rule seems completely different from that of seq.A.

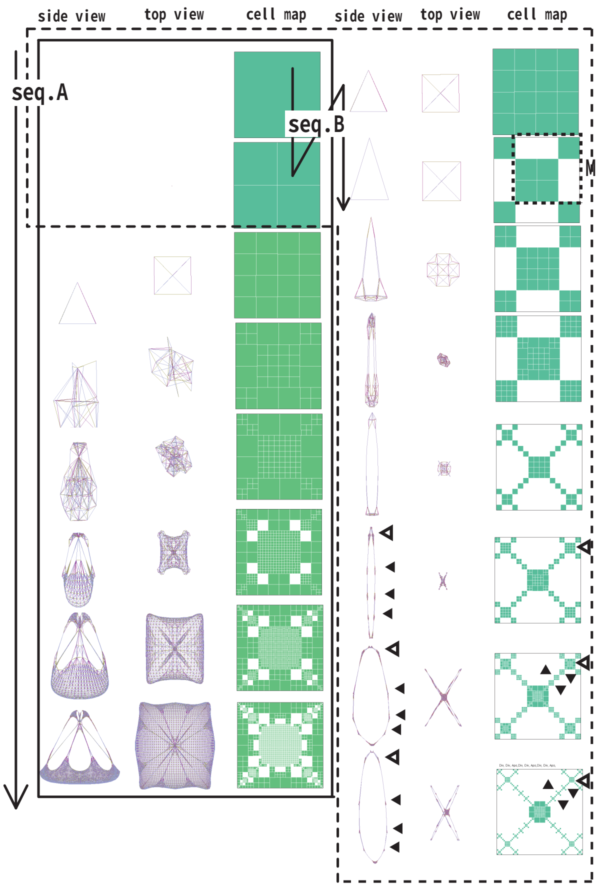

Figure 2: Exponential growth sequences A(left) and B(two left blocks and right).

Self-replication, Annihilation, Stop Growth

Fig.3 shows self-replication process. In this model, if the number of neighbor cells is 0,2,5,7, or 9, the cell is divided. And if the number of neighbors is 1,3,4,6, or 8, the cell is deleted. Each group keeps changing the number of cells which consist its network one and four generating new groups. Several model in other parameters showed annihilation and stop growth behaviors. The simplest model of annihilation behavior can be observed when we set the number of neighbors 0 for cell division and 2 for cell deletion applying division rule and deletion rule one after another. And the simplest growth saturation model can be observed by settling 0 for cell division and any numbers except for 2 for cell deletion.

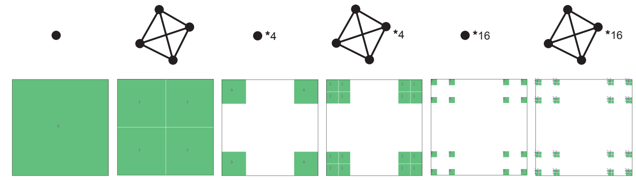

Figure 3: Self-replication.

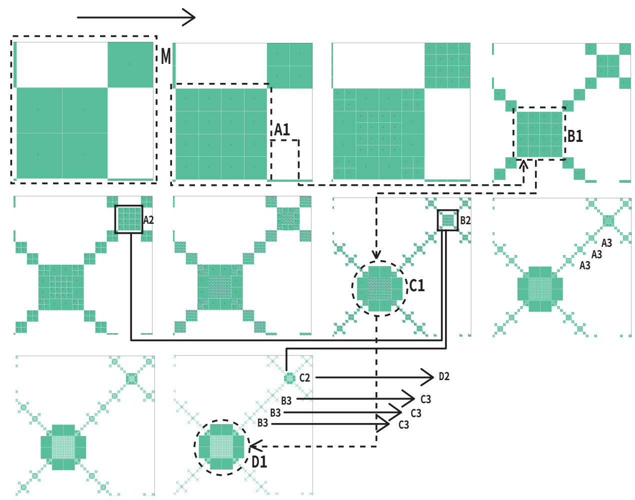

Figure 4: Detail of exponential growth sequences B.

4 Discussions

Figure 4 represents the magnification of the part of cell connection map in Figure 2 (as marked "M"). After 16 cells, which are arrayed in square grid appears (A1 and B1), this part gets rounded (C1). Once this form is created, all internal cells have four-neighbors thus keep dividing. And "big" eight cells surrounding the cells have more than at least 10cells. Therefore these cells won't be divided any more. This is a kind of "expanding bag". And this bag can be seen at other part of the body (A2,B2,C2, and A3,B3,C3 and so on). This shows that the system is growing creating many expanding bags around the body.

Figure 5 represents the same part of cell connection map under the different condition of cell division and cell deletion. This time, cell is divided if the number of neighbor cells is 0,2,6, or 8. Cell is deleted if it is 1,3,5,7, or 9. Although most of the condition are the same between seq.A and seq.B, the morphogenetic processes are essentially different. See the part marked "A". Once this shape is created, the shape doesn't change any more. That means that the number of cells included in this part doesn't change. (This

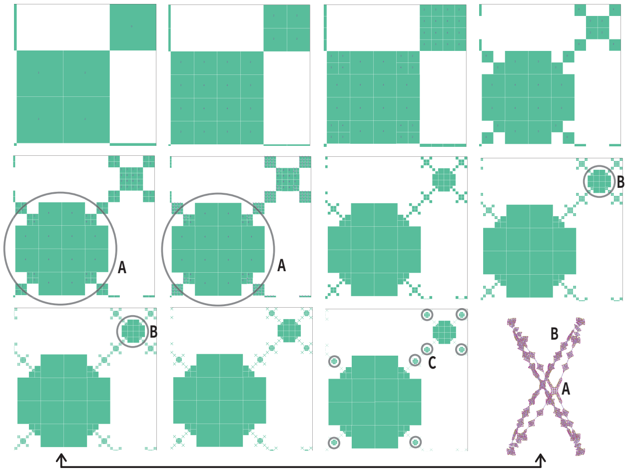

Figure 5: Detail of exponential growth sequence C.

is seen in other parts of sequences B and C and so on.) This system keeps generating many "gnarls" in different positions. The X-Y view is shown in the same figure. It can be seen that many gnarls are created in the form. Sizes of each gnarl are the same.

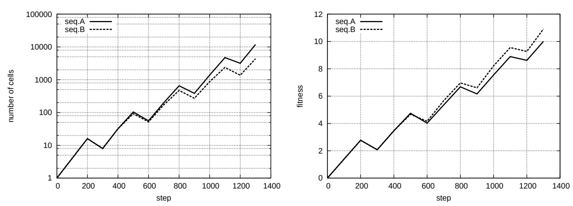

Figure 6: Left: Fitness value transition graph. Right: Number of cells transition graph.

We show the number of cells and fitness value transition graph in Fig.6 in order to quantify the difference of the characteristics of these forms between sequence B and C. In Fig.6 left, the X-axis and Y-axis represents steps and the number of cells, respectively, comparing sequence B and C. As the figure shows, the fitness in seq. B is smaller than that in seq. C although the number of cells in seq. B is larger than that of seq. C in each time. This means uniformity of the whole system of seq.C par cell is larger than that of seq.B. Hence, it suggests that many kinds of differentiation rules are not needed in order to get complicated forms. In other words, sustaining an adequate cell differentiation rule is necessary for the morphogenesis of the model.

5 Conclusion

These results lead to the following conclusion.

1. Several types of morphogenetic behaviors of three-dimensional sheets can be realized in autonomous and distributed way - just by counting the number of neighbors.
2. The form can be quantified easily by evaluating cell connection map.

Some fundamental morphogenetic behaviors are observed; two types of exponential growth, self-replication, stop growth and annihilation process. Those models were sensitive to the cell differentiation rules, to put it another way, sensitive to the topology of cell connections. What we intended to show in this paper is the abundant power of morphogenetic expression supported by the condition of spatial constraint, and the possibility that we can evaluate complicate forms by mapping it into other method, cell connection map.

Acknowledgements

Many thanks to Peter Eggenberger Hotz for helpful suggestions. This research is supported by Swiss National Science Foundation, project #200021-105634/1.

References

[1] A.M.Turing: A reaction-diffusion model for development, The chemical basis of morphogenesis, Phil Trans. Roy. Soc. of London, Series B; Biological Sciences, **237**, 5,PP.37-72 (1952)

[2] L.Wolpert Positional Information and the Spatial Pattern of Cellular Differentiation, J. Theoret. Biol., **25**, PP.1-47 (1969)

[3] H.Honda: The mathematical and physical analysis of morphogenesis, Kyoritsu-shuppan (2000)

[4] A. Lindenmayer: Mathematical Models for Cellular Interaction in Development, Journal of theoretical Biology, **18**, PP.280-300 (1968)

[5] C.G.Langton: Self-reproduction in cellular automata, Physica D: Nonlinear Phenomena, **10**, Issues 1-2, PP.135-144 (1984)

[6] M.Odell, G.Oster, P.Alberch: The Mechanical Basis of Morphogenesis, Developmental Biology **85**, PP.446-462 (1981)

[7] K.Sims: Evolving 3d morphology and behavior by competition. Artificial Life, **1**, Issue 4, PP.353-372 (1995)

[8] K.Tomita, H.Kurokawa, S. Murata: Graph Automata: Natural Expression of Self-reproduction, Physica D: Nonlinear Phenomena, **171** No.4, PP.197-210 (2002)

[9] Martin Gardner: Mathematical games - the fantastic combinations of john conway's new solitaire game, life. Scientific American, PP.120-123(1970)

The Eleventh International Symposium on Artificial Life and Robotics 2006 (AROB 11th'06),
B-con Plaza, Beppu, Oita, Japan, January 23-25, 2006

Sexual Reproduction in Digital Organisms

Ai Dongmei
School of Applied Science
University of Science and Technology Beijing
Beijing , 100083

Ban Xiaojuan,Yin Yixin,Tu Xuyan
School of Information Engineering
University of Science and Technology Beijing
Beijing , 100083

Abstract

Artificial life platform is an emulational system which uses computer software to study the behaviors characteristics such as reproduction, evolution, mutation, and emergence of digital organisms. After studying the parameter and functioning capability of Avida, the artificial life platform, aiming at the asexual reproduction in digital organisms, We designed the sexual reproduction mechanism of digital organisms by utilizing the genetic programming principle, introduced the cross breeding mechanism of natural organisms into digital organisms, and designed the cross breeding mechanism of digital organisms, so as to avoid the disadvantage of inbreeding reproduction. Our results demonstrate that sex is advantageous for population survival under some conditions, the mean fitness of surviving sexual populations was greater than in asexual population.

1 Introduction

Artificial life platform is a system using computer as tool and medium, utilizing software to emulate organisms features [1]. Tierra, developed by Thomas S. Ray, is the representative of this field. He introduced the concept of organisms evolution in biology into computer science [2][3]. Every cell in computer multiplies, mutates, and evolves. They all keep to survival of the fittest in Charles Darwin's Evolutionism and fight for the resource in computer. These so-called cells characterized by organisms features are in fact programs. Therefore these cells are also called digital organisms. Afterwards, inspired by the ideas in Tierra, some other artificial life platforms are developed [4], among which Avida is the most influential one.

In Avida system [5], digital organisms is asexual reproductive. They self-replicate and mutate in the process of reproduction so as to form organisms with different genes. They keep to survival of the fittest; fight for the memory and the resource of CPU in the same environment. But whether among animals or plants in nature, sexual reproduction is the most common way. Biologically, asexual reproduction is a primitive reproduction. Sexual reproduction, on the other hand, synthesizes both the advantages and disadvantages from both parents, so that it could partly conceal the hereditary defects. Compared to the organisms produced by asexual reproduction, organisms from sexual reproduction is more adaptable and has stronger vitality [6]. Based on sexual reproductive, SEBRED is developed. It brings sexual reproduction and cross breeding mechanism into digital organisms. This system aims at improving the fitness of populations, and further

Supported by NSFC(No:60374032,60503024)

improving the organisms features of digital organisms.

2.The Genetic Operate Design of Digital Organisms in SEBRED

There are various reproduction methods to raise up seed in nature organisms. Primitive monad usually raises up seed by asexual reproduction. But, most of plants and animals and human beings raises up seed by sexual reproduction. In sexual reproduction, the creature individual is divided into male and female. The offspring reproduced by sexual reproduction have more mutations. The offspring from sexual reproduction become more fit the environment than those offspring from asexual reproduction. In natural selection, sexual reproduction is beneficial mutations and fit environment.

2.1 The Reproduction Model of Primitive Digital Organisms in SEBRED

In SEBRED, digital organisms is divided into primitive digital organisms and advanced digital organisms. First of all, an ancestor of digital organisms begins to self-replicate and many offspring come into being. In the process of reproduction, the mutations of gene result in the different genes of the offspring. The offspring also reproduce a large number of offspring as their ancestors do. Of course different digital organisms has different fitness that even changes in different periods. Those digital organisms with strong fitness reproduce more offspring, and those with low fitness reproduce less.

In the reproduction process of these primitive digital organisms, improved genetic algorithm is used. In this process digital organisms has experienced three evolutional models—digitally set fitness and natural selection, mutation, and self-replicate. These organisms have experienced 250 generations, so their fitness has improved; their organisms structure becomes more complicated compared to their ancestors. This is the evolutional process of primitive digital organisms. We regard this biological species as the preliminary species of advanced digital organisms, and those organisms after 250 generations as the advanced digital organisms. Biologic experiments turn out in biology that sexual cross is not beneficial to simple organisms but beneficial to the complicated organisms developed from simple organisms. Digital organisms before the 250th generation have never experienced sexual reproduction (cross or exchange), so they have the same way of reproduction as in Avida. But the difference is that in SEBRED, although organisms before 250th generation have no sexual reproduction, when each organism comes into being, its sex property randomly has two sex divisions—female and male.

2.2The Sexual Reproduction Algorithm of Advanced Digital Organisms Based on Genetic Programming

In SEBRED, after running 250 generations, there will be almost 3600 organisms. They have very different genotypes and chromosomes, so the programs (or organisms) length are also different. In this system, the hereditary individuals have two sex divisions: female and male. Some sexual organisms have come into being at random in this system. After the 250 generations, the reproduction mechanism has become sexual reproduction. So in SEBRED, the intercrossed digital organisms have different sizes (programs with different length). Moreover, during the process of evolution, program (organisms) will change it's size according to the environment [7]. But the string with set length which frequently used by genetic algorithm to illustrate questions has restrained the application of genetic algorithm. Lacking of dynamic changeability. String with set length of genetic algorithm has no dynamic changeability, so once the length of string is set, it is very hard to dynamically express the change of the state or the behavior.

So the copulation mechanism of digital organisms in SEBRED adopts genetic programming to make two organisms exchange.

In SEBRED, the advanced digital organisms structure adopts linear structure. Every digital organisms performs the program of its own chromosome during the process of evolution. When two digital organisms copulate, the length of their chromosomes is different. With the evolution of the species, the length of digital organisms' chromosomes will change. The following part is about the principles and methods of digital organisms' copulation:

1.Organisms with same sex cannot mate up; the female individual can only mate up with the male individual randomly(the male individual can only mate up with the female individual randomly).

2.Each individual mates up with four different individuals around with opposite sex., there will be eight filial individuals. Then choose two best ones as the filial individuals and add them into the environment, and this is sitting combination.

If two or more qualified individuals participate in the copulation, the individual should choose the one with the highest fitness. But if they even have the same fitness, the individual should choose the younger one.

3. The Cross Breeding Mechanism of Digital Organisms in SEBRED

In every natural population, many diploidize individuals' genomes keep high proportion of heterozygosity. The hereditary diversities usually are recessive instead of dominant, so it is beneficial to the survival of the species and makes it more adaptable to the environment. Just like the biological system of nature, inbreeding also produces bad offspring. Therefore the program of judging the qualifications of both parents is very essential to the selection process [8].

In SEBRED, the digital organisms involving the sexual copulation have to be compared. Tracing back 4 generations of each side, if they have the same father or mother in the four generations, then this copulation has to be abandoned and select other mating objects once again. But if the selection fails more than 10 times, select another digital organisms around this pair with force and conduct the copulation, as shown in Figure1. Triangle show female, diamond show male, the graphics of shading are the same pedigree.

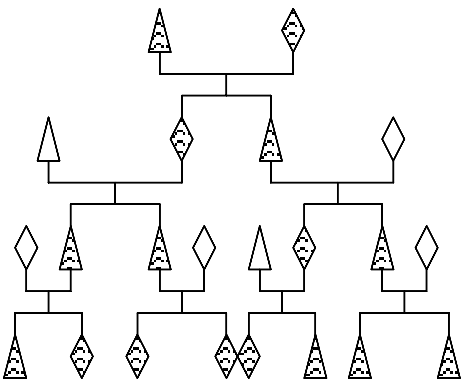

Figure.1 Four-Generation Pedigree

4. Fitness of Digital Organisms in SEBRED System

The factors affecting the fitness of the SEBRED system are different from those affecting Avida. So the fitness of digital organisms in SEBRED system must be reconsidered.

The factors which affect the fitness of digital organisms include merit, gestation time, the number of the "inst_David" instructions contained in the offspring genotype.

Fitness is given by the K multiply M, divide by the gestation time G.

$$\text{Fitness}=K*M/G \qquad (1)$$

1. M(Merit)is a value indicating the CPU time a particular organism has earned, taking into account its length and the tasks that it has successfully completed.
2. G（Gestation time）is the number of instructions an organism must execute to produce a single offspring. This is typically proportional to the length of the genome.
3. K is a coefficient generated by considering both the number of instructions contained in the offspring genotype and Merit.

$$\boldsymbol{K} = 1-(1-\boldsymbol{i}^{\frac{1}{4}})\boldsymbol{e}^{-\frac{0.01}{(i-1)^2}} \qquad (2)$$

i is the number of offspring instructions which contain "inst Divide" instruction.

Summary

This thesis is based on the digital life platform Avida; using genetic algorithm and genetic programming principles, combining the sexual reproduction of advanced life in biology, builds up the sexual reproduction mechanism of digital life; enriches and improves the life features of digital life. Experiments turn out that the fitness of digital life after sexual reproduction is higher than that of asexual reproduction.

References

[1] Chen Hongjuan.: The Research of Theory and Method on Self-Reproduction of Digital Fish. The Doctorial Thesis of USTB, 2002
[2] Wu Jianbing,Yang Jie,Wu Yuehua.: Digital Life and Digital Intelligence. Pattern Recognition and Digital Intelligence (1998) 274-279
[3] Ray,T.S.: An evolutionary approach to synthetic biology: Zen and the art of creating life. In Digital Life Journal, The MIT Press (1994) 179~209
[4] A.N.Pargellis.In: Digital Life Behavior in the Amoeba world.Artifical Life Ⅶ .Cambridge, MA:MIT Press (2001) 63~75
[5] Adami,C. : Introduction to Digital Life. Springer, New York (1998)
[6] Liu Zudong: Genetics. The Higher Education Press (1990)
[7] Wang zhengzhi, Bo Tao.: Evolutionary Computation. Changsha: National University of Defense Technology Press (2000)
[8] Lin Yuan,He Lin,Xu JinLin.: Sex Evolution. Origin and Maintenance. Life Science (2002) 197-200

Development of NC Tool Path Generation System by Absolute and Incremental Type Individual

H. Yamamoto
Faculty of Engineering,
Gifu University,
1-1 Yanagido, Gifu, 501-1193 Japan
E-mail: yam-h@cc.gifu-u.ac.jp

Rizauddin Bin Ramli
Graduate School of Engineering,
Faculty of Engineering, Gifu University,
1-1 Yanagido, Gifu, 501-1193 Japan
E-mail: k3812205@guedu.cc.gifu-u.ac.jp

Abstract

Lately, in order to improve the operating efficiency of automatic production systems such as Flexible Manufacturing Systems (FMS) and Flexible Transfer Lines (FTL), many Numerical Control (NC) lathe machine tools have been used and a few automated programming methodologies of NC machine tools have been researched. The purpose of this research is to develop a system that automatically generates the tool path of the NC lathe machine tools in FTL. The GA methodology of our system adopts the moving points of the tool path as an individual. In the paper, we introduce two original individual expressions. One is an Absolute Expression (AE) and the other is the Incremental Expression (IE). After some simulations, a better machining efficiency for the cylindrical type of work piece obtained in this machining process has been acquired. It has been ascertained that our system is useful.

1. Introduction

Several studies of the tool path of NC machine tools have already been done. Akturk *et al.* [1] proposed a new solution to solve the tool allocation and machining conditions selection problems simultaneously to find the minimum production cost. However, the tool path generation is not considered. Omirou [2] proposed a locus tracing concept which defines a geometric property to generate the tool path. Furthermore, research has been done on an adaptive tool path generation algorithm for precision surface machining [3]. Using this method, however, a high performance CPU processor is required for updating the tool positioning data because the next reference point of the path had to be predicted. In addition, Ko and Kim [4] proposed an iterative learning method and cutting parameters of the process model optimized through GA for the turning process. In spite of using a tool dynamometer for measuring the signal of the cutting force, it is undesirable to adopt this method because it cannot control the cutting depth. Shirase *et al.* [5][6] developed an expert system to improve the productivity in NC lathe tuning where the machining information about cutting parameters, tools and operating time are found in an NC program using a simulator.

In the FTL systems that consist of many NC lathe machine tools, where various types of raw materials are loaded, the development of software for an optimal cutting method of the NC lathe machine tools is essential. Because of that, the generation of the tool path and the decrease of machining time of the NC lathe machine tools are required by the machinist in order to increase the efficiency of the system.

In this research, we propose an NC lathe machine tool path generation system by using the incremental and absolute style of the individual while applying GA when the cycle time and the product shape are given. The effectiveness of the system is verified by a simulation of both methods.

2. Genetic Information of AE and IE

A schematic pathway of the system that we developed is illustrated in Figure 1. The system is divided to 3 segments which consist of an input part, the GA simulation and NC lathe machine tools. In this paper, we will describe the methodology of the GA as our main research. The purpose of the system is to help a production engineer quickly to decide the necessary NC machine tools number under the condition that the target cycle time and product shape is given. In other words, our system is to generate the cutting path from a raw material to a complete work piece just by inputting the product shape and its target cycle time. The information of the product shape is used to code the genetic information as individual or genes in the chromosome.

In our system, we only assume the genetic information in 2 dimensions of *x, y* axis where the individual is expressed as the tool path in *x, y* direction. We assume that the origin of the tool to be as (x_0, y_0) and the arbitrary point within the tool path as (x_n, y_n). According to this assumption, the individual can be expressed as,

$$Ind = \{ (x_0, y_0), (x_1, y_1), \cdots, (x_n, y_n), \cdots, (x_0, y_0) \} \quad (1)$$

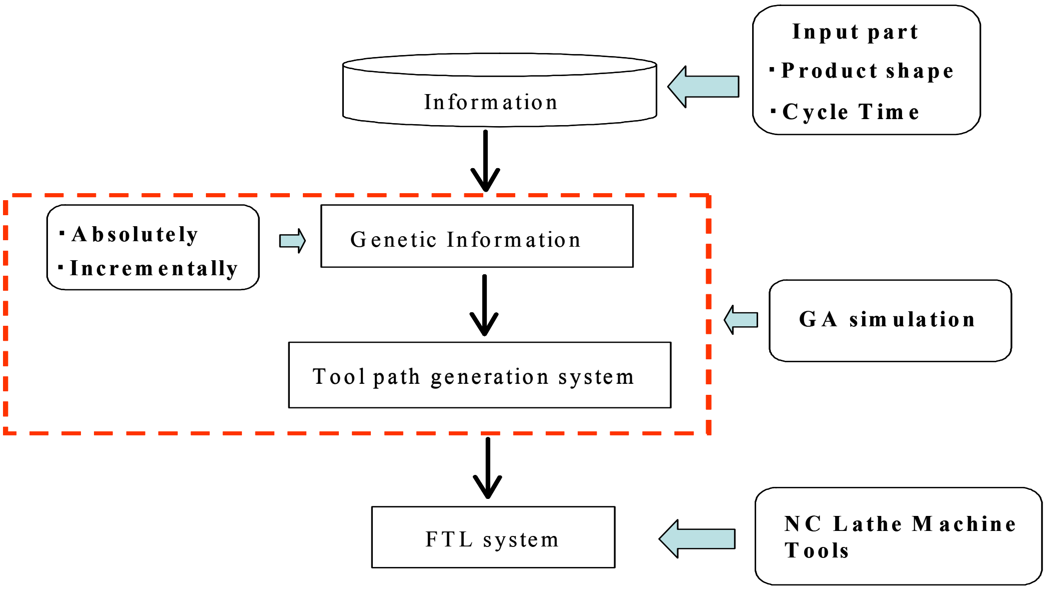

Fig. 1 Schematic pathway of system

In other words, the tool moves from its origin and generates a tool path, return back to its origin as one cycle. In our research, we propose that the tool paths are expressed by two type of individual. First, the tools' origin is considered as the coordinates' origin. In this method, the point on the tool path (x_n, y_n) is considered as the point of *x, y* coordinates as the tool origin is (0, 0). For example, as shown in Figure 2, the tool path is expressed when it moves *f* mm in *x* direction from point A (x_n, y_n) to point B $(x_n + f, y_n)$. We express the individual as an element of tool path which represents by Equation (1) as the Absolute Expression (AE).

Second, the tool path point is expressed as the distances that the tool path moves. In other words, for any arbitrary point A (x_n, y_n), the next tool path point B (x_{n+1}, y_{n+1}) is considered as the distances of *x* and *y* direction while point A still as the origin. For example, as shown in Figure 3, the tool moves *f* mm in the *x* direction from point A (x_n, y_n) to point B $(f, 0)$. We express the individual as an element of tool path which represents by Equation (1) as the Incremental Expression (IE). Each individual in the population is evaluated by a defined fitness function that is given as,

$$Fitness = Cycle \quad time - Total \quad cut \quad time \qquad (2)$$

3. Crossover of Row and Column

In our research, it is difficult to adopt the conventional method of crossover for our IE and AE. Thus, in the operation of crossover, we adopt a peculiar method of crossover. First, as shown in Figure 4, two individuals are randomly selected from the rows of the population. Also the point of the crossover is selected randomly. Parts of rows of the selected individuals are interchanged. We define this type of crossover as the rows crossover.

Second, as shown in Figure 5, two individuals are randomly selected from the columns of the population. Also the point of the crossover is selected randomly. Parts of each column of the selected individuals are interchanged. We define this type of crossover as the columns crossover. In the operation of mutation, the gene in the chromosome that mutates is randomly selected.

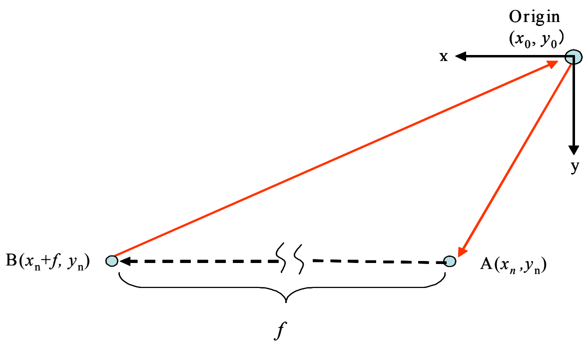

Fig. 2 Tool path generation of AE

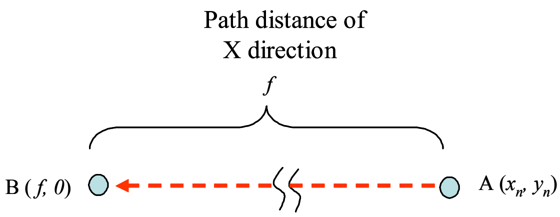

Fig. 3 Tool path generation of IE

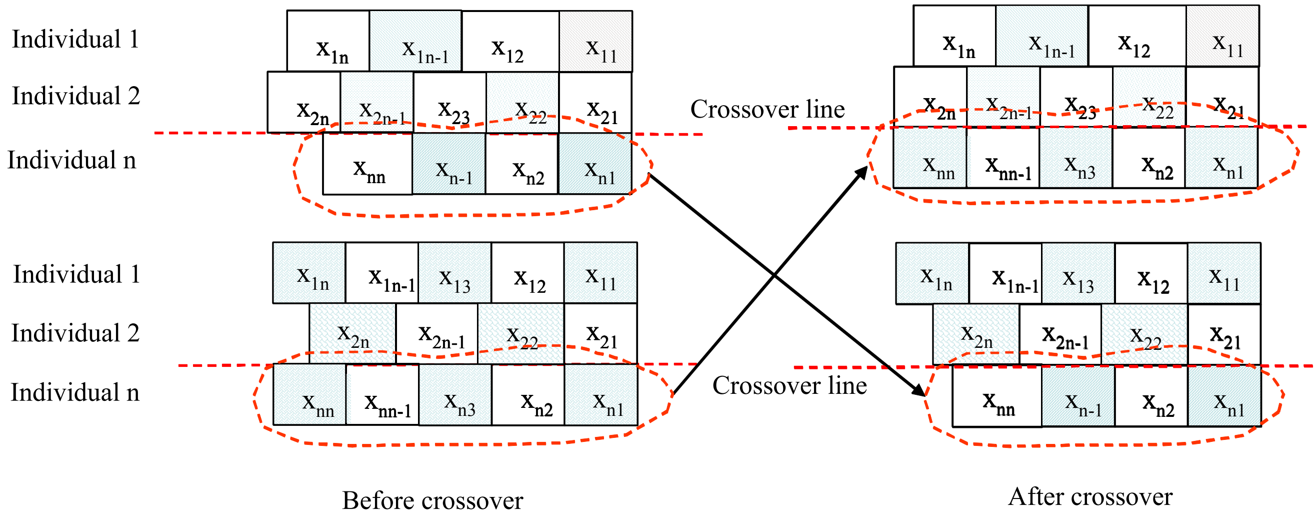

Fig. 4 Row Crossover

4. Simulation Applications

The GA methodology that we developed is then adopted to create the tool path generation system. An example of manufacturing a simple product from a cylinder is shown. We use the system to simulate the machining process of a cylinder with its length is 157mm and diameter is 38 to a demanding product shape as shown in Figure 6. The NC lathe machine will cut the work piece from step A, B, C, D, E, F and G. The distance of step A and D is selected randomly, and when the machine finish cut step A, B and C, the material is reversed and the machine will began to cut D, E, F and G.

The evolution parameters of GA as the simulation of the system runs were used as population size of 100, probability of crossover 0.9 and the probability of mutation 0.05.The tournament selection of next generation with tournament size 5 is used. From our simulation, we found that the cycle time needed to complete the machining process by IE is 22 cycle.
On the other hand, the cycle time needed to complete the machining process by AE is 20 cycle. From the comparison of these results, it is assumed that in IE, the genetic information of each step of individual is highly changed and when the crossover was done to the row, an individual with extremely large number of cycles has been generated. In Figure 7, it is shown that the maximum fitness of AE and IE is 311.01 and 647.92 respectively. The results shows that the AE had a better machining efficiency compare to IE.

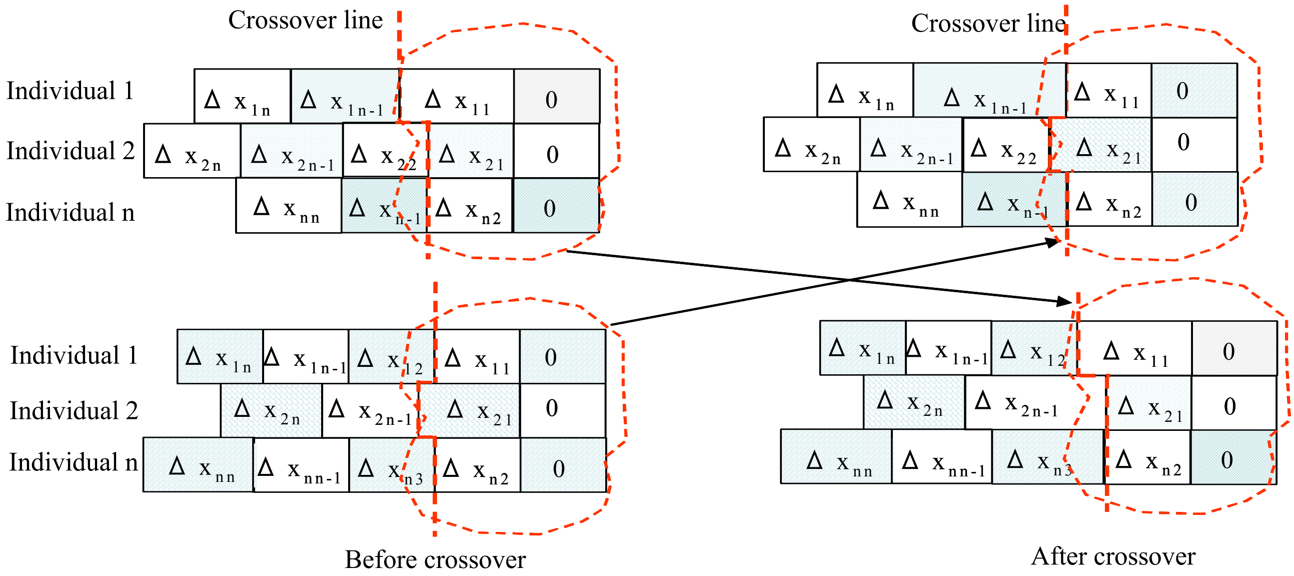

Fig. 5 Column Crossover

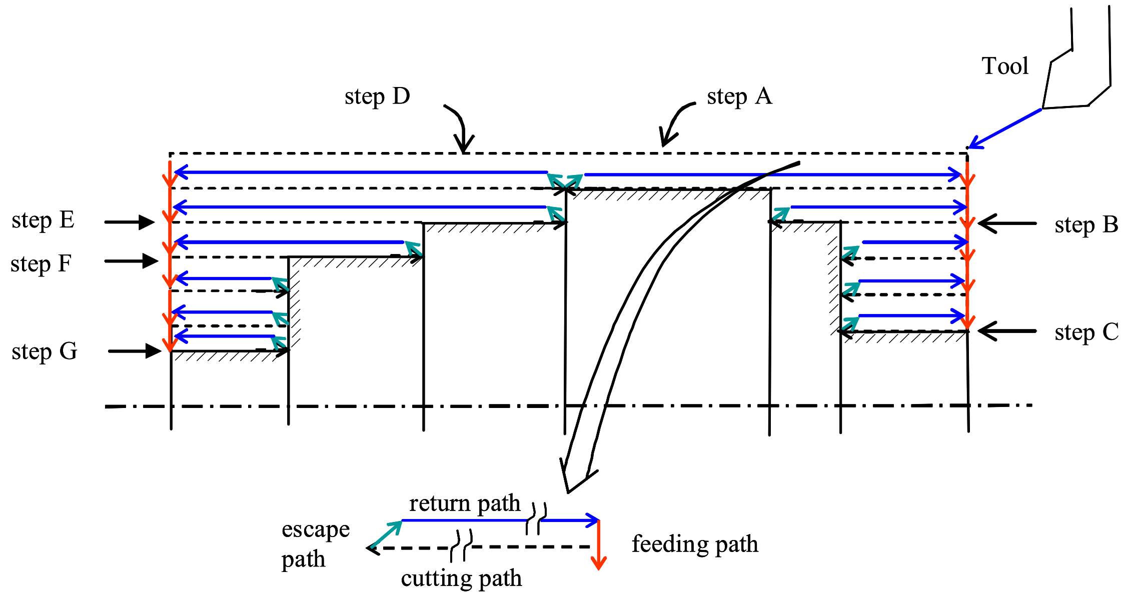

Fig. 6 Example of tool path cutting view

5. Conclusions

In this research, we considered the NC lathe machine tool path generated by the absolute and incremental methods. By comparing the results of each method, we found that the tool path generated by the AE had a small cycle time compare to the IE. This implies to the decreasing of machine quantity which means that only a small space of factory is needed. Then, since that the cycle time is small, the machining time could be reduced, and improve the operating efficiency in the FTL system which leads to low cost production.

Moreover, by just changing the product dimension using our developed GA systems, the machining efficiency of various shapes of product can be realized and it is effective with this system to generate the tool path of the NC lathe machine tools.

6. References

[1] M. S. Akturk, S. Avci, Tool Allocation and Machining Conditions Optimization of CNC Machines, European Journal of Operational Research, Vol. 94, pp. 335-348 (1996).

[2] S. L. Omirou , A locus tracing algorithm for cutter offsetting in CNC machining, Robotic and Computer-Integrated Manufacturing, Vol. 20, pp. 49-55 (2004).

[3] Y. J. Lin, T. S. Lee, An adaptive tool path generation algorithm for precision surface machining, Computer Aided Design, Vol. 31, pp. 237-347 (1999).

[4] T. J. Ko and H. S. Kim, Autonomous cutting parameter regulation using adaptive modeling and genetic algorithms, Precision Engineering, Vol. 22, pp. 243-251 (1998).

[6] K. Shirase, M. Hirao, T. Yasui et al., Improving Productivity in NC Lathe Turning Based on NC Program Diagnosis System(1st Report)-Survey and Improvement on the Productivity in Turning Operation done in the Manufacturing Industries by Using NC Program Simulator, Journal of The Japan Society for Precision Engineering, Vol. 60, No.2, pp. 235-239 (1994). (in Japanese).

[7] H. Kawabata, K.Shirase, K. Sasayama et al., Improving Productivity in NC Lathe Turning Based on NC Program Diagnosis System(2nd Report)-Turning Processes Identification Using Syntax Analysis Approach, Journal of The Japan Society for Precision Engineering, Vol. 60, No. 4, pp. 576-580 (1994). (in Japanese).

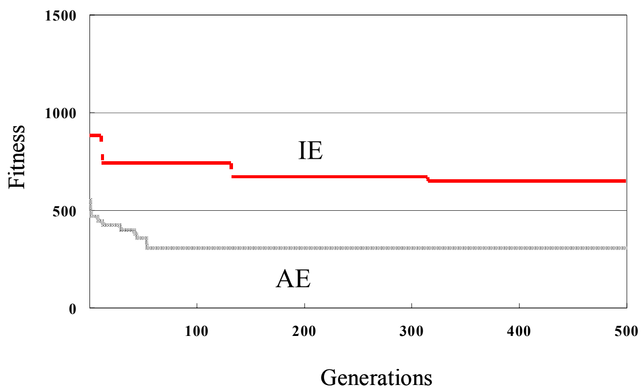

Fig. 7 Maximum fitness of AE and IE

A Study of Selecting Optimal Parameters for Genetic Algorithm

So-Youn Park and Shanshan Jin and Ju-Jang Lee
Electrical Engineering and Computer Science
Korea Advanced Institute of Science and Technology (KAIST)
373-1, Guseong-dong, Yuseong-gu, Daejeon, 305-701, Korea
arashi@odyssey.kaist.ac.kr, shanshan@odyssey.kaist.ac.kr, jjlee@ee.kaist.ac.kr

Abstract

Genetic Algorithms (GA's) are very powerful tool to solve many optimization problems which are difficult for other methodology. But when using it, users have to make a choice of its values of parameter and operations to get a good performance. Many researches investigated the influence of different selection strategies, genetic operators on schema dynamics and developed various GA models, but there exists little information about hierarchical influence of parameter on GA performance. In this paper we will try to take a deeper look on the influence of parameter values on the performance of GA and relationship between them. In experiment, two different types of functions are tested and we find that increasing population size helps GA to find optimal solution most and mutation rate is more effective than crossover rate.

Keywords : *genetic algorithm, parameter, population diversity*

1 Introduction

During several decades, optimization problems are rising as one of the important issues, and GA is powerful tool to solve those problems. It mimics biological evolution to solve problems. Different from hill climbing or simulated annealing, GA uses the current best solution, preserves it, and also travels other possibilities [5],[6],[7]. When using GA, users have to decide genetic operators and values of parameters. These values affect performance of GA and many researches have suggested various strategies to get good a result, but few on hierarchical relationship between these parameters and performance.

The performance of GA can be divided into three aspects - accuracy, convergence speed, and population diversity - generally. Accuracy can be obtained from fitness value of the best individual and convergence speed can be measured by calculating slope of fitness value vs. generation.

Population diversity is related to search space of GA and premature convergence. Premature convergence occurs when GA reaches suboptimal point and cannot escape from that point. Several methods have been proposed to measure population diversity. First one is calculating the occupancy rate of '1' at every chromosome, passing it through a specific threshold function, and adding up all [1]. In this theory maximum population density and chromosome length are exactly same. Second method is getting sum of hamming distance between individuals and dividing it by chromosome length [2]. Third one is calculating ratio between mean and maximum values of fitness function [3]. At each generation, genetic diversity (gdm) lies between 0 and 1 and when gdm approaches 1, this indicates many individuals have same genetic code and reaching its own optimal point (This does not guarantee the solution of problem). We choose third method to measure population density.

In this paper we try to investigate the performance of GA according to three aspects mentioned above with varying values of population size, crossover rate, and mutation rate. In session 2, we define the conditions of GA and explain test functions conducted in this experiment. In session 3, we describe experimental results and discuss them. Finally we summarize and conclude the work and suggest the future work.

2 Methodology

To obtain reasonable values, we use GA in following manner.

In this paper we focus on population size, crossover rate, and mutation rate. Therefore except these parameters, all conditions for GA are fixed. We use Simple Genetic Algorithm (SGA) with Roulette well selection, 1-point crossover, bit flip mutation and Elitism. The ranges of parameters are following: Population size is $10 \sim 100$, pc=$0.1 \sim 0.9$, pm=$0.01 \sim 0.4$. Each GA with specified parameter values is executed 20 times for each function.

Two analytical functions with different characteristics are chosen.

a. Rastrigin function

$$f(x) = 10 \cdot n - \sum (x^2 - 10 \cdot \cos(2\pi x)) \qquad (1)$$

The number of variables for Rastrigin function is 2 and the variable bounds for this function is [-5.12, 5.12] each. This function has global minimum value of 0 at (0,0) and many suboptimal(minimal) points.

b. Dejong function f2

$$f(x, y) = 100 * (x^2 - y)^2 + (1 - x)^2 \qquad (2)$$

The variable bounds for this function is [-2.024, 2.024] each. This function has global minimum value of 0 at (1,1).

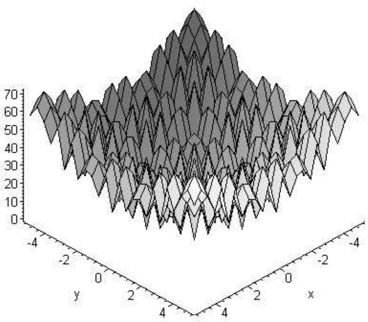

Figure 1: Rastrigin function

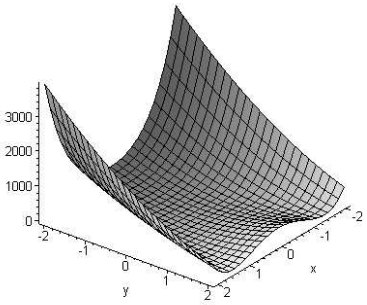

Figure 2: Dejong function f2

Fig. 1 and 2 show 3 dimensional shape of Rastrigin function and Dejong function f2.

3 Results

Through the experimental results there exist some common features.

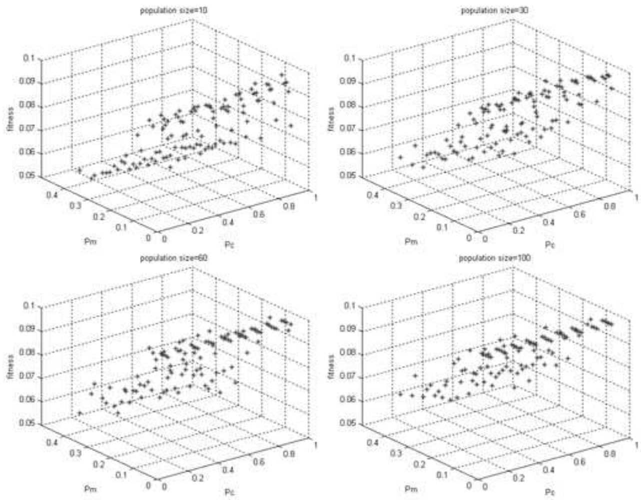

Figure 3: Fitness value of Rastrigin function vs crossover rate vs mutation rate with different population size(10,30,60,100)

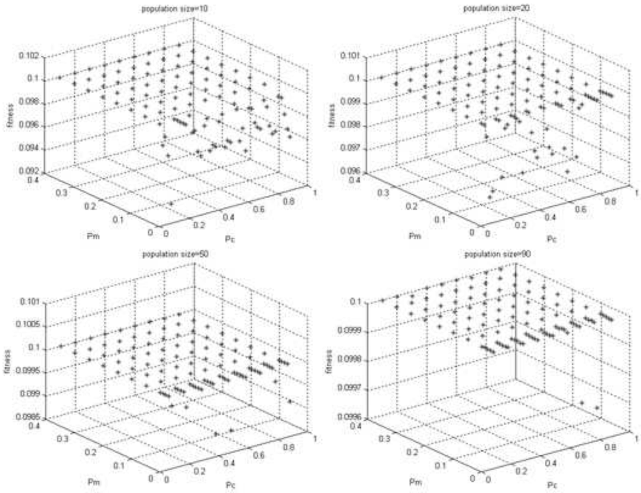

Figure 4: Fitness value of Dejong function vs crossover rate vs mutation rate with different population size(10,20,50,90)

At first, the increase in the population size or mutation rate enhances GA accuracy. When the population size is small, fitness values are smaller than one with large population size and at the same time at the same population size GA with high mutation rate is more accurate than GA with low mutation rate. This is because of the premature convergence. But

The Eleventh International Symposium on Artificial Life and Robotics 2006 (AROB 11th'06),
B-con Plaza, Beppu, Oita, Japan, January 23-25, 2006

too much high mutation rate decline GA accuracy. Roughly speaking crossover corresponds to the near area search and Mutation to the random area search. Therefore even though with small population size, if mutation rate is relatively high, GA has a chance to escape from sub optimal point. But when it increases too much GA travels search space freely and also has little chance to converge in certain point (This should not be the solution). It's very sensitive to the solutions that large population size and high crossover rate cannot overcome (Fig. 3 and 4 show the result).

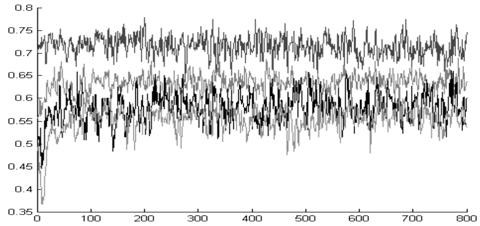

Figure 5: GDM of Rastrigin function with different population size(from top to bottom 10,20,50,90)

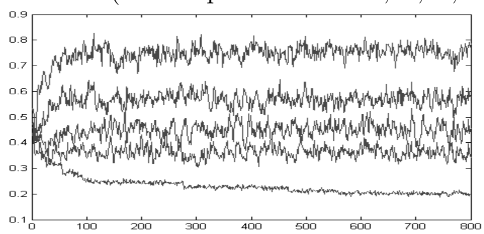

Figure 6: GDM of Rastrigin function with different mutation rate(from top to bottom 0.01,0.02,0.03,0.04,0.2)

Secondly, mutation rate and population size increase population density. Mutation rate increases the average population diversity and also population diversity increases as the generation grows. On the other hand, population size increases the average population diversity, but population diversity does not increase as the generation grows. This is because when the population size is large or the mutation rate is high, GA has more chances to have the variety of individuals. Besides population size cannot change individuals, while mutation can modify the chromosomes of individuals. Therefore the gdm of GA with high mutation rate decreases as generation grows(Fig. 5, 6, 7, and 8 show the result). Crossover rate does not affect population diversity very much.

In [4], Yuri shows that convergence speed decreases as population size grows, but he does not include mutation and elitism in the experiment. In our exper-

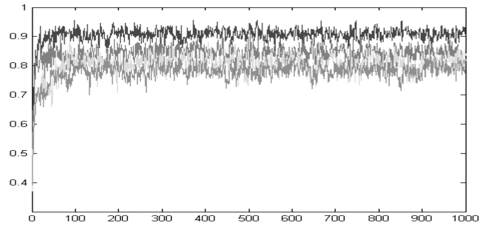

Figure 7: GDM of Dejong function with different population size(from top to bottom 10,30,50,90)

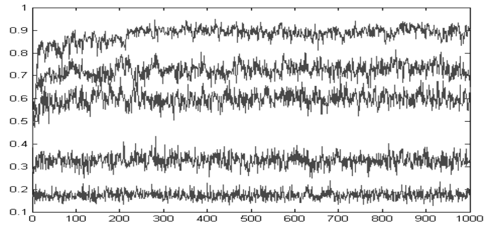

Figure 8: GDM of Dejong function with different mutation rate(from top to bottom 0.01,0.03,0.05,0.15,0.4)

iment we use GA with mutation and elitism, therefore there is little gap between convergence speed with large population size and one with small population size and we cannot deduce general tendency with crossover rate and mutation rate.

4 Conclusion

By the results, generally population size contribute to find the solution most and increase of mutation rate increases accuracy and population diversity. But too high mutation rate disturbs finding the solution.

We checked the functions with different characteristics and there is some difference between test functions. Rastrigin function has many sub optimal points and needs larger search space, therefore it's more sensitive to change in the value of parameters. On the other hand, Dejong function f2 needs smaller search space than Rastrigin function, so it's less sensitive to change in the value of parameters.

We showed that population size affects GA performance most and mutation rate is more effective than crossover rate. If we can consider the function complexity, we can increase GA performance more.

References

[1] Yee Leung, Yong Gao, and Zong-Ben Xu, "Degree of population diversity - a perspective on pre-

mature convergence in genetic algorithms and its Markov chain analysis," *IEEE Trans. Neural Network*,Vol. 8, pp. 1165-1176, 1997.

[2] Chen Tanggong, Wang Youhua, "Adaptive population disappear of genetic algorithm and its application," *Proc. Computational Electromagnetics and Its Applications*, pp. 145-148, 2004

[3] J.A. Vasconcelos, J.A. Ramirez, R.H.C. Takahashi, R.R. Saldanha, "Improvements in genetic algorithms," *IEEE Trans. Magnetic*, Vol. 37, pp. 3414-3417, 2004

[4] Y.R. Tsoy, "The influence of population size and search time limit on genetic algorithm," *Proc. KORUS.*, pp. 181-187, 2003

[5] D.E. Goldberg, Genetic Algorithms in Search, Optimization, and Machine Learning, New York: Addison-Wesely, 1989

[6] Zbigniew Michalewicz, Genetic Algorithms + Data Structures = Evolution Programs, Springer-Verlag, 1999

[7] Melanie Mitchell, An introduction to genetic algorithms, MIT Press, 1996

The Eleventh International Symposium on Artificial Life and Robotics 2006 (AROB 11th'06),
B-con Plaza, Beppu, Oita, Japan, January 23-25, 2006

The new DFM approach based on Genetic Algorithm

Masaya Yoshikawa, Hidekazu Terai
Department of VLSI System Design
Ritsumeikan University
1-1-1, Nojihigashi, Kusatsu, Shiga, 525-8577, Japan

Abstract

As scaling has been continued more than 20 years, it has yielded faster and denser chip with ever increasing functionality. With resent advances technologies, the number of transistors mounted on a VLSI chip is about 10 million gates. In such the advances technology, device feature sizes have become increasingly smaller than the wavelength of light used by available optical-lithography equipment. Therefore, design for manufacturability (DFM) approach has become the most important factor in the design of LSI. In this paper, we propose a new DFM approach as the target for next generations in the layout design phase. Simulation results evaluating the proposed algorithm are shown good performance.

1 Introduction

LSI is widely used in many types of modern electronic products including electric appliances, cellular phones, automobiles, toys, electronic games and robots. Advance LSIs are produced at 0.1-micron design rules, with transistor gate size of 70nm. And then, the number of transistors mounted on the LSI chip is about 10 million gates. In such the nanometer technology, device feature sizes have become increasingly smaller than the wavelength of light used by available optical-lithography equipment. Therefore, design for manufacturability (DFM) approach has become the most important factor in the design of LSI.[1, 2, 3, 4] The Optical Proximity Correction (OPC) is one of the key technologies in DFM approaches. The OPC is the process of modifying the polygons that are drawn by designers to compensate for the non-ideal properties of the lithography process. Given the shapes desired on the wafer, the mask is modified to improve the reproduction of the critical geometry. This is done by dividing polygon edges into small segments and moving the segments around, or by adding additional small polygons to strategic locations in the layout. Since correction parts increase with scaling-down, the correction by OPC can be till 90nm generation. In this paper, we propose a novel DFM approach as the target for next generations in the layout design phase. The proposed algorithm improves manufacture yield by limiting a routing pattern. The proposed algorithm is based on Genetic Algorithm[5, 6, 7]. The GA was proposed by Holland[5] as an algorithm for probabilistic search, learning, and optimization. It is based in part on the mechanism of biological evolution. GA has the three operators of selection, crossover, and mutation. Studies on placement[8], routing[9] and floorplanning[10] have been reported as being applications of GA to the VLSI layout problem. However, no studies have ever seen the effect of applying GA in consideration of DFM.

2 Routing Algorithm

The routing model we assume in this paper is shown in Figure.1. In this routing model, horizontal and vertical routing is possible in all layers. The proposed approach consists of four following steps.

Step1: Division of the routing area

Step2: Global routing

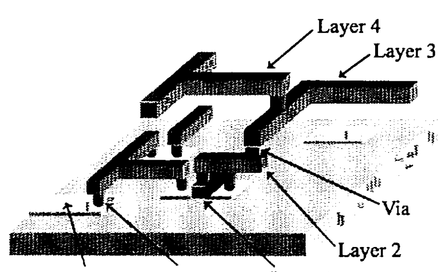

Figure 1: Example of Layout model

The Eleventh International Symposium on Artificial Life and Robotics 2006 (AROB 11th'06),
B-con Plaza, Beppu, Oita, Japan, January 23-25, 2006

Step3: Detail routing by placing block masks

Step4: Final routing by maze router

The first step is division of the area in order t0 produce macro meshes. In this step, it is assumed that there is each terminal at the center of a partial area.

The second step is global routing on the macro meshes. The modified maze routing algorithm is used as base algorithm of the global routing. The maze algorithm, which was developed by Lee[11], is the most widely used algorithm for finding a path between any two vertices on a planar rectangular grid. The search can be visualized as a wave propagating from the source. The source is labeled '0' and the wavefront propagates to all the unblocked vertices adjacent to the source. Every unblocked vertex adjacent to the source is marked with a label '1'. Then, every unblocked vertex adjacent to vertices with a label '1' is marked with a label '2', and so on. This process continues until the target vertex is reached or no further expansion of the wave can be carried out. This maze router is guaranteed to find a path between the source and target, if one exists. In addition, it is guaranteed to be the shortest path between the vertices.[12]

Ordinarily, connected wires become obstacles. That is, the meshes which have been already used by routing, are blocked. However, at this step, since it is global routing, the meshes which connected wires used enlarge the number of labels as shown in Figure.2. Thus, the wire length becomes long when passing through the macro mesh top which has already connected wires. This method disperses wire congestion and raises routability.

The third step is detail routing. In this step, the routing is realized by placing block mask patterns as shown in Figure.3. This placement procedure is based on Genetic Algorithm. Figure.4 shows a flow of this step.

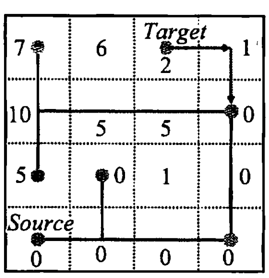

Figure 2: Example of Layout model

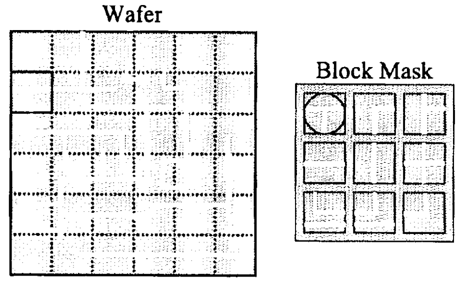

Figure 3: Example of Layout model

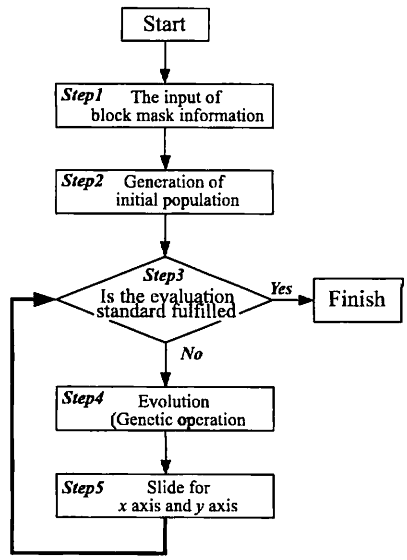

Figure 4: A flow of the third step

It is premised on using partial lithography by the proposed algorithm. As regard to partial lithography, a part of mask block is used for lithography as shown in Figure.5. Thereby, two or more routing patterns with one block mask can be expressed. In order to execute partial lithography, it is necessary to determine the area which executes partial lithography. For that purpose, the area of partial lithography is made to slide in x axis and y axis of a mask block, and the position is determined. It explains using Figure.6 concretely. In the case of Figure.6, the size of a block mask is 5×5, and the size of the area of partial lithography is 3×3. In the case of this example, one grid is possible for a slide for x axis, and two grids are possible for a slide for y axis.

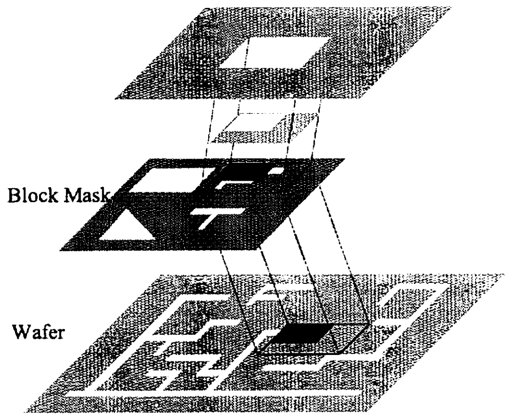

Figure 5: Example of partial lithography

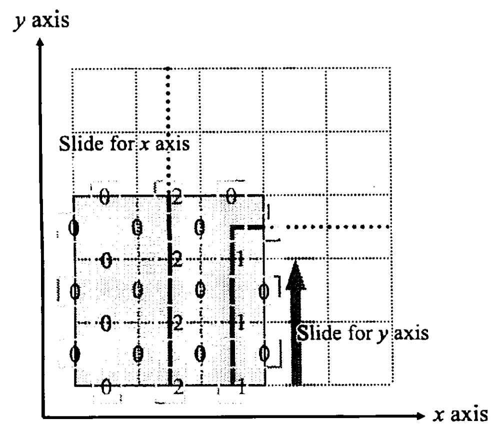

Figure 6: Example of slide for x axis and y axis

Thus, the area of partial lithography is made to slide and the optimal position is determined. And then, as relation to genetic coding, the gene locus corresponds to block mask's ID and each gene gives placement location.

For GA, it is important to set suitable evaluation parameters for controlling the selection of individuals. In order to improve manufacturability, the proposed algorithm introduces new multi-objective functions.

The objective function consists of number of using of block masks, number of placed block masks, total wire length and wire congestion. Preferably, the number of using of block masks also should be small. Moreover, the wire congestion uses the number of wiring on each grid.

Crossover generates an individual by chromosome conversion between two individuals. If excellent partial characteristics, called schemas, of parents can be properly combined and passed to a child, the search performance will be improved greatly.

In proposed algorithm, window areas in parents are prepared and the areas are crossed as shown in Figure.7. Compared with conventional one-point crossover and uniform crossover, the characteristics become easy to be combined and passed to a child. Mutation changes arbitrary genes in an individual. That is, a block mask is exchanged for other block masks.

In the final step(Step4), unconnected wires are routed using the maze router.

3 Experiment and discussion

In order to evaluate the effectiveness of the techniques proposed in this paper, we experimented.

The experimental data is a circuit of 0.35 micron CMOS technology, which has 554 terminals, 186 cells, 223 nets and 4 layers. The proposed algorithm was described using C language and executed on PC-UNIX (Pentium 4 2.4GHz). Parameters of GA are described as follows: The population size is 100, the tournament size is 4, generation gap is 0.7 and the mutation rate is 0.01.

The experimental results are shown in Table.1. An experiment result shows that 90% or more of routing is completed by placement of a block mask (Step3) irrespective of the number of block masks.

Furthermore, the number of the masks used was 100 or less. This means that the manufacturability can

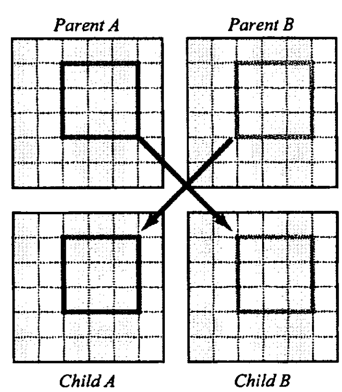

Figure 7: Example of crossover

Table 1: Experimental result

# of BM	Total wire length	Wire congestion	# of using of BM	Ratio of placed BM	Run time
50	$2568nm$	1808.5	35.38	91.91%	$5893.1sec$
100	$2628nm$	1819.0	24.63	92.49%	$5834.3sec$
400	$2609nm$	1648.5	47.75	92.80%	$7178.5sec$
755	$4061nm$	2091.1	98.51	97.18%	$10240.2sec$

be improved. However, the proposed algorithm needs very long computational time, although data size is small.

4 Conclusion

In this paper, we proposed a novel routing algorithm which enables improvement of manufacturability. The proposed algorithm has a four-level hierarchical structure consisting of division of the routing area, global routing, detail routing by placing block masks and final routing by maze router. For selection control, the new multi-objective function was introduced. Experimental results show improvement of manufacturability.

In relation to future research, reducing the run time is the most important priority. We will also experiment using large-scale data.

Acknowledgements

This research is supported by the Nakajima Foundation. The authors would like to thank their supports.

References

[1] Raghvendra, S.; Hurat, P., "DFM: linking design and manufacturing", Proc.18th International Conference on VLSI Design, pp.705-708,(2005)

[2] Keh-Jeng Chang;,"Accurate on-chip variation modeling to achieve design for manufacturability", Proc.4th IEEE International Workshop on System-on-Chip for Real-Time Applications, pp.219-222, (2004)

[3] Pan, D.Z.; Wong, M.D.F.;,"Manufacturability-aware physical layout optimizations", Proc.International Conference on Integrated Circuit Design and Technology, pp.149-153, (2005)

[4] Asami, T.; Nasu, H.; Takase, H.; Oyamatsu, H.; Tsutsui, M.;, "Advanced yield enhancement methodology for SoCs", Proc.IEEE Conference and Workshop Advanced Semiconductor Manufacturing,pp.144-147, (2004)

[5] J.Holland: Adaptation in Natural Artificial Systems,the University of Michigan Press (Second edition ; MIT Press) (1992)

[6] D.Goldberg and R.Lingle, Jr.:"Alleles, loci, and the traveling salesman problem", Proc.of 1st Int. Conf. On Genetic Algorithms and Their Applications, pp. 154–159(1985)

[7] D.E.Goldberg: Genetic Algorithms in search, Optimization and Machine Learning, Addison-Wesley(1989)

[8] L.Zhang, et al., "Analog Module Placement Realizing Symmetry Constraints Based on a Radiation Decoder", Proc. IEEE MWSCAS, pp. I-481-484(2004).

[9] Kanasugi, et al., "A Greedy Router based on Maze Router and Genetic Algorithm", Proc. Int. Conf. on Electronics Packaging, pp.427-430,(2001).

[10] Hung, W.L., et al. "Thermal-aware floorplanning using genetic algorithms", Proc. IEEE Sixth International Symposium on Quality of Electronic Design, pp.634-639, (2005)

[11] C.Y.Lee."An algorithm for path connections and its applications", IRE Transactions on Electronic Computers, (1961)

[12] Naveed Sherwani.:Algorithm for VLSI Physical Design Automation Second Edition, Kluwer Academic Publishers, pp.237-245,(1995)

The Eleventh International Symposium on Artificial Life and Robotics 2006 (AROB 11th'06),
B-con Plaza, Beppu, Oita, Japan, January 23-25, 2006

Design of an Augmented Automatic Choosing Control with Constrained Input by Extremizing a Combination of Hamiltonian and Lyapunov Functions

Toshinori Nawata
Department of Information and Computer Sciences,
Kumamoto National College of Technology,
Kumamoto, Japan. 861-1102

Hitoshi Takata
Department of Electrical and Electronics Engineering,
Faculty of Engineering, Kagoshima University,
Kagoshima, Japan. 890-0065

Abstract

In this paper we consider a nonlinear feedback control called augmented automatic choosing control (AACC) for nonlinear systems with constrained input. Constant terms which arise from sectionwise linearization of a given nonlinear system are treated as coefficients of a stable zero dynamics. Parameters included in the control are suboptimally selected by extremizing a combination of Hamiltonian and Lyapunov functions with the aid of the genetic algorithm.

1 Introduction

A genetic algorithm (GA)[7] is one of evolutionary computing algorithms in engineering sciences. They have been used to solve such complicated tasks as nonlinear global optimization problems. The purpose of this paper is to present a nonlinear feedback control called AACC (Augmented Automatic Choosing Control), which is designed by making good use of the GA.

Generally, it is easy to design the optimal control laws for linear systems, but it is not so for nonlinear systems, though they have been studied for many years[1]~[6]. One of most popular and practical nonlinear control laws is synthesized by applying a linearization method by Taylor expansion truncated at the first order and then the linear optimal control method. This is only effective in a small region around the steady state point or in almost linear systems. Controllers based on a change of coordinates in differential geometry are effective in wider region, but it is not easy to implement them to practical systems. Controllers based on Fuzzy linearization are more practical, but they usually need a lot of complicated divisions. In many physical problems of interest to the control engineer there are various constraints on the control vector. Recently many controls with constraints have been studied.

In this paper we present the AACC with constrained input using the GA for nonlinear systems and its design procedure is as follows. Assume that a system is given by a nonlinear differential equation. Choose a separative variable, which makes up nonlinearity of the given system. The domain of the variable is divided into some subdomains. On each subdomain, the system equation is linearized by Taylor expansion around a suitable point so that a constant term is included in it. This constant term is treated as a coefficient of a stable zero dynamics. The given nonlinear system approximately makes up a set of augmented linear systems, to which the optimal linear control theory is applied to get the linear quadratic (LQ) controls. These LQ controls are smoothly united by sigmoid type automatic choosing functions to synthesize a single nonlinear feedback controller.

This controller is of a structure-specified type which has some parameters, such as the number of division of the domain, regions of the subdomains, points of Taylor expansion, gradients of the automatic choosing functions, and coefficients of the zero dynamics. These parameters must be selected optimally to be just the controller's fit. Since they lead to a nonlinear optimization problem, we are able to solve it by using the GA suboptimally and successfully. The suboptimal values of these parameters are obtained by minimizing the Hamiltonian and maximizing the stable region in the sense of Lyapunov in the paper. This approach is applied to a field excitation control problem of power system to demonstrate the splendidness of the AACC. Simulation results show that the new controller using the GA can improve performance remarkably well.

2 Augmented Automatic Choosing Control

Assume that a nonlinear system is given by

$$\dot{x} = f(x) + g(x)u, \quad x \in \mathbf{D} \tag{1}$$

subject to

$$u_{j,min} \leq u[j] \leq u_{j,max} \quad (j = 1, \cdots, r) \tag{2}$$

where $\cdot = d/dt$, $x = [x[1], \cdots, x[n]]^T$ is an n-dimensional state vector, $u = [u[1], \cdots, u[r]]^T$ is an r-dimensional control vector, $f(x) : \mathbf{D} \to R^n$ is a nonlinear vector-valued function with $f(0) = 0$ and is continuously differentiable, $g(x) : \mathbf{D} \to R^{n\times r}$ is a driving matrix with $g(0) \neq 0$ and is continuously differentiable, $\mathbf{D} \subset R^n$ is a domain , and T denotes transpose.

Considering the nonlinearity of the system (1), introduce a vector-valued function $C : \mathbf{D} \to R^L$ which defines the separative variables $\{C_j(x)\}$, where $C = [C_1 \cdots C_j \cdots C_L]^T$ is continuously differentiable. Let D be a domain of C^{-1}. For example, if $x[2]$ is the element which has the highest nonlinearity of (1), then

$$C(x) = x[2] \in D \subset R \quad (L = 1)$$

(see Section 4). The domain D is divided into some subdomains: $D = \cup_{i=0}^{M} D_i$, where $D_M = D - \cup_{i=0}^{M-1} D_i$ and $C^{-1}(D_0) \ni 0$. $D_i(0 \leq i \leq M)$ endowed with a lexicographic order is the Cartesian product $D_i = \Pi_{j=1}^{L}[a_{ij}, b_{ij}]$, where $a_{ij} < b_{ij}$.

Introduce a stable zero dynamics :

$$\dot{x}[n+1] = -\sigma_i x[n+1] \quad (x[n+1](0) \simeq 1,\ 0 < \sigma_i < 1) \tag{3}$$

where the value of σ_i shall be selected so that $\sigma_i = -\dot{x}[n+1]/x[n+1] \leq -\dot{x}[k]/x[k]$ holds for all $k(k = 1, \cdots, n)$. This tries to keep $x[n+1] \simeq 1$ for a good while when the system (1) is not on $C^{-1}(D_0)$.

Combine (1) with (3) to form an augmented system

$$\dot{\mathbf{X}} = \bar{f}(\mathbf{X}) + \bar{g}(\mathbf{X})u \tag{4}$$

where

$$\mathbf{X} = \begin{bmatrix} x \\ x[n+1] \end{bmatrix} \in \mathbf{D} \times R$$

$$\bar{f}(\mathbf{X}) = \begin{bmatrix} f(x) \\ -\sigma_i x[n+1] \end{bmatrix}, \bar{g}(\mathbf{X}) = \begin{bmatrix} g(x) \\ 0 \end{bmatrix}.$$

Let a cost function be

$$J = \frac{1}{2}\int_0^\infty \left(\mathbf{X}^T\mathbf{Q}\mathbf{X} + u^T\mathbf{R}u\right) dt \tag{5}$$

where

$$\mathbf{Q} = \begin{bmatrix} Q & 0 \\ 0 & q \end{bmatrix}, \quad R \ni q > 0,$$

$Q = Q^T > 0$ and $\mathbf{R} = \mathbf{R}^T > 0$ which denote positive symmetrix matrices. Values of $\mathbf{Q}$ and $\mathbf{R}$ are properly determined based on engineering experience.

On each D_i, the nonlinear system is linearized by the Taylor expansion truncated at the first order about a point $\hat{X}_i \in C^{-1}(D_i)$ and $\hat{X}_0 = 0$:

$$\begin{aligned} f(x) + g(x)u &\simeq A_i x + w_i + B_i u \\ &\simeq A_i x + w_i x[n+1] + B_i u \end{aligned} \tag{6}$$

where

$$\begin{aligned} A_i &= \partial f(x)/\partial x^T\big|_{x=\hat{X}_i},\ B_i = g(\hat{X}_i), \\ w_0 &= 0,\ w_i = f(\hat{X}_i) - A_i\hat{X}_i. \end{aligned}$$

That is, an approximation of (4) is

$$\dot{\mathbf{X}} = \bar{A}_i\mathbf{X} + \bar{B}_i u \quad \text{on } C^{-1}(D_i) \times R \tag{7}$$

where

$$\bar{A}_i = \begin{bmatrix} A_i & w_i \\ 0 & -\sigma_i \end{bmatrix}, \bar{B}_i = \begin{bmatrix} B_i \\ 0 \end{bmatrix}.$$

An application of the linear optimal control theory[2] to (5) and (7) yields

$$u_i(\mathbf{X}) = -\mathbf{R}^{-1}\bar{B}_i^T\mathbf{P}_i\mathbf{X} \tag{8}$$

where the $(n+1) \times (n+1)$ matrix $\mathbf{P}_i$ satisfies the Riccati equation :

$$\mathbf{P}_i\bar{A}_i + \bar{A}_i^T\mathbf{P}_i + \mathbf{Q} - \mathbf{P}_i\bar{B}_i\mathbf{R}^{-1}\bar{B}_i^T\mathbf{P}_i = 0. \tag{9}$$

Introduce an automatic choosing function of sigmoid type:

$$\begin{aligned} I_i(x) &= \prod_{j=1}^{L}\left\{1 - \frac{1}{1+\exp\left(2N_1\left(C_j(x) - a_{ij}\right)\right)}\right. \\ &\left. - \frac{1}{1+\exp\left(-2N_1\left(C_j(x) - b_{ij}\right)\right)}\right\} \end{aligned} \tag{10}$$

where N_1 is positive real value, $-\infty \leq a_{ij}$ and $b_{ij} \leq \infty$. $I_i(x)$ is analytic and almost unity on $C^{-1}(D_i)$, otherwise almost zero(see Figure 1).

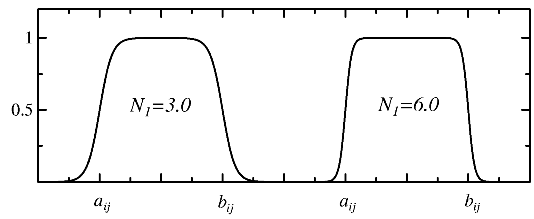

Figure 1: Automatic Choosing Function(N_1=3.0, 6.0)

Uniting $\{u_i(\mathbf{X})\}$ of (8) with $\{I_i(x)\}$ of (10) yields

$$\begin{aligned} \hat{u}(\mathbf{X}) &= [\hat{u}(\mathbf{X})[1], \cdots, \hat{u}(\mathbf{X})[j], \cdots, \hat{u}(\mathbf{X})[r]]^T \\ &= \sum_{i=0}^{M} u_i(\mathbf{X})I_i(x). \end{aligned}$$

We finally have an augmented automatic choosing control which is satisfied with the constraint condition (2) by

$$u(\mathbf{X}) = [u(\mathbf{X})[1], \cdots, u(\mathbf{X})[j], \cdots, u(\mathbf{X})[r]]^T \tag{11}$$

where

$$u(\mathbf{X})[j] = \begin{cases} u_{j,max} & \text{if} \quad \hat{u}(\mathbf{X})[j] \geq u_{j,max} \\ u_{j,min} & \text{if} \quad \hat{u}(\mathbf{X})[j] \leq u_{j,min} \\ \hat{u}(\mathbf{X})[j] & \text{otherwise} \end{cases}$$

$$(1 \leq j \leq r).$$

3 Parameter Selection by GA

The Hamiltonian for Eqs.(4) and (5) is given by

$$H(\mathbf{X},u,\lambda) = \frac{1}{2}\left(\mathbf{X}^T\mathbf{Q}\mathbf{X}+u^TRu\right) + \lambda^T\left(\bar{f}(\mathbf{X})+\bar{g}(\mathbf{X})u\right). \quad (12)$$

Assume that the adjoint vector $\lambda \in R^{n+1}$ is

$$\lambda(\mathbf{X}) = \sum_{i=0}^{M}\{(\bar{B}_i-\bar{g}(\mathbf{X}))\bar{g}(\mathbf{X})^{\dagger}+E\}^T\mathbf{P}_i\mathbf{X}I_i(x) \quad (13)$$

where $\bar{g}(\mathbf{X})^{\dagger}\bar{g}(\mathbf{X}) = E$, E is an appropriate-dimentional unit matrix, † denotes pseudo inverse, and $\mathbf{P}_i$ is the solution of (9).

The necessary condition of the optimality is $\partial H/\partial u = 0$ or $u = -R^{-1}\bar{g}(\mathbf{X})^T\lambda$, which derives Eq.(11) using Eq.(13) and

$$H(\mathbf{X},u,\lambda) = \frac{1}{2}\mathbf{X}^T\mathbf{Q}\mathbf{X}-\frac{1}{2}u^TRu+\bar{f}^T(\mathbf{X})\lambda \quad (14)$$

using Eq.(12).

Next, introduce a Lyapunov function candidate:

$$V(\mathbf{X}) = \mathbf{X}^T\Pi(\mathbf{X})\mathbf{X} \quad (15)$$

where

$$\Pi(\mathbf{X}) = \sum_{i=0}^{M}\mathbf{P}_i\Pi_i(x) \ ,$$

$$\Pi_i(x) = \eta_i\prod_{j=1}^{L}\left\{1-\frac{1}{1+\exp\left(2N_2\left(C_j(x)-a_{ij}\right)\right)} - \frac{1}{1+\exp\left(-2N_2\left(C_j(x)-b_{ij}\right)\right)}\right\}, \quad (16)$$

N_2 and η_i are positive real values.

By the Lyapunov's direct method[3], the equilibrium point 0 is uniformly stable on a connected set:

$$\mathbf{D}_V = \left\{x\in\mathbf{D} : V(\mathbf{X})<\gamma,\, \dot{V}(\mathbf{X})<0\right\}$$

where

$$\gamma = \inf\left\{V(\mathbf{X}) : \mathbf{X}\neq 0,\, \dot{V}(\mathbf{X})=0\right\}. \quad (17)$$

In order to design the optimal control by Hamiltonian and expand the stable region in the sense of Lyapunov as wide as possible, we define a performance

$$PI = \omega_1\int_{\mathbf{D}}|H(\mathbf{X},u,\lambda)|/\mathbf{X}^T\mathbf{X}d\mathbf{X}-\omega_2\gamma \quad (18)$$

where $\omega_i(\omega_i \geq 0; i=1,2)$ is weight.

A set of parameters included in the control (11):

$$\bar{\Omega} = \left\{M,N_1,N_2,a_{ij},b_{ij},\hat{X}_i,\eta_i\right\}$$

is suboptimally selected by minimizing PI with the aid of GA[7] as follows.

<ALGORITHM>

step1:A-priori: Set values $\bar{\Omega}_{apriori}$ appropriately.

step2:Parameter: Choose a subset $\Omega\subset\bar{\Omega}$ to be improved and rewrite it by $\Omega=\{M,N_1,N_2\cdots\} = \{\alpha_k : k=1,\cdot\cdot,K\}$.

step3:Coding: Represent each α_k with a binary bit string of $\widetilde{L}$ bits and then arrange them into one string of $\widetilde{L}K$ bits.

step4:Initialization: Randomly generate an initial population of $\widetilde{q}$ strings $\{\Omega_p : p=1,\cdot\cdot,\widetilde{q}\}$.

step5:Decoding: Decode each element α_k of Ω_p by $\alpha_k = (\alpha_{k,max}-\alpha_{k,min})\,A_k/\left(2^{\widetilde{L}}-1\right)+\alpha_{k,min}$ where $\alpha_{k,max}$:maximum, $\alpha_{k,min}$:minimum, and A_k:decimal value of α_k.

step6:Control: Design $u=u(\mathbf{X})_p \quad (p=1,\cdots,q)$ for Ω_p by using Eq.(11).

step7:Adjoint: Make $\lambda=\lambda(\mathbf{X})_p \quad (p=1,\cdots,q)$ for Ω_p by using Eq.(13).

step8:Lyapunov function: Make $\gamma=\gamma_p$ $(p=1,\cdots,\widetilde{q})$ for Ω_p by using Eq.(17).

step9:Fitness value calculation: Calculate

$$PI_p = \omega_1\int_{\mathbf{D}}\left|\frac{1}{2}\mathbf{X}^T\mathbf{Q}\mathbf{X}-\frac{1}{2}u(\mathbf{X})_p^TRu(\mathbf{X})_p + \bar{f}^T(\mathbf{X})\lambda(\mathbf{X})_p\right|/\mathbf{X}^T\mathbf{X}d\mathbf{X}-\omega_2\gamma_p \quad (19)$$

by Eqs.(14) and (18), or fitness $F_p=-PI_p$. Integration of (19) is approximated by a finite sum.

step10:Reproduction: Reproduce each of individual strings with the probability of $F_p/\sum_{j=1}^{\widetilde{q}}F_j$.

step11:Crossover: Pick up two strings and exchange them at a crossing position by a crossover probability P_c.

step12:Mutation: Alter a bit of string (0 or 1) by a mutation probability P_m.

step13:Repetition: Repeat step5∼step12 until prespecified G-th generation. If unsatisfied, go to step2.

As a result, we have a suboptimal control $u(\mathbf{X})$ for the string with the best performance over all the past generations.

4 Numerical Example

Consider a field excitation control problem of power system which is described[5][6] by

$$\widetilde{M}\frac{d^2\delta}{dt^2}+\widetilde{D}(\delta)\frac{d\delta}{dt}+P_e(\delta)=P_{in}$$

$$P_e(\delta)=E_I^2Y_{11}\cos\theta_{11}+E_I\widetilde{V}Y_{12}\cos(\theta_{12}-\delta)$$

$$E_I+T'_{d0}\frac{dE'_q}{dt}=E_{fd}$$

$$E_I=E'_q+(X_d-X'_d)I_d(\delta)$$

$$I_d(\delta)=-E_IY_{11}\sin\theta_{11}-\widetilde{V}Y_{12}\sin(\theta_{12}-\delta)$$

$$\widetilde{D}(\delta)=\widetilde{V}^2\left\{\frac{T''_{d0}(X'_d-X''_d)}{(X'_d+X_e)^2}\sin^2\delta + \frac{T''_{q0}(X_q-X''_q)}{(X_q+X_e)^2}\cos^2\delta\right\},$$

where δ: phase angle, $\dot{\delta}$: rotor speed, $\widetilde{M}$: inertia coefficient, $\widetilde{D}(\delta)$: damping coefficient, P_{in}: mechanical input power, $P_e(\delta)$: generator output power, $\widetilde{V}$: reference bus voltage, E_I: open circuit voltage, and E_{fd}: field excitation voltage. Put x=$[x[1], x[2], x[3]]^T$=$[E_I - \hat{E}_I, \delta - \hat{\delta}_0, \dot{\delta}]^T$ and $u = E_{fd} - \hat{E}_{fd}$, so that

$$\begin{bmatrix} \dot{x}[1] \\ \dot{x}[2] \\ \dot{x}[3] \end{bmatrix} = \begin{bmatrix} f_1(x) \\ f_2(x) \\ f_3(x) \end{bmatrix} + \begin{bmatrix} g_1(x) \\ 0 \\ 0 \end{bmatrix} u \qquad (20)$$

where $f_1(x) = -\frac{1}{kT'_{d0}}\left(x[1]+\hat{E}_I\right) + \frac{(X_d-X'_d)\widetilde{V}Y_{12}}{k}x[3] \cdot\cos\left(\theta_{12}-x[2]-\hat{\delta}_0\right)$, $f_2(x) = x[3]$, $f_3(x) = -\frac{\widetilde{V}Y_{12}}{\widetilde{M}} \cdot\left(x[1]+\hat{E}_I\right)\cos\left(\theta_{12}-x[2]-\hat{\delta}_0\right) - \frac{Y_{11}\cos\theta_{11}}{\widetilde{M}}\left(x[1]+\hat{E}_I\right)^2 - \frac{\widetilde{D}(x)}{\widetilde{M}}x[3] + \frac{P_{in}}{\widetilde{M}}$, $\widetilde{D}(x) = \widetilde{V}^2\left\{\frac{T''_{d0}(X'_d-X''_d)}{(X'_d+X_e)^2} \cdot\sin^2\left(x[2]+\hat{\delta}_0\right) + \frac{T''_{q0}(X_q-X''_q)}{(X_q+X_e)^2}\cos^2\left(x[2]+\hat{\delta}_0\right)\right\}$, $g_1(x) = \frac{1}{kT'_{d0}}$, $k = 1+(X_d-X'_d)\,Y_{11}\sin\theta_{11}$.

Assume that the constrained input is subject to $u_{min} + \hat{E}_{fd} \leq E_{fd} \leq u_{max} + \hat{E}_{fd}$.

Parameters are $\widetilde{M} = 0.016095[pu]$, $T'_{d0} = 5.09907[sec]$, $\widetilde{V} = 1.0[pu]$, $P_{in} = 1.2[pu]$, $X_d = 0.875[pu]$, $X'_d = 0.422[pu]$, $Y_{11} = 1.04276[pu]$, $Y_{12} = 1.03084[pu]$, $\theta_{11} = -1.56495[pu]$, $\theta_{12} = 1.56189[pu]$, $X_e = 1.15[pu]$, $X''_d = 0.238[pu]$, $X_q = 0.6[pu]$, $X''_q = 0.3[pu]$, $T''_{d0} = 0.0299[pu]$, $T''_{q0} = 0.02616[pu]$.

Steady state values are $\hat{E}_I = 1.52243[pu]$, $\hat{\delta}_0 = 48.57°$, $\hat{\dot{\delta}}_0 = 0.0[deg/sec]$, $\hat{E}_{fd} = 1.52243[pu]$. Set $\mathbf{X} = [x^T, x[4]]^T = [x[1], x[2], x[3], x[4]]^T$, $n = 3$, $\hat{X}_0 = \hat{\delta}_0 = 48.57°$, $C(x)$=$x[2]$, $L = 1$, $\mathbf{Q}$=diag(1, 1, 1, 1), $\mathbf{R}$=1, $\eta_0 = 1$, $\omega_1 = 1$ and $x[4](0) = 1$. Experiments are carried out for the new control(AACC) and the ordinary linear optimal control(LOC)[1][2].

Table 1: Performances $\widetilde{J}$

Method	$x^T(0)$		
	$[0, 0.4, 0]$	$[0, 1.0, 0]$	$[0, 1.44, 0]$
LOC	1.124	×	×
AACC($\omega_2 = 10$)	1.115	2.703	×
AACC($\omega_2 = 500$)	1.489	2.812	4.540

× : very large value

1) AACC($\omega_2 = 10$):
The parameters are suboptimally selected along the algorithm of section 3. $\omega_2 = 10$, Ω=$\{M, N_1, N_2, \hat{X}_i, a_{ij}, b_{ij}, \eta_i\}$, $\widetilde{G}$=100, $\widetilde{q}$=100, $\widetilde{L}$=8, P_c=0.8, P_m=0.03, $\mathbf{D}$=[-0.5,0.5]×[-0.2,0.5]×[-2,2]×[0,1.0]. It results that $M = 3$, $N_1 = 7.18$, $N_2 = 1.56$, $\hat{X}_1 = 60°$, $\hat{X}_2 = 175°$, $\hat{X}_3 = 180°$, $a_1 = b_0 = 53.5°$, $a_2 = b_1 = 147.5°$, $a_3 = b_2 = 177.8°$ and $\eta_1 = \eta_2 = \eta_3 = 2.82$.

2) AACC($\omega_2 = 500$):
The parameters are suboptimally selected by using a similar way of the **AACC**($\omega_2 = 10$). $\omega_2 = 1000$. It results that $M = 2$, $N_1 = 2.24$, $N_2 = 3.33$, $\hat{X}_1 = 95°$, $\hat{X}_2 = 160°$, $a_1 = b_0 = 53.8°$, $a_2 = b_1 = 142.0°$ and $\eta_1 = \eta_2 = 1.37$.

Table1 shows performances by the AACC and the LOC. The cost function of Table1 is $\widetilde{J} = \frac{1}{2}\int_0^{20}\left(\mathbf{X}^T\mathbf{Q}\mathbf{X} + u^T\mathbf{R}u\right)dt$. These results indicate that the AACC is better than the LOC.

5 Conclusions

We have studied an augmented automatic choosing control using zero dynamics for nonlinear systems with constrained input. This approach have been applied to a field excitation control problem of power system. Simulation results have shown that this controller using the GA can improve performance remarkably well.

References

[1] Y. N. Yu, K. Vongsuriya and L. N. Wedman, "Application of an Optimal Control Theory to a Power System", *IEEE Trans. Power Apparatus and Systems*, 89-1, pp.55–62, 1970.

[2] A. P. Sage and C. C. White III, "Optimum Systems Control (2nd edition)", *Prentice-Hall, Inc.*, 1977.

[3] M. Vidyasagar, "Nonlinear Systems Analysis", *Prentice-Hall, Inc.*, 1978.

[4] A.Isidori, "Nonlinear Control Systems : An Introduction (2nd edition)", *Springer-Verlag*, 1989.

[5] Y.Takagi and T.Shigemasa, "An Application of State-Space Linearization to a Power System Stabilizer", *Proc. 29th CDC*, TA8-1, pp.1553–1558, 1990.

[6] H.Takata, "An Automatic Choosing Control for Nonlinear Systems", *Proc. 35th CDC*, FA10-5, pp.3453–3458, 1996.

[7] D. E. Goldberg, "Genetic Algorithms in Search, Optimization, and Machine Learnings", *Addison-Wesley Pub. Co. Inc.*, 1989.

Colour quantisation using Simulated Annealing

Gerald Schaefer, Lars Nolle
School of Computing and Informatics
Nottingham Trent University
Nottingham, U.K.
Gerald.Schaefer@ntu.ac.uk
Lars.Nolle@ntu.ac.uk

Tomoharu Nakashima
School of Computer Sciences
and Intelligent Systems
Osaka Prefecture University
Osaka, Japan
nakashi@cs.osakafu-u.ac.jp

Abstract

Colour quantisation tries to find entries of a colour palette for true colour images to be displayed on hardware with limited colour support while maintaining the best possible image quality. The mapping from true colour entries to the entries in the palette represents an np-complete problem so that colour quantisation algorithms apply various heuristics in order to derive the palette. In this paper we apply a variant of Simulated Annealing (SA) as a generic optimisation algorithm to the colour quantisation problem. Experiments on a series of standard test images show that even without any domain specific knowledge our SA based algorithm is able to outperform conventional quantisation algorithms and hence to provide images with superior image quality.

1 Introduction

Colour quantisation is a common image processing technique that allows the representation of true colour images using only a small number of colours and is useful for displaying images on limited hardware such as mobile devices, for image compression, and for other applications such as image retrieval [11]. True colour images typically use 24 bits per pixel which results in an overall gamut of 2^{24} i.e. more than 16.8 million different colours. Colour quantisation uses a colour palette that contains only a small number of colours (usually between 8 and 256) and pixel data are then stored as indices to this palette. Clearly the choice of the colours that make up the palette has a crucial influence on the image quality of the quantised image However, the selection of the optimal colour palette is known to be an np-hard problem [4]. In the image processing literature many different algorithms have been introduced that aim to find a palette that allows for good image quality of the quantised image [4, 3, 2].

In this paper we apply a variant of Simulated Annealing (SA) as a standard black-box optimisation algorithm to the colour quantisation problem. The main advantage of black-box optimisation algorithms is that they do not require any domain specific knowledge yet are able to provide a near optimal solution. We evaluate the effectiveness of our approach by comparing its performance to the results obtained by several purpose built colour quantisation algorithms [4, 3, 2]. The results obtained show that even without any domain specific knowledge our SA based algorithm is able to outperform standard quantisation algorithms and hence to provide palettised images with superior image quality.

The rest of the paper is organised as follows: Section 2 provides the background for optimisation based on Simulated Annealing. Section 3 explains our application of SWASA, a modified SA algorithm, to the colour quantisation problem. Section 4 provides experimental results based on a set of standard test images while 5 concludes the paper.

2 Simulated annealing

Simulated annealing (SA) was first introduced as a general optimisation method by Kirkpatrick *et al.* [6], based on the work of Metropolis *et al.* [7]. It simulates the annealing of metal, in which the metal is heated-up to a temperature near its melting point and then slowly cooled down. This allows the particles to move towards a minimum energy state, with a more uniform crystalline structure. The process therefore permits some control over the microstructure.

Simulated annealing is a variation of the hill-climbing algorithm. Both start from a randomly selected point within the search space of all the possible solutions. Each point in the search space has a measurable error value, E, associated with it, which indicates the quality of the solution. From the current point in search space, new trial solutions are selected for testing from the neighborhood of the current solution. This is usually done by moving a small step in a random direction. In this application, small and equally distributed random numbers from the interval $[-s_{max}, s_{max}]$ are added to each component of the current solution vector, where s_{max} is called the 'maximum step width'. The values for s_{max} need to be chosen from the interval between 0 and the upper limit of the search space dimension. The decrease in error values is ΔE. If ΔE is negative, i.e. the error of a trial solution is less than the error of the current one, the trial solution is accepted as the current solution.

Unlike hill-climbing SA does not automatically reject a new candidate solution if ΔE is positive. Instead it becomes the current solution with probability $p(T)$ which is usually determined using

$$p(T) = e^{-\Delta E/T} \tag{1}$$

where T is referred to as 'temperature', an abstract control parameter for the cooling schedule. For a given temperature and positive values of ΔE the probability function shown in Equation 1 has a defined upper limit of one, and tends towards zero for large positive values of ΔE. That means, in a practical computer application, the probability $p(T)$ has to be calculated for each candidate solution and to be compared with an equally distributed random number from the interval $[0, 1]$. If the probability $p(T)$ is greater than the random number the candidate solution is accepted as the current solution, otherwise it is rejected.

The algorithm starts with a high temperature i.e. with a high transition probability. The temperature is then reduced towards zero, usually in steps, according to a cooling schedule such as

$$T_{n+1} = \alpha T_n \tag{2}$$

where T_n is the temperature at step n and α is the cooling coefficient (usually between 0.8 and 0.99).

During each step the temperature must be held constant for an appropriate number of iterations in order to allow the algorithm to settle into a 'thermal equilibrium' i.e. a balanced state. If the number of iterations is too small the algorithm is likely to converge to a local minimum.

Step width adapting simulated annealing (SWASA) [8] overcomes the problems associated with constant values for s_{max} by using a scaling function [10] to adapt the maximum step width to the current iteration by

$$s_{max}(n) = \frac{2s_0}{1 + e^{\beta n/n_{max}}} \tag{3}$$

where $s_{max}(n)$ is the maximum step width at iteration n, s_0 is the initial maximum step width, n_{max} the maximum number of iterations and β is an adaptation constant.

3 Simulated Annealing for colour quantisation

In this paper we apply the SWASA algorithm described in Section 2 as a black box optimisation algorithm to the colour quantisation problem. For colour quantisation the objective is to minimise the total error introduced through the application of a colour palette. The colour palette C for an image I, a codebook of k colour vectors, should then be chosen so as to minimise the error function

$$\text{error}(C, I) = \frac{1}{\sum_{j=1}^{k} l_j} \sum_{i=1}^{k} \sum_{j=1}^{l_i} ||C_i - I_j|| + p(C, I) \tag{4}$$

with

$$p(C, I) = \sum_{i=1}^{k} \delta a_i, \quad a_i = \begin{cases} 1 & \text{if } l_i = 0 \\ 0 & \text{otherwise} \end{cases} \tag{5}$$

where l_i is the number of pixels I_j represented by colour C_i of the palette, $||.||$ is the Euclidean distance in RGB space, and δ is a constant ($\delta = 10$ in our experiments). The objective function error(C, I) used is hence a combination of the mean Euclidean distance and a penalty function. The penalty function $p(C, I)$ was integrated in order to avoid unused palette colours by adding a constant penalty value to the error for each entry in the codebook that is not used in the resulting picture.

As can be seen from Equation 4 the objective function is highly non-linear, i.e. it has a high degree of epistasis [1]. Past experience [9] has shown that for this kind of optimisation problems simulated annealing outperforms other generic optimisation algorithms like genetic algorithms [5].

For our colour quantisation algorithm we employ a population based version of the SWASA algorithm with a population size of 10. The start temperature was chosen to be 100 and the cooling coefficient was set to 0.9. The temperature was kept constant over 20 iterations and the maximum number of iterations was set to 10000.

Image	Popularity alg.	Median cut	Octree	Neuquant	Sim. Annealing
Lenna	22.24	23.79	27.45	**27.82**	27.79
Peppers	18.56	24.10	25.80	26.04	**26.16**
Mandrill	18.00	21.52	24.21	**24.59**	24.46
Sailboat	8.73	22.01	26.04	**26.81**	26.69
Airplane	15.91	24.32	28.77	28.24	**29.43**
Pool	19.87	24.57	29.39	27.08	**29.84**
mean	17.22	23.39	26.94	26.73	**27.40**

Table 1: Quantisation results, given in terms of PSNR [dB].

4 Experimental results

In order to evaluate our new method for colour quantisation we have taken a set of six standard images commonly used in the colour quantisation literature (*Lenna, Peppers, Mandrill, Sailboat, Airplane, and Pool*) and applied our optimisation scheme to generate quantised images with a palette of 16 colours.

To put the results we obtain into context we have also implemented four popular colour quantisation algorithms to generate corresponding quantised images with palette size 16. The algorithms we have tested were:

- Popularity algorithm [4]: Following a uniform quantisation to 5 bits per channel the n colours that are represented most often form the colour palette.
- Median cut quantisation [4]: An iterative algorithm that repeatedly splits (by a plane through the median point) colour cells into sub-cells..
- Octree quantisation [3]: The colour space is represented as an octree where sub-branches are successively merged to form the palette.
- Neuquant [2]: A one-dimensional self-organising Kohonen neural network is applied to generate the colour map.

For all algorithms, pixels in the quantised images were assigned to their nearest neighbours in the colour palette to provide the best possible image quality.

The results are listed in Table 1, expressed in terms of peak-signal-to-noise-ratio (PSNR) defined as

$$\mathrm{PSNR}(I_1, I_2) = 10 \log_{10} \frac{255^2}{MSE(I_1, I_2)} \tag{6}$$

with MSE (the mean-squared error) given as

$$\mathrm{MSE}(I_1, I_2) = \frac{1}{3nm} \sum_{i=1}^{n} \sum_{j=1}^{m} [(R_1(i,j) - R_2(i,j))^2 + (G_1(i,j) - G_2(i,j))^2 + (B_1(i,j) - B_2(i,j))^2] \tag{7}$$

where $R(i,j)$, $G(i,j)$, and $B(i,j)$ are the red, green, and blue pixel values at location (i,j) and n and m are the dimensions of the images.

From Table 1 we can see our Simulated Annealing approach to colour quantisation obtains the best results for three of the six images and comes close 2-nd for the other three. Overall a mean PSNR of 27.40 dB is achieved which is significantly better than the 26.94 and 26.73 dB obtained by Octree and Neuquant, the two next best algorithms.

An example of the performance of the different algorithms is provided in Figure 1 which shows part of the *Pool* image together with the same part extracted from the images colour quantised by all algorithms. It is clear that the popularity algorithm performs poorly on this image and assigns virtually all of the colours in the palette to green and achromatic colours. Median cut is better but still provides fairly poor colour reproduction; most of the colours in the quantised image are fairly different from the original. The same holds true for the images produced by Neuquant. Here the most obvious artefact is the absence of an appropriate red colour in the colour palette. A far better result is achieved by the Octree algorithm, although here also the red is not very accurate and the colour of the cue is greenish instead of brown. Clearly the best image quality is maintained by applying our Simulated annealing technique. Although the colour palette has only 16 entries all colours of the original image are accurately presented including the red ball and the colour of the billiard cue.

5 Conclusions

In this work we have applied a variant of Simulated Annealing as a standard black-box optimisation algorithm to the colour quantisation problem. Experimental results obtained on a set of standard test images have demonstrated that this type of optimisation techniques cannot only be effectively employed but is

Figure 1: Part of original *Pool* image (top-left) and corresponding images quantised with (from left to right, top to bottom): Popularity algorithm, Median cut, Octree quantisation, Neuquant, and our Simulated annealing approach.

even able to outperform standard purpose built colour quantisation algorithms.

References

[1] Y. Davidor. Epistasis variance: Suitability of a representation to genetic algorithms. *Complex Systems*, 4:369–383, 1990.

[2] A.H. Dekker. Kohonen neural networks for optimal colour quantization. *Network: Computation in Neural Systems*, 5:351–367, 1994.

[3] M. Gervautz and W. Purgathofer. A simple method for color quantization: Octree quantization. In A.S. Glassner, editor, *Graphics Gems*, pages 287–293. 1990.

[4] P. S. Heckbert. Color image quantization for frame buffer display. *ACM Computer Graphics (ACM SIGGRAPH '82 Proceedings)*, 16(3):297–307, 1982.

[5] J.H. Holland. *Adaptation in Natural and Artificial Systems*. University of Mitchigan Press, 1975.

[6] S. Kirkpatrick, C.D. Gelatt, and M.P. Vecchi. Optimization by simulated annealing. *Science*, 220(4598):671–680, May 1983.

[7] A. Metropolis, W. Rosenbluth, M.N. Rosenbluth, H. Teller, and E. Teller. Equation of state calculations by fast computing machines. *Journal of Chemical Physics*, 21(6):1087–1092, 1953.

[8] L. Nolle. On the effect of step width selection schemes on the performance of stochastic local search strategies. In *18th European Simulation Multi-Conference*, pages 149–153, 2004.

[9] L. Nolle, D.A. Armstrong, A.A. Hopgood, and J.A. Ware. Simulated annealing and genetic algorithms applied to finishing mill optimisation for hot rolling of wide steel strip. *International Journal of Knowledge-Based Intelligent Engineering Systems*, 6(2):104–111, 2002.

[10] L. Nolle, A. Goodyear, A.A. Hopgood, P.D. Picton, and N. Braithwaite. On step width adaptation in simulated annealing for continuous parameter optimisation. In *Computational Intelligence - Theory and Applications*, volume 2206 of *Lecture Notes in Computer Science*, pages 589–598. Springer, 2001.

[11] G. Schaefer, G. Qiu, and G. Finlayson. Retrieval of palettised colour images. In *Storage and Retrieval for Image and Video Databases VIII*, volume 3972 of *Proceedings of SPIE*, pages 483–493, 2000.

The Eleventh International Symposium on Artificial Life and Robotics 2006 (AROB 11th'06),
B-con Plaza, Beppu, Oita, Japan, January 23-25, 2006

Applying Genetic Algorithm to a Programming Training Support System

Eiji Nunohiro, Kenneth J. Mackin, Masanori Ohshiro, Kazuko Yamasaki
Department of Information Systems, Tokyo University of Information Sciences
1200-2 Yatoh-cho, Wakaba-ku, Chiba 265-8501, Japan
{nunohiro, mackin, ohshiro, yamasaki}@rsch.tuis.ac.jp

Abstract

We proposed a programming training support system which understanding programming structure or algorithms. In our proposed training system, a given source code is broken up into separate puzzle pieces, and the user must reconstruct the program by selecting the correct program puzzle pieces in the correct order. In order for the system to break up a program into effective puzzle pieces depending on the proficiency of the user, the system must select how many, and where to set the partition-points to divide the program. For this method, we applied genetic algorithm (GA) search to allow the system to self-organize the problem and select the optimal number of pieces and location of partition-points. We created a prototype system and applied it in a Java programming practice and evaluated the proposed system. As a result, we can show this proposed self-adjusting programming training support system provide tailored programming exercises for students of different achievement levels, and efficiently support the learning environment.

key words: genetic algorithm, e-leaning, programming education.

1 introduction

Computer aided training has become an important method for improving computer education. In the case of early programming training, there are many topics that need to be studied together, such as programming language syntax, programming design methods for example object oriented design, and problem solving algorithms.

It is common to find an emphasis on language syntax or grammar in the early stages of programming training. But the essence of programming education is not mastering the language specification, but understanding programming style or algorithms. For this research, we propose a programming training support system which targets understanding program structures which satisfy required program specifications. In our proposed training system, a given source code is broken up into separate puzzle pieces, and the user must layout the pieces in the correct order to reconstruct the program. The proposed system applies genetic algorithm (GA) and allows the system to self-adjust the difficulty of the programming problems matching the trainee's competency.

2 Programming problem creation

There are many different methods for early stage programming training, for example:

(1) the specification (problem) is supplied and a program which satisfies the specification (solves the problem) must be created.

(2) the specification and partially completed program is supplied, and the program must be correctly completed.

For this research, we follow method 2 and propose a training system which takes into account the proficiency and progress level of the user. Here we emphasize 1) program flow comprehension, 2) program structure comprehension, and 3) program algorithm comprehension, rather than emphasizing memorization of programming language syntax.

Programming training from the viewpoint of program flow comprehension and program structure comprehension can be compared to solving a 2-dimensional puzzle by logically laying out the puzzle pieces. One must comprehend the general structure of the puzzle before laying out the individual pieces. From this standpoint, we propose a training system in which the system breaks up a program into puzzle pieces, and the user must reconstruct the program by selecting the correct program puzzle pieces in the correct order. In order for the system to break up a program into effective puzzle pieces, the system must select how many, and where to set the partition-points to divide the program. For this research, we applied genetic algorithm (GA) search to allow the system to self-organize the problem and select the optimal number of pieces and location of partition-points, depending on the progress level of the user.

3 Program puzzle creation

Depending on the difficulty of the created puzzle pieces, there is a possibility that the created problem becomes too easy or too difficult for the user and fails to improve the user's programming skills, causing an adverse affect to the user's motivation. For this reason it is important that to design the puzzle pieces considering the user's progress. We considered the following automatic puzzle creation algorithm.

【step1】 Analyze the program source code to determine the control depth (control information) and variable reference (reference information) for each line of program.

【step2】 Calculate the difficulty level for each statement using the above control and reference information.

【step3】 Apply genetic algorithm (GA) search to find the optimal combination of partition-points which best match the progress level of the user.

In the following sections, we describe the genetic algorithm search applied.

3.1 Source code analysis

Each line of program source code is analyzed for information to be used in determining the difficulty of the partition. For each line of code, the control depth, and variable reference is calculated to measure the complexity of the source code.

(a) control information analysis
The "control depth" for each statement is calculated. The control depth is the depth of the nest of control statements, such as if, for, and while statements.

(b) reference information analysis
The "variable reference" count for each statement is calculated. The following criteria are used to determine the variable reference for statement S:
- a variable is defined in statement S

Program	Depth	Reference
1:public class EvenOrOdd {	0	0
2: public static void main(String[] args) {	1	1(def:1,use:0)
3: int Evev = 0;	1	1(def:1,use:0)
4: int Odd = 0;	1	1(def:1,use:0)
5: for(int i=0 ; i<=100 ; i++){	1	4(def:2,use:2)
6: if(i % 2 == 0){	2	1(def:0,use:1)
7: Even = Evev+1;	3	2(def:0,use:1)
8: }else{	2	0
9: Odd = Odd+1;	3	2(def:1,use:1)
10: }	2	0
11: }	1	0
12: System.out.println(" Number of Even : "+Even);	1	1(def:0,use:1)
13: System.out.println(" Number of Odd"+Odd);	1	1(def:0,use:1)
14: }	0	0
15:}	0	0

Figure 1: Example of source program analysis

- a variable is used in statement S
The variable reference count for a statement is the total number of times a variable is defined or used in the statement.

An example of source code analysis is shown in Fig.2.

3.2 Relation between Program partition points and difficulty of puzzle

The program puzzle pieces are created by selecting partition points between two lines of code. The difficulty of the puzzle is dependent on the number of pieces and the location of the partition points. If a partition occurs at a location with high control depth and high reference count, the puzzle can be assumed to have a high difficulty. ¿From this assumption, we define the following function to evaluate the difficulty of the partition. Partition point difficulty k is the evaluated difficulty when a partition occurs after program code statement k. Partition point difficulty Ppd_k is defined as follow.

$$Ppd_k = control\_depth * reference\_count \tag{1}$$

The difficulty of the puzzle is also affected by the difficulty of the program algorithm used in the given program source code, but this degree difficulty is dependent on the prior knowledge of the individual user. For this research we let the user decide on the degree of difficulty for an algorithm.

3.3 Program partition by GA

The partition pattern (number of partitions and location of partitions) is selected using the user's

The Eleventh International Symposium on Artificial Life and Robotics 2006 (AROB 11th'06),
B-con Plaza, Beppu, Oita, Japan, January 23-25, 2006

progress level and puzzle difficulty. This puzzle difficulty is calculated using algorithm and language specification which is used in problem and partition difficulty which is sum of partition point difficulty for each partition point. We apply genetic algorithm (GA) to select the partition pattern. GA is a general purpose search algorithm, which is effective in searching a vast search space for an optimal solution when the solution is not known beforehand.

In GA, an initial set of random search points (population) is created, and each point is evaluated for the fitness or effectiveness using a fitness function. The points are then randomly modified using operations such as crossover and mutation. The process of evaluation and modification is repeated until an optimal solution is found. The GA procedure used in this research is described in the following.

【step1】 Creation of initial population
An initial population, where individual (or chromosome) expresses a specific partition pattern, is created randomly.

【step2】 Fitness evaluation
Each chromosome is evaluation with the fitness function.

【step3】 Solution check
If a predefined fitness or number of cycles is achieved, then exit the algorithm.

【step4】 Selection
The fitness values are used in a selection algorithm, where individuals are selected to the next generation. A combination of elite selection, which guarantees individuals with high fitness, and roulette selection, allows individuals with lower fitness to be selected, is used.

【step5】 Crossover
Using a crossover algorithm, a portion of two chromosomes are swapped. A single point crossover algorithm is used.

【step6】 Mutation
Using a mutation algorithm, a portion of a chromosome is modified.

【step7】 Repeat from step2.

3.4 Chromosome expression

The partition pattern expressed as a binary string is used as the chromosome in the genetic algorithm. The length of the chromosome is 1 less than the lines of code (statements) in the program. In the chromosome, the value 1 indicates a partition at that location (line), and 0 indicates no partition at that location. Fig.3 illustrates the relationship between chromosome and partition points. In Fig.3 an example of a 15 line program is shown, and the partition points are the locations where the chromosome value *chr* is 1, i.e. after lines 2,5,6,8,10.

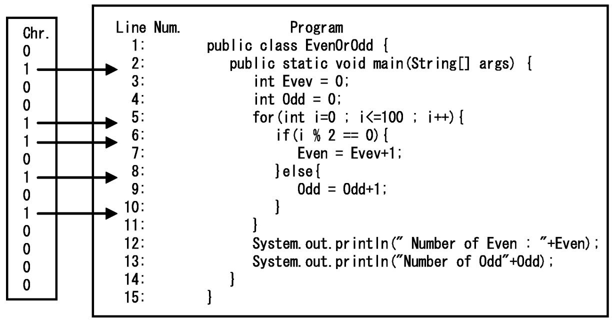

Figure 2: Relationship between chromosome and partition points

3.5 Fitness evaluation

Fitness is evaluated using the user's progress level, target problem difficulty, and difficulty of the created program puzzle. Below we describe the fitness evaluation method.

【puzzle difficulty】
Puzzle difficulty is decided by 3 factors.

① language specification which is being used by a program.

② algorithm which is used in a program.

③ partition difficulty for a program.

The above ① and ② are difficulty about a component of a program, and these are divided into 10 stages as following.

● Level of language specification :$g(1 \leq g \leq 10)$
● Level of algorithm :$a(1 \leq a \leq 10)$

A relationship between a component of a program and degree of difficulty is shown in Fig.4.

The partition difficulty is the sum of the partition point difficulty value for the given program puzzle

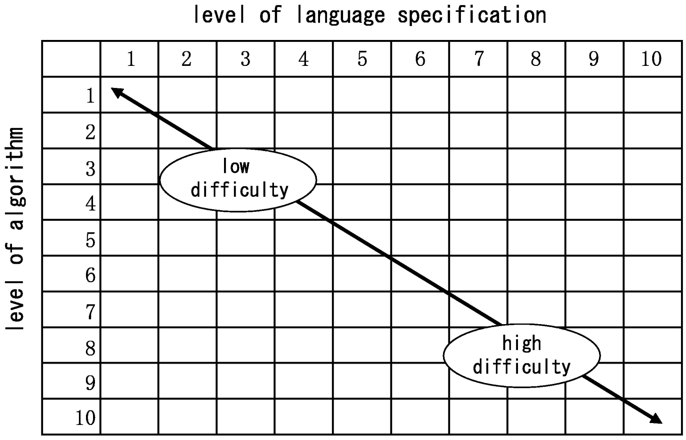

Figure 3: Relationship between a component of a program and degree of difficulty

chromosome, calculated with the following equation.

$$partition\_difficulty(pd) = \sum_{k=1}^{n}(Ppd_k * Chr_k) \quad (2)$$

where: n is number of program, Ppd_k is the partition point difficulty at position k, Chr_k is the value of the chromosome at position k.

Puzzle difficulty is calculated using the above g , a and pd as follows.

$$puzzle\_difficulty(d) = g * a * pd \quad (3)$$

【User's progress level】
User's progress level is defined as the puzzle difficulty of the last cleared problem.

【fitness function】
Fitness evaluation is to evaluate that the level of puzzle difficulty is match the user's progress level.

The fitness function is defined as follow.

$$fitness = |p - d| \quad (4)$$

where : p is user's progress level, d is puzzle difficulty.

The chromosome with the fitness value closest to 0 is selected as the optimal program puzzle combination for the user.

4 Overview of programming training support system

Processing flow of programming training support system is described in the following.

(1) System shows a problem to user according to the learning contents such as a syllabus of program practice or algorithm that user wishes.

(2) User selects a problem to answer from the problem that system showed.

(3) System breaks up a program into puzzle pieces depending on user progress level by using genetic algorithm.

(4) User reconstructs the program by selecting the correct program puzzle pieces in the correct order.

(5) System estimates user's result, and accumulates as the user proficiency.

The basic component of this system to achieve the above mentioned processing is shown in Fig.1.

① **progress status display part** indicates user progress status from user proficiency.

② **progress level evaluation part** estimates user progress from the user proficiency.

③ **problem selection part** selects a problem from the learning item that user whishes or user proficiency.

④ **problem display part** indicates the problem which is proposed by system using the learning item and the user proficiency.

⑤ **puzzle generation part** breaks up a program into puzzle pieces depending on user progress level by using genetic algorithm.

⑥ **answer evaluation part** estimates user's answer.

⑦ **result display part** indicates a result of user.

⑧ **program management part** manages the program used as a problem.

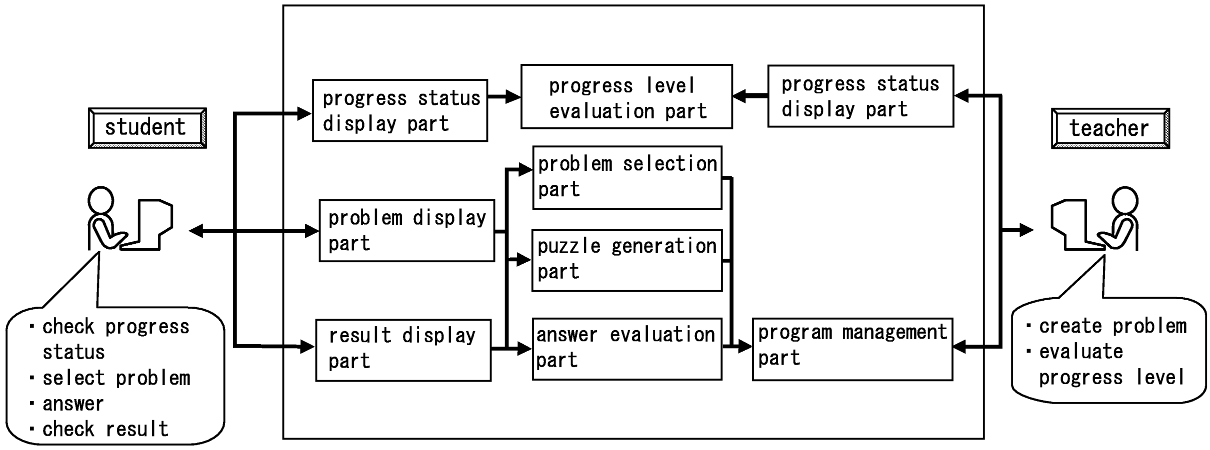

Figure 4: Overview of programming training support system

5 Evaluation results

We execute the following evaluation for some students to estimate this proposed programming training support system.

(1) User choice a problem with difficult level that according to his comprehension level and start training to estimate own comprehension level.

(2) User choice a problem with lowest difficult level and start training to estimate own comprehension level.

(3) User choice a problem with highest difficult level and start training to estimate own comprehension level.

We evaluate the progress level that trainee can clear in the 3 cases and we can get the result that each trainee achieved same progress level for all cases.

6 Conclusion

One of the most important points to carry out an effective programming course, is how to attend to the different skills and levels of each student. For larger classes, it becomes very difficult to teach each of the students individually. The proposed self-adjusting programming training support system can provide tailored programming exercises for students of different achievement levels, and efficiently support the learning environment. The self-organizing nature of the proposed method allows the system to create many different patterns of problems from a limited number of source code, and the genetic algorithm search enables the system to select different problems for repeated trials, and effectively supports the programming training of the user.

The proposed training support system is still in the prototype phase, but we plan to further improve the quality of the system, including reevaluation of the genetic algorithm used.

References

[1] Jain, L.C., et.al. (2002), Virtual Environments for Teaching and Learning, World Scientific.

The Eleventh International Symposium on Artificial Life and Robotics 2006 (AROB 11th'06),
B-con Plaza, Beppu, Oita, Japan, January 23-25, 2006

Automatic generation of B-spline curve using the evolution technique

Mitsutoshi SAITO and Seiichi SERIKAWA
Graduate School of Electric Engineering
Kyushu Institute of Technology
1-1 Sensui-cho, Tobata-ku, Kitakyushu-shi, Fukuoka, 804-8550, JAPAN

Abstract

The B-spline curve is often used as a method to draw an arbitrary curve like a hand-written figure. However, it is difficult to operate the position of the control-point for the faithful drawing. In addition, to arrange the control-points by hand, a lot of experiences needs.

The purpose in this study is to reproduce automatically an arbitrary curve faithfully by using a less control-points. The concept of evolutional method is utilized for the generation of the B-spline curve. The detail process is as follows. The several points on the curve are regarded as the chromosome. The crossover is practiced between two chromosomes. In this study, the individual with the same size of chromosome is regarded as homogeneity, but the one with the different size is defined as heterogeneity. The crossover between homogeneities is called "sexual reproduction". The crossover is not practiced between heterogeneities. The individual without the same size reproduce two its copies. This is called "asexual reproduction". By the strategy, various size of chromosome evolves. For the validity, some hand-written curves are used to generate the B-spline curve. As the result, B-spline curve similar to hand-written curve is automatically reproduced, and it uses a less control-points.

Keywords: hand-written figure, B-spline, genetic algorithm

1. Introduction

The figure is often drawn by hand at the stage of the idea, although it is possible to draw precisely with a computer. A hand-written figure gives man the relief, so there are a lot of hand-written fonts in the word-processor. The B-spline curve is often used as one of the methods to express a hand-written figure. The B-spline curve is generated based on the control-point. When the control-points are arranged automatically with the computer, the number of them becomes large. For the reduction of them, it is possible to arrange them by hand. However, a lot of experiences are needed for it. Thus, it is difficult to operate the number and the position of the control-points [1].

The purpose in this study is to arrange the control-points of B-spline automatically for the faithful representation of an arbitrary curve, and to reduce the control-points as less as possible. For them, the concept of the bug-type of artificial life is introduced [2]. This is one of the extension-models of genetic programming [3].

Chapter 2 explains the method to generate B-spline curve automatically, and chapter 3 shows the results. Some hand-written curves are used to generate the B-spline curve. As the result, B-spline curve similar to hand-written curve is automatically reproduced, and it uses a less control-points. Chapter 4 mentions the conclusion.

2. ethod for the generation of -spline curve

Genetic programming (GP) has been proposed recently[3]. Some unknown functions are discovered by the use of GP. The discovered functions, however, are often very complicated and quite different from those which are discovered by human. For the improvement, a bug type of artificial life, which is called S-system, was proposed [2], [4]. The concept of a sexual / asexual reproduction is introduced. This is very effective for function-search. A part of chromosome changes by mutation. According as the generation proceeds, the bugs with the function adapting to the observation data survive selectively, and find out the function corresponding with the data.

The summary of S-system and the method for the application to generate B-spline curve are mentioned here.

2.1 Design of chromosome

The arbitrary curve is represented by the B-Spline curve. Some points [P_1, P_2,] on the hand written-curve are extracted, and they are called passing points. The

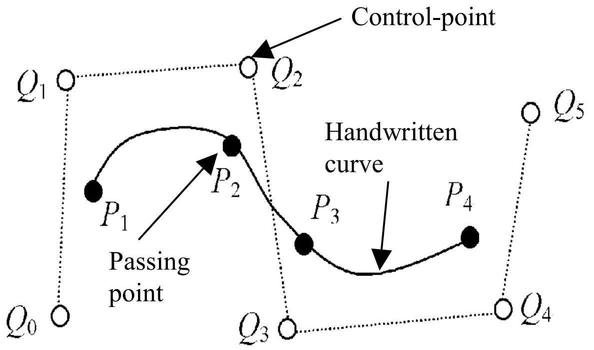

Fig. 1 Relationship among curve, passing points and control-points.

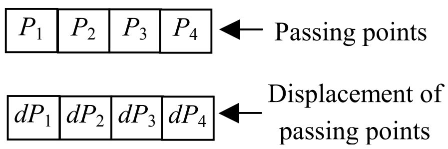

Fig. 2 Definition of chromosome.

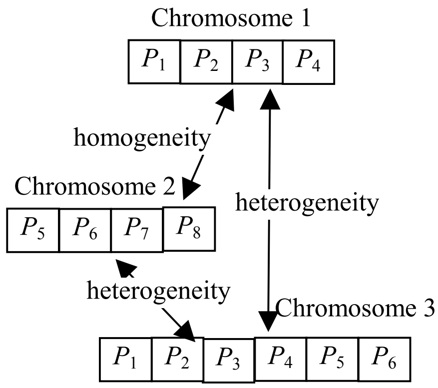

Fig. 3 The difference between homogeneity and heterogeneity.

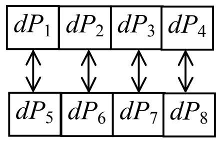

Fig. 4 Crossover using bug type GA strategy.

control-points [$_1$, $_2$,] are obtained by reverse conversion of passing points. The relation is shown in Fig. 1. From the control-points, the B-spline curve can be drawn. In a word, the B-spline curve can be drawn from the passing points.

We define the passing points [P_1, P_2,] as chromosome as shown in Fig. 2. Each point has the displacement. The target of crossover is the displacement. This is the same way of bug type of GA [5]. The number of passing points corresponds to the size of chromosome. In this system, the size of chromosome is not fixed. This is set at random at initial generation, and changes at mutation.

2.2 Sexual reproduction and asexual reproduction

Sexual reproduction and asexual one are introduced in this study. These are important strategy. In the beginning, we have to explain the concepts of homogeneity and heterogeneity. The difference between them is shown in Fig. 3. We define the chromosome with the same size as homogeneity, while the one with different size as heterogeneity. In Fig. 3, chromosome 1 has the same size as chromosome 2, so chromosome 1 and chromosome 2 are homogeneity. The size of chromosome 3 is different from the others, so we call chromosome 3 is heterogeneity against the others. Sexual reproduction is practiced between homogeneities. Heterogeneity cannot reproduce sexually.

The procedure of sexual reproduction is as follows. A chromosome is selected by tournament strategy. It looks for the homogeneity. In case that homogeneity exists, the chromosome with the highest fitness is selected as the partner. The chromosome and its partner reproduce two chromosomes by crossover. As far as sexual reproduction is concerned, the crossover operator is equivalent to that of real GA[2]. This strategy uses displacement dP_i of passing point P_i for a crossover. It means that the target of crossover is the displacement. The example is displayed in Fig. 4.

2.3 imit of the number of homogeneities

According as generation progresses, the number of homogeneities may be almost all. This is because an excellent chromosome survives selectively. In that case, it is hard for the other heterogeneity to appear even if it is very excellent. That is, the search is trapped in a local optimum. For the search being as successful as possible, we limit the number of homogeneities. By this strategy, different many species are in existence at the same time, and each species evolves by sexual reproduction.

2.4 Calculation of fitness

Fitness is the value that shows how the B-Spline curve expressed by the chromosome is similar to original curve. The fitness is high when the B-Spline curve is agreement with the original curve, and the number of passing points is a little. For them, we introduce the degree map. The outline is shown in Fig. 5. Fig.5(a) is the handwritten curve, and Fig. 5(b) represents its degree map. The image size of Fig. 5(a) is the same as Fig. 5(b). In Fig. 5(b), the evaluation value (degree) of each pixel is defined as follow.

$$e\ alulation\ \ alue = 255 \quad s\ \ ift \times gain \qquad (1)$$

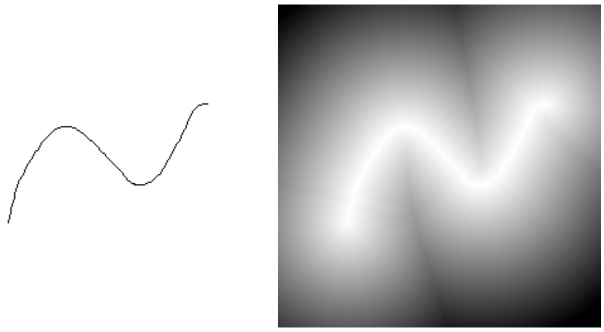

(a) a handwritten curve (b) degree map of (a)

Fig. 5 A handwritten curve and its degree map.

where, *s ift* is the distance-gap from the handwritten curve, *gain* is the constant. As understood from Fig. 5(b), the evaluation value of the pixel on the handwritten curve is 255. The value decreases as parting from the curve. When the value of *gain* increases, the evaluation value rapidly decreases as parting from the curve.

The calculation of fitness is as follows. (i) The B-spline curve is drawn in this map. (ii) The total of evaluation value of each pixel along the curve is calculated. (iii) The average value fit_m per a pixel is obtained. Based on the following definition, the fitness *fit* is obtained.

$$fit = \ _{fit} \cdot fit_m / 255 + (1 \quad _{fit}) \cdot fit_n \tag{2}$$

where, fit_n is the normalized number of passing points, and $_{fit}$ is a constant. This is same concept of MDL[6].

2.5 Algorithm of automatic generation of -spline curve

The flowchart for the generation of B-spline curve is shown in Fig. 6. The summary is as follows.

Extraction of curve The handwritten curve is extracted from the image (BITMAP format), in which a handwritten curve is drawn.

eneration of initial individuals Numerous chromosomes with the arbitrary passing points are generated at random.

ovement By the movement, the passing point in the chromosome changes slightly.

That is to say, the values of P are replaced by $P + dP$ or $P \quad dP$, where P and dP are the chromosome in Fig. 2, and ***k*** 2, 3, , **n**-1, **n** is the number of passing points. This concept is based on Ref. [5].

Calculation of fitness Base on the chapter 2.4, the fitness of each chromosome is calculated.

Descendant-generation-routine At this routine, new chromosomes are generated. For it, generation-gap, selection, crossover, and mutation are practiced.

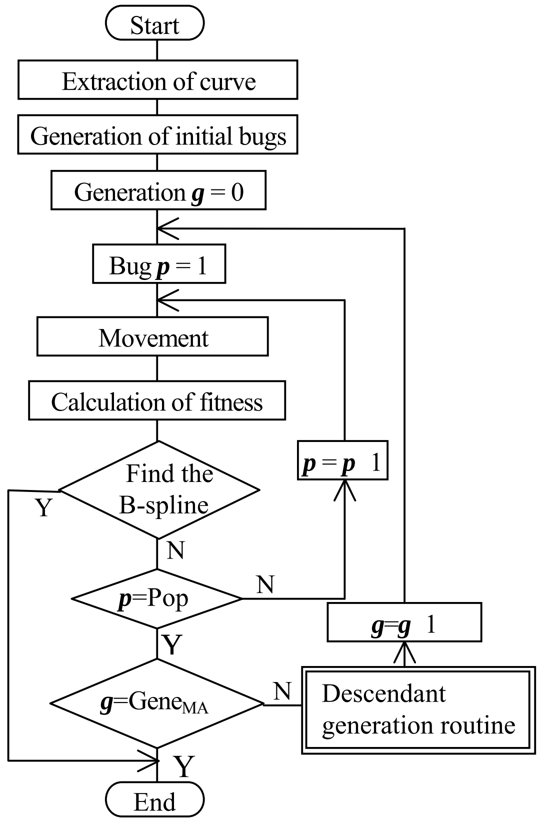

Fig. 6 The flowchart for generating B-spline curve.

Table 1. The value of parameters for simple curve.

Number of passing points	3, 4, , 15
$_{fit}$	0.8
ain	3
Number of chromosomes	300
Maximum generation	100
Range of dP	0, 1, 2
Generation gap	0.5
Crossover rate	0.5
Tournament size	3
Limitation of the number of homogeneities	30
Mutation rate of passing point	0.5
Mutation rate of dP	0.5

eneration-gap The chromosomes of the number of ***Par*** are selected and they are passed down to the next generation. The elite strategy is adopted for it.

Selection An individual is selected by the tournament strategy.

Crossover The selected one is judged whether it has the ability to sexually reproduce. In the case that the selected one has the ability of sexual reproduction,

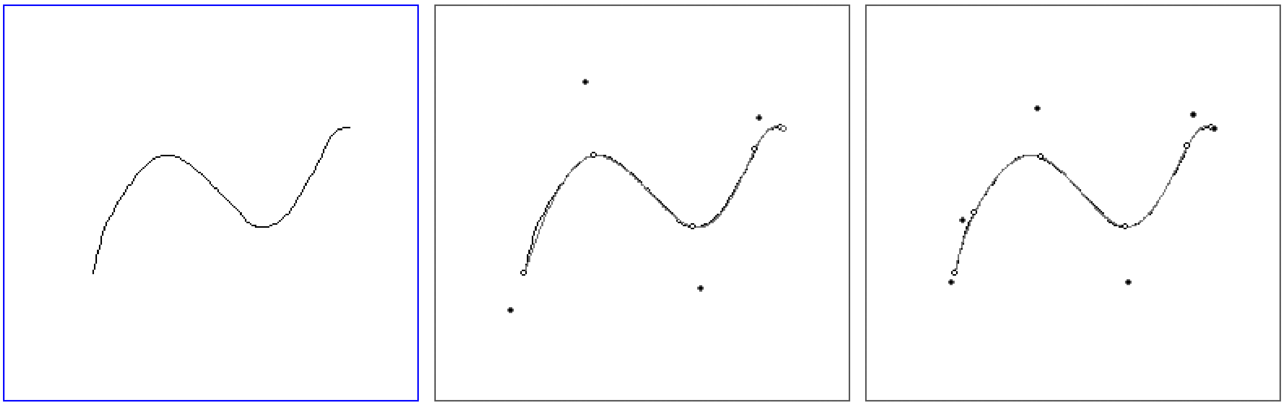

(a) simple handwritten curve (b) B-spline in case of 5 passing points (c) B-spline in case of 6 passing points

Fig. 7 B-spline curve generated from simple curve.

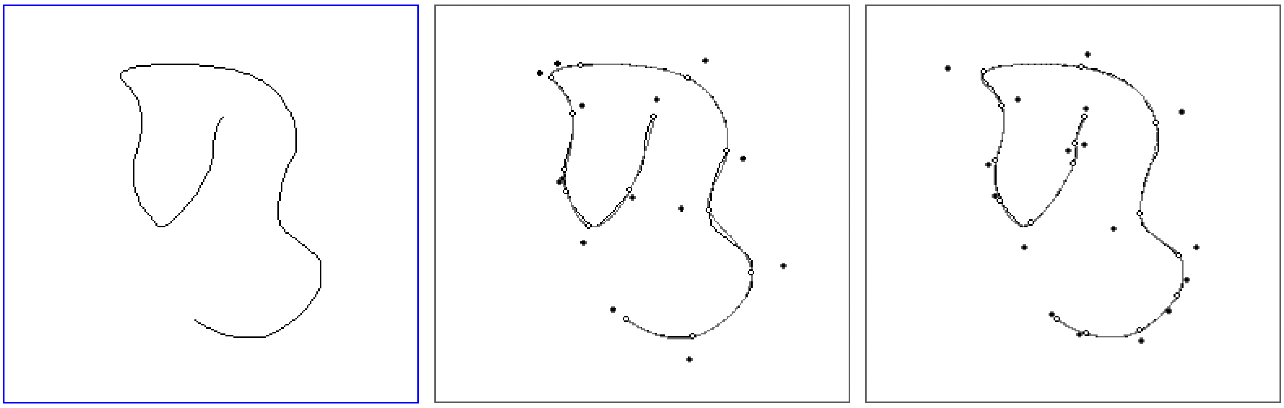

(a) complex handwritten curve (b) B-spline in case of 14 passing points (c) B-spline in case of 16 passing points

Fig. 8 B-spline curve generated from complex curve.

sexual reproduction is performed. In the other case, asexual reproduction is carried out. This is mentioned in chapter 2.2.

utation A part of the chromosome is changed by mutation at a certain rate. In mutation, passing point is added, deleted, or replaced in the chromosome. As far as displacement of passing points dP , the value is replaced by the other value by mutation.

3. Experimental results

For the validity of this algorithm, we practiced the B-spline generation in two cases of curves.

3.1 Simple curve

We tried the generation of B-spline curve 100 times for simple curve. The conditions are listed in Table 1. At one trial, the B-spline curve with the highest fitness is obtained. Because of 100 trials, 100 B-spline curves are gotten. The main breakdown of the number of passing points is as follows. Passing points 5: 15 times, passing points 6: 66 times, Passing points 7: 19 times. The examples are shown in Fig. 7. Fig. 7(a) is the handwritten curve. In Fig. 7(b) and (c), the generated B-spline curves are drawn. In these figures, both handwritten curve and B-spline one are drawn. As understood from them, B-Spline curve is agreement with handwritten one. In addition, the number of passing points is a little. From the comparison of Fig. 7(b) with Fig. 7(c), the B-spline curve drawn with 6 passing points more agrees with the handwritten curve than that of 5 passing points.

3.2 Complex curve

Since the complex curve such as font is used in reality, we tried to generate the B-spline curve for the complex curve. We tried the generation of B-spline curve 100 times. The number of passing points=3,..,31 and $_{fit}$=0.72. The conditions are the same as Table 1 except them. The main breakdown of the number of passing points is shown in Fig. 9. The examples are shown in Fig. 8. Fig. 8(a) is the handwritten curve. In Fig. 8(b) and (c), the generated B-spline curves are drawn. As understood

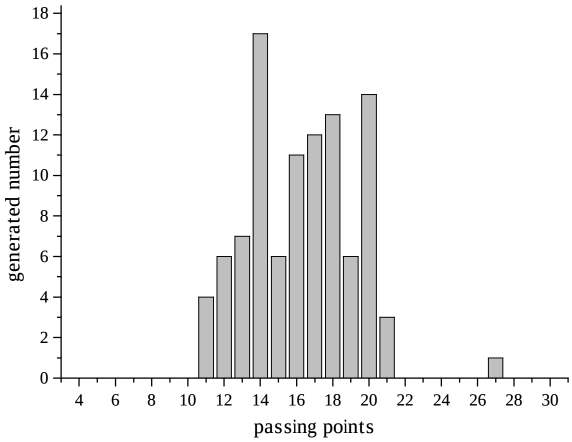

Fig. 9 The distribution of passing points for complex curve.

from them, B-Spline curve is agreement with handwritten one. In addition, the number of passing points is a little for the complex curve. From the comparison of Fig. 8(b) with Fig. 8(c), the B-spline curve drawn with 16 passing points more agrees with the handwritten curve than 14 passing points.

4. Conclusions

The purpose in this study is to arrange automatically the control-points of B-spline for the faithful representation of an arbitrary curve, and to reduce the control-points as less as possible. For them, the concept of the bug-type of artificial life is introduced. As the result, B-spline curve similar to hand-written curve is automatically reproduced, and it uses a less control-points.

In the future, we should investigate the method for the further reduction of control-points, and apply to practical use.

References

[1] Kanemoto, T., *Numeric grap ics processing for C E*, Kyoritsu-shuppan, p.87, p.96 (1994).

[2] S. Serikawa and T. Shimomura, "Proposal of a System of Function-Discovery Using a Bug Type of Artificial Life", *Trans. IEE*, Vol.118-C, 2, p.170, (1998).

[3] J. Koza, *enetic Programming II*, *uto isco ery of Reusa le Su programs*, *MIT Press*, p.109 (1994).

[4] S. Serikawa and T. Shimomura,"Improvement of the Search Ability of S-System (A Function-Discovery System)", *Trans. IEE*, Vol.120-C, 8, *in Press*, (2000).

[5] Iba, H., Higuchi T., de Garis, H, and Sato, T., "Evolutionary Learning Strategy using Bug-Based Search", *Proc. of t e Int. Joint Conf. on rtificial Intelligence IJC I-* , vol.2, pp.960-966 (1993).

[6] Iba, H., *enetic Programming*, Tokyo-Denki -Daigaku shuppan, p.141, p.204 (1996).

The Eleventh International Symposium on Artificial Life and Robotics 2006 (AROB 11th'06),
B-con Plaza, Beppu, Oita, Japan, January 23-25, 2006

A Genetic Approach to the Design of Autonomous Agents for Futures Trading

H. Kitano, T. Nakashima, H. Ishibuchi
Graduate School of Engineering
Osaka Prefecture University
Gakuen-cho 1-1, Sakai, Osaka 599-8531, Japan
{kitano@ci., nakashi@, hisaoi@}cs.osakafu-u.ac.jp

Abstract

This paper proposes a genetic algorithm-based method for designing an autonomous trader agent. The task of the proposed method is to find an optimal set of fuzzy if-then rules that best represents the behavior of a target trader agent. A highly profitable trader agent is used as the target trader agent in the proposed genetic algorithm. A trading history of the target agent is obtained from a series of futures trading. In the antecedent part of fuzzy if-then rules time series data of spot prices are considered while the consequent part indicates the order of trade (Buy, Sell, or No action) with its degree of certainty. The proposed method determines the antecedent part of fuzzy if-then rules. The consequent part of fuzzy if-then rules is automatically determined from the trading history of the target trader agent. The autonomous trader agent designed by the proposed genetic algorithm consists of a fixed number of fuzzy if-then rules. The decision of the autonomous trader agent is made by fuzzy inference from the time series data of spot prices.

1 Introduction

Fuzzy rule-based systems have been successfully applied to various problems such as control [1], function approximation, and pattern classification [2, 3]. The advantage of a fuzzy rule-based system is its interpretability. Since fuzzy if-then rules in a fuzzy rule-based system are written using linguistic values, human users can linguistically understand the meaning of the fuzzy if-then rules.

Recently, virtual economic markets have attracted a great deal of attention for analyzing economic systems and developing autonomous trader agents. U-Mart (Unreal Market as Artificial Research Test-bed) project is one of such virtual markets where multiple trader agents including human traders simultaneously participate in a futures market (Fig. 1).

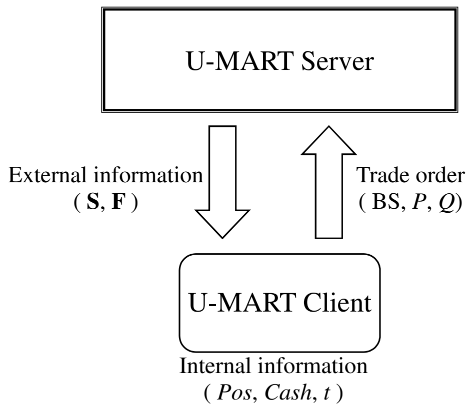

Figure 1: The general view of U-Mart.

In futures markets, the price is determined based on orders made by all trader agents that participate in the market. Thus, it is important for a trader agent to predict the orders of the other trader agents in order to make an optimal trade decision. The aim of this paper is to propose a genetic algorithm-based method for finding an optimal set of fuzzy if-then rules that best represents the behavior of a target trader agent. In the proposed genetic algorithm-based method, an individual represents an autonomous trader agent. A pre-specified number of fuzzy if-then rules are encoded into a string of binary and integer bits. First, an initial population is generated by randomly determining each bit of strings. Then genetic operations such as selection, crossover, and mutation are performed in order to generate new strings. The new strings are used to form the next population together with best strings in the current population. The fitness value of each strategy is evaluated through the rate of matched trading decision during the futures trades. That is, a string has a high fitness value if the autonomous trader agent generated from the string makes decision similar to that of the target trader agent. This procedure is iterated until a pre-specified termination criterion is satisfied. In a series of computational experiments we examine the performance of the proposed method using a time series data of spot prices. It will be shown that the autonomous trader agent designed by the proposed method has a similar behavior to the target trader agent. For example, the autonomous trader agent makes the same decision as the target trader agent, and the profit of the autonomous trader agent is similar to that of the target trader agent if the experimental settings are the same.

2 Fuzzy Rule-Based Systems for Futures Trading

2.1 Handling Trading History

The trading history of the target agent can be converted into a set of training patterns in pattern classification problems. Let us assume that $m+10$ trading actions are included in a trading history data set. That is, the trading history data set consists of two time series data, spot prices and trading actions as follows:

$$TH = \{(s_t, a_t), t = 1, \dots, m+10\}, \tag{1}$$

where TH is the set of trading history, s_t is the spot price at the t-th time step, and a_t is the trading action of the target agent at the t-th time step. We convert the trading history TH into the training data TD as follows:

$$TD = \{\mathbf{x}_p, p = 1, \dots, m\}, \tag{2}$$

where

$$\mathbf{x}_p = (x_{p1}, x_{p2}, \dots, x_{pn}), \quad p = 1, \dots, m. \tag{3}$$

Each attribute in $\mathbf{x}_p, p = 1, \dots, m$ is calculated as follows:

$$\begin{aligned} x_{pi} = s_{p+10} - s_{p+10-i}, \\ i = 1, \dots, n, \quad p = 1, \dots, m. \end{aligned} \tag{4}$$

The class of the p-th training pattern $\mathbf{x}_p$ is determined as the trading action of the target agent at the $(p+10)$-th time step.

2.2 Fuzzy If-Then Rule

We use the following type of fuzzy if-then rules for futures trading:

$$\begin{aligned} R_j: \ &\text{If } x_1 \text{ is } A_{j1} \text{ and } \dots \text{ and } x_{10} \text{ is } A_{j10} \\ &\text{then action is } B_j \text{ with } CF_j, j = 1, \dots, N, \end{aligned} \tag{5}$$

where $A_{j1}, \dots, A_{j10}$ are antecedent fuzzy sets of fuzzy if-then rule R_j, B_j is the consequent action, CF_j is the grade of certainty, and N is the number of fuzzy if-then rules in a fuzzy rule-based system.

Each attribute in the antecedent part of fuzzy if-then rules shows the differences between the spot prices at the latest time and the corresponding time step. For example, x_5 represents the difference of spot prices between the latest and five time steps before. Although we consider only ten attributes in this paper, it is possible to extend the number of attributes. However, since the main focus of this paper is to find an optimal set of fuzzy if-then rules, not to find optimal fuzzy if-then rules, we fix the number of attributes as ten. A modified version with more attributes is left for future research.

As the membership functions for antecedent fuzzy sets $A_{j1}, \dots, A_{jn}$, we use five fuzzy sets and *don't care* shown in Fig. 2.

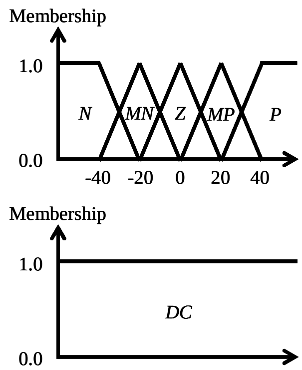

Figure 2: Membership functions for antecedent fuzzy sets.

The consequent part of fuzzy if-then rules can be automatically determined by using a fuzzy rule-generation method in [4] once the antecedent part is fixed.

2.3 Decision Making on Trading Action

Let us assume that we have N fuzzy if-then rules that are obtained by our genetic algorithm-based method. The fuzzy rule-based system is used to determine the trading action such as Buy, Sell, No action.

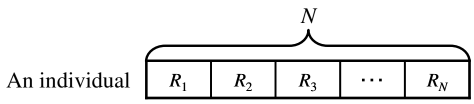

Figure 3: A string for a set of fuzzy if-then rules.

We also assume that an input pattern $\mathbf{x} = (x_1, \ldots, x_n)$ to the fuzzy rule-based system is obtained from the time series of spot prices. The trading action is determined by using a single winner rule where the consequent part of the fuzzy if-then rule $R_{\hat{j}}$ with the maximum product of the compatibility and the degree of certainty is employed:

$$\mu_{\hat{j}} = \max_{j=1,\ldots,N} \mu_j(\mathbf{x}) \cdot CF_j, \tag{6}$$

where

$$\mu_j(\mathbf{x}) = \mu_{j1}(x_1) \cdot \mu_{j2}(x_2) \cdot \ldots \cdot \mu_{jn}(x_n), \tag{7}$$

and $\mu_{ji}(x_i), i = 1, \ldots, n$ is the membership function of fuzzy sets $A_{ji}, i = 1, \ldots, n$ in the antecedent part of the fuzzy if-then rule R_j.

3 Genetic Algorithm for Finding Fuzzy If-Then Rules

In this paper, we use a genetic algorithm-based method for obtaining fuzzy if-then rules. The task of the genetic algorithm is to find an optimal set of fuzzy if-then rules that best represents the behavior of the target trader agent.

3.1 Encoding

An individual represents a set of fuzzy if-then rules in the proposed method. Fuzzy if-then rules in a fuzzy rule-based system are concatenated to form a single string as in Fig. 3. It should be noted that the order of the fuzzy if-then rules in the string does not have any effect on its performance.

Each of fuzzy if-then rules in the string is divided into two parts (see Fig. 4). The first part consists of binary bits that show the inclusion of attributes. That is, the value of 1 in a binary bit means that the corresponding attribute is used in the fuzzy if-then rule. On the other hand, the attribute is not used in the fuzzy if-then rule if the value of the binary bit is 0. It should be noted that whether an attribute is used in fuzzy if-then rules is not common over the set of fuzzy if-then rules. Since the binary bits are used for each

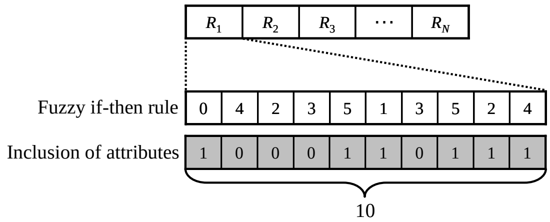

Figure 4: Encoding of a fuzzy if-then rule in the string.

fuzzy if-then rule, whether an attribute is used or not depends on fuzzy if-then rules. The second part shows the antecedent part of fuzzy if-then rules.

Note that the consequent part of fuzzy if-then rules is determined automatically from the trading history of the target agent after determining the antecedent part of fuzzy if-then rules.

3.2 Fitness Function

The task of the proposed genetic algorithm-based method is to find the rule set of fuzzy if-then rules that best represents the behavior of the target trader agent. In the proposed genetic algorithm-based method, we define the fitness of a fuzzy rule-based system S as follows:

$$fitness(S) = \frac{nca(S)}{m}, \tag{8}$$

where $nca(S)$ is the number of correct actions in the training data set TD, m is the number of training data. The fuzzy rule-based systems with higher fitness value best represents the behavior of the target trader agent, thus the fuzzy rule-based systems with a high fitness value are favored in the proposed genetic algorithm-based method.

3.3 Overall Procedure

The procedure of the proposed genetic algorithm-based method can be described as follows:

Step 1: *Initialization.* A pre-specified number of strings are randomly generated to form an initial population of size N_{pop}.

Step 2: *Fitness evaluation.* Each string in the population is evaluated by using the fitness function in (8).

Step 3: *Genetic operations.* We generate new strings through genetic operations such as selection, crossover, and mutation. For the crossover operation, we use rule-wise uniform crossover operation where cut-points occur only between substrings that represent fuzzy if-then rules. In order to select a pair of strings for one crossover operation, we use binary tournament selection where first two strings are selected randomly and then the better string with the higher fitness value in (8) is selected as a parent in the crossover operation. For mutation operation, we use bit-change operation where the value of randomly selected bits is replaced with randomly selected one. It should be noted that only 0 and 1 are possible for binary bits whereas $0 \sim 5$ can be used for the other bits. We generate $N_{\text{pop}} - 1$ new strings by the above genetic operations.

Step 4: *Generation update.* We employ so-called generational version of genetic algorithm with elitist strategy. That is, the new strings generated in the previous step and the best string in the current population are combined to form the next population.

Step 5: *Termination test.* If a pre-specified termination criterion is satisfied, terminate the procedure of the genetic algorithm-based method. Otherwise go to Step 2.

4 Computational Experiments

This section shows the experimental results of the proposed genetic algorithm-based method for obtaining fuzzy rule-based systems that best represent the behavior of the target agent.

4.1 Experimental Settings

The following experimental settings were used in the computational experiments in this paper:

Target agent: ZCrossover
Population size: 50
Crossover rate: 1.0
Mutation rate: 1/6
The number of fuzzy if-then rules in a string: 50
Termination criterion: 5,000 generations

As the target agent in the experiments we use ZCrossover that is an autonomous trader agent developed in Ritsumeikan University.

4.2 Experimental Results

We show the results of the experiments in Fig. 5. From Fig. 5, we can see that the rate of correct actions by the best string in the population (i.e., $fitness(S)$) increases over generations.

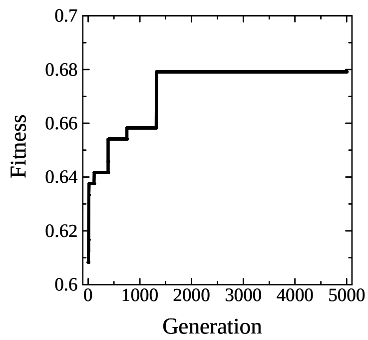

Figure 5: Experimental results.

5 Conclusions

In this paper, we proposed a genetic algorithm-based method. The task of the proposed method is to find a fuzzy rule-based system that best represents the behavior of a target agent in a futures market. Each fuzzy rule-based system is encoded into a string with binary and integer bits. Binary bits show the inclusion or exclusion of the corresponding attributes in each fuzzy if-then rule and the fuzzy sets in the antecedent part of fuzzy if-then rules are specified by integer bits. Through the computational experiments we showed that the proposed genetic algorithm-based method successfully found fuzzy rule-based systems that are consistent with the behavior of the target agent.

References

[1] M. Sugeno, "An Introductory Survey of Fuzzy Control", *Information Science*, Vol. 30, No. 1/2:59-83.

[2] C.C. Lee, "Fuzzy Logic in Control Systems: Fuzzy Logic Controller Part I and Part II", *IEEE Trans. Syst., Man, Cybernetics*, Vol. 20:404-435, 1990.

[3] C.T. Leondes, "Fuzzy Theory Systems", *Techniques and Applications*, Academic Press, San Diego, Vol.1-4, 1999.

[4] H. Ishibuchi, K. Nozaki, H. Tanaka, "Distributed Representation of Ruzzy Rules and its Application to Pattern Classification", *Fuzzy Sets and Systems*, Vol. 52, No. 1:21-32, 1992.

The Eleventh International Symposium on Artificial Life and Robotics 2006 (AROB 11th'06),
B-con Plaza, Beppu, Oita, Japan, January 23-25, 2006

Comparison between Self-organization with Sampling and Genetic Algorithms in multi-modal function

Takayuki Higo
Tokyo Institute of Technology
4259, Nagatuta-cho, Midori-ku
Yokohama-city, Kanagawa, Japan
higo@cas.dis.titech.ac.jp

Keiki Takadama
Tokyo Institute of Technology
4259, Nagatuta-cho, Midori-ku
Yokohama-city, Kanagawa, Japan
keiki@dis.titech.ac.jp

Mitujirou Katuhara
National Maritime Research Institute
6-38-1, Sinkawa
Mitaka-city, Tokyo, Japan
kat@nmri.go.jp

Takahiro Majima
National Maritime Research Institute
6-38-1, Sinkawa
Mitaka-city, Tokyo, Japan
majy@nmri.go.jp

Abstract

In this paper, we propose a novel method for multimodal function optimization. This method can be thought a extension of Adaptive Neighbor Search (ANS) by using simplex neighbor which is a technique of Self-Organization with Sampling. The difference between ANS and the proposed method is the way of defining the neighbor. ANS uses Euclidian distance based neighbor and the proposed method uses spatial relation based neighbor. Through intensive experiments, we confirm the robustness for scaling search space.

1 Introduction

Real-coded Genetic Algorithms (RCGAs) draw attention as general optimization methods for nonlinear continuous function. In RCGAs Unimodal Normal Distribution Crossover (UNDX)[8][5] and Simplex Crossover (SPX)[4] are widely used for crossover , and Minimal Generation Gap (MGG)[9] is used for generation alternation model. Simply using these methods, we encounter the difficulties of multimodality. Especially fast convergence of search points is a serious problem. To over come this problem, island model Genetic Algorithms are proposed. In island model Genetic Algorithms, search points are divided into some groups, and the crossover parents are limited to individuals in same groups. One of the most efficient island model Genetic Algorithms is Adaptive Neighbor Search (ANS)[10]. ANS limits the crossover parents to search points which are near from other parents.

Recently Estimation of Distribution Algorithms (EDAs)[6] was proposed as a model of mathematically interpreted GAs. In EDAs, we represent the search points as a probabilistic distribution. And we use sampling according to the estimated probabilistic distribution instead of crossover. So EDAs can be thought more general framework. Self-organization with Sampling (SOS) is one of the EDA-based optimization method. In SOS, the cost function is estimated from samples drawn according to Boltzmann distribution whose energy is estimated cost function. Using Boltzmann distribution, we can control variety of search points as entropy. So SOS can be thought appropriate method for multimodal function optimization. But SOS has one problem that it is too hard to construct step function approximating cost function in high dimension. We therefore try to propose computable SOS by extending ANS by using simplex neighbor which is used in SOS for finding neighbor search points.

In section 2, we explain ANS. In section 3, we explain SOS. In section 4, we propose a combinatorial method of ANS and SOS. Section 5 is experiments using benchmark problems. Section 6 concludes this paper.

2 Adaptive Neighbor Search

Adaptive Neighbor Search (ANS) is one of the island model GAs. A feature of ANS is to limit the crossover parents to their neighbor search points. We can see this limitation as adaptive clustering based on distance between search points. This mechanism prevent fast convergence and is one way to overcome multimodality.

Figure 1 shows the brief procedure of ANS. The features of ANS can be seen in step 2 of the optimization phase. In step 2, we compute neighbor search points defined as nearest search points in Euclidean distance. Then we apply crossover to neighbor search points and a search point selected in step 1. In crossover we let the search point selected in step 1 be a center of Gaussian (UNDX) or Simplex (SPX).

- Initialization:
  1. Put search points in feasible region
- Optimization:
  1. choose a search point $_0$ randomly
  2. Find neighbor search points $_1 \quad _M$
  3. Operate crossover to $_0 \; _1 \quad _M$ and generate sampling data set D
  4. Alternate generation (exchange $_0$ for best sample in D)
  5. Jump to 1.

Figure 1: ANS procedure

3 Self-Organization with Sampling

Self-Organization with Sampling (SOS) is EDA-based method. SOS estimates the cost function and draws samples according to Boltzmann distribution. Boltzmann distribution is defined as follows:

$$p(\ ) = \frac{\exp(-f(\ )\ )}{Z} \tag{1}$$

$$Z = \int \exp(-f(\ )\ )d \tag{2}$$

where $f(\ )$ is energy function, is inverse temperature and Z is partition function. Controlling the inverse temperature, we can control the variety of search points and generating samples.

Figure 1 shows the brief procedure of SOS. In SOS, we assume that the feasible region is convex polyhedron. This is equivalent to assume the bounded linear constraints. So we put the search points on the vertices of the convex polyhedron. We call these search points "pseudo search points" because they don't move. After putting search points and pseudo search points, we decompose the feasible region into simplexes whose vertexes are the search points or the pseudo search points by Delaunay triangulation[7].

Features of SOS are step 2 and 3. In step 2, SOS generate samples around a search point selected in step 1. This is ensemble of SPX. In step 3, we locally make a sum of probabilistic density in each search point almost equal. In fact, this is not easy. One approximation way is explained in [1]

- Initialization:
  1. Put pseudo search points on the vertices of convex polyhedron defined by linear constraints
  2. Put search points in the convex polyhedron randomly
  3. Apply Delaunay triangulation to search space and generate neighbor simplex set $_{x_i}$.
- Optimization:
  1. choose a search point $_0$ randomly
  2. Draw K samples from each simplex $s_i \in \; _{x_0}$ according to uniform distribution
  3. move $_0$ to make the sum of probabilistic density in each simplex almost equal
  4. Goto 1.

Figure 2: SOS procedure

3.1 Simplex Neighbor

Computation time of Delaunay triangulation, which is used in SOS is exponential in the number of the dimension. So we cannot apply SOS to real problems. In this section we show a polynomial time algorithm which is similar to Delaunay triangulation. This method is introduced in [3] and called simplex neighbor.

Before showing simplex neighbor, we have to know the Delaunay triangulation using a geometric transformation. A geometric transformation which transform a point p in d dimensional space into point $\tilde{p}$ in $d+1$ dimensional space is defined as follows:

$$\tilde{p} = (p \;\; f(p)) \tag{3}$$

$$f(\ ) = \sum_{i=1}^{d} \ _i^2 \tag{4}$$

We can get a $d+1$ dimensional point set $\tilde{S}$ by applying the geometric transformation to a d dimensional point set S. The convex hull $co\ \ v(\tilde{S})$ of $\tilde{S}$ become the Delaunay triangulation. But a computation of convex hull needs exponential time in the number of the dimension. So we try to use another relationship of S and $\tilde{S}$. We focus on a point $_p$ in S and a point set S^- which is S without $_p$. We think of the Delaunay simplexes (triangles) of S^-. If there is a simplex which contains $_p$ in Delaunay Simplexes of S^-, we can compute the simplex by solving a following linear programming:

$$mi \quad f(\ ) = \sum_{\tilde{x}_i \in \tilde{S}^-} \ _i < \tilde{}_i \cdot e_{d+1} > \quad (5)$$

$$s \quad \sum_{x_i \in S^-} \ _i \ _i = \ _p \quad (6)$$

$$\sum_{i=1}^{m} \ _i = 1 \quad (7)$$

$$0 \leq \ _i \quad (8)$$

where e_{d+1} is the unit vector directed to $d+1$th dimension. A vertex of the found simplex are called simplex neighbor.

We show the mean of this linear programming. Let a point set $\tilde{S}^-$ be points which can get by applying the geometric transformation to S^-. If there is a simplex which contains $_p$, a line $l = \{\tilde{}|\tilde{}i \ \ R^{d+1}a \ \ d\tilde{}_i = \tilde{}_{p_i} fori = 1 \ \ 2 \ \ \cdots \ \ d\}$ cross at a face of the convex hull $co\ \ v(\tilde{S}^-)$ of $\tilde{S}^-$. Solving the linear programming, we can find the point at which the line and the face cross. And it's representation is the convex combination of points in S^-. Therefore we can compute the Delaunay simplex contains $_p$ by solving a linear programming. And we will be able to use this method as approximation of Delaunay triangulation.

4 Combination of ANS and SOS

We propose a combinatorial method ANS and SOS. In island model GA, how to limit crossover parents is important problem. ANS uses Euclidian distance based limitation. But this limitation is not good because it is depend on the scale of search space. We therefore propose a ANS-based method which uses simplex neighbor of SOS instead of nearest neighbor of ANS. So in this paper we call this method simplex neighbor method and call ANS nearest neighbor method.

We can assume a case of failure in computing simplex neighbor. There are two reasons to fail. One reason is that there is no simplex contains the selected search point. Another reason is that the arrangement of the search points is singular, for example, some points are on a line or on a face. We can detect these failure by solving the linear programming, because in exceptional case the linear programming have no solution. Then if we detect the exception, we use nearest neighbor instead of simplex neighbor.

5 Experiments

In this section we compare between a nearest neighbor method and a simplex neighbor method. We use two benchmark functions as follows:

- sphere function: $f(\ ) = \sum_{i=1}^{n} \ _i^2$,
- scaled sphere function: $f(\ ) = \sum_{i=1}^{n} i \ _i^2$,

where $\ = 5$ in this experiment.

We apply a nearest neighbor and a simplex neighbor to these function. We use SPX for crossover (sampling) and its expansion rate is recommendation value of [4]. The number of search points is 100 and the Number of samples generated in crossover is 100.

5.1 Results

Figure 3, 4, 5 and 6 show relationship between the number of function evaluations and best value of cost function. The effect of scaling can be seen in the nearest neighbor method but cannot be seen in simplex method. In scaled function the performance of the nearest neighbor method is worse. But the simplex neighbor method stop convergence half way. Applying the simplex neighbor method to 2-dimensional sphere function, we can see the search points splitting up into some clusters. And this is caused by the exception of nonexistence of the simplex.

6 Conclusion

We propose a novel method by combining ANS and simplex neighbor of SOS. Through the experiments, we confirm that the proposed method has an advantage of robustness for scaling. But simplex neighbor has disadvantage that there are cases not to find the simplex. We can develop multimodal function optimization method based on proposed method.

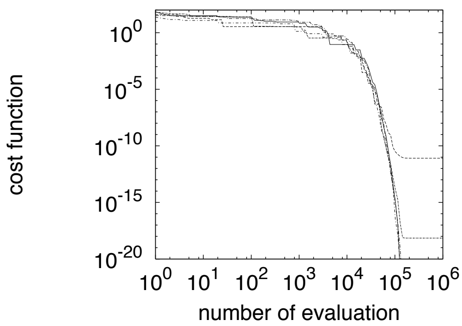

Figure 3: Nearest neighbor for non-scaled function.

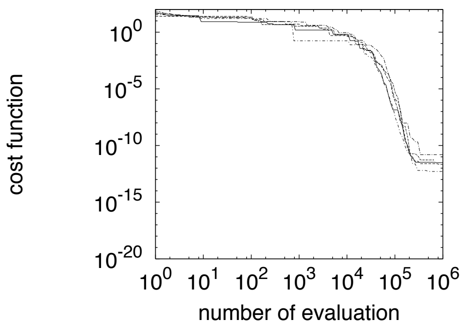

Figure 4: Simplex neighbor for non-scaled function.

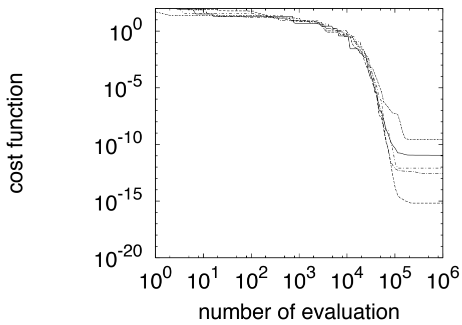

Figure 5: Nearest neighbor for scaled function.

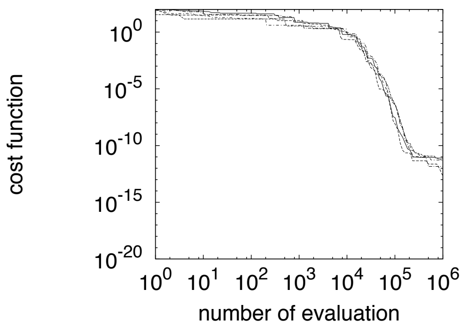

Figure 6: Simplex neighbor for scaled function.

Acknowledgments

The research reported here was supported in part by a Grant-in-Aid for Scientific Research (B, No. 17360424) from the Ministry of Education, Culture, Sports, Science and Technology (MEXT).

References

[1] Higo, T., Takadama, K. (2004), Optimization method based on adaptive search space decomposition: an approach towards multimodal function (in Japanexe). *The Society of Instrument and Control Engineers, Symposium on System and Information 2004*, pp. 95-100

[2] Higo, T., , Takadama, K. (2005), Self-Organized Sampling as an Optimization Method: An Approch towards Multimodal Functions (in Japanexe). *The Japanese Society for Arti cial Intelligence, The 19th Annual Conference of JSAI 2005*

[3] Higo, T., Takadama, K. (2005) Optimization method for high dimensional multimodal function (in Japanexe). *The Society of Instrument and Control Engineers, Symposium on System and Information 2005*

[4] Higuchi, T., Tsutsui, S., and Yamamura, M. (2000), Theoretical analysis of simplex crossover for real-coded genetic algorithms, *Parallel Problem Solving from Nature(PPSN-VI)*, pp. 365-374

[5] Kita, H., Ono, I. and Kobayashi, S. (1999), Multi-parental extension of the unimodal normal distribution crossover for real-coded genetic algorithms, *Proceedings of the 1999 Congress on Evolutionary Computation.* pp. 1581-1587

[6] Larranaga, P., Lozano.J.A. (2001), Estimation of distribution algorithms: a new tool for evolutionary optimization. *Kluwer Academic Publishers*, Boston

[7] Okabe,A., Boots,B. and Sugihara, K. (2000), Spatial Tessellation Concept and Applications of Voronoi Diagrams. *John Wiley & Sons*

[8] Ono, I., and Kobayashi, S. (1997), A A real-coded genetic algorithm for function optimization using unimodal normal distribution crossover. *Proceedings of the Seventh International Conference on Genetic Algorithms(ICGA-7))*, pp.246-253

[9] Satoh, H., Yamamura, M., and Kobayashi, S. (1996), Minimal generation gap model for GAs considering both exploration and exploitation. *Proceedings of the IIZUKA: Methodologies for the Conception, Design, and Application of Intelligent Systems*, pp. 494-497

[10] Takahashi, O. and Kobayashi, S. (2001), An adaptive neighboring search using Crossover-like Mutation for multimodal function optimization. *IEEE International Conference on Systems, Man and Cybernetics*, pp. 261-267

A simple model of evolving ecosystems

Takashi Shimada[†,*] Yosuke Murase[⋆], Satoshi Yukawa[⋆], Nobuyasu Ito[⋆], and Kazuyuki Aihara[†‡]
[†]Aihara Complexity Modelling Project, ERATO, JST
[⋆]Department of Applied Physics, School of Engineering, The University of Tokyo
[‡]Institute of Industrial Science, The University of Tokyo

Abstract

We investigate the structural properties of the system emerged in the ecosystem model which was proposed by the authors and show that the model and the field data shares similar characteristics. In particular, our model suggests that the universal scaling of the "spanning tree", which has been discussed using the field data consists only of less than 100 species, can be valid for larger scale.

1 introduction

Ecosystem, which shows an ineffable balance of wide variety, is generally regarded as a result of the Darwinian competition. Mathematical description will be one promising path to reveal its secret. Many models were proposed to explain its diversity, structure, and temporal or evolutional behavior. However, theoretical studies on such complex ecosystem with many species have been faced with the difficulty of constructing a natural model which can yield a large system. For this reason, properties of large ecosystem such as stability, structure, and extinction have been argued separately.

We have reported that our simple population-dynamics-based model can solve this frustrated situation[1]. In the model, interaction terms between species have nonlinear form but that is scale invariant against the population size. What should be noted is that the system shows spontaneous growth to diverse structure. Furthermore, the system emerged in our model reproduces the q-exponential distribution of the life span of species evaluated from paleontological data[2]. The purpose of this study is to investigate the structural properties of the food web in the model.

*takashi@aihara.jst.go.jp

2 Model

Equations of time-evolution of our model are,

$$
\begin{aligned}
&\text{“plants”}: \\
&\frac{dx_1}{dt} = Gx_1(1-x_1) + \sum_j a_{1j} x_1^{\lambda} x_j^{1-\lambda} \\
&\text{“animals”}: \\
&\frac{dx_i}{dt} = -x_i + \sum_{a_{ij}<0} a_{ij} x_i^{\lambda} x_j^{1-\lambda} + \sum_{a_{ij}>0} a_{ij} x_i^{1-\lambda} x_j^{\lambda} \\
&(a_{ij} = -a_{ji} \in (-1,1), \lambda \in (0,1/2) \quad G>0)
\end{aligned} \tag{1}
$$

where x_i, a_{ij}, G denotes the "population" of the i-th species measured in the unit of energy, the preying interaction coefficient between the i-th and j-th species, and the growth rate of the sole producer in the system called "plants", respectively. The parameter λ represents the saturation effect of the preying rate due to the behavioral adaptation of the animals.

2.1 Transformation of Variables

The transformation of variables as $\{y_i\} = \{x_i^{1-\lambda}\}$ changes the equations (1) into the partly-linearized form as follows.

$$
\begin{aligned}
&\text{“plants”} \\
&\frac{1}{1-\lambda}\frac{dy_1}{dt} = Gy_1(1-y_1^{\frac{1}{1-\lambda}}) + \sum_j a_{1j} y_1^{\lambda} \\
&\text{“animals”} \\
&\frac{1}{1-\lambda}\frac{dy_i}{dt} = -y_i + \sum_{a_{ij}<0} a_{ij} y_j + \sum_{a_{ij}>0} a_{ij} y_i^{\frac{1-2\lambda}{1-\lambda}} y_j^{\frac{\lambda}{1-\lambda}}
\end{aligned} \tag{2}
$$

Then one can classify the property of these equations by the parameter λ to the following three different types.

1. $\lambda > 1/2$: The exponent of the power in eqs.(2) takes a negative value. It is beyond the range $(0, 1)$ which above was assumed to guarantee the convexity of the preying rate. We exclude this

class from our study since the negative value of the exponent of y_i in preying term of y_i means that the species will never become extinct.

2. $\lambda = 1/2$: Interacting terms are linearized. The growth rate of the plants remains nonlinear.

3. $\lambda < 1/2$: The exponent of the power stays in the range $(0, 1)$ so that the eqs.(2) maintain their convexity assumed before. Our study in this work is focused on this class.

2.2 Uniqueness of the Solution

It is worth stressing that we do not require artificial thresholds for the extinction rule in our model. In the Lotka-Volterra model, populations of the unmatched species do not become zero in finite time but they approach zero exponentially in time, therefore a threshold is necessary to cause extinction. In contrast, our size-free interaction causes the algebraic decay of the unmatched species, so the orbits of the unmatched species decrease to zero in finite time. To change the feature of this interaction term, with conserving the finite time extinction property, additional parameters are needed

2.3 Additional Rules for Extinction and Mutation

In addition to Eqs.(1) our model has the following rules of extinction and mutation:

Extinction : If the energy of a species i, x_i becomes zero, the ith degree of the freedom is eliminated. Isolated species are eliminated instantaneously.

Mutation(Invasion) : New species come into the system randomly at time. Initial energy of the new comer is chosen to be very small: we use 10^{-8} as the typical example. The number of the interactions is assigned randomly in the range of $(1, 2m)$, where m is a constant and we take $m = 5$ here. The interaction coefficients are also randomly assigned in $(-1, 1)$.

3 Result: Structure of the Emerged Food Web

As it has been mentioned, the present model yields food webs having large number of species with complex structures(see [1, 2] and Fig.1). The scale invariant interaction term, which permits each species to appear and become extinct independently of bare scales of their population, is the key to get such diverse systems. Besides that, the statistical characteristics such as the temporal fluctuation, the extinction size distribution and the distribution of the life-span of species shows good agreement with field data. As an approach to getting better understanding of the model and ecosystems, we here focus on the structure of the emerged webs.

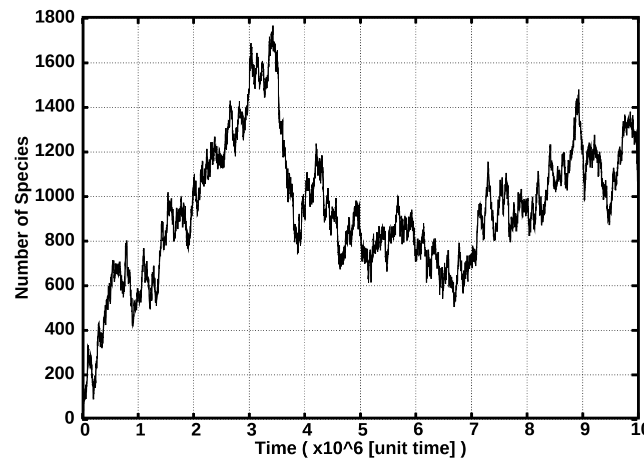

Figure 1: A time development of the number of species in the system with $m = 3$, $\lambda = 0.4$. After the initial transient, the system size goes on fluctuating. The statistical analysis of the web structure in this study is performed for this parameter region.

3.1 Degree Distribution and the Clustering Coefficient

Since the food web generated in the present model is not lattice-like, we first examine the following measures to characterize its topology: the distribution of the degree (in this case, number of interactions of each species) and the clustering coefficient[3]. The degree distribution of the ordinary random graph is Gaussian around the mean value. Another important class recently recognized, which is called scale-free, has a power-law tail in contrast. It is shown that the *growing* and *preferential attachment* of nodes(interactions) are the essential mechanism to evolve such scale-free networks[4]. In the present model, as in a real ecosystems, the network (food web) is indeed constructed by successive growth. There is also the competition which must reflect the preference of adding species and interactions. Therefore the degree distribution is expected to indicate the coarse-grained property of preference in the model.

It turns out that the distribution in our model does not have power-law tails and is well fitted by a Gaussian distribution. In this sense, the food web constructed in our model is rather a random net than a scale-free net. This may mean that there is no positive preference of attaching interaction or the larger number of interaction makes a survival harder. It may be also the reason that the spectrum of eigenvalues of scale-free nets is thought to have broader tail so that such net tends to break down. As to real food web, there are both arguments which support random net [?] and scale-free nets [6] at this point.

The second measure we investigate is the clustering coefficients, which is defined for the node (species) i has k_i of edges (interactions) as

$$C_i = \frac{2T_i}{k_i(k_i-1)}, \tag{3}$$

where E_i represents the number of triangles which includes the node i [3]. This quantity measures the correlation between interactions. In other words, it detects local spatiality with finite dimension in the random-graph-like graphs which can be embedded essentially only in the infinite dimensional space.

The average clustering coefficient over the entire self-organized web in the present model is different order of magnitude compared with the one of random graph with same number of interactions. However, the average except for the *plants* and the interactions related to them is slightly smaller than the one of the random net. These results mean that the triangle structure under competition in the present model is fragile though clustering emerges from the boundary conditions of the energy source.

3.2 Transportation properties of the Spanning Tree

Here we focus on the transportation property[7] of the directed web. To calculate this quantity, one first has to map the web into spanning tree: a loopless and connected tree. Generally the spanning tree of a food web is defined as the collection of the shortest paths from the plants to animals. This mapping is not unique when a species has two or more possibilities for shortest path. In this study we define the spanning tree as the collection of the links from each animal to its most important prey. Then we calculate A_i, the number of species preying the species i directly or indirectly via the tree for all species. Note that we include the species i itself into account: A of the species in the top of the spanning tree is 1 and A_1 is equal to the number of the species in the system. We also calculate the sum $B_i = \sum_j A_j$, where the summation is taken over the tree which was used for the calculation of A_i.

The transportation property of the obtained tree is evaluated from the exponent of the scaling relation $B \propto A^{\eta}$. This exponent η is 2 for chain-like trees(which means the original web has one-dimensional structure) and is 1 for the star-like structures (which imply the original web is random graph). Real networks embedded in the finite dimension has the exponent between 1 and 2 (3/2 for river networks, for example). It was shown that the exponent η of the real food webs is in the range of $1.13 - 16$[7]. This universal scaling is reported to hold both for the partial webs in the certain food web and for the whole networks of the different food webs (B_1 against the total number of species). Note that, since the empirical data available are small and typically has only three trophic level, the validity of this "universality" is open to discussion[8].

We evaluate the scaling relation for the webs emerged in our model (Fig.2). We here choose the parameter such that the number of the species is enough large ($\sim$ 1000) and the number of trophic levels is about 7. The scaling exponent for the trees without the plants, which we call animal trees, is 1.12. The value is consistent with the one estimated in the empirical data. Since the animal trees still have up to 6 trophic levels, this result support the universality in preying interacting system. However, the scaling exponent for the whole web ($B_1 \propto A_1^{\eta=1.064}$) is found to be smaller. It means that the number of the species in the first trophic level is larger than the one expected from the scaling relation while each tree starting from those first consumers shares the same topology as the empirical web. A possible reason why the model system has more species in the first trophic level is that large growth rate of the plants in the model. In the present model, we adopt a large growth rate ($\sim$ 50) to prevent the system from the entire extinction due to the shortage of the energy inflow. Therefore the interactions connecting to the plants are free from the competition among them and hence it may not share the self-similar topology. Assuming that the scaling relation in real food webs is valid, our result implies that the competition towards the energy and resource intake from producers and the environment is as severe as the competition at the higher trophic levels.

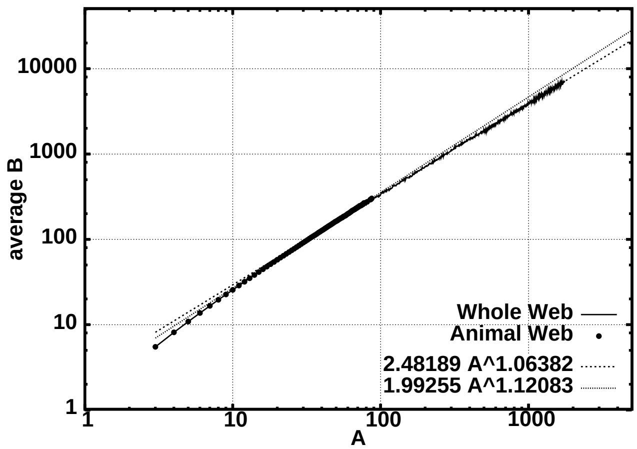

Figure 2: Log-log plot of average C against A.

4 Summary

We have investigated the statistical characteristics of the food web structure of our model. As for the degree distribution and the clustering coefficient, the model and the field data shows good agreement. The spanning trees in our model is also shown to share the same topology with the one of real food webs. The difference is found only in the interactions around the producer species, which implies the severe competition at the first trophic level in real ecosystem.

References

[1] T. Shimada, S. Yukawa, & N. Ito, "Self-organization in an ecosystem" *Artif. Life Robotics*, Vol. 6, pp. 78-81, 2002.

[2] T. Shimada, S. Yukawa, & N. Ito, "Life-span of families in fossil data forms q-exponential distribution" *Int. J. of Mod. Phys. C*, Vol. 14, pp. 1267-71, 2003.

[3] R. Albert & A. L. Barabási, "Statistical mechanics of complex networks" *Rev. Mod. Phys.*, vol. 74, pp. 47-97 2002.

[4] A. L. Barabasi & R. Albert, "Emergence of scaling in random networks" *Science*, vol. 286, pp. 509-512 1999.

[5] J. Camacho, R. Guimerá, & L. A. N. Amaral, "Robust Patterns in Food Web Structure", *Phys. Rev. Lett* vol. 88, 228102 2002

[6] R. V. Solé & J. M. Montoya, "Complexity and fragility in ecological networks" *Proc. R. Soc. Lond. B* vol. 268, pp. 2039-45 2001.

[7] D. Garlaschelli, G. Caldarelli, & L. Pietronero, "Universal scalling relations in food webs" *Nature*, vol. 423, pp. 165-68, 2003

[8] J. Camacho & A. Arenas, "Universal scalling in food-web structure?" *Nature*, vol. 435, pp. E3-E4, 2005

The Eleventh International Symposium on Artificial Life and Robotics 2006 (AROB 11th'06),
B-con Plaza, Beppu, Oita, Japan, January 23-25, 2006

The behavioral adaptation and the diversification in ecosystem

Y.Murase, S.Yukawa, N.Ito
Dept. of Appl. Phys.
School of Eng., Univ. of Tokyo
Bunkyo-ku, Tokyo

T.Shimada
Aihara Complexity Modeling Project
ERATO, JST
Meguro-ku, Tokyo

Abstract

The effect of behavioral adaptation on dynamics of diversity in ecosystems is studied using the size-free model. The behavioral adaptation will be parametrized by value of exponent λ of the interaction in this model. Two phases are observed when this adaptivity parameter, λ, is changed between 0 and 0.5: steady and diversifying phase. For $0 < \lambda < \lambda_c$, where λ_c denotes a critical value, the number of species reaches to a stationary value and fluctuates around it (steady phase). This stational value diverges as $\lambda_c \quad \lambda^{\ -d}$. For $\lambda_c < \lambda < 0\ 5$, it grows monotonously with fluctuation (diversifying phase). The value of λ_c depends on interaction coefficient.

1 Behavioral Adaptation Parameter

An essential feature of ecosystem is its tendency to diversify as a result of the emergence and the extinction of species in the system, which in turn is attributed to the interaction among the species. Many studies have been done to reveal that feature since Darwin's era. Using mathematical models has been one way to understand it.

The most popular model of ecosystem is Lotka-Volterra model. It describe the differential equation of population density. Although this model has contributed to understanding the dynamics of population density, there has been few work of studying dynamics of diversifying of species. This is because of the difficulty of making simple models in which the system self-organize into diverse structure.

Here we adopt size-free model, which Shimada.et.al proposed.[1] This simple model is known to be able to yield species-rich ecosystem. Furthermore the system shows the same statistical properties as in nature, such as the distribution of species' life span and the distribution of extinction size.[2]

Size-free model assumes only prey-predator interaction as inter-species relationships and focus on energy or nutrition transportation in food web structure.

The characteristic feature of this model is nonlinear preying rate. Preying rate per unit predator is assumed to be a function of the ratio of the populations of prey and predator, which is described as

$$a_{ij}\left(\frac{\ \ _j}{\ \ _i}\right) \tag{1}$$

where a_{ij} denotes the preying coefficient of i-th and j-th species, $\ _j$ is the population of prey, and $\ _i$ is the population of predator. λ is the exponent of preying rate which is limited to the range of $(0\ \frac{1}{2}]$.

Using (1), the interaction term between two species is written as

$$a_{ij}\ \ _j\ \ \ _i^{\,1-} \tag{2}$$

Preying term is limited to be convex as a function of prey and predator. This corresponds that preying rate saturates under the condition when prey and predator are abundant. These saturation is not unrealistic and will be common in nature. [3]

A possible explanation for nonlinearlity of preying rate, which is represented by λ in this model, is the behavioral adaptation of species.

Larger λ means larger dependence of the preying rate on the population of the species. When λ is large, predators are more likely to change the interaction rate to eat the prey which has larger population more than the prey which has smaller population. In other words, a predator can choose to eat abundant prey even though preying coefficient remains unchanged. This change of interaction rate can be considered as behavioral adaptation of predator.

For prey, even if the predator has larger population, the preying rate is restricted not to be too large when λ is large. This can also be considered as behavioral adaption of prey to defend themselves from threat of more dangerous predators. [4]

Hence λ is regarded as the parameter of behavioral adaptation in ecological meaning. Species can change their interaction rate, which can be regarded as phenotype, without changing their interaction coefficient, which can be regarded as genotype, when λ is large.

In this model, the system is organized by one plant and many animal species. Plant is sole energy source and animals dissipate energy gained from plant. Only plant has ability to survive alone and have logistic growth rate. On the other hand, animals decrease exponentially without interaction among species. The equation of time-evolution of the popualtion density is described as follows.

Plants:

$$\dot{\ }_0 = G\ {}_0(1 \quad {}_0) + \sum_j a_{0j}\ {}_0\ {}_j^{(1-\ )} \tag{3}$$

Animals:

$$\dot{\ }_i = \quad c_i\ {}_i + \sum_{a_{ij}<0} a_{ij}\ {}_i\ {}_j^{(1-\ )} + \sum_{a_{ij}>0} a_{ij}\ {}_i^{(1-\ )}\ {}_j \tag{4}$$

In this paper, growth rate G was set to 100 and metabolization rate c_i was set to 1.

To see the dynamics of species richness, invasion and extinction are introduced in this model.

If the population of species $i(\ {}_i)$ becomes 0, i-th specie is regarded as being extinct and eliminated from the system. And the animal which becomes to have no prey is also extinct.

Invasion is applied when all the population of the system become stable. The initial population density is chosen to be very weak (10^{-8}). The number of interaction is selected randomly from uniform distribution in the range of $[1\ \ m]$. And the interaction coefficient is also selected randomly from uniform distribution ranging [ ]. m and is the parameter of the strength of interaction. Simulation starts from the situation that there exist only plant in the system.

In this paper, λ is set to uniform in one simulation for any species for simplicity although λ can be variable of species like a_{ij} and can be variable of time.

We studied the effect of behavioral adaptation on diversifying dynamics by investigating the λ dependence.

2 Steady and Diversifying Phases

We carried out numerical simulation and investigated the λ dependence on dynamics of diversity without changing the strength of interaction coefficient. The parameter is set to $\ = 1\ 0$, $m = 5$.

As a result, two phases are observed as λ changes. The first phase is observed when λ is smaller than some characteristic value λ_c. Typical dynamics of diversity is showed in Fig.1. In this phase, the number of species don't increase and fluctuates without time dependency. The system remains to be simple structure. We call this phase 'steady phase'.

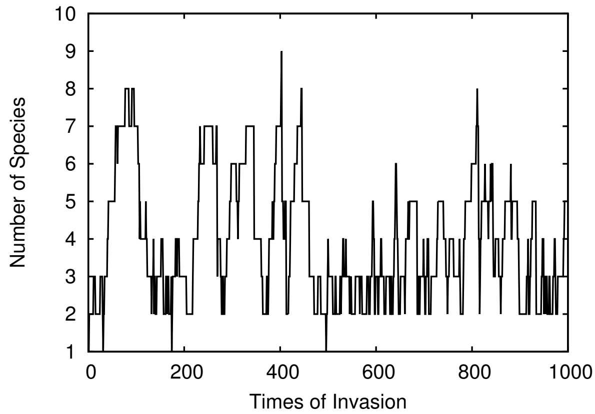

Figure 1: Typical behavior of number of species in steady phase is shown. λ is set to 0 1.

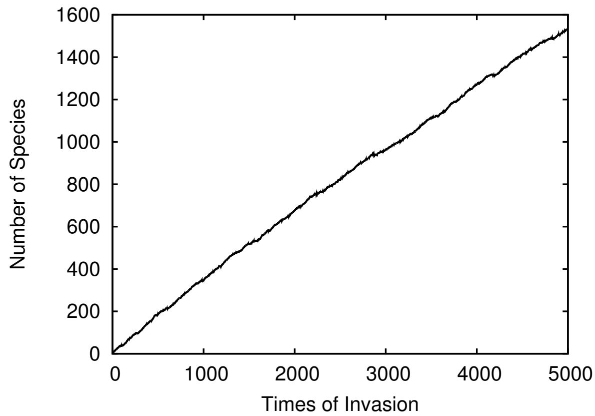

Figure 2: Typical behavior of number of species in diversifying phase is shown. λ is set to 0 5.

The other phase is 'diversifying phase'. This phase is found when λ is larger than λ_c. Typical dyanmics of diversity is showed in Fig.2. In this phase, the species richness continue to increase with fluctuation.

Between these two phases, when $\lambda \quad \lambda_c$, the diversity of the system has neither trend to grow nor trend to collapse and fluctuate widely. Fig.3 shows typical dynamics of species.

The system has tendency to have more species with larger λ in both two phases. λ is considered to have the effect of stabilizing the system. The average number of species in steady phase are plotted as a function of

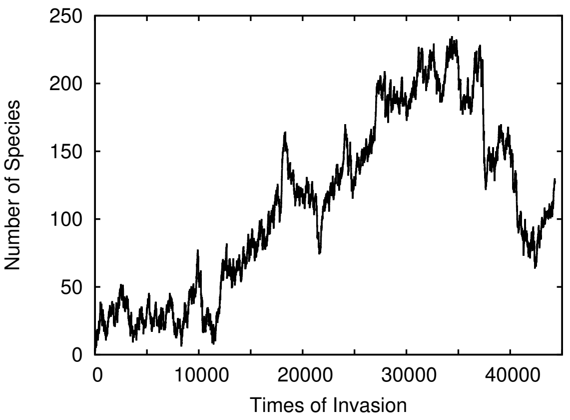

Figure 3: Typical behavior of number of species when λ λ_c is shown. ($\lambda = 0\ 4$)

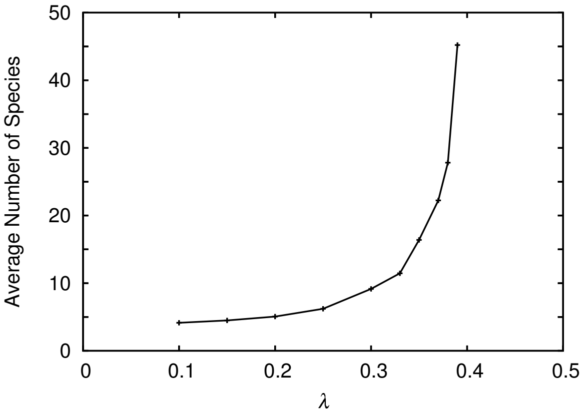

Figure 4: Average number of species in steady phase is plotted as a function of λ. The parameter is $=$ $1\ 0$ $m = 5$. Estimated λ_c from simulation is 0.41.

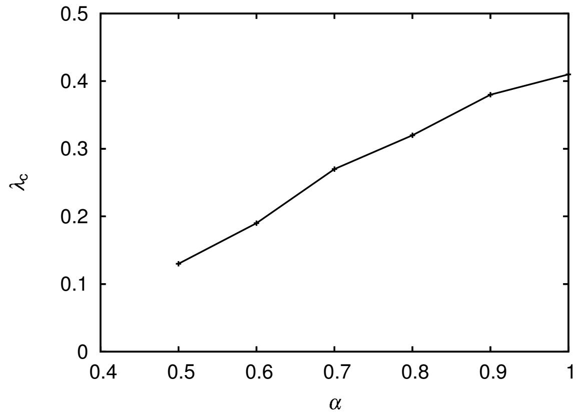

Figure 5: λ_c as a function of parameter of interaction strength, , is shown. The parameter of number of the interaction, m, is set to be 5.

λ in Fig.4. The average number of species diverges as λ_c λ $^{-d}$. The exponent d is about 0.6.

In diversifying phase, increasing rate of species richness also increase with λ. Near λ_c, it is diffucult to measure quantitative amount because the system fluctuate widely.

As R.May and others has insisted[5, 6, 7], stronger interaction leads ecosystem to poorer-species structure. This is also true in this model. Larger m and make the system harder to be stable in diverse structure. The system shows different phase with m, , and λ. In other words λ_c is variable of m and . Fig.5 shows λ_c as a function of . This suggests λ_c monotonusly increase with . This can be explained that λ_c must increase to keep the system enough stable to diversify when m and is larger.

Here it is considerable question that "larger λ means smaller interaction?". In almost all the case, this is not true. For example, let's consider simple food chain with three species like inset of Fig.6. To investigate the effect of λ on the amount of interaction, the interaction coefficients are both set to 0.5 and equilibrium population density is plotted in Fig.6. This suggests that the amount of enegy trasportation term (the amount of interaction) increase with λ monotnously. This is because increase of dependence on prey's population density which is larger than that of predator's in many cases. So in this sense, enforcement of interaction derived from behavioral adaptation (increase of λ) have an effect of the system to being diverse structure. On the other hand, enforcement of interaction derived from increase of interaction coefficient like and m destabilize the system as May and others had

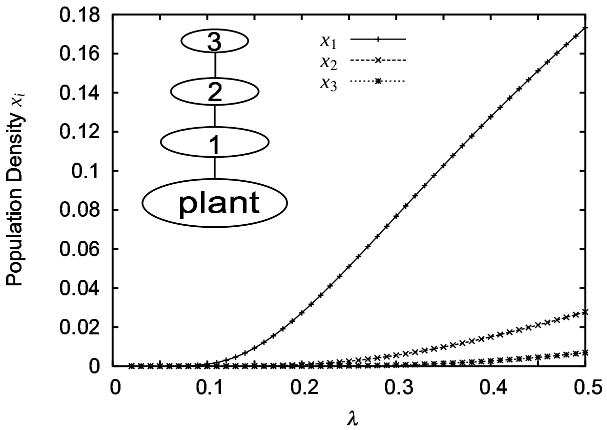

Figure 6: Population density of species as a function of λ. Three species are connecting each other organizing simple food chain like inset. Each interaction is set to 0.5. $\ _i$ is the population of i-th specie.

suggested.

3 Summary and Discussions

We have investigated the effect of interaction rate exponent λ. When λ is large, the dependency of the interaction term on prey increase and the dependency on predator decrease. This can be explained as the parameter of behavioral adaptation. The system tend to be more stable and yield more species-rich system when λ is larger. We found two phases depending on λ. First phase is 'steady phase' in which the system don't grow and remains poor-species community. It appears when λ is smaller than critical value λ_c. The other phase is 'diversifying phase' in which the system continue to grow into species-rich structure. It appears when λ is larger than λ_c.

Large interaction coefficient causes the interaction term large and destabilize the system. On the other hand, increase of λ causes the system to be stabilized though it also causes enforcement of interaction at the same time.

This can be understood using linear stability matrix. The off-diagonal element of Linear stability matrix in this model is as follows.

$$f_{ij} = \begin{cases} a_{ij}\lambda(\frac{x_i^*}{x_j^*})^{1-} & (a_{ij} > 0) \\ a_{ij}(1 \quad \lambda)(\frac{x_i^*}{x_j^*}) & (a_{ij} < 0) \end{cases} \tag{5}$$

Element of stability matrix is not totally random, therefore we can't rigidly apply May's argument. However we can suppose that the system have more probability of being stable when the variance of the value of off-diagonal part is smaller.

When λ is increase, ratio of population density between prey and predator decrease. (Fig.6) Accordingly factor $\frac{x_i^*}{x_j^*}$ decrease and the absolute value of off-diagonal part of Eq.(5) decrease. As a result, the system has more probability of being stable as λ increase.

Species' getting behavioral adaptation is speculated to be great importance to evolutionary process. The effect of behavioral adaptation on evolution is expected to be investigated in real ecosystem.

References

[1] T.Shimada, S.Yukawa, N.Ito, "Self-Organization in an ecosystem", *Artificial Life and Robotics.*, Vol. 6, pp.78-81,2002.

[2] T.Shimada, S.Yukawa, N.Ito, "Life-span of families in fossil data forms q-exponential distribution", *Int.J.Mod.Phys.C*, Vol. 14, pp.1267-1271, 2003.

[3] P.A.Abrams, L.R.Ginzburg, "The nature of predation: prey dependent, ratio dependent or neigher?", *Trends in Ecology and Evolution*, Vol.15, pp.337-341, 2000.

[4] P.A.Abrams, "Why predation rates should not be proportional to predator density", *Ecology*, Vol74, pp726-733, 1993.

[5] R.M.May, "Will a Large Complex System be Stable?", *Nature*, Vol238, pp.413-414, 1972.

[6] A.Roberts, "The stability of a feasible random ecosystem", *Nature*, Vol251, pp.607-608, 1974.

[7] M.E.Gilpin, "Stability of feasible predator-prey systems", *Nature*, Vol254, pp.137-139, 1975.

The Eleventh International Symposium on Artificial Life and Robotics 2006 (AROB 11th'06),
B-con Plaza, Beppu, Oita, Japan, January 23-25, 2006

Stability of Equilibrium State of Multi-type SIS Model on Network with Certain Property

Nobuaki Sugimine[1] and Kazuyuki Aihara[1,2]
[1] Aihara Complexity Modelling Project, ERATO, JST,
45-18 Oyama-cho, Shibuya-ku, Tokyo 151-0065, Japan
E-mail address: sugimine@aihara.jst.go.jp
[2] Institute of Industrial Science, University of Tokyo,
4-6-1 Komaba, Meguro-ku, Tokyo 153-8505, Japan
E-mail address: aihara@sat.t.u-tokyo.ac.jp

Abstract

Whether an epidemic equilibrium state is stable in some sense or not is an important research subject in mathematical epidemics modeling. In a homogeneous population, the basic SIS model has the asymptotical stability of its epidemic equilibrium solution since it can be reduced to the logistic equation. Furthermore, even in the basic SIS model with a non-homogeneous population, the asymptotic stability of its epidemic equilibrium solution is proved [1]. However, this kind of analysis in other models with a non-homogeneous population is not developed so much, even if it is well-known in ones with a homogeneous population. In addition, recent studies of complex networks have revealed that heterogeneity of the link number of vertices drastically changes epidemic thresholds. For these reasons, figuring out roles of heterogeneity becomes major topics in epidemics modeling. Thus, we have analyzed the stability of an epidemic equilibrium solution in a multi-type SIS model on heterogeneous networks.

Key words: multi-type SIS model, stability, scale-free network

1 Introduction

Epidemic processes get more and more complicate both in terms of interactions and networks. In addition to that, heterogeneity in various levels, for example, characteristic of the pathogen, the infectious, and region of outbreak of contagions, would prevent refined data analysis or mathematical modeling to clarify epidemiologically infection diseases for controlling the spread of infection. To give a little help to this, we consider a simple deterministic epidemic model given by ordinary differential equation. For our aim, expressions of effects of networks in differential equation are essence since there are some well-studied simple epidemic models, such as SIS, SIR, and SEIR models, to study infection diseases for a single homogeneous group. Here, S, I, R, and E mean the susceptible, the infectious, the removal, and the exposed, respectively. Further, difference of threshold forms for epidemics caused by effects of networks is an important subject.

In this direction, R. Pastor-Satorras and A. Vespignani first succeeded [2]. They considered a version of SIS models reflecting the scale-free property such that vertex degree distributions in networks obey power-law distributions. This is one of two common aspects that real networks have turned out to possess by last decade studies of complex networks. In a passing remark, the other is the small-world property. They showed that the epidemic threshold of infection rate is zero if vertex degree distributions with finite mean do not have the quadratic moment. In other words, there is an epidemic equilibrium solution on such networks unless the infection rate is zero. Thus, an epidemic equilibrium state always exists on scale-free networks with indices between 2 and 3, which are typically observed in ever investigated real networks with power-law vertex degree distributions. Moreover, several authors' contributions [3, 4] show that epidemics always occur in various models with same networks as R. Pastor-Satorras and A. Vespignani considered.

We are also interested in the situation where the majority cannot sustain epidemics without the presence of the core, individuals who potentially become infectious with the large infection rate [5]. For example, in prevalence of sexually transmitted diseases the core would indicate individuals engaging in risky sexual behavior, and in SARS the core would mean individuals called super-spreader [6]. Hence, we consider a population with two types of individuals: the majority who potentially has the small infection rate and the core who potentially has the large one. To make calculation tractable, we only consider the susceptible and two types of the infectious with no immunes, and do not take into account latent period, incubation period, and so on. We assume that infected people soon become infectious, and have the small infection rate with probability $(1-p)$ or the large one with probability p. In our talk, we introduce such the two-type SIS model originally proposed for regular lattices [5]. We consider this model in networks, and we show a condition for existence of an epidemic equilibrium state, which is locally asymptotically stable. We also show that if the condition does not hold, a disease free equilibrium state is globally asymptotically stable.

2 Model and Result

We introduce the following assumption on vertex degree distributions in networks that is widely accepted in the complex network study [7].

Assumption 1. We define $p(k)$ to be probability that a vertex chosen uniformly at random has vertex degree k. The probability that a given vertex with degree k is linked with a vertex with degree j is proportional to $jp(j)$, which is independent of its own vertex degree k. In other words, whenever $p(k) > 0$,

$$p(j \mid k) = \frac{jp(j)}{\sum_{j'} j'p(j')} \tag{1}$$

holds independently of k.

Further, we need the following technical assumption for mathematical analysis.

Assumption 2. There exists some positive integer K such that $p(k) = 0$ for every $k \geq K+1$.

For simplicity of notations, we set $p(k) > 0$ for every $1 \leq k \leq K$. We denote by $\langle f \rangle$ the expectation of f with respect to $\{p(j)\}_{k=1}^{K}$. We write $q(k) = kp(k)/\langle j \rangle$ for every $1 \leq k \leq K$.

Since we consider a population with two types of individuals such that the majority potentially has the small infection rate λ_1 and the core potentially has the large one λ_2, we treat three relative densities s_k, u_k, and v_k of vertices with degree k; s_k, u_k, and v_k are the ones of the susceptible, the infectious among the majority, and the infectious among the core, respectively. Along the line with [2], we consider the dynamics of $\{(s_k, u_k, v_k)\}_{k=1}^{K}$ given by

$$\begin{aligned}
\frac{ds_k(t)}{dt} &= u_k(t) + \delta v_k(t) - ks_k(t)\big(U(t)+V(t)\big),\\
\frac{du_k(t)}{dt} &= -u_k(t) + ks_k(t)\big(U(t)+V(t)\big)(1-p),\\
\frac{dv_k(t)}{dt} &= -\delta v_k(t) + ks_k(t)\big(U(t)+V(t)\big)p,
\end{aligned} \tag{2}$$

where $\delta > 0$, $p \in [0,1]$,

$$U(t) = \lambda_1 \sum_j q(j)u_j(t),$$

and

$$V(t) = \lambda_2 \sum_j q(j)v_j(t).$$

Although by nature we are supposed to replace U and V with

$$U_k(t) = \lambda_1 \sum_j p(j \mid k)u_j(t)$$

and

$$V_k(t) = \lambda_2 \sum_j p(j \mid k)v_j(t),$$

respectively, we can obtain the more simple expression (2) because of (1).

Let

$$\Omega = \left\{ \{(x_k, y_k, z_k)\}_{k=1}^{K} : \begin{array}{c} \text{for every } 1 \leq k \leq K, \\ x_k, y_k, z_k \geq 0 \text{ and} \\ x_k + y_k + z_k = 1 \end{array} \right\}.$$

Theorem 1. *If*

$$\Big(\lambda_1(1-p) + \lambda_2 \frac{p}{\delta}\Big) \frac{\langle k^2 \rangle}{\langle k \rangle} > 1, \tag{3}$$

then there exists a unique equilibrium solution $\{(s_k, u_k, v_k)\}_{k=1}^{K}$ *of (2) such that* $u_k, v_k > 0$ *for all* $1 \leq k \leq K$. *For* δ *sufficiently close to 1,* $\{(s_k, u_k, v_k)\}_{k=1}^{K}$ *is locally asymptotically stable. Moreover,* $\{(s_k, u_k, v_k)\}_{k=1}^{K}$ *is globally asymptotically stable in* $\Omega \backslash \{(1,0,0)\}_{k=1}^{K}$ *when* $\delta = 1$. *Unless (3) holds, a disease free equilibrium solution* $\{(1,0,0)\}_{k=1}^{K}$ *is globally asymptotically stable.*

3 Sketch of Proof

We first remark that $s_k(t) + u_k(t) + v_k(t) = 1$ for every $1 \leq k \leq K$. We have that for any equilibrium solutions $\{(s_k, u_k, v_k)\}_{k=1}^{K}$ of (2)

$$\begin{aligned}
s_k &= \frac{1}{1 + kW(1-(\delta-1)p^*)},\\
u_k &= ks_kW(1-p),\\
v_k &= ks_kWp^*,
\end{aligned} \tag{4}$$

where $W = \sum_j q(j)\left(\lambda_1 u_j + \lambda_2 v_j\right)$ and $p^* = p/\delta$. From (4), we have that

$$W = \frac{\lambda^*}{\langle k\rangle}\left\langle k^2 \frac{W}{1 + kW(1-(\delta-1)p^*)}\right\rangle, \tag{5}$$

where $\lambda^* = \lambda_1(1-p) + \lambda_2 p^*$. Notice that the right-hand side of (5) consists of the summation of increasing concave functions of W. Thus, (5) has a unique positive solution W if and only if

$$\lambda^* \frac{\langle k^2\rangle}{\langle k\rangle} > 1.$$

Therefore, (2) has a unique equilibrium solution $\{(s_k, u_k, v_k)\}_{k=1}^K$ such that $u_k, v_k > 0$ for all $1 \le k \le K$ if and only if (3) holds.

We consider the linearized dynamics of (2) at $\{(s_k, u_k, v_k)\}_{k=1}^K$:

$$\begin{aligned}
\frac{d\widetilde{s}_k(t)}{dt} &= \widetilde{u}_k(t) + \delta\widetilde{v}_k(t) - k\left(s_k(t)\widetilde{W}(t) + W\widetilde{s}_k(t)\right),\\
\frac{d\widetilde{u}_k(t)}{dt} &= -\widetilde{u}_k(t) + k(1-p)\left(s_k\widetilde{W}(t) + W\widetilde{s}_k(t)\right),\\
\frac{d\widetilde{v}_k(t)}{dt} &= -\delta\widetilde{v}_k(t) + kp\left(s_k\widetilde{W}(t) + W\widetilde{s}_k(t)\right),
\end{aligned} \tag{6}$$

where

$$\widetilde{W}(t) = \sum_j q(j)(\lambda_1\widetilde{u}_j(t) + \lambda_2\widetilde{v}_j(t)).$$

Notice that $\widetilde{s}_k(t) + \widetilde{u}_k(t) + \widetilde{v}_k(t) = 0$ for every $1 \le k \le K$.

From now on, we set $\delta = 1$. Since we obtain from (4) and (6) that

$$\frac{d\widetilde{W}(t)}{dt} = \frac{\lambda^* W}{\langle k\rangle}\left(\sum_k k^2 p(k)\widetilde{s}_k(t)\right),$$

we consider the linear dynamics

$$\frac{d}{dt}\begin{pmatrix}\widetilde{W}(t)\\ \widetilde{s}_1(t)\\ \vdots\\ \widetilde{s}_K(t)\end{pmatrix} = \mathbf{A}\begin{pmatrix}\widetilde{W}(t)\\ \widetilde{s}_1(t)\\ \vdots\\ \widetilde{s}_K(t)\end{pmatrix}, \tag{7}$$

where

$$\mathbf{A} = \begin{pmatrix} 0 & a_1 & \cdots & a_K\\ -s_1 & -1-W & & \\ \vdots & & \ddots & \\ -Ks_K & & & -1-KW\end{pmatrix}$$

and $a_j = \lambda^* W j q(j)$.

We will show that real parts of all eigenvalues of $\mathbf{A}$ are negative. Let $c_j = j s_j a_j$. The characteristic equation $\Phi_{\mathbf{A}}$ of $\mathbf{A}$ is as follows:

$$\begin{aligned}
&\Phi_{\mathbf{A}}(x)\\
=&x(x+1+W)\cdots(x+1+KW)\\
&+c_1(x+1+2W)\cdots(x+1+KW)\\
&+c_2(x+1+W)(x+1+3W)\cdots(x+1+KW)\\
&\vdots\\
&+c_K(x+1+W)\cdots(x+1+(K-1)W).
\end{aligned} \tag{8}$$

The expression (8) of $\Phi_{\mathbf{A}}(x)$ shows that

$$\Phi_{\mathbf{A}}(0) > 0, \tag{9}$$

and the coefficient of degree K is

$$\sum_{j=1}^K (1 + jW). \tag{10}$$

The expression (8) of $\Phi_{\mathbf{A}}(x)$ also shows that for every $2 \le j \le K$

$$\Phi_{\mathbf{A}}\big(-1 - jW\big)\Phi_{\mathbf{A}}\big(-1-(j-1)W\big) < 0,$$

which implies that for every $2 \le j \le K$ there exists at least one root $-\alpha_j$ of $\Phi_{\mathbf{A}}(x) = 0$ in $(-1-jW, -1-(j-1)W)$. Then we obtain that

$$\Phi_{\mathbf{A}}(x) = (x+\alpha_2)\cdots(x+\alpha_K)(x^2+\beta x+\gamma)$$

for some real numbers β and γ. In this expression, the coefficient of degree K is

$$\sum_{j=2}^K \alpha_j + \beta. \tag{11}$$

From (10) and (11), we see that

$$\sum_{j=2}^K \alpha_j + \beta = \sum_{j=1}^K (1+jW),$$

which together with the fact that $\alpha_j < 1 + jW$ implies that

$$\beta = \sum_{j=2}^K (1+jW) - \sum_{j=2}^K \alpha_j > 1 + W > 0. \tag{12}$$

When the equation

$$x^2 + \beta x + \gamma = 0 \tag{13}$$

has no real-valued solutions, real parts $-\beta/2$ of the two solutions are negative. Suppose that the equation (13) has two real-valued solutions. Notice that the equation (13) has never a zero solution because of (9). By the fact that $\beta > 0$, there is no possibility that both the two solutions are positive. If the equation (13) has one negative solution and one positive solution, the equation $\Phi_{\mathbf{A}}(x) = 0$ has only one positive solution. This and (9) contradict that the maximal coefficient of $\Phi_{\mathbf{A}}(x)$ is equal to 1. Then both the two solutions are negative. Therefore, we showed that real parts of all eigenvalues of $\mathbf{A}$ are negative. In other words, the linear dynamics (7) is asymptotically stable.

Recall that we consider the case where $\delta = 1$ in the linearized dynamics (6). The second and the third equations of (6) together with the asymptotic stability of $(\widetilde{W}(t), \widetilde{s}_1(t), \ldots, \widetilde{s}_K(t))$ imply that the linearized dynamics (6) is also asymptotically stable, which is equivalent to that real parts of all eigenvalues of the corresponding matrix to (6) are negative. By continuity, this is still true for δ sufficiently close 1. Therefore, the dynamics (2) is local asymptotically stable at $\{(s_k, u_k, v_k)\}_{k=1}^K$ for δ sufficiently close 1.

To obtain the global asymptotic stability of $\{(s_k, u_k, v_k)\}_{k=1}^K$ for $\delta = 1$, we need a slight modification to the argument in [1]. Key ingredients are the following:

$$pu_k(t) = (1-p)v_k(t) + z_k e^{-t},$$
$$z_k = pu_k(0) - (1-p)v_k(0),$$

and

$$ps_k(t) + v_k(t) = p - z_k e^{-t}.$$

By using the argument in [1], we see that unless (3) holds, a disease free equilibrium solution is globally asymptotically stable.

4 Conclusion

Since late 1990s, many real networks have been recognized to have the scale-free property that leads the divergence of the quadratic moment $\langle j^2 \rangle$ of their vertex degree distributions often times. When $\langle j^2 \rangle$ is so large, according to (3) (or [2, 3, 4]), epidemic thresholds become so small. Thus, even if epidemics do not still occur, they are suppressed by a narrow margin. For this reason, it is possible that a little rise of the proportion of the core members causes epidemics. Especially, in the situation with $\delta = 1$, this is inevitable since the epidemic state is globally asymptotically stable. This suggests that decreasing the proportion of the core members at any time might be a required strategy.

References

[1] A. Lajmanovich and J.A. Yorke, "A deterministic model for gonorrhea in a nonhomogeneous population," *Math. Biosci.*, Vol. 28, pp. 221-236, 1976.

[2] R. Pastor-Satorras and A. Vespignani, "Epidemic spreading in scale-free networks," *Phys. Rev. Lett.*, Vol. 86, pp. 3200-3203, 2001.

[3] J. Joo and J.L. Lebowitz, "Behavior of susceptible-infected-susceptible epidemics on heterogeneous networks with saturation," *Phys. Rev. E*, Vol. 69, 066105, 2004.

[4] J. Liu, J. Wu, and Z.R. Yang, "The spread of infectious disease on complex networks with household-structure," *Physica A*, Vol. 341, pp. 273-280, 2004.

[5] R.B. Schinazi, "On the importance of risky behavior in the transmission of sexually transmitted diseases," *Math. Biosci.*, Vol. 173, pp. 25-33, 2001.

[6] N. Masuda, N. Konno and K. Aihara, "Transmission of severe acute respiratory syndrome in dynamical small-world networks," *Phys. Rev. E*, Vol. 69, 031917, 2004.

[7] M.E.J. Newman, "The structure and function of complex networks," *SIAM Review*, Vol. 45, pp. 167-256, 2003.

The Eleventh International Symposium on Artificial Life and Robotics 2006 (AROB 11th'06),
B-con Plaza, Beppu, Oita, Japan, January 23-25, 2006

On Chaos Suppression by Resonant Parametric Perturbation

M. Sekikawa
Aihara Complexity Modelling Project
ERATO, JST
Tokyo, Japan

N. Inaba
Faculty of Engineering
Utsunomiya University
Tochigi, Japan

K. Aihara
Institute of Industrial Science
The University of Tokyo
Tokyo, Japan

Abstract

Chaos suppression is a phenomenon in which a chaotic attractor is suppressed and a periodic attractor is generated by a weak harmonic perturbation. We assert that the phenomenon is caused by a slight shift of a bifurcation curve. In this paper, we show that the mechanism is applicable to the Duffing-Holmes equation with parametric perturbation in which the taming chaos phenomenon was originally discovered.

1 Introduction

Chaos is sometimes suppressed and a periodic orbit is generated by the second weak harmonic perturbation in nonautonomous differential equations. This phenomenon is called "chaos suppression" or "taming chaos," and has been investigated intensively with great interest [1]–[6]. The taming chaos phenomenon was originally discovered in the following Duffing-Holmes equation:

$$\ddot{x} - x + \beta\left[1 + \eta\cos(\Omega t)\right]x^3 = -\delta\dot{x} + \gamma\cos(\omega t), \quad (1)$$

where parameters η and Ω denote the amplitude of a parametric perturbation and its angular frequency, respectively. We consider the case in which the parameter η satisfies the following condition: $0 \leq \eta \ll 1$. Parameters β, δ, γ and ω are chosen so as to generate chaos in Eq. (1) when η equals zero. Figure 1, which is the re-creation of FIG. 4 in Ref. [1], depicts the behavior of the maximum Lyapunov exponent with $\eta = 0.03$ ($\ll 1$) when the parameter Ω is varied. We describe the calculation method of the Lyapunov exponent in Chap. 2. The maximum Lyapunov exponent vanishes and entrainments are generated when the angular frequency of the second weak perturbation Ω is an integral multiple of that of primary perturbation ω as can be seen from Fig. 1.

The taming chaos phenomenon has been studied by many scientists since 1990, and it is introduced as an effective method of taming chaotic behavior without

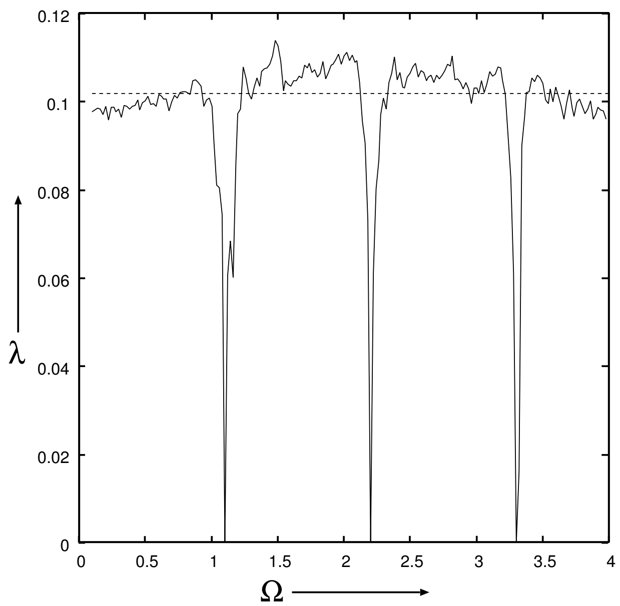

Figure 1: Maximum Lyapunov exponent with $\beta = 4.0$, $\delta = 0.154$, $\gamma = 0.088$, $\omega = 1.1$, and $\eta = 0.03$. The dotted line refers to $= 0.1017$ in the unperturbed case.

any feedback [2]–[6]. Contrary to this claim, we provide a hypothesis for the taming chaos phenomenon caused by weak resonant perturbation [7]. According to the hypothesis, the mechanism of the taming chaos phenomenon is extremely simple, and taming chaos is not exactly an effective method of controlling chaos. The hypothesis based on our insights on the mechanism of taming chaos is illustrated as follows.

Figure 2 shows a schematic bifurcation diagram of Eq. (1), where the abscissa denotes the angular frequency of the primary perturbation ω, and the ordinate denotes its amplitude γ. The bifurcation curves denoted as **G** and **I** are the saddle-node bifurcation curve with $\eta = 0$ and the period doubling bifurcation curve with $\eta = 0$, respectively. The region with

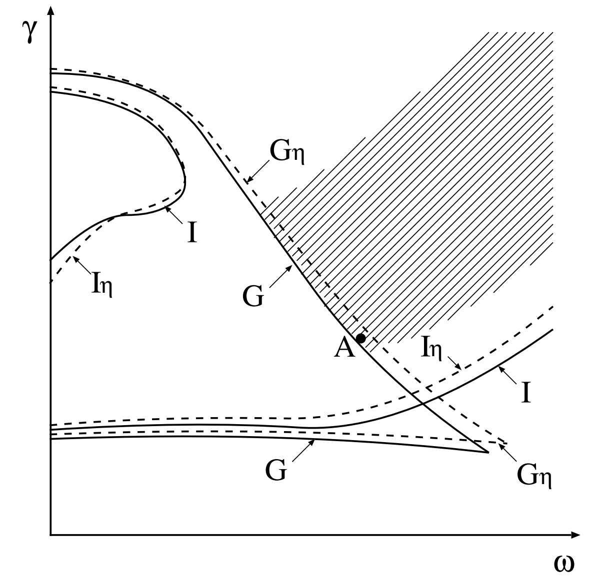

Figure 2: Schematic bifurcation diagram of Eq. (1).

the oblique lines corresponds to the parameter sets in which the chaotic attractors are observed. We consider the case in which the parameter Ω satisfies the following condition: $\Omega = k\omega$, where k is a natural number, because the taming chaos phenomenon occurs when the weak resonant perturbation is in harmony with the primary perturbation. What happens if the parameter η is changed from zero to $0 < \eta \ll 1$? For instance, the saddle-node bifurcation curve **G** and the period doubling bifurcation curve **I** move slightly to $\mathbf{G}_\eta$ and $\mathbf{I}_\eta$, respectively with $k = 1$ as shown in Fig. 2. What happens if we choose the parameter k as two, three, four and so on? This is not a mathematical proof, but intuitively, it is natural to imagine that a similar phenomenon will occur as in the case with $k = 1$, since the weak resonant perturbation is in harmony with the primary perturbation; that is, it is synchronized with the primary perturbation. Let us choose an initial parameter set at the point marked with **A** in Fig. 2. Chaos is generated for $\eta = 0$ since point **A** is outside the entrainment with $\eta = 0$. Meanwhile, for small but nonzero η, the former chaos changes into the periodic orbit since point **A** is inside the entrainment. This is the *trick* of the taming chaos phenomenon [7].

In this paper, we make a two-parameter bifurcation diagram of Eq. (1) in order to verify the hypothesis. We show that the mechanism is applicable to the Duffing-Holmes equation with parametric perturbation in which the taming chaos phenomenon was originally discovered.

2 Analysis method

The maximum Lyapunov exponent shown in Fig. 1 is calculated using Shimada's algorithm [8]. We transform Eq. (1) into the 6th-dimensional autonomous equation (2) in order to calculate the Lyapunov exponent, because Eq. (1) has two force terms.

$$\left\{ \begin{array}{lcl} \dot{x} & = & y \\ \dot{y} & = & x - \beta\,(1 + \eta\theta)\,x^3 - \delta y + \gamma\phi \\ \dot{\phi} & = & -\omega\Phi \\ \dot{\Phi} & = & \omega\phi \\ \dot{\theta} & = & -\Omega \\ \dot{} & = & \Omega\theta. \end{array} \right. \tag{2}$$

The initial condition of the state variables $(\phi, \Phi, \theta, \ )$ is $(1, 0, 1, 0)$ in Eq. (2).

We use the method presented in Ref. [9] to make a two-parameter bifurcation diagram. We summarize this method here. If we note that both forces in Eq. (1) are periodic functions of $2\pi/\omega$, the phase plane at $\ = 0$ and that at $\ = 2\pi/\omega$ can be considered to be the same. The following Poincaré map T_λ is defined as

$$\begin{array}{lcl} \mathrm{T}_\lambda & : & \mathbb{R}^2 \to \mathbb{R}^2 \\ & & \boldsymbol{u} \mapsto \mathrm{T}_\lambda(\boldsymbol{u}) = \boldsymbol{\varphi}(2\pi/\omega, \boldsymbol{u}, \ ), \end{array} \tag{3}$$

where $\boldsymbol{\varphi}(\ , \boldsymbol{u}, \ )$ is the solution of Eq. (1) for the initial value $\boldsymbol{x} = \boldsymbol{u}$.

If $\boldsymbol{u}$ is the m-th periodic point of T_λ, then $\boldsymbol{u}$ satisfies the following equation:

$$\mathrm{T}_\lambda^m(\boldsymbol{u}) - \boldsymbol{u} = 0. \tag{4}$$

T_λ^m denotes the m composite map of T_λ. The properties of $\boldsymbol{u}$ are classified according to the root μ of the following characteristic equation:

$$\left| \frac{d}{d\boldsymbol{u}} \mathrm{T}_\lambda^m(\boldsymbol{u}) - \mu \boldsymbol{I} \right| = 0, \tag{5}$$

where $\boldsymbol{I}$ is the identity matrix.

3 Influence of weak parametric resonant perturbation

A two-parameter bifurcation diagram of the Duffing-Holmes equation with parametric perturbation (1) is analyzed in order to clarify the mechanism of the taming chaos phenomenon observed in Eq. (1) in this chapter. We fix parameters β and δ at 4.0 and 0.154, respectively. Figure 3 shows the two-parameter bifurcation diagram of Eq. (1), where the abscissa denotes ω, and the ordinate denotes γ. The bifurcation

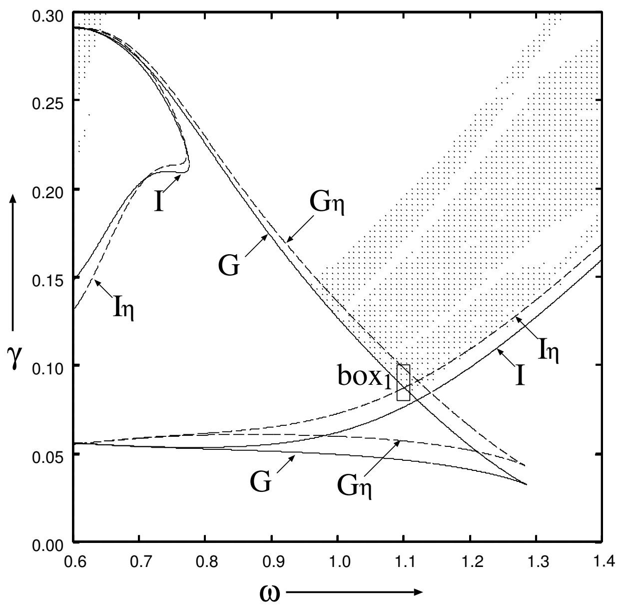

Figure 3: Two-parameter bifurcation diagram with $\beta = 4.0$ and $\delta = 0.154$.

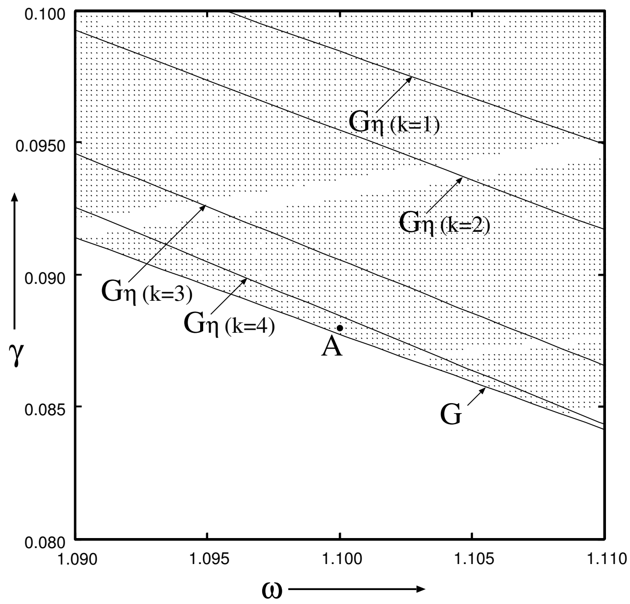

Figure 4: Enlargement of box_1 in Fig. 3 (box_1).

curves denoted as **G** and **I** are the saddle-node bifurcation curve with $\eta = 0$ and the period doubling bifurcation curve with $\eta = 0$, respectively. The parameter values that generate the saddle-node bifurcation and period doubling bifurcation are determined by simultaneously solving Eqs. (4) and (5) with $\mu = 1$ and $\mu = -1$, respectively. The simultaneous equation is solved by Newton's method. The dotted regions where the maximum Lyapunov exponent is positive are the regions where chaos occurs in the bifurcation diagrams. We verify that the structure of the bifurcation diagram and the regions where chaos occurs are consistent.

What happens if the weak resonant perturbation is added to the Duffing-Holmes equation? We consider the case in which the parameter Ω satisfies the following condition: $\Omega = k\omega$, where k is a natural number, because the taming chaos phenomenon occurs when the weak resonant perturbation is in harmony with the primary perturbation. The bifurcation curves **G** and **I** move slightly to $\mathbf{G}_\eta$ and $\mathbf{I}_\eta$, respectively, in the case of the weak resonant perturbation with $\eta = 0.03$ and $\Omega = 1.1 (k = 1)$ as shown in Fig. 3. The behavior of the maximum Lyapunov exponent of Fig. 1 is observed at point **A** in Fig. 4. The bifurcation curve **G** is the saddle-node bifurcation curve without weak resonant parametric perturbation ($\eta = 0$) in Fig. 4. Chaos is generated for $\eta = 0$ since point **A** is outside the entrainment (See Fig. 5(a)). The saddle-node bifurcation curve **G** moves to $\mathbf{G}_{\eta(k=1)}$ in the case of the weak resonant parametric perturbation with $\eta = 0.03$ and $\Omega = 1.1$. Then, the former chaos changes into the periodic orbit as shown in Fig. 5(b) since point **A** is inside the entrainment. The saddle-node bifurcation curve **G** moves slightly and point **A** is inside the entrainment as in the case with $k = 1$ when we choose the parameter k as two, three, or four. Therefore, the phenomenon observed in Fig. 1 is realized by the slight shift of the saddle-node bifurcation curve when the weak resonant perturbation is in harmony with the primary perturbation.

4 Conclusion

In this paper, we clarified that the taming chaos phenomenon observed in the Duffing-Holmes equation with parametric perturbation is caused by a slight shift of the saddle-node bifurcation curves.

References

[1] R. Lima and M. Pettini, "Suppression of chaos by resonant parametric perturbations," *Phys. Rev. A*, **vol. 41**, no. 2, pp. 726–733, Jan., 1990.

[2] Y. Braiman and I. Goldhirsch, "Taming chaotic dynamics with weak periodic perturbations," *Phys. Rev. Lett.*, **vol. 66**, no. 20, pp. 2545–2548, May, 1991.

[3] R. Chacón and J.D. Bejarano, "Routes to suppressing chaos by weak periodic perturbations," *Phys. Rev. Lett.*, **vol. 71**, no. 19, pp. 3103–3106, Nov., 1993.

[4] P. Colet and Y. Brainman, "Control of chaos in multimode solid state lasers by the use of small periodic perturbations," *Phys. Rev. E*, **vol. 53**, no. 1, pp. 200–206, Jan., 1996.

[5] R. Chacón, M. Sánchez, and J. A. Martínez, "Geometrical resonance analysis of chaos suppression in the bichromatically driven van der Pol oscillator", *Phys. Rev. E*, **vol. 56**, no. 2, pp. 1541–1549, Aug., 1997.

[6] R. Chacón,"General results on chaos suppression for biharmonically driven dissipative systems," *Phys. Lett. A*, **vol. 257**, no. 5-6, pp. 293–300, July, 1999.

[7] N. Inaba, M. Sekikawa, T. Endo, and T. Tsubouchi, "Revealing the trick of taming chaos by weak harmonic perturbations," *Int. J. Bifurc. Chaos*, **vol. 13**, no. 2, pp. 2905–2915, Oct., 2003.

[8] I. Shimada and T. Nagashima, "A numerical approach to ergodic problem of dissipative dynamical systems," *Prog. Theor. Phys.*, **vol. 61**, no. 6, pp. 1605–1615, June, 1979.

[9] H. Kawakami, "Bifurcation of periodic responses in forced dynamic nonlinear circuits: computation of bifurcation values of the system parameters," *IEEE Trans. Circuits Syst.*, **vol. CAS-31**, no. 3, pp. 248–260, Mar., 1984.

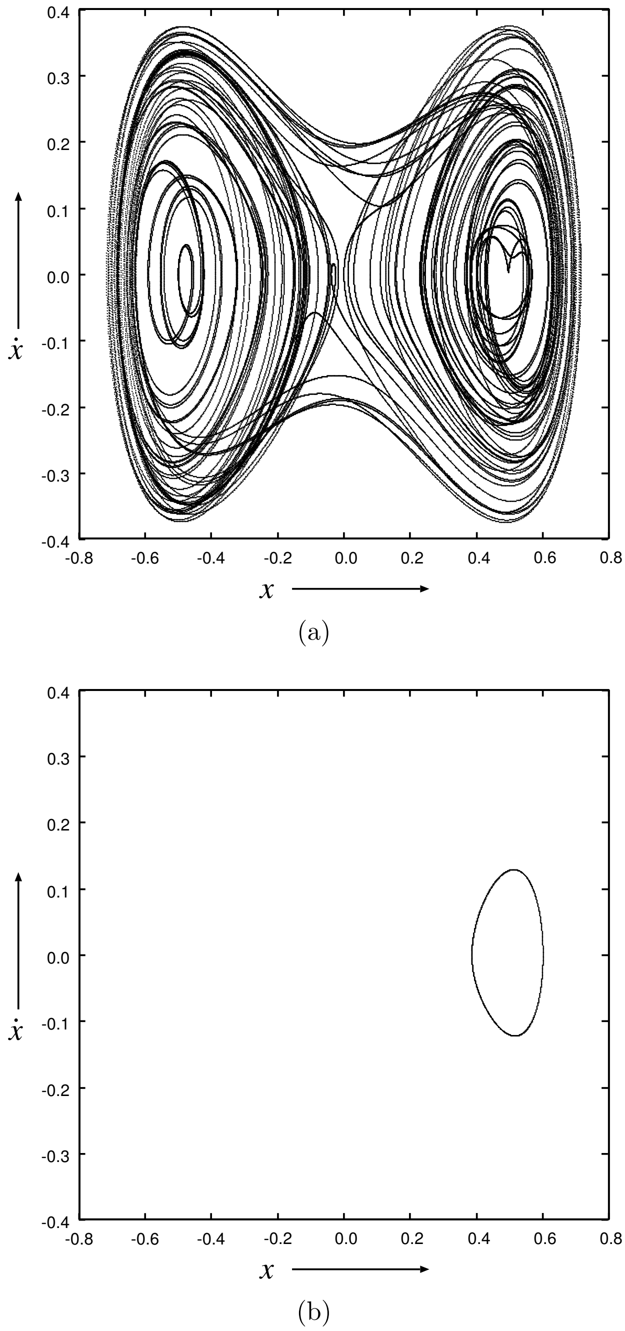

Figure 5: Attractors observed at point **A** in Fig. 4 with $\beta = 4.0$, $\delta = 0.154$, $\gamma = 0.088$ and $\omega = 1.1$: (a) Chaotic attractor with $\eta = 0.0$; (b) Periodic attractor with $\eta = 0.03$ and $\Omega = 1.1$.

The Eleventh International Symposium on Artificial Life and Robotics 2006 (AROB 11th'06),
B-con Plaza, Beppu, Oita, Japan, January 23-25, 2006

State Estimation with Finite Data Rates and Information Pattern

Hidetoshi Shimokawa*

Kazuyuki Aihara†*

*Aihara Complexity Modelling Project
ERATO JST
Meguro-ku, Tokyo 151-0064, Japan
simokawa@ieee.org

†Institute of Industrial Science
The University of Tokyo
Meguro-ku, Tokyo 151-0064, Japan
aihara@sat.t.u-tokyo.ac.jp

Abstract

Many sensor networks carry quantized data these days and it is interesting problem to know how much data rate is necessary and how we can encode efficiently for estimating state of a linear system. Preceding study shows that if full information is available at the encoder, we can estimate the state in arbitrary precision asymptotically with finite data rate which is determined by instability of the plant. In this paper, we propose a new quantization method which achieves near-optimum data rate even if the encoder is memoryless and doesn't know the input to the plant. This result is related to so-called side information problem in Information Theory. We can consider that the input to the plant is side information available only at the decoder.

1 Introduction

Motivated by recent development of digital technology and communication, estimation and control in the presence of information constrains have received considerable attention. This problem introduces the information theoretical view point and the question how to choose the bits of information that would be most useful for estimation and control. In recent years, a number of researches have analyzed various version of this problem ([1], [2], [3]).

In this paper, we focus on state estimation of one-dimensional, unstable, deterministic, discrete time, linear, time invariant system with a digital channel connecting the sensor to the estimator. The system may have bounded process noise. Our problem formulation follows that of Tatikonda and Mitter[2]. We consider the following linear time-invariant system:

$$x_{t+1} = ax_t + u_t,$$

where x_t is the state and u_t is the input at time $t \in \{0, 1, \dots\}$. We assume that we can directly observe the state x_t but the estimator get the information of the state only via digital link with a finite data rate.

- Encoder: The encoder at time t is a map

  $$\mathcal{E}_t : (x^t, \sigma^{t-1}, u^{t-1}) \to \sigma_t,$$

  where codeword σ_t takes its value in a finite set.

- Decoder: the decoder at time t is a map

  $$\mathcal{D}_t : (\sigma^t, u^{t-1}) \to \hat{x}_t,$$

  where $\hat{x}_t$ is the estimator of x_t.

We denote $(x_0, x_1, \dots, x_t)$ by x^t and so on. We can consider several configurations depending on which information is available at the encoder. They are called the *Information Pattern* of the encoder([2],[4]). Tatikonda and Mitter[2] discuss two classes of Information Pattern.

- Encoder Class One:

  $$\mathcal{E}_t : (x^t, \sigma^{t-1}, u^{t-1}) \to \sigma_t.$$

  This encoder has full access to information.

- Encoder Class Two (Figure 1):

  $$\mathcal{E}_t : x_t \to \sigma_t.$$

  This encoder has no access to the input, moreover, no access to past observation and past encoded symbols, that is, it is memory-less.

In both classes, the encoder and the decoder have knowledge of the dynamics of the plant and knowledge of the encoder and the decoder each other. Tatikonda and Mitter[2] show that the state can be estimated with zero-error asymptotically for class one, but they state, in Proposition 6.1, that it is impossible to estimate the state with bounded error for class two if the encoding rate is finite. In this paper, we introduce a new quantization method and demonstrate that we can achieve zero-error asymptotically even for class two with a finite data rate. Moreover, we can bound estimation error even if the bounded process noise is present.

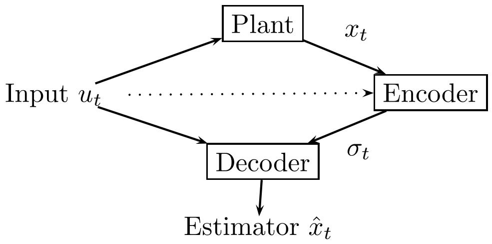

Figure 1: Information Pattern

2 Simple Example

We construct a simple plant and a encoder/decoder pair to illustrate that we can determine the system state with bounded error even if the encoder is memory-less.

- Plant:
$$x_{t+1} = 2x_t, \qquad x_0 \in [0, 2).$$
- Encoder:
$$\sigma_t = \lfloor x_t \rfloor \bmod 2$$
- Decoder: Let
$$\hat{x}_{-1} = 0, \quad \hat{x}_t = 2\hat{x}_{t-1} + \sigma_t \quad (t \geq 0).$$

Where $\lfloor x \rfloor$ denotes the maximum integer which is less than or equal to x. Apparently, $\{\sigma_t\}_0^\infty$ represent the binary expansion of x_0 and $\hat{x}_t = \lfloor x_t \rfloor$. It follows that

$$\hat{x} \leq x_t < \hat{x}_t + 1.$$

This shows that the error $|\hat{x}_t - x_t|$ is bounded even if the encoder is memory-less. This is a counter example of Proposition 6.1 ([2]).

3 Main Result

In this section, we state stronger result than the counter example in the previous section. In the previous example, we assume that the input to the plant is always zero, but here, we allow some variable input which is known only to the decoder and bounded process disturbance. Moreover, we show that the estimation error can vanish asymptotically with sufficiently large encoding rate if disturbance is not present.

Let consider the following one-dimensional unstable linear system with input u_t and bounded disturbance w_t.

$$x_{t+1} = ax_t + u_t + w_t, \tag{1}$$

where $|a| > 1$ and $|w_t| \leq D$. We assume that the initial value x_0 is also bounded:

$$x_0 \in [\tilde{x}_0, \tilde{x}_0 + L_0]. \tag{2}$$

We define system parameters K, L_t and δ_t to construct a encoder and a decoder as follows.

- Let K be an integer which satisfies that
$$K > |a| + 1. \tag{3}$$
For example, we can choose K such that
$$K = \lfloor |a| \rfloor + 2.$$
- For $t \geq 0$, let
$$\delta_t = \frac{L_t}{K-1}. \tag{4}$$
- For $t \geq 1$, let
$$L_t = |a|\delta_{t-1} + 2D. \tag{5}$$

Note that these parameters doesn't depend on observation and can be computed without memory. Now we construct a encoder and a decoder.

- Encoder:
$$\sigma_t = \mathcal{E}_t(x_t) = \lfloor \frac{x_t}{\delta_t} \rfloor \bmod K. \tag{6}$$
Because $\sigma_t \in \{0, \cdots, K-1\}$, the encoding rate is $\lceil \log_2 K \rceil$.
- Decoder:
$$\hat{x}_t = \lfloor \frac{\tilde{x}_t}{\delta_t} \rfloor + \left\{ \left(\sigma_t - \lfloor \frac{\tilde{x}_t}{\delta_t} \rfloor \right) \bmod K \right\}, \tag{7}$$
where, for $t \geq 1$,
$$\tilde{x}_t = \begin{cases} a\hat{x}_{t-1} + u_{t-1} - D & (a > 1), \\ a(\hat{x}_{t-1} + \delta_{t-1}) + u_{t-1} - D & (a < -1). \end{cases} \tag{8}$$

The following theorem states that the estimation error of $\hat{x}_t$ and $\tilde{x}_t$ is bounded as far as (3) is established.

Theorem 3.1. *For $t > 0$,*

$$\tilde{x}_t \le x_t \le \tilde{x}_t + L_t, \tag{9}$$
$$\hat{x}_t \le x_t < \hat{x}_t + \delta_t, \tag{10}$$

$$\delta_t = \gamma^t L_0 + \frac{1-\gamma^t}{1-\gamma}\frac{2D}{K-1}, \tag{11}$$

and

$$\lim_{t\to\infty} \delta_t = \frac{2D}{K-1-|a|}, \tag{12}$$

where $\gamma = |a|/(K-1) < 1$.

Corollary 3.1. *If there is no disturbance, i.e. $D = 0$, then the estimation error vanishes asymptotically.*

Tatikonda and Mitter[2] show that even if the encode has memory and knows the input, the encoding rate must be greater than $\log_2 |a|$ so that the error vanishes. The encoding rate of the above memory-less encoder is:

$$\lceil \log_2(\lfloor |a| \rfloor + 2) \rceil, \tag{13}$$

where $\lceil x \rceil$ denotes the minimum integer which is greater than or equal to x. For large $|a|$, the difference of these two rates is relatively small.

To prove this theorem, we prove the following lemma first.

Lemma 3.1. *Let x, $\tilde{x}$ and $\delta > 0$ are real variables and $K \ge 2$ is a integer. If*

$$\tilde{x} \le x \le \tilde{x} + (K-1)\delta,$$

then

$$\left(\lfloor \frac{x}{\delta} \rfloor - \lfloor \frac{\tilde{x}}{\delta} \rfloor\right) \bmod K = \lfloor \frac{x}{\delta} \rfloor - \lfloor \frac{\tilde{x}}{\delta} \rfloor. \tag{14}$$

Proof. Because $x \ge \tilde{x}$,

$$\lfloor \frac{x}{\delta} \rfloor - \lfloor \frac{\tilde{x}}{\delta} \rfloor \ge 0.$$

Using a basic inequality:

$$x - 1 < \lfloor x \rfloor \le x,$$

it follows that

$$\begin{aligned} \lfloor \frac{x}{\delta} \rfloor - \lfloor \frac{\tilde{x}}{\delta} \rfloor &< \frac{x}{\delta} - \frac{\tilde{x}}{\delta} + 1 \\ &\le \frac{(K-1)\delta}{\delta} + 1 = K. \end{aligned}$$

Therefore,

$$0 \le \lfloor \frac{x}{\delta} \rfloor - \lfloor \frac{\tilde{x}}{\delta} \rfloor < K,$$

and

$$\left(\lfloor \frac{x}{\delta} \rfloor - \lfloor \frac{\tilde{x}}{\delta} \rfloor\right) \bmod K = \lfloor \frac{x}{\delta} \rfloor - \lfloor \frac{\tilde{x}}{\delta} \rfloor. \tag{15}$$

□

Now, we prove the Theorem 3.1.

Proof. Because of definition of $\tilde{x}_0$ and L_0, it is obvious that (9) is established for $t = 0$. We assume (9) is established for some t, and then show that (10) is established for t and (9) is established for $t+1$.

Substituting (7) by (6),

$$\begin{aligned} \hat{x}_t &= \lfloor \frac{\tilde{x}_t}{\delta_t} \rfloor + \left\{ \left(\left(\lfloor \frac{x_t}{\delta_t} \rfloor \bmod K \right) - \lfloor \frac{\tilde{x}_t}{\delta_t} \rfloor \right) \bmod K \right\} \\ &= \lfloor \frac{\tilde{x}_t}{\delta_t} \rfloor + \left\{ \left(\lfloor \frac{x_t}{\delta_t} \rfloor - \lfloor \frac{\tilde{x}_t}{\delta_t} \rfloor \right) \bmod K \right\}. \end{aligned}$$

It follows from (4), (9) and Lemma 3.1 that

$$\hat{x}_t = \lfloor \frac{\tilde{x}_t}{\delta_t} \rfloor + \lfloor \frac{x_t}{\delta_t} \rfloor - \lfloor \frac{\tilde{x}_t}{\delta_t} \rfloor = \lfloor \frac{x_t}{\delta_t} \rfloor,$$

which implies (10).

For the case $a > 1$, it follows from (1) and (10) that

$$\begin{aligned} a\hat{x}_t + u_t - D \le x_{t+1} &= ax_t + u_t + w_t \\ &< a(\hat{x}_t + \delta_t) + u_t + D. \end{aligned}$$

and from (5) that

$$a\delta_t = L_{t+1} - 2D.$$

Therefore, (9) follows for $t+1$ by (8).

For the case $a < 1$, it follows from (1) and (10) that

$$\begin{aligned} a(\hat{x}_t + \delta_t) + u_t - D < x_{t+1} &= ax_t + u_t + w_t \\ &\le a\hat{x}_t + u_t + D \\ &= a(\hat{x}_t + \delta_t) + u_t - a\delta_t + D. \end{aligned}$$

and from (5) that

$$-a\delta_t = L_{t+1} - 2D.$$

By (8), we have

$$\tilde{x}_{t+1} < x_{t+1} \le \tilde{x}_{t+1} + L_{t+1}.$$

Finally, it follows from (4) and (5) that

$$\delta_{t+1} = \gamma\delta_t + \frac{2D}{K-1},$$

which leads to (11) and (12). □

4 Summary

In this paper, we show that we can construct a encoder and a decoder which can estimate the state with bounded error even if the encoder is memory-less and doesn't have access to the input of the plant. This is stronger result for encoders in class two than the result by Tatikonda and Mitter[2]. As far as we know, this type of quantization is new in this field and we believe that this method gives us new insight to understand which information bits are important for estimation and control.

Finally, we point out some relation between our result and studies in Information Theory. Encoders in class two has two limitations. One is memory-less and the other is unavailability of the input. Our result suggests that we can construct a memory-less encoder at the expense of optimal rate, that is, we need a slightly higher rate (13) than $\log_2 |a|$ bits. This is the same situation in source coding that we can achieve optimum compression rate with the long block length which requires long memory. The latter limitation has a strong connection with problem of side information. We can consider the input to the plant as side information available only at the decoder. In lossless source coding, it is shown that the optimum encoding rate doesn't change whether side information is available at the encoder or not ([5],[6],[7]). Our result is consistent with this because we can achieve optimum rate asymptotically if the encoder is allowed to have memory. The quantizer we proposed here is inspired by bin-coding([8]). Though bin-coding is a random coding and ours is deterministic, the idea that the source symbols should be spread over the codewords uniformly is the same. We should emphasize that our result is not direct consequence of source coding with side information. It should be noted that for lossy source coding([9]), the optimum coding rate can be different whether the input is available at the encoder or not. Actually, our method can not be applied to the case when unbounded disturbance is present([3]).

We consider that extension to multi-dimensional system is not a problem by means of real Jordan canonical form as [3] and [2]. Application to a non-linear plant([10],[11]) is a future work.

Acknowledgements

The authors would like to thank Prof. Tsumura for his useful comments.

References

[1] Wing Shing Wong and Roger W. Brockett. Systems with finite communication bandwidth constraints – part I: State estimation problems. *IEEE Trans. Automat. Contr.*, 42(9):1294–1299, Sep. 1997.

[2] Sekhar Tatikonda and Sanjoy Mitter. Control under communication constraints. *IEEE Trans. Automat. Contr.*, 49(7):1056–1068, July 2004.

[3] Girish N. Nair and Robin J. Evans. Stabilizability of stochastic linear systems with finite feedback data rates. *SIAM J. Control Optim.*, 43(2):413–436, 2004.

[4] Hans S. Witsenhausen. Separation of estimation and control for discrete time systems. *Proceedings of the IEEE*, 59(11):1557–1566, Nov. 1971.

[5] D. Slepian and J. K. Wolf. Noiseless coding of correlated information sources. *IEEE Trans. Inform. Theory*, 19:471–480, Jul. 1973.

[6] Aaron D. Wyner. On source coding with side information at the decoder. *IEEE Trans. Inform. Theory*, 21(3):294–300, May 1975.

[7] Rudolf Ahlswede and János Körner. Source coding with side information and a converse for degraded broadcast channels. *IEEE Trans. Inform. Theory*, 21(6):629–637, Nov. 1975.

[8] T. M. Cover. A proof of the data compression theorem of Slepian and Wolf for ergodic sources. *IEEE Trans. Inform. Theory*, 21:226–228, Mar 1975.

[9] Aaron D. Wyner and Jacob Ziv. The rate-distortion function for source coding with side information at the decoder. *IEEE Trans. Inform. Theory*, 22(1):1–10, Jan. 1976.

[10] Girish N. Nair, Robin J. Evans, Iven M. Y. Mareels, and William Moran. Topological feedback entropy and nonlinear stabilization. *IEEE Trans. Automat. Contr.*, 49(9):1585–1597, Sep. 2004.

[11] Claudio De Persis and Alberto Isidori. Stabilizability by state feedback implies stabilizability by encoded state feedback. *Systems & Control Letters*, 53:249–258, 2004.

The Eleventh International Symposium on Artificial Life and Robotics 2006 (AROB 11th'06),
B-con Plaza, Beppu, Oita, Japan, January 23-25, 2006

Modeling of Birdsong Learning with Chaotic Elman Network

M. Funabashi
Graduate School of Frontier Sciences
University of Tokyo

K. Aihara
Institute of Industrial Science
University of Tokyo

Abstract

Among passerines, Bengalese finches are known to sing extremely complex courtship songs, with 3 hierarchical structures: the element, the chunk, and the syntax. To elucidate the complex mechanism of the song of Bengalese finches, Okanoya and his colleagues have launched numerous studies based on Tinbergen's four questions for ethologists.

To offer a more dynamic view on the development of birdsong learning, we first construct a model using the Elman network with chaotic neurons, that successfully learned the supervisor signal defined by a simple finite-state syntax.

Second, We focus on the process of individual-specific increases in the complexity of song syntax. We propose a new learning algorithm to produce the intrinsic diversification of song syntax without a supervisor based on the itinerant dynamics of chaotic neural networks and the Hebbian learning rule. The emergence of a novel syntax modifying the acquired syntax is demonstrated.

The significance of this model is discussed.

1 Introduction

Courtship songs of passerines have been recently considered to be an evolutionary model of human language, if taken only in terms of syntactical structure. Among passerines, Bengalese finches are known to sing extremely complex songs compared with its ancestor species. The courtship song can be expressed in the form of a finite-state syntax with three hierarchical structures: the element, the chunk, and the syntax, based on sonogram analysis and the variable N-gram model [5][6]. To elucidate the mechanism of such an increase in the complexity of Bengalese finch song, Okanoya and his colleagues have launched numerous studies based on Tinbergen's four questions for ethologists [8].

Besides these traditional approaches, there has recently been an insistence to construct an abstract mathematical model as an analogy that would be fruitful to understand the developmental dynamics of birdsong in a comprehensive manner [4]. For this purpose, modeling with a neural network is considered to be appropriate because of the possibility to implement several biological concepts in the model structure and learning algorithm.

2 Modeling with chaotic Elman network

The following three conditions are naturally assumed as the abstract conditions of neural network modeling. First, we externally give the network the supervisor signal to learn, which coresponds to the song of a male parent. Second, the network must have the capability to generate song as a temporal sequence. Third, the network must also have the capability to express stochastic finite-state automaton, which is the class of syntax to learn. In addition, to implement the notion of chaos as a learning catalyst[7], which is the driving force of the intrinsic diversification of syntax, the use of chaotic neurons is assumed to be the fourth condition.

Considering these four conditions, we first constructed a model of birdsong learning based on the Elman network [2]. The Elman network is a discrete time system that consists of four layers: Input, Hidden, Context, and Output. We used the Output layer consisting of eight analog neurons, each one representing a different alphabetical element that appears in the song, e.g., the first neuron represents element " A ", the 2nd neuron " B ", . . . , and the eighth neuron represents the end signal " = " of the song. The analog neuron is defined as follows:

$$y_i(t) = f(\sum_{j=1}^{n} w_{ij} x_j(t) + \theta_i^{out}).$$

At time t, $x_j(t)$ is the output of the jth neuron of the Hidden layer, $y_i(t)$ is the output of the ith neuron of the Output layer, and w_{ij} is the connection weight between the ith neuron of the Output layer and the jth neuron of the Hidden layer. n is the number of neurons in the Hidden layer. θ_i^{out} is the threshold of the ith Output layer neuron, and the function, $f(x)$, is defined as follows with the increment parameter β:

$$f(x) = \frac{1}{1 + \exp(-\beta x)}.$$

To express the stochastic bifurcation of song syntax, as we run the network simulation to generate element sequences after learning, only one neuron among eight of the Output layer was finally chosen to fire 1 which represents one alphabetical element, and the rest were set to remain 0. This winner-take-all selection is made with a quasi-random variable and is proportional to the analog output value, $y_i(t)$, of each Output layer neuron. The eight binary outputs from the Output layer are then copied on a one-to-one basis to the eight outputs of the Input layer for the next time step. This stochastic winner-take-all feedback allows the network to express stochastic branches of finite-state syntax and to produce the time series of alphabetical elements. This can be interpreted as the self-auditory feedback of Bengalase finches, which is necessary to maintain the song syntax.

Each neuron of the Input and Context layer is connected to all neurons in the Hidden layer, and each neuron of the Hidden layer is connected to all neurons in the Output layer. The output of the Context layer at time t is identical to that of the Hidden layer at time $t-1$.

For the Hidden layer, we used chaotic neurons that can be taken as an expansion of the analog neuron based on the physiological property of the giant axon of a squid[1]. The chaotic neurons that we used in this model were defined as follows:

$$x_i(t+1) = f(\sum_{j=1}^{8} \upsilon_{ij} \sum_{d=0}^{t} k_e^d \iota_j(t-d)$$
$$+ \sum_{j=1}^{n} w_{ij} \sum_{d=0}^{t} k_f^d x_j(t-d) - \alpha \sum_{d=0}^{t} k_r^d x_i(t-d) + \theta_i^{hidden}),$$

where υ_{ij} is the connection weight between the jth Input layer neuron and the ith Hidden layer neuron, $\iota_j(t)$ is the output of the jth Input layer neuron at time t, and θ_i^{hidden} is the threshold of the ith Hidden layer neuron. The parameters α and k_r are set to 0 at the beginning, which makes the dynamics similar to that of the analog neuron, but the influences of past inputs (outputs of the Input layer) and outputs (outputs of the Context layer) are controlled by k_e and k_f. By assuming the time scale resolution $2^k (k = 0, 1, 2, \cdots)$ of the past influence, we distributed the values of k_e and k_f among the values set by $k_e^d = k_f^d = 0.1$, where $d = 2^k - 1$ when $k \geq 1$, and $k_e = k_f = 0$ when $k = 0$. The number of neurons for each value of k_e and k_f was set inversely proportional to the time scale resolution.

We call this the chaotic Elman network model.

Using the back propagation method, the connection weight and thresholds of the network were trained to predict the next element of each supervisor song at each time step, t. The previous element of each song was used as the outputs from the Input layer for every t. The initial outputs of the Input and Context layers at the beginning of a song were set to 0.5. Ten thousand songs generated from the supervisor syntax were used to train the network. As a result, the network successfully learned the supervisor signal, which was defined by simple finite-state syntax, as seen in Fig. 2. For example, from the supervisor defined in Fig. 2, Sequences such as AABBDD=, AABBCCBBDD=, AABBCCBBCCBBDD=,$\cdots$ were generated randomly. This stage could be regarded as the sensory-motor phase of the birdsong development, which is considered to be the process to acquire the song of a male parent. This stage can be interpreted as the decrease of randomness of the song compared to that of the male parent, as seen in Fig. 3. The song that the network acquired corresponded to the crystallized full song in the development.

3 Modeling of individual-specific diversification of syntax

Second, we focused on the process of individual-specific diversification of syntax that the song of Bengalese finches can go through even after the crystallization, about 90 days after hatching, which somewhat implies an internal mechanism of an increase in complexity without the supervisor, as shown in Fig. 3. (Kawamura, T. and Okanoya, K. in preparation, and personal communication with Sasahara, K.).

As an analogy of such an intrinsic diversification of syntax, we proposed a new learning algorithm based on itinerant dynamics of chaotic neural networks and the Hebbian learning rule. Setting the network in the retrieval mode, we increased the value of parameters α and k_r, which represent the scale and the decay by the time of refractoriness, respectively. The increase of the refractoriness of chaotic neural networks can cause network itinerant dynamics among the learned attractors[3]. In this model, dynamics which seem to be caused by this chaotic wandering appeared at certain parameters, as shown in Fig. 4. The syntax of itinerant dynamics implies that the network partially follows the orbit near the acquired attractor, but randomly slips off the learned track because of refractoriness and returns to another part of the attractor. During this chaotic retrieval process, we added the modification of the connection weight w_{ij}(between the Hidden and Context layer) and υ_{ij} (between the Hidden and Input layer) according to the Hebbian learning rule. The Hebbian learning rule was defined as follows:

$w_{ij}(t+1) = w_{ij}(t) + \epsilon(2x_i(t) - 1)(2x_j(t-1) - 1)$ and
$\upsilon_{ij}(t+1) = \upsilon_{ij}(t) + \epsilon(2x_i(t) - 1)(2\iota_j(t) - 1),$

where ϵ is the learning coefficient.

This algorithm can be taken as an application of the concept of chaos as a catalyst of learning that was proposed in olfactory system[7]. There is already a neural network olfactory bulb model with multiplicative noise[9], which exhibited itinerant dynamics among autoassociative memories. Additional learning in this stage was also shown to recombine memorized attractors to produce novel ones. Our modeling has an aspect that can be expanded to cross-associative memories.

As a result, based on the syntax acquired from a supervisor by back propagation, some new syntactical structures were obtained after additional Hebbian learning in the chaotic retrieval process, as shown in Fig. 5. Interestingly, the segmentation and convergence of chunk sequences were observed. Forming novel branches from/into the middle of supervisor's chunks, chunks AA, BB, and DD were segmented, and chunks BB and CC were converged to form a novel chunk, BBCC. The entropy measured as a Markov source increased from 1.162879 to 1.224444, which follows the notion of abstract dynamics of birdsong development, as shown in Fig. 3. Syntactical structures vary depending on the amount of change of parameters α and k_r, the learning coefficient ϵ, and the Hebbian learning period. If the Hebbian learning period is too long, the acquired supervisor syntax attractors seemed to be completely destroyed.

4 Discussion

In this model, we demonstrated that dynamics of the chaotic Elman network can serve as an abstract mechanism of individual-specific diversification of birdsong syntax. Although two kinds of learning algorithms, back propagation and Hebbian learning, are switched externally, the result provides the basis to construct a more consistent model of birdsong development. There is a recent estimate that certain neurons in the HVc nucleus of Bengalese finches refer to the error rate of their song compared to that of their male parent, and the HVc nucleus is connected to the motor pathway that controls vocalization (personal communication with Nishikawa, J.). Considering this possibility, by assuming the feedback between the error rate of back propgation and learning coefficient ϵ of Hebbian learning, there might be a possibility to construct a consistent model that can autonomously reproduce several types of birdsong development, as shown in Fig. 3.

The convergence of learning to achieve a more complex syntax is a future task to be implemented in this model. The network seems to confront the local minima problem because a simple increase in the number of neurons of the Hidden layer(n) does not guarantee the acquisition of a more complex syntax that often appears in the song of Bengalese finches. In the cerebrum of Bengalese finch, there are three nuclei, NIF, HVc and RA, that were found to control the structure of the syntax, the chunk, and the element of their song, respectively[6]. For anatomical and physiological plausibility and the advancement of the ability of learning, this modularity of the brain which corresponds to three hierarchical structures of the song should be further implemented. For this purpose, the definition or the distribution of parameters k_e and k_f, which represent the time scale of the influence from the past inputs, could be reconsidered.

For further research, more precise dynamics of the chaotic Elman network need to be analyzed. Expanding the dynamics of chaotic neural networks to a structure with nonlinear feedback (in this case stochastic neurons) would be fruitful becausse the brain is a system composed of various types of neurons.

At the same time, the diversification of the song syntax in evolutionary context is also influenced by the interaction with females, so that process can be implemented in the network model. The expansion will enable to connect the level of neuroscience and ethology in this model, aiming to find the actual degree of complexity of the song based on social interaction, which has not been sufficiently modeled by entropy.

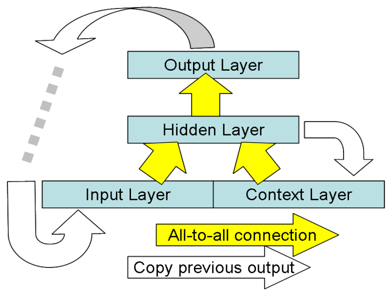

Figure1. Architecture of chaotic Elman network.

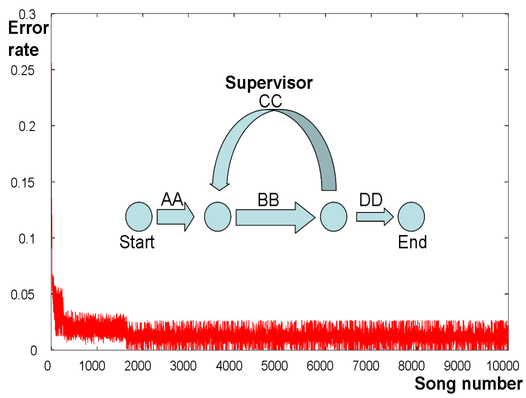

Figure 2. Definition of supervisor syntax and root mean squared error rate of learning by back propagation.

The supervisor song consists of elements A, B, C, and D, and chunks AA, BB, CC, and DD, with the end signal " = ". Cutting off branches of probability less than 0.05, the network successfully acquired the supervisor syntax. The entropy of syntax as a Markov source after learning was 1.162879. The number of neurons in the Hidden layer(n) was set to 20.

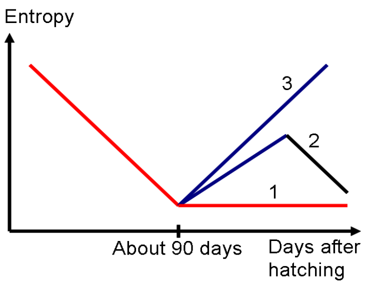

Figure 3. Schematic diagram of birdsong development of Bengalese finches in terms of randomness and complexity. Several types of development are observed. After the acquisition of syntax of the male parent until about 90 days after hatching, the song, 1: maintains the acquired synax, 2: goes through the process of intrinsic diversification but returns to the syntax of the male parent, 3: diversifies intrinsically and a more complex syntax is produced. Considering the change of syntactical structure, the change of syntax entropy can be interpreted in two ways: as the decrease of randomness (red line) and the increase of complexity (blue line).

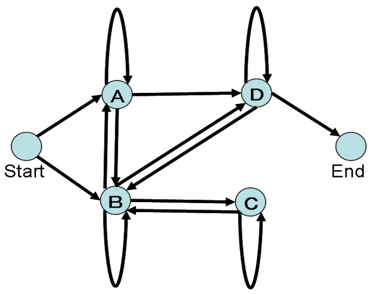

Figure 4. Example of itinerant dynamics of chaotic Elman network. After the succesful acquisition of the supervisor syntax, the refractoriness parameters, α and k_r, are both increased to 0.25. Branches of probability less than 0.05 are cut off.

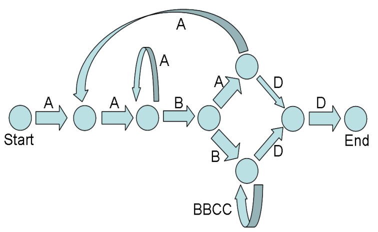

Figure 5. Example of novel syntax after additional Hebbian learning during chaotic itinerancy. The novel syntax was obtained after Hebbian learning of 120 itinerant songs at parameters $\epsilon = 0.00001$, $\alpha = 0.25$, and $k_r = 0.25$. After the learning, parameters α and k_r were again set to 0, and the network produced a novel syntax. Branches of probability less than 0.05 are cut off. The entropy of syntax as a Markov source after the additional learning was 1.224444.

Acknowledgements

This study was partially supported by the Advanced and Innovative Research program in Life Sciences from MEXT of Japan.

References

1. Aihara K., Takabe T. and Toyoda T." Chaotic neural networks. "*Phys. Lett. A*, 144, pp. 333-340, 1990.
2. Elman J. L." Finding Structure in Time. "*Cognitive Science*, 14, pp. 179-211, 1990.
3. Kitajima H." Itinerant memory dynamics and global bifurcations in chaotic neural networks. "*CHAOS*, Vol. 13, No. 3, pp. 1122-1132, 2003.
4. Okanoya K., Yoneda T. " Phonetic Development of Avian Species -Analysis by an Analogy with Neural Networks-. "(in Japanese)*Comparative Physiology and Biochemistry* (in Japanese), Vol. 12, No. 1, pp. 3-13, 1995.
5. Okanoya K. *The Transition to Language*, Oxford University Press, Oxford, 2002.
6. Okanoya K. *From Birdsong to Human Language.* (in Japanese), Iwanami, Tokyo, 2003.
7. Skarda C. A. and Freeman W. J." How brain s make chaos in order to make sense of the world. "*Behavioral and Brain Sciences*, 10, pp. 161-195, 1987.
8. Tinbergen, N. " On aims and methods of ethology. " *Zeitschrift fur Tierpsychologie*, 20, pp. 410-433, 1963.
9. Tsuda I. " Dynamic Link of Memory -Chaotic Memory Map in Nonequilibrium Neural Networks. "*Neural Networks*, 5, pp. 313-326, 1992.

The Eleventh International Symposium on Artificial Life and Robotics 2006 (AROB 11th'06),
B-con Plaza, Beppu, Oita, Japan, January 23-25, 2006

Classification of the spike sequences by discriminating their sources of time correlation

Kantaro Fujiwara , Kazuyuki Aihara
Department of Mathematical Informatics, Graduate School of Information Science and Technology, The University of Tokyo
Institute of Industrial Science, The University of Tokyo, and ERATO, JST, Japan
4-6-1 Komaba, Meguro-ku, Tokyo, 153-8505 Japan

Abstract

Irregular spike sequences of cerebral cortex in vivo are observed in numerous number of previous studies. Those spike sequences generally differ from an entirely random sequence, and exhibit temporal correlations. There are two possible origins in producing the temporal correlation: (1) temporal correlations of the incoming synaptic inputs; (2) neuronal integration mechanism. The temporal correlation of the neuronal output is produced by (1), (2), or the mixture of them.

In this paper, we propose an algorithm that discriminates the origin of the temporal correlations of spike sequences. Statistical characteristics of the spike sequences plays a key role in this algorithm. This algorithm helps classify the spike sequences by discriminating their sources of time correlation.

1 Introduction

Neurons are speciallized cells that enable specific information processing mechanisms in the brain. Neurons can receive signals from many other neurons, typically on the order of 10,000 neurons. There are examples of cells that receive more inputs such as pyramidal cells in the hippocampus, which have been estimated to receive on the order of 50,000 inputs. The sending neurons contact the receiving neuron at either at the cell body or the dendrites. It is known that various mechanisms are utilized to transfer information between the presynaptic neuron (the neuron sending the signal) and the postsynaptic neuron (the neuron receiving the signal). The general information processing feature of synapses is that they enable signals from a presynaptic neuron to alter the state of a postsynaptic neuron, and eventually to trigger the generation of an electric pulse in the postsynaptic neuron.

One may think that neurons generate regular spike sequences since the number of incoming spikes are large and the fluctuation in the accumuated potential is expected to be small. However, cortical neurons do not actually generate regular spike sequences, although motoneurons do. Until recently, the biological meaning of model parameters had not been throughly examined, for example why neurons spike irregularly.

Spike production can be considered as a two-step process. First, synaptic inputs are integrated by an extensive and complex dendritic trees resulting in a total synaptic current. Second, the cell emits spikes in response to this synaptic current. A numerous number of single neuron models that can reproduce some aspects of spiking statistics of biological neurons, such as the probability density of interspike intervals (ISIs) have been produced, and most of them have largely focused on the latter.

Many biological data exhibit non-zero value of correlation. What is the origin of producing temporal correlation? There are two possibilities. First, incoming synaptic inputs may cause the output temporal correlation. In most of the previous studies, temporal properties of inputs were taken into account. Second, neuronal integration mechanism may cause the output temporal correlation. We now define the terms we use in this study.

If the dynamics is entirely independent of the event of spike production, we identify this dynamics as the "*input*". Incoming synaptic input is the typical example.

If the dynamics entirely depends on the event of spike production, we identify this dynamics as the "*neuronal integration mechanism*". In this case, entirely dependent means that the dynamics is reset by every spike event. Membrane potential is the typical example.

If the dynamics partly depends on the event of spike production, we identify this dynamics as the "*mixture*". This is the mixture of the input and the neuronal integration mechanism. Dynamics as Ca^{2+} dependent channels which are partly dependent on voltage dynamics is also included in this term.

We suggest an algorithm to discriminate the three sources of temporal correlations in this study. By using this algorithm, we can classify the spike sequences and the neurons that produces them by differences of the neuronal spiking mechanism.

1.1 Spike auto correlation

Auto correlation is defined as a function of lag l.

$$A(l) \cdot \quad \frac{\lambda(\ )\lambda(\ +l)\ _t \quad f^2}{f^2} \qquad (1)$$

$\lambda(\ )$ is the firing rate defined as the probability of a spike event per infinitesimal unit time t, f is the mean firing rate, and the notation represents a temporal averaging operation. The value of the auto correlation determines the correlation of the spike sequences, positive or negative.

k-th moment of auto correlation is defined as

$$A_k \cdot \quad \int_0^\infty l^k A(l) dl \qquad (2)$$

If all of the A_k are equal to zero, the sequence has no correlation. If each A_k has a positive value, the ratio A_{k+1}/A_k characterizes the sustaining time scale of positive correlation.

1.2 Spiking irregularity C_V

Coefficient of variation C_V indicates the spiking irregularity.

$$C_V \cdot \quad \frac{\sqrt{\frac{1}{n-1}\sum_{i=1}^{n}(T_i \quad \overline{T})^2}}{\overline{T}} \qquad (3)$$

T_i is the duration of the ith ISI, is the total number of ISIs, and $\overline{T}=\frac{1}{n}\sum_{i=1}^{n}T_i$ is the mean ISI. C_V take 1 for purely Poisson process, and 0 for perfectly regular sequences.

2 Discriminating the sources of time correlation

2.1 Renewal process

If the *input* is temporally uncorrelated, temporal correlation in a spike sequence is generated by only the *neuronal integration mechanism.* The integrated quantities in the neuron are reset at a spike event, so an event after a spike is uncorrelated to any event before the spike, so called a renewal process. If it is a renewal process, there is one-to-one correspondence between the ISI distribution and the spike auto correlation. In this case, the time scale of the auto correlation must have a positive correlation to the mean intervals, as long as the shapes of ISI are similar. We can determine whether the shape of the ISI distribution has changed or not by measuring C_V and the other higher dimensional statistical values. Thus, the following property is to be true.

Property 1
If the ISI distribution is constant for $\bar{T}$ modulation and $A_{k+1}/A_k \quad \bar{T}$, time correlation is produced by the *neuronal integration mechanism.*

2.2 Non-renewal process

From *property 1*, we can recognize the *neuronal integration mechanism* when the ISI distribution is constant under rate modulation. Therefore, in the case of the ISI distribution constant, but A_{k+1}/A_k does not have a positive correlation with $\bar{T}$, there are two possible sources of time correlation, the *input* or the *mixture.* How can we discriminate them?

The difference of the correlation from the *mixture* and the *input* is, whether it affects the firing rate or not. Therefore, the ratio of the moment of auto correlation A_{k+1}/A_k is constant when there is only the *input* correlation[1]. If there exists a term which affects the firing rate, A_{k+1}/A_k fluctuates. This property is to be true in any case, even if the ISI distribution fluctuates with rate modulation.

Property 2
If A_{k+1}/A_k is constant for $\bar{T}$ modulation, time correlation is produced by the *input.*

2.3 Inconstant auto correlation

If A_{k+1}/A_k fluctuates with $\bar{T}$ modulation, there are two possible sources of time correlation, the *neuronal integration mechanism* or the *mixture*. How can we discriminate them?

The difference of the correlation from the *neuronal integration mechanism* and the *mixture* is, whether it resets its dynamics after the spike event or not. It is known that the positive correlation between C_V and $\bar{T}$ is not produced only by the neuronal resetting mechanism [2].

However, the case that there is no positive correlation between C_V and $\bar{T}$ even in the presence of the temporal correlation by the *mixture* still exists. In this case, comparison of $\bar{T}$ and A_{k+1}/A_k make sense. If $A_{k+1}/A_k \quad \bar{T}$, the temporal correlation is produced by the *mixture*. Temporal correlation produced by the *neuronal integration mechanism* lasts for the spike interval $\bar{T}$, since neuronal resetting mechanism vanishes the correlation between spikes. Thus, the following property is to be true.

Property 3
If $C_V \quad \bar{T}$ or $A_{k+1}/A_k \quad \bar{T}$, time correlation is produced by the *mixture*.

3 Algorithm for the classification

From the properties 1, 2 and 3, we can obtain the algorithm to discriminate the sources of time correlation for arbitrary spike sequences. Figure 1 shows the algorithm.

The algorithm begins from the determination of the correlation between A_{k+1}/A_k and $\bar{T}$. If there exists only the *input* correlation, A_{k+1}/A_k is constant under rate modulation, since the *input* correlation doesn't affect firing rate (ref. *property 2*).

The second determination is that whether the ISI distribution is constant under rate modulation or not. If the ISI distribution is constant under rate modulation, one can determine whether the spike sequence is a renewal process or not by the existence of the correlation between A_{k+1}/A_k and $\bar{T}$. Renewal process is only produced by the *neuronal integration mechanism* (ref. *property 1*). If the ISI distribution is inconstant, the measure of C_V and the value of the A_{k+1}/A_k make sense as in the *property 3*.

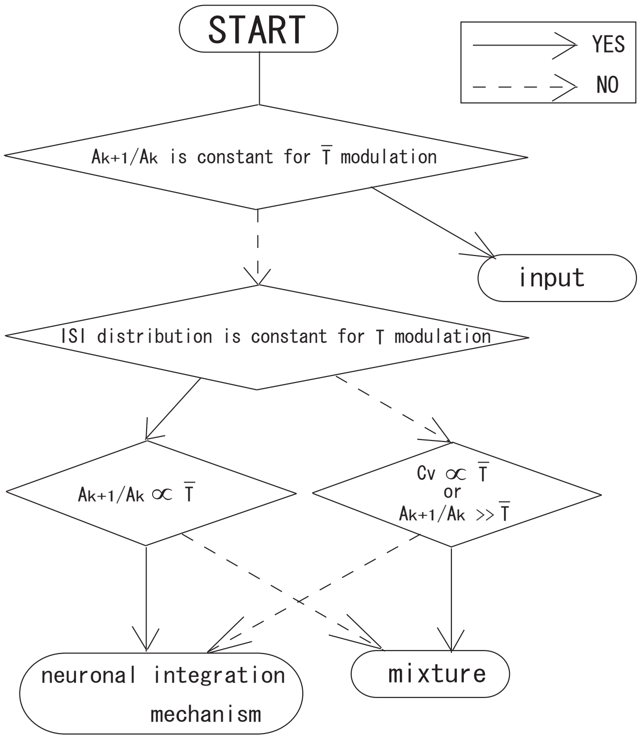

Figure 1: Flow chart of the algorithm to discriminate the sources of temporal correlation. Arbitrary spike sequence is classified into 3 groups.

4 Application to the experimental data

We applied the algorithm to the experimental data. The ISI data is recorded from the gustatory cortex of rats during taste-aversion learning experiment. The data we analyzed was the spike sequence that exhibits bursting patterns.

For the first step, A_{k+1}/A_k was inconstant with modulating $\bar{T}$. Furthermore, the ISI distribution is inconsistent under $\bar{T}$ modulation since C_V had a positive correlation with $\bar{T}$ (figure 2).

These results show that the temporal correlation of this spike sequence from gustatory cortex is produced by the *mixture* according to this discriminating algorithm.

Several slow inward currents have been implicated in the generation of somatic bursts in cortical neurons, including voltage-sensitive calcium[3] and sodium currents[4], and a calcium-activated cationic current[5]. Therefore, the result from the algorithm that the temporal correlation is produced by the correlation of the *mixture* is a natural result. The *mixture* partly depends on the event of spike production,

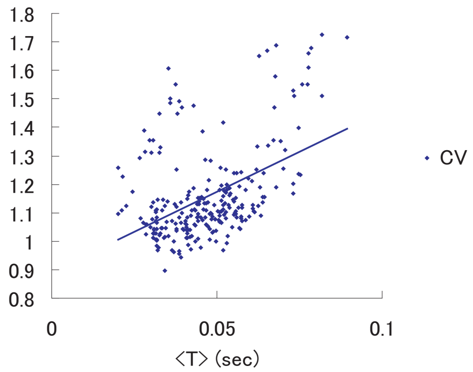

Figure 2: Cv under $\bar{T}$ modulation

including the slow dynamics that is not reset but influenced by every spike event.

5 Conclusion

We proposed an algorithm that discriminates the origin of the temporal correlations of spike sequences. We confirmed its usefulness by applying to the experimental data.

In the experimental studies, it is difficult to obtain the information of the input. This algorithm helps classify the spike sequences by discriminating their sources of time correlation even in those cases. It is interesting to develop this brief algorithm more precisely.

Acknowledgements

We are thankful to Hiroki Fujiwara and Minoru Tsukada for providing me the precious experimental data. This study is partially supported by the Superrobust Computation Project in 21st Century COE Program on Information Science and Technology Strategic Core and by the Advanced and Innovational Research program in Life Science from the Ministry of Education, Culture, Sports, Science, and Technology, the Japanese Goverment.

References

[1] Y. Sakai, "Neuronal integration mechanisms have little effect on spike auro-correlations of cortical neurons," *Neural Networks*,Vol. 14, pp. 1145-1152, 2001.

[2] K. Fujiwara, K. Aihara, "A Simple Neuron Model with Memory of Firing," *Proceedings of 2004 international symposium on nonlinear theory and its applications* (NOLTA2004), pp497–500, 2004.

[3] R. K. Wong, D. A. Prince, "Afterpotential generation in hippocampal pyramidal cells," *Journal of Neurophysiology,* vol.45, pp86–97, 1981.

[4] R. Azouz, M. S. Jensen, Y. Yaari, "Ionic basis of spike afterdepolarization and burst generation in adult rat hippocampal CA1 pyramidal cells," *Journal of Physiology,* vol.492, pp211–223, 1996.

[5] Y. Kang, T. Okada, H. Ohmori, "A phenytoin-sensitive cationic current participates in generating the afterdepolarization and burst afterdischarge in rat neocortical pyramidal cells," *European Journal of Neuroscience,* vol.10, pp1363–1375, 1998.

The Eleventh International Symposium on Artificial Life and Robotics 2006 (AROB 11th'06),
B-con Plaza, Beppu, Oita, Japan, January 23-25, 2006

Spike train surrogates and dual coding

Yoshito Hirata[1,*], Hideyuki Suzuki[1,2], and Kazuyuki Aihara[1,2,3]
[1]Department of Mathematical Informatics, The University of Tokyo,
7-3-1 Hongo, Bunkyo-ku, Tokyo 113-8656, Japan
[2] Institute of Industrial Science, The University of Tokyo,
4-6-1 Komaba, Meguro-ku, Tokyo, 153-8505, Japan
[3] Aihara Complexity Modelling Project, ERATO, JST,
45-18 Oyama, Shibuya-ku, Tokyo 151-0065, Japan
* yoshito@sat.t.u-tokyo.ac.jp

Abstract

For information coding for a neuron, there are two major hypotheses. In the rate coding hypothesis, the information is believed to be coded in the average firing rate. Under the temporal coding hypothesis, on the other hand, each timing of spikes is considered to contain the information. A problem is that each neuron in a different region of the brain may use a different coding mechanism. There also appeared a comprehensive hypothesis called dual coding, under which the same neural network selects the rate coding and temporal coding depending on noise level, heterogeneity of networks, or input correlations. We recently proposed spike train surrogates that distinguish the rate coding from the temporal coding. In this paper, we apply this method to numerical examples based on the dual coding and test how sensitive the method is to the temporal part of the dual coding.

Key words

Neural coding, rate coding, temporal coding, surrogate data, hypothesis testing, experimental design

1 Rate, temporal, and dual codings

Although the measurement techniques have been improved, still unclear is how the brain processes information. We are not even sure how the information is encoded in the brain. It has been a strong belief that spikes contain the information. It was proved that under certain conditions, a dynamics of a neuron is completely described by a sequence of firings and non-firings [1]. It was also argued that an embedding using interspike intervals can reconstruct the original states [2]. Therefore, it may be reasonable to assume that spikes retain all the information. Then our problem is how the information is encoded on spikes. For the neural coding, it has been widely believed that the information is coded in the average firing rate. This hypothesis is called rate coding. Even now this hypothesis is believed to be true in codings for sensory neurons. Although for a neuron we need some time to average over spikes to find the average firing rate, we only need a short time to find the average firing rate if we prepare an ensemble of neurons and find the average firing rate by taking the average over the ensemble. This variant of rate coding is called population rate coding [3, 4, 5].

By following the improvements of the measurement techniques, we started observing that some neurons reproduce the outputs exactly to certain stimuli [6, 7, 8, 9, 10, 11]. Based on this fact, a new hypothesis, the temporal coding hypothesis, has been developed. Under this hypothesis, each timing of spikes is believed to convey the information. This hypothesis was argued to enable speedy and energy saving computations [12, 13], while it is still unclear how each timing of spikes deals with the information processing.

The situation under these two hypotheses is a bit complicated because they are not completely exclusive: It is easy to imagine that neurons in the central nerve system uses a different coding from those in the peripheral systems. It has been also argued that the same neuron may use both codings depending on noise level, heterogeneity of networks, or input correlations [5, 12, 14, 15, 16, 17, 18, 19]. This comprehensive hypothesis is called dual coding [17, 18, 19]. Even if the dual coding hypothesis is true, it is still important when a certain neuron uses which coding.

Recently we proposed a hypothesis testing distinguishing the rate coding from the temporal coding [20]. We extended the idea of surrogate data [21, 22, 23, 24] to this problem of neural codings. Surrogate data are the common techniques in nonlinear linear time series for testing the properties of time series data. First we calculate a statistic from the original data. For a hypothesis we chose, we generate random data that preserve some properties of the original data which correspond to the hypothesis. Then, we calculate the same statistic from each surrogate. If the statistic obtained from the original data is out of the range for those obtained from the surrogate data, then our hypothesis should be rejected. The common surrogate tests include those for serial dependence [21], nonlinearity [22, 23], and long term correlation [24].

In our method of Ref. [20], we assume that the neural coding we want to test is based on the rate coding. Then we generate random spike trains that preserve the average firing rate and the distribution of interspike intervals. If the original data have a significant difference from the corresponding spike train surrogates, then we reject the hypothesis that the coding of the original spike train is based on the rate coding.

In this paper, we applied the above spike train surrogates for testing the rate coding hypothesis to artificial data that are generated based on the dual coding. Since the dual coding contains the aspect of the temporal coding, the hypothesis that the coding is the rate coding should be rejected. However, when the original spike train is too short and it just contains few spikes, it would be impossible to reject the hypothesis even if the original spike train is based on the dual coding. We test the limit of the method of Ref. [20] for discriminating the dual coding from the rate coding.

2 Spike train surrogates

In this section, we briefly review here the method of Ref. [20] for testing the rate coding. The method starts by assuming that the neural coding we want to examine is the rate coding. Then we randomize the spike train so as to preserve the important properties of the rate coding. Since the rate coding is characterized by the average firing rate, and the dynamics of neurons should be constrained by the distribution of interspike intervals, the quantities that should be preserved during the randomization are the average firing rate and the distribution of interspike intervals. Preserving the second quantity, the distribution of interspike intervals, is easy. It can be realized by exchanging the order of the interspike intervals. However, preserving the first quantity, the average firing rate, is hard. To do it, we need to use a fancy numerical optimization.

We formulate the problem as the following minimization problem. To describe the problem, we have to define the average firing rate mathematically. Let τ be the time window for finding the average firing rate, and s and $\tilde{s}$ be spike trains in time period $[0, T)$. In addition, let $s_{[t_1,t_2)}$ denote the number of spikes in time period $[t_1, t_2) \subset [0, T)$. We write the number of spikes in $s_{[t_1,t_2)}$ by $\#s_{[t_1,t_2)}$. We choose the minimum integer M such that $M\tau \geq T$. Then the average firing rate can be defined as $\{\#s_{[i\tau,(i+1)\tau)}/\tau | i = 0, 1, \cdots, M-1\}$.

To define the algorithm, we also need to define a distance between two spike trains, which should be based on the average firing rate. We use the following d_τ:

$$d_\tau(s, \tilde{s}) = \frac{1}{M} \sum_{i=1}^{M} (\#s_{[(i-1)\tau,i\tau)} - \#\tilde{s}_{[(i-1)\tau,i\tau)})^2. \quad (1)$$

Let p be the permutation of order of interspike intervals. Let s^p be the spike train that can be obtained by reordering the interspike intervals of s using p. Since interspike intervals are reordered, the timings for the first and last spikes stay the same. If $d_\tau(s, s^p) = 0$, then s^p is a surrogate, or s^p preserves the distribution of interspike intervals and the average firing rate of s. If $d_\tau(s, s^p) \ll 1$, then s^p is its good approximation. Therefore, we minimize $d_\tau(s, s^p)$ over all the permutations p.

This formulation for obtaining surrogate data is similar to that of Schreiber and Schmitz [23] since they formulated a problem for generating surrogate data of general class as a minimization problem. Therefore, by following them, we use the simulated annealing to solve our problem. The algorithm can be stated as follows:

1. Generate s_0 by randomly exchanging the order of interspike intervals of the original spike train.
2. Generate s_{i+1} from s_i by exchanging two randomly chosen interspike intervals.
3. If $d_\tau(s, s_i) \leq d_\tau(s, s_{i+1})$, then replace s_{i+1} by s_i with probability $1 - \exp(-\beta i(d_\tau(s_{i+1}) - d_\tau(s_i)))$, where β is the parameter for the simulated annealing.
4. If $d_\tau(s, s_{i+1})$ does not satisfy a desirable accuracy, then increment i and go back to Step (2).

Since we try to preserve the key quantities that characterize the rate coding, the algorithm is a

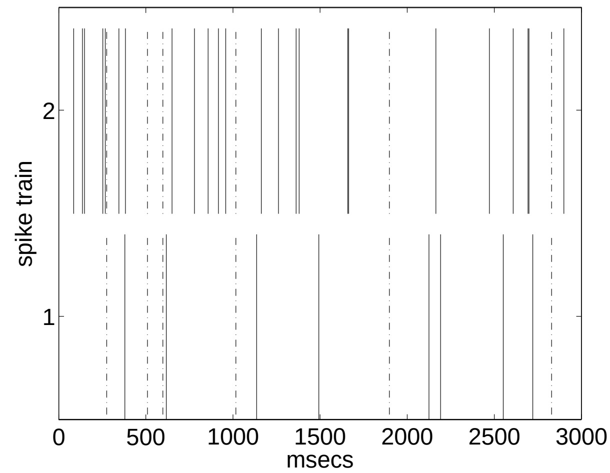

Figure 1: Example of spike trains 1 and 2. Solid lines correspond to spikes generated based upon rate coding and dashed lines, those based upon temporal coding.

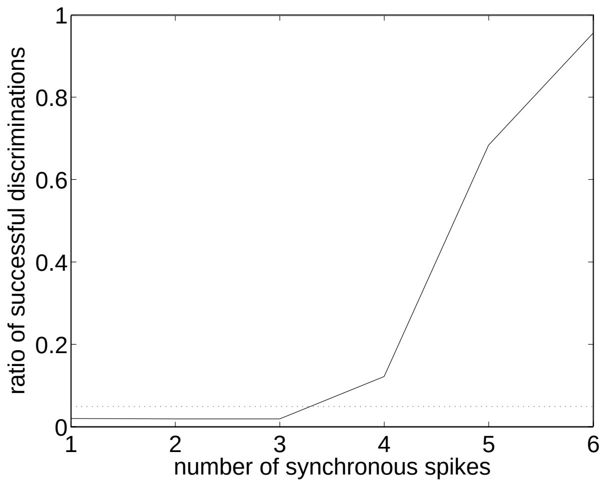

Figure 2: Ratio of successful discrimination v the number of synchronous spikes.

constrained realization. According to Theiler and Prichard [25], we can have a freedom for choosing a discrimination statistic when we use a constrained realization for generating surrogate data.

3 Simulation results

We applied the algorithm stated in the previous section to spike trains based on the dual coding. To generate spike trains based on the dual coding, we did in the following way:

1. First we generated three spike trains. The first spike train contains 24 spikes, and the second contains 8 spikes. The third spike train contains spikes, whose total number varies between 1 and 6.
2. We combine the first and third spike trains to make spike train 1. In the similar way, we combine the second and third spike trains to obtain spike train 2.

An example of the spike trains is shown in Fig. 1. The first and second spike trains correspond to spikes based on the rate coding. The third spike train corresponds to spikes based on the synchronous temporal coding. Therefore, since spike trains 1 and 2 contain the aspects of both the rate coding and the temporal coding, they are based on the dual coding. Because they are based on the dual coding, the surrogate data test should reject the hypothesis that spike trains are based on the rate coding. By changing the number of spikes in the third spike train, we would like to check the sensitivity of the method of Ref. [20].

We applied the following hypothesis testing to this data set. First we calculated the cross-correlogram [26] with width 5 ms for the original pair of spike trains and found the peak. Second for spike train 1, we generated 19 spike train surrogates. We used the bin width of 100 and maximum d_τ of 0.2. For each surrogate, we calculated the cross-correlogram with spike train 2 and found the peak. If the peak for the original pair is greater than the maximum for the pair of each surrogate and spike train 2, then we can reject the hypothesis that these spike trains are based on the rate coding.

The result is summarized in Fig. 2. When the number of the synchronous spikes is greater than 3, the ratio of successful discrimination is above 0.05. It means that when the number of the synchronous spikes is equal to or greater than 4, we can identify that the codings are different from the rate coding, while we cannot correctly show that the codings are not the rate coding when the number of the synchronous spikes is less than 4. Moreover, when the number of the synchronous spikes is 4, the rate of rejections is 0.123. If we want to test the rate coding hypothesis using a set of trials with the confidence interval of 99 %, the number of trials should be more than 48 because since the possibility of rejection for each trial is now 5% and the probability follows the binomial distribution, given the number N of trials the 1% bound is given by $(0.05 + 2.316\sqrt{0.05 \cdot 0.95/N})$.

4 Conclusions

The method of Ref. [20] has some limits when we try to discriminate the dual coding from the rate coding. To be discriminated correctly, spike trains based on the dual coding should contain the spikes based on the temporal coding more than a certain ratio. By investigating artificial data sets like ones we used here and finding out the necessary and sufficient conditions, we can design real experiments, which will reveal actual neural codings in humans and animals.

Acknowledgments

This research is partially supported by Grant-in-Aid for Scientific Research on Priority Areas -Higher-Order Brain Functions-(17022012) and the Advanced and Innovational Research program in Life Sciences from MEXT of Japan, and the Industrial Technology Research Grant Program in 2003, from the New Energy and Industrial Technology Development Organization (NEDO) of Japan.

References

[1] Y. Hirata, K. Judd, and K. Aihara, *Phys. Lett. A* **346**, 141 (2005).

[2] T. Sauer, *Phys. Rev. Lett.* **72**, 3811 (1994).

[3] M.N. Shadlen and W. T. Newsome, *J. Neurosci.* **18**, 3870 (1998).

[4] D. J. Mar, C. C. Chow, W. Gerstner, R. W. Adams, J. J. Collins, *Proc. Natl. Acad. Sci. USA* **96**, 10450 (1999).

[5] M. C. W. van Rossum, G. G. Turrigiano, S. B. Nelson, *J. Neurosci.* **22**, 1956 (2002).

[6] H. K. Bryant and J. P. Segundo, *J. Physiol.* **260**, 279 (1976).

[7] Z. F. Mainen and T. J. Sejnowski, *Science* **268**, 1503 (1995).

[8] R. R. D. van Steveninck, G. D. Lewen, S. P. Strong, R. Koberle, and W. Bialek, *Science* **275**, 1805 (1997).

[9] S. P. Strong, R. Koberle, R. R. D. van Steveninck, and W. Bialek, *Phys. Rev. Lett.* **80**, 197 (1998).

[10] P. Reinagel and R. C. Reid, *J. Neurosci.* **20**, 5392 (2000).

[11] K. MacLeod, A. Bäcker, and G. Kaurent, *Nature* **395**, 693 (1998).

[12] M. Abeles, *Corticonics*, Cambridge University Press, Cambridge, UK.

[13] S. Thorpe, D. Fize, and C. Marlot, *Nature* **381**, 520 (1996).

[14] O. Araki and K. Aihara, *Neural Comp.* **13**, 2799 (2001).

[15] T. Lu, L. Liang, X. Wang, *Nature Neurosci.* **4**, 1131 (2001).

[16] P. H. E. Tiesinga, J-M. Fellis. J. V. José, T. J. Sejnowski, *Network* **13**, 41, (2002).

[17] N. Masuda and K. Aihara, *Phys. Rev. Lett.* **88**, 248101 (2002).

[18] N. Masuda and K. Aihara, *Neural Comp.* **15**, 103 (2003).

[19] N. Masuda and K. Aihara, *Neurocomputing* **58–60**, 33 (2004).

[20] Y. Hirata, Y. Katori, H. Suzuki, and K. Aihara, Mathematical Engineering Technical Reports, METR 2005-35, 2005.

[21] J. A. Scheinkman and B. LeBaron, *J. Business* **62**, 311 (1989).

[22] J. Theiler, S. Eubank, A. Longtin, B. Galdrikian, and J. D. Farmer, *Physica D* **58**, 77 (1992).

[23] T. Schreiber and A. Schmitz, *Phys. Rev. Lett.*, **77**, 635 (1996).

[24] M. Small, D. Yu, and R. G. Harrison, *Phys. Rev. Lett.* **87**, 188101 (2001).

[25] J. Theiler and D. Prichard, *Physica D* **94**, 221 (1996).

[26] C. D. Brody, *Neural Comp.* **11**, 1537 (1999).

The Eleventh International Symposium on Artificial Life and Robotics 2006 (AROB 11th'06),
B-con Plaza, Beppu, Oita, Japan, January 23-25, 2006

Dynamic Switching of Neural Coding Schemes in a Network with Gap Junctions

Yuichi Katori[1], Naoki Masuda[1,2] and Kazuyuki Aihara[1]
[1] Aihara Complexity Modelling Project, ERATO,JST,
3-23-5 Uehara, Shibuya-ku, Tokyo 151-0064, Japan
[2] Laboratory for Mathematical Neuroscience, RIKEN Brain Science Institute,
2-1, Hirosawa, Wako, Saitama 351-0198, Japan

Abstract

How neurons code information in our brain is one of the most important themes in neuroscience. Population rate coding and temporal coding are two common neural coding schemes. Recent studies have pointed out that these two coding schemes may coexist [1][2]. Experiments have revealed a massive number of gap junctions in various regions of the brain. Neurons connected with gap junctions induce synchronous spiking. Moreover, theoretical works indicate that gap junction induce not only synchronous activity but also a switching behavior between synchronous states and desynchronous states [5]. We used information theory and computer simulations to investigate how this kind of switching behavior relates to the neural coding. First, we demonstrated that even under time-varying inputs, neurons coupled with gap junctions induced switching behavior between synchronous and desynchronous states. Then, we used three types of mutual information to separate the contribution of each coding scheme from the information carried on a network. We measured these mutual information carried in sepatate periods of synchronous and desynchronous states. Our results show that the population rate coding has an advantage in periods of desynchronous states and the temporal coding has an advantage in periods of synchronous states. We found that these two types of coding schemes emerge alternately with switching between synchronous and desynchronous states.

Key words: Neural coding, gap junction, chaotic itinerancy, population rate coding, temporal coding, mutual information.

1 Introduction

Many studies in the past few decades have investigated how neurons code information. However, no established theory fully addresses to answer this question. One of the most plausible coding schemes is population rate coding, which represents information as a firing rate averaged over hundreds of neurons. This makes it possible to transmit a signal within a short time and to have robustness against spike failure. Another plausible scheme is temporal coding, which indicates that information is coded by precise temporal patterns of spikes, such as in synchronous firing. Synchronous firing with millisecond precision has been observed in experiments as in multi-channel recording [3]. Many theoretical works have discussed what structures induce this synchronous firing and how these activities are relevant to neural coding. Furthermore, recent studies have found the possibility of the coexistence of these two coding schemes which is controlled by noise intensity [1][2].

Furthermore, recent experiments have shown a massive number of gap junctions. These gap junctions are specialized areas of the cell membranes connecting neighbor cells; they induce synchronous firing [4]. In addition to the synchronous activity, theoretical studies suggest that gap junctions induce chaotic activities [6] and transitions between synchronous and desynchronous states. However, little is known about how this transient activity is associated with neural coding. We have used numerical simulations and information theory to investigate how the transitions between synchronous and desynchronous states is connected with neural coding.

2 Analysis

We investigated a neural network coupled with gap junctions. We used a simple two-variable neuron model called a μ-model, which is more plausible than a one-variable neuron model like the integrate-and-fire model [5]. The model is composed of two variables x_i and y_i, where the first variable represents the membrane potential and the second variable represents activation of some ion channels. Here we chose $\mu = 1.65$.

$$\frac{dx_i}{dt} = -y_i - \mu x_i^2(x_i - \frac{3}{2}) + I(t) + J(t) \quad (1)$$

$$\frac{dy_i}{dt} = -y_i + \mu x_i^2 \quad (2)$$

$$(i = 1, \cdots, N),$$

where $J(t)$ is a current induced by gap junction coupling with neighbor neurons:

$$J(t) = \begin{cases} G(x_{i+1} - xi) & (i = 1) \\ G(x_{i+1} + x_{i-1} - 2x_i) & (i = 2, \cdots, N-1) \\ G(x_{i-1} - x_i) & (i = N). \end{cases} \quad (3)$$

In this simulation, we used a chain network of 40 neurons, where, G is the coupling constant of the gap junctions, assumed to be identical for all connections in the network. This kind of network shows an alteration of synchronous and desynchronous states even with a constant input [5]. In the field of nonlinear science, several studies have examined the mechanism of this phenomenon. However, our interest is how this phenomenon is associated with the neural coding. We used mutual information as a measure of efficiency of information transmission between inputs and output spike trains. To investigate this, we applied time-varying input to this neural network and measured how neurons carry information. We chose the input $I(t)$ to be the Ornstein-Uhlenbeck (OU)-process generated by the stochastic differential equation: $dI = -mIdt + \sigma dW$, where dW denotes the Wiener process. We set the amplitude of inputs small enough not to break alteration of synchronous and desynchronous states. We set $m = 0.05$ and $\sigma = 0.005$.

Figure 1 shows the simulation results of the network with the coupling constant $G = 0.1$ and the inputs specified above applied. Figure 1(a) shows the time series of the input generated by the OU-process. Figure 1(b) shows a superimposed time series of the membrane potentials of the 40 model neurons. The time series shows the alteration of synchronous and desynchronous states even with the time-varying input. Figure 1(c) shows a time series of a moving average of standard deviation of the 40 neurons's membrane potentials $D(t)$ as a degree of a desynchrony of membrane potentials.

To analyze how the information is transmitted on the network, we used three types of mutual information to determine the contribution of the two coding schemes. The first type of information was the full temporal information, which is associated with all possible patterns of spike occurrence in the population. Second was the spike count information which corresponds to the information carried by the firing rate of the neural population. The spike count information is based on the number of spikes in the population in an arbitrarily chosen time window. Third was pure temporal information. This is given as a subtraction of the spike count information from the full temporal information.

Consider a time duration T, which corresponds to a period to apply the input to the network. Let us denote each input time series over the duration as $s_i(\tau)$. Each time-varying input is generated by a different random seed and indexed by $i(i = 1, ..., M)$. Here, we set $M = 50$. We ran 100 simulations for different initial states of x and y for each signal and record spike train $\{t^i\}$ generated by the population of neurons. Simultaneously, we calculated a trial average of spike train density of the population under the input time series s as

$$r(\tau; s) = \sum_k \frac{\delta_{t,t^k}}{\Delta t}, \quad (4)$$

where δ_{t_1,t_2} is the Kronecker delta function (1 if t_1 and t_2 label the same time bin and zero otherwise). The index k indicates spike number and Δt is small time bin (we chose $\Delta t = 0.1$). We considered a time window of width W to measure the mutual information. The full temporal information is given by integrating the instantaneous information in this time window: [7]

$$I_{full}(W) = \int_0^W dt \left\langle r(t; s) \log_2 \frac{r(t; s)}{\langle r(t; s') \rangle_{s'}} \right\rangle_s, \quad (5)$$

where the brackets $\langle\rangle_s$ indicate the average across stimuli s. The spike count information was calculated using a spike count in the time window as

$$I_{rate}(W) = \left\langle R(t; s) \log_2 \frac{R(t; s)}{\langle R(t; s') \rangle_{s'}} \right\rangle_s, \quad (6)$$

where $R(t; s)$ is the integration of number of spikes in the time window W:

$$R(t; s) = \int_0^W r(t; s) dt. \quad (7)$$

Here, $I_{full}(W)$ and $I_{rate}(W)$ satisfy $I_{full}(W) \geq I_{rate}(W)$. The pure temporal information is given as the subtraction of the spike count information from the full temporal information:

$$I_{temporal}(W) = I_{full}(W) - I_{rate}(W). \quad (8)$$

To investigate the difference between the coding schemes in the synchronous and desynchronous states,

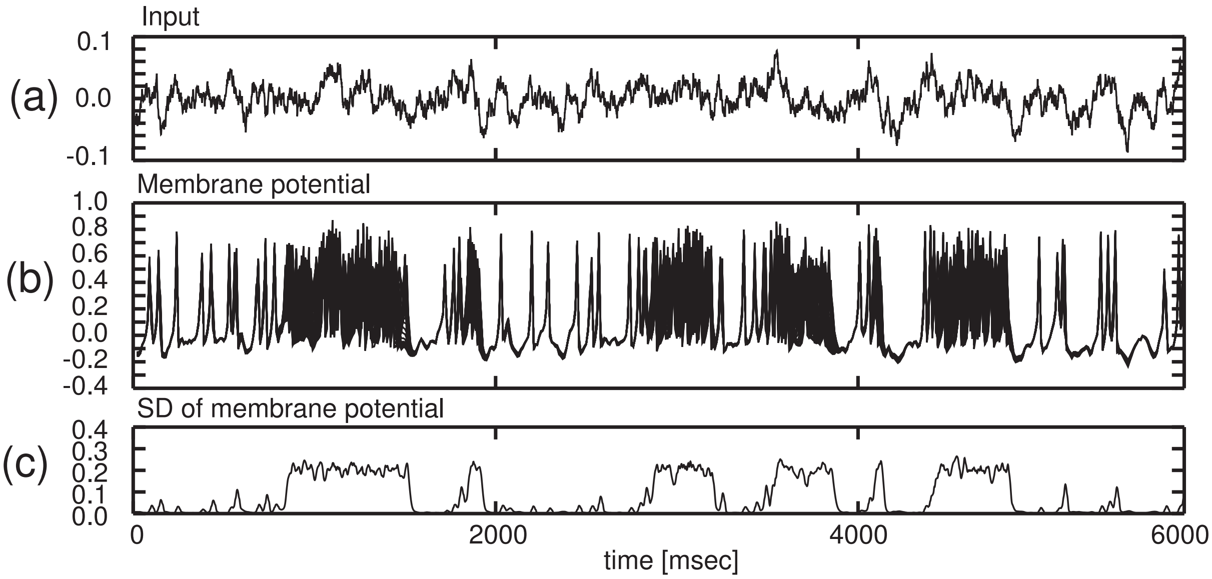

Figure 1: A typical response of 40 model neurons coupled with gap junctions when applying the input generated by Ornstein-Uhlenbeck (OU)-process. (a) Times series of input applied for this neural network. (b) Superimposed plot of membrane potential of 40 neurons. (c) Time series of standard deviation of membrane potential of 40 neurons.

we needed to categorize these spikes by whether they were generated in synchronous or in desynchronous states. To do this, we defined each state using the standard deviation of membrane potential $D(t)$. We defined the synchronous state as $D(t) < 0.1$ and the desynchronous state as $D(t) \geq 0.1$. Then we calculated the three types of mutual information using the spike trains generated in the separate periods of synchronous and desynchronous states.

As a result of this calculation, we obtained the spike count information, revealing the efficiency of the population rate coding, and the pure temporal information revealing the efficiency of the temporal coding. Figures 2 (a) and (b) show how these quantities depend on the coupling constant of the gap junction. Figure 2(c) shows degrees of synchrony of the network. The (+) sign indicates the temporal average of the standard deviation of membrane potentials. The (x) sign shows the synchrony of the spikes. This quantity is defined as the ratio of spikes that occurred in a short time window around each spike to the number of neurons in the network. The square sign shows the ratio of duration of synchronous states to duration of desynchronous states.

In the synchronous states, the temporal coding was shown to have an advantage, the information carried by the temporal coding increased as the coupling constant of the gap junctions increased. In contrast, the spike count information did not increase as much as the pure temporal information. This was caused by an improvement of the reproducibility of precise spike timing, which depends on the synchrony of the neurons; the synchrony increased as the coupling constant of gap junctions strengthen.

In the desynchronous states, the spike count information had an advantage. In population rate coding, the amplitude of the input sequence is reproduced in the firing rate of the output spike train. Information carried by population rate coding increased in the region of $G < 0.3$. However, in the region of $G \geq 0.3$, each spike tended to synchronize and could not maintain the information about the amplitude. This is because, the spike count information decrease in this region. These results indicated that the two coding schemes emerge alternately with the switching of the synchronous and desynchronous states.

3 Summary

We have shown that a neural network coupled with gap junctions induces the alteration of synchronous and desynchronous states even under time-varying inputs and that two coding schemes, population rate coding and temporal coding emerge alternately along with the changing of these states. Our findings about

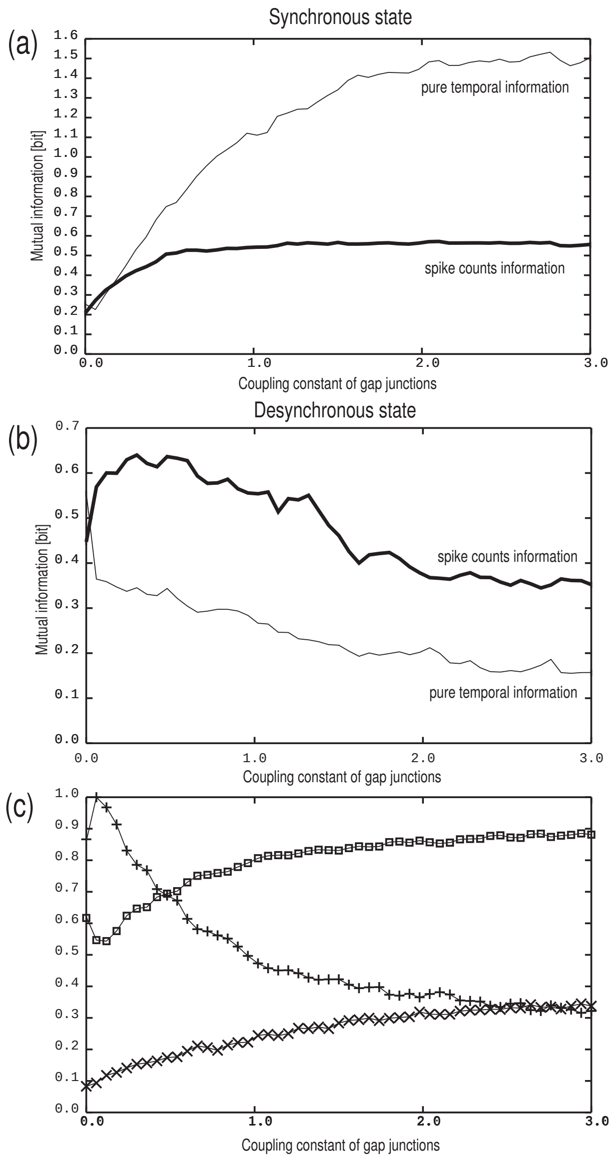

Figure 2: Mutual information and synchrony as a function of coupling constant of gap junctions. (a),(b) Spike count information as a measure of population coding efficiency (bold line) and pure temporal information as a measure of temporal coding efficiency (thin line). (a) Information carried in the periods of synchronous states. (b) Information carried in the periods of desynchronous states. (c) Degree of synchrony. Temporal average of standard deviation of membrane potentials of these neurons (+). Spike synchrony (x). Ratio of duration of synchronous states to duration of desynchronous states (square).

the functions examined here may contribute to information processing in the cortical network. In cortical neurons, ceaseless transitions of state take place as signals are received from sensory neurons and other parts of the brain. These states may represent memory patterns. This memory pattern becomes other pattern. The population rate coding could be used efficiently in the process of collecting signals from various parts of the brain. Then, the temporal coding could be used to recall a memory in the synchronous state. After recalling the memory, the state could desynchronize to collect new signals again. The states-switching behavior with gap junctions may contributes to such brain functions.

References

[1] N.Masuda and K.Aihara (2002), "Bridging rate coding and temporal spike coding by effect of noise", *Rhysical Review Letters*,88,248101

[2] N.Masuda and K.Aihara (2003), "Duality of rate coding and temporal coding in multilayerd feedforward networks",*Neural Computation*,15,103-125.

[3] A.K.Engel, P.Fries and W.Singer (2001),"Dynamic predictions: oscillations and synchrony in top-down processing"*Nature Reviews Neuroscience*,2,880-888.

[4] M.Galarreta and S.Hestrin (1999),"A network of fast-spiking cells in the neocortex connected by electrical synapses" *Nature*,402,72-75.

[5] I.Tsuda, H.Fujii, S.Tadokoro, et al (2004). "Chaotic itinerancy as a mechanism of irregular changes between synchronization and desynchronization in a neural network" *Journal of Integrative Neuroscience*,3,159-182.

[6] N.Schweighofer, K.Doya, H.Fukai, et al.(2004), "Chaos may enhance information transmission in the inferior olive", *PNAS*, Vol.101, no.13, 4655-4660.

[7] S.Panzeri and S.R.Schults (2001), "A unified approach to the study of temporal, correlational, and rate coding", *Neural computation*, 13,1311-1349.

The Eleventh International Symposium on Artificial Life and Robotics 2006 (AROB 11th'06),
B-con Plaza, Beppu, Oita, Japan, January 23-25, 2006

MOSFET Implementation of Two-dimensional Neuron Model

Takashi Takemoto*, Takashi Kohno† Shigeki Tsuji† and Kazuyuki Aihara† ‡
*Complexity Science and Engineering Frontier Science, The University of Tokyo.
† Aihara Complexity Modeling Project, ERATO, JST.
‡ Institute of Industrial Science, The University of Tokyo.

Abstract

We propose a two-dimensional neuron model using metal-oxide-semiconductor field-effect-transistors (MOSFET). Two-dimensional models are tractable mathematically because the temporal evolution of the variables can be visualized in the phase plane. Our circuitry were designed according to the mathematical structure determined using phase plane analysis and bifurcation theory. Hence, our circuitry is compact and biologically plausible. Our circuitry can achieve class I mode without narrow channel, class II, and I* mode when a few circuit parameters are changed. Class I* neurons are mainly characterized by a phase plane structure with a narrow channel and exhibit spatio-temporal chaos when coupled with gap junctions. We analyzed the responses to singlet pulse, and demonstrated the threshold mechanism in class I, II, and I* modes. Moreover, we showed that class II and I* neurons not only exhibit periodic but also chaotic responses to periodic pulse stimuli.

1 Introduction

Various silicon neurons that reproduce the properties of biological neurons have been proposed to create some new possibilities in neuroscience, computer science and electronics. Conventionally, silicon neurons have been designed according to the two major principles: phenomenological and conductance-based designs. Recently, Kohno and Aihara proposed mathematical-model-based design that is based on mathematical structures revealed using phase plane analysis and bifurcation theory [1]. It allows us to implement simple and biologically realistic silicon neurons. Our circuitry is designed according to this design principle.

Neurons are classified into two classes according to their responses to sustained current stimuli: class I and II. The firing frequency of class I neurons at the onset is asymptotically zero, whereas that of class II neurons is nonzero. Two-dimensional neuron models are tractable mathematically because their dynamic behaviors can be visualized in phase planes. It is well known that saddle-node on invariant circle bifurcation produces class I excitability, and the subcritical Hopf bifurcation class II. These bifurcations can be generated in two-dimensional systems.

The responses to periodic pulses of squid giant axons and the Hodgkin-Huxley (HH) model have been intensively studied. Class II models such as the HH model are well known to exhibit not only periodic but also aperiodic responses to periodic stimuli depending on their amplitudes and frequencies. Complex responses to simple inputs may play important roles in neural codings.

Our silicon neuron can achieve class I, II, and I* neurons when a few circuit parameters are changed. The essential nonlinearity of class I* is mainly characterized by a phase plane structure with a narrow channel [2]. In the following section, we describe how our circuitry was designed. In Sec. 3, we present its responses to singlet and periodic pulse stimuli. Finally, in Sec. 4, we make concluding remarks.

2 Modeling the Electronic Neuron Model

Our circuitry mainly consists of three blocks: the V-I converter, the inverted-N-shaped nonlinear characteristics circuitry, and the U-shaped nonlinear characteristics circuitry (see Fig. 1). We designed these blocks using enhanced MOSFETs, resistors, and capacitors.

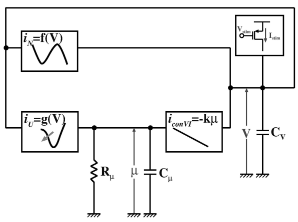

Fig. 1: Block diagram of electronic neuron model.

The circuit equations are as follows:

$$\begin{cases} C_V \dfrac{dV}{dt} &= f(V) - E\mu + I_{stim} \\ C_\mu \dfrac{du}{dt} &= g(V) - K\mu \end{cases} , \qquad (1)$$

where

$$f(V) = Aexp\left(\frac{B}{1+exp(-\kappa_n V/U_T)} - C\frac{\kappa_n}{U_T}V\right) + D,$$

$$g(v) = \frac{F}{1+exp(-\kappa_n V/U_T + G)} + Hexp\left(-I\frac{\kappa_n}{U_T}V\right) + J.$$

We can adjust the parameters, A to K, in these equations by adjusting the resistances, the voltages, and the current sources in the three main blocks in our circuitry.

A schematic of the V-I converter is shown in Fig. 2. The source-follower, M29-M30, shifts the input voltage according to $V'_{IN} = V_{IN} + V_{DD} - V_{conVI}$, where V_{IN} is the input voltage and V_{conVI} is a constant bias voltage that we can control. The feedback structure composed of M32-M33 suppresses the nonlinearity of the input/output (IO) characteristics intrinsic to MOSFETs. The IO characteristics of this circuit are very linear.

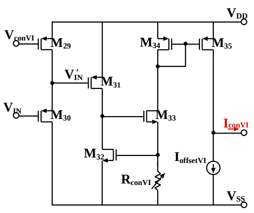

Fig. 2: Schematic of V-I converter.

A schematic of the inverted-N-shaped nonlinear characteristics circuitry is shown in Fig. 3. It mainly consists of a differential pair, M1-M2, V-I converter, M5-M9, and common-source (CS) amplifier. The combined output current of M1-M2 and M5-M9 has flatter N-shaped I-V characteristics. These currents are applied to MOSFET M12 as the input voltage via resistor R_{sN} and converted exponentially. This makes the ratio of the N-shaped I-V characteristics increase more in regions with small input voltages, V_{IN}. The ratio of the increase depends on the resistance, R_{sN}, and the current source, I_{sN}. The output current of this circuit represents the V-nullcline in our silicon neuron.

A schematic of the U-shaped nonlinear characteristic circuitry is shown in Fig. 4. It mainly consists of a differential pair, M15-M18, and a scalable CS amplifier, M19-M26. The latter consists of a V-I converter to convert the scale of the input voltage. The input voltage is applied to the differential pair and the scalable CS amplifier. One applied to the latter is scaled by the V-I converter. Its output

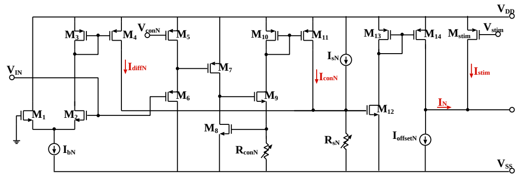

Fig. 3: Schematic of inverted-N-shaped circuit.

current, I_{conU}, is applied to MOSFET M26 via resistor R_{sU} and converted exponentially. The slope of output current, I_{CSU}, can be altered by R_{sU} and the current source, I_{sU}. The output current of this circuit represents the μ-nullcline in the silicon neuron.

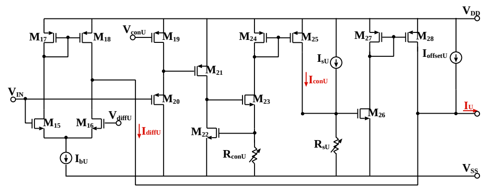

Fig. 4: Schematic of U-shaped circuit.

A plot of the nullclines of our electronic neuron model obtained using the circuit equations is shown in Fig. 5. Our circuitry can achieve three neuron modes, namely, class I without a narrow channel and class II and I*. These neuron modes have a common inverted N-shaped V-nullcline and different μ-nullclines depending on only two circuit parameters, I_{sU} and V_{diffU}.

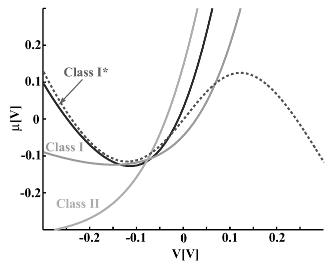

Fig. 5: Phase plane structure of electronic neuron model. Dashed line is V-nullcline and solid lines are μ-nullclines.

3 Circuit Operation and Characteristics

In this section, we give the responses of our circuitry to singlet and periodic pulse stimuli. We focused on the three neuron modes: class I, II, and I*. We used the fourth-order Runge-Kutta method for numerical simulations.

3.1 Responses to singlet pulse stimuli

Plots of the responses to singlet pulse stimuli are shown in Fig. 6. We stimulated our circuitry with singlet pulses of various strengths. When the pulses were weak, the system immediately returned directly to the resting state. When the strength was over the threshold, the membrane potential rapidly increased and then plunged below its resting state before returning to it. The time interval between the onset of the action potential and the peak is obviously shorter than that between the peak and the desinence.

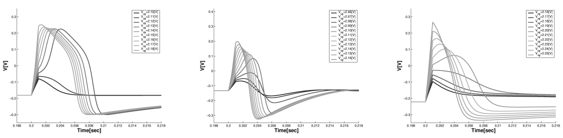

(a) Class I mode. (b) Class II mode. (c) Class I* mode.

Fig. 6: Responses to singlet pulse stimuli.

The phase plane structure of class I mode is shown in Fig. 7. When the system is near a saddle-node on the invariant circle bifurcation, the nullclines of this mode have three intersections: (S) is a stable equilibrium (resting state), (T) is a saddle, and (U) is an unstable equilibrium. In this case, the system has a pair of incoming trajectories: stable and unstable manifolds of the saddle. The stable manifold defines a separatrix curve (threshold), and it results in all-or-none behaviors. When the input pulse is strong enough to pitch the system state over the separatrix, an action potential is generated. Its trajectory follows along the unstable manifold and eventually returns to the resting state. The peak voltages of action potentials are approximately constant regardless of the stimulus voltage.

The phase plane structure of class II mode is shown in Fig. 8 . The two nullclines have an intersection: (S) is a stable equilibrium (resting state). The ascending limb of the V-nullcline plays a role as a threshold. However, the membrane potential does not always overshoot if the stimulus voltage is over it. Phenomenologically, Class II neurons are well known to not have a well-defined threshold, but a graded one [3]. The peak voltage of the action potential largely depends on the ratio between the two time constants, C_V and C_μ.

The phase plane structure of class I* mode is shown in Fig. 9 . As is the case for the class I mode, a stable manifold defines a separatrix. However, when the stimulus shifts the system state beyond the ascending limb of the V-nullcline, the membrane potential overshoots even if it is inside of the unstable manifold. This excitation mechanism is similar to class II mode, and the threshold is graded in this region.

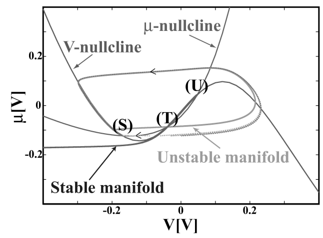

Fig. 7: Phase plane dynamics in class I mode.

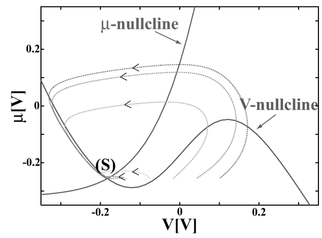

Fig. 8: Phase plane dynamics in class II mode.

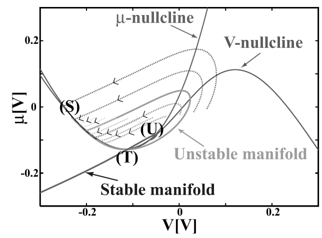

Fig. 9: Phase plane dynamics in class I* mode.

3.2 Responses to periodic pulse stimuli

The responses to periodic pulses of squid giant axons and the HH equations have been studied in detail. Class II models such as the HH model are well known to not only exhibit periodic but also aperiodic responses to periodic pulse stimuli depending on their amplitudes and interstimulus intervals, T_{stim}. In this section, we demonstrate that our circuitry exhibits chaotic responses to applied periodic pulses in several parameter regions.

We fixed the pulse width, W, to 0.5 msec and T_{stim} to 7.0 msec in class II mode and 11.0 msec in class I* mode. The stimulus strength, V_{stim}, was varied. When V_{stim} was low, our circuit did not fire. As V_{stim} was slightly increased, nonperiodic responses occurred. A typical nonperiodic response in class II mode is shown in Fig. 10. The trajectory is not a closed curve but a complex pattern.

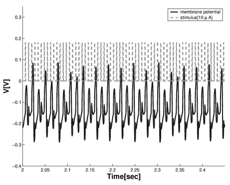

(a) Time series.

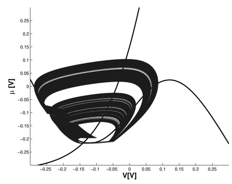

(b) Trajectory in μ-V phase plane.

Fig. 10: Nonperiodic responses to periodic pulse stimuli (class II mode).

As we can see from Fig. 11, class I* mode also generated nonperiodic responses. We examined the responses to periodic pulse stimuli in class I mode. However, we did not find any parameter sets that caused nonperiodic responses. The generation of nonperiodic responses may need the threshold to be graded as in the case of class II neurons. Class I* mode has this kind of threshold as noted earlier.

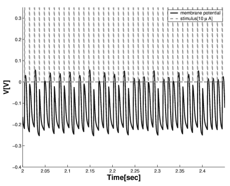

(a) Time series.

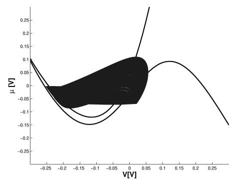

(b) Trajectory in μ-V phase plane.

Fig. 11: Nonperiodic responses to periodic pulse stimuli (class I* mode).

We focused on the membrane potential at 0.5 msec after the falling edge of stimulus current. We call this voltage V_{delay}. Figure 12 shows return maps for V_{delay} corresponding to Figs. 10 and 11, and $V_{delay}(n)$ is plotted versus $V_{delay}(n+1)$. Both modes represent single-valued maps. The Lyapunov exponents we estimated for the class II and I* modes were 1.833 ± 0.00246 and 1.691 ± 0.00013. Note that both are positive, which indicates that these nonperiodic responses are chaotic with orbital instability.

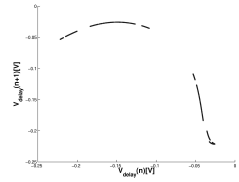

(a) Class II mode.

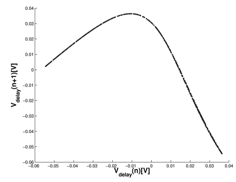

(b) Class I* mode.

Fig. 12: Return map of V_{delay}.

4 Concluding Remarks

We developed a two-dimensional electronic neuron model using MOSFETs that can achieve the three significant neuron modes: class I, II and I*. We reported numerical simulation results for responses to singlet and periodic pulse stimuli. We showed that class II and I* modes have graded threshold mechanisms, and that they exhibit chaotic responses to periodic pulse stimuli. Our circuitry is compatible with standard CMOS processes. Hence, it can be easily implemented in an analog very-large-scale integrated circuit (VLSI), and large-scale network can be constructed.

Acknowledgments

This study was partially supported by the Superrobust Computation Project in 21st Century COE Program on Information Science and Technology Strategic Core and by the Advanced and Innovational Research program in Life Science from the Ministry of Education, Culture, Sports, Science, and Technology, the Japanese Government.

References

[1] Takashi Kohno and Kazuyuki Aihara, "A MOSFET-based model of a Class 2 Nerve membrane.", *IEEE Trans. Neural Networks*, Vol. 16(3), pp. 754-773, 2004.

[2] H. Fujii and I. Tsuda, "Itinerant dynamics of class I* neurons coupled by gap junctions.", *Computational Neuroscience: Cortical Dynamics Lecture Notes In Computer Science*, Vol. 3146, pp. 140-160, Springer-Verlag, 2004.

[3] Rinzel J. and Ermentrout G. B., "Analysis of Neural Excitability and Oscillation.", *In Koch C., Segev I.(eds) Method in Neuronal Modeling, The MIT Press, Camblige Mass.*, 1989.

The Eleventh International Symposium on Artificial Life and Robotics 2006 (AROB 11th'06),
B-con Plaza, Beppu, Oita, Japan, January 23-25, 2006

A Stepping motor control for Electric Vehicle

Masanori Sugisaka , Khairunizam Ahmad
Department of Electric and Electronic Engineering
Oita University
700 Oaza Dannoharu, Oita, Japan
Tel: +81-97-554-7831
Fax: +81-97-554-7841

Email: msugi@cc.oita-u.ac.jp, hinagata96@hotmail.com

Abstract

This paper is discussing about a stepping motor, which is used to control acceleration and brake's paddle of an electric vehicle. The moving angle of the stepping motor will decide a position of the paddles and also the electric vehicle itself. As a conventional electric vehicle, the user controls the position of the acceleration and brake paddle manually by pushing or releasing it to a desire position. In this project I used the electric vehicle called MINI-SWAY, which is restructured to be fully controlled by computer mode that play the same role as a user in a conventional electric vehicle.

1. Introduction

The twenty first century will be the environmentally century. One of the most pressing needs of our life is an alternative clean, efficient, intelligent and environmentally friendly for urban transport system. Electric vehicle (EV) offer a solution for improving air quality, reducing the reliance on fossil fuel, and enhancing energy efficiency. Furthermore, electric vehicle equipped with artificial intelligent, intelligent navigation, advanced control and communication, positioning system can improve traffic safety and road utilization. The main important reasons why we are thinking about automatics or intelligent vehicle are to prevent incident happen on road and also to avoid traffic control such in a big city [1]. The long-term goal of the EV is the implementation of the Automated Highway System (AHS), which will include completely "hand-off" driving in which vehicles are fully automatically controlled once they enter the system. Achieving this goal requires significant research in system modeling, lateral (steering) control [2][3], speed control, and combined lateral and speed control of the vehicles. This paper is the initial step in solving the problem of combining a lateral control and a speed control of the electric vehicles. As mentioning in the title of this paper, a detail research on the steeping motor must be done in term of the stability of the system. This paper describes a characteristic of the stepping motors, which are used as a speed and brake control for EV to move a long a target line using a lateral control algorithm. The second section will introduce the devices that are used to control the stepping motors, which is played an important role that must be understand and to suit with a lateral control. The third section will show a characteristic of the steeping motors used in our EV, which is the result of the experiment. The forth section will be the conclusion and a further research related to the complete EV system will also be introduced.

2. Devices

Sensor technology will have a critical role in intelligent EV operation and safety. Sensors will be needed for lateral position, speed, and brake etc for vehicle control. As in lateral control, discrete markers [4] were introduced that shows a great promise on control sensing of EV. For a better image of my project equipments, lets introduce all of the important devices in general. Electric vehicle in our laboratory is composed of 6 ultrasonic sensor E4B-LS704 having 70cm as detection distance. The sensor can automatically slow down the speed when detecting unexpected thing. The host computer CPU II Celeron 466MHz does the control of all motors and devices connected to motor driving card PCI-7208 and input output port IBX-2726C as an interface to the controller. The NEC computer is used for image processing having a Liquid Crystal Display touch panel. These PCs are connected to hardware via controller card. The hardware uses are stepper motors, a servomotor [5]; drive frame grabber and a serial port for camera control. In addition 40x of chip ROM and 256 Mbytes of RAM and 10/100m of LAN are used. A 24V lead acid is used as the main power supply for all motors and devices on the vehicle. According to this DC supply 24V is directly used for motors, sensors and LED while the computer responsible for processing the image receives an AC 100V from AC/DC inverter. In our MINI-SWAY EV the steeping motor is used to drive a DC brush less motor to rotate a rear tire before moving. As a feedback to us, a rotary encoder E6C2-CWZ6C from OMRON is used. The rotation numbers of the tire is determined depending on the output pulse from rotary encoder to a controller board PCI-7208. The encoder is used as a sensor to detect the direction and the numbers of rotation of the rotating tire. It has a specification 100 Pulse Per Revolution. It is means that for a complete one revolution of the rotary encoder will produce 100 pulses as an input to a motor controller board. Figure 1 shows a construction of the encoder basis, which is used in our experimental equipment.

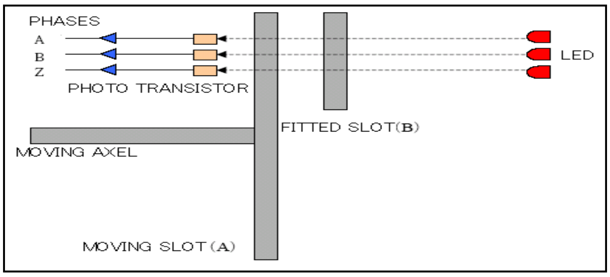

Fig. 1 Rotary Encoder

There are two stepping motors used in our EV system. It is needed for controlling a DC Brush less motor for rotating a rear tire and also for pulling the brake pedal up and down. In this paper, the experiment is done on the steeping motor, which is control, the DC Brush less motor only. Let see the parameters of the signal commands (Table 1) that we set to create an input pulse from a controller board to stepping motor driver.

Table 1 Signal Parameters of the commands

PARAMETER	DISCRIPTION
dwMode	MTR_ACC_SIN/S curve action
dwLowSpeed	Start up speed range from1-1,000,000[Hz]
dwSpeed	Stable speed of the motor range from 1-1,000,000[Hz]
dwAcc	Acceleration pulse numbers PULSE/mSec
dwDec	Decleration pulse numbers PULSE/mSec
dwSSpeed	Speed for S curve range from 1-499,999[Hz]
nStep	The number of pulse

The signal parameter as describes in Table 1 is very important because the changes of it will cause a huge changing of the tire rotation. As in the lateral control for a machine vision [6], the same parameters were used for controlling a steering angle while running on line. For a detail understanding, Figure 2 shows a graph related to the signal parameters.

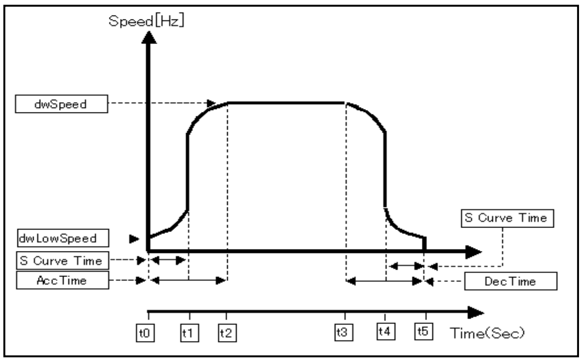

Fig. 2 The Relation Between Signal Parameters

In combining the lateral control and the speed control for getting a single complete intelligent EV system dwSpeed (Hz) and nStep (Number of Pulse) play an important role that must be taken onto account. The characteristic of the stepping motor that drive a DC Brush less motor should be studied in detail to suit the condition of the lateral (steering) control. In my research, the main target is to archive a perfect steering control and at the same time another control strategies will be added such as brake, speed, signal etc in term of stability and safety of the system [7]. The next is a third section that will discuss the experimental method and the experimental result.

3. Experimental method and result

In the explanation as above, the purpose of this paper is to find the characteristic of the steeping motor that drive a DC Brush less motor and running the rear tire of the EV. Also, that characteristic must fulfill the requirement or suit with the lateral algorithm, which is becoming the main objective of the project. To archive this, giving a certain pulse to a steeping motor driver was done in the experiment. As a feedback to us, the algorithm has also been studied on how to obtain the present situation of the rear tire after giving a certain pulse to a steeping motor. Later, in the next project the result will be an important factor in determining the stability of the EV by combining a lateral control and a speed control. The rotational speed of the rear axle can be deduced by taking definite difference of the rear encoder position, and normalizing for the number of pulse per revolution n as below,

$$\boxed{\omega = \frac{1}{n}\frac{p_a - p_{a-1}}{t_a - t_{a-1}}} \qquad (1)$$

For a successive reading of the axle encoder p_{a-1} and p_a at time t_{a-1} and t_a. The Rotation Per Minutes of the tire can be derive as below,

$$\boxed{RPM = \frac{1}{n}\frac{\Delta Pulse}{\Delta Time}} \qquad (2)$$

$$\boxed{\begin{aligned} \Delta Pulse &= P_t - P_{t-1} \\ \Delta Time &= t - (t-1) \end{aligned}} \qquad (3)$$

$$\boxed{n = EncoderSlot \times RatioValue}$$

(4)

Equation from eq.1-eq.4 is used to determine the rotation of the tire in RPM. The result of the experiment is shown by plotting a graph of RPM versus Time after giving a certain pulse to a steeping motor. Ten times experiment was done with a different output pulse from a controller board, but here I will shows one of the results with output pulse is 600 Pulse.

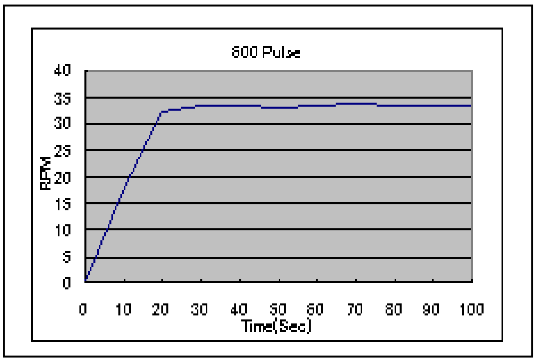

Fig. 3 RPM Vs Time

From the experiment the relation between RPM and PULSE was also obtained by plotting the graph RPM versus PULSE as shown Figure 4.

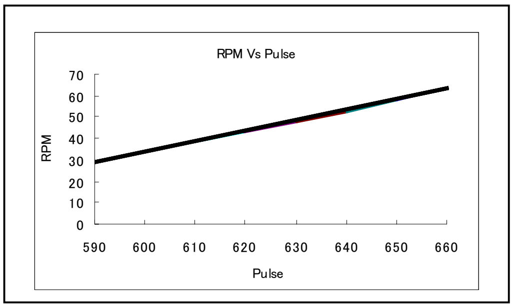

Fig. 4 RPM Vs Pulse

4. Conclusion

The characteristic of the steeping motor, which is driven a DC Brush less motor has been studied and give a good response for combining with a lateral control in the next project. The feedback of the running tire is obtained by using a sensor, rotary encoder. But a detail studies should be done on mechanical devices, which is connected from DC Brush less motor to a rear tire. Even a small failure happens on it, will cause a precision problem while comparing a desire position of process and a present process. Before combining with a steering control, which is the main objective on my project, a single motor control is also important and the experiment is planned after this. The use of control methodology in motor control has been discussed in a numbers of papers. A PID or Fuzzy control methodology may be applicable for controlling motor in EV. The main problem may be happen because the steeping motor is not directly control the rear tire. A steeping motor is easy to control because it move step by step of angle. The problem is DC Brush less motor. It will be discussed in the next paper.

References

[1] T.A. Lasky, B. Ravani (1993), *A Review of Research To Automated Highway System*, AHMCT Research Report, pp. 5-7

[2] Hessburg. T and Tomizuka. M (1991), *A fuzzy rule-based controller for automotive vehicle guidance*. Technical Report UCB-ITS-PRR-91-8

[3] S. Tsugawa, I. Mori, S. Kato (1998), *A Lateral Control Algorithm for Vision-Based Vehicle with a Moving Target in the Field of View*, IEEE International Conference on Intelligent Vehicles, pp. 41-45

[4] Zhang W.B (1991), A Roadway information system for vehicle guidance/control, Vehicles Navigation & Information System Conference Proceedings, pp. 1111-1116

[5] M. Sugisaka, M. Zacharie (2002), *The Control of the EV Steering Wheel using an AC Servomotor,* The 21st SICE, pp.39-42

[6] T. Tokuda (2005), *A Machine Vision for Electric Vehicle,* Masters thesis Oita Uni.

[7] Novak, R. J (1992), *Diagnosis of System Fault, Vehicle Electronic Meeting Society's Need: Energy, Environment, Safety,* pp.163-170

The Eleventh International Symposium on Artificial Life and Robotics 2006 (AROB 11th'06),
B-con Plaza, Beppu, Oita, Japan, January 23-25, 2006

Reinforcement Learning with Self-Instruction by using dual Q-tables

Osamu NISHIMURA[1)] Hirokazu MATSUI[2)] Chieko HIOKI[3)] Yoshihiko NOMURA[2)]
1) Graduate School of Engineering, Mie University. 2) Faculty of Engineering, Mie Univ.
3)Toyota Communication Systems Co., Ltd.
Address Kurima-machiya 1577, Z, 514-8507, Japan
voice: +81-59-231-9692; E-Mail: nosamu@robot.mach.mie-u.ac.jp

Abstract

In this paper, we propose the Q-learning method that selects proper actions of robot in unknown environment by using the Self-Instruction based on the experience in known environment. Concretely, it has two Q-tables, that are updated at the same time. One is smaller, based on a partial space of the environment. The other is lager, based on the whole space of the environment. The smaller is used for the knowledge storing as self-instructing. The larger is used for the experiment storing.

We simulated and compared the proposed method with the simple method under conditions with several rates of proper actions by self-instruction. As a result of the simulation, we showed that the proposed method is more effective than the ordinaries.

1 Introduction

In this paper, we propose an efficient learning algorithm using a Self-Instruction for an autonomous robot. When human being encounters a known environment, he acts based on his experience. When he encounters an unknown environment, he acts based on his knowledge, that is compressed his experience. In many cases, his knowledge is effective, and he can acquire his target. Even if not effective, he stacks the experience for the next chance. We think that human being has two kinds of tables for his effective actions, which are for knowledge storing and for experience storing. We aim at making an efficient learning algorithm by adding the human inference [Hioki:01]. The reduction on the trial frequency is important for reinforcement learning under an actual environment. In the researches such as [Takahashi:03] [Uchibe:04], learning modules are arranged hierarchically. In the researches such as [Katayama:04], the learning is gradually changing based from on prior knowledge to on profit sharing. We propose the method based on Q-learning, that has two Q-tables for knowledge and for experience, and updates two Q-tables at the same time, so that the trial frequency tries to be decreased.

2 Principle

2.1 Concept

Here, we describe the proposed reinforcement learning method with Self-Instruction. The proposed methods make two Q-tables update at the same time, one is larger for experience storing, the other is smaller for knowledge storing. We think the following, an experience is one example in the environment, so we set the Q-table for the experience to the whole space of the environment, and knowledge is compressed the experience in the environment, so we set the Q-table for the knowledge to a partial space of the environment, The smaller Q-table (for the knowledge storing) makes the learning finish earlier. The larger Q-table (for the experience storing) makes the learning be even in more detail.

This research aims at the method that makes be learned the environment earlier and in more detail by using these two Q-tables at the same time while switching by information entropy by each Q-table.

2.2 Materialization

Here, we materialize the concept in the above paragraph to the algorithm of the proposed method, as shown in **Fig. 1**.

(1) Set Environment: The learning environment is prepared for a learning agent. In the environment, the proper action is defined. The agent can know indirectly the environment by getting rewards.

(2) Init Q-tables: The agent initializes the two Q-tables to set each Q-value to an init value.

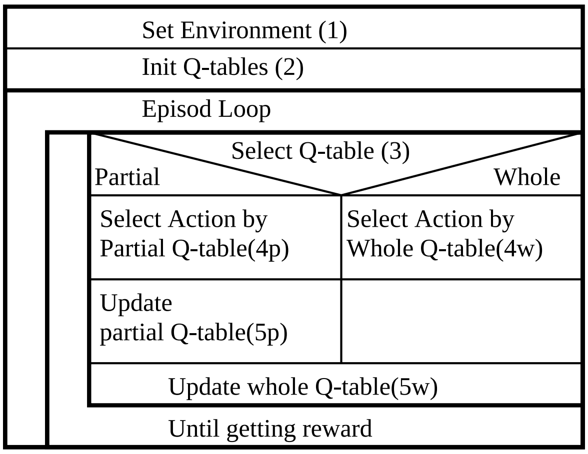

Fig. 1 NS chart of the proposed method

(3) Select Q-table: The agent selects the Q-table with lower information entropy$H(s)$, out of the partial and the whole Q-table, that is calculated by **Eq. 1**.

$$H(s) = \sum_{a \in A} p(a \mid s) \log_2 \frac{1}{p(a \mid s)} \qquad (1)$$

where $p(a \mid s)$ is a probability of selecting action a at the state s, that is defined by the following **Eq. 2**. We think that it means Q-table is effective, that the entropy of Q-table is low.

(4) Select Action (for both Q-tables): The agent decides the action by the Boltzmann selection used generally on Q-learning. The selection probability of action a is shown by **Eq. 2**.

$$p(a \mid s^k) = \frac{\exp(\frac{Q(s^k,a)}{T})}{\sum_{a' \in A} \exp(\frac{Q(s^k,a')}{T})} \qquad (2)$$

where $p(a|s^k)$ is probability of selecting action a on state s^k, k is times, T is temperature.

(5) Update Q-table (for both Q-tables): Q-value is updated by **Eq. 3**. The set of equations is used standard with updating Q-value.

$$\begin{array}{rcl} Q(s^k,a) & \leftarrow & (1-\alpha)Q(s^k,a) + \alpha(r + \gamma V(s^{k+1})) \\ V(s^{k+1}) & = & \max_{a \in A} Q(s^k,a) \end{array} \qquad (3)$$

where s^k is current state, s^{k+1} is the next state, a is selected action, r is reward, α is learning rate, γ is discount rate.

3 Experiment

We compare the proposed method with the ordinary method by simulation in the three environment. We simulate the proposed method with the two Q-tables, one is smaller, based on the partial space of the environment, the other is larger, based on the whole space of the environment, and simulate the ordinary method with the Q-table for the partial space, and the ordinary method with the Q-table for the whole space. Here, the Q-table for the whole space can represent perfectly for the three environments, but the Q-table for the partial space can represent perfectly for one environment (case 1), half for another (case 2), not at all for the other(case 3). We verify that the proposed method is effective in the above three cases.

3.1 Experiment condition

We simulate the methods in the environment of 20 cells arranged like a ring, as shown in **Fig. 2**.

Fig. 2 Experimental Environment at certain time

An agent exists on a cell. The agent can move from 1 step to 5 steps forward at a time. Each cell has 1 out of 6 colors (Red, Yellow, Green, Cyan, Blue, Magenta), the color is changed by each unit time. The agent gets reward, in the case that continuous 3 times, agent's actions are matched with the actions that are pre-decided by the current cell and the current color of the cell. An agent starts at a random cell. We define an episode to be time until getting reward, and define one trial to be 100 episodes.

The proposed method has two Q-tables, as shown in **Fig. 3**. and the ordinary method has each Q-table. We define Q-tables for the whole space and for the partial space to be the following. Q-table for the whole space: It has 3 axes, one is positions(20), another, colors(6), the other, actions(5). Q-table for the partial space: It has 2 axes, one is positions(20), the other, actions(5). We simulate in the three types of the environments:

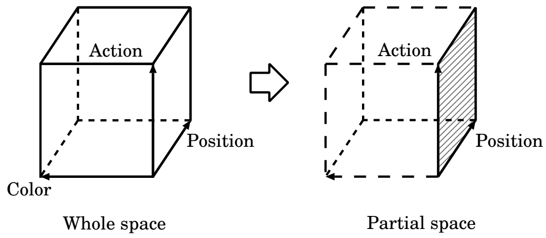

Fig. 3 Q-tables for the partial space and the whole space

Case 1 : The environment is enough represented by the Q-table for the partial space. Concretely, in this environment, the agent can decide the optimal action only with information of position, without information of colors. In other words, all the optimal actions are decided only by the Q-table for the partial space in the environment. We think that Self-Instruction is perfect effective.

Case 2 : The environment is half represented by the Q-table for the partial space. Concretely, in this environment, the agent can decide the optimal action at 10 out of 20 positions on the ring, only with information of positions, and cannot at the rest. In other words, half actions are decided by the Q-table for the partial space, but the other half actions can be decided only by the Q-table for the whole space. We think that Self-Instruction is half effective. In this case, we expect that the proposed method is more effective than the ordinary.

Case 3 : The environment is not represented at all by Q-table for the partial space. Concretely, in this case, the agent cannot decide the optimal action only with information of positions, and it needs information of the color at that time more. In other words, no action is decided only by the Q-table for the partial space. All the actions are decided only by the Q-table for the whole space. In short, Self-Instruction is not effective at all.

The Q-values are initialized to 0.0, the reward$r$ is set to 1.0, the learning rateα is set to 0.9, the discount rateγ is set to 0.005, The threshold of the learning degree of each space is set to 0.1. The temperature T of Boltzmann selection is set to 0.1.

3.2 Results and discussion

Here, we simulated the proposed method with the Q-table for the partial space and the Q-table for the whole space(PM), the ordinary method with the Q-table for the partial space(OMP), and the ordinary method with the Q-table for the whole space(OMW) in each case from 1st episode to 100th. Each graph is the average of 1000 trials.

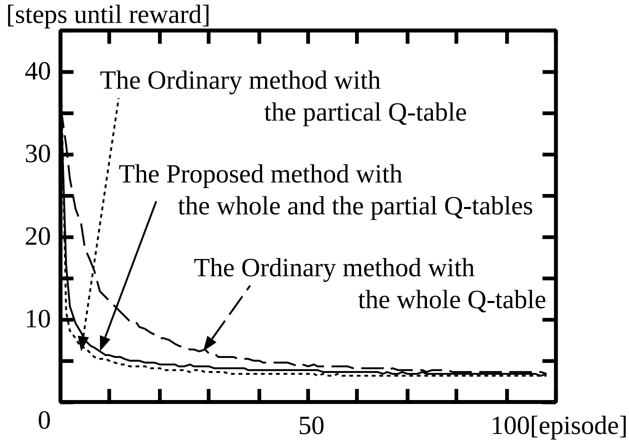

Fig. 4 Case1: Self-Instruction is perfect effective.

The result of the case 1 is shown in **Fig. 4**. In the case 1, the agents with all the three methods, PM, OMP and OMW, acquired the optimal value respectively. The agent with OMP converged earlier than the agents with PM and OMW, but the agent with PW converged almost as early as the agent with OMP. The agent with OMP learned the environment the most efficiently, since the partial space was optimal for the environment. The agent with OMW learned it not efficiently, since the whole space was redundant. The agent with PM learned it almost efficiently, since the Q-table for the partial space is almost used, the Q-table for the whole space is a few used. In the case 1, PM was almost as effective as OMP, more effective than OMW.

The result of the case 2 is shown in **Fig. 5**. In the Case 2, the agents with PM and OMW acquired the optimal value respectively. But the agent with OMP acquired not optimal value, since the agent with OMP was able to decide only half actions and had to select the rest half actions at randam. The agent with PM learned earlier than the agent with OMW, since at first the agent with PM depended on the Q-table for the partial space. The agent with PM learned the optimal

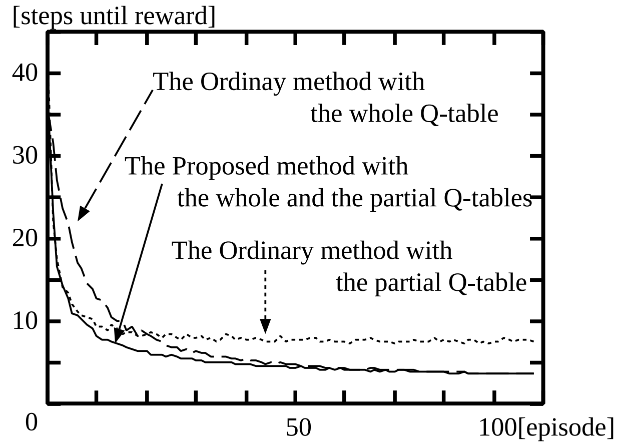

Fig. 5 Case2: Self-Instruction is half effective.

value since at last the agent with PM depended on the Q-table for the whole space. In the case 2, PM was more effective than the ordinary methods.

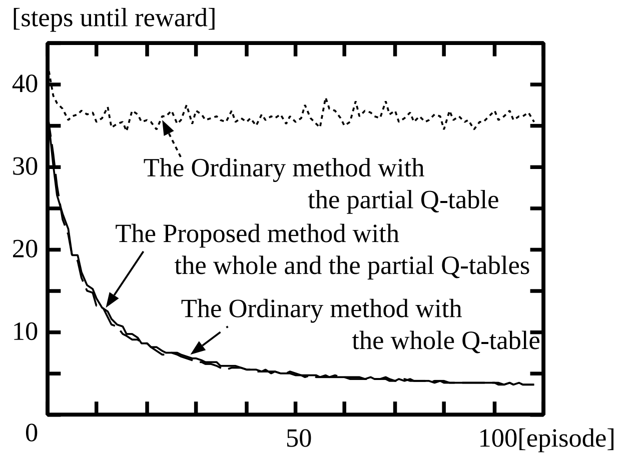

Fig. 6 Case 3: Self-Instruction is not effective at all.

The result of the case 3 is shown in **Fig. 6**. In the Case 3, the agents with PM and OMW acquired the optimal value respectively. But the agent with OMP did not learned it at all, since the agent with OMP was able to decide no actions or had to select any action at randam. The agent with PM learned the optimal value since the agent with PM learned the environment with using the Q-table for the whole space without using the unavailable Q-table for the partial space. In the case 3, PM was almost as effective as OMW, more effective than OMP.

We verified that PM is more effective in any case, by simulating in the above three cases, that represent any cases.

4 Conclusion

In this paper, we proposed the Reinforcement Learning Algorithm with Self-Instruction by using dual Q-tables for a partial space and for a whole space. and verified that the proposed method is more effective than the ordinaries. In the future, we will study a method that finds an effective partial space on learning. We will expand the relation between a partial space and a whole space to multilayer.

References

[1] Chieko HIOKI, Hirokazu MATSUI, Yoshihiko NOMURA, "Reinforcement Learning by Using a Self-Instruction for Actions in Unknown Environment," *The 44th technical committee of Special Interest Group on Fundation of Artificial Intelligence(SIG-FAI)*,2001.

[2] Yasutake Takahashi, Minoru Asada, 'State-Action Space Construction for Multi-Layered Learning System," *Journal of the Robotics Society of Japan*, Vol. 21 No. 2, pp.164–171, 2003.

[3] Eiji Uchibe, Kenji Doya, "Hierarchical Reinforcement Learning for Multiple Reward Functions," *Journal of the Robotics Society of Japan*, Vol. 22 No. 1, pp.120–129, 2004.

[4] K. Katayama, T. Koshiishi, H. Narihisa, "Reinforcement Learning Agents with Analystic Hierarchy Process," *Transactions of the Japaneses Society for Articicial Inttelligence*,Vol. 19, No. 4, pp.279–291, 2004.

The Eleventh International Symposium on Artificial Life and Robotics 2006 (AROB 11th'06),
B-con Plaza, Beppu, Oita, Japan, January 23-25, 2006

Position Estimation of a Mobile Robot Using U-SAT (Ultrasonic Satellites)

Su Yong Kim, Chang Sup Kim
Department of Mechanical and Intelligent Systems Engineering
Pusan National University
Busan, 609-735, KOREA

Sang Min Kim
Department of Interdisciplinary Program in Mechatronics
Pusan National University,
Busan, 609-735, KOREA

Man Hyung Lee
School of Mechanical Engineering,
Pusan National University,
Busan, 609-735, KOREA

Abstract

In this paper, we propose a new method to find an absolute position by using ultrasonic sensors. In order to evaluate the performance, U-SAT (Ultrasonic Satellites) is compared with the RTK (Real Time Kinematics)-DGPS (Differential Global Positioning System). As a result, the possibility of using U-SAT can be discussed as pseudolites or pseudo-satellites in the place where GPS is not available. Experiment was performed in the case that the mobile robot moves to the target point using U-SAT, that is, absolute positioning method. The performance of U-SAT is estimated from the result of the experiment.

1 Introduction

The process of finding robot in environment is a major concern in mobile robot navigation. To measure the position of a mobile robot, a variety of studies are going on and robot positioning has been done in two basic methods. They are not only absolute and relative positioning but also a combination of them.

The dead-reckoning method has been widely used as one of the methods of relative positioning. Dead-reckoning method uses the encoded information which gains the wheels to determine the position of the robot. But because of wheel slippage, mechanical tolerance and surface roughness, this method has its unbounded accumulation of errors. So the real position is hardly maintained as it moves longer distance [1]. Other methods use sensors such as a rate-gyro and a magnetic compass. A rate-gyro accumulates errors continuously with the passage of time and a magnetic compass does not function well at the place where the magnetic fields vary from position to position. For these reasons, it is hard to find accurately the location of the robot moving far away only by using relative positioning.

On the other hand, absolute positioning is accomplished by using a CCD camera, infrared light, global positioning system (GPS), and ultrasonic sensor. Vision system by CCD camera requires complicated signal processing to analyze images. In addition, it is expensive and highly depends on camera calibration and image sensitivity [2]. Positioning by using infrared light is easy and inexpensive. However, this method leads to problems such as low performance and limitations in terms of its application in an outdoor environment [3]. The GPS can give accurate information to identify locations. By a differential GPS, the accuracy of positioning is also improved. However, this type of sensor usually provides measurements at 1-10 Hz. This sampling rate may not be sufficient if the dynamics of a positioning object changes relatively fast. Besides, it does not operate well in the place where no GPS satellite signal is available or where there are less than four visible satellites [4]. In addition, pseudo-satellites for indoor or outdoor places have been re-searched. Ultrasonic ranging systems, which are similar to the basic concept of GPS, have advantages such as low costs and a high update rate a disadvantage is its low accuracy which is caused by air turbulence, humidity, temperature dependence, transmitter misalignment and transmitter bandwidth [5]. In contrast to the conventional GPS, it is possible to build up cell structures in widely ramified buildings.

In the measurement of the distance using direct ultrasonic waves, the method with high precision is proposed [6]. Absolute positioning system using ultrasonic sensors based on this method is represented as U-SAT (Ultrasonic Satellites). So in order to evaluate the performance of U-SAT, it is compared with RTK-DGPS that is more accurate than any other absolute positioning system. The possibility of using U-SAT as pseudolites in the place where GPS is not available is discussed. And Experiment was performed in the case that the mobile robot moves to the target point using U-SAT. The performance of U-SAT is estimated from the result of the experiment.

2 Concept of U-SAT

The measurement of the distance using the ultrasonic waves is calculated with sound velocity and the delivering time. TOF (Time of Flight) is defined as the time difference between transmitter and receiver. It is shown in Fig.1. The distance is

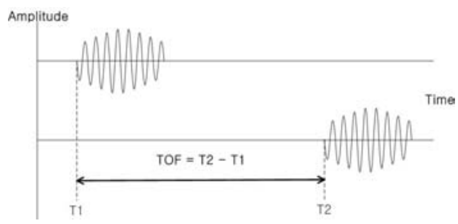

Fig.1 Definition of TOF

determined in Equation (2) and sound velocity is represented as a function of temperature.

$$TOF = T2 - T1 \tag{1}$$

$$d = c \times TOF + d_0 \tag{2}$$

$$c = 331.5 + 0.60714T \tag{3}$$

Where, d is distance and c is sound velocity in the air temperature of T.

This shows the detection accuracy of about 2mm by the ultrasonic frequency detection method [6]. And the distance between separated transmitter and receiver is calculated by direct ultrasonic waves. U-SAT is based on this method. Ultrasonic transmitters function as ultrasonic satellites and locate on the fixed places whose coordinates are known. So ultrasonic receivers receive ultrasonic waves transferred from ultrasonic satellites and the distance between ultrasonic receivers and ultrasonic satellites is calculated. The basic idea of U-SAT is similar to that of GPS. Although ultrasonic receivers exist in the ultrasonic satellites, the position of ultrasonic receiver is calculated respectively. Therefore multiple mobile robots can be used.

In Fig.2, U-SAT consists of four ultrasonic satellites. In order to calculate the distance using ultrasonic waves, the time when ultrasonic satellite radiates ultrasonic waves must be measured. U-SAT does not inform the transmission time. So transmission time is known by using RF signal. U-SAT calculates the distance by measuring the time when the ultrasonic waves is received. It is supposed that there is no time delay during receiving RF signal. In Fig.2, U-SAT transmitter (1) transfers synchronized RF signals to other U-SAT transmitters and U-SAT receiver at the period of 83ms. They receive synchronized RF signals and find when ultrasonic waves are radiated. In accordance with this period, ultrasonic satellites radiate ultrasonic waves by turns and U-SAT receiver calculates the distance by using Equation (2). Synchronized RF signals are transferred with the period of 83ms in order to avoid the interference of ultrasonic waves and the influence of the reflection of them and this period can be flexibly regulated according to the environment.

Fig.3 shows the timing diagram for ultrasonic receiver to be synchronized by RF signal. After U-SAT receiver receives ultrasonic waves which radiated ultrasonic satellites respectively, each distance d1, d2, d3, and d4 between ultrasonic radiated ultrasonic satellites respectively, each distance d1, d2, d3, and d4 between ultrasonic

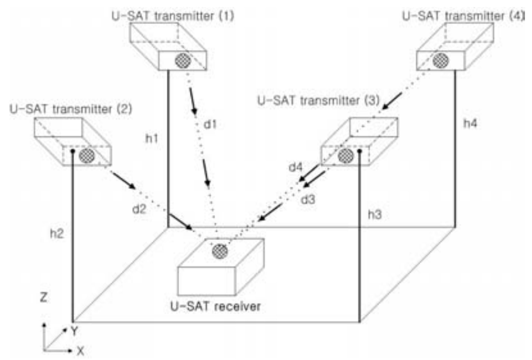

Fig.2 System description

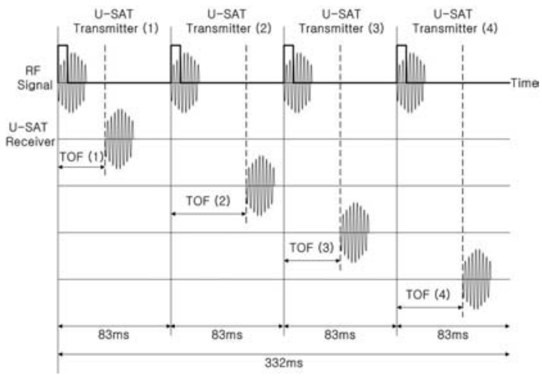

Fig.3 Timing diagram

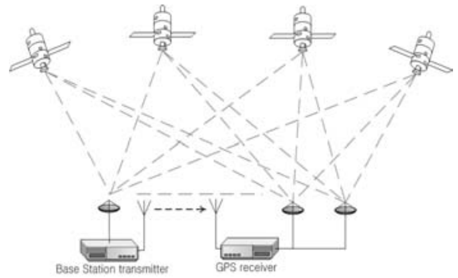

Fig.4 RTK-DGPS

waves and its satellites are calculated. The coordinate of the ultrasonic receiver can be obtained by L.M.S (Least Mean Square method). The sampling time of GPS is 1Hz while that of U-SAT is 3Hz shown in Fig.3. Since U-SAT is more flexible and faster than GPS, it can frequently acquire the position information.

3 RTK-DGPS

GPS is a space-based positioning, navigation, and timing system developed by U.S. Department of Defense (DoD). GPS receiver receives GPS signals from more than four GPS satellites and calculates its position real time. But it doesn't function well in the place where GPS satellite signal doesn't reach or visible satellites are less than four.

In order to increase the accuracy of the position error, DGPS is most frequently studied around the world. Usually, code differential positioning can satisfy positioning accuracy of meter level, while carrier phase differential positioning can achieve positioning accuracy of centimeter level for the real-time positioning in three dimensions. RTK realizes real-time positioning by the carrier-phase differencing algorithm in moving. As shown in Fig.4, its principle is that, the reference station transmits the collected raw carrier-phase and pseudorange measurements to the rover station, thus the rover station can calculate the coordinate by differencing algorithm. The accuracy of RTK-DGPS used in this experiment is 1.6 cm.

4 System Configuration

A system configuration is shown in Fig.5 in order to analyze the performance of U-SAT using DGPS. Four U-SAT transmitters are located on the four points of the rectangular in 1m height whose length and width are 5m and 3m respectively. And they are the ultrasonic receiver, GPS receiver, and the turntable which is used to evaluate the position information of U-SAT and GPS. The turntable rotates constant speed in proportion to the voltage and the length of the arms installed at the turntable is 1m. GPS and the ultra-sonic receiver are connected with the turntable by the arms on both sides. The performance of U-SAT using DGPS is analyzed. So the accuracy of U-SAT has been estimated comparing with GPS.

5 Experimental Results

In this experiment, the position information of GPS and U-SAT is respectively measured using the consisted experimental system. Since two positions information are represented in different coordinate system, centers of the circle created by each position information are accorded using transformation.

First the GPS and U-SAT receiver is fixed and the static position is measured during a few minutes. Shown in Fig.6, the errors of U-SAT are wider range than those of GPS. However the position information of GPS and U-SAT does not obtain the accumulative errors. Second in case the turntable rotates the constant speed the position information of U-SAT is compared with that of GPS. The experiment has been implemented at constant speed of 0.1 m/s, 0.2 m/s, 0.3 m/s, and 0.4 m/s. The circles of the position information using GPS and U-SAT are U-SAT does not obtain the accumulative errors. Second in case the turntable rotates the constant speed the position information of U-SAT is compared with that of GPS. The experiment has been implemented at constant speed of 0.1 m/s, 0.2 m/s, 0.3 m/s, and 0.4 m/s. The circles of the position information using GPS and U-SAT are shown in Fig.7.

In Fig.7, The errors of GPS are not influenced by the speed but those of U-SAT are increased as the speed is increased. Since the four U-SAT transmitters radiate ultrasonic waves by turns, the receiver can determine the position after U-SAT receiver finishes receiving the signals from all four

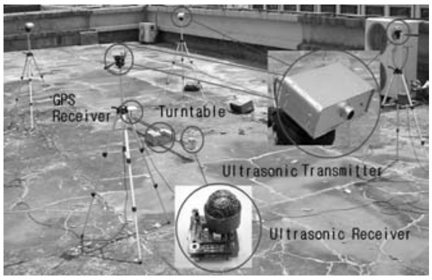

Fig.5 Experiment configuration

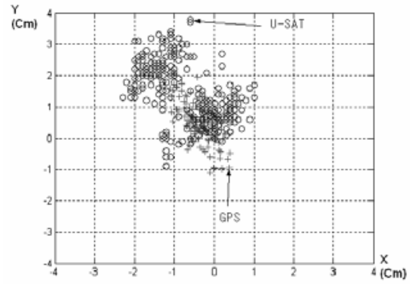

Fig.6 Experimental results of the static position (GPS: +, U-SAT: o)

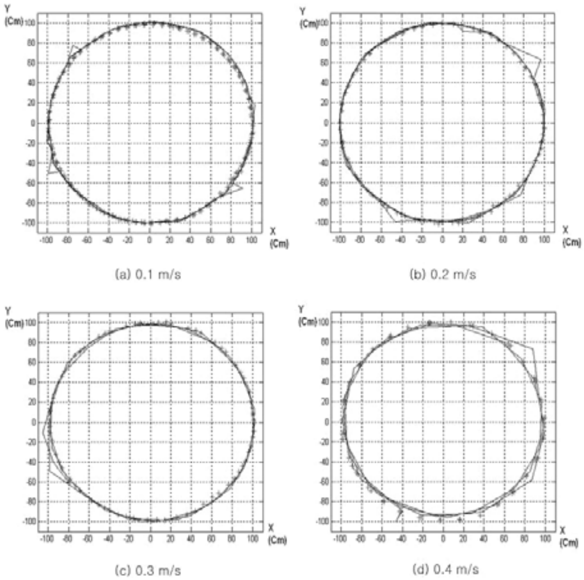

Fig.7 Experimental results of the dynamic position (GPS: +, U-SAT: line)

transmitters. Therefore the errors of U-SAT are influenced by the speed. It causes many problems at the high speed. To solve this problem, the sampling time of the system should be change or more U-SAT transmitters have to be used for faster reception. At the above experiment, the performance of GPS is better than that of U-SAT. However, U-SAT shows a good performance concerning price and has an improvement possibility through more researches. In case that several U-SAT receivers exist, the position of U-SAT receiver can be calculated respectively. Therefore U-SAT is very suitable for pseudolite system in the place where GPS is not available. Although U-SAT is affected by the condition of the outdoor environment, it is more stable at the indoor environment.

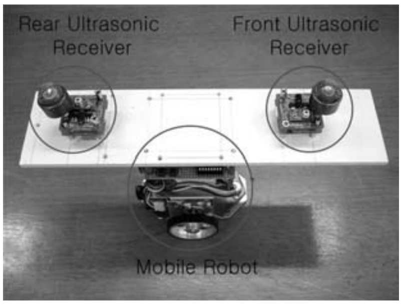

Fig.8 Configuration of the mobile robot

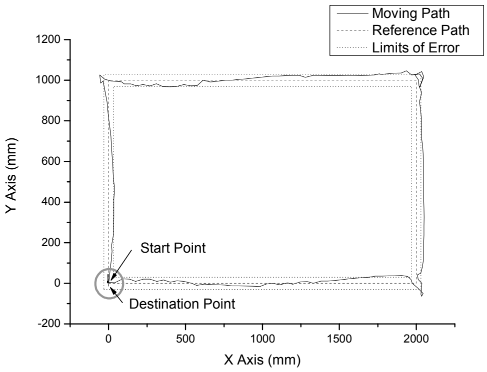

Fig.9 Position estimation result of the mobile robot

6 Position Estimation of a Mobile Robot

Fig.8 depicts the configuration of the mobile robot. Two ultrasonic receivers are mounted on the mobile robot so that they can obtain the position information and orientation. The localization information is sent to PC via bluetooth. And PC executes its trajectory tracking control. So the mobile robot moves along the reference path in a counterclockwise direction. As seen in Fig.9, the reference path is situated on the four points of the rectangular whose length and width are 2m and 1m respectively [7].

Experiment was conducted in order to verify that the mobile robot can move accurately along the reference path using U-SAT. Fig.9 shows the experimental result. A maximum translational velocity of 0.1m/s was used for this experiment, resulting in a maximum error of 3cm for this run. Experimental result using U-SAT shows that the position estimation of the mobile robot using U-SAT is closed for closed reference path. However, the accumulative error can be eliminated for this method using U-SAT. The experimental result shows good performance and is acceptable.

7 Conclusion

In this paper, the performance of U-SAT has been evaluated using RTK-DGPS that is more accurate than any other absolute positioning system. Though the performance of RTK-DGPS is better than that of U-SAT, the result of U-SAT is also acceptable. In case of the mobile robot which moves slowly or stops, the position information guarantees very stable performance. In Addition, U-SAT can be used as a proper system in the place where GPS is not available, such as indoor area. Finally Experiments were performed in the case that the mobile robot moves to the target point using U-SAT. The performance of U-SAT is estimated from the results of the experiment. The mobile robot can move accurately along the reference path using U-SAT. As a result of experiment, this method using U-SAT shows good performance and is suitable. Absolute positioning method using U-SAT can be applied to any indoor system that need absolute position information. There exist many problems mentioned above to solve such influences of speed and environmental conditions. Many researches are being implemented to improve the accuracy of U-SAT.

References

[1] Jae Hwan Kim and Poong Hyun Seong, "Experiments on orientation recovery and steering of autonomous mobile robot using encoded magnetic compass disc," *IEEE Transactions on, Instrumentation and Measurement*, Vol. 45, Feb, 1996, pp. 271~274.

[2] Kai-Tai Song and Wen-Hui Tang, "Environment perception for a mobile robot using double ultrasonic sensors and a CCD camera," *IEEE Transactions on, Industrial Electronics*, Vol. 43, June, 1996, 5293219, pp. 372~379.

[3] Y. Arai and M. Sekiai, "Absolute position measurement system for mobile robot based on incident angle detection of infrared light," *2003. (IROS 2003). Proceedings. 2003 IEEE/RSJ International Conference on, Intelligent Robots and Systems*, 2003, pp. 986~991.

[4] Alan G. Evans, Everett R. Swift, James P. Cunningham, Robert W. Hill, Geoffrey Blewitt, Thomas P. Yunck, Stephen M. Lichten, Ron Hatch, Stephen Malys, and John Bossler, "The Global Positioning System Geodesy Odyssey," *Navigation : Journal of The Institute of Navigation*, Vol. 49, No. 1, Spring, 2002, pp. 7~33.

[5] S. Y. Yi and J. H. Jin, "Self-localization of a mobile robot using global ultrasonic sensor system," *Journal of Control, Automation, and Systems Engineering*, Vol. 9, No.2, Feb, 2003, pp. 145~151.

[6] D. H. Lee, H. T. An, K. R. Baek, and M. H. Lee, "A study on resolution Enhancement in the detection of ultrasonic signal," *The KSAE Annual Fall Conference, Branch of Busan·Ulsan·Gyeongnam*, 2003, pp. 95~102.

[7] Y. Kanayama, Y. Kimura, F. Miyazaki, T. Noguchi, "A stable tracking control method for an autonomous mobile robot," *Robotics and Automation, 1990. Proceedings., 1990 IEEE International Conference on*, Vol. 1, 1990, 3863661, pp. 384~389.

Robotics Safety Issues For Human Welfare in an Automated Manufacturing System

Dr.Bhuvenesh Rajamony
Program Chairman
School of Manufacturing Engineering
Northern Malaysia University College of Engineering
01000, Kangar, Perlis, Malaysia
Email: bhuvenesh@kukum.edu.my

Dr.Mohd Rizon Juhari
Associate Professor
School of Mechatronic Engineering
Northern Malaysia University College of Engineering
01000, Kangar, Perlis, Malaysia
E-mail: rizon@kukum.edu.my

Abstract

The high degree of automation, that until recently was reserved for mass production only, is applied now, with the aid of robots and computer, also to small batches. This requires a change from hard automation in the production line to a flexible manufacturing system which can be more readily rearranged to handle new market requirements. Safety is an important factor in design for robots working in this manufacturing environment. The issue of robot safety in an automated manufacturing system deals with the design of a reliable control system to prevent malfunctions and operator's safety. Industrial robots have a wide range of potential applications in manufacturing systems because they are flexible and programmable themselves. Different robot configuration generates different characteristic working envelop shapes .The design of the work station layout and training of plant personnel are important. Robot application designers need to give more careful thought to persons who work within the confines of the robot workspace. The worker and the operator safety is the most important concern. The discussion follows the practical sequence in which one must think when designing a piece of automatically acting equipment. This paper highlights the safety issues of robots for human welfare in an automated manufacturing system.

Keywords:
Automated, Robotic design, Manufacturing, Plant personnel, Work safety

1. INTRODUCTION

The high degree of automation, that until recently was reserved for mass production only, is applied now, with the aid of robots and computer, also to small batches. This requires a change from hard automation in the production line to a flexible manufacturing system which can be more readily rearranged to handle new market requirements. The supervision of this factory will be performed by computer-integrated manufacturing (CIM) system, in which the production flow, from the conceptual design through the finished product, will be entirely under computer control and management. This involves the steps of design, including analysis and simulation, documentation, manufacturing planning and control, including material and machine scheduling, and factory automation, including materials processing, inspection, assembly, and materials handling. The application of robotics in companies implementing CIM requires that robot system become a part of the total CIM concept. Implementing a CIM system enterprise-wide requires extensive planning, many months and hard work, and a substantial investment in people and their welfare, hardware and software.

2. ROBOT ELEMENTS FOR SAFETY CONSIDERATION

An industrial robot is essentially a device that can move materials, parts, or tools from one point to another under programmed control without human intervention. It can also be easily taught to perform simple tasks such as pick-and-place or spot welding or painting. The types of servomechanisms used to control the motion along each axis are similar in each case. There are three basic components of an industrial robot for safety consideration: Manipulator, Controller, and Tooling.

(i) **Manipulator:** The manipulator consists of the base and arm of the robot, including the power supply, which may be electrical, hydraulic, or pneumatic. The manipulator is the device that provides movement in any number of degrees of freedom. The movement of the manipulator can be described in relation to its coordinate system, which may be cylindrical, spherical, anthropomorphic, or Cartesian. Depending on the controller, movement can be point-to-point motion or continuous-path motion.

(ii) **Controller:** The versatility of a robot arises from its multi-axis mechanical configuration and the robot controller. The ability to reprogramme the robot controller gives the flexibility to the robot to perform a wide range of actions. The controller contains various interfaces with both command devices and sensing units. The controller has to define the trajectory of the robot gripper with time and transform this trajectory, which is in Cartesian, into its base-frame coordinate system and finally into joint movements. Many of these tasks are to be performed in real time.

(iii) Tooling: Tooling is what enables the robot to do a particular job. Tooling is sometimes used synonymously with end effectors, although the latter has a more restricted meaning to apply to end-of-arm fixturing to grasp, lift, or turn. Tooling, on the other hand, has a broader context which can apply to power tools for drilling and grinding, as well as for painting and welding guns. Typical end effectors include electromagnets, hooks, vacuum cups, adhesive fingers, and bayonet sockets. Different robot configuration generates different characteristic working envelop shapes. The work volume refers to the space within the robot can operate.

3. APPLICATIONS OF ROBOTS IN MANUFACTURING

Industrial robots have a wide range of potential applications in manufacturing systems because they are flexible and programmable themselves. The use of sensors allows the robots to see, hear, and smell the environment. The robot controllers can be generally integrated easily into the manufacturing system environment and are capable of communicating with other programmable controllers. In hostile environments, such as foundries or forges, robots are often used for high-temperature handling, particularly in stamping operations. Feeding and unloading of machine tools is an area in which robots are used, especially with automatic lathes.

Automated assembly operations using industrial robots and circular and linear transfer lines.

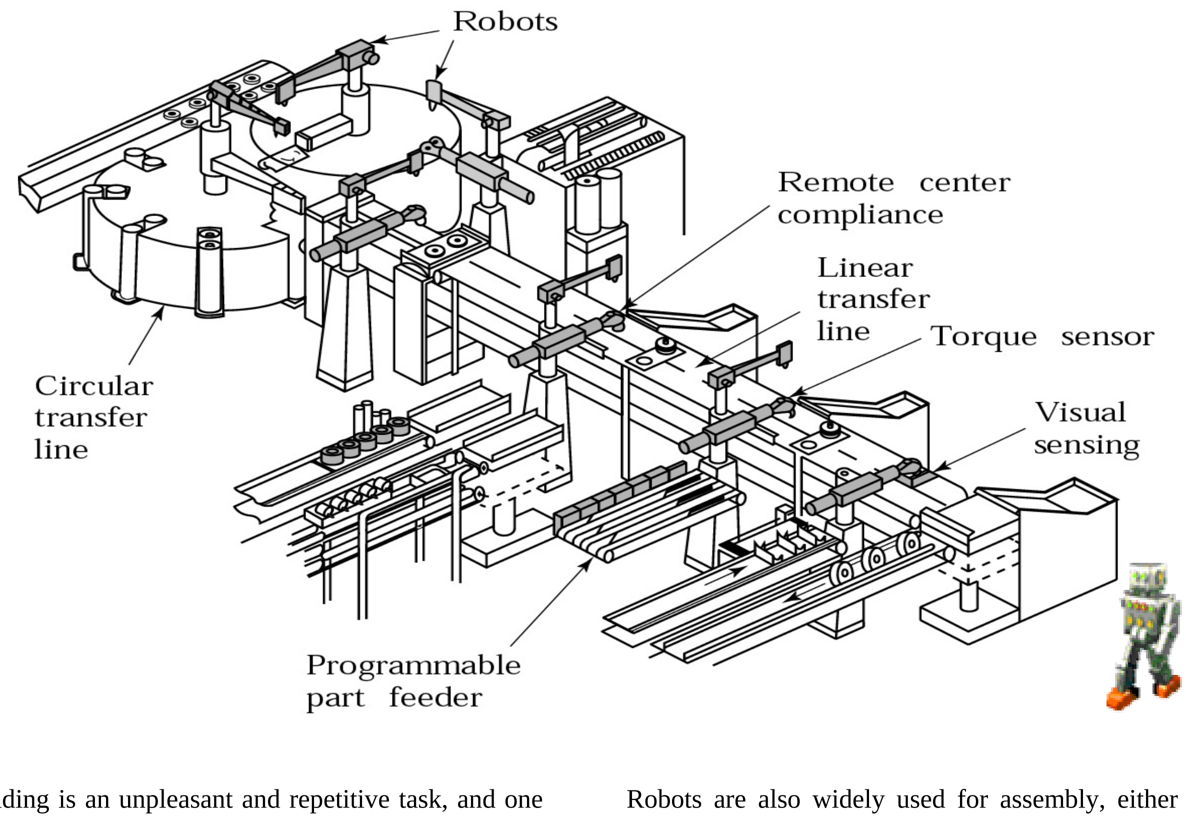

Welding is an unpleasant and repetitive task, and one for which robots are already widely used, and are likely to be used more extensively, due to the progress made in the development of sensors. The technique of spot welding is well developed, and is used frequently, especially in the motor industry. Continuous arc welding is a far more delicate operation, the main problems being to follow the joint, and find a sensor which can function properly near a welding torch. The market for robots in continuous welding is optimistic. Some manufacturing offer robots specifically designed for this purpose.

Robots are also widely used for assembly, either of printed circuit boards, into which components are automatically installed, or of small systems. The scale of use of robot in painting operations has not been spectacular, even though the task is unpleasant, and potentially dangerous. There are however several robots available which have been designed solely for this function.

4. EMPHASIS FOR HUMAN SAFETY

Strong emphasis is given to the following laws:
1. A robot must not harm a human being, nor through inaction allow one to come to harm.
2. A robot must always obey human beings, unless that is in conflict with the first law.
3. A robot must protect itself from harm, unless that is in conflict with the first and second laws.

It is, therefore, the responsibility of the designers to consider measures to diminish the possibility of accidents to both hardware and humans. A robotics installation is still a new occurrence in most factories, therefore, that some type of protective barrier be placed around the work envelope to prevent unauthorized workers from getting too close to the robot work cell and to restrict traffic flow in the area. Both physical barriers and electronic detectors can be employed. Some examples are:

- Painted lines on the floor
- Chains and guard posts
- Safety rails
- Wire mesh fencing
- Presence –sensing device, with light beams forming a curtain across the zone of operation.
- Breaking the curtain of light beams by operator's presence sets the robot off.

In addition to physical barriers, detectors such as electronic curtains, motion detectors, and pressure - sensitive floor pads can also provide protection. A typical robotic installation might include a combination of barriers and protection devices. Another approach states that only robots themselves are able to detect the approach of humans. Therefore, the solution to the safety problem is to provide sensor systems, which can detect intruders that enter the robot area while it is operating.

5. CONCLUSION AND FUTURE TREND

Safety is an important factor in robotic design, from the beginning of the design to the implementation of the process. Specific areas of safety awareness in a robotic installation include types of barriers for worker protection, general personnel safety, and operator and maintenance personnel safety. The uses of robotics in the manufacturing no doubts will bring a lot of benefits as mentioned above. But the introduction of the robot into the work place may have a significant impact on the workers, management, and the organizational unit. To effectively use this new technology, managers need to identify the critical points of impact and develop mechanisms to effectively adjust to this new technology.

BIBLIOGRAPHY

.

1. James A.Rehg, Henry W. Kraebber, "Computer Integrated Manufacturing", Prentice Hall,2001..
2. Mikell P.Groover ,"Automation, Production Systems, and Computer-Integrated Manufacturing, Prentice Hall International, Inc.2001
3. E.Paul Degarmo, J T.Black,Ronald A.Kohser(2003):Materials and Processes in Manufacturing, John Wiley & Sons. Inc.
4. Bhuvenesh Rajamony, "Safety Issues of Robotics in an Automated Manufacturing System, Proceedings of the 1st International Workshop on Artificial Life and Robotics Vol 1,pp. 113-116, 2005.

The Eleventh International Symposium on Artificial Life and Robotics 2006 (AROB 11th'06),
B-con Plaza, Beppu, Oita, Japan, January 23-25, 2006

Asymmetry Analysis of Human Motions for Examining Rehabilitation Training

Keiko NODA , Joo Kooi TAN , Seiji ISHIKAWA

Nobuhiro KITO , Koji OKUMURA

Department of Control Engineering, Kyushu Institute of Technology
Sensuicho 1-1, Tobata, Kitakyushu 804-8550, Japan
E-mail: {noda, etheltan, ishikawa}@ss10.cntl.kyutech.ac.jp

Kawashima Orthopedic Hospital
Miyao 14-1, Nakatsu, Oita 871-0012, Japan

Abstract

Rehabilitation is to make a recovery from the impediment as much as possible with the people whose normal life is difficult with the natural disabilities or the sequelae due to some disease or injury, and to help them gaining independent life as much as possible. In medical rehabilitation training, it is requested to establish the method of evaluating training effect quantitatively employing the motion capture technique.

This paper proposes a method of examining a walking motion by asymmetry analysis. In the experiment, three-dimensional recovery is performed of three patients' walking motions. We analyze the walking motions using the data obtained by the 3-D recovery. A normal walking motion is assumed to have equal variances between the angles of the right-hand side and the left-hand side of a human body. Hence the motion is symmetric. Since one of the major purposes of the rehabilitation training is regarded as to recover symmetry in human motions, examination of the degree of asymmetry employing the proposed technique is expected to contribute to evaluating the training effects and therefore the training strategies in rehabilitation properly.

Keywords: asymmetry analysis, rehabilitation, 3-D recovery, factorization

1. Introduction

Three-dimensional recovery of human motions is applicable to the analysis and the examination of human motions and the technique is therefore requested for use in various human motions related fields. For example, it can be used to evaluate the effect of the rehabilitation training in the medical field.

In medical rehabilitation training, it is requested to establish the method of evaluating training effect quantitatively employing a motion capture technique. It is, however, note very easy in a small hospital to introduce motion capture systems commercially available, because they are extremely expensive and need a large space like a drama studio to take images by multiple cameras. Operations of such motion capture systems are also not very easy for those who are unfamiliar with this field, since they include camera calibration. A cheap motion capture system with simple operation is expected in the communities that want to analyze human motions.

We have developed a novel motion capture system based on the factorization method [1]. It allows simple manipulation in video image taking, as it does not have to perform camera calibration before image capture. We apply this motion capture system to a patient's motion recovery and analysis in rehabilitation training. They all suffer from coxalgia The motion is analyzed with respect to the variances of the right-hand side as well as the left-hand side joint angles of some human portions. Their symmetry/asymmetry is examined to understand the degree of asymmetry with each patient. By the inspection of this asymmetry degree with a patient periodically, we expect that the effectiveness of rehabilitation training is evaluated properly.

2. Technique of 3-D Recovery

The developed 3-D motion recovery technique based on uncalibrated cameras is briefly described in this section. $F\,(\geq 3)$ video cameras are fixed around an object with the feature points and obtain the images of an object. We extract the feature points $P_t\ (t = 1, 2, \cdots, T)$ that are observed among F video camera images and every sample time $t\,(t = 1, 2, \cdots, T)$. Let the 2-D coordinates of the feature point p on the image be denoted by $(x_{fp}(t), y_{fp}(t))$. Then the matrix $W(t)$ at sample time t is defined as

$$W(t) = \begin{pmatrix} x_{11}(t) & \cdots & x_{1P_t}(t) \\ \vdots & \ddots & \vdots \\ x_{F1}(t) & \cdots & x_{FP_t}(t) \\ y_{11}(t) & \cdots & y_{1P_t}(t) \\ \vdots & \ddots & \vdots \\ y_{F1}(t) & \cdots & y_{FP_t}(t) \end{pmatrix}, \qquad (1)$$

where $t = 1, 2, \cdots, T$.

When the matrix $W(t)$ is arranged from t=1 to T, it is expressed by

$$W = \begin{pmatrix} W(1) & W(2) & \cdots & W(T) \end{pmatrix}. \qquad (2)$$

Subtracting the mean quantity of each line from each element of the matrix W, the matrix W is defined by

$$\begin{aligned} W &= W - \frac{1}{Q} WE \\ &= \begin{pmatrix} W(1) & W(2) & \cdots & W(T) \end{pmatrix}, \end{aligned} \qquad (3)$$

where Q is the number of all the feature points, and E is a $Q \times Q$ matrix each element of which is unity.

Equation (3) results in the decomposition of the matrix W into two matrices such as

$$W = MS. \qquad (4)$$

The matrix M, an orientation matrix, contains the information on the directions of the light axes of employed video cameras, whereas the matrix S, a shape matrix, gives the 3-D coordinates of all the feature points registered in the matrix W.

3. Recovery and Analysis of Walking Motion

Three-dimensional recovery is performed of the walking motion of the three patients suffering from coxarthrosis and receiving rehabilitation training. The number of markers attached to these patients is 23. They are instructed to walk on a rectangle mat of about 5 meters long in a straight and natural way. The video images of the walking motion of the patients are obtained by three video cameras that are placed fixed and distant around the patient. The frame rate is 60 [fps], and the measurement time is 5 seconds. The walking cycles within the measurement time are about four cycles. The images are successively taken into a PC, and the matrix W of Eq.(3) is defined from the marker locations on the images. The matrix W then receives decomposition as shown in Eq.(4). **Figure 1** shows the three-dimensional recovery result of the walking motion of Patient A.

We analyze the walking motions using the data obtained by the 3-D recovery. The employed parameters are the angle of a knee joint on each side, the angle of a hip joint on each side, the angle of an elbow on each side, the angle of an upper arm on each side (See **Fig.2a**), the rotation angle around the medial axis of the body (See **Fig.2b**), and the slope of the medial axis of the body against the vertical line (See **Fig.2c**).

We analyze two walking cycles in order to obtain stable walking data. The data are examined using the average and the standard deviation of these parameters. We analyze whether or not the average of each parameter values distribution is mutually different between the right-hand side and the left-hand side of the body statistically. The significant difference equation is defined by

$$u = \frac{\mu_R - \mu_L}{\sqrt{\frac{\sigma_R}{m}} + \sqrt{\frac{\sigma_L}{n}}}. \qquad (5)$$

The quantities μ_R and μ_L are the average of the parameter values distribution on the respective side of the body. The values σ_R and σ_L are the standard deviation of the parameters on the respective side of the body. The number of frames (the number of data) are denoted by m and n on the respective side. In Eq.(5), under 5[ ] level of significance, there is significant difference between the right-hand side and the left-hand side, if $|u| \geq 1.96$ holds. Otherwise, i.e., in case of $|u| < 1.96$, there is no significant difference between them.

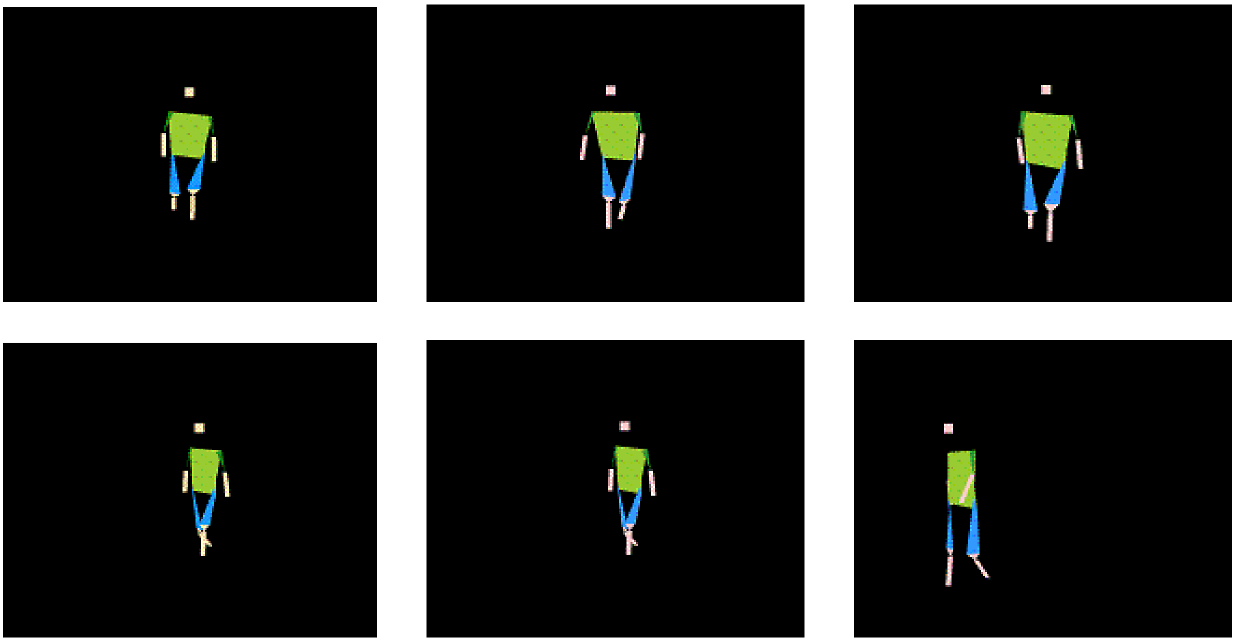

Fig. 1 3-D recovery result of the walking motion with respect to Patient A.

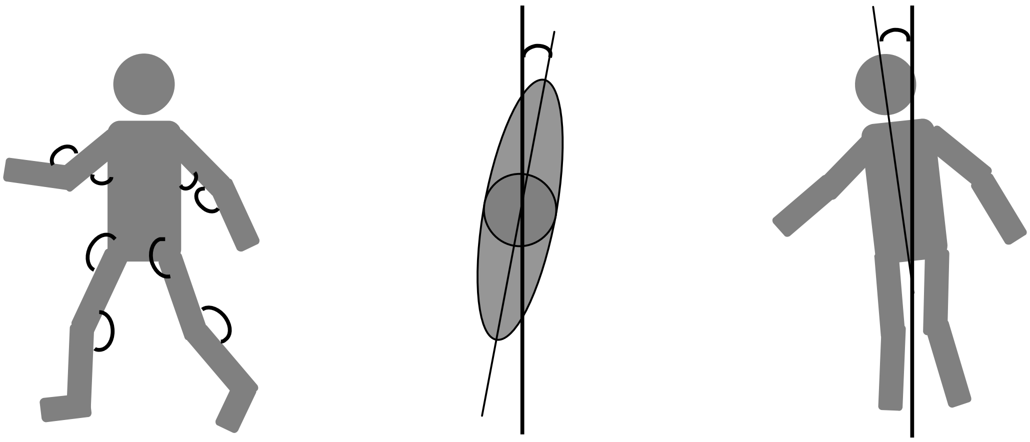

(a) **(b)** **(c)**

Fig. 2 The analyzed parameters.

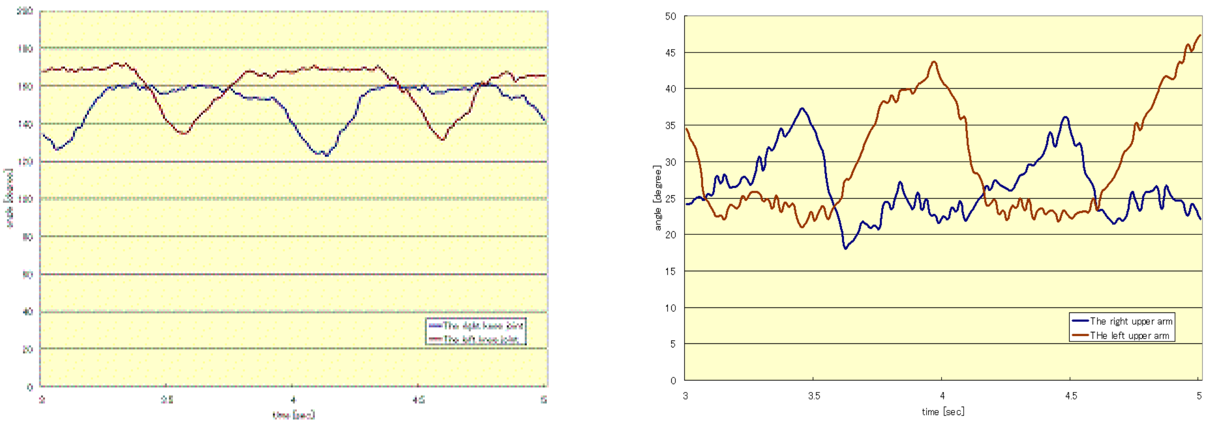

(a) **(b)**

Fig. 3 (a) The angle of knee joints, and (b) the angle of upper arms with respect to Patient A.

Table 1 Analysis of the angles of knee joints, the angles of crotch joints, the angles of elbow joints and the angles of upper arms with respect to Patient A.

		Average [degree]	Standard deviation	Significant difference
Knee joints	Right	151.04	11.10	○
	Left	160.20	11.36	
Crotch joint	Right	153.19	4.67	○
	Left	170.47	4.97	
Elbow joint	Right	150.80	8.63	○
	Left	157.92	9.22	
Upper arms	Right	26.50	4.33	○
	Left	29.98	7.59	

4. Experimental Results

Figure 3 shows the change of the angles of knee joints, and the angles of upper arms of Patient A as time passes. The blue line represents the right knee joint angle, whereas the red line gives the left knee joint angle. Obviously the left knee joint angle is larger than the right in average.

Table 1, on the other hand, gives the average and the standard deviation of the angles; angle of a knee joint on both sides, the angle of a crotch on both sides, the angle of an elbow on both sides, and the angle of an upper arm on both sides. We have analyzed statistically the significant difference of these angles between the right-hand side and the left-hand side. As a result, it has been proved that there is the significant difference between them. Therefore, we judge that the walking motion of the patient A is asymmetric.

5. Discussion and Conclusions

Patient A is suffering from a disease in the left crotch joint. From Table 1, in regard to Patient A's walking motion, it was found that the left knee joint is not bent enough in comparison with the right knee joint. And it was found in regard to the upper arms that the left arm is shaken more largely than the right arm. These facts indicate that Patient A tries to balance the walking by shaking the left arm wide, since the right knee doesn't bend much. In this way, the patient unconsciously establishes the optimal walking motion under the disease, when walking.

A normal walking motion is assumed to have equal variances between the angles of the right-hand side and the left-hand side of a human body. Hence the motion is symmetric. Since one of the major purposes of the rehabilitation training can be regarded as to recover symmetry in human motions, examination of the degree of asymmetry employing the proposed technique is expected to contribute to evaluating the training effects and therefore the training strategies in rehabilitation properly.

The developed motion capture system has an advantage over others in that calibration-free cameras can be employed in motion capture. By the refinement of the proposed technique, it may possible to produce a motion capture system of simpler manipulation. This may therefore lead to wide spread of a motion capture technique.

Acknowledgement

We wish to express our sincere gratitude to the patients who cooperated as subjects in the experiment.

Reference

[1] Tan, J. K., Ishikawa, S.: " Human motion recovery by the factorization based on a spatiotemporal measurement matrix ", *Computer Vision and Image Understanding*, vol.82, no.2, pp.101-109, 2001

The Eleventh International Symposium on Artificial Life and Robotics 2006 (AROB 11th'06),
B-con Plaza, Beppu, Oita, Japan, January 23-25, 2006

Optimization of Coordinated Control Parameters of Traffic Signals Using ACO

Manami Shinohara
Graduate School of Engineering
Utsunomiya Univ.
Utsunomiya-city,
321-8585 Japan

Kenji Shoji Toyama Fubito Juichi Miyamichi
Faculty of Engineering
Utsunomiya Univ.
Utsunomiya-city,
321-8585 Japan

Abstract

In this paper, we focus attention on offset that is one of coordinated control parameters, optimize the offsets by ant colony optimization(ACO). Finding an optimal solution is carried out by repeating the above procedure. Experimental results show the good coincidence with the solutions of traffic signal control theories in offset. And, the offsets optimized by the proposed method gave a better evaluation than a current offsets under the road traffic condition of an area of our city. In addition, as experimental comparison of optimization methods, we applied a genetic algorithm (GA) to the problem of interest.

1 introduction

Increasing number of vehicles in use generates serious problems such as traffic accidents and congestion. It is deeply desired that automobile traffic safety and smooth traffic flow are realized by appropriate traffic light control. There are three types of traffic light control: independent control handling a single signal, coordinated control in which two or more signals on a arterial road work in association with each other, and area traffic control which is a two dimensional version of coordinated control. Especially, a large effect of traffic light control can be expected in coordinated control and area traffic control if they go well. The object of this study is to improve the performance in coordinated control. The parameters of coordinated control consist of common length, split, and offset. We focus attention on the offset. Within the parameters of coordinated control, common cycle length, split, and offset, we focus attention on the offset. The decision of offsets is defined as a combinatorial problem. In deciding combination of offsets, the total number of combinations of intege offsets becomes the possible number of offsets to the power of N-1, where N is the number of intersections. If the number of intersections increases, the number of combinations becomes huge, and it is difficult to find an optimal solution. Therefore, we have to solve the problem by some heuristic method. In this work, we optimized the offsets of coordinated control by ACO. ACO is a metaheuristics for combinatorial optimization problem. Applyingit to several combinatorial optimization problems, e.g. traveling salesman problem and graph coloring problem, its availability is confirmed. There are several works of optimizing the control parameters of traffic lights with algorithms imitating swarm behavior such as ACO. However, it is difficult to newly apply the algorithms into the present signal systems of Japan, because the scale of the systems that the algorithms assume is large. The purpose of this research is to optimize the offsets of local systems having several signals on the assumption that such optimizations are introduced in existing systems in Japan.

2 Coordinated control

Two or more signals on a arterial road work in association with each other shown in the upper of figure 1 called coordinated control. Common cycle length and offset are particular parameters of coordinated control. Cycle length is a total time to complete one cycle. The system needs a common cycle length. Offset is the delay time to star the green phase between the reference signal at the intersection 1 in figure 1 and the signal concerned.

According to the manual of JSTE [1] , if round trip time T of a link in overall speed is multiple integer of cycle length C ($T = nC$), vehicle delay time can be minimal.

3 ACO

ACO algorithm is shown in figure 2.

Pheromone $\tau_{ij}(t)$ on route (i, j) from condition i to j in time t evaporats at the rate of ρ, and increases to $\tau_{ij}(t+1)$ by each ant agent $k(k = 1, \cdots, m)$. Hence, pheromone volume $\tau_{ij}(t+1)$ in time $(t+1)$ is calculated by equation 1.

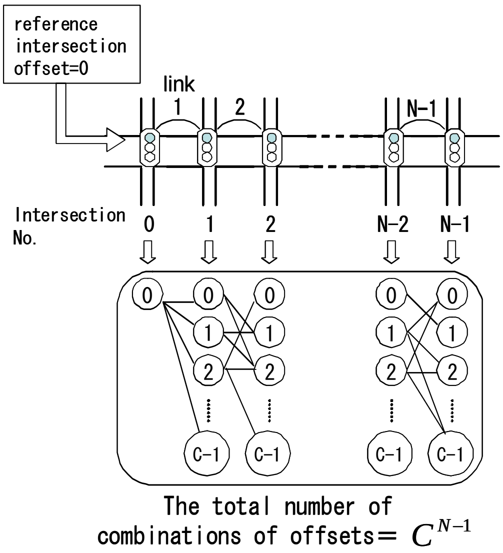

Figure 1: Coordinated control(upper) and the set of offsets(lower)

```
1.   Initialize (initialized pheromone)
2.   Loop until fulfill condition (repeat time of colony) to end
       2. 1  Loop until M agents end
               i   Selecting a route probabilistically
               ii  Updating pheromone
       2. 2  Evaluating all solutions
       2. 3  Updating pheromone  (to excellent solution of colony)
3.   End.
```

Figure 2: ACO algorithm

$$\tau_{ij}(t+1) = (1-\rho)\tau_{ij}(t) + \sum_{k=1}^{m} \Delta\tau_{ij}^{k}(t) \qquad (1)$$

4 Applying ACO to coordinated control[3]

In this paper, we optimized the offsets of coordinated control along a road with N traffic signals. For coordinated control with N signals, $N-1$ links as shown in the upper half of Figure 1, we restrict the offset of each signal to integer. So, in the case where common cycle length is the integer value C [s], the offset can be chosen is one of C integer values ranging from 0 to $C-1$. The offset of one of the N traffic signals is fixed to 0, and for the rest of the signals the number of combination of their offsets is C^{N-1} as shown in the lower half of Figure 1. A combination of offsets generated by ACO as a feasible solution is evaluated by a microscopic traffic simulator CORSIM. From the result of the simulation we calculate a cost index CI based on Vt, Tt, Dt, and Sp as

$$CI = \sum_{n=1}^{N-1} \left\{ \frac{\mathrm{Dt}}{\mathrm{Tt}} \times \mathrm{Vt} \times \frac{1}{\mathrm{Tt}} + K \times \frac{\mathrm{Sp} \times \mathrm{Vt}}{\mathrm{Tt}} \right\} \qquad (2)$$

where Vt is the number of vehicles that have been discharged from the links, Tt is total time on the link for all vehicles, Dt is the time that vehicles are delayed if they cannot travel at the free flow speed, Sp is the ratio of the number of vehicles that have stopped at least once on a link to the total link trips, and K is weight coefficient of Sp. The CI is the weighted sum of delay and stop. So, the smaller the CI thebetter the offsets.

The CI is used to find the best solution in the colony at time t. The pheromone amount on the path of best solution is additionally increased. Moreover, the pheromone amount on the paths neighboring the best are also increased. Let τ_q be a pheromone amount on the path from the offset p at n-th signal to the offset q at (n+1)-th in the best solution at time t. The additional increment for the pheromone amount on the paths neighboring the best is expressed as

$$\tau_{q+x} \leftarrow \tau_{q+x} + 0.1e^{-\frac{x^2}{\sigma^2}} \qquad (3)$$

where x is the integer representing the displacement from the best offset, and σ is the standard deviation of Gaussian function. In our experiments we use σ=5.0. After the increments we limit all the pheromone amounts to the range between lower and upper limits preventing the ACO from concentrating the pheromone into a specific path based on MAX-MIN Ant System.

$$\tau_{min} \leq \tau \leq \tau_{max} \qquad (4)$$

5 Applying GA to coordinated control

Under the same traffic condition as on the previous section, the offsets are optimized by a simple GA according to the research [5] . The chromosome for the GA consists of 3(N-1) bits as shown in Figure 3, where the offset of each signal is represented 3-bit binary number.

In the case of 5 signals and 4 links in Figure 3, the length of the chromosome becomes 12 bits. In order to evaluate a set of offsets represented by a chromosome, we define a fitness function. The fitness F is defined by the inverse of CI as

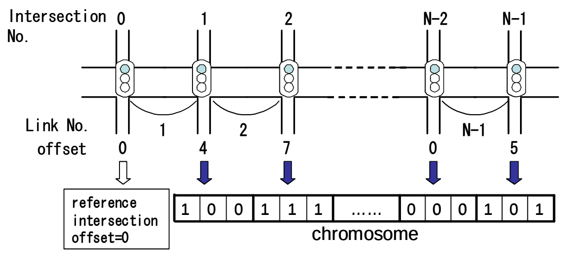

Figure 3: coding

$$F = \frac{1}{CI} \qquad (5)$$

Before starting the GA, we must generate an initial population. Each individual is generated from uniform random bits. In GA, after the evaluation of all individuals of current generation, the operations based on the genetic rules are applied to them for the construction of next generation. As the genetic rules, we adopt elitism, and apply crossover and mutation to the individuals selected by roulette. Elitism is a mechanism that protects the chromosomes of the most-highly-fit population from the genetic operation. In experiments, the top of the individuals become elite. Crossover is the main mechanism of GA which expects the more-highly-fit children than their parents. In experiments, a parent is chosen from all individuals based on the roulette selection at the probability proportional to the F value. From a pair of parents, their copies are made as children, and one-point crossover is applied for the children in the probability of 0.5. The mutation inverts each(a one of) bit in the chromosome according to the probability of 0.1. The set of offsets with most highly fitness at 100th generation is made to be the best solution. The case of 5 signals and 4 links as Figure 3, feasible solution can be expressed at binary number 12 digits. The GA optimizes the offset of each signal in the resolution of 3 bits. So, we apply coarse-to-fine method. That is, in the first stage we coarsely obtain the upper 3 bits of each offset using the GA, and in the second stage we find the optimal lower 3 bits of the coarse offsets obtained in the first stage using the same GA.

6 Experimental Results

First, we compare the offsets derived from the traffic engineering theory [1] with those optimized by the ACO under the traffic condition with an undersaturated bottleneck intersection. Experiments are performed on the settings of 5 signals, 4 links equally spaced at 3 types of link length, and no turn vehicles at main road

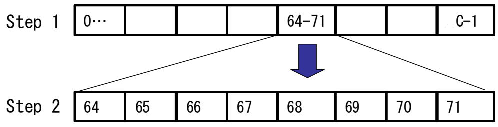

Figure 4: coarse-to-fine

which are the simplified versions of real traffic roads. The optimal offsets by the ACO and the offsets derived from the theory are shown in Table 1 with their CI.

Table 1: comparison with theory solution

link length,cycle length	offsets by ACO	CI
1000[ft],50[s]	0 16 34 32 23	145.0
1300[ft],66[s]	0 22 46 38 43	115.6
1650[ft],84[s]	0 29 56 53 49	92.7
	offsets by theory	CI
1000[ft],50[s]	0 25 0 25 0	171.9
1300[ft],66[s]	0 33 0 33 0	128.6
1650[ft],84[s]	0 42 0 42 0	107.0

Next, we compare the CIs obtained from the ACO with that from the GA under the same conditions of the above in the case of link length of 1300[ft] and common cycle length of 66[s]. The ACO and the 2-stage GA are performed 5 times with randomly generated initial values. In the ACO, the number of ants is made to be 10 and the number of ant-cycles to be 10. In the 2-stage GA, the number of individuals is made to be 10 and the number of generation to be 5. In the both of the algorithms, the total number of evaluation by the simulator CORSIM becomes 100 times. The best offsets by the ACO and the 2-stage GA of each execution are shown in Figure 5 and their CIs are shown in Table 2.

Table 2: comparison with CI by GA solution

CI by ACO	CI by GA
117.05	124.83
117.80	125.26
118.06	134.10
118.80	135.59
119.95	139.23

Thirdly, we compare the actual offsets of the existing system with those optimized by the ACO for the

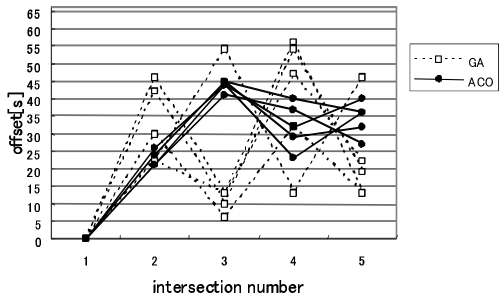

Figure 5: comparison with offsets by GA

actual data of link length, cycle length and traffic flow taken from an arterial road in Utsunomiya city, Japan. Figure 6 shows the graph of offsets and CIs.

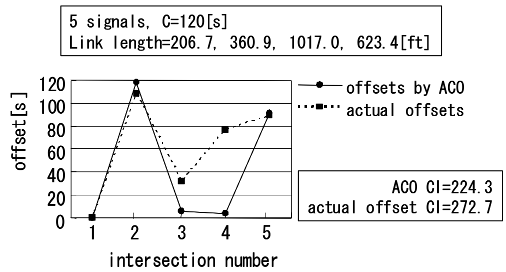

Figure 6: comparison with actual offsets of a coordinated control in a city of Japan

7 Discussion

We obtained lower CI values of solutions by the ACO than those of the theoretical solutions in the first experiments. These results seem to be because the evaluation function CI includes the item of starting delay which is one of the factors simulated by the simulator CORSIM and which is out of scope in the theoretical solutions. In the comparison of the ACO with the 2-stage GA, the difference between the solutions of the ACO and those of the GA is clear. In Figure 5 of the results of 5 trials of both methods, we can see the relatively convergent offsets by the ACO at every intersection, while the offsets by the GA are scattered. The value of offset in each intersection has been scattered in comparison with GA on ACO. In addition we obtained lower CI values of solutions by the ACO than those by the GA as shown in Table 2. From the above, it is considered that the number of evaluations (100 times in the experiments) is not enough for the GA to search solutions and that it is acceptable for the ACO. Therefore, the number of evaluations necessary to obtain a good solution for the ACO is smaller than that for the GA. The result of the last experiment shows the potential of the ACO applied to an actual coordinated control, that is, the best offsets selected by the ACO is near to the actual ones and the CI value of the best solution by the ACO is smaller than that of the actual offsets.

8 Conclusion

In this paper, we focus attention on offset that is one of coordinated control parameters, optimized the offsets by ACO, and examined the efficacy of the ACO for the optimization of the coordinated control parameters. As future works, we plan (1) to improve the ACO program such that it can be applied to coordinated control under more realistic conditions, (2) to expand it such that it can optimize the other signal parameters of split and cycle length, and (3) to apply ACO to area traffic control.

Acknowledgements

We would like to thank Tochigi Prefectural Police Traffic Control Center in Japan for offering us the actual data set of a coordinated control.

References

[1] Japan Society of Traffic Engineers ed. (1994). Manual on Traffic Signal Control, Tokyo, Japan(in Japanese).

[2] Bonabeau, E., Dorigo, M. and Theraulaz, G., "Inspiration for Optimization from Social Insect Behaviour", Nature, vol.406, pp.39-42(2000).

[3] Manami Shinohara, Kenji Shoji, Fubito Toyama, "Optimization of Coordinated Control Parameters of Traffic Signals Using ACO", Forum on Information Technology (FIT2004), vol.2, p259-260(2004)(in Japanese).

[4] Oliveira,D., Ferreira,P., and Bazzan,A., " A Swarm-Based Approach for Selection of Signal Plans in Urban Scenarios", In Proceeding of Fourth International Workshop on Ant Colony Optimization and Swarm Intelligence-ANTS 2004, vol. 3172 of LNCS, pp.416-417, Springer-Verlag, Berlin, Germany(2004).

[5] Masakazu Odawara, Mamoru Hisai, "A Study on Common Cycle Length of Coordinated Signal System through Genetic Algorithm", The Infrastructure Planning Committee, JSCE, vol.20(2), pp815-818(1997)(in Japanese).

The Eleventh International Symposium on Artificial Life and Robotics 2006 (AROB 11th'06),
B-con Plaza, Beppu, Oita, Japan, January 23-25, 2006

Evolution Strategies Based Gaussian Sum Particle Filter for State Estimation of Nonlinear Stochastic Systems*

Katsuji Uosaki Toshiharu Hatanaka
Department of Information and Physical Sciences
Graduate School of Information Science and Technology, Osaka University
Suita, Osaka 565-0871, Japan

Abstract

Recently, particle filters have drawn much attentions for optimal filtering of nonlinear systems. Particle filters evaluate a posterior probability distribution of the state variable based on observations in Monte Carlo simulation using so-called importance sampling. However, degeneracy phenomena in the importance weights deteriorate the filter performance, and Evolution strategies based particle filter, in which selection process in evolution strategies is applied, has been proposed to overcome this difficulty. In this paper, we propose a novel particle filter, which combines the ideas of Gaussian sum filter and Evolution strategies based particle filter. Numerical simulation study exemplifies the applicability of this approach to nonlinear filtering.

1 Introduction

Optimal filtering for stochastic systems has a lot of applications in signal processing, control system sciences and related areas. It can be carried out by evaluating recursively the evolving posterior probability density function (pdf) with a prior pdf for the unknown state and a likelihood function relating them to the observations. However, the posterior pdf do not admit a closed-form expression except for simple models such as linear Gaussian state space models where well-known Kalman filter [1] can be applied. In many realistic problems, where state space models include nonlinear and non-Gaussian elements that preclude a closed form of expression for the optimal filters, several approximations have been proposed. A class of filters called Gaussian filters provide Gaussian approximations to the filters including the extended Kalman filter (EKF) and its variation [2], and other filters such as Gaussian sum filters [3], where the posterior pdf's are approximated by the Gaussian mixtures, have been attempted. Recent massive increase of the computational power allowed to the rebirth of Monte Carlo integration and its application of Bayesian filtering, or "particle filtering" [4]. In this approach, pdf's are represented by a weighted sum based on the discrete grid sequentially chosen by the importance sampling and the estimates are obtained based on corresponding importance weights. We propose here a novel particle filter, which combines the ideas of Gaussian sum filter [3] and Evolution strategies based particle filter (ESP) [5], which substitutes selection rule in Evolution strategies to resampling in the conventional particle filter to overcome the degeneracy phenomenon. Numerical simulation studies have been conducted to indicate the potential to create high performance filters for nonlinear state estimation.

*This work is partially supported by the Grant-in-Aid for Scientific Research from the Japan Society for the Promotion of Science (C)(2)14550447.

2 Gaussian Sum Filter

Consider the following nonlinear state space model.

$$x_{k+1} = f(x_k) + v_k, \tag{1}$$
$$y_k = g(x_k) + w_k, \tag{2}$$

where x_k, y_k, v_k and w_k are the state variable, observation, system noise and observation noise sequences, respectively, and f and g are known possibly nonlinear functions. We assume v_k and w_k are independently identically distributed (i.i.d.) and mutually independent. Problem to be considered here is to find the best estimate of the state variable x_k in some sense based on the all available data of observations $y_{1:k} = \{y_1, y_2, \dots, y_k\}$. We can solve the problem by calculating the posterior pdf of the state variable x_k of time instant k based on $y_{1:k}$.
The posterior pdf $p(x_k|y_{1:k})$ of x_k based on the observation sequence $y_{1:k}$ satisfies the following recursions:

Time update:

$$p(x_k|y_{1:k-1}) = \int p(x_k|x_{k-1})p(x_{k-1}|y_{1:k-1})dx_{k-1}, \tag{3}$$

Observation update:

$$p(x_k|y_{1:k}) = \frac{p(y_k|x_k)p(x_k|y_{1:k-1})}{p(y_k|y_{1:k-1})} \tag{4}$$

with a prior pdf $p(x_0|y_0) \equiv p(x_0)$ of the initial state variable x_0. Here normalizing constant

$$p(y_k|y_{1:k-1}) = \int p(y_k|x_k)p(x_k|y_{1:k-1})dx_k$$

depends on the likelihood $p(y_k|x_k)$, which is determined by the observation equation (2).

Since a closed analytical form solution is not admitted except in very restrictive cases such as linear Gaussian state space models, some approximations should be introduced. The most common approximation approach is the extended Kalman filter (EKF) [2], where a linearization technique based on a first order Taylor expansions of the nonlinear system and observation equations about the current estimate is used. Another one is the Gaussian sum filter, where the following Gaussian sum representation of the posterior and the predictive pdf's is used [3],

$$p(x_k|y_{1:k}) = \sum_{i=1}^{p} w_{k|k}^{(i)} \mathcal{N}(x_k;\, \mu_{k|k}^{(i)}, \Sigma_{k|k}^{(i)}), \tag{5}$$

$$p(x_{k+1}|y_{1:k}) = \sum_{i=1}^{p} w_{k+1|k}^{(i)} \mathcal{N}(x_{k+1};\, \mu_{k+1|k}^{(i)}, \Sigma_{k+1|k}^{(i)}), \tag{6}$$

where $\mathcal{N}(x;\, \mu, \Sigma)$ is Gaussian pdf with expectation μ and covariance Σ,

$$\mathcal{N}(x;\, \mu, \Sigma) = \frac{1}{(2\pi)^{\frac{n}{2}} |\Sigma|^{\frac{1}{2}}} \exp\left(-\frac{1}{2}(x-\mu)^T \Sigma^{-1} (x-\mu)\right). \tag{7}$$

The weight $\{w_{k|k-1}^{(i)}, w_{k|k}^{(i)},\ (i = 1, \ldots, p)\}$ are non-negative and satisfy $\sum_{i=1}^{p} w_{k|k-1}^{(i)} = 1,\ \sum_{i=1}^{p} w_{k|k}^{(i)} = 1$. Then, the means and covariances are updated by

$$\begin{aligned}
&\mu_{k|k}^{(i)} = \mu_{k|k-1}^{(i)} + K_k^{(i)}(y_k - g(\mu_{k|k-1}^{(i)})),\\
&\Sigma_{k|k}^{(i)} = (I - K_k^{(i)} \tilde{C}_k^{(i)}) \Sigma_{k|k-1}^{(i)},\\
&K_k^{(i)} = \Sigma_{k|k-1}^{(i)} \tilde{C}_k^{(i)T} (\tilde{C}_k^{(i)} \Sigma_{k|k-1}^{(i)} \tilde{C}_k^{(i)T} + R_k)^{-1},\\
&\mu_{k+1|k}^{(i)} = f(\mu_{k|k}^{(i)}),\\
&\Sigma_{k+1|k}^{(i)} = \tilde{A}_{k+1}^{(i)} \Sigma_{k|k}^{(i)} \tilde{A}_{k+1}^{(i)T} + Q_k,\\
&\tilde{C}_k^{(i)} = \frac{dg(x)}{dx}\Big|_{x=\mu_{k|k-1}^{(i)}}, \qquad \tilde{A}_k^{(i)} = \frac{df(x)}{dx}\Big|_{x=\mu_{k|k}^{(i)}},\\
&w_{k|k}^{(i)} = \frac{w_{k|k-1}^{(i)} \beta_k^{(i)}}{\sum_{i=1}^{p} w_{k|k-1}^{(i)} \beta_k^{(i)}}, \qquad w_{k+1|k}^{(i)} = w_{k|k}^{(i)},\\
&\beta_k^{(i)} = \mathcal{N}(y_k;\, g(\mu_{k|k-1}^{(i)}), \tilde{C}_k^{(i)} \Sigma_{k|k-1}^{(i)} \tilde{C}_k^{(i)T}).
\end{aligned} \tag{8}$$

In Gaussian sum filter, the mean and covariance evaluation (8) may be tedious and time-consuming, and divergence may occur due to the linearizations in (8) when severe non-linearities exist in the models. To resolve these difficulties, Gaussian sum particle filter has been proposed [6], which will be briefly explained in the following.

3 Gaussian Sum Particle Filter

Gaussian sum particle filter assumes the posterior and predictive pdf's by Gaussian sum as (5) and (6) in Gaussian sum filter instead of grid approximation,

$$p(x_k|y_{1:k}) \approx \sum_{i=1}^{p} w_k^{(i)} \delta(x_k - x_k^{(i)}) \tag{9}$$

with Dirac's delta function $\delta(\cdot)$ such that $\delta(x) = 1$ for $x = 0$ and $\delta(x) = 0$ otherwise, in the conventional particle filter [4]. Here, the particles $\{x_k^{(i)},\ (i = 1, \ldots, p)\}$ are generated and associated weights $\{w_k^{(i)},\ (i = 1, \ldots, p)\}$ are chosen using the principle of "importance sampling." Under the assumption $w_{k+1|k}^{(i)} = w_{k|k}^{(i)},\ (i = 1, \ldots, p)$ the mean $\mu_{k+1|k}^{(i)}$ and covariance $\Sigma_{k+1|k}^{(i)}$ of Gaussian pdf $\mathcal{N}(x_k;\, \mu_{k+1|k}^{(i)}, \Sigma_{k+1|k}^{(i)})$ corresponding to

$$\int \mathcal{N}(x_k;\, \mu_{k|k}^{(i)}, \Sigma_{k|k}^{(i)}) p(x_{k+1}|x_k) dx_k \tag{10}$$

are estimated through the following Monte Carlo sampling in stead of mean and covariance update (8) in Gaussian sum filter.
For each $i = 1, \ldots, p$, we draw m samples $\{x_k^{(i,j)},\ (j = 1, \ldots, m)\}$ from $\mathcal{N}(x_k;\, \mu_{k|k}^{(i)}, \Sigma_{k|k}^{(i)})$, and then draw $x_{k+1|k}^{(i,j)}$ from $p(x_{k+1}|x_k^{(i,j)})$. Mean and covariance are then computed by

$$\begin{aligned}
\mu_{k+1|k}^{(i)} &= \frac{1}{m} \sum_{j=1}^{m} x_{k+1|k}^{(i,j)},\\
\Sigma_{k+1|k}^{(i)} &= \frac{1}{m} \sum_{j=1}^{m} (x_{k+1|k}^{(i,j)} - \mu_{k+1|k}^{(i)})(x_{k+1|k}^{(i,j)} - \mu_{k+1|k}^{(i)})^T.
\end{aligned} \tag{11}$$

On the other hand, observation update (4) with (5) is carried out by importance sampling. We first draw samples $\{x_k^{(i,j)},\ (j = 1, \ldots, m)\}$ from the importance function $q(x_k|y_{1:k})$, then compute the corresponding weights by

$$\tilde{w}_{k|k-1}^{(i,j)} = \frac{p(y_k|x_k^{(i,j)}) \mathcal{N}(x_k^{(i,j)};\, \mu_{k|k-1}^{(i)}, \Sigma_{k|k-1}^{(i)})}{q(x_k^{(i,j)}|y_{1:k})}. \tag{12}$$

We compute the estimates of the mean and covariance as

$$\begin{aligned}
\mu_{k|k}^{(i)} &= \sum_{j=1}^{m} w_{k|k-1}^{(i,j)} x_k^{(i,j)},\\
\Sigma_{k|k}^{(i)} &= \sum_{j=1}^{m} w_{k|k-1}^{(i,j)} (x_k^{(i,j)} - \mu_{k|k}^{(i)})(x_k^{(i,j)} - \mu_{k|k}^{(i)})^T,
\end{aligned} \tag{13}$$

with the normalized weights $w_{k|k-1}^{(i,j)} = \tilde{w}_{k|k-1}^{(i,j)} / \sum_{i=1}^{p} \tilde{w}_{k|k-1}^{(i,j)}$, and then update the weights by

$$w_{k|k}^{(i)} = \frac{\sum_{j=1}^{m} \tilde{w}_{k|k-1}^{(i,j)} w_{k-1|k-1}^{(i,j)}}{\sum_{i=1}^{p} \sum_{j=1}^{m} \tilde{w}_{k|k-1}^{(i,j)} w_{k-1|k-1}^{(i,j)}}. \tag{14}$$

Since this filter approximates the posterior pdf by a weighted sum of continuous functions (Gaussian pdf's) while the conventional filter approximates it with a set of grid points, this filter can approximate the pdf with smaller number of summands p than the conventional filter, and it leads smaller computation burden. However, there may exist the degeneracy phenomenon as in the conventional particle filter [4], that is, after several updates, the posterior pdf's are approximated by a single Gaussian. It leads poor approximation and a large computation effort is wasted in updating Gaussians whose contributions to approximate the posterior pdf $p(x_k|y_{1:k})$ is negligible.

4 Evolution Strategies Based Gaussian Sum Particle Filter

In order to reduce the effects of degeneracy in Gaussian sum particle filter, resampling process [7] can be applied as in the conventional particle filter.
The basic idea of resampling is to eliminate the factors with small weights and to concentrate on the factors with larger weights. In conventional particle filter, a new set of particles $\{x_k^{(i)},\ (i=1,\dots,p)\}$ are generated by resampling from an approximate representation of $p(x_k|y_{1:k})$ given by (9) so that $\Pr(x_k^{(i)}=x_k^{(j)})=w_k^{(j)}$, and the weights are reset as $w_k^{(i)}=1/p$. This filter is called as "Sequential importance sampling resampling filter" (SIR) [7]. Resampling process in SIR can be applied to Gaussian sum particle filter as follows:
A new set of Gaussian pdf's $\{\mathcal{N}(x_k;\ \mu_{k|k}^{(i)},\Sigma_{k|k}^{(i)},\ (i=1,\dots,p)\}$ are generated by resampling from the set of Gaussian pdf's generated by (12)–(14) in the approximate representation of $p(x_k|y_{1:k})$ (5) so that

$$\Pr(\mathcal{N}(x_k;\mu_{k|k}^{(i)},\Sigma_{k|k}^{(i)})=\mathcal{N}(x_k;\mu_{k|k}^{(j)},\Sigma_{k|k}^{(i)}))=w_{k|k}^{(j)}. \tag{15}$$

The weights are reset as $w_{k|k}^{(i)}=1/p$. We can call this filter as "Gaussian sum resampling particle filter" (GSR) [6]. Fluctuation of the computation time in GSR may become large since the choice of particles in GSR is probabilistic.
We propose here a novel particle filter combining the idea of Gaussian sum filter and Evolution strategies (ES) by Rechenberg and Schwefel [8] as in Evolutionary strategies based particle filter (ESP) [5]. ES is one of the Evolutionary Computation (EC) approaches, computational models simulating natural evolutionary processes to design and implement computer-based problem solving systems [9]. It has been applied to continuous function optimization in real-valued n-dimensional space via processes of selection and perturbation such as recombination and mutation depending on the perceived performance (fitness) of the individual structures. Mutation process, which is realized by additive process of random fluctuations, introduces innovation into the population. Then, selection process is carried out by choosing deterministically the individuals of higher fitness from the union of parents and offspring or offspring only to form the parents of the next generation in order to evolve towards better search region. Two main selection processes have been proposed, i.e., $(\mu+\lambda)$-selection and (μ,λ)-selection. In these selection processes, λ offspring are created from μ parents and the μ best individuals are selected out of the union of parents and offspring, and offspring only, respectively.
The deterministic selection rules in ES can make the fluctuations of computation time smaller, then they are substituted to resampling process in GSR to derive a novel filter, "Evolution strategies based Gaussian sum particle filter" (ESGSP). The filter implements the observation update (4) with (5) as follows:
For each $i=1,\dots,p$, $\ell=1,\dots,r$, samples $\{x_k^{(i,j,\ell)},\ (j=1,\dots,m)\}$ are drawn from the importance function $q(x_k|y_{1:k})$, and the corresponding weights are computed by

$$\tilde{w}_{k|k-1}^{(i,j,\ell)}=\frac{p(y_k|x_k^{(i,j,\ell)})\mathcal{N}(x_k^{(i,j,\ell)};\ \mu_{k|k-1}^{(i)},\Sigma_{k|k-1}^{(i)})}{q(x_k^{(i,j)}|y_{1:k})} \tag{16}$$

and normalized as $w_{k|k-1}^{(i,j,\ell)}=\tilde{w}_{k|k-1}^{(i,j,\ell)}\ /\sum_{i=1}^{p}\tilde{w}_{k|k-1}^{(i,j,\ell)}$. The estimates of the mean and covariance are computed by

$$\begin{aligned}\mu_{k|k}^{(i,\ell)}&=\sum_{j=1}^{m}w_{k|k-1}^{(i,j,\ell)}x_k^{(i,j,\ell)},\\ \Sigma_{k|k}^{(i,\ell)}&=\sum_{j=1}^{m}w_{k|k-1}^{(i,j,\ell)}(x_k^{(i,j,\ell)}-\mu_{k|k}^{(i,\ell)})(x_k^{(i,j,\ell)}-\mu_{k|k}^{(i,\ell)})^T,\end{aligned} \tag{17}$$

The weights are then updated by

$$w_{k|k}^{(i,\ell)}=\frac{\sum_{j=1}^{m}\tilde{w}_{k|k-1}^{(i,j,\ell)}w_{k-1|k-1}^{(i)}}{\sum_{i=1}^{p}\sum_{j=1}^{m}\tilde{w}_{k|k-1}^{(i,j,\ell)}w_{k-1|k-1}^{(i)}}. \tag{18}$$

We sort the set of $p\times r$ pairs of Gaussian pdf's and corresponding weights, $\{(\mathcal{N}(x_{k|k};\ \mu_{k|k}^{(i,\ell)},\ \Sigma_{k|k}^{(i,\ell)}),\ w_{k|k}^{(i,\ell)},\ (i=1,\dots,p,\ \ell=1,\dots,r)\}$ according to the weights $w_{k|k}^{(i,\ell)}$ in descending order. We retain the first p pairs with larger weights, and denote them $\{\mathcal{N}(x_{k|k};\ \mu_{k|k}^{(i)},\ \Sigma_{k|k}^{(i)}),\ \tilde{w}_{k|k}^{(i)},\ (i=1,\dots,p)\}$. The weights are normalized as $w_{k|k}^{(i)}=\tilde{w}_{k|k}^{(i)}/\sum_{i=1}^{m}\tilde{w}_{k|k}^{(i)}$. This process corresponds to (p,pr)-selection in ES.

5 Numerical Example

A numerical simulation is carried out to exemplify the applicability of the proposed ESGSP filter. The following

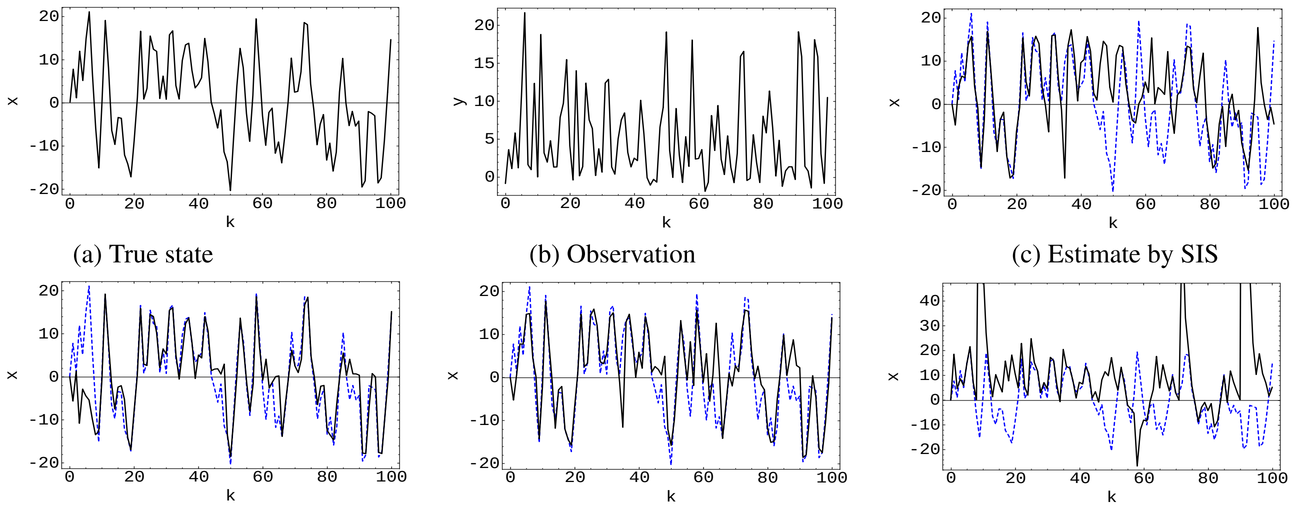

(a) True state (b) Observation (c) Estimate by SIS

(d) Estimate by GSP (e) Estimate by ESGSP (f) Estimate by EKF

Figure 1: Sample behavior of state and observation processes, and the state estimates (solid line: estimate, dashed line: true state)

nonlinear state space model with known parameters is considered.

$$\begin{aligned} x_k &= \frac{x_{k-1}}{2} + \frac{25x_{k-1}}{1+x_{k-1}^2} + 8\cos(1.2k) + v_k \\ &= f(x_{k-1}) + v_k, \qquad (19) \\ y_k &= \frac{x_k^2}{20} + w_k, \end{aligned}$$

where v_k and w_k are i.i.d. zero-mean normal random variables with variance 10 and 1, respectively. The normal distribution with mean $f(x_{k-1}^{(i)})$ and variance 10 is chosen as the importance density $q(x_k|x_{k-1}^{(i)}, y_{1:k})$. Sample paths of the observation process and the state estimates by the particle filters (SIS ($n = 50$), GSP ($p = 5, m = 10$), and the proposed ESGSP ($p = 5, m = 5, p = 2$)) are given in Fig.1, and that of EKF as well for comparison. Particle filters, especially GSP and proposed ESGSP filters, show better behaviors in nonlinear state estimation, while the estimate by EKF cannot follow the true state.
The other choice of design parameters and evolution processes may improve the performance, and their better choice will be pursued.

6 Conclusions

A novel filter, Evolution strategies based Gaussian sum particle filter (ESGSP), has been proposed by combining the ideas of Gaussian sum filter and Evolution strategies based particle filter (ESP). Since this filter employs the Gaussian sum approximation of the posterior probability distribution with the mean and covariance evaluated by Monte Carlo sampling, it can be applied any type of nonlinear systems and non-Gaussian noise cases. Introducing of other evolution operations and better choice of design parameters will lead the particle filters with better performance.

References

[1] Sorenson, H. W. (1985), *Kalman Filtering: Theory and Application*, IEEE Press

[2] Jazwinski, A. H. (1970), *Stochastic Process and Filtering Theory*, Academic Press

[3] Alspach, D. L. and Sorenson, H. W. (1972), "Nonlinear Bayesian estimation using Gaussian sum approximation," *IEEE Trans. on Automatic Control*, AC-17 (4): 439–448

[4] Doucet, A., de Freitas, N. and Gordon, N. (Eds.) (2001), *Sequential Monte Carlo Methods in Practice*, Springer

[5] Uosaki, K., Kimura, Y. and Hatanaka, T. (2004), "State estimation of nonlinear stochastic systems by evolution strategies based particle filter," *Proc. 9th Int. Symposium on Artificial Life and Robotics*: 406–409

[6] Kotecha, J. H. and Djurić, P. M. (2003), "Gaussian sum particle filtering," *IEEE Trans. on Signal Processing*, SP–51 (10): 2602–2612

[7] Liu, J. and Chen, R. (1998), "Sequential Monte Carlo Methods for Dynamic Systems," *J. of American Statistical Association*, 93: 1032–1044

[8] Schwefel, H.-P. (1995) *Evolution and Optimum Seeking*, J. Wiley

[9] Bäck, T. (1996), *Evolutionary Computation*, Oxford Press

The Eleventh International Symposium on Artificial Life and Robotics 2006 (AROB 11th'06),
B-con Plaza, Beppu, Oita, Japan, January 23-25, 2006

A New Algorithm for Obtaining Molecular Information Based on TaqMan® Real Time PCR

Zuwairie Ibrahim[1&2], Yusei Tsuboi[2], Sasaki Shinya[2], Yamaguchi Tomohiro[2], and Osamu Ono[2]

[1]Department of Mechatronics and Robotics
Faculty of Electrical Engineering
Universiti Teknologi Malaysia
81310 UTM Skudai, Johor Darul Takzim
Malaysia
zuwairie@fke.utm.my

[2]Institute of Applied DNA Computing
Meiji University
1-1-1 Higashi-mita, Tama-ku
Kawasaki-shi, Kanagawa-ken
214-8571 Japan
(zuwairie, tsuboi, ee21008, ee21012, ono)@isc.meiji.ac.jp

Abstract

We investigated a novel algorithm for obtaining molecular information based on TaqMan real time polymerase chain reaction (PCR). Two kinds of double-stranded DNAs (dsDNAs) of 120 base-pairs (bp) and 170-bp are chosen as the input of the algorithm, which reflects the output of Hamiltonian Path Problem (HPP) and the shortest path problem, based on Adleman's DNA computing and direct-proportional length-based DNA computing, respectively. This study explores that after a combination of TaqMan real time PCR is performed, a step-by-step analysis is important to analyze the result of TaqMan real time PCR, which in turn, make extraction of molecular information possible.

Keywords: Real Time PCR, TaqMan, Hamiltonian Path Problem, DNA Computing

1 Introduction

The innovation of the real-time polymerase chain reaction (PCR) technique played a crucial role in molecular medicine and clinical diagnostics [1]. Examples are the quantitation of relative gene expression [1], detection of minimal residual disease [2], cancer diagnostics [3], pathogen detection [4], and quantitation of viral load [5]. Other applications include detection of genetically modified organisms in food samples [6], and allelic discrimination [7].

Even though the use of real time PCR in molecular medicine and clinical diagnostics has gain its obvious popularity, the application of real time PCR in an unconventional DNA computing system is still questionable. In DNA computing point of view, a problem of obtaining molecular information is frequently occurs, especially in the case of molecular search, such as Hamiltonian Path Problem (HPP), Traveling Salesman Problem (TSP), and the shortest path problem. In these cases, for an optimal path, obtaining molecular information that is defined as the intermediate nodes between the start node and the end node, and also the order of these nodes is commonly required during the *in vitro* computation. Normally, in practice, two conventional methods: DNA sequencing and graduated PCR are employed in order to obtain the molecular information. The need for an automated, simple, and innovative approach for obtaining the molecular information is the driving force of this research. Hence, we propose the use of real time PCR and its associate algorithm in DNA computing, especially for obtaining molecular information. For real time PCR, several detection methods have been designed and developed such as hydrolysis or TaqMan probes, scorpions, hybridization probes, SYBR Green I, and molecular beacon [8]. In this research, TaqMan probe is chosen due to its capability to perform real time PCR with high specificity.

2 TaqMan Chemistry

A TaqMan DNA probe is a modified dual-labeled of oligonucleotides. The 5' and 3' end of oligonucleotides is attached with a reporter and quencher fluorescent molecule, respectively [9] as shown in Figure 1. Examples of common quencher fluorophores include TAMRA, DABCYL, and BHQ, whereas FAM, VIC, and NED are frequently used as reporter fluorophores [10].

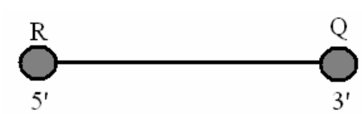

Figure 1: The structure of TaqMan DNA probe.

3 Real Time PCR with TaqMan Probe

The presence of dual-labeled TaqMan DNA probes with forward and reverse primers is important during real time PCR. As PCR is a repeated cycles of three steps: denaturation, annealing, and polymerization, TaqMan DNA probe will anneal to a site of DNA template in between the forward and reverse primers during annealing step, if the sequences of the site of DNA template is complement to the sequences of DNA probe. During polymerization, *Thermus aquaticus* (*Taq*) DNA polymerase will extend the primers in 5' to 3' direction. At the same time, the *Taq* polymerase acts as a "scissor" to cleave the probe and thus, separating the reporter from the quencher. As a result, the separation allows the reporter to emit its fluorescent as shown in Figure 2 [11]. As a result of PCR, the number of DNA template increases exponentially and at the same time, the intensity of fluorescent emitted by TaqMan probes is increases exponentially as well. The increasing of amplified DNA template with respect to fluorescent intensity can be detected and visualized by a real time PCR instrument such as Rosche LightCycler® 2.0.

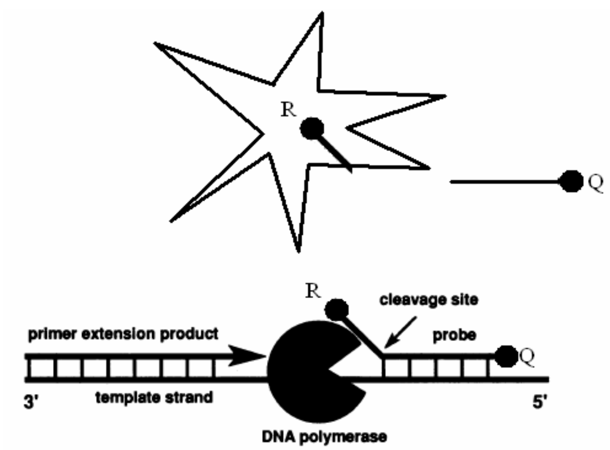

Figure 2: Sequence specific amplification detection by TaqMan real time PCR.

4 Notations

We introduce several notations in this paper. Firstly, $a_g b_h c_i d_j e_k f_l$ denotes a dsDNA which contains subsequences a, b, c, d, e, and f, consequently. The subscripts g, h, i, j, k, and l indicate the length of each respective subsequence. As such, a_{20} means the length of subsequences a is 20-mer. A dsDNA can also be represented without indicating the length of each segment as *abcdef*.

Reaction called TaqMan(a,b,c) means amplification is performed using forward primer a, reverse primer $\overline{c}$, and TaqMan probe b. TaqMan(a,b,c)=YES if an amplification is detected and the amplification graph is obtained. An example of amplification graph is shown in Figure 3 [12]. The condition of TaqMan(a,b,c)=YES is graphically explained in Figure 4. Note that the specific amplification is detected if the TaqMan probe, forward and reverse primers anneal to their complement sequences in the DNA template. On the other hand, TaqMan(a,b,c)=NO if no amplification is detected and the condition of this case is graphically described in Figure 5. Note that in this case, the DNA template does not contain complement sequences $\overline{b}$, which is required for DNA probe to anneal at the specific location in the DNA template.

5 The Proposed Algorithm based on TaqMan Real Time PCR for Hamiltonian Path Problem

Let say the output of the *in vitro* computation of HPP is represented by a 120-mer dsDNA:

$a_{20}x_{20}z_{20}w_{20}y_{20}b_{20}$

where the Hamiltonian path begin at node a, end at node b, and the intermediate nodes are x, z, w, and y, consequently. But in practice, one only knows the start node, the end node, and the intermediate nodes. However, the order of these intermediate nodes is not known.

The algorithm based on TaqMan real time PCR for this case consists of several reactions as follows. Note that for every reaction, the amplification output, which is indicated by YES or NO, is also given.

- TaqMan(a,w,x) = NO
- TaqMan(a,w,y) = YES
- TaqMan(a,w,z) = NO
- TaqMan(a,x,w) = YES
- TaqMan(a,x,y) = YES
- TaqMan(a,x,z) = YES
- TaqMan(a,y,x) = NO
- TaqMan(a,y,w) = NO
- TaqMan(a,y,z) = NO
- TaqMan(a,z,w) = YES
- TaqMan(a,z,x) = NO
- TaqMan(a,z,y) = YES

Importantly, real-time PCR itself does not provide direct molecular information as we need. In order to obtain molecular information based on this method, a series of step-by-step analysis is done to compute the order of the intermediate nodes, based on the results of previous reactions. During the step-by-step analysis, only the reaction with the result YES is taken into account. By referring to the expected output of the real time PCR, step-by-step analysis is performed as below:

1. TaqMan(a,w,y)	= YES	*awyb*	
2. TaqMan(a,x,w)	= YES	*axwyb*	
3. TaqMan(a,x,y)	= YES	*axwyb*	(no change)
4. TaqMan(a,x,z)	= YES	*ax*(*w*/*z*)(*y*/*z*)*b*	
5. TaqMan(a,z,w)	= YES	*a*(*x*/*z*)*wyb*	

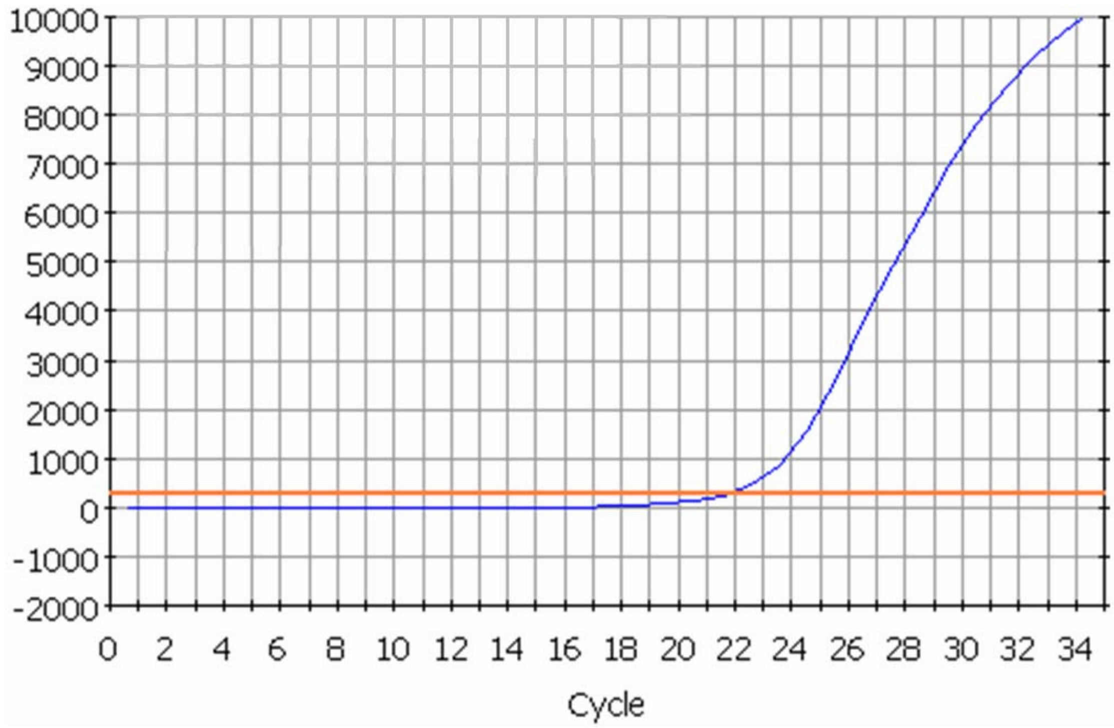

Figure 3: An example of amplification plot obtained using real time PCR.

6. TaqMan(a,z,y) = YES $a(x/z)wyb$ (no change)
7. Refer again to TaqMan(a,x,z) = Yes $axzwyb$
8. Output of step-by-step analysis = $axzwyb$

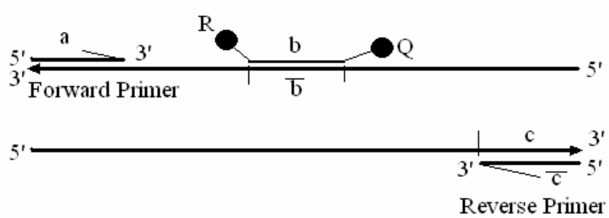

Figure 4: Graphical description of TaqMan(a,b,c)=YES.

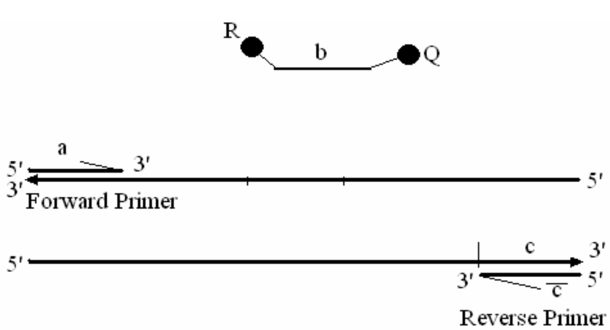

Figure 5: Graphical description of TaqMan(a,b,c)=NO.

6 The Proposed Algorithm based on TaqMan Real Time PCR for the Shortest Path Problem

Let say the output of the *in vitro* computation of the shortest path problem based on direct-proportional length-based DNA computing [13] is represented by a 170-mer dsDNA:

$a_{20}m_{10}x_{20}n_{30}w_{20}o_{20}y_{20}p_{10}b_{20}$

where the shortest path begin at node a, end at node b, and the intermediate nodes are x, w, and y, consequently. In this case the node z is not part of the intermediate nodes. But in practice, one only knows the start node and the end node only. Unlike HPP, information such as the number of the intermediate nodes, the presence or absence of a node in between the start and end node, and the order of the intermediate node are not known.

The algorithm based on TaqMan real time PCR for this case consists of several reactions as follows. Note that for every reaction, the amplification output, which is indicated by YES or NO, is also given.

- TaqMan(a,w,b) = YES
- TaqMan(a,x,b) = YES
- TaqMan(a,y,b) = YES
- TaqMan(a,z,b) = NO

- TaqMan(a,w,x) = NO
- TaqMan(a,w,y) = YES
- TaqMan(a,x,w) = YES
- TaqMan(a,x,y) = YES

Similar to the previous case, by referring to the expected output of the real time PCR, step-by-step analysis is performed as below:

1. TaqMan(a,w,b) = YES
2. TaqMan(a,x,b) = YES
3. TaqMan(a,y,b) = YES
4. TaqMan(a,z,b) = NO
   Thus, node z is not included.
5. TaqMan(a,w,y) = YES *awyb*
6. TaqMan(a,x,w) = YES *axwyb*
7. TaqMan(a,x,y) = YES *axwyb* (no change)
8. Output of step-by-step analysis = *axwyb*

7 Discussions and Concluding Remarks

Step-by-step analysis after the real time PCR is done is crucial because real time PCR did not provide the DNA information directly. It is shown that based on this example, the step-by-step analysis consists of 8 steps, where the order of subsequences, or molecular information, is updated after each step. However, it is also possible that the updated molecular information is similar to the previous updated molecular information of previous step. According to the expected results of real time PCR, after step 6 of step-by-step analysis, the final order of subsequences still can not be obtained. Thus, additional steps are required to refer to the step 4 before the order of subsequences can be finalized.

For the case of the shortest path problem, steps 1-4 are importance for confirmation whether a particular node exist in between the start and end node. Hence, based on the expected output of real time PCR, it can be conclude that the node z is not exist in between the start and end node and not part of the intermediate nodes. After that, the steps 5-8 are performed to extract the molecular information of the shortest path.

A combination of TaqMan real time PCR could be performed for extracting molecular information, instead of using DNA sequencing method and graduated PCR. Since the proposed algorithm appears more automated and simple, this study strongly encourages the use of real-time PCR for obtaining molecular information in DNA computing

References

[1] L. Overbergh, A. Giulietti, D. Valckx, B. Decallonne, R. Bouillon and C. Mathieu, "The use of real-time reverse transcriptase PCR for the quantification of cytokine gene expression," *Journal of Biomolecular Techniques*, Vol. 14, pp. 33-43, 2003.

[2] A. Li, E. Forestier, R. Rosenquist, and G. Roos, "Minimal residual disease quantification in childhood acute lymphoblastic leukemia by real-time polymerase chain reaction using the SYBR Green dye," *Experimental Hematolology*, Vol. 30, pp. 1170-1177, 2002.

[3] P. S. Bernard and C. T. Wittwer, "Real-time PCR technology for cancer diagnostics," *Clinical Chemistry*, Vol. 48, pp. 1178-1185, 2002.

[4] D. M. Norton, "Polymerase chain reaction-based methods for detection of Listeria monocytogenes: toward real-time screening for food and environmental samples," *Journal of AOAC International*, Vol. 85, pp. 505-515, 2002.

[5] H. G. Niesters, "Quantitation of viral load using real-time amplification techniques," *Methods*, Vol. 25, pp. 419-429, 2001.

[6] F. E. Ahmed, "Detection of genetically modified organisms in foods," *Trends in Biotechnology*, Vol. 20, pp. 215-223, 2002.

[7] J. S. Sevall, "Rapid allelic discrimination from real-time DNA amplification," *Methods*, Vol. 25, pp. 452-455, 2001.

[8] A. Giulietti, L. Overbergh, D. Valckx, B. Decallonne, R. Bouillon, and C. Mathieu, "An overview of real-time quantitative PCR: application to quantify cytokine gene expression," *Methods*, Vol. 25, pp. 386-401, 2001.

[9] N. J. Walker, "A technique whose time has come," *Science*, Vol. 296, pp. 557-559, 2002.

[10] M. A. Valasek and J. J. Repa, "The power of real-time PCR," *Advances in Physiology Education*, Vol. 29, pp. 151-159, 2005.

[11] P. M. Holland, R. D. Abramson, R. Watson, and D. H. Gelfand, "Detection of specific polymerase chain reaction product by utilizing the 5'→3' exonuclease activity of *Termus aquaticus* DNA polymerase," *Proceedings of the National Academy of Sciences of the United States of America*, Vol. 88, pp. 7276-7280, 1991.

[12] http://pathmicro.med.sc.edu/pcr/realtime-home.htm

[13] Z. Ibrahim, Y. Tsuboi, O. Ono, and M. Khalid, "Experimental implementation of direct-proportional length-based DNA computing for numerical optimization of the shortest path problem", *European Conference on Artificial Life 2005: Workshop on Unconventional Computing*, pp. 35-46, 2005.

The Eleventh International Symposium on Artificial Life and Robotics 2006 (AROB 11th'06),
B-con Plaza, Beppu, Oita, Japan, January 23-25, 2006

Automatic evolution of bipedal locomotion in a simulated humanoid robot with many degrees of freedom

Malachy Eaton, T.J. Davitt
Department of Computer Science and Information Systems,
College of Informatics, University of Limerick, Ireland
email: malachy.eaton@ul.ie

Abstract:

This paper describes a methodology together with an associated series of experiments employing this methodology for the evolution of walking behaviour in a simulated humanoid robot with eighteen degrees of freedom. The robots evolved in this study learn to walk smoothly in an upright or near-upright position and demonstrate a variety of different locomotive behaviours, including 'skating', 'limping' and walking in a manner curiously reminiscent of a mildly or heavily intoxicated person. A previous study [5] demonstrated the possible potential utility of this approach while evolving controllers based on simulated humanoid robots with a restricted range of movements. Although walking behaviours were developed, these were slow and relied on the robot walking in an excessively stooped position similar to the gait of a stooped elderly person. This paper extends the previous work to a robot with many degrees of freedom, up to eighteen in total (arms, elbows, legs, hips, knees, etc.) and demonstrates the automatic evolution of fully upright bipedal locomotion in a humanoid robot using an accurate physics simulator.

Introduction

The humanoid robot is simulated using the Webots mobile robot simulation package [7,11]. The humanoid robot is broadly modeled on the Sony QRIO humanoid robot [8].

For each motor (or joint) a number of keyframe values can be defined. These keyframe values are passed to a separate existing utility; the sequence manager. The keyframes are values that must be reached at a specific point in the movement. The interpolation function in the sequence manager divides up the distance between keyframes into the specified number of interpolation values. Every keyframe must be passed through in turn; once the final frame is reached the cycle repeats.

A genetic algorithm using the crossover, mutation, and selective reproduction operators provides the values for the individual keyframes. The fitness function employed is a simple function mainly based on the robot remaining standing together with the distance traveled by the robot in a forward direction. Using this fitness function together with the genetic algorithm the simulated humanoid robot evolves sophisticated movements over time for up to eighteen degrees of freedom and four keyframes per degree of freedom.

In order to get the robot to walk a fitness function based on the product of the length of time the robot remains standing by the total distance traveled by the robot was devised. This was later modified to reward walking in a forward (rather than backward or sideways direction) and also to promote walking in a more upright position, by taking the robots final height into account.

The current length of chromosome is 288 bits comprising 4 bits determining the position of the 18 motors for each of 4 keyframes. Twenty strings are used per generation. The genetic algorithm uses roulette wheel selection with elitism; the top string being guaranteed safe passage to the next generation, together with standard crossover and mutation.

We consider these results obtained to demonstrate the utility and possible future potential of this approach to the automatic development of bipedal locomotion together with other complex control applications for future humanoid robots.

For a good introduction to the general topic of evolutionary robotics see [9]. For a discussion on the general topic of the performance evaluation of bio-inspired embodied and simulated artifacts see [4]. For other work in this general area see references [1,2,3,6,8,10,12] We consider one of the advantages of our approach to be the relative simplicity of application and also the potential ease of extensibility to other control functions and robot bodies.

The Webots World

We a mobile robot simulation package called Webots. It allows you to create and modify various robot worlds ranging from offices to football pitches. The package also provides sample controllers for the robots which range from two wheeled machines with no sensors to highly sophisticated humanoid robots with several sensors, cameras etc. Using the package you can create new robot worlds with relative ease as well as modify the existing ones. Similarly you can create and/or modify robot controllers. using C, C++ or Java.

The provided worlds are of great importance in assisting you in your development of robot controllers. Inside the robot world you can change the angle of the image you are see or move the robot to any point inside the world. Figure 1 shows the robot in the simulated world modelled for this work.

The world also contains a facility where by you can try out various movements with the robot without having to actually program it. While this can be slow and at times tedious it is vital in understanding the robots functionality. A controller menu is available from which you can control all the robots joints. The joints operate in a similar (but simplified manner) to human joints. By this we mean that the knee only moves in one way i.e. back/forward whereas the shoulder moves in three ways: Up/Down, Left/Right and in circular motions.

The sequence manager is an existing utility which gets sent an integer value corresponding to the sequence to be performed. Once it has this it reads in the servo positions from a file and moves the joints to the desired position at the desired speed. A key feature of the sequence manager is the ability to use interpolation values. These greatly cut down on the amount of positions to be defined. It does this by taking in a series of keyframes. The keyframes are the values which must be reached at a specific point in the movement. The interpolation function in the sequence manager divides up the distance between keyframes into the specified number of interpolation values. Every keyframe must be passed through.

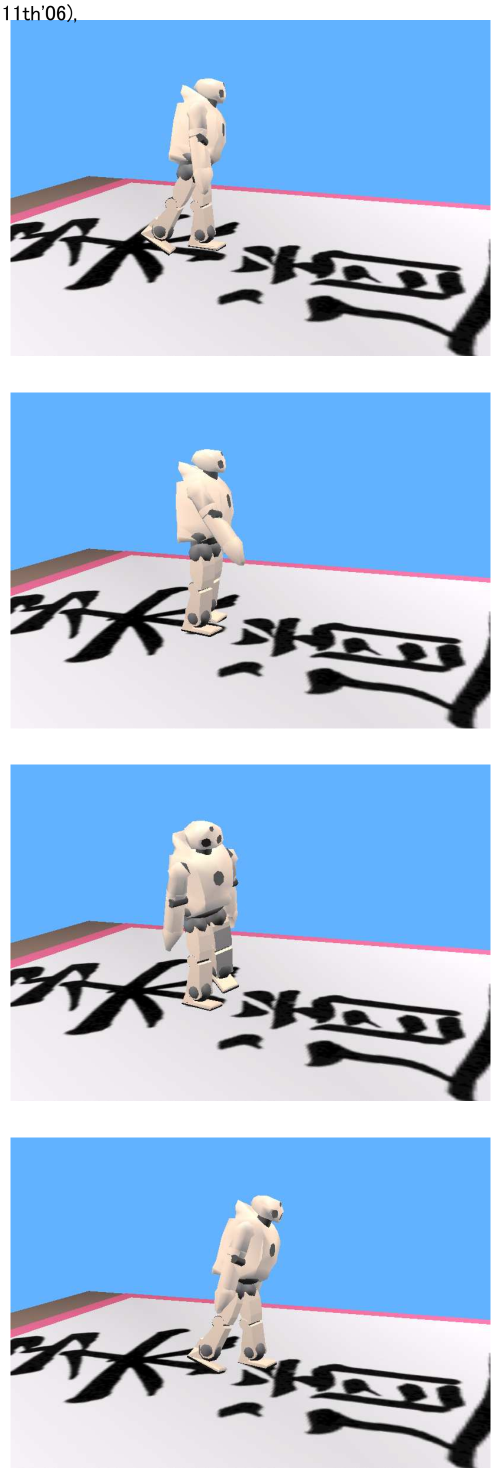

Figure 1. The Robot walking with a limping gait; this can be seen in the third frame in this sequence, although overall forward motion is quite good. Notice also the right arm moving forward in a steadying motion in frame 2.

The Genetic Algorithm

A genetic algorithm was used to develop robot walking sequences. The string length of the chromosomes is 288 bits. This encompasses 4 keyframes representing 18 motors. Four bits are used to determine the position of each motor. There are fifty strings per generation and up to five hundred generations. The basic GA algorithm is as follows.

- Firstly a random number generator is used to give random binary values to each string.
- Minimum values and range values for each joint to be included in the algorithm are entered.
- The string is broken into values for each four bit section giving a value of between 1 and sixteen.
- The range of each motor is divided by the number obtained in the previous step and added onto the minimum motor value to give a set motor position.
- This process is continued until all motors have assigned values.
- Once the motors have their assigned values, a sequences file is automatically produced to be read by the sequence manager.
- This sequence is then tested until the robot falls over, or a sufficient amount of time has passed corresponding to approximately 30 seconds of 'real' time
- After the robot has reached one of the above conditions it is reset to a standing position and the fitness of the walking attempt is calculated.This is done for each string in the given generation.
- Once all strings have been tested the fitness function is applied to determine which strings will be allowed to reproduce, together with the genetic operators of mutation and crossover with specified probabilities. This is carried out for each generation.

Roulette wheel selection was used where the probability of selection is proportional to the strings' fitness was used, with or without elitism. Elitism is also used which means that the top string is guaranteed safe passage into the next generation. These strings were also available for selection for crossover and mutation. Two point crossover is applied with a probability of 0.5 and the probability of a bit being mutated is 0.04. These values were arrived at after some experimentation.

Fitness function and initial results

The original fitness function used was based on the product the length of time the robot stayed standing and the distance travelled. This was determined by calculating the amount of movement frames the robot had travelled and multiplying it by the distance travelled. The distance travelled was computed using the formula for measuring a straight line i.e. $\sqrt{((x2-x1)^2 + (y2-y1)^2)}$. The points used were the robots initial position and the position where it eventually fell.

At this stage the robot was effectively mostly learning to dance on the spot. Also sequences that walked backwards scored equally well as those that went forward. To remedy this, a weight was used to increase the value of all walks that go directly forward: the fitness was multiplied by a factor (2.0) if it moved in the direction it was facing to promote forward walking as it was the main goal.

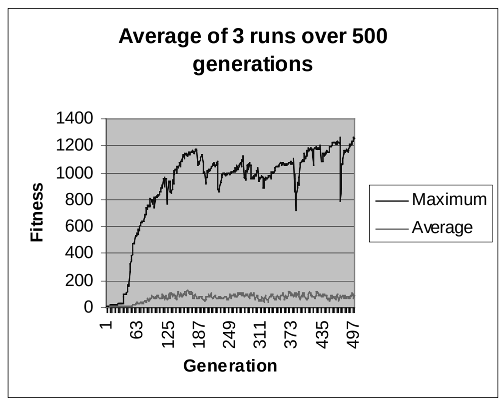

Figure 2. Average and maximum fitness

The fitness function then was the product of the number of timesteps completed up to a maximium (800) by the distance moved from the starting point multiplied by two if the final resting position of the robot was ahead of where it started. In order to promote walking in an upright position the robots height was also taken into account. This used the Y value returned by the GPS sensor to determine the posture of the robot; the more upright the robot was the higher it was rewarded.

Figure 2 shows the average and maximum fitness values for the robot over 500 generations. These figures are averaged over 3 runs. Each run took several days of actual computer simulation corresponding to about a week of simulated time (the simulation runs at about three times faster than an actual robot).

A value over about 100 corresponds to the robot at least staying standing for some period of time, over 500 corresponds to a walk of some description. We see that for about 50 generations no walk develops, then there is a nice steady increase in fitness up to about generation 500, followed by an up and down pattern with a gradual upward trend. Note that although elitism was employed, because of the accurate physics simulation with noise etc. this allows for the maximum fitness to fall as well as rise from generation to generation. Any fitness above about 800 will generally correspond to a reasonable walk in the forward direction, 1200 or above corresponding to quite good, stable walks. The maximum fitness generated was in generation 470 of the second test run with a value of 1860 corresponding to a fine forward walk with a slight limping gait (see Figure. 1).

Other patterns of locomotion included 'skating', with the robot keeping one foot constantly in contact with the ground and pushing along with the other, and walking in a manner reminiscent of an intoxicated person, with arms and legs akimbo, however still walking in a surprisingly effective manner. The simulations, while running, have provoked comments on the various human-like attributes of the walking patterns developed, especially in the later stages of evolution.

Summary and future work

Using a genetic algorithm a simulated robot has been able to teach itself how to walk. The section on the Genetic Algorithm explains how the controller file was able to process binary strings in order to develop walking sequences through the manipulation of 18 of the 22 motors used in the robot.

The different evolutionary techniques used such as roulette wheel and elitism are explained. The development of the fitness function used to determine the best walk sequences has been described in a little detail. To our knowledge this is one of the first published papers to allow for the automatic generation of walking behaviour in a robot with such a large number of degrees of freedom. Work is continuing on the development of controllers for humanoid robots, by extending again the number of degrees of freedom, and by the application of the techniques described here to different humanoid robot morphologies.

References:

[1] Boeing A, Hanham S, Braunl T (2004)"Evolving autonomous biped control from simulation to reality" in Proc. 2nd International Conference on Autonomous Robots and Agents" December 13-15, 2004, pp. 440-445.

[2] Boeing A, Braunl T (2002) "Evolving Splines: An alternative locomotion controller for a bipedal robot" in Proc. 7th International Conference on Control, Automation, Robotics and Vision (ICARCV'02), Dec. 2002, pp.898-802.

[3] Busch J et al (2002) "Automatic Generation of Control Programs for Walking Robots using Genetic Programming" Proc 5th European Conference on Genetic Programming (EUROGP), LNCS 2278, J.A Foster et al. (Eds.) pp. 258-267, 2002.

[4] Eaton M, Collins JJ, Sheehan L (2001), "Towards a benchmarking framework for research into bio-inspired hardware-software artefacts", in *Artificial Life and Robotics*, Vol. 5 No. 1, 2001 pp. 40-46.

[5] Eaton, M. and Davitt, T.J. (2005) "Evolution of walking behaviour in a simulated humanoid robot" in Proceedings of the 9th International Conference on Cognitive and Neural Systems, Boston University May 2005, page 26.

[6] Hornby, G.S., Fujita, M., Takamura, S., Yamamoto, T. and Hanagata, O. (1999). "Autonomous evolution of gaits with the Sony quadruped robot." *Proceedings of 1999 Genetic and Evolutionary Computation Conference (GECCO).* Banzhaf, Daida, Eiben, Garzon, Honavar, Jakiela, Smith, eds., Morgan Kauffmann, pp. 1297-1304.

[7] Michel O (2004), "Webots: Professional Mobile Robot Simulation", International Journal of Advanced Robotic Systems, Vol. 1, No. 1, pages 39-42.

[8] Mojon S (2003) "Realization of a Physic Simulation for a Biped Robot" Semester project, School of Computer and Communication Sciences EPFL, Switzerland 2003.

[9] Nolfi S, Floreano D.(2000) "Evolutionary Robotics: The Biology, Intelligence, and Technology of Self-Organizing Machines". MIT press, 2000.

[10]Wolff K and Nordin P (2002)"Evolution of Efficient Gait with an Autonomous Biped Robot using Visual Feedback, Proceedings of the 8th Mechatronics Forum International Conference pp 504-513. 2002 .

[11] Webots. http://www.cyberbotics.com. Commercial Mobile Robot Simulation Software.

[12] Zykov V, Bongard J, Lipson H (2004) "Evolving Dynamic Gaits on a Physical Robot" Proceedings of Genetic and Evolutionary Computation Conference, Late Breaking Paper, GECCO'04, 2004.

Interpretability-Accuracy Tradeoff by Multiobjective Genetics-Based Machine Learning for Pattern Classification Problems

Yusuke Nojima, Hisao Ishibuchi
Dept. of Computer Science and Intelligent Systems
Osaka Prefecture University
Gakuen-cho 1-1, Sakai, Osaka 599-8531
{nojima, hisaoi}@cs.osakafu-u.ac.jp

Abstract

This paper examines the interpretability-accuracy tradeoff of fuzzy rule-based classifiers obtained by a multiobjective genetics-based machine learning (GBML) algorithm. Our GBML algorithm is a hybrid version of Michigan and Pittsburgh approaches. Each candidate classifier is evaluated in the framework of evolutionary multiobjective optimization (EMO). The main advantage of EMO is a number of non-dominated solutions with respect to multiple objectives can be obtained in its single run. In our GBML, we employ three objectives corresponding to the accuracy and interpretability of classifiers: to maximize the number of correctly classified training patterns by a classifier, to minimize the number of fuzzy rules in a classifier, and to minimize the rule length of a classifier. From these three objectives, we define three types of formulations and compare three interpretability-accuracy tradeoffs.

1 Introduction

There are two goals in the design of fuzzy rule-based classifiers: One is the accuracy maximization and the other is the complexity minimization [1, 2]. The complexity minimization is directly related to the interpretability of the classifier. Some researchers had tried to simultaneously perform the accuracy maximization and the complexity minimization. Then the existence of the interpretability-accuracy tradeoff in the design of fuzzy rule-based classifiers has been realized by some researchers.

This paper examines the interpretability-accuracy tradeoff of fuzzy rule-based classifiers obtained by a multiobjective genetics-based machine learning (GBML) algorithm. In general, GBML algorithms are divided into two approaches: Michigan and Pittsburgh approaches. A single fuzzy rule is handled as an individual in the Michigan approach, while a rule set (i.e., a fuzzy rule-based classifier) is handled as an individual in the Pittsburgh approach. Our multiobjective GBML algorithm is a hybrid version of Michigan and Pittsburgh approaches, which is implemented in the framework of evolutionary multiobjective optimization (EMO) [3]. Thus, each classifier is evaluated in Pittsburgh approach based on EMO algorithm, while each rule of the rule set is evaluated in Michigan approach as a local search. We employ NSGA-II algorithm that is one of the state of the art EMO algorithms [4]. In our multiobjective GBML algorithm, we assume three objectives: to maximize the number of correctly classified training patterns by a classifier, to minimize the number of fuzzy rules in the classifier, and to minimize the number of antecedent conditions of fuzzy rules in the classifier. The first objective corresponds to accuracy maximization. The second and third objectives correspond to interpretability maximization. The reason why we assume the second and third objectives as interpretability maximization is that we intend to prefer simple classifiers with a small number of rules rather than complex classifiers with a large number of rules. Thanks to these three objectives, we can obtain a number of non-dominated fuzzy rule-based classifiers with different accuracy and interpretability. That is, we can obtain not only complicated classifiers with high accuracy but also simple classifiers with high interpretability by our GBML algorithm.

In this paper, through some computational experiments, we demonstrate that we can obtain a number of non-dominated fuzzy rule-based classifiers by our GBML algorithm and there exist the clear tradeoff between interpretability and accuracy of obtained classifiers. Also, we show that some of obtained classifiers are overfitting to the training patterns. Furthermore, we show the effect of each objective comparing three-objective formulation consists of all three objectives with two-objective formulations consist of the first objective and either the second or third objective.

2 Multiobjective Genetics-Based Machine Learning

2.1 Fuzzy Rule-Based Classifier

Let us assume that we have m training patterns $\mathbf{x}_p = (x_{p1}, ..., x_{pn})$, $p = 1, 2, ..., m$ from M classes where x_{pi} is the attribute value of the p-th training pattern for the i-th attribute ($i = 1, 2, ..., n$). We also assume that the n-dimensional pattern space has already been normalized into the n-dimensional unit hyper-cube $[0, 1]^n$. That is, we assume that we have an M-class pattern classification problem with m training patterns in the n-dimensional pattern space $[0, 1]^n$. We use fuzzy rules of the following form:

Rule R_q: If x_1 is A_{q1} and ... and x_n is A_{qn}
then Class C_q with CF_q

where R_q is the label of the q-th rule, $\mathbf{x}= (x_1, ..., x_n)$ is an n-dimensional pattern vector, A_{qi} is an antecedent fuzzy set, C_q is a class label, and CF_q is a rule weight. We use 14 homogenious fuzzy partitions as antecedent fuzzy sets (Fig.1). We also use "don't care" as an additional antecedent set. According to the compatibility grade of each training pattern (see the textbook on fuzzy data mining [5]).

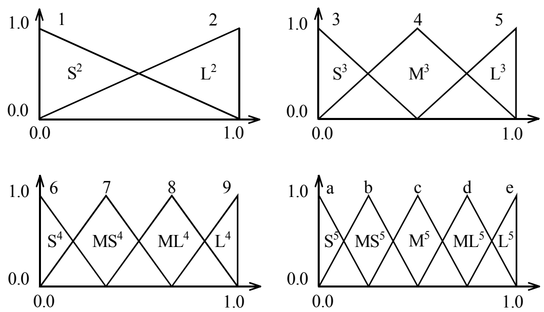

Figure 1: Homogeneous fuzzy partitions.

Let S be a fuzzy rule-based classifier (i.e., a set of fuzzy rules). When an input pattern is to be classified by the fuzzy rule-based classifier S, a single winner rule with the maximum compatibility grade multiplied by rule weight CF is chosen from S. The input pattern is assigned to the consequent class of the winner rule. When multiple rules with different consequent classes have the same maximum value, the classification of the input pattern is rejected. The classification of $\mathbf{x}_q$ is also rejected when there is no compatible fuzzy rules with positive compatibility grades for $\mathbf{x}_q$ [5].

Because the consequent class and rule weight are specified by the compatibility grade of training patterns automatically, the main issue of this problem is to find the appropriate combination of antecedent fuzzy sets. To this end, we apply our multiobjective GBML algorithm to the design of fuzzy classifiers.

2.2 Multiobjective Formulations of Fuzzy Rule-Based Classifier Design

To obtain a large number of non-dominated classifiers with different accuracy and different complexity, we consider the following three objectives:

$f_1(S)$: The number of correctly classified training patterns by S,

$f_2(S)$: The number of fuzzy rules in S,

$f_3(S)$: The total number of antecedent conditions of fuzzy rules (i.e., total rule length) in S.

From these objectives, we define the following three formulations of multiobjective optimization problems (MOPs) for the interpretability-accuracy tradeoff analysis:

MOP-1: Maximize $f_1(S)$, minimize $f_2(S)$,

MOP-2: Maximize $f_1(S)$, minimize $f_3(S)$,

MOP-3: Maximize $f_1(S)$, minimize $f_2(S)$ and $f_3(S)$.

2.3 Hybrid Multiobjective Fuzzy GBML Algorithm

We use a hybrid multiobjective fuzzy GBML algorithm to efficiently find a large number of non-dominated fuzzy rule-based classifiers of the three multiobjective optimization problems: MOP-1, MOP-2 and MOP-3. Our GBML algorithm can be viewed as a Pittsburgh-style algorithm except that a Michigan-style algorithm is applied to each rule set as a kind of mutation. Our GBML algorithm is implemented in the framework of the NSGA-II algorithm as follows:

Step 1: Generate an initial population of N_{pop} classifiers where N_{pop} is the population size.

Step 2: Generate an offspring population by iterating the following procedures N_{pop} times:
(1) Select a pair of parent classifiers from the current population using binary tournament selection.
(2) Generate an offspring from the selected pair of parent classifiers by crossover and mutation.
(3) Apply a single iteration of a Michigan-style GBML algorithm to the offspring classifier with a prespecified probability.

(4) Remove meaningless fuzzy rules with non-positive rule weights from the classifier.

Step 3: Combine the current population and the offspring population into a merged one. Then choose the best N_{pop} classifiers from the merged population to construct the next population.

Step 4: If a prespecified stopping condition is not satisfied, return to Step 2. Otherwise terminate the execution of the algorithm. In the latter case, we choose all the non-dominated classifiers in the merged population in Step 3 as the final solutions.

In the following, we explain our GBML algorithm in detail. Each fuzzy rule is represented by its antecedent part $\mathbf{A}_q$ as an integer string of length n where n is the dimensionality of the pattern space (i.e., n is the number of attributes). We use 15 symbols (e.g., 0, 1, ..., 9, a, b, c, d, e) for representing don't care and the 14 antecedent fuzzy sets in Fig. 1. A rule set S of classifier is handled as an individual and coded as a concatenated integer string where each substring of length n represents a single fuzzy rule.

We use a heuristic method to generate an initial population of classifiers in Step 1 of our GBML algorithm. First we randomly select a prespecified number of training patterns (say, N_{rule} training patterns). Next we generate a fuzzy rule from each training pattern by probabilistically choosing an antecedent fuzzy set for each attribute value from the 14 candidate fuzzy sets based on softmax method. That is, the antecedent fuzzy set with a large compatibility grade with the training pattern tends to be selected. Then each antecedent fuzzy set of the generated fuzzy rule is replaced with don't care using a prespecified probability $P_{don't\,care}$. In this manner, N_{rule} initial fuzzy rules are generated. An initial rule set consists of these fuzzy rules. By iterating this procedure, we generate N_{pop} initial classifiers (i.e., an initial population).

In Step 2 (1) of our GBML algorithm, a pair of parent rule sets are selected from the current population by binary tournament selection based on the Pareto ranking and the crowding measure as in the NSGA-II algorithm [4]. Let the selected classifiers be S_1 and S_2. Some fuzzy rules are randomly selected from each parent to construct a new classifier by crossover in Step 2 (2). The number of fuzzy rules to be inherited from each parent to the new classifier is randomly specified in the intervals $[1, |S_1|]$ and $[1, |S_2|]$, respectively. Thus, the string length is not fixed in our method. In our computational experiments, we use an upper limit on the number of fuzzy rules in each classifier for finding compact classifiers with high interpretability. The upper limit is specified as 40 in this paper. This crossover operation is applied to the selected pair of parent classifiers using a prespecified crossover probability P_C. When the crossover operation is not applied, one of the two parent classifiers is viewed as an offspring. Each antecedent fuzzy set of the newly generated offspring classifier is randomly replaced with a different antecedent fuzzy set using a prespecified mutation probability P_M.

After the crossover and mutation operations in Step 2 (2), a single iteration of the following Michigan-style algorithm is applied to the newly generated offspring classifier in Step 2 (3):

(3)-1: An offspring classifier S is given by the main part of our GBML algorithm.

(3)-2: Classify each training pattern by the classifier S. The fitness value of each rule is the number of correctly classified training patterns by that rule.

(3)-3: Generate $N_{replace}$ fuzzy rules from the existing rules in S by genetic operations and from misclassified and/or rejected training patterns.

(3)-4: Replace the worst $N_{replace}$ fuzzy rules in S with the newly generated $N_{replace}$ rules.

(3)-5: Return the updated classifier S to the main part of our GBML algorithm.

The fitness of each fuzzy rule R_q is the number of correctly classified training patterns by R_q in (3)-2 of our Michigan-style algorithm. For selected offspring, we generate at least a half of new fuzzy rules by genetic operations from the existing rules in S. The other rules are generated from the misclassified and rejected training patterns by the classifier as in the initialization of our GBML (see [3]).

When a new classifier includes meaningless fuzzy rules with non-positive rule weights, those fuzzy rules are removed from the classifier (Step 2 (4)). This procedure is iterated N_{pop} times to generate an offspring population of N_{pop} classifiers. After generating the next population is constructed from the merged population of the current and offspring populations in the same manner as the NSGA-II algorithm [4]. When a prespecified stopping condition is satisfied, our GBML algorithm returns all the non-dominated classifiers in the merged population.

3 Experiments

We examined six data sets with many numerical attributes. But, due to the page limitation, we show one of the typical results in the design of fuzzy rule-based classifiers by our GBML algorithm. The performance of each variant was evaluated by ten independent iterations (with different data partitions) of the whole ten-fold cross-validation (10-CV) procedure. That is, our GBML algorithm was executed 100 times.

We use the following parameter specifications in our GBML algorithm: number of fuzzy rules of a initial classifier: 20 rules, probability of don't care: 0.8, population size: 200 rule sets, crossover probability in the main part: 0.9, crossover probability in the Michigan part: 0.9, mutation probability in the main part: $1/n$, mutation probability in the Michigan part: $1/n$, stopping condition: 5000 generations.

Figure 2 shows the average error rates on training patterns of the diabetes data set. This data set has 768 patterns with 8 attributes and 2 classes. The average error rates in MOP-1 are calculated from classifiers with the same number of rules. As in MOP-1, the average error rates in MOP-2 are calculated from classifiers with the same rule length. The average error rates in MOP-3 are calculated from classifiers with the same number of rules and the same rule length. However, when rule sets with the same number of rules and/or rule length were obtained only from 50 or less runs, the average error rate is not reported in this paper since such an average result is not reliable. From Fig.2, we can see that there exist the clear interpretability-accuracy tradeoffs and each tradeoff has a similar structure to one another.

Figure 3 shows the average error rates on test patterns of the diabetes data set. We can see that the obtained classifiers with high generalization ability were obtained from MOP-3. This observation suggests a potential usefulness of the use of both complexity measures (i.e., the number of fuzzy rules and the total rule length) as a safeguard against the overfitting of fuzzy rule-based classifiers to training patterns.

4 Summary

In this paper, we examined the interpretability-accuracy tradeoff of fuzzy rule-based classifiers through computational experiments using a hybrid multiobjective fuzzy GBML algorithm. Experimental results showed that there exists a clear interpretability-accuracy tradeoff structure with respect to error rates on training patterns. Our experimental results also suggested potential advantages of three-objective formulation over two-objective ones.

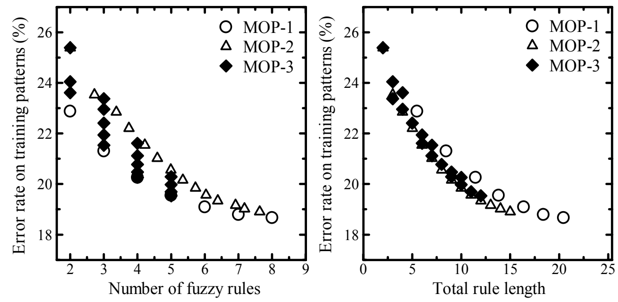

Figure 2: Experimental results on training patterns of the diabetes dataset.

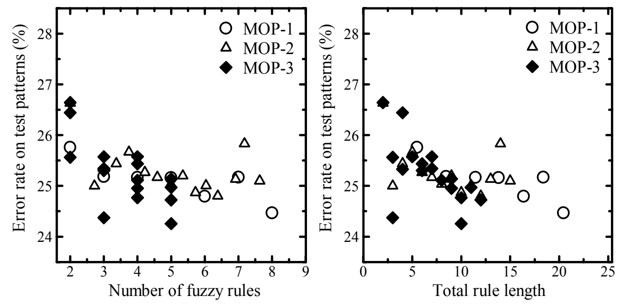

Figure 3: Experimental results on test patterns of the diabetes dataset.

References

[1] J. Casillas, O. Cordon, F. Herrera, L. Magdalena (eds.), *Interpretability Issues in Fuzzy Modeling*, Springer, Berlin, 2003.

[2] J. Casillas, O. Cordon, F. Herrera, L. Magdalena (eds.), *Accuracy Improvements in Linguistic Fuzzy Modeling*, Springer, Berlin, 2003.

[3] H. Ishibuchi, T. Yamamoto, T. Nakashima, Hybridization of fuzzy GBML approaches for pattern classification problems, *IEEE Trans. on Systems, Man, and Cybernetics*: Part B 35 (2) (2005) 359- 365.

[4] K. Deb, A. Pratap, S. Agarwal, T. Meyarivan, A fast and elitist multiobjective genetic algorithm: NSGA-II, *IEEE Trans. on Evolutionary Computation* 6 (2) (2002) 182-197.

[5] H. Ishibuchi, T. Nakashima, M. Nii, *Classification and modeling with linguistic information granules: Advanced approaches to linguistic data mining*, Springer, Berlin, 2004.

Recovering the Network through Mutual Recognition and Copying

Yoshiteru Ishida and Yuuki Sugawara
Department of Knowledge-based Information Engineering
Toyohashi University of Technology
Toyohashi, Aichi, 441-8580 Japan

Abstract

We studied a self-repair network by mutual copying. This paper further considers a model that involved mutual recognition among nodes before repairing. Although the repairing with recognition outperforms the repairing without recognition, there are cases that recognition hampers cleaning. It is reported that there is an adequate frequency of mutual recognition that enables the best result of cleaning the network.

1 Introduction

Although many networks, artificial or natural, have been studied from the viewpoint of their structure and topology, and their structural properties such as "scale-free" or "small-world" has been paid attention, studies on the interaction in the network or "semantics" of the network (as opposed to syntax) have been paid little attention. For example, "scale-free" network [1] focuses on the spatial scale-freeness; however, temporal scale-freeness seems also important.

We have been studying the interaction of the network and proposed the framework of immunity-based systems, "semantics" of the network. In our framework, the network is double-sided and would raise the self-referential paradox in a flat logic without distribution, and hence subtle tuning is needed as in the immune system. The drastic change of the aspect of faults, as seen in malicious faults such as computer viruses, calls for the design paradigm of the immune system which has the "self" that is adaptive to the environment.

The self-nonself discrimination problem dealt in the immune system would raise self-referential problem as often mentioned in the statements such as: "I am a liar" and "This statement is false". To resolve this paradox, hierarchical logic or distribution of subject could be done. We use the latter approach.Dividing subject and placing them inside the system has been often discussed in Autopietic Systems [2] and other complex systems. Placing the distributed subjects in the system implies that the subjects have only local and unlabelled information in solving problems. Also, and more importantly, the subject can be the object to which subject operates and interacts. It is still controversial whether the immune system actually need to discriminate self and nonself in order to eliminate nonself [3], however, elimination is done actually and hence the double-sided property that the subject must be the object is imperative. Thus, the immune system is "double-edged sword".

2 Self-Repair by Copying: The Double Edged Sword

2.1 A Model of Self-Repair Network

This paper concentrates on the naive problem of cleaning up the network by mutually copying: When can a contaminated network be cleaned up by mutually copying? We have studied the immunity-based systems, and pointed out the possibility that they will be the double edged sword [4]. For example, the system based on the Jerne's idiotypic network framework has recognizing units that are also being recognized. Self-nonself recognition involving self-referential paradox could also lead to the situation of the double edged sword: recognition done by units credible enough is credible, but not credible otherwise. The repair by copying in information systems is also the "double edged sword" and it is engineering concern to identify when it can really eradicate abnormal elements from the system. This paper considers CA (cellular automata), probabilistic CA specifically, to model the situation where computers in a LAN mutually repair by copying their content. We will give clear priorities on simplicity over reality of the system. The studying the reliability of information systems by a probabilistic CA is not new. The results by Peter Gacs [5] for his probabilistic CA proving positive error rate conjecture.

2.2 A Model by Probabilistic Cellular Automata

In our model, the system consists of units capable of repairing other units connected. We call the connected units as neighbor units based on the terminology of CA. The repairing may be done by copying its content to the other units, since the application to a computer network by LAN in our mind. Although mutual repairing and testing may be done in an asynchronous manner, our model considers synchronous interactions for simplicity and for comparison with existing probabilistic CA models [6, 7, 8].

The structure of the array is a ring with unit 1 adjacent to the unit N (Figure 1). Also, we restrict the case where each unit has a binary state: normal (0) and abnormal (1).

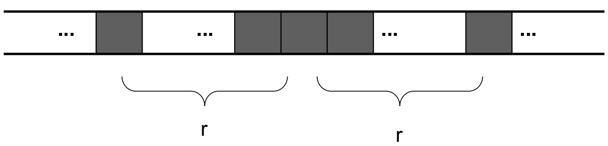

Figure 1: One-dimensional array with the neighborhood radius r. The next state of the cell will be determined by $2r + 1$ nodes in the neighborhood.

The specific feature of the self-repair network is that repairing by the abnormal unit has an adverse impact. This adverse impact is implemented as higher probability of contamination than that of successful cleaning in the model by probabilistic cellular automata. Each unit tries to repair the units in the neighborhood in a synchronous fashion with a probability P_r. As shown in Figure 5, the repairing will be successful with the probability P_{rn} when it is done by a normal unit, but with the probability P_{ra} when by an abnormal unit ($P_{ra} \leq P_{rn}$). In this paper, we assume $P_{rn} = 1$. The repaired units will be normal when all the repairing is successful. Thus, when repairing is done by the two adjacent units, all these two repairing must be successful in order for the repaired unit to be normal. In such models, it is of interest to determine how the repairing probability P_r should be set when the success probability by abnormal unit P_{ra} is given. Also, when P_r is fixed to some value and P_{ra} moves continuously to large value, does the number of abnormal units change abruptly at some critical points or does it just gradually increase? Further, when given some value of P_{ra}, P_r should always be larger, which requires more cost. Domany-Kinzel model [6] is a one-dimensional two state and totalistic probabilistic cellular automaton (PCA).The interaction rule is as follows:

$(0{*}0) \rightarrow 0{:}1$, $(0{*}1) \rightarrow 1{:}p1$, $(1{*}1) \rightarrow 1{:}p2$

Our PCA model can be equated with the DK model when $P_r = 1$ (i.e. units always repair).

2.3 Recognizing Abnormal Units Before Repair

The original model of a self-repair network does not involve recognition of abnormal units. Rather, the model is intended to show when and how the cleaning of the network can be done without recognition. The model in this paper, however, focuses the impact of recognition for diminishing useless repair or repair with adverse effect. Thus, a new model involves recognition of the states (normal or abnormal) of a target node before trying to repair the node. For simplicity, frequency of recognition is controled by a recognition rate P_{rec}. When recognition is done (with a probability P_{rec}), successful recognition occurs with a recognition success rate P_{recn} when done by normal nodes, and P_{reca} by abnormal nodes. If the target node is identified as abnormal, repair action take place. When recognition does not occur (with a probability $1 - P_{rec}$), the repair action takes place with the probability P_r. Thus, if the recognition is completely suppressed ($P_{rec} = 0$), this new model gets back to the original model. Figure 2 shows the procedure of recognition and repair.

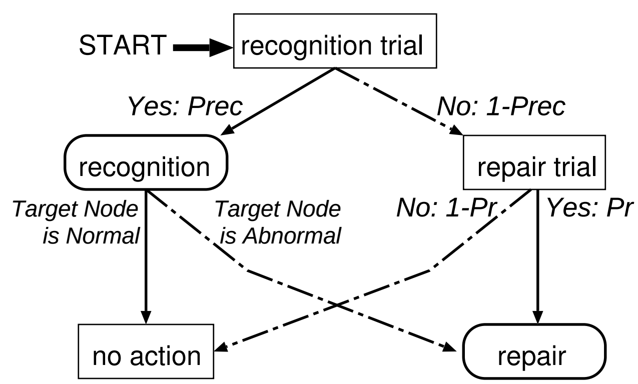

Figure 2: Procedure for Recognition and Repair

Figure 3 depicts a scenario of the state change by recognition and repair. When the center node is focused, recognition is done by the left node and the state of the center node is successfuly identified. Since the center node is normal, no repair action take place from the left node. On the other hand, recognition does not take place from the right node, and repair action take place in this scenario. Since the repair by the right node fails, the center node is made abnormal.

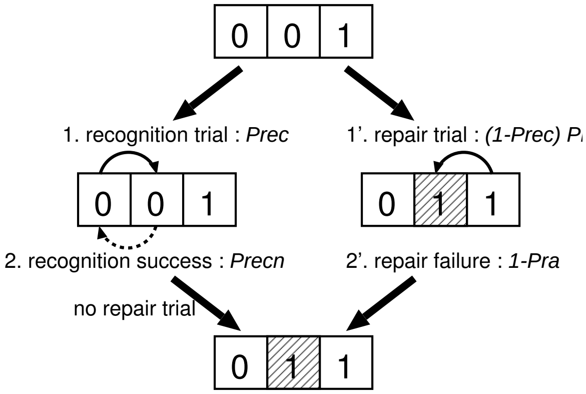

Figure 3: An Example of Recognition and Repair in the Neighborhood

3 Simulation Results

3.1 Impact of Recognition

Computer simulations are conducted in a one-dimensional array with a ring structure (periodic boundary condition). Parameters listed in Table 1 are fixed throughout simulations. Other parameters: P_{rec}, P_{reca}, P_r, and P_{ra} are varied to observe the impact of recognition.

Table 1: List of Parameters for Simulations

	Description	Value
N	Number of Nodes	500
$N_f(0)$	Initial Number of Failure Nodes	250
r	Radius of Neighborhood	1
T	Time Steps for Each Trial	5000
N_T	Number of Trials Averaged for One Plot	10
P_{rn}	Repair Success Rate by Normal Nodes	1
P_{recn}	Recognition Success Rate by Normal Nodes	1

We are concerned with a problem: Is recognition really necessary? If yes, when and how the recognition should be incorporated? In the following simulations, we persue the problem of identifying an appropriate level of recognition (i.e. P_{rec}) when the adverse effect of abnormal units (i.e. P_{reca} and P_{ra}) is given.

3.2 The Worst Case

Let us first observe the worst case when there will be no successful repair by abnormal nodes (i.e. $Pra = 0$ is fixed). Let us further divide the case into two extreme cases: there will be no repair action at all when recognition is not carried out (i.e. $Pr = 0$ is fixed); and there will be always repair when recognition is not carried out. Figure 4 plots the former case (*no repair*), and Figure 5 the latter case (*always repair*). In the *no repair* case, there is not blind repair and repair takes place only after recogntion. In the original model [9] where no recognition is involved, all the nodes will eventually become abnormal in the worst case. However, the abnormal nodes can be even eradicated in the model with recognition when $Preca$ exceeds 0.4. It is also observed that level of recognition ($Prec$) should be kept small to control the number of abnormal nodes when $Preca$ is less than 0.4.

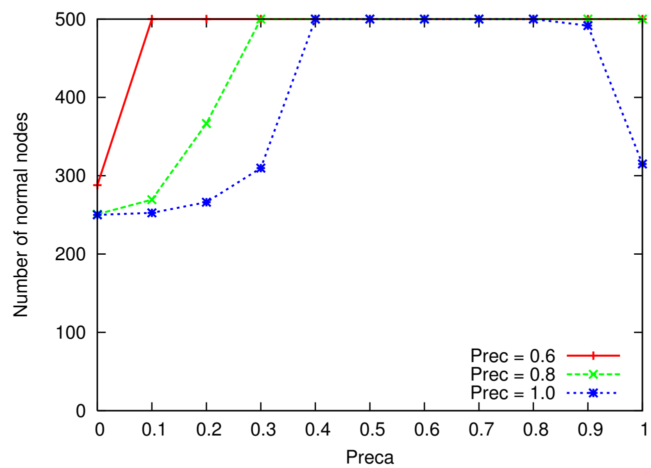

Figure 4: Time Evolution of the Number of Normal Nodes when $Preca$ is varied; and $Pr = 0, Pra = 0$ are fixed.

In the case of *always repair*, both normal nodes and abnormal nodes can go extinct. There is a threshold value of $Preca$ between 0.9 and 0.8 over which abnormal nodes can be eradicated. Below the threshold, however, normal nodes will go extinct when $Preca$ is increased.

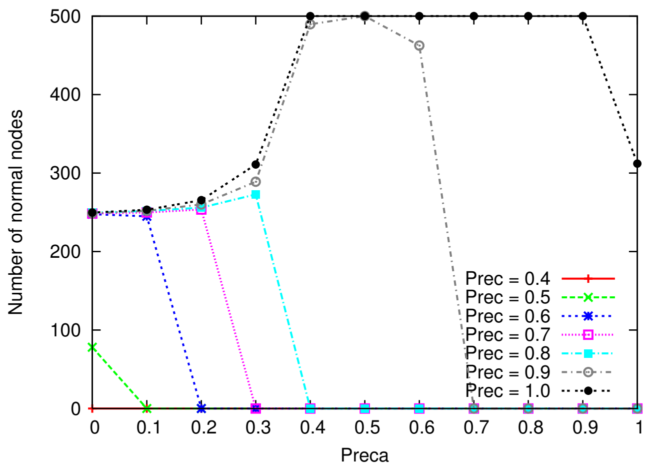

Figure 5: Time Evolution of the Number of Normal Nodes when $Preca$ is varied; and $Pr = 1, Pra = 0$ are fixed.

3.3 Level of Recognition Required for Abnormal Nodes Eradication

When the rate of successful repair by abnormal nodes (i.e. P_{ra}) is given, what is the minimum level of recognition (i.e. P_{rec}) required for abnormal nodes eradication? Figure 6 plots the minimum level of P_{rec}. As observed and already reported, we do not care the level of repair [9] and the level of recognition when P_{ra} exceeds 0.4. When P_{ra} is less than 0.4, however, recognition is needed (P_{rec} is positive) to eradicate abnormal nodes. Further, the smaller the level of repair (P_r), the smaller the level of recognition (P_{rec}) can be.

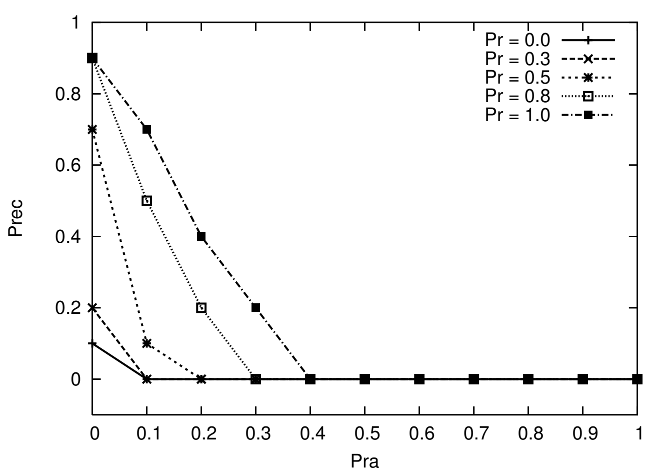

Figure 6: Minimum level of P_{rec} to eradicate abnormal nodes when P_{ra} is given.

4 Conclusion

A new model involving not only repair but also recognition is investigated to observe the impact of recognition. Only repair by copying suffices for abnormal nodes eradication when the rate of successful repair by abnormal nodes exceeds some level. However, recognition before repair is required when the rate does not exceed the level.

Acknowledgements

This work was partly supported by Grants-in-Aid for Scientific Research (B), 16300067, 2004; and by the 21st Century COE Program "Intelligent Human Sensing" from the Ministry of Education, Culture, Sports, Science and Technology of Japan.

References

[1] A.-L.Barabasi, Linked: The New Science of Networks , Perseus, 2002.

[2] H. Maturana, and F. Varela, Autopoiesis and Cognition: the Realization of The Living, D. Reidel, Dordrecht, 1980.

[3] R.E. Langman and M. Cohn (eds.) Seminars in Immunology. (http://www.idealibrary.com) , 2000.

[4] Ishida, Y.: Immunity-Based Systems: A Design Perspective, Springer, GmbH (2004)

[5] Gacs, P.:Reliable Cellular Automata with Self-Organization, J. Stat. Phys. 103(2001), pp. 45-267

[6] Domany, E. and Kinzel, W.: Equivalence of cellular automata to Ising models and directed percolation, Phys. Rev. Lett. 53 (1984) pp. 311

[7] Bagnoli, F., Boccara N. and Palmerini, P.: Phase Transitions in a Probabilistic Cellular Automaton with Two Absorbing States, arXiv:cond-mat/9705171 v2 (1997)

[8] Vichnicac, G.Y., Tamayo P. and Hartman, H.: Annealed and quenched inhomogeneous cellular automata, J. Statist. Phys. 45 (1986) pp. 875.

[9] Y. Ishida, A Critical Phenomenon in a Self-Repair Network by Mutual Copying, Lecture Notes in Artificial Intelligence (LNAI 3682) (2005) 86-92

The Eleventh International Symposium on Artificial Life and Robotics 2006 (AROB 11th'06),
B-con Plaza, Beppu, Oita, Japan, January 23-25, 2006

Dynamics of Spatial Strategies in Regulating Copying Strategies in a Self-Repair Network

Yoshiteru Ishida and Masakazu Oohashi
Department of Knowledge-based Information Engineering
Toyohashi University of Technology
Toyohashi, Aichi, 441-8580 Japan

Abstract

We have studied a framework of "Spatial Prisoner's Dilemma" that will control the frequency of repairing in a self-repair network. The framework demonstrated an adaptability of the spatial strategies to the environment of the network: whether or not the node in the network is prone to be abnormal. Among spatial strategies, several ecological relations, such as symbiotic relation, have been identified.

1 Introduction

Many networks, artificial or natural, have been studied from the viewpoint of their structure and topology, and their structural properties such as "scale-free"[1] or "small-world"[2] has been paid attention, studies on the interaction in the network or "dynamics" of the network (as opposed to structure) also becomes important topic. For example, "scale-free" network focuses on the spatial scale-freeness; however, temporal scale-freeness seems also important. From the context of fault-diagnosis, impact of the "scale-free" network theory is that it pointed out the internet is robust against random faults but vulnerable to the attacks targeted the hub [3], and that viruses and worms may not eradicated since the "epidemic threshold" is absent in the "scale-free" network[4, 5]. Another point that the viruses and worms bring about is that they completely changed the nature of faults. Machine faults usually belong to the random faults, since they are not "selective" to occur, and also they correspond to designed function and hence recovered when the parts covering the function are replaced. The point is that viruses and worms do change the intended function rather than causing malfunction, hence cannot be treated by usual redundancy and/or stand-by techniques. This drastic change of the aspect of faults calls for the design paradigm of the immune system which has the "self" that is adaptive to the environment. We have been studying the interaction of the network and proposed a dynamic relational network based on the immune network to increase robustness and adaptability to the dynamic environment. In the framework, the network is double-sided and would raise the self-referential paradox in a flat logic without distribution, and hence subtle tuning is needed as in the immune system. Organizing treatments to faults in large-scale systems has been proposed in a new approach of recovery-oriented computing [6]. Self-repair systems with autonomous distribution, abnormal units may adversely affect the system when they try to repair other normal units. Thus, the problem involves the "double edged sword" similar to the immune system. When the self-repair is done in an autonomous distributed manner, each unit does not voluntarily repair other units to save their own resources, thus leaving many abnormal units not repaired. This situation is similar to the dilemma that would occur in the Prisoner's Dilemma. Thus, we use an approach of a spatial version of Prisoner's Dilemma [7, 8] for emergence of cooperative collectives and for controlling copying to save resources.

2 A Framework for Self-Repairing

2.1 Spatial Prisoner's Dilemma and Spatial Strategies

The Prisoner's Dilemma (PD) is a game played just once by two players with two actions (cooperation, C, or defect, D). Each player receives a payoff (R, T, S, P) (Table 1) where $T > R > P > S$ and $2R > T + S$. In IPD, each iterated action is evaluated. In SPD, each site in a two-dimensional lattice corresponding to a player plays PD with the neighbors, and changes its action by the total score it received.

Spatial Prisoner's Dilemma has been studied to investigate when, how, and why the cooperation emerges

Table 1: The Payoff Matrix of the Prisoner's Dilemma. R, S, T, P are payoff to the player A.

		Player B	
		C	D
Player A	C	R	S
	D	T	P

among selfish agents. Our SPD [9, 10] is done with spatial strategies: the next action will be determined based on the pattern of neighbors' actions. Score is calculated by summing up all the scores received from PD with 8 neighbor players. After r (strategy update cycle) steps of interactions with neighbors, the strategy will be chosen from the strategy with the highest score among the neighbors. The strategy code of the unit is expressed as a string consisting nine character of C's and D's [11] whose l-th element is C (D) if the action C (D) is taken when the number of D of the neighbor players is l (l=0,1,$\cdots$,8). For example, All-C is [CCCCCCCCC], All-D is [DDDDDDDDD]. In the simulations to come, strategies are restricted to the kC strategy, which is composed of only 9 among the 512 existing strategies. In the kC strategy, the unit does the action of D if the number of D units is less than k; and it does the action of C if the number of D units is greater or equal to k. The kD strategies can be similarly defined. For example, 4C is [DDDDCCCCC] as shown in Figure 1. A snapshot of SPD in a 2-d lattice is shown in Figure 2.

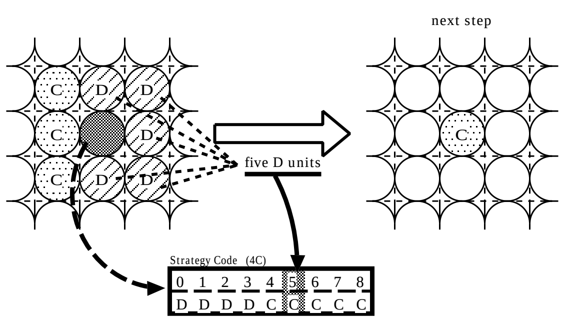

Figure 1: A Spatial Strategy 4C and Its Action

2.2 A Model Incorporating SPD

In the model by probabilistic cellular automaton, units do not have a failure rate and do not become abnormal by themselves, however, the units in the model here implement failure rate. The adverse impact by the abnormal units is implemented as raising the failure rate of the repaired units (when repaired by the abnormal units). Further, the units are assumed to use some resources while repairing. The units have to do the tasks assigned to them; but without doing repair, abnormal units increase and hence the performance in the system decreases; hence a dilemma.

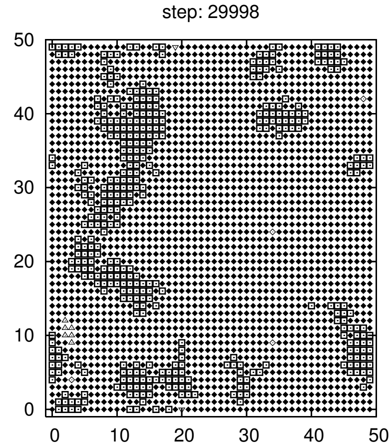

Figure 2: A Snapshop of SPD in the 50×50 2-d lattice

The unit becomes abnormal with a failure rate λ. Each unit has a spatial strategy and repairs (C) or does not repair (D) neighbor units according to it. Repairing is done depending on the repairing rate γ and a repaired unit becomes normal. Also the unit uses the quantity of resource R_λ for repairing. The unit is able to repair more than one unit, provided that the quantity of maximum resource R_{max} is not exceeded. We call the resource that is not used for repairing the available resource R_a, and consider it as score of a unit. If an abnormal unit repairs another unit, the failure rate λ of the repaired unit is increased by damage rate δ. Through the strategy update cycle r, the strategy of unit is updated to that of the strategy that got the highest profit among the Moore neighborhood units. When the unit copies its content (software that can be copied and be contaminated), the strategy of the unit is also copied. Thus, the strategy will be changed at copying in addition to every strategy update cycle. The strategy can mutate by flipping over an element of the code at every strategy update cycle with mutation rate μ.

3 Computer Simulations with a Square Lattice

Computer simulations are conducted in a two-dimensional lattice space with a unit existing in each lattice. Parameters are listed in Table 2.

Table 2: List of Parameters for Simulations

	Description	Value
$L \times L$	Size of the Space	50×50
N	Number of Nodes	2500
$N_f(0)$	Initial Number of Abnormal Nodes	0
λ	Failure Rate	0.001
γ	Repair Rate	0.01
δ	Damage Rate	0.1
μ	Mutation Rate	0.001
r	Strategy Update Cycle	200
R_{max}	Maximum Resource	8
R_λ	Resource used for Repairing	2

3.1 Spatial Strategies kD and kC

In regurating repairing, kC strategies outperform kD strategies. When the number of units taking D action increases, kD strategies stuch at high level of D (and hence abnormal units increase). Whereas the kC strategies, however, could take C because of "contrariness", hence D dominant situation can be changed to C dominant situation. Figure 3 plots the number of units with D action and that of abnormal units when spatial strategies are restricted to kD. We also found that kC strategies outperfom the case when kC and kD are mixed. Hence, hereafter spatial strategies are restricted to kC only.

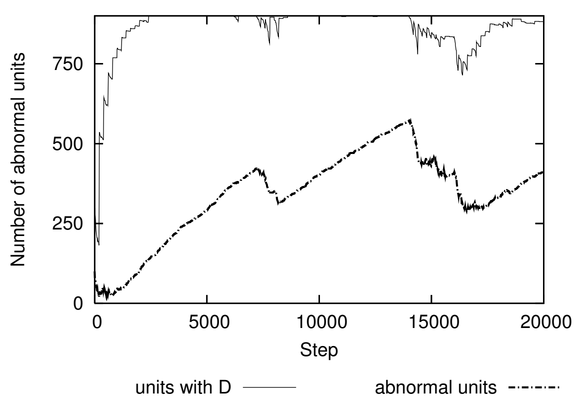

Figure 3: Evolution of the number of units with D action and that of abnormal units in kD. Lattice size is 30×30.

3.2 Adaptive nature of the strategic repair

Figure 13 shows the number of units in each strategy of the strategic repair. It is observed that when the number of abnormal units increases, units with easily repairing strategies like 0C also increase. Otherwise, units using hardly repairing strategies like 8C increase. This result suggests that the units choose an appropriate strategy depending on the environment. In fact, the efficacy (with respect to resource saving and abnormal units eradication) of each strategy depends on the environment such as the failure rate and the number of abnormal units. The adaptability of the strategic repair can be more obvious when comparing Figures 4 which is the case with a high failure rate (0.002) and a low failure rate (0.001). More interestingly, Figure 4 (above) indicates that the strategy 8C and 0C (or 1C) mutually support and are in a symbiotic relation.

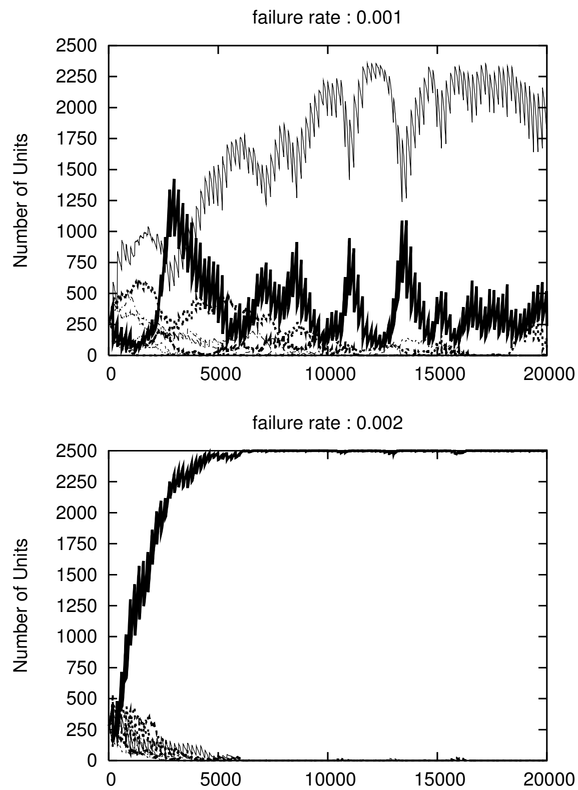

Figure 4: Time Evolution of the Fraction of Units with Spatial Strategies with failure rate 0.001(above) and 0.002(below)

3.3 Symbiotic Relation

The strategy 8C at a glance is dominant and may be sufficient as the optimal strategy in this environment, however, 8C alone could not even survive.Figure

5 shows the case when 0C and 1C are suppressed, and the case 8C is supressed. When 0C and 1C are suppressed, 2C becomes dominating strategy and 8C fades out. This implies that the dominating strategy depends on not only the failure rate but on the available strategies. When 8C is supressed, 7C dominates as a substitute of 8C, and 0C becomes supporting strategy. These simulations suggest that even in the environment restricted to kC strategies, many relations appear and yet adaptive nature could be preserved to regulate frequency of repairing.

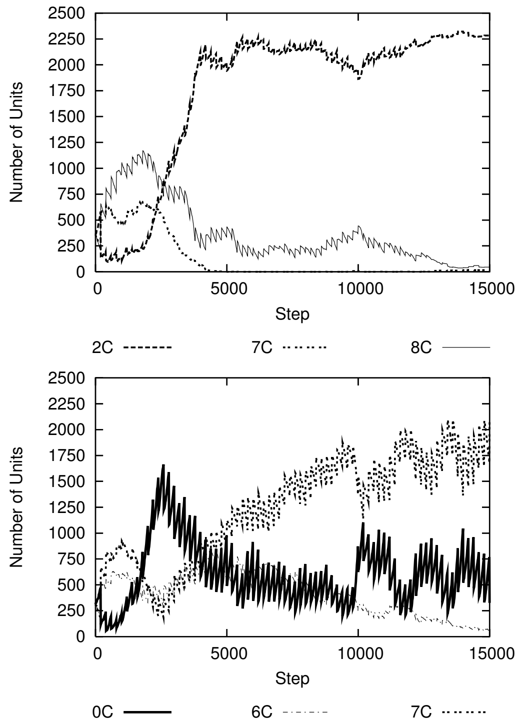

Figure 5: Time Evolution of the Fraction of Units with Spatial Strategies when 0C and 1C are suppressed (above) and 8C is supressed(below)

4 Summary and Conclusion

A framework of regulating mutual copying so that nodes (corresponding to computers) do not become selfish by only being repaired and also do not consume resources too much by often repairing. The framework involving a game theoretical approach of spatial Prisoner's Dilemma turned out to be adaptive to the environment: strategies encouraging repairing emerges when the environment allows many abnormal nodes and opposite strategies when the environment does not permit many abnormal nodes. Similarly to the ecological systems, symbiotic relation can be observed in the strategies emerged. Similarity and difference from the biological systems may be carefully investigated in the future work.

Acknowledgements

This work was partly supported by Grants-in-Aid for Scientific Research (B), 16300067, 2004; and by the 21st Century COE Program "Intelligent Human Sensing" from the Ministry of Education, Culture, Sports, Science and Technology of Japan.

References

[1] A.-L.Barabasi, Linked: The New Science of Networks , Perseus, 2002.

[2] D.J. Watts, Six Degrees: The Science of a Connected Age, W.W. Norton & Company, 2003.

[3] Z. Dezso and A.-L.Barabasi, Halting viruses in scale-free networks, Phys. Rev. E 65, 055103, (2002)

[4] R. M. May and A. L. Lloyd, Infection dynamics on scale-free, Phys. Rev. E, 64, (2001) 066112.

[5] R. Pastor and A. Vespignani, Epidemic spreading in scale-free networks, Phys. Rev. Lett, 86, (2001) 3200.

[6] A. Brown and D. Patterson, Embracing Failure: A Case for Recovery-Oriented Computing (ROC), High Performance Transaction Systems Workshop (TTPS '01) (2001)

[7] R. Axelrod, The Evolution of Cooperation, Basic Books, New York (1984)

[8] M.A. Nowak and R.M. May, Evolutionary games and spatial chaos, Nature, Vol. 359 (1992) 826-829

[9] Y. Ishida and T. Mori, A Network Self-Repair by Spatial Strategies in Spatial Prisoner's Dilemma, Lecture Notes in Artificial Intelligence (LNAI 3682) (2005) 79-85

[10] Y. Ishida and T. Mori, Spatial Strategies on a Generalized Spatial Prisoner's Dilemma, J. of Artificial Life and Robotics, Vol. 9, No. 3 (2005) 139–143

[11] K. Matuo and N. Adachi, N. Metastable Antagonistic Equilibrium and Stable Cooperative Equilibrium in Distributed Prisoner's Dilemma Game, Proc. Int. Symp. Syst. Res., Infor. Cybern. (1989)

The Eleventh International Symposium on Artificial Life and Robotics 2006 (AROB 11th'06),
B-con Plaza, Beppu, Oita, Japan, January 23-25, 2006

Sensor Data Mining System with Multiagent Approach for Metrological Data and Pachinko System

Ayahiko Niimi
Department of Media Architecture
Future University-Hakodate
116-2 Kamedanakano-cho, Hakodate-shi, Hokkaido 041-8655, JAPAN

Abstract

In this paper, we proposes the technique of the sensor data mining with multiagent approach. In the sensor data mining by multiagent approach, we define the source to which sends sensor data as agent, and sensor data analyze system including sensors and mining programs is defined as multiagent sensor data mining system. We discuss proposed multiagent system which is applied to the meteorological observation data and the data of the store system of pachinko. The meteorological observation data contains a large amount of the numerical data. The meteorological observation data also contains both of data only before and after the data observed at the regular time and the time at which special event is occurred. The purpose of the data analysis is defined as to extract the observation data of the regular time when the relation is strong to the event of thunder or lightning. The pachinko data composed the stream data of the number of pachinko bolls used to play a game with each pachinko machine and the number of balls at jackpot, etc. It is used to investigate prevention of the user from illegal using and a popular pachinko machine model.

Keyword:

Sensor Data Mining System, Multiagent Approach, Metrological Data, Pachinko Data

1 Introduction

Recently, we can obtain various data easily by a high performance of computer and the Internet. Data mining that extracted significant knowledge from a large amount of data become popular. The technique for applying data mining to text information such as Web page is developed recently though the data stored in databases was targeted in normal data mining. In the Internet, various time series data can be obtained. For instance, the image data of the weather satellite and the data of various sensors can be obtained. The feature of these data is continuous data in the time series.

The techniques which applied data mining from databases are used for time series data, but some techniques were improved for time series data.

In this paper, we proposes the technique of the sensor data mining with multiagent approach. In the sensor data mining by multiagent approach, we define the source to which sends sensor data as agent, and sensor data analyze system including sensors and mining programs is defined as multiagent sensor data mining system. The advantage of multiagent system is scalavirity of the number of sensors. It becomes to be able to correspond to the change in the number of sensors easily by constructing the multiagent system.

We discuss proposed multiagent system which is applied to the meteorological observation data and the data of the store system of pachinko. The meteorological observation data contains a large amount of the numerical data. The meteorological observation data also contains both of data only before and after the data observed at the regular time and the time at which special event is occurred. The purpose of the data analysis is defined as to extract the observation data of the regular time when the relation is strong to the event of thunder or lightning.

The pachinko is Japanese pinball. The pachinko data composed the stream data of the number of pachinko bolls used to play a game with each pachinko machine and the number of balls at jackpot, etc. It is used to investigate prevention of the user from illegal using and a popular pachinko machine model.

The advantage of the proposal approach is that it is easy to correspond to the change in the number of data sources. The change of the system is not to hard even when the composition of the sensor changes. Moreover, the data acquisition system from the sensor in the remote place can be easily constructed by constructing the system on the Internet.

2 Sensor Data Mining using Multiagent

In KES2003, the multiagent technology is defined as a technology that processed information by cooperatively operating two or more independent programs (agent). [1]

Generally, multiagent technology is discuss with an autonomous control of an individual agent, but in this paper, we do not discuss it mainly.

A communication between agents between one to one, one to multi, multi to multi. In this paper, we use one to one communication by UNIX process communication, one to multi by Black board model.

2.1 Agent Definitions

The definition of agent which is used for data mining in this paper is defined as follows.

Query agent: Query agent receives used the database and the data mining algorithm from a user, and generates other agents. Query agent is generated at each demand of a user.

Mining agent: Mining agent generates DB-access agent, acquires data from DB-access agent, and applies data mining algorithm. Mining agent is generated of each applied mining algorithm.

DB-access agent: DB-access agent acquires data from the database, and sends it to mining agent. DB-access agent is generated of each database and of each mining agent.

Result agent: Result agent observes a movement of mining agents, and obtains result from mining agents. When result agent obtains all results, result agent arrangement/integrates, and shows it to a user.

Black board(BB): Place where results from data mining agent is written.

2.2 Flow of System

A flow of proposed system is defined as follows. (Fig. 1 shows flowchart of proposed system.)

1. A user generates Query agent, with setting the used database and the used data mining algorithm as its parameter.
2. The place of black board(BB) is set with Query agent.
3. Query agent generates Mining agent, and the place of BB is transmitted.
4. Query agent generates Result agent, and the place of BB is transmitted.
5. DB-access agent is generated, and Mining agent is accessed to the database.
6. DB-access agent gets data from the database.
7. Mining agent receives data from DB-access agent, and applies the data mining algorithm.
8. Mining agent writes the result of data mining on BB.
9. Result agent checks BB, and if all results are written, arranges the results and presents to the user.
10. All agents are eliminated.

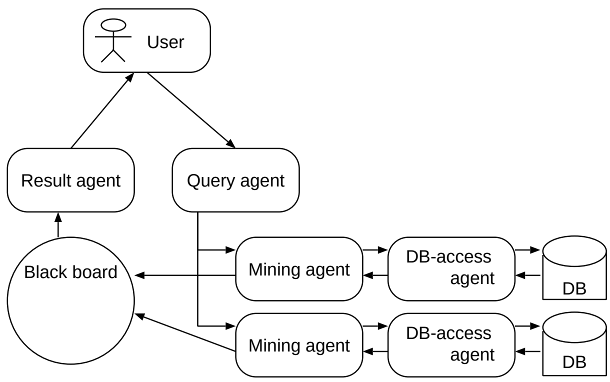

Figure 1: Flowchart of Proposed System

2.3 Feature of Proposed Method

The proposal method has the following features.

The result of data mining can be made for more meaning result by building in the thesaurus agent as Mining agent, and making it can access the thesaurus database.

Query agent generates two or more Mining agent, it becomes possible to execute data mining algorithms in parallel. Moreover, it becomes possible that constructing the system and the access to the database and the processing of data are divided by separating

DB-access agent accessed the database with Mining agent that processes data.

It becomes possible that the processing of each data mining algorithm and its arrangement/integration are separately thought by setting the agent which arranges the result. Moreover, it becomes easy to build arrangement/integration according to user's purpose into the system.

The system user comes to be able to construct the system corresponding to the purpose by recycling DB Agent and Mining Agent, and do tuning of Query agent and Result agent.

In this paper, the black board model with the file was handled with the interprocess communication on UNIX, but it can be easily enhanced to the communication on TCP/IP. Then, it is possible to enhance proposed approach to application to database that has been distributed on Internet. The problem of proposed approach is not using interprocess communication on UNIX but using black board model. Writing in the black board becomes a problem when the number of databases and data mining algorithm used increase, then the entire operation is influenced from the operation of the slowest agent. Therefore, the access to database and the processing of the data mining algorithm can be run parallel, but processing stops when checking results in the blackboard. It is necessary to consider that the maximum time is set to the black board writing check, and the system can show the result after each agent process.

2.4 Adapt for Sensor Data Mining

The proposed multiagent system was for database system. Then, we expanded the proposed system for sensor data mining. In this expansion, sensor units which are data sources treat as databases, and sensor units have both sensor part which measurement system and send part which send measurement data. If the sensor units can send data for the Internet, the expanded multiagent system can easy to construct. A lot of recent sensor units can make network and send measurement data for the network. So, the proposed multiagent sensor data mining system can build into an existing sensor network system.

3 Metrological Data Mining System

We construct the meteorological data analysis system as one of the examples of applying the proposal technique, and verify the effectiveness of the proposal technique. We construct the data mining system that does data mining collecting data on the network by using the sensor network where the fixed point observation data has been disclosed on the Internet named Teiten2000.[3, 4]

In Teiten2000, the information such as temperature, humidity, and the fixed point image are collected with each sensor unit, and sensor unit preserves data in local database. In the Teiten2000 sensor network, the data of each local database ties on the network. The system by which the meteorological data analysis system that proposes it collects data from a local database of each sensor unit, and does data mining from this network. Data mining that uses the data of Teiten2000 has already been evaluated.[4]

The agent which collect data from the sensor unit and the agent which chooses two or more sensor data are being constructed now. It is scheduled that data mining from the Teiten2000 network is done after the agents are constructed, and an effective output is evaluated.

4 Pachinko Data Mining System

We construct the data mining system of the pachinko(Japanese pinball) data as an example of applying the proposal technique, and verify the effectiveness of the proposal technique.

The data mining system of the pachinko data is a system that analyzes the movement of the ball of the pachinko stand in the pachinko parlor by data mining. The sensor that examines the opening and shutting door of pachinko stand and number of output balls, the big hit(jackpot) frequency, etc. is built in and it is called stand computer("DaiCom") in each pachinko stand. Data is collected by the computer that is called island computer("ShimaCom") brings several stand computer together. In addition, the computer that is called hall computer("HallCom") collects the data of the pachinko stand of the parlor.

We build multiagent sensor mining system into this system, and construct the system that in real time moves the number of ball in data mining. It aims to detect illegal play by the outlier analysis of the movement of the number of ball, to examine the model of a popular pachinko stand, and to analyze how for the customer to play by using the constructed system.

While with the data mining system as a system that collects data from the pachinko stand by the network the system that collects the data of several stand computer("DaiCom") directly is constructed under the present situation. It is scheduled that the network where island computer("ShimaCom") and hall computer("HallCom") were used for the pachinko stand of an actual parlor to correspond is constructed, and the multiagent sensor data mining system is built into the system.

5 Conclusion and Future Works

In this paper, we proposes the technique of the sensor data mining with multiagent approach. In the sensor data mining by multiagent approach, we define the source to which sends sensor data as agent, and sensor data analyze system including sensors and mining programs is defined as multiagent sensor data mining system. The advantage of multiagent system is scalavirity of the number of sensors. It becomes to be able to correspond to the change in the number of sensors easily by constructing the multiagent system.

We discuss proposed multiagent system which is applied to the meteorological observation data and the data of the store system of pachinko. The pachinko data composed the stream data of the number of pachinko bolls used to play a game with each pachinko machine and the number of balls at jackpot, etc. It is used to investigate prevention of the user from illegal using and a popular pachinko machine model.

The advantage of the proposal approach is that it is easy to correspond to the change in the number of data sources. The change of the system is not to hard even when the composition of the sensor changes. Moreover, the data acquisition system from the sensor in the remote place can be easily constructed by constructing the system on the Internet.

Each system is being constructed now. The effectiveness of the system is scheduled to be verified by constructing the multiagent sensor mining system, and using actual data in the future.

Acknowledgements

We thanks Dr. Masashi Toda of Future University-Hakodate for helpful discussion about sensor system of Teiten 2000. We thanks Dr. Masaaki Wada and Dr. Kei Ito of Future University-Hakodate for helpful discussion about Pachinko data store system.

References

[1] Niimi, A., Konishi, O.: Data Mining for Distributed Databases with Multiagents. KES'2003, Proceedings, PartII, Lecture Notes in Artificial Intelligence 2774, Springer:pp.1412–1418 (2003)

[2] Niimi, A., Konishi, O.: Extension of Multiagent Data Mining for Distributed Databases. KES'2004, Proceedings, PartIII, Lecture Notes in Artificial Intelligence 3215, Springer:pp.780–787 (2004)

[3] Teiten 2000 Project, http://www.teiten2000.jp/

[4] Toda, M., Osanai, A., Niimi, A., Akita, J., Kimura, K., Konishi, O.: Information Access Method to Meteorological Data for Educational Application, World Conference on Education Multimedia, Hypermedia and Telecommunications (ED-MEDIA2005), Association for the Advancement of Computing in Education, Montre'al, Canada, Proceedings: pp.4404–4408, June 2005.

Application of Graduated PCR in Concentration-Controlled Direct-Proportional Length-Based DNA Computing

Zuwairie Ibrahim[1&2], Yusei Tsuboi[2], and Osamu Ono[2]

[1]Department of Mechatronics and Robotics
Faculty of Electrical Engineering
Universiti Teknologi Malaysia
81310 UTM Skudai, Johor Darul Takzim
Malaysia
zuwairie@fke.utm.my

[2]Institute of Applied DNA Computing
Meiji University
1-1-1 Higashi-mita, Tama-ku
Kawasaki-shi, Kanagawa-ken
214-8571 Japan
(zuwairie, tsuboi, ono)@isc.meiji.ac.jp

Abstract

Graduated polymerase chain reaction (PCR) is a method to obtained molecular information in DNA computing, especially in the case of molecular search for weighted graph problems based on length, concentration, and melting temperature. Graduated PCR is not new in the area of DNA computing. In fact, graduated PCR has been performed by Adleman, when he demonstrated a DNA computer for solving an instance of 7-nodes Hamiltonian path problem. We report here the use of graduated PCR in concentration-controlled direct-proportional length-based DNA computing and the importance of graduated PCR is discussed.

Keywords: DNA Computing, Molecular Information, Graduated PCR

1 Introduction

In the area of DNA computing, there are two kinds of methods that are useful to extract the information from DNA: DNA sequencing and graduated PCR. DNA sequencing is done by a machine called sequencer, which is able to reveal every nucleotide in DNA. Lee *et al.* [1] have employed this method at the end of their algorithm of temperature gradient based DNA computing (TG-DNAC). Nevertheless, it seems likely that it is quite hard to analyze the output of the sequencer. The second method, which is graduated PCR, is less expensive than DNA sequencing and not able to reveal every nucleotide of DNA, but adequate to visualize the desired information. Moreover, the interpretation is easier to understand compared to DNA sequencing. Therefore, graduated PCR is more preferred as an extended protocols in concentration-controlled direct-proportional length-based DNA computing (CCDPLB-DNAC). Graduated PCR consists of several protocols, such as DNA extraction from a gel, polymerase chain reaction (PCR), and polyacrylamide gel electrophoresis (PAGE). Graduated PCR, in fact, has been used by Adleman to visualize the computation output of Hamiltonian path problem (HPP) [2].

2 Concentration-Controlled Direct-Proportional Length-Based DNA Computing

A new hybrid approach called concentration-controlled direct-proportional length-based DNA computing (CCDPLB-DNAC) has been proposed [3]. The hybrid approach combines two characteristics: length and concentration, for encoding and at the same time, effectively control the degree of hybridization of DNA. The encoding by length is realized whereby the cost of each path is encoded by the length of the oligonucleotides (oligos) in a proportional way. This kind of encoding is exactly the same as the previously proposed direct-proportional length-based DNA computing (DPLB-DNAC). On the other hand, the control of hybridization by concentration is done by varying the amount of oligos, as the input of computation. The main objective of this approach is the same as DPLB-DNAC, which is to compute the shortest path of a weighted graph *in vitro*.

The origin of DNA computing by concentration-controlled can be traced back to the work by Oliver in which, concentration of DNA has been proposed for a calculation of multiplication of Boolean matrix [4]. The principle underlying the concentration-controlled DNA computing for weighted graph problems is that during the initial pool generation, the rate of biochemical reactions depends heavily on the reaction rate constants and reactant concentrations. Thus, as the concentration of DNA strands increase, the paths including them can be generated more frequently and the hopeful DNA paths can be generated with high concentration.

The experimental protocol, in fact, is almost the same with the previously proposed DPLB-DNAC, however, the difference is that the amount of oligos poured into the initial test tube is relatively different depending on the relative concentration, which is calculated using Equation 1 [5], such that:

$$D_{ij} = \left(\frac{Min}{C_{ij}}\right)^2 \quad (1)$$

where Min is the minimum weight of the graph, C_{ij} is the weight of an edge, $E(V_i,V_j)$, and D_{ij} denotes relative concentration of the corresponding edge. The relative concentrations can then be translated into the actual amount by the following equation:

$$A_{ij} = D_{ij} A_{ref} \quad (2)$$

where A_{ij} is the actual amount of oligos for an edge $E(V_i,V_j)$ and A_{ref} denotes the reference amount.

Based on CCDPLB-DNAC, if the input of the shortest path problem is shown in Figure 1, the output of the *in vitro* computation is shown in Figure 2.

3 Output Visualization by Graduated PCR

For the sake of explanation, the DNA molecule representing the answer of the shortest path $V_1 - V_3 - V_4 - V_5$ is taken again for an instance. For this purpose, it is important to extract the shortest band of DNA from the gel, and graduated PCR can be performed by running four different PCR operations to the solution containing DNA duplex $V_1 - V_3 - V_4 - V_5$ separately. The pair of primers used for every PCR reaction are $V_1 - \overline{V_2}$, $V_1 - \overline{V_3}$, $V_1 - \overline{V_4}$, and $V_1 - \overline{V_5}$. It is expected that for the final solution containing the strand $V_1 - V_3 - V_4 - V_5$ with length of 100 base-pairs (bp), graduated PCR will produce bands of x, 50 bp, 75 bp, and 100 bp in successive lanes of a gel as depicted in Figure 3. The symbol x denotes the absence of a band corresponding to the omission of nodes V_2 along the DNA duplex. This means that there are intermediate nodes, V_3 and V_4 in between the start node V_1 and the end node V_5. Therefore, the shortest path of the graph can be readout as $V_1 \rightarrow V_3 \rightarrow V_4 \rightarrow V_5$.

4 Experimental Protocols and Results

Based on gel image of Figure 2, four DNA mixtures, which are the product of PCR, were subjected to PAGE for 40 minutes at 200V. After that, the gel was stained by SYBR Gold (Molecular Probes, USA) and the bands of DNA were viewed by a 312nm UV Transluminator. Quantum Prep™ Freeze 'N Squeeze DNA Gel Extraction Spin Columns (Bio-Rad, Japan) was used for the purpose of DNA extraction from the polyacrylamide gel. By using a clean razor blade, the band of interest, which is the shortest band, was carefully excised from the gel. The gel slice was chopped and placed into the filter cup of the Quantum Prep Freeze 'N Squeeze DNA Extraction Spin Column. Then, the filter cup was placed into a dolphin tube. The Quantum Prep Freeze 'N Squeeze DNA Extraction Spin Column was placed in a -20ºC freezer for 5 minutes and the sample was spun at 13,000 x g for 3 minutes at room temperature. The purified DNA was collected from the collection tube and ready for PCR. A gel image of the purified DNA is depicted in Figure 4. After the DNA extraction from the polyacrylamide gel is done, four different PCR, namely PCR12, PCR13, PCR14, and PCR15, were ran to the purified solutions. The pair of primers used for every PCR is listed in Table 1.

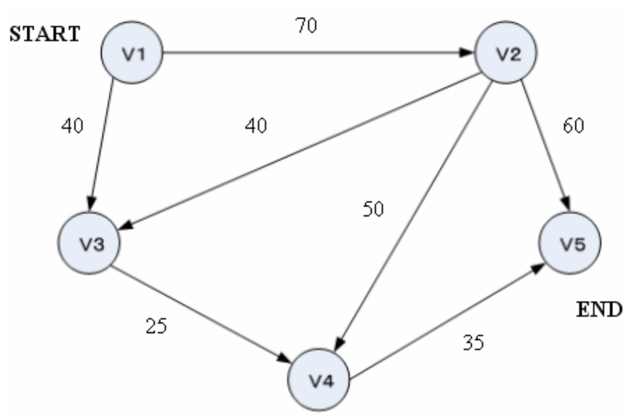

Figure 1: An example of the input of the shortest path problem.

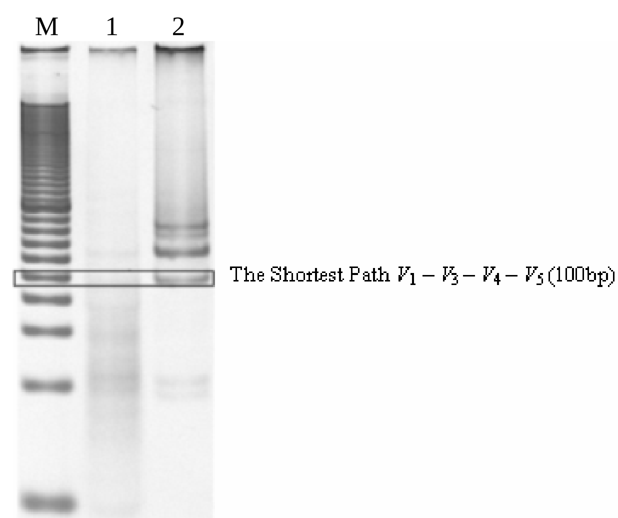

Figure 2: Experimental results of gel electrophoresis on 10% PAGE in the case of DPLB-DNAC. Lane M denotes 20-bp ladder, lane 1 is the product of POA, and lane 2 is the product of PCR.

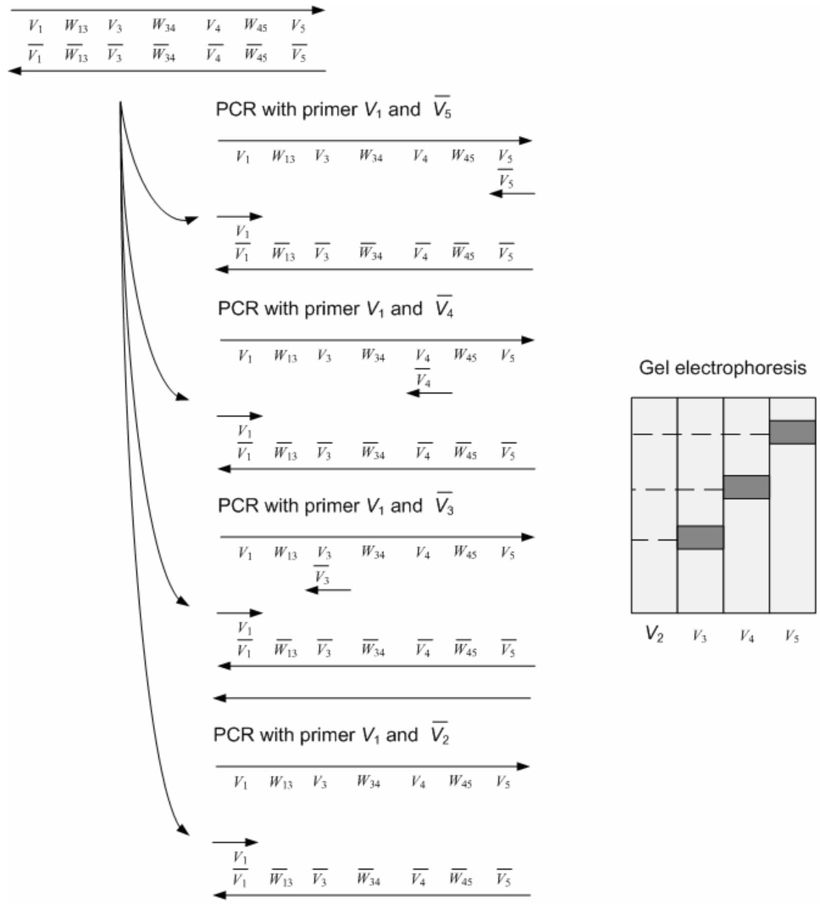

Figure 3: Example showing a brief protocol and the expected results of graduated PCR for CCDPLB-DNAC.

Each PCR was performed in a 25 µ*l* solution consisted of 2.5 µ*l* of each primers, 1 µ*l* template, 2.5 µ*l* dNTP (TOYOBO, Japan), 2.5 µ*l* 10x KOD dash buffer (TOYOBO, Japan), 0.125 µ*l* KOD dash (TOYOBO, Japan), and 13.875 µ*l* ddH_20 (Maxim Biotech, Inc., Japan). The reaction consisted of 25 cycles and for each cycles, the appropriate temperature were 94ºC for 30s, 55ºC for 30s, and 74ºC for 10s.

Again, the product of graduated PCR was subjected to PAGE for 40 minutes at 200V and the gel was stained by SYBR Gold (Molecular Probes, USA). The band of DNA was viewed by 300nm FOTO/Phoresis® UV Transilluminator (Fotodyne Inc., USA) and the resulted gel image was captured. Figure 5 shows the gel image of the product of graduated PCR.

5 Discussions

Based on the shortest length dsDNAs, one only knows that the shortest path begins from V_1 and ends at V_5. However, the information does not contain the nodes that pass through the shortest path and the order of those nodes. The information regarding all the nodes in the shortest path and the order can be obtained by applying graduated PCR. By referring to the experimental results in Figure 5, it is proved that graduated PCR is able to produce bands of *x*, 50, 75, and 100 in successive lanes of a polyacrylamide gel. The symbol *x* denotes the absence of a band corresponding to the omission of nodes V_2 along the DNA duplex. This means that there are intermediate nodes, V_3 and V_4 in between the node V_1 and V_5, and the order of those intermediate nodes can be known. Therefore, the shortest path of the graph can be readout as $V_1 \rightarrow V_3 \rightarrow V_4 \rightarrow V_5$.

Two significant benefits of graduated PCR for CCDPLB-DNAC are identified. The first is due to its capability to show and visualize the detailed output of the shortest path computation based on CCDPLB-DNAC. The other benefit is that at the same time, the correctness of the proposed CCDPLB-DNAC for the computation of the shortest path problem can be proved. Hence, it is found that graduated PCR should be essentially incorporated in the CCDPLB-DNAC in order to improve the overall performance of CCDPLB-DNAC.

Figure 4: Experimental results of gel electrophoresis on 10% polyacrylamide gel. Lane M denotes 20-bp ladder, and lane 1 is the purified DNA of gel extraction.

Table 1: Four sets of primers used for the graduated PCR.

Solution	Forward Primers (F) and Reverse Primers (R) (5'-3')
PCR12	F = AAAGCTCGTCGTTTAGGAGC R = CGTGATCCCTAAACCTCCAA
PCR13	F = AAAGCTCGTCGTTTAGGAGC R = CGATACGGCATCATCTCGCT
PCR14	F = AAAGCTCGTCGTTTAGGAGC R = GCTATGGCTTGACTATTCGC
PCR15	F = AAAGCTCGTCGTTTAGGAGC R = GCACCCACCGAGACATTATC

6 Concluding Remarks

In this paper, we presented graduated PCR, as an option to extend the protocol of CCDPLB-DNAC. Based on the proposed approach, the product of CCDPLB-DNAC is subjected to DNA extraction from polyacrylamide gel, PCR, and PAGE. As supported by the experimental results, a series of bio-molecular reactions have been successfully carried out in laboratory. Further, it is showed that graduated PCR is also able to visualize detail additional information of the shortest path, such as the intermediate vertices and the order of these vertices in the shortest path and at the same time, proved the correctness of the CCDPLB-DNAC.

Acknowledgements

This research was supported partly by the IEEE Computational Intelligence Society (IEEE-CIS) Walter J Karplus Student Summer Research Grant 2004 for a research visit in September 2004 at the DNA Computing Laboratory, Graduate School of Information Science and Technology, Hokkaido University, Sapporo, Hokkaido, Japan. The first author would like to thank Masahito Yamamoto for discussions that led to improvements in this work. Also, the first author is sincerely grateful to Atsushi Kameda, Satoshi Kashiwamura, and members of DNA Computing Laboratory of Hokkaido University for fruitful explanations and kind assistance during the practice of biochemical experiments. Lastly, the first author is very thankful to Universiti Teknologi Malaysia (UTM) for granting a study leave at Meiji University under JPA-SLAB scholarship.

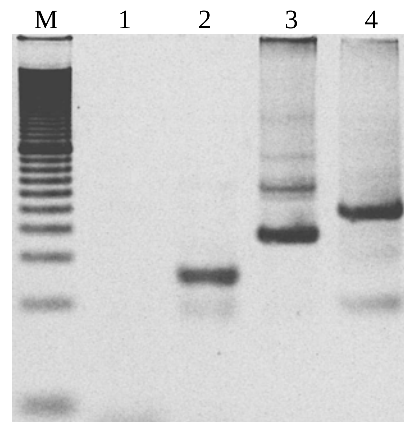

Figure 5: Experimental results of graduated PCR. Lane M denotes 20-bp molecular marker, lane 1, lane 2, lane 3, and lane 4 are the product of PCR on DNA mixtures PCR12, PCR13, PCR14, and PCR15, respectively.

References

[1] J. Y. Lee, S. Y. Shin, T. H. Park, and B. T. Zhang, "Solving traveling salesman problems with DNA molecules encoding numerical values," *BioSystems*, Vol. 78, Issue 1-3, pp. 39-47, 2004.

[2] L. Adleman, "Molecular computation of solutions to combinatorial problems," *Science*, Vol. 266, pp. 1021-1024, 1994.

[3] Z. Ibrahim, Y. Tsuboi, O. Ono, and M. Khalid, "Hybrid concentration-controlled direct-proportional length-based DNA computing for numerical optimization of the shortest path problem," *Second International Workshop on Biologically Inspired Approaches to Advanced Information* (accepted)

[4] J. Oliver, "Computation with DNA: matrix multiplication," *DNA Based Computers 2: DIMACS Series in Discrete Mathematics and Theoretical Computer Science*, Vol. 44, pp. 113-122, 1999.

[5] M. Yamamoto, A. Kameda, N. Matsuura, T. Shiba, Y. Kawazoe, and A. Ahochi, "A separation method for DNA computing based on concentration control," *New Generation Computing*, Vol. 20, pp. 251-262, 2002.

Molecular Computing Approach for Constraint Assignment Problem

Zuwairie Ibrahim[1&2], Yusei Tsuboi[2], and Osamu Ono[2]

[1]Department of Mechatronics and Robotics
Faculty of Electrical Engineering
Universiti Teknologi Malaysia
81310 UTM Skudai, Johor Darul Takzim
Malaysia
zuwairie@fke.utm.my

[2]Institute of Applied DNA Computing
Meiji University
1-1-1 Higashi-mita, Tama-ku
Kawasaki-shi, Kanagawa-ken
214-8571 Japan
(zuwairie, tsuboi, ono)@isc.meiji.ac.jp

Abstract

The concept of direct-proportional length-based DNA computing is considered in order to solve a constraint assignment problem on an unconventional molecular computer. Constraint assignment problem is an extended version of unconstraint assignment problem, where a constraint that is the cost of an assignment is taken into account during the optimization. This paper shows that the complexity of constraint assignment problem could be reduced to a path-finding problem and an algorithm based on direct-proportional length-based DNA computing is design for searching the optimal assignment.

Keywords: Constraint Assignment Problem, Optimization, Direct-Proportional Length-Based DNA Computing

1 Introduction

In the previous paper [1-2], we proposed a DNA-based computing algorithm for solving unconstraint assignment problem. The objective of the unconstraint assignment problem is to establish a full one-to-one correspondence between two set E (employees) and J (jobs), both of which have N elements. An assignment is a one-to-one mapping, $\alpha: E \rightarrow J$ [3]. The assignment problem is so fundamental in operations research as well as in engineering field. It is very useful because assigning n tasks to n people is a basic primitive in many applications [4].

Based on the constraint assignment problem, a constraint is considered that is the cost of assigning an element in E to an element in J, and thus, the objective of the assignment now is to find one-to-one correspondence between two set E and J, both of which have N elements with the lowest cost.

Basically, from the DNA computing point of view, there are several characteristic of DNA that could be manipulated in order to solve a weighted graph problem. Those are length [5], concentration [6], and melting temperature [7]. However, a length-based DNA computing called direct-proportional length-based DNA computing is chosen and extended for the development of a DNA algorithm for the computation of a constraint assignment problem.

2 Modified Graph

A simple input of a constraint assignment problem is depicted in Figure 1. This input consists of a set employees, $E = \{a, b, c\}$ and a set jobs, $J = \{d, e, f\}$. The cost of an assignment is also shown. Based on the input, the optimal assignment is *a*-*d*, *b*-*e*, and *c*-*f*, where the assignment cost is 5.

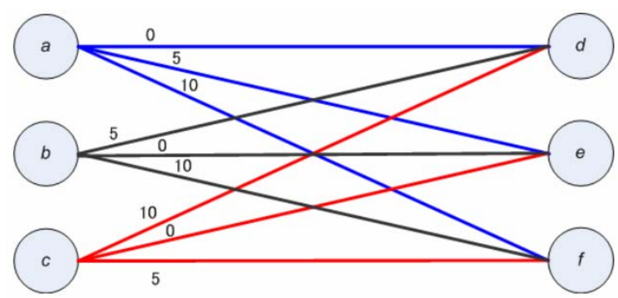

Figure 1: Input of a constraint assignment problem.

In order to reduce the constraint assignment problem to a path-finding problem, the input graph in Figure 1 is visualized slightly different into a modified graph as shown in Figure 2. According to the input, it is clear that the nodes *a*, *b*, and *c* are connected to nodes *d*, *e*, and *f*. The modified graph is constructed in such as way that the nodes *d*, *e*, and *f* that belong to node *a* are connected by connective edges to node *b*. Similarly, nodes *d*, *e*, and *f* that belong to node *b* are connected by connective edges to node *c*. Lastly, nodes *d*, *e*, and *f* that belong to node *c* are connected by connective edges to node *end*. We introduce a node *end* as a stopper. The costs of connective edges are set to 0. According to the modified graph, the constraint assignment problem can be solved *in vitro* on a molecular computer by computing the shortest path problem employing direct-proportional length-based DNA computing as shown in Figure 3.

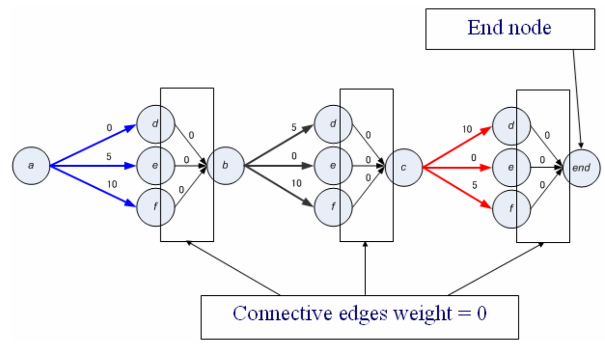

Figure 2: A modified graph.

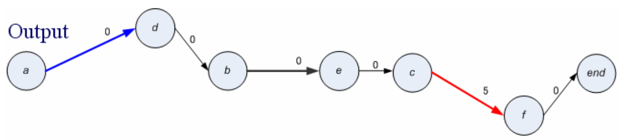

Figure 3: The shortest path as solution to a constraint assignment problem.

3 DNA sequence design

The sequence design is exactly the same as direct-proportional length-based DNA computing as follows:

a. If there is a connection between V_1 to V_j, where $j \neq n$, synthesize the oligo for edge as
$V_1(20) + W_{1j}(\omega - 30) + V_j(20)$

b. If there is a connection between V_i to V_j, where $i \neq 1$, $j \neq n$, synthesize the oligo for edge as
$V_i(20) + W_{ij}(\omega - 20) + V_j(20)$

c. If there is a connection between V_i to V_n, where $i \neq 1$, synthesize the oligo for edge as
$V_i(20) + W_{in}(\omega - 30) + V_n(20)$

where V, W, and '+' denote the DNA sequences for nodes, DNA sequences for weight, and 'join' respectively. The synthesized oligos consist of two node segments and an edge segment. 'ω' denotes the weight value for corresponding DNA sequences for weight W_{ij}, where W_{ij} denotes the DNA sequences representing a cost between node V_i and V_j. The value in parenthesis indicates the number of DNA bases or nucleotides for each segment. Table 1 lists all the oligos designed using DNASequenceGenerator [8] for the *in vitro* computation.

4 *In vitro* computation

In this research, POA is performed for initial pool generation. After parallel overlap assembly is done, all possible solutions of the constraint assignment problem as shown in Figure 4 could be generated. The values in parenthesis indicate the cost of each assignment. Polymerase chain reaction (PCR) is performed to amplify exponentially generated double stranded DNAs (dsDNAs) that begin from node *a* and end at node *end*.

a-d-b-d-c-d-end (15)	a-e-b-d-c-d-end (20)	a-f-b-d-c-d-end (25)
a-d-b-d-c-e-end (5)	a-e-b-d-c-e-end (10)	a-f-b-d-c-e-end (15)
a-d-b-d-c-f-end (10)	a-e-b-d-c-f-end (15)	a-f-b-d-c-f-end (20)
a-d-b-e-c-d-end (10)	a-e-b-e-c-d-end (15)	a-f-b-e-c-d-end (20)
a-d-b-e-c-e-end (0)	a-e-b-e-c-e-end (5)	a-f-b-e-c-e-end (10)
a-d-b-e-c-f-end (5)	a-e-b-e-c-f-end (10)	a-f-b-e-c-f-end (15)
a-d-b-f-c-d-end (20)	a-e-b-e-c-d-end (25)	a-f-b-e-c-d-end (30)
a-d-b-f-c-e-end (10)	a-e-b-e-c-e-end (15)	a-f-b-e-c-e-end (20)
a-d-b-f-c-f-end (15)	a-e-b-e-c-f-end (20)	a-f-b-e-c-f-end (25)

Figure 4: All possible solutions of the constraint assignment problem.

In constraint assignment problem, an employee should be assigned only to one machine, either *d*, *e*, or *f*. In order to select only possible solutions that satisfy this rule, magnetic bead separation can be applied three times, particularly, for extraction of subsequences *d*, *e*, and *f*. Magnetic bead separation is a biotechnology tool to extract dsDNAs that contain certain subsequences from a solution. Possible solutions that survived after the magnetic bead separation are shown in Figure 5.

a-f-b-d-c-e-end (15)
a-e-b-d-c-f-end (15)
a-d-b-e-c-f-end (5)
a-f-b-e-c-d-end (20)
a-d-b-f-c-e-end (10)
a-f-b-e-c-d-end (30)

Figure 5: Possible solutions survived after magnetic bead separation of subsequence *d*, *e*, and *f*.

All possible solutions survived after the previous reactions contain one-to-one assignment of employees and jobs with various costs. The solution of the constraint assignment problem is the one-to-one assignment with the lowest cost. The selection of that kind of assignment is possible by performing a method called gel electrophoresis. Gel electrophoresis, in fact, is a method to separate and list dsDNAs according to their lengths, in an agarose or polyacrylamide gel. The separation by gel electrophoresis is shown conceptually in Figure 6.

After the gel electrophoresis is successfully done, the shortest band appears in the gel represents the solution of the constraint assignment problem. However, a method to extract the information represented by dsDNAs in the shortest band is required. Fortunately, it is possible to extract the information by using a method called graduated PCR. Graduated PCR can be performed by extracting the dsDNAs of interest from the gel and applying three different PCRs with three different set of

Table 1: DNA sequences required for the *in vitro* computation

Nodes		
Name	DNA sequences (5'-3')	Length
a	CGTCTGTCTAGCGGACCTTA	20
b	TACACCGACTACCCATGTGC	20
c	GATCCCTGAGAGGTGAATGG	20
d	GTTCAACTGACAGGTGTGCC	20
e	CTAAGTTGTGGTGAGTGGGC	20
f	GAATATCCCGTCCTCTACGC	20
end	TGGTCCCAGTGATACCAGTC	20
Complements of nodes		
Name	DNA sequences (5'-3')	Length
a	TAAGGTCCGCTAGACAGACG	20
b	GCACATGGGTAGTCGGTGTA	20
c	CCATTCACCTCTCAGGGATC	20
d	GGCACACCTGTCAGTTGAAC	20
e	GCCCACTCACCACAACTTAG	20
f	GCGTAGAGGACGGGATATTC	20
end	GACTGGTATCACTGGGACCA	20
Edges		
Name	DNA sequences (5'-3')	Length
a-d	CGTCTGTCTAGCGGACCTTAGTTCAACTGACAGGTCTCGG	40
a-e	CGTCTGTCTAGCGGACCTTAACGTGCTAAGTTGTGGTGAGTGGGC	45
a-f	CGTCTGTCTAGCGGACCTTACCGTCTTTTAGAATATCCCGTCCTCTACGC	50
b-d	TACACCGACTACCCATGTGCAGGTCGTTCAACTGACAGGTGTGCC	45
b-e	TACACCGACTACCCATGTGCCTAAGTTGTGGTGAGTGGGC	40
b-f	TACACCGACTACCCATGTGCGCGTGCTCTCGAATATCCCGTCCTCTACGC	50
c-d	GATCCCTGAGAGGTGAATGGACGTGTTTTGGTTCAACTGACAGGTGTGCC	50
c-e	GATCCCTGAGAGGTGAATGGCTAAGTTGTGGTGAGTGGGC	40
c-f	GATCCCTGAGAGGTGAATGGGCGTGGAATATCCCGTCCTCTACGA	45
d-b	GTTCAACTGACAGGTGTGCCTACACCGACTACCCATGTGC	40
e-b	CTAAGTTGTGGTGAGTGGGCTACACCGACTACCCATGTGC	40
f-b	GAATATCCCGTCCTCTACGCTACACCGACTACCCATGTGC	40
d-c	GTTCAACTGACAGGTGTGCCGATCCCTGAGAGGTGAATGG	40
e-c	CTAAGTTGTGGTGAGTGGGCGATCCCTGAGAGGTGAATGG	40
f-c	GAATATCCCGTCCTCTACGCGATCCCTGAGAGGTGAATGG	40
d-end	GTTCAACTGACAGGTGTGCCTGGTCCCAGTGATACCAGTC	40
e-end	CTAAGTTGTGGTGAGTGGGCTGGTCCCAGTGATACCAGTC	40
f-end	GAATATCCCGTCCTCTACGCTGGTCCCAGTGATACCAGTC	40

forward and reverse primers. After that, gel electrophoresis is applied again to the three different products of PCRs and the resultant lengths are observed. The conceptual description of graduated PCR is shown in Figure 7. If the expected product of gel electrophoresis shown in Figure 7 is observed, one can conclude that the best assignment is *a-d*, *b-e*, and *c-f*.

6 Concluding Remarks

This research concerning with an extended version of DNA-based algorithm based on direct-proportional length-based DNA computing for solving an example of engineering problem, namely, constraint assignment problem. A constraint that is the cost for each assignment is taken into account in this paper. It has been shown that the complexity of the constraint assignment problem could be reduced to path-finding problem and the direct-proportional length-based DNA computing could be performed for the *in vitro* computation. For this purpose, direct-proportional length-based DNA computing is improved by additional reactions called magnetic bead separation and graduated PCR. For the future works, the proposed algorithm will be implemented in laboratory experiments.

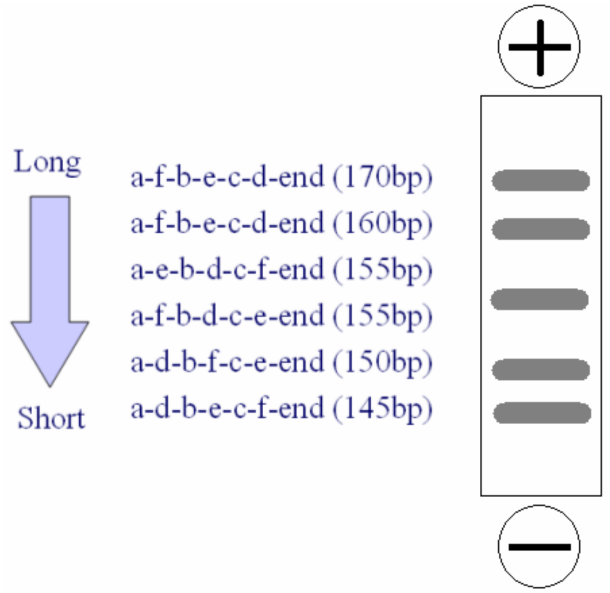

Figure 6: Separation by gel electrophoresis of possible solutions after magnetic bead separation of subsequence *d*, *e*, and *f*.

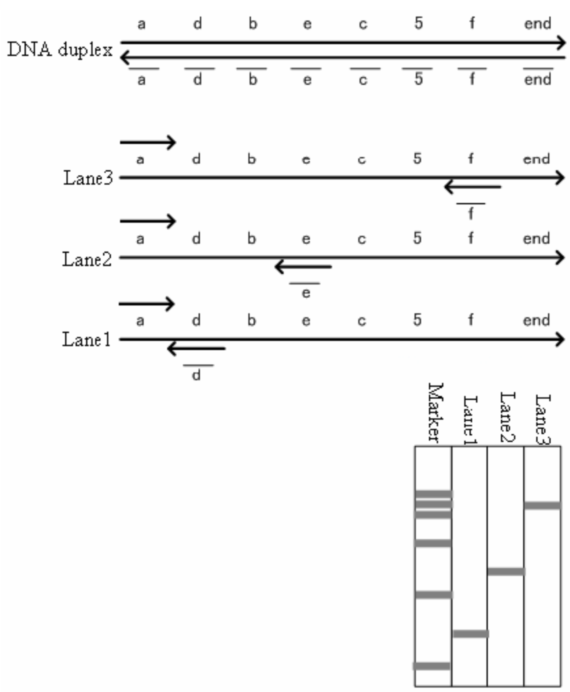

Figure 7: Expected output of graduated PCR for extraction of molecular information of the constraint assignment problem.

Acknowledgments

The first author is very thankful to Universiti Teknologi Malaysia for granting a study leave in Meiji University under JPA-SLAB scholarship.

References

[1] Z. Ibrahim, Y. Tsuboi, and O. Ono, "Solving unconstraint assignment problem by a molecular-based computing algorithm," *IEEE International Symposium on Industrial Electronics 2004*, pp. 1473-1478, 2004.

[2] Z. Ibrahim, Y. Tsuboi, O. Ono, and M. Khalid, "Unconstraint assignment problem: a molecular computing approach," *International Arab Journal of Information Technology*, Zarqa Private University, Vol. 3, No. 2, pp. 183-188, 2006.

[3] G. Liu and R.M. Haralick, "Assignment problem in edge detection performance evaluation," *Proceedings of the IEEE Conference on Computer Vision and Pattern Recognition*, Vol. 1, pp. 26-31, 2000.

[4] A. Arora, A. Frieze, and H. Kaplan, "A new rounding procedure for the assignment problem with applications to dense graph arrangement problems," *Proceedings of the 37th Annual Symposium on Foundations of Computer Science*, pp. 21-30, 1996.

[4] D. M. Norton, "Polymerase chain reaction-based methods for detection of Listeria monocytogenes: toward real-time screening for food and environmental samples," *Journal of AOAC International*, Vol. 85, pp. 505-515, 2002.

[5] Z. Ibrahim, Y. Tsuboi, O. Ono, and M. Khalid, "Experimental implementation of direct-proportional length-based DNA computing for numerical optimization of the shortest path problem", *European Conference on Artificial Life 2005: Workshop on Unconventional Computing*, pp. 35-46, 2005.

[6] M. Yamamoto, A. Kameda, N. Matsuura, T. Shiba, Y. Kawazoe, and A. Ohuchi, "Local search by concentration-controlled DNA computing," *International Journal of Computational Intelligence and Applications*, Vol. 2, No. 4, pp. 447-455, 2002.

[7] J.Y. Lee, S.Y. Shin, S.J. Augh, T.H. Park, B.T. Zhang, "Temperature gradient-based DNA computing for graph problems with weighted edges," *Lecture Notes in Computer Science*, Vol. 2568, pp. 73-84, 2003.

[8] F. Udo, S. Sam, B. Wolfgang, and R. Hilmar, "DNA sequence generator: a program for the construction of DNA sequences," *Proceedings of the 7th International Workshop on DNA Based Computers*, pp. 23-32, 2001.

Matrix Multiplication by DNA Computing

Kasai Nobuyuki[1], Zuwairie Ibrahim[1&2], Yusei Tsuboi[1], and Osamu Ono[1]

[1]Institute of Applied DNA Computing
Meiji University
1-1-1 Higashi-mita, Tama-ku
Kawasaki-shi, Kanagawa-ken
214-8571 Japan
(ce55024, zuwairie, tsuboi, ono)@isc.meiji.ac.jp

[2]Department of Mechatronics and Robotics
Faculty of Electrical Engineering
Universiti Teknologi Malaysia
81310 UTM Skudai, Johor Darul Takzim
Malaysia
zuwairie@fke.utm.my

Abstract

In this paper, a method to do binary multiplication with DNA molecules based on DNA computing is presented. The first proposal on matrix multiplication with DNA has been presented by John S. Oliver. In this paper, the scheme of Boolean matrix multiplication, which has been proposed by Oliver is improved, simplified, and realized in laboratory experiments. During the *in vitro* implementation, parallel overlap assembly is employed to construct every possible path in the directed graph in massively parallel fashion. A test of the reaction to identify the existence of a path is done by polymerase chain reaction. After that the product of polymerase chain reaction is subjected to polyacrylamide gel electrophoresis in order to visualize the result of the computation. By analyzing the existence of the bands of gel electrophoresis, it is able to read the output of the Boolean matrix multiplication. The experimental results prove the performance of a mathematical calculation based on DNA computing.

1 Introduction

In 1994, L. Adleman's [1] ground-breaking work demonstrated the way to use DNA molecules for computational purposes. This experience also contributed into a better understanding where to go with DNA machines, namely, to try to develop memory machines that are machines with very large memory that implements rather simple search operations.

In 1997, a method to perform this calculation using DNA to represent the edges, vertices, and paths in the graph above has been proposed by John S. Oliver [2]. The method used restriction enzymes, which cut DNA sequences which represented the edges, vertices, and paths in the graph. To solve an 10×10 matrix, 100 types of restriction enzymes are used. However, all types of restriction enzymes are approximately no more than 230 types. This method can not be used to solve a large matrix. Thus a method to do the Boolean matrix multiplication based on DNA computing without restriction enzymes is proposed in this paper. We carried out an experiment on the method.

The main strategy behind the in vitro implementation is by representing the Boolean matrices and their product by a directed graph, which consists of a set of vertices and edges. If an element in the input matrix is the symbol '1', we can draw an edge that is connecting two vertices in the directed graph and vice versa. Since it is possible to construct any consecutive matrices and the multiplication product of those matrices, then it is certainly possible to do the Boolean matrix multiplication based on DNA computing.

2 Boolean Matrix

Two Boolean matrices and their product can be represented by a directed graph (kim 1982; Robinson and Foulds 1980).For example, the product of two Boolean matrices, X and Y and the directed graph representation are shown in Figure 1.

In this graph, the initial vertices, "1" and "2" represent the row identifiers for the first matrix and the product matrix. The terminal vertices "A" and "B" represent the column identifiers for the second and product matrix. Based on the definition of matrix multiplication, the number of columns in the first matrix must equal the number of rows in the second matrix. The intermediate vertices "a" and "b" represent the columns of the first matrix and the rows of the second matrix.

Nonzero elements in the first or second matrix are represented by a directed edge (vector connection) in the graph. Connections between initial and intermediate vertices represent nonzero elements in the first matrix. Connections between intermediate and terminal vertices represent nonzero elements in the second matrix.

Such as, in the first matrix, the element at the intersection of row "1" and column "b" is the symbol '1'. Thus, we draw an edge proceeding from vertex "1" to vertex "b". Again, in the first matrix, the element at the intersection of row "1" and column "a" is the symbol 'zero'. Thus, there is no edge proceeding vertex "1" and vertex "a". Similarly, we can construct edges between vertex "a", "b", "A" and "B" to represent symbols of one in the second matrix. Each of the constructed edge has its own directionality indicated by an arrowhead.

The elements of the product matrix symbolize the existence or nonexistence of paths made form continuous linkages of edges between initial and terminal vertices. Paths can only be constructed by proceeding along edges in the direction indicated by the arrowhead associated with each edge. In essence, one is asking if it is possible to form a path from each initial vertex to each of terminal vertices. The problem of evaluating the elements in Z can be reduced to determining a compete set of paths from the initial vertices "1", "2" to terminal vertices "A", "B".

$$\underbrace{\begin{array}{c c} & \begin{array}{cc} a & b \end{array} \\ \begin{array}{c} 1 \\ 2 \end{array} & \begin{bmatrix} 0 & 1 \\ 1 & 0 \end{bmatrix} \end{array}}_{X} \underbrace{\begin{array}{c c} & \begin{array}{cc} A & B \end{array} \\ \begin{array}{c} a \\ b \end{array} & \begin{bmatrix} 0 & 1 \\ 1 & 0 \end{bmatrix} \end{array}}_{Y} = \underbrace{\begin{array}{c c} & \begin{array}{cc} A & B \end{array} \\ \begin{array}{c} 1 \\ 2 \end{array} & \begin{bmatrix} 1 & 0 \\ 0 & 1 \end{bmatrix} \end{array}}_{Z}$$

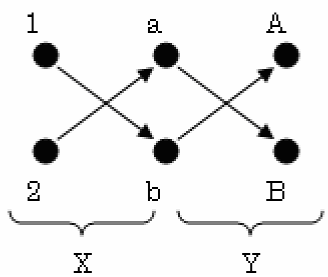

Figure 1: Multiplication of matrix and the graph represented the matrix.

3 The Proposed Methodology and Experiments

3.1 DNA Sequence Design

In order to perform the calculation using DNA, single-stranded DNA (ssDNA) of each vertex in the constructed directed graph is assigned with a unique 20-mer DNA sequences generated using DNA Sequence Generator. As Adleman's experiment, DNA sequences of ssDNA of each edge connecting two particular vertices are represented by DNA sequences assigned those two vertices. For example, an edge connecting vertices "i" and "j" is represented by complementary sequences used the second half of the sequences assigned vertex "i" and the first half of the sequences assigned vertex "j". Consequently, the ssDNA of the edge link these two ssDNAs of vertex "i" and "j", making an incomplete double-stranded DNA (dsDNA). Similarly, all of vertices and edges are represented by ssDNAs. Nonzero elements in the product of two Boolean matrices, X and Y connect initial, intermediate and terminal vertices with edges in graph. Therefore these ssDNAs make a unique 60-mer incomplete dsDNA.

For example, three ssDNAs of vertices "1", "b" and "A" are linked by two ssDNAs of edges "1b" and "bA". Their ssDNAs make a unique 60-mer dsDNA. So the element in row "1" column "a" of the product matrix is nonzero. Two ssDNAs of vertices "1", "a" aren't linked because of no edge. Similarly, other ssDNAs are linked.

3.2 Analysis

Parallel overlap assembly (POA) [3-5] is employed to generate complete dsDNAs, which represent all the possible paths of the graph. The reaction mixture is called template. The template is distributed into reaction test tubes. The number of the reaction test tubes is the same as the number of element in the product matrix. Each reaction test tubes is represented each elements in the product matrix. Two primers corresponding to the initial and terminal vertices in the graph are added to one of the reaction test tubes (Figure 2). A test of the reaction to identify the existence of a path is done by polymerase chain reaction (PCR). If the two primers corresponding to the initial and terminal vertices of a path exist in the reaction test tube, the dsDNA represented the path is amplified by PCR. To amplify, the reaction test tube has a path. Thus the element in the product matrix is symbol '1'. For example, if a dsDNA represented a pass that connects vertex "1" to vertex "A" and two primers corresponding to vertex "1" and vertex "A" exist in a reaction test tube, the dsDNA are amplified in the tube by PCR. The reaction test tube has a path. The element at the intersection of row "1" and column "A" is the symbol '1'. After that, the product of polymerase chain reaction is subjected to polyacrylamide gel electrophoresis in order to visualize the result of the computation. By analyzing the existence of the bands of gel electrophoresis, we are able to read the output of the Boolean matrix multiplication.

3.3 Experimental Protocols

We solved Boolean matrix in Figure 3. To generate all the possible paths of the graph by POA was performed in a 108μℓ solution containing 20μℓ oligos, 10μℓ dNTP (TOYOBO, Japan), 10μℓ 10x KOD dash (TOYOBO, Japan), 0.5μℓ KOD dash (TOYOBO, Japan), and 67,5μℓ ddH2O(Maxim Biotech). The reaction consisted of 25 cycles and for each cycles, the appropriate temperature were as follow:

- 94℃ for 30s
- 55℃ for 30s

- 74℃ for 10s

The product of parallel overlap assembly is called template.

The number of reaction test tubes was four. In each tube added two primers corresponding to the initial and terminal vertices of a path, DNA amplification was done by PCR. The PCR was performed in a 22.5μℓ solution consisted of 2.5μℓ for each primers, 1μℓ template, 2.5μℓ dNTP (TOYOBO, Japan), 2.5μℓ 10x KOD dash buffer (TOYOBO, Japan), 0.125μℓ KOD dash (TOYOBO, Japan), and 13.875μℓ ddH2O (Maxim Biotech). The reaction consisted of 25 cycles and for each cycles, the appropriate temperature were as follow:

- 94℃ for 30s
- 55℃ for 30s
- 74℃ for 10s

In order to visualize the result of the computation, the product of PCR was subjected to polyacrylamide gel electrophoresis for 40 minutes at 200V. After that, gel electrophoresis, the gel was stained by SYBR Gold (Molecular Probes) and the gel image was captured.

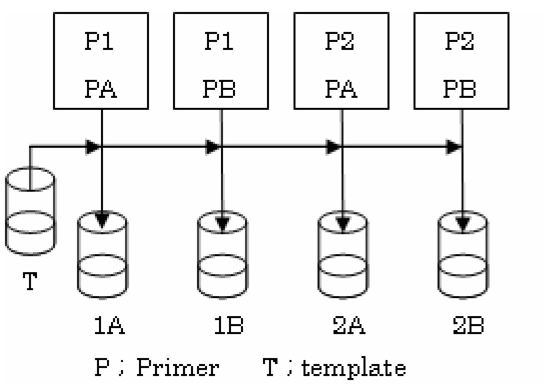

Figure 2: Add two primers in each tubes.

$$\begin{array}{c|cc} & c & d \\ \hline a & 0 & 1 \\ b & 1 & 0 \end{array} \begin{array}{c|cc} & e & f \\ \hline c & 1 & 0 \\ d & 0 & 1 \end{array} \begin{array}{c|cc} & g & h \\ \hline e & 0 & 1 \\ f & 1 & 0 \end{array} \begin{array}{c|cc} & i & j \\ \hline g & 1 & 0 \\ h & 0 & 1 \end{array} = \begin{array}{c|cc} & i & j \\ \hline a & 1 & 0 \\ b & 0 & 1 \end{array}$$

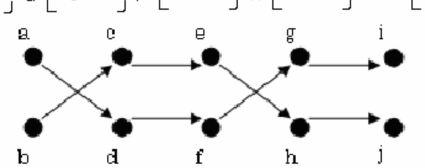

Figure 3: Multiplication of matrix and the graph represented the matrix.

Table 1: DNA sequence.

Name	20-mer Sequences (5'-3')
a	AAAGCTCGTCGTTTAAGGAA
b	GAAGCCTACTGTACTCTGCG
c	TACCCAATCGAACTGATAAG
d	CAGCCACGTAGTAGAGCTAG
e	GCCCAAGGTGCGTCAGTAAT
f	TCGGTCAACGGAGGGGTATA
g	TGGAATGGGTCAGAGAGCAC
h	GCACGAAGATAATCCGCAAC
i	ATGCCTGGCTAAAGTGAGAC
j	TAATAAATTCGTATCCACGG
Ead	TACGTGGCTGTTCCTTAAAC
Ebc	CGATTGGGTACGCAGAGTAC
Edf	CGTTGACCGACTAGCTCTAC
Ece	CACCTTGGGCCTTATCAGTT
Efg	ACCCATTCCATATACCCCTC
Eeh	ATCTTCGTGCATTACTGACG
Ehj	GAATTTATTAGTTGCGGATT
Egi	AGCCAGGCATGTGCTCTCTG
primer a	AAAGCTCGTCGTTTAAGGAA
primer b	GAAGCCTACTGTACTCTGCG
primer i	GTCTCACTTTAGCCAGGCAT
primer j	CCGTGGATACGAATTTATTA

4 Results

In each tube added two primers corresponding to the initial and terminal vertices of a path, DNA amplification was done by PCR. The product of PCR was subjected to polyacrylamide gel electrophoresis. The gel image of the result is showed Figure 4. Lane 1 was represented the element at the intersection of row "a" and column "i" in the product matrix. Similarly, other Lanes were represented the element in the product matrix. Lane M denoted 20-bp ladder. The existence of the bands of gel electrophoresis was observed at 100-bp on each Lane. Each bands differed from the shade of color. Lane 1 and Lane 4 were dark. The dsDNAs of these Lanes amplified. Lane 2 and Lane 3 were light. The dsDNAs of these Lanes didn't amplify. Consequently, in the product matrix, the element at the intersection of row "a" and column "i" was the symbol '1'. The element at the intersection of row "a" and column "j" was the symbol '0'. Similarly, other elements were found.

5 Discussions

We proposed the method to do the Boolean matrix multiplication based on DNA computing without restriction enzymes and carried out the experiment. As a result of the experiment, each bands of gel electrophoresis at 100-bp differed from the shade of color. When POA was conducted, two dsDNAs represented paths between "a" and "i" vertices and between "b" and "j" vertices were generated. PCR was known that a dsDNA existing the two primers corresponding to the initial and terminal vertices of a path in the reaction test tube, is amplified faster than existing the primer corresponding to the initial or terminal vertices of a path in the reaction test tube. If dsDNA amplifies, a band of gel electrophoresis is dark. A band which is light doesn't amplify dsDNA. Thus each bands differed from the shade of color. Consequently, we found, in the product matrix, the element at the intersection of row "a" and column "i" was the symbol '1' and element at the intersection of row "a" and column "j" was the symbol '0'. Similarly, other elements were found.

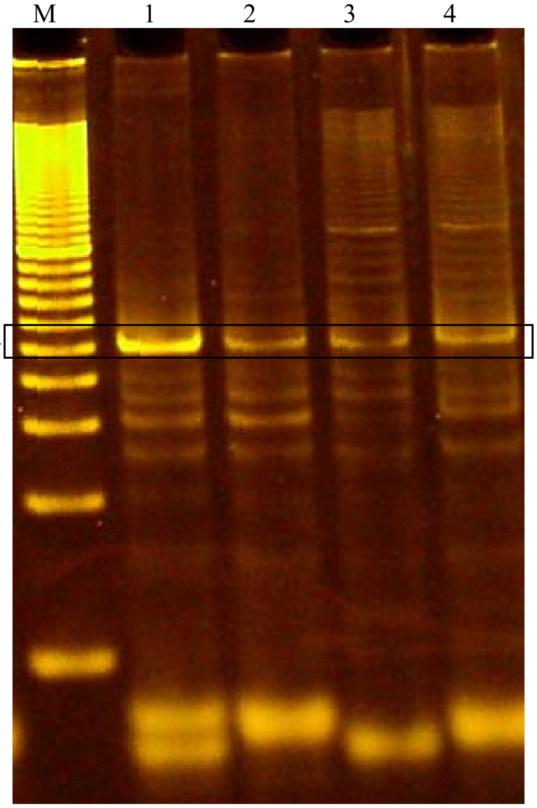

Figure 4: Experimental results of gel electrophoresis on 10% polyacrylamide gel. Lane M denotes 20-bp ladder. Lane 1 was represented the element at the intersection of row "a" and column "i" in the product matrix. Lane 2 was represented the element at the intersection of row "a" and column "j" in the product matrix. Lane 3 was represented the element at the intersection of row "b" and column "i" in the matrix. Lane 4 was represented the element at the intersection of row "b" and column "j" in the matrix.

As a conclusion, we were able to calculate Boolean matrix multiplication based on DNA computing without the use of restriction enzymes. In future, the same methodology will be used to perform a 10×10 matrix multiplication on a molecular computer.

References

[1]L.Adleman, "Molecular computation of solutions to combinatorial problems", Science 266, pp.583-585, 1994.

[2]John S.Oliver, "Matrix Multiplication with DNA", J Mol Evol 45, pp161-167, 1997

[3]Lee,J.Y., Lim, H.W., Yoo, S.I, Zhang, B.T., Park, T.H., "Efficient Initial Pool Generation for Weighted Graph Problems using Parallel Overlap Assembly," in Preliminary Proceedings of the Tenth International Meeting on DNA Based Computers, pp.357-364, 2004

[4]Ibrahim, Z., Tuboi, Y., Ono, O., and Khalid, M., "Experimental Implementation of Direct-Proportional Length-Based DNA Computing for Numerical Optimization of the shortest path Problem", Workshop on Unconventional Computing, 18th European Conference on Artificial Life, Luniver Press, pp. 35-46,2005

[5]Kaplan, P.D., Ouyang, Q., Thaler, D.S., Libchaber, A., "Parallel Overlap Assembly for the Construction of Computational DNA Libraries", Journal of Theoretical Biology, Vol. 188, Issue 3, pp.333-341, 1997

The Eleventh International Symposium on Artificial Life and Robotics 2006 (AROB 11th'06),
B-con Plaza, Beppu, Oita, Japan, January 23-25, 2006

Independent Agents in a Globalized World Modelled by Tissue P Systems

Marion OSWALD
Faculty of Informatics
Vienna University of Technology
Vienna, Austria

Abstract

For modelling the interactions of independent agents (only interacting via a common environment, but not depending on any direct physical interactions with other agents) in the globalized world, we here consider so-called agent tissue P systems (ATP systems for short). Based on the model of tissue P systems, such ATP systems consist of cells (independent agents) with specific programs which allow for changing the objects inside the agent or for exchanging objects from inside the agent with objects from the environment through the cell membrane. We investigate the computational power of specific variants of ATP systems and also discuss the special decidability problem whether or not a given ATP system of specific type from its initial contents can ever reach a configuration where all objects in the system are contained in a specific subset of the set of objects.

1 Introduction

In a globalized world, the actions of an individual (in the following called agent) may affect not only its direct environment, but instead also other agents in an arbitrary (physical) distance. In this paper we only investigate the part of interactions between the agents which does not rely on the physical distance, but due to the modern communication facilities, like email, web, etc., allows for interactions independent from the physical distance of the agents. (In what follows we shall refer to this part of the world we are going to model as "the globalized world".)

For modelling the interactions of independent agents (only interacting via the environment, but not depending on any direct physical interactions with other agents) in the globalized world we use a specific model of tissue P systems.

Tissue P systems first were considered in [5]; they are a variant of membrane systems as introduced by Gheorghe Păun in 1998 (for a detailed description see [6], for the actual state of research see [7]).

Here we consider agent tissue P systems (ATP systems for short) consisting of cells (independent agents) with specific programs which allow for changing the objects inside the agent or for exchanging objects from inside the agent with objects from the environment through the cell membrane. The environment only acts as a communication medium but cannot change the objects it communicates.

The agents may carry different programs which may be chosen to be run non-deterministically. In each evolution step of the whole system, an arbitrary number of agents may run one of its programs which we call the *partially parallel* or *asynchronous* derivation mode (see [1]). We may also consider the *maximally parallel* derivation mode, often used in the area of P systems, where in every cell (agent) one of the programs has to be run, or the *sequential* mode where, in each evolution step, only one agent runs one of its programs.

A model of tissue P systems closely related to the model considered in this paper is the model of P colonies as it was first introduced in [4], where the programs of the agents are very simple, just allowing for exchanging two symbols between the agent and the environment and changing a second symbol inside the agent to another symbol at the same time.

In the generating case, even one agent with a suitable number of such programs turned out to be computationally complete (see [2]). But in contrast to the usual investigations in the area of P systems where the generative and accepting power of those systems is investigated we here are interested in the time development of our ATP systems. Special questions concern the probability of events to happen in a given time interval. Theoretically these questions may turn out to be quite difficult, as for example even the simple question whether a specific event may ever happen or not may turn out to be undecidable at all. Hence, it is a challenging problem to find ATP systems with simple programs in the agents that allow at least for deciding some specific questions.

As an extension of the static variant described before, we may also consider a dynamic variant, where agents may die or may be newly born. Moreover, as a normal feature of artificial intelligence, the programs of the agents also may undergo dynamic changes.

2 Definitions

2.1 Preliminaries

An *alphabet* V is a finite non-empty set of abstract *symbols*. Given V, the free monoid generated by V under the operation of concatenation is denoted by V^*; moreover, we define $V^+ := V^* \setminus \{\lambda\}$, where λ denotes the empty word. A multiset over V is represented as a string over V (and any of its permutations). By $\mid x \mid$ we denote the length of the word x over V as well as the number of elements in the multiset x.

A *deterministic finite automaton* (*DFA* for short) is a quintuple $M = (Q, T, \delta, q_0, F)$ where Q is the finite set of *states*, T is the *input alphabet*, $\delta : Q \times T \to Q$ is the *state transition function*, $q_0 \in Q$ is the *starting state* and $F \subseteq Q$ is the set of *final states*. The transition function δ can be extended in a natural way to a function $\delta : Q \times T^* \to Q$. The language accepted by the DFA M is the set of all strings $w \in T^*$ that are accepted by M in such a way that $\delta(q_0, w) \in F$.

For more notions from the theory of formal languages, the reader is referred to [3].

2.2 ATP Systems

An *agent tissue P system (ATP system)* is a construct

$$\Pi_{ATP} = (O, O_T, E, B_1, ..., B_n)$$

where V is an alphabet (its elements are called objects), E is a set of environmental objects (i.e., the initial contents – or initial state – of the environment), $O_T \subseteq O$ is a set of final objects, and $B_1, ..., B_n$ are agents; each agent B_i is a pair $B_i = (O_i, P_i)$, where O_i is a multiset over O (the initial contents – or initial state – of the agent), and P_i is a finite sequence of evolution and/or communication rules. An evolution rule from P_i changes one object from O inside the cell (the agent) to another one, whereas a communication rule exchanges one object from the environment with an object from inside the cell.

A *computation* in the ATP system Π_{ATP} starts with O_i in the corresponding agent and with E and eventually some additional multiset as the input of the system in the environment. Throughout the computation, a *configuration* of Π_{ATP} is described by the contents (state) of the environment and the contents (states) of the agents.

In the sequential derivation mode, a derivation step of Π_{ATP}, i.e., passing from one configuration of Π_{ATP} to another one, means that one agent carries out one of its programs, non-deterministically chosen. In the asynchronous derivation mode, Π_{ATP} may run one program in an arbitrary number of cells (agents). In the maximally parallel derivation mode, every agent (cell) has to carry out one of its programs (if possible).

2.3 A Special Variant of ATP Systems - P Colonies

As a special variant of ATP systems, we consider the model of P colonies introduced in [4] and further investigated in [2]. A *P colony* is a construct

$$\Pi_C = (V, e, T, B_1, ..., B_n)$$

where V is an alphabet (its elements are called objects), e is a distinguished object of V (the environmental object), $T \subseteq V - \{e\}$ is a set of final objects, and $B_1, ..., B_n$ are agents; each agent B_i is a pair $B_i = (O_i, P_i)$, where O_i is a multiset over V (the initial state of the agent), and P_i is a finite set $\{p_{i,1}, ..., p_{i,k_i}\}$ of programs; each program $p_{i,j}$ is either a non-checking program of the form $\langle a \to b, c \leftrightarrow d \rangle$, or a checking program of the form $\langle a \to b, c \leftrightarrow d / c' \leftrightarrow d' \rangle$. In the generating case, we always assume that each O_i consists of two copies of e. A P colony can be written as the ATP system

$$\Pi_{ATP} = \left(V^*, T^*, \{e\}^*, B_1, ..., B_n\right).$$

At the beginning of a computation performed by a given P colony, the environment contains arbitrarily many copies of e; moreover, each agent contains two copies of e. At each step of the computation, the contents of the environment and of the agents change in the following manner: In the maximally parallel derivation mode, each agent which can use any of its programs should use one (non-deterministically chosen), whereas in the sequential derivation mode, one agent uses one of its programs at a time (non-deterministically chosen). By using a program $\langle a \to b, c \leftrightarrow d \rangle$, an agent with objects ac inside and with d in the environment will get the objects bd inside and c will now be placed into the environment. Using a program $\langle a \to b, c \leftrightarrow d / c' \leftrightarrow d' \rangle$ means to pass from ac inside and d outside to bd inside and c outside, and this should be done whenever possible; if the interchange $c \leftrightarrow d$ cannot be done, then we pass from ac' inside and d' outside to ad' inside and c' outside. Note that the first rule is always applied, and that either the first or the second communication rule has to be applied, with priority for the first one.

Any copy of an object can be involved in only one rule. Using the programs in this way, with all agents acting simultaneously or sequentially, nondeterministically choosing the program(s) to be applied, we can pass from one configuration of the system (represented by the contents of the agents and of the environment) to another configuration. Formally, a configuration can be written as an $(n+1)$-tuple $(w_1, ..., w_n; w_E e^{\omega})$, with $w_i \in V^2$ representing the objects from agent i, $1 \le i \le n$, and $w_E \in (V - \{e\})^*$, representing the objects from the environment different from the "background" object e; e^{ω} is used as notation for the arbitrarily many copies of the object e that are always contained in the environment; the initial configuration of a system is always $(ee, ..., ee; e^{\omega})$. A sequence of transitions is called a *computation.* A computation is said to be *halting,* if a configuration is reached where no program can be applied anymore. With a halting computation we associate a *result* which is given as the number of copies of the objects from T present in the environment in the halting configuration.

Because of the non-determinism in choosing the programs, starting from the initial configuration we obtain several computations, hence, with a P colony we can associate a set of (vectors of) numbers, denoted by $N(\Pi)$, computed by all possible halting computations of Π.

2.3.1 Computational power of P colonies

In [2], P colonies working in the sequential mode with checking programs of height at most 5 were shown to be computationally complete, whereas when working in the maximally parallel mode, P colonies using programs again with height 5 but without priorities on the communication rules (i.e., without checking programs) achieve the same computational power, too.

Already one agent using checking programs is enough to obtain computational completeness in P colonies working in the sequential mode, which is a quite surprising result optimal with respect to the number of agents. If only non-checking programs are used, even P colonies with only one agent as well as P colonies with an arbitrary number of agents working in the sequential mode characterize the family of languages generated by matrix grammars without appearance checking.

3 Undecidability / Decidability for ATP Systems

The general variant of decidability problems we consider here is the following: Given an ATP system with specific initial contents, is it decidable whether it ever can reach a configuration where all objects in the system are contained in a specific subset of the set of objects?

3.1 Undecidability for P Colonies

Can a configuration fulfilling specific constraints ever be reached (e.g., the objects occurring in the system all are included in a specific subset of the set of objects)? This question in general is not decidable. For a given P colony, the question whether such a system will ever produce anything, i.e., whether $N(\Pi) = \emptyset$, corresponds with the famous halting problem (e.g., see [3]), hence this question is undecidable.

3.2 Decidability for ATP Systems

We now consider a specific variant of ATP systems that model finite automata, and in this framework we consider some problems which are easily decidable.

Let $M = (\{q_1, ..., q_n\}, T, \delta, q_1, F)$ be a finite automaton. Then we construct the ATP system

$$
\begin{array}{lcl}
\Pi_{ATP} & = & (O, O_T, \emptyset, B_1, ..., B_n), \\
O & = & \hat{Q} \cup QT^*, \\
O_T & = & F \cup \hat{Q}, \\
O_i & = & \{\hat{q}_i\}, 1 \le i \le n, \\
P_i & = & \{\langle \hat{q}_i \leftrightarrow q_i u \rangle, \langle q_i a w \rightarrow q_j w \rangle, \langle q_j w \leftrightarrow \hat{q}_i \rangle \\
 & & \mid \delta(q_i, a) = q_j, 1 \le i, j \le n, u, w \in T^* \}.
\end{array}
$$

The programs in the agents consist of single communication rules ($\hat{q}_i \leftrightarrow q_i u$ and $q_j w \leftrightarrow \hat{q}_i$) and single evolution rules ($q_i a w \rightarrow q_j w$); as only the beginning of the strings is changed, these rules could also be written in the form $\hat{q}_i \leftrightarrow q_i$ and $q_j \leftrightarrow \hat{q}_i$ as well as $q_i a \rightarrow q_j$ which shows that the infinite set of rules P_i can be described in a finite way.

Observe that the information processing in ATP systems (other than in finite automata), only takes place via the environment without any direct communication between the cells (agents), which here can be seen as parallel processors working in an asynchronous (sequential) manner.

We now want to know whether the system started with the input $q_1 w_k$ for some $w_k \in T^*$, $1 \leq k \leq m$, $m \geq 1$, can ever reach a configuration where all objects in the system are contained in O_T (indicating that all the input string(s) $w_1, ..., w_m$ are accepted). This problem is easily decidable in a reasonable amount of time: after at most $(|w_1| + ... + |w_m|)*3$ steps we know the answer. Moreover, in the affirmative case, we know that the input string(s) have been accepted, while in the negative case, at least one input string has not been accepted. In fact, we even know exactly how many input strings have been accepted by counting the objects $q_i \in F$. Hence, by just looking at the environment, we can figure out the desired result and thus, after a period that can easily be computed, can decide the given problem.

4 Variants

One variant of ATP systems is taking the environment not only as a communication medium, but also enabling it to change the objects it communicates. Formally, this, for example, could be done by defining an additional agent (symbolizing the environment) with its own corresponding programs.

On the other hand, as an extension of the static variants described above, we may also consider a dynamic variant, where agents may die or may be newly born, i.e., we can consider cell deletion, cell division and cell generation. When a cell is deleted, the exchange of a specific element between the environment and the cell or the evolution of an element inside the cell may cause the death of the cell (with variants where all the elements inside the cell also die or else the contents of the deleted cell is added to the environment). By cell division, one cell can be reproduced with its whole contents and the corresponding programs, whereas new cells can be generated with explicitly stated contents and new or modified programs. Moreover, as a normal feature of artificial intelligence, the programs of the agents also could undergo dynamic changes.

5 Conclusion

We have introduced the computing model of agent tissue P systems (ATP systems) and investigated some decidability problems concerning questions whether a specific event may ever happen or not in these systems.

As we have seen in the generating case of P colonies, even simple questions may be highly undecidable, yet for a specific accepting variant of ATP systems some problems were shown to be easily decidable. Using suitable representations and systems, in general also the question whether $w \in L$ can be decided for any recursive language L. One of the most challenging questions for future research is to find variants of ATP systems between these two extremes of decidable problems. Another question not yet investigated in detail in the area of P systems is concerned with permitted and forbidden configurations (e.g., given by complementary subsets of O): Given an initial configuration, can the systems always stay within the permitted configurations, or is it possible that it may reach a forbidden configuration?

Acknowledgements

We gratefully acknowledge interesting and fruitful discussions with Rudolf Freund.

The work of Marion Oswald is supported by FWF-project T225-N04.

References

[1] R. Freund, Asynchronous P systems, *Proceedings WMC5,* 2004, 12–28.

[2] R. Freund, M. Oswald, P Colonies working in the maximally parallel and in the sequential mode, in: G. Ciobanu, Gh. Păun (Eds.), *TAPS'05*, Timişoara, Romania, 2005, 49–56.

[3] J. Hopcroft, J. Ullman, *Introduction to automata theory, languages, and computation,* Addison-Wesley, 1979.

[4] J. Kelemen, A. Kelemenová, Gh. Păun, On the power of a biochemically inspired simple computing model: P colonies, in: M. Bedan et al. (Eds.), Workshop on Artificial Chemistry, *ALIFE9*, Boston, USA, 2005, 82–86.

[5] C. Martín-Vide, J. Pazos, Gh. Păun, A. Rodriguez-Paton, Tissue P systems, *Theoretical Computer Science* 296 (2) (2003) 295–326.

[6] Gh. Păun, *Membrane computing - an introduction*, Springer-Verlag, Berlin, 2002.

[7] The P systems webpage: http://psystems.disco.unimib.it

A Bioinformatics Method for Signaling Pathways in Cells

Jian-Qin Liu and Katsunori Shimohara
ATR Network Informatics Laboratories
2-2-2, Hikaridai, "Keihanna Science City,"
Kyoto 619-0288, Japan
e-mail: {jqliu, katsu}@atr.jp

Abstract

In this paper, a new bioinformatics method for modeling cellular pathways is proposed based on graph rewriting and network reconstruction. The simulation result shows that the graph rewriting operators and networking structure are beneficial to quantitatively describe the signaling mechanism of GEF/GAP/kinase/phosphatase pathway networks.

1. Introduction

The motivation of the research work presented here is to study the mechanism of molecular computers made from molecular biochemical reaction and to design new bioinformatics simulation methods based on this mechanism for application to bioinformatics analysis. Bioinformatics simulation modeling and methods are more difficult than one might expect, even though many simulation models and methods have recently been proposed. It is imperative to design new models and to use them in discovering biological knowledge [1].

As a highlighted theme in the field of genomics and proteomic bioinformatics, pathway modeling with complex behaviors due to non-linear interactions is one of the most important remaining tasks [2~7]. For example, "pathway logic" [8] directly handles pathway modeling. The "Maude system" [11] is software that can realize pathway logic by adopting the function of "rewriting". The software is based on rigorous theoretical computer science, and it is helpful for discovering pathways. This work has encouraged us to explore a formal modeling method for pathway analysis.

The rapid progresses in experimental molecular biology are providing us much knowledge in theory and tools for biological cell experiments where many biochemical reactions are carried out with an enormous number of bio-molecules. Abstraction is not only a way to represent data for theoretical study but also a necessary method for simulation, especially in large-scale bio-informatics systems. From experiments on molecular computers, we can gain some insight. For example, in DNA computers, the operators are carried out in test tubes to accomplish specific computing tasks so that the relationship between input and output is exactly determined. This process acts as a kind of bottom-up wetware-level inference machine for synthesis of the biochemical reactions in vitro. Based on the formalization of this physically feasible computing process, the formal models, operators and algorithms extracted will be beneficial to extending our knowledge of mechanism behind the underlying biological objects verified from experimental data to the broader domain of biological systems that include the underlying molecules in the reactions. This knowledge would act as a bridge toward top-down knowledge discovery.

2. Structural Scheme for Bioinformatics

Toward the goal of analysis-based pathway simulation, this paper proposes a formal system defined as a type of graph rewriting to unify different jobs in pathway modeling, since graphs can provide efficient representation and related semantic explanation.

Here we focus on pathway simulation. In the study of the signaling pathways in cells, it is meaningful to work out a unified formal method based on a molecular mechanism, where the mechanism of modeling bio-pathways and the structure of simulating pathways are consistent. For this purpose, a graph-rewriting method for pathway simulation is discussed in terms of corresponding formal characteristics, representation schemes and simulation issues. This is one of the efforts being made toward automatic analysis for bioinformatics in which multidisciplinary fields can be integrated into computer-aided systems for bioinformatics. Great progresses have been made in the field of bioinformatics. However, much difficulty would remain in integrating these fields in order to make breakthrough in new knowledge discovery based on theory and by software. In a word, we are trying to tackle this topic by a unified model -- graph rewriting -- that is supported by computer science theory and programming technology. Furthermore, we expect to extend this model to a powerful technology.

On an abstract level, the corresponding formal model can be constructed as a graph rewriting system. Now, we define the graph rewriting in a formal way as:

Let G = < V, E>

where

A -- the alphabet set;

V -- the set of vertexes;

E -- the set of edges.

Consequently, from the above model, we can derive the following writing processes on graphs:

$$G \rightarrow G'$$

where G and G' refer to the graphs.

3. Simulation for Cellular Pathways

In order to elucidate this network's behavior quantitatively, we discuss an example of simulated pathways (Cf. Fig. 1) in which the atomic pathway set of Rho-MBS-MLC is defined as the set of {pathway of Rho, pathway of MBS, pathway of MLC}. In the normal case, the interaction-rating array (symmetric form) is set in an empirical way, that is, the mutual links are designed to reflect the reversibility of phosphorylation/dephosphorylation of related reactants in the pathways. The concentration representation for signaling proteins of Rho GTPase in the set of {MLC+, MLC-, MBS+, MBS-} can be defined in different ways, such as digital, continuous or symbolic values, where + and – refer to the phosphorylation and dephosphorylation states, respectively. In the simulation, initialized values of concentration can be set in a random way. The activation rule of cellular agents on quantified concentration is defined in the following form: IF *perception* THEN *action*. Here, the related threshold function and fitness function are defined in an empirical way.

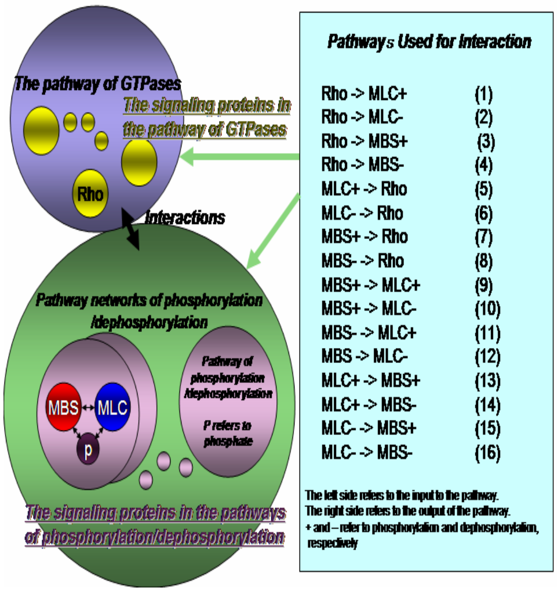

Fig. 1 Relations among the pathways

The kernel of the algorithm is the mechanism of selection and variation by the estimation of interaction rating. The interaction algorithm of two pathways is outlined in a stochastic way by the following steps:

Step 1: The probability Pp (x, t) is simulated by a logistics function (a = 4, X_0 = 0.05).

Step 2: The two classes of the population are estimated based on a uniform distribution assumption such that the classes are given as class1 ranges in [0,0.5]; class2 ranges in (0.5,1]. The mean *m(t)* and variance *v(t)* are the main measures for the two classes. The element numbers of the two classes are L1(t) and L2 (t).

Step 3: Two individuals are selected from the class with the largest probability.

The two pathways (individuals) are selected to be combined into a new pathway by the interaction operation. The new pathway is then placed in the pathway set (pool). The probability of a new pathway is estimated by the weight summation of the probability of the two individual pathways, and its simulated interacting-rate is assigned by this value.

Step 4: The martingale measure Mp for the termination is defined as: Mp = INP – ANP, where INP denotes the interaction rate of the new pathway and ANP denotes the average of the interaction rating of the pathway set. In this example, the measure is estimated by weighted summation of the probabilities of the two pathways.

Step 5: If this measure is supermartingale (increased), then goto step 2. If submartingale (decreased), goto next step.

Step 6: Stop and output the current pathway set as the final result.

Because it is impossible to quantitatively measure all of the coefficients of biochemical reactions for pathways through biochemical experiments, in the sense of local concentration of the related signaling molecules, simulation is very important to understanding the quantitative effect of the interaction functions of pathways.

Considering the importance of the interaction operation in the entire simulation work, let us select one sample from the pathway pool of the interacting processes. This is a snapshot of a randomly selected episode from the current moment to next moment in a continuous interacting process. Here we have 19 pathways in the pathway set. They are clustered into two classes whose concentrations vary at (0, 0.5] and (0.5, 1.0). Here, 'concentration' refers to the estimated average concentration of the signaling protein, such as MBS in the MBS pathway and MLC in the MLC pathway, which act as function effectors of the phosphorylation/dephosphorylation in the underlying pathway. The pathway index of class 1 is 6, and that of class 2 is 13. Two pathways with larger probability than the others in the pathway pool, indexed as 2 and 15, are selected for combining to generate a new pathway.

The new pathway is assigned an average concentration -- 0.493133 -- of the signaling proteins to connect the signaling proteins in the two pathways. Then, this pathway is classified as class 1 and its probability is estimated as 0.853140, according to the following formula:

$$Pr' = Pr1 * Pr1/(Pr1+Pr2) + Pr2 * Pr2/(Pr1+Pr2),$$

where Pr' refers to the probability of the new pathway. Pr1 and Pr2 refer to the probabilities of the original pathways indexed as 2 and 15, respectively. We find that Pr' is bigger than the average probability of class 1 -- 0.184589, which means it is more plausible from the viewpoint of interaction-rating measurement.

The termination for the interacting process is as follows:

If the new pathway has a higher probability than the average value, the computing process will be continued.

If the total allowed time or the new probability is lower than the average probability, the computing process will be terminated.

As Fig. 2 (a), (b), (c) and (d) shown, the two states of pathways can be obtained.

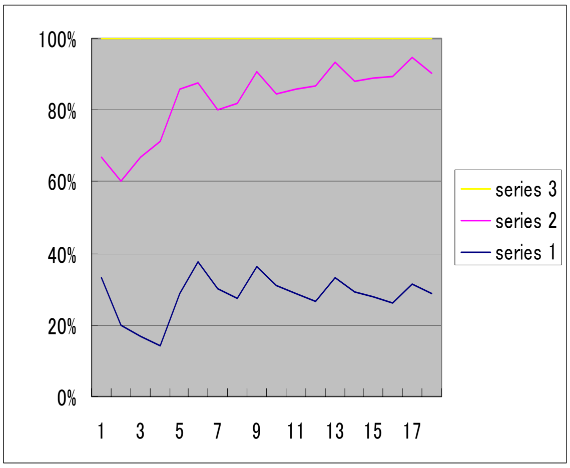

Fig. 2 (a) Concentration vs. time curves that correspond to the two states of the pathways

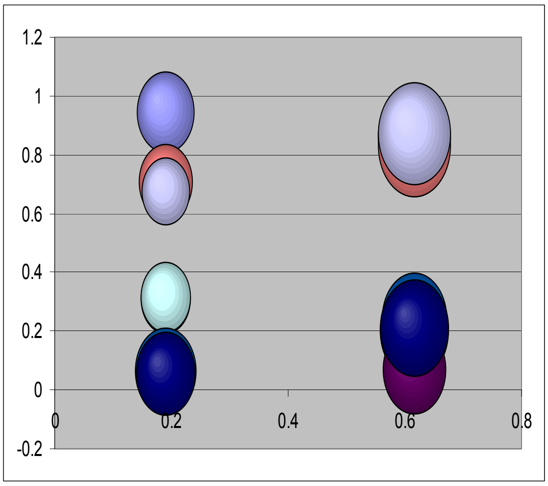

Fig. 2 (b) Size of the signaling molecules

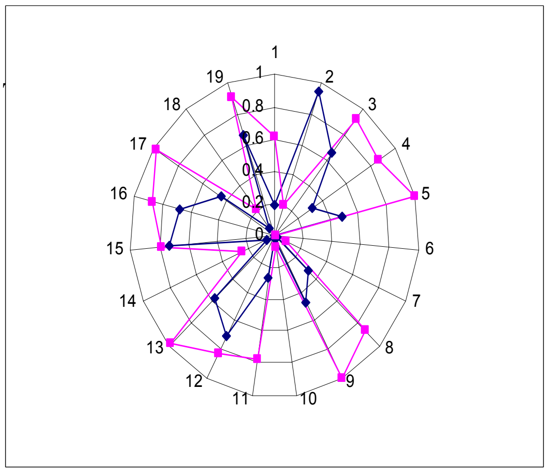

Fig. 2 (c) Partial interaction network reconstructed by estimation

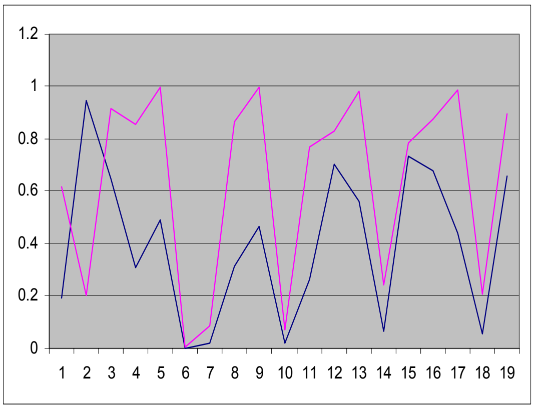

Fig. 2 (d) Concentration vs. time under the dynamical environment

In a word, the interaction operators based on estimation can generate stable states of the simulated pathways under certain conditions. As a result, the proposed method is efficient.

4. Conclusion

The simulation method based on graph data-structure and related rewriting operators is discussed. Through pathway simulation in bioinformatics, new knowledge may emerge and will surely be beneficial to develop computer-aided system for proteomics [10].

Acknowledgement

This research was conducted as part of "Research on Human Communication" with funding from the National Institute of Information and Communications Technology, Japan.

(Main) References

[1] Nir Friedman, Inferring Cellular Networks Using Probabilistic Graphical Models, Science, Vol. 303, 6 February 2004; pp.799-805.
[2] O. Wolkenhauer, et al., Control and coordination in biochemical networks, IEEE Control Systems Magazine, 24 (4) Aug. 2004; 30-34.
[3] Saez-Rodriguez et al., Modular analysis of signal transduction networks, IEEE Control Systems Magazine, 24 (4) Aug. 2004; 35-52.
[4] S. Y. Shvartsman, et al., Epidermal growth factor receptor signaling in tissues, IEEE Control Systems Magazine, 24 (4) Aug. 2004; 53-61.
[5] M. Khammash and H. El-Samad, Systems biology: from physiology to gene regulation, IEEE Control Systems Magazine, 24 (4) Aug. 2004; 62-76.
[6] S. Paliwal, et al., Responding to directional cues: a tale of two cells [biochemical signaling pathways], IEEE Control Systems Magazine, 24 (4) Aug. 2004; 77-90.
[7] H. Schmidt and E. W. Jacobsen, Identifying feedback mechanisms behind complex cell behavior, IEEE Control Systems Magazine, 24 (4) Aug. 2004; 91-102.
[8] C. Talcott, S. Eker, M. Knapp, P. Lincoln, K. Laderoute, Pathway Logic Modeling of Protein Functional Domains in Signal Transduction, PSB 2004.
[9] John S. McCaskill and Ulrich Niemann, Graph Replacement Chemistry for DNA Processing, in A. Condon (Ed.): DNA 2000, LNCS 2054, pp.103-116, 2001. Springer-Verlag, Berlin, Heidelberg, 2001.
[10] Carol Ezzell, Proteins rule, Scientific American, 286 (4), April 2002; pp. 26-33.
[11] http://www.csl.sri.com/projects/maude/

The Eleventh International Symposium on Artificial Life and Robotics 2006 (AROB 11th'06),
B-con Plaza, Beppu, Oita, Japan, January 23-25, 2006

3-D Modeling of Remote Dynamic Situations Using Mobile Stereo Cameras

Iku Yamaguchi, Joo Kooi Tan, and Seiji Ishikawa
Department of Control Engineering, Kyushu Institute of Technology
Sensuicho 1-1, Tobata, Kitakyushu 804-8550, Japan
E-mail: {yamaguti, etheltan, ishikawa}@ss10.cntl.kyutech.ac.jp

Abstract

This paper proposes a technique for recovering 3-D shape of the objects in remote dynamic situations employing mobile cameras. Since the proposed technique allows independent move of the employed cameras, 3-D recovery under various environments such as remote places can be realized. Our technique has an advantage over others in that camera calibration before taking images is not prerequisite to the recovery. A system is described that captures images of remote objects by the proposed motion capture technique, transfers the images by analog airwaves, and recovers 3-D shape of the objects from the images. It is expected that this technique will improve the efficiency of image information transfer. In the performed experiment, a human walking motion captured at a remote place recovered its 3-D motion successfully at a laboratory by image transfer.

Keywords— Motion capture, Mobile cameras, Image transfer, Factorization.

1. Introduction

Three-dimensional (abbr. as 3-D hereafter) modeling techniques of non-rigid objects have quite considerably developed in recent years. On the other hand, it has become possible to transmit images by using the Internet, as long as the image of a video camera can be converted into digital data. Therefore it will be useful to develop a 3-D modeling technique with video images acquired from mobile camera at remote dynamic situations.

This paper presents a technique for 3-D modeling of remote dynamic situations containing non-rigid as well as rigid objects employing mobile stereo cameras. We have developed this technique as a new motion capture technique whose cameras can move around the objects independently.

We have already proposed a shape recovery technique of 3-D non-rigid objects based on multiple uncalibrated cameras [1]. This technique has an advantage over others in that camera calibration before taking images is not prerequisite to the modeling. Instead, the camera calibration is done by employing the 2-D coordinates of the feature points of rigid object in the images of a video stream. This leads us to the modeling of any events and performances that need immediate understanding of the situation. In recent years, dynamic calibration techniques [2] that can calibrate the employed cameras speedier than the conventional techniques are employed in several commercial motion capture systems. However they actually need some preparation before starting of taking images even if it is possible to calibrate cameras in a short time. Therefore, if they are employed, a decisive moment may be missed after fixation and calibration of cameras.

In this paper, we propose a mobile motion capture system that recovers 3-D shape of remote objects in an arbitrary environment. Moreover, in order to perform an efficient 3-D recovery from image data obtained at a remote environment, an image transfer system is also described. Some experimental results are shown and discussion is given.

2. Proposed 3-D modeling technique

In the first place, the 3-D coordinates of objects are necessary in order to realize 3-D modeling. This section shows how to obtain the 3-D coordinates of objects for 3-D modeling.

The technique proposed in this paper recovers the 3-D coordinates of rigid objects and non-rigid objects, if more than or equal to two mobile cameras are employed for motion capture. **Figure 1** shows the outline of the image capture system.

This system adopts a method of taking images of rigid objects and non-rigid objects simultaneously, while $F (F \geq 2)$ cameras move in $l (l = 1,2,\cdots, L)$ directions. Some feature points are put on the surface of each object.

Fig.1 System overview.

We call the feature points on rigid objects as *rigid points* and those on non-rigid objects as *non-rigid points* hereafter. Camera orientations are all different through the camera movement from $l=1$ to $l=L$. Therefore the cameras need calibration to obtain 3-D information of the object. Although conventional 3-D recovery techniques need camera calibration employing particular tools, the proposed technique doesn't have to employ such tools for the camera calibration. Instead it employs rigid points observed in the captured images. Details of the procedure are described below. There are two important phases in the procedure.

2.1 Recovery of Rigid Objects

The 2-D coordinates (x, y) of the feature points in the image obtained from the camera whose orientation is l are stored in the measurement matrix as follows;

$$W_l = \begin{pmatrix} x_1^l & \cdots & x_{R_n}^l & x_{R_n+1}^l & \cdots & x_{R_n+N_n}^l \\ \hline y_1^l & \cdots & y_{R_n}^l & y_{R_n+1}^l & \cdots & y_{R_n+N_n}^l \end{pmatrix} \tag{1}$$

where the number of rigid points is denoted by $R_n (R_n \geq 6)$ and the number of non-rigid points by N_n. Here at least not less than six rigid points are required to the calculation. Let the sub-matrix containing rigid points be denoted by W_l^{R} and the sub-matrix containing non-rigid points be denoted by W_l^{N} with respect to the matrix of Eq.(1). Then Eq.(1) can be rewritten as

$$W_l = \left(W_l^{\mathrm{R}} \quad W_l^{\mathrm{N}}\right). \tag{2}$$

Since camera orientation changes from l=1 to L, the measurement matrix W at all the observation time is described as follows;

$$W = \begin{pmatrix} W_1^{\mathrm{R}} & W_1^{\mathrm{N}} & & & & & \\ & & W_2^{\mathrm{R}} & W_2^{\mathrm{N}} & & & \\ & & & & \ddots & & \\ & & & & & W_L^{\mathrm{R}} & W_L^{\mathrm{N}} \end{pmatrix}. \tag{3}$$

It should be noted that the data don't exist at blank elements in the matrix W, except for W_l^{R} and W_l^{N}.

Matrix W_l^{R} is a measurement matrix of rigid points. Since we assume that same rigid points are always tracked and taken images during image capturing, even if the camera moves, this matrix with superscript R contains the coordinates of the same rigid points. Therefore it is possible to transform Eq.(3) as follows with respect to the coordinates of rigid points;

$$W = \begin{pmatrix} W_1^{\mathrm{R}} & W_1^{\mathrm{N}} & & & \\ W_2^{\mathrm{R}} & & W_2^{\mathrm{N}} & & \\ \vdots & & & \ddots & \\ W_L^{\mathrm{R}} & & & & W_L^{\mathrm{N}} \end{pmatrix} \equiv \left(W^{\mathrm{R}} \quad W^{\mathrm{N}}\right). \tag{4}$$

Applying the factorization method [3] to Eq.(4), we have

$$W^{\mathrm{R}} = M \cdot S^{\mathrm{R}}. \tag{5}$$

Thus the 3-D coordinates of rigid points S^{R} are obtained.

2.2 Recovery of non-rigid objects

In Eq.(5), matrix M is a camera orientation matrix at all the observation time. When 3-D coordinates of the non-rigid points at position l are denoted by S_l^{N}, the following relation holds.

$$W_l^{\mathrm{N}} = M_l \cdot S_l^{\mathrm{N}}, \tag{6}$$

where M_l denotes a camera orientation matrix at position l. Therefore S_l^{N} is obtained as

$$S_l^{\mathrm{N}} = M_l^{+} \cdot W_l^{\mathrm{N}} \tag{7}$$

by using the pseudo-inverse matrix M_l^{+} of M_l. Thus 3-D coordinates of non-rigid objects are given by S^{N}. In this way, 3-D recovery of both feature points is achieved.

3. Transferring images from a remote place

The method of transferring images obtained by a mobile camera is important for 3-D recovery of the objects at a remote place.

In recent years, it has become possible to transmit images by using various ways such as the Internet, as long as the image of a video camera can be converted into digital data. This leads us to obtaining images from a remote place immediately. Thus we construct an image transfer system for a mobile motion capture system. The protocol of image transfer includes analog airwave, wireless LAN, and Internet. Alternatively there is of course a method of storing images once into a video tape and mailing them to another place, we choose a more effective way in this study. In order to use a larger space efficiently for 3-D recovery outdoors, we construct an image transfer system which employs an analog airwave, although wireless LAN is also effective for some outdoor experiments.

We construct the following system. **Figure 2** shows the overview of the image transfer system.

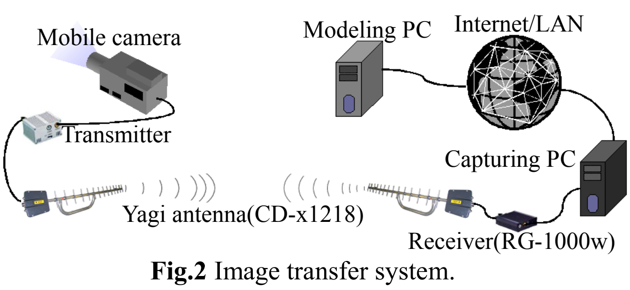

Fig.2 Image transfer system.

3.1 Transferring images to PC for capture

The analog image output of the video camera is transmitted to PC with a transmitter (RG-1000w) for performing 3-D modeling.

The signal is amplified and transferred by employing Yagi antenna (CD-x1218) that is one of the high-directivity antennas. The signal of the camera of each channel is transmitted and received with an individual antenna. The reception side of the antenna is connected to a receiver (RG-1000w).

3.2 Capturing images to PC via a capture board

Images of the objects concerned are captured into PC via a capture board. The maximum frame rate is 30 fps and its resolution is 640×480 pixels. The captured images are transferred through Internet to a modeling PC in a remote laboratory for recovery calculation and display of the result.

3.3 3-D recovery from obtained images

Applying the proposed technique to the obtained images, we finally get recovered human motions. For 3-D expression with high reality, we create human models employing OpenGL.

4. Experimental results

In the experiment, a human moving motion captured at a remote place was modeled its 3-D shape successfully. **Figure 3** and **Figure 4** show the captured images and its 3-D modeled results, respectively. In both figures, time proceeds as indicated by arrows.

5. Conclusions

This paper proposed a technique for 3-D modeling of remote dynamic situations employing mobile stereo cameras.

One of the largest advantages of the proposed technique is the degrees of freedom for the applicable situations. Some of its reasons are described as follows.

i) In the proposed system, ordinary camera calibration is not necessary before taking images for the recovery. Therefore, we can start the experiment immediately, which may be applicable to broadcasting of an accident at a remote place promptly in a 3-D way.

ii) Even if the object concerned moves widely, we can also track along its moving, because the system doesn't have a limit with the range of motion capture, unlike the existing methods employed in a studio.

In this way, the proposed technique, 3-D modeling of remote dynamic situations, has finally been realized.

This study was partly supported by Kayamori Foundation of Information Science Advancement, which is greatly acknowledged.

References

[1] J. K. Tan, S. Ishikawa, "Recovering 3-D motion of team sports employing uncalibrated video cameras", *IEICE Trans. on Information and Systems*, **E84-D**, 12, 1728-1732, 2001.

[2] Borghese N.A., Cerveri P. "Calibrating a video camera pair with a rigid bar", *Pattern Recognition*, **33**, 1, 81-95, 2000.

[3] C. Tomasi, T. Kanade, "Shape and motion from image streams under orthography: A factorization method", *Int. J. Computer Vision*, **9**, 2, 137-154, 1992.

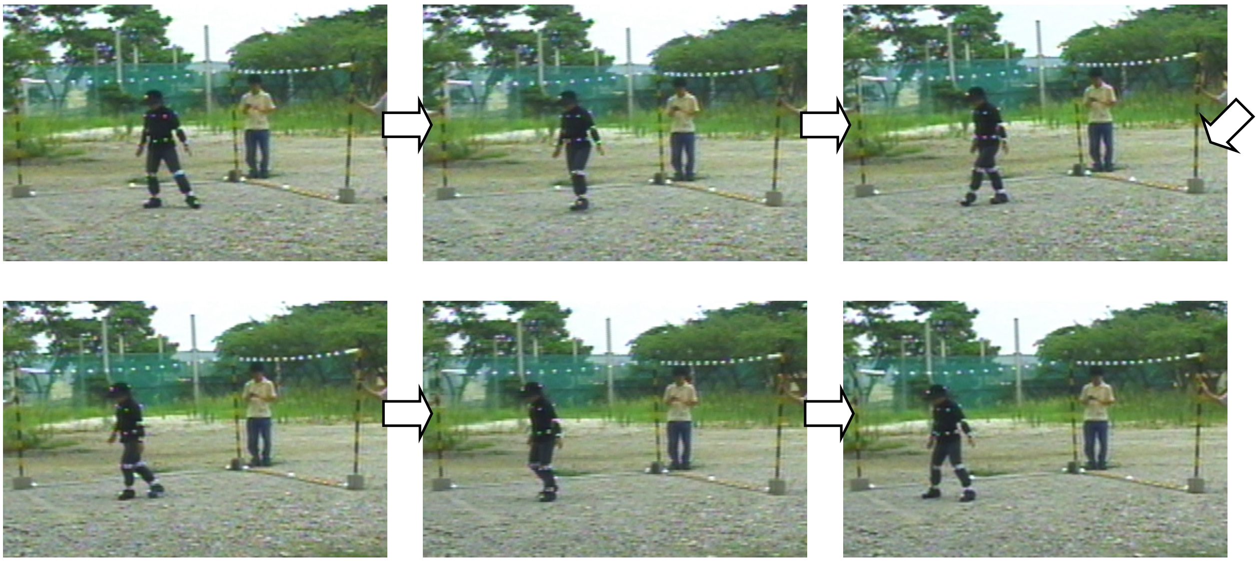

Fig.3 Video images of a person in an action.

Fig.4 Recovered motion and the environment.

The Eleventh International Symposium on Artificial Life and Robotics 2006 (AROB 11th'06),
B-con Plaza, Beppu, Oita, Japan, January 23-25, 2006

Tracking an Object Using an Update Type Two-dimensional Histogram

Hirofumi UEMURA **Joo Kooi TAN** **Seiji ISHIKAWA**

Department of Mechanical Control Engineering

Kyushu Institute of Technology

Sensuicho 1-1, Tobata, Kitakyushu 804-8550, Japan

uemura@ss10.cntl.kyutech.ac.jp, {etheltan, ishikawa}@cntl.kyutech.ac.jp

Abstract: In this paper, we propose a new technique for tracking an object under changeable illumination. In object tracking that use color information, illumination change is a serious problem. The reason is that the color to be tracked usually changes, when the illumination changes. The robustness of the tracking performance can be improved to a large extent by the employment of an update-type color histogram. The weight imposed by the Gaussian distribution is used together with the update of the histogram. The Gaussian distribution is made from the initial color model of the object. The distribution near the initial color model is added to the histogram with higher weight. As a result, the color model can be updated with better accuracy. The effectiveness of the proposed technique is confirmed by experiments.

Keywords: Human tracking, Two-dimensional color histogram, Anisotropic Gaussian distribution, Robot vision.

1. Introduction

Color is an important cue as well as shape or texture in finding an object in a scene. A mother can identify her child easily in a park among lots of children by the color of her child's upper or lower clothes. A computer vision system searches for skin color regions in an image to extract human faces or hands in order to find out a human. Many studies have been performed until now for the purpose of detecting or segmenting objects from images using color information [1,2]. The difficulties of employing color information in computer vision problems is, however, it is not very stable as a feature to be detected, since it is normally influenced by illumination conditions caused by weather, time in a day, lights, shade, etc. A robust color detection technique hasn't been proposed yet in the computer vision field.

When a computer vision system performs color extraction, it needs to make a color model. There have been many methods for the color model making [3]. The employment of two-dimensional (2-D) color histogram on the chrominance space seems promising for color extraction, since it clearly describes the shape of color distribution. Already reported technique [4] employs the color histogram with normalized rg expression. But it is not very easy to understand the distribution intuitively, as it doesn't match the human sense of color.

In this paper, we propose a new technique for color detection employing the 2-D color histogram on the chrominance space. Illumination change of a given environment is also taken into account by the employment of an anisotropic Gaussian distribution in the modeling of a 2-D color histogram. We employ HSV system for color expression because of its popularity among computer vision researchers and the similarity to human sense.

2. A color tracking system

Object tracking systems normally employ shape and texture information in order to calculate correlation between successive image frames. The reason why the employment of color information is not very popular is that it is not robust to illumination change. The color information is, however, advantageous when a human is searched in an image, because the skin color is an intrinsic nature to a human.

Illumination change occurs gradually in the time lapse of the day, but it occurs suddenly, if one turns on or turns off the light in the room or goes into a shadow/shade spot from a san light spot outdoors. Although both situations should be overcome in order to employ color in the tracking, the former is taken into consideration in this particular paper.

We have developed a color tracking system based on a 2-D color histogram. It can track a specified color in a room with moderate illumination change. It achieves it by acquiring the changing color, and updating 2-D color histogram. Overview of the system is given in **Fig.1**.

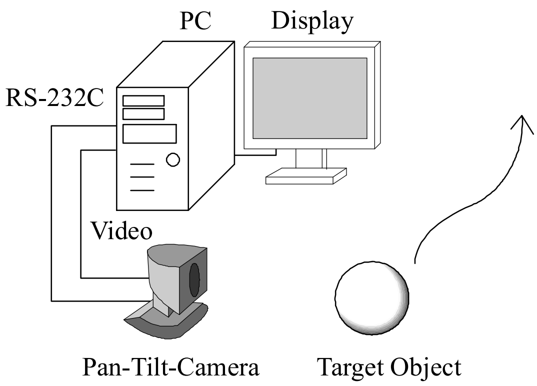

Fig.1 Overview of the developed color tracking system.

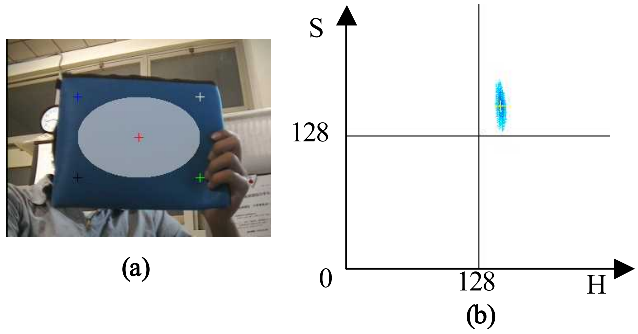

Fig.2 Target image (a) and its histogram (b).

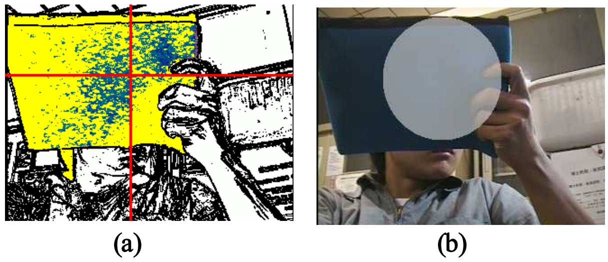

Fig.3 The extracted area (a) and the oval window (b).

2.1 A histogram model of color

In the proposed technique, we use a 2-D histogram model based on parameter H and S among the HSV color space. Note that, both H and S are sampled by the 8bit level. Histogram H_I of the object area is acquired from the input image by an oval window. However, it adds it to the histogram only when S 30 holds. Moreover, the frequency value of H_I is normalized so that max(H_t)=255. The example of the input image and the histogram are shown in **Fig.2**.

2.2 Update of the histogram model

In the first place, we extract the object area using H_I. At this time, the density value of the extracted pixel is assumed to be a frequency value of H_I. As a result, it will have the high-density value with a pixel that represents the color of the object. Afterwards, the area in the image obtained to update the histogram is decided by the following procedure.

1) The centroid C of the extracted area is calculated.
2) The edge image is obtained from the input image.
3) If the extracted area exists in four top and bottom of the centroid and right and left directions, it makes a starting point there and the extracted area is enhanced.
4) The width from the centroid of the enhanced area and the width in the oval window used with a former frame are compared. If it is long,, α is multiplied. If it is short, β is multiplied.

A new histogram $H_N(t)$ is acquired from the new oval window area decided above. The image which piles up the extracted area, the enhanced area and the centroid position to the edge image is shown in **Fig.3(a)** and the new oval area is shown in **Fig.3(b)**.

2.3 Limitation of update area with the anisotropic Gaussian distribution

The newly acquired $H_N(t)$ is added and the histogram is updated. However, it is not preferable that the color area which is quite different from the area of H_I is added. Because there is a possibility that the color model of the background area is added. It is likely that the color change takes place around the color distribution of H_I. Then, decentralization of each direction is requested in addition based on the color distribution around the centroid position of H_I. Anisotropic Gaussian distribution H_G given by Eq.(1) is multiplied to $H_N(t)$ as the weight. The update calculation of the histogram is defined by Eq.(2).

$$H_G(H,S) = e^{-\frac{\sqrt{H^2+S^2}}{2 f_\sigma^2(\theta)}} \tag{1}$$

$$H_U(t+1) = H_U(t) + H_N(t) \cdot H_G + H_I \tag{2}$$

$$H_U(0) = H_I \tag{3}$$

Here $H_U(t)$ is a histogram used to extract color at frame t. The function $f_\sigma(\theta)$ gives the variance dependent on the orientation θ on the 2-D histogram.

3. Experimental results

The results of tracking experiments are shown in **Fig.4**. The tracking object is human clothes. In the experiment, the illumination of the room has been made variable. The tracking screen, the state of the histogram model and the appearance of the enhanced area in each frame are shown at each sample time. Note that: $\alpha = 1.1, \beta = 0.9$

As a result, the proposed system was possible to track the object without losing the sight of the object, even if the illumination of the room changed. The background area was not added to the histogram model when the oval window area in the tracking screen included it. This is an effect of the weight imposed by the Gaussian distribution. Moreover, more effective setting of the oval window has become possible, because it enhanced the color extraction area. Therefore, the update of the histogram has been achieved with high accuracy.

4. Discussion and conclusions

We have proposed a color tracking system employing a 2-D color histogram under changeable illumination. It is possible to update the histogram by adding a new color area that change according to the illumination. This suggests that the proposed technique is able to track an object in an unknown illumination environment. When the illumination change becomes larger, an integrated 2-D histogram has a large region on the HS plane and this may cause inclusion of various colors around the specified color. Then the result of the specified color extraction may become worse as it may contain undesirable noise. In the proposed technique, the possibility of including the undesirable noise is reduced to a large extent by making limitation by the Gaussian distribution around the initial color distribution.

Applications of the proposed color tracking system may include monitoring a particular person. We know parents dress their small child with loud colors, e.g., a red sweater with blue pants, so that they can easily find out their child among lots of children in a children's park. The present system may be employed in place of the parents to monitor their child while they are busy chatting.

References

[1] Russ, J. C.: The Image Processing Handbook, CRC Press (1999).

[2] Ishikawa, S., Tabusa, T., Kawaguchi, E: "Recognizing clothes of a person in an image", The 5th Int. Conf. on Control, Automation, Robotics and Vision, pp.56-60 (Dec., 1998).

[3] Terrillon, J.C., Akamatsu, S.: "Comparative performance of different chrominance spaces for color segmentation and detection of human faces in complex scene images", Proc. 12th Conf. on Vision Interface (VI '99), Vol. 2, pp. 180-187 (1999).

[4] Kawato, S., Tetsunari, N.: "Skin-color model and face region extraction", Technical Report of IEICE. PRMU2001-59, pp.143-148 (July, 2000).

(a) Tracking images

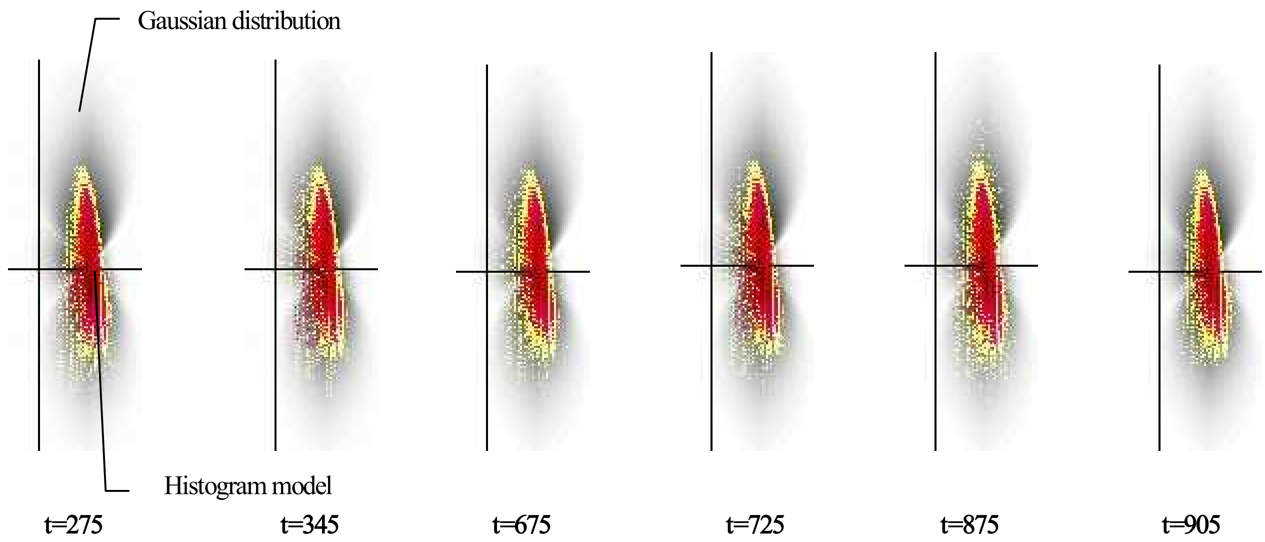

(b) History of histogram

Fig.4 Experimental results.

The Eleventh International Symposium on Artificial Life and Robotics 2006 (AROB 11th'06),
B-con Plaza, Beppu, Oita, Japan, January 23-25, 2006

Detecting Method of Coconuts Location using Circular Hough Transform

Mohamed Rizon[1], Haniza Yazid[2], Puteh Saad[2], Ali Yeon Md Shakaff[2], Abdul Rahman Saad[2], Masanori Sugisaka[3,4], Sazali Yaacob[1], M. Rozailan Mamat[5], M. Karthigayan[1], Desa Hazry[4] and Muhammad Firdaus Hashim[2]

[1]*School of Mechatronic Engineering*
[2]*School of Computer Engineering*
Northern Malaysia University College of Engineering
01000 Kangar, Perlis, Malaysia
[3]*Advanced Research Institute for Science and Enginering, Waseda University*
3-4-1 Okubo, Shinjuku, Tokyo, 169-8555 Japan
[4]*Department of Electrical and Electronics Engineering*
Faculty of Engineering, Oita University
700 Dannoharu, Oita-shi, 870-1192 Japan
[5]*Terengganu Advanced Technical Institute (TATI)*
Jalan Panchor, Teluk Kalong, 24000 Kemaman, Terengganu, Malaysia
Email: rizon@kukum.edu.my

Abstract

The goal of this research is to develop efficient coconuts detection in an image. In this work, two main techniques have been used for solving coconuts detection and recognition. The first technique comes with the separability filter which will obtain the most possible points to be the coconut candidates. Next, Hough transform (HT) has been applied to the extracted points by the separability filter. This Hough transform has been widely applied to extract analytical features such as circles, lines and ellipses. The Hough transform method and several modified versions have been known as robust techniques for curve detection. In this research the modified version of the HT is used to detect the circular regions. The Circular Hough Transform (CHT) is a modified version of HT that will use the edge information to minimize the computational requirement of the HT.

Keywords: separability filter, Circular Hough Transform, edge detection, mathematical morphology

1 Introduction

Coconut is known in scientific as coco nucifera and is a member of Family Arecaceae (palm family). Coconut is an important plant in the lives and economies of people in South East Asia like Burma, Indonesia, Philippines and Malaysia. In Malaysia, coconut is planted either for personal use or commercialize. There are varieties of commercial coconut that had been planted in Malaysia such as Malayan Tall (MT), Malayan yellow Dwarf (MYD), Malayan Green Dwarf (MGD), Rennel Tall, Malayan Red Dwarf (MRD) and Pandan. Coconut provides almost all necessities of life like food, drink, oil, medicine, timber, thatch, mats, fuel and domestic utensils. For a good reason, it has been called the "tree of heaven" and "tree of life". A 40 year old palm typically attains a height of 20-22m and an 80 year old palm may attain a height of 35-40m. Due to the increasing usage of coconut, new method had to be explored to assist the coconut gripping process. In this research, automatic coconut recognition has been done to assist the coconut gripping. Two techniques had been considered to solve the detection and recognition process, the separability filter and the CHT. The separability filter was introduced by Fukui [1] and had been used in iris detection. Meanwhile the CHT is a kind of HT that can extract circular objects from an image. The CHT had been used in several researches in detecting fingertips position, automatic ball recognition, and iris detection for face recognition [2-3]. The application of the two techniques for the coconut detection is the main contribution of this research. Figure 1 shows the block diagram of the system.

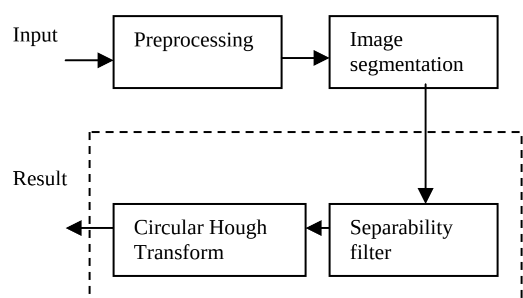

Figure 1: Coconut recognition system

2 Detecting method

Images used in this paper have 320 pixels wide and 240 pixels high. The input image is in gray scale using portable gray map (PGM) file format. The image had to be enhanced using histogram equalization. Histogram equalization tends to increase the contrast of the image. Histogram equalization produced a better result for region-based feature extraction. Then, the image segmentation is done. In this segmentation step, the edge detection and mathematical morphology had been employed. The edge detection process is very important as the edge information will be used by the CHT technique. There are lots of edge detectors that can be used. Canny edge detector has been employed to the image and Canny can give thin edge compared to Sobel [4]. Beside that, the opening and closing morphology are employed to minimize the points to apply the template matching. The closing tends to close small gaps and removes much of the white pixel noise, giving a fairly clean image. Opening on the other hand tends to open small gaps or spaces between touching objects in an image. The closing has been applied first then the opening. The closing 'close' small gaps and make the region is clearly seen but it still consist lots of unnecessary information. Then, the opening took place. The opening will eliminate some of the unwanted information.

After the segmentation process, both the proposed techniques are applied. The separability filter, describe in section 2.1 had been applied to the image to obtain the most possible coconut coordinates.

The CHT has explained in section 2.2, is applied to image after the separability technique had been employed. When using the CHT, the radius r is known in advanced because of the coconut's shape is peculiar feature by each other, so the radius r can be treated as known parameter. In this work, the radii for the coconut largeness have been set to 30, 40 and 50 pixels.

2.1 Separability filter

The separability filter is a template-based method. The proposed technique will place the template of figure 2 at each point (x_i, y_i) and then compute the separability between the two regions R_1 and R_2 in the template with size r.

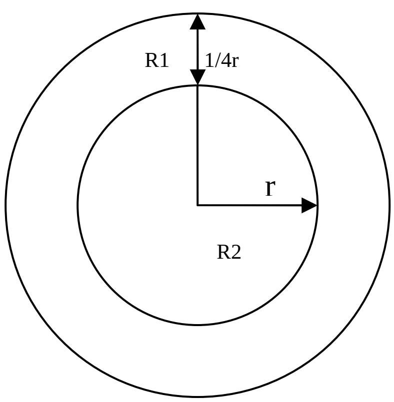

Figure 2: circle template to detect coconut candidate

The circle give the local maxima of the separability η is selected as the best possible coconut candidates.

2.2 Circular Hough Transform

The HT and several modified versions have been recognized as robust techniques for curve detection. This method can detect object even polluted by noise. The CHT was sketched by Duda et al [5]. The CHT is one of the modified versions of the HT. The CHT aims to find circular patterns within an image. The CHT is used to transform a set of feature points in the image space into a set of accumulated votes in a parameter space. Then, for each feature point, votes are accumulated in an accumulator array for all parameter combinations. The array elements that contain the highest number of votes indicate the presence of the shape. A circle pattern is described by Equation 1

$$(x_p - x_0)^2 + (y_p - y_0)^2 = r^2 \tag{1}$$

where x_0 and y_0 are the coordinates of the center and r is the radius of the circle. An example of conventional CHT is shown in figure 3.

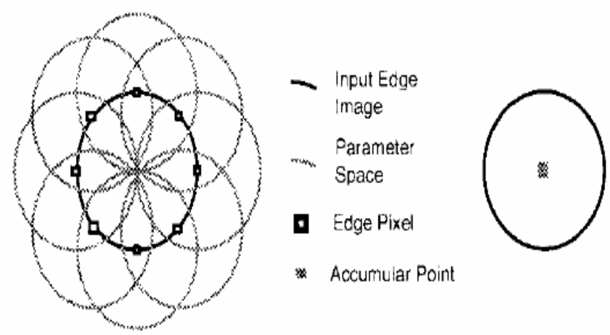

Figure 3: The contribution of the edge points to the accumulator space

The black circles indicate a set edge points within the image. Each edge point contributes a circle of radius R to an output accumulator space indicated by the grey circles. The output accumulator space has a peak where these contributed circles overlap at the center of the original circle. Modification to the CHT has been widely implemented to either increase the detection rate or reduce its computational complexity [6-8]. In this work, the edge orientation information is used to increase the CHT performance. This method was fist proposed by Kimme et al [6]. The use of the edge orientation information limits the possible positions of the center for each edge point. Using this method, only an arc needs to be plotted perpendicular to the edge orientation at a distance R from the edge point.

3.0 Result

The best template moving is 20 pixels to the right and 20 pixels down. The graph below has summarized the detection rate of 25 images that has been tested. The best template moving is 20 pixels with the highest percentage 96 % is as shown in figure 4 and tabulated as in table 1.

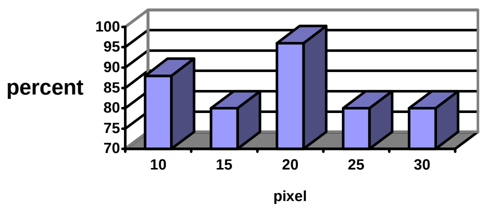

Figure 4: the best pixel for template moving

Table 1: percentage of the tested template moving

Pixel	Percent
10	88
15	80
20	96
25	80
30	80

To validate the both techniques, 30 images have been tested. For now, maximum voting to detect the presence of circular shape for the CHT technique is selected manually for each image. Summarized result for the tested images as shown in figure 5.

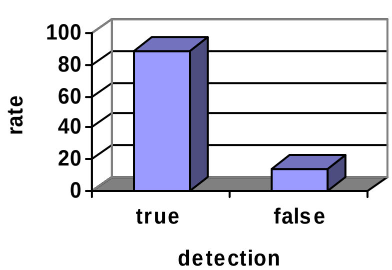

Figure 5: the detection rate for 30 images

It has been tested for 30 images and detected 86.67% of coconut location. The successful detections are shown in figure 6-9. The error occurred when the image that had been captured is far from the coconut palm.

Figure 6: coconut detection with maximum voting= 55

Figure 7: coconut detection with maximum voting=65

Figure 8: coconut detection with maximum voting=71

Figure 9: coconut detection with maximum voting=68

As discussed above, the coconut largeness had been fixed from 30-50 pixels. If the image taken from far, the coconut image tends to be small and difficult to be detected as shown in figure 10.

Figure 10: undetected coconut location

4.0 Conclusion

The separability filter tends to detect the possible coordinates of the coconut. Then, using the CHT, the obtained coordinates that are not considered as circle will be eliminated. In this research the coconut location can be detected but some constraint had been exposed. The main constraint is the size of the coconut. Template is used to get the radius of the coconut largeness. The radius is fixed between 30 to 50 pixels. The problem arises if the coconut image had been captured far away and the image tends to be small. Beside that, some of the coconuts are in a bunch and it overlaps between each other. These make the detection method difficult in carrying out the task. In the future, automatic threshold will be applied to the CHT for the voting process to detect the presence of circular shape.

Acknowledgements

The authors wish to thank Northern Malaysia University College of Engineering for their supports throughout this research.

References

[1] K. Fukui, O. Yamaguchi, "Facial feature points extraction method based on combination of shape extraction and pattern matching", *Trans. IEICE Japan J80-D-II.* Vol 8 (1997) 2170-2177.

[2] T. D'Orazio, C.Guaragnella, M.Leo, A. Distante,"A new algorithm for ball recognition using circle Hough transform and neural classifier", *Pattern Recognition*, vol 37, (2004), 393-408.

[3] Tsuyoshi Kawaguchi, Daisuke Hidaka, M.Rizon, "Detection of eyes from human faces by Hough transform and separability filter" , *Proceeding of IEEE ICRP*, vol 1, (2000), 49-52.

[4] Haniza Yazid, Mohamed Rizon, Puteh Saad, Ali Yeon Md Shakaff, Sazali Yaacob, Abdul Rahman Mohd. Saad and Masanori Sugisaka**,** "An approach of coconuts detection using edge information", sub'd to *Conference of Intelligence System and Robotic (iCISAR2005)*, Universiti Putra Malaysia,2005

[5] R.O Duda, P.E Hart, "Use of the hough transformation to detect lines and curves in picture", *Commun. ACM* (1972)11-15.

[6]C. Kimme, D. Ballard, J. Sklansky, "Finding circles by an array of accumulators", *Proc. ACM* vol 18(1975)120-122.

[7] D.Ioannou, W.Duda and F.Laine,"Circle recognition through a 2D Hough Transform and radius histogramming",*Image and Vision Computing*, vol 17, (1999), 15-26.

[8] N Guil, E.L.Zapata, "Lower Order Circle and Ellipse Hough Transform", *Pattern Recognition*, vol 30, (1997), 1729-1744.

Brain regions related to odor learning and memory in terrestrial slug, *Inciralia fruhstorferi*: Two lobes of the cerebral ganglion show different spatio-temporal activities.

Yoshinari Makino†, Hisanori Makinae, Tsukasa Obara, Masafumi Yano

Research Institute of Electrical Communication, Tohoku University,
2-1-1 Katahira, Aoba-ku, Sendai, 980-8577, Japan

† e-mail: tei@riec.tohoku.ac.jp

Abstract

Learning and memory are brain functions that emerge from simultaneous and cooperative information processing of various brain regions. To understand mechanisms of learning and memory, it is necessary to investigate the brain as a whole. For this purpose, terrestrial mollusks, slugs and snails, are good model because of the simple structure of their brain, i.e., the cerebral ganglion, and their high ability to learn odor information. In this paper, we describe two aspects of a global network for olfactory functions in the cerebral ganglion of the slug, *Inciralia fruhstorferi*. Anatomical distributions and projections of dopamine-containing neurons indicated that the posterior region of the metacerebrum can affect the procerebrum. Optical recordings of the activities evoked by olfactory nerve stimulations indicated that a process in the metacerebrum would precede a process in the procerebrum, and that each of the superior and inferior tentacle nerves would provide different afferent inputs to the metacerebrum. These results consistently suggest that both of the procerebrum and the metacerebrum may play an important role in olfactory functions.

Key Words: Learning and memory, Terrestrial slug, Olfactory functions, Neuromodulator, Optical recording,

1 Introduction

Learning and memory are brain functions that emerge from simultaneous and cooperative information processing of various brain regions. For understanding the mechanisms of learning and memory, it is necessary to investigate the brain as a whole. From this point of view, the terrestrial mollusks, slugs and snails, are good model for investigating neural mechanisms for learning and memory. In the slugs and snails, olfaction is the dominant sensory modality guiding various kinds of behavior. These animals not only can identify and orient to odors but also have an ability to learn odors based on events associated odor stimulation [1][2][3][4].

Olfactory information is received by olfactory epithelia located on two pairs of tentacles, i.e., the superior and inferior tentacles (STs and ITs). The ST and IT are connected with cerebral ganglion via superior and inferior tentacle nerves (STN and ITN), respectively. The cerebral ganglion is a higher center of the mollusk's brain, and in terrestrial slugs and snails it is comprised of three lobes: the procerebrum (PC), the mesocerebrum (MsC) and the metacerebrum (MtC) [5]. The tentacle nerves project their afferent fibers mainly into the PC and the MtC. Thus, we can hypothesize that the olfactory functions, including learning and memory, may emerge from parallel processes in each of the PC and the MtC and their interactions. Many of studies have focused attentions to the PC because parts of projections from the STN and ITN evidently converge into the PC. A body of evidence indicates that the PC would be a network specialized in olfaction function [6]. Compared to the PC, however, there are few studies to investigate functions of the MtC probably because it has no distinctive anatomical features and its cellular population appears heterogeneous compared to that of the other lobes [5].

In this paper, we describe two aspects of a global network for olfactory functions in the cerebral ganglion of the terrestrial slug, *Inciralia fruhstorferi*. One is concerned with anatomical distributions and projections of the dopamine-containing neurons and their projections in the cerebral ganglion, and the other is concerned with spatio-temporal activities of the cerebral ganglion evoked by the STN and ITN stimulations.

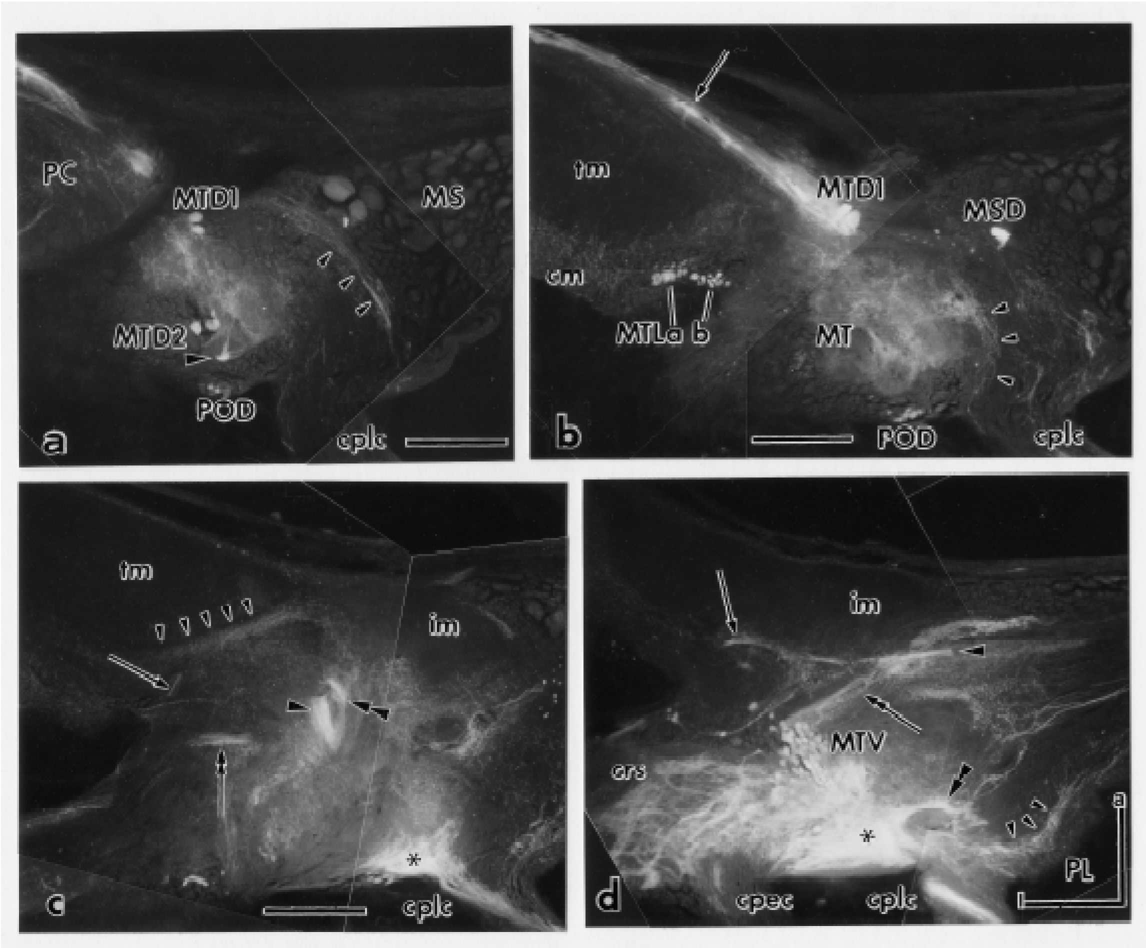

Figure 1: Series of horizontal sections of the cerebral ganglion stained by the FaGlu method.

2 Distribution of dopamine-containing neurons in the cerebral ganglion

Dopamine is one of biogenic monoamines that are widely distributed in vertebrate and invertebrate brains. The monoamines are known to have an important role with respect to emergent properties of neural networks [7] or global functions of the brain as a whole, including learning and memory [8][9]. Thus, examining the anatomical structure of the monoamine-containing neurons might reveal a functional architecture of the brain.

By using the formaldehyde-glutaraldehyde (FaGlu) histofluorescence method, we stained dopamine-containing neurons in the cerebral ganglia. Figure 1 shows a series of horizontal sections of the cerebral ganglion (about 20 micrometer in thick) stained by FaGlu. In these, the dopamine-containing neurons appears intense blue-green. There were about 200 cell-bodies in each hemiganglion. These were arranged as several clusters in the MtC. The PC was devoid of the dopamine-containing cell-bodies. Most of fibers from these cell–bodies seemed to converge into the posterior region of the MtC and then diverge to various regions, such as the PC, the opposite cerebral ganglion, other ganglia including the tentacle ganglion, and the lips. Within the posterior MtC, the density and pattern of the fiber- distribution were different between its medial and lateral regions.

The posterior regions of the MtC are known as the regions where afferent fibers from the sensory organs (the tentacles and lips) projects into. Thus, the revealed anatomical features of the dopamine–containing neurons suggest that the emergent properties of the network such as the PC would be modulated by the dopamine-containing neurons that might be activated by the sensory inputs.

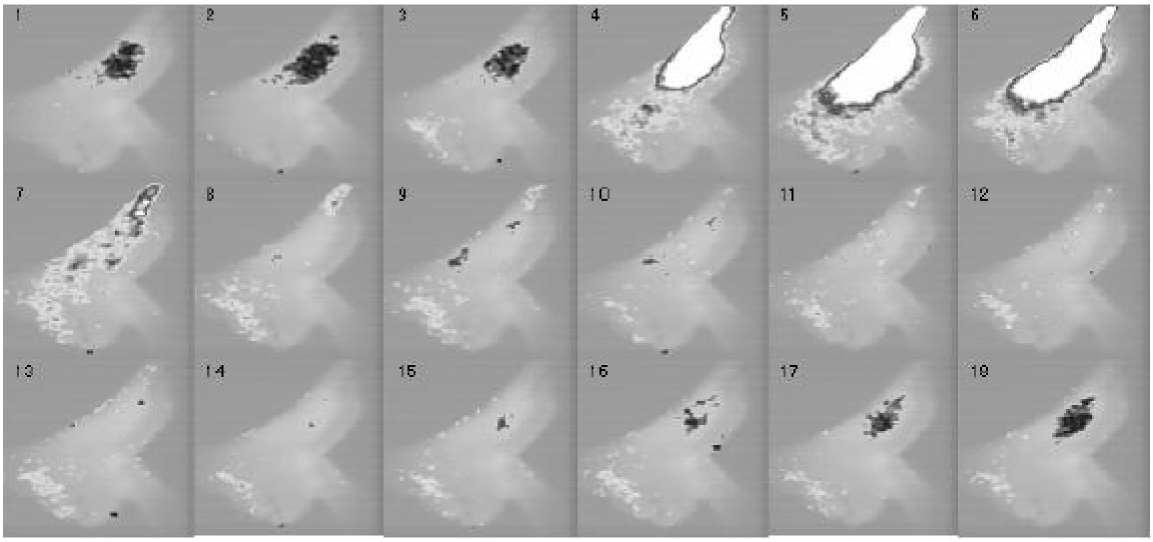

Figure 2: An example of the spatio-temporal response of the cerebral ganglion to the STN stimulation.

3 Optical recording for the cerebral ganglion

Optical recording technique is a suitable way for clarifying the spatio-temporal activity of large area of the brain. By using the voltage sensitive dye (di-4ANEPPS), we observed activities of the whole cerebral ganglion when the STN or ITN was electrically stimulated. An example of the evoked activity by STN stimulation is shown in Figure 2. The neuropile region of the posterior-medial MtC was firstly depolarized and then the PC was depolarized. In the PC, depolarization was followed by hyperpolarization that slowly returned back to the resting level, whereas in the MtC, the depolarization was almost monotonically returned back to the resting level. These temporal profiles were commonly observed for each of the STN and ITN stimulations.

Concerning the spatiotemporal patterns within the PC, all region of the terminal mass (known as a region receiving olfactory inputs) was firstly activated almost simultaneously, and then the activity of the internal mass (knows as a output region of the PC) and probably of the cell mass (a layer of intrinsic cell bodies of the PC) was followed. Timings of the peak of depolarization and hyperpolarization seemed to slightly vary depending on the stimulation timing to the spontaneous activities.

The signals observed in the MtC were smaller than those in the PC so that the activated area in the MtC seemed to be unclear in the image data of the Figure 2. To clarify an activated area, we summed the signals for post-stimulus period within the MtC and subtracted a summed signal for the pre-stimulus period from it. Regardless of the stimulated nerves or stimulus intensities, the activated area seemed to be within the posterior-medial region of the MtC. Figure 3 shows the spatial patterns of the enhanced signal for each of STN and ITN stimulations. In this preparation, the ITN stimulation strongly activated a lateral-half of the posterior-medial MtC rather than its medial-half, whereas the STN stimulation activated both halves almost evenly.

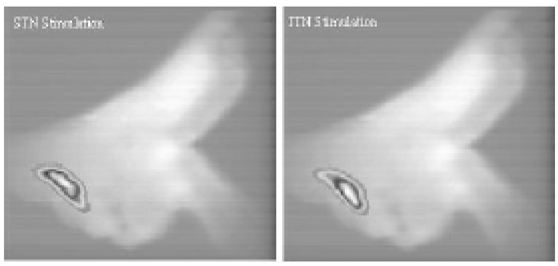

Figure 3: Examples of the enhanced signals of the MtC activities to the STN and ITN stimulations.

4 Discussion

The distributions and projections of the dopamine-containing neurons in the cerebral ganglion suggest that the posterior region of the MtC would alter emergent properties of the PC through the neuromodulatory effects of dopamine. This anatomically suggested role of the MtC was consistent with our physiological observations. The optical recording for the whole cerebral ganglion indicated that the PC and the posterior-medial region of the MtC would relate to the olfactory function. The temporal profiles of the evoked activities of each lobe suggest that the processes in the MtC would precede those in the PC, and the spatial patterns within the MtC suggest that each of the STN and ITN would provide different afferent inputs to the cerebral ganglion. These findings are very interesting with respect to the olfactory functions, because functional differences between the ST and the IT have been suggested in odor learning [10][11], but the physiological studies focusing on the PC have failed to show clear difference between the afferent inputs to the PC from the ST or IT.

Concerning the quick response of the MtC compared with the PC, we think that each olfactory pathway through the MtC and the PC may contribute coarse categorizations and fine discriminations of odors, respectively. If the coarse categorizations process can quickly evaluate potentially important odors such as foods' odors or appetitively or aversively learned odors, it may efficiently limit the odors that should be processed thorough the fine discrimination pathway. Because various odors exist in the real world, such parallel processes may be ecologically advantageous.

5 Conclusion

We can conclude that both of the PC and the MtC in the slug's brain are necessary for olfactory functions including learning and memory. Regardless of sensory modalities, the parallel information processing is a common characteristic of the brain, and it is a fundamental question how the brain integrates such information and determines a behavioral output in various environments. For addressing these issues, the brain of the terrestrial mollusks is a good model. Further studies to clarify the roles of the MtC on olfactory processing and interactions between the MtC and the PC pathways will reveal a fundamental principle of the sensory information processing in the brain.

Acknowledgements

This work was supported in part by Grant-in-Aid #17075003 of the Ministry of Education, Culture, Sports and Technology of Japan.

References

[1] Sahley CL, Rudy JW, Gelperin A (1981), One-trial associative learning modifies food odor preferences of a terrestrial mollusc. *Proc Natl Acad Sci USA*, 78, 640-642.

[2] Sahley CL, Rudy JW, Gelperin A (1981), An analysis of associative learning in a terrestrial mollusc. I. Higher-order conditioning, blocking and a transient US pre-exposure effect. *Journal of Comparative Physiology*, 144, 1-8.

[3] Chase R (1982), The olfactory sensitivity of snails, Achatina fulica. *Journal of Comparative Physiology,* 145, 447-457.

[4] Yamada A, Sekiguchi T, Suzuki H, Mizukami A (1992), Behavioral analysis of internal memory states using cooling-induced retrograde amnesia in *Limax flavus*. *Journal of Neuroscience,* 12, 729-735.

[5] Chase R (2000), Structure and function in the cerebral ganglion. *Microscopy Research & Technique*, 49, 511-520.

[6] Gelperin A, Tank DW (1990), Odour-modulated collective network oscillations of olfactory interneurons in a terrestrial mollusk. *Nature*, 345, pp. 437-440.

[7] Makino Y, Akiyama M, Yano M (2000), Emergent mechanisms in multiple pattern generation of the lobster pyloric network. *Biological Cybernetics*, 82, 443-454.

[8] Schultz W (1998), Predictive reward signal of dopamine neurons. *Journal of Neurophysiology,* 80, 1-27.

[9] Hammer M (1993), An identified neuron mediates the unconditioned stimuli in associative olfactory learning in honeybees. *Nature,* 366, 59-63.

[10] Kimura T, Toda S, Sekiguchi T, Kawahara S, Kirino Y, (1998), Behavioral modulation induced by food odor aversive conditioning and its influence on the olfactory response of an oscillatory brain network in the slug *Limax marginatus*. *Learning & Memory*, 4, 365-375.

[11] Friedrich A, Teyke T (1998), Identification of stimuli and input pathways mediating food-attraction conditioning in the snail, Helix. *Journal of Comparative Physiology A,* 183, 247-254.

The Eleventh International Symposium on Artificial Life and Robotics 2006 (AROB 11th'06),
B-con Plaza, Beppu, Oita, Japan, January 23-25, 2006

Natural Intelligence: Noise-resistance of Neural Spike Communication

Noriyasu Homma
Facl. of Medicine
Tohoku University
Sendai, 980-8575

Koh Fuchigami
Toshiba Med. Sys. Corp.
3-26-5, Hongo, Bunkyo-ku
Tokyo, 113-8456

Masao Sakai
Grad. Sch. of Inf. Sci.
Tohoku University
Sendai, 980-8576

Kenichi Abe
College of Eng.
Nihon University
Koriyama, 963-8642

Abstract

In this paper, we analyze neural spike dynamics of a double feedback neural unit (DFNU). An essential emphasis of the DFNU is not only on its simple formulations that can provide quantitative analytic results, but also on physiological plausibility of the dynamics that is comparable to that of Hodgkin-Huxley's model. The results suggest that a proportional coding of neural information on firing frequency may not be always reasonable due to sensitivity to noisy inputs especially for low-frequency neural firings. On the other hand, high-frequency firings are relatively appropriate for a neural informational carrier due to the reliability and robustness to noisy inputs.

1 Introduction

A typical engineering neural network deals with non-spiking or *analog* signals as the medium of informational communication. In the nervous system, neural spikes are used as the medium of communication instead of the analog signals. Neural spikes can therefore be the essential element of the mechanism for communication in brain [1]. Thus, analyzing the dynamics of the neural network with pulse sequence is one of the approaches to investigate the mechanism of neural signal transmission, and to construct a biologically-plausible model of nervous systems.

Various models that include Hodgkin-Huxley's (H-H) model [2] and pulse-coupled neural networks [3] have been designed to take advantage of neural spikes. Although behavior of these models are physiologically plausible, it is often very hard to analyze the models' dynamics due to their structural and dynamical complexity. Thus, it is difficult to design and control the dynamics as well.

To overcome this problem, we have proposed a double feedback neural unit (DFNU) [4]. An advantage of the proposed DFNU is that the dynamics is not only sufficiently physiologically plausible, but also analyzable due to its simple formulations. We then conduct qualitative and quantitative analysis of the firing dynamics of the DFNU in this paper. The results suggest some new aspects that the neural information may not be always carried by the firing frequency due to sensitivity to noisy inputs.

2 Double feedback neural unit

The DFNU is a model to generate pulse sequences, based on a dynamic neural unit (DNU) [5], and represented by the following difference equations with discrete time $n = 1, 2, \dots$

$$s(n+1) = y(n) + \alpha s(n) \quad (1)$$

$$y(n) = f\left(u(n) - s(n)\right) \quad (2)$$

where $u(n)$ and $y(n)$ represent the input and output of the DFNU, respectively. $s(n)$ denotes the internal feedback state variable and $\alpha, 0 < \alpha < 1$, is a decreasing rate of the feedback. f is the following nonlinear sigmoidal function with a slant β

$$f(x) = \frac{1}{1 + \exp(-\beta x)}$$

The block diagram of DFNU is illustrated in Fig. 1. In this paper, $0 \le u < 1$, $\alpha = 0.6$, and $\beta = 1.0 \times 10^5$ unless otherwise specified. For such slant value, the sigmoidal function is a step function approximately. In this case, from (2), the output $y = 1$ only when the input u is larger than

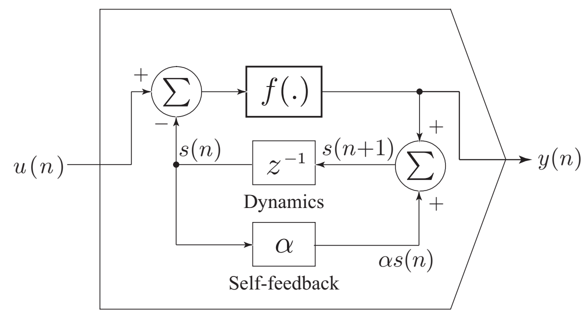

Figure 1: Block diagram of the DFNU given by (1) and (2).

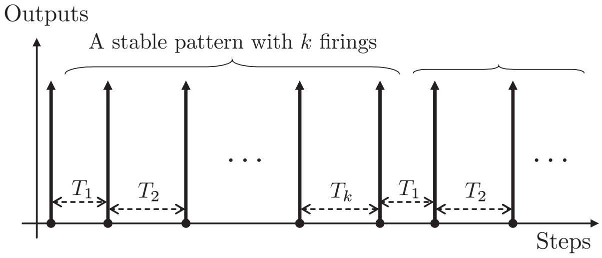

Figure 2: A stable pattern with k firings of intervals $(T_1, T_2, \ldots, T_k)$ steps, $T_j \in \{T, T+1\}$, $j = 1, 2, \ldots, k$, $T \in \{2, 3, \ldots\}$.

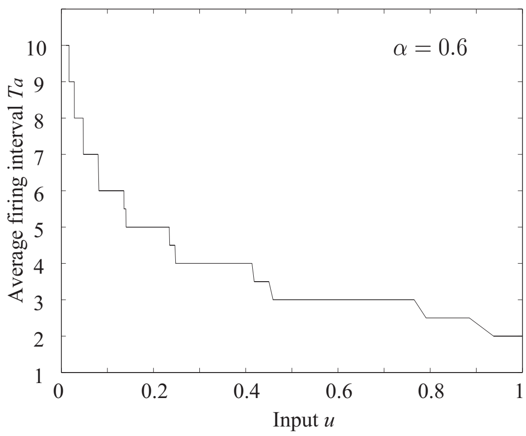

Figure 3: The average firing interval T_a as a function of the constant input u.

the state variable s, otherwise $y = 0$. That is, the DFNU fires only if $u > s$.

Previous work [6] showed that the firing dynamics of DFNUs with constant inputs becomes stable after progress of enough time, namely, firing patterns of DFNUs converge. A generic stable firing intervals are combinations of intervals T and $(T+1)$ steps with k firings as shown in Fig. 2. Here, the interval, $T \in \{2, 3, \ldots\}$, and the number of firings within the stable pattern, $k \in \{1, 2, \ldots\}$, are changed depended on the input u and the parameter α in (1). Although the firing dynamics of DFNU is dominated by the parameter α, a qualitative relation between the average firing interval $T_a = \sum_{i=1}^{k} T_i/k$ and the input u is not changed regardless of α. Figure 3 shows a typical relation between T_a and u.

3 Analysis of firing dynamics

3.1 Formulation of DFNU's internal state for constant inputs

For simplicity, let us consider a simple firing pattern of $k = 1$ with constant firing periods $T \in \{2, 3, \ldots\}$. Noting that the output $y = 0$ when the DFNU does not fire, the state variable $s(n+1) = \alpha s(n)$ from (1). Since $0 < \alpha < 1$, s decrease every step in this case. In the stable state, the state s thus takes a peak value s_{p_T} at one-step after the firing, and after that it decrease until the next firing. That is, letting $n = 1$ denote a discrete time at one-step after a firing, the state $s(1) = s_{p_T}$. At the next step $n = 2$, the state $s(2) = y(1) + \alpha s(1) = \alpha s(1)$ since $y(1) = 0$ in (1) if the neuron does not fire. Similarly, the states $s(T)$ at the next firing and $s(T-1)$ at one-step before the next firing are given as

$$s(T-1) = y(T-2) + \alpha s(T-2) = \alpha^{T-2} s_{p_T} \quad (3)$$
$$s(T) = y(T-1) + \alpha s(T-1) = \alpha^{T-1} s_{p_T} \quad (4)$$

In the stable state, the state at one-step after the next firing is also the same peak value s_{p_T}. Thus, $s(T+1) = s_{p_T}$. On the other hand, $s(T+1) = 1 + \alpha^T s_{p_T}$ since the output at the next firing $y(T) = 1$ in (1). Therefore, the peak value of the state can be given by

$$s_{p_T} = \frac{1}{1 - \alpha^T} \quad (5)$$

3.2 Design of firing patterns

Let us consider a constant input u for generating neural spikes with a stable firing period T. For this purpose, the state at a firing, $s(T)$ for example, must be less than the input u, and the state at one-step before the firing, $s(T-1)$, must be larger than the input u. Therefore, from (3)–(5),

$$\frac{\alpha^{T-1}}{1 - \alpha^T} < u < \frac{\alpha^{T-2}}{1 - \alpha^T} \quad (6)$$

4 Noise resistance of neural spikes

In digital communication by using pulse signals, communication can be robust to distortion of the pulse shape since the information may not be carried by the pulse shape, but encoded on whether the pulse exists or not at that moment. Physiological aspects of the signal transmission at synaptic connections also suggest that the neural information is not carried by the pulse shape, but by the pulse frequency (period) [5].

On the other hand, a relatively simple firing pattern requires the input with extremely great accuracy for biological information [4]. In order to generate more complex firing patterns such as chaotic ones, the input with infinite great accuracy may be needed. Even if the great accuracy can be realized, such systems are too sensitive to noise [7]. In other words, if the pulse frequency by which the neural signal may be transmitted is sensitive to noise, the neural communication system is not robust to noise even the neural communication through spike signals is robust to distortion of the pulse shape.

4.1 Analysis of noise-resistance of neural spike signals

Using the theory derived in the previous section, we will now analyze robustness of spike signals to noisy inputs by evaluating the input accuracy required for generating a desired firing pattern. For simplicity, let T be a constant period of the stable firing pattern with $k = 1$. In this case, from the condition in (6)

$$\frac{1}{\alpha^2(\alpha^{-T} - 1)} > u \tag{7}$$

and

$$u > \frac{1}{\alpha(\alpha^{-T} - 1)} \tag{8}$$

Noting that $0 < \alpha < 1$ and thus $a \equiv 1/(\log \alpha) < 0$, then from (7)

$$T < a \log \alpha^2 u - a \log(1 + \alpha^2 u) \tag{9}$$

Since $-a > 0$ and $0 < \log(1 + \alpha^2 u) < \log(1 + \alpha^2)$ for $0 < u < 1$

$$T < a \log u + 2 - a \log(1 + \alpha^2) \tag{10}$$

Similarly, from (8), by using the relation $\alpha^{-T} - 1 < \alpha^{-T}$

$$T > a \log u + 1 \tag{11}$$

Finally, from (10) and (11)

$$a \log u + 1 < T < a \log u + 2 - a \log(1 + \alpha^2) \tag{12}$$

Letting $1 < b < 2 - a \log(1 + \alpha^2)$, the firing period T can be given as the following logarithmic function of input u.

$$T = a \log u + b \tag{13}$$

From (13), $dT/du = a/u$. Note that the differential coefficient of the function is in inverse proportion to the input u. In other words, neural spikes of a relatively larger period or lower frequency generated by a smaller input are sensitive to the input noise, while spikes of the smaller period (higher frequency) are relatively robust to the noise.

Since firing outputs are inputs to other neurons, the sensitivity to noise suggests that neural information uniformly encoded on a wide band of the firing frequency from high to low is not always reasonable. This implies that a proportional expression of neural information by using the firing frequency or period may not be appropriate for the model of neural communication, although such proportional encoding has been widely used in many engineering neural models. A manner of neural communication that is robust to noisy environments seems to be more plausible as important control signals for life to survive.

4.2 Plausibility of DFNU's dynamics

The hypothesis that a proportional encoding of the neural information by using the firing frequency is not always reasonable is derived from the analytic results of DFNU's dynamics, instead of real neural dynamics. It is thus important to verify how much the DFNU's dynamics is physiologically plausible. For this purpose, we will compare the DFNU's dynamics with that of H-H model [2] as the most familiar and physiologically plausible model of real neurons.

By conducting simple simulations, we can find that firing intervals of the H-H model become smaller as the input to the model is larger [4]. This is summarized in Fig. 4 illustrating the average firing interval T_a as a function of the input's amplitude I_a. Note that comparing Fig. 4 with Fig. 3, the qualitative relation between the average firing interval and input amplitude is the same. That is, (i) the relation is *not* in inverse proportion, namely, the firing frequency is *not* proportional to the input, and (ii) a larger interval or lower frequency of firings is relatively more sensitive to the input amplitude than a smaller interval or higher frequency.

Since H-H model is a continuous time system while the DFNU model is a discrete time system, we need a quantitative relation between these two models to compare the models with each other. For simplicity, let us consider constant firing periods T as calculated in Section 3.1. In this case, the average firing period is T, and thus let T denote the average period of the DFNU to discriminate between T of the DFNU and T_a of H-H model. Supposing that $(I_a, T_a) \simeq (30, 10)$ in Fig. 4 of H-H model corresponds to $(u, T) = (0.2, 5)$ in Fig. 3 of the DFNU model,

$$T = T_a/2, \quad u = I_a/150 \tag{14}$$

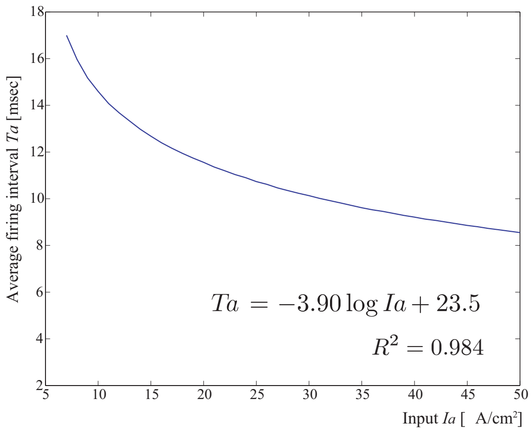

Figure 4: The average firing interval T_a as a function of the input amplitude I_a.

Substituting $\alpha = 0.6$ and (14) into (12),

$$-3.915 \log I_a + 21.62 < T_a < -3.915 \log I_a + 24.82 \quad (15)$$

On the other hand, an approximate equation derived from Fig. 4 is as follows.

$$T_a = -3.90 \log I_a + 23.5 \quad (16)$$

In spite of DFNU's simple formulations that do not include detailed and explicit membrane dynamics consisting of several ionic channels represented in H-H model, both relations between the average period and the input are almost equal.

From this point of view, the simple DFNU model, explaining the logarithmic relation between the average firing period and the input of the H-H model, is physiologically plausible. We can therefore expect that the analytic results of the proposed model can estimate quantitative behavior of the H-H model and real neuron's dynamics. A new neuron model based on the results reported in this paper will be presented at the conference.

5 Conclusions

We have studied dynamics of the DFNU. Using the simple formulations of the DFNU, we have conducted quantitative analysis of the model. Comparing the DFNU's dynamics to that of H-H model as the most familiar and physiologically plausible model of real neurons, it has been shown that dynamics of DFNU is also physiologically plausible.

Note that although most engineering analog neurons assume a proportional relation between inputs and firing frequency, the analytic results reported in this paper suggest different coding of the neural information that is more plausible from the viewpoint of noise-resistance of neural spikes as important control signals for life to survive. Using the results presented in this paper, we can develop a novel informational processing tool that is robust to noisy environments.

Acknowledgment

This work was partially supported by Grant-in-Aid for Scientific Research #15700119 and #17500083.

References

[1] F. Delcomyn, *Foundations of Neurobiology*, W. H. Freeman and Co., New York, 1997.

[2] A. L. Hodgkin, *et al.*, "A Quantitative Description of Membrane Current and Its Application to Conduction and Excitation in Nerve," *J. Physiol.*, Vol. 117, pp. 500, 1952.

[3] R. D. Broussard, S. K. Rogers, M. E. Oxley, and G. L. Tarr, "Physiologically Motivated Image Fusion for Object Detection using a Pulse-Coupled Neural Network," *IEEE Trans. Neural Networks*, Vol. 10, No. 3, pp. 554–563, 1999.

[4] K. Fuchigami, N. Homma, M. Sakai, and K. Abe: "Is Neural Firing Frequency an Informational Carrier in Neural Systems?", *Proc. SICE 2005*, pp. 2067–2072, 2005.

[5] M. M. Gupta, L. Jin, and N. Homma, *Static and Dynamic Neural Networks: From Fundamentals to Advanced Theory*, IEEE Press & Wiley, New York, 2003.

[6] K. Fuchigami, N. Homma, M. Sakai, and K. Abe, "Analysis of Firing Dynamics by Using a Double Feedback Neural Unit," *Bull. Coll. Med. Sci. Tohoku Univ*, Vol. 13, No. 1, pp. 33–41, 2004. (in Japanese)

[7] J. K. Douglass, L. Wilkens, E. Pantazelou, and F. Moss: "Noise Enhancement of Information Transfer in Crayfish Mechanoreceptors by Stochastic Resonance," *Nature*, Vol. 365, pp. 337–340, 1993.

The Eleventh International Symposium on Artificial Life and Robotics 2006 (AROB 11th'06),
B-con Plaza, Beppu, Oita, Japan, January 23-25, 2006

Acquisition of Deterministic Exploration Behavior by Reinforcement Learning

Katsunari Shibata
Dept. of Electrical and Electronic Engineering, Oita University, 700 Dannoharu, Oita 870-1192
shibata@cc.oita-u.ac.jp

Abstract
Exploration is an important factor that influences the performance in reinforcement learning, and random factors are usually used to realize it. However, the exploration that real lives are doing does not seem just random actions, but seems a kind of deterministic and intelligent actions using their knowledge and considering the context. In this paper, the author tries to explain such explorations as a deterministic behavior and propounds a novel approach that effective exploration is acquired by reinforcement learning. It is shown that an agent with a recurrent neural network trained based on reinforcement learning becomes to explore effectively to some extent in some simple problems.
Keywords: exploration, reinforcement learning, recurrent neural network, context

1. Introduction
Reinforcement learning is an autonomous and purposive learning based on reward and punishment by trial and error. The trial and error is usually called "exploration" and it is an important factor that has a large influence on the performance of reinforcement learning. Usually, it is realized by stochastic action selections using random numbers, such as ε-greedy or Boltzmann selection[1]. However it is difficult to decide the ratio of the random factors in the action selection due to the "exploration-exploitation dilemma".

This research was triggered by the simple questions as "Do we take stochastic actions?" and "Is there a random number generator in our brain?" For example, if we are put in an unknown maze, we try not to pass the same way as we have already passed, and try to imagine a two-dimensional map in our brain. In other words, we explore the maze using the knowledge we have and considering the context. When we are at a branch, we don't move our fingers, jump, or go to the midway of the two paths, and choose one of the two paths. From this fact, our "exploration" is not just random actions, but seems very intelligent actions. When we don't have any idea about which way we should go, we sometimes shoot a dice. However, even in such a situation, the decision itself can be considered to be deterministic.

Against the above interpretation, the following discussions can be accepted. One of them is that that is the result of a stochastic action selection with a high probability for the action with a high action value after representing appropriate action values using knowledge and/or context. Another is that the exploration is not done at each actuator level, but is the result of the stochastic action selection on higher abstracted space. Actually, abstraction of action space has been discussed as temporal abstraction[2].

It is certainly difficult to deny the possibility of the existence of stochastic action selection. However, there seems no rational reason why stochastic action selection must be employed except for "the concern that an agent cannot explore all the unknown states without stochastic factors" or "easiness of statistical analysis". When our "exploration" mentioned above is considered, it is thought that exploration can be realized without stochastic factors. If exploration is a result of deterministic decision making, it is considered as one of the actions in a wide meaning. Then it is expected that appropriate explorations can be learned through experiences as well as the other functions. The author has been thinking that the reinforcement learning is useful not only for the learning of actions but for the learning of a variety of functions including recognition and memory, and plays an important role in the emergence of our intelligence as living creatures[3].

According to the above discussion, in this paper, based on the hypothesis that "exploration" by real lives is not realized by stochastic action selections, but a kind of deterministic ones, it is propounded that the actions that can be interpreted as exploration are acquired by reinforcement learning. However, since the learning without using random number generator is another ongoing research subject, this paper is focused only on the acquisition of non-random exploration and random numbers are used for learning. Since context is useful to realize effective "exploration" as mentioned above, a recurrent neural network is used[4]. Two kinds of very simple tasks are picked up, and the acquisition of exploration behavior is examined. In one of them, the goal cannot be known explicitly, but effective exploration using knowledge and context is required. The other task is mainly focused on the acquisition of knowledge by explorations.

2. Learning
Here, Elman-type recurrent neural network whose hidden outputs are fed back to the input layer at the next time step is employed as the most general recurrent neural network. The present observation signals s_t are the input of the network. The number of output neurons is the same as the number of actions, and each output is used as Q value for the corresponding action. After forward computation of the output for the previous input signals, the training signal $Q_{s,a_{t-1}}$ for the Q value of the previous action $Q_{a_{t-1}}(s_{t-1})$ is generated autonomously based on Sarsa algorithm[1] as

$$Q_{s,a_{t-1}} = r_t + \gamma Q_{a_t}(s_t) \tag{1}$$

where r is a given reward and γ is a discount factor.

The training signal is given only to the corresponding output, and the network is trained by BPTT (Back Propagation Through Time)[5]. The output function used in the hidden and output layer is the sigmoid function whose value ranges from -0.5 to 0.5, so the output of the network after adding 0.4 is used as Q value, and the training signal is used after subtracting 0.4 from the signal generated by Eq. (1).

The learning is done independently for each episode (trial). Before each episode, all the hidden outputs are reset to 0.0, and all the Q values after reaching a goal are 0.0. When the agent reaches the goal, it can get a reward $r = 0.8$, and otherwise $r = 0.0$ always.

3. Simulation

3.1 Exploration on branch situation

At first, the branch situation is simulated in which only one of two marked states among many states is the real goal, but there are no information about which is the real one between the two marked states. As shown in Fig. 1, an agent is located at the center of the 5x5 grid world, and two landmarks are put randomly on two states on the four sides of the world. The real goal is chosen randomly from the two marked states, but the agent does not know that. The two points that should be observed are whether the agent can go to one of the marked states by its intention and also whether the agent can change its moving direction after reaching the state and finding that it is not the real goal.

The agent can choose one of the four actions, moving up, right, down, and left, and the state transition is deterministic. If the agent hits against a wall, it stays at the same state. The agent can observe whether the state is marked or not for each of 9x9 grid world whose center is fixed at the agent location. This enables the agent to catch the both landmarks wherever the agent exists. The input signals to the network are 9x9=81 binary signals. The neural network has three layers, and the number of hidden neurons is 20. The maximum time steps traced back through time for BPTT is 30. ε-greedy is used as stochastic action selection during learning. ε is fixed at 0.1 and discount factor γ is 0.92. The initial weight for each hidden-output connection is 0.0 and that for each non-feedback input-hidden connection is chosen randomly from -0.5 to 0.5. For the self-feedback connections, the initial weight is 4.0, while that for the other feedback connections is 0.0. The learning constant for BPTT is 0.2.

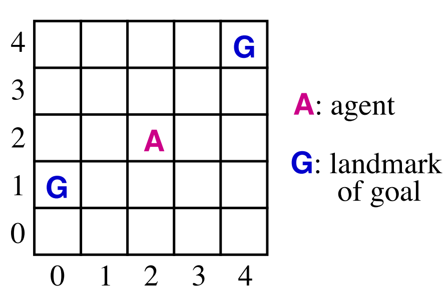

Fig. 1 The task in which there are two landmarks of goal, but no information about which is the real goal.

At the early phase of the learning, even though the agent reached one marked state, it was difficult to go toward the other marked state. Sometimes it took several thousands of steps to reach the real goal, but the number decreased as the learning progressed. After learning of 100000 episodes, the agent still failed to reach the goal for 5 combinations of real and fake goal locations, but it successfully reached the real goal 251 combinations among the total of 256 combinations.

Successful sample behaviors for 4 combinations are shown in Fig. 2. It is seen that the agent heads to one of the marked states at first, and then after finding the state is not the real goal, it changes its moving direction to the other marked state even though one redundant action is seen just after reaching the first marked state in the case of Fig. 2 (a) (b). In these cases, the distance from the center to each marked state is the same with each

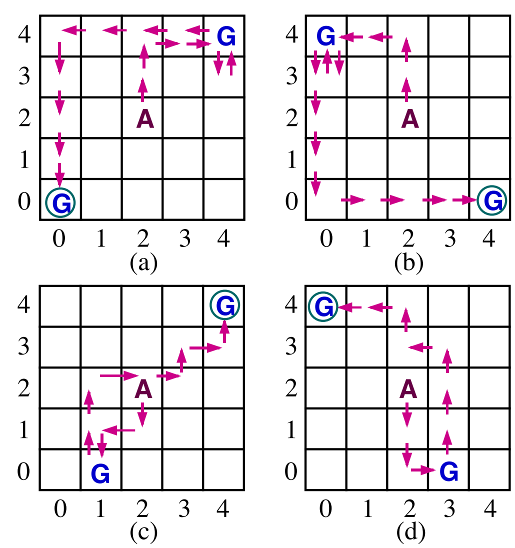

Fig. 2 The behaviors after learning. 'G' indicates the landmark of goal and circled one indicates the real goal.

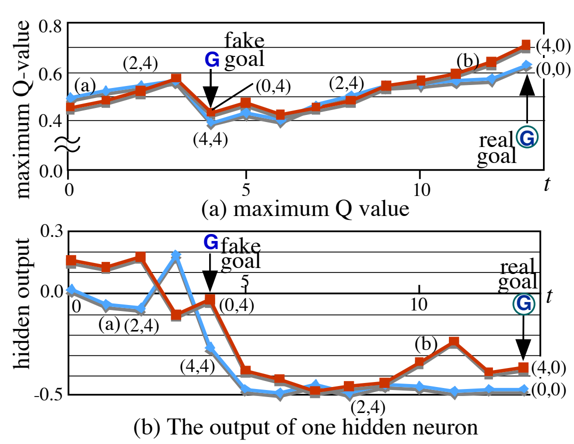

Fig.3 The change of the maximum Q value and one hidden neuron's output in one trial for the case of Fig.2 (a) and (b). 'G' indicates the landmark of goal and circled one indicates the real goal.

other, but when one of the marked state was moved closer to the center, it visited to the closer marked place at first as shown in Fig. 2 (c) (d) with some exceptions.

Fig. 3 shows the change of the maximum Q value and the output of one hidden neuron in one trial for the both cases of Fig. 2 (a) and (b). It is seen that the maximum Q value increased as the agent approached to the marked place, but once it found the marked state was not the real goal, the Q value went down. However, it increased again as the agent approached to the other marked state. In the case of Fig. 2 (a), it passed on the state (2,4) twice, and the observation is completely the same between before and after reaching the fake goal at the state (4,4). Nevertheless, the Q value on the state (2,4) is 0.54 for the right move and 0.45 for the left move before reaching the fake goal, while it changes to 0.42 for the right move and 0.50 for the left move. This means that the recurrent network extracted and kept the information that the first marked state was the fake goal, and the network reflected the information to the Q value. The hidden neuron in Fig. 3 (b) took the value around 0.0 at first, but once it reached the fake goal, the value went down around -0.4. For the other combination of the marked states, the same tendency can be seen in this neuron. It can be considered that the neuron is representing the passing of the fake goal.

3.2 Exploration without information of goal location

A mouse in a maze explores effectively without any information about food location. There appears to be a problem whether such exploration behavior can be acquired by reinforcement learning. Then this section is focused on the exploration without information of goal location, and it is examined whether actions that can be called as exploration can be acquired through learning.

As shown in Fig. 4, five 2x2 mazes are prepared. Four of them have one wall inside, and the other has no walls. One of the five is chosen randomly at every trial, and the agent is located randomly at one of four states. The agent can take one of the five actions each of which is move to one of the four directions or stay at the same state. The state transition is deterministic and if the agent chooses the action to move against a wall, it stays at the same state. A total of 17 observation signals can be divided into four kinds. The first four signals indicate whether a wall exists in one of the four directions, and other eight signals indicate whether the goal exists at each of eight neighbor states. The other 5 signals indicate the previous action that is one of the five actions. Each signal is binary signal and is put into the recurrent network. At the beginning of a trial, all the observation signals representing previous actions are 0. Action selection method is ε-greedy and ε is 0.1 at the beginning of learning, and is gradually decreased to 0.0 by a constant value until the end of the learning. This means that the agent selects its action greedy at the end of the learning. The number of layers in the network is four and each of which has 17 (except for the feedback input), 20, 10, 5 neurons respectively from the input layer to the output layer. All the outputs of the

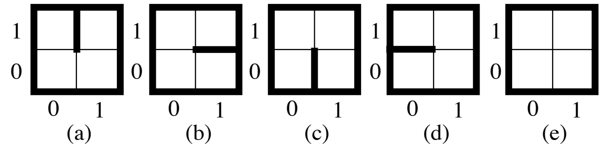

Fig. 4 Five 2x2 mazes used in the simulation

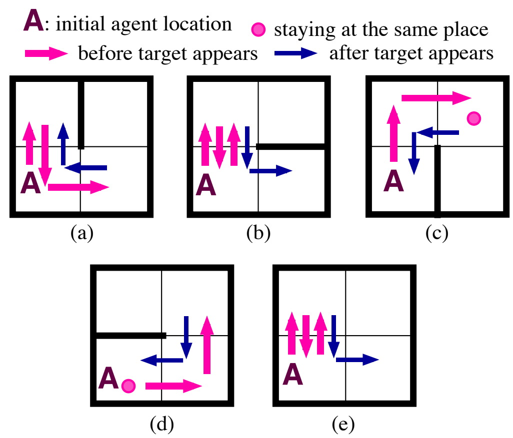

Fig. 5 Acquired exploration behaviors before and after the goal appears.

upper hidden neurons are also the input at the next time step together with the 17 external input signals. The network is trained by BPTT with the training signal as Eq. (1). The number of time steps traced back to the past is 10 here. The initial weight value is 0.0 for all the connections from the upper hidden layer to the output layer, and that for the other connections is chosen randomly from -1.0 to 1.0. The discount factor γ is 0.9 and learning rate for BPTT is 0.2.

The goal appears randomly one of the three states where the agent does not exist after three state transitions by the agent action. For example, if the agent is located initially at (0, 0) and no wall is detected, it cannot identify whether the maze is (a), (b) or (e). Accordingly, unless it moves, it cannot know whether it should go up or right when the goal appears on the diagonal state (1, 1). However, if the agent moves beforehand and identifies the maze, it can go to the correct direction even though the goal appears on the diagonal state. Furthermore, if the agent exists at the next of the inner wall when the goal appears, it has to move three times to reach the goal if the goal was put behind the inner wall. Accordingly, it should be on a state that is not next to the inner wall just before the appearance of the goal and should remember where is the inner wall.

The average time steps from the appearance of the goal for 1000 trials after 100000 trials of learning is 1.35 for the four-layer Elman network case, 1.55 for three-layer Elman network case, and 1.57 for four-layer regular network case. The optimal number of expected steps is 1.33. The behavior of the agent using four-layer Elman network is shown in Fig. 5. In this figure, the initial agent location is (0, 0), and a thick arrow or point indicates the action before the appearance of the goal, and a thin line indicates the action after the goal appeared on the diagonal state of the agent. In all the cases, the agent existed on the state that is not next to the inner wall after some actions before the appearance of the goal, and when the goal appeared on the diagonal state, it could go to the way that the inner wall did not block. Comparing with (a) and (b), the agent went up to (0, 1) at first, and then returned to (0, 0) in the both cases, but the third action is to go right in the case of (a), while to go up in the case of (b) even though the observation signals are the same between them. This means that the recurrent network memorized whether the inner wall existed or not on the state (0, 1), and the memorized information was reflected to the third action.

Finally, in order to examine whether the state value increases by knowing the maze shape and it promotes the exploration behaviors, the maze shape is made to be more complicated and the sight of the goal is completely deprived. Here, the shape of 3x3 maze such as shown in Fig. 6 is decided randomly at every trial, and the agent is put on the center of the maze. The goal is also located randomly, but the agent cannot know the location. The agent's observation has eight signals. Four of them represent the wall presence in each of 4 directions, and the other four represent the previous action. The Elman network has three layers, and the number of hidden neurons is 30. The initial weight values are the same as in the previous simulation. The learning rate for BPTT is 0.01, and the number of time steps traced back to the past is truncated at 30 steps. ε in the ε-greedy is 0.1, and the discount factor γ is 0.9.

Fig. 6 shows the learning result. Even though the maze shape changes randomly at every trial, the exploration behavior to go everywhere effectively can be obtained as shown in the figure with some exceptions. In this case, since there is certainly a goal in the maze, if exploration progresses and the number of non-visited states becomes small, the possibility to reach the goal at the next time step becomes large when it goes to a non-visited state. Accordingly, it is expected that the recurrent network learns the fact, and the maximum Q value that is the state value increases gradually according to the progress of exploration. However, the increase of the Q value could not be observed.

Then the goal location was limited at one of four corners. The learning of exploration behavior could not be obtained. For example, in the case of Fig. 6 (a), if the goal is located on one random state on the four sides, there is a possibility to reach the goal whatever direction the agent goes to. However, if the goal is located only on one of the four corners, there is no possibility to reach the goal at the next time step from the center of the maze. That might be the reason that the agent could not learn an appropriate exploration behavior such that the agent goes to the left since it has been to the right before. If the recurrent network memorizes the information about all the visited states in the maze, a proper state value function might be obtained. The recurrent network is difficult to learn the function of a counter or multiple state transitions. The problem might be originated from the learning ability of the recurrent network. However, hereafter, more detailed analysis is necessary to know the cause correctly.

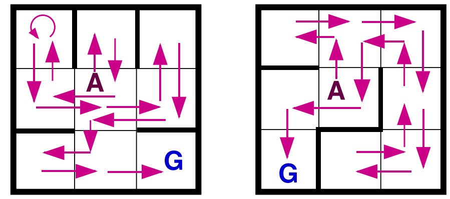

(a) (b)

Fig. 6 Exploration behavior after learning in the case of no sight of the goal.

4. Conclusion

It is propounded that by not treating "exploration" in reinforcement learning as simple stochastic actions but treating it as a kind of intended actions, effective "exploration" is acquired by reinforcement learning. This idea was introduced in the task that the goal information is not clear and also in the task in which "exploration" is required with no information about the goal location, and effective "exploration" can be obtained to some extent by reinforcement learning.

It is thought that this idea is deeply relating to the temporal and spatial "abstraction" and also to the "curiosity" that has a possibility to make actions emerge without reward. It is desired to construct a system to explain these items consistently.

Acknowledgement

This research was supported by JSPS Grant in Aid in Scientific Research (B) #14350227and #15300064, and also Overseas Advanced Education and Research Application Assistance Program. I would like to say thank to Prof. R. S. Sutton at Univ. of Alberta, Canada for useful comments.

Reference

[1] Sutton, R.S. and Barto, A.G., "Reinforcement Learning: An Introduction", MIT Press, Cambridge, MA (1998)

[2] Sutton, R.S., Precup, D., and Singh, S., "Between MDPs and semi-MDPs: A Framework for Temporal Abstraction in Reinforcement Learning". *Artificial Intelligence 112*:181-211 (1999).

[3] Shibata, S., "Reinforcement Learning and Intelligence of Robots", Proc. of the 16th Annual Conf. of JSAI, 2A1-05 (2002) (in Japanese)

[4] Shibata, K. and Sugisaka, M., "Dynamics of a Recurrent Neural Network Acquired through the Learning of a Context-based Attention Task", *Artificial Life and Robotics*, Vol. 7, pp. 145-150, (2004)

[5] Rumelhart, D.E, Hinton, G.E., and Williams, R.J., "Learning Internal Representations by Error Propagation". *Parallel Distributed Processing,* The MIT Press, pp. 318-362 (1986).

Hierarchical Q-learning in POMDP Environments

Hiroyuki Kamaya
Dept. Electrical Eng.
Hachinohe National College of Tech.
Tamonoki, Hachinohe 039-1192, Japan

Kenichi Abe
Dept. Computer Science
College of Eng. Nihon Univ.
Tamura-machi, Koriyama 983-8642, Japan

Abstract

This paper presents a new hierarchical reinforcement learning (RL) algorithm to speed up learning, to make it more robust to hidden states, and to handle non-deterministic problems. This on-line RL algorithm is called $SSS(\lambda)$, which extended Sun and Sessions's original *Self-Segmentation of Sequences* (SSS) algorithm using eligibility traces. $SSS(\lambda)$ is compared with HQ-learning, which is a hierarchical RL algorithm proposed by Wiering and Schmidhuber, for partially observable navigation tasks. The results of extensive simulations demonstrate that $SSS(\lambda)$ is clearly outperforming HQ-learning.

1 Introduction

Reinforcement learning (RL) is a general framework for describing learning problems in which an autonomous agent learns strategies for interacting with its environment[1]. A key assumption underlying many studies on RL is that the agent-environment interaction can be viewed as Markov decision processes (MDPs). In many domains, e.g., in mobile robotics, in multi-agent and distributed control environments, etc., however, it will not be possible for the agent to have perfect and complete perception of the state of the environment. This problem is also referred to as the problem of *incomplete perception*, *perceptual aliasing*, or *hidden state*. And their problem can be formulated as partially observable Markov decision processes (POMDPs). In POMDPs, the mapping from the set of environmental states to a finite set of observations is not one-to-one. Therefore, different environmental states may be in the same observation. Recent research on hidden state RL problems has been concentrated on overcoming partial observability by using memory of previous actions and observations to disambiguate the current state[2]. Such methods, however, require huge computational burden, and so result in very limited applicability.

To reduce the computational complexity, several hierarchical approaches for RL have been proposed. Wiering and Schmidhuber have presented the interesting method, called *HQ-learning*[3]. In HQ-learning, a *non-Markovian* task is automatically decomposed into simpler subtasks that can be solved by multiple Q agents. Sun and Sessions have proposed a more general algorithm, called *Self-Segmentation of Sequences* (SSS) *algorithm*[4]. The SSS algorithm segments action sequences to reduce *non-Markovian* temporal dependencies and to create hierarchical structures based on reinforcement received during task execution.

In this paper, we propose a new hierarchical RL algorithm to speed up learning, to make it more robust to hidden states, and to handle non-deterministic problems. This on-line RL algorithm is called $SSS(\lambda)$, which extended the SSS algorithm using eligibility traces. Compared with HQ-learning, it is demonstrated that $SSS(\lambda)$ can outperform in a partially observable navigation task.

The rest of this paper is organized as follows. Section 2 introduces the bases of reinforcement learning. Section 3 reviews the proposed $SSS(\lambda)$ algorithm. Section 4 describes the empirical results. Finally, section 5 concludes this paper.

2 Reinforcement Learning

At each time step $t(\in 0, 1, 2, ...)$, the agent observes its environmental *state*, $s_t \in S$, where S is the set of possible states, and selects an *action*, $a_t \in A(s_t)$, where $A(s_t)$ is the set of actions available in state s_t. As a consequence of its action, the agent receives a scalar reinforcement signal, referred as *reward*, $r_t \in R$. One time step later, the agent observes a new state, s_{t+1}.The aim of the agent, based on its experience with the environment, is to find a strategy or an optimal *policy* for choosing actions that maximizes the expected discounted reward $E\{\sum_{t=0}^{\infty} \gamma^t r_t\}$, where γ is a parameter, $0 \le \gamma \le 1$, called the discount factor. Q-

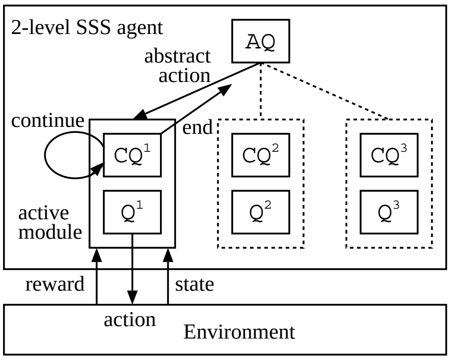

Figure 1: SSS agent with two level hierarchy.

learning, TD(λ), and Sarsa are widely known as the RL algorithms.

The Sarsa(λ) algorithm is multi-step version of the Sarsa. In Sarsa(λ), on experiencing transition $< s_t, a_t, r_t, s_{t+1}, a_{t+1} >$, where a_{t+1} is the selected action in s_{t+1}, the following updates are performed in order:

$$\eta(s, a_i) \leftarrow \begin{cases} 1, & \text{for } a_i = a_t \\ 0, & \text{for all } a_i \neq a_t \end{cases} \quad (1)$$

$$\delta = r_t + \gamma Q(s_{t+1}, a_{t+1}) - Q(s_t, a_t), \quad (2)$$

for all s_i and a_i

$$Q(s_i, a_i) \leftarrow Q(s_i, a_i) + \alpha\delta\eta(s_i, a_i), \quad (3)$$

$$\eta(s_i, a_i) \leftarrow \gamma\lambda\eta(s_i, a_i), \quad (4)$$

where α $(0 < \alpha \leq 1)$ is the learning rate, $\eta(s, a)$ is the eligibility trace function, and λ $(0 \leq \lambda \leq 1)$ is the eligibility factor.

3 $SSS(\lambda)$ Algorithm

The SSS algorithm involves three types of learning modules:

- Individual action module Q: Each discovers a local control policy,
- Individual controller CQ: For each Q module, there is a corresponding controller CQ. Each CQ learns whether the Q module should continue its control or give up the control,
- Abstract controller AQ: It performs and learns abstract control action, that is, selects which Q module should be taken under given circumstances.

Behavior of a 2-level SSS agent which has one higher-level controller AQ and three pairs of Q/CQ modules is demonstrated as an example (Fig.1). The agent operates as follows: when the system first starts, AQ decides which Q/CQ module should be taken over next from a starting state (Q^1/CQ^1 is chosen in Fig.1); at a given time, only one pair of Q/CQ can be active; when the CQ selects *continue*, the active Q will select an action with regard to the current state that will be affected with the environment and thus receive reinforcement from the environment; conversely, when the CQ selects *end*, the active Q relinquishes its control, and the control is returned to AQ, which will decide which Q/CQ module should be taken over next from the current point; this procedure then is repeated in the same way.

In order to speed up learning, we extend the original SSS algorithm using eligibility traces. This new algorithm is called $SSS(\lambda)$[5]. The 2-level $SSS(\lambda)$ algorithm is listed below (we use k to denote the abstract action at the higher-level and the pair of active controllers simultaneously).

- Initialize Q, CQ, and AQ
- **Repeat** (for each trial)
-   η_Q, η_{CQ}, and η_{AQ} are initialized to zero
-   Observe s
-   $k \leftarrow AQ$ (AQ selects Q/CQ from s), $\tilde{s} \leftarrow s$
-   $a \leftarrow Q^k$ (Q^k selects an action from s)
-   **Repeat** (for each step of trial)
-     Take action a, observe r, s'
-     $ca' \leftarrow CQ^k$ (CQ^k selects *continue* or *end* from s')
-     Update CQ^k, $ca \leftarrow ca'$
-     **if** ca is *continue* **then**
        $a' \leftarrow Q^k$ (Q^k selects an action from s')
        Update Q^k
-     **else** (that is, ca is *end*)
        $k' \leftarrow AQ$ (AQ selects Q/CQ from s')
        Update Q^k, CQ^k and AQ, $\tilde{s} \leftarrow s', k \leftarrow k'$
        η_Q and η_{CQ} are reset to zero
        $a' \leftarrow Q^k$ (Q^k selects an action from s')
-     $s \leftarrow s', a \leftarrow a'$
-     **until** s is the terminal

We can extend the two level hierarchy to more levels. In our previous paper, we implemented the 3-level SSS algorithm[6]. In such a case, on the top of AQ_0(=Q)'s, CQ_0 (=CQ)'s, and AQ_1(=AQ)'s, we introduce AQ_2 for selecting among AQ_1's as well as CQ_1 that determines whether the corresponding AQ_1 should continue its control or give up the control. By the same manner, we can extend the 3-level $SSS(\lambda)$ to more levels.

4 Empirical Results

In order to evaluate the robustness and the ability to handle hidden states problems, we test both of the 3-level $SSS(\lambda)$ algorithm and the HQ algorithm for a partially observable maze navigation task. In this task, the agent has to discover paths leading from the starting location to the goal location, while the agent has no information about maze environment.

Fig.2 shows a partially observable 26 × 23 maze[3]. Starting at "S", the agent has to (1) fetch a key at position "K", (2) move towards the "door" (the gray area) which normally behaves like a wall and will open (disappear) only if the agent is in possession of the key, and (3) proceed to goal "G". There are only 11 different, highly ambiguous inputs; the key (door) is observed as a free field (wall). The optimal path takes 83 steps.

The agent can only perceive if the four adjacent cells are free spaces or walls. Note that the agent can't perceive the true state such as agent's global position. Therefore, many locations, from which the agent should execute different actions, may be perceived as identical.

In each location, there are four possible actions: *go left*, *go right*, *go up*, and *go down*, which deterministically (or non-deterministically) cause the agent to move one location in the corresponding direction on the grid, except a movement taking the agent to a wall. In that case, agent's location is not changed.

The reward is 500 if the agent reaches the goal location, and -0.1 otherwise.

The parameter settings for 3-level $SSS(\lambda)$ were following: the discount factor γ was 0.97, the learning rates were $\alpha_{AQ_0} = \alpha_{CQ_0} = 0.05$, $\alpha_{AQ_1} = \alpha_{CQ_1} = \alpha_{AQ_2} = 0.2$ and the eligibility factor was $\lambda = 0.9$. The AQ_2 and AQ_1 modules select one pair of Q/CQ module according to the ϵ-greedy rule, where ϵ was initially set to 0.1 and then linearly decreased to 0. Q/CQ's action choice depends on the current observation. During learning, at time t, the active CQ_1, AQ_0 and CQ_0 modules select an action according to the Max-Boltzmann rule, where p_{max} was initially set to 0.9 and then linearly increased to 1. The temperatures were $\tau_{AQ_0} = \tau_{CQ_0} = 0.1$, $\tau_{CQ_1} = 0.2$.

The parameter settings for HQ were similar to [3].

Each simulation consists of $20,000$ trials. In each trial, the number of steps is limited up to $1,000$. The trial is stopped either when agent's goal is achieved, or after time runs out.

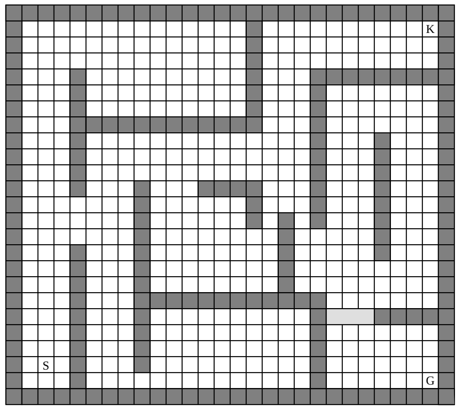

Figure 2: 'key and door' problem.

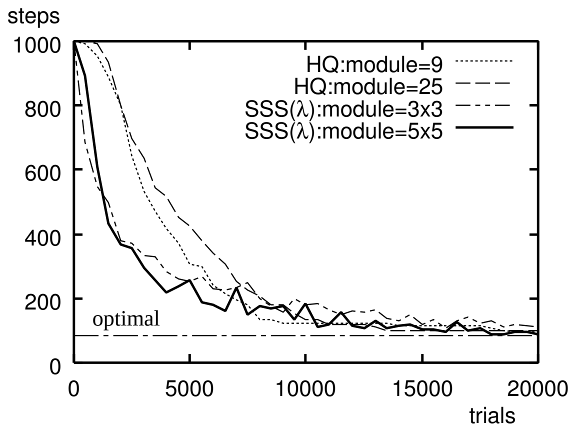

Figure 3: Estimated performance.

4.1 Noiseless Environment

Fig.3 shows the average performance of $SSS(\lambda)$ and HQ, respectively, over 100 simulations. The X-axis indicates the number of trials the agent has attempted so far. The Y-axis indicates the number of steps to the goal. In all cases, the better the performance becomes, the lower the curve is. The $SSS(\lambda)$ agent achieved much better results in term of the number of trials than did the HQ agent.

Table 1 shows the performance after learning over 100 independent runs. The 2nd column is the number of modules, the 3rd column is average path lengths over simulations, the 4th column is the percentage to achieve the optimal steps, the 5th column is the percentage to reach the goal, and the 6th column shows average path lengths of solutions. As listed in Table 1, $SSS(\lambda)$ with 5×5 modules could find the optimal path at the rate of about 34%. On the contrary, HQ with 25 modules could find the optimal path at the rate of about 11%. It is obvious from the experiments that $SSS(\lambda)$ could usually find good solutions.

Table 1: Performance of HQ and $SSS(\lambda)$ after learning.

Algorithms	Modules	Av. steps	(%)Opt.	(%)Goal	Av. sol.
HQ	9	97.7	13	99	88.6
HQ	25	99.9	11	99	90.8
$SSS(\lambda)$	3×3	111.5	19	98	93.4
$SSS(\lambda)$	5×5	88.3	34	100	88.3

Table 2: Performance of HQ and $SSS(\lambda)$ after learning in the noisy case.

Algorithms	Modules	Av. steps	(%)Opt.	(%)Goal	Av. sol.
HQ	9	405.3	0	88	324.2
HQ	25	458.2	0	83	347.2
$SSS(\lambda)$	3×3	299.0	0	86	184.8
$SSS(\lambda)$	5×5	192.7	0	96	159.0

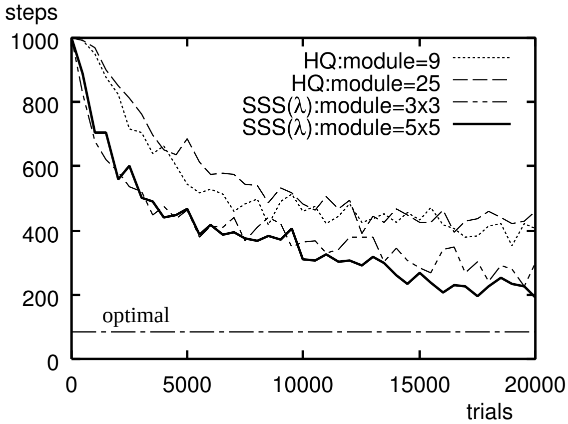

Figure 4: Estimated performance in the noisy case.

4.2 Noisy Environment

In addition to the hidden state problem described above, we also evaluate learning performance for the case that the state transitions are noisy; random actions are executed at 10% probability. The parameter settings were similar with the noiseless case.

Fig.4 shows the average performance for the noisy case. Table 2 shows the performance after learning. In many cases, long paths were found. A little noise did decrease performance; however, the agent almost reached the goal in the simulations. It is obvious from these experiments that $SSS(\lambda)$ performs significantly much better than HQ.

5 Summary

In this paper, we have presented a new hierarchical RL algorithm, called $SSS(\lambda)$, to deal with non-Markovian temporal dependencies. The algorithm has been tested on a partially observable navigation task. Even in a noisy POMDP environment, the proposed $SSS(\lambda)$ algorithm can usually find good solutions. Furthermore, $SSS(\lambda)$ can achieve much faster convergence property than HQ in both of noiseless and noisy environment. As confirmed by the results of our experiments, $SSS(\lambda)$ can be clearly outperforming HQ-learning.

References

[1] R.S.Sutton and A.G.Barto, "*Reinforcement Learning: An Introduction*," MIT Press, 1998.

[2] L.P.Kaelbling, M.L.Littman and A.W.Moore, "Reinforcement Learning: A Survey," *Journal of Artificial Intelligence Research* 4, pp. 237–285, 1996.

[3] M.Wiering and J.Schmidhuber, "*HQ*-learning," *Adaptive Behavior*, **6**-2, pp. 219–246, 1997.

[4] R.Sun and C.Sessions, "Self-Segmentation of Sequences: Automatic Formation of Hierarchies of Sequential Behaviors," *IEEE Trans.*, SMC-B-**30**, pp. 403–418, 2000.

[5] H.Kamaya and K.Abe, "Self-Segmentation of Sequences Algorithm with Eligibility Traces in POMDPs," *Proc. of ASCC 2002*, pp. 408–413, 2002.

[6] H.Kamaya and K.Abe, "Hierarchical Self-Segmentation Algorithms for *Q*-learning in Non-Markovian Environments," *SNPD'01*, pp.55–62, 2001.

Improvement of Finishing Quality on Blow Mold's Constriction Parts by Using an Intelligent Finishing Robot

F. Nagata
Fukuoka Ind. Tech. Center
Kitakyushu, Fukuoka, Japan

T. Hase, M. Omoto, Z. Haga
Meiho Co. Ltd.
Nohgata, Fukuoka, Japan

K. Watanabe
Saga University
Saga, Japan

Abstract

We have already proposed a few types of mold polishing robots which have a high relationship with 3D CAD/CAM and can regulate the feed rate due to a simple fuzzy reasoning. In this paper, in order to improve the finishing quality on blow mold's constriction parts, a compact spindle driven by an electric servo motor is first introduced at the tip of the robot arm. The spindle can rotate with a low speed within from 0 to 3000 rpm. We also consider a scheme that can suppress the undesirable tool slide by applying a weak coupling control to between position feedback control loop and force feedback control loop. The effectiveness and promise are shown through an experiment.

1 introduction

We have already proposed a mold finishing robot that has a high relationship with 3D CAD/CAM systems. The robot can also regulate the tip feed rate (tangential velocity) by means of a simple fuzzy reasoning. In this paper, in order to improve the surface quality around blow mold's constriction part, a compact spindle driven by an electric servo motor is first introduced at the tip of the robot arm. The spindle has an ability of low speed rotation within from 0 to 3000 rpm. We also consider a hybrid position/force control scheme that has a delicate cooperation (i.e., weak coupling between force feedback loop and position feedback loop) only in pick feed direction so that undesirable phenomena on tool slide can be suppressed. The force feedback loop controls the polishing force which is the resultant force consisting of tool contact force, friction force due to translational motion and another friction force due to rotational motion. The result allows the finishing root to perform stable polishing force control precisely following desired trajectory on the blow mold's constriction part.

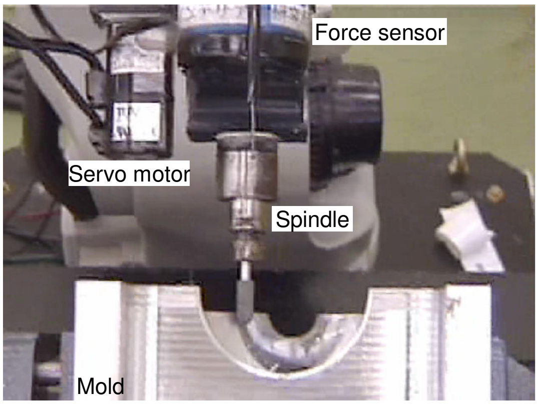

Figure 1: Servo spindle attached to the tip of the robot arm.

2 Polishing Strategy

When conventional air-driven spindles are used with a specified rotational velocity about 20,000 rpm, undesirable over-polishing tends to occur. On the other hand, enough driving torque can't be performed in the case of under the specified velocity. Besides the detection and control of the rotational velocity and torque are also not easy. In order to solve such problems, it is effective to drive the spindle with an electric servo motor. Figure 1 shows a polishing spindle provided by Yaskawa Electric Corp., attached to the tip of the robot arm via a force sensor. The position of the servo motor is designed parallel to the spindle to transfer the driving torque through a pulley and velt. A ball-end abrasive tool is fixed to the spindle and rotated within from 0 to 3000 rpm by the servo motor. The spindle torque is also monitored with the servo amplifier.

A representative polishing image using the ball-end abrasive tool is illustrated in Fig. 2. Position of the abrasive tool is controlled following a zigzag path generated from a 3D CAD/CAM, and concurrently the

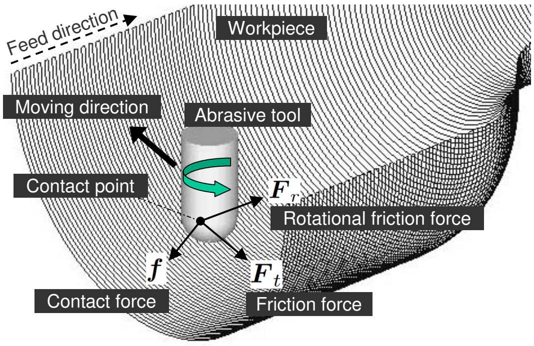

Figure 2: Polishing strategy considering friction forces.

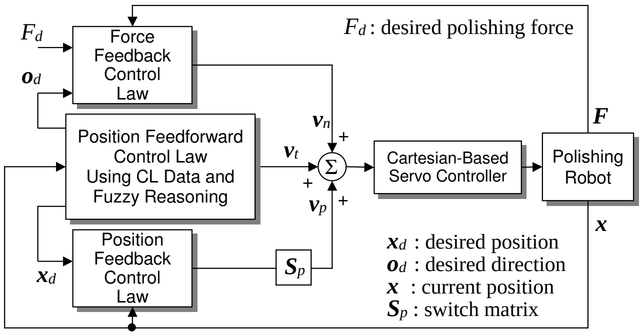

Figure 3: Block diagram of the proposed hybrid position/force controller.

polishing force acting between the tool and the workpiece is regulated to a desired value F_d. The polishing force vector $\boldsymbol{F} = [F_x\ F_y\ F_z]^T$ is the resultant force among of the contact force $\boldsymbol{f} = [f_x\ f_y\ f_z]^T$, friction force $\boldsymbol{F}_t = [F_{tx}\ F_{ty}\ F_{tz}]^T$ yielded by translational motion and another friction force $\boldsymbol{F}_r = [F_{rx}\ F_{ry}\ F_{rz}]^T$ generated by rotational motion, which is given by

$$\boldsymbol{F} = \boldsymbol{f} + \boldsymbol{F}_t + \boldsymbol{F}_r \tag{1}$$

where each component of the vectors is composed in base coordinate system. It is assumed that the friction force in Fig. 2 consists of Coulomb friction and viscous friction forces, so that $\boldsymbol{F}_t + \boldsymbol{F}_r$ is represented by

$$\boldsymbol{F}_t + \boldsymbol{F}_r = \mathrm{diag}\big(\mu_x, \mu_y, \mu_z\big)\|\boldsymbol{f}\|\frac{\boldsymbol{v}_t}{\|\boldsymbol{v}_t\|} \\ +\mathrm{diag}\big(\eta_\mathrm{x}, \eta_\mathrm{y}, \eta_\mathrm{z}\big)\boldsymbol{v}_\mathrm{t} + \mathrm{diag}\big(\eta_x, \eta_y, \eta_z\big)\boldsymbol{v}_r \tag{2}$$

where μ_i and η_i $(i = x, y, z)$ are the coefficients of Coulomb friction per unit contact force and viscous friction, respectively. $\boldsymbol{v}_t = [v_{tx}\ v_{ty}\ v_{tz}]^T$ and $\boldsymbol{v}_r = [v_{rx}\ v_{ry}\ v_{rz}]^T$ are the translational (tangential) velocity and circumferential velocity at the contact point.

As can be guessed, it is not easy to independently measure $\boldsymbol{f}$, $\boldsymbol{F}_t$ or $\boldsymbol{F}_r$ constructing the polishing force. However, those resultant force norm, i.e., polishing force norm, can be referred by

$$\|\boldsymbol{F}\| = \sqrt{\left\{{}^SF_x\right\}^2 + \left\{{}^SF_y\right\}^2 + \left\{{}^SF_z\right\}^2} \tag{3}$$

where the superscript S denotes the value in sensor coordinate system, and the components ${}^SF_i$ $(i = x, y, z)$ are obtained from the force sensor shown in Fig. 1. Although there exist an attachment, spindle, tool axis and ball-end abrasive tip between the force sensor and tool contact point, the force control system used in experiment has a stiff and linear property about 12 kgf/mm in case that the displacement in normal direction after a contact motion is under 1 mm. Therefore, the system can be regarded as an almost rigid body when the polishing force is given around 3 kgf. When the robot runs, $\|\boldsymbol{F}\|$ is controlled to F_d to obtain a uniform surface quality.

3 Control Strategy

3.1 Hybrid position/force control with weak coupling

In this section, a hybrid position/force control method is proposed to realize the polishing strategy described in previous section. Figure 3 shows the block diagram of the proposed control system in Cartesian coordinate space. $\boldsymbol{x}_d$ and $\boldsymbol{o}_d$ are desired position and direction vectors minutely obtained from cutter location (CL) data [1]. The CL data are calculated from the main-processor of CAM. $\boldsymbol{x}$ is the current position at the tip of the abrasive tool obtained from the forward kinematics. $\boldsymbol{F}$ is the force sensor measurement given by eq. (3).

The key idea is a weak coupling control between the position feedback loop and force feedback loop. Directions to perform such a weak coupling control are selected by a switch matrix $\boldsymbol{S}_p = \mathrm{diag}(S_x, S_y, S_z)$. If the position feedback loop makes interfere with the force feedback loop, then corresponding diagonal element of $\boldsymbol{S}_p$ should be set to 1. The force feedback loop regulates the polishing force. Normal velocity $\boldsymbol{v}_n = [v_{nx}\ v_{ny}\ v_{nz}]^T$ at the contact point is the manipulated variable from the force feedback control law [2].

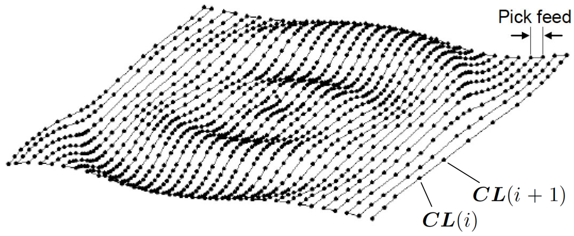

Figure 4: Example of CL data composed of position and normal direction components.

The position control is carried out by applying both the feedback control and feedforward control. The feedforward control using CL data and a fuzzy reasoning is used to make the abrasive tool move with a variable velocity norm along desired trajectory, whose manipulated variable is given by $\boldsymbol{v}_t$. Since $\boldsymbol{v}_t$ is generated from the feedforward control law, the force feedback loop is not disturbed.

The manipulated variable $\boldsymbol{v}_p = [v_{px}\ v_{py}\ v_{pz}]^T$ in pick feed direction is generated for position feedback control which has an important function to exactly move the abrasive tool with a constant pitch. Consequently, high quality surfaces without irregularity can be obtained. Finally, the summation $\boldsymbol{v} = [v_x\ v_y\ v_z]^T$ of three manipulated variables written by following equation is given to the reference of the robotic servo controller.

$$\boldsymbol{v} = \boldsymbol{v}_n + \boldsymbol{v}_t + \boldsymbol{v}_p \tag{4}$$

3.2 Update timing of CL data

Here, we describe how to update the current step i of the CL data, i.e., when the next step i+1 should be set to i, to realize a smooth feed motion. The main-processor of the CAM generally produces the CL data $\boldsymbol{CL}(i) = [\boldsymbol{p}^T(i)\ \boldsymbol{o}^T(i)]^T$ as shown in Fig. 4 so as to machine a workpiece within a given tolerance to a designed model. $\boldsymbol{p}(i) = [p_x(i)\ p_y(i)\ p_z(i)]^T$ and $\boldsymbol{o}(i) = [o_x(i)\ o_y(i)\ o_z(i)]^T$ $(i = 1, 2, 3, \ldots, l$: l is the number of steps) are the position and normal direction components, respectively. Figure 5 shows an image of the proposed polishing strategy where the tool contour is efficiently utilized. One of the key points is that the tool doesn't go up over the situation (1) or (5) shown in Fig. 5 in order to avoid an undesirable over polishing around the edge.

Actually, the tangential velocity of the ball end abrasive tool is linearly calculated based on the following direction vector.

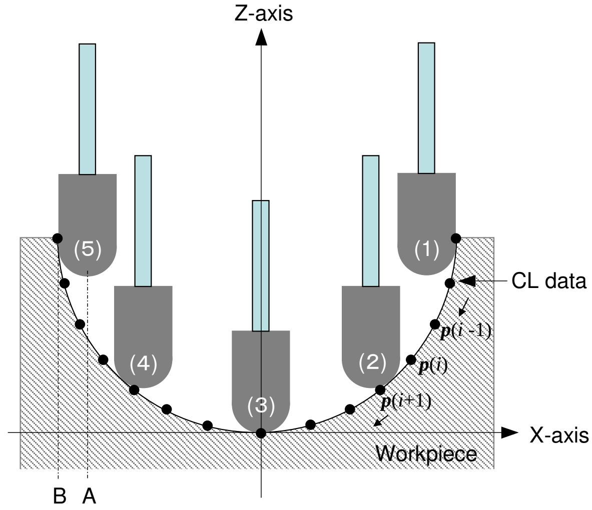

Figure 5: Relation between the tool's center and CL data.

$$\boldsymbol{t}(i) = \boldsymbol{p}(i+1) - \boldsymbol{p}(i) \tag{5}$$

In this case, it is very important to realize a smooth feed motion that when the step number i should be updated: how to decide the timing of reading the next step i+1. After here, the following three conditions are evaluated.

1) Detecting from the current position $\boldsymbol{x}(k)$ of tool tip
2) Considering the force measurement in normal direction besides the condition 1).
3) Detecting from the sum of the manipulated variable $\boldsymbol{v}_t(k)$

Concerning the condition 1), when the tool tip $\boldsymbol{x}(k)$ becomes out of $[\boldsymbol{p}(i), \boldsymbol{p}(i+1)]$, i.e., $\boldsymbol{x}(k)$ goes over $\boldsymbol{p}(i+1)$, i is updated. However, it doesn't work well around the situations (1) and (5) in Fig. 5. The reason is that a constraint caused by a contact between the tool contour and workpiece prevents the tool tip from going over $\boldsymbol{p}(i+1)$. For example, even if the tool tip approaches to the point A in situation (5) through (4), it can't arrive at the point B. Consequently, the next step is not read out.

In the condition 2) to solve the problem, the force measurement is further considered in addition to the condition 1). In other words, when a large x-directional force such as $|f_x| > F_d$ is detected, then the next step is immediately read in. In this case also, however, an incorrect detection tends to occur. Because the force control system in the finishing robot

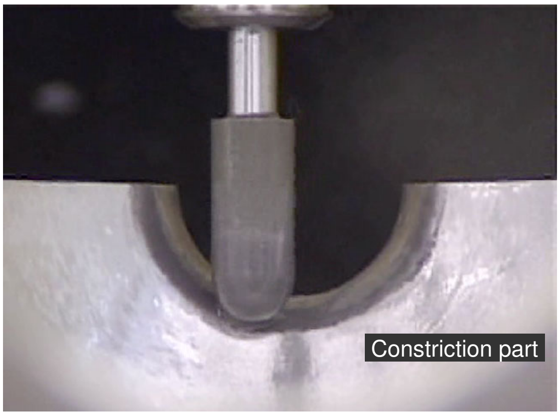

Figure 6: Finishing scene of blow mold's constriction part.

is considerably high: its stiffness in the tool contact direction is about 12 kgf/mm, so that an undesirable spike over F_d sometimes breaks out.

Through the try and error mentioned above, the condition 3) is now introduced. In the condition 3), if the following equation is satisfied, then i is updated to $i+1$.

$$\sum_{n=k_i}^{k} \|\boldsymbol{v}_t(n)\| \geq \|\boldsymbol{t}(i)\| \tag{6}$$

where k_i is the discrete time when the last updating was conducted. In eq. (6), when the sum of the manipulated variable in the tangential direction, which has been given to the servo system after the last updating, goes beyond the current distance $\|\boldsymbol{t}(i)\|$ between two adjacent steps, i is updated to $i+1$. Due to the detection of the update timing by using eq. (6), the feed motion can be smoothly carried out even under the constrained situations (1) and (5) shown in Fig. 5.

4 Experimental Results

In this section, an experiment was conducted using an aluminum blow mold with a constriction part in order to evaluate the effectiveness of the proposed system. Figure 6 shows the finishing scene of the constriction part. It was observed from the result that the tip of the abrasive tool could move along the desired trajectory without sliding down the constriction part. In this case, the pick feed in the CL data was given 0.2 mm along the constriction part.

5 Conclusions

In this paper, a compact spindle with a function of low speed regulation is first introduced at the tip of the robot arm to suppress undesirable over-polishing. We also proposed a hybrid control scheme in which the position feedback loop delicately contributed to the force feedback loop only in the pick feed direction. Consequently, fatal phenomenon concerning tool sliding down disappeared and the finishing quality around the blow mold's constriction part could be successfully improved.

References

[1] F. Nagata, K. Watanabe and K. Izummi, "Furniture Polishing Robot Using a Trajectory Generator Based on Cutter Location Data," *Procs. of IEEE International Conference on Robotics and Automation*, pp. 319–324, 2001.

[2] F. Nagata, K. Watanabe, Y. Kusumoto, et al., " Generation of Normalized Tool Vector from 3-Axis CL Data and Its Application to a Mold Polishing Robot," *Procs. of IEEE/RSJ International Conference on Intelligent Robots and Systems*, pp. 3971–3976, 2004.

The Eleventh International Symposium on Artificial Life and Robotics 2006 (AROB 11th'06),
B-con Plaza, Beppu, Oita, Japan, January 23-25, 2006

Self-Organizing Neural Networks for Incremental Category Learning

Masao Sakai*1, Kazunori Takei*1, Noriyasu Homma*1, Yosuke Koyanaka*2, and Kenichi Abe *3

*1 Tohoku University,
Kawauchi, Aoba-ku,
Sendai,
980-8576, JAPAN

*2 FANUC LTD,
Oshino-mura,
Yamanashi,
401-0597, JAPAN

*3 Nihon University,
1 Nakagawara, Tokkusada,
Tamura-machi, Koriyama,
963-8642, JAPAN

Abstract

In this paper, we develop a neural model that forms categories of inputs for some practical applications such as pattern recognition, learning, image processing, and trend analysis.

The model is based on Ward's hierarchical and K-means clustering algorithms[1, 2], thus carries out the category formation under an incremental and unsupervised learning environment. In addition, the model can also make use of discontinuous teach data for forming ideal categories. Simulation results demonstrate the usefulness of the model for a category formation task.

1 Introduction

"Category" is defined as a group of people or things with particular features in common [3]. Human autonomously forms the categories from acquired information, thus can recognize and divide various things by using the self-formed categories. Therefore it is often said that the category formation is one of the most important ability of human.

In this paper, we develop a neural model to carry out the category formation. The developed model is based on Ward's hierarchical and K-means clustering algorithms. Ward's method[1] is a hierarchical clustering algorithm for sequential inputs under an incremental and unsupervised learning environment; hence the model can actually self-organize an appropriate set of clusters corresponded to human categories without teach data such as an ideal classfication of the inputs.

In contrast, we have to consider individual variations in the classification formed without the teach data. The classfication and recognition are depend on a number of the formed categories; thus to manage the number is important for the design of the ideal classfication. The teach data can be available to estimate the ideal number; hence we improve on the developed model based on the Ward's method to take advantage of this. Furthermore, the K-means clustering algorithms is introduced into the developed model to manage the drastic reclassification of formed clusters due to the discontinuous teach data.

In this paper, the category formation ability of the developed model is demonstrated on a practical image recognition task under an incremental and unsupervised learning environment. In addition, the adequacy of the formed category is evaluated by using principal component analysis.

2 Category Formation Model

2.1 Problem Definition

In this research, a vector representation $\boldsymbol{x}$ for a thing is defined as

$$\boldsymbol{x} \quad = \quad [x_1, x_2, \cdots, x_n]^T \in \Re^n, \tag{1}$$

where x_i, $i = 1, 2, \cdots, n$, denote features of the vector $\boldsymbol{x}$, the superscript T means transpose, and n is the number of features. For simplicity, we consider normalized features value $x_i \in [0, 1]$.

The goal here is to make appropriate clusters corresponded to the proper categories from the set $X(t)$ of all input vectors $\{\boldsymbol{x}(1), \cdots, \boldsymbol{x}(T)\}$, where $\boldsymbol{x}(t)$ is a vector at time $t = 1, 2, \cdots, T$. Clusters $S^\ell, \ell = 1, 2, \cdots, L$, can be defined as sets of things that satisfy specific conditions depending on the set X

$$S^\ell \quad = \quad \{\boldsymbol{x} \in X \mid \boldsymbol{x} \text{ satisfy a condition } \ell\}, \tag{2}$$

where L is the number of clusters.

The cluster S^ℓ are memorized by a set of neural parameters $\{\boldsymbol{w}^\ell, r^\ell, N^\ell, T^\ell\}$ stored in the ℓth neuron, where $\boldsymbol{w}^\ell, r^\ell, N^\ell$, and T^ℓ are the center, scale, number

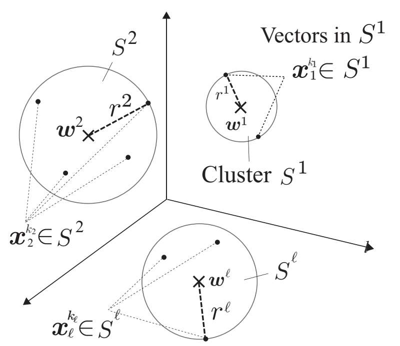

Figure 1: Vectors $\boldsymbol{x}$ and clusters S^l in a vector space.

of the constituent vectors, and proper category information such as name or number obtained from teach data of the cluster S^ℓ, and M is the number of neurons. If the proper category information T^ℓ is unknown, we set $T^\ell = 0$. In general, M is equal to L.

For simplification, we consider only a sphere with center $\boldsymbol{w}^\ell \in \Re^n$ and radius r^ℓ as a shape of the cluster S^ℓ, as show in Figure 1. It generally seems reasonable to suppose that all the vectors of a same category exist in close proximity; hence the model must satisfy that for any vectors $\boldsymbol{x} \in X$, $\boldsymbol{x}$ is in a cluster $S^{\ell(\boldsymbol{x})}$ and the memory $\boldsymbol{w}^{\ell(\boldsymbol{x})}$ in the $\ell(\boldsymbol{x})$th neuron is the nearest one among neural networks and $\|\boldsymbol{w}^{\ell(\boldsymbol{x})} - \boldsymbol{x}\|$ is less than the radius $r^{\ell(\boldsymbol{x})}$. That is,

$$^\forall \boldsymbol{x} \in X, \quad ^\exists \ell(\boldsymbol{x}) \in \{1, 2, \cdots, M\} \quad \text{such that } \boldsymbol{x} \in S^{\ell(\boldsymbol{x})},$$

$$\|\boldsymbol{w}^{\ell(\boldsymbol{x})} - \boldsymbol{x}\| = \min_{\ell \in \{1,2,\cdots,M\}} \|\boldsymbol{w}^\ell - \boldsymbol{x}\| \leq r^{\ell(\boldsymbol{x})}. \tag{3}$$

Therefore, the center and radius of the cluster S^ℓ are defined as

$$\boldsymbol{w}^\ell = \sum_{k=1}^{N^\ell} \boldsymbol{x}_\ell^k \,/\, N^\ell, \tag{4}$$

$$r^\ell = \max_{k \in \{1,2,\cdots,N^\ell\}} \|\boldsymbol{w}^\ell - \boldsymbol{x}_\ell^k\|, \tag{5}$$

where $\boldsymbol{x}_\ell^k, k = 1, 2, \cdots, N^\ell$, are vectors belonging to claster S^ℓ.

2.2 Neural Structure

We explains the neural structure and recognition process for input $\boldsymbol{x}$ of the model. In this paper, the ℓth neural output for the input $\boldsymbol{x}$ is defined as

$$y^\ell(\boldsymbol{x}) = \exp\left(-\alpha \frac{\|\boldsymbol{w}^\ell - \boldsymbol{x}\|}{r^\ell}\right), \tag{6}$$

where α is a large positive constant. If the distance between the neural memory $\boldsymbol{w}^\ell$ and the input $\boldsymbol{x}$ is small, then the neuron activates strongly, that is, the neural output is large.

The recognition algorithm for the input $\boldsymbol{x}$ is explained as follow. We select a neuron c whose output is the largest among the neural networks

$$c = \arg\max_\ell y^\ell(\boldsymbol{x}). \tag{7}$$

If there are some neurons c_ℓ, $\ell = 1, 2, \cdots$, that satisfy Eq. (7), then the candidate neuron is selected randomly.

Here, we introduce a boundary value, τ, $0 < \tau < 1$, for evaluation of the neural output. If $y_c(\boldsymbol{x}) > \tau$, then the input vector $\boldsymbol{x}$ is within the region of the candidate category S^c, otherwise is not within that. Therefore we can quantitatively evaluate similarities of the input $\boldsymbol{x}$ among the already-formed categories S^ℓ. In this research, τ is defined by the following equation.

$$\tau = \exp(-\alpha\beta), \tag{8}$$

where β is an arbitrary positive constant. The output vector $\boldsymbol{Y}$ of the model is defined as

$$\boldsymbol{Y} = \begin{cases} \boldsymbol{w}^c, & (y^c \geq \tau), \\ \vec{0}, & (y^c < \tau). \end{cases} \tag{9}$$

2.3 Category Formation Algorithm

In this section, we explains the algorithm to form suitable categories autonomously from sequential inputs. The algorithm is based on the Ward's hierarchical and K-means clustering algorithms, and make use of discontinuous teach data for forming ideal categories.

The category formation algorithm will now be proposed as follow:

1. Initialize time $t = 0$ and the number of neurons $M = 1$.
2. Select a input vectors $\boldsymbol{x}(t)$ for a thing randomly, and store it with a set $X(t) = \{\boldsymbol{x}(1), \boldsymbol{x}(2), \cdots, \boldsymbol{x}(t)\}$.
3. Is the time t equal to 0 ? If so, go to step 4; if otherwise, go to step 5.
4. Create a new cluster by input vector $\boldsymbol{x}(t)$ as the following: $M \leftarrow M + 1$, $\boldsymbol{w}^M \leftarrow \boldsymbol{x}(t)$, $T^M \leftarrow Q(\boldsymbol{x}(t))$, and go to Step 13.
5. Is the proper category number $Q(\boldsymbol{x}(t))$ obtained for the input $\boldsymbol{x}(t)$? If yes, go to Step 6; if no, go to Step 7.

6. Is there a candidate cluster S^c satisfied $T^c = Q(\boldsymbol{x}(t))$? If yes, go to Step 11; if no, go to Step 7.

7. Whether or not at least one of the following conditions holds ?

   (a) $M < M_L$,

   (b) $\min_{\ell} \|\boldsymbol{w}^\ell - \boldsymbol{x}(t)\| > \min_{\ell_1,\ell_2} \eta_1 \cdot \|\boldsymbol{w}^{\ell_1} - \boldsymbol{w}^{\ell_2}\|$,

   (c) $\begin{cases} \sum_\ell N^\ell > \eta_2 \cdot M, \\ \text{and} \\ \min_\ell \|\boldsymbol{w}^\ell - \boldsymbol{x}(t)\| > \max_\ell \eta_3 \cdot r^\ell, \end{cases}$

   where M_L is an arbitrary positive integer, η_1, η_2, and η_3 are arbitrary positive constants, ℓ, ℓ_1, and ℓ_2 denote $\ell \in \{1, 2, \cdots, M\}$, $\ell_1 \in \{1, 2, \cdots, M-1\}$, and $\ell_2 \in \{\ell_1+1, \ell_1+2, \cdots, M\}$. If yes, go to Step 4; if no, go to Step 8.

8. Evaluate influences of the input vector $\boldsymbol{x}(t)$ on the already-formed categories $S^\ell, \ell = \{1, 2, \cdots, M\}$ at the two following cases:

   CASE 1: The influences $F^\ell(t)$ adding $\boldsymbol{x}(t)$ to the already-formed categories S^ℓ are calculated by the following equation.

$$F^\ell(t) = \begin{cases} \dfrac{N^\ell \cdot \|\boldsymbol{w}^\ell(t) - \boldsymbol{x}(t)\|}{N^\ell + 1}, \\ \qquad \cdots (Q(\boldsymbol{x}(t)), \cdot T^\ell = 0), \\ \infty, \quad \cdots (\text{otherwise}). \end{cases} \tag{10}$$

   CASE 2: Any two already-formed categories S^{ℓ_1} and S^{ℓ_2} combine as a revised cluster S^{ℓ_1}, where $\ell_1 \in \{1, 2, \cdots, M-1\}$, $\ell_2 \in \{\ell_1+1, \ell_1+2, \cdots, M\}$, the cluster S^{ℓ_2} is deleted, and a new clusters is created by $\boldsymbol{x}(t)$. In these case, the influences $G^{\ell_1}_{\ell_2}(t)$ are calculated by the following equation.

$$G^{\ell_1}_{\ell_2}(t) = \begin{cases} \dfrac{N^{\ell_1} \cdot N^{\ell_2} \cdot \|\boldsymbol{w}^{\ell_1}(t) - \boldsymbol{w}^{\ell_2}(t)\|}{N^{\ell_1} + N^{\ell_2}}, \\ \qquad \cdots (T^{\ell_1} \cdot T^{\ell_2} = 0), \\ \infty, \cdots (\text{otherwise}). \end{cases} \tag{11}$$

9. Which is smaller;

$$\min_{\ell \in \{1,2,\cdots,M\}} F^\ell(t) \quad \text{or} \quad \min_{\substack{\ell_1 \in \{1,2,\cdots,M-1\} \\ \ell_2 \in \{\ell_1+1, \ell_1+2, \cdots, M\}}} G^{\ell_1}_{\ell_2}(t) \ ?$$

   If the former, go to Step 12; if the latter, go to Step 10.

10. Select a candidate cluster S^c satisfied the following equation

$$c = \arg \min_{\ell \in \{1,2,\cdots,M\}} F^\ell(t), \tag{12}$$

   and revise T^c of the candidate cluster S^c as the following:

$$T^c \leftarrow Q(\boldsymbol{x}(t)). \tag{13}$$

11. Revise the center of the candidate cluster S^c as the following:

$$\boldsymbol{w}^c \quad \leftarrow \quad \frac{N^c \boldsymbol{w}^c + \boldsymbol{x}(t)}{N^c + 1}, \tag{14}$$

   and go to Step 13.

12. The combination of S^{ℓ_2} with S^{ℓ_1} revises the center $\boldsymbol{w}^{\ell_1}$ and proper category information T^{ℓ_1} of the cluster S^{ℓ_1} by the following equations.

$$\boldsymbol{w}^{\ell_1} \quad \leftarrow \quad \frac{N^{\ell_1} \boldsymbol{w}^{\ell_1} + N^{\ell_2} \boldsymbol{w}^{\ell_2}}{N^{\ell_1} + N^{\ell_2}}, \tag{15}$$

$$T^{\ell_1} \quad \leftarrow \quad T^{\ell_1} + T^{\ell_2}, \tag{16}$$

   and let the input vector $\boldsymbol{x}(t)$ be the cluster S^{ℓ_2} as the following: $\boldsymbol{w}^{\ell_2} \leftarrow \boldsymbol{x}(t)$, $T^{\ell_2} \leftarrow Q(\boldsymbol{x}(t))$, and go to Step 13.

13. Reclassify all the vectors $\boldsymbol{x}(1), \boldsymbol{x}(2), \cdots, \boldsymbol{x}(T)$ of the set $X(t)$ by the K-means clustering algorithm with initial centers, and compute the centers and numbers of the constituent vectors for the clusters.

14. Increase time $t \leftarrow t + 1$ and return to Step 2.

3 Character Recognition

3.1 Preprocessing of Character Images

We applied the developed neural model to a character recognition task. We prepared images of three alphabet characters, "A", "C", "F", for several font styles and regarded the images of the same character as patterns belonging to the same category. The category formation was an incremental learning task, and thus the model required to acquire categories with sequential input of the images and simultaneously to recognize the inputs based on already-formed underdeveloped categories S^ℓ represented by a set of neural memories $\{\boldsymbol{w}^\ell, r^\ell, N^\ell, T^\ell\}$.

In this task, we prepared 15 images with 32 × 32

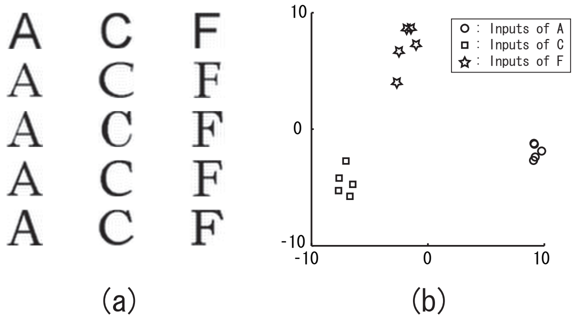

Figure 2: (a)Images of three alphabet characters, "A", "C", "F" for 5 font styles for learning. (b)Distribution of the first two principal components for all the 15 input images. The contributions of the two axes were 47% and 25% respectively, giving a cumulative contribution of 72%.

pixels and gray-scale (8-bit) for 5 font styles as shown Figure 2 (a). In order to reduce the computational cost, the size of the images is compressed into 22 × 22 pixels by 2-dimensional discrete cosine transformation (2-D DCT) method, and then let the compressed data be the input vectors $\boldsymbol{x} = [x_{1\text{x}1}, \cdots, x_{22\text{x}22}] \in \Re^{484}$ to the model.

Figure 2 (b) shows the distribution of the first two principal components for all the 15 inputs. Note that inputs of same characters exist in close proximity. In contrast, the clusters of each character separately exist. This implied that the inputs can be recognized and divided fundamentally.

3.2 Simulation results

The goal of this simulation were to form clusters corresponded to the proper categories. The order of the sequential inputs was decided randomly, and the parameters, $M_L = 1,\ \eta_1 = 1,\ \eta_2 = 3,\ \eta_3 = 1$, were set experimentally.

Figure 3 showed results of the category formation task. The model probably succeeded to form such suitable clusters corresponded to the proper categories as shown in Figure 3 (a) by using only one teach data for each character, not to mention the perfect one. The model, however, failed in the rare cases, for example, the typical failure case shown in Figure 3 (b). In this case, two clusters, $S^{F'}$ and $S^{F''}$, were formed as to the character F by accident. The unsuitable number of formed categories probably depended on values of the above parameters M_L, and $\eta_i, i \in \{1, 2, 3\}$.

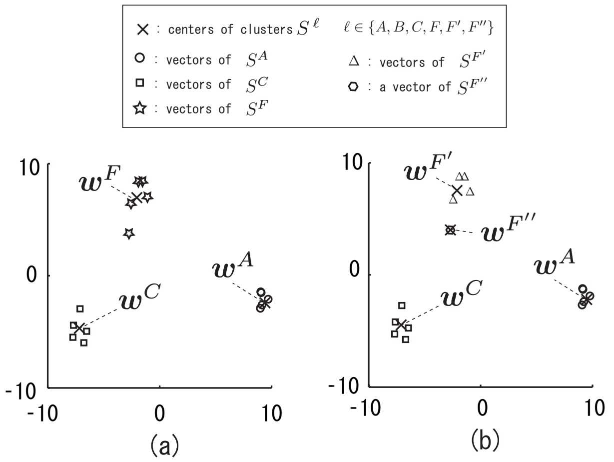

Figure 3: Distribution of the first two principal components for the constituent vectors $\boldsymbol{x}$ and center $\boldsymbol{w}$ of formed categories. (a) The success case. (b) A typical failure case.

4 Conclusion

In this paper, we have developed a new neural model for the category formation. It has been shown that the model can self-organize an appropriate set of clusters from character images with few teach data and recognize the character images adequately by the relation among an input vector and formed clusters. However, we have to determine the key parameters such as $M_L, \eta_i, i \in \{1, 2, 3\}$, and β by trial and error for unsupervised formation of unknown complex categories. The development of the determination method will be the future work of this study.

References

[1] Joe H. Ward (1963). Hierarchical Grouping to optimize an objective function. Journal of American Statistical Association, 58(301), 236-244.

[2] J. B. MacQueen (1967): "Some Methods for classification and Analysis of Multivariate Observations, Proceedings of 5-th Berkeley Symposium on Mathematical Statistics and Probability", Berkeley, University of California Press, 1:281-297

[3] Oxford Advanced Learner's Dictionary, Oxford University Press 2000.

The Eleventh International Symposium on Artificial Life and Robotics 2006 (AROB 11th'06),
B-con Plaza, Beppu, Oita, Japan, January 23-25, 2006

Simplified Geometric Models in Skill-Based Manipulation for Practical Use

Akira Nakamura*, Kosei Kitagaki*, and Takashi Suehiro*

Intelligent Systems Research Institute
National Institute of Advanced Industrial Science and Technology (AIST)
Central 2, 1-1-1 Umezono, Tsukuba, Ibaraki, 305-8568 Japan
a-nakamura@aist.go.jp, k.kitagaki@aist.go.jp, t.suehiro@aist.go.jp

Abstract

Dexterous manipulation plays an important role in working robots. Manipulator tasks such as assembly and disassembly can generally be divided into several motion primitives. We call these "skills" and explain how most manipulator tasks can be composed of skill sequences. Skills are also used to compensate for errors both in the geometric model and in manipulator motions. There are dispensable data in the shapes, positions and orientations of objects when achieving skill motions in a task. Therefore, we can simplify geometric models by considering the dispensable data in a skill motion. We call such simplified models "false models." This paper describes our definition of false models in planning and visual sensing and shows application to tasks performed by maintenance robots.

Key words: manipulation skill, geometric model, false model, planning, visual sensing

1. Introduction

For manipulation robots to be useful in several fields, it is necessary for a robot to achieve various tasks by using special techniques. By analyzing human motions in tasks such as assembly and disassembly, movements were found to consist of several significant motion primitives. We called these "skills" and showed that most of the tasks of the manipulator can be composed of sequences of skills [1]-[4]. That is, we demonstrated that robots can perform various human tasks by using the concept of skill. This skill level control is placed between the task level control and the servo level control in the hierarchy of manipulator control, and a programmer is able to describe a task program easily as a sequence of these skills, without taking account of the servo level control.

Skill technique is also used to compensate for errors both in the geometric model and in manipulator motion. The move-to-touch skill can cancel model errors in the direction of the transition. Similarly, the rotate-to-level skill and the rotate-to-insert skill can cancel model errors in the direction of rotation. Furthermore, we can derive simplified geometric models by allowing for a maximum error or margin in a task that is composed of skill motions. We call such robust geometric models "false models" and have shown their effectiveness as follows [5]. False models are constructed using only the data necessary in planning for manipulation and visual sensing for model matching. Since a smaller number of data with respect to shapes, positions and orientations of objects are needed, visual sensing is easier.

The topics of this paper are false models in skill-based manipulation for practical use. It is expected that maintenance robots for domestic appliances will greatly take an active part in the future (Fig. 1). Therefore, we take up maintenance robots that carry out repair, inspection and so on as practical use. The robots open and close the enclosure, and replace the parts (Fig. 2). Therefore, it is necessary for the robots to perform tasks related to a screw

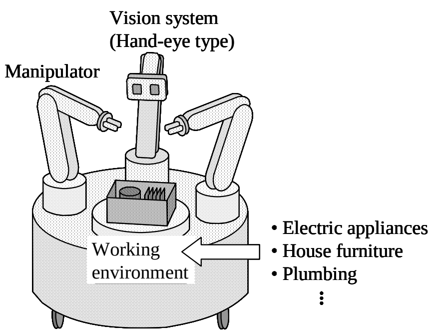

Fig. 1 Maintenance robot for domestic appliances

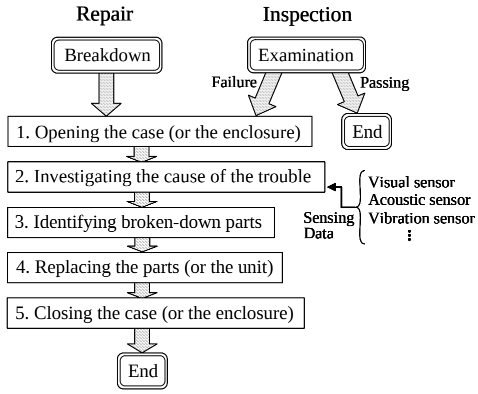

Fig. 2 Procedure of maintenance

and a bolt. In this paper, we will explain definition of false models and show false models throughout tasks such as loosening a screw and unfastening a bolt for practical use of our technique. Then, degrees of difficulty of executing a task can be derived using complexity of skill sequence and false models.

The next section explains manipulation skills and the composition of skill sequences. The processes of visual sensing, geometric modeling and execution of a task are explained for task and skill levels in section 3. False models in planning and visual sensing are defined in section 4. Our proposed method is demonstrated using two examples of tasks performed by maintenance robots in section 5.

2. Manipulation Skills

This section explains our concept of skills. See References [1]-[3] for more details.

In assembly and disassembly tasks, skills in which the contact states vary are particularly significant. In References [4], [6], we considered three skills, "move-to-touch," "rotate-to-level" and "rotate-to-insert," which play an important part in such tasks.

(1) Move-to-touch Skill

The move-to-touch skill is defined as the transition of a grasped object *P* in a constant direction that continues until contact with another object *Q* occurs (Fig. 3).

(2) Rotate-to-level Skill

This skill is defined as rotation around either a contact point or a contact edge to match the face of the grasped object *P* with the face of another object *Q* (Fig. 4).

(3) Rotate-to-insert Skill

This skill is this motion of rotating the object *P* obliquely into the hole in another object *Q* to insert it accurately (Fig. 5).

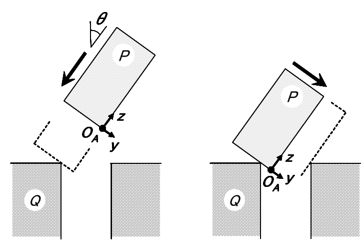

(a) Move-to-touch$_f$ skill (b) Move-to-touch$_c$ skill

Fig. 3 Move-to-touch skills

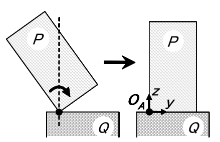

Fig. 4 Rotate-to-level skill

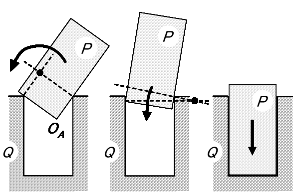

(a) (b) (c)

Fig. 5 Rotate-to-insert skill

A specific task is composed of sequences of skill primitives such as move-to-touch, rotate-to-level and rotate-to-insert skills. The skill sequences can be decided by several methods. We showed a method using variations of the number of contact points in skill primitives [4].

3. Process of Sensing, Planning and Execution

The procedures for sensing, modeling, planning and execution are shown in Fig. 6. In this scheme, the planning of the task level is first performed, and then the executions of the skill level are performed according to the sequences derived from the task planning. See References [5] for more details.

(Step 1) Task Level

At the task level, the skill sequence composing the task is decided. First, visual sensing of the working environment of the robot is performed using a vision system and modeling is done. Next, planning follows, and skill command sequences and the initial position and orientation of a grasped object are derived.

(Step 2) Skill Level

At the skill level, each skill in the command sequence $\{Skill_1, Skill_2, \ldots\}$ is executed successively. Before this sequence is performed, the transition of the grasped object *P* to the initial state is done. We represent the transition as $PreSkill_1$.

4. Concept of False Models

In planning for manipulation and visual sensing for model matching, it is not necessary to use geometric models that express real objects completely. By constructing geometric models using only the data necessary for planning and visual sensing, it is possible to facilitate these processes. We call such robust models "false models" *(FM)*. False models in planning and visual sensing are defined as follows.

(i) False models in planning (FM_p) are geometric models composed only of the necessary and minimum data for

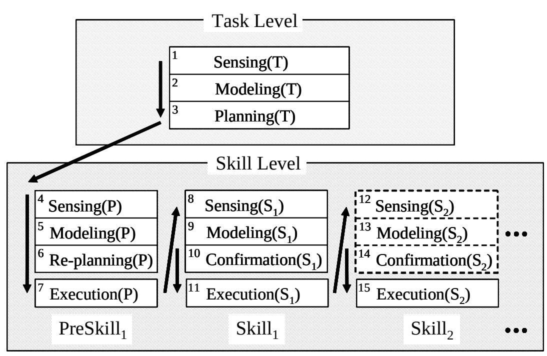

Fig. 6 Process flow

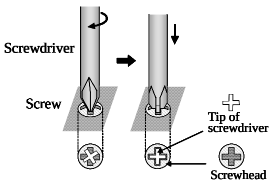

Fig. 7 Rotate-to-bite skill

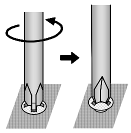

Fig. 8 Rotate-to-loosen skill

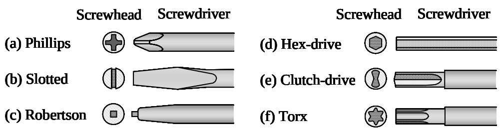

Fig. 9 Screwdrivers

shape, position and orientation to perform skill-based planning.

(ii) False models in visual sensing *(FM_v)* are geometric models composed only of the necessary and minimum data for shape, position and orientation to perform model matching. False models in planning *(FM_p)* are constructed from the data of false models in visual sensing *(FM_v)*.

5. Examples of False Models

We will also consider several skills related to the tasks in the examples mentioned later. In these skills, we use a cross-head screwdriver and screw according to tasks as examples.

(4) Rotate-to-bite Skill

This skill is a rotation around the axis of the screwdriver to fit the tip of the screwdriver into the flutes of the screw head (Fig. 7). This skill is performed with pushing force.

(5) Rotate-to-loosen Skill

This skill is defined as an initial rotation to loosen the fixed screw (Fig. 8). This is performed by matching the axes of rotation of a part and a tool. If these axes do not correspond, the tool is moved to the position before rotation is executed. In this paper, we assume that this skill also includes the transition to remove an error before rotating.

(6) Rotate-to-extract Skill

This skill is defined as revolutions to pull the screw out. The skill continues after rotate-to-loosen skill.

(7) Move-to-remove Skill

This skill is the transition to remove the screw.

5.1. Loosening a Screw Using a Screwdriver

We will consider the task of loosening a screw using a screwdriver [6]. Although there are many kinds of screws and screwdrivers as shown in Fig. 9 [7], we will consider this task by unifying the skill sequences in the following examples.

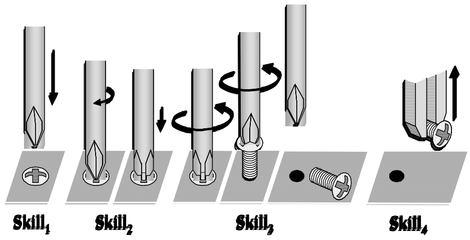

Fig. 10 Skill sequence of loosening with a cross-head screwdriver

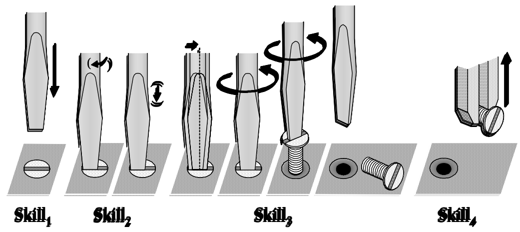

Fig. 11 Skill sequence of loosening with a slotted screwdriver

We assume that the task of loosening a screw using a screwdriver is composed of the following skills (Fig. 10 and Fig. 11); $Skill_1$: Move-to-touch skill, $Skill_2$: Rotate-to-bite skill, $Skill_3$: Rotate-to-(loosen ／ extract) skill (without interruption), $Skill_4$: Move-to-remove skill. False models are shown in Table 1; (a): case of a cross-head screw, (b): case of a slotted screw, (c): cases of Robertson, hex-drive, clutch-drive, torx screws.

5.2. Unfastening a Bolt Using a Wrench

Let us consider the task of unfastening a bolt using a wrench.

We assume that this task is composed of the following skills (Fig. 12); $Skill_1$: Move-to-touch skill, $Skill_2$: Rotate-to-insert skill, $Skill_3$: Rotate-to-loosen skill, $Skill_4$: Rotate-to-extract skill, $Skill_5$: Move-to-remove skill. False models are shown in Table 2. (r_V is $(3 \ln 3 \cdot m) / \pi$ (= about $1.049\ m$), which is derived by the least mean-square method.)

A skill sequence has been considered in each example. However, the following can be shown in general.

(i) The skill sequence that composes the task is not necessarily uniquely decided.

(ii) False model FM_p, FM_v in each skill primitive is not necessarily unique.

The degrees of difficulty of executing a task can be derived using complexity of skill sequence and false models. It is important to select simple skill sequence and simple false models for practical use.

6. Conclusions

We have shown false models for planning skill-based manipulation. It is possible to perform planning efficiently, since the false models are composed of only indispensable data. We also showed the application of the false models to tasks which are often performed by maintenance robots.

In the future, we will further study false models for various skill-based tasks and attempt to apply our method to real systems.

Acknowledgment

A part of this study was financially supported by the Budget for Nuclear Research of the Ministry of Education, Culture, Sports, Science and technology, based on the screening and counseling by the Atomic Energy Commission.

References

[1] Hasegawa T, Suehiro T, Ogasawara T, Matsui T, Kitagaki K, Takase K (1990), An integrated tele-robotics system with a geometric environment model and manipulation skills. In: Gotoh T, Kato I, Paul RP (eds) Proceedings of the IEEE International Workshop on Intelligent Robots and Systems (IROS '90), Tsuchiura, Japan, July 3-6, 1990, pp.335-341

[2] Suehiro T, Takase K (1990), Skill based manipulation system (in Japanese). J Robotics Soc Jpn 8:551-562

[3] Hasegawa T, Suehiro T, Takase K (1992), A model-based manipulation system with skill-based execution. IEEE Trans Robotics Autom 8(5):535-544

[4] Nakamura A, Ogasawara T, Suehiro T, Tsukune H (1996), Skill-based backprojection for fine motion planning. In: Asada M, Arai T, Kak A, Sandini G (eds) Proceedings of the IEEE/RSJ International Conference on Intelligent Robots and Systems (IROS '96), Osaka, Japan, Nov 4-8, 1996, pp.526-533

[5] Nakamura A, Ogasawara T, Kitagaki K, Suehiro T (2001), Using robust and simplified geometric models in skill-based manipulation. In: Tarn T J, Burdick J, Papanikolopoulos N (eds) Proceedings of the IEEE/RSJ International Conference on Intelligent Robots and Systems (IROS 2001), Hawaii, USA, Oct 29-Nov 3, 2001, pp.138-145

[6] Nakamura A, Ogasawara T, Suehiro T, Tsukune H (1998), Fine motion strategy in three-dimensional space using skill-based backprojection. Artificial Life and Robotics 2(3):134-137

[7] Jackson A and Day D (1992), Tools and how to use them. Wings books, New Jersey, p.221

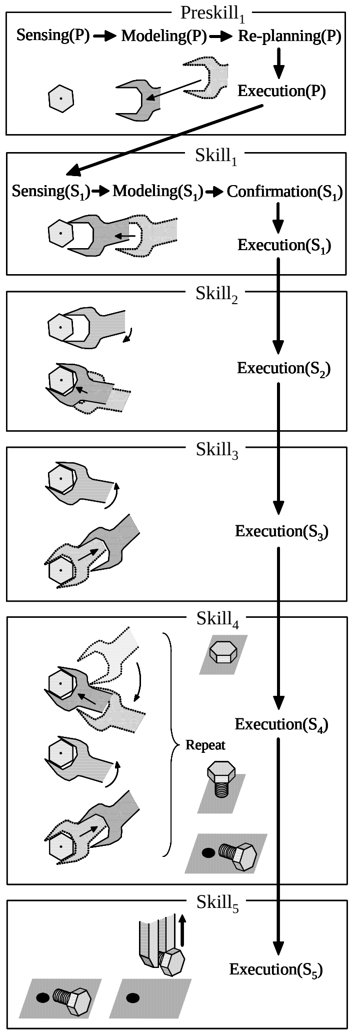

Fig. 12 Procedure of unfastening

Table 1 False models in loosening a screw using a screwdriver

			Skill$_1$ (Preskill$_1$)		Skill$_2$		Skill$_3$		Skill$_4$	
		RO	FM$_p$	FM$_v$	FM$_p$	FM$_v$	FM$_p$	FM$_v$	FM$_p$	FM$_v$
I	(a) Phillips				Not needed	Not needed	Not needed	Not needed		or
II	(b) Slotted				Not needed	Not needed				or
III	(c) Robertson				Not needed	Not needed	Not needed	Not needed		or

RO : Real objects
FM$_p$: False models for planning
FM$_v$: False models for visual sensing and model matching

Table 2 False models in unfastening a bolt using a wrench

		Skill$_1$ (Preskill$_1$)		Skill$_2$		Skill$_3$		Skill$_4$		Skill$_5$	
	RO	FM$_p$	FM$_v$	FM$_p$	FM$_v$	FM$_p$	FM$_v$	FM$_p$	FM$_v$	FM$_p$	FM$_v$
Bolt	M m	M m	r_v	Not needed	Not needed	Not needed	Not needed	Not needed	Not needed		or r_v

RO : Real objects
FM$_p$: False models for planning
FM$_v$: False models for visual sensing and model matching

The Eleventh International Symposium on Artificial Life and Robotics 2006 (AROB 11th'06),
B-con Plaza, Beppu, Oita, Japan, January 23-25, 2006

Constructing technique of state space with low dependence on sensor configurations for autonomous mobile robots

Takeshi SHIBUYA and Tomoki HAMAGAMI
Graduate School of Engineering
Yokohama National University
Yokohama, Japan

Abstract

The goal of this study is to develop heterogeneous mobile robots which realize cooperative actions to accomplish each task in an environment. An important part of achieving the goal is that the agent controlling the robots can realize suitable state space automatically. In particular, domestic robots equipped low-cost, discrete simple range sensors have difficulties of efficient learning of environment because the deviation of sensor configuration in each robot causes serious problem in which the learning policies can not be shared among them. To overcome this problem, a new technique of constructing effective state space with low dependence on sensor configurations is conducted. The technique consists of two parts: those are rectangle-model abstracting real environment and self-constructing universal state environment with SOM map. The simulation experiment results have shown the technique gives an agent controlling an intelligent wheelchair robot an ability of autonomous construction of environment.

1 Introduction

For realising ubiquitous network robots and constructing their society,the novel technique for autonomous mobile robot and agent becomes increasingly significant. In this future environment with the robots, various type of robots can cooperate and collaborate each other, then will emerge a new service for our welfare.

As one of the application of the service, we have studied an intelligent wheelchair (IWC)[1]. The IWC is defined as a domestic mobile robot which can explore the environment autonomously, observe the state space through sensors, and learn suitable behavior. In order to realize the functions, an agent controlling on IWC robot needs to acquire environmental information through sensors and to construct state space. However, domestic robots like the IWCs equipping low-cost, simple, and discrete range sensors have difficulty of efficient learning of environment[2].

The first difficulty is a dilemma of sensor orders in which how many sensor can be equipped and how many dimension of state space is required. If the sensors are equipped without restriction, the rapidly increasing computational cost, so called curse of order, will be raised by using high-order and precise environmental information. Otherwise, limited sensors will raise several aliasing state in an environment called perceptual aliasing.

Another difficulty is that the deviation of sensor configuration in each robot causes serious problems in which each learning policy can not be commonized among them. This problem prevents reusing of the learning results of a robot to other robots, and becomes a barrier of development of ubiquitous network robot.

In order to solve the problems, this study has an assumption that each robot has a different sensor configuration between them. Under this assumption, in order to realize efficient learning through the cooperative behavior of each robot, the communizing of internal state between them is significant technique.

The primary objective of this paper is to propose a simple and effective technique of partitioning state space for efficient learning independent of sensor specification and configuration.

2 Autonomous mobile robot platform: Intelligent wheelchair

We have been developing prototype of IWC which is named ACCoMo (intelligent wheelchair as autonomous, cooperative, and collaborative mobile robot)[1]. Appearance of an ACCoMo is shown in

Figure 1. The IWC has several range sensors (PSD: Position Sensitive Detector sensors) equipped around the frame of the platform wheelchair and moves with a direct drive servo motor in each wheel. An agent software observes environment as space of several dimensions with these sensors, and decide an action in each step, then controls these motors. The rule set of deciding an action from sensor inputs is called *policy*. The goal of the learning of agent is acquire a suitable policy through exploring in the environment. In our previous study, we have designed the ACCoMo as an intelligent mobile robot acquiring intelligent behavior with the reinforcement learning (RL); the neural network (NN) evolved by the genetic algorithm (GA) and their decision tree evolved by the genetic programming.

However, we have encountered some problems which have been caused by the deviation of sensor configuration (the number of sensors, the type of sensors) when the ACCoMo is applied in several environments. One example of the problems is that each agent recognizes a state of real environment as a different state because the accuracy and attachment positions of sensors are different among each IWC even though the IWCs have same sensors. The problem is a kind of *perceptual aliasing*[3] which is caused by a lack of sensor precisions. Although many approaches have been proposed to compensate for the problem, to realize sufficient sensor precisions is difficult problem under real environment. Another example is that the policy acquired by an agent through the experience with an IWC does not work in other IWCs which have different sensor configuration from it. These problems cause a serious problem in which a policy is limited to a specific hardware, and inefficiency of learning.

One possible method to have the policy in common among agents according to various IWC is that high accuracy and enough sensors are attached to identify the state of real environment. However, so many sensors can not be attached because IWC platform has a limitation of attachment positions. Furthermore, so many sensors lead so many space dimensions which cause fail of learning , so-called *curse of dimensionality*.

In order to solve these problems, following proposed techniques are combined. The first part models the environment as rectangles to abstract obstacles layout, which rectangles can be synthesized directly from sensor outputs by using dimension free algorithm for one thing.

Figure 1: Prototype of the Intelligent Wheelchair

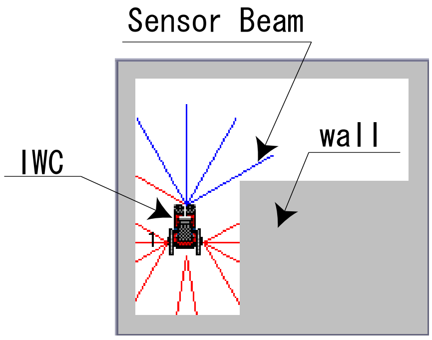

Figure 2: IWC simulator

3 Methodology

3.1 Rectangle model representing abstract environment

As shown in Figure 3 , i denotes range sensor number, $\hat{l}_i$ denotes the output of sensor i which means the measured distance between the sensor and sensed obstacle. $\hat{h}_i$ denotes the distance between the obstacle and the center of rotation of the robot. Each $\hat{h}_i$ called hazard vector which is recognized in the agent as abstract image of neighboring environment is calculated by geometric operation with these parameters in each step. Moreover, each $\hat{h}_i$s are classed in valid or invalid values with threshold. Where, the valid value means that the sensed obstacle is in the attention distance. Then, collecting adjacent valid vectors and surrounding them by rectangle as few number, these vectors are modeled by surrounding with suitable size rectangles. Figure 4 shows how the vectors are surrounded by the model. As shown in the figure, this model can work well to represent abstraction image of obstacles. This abstraction technique can enable an agent free from

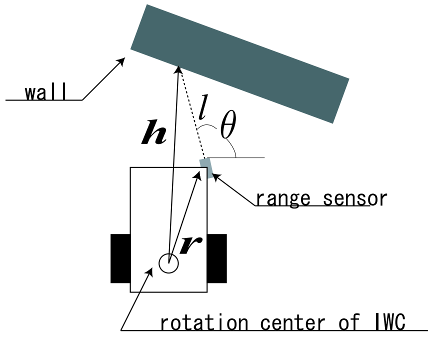

Figure 3: Parameters for geometric positioning between a robot and walls.

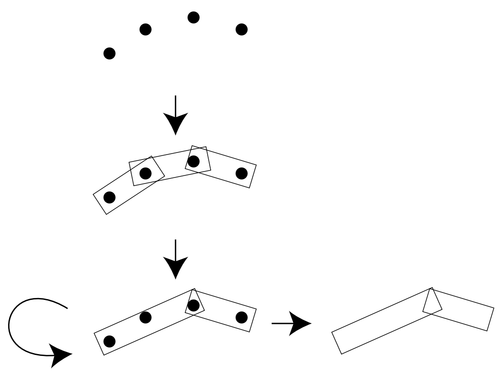

Figure 4: Methodology of making rectangle from hazard vector.

dependencies from various sensor configuration, how many sensors are equiped or how much precise sensors are required.

3.2 Constructing state space with self organization map

In order to construction state space with the rectangle model as mention above, this study applies image-based self organization technique: self organization map(SOM)[4].

First, a 2-D image which consists of rectangles generated by the model is synthesized. The image is a layout as if the agent looks down him/herself image from the overhead. During exploring the environment with acquiring various images, then clustering the image into some class by SOM, the agent can construct state space autonomously. Furthermore, in order to construct state space effectively, each image needs to be normalized for rotation. In particular, the central moment is applied.

3.3 The State of the arts

Proposed technique provides mapping a environmental information to the agent's state with low dependency on the sensor configuration. This enables agent to decide behavior using common state space among robots with different sensor configuration.

Then, this technique can represent the environment with some simple figures in the model.

This advantage realizes robustness for noises when the agent maps the environmental information to a state. Furthermore, state space constructed with our proposed technique has a topological structure.

This structure will be useful for effective learning because the group of states in which suitable action is similar is neighbor in each other in the map, that is the propagation of reinforcement value can be realized on the map.

4 Simulation Experiments and Results

Two simulation experiments are conducted to demonstrate the effectiveness of our proposed technique.

The purpose of the first experiment is to verify that the agent can construct state space through sensor outputs as the environmental information. Another experiment makes another agent evaluate the constructed state space, the agent which controls another IWC with different sensor configuration.

As simulation environment, an simple aisle shown in Figure 2 is explored. An agent that controls the simulated IWC behaves in the environment and constructs state space autonomously.

The agent acquires $\hat{h}_i$ as environmental information during random exploring. Then, the agent generates rectangle images from vector $\hat{h}$. Figure 5 shows the example of acquiring the environment information and modeling it.

The image is classified into a class on SOM map, and the map is reorganized when 200 images are obtained. Figure 6 shows the SOM map constructed state space in Figure 5. Each state shows typical obstacle alignment shown in Figure 5.

Figure 7 shows the mapping between environment positions and the states, where (a) is a mapping constructed by the agent which has 16 range-sensors, (b) is a observed state by the agent which has 12 range-sensors.

The results show that the state space which has constructed 16 sensors can be reused for the agent with another sensor configuration. Consequently, the proposed technique enables the agent to constructed generalized state space for autonomous learning.

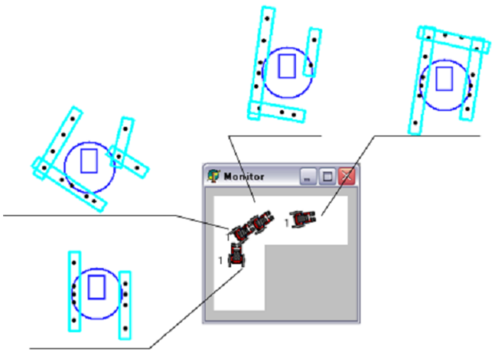

Figure 5: The example of acquiring the environmental information.

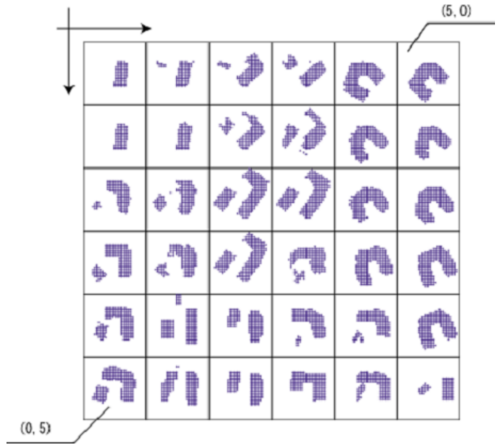

Figure 6: The SOM map constructed state space in Figure 2

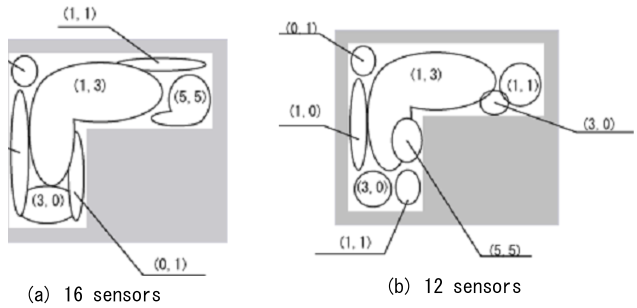

Figure 7: The mapping between environment positions and the states by agents with different sensor configuration. Each coordinate is corresponded to the one of the state of SOM map

5 Conclusion

A new constructing technique of state space with low dependence on sensor configurations for autonomous mobile robots is proposed. The advantage of the technique is that the state space can be constructed from simple, low precise sensors on domestic robots like IWC. It enables us to realize various application by using cooperative action within ubiquitous network robot. In future plan, we plan to conduct the technique to adapt effective reinforcement learning in real environment.

References

[1] T.Hamagami, H.Hirata, "Development of Intelligent Wheelchair Acquiring Autonomous, Cooperative, and Collaborative Behavior," Proc of IEEE International Conference on Systems, Man and Cybernetics, pp.3235-3530 (2004).

[2] T.Hamagami, H.Hirata, "State Space Partitioning and Clustering with Sensor Alignment for Autonomous Robots," Proc of IEEE International Conference on Systems, Man and Cybernetics, CD-ROM (2005).

[3] L.P.Kaelbling,M.L.Littman,A.P.Moore, "Reinforcement Learning: A Survey," Journal of Artificial Intelligence Research, Vol.4, pp.237–285, 1996.

[4] T.Kohonen,Self-Organizing Maps, Springer Verlag,2000.

Emergent Societies: An Advanced IT Support of Crisis Relief Missions

Peter Sapaty [1] Masanori Sugisaka [2] Robert Finkelstein [3] Jose Delgado-Frias [4] Nikolay Mirenkov [5]

[1] Institute of Mathematical Machines and Systems, National Academy of Sciences,
Glushkova Ave 42, 03187 Kiev, Ukraine, +380-44-5265023, +380-44-5266457 (fax)
sapaty@immsp.kiev.ua

[2] Department of Electrical and Electronic Engineering, Oita University
700 Oaza Dannoharu 870-1192 Japan, tel. 097-554-7831 fax. 097-554-7841
msugi@cc.oita-u.ac.jp

[3] Robotic Technology Inc., 11424 Palatine Drive, Potomac, Maryland 20854
301-983-4194 Voice, 301-983-3921 Fax
RobertFinkelstein@compuserve.com

[4] School of Electrical Engineering & Computer Science, Washington State University
Pullman, WA 99164-2752, Ph: (509)335-1156, Fax: (509)335-3818
jdelgado@eecs.wsu.edu

[5] University of Aizu, Aizu-Wakamatsu, Fukushima-ken 965-8580 Japan
+81-242-37-2500, +81-242-37-2528 (fax)
nikmir@u-aizu.ac.jp

Abstract

A novel distributed control ideology and technology will be described for management of advanced crisis relief missions. The approach is based on the installation of a universal "social" module in massively wearable electronic devices, like laptops and mobile phones, which can collectively interpret a spatial scenario language, exchanging high-level program code (waves), data, and control with other modules in parallel. This can dynamically integrate any scattered post-disaster human and technical resources into an operable distributed system capable of solving autonomously complex survivability, relief, and reconstruction problems.

Keywords: critical infrastructures, key resources, emergency management, emergent societies, crisis relief, information technologies, distributed control, WAVE-WP model, wearable electronic devices, mobile robotics.

1 Introduction

1.1 The Grim Big Picture

Millions of people are on the move, traffic jams everywhere. Houses destroyed, infrastructures gone, winds hundreds kilometers per hour, flooding and fires. No electricity, shortage of food and fuel, usual ties broken, businesses vanished, jobs lost. No central authorities or services, looting and lawlessness… This is becoming a familiar picture throughout the world, especially due to global warming and climate change. Katrina and Rita are recent very sad examples. Earthquakes are another disaster area, like the recent one in Pakistan, and the tsunami a year before. Manmade disasters caused by armed conflicts and terrorist attacks are effectively contributing to this black list too.

How to regain integrity, restore law and order, and assemble scattered resources for a collective survival? How to rebuild the damaged territory, revive the previous infrastructures or create new ones, and return to normal life?

In Fig.1, a symbolic picture of the post-disaster area, once representing an integral organism, is shown with the wreckage of living quarters, organizations and infrastructures, also separated and scattered individuals and their emergent grouping.

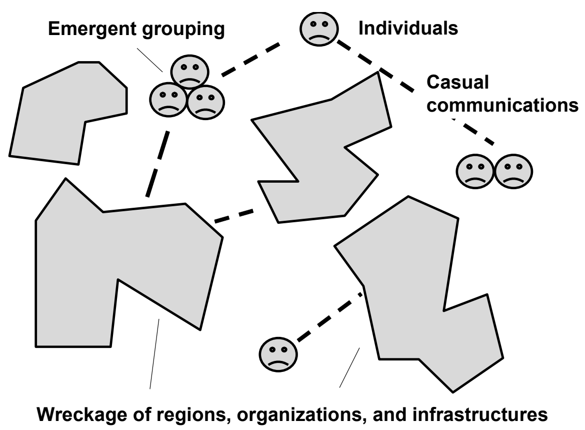

Figure 1. A grim picture of the disaster area.

Despite indiscriminate damages, the disaster area can still hold key human, technical, and natural resources, and its parts can still be able to communicate with each other (for example, if cellular towers, at least some of them, are still operating, and/or access to internet remains available). Radio communications, local however, can be helpful too, and some units in the area may have satellite phones. The electric grid power may still be available, and the same grid can potentially be used for data communications (such promising projects already exist). So there may be sufficient resources for self-survival and even self-recovery, especially with an external aid hurrying, but they are pretty much scattered and disorganized. Restoring *integrity and coordination* in the disaster area is becoming a primary goal.

1.2 Emergency Management

Emergency management [1], due to the increased world dynamics, is one of the hottest topic today. The emergency managers around the world are faced with new threats, new responsibilities, and new opportunities. It is widely believed [2] that the combination of novel technologies and data bases can allow law enforcement and intelligence investigators to identify potential terrorist plots, use a multitude of data bases that may contain hidden patterns of information about transactions needed to execute plots, and then mount preemptive strikes to stop their plans.

The National Response Plan [3] establishes a comprehensive all-hazards approach to enhance the ability to manage domestic incidents. The plan incorporates best practices and procedures from different incident management disciplines. Another prominent document, The National Infrastructure Protection Plan (NIPP) [4] provides a unifying structure for the integration of all critical infrastructures and key resources protection efforts into a single national program.

However the existing efforts are actually offering yet another infrastructures, to be built on the same principles as the existing ones, i.e. consisting of *specialized components* located in *certain places* and *communicating* with each other, with a good deal of *central control* over them. Due to this, they may inevitably be as (if not more) vulnerable to attacks and failures as other infrastructures, and may become a burden rather than savior.

Even in the relatively modest Katrina case, local infrastructures were indiscriminately fragmented and totally inoperable (while malicious ones thriving), and federal bodies showed clumsiness and inefficiency. The new global infrastructures outlined, like what we see in NIPP, may result in a similar performance in case of major disasters caused by hurricanes, earthquakes, or WMD attacks.

1.3 Towards New Emergency Management Approaches

We believe that the critical infrastructure protection, recovery, and relief ideologies and technologies should be based on quite different, *revolutionary rather than evolutionary*, principles, and they should evolve and operate in *other time-space dimensions* than the traditional infrastructures and forces that can harm them, in order to be incomparably superior and unaffected themselves in case of major crises.

A completely different approach is being developed of how to penetrate into any distributed and open systems and establish an overwhelming power over them (destruction of malicious infrastructures in these systems being an option). Any global or local scenario we want to implement over any area or system is formulated in a special *spatial control language*, which is interpreted cooperatively in a distributed system widely using *smart mobile program code* covering the system or its parts in parallel. This provides spatial *hologramlike* algorithms, which dynamically exist in between system components rather than inside them, thus being *totally unobservable and unreachable* by conventional means.

Actually, this work follows a sort of an *intelligent supervirus* ideology, with its potentially unlimited self-penetration and self-recovery possibilities. The approach can also setup, at runtime, any needed infrastructures over scattered post-disaster human or technical resources, and these infrastructures can evolve and freely migrate in both physical and virtual worlds, self-recovering after damages and preserving integrity and goal orientation.

This paper summarizes the technology called WAVE-WP that serves these purposes, outlines its main applications and possible implementation with the use of massively wearable devices. Examples of spatial programming of some exemplary crisis relief operations will be demonstrated too.

2 WAVE-WP Model and Technology

The distributed computation and control WAVE-WP (or World Processing) model and technology [5-7] are based on a higher-level language describing parallel distributed solutions in computer networks *as a single seamless spatial process* rather than traditional collection and interaction of parts (agents), while shifting these and other routines to an efficient automatic implementation. Communicating copies of the WAVE-WP language interpreter (WI) should be installed in most *sensitive points* of the system to be governed (like internet hosts, robots, troop carriers, dismounted soldiers, laptops, mobile phones, etc.).

Parallel spatial scenarios (or waves) written in the language can start from *any interpreter*, covering the network at runtime and cooperating with each other in the distributed space. The approach often provides *hundreds of times application code reduction* and simplification, allowing us to concentrate on efficient *global solutions* rather than implementation details.

Spreading via networked WIs, waves can create *dynamic knowledge infrastructures* arbitrarily distributed between the system components. Subsequently or simultaneously navigated by same or other waves, they can effectively support distributed databases, advanced command and control, global situation awareness, parallel inference, and autonomous decisions. It is convenient to operate in this seamless virtual world fully ignoring its physical distribution, whereas virtual networks can migrate (partially or as a whole) in physical networks while being processed.

Installed in advance in different components that may happen to be located in a disaster area, with possibilities of their communication using any remaining channels, WIs can convert the whole area (like the one shown in Fig. 1) into an *operable self-organized system*. The latter will be able to solve complex tasks on itself (see Fig.2), where high-level relief scenarios in WAVE-WP can start and evolve from any interpreter, *covering the whole system* or its needed parts at runtime, while establishing full control over it.

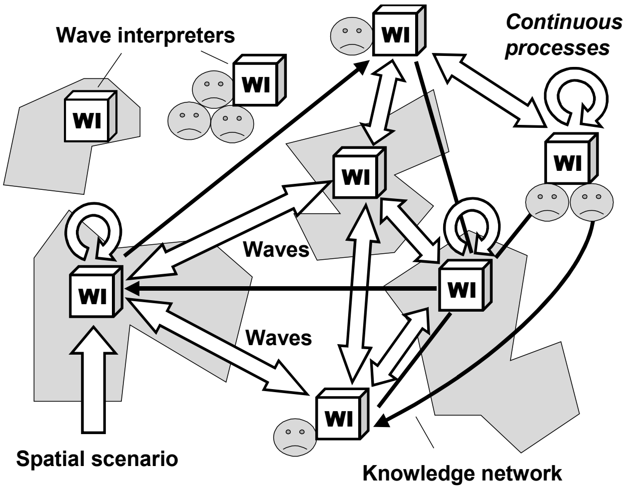

Figure 2. Converting the disaster area into an operable system.

3 The WAVE-WP Language

3.1 Language Basics

We are considering here only the top definition of the WAVE-WP language, shown in Fig. 3, with details in [5, 6].

wave	→	{ *advance* ; }
advance	→	{ *move* , }
move	→	{ *unit act* }
unit	→	*constant* | *variable* | [*rule*] (*wave*)
variable	→	*nodal* | *frontal* | *environmental*
rule	→	*forward-rule* | *echo-rule*
act	→	*fusion-act* | *flow-act* | *application*
constant	→	*information* | *physical-matter* | *program-code*

Figure 3. WAVE-WP language syntax.

Starting from a certain position, the program, or *wave*, navigates in physical or virtual space, with successive *advances* starting from positions reached by the previous advances. An advance may consist of *moves*, which can develop in parallel. Moves may be data processing and/or space propagation expressions of *units* separated by *acts*. A unit can represent a value directly, as *constant* or *variable*, or may be an arbitrary *wave in parentheses*, optionally prefixed by a *rule*. Variables may be: *nodal,* dynamically associated with space positions and shared by waves; *frontal,* moving in space with control; and *environmental*, accessing the navigated environment in points reached.

Rules being *forward rules*, coordinating spreading of waves or setting up special navigation contexts, or *echo rules* detailing the fusion and return of (remote) states and data. Acts classify as *fusion acts* producing new values from operands, *flow acts* moving data and control in space, and *application acts* activating alien or native procedures. Constants and variables may represent both *information* and *physical matter*; they may also represent *program code* to be created, processed or modified with a subsequent execution as waves, thus providing high programming flexibility in dynamic environments.

3.2 Spatial Interpretation

What follows from this language definition, is the *unwrapping and replication* of the recursive formulae, rather than traditional *reduction*, as shown in Fig. 4. The wave program *matches*, *conquers*, *floods*, *covers* the distributed physical or virtual world *in parallel*, establishing full control over the space. Each act is performed in the space *positions reached* on *local data* there, or on what is obtained and returned by other waves of the expression. The resultant value on any construct comprises *all values* obtained in the points of space reached by it. All constructs return *control states*, which are *merged* and *generalized* at higher levels with the use of *rules* for making hierarchical spatial decisions.

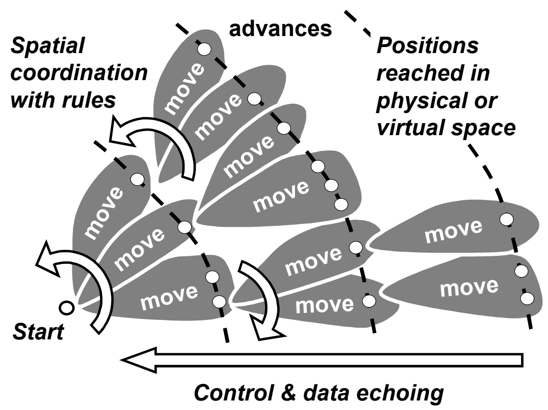

Figure 4. Spatial evolution of waves.

A number of successful implementations of this approach have been made in different countries, with public domain available on the internet [5]. The new, advanced version is currently being re-implemented and patented, with orientation on both software product and direct "wave chip".

4 Current and Prospective Applications

Let us mention some applications of this technology that may be directly or indirectly helpful for the advanced emergency management, with more details and other areas presented in [5-7].

Distributed Robotic Brain. WAVE-WP interpreters put on top of (and integrated with) the usual robotic functionality may effectively convert any group of robots into an integral spatial machine capable of doing complex jobs simultaneously and cooperatively. Individual robots may be of any type (from most advanced to primitive) devices, some can even fail at runtime, but the group as a whole may remain functional and goal-oriented.

Future Combat Systems. Installed in main components of FCS, WAVE-WP can provide global vision of the territory and overall situation awareness, despite limitations of individual sensors and control facilities. It optimizes fusion and distribution of scattered targets, provides flexible command and control, where the CC infrastructure may be adaptable at runtime.

Tracing Physical Objects. The technology enables an efficient chase of (aerial or ground) physical objects by self-navigating and replicating program agents following them via computer networks. The multiple mobile intelligence, migrating in computer networks, provides a new level of flexibility for various management systems. It may guide, for example, the destruction of unwanted objects after individual investigation of their routes and behavior.

Global Fighting of Network Intrusions. WAVE-WP interpreters installed in internet hosts and accessing usual management tools, can form a higher layer converting large volumes of raw data into the seamless distributed knowledge for global network analysis and optimization. The WI network can simultaneously discover and analyze viruses throughout the whole world, blocking their spread and inferring attack sources.

National and International Infrastructures. The technology can effectively support vital infrastructures of national and international scale, solving complex problems in them in parallel. These may relate to politics, economics, demographics, weather prediction, environmental pollution, postal service, transport, industrial goods flow, tracing international criminals, and air and space defense, with optimized solutions without central resources.

5 Using Massively Wearable Devices

Emergency management may be fundamentally assisted by the massively wearable individual data processing and communication devices, which are expected to remain with individuals under any circumstances. WIs, installed in them (this can be done without problems, taking into account the existing experience of implementation of the WAVE system on different platforms and compactness of the language interpreter) can make the whole societies, especially emergent ones in the disaster areas, to be programmable and controllable in the way required, despite the scattering of resources and limited communications.

Mobile phones, the undisputed leader among wearables, are expected to be the most common consumer electronics device on the planet [8]. By the end of 2009, some 2.6 billion mobiles will be in regular use around the world. Mobiles, for example, are catapulting rural Africa into the 21st century, making it the world's fastest-growing cellphone market [9]. They are enabling millions of people to skip a technological generation and bound straight from letter-writing to instant messaging. Asia is the next fastest-expanding market.

Many also use GPS, digital cameras, portable PCs along with mobile phones, and there already exist advanced products that combine all these and many other features within a single piece (including also Bluetooth, WiFi, phone radio and TV [10,11]). 3G, or third generation, brings broadband for mobiles too [12]. Also, the recently unveiled sub-$100 laptop design [13], with its internet wireless access and a hand crank for when there is no power supply, is expected to contribute drastically to the unprecedented electronic integration of the whole world.

We may assume that these devices (at least some of them) would remain able to communicate with each other during and after the disasters via the wireless networks, internet, radio or any other channels, and in the worst case even via humans (who, using voice, handwriting or gestures, can pass manually the needed code and data, with the return to an electronic WI level at the reception end).

6 Emergency Management Code Examples

We will consider here only elementary examples of spatial programming in WAVE-WP for some tasks that may relate to emergency management, with simplifications necessary for showing program code within the limited paper space.

6.1 Spatial Counting of All Casualties

Let us consider a fully distributed and parallel counting of the total number of casualties in the disaster area, on all affected regions, assuming for simplicity that only a single WI is available in each region or group of individuals (the interpreter-participant can be negotiated locally if more than one).

The following program can be applied from any available WI as an entry one, which can be away from the disaster area (say, located in a federal center) or can reside within the area, as a special or emergently selected body or individual. (Characters `#`, `_`, `?`, and `!` are serving, respectively, as hop, aggregation, external procedure call, and halt acts; whereas `grasp` and `repeat` being forward rules , and `sum` as an echo rule of the language.)

```
Farea = disasterarea;
USER = sum(
 direct # any _ Farea;
 repeat(
  grasp(Nmark == nil; Nmark = 1);
  ? casualtiesinfo ! done,
  any # Farea
 )
)
```

Within the identified `disasterarea`, assigned to and subsequently carried in frontal variable `Farea` (names of frontal variables must begin with `F`) the program first hops into `any` directly reachable units within the area. Then from all these units it repeatedly (in parallel to all reachable neighbors) navigates the area using `any` available local channels between the interpreters (manual communications are not excluded too). The program enters nodes only once, marking each with an individual nodal variable `Nmark` (which names should start with `N` in the language), grasping nodal resources for performing an indivisible check-assignment sequence.

This parallel spatial process forms a spanning tree covering (if communications permit) the whole disaster area via the reached WIs in it. In each WI reached by the waves, an external procedure `casualtiesinfo` (which can be performed manually, by humans or groups of them sharing the same WI) returns the number of detected casualties in this region. These collected numbers are then summed up in parallel in the tree nodes and moved up the tree in the global echo process, receiving finally the total number of casualties on the whole area, output to the `USER` owning the entry WI.

As can be seen, the whole disaster area had been dynamically converted into a parallel spatial machine capable of solving the problem in a fully distributed manner, without central computational resources, as shown in Fig. 5.

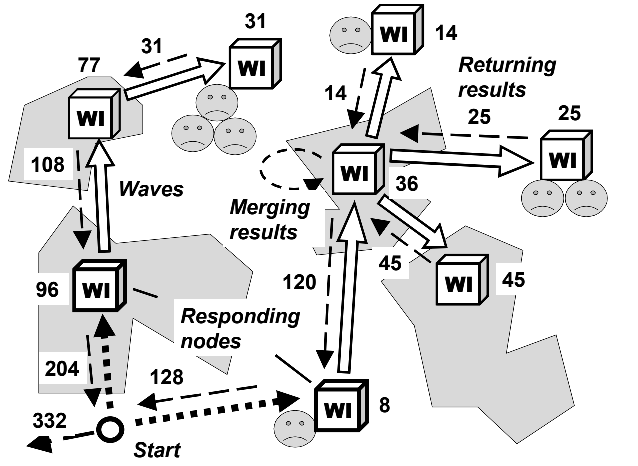

Figure 5. Spatial counting of the total number of casualties.

6.2 Relief Delivery to the Most Affected Region

If to use echo rule `max` instead of `sum` of the previous program, and also lift physical coordinates of the regions navigated (via environmental variable `WHERE` associated, say, with GPS devices), it is possible to get the final result on the disaster area as the following aggregated value. The first part of it will give the number of casualties of the most affected region, and the second one providing physical coordinates of this region (as measured from the related WI). The following program records this two-value result in the nodal variable `Nmax` associated with the entry node.

```
Farea = disasterarea;
Nmax = max(
 direct # any _ Farea;
 repeat(
  grasp(Nmark == nil; Nmark = 1);
  number ? casualties _ WHERE ! done,
  any # Farea
 )
)
```

Using the obtained first value in `Nmax`, it is easy to describe in WAVE-WP the assemblage of needed number of relief packages (storing all physical packages in frontal variable `Fsupply`). This can be succeeded by a direct movement into the physical location in space (by the second value in `Nmax`), distributing afterwards the relief packages between the suffered individuals (using external manned procedure `distribute`), as follows:

```
Fsupply = "reliefpackage" * Nmax : 1;
direct # Nmax : 2;
Fsupply ? distribute
```

In this program, `:` is an indexing act of the language, being superior to multiplication `*`, the latter working on physical matter at the left (`"reliefpackage"`) and information at the right (number of packages needed, same as number of casualties).

6.3 The Delivery to All Regions

It is easy to modify and merge into one the previous two programs in order to find casualty numbers separately on all affected regions, with corresponding coordinates of these regions, and then assemble the needed amount of goods for every region and forward all these to the proper destinations, with a subsequent manual distribution, as follows.

```
Farea = disasterarea;
Nall = (
 direct # any _ Farea;
 repeat(
  grasp(Nmark == nil; Nmark = 1);
   number ? casualties _ WHERE ! done,
   any # Farea
 )
);
Nall; N = VALUE;
Fsupply = "reliefpackage" * N : 1;
direct # N : 2;
Fsupply ? distribute
```

The needed number of packages will be delivered to all related destinations via the rotes available, which may happen to be complex, taking into account the remaining usable road infrastructures and peculiarities of the terrain. This delivery may be performed by manned vehicles or convoys, or by advanced unmanned mobile ground systems, like those described in [14], with omission of further details on this within this short paper. Any detailed delivery, including path finding and avoidance of obstacles, can be effectively represented in WAVE-WP, with related examples discussed in [5-7]. The general picture of parallel physical delivery to the needed destinations may look like the one shown in Fig. 6.

In a similar way, it is easy to describe and execute much more complex scenarios of self-organization of affected regions, including massive evacuation, forming new emergency infrastructures, fighting malicious post-disaster infrastructures (like looting), movement and spreading of communicating relief teams, cooperating with the self-organizing disaster area, and so on. As WAVE-WP technology allows us to set up a formal description of what was considered as predominantly human before, the relief scenarios can be effectively performed by any combination of manned and unmanned units, with humans and robots sharing responsibility for the key decisions in different space-time locations.

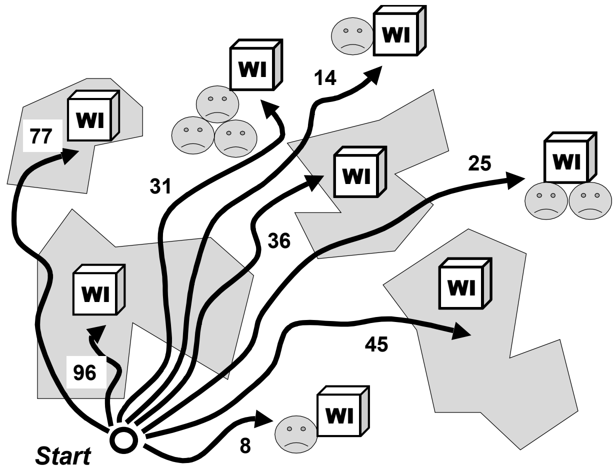

Figure 6. Delivery of the needed goods to affected regions.

7 Conclusions

A ubiquitous, supervirus-like approach for emergency management and critical infrastructure and key resources protection has been proposed, based on the universal distributed processing and control technology WAVE-WP. Effectively operating in a different space-time continuum than the existing systems or forces that can harm them, it can dynamically set up an *unlimited power over the distributed worlds*, being itself much less vulnerable to damages than other systems.

The compactness and simplicity of relief scenarios in the WAVE-WP language allow us to program them on the fly, reacting timely on rapidly changing situations. The technology can effectively convert scattered human and technical resources into *highly operable distributed systems* capable of organizing relief missions in other systems or autonomously solving complex self-survivability and self-recovery problems.

The implementation of the technology can be easily done on any existing software or hardware platform, and the corresponding *"social" module*, as a software or hardware wave interpreter, can be readily installed in many wearable devices, and first of all mobile phones and handheld and laptop PCs.

Massive use of *advanced mobile robotics* in the future relief missions, and its integration with manned components under the unified command and control, can be drastically simplified by this flexible control model too.

References

[1] J. A. Bullock; G. D. Haddow, "The future of emergency management", Journal of Emergency Management, Winter 2004, Volume 2, Number 1, pages 19-24, http://www.pnpco.com/.

[2] S. Nunn, "Preventing the Next Terrorist Attack: The Theory and Practice of Homeland Security Information Systems", Journal of Homeland Security and Emergency Management, ISSN 1547-7355 Vol. 2 (2005), Iss. 3, http://www.bepress.com/jhsem/.

[3] National Response Plan, US Department of Homeland Security, December 2004, 95p., http://www.dhs.gov/interweb/assetlibrary/NRPbaseplan.pdf

[4] Draft National Infrastructure Protection Plan, US Department of Homeland Security, Office of the Assistant Secretary for Infrastructure Protection, November 2, 2005, 2005, 161p., www.dhs.gov (unpublished yet).

[5] P. S. Sapaty, Mobile Processing in Distributed and Open Environments, John Wiley & Sons, ISBN: 0471195723, New York, February 1999, 436 p.

[6] P. S. Sapaty, Ruling Distributed Dynamic Worlds, John Wiley & Sons, ISBN 0-471-65575-9, New York, May 2005, 256p.

[7] P. Sapaty, M. Sugisaka, N. Mirenkov, M. Osano, R. Finkelstein, "Grasping the Distributed Entirety", Proc. Tenth International Symposium on Artificial Life and Robotics (AROB 10th), Beppu, Japan, February 4-6, 2005.

[8] "Mobiles Head for Sales Milestone", BBC NEWS, Technology, 19 July 2005, http://news.bbc.co.uk/.

[9] S. LaFraniere, "Cellphones Catapult Rural Africa to 21st Century", The New York Times, August 25, 2005, www.NYTimes.com.

[10] "Samsung i730", http://www.vzwshop.com/samsungi730info/.

[11] "GPS Mobile Phone", http://www.easydevices.co.uk/pcp/Mobile_Phone.html.

[12] "3G Industry Optimistic for 2006", BBC NEWS, Technology, Friday, 25 November 2005, http://news.bbc.co.uk/.

[13] "Sub-$100 Laptop Design Unveiled", BBC NEWS, Technology, 29 September 2005, http://news.bbc.co.uk/.

[1] Joint Robotics Program, Master Plan FY 2005, US Department of Defense, http://www.jointrobotics.com/activities_new/masterplan.shtml.

The Eleventh International Symposium on Artificial Life and Robotics 2006 (AROB 11th'06),
B-con Plaza, Beppu, Oita, Japan, January 23-25, 2006

Cognitive Contour Detection for Negative Filtering

Zoltán Petres [1,2] Barna Reskó [1,2] Hideki Hashimoto [1]

[1] Institute of Industrial Science, The University of Tokyo
[2] Computer and Automation Research Institute, Hungarian Academy of Sciences

Abstract

This paper presents a cognitive model based on the mammalian visual cortex, which is able to perform image contouring by the means of extracting contour line segments as abstract objects. The line segments are organized by their orientation and length in a three-dimensional array, the Visual Feature Array, which allows image processing and transformations along new dimensions, such as orientation or length. Negative Filtering is the process when the Visual Feature Array is used to reconstruct the original contour image by redrawing the stored line segments, thus removing noise from the image. The presented approach is strongly based on cognitive psychology and neurobiology. The processing model has a strictly parallel architecture in order to mimic its biological inspirator, and to allow constant time processing on a parallel computational hardware.

1 Introduction

In order to show why cognitive models can give the necessary boost in computation, consider the example where a person has to decide whether there is a cat or something else on an image. Such a task is impossible for a computer to perform today, yet a human can do it reliably in half a second or less. This result is very interesting when considering that the "processing time" of a typical neuron is in the range of milliseconds while that of a logic gate of a modern silicon-based computer is in the range of nanoseconds. The computational capacity of the brain thus has to lie in its special architecture and particular information representation and processing, rather than in the speed of its processing elements. It is our belief that in order to step beyond the borders of today's computer systems' architectures the basic way of information representation and processing has to be changed. For new ideas we turn to existing cognitive systems in biological architectures to study them, because they already bear the solutions that we are seeking for. Hubel and Wiesel first described the visual system [1], and suggested that iso-orientation domains are packed in essentially linear parallel stripes, which Hubel [2] subsequently referred to as the "ice-cube" model. The model of Hubel, and later V1 models [3] suggest that cells in the visual cortex are organized in a 3D structure, where a location on the visual field and an input stimulus preference (*e.g.* orientation preference) can be assigned to each cell. A cognitive system is implemented in a biological neural network, where simple units of computation are connected in a very complex structure. Our research goal is to turn the cognitive information processing system into engineering models which can later be organized into a cognitive psychology inspired model running on a biology related computational architecture.

This paper introduces a model strongly based on the cognitive functions of the visual cortex for image contour detection. The model was elaborated on the analogy of the mammalian visual system. Each phase from the retina to the visual cortex is represented in the model by imitating the biological structures and cognitive functions in order to perform similar image transformations and operations. In classical image processing algorithms, such as edge detection using a sobel filter, both the input and the output are matrices containing pixels. These algorithms thus represent a pixel-to-pixel transformation between two matrices. Similarly to the neural networks in the cerebral cortex, the model proposed in this paper implements a pixel-to-feature transformation, where *feature* refers to a more abstract visual object, such as a line segment of a certain length and orientation, or a line crossing. The result of the transformation is thus a feature-level abstraction of the input image. The abstract features can also be re-transformed into the pixel level by a feature-to-pixel inverse transformation, allowing a visual representation of the feature-level abstraction. The re-transformation of features into pixels will exclude noise from the result, thus it can be used as a filtering technique, described later in this paper. The presented model can be applied in many practical applications. One of them is the Intelligent Space, detailed in [4].

The rest of the paper is organized as follows. Section 2 describes the proposed architecture of the model for high speed image processing. Section 3 is devoted to the model evaluation and experimental results. Finally, Section 4 concludes the paper.

2 Cognitive model of the visual pathway

A scene projected to the retina becomes a two-dimensional image, which is transferred to the brain for further processing. Such an image is composed of image features like regions of a certain color and texture, their boundaries as segments of different orientation and length. The image features make part of more abstract features like simple shapes, curves, circles.

The main goal of the present model is to *understand* the basic primitives of an image, on the analogy of the cerebral cortex as a complex cognitive system. The *understanding* of a feature in biology is defined as the firing of a set of neurons, which tend to fire when that particular feature is presented on the input as a stimulus. In the proposed model a feature is represented by the activation of a single neuron instead of a set, and it is considered *understood* when the corresponding neuron fires. The neurons of the understood features can project their outputs to higher and lower levels in the neural hierarchy. Projecting the output further up allows the neurons in higher levels to understand more abstract features as the composition of lower level features. On the other hand, a neuron that projects its output to lower levels in the neural hierarchy can be considered as an *expectation* from above, and will help the low-level neurons to understand the lower level features.

This paper concentrates on how primitive image features are understood, and how they can be used as an expectation in lower levels.

The proposed model in this paper receives an image on its input, which is immediately subjected to an edge detection filter. This filter is based on the receptive field characteristics of the retinal ganglion cells. In the small region of the visual field which is centered around the position of the ganglion cell the afferent connections have a relatively high positive weight, while in the surrounding regions the synapse weights are inhibitory. The receptive field is modeled with a 3×3 matrix M_1 with higher positive input weight values in the middle and small negative values in the surrounding regions.

$$M_1 = \begin{pmatrix} -\frac{1}{8} & -\frac{1}{8} & -\frac{1}{8} \\ -\frac{1}{8} & 1 & -\frac{1}{8} \\ -\frac{1}{8} & -\frac{1}{8} & -\frac{1}{8} \end{pmatrix} \tag{1}$$

The output pattern of the cells with input weights of M_1 will be an edge detected image of the original image. It is to note that at this level of neural processing the image features understood (or represented by neural activation) are pixels of an edge detected image, edge elements.

Going further on the visual pathway we find that the receptive fields of the neurons in LGN are also circular like those in the retina. This suggests that the LGN does not add any extra image processing functionality to the visual pathway. It rather has an important role in modulating the input to the cortex by attention, but the exact functionality is still a subject of research.

For the above reason we consider the retinal and LGN-neurons as primary edge detectors, and their overall functionality in the aspects of image processing is covered by the M_1 matrix in the model. The input from the cells of such receptive fields project into the visual cortex, where further image processing takes place.

The image representation in the visual cortex is retinotopic, which means that neighboring regions of the visual field are projected to neighboring regions in the cortex. The neurons of such a region are tuned to respond to a variety of input stimuli described by different receptive fields characteristics. This implies that a vast variety of receptive fields belong to one small region of the visual cortex, and thus to a small region of the visual field. The variety of receptive fields representing different visual features (*e.g.* line orientations) can be organized along new dimensions.

After an edge detection discussed above, an edge detected image is available in the matrix I where

$$I \in \mathbb{R}^{n \times m}, \tag{2}$$

n and m representing the image dimensions.

According to the visual cortex, several different features can be extracted from the edge detected image I. The extraction of the features begins with those having the largest number of pixels, *i.e.* the longest lines. When the first feature is extracted from the edge detected image I, the feature pixels are removed from I, resulting a new matrix that we refer to as $I^{(1)}$. After extracting and removing the k^{th} feature from $I^{(k-1)}$ the matrix $I^{(k)}$ remains. Using this notation the original edge detected image is denoted $I^{(0)}$. This step is necessary to ensure that only one of many possible similar features is extracted from the edge detected image $I^{(0)}$. The k^{th} feature is removed from $I^{(k-1)}$ and added to a two-dimensional matrix F_k, such that

$$\forall i, j, k : (F_k)_{i,j} \in \{0; 1\}, \tag{3}$$

and the value $(F_k)_{i,j}$ indicates if any pixel of the detected feature k is present in the edge detected image at the position $I_{i,j}^{(k-1)}$.

It is important to note that the features to extract are ordered by the number of pixels they contain in order to ensure that

$$\mathcal{F}_k \supseteq \mathcal{F}_l, k < l, \tag{4}$$

where $\mathcal{F}_k$ is the set of pixels contained by the k^{th} feature. Since there are several image features to be extracted from the image, there will be a matrix F for each of these features. We define the three-dimensional array with the F matrices overlapped along a third dimension as follows:

$$\mathcal{V} \in \mathbb{R}^{n \times m \times r} \tag{5}$$

For the three-dimensional matrix $\mathcal{V}$ we introduce the notion of *Visual Feature Array* or *VFA*, where r represents the total number of visual features. By construction, the element $\mathcal{V}_{i,j,k}$ of the VFA represents if an edge pixel $I_{i,j}^{(k-1)}$ belongs to the k^{th} visual feature.

In the VFA each element corresponds to the response of a cortical neuron tuned to a certain feature in a certain location. In the VFA the features are organized along a third dimension, orthogonal to the other two dimensions. Such a system of visual features yields a 3-dimensional neural array model of the primary visual cortex.

In the visual cortex there are neurons tuned to a whole variety of visual features. The present model includes the orientation selective cortical cells with end-inhibition characteristics. Each feature in the VFA can thus be described by an orientation angle and an optimal length. The possible orientations are equally distributed with a specified angular resolution. The angles represented in the VFA are defined with the angle α and angular resolution θ, such that

$$\alpha \in [0 \ldots \pi], \alpha = k \cdot \theta, k \in \mathbb{N}, \tag{6}$$

and thus the matrix elements $(F_{\alpha=\pi/5})_{i,j}$ will be values of 1 where an edge line segment with an orientation close to $\pi/5$ is found in the edge detected image at $I_{i,j}$.

The end-inhibition property of the neurons is also formalized in the model. An optimal length l of a neuron is a length to which it gives a maximal response. The different lengths are distributed between the shortest length and the longest length, and their number is h. Since the line lengths are measured in pixels, the shortest possible line segment is 3 pixel long. The maximal length can be chosen taking the requirements of the input image and the available computational capacity into consideration. Normally this value is between 20 and 30 pixels.

Given an angular resolution of θ and the number of different length values h, the number of possible visual features r can be assessed as follows:

$$r = \frac{\pi}{\theta} \cdot h. \tag{7}$$

A visual feature k is thus characterized by two values, an orientation α and length l. The matrix elements $(F_k)_{i,j}$ will thus have a value of 1 if the edge pixel on the edge detected image $I_{i,j}$ belongs a feature with the characteristics of k.

In the visual cortex there are receptive field characteristics that actually define the visual feature the particular neuron is responsive to. In order to extract the desired features from an edge detected image, for each feature k a mask matrix R_k obtained from a corresponding receptive field has to be defined. In the proposed model the visual features are extracted by a convolution of the edge detected image and a matrix R_k. In the present case the receptive fields are modeled by binary matrices instead of matrices with real values. These matrices contain the sought feature as it may appear on the binary edge detected image.

Consider a grouping transformation on the VFA, which simply groups all the layers into one final layer containing all the extracted features. This transformation equals sending the output of the VFA neurons *down* in the neural hierarchy, and can be used to reconstruct an image by redrawing the detected visual features. This reconstruction will include only the features that were extracted from the original image. This implies that the noise (pixels not considered as the part of any feature) will not be present in the reconstructed edge detected image.

We have introduced the notion of *negative filtering* as the process of understanding image primitives and reconstructing the image from them. The notion arose from the fact that on contrary to a filtering process, the above defined process adds useful information to the image, instead of subtracting it.

3 Model evaluation, results

The proposed model has two important advantages compared to classical solutions. By virtue of the simple but numerous computational units (neurons) that work parallel on the solution, the model can perform the proper activation of the VFA and the negative filtering in constant time. This, however requires a parallel hardware implementation of the model.

In our case only a computer simulation of the model was available, which allowed to evaluate the functionalities of the model, but not its performance.

The input test image used to evaluate the model is shown in Figure 1a. This image is subjected to a primary edge detection according to the model. The result is a binary image of edge elements, with white dots representing high-contrast points on the original image. This edge-detected image is shown in Figure 1b.

The edge-detected image in our model corresponds to the image that is projected to the visual cortex. In the model, this image is used as the input to the neurons in the VFA. In the present implementation 5 different line lengths were used with the possible orientations to calculate the values of the VFA. These lengths were 3, 5, 9, 17, and 33 pixels.

The VFA layers of two different orientations and the

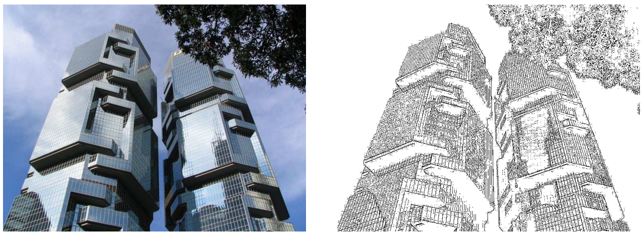

(a) (b)

Figure 1: Original test image (a) and the result of the primary edge detection (b)

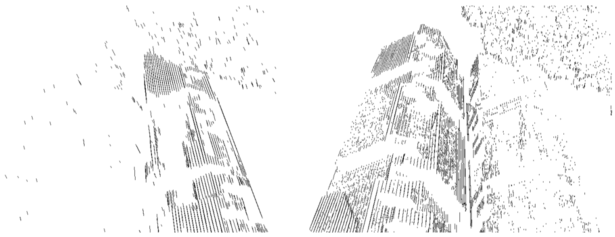

(a) (b)

(c) (d)

Figure 2: The segments of two different orientations (a)–(b) and the segments of two different line lengths (c)–(d).

segments of two different line lengths are shown in Figure 2.

The union of the VFA layers yields the top-down reconstruction of the edge detected image from the detected line segments. The reconstruction will exclude the edge elements detected as noise noise, which was not recognized as a visual feature (a line segment of certain length and orientation).

4 Conclusion

A model for intelligent contour detection was presented in this paper. The basic structure and functionality of the model is based on the mammalian primary visual cortex, which can perform edge contour extraction on an edge detected image. The extracted contour pixels are clustered into visual features which are more abstract representations of the visual information. The features are organized into a three-dimensional orthogonal array (the VFA) according to their properties. The extracted features are used in two ways: further abstraction or top-down image reconstruction. This latest adds an augmented information space to the original edge detected image, which we refer to as negative filtering.

The VFA containing different features can be submitted to grouping transformations, that merge layers of the VFA according to certain rules, such as similar line length or orientation. The grouping transformations are necessary for further transformations, such as line crossing and vertex detection.

The model and especially the VFA has been designed to operate in a fully parallel manner. In the present system binary array values were used for the sake of easy hardware implementation. An FPGA or other parallel implementation of the model yields a constant time contour detection and visual feature extraction.

References

[1] D. H. Hubel and T. N. Wiesel. Receptive fields, binocular interaction and functional architecture in the cat's visual cortex. *J. Physiology*, 160:106–154, 1962.

[2] D. Hubel. *Eye, Brain and Vision*. W.H. Freeman & Company, 1995.

[3] A. Grinvald, D. Malonek, A. Shmuel, D. Glaser, I. Vanzetta, E. Shtoyerman, D. Shoham, and A. Arieli. *Imaging of Neuronal Activity*. Cold Spring Harbor Laboratory, 1999.

[4] Zoltán Petres, Barna Reskó, Péter Baranyi, and Hideki Hashimoto. Biology Inspired Intelligent Contouring Vision Device in Intelligent Space. In *Proceedings of the 6th International Symposium on Advanced Intelligent Systems (ISIS 2005)*, pages 865–870, Yeosu, Korea, Sept 28–Oct 1 2005.

Multistable Perception Model by Multilayered Bidirectional Associative Memory

Kazuyuki Kitamura†, Teijiro Isokawa†, Haruhiko Nishimura‡,
Naotake Kamiura†, and Nobuyuki Matsui†

†Graduate School of Engineering, University of Hyogo,
2167 Shosha, Himeji, Hyogo, 671-2201, JAPAN
‡Graduate School of Applied Informatics, University of Hyogo,
1-3-3, Chuo-ku, Kobe, 650-0044, JAPAN

Abstract

Multistable perception phenomena in seeing ambiguous figures have been observed and their distribution curves of alternation durations are well-known as the Gamma distribution through psychophysical experiments. It is important and interesting to investigate its describable model for clarifying brain functions. In this paper, we propose a model based on the multilayered bidirectional associative memories and report good simulation results on the distribution of alternation durations.

1 Introduction

Multistable perception is perception in which two (or more) interpretations of the same ambiguous image alternate spontaneously while an observer looks at them. Three kinds of this phenomenon, figure-ground, perspective (depth), and semantic ambiguities are well known (As an overview, for example, see[1]). In this circumstance the external stimulus is kept constant, but perception undergoes involuntary and random-like change. The measurements have been quantified in psychophysical experiments and it has become evident that the frequency of the time intervals spent on each percept is approximately Gamma distributed[2, 3].

Figure-ground reversal is an automatic process which happens even if there is no premise knowledge about the object form. However, the others are processes depending on conceptual knowledge. This indicates a possibility that each perceptual conflict happens similarly in the individual (different) place within the large region from the initial vision process to the higher cognitive reasoning process. Therefore, existence of some neural mechanism common to all is suggested.

In this work, we propose a perception model of ambiguous patterns based on the multilayered bidirectional associative memory, aiming at the explanation of the above facts. This model has two main features, one of which is a bottom-up and top down information (signal) flow between the lower layers and higher ones by expansion of the bidirectional associative memory scheme[4]. The other is a checking process of the conformity of the bidirectional signals. According to the input signal from the lower level, the higher level feeds back a suitable candidate among the stored templates to the lower level. If the lower area cannot get a good match, the process starts over again and lasts until a suitable interpretation is found. We analyze temporal behaviors of the system under this framework through computer simulations.

2 Multistable Perception and brain mechanism

2.1 Multistable Perception

Multistable perception (or so-called perceptual alternation) is a phenomenon occurred in our brains in which there are plural candidates of interpretations whereas retinal input is not changed, and only one interpretation of them arises in our brains at a time. Interpretations are autonomously exchanged over time and the timing of exchanges is known to be random. This phenomenon usually occurs when we see ambiguous figures, such as the Necker-cube in Fig. 1. We have two interpretations on this cube. From psychophysical experiments, the distribution of the perceptual durations can be obtained. It is known that this distribution follows well the Gamma distribution defined by

$$f(x) = \frac{1}{a^b\Gamma(b)}x^{b-1}\exp(-x/a) \qquad (1)$$

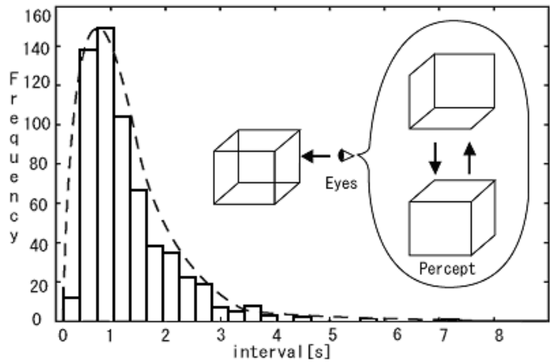

Figure 1: Frequency distribution of the duration of the Necker cube for a subject

In Fig. 1, we also show a typical example of the distribution of the perceptual duration by seeing Necker-cube and its corresponding Gamma distribution.

2.2 Brain Mechanisms for Multistable Perception

The mechanism for multistable perceptions should be functional in the wide range of cerebral cortex beyond primary visual cortex, since there exists several levels (kinds) of multistable perceptions, such as figure-ground, perspective, and semantic ambiguities. The cortico-cortical fibers connect among areas on cortex and their circuitry is uniform over it, without their functions or locations. Information processing in neocortex is performed by the interactions among areas through fibers.

In recognizing an object in a scenery, this type of interactions between higher-order and lower-order cortex areas could be also used. Higher-order cortex receives signals from lower cortex, based on these signals it retrieves the pattern from stored templates that is most feasible for them, and transmits this pattern as a feedback to lower cortex. An interpretation for the object is achieved by making a match of information from the higher and lower cortex. Ping-pong style of matching process based on interactions in the brain [5] is expected to serve as a candidate for the general (common) neural mechanism of multistable perception. The brain mechanism proposed in [6], in which the top-down prediction from inferotemporal cortex confronts with the bottom-up recognition from primary visual cortex, also corresponds to this matching process.

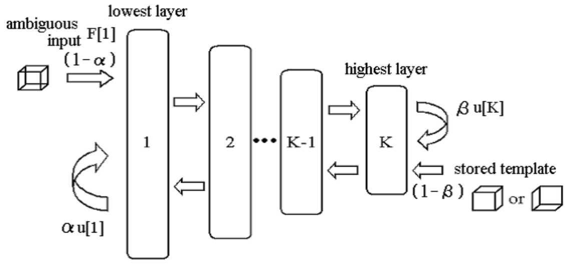

Figure 2: The structure of the multilayered BAM module for multistable perception

3 Multilayered Bidirectional Associative Memory

Bidirectional Associative Memory (BAM) network is a kind of associative memory with capability of retrieving input patterns from target patterns, as well as target patterns from input patterns[4]. It consists of two layers of neurons, U-layer and V-layer, connected through weights. The outputs of neurons in the U-layer are input to those in the V-layer through weight $\boldsymbol{w}$ and the outputs in the V-layer make feedback to the U-layer through $\boldsymbol{w}^T$, so the information flows between these layers repeatedly. The states of network converges to the input pattern and its corresponding target pattern by updating the states of neurons.

In this paper, we introduce a multilayered BAM module, which allows more layers in the BAM network. Figure 2 shows the structure of multiple BAM module, the information flows from lowest layer to highest layer and vice versa. The lowest layer of the network corresponds to visual receptor that accepts ambiguous inputs from outside, and The highest layer represents interpretations for the input signals.

The connection weight between the i-th neuron in the k-th layer and the j-th neuron in the $k+1$-th layer, w_{ij}, is defined as

$$w[k]_{ij} = \sum_{l=1}^{L} u[k]_i^l \cdot u[k+1]_j^l. \tag{2}$$

where $u[k]_i^l$ is the state of the i-th neuron in the k-th layer, given the l-th pattern.

The state of a neuron is updated by

$$u[k+1]_i = \begin{cases} f(x[k]_i) & (\text{with } p = g(x[k]_i)) \\ -f(x[k]_i) & (\text{with } 1-p) \end{cases} \tag{3}$$

where

$$f(x[k]_i) \quad = \quad \tanh(x[k]_i/\epsilon),$$

$$g(x[k]_i) = \frac{1}{1+\exp(-|x[k]_i/T)},$$
$$x[k]_i = \frac{1}{m}\sum_{j=1}^{m} w[k]_{ji} \cdot u[k]_j.$$

At the lowest layer and the highest layer of the network, the ambiguous input and the candidate of interpretations is fed respectively by these equations:

$$u[1]_i(t+1) = \alpha u[1]_i(t) + (1-\alpha)F[1]_i \quad (4)$$
$$u[K]_i(t+1) = \beta u[K]_i(t) + (1-\beta)u[K]_i^l \quad (5)$$

where α and β are called loop-input rates in the lowest layer and the highest layer respectively. $F[1]$ represents ambiguous input signal, which has intermediate states between $u[1]^1$ and $u[1]^2$. When the states of the highest layer are changed by Eq.(5), $u[K]^1$ or $u[K]^2$ is chosen as a new interpretation $u[K]$ according to the current interpretation of the network. The initial interpretation (at the first application of Eq.(5)) is set to the one that is more resemblant to $u[K]^1$ or $u[K]^2$. The interpretation is not changed until the counter exceeds a certain value (called upper-bound of disagreement, L_{upper}). This counter increments by one whenever the interpretation and the states in the highest layer are different.

We prepare the patterns that contain the same number of 1's and -1's and their inverse for the stored templates for each layer. The template patterns for the k-th layer is represented by

$$u[k]^1 = \{\quad 1,\cdots,1 \quad -1,\cdots,-1 \quad\},$$
$$u[k]^2 = \{\quad -1,\cdots,-1 \quad 1,\cdots,1 \quad\}.$$

For the measurement of interpretation represented at the highest layer, we introduce an overlap value $M(t)$ as

$$M(t) = \frac{1}{N}\left(\sum_{i=1}^{N} u[K]_i(t)\cdot u[K]_i^1\right) \quad (6)$$

where N is the number of neurons in the highest(K-th) layer.

4 Simulation Results

4.1 Experimental Setup

We explore the behaviors of our BAM module by the computer simulations. An BAM module with 4 layers whose number of neurons in all the layers is 4, i.e., 4-4-4-4 network, is applied. We employ $\epsilon = 10^{-10}$ and $T = 0.10$ in Eq.(3) in the simulations.

We run multilayered BAM modules for acquiring 10,000 durations in interpreting the pattern #1 ($u[K]^1$). The input pattern $F[1]$ at the lowest layer is always set to the intermediate pattern between two stored pattern, i.e., $F[1] = \{1,\cdots,1\}$, and initial interpretation at the highest layer of the network is determined by information from lower layers. The interpretation is changed to another one when the number of disagreements at the highest layer reaches the upper-bound of disagreements, and at the same time we get one duration of this interpretation.

We introduce Kolmogorov-Smirnov test with 0.05 of significant level for determining whether these durations follow the Gamma distribution. The parameters of Gamma distribution, a and b, are calculated by

$$a = \sigma/\mu, \quad b = \mu/a,$$

where σ and μ are variance and average of the duration data, respectively. The maximum difference between the duration data and the Gamma distribution with the parameters a and b is defined as

$$D_n = \max_x |F(x) - S_n(x)|$$

where $F(x)$ and $S_n(x)$ are cumulative frequency functions of Gamma distribution and the duration data, respectively. The critical value at 0.05 of significant level, $D_n^{0.05}$, is given by

$$D_n^{0.05} = 1.358/\sqrt{n}.$$

When $D_n < D_n^{0.05}$, the duration data is regarded as following a given Gamma distribution.

4.2 Results

First we show an example of temporal behavior of the network as the transition of $M(t)$ at the highest layer in Fig. 3. In this simulation, the upper bound of disagreement L_{upper} is 40, $\alpha = 0.1$ and $\beta = 0.2$, are used for the parameters. The durations for an interpretation are different each other. From these durations, we get frequencies and a Gamma distribution that is most fitted to them, as shown in Fig. 4.

We perform K-S tests with respect to the results for various β and L_{upper} parameters, in order to check whether the durations from our model follow the Gamma and normal distribution. Table 1 shows the number of acceptance by K-S test, where the number of trials is 10 for each parameter and $\alpha = 0.1$. The numbers without brackets in this table indicate the number of acceptance for Gamma distribution and the

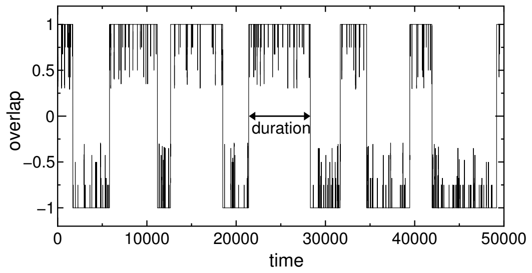

Figure 3: Temporal behavior of the highest layer's state under ambiguous input

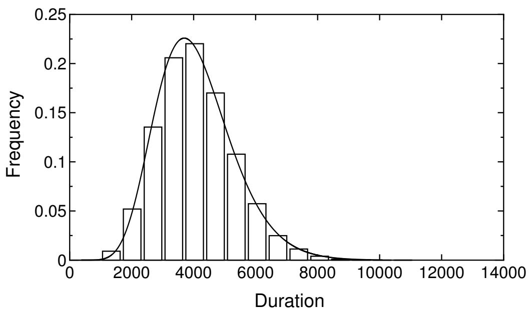

Figure 4: Frequencies of duration data (bar) and a Gamma distribution that is most fitted (solid line)

number with brackets show those for normal distribution. It is found that the distribution of durations follow the Gamma distribution, rather than the normal distribution.

5 Conclusion

We have proposed a model scheme for representing multistable perception in the visual system. Our model can represent interactions between the lower and higher cortical area in the brain by introducing a multilayered associative memory and its information flow. From the simulation results, the durations from our model well follows Gamma distributions that is one of characteristics in multistable perception, thus our model can represent the temporal structure for multistable perception.

In the future researches, we further explore the agreement with the cortical architecture and brain-like computation. Moreover, a new finding was recently reported that a shape-defining parameter of Gamma distribution fitted to time intervals data takes a quantal and natural number [7]. We are now proceeding to investigate our model for this result.

Table 1: The number of acceptance by K-S test for Gamma (without brackets) and normal (with brackets) distributions

	β		
Lupper	0.1	0.2	0.3
10	0 (0)	0 (0)	0 (0)
20	1 (0)	2 (0)	0 (0)
30	1 (0)	3 (0)	2 (0)
40	3 (0)	4 (0)	4 (0)
50	3 (0)	9 (0)	7 (0)
60	5 (0)	4 (0)	7 (0)
70	10 (0)	10 (0)	8 (0)
80	8 (0)	8 (0)	5 (0)
90	9 (0)	9 (0)	10 (0)
100	8 (0)	9 (0)	10 (0)
110	10 (0)	6 (0)	8 (0)
120	9 (0)	9 (0)	9 (0)

References

[1] Attneave F (1971), "Multistability in perception," *Scientific American*, vol. 225, pp. 62–71.

[2] Borsellino A, Marco AD, Allazatta A, Rinsei S, Bartolini B (1972) "Reversal time distribution in the perception of visual ambiguous stimuli", *Kybernetik*, vol.10, pp.139–144.

[3] Borsellino A, Carlini F, Riani M, Tuccio MT, Marco AD, Penengo P, Trabucco A (1982), "Effects of visual angle on perspective reversal for ambiguous patterns", *Perception*, vol. 11, pp. 263–273.

[4] Kosko B (1988), "Bidirectional Associative Memory", *IEEE Transaction on System, Man, and Cybernetics*, vol. 18, No. 1, pp. 49–60.

[5] Mumford D (1992), "On the computational architecture of the neocortex II.the role of cortico-cortical loops", *Biological Cybernetics*, vol. 66, pp. 241–251.

[6] Koerner E, Matsumoto G (2002), "Cortical Architecture and Self-Referential Control for Brain-like Processing in Artificial Neural Systems", *IEEE Engineering in Medicine and Biology Magazine*, vol. 21, No. 5, pp. 121–133.

[7] Murata T, Matsui N, Miyamoto S, Kakita Y, Yanagida T (2003), "Discrete stochastic process underlying perceptual rivalry", *NeuroReport*, vol. 14, No. 10, pp. 1347–1352.

The Eleventh International Symposium on Artificial Life and Robotics 2006 (AROB 11th'06),
B-con Plaza, Beppu, Oita, Japan, January 23-25, 2006

Comparative Study on Fuzzy and Non-Fuzzy Cost-Sensitive Classification Systems

T. Nakashima, Y. Yokota, H. Ishibuchi
Graduate School of Engineering
Osaka Prefecture University
Gakuen-cho 1-1, Sakai, Osaka 599-8531, Japan
{nakashi, hisaoi}@cs.osakafu-u.ac.jp
yokota@ci.cs.osakafu-u.ac.jp

G. Schaefer
School of Computing and Informatics
Nottingham Trent University
Nottingham, U.K.
Gerald.Schaefer@ntu.ac.uk

Abstract

In this paper we compare the performance of fuzzy and non-fuzzy classification problems. We particularly focus on the case where the cost of misclassification/rejection is considered as the performance measure of classification systems. Computational experiments show the comparative results of these classification systems on real-world pattern classification problems.

1 Introduction

Various methods have been proposed for pattern classification systems [1]. In many cases the classification rate is considered as the performance measure of classification systems. In this paper, we consider the situation where the cost of misclassification/rejection is necessary. Through the computational experiments we examine the performance of cost-sensitive fuzzy classification systems proposed in [2] comparing with non-fuzzy cost-sensitive classification systems.

2 Pattern Classification Problems with Cost

Let us assume that our pattern classification problem is an n-dimensional problem with C classes and m given training patterns $\mathbf{x}_p, p = 1, 2, \ldots, m$. Without loss of generality each attribute of the given training patterns is normalized into a unit interval $[0, 1]$. That is, the pattern space is an n-dimensional unit hypercube $[0, 1]^n$. In this paper we consider a situation where a cost of misclassification/rejection is associated with each training pattern. That is, the task in our pattern classification problems in this paper is to minimize the cost of misclassification/rejection as well as to minimize the number of misclassifed patterns. Let $w_p, p = 1, 2, \ldots, m$ be the cost of the p-th training pattern. We define the cost of misclassification/rejection caused by a classification system S as follows:

$$Cost(S) = \sum_{p=1}^{m} cost(\mathbf{x}_p, S), \tag{1}$$

where

$$cost(\mathbf{x}_p, S) = \begin{cases} 0, & \text{if } \mathbf{x}_p \text{ is correctly classified,} \\ w_p, & \text{otherwise.} \end{cases} \tag{2}$$

3 Cost-Sensitive Fuzzy Classification System

This section describes the generation of fuzzy if-then rules from given training patterns. Our fuzzy rule-based classification system consists of N fuzzy if-then rules each of which has the following form:

$$R_j : \text{ If } x_1 \text{ is } A_{j1} \text{ and } \ldots \text{ and } x_n \text{ is } A_{jn} \text{ then } C_j \text{ with } CF_j, \tag{3}$$

for $j = 1, \ldots, N$ where A_{jn} is an antecedent fuzzy set, C_j is a consequent class, and CF_j is the grade of certainty. There are two steps in the generation of fuzzy if-then rules: specification of the antecedent part and determination of the consequent class C_j and the grade of certainty CF_j. The antecedent part of fuzzy if-then rules is specified manually. Then the consequent part (i.e., consequent class and the grade of certainty) is determined from the given training patterns.

3.1 Fuzzy Rule Generation

Let us assume that m training patterns $\mathbf{x}_p = (x_{p1}, \ldots, x_{pn})$, $p = 1, \ldots, m$, are given for an n-dimensional C-class pattern classification problem. We also assume that a weight w_p, $p = 1, \ldots, m$, is assigned to each training pattern a priori. The consequent class C_j and the grade of certainty CF_j of the if-then rule are determined in the following manner:

Step 1: Calculate $\beta_{\text{Class } h}(j)$ for Class h as

$$\beta_{\text{Class } h}(j) = \sum_{\mathbf{x}_p \in \text{Class } h} \mu_j(\mathbf{x}_p) \cdot w_p, \tag{4}$$

where

$$\mu_j(\mathbf{x}_p) = \mu_{j1}(x_{p1}) \cdot \ldots \cdot \mu_{jn}(x_{pn}), \tag{5}$$

and $\mu_{jn}(\cdot)$ is the membership function of the fuzzy set A_{jn}.

Step 2: Find Class $\hat{h}$ that has the maximum value of $\beta_{\text{Class } h}(j)$:

$$\beta_{\text{Class } \hat{h}}(j) = \max_{1 \leq k \leq C} \{\beta_{\text{Class } k}(j)\}. \tag{6}$$

We note that this fuzzy rule generation method can also be applied to the standard pattern classification problems where there are no pattern weights. In this case, the class and the grade of certainty are determined from training patterns by specifying a pattern weight as $w_p = 1.0$ for $p = 1, \ldots, m$.

If two or more classes take the maximum value, the consequent class C_j of the rule R_j cannot be determined uniquely. In this case, specify C_j as $C_j = \phi$. If a single class $\hat{h}$ takes the maximum value, let C_j be Class $\hat{h}$. The grade of certainty CF_j is determined as

$$CF_j = \frac{\beta_{\text{Class } \hat{h}}(j) - \bar{\beta}}{\sum_h \beta_{\text{Class } h}(j)} \tag{7}$$

with

$$\bar{\beta} = \frac{\sum_{h \neq \hat{h}} \beta_{\text{Class } h}(j)}{C - 1}. \tag{8}$$

3.2 Fuzzy Reasoning

Using the rule generation procedure outlined above we can generate N fuzzy if-then rules as in (3). After both the consequent class C_j and the grade of certainty CF_j are determined for all N rules, a new pattern $\mathbf{x} = (x_1, \ldots, x_n)$ can be classified by the following procedure:

Step 1: Calculate $\alpha_{\text{Class } h}(\mathbf{x})$ for Class h, $j = 1, \ldots, C$, as

$$\alpha_{\text{Class } h}(\mathbf{x}) = \max\{\mu_j(\mathbf{x}) \cdot CF_j | C_j = h\}, \tag{9}$$

Step 2: Find Class h' that has the maximum value of $\alpha_{\text{Class } h}(\mathbf{x})$:

$$\alpha_{\text{Class } h'}(\mathbf{x}) = \max_{1 \leq k \leq C} \{\alpha_{\text{Class } k}(\mathbf{x})\}. \tag{10}$$

If two or more classes take the maximum value, then the classification of $\mathbf{x}$ is rejected (i.e. $\mathbf{x}$ is left as an unclassifiable pattern), otherwise assign $\mathbf{x}$ to Class h'.

4 Cost-Sensitive Non-Fuzzy Classification Systems

We also examined the performance of non-fuzzy classification methods such as neural network and nearest neighbor classification. Both the two classification methods are modified so that they can handle training patterns with misclassification/rejection costs.

4.1 Neural Network Classification

Neural network classification systems are one of the most well-known systems. We convert common neural network classification systems into cost-sensitive ones. Let us assume that a neural network classification system has n input units, N_h hidden units, and N_o output units. We also assume that an output vector $\mathbf{o} = (o_1, \ldots, o_{N_o})$ is obtained by the neural network classification system from an input pattern $\mathbf{x} = (x_1, \ldots, x_n)$. The input pattern is classified as Class $\hat{i}$ if and only if the following equation holds:

$$o_{\hat{i}} > o_k, \quad \text{for } \forall k, \ k \neq \hat{i}, \tag{11}$$

For the learning of the weights of neural network classification systems the error-backpropagation algorithm is normally employed in which the following error function is used to calculate the amount of weight adjustment:

$$E_p = \frac{1}{2} \sum_{k=1}^{N_o} (o_k - t_{pk})^2, \tag{12}$$

where $\mathbf{t}_p = (t_{p1}, \ldots, t_{pN_o})$, $p = 1, \ldots, m$ is the target signal for the p-th training pattern and is defined as follows:

$$t_{pk} = \begin{cases} 1, & \text{if the class of } \mathbf{x}_p \text{ is } k, \\ 0, & \text{otherwise.} \end{cases} \tag{13}$$

We construct cost-sensitive neural network classification systems by modifying the error function as follows:

$$E_p = \frac{1}{2} w_p \sum_{k=1}^{N_o} (o_k - t_{pk})^2, \quad (14)$$

where w_p is the cost of misclassification/rejection for $\mathbf{x}_p$. The amount of weight adjustment is calculated by using the modified error function in (14).

4.2 Nearest Neighbor Classification

We use 1-NN where an n-dimensional unknown pattern $\mathbf{x}$ is classified as the class of its nearest neighbor training pattern $\mathbf{x}_{\hat{p}}$. Euclidean distance is used to determine the nearest neighbor training pattern as follows:

$$d(\mathbf{x}, \mathbf{x}_{\hat{p}}) = \min\{d(\mathbf{x}, \mathbf{x}_p)\}, \quad (15)$$

$$d(\mathbf{x}, \mathbf{x}_p) = \sqrt{\sum_{i=1}^{n} (x_i - x_{pi})^2}, \quad (16)$$

where $\mathbf{x}_p$, $p = 1, \ldots, m$, is the p-th training pattern and $d(\mathbf{x}, \mathbf{x}_p)$ is a distance measure between $\mathbf{x}$ and $\mathbf{x}_p$. We also consider a modified version of the 1-NN where the weight of training patterns is used in the determination of the nearest neighbor training patterns. In the modified 1-NN we use a modified distance measure given by (15):

$$d'(\mathbf{x}, \mathbf{x}_p) = \frac{d(\mathbf{x}, \mathbf{x}_p)}{w_p}, \quad (17)$$

where w_p is the weight of the p-th training pattern. From (17) we can see that those training patterns with large weight have smaller distance measure than the case of Euclidean distance. On the other hand, the modified distance becomes larger than the Euclidean distance when the weight of a training pattern is small (less than 1).

5 Computational Experiments

We compare the performance of the three cost-sensitive classification methods: fuzzy rule-based systems, neural network classification systems, and nearest neighbor classification systems.

5.1 Data Sets

In the experiments in this paper we use nine data sets to evaluate the performance of the three cost-sensitive classification systems. We show the data sets in Table 1.

Table 1: Data sets.

Data set	# of attributes	# of classes
Breast cancer	9	2
Haberman	3	2
Sonar	60	2
Balance scale	4	3
CMC	9	3
Glass	9	7
Hayes roth	4	3
Iris	4	3
Wine	13	3

Since the original data sets do not have weights associated with the training patterns, we temporarily assign them for our experiments. For two-class pattern classification problems (i.e., Breast cancer, Haberman, Sonar), we consider two weight assignment schemes. The first scheme is called Class-1-focused scheme where the cost of training pattern $\mathbf{x}_p$, $p = 1, \ldots, m$ is specified as $w_p = 1.0$ if $\mathbf{x}_p$ belongs to Class 1 and $w_p = 0.5$ otherwise. On the other hand, we specify the cost as $w_p = 1.0$ for Class 2 training patterns and $w_p = 0.5$ otherwise in the second weight assignment scheme called Class-2-focused scheme.

For pattern classification problems with more than two classes, we assign the cost of misclassification/rejection of training patterns by the degree of class overlap between different classes. We specify the weight of training patterns as follows:

$$w_p = \frac{N_p^{\text{same}}}{N_{\text{size}}}, \quad (18)$$

where N_{size} is the number of selected neighboring patterns and N_p^{same} is the number of training patterns from the same class as $\mathbf{x}_p$ in the N_{size} selected patterns.

In the experiments the 10-fold cross validation technique is used to examine the performance of classification systems on test data. In 10-fold cross validation data sets are partitioned into ten disjoint subsets. Nine subsets out of the ten were used as training data and the other subset is used as test data. This procedure is iterated until all the ten subsets have seen as test data. In the computer simulation in this subsection we performed the 10-fold cross validation 100 times. The average results (both classification results and costs) over the 100 10-fold cross validations are then calculated. We also performed one-side t-test to examine the difference between every pair of classification methods.

5.2 Experimental Results

Tables 2 and 3 show the results of the experiments for two-class and multiclass problems. The costs of misclassification/rejection in (1) obtained by the three classification methods are shown in these tables.

Table 2: Results for two-class problems.

Class-1-focused Data set	Fuzzy	Neural	1-NN
Breast cancer	2.17	8.01	1.74
Haberman	4.15	8.03	5.53
Sonar	4.44	4.85	4.54
Class-2-focused Data set	**Fuzzy**	**Neural**	**1-NN**
Breast cancer	1.76	1.44	1.94
Haberman	7.05	4.05	8.12
Sonar	4.68	5.55	4.15

Table 3: Results for multi-class problems.

Data set	Fuzzy	Neural	1-NN
Balance scale	4.09	2.01	0.99
CMC	22.86	39.24	25.08
Glass	1.98	5.82	1.64
Iris	0.61	9.31	0.23
Hayes roth	1.72	2.40	2.31
Wine	0.71	11.44	0.23

Then we performed one-side t-test for every pair of the three classification methods. The results of the t-test are shown in Tables 4 and 5. We only show the comparison between fuzzy and non-fuzzy classification methods (i.e., fuzzy-neural and fuzzy-1-NN).

Table 4: Results of t-test for two-class problems.

Class-1-focused Data set	Fuzzy $\succ$ Neural	Fuzzy $\succ$ 1-NN
Breast cancer	×	○
Haberman	○	○
Sonar	○	–
Class-2-focused Data set	**Fuzzy $\succ$ Neural**	**Fuzzy $\succ$ 1-NN**
Breast cancer	×	–
Haberman	×	○
Sonar	○	×

Table 5: Results of t-test for multi-class problems.

Data set	Fuzzy $\succ$ Neural	Fuzzy $\succ$ 1-NN
Balance scale	×	×
CMC	○	○
Glass	○	×
Iris	○	×
Hayes roth	○	○
Wine	○	×

From Tables 4 and 5 we can see that the fuzzy classification systems are better than the neural network classifiation systems for almost all data sets. For the comparison between the fuzzy and the 1-NN classification systems, we can say that the fuzzy classification systems are better than the 1-NN classification systems for two-class problems while it is not the case for multi-class problems.

6 Conclusions

In this paper, we compare the performance of three cost-sensitive classification systems: fuzzy classification systems, neural network classification systems, and 1-NN classification systems. We particularly focused on the comparison between fuzzy and non-fuzzy classification systems, that is, comparison between fuzzy and neural network classification systems, and between fuzzy and 1-NN classification systems. The results of the computational experiments showed that the fuzzy classification systems are better than the neural network classification systems. We also showed that the fuzzy classification systems are better than the 1-NN classification systems for two-class problems while the 1-NN classification systems are better than fuzzy classification systems for multi-class problems. Further research is necessary to investigate the reason of these results.

References

[1] R. O. Duda, P. E. Hart, and D. G. Stork, *Pattern classification*, John Wiley & Sons, 2001.

[2] T. Nakashima, Y. Yokota, H. Ishibuchi, and A. Bargiela, "Effect of Data Weighting Methods on the Performance of Fuzzy Classification Systems," *Proc. of 2005 NAFIPS*, pp. 216-221, Michigan, USA, 2005.

The Eleventh International Symposium on Artificial Life and Robotics 2006 (AROB 11th'06),
B-con Plaza, Beppu, Oita, Japan, January 23-25, 2006

Emergent design of a control system for cooperation between robots

Koichi NAKAYAMA[1] Hirokazu MATSUI[2] Katsunori SHIMOHARA[1]
1) ATR Network Informatics Lab. 2) Faculty of Engineering, Mie Univ.
Address 2-2-2 Hikari-Dai, Keihanna Science City, Kyoto 619-0288, Japan
voice: [+81](0774)95-1098; e·mail: `knakayama@atr.jp`

Abstract

We describe sLs-GA (Serial and List-structural Genetic Algorithm) that designs control systems. Generally, the short term optimality of output is different from long term optimality. In this paper, we describe the characteristics of sLs-GA, which obtains not only the optimal control parameters but also the optimal structures of control system for the long term. We verify experimentally that the sLs-GA is applicable, using a target tracing problem with the physical robot "Movable Intelligent Evolutional Computer (MieC)".

1 Introduction

In this paper, we propose a Serial and List-structural Genetic Algorithm (sLs-GA) that uses list structures to represent the genes of agents for the design of robot control systems. The designed control system is modeled as a Multi-Agent oriented Control System (MACS).

In the conventional design of control systems, accurate modeling or analyzing of the controlled object is necessary to design a control system. However, accurate modeling and analyzing are difficult because error margins between the model and the actual controlled object are unavoidable. We propose an adaptive designing algorithm for the control system without modeling and analyzing the controlled object. We aim at the automatic design of an entire control system, including the controlled object.

In our previous research, we modeled as an agent, unknown parameters of a control system. We proposed a Serially and Dynamically Separating Genetic Algorithm (sDS-GA)[1], and applied it to optimize the parameters of the robot control system[2]. The sDS-GA obtained not short-term but long-term optimal parameters under an unknown and dynamic environment. But the sDS-GA must have a pre-fixed colony size which depends on the range of the agent's timely influence. In this paper, we propose the Serial and List-structural Genetic Algorithm. In the sLs-GA, the agents act one by one in order on a list. As a result, the nearer agents on the list have a bigger infuluence on each other. The sLs-GA automatically adjusts the influence so we don't have to consider the range of the influence. We optimize not only the control parameters but also the structures of control system by sLs-GA. And we show that a MACS applying the sLs-GA is designed to work stably, even if the characteristics of the controlled object are changed unexpectantly.

2 Serial and List-structural Genetic Algorithm (sLs-GA)

In this section, we propose the List-structural Genetic Algorithm (sLs-GA) to design robot control systems.

The basic idea of sLs-GA is as follows. In sLs-GA, control-agents are positioned as the list-structure. In a certain period, one control-agent is chosen, according to the list order, and it controls the system. In the next period, the next control-agent in order is chosen from the list, and it controls the system.

Each agent is evaluated each period. When an agent has a high evaluation, the agent splits into two agents, And when an agent has a low evaluation the agent is extinguished.

We show the main routine of the algorithm using sLs-GA in **Fig. 1**.

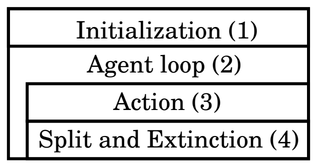

Figure 1: Main routine of the sLs-GA shown by NS chart.

The learning algorithm used by the sLs-GA is as follows.

(1) Initialization: $N_A(t)$ agents at $t = 0$ are created and positioned as the list-structure. The evaluation value of an agent a, $E_A(a,t)$, is initially set to $E_A(a,0)$ and its action determination gene, $Gene_{Act}(a)$, is initially randomly chosen.

(2) Agent Loop: Every agent takes charge of the control in order for robot control.

(3) Action (Robot control by agent): The agent acts for robot control. Details are shown in section 3. The agent changes its own evaluation value based on the result of the action.

(4) Split and Extinction of Agents: An agent is split into two agents when the evaluation value by an agent becomes more than twice the initial value ($E_A(a,0)$). One split agent stays in the same position on the list, and the other is inserted at the next position (**Fig. 2**(A)). The two agents inherit half of the original agent's evaluation value. An action gene is mutated according to the mutation probability P_{mut}.

An agent is extinguished when its evaluation value becomes less than or equal to zero. The current position of the agent is omitted on the list, and the order(the previous, the current and the next) is changed to the previous and the next (**Fig. 2**(B)).

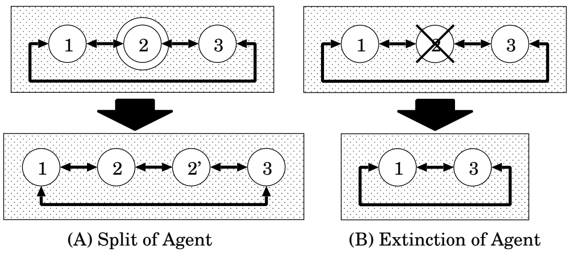

Figure 2: Splitting and Extinction of the sLs-GA.

3 Experiment

In this section, we verify experimentally that the sLs-GA is applicable using the physical robot.

3.1 Experimental Model

3.1.1 Physical structure of MieC

We use MieC (Movable Intelligent Evolutional Computer) as the physical robot, that is a kind of autonomic vehicle. MieC has two motors as movable actuators, two encoders for the motors as internal sensors, and a camera as an external sensor (**Fig. 3**), and has batteries as a power supply. The traced target is one of three colored balls, red, green and blue. These are projected on a screen. Each ball swings by each ten seconds. The phase between two balls is 120 degrees (**Fig. 4**). It is not specified for MieC which colored ball should be traced. MieC learns this from the obtained reward.

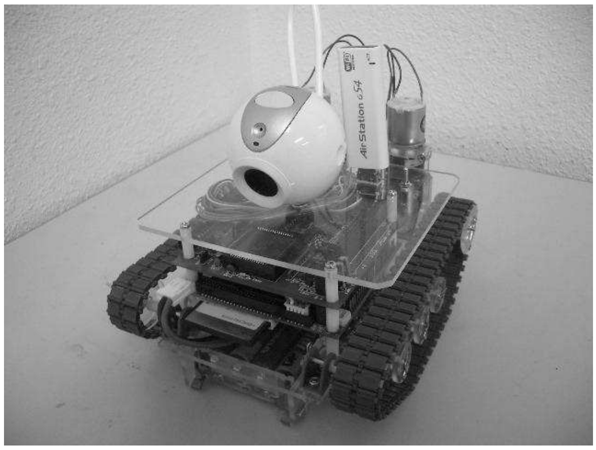

Figure 3: Movable Intelligent Evolutional Computer (MieC)

3.1.2 Control System for the Target Tracing Problem

The flow of target tracing control is shown in **Fig. 5**. This control flow is one of the simplest in this case.

(1) The current position of the target decided by Switch $S_C \in \{Red, Green, Blue\}$ is solved by processing an image from the camera. (2) The position command of MieC is determined by the error between the target position and the current position. (3) The target rotation angles of the left and the right tracks are calculated from the position command, considering the inverse kinematic of MieC. (4) The voltage commands to motors are determined by the errors between the target positions and the value current positions, respectively. (5) The motors are rotated by the voltage

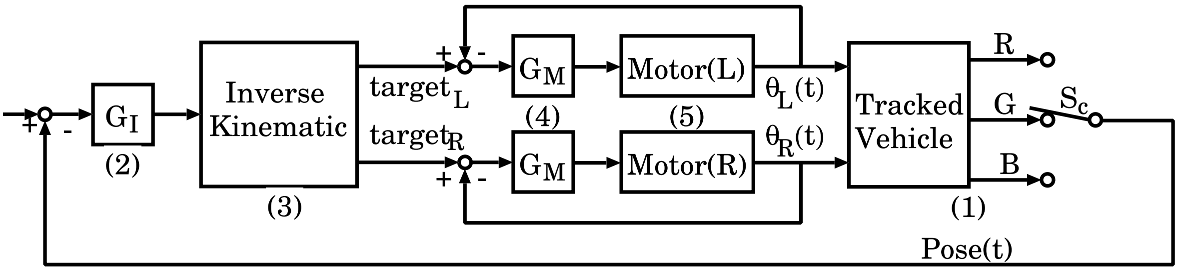

Figure 5: A block diagram showing the target tracking of the traced vehicle

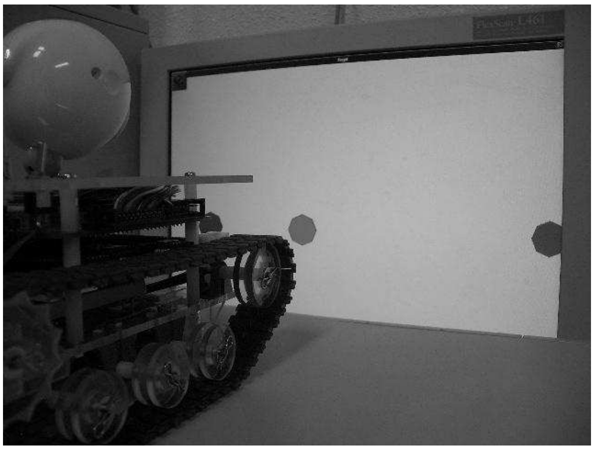

Figure 4: Tracing Target (Balls of red, blue and green)

commands, respectively. (6) Return to (1).

In steps (2) and (4), the commands are determined by the errors and the gains G_I and G_M. Here we treat the gains G_I and G_M as proportionality constants, although the gains have to be determined, considering the weight and the inertia moment of MieC and the characteristics of the motors, etc. The execution cycle (1)-(3) and the execution cycle (4)-(5) depend on the execution speeds of image-processing and motor-control, respectively. These execution cycles are considered to determine the gains G_I,G_M. Here, these parameters G_I,G_M are optimized applying sLs-GA.

3.1.3 Agent Action

One agent controls MieC during 0.1 second in the order of the list. We give each agent three genes S_C, G_I and G_M. S_C takes one of 3 values {R, G, or B}. G_I takes one of 10 quantized values {0.0, 0.2, 0.4, $\cdots$, 1.8}. G_M takes one of 10 quantized values {0.0, 0.6, 1.2, $\cdots$, 5.4}. S_C shows the color MieC traces. The agents with gene G_I and gene G_M can call the cycle (1)-(3) and the cycle (4)-(5), respectively. However, the agent cannot call a cycle before the same cycle is completed.

3.1.4 Agent Evaluation

Each agent is evaluated by how much MieC can trace the target during the time in its duty. An agent is evaluated by the following equation at the time it finishes the control.

$$Evaluation = 1.0 - (B_P(X))^2 \qquad (1)$$

where X is color {Red,Green,Blue}. $B_P(X)$ is the horizontal position of the ball X. The value is -1 when the ball X is at the left end, The value is 1 when the ball X is at the right end,

The equation includes the effect of the previous agents' actions, because the current ball position is influenced by the previous agents' actions.

In this experiment, the number of initial agents was set to $N_A(0) = 100$, and the mutation probability $P_{mut} = 0.1$.

3.2 Experiments and Discussion

In this experiment, all 100 agents act for 10 seconds. Up to 1,000 seconds, X is Red. After 1,000 seconds, X is Blue.

We gained the following results. The history of the population ratio of $S_C \in \{R, G, B\}$ is shown in **Fig. 6**. The histories of the population ratios of $G_I \in \{0.0, 0.2, 0.4, \cdots, 1.8\}$ and $G_M \in \{0.0, 0.6, 1.2, \cdots, 5.4\}$ are shown in **Fig. 7**, respectively. The horizontal axes express the time [in seconds]. The vertical axes express the ratios of genes, respectively.

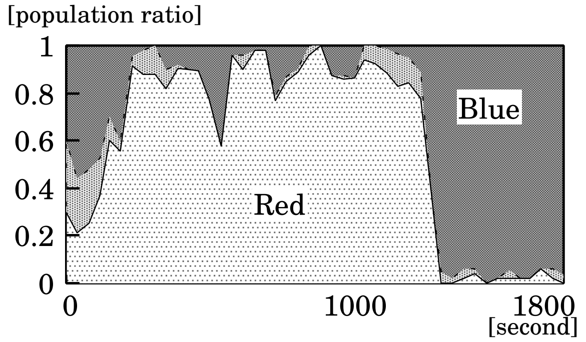

Figure 6: The history of the population ratio of S_C

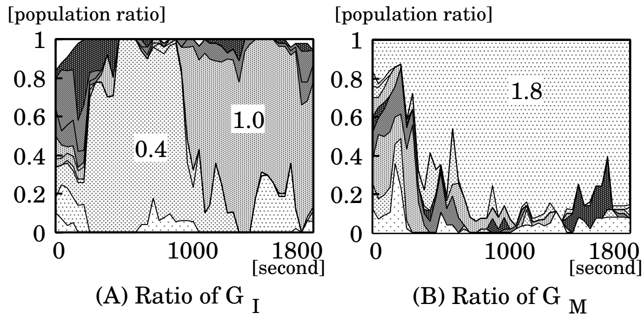

Figure 7: The history of the population ratio of G_I and G_M

In **Fig. 6**, up to 200 seconds, S_C converged on the optimal value R. After 1,000 seconds, X is Blue. Then, most S_C are changed to B around 1,200 seconds.

In **Fig. 7**(B), up to 600 seconds, G_M converged on 1.8. These genes are unaffected by the difference of the tracing targets. Then the learned value of G_M that is for red ball tracing is used for blue ball tracing.

In **Fig. 7**(A), up to 200 seconds, G_I converged on 0.4. At around 900 seconds, most G_I are changed to 1.0. That result shows that the control system of MieC adapts to the lowering of the battery voltage. When the battery voltage of MieC lowers, motor gain G_M should be a bigger value. However, in this experiment, G_M is already maximum. For this reason, G_I was changed.

From the above discussion, it is believed that sLs-GA can optimize not only the control parameters but also the structures of the control system. The sLs-GA is efficient for the optimization of a control system for MieC as an actual intelligent robot under an unknown environment.

4 Conclusion

In this paper, we verified the effectiveness of the adaptive design of a control system by a physical experiment. The experimental result showed that the proposed sLs-GA designed not only the optimal control parameters but also the optimal structures of a control system for a tracing problem of a physical robot.

Acknowledgements

This research was supported in part by the Telecommunications Advancement Organization of Japan.

References

[1] K. Nakayama, H. Matsui, K. Shimohara, O. Katai, "Proposal of Serially and Dynamically Separating Genetic Algorithm and Its Application to Optimization of Robot Control Systems," *Proceedings of the Tenth International Symposium on Artificial Life and Robotics*, pp. GS12-2(CD-ROM), 2005.

[2] K. Nakayama, H. Matsui, K. Shimohara, "Emergence System Design by Serially and Dynamically Separating Genetic Algorithm (In Japanese)," *IPSJ Symposium Series*, Vol. 2005, No. 11, pp. 79-82, 2005.

A Design of Mass Estimated Adaptive Friction Compensator for Position Control of Linear Motor System

Jin Woo Lee
Dept. of Electrical Engineering
Dong-A University
840, Hadan-dong, Saha-gu, Busan, Korea
jinwoo@donga.ac.kr

Jin Ho Suh
Dept. of Electrical Engineering
Dong-A University
840, Hadan-dong, Saha-gu, Busan, Korea
suhgang@donga.ac.kr

Kwon Soon Lee
Dept. of Electrical Engineering
Dong-A University
840, Hadan-dong, Saha-gu, Busan, Korea
kslee@dau.ac.kr

Keywords: Linear motor servo system, Friction, Adaptive control, Mass estimator

Abstract

In this paper, we propose an adaptive control algorithm to improve the position accuracy and reduce the nonlinear friction effects for linear motion servo system. Especially, the considered system included not only the variation of the mass of mover but also the friction change by the normal force. To adapt these problems, we designed the controller with the mass estimator and the compensator by observing the variation of normal force.

1. Introduction

In the general mechanical servo system, the friction deteriorates the performance of the controller by its nonlinear characteristics. Especially, the friction phenomenon causes steady-state tracking errors, limit cycles in the position and velocity control system, even though gains of the controller are tuned well in the linear system model. Even if the sensor is used higher accuracy level, it is difficult to improve the tracking performance of the position to the same level with a general control method such as PID type. Therefore, many friction models were proposed and compensation methods have been researched actively [1].

In this paper, we consider that the variation of mover's mass is various by loading and unloading. The normal force variation occurs by it and other parameters. Then, we performed simulation to evaluate its adaptation and performance of position accuracy for control systems for other control systems.

2. Mathematical modeling

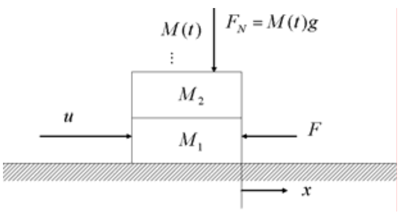

Fig. 1 Configuration of the considered system and each component

The linear motion servo system with nonlinear friction and variation of mover's mass can be shown as Fig. 1. Fig. 1 shows mover's mass M_1 is changed to $M_1 + M_2$. The system dynamic equation can be described by Eq. (1).

$$M\frac{d^2x}{dt^2} = u - F \tag{1}$$

where, x is mover position, M is mass, u and F are control input(thrust force) and friction force, respectively. LuGre dynamic friction model F is considered the model of bristles reaction between two surfaces. And it based on the average deflection behavior of the elastic bristles. It can be described by Eq. (2).

$$F = \sigma_0 z + \sigma_1 \frac{dz}{dt} + \sigma_2 v \tag{2}$$

where, z is average deflection of elastic bristles, v is mover's velocity. σ_0, σ_1, and σ_2 are coefficient of stiffness, damping coefficient, and coefficient of viscous, respectively.

The equation of bristle deflection z and the positive definite function that relies on factors such as surface material characteristics can be described by Eqs. (3) and (4) respectively.

$$\frac{dz}{dt} = v - \frac{\sigma_0 |v|}{g(v)} z \tag{3}$$

$$g(v) = F_C + (F_S - F_C)e^{-(v/v_s)^2} \tag{4}$$

where, F_C is Coulomb friction level, F_S is stiction force level, and v_s is Stribeck velocity. The steady state relation is $\dot{z} = 0$, the steady state friction F_{SS} can be rewritten as Eq. (5). Fig. 2 shows the surface of steady state friction model for the mass, velocity, and friction force.

$$\begin{aligned} F \approx F_{SS} &= g(v)\operatorname{sgn}(v) + \sigma_2 v \\ &= \{F_C + (F_S - F_C)e^{-(v/v_s)^2}\}\operatorname{sgn}(v) + \sigma_2 v \end{aligned} \tag{5}$$

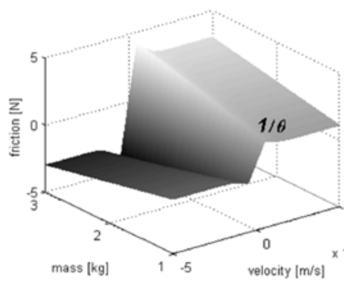

Fig. 2 Steady state friction surfacel for scale factor θ

3. Adaptive Controller Design with Mass Estimator

Let assume the parameters of dynamic friction and the initial mover's mass are known. But, these are change during the time of control because of loading and unloading. Therefore, we designed the mass estimator that can scale the position controller H(s) and constrict the estimates of the normal force factor more rapidly.

Fig. 3 shows the proposed control system and the system equation with control is described as follows:

$$M\frac{d^2x}{dt^2} = u - F = -\hat{M}H(s)e + \hat{M}\frac{d^2x_d}{dt^2} + \hat{F} - F \tag{3}$$

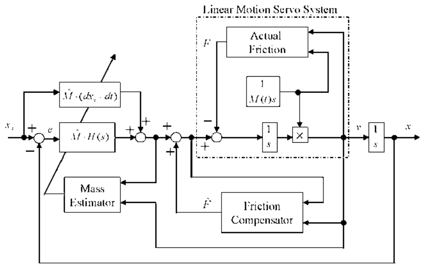

Fig. 3 Control system structure with the mass estimated adaptive controller and compensator

To design the mass estimator, it needs to assume there are not any more the friction and other external forces in the system by the ideal compensator. Then, the relation can be obtained as follows:

$$u = M\frac{d^2x}{dt} = Ma = \frac{a}{\theta_2} \tag{4}$$

where, θ_2 is the estimates of mass, and we can know $\theta_2 = 1/M = a(t)/u(t)$. Then, its estimate can be written as Eq. (5) and shown by Fig. 4.

$$\hat\theta_2 = \frac{1}{\hat M(t)} = \frac{\hat a(t)}{u(t)} \tag{5}$$

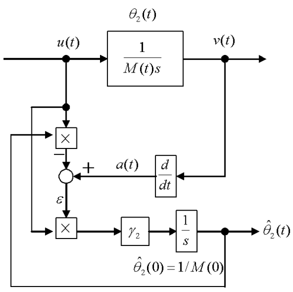

Fig. 4. Block diagram of the mass estimator for the plant without actual friction and compensator

To analysis the convergence of the mass estimator, let define the estimate of system output is $\varepsilon = a - \hat a$, and the error of estimate is $\tilde\theta_2 = \hat\theta_2 - \theta_2$. Then, ε can be rewritten as follows:

$$\varepsilon = a - \hat a = \theta_2 u - \hat\theta_2 u = -\tilde\theta_2 u \tag{6}$$

In order to minimize ε, the cost function is defined by

$$J(\hat\theta_2) = \frac{\varepsilon^2}{2} = \frac{(a - \hat\theta_2 u)^2}{2} \tag{7}$$

When $\nabla J(\hat\theta_2)$ is $(a - \hat\theta_2 u)u = 0$, $J(\hat\theta_2)$ has a minimum. Therefore, the equation of $\tilde\theta_2$ can be rewritten as Eq. (8) by using the gradient method.

$$\frac{d\hat\theta_2}{dt} = -\gamma_2\nabla = \gamma_2(a - \hat\theta_2 u)u = \gamma_2\varepsilon u \tag{8}$$

where, $\hat\theta_2(0) = 1/M(0)$ and $\gamma_2 > 0$. To analysis the stability of the whole system, it can be chosen *Lyapunov function candidate* V as follows:

$$V = \zeta^T P\zeta + \frac{1}{\gamma_1}\tilde\theta_1^2 + \frac{\tilde z^2}{k} + \frac{1}{\gamma_2}\tilde\theta_2^2 \tag{9}$$

Then, dV/dt can be obtained as Eq. (10) under the conditions that are $\dot{\tilde\theta}_2 = \dot{\hat\theta}_2 - \dot\theta = \gamma_2\varepsilon u - \dot\theta_2 = -\gamma_2 u^2\tilde\theta_2$ and $\dot\theta_2 = 0$.

$$\frac{dV}{dt} = -\zeta^T Q\zeta - \theta_1\frac{\sigma_0|v|}{g(v)}\tilde z^2 + \tilde\theta_1\left(-\tilde z\frac{\sigma_0|v|}{g(v)}\tilde z + \frac{1}{\gamma_1}\frac{d\tilde\theta_1}{dt}\right) + \frac{2\tilde\theta_2\dot{\tilde\theta}_2}{\gamma_2}$$

$$= -\zeta^T Q\zeta - \theta_1\frac{\sigma_0|v|}{g(v)}\tilde z^2 - 2u^2\tilde\theta_2^2$$

$$= -\zeta^T Q\zeta - \theta_1\frac{\sigma_0|v|}{g(v)}\tilde z^2 - 2\varepsilon^2 \le -\zeta^T Q\zeta < 0 \tag{10}$$

4. Simulation Results

In this paper, we performed the numerical simulations to verify the proposed control system about the position tracking control using Matlab/Simulink module. These results included the asymptotic tracking performances for the distance errors, the friction estimates, and the mass and normal force estimate, etc. Fig. 5 and Fig. 6 show the results of the displacement and its error, respectively.

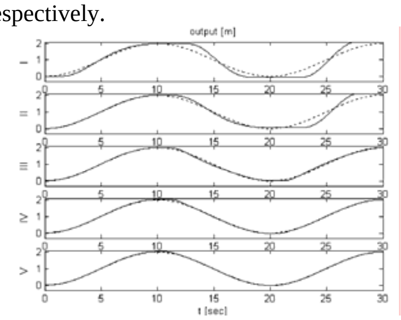

Fig. 5. Distance variations(solid line) for the reference trajectory (dotted line)

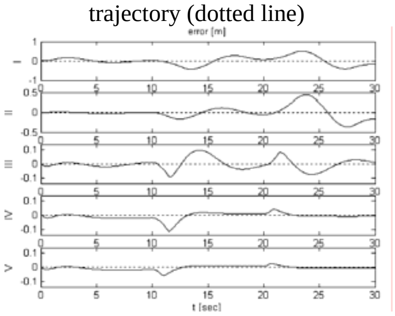

Fig. 6. Variations of the position error

5. Conclusions

In this paper, we consider that the variation of mover's mass is various by loading and unloading. The normal force variation occurs by it and other parameters. Therefore, the proposed control system was composed of the main position controller and the friction compensator part. And a mass estimator was designed by the adaptive control law.

Acknowledgement

This work was supported by grant No. R01-2005-000-10418-0 from Korea Science and Engineering Foundation in Ministry of Science & Technology.

References

[1] B. Armstrong-Helouvry, et. al., "A Survey of Models, Analysis Tools and Compensation Methods for the Control of Machines with Friction," *Automatica*, Vol. 30, No. 7, pp. 1083-1138, 1994.

[2] C. Canudas de Wit, et. al., "A New Model for Control of Systems with Friction," *IEEE Trans. on Automatic Control*, Vol. 40 , No. 3, pp. 419 - 425, 1995.

[3] C. Vivas, et. al., "Gain-scheduling Control of Systems with Dynamic Friction," in *Proceedings of the 41st IEEE Conference on Decision and Control*, pp. 89-94, 2002.

[4] K. K. Tan, et. al., "Robust Adaptive Numerical Compensation for Friction and Force Ripple in Permanent-Magnet Linear Motors," *IEEE Trans. on Magnetics*, Vol. 38, No. 1, pp. 221- 228, 2002.

Implicit Principle Discovery in Tourism Geography Information Based on Data Mining

Du Junping
School of Computer Science
Beijing Technology and Business University, Beijing, 100037

Guo Wensheng
School of Information Engineering
University of Science and Technology, Beijing, 100083

Abstract

We made study in geography data sets using data mining technology and established a semantic network with the use of implicit information in the data. We got implicit principles in geography information with supervised classification technology and unsupervised classification technology. Some valuable conclusions are presented.

1 Introduction

China has large amount of tour resources and tourism grows up rapidly. In order to provide tour destination information to the tourists, including tour resources, facilities, tour lines, enterprises and products, each tour destination has set up GIS. But GIS provide only the search service of geography features to the users, and it can not meet the complicated semantic search demand.

Semantic search in the geography information requires the implicit principles in the information. This implicit information does not exist in the level of pure geographical features, but in the level of the relationships among the features, their extent, density, frequency, neighborhood, uniqueness and more. This knowledge often is well known by humans with their background information, however is has to be made explicit for the computer. Based on the data mining theory, we tried to discover the implicit principles in the geography information with the consideration of the features of the tourism industry.

2 Patterns In the Geography Information

In GIS, there is some knowledge about the distribution and location of the geometrical elements, their connections to each other, their accumulation in special places and so on. Those characteristics make the information of a data set complete and allow humans to interpret data. In order to make this knowledge to be interpretable by computer, we need a translation in two respects: first a language translation, but moreover a semantic translation. Those catalogues, which describe the meaning of a word and determine its sense depending on the context, are called ontologies. To enrich the ontology, our ambition is focused on teaching the computer to learn spatial concepts and to combine knowledge with higher concepts automatically. Some are hidden in the spatial data, some exist in pure geometry and most of them are exist in the combination and interaction of the spatial elements. Spatial data mining is the approach to extract the implicit information.

Using typical queries using search engine and user scenarios with spatial background, there is a lot of useful information stored in the geographical data sets. If a user wants to search for a hotel in the centre of the city, at least the

Supported by Beijing Natural Science Foundation of China (4042012), Key Project of Beijing Educational Committee（KZ200510011009） and Project of National Science Foundation of China (60442003)

search engine has to know, where the city center is. This knowledge can be discovered in vector data, but it is usually not explicitly stored in the database.

Indeed we recognize streets and houses and we are able to get further facts. Humans can locate the theater or museum by the special shape of this building. The interaction of the streets and houses and their concentration induces at least the information, that it is a town. We also can identify larger buildings in the upper part and distinguish them from smaller ones in the south. A computer can calculate these facts too. The big challenge is the following reasoning process. Humans interpret the larger buildings as the inner part of the town, because they know about old farmyards and the typical formation of a town. The smaller buildings represent a courtyard of one family house. We are able to locate the main street leading through the town as well, because of the structure of the settlement. Therefore humans can detect the city centre approximately without difficulty.

Some characteristics of the elements can be determined with simple GIS functionality, such as to calculate an area/size or to count the existence of special objects. The evaluation of other properties, such as density, distribution or neighborhood is more complicated. The analysis of distances is an essential part to get knowledge of these aspects. However, the handling of threshold values or absolute numbers is less helpful, because it depends on the context, if an attribute or a characteristic is really specific and outstanding. Most of the time those values are of interest and shed light on something. Clustering algorithms can be used to identify groups of elements respectively to their neighborhood. Among clustering algorithms, those are preferable that do not need threshold values. Moreover the combination of properties and their calculated values raise a problem. Logic operations have to be extended by weighting and quantifiers, which depend on the importance, relevance, quality of the attribute values and significance of elements.

3 Data Mining and Principles Discovering

As mentioned above there are rules implicit in spatial data, however there are two different ways of approaching the goal of extraction implicit knowledge. These two kinds of extraction models are on the one hand, to define the rules a priori (association rules) and to apply them to the data, on the other hand, to let the computer find the rules by itself by exploring the data. Both ways can get more knowledge. The second case brings up unknown knowledge or inherent information, which may be useful to learn more about the data set, but can not be useful as well. Both methods are usually known as data mining and will be described and examined. They are discerned into supervised and unsupervised classification.

3.1 Supervised Classification

The supervised classification implies knowledge discovery on the basis of predetermined models respectively spatial association rules. Supervised classification starts from a set of classified examples for a concept to be learnt. From this set classification schemes for the concepts are derived, e.g. using machine learning approaches, or also Maximum Likelihood classification. In principle every kind of knowledge representation can be used to form a classification scheme, especially rule-based systems or semantic networks. We will depict the process by the help of decision trees. Every branch represents the existence of a distinctive classification feature. Depending on the result of the inquiry, the adequate branch will be followed further. In the end, the model leads to a classification into different categories of one issue. However the scheme includes some essential problems. The sequence of the validation of a distinctive classification feature is one determining factor. The need of high quantitative and qualitative data is necessary to be able to calibrate the model. The concept of “city center” can be implemented by such method. For example, if a point satisfies such condition, we can define it as the center of the city.

On the contrary, we could have included distinctive features, which do not correspond to the reality, and have only been valid for a small test data set. This implies, that the setup of such models has to be done very carefully, possibly using large test data sets in order to gain the information from and to perform tests for verification of the derived rules. Furthermore, a specific inference scheme has to be designed to apply the rules to the data, which takes the probability or the importance of a condition to a rule into account.

3.2 Unsupervised Classification

The method aims at leaving the process of knowledge discovery to the computer itself. That means the computer has to discover rules, separations into categories, similarities in data sets without any predefined restrictions. Since such rules are induced from a finite set of examples, they cannot be verified, but only falsified. Thus, there has to be a validation of the utility of the detected information. It may happen, that rules will be found, which are obvious and do not give further knowledge. It is another process of learning to distinguish useful and non-useful rules.

A way to analyze geometric objects is to determine their characteristics and to try to find regularities among them. Such regularities then, in turn, can be considered as representatives for a certain class of objects or a class of objects in a certain context or environment. For linear objects or even networks of linear objects, the nodes are such a characteristic, including the node degree, i.e. the number of outgoing lines from the node. Furthermore, also the angles of the outgoing lines can be important. Different types of nodes can be distinguished and classified.

While investigating the concept of the city centre with supervised models, we introduced the criteria of crossroads in the centre. A crossroad is a node with at least four outgoing lines, which were expected primarily in the city centre, as there many roads come together. The tests turned out in an unexpected result of this investigation. The condition to find crossroads in the city centre depends on the size of the town. There seems to be a rule regarding the relation between the structure of the centre, the spatial arrangement of streets and the size of the city.

Typical structures in the city centre are shown, depending on the dimension of the town. In small towns, often a big street leads through and mainly TEE-junctions can be found, whereas in medium size cities the expected structure dominate, meaning that three or more major roads will meet in the city centre. In large cities the opposite trend can be observed: major streets will run around the city but in the centre itself only minor streets or even pedestrian areas will be located.

The intention was to look into detail, if there are reasoning mechanisms to cut settlement areas into partitions, especially if the lines will meet approximately orthogonal. Among other things it came up, that highways will be represented by separate clusters with solely one edge (ELLjunctions), with the exception of the access roads. Naturally there are only a few intersections with highways, the parts between are direct polylines without branches.

It could be one of a criteria to determine highways respectively to distinguish their access roads from their carriage-ways in data sets. It can be very helpful to validate further structures like the neighborhood of settlement areas in the vicinity of a highway access.

On the basis of described processes, we are able to examine the data sets and the above mentioned results in more detail, whereby supervised and unsupervised models can hardly be kept apart at this stage. The following factors could be decisive for further (supervised and unsupervised) interpretations: size of a single mesh, length of segments between nodes, frequency of occurrence of high-order respectively significant nodes, in depth study of the type/shape of the nodes. To get on without predefinition of thresholds or the preliminary fixing of minimal and maximal values, it is our aim to continue the search for broader regularities, for example in the combination between above mentioned criteria.We will concentrate on both ways, supervised and unsupervised methods. Both can support knowledge discovery and during the implementation of algorithms, both data mining models will influence each other.

4 Conclusion

This paper explains the data mining in the spatial database of the GIS using two classified methods of the data mining. Some valuable implicit principles are also presented. These principles contribute to the establishment of the geography information search engine based on the semantic net, meeting the requirements of the semantic search demanded by users. In practice, the conclusions from the data mining are a powerful tool by which the tourists can know about the destination and the prospect of this application will be very wide.

References

[1] David Hand, Heikki Mannila, Padhraic Smyth. Principles of Data Mining，2003

[2] Wu Mingrui, A neural network algorithm used in the pattern rogognition. Software Journal，2001

[3] Olivia Parr Rud. Data Mining Cookbook，Modeling Data for Marketing, Risk, and Customer Relationship Management，2003

The Eleventh International Symposium on Artificial Life and Robotics 2006 (AROB 11th'06),
B-con Plaza, Beppu, Oita, Japan, January 23-25, 2006

Development of Neural Network Based Pattern Classification System for cDNA Micro Array

Dae-Wook Kim Chang-Hyun Park Hyun-Chang Yang Kwee-Bo Sim
School of Electrical and Electronics Engineering
Chung-Ang University
221 Heuseok-dong, Dongjak-gu, Seoul 156-756, Korea

Abstract

DNA chip is able to show DNA-data that includes diseases of sample to user by using complementary characters of DNA. So this paper studied neural network algorithm for image data processing of DNA chip. DNA chip outputs image data of colors and intensities of lights when some sample DNA is putted on DNA chip, and we can classify pattern of these image data on user pc environment through artificial neural network and some of image processing algorithms. Ultimate aim is developing of pattern classifying algorithm, simulating this algorithm and so getting information of one's diseases through applying this algorithm. Namely, this paper study artificial neural network algorithm for classifying pattern of image data that is obtained from DNA chip. Also, by using histogram, gradient edge, ANN and learning algorithm, we can analyze and classifying pattern of this DNA chip image data. So we are able to monitor, and simulating this algorithm.

1 Introduction

In this paper, we perform the experiment processing that includes shrinking noise, edge detection and subtract perimeter background intensity from spots intensity. Setting up some regional spots and grids, summation their pixel values if they are under threshold. Then we are able to deal with the Image as lattice which has binary values 1 or 0. Also the binary values demonstrate the whole the image as binary code in its rows or columns. Therefore we can apply the data into the Artificial Neural Network (ANN). The ANN is trained by backpropagation algorithm. The former all processing is performed on the gray level image and color image. When we use gray level image, we are able to classify for the shape with revelation spots. Also when we use color element of the image, we can get pattern data more precisely. It makes the result more exact. Moreover we saw special revelation characteristics by using color image data. DNA chips are designed to identify hybridization products in the same format as with traditional sequencers. Once hybridization has been completed, phosphorescent chemicals that bind to the hybridized sequences are scanned with a light source by laser scanner or CCD cameras, making it easy to detect their revelation with automated colorimetric or fluorimetric equipment [1][2]. Namely, the concept behind DNA chips is simply that of miniaturizing the gene sequencing technologies already being developed, so that many assays and their related procedures can be performed together. DNA chips will give researchers the ability to analyze thousands of genes at once, and may also make it possible to conduct very elaborate diagnostic procedures in such small settings as a physician's office or even with mobile equipment used at the point of care. We perform the procedures in normal user pc. So, This Paper is about DNA chip Image analysis system. We use neural network and some image processing algorithms on analysis of DNA chip image data. In section II, we explain DNA chip and its analysis system that we performed experiment. In section III, we show the current research issues, especially, Segregation spot from background, cutting noise and method to solve them. Also in section IV, we will show the process of experimental. We can get someones DNA information using DNA chip image data. It includes information of diseases and mutations.

2 cDNA Micro Array Image Analysis

2.1 DNA Chip

The DNA chip (especially, we call it another name, cDNA micro array) is a revolutionary new tool used to identify mutations and diseases in gene. The chip, which consists of a small glass plate encased in plastic, is manufactured somewhat like a computer microchip. On the surface, each chip contains thousands of short, synthetic, single-stranded DNA sequences, which together, add up to the normal gene in question. Fig. 1 depicts that sample cDNA micro-array image data that is a kind of DNA chip which has ability to show a specific disease or DNA mutation.

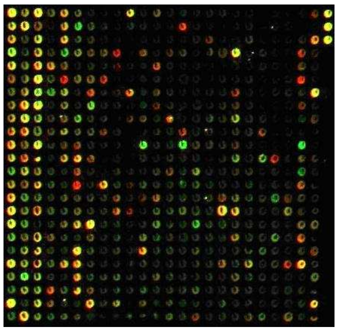

Figure 1: cDNA image that is used in our experiment

2.2 Concept of cDNA Micro Array

We can use purified single-stranded cDNA (complementary DNA) from an individual with a known genetic disease, requiring the use of touch or fine micropipetting, to spot the cDNA onto the surface of the chip. The cDNA immobilizes on the chip through covalent bonds, due to the positively charged surface, produced by amino silane or polylysine. For all types of chips, a potential DNA target sequence, from on to interact with the probes. Hybridization will occur at complementary sequences between the two samples resulting in a fluorescent image, which is then scanned by a laser beam or CCD Camera, and analyzed by a computer. The intensity of fluorescent light varies with the strength of the hybridization, thus providing a quantitative 'snapshot' of gene expression [3][4].

2.3 Image Analysis of cDNA Micro Array

First of all, we have to get cDNA image data through CCD, CMOS camera or laser scanner. we can perform some preprocessing and classification of image pattern. So we are able to know the information of sample DNAs mutation or disease on user computer environment. The cDNA chip has 24 x 24 grids and we will do image processing for its shape and individual colors. Fig. 2 shows a typical DNA chip image analysis system.

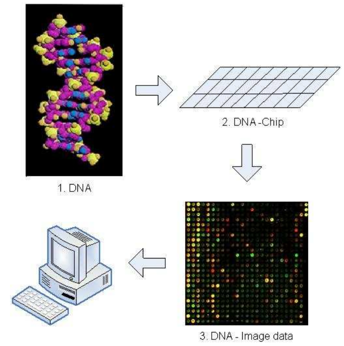

Figure 2: cDNA image analysis

3 Research Issue of cDNA Image Analysis

3.1 Segregation Spot from Background

Currently, there are some methods. Imagene an-Genepix in Axon Instrument,ScanAnalyze developed by Stanford Univ and they separate spots from background by circle shape. Also ArraySuit developed by Dr. Yi dong Chen in NIH separate spot from background by recognition pattern of whole spot [4][5] At this time, we are able to separate spot from background by edge detection and partition of grids which we already know. So we can make template spot Image.

3.2 Cutting Noise

Currently, general methods delete noise by cutting upper 15% and lower 15% pixels. However it is not enough because it cuts normal image pixels. So, in this paper we use preprocessing method that includes binary and morphology. Also we cluster image data to some parts using ANN which is robust for noise. So we estimate revelation of special DNA from image data which has ANN output values in acceptable range of error. Therefore, it is possible that gaining information from cDNA micro array which includes some noises. Also, to delete fluorescent light that is not wanted, we subtract perimeter pixel values from target spot pixel values. So we can shrink noise which is caused by polluted materials. When distribution of brightness is accordance with normal distribution, typical summation value of whole individual brightness is similar to typical summation value of two pixels brightness. So, to subtract perimeter background pixel values from target spot values, we have to prove that distribution of brightness is normal distribution. To prove this, assuming that cDNA chip is using glass as plate (glass is known base material that rarely creates normal (not wanted) fluorescent light). Major factor of not-wanted fluorescent light is some polluted material which attached on the plate. In the process of hybridization, it is possible that surface of chip is polluted with some not-wanted material. So there are van der waals forces between base glass and not-wanted material. But the washing process that is after hybridization process omits the not-wanted material in the high dense region more than in the low dense region. Eventually, regional variation of not-wanted material will decrease. So, it proves that not-wanted material distribution of brightness is approximate to normal distribution [4][5]. First of all, we subtract perimeter background pixel values from target spot values to shrink noise [4]. Second, we use ANN algorithm which has robust pattern classification ability. Typical value of spot brightness is known (1) where i

$$t_{ij} = a_i d_j \theta_{ij} e^{\varepsilon_{ij}} + b_{ij}' \qquad (1)$$

is a sample comparison group or standard group, a_i is total summation value of mRNA extracted from individual groups, d_j is revelation quantity of cDNA on j-th spot, θ_{ij} is proportion of mRNA quantity created by j-th gene for total mRNA quantity of all group, b_{ij} is background brightness that is included in spot brightness. According to former intuitive proof, we can regard that b_{ij} is the perimeter background brightness [4], [5]. Glass and nylon is most used as base material of cDNA. Specially, glass is more adaptive and useful because it creates fewer singular fluorescent lights than other material

4 Experimental Procedure of cDNA Micro Array Image Analysis

4.1 Preprocessing

Two ways process are performed. First, we can handle the image data in its shape. We make the color image to gray level image. And we can make binary image [6]. Then we manipulate the image for its shape pattern classification and noise cutting. Fig. 3 shows a binary image of cDNA micro array, and we can decrease the noise. Second, we abstract its color element of image data. Its to classify the pattern in its colors. All the way is on the pixel based. We

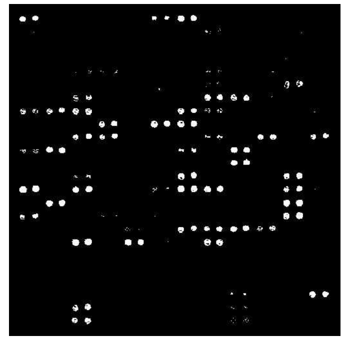

Figure 3: Binary image of cDNA micro array

can input the data in R G and B format because we know target pixels R, G and B values. Processing of RGB values in pattern classification will make the result more precisely, and its a valid method because its on the basis of color space and the revelation is in color and shape space. Also special color will indicate special revelation. So we can get more information of cDNA micro array.

4.2 Edge Detection and Cutting Noise

We use nonlinear spatial filter to detect spot?s edge, and subtract perimeter background pixel values from target spot values. It?s related with not-wanted fluorescent light problem.

4.3 Setting up Uniform Boundaries on cDNA Image

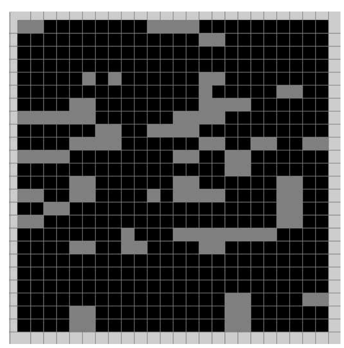

Figure 4: Block image of cDNA micro-array

Assuming only one type cDNA image data is used in experiment. There are so many DNA image types but, actually we use only one type cDNA micro array image. Also we summate all of pixel values in the uniform boundary. Setting up uniform boundary is an establishment of lattice on Image data. So, we cut pixels its summation values are under threshold value for obtaining special points of Image. Fig. 4 is a Block image of cDNA micro array, and we can apply the data into the neural network.

4.4 Input Special Point Value into ANN

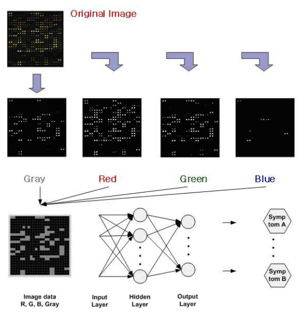

Figure 5: Input-output data of neural network classifier

To learn the task, we exercise the net by back propagation algorithm. Also we use MLNN. At this point, to reduce operation load, we except some region that is clear its not-revelation. In other words, there are losses of efficiency because of operation load on ANN pattern recognition. So we except some region that is clear its not-revelation. Also we can separate image into uniform region, and input its handled value into ANN. It is not able to cut the regional value that has over revelation for comparison image. However it has long odds that over revelation data are recognized as correct pattern, when we divide in block and input this data into ANN. It is on two reasons. First, even if we get over revelation data, naturally, it has positive character because it has target characteristics. Second, it is not matter on the actual experiment because many other spot regional data that we are able to input ANN. So we can cut the data is not wanted. Fig. 5 is a pattern classification system that we suppose.

5 Experimental Result and Conclusion

We got the neural network weights for cDNA micro array analysis. The systems training count is over than 2,000,000 when training error is 0.00001. Its trained by backpropagation algorithm, it takes about 20 sec. So the system can classify the pattern that has very small differences on the cDNA micro array. The cDNA micro array has 24 x 24 spots. We demonstrated the validity of pattern classification through the ANN. Also we demonstrated that ANN is a valid method for cDNA pattern classification, and the ANN was robust against the noise in the experiment. So we can find extended application of cDNA micro-array using artificial neural network. The only question is how to decrease the training time. Its the characteristic of the backpropagation algorithm. So we will compare and apply the other ANNs and training algorithms, and we will get the more powerful ability of pattern classification. In this paper, we suggested the method that classify pattern of cDNA chip image using image processing and ANN. Finally, we could get corrected image pattern from cDNA chip image data through the method spatial filter and ANN on gray and color space. Also we could classify the image data. So its simple and easy to realize.

Acknowledgements

This research was supported by the project of Developing SIC (Super Intelligent Chip) and its Applications under the program of Next generation technologies in 2000 of Ministry of Commerce, Industry and Energy.

References

[1] Jang B. Rampal, em DNA Arrays Methods and Protocols , Humana Press , 2001.

[2] Tom M. Mitchell, em Machine Learning , The McGraw-Hill Companies, Inc., 1997.

[3] DNA-chip Technologies (Part 1): Research Fundamentals and Industry Catalysts (1998, Sep) [Online]. Available: http://www.devicelink.com/ivdt/archive/98/09.html.

[4] Han-Yang Univ., em Development for DNA image analysis software through deconvolution method, Technical report, Ministry of Science and Technology of Korea , 2004 .

[5] Eng, Charis and Jan Viig, " Genetic Testing: The problems and the promise," *Nature Biotechnology* ,Vol. 15, pp. 422-426, 1997

[6] Rafael C. Gonzalez and Richard E. Woods, em Digital Image Processing , Prentice Hall, 2002.

The Eleventh International Symposium on Artificial Life and Robotics 2006 (AROB 11th'06),
B-con Plaza, Beppu, Oita, Japan, January 23-25, 2006

Remarks on tracking method of neural network weight change for adaptive type neural network direct controller

Takayuki Yamada
Department of Computer and Information Sciences
Faculty of Engineering
Ibaraki University
4-12-1 Nakanarusawa, Hitachi, Ibaraki, 316-8511, Japan

Abstract

A neural network usually learns so as to minimize a scalar value such as a cost function. This scalar value is useful for a confirmation of neural network learning performance. However, this confirmation may not be correct for neural network controllers because a plant dynamics affects the cost function. My previous paper proposed a new tracking method of the neural network weight change as an examination of the neural network controller learning performance and it was applied to a learning type neural network direct controller. This paper shows the simulation results when the tracking method is applied to an adaptive type neural network direct controller.

1. Introduction

Many studies have been undertaken in order to apply both the flexibility and the learning capability of neural networks to control systems.[1]-[3] Learning rules of neural network weights are usually designed so as to minimize the error between a plant output (or neural network output) and a desired output (teaching signal). The essence of neural network learning is nothing but the change of the neural network weights. However, in order to examine the performance of the neural network learning, most researchers use a cost function (squared error between the desired output and the neural network output (or the plant output)). This is because it is not practical to examine the huge number of the neural network weights and the cost function is a scalar value which is easily dealt with. However, the neural network weight change is not always reflected in the cost function. This problem is especially serious in neural network controller applications. This is because the performance of the cost function is affected by dynamics of the plant. My previous paper[1] proposed a new tracking method of the neural network weight change as an examination of the neural network controller learning performance. This tracking method can realize to observe the neural network weight change directly. It was also applied to a learning type neural network direct controller and its usefulness was confirmed. The learning type of the neural network controller is useful to confirm the characteristics of the proposed tracking method. This is because it is simplest and the neural network weight changes slowly in comparison with an adaptive type controller[2]. On the other hand, the adaptive type neural network controller requires less convergence time. This is because the neural network weights of the adaptive type controller are changed at every sampling time and we can realize an on-line neural network controller when this type controller can be applied to practical systems.

This paper applies the tracking method of the neural network weight change to the adaptive type neural network direct controller for a second order discrete time SISO (single input and single output) plant. The simulation results confirm the usefulness of the tracking method for the adaptive type neural network direct controller. I also obtain interesting phenomena which are not observed on the simulation for the learning type neural network direct controller.

2. Tracking method of neural network weight change

This section explains the tracking method of the neural network weight change briefly. This tracking method is applied to the adaptive type neural network direct controller for SISO plant. For this selection, an output layer of the neural network has one neuron, the weights between the output layer and a hidden layer can be expressed as a vector ω and the weights between the hidden layer and an input layer can be expressed as a matrix W. To simplify, the neuron number of the input layer is equal to that of the hidden layer. That is, the weight matrix W is the square matrix. The tracking method uses the following steps.

(Tracking method of neural network weight change)

(1) We can derive one weight vector Γ from the neural network weight vector ω and weight matrix W as follows:

$$\Gamma^T = [\omega_1 \cdots \omega_n \; W_{11} \cdots W_{1n} W_{21} \cdots W_{2n} \cdots W_{n1} \cdots W_{nn}] \quad (1)$$

where n is the neuron number both the input layer and the hidden layer.

(2)We must define a standard vector Γ_0. Any vector, which has same order as that of the weight vector Γ, can be selected as this standard vector, for example, the weight vectors derived from the initial neural network weights, the final neural network weights and so on.

(3) We can calculate an inner product of the weight vector Γ and a standard vector Γ_0 because these vectors have same order. We can also calculate an angle between the weight vector Γ and the standard vector Γ_0 as follows:

$$X = |\Gamma| \cos\theta, \quad Y = |\Gamma| \sin\theta \quad (2)$$

$$\theta = \cos^{-1}\left(\frac{<\Gamma_0 \quad \Gamma>}{|\Gamma_0| \; |\Gamma|}\right) \quad (3)$$

Where $<\Gamma_0 \quad \Gamma>$ is the inner product between the vector Γ_0 and the vector Γ, and $|\Gamma|$ is the norm of the vector Γ.

(4) We can draw a new weight performance on the 2D plane by the use of X and Y in equations (2) and (3).

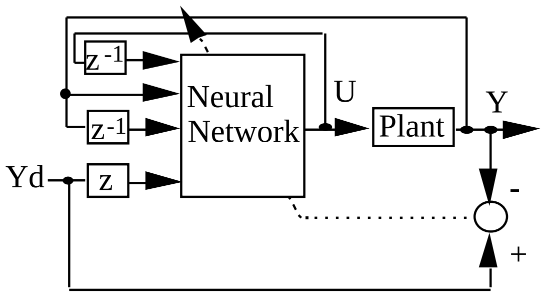

Fig.1 Block diagram of neural network direct controller for second order discrete time plant.

3. Simulation

This paper applies the tracking method of the neural network weight change to the adaptive type neural network direct controller. The simulated plant is follows:

$$Y(k) = -a_1 Y(k-1) - a_2 Y(k-2) + U(k-1) + bU(k-2) - a_3 Y(k-3) + C_{non} Y^2(k-1) \quad (4)$$

Where Y(k) is the plant output, U(k) is the plant input, k is the sampling number, a_1, a_2 & b are the plant parameters, a_3 is the parasite term and C_{non} is the nonlinear term. For this simulation, a_1=-1.3, a_2=0.3, b=0.7, a_3=-0.03 and C_{non}=0.2 are selected. The rectangular wave is also selected as the desired value Yd. The output error ε is defined as follows:

$$\varepsilon(k) = Yd(k) - Y(k) \quad (5)$$

For this simulated plant, the neuron number n in both the input and hidden layers is 4. The neural network input vector I is defined as the following equation.

$$I^T(k) = [Y_d(k+1) \; Y(k) \; Y(k-1) \; U(k-1)] \quad (6)$$

We select the following sigmoid function f(x) as the input output relation of the hidden layer.

$$f(x) = \frac{X_g\{1-\exp(-4x/X_g)\}}{2\{1+\exp(-4x/X_g)\}} \quad (7)$$

Where Xg is the parameter which defines the sigmoid function shape. The plant input U(k) equals the neural network output composed as follows:

$$U(k) = \omega^T(k) f\{W(k) I(k)\} \quad (8)$$

The block diagram of the adaptive type neural network direct controller is shown in Fig.1. The learning rule of this neural network controller is shown in the following equations.

$$W_{ij}(k+1) = W_{ij}(k-1) + \eta\varepsilon(k)\omega_i(k-1) I_j(k-1) \times f'\{\sum_{j=1}^{n} W_{ij}(k-1) I_j(k-1)\} \quad (9)$$

$$\omega_i(k+1) = \omega_i(k-1) + \eta\varepsilon(k) f\{\sum_{j=1}^{n} W_{ij}(k-1) I_j(k-1)\} \quad (10)$$

Where η is the parameter to determine the neural network convergence speed. We select the weight vector derived from the initial neural network weights as the standard vector Γ_0 of the equations (2) and (3)

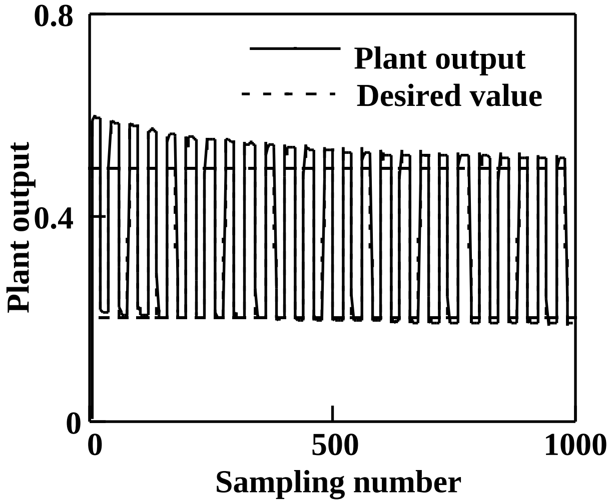

Fig.2 Plant output (k=1~1000).

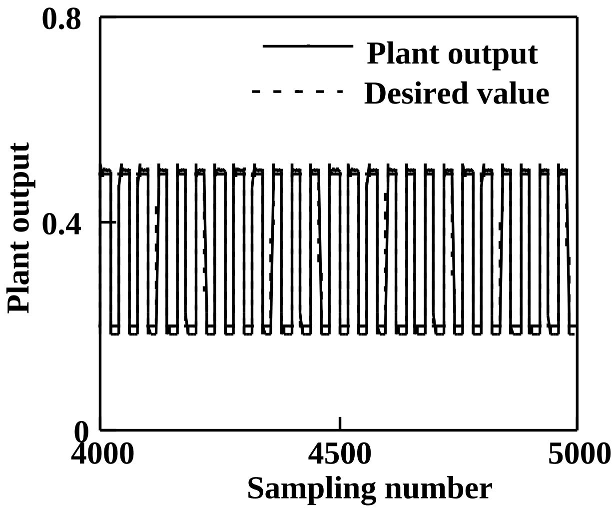

Fig.3 Plant output (k=4000~5000).

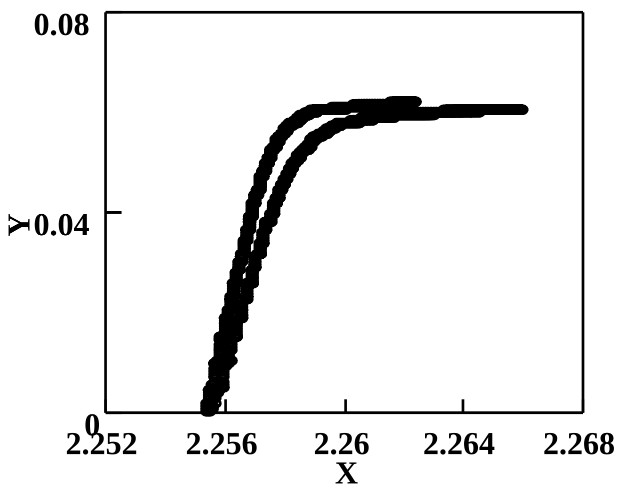

Fig.4 Track of neural network weight change.

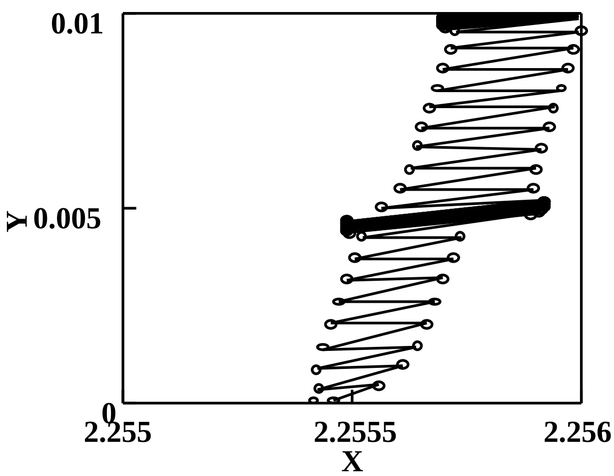

Fig.5 Expansion of track around initial stage of learning.

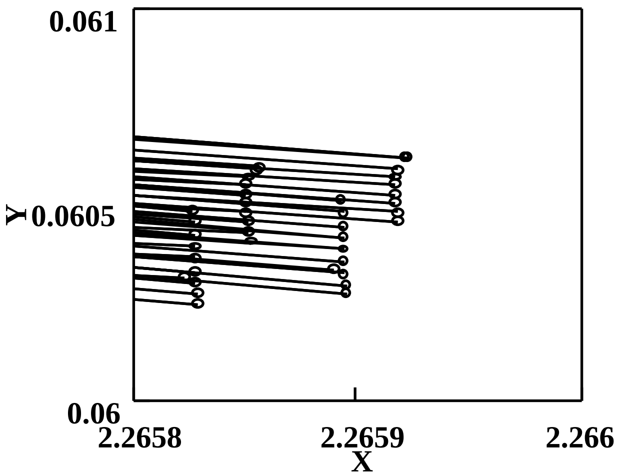

Fig.6 Expansion of track around final stage of learning.

There is less meaning in the cost function for the adaptive type neural network controller. This is because the neural network weights are changed at every sampling time. We usually use the plant output as an examination of the neural network performance. Figure 2 shows an example of the plant output (k=1~1000). The solid line and the broken line show the plant output and the desired value respectively. As shown here, the plant output converges with the desired value. Figure 3 shows the plant output (k=4000~5000) of this example. As shown here, a small error remains, but the plant output converges with the desired value and whole control system is stable. As shown in these figures, the neural network learning seems to be well performed. Figure 4 shows the track of the neural network weight change. It is drawn by the use of our tracking method explained in the section 2. In this figure, I draw a circle at the point (X,Y) of eqs.(2)&(3). Since we select the vector derived from the initial neural network weights as the standard vector Γ_0, the neural network learning begins on the X axis. As shown in this figure, the track of the neural network weight change separates into two trajectories as learning progresses. The difference between two trajectories becomes to be large and they do not converge in this example. Figure 5 shows the expansion of the track around the initial neural network learning stage. The circle is drawn and the solid line shows the sampling time sequence. As shown here, the track of the neural network weights change separates after several sampling time. Figure 6 shows the expansion of the right trajectory of the track around the final neural network learning stage. As shown here, the neural network weight change is not finished although the plant output converges with the desired value. Figure 7 shows an another example of the track of neural network weight change (a_3=0, C_{non}=0). Figures 8 and 9 show the expansions of Fig.7. As shown in these figures, the track of neural network weight change is separated into two trajectories. Above phenomena are not observed in the application to the learning type neural network direct controller.

4. Conclusion

This paper applied the tracking method of the neural network weight change to the adaptive type neural network direct controller. The simulation results confirm the usefulness of the tracking method for the adaptive type neural network direct controller. I also obtain interesting phenomena which are not observed on the simulation for the learning type neural network direct controller. The track of the neural network weight change are separated into two trajectories.

Acknowledgment

The author wishes to express his thanks to Mr.Yasuhiro Uematsu, graduated student, Ibaraki University, for his programming and simulation.

References

[1] Takayuki Yamada, "Remarks on tracking method of neural network weight change for learning type neural network direct controller", Proceedings of AROB 10th '05 (The Tenth International Symposium on Artificial Life and Robotics 2005), pp.624-627(2005)

[2]T.Yamada and T.Yabuta, "Some Remarks on characteristics of Direct Neuro-Controller with Regard to Adaptive Control", Transactions of the Society of Instrument and Control Engineers, Vol.27, No.7, pp.784-791(1991)(in Japanese)

[3]K.S.Narendra and K.Parthictsarathy, "Identification and Control of Dynamics System Using Neural Networks", IEEE Transaction on Neural Networks, Vol.1, No.1, pp.4-27, 1990

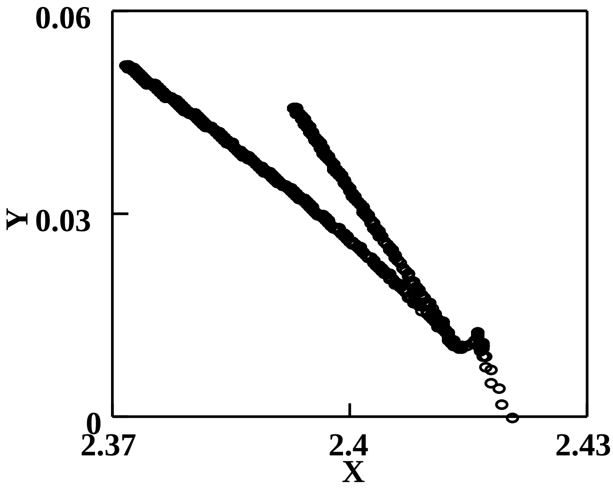

Fig.7 Track of neural network weight change.

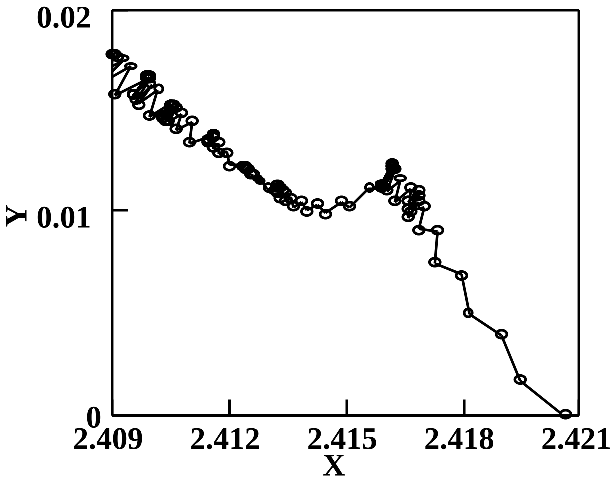

Fig.8 Expansion of track around initial stage of learning.

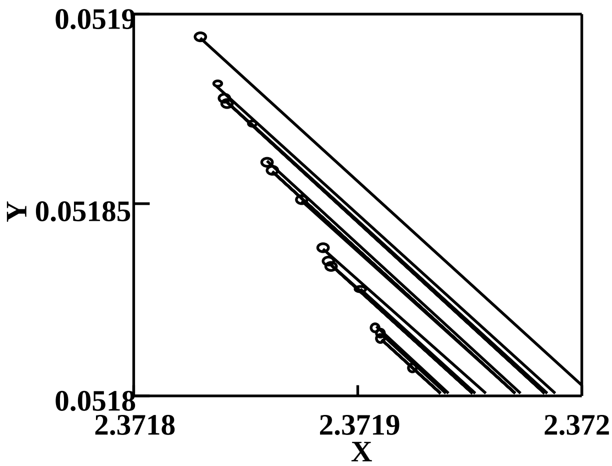

Fig.9 Expansion of track around final stage of learning.

The Eleventh International Symposium on Artificial Life and Robotics 2006 (AROB 11th'06),
B-con Plaza, Beppu, Oita, Japan, January 23-25, 2006

Situation Recognition Mechanism Based on the Fuzzy ART for a Communication Robot

K. Iwatsubo* Y. Haga** Y. Hoshi* B.T. Nohara*

*Musashi Institute of Technology
1-28-1 Tamazutsumi, Setagaya-ku
Tokyo, 158-8557, Japan

**Bandai Co.,Ltd.
1-4-8 Komagata, Taito-ku
Tokyo, 111-8081, Japan

Abstract

In this paper, we propose the new method of categorizing the perceptual space using the Fuzzy ART (Adaptive Resonance Theory) algorithm. The Fuzzy ART, which is a kind of the neural network, is an architecture to classify the vector. To categorize the perceptual space is to classify the information of environment acquired by a robot. When a robot properly categorizes the information of environment, a robot can recognize present situation around a robot itself. We also demonstrate the usefulness of the proposed method by applying the function of the human body detection to a communication robot.

Keywords: Back Propagation, Communication Robot, Fuzzy ART Neural Network, Human Body Detection, Pyroelectric Sensor, Situation Recognition

1 Introduction

The technology of robots has made rapid progress. Recently developed robots are able to do more complex actions compared with traditional one. However, considering many applications of robots in the future, the development of a well behavior based robot is desirable. To achieve autonomous behavior of a robot, a robot should recognize a present situation around a robot itself using sensors installed in a robot. Then a robot selects a suitable behavior for the recognized situation, and executes the appropriate action. Up to now, the field of the artificial intelligence has been studied from the viewpoint of acquiring an appropriate action for the situation. However, the definition of the situation needed a human's design in order to acquire actions of a robot in past studies.

The number of sensors installed in the robot and the resolution quantization determine the volume of perceptual space for a robot. Increasing the number of sensors and improving the resolution quantization of the sensors for the achievement of the high recognizable accuracy explode the perceptual space of a robot. When the perceptual space is exploded, we face on the difficulty that defines each situation. Therefore it is desirable that a robot categorizes the perceptual space autonomously. In this paper, we propose the method of categorizing the perceptual space using Fuzzy ART algorithm. The Fuzzy ART has a feature which is creating new neurons. The proposed system is expected to improve the recognizable accuracy of a robot by utilizing this feature.

We demonstrate the usefulness of the proposed method by applying the function of the human body detection to a communication robot. The human body detection system is accomplished by the integration of the Fuzzy ART and BP (Back Propagation). The heat detection sensor called 'pyroelectric sensor' is installed in the robot, and the human body detection is achieved by measuring body temperature. After the learning, a robot can distinguish a human body and an obstacle using the integration of the Fuzzy ART and BP.

2 The Fuzzy ART Neural Network

2.1 Outline

The ART network, which is a kind of the neural network, was originally proposed by Carpenter and Grossberg[1]. The ART network uses binary inputs. For analog inputs the Fuzzy ART was designed[2][3]. In this study, we use the Fuzzy ART since input is analog value and the perceptual space is easily constructed by the Fuzzy ART. Fig.1 shows the structure of the Fuzzy ART used in this study. The Fuzzy ART consists of the comparison layer, named F1-layer, and the recognition layer, named F2-layer.

An input vector to the F1-layer fits a neuron in the F2-layer. When no neuron is fitted, a new neuron is

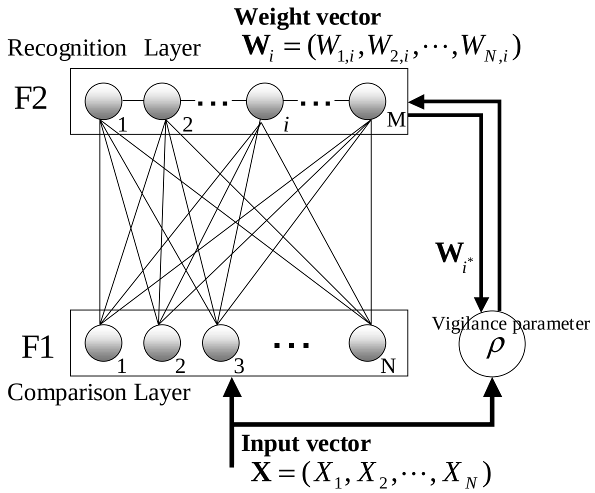

Fig. 1: Structure of the Fuzzy ART

created in the F2-layer. The significant feature of the Fuzzy ART is to create new neurons. Neurons in the F2-layer have the weight vector as a template of memory pattern. The fitness is calculated by comparing with the input vector and the weight vector in the F2-layer. The vigilance parameter ρ $(0 < \rho < 1)$ is a threshold value which decides whether a new neuron should be created.

2.2 Operation

An input vector $\mathbf{X}(0 < X_i < 1)$ to the F1-layer is represented as a N-dimensional vector, where N is the number of perceptual input of a robot. After the input vector $\mathbf{X}$ is put to the F1-layer, the weight vector $\mathbf{W}_i$ of the $i-$th neuron in the F2-layer is compared with the input vector $\mathbf{X}$. The weight vector $\mathbf{W}_i$ has the same dimension of the input vector. The value of selection intensity T_i, which is the level of excitation of the i-th neuron in the F2-layer, is calculated as follows:

$$T_i = \frac{|\mathbf{X} \wedge \mathbf{W}_i|_N}{\alpha + |\mathbf{W}_i|_N}, \tag{1}$$

where $\alpha(0 < \alpha < 1)$ is the choice parameter, and $|\mathbf{W}_i|_N$ and $\mathbf{X} \wedge \mathbf{W}_i$ are defined by $|\mathbf{W}_i|_N = \sum_{i=1}^{N} |W_i|$ and $\mathbf{X} \wedge \mathbf{W}_i = [\min(X_1, W_{1,i}), \cdots, \min(X_N, W_{N,i})]$, respectively.

The neuron with the largest value of selection intensity is selected as the best match neuron i^*, and the fitness A_{i^*} of the best match neuron is calculated as follows:

$$A_{i^*} = \frac{|\mathbf{X} \wedge \mathbf{W}_{i^*}|_N}{|\mathbf{X}|_N}. \tag{2}$$

Then the fitness is compared with the value of vigilance parameter ρ. If $A_{i^*} \geq \rho$, then the input vector fits the best match neuron, and the weight vector of the best match neuron is updated as follows:

$$\mathbf{W}_{i^*}^{\mathrm{new}} = \beta(\mathbf{X} \wedge \mathbf{W}_{i^*}^{\mathrm{old}}) + (1-\beta)\mathbf{W}_{i^*}^{\mathrm{old}}, \tag{3}$$

where β $(0 < \beta < 1)$ is the learning speed ratio.

If $A_{i^*} < \rho$, which means that the input vector does not fit the best match neuron, then the next best match neuron is searched again. The search for the best match neuron is repeated until $A_{i^*} \geq \rho$ is satisfied as follows:

- to select the second largest $T_{i'}$ (Eq.(1)) (*)
- to calculate $A_{i^{*\prime}}$ (Eq.(2)) corresponding to $T_{i'}$
- if $A_{i^{*\prime}} \geq \rho$, then $\mathbf{W}_{i^{*\prime}}^{\mathrm{new}} = \beta(\mathbf{X} \wedge \mathbf{W}_{i^{*\prime}}^{\mathrm{old}}) + (1-\beta)\mathbf{W}_{i^{*\prime}}^{\mathrm{old}}$ (Eq.(3))
- if $A_{i^{*\prime}} < \rho$, then go to (*)

If there is no neuron that should be fitted in the F2-layer, a new neuron is created in the F2-layer. The weight vector of a new neuron is set to the input vector as follows:

$$\mathbf{W}_{M+1} = (X_1, X_2, \cdots, X_N). \tag{4}$$

The Fuzzy ART network is constructed by repeating the renewal of the weight vector $\mathbf{W}_i$ and the creation of a new neuron in the F2-layer.

2.3 Perceptual space represented by the Fuzzy ART

We consider the perceptual space of a robot. The perceptual space represented by the Fuzzy ART is accomplished using the complement coding. The extended input vector $\widehat{\mathbf{X}}$ modified from the original input vector $\mathbf{X}$ is written using the complement coding as follows:

$$\widehat{\mathbf{X}} = (\underbrace{X_1, \cdots, X_N}_{\mathbf{X}}, 1-X_1, \cdots, 1-X_N). \tag{5}$$

Note that $\widehat{\mathbf{X}}$ is a 2N-dimensional vector. Let the extended weight vector $\widehat{\mathbf{W}}_i$ corresponding to $\widehat{\mathbf{X}}$ be denoted by

$$\widehat{\mathbf{W}}_i = (W_{1,i}, \cdots, W_{N,i}, \overline{W}_{1,i}, \cdots, \overline{W}_{N,i}). \tag{6}$$

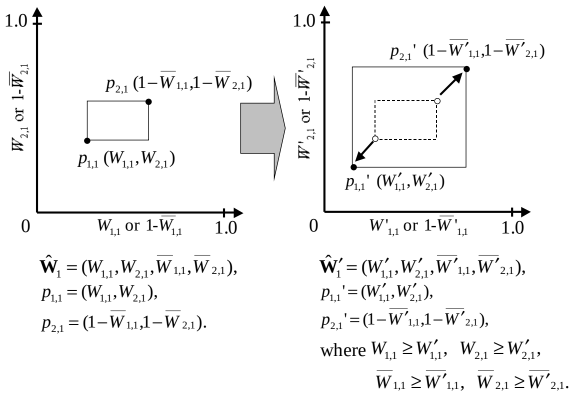

Fig. 2: Perceptual space in the Fuzzy ART

Here, we define the following two points $p_{1,i}$ and $p_{2,i}$ in the N-dimentional space using the complement coding:

$$\begin{aligned} p_{1,i} &= (W_{1,i},\cdots,W_{N,i}), \\ p_{2,i} &= (1-\overline{W}_{1,i},\cdots,1-\overline{W}_{N,i}). \end{aligned} \tag{7}$$

The perceptual space categorized by the Fuzzy ART becomes the linear space spanned maximally by the two points $p_{1,i}$ and $p_{2,i}$. Fig.2 shows an example of the two-dimensional perceptual space. We update the extended weight vector based on Eq.(3). So, the norm of the weight vector decreases and the created perceptual space expands gradually.

3 Experiment

3.1 The human body detection and a pyroelectric sensor

We demonstrate the usefulness of the proposed method by applying the function of the human body detection to a communication robot. The function of human body detection is necessary for a communication robot since a robot works required tasks ordered by a robot's user. Many industrial applications perform the function of human body detection using an image sensor so far. However the system using an image sensor is too expensive to apply to the consumer market of communication robots. Therefore we utilize a 'pyroelectric sensor' instead of an image sensor as the detection of human bodies.

The pyroelectric sensor detects the change of temperature caused by infrared rays radiated from human or animals. In the pyroelectric sensor used in this study, the detectable distance is 1.0[m], and the horizontal, detectable range is -30[deg]$\sim$+30[deg].

3.2 Communication robot

Fig.3 shows our communication robot 'BN-16' used in this study. This robot has two driving wheels installed in both sides and a free wheel in the rear side. The pyroelectric sensor and the infrared sensor are installed in three directions (the front, the front-left, and the front-right) of the robot as shown in Fig.4. In the infrared sensor used in this study, the detectable distance is 1.3[m], and the horizontal, detectable range is -15[deg]$\sim$+15[deg]. The function of human body detection is accomplished by using pyroelectric sensors and infrared sensors.

3.3 Total system

The proposed method stated in Section 2 is applied to the perceptual space of BN-16. The human body detection system is accomplished by the integration of the Fuzzy ART and Neural Network that uses BP (Back Propagation). In the human body detection system, the perceptual space of BN-16 is categorized using the Fuzzy ART, and each categorized space is recognized using BP. Fig.5 shows the outline of the system of human body detection by the integration of the Fuzzy ART and Neural Network. Total system consists of the F1-layer, the F2-layer, and the F3-layer. The network between the F1-layer and the F2-layer is constructed by the Fuzzy ART, and the network between the F2-layer and the F3-layer is assembled by Neural Network that uses BP. The pyroelectric sensor detects the difference of the temperature, so we let the

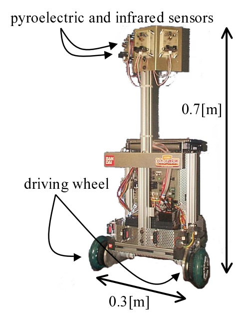

Fig. 3: Communication robot: BN-16

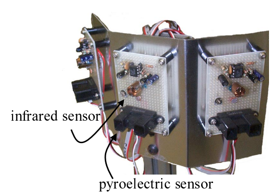

Fig. 4: Robot's sensors: Pyroelectric sensor and Infrared sensor

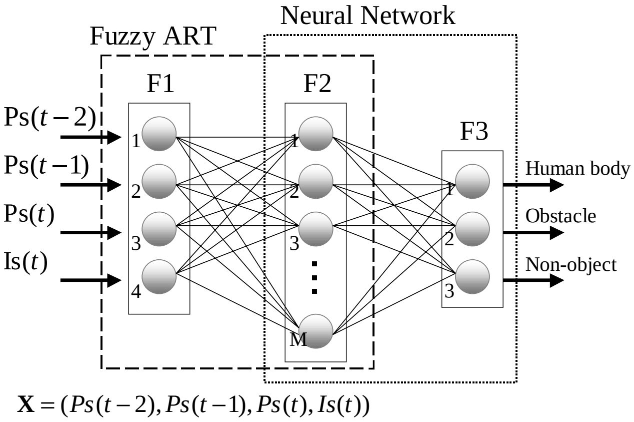

Fig. 5: The system of human body detection

input vector be

$$\mathbf{X}(t) = (\mathrm{Ps}(t-2), \mathrm{Ps}(t-1), \mathrm{Ps}(t), \mathrm{Is}(t)), \qquad (8)$$

where $\mathrm{Ps}(t), \mathrm{Ps}(t-i)$ are the value of the pyroelectric sensor at time t and the value of i-sampling earlier time, respectively and $\mathrm{Is}(t)$ is the value of the infrared sensor at time t.

The output of this system is as follows: whether a human body is detected or whether an obstacle is detected or whether nothing is detected. In the learning process, to obtain a desirable output, the neuron of the F2-layer is created as occasion demands and the weight vector between the F2-layer and the F3-layer is updated using the teacher data.

The total system works as follows: the vector $\mathbf{X}$ is inputted to the F1-layer. Then the fitness A_i in the F2-layer is calculated. The output value of the F3-layer is obtained as the product-sum of the fitness and the weight vector between the F2-layer and the F3-layer. The largest value in the output of the F3-layer is the recognition result of the total system. If the output of the F3-layer is not a correct result, the weight vector between the F2-layer and the F3-layer is updated to output a correct recognition result.

3.4 Results in the experiments

After the learning process, the recognizable accuracy reaches about 90[%], and the robot can distinguish between a human body, an object, and non-object with high rate. Fig.6 and Fig.7 shows the perceptual space constructed by $\mathrm{Ps}(t)$ and $\mathrm{Is}(t)$, in the early learning stage, and after the learning, respectively. The robot can autonomously categorize the perceptual space using the proposed method. We applied the proposed system to the robot with the function of tracking a human body to demonstrate the usefulness. The communication robot can track a human body while avoiding obstacles in the experiments. The robot can distinguish between a human body and an object.

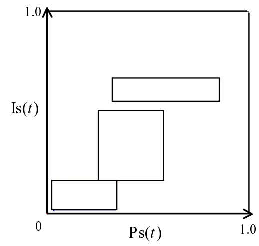

Fig. 6: Perceptual space in the early learning stage

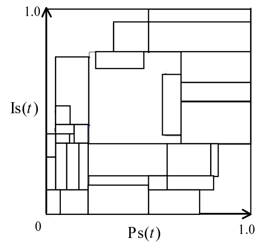

Fig. 7: Perceptual space after the learning

4 Concluding remarks

In this paper, we propose the new method of categorizing the perceptual space using the Fuzzy ART algorithm. We demonstrate the usefulness of the proposed method by applying the function of the human body detection to a communication robot. The proposed method is effective as the method of categorizing the perceptual space. We have such an advantage of the proposed method that the perceptual space of a mobile robot is categorized in real time. The proposed method is expected to be applied to the situation recognition mechanism of the controlled object such as mechanical pets and the industrial robots, etc.

References

[1] G.A. Carpenter, S. Grossberg "The ART of Adaptive Pattern Recognition," *IEEE Computer*,Vol. 21, No.3, 1988.

[2] G.A. Carpenter, S. Grossberg, and D.B. Rosen "Fuzzy ART: Fast Stable Learning of Analog Patterns by an Adaptive Resonance System," *Neural Networks*,Vol. 4, pp. 759-771, 1991.

[3] Russell Beale, and Tom Jackson *Neural Computing: An Introduction*, KAIBUNDO, 1993.

The Eleventh International Symposium on Artificial Life and Robotics 2006 (AROB 11th'06),
B-con Plaza, Beppu, Oita, Japan, January 23-25, 2006

ulti-module neural network system with concept formation and primitive consciousness

Yasuo Kinouchi , Katsumasa Masuda , and Shoji Inabayashi
Tokyo University of Information Sciences, 1200-2 Yatoh-cho Wakaba-ku Chiba-shi 265-8501 Japan,
kinouchi@rsch.tuis.ac.jp
Pacific Technos Corp., 8-4-19 Tajima Sakura-ku Saitama-shi 338-0837 Japan,
ina@pacific-systems.co.jp

Abstract

To develop an information processing system that works in a way similar to primitive "thinking," we designed an adaptive system with concept formation and primitive consciousness in a working memory. This system is mainly composed of concept-formation modules, episodic memory, and integration modules. A number of micro features are input into the concept formation modules, and converted into a small number of signals representing concepts. These conversions corresponding to recognition are formed slowly through learning in the entire system, and details of the conversion function are memorized on weights as average occurrence ratio of micro features. The episodic memory module quickly memorizes two or more signals corresponding to concepts that occur at the same time as one scene. The integration module selects efficient and useful concepts for the entire system by means of a two-cycle voting method. Selected concepts are sent back to the concept formation modules. The module that originally output the returned concept reversely converts them into a kind of micro feature signal representing an imagery of the concept; that is, this reverse conversion corresponds to recollection, and displays the imagery in the working memory. These virtual and dim imageries reproduced in a working memory and the mechanism of reproducing the imageries are principal parts of our primitive consciousness.

1. Introduction

We have designed a multi-module neural network system that adapts to the environment using concept formation and primitive consciousness with a working memory. A lot of discussions about consciousness have been done so far. However, understanding consciousness still faces many problems. Haikonen has already paid attention to the importance of inner speech, and has developed an implementation method based on a neural network [1], but this method is not necessarily clear because of the structure of a main association unit is not concrete. Though Taylor[2] and Koch[3] explained consciousness in the brain after a detailed research of brain functions, both explanations are not enough to clarify a structure based on neural networks. Although a system with primitive consciousness must be capable of concept formation, recollection of concepts as an inverse operation of recognition, and association between concepts that can be controlled in detail, they did not consider these functions.

Since these functions are difficult to execute on current neural networks, such as the widely used back-propagation type, we paid attention to the necessity of links between nodes and devised a simple neural network. In this new neural network, the weight between nodes is changed by a similar way to Hebb's rule. After learning, when a link between nodes is necessary, the value of its weight is given as 1. When a link is unnecessary, it is given as 0. When the necessity is uncertain, it is given as . Under the assumption that input signals of the modules are expressed by 1 or 0, depending on the presence of micro features, the group of weight values expresses concepts or images. By outputting the weight value, concepts and images can be recollected as sets of micro features. Combining concept formation and recollection functions of the neural network allowed us to create an associative memory system that can be minutely controlled.

The above neural networks were used to design a module with concept formation and association, a module for episodic memory, and a module for integration. The module for integration selects efficient and useful concepts for the system by using a two-cycle voting method that we devised. The concepts selected by this module are returned to the module which recognized the concept, and displayed as a dim imagery on a working memory by using the recollection function. The content in the working memory is again input to the module for concept formation together with the input from the external world. This means that the system considers the images on working memory to be a kind of reality similar to the images from the surrounding environment. Repeating this process, the system can adapt to the environment autonomously.

2. Consciousness, concepts, and images

We assumed that our consciousness is classified into two displays of inner spaces according to our senses in daily life.

(1) Real world and real-time spaces: This space displays the external environment and the state inside of our body. We feel this display as a reality through senses such as sights and sounds. Each sense is independent, and each space is not integrated across two or more senses. The system itself cannot change the displayed content. The content of these spaces does not influence an action decision of the system directly.

(2) Thinking space: In the thinking space, all senses, such as sight and sound, are integrated, and images and

concepts considered the most important by the system are displayed on each occasion. When we recall a past scene or imagine a future forecast, images are displayed. The content displayed here is information that has spread not in the real-time world but in the wide space-and-time world. Moreover, the system itself can change the content of the space. The display shows information integrated at the highest level in a system. The content influences an action decision of the system directly. The thinking space is a kind of "virtual space" where our thinking is displayed.

We think that an important part of consciousness belongs to the thinking space, which is therefore mainly discussed in this paper. However, to treat this thinking space independently of the usual word "thinking", it is called "virtual space" in this paper.

We consider primitive consciousness to be a kind of virtual space with the following functions.

a. Useful information for the system is selected and generated by the integration of several senses, past experiences, and forecasts about the future.

b. The selected and generated information are displayed in virtual space as a dim imagery.

c. The displayed content influences the action of the system and the content of virtual space.

d. The system associates various concepts and images from the content of virtual space.

e. The system intentionally simulates and forecasts future events by operating the images in virtual space.

f. The system displays the system itself in virtual space as an image.

In regards to the above functions, images and concepts become important basic units. Images usually range widely from an extremely ambiguous image to a clear image. An image that is clear and general is called a concept in this paper. That is, the concept is treated as a subset of the image. Moreover, the function for generating and controlling images and concepts is indispensable in order to achieve the function of consciousness. In this study, we used Kinouchi and Inabayashi's methods [4][5] for generating concepts from images and associating between images and concepts in a simple layered neural network.

3. Configuration and functions of system

As shown Figure 1, this system is mainly composed of three kinds of modules: concept formation, log(episodic memory), and integration. Parallel stimulations are input to the system as a time series. The inputs from the environment are converted into signals of micro features by sensors and preprocessing.

3.1 Concept formation module

This module is composed of a visual sub-module, an auditory sub-module, and a body sub-module. Micro features are input into these sub-modules, and each sub-module has two layer as shown Figure 2.

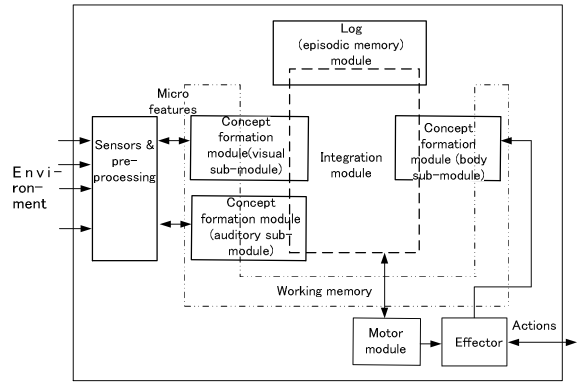

Fig. 1 system configuration

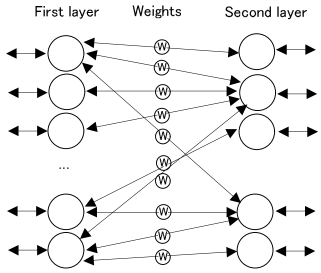

Figure 2 Configuration of Concept formation module

The nodes on the first layer are connected with all the nodes on the second layer. There are weights between the two layers. The input, a cluster of micro features, at time t from the preprocessing module to the first layer is given by (t) = $(x_1,x_2,\ldots,x_i,\ldots,x_m)$. Here, x_i has three states: "1", "0", and " ". When the i-th feature exists in image , x_i is given as 1. When the i-th feature is absent, x_i is given as 0. The mark shows that image is not influenced by the existence of the i-th feature. In the basic processing mode, the first layer outputs R(t) = $(r_1,r_2,\ldots,r_i,\ldots,r_m)$, which is R(t)= (t), to the second layer. The weights of the links between the first layer and the second layer are given by $W^C_j(t) = (w^C_{1j},w^C_{2j},\ldots,w^C_{ij},\ldots,w^C_{mj})$. Here, $w^C ij$ ($0 \leqq w^C ij \leqq 1$) is the weight of the link that connects node i on the first layer and node j on the second layer. The total input of node j on the second layer is calculated from

$$E^C_j = \Sigma\ (r_i \quad f(w^C_{ij})\ )\ /m \quad (i=1,m), \qquad (1)$$

where $f(w^C_{ij})$ is a step function that converts analog variable w^C_{ij} to discrete variables "1", "0", and " " according to the following equations.

$$f(w^C_{ij}) = 0 \quad (0 \leqq w^C_{ij} \leqq d),$$
$$f(w^C_{ij}) = \quad (d \quad w^C_{ij} \leqq 1-d),$$
$$f(w^C_{ij}) = 1 \quad (1-d \quad w^C_{ij} \leqq 1)$$

The operation "*" means comparing two inputs, as shown in Table 1.

Table 1.

Input A	0	0	0	1	1	1			
Input B	0	1		0	1		0	1	
Output	1	0	d	0	1	d	d	d	d

($0 \leqq d \leqq 1$)

Only one node j with the highest value E^C_j becomes excited and emits signal 1 to other modules. And it varies weights w^C_{ij} according to the next equation, in which constant k_C is a learning rate coefficient with a small value.

$$w^C_{ij}(t+1)= w^C_{ij}(t) + k_C\,(x(t) - w^C_{ij}(t)) \qquad (2)$$

As this process is repeated, w^C_{ij} slowly approaches the average value of occurrence rate of $x_i=1$, under the condition that node j is excited. When $f(w^C_{ij})$ of node j equals 1, micro feature x_i belongs to those images or concepts represented by node j. When $f(w^C_{ij})$ of node j equals 0, x_i does not belong to those images or concepts. And when $f(w^C_{ij})$ of node j equal #, x_i does not affect the images or concepts. As a whole, images and concepts are formed and memorized slowly in concept formation modules. After the concepts and images are formed, they are used for recognition and association between them.

3.2 Integration module

The main function of the integration module is selecting efficient and useful images and concepts for the entire system from outputs of the concept formation modules and the episodic memory module. This function is formed in a two-step process on the structure shown in Figure 3, in which node i and node j are mutually connected and have links in the both directions. The link from node i to node j has a weight w^I_{ij} ($0 \leqq w^I_{ij} \leqq 1$).

First step: Efficient images and concepts are selected according to the weights determined in the first step. This step is comprised of two-cycle actions.

First Cycle: Each node in the concept formation modules is excited according to the E^C_j, and outputs of the modules are input to the integration module, and propagate to other nodes. Then gain of nodes j, E^I_j, are calculated by each output of node i, $y_i(t)$, according to next equation.

$$E^I_j = \Sigma\,(y_i(t) \cdot w^I_{ij}(t)) / n \quad (i=1,n). \qquad (3)$$

E^I_j shows the degree how the excitation of node j expected according to past selection results.

Second Cycle: Excitation of each node j is determined according to the E^C_j calculated in the concept formation module and E^I_j calculated in first cycle. Only several nodes exciting with a large value of $g(E^I_j) + E^C_j$ are selected in the integration module based on modified "winner takes all" rule, where $g(E^I_j) = 2E^I_j - 1$. Using function g, E^I_j has both excitation and suppressing effect. Selected nodes are not only corresponding to concepts recognized in a concept formation module to which nodes belong but also supported from other modules according to coincidence of nodes excitation.

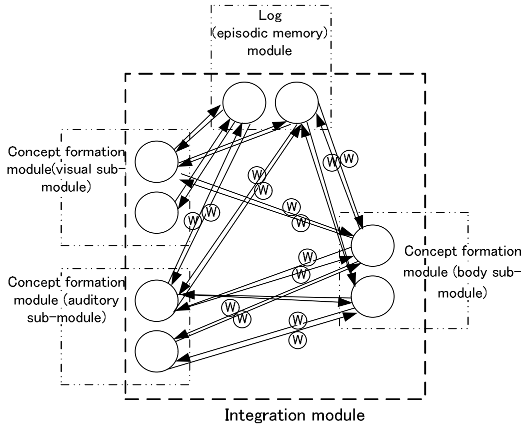

Fig. 3 Configuration of Integration module

In the concept formation module, selected nodes act in the reverse direction, and output values of $f(w^C_{ij})$ are put into working memory. Images or concepts represented as the weights $f(w^C_{ij})$ are therefore displayed on the working memory, so we can feel imageries in a virtual space or thinking space. Using the two-cycle action, even when many conditions exist at the same time, a useful node for the system can be appropriately selected. Moreover, signal propagation in the reverse direction is a kind of positive or negative feedback, so this process sustains "attention" at the micro feature level.

Second step: The results of selection signals in the first step are sent to the motor module, and action of system is determined and executed in the environment. Only when $y_i(t)$, output of node i, equals 1, w^I_{ij} is corrected based on the following equation corresponding to the $y_j(t)$, output of node j. Constant k_C is a learning rate coefficient with a small value.

$$w^I_{ij}(t+1) = w^I_{ij}(t) + k_I\,(y_j(t) - w^I_{ij}(t))$$

On repeating these operations, w^I_{ij} approaches conditional probability $p(y_j=1 \mid y_i=1)$.

3.3 Log (episodic memory) module

The log module memorizes a group of concepts that the integration module selected each time in order of occurrence. The group of concepts selected by the integration module corresponds to one scene of our consciousness, and the log module functions like an episodic memory. Figure 4 shows the configuration of the log module consisting of a two layer neural network with feedback. Concept-formation modules memorize the value of the average input by using a small learning coefficient. However, the log module memorizes a momentary value of the input in every case by using a large learning coefficient. Moreover, the log module has a recollection function as well as a memorizing function. The log module recalls a similar scene to the scene memorized in the past, the scenes that are associated with the first recalled scene are recollected one after another, and they are output to the integration module.

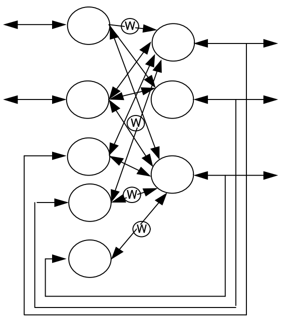

Fig. 4 Configuration of log module

4. Total system operation

4.1 Three-stage growth of the system

The functions of the entire system "grow up" by three-stage learning as explained below.

First stage: This stage corresponds to that of a baby in the human analogy. Only concept formation modules work at this time. Images and concepts are formed in learning without a teacher. The system at this time does not have decision ability, and episodic memory does not function.

Second stage: This stage corresponds to an infant. The integration module forms links based on the degree of simultaneous occurrence of images and concepts that the concept formation modules formed before. The concept formation modules start learning with a teacher. At this time, the output signal of another concept-formation module is used as a teacher signal. The system at this time has only low level decision ability, and the episodic memory does not function sufficiently.

Third stage: This stage corresponds to a child. High level decision becomes possible by using the links in the integration module with the images and concepts in the concept-formation modules, which actively learn with the teacher signal. The episodic memory functions sufficiently.

4.2 Conscious operation in the system

The functions of consciousness are completed in the third stage. Important information selected by the integration module influences states of the system through the working memory and concept-formation module. When information in the working memory is more important than that of the stimulation from the environment, the information relating to the working memory is recalled to the working memory again. The circulating operation, that is, the concept formation module, integration module, and working memory execution, is a kind of association operation. In addition, if the log module joins this circulation, it becomes association based on episodic memory.

The concept selected by the integration module is output to the motor module and influences the action decision directly. Though the decided action acts on the environment through an effector (a kind of muscle), the sensor in the effector perceives movement, and sends the sensed signal to the body sub-module at the same time. This signal influences the integration module and working memory. This means that the system can change the content of the working memory by intentional action. These actions correspond to human intentional thinking or simulating the future.

Micro features of e.g. an apple are bundled and represented by a node in a second layer in the visual sub-module. When the node is stimulated, an image of an apple is recollected and we feel an apple in the working memory. Similarly, micro senses in our body bundled and represented by a node in a second layer in the body sub-module. When the node in the body sub-module is stimulated, an image of something is recollected. We expect that something felt in the working memory is a kind of sense of self.

5. Conclusion

We have designed an adaptive system with concept formation and primitive consciousness that can be executed as thinking. This system uses a simple linkage-oriented neural network. We are now developing a simulation program of the entire system on a computer to clarify its operational characteristics.

Acknowledgments

We thank Mr. Ryohei Kobayashi for his useful suggestion.

References

[1] Haikonen P (2003), The cognitive approach to conscious machines. Imprint Academic
[2] Taylor JG et al. (2000), The frontal lobes and executive function, IJCNN2000
[3] Koch C (2004), The quest for consciousness. Roberts Company Publishers
[4] Kinouchi Y, Inabayashi S, and Sasho T et al. (2001), A structure of an associative memory system with concept formation based on mutual feature reactions. IJCNN'01
[5] Kinouchi Y, Inabayashi S, and Sasho T et al. (2000), An adaptive associative memory system based on autonomous reaction between image memories. Artificial Life and Robotics, Vol.4, pp.53-56, Springer

The Eleventh International Symposium on Artificial Life and Robotics 2006 (AROB 11th'06),
B-con Plaza, Beppu, Oita, Japan, January 23-25, 2006

A Bayesian approach to blind source separation with variable number of sources

Jun-ichiro Hirayama, Shin-ichi Maeda and Shin Ishii

Graduate School of Information Science
Nara Institute of Science and Technology
8916-5, Takayama, Ikoma, Nara, 630-0192, Japan
E-mail: {junich-h, ichi, ishii}@is.naist.jp

Abstract

Most of the existing independent component analysis (ICA) algorithms assume that the number of true sources is constant for all samples. In practical situations, however, signals often have difficult non-stationarity such that each source signal abruptly appears or disappears and hence the number of presented sources changes with time. In this article, we propose a novel ICA method, called Switching ICA, to address the blind source separation with unknown and variable number of sources in noisy situations. We incorporate a dynamical model of non-stationary sources that may abruptly appear or disappear through time into the generative model of noisy ICA, and the variational Bayes (VB) method is employed to realize an effective Bayesian inference for this model. In a simulation experiment using an artificial dataset, our method correctly recovers the original source signals and their varying number, showing a superior performance compared to the existing ICA algorithms in the presence of noise.

1 introduction

Blind source separation (BSS) is the problem of recovering unknown source signals when only their mixtures are observed, without knowing the actual mixing process. Independent component analysis (ICA) [8] is currently the most promising approach to BSS, which recovers original source signals by exploiting the statistical independence among them, which can be assumed in many situations.

Most of the existing BSS/ICA algorithms assume that the number of true sources is known and constant for all samples. In practical situations, however, the number of sources is rarely known a priori, and real-world signals often have difficult non-stationarity such that each source signal abruptly appears or disappears and hence the number of presented sources changes with time. This may degenerate the performance of source separation without considering it.

In this article, we propose a novel BSS/ICA method, called Switching ICA, to address the BSS with unknown and variable number of sources in noisy situations. We incorporate a dynamical model of non-stationary sources that may abruptly appear or disappear through time into the generative model of noisy ICA. The generative model then becomes a kind of hidden Markov model (HMM) in which the observation process is described as the data generation process of noisy ICA. We employ the variational Bayes (VB) method to derive a deterministic and computationally-effective approximation of the Bayesian inference for this model.

2 Switching ICA

2.1 Generative model

Let $\ _{j\,t}$ $(j = 1 \quad d)$ denote observations from d channels at time step , which are linear mixtures of unknown and mutually independent source signals from   channels, $s_{i\,t}$ $(i = 1 \quad)$, plus Gaussian noise. The probabilistic generative model of an observation vector $\boldsymbol{x}_t = (\ _{1\,t} \quad _{2\,t} \quad \quad _{d\,t})'$ is then given by

$$\boldsymbol{x}_t = \boldsymbol{A}\boldsymbol{s}_t + \ _t \tag{1}$$

where $\boldsymbol{s}_t = (s_{1\,t}\ s_{2\,t} \quad s_{n\,t})'$ is the source vector, $d \times$ matrix $\boldsymbol{A}$ is the mixing matrix, and $\ _t$ is the noise vector which is assumed to be distributed as an isotropic Gaussian with a mean zero and a variance $\ ^{-1}$.

2.2 Source model

Each source signal $s_{i\ t}$ is modeled as

$$s_{i\ t} = z_{i\ t} u_{i\ t} \tag{2}$$

where $z_{i\ t}$ is an indicator variable which takes zero (inactive) or one (active), called *switching variable*, and $u_{i\ t}$ is the original signal of source i. To represent the original signal, $u_{i\ t}$, we use a mixture of Gaussian (MoG) as in existing studies [11, 4]. For simplicity, we use a scale mixture [3] of two Gaussian distributions to represent super-Gaussian signals with its parameters being fixed and not adjusted by learning. Then the conditional model of $s_{i\ t}$ given $z_{i\ t} = 1$ is

$$p(\ _{i\ t}) = \ _i(\ _{i\ t}) \tag{3a}$$

$$p(s_{i\ t} \mid \ _{i\ t}\ z_{i\ t} = 1) = \mathrm{N}(s_{i\ t} \mid 0\ \phi_i(\ _{i\ t})) \tag{3b}$$

where $\ _{i\ t} \in \{0\ 1\}$ is a latent variable to indicate each of the two Gaussian components, and $\ _i(\ _{i\ t})$ and $\phi_i(\ _{i\ t})$ respectively represent the mixing rates and component variances depending on $\ _{i\ t}$. On the other hand, the source $s_{i\ t}$ takes consistently zero when $z_{i\ t} = 0$, as represented by

$$p(s_{i\ t} \mid z_{i\ t} = 0) = \ (s_{i\ t}) \tag{4}$$

where $\ (\cdot)$ denotes the Dirac's Delta function.

2.3 Markov switching

We assume a Markov process on the switching variables. Following strictly the assumption of mutual independence among sources, we assume $z_{i\ t}$ for $i = 1\ 2$ are independent of each other. The initial and transition probabilities of the switching variables are then given by $p(\boldsymbol{z}_1) = \prod_{i=1}^{n} p(z_{i\ 1})$ and $p(\boldsymbol{z}_t \mid \boldsymbol{z}_{t-1}) = \prod_{i=1}^{n} p(z_{i\ t} \mid z_{i\ t-1})$, respectively, where we assume

$$p(z_{i\ 1}) = \pi_i^{z_{i,1}} (1 - \pi_i)^{1 - z_{i,1}} \tag{5a}$$

$$p(z_{i\ t} \mid z_{i\ t-1}) = \left[(1 - r_{0i})^{z_{i,t}}\, r_{0i}^{1 - z_{i,t}}\right]^{z_{i,t-1}} \times \left[r_{1i}^{z_{i,t}} (1 - r_{1i})^{1 - z_{i,t}}\right]^{1 - z_{i,t-1}} \tag{5b}$$

Here, π_i is the probability for initial presence of the i-th source, and r_{0i}, $r_{1i} \in [0\ 1]$ are probabilities that the i-th source switches from active to inactive and from inactive to active, respectively. The parameters, $\ = (\pi_1\ \pi_2\ \ \ \pi_n)'$, $\boldsymbol{r}_1 = (r_{11}\ r_{12}\ \ \ r_{1n})'$ and $\boldsymbol{r}_0 = (r_{01}\ r_{02}\ \ \ r_{0n})'$, are unknown and estimated.

2.4 Variational Bayesian inference

A Bayesian inference for the model described above is performed by the variational Bayes (VB) method [5]. Let $\ = \{\boldsymbol{s}_t\ \boldsymbol{y}_t\ \boldsymbol{z}_t \mid\ = 1\ \ \ T\}$ denote the set of latent variables, $\mu = \{\boldsymbol{A}\ \ \}$ the set of observation model parameters, and $\ = \{\pi_i\ r_{1i}\ r_{0i} \mid i = 1\ \ \ \}$ the set of dynamics model parameters. The VB method solves a functional optimization problem to obtain the probability distribution $q(\ \ \mu\ \ )$ that well approximates the true posterior $p(\ \ \mu\ \ \mid \boldsymbol{X})$, where $\boldsymbol{X} = (\boldsymbol{x}_1\ \boldsymbol{x}_2\ \ \ \boldsymbol{x}_T)$. We introduce the factorization assumption: $q(\ \ \mu\ \ ) \approx q(\ )q(\mu\ \ )$ to allow the solution to have closed forms with respect to $q(\ )$ and $q(\mu\ \ )$. For the parameters μ, we assume a matrix normal-Gamma conjugate prior:

$$p_0(\mu) = \mathrm{N}_{d\times n}\ \boldsymbol{A} \mid \boldsymbol{M}_0\ \ ^{-1}\boldsymbol{I}_d\ \boldsymbol{G}_0^{-1}\ \ \mathrm{Ga}(\ \mid \kappa_0\ \lambda_0) \tag{6}$$

where $\mathrm{N}_{d\times n}(\cdot \mid \cdot\cdot\cdot)$ denotes a matrix normal distribution [1], and $\mathrm{Ga}(\cdot \mid \cdot\ \cdot)$ is a Gamma distribution. For , we also use a conjugate prior which is given by a product of Beta distributions.

According to the VB method, the approximate posterior for $\boldsymbol{s}_t$, conditional on $\boldsymbol{y}_t$ and $\boldsymbol{z}_t$, is derived as

$$q(\boldsymbol{s}_t \mid \boldsymbol{y}_t\ \boldsymbol{z}_t) = \frac{\ (\boldsymbol{x}_t\ \boldsymbol{s}_t)\, p(\boldsymbol{s}_t \mid \boldsymbol{y}_t\ \boldsymbol{z}_t)}{\int d\boldsymbol{s}_t\ \ (\boldsymbol{x}_t\ \boldsymbol{s}_t)\, p(\boldsymbol{s}_t \mid \boldsymbol{y}_t\ \boldsymbol{z}_t)} \tag{7a}$$

$$= \mathrm{N}_n(\boldsymbol{s}_t \mid \ \ _t(\boldsymbol{y}_t\ \boldsymbol{z}_t)\ \hat{\boldsymbol{V}}_t(\boldsymbol{y}_t\ \boldsymbol{z}_t)) \tag{7b}$$

$$\hat{\boldsymbol{V}}_t(\boldsymbol{y}_t\ \boldsymbol{z}_t) = \ \ \ \boldsymbol{A}'\boldsymbol{A}\ \ + \boldsymbol{V}_t(\boldsymbol{y}_t\ \boldsymbol{z}_t)^{-1}\ \ ^{-1} \tag{7c}$$

$$\ _t(\boldsymbol{y}_t\ \boldsymbol{z}_t) = \hat{\boldsymbol{V}}_t(\boldsymbol{y}_t\ \boldsymbol{z}_t)\,\langle\ \ \boldsymbol{A}\rangle'\,\boldsymbol{x}_t \tag{7d}$$

where $\ (\boldsymbol{x}_t\ \boldsymbol{s}_t) \equiv \exp(\langle \log p(\boldsymbol{x}_t \mid \boldsymbol{s}_t\ \boldsymbol{A}\ \ \ )\rangle_{\boldsymbol{A}\ \ }\ )$. $\boldsymbol{V}_t(\boldsymbol{y}_t\ \boldsymbol{z}_t)$ is the prior covariance matrix for $\boldsymbol{s}_t$, which is a diagonal matrix whose i-th diagonal element is $z_{i\ t}\phi_{i\ t}(\ _{i\ t})$. Note that both the prior and posterior variances for a source i degenerate to zero if $z_{i\ t} = 0$. The expectations $\langle\ \ \boldsymbol{A}\rangle$ and $\langle\ \ \boldsymbol{A}'\boldsymbol{A}\rangle$ are given by Eq. (10) below. Let $l(\boldsymbol{x}_t\ \boldsymbol{y}_t\ \boldsymbol{z}_t)$ denote the denominator in Eq. (7a). The marginal likelihood of $\boldsymbol{z}_t$ is given as

$$e(\boldsymbol{x}_t\ \boldsymbol{z}_t) = \sum_{\boldsymbol{y}_t} l\,(\boldsymbol{x}_t\ \boldsymbol{y}_t\ \boldsymbol{z}_t)\, p(\boldsymbol{y}_t) \tag{8}$$

---

[1] A matrix normal distribution is defined as

$$\mathrm{N}_{d\times n}(\boldsymbol{A}\ \ \boldsymbol{M}\ \boldsymbol{V}\ \boldsymbol{K}) = (2\ \ )^{-\frac{dn}{2}}\ \ \boldsymbol{K}\ ^{-\frac{d}{2}}\ \ \boldsymbol{V}\ ^{-\frac{n}{2}}$$
$$\exp\ \ \ \frac{1}{2}\mathrm{tr}\ \ (\boldsymbol{A}\ \ \ \boldsymbol{M})'\,\boldsymbol{V}^{-1}(\boldsymbol{A}\ \ \ \boldsymbol{M})\,\boldsymbol{K}^{-1}$$

where $\boldsymbol{A}\ \ \ ^{d\times n}$, $\boldsymbol{M}\ \ \ ^{d\times n}$, $\boldsymbol{K}\ \ \ ^{n\times n}$, and $\boldsymbol{V}\ \ \ ^{d\times d}$. $\boldsymbol{M}$ denotes the mean of $\boldsymbol{A}$; $\boldsymbol{K}$ and $\boldsymbol{V}$ are two covariance matrices of $\boldsymbol{A}$ [10].

which is the summation over 2^n possible values of the -dimensional binary vector $\boldsymbol{y}_t$. Using the marginal likelihood, the approximate joint posterior of $\boldsymbol{z}_t$ for all is

$$q(\boldsymbol{z}_1 \ \boldsymbol{z}_2 \quad \boldsymbol{z}_T)$$
$$= \frac{1}{C_{\boldsymbol{\xi}}} e(\boldsymbol{x}_1 \ \boldsymbol{z}_1) \quad (\boldsymbol{z}_1) \prod_{t=2}^{T} e(\boldsymbol{x}_t \ \boldsymbol{z}_t) \ _r(\boldsymbol{z}_t \ \boldsymbol{z}_{t-1}) \quad (9)$$

where $(\boldsymbol{z}_1) \equiv \exp(\langle \log p(\boldsymbol{z}_1 \mid \quad) \rangle_{\boldsymbol{\pi}})$ and $_r(\boldsymbol{z}_t \ \boldsymbol{z}_{t-1}) \equiv \exp(\langle \log p(\boldsymbol{z}_t \mid \boldsymbol{z}_{t-1}) \rangle_{\boldsymbol{r}_0 \ \boldsymbol{r}_1})$. $C_{\boldsymbol{\xi}}$ is the normalization term. Because Eq. (9) is a simple HMM whose transition and observation processes are given by $_r(\boldsymbol{z}_t \ \boldsymbol{z}_{t-1})$ and $e(\boldsymbol{x}_t \ \boldsymbol{z}_t)$, respectively, the marginal distributions, $q(\boldsymbol{z}_1) \quad q(\boldsymbol{z}_T)$, are exactly calculated by the standard Forward-Backward algorithm [12]. The pairwise posteriors $q(\boldsymbol{z}_t \ \boldsymbol{z}_{t-1})$ can also be exactly calculated for updating the approximate posterior for $\pi_i \ r_{1i} \ r_{0i}$ which are given as Beta distributions. The detail of Bayesian learning of HMM can be found in [9]. Taking expectations with respect to the posteriors, the following statistics are calculated: $\boldsymbol{R}_{ss} = \langle \boldsymbol{S}\boldsymbol{S}' \rangle + \boldsymbol{G}_0$, $\boldsymbol{R}_{xs} = \boldsymbol{X}\langle \boldsymbol{S} \rangle' + \boldsymbol{M}_0\boldsymbol{G}_0$, $\boldsymbol{R}_{xx} = \boldsymbol{X}\boldsymbol{X}' + \boldsymbol{M}_0\boldsymbol{G}_0\boldsymbol{M}_0'$ and $\boldsymbol{R}_{x|s} = \boldsymbol{R}_{xx} - \boldsymbol{R}_{xs}\boldsymbol{R}_{ss}^{-1}\boldsymbol{R}_{xs}'$, where $\boldsymbol{S} = (\boldsymbol{s}_1 \ \boldsymbol{s}_2 \quad \boldsymbol{s}_T)$. Then the approximate posterior for $\boldsymbol{A}$ and is given as

$$q(\mu) = \mathrm{N}_{d \times n}(\boldsymbol{A} \mid \hat{\boldsymbol{M}} \quad ^{-1}\boldsymbol{I}_d \ \hat{\boldsymbol{G}}^{-1})\mathrm{Ga}(\quad \mid \hat{\kappa} \ \hat{\lambda}) \quad (10)$$

where

$$\hat{\boldsymbol{M}} = \boldsymbol{R}_{xs}\boldsymbol{R}_{ss}^{-1}; \quad \hat{\boldsymbol{G}} = \boldsymbol{R}_{ss} \quad (11a)$$
$$\hat{\kappa} = \kappa_0 + \frac{d(\ + T)}{2}; \quad \hat{\lambda} = \lambda_0 + \frac{1}{2}\mathrm{tr} \ \boldsymbol{R}_{x|s} \quad (11b)$$

3 Simulations

We examined the basic performance of Switching ICA with a dataset synthesized by the mixing process in Eq. (1) from artificially-generated source signals. The number of mixtures and that of all potential source signals were set as $d = \ = 3$, and the time-series length was $T = 300$. The three source signals were generated from the scale-MoG in Eq. (3) with $\phi_0 = 0\ 5$, $\phi_1 = 2\ 5$ and $= 0\ 25$ (which were assumed to be known) under a specific switching assumption with an unknown mixing matrix. The switching values and source signals used to synthesize the observations are shown in the left panel of Fig. 1. The bar graph at the top of each panel shows the value of the true switching variables, $z_{i\ t}$ for $= 1\ 2 \quad T$ (denotes the true value), where the white color represents $z_{i\ t} = 1$ and the black color $z_{i\ t} = 0$. The number of active source signals varied with time: two, one and three for $\in [1\ 100]$, $\in [101\ 200]$ and $\in [201\ 300]$, respectively. We set the inverse variance of Gaussian noise at $= 6$ (SNR $\approx 16\ 81$). The prior hyperparameters were set at: $\boldsymbol{M}_0 = \boldsymbol{0}$, $\boldsymbol{G}_0 = 0\ 01\boldsymbol{I}_n$, $\kappa_0 = \lambda_0 = 1 \times 10^{-3}$, $u. = w. = 0\ 5$, and the process was iterated 500 times to converge. The hyperparameters in the trial distributions were determined randomly, except that the mean parameter of the mixing matrix $\boldsymbol{M}$ was initialized by the one estimated by an existing ICA algorithm, in order to avoid poor local maxima.

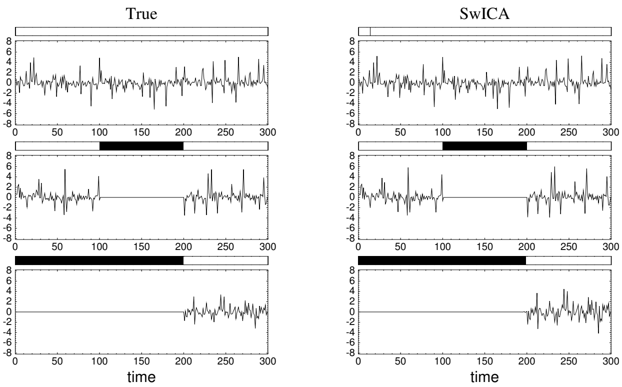

Figure 1: Examples of true and estimated source signals and the switching variables

The right panel of Fig. 1 shows a typical example of recovered source signals and the switching variables. The bar graph denotes the maximum a posteriori (MAP) estimate of the switching variables, where the black color and white colors represent zero and one, respectively. We can see that our Switching ICA (SwICA) correctly recovered the three source signals and the changes in their number by identifying the active/inactive terms for each source.

We then compared our SwICA with three ICA methods. One is JADE [6], a well-known ICA algorithm which tries to minimize cross-cumulant, and the second is an ICA using natural gradient with a nonholonomic constraint [1] (referred to as NG-N). It has been reported that NG-N correctly performed BSS in low-noise situations even when some source signals abruptly disappeared. The other one is a restricted version of our Switching ICA such that the model no longer assumes dynamics on the switching variables (referred to as NoDyna). In NoDyna, the switching variables, $z_{i\ t}$ for $= 1\ 2 \quad T$, were considered as independent Bernoulli samples as $p(z_{i\ t} = 1) = 1 - p(z_{i\ t} = 0) = r_{zi}$, instead of obeying the

Markov process in Eq. (5); the parameters, r_{zi} for $i = 1\ 2$, were simply estimated using a conjugate prior given as the Beta distribution, in a similar way to learning the dynamics parameters in the Markov process. The NoDyna algorithm used the same setting as that of SwICA described above.

Each of the four algorithms was conducted for 50 runs, by applying different Gaussian noises and using different initial hyperparameters for SwICA and NoDyna. To evaluate the estimation performance, we used the following two performance measures: average Source-to-Distortion Ratio (aSDR) and Amari's Performance Index (PI) [2], which measure the estimation performance of source signals and mixing matrix, respectively. The former was a slight modification of the Source-to-Distortion Ratio proposed in [7], which becomes high when the absolute correlation between true and estimated sources for every i is high, while it becomes low when the absolute correlation is low. The latter evaluates the reproducibility of the recovered mixing matrix up to scale and permutation ambiguities, which is zero when the mixing matrix was appropriately recovered.

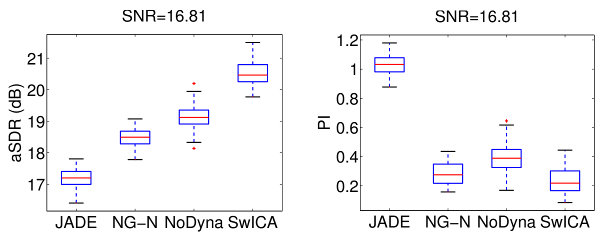

Figure 2: Comparison of the four algorithms' performances for 50 runs.

In Fig. 2, the left and right panels respectively show the box-plots of aSDR and PI for the four algorithms. We can see that the aSDR of NG-N is apparently higher than that of JADE and the PI of NG-N is lower than that of JADE. This result confirmed the effectiveness of NG-N when the number of sources changes with time in comparison to the standard ICA method. It can be seen that, however, SwICA exhibits the best performance among the four algorithms, by further improving both aSDR and PI. Especially, the improvement in PI is not shown by NoDyna, which implies the importance of assuming Markov dynamics on switching variables.

4 Conclusion

In our experiments, the Switching ICA showed a high performance of source separation in highly non-stationary situations where the number of presented sources dynamically changes over time. We are currently working on applying our method to more difficult, i.e., realistic, situations.

A major deficit of the Switching ICA is its high computational cost. Actually the cost grows in an exponential order of the number of potential sources, ; then, it is intractable when is large. This difficulty may be addressed by assuming further factorization on the trial distributions, as utilized in [4], or by some Monte Carlo techniques.

References

[1] S. Amari, T. P. Chen, and A. Cichocki. Nonholonomic orthogonal learning algorithms for blind source separation. *Neural Computation*, 12(6):1463–1484, 2000.

[2] S. Amari, A. Cichocki, and H. H. Yang. A new learning algorithm for blind source separation. In *Advances in Neural Information Processing Systems*, volume 8, pages 753–763, Cambridge MA, 1996. MIT press.

[3] D. F. Andrews and C. L. Mallows. Scale mixtures of normal distributions. *J. Royal Stat. Soc. B*, 36:99–102, 1974.

[4] H. Attias. Independent factor analysis. *Neural Computation*, 11(4):803–851, 1999.

[5] H. Attias. Inferring parameters and structure of latent variable models by variational Bayes. In *Proc. 15th Conf. on Uncertainty in AI*, pages 21–30, 1999.

[6] J. F. Cardoso and A. Souloumiac. Blind beamforming for non-Gaussian signals. *IEEE Proc. -F*, 140(6):362–370, 1993.

[7] R. Gribonval, L. Benaroya, E. Vincent, and C. Févotte. Proposals for performance measurement in source separation. In *Proc. 5th International Conference on Independent Component Analysis and Blind Signal Separation (ICA)*, number 763–768, 2003.

[8] A. Hyvarinen, J. Karhunen, and E. Oja. *Independent Component Analysis*. Wiley, 2001.

[9] D. J. C. MacKay. Ensemble learning for hidden Markov models. Technical report, Cavendish Laboratory, University of Cambridge, 1997.

[10] T. Minka. Bayesian linear regression. Technical report, MIT, 2000.

[11] E. Moulines, J.-F. Cardoso, and E. Gassiat. Maximum likelihood for blind separation and deconvolution of noisy signals using mixture models. In *Proc. ICASSP*, volume 5, pages 3617–3620, 1997.

[12] L. R. Rabiner. A tutorial on hidden Markov models and selected applications in speech recognition. *Proceedings of the IEEE*, 77(2):257–286, 1989.

The Eleventh International Symposium on Artificial Life and Robotics 2006 (AROB 11th'06),
B-con Plaza, Beppu, Oita, Japan, January 23-25, 2006

A Controller Design for a Motion Generator Based on Dual Linear Motors

Dong Hoon Lee
Sang Yeol Seo, Woo Seok Choi
Dept. of Mechanical Design, Graduate School,
Kyungnam University,
Masan, Gyeongnam, 631-701, Korea

Se-Han Lee, Han Sung Kim
School of Mechanical and Automation Eng.,
Kyungnam University,
Masan, Gyeongnam, 631-701, Korea

Abstract

In this research a 2-dimensional arm motion generator composed of two linear motors was developed. The inertia, damping and/or stiffness characteristics of the motion generator can be changed on the real-time basis by properly regulating the force generated by the linear motors. That is, active impedance is implemented without actual change in the physical structure of the motion generator. A motor force control is carried out by regulating the input currents supplied to the linear motors. In the control system the time delay due to the sampling period has an adverse effect on the stability of the system. Furthermore, disturbances caused by characteristics of the motion generator exist.

To cope with these difficulties, 2-DOF controller combined with the LQ-servo and H-infinity controller was used. This motion generator can be used to measure kinesthetic sense associated with the human arm and thus leads to developing the products for which the kinesthetic sense is taken into account.

1. Introduction

As lifestyles modernize, products with not only function in its mind but products with kinesthetic sense along with its function draw attention to customers. That is, people consider the sensibility of a product as well as its performance. In recent years, there are lots of efforts and considerations to apply this even from the designing and early stages of development.

The object of this research is to develop an arm motion generator necessary for quantification and implementation of kinesthetic sense, which mainly relates to arm movement. In most mechanical systems, motion has close relations with mechanical impedance, which consists of inertia, stiffness, and damping. The arm motion generator developed in this research must measure the kinesthetic sense difference experienced by a person by alternating the impedance or must let the person experience the desired 'sense'. But varying the impedance physically is very tedious, costly, and time demanding. The arm motion generator controls the force outputs of the linear motors as to have the same effect as to physically changing the impedance.

These kinds of motion generators are used in various flight and vehicle simulators and vigorous research of this continues today. However, these motion generators mainly use pneumatic systems to generate an entire body movement, and thus systems get complicated and manufacturing gets costly. But since the motion generator developed in this research only deals with arm movement, it makes the use of electrical motor possible, which brings system composing and controlling simple.

And the similar concept of active impedance used in this research has been widely studied in robot engineering. In robotics, when a manipulator is in contact with an object, the relation between the force exerted on the object by the manipulator and the motion at the contact point is modeled with impedance such as inertia, damping and stiffness and then the appropriate position/force control is carried out.[1]

The concept of active impedance in this research is basically the same with the impedance in robotics, but has many differences in application purpose and method.

2. Implementation of Active Impedance

A motion generator capable of implementing two dimensional plane motion is made by combining two linear motors perpendicularly as shown in Fig. 1. As an operator moves the lever with his hand to generate some movement pattern, displacement, velocity, and acceleration involved in this pattern are detected. Based on this information, motor driving current is regulated to get desired active impedance that is active inertia, active damping, and/or active stiffness. By implementing this kind of active impedance, by varying inertia, stiffness, and/or damping, one can measure the kinesthetic sense most suitable for the operator.

This chapter will explain about implementation of active impedance using the motion generator mentioned above.

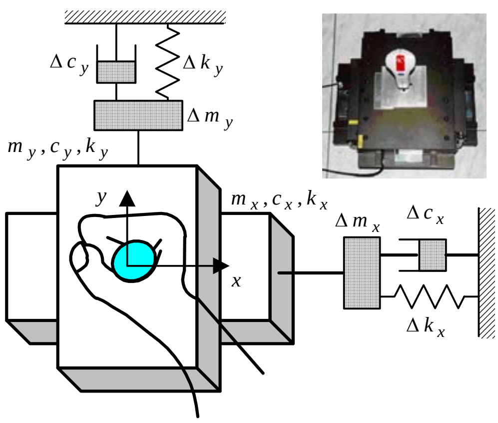

Fig.1. Configuration of the motion generator and concept of active impedance

2.1 Active Impedance

Impedance in an electrical system is a measure of current response in a circuit to certain AC voltage. Electrical impedance consists of inductance, capacitance, and/or resistance. Impedance in a mechanical system is defined in similar concept as a measure of motion response to force applied to the system, and consists of inertia, damping, and stiffness. Active impedance, mentioned in this research, means getting the same effect of physically changing the impedance of the moving part of the linear motor with only generating proper force from the motor.

Let us first consider active inertia. When an operator applies force F to the lever of the linear motor in which moving part has mass of m and no energy is supplied, acceleration of $a_O = F / m$ is experienced. Assuming that we add active inertia of Δm to mass m of actual moving part,

$$M = m + \Delta m \quad (1)$$

the operator must experience acceleration of $a = F/(m+\Delta m)$ ($< a_O$) for the same input of F. If appropriate current is supplied to the motor to generate force of $F_1 = \Delta m \cdot a$ to the opposite direction of the force given by the operator, the net force input on the moving part becomes

$$F - F_1 = (m + \Delta m)\, a - \Delta m \cdot a = m \cdot a \quad (2)$$

and so the acceleration felt by the operator is not a_o but a, which is the acceleration earned from force F applied on active inertia M, even when the operator puts force F on mass m. In this way, active inertia larger than actual inertia can be implemented.

While, given torque constant (force constant in case of linear motor) of the motor K_T and current supply i, the force generated by the linear motor F_m becomes $F_m = K_T \cdot i$. And supplying the current of

$$i_m = -\Delta m \cdot a / K_T \quad (3)$$

to the motor could generate the effect of active inertia M. Here, the letter m at the current stands for the current relating to mass(active inertia). Also, the negative sign means that the force generated by the motor should be in the opposite direction to the force applied by the operator. A plus sign(+) should be used as to get active inertia less than the actual inertia, because the force from the motor should be in the same direction with the force applied by the operator.

Active damping C and active stiffness K can be presented in the same manner,

2.2 Complex Active Impedance Implementation

Inertia, damping, and stiffness do not exist in simple forms but rather in complex structures in actual mechanical systems. That is why implementing complex active impedance is required to let us reach closer to actual systems. When an operator applies force to the arm motion generator (to the lever connected to the linear motor), the motion generator also exerts the same amount of force to the opposite direction, as noted in the Newton's law of action-reaction. This force is called reaction force. Thus, when the operator generates motion by exerting force on the lever connected to the motor, the operator will experience reaction to inertia, damping, and stiffness all in complex. Expressing this in an equation gives,

$$\begin{aligned} F_{\text{total}} &= F_{\text{inertia}} + F_{\text{damping}} + F_{\text{stiffness}} \\ &= M \cdot a + C \cdot v + K \cdot x \end{aligned} \quad (4)$$

When considering a reaction of an instant, the complex form of the inertia, damping, and stiffness would not be known. But by considering that the reaction due to inertia be proportional to acceleration, damping to velocity, and stiffness to position, one can measure the form of time-varying reaction, which leads to classification of the each component of the total reaction.

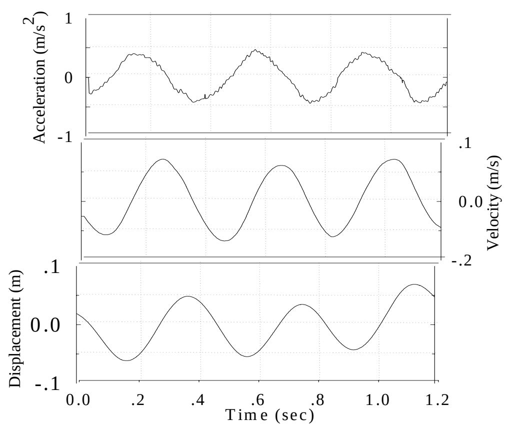

Fig. 2 Displacement, velocity and acceleration due to the arbitrary motion generated by the operator

Consider the case where an operator intentionally creates vibration by holding the lever of the motion generator as shown in Fig. 2. The velocity and acceleration in the figure can be obtained by using the basics of the measurement of the position of the linear motor moving part using the encoder. First, when the values of active impedance M, C, K which are to be implemented are set, additional impedance Δm, Δc, Δk can be calculated by using Eqn. (4). By multiplying these values of additional mass, damping, and stiffness by the acceleration, velocity and displacement obtained above and then adding this value would get the force which the linear motor should generate. At this time, the total reaction felt by the operator is expressed in Eqn (5), but for this to happen, the motor has to generate the following force.

$$F_{\text{motor}} = \Delta m \cdot a + \Delta c \cdot v + \Delta k \cdot x \quad (5)$$

To generate this force, the current that must be supplied to the linear motor is

$$i_{\text{total}} = i_m + i_c + i_k = \frac{-(\Delta m \cdot a + \Delta c \cdot v + \Delta k \cdot x)}{K_T} \quad (6)$$

3. Motion Generator System

3.1 Motion Generator System Structure

Fig. 3. shows an arm motion generator composed of the two linear motors, drive circuit to run linear motors, TMS320 DSP board used as controller, and parallel port connected PC used to collect and analyze experimental data. A voltage driven BLDC (Brushless DC) drive, exclusively for motors, is used to drive the linear motor.

The main controller TMS320 DSP board can be operated at 40MHz speed and it carries out algorithms necessary to control the motor. An A/D converter measures analog current supplied to the motor and digitizes it, then sends it to the DSP, while the D/A converter transforms the output digital signal from the controller to analog voltage to send it to the motor drive.

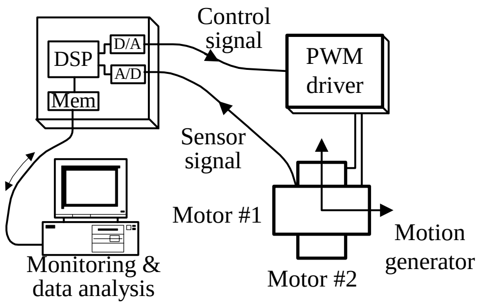

Fig. 3. Schematic of experimental setup

3.2 Motion Generator Control System

The force for the active impedance is proportional to the current supplied to the motor. But since most motor drivers are usually voltage-driven, the current is not directly controlled but it is controlled indirectly by controlling the voltage. That is, to supply desired current, the voltage of the linear motor must be controlled by the controller. The relation between the allowed input voltage u, and the current flowing through the motor i is commonly known as

$$u - K_E\, v = L\frac{di}{dt} + Ri \tag{7}$$

where L and R denote the inductance and resistance of the linear motor winding, respectively, and K_E the back emf constant. Since the motion is produced by combination of force the operator applies and force the motor generates, the displacement, velocity and acceleration of the motion generator depends mostly upon the force arbitrarily applied by the operator. Therefore, the term $K_E\, v$ on the left-hand side of Eqn. (7) varies arbitrarily, and this is treated as a disturbance in the control system. In this case the plant can be represented by

$$G_p(s) = \frac{1}{Ls + R} \tag{8}$$

Since the current output for motor drive is measured by the A/D converter and fed back to the control system, the time delay of at least the sampling period T due to A/D conversion and computation time occurs. As for the linear motor, the electric time constant τ_e is about 1,250μs, while the sampling period of the controller is T_s = 400μs. It is generally preferable that the sampling period be less than 1/10 of the plant time constant.

It is interesting to investigate the effect of this time delay scale on the control system. First take z-transform Eqn. (9) then ,

$$G_p(z) = \frac{0.10784 z^{-1}}{1 - 0.72615 z^{-1}} \tag{9}$$

roots locus corresponding to Eqn. (9) can say that K_p gain is to be limited less than 16 according to gain limitation characteristic depending on sampling period in discrete system,

To cope with such a problem, 2-DOF control system including internal plant and H-infinity controller, which is to regard modeling error, shown in Fig. 4. was employed in this research. Time delay mentioned before will be absorbed in modeling error.

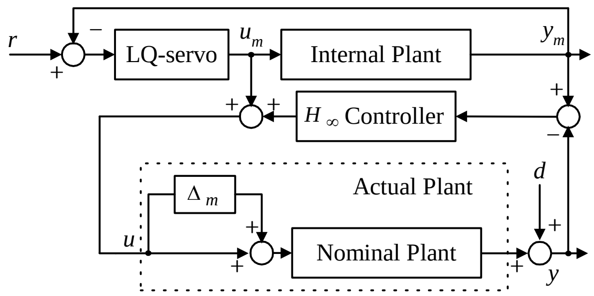

Fig. 4. Block diagram of 2-DOF current controller including internal plant and H-infinity controller.

3.3 H-infinity Control Formulation

Time delay was considered multiplicative modeling error Δ_m in Fig. 4. before. The multiplicative modeling error is generally accepted as a problem related to sensor noise system.[2]

A proper weight functions $W_S(s)$, $W_T(s)$ may be used to mixed sensitivity H-infinity control problem as following.

$$\left\| \begin{matrix} W_S(s)S(s) \\ W_T(s)T(s) \end{matrix} \right\|_\infty < \gamma \tag{10}$$

where $S(s)$, $T(s)$ is sensitivity and co-sensitivity function. γ is positive real number.

Generalized plant corresponding for Eqn. (10) and its block diagram are as following At $\gamma \approx 0.14$, obtained controller $K(s)$ satisfying Eqn. (10) and block diagram in Fig. 4. [3]

3.4 LQ-Servo Formulation

LQ-servo is used to control internal plant. Though LQ-servo problem is a kind of trial and error, LQ-servo has merit to obtain control gain considering control input constraint.[4] In this research, control input weight matrix **R** was chosen not to over maximum motor drive output.

4. Performance of the Motion Generator

The experimental condition is as following, when active stiffness, 500 N/m, active damping, 100 Ns/m, and active inertial, 5kg, are applied respectively, an operator activates the motion generator with arbitrary reciprocal motion.

In the plots, Fig. 5., Fig. 6., Fig. 7., dotted lines labeled ref. are current corresponding to displacement, velocity, and acceleration respectively caused by the operator and solid lines are current controlled by the controller proposed in this research. Though a conventional PI controller in itself is good controller, gain adjust constraint due to discretization exists.

Feed forward controller, having LQ-servo form, has no feed back loop and H-infinity controller to compensate the difference between internal plant and nominal plant has properties to guarantee robust stability against time delay characteristic, which was obstacle factor to give high gain in PI controller. By the reason mentioned before, no stability problem may occur and sufficient performance may be forecasted. The experimental results shown in Fig. 5., Fig. 6., Fig. 7. can back up the performance of controller proposed in this research.

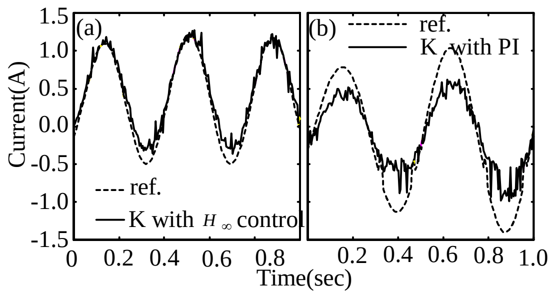

Fig. 5. Following response of Current corresponding to active stiffness using 2-DOF controller including H-infinity controller (a) and conventional PI controller (b), respectively.

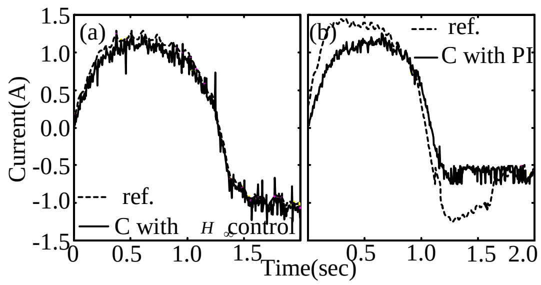

Fig. 6. Following response of Current corresponding to active damping using 2-DOF controller including H-infinity controller (a) and conventional PI controller (b), respectively.

5. Conclusions

In this research, an arm motion generator capable of two-dimensional movement is made by perpendicularly connecting two linear motors. By controlling the force generated by these motors on the motion generator, the active impedance is implemented, which has the same effect as physically changing the inertia, damping, and stiffness of the motion generator. Numerous kinesthetic senses relating to arm movement can be measured due to the ability to change the impedance, such as inertia, damping, and stiffness, on real-time basis.

In this research, a 2-DOF controller was employed to cope with some inherent problems with current control of the linear motor. The control system shows reasonable performance on both disturbance rejection and tracking. This type of research can be related to virtual reality engineering and give a user the chance to experience various kinds of virtual kinesthetic senses, and it is also expected to be applied to mechanical structures that generates various forms of forces.

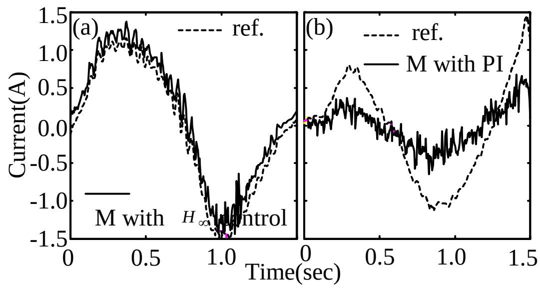

Fig. 7. Following response of Current corresponding to active inertia using 2-DOF controller including H-infinity controller (a) and (conventional PI controller (b), respectively.

Acknowledgements

This research was supported by the **N**ew **U**niversity for **R**egional **I**nnovation program of the Ministry of Education & Human Resources Development (NURI MECHANO 21).

References

[1] M. W. Spong, M. Vidyasagar, *Robot Dynamics and Control*, Wiley & Sons, pp.252-254, 1989.
[2] S. Bahram, and M. Hassel, *CONTROL SYSTEM DESIGN USING MATLAB*, Prentice-Hall, New Jersey, pp.404, 1993.
[3] Z. H. Kemin, J.C. Doyle and K. Glover, *ROBUST and OPTIMAL CONTROL*, Prentice-Hall, New Jersey, pp.459-pp.462, 1996.
[4] D. Ken, S. Thompson and B. Barraclough, *The Art of CONTROL ENGINEERING*, Addison-Wesley, England , pp.603 – 604, 1997.

The Eleventh International Symposium on Artificial Life and Robotics 2006 (AROB 11th'06),
B-con Plaza, Beppu, Oita, Japan, January 23-25, 2006

Stiffness Analysis of a Limited-DOF Parallel Manipulator including the Compliance of Both Joints and Links

Han Sung Kim*, Chang-Rok Shin, Joon-Wu Kim, and Se-Han Lee

School of Mechanical and Automation Engineering
Kyungnam University
449 Wolyoung Dong, Masan, Kyungnam, 631-701, Korea (hkim@kyungnam.ac.kr)

Abstract

This paper presents a stiffness analysis method for a limited-DOF parallel manipulator, which takes into account of elastic deformations of joints and links. A limited-DOF parallel manipulator is defined as a spatial parallel manipulator which has less than six degrees of freedom. Differently from the case of a 6-DOF parallel manipulator, the serial chains in a limited-DOF parallel manipulator are subject to constraint forces as well as actuation forces. The reaction forces due to actuations and constraints in each limb can be determined by making use of the theory of reciprocal screws. It is shown that the stiffness model of an *F*-DOF parallel manipulator consists of *F* springs related to the reciprocal screws of actuations and 6-*F* springs related to the reciprocal screws of constraints, which connect the moving platform to the fixed base in parallel. The 6×6 stiffness matrix is derived, which is the sum of the stiffness matrices of actuations and constraints. The six spring constants can be precisely determined by modeling the compliance of joints and links in a serial chain as follows; the link can be considered as an Euler beam and the stiffness matrix of rotational or prismatic joint can be modeled as a 6×6 diagonal matrix, where one diagonal element about the rotation axis or along the sliding direction is zero. By summing the elastic deformations in joints and links, the compliance matrix of a serial chain is obtained. Finally, applying the reciprocal screws to the compliance matrix of a serial chain, the compliance values of springs can be determined.

1 Introduction

A Parallel manipulator typically consists of a moving platform that is connected to a fixed base by several serial chains, called limbs. In general, parallel manipulators have some advantages of high speed, payload, accuracy and stiffness over serial manipulators. Among various parallel manipulators, the 6-DOF Stewart-Gough platform has attracted the most interests of researchers and industries, since all the linear actuators are under only tensional/compressive forces. [1,2] However, the manipulator has some disadvantages such as complex forward kinematics, small workspace, and requiring many parts.

To overcome the above shortcomings, parallel manipulators with fewer than six degrees of freedom have been investigated.[3~12] Limited-DOF parallel manipulators have the advantages of relatively simple forward-kinematics, larger workspace, lower inertia, and requiring less parts over 6-DOF counterparts. A limited-DOF parallel manipulator costs less than a 6-DOF counterpart and, hence, it may be more economic to employ such manipulators for applications for which 6-DOF is not necessary. Among limited-DOF parallel manipulators, 3-DOF translational parallel manipulators[6~9] and 3-DOF rotational parallel manipulators[10,11] have been focused.

In the beginning design stage of manipulators requiring high speed, accuracy, and stiffness, the stiffness analysis may be very essential and the most important step. For 6-DOF parallel manipulators, various methods of the stiffness analysis have been published.[12~14] However, the stiffness analysis for limited-DOF parallel manipulators has been a little investigated. Among the research results, Zhang and Gosselin[15~18] analyzed limited-DOF parallel manipulators with passive constraining limbs. However, the method of using virtual joints is not systematic. It is well known that the Jacobian and stiffness matrices of a 6-DOF parallel manipulator are 6×6 matrices. However, it is not clear as to what is the best way to express the Jacobian and stiffness matrices of a limited-DOF parallel manipulator. For the Jacobian matrix, Joshi and Tsai[19] presented that a 6×6 Jacobian matrix including actuations and constraints should be used in order to analyze all the singularities and to prevent an erroneous design.[20,21] Since the stiffness matrix is basically based on the Jacobian matrix, the stiffness matrix should contain the information on the stiffness due to actuations and constraints and should be a 6×6 matrix even for a limited-DOF parallel manipulator.

In this work, the reciprocal screws of actuations and constraints are determined by using the theory of reciprocal screws. The reciprocal screws are the reaction forces due to actuations and constraints, which eventually result in the infinitesimal deflections of joints and links in a serial chain. Using the 6×6 Jacobian matrix, the stiffness matrix becomes the sum of the stiffness matrices of actuations and constraints. The joint stiffness values can be precisely determined by modeling the compliance of joints and links in each serial chain. The stiffness values of a joint can be precisely determined by using the analytic or experimental data of bearings, and the stiffness matrix for revolute and prismatic joints becomes a 6×6 diagonal matrix, where one diagonal element about the rotation axis or along the sliding direction is zero. The links in a serial chain are modeled as Euler-Bernoulli beams. Summing the elastic deformations in all the parts, the total compliance matrix of a serial chain can be obtained. Since the total compliance matrix is generally singular, it is impossible to get the inverse matrix. Instead, multiplying the total compliance matrix by the reciprocal screws yields finite deflections about or along the reciprocal screws. From the finite deflections, the compliance values of springs can be obtained.

2 Stiffness Analysis

In this work, a limited-DOF spatial parallel manipulator with *F*-DOF ($3 \le F < 6$) is considered. As shown in Fig. 1, it is assumed that the moving platform is constrained by m number of serial-kinematic chains and each limb may have at most one actuator. The limbs having an actuator are indexed first such as $i = 1, 2, \ldots, F$, and the other limbs with no actuator are indexed as $i = F+1, F+2, \ldots, m$. Let the degree-of-freedom associated with all the joints of the *i*th limb be defined as the connectivity, C_i, of that limb.[22,23] Each limb constrains the moving platform by $6 - C_i$ number of constraints, and the total number of all the independent constraints should be six.

The overall Jacobian matrix for a limited-DOF parallel manipulator can be expressed by[19]

$$J = \begin{bmatrix} J_a & J_c \end{bmatrix} \in R^{6\times 6}, \qquad (1)$$

where the Jacobian matrix of actuations and the Jacobian matrix of constraints are given by[19]

$$J_a = \begin{bmatrix} \hat{\boldsymbol{s}}_{a,1} / \hat{\boldsymbol{s}}_{a,1}^T \hat{\boldsymbol{S}}_{a_1,1} & \cdots & \hat{\boldsymbol{s}}_{a,F} / \hat{\boldsymbol{s}}_{a,F}^T \hat{\boldsymbol{S}}_{a_F,F} \end{bmatrix} \in R^{6\times F} \text{ and,} \qquad (2)$$

$$J_c = \begin{bmatrix} \hat{\boldsymbol{s}}_{c,1,1} & \cdots & \hat{\boldsymbol{s}}_{c,6-C_1,1} & \cdots & \hat{\boldsymbol{s}}_{c,1,m} & \cdots & \hat{\boldsymbol{s}}_{c,6-C_m,m} \end{bmatrix} \in R^{6\times(6-F)}. \qquad (3)$$

In the Jacobian matrix, $\hat{\boldsymbol{s}}_{c,k,i}$ are the reciprocal screws of constraints that are reciprocal to all the joint screws, and $\hat{\boldsymbol{s}}_{a,i}$ are the reciprocal screws of actuations that are reciprocal to all the joint screws except the active joint screw, $\hat{\boldsymbol{S}}_{a_i,i}$. It is noted that the overall Jacobian matrix of a limited-DOF parallel manipulator consists of the actuation and constraint parts and the rank should be six.

It is well known that the stiffness mapping between applied wrench and infinitesimal twist at the end-effector is expressed in terms of the stiffness matrix, K

$$\hat{\boldsymbol{w}} = K\,\delta\hat{\boldsymbol{D}}, \qquad (4)$$

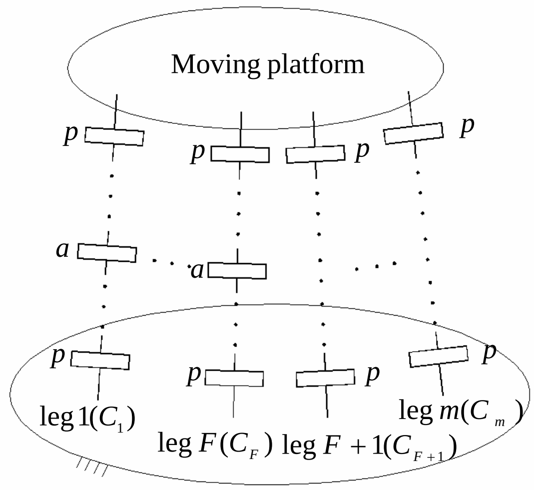

Fig. 1 Structure of an *F*-DOF parallel manipulator. (Note: *a*: active joint, *p*: passive joint)

and the stiffness matrix is given by

$$K = J[k]J^T \qquad (5)$$

Using Eqs. (2) and (3), the stiffness matrix can be expressed in terms of the Jacobian matrices of actuation and constraints by

$$K = J_a[k_a]J_a^T + J_c[k_c]J_c^T \qquad (6)$$

where $[k_a]$ and $[k_c]$ are the diagonal matrices of which the diagonal elements are the spring constants related to actuations and constraints, respectively.

When pure force is exerted on a limb with some compliance, it generates infinitesimal translational motion along the line of the force. On the other hand, when pure couple is applied to a limb, it generates infinitesimal rotational motion about the axis of the couple. Hence, the infinitesimal translational and rotational motions can be modeled as the deflection of a linear spring placed along the line of the force, and the deflection of a rotational spring with the axis of the couple, respectively. The stiffness of a limited-DOF parallel manipulator can be modeled that the moving platform is supported by six independent springs, since there exist six reciprocal screws in a general case. Among the springs, *F* springs are related to the actuations and 6-*F* springs are related to the constraints.

3 Compliance Modeling of Serial Chains

In this section, we present a method to determine the spring constants related to actuations and constraints in a serial chain. In deriving the compliance model of a serial chain, the flexibility in joints and links is considered. First, without loss of generality, only revolute and prismatic joints are considered, since a spherical joint is equivalent to three intersecting non-coplanar revolute joints, a universal joint is equivalent to two intersecting revolute joints, a cylindrical joint is equivalent to the sum of a revolute joint and a prismatic joint along the revolute joint axis, and so on. The compliance matrix of a 1-DOF joint is given by

$$C_J = \begin{bmatrix} c_{l,r} & 0 & 0 & 0 & 0 & 0 \\ 0 & c_{l,r} & 0 & 0 & 0 & 0 \\ 0 & 0 & c_{l,a} & 0 & 0 & 0 \\ 0 & 0 & 0 & c_{\theta,r} & 0 & 0 \\ 0 & 0 & 0 & 0 & c_{\theta,r} & 0 \\ 0 & 0 & 0 & 0 & 0 & c_{\theta,a} \end{bmatrix} \tag{7}$$

where the axis of a joint is aligned with the z-axis of a local frame, and the radial direction of a joint is placed on the xy plane of a local frame as shown in Fig. 2. The subscripts, l and θ denote the linear and rotational stiffnesses, and the following subscripts, a and r denote the axial and radial directions. It is noted that $c_{\theta,a} = \infty$, for a revolute joint, and $c_{l,a} = \infty$, for a prismatic joint.

Second, the links in a serial chain are considered as Euler-Bernoulli beams, implying that the shear effect and inertia of rotation of the beam section are ignored, and beam sections stay plane and perpendicular to the neutral axis. Forces and moments elastically deform the tip of each link. The elastic deformations at the tip of a link are written as follows:

$$\begin{aligned} \delta_x &= \frac{L^3}{3EI_x}F_x + \frac{L^2}{2EI_y}M_y \\ \delta_y &= \frac{L^3}{3EI_y}F_y - \frac{L^2}{2EI_x}M_x\,,\ \delta_z = \frac{L}{AE}F_z\,, \\ \theta_x &= -\frac{L^2}{2EI_y}F_y + \frac{L}{EI_x}M_x\,, \\ \theta_y &= \frac{L^2}{2EI_x}F_x + \frac{L}{EI_y}M_y\,,\ \theta_z = \frac{L}{GI_p}M_z \end{aligned} \tag{8}$$

where A and L are the area and length of a link, E is the modulus of the longitudinal elasticity, G is the modulus of the transverse elasticity. I_x, I_y and I_z are the moment of inertias about the x, y, and z axes, respectively. I_p is the polar moment of inertia. Then, the compliance matrix of a link is given by

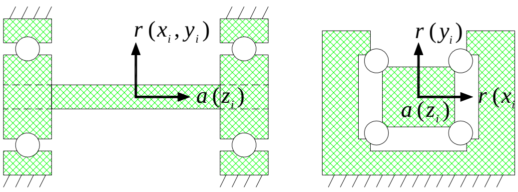

Fig. 2 Compliance model of 1-DOF joints.

$$C_L = \begin{bmatrix} \frac{L^3}{3EI_x} & 0 & 0 & 0 & \frac{L^2}{2EI_y} & 0 \\ 0 & \frac{L^3}{3EI_y} & 0 & -\frac{L^2}{2EI_x} & 0 & 0 \\ 0 & 0 & \frac{L}{AE} & 0 & 0 & 0 \\ 0 & -\frac{L^2}{2EI_y} & 0 & \frac{L}{EI_x} & 0 & 0 \\ \frac{L^2}{2EI_x} & 0 & 0 & 0 & \frac{L}{EI_y} & 0 \\ 0 & 0 & 0 & 0 & 0 & \frac{L}{GI_p} \end{bmatrix}. \tag{9}$$

The infinitesimal twist at the ith joint or the ith link expressed in the ith local frame can be expressed by

$${}^i\delta\hat{\mathbf{D}}_i = {}^iC_i\,{}^i\hat{\mathbf{w}}_i \tag{10}$$

where ${}^iC_i$ denotes the compliance matrix of the ith part expressed in the ith local frame and ${}^i\hat{w}_i$ denotes the wrench applied on the ith part expressed in the ith local frame. Expressing the infinitesimal twist and wrench with respect to the moving frame (P) gives

$$\delta\hat{\mathbf{D}}_i = {}^P_iT\;{}^i\delta\hat{\mathbf{D}}_i \text{ and } \hat{\mathbf{w}}_i = {}^P_iT^{-T}\;{}^i\hat{\mathbf{w}}_i \tag{11}$$

where the transformation matrix of screws from the ith frame to the moving frame is given by

$${}^P_iT = \begin{bmatrix} {}^P_iR & {}^P\hat{p}_i\,{}^P_iR \\ 0_{3\times3} & {}^P_iR \end{bmatrix} \tag{12}$$

where ${}^P_iR$ denotes the rotation matrix from the ith frame to the moving frame and ${}^P\hat{p}_i$ denotes the skew-symmetric matrix representing the vector from the origin of the moving frame to that of the ith local frame expressed in the moving frame. The total deflection of a serial chain can be calculated by the sum of all the deflection in joints and links given by

$$\delta\hat{\mathbf{D}} = \sum_{i=1}^{n} ({}^P_iT\;{}^iC_i\;{}^P_iT^T)\hat{\mathbf{w}}\,. \tag{13}$$

Therefore, the compliance of a serial chain expressed in the moving frame can be written by

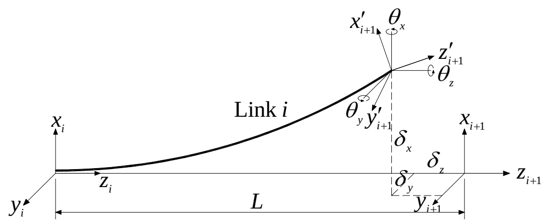

Fig. 3 Compliance model of a link.

$$C = \sum_{i=1}^{n} ({}^{P}_{i}T \; {}^{i}C_{i} \; {}^{P}_{i}T^{T}) \cdot \qquad (14)$$

The joint compliance values related to the reciprocal screws of actuations and constraints are calculated by

$$c_l = \delta \boldsymbol{x} \cdot \boldsymbol{f} \text{ and } c_\theta = \delta\theta \cdot \boldsymbol{m} \qquad (15)$$

where $\|\boldsymbol{f}\| = 1$ and $\|\boldsymbol{m}\| = 1$.

4 Conclusions

In this paper, the stiffness analysis for a limited-DOF parallel manipulator using the theory of reciprocal screws and considering the elastic deformation in joints and links by the reciprocal screws is presented. For an *F*-DOF parallel manipulator, it is derived that there exist *F* number of reciprocal screws related to actuations and 6-*F* number of reciprocal screws related to constraints. The stiffness matrix for a limited-DOF parallel manipulator becomes the sum of the stiffness matrices of actuations and constraints. The practical values of spring constants are obtained by modeling the compliances of joints and links in each serial chain. In the further works, this analytic method will be used in the design optimization of a parallel-kinematic machine tool and the effectiveness of the suggested stiffness analysis method will be verified through experiments.

REFERENCES

[1] Stewart, D., 1965, "A Platform with Six Degrees of Freedom," *Proc. Institute of Mechanical Engr.*, London, England, Vol. 180, pp. 371~386.

[2] Gough V. E., and Whitehall S. G., 1962, "Universal Tire Test Machine," *Proceedings 9th Int. Technical Congress F.I.S.I.T.A.*, Vol. 117, pp.117~135.

[3] Clavel, R. 1988, "Delta, a Fast Robot with Parallel Geometry," *18th International Symposium on Industrial Robots*, Sydney, Australia, pp. 91-100.

[4] Pierrot, F., Reynaud, C., and Fournier, A., 1990, "DELTA: A Simple and Efficient Parallel Robot," *Robotica*, Vol. 8, pp. 105~109.

[5] Siciliano, B., 1999, "The Tricept Robot: Inverse Kinematics, Manipulability Analysis and Closed-Loop Direct Kinematics Algorithm," *Robotica*, Vol. 17, pp. 437~445.

[6] Tsai, L. W. and Joshi, S., 2000, "Kinematics and Optimization of a Spatial 3-UPU Parallel Manipulator," *ASME Journal of Mechanical Design*, Vol. 122, No. 4, pp. 439~446.

[7] Wenger, P., and Chablat, D., 2000, "Kinematic Analysis of a New Parallel Machine Tool: The Orthoglide," *Advances in Robot Kinematics*, Edited by J. Lenarcic and M. L. Stanisic, Kluwer Academic Publishers, London, pp. 305~314.

[8] Kim, H. S., and Tsai, L. W., 2003, "Design Optimization of a Cartesian Parallel Manipulator," *Journal of Mechanical Design*, Vol. 125, No. 1, pp. 43~51.

[9] Kim, H. S., and Tsai, L. W., 2002, "Evaluation of a Cartesian Parallel Manipulator," *8th International Symposium on Advances in Robot Kinematics*, 24~28 June, Caldes de Malavella, Spain, pp. 21~28.

[10] Gosselin, C. M., and Angeles, J., 1989, "The Optimum Kinematic Design of a Spherical Three-Degree-of-Freedom Parallel Manipulator," *ASME Journal of Mechanisms, Transmissions, and Automation in Design*, Vol. 111, No. 2, pp. 202~207.

[11] Fang, Y. F., and Tsai, L. W., 2004, "Structure Synthesis of a Class of 3-DOF Rotational Parallel Manipulators," *IEEE Trans. on Robotics Automation*, Vol. 20, No. 1, pp. 117~121.

[12] Gosselin, C., 1990, "Stiffness Mapping of Parallel Manipulators," *IEEE Transaction on Robotics and Automations*, Vol. 6, pp. 377~382.

[13] Griffis, M., and Duffy, J., 1993, "Global Stiffness Modeling of a Class of Simple Compliant Couplings," *Mechanism and Machine Theory*, Vol. 28, No. 2, pp. 207~224.

[14] Tahmasebi, F. and Tsai, L. W., 1995, "On the Stiffness of a Novel Six-Degrees-of-Freedom Parallel Manipulator," *Journal of Robotic Systems*, Vol. 12, No. 12, pp. 845~856.

[15] Zhang, D., and Gosselin, C. M., 2001, "Kinetostatic Modeling of N-DOF Parallel Mechanisms with a Passive Constraining Leg and Prismatic Actuators," *ASME Journal of Mechanical Design*, Vol. 123, pp. 375~381.

[16] Zhang, D., and Gosselin, C. M., 2002, "Kinetostatic Modeling of Parallel Mechanisms with a Passive Constraining Leg and Revolute Actuators," *Mechanism and Machine Theory*, Vol. 37, pp. 599~617.

[17] Zhang, D., and Gosselin, C. M., 2002, "Kinetostatic Analysis and Design Optimization of the Tricept Machine Tool Family," *ASME Journal of Manufacturing Science and Engineering*, Vol. 124, pp. 725~733.

[18] Zhang, D., and Gosselin, C. M., 2002, "Parallel Kinematic Machine Design with Kinetostatic Model," *Robotica*, Vol. 20, pp. 429~438

[19] Joshi, S. A., and Tsai, L. W., 2002, "Jacobian Analysis of Limited-DOF Parallel Manipulators," Journal *of Mechanical Design*, Vol. 124, pp. 254~258.

[20] Zlatanove, D., Bonev, I., and Gosselin, C., 2002, "Constraint Singularities as C-Space Singularities," *Proceedings of the 8th Advances in Robot Kinematics*, edited by J. Lenarcic and F. Thomas, Kluwer Academic Publishers, pp. 183~192.

[21] Han, C., Kim, J., Kim J., and Park, F. C., 2002, "Kinematic Sensitivity Analysis of the 3-UPU Parallel Mechanism," *Mechanism and Machine Theory*, Vol. 37, pp. 787~798.

[22] Tsai, L. W., 1999, *Robot Analysis: The Mechanics of Serial and Parallel Manipulators*, John Wiley & Sons, New York, NY.

[23] Tsai, L. W., 2000, *Mechanism Design: Enumeration of Kinematic Structures According to Function*, CRC Press, pp. 221~247.

The Eleventh International Symposium on Artificial Life and Robotics 2006 (AROB 11th'06),
B-con Plaza, Beppu, Oita, Japan, January 23-25, 2006

A Robust Adaptive Control of Robot Manipulator Based on DSPs

Sung Hyun Han, Uhn Zoo Na, Woo Song Lee, Haeng Bong Shin, and Yoon Kyu Kim

Division of Mechanical and Automation Eng., Kyungnam Univ., Masan, 631-701, Korea.
E-mail: shhan@kyungnam.ac.kr Tel: +82-55-249-2624 Fax: +82-55-249-2617

ABSTRACT

We describe a new approach to the design and real-time implementation of an adaptive controller for robotic manipulator based on digital signal processors in this paper. The Texas Instruments DSPs(TMS320C80) chips are used in implementing real-time adaptive control algorithms to provide enhanced motion control performance for dual-arm robotic manipulators. In the proposed scheme, adaptation laws are derived from model reference adaptive control principle based on the improved direct Lyapunov method. The proposed adaptive controller consists of an adaptive feed-forward and feedback controller and time-varying auxiliary controller elements. The proposed control scheme is simple in structure, fast in computation, and suitable for real-time control. Moreover, this scheme does not require any accurate dynamic modeling, nor values of manipulator parameters and payload. Performance of the proposed adaptive controller is illustrated by simulation and experimental results for robot manipulator consisting of dual arm with four degrees of freedom at the joint space and cartesian space.

Keywords : Adaptive Control, DSP(TMS320C80), Dual-Arm Robot, Real Time Control, Real-Time Implementation

I. INTRODUCTION

At recent there are mach advanced techniques that are suitable for servo control of a large class of nonlinear systems including robotic manipulators (P.C.V. Parks, 1966; Y.K.Choi et al., 1986; Y.M.Yoshhiko, 1995). Since the pioneering work of Dubowsky and DesForges (1979), the interest in adaptive control of robot manipulators has been growing steadily (T. C. Hasi, 1986; D. Koditschck, 1983; A. Koivo et al., 1983; S. Nicosia et al., 1984). This growth is largely due to the fact that adaptive control theory is particularly well-suited to robotic manipulators whose dynamic model is highly complex and may contain unknown parameters. However, implementation of these algorithms generally involves intensive numerical computations (J. J. Craig, 1988; H. Berghuis et al., 1993).

Current industrial approaches to the design of robot arm control systems treat each joint of the robot arm as a simple servomechanism. This approach models the time varying dynamics of a manipulator inadequately because it neglects the motion and configuration of the whole arm mechanism. The changes in the parameters of the controlled system are significant enough to render conventional feedback control strategies ineffective. This basic control system enables a manipulator to perform simple positioning tasks such as in the pick-and-place operation. However, joint controllers are severely limited in precise tracking of fast trajectories and sustaining desirable dynamic performance for variations of payload and parameter uncertainties (R. Ortega et al., 1989; P. Tomei, 1991). In many servo control applications the linear control scheme proves unsatisfactory, therefore, a need for nonlinear techniques is increasing.

Digital signal processors (DSP's) are special purpose microprocessors that are particularly suitable for intensive numerical computations involving sums and products of variables. Digital versions of most advanced control algorithms can be defined as sums and products of measured variables, thus can naturally be implemented by DSP's. DSPs allow straightforward implementation of advanced control algorithms that result in improved system control. Single and/or multiple axis control systems can be controlled by a single DSP. Adaptive and optimal multivariable control methods can track system parameter variations. Dual control, learning, neural networks, genetic algorithms and Fuzzy Logic control methodologies are all among the digital controllers implementable by a DSP (N. Sadegh et al., 1990; Z. Ma et al., 1995). In addition, DSP's are as fast in computation as most 32-bit microprocessors and yet at a fraction of their prices. These features make them a viable computational tool for digital implementation of advanced controllers. High performance DSPs with increased levels of integration for functional modules have become the dominant solution for digital control systems. Today's DSPs with performance levels ranging from 5 to 5400 MIPS are on the market with price tags as low as $3 (P. Bhatti et al., 1997; T. H. Akkermans et al., 2001). In order to develop a digital servo controller one must carefully consider the effect of the sample-and-hold operation, the sampling frequency, the computational delay, and that of the quantization error on the stability of a closed-loop system (S. A. Bortoff, 1994). Moreover, one must also consider the effect of disturbances on the transient variation of the tracking error as well as its steady-state value (F. Mehdian et al., 1995; S. H. Han et al., 1996).

This paper describes a new approach to the design of adaptive control system and real-time implementation using digital signal processors for robotic manipulators to achieve the improvement of speedness, repeating precision, and tracking performance at the joint and cartesian space. This paper is organized as follows : In Section Ⅱ, the dynamic model of the robotic manipulator is derived. Section Ⅲ derives adaptive control laws based on the model reference adaptive control theory using the improved Lyapunov second method. Section Ⅳ presents simulation and experimental results obtained for a dual-arm robot. Finally, Section Ⅴ discusses the findings and draws some conclusions.

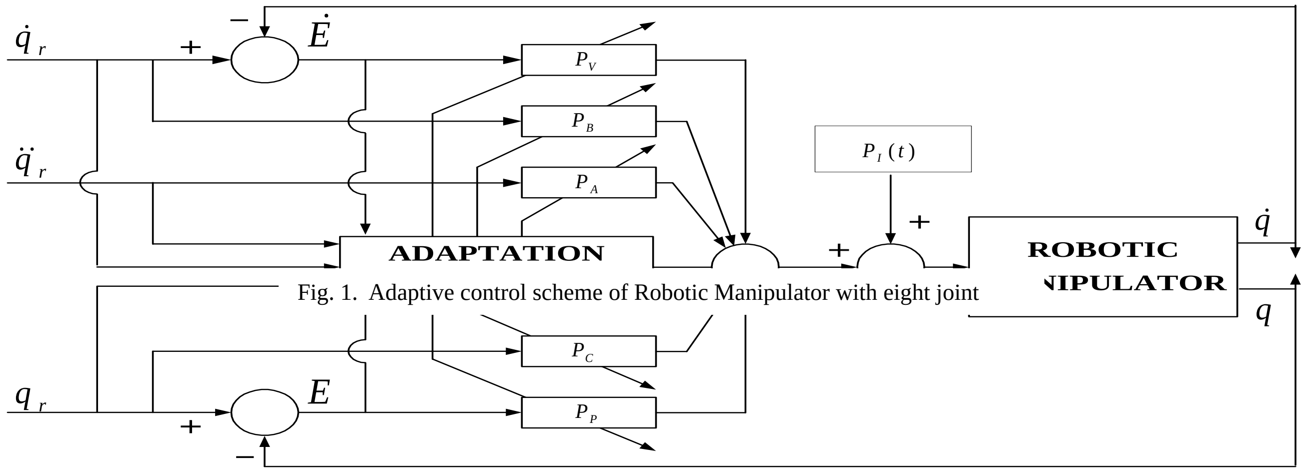

Fig. 1. Adaptive control scheme of Robotic Manipulator with eight joint

II. MODELING

The dynamic model of a manipulator-plus-payload is derived and the tracking control problem is stated in this section.

Let us consider a nonredundant joint robotic manipulator in which the n×1 generalized joint torque vector τ (t) is related to the n×1 generalized joint coordinate vector q(t) by the following nonlinear dynamic equation of motion

$$D(q)\,\ddot{q} + N(q,\dot{q}) + G(q) = \tau(t) \tag{1}$$

where $D(q)$ is the n×n symmetric positive-definite inertia matrix, $N(q,\dot{q})$ is the n×1 coriolis and centrifugal torque vector, and $G(q)$ is the n×1 gravitational loading vector.

Equation (1) describes the manipulator dynamics without any payload. Now, let the n×1 vector X represent the end-effector position and orientation coordinates in a fixed task-related cartesian frame of reference. The cartesian position, velocity, and acceleration vectors of the end-effector are related to the joint variables by

$$\begin{aligned} X(t) &= \Phi(q) \\ X(t) &= J(q)\,\dot{q}(t) \\ X(t) &= \dot{J}(q,\dot{q})\,\dot{q}(t) + J(q)\,\ddot{q}(t) \end{aligned} \tag{2}$$

where Φ(q) is the n×1 vector representing the forward kinematics and J(q) = [$\partial\Phi(q)/\partial q$] is the n×n Jacobian matrix of the manipulator.

Let us now consider payload in the manipulator dynamics. Suppose that the manipulator end-effector is firmly grasping a payload represented by the point mass ΔM_p. For the payload to move with acceleration $\ddot{X}(t)$ in the gravity field, the end-effector must apply the n×1 force vector $T(t)$ given by

$$T(t) = \Delta M_p\,[\,\ddot{X}(t) + g\,] \tag{3}$$

where g is the n×1 gravitational acceleration vector.

The end-effector requires the additional joint torque

$$\tau_f(t) = J(q)^T\,T(t) \tag{4}$$

where superscript T denotes transposition. Hence, the total joint torque vector can be obtained by combining equations (1) and (4) as

$$J(q)^T\,T(t) + D(q)\,\ddot{q} + N(q,\dot{q}) + G(q) = \tau(t) \tag{5}$$

Substituting equations (2) and (3) into equation (5) yields

$$\begin{aligned} &\Delta M_p\,J(q)^T[\,J(q)\,\ddot{q} + \dot{J}(q,\dot{q})\,\dot{q} + g\,] \\ &+ D(q)\ddot{q} + N(q,\dot{q}) + G(q) = \tau(t) \end{aligned} \tag{6}$$

Equation (6) shows explicity the effect of payload mass ΔM_p on the manipulator dynamics. This equation can be written as

$$\begin{aligned} &[D(q)+\Delta M_p\,J(q)^T\,J(q)]\,\ddot{q} + [N(q,\dot{q}) \\ &+\Delta M_p J(q)^T\,\dot{J}(q,\dot{q})\,\dot{q}] + [G(q)+\Delta M_p J(q)^T g] = \tau(t) \end{aligned} \tag{7}$$

where the modified inertia matrix $[D(q)+\Delta M_p J(q)^T J(q)]$ is symmetric and positive-definite. Equation (7) constitutes a nonlinear mathematical model of the manipulator-plus-payload dynamics.

III. ADAPTIVE CONTROL SCHEME

The manipulator control problem is to develop a control scheme which ensures that the joint angle vector *q*(*t*) tracks any desired reference trajectory $q_r(t)$, where $q_r(t)$ is an n×1 vector of arbitrary time functions. It is reasonable to assume that these functions are twice differentiable, that is, desired angular velocity $\dot{q}_r(t)$ and angular acceleration $\ddot{q}_r(t)$ exist and are directly available without requiring further differentiation of $q_r(t)$. It is desirable for the manipulator control system to achieve trajectory tracking irrespective of payload mass ΔM_p.

The controllers designed by the classical linear control scheme are effective in fine motion control of the manipulator in the neighborhood of a nominal operating point P_o. During the gross motion of the manipulator, operating point P_o and consequently the linearized model parameters vary substantially with time. Thus it is essential to adapt the gains of the feedforward, feedback, and PI controllers to varying operating points and payloads so as to ensure stability and trajectory tracking by the total control laws. The required adaptation laws are developed in this section. Fig. 1 represents the block diagram of adaptive control scheme for robotic manipulator.

Nonlinear dynamic equation (7) can be written as

$$\tau(t) = D^*(\Delta M_p, q, \dot{q})\, \ddot{q}(t) + N^*(\Delta M_p, q, \dot{q})\, \dot{q}(t) + G^*(\Delta M_p, q, \dot{q})\, q(t) \tag{8}$$

where D^*, N^*, and G^* are n×n matrices whose elements are highly nonlinear functions of ΔM_p, q, and $\dot{q}$.

In order to cope with changes in operating point, the controller gains are varied with the change of external working condition.

This yields the adaptive control law

$$\tau(t) = [P_A(t)\, \ddot{q}_r(t) + P_B(t)\, \dot{q}_r(t) + P_C(t)\, q_r(t)] + [P_V(t)\, \dot{E}(t) + P_P(t)\, E(t) + P_I(t)] \tag{9}$$

where $P_A(t)$, $P_B(t)$, $P_C(t)$ are feedforward time-varying adaptive gains, and $P_P(t)$ and $P_V(t)$ are the feedback adaptive gains, and $P_I(t)$ is a time-varying control signal corresponding to the nominal operating point term, generated by a feedback controller driven by position tracking error $E(t)$ defined as $q_r(t) - q(t)$.

The gains of adaptive control low in equation (9) are defined as follows:

$$P_A(t) = a_1[p_{a1}E + p_{a2}\dot{E}][\ddot{q}_r]^T + a_2\int_0^t [p_{a1}E + p_{a2}\dot{E}][\ddot{q}_r]^T dt + p_a(0) \tag{10}$$

$$P_B(t) = b_1[p_{b1}E + p_{b2}\dot{E}][\dot{q}_r]^T + b_2\int_0^t [p_{b1}E + p_{b2}\dot{E}][\dot{q}_r]^T dt + p_b(0) \tag{11}$$

$$P_C(t) = c_1[p_{c1}E + p_{c2}\dot{E}][q_r]^T + c_2\int_0^t [p_{c1}E + p_{c2}\dot{E}][q_r]^T dt + p_c(0) \tag{12}$$

$$P_I(t) = \lambda_2[p_{i2}E] + \lambda_1\int_0^t [p_{i1}E]^T dt + p_i(0) \tag{13}$$

$$P_P(t) = p_1[p_{p1}E + p_{p2}\dot{E}][E]^T + p_2\int_0^t [p_{p1}E + p_{p2}\dot{E}][E]^T dt + p_p(0) \tag{14}$$

$$P_V(t) = v_1[p_{v1}E + p_{v2}\dot{E}][\dot{E}]^T + v_2\int_0^t [p_{v1}E + p_{v2}\dot{E}][\dot{E}]^T dt + p_v(0) \tag{15}$$

where $[p_{p1}, p_{v1}, p_{c1}, p_{b1}, p_{a1}]$ and $[p_{p2}, p_{v2}, p_{c2}, p_{b2}, p_{a2}]$ are positive and zero/positive scalar adaptation gains, which are chosen by the designer to reflect the relative significance of position and velocity errors E and $\dot{E}$.

IV. SIMULATION AND EXPERIMENT

A. Simulation

This section represents the simulation results of the position and velocity control of a four-link robotic manipulator by the proposed adaptive control algorithm, as shown in Fig.2, and discusses the advantages of using joint controller based-on DSPs for motion control of a dual-arm robot. The adaptive scheme developed in this paper will be applied to the control of a dual-arm robot with eighth axes. Fig.2 represents link coordinates of the dual-arm robot.

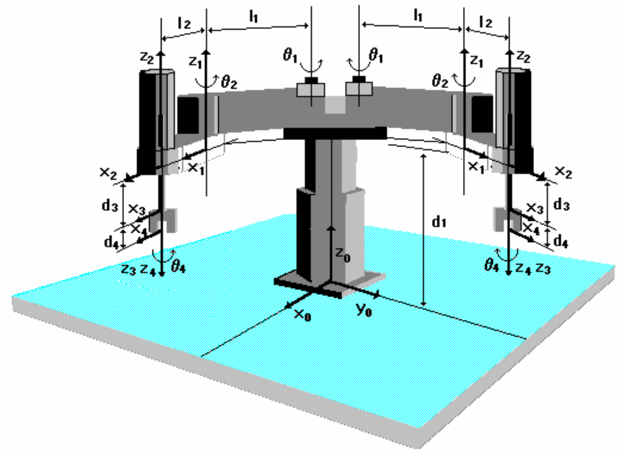

Fig.2. Link coordinates of dual-arm robot

Table Ⅰ Link parameters of robot.

Mass of link(kg)		Length of link(kg)		Inertia of link(kg)		Gear ratio of link	
m1	15.0067	I1	0.35	I1	0.1538	r1	1/100
m2	8.994	I2	0.3	I2	0.0674	r2	1/80
m3	3.0	I3	0.175	I3	0.045	r3	1/200
m4	1.0	I4	0.007	I4	0.0016	r4	1/75
m5	15.067	I5	0.35	I5	0.1538	r5	1/100
m6	8.994	I6	0.3	I6	0.0674	r6	1/80
m7	3.0	I7	0.175	I7	0.045	r7	1/200
m8	1.0	I8	0.007	I8	0.0016	r8	1/75

Table Ⅱ Motor parameters of robot

Rotor inertia (kg · m^2)		Torque constant (K m/a)		Back emf constant (V s/rad)		Amaturewinding resistance(ohms)	
Jm1	5.0031×10^{-5}	Ka1	21.4839×10^{-2}	Kb1	214.8592×10^{-3}	Ra1	1.5
Jm2	1.3734×10^{-5}	Ka2	20.0124×10^{-2}	Kb2	200.5352×10^{-3}	Ra2	4.2
Jm3	0.8829×10^{-5}	Ka3	20.0124×10^{-2}	Kb3	200.5352×10^{-3}	Ra3	9
Jm4	0.2256×10^{-5}	Ka4	17.6580×10^{-2}	Kb4	176.6620×10^{-3}	Ra4	20
Jm5	5.0031×10^{-5}	Ka5	21.4839×10^{-2}	Kb5	214.8592×10^{-3}	Ra5	1.5
Jm6	1.3734×10^{-5}	Ka6	20.0124×10^{-2}	Kb6	200.5352×10^{-3}	Ra6	4.2
Jm7	0.8829×10^{-5}	Ka7	20.0124×10^{-2}	Kb7	200.5352×10^{-3}	Ra7	9
Jm8	0.2256×10^{-5}	Ka8	17.6580×10^{-2}	Kb8	176.6620×10^{-3}	Ra8	20

B. Experiment

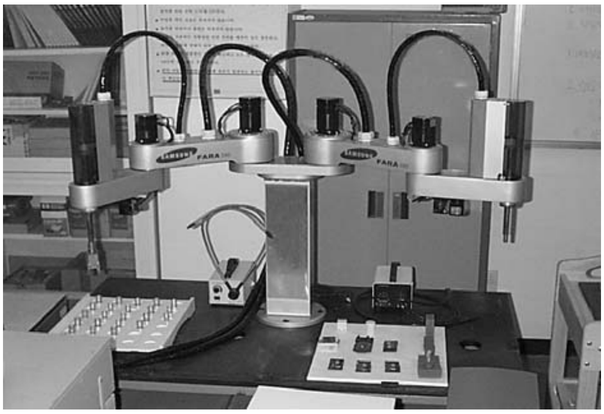

Fig. 3. Experimental set-up

The performance test of the proposed adaptive controller has been performed for the dual-arm robot at the joint space and cartesian space. At the cartesian space, it has been tested for the peg-in-hole tasks, repeating precision tasks, and trajectory tracking for B-shaped reference trajector. At the joint space, it has been tested for the trajectory tracking of angular position and velocity for a dual-arm robot made in Samsung Electronics Company in Korea. Fig. 3 represents the experimental set-up equipment. To implement the proposed adaptive controller, we used our own developed TMS320C80 assembler software. Also, the TMS320C80 emulator has been used in experimental set-up. At each joint of a dual-arm robot, a harmonic drive (with gear reduction ratio of 100 : 1 for joint 1 and 80 : 1 for joint 2) has been used to transfer power from the motor, which has a resolver attached to its shaft for sensing angular velocity with a resolution of 8096 (pulses/rev). Fig. 4 represents the schematic diagram of control system of dual-arm robot. And Fig. 5 represents the block diagram of the interface between the PC, DSP, and dual-arm robot.

The performance test in the joint space is performed to evaluate the position and velocity control performance of the four joints under the condition of payload variation, inertia parameter uncertainty, and change of reference trajectory.

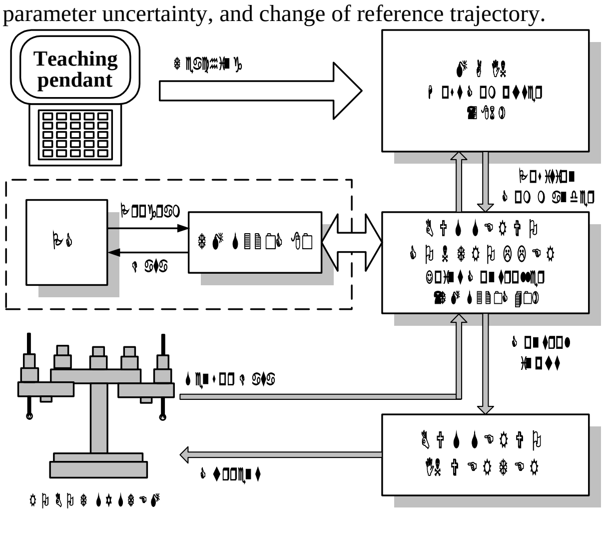

Fig. 4. The block diagram of the interface between the PC. DSP, and dual-arm robot.

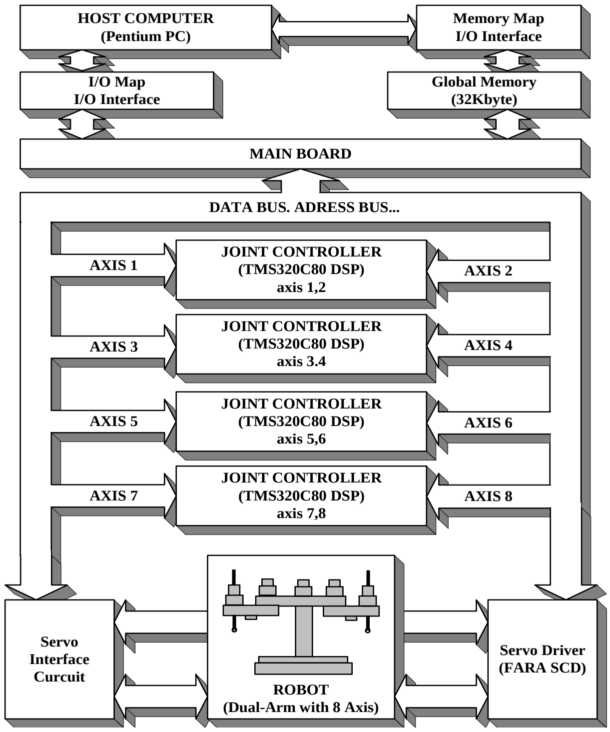

Fig. 5. The schematic diagram control system of dual-arm robot.

Fig.6 represents the B-shaped reference trajectory in the cartesian space. Fig. 7 shows the experimental results of the position and velocity control at the first joint with payload 4 kg and the change of reference trajectory. Fig. 8 shows the experimental results for the position and velocity control at the second joint with 4 kg payload. Fig.'s 9 and 10 show the experimental results for the position and velocity control of the PID controller with 4 kg payload. As can be seen from these results, the DSP-based adaptive controller shows extremely good control performance with some external disturbances. It is illustrated that this control scheme shows better control performance than the exiting PID controller, due to small tracking error and fast adaptation for disturbance.

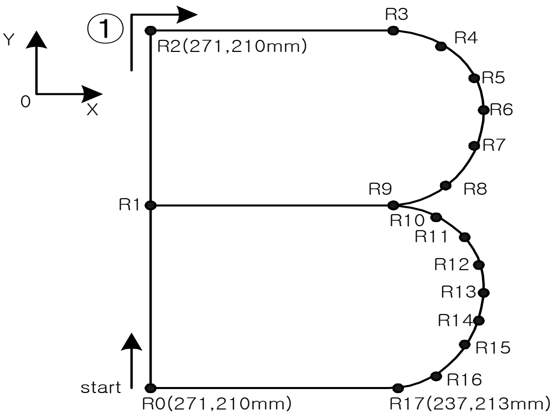

Fig. 6. The B shaped reference trajectory in the cartesian space.

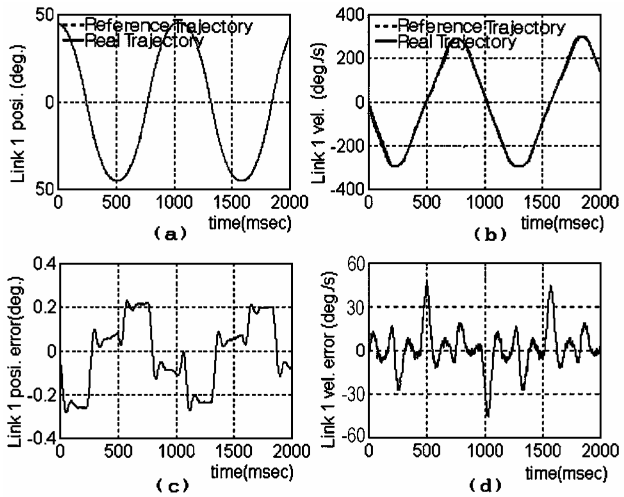

Fig. 7. (a)-(d) Experimental results for the position and velocity tracking of adaptive controller at the first joint with 4kg payload.

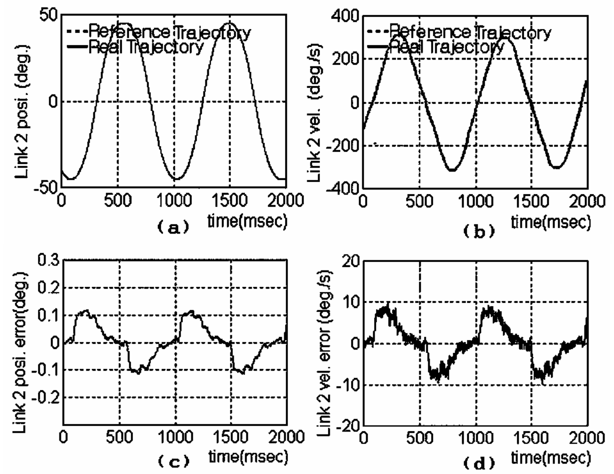

Fig. 8. (a)-(d) Experimental results for the position and velocity tracking of adaptive controller at the second joint with 4kg payload.

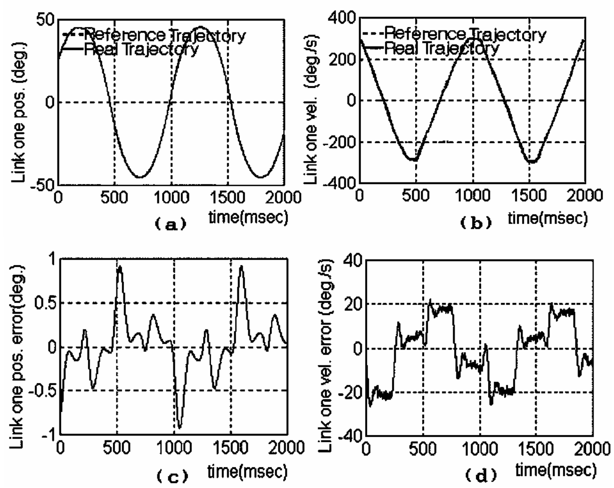

Fig. 9. (a)-(d) Experimental results of PID controller for the position and velocity tracking at the first joint with 4kg payload.

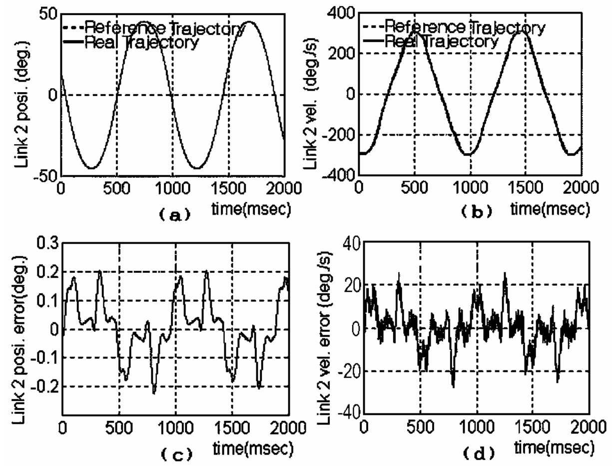

Fig. 10. (a)-(d) Experimental results of PID controller for the position and velocity tracking at the second joint with 4kg payload.

Ⅴ. DISCUSSION AND CONCLUSIONS

A new adaptive digital control scheme is described in this paper using DSP(TMS320C80) for robotic manipulators. The adaptation laws are derived from the direct adaptive technique using the improved Lyapunov second method. The simulation and experimental results show that the proposed DSP-adaptive controller is robust to the payload variation, inertia parameter uncertainty, and change of reference trajectory. This adaptive controller has been found to be suitable to the real-time control of robot system. A novel feature of the proposed scheme is the utilization of an adaptive feedforward controller, an adaptive feedback controller, and a PI type time-varying control signal to the nominal operating point which result in improved tracking performance. Another attractive feature of this control scheme is that, to generate the control action, it neither requires a complex mathematical model of the manipulator dynamics nor any knowledge of the manipulator parameters and payload. The control scheme uses only the information contained in the actual and reference trajectories which are directly available. Futhermore, the adaptation laws generate the controller gains by means of simple arithmetic operations. Hence, the calculation control action is extremely simple and fast. These features are suitable for implementation of on-line real-time control for robotic manipulators with a high sampling rate, particularly when all physical parameters of the manipulator cannot be measured accurately and the mass of the payload can vary substantially. The proposed DSP-based adaptive controllers have several advantages over the analog control and the micro-computer based control. This allows instructions and data to be simultaneously fetched for processing. Moreover, most of the DSP instructions, including multiplications, are performed in one instruction cycle. The DSP tremendously increase speed of the controller and reduce computational delay, which allows for faster sampling operation. It is illustrated that DSPs can be used for the implementation of complex digital control algorithms, such as our adaptive control for robot systems.

REFERENCES

P.C.V. Parks, July 1966, "*Lyapunov Redesign of Model Reference Adaptive Control System*," IEEE Trans. Auto. Contr., Vol. AC-11, No. 3, pp. 362-267.

Y.K. Choi, M.J. Chang, and Z. Bien, 1986, "*An Adaptive Control Scheme for Robot Manipulators*." IEEE Trans. Auto. Contr., Vol. 44, No. 4, pp. 1185-1191.

Y.M. Yoshhiko, June 1995, "*Model Reference Adaptive Control for Nonlinear System with unknown Degrees*, "In the proceeding of American Control Conference, pp.2505-2514, Seatle.

S. Dubowsky, and D.T. DesForges, 1979, "*The Application of Model Reference Adaptation Control to Robot Manipulators*," ASME J. Dyn. Syst., Meas., Contr., Vol. 101, pp. 193-200.

T.C. Hasi, 1986, "*Adaptive Control Scheme for Robot Manipulators-A Review*." In Proceeding of the 1987 IEEE Conference on Robotics and Automation, San Fransisco, CA.

D. Koditschek, 1983, "*Quadratic Lyapunov Functions for Mecanical Systems*," Technical Report No. 8703, Yale University, New Haven, CT.

A. Koivo and T. H. Guo, 1983, "*Adaptive Linear Controller for Robot Manipulators.*" IEEE Transactions and Automatic Control, Vol. AC-28, pp. 162-171.

S. Nicosia and P. Tomee, 1984, "*Model Reference Adaptive Control Algorithm for Imdustrial Robots*," Automatica, Vol. 20, No. 5, pp. 635-644.

J. J. Craig, 1988, "*Adaptive Control of Meduanical Manipulator*," Addison-wesley.

H. Berghuis, R.Orbega, and H.Nijmeijer, 1993, "*A Robust Adaptive Robot controller*," IEEE Trans., Robotics and Automation, Vol. 9, No. 6, pp. 825-830.

R. Ortega and M.W. Spong, 1989, "*Adaptive Motion Control of Rigid Robots: A Tutorial*," Automatica, Vol. 25, pp. 877-888.

P. Tomei, Aug. 1991, "*Adaptive PD Controller for Robot Manipulators*," IEEE Trans. Robotics and Automation, Vol.7, No.4.

N. Sadegh and R. Horowitz, Aug. 1990, "*An Exponentially Stable Adaptive Control Law for Robot Manipulators*," IEEE Trans. Robotics and Automation, Vol. 9, No. 4.

Z. Ma, J. shen, A. Hug, and K. Nakayama, October 1995, "*Automatic optimum Order Assignment in Adaptive Filters*," international conference on signal Processing Applications & Technology, Boston pp. 629-633.

T. A. Lasky and T. C. Hsia, July 1994, "*Application of a Digital Signal Processor in Compliant Control of an Industrial Manipulator*," Proceedings of American Control Conference.

K. Michael and P. Issa, June 1995, "*Digital Signal Processor : A Control Element*," In Proceedings of American Control Conference, Seatle, pp. 470-474.

S. A. Bortoff, Feb. 1994, "*Advanced Nonlinear Robotic Control Using Digital Signal Processing*," IEEE Trans. Indust. Elect., Vol. 41, No. 1.

F. Mehdian and M. Wirth, June 1995, "*Adaptive Control of Robotic Manipulators Using DSPs*," In Proceedings of American Control Conference, Seatle, pp.480-481.

S. H. Han, J. Lee, D. Ahn, M. Lee, and K. Son, July 1996, "*Implementation of Robust Adaptive Controller of Robotic Manipulator using DSPs*, "In Proceedings of Eleventh International Conference on System engineering, Lasvegas, pp. 668-673.

T. H. Akkermans and S. G. Stan, 2001, "*Digital servo IC for optical disc drives*", *Contr. Eng. Pract.*, vol. 9, no. 11, pp. 1245-1253.

P. Bhatti and B. Hannaford, 1997, "*Single-chip velocity measurement system for incremental optical encoders*", IEEE Trans. Contr. Syst. Techn., vol. 5, no. 6, pp. 654-661.

A Study on Image Based Visual Feedback Control of Robot System

Sung Hyun Han and Uhn Zoo Na
Division of Mechanical and Automation Eng., Kyungnam Univ., Masan, 631-701, Korea.
E-mail: shhan@kyungnam.ac.kr Tel: +82-55-249-2624 Fax: +82-55-249-2617

Hong Rae Kim,Yoon Kyu Kim, and Chang Rok Shin
Dept. of Mechanical Eng.,Graduate School, Kyungnam Univ., Masan, 631-701, Korea.
Tel: +82-55-249-2590 Fax: +82-55-249-26

Abstract

This paper presents how it is effective to use many features for improving the speed and the accuracy of the visual servo systems. Some rank conditions which relate the image Jacobian and the control performance are derived. It is also proven that the accuracy is improved by increasing the number of features. Effectiveness of the redundant features is evaluated by the smallest singular value of the image Jacobian which is closely related to the accuracy with respect to the world coordinate system. Usefulness of the redundant features is verified by the real time experiments on a Dual-Arm Robot manipulator made in Samsung Electronic Co. Ltd..

Key Words : Visual Feedback Control, Robot System, Image Based, Visual Tracking, Real Time Control.

1. Introduction

Recently, robots can perform assembly and material handling jobs with speed and precision yet, compared to human workers robots, are hampered by their lack of sensory perception. To address this deficiency considerable research into force, tactile and visual perception has been conducted over the past two decades.

Visual servoing is the fusion of result from many elemental areas including high-speed image processing, kinematics, dynamics, control theory, and real-time computing. It has much in common with research into active vision and structure from motion, but is quite different from the often described use of vision in hierarchical task-level robot control systems. Many of the control and vision problems are similar to those encountered by active vision researchers who are building robotic heads. However the task in visual servoing is to control a robot to cope with its environment using vision as opposed to just observing the environment.

Most visual servoing problems can be considered as nonlinear control problems with the gray level of each two dimensional pixel array being an observation. The difficulty of the problem is the size and the nonlinearity. The size of the observation is larger than ten thousand and they have nonlinear interaction with each other. A few researches based on the stochastic models of the two-dimension observation are found, but most visual servoing schemes uses the features of the image as the observation. To manipulate objects with complex shapes, it is important to deal with complex features such as spheres and cylinders. However, the time extracting complex features will become too long based on limited hardware. Accordingly, visual servoing scheme which utilizes many features effectively is required. Furthermore exploiting the information carefully from the features will give robust and accurate control performance [2],

Sanderson et al. proposed a feature-based approach and defined the Jacobian of ideal inverse interpretation which was considered as the infinitesimal change of the relative position and orientation between the camera and the object in the environment.

Newman et al. proposed an adaptive control law based on a single input single output model and a feature selection criterion were proposed [1], [2]. The criterion addressed the choice of which feature should be used to control each actuator, where the number of selected features is equal to the number of the actuator. Feddema et al. [3], also studied the selection method of the features to make the Jacobian good condition. Real time experiment of gasket tracking showed that the proper selection of features is necessary to minimize the effect of image noise.

Papanikolopoulos et al. [2], [3] experimentally examined many control algorithms including Proportional-Plus- Integral, pole assignment and linear quadratic gaussian. Some adaptive control schemes were also examined in [8]. These approaches do not consider to use the redundant features which are defined as the features whose number is more than the degrees of freedom of the robot manipulator.

Chaumette el al. [2] and Espiau el al. [3] derived the interaction matrix, and introduced the concept of task function. Chaumette [2] extended the task function approach to the complex features. Jang and Bien [10] mathematically defined the "feature", and derived the feature Jacobian matrix. The authors [2] derived the image Jacobian, and used its generalized inverse and PD control to generate the hand trajectory. These schemes are based on the generalized inverse of the Jacobian. Redundant features can be used. However, the parameters to improve the control performance are very limited and the controllability of the redundant features are not discussed.

The authors proposed a linearized dynamic model of the visual servo system and linear quadratic control scheme for redundant features [1], [3]. The controllability problem was discussed but the performance improvement by utilizing the redundant features was not presented.

This paper presents how the control performance of the feature-based visual servoing system is improved by utilizing redundant features. Effectiveness of the redundant features is evaluated by the smallest singular value of the image Jacobian which is closely related to the accuracy in the world coordinate system. Usefulness of the redundant features is verified by the real time control experiments. To illustrate the accuracy of the redundant visual servo system, real time experiments on the Dual-Arm robot with eight joints are carried out. Translation and rotation step response with three, four and five features are examined in this experiment.

2. System Modeling and Formullation

The object image moves with the joint angle to the object image, which is composed of the kinematic model and the camera model as shown in Fig.1. Suppose that a camera is mounted on the robot hand and the object does not move. The kinematic model is a map from the joint angle to a position of the camera. Since the camera is on the robot hand, the camera position is uniquely defined by the joint angle θ based on the kinematic structure of the robot. The camera model is a map from the position of the camera to the camera to the image of the object. The object image is generated by the perspective of the relative position between the camera and the object. The perspective projection is a map between two different representations of the position of the object, i.e., the representations in the camera coordinate system $[XYZ]^T$ and in the image plane $[xy]^T$.

The perspective projection with f being the focal length of the lens is given by

$$[x \quad y]^T = [X \quad Y]^T (f/z) \tag{1}$$

Suppose that there are n feature points, namely $p_i = [X_i Y_i Z_i]^T \quad (i = 1,....,n)$, on an object and the corresponding positions in the image plane are $\xi_i = [x_i y_i]^T \ (i = 1,....,n)$. Assume that the shape and the size of the object are known and constant (i.e., the object is a rigid body). Then ξ_i for $i = 1,....,n$ become functions of the joint angle θ. Let us define a $2n$ dimensional feature vector by $\xi \cong [\xi_1^T \cdots \xi_n^T]^T$. Then the system model for n feature points is defined by the map $\psi : \mathbf{R}^m \to \mathbf{R}^{2n}$ from the joint angle θ to the feature vector ξ as follows:

$$\psi(\theta) \cong \xi \tag{2}$$

where m is the number of the joints of the robot.

Since the task must be carried out in the nonsingular region of the robot, the nonsingular region is called the operation region $\mathrm{M}_\theta \subset \mathbf{R}^m$. We restrict the robot motion in the operation region. Thus the robot Jacobian J robot is invertible in the working area. It is useful to introduce the feature manifold M, which is defined by

$$\mathrm{M} = \{\xi \in \mathbf{R}^{2n} : \xi = \psi(\theta), \theta \in \mathrm{M}_\theta\} \tag{3}$$

The features on the feature manifold is called the admissible features. If the features are admissible, then the robot Jacobian is invertible by definition. In equation (3), θ represents joint angle.

Differentiation of the system model yields

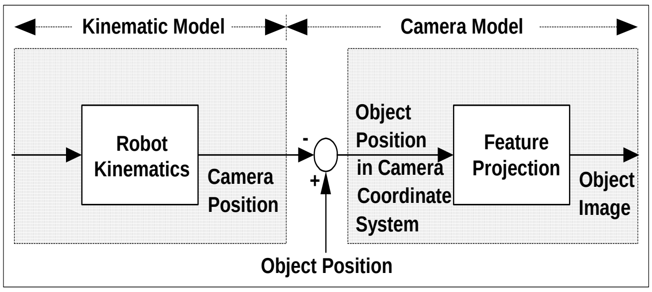

Fig. 1. System Modeling

$$\dot{\xi} = J\dot{\theta} \tag{4}$$

where the $2n \times m$ matrix J is defined by

$$J \cong \begin{bmatrix} J_{im}^{(1)} \\ \vdots \\ J_{im}^{(n)} \end{bmatrix} {}^c J_{ARM} \tag{5}$$

The matrix $J_{im}^{(i)}$ is given by [14], [12]

$$J_{im}^{(i)} \cong \begin{bmatrix} -\frac{f}{z_i} & 0 & \frac{x_i}{Z_i} & \frac{x_i y_i}{f} & -\frac{x_i^2 + f^2}{f} & y_i \\ 0 & -\frac{f}{z_i} & \frac{y_i}{Z_i} & \frac{y_i^2 + f^2}{f} & \frac{x_i y_i}{f} & -x_i \end{bmatrix} \tag{6}$$

and called the image Jacobian [12]. ${}^c J_{ARM}$ is the robot Jacobian expressed in the camera coordinate system. Since the vector ${}^c J_{ARM}\dot{\theta} \in \mathbf{R}^6$ is the linear and angular velocities of the camera expressed in the camera coordinate system, $J_{im}^{(i)}$ becomes the infinitesimal change of the position of the camera. Moreover, $J(i) \cong J_{im}^{(i)}\, {}^{c}J_{ARM}$ becomes the infinitesimal change of the features according to the infinitesimal change of the joint angles.

The degenerated features are the features for which the extended image Jacobian is not full rank. The degenerate features should be avoided because the inverse map (the map from ξ to θ) becomes singular. Thus, when the number of joints is m,

$$rank\ J(\theta) = m \qquad \forall \theta \in \mathrm{M}_{\theta} \tag{7}$$

is required for all admissible features. To satisfy this condition $n \geq m/2$ is an obvious necessary condition, but it is not sufficient for some cases.

For example, consider a general six degree of freedom $(m = 6)$. In this case, $n \geq 3$ is necessary. If $n = 3$, $rank\ J \langle 6$ the camera lies on the cylinder(Fig. 2) which includes the three points and the axis of which is perpendicular to the plane containing these points. For any attitude of the camera, J is singular. Thus $n = 3$ is not sufficient and $n \geq 4$ is desirable. For the case of $n = 4$, we have the following theorem.

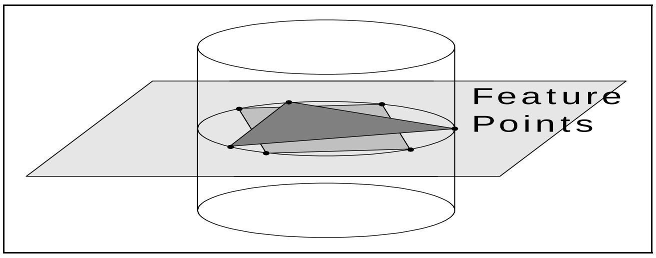

Fig. 2. Singular Cylinder

Theorem 1: Suppose that there are four points on a plane and the corresponding feature vector is admissible. Then the extended image Jacobian is full rank if any three feature points out of them are not collinear in the image plane.

Proof : Let the plane on which the four points exist be $Z = pX + qY + r$. Then Z_i satisfies $Z_i = pX_i + qY_i + r$ for $i = 1, \cdots, 4$. Substituting (1) into this yields

$$\frac{f}{Z_i} = \frac{f - px_i - qy_i}{r} \tag{8}$$

And substituting this into (6) yields

$$J_{im}^{(i)} = M_i N \tag{9}$$

where M_i and N are defined by

$$M_i = \begin{bmatrix} f & 0 & x_i & y_i & 0 & 0 & x_i^2/f & x_i y_i/f \\ 0 & f & 0 & 0 & x_i & y_i & x_i y_i/f & y_i^2/f \end{bmatrix},$$

$$N = \frac{1}{r}\begin{bmatrix} -1 & 0 & 0 & 0 & -r & 0 \\ 0 & -1 & 0 & r & 0 & 0 \\ p & 0 & 1 & 0 & 0 & 0 \\ q & 0 & 0 & 0 & 0 & r \\ 0 & p & 0 & 0 & 0 & -r \\ 0 & q & 1 & 0 & 0 & 0 \\ 0 & 0 & -p & 0 & -r & 0 \\ 0 & 0 & -q & r & 0 & 0 \end{bmatrix} \tag{10}$$

Then we obtain $J = MN\,{}^{c}J_{ARM}$, where $M = \begin{bmatrix} M_1^T & M_2^T & M_3^T & M_4^T \end{bmatrix}^T$. It is straightforward to see that

$$\det M = \begin{vmatrix} 1 & x_1 & y_1 \\ 1 & x_2 & y_2 \\ 1 & x_3 & y_3 \end{vmatrix} \bullet \begin{vmatrix} 1 & x_2 & y_2 \\ 1 & x_3 & y_3 \\ 1 & x_4 & y_4 \end{vmatrix} \bullet \begin{vmatrix} 1 & x_3 & y_3 \\ 1 & x_4 & y_4 \\ 1 & x_1 & y_1 \end{vmatrix} \bullet \begin{vmatrix} 1 & x_4 & y_4 \\ 1 & x_1 & y_1 \\ 1 & x_2 & y_2 \end{vmatrix} \tag{11}$$

Thus M is invertible because any three feature points are not collinear. On the other hand, if $p^2 + q^2 \neq 0$, the first six rows of N is linearly independent. If $p = q = 0$, the first four and the last two rows are linearly independent. Thus rank $N = 6$. finally, since all features are admissible, ${}^{c}J_{ARM}$ is invertible. Therefore, the extended image Jacobian J is full rank.

3. Visual Feedback System

For evaluating the performance of the feature-based visual feedback system, it is useful to discuss the ratio of the joint angle error to the feature vector. The following theorem shows that increasing the number of the feature point is an effective way to improve the performance.

Let the joint error be $\Delta\theta = \theta - \theta_d$ and the feature error be $\Delta\xi = \xi - \xi_d$. Define the worst joint/feature error ratio ER, called sensitivity, as follows:

$$ER = \sup_{\|\Delta\xi \neq 0} \frac{\|\Delta\theta\|}{\|\Delta\xi\|} = \frac{1}{\beta_{\min}(J)} \tag{12}$$

where $\beta_{\min}(J)$ is the minimum singular value of J. Then the sensitivity ER decreases strictly by increasing the number of non-degenerated features on the object.

Let J_n be the image Jacobian for n feature points and J_{n+1} be the image Jacobian obtained by adding an extra feature point to the already existing feature points.

Then we have

$$J_{n+1} = \begin{bmatrix} J_n \\ J^{(n+1)} \end{bmatrix} \tag{13}$$

where $J^{(n+1)}$ is the $2\times m$ image Jacobian corresponding to the newly added feature point. It is straightforward to see that

$$\beta_{\min}(J_n) \le \beta_{\min}(J_{n+1}) \tag{14}$$

The equal sign holds only if each row of $J^{(n+1)}$ is linearly dependent to J_n, i.e., only if J_{n+1} is not full rank. Since we assumed that the features are not degenerated, the equal sing should be dropped. Thus adding extra feature points strictly increases the minimum singular value.

This theorem says that we can reduce the joint angle error by increasing the number of feature points.

Linearizing the model (2) with the feature vector being the state vector yields an uncontrollable model because ξ can not move arbitrarily in $\mathbf{R}^{2n}$ [13]. A simple way to avoid this problem is to map $\xi \in \mathrm{M}$ onto the tangent space of M by using the following transformation.

$$z = J_d^T(\xi - \xi_d) \tag{15}$$

where $J_d = J(\theta_d)$ is the image Jacobian at the desired point[16]. Note that z and θ are one-to-one in the neighborhood of θ_d. The dynamics of the feature error on the tangent space of the manifold M is given by

$$\dot{z} = J_d^T J(\theta)\dot{\theta} \tag{16}$$

Thus, for a simple continuous time control law $\dot{\theta} = -Kz$ with a positive definite constant matrix K yields an asymptotic stability if $J_d^T J(\theta)$ is positive definite. It is shown that this condition is satisfied fairly large region about θ_d [13].

4. Experiments and Discussion

As shown in Fig.3, the objects are white boards with three, four and five black marks. Three points are arranged to make a regular triangle with edge length 120mm. Four points are on corners of a square with edge length 120mm. All marks are on a plane except the one of five points at the center of the square, which has height 60mm. Dual-Arm robot holds the objects and a camera(Fig.4). The world coordinate system $\omega_X - \omega_Y - \omega_Z$ is at the base of the Dual-Arm robot. A nominal camera position is almost in front of the plane on which the marks exist. To avoid the singular cylinder(Fig.2) the optical axis and the normal axis of the object plane are not aligned. The distance is about 1000mm. The features are the x and y coordinates of the center of the image of each mark. Computing their minimum singular values at the reference position gives

$$\begin{aligned}\beta_{\min} &= (J_3) = 0.35, \\ \beta_{\min} &= (J_4) = 0.65, \\ \beta_{\min} &= (J_5) = 3.60\end{aligned} \tag{17}$$

Thus accuracy of the position control of the camera in the 3D work space will be improved by using 5 features. We carried out many step tests to this observation.

The first experiment is a step motion in vertical axis. The object is moved upward for 120mm (i.e., in ω_Z direction). The camera is controlled to keep the features at the initial positions. Thus the initial values and the reference values are the same. The object motion is considered as a disturbance for the plots of the features in the image plane. On the other hand, the object motion becomes the step change of the reference position for the plots of the camera motion in the world coordinate system. Since Dual-Arm robot has only 6 degrees of freedom, the orientation of the object changed slightly. Thus, the reference orientation is [2.8, 0, -1.8] degrees expressed in the Euler angles, say p, η, ϕ.

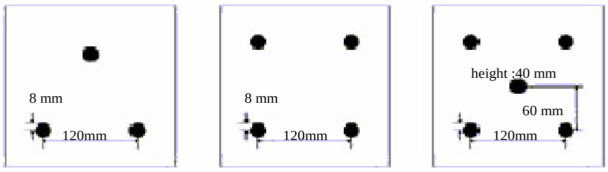

Fig. 3. Configuration of Feature Points

Fig. 4. Experimental Setup

Table 1. Specification of Dual Arm Robot

Content		Unit	Spec.	Remark
Workspace	1st Arm	Deg	180	
	2nd Arm	Deg	450	
	Z Axis	Mm	150	
	R Axis	Deg	±180	
Maximum Reach		Mm	(350+260)	
Payload		Kg	2.5	High-speed
Max. Resultant Vel.		m/sec	5.4	1,2 Axis
Position Repeatability	Plane	Mm	0.05	1,2 Axis
	Z Axis	Mm	0.02	
	M Axis	Deg	0.05	
Weight		Kg	200	
Coincident Control Axis No.		EA	8Axis (4+4)	

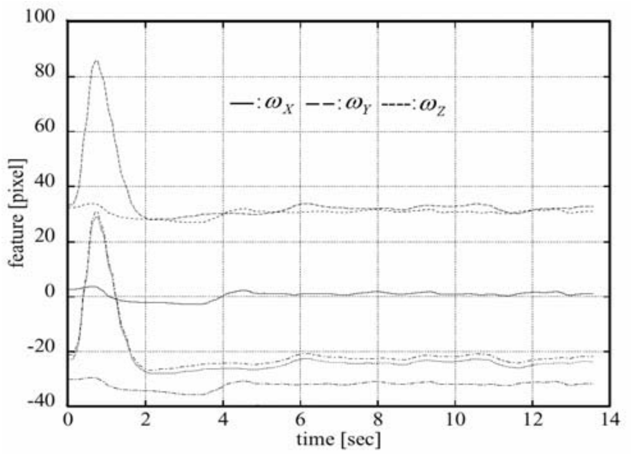

Fig.4. Response in Image Plane for 3 Points.

5. Conclusions

In this paper, it has been presented how the control performance of the feature-based visual servo system is improved by utilizing redundant features. Effectiveness of the redundant features is evaluated by the smallest singular value of the image Jacobian which is closely related to the accuracy in the world coordinate system. It shows that the accuracy of the camera position control in the world coordinate system was increased by utilizing redundant features. Real time experiments on dual-arm-robot were carried out to evaluate the improvement of the accuracy and speed by utilizing the redundant features. The results verifies that the minimum singular value of the extended image Jacobian plays an important role for performance improvement of the feature-based visual servoing.

References

[1] K. Hashimoto et al.,1991, "Image-based dynamic visual servo for a hand-eye manipulator," in *MTNS-91*, Kobe, Japan, pp. 609~614.

[2] Sung Hyun Han, Man Hyung Lee, Hideki Hashimoto, 2000, "Image-Based Servoing Control of a SCARA Robot" *KSME International Journal*, Vol. 14, No. 7, pp. 782~788.

[3] P. K. Allen, A. Timccnko, B. Yoshimi, and P. Michelman, 1993, "Automated tracking and grasping of a moving object with a robotic hand-eye system," *IEEE Trans. Robotics and Automation*, vol. 9, no. 2, pp. 152~162.

The Eleventh International Symposium on Artificial Life and Robotics 2006 (AROB 11th'06),
B-con Plaza, Beppu, Oita, Japan, January 23-25, 2006

Lateral-shearing Interferometer for optical testing of DVD pick-up lenses

Byoung Chang Kim*, Seo Heon Kim, Yong Kwan Kwon and Won Il. Kim

School of Mechanical and Automation Engineering
Kyungnam University
449 Wolyoung Dong, Masan, Kyungnam, 631-701, Korea(bckim@kyungnam.ac.kr)

Abstract

We present a lateral-shearing interferometer specially devised for production-line inspection of aspheric lenses. The interferometer constitutes four right-angle prisms, whose relative sliding motions provide the lateral shear and phase shifts necessary for measuring the beam wavefront collimated by the lens under test. The prisms are held together face to face using index-matching oil, so environmental disturbances from external vibration and atmospheric turbulence can be minimized. Further, a special phase-measuring algorithm of least-squares is adopted to compensate for the phase shift error caused by the thickness variation in the index-matching oil holding the prisms. Experimental results prove that the interferometer provides a measuring repeatability in the order of one hundredth of the light wavelength.

1. Introduction

Optical pickup objectives used in data storage devices such as compact discs (CD) or digital versatile discs (DVD) are made in aspheric shape and fabricated in large volumes using the injection molding process. In this mass-production, one critical problem is the optical testing of produced lenses especially for production-line quality assurance. The optical testing involves measuring the converging or collimated wavefront from the objectives to reveal any surface defects and aberrations. In fact, a wide variety of interferometric techniques are available for the purpose.[1] Among them, the Fizeau interferometry is most popularly used in industry, being well incorporated with latest computer-vision technology.[2] As the objective has been designed to focus the incoming parallel beam at a certain depth location underneath a protective disc layer, a blank disc plate with controlled thickness is included in the testing. Without the disc plate, an excessive amount of spherical aberration would dominate in the generated wavefront, leaving out other types of aberrations such as astigmatism and coma rarely observable. Consequently, three optical components of the objective itself, the disc plate, and the reflecting mirror should be precisely aligned along the optical axis to obtain accurate testing results. A thorough analysis of alignment errors in this particular double-pass interferometry reveals that 10 out of the entire 18 degrees-of-freedom of the three components have significant effects on measurement results.[3] For that reason, the testing method turns out to be a time-consuming, laborious task even to the skillful operator and hardly ever applicable to the total quality inspection of all the produced lenses.

In recent years various types of lateral-shearing interferometer have been investigated with particular intention of testing of aspheric lenses and surfaces.[4] They all allow single-pass wavefront measurement without the reflecting mirror needed in the Fizeau interferometry. This advantage reduces necessary alignment work significantly and subsequent total measuring time. In this paper we presents a special lateral-shearing interferometer, which has been devised for production-line inspection of aspheric objective lenses. This interferometer has a high immunity to external vibration and atmospheric disturbance, since the whole interferometer is composed of four pieces of square prisms held together face to face using index-matching oil. The relative sliding displacements of the prisms can readily generate both the lateral shear and phase shifts necessary to determine the wavefront to be measured. As a result, the lateral-shearing interferometer provides a great flexibility in handling various types and sizes of aspheric lenses. In addition, the latest computer-vision technology can be well incorporated so that necessary testing operation can be implemented automatically in unmanned manner.

2. Interferometer design

The lateral-shearing interferometer configured in this investigation is shown in Figure 1. A coherent HeNe laser is used as light source. The laser beam is focused using a microscope objective and then collimated by the lens being tested. A disc plate is placed before the lens for the same reason as in the Fizeau interferometer of Figure 1 to avoid excessive spherical aberration. The collimated beam would be a plane wave if the lens were perfect being free from aberrations; otherwise it would have a distorted wavefront.

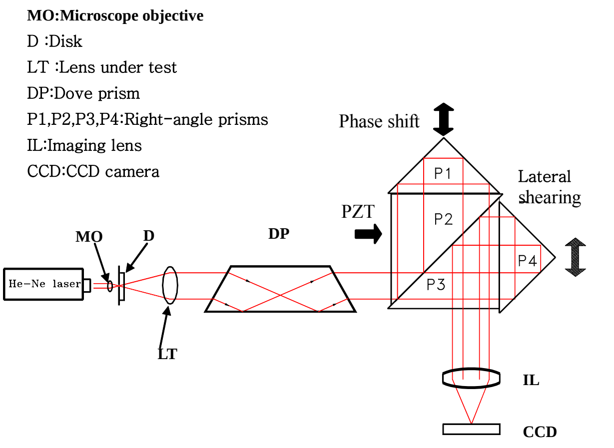

Figure 1. Optical configuration of the lateral-shearing interferometer under investigation

The lateral-shearing interferometer measures the wavefront using four pieces of square prisms. The prisms are attached face to face using index-matching oil to allow their relative sliding motions necessary for lateral shear and phase-shift. For convenience, the prisms are referred to as P1, P2, P3, and P4, respectivel. The prism P3 is fixed stationary at center in the assembly, and its inclined surface divides the incoming beam 50:50, half the beam to reflect and the other half to transmit. The separated beams are then reflected back by P1 and P4 respectively, and combined together with a predetermined amount of lateral shear to produce interferometric fringes.

The amount of lateral shear is adjusted by sliding P4 in the z-direction, being twice the displacement of P4. The direction of lateral shear in the xy-plane is also variable by rotating the dove prism placed between the test lens and the interferometer; the collimated beam swivels twice the angular rotation of the dove prism. Another important aspect of the interferometer design is that phase shifting necessary for effective fringe analysis is simply introduced by pushing P2 along the inclined surface of P3. P1 is constrained to move only in the z-direction. The movement of P2 in the x- and z-directions causes no lateral shear in the x-direction, but only changes the optical path in the z-direction to induce phase shift. A micrometer is used to set the position of P4 with a predetermined amount of lateral shear. And a piezoelectric ceramic actuator is used to push P2 in steps during measurement to generate a series of phase shifts. A ball joint is inserted between the actuator and P2, so that P2 can slide along the inclined surface of P3 in the x- and z-directions while the actuator elongates only in the x-direction. The motion of P1 is kinematically guided by a set of preloaded springs to move only in the z-direction. The refractive index of the index-matching oil is selected to be the same as that of the prisms.

3. Phase measurement

Figure 2 shows the wavefronts of the two beams involved in the lateral-shearing interferometry. Let the wavefront of one beam be represented by z=w(x,y). Then the other wavefront can be expressed as w(x-s,y)+d, where s is the amount of lateral-shear in the x-direction and d is the path difference between the beams along the optical axis. When the two wavefronts are combined, the intensity of interferometric fringes is obtained as

$$I(x,y) = D(x,y) + V(x,y) \cos[k(\Delta w_x(x,y) - d)] \qquad (1)$$

where $\Delta w_x(x,y) = w(x,y) - w(x-s,y)$; k is the wavenumber, $k=2\pi/\lambda$; and D(x,y) and V(x,y) are the intensity mean and modulation amplitudes, respectively. The phase term $\Delta w_x(x,y)$, defined as the wavefront difference, has to be determined from the measured intensity of interferometric fringes. In doing that, there are additional unknowns of D(x,y) and V(x,y) as in Eq.(1), so $\Delta w_x(x,y)$ can not simply be extracted from single intensity measurement. Therefore, multiple intensity measurements are necessary to be made with different phase shifts. Let the path differences be varied with phase shifts such as $d=d_o$, d_1, ..., d_m. Then Eq.(1) is extended as

$$I_{ij} = D_i + V_i \cos(\phi_i - \phi_j) \qquad (2)$$

where $\phi_I = k\Delta w_x(x,y)$ and $\delta_j = kd_j$. For convenience of expression, the subscript i implies the location of (x,y) and j indicates the j-th phase shift.

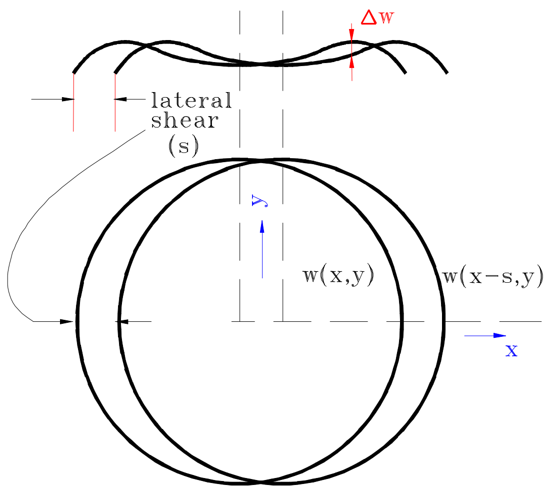

Figure 2. Two wavefronts involved in the lateral-shearing interferometry

In determining ϕ_i from Eq.(2), a suitable phase-measuring algorithm is required. Much work has in fact been done on establishing effective phase-measuring algorithms, and as results many novel algorithms are available.[5] Most existing algorithms have their own advantages and are distinguished from each other by the required number and spacing of phase shifts. However, they all assume that phase shifts be exactly induced as intended. If there are errors in actual phase shifts due to miscalibration or external disturbance, no accurate measurement is guaranteed. In our lateral-shearing interferometer, one problem is that the amounts of phase shifts are not easy to be precisely controlled. The reason is that the index-matching oil is squeezed in and out when the prisms are moved for phase shifting. Consequently the oil thickness does not remain constant, causing a significant level of inaccuracy in phase shifting. This problem can be overcome by adopting an adaptive algorithm in that actual true values of phase shifts are identified directly from interferograms. Here we adopt a least-squares algorithm in which a residual error function related to phase shift errors is to be minimized to determine true solutions of phase shifts.[6]

The first step of the least squares phase-measuring algorithm is to define the differential intensity such as

$$J_{ij} = I_{ij} - I_{i0} = C_i(\cos\delta_j - 1) + S_i \sin\delta_j \qquad (3)$$

where C_i and S_i are obtained from Eq.(2) such as $C_i = V_i \cos\phi_i$ and $S_i = V_i \sin\phi_i$. In fact, the differential intensity J_{ij} represents the variation of intensity induced by the phase shift δ_j, assuming $\delta_0 = 0$. Then, besides C_i and S_i, δ_j is also treated as unknowns and determined so as to minimize the residual function of

$$E = [J_{ij} - J_{ij}^*]^2 = [C_i(\cos\delta_j - 1) + S_i \sin\delta_j - J_{ij}^{*2} \quad (4)$$

where J_{ij}^* denotes the measured value of J_{ij}. The necessary conditions for the minimization of the function E are given by the equations of

$$E/\partial C_i = \partial E/\partial S_i = \partial E/\partial_j = 0. \qquad (5)$$

Adopting the special numerical method that has been thoroughly described by the authors in the reference, the above equations can readily be solved. When δ_j, C_i, and S_i are obtained, the wavefront difference $\Delta w_x(x,y)$ is finally determined as

$$\Delta w_x(x,y) = \phi_i/k = (1/k)\tan^{-1}(S_i/C_i). \quad (6)$$

4. Wavefront reconstruction

Now the wavefront field w(x,y) is to be obtained from the computed $\Delta w_x(x,y)$. One drawback of the lateral-shearing interferometry is that w(x,y) can not be determined simply by unwrapping $\Delta w_x(x,y)$. The reason is that $\Delta w_x(x,y)$ represents the phase differences between w(x,y) and a shifted part of itself, i.e., $\Delta w_x(x,y) = w(x,y) - w(x-s,y)$, not being the phase deviations from a reference as in the Fizeau interferometry. Therefore, a special phase-reconstruction algorithm is needed to estimate w(x,y) from $\Delta w_x(x,y)$. As results of recent rigorous work on the subject, several estimation algorithms are available and they may be categorized as either modal or zonal phase-reconstruction techniques. [7] In the former, w(x,y) is described as a sum of modal functions, such as the Zernike polynomials. Then the coefficients of the modal functions are determined by approximating the measured $\Delta w_x(x,y)$ in terms of the sheared forms of the model functions considering the amount of lateral shear. On the other hand, in zonal phase-reconstruction technique, w(x,y) is computed point by point on a grid of measured phase difference points by the application of a least-squares fit to the measured $\Delta w_x(x,y)$. The two phase-reconstruction techniques are capable of minimizing the propagation of measurement errors of $\Delta w_x(x,y)$ in determining w(x,y). However, they require a considerable amount of computation especially for large size matrix inversion or recursive multi-dimensional steepest search. In addition, due to computational truncation errors, they tend to fail to give out precise solutions when w(x,y) is a nearly plane wave with small aberrations. The DVD objectives generally have minute aberrations whose total root-mean-square values range within a few hundredth wavelength, so the problem of computational truncation errors becomes significant. [3]

In this investigation, a simple phase-reconstruction algorithm with less computation is employed which is well suited for fast inspection of DVD objectives. When the amount of lateral shear s is taken small, the tangential slope of the wavefront may be well approximated such as

$$\frac{\partial w(x,y)}{\partial x} \approx \frac{1}{s}\Delta w_x(x,y). \qquad (7)$$

This approximation becomes more valid if the measured $\Delta w_x(x,y)$ bears no drastic changes, which is generally the case of DVD objectives. Recovering the whole wavefront w(x,y) can then be done using two wavefront slopes along two orthogonal directions such as

$$w(x,y) = \int\left[\frac{\partial w(x,y)}{\partial x}dx + \frac{\partial w(x,y)}{\partial y}dy\right] \quad (8)$$

in which $\Delta w_y(x,y)$ represents the tangential slope of wavefront along the y-direction. As previously explained in Figure 1, in our interferometer the direction of lateral shear is simply switched to the y-direction by swiveling the dove prism by 45 degrees. Then $\Delta w_y(x,y)$ can be measured following exactly the same procedure for $\Delta w_x(x,y)$.

Reconstruction of the whole field of wavefront is performed by integrating the measured values of $\Delta w_x(x,y)$ and $\Delta w_y(x,y)$ as in Eq.(8). In doing that, many integration paths may be taken to reach a certain point (x,y). In nature, w(x,y) is supposed to be a point function, thus its computed result should be identical regardless of integration paths. In practice, the errors in $\Delta w_x(x,y)$ and $\Delta w_y(x,y)$ tend to propagate as the integration proceeds. If this is the case, the reconstructed w(x,y) varies with integration paths and becomes inaccurate. The concept is that every point value of w(x,y) is determined by making the most of two orthogonal paths; one incremented from the x-neighbor point and another from the y-neighbor point. This is logically expressed as

$$w(x,y) = \frac{1}{2}[\{w(x-dx,y) + \frac{dx}{s}\Delta w_x(x-dx,y)\} + \{w(x,y-dy) + \frac{dy}{s}\Delta w_y(x,y-dy)\}] \tag{9}$$

This averaging is performed for every point in recursive manner. As results, errors residing in $\Delta w_x(x,y)$ and $\Delta w_y(x,y)$ are averaged out as the integration progresses.

Once the whole field of w(x,y) is obtained, the aberrations of the test lens is identified by fitting the Zernike circular polynomials.[1] For that, it is necessary to fit the computed data points of w(x,y) in unit radius circle by rescaling their the x- and y-coordinates. The amount of shear is taken usually as 5 % the pupil diameter of the lens being measured. Thus interference occurs only in an ellipsoidal area contracted in the sheared direction, so different scale factors are needed for rearranging the x- and y-coordinates. Further, the Gram-Schmidt orthogonalization is needed to convert the Zernike polynomials to be orthogonal over the rescaled discrete data points.[1]

5. Experimental results

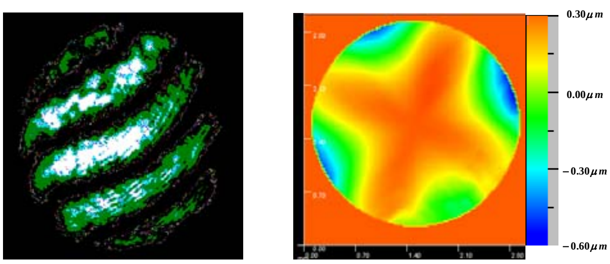

(a) A representative shearing interferogram **(b)** A reconstructed wavefront

Figure 3. Experimental results obtained from a DVD objective

An exemplary shearing interferogram obtained from DVD objectives is shown in Figure 3, together with its corresponding wavefront finally reconstructed. The level of total wavefront distortion of the objectives is usually in the range of a few hundredth wavelength in root-mean-square values. For phase-shifting fringe analysis, 5 interferograms are sequentially measured with different amounts of phase shift. Then the phase-measuring algorithm of least squares determines the wavefront difference

6. Conclusions

A lateral-shearing interferometer has specially been devised and tested for the optical testing of aspheric lenses. The interferometer is configured with four square prisms whose relative sliding motions readily provide lateral-shearing and phase-shifting necessary for evaluating the beam wavefront collimated by the lens under test. The prisms are attached face to face using index-matching oil, so undesirable disturbances from external mechanical vibration and atmospheric turbulence can be minimized. Further, a special phase-measuring algorithm of least-squares has been adopted to compensate for the phase-shifting errors caused by the thickness variation in the index-matching oil holding the prisms. Measurements results proved that the interferometer has a repeatability of less than $\lambda/100$.

Acknowledgements

This work is supported by the New University for Regional Innovation (NURI) program from the Minister of Education and Human Resources Development, Korea.

References

[1] D. Malacara(1992), Optical Shop Testing, John Wiley & Sons, Inc., 2nd edition.
[2] P.F. Forman(1979), Interferometric examination of lenses, mirrors and optical systems, Proc. SPIE, **163**, pp.103.
[3] B.C. Kim(1998), Performance test of aspheric lenses using optical interference, Korea Advanced Institute of Science and Technology, MSC thesis.
[4] M. Murty(1970), A compact lateral shearing interferometer based on the Michelson interferometer,, Appl. Opt. **9**(5), pp.1146.
[5] K. Creath(1988), Phase-measurement interferometry techniques, Progress in Optics, **26**, pp.349.
[6] G. Han and S. Kim(1994)., Numerical correction of reference phases in phase-shifting interferometry by iterative least-squares fitting, Appl. Opt. **33**(31), pp.7321.
[7] G. Harbers, P. Kunst, and G. Leibbrandt(1996), Analysis of lateral shearing interferograms by use of Zernike polynomials, Appl. Opt. **35**(31), pp.6162.

Permanent Magnet Biased Magnetic Bearings and Robotic Applications

Jin Seok Won

Dept. of Mechanical Design, Graduate School,
Kyungnam University,
Masan, Gyeongnam, 631-701, Korea

Tae Hyun Son

School of Mechanical and Automation Eng.,
Kyungnam University,
Masan, Gyeongnam, 631-701, Korea

Uhn Joo Na

Dept. of Mechanical Design, Graduate School,
Kyungnam University,
Masan, Gyeongnam, 631-701, Korea

Sung Hyun Han

School of Mechanical and Automation Eng.,
Kyungnam University,
Masan, Gyeongnam, 631-701, Korea

Abstract

The theory for a novel fault-tolerant 4-active-pole homopolar magnetic bearing is developed. If any one coil of the four coils in the bearing actuator fail, the remaining three coil currents change via an optimal distribution matrix such that the same opposing pole, C-core type, control fluxes as those of the un-failed bearing are produced. The hompolar magnetic bearing thus provides unaltered magnetic forces without any loss of the bearing load capacity even if any one coil suddenly fails. Numerical examples are provided to illustrate the novel fault-tolerant, 4-active pole homopolar magnetic bearings.

1 Introduction

A magnetic bearing system is an active control device that suspends the spinning rotor magnetically without physical contact as well as suppresses vibrations. Magnetic bearings find greater use in high speed, high performance applications such as flywheel energy storage systems since they have many advantages over rolling element bearings (Bitterly, 1997). Unlike electromagnetic heteropolar bearings shown in the previous works (2003, Na, 2005), permanent magnet biased homopolar magnetic bearings have a unique biasing scheme that directs the bias flux flow into the active pole plane where it energizes the working air gaps, and then returns through the dead pole plane and the shaft sleeve. Use of rare earth permanent magnets such as Samarium-Cobalt and Neodymium-Iron-Boron yields a very high efficiency when the permanent magnets are used as the source of bias flux to energize the air gaps and electromagnets are used to supply control fluxes in the active plane. Sortore et al (1990) and Allaire et al (1992) presented design methods and experimental verifications for permanent magnet biased magnetic bearings. Similarly, Maslen et al (1996) also showed both analytical and experimental results on the design and construction of permanent magnet biased magnetic bearings. Lee et al (1994) provides design, testing and performance limits of the permanent magnet biased magnetic bearings. Fan et al (1997) presented systematic design procedures for permanent magnet biased magnetic bearings. Fukada and Yutani (1998) studied the frequency response of permanent magnet biased magnetic bearings.

Fault-tolerance of the magnetic bearing system is of great concern for highly critical applications of turbo-machinery since a failure of any one control components may lead to the complete system failure. Maslen and Meeker (1995) introduced a fault tolerance of an 8-pole heteropolar magnetic bearing actuator with independently controlled currents and experimentally verified it (Maslen et. al., 1999). They utilized flux coupling in a heteropolar magnetic bearing that allows the remaining coils to produce force resultants identical to the unfailed bearing. Na and Palazzolo (2001) provided the optimized realization of fault-tolerant magnetic bearing actuators so that fault-tolerant control can be realized for an 8-pole bearing for up to 5 coils failed, and experimentally verified it (Na et. al, 2002).

Fault tolerant scheme applied to heteropolar magnetic bearings was modified and extended to permanent magnet biased homopolar magnetic bearings in Na's work (Na, 2004). He presented the optimized realization of fault tolerant 8-pole homopolar magnetic bearings, so that the same magnetic forces can be realized up to any combination of 5 coils failed out of 8 coils. However, the overall load capacity of the bearing is reduced as coils fail. The same magnetic forces are then preserved up to the load capacity of the failed bearing.

2 Bearing Model

A 4-active pole, permanent magnet biased homopolar magnetic bearing is analyzed. Assuming that eddy current effects and material path reluctances are neglected, Maxwell's equations are reduced to the equivalent magnetic circuit for the homopolar magnetic bearing. The reluctance in air gap j of the active pole plane is;

$$R_j = \frac{g_j}{\mu_0 a_0} \tag{1}$$

where

$$g_j = g_0 - x\cos\theta_j - y\sin\theta_j \tag{2}$$

Applying flux conservation law to the magnetic circuit results in one more equation. Flux to current relations on the magnetic bearings is described as,

$$R\Phi = H + NI \tag{3}$$

The 4-active pole homopolar magnetic bearing utilizes 4 independent coils each driven by its power amplifiers so as to obtain the flexibility of a coil failure.

$$B = \varsigma A^{-1}R^{-1}(H + NI) \tag{4}$$

The magnetic forces developed in the active pole plane are described as;

$$f_x = B^T \frac{\partial D}{\partial x} B \tag{5}$$

$$f_y = B^T \frac{\partial D}{\partial y} B \tag{6}$$

3 Fault Tolerant Control

The 3-D magnetic field model is constructed for the designed homopolar magnetic bearing. A commercial magnetic field software (OPERA3D) is used for the 3-D field calculation. Two cases of currents, which are the normal current $I_1 = \tilde{T}v_c$ and the 4th coil failed current $I_2 = T_4 v_c$, are applied on the 3-D magnetic bearing model at the centered position to calculate magnetic fluxes and magnetic forces. The feedback voltages are simply assumed to be $v_{cx} = 3.0\cos\Omega t$, $v_{cy} = 3.0\sin\Omega t$, $t \in [0, 2\pi/\Omega]$. 12 current sets of I_1 and I_2 at $t = [\pi/(6\Omega), 2\pi/(6\Omega), \ldots, 12\pi/(6\Omega)]$ are applied on the model such that the corresponding magnetic fluxes as well as magnetic forces should be calculated at each current sets. Flux distribution in the active pole plane driven with the current set is shown in Fig. 1.

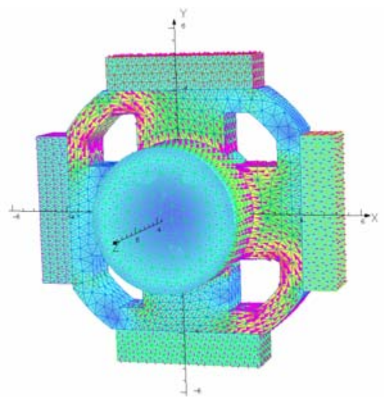

Fig. 1 Flux Distribution Calculated with 3-D Finite Element Model by Current Set

The fault tolerant control system consists of two independent parts, which are a feedback voltage control law and an adaptive current distribution mechanism. A simple PD feedback control law is used to stabilize the system. While the feedback control law remains unaltered during the failure the appropriate current distribution matrix T can be continuously updated according to the failure status of coils (Na et. al., 2002).

The fault-tolerant control system is simulated on a horizontal rigid rotor supported on the 4-active pole homopolar bearings. The symmetric rotor used in this analysis has mass of 12 kg, the polar moment of inertia of 0.05 kgm^2, and the transverse moment of inertia of 0.36 kgm^2 about the mass center. Two magnetic bearings are located at 0.22 m either side of the mass center. An unbalance eccentricity of $1.0\times 10^{-5} m$ is applied at both bearing locations with relative phase angle 90°. The power amplifiers are simply modeled with the DC gain of 1 Ampere/Volt. The sensors are also simply modeled with a DC sensor gain of 7874 volt/m. The closed loop bearng stiffness and damping can be adjusted by tuning the PD control gains (Keith et. al., 1990). The designed PD controller has the proportional gain of 60 and the derivative gain of 0.05. The proportional control gain of K_p is tuned to produce the positive closed loop bearing stiffness. The derivative control gain of K_d is tuned to add enough closed loop bearing damping.

The transient response from normal operation with no failure to fault-tolerant control with the 4th coil failed for both bearings was simulated for nonlinear force modeled bearings at 10,000 RPM. The nonlinear magnetic bearings are used for a more stringent test. Figure 2 shows transient current inputs from the normal unfailed operation through failure of the 4th coil of the bearing A failed at 0.05 sec. The transient response of the displacements at the bearing A is shown in Fig. 3. Displacements and flux density variation at Bearing A remain unchanged even after the 4th coil fails, while the three remaining currents are redistributed via T_4 after the 4th coil fails at 0.05 seconds. This means that any one coil out of four coils is free to fail while bearing properties such as the load capacity and stiffness remain invariant, if $\tilde{T}$ is replaced by T_1, T_2, T_3, and T_4 shortly after failure.

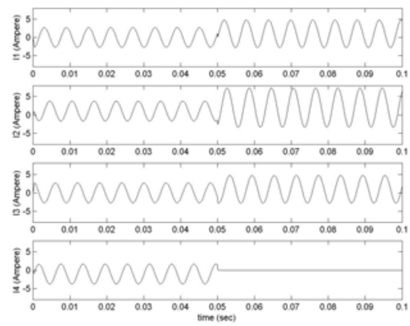

Fig. 2 Current Plot for Normal Operation to the 4th Coil Failed Operation

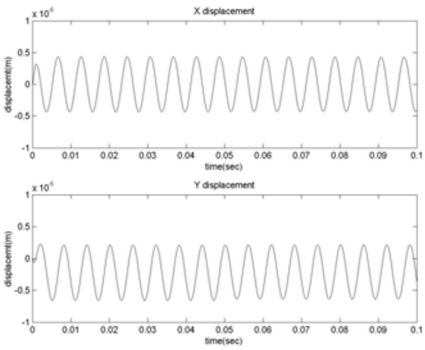

Fig. 3 Displacement Plot for Normal Operation to the 4th Coil Failed Operation

4 Conclusion

A fault-tolerant control scheme is developed for the permanent magnet biased, 4-active-pole homopolar magnetic bearings. The present work extends Na's previous result (Na, 2004) such that unique fault tolerant schemes are realized for 4 active pole homopolar magnetic bearings. If any one coil out of four coils suddenly fails, the remaining three coil currents can be redistributed in a way such that the same C-core type, control fluxes as those of an un-failed bearing are preserved in the active-pole plane.

The bias voltage linearization can be realized for the failed bearing in a manner such that the magnetic forces are decoupled by using a modified current distribution matrix after a coil failure. The Lagrange Multiplier optimization with equality constraints is utilized to calculate the optimal distribution matrices for the failed bearing.

Three dimensional finite element magnetic bearing model is also constructed. The magnetic forces calculated with the 3-D finite element model are well matched with those calculated with the 1-D circuit model. The fault-tolerant control system is simulated on a horizontal rigid rotor supported on the 4-active pole homopolar bearings. Dynamic simulation shows that very much the same vibrations as well as the same fluxes are maintained throughout the failure event.

Acknowledgements

This research was supported by the **N**ew **U**niversity for **R**egional **I**nnovation program of the Ministry of Education & Human Resources Development (NURI MECHANO 21).

References

Allaire, P.E., Maslen, E.H., Humphris, R.R., Sortore, C.K., Studer, P.A., 1992, "Low Power Magnetic Bearing Design for High Speed Rotating Machinery," *Proceedings of the NASA International Symposium on Magnetic Suspension Technology*, pp. 317-329.

Allaire, P.E., Mikula, A., Banerjee, B.B., Lewis, D.W., and Imlach, J., 1989, "Design and Test of a Magnetic Thrust Bearing," *Journal of the Franklin Institute*, Vol. 326, pp. 831-847.

Bitterly, J.G, and Bitterly, S.E., 1997, "Flywheel Based Energy Storage System," U.S. Patent No. 5,614,777.

Fan, Y., Lee, A., and Hsiao, F., 1997, "Design of a Permanent/Electromagnetic Magnetic Bearing-Controlled Rotor System," *Journal of the Franklin Institute*, Vol. 334B, pp. 337-356.

Fukata, S., and Yutani, K., 1998, "Characteristics of Electromagnetic Systems of Magnetic Bearings Biased with Permanent Magnets," *Proceedings of the Sixth International Symposium on Magnetic Bearings*, pp. 234-243.

Keith, F. J., Williams, R. D., and Allaire, P. E., 1990, "Digital Control of Magnetic Bearings Supporting a Multimass Flexible Rotor," *STLE Tribology Transactions* , Vol. 33, pp. 307-314.

Lee, A.C., Hsiao, F.Z., and Ko, D., 1994, "Analysis and Testing of a Magnetic Bearing with Permanent Magnets for Bias," *JSME International Journal, Series C* , Vol. 37, pp. 774-782.

Lee, A.C., Hsiao, F.Z., and Ko, D., 1994, "Performance Limits of Permanent-Magnet-Biased Magnetic Bearings," *JSME International Journal, Series C* , Vol. 37, pp. 783-794.

Maslen, E.H., Allaire, P.E., Noh, M.D., and Sortore, C.K., 1996, "Magnetic Bearing Design for Reduced Power Consumption," *ASME Journal of Tribology* , Vol. 118, pp. 839-846.

Maslen, E.H., Meeker, D.C., 1995, "Fault Tolerance of Magnetic Bearings by Generalized Bias Current Linearization," *IEEE Transactions on Magnetics*, Vol.31, pp. 2304 – 2314.

Maslen, E. H. , Sortore, C. K., Gillies, G. T., Williams, R. D., Fedigan, S. J., and Aimone, R. J., 1999, "A Fault Tolerant Magnetic Bearings," *ASME Journal of Engineering for Gas Turbines and Power*, Vol. 121, pp. 504-508.

Na, U.J., 2004, "Fault Tolerance of Homopolar Magnetic Bearings," *Journal of Sound and Vibration*, Vol. 272, pp. 495-511.

Na, U.J., 2005, "Fault Tolerant Control of Magnetic Bearings with Force Invariance," *Journal of Mechanical Science and Technology*, Vol. 19. pp. 731-742.

Na, U.J., Palazzolo, A.B., and Provenza, A., 2002, "Test and Theory Correlation Study for a Flexible Rotor on Fault-Tolerant Magnetic Bearings," *ASME Journal of Vibration and Acoustics*, Vol. 124, pp. 359-366.

Sortore, C.K., Allaire, P.E., Maslen, E.H., Humphris, R.R., Studer, P.A., 1990, "Permanent Magnet Biased Magnetic Bearings – Design, Construction and Testing," *Proceedings of the Second International Symposium on Magnetic Bearings*, pp. 175-182.

The Eleventh International Symposium on Artificial Life and Robotics 2006 (AROB 11th'06),
B-con Plaza, Beppu, Oita, Japan, January 23-25, 2006

A Free-scale model of knowledge growth

Y. G. Zhang
Institute of Systems Science, Academia Sinica, Beijing, China, 100080
yzhang@iss.ac.cn

M.Sugiasaka
Dept. of Electrical & Electronic Engineering , Oita University, Japan, 870-1192
msugi@cc.oita-u.ac.jp

L. Tang
Institute of Systems Science, Academia Sinica, Beijing, China, 100080
tanglu111@hotmail.com

Abstract
In this paper we try to discuss the knowledge with certain structure and similar to human's knowledge, or the evolutionary configuration of knowledge. In fact, we could observe the process of mother teaching baby language and you could find that "mother" use natural language to make a link of schemes stored in baby's brain. Natural language is the link between scheme and human baby knowledge. At beginning the human baby could know mother's face, the taste of mother's milk, some toys and mother's sound, and then they try to understand some very simple repetitive worlds. The baby gradually learned them and could repeat them. Thus baby got some schemes and obtained primitive knowledge about the surrounded world. Later they could understand some simple sentence; they start to get complete knowledge.

So, we say that the natural language is the key from scheme to presentative knowledge.

Key waords:

I. Introduction

So far, there are many works in literature about the relation between intelligence and knowledge; depends on our research we define intelligence as the abilities to obtain knowledge, to use knowledge and to operate knowledge. We have done certain research on the expression of knowledge[ ]. We also think of that knowledge in brain has some network based structure. This network is changing as knowledge growing in two ways; one way is that some new nodes are added or the network extends to more complicate; the another way is appearance of aggregation of knowledge. In fact, knowledge emergence or knowledge aggregation is very important when knowledge growing, otherwise the structure of network is getting bigger and bigger, so that we cannot easily retrieve any knowledge from this network structure. In this paper we would like to discuss the process of changing of the network model when knowledge growing.

① This work is partially supported by Chinese Natural Science Foundation (CNSF). #60275016

II. Perception and presentative knowledge

To explain the aggregation of knowledge we limit our discussion on the presentative knowledge, that is more intuitive. Usually, perception comes from the sensing organs in a body, for example, eyes, ears, tongue and nose. They obtain some real signals and transfer them into perceptual information, and then store it in some region of brain. The perceptual information is a kind of primitive knowledge. This primitive knowledge is mapped or related with some scene that stored in impression, feeling or sensing. We call this primitive knowledge as presentative knowledge. This is proved by many cognitive experiments on animals and human being. This sort of primitive knowledge is usually called as "schema". It might mean a noun or a verb, and it is very concrete. It is the element of presentative knowledge or the start of growth of knowledge. Also, it especially is the type of knowledge in babyhood for both human and mammal animals. As the baby of human and animal growing up, they learned more and more and the structure of their primitive knowledge is changing in the two ways.

III. The homogeny of knowledge and "lanquadge"

There are two paths to obtain presentative knowledge, one is learn from "mothers" and the other is learn himself. For animals, the mother's teaching use "body language" and very simple sounds (primitive language), and it is enough for survival of their offspring because they just need knowledge that how to find food and avoid the enemies. For human baby it was very similar to animal at the early beginning stage. But the situation is getting different more and more when human baby growing up. Human baby obtains knowledge moiré and more as he/she has better language abilities. They do not need only food and avoiding enemies. They had more wide (primitive) knowledge and they learned more from mother and society. We think of that it is homogeneously evolution both growth of knowledge and natural language. Thus, the representation of knowledge and its construction is related with language.

IV. Structure of presentative knowledge

Based on the analysis above we try to explain the structure of presentative knowledge. First, the schemas are divided into several groups according to the noun, verb, adjective, and adverb and so on. The relations are defined according to grammar. The relations are grouped as several layers, such that "fragment", "very simple", "simple", "usual", "complex", "very complex", etc. any relation in those groups will combine some schemas, this combination is very similar to the structure of a sentence but it is not a sentence. A combination corresponds a mapping between the semantic and a real scene or subject. So, the knowledge expression is to define those "rules" grouped schemas as different layers. Examples of the relations:

"fragment":

(Food--Noun schema);
(Eating--Action schema);
(Color—Adjective schema).

"very simple":

(Eating) + (food).

"usual":

(Look) + (at) + (here).

The presentation of knowledge is a very important problem. However, it is not enough for the emergence of intelligence. Essentially, it is a process to from a network with knowledge growth. It is an evolutionary process. (see the attached figure). In this paper we try to build up a model to describe this process.

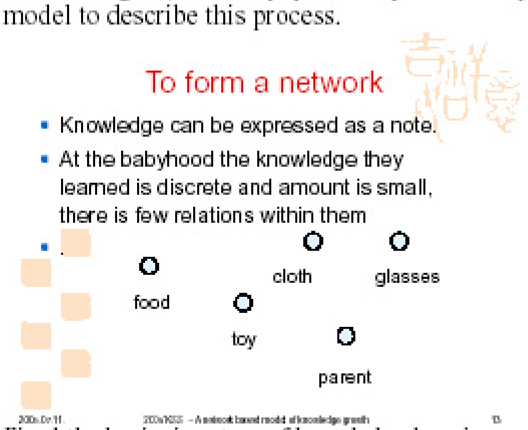

Fig. 1 the beginning stage of knowledge learning

Between the discrete notes some aggregation appears after learning with supervised and unsupervised

For example, Between the discrete notes some link appears after learning with supervised and unsupervised. "apple" is eatable, "milk" is eatable either, thus there is link between apple and milk. Some link has got by "mothers'" teaching, this occurs in supervised learning.

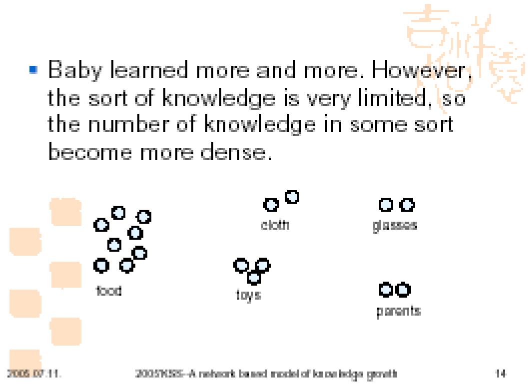

Fig. 2 the dense stage of knowledge growth

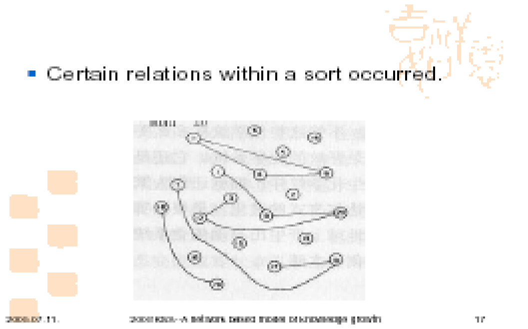

Fig. 3 The aggregation effect of knowledge growth

The link is getting denser and concept appears. And then a part of the network is replaced. See fig 4 and 5.

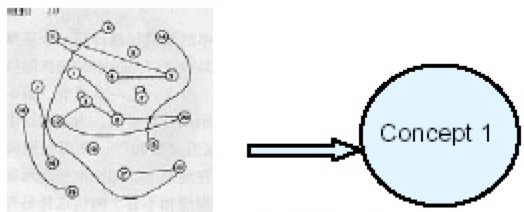

Fig. 4 Forming of concept and its replacement

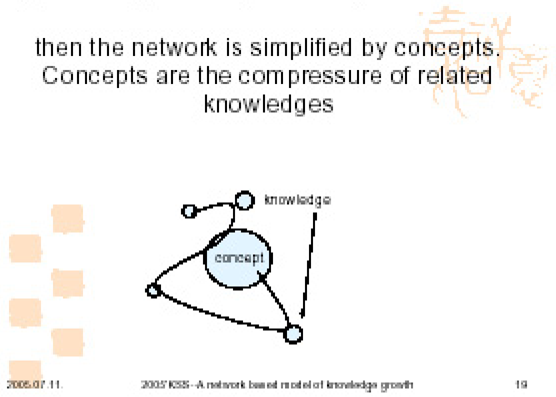

(a)

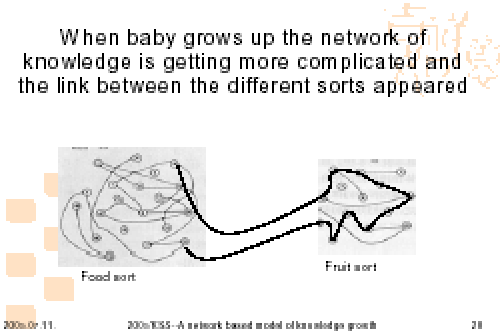

Fig. 5 (a) and (b) The network is reducing after conception replacement

V. Some Concepts of Complex Networks

The research of complex networks [1,2,3,4,5,9,11] has lead to a tremendous amount of interest in the study of complex systems in real world, including the Internet and World Wide Web[5,6,7,8], food chain web[10], social networks[12] and biological networks[13], etc. It is naturally to use this tools to study the networks exist in nature language. Some research about English has been done in recent years concerning the networks structure of language and semantic networks.

The most interesting features of complex networks are the small-world and scale-free. The statistical quantities characterizing small-world networks are clustering coefficient C and the average length of shortest path L. The clustering coefficient is the probability that any two nodes are connected to each other, given that they are both connected to a common node, and the latter measures the minimal number of links connecting two nodes in the network. Following Watts and Strogatz [4], we calculate C by taking the average over all nodes i of the quantity

$$Ci = \frac{2Ti}{Ki(Ki-1)} \qquad (1)$$

where T_i denotes the number of connections between the neighbors of node I, and $k_i(k_i-1)/2$ is the number of connections in a fully connected graph with k_i nodes. C is normalized to range $[1,0]$. $C=0$ means no nodes have common neighbors with their neighbors, no triangles exist in the graph. In a fully connected graph, $C=1$. A path is a sequence of edges that connected one node to another. The path length is the number of edges along the path. The average length of shortest path L measures the average minimal path connecting two nodes in the network.

Regular network have high clustering coefficient and large average length of shortest path, opposite to random graph which have low clustering coefficient and small average length of shortest path. Between these two extremes somewhere, the clustering coefficient is almost as high as that of a regular network while the average length of shortest path is almost as small as that of a random network with the same number of nodes and edges. This type of networks is called as "small-world" for it is similar to the small-world phenomenon.

The study of scale-free networks concerns behavior in the probability distribution of degree, the possible number of links at a random chosen node in the network. Unlike the Poisson degree distribution for random networks, in a scale-free network, the distribution of degree follows a power law in that most nodes have only a few connections and few nodes have very large number of neighbors [10]. Barabasi and Albert demonstrated that the power law distribution could be caused by two basic factors: growth and preferential attachment. Growth means the number of nodes keeps increasing and the preferential attachment means, as the new nodes appear, they tend to connect to the more connected nodes. The probability for a new node to be connected to an existing node is proportional to the degree of the existing node.

It has been discovered recently that aggregation and regeneration of nodes can also leads to the power law distribution of degree, which means that preferential attachment is not a necessary condition for the formation of scale-free networks. Kim and his cooperators propose a network model. In their model, nodes can merge with one of their neighbors and new nodes been added to the network to maintain the number of nodes (Fig. 6). Another model proposed by Alava and Dorogovtsev permit to aggregate nodes which are selected at random (Fig. 7)

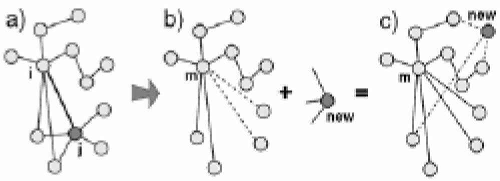

Fig. 6

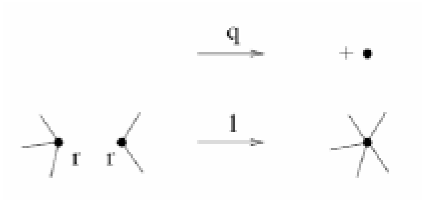

Fig. 7

VI. Structural Analyses of HowNet

We used the Chinese semantic network HowNet as source of semantic knowledge in Chinese. HowNet was developed by Dong. Similar with WordNet, it also has words and basic meaning units, called sememes. There are 65,000 Chinese concepts and 75,000 English equivalents defined with a set of 1503 sememes. In this Dictionary, every concept of a word or phrase and its description form one entry. An entry will comprise four items. The items are arranged in the following sequence:

W_X= word / phrase form
G_X = word / phrase syntactic class
E_X = example of usage
DEF = concept definition

"X" represents some language and each language has three specific items: W_X, E_X and G_X. Therefore, W_C, E_C and G_C would be entries for the words, the examples and the parts-of-speech respectively in Chinese, whereas W_E, E_E and G_E are the corresponding entries for English. Definition of concepts in HowNet is to present the inter-relation between concepts and that between their attributes. HowNet knowledge base gives for every entry a structure of sememes that forms an explanation of a concept. Figure 3 shows an example entry, "陪床", a word don't has directly corresponding word in English, which means "stay in a hospital ward to look after a patient".

W_C=陪床
G_C=V
E_C=
W_E=stay in a hospital ward to look after a patient
G_E=V
E_E=
DEF={stay|停留:location={room|房间:domain={medical|医}, {doctor|医治:location={~}}}, purpose={TakeCare|照料:patient={human|人: domain={medical|医}, {SufferFrom|罹患: experiencer={~}}, {doctor|医治:patient={~}}}}}

Fig. 8 An example of entry in HowNet

We extract a network from HowNet. Each entry is a node, and two nodes are connected if one of the corresponding words is embedded in the definition of the other one. After eliminate those nodes which have the same word and semantic, we get a network with 55435 nodes and 153040 connections.

We analysis 5 properties of the network: sparsely, diameter, shortest path length clustering coefficient and degree distributions.

	N	*CN*	*<k>*	*D*	*L*	*C*
HowNet	55435	100%	5.52142	10	3.896608	0.217915
Random Graph	55435	59%	5.52142	9	2.895111	0.000146

Table 1. Statistics for HowNet, and a comparison with a random network with size and connection density equal to HowNet. *N* is the number of nodes, *CN* is the connectedness, *<k>* is the average number of connections, *D* is the diameter of networks, L is the average shortest path length, and C is the clustering coefficient.

We first examined the static properties of network. As showed in table 1, this network is sparse. A node has only 5.5 neighbors on average, a very small percentage compared with the total number of nodes. Despite the sparsity, all of the nodes compose a single large connected component, while the largest connected component of random network only consists of 59% of all nodes.

Contrast with the large component, network exhibits very low diameter and short average path length. The diameter of HowNet is 10, and average shortest path length is 3.897. That means it only needs average 4 links to associate two nodes.

The clustering coefficient of HowNet is 0.217915, which is very high compared in table 1 with the corresponding value of a random network with the same scale.

The degree distribution could tell us something about the possible dynamical feature of HowNet. Fig. 9 is the degree distribution of HowNet. The distribution was measured by grouping all values of k into 10 bins of consecutive values and computing the mean value of k for each bin. The exponent of the best fitting power law is 1.13. There are several "hubs" in HowNet with degrees more than 1000 (see table 2). We could see that those "hubs" are the more kernel concepts in human thought.

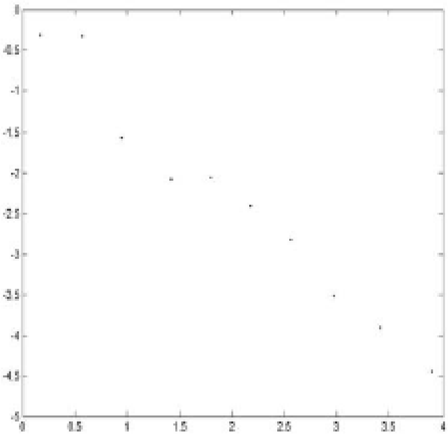

Fig.9 The degree distribution of HowNet show in log-log coordinates

V. The properties of the network formed by knowledge growth

Regular network have high clustering coefficient and large average length of shortest path, opposite to random graph which have low clustering coefficient and small average length of shortest path [21]. Between these two extremes somewhere, the clustering coefficient is almost as high as that of a regular network while the average length of shortest path is almost as small as that of a random network with the same number of nodes and edges. This type of networks is called as "small-world" for it is similar to the small-world phenomenon [22].

The study of scale-free networks concerns behavior in the probability distribution of degree, the possible number of links at a random chosen node in the network. Unlike the Poisson degree distribution for random networks, in a scale-free network, the distribution of degree follows a power law in that most nodes have only a few connections and few nodes have very large number of neighbors [10]. Barabasi and Albert demonstrated that the power law distribution could be caused by two basic factors: growth and preferential attachment. Growth means the number of nodes keeps increasing and the preferential attachment means, as the new nodes appear, they tend to connect to the more connected nodes. The probability for a new node to be connected to an existing node is proportional to the degree of the existing node.

It has been discovered recently that aggregation and regeneration of nodes can also leads to the power law distribution of degree, which means that preferential attachment is not a necessary condition for the formation of scale-free networks. Kim and his cooperators propose a network model. In their model, nodes can merge with one of their neighbors and new nodes been added to the network to maintain the number of nodes (Fig. 5). Another model proposed by Alava and Dorogovtsev permit to aggregate nodes which are selected at random.

Reference

[1] R. Albert, H. Jeong, A. L. Barabasi. Diameter of the world wide web. *Nature* 401, 130-131 (1999).

[2] B.A. Huberman, L.A. Adamic. Growth dynamics of the World Wide Web. *Nature* 401, 131 (1999).

[3] A.-L. Barabasi, R. Albert. Emergence of scaling in random networks. *Science* 286, 509-512 (1999).

[4] S. H. Strogatz. Exploring complex networks. *Nature* 410, 268- 276 (2001).

[5] D. J. Watts. *Small Worlds: The Dynamics of Networks between Order and Randomness*. Princeton University Press, Princeton, 1999.

[6] B.A. Huberman, P.L.T. Pirollo, J.E. Pitkow, R.M. Lukose. Strong regularities in world wide web surfing. *Science* 280,95-97 (1998).

[7] Steve Lawrence, C. Lee Giles. Searching the World Wide Web. *Science* 280, 98-100 (1998).

[8] Steve Lawrence, C. Lee Giles. Accessibility of information on the Web. *Nature* 400,107-109 (1999).

[9] R. Albert, H. Jeong, A. L. Barabsi. Error and attack tolerance of complex networks. *Nature* 406, 378 –382 (2000).

[10] R. J. Williams, N. D. Martinez. Simple rules yield complex food webs. *Nature* 404, 180-183(2000).

[11] D. J. Watts, S. H. Strogatz. Collective dynamics of small-world networks. *Nature* 393, 440—442 (1998).

[12] M. E. J. Newman. The structure of scientific collaboration networks. *Proc. Natl. Acad. Sci.* USA 98, 404-409 (2001).

[13] H. Jeong, B. Tomber, R. Albert, Z.N. Oltvai, and A.-L. Barabasi. The large-scale organization of metabolic networks. *Nature* 407, 651 (2000).

The Eleventh International Symposium on Artificial Life and Robotics 2006 (AROB 11th'06),
B-con Plaza, Beppu, Oita, Japan, January 23-25, 2006

Fundamental Study of Dielectric Elastomer as Artificial Muscle

Junnici Hayashida (Matsue National College of Technology)
Fengzi Dai (Matsue National College of Technology)
Yutaka Fujihara (Matsue National College of Technology)

Abstract

In this paper, we focus attention on the soft actuator that generally called artificial muscle. The artificial muscle can move linearly and is small and lightweight. Also, a basic experiment was done for the aim of the application of the dielectric elastomer EAP (Electro Active Polymer) as the artificial muscle.

Key word: EAP, Artificial Muscle

1. Introduction [1]

Presently, the needs of small size and weight saving for actuator are increased further by the development of the technology. For example, the miniature camera mounted in the cellular phone needs a small actuator. At the same time, the robot that mimics human begins to arrive on market. However, the movement of that robot is a little awkward motion. It is believed that the rotation movement by the servo motor causes the awkward motion of robot. Contrarily, the human muscle moves linearly in contrast to the robot. From this example, we see that the actuator which make a linearly movement is necessary.

2. Dielectric elastomer EAP artificial muscle [2] [3]

The dielectric elastomer EAP artificial muscle is structured to hold a soft electrode between two sheets of dielectric elastomer as shown in Fig.1. The thickness of the film is 100 μ m. A soft electrode is used to avoid disturbing the expansion and contraction of the artificial muscle. In the experiment, the dielectric elastomer film is impressed about 4kV. The large electric field is occurred between the electrodes. And both electrodes attract each other. In our experiments, the three kinds of film of silicon rubber, acrylic form elastomer and urethane rubber are used. These films occur elastic deformation, and expand in the horizontal direction.

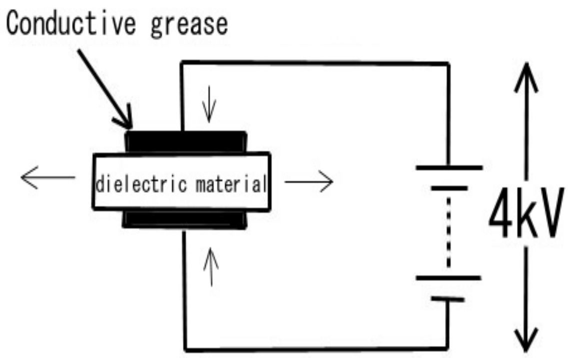

Fig.1 Structural drawing

3. Basic experiment [2] [3] [4]

The stress that occurs between the electrodes can be expressed by the equation (1).

$$P = \varepsilon_0 \varepsilon_r E^2 \tag{1}$$

where,
P:stress, ε_r :relative permittivity, ε_0 : permittivity in vacuum, and E :electric field strength.

By the experiment, we confirm that the displacement of the film and the relationship between the electric field strength and the stress are correspond to the equation(1). And also we examined that which film among the three materials is suitable for artificial muscle.

Fig.2 Photograph of experimental sample

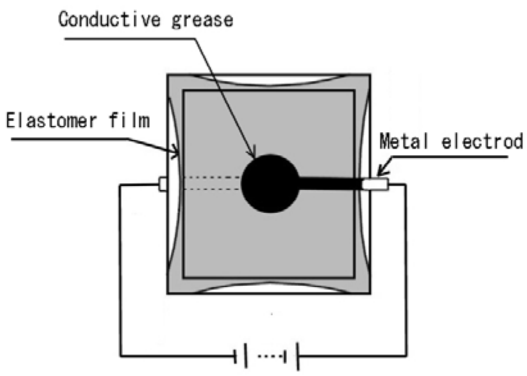

Fig.3 Structural drawing of experimental sample

The three kinds of material, silicon rubber, acrylic form elastomer and urethane rubber were used as the experimental sample. Each sample was fixed on the acrylic frame shown in Fig.2. Fig.3 is the structural drawing of Fig.2. The reason of the fixation to the flame is to prevent the film from the slackening and to guard against the failure of the electric discharge that happens easily in the experiment using the high voltage.
Conductive grease was used for the electrode. And the diameter of the electrode is 15mm. The voltage of 0V~4kV was applied to the space of the electrode. The displacement of the film was measured by image processing from the computer. By another experiment, an influence to the displacement can be examined when conductive grease is used for electrode and when carbon powder is used for electrode. But this experiment is not done because material was not enough as for the urethane rubber.

4. Experimental result and consideration

Fig.4 indicates the relationship between the displacement of film and the electric field strength from the result of the experiment. This figure shows that the displacement of film increases according to the curve of parabola. Therefore, the result of the relationship between the displacement and the electric field strength is coincided with the equation (1).

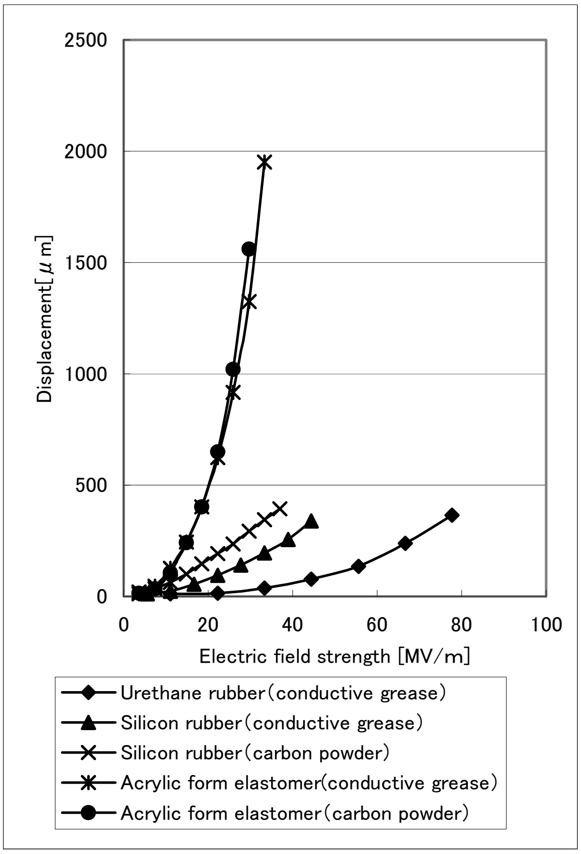

Fig.4 Graph of electric field strength displacement

And it is clarified that acrylic form elastomer has the biggest displacement among these three materials the second is the silicon rubber, and urethane rubber became the smallest. In other preliminary experiment, we have got the result that the relative permittivity of silicon rubber is 3.18 and the relative permittivity of acrylic form elastomer is 3.98. Supposing the relative permittivity of the material had a much effect on the displacement, the acrylic form elastomer and the silicon rubber would be similar of displacement.

But, the result clearly shows that the size of the displacement of silicon rubber and the acrylic form elastomer is different. Therefore, it can be estimated that not only the electric character but also the mechanical character such Young's module greatly influence the displacement.

Dose the electrode also has any effect on the displacement. In Fig.4, the displacement using powder electrode was bigger than that using conductive grease. When the powder electrode is used, the contact point of the conductive particle is conducting mode. But, when conductive grease was used, the grease exists between the conductive particles. Therefore, it can be assumed that the displacement of conductive grease is smaller than that of the conductive powder.

From these results, acrylic form elastomer is suitable as the material for artificial muscle. Because the displacements of other materials are small, application is limited. However, the conductive grease is used for the electrode because the conductive grease is easy to be used in the experiment.

Furthermore, by the visual observation, it is confirmed that the response of acrylic form elastomer is slower than silicon. However, the response time of acrylic form elastomer is about in one second, acrylic form elastomer had no problem to use as the actuator that is linearly motion type.

5. The application example as actuator

In this paper, the actuator is used for the focal control of the lens as application example. And, the trial production of application was made.

In the past, the focal control of lens used the electromagnetic motor or the ultrasonic motor that consist of many machine parts. These motors can accurately decide the position for focal adjustment. While on the other hand, these systems need high reliability, complex mechanisms and precise parts to move accurately.

When the dielectric elastomer EAP artificial muscle was used, both complex mechanism and precise parts are not needed. Because the artificial muscle can operates linearly, therefore the weight saving and the small sizing can be done. The structural and the cross section drawings are shown respectively in Fig.5 and Fig.6.

Fig.5 The structural drawing

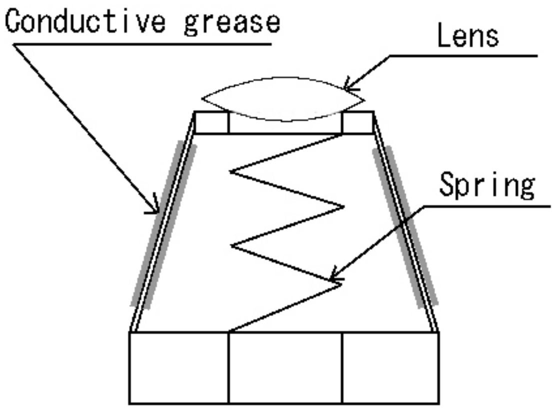

Fig.6 Cross section

The parts that fix the lens are wrapped with the elastomar film. And the parts are pushed up by the spring. Therefore, the structure is very simple. And, there is an advantage that the number of parts used decreases. However, because the high voltage power supply is used, it is necessary to pay attention to need the electrical discharge.

The movement for focus adjustment responds at once when the voltage was applied. And the mechanical noise and electromagnetic waves can be prevented.

6. Conclusions

In this paper, the possibility of the soft actuator by the dielectric elastomar EAP artificial muscle was researched. The basic experiment of artificial muscle was done. And the possibility of the application of artificial muscle was confirmed. The results obtained by the experiment were shown as follows.

1) The displacement of acrylic form elastomer occurred the biggest of experiment sample.

2) The acrylic form elastomer is suitable as the material of the application.

3) The actuator for the focal control of the lens was produced, and the operation was confirmed.

Reference

[1] Haruo Sugi, The muscle is mysterious (Japanese), p.p16-64, Koudansya, (2003)
[2] Yoshihito Osada, The front of soft actuator development (Japanese), NTS, (2004))
[3] Scott Stanford, Neville Bonwit, Ron Pelrine, Roy Kornbluh, Oibing Pey, Seiki Chiba, "Electroactive Polymer Artificial Muscle (EPAM) for Biomimetic Robotics", Second conference on artificial muscle, National Institute of Advanced Industrial Science and Technology, (2004)
[4] Yoseph Bar-Cohen, Electroactive Polymer [EAP] Actuators as Artificial muscles, p.p529-581, SPIE, (2004)

A State Space Filter for Reinforcement Learning

Masato Nagayoshi[ab], Hajime Murao[c] and Hisashi Tamaki[d]

[a] Grad. School of Sci. and Tech., Kobe Univ. Rokko-dai, Nada-ku, Kobe 657-8501, Japan
nagay@al.cs.kobe-u.ac.jp

[b] Hyogo Assistive Technology Research and Design Institute, 1070, Akebono-cho, Nishi-ku, Kobe 651-2181, Japan

[c] Faculty of Cross-Cultural Studies, Kobe Univ. 1-2-1, Tsurukabuto, Nada-ku, Kobe 657-8501, Japan
murao@i.cla.kobe-u.ac.jp

[d] Dept. Computer and Systems Engr., Kobe University, Rokko-dai, Nada-ku, Kobe 657-8501, Japan
tamaki@al.cs.kobe-u.ac.jp

Abstract

Reinforcement Learning (RL) attracts much attention as a technique of realizing computational intelligence such as adaptive and autonomous decentralized systems. However, in general, it is not easy to put RL into practical use. This difficulty includes a problem of designing a reasonable state space of an agent, i.e., satisfying two requirements in trade-off: to reduce the search space for making a learning process be fast and to keep the characteristics of the search space for seeking better strategies. In this paper, in order to overcome the above difficulty, we propose a concept of a "state space filtering", and a method of adjusting the search space adaptively by referring to an entropy. Then, through a computational experiment by using a robot navigation problem with continuous state space, the validity and the potential of the proposed method have been comfirmed.

1 Introduction

In recent years, artificial systems has become extremely complicated and enlarged. A conventional way in which systems are controlled in a top-down manner mainly by human is facing up the difficulty of adaptability and flexibility. As one of the solutions against this issue, the development of autonomous systems has been undergoing, and engineers and researchers are paying attention to Reinforcement Learning (RL)[1] as a technique of realizing the autonomous systems. However, in general, it is not easy to put RL into practical use. This difficulties include such issues as satisfying the requirement on learning speed, resolving the perceptual aliasing problem, designing a reasonable state space of an agent, etc. In this paper, we deal with the problem of designing the state space. The other two problems are resovable by designing suitably (adaptively) the state space. The problem of designing the state space contains the following two requirements, that is, to reduce the search space as much as possible in order to make a learning process be fast and to keep the characteristics or the structure of the search space as much as possible in order to seek such strategies as being closer to the optimal. Here, these requirements are in trade-off.

Some possible solutions for the problem have been proposed recently, which include such an approach where function approximation techniques are used[2, 3], and an approach in which the state space are divided and integrated on the way of learning [4, 5, 6, 7, 8, 9]. Almost all methods in both approaches are designed for specific RL technique and pay attention to the quality of learning not to speed up the learning process.

In this paper, it is considered to satisfy the above requirements in trade-off arising in designing a state space of an agent. First, a concept of a "state space filtering" is newly introduced, and, based on this concept, the acquisition problem of a state space filter is defined. The proposed framework makes it possible to classify the related methods proposed so far and also to clarify the characteristics of them. Then, an acquisition method which is to adjust the search space adaptively by referring to an entropy is proposed. Through some computational experiments by using a robot navigation problem, the proposed method is compared with the existing methods with respect to the efficiency of the state space filtering.

2 State Space Filter

2.1 Framework of a Learning System with a State Space Filter

In this paper, we propose a computational model where a concept of a "state space filtering" is introduced. In conventional reinforcement learning methods, it is typical that an action module is adjusted by

The Eleventh International Symposium on Artificial Life and Robotics 2006 (AROB 11th'06),
B-con Plaza, Beppu, Oita, Japan, January 23-25, 2006

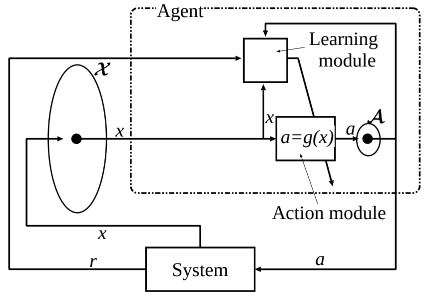

Figure 1: A conventional framework.

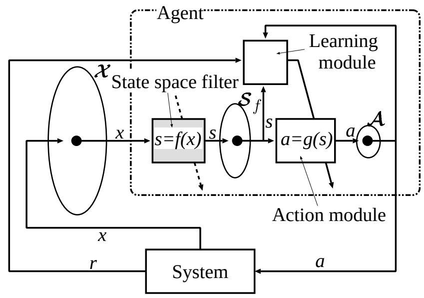

Figure 2: A framework with a state space filter.

a learning module which is to adjust the appropricate mapping between a system's state space $\boldsymbol{\mathcal{X}}$ (hereafter called "input state space") and an action space $\boldsymbol{\mathcal{A}}$, as shown Fig.1. In contrast, the mapping between $\boldsymbol{\mathcal{X}}$ and $\boldsymbol{\mathcal{A}}$ is broken down to a mapping f and a mapping g, where f is a mapping between $\boldsymbol{\mathcal{X}}$ and a agent's state space $\boldsymbol{\mathcal{S}}$ (hereafter called "inner state space"), and g is a mapping between $\boldsymbol{\mathcal{S}}$ and $\boldsymbol{\mathcal{A}}$. Here, the learning module takes on the adjustment of g. The mapping f corresponds to a "filtering" in the sense that it retrieves the useful characteristics from an input state $x \in \boldsymbol{\mathcal{X}}$, and a module of f is described as "a state space filter". The proposed framework of the learning system with the state space filter is shown in Fig.2.

2.2 A Definition of the State Space Filter and an Ideal State Space Filter

As mentioned above, the state space filter is defined as a module taken on the mapping $f : \boldsymbol{\mathcal{X}} \rightarrow \boldsymbol{\mathcal{S}}$. Besides, an ideal state space filter is defined as a module that satisfies the following requirements.

1. If an optimal mapping $y^* : \boldsymbol{\mathcal{S}} \rightarrow \boldsymbol{\mathcal{A}}$ is given, $\boldsymbol{\mathcal{S}}$ should be constructed in the form of mapping between input states $\{x | a = y^*(x)(x \in \boldsymbol{\mathcal{X}})\}$ and an identical inner state $s \in \boldsymbol{\mathcal{S}}$.

2. Any two input states, whose optimal action is the same and which are directly transitable with each other, are to be mapped to one inner state. Namely if $y^*(x_i) = y^*(x_j) : (x_i, x_j \in \boldsymbol{\mathcal{X}}, x_i \neq x_j)) \wedge (x_i \in \mathcal{X}_j \vee x_j \in \mathcal{X}_i)$, then $f(x_i) = f(x_j)$, where $\mathcal{X}_i \subseteq \boldsymbol{\mathcal{X}}$ is defined as a set of input states able to transit directly from an input state $x_i \in \boldsymbol{\mathcal{X}}$.

Here, in general the optimal mapping y^* is not given beforehand. Thus, it's necessary to adjust the state space filter and to learn the action module simultaneously in the course of learning process.

3 A Method to Acquire Adaptively a State Space Filter with an Entropy

A variety of methods to acquire the state space filter can be considered. In this paper, we propose an acquisition method where an Entropy is taken into consideration. Here, it is expected that (i) is able to learn in parallel the state space filter and an action module, (ii) is not requirng the specific RL methods as the learning module.

3.1 Basic Idea

The state space filter is adjusted toward the direction of both minimizing a size of the inner state space $|\boldsymbol{\mathcal{S}}_f|$ and a sum entropy of action selection probability distributions in an inner state:

$$\phi(f) = \sum_{s \in \boldsymbol{\mathcal{S}}_f} H(s) \tag{1}$$

where $\boldsymbol{\mathcal{S}}_f$ is an inner state space constructed by a state filter$f$, and $H(s)$ is an entropy defined for an inner state s:

$$H(s) = -(1/\log|\boldsymbol{\mathcal{A}}|) \sum_{a \in \boldsymbol{\mathcal{A}}} p(a|s) \log p(a|s) \tag{2}$$

where $p(a|s)$ is a probability an action a is selsected in an inner state s, $\boldsymbol{\mathcal{A}}$ is an action space, and $|\boldsymbol{\mathcal{A}}|$ is a number of available actions.

The state space filter is adjusted by treating this entropy $H(s)$ as an index of a correctness of state aggregation in an inner state$s$. In particular, in case of mapping from the input state space roughly digitized to the inner state space, a perceptual aliasing problem is happened. That is, the action which an agent should select can not be identified clearly. Thus, the above entropy may not be small in the inner state space should be divided. If entropy get smaller despite being the action module learned a enough number of time in the inner state, the state space filter is adjusted by dividing the inner state due to that the perceptual aliasing problem is happened in the inner state.

Similarly, if entropy is small in an inner state and a different inner state mapping from a transited input

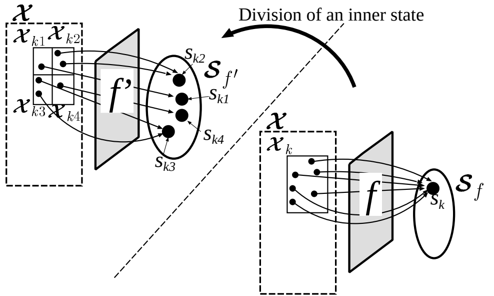

Figure 3: Division of an inner state.

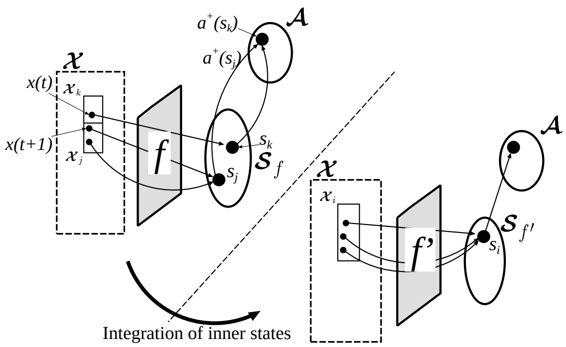

Figure 4: Integration of inner states.

state, and representative actions in each other's inner states are same, the state space filter is adjusted by integrating the inner states due to that the inner state is divided, where the representative action in an inner state is such an action that possesses a most strong select probability in the inner state.

3.2 Division of an Inner State

If $L(s) > \theta_L$ and $H(s) > \theta_H$, where $L(s)$ is a number of time the action module learned in an inner state s, then the state space filter is adjusted by dividing an range field of the input state mapping to the inner state s into 2 parts with respect to each dimension, and mapping it to a different inner state respectively as shown Fig.3, where θ_L is a threshold value of a number of time the action module learned in an inner state, and θ_H is a threshold value of an entropy. Through this operation, a size of the inner state space after divided increases by $(2^N - 1)$, where N is a number of dimension.

Also note that the values of the new 2^N inner states are those of the inner state before divided.

3.3 Integration of Inner States

If $s \neq s'$, $H(s) > \theta_H$, $H(s') > \theta_H$ and $a(s)^+ = a(s')^+$, then the state space filter is adjusted by integrating the inner states s and s' to an inner state as shown Fig.4, where s is an inner state mapping from an input state, s' is an inner state mapping from a transited input state next time, θ_H is the same value as used when the approach to division of an inner state, $a(s)^+$ is a representative action in the inner state s. In addition, if an inner state s, which never, not once, mapped during a certain period θ_t, exists, then the state space filter is adjusted by integrating the inner state s and an adjacent inner state (namely, whose range is adjacent) to s into an inner state. Through this operation, a size of the inner state space after divided decreases by 1.

Also note that the value of the new inner state is an average of the values of the 2 inner states before integrated.

Table 1: Parameters for a Simulation.

Method	Parameter	Value
all	α	0.1
all	γ	0.9
all	τ	0.1
A	θ_H	0.3
A	θ_L	1000
A	θ_t	100[episode]
B	$\{\ \alpha_B,\ \gamma_B\}$	{1.0, 0.1}
B	ρ	0.95

4 Computational Example

The proposed method is applied to so-called "robot navigation problem" navigating a learning agent from a start to a goal. In continuous space: 1000×1000[mm] bounded by the wall, the goal of 15[mm] in radius is located at the center of the space: $(x, y) = (500, 500)$. The agent of 25[mm] in radius is placed and a direction of the agent is decided initially at randomly. The positive reinforcement signal $r_t = 10$ (namely reward) is given to the agent only when the front of the agent arrives at the goal and the reinforment signal $r_t = 0$ at any other time steps. This process, called as one episode, is repeated.

The learning agent has two wheels, and can move to various directions . A set $\boldsymbol{\mathcal{A}}$ of actions of the agents is defined as

$$\boldsymbol{\mathcal{A}} = \{\text{forward, left forward, right forward, left rotation, right rotation}\} \quad (3)$$

Moreover, the agent has two sensors measuring the distance and the direction to the goal.

The proposed method (hereafter called "method A") is compared with a method based on Handa et al. [7] (hereafter called "method B") and some grid-partition methods that divide the inner state space evenly into 2, 4, 8 space dimentions (hereafter called

Table 2: Time for Learning.

Method	Time[sec]
A	0.530
B	0.743
2	0.708
4	0.300
8	0.354

"method 2", "method 4", "method 8", respectively). Here, B is used with parameters for selection intensity α_B, γ_B and a warning rate ρ.

All methods adopt Q-learning, using softmax action selection with Boltzmann distribution, with same parameters in each learning module. Computer simulations have been done with paramters as shown in Table 1. Here, θ_H was set referring to about 0.288 : a maximal value of an entropy when the highest selection probability for one action is 0.9.

The number of steps required to accomplish the task has been observed during learning, and its averages over 20 simulations with various methods are described in Fig.5. The average size of the inner state space to obtain has been observed during learning over 20 simulations with various methods are described in Fig.6. Computational times averaged over 20 simulations with various methods are described in Table 2.

The average size of the inner state space in method A is smaller than method B and method 8 at every episode, moreover the computational time in method A is shorter than method B, even though method A finally converges to the same performance with method B and method 8.

On the other hand, the computational times in method 2 and method 4 are shorter than method A. However, it is very difficult to select a proper grid-partition methods without prior knowledge in advance. In contrast, method A and method B avoid the need to the proper grid-partition.

5 Conclusion

In this paper, we propose a concept of a "state space filtering", and a method to acquire adaptively the state space filter based on an Entropy. Then, through some computational experiments by using a robot navigation problem with continuous state space, the validity and the potential of the proposed method have been comfirmed.

Our future projects includes : 1) to estimate the state space filter theoretically or Experimentally, 2) to acquire the state space filter for partially observable environments, 3) to apply real world problems, etc.

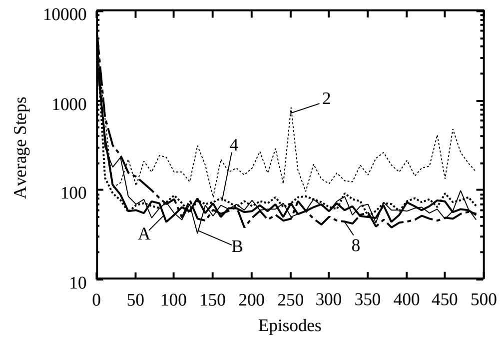

Figure 5: Number of steps required.

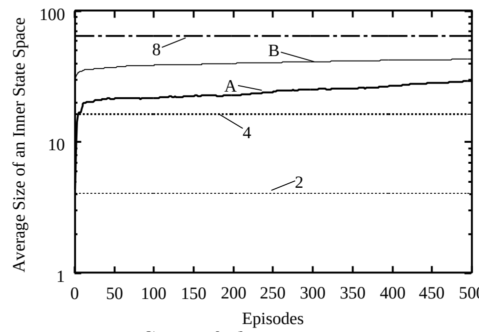

Figure 6: Size of the inner state space.

References

[1] R.S. Sutton and A.G. Barto: Reinforcement Learning, A Bradford Book, MIT Press (1998)

[2] R.S. Sutton: Generalization in Reinforcement Learning: Successful Examples Using Sparse Coarse Coding, *Advances in Neural Information Processing Systems: Proc. of the 1995 Conf.*, 1038-1044 (1996)

[3] K. Doya: Temporal Difference Learning in Continuous Time and Space, *Advances in Neural Information Processing Systems: Proc. of the 1995 Conf.*, 1073-1079, MIT Press (1996)

[4] T. Yairi, K. Hori and S. Nakasuka: State Generalization Based on Maximum Likelihood Estimation Considering Multiple Behavior Outcomes, *JSAI Jour.*, **16**(1)V, 128-138 (2001)(in Japanese)

[5] H. Murao and S. Kitamura: QLASS: an enhancement of Q-learning to generate state space adaptively, *Proc. of Fourth European Conf. on Artificial Life(ECAL97)* (1997)

[6] T. Hamagami, S. Koakutsu and H. Hirata: An Adjustment Method of the Number of States on Q-Learning Segmenting State Space Adaptively, *T.IEICE Japan*, **J86-D-I**(7), 490-499 (2003)(in Japanese)

[7] H. Handa, A. Ninomiya, T. Horiuchi, T. Konishi and M. Baba: An Incremental State-Space Construction Based on the Notion of Constradiction for Reinforcement Learning, *T.SICE*, **38**(5), 469-476 (2002)(in Japanese)

[8] J. Morimoto and K. Doya: Learning Dynamic Motor Sequence in High-dimensional State Space by Reinforcement Learning: Learning to Stand Up, *T.IEICE Japan*, **J82-D-II**(11), 2118-2131 (1999)(in Japanese)

[9] M. Nagayoshi, H. Tamaki, H. Murao and S. Kitamura: A Method of Adaptive State Space Construction for a Modular Reinforcement Learning, Mem. Grad. School Sci. & Tchnol.,Kobe Univ., 23-B, 13-20 (2005)(in Japanese)

The Eleventh International Symposium on Artificial Life and Robotics 2006 (AROB 11th'06),
B-con Plaza, Beppu, Oita, Japan, January 23-25, 2006

Prediction of the Aperiodic Time Series of a Visual Target by Humans

Manabu Shikauchi, Shin Ishii and Tomohiro Shibata
Graduate School of Information Science,
Nara Institute of Science and Technology,
8916-5 Takayama, Ikoma, Nara 630-0192, JAPAN

Abstract

It is advantageous for animals and humans to predict changes in the environment. To uncover mechanisms for such a prediction is one of the most important topics in brain science.

In our study, aperiodic time series generated by an AR process were sequentially presented by means of a small target at a regular time interval, and subjects were asked to predict the next target position. The result shows that the effects of learning were not clearly observed, while it was observed that the subjects tried to predict the next target position based on a low-order AR model, and some performance-improvement was also observed through long-term trials.

Keywords
Aperiodic time-series, auto-regressive process, online learning, prediction.

1 Introduction

It is advantageous for animals and humans to predict changes in the environment. To uncover mechanisms for such a prediction is one of the most important topics in brain science. We are concerned that humans learn the underlying dynamics of objects and that humans can do the most suitable prediction when the time series from the objects are aperiodic but have hidden linear dynamics.

Shibata et al.[1] investigated the ability of prediction in humans utilizing smooth pursuit eye movements which are specific to primates. They conducted a task in which each subject was asked to pursue aperiodic target motions generated by an Auto-Regressive (AR) process. Their results suggested that subjects were capable of (1) online learning of a hidden linear dynamics in the AR process (the AR model), and (2) performing predictive tracking similar to the optimal filtering to some extent.

This study aims at investigating whether such predictive ability of humans as reported by Shibata et al. works for visual perception as well. In our study, discrete time series was used in contrast to Shibata et al's work using a continuously moving target.

2 Methods

2.1 Visual stimulus

We used the AR process to produce the time series presented to the subjects (the left panel of Figure 1), because the AR process is aperiodic, and then the possibility that the subjects predict based only on memorized patterns can be excluded. In addition, a quantitative analysis becomes possible by using the AR process; if the optimal prediction defined later is achieved by subjects, the distribution of the prediction error would be close to the noise distribution that the AR process employed. If subjects have no knowledge about the AR model and its parameters, then the subjects have to learn the model based on the presented time series in order to achieve the optimal performance.

In this study, we adopted a first-order AR model as the simplest case:

$$S \qquad S \qquad + \xi \tag{1}$$

where S and ξ denote the target position and the system noise following the normal distribution $\mathcal{N}$ $_s$ $_s$, at time . In this study, the mean $_s$ and the standard deviation (SD) $_s$ were set to -0.4 [mm] and 18.8 [mm], respectively.

As contrasted to the task using the AR model (AR task), we prepared a task in which the time series produced by the corresponding AR process were shuffled (Random task), as shown in Figure 1. The linear prediction theory tells us that the following prediction is optimal in the AR task:

$$P \qquad P \tag{2}$$

where P is the predicted position at time . The prediction error distribution in this case follows the system noise distribution $\mathcal{N}$ $_s$ $_s$.

2.2 Subjects

Two healthy male subjects (MO and TU), whose eyesights were normal (the subject TU had corrected eyesight), were participated in the experiment.

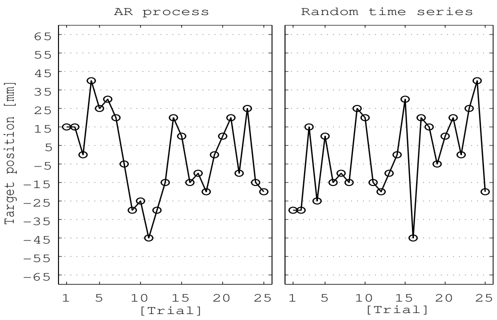

Figure 1: Target time-series of the AR task (left) and the random task (right).

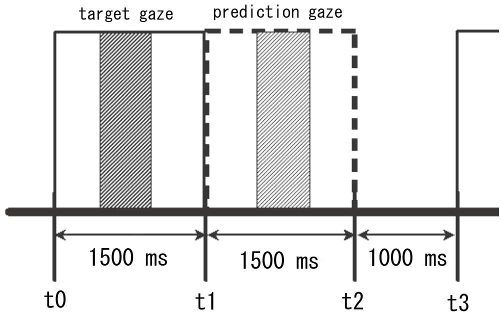

Figure 2: One trial consisting of a fixation period of 1500 [ms] and a prediction period of 1500 [ms]. See the text for more detail.

2.3 Procedure

Each subject was required to predict the target position at the next discrete time step, but not informed about the way to generate the target time-series. Subjects presented their prediction by their gaze at a point on a monitor. Although this study does not focus on the eye movement, we chose an eye movement as a device for pointing out the prediction rather than, for example, a hand movement, because one-dimensional eye movement was considered to have higher measurement accuracy with less physical efforts.

A horizontal graduated ruler was presented on the monitor because subjects participated in a pre-experiment reported the difficultly to gaze at a certain point without the ruler. The ruler was presented just beneath the horizontal location where the target was presented. The scale resolution of the ruler was 5 [mm] and the range was [mm] (view of [deg]).

We also needed to correct the time series generated by the continuous-valued AR process to fit the discrete-valued scales. In this study, we took a very simple correction method that each original position was shifted to the nearest scale. Then, every position in the time series took one of 27 quantized values.

A target was presented by a standard PC (DELL, Pentium -746 [Hz]) on a TFT color LCD monitor of 15.4 [inch]. Subjects sat down, and fixed their head on the position of 80 [cm] from the monitor. To fix the subject head, we used a bite bar and a chin rest. Eyelink (SR Research company) was used for measurement of eye movements, and a sampling frequency was 250 [Hz].

Figure 2 shows one trial consisting of a pair of a fixation period and a prediction period. In a fixation period in the -th trial, a fixation target S appeared on the monitor, and the subject gazed at the target (target gaze) until the target disappeared 1500 [ms] later with a notification sound. Then, a prediction period of 1500 [ms] was started and finished with another sound. In the prediction period, each subject was required to predict the next target position and keep gazing at the position (prediction gaze) until the subject heard a sound. After a 1000 [ms] rest, the next trial was started.

One block consisted of 25 trials, and two block types were designed. One was **the AR block** where the time series were generated by an AR process, and the other was **the random block** where the time series were an order-shuffled variation of the ones produced by the AR process. Each subject took part in the experiment of 48 blocks (1200 trials) where 24 random blocks and 24 AR blocks were randomly aligned.

Note that all time series were different in each block with the others, due to the probabilistic nature of the AR process, although they were generated by the same AR model with the same noise function ξ .

2.4 Analysis

We conducted two types of analyses. One was to examine whether humans were able to perform good prediction based on some learning related to the hidden linear dynamics of the AR model. The other was to investigate how much complicated model humans actually utilized.

For the former analysis, the SD of the prediction error was used as an indicator to evaluate human's prediction and learning. The SDs of prediction error over trials and blocks were defined respectively as

$$SD_{trial} \qquad \sqrt{\ /\ _{block} \qquad \sum_{n=1}^{N_{block}} E_n \qquad ^2} \qquad (3)$$

$$SD_{block} \quad \sqrt{/ \quad _{trial} \quad \sum_{t=1}^{N_{trial}} E_n \quad \nu^{2}} \qquad (4)$$

where E_n denotes the prediction error in the -th trial of the -th block, $_{trial}$ the number of trials in each block, $_{block}$ the number of blocks in each task, and $/ \ _{block} \sum_{n=1}^{N_{block}} E_n$. $_{trials}$ and $_{block}$ were set to and , respectively, throughout the experiment. Note that $E_n \quad S_n + \quad P_n +$, because subjects predicted the next position $S_n +$ in the -th trial.

Analysis of variance (ANOVA) was used for statistical analysis. We detected significant difference with the condition of p-value $<$.

As for the second analysis to investigate how much complicated model humans actually utilized, AR models were fitted to the subject's behavioral data, and the selection of the model's order was performed according to the Akaike's information criterion [2]: $AIC \ q \quad _{trial} \ log \ _s^2 + \quad q +$, where q is the order of the estimated model. Note that the choice of the 0-th order model means the preference of a model with no-dynamics but drove only by a noise.

Matlab (Mathworks) and its statistics toolbox were used for all statistical analyses.

3 Results

Figures 3 and 4 show the results of SD_{trial} and SD_{block} , respectively, in the AR task and the random task done by the two subjects.

The results show that the difference between the AR task and the random task was not statistically significant in most trials and blocks for both the subjects.

Because, as Figure 3 indicates, a monotonic decrease of SD_{trial} was not observed, SD_{trial} was divided into 5 sections of every 5 trial, and multiple comparison (Scheffe's) was used in each trial section for a statistical analysis. For subject MO, there was no significant difference in SD_{trial} section. For subject TU, SD_{trial} of solely the 4th section decreased temporarily. In short, there was no learning effect observed between trials.

Because, as Figure 4 indicates, a monotonic decrease of SD_{block} was not observed, SD_{block} was divided into 4 sections of every 6 block, and multiple comparison (Scheffe's) was used in each block section for a statistical analysis. For subject TU, a tendency to decrease was observed. In short, there was a learning effect between blocks for this subject.

The block count was collected about the AR order of prediction time series, which was identified based on AIC (Table 1). The block count was 0 about the identified orders being 7th- 24th. The number of blocks with the 0-th order was the largest for both the subjects and each task. The rates of blocks with the 0-th, the 1st, and more than the 2nd in the AR task were each 63%, 17% and 21% for subject MO, and were each 50%, 29% and 21% for subject TU.

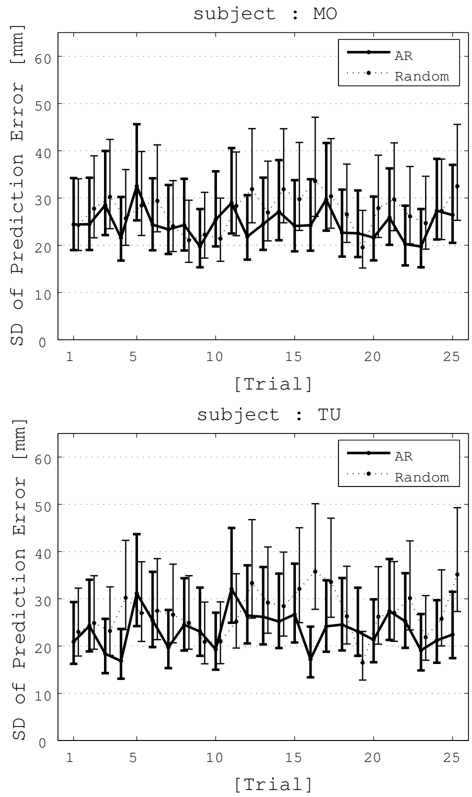

Figure 3: SD_{trial} of MO and TU. The solid line shows the SD_{trial} of the AR task, while the broken line SD_{trial} of the random task. Error-bars show 95% confidence intervals.

4 Discussions

The results have shown that the effects from learning were not clearly observed, but some performance-improvement was observed through long-term trials. Figure 3 exhibits wide error-bars corresponding to 95% confidence intervals. These wide error-bars might be a reason why we were not able to see the different in performance between the AR task and the random task as well as the decrease in errors over trials, part of which could be due to the small number of samples. We also found that there was no large difference between the system noise input to the AR task and the random task, which might prevent us from finding the difference in the subject's behaviors between these tasks.

Another analysis has suggested that the subjects tried to

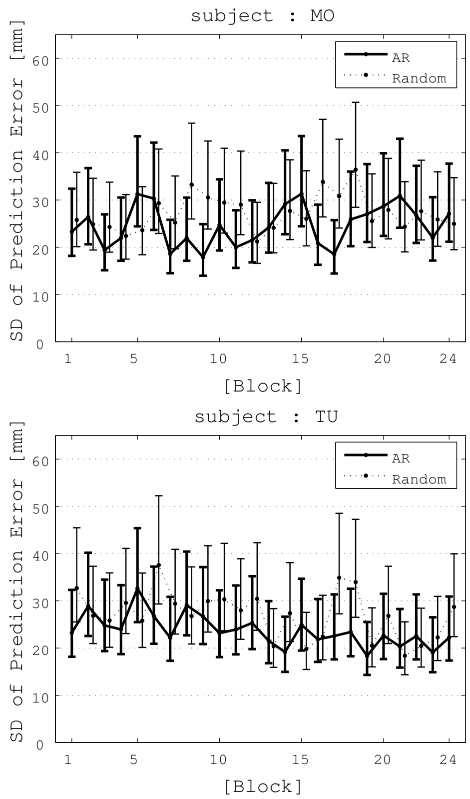

Figure 4: SD_{block} of prediction error with each block. there are the result of MO, TU from the top. The AR(solid line) is of the AR task and the random (broken line) is of the random task. Error-bar is 95% confidence intervals.

predict the next target position by using some dynamics, because the -th order was much identified in the random task compared to in the AR task, and in contrast, the first or later order was much identified in the AR task compared to the random task. The retrospective reports of the subjects revealed that they did not imagine an underlying AR model nor the fact that two types of the task were mixed. The identified order higher than the first order in the case of the AR task may suggest that they tried to use a complicated rule and/or switched their strategies, which utilized the memory of past time-series.

Our current study is based on the Shibata et al.'s study which examined smooth pursuit eye movements of humans. They showed that humans were able to predict the target motion generated by a third-order AR process with the help of online learning of the AR model. Comparing this study to the Shibata et al.'s study, the most salient difference seems to lie on the perception of the target motion, i.e., their presented stimuli were perceived as a motion explicitly driving motion perception pathways in the brain [3, 4], while, in our study, the time series were carefully designed not to be perceived as apparent motion [5]. Therefore, our study would suggest that perception of underlying continuous motions is necessary for accurate prediction and learning of discrete time series. To make sure this conjecture will be an interesting future work.

Table 1: The number of blocks with 0-th-6th.

the AR task

	0th	1st	2nd	3rd	4th	5th	6th
MO	15	4	3	2	0	0	0
TU	12	7	4	0	0	0	1

the random task

	0th	1st	2nd	3rd	4th	5th	6th
MO	20	2	1	1	0	0	0
TU	18	4	0	2	0	0	0

Acknowledgement

A part of this study has been supported by the Inamori research grant.

References

[1] T. Shibata, D. Kawawaki, Y. Fujiwara, K. Doya and M. Kawato: "Prediction and learning of aperiodic visual target motion in human smooth-pursuit eye movements", Technical report of IEICE, **103**, 602, pp. 13–18 (2004).

[2] H. Akaike: "On the use of a linear model for the identification of feedback systems", Ann Inst Statist Math, **20**, pp. 425–439 (1968).

[3] H. Komatsu and R. Wurtz: "Relation of cortical areas MT and MST to pursuit eye movements. I. Localization and visual properties of neurons", J Neurophysiol, **60**, 2, pp. 580–603 (1988).

[4] D. Kawawaki, T. Shibata, N. Goda, K. Doya and M. Kawato: "Anterior and superior lateral occipito-temporal cortex responsible for target motion prediction during overt and covert visual pursuit", Neurosci Res (in press).

[5] J. v. d. Steen, E. Tamminga and H. Collewijn: "A comparison of oculomotor pursuit of a target in circular real, beta,, or sigma motion", Vis Res, **23**, 12, pp. 1655–61 (1983).

The Eleventh International Symposium on Artificial Life and Robotics 2006 (AROB 11th'06),
B-con Plaza, Beppu, Oita, Japan, January 23-25, 2006

Robotic Emotion Generation using Dynamics-based Information Processing

Minoru HASHIMOTO
Department of KANSEI Engineering
Shinshu University
3-15-1 Tokida, Ueda, Nagano 386-8567, Japan
hashi@shinshu-u.ac.jp

Yuki KATOH
Mechatronics Division
Harmonic Drive Systems Inc.
1856 —1 Maki, Hotaka, Azumino, Ngano 399-8305, Japan
yuki. kato@hds.co.jp

Abstract

This paper provides a framework to generate robotic emotions during human-robot communication. The proposed method utilizes dynamic systems to make continuous information processing for emotion generation. The synchronization and entrainment of the dynamic system are used for information processing. The emotion generation system consists of discrimination, emotion and expression parts. This paper describes the design of the vector filed for the continuous discrimination of stimuli and emotion generation. We realize dynamic discrimination simply by using the proposed method. By introducing a conditioning the emotional response develops over time. The proposed method is examined by the simulations and experiments. The results show the effectiveness of the continuous discrimination, the emotion generation and the expression.

Index Terms - Dynamics, Facial recognition, Communication robot, Robotic emotion, Human-robot interaction.

1 Introduction

Emotion plays a very important role in our daily communication. Although there are many communication robots, which have emotion-like responses [1], in most cases these responses do not react to the external stimuli that are not pre-programmed. In order to make human-like emotion it is important that the robot develops the intrinsic emotional states based on the communication with human, and changes the response according to the intrinsic emotional state.

On the other hand neural scientists investigate the information processing of emotions in the brain. The emotional states we subjectively experience are the end result of information processing that occurs unconsciously as the brain decodes the significance of stimuli in order to shape appropriate behaviour. LeDoux [2] finds that the amygdala structure within the brain is important in responding to emotions, particularly fear. The amygdala mediates fear and other responses and actually processes information more quickly than other parts of the brain, allowing for a rapid responses that can by life saving before other parts of the brain have had a chance to react. The roles of amygdala structure are discriminations of stimuli, combinations between stimuli and responses, and generations of commands for responses [3]. The relationships between stimuli and responses are installed inherently in the human body. The relationship develops by conditioning from experiences. Information processing is performed by dynamic processes. Freeman [4] finds that there is chaotic dynamics in biological pattern recognition of the olfactory system.

Okada et al. [5]-[7] proposed a polynomial design of the nonlinear dynamics for brain-like information processing of whole body motion of robots. This technique allows us to perform dynamic information processing using the nonlinear dynamics network with the polynomial configuration. Therefore, this method is useful, not only for motion generation of humanoids, but also for information processing of the robotic emotional generation.

In this paper we propose a framework to generate robotic emotions based on the dynamics-based information processing with the polynomial design during human-robot communication. We assume face to face communication as a human-robot interaction. The human facial expression is used as an external stimulus for the robot. The robot reacts continuously to the human facial expression.

This paper will address the following issues: In section 2 the emotion system that we utilized is explained. In section 3 the computation method of the vector field is described based on the polynomial approximation. In section 4 the design of dynamics for discrimination is proposed. In section 5 we describe conditioning of the emotion part. In section 6 the method of the robotic facial expression based on the emotional state is addressed. Then we report on the experimental results in section 7. Lastly, we make the conclusion in section 8.

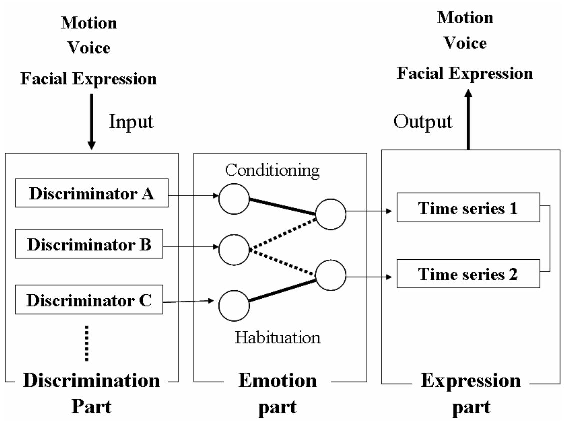

Fig.1 Structure of the emotional system.

2 Emotional Generation System

Figure 1 shows a structure of an emotional system which consists of a discrimination part, an emotion part and expression part. The discrimination part identifies the kind of stimuli such as facial expressions in the environment. In the emotion part the discriminated stimulus is examined the internal state, and the combinations between stimuli are generated by classical conditioning. Lastly, in the expression part the expression command trajectories are generated based on the emotional state that is output from the emotion part.

.

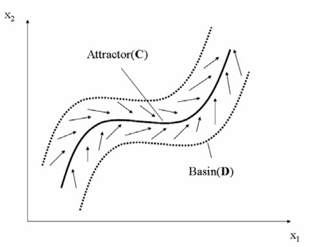

Fig.2 Schematic drawing of the vector field.

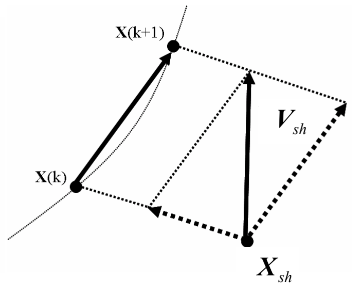

Fig.3 Making the vector field.

3 Making Vector Field

An example of a vector field in the two dimensional space is shown in Fig.2. The vector filed is formed around arbitrary curve C. The curve C is assumed as an attractor, and region D is a basin of entrainment around the attractor. The curve C is a function of discrete time t and consists of $\mathbf{X} = \{\mathbf{X}(1), \cdots, \mathbf{X}(t), \cdots, \mathbf{X}(m)\}, (\mathbf{X} \in \mathbf{R}^N)$, where N expresses the dimension of the state space. We make a vector $\boldsymbol{V}_{sh}$ which directs from arbitrary point $\boldsymbol{X}_{sh}$ in the basin D to the curve C as shown in Fig.3. The vector is defined by the following equation.

$$\boldsymbol{V}_{sh} = \gamma(\boldsymbol{X}(k) - \boldsymbol{X}_{sh}) + (\boldsymbol{X}(k+1) - \boldsymbol{X}(k)) \qquad (1)$$

where, γ is a constant, $0 \le \gamma \le 1$. We make many vectors $\boldsymbol{V}_{sh}\ (h = 1,2 \cdots L)$ in the basin D in this way and approximate them by a polynomial expression. When $\boldsymbol{X} \in \boldsymbol{R}^2$, the polynomial is as follows,

$$\begin{aligned} v_{sh1} &= \dot{x}_{sh1} = \sum_{i=0}^{n}\sum_{j=0}^{n} a_{1ij} x_{sh1}^{i} x_{sh2}^{j} \\ v_{sh2} &= \dot{x}_{sh2} = \sum_{i=0}^{n}\sum_{j=0}^{n} a_{2ij} x_{sh1}^{i} x_{sh2}^{j} \end{aligned} \qquad (2)$$

where, $\boldsymbol{V}_{sh} = (v_{sh1}, v_{sh2})^T$ and $\boldsymbol{X}_{sh} = (x_{sh1}, x_{sh2})^T$. The values of the parameters a_{1ij}, a_{2ij} can be obtained by the least-squares method.

$$\boldsymbol{A} = \boldsymbol{V}\boldsymbol{\Theta}^{\#} \qquad (3)$$

where,

$$\mathbf{A} = \begin{pmatrix} a_{100} & a_{101} & \cdots & a_{1nn} \\ a_{200} & a_{201} & \cdots & a_{2nn} \end{pmatrix}$$

$$\mathbf{V} = \begin{pmatrix} \mathbf{V}_{s1} & \mathbf{V}_{s2} & \mathbf{V}_{s3} & \cdots & \mathbf{V}_{sL} \end{pmatrix}$$

$$\mathbf{\Theta} = \begin{pmatrix} \boldsymbol{\theta}(\mathbf{X}_{s1}) & \boldsymbol{\theta}(\mathbf{X}_{s2}) & \boldsymbol{\theta}(\mathbf{X}_{s3}) & \cdots & \boldsymbol{\theta}(\mathbf{X}_{sL}) \end{pmatrix}$$

$$\boldsymbol{\theta}(\mathbf{X}_{sk}) = \begin{pmatrix} 1 \\ x_{sk2} \\ x_{sk1} x^2{}_{sk2} \\ \vdots \\ x^n{}_{sk1} x^n{}_{sk2} \end{pmatrix}$$

$\boldsymbol{\Theta}^{\#}$ means a pseudo inverse matrix of $\boldsymbol{\Theta}$.

4 Design of Vector Field for Discrimination

4.1 Discrimination using vector fields

The discrimination part distinguishes between stimuli by using vector fields. The time series data of a stimulus is obtained through the sensors such as a camera. The robot has to identify a kind of stimuli from the time series data. Then a vector field of dynamics is used. The vector field consists of input dimensions and output dimensions. Figure 4 shows an example of facial expression discriminations in which there are two input dimensions and one output dimension. The axes of the input dimensions, X1 and X2, show the data of mouth width and eye height, respectively. We make a trajectory of the attractor based on the time series data of the facial expression as shown in Fig.5 (a). The output dimension indicates the symbol of the facial expression. The output dimension is constructed by time series data which increase linearly as time (Fig.5 (b)). Combining the input and output dimensions a discrimination vector field such as in Fig.6 is obtained. The vector field is written by equation (4). The vector field with the region of the entrainment is generated by a polynomial design method described in the former session.

$$\begin{aligned} \dot{x}_1 &= f_1(x_1, x_2, y) \\ \dot{x}_2 &= f_2(x_1, x_2, y) \\ \dot{y} &= f_3(x_1, x_2, y) \end{aligned} \qquad (4)$$

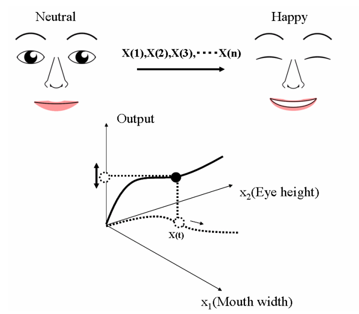

Fig.4 Discrimination using dynamics.

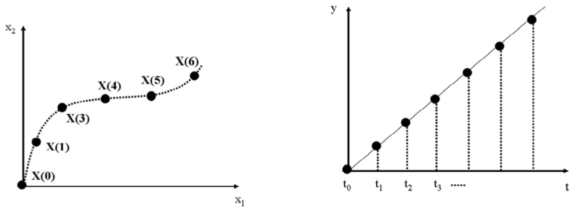

(a) (b)

Fig. 5 Attracter of input and output spaces. (a)Input space. (b)Output space.

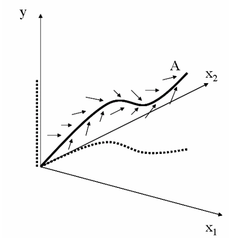

Fig.6 Vector field of discrimination space.

4.2 Stabilization

When the input data is located in the entrainment region, the discrimination vector field outputs a correct symbol of the output dimension. However, if the input data is located outside of the entrainment region of the attractor in the input dimension, the output signal diverges, since the vector field is not defined outside of the entrainment region. In order to stabilize the output signal we introduced another vector field outside of the initial entrainment region. The new vector field has an attractor located on the origin of the space as shown in Fig.7. We call this space a stabilized vector field.

An example of the stabilized vector field is shown in Fig.8. The initial attractor increases in a monotone in the input space as an example. The stabilized vector field whose attractor is located on the origin is constructed on the outside of the initial entrainment region. The behaviour of the discrimination space is examined with the sample input data. The sample input data $x_1(t), x_2(t)$ is given, and the output data $y(t)$ is computed. At first, the input signal behaves on the outside of the entrainment region, and then the input signal follows the trajectory of the attractor as shown in Fig.9(a). The black spot is starting point of the state. There is no divergence on the output signal, and the output signal increases after the input signal goes into the entrainment region. The other example is shown in Fig.9(b). The input signal follows the trajectory of the attractor at the beginning, and then the signal changes the direction of motion to the reverse direction. The output signal increases as the input signal increases at first, and then the output signal decreases after the direction changes.

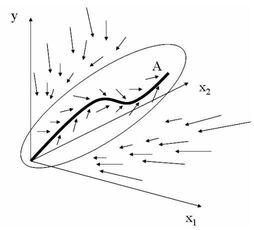

Fig. 7 Stabilized vector field.

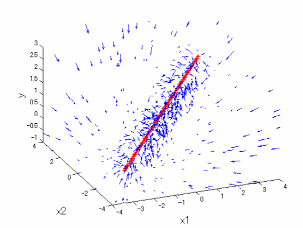

Fig.8 An example of stabilized vector field.

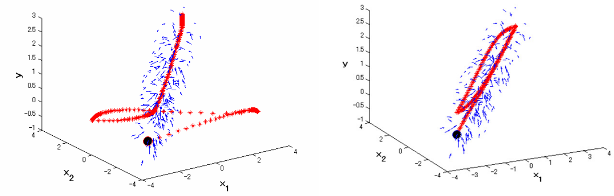

(a) (b)

Fig. 9 Examples of the stabilized discrimination space.

5 Emotion Part

The emotion part recognizes the meaning of the stimulus and evaluates the value based on the viewpoint of self-preservation. The meaning recognition gives a relationship that the input stimulus is connected to the output response. We design the basic relationships between stimuli and responses according to the biological inherent responses. Relationships are developed by classical conditioning. The information processing of the conditioning is performed in the emotion part using the symbols of the stimuli which are obtained from the discrimination part (Fig.10).

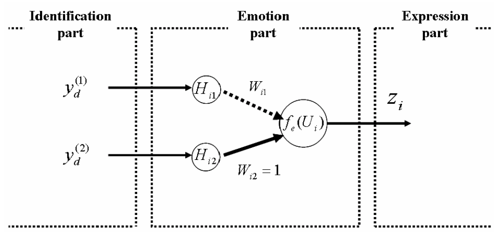

Fig. 10 Schematic drawing of the emotion part.

Figure 11 shows an example of the relationships of stimuli and responses. We obtain symbols of stimuli from the discrimination part such as $y_d^{(1)}$, $y_d^{(2)}$ and $y_d^{(3)}$. The emotion part outputs the symbols of responses, z_1 and z_2, related to the stimulus symbols. In the figure the solid lines show the inherent relation that we design in advance. The weight coefficients for the stimuli $y_d^{(1)}$ and $y_d^{(2)}$ are written by the following equation.

$$\boldsymbol{w}_1 = (1 \;\; 0)^T \;,\quad \boldsymbol{w}_2 = (0 \;\; 1)^T \qquad (5)$$

The stimulus $y_d^{(3)}$ does not have any relationship to the response at first. Now we give meaning to the stimulus $y_d^{(3)}$ through conditioning. The stimulus $y_d^{(3)}$ is input first, and then the stimulus $y_d^{(1)}$ is input. In this case an inherent response z_1 occurs. If the input-output response $y_d^{(3)} \to y_d^{(1)} \to z_1$ is repeated, then the new relation $y_d^{(3)} \to z_1$ is generated. Namely, the stimulus $y_d^{(3)}$ is given meaning.

$$\boldsymbol{w}_3 = (1 \;\; 0)^T \qquad (6)$$

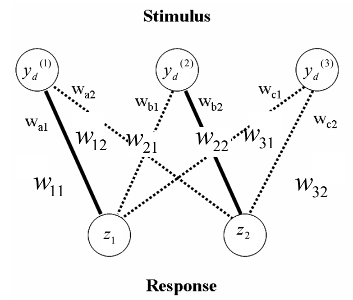

Fig.11 Classical conditioning of stimuli

We need a learning algorism for the conditioning. The information processing of the conditioning is performed by the output-dependent learning based on Hebb learning [8].

$$H_{ij}(t+1) = a y_d^{(j)} + b H_{ij}(t) \tag{7}$$

$$U_i(t) = \sum_j W_{ij}(t) y_d^{(j)} \tag{8}$$

$$z_i(t) = f_e(U_i(t)) \tag{9}$$

$$\Delta W_{ij}(t) = c(1 - W_{ij}(t))(H_{ij}(t) - H_2) z_i(t) \tag{10}$$

where, $y_d^{(j)}$ is a stimulus input signal to the emotion part, H_{ij} is a variable determined by equation (6), U_i is the internal state, z_i is an output of the emotion part, ΔW_{ij} is a change rate of the weight coefficient W_{ij}, a, b and c are constants.

We simulate an example of the conditioning by using the learning algorism described above. The input-output response $y_d^{(1)} \to y_d^{(2)} \to z_i$ is repeated, where $y_d^{(1)}$ and $y_d^{(2)}$ are the conditioned and unconditioned stimuli to the response z_i, respectively. The value of the constants are $a = 0.03, b = 0.99, c = 0.05$ and $H_2 = 0.1$. The simulated result is shown in Fig.12. The variable H_{i1} changes after the conditioned stimulus is input. The weight coefficient w_{i1} increases over time, and then the response z_i occurs by not only $y_d^{(2)}$ but also $y_d^{(1)}$.

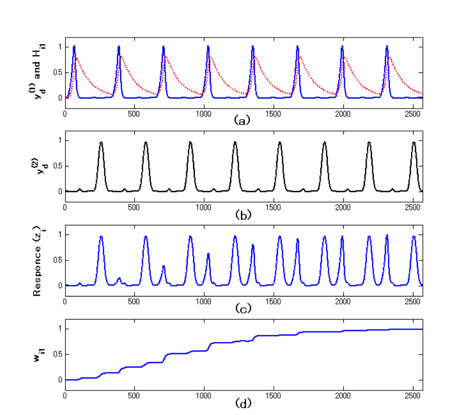

Fig.12 Simulated result of conditioning. (a)Conditioned stimulus and the variable, (b) Unconditioned stimulus, (c) Response, (d) Weight coefficient between the conditioned stimulus and the response.

6. Expression Part

The expression part generates the actual data to control the robotic facial expression. Input signal of the expression part is the output signal from the emotion part. By using the emotional state we compute the output data in the expression part, and we combine the data of each emotion to make the actual trajectories of the robot expression. Since the output signal from emotion part is continuous, we obtain the continuous trajectory of the robot expression by mapping the emotional state. The function is written by the following equations.

$$o^{(p)} = \sum_i s_i g_i^{(p)}(z_i) \tag{11}$$

$$g_i^{(p)}(z_i) = a_{i,p} + b_{i,p} z_i + c_{i,p} z_i^2 + d_{i,p} z_i^3 \tag{12}$$

where, $o^{(p)}$ is the p th characteristic quantity for the facial expression. $g_i^{(p)}(z_i)$ is a mapping function from the i th emotional state to the p th characteristic quantity. s_i is a coefficient for normalization. The value of z_i changes 0 to 1. By using the equations (11) and (12), we computed an example of a facial expression. We use five characteristic quantities for the facial expression as shown in Fig.13. Figure 14 shows the trajectories of the characteristic quantities and the facial expression when $z_1 = 0 \to 0.4$, and $z_2 = 0 \to 1.0$, linearly.

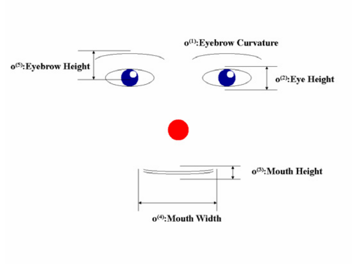

Fig.13 Characteristic quantities for the facial expression.

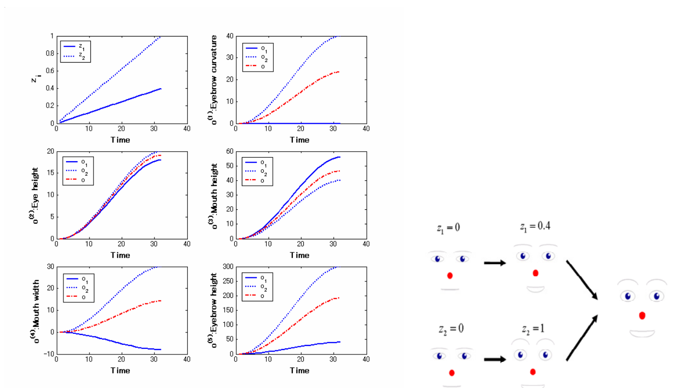

(a) (b)

Fig.14 An example of the facial expression. (a) Trajectories. (b) Facial expression.

7 Experiment

Figure 15 shows the experimental setup for the emotional generation system. We use two PC's to construct a discrimination part, an emotion part and an expression part. The discrimination is performed by PC1. The image signal from a CCD camera is connected to an image processing board (IP 5005 made by Hitachi) in PC1, and the characteristic quantities are obtained. PC2 computes the emotion and expression parts and shows the robotic facial expression on the display.

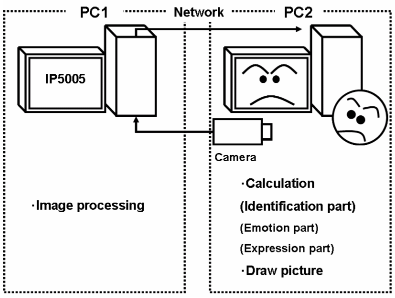

Fig.15 Experimental setup.

7.1 Design of the vector fields for facial expression

We use four characteristic quantities for facial discrimination, i.e., height of eye, distance between eye and eyebrow, width of mouth, height of mouth. We measure changes in the characteristic quantities from a neutral expression to another expression using the former extraction method, and then we obtain time series data of the characteristic quantities. The time series data become the sample data of the attractors of the dynamics. We measured it five times for the same expression. We compute the average of the data. The average data is approximated with fifth order polynomial to get a smooth curve. We use one dimensional data as the output signal. The output signal increases from 0 to 1 in a monotone as shown in Fig.5. We make an attractor in five dimensional vector filed. The space consists of four dimensional data of characteristic quantities and one dimensional data of the output signal. We designed the entrainment region of the attractor so that the actual measurement data of characteristic quantities are included in the region.

7.2 Discrimination of facial expression

We conduct identification experiments of facial expressions in real time with an animated image of a human face. We used four kinds of expression change from Neutral to four characteristic expressions of A,B,C,D as shown in Fig.16. We designed four vector fields using the trajectories beforehand and considered it identification device for expressions. We input the characteristic quantities provided from face image processing into each identification device continually. The face image change in time series is shown in Fig.17. In addition, the output signals from each identification device are shown in Fig.18.

The output signal of each identification device changes from 0 to 1, when the memorized change of facial image occurs. On the other hand, the output signal keeps around 0, when the facial image is not a memorized one. We can find that expressions A and D are distinguished precisely, but the identification precision between expressions B and C is not as good. As we can find in Fig.16, the trajectories of attractors of expressions B and C are located in closed area. We believe that this is the reason why the separation between B and C is not precise. The problem may be solved by adding another dimension in the input space, so that the separation of the trajectories can be exactly determined. In addition, if we can detect the characteristic quantities precisely, then the separation between B and C improves. In our experiment we used a simple extraction method for the characteristic quantities.

7.3 Conditioning and robotic facial expression

We conducted experiments of the robotic emotional generation to evaluate the proposed information processing. We determined the initial relationships between the external stimuli and the robotic facial expressions as shown in Fig.19. The relationships are changed by conditioning. Figure 20 shows the results of the conditioning between the stimuli (2) and (4). The stimuli $y_d^{(2)}$ and $y_d^{(4)}$ are conditioned by it being repeated in turn. Figure 21 shows the expressions in the segments T_A and T_C. In the case of segment T_A, the expression is determined by the initial relationships. On the other hand, in segment T_C the expression is changed from the initial relationships due to conditioning.

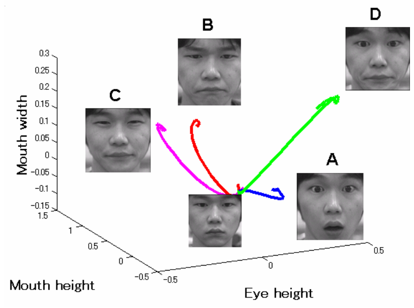

Fig.16 Attractors of facial expressions

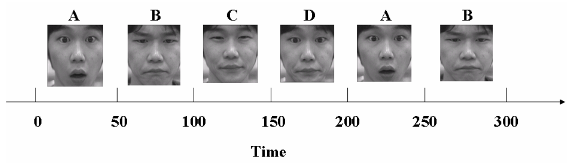

Fig.17 Sequence of facial expressions in discrimination experiment

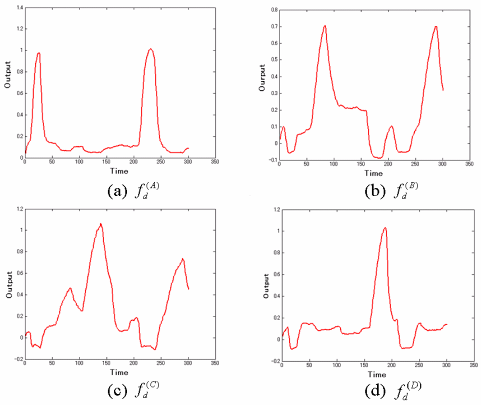

Fig.18 Experimental results of facial discrimination

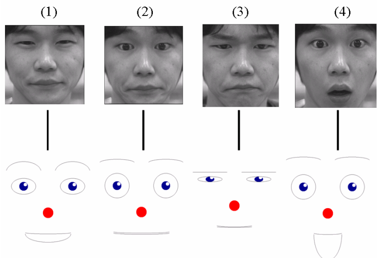

Fig.19 Initial relationships between the stimuli and the expressions.

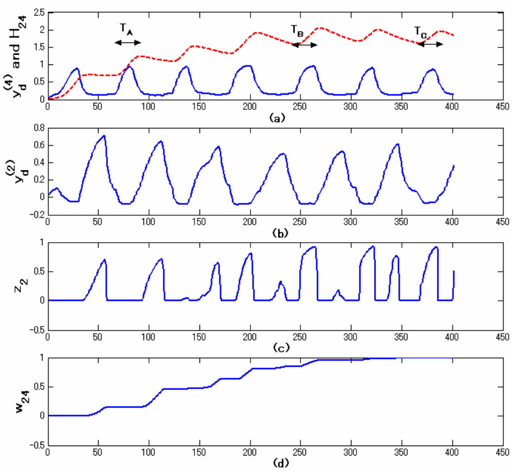

Fig.20 Experimental results of conditioning.

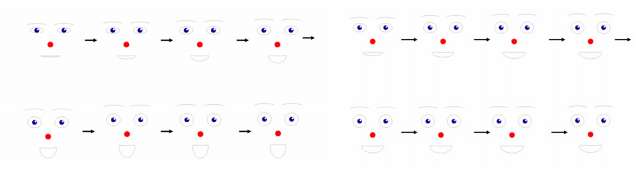

(a) (b)

Fig.21 Experimental results of expression. (a) Expression during T_A. (b)Expression during T_C.

8 Conclusion

We propose a framework to generate robotic emotion for human-robot communication based on the dynamics-based information processing. The proposed method utilizes dynamic systems to make continuous information processing for emotional generation. The synchronization and entrainment of the dynamic system are used for information processing. The vector fields are utilized to make information processing of time series data continuously. The emotional generation system consists of discrimination, emotion and expression parts. We realized dynamic discrimination simply by using the proposed method. By introducing a conditioning the emotional response developed at time. We showed that the new computational framework was effective for face to face communications based on an experimental work.

Acknowledgement

We are grateful to Assoc. Prof. Michael Honywood of Shinshu University who provided critical assistance on our manuscript. This research was supported by The Mitsubishi Foundation.

Reference

[1] For example: Masahiro Fujita, "AIBO: Toward the Era of Digital Creatures," *The International Journal of Robotics Research*, Vol.20, No.10, pp.781-794, 2001.

[2] Joseph Ledoux, *The Emotional Brain: The Mysterious Underpinnings of Emotional Life*, Touchstone Books, 1998.

[3] Gen Matsumoto and Taketoshi Ono, *Brain Science of Emotion and Consciousness -what is human beings-*, Baifukan Pub., 2002. (in Japanese)

[4] W.J.Freeman, "Simulation of Chaotic EEG Pattern with a Dynamic Model of the Olfactory System," *Biol.Cybern.*56, pp.139-150,1987.

[5] Masafumi Okada, Koji Tatani and Yoshihiko Nakamura, "Polynomial Design of the Nonlinear Dynamics for the Brain-Like Information Processing of whole Body Motion," *Proceedings of the 2002 IEEE International Conference on Robotics and Automation,* Washington, DC, May, pp.1410-1415, 2002.

[6] Masafumi Okada, Daisuke Nakamura and Yoshihiko Nakamura, "Hierarchical Design of dynamics Based Information Processing System for Humanoid Motion Generation," *Proceedings of the 2nd International Symposium on Adaptive Motion of Animals and Machines*, Kyoto, March, SaP-III-1, 2003.

[7] Masafumi Okada and Yoshihiko Nakamura, "Design of the Continuous Symbol Space for the Intelligent Robots using the Dynamics-based Information Processing," *Proceedings of the 2002 IEEE International Conference on Robotics and Automation*, New Orleans, LA, April, pp.3201-3206, 2004.

[8] Yukifumi Shigematsu, Hiroshi Okamoto,Kazuhisa Ichikawa,Gen Matsumoto: Temporal Event Association and Output-Dependent Learning. A Proposed Scheme of Neural Molecular Connections, Journal of Advanced Computational Imtelligence,Vol.3, No.4, 1999.

The Eleventh International Symposium on Artificial Life and Robotics 2006 (AROB 11th'06),
B-con Plaza, Beppu, Oita, Japan, January 23-25, 2006

Data Manipulation of DNA Relational Database

Yutaka Kita , Satoshi Kashiwamura , Atsushi Kameda , Masahito Yamamoto , and Azuma Ohuchi

*Graduate School of Information Science and Technology, Hokkaido University
Nishi 9, Kita 14, Kita-ku, Sapporo, Hokkaido, 060-0814, Japan
{ki-yu, kashiwa, masahito, ohuchi}@complex.eng.hokudai.ac.jp

**CREST, Japan Science and Technology Agency (JST)
Honmachi 4-1-8, Kawaguchi 332-0012, Japan
kameda@complex.eng.hokudai.ac.jp

Abstract

DNA memory is a recording medium that utilizes the advantages of DNA molecules. However, only a few article have studied the possibility of DNA databases. In this paper, we suggest a DNA relational database with a simple data model. We show a mathematical model and chemical experimental results that consist of data manipulation and relational algebra.

key words: DNA database, simple data model, relational algebra

1 Introduction

Recently, many papers have dealt with DNA memory, which is a recording medium that utilizes the stability and minute characteristics of DNA molecules. Kashiwamura et al. described the use of nested PCR to do hierarchical memory operations to construct large DNA memory [1]. However, most DNA memory is memory as storage, and so there are insufficient points to manage the data as a database.

Storing data in DNA molecules represent data as arrangement of base sequences. It is easy to deal with genome DNA in a DNA database because they can be directly manipulated by chemical reactions. In addition, storing and processing individual genetic information in electronic data has many problems from the viewpoint of the protection of individual information. Reif et al. invented a method that makes a database of DNA molecules without changing them into digital media and retrieves the data from DNA molecules [2]. Even in a large DNA database, the processing time is fairly constant because chemical reactions are fairly constant due to massive parallel reaction of DNA molecules.

In studies of DNA relational database, Arita et al. showed the feasibility of relational algebra (RA) through *i vi ro* experiments [3], and Katsányi showed the feasibility of relational algebra with theoretical models that consist of basic biomolecular reactions [4]. However, in their data models, one DNA molecule is represented as the tuple of relational databases. Therefore, such operations as the extraction of only information of attributes will become troublesome.

In this paper, we construct a DNA relational database with a simple data model in which one DNA molecule stores one data. Therefore, our data model simply extracts only information of attributes, much easier than conventional models. We showed some experimental results that are considered important parts and discussed possibility of practical application of the proposed model as well as the limit of it.

2 Model

2.1 datamodel

A relation is denoted by R, and a test tube that consists of DNA molecules representing R is denoted by U. Given two variables $i = 1 \;\; 2 \qquad$ and $j = 1 \;\; 2 \qquad m$,

$$\begin{aligned} R(A_1 \;\; A_2 \qquad A_n) \;\; = \;\; \{ & (v_1^{(1)} \;\; v_2^{(1)} \qquad v_n^{(1)}) \\ & (v_1^{(2)} \;\; v_2^{(2)} \qquad v_n^{(2)}) \\ & (v_1^{(m)} \;\; v_2^{(m)} \qquad v_n^{(m)}) \} \end{aligned}$$

where A_i is an attribute value, and $v_i^{(j)}$ is a element of the relation. A tuple of attributes is denoted by

$_j = (v_1^{(j)}\ v_2^{(j)}\quad v_n^{(j)})$. Given $_j$, we denote ID_j that stores the value of j. All data are represented by single-stranded DNA (ssDNA) with the attribute and the tuple information shown in Fig. 1.

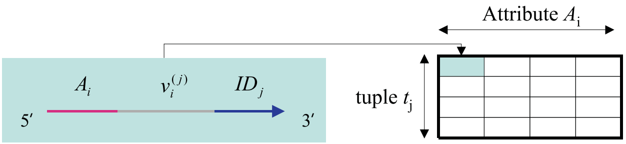

Figure 1: Representation of data with ssDNA

2.2 Basic Operations

We define the basic experimental operations for database processing and use a mathematical model based on Reif's RDNA model [5], which has slightly different notation for operations than the models of Reif's and Katsányi's.

- $Merge(U_x\ U_y)$: Mix the DNA molecules in the test tubes U_x and U_y.
- $Amplif\ \ (U\ FW\ RE)$: Execute amplification reactions for DNA molecules in test tube U with sequence sets of forward primers FW and reverse primers RE.
- $Appe\ \ d(U\ S\ E))$: Append corresponding sequence set S to DNA molecules in test tube U and contain any subsequence E at the 3' end.

For the double-stranded DNA (dsDNA) in test tube U and one of the ssDNA's end is biotinylated, operations are following:

- $Separa\ \ e_+(U)$: Extract ssDNA whose ends are not biotinylated.
- $Separa\ \ e_-(U)$: Extract ssDNA whose ends are biotinylated.

For the DNA molecules in test tube U, operations are following:

- $Ge\ \ (U\ +S)$: Extract ssDNA that contains any subsequence S.
- $Ge\ \ (U\ -S)$: Extract ssDNA that does not contain any subsequence S.

Using the basic operations, we can describe data manipulations (Insert, Delete, Update, and Select). Here, Select means referring to one data. For selecting tuples, we describe in RA operation.

3 RA Operations

In this section, we describe packaging methods for five RA operations (Union, Difference, Projection, Selection, and Cartesian product) in test tubes with basic operations. The other operations can be expressed by utilizing these ones.

3.1 Union

Take the union of sets with two union compatible relations R_x and R_y.

$$R_z := R_x \cup R_y\ do:$$
$$U_z := Merge(U_x\ U_y)$$

This program can be executed by mixing two tubes that represent R_x and R_y.

3.2 Difference

Take the difference of sets with two union compatible relations R_x and R_y.

$$R_z := R_x - R_y\ do:$$
$$S_1 := Amplif\ \ (U_y\ \emptyset\ RE)$$
$$where\ RE = \{\overline{ID}_j | j = (1\ 2\quad m)$$
$$5'\ e\ \ d\ bio\ i\quad la\ ed\}$$
$$S_2 := Separa\ \ e_-(S_1)$$
$$U_z := Ge\ \ (U_x\ -S_2)$$

where, $\overline{ID}_j$ represents comprementary strands of ID_j. $Amplif\ \ (U_y\ \emptyset\ RE)$ operation is an extension reactions. Moreover, we utilize affinity separation to execute $Separa\ io\ \ _-(S_1)$ and $Ge\ \ (U_x\ -S_2)$ operations.

3.3 Projection

In relation R, an arbitrary subset of $\{A_1\ A_2\quad A_n\}$ is denoted by X. Create a new relation to abstract attributes, that are assigned by subset X, from relation R.

$$R' := \Pi_x R\ do:$$
$$S_1 := Amplif\ \ (U\ X\ RE)$$
$$where\ X = \{A_i | i = \{1'\ 2'\quad k'\} \subseteq \{1\ 2\qquad\}\}$$
$$RE = \{\overline{ID}_j | j = (1\ 2\quad m)\ \ 5'\ e\ \ d\ bio\ i\quad la\ ed\}$$
$$U' := Separa\ \ e_+(S_1)$$

$Amplif\ \ (U\ X\ RE)$ operation is a simple polymerase chain reaction (PCR), and $Separa\ io\ \ _+(S_1)$ operation is executed by affinity separation.

3.4 Selection

We denote selection condition as F. Abstract tuples that satisfy condition F from relation R.

$$R' := \ _F R\ do:$$
$$S_1 := Amplif\ \ (U\ FW\ F)$$
$$where\ FW = \{A_i | i = (1\ 2\ \ \ \ )\}$$
$$F = \{\overline{ID}_j | P_F(\ _j)\ \ 5'\ e\ \ d\ bio\ i\ \ \ la\ ed\}$$
$$U' := Separa\ e_+(S_1)$$

$P_F(\ _j)$ is predicate that become true when tuple $_j$ satisfies condition F. This Selection program can be executed in similar chemical operations of the Projection program.

3.5 Cartesian Product

The multiplication of two relation $R_x(A_1\ A_2\ \ \ \ A_n)$ and $R_y(A_{1'}\ A_{2'}\ \ \ \ A_{n'})$. In other words, create $R_x \times R_y(A_1\ A_2\ \ \ \ A_n\ A_{1'}\ A_{2'}\ \ \ \ A_{n'})$

$$R_z := R_x \times R_y\ do:$$
$$S_1 := Appe\ \ d(U_x\ S\ E_x)$$
$$S_2 := Appe\ \ d(U_y\ S\ E_y)$$
$$where\ E_x = \{ID_j | j = (1\ 2\ \ \ \ m)\}$$
$$E_y = \{ID_{j'} | j' = (1'\ 2'\ \ \ \ m')\}$$
$$S = \{ID_{f(j\ j')} |\ _j \in R_x\ \ \ _{j'}' \in R_y\}$$
$$U_z := Merge(S_1\ S_2)$$

here, we define $f(j\ j')$ that returns specified value that depends on j and j' that distinguish tuple $(\ _j\ \ _{j'}')$ that represents the concatenation of tuples of $_j$ and $_{j'}'$. We utilize State Transition PCR (ST-PCR) [6] to execute $Appe\ \ d(U\ S\ E)$ operation. By ST-PCR, we prevent DNA molecules from forming complete dsDNA.

4 Experiments

We set two relations $R_1(3 \times 3)$ and $R_1'(2 \times 2)$ to verify whether we can execute RA operations $i\ \ \ vi\ ro$. Here, we showed experiments of Cartesian product. We also describe ssDNA that contains A_i and ID_j as $da\ a(i\ \ j)$, a set of primers that correspond A_i and ID_j as $p(i\ \ j)$, and transition molecule for R_i as $\ R_i(j\ j')$.

In this paper, we consider 16-mer ssDNA as 1 unit and assign these units to attribute A_i, tuple information ID_j and data element $v_i^{(j)}$. We employed a sequence set of GC-Templates in Template Method [7]. However, since sequences of GC-Templates aren't designed to consider a thermodynamic viewpoint, some sequences may form secondary structure in which DNA molecule anneals with itself and may prevent the intended experimental reactions. To solve this problem, we predict free energy ($\ G$) and secondary structure of combined sequences of GC-Templates by Mfold [8] and generated data strands and transition molecules. To examine the success of the experiments, we used PolyAcrylamide Gel Electrophoresis (PAGE).

For two relations (R_1 and $R_{1'}$), we performed Cartesian product operations shown in Fig. 2. First, we mixed the corresponding transition molecules with each test tube that represent R_1 and $R_{1'}$ and performed ST-PCR to execute $Appe\ \ d(U\ S\ E)$. The appropriately reacted data strands were 64-mer, which we checked by measuring their length with gel electrophoresis.

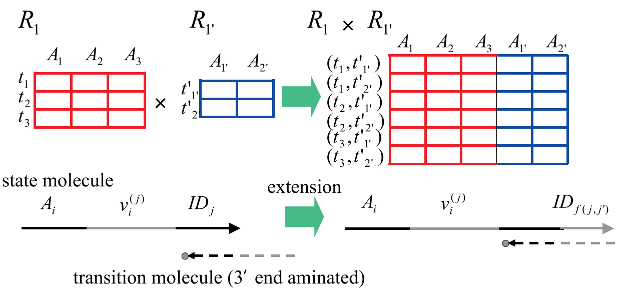

Figure 2: Cartesian product between $_1$ and $_{1'}$ and example of ST-PCR. State molecules corresponding to data represent strands and transition molecules to strands that consist of $\overline{ID}_j$ and $\overline{ID}_{f(j\ j')}$. After ST-PCR, only state molecules are extended because 3' end of transition molecules are aminated.

To complete Cartesian product operations, we mixed post-ST-PCR samples and described the relation of after Cartesian product between R_1 and $R_{1'}$ as R_2. However, this experiment was insufficient to verify the operation. Therefore, we executed additional relational Selection operations that extracted the elements of tuple $(\ _1\ \ _{1'}')$ from relation R_2. We perfromed PCR with forward primer mix solution (A_1, A_2, A_3, $A_{1'}$, and $A_{2'}$) and reverse preimer $\overline{ID}_{f(1\ 1')}$. Target bands of data strands of relation R_2 (64-mer) were amplified, as shown in Fig. 3.

However, we could not verify whether only data strands of tuple $(\ _1\ \ _{1'}')$ were amplified from this experiment. Thierefore, we executed a second PCR for post-Selection solution. However, since R_2 consisted of 30 data strands, it's difficult to perform and show PCR with all primer sets. Therefore, we selected five primer sets ($p(1\ \ f(3\ 2'))$, $p(2\ \ f(1\ 1'))$, $p(3\ \ f(3\ 1'))$, $p(4\ \ f(1\ 1'))$, and $p(5\ \ f(2\ 1'))$). Assuming that Selection operation was succeeded, amplification reaction

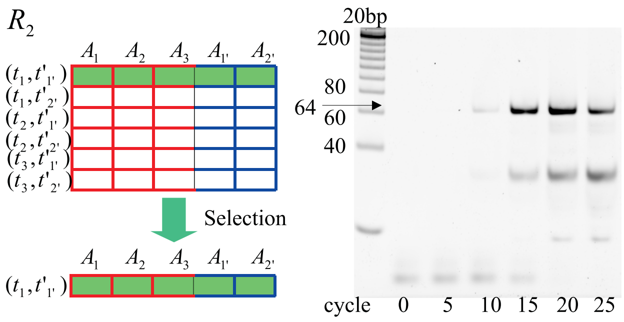

Figure 3: Results of Selection operation extracting elements of tuple $(t_1\ t'_{1'})$ from relation $_2$. Bands show data strands of $_2$ (64-mer) were amplified. However, amplified data strands were not ensured as elements of tuple $(t_1\ t'_{1'})$.

is observed in case of using $p(*\ f(1\ 1'))$ and not other primer sets. The results of the second PCR shown in Fig. 4. The target bands of data strands (64-mer) appeared in samples of PCR with $p(*\ f(1\ 1'))$, while few data strands were amplified with other primer sets. These experiment results show that Cartesian product and Selection operations could be executed. We considered Projection operation feasible operation because the operation of Selection and Projection operations use similar chemical experiments except the primer sets. Moreover, we showed the feasibility of the RA Join operation because Selection after Cartesian product corresponded to Join.

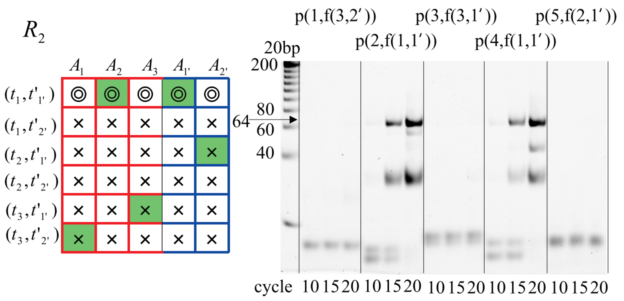

Figure 4: Result of the second PCR for relation $_2$ and a series of experiments corresponding to RA Join operation. We used five primer set (two target and three non-target) described in the relation table. After the first PCR, most data strands in the test tube were element of tuple $(t_1\ t'_{1'})$, data strands amplified only with $p(*\ f(1\ 1'))$. Moreover, proportion of data strands remained fairly constant through consecutive operations.

5 Discussion & Conclusion

We proposed a DNA relational database model in which one DNA molecule stored one data and showed a mathematical model of data manipulation and RA operations. A simple data model contributes to simplicity of data manipulation experiments compared to existing models. We confirmed successful data reference and RA operations *i vi ro* and showed results of Cartesian product operation. In experiments of Cartesian product, we demonstrated the robustness of our model in terms of continuous PCR reactions. This result will be a stepping stone to continuous action of DNA relational database.

However, to realize a DNA relational database, many problems need to be solved. To realize reference of database, we must check robustness for continuous affinity separation and verify feasibility that we can obtain tuple information using data element. In addition, the size of our database is still too small to use bioinformatics. We must cooperate with large DNA memory on this point. As the future work, we will solve these problems and construct DNA relational database system.

References

[1] S. Kashiwamura, M. Yamamoto, A. Kameda, T. Shiba, and A. Ohuchi, "Hierarchical DNA memory based on nested PCR", *8th International Workshop on DNA-based Computers (DNA8), in Lecture Notes In Computer Science*, pp. 112-123, 2003.

[2] J. H. Reif, T. H. LaBean, M. Pirrug V. S. Rana, B. Guo, C. Kingsford, and G. S. Wickham, "Experimantal Construction of Large Scale DNA Databases with Associative Search Capability", *7th International Meeting on DNA-Based Computers (DNA7), in Lecture Notes in Computer Science*, pp. 231-247, 2002.

[3] M. Arita, M. Hagiya, and A. Suyama, "Joining and Rotating Data with Molecules", *Proc. of IEEE 4th International Conference on Evolutional Computaion (ICEC'97)*, pp. 243-248, in IEEE press, 1997.

[4] I. Katsányi, "On implementating Relational Database on DNA Strands", *Acta Cybernetica*, vol. 16(2), pp. 259-270, 2003.

[5] J. H. Reif, "Parallel biomolecular computation:Models and simulations", *Algorithmica*, vol. 25, no. 2-3, pp.142-175, 1995.

[6] K. Hasimoto, A. Kameda, M. Yamamoto, and A. Ohuchi, "State Transition Model Based on DNA Polymerization", *Proc. of the International Technical Conference on Circuit/Systems, Computers and Communications (ITC-CSCC'03)*, pp. 1889-1892, 2003.

[7] M. Arita and S. Kobayashi, "DNA Sequence Design Using Templates", *New Generation Computing*, vol. 20, pp. 263-277, 2002.

[8] M. Zuker, "Mfold web server for nucleic acid folding and hybridization prediction", *Nucleic Acids Research*, vol. 31, pp. 3406-3415, 2003.

The Eleventh International Symposium on Artificial Life and Robotics 2006 (AROB 11th'06),
B-con Plaza, Beppu, Oita, Japan, January 23-25, 2006

Stability evaluation method of DNA tile structure

Naoki Iimura[1], Masahito Yamamoto[1,2], Fumiaki Tanaka[1]
Atsushi Kameda[2], Azuma Ohuchi[1,2]

[1]Graduate School of Engineering, Hokkaido University
North 13, West 8, Kita-ku, Sapporo 060-8628, Japan
http://ses3.complex.eng.hokudai.ac.jp
Tel:+81-11-716-2111(ext.6498),Fax:+81-11-706-7834
[2] CREST, Japan Science and Technology Cooperation (JST)
Honmachi 4-1-8, Kawaguchi 332-0012, Japan
E-Mail : {i˜mu, masahito, ,fumi95,kameda,ohuchi}@complex.eng.hokudai.ac.jp

Abstract

DNA tiles formed from self-assembly by a hybridization property of DNA molecules have attracted attention as a new calculation technique and new nanostructures. When nanostructures are composed of DNA tiles, base sequences that correctly and stably hybridize are required. We have to design base sequences (the row of the base) that become such stable tiles. In conventional research, however, sequence design that considers the structure stability of tiles can not be carried out. The purpose of this paper is to propose an evaluation method for the structure stability of DNA tiles.

key words - DNA tile, DNA nano-structure, DNA computing, sequence design, free energy

1 Introduction

DNA is a double helix consisting of two single strand DNA molecules held together by specific bonded base pairs: guanine (G) and cytosine (C) sticks, and adenine (A) and thymine (T) sticks. DNA forms one spiral double strand DNA molecule from two single strand DNA molecules when this property acts in parallel. This complementary chemical bond is called "hybridization."

Winfree *et al.* generated DNA tile conformation by making two or more DNA molecules meet[1][2]. Each tile has an adhesive end called "sticky end" that associates according to complementarity. Branched DNA tiles with sticky ends constitute nanostructure. (Figure1)

Binary counter and silver nanowire with DNA nanostructure have been researched [3]. Nanodevices and smaller circuits for application are expected.

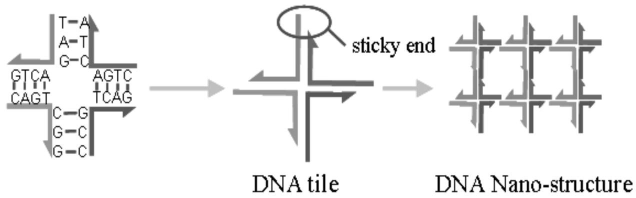

Figure 1: DNA Nano-structure made by DNA tiles

Sequences tightly bonding in tile conformation are indispensable and must be designed to constitute DNA tiles. Conventional research SEQUIN considers only complementary sequences in designing sequences [4]. However, it is difficult to see that the tile is well generated because tile structure may not be stable thermodynamically.

In DNA computing, many base sequence design techniques for constituting a desired structure have been studied. An evaluation of a sequence by the temperature at which a double strand DNA molecular comes off to two single strand DNA moleculars (Melting temperature : Tm) or free energy (ΔG) calculated by the adjoining base is emphasized [5]. Despite that free energy can be used as a standard of the stability of hybridization, it has never been used for the sequence design of DNA tiles by the above evaluation methods.

We propose an evaluation method for the structure stability of DNA tiles, in which a thermodynamically stabilized tile structure can be designed by hybridization prediction based on free energy. This method is effective, especially, when more complicated nanostructures are required and two or more kinds of tiles are required.

2 Proposal method

We use free energy (ΔG) based on the Nearest Neighbor method [7] [8] for evaluation. Free energy changes with base sequences because it depends on secondary structure and hybridization strength between molecules. ΔG becomes lower as the structure (hybridization) is stabilized. Furthermore, ΔG generally becomes lower as the number of bonded base pairs increases in single strand DNA molecule and between two single strand DNA molecules.

ΔG when a single strand DNA has secondary structure is lower than when it does't have secondary structure. Moreover, if the number of base pairs is the same, ΔG becomes lower as the number of G and C base pairs increases because hybridization strength when G and C hybridize is stronger than when A and T hybridize.

We evaluate stability based on ΔG when single strand DNA molecules have secondary structure, when desired hybridizations react, and when undesired hybridizations react.

2.1 Points of evaluation

To produce a stable tile hybridized desirably and that doesn't hybridize undesirably, ΔG hybridized desirably is reduced, and ΔG hybridized undesirably is heightened.

The primary consideration in designing stabler tiles are the following two points.

1. The bond of the desirable complementary sequence is tight.
2. No sequence easily has secondary structure.

2.2 Evaluation items

Taking the above points into consideration, we propose evaluation items. The tile structure becomes more stable as the value of each item becomes larger.

(1) The sum of ΔG When each single strand DNA molecule has the stablest secondary structure

Hybridization between single strand DNA molecules may be obstructed by secondary structure. Because a sequence that has large ΔG cannot easily have secondary structure, necessary hybridization between molecules for tile construction reacts surely, and so tile can form efficiently.

(2) The sum of ΔG when two single strand DNA molecules mis − hybridize for tile comformation

Sequences that hybridize undesirably may become competition that obstructs necessary hybridization. Therefore, since hybridization undesirably must be unstable, ΔG has to be high.

(3) The sum of the absolute value of ΔG when two single strand DNA molecules hybridize desirably

Necessary hybridization must react more accurately and be tighter. ΔG has to be low. Because this item is the absolute value of ΔG, the ΔG becomes lower as the tile is more stable.

We need to find the sequence that increases the value of the above items heuristically or the design sequence by optimization.

3 Validity of evaluation items

In this section, we show that a tile designed by the proposed evaluation items is more stable than a conventional tile. We compared tiles generated randomly with conventional tiles by our evaluation items.

We used 4×4 DNA tiles as a subject of verification (Figure 2). This 4×4 DNA tile, which consists of one long sequence CORE, four short SHELLs and ARMs (Figure 3), needs the most sequences and is the most complicated of any DNA tiles. In addition, this tile creates a silver nanowire and arranges protein regularly [3].

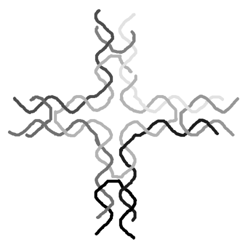

Figure 2: 4×4DNA tile

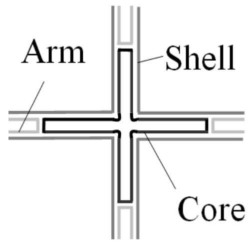

Figure 3: The kinds of sequene in 4×4 DNA tile

We generated 10,000 sets of tiles randomly and then evaluated them by the above evaluation items. At this time, complementary bases were arranged on a position that should be arranged as complementary bases for tile formation.

The length of the sequence was the same as the conventional tile (Yan et al [6]) and the GC% (the contents of G and C) was set to 55-65% (in conventional work, 59%) to compare with tiles made by conventional work SEQUIN.

3.1 Application to 4×4 DNA tiles

In 4×4 DNA tiles, the longest sequence CORE easily tends to have secondary structure. We examined a distribution of CORE's ΔG beforehand, when CORE had secondary structure. Then, we adopted CORE, which is in the lowest 10% of distribution when sequences are generated randomly.

Item 1: (I_1) is the sum of ΔG when nine single strand DNA molecules have the stablest secondary structure.

Item 2: (I_2) is the sum of ΔG of single strand DNA molecules that mis-hybridize with each other undesirably. We don't want to allow Core and Core (and Arm and Arm ,and Shell and Shell) to hybridize with each other. If this ΔG is low, undesirable hybridization reacts.

Item :3 (I_3) is the sum of ΔG of single strand DNA molecules that desirably hybridize with each other. In this case, sequences that hybridize with SHELL (a) are three sequences: (b), (c), and (d) (Figure 4). However, these three sequences have to hybridize to sequences except SHELL (a), that is , a duplication occurs. We divided SHELL (a) into four partitions and used the subsequences to avoid such duplication (Figure 5).

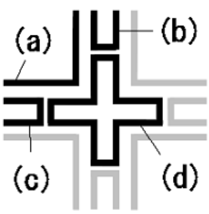

Figure 4: Before partition

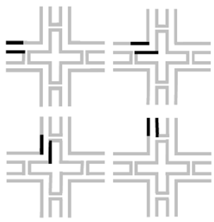

Figure 5: After partition

4 Results

The graph in Figure 6 illustrates the distribution of I_1 and the evaluation values of the conventional tile (Yan et al [6]). As the value of the graph becomes large, sequence doesn't easily have the secondary structure. We discovered sequences that make the value larger than the conventional sequence.

The graphs in Figures 7 and 8 show the distribution of I_2 and I_3. There are also more stable tiles than the conventional tile in each graph. In I_2, Yan's tile is in the top 2%, so we revealed that conventional work can design a sequence that doesn't hybridize undesirably. In I_3 we revealed that sequence design based on only complementary sequence improved hybridization strength.

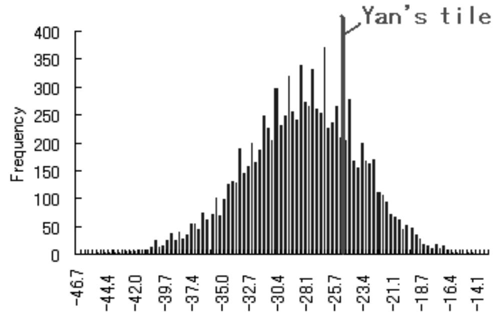

Figure 6: Distribution of I_1

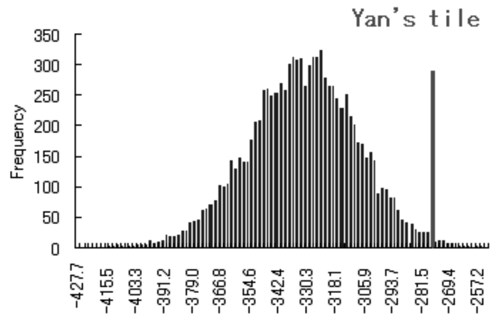

Figure 7: Distribution of I_2

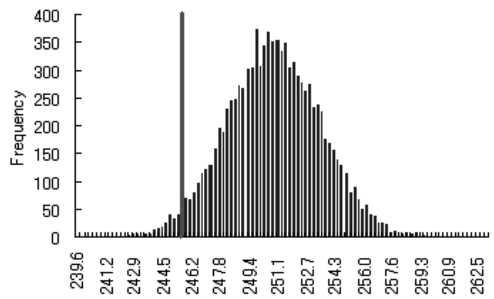

Figure 8: Distribution of I_3

The value of each item was uneven. Figure 9 shows an average of each evaluation value. The effect of I_2

inevitably, became stronger, in particular because calculation time to calculate the value of I_2 increased. Based on Figure 9, weight was adjusted as the absolute value of each item's average became equal. Figure 10 shows the sum of each item weighted by the above weight.

The results of our experiment show that we can design more stable tiles based on our three items. However, we can do so only if I_2 is taken into consideration. From this point we might proceed to examine the influence of each item with chemical experiments.

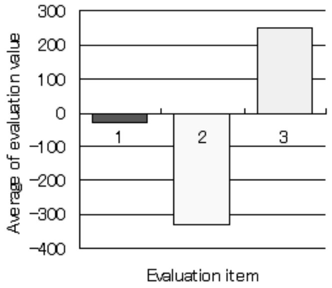

Figure 9: Average of evaluation items

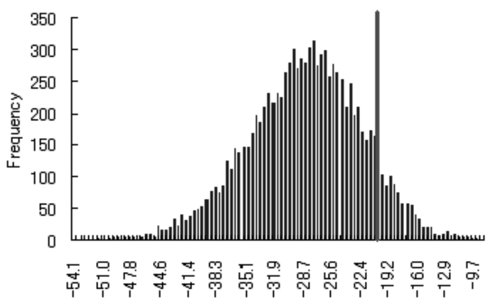

Figure 10: Distribution of the sum of evaluation items

5 Summary

We proposed a stability evaluation method for DNA tiles. Our method designed stabler sequences thermodynamically. We also investigated that a sequence designed by our method is expected to be more stable than the conventional tile.

We will design a tile sequence based on our method and actually validate that tiles will be constituted well by chemical experiments and visualized by atomic force microscopy (AFM).

References

[1] Erik Winfree, Furong Liu, Lisa A.Wenzler and Nadrian C.Seeman, "Design and self-assembly of two-dimensional DNA crystals", Nature, Vol.394, pp.539-544, 1998.

[2] Erik Winfree, "DNA Computing by Self-assembly", in NAE's The Bridge33(4):pp.31-38, 2003.

[3] Hao Yan, Sung Ha Park, Gleb Finkelstein, John H.Reif, Thomas H.LaBean, "DNA-Templated Self-Assembly of Protein Arrays and Highly Conductive Nanowires", Science, val.301, pp.1882-1884, 2003.

[4] Nadrian C.Seeman, "DeNovo Design of Sequence for Nucleic Acid Structural Engineering", Jornal of Biomolecular Strucure & Dynamics, ISSNO. 739-1102, Vol.8, 1990.

[5] Fumiaki Tanaka, Atsushi Kameda, Masahito Yamamoto, Azuma Ohuchi, "Design of nucleic acid sequence for DNA computing based on a thermodynamic approach", Nucleic Acids Research, val.33, pp.903-911, 2005.

[6] http://www.sciencemag.org/cgi/data/301/5641/1882/DC1/1

[7] A.M.Zuker, B.D.H.Mathews, C.D.H.Turner, "ALGORITHMS AND THERMODYNAMICS FOR RNA SECONDARY STRUCTURE PREDICTION: A PRACTICAL GUIDE", In RNA Biochemistry and Biotechnology, J. Barciszewski & B.F.C. Clark, eds., NATO ASI Series, Kluwer Academic Publishers, 1999

[8] Mirela Andronescu, Rosalia Aguirre-Hernandez, Anne Condon, Holger H.Hoos, "RNA soft:a suite of RNA secondary structure prediction and design software tools", Nucleic Acids Research, val.31, No.13, pp.3416-3422, 2003.

The Eleventh International Symposium on Artificial Life and Robotics 2006 (AROB 11th'06),
B-con Plaza, Beppu, Oita, Japan, January 23-25, 2006

Evolutionary emergence of the 16S /18S-ribosomal RNA from a poly-tRNA structure containing a "(5') $tRNA^{Gly}$-spacer-$tRNA^{Cys}$-spacer-$tRNA^{Leu}$ (3')" region.

Koji Ohnishi [1, 2,3] Shouken Hokari [2]

ohnishi@sc.niigata-u.ac.jp hokari_s@mail.goo.ne.jp

[1] Department of Biology, Faculty of Science, [2] Graduate School of Natural Sciences, and [3] Center for Interdisciplinary Research,

Niigata University, Ikarashi-2, Niigata, 950-2181, Japan

ABSTRACT: Small subunit (SSU- or 16S/18S-) rRNAs were found to have a base-sequence region homologous to the "(5') $tRNA^{Gly}$-spacer-$tRNA^{Cys}$-spacer-$tRNA^{Leu}$ (3')" region of the *Bacillus subtilis trnD* tRNA cluster and its homologue tRNA-clusters in other bascteria (such as the *E. coli trnGCL* tRNA cluster). Furthermore, the codon-interacting helix 28 region of the ribosomal A site in both *E. coli* and *Saccharomyces cervisiae* SSU-16S-/18S-) rRNAs were found to be homologous to tRNA (especially, $tRNA^{Gly}$) and proto-$tRNA^{Gly}$. These results strongly suggest that earliest peptide-making apparatus would have been a poly-tRNA ribozymic biomachine.

1. Introduction

The *trnD*-tRNA gene cluster of the *Bacillus subtilis trrnD* operon has been proposed to be a relic of an earliest peptide-synthesizing RNA biomachine for synthesizing a "*trnD*-peptide" (= "NSEVM DFTYWHQBCLL") whose amino acid (aa) sequence is in the order of aa specificities of the 16 tRNAs in the *trnD* tRNA gene cluster (Poly-tRNA theory, See [1] ~[4] for details.). In this paper, evolutionary origin of SSU-rRNA from poly-tRNA structure was analyzed based on sequence similarity analyses.

2. Homology between 16S rRNAs and (5') $tRNA^{Gly}$-spacer-$tRNA^{Cys}$-spacer-$tRNA^{Leu}$(3') region

The(5')$tRNA^{Gly}$-spacer-$tRNA^{Cys}$-spacer-$tRNA^{Leu}$ (3') region of the *trnD* tRNA cluster in the *trrnD* operon was aligned against the *trnGCL* tRNA cluster in *E. coli*,, which evidently shows strong homology with each other (Figure 1). Since the *trnGCL* cluster is widely distributed in eubacteria, this tri-tRNA region was shared by the latest primitive organism commonly ancestral to all of the living biotic phyla. On the other hand, the SSU- and LSU-rRNAs were analyzed by Harr-Plot similarity search, resulting in a finding that a most similar region between SSU/LSU rRNAs and the *B. subtilis trnD*-tRNA cluster (containing 16 tRNAs and spacers) was discovered to reflect

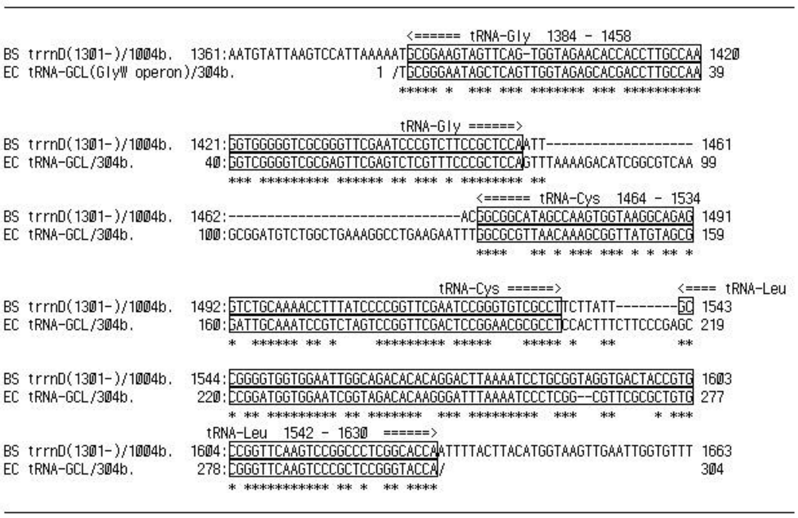

Figure 1. Alignment of $tRNA^{Gly}$-$tRNA^{Cys}$-tRN^{Leu} regions in *B. subtilis* (BS) *trnD* tRNA gene cluster (in *trrnD* operon from GenBank locus BACTGTRND) and the *E. coli* (EC) *trn*GCL tRNA gene cluster. Asterisks indicate base-matches.

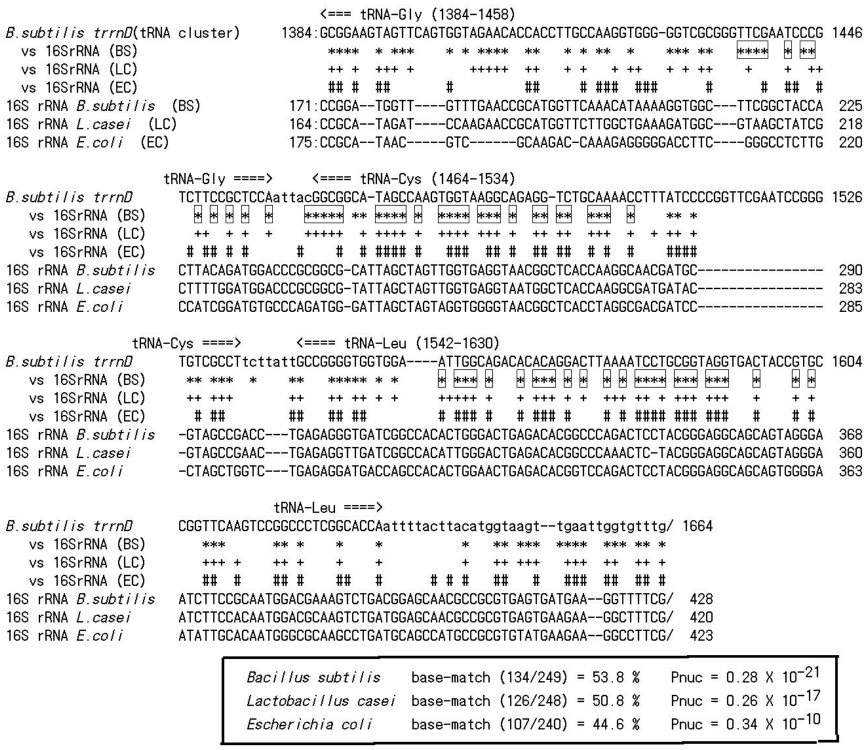

Figure 2. Alignment of $tRNA^{Gly}$-$tRNA^{Cys}$-tRN^{Leu} regions against eubacterial 16S rRNAs. Base-match levels are evaluated by $P_{nuc}(m,n)$ values (ref.[2]-[4]) shown in the box, meaning the probability that *m* or more base-matches occurs by chance in randomly selected *n*-base-long alignments. Data from BenBank.

significant homology between 16S-(SSU-)rRNA and the GCL tri-tRNA cluster region of the *trnD* tRNA-cluster. As shown in Figure 2 and Figure 3, the *B. subtils* tri-tRNA region shows a 53.8% (134/249) base-match and $P_{nuc}(134,249) = 0.28$ E-21 (See refs. [2]-[4] for the P_{nuc} value.). Thus the 16S-(and SSU-)rRNA region aligned against the tri-tRNA (Fig.2) is now concluded to have been derived from *trnGCL* tRNA cluster.

3. Origin of the codon-recognizing A-site helix 28 of the SSU-rRNA from tRNA

Helix 28 of the ribosomal A site is known to have critical role in recognizing codons in mRNA, and is a portion of the 3' minor domain of SSU-rRNA (ref. (5)). In the *E. coli* 16S rRNA, the helix 28 is constructed by base-pairing a sequence region, 921 /UGACGGGGGCCCCB/ 934 (over-lined in Figure 4), with another sequence region, 1384 /CGGGCCUUGUACA/ 1396.

The helix 28 and its vicinities in SSU-rRNAs were analyzed for finding sequence region(s) of rRNAs possibly homologous to some tRNA(s) or tRNA-clusters. Finally, the former region (E. coli 921-934) and its downstream region was found to show close sequence similarity to tRNA, as shown in Figure 4. An alignment of the bases 915-1001 of the *E. coli* 16S rRNA with the $tRNA^{Gly}$ region of the *E. coli trnGCL* tRNA cluster elucidated a 50.0 % base-match (= 41/82), and a base-matching probability by chance, $P_{nuc}(41,82) = 0.97$ E-6. A similar level of base-identity was also found between the *E. coli* 16S rRNA helix 28 region and the reconstructed proto-$tRNA^{Gly}$.(reconstruction in [4]). The corres-ponding helix 28-containing region of the *S. cervisiae* 18S rRNA is also aligned in Figure 4, together with the *trnGCL* homologue region of eubacterial 16S rRNAs found in Figure 2. These results strongly tell us a genuine homology of the helix 28 with tRNA from which the A site would have been derived.

4. References:

[1] Ohnishi K.(1993), Evolution from semi-tRNA to early protein-synthesizing RNA molecule. In: *Endocytobiology V* (Sato S. et al., eds), Tubingen Univ.Press. Tubingen, pp.407-414.

[2] Ohnishi K. et al.(2002a), *Viva Origino* 30: 63-78.(http://www.origin-life.gr.jp/3002/3002063/3002063.html)

[3] Ohnishi K. et al. (2002b), Origin of most primitive mRNAs and genetic codes via interactions between primitive tRNA ribozymes. *Genome Informatics* 13: 71-81 (http://www.jsbi.org/journal/GIW02/GIW02F008.html)

[4] Ohnishi,K., Ohshima,M., Furuichi,N.(2005), Evolution from possible primitive tRNA-viroids to early poly-tRNA-derived mRNAs. A new approach from the poly-tRNA theory, *Genome Informatics* 16(2): 94-103.

[5] Bulygin, K. et al. (2005) The first position of a codon placed in the A site of the human 80S ribosome contacts nucleotide C1696 of the 18S rRNA as well as positions S2, S3, S3a, S30, and S15. *Biochemistry* 44: 2153-2162.

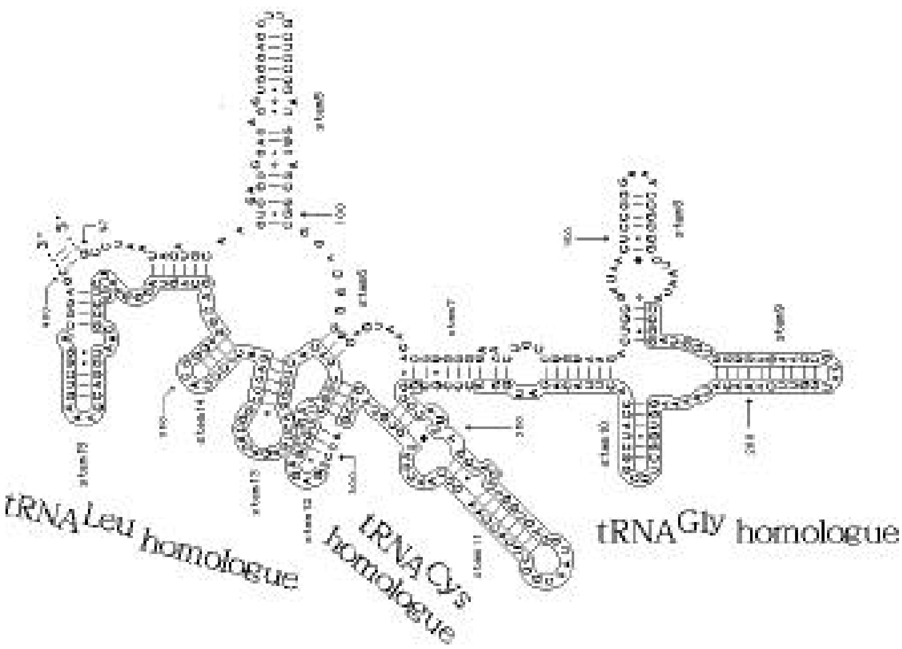

.

Figure 3. Homologue of the tRNA^{Gly}-tRNA^{Cys}-tRN^{Leu} region of the *B. subtilis trnD*-tRNA cluster in the secondary structure of the *E. coli* 16S rRNA. Based on the alignment in Figure 2.

```
18S rRNA helix 28
        (S. cerevisiae)    1134/AAAGGAATTGACGGAAGGGCACCACTAGGAGTGGAGCCTGCGGC-TAATTTGACTCAACA-CGGGGAAACTCACCAGG 1209
 vs E. coli helix 28 (|)        ||| ||||||||||  |  |  ||| || |||||||| |  ||  ||||| ||  ||||  ||  ||| || ||| ||
16S rRNA helix 28 (E.coli)  913/AAATGAATTGACGGGGGCCCGCACAAGCGGTGGAGCATGTGGTTTAATTCGATGCAACG-CGAAGAACCTTACCTGG  989
  vs proto-tRNA-Gly (+)         /+   + ++ +++  +     ++    ++++ +  ++++ ++ ++     + ++    + ++  +   +  + +  +
  vs EC trnGCL (=)              /===== == ====     = ==    === ===== =   ===     = =    = ==      =    == =
  vs B.s. trrnD (*)             /*  ** ** ***  *     **    *** ** ****    **     * **    * **  *   *  * *  *

                                       <==== tRNA-Gly
Proto-tRNA-Gly              -9 ttagcgaauG-CGGAAGUAGUUCAGUU=CGGUAGCUCAUGAGGGTTGCCAAGGUGGG-GGUCGCGGGUUCGAAUCCCG
                                       <==== tRNA-Gly
trnGCL, E. coli             -8 tgatgaa-tG-CGGGAATAGCTCAGTT=-GGTAGAGCACGACCTTTGCCAAGGTCGG-GGTCGCGAGTTCGAGTCTCG   65
B.subtilis trrnD(tRNA cluster)         <==== tRNA-Gly (1384-1458)
                          1376 ttaaaaa-tG-CGGAAGTAGTTCAGT==-GGTAGAACACCACC-TTGCCAAGGTGGG-GGTCGCGGGTTCGAATCCCG 1446
16S rRNA B.subtilis               171: T-CGGA--TGGTT-----=-GTTTGAACCGCATGGTT-CAAACATAAAAGGTGGC---TTCGGCTACCA  225
16S rRNA E.coli                   175: T-CGCA--T-AAC-----=-GTC------GCAAGAC--CAAAGAGGGGGACCTTC----GGGCCTCTTG  220
16S rRNA L.casei                  164: T-CGCA--TAGAT-----=-CCAAGAACCGCATGGTT-CTTGGCTGAAAGATGGC---GTAAGCTATCG  218
16S rRNA M.xanthus                167: T-CGGA--TAAGCCCAC==-GGTTTCTTCGGAGACTG-AGGGAAAAGGTGGCCTCTGTATTACAAGCTAT  228

18S rRNA (S. cerev.)  T-CCA-GACA-CAATAA(49gaps )GGATTGACA-GA-TTGAG/ 1239
 vs E. c. helix 28(|) | |   |||| | |              ||  || ||  ||||
16S rRNA helix 28(EC) T-CTT-GACAUCCACGG(49gaps )AAGTTTTCA-GAGATGAG/ 1020
vs proto-tRNA-Gly(+)  + +++     ++++/ (EC helix 28 vs proto-tRNA-Gly (-7 ~ +78): 42/84 = 50.0 %,Pnuc(42,84) = 0.72 x 10^-6
  vs EC trnGCL (=)    =  =      ====/ (EC helix 28 vs trnGCL(-6 ~ +77):  41/82 = 50.0 %, Pnuc(41,81) = 0.97 x 10^-6
  vs B.s. trrnD (*)      *   * **  */

Proto-tRNA            U-CUU-CCGCUCCA 78
                      tRNA-Gly ====>              <==== tRNA-Cys (1464-1534)
trnGCL, E. coli    66:T-TTC-CCGCTCCAGTT(49bases)TTGGCGCGT-TAACAAAGCGGTTATGTAGCGG-ATTGCAAATCCGTCTAGTCCGGTTCGACTCCGGA  194
                      tRNA-Gly ====>              <==== tRNA-Cys (1464-1534)
B.subtilis trrnD 1447 T-CTT-CCGCTCCAatt(49gaps )acGGCGGCA-TAGCCAAGTGGTAAGGCAGAGG-TCTGCAAAACCTTTATCCCCGGTTCGAATCCGGG 1526
16S rRNA B.subtilis   C-TTA-GAGATGGACCC(49gaps )GCGGCG-CATTAGCTAGTTGGTGAGGTAACGGCTCACCAAGGCAACGATGC---------------  290
16S rRNA E.coli      C-CAT-GGGATGTGCCC(49gaps )AGATGG-GATTAGCTAGTAGGTGGGGTAACGGCTCACCTAGGCGACGATCC---------------  285
16S rRNA L.casei      C-TTT-TGGATGGACCC(49gaps )GCGGCG-TATTAGCTAGTTGGTGAGGTAATGGCTCACCAAGGCGATGATAC---------------  283
16S rRNA M.xanthus    CACATTCAGATGAGTCC(49gaps )GCGGCC-CATCAGCTAGTTGGCGGGGTAATGGCCCACCAAGGCAACGACGG---------------  295
```

Figure 4.Alignment of the A site helices 28 of the *E. coli* 16S- and the *Saccharimyces cervisiae* 18S-rRNAs against the tRNA^{Gly}-tRNA^{Cys}- regions from eubacterial tRNA^{Gly}-tRNA^{Cys}-tRN^{Leu} regions. Base-matche levels are given in the Figure. See text for the overlined regions (helix 28) of SSU-rRNAs,

Stochastic Analysis of Schema Distribution in Multiplicative Landscape

Hiroshi Furutani, Susmu Katayama
Makoto Sakamoto
University of Miyazaki
Miyazaki City, 899-2192

Takao Ito
Ube National College of Technology
Ube City, 755-8555

Abstract

In this study, we investigated the influence of genetic drift on the performance of a GA on the multiplicative landscape. We performed the theoretical investigation of frequencies of the first order schemata, and calculated their changes in time by using the Wright-Fisher model. We showed that this mathematical theory reasonably predicts various quantities including the ultimate distribution of the first order schemata.

1 introduction

In this paper, we study the influence of finite population size on the performance of genetic algorithms (GAs). We focus on the effect of genetic drift by the random sampling in the selection process. When we apply a GA to a given problem, we choose the population size N intuitively. We do not have any applicable theory to guide the choice of N. If we choose a small N to reduce the cost of calculations, there appears the problem of genetic drift. The main part of the effect of genetic drift may disappear by averaging repeated trials. However there are several cases in which its effect remains finite even after averaging. An example of such cases is a GA on the multiplicative landscape. If one uses a small N, the risk of poor performance becomes high by the undesirable effect of genetic drift.

The theoretical analysis of GAs with finite N is far more complicated than the deterministic approach assuming infinitely many N. The most representative approach is Markov chain analysis of Nix and Vose [1]. The Nix and Vose Markov model includes selection, mutation and crossover and can calculate the exact transition matrix. However, it is in general difficult to obtain an analytical expression of Markov process in closed form. Furthermore the dimension of the transition matrix increases exponentially with string length ℓ and population size N. This makes numerical simulations impossible for realistic values of ℓ and N.

In population genetics, researchers also encountered this type of difficulties in treating the evolution of a finite population by Markov chain model [2]. One of the approaches to avoid this problem is to restrict the search space within the first order schemata [3]. We apply this approach to the present problem, and consider the evolution of first order schemata in the GA on the multiplicative landscape with the finite population size.

2 Mathematical Model

We consider the processes of selection, mutation and crossover, and investigate the influence of the population size N. We use the fitness proportionate selection and uniform crossover. The population evolves in discrete and non-overlapping generations.

Individuals are represented by binary strings of the fixed length ℓ. The number of genotypes is $n = 2^\ell$, and the ith genotype is identified with the integer i. We use the representation $i =< i(\ell), \cdots, i(1) >$.

The population size N is fixed, and $N = \sum_{i=0}^{n-1} N_i(t)$. Here $N_i(t)$ is the frequency of the ith genotype at generation t. The relative frequency $x_i(t)$ is $x_i(t) = N_i(t)/N$.

The average fitness of the population $\bar{f}(t)$ is

$$\bar{f}(t) \equiv \sum_{j=0}^{n-1} f_j \, x_j(t), \qquad (1)$$

where f_i is a fitness of the ith genotype. We use the fitness function of multiplicative form

$$f_i = \prod_{k=1}^{\ell} (\, 1 \,+\, i(k)\, s\,), \quad (s \geq 0). \qquad (2)$$

Here the parameter s represents selection strength.

2.1 Deterministic Equations

The deterministic equations for selection and mutation are described here. For proportionate selection, the relative frequency at the next time step $x_i(t+1)$ is given by

$$x_i(t+1) = \frac{f_i}{\bar{f}(t)} x_i(t) \quad (i = 0, \ldots, n-1), \qquad (3)$$

To show equation (3) is under the action of selection, we use the notation

$$\widehat{S} x_i(t) \;=\; \frac{f_i}{\bar{f}(t)} x_i(t),$$

where $\widehat{S} x_i$ means the frequency x_i after selection.

2.2 Schema Theorem

A schema $\mathcal{H}$ is the set of all strings with certain defining values at fixed positions. It is represented by three types symbols, 0,1 and $*$ [4]. The bits 0 and 1 are defining bits, and $*$ is a wild card. The order of schema $\mathcal{O}(\mathcal{H})$ is the number of defining bits.

We also use the notation showing explicitly the order of schema, the positions of defining bits, and their binary values, $\mathcal{H} = \mathcal{H}^{(k)}[i(b_1), \ldots, i(b_k)]$. Here, $k = \mathcal{O}(\mathcal{H})$, and $b_1 < \ldots < b_k$ are positions of defining bits. In the similar manner, we use the notation for the relative frequency $h(\mathcal{H})$,

$$h(\mathcal{H}) = h^{(k)}[i(b_1), \ldots, i(b_k)].$$

We will use a shorthand notation

$$h^{(1)}[i(k) = 1] \rightarrow h[1_k], \quad h^{(1)}[i(k) = 0] \rightarrow h[0_k].$$

In this analysis, the notion of linkage is very important, and the second order linkage disequilibrium coefficient D is defined as [5]

$$D[k, m] = h^{(2)}[i(k) = 1, i(m) = 1] - h[1_k] h[1_m]. \quad (4)$$

When each gene evolves independently, a population is in linkage equilibrium, while if there are any correlations among genes at different loci, it is in linkage disequilibrium. When the population is in linkage equilibrium, all D coefficients are zero, $D[k, m] = 0$. In this state, the frequency of genotypes i is given in terms of the first order schema frequencies

$$x_i \;=\; \prod_{k=1}^{\ell} h[i(k)]. \qquad (5)$$

3 Deterministic Model

We consider the evolution of the GA on the multiplicative landscape in the deterministic model[6].

3.1 Multiplicative Landscape

It is natural to assume that the population is in linkage equilibrium at $t = 0$, and the deterministic theory predicts that the population is in linkage equilibrium at all generations under the action of selection and crossover. Using equation (5), we have the average fitness in the product form

$$\bar{f}(t) = \prod_{k=1}^{\ell} \{h[0_k] + (1+s) h[1_k]\} = \prod_{k=1}^{\ell} (1 + s\, h[1_k]). \quad (6)$$

Then we may define the fitness function of the first order schemata

$$g_k = 1 + s\, h[1_k]. \qquad (7)$$

To show the assumption of linkage equilibrium explicitly, we give

$$\bar{f}^{(\mathrm{eq})} \;=\; \prod_{k=1}^{\ell} g_k.$$

The Walsh transform of the fitness function is obtained as

$$\tilde{f}_i = \prod_{k=1}^{\ell} \{1 + (-1)^{i(k)} (1+s)\} \qquad (8)$$

Under the assumption of linkage equilibrium, we can obtain the schema equation of the first order schemata for selection. The evolution equation of $h[1_k]$ is

$$\widehat{S}\, h[1_k](t) \;=\; \frac{(1-s)\, h[1_k](t)}{h[0_k](t) + (1-s) h[1_k](t)}. \qquad (9)$$

If mutation is included in the GA, the evolution equation is

$$h[1_k](t+1) = (1-\mu) h[1_k](t) + \mu h[0_k](t),$$

with mutation rate μ, and $h[0_k] = 1 - h[1_k]$.

4 Stochastic Models

We review here the Wright-Fisher model for the evolution of a haploid population whose size remains constant at N. The number of the first genotype N_0 takes the values of $\{0, 1, \ldots, N\}$, and that of the second genotype is given by $N_1 = N - N_0$.

We consider the selection process of random sampling. Let us assume there are $N_1(t) = i$ copies of the first genotype at the current generation. If we randomly choose the offspring from the population, the probability $P(j|i)$ of $N_1(t+1)$ taking the value of j from the possible values of $\{0,\ldots,N\}$ is given by the binomial distribution,

$$P(j|i) = \binom{N}{j}\left(\frac{i}{N}\right)^j\left(1-\frac{i}{N}\right)^{N-j}. \qquad (10)$$

The probability $P(j|i)$ specifies the process of random sampling, and the future behavior of the process only depends on its current frequencies. Thus this process is a Markov chain. The states $i = 0$ and $i = N$ are absorbing states, and other states are transient states. If the process enters either of the absorbing states, it will stay there forever. The state $i = N$ means the allele 1 is fixed while the allele 0 is lost in the population.

Let $q_i(t)$ be the probability that the population is in $N_1 = i$ at t, with the condition $\sum_{i=0}^{N} q_i(t) = 1$. The process is described by

$$q_j(t+1) = \sum_{i=0}^{N} P(j|i)\, q_i(t). \qquad (11)$$

The generalization of the Wright-Fisher model to the alleles with different fitness values is straightforward. We define the fitness values as

$$f_i = \begin{cases} 1 & (i=0) \\ 1+s & (i=1). \end{cases}$$

We assume $s \geq 0$, and $i = 1$ is the favorable allele. The transition probability is given by

$$\begin{aligned} P(j|i) &= \binom{N}{j} b^j (1-b)^{N-j}, \qquad (12) \\ b &= \frac{(1+s)i}{(1+s)i+N-i}. \end{aligned}$$

It is to be noted that both $N_1 = 0$ and $N_1 = N$ are also absorbing states, and there is a finite risk of the loss of favorable allele 1.

If mutation is included, we modify this equation by the analogy

$$\begin{aligned} P(j|i) &= \binom{N}{j} c^j (1-c)^{N-j}, \qquad (13) \\ c &= (1-\mu)b + \mu(1-b) \\ b &= \frac{(1+s)i}{(1+s)i+N-i}. \end{aligned}$$

5 Numerical Results

We carried out GA calculations on the multiplicative landscape with the fitness proportionate selection.

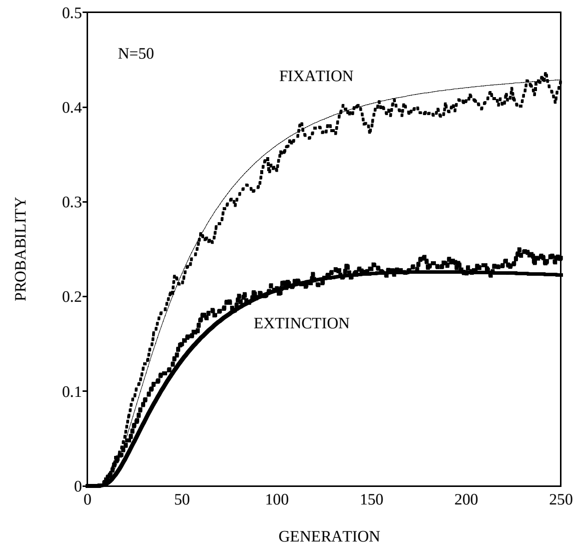

Figure 1: Fixation and extinction Probabilities of the favorable schema. $N = 50$.

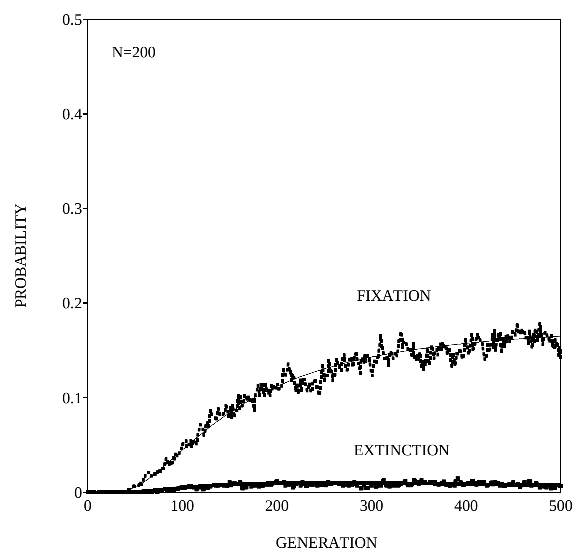

Figure 2: Fixation and extinction Probabilities of the favorable schema.$N = 200$.

The crossover was included by uniform crossover with the crossover rates $\chi = 1$, and mutation rate was $\mu = 0.001$. The string length was $\ell = 8$. The calculations were performed repeatedly, and results were averaged over 1000 runs.

Figures 1 and 2 also show the fixation and extinction probabilities of the first order schema $h[1_k]$ with $N = 50$ and $N = 200$, respectively. In the result of $N = 50$, the figure tells that about 20% of the favorable schema is lost On the other hand, with the larger population size of $N = 200$, the extinction probability is very small, meaning the effect of genetic drift is very weak.

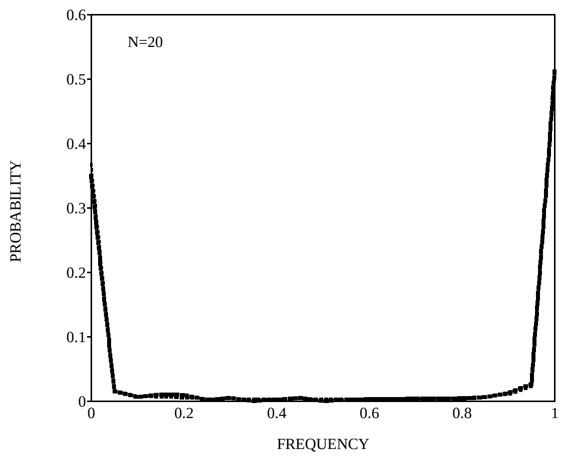

Figure 3: Ultimate distribution of the favorable schema. $N = 20$. Abscissa is the relative frequency of the first order schema $h[1_k]$.

Figures 3 and 4 show the ultimate distributions of the first order schema $h[1_k]$ at $t = 500$ for $N = 20$ and 200. These figures suggest that the genetic drift causes a force to push members of the population to undesirable direction. We also note that the predictions of Wright-Fisher model reproduce the numerical results very well.

6 Summary

We studied the evolution of the GA on the multiplicative landscape by investigating the influence of genetic drift. Within the framework of the infinite population model, the assumption of linkage equilibrium holds at all generations if the initial state is at linkage equilibrium. Therefore, the system is completely determined by the first order schema frequencies $h[1_k]$.

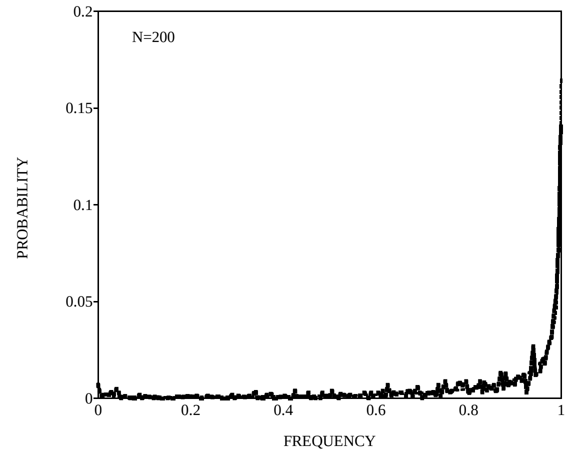

Figure 4: Ultimate distribution of the favorable schema. $N = 200$.

In the GA calculation with crossover, the evolution of the first order schema $h[1_k]$ is well reproduced by the stochastic model. The genetic drift gives undesirable effect on it when N is small. The analysis of the first order schema shows that this problem is caused by the extinction of the favorable schema. .

References

[1] Nix, A. E., Vose, M. D.: Modelling Genetic Algorithm with Markov Chains. Annals of Mathematical and Artificial Intelligence. **5** (1992) 79–88

[2] Ewens, J.W. J.: Mathematical Population Genetics. I. Theoretical Introduction, Second Edition. Springer-Verlag, New York (2004)

[3] Asoh, H., Mühlenbein, H.: On the Mean Convergence Time of Evolutionary Algorithms without Selection and Mutation. Parallel Problem Solving from Nature, Lecture Notes in Computer Science, **866**, Springer-Verlag, New York, (1994) 88-97

[4] C. R. Stephens and H. Waelbroeck, *Evolutionary Computation*, **7**, 109 (1999).

[5] H. Furutani, in *Foundations of Genetic Algorithms* 7, (Morgan Kaufmann, San Francisco, 2003), p.9.

[6] H. Furutani, *Proceedings of the Simulated Evolution and Learning Conference, SEAL'02*, 230 (2002).

The Eleventh International Symposium on Artificial Life and Robotics 2006 (AROB 11th'06),
B-con Plaza, Beppu, Oita, Japan, January 23-25, 2006

Integrated multimedia understanding based on ental Image Directed Semantic Theory

Masao Yokota
Fukuoka Institute of Technology
yokota@fit.ac.jp

Genci Capi
Fukuoka Institute of Technology
capi@fit.ac.jp

Abstract

The authors have proposed the Mental Image Directed Semantic Theory (MIDST) and have been developing the integrated multimedia understanding system IMAGES-M as robotic intelligence. This paper focuses on the semantic processing of sensory and motory data in IMAGES-M, simulating the interactions between robots and their environments including humans.

1. Introduction

Recently, there have been developed various kinds of robots intended for practical use. We assume that robots suitable for collaboration with humans should be equipped with good capabilities for

(C1) understanding of real environments, and

(C2) communication with ordinary people.

More concretely, these robots can recognize well their environments by their miscellaneous sensory organs to act appropriately by their miscellaneous actuators, and avail themselves of miscellaneous kinds of communication media such as natural language, body language, map, etc.

For such a purpose above, we think it is most essential to develop a formal language for representing and computing semantic contents conveyed by various information media such as text, picture, sensory and motory data, etc. This kind of formal language should have at least a descriptive power for spatio-temporal events that people or robots perceive in the real world.

Yokota, M. ([1], [2]) has proposed a semantic theory for natural languages so called Mental Image Directed Semantic Theory (MIDST)'. In the MIDST, word concepts are associated with omnisensual mental images of the external or physical world and are formalized in an intermediate language $\boldsymbol{L_{md}}$, based on first-order predicate logic while the other knowledge description schema such as [3], [4] are too linguistic (or English-like) to formalize omnisensual mental images.

The $\boldsymbol{L_{md}}$ is employed for many-sorted predicate logic and has been implemented on several types of computerized intelligent systems [1], [5]. There is a feedback loop between them for their mutual refinement unlike other similar theories [6], [7].

In this paper we focus on the semantic processing of sensory and motory data represented in the formal language $\boldsymbol{L_{md}}$, simulating the interactions between robots and their environments including humans.

2. rief sketch of $\boldsymbol{L_{md}}$

The MIDST has modeled mental images as "Loci in Attribute spaces" [1], [2]. An attribute space corresponds with a certain measuring instrument just like a barometer, a map measurer or so and the loci represent the movements of its indicator.

A general locus is to be articulated by "Atomic locus" formalized as the expression (1) in first-order logic, where "L" is a predicate constant.

$$L\ x,y,p,\ \ ,a,g, \qquad (1)$$

The expression (1) is called "Atomic locus formula" whose arguments are referred to as Event Causer', Attribute Carrier', Initial Attribute Value', Final Attribute Value', Attribute Kind', Event Kind' and Standard Attribute Value', respectively.

The interpretation of (1) is as follows, where "matter" means "object " or "event".

"Matter 'x' causes Attribute 'a' of Matter 'y' to keep (p=q) or change (p ≠ q) its values temporally (g=Gt) or spatially (g =Gs) over a time-interval, where the values 'p' and 'q' are relative to the standard 'k'."

When g=Gt and g=Gs, the locus indicates monotonous change or constancy of the attribute in time domain and in space domain, respectively. The former is called temporal event' and the latter, spatial event'.

For example, the motion of the bus' represented by S1 is a temporal event and the ranging or extension of the road' by S2 is a spatial event whose meanings or concepts are formalized as expressions (2) and (3), respectively, where the attribute is "physical location" denoted as .
We think that the verb run' used in S2 must reflect the motion of the observer's attention [2].

(S1) The bus runs from Tokyo to Osaka.

$$\exists x,y,\ \ L\ x,y,To\ yo,\ \ sa\ a,\ \ \ ,\ t,\ \wedge\ us\ y \qquad (2)$$

(S2) The road runs from Tokyo to Osaka.

$$\exists x,y,\ \ L\ x,y,To\ yo,\ \ sa\ a,\ \ \ ,\ s,\ \wedge road\ y \qquad (3)$$

The expression (4) is the conceptual description of the English word "fetch", implying such a temporal event that x1' goes for x2' and then comes back with it, where Π' and •' are instances of the tempo-logical connectives, SAND' and CAND', standing for "Simultaneous AND" and "Consecutive AND", respectively.

In general, a series of atomic locus formulas with such connectives is called simply Locus formula'.

$$\exists x\ ,x\ ,p\ ,p\ ,\quad L\ x\ ,x\ ,p\ ,p\ ,\quad ,\ t,$$
$$\bullet\ L\ x\ ,x\ ,p\ ,p\ ,\quad ,\ t,\ \ \Pi L\ x\ ,x\ ,p\ ,p\ ,\quad ,\ t,$$
$$\wedge x\ \neq x\ \ \wedge p\ \neq p \tag{4}$$

In order for complete representation of temporal relations, we have introduced a concept called Empty Event (EE)' and symbolized as ε' which stands exclusively for time elapsing. For example, (5) represents $_1$ during $_2$'.

$$(\varepsilon_1 \bullet\ _1 \bullet \varepsilon_2)\ \Pi\ \ _2 \tag{5}$$

The image model presented here is also valid for formalizing word concepts (i.e. coding) of actions because any action must be measured with sensors for its formalization. That is, ***grounding words on actions is equivalent to grounding words on sensations of actions***

Sensors and actuators are assumed to collaborate very closely in feedback or feed-forward ways in cybernetics and there is a hypothesis that some kinds of sensations (or perceptions) and actions are encoded in the same way in organisms [12]. If not, real-time coordination of multiple sensors and actuators would be impossible. Mimicking' may be a good support for this hypothesis.

3. Systematic computation of L_{md}

The integrated multimedia understanding system IMAGES-M works as the main intelligence of a robot, employing locus formulas as intermediate conceptual representations through which it can integrally understand and generate sensory data, speech, visual image, text, and motory data.

IMAGES-M is one kind of expert system equipped with five kinds of user interfaces for multimedia communication, that is, Sensor Data Processing Unit (SDPU), Speech Processing Unit (SPU), Image Processing Unit (IPU), Text Processing Unit (TPU), and Action Data Processing Unit (ADPU) besides Inference Engine (IE) and Knowledge Base (KB). Each processing unit in collaboration with IE performs mutual conversion between each type of information medium and locus formulas.

The fundamental computations on L_{md} by IMAGES-M are to detect semantic anomalies, ambiguities and paraphrase relations. These are performed as inferential operations on locus formulas at IE.

Detection of semantic anomalies is very important to avoid succession of meaningless computations or actions. For an extreme example, consider such a report from certain sensors as (6) represented in L_{md}, where A29' is the attribute taste'. This locus formula can be translated into the English sentence S3 by TPU, but it is semantically anomalous because a desk' has ordinarily no taste.

$$\exists x\ L\ \ ,x,S\ \ eet,S\ \ eet,\quad ,\ t,\ \ \wedge des\ \ x \tag{6}$$

(S3) The desk is sweet.

These kinds of semantic anomalies can be detected in the following processes.

Firstly, assume the postulate (7) as the commonsense or default knowledge of "desk", stored in KB, where A39' refers to the attribute vitality', and the special symbols ' and /' are defined as (8) and (9) representing always' and no value', respectively.

$$\lambda x\ \ des\ \ x\ \Leftrightarrow \lambda x\quad L\quad ,x,\ ,\ ,\quad ,\ t,$$
$$\wedge\quad \wedge L\quad ,x,\ ,\ ,\quad ,\ t,\quad \wedge \tag{7}$$
$$\Leftrightarrow\ \forall p,\quad \Pi\ \varepsilon\ p, \tag{8}$$
$$L\quad ,\ ,\quad \Leftrightarrow\ \ \exists p\ \ L\quad ,p, \tag{9}$$

Secondly, the postulates expressed by (10) and (11) in KB are utilized. The formula (10) means that ***<u>if one of two loci exists every time interval, then they can coexist</u>***. The formula (11) states that ***<u>a matter has never different values of an attribute at a time</u>***.

$$\wedge\quad \supset.\quad \Pi \tag{10}$$
$$L\ x,y,p,\ \ ,a,g,\quad \Pi L\ \ ,y,r,s,a,g,\quad \supset.\ p\ \ r \wedge\quad s \tag{11}$$

Lastly, IE detects the semantic anomaly of "sweet desk" by using (7)-(11). That is, the formula (12) below is finally deduced from (7)-(11), which violates the postulate (16), that is, " $S\ \ eet \neq /$ ".

$$L\quad ,x,S\ \ eet,S\ \ eet,\quad ,\ t,\quad \Pi L\ \ ,x,\ ,\ ,\quad ,\ t, \tag{12}$$

These processes above are also employed for dissolving syntactic ambiguities in people's utterances such as S4. IE rejects sweet desk' and eventually adopts sweet coffee' as a plausible interpretation.

(S4) Bring me the coffee on the desk,
which is very sweet.

If multiple plausible interpretations of a text or another type of information are represented in different locus formulas, it is semantically ambiguous. In such a case, IMAGES-M will ask for further information in order for disambiguation.

Furthermore, if two different representations are interpreted into the same locus formula, they are paraphrases of each other. The detection of paraphrase relations is very useful for deleting redundant information, for cross-media translation, etc. [8].

4. Interaction between a robot and its world

A robot is to solve some kinds of problems in its world. Such problems can be classified roughly into two categories as follows.

(CP) Creation Problem:
e.g.) house building, food cooking, etc.

and

(MP) Maintenance Problem:

e.g.) fire extinguishing, room cleaning, etc.

In general, an MP is relatively simple one that the robot can find and solve autonomously while a CP is relatively difficult one that is given to the robot, possibly, by humans and to be solved in cooperation with them.

4.1 Definition of a problem and a job for a robot

A robot must determine its job to solve a problem in the world. In general, the robot needs to interpolate some transit event $_T$ between the two events, namely, Current Event ($_C$)' and Goal Event ( )' as shown by (13).

$$_C\bullet\ _T\bullet \qquad (13)$$

According to this formalization, a problem $_P$ is defined as $_T\bullet$ and a job for the robot is defined as its realization.

The events in the world are described as loci in certain attribute spaces and a problem is to be detected by the unit of atomic locus by the inference employing such a postulate as (14) implying Continuity in attribute values'. Therefore, the problem $_P$ in (15) is to be inferred as (16).

L x,y,p ,p ,a,g, $\bullet$*L ,y,p ,p ,a,g, .⊃. p p* (14)

L x,y,p ,p ,a,g, $\bullet\ _P\bullet$ *L ,y,p ,p ,a,g,* (15)

L ,y,p ,p ,a,g, $\bullet$ *L ,y,p ,p ,a,g,* (16)

4.2 CP finding and solving

Consider a verbal command such as S5 uttered by a human. Its interpretation is given by (17) as the goal event . If the current event $_C$ is given by (18), then (19) with the transit event $_T$ underlined can be inferred as the problem corresponding to S5.

(S5) Keep the temperature of room C9' at 20.

L ,C , , , , t, $\wedge$ *room C* $\wedge$ *actor* (17)

L x,C ,p,p, , t, $\wedge$ *room C* (18)

<u>*L ,C ,p, , , t,*</u> $\bullet$ *L ,C , , , , t,*
$\wedge$ *room C* $\wedge$ *actor* (19)

For this problem, the robot is to execute a job deploying a certain thermometer and actors z1' and z'. The selection of the actor z1' is performed as follows:

If -p t en is a cooler, ot er ise
if -p t en is a eater, ot er ise
-p and no actor is deployed as .

The selection of z' is a job in case of MP described in the next section.

4.3 P finding and solving

In general, the goal event for an MP is that for another CP such as S5 given possibly by humans and solved by the robot in advance. That is, the job in this case is to autonomously restore the goal event created in advance to the current event $_C$ as shown in (20), where the transit event $_T$ is the reversal of such $-_T$ that has been already detected as abnormal' by the robot.

For example, if is given by (17) in advance, $_T$ is also represented as the underlined part of (19) while $-_T$ as (21). Therefore the job here is quite the same that was described in the previous section.

$$\bullet\ -_T\bullet\ _C\bullet\ _T\bullet \qquad (20)$$

L ,C , ,p, , t, $\wedge$ *room C* $\wedge$ *actor* (21)

5. Application to robot manipulation

The intelligent system IMAGES-M, still under development, is intended to facilitate integrated multimedia information understanding, including cross-media operations. At present, IMAGES-M, installed on a personal computer, can deploy SONY AIBOs, dog-shaped robots, as actors and gather information about the physical world through their microphones, cameras and tactile sensors. Communications between IMAGES-M and humans are performed though the keyboard, mouse, microphone and multicolor TV monitor of the personal computer.

Consider such a verbal command as S6 uttered to the robot, SONY AIBO, named John'.

(S6) John, walk forward and wave your left hand.

Firstly, late in the process of cross-media translation from text to AIBO's action, this command is to be interpreted into (22) with the attribute shape ( )' and the values *Wal f-* ' and so on at the standard of *I* ', reading that John makes himself walk forward and wave his left hand. Each action in AIBOs is defined as an ordered set of shapes (i.e., time-sequenced snapshots of the action) corresponding uniquely with the positions of their actuators determined by the rotations of the joints. For example, the actions walking forward (***Wal f***)' and waving left hand (***Wa el***)' are defined as (23) and (24), respectively.

L Jo n,Jo n,Wal f- ,Wal f-m, , t, I $\wedge$
L Jo n,Jo n,Wa el - ,Wa el -n, , t, I (22)

Wal f *Wal f- , Wal f- , ,Wal f-m* (23)

Wa el *Wa el - , Wa el - , , Wa el -n* (24)

Secondly, an AIBO cannot perform the two events (i.e., actions) simultaneously and therefore the transit event between them is to be inferred as the underlined part of (25) which is the goal event here.

L Jo n,Jo n,Wal f- ,Wal f-m, , t, I
$\bullet$<u>*L Jo n,Jo n,Wal f-m,Wa el - , , t, I*</u> $\bullet$
L Jo n,Jo n,Wa el - ,Wa el -n, , t, I (25)

Thirdly, (26) is to be inferred, where the transit event, underlined, is interpolated between the current event and the goal event (=(25)).

L Jo n,Jo n,p ,p , , t, I
<u>$\bullet$*L Jo n,Jo n,p ,Wal f- , , t, I*</u> $\bullet$ (26)

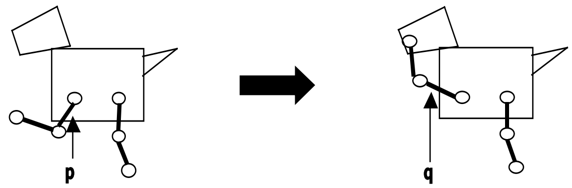

Fig.1. Actions as temporal changes in angularities of the joints in an AIBO (Sony)

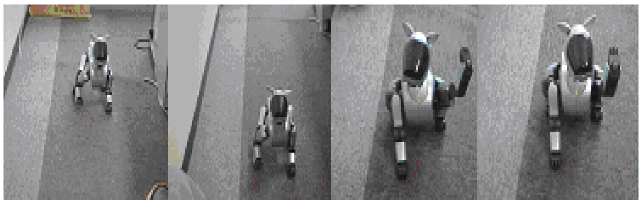

Fig.2. AIBO behaving in accordance to the command Walk forward and wave your left hand'

Finally, (26) is interpreted into a series of the joint angles in the AIBO as indicated by the values p' and q' of Angularity (A45)' in Fig.1 and it acts as shown in Fig.2.

. Discussions and conclusions

The authors formalized the performances of a robot in L_{md} and applied it to robot manipulation by text as a simulation of robot-world interaction. This is one kind of cross-media operation via locus formulas as already reported [8], [11]. At our best knowledge, there is no other system that can perform cross-media operations in such a seamless way as ours, which leads to the conclusion that employment of atomic locus formulas has made the logical expressions of event concepts remarkably computable and has proved to be very adequate to systematize cross-media operations. This is due to their medium-freeness and good correspondence with the performances of miscellaneous devices, which in turn implies that locus formula representation may make it easier for the devices to share a task than macro-command representation.

From the simulation results, we conclude that L_{md} can be a universal language for robots. Our future work will include establishment of learning facilities for automatic acquisition of word concepts from sensory data and human-robot communication by natural language under real environments.

Acknowledgements

This work was partially funded by the Grants from Computer Science Laboratory, Fukuoka Institute of Technology and Ministry of Education, Culture, Sports, Science and Technology, Japanese Government, numbered 14580436 and 17500132.

References

[1] M.Yokota: "An approach to natural language understanding based on a mental image model," Proc. of the 2nd International Workshop on Natural Language Understanding and Cognitive Science, pp.22-31, 2005.

[2] M. Yokota, et al: "Mental-image directed semantic theory and its application to natural language understanding systems", Proc. of NLPRS'91, pp.280-287, 1991.

[3] J.F. Sowa: Knowledge Representation: Logical, Philosophical, and Computational Foundations, Brooks Cole Publishing Co., Pacific Grove, CA, 2000.

[4] G.P. arri: "NKRL, a Knowledge Representation Tool for Encoding the Meaning' of Complex Narrative Texts", Natural Language Engineering - Special Issue on Knowledge Representation for Natural Language Processing in Implemented Systems, 3,pp.231-253, 1997.

[5] S.Oda, M.Oda M.Yokota : "Conceptual Analysis Description of Words for Color and Lightness for Grounding them on Sensory Data", Trans.of JSAI,16-5-E,pp.436-444, 2001.

[6] R.W. Langacker : Concept, Image and Symbol, Mouton de Gruyter, Berlin/New York, 1991.

[7] G.A. Miller P.N.: Johnson-Laird : Language and Perception, Harvard University Press, 1976.

[8] M.Yokota G.Capi: "Cross-media Operations between Text and Picture Based on Mental Image Directed Semantic Theory," WSEAS Transactions on Information Science and Applications, 10-2, pp.1541-1550, 2005.

[9] M.Amano, et al : "Linguistic Interpretation of Human Motion Based on Mental Image Directed Semantic Theory," Proc. of IEEE AINA2005, pp.139-144, Taipei , 2005.

[10] M.Amano, et al : "Cross-media Translation between Human Motions and Texts Based on Mental Image Directed Semantic Theory," Proc. of IEEE ICDCSworkshop2005, pp.707-713, Ohio, 2005

[11] M.Yokota G.Capi: "Integrated Multimedia Understanding for Ubiquitous Intelligence Based on Mental Image Directed Semantic Theory," IFIP EUC'05 UISW2005, Nagasaki, 2005 (*to e presented*).

[12] W. Prinz : "A common coding approach to perception and action", In *Relations ips et een perception and action* (Neumann, O. and Prinz, W. eds.), pp.167-201, Springer-Verlag, 1990.

The Eleventh International Symposium on Artificial Life and Robotics 2006 (AROB 11th'06),
B-con Plaza, Beppu, Oita, Japan, January 23-25, 2006

Associative Learning Method in Hyper-Column Model

Atsushi Shimada
Department of Intelligent Systems
Kyushu University
6-1 Kasuga-koen Kasuga Fukuoka 816-8580

Naoyuki Tsuruta
Department of Electronics Engineering
and Computer Science
Fukuoka University
8-19-1, Nanakuma, Johnan, Fukuoka 814-0180

Rin-ichiro Taniguchi
Department of Intelligent Systems
Kyushu University
6-1 Kasuga-koen Kasuga Fukuoka 816-8580
8-19-1, Nanakuma, Johnan, Fukuoka 814-0180

Abstract

In this paper, we propose an associative learning method in Hyper-Column Model (HCM). HCM is a model to recognize images, and consists of Hierarchical Self-Organizing Maps (HSOM) and Neocognitron (NC). HCM complements disadvantages of HSOM and NC, and inherits advantages from them. There is a problem, however, that HCM does not suit general image recognition in HCM since its learning method is an unsupervised one with competitive learning which is used by Self-Organizing Map (SOM). Therefore, we extended HCM to a supervised learnable model with an associative learning of SOM. We have found that an ability of HCM with the associative learning is superior to the one with unsupervised learning.

1 Introduction

Recently, applications of Artificial Neural Networks (ANNs) have expanded into general image recognition such as face recognition and visual surveillance. In these applications, there are three problems.

1. In spite of the high dimension of the input images, the regions of object parts occupy small areas of the whole space. Therefore, it is necessary to reduce the dimension to eliminate the redundancy and to allow the network to learn according to the region actually expanding the object.

2. The absolute dimensionality of the image region is very large even if the redundancy is eliminated, since images have large variations as a function of object locale, illuminant, and so on. Therefore, techniques to reduce the system size to a realizable scale are necessary.

3. In such cases, ANNs need a very large number of neurons. Therefore, learning methods which depend on the initial states of the connection weights cannot perform well, even if a network model such as the multilayered perceptron is theoretically very powerful. Thus, learning methods whose performance does not depend on the initial states of connection weights are needed.

Tsuruta proposed Hyper-Column Model (HCM)[1] which is a new image recognition model combining Hierarchical Self-Organizing Map (HSOM)[2] and Neocognitron (NC)[3]. The learning method is quite simple with unsupervised learning, but it is powerful enough since it does not depend on the initial states of the connections. In addition, HCM can reduce the dimensionality of general images and can perform better than HSOM and NC, since HCM overcomes the disadvantages of HSOM and NC and inherits their advantages directly. HCM cannot, however, show high ability when the boundary between categories is very complicated, such a case that objects of different categories have similar features. Therefore, a new learning algorithm for the HCM is proposed. The proposed algorithm is associative learning method, which is very powerful to separate the similar input data which should belong to different categories on the feature map.

The Eleventh International Symposium on Artificial Life and Robotics 2006 (AROB 11th'06),
B-con Plaza, Beppu, Oita, Japan, January 23-25, 2006

2 HSOM and NC

2.1 Hierarchical Self-Organizing Map (HSOM)

The HSOM is a two layers of SOM network connected as any feedforward neural network: every unit in the sending layer is connected to every unit in the receiving layer. The basic SOM defines a mapping from the input data space onto a regular array of neurons. All neurons ($1 \quad u \quad$) are fed the same input data $\boldsymbol{I}$. Each neuron has a weight vector $\boldsymbol{W}_u$. When the neurons are fed $\boldsymbol{I}$, they are activated according to the similarity between $\boldsymbol{I}$ and $\boldsymbol{W}_u$. In practical applications the Euclidian distance is usually used as the similarity measure, only neuron c can be activated, where

$$\boldsymbol{I} \quad \boldsymbol{W}_c \; = \min_u(\; \boldsymbol{I} \quad \boldsymbol{W}_u \;) \qquad (1)$$

In the training phase, each time a training data item is input, te winner is selected according to Eq. (1) and is trained according to the following equations:

$$\boldsymbol{W}_u(\; +1) = \boldsymbol{W}_u(\;) + h_{cu}(\boldsymbol{I}(\;) \quad \boldsymbol{W}_u(\;)) \qquad (2)$$

$$h_{cu} = \quad (\;) \; \exp\left(\frac{ \; r_c \quad r_u \; ^2}{2 \; ^2(\;)} \right) \qquad (3)$$

h_{cu} is a neighborhood kernel function. With increasing $r_c \quad r_u$ and , h_{cu} converges to zero. $(\;)$ is a monotonically decreasing function of $(0 < \; (\;) < 1)$, and $^2(\;)$ defines the width of the kernel.

In the case of HSOM, the neurons ($1 \quad v \quad M$) in the second layer are fed the index of the winner neuron in the first layer as input data. The training algorithm in the second layer is same as that in the first layer but the number of neurons M is smaller than . This small number of neurons help the HSOM to integrate the features extracted in the first layer.

Characteristics of the HSOM are summarized in the following points.

1. HSOM solves the complex region problem, when a sufficiently dense data set is given for continuous variation of the input data.

2. HSOM cab be a good preprocess to resolve the dimensional reduction problem.

In case where the HSOM is used directly for general image recognition, the following three problems, however, arise.

1. Image recognition methods based on HSOM are regarded as a memory-based method. Therefore, in case where the dimension and the size of data distribution are large, the network size increases.

2. Maps are organized according to the continuity of data distribution in the space defined by the distance between images using template matching. Therefore, it is hard to organize maps in cases where the distance between images does not smoothly vary with locale and scale of target object. In such cases, a heuristic, such as image blurry, must be adapted or the number of training samples must be increased so that the variations of distance are smooth enough.

3. The recognition method is also based on the distance of images and, therefore, is regarded as one of nearest neighbor method. Therefore, a high accurate segmentation of target region and a normalization of locale and size should be needed.

2.2 Neocognitron (NC)

Neocognitron (NC) is proposed by Fukushima[3] as a hierarchical network consisting of several layers of neuron-like cells. The lowest stage of the network is the input layer. Each succeeding stage has a layer consisting of cells called S-cells followed by another layer of cells called C-cells. S-cells are the feature-extracting cells. The C-cells are inserted on the network to allow for positional errors in the features.

The "structural" advantages of NC are summarized in the following two points, which can alleviate the disadvantages of HSOM.

1. Every feature map is rather small since NC has a hierarchical structure of divide-and-conquer type. This characteristic resolves the disadvantage 1 of HSOM.

2. Toward the disadvantage 2 and 3 of HSOM, NC does not need any preprocesses of blurring nor normalization due to its shift invariant recognition mechanism. NC, also, needs small number of training sample data because of its learning mechanism.

The original NC has the following two disadvantages when it is directly applied to general image recognition. The advantages of HSOM match with those disadvantages.

1. The learning process of NC is strongly depends on the initial state of weight vectors, and the feature extraction does not often perform well due to its simple competitive learning without neighborhood learning.

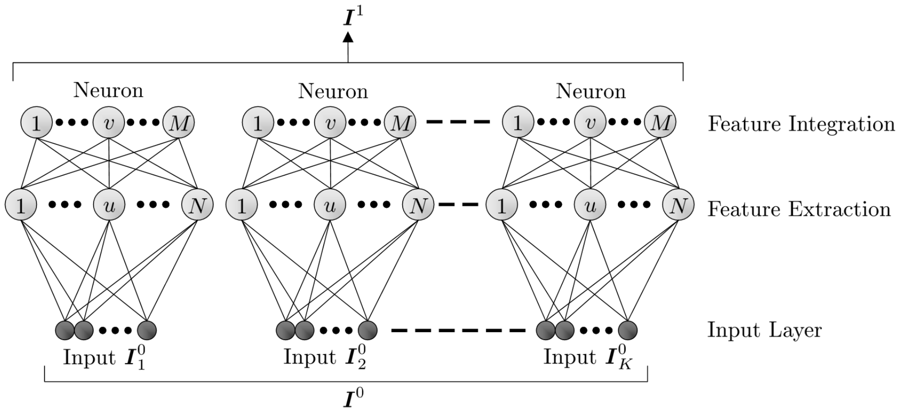

Figure 1: Structure of HCM

2. The shift integration layer integrates only shifted patterns, and does not requantize feature spaces. Therefore, its dimension reduction is not enough for variation of target shape, which requires large number of network neurons.

3 Hyper-Column Model (HCM)

Hyper-Column Model (HCM) is proposed for visual recognition of objects with variations in its position, size, and orientation[1]. HCM is a kind of competitive neural networks with unsupervised learning. The network is composed of hierarchical layers derived from NC by replacing the unit cell plains (each C-cells and the lower directly connecting S-cells) in NC with two-layers HSOM. These HSOM cell plains allow features extraction through the first SOM layer followed by features integration in the second SOM layer, as shown in Fig. 1. This feature integration process allows the cell plains to integrate more features in lower number of neurons. NC does not perform such feature integration process.

3.1 Associative Learning in HCM

The structure of HCM is similar to the one of NC, but HCM uses unsupervised learning algorithm that is used in SOM. In general image recognition problems, it is known that the recognition ability with supervised learning method is superior to the one with unsupervised learning method. Therefore, introducing a supervised learning method into HCM is needed.

We introduce a method of supervised learning in SOM proposed by Ichiki[4] into HCM. In this learning method, we can regard the input vector as the one which is composed of different two components; an input part $\boldsymbol{I}$ and an associative part $\boldsymbol{T}$. As a result, the networks can be considered as a supervised learning machines.

$$\boldsymbol{X} = a\begin{pmatrix} \boldsymbol{I} \\ 0 \end{pmatrix} + \begin{pmatrix} 0 \\ \boldsymbol{T} \end{pmatrix} \tag{4}$$

where $a > 1$ in order that the input part can affect the information of the map more than the output part does. The weight vector $\boldsymbol{W}_u$ is represented as follows,

$$\boldsymbol{W_u} = \begin{pmatrix} \boldsymbol{W}_u^I \\ \boldsymbol{W}_u^T \end{pmatrix} \tag{5}$$

4 Experimental Results

4.1 Condition

The input data were images of human hands which consist of 10 categories shown in Fig. 2. Each category has 10 images for training data, and 500 images for test data. The size of images was 100 100, and each pixel had an 8-bit gray value. The neurons in each feature extraction layer were arranged in a ring shape. In experiment, training data were learned by the traditional learning (HCM) and by the associative learning (AHCM).

4.2 Learning result

The maps generated by each HCM are shown in Fig. 3. The horizontal axis shows the sample number. From number 0, each 10 samples belong to the same category. The vertical axis shows the neuron number. HCM cannot generate one neuron cluster for the whole of one category 1, 2, 6, 7 and 8. On the other hand, AHCM can do it in most cases.

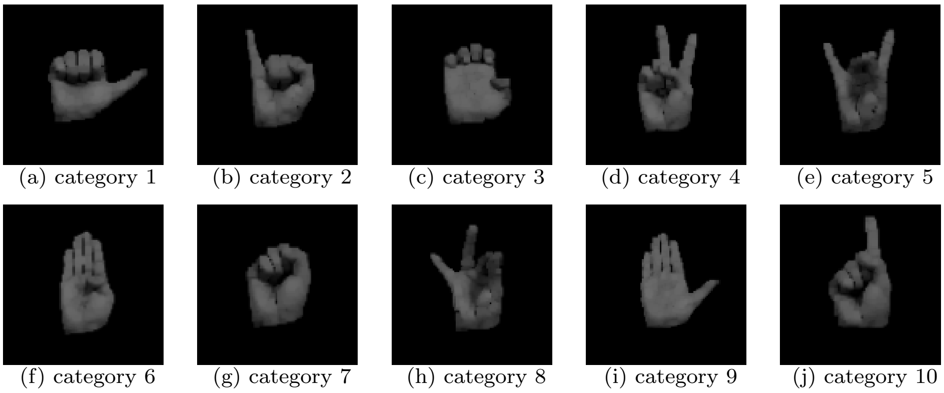

(a) category 1 (b) category 2 (c) category 3 (d) category 4 (e) category 5
(f) category 6 (g) category 7 (h) category 8 (i) category 9 (j) category 10

Figure 2: Training images

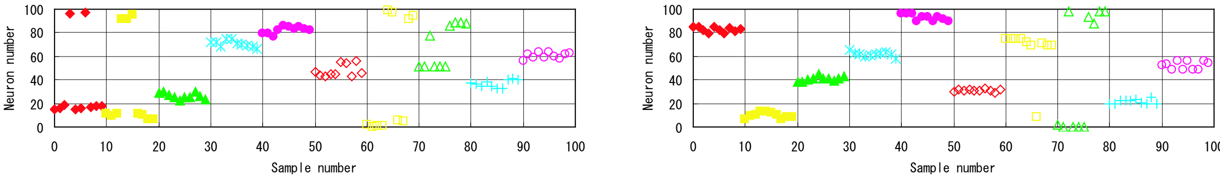

(a) Traditional learning (b) Associative learning

Figure 3: Correspondence between maps of HCM and sample data in experiment

4.3 Recognition accuracy

The average rate of correct recognition of HCM was 72 5%. The images of category 7 tended to be misunderstood as category 2. There are some overlaps between the neurons which belong to category 2 and category 7 as can be expected from Fig. 3(a). The images which belong to category 9, also, tended to be misunderstood as category 6. In most images which were not recognized correctly, the position of thumb was nearby the palm. We think that HCM with unsupervised learning could not create an appropriate boundary between category 6 and category 9 since the images of category 9 are similar to the ones of category 6.

On the other hand, the average rate of correct recognition of AHCM was 93 3%. The associative learning method gave good results without decreasing the recognition rates.

5 Conclusions

An associative learning method in Hyper-Column Model (HCM) was proposed. In the experiments described in this paper, the recognition ability of HCM with the associative learning was superior to the traditional learning. However, HCM has a problem that it runs out of neuron when the number of category increases. We are now researching for reconstruction of the network and incremental learning.

References

[1] Naoyuki Tsuruta, Rin-ichiro Taniguchi, and Makoto Amamiya. "Hypercolumn Model: A Combination Model of Hierarchical Self-Organizing Maps and Neocognitron for Image Recognition". *Systems and Computers in Japan*, 31(2):49–61, 2000.

[2] J. Lampinen and E. Oja. "Clustering properties of hierarchical self-organizing maps". *Journal of Mathematical Imaging and Vision*, 2(3):261–272, 1992.

[3] K. Fukushima. "Neocognitron: A self-organizing neural network model for a mechanism of pattern recognition unaffected by shift in position". *Biological Cybernetics*, 36(4):193–202, 1980.

[4] Ichiki H., Hagiwara M, and Nakagawa M. "Kohonen feature maps as a supervised learning machine". *Proc. of International Conference on Neural Networks*, pages 1944–1948, 1993.

The Eleventh International Symposium on Artificial Life and Robotics 2006 (AROB 11th'06),
B-con Plaza, Beppu, Oita, Japan, January 23-25, 2006

Incremental acquisition of behavioral concepts through social interactions with a caregiver

T. Taniguchi
Dept. of Mechanical Eng. and Sci.
Kyoto University
Kyoto, Yoshida-honmachi 606-8501

T. Sawaragi
Dept. of Mechanical Eng. and Sci.
Kyoto University
Kyoto, Yoshida-honmachi 606-8501

Abstract

We describe a novel modular reinforcement learning architecture, the reinforcement learning schemata model (RLSM), based on the schema model proposed by Piaget. In our previous work, we described the dual-schemata model, which enables autonomous robots to obtain concepts representing their environment and/or surrounding objects incrementally, based on sensory-motor interaction with their environment. By applying this basic idea to reinforcement learning, we have developed an incremental reinforcement learning architecture. The results shows that by using RLSM, autonomous robots can obtain several behaviors incrementally through interactions with their caregiver, who designs various reward functions.
Keywords: Reinforcement learning, schema model, social interaction.

1 Introduction

How can we enable autonomous robots to acquire behaviors incrementally through natural interactions with their environment? To give a reasonable solution to this problem in the context of reinforcement learning is the main purpose of this paper. Here, "environment" includes not only the physical environment but also the human caregiver interacting with the robot. Human infants acquire a number of behaviors through interactions with their surroundings, particularly their mothers, who interact kindly with them very frequently. However, an autonomous robot cannot obtain behavioral concepts incrementally through such interactions because reinforcement learning usually requires that a reward function, which represents a behavior that should be acquired by the robot, be fixed during the robot's learning phase. To overcome this problem, we propose a novel incremental modular reinforcement learning method, the reinforcement learning schemata model (RLSM), which enables an

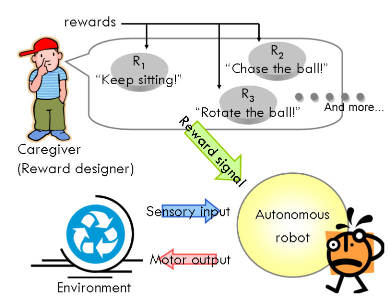

Figure 1: Abstract diagram of social interaction

autonomous robot to obtain behavioral concepts incrementally by differentiating its behavioral concept when it encounters an environment that has not been experienced before. In the next section, we discuss social interaction in the context of reinforcement learning. In the third section, we describe our RLSM. Finally, we describe the results of testing RLSM under the condition that an autonomous robot's caregiver sometimes switches reward functions.

2 Social interaction based on reinforcement learning

Social interaction has many features on which focus can be placed. In the human cognitive development process, the first social interactions emerge between an infant and his or her mother. The infant learns several behaviors, which are considered somewhat meaningful and different by his or her mother, through interaction. However, an infant cannot recognize explicit differences between various behaviors. It may be very difficult to notice the overt differences because they do not exist in the physical phenomena, only in the mother's covert intentions. Therefore, it is important for the infant to recognize the differences of the mother's intentions from the series of interactions with his or her mother, or other caregivers.

From the viewpoint of reinforcement learning, this time series can be represented by a series of two vectors and a scalar: sensor vector s_t, motor vector a_t, and reward signal r_t. We assume that the differences in the caregiver's intentions are encoded in this time series data (Fig. 1). Caregivers usually control reward functions to communicate their intentions to an infant. A cognitive development autonomous robot should thus be able to learn several behavioral concepts by receiving corresponding rewards.

3 RLSM: reinforcement learning schemata model

A modular learning architecture manages several learning modules to learn dynamics and/or multiple objective behaviors. The "mixture-of-experts" modular learning architecture proposed by Jacobs et al.[5] is widely used for pattern matching problems and state-prediction problems. In the context of reinforcement learning, Singh proposed the compositional Q-learning architecture which extends mixture-of-experts to reinforcement learning [3]. In this architecture, a compositional task is decomposed into several elemental tasks, and each elemental task is learned by an expert. The achitecture has several Q-tables, and a Q-table is considered as an expert. However, the number of experts is fixed. Since a cognitive development autonomous robot has to learn new behaviors incrementally, the number of experts should be flexible. Takahashi et al. proposed a modular reinforcement architecture [2], in which a new Q-table is created for each interaction context. However, the criteria are based on the environmental dynamics, which are not related to r_t, but to s_t and a_t. Therefore, the tables do not reflect the intentions of the caregiver who designed the reward functions.

3.1 Basic concepts

In the context of a developmental learning, we previously proposed the dual-schemata model which enables an autonomous robot to obtain an environmental model incrementally [1]. By "schema" we mean a term in Piaget's developmental psychology [6]. By extending this concept to reinforcement learning, we developed our reinforcement learning schemata model (Fig. 2), in the sameway that Singh extended mixture-of-experts to reinforcement learning. A schema assimilates experiences that are predicted correctly by its inner prediction function. The experiences accommodate its inner functions.This cyclic process is called an equilibration process. However, if every schema refuses to assimilate a novel experience, the RLSM creates a new schema for the situation which produces that experience. This process is called differentiation. These equilibration and differentiation processes are the basic concepts of our schemata model.

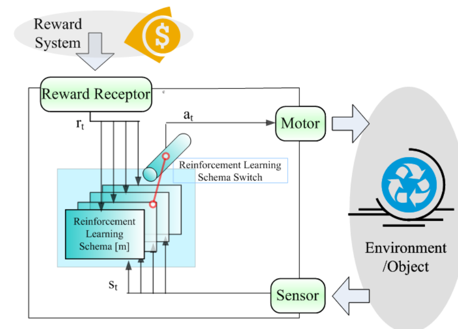

Figure 2: Reinforcement learning schemata model

3.2 Algorithm

RLSM is formulated based on Q-learning. The λ-th schema has three functions: state-action-value function Q^λ, standard deviation estimator function σ^λ, and Q^λ's second order statistics function $Q^{(2)\lambda}$. $Q^{(2)\lambda}$ is a supplementary function used to calculate σ^λ. In temporal difference (TD) learning including Q-learning, errors in the value function cannot been observed directly, so the TD errors must be considered. Therefore, $Q^{(2)\lambda}$ is considered for the purpose of estimating Q^λ's standard deviation. TD-error δ_t and secondary TD-err $\delta_t^{(2)}$ for each λ-th schema are calculated using

$$\delta_t^\lambda = r_t + \gamma V^\lambda(s_{t+1}) - Q^\lambda(s_t, a_t) \; and \qquad (1)$$

$$\delta_t^{(2)\lambda} = r_t^2 + 2\gamma r_t V^\lambda(s_{t+1}) + \gamma^2 Q^{\lambda(2)}(s_{t+1}, a_{t+1}^*) - Q^{\lambda(2)}(s_t, a_t), \qquad (2)$$

where

$$V^\lambda(s_t) = Q(s_t, a_t^*), \qquad (3)$$

$$a_t^* = argmax_a Q^\lambda(s_t, a), \qquad (4)$$

and γ is a discount parameter. Each function is updated using these errors:

$$Q^\lambda(s_t, a_t) \leftarrow Q(s_t, a_t) + \alpha\delta_t \qquad (5)$$

$$Q^{(2)\lambda}(s_t, a_t) \leftarrow Q^{(2)}\lambda(s_t, a_t) + \alpha\delta_t^{(2)} \qquad (6)$$

$$\hat{\sigma}^\lambda = \sqrt{Q^{(2)\lambda} - (Q^\lambda)^2}. \qquad (7)$$

By dividing δ_t by estimated standard deviation $\hat{\sigma}_t$, we obtain a dimensionless number, R_t^λ, as the subjective error:

$$\begin{aligned} R^\lambda(t) &\equiv |\delta_t^\lambda / \hat{\sigma}_t^\lambda| & (8)\\ \breve{R}^\lambda(t+1) &= (1-p)R^\lambda(t) + p\breve{R}^\lambda(t) & (9)\\ &\sim \int_0^\infty \frac{1}{\tau} exp(-\frac{s}{\tau}) R^\lambda(t-s)ds & \\ \mathsf{V}^\lambda(\mathsf{t}) &= \chi_c(n_p \breve{R}^\lambda(t), n_p) & (10)\\ n_p &= \frac{1+p}{1-p}, & (11) \end{aligned}$$

where $\chi_c(x,n)$ is a chi-squared one-sided cumulative function, $P(X < x)$, $\breve{R}^\lambda$ is a temporal weighted average of the subjective errors, and V^λ is the λ-th schema activity. "Schema activity" means how near the robot's facing environment and reward function are to the λ-th reinforcement learning schema. The p is a parameter representing how long a schema retains a previous recognition. In continuous time, time constant $\tau = \triangle t/(1-p)$ corresponds to p; $\triangle t$ is the continuous time for one step in discrete time.

A reinforcement learning schema decides whether to assimilate an experience or reject it by referring to schema activity V^λ. If all the schemata reject an incoming experience, differentiation is inisiated and a new schema is created. This algorithm enables an autonomous robot to notice qualitative changes in a time series of s_t, a_t and r_t and to obtain novel behavioral concepts incrementally. Significance parameter α is set, and the probability, $P(\lambda)$, with which λ-th schema is selected is defined as

$$\begin{aligned} \mu(H^\lambda) &= sgn(\mathsf{V}^\lambda(\mathsf{t}) - \alpha) & (12)\\ P(\lambda) &= \mu(H^\lambda)\prod_{k=0}^{\lambda-1}(1-\mu(H^k)), & (13) \end{aligned}$$

where

$$sgn(x) = \begin{cases} 1 & if \quad x > 0, \\ 0 & otherwise \end{cases} \qquad (14)$$

and $\mu(H^\lambda)$ is the truth value of hypothesis H^λ, which means that the robot's facing environment corresponds to the λ-th schema. H^0 is a dummy hypothesis defined to simplify the equation ($\mu(H^0) = 0$).

4 Evaluation

We evaluated RLSM by using 2D simulation for the Khepera mobile robot [7].

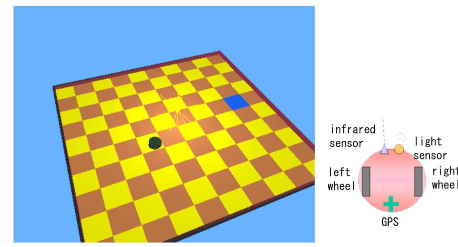

Figure 3: Left: simulation space; right: Khepera's sensory-motor system

4.1 Conditions

The simulation space and a Khepera's sensory-motor system are illustrated in Fig. 3. We used Webots, produced by cyberbotics, to simulate Khepera's dynamics. The square simulation space was enclosed by walls 2 m long and 10 cm high. A light source was located at a height of 10 cm at the center of the space. Khepera has two wheels as a motor system, and their rotational velocities can be set independently at each time step. Khepera's sensory system comprises an infrared sensor, a light sensor, and a GPS. Q-learning usually requires a discrete state space. Therefore, we divided Khepera's x,y coordinates and its angle of direction, obtained from the GPS, into six parts, and defined $216 (= 6 \times 6 \times 6)$ states. The action space was also made discrete by defining five representative motor outputs: i.e. forward, back, right, left, and stop. Forward and back move the robot about 30 cm per step, and right and left rotate it about 60° per step. The values of the infrared sensor (ds) and the light sensor (ls) were limited to between 0 and 1. They were used only to calculate the rewards.

We prepared three reward functions:

$$\begin{aligned} r^1 &= ds & (15)\\ r^2 &= 1.5 * ls & (16)\\ r^3 &= 1.8 * v_{forward}, & (17) \end{aligned}$$

where $0 \leq v_{forward} \leq 1$ is the value given when Khepera advances. These reward functions mean that the caregiver wants the robot to face a wall, to receive more light, and to go forward, respectively. The meta parameters for reinforcement learning were set to $\alpha = 0.2$ and $\gamma = 0.8$. The meta parameters for the schemata model were set to $p = 0.999$ and $\alpha = 0.0001$.

We investigated whether RLSM enabled Khepera to obtain several behavioral concepts, i.e. reinforcement learning schemata, and recall them while it was interacting with the environment, in which the reward

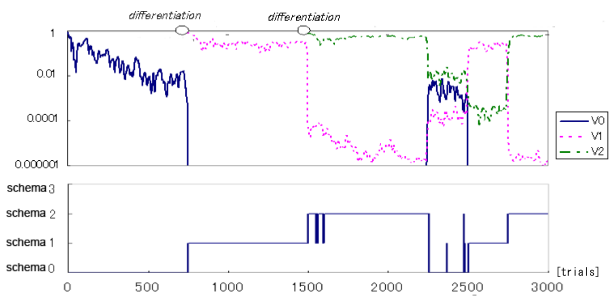

Figure 4: Top: schema differentiation process and transition of schema activities; bottom: selected reinforcement learning schema

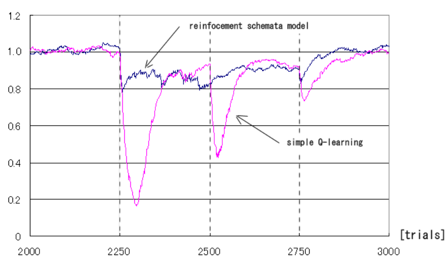

Figure 5: time course of averaged rewards after Khepera experienced three reward functions

functions were switched in turn. Each trial consisted of 200 steps. Khepera's action at each step was determined by Boltzmann selection. In each trial, the inverse temperature was set to $\beta = 0$ during thefirst 100 steps, to $\beta = 1$ during the next 50 steps, and to $\beta = 3$ (almost greedy) during the final 50 steps. The reward functions were set to r^1 for $(0 < trial \leq 750)$, r^2 for $(750 < trial \leq 1500)$, and r^3 for $(1500 < trial \leq 2250)$. Subsequently, each reward function was used for 250 trials in turn.

4.2 Result

As shown in Fig. 4, each schema activity, V^λ, transited successfully, and the schema, initially only one, differentiated into three, and three behavioral concepts corresponding to the three reward functions were organized. Each schema was selected as shown in Fig. 4, and the averaged rewards transited remaining at a high level as compared with simple Q-learning as shown in Fig. 5. This shows that RLSM is better than simple Q-learning in a dynamically changing environment.

5 Summary

We have described a novel reinforcement architecture, RLSM, for a dynamic environment in which a caregiver designs several reward functions to train an autonomous robot. Using RLSM enables a robot to obtain several learning modules, called reinforcement learning schemata, without any explicit indication except for sensor vectors, motor vectors, and rewards, which are usually given in reinforcement learning. This kind of constructive learning process will enable development of cognitive development autonomous robots.

Acknowledgements

This work was supported in part by the Center of Excellence for Research and Education on Complex Functional Mechanical Systems. (The 21st Century COE program of the Ministry of Education, Culture, Sports, Science and Technology, Japan).

References

[1] T. Taniguchi, T. Sawaragi (2004), "Design and Performance of Symbols Self-Organized within an Autonomous Agent Interacting with Varied Environments ", IEEE International Workshop on RO-MAN, in CD-ROM

[2] Y. Takahashi et al.(2004), "Modular Learning System and Scheduling for Behavior Acquisition in Multi-Agent Environment." RoboCup 2004 Symposium papers and team description papers, in CD-ROM

[3] S. P. Singh (1992),"The Efficient Learning of Multiple Task Sequences", Neural Information Processing System 4, pp. 251–258

[4] R.S. Sutton, A.G. Barto (1998),"Reinforcement Learning: An Introduction", MIT Press

[5] R.A. Jacobs et al.(1991),"Adaptive Mixtures of Local Experts", Neural Computation, vol. 3, no. 1, pp. 79–87

[6] J.H. Flavell (1963), "The Developmental Psychology of Jean Piaget", Van Nostrand Reinhold

[7] Webots. http://www.cyberbotics.com. Commercial Mobile Robot Simulation Software.

The Eleventh International Symposium on Artificial Life and Robotics 2006 (AROB 11th'06),
B-con Plaza, Beppu, Oita, Japan, January 23-25, 2006

A Step towards Artificial 'Kansei'

Kaoru Sugita Genci Capi Masao Yokota
Fukuoka Institute of Technology
{sugita, capi, yokota}@fit.ac.jp

Abstract

Various types of robots developed in recent years can play their roles according to programmed actions to stimuli. However, they have not yet come to understand such a mental function of their human partners as is called *Kansei*. In this paper, *Kansei* for a robot, so called, 'Artificial *Kansei*' is proposed as one of the functions of a multi-agent mind model in the view of artificial or robotic individuality.

1. Introduction

In recent years, there have been developed various types of robots in Japan. However, they are to play their roles according to programmed actions to stimuli and have not yet come to understand such a mental function of their human partners as is called *Kanse*i. The authors have proposed a human mind model of human mind consisting of Stimulus, Knowledge, Emotion and Response Processing Agents (see Fig.1) and simulated human-robot communication based on it [1]. Besides this, we have tried to describe the meanings of *Kansei* expressions such as 'heart-calming', 'fantastic', 'soft', 'thick', 'grotesque', etc related to visual images of crafts and to retrieve them by these expressions as queries [4, 5, 6]. In this paper, we describe 'Artificial *Kansei* (AK)', namely, *Kansei* for a robot as tight collaboration of Knowledge and Emotion Processing Agents of our mind model, and verbalization of *Kansei* information so called '*Kansei* expression' by Response Processing Agent in the view of artificial or robotic individuality.

2. Multi-agent mind model

Figure1 shows the multi-agent mind model proposed by the authors [1]. This is a functional model of human central nervous system consisting of the brain and the spine. The basic performances of its agents are as follows.

(1) **Stimulus Processing Agent** (**St**) receives stimuli from the world (**W**) and encodes them into mental images (i.e. encoded sensations) such as *"I sensed something oily."* (if verbalized in English.)
(2) **Knowledge Processing Agent** (**Kn**) evaluates mental images received from the other agents based on its memory (e.g. knowledge), producing other mental images such as *"It is false that the earth is flat."*
(3) **Emotion Processing Agent** (**Em**) evaluates mental images received from the other agents based on its memory (e.g. instincts), producing other mental images such as *"I like the food."*
(4) **Response Processing Agent** (**Re**) converts mental images (i.e. encoded physical actions such as *"I'll walk slowly."*) received from the other agents into real physical actions against **W**.

A *performance* ***P*** for a *stimulus X* with a *result Y* at each agent can be formalized as a function by the expression (1).

$$Y=\boldsymbol{P}(X), \qquad (1)$$

where

P: a combination of ***atomic performances*** described later,
X: a spatio-temporal distribution of stimuli from **W** to **St** or a mental image for another agent, and
Y : a series of signals to drive an actuator for **Re** or a mental image for another agent.

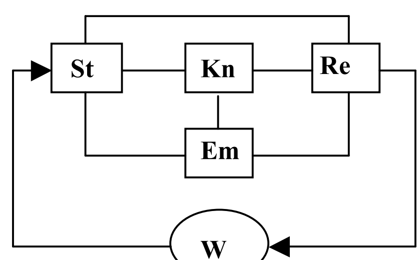

St: Stimulus Processing Agent.
Kn: Knowledge Processing Agent.
Em: Emotion Processing Agent.
Re: Response Processing Agent.
W: World surrounding human mind, including his/her body.

Fig.1. Multi-agent model of human mind.

A performance ***P*** is assumed as a function formed either consciously or unconsciously. In a conscious case, a set of atomic performances are to be chosen and combined according to X by a meta-function, so called, '***Performance Selector*** (PS)' assumed as '***Conscience***'. On the contrary, in an unconscious case, such a performance as associated most strongly with X is to be applied automatically [8]

3. Mental image description

The Mental Image Directed Semantic Theory (MIDST) has modeled mental images as "Loci in Attribute spaces" [3], [7]. An attribute space corresponds with a certain measuring instrument just like a thermometer, map measurer or so and the loci represent the movements of its indicator. The performance of 'Attribute space' is the model of '***Atomic performance***' introduced in Section 2.

A general locus is to be articulated by "Atomic locus" formalized as the expression (2) in first-order logic, where "L" is a predicate constant.

$$L(x,y,p,q,a,g,k) \quad (2)$$

The expression (2) is called "Atomic locus formula" whose arguments are referred to as 'Event Causer', 'Attribute Carrier', 'Initial Attribute Value', 'Final Attribute Value', 'Attribute Kind', 'Event Kind' and 'Standard Attribute Value', respectively.

The interpretation of (2) is as follows, where "matter" refers to "object" or "event".

"Matter 'x' causes Attribute 'a' of Matter 'y' to keep (p=q) or change (p ≠ q) its values temporally (g=Gt) or spatially (g =Gs) over a time-interval, where the values 'p' and 'q' are relative to the standard 'k'."

When $g=Gt$ and $g=Gs$, the locus indicates monotonic change or constancy of the attribute in time domain and in space domain, respectively. The former is called 'temporal event' and the latter, 'spatial event'.

For example, the motion of the 'bus' represented by S1 is a temporal event and the ranging or extension of the 'road' by S2 is a spatial event whose meanings or concepts are formalized as expressions (3) and (4), respectively, where the attribute is "physical location" denoted as $A12$. We think that the verb 'run' used in S2 must reflect the motion of the observer's attention [4].

(S1) The bus runs from Tokyo to Osaka.

$$(\exists x,y,k)L(x,y,Tokyo,Osaka,A12,Gt,k)\wedge bus(y) \quad (3)$$

(S2) The road runs from Tokyo to Osaka.

$$(\exists x,y,k)L(x,y,Tokyo,Osaka,A12,Gs,k)\wedge road(y) \quad (4)$$

The expression (5) is the conceptual description of the English word "fetch", implying such a temporal event that 'x1' goes for 'x2' and then comes back with it, where 'Π' and '•' are instances of the tempo-logical connectives, 'SAND' and 'CAND', standing for "Simultaneous AND" and "Consecutive AND", respectively.

In general, a series of atomic locus formulas with such connectives is called simply 'Locus formula'.

$$\begin{aligned}&(\exists x1,x2,p1,p2,k)\ L(x1,x1,p1,p2,A12,Gt,k)\\ &\bullet (L(x1,x1,p2,p1,A12,Gt,k)\Pi L(x1,x2,p2,p1,A12,Gt,k))\\ &\wedge x1\neq x2\ \wedge p1\neq p2\end{aligned} \quad (5)$$

In order for complete representation of temporal relations, we have introduced a concept called 'Empty Event (EE)' and symbolized as 'ε' which stands exclusively for time elapsing. For example, (6) represents 'X_1 during X_2'.

$$(\varepsilon_1 \bullet X_1 \bullet \varepsilon_2)\ \Pi X_2 \quad (6)$$

The image model presented here is also valid for formalizing word concepts (i.e. coding) of actions because any action must be measured with sensors for its formalization. That is, ***grounding words on actions is equivalent to grounding words on sensations of actions.***

Sensors and actuators are assumed to collaborate very closely in feedback or feed-forward ways in cybernetics and there is a hypothesis that some kinds of sensations (or perceptions) and actions are encoded in the same way in organisms [7].

4. Artificial *Kansei*

It is well known that emotion in a human can be affected by his/her world, namely, ***W*** in Fig.1. For example, a person's evaluation of live image of an object (i.e. image output from **St**) expressed by such words as 'favorite', 'beautiful', 'tasty', etc can vary depending on his/her emotional bias such as 'hungry', 'depressed', etc.

Kansei is one of mental functions with emotion involved but has a more complicated phase than pure emotion originated from instincts or imprinting. For example, sweet jam may be nice on toast but not on pizza for certain people knowledgeable about these foods. For another example, people can be affected on their evaluation of an art by its creator's name, for example, 'Picasso'. These are good examples of *Kansei* processing as emotional performance affected by knowledge in humans.

Therefore, *Kansei* can be defined as human emotion toward an object affected by its information for him/her, so called, 'concept', including his/her intellectual pursuits, traditions, cultures, etc concerning it. In this sense, *Kansei* is assumed to be reasonable among the people sharing such concepts unlike pure emotion. These hypothetic considerations are formalized as (7) and (8).

$$I_P(\mathrm{x}) = \boldsymbol{P_E}(\mathrm{S(x)}) \quad (7)$$

$$I_K(\mathrm{x}) = \boldsymbol{P_E}(\mathrm{S(x)} \wedge \mathrm{O(x)}) = \boldsymbol{P_E}(\mathrm{S'(x)}) \quad (8)$$

where

$\boldsymbol{P_E}$(X): Performance of **Em** for mental image 'X',

I_P(x): Mental image as pure emotion for object 'x',

I_K(x): Mental image as *Kansei* for object 'x',

S(x): Live image of object 'x' from **St**,

O(x): Concept of object 'x' from **Kn**,
S'(x): Unified image of live image and concept.

Figure 3 shows an example of *Kansei* processing in our mind model, where perceived, induced and inspired images correspond to S(x), S'(x) and $I_K(x)$, respectively, while Fig.2 is for pure emotion with $I_P(x)$ as the inspired image.

These two inspired images are to be verbalized in **Re** as 'Fragrant!' and 'Appetizing!', labeled in Fig.2, respectively. The essential difference between them is assumed to reside in whether or not they are affected by O(x), namely, the concept of 'chocolate cream bread', inferred by **Kn** from the shape and the smell. Whereas, pure emotion for an object can be a special case of *Kansei* processing without knowing or recognizing what it is.

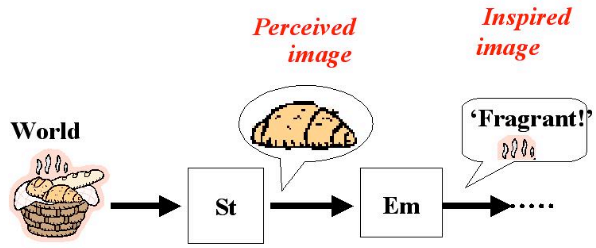

Fig.2. Example of pure emotion

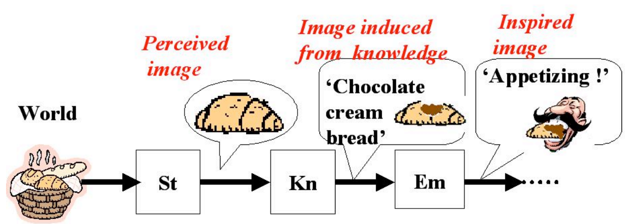

Fig.3. Example of *Kansei* processing

In the MIDST, the concept of an object '*x*' is given as an integrated omnisensory mental image of its properties and its relations with other objects involved. For example, the concept of 'chocolate cream bread' can be given by (9), reading that *x* is bread, sweet due to chocolate cream, fragrant of itself, etc, where A29 and A30 refer to 'Taste' and 'Odour', respectively.

$$(\lambda x)chocolate\_cream\_bread(x) \Leftrightarrow (\lambda x\exists y,k1,k2)L(y,x,Sweet,Sweet,A29,Gt,k1)\Pi L(x,x,Fragrant,Fragrant,A30,Gt,k2) \wedge bread(x) \wedge chocolate\_cream(y) \wedge \ldots \quad (9)$$

5. Human-robot communication

For comprehensible communication with humans, robots must understand natural language *semantically* and *pragmatically*. Here, semantic understanding means connecting symbols to conceptual images of objects and pragmatic understanding means connecting symbols to real objects by unifying conceptual images with perceptual images as shown in Fig.4.

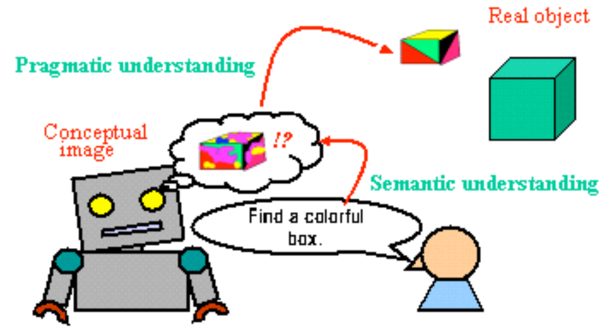

Fig.4. Semantic and pragmatic understanding

However, humans and robots can be equipped with sensors, actuators and brains of different performances and their vocabularies may well be grounded on quite different sensations, physical actions or mental actions. And in turn such a situation may bring inevitably different kinds of semantics to them, so called, "Natural Semantics (NS)" for humans and "Artificial Semantics (AS)" for robots.

For example, consider such a scenario as follows.

...A human 'Kate' and a humanoid robot 'Robbie' encounter at the terrace in front of the room where a Christmas party is going on merrymaking. Kate says "Robbie, please fetch me some delicious food from the noisy room." Robbie replies "OK, Kate."….

For a happy end of this dialog, Robbie must have a good knowledge of Kate's NS for *Kansei* and translate it into its AS appropriately enough to find out the real objects referred to by her words. In this case, Robbie need at least to interpret Kate's statement as the expression (10) reading "If *Robbie* fetches *Kate* some food delicious ***for her*** from the room noisy ***for her*** (***E1***), then consecutively it makes *Kate* happier (***E2***)," or as its logical equivalent, the expression (11) reading "It is not the case that *Robbie* fetches *Kate* the food … and consecutively it does not make *Kate* happier." Both the expressions are adopted in MIDST as the canonical conceptual structures of an imperative sentence.

$$\boldsymbol{E1 \rightarrow_c E2} \quad (10)$$

$$\boldsymbol{\sim(E1 \bullet \sim E2)} \quad (11)$$

where

$$\boldsymbol{E1} \Leftrightarrow (\exists x1,x2,k1,k2,k3,k4)\ (L(R,R,K,x2,A12,Gt,k1)\bullet (L(R,R,x2,K,A12,Gt,k1)\Pi L(R,x1,x2,K,A12,Gt,k1))) \Pi(L(K,x1,Delicious,Delicious,B08,Gt,k2)) \Pi L(K,x2,Noisy,Noisy,B08,Gt,k4)) \wedge food(x1) \wedge room(x2)$$

$$\boldsymbol{E2} \Leftrightarrow (\exists e1,e2,k7)\ L(\boldsymbol{E1},K,e1,e2,B04,Gt,k7) \wedge e2>e1.$$

The special symbols and their meanings in the expressions above are:

'$X \rightarrow_c Y$' ='If *X* then consecutively *Y*', *R*='Robbie', *K*='Kate', *A31*='Sound', *A32*='Color', *B08*='*Kansei*' and *B04*= 'Happiness (=degree of happiness)'.

As easily imagined, these values of the attribute *Kansei* (*B08*) greatly depend on their standards (i.e. *k2* and *k4*) that are most closely related to 'Individual' or 'Purposive' standard shown in Table 1 (see APPENDIX).

By the way, Robbie's task is only to make ***E1*** come true where each atomic locus formula is associated with his actuators/sensors. Of course, Robbie believes that he will become happier to help Kate, given by expression (12) where 'B03' is 'trueness (=degree of truth)'and 'K_B' is a certain standard of 'believability'. That is *emotionally* to say, Robbie likes Kate. Therefore, this example is also very significant for intentional sensing and action of a robot driven by logical description of its belief.

$$(\exists p)L(R,\boldsymbol{E},p,p,B03,Gt,K_B) \wedge p>K_B \wedge \boldsymbol{E} = \boldsymbol{E1} \rightarrow_c \boldsymbol{E2} \quad (12)$$

6. Discussion and conclusion

Our mind model is much simpler than Minsky's [2] but the locus formula representation can work for representing and computing mental phenomena fairly well [1, 3]. For realizing a plausible *Kansei*, it is most essential to find out functional features of **Em** and to deduce from them such laws that rule $\boldsymbol{P_E}$. The most important problems to be solved are how to realize the attribute space of *Kansei* and how to build its corresponding atomic performance. In order to solve these problems, we will consider the application of soft computing theories such as neural network, genetic algorithm, fuzzy logic, etc. in the future.

References

[1] Yokota,M., Shiraishi,M. and Capi,G.: "Human-robot communication through a mind model based on the Mental Image Directed Semantic Theory," Proc. of the 10th International Symposium on Artificial Life and Robotics (AROB '05), pp.695-698, 2005.

[2] Minsky, M: The society of mind, Simon and Schuster, New York, 1986.

[3] Yokota, M. & Capi,G.: "Cross-media Operations between Text and Picture Based on Mental Image Directed Semantic theory," WSEAS Trans. on INFORMATION SCIENCE and APPLICATIONS, Issue 10, 2, pp.1541-1550, Oct. 2005.

[4] M.Fukuda, K.Sugita and Y.Shibata, "Perceptional Retrieving Method for Distributed Design Image Database System," IPSJ Journal, Vol.39, No.2, pp.158-169, 1998.

[5] K.Sugita, A.Miyakawa and Y.Shibata, "Relation Between Kansei Words and the Room Space in Digital Traditional Japanese Crafting System," The International Conference on Advanced Information Networking and Applications (AINA), 159-162, 2003.

[6] K.Sugita, T.Ishida, A.Miyakawa, Y.Shibata, "Kansei Retrieval Method using the Quantitative Feature of Traditional Japanese Crafting Object," Proc. of The 6th International Workshop on Multimedia Network Systems and Applications (MNSA'2004), 112-117, 2004.

[7] Prinz, W.: "A common coding approach to perception and action", In *Relationships between perception and action* (Neumann, O. and Prinz, W. eds.), pp.167-201, Springer-Verlag, 1990.

[8] Brooks, R. A.: "A robust layered control system for a mobile robot", IEEE Journal of Robotics and Automation, RA-2, pp.14-23, 1986.

APPENDIX

Table 1 Examples of standards.

Categories of standards	Remarks
Rigid Standard	Objective standards such as denoted by measuring *units* (meter, gram, etc.).
Species Standard	The *attribute value ordinary* for a species. A *short train* is ordinarily longer than a *long pencil*.
Proportional Standard	'*Oblong*' means that the width is greater than the height at a physical object.
Individual Standard	*Delicious* food for one person can be too *poor* for another.
Purposive Standard	One room *comfortable* enough for a person's *sleeping* may be *uncomfortable* for his *jogging*.
Declarative Standard	The origin of an order such as 'next' must be declared explicitly just as 'next *to him*'.

The Eleventh International Symposium on Artificial Life and Robotics 2006 (AROB 11th'06),
B-con Plaza, Beppu, Oita, Japan, January 23-25, 2006

A Spoken Language Interface to a Mobile Robot

Johan Bos
Dipartimento di Informaticà
Universita di Roma "La Sapienza"
via Salaria 113 00196 Roma, Italy

Tetsushi Oka
Dept. of Information and Systems Engineering
Fukuoka Institute of Technology
3-30-1 Wajiro-higashi, Fukuoka 811-0295 Japan

Abstract

We describe a spoken dialogue interface to a mobile robot, which a human can direct to specific locations, ask for information about its status, and supply information about its environment. The robot uses an internal map for navigation, and communicates its current orientation and accessible locations to the dialogue system. In this paper, we focus on linguistic and inferential aspects of the human-robot communication process.

1 Introduction

The use of spoken language is arguably the most natural way of establishing a communication channel between a human and a robot. A successful implementation of a talking robot requires a good understanding of many different aspects of conversation, ranging from acoustic signals, the syntactic structure of the language, the meaning associated it, and the underlying goals derived from it. This paper presents an approach to human-robot dialogue understanding. In the framework that we introduce, the meaning of utterances of the dialogue participants and other information of the situation are represented as logical forms of compositional semantics, and logical inferences are drawn to manage the direction of the dialogue from the robot's point of view: when to perform which actions, how to answer a question, and whether to show agreement or disagreement towards the user's contribution.

*This work was conducted at ICCS, School of Informatics, University of Edinburgh.

2 Natural Language Understanding

2.1 Speech Recognition

The robot that we developed is able to communicate with humans in spoken language, rather than typed. In our system, we use Nuance's speaker-independent speech recognition system (`www.nuance.com`), which allows language models to be specified in the GSL (Grammar Specification Language), a form of context free grammars. Rather than coding the grammar-based language model in GSL directly, we use a generic domain-independent, but linguistically motivated grammar as a starting point. The grammar in question is a unification grammar for English, which gets translated into GSL, using the UNIANCE compiler [1]. We did not adopt the standard slot-filling paradigm for semantic interpretation, but used UNIANCE's feature to employ a sophisticated compositional semantics involving λ terms which are passed as the value of a single slot for the recognised sentence. As a result the output of the speech recognition component is a genuine semantic representation, and no further parsing is required before handing it over to the dialogue manager.

2.2 Semantic Interpretation

Discourse Representation Theory (DRT) [5] is used for meaning representation in the system. It is a formal theory of discourse interpretation, covering a wide variety of natural language phenomena including referring anaphoric and deictic expressions, quantified expressions, plural noun phrases, and a wide spectrum of presuppositional expressions [3].

We use Discourse Representation Structures (DRSs) to represent the meaning of the dialogue between user and system. There are computational implementations that provide means to extend existing linguistic grammars with DRS-construction tools that we use to design the semantic interpretation component. There is a standard translation from DRSs to formulas of first-order logic that behaves linear on the size of the input, which gives us the means to implement logical inference.

DRT was initially designed to deal with texts, so we use an extension of standard DRT that enables us to cope with the semantics of imperatives and interrogatives. We use a modified DRS-language covering these extensions:

Syntax of DRSs

1. If x_1 x_n is a set of discourse referents, and $_1$ $_m$ is a set of DRS-conditions, then the ordered pair x_1 x_n $_1$ $_m$ is a DRS;
2. If B_1 and B_2 are DRSs, then so is (B_1;B_2). (merge of DRSs)

In DRS conditions, DRS-action-terms are used to deal with imperatives in dialogue, following [4]. We distinguish between atomic and composite DRS-action-terms:

Syntax of DRS-action-terms:

1. If B is a DRS, then B is a DRS-action-term;
2. If A_1 and A_2 are DRS-action-terms, then so are (A_1;A_2) (sequence) and (A_1 A_2) (free choice).

Syntax of DRS-conditions:

1. If R is a relation symbol for an -place predicate and $x_1 \ldots x_n$ are discourse referents then $R(x_1,\ldots,x_n)$ is a DRS-condition;
2. If x_1 and x_2 are discourse referents, then $x_1 = x_2$ is a DRS-condition;
3. If B is a DRS, then B, $\Box$B, $\Diamond$B, ?B are DRS-conditions;
4. If B_1 and B_2 are DRSs, then B_1 B_2, B_1 B_2, B_1?B_2 are DRS-conditions;
5. If x is a discourse referent and B a DRS, then x:B is a DRS-condition;
6. If A is a DRS-action-term, and B a DRS, then [A]B and A B are DRS-conditions;
7. If A is a DRS-action-term then !A is a DRS-condition.

Clauses 1 and 2 deals with basic DRS-conditions as in standard DRT [5]. Clause 3 introduces negation, the modal operators, and yes-no questions. Clause 4 covers disjunction, conditionals, and wh-questions. Hybrid DRS-conditions, formed by combining a discourse referent and a DRS, are introduced in clause 5. Clause 6 describes necessary and possible effects of actions, and clause 7 introduces DRS-conditions that describe actions that are commanded.

2.3 Inference

The DRS-language used for representing the semantic content is useful for dealing with various linguistic phenomena, but there are no efficient inference engines available that work directly on DRSs. Since there are a couple of efficient theorem provers and model builders for first-order logic available, we translate the DRSs to first-order formulas for inference tasks.

The core of the translation to first-order covering our extended DRS-language is based on the "standard translation" from DRT to first-order logic [5]. Basically, it introduces existential quantifiers for discourse referents, unless discourse referents are declared in the universe of the antecedent DRSs of an implication, in which case they will undergo universal quantification. Sets of DRS-conditions are translated into a conjunction of first-order formulas. To deal with the modal operators in our extended DRS-language, we use the ideas of the relational translation for modal logic to first-order formulas [6]. This means that all basic DRS-conditions of arity are translated into first-order relations of arity $+1$, where the additional argument plays the role of a possible world (a state). DRS-action-terms are translated into three-place relations where the first argument denotes the current state, the second argument describes the actions, and the third argument denotes the resulting state. The full translation is given in [7]. We illustrate the translation with an example.

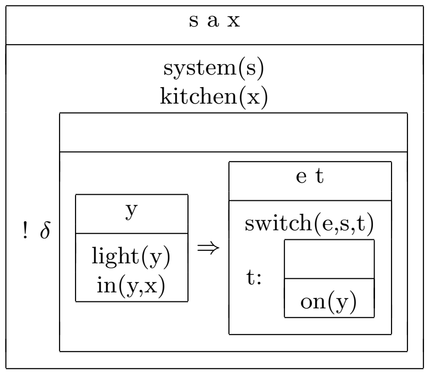

Figure 1: Example DRS paraphrasing the utterance "Switch every light in the kitchen on".

Consider the DRS for *Switch every light in the kitchen on!* in Figure 1. This example will get the following first-order translation:

$$w \;\; s \;\; a \;\; x \; (\text{possible\_world}(w) \quad \text{system}(w,s)$$
$$\text{kitchen}(w,x) \quad v \;\; a \; (\text{action}(w,a,v) \quad y$$

(light(a,y) in(a,y,x) e t
(switch(w,e,s,t) on(t,y)))))

We make use of two kinds of inference engines: theorem provers, and model builders. A theorem prover, when given a first-order formula, tries to decide whether it is true in all possible models. A model builder, on the other hand, tries to construct a possible model for the input formula. Figure 2 describes this idea in the form of an algorithm. Step 1 illustrates the fact that due to potential ambiguities appearing in the utterances conveyed by the user, semantic interpretation normally result in a set of DRSs. In Step 2, we make interpretation of the dialogue sensitive to context (see Section 2.4). We start with the empty set of interpretations (Step 3) and attempt to find consistent interpretations for each of the DRSs (Step 4). The theorem prover and model builder work in a complementary way. As soon as a proof is found the model builder does not need to further attempt to find a model because it will never succeed in doing so. However, if a model is found, the theorem prover can stop its attempt to find a proof, because it will never be able to do so. Finally, the system is instructed on how to react on the set of interpretations found (Step 5 and 6).

As the algorithm implies, the models generated by the model builder play a crucial role in interpretation. Figure 3 shows the model generated for the DRS of Figure 1. There are two interesting things about models. First, the flat representations of these models (they contain no recursion, in contrast to DRSs) ensure that they are extremely easy to process— all quantification and boolean structures are explicit in models. Second, the models produced by the model builder are minimal models, and contain no irrelevant information.

We use the model to deduce what actions need to be performed by the robot, or to answer questions posed by the user. For instance, in the model in Figure 3 a desired action for the robot is to supply power to the lights `d6` and `d7`.

The algorithm itself is implemented on top of the information-state approach to dialogue modelling [8], in which an agent's information state is updated on the basis of observed dialogue moves, leading to the selection of a new dialogue move to be performed by the agent. This is realised by a set of update rules, linking preconditions to effects. The dialogue manager repeatedly computes the effects of those update rules whose preconditions are satisfied by the current information state. Preconditions are expressed in terms of current values in the information state, while the ef-

1. Construct a (finite) set of DRSs $\mathcal{B}$ for a new utterance with respect to the previous DRS B_{old};
2. Construct a DRS C representing situational knowledge;
3. Initialise the set of interpretations $\mathcal{I}$ to $\emptyset$;
4. For each $B_i \in \mathcal{B}$:
   (a) Translate the compound DRS $(B_i; C)$ to the first-order representation $_i$;
   (b) Compute appropriate background knowledge stated as the first-order theory $_i$ for $_i$;
   (c) Attempt to build a model for ($_i \wedge$ $_i$) by simultaneously performing:
      i. Give ($_i \wedge$ $_i$) to a model builder, possibly resulting in a model M_i; (for consistent interpretations).
      ii. Give $\neg$($_i \wedge$ $_i$) to a theorem prover, possible resulting in a proof (for inconsistent interpretations);
   (d) If a proof is found cancel $4(c)i$. If a model is found add $\langle B_i \; M_i \rangle$ to $\mathcal{I}$ and cancel $4(c)ii$;
5. If $\mathcal{I} = \emptyset$ perform a misunderstanding act and quit. Else perform an understanding act and select a preferred interpretation $\langle B_p \; M_p \rangle$ from $\mathcal{I}$;
6. Use the information in M_p to decide whether to perform any actions. Replace B_{old} by B_p.

Figure 2: Update algorithm for inference-based dialogue management

```
D={d1,d2,d3,d4,d5,d6,d7,d8}
F(possible_world)={d1,d2,d3}
F(system)={(d1,d4),(d2,d4),(d3,d4)}
F(kitchen)={(d1,d5),(d2,d5),(d3,d5)}
F(action)={(d1,d2,d3)}
F(light)={(d1,d6),(d2,d6),(d3,d6),(d1,d7),
          (d2,d7),(d3,d7)}
F(in)={(d1,d6,d5),(d2,d6,d5),(d3,d6,d5),
       (d1,d7,d5),(d2,d7,d5),(d3,d7,d5)}
F(poweron={(d2,d6),(d2,d7)}
F(off)={(d1,d6),(d1,d7)}
F(on)={(d3,d6),(d3,d7)}
```

Figure 3: Example model

fects will change these values. The 26 update rules in our current system deal with establishing contact with the user, initiating clarification dialogues (when the recognition confidence score is below a certain threshold), answering questions, acknowledging requests and confirming or denying statements.

2.4 Background Knowledge

The interpretation algorithm in Figure 2 integrates background knowledge in two ways: in Step 2 situational knowledge is combined with the DRS; and in Step 4b other background knowledge is computed. These other sources of background knowledge can be divided in ontological knowledge, world knowledge and knowledge linking language to robot primitives.

Ontological knowledge comprises the various relationships between concepts that appear in the application domain. The two main relations that are expressed are subsumption and disjointness. For instance, we need to express that in all possible worlds a kitchen is a region, and that in all possible worlds a kitchen is not a corridor. Both can easily be coded in first-order logic:

w x(kitchen(w,x) region(w,x))
w x(kitchen(w,x) corridor(w,x))

World knowledge subsumes all generalisations relevant to the application domain. The so-called 'frame axioms' belong to this class, and rules expressing physical laws. The frame axioms state properties of objects when certain actions are performed. For instance, if a robot moves from one region to another, its position will be different, but the positions of all other objects normally remain unaltered. Again, this can be relatively easily coded in first-order logic.

Knowledge linking natural language to robot primitives can be seen as a set of meaning postulates, rules that map non-logical symbols expressing the meaning of actions to symbols understood by the robot. Put differently, these rules establish the interface between the instruction language (i.e., English) and the hardware of the robot. An example of such a rule is "to switch on a device" and its translation into a DRS (Figure 1), which is mapped to the action `poweron`, as can be seen in the model generated for it (Figure 3).

Situational knowledge, finally, comprises the information of a specific situation in time. In the application domain of mobile robots, this typically consists of the regions and objects that are accessible to the robot, and the current positions of movable objects (including the robot itself). We do not code this knowledge directly into first-order knowledge, but rather use DRSs. This allows us to combine the situational knowledge with the information from the dialogue, enabling to interpret actions directly in the current situation.

3 Mobile Robot Control

3.1 Control Architecture

The control system is a looping algorithm reading sensory input and writing motor output at regular intervals. The sensory input comprises the readings of sonars, infrared sensors, bumpers and odometry. The sonars and infrared sensors are used for detecting occupied space and obstacles, and the bumpers notify if the robot hit an obstacle or wall. The odometry component measures the position and orientation of the robot. The motor output comprises translational and rotational velocity of the robot, and pan-tilt-zoom information for the camera unit.

We use units called "behaviours" to implement robot control. A behaviour has its own internal memory and uses the sensory input and motor output of the control system. While executing, it computes the motor output based on the sensory input and internal memory and updates the memory at regular intervals. It terminates when certain conditions are fulfilled. For example, a behaviour to move forward repeatedly sends velocity commands in a forward direction and terminates when an obstacle is detected or the robot has reached a specified location.

Behaviours are described as object-oriented classes (Figure 4). An instance of a behaviour class can be created using different parameters such as speed, direction, duration, or goal.

The robot needs to be able to deal with multiple goals. For instance, the robot may receive a new verbal command from the user when it is already undertaking an action. In that case, the robot must suspend the current behaviour and create and execute another. In our control system, we use a stack of behaviour instances to pursue multiple goals given by the user. The control system creates instances of behaviour classes, pushes them into the stack and deletes them when they terminate.

The behaviour that is executed is the one on the top of the stack. Any new command suspends the current executing behaviour and starts a new behaviour. When the new behaviour terminates, it is popped of the stack and the previous one resumes execution. The use of a stack simplifies the way the dialogue system sends commands to the control system. It doesn't need

The Eleventh International Symposium on Artificial Life and Robotics 2006 (AROB 11th'06),
B-con Plaza, Beppu, Oita, Japan, January 23-25, 2006

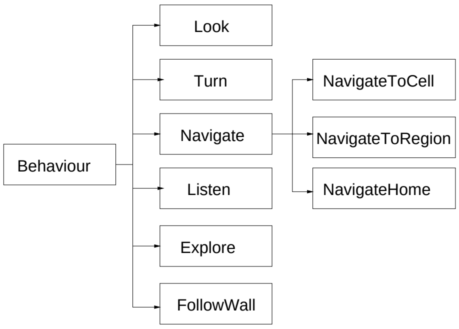

Figure 4: Part of behaviour class hierarchy

send commands to explicitly suspend, resume, terminate or remove behaviours to achieve multiple goals.

There are robot primitives creating simple behaviours such as *go(Distance, Speed)*, *turn(Angle, Speed)* and *look(Pan,Tilt)*, as well as commands introducing complex behaviours like *follow_wall(Distance)* and *move_to_region(N)*. In addition, sequences of actions such as *seq(zoom(100), look(0, 20), turn(90, 20))* can be commanded, in which case three behaviour instances are created and pushed into the stack.

3.2 Internal Map and Situational Knowledge

An internal map of the environment is used to plan a path to the target location and navigate the robot there following the path and avoiding obstacles. There are three layers in the map. The geometrical layer uses an occupancy grid to represent occupied and free space in the environment. The topological layer is automatically constructed from the occupancy grid by subdividing the free space into distinct topological regions corresponding to rooms or parts of the corridor (Figure 5). This is possible by creating a Generalised Voronoi Diagram [9, 10, 11].

The numbers in the geometrical map shown in Figure 5 are identifiers of topological regions which can be seen as nodes of an undirected graph. A further layer of representation connects the map of the navigation system with a vocabulary of semantic symbols used by the dialogue system. This is done by associating semantic descriptions to regions (Table 1). These descriptions can be arbitrarily complex. For instance, the DRS $\lambda p\ (\ [\quad]\ [\mathit{office}(x)\ \ \mathit{of}(x\ \ y)\ \ \mathit{tim}(y)]\ ;\ p(x))$ could be used to denote Tim's office.

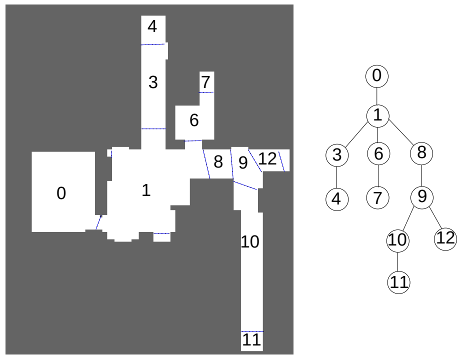

Figure 5: Representation of the environment

Table 1: Semantic labels

Region	Description	Semantic label
0	the office	p.([x] [OFFICE(x)] ;p(x))
1	the hallway	p.([x] [HALLWAY(x)] ;p(x))
3, 4, 8-12	the corridor	p. [x] [CORRIDOR(x)] ;p(x))
6	the rest room	p.([x] [REST_ROOM(x)] ;p(x))

4 Implementation and Evaluation

We implemented a talking mobile robot system, Godot, integrating a dialogue interface and a control system on an RWI Magellan Pro mobile robot platform with an on-board PC and a laptop computer on the top (Figure 6).

Godot is a complete end-to-end system for human-robot communication, where users can start a new dialogue simply by addressing the robot in spoken language, with the robot responding in real time. Although we have not yet reached the stage of carrying out formal usability studies, we have tested Godot when visitors to our department unfamiliar with Godot have controlled its movements and its camera with success. Another evaluation took place over two days in the Scottish museum, where museum visitors could address the Godot in a simulated house. This was a different environment from Godot's usual one (the basement of our department) but our modular approach allowed us to quickly adapt it—in fact we only needed to change the internal map. In these interactions with new users we collected the spoken data and used that to improve the system, by extending the vocabulary and grammar constructions. We have published videos of Godot in action at `http://www.ltg.ed.ac.uk/godot/`.

Figure 6: Godot, the mobile robot

5 Conclusions

We have developed an effective interface between natural language semantics and the robot control layer, thus enabling users to refer to locations in a natural way, rather than resorting to expressions like *go to grid cell 45-66* or *you are in region 12.* The framework is practically domain-independent: a change of environment would only require a change of the internal map and possibly a new lexicon.

Our robot employs an inference-based approach to dialogue understanding, with the aim to find a *consistent* semantic representation capturing the meaning of the dialogue. If a consistent interpretation cannot be found, we have got a signal that something is going wrong in communication. Such a situation might arise from disagreement or misunderstanding between dialogue participants. Inference also contributes to ambiguity resolution (for instance the resolution of pronouns and other anaphoric expressions) and helps finding preferred interpretations. Moreover, with the help of *model building*, inference can be used for performing actions and answering questions, too. The resulting dialogue system is formulated on an abstract level, and is easily portable to robots in new domains or with different applications.

Future work will address the interpretation of vague expressions (*the end of the corridor*), metonymic expressions (*go to the door*, where an artifact is interpreted as a location), together with commands which require Godot to reason and talk about its current activities (*continue going to the kitchen*).

Acknowledgements

This work was supported by IBL for mobile robots (EPSRC GR/M90160) and the EU Project Magicster (IST 1999-29078). We thank Nuance for permission to use their software and tools.

References

[1] Johan Bos, "Compilation of Unification Grammars with Compositional Semantics to Speech Recognition Packages," *COLING 2002. Proceedings of the 19th International Conference on Computational Linguistics*, 106–112, 2002. 1982.

[2] Hans Kamp, "A Theory of Truth and Semantic Representation," *Formal Methods in the Study of Language*, 277–322, 1982.

[3] A. Rob Van der Sandt, "Presupposition Projection as Anaphora Resolution," *Journal of Semantics*, vol.9 333-377, 1992.

[4] Alex Lascarides, "Imperatives in Dialogue," *Proceedings of the 5th International Workshop on Formal Semantics and Pragmatics of Dialogue (BIDIALOG)*, 1–16, 2001.

[5] H. Kamp and U. Reyle, *From Discourse to Logic; An Introduction to Modeltheoretic Semantics of Natural Language, Formal Logic and DRT*, Kluwer, 1993.

[6] Robert C Moore, "Reasoning about Knowledge and Action," *SRI International Technical Report*, 1980.

[7] Johan Bos, "Implementing the Binding and Accommodation Theory for Anaphora Resolution and Presupposition Projection," *Computational Linguistics*, vol.29, 2, 179–210, 2003.

[8] David Traum et al, "A model of dialogue moves and information state revision," *Trindi Technical Report D2.1,* 1999.

[9] Jean Claude Latombe, "Robot Motion Planning," *Kluwer Academic Publishers*, 1991.

[10] Sebastian Thrun, "Learning Maps for Indoor Mobile Robots," *Artificial Intelligence*, vol.99(1), 21–71, 1998.

[11] Christian Theobalt, "Navigation on a Mobile Robot," *Master's Thesis, University of Edinburgh*, 2000.

The Eleventh International Symposium on Artificial Life and Robotics 2006 (AROB 11th'06),
B-con Plaza, Beppu, Oita, Japan, January 23-25, 2006

Performance Evaluation of Evolutionary Multiobjective Optimization

Genci Capi[1], Koco Bode[2] and Masao Yokota[1]

[1]Faculty of Information Engineering
Fukuoka Institute of Technology
3-30-1 Wajiro-Higashi, Higashi-ku, Fukuoka, 811-0195, Japan

[2] Faculty of Mechanical Engineering
Polytechnic University of Tirana
Sheshi Nene Tereza, Tirana, Albania

capi@fit.ac.jp

Abstract
In this paper, we focus on the performance of evolutionary multiobjective optimization algorithm. Especially, how the population size and number of interactions affect the quality and distribution of optimal Pareto solution. The performance is tested in humanoid robot gait generation task. The humanoid robot gait is generated based on two conflicting objectives: minimum energy and minimum torque change. The preliminary results show that population size and number of interactions greatly effect the performance of multiobjective evolutionary algorithm.

KEY WORDS
Actor-critic Reinforcement Learning, Genetic Algorithm, metaparameters.

1. Introduction

In most of real world problems several objectives, often conflicting ones, must be satisfied simultaneously in order to obtain an optimal solution. Evolutionary algorithm is one of the most prominent class of metaheuristics for tracking multiobjective optimization problems.

In order to solve multiobjective problems different approaches have been proposed. Syswerda and Palmucci ([1]) proposed a combination of all objectives into a single one using different weighting coefficients for each one of them. Charnes and Cooper ([2]) and Ijiri ([3]) developed a method where the targets or goals are incorporated into the problem as additional constraints. However, both these methods require accurate information on the objectives, to determine the appropriate weights.

Recently multiobjective evolutionary algorithm (EA) ([4], [5]) has been proven to give good results by finding better tradeoffs between different objective functions. However, a crucial issue is to determine the EA parameters like the population size, number of interactions, crossover and mutation probability, in order to improve the performance..

In order to see the effect of these parameters on the performance of multiobjective EA, we considered a the humanoid robot gait generation based on two conflicting objective functions: minimum consumed energy (MCE) and minimum torque change (MTC) ([6]). In our previous works, we considered the humanoid robot gait generation during walking and going up-stairs ([7]) and a real time gait generation ([8]), where each criteria was satisfied separately. The results showed that MCE gait has different characteristics compared to MTC. MCE gait was similar with that of human. Another advantage of MCE criteria is also related to the operation time when a battery actuates the motors. On the other hand, due to smooth change of torque and consequently of link accelerations, the disturbance of robot stability was small in MTC humanoid robot gait. Based on these observations, it would be effective to generate a humanoid robot gait utilizing the advantages of each optimization criteria. Our method produces a set of non-dominated Pareto front solutions from which we can select the preferable humanoid robot gait.

Some preliminary results presented in this paper show that performance of multiobjective EA is greatly affected by the parameters such as population size and termination criteria. Especially, the number of interactions influences the quality of the solution and the distribution of nondominated solutions in the obtained Pareto optimal set.

2. Multiobjective Evolutionary Algorithm

In multiobjective optimization problems there are many (possibly conflicting) objectives to be optimized, simultaneously. Therefore, there is no longer a single optimal solution but rather a whole set of possible solutions of equivalent quality. In contrast to fully ordered scalar search spaces, multidimensional search spaces are only partially ordered, i.e. two different solutions are related to each other in two possible ways: either one dominates the other or none of them is dominated. Consider without loss of generality the following multiobjective maximization problem with m decision variables x (parameters) and n objectives:

$$y = f(x) = (f_1(x_1, \ldots\ldots x_m), \ldots, f_n(x_1, \ldots\ldots x_m)) \tag{1}$$

where $x = (x_1, \ldots\ldots x_m) \in X$, $y = (y_1, \ldots\ldots y_n) \in Y$ and where x is called decision (parameter) vector, X parameter space, y objective vector and Y objective space. A decision vector $a \in X$ is said to dominate a decision vector $b \in X$ (also written as $a \succ b$) if and only if:

$$\forall i \in \{1, \ldots, n\} : f_i(a) \geq f_i(b) \wedge \exists j \in \{1, \ldots, n\} : f_j(a) > f_j(b) \tag{2}$$

The decision vector a is called Pareto-optimal if and only if a is nondominated regarding the whole parameter space X. Pareto-optimal parameter vectors cannot be improved in any objective without causing degradation in at least one of the other objectives. They represent in that sense globally optimal solutions. Note that a Pareto-optimal set does not necessarily contain all Pareto optimal solutions in X. The set of objective vectors corresponding to a set of Pareto-optimal parameter vectors is called "Pareto-optimal front".

In extending the ideas of single objective EAs to multiobjective cases, two major problems must be addressed: 1. How to accomplish fitness assignment and selection in order to guide the search towards the Pareto-optimal set. 2. How to maintain a diverse population in order to prevent premature convergence and achieve a well distributed, wide spread trade-off front. Note that the objective function itself no longer qualifies as fitness function since it is a vector valued and fitness has to be a scalar value. Different approaches to relate the fitness function to the objective function can be classified with regard to the first issue. The second problem is usually solved by introducing elitism and intermediate recombination. Elitism is a way to ensure that good individuals do not get lost (by mutation or set reduction), simply by storing them away in an external set, which only participates in selection. Intermediate recombination, on the other hand, averages the parameter vectors of two parents in order to generate one offspring.

3. Humanoid Robot Gait Generation

During motion, the arms of the humanoid robot will be fixed on the chest. Therefore, it can be considered as a five-link biped robot in the saggital plane, as shown in Fig. 1. The motion of the biped robot is considered to be composed from a single support phase and an instantaneous double support phase. The friction force between the robot's feet and the ground is considered to be great enough to prevent sliding. In addition, the posture at the beginning and at the end of the step is considered the same.

The humanoid robot gait synthesis problem during walking, consists on finding the joint angle trajectories, to connect the first and last posture of the biped robot for which the CE or TC is minimal. For the MCE cost function, it can be assumed that the energy to control the position of the robot is proportional to the integration of the square of the torque with respect to time, because the joint torque is proportional with current. Therefore, minimizing the joint torque can solve the MCE problem. The cost function J, which is a quantity proportional to the energy required for the motion, is defined as follows:

$$\mathrm{En} = \frac{1}{2}\left(\int_0^{t_f} \tau^T \tau \mathrm{dt} + \Delta\tau_{\mathrm{jump}}^2 \Delta t + \int_0^{t_f} \mathrm{Cdt}\right), \tag{3}$$

where: t_f is the step time, τ is the torque vector, $\Delta\tau_{\mathrm{jump}}$ and Δt are the addition torque applied to the body link to cause the ZMP to jump in the ne supporting foot and its duration time, and C is the constraint function, given as follows:

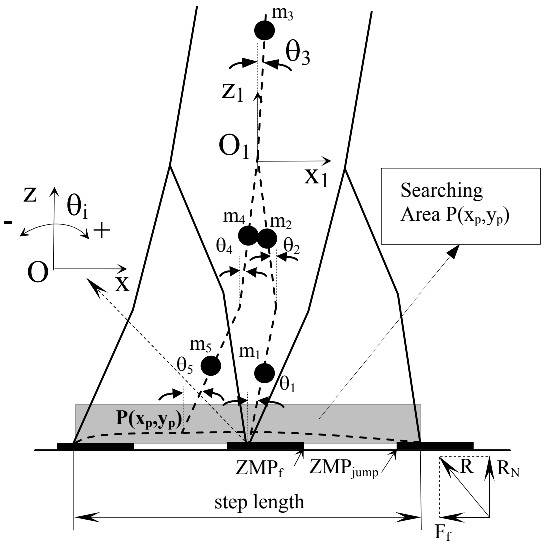

Fig.1 Five link biped robot in the saggital plan.

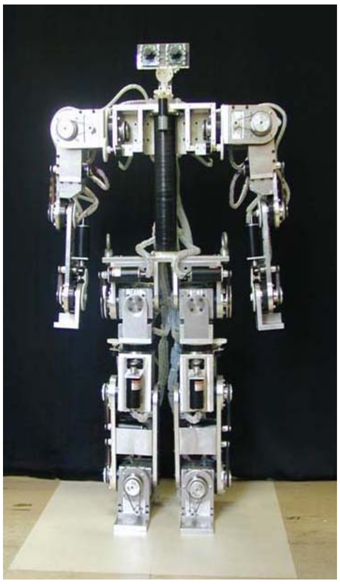

Fig.2. "Bonten-Maru" humanoid robot.

$$C = \begin{cases} 0 \text{ - if the constraints are satisfied,} \\ c_i \text{ - if the constraints are not satisfied,} \end{cases}$$

c denotes the penalty function vector. The individuals that not satisfy the constraints have a low probability to survive in the next generation. We consider the following constraints during the humanoid robot gait generation:

- The walking to be stable or the ZMP to be within the sole length.
- The distance between the hip and ankle joint of the swing leg must not be longer then the length of the extended leg.
- The swing foot must not touch the ground prematurely.

The MTC model is based on smoothness at the torque level. Uno et al., 1989 argue that human arm motion is generated based on MTC cost function. The cost is the integrated squared torque change summed over the joints and the movement. In the MTC, the objective function to be minimized is expressed as follows:

$$J_{torquechange} = \frac{1}{2}\left(\int_0^{t_f} \left(\frac{d\tau}{dt}\right)^T \left(\frac{d\tau}{dt}\right) dt + \left(\frac{\Delta\tau}{\Delta t}\right)^2 + \int_0^{t_f} C dt\right). \quad (4)$$

4. Results

In the simulations, we use the parameters of the "Bonten-Maru" humanoid robot (Fig. 2). The "Bonten-Maru" is 1.2m high, each leg has 6 degrees of freedom and is composed by three segments: upper leg, lower leg and the foot. The foot length is 0.18m. A DC servomotor actuates each joint. The control platform is based on Common Object Request Broker Architecture (CORBA), which allows an easy updating and addition of new modules.

Due to difficulties of binary representation when dealing with continuous search space with large dimension, real coded GA [8] is used in this study. The decision variables are represented by real numbers within their lower and upper limits. We employed a standard crossover operator and the non-uniform mutation. In all optimization runs, crossover and mutation probabilities were chosen as 0.9 and 0.3, respectively. On all optimization runs, the population size was selected as 50 individuals and the optimization terminated after 100 generations. The maximum size of the Pareto-optimal set was chosen as 50 solutions.

In the following, we present the results for the step length 0.42m and step time 1.2s. Fig. 3 shows the Pareto-optimal trade-off front after 100 generations. We can observe the existence of a clear tradeoff between the two objectives. In addition, the obtained reference solution set has a good distribution (similar to uniform distribution). One of the interesting features of the resulting Pareto front is the almost exponential relation between the MCE and MTC cost functions. Results in Box 1 and Box 5 are at the extreme ends of the Pareto front. Box1 represents Pareto solutions with high value of MTC function, but low energy consumption. Based on the Pareto-optimal solutions, we can choose whether to go for minimal CE (Box 1 in Fig. 3) at the expense of a less smoothness in the torque or choose some intermediate result. If we are interested for a low consumed energy humanoid robot gait, without neglecting the smoothness in the torque change, the results shown in Boxes 2, 3 are the most important. The results in Box 2, show that by a small increase in the energy consumption (2.2%), we can decrease the MTC fitness function by around 12.1%. Also, the energy can be reduced by 14.5% for a small increase in the MTC cost function, as shown by Box 4 solution.

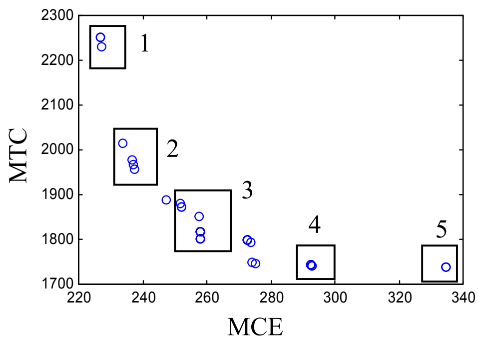

Fig. 3. Pareto front after 100 generations.

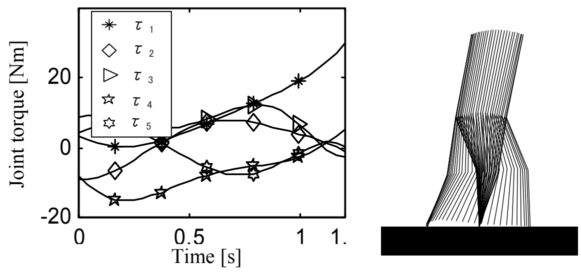

(a) Box 1 results (MCE).

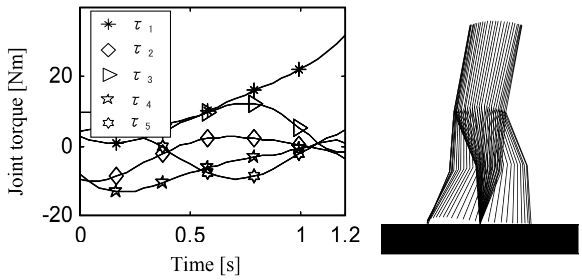

(b) Box 3 results.

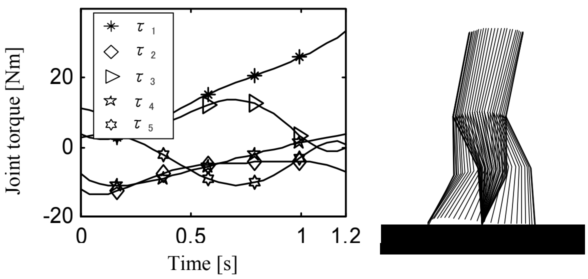

(c) Box 5 results (MTC).

Fig. 4. Torque vector and optimal gait of different optimal solutions selected from Pareto-front.

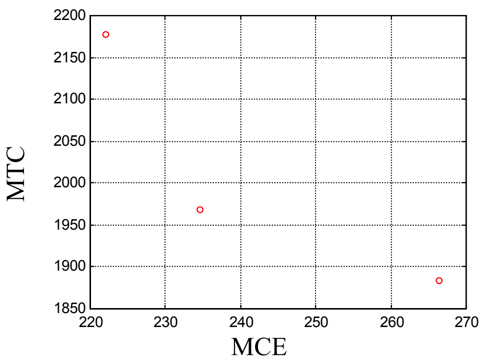

Fig. 5. Performance of EA with 40 interactions.

In the following we changed the number of interactions to 40 while the population size is considered 50, the same with previous simulation. The optimal Pareto solution is shown in Fig. 5. This figure shows that nondominated solutions in the obtained Pareto optimal set are not well distributed. The fitness values of both objective functions are nearly the same with the results shown in Fig. 3. The performance of EA with 100 interactions is slightly better for MTC cost function.

5. Conclusion

In this paper we gave some preliminary results on how parameters such as number of interactions, population size influence the performance of multiobjective EA. We checked the performance on a humanoid robot gait generation task based on two conflicting objective functions. The results show that the proposed approach is efficient for solving multiobjective optimization in that multiple Pareto-optimal solutions can be found in one simulation run. In addition, number of interactions greatly affects the distribution of nondominated solutions in the obtained Pareto-optimal. In addition, the results show that the optimal gait reduces the energy consumption and increases the stability during the robot motion.

References:

[1] Syswerda, G., and Palmucci, J., 1991, The application of genetic algorithms to resource scheduling, in: *Proc. of the Fourth Int. Conference on Genetic Algorithms*, R. K. Belew and L. B. Brooker, ed., Morgan Koufmann, California, pp. 502-508.

[2] Charnes, A., and Cooper, W. W., 1961, Management models and industrial application of linear programming, Vol. 1, John Wiley, New York.

[3] Ijiri, Y., 1965, "Management goals and accounting for control", North-Holland, Amsterdam.

[4] Coello, C. A. C., 1999, "A cornprehensive survey of evolutionary based multiobjective optimization techniques," *Knowledge and Information Systems*, 1(3):269-308.

[5] Herrera, F., Lozano, M., and J. L. Verdegay, 1998, Tackling real-coded genetic algorithms: operators and tools for behavioral analysis, *Artificial Intelligence Review*, 12(4), 265-319.

[6] Uno, Y., Kawato, M., and Suzuki, R., 1989, Formulation and control of optimal trajectory in human multijoint arm movement, *Biol. Cybernet*. 61:89-101.

[7] Capi, G., Nasu, Y., Barolli, L., and Mitobe, K., Takeda, K., 2001, Application of genetic algorithms for biped robot gait synthesis optimization during walking and going up-stairs", *Advanced Robotics Journal*, 15(6):675-695.

[8]Capi, G., Nasu, Y., Barolli, L., and Mitobe, K., 2003, "Real time gait generation for autonomous humanoid robots: a case study for walking", *Robotics and Autonomous Systems*, 42(2):107-116.

Mobile Robot Navigation by Visual Perception with Vision Decision Agent in an Unstructured Environment

Chandima Dedduwa Pathiranage
Dept. of Advanced Systems Control Eng.
Graduate School of Science and Eng.
Saga University
1-Honjomachi, Saga 840-8502, Japan

Keigo Watanabe, Kiyotaka Izumi
Dept. of Advanced Systems Control Eng.
Graduate School of Science and Eng.
Saga University
1-Honjomachi, Saga 840-8502, Japan

Abstract

We present a vision-based robot navigation system in an unstructured environment. This system operates under two stages: namely online path planning upon receiving the current image and robot navigation related to the current planned path. We make a simulator that can simulate the minimum path upon giving the starting and the goal point. The robot using this system can acquire the coordinates of the planned path and navigate along the path smoothly. The intent of this project is to create a system that allows robot to navigate in a dynamic environment in a way that facilitates path planning and goal oriented tasks with the minimum hardware requirements.

1 Introduction

Digital image processing [1] has been used in the field of robotics to find out many solutions for the robot navigation problems. This is due to the fact that digital image processing provides a rich set of features of the environment at anytime which will direct a robot to the goal controlling the navigation behavior of the robot in real time. Many robot navigation systems also focus on producing a detailed metric map of the world using expensive hardware, such as a laser scanner. The system we introduce here facilitates path-planning and does not require expensive range sensors. Some vision-based systems [2][3] require expensive and complicated hardware. We have to reduce the amount of hardware so that it will not affect performances of the navigation system since our priority goes to system performances. The present navigation system we have designed relies on the image data received from the camera as the sole input to navigate the robot. This is the highlighting point in our system.

In path planning problems, conventional vision systems have used different planning methods such as visibility graphs, Voronoi diagram, cell decomposition method, potential field method, etc. Some of those methods do not give the minimum path to the goal and when there are many sharp turning points in the path, it makes navigation complicated. One of the advantages in our navigation system is that we can reduce the number of sharp turning points and guarantee the smooth navigation along the path.

Our navigation system is capable of identifying the obstacle locations, shapes of the obstacles and sizes of obstacles. It can readily make the shortest path upon giving the goal. Introducing circular object modeling and tangential path planning methods, we can add additional advantages to our navigation system, compared to the previous work on vision-based navigation systems [2][3][4]. This leads to the processing time to be small and to reduce the complexity of the system. A vision decision agent is introduced into the navigation system so that it can learn the dynamic behavior of the environment. Simplicity, reliability, accuracy and quickness of our navigation system result in a successful result in a dynamic environment.

2 The Present System Overview

Our experimental setup includes a USB camera, a test bed and a computer. Khepera miniature robot is used in this experiment. The plan view of the robot environment is captured by the camera and is read by the computer where the robot is connected through a serial line to process the captured image. The image processing part of the system processes the image for detailed information of the robot environment. In identifying the edges of objects, Canny edge detection method is performed. To ensure faster navigation and to ease path planning, each detected obstacle is modeled by a circle in the path planning part of the system so that each circle just fits each obstacle.

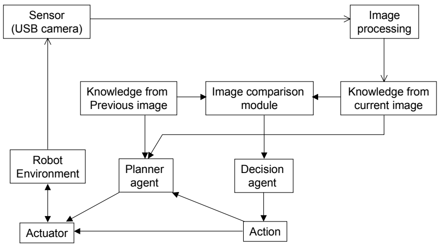

Figure 1: System architecture

Modeled obstacle can now be considered as circular obstacles. To make sure safe navigation of the robot, modeled obstacles are further expanded to keep an adequate clearance between the obstacle and the robot. The navigation system reads the coordinates of the planned path and converts the coordinates to real axis coordinates. The robot is then fed with the real axis coordinates and smooth navigation could be obtained along the planned path. The robot navigation is executed in parallel with decisions made by the vision decision agent implemented to observe the changes of the environment.

3 Architecture of Vision-Based Navigation System

The present vision-based navigation system can be split into three main parts, namely

1. Image processing,
2. Path planning, and
3. Robot navigation.

The architecture of our navigation system can be illustrated as shown in Fig. 1.

3.1 *Image Processing*

3.1.1 Image acquisition and conversion

Plan image of the robot environment is acquired through a USB camera. Software program is set to capture the image continuously with a given time interval. The captured image is RGB image as shown in Fig. 2(a). The RGB image is then converted to a gray level image.

3.1.2 Morphological dilation

Dilation adds pixels to the boundaries of objects in an image. An essential part of the dilation operation is

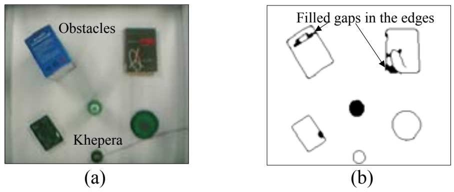

Figure 2: (a): Robot environment and (b): Edge detected, dilated image

the structuring element used to probe the input image. The pixels in the structuring element containing 1's define the neighborhood of the structuring element. Due to some light-colored, small clusters of pixels in the image can end up with breaking edges. Therefore the edge detected image is passed through the process of morphological dilation to obtain the continuous edges for all the objects in the image (see Fig. 2(b)). The size and the shape of the structuring element (see Fig. 3(a)) are selected to be "3" and "disk" respectively.

3.1.3 Morphological filling

The navigation system needs the understanding of exact number of objects in the image to proceed from the edge detection and the dilation. Morphological dilated edge detected image shows the clear and continuous boundaries of objects. Due to the irregular shape of the body of a particular object, it tends to locate the edges inside the main boundary of an object. This may mislead the navigation system that there may be many objects than the actual number of objects. To overcome this problem, morphological filling is carried out in the entire dilated edge detected image so that this filling technique will fill out all the area inside the main boundary of each object. Morphologically filled image; binary image looks similar to the figure in Fig. 4(a).

3.1.4 Labeling the objects

Objects in the binary image are labeled so that the navigation system can easily obtain the necessary information of the relevant objects when needed to proceed. Labeling the objects helps the system to distinguish the objects, their locations, boundary coordinates and area, etc. With the fact that the pixels of a particular object (1's) are connected together, the system can group the connected pixels and label connected component accordingly. Each set of connected pixel components represents the objects in the image. Fig. 3(b) shows the method of labeling the connected

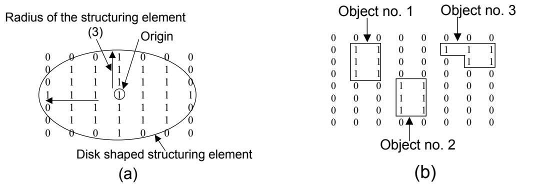

Figure 3: (a): Structuring element and (b): Labeling the connected components in a binary image

components in the binary matrix of a particular image. Labeling the objects in the image is shown in Fig. 4(a).

3.1.5 Object modeling

Path planning process may be complicated if the shapes of objects are irregular. It is desirable to make the irregular shaped objects in the image have regular shaped objects. Modeling of objects helps to ease the path planning and reduce the complexity in calculation. Modeling objects as circular objects is found to be one of the simplest methods in object modeling. It is needed to find out the center of each object in modeling the objects into circular objects. The center of objects is taken as the center of the circle which is used to model the objects. Since the objects are in irregular shapes, exact center of an object can not be found but the near center of an object can be found by securing the near symmetry of the object. For this purpose, the system finds rectangular bounding boxes which can just fit the objects and the center of each bounding box is taken as the near center of each object. And this near center of an object is treated as the center of modeling circle (see Fig. 4(a)). The navigation system is fed with these modeled circular objects for the next stage of path planning process. Object modeling and approximation are shown in Fig. 4(b).

3.2 *Path Planning*

The present navigation system uses the tangential method to make the path planning. The path planning part of our navigation system first identifies the closest obstacle to the starting point which lies on the line joining starting point and the goal point. It finds the two optimum tangential points of the interested circle; one is related to the starting point and the other is related to the goal point which give the minimum path between the starting and goal points when avoiding the first obstacle. At this stage, it records a part of this path from the starting point up to the tangential point which is related to the goal point. Between these

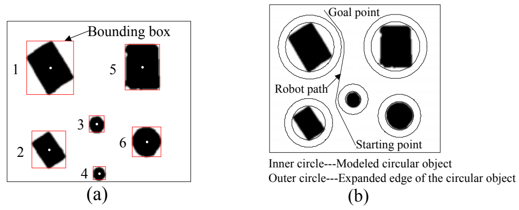

Figure 4: (a): Labeling the objects in the image and (b): Object modeling and path planning

tangential points, robot will follow the circle. And this resultant path is taken as the first segment of the final path. The tangential point, related to the goal point, of this segment of the path is made as the starting point for the next stage of path planning. This process is repeated until the path planning part of the navigation system finds the minimum path up to the goal point. A planned path upon giving the goal point is shown in Fig. 4(b).

3.3 *Robot Navigation*

We have first performed our experiment in the static environment. Coordinates of the planned path are in the pixel coordinates pertaining to the image axes. And these pixel coordinates have to be converted to the real coordinate system of the test bed to get the exact location of the path in the test bed. To make the robot navigate through the planned path, the navigation system obtains the key turning points in the final path and calculates the initial position of the robot, the initial direction of the robot, angles of the lines joining two adjacent turning points of the final path to the horizontal axis and the distances between adjacent turning points. All measurements are made with reference to the real test bed axis. The robot understands the distance to be traveled and the angle to be turned in terms of the time. The robot navigation takes place along the path shown in Fig. 4(b). Although our navigation system mainly works on image data retrieved from the captured image without any expensive hardware, we have shown the accuracy and simplicity of our system.

4 Dynamic Navigation

We have designed our navigation system to take changes in the environment into account. A vision decision agent is introduced to facilitate the robot navigation under dynamic conditions. The vision decision agent decides the suitable action that the robot should

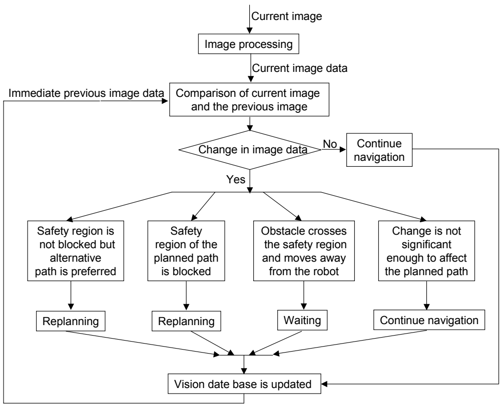

Figure 5: Flow chart of vision decision agent

undergo. The vision decision agent constitutes of image comparison network which uses the priori knowledge and the current knowledge of the environment to study for possible changes in the environment while updating the knowledge base of the environment each time when it receives a new image. The architecture of the vision decision agent is shown in Fig. 5. Based on the outcome of the image comparison module, the vision decision agent decides the three actions that should be executed by the navigation system. Three decisions are:

- **Continue navigation:** Robot navigates continuously unless the safe region of the planned path is blocked or the navigation system did not find any significant changes in the environment.
- **Waiting:** The robot waits if an obstacle crosses the safe region of the planned path and moves away from the robot.
- **Replanning:** The navigation system plans an alternative path from its current position if the safety region of the planned path is blocked by obstacles or the environment has changed significantly so that the system can find an alternative minimum path.

Navigation along the newly planned path when the object no. 1 left the environment is shown in Fig. 6. The navigation system executes the decision given by the vision decision agent and guides the robot accordingly until it reaches the goal point.

5 Conclusion

The present vision-based navigation system was capable of identifying the changes in the environment

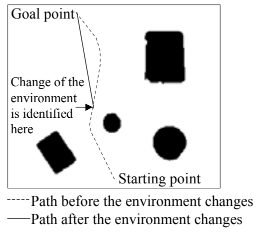

Figure 6: Dynamic path planning

while robot navigating in its environment. For example, the system can detect when the objects move in the environment and the existing objects leave the environment and the new objects enter into the environment. The proposed navigation system was able to navigate the robot under the dynamic conditions. The highlighting points of this work were that our system mainly worked on the vision data and we have used the minimum number of hardware requirements thus allowing the system to be simple but to performed well without any drawbacks. We have shown the faster path planning method and the safer navigation method by incorporating circular object modeling and tangential path planning method. This has reduced the calculation time to a considerable extent. Thus, we have presented a vision-based navigation system with a reduced complexity and faster response.

References

[1] R. C. Gonzalez and R. E. Woods, *Digital Image Processing*, New York, NY: Addison-Wesley, 1992.

[2] I. Ohya, A. Kosaka and A. Kak, "Vision-based navigation by a mobile robot with obstacle avoidance using single-camera vision and ultrasonic sensing," *IEEE Trans. on Robotics and Automation*, vol. 14, no. 6, pp. 969–978, December 1998.

[3] J. Gaspar, N. Winters and J. S. Victor, "Vision-based navigation and environmental representations with an omnidirectional camera," *IEEE Trans. on Robotics and Automation*, vol. 16, no. 6, pp. 890–898, December 2000.

[4] J. Weng and S. Chen, "Visual learning with navigation as an example," *IEEE Intelligent Systems*, vol. 15, no. 5, pp. 63–71, Sep-Oct. 2000.

Guiding Mobile Robots in Ubiquitous Environment Using Binocular Vision System and Intelligent Decision Making

Janaka Chaminda Balasuriya, Keigo Watanabe and Kiyotaka Izumi
Department of Advanced Systems Control Engineering
Graduate School of Science and Engineering
Saga University, 1-Honjomachi, Saga 840-8502, Japan
jcbala@lycos.com, {watanabe, izumi}@me.saga-u.ac.jp

Abstract

This paper describes an intelligent ubiquitous environment that is comprised of binocular vision system and adaptive fuzzy neuro based decision-making system for guiding a mobile robot. The integrated binocular vision system is mounted in the environment (rather than on one single robot) so as to get information about the whole area. This information after analyzing and processing is distributed among the robot units for navigation purposes. Potential field path planning techniques including mapping and navigation, allow safe navigation through the dynamic environment when carrying out dynamic target tracking forming a robust and cohesive intelligent ubiquitous system.

1 Introduction

Target tracking and path planning are used in many fields such as robotics, intelligent systems, autonomous vehicles, guidance systems, etc. There are many approaches in the areas of research to fulfill the dream of a fully functional automated moving system in a real-time environment. This simplest form of a tracking and guidance system can be considered as guiding a robot to a stationary position in a static environment. But, there will be many critical issues to consider when the target is moving and the environment is dynamic. According to Luo et al. [1], in addition to the sensory detection module in a general position based tracking system, there are many limitations to address, such as estimation/prediction of the object position from noisy sensory measurements, motion control of the tracker to track the moving object, etc.

When the target is a dynamic object with a complex nature of movement or target tracking is performed in a dynamic environment, accurate detection and fast responses are a must. These need much more advanced features such as fast response sensors, high speed processing equipment, etc. On the contrary, if the sensors have a slower response time, the estimation is no longer sufficient for a real-time target tracking [2].

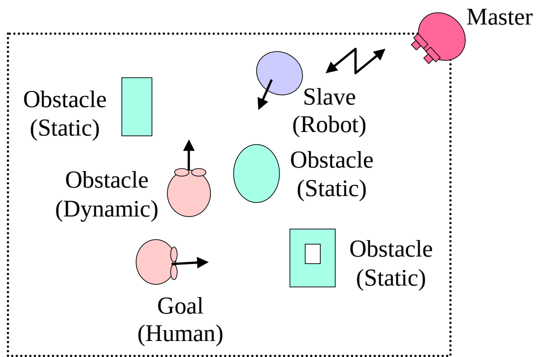

Figure 1: Target tracking in dynamic environment, where master, central intelligent system consists of binocular vision system and fuzzy logic decision making.

Hence many real-time tracking systems use intelligent prediction strategies based on fuzzy logic decision making to predict the potential object position at the next time period. Information gathered in such a way is used to speed up the detection procedure and to control motion parameters of a tracker device.

2 Target System

Navigate a slave (e.g. robot) to meet a goal (e.g. human) in motion while avoiding static and dynamic objects in the surrounding environment according to commands issued by a master (intelligent system consisting of fixed binocular vision system and fuzzy logic decision-making).

The environment is continuously monitored by the binocular vision system to identify static and dynamic objects. Here, objects like desks, chairs, standstill humans, robots, etc. are identified as static objects, whereas moving humans, robots, vehicles, animal, etc. are identified as dynamic objects. Next a goal (e.g. a human, vehicle, etc.) and a slave (e.g. a ubiquitous robot, a blind person, autonomous vehicle, etc.) are identified within this environment. Once a goal and a slave are identified, all the other objects (static or dynamic) in the environment will be considered as obstacles. Continuously analyzing the changes in the environment, master guides the slave until the slave reaches the goal by fuzzy logic decision-making (see Figure 1).

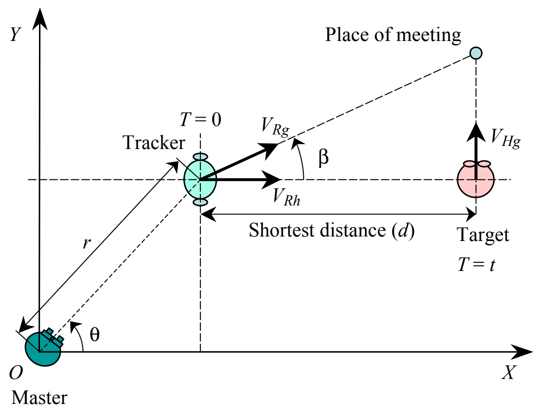

Figure 2: Position and velocity analysis.

3 Intelligent Space

In an era of "intelligent objects", it is also possible to think about "intelligent space", as proposed by Hashimoto et al. [3]. Intelligent space is an environmental system, which is able to support human in informative and physical ways. Most of intelligent systems interact with humans in a passive space, but in intelligent space, an environment containing humans and artificial systems is capable of self-sufficient. Artificial systems like sensors, cameras, etc. become agents of intelligent space and simultaneously humans and artificial systems like robots become "clients" of it. Consider a situation where a robot is lacking in sensors to navigate around an intelligent space. At such instance it can get the necessary guidance from the intelligent space very easily. The ultimate goal of intelligent space is to accomplish an environment that comprehends intentions of humans and assist them [4].

4 Position and Velocity Analysis

Position and velocity of the target, tracker and obstacles (static and dynamic) are obtained in the manner as illustrated in Figure 2. (Only target and tracker are shown). Master is positioned at one end of the concerned area, looking at the entire place. Give the coordinates of the tracker R with reference to its position, which can simply be written as equation (1) omitting z components considering the ground plane:

$$R = (x, y) = (r\cos\theta, r\sin\theta) \qquad (1)$$

Similarly velocity of each dynamic object is obtained, concerning one object at a time, one after each other. This process continues in a loop updating the decision-making systems. Since there can be many objects in the concerned area in many sizes and shapes, considerable amount of time can be expected to be wasted for one round of analysis. In order to minimize such time, simplification process is applied initially as described below.

5 Experimental Setup

Experimental setup to check the objective functionality of the software modules is shown in Figures 3 (a) and 3 (b), where Figure 3 (a) shows the real setup while Figure 3 (b) shows more generalized/simplified version of the same. Figure 3 (a) illustrates a "target" (movable toy), "tracker" (Khepera, programmable mobile robot for target tracking) and one obstacle (as the first stage). The simplification process includes the same objects (as in Figure 3 (a)) covered with specific colour top. This conversion is used to decrease the excessive burden on calculations involved, so that it will permit the initial identification of "target" (in blue colour), "tracker" (in green) and "obstacle" (in red) and later obtain the locations of them. In this way, it will be possible to search for colour matching/searching, without using complex object matching algorithms.

Some results obtained from the stereo vision-system, while trying to catch the motion of the target are shown in Figure 4. Here the target is tracked and its outer regions are marked with white colour and

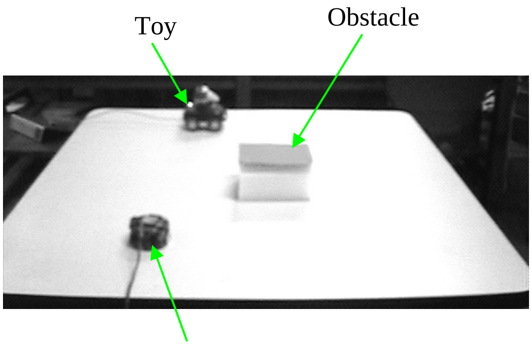

(a) Real situation

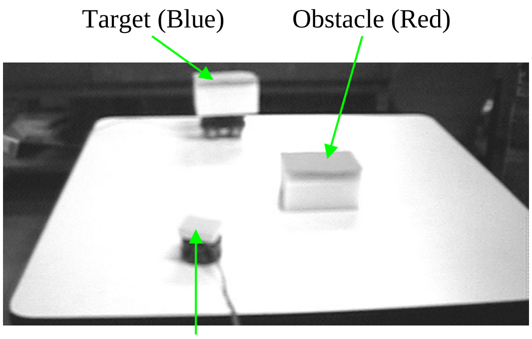

(b) Modified for simplification

Figure 3: Experimental setup to check the functionality of the software modules. Real objects are covered in special colours to make the identification and tracking processes more easier.

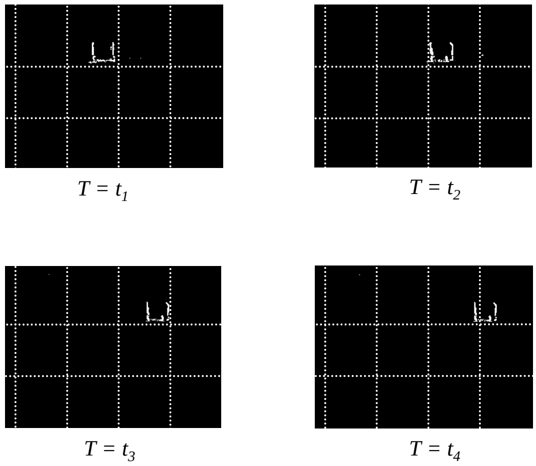

Figure 4: Tracking target.

all the other surrounding area is indicated by black colour. (Grid lines are added later for clarification).

6 Fuzzy and Relative Velocity

In the case of dynamic motion analysis, it is necessary to apply relative motion mechanisms. Once the robot starts to move, its speed and direction should be adjusted appropriately according to relative motion. Although the main objective is to track the target (i.e. to go and meet the moving human), necessary adjustments should be performed considering the relative motion as given by

$$V_{Rg} = V_{Rh} + V_{Hg} \tag{2}$$

where V_{Hg} is velocity of the target (human) with reference to the ground, V_{Rh} is velocity of the tracking robot with relative to the human and V_{Rg} is velocity of the tracking robot with reference to the ground.

In order to make V_{Rh} positive, i.e. the robot be able to meet the human (in case of following the human in straight behind), magnitude of V_{Rg} should be higher than magnitude of V_{Hg}. Also, magnitude of V_{Rh} will decide the time taken for the meeting of the two parties.

7 Environment with Obstacles

In an environment with continuously changing surroundings, it is necessary to make the necessary corrections from time to time. Once obtained the initial calculations of the relative velocity (speed, direction and hence by having a rough idea of time taken for the whole tracking job), it is necessary to apply it to the tracking device. Next it is necessary to adjust it as time proceeds or environment changes. This may be necessary to analyze target details as well as obstacles in the vicinity as described as follows.

Figure 5 illustrates path planning with respect to the obstacle position and motion. In the event of finding the most suitable path in a dynamic environment, it is necessary to consider all possible paths at a specific time. Consider the tracker position at $T = 0$ with the target position at $T = t$ (next position prediction of the target). For quick target tracking, next position of the target is considered with the current position of

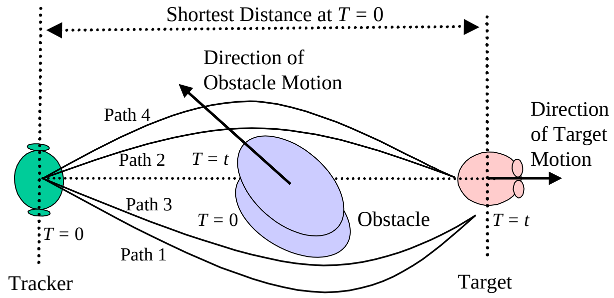

Figure 5: Path selection.

the tracker. With reference to the obstacle position at $T = 0$, path 1 or 2 seems to be acceptable. At $T = t$, obstacle moves a little bit and path 2 will no longer be acceptable as safe and it should be shifted as path 4 to avoid any possibility of collision. At the same time, path 1 can be re-adjusted to path 3 making it little shorter than path 1 to reach the target.

8 Summary

Attempt of implementing an intelligent decision-making system has been presented for guiding an autonomous mobile robot in ubiquitous environment using binocular vision system. Although much work has to be performed in the future in this regard, much benefit as well as certain parts that need improvements had been identified as follows. Time consumed for the studious calculations and processing of the vast amount of software programs is a major problem in the real time system. It has created a delay in taking the correct decision at the specific instance of time. In order to overcome such drawbacks, minimizing the total number of software programs or making them much easier for processing is currently under consideration. Application of a sense of "experience" to the central system (i.e. to keep certain instruction for a specific instance such as how the system responded for a particular situation in the past so as to apply them again if a similar situation occurs in the future. So in that case, it is not necessary to re-calculate once again minimizing the processing time to a great extent) is also being analyzed.

References

[1] R. C. Luo, T. M. Chen, and K. L. Su, "Target tracking using hierarchical grey-fuzzy motion decision-making method," *IEEE Transactions on Systems, man, and Cybernetics - Part A: Systems and Humans*, vol. 31, no. 3, May 2001, pp. 179–186.

[2] R. C. Luo and T. M. Chen, "Target tracking by grey prediction theory and look-ahead fuzzy logic control," in *Proc. IEEE Int. Conf. Robotics and Automation*, vol. 2, Detroit, MI, USA, May 10–15, 1999, pp. 1176–1181.

[3] H. Hashimoto, P. T. Szemes, and K. Morioka, "Intelligent space — Robots and spaces —," in *Proc. International Symposium on Electronics for Future Generations*, Tokyo, March 2004, pp. 383–388.

[4] H. Hashimoto, J. H. Lee, and K. Morioka, "Human robot interaction via intelligent space," in *Proc. International Conference on Control, Automation and Systems (ICCAS2002)*, Jeonbuk, Korea, October 2002, pp. 512–517.

[5] D. J. Coomb, "Real time gaze holding in binocular robot vision," *Technical Report, University of Rochester*, Dept. of Computer Science, 1992.

[6] J. Chung and H. S. Yang, "Fast and effective multiple moving targets tracking method for mobile robots," in *Proc. IEEE Int. Conf. Robotics and Automation*, vol. 3, Nagoya, Japan, May, 1995, pp. 2645–2650.

[7] Z. Lin, V. Zeman, and R. V. Patel, "On-line robot trajectory planning for catching a moving object," in *Proc. IEEE Int. Conf. Robotics and Automation*, vol. 3, Scottsdale, AZ, 1989, pp. 1726–1732.

[8] B. R. Chang and S. F. Tsai, "An intelligent prediction method for short-term time series forecast on engineering education," in *Proc. International Conference on Engineering Education*, Manchester, U.K. August 2002.

[9] J. Spletzer and C. J. Taylor, "Sensor planning and control in a dynamic environment," in *Proc. of IEEE International Conference on Robotics and Automation (ICRA '02)*, vol. 1, May 2002, pp. 676–681.

Kansei and Human Experience Analysis for Mobile Robot Navigation in Ubiquitous Environment

Janaka Chaminda Balasuriya,* Chandrajith Ashuboda Marasinghe,** Keigo Watanabe*
and Kiyotaka Izumi*
*Department of Advanced Systems Control Engineering
Saga University, 1-Honjomachi, Saga 840-8502, Japan
**Software Engineering Lab, Department of Computer Software
University of Aizu, Aizu-Wakamatsu, Fukushima, Japan
*jcbala@lycos.com, {watanabe, izumi}@me.saga-u.ac.jp
**ashu@u-aizu.ac.jp

Abstract

Researchers are trying to construct an intelligent system with the help of the advance in technology. There were many successful milestones that had passed achieving 'humanoid robots', that are little closer to humans but not at whole. Although, the expectation level of the intelligence of these new systems is still unknown, it can be fairly assumed that reaching a goal at least up to an intelligence level of a human being, may be a big success. In order to be more close to the human, it is necessary to analyze the behavioral patterns of humans in order to apply those for the other artificial intelligent machines. Especially, decision making of humans should be thoroughly analyzed. We humans take a decision not just thinking about the current situation but considering many previous similar instances, simply known as 'experience'. Will there be any improvement to intelligent systems, if they also have this 'experience'? This research project discusses the possibility of applying 'experience' to path planning for mobile robots in ubiquitous environments.

1 Introduction

Being a human, have you ever noticed or did you ever consider how easy for us to walk along a crowded pathway? Crossing at the correct place avoiding incoming traffic, selecting the speed, as we desired or according to the environment are not complicated task for any normal human. It is just another matter or day today life styles and we do not even bother to think about it. But how about making a robot to do the same thing? Needless to say, it will be very complicated task comprising of many analysis, calculations and procedures.

As Simmons et al. [1] describe, recent research in mobile robot navigation has utilized autonomous mobile robots in service fields. To operate them in an environment with people, it requires more than just navigation. The robots should recognize and act according to human social behavior to share the resources without conflict [2]. Sometimes, even when humans interact with each other, it leads to resource conflict. At such times humans use social rules to maintain order [3] [4].

2 Experience Analysis

In experience analysis, the reasoner remembers previous situations similar to the current one and uses them to help to solve the new problem. Remembered cases are used to suggest a means of solving the new problem, suggest a means of adapting a solution that does not fit, warn of possible failures, and interpret a situation. Reasoning based on previous experience is another word for using old solutions to solve new problems and demands. Using old cases it is possible to explain new situations, argue new solutions, reasoning from precedents to interpret a new situation, create an equitable solution to a newer problem, etc. [5].

While analyzing the way that how people solve problems, it can be seen that reasoning based on experience is in continuous use. For obvious cases, the way attorneys, doctors, and mediators work can be seen. It can also be seen using extensively in day today living by general public such as meal planning, shopping, traveling, etc. Although it is imprudent to think that old solution will be valid for the new case each time, it can still be validated for the new case since the old case facilitates to generate a plausible answer easily. This reduces considerable time of processing the whole situation once again.

3 Social Rules

As Nakauchi and Simmons [2] explained, there are many aspects to the social rules and behaviors in human society. Among them, standing in line is one such example for the most highly socialized and crucial skills required for autonomous robots that operate in an environment with humans. For example, at various supermarkets, grocery stores, post office, banks, etc., humans stand in line and wait their turn. If a person does not understand or obey the social rules, he will not be able to get those services. This is true for an autonomous robot. If the robot does not 'understand' the social behaviors of humans and if it treats the humans in front of it as obstacles, then it will never be able to achieve its goals. Hence automated robots should be designed to 'understand' the social behaviors of humans and to work in accordance to them.

4 Personal Space

Personal space can be considered as a person's own territory/area which is very close to his physical body. The person feels uncomfortable if other people moved into this area and always tries to keep it restricted to others in the vicinity. This 'personal space' or 'human territory' has been studied in the field of cognitive science as mentioned by Malmberg [4], Sack [3] and many others. The shape of this space can be modeled as an oval, which has wider space towards the direction of one's own eyes as shown in Figure 1. A typical example for the effect of personal space can be seen in many day today activities of humans such as people forming and moving in lines. When people form a line, in general, they keep a certain distance away from each other people. They also usually stand so that they face towards the person in front. These phenomena can be described based on the concept of personal space. The idea is that the person who is standing in line keeps enough distance to the person in front so that person in front does not feel uncomfortable. On the other hand, he stands close enough to the person in front to avoid other people cutting in the line [2].

Although the actual size or distances to the sides of this personal space vary drastically with culture, work performed, environmental conditions, etc., a robot working with humans should have an understanding of it in order to prevent unnecessary repercussions.

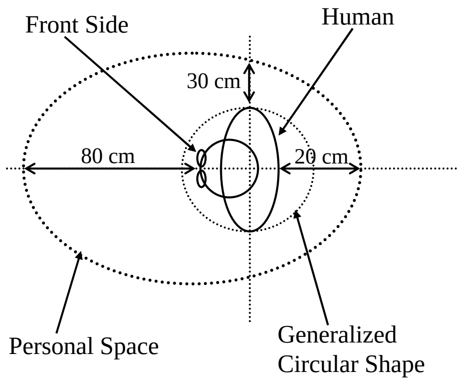

Figure 1: Personal human space.

4.1 Size and distance

Personal space can be generalized to an average size of 80 cm in front, 20 cm behind, and 30 cm in sides for a human as shown in Figure 1. Calculating the above, Nakauchi and Simmons [2] had assumed that the personal space of the person in front is identical to the personal space of the subject (who is going closer). But having different size subjects (such as different size robots), this should be varied and adjusted appropriately. Consider a human, generalized to a circular shape of 45 cm of diameter. Then these distances can be considered as a percentage of 177.8% in front, 44.4% behind and 66.7% in sides as the following propotion yields:

$$(a\_dist/gcd) \times 100\% \tag{1}$$

where a_dist is average distance and gcd is generalized circular diameter. Hence for any sized subject (robot), appropriate personal space can be obtained by using the above propotion.

4.2 Safe and personal distance

It is not necessary to consider this personal space while in motion because it involves many calculations and precautional stages. Rather, while in motion, safe distance (sd) from the nearest object is analyzed. Consider a situation as given in Figure 2. When robot R requires travel to the human A, within a path where there is an obstacle and other humans. At time $T = 0$, obtaining the positions of target (human A) and Tracker (Robot R), tentative safest and shortest path is obtained (for this, previous experiences if any can be used for fast accessing and reducing unnecessary calculations to speed up the process). Then considering the generalized circular diameter (gcd) of the tracker (robot R) at that instance, already obtained path is readjusted keeping the safe distance. The gcd is not a constant due to the fact that many postures that the robot can have such as stretching arms, carrying some objects, etc. but as a general rule, once calculated, the gcd can be considered as a constant throughout an operation. This safe distance has been considered as half of the generalized circular diameter (i.e. if $gcd = d$, then $sd = d/2$). Once this is done, the whole path will be considered as a strip of width $gcd+2sd$ or simply $2gcd$ in order for the robot to travel along that path.

Now consider an instance that robot R meets a human B while traveling along the path. At such times it is unnecessary to change 'safe distance' to 'personal space' as this human is just another obstacle along the path and that the robot has no intentions of interacting with him. Further having a distance of sd is enough to move along the way. (If the robot has to consider personal space every time it meets a human, it will cause many problems due to certain space restrictions of a particular area, unnecessary calculations involved, etc.) Finally when the robot reaches its target human A at $T = t$, it needs to consider personal space so that interaction is going to take place. Then, robot motion is decided so as to arrange the space around it, according to the personal space criteria.

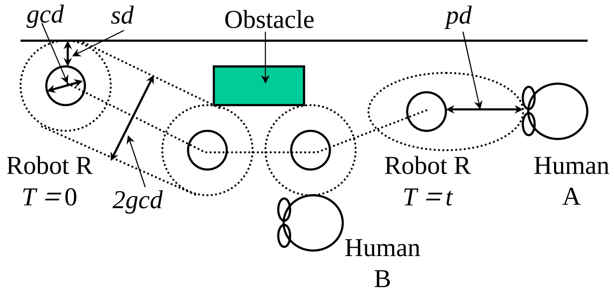

Figure 2: Safe and personal path planing.

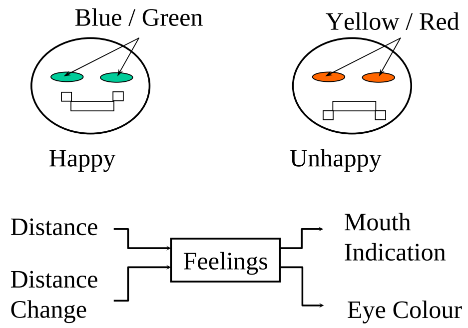

Figure 3: Two human feelings in 'Feelings' fuzzy model.

5 Emotional States

Humans are full of emotions and they show them in many direct or indirect ways even without consciousness. Many such feelings are expressed in human face and recognized by fellow companions without much difficulty. Understanding of these emotional states is very useful in interaction and communication with humans. While in conversation, idea is expressed in voice means by humans (whether the speaker really means it or not) but the true intentions are shown by other means of the body such as special gestures of hands, change in face, pupil dilation of eyes, direction of face/eyes, etc. Sometimes these gestures are used by experts to find out the true nature of individuals. Although specialized knowledge is required to do such things, just by having basic instinct, ordinary people do the interactions without much effort or rather unintentionally. Consider few cases as follows:

If a person is frowning, others try to get away and nobody dares to move closer (understanding that, that person is in anger and unable to have any deals with him). Sometimes, the same reaction may be returned by the viewer. In another situation, 'smile' indicates the gesture of goodwill (can be misused as well). In an event of meeting, indicate friendliness, etc., smiling is used always. There is no doubt reaching a person with a smile. It is always better to have a smile in return in order to indicate the same good feeling. Although such a behaviour is not unusual to a human being, how about to a robot (when interacting with humans)? Will not it be much easier and more comfortable for us to have a robot companion that shows its feelings as well? Even without speaking a single word, a single gesture of the robot may represents thousand words that we humans understand.

5.1 Indication of feelings

In a human face, a large number of muscles support to show many feelings. Although it will not be possible to have a similar face mechanism for a robot as an initial stage, an indication of eye colour (shades of different colours) and the shape of the mouth as shown in the Figure 3 can be used to indicate basic feelings of a robot.

Consider a situation where a robot is moving along a pathway and a human is coming closer to it (or rather blocking the pathway). Having a sense of 'personal space' (or 'feeling' danger to own motion or to the self), robot can indicate its unhappy or unstable state by indicating the colour 'yellow' in his eyes. If the person continues his motion and the level of uncertainty of the robots gets increased, then the eye colour can be changed towards 'orange' ('red' can be used to indicate extreme unhappiness).

Once the 'unhappy' situation is subsidized, the eye colour can be returned back to its normal. Similarly, happy or good feeling can be indicated by green followed by blue. In this way, robot is capable of showing its inner 'feelings 'in certain extinct to the surrounding human beings.

5.2 Fuzzy and feelings

The complete system will be comprised of several fuzzy models for initial path planning, obstacle detection, path adjustments, etc. One such module used to anticipate the feelings due to personal space is shown in Figure 3. The input membership functions for distance and rate of change of distance with output functions for mouth indication and eye colour are shown in Figure 4, where rule viewer for some input values for the above system is given.

6 Summary

In this research project, giving a robot a sense of feelings (that we humans understand) according to certain experiences has been analyzed. The robot gets this feeling as an experience while it moves with other subjects including humans. Although it seems to be easy to reach a human (for us), it is not so for an artifact such as a mobile robot. There are many other factors that should be considered in addition to the safe distance. They include reaching speed, angle of meeting (such as face to face, side to side, from behind), etc. and these are also should be analyzed for a better system.

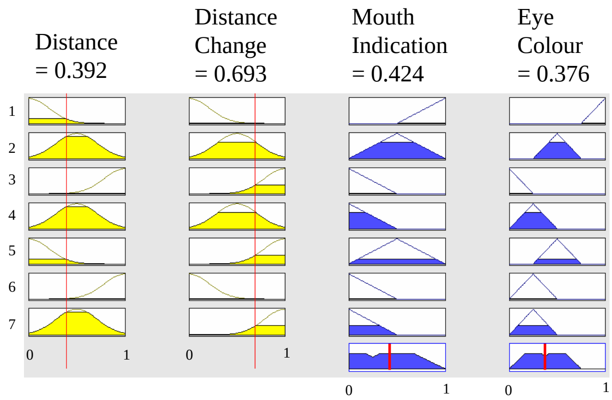

Figure 4: Rule viewer for 'Feelings' fuzzy system.

Similar to the human nature, experience is gathered in many acquaintances with similar situations and this requires many involvements with time. Although there may be specific instances slightly different to the previous, having an intelligent decision-making can be supposed to assist such times. These are currently under consideration.

References

[1] R. Simmons, R. Goodwin, K. Z. Haigh, S. Koenig, and J. O'Sullivan, "A layered architechture for office dilivery robots," in *Proc. of Autonomous Agents*, 1997, pp. 245–252.

[2] Y. Nakauchi and R. Simmons, "A social behavioral robot that stands in line," *Autonomous Robots*, vol. 12, 2002, pp. 313–324.

[3] R. Sack, *Human Territory*, Cambridge University Press, UK, 1986.

[4] M. Malmberg, *Human Territoriality: Survey of behavioural territories in man with preliminary analysis and discussion of meaning*, Mouton Publishers, 1980.

[5] J. L. Kolodner, "Improving human decision making through case-based decision aiding," AAAI, AI Magazine, Summer 1991, pp. 52–68.

[6] T. Gilovich, "Seeing the past in the present: The effects of associations to familiar events on judgments and decisions," *Journal of Personality and Social Psychology*, vol. 40, no. 5, 1981, pp. 797–808.

The Eleventh International Symposium on Artificial Life and Robotics 2006 (AROB 11th'06),
B-con Plaza, Beppu, Oita, Japan, January 23-25, 2006

A Natural Language based Human Friendly Network Robotic System

Chandimal Jayawardena Keigo Watanabe Kiyotaka Izumi
Department of Advanced Systems Control Engineering
Saga University
Saga 840-8502, Japan

Abstract

Network robotic systems, specially which are operated over the Internet, are meant to be used by non-experts. Therefore, user-friendly interfaces would provide many advantages. In developing user friendly interfaces, natural language communication is mandatory. This paper presents a network robotic system in which a user can command a robot manipulator to identify and pick objects placed on a table. Some toys are used as objects. User may use commands such as "*pick the elephant*." The objects having complicated shapes are identified independent of their location and the orientation. To do this, two dimensional object recognition techniques are extended to three dimensional object recognition utilizing a standard feed-forward neural network.

1 Introduction

Network robotic systems are very important in the sense that they combine robots, which are fast and precise, with remote control capabilities. Specially, with the advent of the Internet, a new class of robots has emerged with new advantages and features. During the last one and half decades, there have been a number of Internet robotic systems. Using Internet as the medium of communication for network robotic systems has become increasingly popular due to advantages such as, low cost, easy accessibility, easy maintenance, possibility of allowing public participation, etc.

Since Internet based tele-robots are meant to be used by non-experts and the expected user base is very high and diverse, the human-robot interaction should be as natural and user-friendly as possible. In most existing Internet based robotic systems [1][2][3][4],user interaction with robot is via filling forms, selecting commands, clicking with mouse, etc. In contrast, a user-friendly framework for tele-operation using natural language commands would be more appropriate.

Sanz et al. [5] proposed for the first time, the importance of using natural words to refer to objects in tele-operation systems. However, there, the authors' concentration was on object recognition aspects.

Online robots are controlled through a web browser. They are different from conventional teleoperation in several aspects. In addition to the well known problems related to time delay, supervisory control, and stability, online robots need to be designed to be operated by non-specialists around the clock via human-friendly interfaces. Therefore, new strategies are needed to coordinate simultaneous users handling large variations in demand and time delay.

In most existing network or online robotic systems, input to the robot is given by filling forms or selecting commands. In some recent research, integrating object recognition capabilities with online robots has been addressed [5].

2 System Overview

The network robotic system presented in this paper allows the manipulation of objects of different shapes located on a table using a sub-set of the natural language. The objects used have complicated three dimensional shapes.

User can see the table and may ask the robot to pick any one of the toys. For example, user may say "*pick the elephant*." This kind of user interaction is important in network or online robotic systems because it enhances the user-friendliness. However, efficient object recognition is one of the challenges. In [5], an object recognition systems for online robots which was based on two dimensional information of an image was presented. The objective of the approach presented in this paper is to integrate three dimensional object identification to the online robotic system. Considering the restrictions imposed on online robotic systems which operates over the Internet, this approach needs to be simple and efficient.

The modules of the system are shown in the Fig. 1. They are, image acquisition, object feature extraction, neural network module, knowledge base, lexical symbol identification, command execution and communication module. The

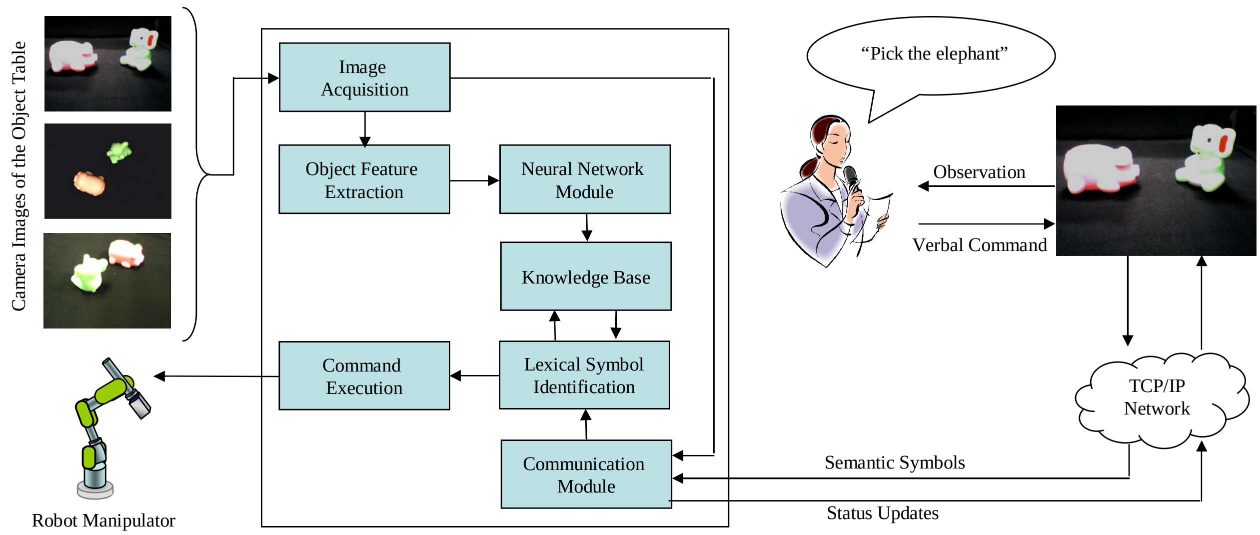

Figure 1: System overview.

functions of these modules are discussed in the next sections.

3 Implementation

3.1 Experimental Setup

The system shown in the Fig. 1 has a client-server architecture. The server side consists of a PA-10 industrial manipulator and the controller, object table, three USB cameras, and a PC running WindowsXP. The three cameras were placed over, in front of, and in a side of the object table.

The client side consists of a PC running WindowsXP and a microphone. Voice recognition was performed using IBM ViaVoice SDK.

Both the server and the client were connected to an Ethernet network and the communication was performed using TCP/IP sockets.

3.2 Image Acquisition

For the image acquisition DirectX technology was used. Camera images taken from all three cameras are further processed to extract object features. Low resolution versions of images are sent to the communication module and they are sent to the user in order to provide 3 dimensional details of the workspace.

3.3 Object Recognition

The challenge in object recognition is to identify object with complicated three dimensional shapes placed on the table. However, considering the constraints imposed on online network robotic systems, the approach needs to be simple and efficient. Since the object can be placed in arbitrary orientations and in arbitrary places, the object descriptors used should be invariant to rotation and translation.

Hu descriptors are well-known for two dimensional shape recognition. They have the particularity of being invariant to scale, translation and rotation [6]. In our approach, we have tried to approximate 3D object identification with 2D information obtained from orthogonal camera images. To achieve this a neural network technique was used.

3.4 Learning

To train the neural network, first a set of training data was collected. Each object was placed in different orientations and images were taken from all three cameras simultaneously. Some of those images are shown in Fig. 2. Then, those images were binarized and the first and second Hu descriptors of the shapes were found as follows.

For a two dimensional function $f(x, y)$, the moment of order $(p + q)$ is defined as:

$$m_{pq} = \int_{-\infty}^{+\infty} \int_{-\infty}^{+\infty} x^p y^q f(x, y) dx dy \qquad (1)$$

for $p, q = 0, 1, 2, ...$

Table 1: Object representaion.

	Object Descriptor					
	Front		Up		Side	
	H1	H2	H1	H2	H1	H2
Elephant-1	0.017479	0.033349	0.015421	0.029573	0.022898	0.039438
Elephant-2	0.018220	0.033008	0.014670	0.029938	0.023288	0.043842
...	...	...	...	...	...	...
Pig-1	0.016445	0.029444	0.018702	0.031850	0.018614	0.031869
Pig-2	0.014417	0.031383	0.015995	0.037169	0.016219	0.029566
...	...	...	...	...	...	...
Car-1	0.015429	0.028767	0.016730	0.031066	0.050733	0.072174
Car-2	0.017421	0.043342	0.016040	0.035854	0.029486	0.046491

H1: Fist Hu descriptor, H2: Second Hu descriptor.

If $f(x, y)$ is piecewise continuous and has nonzero values only in a finite part of the xy-plane, moments of all orders exist, and the moment sequence (m_{pq}) is uniquely determined by $f(x, y)$. Conversely, m_{pq} uniquely determines $f(x, y)$.

The central moments are defined as:

$$\mu_{pq} = \int_{-\infty}^{+\infty} \int_{-\infty}^{+\infty} (x - \overline{x})^p (y - \overline{y})^q f(x, y) dx dy \quad (2)$$

where $\overline{x} = m_{10}/m_{00}$ and $\overline{y} = m_{01}/m_{00}$.

If $f(x, y)$ is a digital image, the Eq. (2) becomes:

$$\mu_{pq} = \sum_x \sum_y (x - \overline{x})^p (y - \overline{y})^q f(x, y) \quad (3)$$

The normalized central moments are defined as:

$$\eta_{pq} = \frac{\mu_{pq}}{\mu_{00}^{\gamma}} \quad (4)$$

where $\gamma = \frac{p+q}{2} + 1$.

From the normalized moments of order up to three, it is possible to derive seven invariant moments or Hu descriptors. In this work, the first and second Hu descriptor, ϕ_1 and ϕ_2 were used such as

$$\phi_1 = \eta_{20} + \eta_{02} \quad (5)$$

$$\phi_1 = (\eta_{20} + \eta_{02})^2 + 4\eta_{11}^2 \quad (6)$$

Vectors of all six descriptors were used as the training vectors of the neural network. For each object, sixteen samples were collected. Table 1 shows some such examples of objects.

The neural network used was a standard feed forward back-propagation neural network. Number of neurons in the output layer is equal to the number of object classes. In this case, it is three to classify the three object classes "*elephant*," "*pig*," and "*car*."

3.5 Results

After the network was trained, it was tested with some test data. Test images were obtained by placing all objects on the table in arbitrary orientations and positions. As explained above, three images were taken from the three cameras and the Hu descriptors were calculated as before. Some sample test images are shown in the Fig. 3.

In addition to the Hu descriptors, from the top camera view, center of area of each object is calculated and each object is marked with an object number. However, without identifieng which object is the "*elephant*," a user command such as "*pick the elephant*" cannot be executed. For that, Hu descriptor vector for each object is fed to the previously trained neural network and the objects are identified. Some test data are shown in the Table 2.

The trained neural network was tested with twenty test images and it was found that these two object can be correctly identified with 100% accuracy. Once a user issue a command such as, "*pick the elephant*," the correct object can be identified and picked independent of the object location and the orientation.

4 Summary

In this paper, possibility of introducing three dimensional object recognition capabilities to network robotic systems was discussed. Although it is only a portion of the total network robotic system, it is vital in providing user-friendly natural language controlled interfaces.

Table 2: Test Data.

Object No.	Object Center		Object Descriptor						Object Ident.
	x	y	Front		Up		Side		
	$(pixels)$	$(pixels)$	H1	H2	H1	H2	H1	H2	
1	169	99	0.0172438	0.030375	0.0199281	0.041321	0.0182495	0.033830	elephant
2	196	134	0.0176682	0.034507	0.0275677	0.080579	0.0259410	0.080527	car
3	226	62	0.0179100	0.032484	0.0180720	0.032840	0.0175880	0.033244	pig

H1: Fist Hu descriptor, H2: Second Hu descriptor.

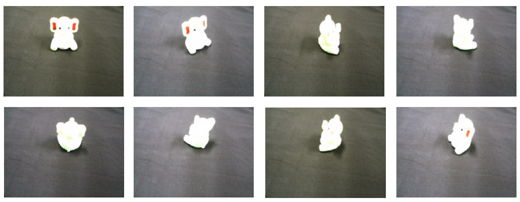

(a) Front camera view

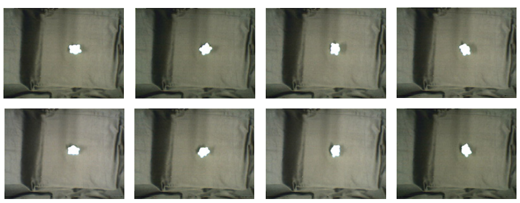

(b) Up camera view

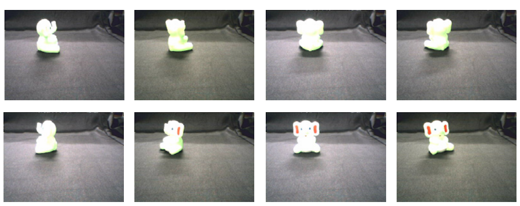

(b) Side camera view

Figure 2: Sample training images — elephant.

In this approach, main objective was to develop a system which was able identify objects with complex shapes irrespective of the object location and orientation; but at the same time, the simplicity and the efficiency of the approach was considered. Therefore, a well known technique for two dimensional shape recognition was extended two identify three dimensional object by utilizing a standard feed-forward back-propagation neural network.

It was found that once trained, the neural network could correctly classify the objects. However, in this experiment only three objects were used.

(a) Front view (a) Up view (a) Side view

Figure 3: Sample test images — elephant, pig and car.

References

[1] K. Goldberg, M. Mascha, S. Gentner, N. Rothenberg, C. Sutter, and J. Wiegley, "Desktop teleoperation via the world wide web," in *Proc. IEEE Int. Conf. Robotics Automation*, 1995, pp. 654–659.

[2] K. Goldberg, J. Santarromana, G. Bekey, S. Gentner, R. Morris, J. Wiegley, and E. Berger, "The telegarden," in *Proc. Assoc. Computing Machinery Special Interest Group Computer Graphics Interactive Techniques*, 1995, pp. 135–1140.

[3] P. Saucy and F. Mondana, "KhepOnTheWeb: Open access to a mobile robot on the internet," *IEEE Robot. Autom. Mag.*, vol. 7, no. 1, pp. 41–47, Mar. 2000.

[4] D. Schulz, W. Burgard, D. Fox, S. Thrun, and A. B. Cremers, "Web interface for mobile robots in public places," *IEEE Robot. Autom. Mag.*, vol. 7, no. 1, pp. 48–56, Mar. 2000.

[5] P. J. Sanz, R. Marín, and J. S. Sánchez, "Including efficient object recognition capabilities in online robots: From a statistical to a neural-network classifier," *IEEE Trans. on Systems, Man, and Cybernetics-Part C: Applications and Reviews*, vol. 35, no. 1, pp. 87—96, 2005.

[6] M. K. Hu, "Visual pattern recognition by moment invariants," *IRE Trans. of Info. Theory*, vol. 8, pp. 179–187, 1962.

The Eleventh International Symposium on Artificial Life and Robotics 2006 (AROB 11th'06),
B-con Plaza, Beppu, Oita, Japan, January 23-25, 2006

Some Properties of Coupled Van del Pol Oscillators with Inhibitory or Excitory Connections

Kiyotaka Izumi, Akihito Tajima, Guang Lei Liu, and Keigo Watanabe
Dept. of Advanced Systems Control Engineering,
Saga University
1-Honjomachi, Saga, 840-8502, Japan

Abstract

Fundamental properties of a central pattern generator (CPG) using Van del Pol oscillators are examined to generate some locomotion patterns for a semi-looper-like worm robot, where such a robot adopts a locomotion of green caterpillar as a basic locomotion pattern, but sometimes it can realize a locomotion of looper. Assume that the robot is composed of simple three serial links, as a fundamental research. Several simulations are conducted for examining how to design the CPG by using inhibitory or excitory connections to obtain a stable rhythmic response, and for searching the design parameters to produce valid amount of amplitude and frequency.

1 Introduction

Robots which move any narrow passage such as a tube is considered in our study. Those robots are being materialized by various mechanisms and the research is advanced toward commercialization. The present research handles a semi-looper type robot that can be composed of a serial link structure that is the most simple structure. The semi-looper type robot can realize both of the motion patterns for the looper and the green caterpillar. We examine a method for realizing a motion pattern generation based on a CPG for the semi-looper type robot.

There is a Van del Pol oscillator as one of the realization methods of an oscillator[1]-[4]. It is very difficult to deduce design parameters for an analysis target, because the Van del Pol oscillator is expressed with a nonlinear equation of motion. Most of conventional research analyze the oscillator by numerical analysis, and decide the final design parameters by trial and error when the object to be applied is fixed. An example of its application is the gait acquisition of leg type robots.

Also, it is known that the output of the Van del Pol oscillator is sensitive to a design parameter. The response is largely changed to a slight change of parameters. The output is sometimes in the inclination diverged. Therefore, the parameters need to be designed carefully, when this oscillator is applied to a real system.

We examine the influence that the design parameter in a single Van del Pol oscillator gives to the oscillation generated in this paper. Furthermore, we discuss the influence of connection weights for output oscillations, in which two Van del Pol oscillators are coupled with such connection weights. The effectiveness of the systematic design of the Van del Pol oscillator is examined by some numerical simulations, though we need to examine about the stability condition of Lyapnov to discuss the stability of oscillations rigorously.

2 Van del Pol Oscillator

When some Van del Pol oscillators are coupled respectively, the dynamics of ith oscillator is given by

$$\ddot{x}_i = a_i\left(b_i^2 - x_{ai}^2\right)\dot{x}_i - c_i^2 x_{ai} + d_i, \tag{1}$$

where x_{ai} denotes the connection variable and λ_{ij} denotes the connection weight which are related by

$$x_{ai} = \sum_{j=1}^{n} \lambda_{ij} x_j, \tag{2}$$

where n is the number of oscillators. Coefficients a_i, b_i, c_i and d_i in equation (1) have to be designed in an appropriate manner. In particular, b_i is called the amplitude parameter, c_i is called the frequency parameter and d_i is called offset parameter; those characterizes the shape of an output oscillation.

The analysis of Van del Pol oscillator is difficult, because its dynamics include the nonlinear term which is the product of x_{ai}^2 and $\dot{x}_i$. Most conventional researches discuss the results of numerical analysis. There are no results on the systematic design of any oscillators; parameters of an oscillator are designed through trial and error.

Here, a single oscillator is analyzed by a numerical approach to design parameters. The amplitude parameter b

Table 1: Conditions for the analysis of amplitude parameter

Parameters	Values
a	7
d	20
b^2	1 ~ 93
c^2	21 ~ 1600
Sampling interval	12.5 [ms]

Table 2: Conditions for the analysis of frequency parameter

Parameters	Values
a	7
d	20
b^2	5 ~ 80
c^2	6.25 ~ 6400
Sampling interval	12.5 [ms]

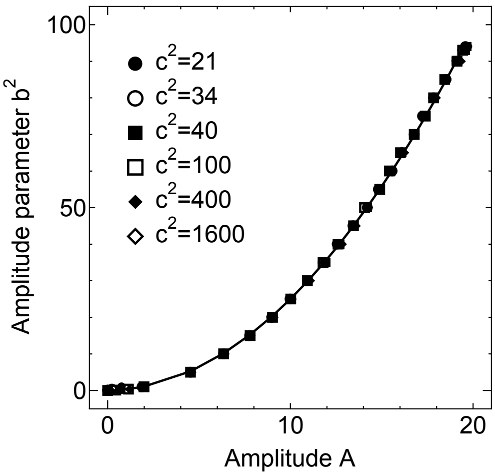

Figure 1: Property of amplitude parameter b

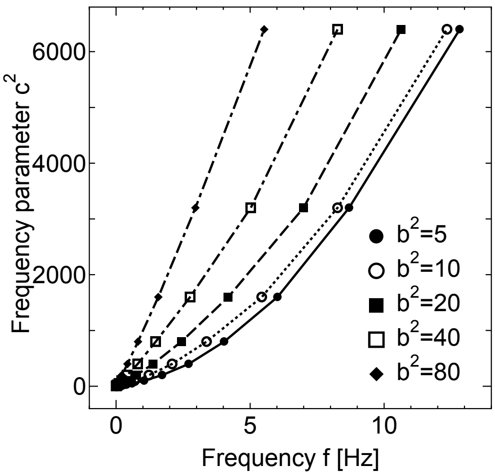

Figure 2: Property of frequency parameter c

is analyzed by the results of some simulations. Simulation conditions are tabulated in **Table 1**. The corresponding results are shown in **Fig. 1**. It is found from the results that the amplitude of an output depends on the amplitude parameter b^2 and is independent of the frequency parameter c^2. The solid line in Fig. 1 is the fitted curve approximated with a quadratic polynomial as shown by

$$b^2 = 2.4400445 \times 10^{-1} A^2 + 6.8580147 \times 10^{-2} A - 7.1860883 \times 10^{-2} \quad (3)$$

The parameter a can alter the output amplitude, but it is more sensitive to its variation than the parameter b^2. In our check, the region of a for generating a periodic signal is about from 7 to 55. If the parameter a is set to a large value, then the output of the oscillator diverges. It is found from this discussion that we have to adjust the parameter b^2 to alter the output amplitude, fixing the parameter a in a small value.

Next, the frequency parameter c is analyzed by using the results of some simulations. Simulation conditions are listed in **Table 2**. The corresponding simulation results are shown in **Fig. 2**. When the amplitude parameter b^2 is fixed, the output frequency becomes high depending on the frequency parameter. Moreover, if the frequency parameter is fixed, then the output frequency becomes high, setting the amplitude parameter in a small value. Note however that, when the amplitude parameter is set in a small value, the output amplitude becomes small.

Considering with the application for a real system, we may not generate desired amplitude and offset by setting any parameters. In this situation, the desired amplitude and offset can be realized by using an output equation

$$y_i = k_i x_i + o_i \quad (4)$$

where k_i denotes an amplitude coefficient and o_i denotes an offset.

From discussions aforementioned, the design approach of a single Van del Pol oscillator is summarized as follows:
.

1. Set parameters a and d. The parameter a is set to 7 and the parameter d is set to 20 in all simulations of this paper.

2. Design the amplitude parameter b^2 using equation (3). Note that the output amplitude becomes large with increasing the amplitude parameter b^2, though the designed b^2 has to be readjusted.

Table 3: Designed parameters of two VDP oscillators

VDP i	a_i	b_i^2	c_i^2	d_i
VDP 1	7	24.7	334.2	20
VDP 2	7	6.08	46.2	20

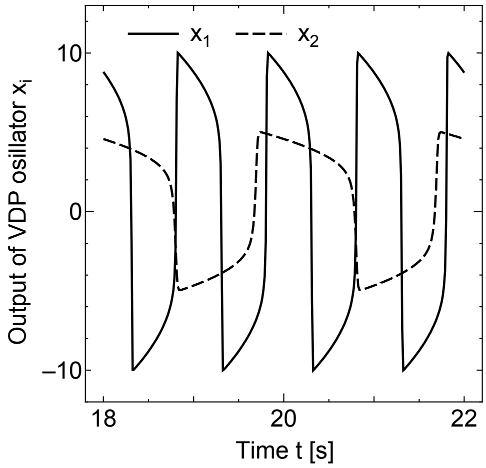

Figure 3: Output of VDP oscillator with $\lambda_{12} = \lambda_{21} = 0$

3. Design the frequency parameter c^2 according to the discussions of Fig. 2.
4. Adjust the output amplitude and offset using equation (4), if necessary.

3 Connection Weights of Coupled Oscillator

The 1st oscillator (VDP1) is designed by the proposed design approach, whose amplitude is 10 and frequency is 1 [Hz]. The 2nd oscillator (VDP2) is designed, in which the amplitude is 5 and the frequency is 0.5 [Hz], using the same manner. Designed parameters are listed in **Table 3**. The VDP1 response is represented by x_1, and the VDP2 response is represented by x_2 as shown in **Fig. 3**. According to the notations of the equation (1), Fig. 3 can be obtained by using

$$\lambda_{11} = 1,\ \lambda_{12} = 0,\ \lambda_{21} = 0,\ \lambda_{22} = 1$$

in equation (2). The VDP1 and the VDP2 can generate each desired oscillation as found from Fig. 3. The effect of connection weight is analyzed by simulation results in four cases such that λ_{11} and λ_{22} are set to 1 in all cases; the first case is $\lambda_{12} = \lambda_{21} = 0.1$; the second case is $\lambda_{12} = 0.1$ and $\lambda_{21} = -0.1$; the third case is $\lambda_{12} = -0.1$ and $\lambda_{21} = 0.1$; and the fourth case is $\lambda_{12} = \lambda_{21} = -0.1$.

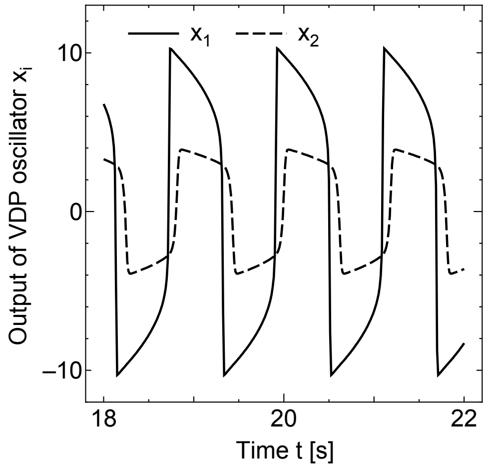

Figure 4: Outputs of VDP oscillator with $\lambda_{12} = \lambda_{21} = 0.1$

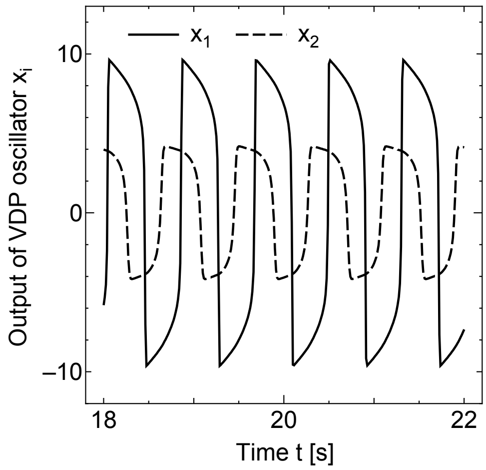

Figure 5: Outputs of VDP oscillator with $\lambda_{12} = 0.1$ and $\lambda_{21} = -0.1$

The result of the first case is shown in **Fig. 4**. Each oscillator has the same frequency as about 0.75 [Hz] which is average value of each desired frequency. The phase difference between the VDP1 and VDP2 becomes constant. The amplitude of the VDP2 becomes smaller than the desired value.

Figure 5 is the result of the second case. The frequency of the VDP1 is identical with the VDP2, as in the first case. The frequency is about 1.3 [Hz] which is the reciprocal value of the averaged frequency for both oscillators. The phase lag in the VDP2 relative to the VDP1 is 1/4 period. The trend on the output amplitude is similar to the first case.

The frequency of the third case is the same as that of the

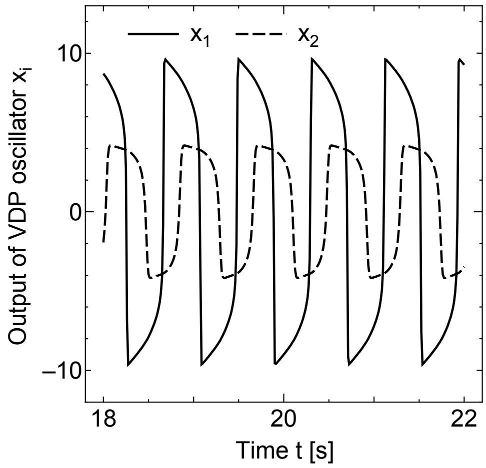

Figure 6: Outputs of VDP oscillator with $\lambda_{12} = -0.1$ and $\lambda_{21} = 0.1$

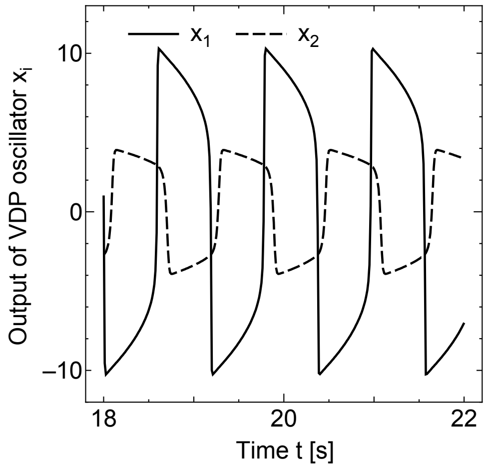

Figure 7: Outputs of VDP oscillator with $\lambda_{12} = \lambda_{21} = -0.1$

second case, as shown in **Fig. 6**. However, the phase lead in the VDP2 relative to the VDP1 becomes 1/4 period. Other characteristics of oscillations are substantially the same as those of other cases.

Finally, for the fourth case, we have similar discussions about the amplitude and the frequency to the first case. The only difference from the first case is that the present phase shift is 1/2 period as shown in **Fig. 7**.

From discussions mentioned above, the following points are summarized about the sign combination of connection weights in two Van del Pol oscillators:

- **About the frequency:** Each oscillator has the same frequency. When the sign of λ_{12} and λ_{21} is identical, the frequency becomes the averaged value between the VDP1 and the VDP2. If these signs are different then the frequency becomes the reciprocal value of the average between the VDP1 and the VDP2.

- **About the phase shift:** The phase shift is 0, when the sign of both connection weights is plus. When λ_{12} is plus and λ_{21} is minus, the phase lag becomes 1/4 period. If λ_{12} is minus and λ_{21} is plus, then the phase lead becomes 1/4 period.

- **About amplitude:** The amplitude of the oscillator, designed with smaller amplitude than other one, becomes a little bit small in the actual response.

As very important results, it is suggested that the phase shift can be designed by the sign combination of connection weights.

4 Conclusions

In this paper, we have studied on the design approach to a single Van del Pol oscillator and on the numerical analysis of coupled two Van del Pol oscillators with connection weights. The systematic design approach was demonstrated in a single oscillator in order to generate the desired oscillation. The relationship between the connection weights and the output responses was clarified through some simulations. Results obtained here gave some important points to design the Van del Pol oscillator.

In future works, the present results will have to be discussed with other conditions and three or more coupled oscillators.

References

[1] J. S. Bay and H. Hemami, "Modeling of a Neural Pattern Generator with Coupled Nonlinear Oscillators, " *IEEE Trans. on Biomedical Engineering*, Vol. 34, No. 4, pp. 297–306, 1987.

[2] J. J. Collins and S. A. Richmond, "Hard-Wired Central Pattern Generators for Quadrupedal Locomotion," *Biological Cybernetics*, Vol. 71, pp. 375–385, 1994.

[3] T. Zielińska, "Coupled Oscillators Utilised as Gait Rhythm Generators of a Two-Legged Walking machine," *Biological Cybernetics*, Vol. 74, pp. 263–273, 1996.

[4] L. Liu, A. B. Wright, and G. T. Anderson, "Trajectory Planning and Control for a Human-Like Robot Leg with Coupled Neural-Oscillators," *Proc. of The 7th Mechatronics Forum International Conference and Mechatronics Educational Workshop*, Paper ID M2000-72, 2000.

The Eleventh International Symposium on Artificial Life and Robotics 2006 (AROB 11th'06),
B-con Plaza, Beppu, Oita, Japan, January 23-25, 2006

Optimal Design Method for Region Setting in Fuzzy Energy Switching Control of Underactuated Manipulators

Keisuke Ichida, Kiyotaka Izumi, Keigo Watanabe, and Nobuhiro Uchida
Department of Advanced Systems Control Engineering,
Graduate School of Science and Engineering, Saga University,
1-Honjomachi, Saga 840-8502, Japan
E-mail: 05633001@edu.cc.saga-u.ac.jp; {izumi, watanabe}@me.saga-u.ac.jp

Abstract

Underactuated manipulators have some passive or free joints in general, where the number of inputs is less than the degrees of freedom. These systems have complex structural properties, and they have to control a lot of generalized coordinates by few inputs. However, reducing the number of actuators brings some advantages such as lightweighting, compactification and cost reduction. We here propose a switching control method based on fuzzy energy regions. We also discuss the application of a logic-based approach to underactuated manipulators with drift terms as considered in this research. Then we compare a switching control method based on a logic method with that based on the present fuzzy energy regions. The effectiveness of the proposed method is demonstrated with some simulations.

1 Introduction

In general, manipulators used for industry and academic laboratory have actuators to drive each joint. Then, these actuators are appropriately controlled to achieve the desired motion. On the other hand, underactuated manipulators handled by our research have some passive or free joints without actuators and brakes. These passive or free joints cannot generate dynamic torque at all. Due to the existence of such underactuated joints, the desired reference cannot be designed arbitrary, so that we cannot use the same control approach as used for the manipulators with fully actuated joints. To control underactuated manipulators a lot of researches have been studied.[1, 2, 3].

The present authors have also already proposed a switching control, in which some partly stable controllers were designed by computed torque method and switching low was obtained as the index of controller directly by fuzzy reasoning. In our method, it needs to design parameters related to energy regions and gains of some partial stabilizing controllers based on the computed torque method[4]. It is interesting to discuss about the energy region related parameters. In particuler, we are here concerned with a logic-based switching method that has been proposed by Hespanha et al[5]. Note however that this method was applied to nonholonomic systems without drift terms in the original paper.

In this paper, we thus discuss the application of the logic-based switching method to underactuated manipulators with drift terms. Here, we compare it with a switching control method based on fuzzy energy region. We show the effectiveness of design parameters through some simulations.

Table 1: Definition of input torque, generalized coordinates and physical parameters

Symbols	Physical meaning
$_1$	Input torque [Nm]
$_1$ $_2$	Link angles [rad]
m_1 m_2	Mass of link [kg]
l_1 l_2	Link length [m]
l_{g1} l_{g2}	Distance between joint and center of gravity [m]
I_1 I_2	Moment of inertia [kgm^2]
$_1$ $_2$	Viscous coefficient [Ns/m^2]

2 Underactuated Manipulator

Figure 1 shows two-link underactuated manipulator where the first joint is active and the second joint consists of a passive joint. In Table 1, $_1$ denotes the applying torque of 1st joint, $_1$, $_2$ denote the angle of each link, and the physical parameters are shown in

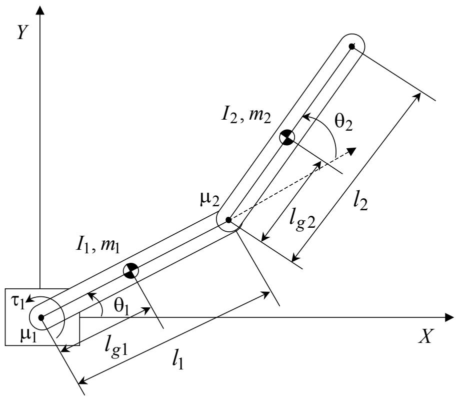

Figure 1: Two link underactuated manipulator

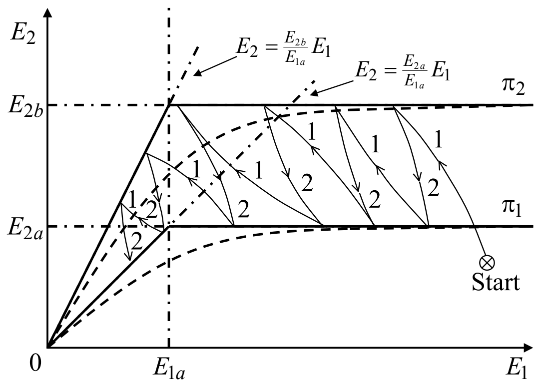

Figure 2: Region approximations for a logical switching

it. The dynamical model of the underactuated manipulator is given as follows:

$$M(\theta)\,\ddot{\theta} + \boldsymbol{h}(\theta \quad \dot{\theta}) = \qquad (1)$$

where

$$\begin{aligned}
M(\theta) &= \begin{bmatrix} M_{11}(\theta) & M_{12}(\theta) \\ M_{12}(\theta) & M_{22}(\theta) \end{bmatrix} \\
M_{11}(\theta) &= (m_1 l_{g2}^2 + m_2 l_1^2 + I_1) + (m_2 l_{g2}^2 + I_2) \\
&\quad + 2 m_2 l_1 l_{g2} \cos {}_2 \\
M_{12}(\theta) &= (m_2 l_{g2}^2 + I_2) + m_2 l_1 l_{g2} \cos {}_2 \\
M_{22}(\theta) &= m_2 l_{g2}^2 + I_2 \\
\boldsymbol{h}(\theta \quad \dot{\theta}) &= [h_1(\theta \quad \dot{\theta}) \; h_2(\theta \quad \dot{\theta})]^T \\
h_1(\theta \quad \dot{\theta}) &= -(m_2 l_1 l_{g2})(2 \dot{}_1 \dot{}_2 + \dot{}_2^2) \sin {}_2 + \; {}_1 \dot{}_1 \\
h_2(\theta \quad \dot{\theta}) &= m_2 l_1 l_{g2} \dot{}_1^2 \sin {}_2 + \; {}_2 \dot{}_2
\end{aligned}$$

3 Energy Regions

3.1 De nition of energy

Energy is defined by using general coordinates. Desired joint angle of each link is ${}_{di}$, and the error of joint angle is denoted by

$$e_i \triangleq {}_{di} - {}_{i} \qquad (2)$$

Then, the energy of each link is defined by

$$E_i \triangleq e_i^2 + \dot{e}_i^2 \qquad (3)$$

4 Switching Control

4.1 Logic based switching

Boundary curves π_i, $(i = 1 \quad 2)$ are defined by

$$\pi_i(E_1) = A_i \quad 1 - e^{-E_1 \quad T} \qquad (4)$$

where A_i is the amplitude of π_i and T is the convergence ratio. It is assumed that E_i's converge monotonically when the partly stable controllers C_i are applied for a system. The logic based switching function is defined by

$$\hat{I} = \begin{matrix} j & \text{if } E_1 \in \mathcal{R}_j \\ \max\{i(=1 \quad 2) : E_1 \in \mathcal{R}_i\} & \text{if } E_1 \notin \mathcal{R}_j \end{matrix} \qquad (5)$$

Then, the ideal energy response becomes as shown in Figure 2.

4.2 Fuzzy energy region based switching

We design controller 1 (C_1) and controller 2 (C_2) for a two link manipulator. They are used as partial stabilizing controllers to stabilize each link. We can define energy region by each controller.

If an exponential function is used, design parameters of boundary curve to divide energy region are denoted by the amplitude and the time constant. Control responses of manipulators depend on these parameters. Such parameters need to be set in ideal way. But it is difficult to set at once. Therefore, the boundary curve is denoted by fuzzy expression in this research. If a boundary curve has fuzziness denoted by the present fuzzy reasoning, then there appears an advantage of present method in setting the design parameters roughly. We first consider a straight line approximation shown in Figure 2. After such an approximation, fuzzy sets for E_2 can be defined for $E_1 \leq E_{1a}$

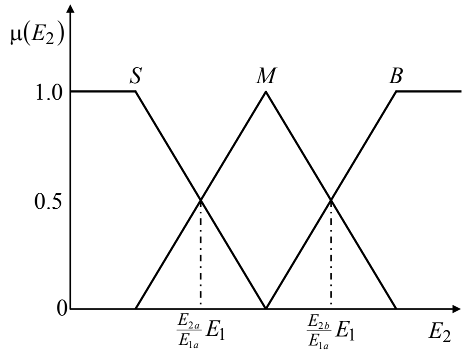

Figure 3: Membership functions for $E_1 \leq E_{1a}$

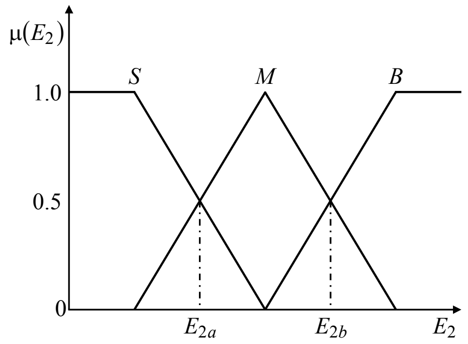

Figure 4: Membership functions for $E_1 > E_{1a}$

and $E_1 > E_{1a}$ cases as shown in Figure 3 and Figure 4, where E_{1a}, E_{2a} and E_{2b} are the design parameters of fuzzy sets. In order to realize ideal energy responses, fuzzy rules are given as follows:

Rule 1:	If $E_2 = S$	Then $s_1 = 1$		
Rule 2:	If $E_2 = M$	and $I_{t-1} = 1$	Then $s_2 = 1$	
Rule 3:	If $E_2 = M$	and $I_{t-1} = 2$	Then $s_3 = 2$	
Rule 4:	If $E_2 = B$	Then $s_4 = 2$		

Here, a parameter I_{t-1} which means the index of controller for one-step delay, is introduced, because one-step delayed controller must be retained in the overlapped energy region according to the ideal energy response. s_i is the index of controller that must be used in the fuzzy rule i.

5 Simulations

For partial stabilizing controller, set the ith link proportional gain K_{pi}, derivative gain K_{vi}, and region parameters E_{1a}, E_{2a}, E_{2b}. At this stage, the

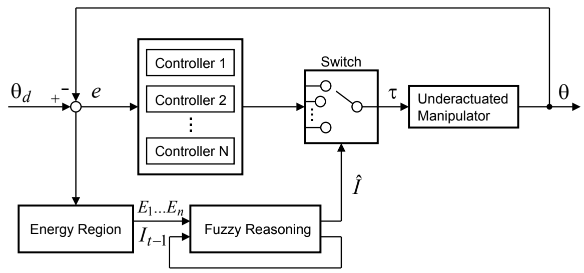

Figure 5: Switching control system

value of each gain is fixed, region set parameters are changed. Actually, each gain parameter is set to K_{p1}=25.0, K_{v1}=10.0, K_{p2}=25.0, K_{v2}=10.0. Parameters of fuzzy energy region (method A) are set to E_{1a}=4.0, E_{2a}=1.0, E_{2b}=3.5, and parameters of logic based (method B) are set to T=2.5, A_1=1.0, A_2=3.5. The initial state vector is set to

$$\begin{aligned} \boldsymbol{x}(0) &= [\theta^T(0)\ \dot{\theta}^T(0)]^T \\ &= [\ 0\ \ \pi/4\ \ 0\ \ 0\ ]^T \end{aligned}$$

To compare the logic based switching with the fuzzy energy region based switching, we evaluate the total error energy of each link. The evaluation function was applied for last 15 seconds when the control converged to zero roughly. Results using the fuzzy energy based switching are shown in Figure 6 and Figure 7, and the results of logic based switching are shown in Figure 8 and Figure 9. Then, the evaluation function in method A was 6.819, whereas the evaluation function in method B was 2.525. Thus, both methods converged with a satisfied condition. Note however that the convergence result of method B is a little better than that of method A.

6 Conclusions

In this paper, a control method of underactuated manipulator using partly stable controllers has been designed by computed torque method. For switching mechanism, we compared the fuzzy energy region based switching with the logic based switching. Fuzzy energy region based switching was better in the number of switching times than logic based one. Regarding the joint angle response, the fuzzy energy region based switching was better than the logic based one. However for the evaluation of convergence by using a cost function, the logic based switching was a slightly better than the fuzzy energy region based one.

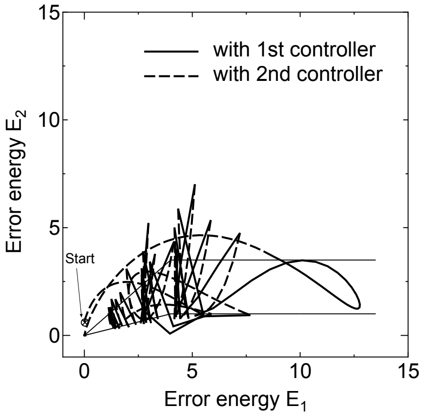

Figure 6: Energy with the fuzzy energy based switching

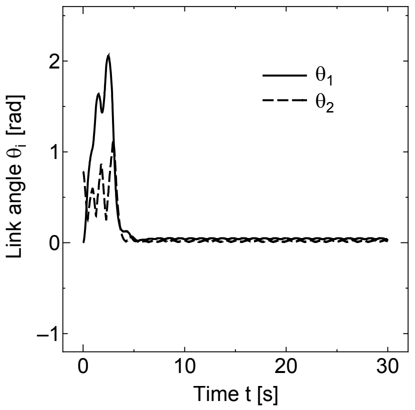

Figure 7: Link angles with the fuzzy energy based switching

References

[1] Y. Nakamura, T. Suzuki, and M. Koinuma, "Nonlinear behavior and control of a nonholonomic free-joint manipulator," *IEEE Trans. on Robotics and Automation*, vol. 13, no.6, pp. 853–862, 1997.

[2] H. Arai, K. Tanie, and N. Shiroma, "Nonholonomic control of a three-DOF planar underactuated manipulator," *IEEE Trans. on Robotics and Automation*, vol. 14, no. 5, pp. 681–695, 1998.

[3] I. Fantoni, R. Lozano, and M. W. Spong, "Energy based control of the pendubot," *IEEE Trans. on Automatic Control*, vol. 45, no. 4, pp. 725–729, 2000.

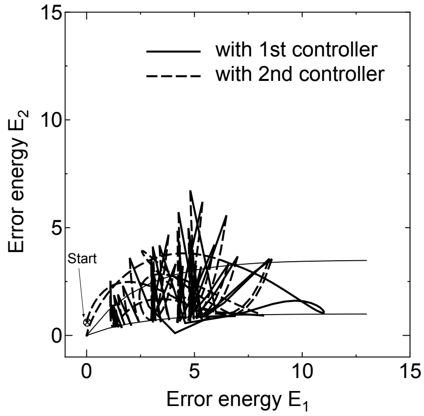

Figure 8: Energy with the logic based switching

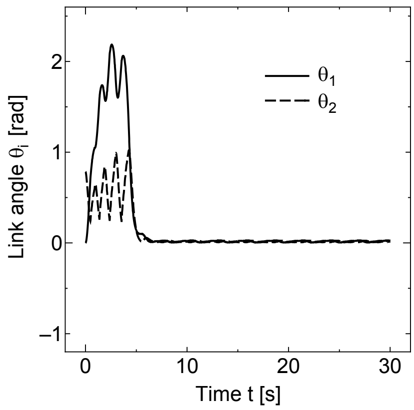

Figure 9: Link angles with the logic based switching

[4] L. Udawatta, K. Watanabe, K. Izumi, and K. Kiguchi, "Control of underactuated manipulators using fuzzy logic based switching controller," *J. of Intelligent and Robotic Systems*, vol. 38, pp. 155–173, 2003.

[5] J. P. Hespanha and A. S. Morse, "Stabilization of nonholonomic integrators via logic-based switching," *Automatica*, vol. 35, pp. 385–393, 1999.

The Eleventh International Symposium on Artificial Life and Robotics 2006 (AROB 11th'06),
B-con Plaza, Beppu, Oita, Japan, January 23-25, 2006

Design of an home / office automation for the physically handicapped using mobile robots

T.C.Manjunath

Research Scholar, IEEE / SPIE / IOP / ISSS Student member,
101 B, Interdisciplinary Programme in Systems and Control Engineering, ACRE Building,
Indian Institute of Technology Bombay, Powai, Mumbai-400076, Maharashtra, India.
Email : tcmanju@sc.iitb.ac.in ; Phone : +91 22 25780263 ; FAX : +91 22 25720057

Abstract

This paper deals with the design, fabrication and implementation of an efficient method of part-feeding mechanism (work-space fixture) for a stationary 2-DOF cylindrical coordinate robot. The aim was to design, fabricate each part of the unit with indigenous components and construct a prototype of an part-feeding mechanism such as a conveyer belt for a robotic system to pick up parts from one place and keep it at another place, say in a container. This is achieved by means of a robot which is used in conjunction with the conveyor belt mechanism for performing an assembly operation, say, a PNP operation and interacting with each other and control it with a Graphical User Interface (GUI) software written in Visual Basic (VB) language while performing an assembly operation avoiding all the obstacles in its path of motion from the source to the destination.

The objective of this work was to build a low cost part-feeding mechanism to the robot that could perform simple industrial manipulation tasks like picking up of manufactured components from conveyer belt and placing in a bin or a container. The simulation, design, fabrication and implementation of the work is divided into different stages, viz., Design and fabrication of the mechanical hardware of the robotic system, Design of the electrical / electronic hardware for the robot system, Development of the control software and various algorithms by developing a user friendly GUI using Visual Basic language in order to control the entire designed and fabricated robotic system, Integration of all the above three stages to perform an application such as grasping of objects which are arriving on a conveyor belt and placing in an container such as a bin and repeating the same task again and again.

1. Introduction

In any robotic industry , only robot will not be there. Along with the robot , some accessories are present . These accessories of the robot are called as *t e or space fixtures*. Any assembly line automation or a Flexible Manufacturing System [FMS] consists of a number of robotic work cells. Each cell is being assigned to do a particular job. Each cell consists of a number of devices called as *or space fixtures of t e ro ot*. These work space fixtures are nothing but the accessories of the robot For the job to be successfully done by the robot, environment of the robot external to it is very very important. Importance has to be given to the design and layout of the work space fixtures external to the robot. Many a times, the cost of the design of the work space fixtures is more than that of the robot itself [1]. Some of the examples of work space fixtures used in the work space of robot external to it are :

(a) Part feeders
(b) Transport devices
(c) Part holding devices / Fixed tools
(d) Part storage devices / Bins / Containers

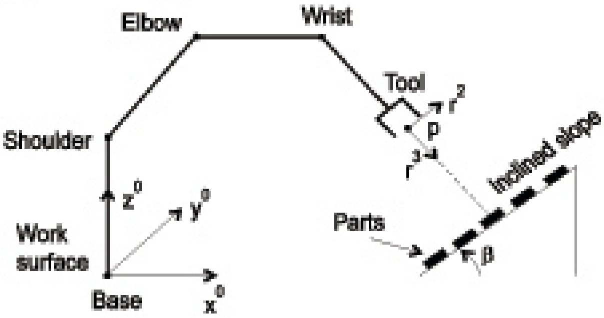

Fig. 1 A gravity fed part feeder aligned in x-z plane

Part Feeders Devices which feeds the part to the robot for manipulation (gravity fed part feeder). Part feeders are defined as the devices used to feed the parts or objects to the robot for gripping / grasping / picking or for doing any robotic manipulation. If a object or part has to be successfully grasped by the robot ; then , the part must be presented to the robot in a manner that is compatible with the tool . Generally, part feeders are arranged concentrically around the robot base as shown in Fig. 1 or on the periphery of work envelope or in between or vertically or horizontally.

A gravity fed part feeder is defined as one in which all the parts are falling or sliding one after another due to gravity on a inclined slope which is inclined at an angle of β with the work surface and the part feeder is situated at a distance of f from the base of the robot , where $\beta = \tan^{1}(\mu , 1)$, where μ is the coefficient of friction between the object and the work surface.

Transport Devices Devices which transport the parts from one work cell to another work cell of the robot (for e.g., conveyors and carousels).

Con eyors are the linear type of part feeders and called as linear transport devices. Their function is to present the parts or objects to the robot for manipulation. They are used to transport the parts linearly from robot to robot or from one robotic work cell to another robotic work cell. They are used to transport parts / objects for manipulation either from left to right or from right to left and are driven by electric motors at either ends. It can be used for a multi robot work cell.

Example : automated assembly lines. The parts are approached from the above with r^3 = i^3 i.e., approach vector opposite to z^0 of base. A four axis robot is sufficient instead of a Five axis robot. The 1st and 2 nd axis are used to position the tool over the belt. The 3 rd axis places the tool at proper elevation above the object. The 4th axis orients the tool in the direction of the object. Exchange of parts (swapping) between two robots is not possible. It is possible if the conveyor belt is driven in reverse direction. Any number of robots can be accommodated on either sides of the conveyor belts [2].

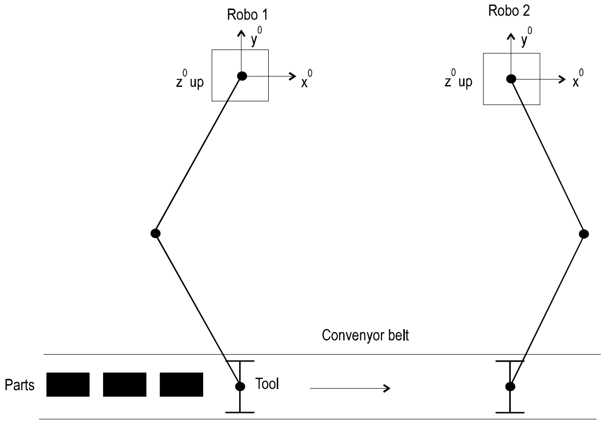

Fig. 2 A conveyor belt mechanism

Carousels are rotary transport devices (rotary part feeders). They transfers parts back and forth between two or more than two robots. The parts are approached from above. SCARA' s are sufficient. A carousel consists of a rotating table with a central pedestal. Robots are mounted in a circular fashion around the rotary turn table. Swapping of parts between robots is possible, since the table can be rotated or turned in the reverse direction. They are used to accommodate only a few robots since the diameter of rotary turn table places a restriction on number of robots. If the number of robots has to be increased , then the diameter of the turn table has to be increased . Then, eccentricity, i.e., balancing of the table comes into picture. Carousel is shown in Fig. 2 below.

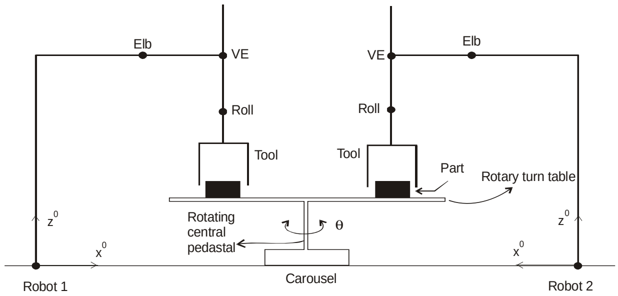

Fig. 3 A carousel

Part olding Devices Fixed Tools Devices which are used to hold a sub part in proper position and orientation (clamps , jigs , vices).

Part Storage Devices Devices which are used to store the manufactured parts (bins / containers).

2. Design of mechanical fixture robot

I RI is a cylindrical coordinate robotic unit having its workspace as a solid cylinder and has two positional axes, viz., the base and the vertical prismatic motion (termed as the major axes) and one orientation axes, viz., the roll (termed as minor axes) which allows the wrist to be oriented in the direction of the object. The robot designed is capable of sensing and picking of objects and placing them in its work volume in a particular position and orientation with a high degree of precision and accuracy.

A part feeding mechanism for the robotic system, viz., a conveyor belt on which the parts are arriving one after the other is to be designed and fabricated along with the robotic system. Though thought of this work as a technology demonstration project, the INRI can be put to many uses such as in assembly operations or in the educational field. There is also plenty of scope for future enhancements such as remote controllability of the system, internet based controllability and the object sensing / obstacle avoiding techniques such as using the computer vision for mechanical systems.

The entire mechanical assembly of the robotic system is being divided into three parts, viz., Base assembly, Arm assembly, End-effector (Gripper) assembly, Conveyor belt assembly. The entire mechanical assembly of the designed and fabricated robotic system is shown in Fig. A conveyor mechanism is a one DOF system which is moving in a linear fashion along a straight line and is driven by a conveyor DC servomotor with a 90 power transmission and which has the same specifications as that of the vertical extension / roll motor.

A conveyor mechanism is a one DOF system which is moving in a linear fashion along a straight line and is driven by a conveyor DC servomotor with a 90 power transmission and which has the same specifications as that of the vertical extension / roll motor. It consists of a belt which is moving on rollers (in order to prevent the sag) over which the objects are coming one after the other and is as shown in Fig. 5.1. The length of the conveyor belt being (45×5) cms. The speed of movement of the conveyor belt mechanism being approx. 12 cms / min. The electronic unit serves as an driver interface between the mechanical hardware and the computing system [3]. The electronic circuitries designed and fabricated by us consists of the following sub-parts, viz.,

1. **Driver interfacing unit** - is used to drive the actuators (motors) and consists of the drive power amplifiers with its peripheral chips such as the decoders and the buffers . The driver unit consists of two L293D IC's , each driver IC being used to drive two motors . The conveyor belt is driven by a FET IRF z 44 N. The designed and fabricated driver unit acts as the interface between the computer system and the mechanical unit (robot) and was tested on a general purpose PCB .

2. **Controller unit** - which consists of a IC circuitry (such as decoders 74138, buffers 74LS245) to give proper control signals to the robotic system for satisfactory operation. The data to the control unit comes from computer through the parallel port interface .

3. **Sensing unit** - to sense the objects (using limit switches , etc.,.) and to avoid the collisions of the robot with the obstacles , to find whether the object has been gripped properly or not. When both the limit switches (which are connected in series) gets closed after grasping the object, a signal will be sent to the parallel port through the status pin which makes the gripper motor cut off from the supply preventing further motion of the gripper and a message will be displayed on the GUI indicating that the object has been gripped.

4. **Power supply unit** - to supply power to the various electronic circuitries. The power to the driver cards and the driver IC's is obtained from the standard laboratory made regulated power supply . A 7805 regulator IC is used to provide 5 volts to the various IC chips .

The robotic system developed and controlled by the computer employs a GUI developed in Visual Basic 6.0. VB is selected as it is a simple, yet powerful, windows platform based programming language, which provides us with a complete set of tools to simplify complex rapid application development [4].

3. Software design application

An efficient VB GUI was developed to do the Pick aNd Place (PNP) application by using the robot [5]. The GUI developed consists of various menu boxes, instructions such as File menu, motor selection list box, motor selected text box, direction option buttons, start button, Stop button, reset button, conveyor on / off, auto teach facility, The run screen, single stepping feature, run through, code box, clear, step, run and stop (Fig. 5).

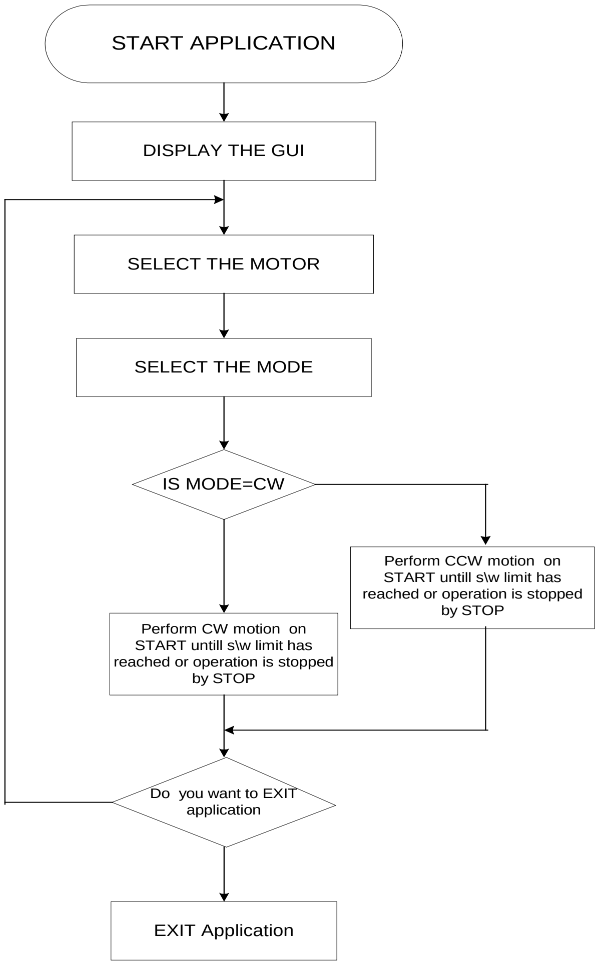

Fig. 4 Flow chart module of software to do PNP job

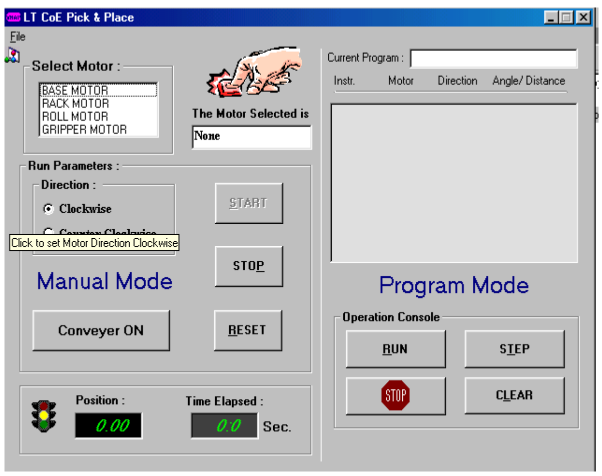

Fig. 5. GUI to do PNP operation

5. APP ICATIO OF I RI P P OPERATIO

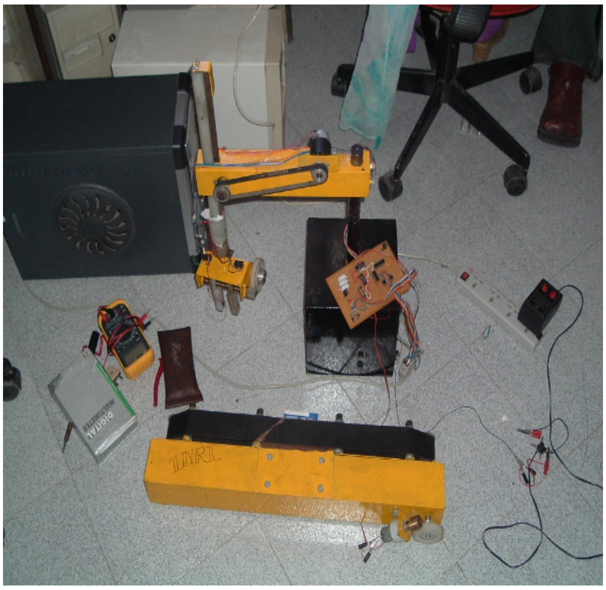

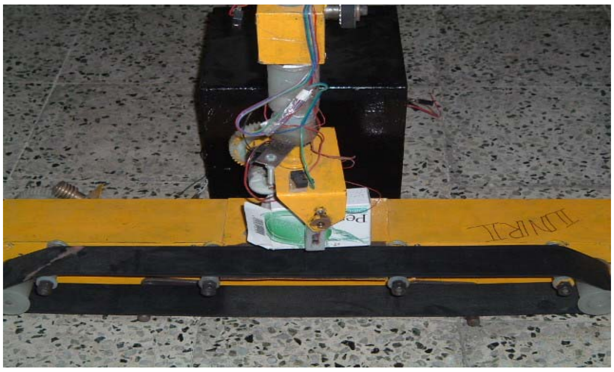

Fig. 6 Robot picking up the object form the conveyor belt, transporting the object to the destination (container) placing the object in the container

. Conclusions

A novel design and implementation of a work space fixture for a 2 DOF cylindrical robot was done successfully and the work space fixture, i.e., the 1 DOF conveyor belt mechanism was tested for various types of operations.

References

[1] Robert Schilling, Fundamentals of robotics, PHI.
[2] Hodges Bernard, Industrial Robotics, Jaico Pub.
[3] T.C.Manjunath (2005), Fast Track to Robotics, 2nd edition, Nandu Publication, Mumbai, India.Fu, Gonzales, Lee, Robotics-Control Sensing Vision, Mcgraw Hill.
[4] T.C.Manjunath (2005), Fundamentals of Robotics, 3rd edition, Nandu Publication, Mumbai, India.
[5] Groover *et.al.*, Industrial Robotics, MGH.

The Eleventh International Symposium on Artificial Life and Robotics 2006 (AROB 11th'06),
B-con Plaza, Beppu, Oita, Japan, January 23-25, 2006

Remarks on texture synthesis and texture segmentation with the aid of multi-level logistic model of Markov Random Field

Tomasz Kubik† Masanori Sugisaka*

† Institute of Computers, Control and Robotics, Wrocław University of Technology,
Janiszewskiego 11/17, Wrocław 50-372, Poland
E-mail: Tomasz.Kubik@pwr.wroc.pl
* Department of Electrical and Electronic Engineering, Oita University,
700 Dannoharu, Oita 870-1124, Japan
E-mail: msugi@cc.oita-u.ac.jp

Keywords: texture synthesis, texture segmentation, Markov Random Field

Abstract

Markov Random Field (*MRF*) method is used for texture modeling. This method makes use of parameterized random field models. The article concerns *MRF* method from two points of view: texture synthesis and texture segmentation. Texture synthesis, in general, relies on a joint distribution sampling while the model of a random field is fully known. The common algorithms employed here are: Metropolis sampler and Gibbs sampler. Texture segmentation can be done in two ways. Assuming, that unknown parameters of known distribution can be estimated and classified within regions of interest, the classification results for all regions in the image analyzed provide the clue for the final segmentation. The other proposition assumes, that there are several reference random fields models which are fully known. The model that fits the best to the region of interest defines the results of classification. Thus the segmentation comes from the classification performed for the whole image.

1 Introduction

The method of MRF is based on the random field model where the form of its joint and parameterized distribution is known. This section provides some basic definitions used in the model definition (plese refer to [1] for details).
Let *field of view* S be a regular, 2 dimensional, and discrete lattice:

$$S = \{(i,j) : 1 \leq i \leq N_1, 1 \leq j \leq N_2\} \tag{1}$$

Let pallet $\mathcal{L}$ be a finite set of n *colors*: $\mathcal{L} = \{1, \ldots, n\}$. The function $x : S \to \mathcal{L}$ defines an *image*. The value of this function for $s \in S$ is denoted as x_s (color assigned to the *pixel* s). The neighborhood system for S is:

$$\sigma = \{\sigma_s \mid \forall s \in S\} \tag{2}$$

where σ_s stands for the set of neighbors of s. The neighborhood systems of 1st, 2d, 3rd, ..., kth order can be defined as in the Figure 1a). The pair (S, σ) constitutes a graph, in which elements S are nodes, and arcs are defined by the neighborhood system σ. A clique c for (S, σ) is a subset of S. The clique can contain one pixel, $c = \{s\}$, or a pair of neighboring pixels, $c = \{s, s'\}$, or a triple of neighboring pixels, $c = \{s, s', s''\}$, etc. The cliques containing single pixels, pairs, and triplets are denoted, respectively, as:

$$\begin{aligned}
&C_1 = \{s \mid s \in S\} \\
&C_2 = \{\{s, s'\} \mid s' \in \sigma_s, s \in S\} \\
&C_3 = \{\{s, s', s'''\} \mid s, s', s'' \in S \text{ all are neighbors}\}
\end{aligned} \tag{3}$$

The collection of cliques is denoted as $C = C_1 \bigcup C_2 \bigcup C_3 \cdots$. The different types of cliques corresponding to the neighborhood system of the 2nd order, are shown in the Figure 1b).

1.1 Random field model

Let $X = \{X_1, \ldots, X_m\}$ $(m = N_1 \cdot N_2)$ be the family of probabilistic variables defined on the set S, and let each variable X_s can take a value $x_s \in \mathcal{L}$. Family X is called a *random field*. The probability that random variable X_s takes the value x_s is denoted as $P(X_s = x_s)$, what can be written as $P(x_s)$. The joint probability is denoted as $P(X_1 = x_1, \ldots, X_m = x_m)$, what can be shortened to $P(X = x)$, where $x = \{x_1, \ldots, x_m\}$ and $X = \{X_1, \ldots, X_m\}$, or written simply as $P(X)$. Thus any image can be regarded as a realization of a random field where pixel colors follows the random field joint probability distribution.

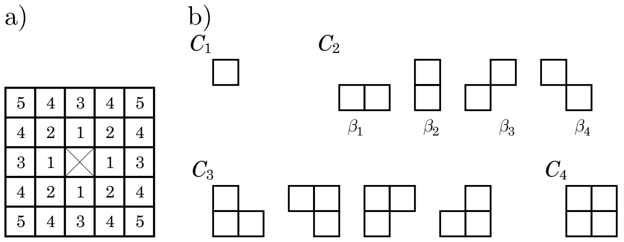

Figure 1: a) Neighborhood systems of nth order (fields marked with 1 denotes the neighboring system of the 1st order, fields marked with 1 and 2 - neighboring system of the 2nd order; 1,2 i 3 - of the 3rd order, etc.) b) Cliques for the neighborhood system of the 2nd order with parameters β_k, $k = 1, 2, 3, 4$, related to the four different clique types.

1.2 *MRF* model

The joint probability distribution design is a basic task in the *MRF* based texture modelling. X is called *MRF* on S with respect to σ iff the following conditions holds, [**?**]:

$$P(x) > 0, \forall x \in X \quad \text{(positivity)} \tag{4}$$

$$P(x_s | x_{S-\{s\}}) = P(x_s \mid x_{\sigma_s}) \quad \text{(Markovianity)} \tag{5}$$

where $S - \{s\}$ denotes all pixels in S except s, $x_{S-\{s\}}$ denotes colors of all pixels in S except s, and $x_{\sigma_s} = \{x_{s'} \mid s' \in \sigma_s\}$ denotes the colors of neighbors of s.

The conditional probability $P(x_s \mid x_{S-\{s\}})$ is defined as:

$$P(x_s \mid x_{S-\{s\}}) = \frac{e^{-\sum_{c\in\mathcal{A}} V_c(x_s)}}{\sum_{x'_s\in\mathcal{L}} e^{-\sum_{c\in\mathcal{A}} V_c(x'_s)}} \tag{6}$$

where x'_s takes all possible values of colors which can be assigned to the pixel s, and $\mathcal{A}$ is a set of cliques including pixel s. $V_c(\cdot)$ represents the potential of a clique c. The potentials of cliques containing more then one pixel, in a multi-level logistic model (*MML model*), are defined as follows:

$$V_c(x) = \begin{cases} \zeta_c & \text{if all pixels in the clique } c \\ & \text{have the same color,} \\ -\zeta_c & \text{otherwise.} \end{cases} \tag{7}$$

where ζ_c is a potential of a clique c. Let potential of a clique containing a pair of pixels (a cliques in C_2) for the neighborhood system of the 2nd order, where parameters β_k, $k = 1, 2, 3, 4$ are assigned as in Figure 1b), is defined as follows:

$$V_2(x_s, x_{s'}) = \begin{cases} -\beta_k & \text{if } x_s = x_{s'} \\ \beta_k & \text{otherwise} \end{cases} \tag{8}$$

To highlight that this potential depends on parameters, it can be rewritten as $V_2(x_s, x_{s'}, \bar{\beta})$, where $\bar{\beta} = (\beta_1, \ldots, \beta_4)$. Finally, considering only cliques included in C_2, the conditional probability $P(x_s \mid x_{S-\{s\}})$ is given by:

$$P(x_s \mid x_{S-\{s\}}) = \frac{e^{-\sum_{s'} V_2(x_s,x_{s'})}}{\sum_{x'_s} e^{-\sum_{s'} V_2(x'_s,x_{s'})}} \tag{9}$$

where $\sum_{s'}$ denotes the sum over all neighbors of s, for which (s, s') is a clique in C_2. Using double indexing this probability can be rewritten as follows:

$$P(x_{i,j} \mid x_{S-\{(i,j)\}}) = \frac{e^{-L(x_{i,j})}}{\sum_{x'_{i,j}} e^{-L(x'_{i,j})}} \tag{10}$$

where

$$\begin{aligned} L(a_{i,j}) \quad = \quad & V_2(a_{i,j}, a_{i-1,j}) + V_2(a_{i,j}, a_{i+1,j}) \\ & +V_2(a_{i,j}, a_{i,j-1}) + V_2(a_{i,j}, a_{i,j+1})+ \\ & V_2(a_{i,j}, a_{i-1,j-1}) + V_2(a_{i,j}, a_{i+1,j+1})+ \\ & V_2(a_{i,j}, a_{i+1,j-1}) + V_2(a_{i,j}, a_{i-1,j+1}) \end{aligned} \tag{11}$$

Thus, if all pixels in a clique have the same color, $L = 2\beta_1 + 2\beta_2 + 2\beta_3 + 2\beta_4$. If all colors are different, then $L = -2\beta_1 - 2\beta_2 - 2\beta_3 - 2\beta_4$

2 Texture syntesis

If a model of a random field is fully known, texture synthesis can be realized as the joint distribution sampling. The common algorithms used for such sampling are: Metropolis sampler [2, 3], and the Gibbs sampler [4]. Both algorithms produce an image with a texture in an iterative way, starting from an image with pixel colors generated from a palette $\mathcal{L}$ with uniform random distribution function. The iterations continue arbitrary number of times.

In the Metropolis sampler at each iteration step a copy of a current image is generated. In this copy a color for a chosen pixel is generated randomly from $\mathcal{L}$ with uniform random distribution function. Then the copy becomes a new current image, if the probability obtained from a model is higher for it then for the current image.

The scheme of a Gibbs sampler is following. For a randomly chosen pixel at each iteration step all possible colors are tested. The color which agree the most with a model of a random field (under condition, that colors of the pixels in the neighborhood of the pixel of interest are are known) is accepted as a new color.

3 Texture segmentation

Texture segmentation can be done in two ways: 1) by the estimation of unknown parameters of the known random field model, followed by their classification (estimation method), 2) by the choice of such random field model from a set of models, which fits the best to the samples observed (best fit method).

In both solution an image being segmented is scanned with a moving window. The size and the position of this window defines a region of interest containing the texture. The texture is recognized by the parameters classification (estimation method) or by the best candidate selection (best fit method). The position of the center of the moving window defines the pixel in the original image, which should labelled according to the texture recognized. The outcome of this procedure is a segmented image.

The estimation method requires some computation to be performed. Such computation can be regarded as *MRF* parameters recovering on the base of an observed texture, where this texture is *MRF* realization. Classification, that follows parameters estimation, takes vector of parameters as a feature vector. The result of the classification is a label corresponding to the texture.

The best fit method (by means of the highest likelihood function value) requires that all *MRF* models of textures are known. If they are known, the result of the method are labels, which correspond to the best fitting texture models found. The texture models can be supplied by an expert user (by specifying parameters) or build on the base od samples. The set of samples for all distinguishable textures can be created by cutting homogeneous regions from a test image. Then, the parameters of the models can be recovered in the same way as in the estimation method. After averaging they can be used for segmentation in the best fit method.

4 Experiments

In the experiments conducted *MLL model* of random field was employed (see equation (10)). The model was described by four parameters: β_1, β_2, β_3, β_4. Texture synthesis method was based on the Gibbs sampler. Parameters estimation procedure used in the article was an implementation of kind of gradient search algorithm, [5]. Classification of the parameters estimated was done with the aid of artificial neural network based classifier. The classifier was trained with data provided from the reference textures models.

The results of segmentation with respect to the segmentation method are shown in the Figure 3. The size of the moving window used was 12×12, 15×15, 20×20.

5 Conclusions

Texture synthesis and texture segmentation by the use of the *MLL* model of the *MRF* and the segmentation method presented is easy to implement for the case of artificial textures. It has been observed, that the best fit method of texture segmentation is much faster then the estimation method. The only step that cost much of the computation time is the initial set of texture model parameters approximation (if they are not known from the begining). Nevertheless, the results of two segmentation methods are comparable.

Working with a moving window gives bad segmentation result on the borders of two textures. Thus a kind of a method that gives better accuracy in such case should be applied.

The use of the method proposed for natural textures is not so promising. The reason is that natural textures have models that are unknown, and must be discovered first. This brings much more difficulty in the method application. It was tested (result not shown) that the *MLL* model used does not fit to the natural textures. For natural texture modelling please refer to [6].

References

[1] S. Z. Li: *Markov Random Field Modeling in Computer Vision* Spinger-Verlag, London, UK, (1995).

[2] N. Metropolis, A. W. Rosenbluth, M. N. Rosenbluth, A. H. Teller, and E. Teller: Equations of state calculations by fast computational machine. *Journal of Chemical Physics*, 21:1087–1091, (1953).

[3] J. M. Hammersley and D. C. Handscomb: *Monte Carlo Methods* Wiley, New York, (1964).

[4] S. Geman and D. Geman: Stochastic relaxation, Gibbs distribution and the Bayesian restoration of images. *IEEE Transactions on Pattern Analysis and Machine Intelligence*, 6(6):721–741, (1984).

[5] Y. Yu and Q. Cheng: MRF parameter estimation by an accelerated method. *Pattern Recognition Letters*, 24:1251–1259, (2003).

[6] R. D. Paget: Nonparametric Markov Random Field Models for Natural Texture Images. Master's thesis, The University of Queensland, St Lucia, Queensland 4072, Australia, (1999).

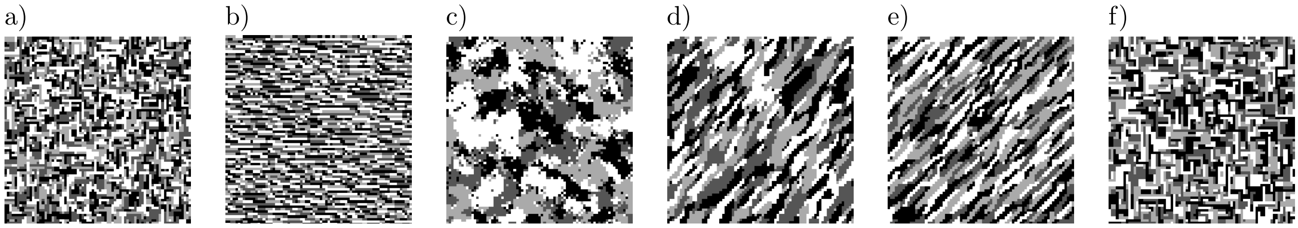

original parameters					estimated parameters				
	β_1	β_2	β_3	β_4		β_1	β_2	β_3	β_4
a)	1.0	1.0	-0.5	-0.5	a)	1.08717	1.09241	-0.565433	-0.566961
b)	1.0	-0.8	0.5	-0.5	b)	1.04465	-0.899957	0.558655	-0.54535
c)	0.3	0.3	0.3	0.3	c)	0.320296	0.314226	0.288998	0.281211
d)	0.5	1.0	-0.5	0.7	d)	0.74194	1.30031	-0.843298	0.704515
e)	1.0	1.0	-1.0	1.0	e)	1.53794	1.48114	-1.6005	1.53289
f)	2.0	2.0	-1.0	-1.0	f)	2.4197	2.45401	-1.24345	-1.30294

Figure 2: Synthesized artificial textures along with the parameters used for their synthesis (original parameters), and parameters that were estimated for them (inside a moving window of the size 20×20). The images are enlarged for better visualization.

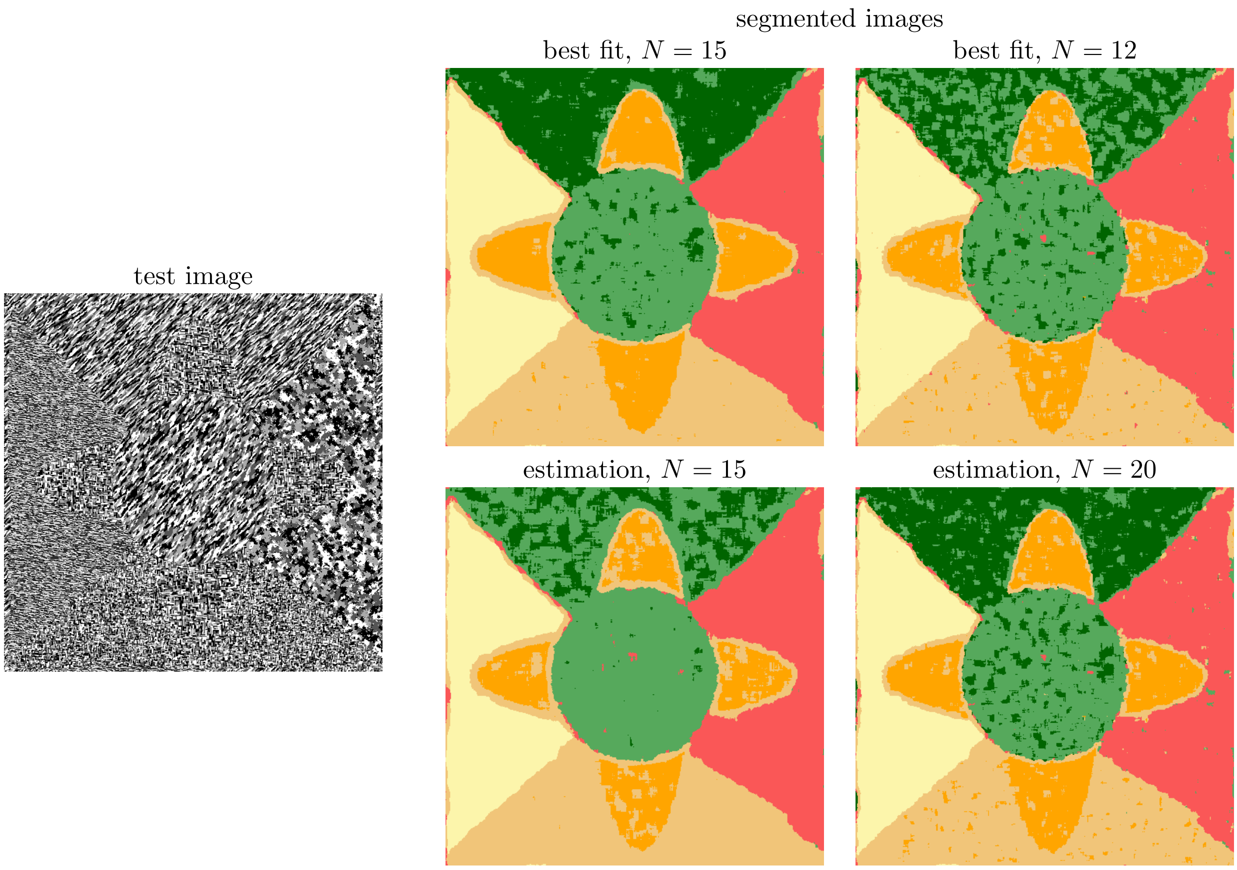

Figure 3: Results of texture segmentation with respect to the segmentation method, where N comes from the size of the moving window used which was $N \times N$.

Tension-based Movement Corrections of the Artificial Agent

Matosiuk B., Grzyb B.
Faculty of Mathematics, Physics and Computer Science
Maria Curie-Sklodowska University
pl. Marii Curie-Skodowskiej 1, 20-031 Lublin, Poland
bartosz@matosiuk.net, beata@gabri.pl

Abstract

This paper presents results of an experiment with a simulated mobile robot equipped with a psychodynamic-like controller called PreBrain-M we have built. The theory of machine psychodynamics, inspired by the works by Sigmund Freud, deals with pleasure-seeking robots, where the pleasure is a variable that substantially increases when a certain tension rapidly discharges. The PreBrain-M is a modular system that contains two types of devices: tension accumulators and tension dischargers. The communication between the devices is based on time-series called spiketrains. The most essential part of our PreBrain-M is the circuit responsible for smart chasing of objects. Owing to this circuit the robot moves toward anticipated location of the pursued object. The PreBrain's performance was compared with the performance of a controller which always moves in the direction it currently sees the object of chasing.

1 Introduction

The theory of machine psychodynamics, inspired by the works by Sigmund Freud, is being developed at the Advanced Telecommunications Research Institute (ATR), Kyoto, Japan in the framework of the Artificial Brain Project [1]. In his work Beyond the Pleasure Principle Freud proposes that the course taken by mental events is invariably set in motion by an unpleasurable tension, and that it takes a direction such that its final outcome coincides with a lowering of that tension [2, p.3]. Hence, machine psychodynamics deals with pleasure-seeking robots, called psychodynamic robots, where the pleasure is a variable that substantially increases when a certain tension rapidly discharges [3]. PreBrains is the name of a family of controllers for psychodynamic robots.

Psychodynamic architecture employs two types of devices: tension accumulators and tension dischargers. A tension accumulator produces a spiketrain whose frequency is proportional to the current tension level. The tension dischargers cause such motions of the robot that it can get sensory patterns causing possibly rapid discharge of a tension accumulated at a given accumulator. The corner-quitting module shown in Fig. 1 is a simple example of cooperation between a tension accumulator and a tension discharger.

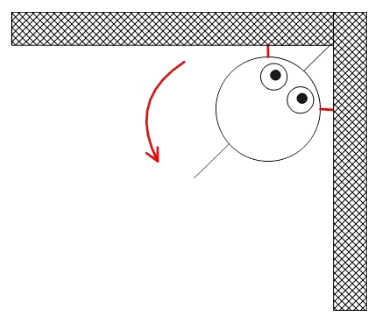

Figure 1: *The corner-quitting module gets activated when simultaneous signals come from both left and right IR sensor, which means that the robot stuck in the corner. In such a case a related tension is being accumulated. Then the module's tension discharger sends appropriate signals to the drivers of the robot's motors.*

Although such approach is a great simplification of the processes taking place in a human brain it is possible that during growth of the controller's complexity some extraordinary features would emerge. An example that confirms such statement is an experiment performed by the ATR Artificial Brain Group members that showed how easy the complex phenomenon of the robot's hesitation could occur when an agent were controlled by a PreBrain in which contradictory tensions fought for dominance [4]. The PreBrain-M we present contains modules for corner quitting and smart chasing of objects of interest..

2 PreBrain-Building Platform

PreBrain controllers are being created using the BrainCAD - a CAD-style toolkit for rapid prototyping of distributed data-processing systems. It offers a library of ready-made tension accumulators and dischargers, as well as a convenient GUI for designing connections among arbitrary number of tension accumulators and dischargers. Under the current version of the BrainCAD, the designs can be run on multiple stations in real-time regime in synchronous mode. The toolkit also containins several useful, build-in modules, a number of generic mathematical functions and a simulator of a mobile robot (for a visual observation of the behavior of the agent controlled by the PreBrain).

The tension is a function of the sum of received excitations, discharging signals, and spontaneous leakage. In the PreBrain-M it is defined the same way as in [6], i.e. by a set of values representing the accumulation/discharge time. During every clock, which is a PreBrain's measure of time, each tension accumulator produces a spiketrain whose frequency changes according to the formula:

$$\Theta_{i,t+1} = G\left(\Theta_{i,t} + \frac{\frac{u}{S_i} + \frac{A_{i,t}}{T_{A,i,t}} + \frac{D_{i,t}}{T_{D,i,t}}}{f}\right)$$

t - time (in clocks),
Θ_t - tension volume,
u - parameter determining the direction of uncontrolled change of tension (1 - increase, -1 - decrease),
$A_{i,t} = (A_{i,t,0} + ... + A_{i,t,7})$ - i-th tension accumulation signal,
$D_{i,t} = (D_{i,t,0} + ... + D_{i,t,7})$ - i-th tension discharge signal,
S_i - time of uncontrolled charge/discharge,
$T_{A,i,t}$ - accumulation time (from 0 to 1) assuming that $A_{i,t}$ contains only 1s,
$T_{D,i,t}$ - discharge time (from 1 to 0) assuming that $D_{i,t}$ contains only 1s,
f - frequency of clocking (clocks per second).

Function G(x) will return

$$G(x) = \begin{cases} 1 & x \geq 1 \\ x & x \in (0,1) \\ 0 & x \leq 0 \end{cases}$$

In PreBrain the spiketrains are used to exchange information within the PreBrain elements. It is necessary to employ such data carrier since the tension dischargers could be implemented in two different ways; a C++ client or a Pulsed Para-Neural Network module.

PPNNs are graphs composed with axons that represent delays and nodes that process received spiketrain. Although it was proved that a PPNN could be built for every Boolean function [5], this paradigm does not provide a natural method to synthesize more complex arithmetical operations on spiketrains. Hence when it is necessary (i.e. when a design requires more than the BrainCAD library devices) the programmed C++ modules are being used. The designer's task is to define a module's output upon values read from the input. Created functions are still operating on the spiketrains sent to each destination module during every clock.

An intrinsic element of the PreBrain platform is a simulated agent representing a Breitenberg-style robot. In its basic version the robot equipped with a set of IR sensors that enables it to receive a signals from the environment and two motors - each equipped with a FCV (frequency-to-voltage) module. Since PreBrain controller can only excite the motors with unary spike trains, each FCV has a positive and negative input and produces a positive or negative voltage depending on the difference between the frequencies provided to its inputs. Hence, the speed and direction of rotation of each of the robot's wheels depends on the distribution of the frequencies of the four spiketrains sent to FCVs.

3 Motion-Corrector Module

The Motion-Correction Module (MCM) has been written in C++ and compiled as a BrainCAD-library module. Attached to the PreBrain together with a handful of dedicated tension-accumulation devices, MCM enables the robot to estimate the future position of the object that is being chased [Fig. 2].

MCM uses the V-Green module (from the BrainCAD library), which simulates a camera-based tracking of a movement of a small green object. The output data is an angle-range within which the robot sees the object. The camera's visual field is divided into five sectors. The appearance of the object in a given sector results in an increase of a related tension (T1, T2, T3, T4, or T5). This event implies the accumulation of the tension Tlr or Trr (depending on the side of the visual field where the object was detected) or the discharge of all tensions (when the object was detected in the central sector). Figure 3. shows a scheme of the PreBrain-M and explains the role of MCM.

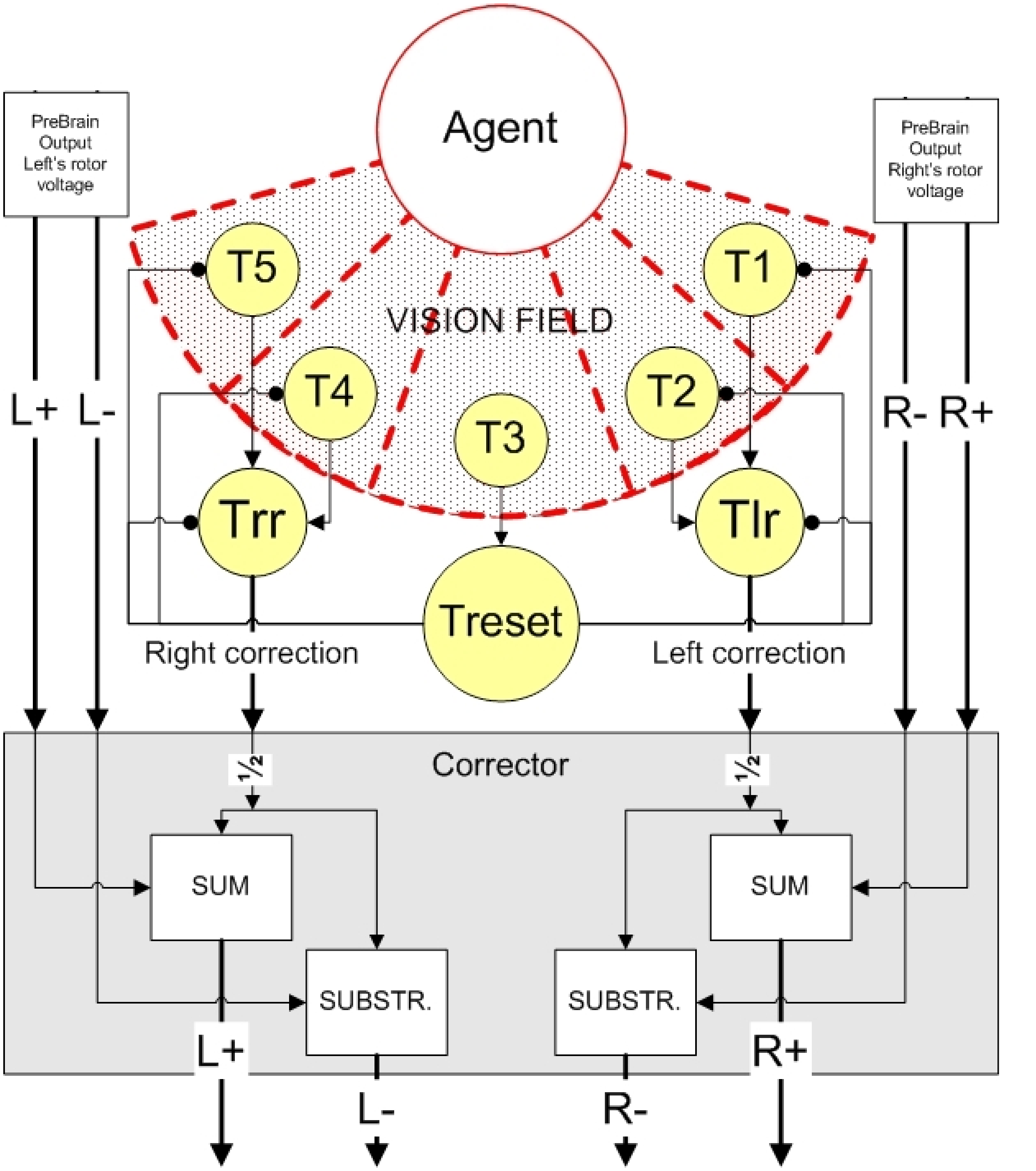

Figure 3: *A scheme of PreBrain-M. The controlled agent's visual field is divided into 5 sectors related to five basic tension accumulators (T1, T2,..., T5). When the object of interest is seen in a particular sector, a related tension gets increased, which causes an increase of one of three auxiliary tensions - Tlr for the left side of the vision field, Trr for the right side, and Treset for the central sector. An increase of Treset causes decrease of all the other tensions, which results in a repeatitive work of the system. The frequency resulting from the tension accumulated in Tlr or Trr is appropriately weakened to avoid harmful oscillations and the obtained sub-frequencies are added to and subtracted from the positive and negative input, respectively, for both motors.*

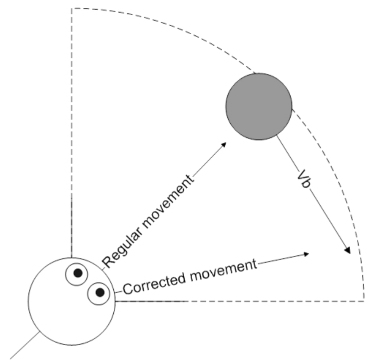

Figure 2: *Motion-Correction Module's goal is to increase the effectiveness of chasing the object of interest through enabling the robot to move towards not the actual position of the object but toward an estimated position.*

4 Experiment

The goal of our experiment was to find out whether the efficiency of the PreBrain could be substantially increased by a support of the tension-driven MCM (Motion-Corrector Module).

We used the controller described in [6], which is equipped with the circuit allowing robot to follow a green ball by always heading straight toward it. We also used the feature build-in the simulated robot that records the distance between the robot and the ball in every clock during the 30 minutes pursue. For the second run the same initial conditions were assured but this time MCM was attached to the PreBrain. The log files analysis revealed that the tensions based motion-corrector module increased the frequency of the robots rendezvous with the ball almost twice. The research is being continued. The next generation of the PreBrains should be able to learn the described behaviors. The learning should be psychodynamic, i.e. reinforced by pleasure signals.

Acknowledgements

This research was supported by Gdansk Artificial Brain Research Initiative (GABRI; http://www.gabri.pl). The authors would also like to express their gratitude to Dr Andrzej Buller for his great help in editing this paper.

References

[1] Buller A. (2004) From q-cell to artificial brain, *Artificial Life and Robotics, 8 (1), pp. 89-94.*

[2] Freud S. (1920/1990) *Beyond the Pleasure Principle*, W.W.Norton & Co, pp. 3-4.

[3] Buller A., Hemmi H., Joahimczak M., Liu J., Shimohara K., Stefanski A (2004) ATR Artificial Brain Project: Key Assumptions and Current State *Proceedings, Ninth International Symposium on Artificial Life and Robotics (AROB 9th '04), January 28-30, 2004, Beppu, Japan, pp:166-169.*

[4] Liu J. & Buller A. (2004) Tensions and Conflicts: Toward a Pleasure-Seeking Artifact, *The 5th IFAC Symposium on Intelligent Autonomous Vehicles (IAV'2004), July 5-7, Lisbon, Portugal.*

[5] Eeckhaut H. & Van Campemhout J. (2003) Handcrafting Pulsed Neural Networks for the CAM-Brain Machine, *The Eight International Symposium on Artificial Life and Robotics (AROB 8th '03), January 24-26, Beppu, Japan, 494-498.*

[6] Li J., Buller.A, Liu J (2004) Robot's behavior driven by internal tensions regulated by pulsed para-neural networks, *Tenth International Symposium on Artificial Life and Robotics (AROB 10th '05) February 4-6, 2005 at Beppu, Japan.*

The Eleventh International Symposium on Artificial Life and Robotics 2006 (AROB 11th'06),
B-con Plaza, Beppu, Oita, Japan, January 23-25, 2006

Development of a Mobile Robot for Video and Thermal Monitoring of Railway Tunnels

N. M. Bykova bykova@iriit.irk.ru
S. V. Yeliseev eliseev_s@rkt.iriit.irk.ru
A. A. Loukianov aloukian@iriit.irk.ru
A. P. Khomenko khomenko@rkt.iriit.irk.ru

Research and Development Department,
Irkutsk State University of Railway Transport,
664074, Chernyshevsky st. 15, Irkutsk, Russia.

Abstract

The paper presents a project for development a railway mobile robot for inspection and monitoring of railway tunnels. The mobile robot has to be equipped with a number of sensors and instruments and a computer system to process and store collected sensory information. The basic set of sensors includes video cameras, infrared cameras, railway track inspection sensors, positioning sensors. Additional sensors and instruments can be installed. The paper discusses the structural and hardware layout of the mobile robot, the architecture of robot control system and sensory information processing and storage system. The mobile robot functions, operation modes and control principles are considered. The paper focuses on advantages of automatic inspection and monitoring compared to usual visual checkups performed by a human operator. A special emphasis is placed on the problem of reliable mobile robot positioning inside the tunnel using visual information.

Keywords: mobile robot, image processing, monitoring, defect detection

1 Introduction

A joint use of video and thermo cameras when examining constructions and equipment allows not only to control them in optical and infrared wave bands but promotes automation of data processing of thermal imaging monitoring. This is particularly actual for constant temperature images of lengthy constructions: tunnels, bridges, reservoirs, tubings, etc.

The present article considers the development and use of automated monitoring and diagnostic system, based on mobile rail robot, for automated technical state monitoring of railway tunnels, in particular the Severo-Muisk railway tunnel. The considered system is designed to collect and process large amount of sensory and measurement data when carrying out video and thermal-imaging inspections in the tunnel. It is possible to add additional sensors and instruments to the system (ultrasonic, radio-locating, etc.) and extend a set of data parameters to be monitored.

The Severo-Muisk railway tunnel is one of the most complex railway tunnels in the world. Its peculiarity is not only its large length (15,3km), the most laying depth (1km) but as well extremely adverse geological, hydrological, seismic, and mining conditions of the region where it is situated; moreover, there were considerable problems and delays in the process of its building. Dependable and safe exploitation of the Severo-Muisk tunnel (SMT) largely depends on the effectiveness of the measures on monitoring and assessing of its technical state [1]. One of the important methods of monitoring of the state of the tunnel is a visual examination, i.e. examination of state, defects and damages of its internal vault (destructions, corrosion, cracks, etc.) and rail way. Valuable information of the current state of the tunnel may be got applying the thermal imaging monitoring in infrared frequency range, it allows to reveal humidification and cracks with subterranean water leaking. Also there is a problem that is extremely important for safe exploitation of the tunnel and it is monitoring of the drainage system state. The drainage system is designed to offtake water that is one of the main factors of destruction. Drainage system monitoring as well as revealing of its defects (leakings, wet spots) can be carried out by both visual and thermal imaging examinations (monitoring of thermal springs). A serious danger is interstices in the space behind the lining of the tunnel, they can be revealed by radiolocation approach.

2 Mobile robot for monitoring

The suggested mobile robot (Fig. 1) represents a moving (on the rail way) autonomous platform (truck) (1) equipped with a power unit (2) to set the truck in motion and provide the installed equipment with energy. The equipment of the mobile robot includes: lighting equipment (3), video cameras (4), thermal imaging cameras (5), additional monitoring

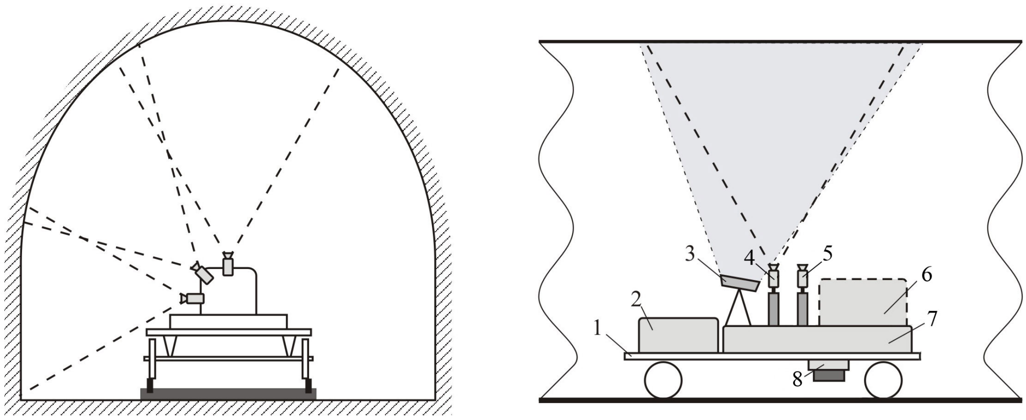

Figure 1: The scheme of proposed mobile robot

subsystems (6); a complex of subsystems: a) a computer vision subsystem, b) a measuring data logging subsystem and c) the platform movement control subsystem (7); subsystems and transducers of the platform positioning (8).

The obtained data are bound by location with the use of an odometer with periodical adjustment to external labels. The logged information is recorded in external media or processed in real time.

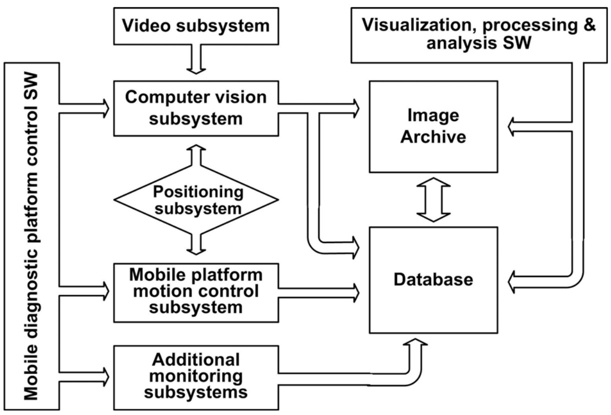

Figure 2: Architecture of the system for sensory information processing

The automated monitoring and diagnostic system has in its structure the following components (Fig. 2):

- Video subsystems consisting of the set of video cameras.
- Thermal imaging subsystem consisting of the set of thermal imagers.
- Computer vision subsystem processing the images, coming from the video cameras, in real time.
- Subsystems for comparison and matching of video and thermal images.
- The platform positioning subsystems allowing to bind the obtained information to the coordinates of a monitored section of the SMT. Approximate estimate of robot location can be obtained with the help of platform wheel encoder sensors. The accurate positioning is accomplished with the help of external labels on the tunnel surface or railway crossties. We are developing electronic counter device in order to use crossties for positioning purposes.
- Database for storing numerical results of image processing, thermal images, monitoring protocols, and other data. The database is to store the processing results with coordinate binding to a definite section of the SMT.
- Digital archive of tunnel surface images.
- The platform movement control subsystems.
- Software for automated control of diagnostic mobile robot, system setup and diagnostics.
- Software for visualization, processing and analysis of collected sensory data, automatic report generation.

3 Functions of mobile robot

Visual detection of defects of the tunnel lining. Detecting of defects in the images obtained by the video subsystem is carried out by the computer vision subsystem with the help of image processing algorithms (pattern recognition). The image processing algorithms may be directed to detecting of typical defects of the tunnel lining which can be detected visually. When a defect is detected the computer vision subsystem saves its image in the archive and makes a corresponding record in the current inspection protocol.

Temporal visual monitoring of the tunnel lining. In order to perform this task, primarily the system saves the initial state of the lining in the database in the form of coordinate-bound archive images and their processing results. These saved initial data then are used as reference data to compare with the data of the following video inspections. If there are any distinctions between the current and reference data the system makes a record in the protocol of video inspection (about the disparities found), also an image is saved in the archive for visual comparison.

Temporal thermal monitoring of the tunnel surface. The obtained thermal images are analyzed and compared to the reference data in the database. At the same time the thermal images are matched to video images of the same scene. The temperature anomalies are revealed by searching irregular temperature patterns in thermal images or by comparing averaged measurements to the reference data or data from previous inspections. Discovered temperature anomalies are saved in the database and logged in the inspection protocol.

Collection of statistics. The repeating inspections will help to build a rich quantitative and qualitative statistics on tunnel lining conditions and their changes over tunnel life. The quantitative statistics will be collected for numerical analysis results. The qualitative statistics will be collected in form of digital images archive. The statistics will help to understand and predict the dynamics of the development of tunnel conditions changes and defects.

Monitoring of railway tracks. If proper instruments and sensors are installed on a mobile robot it can be used to monitor the condition of railway tracks inside the tunnel.

The functions of the considered system may be expanded by installing additional sensors and instruments, namely: (a) laser rangefinders for monitoring of the tunnel lining geometry; (b) radio-locating devices in order to detect water- or air-filled openings (interstices) in the space behind the tunnel lining.

The components and software of the monitoring and diagnostic mobile robot may become reference prototypes for building the automated mobile robots to monitor the state of other railway objects.

4 Operation principles and the efficiency of the mobile robot

The suggested automated monitoring and diagnostic system will operate in one of the following modes:

– **Complete automated monitoring of the SMT state along its whole length.** The characteristic feature of this mode is the large amount of collected and processed data as well as the time needed for this operation since the inspection is carried out at slow speed.

– **Complete automated monitoring of the SMT carried out for specific sections of the tunnel.** Transition of the mobile robot into a specified section is carried out automatically at full speed.

– **Multilevel monitoring of the SMT state.** At the first level the monitoring of a limited set of parameters is carried out by an accelerated technique, the sections for a complete monitoring are selected automatically or semiautomatically according to the results of this monitoring.

– **Sampling monitoring of a number of the SMT sections.** The parameters and sections for sampling are determined by the monitoring program or in a random way.

The proposed mobile robot and its information processing system offer the following advantages over manual inspection procedures:

- Increasing of productivity and improving the quality of monitoring procedures;
- Automating monitoring procedures;
- Recording of the initial conditions in the tunnel and their temporal changes to give exhaustive evaluation of the tunnel state at any moment;
- Automatic collection of digital images archive for any section of the tunnel in order to help visual assessment of the lining state for any section of the tunnel at any time.
- Building up of the statistics and dynamics of the parameter changes of the tunnel state during its exploitation;
- Collected statistics can be used to analyze, assess and predict tunnel conditions in order to improve safety and perform damage and preventive repairs.
- Collected statistics can be used in future research and design works to build long railway tunnels.

5 Robust and accurate mobile robot positioning using computer vision data

Robust and accurate positioning of the mobile robot is one of the principal tasks of its control system. If this problem is not solved, the monitoring and diagnostic data collected by the robot cannot be bound to a concrete section of the tunnel. Positioning system based on wheel encoders and electronic counter for crossties can fail or receive incorrect initial data. In order to increase robustness and fault tolerance it is necessary to develop a robust method for robot positioning that can recover the correct position autonomously.

This task may be solved with the help of computer vision data. The robot's position in the tunnel is defined by distance x between the robot and one of the tunnel portals. In order to find x it is suggested [2] to use one-dimensional particular case of probabilistic approach of localization:

$$x = H(P(x)), \tag{1}$$

where $P(x)$, $x \in \boldsymbol{X}$ – probability density function; $H(\cdot)$ – statistical estimator function (here $\arg\max P(x)$ can be used). Function $P(x)$ is estimated as a conditional probability density function $P(x|a_1, \ldots, a_N,\ L_1, \ldots, L_N)$ that depends on the robot movements a_i and computer vision data L_i, obtained at specific location in the tunnel. The computer vision data can be composed from the image parameters and primitives extracted by image processing and pattern recognition algorithms [3].

After the platform makes a movement a_k the probability density function $P(x)$ is updated by the following recursive formula

$$P(x)_k = \int_{\boldsymbol{X}} P(x_k|x_{k-1})\ P(x)_{k-1}\ dx_{k-1}, \tag{2}$$

where $P(x_k|x_{k-1})$ – conditional probability density function for movement a_k that changed the position of the platform from the coordinate x_{k-1} to coordinate x_k. This conditional PDF is calculated on basis of an error model for robot positioning system and sensors.

When the computer vision data L_k is received the function $P(x)$ is changed by the following recursive update formula

$$P(x)_k = \mu\ P(L_k|x)\ P(x)_{k-1}, \tag{3}$$

where $P(L_k|x)$ is the conditional probability density for obtaining vision data L_k at position x, $\mu = \left[\int_X P(x)_k\right]^{-1}$ – normalizing multiplier. Conditional PDF $P(L_k|x)$ is derived from the results of the previous inspections, which are stored in the system database. Expressions (2) and (3) imply that the movements and observations correspond to Markov assumptions, which are easily satisfied under conditions of a single-track tunnel.

The considered above method allows to solve a problem of the global localization of the mobile robot in the tunnel. It also allows to recover correct mobile robot position after sensor system failure or incorrect initial position data. But the accuracy of this method is not so high.

For accurate positioning of the robot (position error within 4 to 7 cm) it is suggested by [4] to use local positioning technique. This technique is based on the visual servo control [5, 6]. Mismatching between coordinates of visual landmarks on the initial (made from the target robot position) and current video images is used as an error signal for the servo controller. In order to compare and match the visual landmarks the probabilistic approach, based on [7], was proposed in [4].

6 Conclusions

The subject of our paper is the development of automated monitoring and diagnostic system on the basis of a mobile robot moving on a railway tracks and equipped with a set of sensors and instruments. This mobile robot system is intended to monitor the state of the Severo-Muisk railway tunnel. The structural layout, control principles and operating modes are considered here. We suggest the scheme of a control system and the system architecture for sensor information processing of the robot. A special attention is given to the system of the robot positioning in the tunnel. We have succeeded in showing that the probabilistic approach of localization with the use of the computer vision data can be applied for solving the problem of position estimation of the robot in the tunnel (in case of an error or failure).

References

[1] S.V. Eliseev et al, "Inspection Results and Expertise of Technical Condition of Severomuisk Railway Tonnel," Technical report, Irkutsk State University of Railway Transport, Irkutsk, 2003.

[2] A.A. Loukianov, M. Sugisaka, "A Selective Vision and Landmark based Approach to Improve the Efficiency of Position Probability Grid Localization," *Trans. of IEEJ Journal (C: Electronics, Information and Systems)*, Vol. 123, No. 4, pp. 804-809, 2003.

[3] K.Rohr, "Landmark-Based Image Analysis: Using Geometric and Intensity Models," Computational Imaging and Vision Series, Dordrecht: Kluwer Academic Publishers, Vol. 21, 2001.

[4] A.A. Loukianov, "A Probabilistic Relaxation Method for Visual Landmarks Matching in Accurate Positioning of Mobile Robots," *Int. Journal of Computer and Systems Science*, No. 1, 2006.

[5] G.D. Hager, S. Hutchinson, P. Corke, "A Tutorial on Visual Servo Control," *IEEE Trans. on Robotics and Automation*, Vol. 12, No. 5, 1996.

[6] J. Chen, W. E. Dixon, D. M. Dawson, "Homography-based visual servo tracking control of a wheeled mobile robot," In *Proc. Of IEEE Conf. on Intelligent Robots and Systems*, Vol. 2, 2003.

[7] W. J. Christmas, J. Kittler, M. Petrou, "Structural matching in computer vision using probabilistic relaxation," *IEEE Trans. Pattern Analysis and Machine Intelligence*, Vol. 17, No. 2, 1996.

The Eleventh International Symposium on Artificial Life and Robotics 2006 (AROB 11th'06),
B-con Plaza, Beppu, Oita, Japan, January 23-25, 2006

A Unique Design and Implementation of A Mobile Octagon

Deepali Trivedi*, Amit Joshi*, S.A. Patekar[1], T.C. Manjunath[2]

*Post-graduate (M.E.) Students, Computer Science Engg., VJTI, Matunga, Mumbai-19, India.
[1] Professor and Head, Computer Science Engg., VJTI, Matunga, Mumbai-19, India.
[2] Research Scholar (doing Ph.D), IEEE / SPIE / ISOI / SSI Student Member,
Interdisciplinary Programme in Systems and Control Engineering, 101 B, ACRE Building,
Indian Institute of Technology Bombay, Powai, Mumbai-400076, Maharashtra, India.
Emails : deepalitrivedi@yahoo.com ; miamitjoshi@rediffmail.com ; patekar@yahoo.com ; tcmanju@sc.iitb.ac.in
Phone : +91 22 25780263 ; FAX ; +91 22 25720057

Abstract

The paper presents the modeling, simulation, design and fabrication of each part and construction of a four axes mobile robot with indigenous components and to control it with a personal computer using the java language. The main objective of this work is to design, fabricate a modular simple low-cost indigenously developed educational full fledged robotic control system named as "OCTAGON" that could accomplish 2 dimensional motion in a Y plane equipped with intelligence system and a 4 DOF manipulator arm for Pick aNd Place (PNP) operations from the source to the destination provided by the user. The robot is simulated and modeled using the graphic simulators and the AutoCAD simulation package. A user-friendly module is designed for the operation of the entire system. The design of the OCTAGON is done at 3 levels, viz., Mechanical sub-system, Electronic sub-system, Software and working.

1. Introduction

Imagine a day in your life when you wake up in the morning and find a machine walking up to you and saying "GOOD MORNING SIR Have a cup of tea". How would you respond to such a situation With so much progress made in the filed of science, engineering and technology, this dream is absolutely realizable in the automation age. Keeping in pace with the current technology, we have designed and fabricated a mobile robot named OCTAGON as shown in Fig. 1, which is basically a moveable mobile trolley on which the articulated robotic manipulator arm is mounted to perform Pick aNd Place (PNP) operations. These operations are defined by the program typed in by the user using a user friendly language specifically developed for this robot in JAVA. Mobile robots finds a lot of applications in almost each and every field today ranging from space applications, nuclear, war, industrial fields to the domestic and to the educational field. Here, a modest attempt is made to design and fabricate a mobile robot using the indigenously available components starting from scratch. This work was taken up as a research project work by the students under the guidance of the professors from VJTI and IIT. The paper is organized as follows. First, a introduction to robotics and robots is given. Second, the design of the mechanical assembly is presented. A brief introduction to the electronic design is given in section 3. Fourth, the computer control of the robotic system using the visual basic language is presented. Finally, the conclusions are drawn followed by the references.

Fig. 1 The designed OCTAGON

2. echanical Design

The mechanical design of the system is divided into 3 parts, viz., the mobile base assembly (vehicle), the arm assembly and the gripper assembly. The designed robot arm mounted on the vehicle has R-R-R (Rotary-Rotary-Rotary) type of axes and is an articulated one. The designed and fabricated mobile robotic system consists of a mobile trolley made of hard hylam over which the arm and the necessary interfacing circuitries, electronic and electrical components are mounted [1]. Hylam sheet was chosen keeping in mind the following properties, viz., good insulating medium, light in weight, can be easily cut into required shape and size, provides a platform for the arm and the entire structure including the electronic circuitries. A electronic circuitry consisting of drivers, amplifiers, power-supply, etc.,. is used as the controller. Bi-directional AC synchronous motors with relay bank switching and DC servos are used to impart motion to the robot. A computer is used for the visual display of the user program.

AC synchronous motors capable of generating a torque of 10 kg-cm at 60 rpm are used to drive the wheels. Specification of AC motor used for mobile base, arm base, arm shoulder are 230 V AC, 60 rpm, torque 7 kg-cm, weight 1.5 kg, and the specifications of the elbow motor, roll and gripper motor are DC Motor, 4 kg-cm torque, 0.5A current rating, bi-directional, 60 r.p.m. The mobile AC motors are mounted on the lower surface of the hylam sheet with the help of brackets made from aluminum in order to reduce the weight [2].

The two wheels of diameter 12 cms, plastic made with a rubber tyre over it is coupled to the main driving motors using a chain of gearing systems and supported between two ball bearings. The motors are coupled to the wheels using aluminum shafts via the spur gears of 12 and 48 teeth's. Since the hylam base has to carry the entire weight of the robot, it was necessary for us to increase the torque rating at the wheel shafts. This was achieved by using spur hard nylon gears of 1:4 ratios. The smaller gear attached to motor has 12 teeth's and the bigger gear attached to the wheel has 48 teeth's. The two driving wheels of 10 inches are placed along the diameter of the circular hylam sheet below it . The rubber tyre helps the robot better gripping of the surface.

Two castor wheels are used as guiders, one at the front and the other at the back. A 1:4 spur gear arrangement is used for reducing the speed to 15 rpm and increases the torque by 40 kg-cm at the wheels. The arm mounted on the trolley has a 4 DOF and consists of arm base; arm shoulder, arm elbow and the arm roll motion with the grip motion. Worm and worm wheel arrangement is used for the shoulder and elbow joints because even when the arm is in the intermediate position, it won't fall down and thus acts a locking mechanism. The fabricated length of the upper arm and the forearm is 24 cms and 20 cms.

ase assem ly of the 3 axis robot arm is slightly off center of the octagonal acrylic platform. It consists of two small circular plates one above the other (bottom plate being fixed and the upper one rotating w.r.t. the bottom) with a thrust bearing in between them to provide a smooth base rotation of 300 either in the clockwise or in the anticlockwise direction. A big AC synchronous motor is attached at the bottom of the acrylic platform. A worm and a worm wheel assembly of 1:30 ratio is keyed to the motor shaft in the horizontal plane. A central rotating shaft is attached to the big rotating worm wheel. This shaft is extended from the bottom of the platform to the top circular plate and is welded at the center. Limit switches may be used at the extreme ends of the double plates. The entire arm (with the shoulder assembly, elbow assembly and the gripper assembly) is mounted on the upper rotating plate [3].

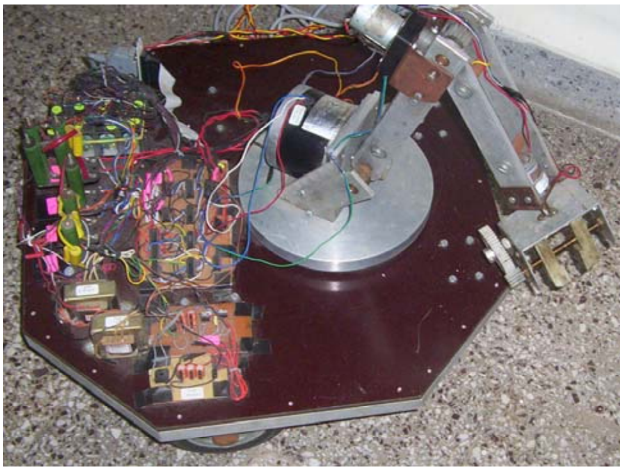

Fig. 2 : A pictorial view of the designed fabricated mobile OCTAGON

S oulder assem ly : The shaft is fitted with a pair of parallel aluminum plates that move along with the shaft. The motion is actuated by a very compact mechanism of worm and worm wheel. The double helical worm is fitted on the motor shaft, while the worm wheel is fitted on the shaft, which provides elbow rotation. The speed ratio of this arrangement is 1:15, that is, the worm wheel makes one complete revolution when the worm makes 15 revolutions. The motor is fixed on the circular aluminum plate on the base assembly. To shoulder axis, 1st link of length 250mm is attached. Limitation of the shoulder motion is 90 .

El o oint motion : The motion is actuated by a very compact mechanism of worm and worm wheel. The double helical worm is fitted on the motor shaft, while the worm wheel is fitted on the shaft, which provides elbow rotation. The speed ratio of this arrangement is 1:30, that is, the worm wheel makes one complete revolution when the worm makes 30 revolutions. The motor is fixed on the lower plate of the inner arm. The position of the motor is so adjusted that it does not obstruct the rotation of the outer arm. The plates of both the arms are coupled to the shaft with the outer arm plates inside the inner arm plates. The shaft moves in a pair of Brass bushes in the inner arm plates. Contact between the two plates is avoided by a pair of thrust bearings between them. The upper plate of the outer arm is pinned to the shaft motor. Actuating the motion is a AC motor; small in size with considerable torque and speed. The motor is light in weight (200 gm) and easy to control, thus making it an ideal choice for actuation. Limitation of the elbow motion is 120 .

ripper : The robot being a PNP-type has a gripper as the end-effector (Fig. 3). The gripper is of parallel jaw type, which works on the principle of left-hand / right-hand screw. These 2 jaws run on the LH / RH screw. The LH / RH screw is made by tapping a brass rod with LH die from one end and RH die from other end. This ensures that the gripper jaws move in the opposite direction, that is, the jaws move either towards each other to grip an object or away from each other to release it. The LH / RH screw is coupled to a small DC tape motor shaft (12V, 1A) via a bevel gear arrangement in the ratio 1:1 as shown in the Image. One limit switches are placed at the inner ends of the finger. This limit switch is connected to the controller card and is used to prevent the further closing of the fingers after the object has been gripper properly. Another limit switch is attached to the extreme end of the maximum opening of the gripper which is also connected to the controller card. The maximum opening of the gripper is 75 mm [4].

Fig. 3. Designed gripper and motor mounting

3. Electronics Design

The mechanical set up forms the skeleton of the robot and what adds intelligence to it is the electronics and the software module. The block diagram of the designed robotic control system is shown in Fig. 4. The electronic design is divided into various sections and finally, the integration is done. Electronic system consists of various cards like the power supply card, controller card, and driver card, interfacing card, sensing and the feedback cards. The software module is designed for maximum robot control working efficiency in a user-friendly java environment. It is so designed that the user can have complete control over each movable part of the robot. Also the user can easily maneuver the robot make it traverse a path towards the object to be picked. He / she can then manipulate the different limbs of the robotic arm so that the gripper comes closer to the object eventually picks it up. Throughout this process the software interface guides the user through the usage of various parts of the robot provides him with responses from the robot. The robot is interfaced to the computer using the parallel port. If there are obstacles in the path of motion of the robot, then the software takes care of this by initiating an alternative path around the obstacles making sure that the robot reaches the desired destination. The design of the software is kept modular and structured properly. The robot can be controlled in 18 modes as given in Table 1. The various electronic circuitries designed are

Motor dri er circuit : is the interface medium between the PC and the Robot as shown in Fig. 4. It is designed using IC's L293D and consists of an :

Input section : in the motor driver circuit which consists of a 25 pin D male connector which connects the driver circuit to the PC through the parallel port using the RS232C. The program sends the byte combination to energize the desired motors, which reaches the driver circuit through the 3-meter data cable to the input of the driver circuit. The i/p section has also a T T L short circuit prevention logic. This circuit is employed to ensure that the motor driver IC does not receive a logic 1 signal on both the CW / CCW inputs which may cause the motors to get stalled. The L293D has 2 direction inputs for each motor, which should be activated exclusively and not simultaneously. The TTL short circuit prevention logic makes sure that if both signals (CW / CCW) for a motor are high simultaneously then input to the driver on both the direction lines will be Logic 0. The Ex-OR gate output will be logic 1 only if one of the inputs is Logic 1. Output is then logically ANDed with the 2 inputs to yield the final outputs for CW (clockwise) and CCW. The input connector is used to connect any input signal to be fed back to the PC from the driver circuit. It sends them to the PC via the unused lines of the parallel port. We use 3 lines from the status port of the parallel port connector as feedback signals to indicate Base Reset position, Elbow Reset position and Gripper status (limit switch) [5].

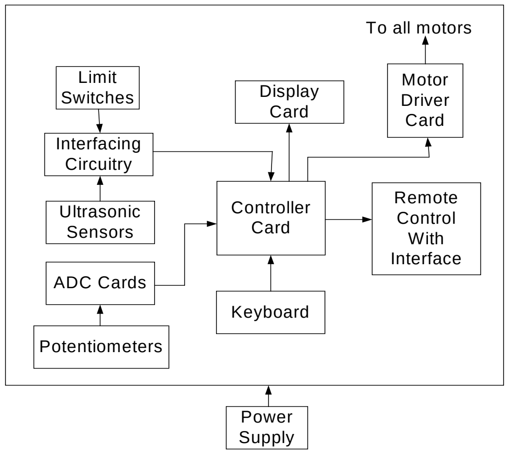

Fig. 4 : Designed and fabricated interfacing card

utput section : consists of the dual motor driver IC L293D, a quad push-pull driver capable of delivering output currents of up to 1A or 600mA per channel respectively. Each channel is controlled by a TTL-compatible logic input and each pair of drivers (a full bridge) is equipped with an inhibit input which turns off all four transistors. A separate supply input is provided for the logic so that it may be run off a lower voltage to reduce dissipation. Additionally, the L293D includes the output clamping diodes within the IC for complete interfacing with inductive loads. Both devices are available in 16-pin Batwing DIP packages. They are also available in Power S0IC and Hermetic DIL packages. The enable lines for the ICs are kept at logic 1 to enable all the ICs. The outputs of the ICs are given to diode bridges, which are used to interface to inductive loads [6]. The motors are connected across the bridges. Electronic views are shown in Fig. 5.

Po er supply circuit : is designed to give a 12V output at 5A and 5V at 1A. A 5V / 12V supply is chosen because the cumulative current drawn when all the motors are energized is around 3A. Thus as a safety measure, a 5A supply is selected. The power supply consists of the step down transformer, the filter circuit, the bridge rectifier and the regulator circuit. A fuse of 5 A is used to protect the circuit from an overload of current drawn from the mains. The power supply unit consists of two circuits namely, a 5V / 1A supply employing a 78L05 IC regulator and a 12V / 5A supply employing a 338K IC regulator [7].

Fig. 5 Various views of the robot / electronics

obile	Arm
Forward	Arm base clockwise
Backward	Arm base anticlockwise
Forward Left	Arm shoulder up
Forward Right	Arm shoulder down
Backward Left	Arm elbow up
Backward Right	Arm elbow down
Spin Clockwise	Arm roll clockwise
Spin Anti-clockwise	Arm roll counter-clockwise
	Arm gripper open
	Arm gripper close

Table 1 : Table to show 18 motions of OCTAGON

4. Software Design

OCTAGON system employs a sophisticated application controlling interface created in JAVA as it is a fantastic programming language for any application software development. The developed software module for controlling the robot is shown in Fig. 6. The software module application facilitates the user interaction with OCTAGON and has many in built features [8].

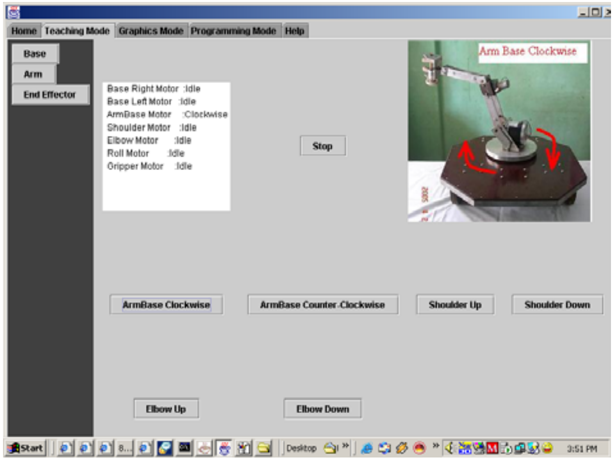

Fig. 6 : Java based graphical user interface for maneuvering the robot

5. Conclusions

A mobile octagon with a 4 axes robot arm was modeled, simulated, designed, fabricated indigenously with the local available components and successfully implemented and is in operation. The mechanical assembly was divided into 3 units, viz., base, arm and the end-effector assembly. The electronic section was done in 3 stages, viz., power supply, controller and the driver unit. The robot was controlled using a GUI developed in JAVA in various modes. A brief kinematic analysis of the robot was also carried out. A number of pick and place operations were successfully performed by the developed robot by using teaching mode, manual mode and programming modes.

References

[1]. Robert, J. S., "Fundamentals of Robotics : Analysis and Control", PHI, New Delhi.

[2]. Klafter, Thomas and Negin, "Robotic Engineering" PHI, New Delhi.

[3]. Fu , Gonzalez and Lee, "Robotics : Control , Sensing , Vision and Intelligence", McGraw Hill.

[4]. Ranky, P. G., C. Y. Ho, "Robot Modeling, Control Applications", IFS Publishers, Springer, UK.

[5]. T.C.Manjunath (2005), "Fundamentals of Robotics", Nandu Publishers, 3rd Revised Edition, Mumbai.

[6]. T.C.Manjunath (2005), "Fast Track To Robotics", Nandu Publishers, 2nd Edition, Mumbai.

[7]. Ranky, P. G., C. Y. Ho, "Robot Modeling, Control Applications", IFS Publishers, Springer, UK.

[8]. Groover , Weiss , Nagel and Odrey, "Industrial Robotics", McGraw Hill.

The Eleventh International Symposium on Artificial Life and Robotics 2006 (AROB 11th'06),
B-con Plaza, Beppu, Oita, Japan, January 23-25, 2006

Design of an home / office automation for the physically handicapped using mobile robots

T.C.Manjunath

Research Scholar, IEEE / SPIE / IOP / ISSS Student member,
101 B, Interdisciplinary Programme in Systems and Control Engineering, ACRE Building,
Indian Institute of Technology Bombay, Powai, Mumbai-400076, Maharashtra, India.
Email : tcmanju@sc.iitb.ac.in ; Phone : +91 22 25780263 ; FAX : +91 22 25720057

Abstract

In this paper, the design and implementation of a automated blind navigator for the physically handicapped persons is presented. In this project, we have attempted to design an automation solution, keeping in mind the needs of the physically challenged, which in our context includes the elderly and the disabled.

1. Introduction

There are millions of people with some form of physical disability in the world - some are born with debilitating disorders and some are unlucky enough to acquire bodily defects as a result of an unfortunate circumstance. Regardless of what disability one may have, technology strives to perform as a surrogate of the bodily function that was lost, or never was in the first place. What is technology if it cannot ease away the hurdles felt on a daily basis by a portion of our society? Be it through medicine, physical aids or electronically, technology and the proponents behind it have a responsibility to not ignore those who can truly make the most use from it.

Today it is possible for a blind person to see with the creation of the world's first artificial eye. This was achieved by directly wiring a CCD camera to the brain. Using this camera, which was mounted on a pair of sunglasses, partial vision was restored in the first recipient of this technology. Those suffering from debilitating diseases or with missing limbs can take respite in what today's expertise can offer. Getting mobile means making use of specially designed scooters, keeping in mind the needs of the immobile, such as ease of access and control. But living in a country where two-thirds of the population is below the poverty line presents a whole new challenge for marketing such a technology to the masses [1].

The only solution would seem to design a cost-effective, need-oriented, specifically designed system that could be adapted to suit the individual needs of each and every disabled person. The logical solution would be to develop a system, which could be assembled as per the specific needs of the individual. A diagrammatical representation of the above proposal is done in this paper and is proposed and implemented for a blind navigator. In this project, we have attempted to design an automation solution, keeping in mind the needs of the physically challenged, which in our context includes the elderly and the disabled. To be very specific, we have designed this system keeping in mind people who have no mobility from the waist down, i.e., they have no use of their legs. However, this system can be modified, using suitable peripherals to suit even those handicaps with no movement of the body at all, i.e., people who have no motor functions from the neck down. This has been left as a future prospect of the project left open to those interested. Basic block-diagram of the proposed system is as shown below in Fig. 1.

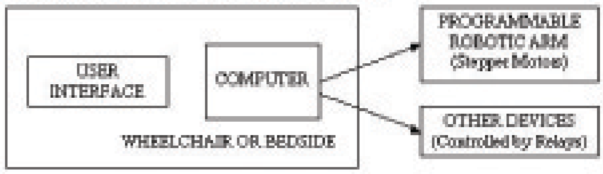

Fig. 1 System block diagram

Fig. 2 GUI developed

Basically, a computer strapped onto a wheelchair with a suitable input peripheral such as a PDA or a keyboard may be used to interact with the system. This system has been designed keeping in mind those individuals who have motor function in their hands so that they may be able to operate the input peripherals like a keyboard or a hand-held input device like a PDA, etc. [1].

2. Feasibility Analysis

The project implementation has been divided into three phases:

Designing the Relay controller for the O OFF control of various devices

In this phase, we will design a controller to switch ON or OFF a series of relays so as to be able to operate a large variety of devices including motors, pneumatic or hydraulic actuators or even switching ON / OFF electronic equipment. Here, we have actually interfaced relays with the computer.

Designing the robotic arm using stepper motors.

This phase includes the interfacing of a pair of stepper motors with the computer to allow for a two-axis motion of an artificial arm so as to perform tasks, which are out of the reach of the individual.

Creating a Front-End software interface or I.

The third and final phase of the project includes the creation and implementation of a user-friendly, pointing-device compatible (mouse operable), GUI - Graphical User Interface. By far the most challenging part of this whole undertaking has been to get the devices to work upon interfacing with the computer. The Visual C codes used for development and the preliminary failures during the course of this project were a challenge in itself [2].

The Front-End Software has been designed using the Microsoft Visual Studio©. Using Visual C++, which is one of the most powerful developer tools available in the market today, we were able to create a good-looking Graphical User Interface (GUI) to allow a user to interact with both : The Robotic Arm & The Relay Controller simultaneously. This was a challenge in itself, as initially we were finding new ways to be able to multiplex the computer signals so as to operate both of the circuits at once. The front-end software program executable called "ROBO.EXE" is used to run the interfaced devices. A detailed view followed by a brief description of each function of the interface follows suit.

4. echanical design of the robot arm

As mentioned earlier, the robotic arm is made out of a compressed fibrous plastic material and is popularly known as foam-board. The foam-board used for our designing purpose was 3 mm thick. The whole process of creating the robotic arm involves the following steps :

First, based on the requirements of the process that the arm is going to be used for, the arm is designed on paper and also using some CAD (Computer Assisted Design) software. The arm needs to be simulated, its trajectories need to be calculated, its work-envelope geometry needs to be thought out before actually starting to build the arm. Why this needs to be stressed is because, we need to design the arm keeping in mind the needs of a disabled individual. What he / she can and cannot do. For the purpose of simplicity however, we have kept the design of the robotic arm as minimal and simple as possible. The following points need to be kept in mind while designing the robotic arm:

- The specific disability / disabilities of the individual. (The arm may be customized according to the disability of the individual.)
- The requirements and purposes the arm must be able to fulfill. (i.e., the maximum and minimum reach of the arm.)
- The tasks that need to be performed by the arm. (such as lifting an object, or stirring a spoon, etc.)
- The workspace geometry of the arm. (i.e., the workspace allowed to the arm due to the close proximity with the human operator.
- The load bearing capacity of the actuator.
- The environment in which the arm is subject to operate.
- The budget of the individual.

It would be fair to say that depending upon the custom requirements of each individual, the robotic arm may be modified to suit the needs of the person. The arm needs to be made sturdy so as to be able to handle the rigorous everyday chores put to it by the user. The actuators need to have a long life and need to be able to handle worst-case scenario handling conditions. Therefore, the materials used to construct the arm need to be able to handle large loads without shearing. However, for building our prototype, we have made use of a lightweight, sturdy material that is equally effective. First, corresponding to the design, a 1:1 template is traced onto the material and the material is cut at these traced edges. The cutout parts are then attached together in their specific sequence so as to create the individual sections of the arm. Starting from the base each section is attached to its corresponding sections using the required joint structure. The completed frame of the robot is now ready to be fitted with the actuators.

The actuators are attached to the arm in such a way that they do not hinder the motion of the arm itself. For this purpose, generally they are placed away from the work envelope of the arm itself. Moreover, the actuators need to be powerful enough to be able to drive the arm without causing any backlash or slip. This needs to be taken care of especially because we do not want the arm to slip from its position while lifting a heavy load. The actuators we have used are of the digital type (Stepper Motors X2). Thus, a suitable drive mechanism needs to be implemented to run the arm itself [2].

The robotic arm is made out of a compressed fibrous plastic material and is popularly known as foam-board. The foam-board used for our designing purpose was 3mm thick. An important feature of the arm that might not appear at first sight is the mutual coupling of two joints; namely the shoulder and the wrist. The shoulder and wrist joints are mutually coupled by a parallel bar arrangement so as to provide compliant motion to the gripper when it is lifting or placing level-sensitive objects like a glass of water or the like.

Thus, this eliminates the need to have sophisticated trajectory calculation for the wrist and also the need to place a heavy motor at that point. The material used for constructing the robotic arm needed to be light and durable. The most suitable material we could find for this purpose was a fibrous plastic created by compacting a resin called "foam-board". This foam board can be easily cut and pasted like ordinary cardboard but has the strength of a hard plastic. Therefore it can withstand a lot of shear-force as compared to cardboard.

It is clear from the schematic shown in the GUI that the robotic arm has three degrees of freedom from just two axes. The two axes being the rotary axis passing through the base' revolute joint and that passing through the shoulder's revolute joint. Both the axes are rotational and hence this robotic arm can also be described as an RR-Robotic arm. The material used for constructing the robotic arm needed to be light and durable. The most suitable material we could find for this purpose was a fibrous plastic created by compacting a resin called "foam-board". This foam board can be easily cut and pasted like ordinary cardboard but has the strength of a hard plastic. Therefore it can withstand a lot of shear-force as compared to cardboard [3].

An important feature of the arm that might not appear at first sight is the mutual coupling of two joints; namely the shoulder and the wrist. The shoulder and wrist joints are mutually coupled by a parallel bar arrangement so as to provide compliant motion to the gripper when it is lifting or placing level-sensitive objects like a glass of water or the like. Thus this eliminates the need to have a sophisticated trajectory calculation for the wrist and also the need to place a heavy motor at that point. The arm is controlled with the help of a pair of stepper motors, one each for the base and the shoulder. The base motor has its axis vertical and is attached directly into the base, while the shoulder motor has its axis horizontal and is attached just below the shoulder joint.

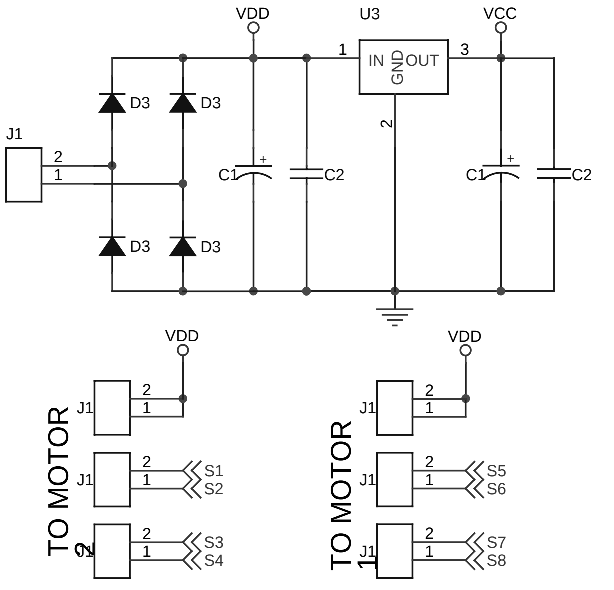

Fig. 3. Power supply circuitry

It was possible to use ordinary DC motors for this purpose with a suitable reduction ratio. But, that would greatly diminish the precision of the arm. Moreover, to avoid subjecting the arm to sudden strains or even locking due to limited motion of the joints, it was decided to use stepper motors instead. However, we do make use of a DC motor for the gripper, which is being controlled by a relay.

5. Design of the power supply

The performance of the controller depends on the proper functioning of the power supply unit. The power-supply not only converts A.C into D.C, but also provides output voltage of 5V, 1A DC to run the motors. Note that the relays operate directly on the 12V supply. The essential components of the power supply are transformer, rectifier, filters and regulators (Fig. 3).

. Interfacing unit

The robot is interfaced to the computer's parallel port using a interfacing device. The original IBM-PC's Parallel Printer Port had a total of 12 digital outputs and 5 digital inputs accessed via 3 consecutive 8-bit ports in the processor's I/O space. The ports have been color-coded for ease of reference. The Blue pins refer to the Output ports, while the Red pins refer to the input ports. The Green pins denote ground.

- 8 output pins accessed via the **DATA Port** .
- 5 input pins (one inverted) accessed via the **STAT S Port** .
- 4 output pins (three inverted) accessed via the **CO TRO Port** .
- The remaining 8 pins are grounded.

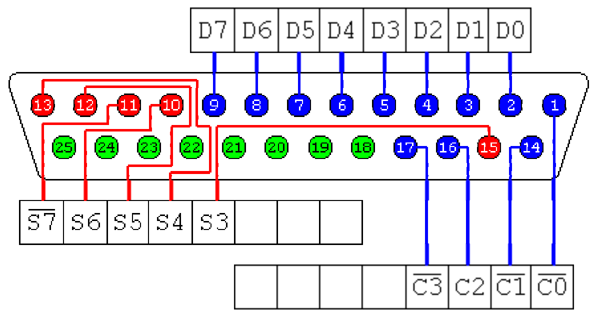

Fig. 4. Parallel port

. Relay controller stepper controller

The control circuit used for controlling the robotic arm is one of the most intriguing and complex parts of this entire undertaking. The task facing the designer was to create a circuit, which would perform a two-fold task for serving the purpose. Firstly, it needed to isolate the low-power output-port signals of the LPT1 port. Secondly, it needed to be able to drive the motor after this isolation, which would definitely require a complex switching mechanism. A schematic of the control circuit is shown in Fig. 5. Here too, the signals arriving from the port are first isolated to disallow any stray voltages or currents from passing back to the sensitive computer port [3].

These isolated signals are then given a driving capability using a buffer. Subsequently, the buffered signals move on to the GATE terminal of an N-channel MOSFET. On receiving the requisite level of GATE voltage, the NMOS switches ON thus allowing the drive to that particular winding of the stepper motor. However, since the signal arriving from the port is in the form of a square pulse, so too at the output of the NMOS we would observe a square pulse but of a higher driving capability. Now, these square pulses arrive in succession to the coils of the stepper motor, thus rotating the motor depending upon the sequence of their excitation.

The Relay Controller is intended for use mainly in switching applications. Initially, there were plans to make use of a series of 8 relays dedicated for switching ON / OFF the various devices, but since the robotic arm was making use of the same parallel port LPT1, a solution had to be found to multiplex the relay control signals as well as the robotic arm control signals. This was achieved by cutting down the required number of relays to 4. Moreover, the initial circuit proposed was that of a logical device controller, which made use of an array of combinational logic devices to switch the relays, as well as to sense the present condition of the relay (whether the device is actually ON or OFF). This idea was abandoned after the failure of the design during testing phase [4].

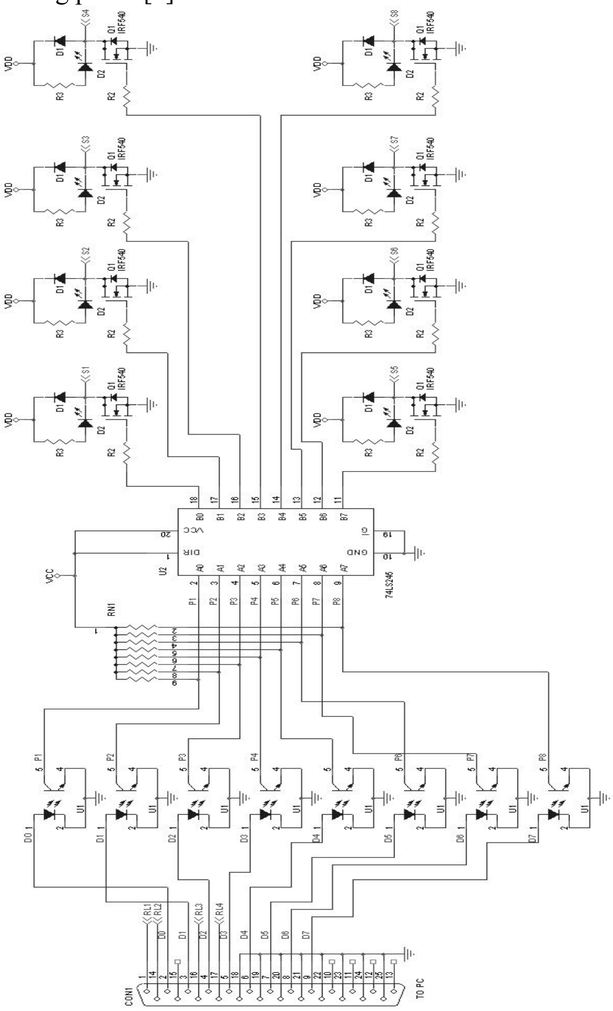

Fig. 5 Stepper motor controller circuit diagram

However, a new and improved version of the circuit was developed, to ensure fail-safe operation even in extreme conditions. Where the previous circuit failed to operate due to its complex logic involved, the new version of the circuit performed outstandingly due to its much more simpler and rugged design.

Another modification was that of the software used for the switching purpose. The native C-language initially used, was scrapped. Instead, modules of the software were created in Visual C++, which were then linked in a compiler and run in compatibility mode with the operating system. Each module contained reference to various classes used mainly for designing the front-end of the interface. The schematic below shows the circuit used for relay switching:

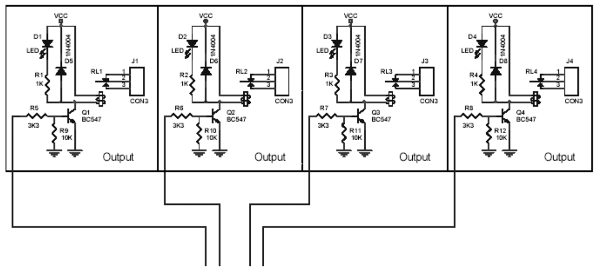

Fig. 4 Relay controller / switching circuit

The switching circuit is basically used for switching ON / OFF those devices that are connected to the supply through the relay. When the relay switches ON, the device will obtain the required drive and will thus switch ON. The relays used for this project have a rating of 12V / 200 Ω. A transistor BC548 controls the relays, which perform the switching depending upon the BASE drive they are given. The resistors are used for biasing the transistor and also limiting the current to the LED, which displays the status of the relay. A flywheel diode is used to dissipate the residual EMF present in the relay coils.

A supply of 12V DC is given to the P-terminal of the LED, while the loose ends of the biasing resistors are connected to ground. Now, when an ON signal arrives from the port pin to the BASE of the transistor, the NPN transistor tends to switch ON allowing the supply current to flow through it. This supply current in-turn energizes the plunger-coil of the relay. When the plunger-coil is energized, the electro-magnetic coil forces the plunger to switch from its N/C terminal to its N/O terminal. This in-turn allows the supply to be given to the device, which is connected between the terminals of the relay. The device thus switches ON [4].

8. Conclusions

The design and implementation of a automated blind navigator for the physically handicapped persons using mobile robots is presented in this paper.

REFERE CES

[1] Robert Schilling, Fundamentals of robotics, PHI.

[2] Hodges Bernard, Industrial Robotics, Jaico Pub.

[3] T.C.Manjunath (2005), Fundamentals of Robotics, 3rd edition, Nandu Publication, Mumbai, India.

[4] Fu, Gonzales, Lee, Robotics-Control Sensing & Vision, Mcgraw Hill.

An Efficient Path Planning Mechanism For A Micro-Robot

T.C.Manjunath

Research Scholar, IEEE / SPIE / IOP / ISSS Student member,
101 B, Interdisciplinary Programme in Systems and Control Engineering, ACRE Building,
Indian Institute of Technology Bombay, Powai, Mumbai-400076, Maharashtra, India.
Email : tcmanju@sc.iitb.ac.in ; Phone : +91 22 25780263 ; FAX : +91 22 25720057

Abstract

This paper deals with the design, fabrication and implementation of a micromouse robot controlled using a microcontroller. Micromouse is a mobile robot designed and programmed to navigate through a maze using the learning route. The project was to design and construct a miniature path follower to ease the development of moving object tracking system. The first stage in the project was to design and construct the micromouse. Electric motors have been added to provide a load torque. The electronics were tackled next and were controlled by Micromouse microcontroller to transmit and receive the positional information to make the tracking possible. The communication is done through the RF Transmitter and receiver module. The majority of the development associated with the torque . Overall, the project was a success and all the design concepts have been proven. Further improvements / adjustments to perfect the tracking are suggested and a possible future extension to the project would be to develop it to the perfection from the practical implementation view.

Keywords : Micromouse Robot, Path Planning, Microcontroller, Driver, Stepper motors.

1. INTRODUCTION

Micro mouse is a mobile robot designed to navigate through a maze. In this project, two micromices are designed. The first working mouse must quickly roam around the maze and learn the route, then travel from a designated maze. The second working mouse must quickly roam around the maze by learning the route, then travel from a designated maze corner to catch the first micro mouse as rapidly as possible. The standard Micro mouse has a series of standard core components: A motor drive module which consists of two motors drive wheels, a microcontroller board that consists of a microcontroller, external RAM and components to drive these and finally a motor control board which drives the motors. Once the Micro mouse is built, a control algorithm to steer the Micromouse and to allow the Micromouse to sense its position is developed. Once this is accomplished, a second control algorithm is developed that will allow the maze to be solved.

In the development of these algorithms, certain parameters of the Micromouse need to be measured or obtained from the Micromouse hardware. These are obtained by taking measurements from the Micromouse whilst it is running in the maze. The project requires mechanical, electronic and software design and development. The 1st step towards the completion of the project is the design and construction of a mechanical structure of the Micromouse. Electronics is then developed as well as an interface with the mechanical hardware to allow the control and communication. The final component of the project is the software design. A program is written to interpret and control the electronics.

2. OBJECTIVE

Objective of the project is to develop a system that can trace a moving object , follow and catch up with it. The proto here is constructed with the help of two micromouse. The first micromouse is free moving object. The 1st micromouse transmit information about it's current location. This information is captured by the 2nd micromouse and follows the 1st with best suitable path. The path traced by the 2 micromouses is constructed in the form of maze. The prototype maze layout is shown in Fig. 1 with software.

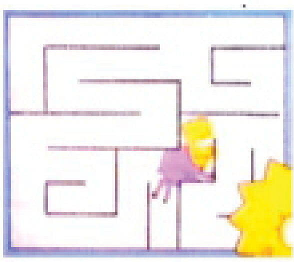

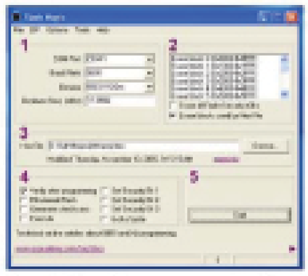

Fig. 1 Design of the path for the micromouse using the developed GUI in flash

Physical Dimensions

The maze is constructed with a dimension of 72 x 72 cm and virtually divided into 16 cells each of 18 x 18 cm. As per the standard maze construction maze path is 16.2 cm wide with added walls of thickness 1.8cm, thus it is 18 cm wide with walls. Micromice has a size of 18 x 22 cm in full length whereas the sensor size is 18 x 18 cm. In order to male it compact the sensor module is overlapped on the micromice. The wheels are design through a lightweight metal like aluminum. The circumference of the wheel is 13 cm and hence the diameter is 4.2 cm.

3. CO STR CTIO IDEAS

Two complete different ways of designing the micromouse are possible. One is the conventional analogue method with comparators and analogue control of the motors. The second, the digital way can either be realized by using digital logic devices or by using a microprocessor. The opportunity of using a microprocessor is the easy and convenient adjustment of the software for different tasks and to increase the overall speed without any change of hardware or the trial and error method with a lot of variable resistors.

Therefore, we used a microcontroller, which is very fast in operation and because of its reduced instruction set easy to handle. The hardware architecture allows execution of one instruction in only one processor cycle, because the data and the address bus are completely separated. Also, input and output of the microcontroller are very easy to use, because they can be directly accessed by the program. The motor control will be realized with two half bridges, which contain each 2 logic level MOSFET's one for running and one for braking. These transistors can be directly driven by CMOS-Logic devises and are capable of high voltages and high current.

Driving backwards was thought not to be necessary during the design process. For wall detecting, pulsed infrared sensors are used. The pulsing of the sensors increases their working distance enormously and makes variable resistors unnecessary. With these sensors, it is also possible to read out wheel reflectors. We tried to built up the micromouse as compact and light as possible for having sufficient space for turning and running the micromouse between the walls of the maze. Reduction of weight results in a better mobility.

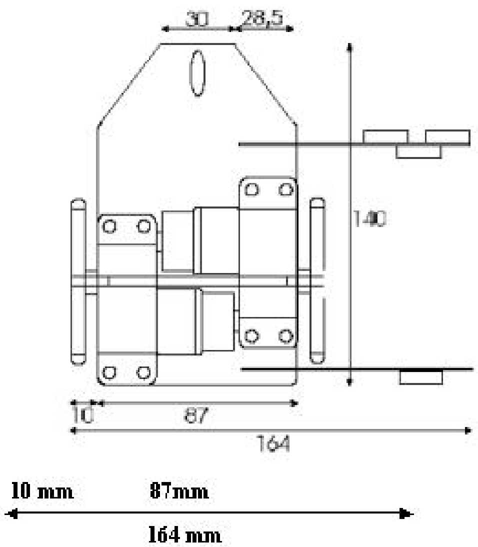

Fig. 2 : Mouse layout - Top view

echanical Construction

From the Fig. 2, it can be seen that the gearboxes are mounted as close as possible to reduce the size of the chassis. Everything on the chassis was mounted in a way that we could get as close as possible to the maze ground to get the centre of gravity down. For minimum weight the sensor arms are build out of epoxy (the same material as the chassis) and soldered to the ground plate. The ball-bearing we used first was replaced by a cloth hanger. This also led to better steering of the micromouse because of the reduced weight in the front .

4. Stepper otor

A stepper, or stepping motor converts electronic pulses into proportionate mechanical movement. Each revolution of the stepper motor's shaft is made up of a series of discrete individual steps. A step is defined as the angular rotation produced by the output shaft each time the motor receives a step pulse. These types of motors are very popular in digital control circuits, such as robotics, because they are ideally suited for receiving digital pulses for step control. Each step causes the shaft to rotate a certain number of degrees.

A step angle represents the rotation of the output shaft caused by each step, measured in degrees. Fig. 3 below illustrates a simple application for a stepper motor used. Each time the controller receives an input signal, the motor is driven a certain incremental distance. Like in addition to the drive mechanism in a printer, stepper motors are also popular in machine tools, process control systems, tape and disk drive systems, and programmable controllers. The most popular types of stepper motors are permanent magnet (PM) and variable reluctance (VR).

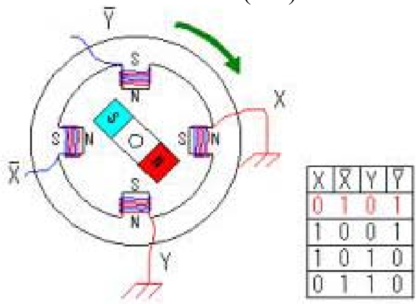

Fig. 3 Stepping motor (CW / CCW) used in our work

Fig. 3 above shows a permanent magnet stepper motor with four stator windings. By pulsing the stator coils in a desired sequence, it is possible to control the speed and direction of the motor. The figure also shows the timing diagram for the pulses required to rotate the PM stepper motor. This sequence of positive and negative pulses causes the motor shaft to rotate counterclockwise in 90° steps. The waveforms of Fig. 3 above illustrate shows how the pulses can be overlapped and the motor made to rotate counterclockwise at 45° intervals.

The direction of rotation is determined by applying the pulses to either the clockwise or counter clockwise drive circuits. Rotor displacement can be very accurately repeated with each succeeding pulse. Stepping motors are generally operated without feedback, which simplifies the control circuit considerably. One of the most common stepper motor drive circuits is the unipolar drive, shown in Fig. 3. This circuit uses bifilar windings and four Darlington transistors to control the direction of rotation and the stepping rate of the motor.

5. OCK DIA RA

- As shown in the block diagram port 0 is connected to IR sensor module through the Schmitt trigger 74HCT14 which is used for the TTL compatibility.
- The Port 1 is also connected to the IR sensor module through the Schmitt trigger.
- Port 2 is connected to the RF communication module
- Port 3 is connected to the Stepper Motor through ULN2803 which is used as a current boosters

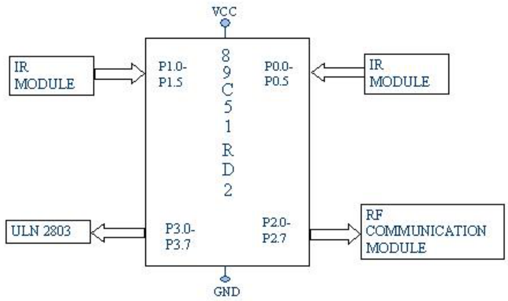

Fig. 4 Block diagram of the system

Components ist

- ✓ 89C51RD2 - (2 in number)
- ✓ ULN2803 - (6 in number)
- ✓ Schmitt Trigger - 74HCT14 - (4 in number)
- ✓ IR Sensors Module - (24 in number)
- ✓ Transmitter Module - (24 in number)
- ✓ Resistances - 1K & 5K
- ✓ Stepper Motor (MACT) - (2 in number)
- ✓ 9 Voltage battery

icrocontroller 89C51RD2

For controlling the micromice, we are using microcontroller, i.e. 89C51RD2 one for each micromice. 89C51RD2 is a high performance CMOS flash version of the 80C51 CMOS single chip 8-bit microcontroller. It contains a 64k byte flash memory block for code and for data. The 64kb flash memory can be program either in parallel mode or serial mode with the ISP capability or with the software. The programming voltage is internally generated from the standard V_{cc} pin.

Here, we are using all the 4 ports of the controller.

- For programming we assert the pin no 29 low.
- External crystal is connected to the pins 18 and 19.
- Pins 10 and 11 are used to program the controller serially into the flash RAM which is 64K bytes.
- To reset the system we give high voltage to the pin 9.

lock Diagram

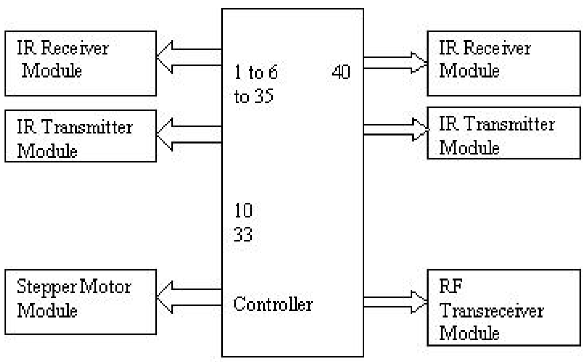

Fig. 5 Overall block diagram of the system

Crystal Tuned P ased ASK odule

This module uses the technique of On-Off keyed modulation. Local Oscillator is based on PLL. The module is high performance, simple to use and miniaturized.

SC ITT TRI ER

It is used to provide TTL compatibility it eliminates noise. It provides 6 inverting buffers with Schmitt trigger action. They are capable of transforming slowly changing input signal into sharply defined distortion free output signals.

28 3

It is a current amplifier. The required current rating for stepper motor is 0.7 ampere per phase. One ULN can give current rating of 0.22 to 0.28 amperes. Thus to get the required rating of 0.7 amp we are using three ULN which are mounted one over the other. ULN2803 is a 18 pin IC which provides current stability and is easily available.

SE SORS

The Fig. 6 shows the circuit diagram of one of the sensors. The IR-Diode is pulsed by the MOSFET (small duration pulses are given). When the IR-Transistor detects reflected light (which means a wall), the input of the comparator LM339 (very high current stability & acting as a comparator) is pulled to ground and at the output of the comparator occurs a high impulse. The 100nF coupling capacitor blocks DC and low frequent signals. Therefore, ambient light cannot interfere. We are using common anode sensors. These are infrared sensors. The number of the IR sensor is TSOP series IR DIODES. Voltage rating of IR sensor is 3.3 volt. We are using these sensors because it has affordable cost with good sensitivity. Actually, we need accuracy and not larger range i.e. the sensor should not sense anything beyond 2.5 cm range.

Arrangement of sensors

12 sensors are used in one micromice .two are at the front side, 5 for left stepper motor and 5 for right stepper motor. Out of this 5 sensors the central one is used for the right or left turn. The other two sensors besides the center one are used to control the straight. The extreme two sensors normally not used and are there for corner point detection.

Communication odule

The communication between the two mouse is achieved through a Crystal Tuned PLL Based ASK Module.

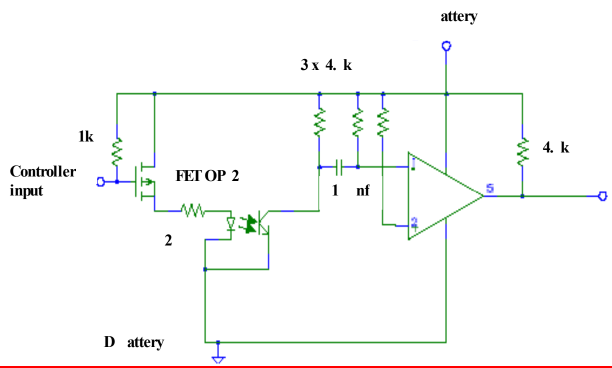

Fig. 6. Schematics of one Sensor-stage

. The Software Design

The software for the vehicle must be able to drive the mouse straight ahead and to turn right around the corner. For driving straight ahead the software has to control the motors in an suitable way. Therefore a PWM (Pulse Width Modulation) with a resolution of 16 bits for each wheel was developed. The program has to check the sensors in order to control the vehicle by detecting the walls. During the initialization the I/P's and O/P's are set. Also, all the needed variables are presetted or cleared and the ISR (Interrupt Service Routine) for PWM is started. Then the program waits for the START button (Input RA2 of the controller to be pressed. After that the microcontroller drives the vehicle along the wall, until no sensor has wall detection. Then, the TURN subroutine is started and the wallcounter decreased by one. The mouse stops and if not all walls are done, the mouse starts with the next straight driving process.

The ISR is called with every timer overflow. At first a helping counter is increased. The ISR checks now, if the desired PWM value is higher or less than the helping counter. If the desired PWM value is less, the appropriate PWM output is set to low and otherwise to high level. With every call of the ISR the timer has to be presetted again. The above diagram shows in an elegant way, how the PWM actually works. The bits Q1 .. .. Q4 represent the corresponding bits of the PWM helping counter. The ISR compares them with the desired PWM and switches the outputs high or low, depending on the result of the comparison.

Driving along the wall :

Depending on the sensors, the mouse has either to drive straight on or to steer left or right. The control algorithm is a modified bang-bang mechanism.

T ere are different stages :

Stage 1 Only mid sensor has contact - drive ahead.
Stage 2 Mid and right sensor has contact - drive slightly right.
Stage 3 Only right sensor has contact - drive right
Stage 4 Mid and left sensor has contact - drive slightly left.
Stage 5 Only left sensor has contact - drive left.

When none of the sensors have contact, a gap counter is decreased and when this counter is equal to zero, the mouse starts the stop and then the turning process. The turning process is a very simple subroutine, which brakes the right wheel and turns with the left one around, until the first (the right) wall-sensor has contact. Due to the force of inertia and the wheel-slip the vehicle turns a bit further and the as next started straight driving routine adjusts the car again straight towards the wall. The Maze Logic is resolved using the matrix positional coordinates.

Two types of software s design

KEIL - has simulator which contain functionally rich library and good support and compatibility with 89C51. CX51 provides the flexibility of programming in C and the code efficiency and speed of assembly language. It is ground up implementation dedicated to generating extremely fast and compact code for the 8051 microprocessor. FLASH- FLASH is the software that is used by us for the downloading of the program that is stored in the computer in to the micro controller through the bus called RS232. The screen shot of the software is as shown in Fig. 1.

. ORKI OF T E SYSTE

icromouse One

The first micromouse is designed to since the magnetic ink path and propagate along the same. The micromouse is composed of three sensors, viz. central, right, and left. As long as the central sensor is assorted the micromouse will propagate straight line path. If any one of the right or left sensors gets asserted the respective rotational motion will be initiated at the directive stepper motor so that the mouse will take turn. As soon as the left / right sensors gets disserted the mouse will continue the straight line path. The action and motion of the first mouse is transmitted using transmitting mechanism.

icromouse Two

Micromouse two receives the signals forwarded by micromouse one. Micromouse two detects the shorts path towards micromouse one by reading the position of micromouse one and traverse it. Micromouse two is well equipped with the wall sensors with the help of wall sensors directing path to it self.

8. Conclusions

Overall, it was felt that the project was successful in all areas; mechanics, electronics and software. All the primary aims were achieved and in addition the majority of the secondary aims were achieved. The project tackled new areas of design that required innovative ideas.. Its construction has proved the design concepts used and with some minor adjustments and improvements, these could be taken forward to produce an even better test bed. A possible extension to this project has been proposed and concerns the processing. An application was considered using the designed micromouse.

APP ICATIO

The concept of our project was implemented for the purpose of identifying vehicles over a decided territory. This particular project developed as per the requirement put forward by the MUMBAI traffic police department hence the application has to be enhanced to the realistic implementation. As far as the implementation is concerned an ordinance has to be established where in all vehicles should be equipped through the identity transmitting module. The reception can be established through cells defined and established by private and government cellular communication provider. Since it is in the public interest the police department is into process to sanction an ordinance and by 2010 the ordinance will be implemented in full proof manner.

References

[1]. Ayala, K.J. : *T e Microcontroller rc itecture, Programming and pplications*, 2nd Edition. Minneapolis: West Publishing Company, 1997.Calcutta.
[2]. Hughes, F.W. *p mp and oo* . 1st Edition. Englewood Cliffs: Prentice-Hall Inc., 1981.

Design Of A Intelligent Sensing Interface For A Flexible Manufacturing System

T.C. anjunath

Research Scholar, IEEE / SPIE / IOP / ISSS Student member,
101 B, Interdisciplinary Programme in Systems and Control Engineering, ACRE Building,
Indian Institute of Technology Bombay, Powai, Mumbai-400076, Maharashtra, India.
Email : tcmanju@sc.iitb.ac.in ; Phone : 91 22 25780263 ; FA : 91 22 25720057

Abstract

This paper deals with the design, fabrication and implementation of a sensor interface for a Flexible Manufacturing System (FMS) which is capable of sensing the dead ends of the rail track on which the mobile robot system is moving and does some manipulation task. A provision for sensing the limits of the joints, the hard home position of the flexible manufacturing system is designed and developed as a project work. The developed sensor system consists of limit switch sensing circuit, a reset detection circuitry for the mobile flexible manufacturing system, a infra-red detection circuitry and a ultrasonic obstacle avoidance circuitry, thus making the system a closed loop control system.

Keywords Flexible manufacturing system, Limit switches, Computer, Infra-red detection circuitry.

1. Introduction

Sensors are feedback devices which are used to sense the maximum limits of various actions of the robots like the gripper close / open, sense the dead ends of the joints of a robot, thus making it very intelligent. They are used to sense the changes in the environment (detect the obstacles) and get adaptable to the environment (overcome the obstacle and proceed to the destination). There are various types of sensors such as limit switches, IR detectors, proximity switches, cameras, tachometers, thermocouples, thermistors, potentiometers, range sensors, ultrasonic sensors, inductive sensors, light sensors, hall effect sensors, gyroscopes, laser sensors, light sensors, opto-couplers, encoders, incremental encoders, positional encoders, shaft encoders, synchros, etc., [1].

Sensors make the robotic system a close loop feedback control system. Here, in our work, we have designed a powerful sensing system for a mobile robotic system, which is moving on a railway track. In this work, a full-fledged autonomous flexible manufacturing system (FMS) is designed, fabricated and implemented using good sensing techniques with an artificial intelligence provider algorithm. Various type of sensing circuitries is used to make the system closed loop and provide intelligence to the automated system, INARMS which is shown in Fig. 1.

The paper is organized as follows. Section 2 gives a brief introduction to the input section of the sensors. Section 3 discusses about the infra-red detection circuitry. In section 4 , the sensor block diagram interface to the robotic system and to the computer is presented. Working of the comparator circuit and the limit switches is discussed in section 5. The obstacle avoidance algorithm is presented in section 6. Ultrasonic sensing system design is given in section 7. The paper concludes with the conclusions in section 8 followed by the references.

2. Input section

The input card is used to give inputs to computer from robot. The inputs to computer are actually the status of various limit switches, IR detectors circuit to take appropriate action to stop further movement of motor and rather stop at that particular position. The input card composes of various IC's like LM324, 74LS76, 74LS245 and transistor, resistor and LED [2]. Transistors and LED's are used to indicate weather desired position is reached or not. In our circuit, we have used the limit switches for

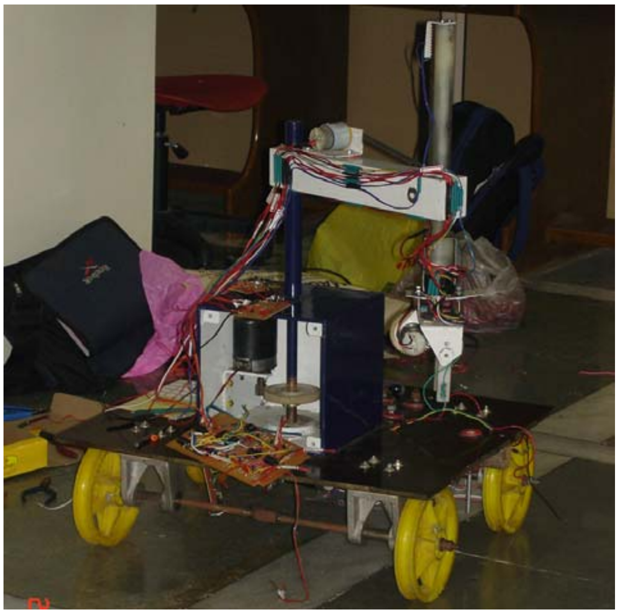

Fig. 1 The designed and assembled flexible manufacturing system with the sensing interface.

RIPPER :-Two limit switches are connected in parallel for detecting closing action and one for detection the extreme limit. In the home position, the gripper remain in fully opened position so that limit switches used for detecting extreme and goes to NO position.

RO ACTIO :- Two limit switches are used for detecting the home position of roll motor .In the home of roll motor and 90° rotation (clockwise) of roll motor, the home roll limit switch get to it's NO position .

PRIS ATIC ACTIO :- Two limit switch are installed at extreme end of vertical extension assembly to detect two end limits. In home position of robo the VE goes to fully upward position, so that bottom limit switch of VE goes to it's NO position.

In this way, two limit switches are used for controlling individual action of gripper, roll and prismatic motion.

3. Infra-red detection circuit

The IR detector circuit is used to detect maximum minimum limit of the base assembly. IR circuit is also used for detecting forward reverse stop point. We are using pair of IR detector's to detect base minimum limit (0 degree) maximum limit (180 degree).

A pair of IR detector's to detect forward reverse stop point are used. Hence in all there are 10 inputs but since we are using parallel port in SPP mode number of inputs to computer get reduced to 5. So we multiplexed all the inputs such that two states of each action are given to two inputs of J-K flip flop, taking single ' output [3].

As the infrared sensor device, P T (Lead [Pb:Plumbum] irconate Titanate) is used. This material has the nature that the electric charge in the surface is divided into the positive electric charge and the negative electric charge in the usual condition (Spontaneous polarization). The distribution of the electric charge is disordered when the infrared rays lash this material and the voltage occurs. The infrared sensor outputs the change of this voltage.

The infrared sensor has the kinds such as the single type, the dual type, the quad type. The dual type is often used to detect the move of the person or the animal. The two identical shape elements are used for the dual-type sensor. And, it is put for the pole of the element to become opposite.

When the change of the infrared quantity occurs, being simultaneous with the element which was put in this way, because the occurring voltage is opposite, it denies each other and the voltage doesn't appear in the output. The output voltage changes only when there is a difference in the quantity of the infrared rays which enter both elements.

Because the same change occurs to both elements even if the infrared quantity of the background in the place to detect with the sensor changes, little change of the output occurs even if it occurs. When the person or the animal crosses the sensor, the quantity of the infrared rays which enter both elements becomes not equal and the change of the voltage appears in the output. IR circuit used is shown in Fig. 2.

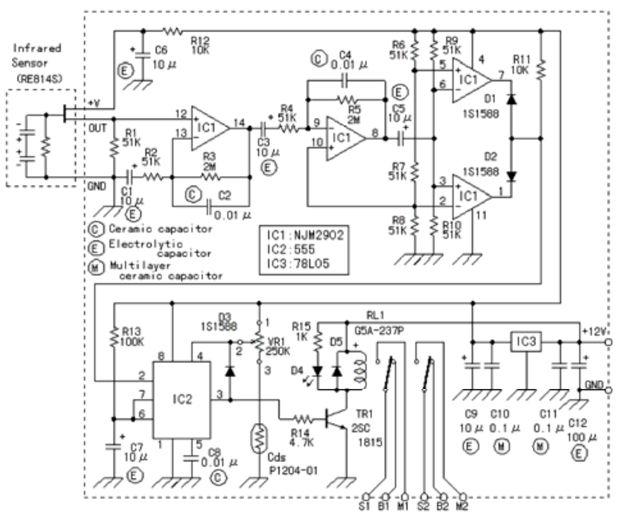

Fig. 2. Designed and fabricated IR circuitry

4. lock-diagram for the sensor interface

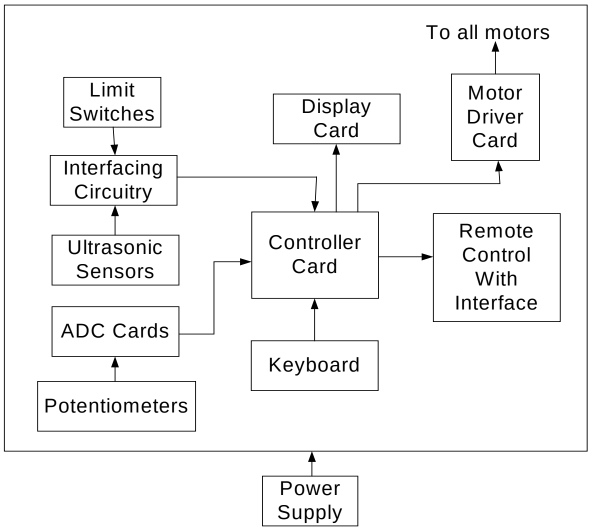

Fig. 3. Designed and fabricated sensing interfacing card

5. orking of comparator circuit for the limit switches

The input to computer requires proper logic states, that is 0 or 1. Hence, to achieve this, we have used comparator circuit for each limit switches [4]. The comparator action is achieved by connecting resistive bridge at input of comparator (LM 324) placing the limit switches in bridge arm connected to inverting input of comparator as shown in Fig. 4. When the switch is closed then voltage at inverting input is high then non-inverting input. Hence output is logic 0. But when the limit switch get into it's NO position, then voltage at non-inverting is high output goes to logic 1 , indicating extreme limit reach.

Consider limit switch state for prismatic motion. When the robot is in home position then lower prismatic limit switch will be in NO position upper limit switch will be in NC position. Hence output of lower comparator will be logic 1 that of the upper comparator will be logic 0.This two inputs are given to k j inputs of J-K flip flops respectively. This causes output to be logic 0 indicating home position [5].

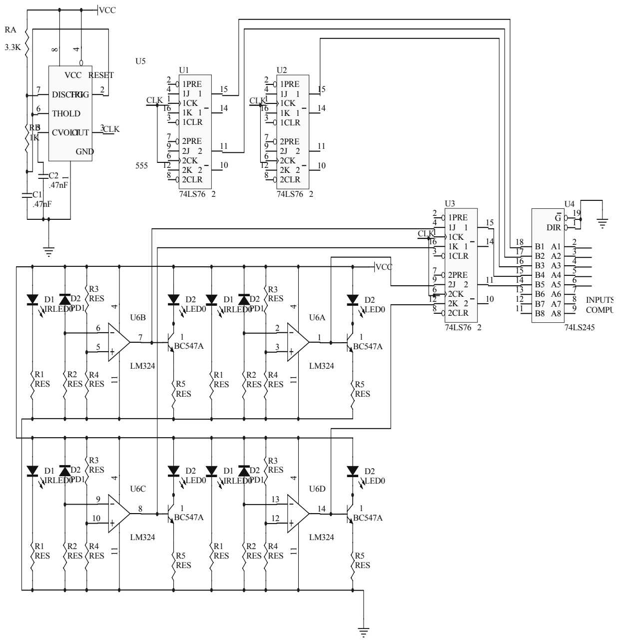

Fig. 4 Reset detection sensing system

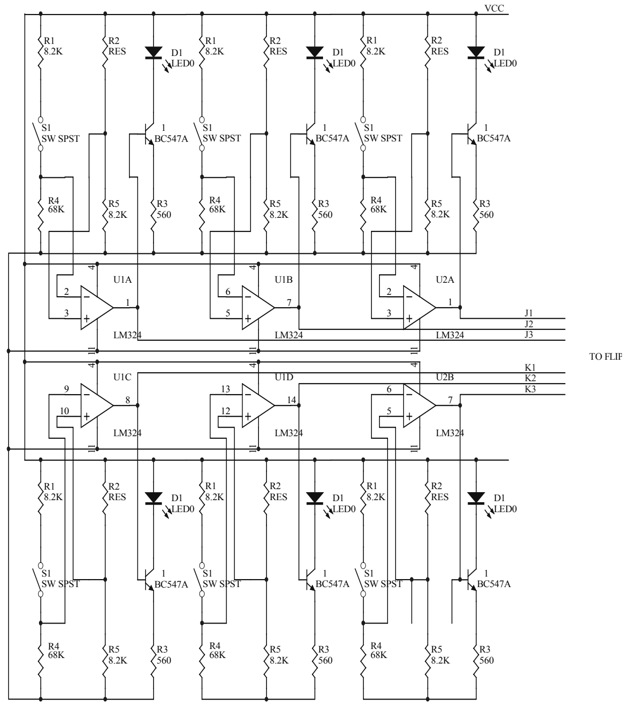

Fig. 5 Limit switch sensing circuitry

On the other hand when VE comes to it's extreme lower position then state of comparators will be exactly reverse of previous case. Hence, output of flip flop goes to logic 1, indicating / detecting extreme lower end. This output is used to signal computer to stop rack motor via IC 74245 buffer. In this way all the output of individual comparator are to given to J-K flip flops output 's of all J-K are given to computer indicating to take stop action's.

. Obstacle Sensing Avoidance Algorithm

Here, the operations are actually carried out or taught to the robot instead of just assuming the parameters. Here in lies the advantage of using remote control over the keyboard to program the robot, however typing the program through the keyboard based on assumed parameters is faster method of programming. If there are obstacles in the path of motion of the robot, then the software takes care of this by initiating an alternative path around the obstacles making sure that the robot reaches the desired destination. However, if there are too many obstacles then the robot may not reach the desired position according to the program [6].

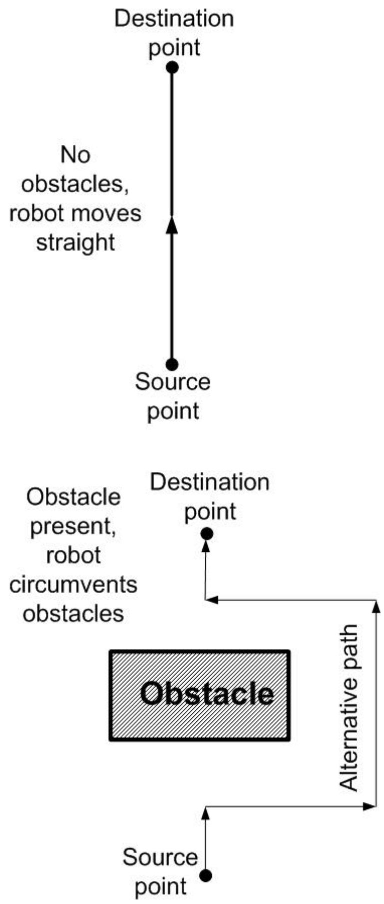

Fig. 6 Obstacle avoidance algorithm

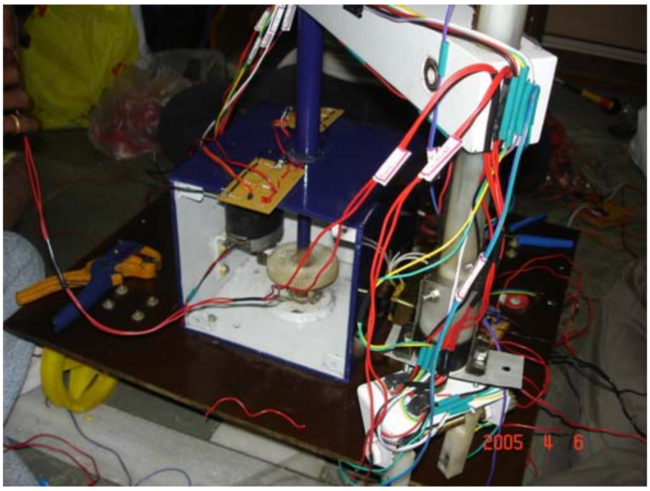

Fig. 7 Reset detection sensing unit PCB's

If you drive an automobile, you know the practical application of the Pauli exclusion principle: Two objects cannot occupy the same space at the same time. What's true for automobile is even true for robots. An autonomous robot has to keep itself from colliding with obstacles. Obstacles might take the form of a wall or post, or they may be mobile like a dog, a person, or another robot.

Since robot can't know the position of moving object in advanced, it must have some way of detecting obstacles in real time. Luckily, detecting obstacles doesn't require anything as sophisticated as machine vision. A much simpler system will suffice. Some robots use SONAR (sometimes called SODAR when used in air instead of water) or RADAR. An simple system is to use ultrasonics.

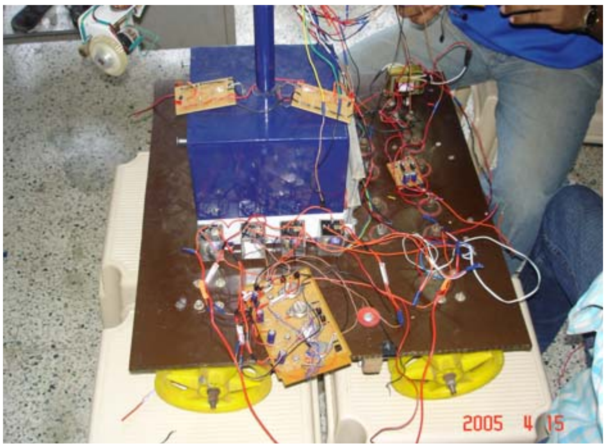

Fig. 8 Limit switches sensing unit PCB's

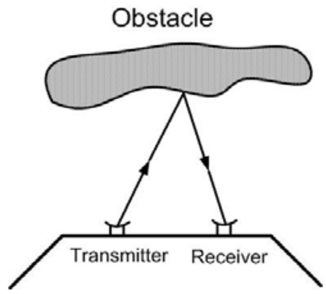

Fig. 9 Ultrasonic transmitter receiver pair

. ltrasonic Sensors imit Switches Pots

Ultrasonic sensors [7] are mounted at four points on the links to prevent the collision of the robot with the obstacles. These sensors give a signal to the computer through the parallel port and the computer in turn processes this signal and in turn avoids the collision by turning the arm in another direction. Limit switches are used at the inner surfaces of the grippers to sense whether the gripper has held / picked up the object or not. Potmeters are mounted at the joints to accurately measure the movement.

8. Conclusions

A sensor interface was designed and installed in the flexible manufacturing system which is used to provide closed loop feedback action of the system, thus avoiding collision of the system with the obstacles. The sensing inputs are taken to the computer, processed and necessary action is taken, thus providing artificial intelligence to the FMS.

References

[1] Robert Schilling, Fundamentals of robotics, Prentice hall.
[2] Hodges Bernard, Industrial Robotics, Jaico publication.
[3] Klafter, Cheimieleswski, Negin, Robotics Engineering Approach , Prentice hall.
[4] Fu, Gonzales, Lee, Robotics-Control Sensing Vision, McGraw Hill.
[5] T.C.Manjunath (2005), Fundamentals of Robotics, 3rd edition, Nandu Publication, Mumbai, India.
[6] T.C.Manjunath (2005) , Fast Track to Robotics, 2nd edition, Nandu Publication, Mumbai, India.
[7] National Semiconductor , Data sheets for linear IC's.

The Eleventh International Symposium on Artificial Life and Robotics 2006 (AROB 11th'06),
B-con Plaza, Beppu, Oita, Japan, January 23-25, 2006

Application of Uncertain Variables to Knowledge-based Decision Making in Complex Systems with Uncertain and Random Parameters[1]

Z.Bubnicki
Institute of Information Science and Engineering, Wroclaw University of Technology
Wyb. Wyspianskiego 27, 50-370 Wroclaw, POLAND
e-mail: zdzislaw.bubnicki@pwr.wroc.pl

Abstract

The paper is concerned with the application of uncertain variables to decision making based on an uncertain knowledge. The system under consideration contains two kinds of parameters: uncertain parameters characterized by an expert in the form of certainty distributions and random parameters described by probability distributions. The general formulation of the decision problem using uncertain and random variables is described. The decision making for a hybrid system with the cascade structure is presented. The possibilities of the application to allocation problem in a complex of parallel operations are discussed. A simple example illustrates the approach presented.

Keywords: uncertain systems, uncertain variables, knowledge-based systems, decision making systems

1 Introduction

The uncertain variables have been introduced and developed as a tool for analysis and decision making in a class of uncertain systems described by traditional mathematical models or by relational knowledge representations with unknown parameters characterized by an expert [1–5]. In the paper [6] an approach for the system with uncertain and random parameters has been presented. The purpose of this paper is to extend this approach and to show how the uncertain variables may be applied to a class of complex systems consisting of two subsystems with different descriptions of the uncertainty. Section 3 is devoted to a hybrid system with a cascade structure containing random and uncertain parts. Section 4 presents some remarks concerning the complex of parallel operations. We shall start with the short presentation of the decision problem based on the uncertain variables. Details of the uncertain variables theory and its applications may be found in the author's books cited above.

2 The general formulation of the decision problem using uncertain and random variables

In the definition of the uncertain variable $\bar{x}$ we consider two soft properties (i.e. such properties $\varphi(x)$ that for the fixed x the logic value $v[\varphi(x)] \in [0,1]$): "$\bar{x} \cong x$" which means "$\bar{x}$ is approximately equal to x" or "x is the approximate value of $\bar{x}$," and "$\bar{x} \,\tilde{\in}\, D_x$" which means "$\bar{x}$ approximately belongs to the set D_x" or "the approximate value of $\bar{x}$ belongs to D_x". The *uncertain variable* $\bar{x}$ is defined by a set of values X (real number vector space), the function $h(x) = v(\bar{x} \cong x)$ (i.e. the certainty index that $\bar{x} \cong x$, given by an expert) and the following definitions for $D_x, D_1, D_2 \subseteq X$:

$$v(\bar{x} \,\tilde{\in}\, D_x) = \max_{x \in D_x} h(x),$$

$$v(\bar{x} \,\tilde{\notin}\, D_x) = 1 - v(\bar{x} \,\tilde{\in}\, D_x),$$

$$v(\bar{x} \,\tilde{\in}\, D_1 \vee \bar{x} \,\tilde{\in}\, D_2) = \max\{v(\bar{x} \,\tilde{\in}\, D_1), v(\bar{x} \,\tilde{\in}\, D_2)\},$$

$$v(\bar{x} \,\tilde{\in}\, D_1 \wedge \bar{x} \,\tilde{\in}\, D_2) = \min\{v(\bar{x} \,\tilde{\in}\, D_1), v(\bar{x} \,\tilde{\in}\, D_2)\}.$$

The function $h(x)$ is called a *certainty distribution*. In the case of *C-uncertain variable* $\bar{x}$, the certainty index that $\bar{x}$ approximately belongs to D_x is defined as follows:

$$v_c(\bar{x} \,\tilde{\in}\, D_x) = \frac{1}{2}[v(\bar{x} \,\tilde{\in}\, D_x) + 1 - v(\bar{x} \,\tilde{\in}\, \overline{D}_x)] \quad (1)$$

where $\overline{D}_x = X - D_x$. The application of *C*-uncertain variable means better using of the expert's knowledge, but may be more complicated.

Let us consider a static plant with the input vector $u \in U$ and the output vector $y \in Y$, described by a relation $R(u, y; x) \subset U \times Y$ where the vector of unknown parameters $x \in X$ is assumed to be a value of an uncertain variable described by the certainty distribution $h(x)$ given by an expert. If the relation R is not a function then the value u determines a set of

[1] This work was supported by the Polish State Committee for Scientific Research under Grant No. 3T11A 031 28 (2005-2007)

possible outputs

$$D_y(u;x)=\{y\in Y:(u,y)\in R(u,y;x)\}. \quad (2)$$

For the requirement $y\in D_y\subset Y$ given by a user, we can formulate the following **decision problem**: For the given $R(u,y;x)$, $h(x)$ and D_y one should find the decision u^* maximizing the certainty index that the set of possible outputs approximately belongs to D_y (i.e. belongs to D_y for an approximate value of $\bar{x}$). Then

$$u^*=\arg\max_{u\in U} v[D_y(u;\bar{x})\,\tilde{\subseteq}\, D_y]=\arg\max_{u\in U}\max_{x\in D_x(u)} h(x) \quad (3)$$

where $D_x(u)=\{x\in X: D_y(u;x)\subseteq D_y\}$.

Let us now consider the system described by a relation $R(u,y;x,w)$ where $x\in X$ and $w\in W$ are the vectors of uncertain and random parameters, respectively. If $\bar{x}_i$ and $\tilde{w}_i$ are independent uncertain and random variables for different *i*, respectively then

$$h(x)=\min_i h_i(x_i), \qquad f(w)=\prod_i f_i(w_i).$$

For the system as a whole one may apply the following general approach described for one element in [4, 7]:
1. To determine $D_y(u;x,w)$ and

$$v[D_y(u;\bar{x},w)\,\tilde{\subseteq}\, D_y]\overset{\Delta}{=}v(u,w) \quad (4)$$

according to (2) and (3), with $R(u,y;x,w)$ in place of $R(u,y;x)$.
2. To find u^* maximizing

$$\mathrm{E}[v(u,\tilde{w})]=\int_W v(u,w)f(w)dw$$

(version I), or to find u^* as the expected value $\mathrm{E}[u(\tilde{w})]$ where $u(w)$ is obtained by maximization of (4) (version II). In the next section a particular form of the structure and a special approach to our problem based on a decomposition will be presented.

3 Hybrid system with cascade structure

Let us consider the system with the cascade structure (Fig. 1) in which the elements 1 and 2 are described by the relations $R_1(u_1,z;w)$ and

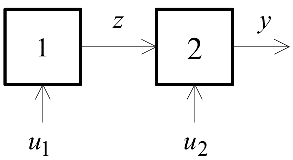

Fig. 1. Cascade structure

$R_2(u_2,z,y;x)$, respectively, where *w* is a value of a random variable $\tilde{w}$ with the probability density $f(w)$ and *x* is a value of an uncertain variable $\bar{x}$ with the certainty distribution $h(x)$. Let us apply an approach taking into account the additional requirement for the first element: $z\in D_z$ were D_z is given by a user. The probability that the requirement is satisfied

$$P(z\in D_z)=P(\tilde{w}\in D_w(u_1))\overset{\Delta}{=}p(u_1) \quad (5)$$

where $D_w(u_1)=\{w\in W: D_z(u_1;w)\subseteq D_z\}$. Then two cases of the decision problem may be formulated:
1. To determine u_2^* using according to version I or II, with $u_1=u_1^*$ where u_1^* is the value of u_1 maximizing (5).
2. To determine (u_1^*,u_2^*) according to version I or II, subject to the constraint $p(u_1)\ge\bar{p}$ where $\bar{p}$ is a given value.

Example 1. Consider very simple example with $u_1,u_2,z,y,x,w\in R^+$ (one-dimensional, non-negative variables) and the relations in the form of inequalities:

$$wu_1\le z\le 2wu_1, \quad xu_2+z\le y\le 2xu_2+z \quad (6)$$

The elements 1, 2 may be for example production units, $u_{1,2}$ may denote amounts of raw materials and z,y – amounts of products where *z* is used as an additional raw material for the second element. The inequalities (6) are reduced to $xu_2+wu_1 \le y\le 2(xu_2+wu_1)$. Let $D_y=[y_1,y_2]$. Then

$$v(u_1,u_2,w)=\max_{x\in D_x(u,w)} h(x) \quad (7)$$

where the set $D_x(u,w)=D_x(u_1,u_2,w)$ is determined by the inequality

$$(y_1-wu_1)u_2^{-1}\le x\le 0.5(y_2-2wu_1)u_2^{-1}. \quad (8)$$

Assume that $\bar{x}$ has a triangular certainty distribution presented in Fig. 2. Let us apply *C*-uncertain variables.

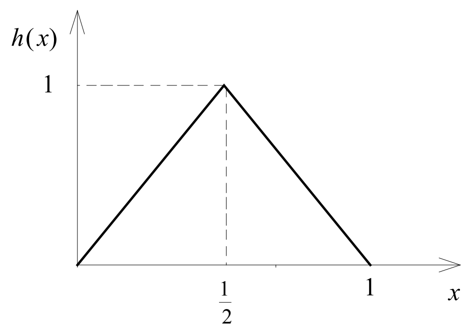

Fig. 2. Example of certainty distribution

Then, using (1), (7) and (8), under the assumption $y_2\ge 2y_1$, we can obtain the following function $v_c(u_1,u_2,w)$:

$$v_c(u_1,u_2,w) = \begin{cases} 0.5(y_2 - 2wu_1)u_2^{-1} & \text{for } u_2 \geq y_1 + 0.5y_2 - 2wu_1 \\ 1-(y_1 - wu_1)u_2^{-1} & \text{for } y_1 - wu_1 \leq u_2 \leq y_1 + 0.5y_2 - 2wu_1 \\ 0 & \text{for } u_2 \leq y_1 - wu_1 \,. \end{cases}$$

It may be shown that $u_2(u_1,w)$ maximizing v_c for the fixed value u_1 is as follows:

$$u_2(u_1,w) = y_1 + 0.5y_2 - 2wu_1 \qquad (9)$$

and v_c is then the following

$$v_c(u_1,w) = (y_2 - 2wu_1)(2y_1 + y_2 - 4wu_1)^{-1} \,. \qquad (10)$$

It is easy to show that for $y_2 \geq y_1$, (10) is an increasing function of u_1. Assume that $w \leq w_m$, i.e. $f(w) = 0$ for $w \geq w_m$. Using the assumption $y_1 - wu_1 \geq 0$ (see (8)) we obtain $u_1^* = y_1 w_m^{-1}$, and putting u_1^* into (9) yields $u_2^*(w) = y_1 + 0.5y_2 - 2wy_1 w_m^{-1}$. Finally, $u_2^* = \mathrm{E}[u_2^*(\tilde{w})] = y_1 + 0.5y_2 - 2\mathrm{E}(\tilde{w})y_1 w_m^{-1}$. Let us take into account the additional requirement for the first element: $z \in D_z = [z_1, z_2]$, $z_{1,2} \geq 0$, $z_2 \geq 2z_1$. In this case $D_w(u_1)$ is determined by the inequality $z_1 u_1^{-1} \leq w \leq z_2(2u_1)^{-1}$. For example, assume the rectangular probability density: $f(w) = w_m^{-1}$ for $0 \leq w \leq w_m$ and $f(w) = 0$ otherwise. Then, according to (5)

$$p(u_1) = \begin{cases} (0.5z_2 - z_1)(w_m u_1)^{-1} & \text{for } u_1 \geq 0.5 z_2 w_m^{-1} \\ 1 - z_1(w_m u_1)^{-1} & \text{for } z_1 w_m^{-1} \leq u_1 \leq 0.5 z_2 w_m^{-1} \\ 0 & \text{for } u_1 \leq z_1 w_m^{-1} \,. \end{cases} \qquad (11)$$

Now we can consider two approaches:

1. We determine

$$u_1^* = \arg\max_{u_1} p(u_1) = 0.5 z_2 w_m^{-1}$$

and by using (9) with $u_1 = u_1^*$ we have $u_2^* = y_1 + 0.5y_2 - \mathrm{E}(\tilde{w}) z_2 w_m^{-1} = y_1 + 0.5y_2 - 0.5z_2$ which may be used when $z_2 \leq 2y_1 + y_2$. For example, for $z_1 = 1$, $z_2 = 3$, $y_1 = 2$, $y_2 = 5$, $w_m = 0.75$ we obtain $u_1^* = 2$, $u_2^* = 3$ and $p(u_1^*) = 1 - 2z_1 z_2^{-1} = \frac{1}{3}$ which means that the requirement $z \in [z_1, z_2]$ is too strong. For $z_1 = 0.5$ we obtain $p(u_1^*) = \frac{2}{3}$. Hence, u_1^* is the decision for which the requirement concerning the first element is satisfied with the greatest probability equal to $\frac{2}{3}$.

2. For the requirement $p(u_1) \geq \overline{p}$ we obtain from (11) the greatest possible value $u_1^* = (0.5z_2 - z_1)(\overline{p} w_m)^{-1}$ and by using (9) with $u_1 = u_1^*$ we have

$$u_2^* = y_1 + 0.5y_2 - 2\mathrm{E}(\tilde{w})u_1^* = y_1 + 0.5y_2 - (0.5z_2 - z_1)\overline{p}^{-1}.$$

4 Task allocation problem

The similar approach may be applied to an allocation problem in a complex of operations. To explain To explain the idea for the hybrid complex with uncertain and random parameters, let us start with the uncertain complex ([4]) containing k parallel operations described by the inequalities $T_i \leq x_i u_i$ $(i \in \overline{1,k})$ where u_i is the size of a task assigned to the i-th operation, T_i is the execution time, $x_i > 0$ is assumed to be a value of an uncertain variable $\overline{x}_i$ described by a certainty distribution $h_i(x_i)$ given by an expert and $\overline{x}_1, ..., \overline{x}_k$ are independent variables. The complex may be considered as a decision plant described in Sec. 2 where y is the execution time of the whole complex $T = \max\{T_1, ..., T_k\}$, $x = (x_1, ..., x_k)$, $u = (u_1, ..., u_k) \in \overline{U}$. The set $\overline{U} \subset R^k$ is determined by the constraints: $u_i \geq 0$ for each i and $u_1 + ... + u_k = U$ where U is the total size of the task to be distributed among the operations (Fig. 3). The initial requirement given by a user is $T \leq \alpha$ for the given α.

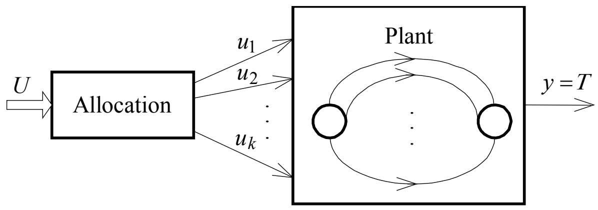

Fig. 3. Complex of parallel operations as a decision plant

According to the general formulation of the decision problem presented in [4], the allocation problem may be formulated as an optimization problem consisting in finding the optimal allocation u^* that maximizes the certainty index of the soft property: "the set of possible values T approximately belongs to $[0, \alpha]$" (i.e. belongs to $[0, \alpha]$ for an approximate value of $\overline{x}$).

Now let us consider the complex consisting of two subcomplexes: the uncertain subcomplex described by $T_i \leq x_i u_i$ for $i \in \overline{1, k_1}$ and the random subcomplex described by $T_i \leq w_i u_i$ for $i \in \overline{k_1 + 1, k_1 + k_2}$ $(k_1 + k_2 = k)$ where $w_i \geq 0$ are values of random variables $\tilde{w}_i$ described by the probability density

$f_i(w_i)$, $(w_{k_1+1},..., w_{k_1+k_2}) \triangleq w$. The **allocation problem** corresponding to version II in Sec. 2 is then as follows: To find the decisions $u_i^* = \mathrm{E}[u_i(\widetilde{w})]$ where $u_i(w)$ are the decisions maximizing the certainty index that the requirement $T \le \alpha$ is approximately satisfied for the fixed *w*, E denotes the expected value.

Let us introduce the notation

$$\tau_i(u_i) = \begin{cases} x_i u_i & \text{for} \quad i \in \overline{1, k_1} \\ w_i u_i & \text{for} \quad i \in \overline{k_1+1, k_1+k_2} \end{cases}.$$

In the first subcomplex τ_i is a value of $\overline{\tau}_i = \overline{x}_i u_i$ and $v_i(u_i) = v[\overline{\tau}_i(u_i) \,\widetilde{\le}\, \alpha]$. In the second subcomplex τ_i is a deterministic variable and $v_i(u_i) = 1$ for $u_i \le \alpha\, w_i^{-1}$, $v_i(u_i) = 0$ otherwise. For the triangular certainty distribution it is easy to show [4] that the solution of our distribution problem is as follows:

1. If

$$\sum_{i=k_1+1}^{k_1+k_2} \frac{\alpha}{w_i} < U \tag{12}$$

then in the second subcomplex $u_i(w_i) = \alpha\, w_i^{-1}$ and in the first subcomplex $u_i(w_i)$ should be determined in the same way as for the uncertain complex described above with

$$U - \sum_{i=k_1+1}^{k_1+k_2} \frac{\alpha}{w_i} \tag{13}$$

instead of *U*.

2. If (12) is not satisfied then in the first subcomplex $u_i = 0$ and in the second subcomplex u_i may be any number satisfying the condition $u_i \le \alpha\, w_i^{-1}$ and

$$u_{k_1+1} + u_{k_1+2} + ... + u_{k_1+k_2} = U .$$

Then the requirement $T \le \alpha$ is exactly satisfied $(v(u) = 1)$ for the given values w_i. As a particular solution one may accept $u_i = \alpha\, c w_i^{-1}$ where

$$c = U\Big(\sum_{i=k_1+1}^{k_1+k_2} \frac{\alpha}{w_i}\Big)^{-1} .$$

In such a way in the cases 1 and 2 we obtain the solution $u_i(w)$ for the fixed *w*. Finally, one should determine $u_i^* = \mathrm{E}[u_i(\widetilde{w})]$.

The similar approach may be applied for a resource distribution problem, i.e. when the operations are described by $T_i \le x_i u_i^{-1}$ and $T_i \le w_i u_i^{-1}$ where u_i is the amount of the resource assigned to the *i*-th operations. If

$$\sum_{i=k_1+1}^{k_1+k_2} \frac{w_i}{\alpha} < U \tag{14}$$

then in the second subcomplex $u_i(w_i) = w_i \alpha^{-1}$ and in the first subcomplex $u_i(w_i)$ should be determined with $D_i(u_i) = [0, \alpha\, u_i]$ and

$$U - \sum_{i=k_1+1}^{k_1+k_2} \frac{w_i}{\alpha} \tag{15}$$

instead of *U*. If (14) is not satisfied then $v(u) = 0$ for any distribution *u*.

5 Conclusions

It has been shown how to apply the uncertain variables as a tool for decision making in a complex system consisting of two parts: the part with uncertain parameters characterized by an expert and the part with random parameters described by probability distributions. The approach presented in the paper has been applied to the control of a production process described by uncertain relational knowledge representation and to a load distribution in a multiprocessor system. The approach may be extended for a complex computer system with distributed knowledge [8].

References

[1] Bubnicki Z (2001), Uncertain variables and their applications for a class of uncertain systems. International Journal of Systems Science 5:651-659

[2] Bubnicki Z (2001), Uncertain variables and their application to decision making. IEEE Trans. on SMC, Part A: Systems and Humans 6:587-596

[3] Bubnicki Z (2002), Uncertain logics, variables and systems. Springer-Verlag, Berlin, London, N. York

[4] Bubnicki Z (2004), Analysis and decision making in uncertain systems. Springer-Verlag, Berlin, London, N. York

[5] Bubnicki Z (2005), Modern control theory. Springer-Verlag, Berlin, London, N. York

[6] Bubnicki Z (2005), Learning algorithms and uncertain variables in knowledge-based pattern recognition. Proceedings of the 10th International Symposium on Artificial Life and Robotics, Oita, Japan, Feb 4-5, 2005, pp. 236-239

[7] Bubnicki Z (2003), Application of uncertain variables in a class of control systems with uncertain and random parameters. Proceedings of the European Control Conference, Cambridge, UK, 2003.

[8] Bubnicki Z (2002), Application of uncertain variables to decision making in a class of distributed computer systems. Proceedings of 17th IFIP World Computer Congress, Montreal, Canada, Aug 25-30, 2002, Kluwer Academic Publishers, Norwell, MA, Vol. “Intelligent Information Processing”, pp. 261-264

Firing Cell: An Artificial Neuron with a Simulation of Long-Term-Potentiation-Related Memory

Jacek Bialowas
Dept. of Anatomy and Neurobiology
Medical University of Gdansk
Debinki 1, 80-211 Gdansk, Poland

Beata Grzyb
Faculty of Mathematics, Physics and Computer Science
Maria Curie-Sklodowska University
Pl. Marii Curie-Sk odowskiej 1
20-031 Lublin, Poland
E-mail: beata@gabri.pl

Pawel Poszumski
Institute of Oceanology
Polish Academy of Science
Powstancow Warszawy 55
81-712 Sopot, Poland

Abstract: We propose a computational model of neuron, called firing cell (FC), properties of which cover such phenomena as attenuation of receptors for external stimuli, delay and decay of postsynaptic potentials, modification of internal weights due to propagation of postsynaptic potentials through the dendrite, modification of properties of the analog memory for each input due to a pattern of short-time synaptic potentiation or long-time synaptic potentiation (LTP), output-spike generation when the sum of all inputs exceeds a threshold, and refraction. The cell may take one of the three forms: excitatory, inhibitory, and receptory. The computer simulations showed that, depending on the phase of input signals, the artificial neuron's output frequency may demonstrate various chaotic behaviors.

1. Introduction

The paper presents a new approach to building computational models of selected brain circuits, aimed to develop a tool supporting an interpretation of recordings of electric potentials in living neural tissue. Such computational models must reflect the most essential properties of biological neurons and their assemblies, but, in order to not to increase the necessary computational power beyond necessity, not too much more.

We propose that, as for a single neuron, at least the following neurophysiological facts should be covered in an model of the discussed kind:

1. Each input signal causes some changes of the postsynaptic potential at the area of the input point; there are typical patterns of the increment and decay of the excitatory (EPSP) and inhibitory (IPSP) potential [1][2],
2. There is a set of commonly accepted neuro-physiological data: time courses, amplitudes of various postsynaptic potentials, action-potential amplitude, and the thresholds for neural activation causing action potentials and removing the block of NMDA canals [1][3],
3. If (after an arrival of an action potential at a particular input) the accumulated local potential for postsynaptic region of each input synapse increase beyond the value of the local threshold (about -70mV), the NMDA receptor causes an opening of the previously blocked channel for an influx of calcium ions [4][5][6], and thus the phenomenon of *Long–Term Potentiation* (LTP),
4. On the most excitatory neural inputs the long-term memories can be activated, which results in an increase of LTP through an activation of NMDA receptors,
5. The amplitude of the single excitatory postsynaptic potential (EPSP) is not an absolute constant; indeed, several values has been proposed by neurophysiologists (see Andersen [3]),
6. Internal weights change due to propagation of postsynaptic potentials through the dendrite [7].

Some properties of the real neuron such as transiently after hyperpolarisation in refractory time and presynaptic regulatory mechanisms as reuptake of released neurotransmitters we did not take into consideration.

As for currently available simulators of life-like neural circuits, they allow to simulate the circuits built of thousands of cells, but neglect some important properties of single cell (see Ambros & Ingerson [8]; Izhikevich [9] or tend to go deeply into detailed biophysics and biochemistry of a single neuron; so, in case of simulation of large neural networks, the complexity of the neuron's mathematical description requires hardly available computational power e.g. Hines [10]; Sikora [11]; Traub et al. [12]).

It seems to be commonly believed in the research that a useful neural model must be of "channel-type" i.e. it must reflect opening of ionic channels at the cell membrane of dendrite as a reaction to action potential arrival at the synapse and opening ionic channels at the initial segment of axon for generation and propagation of action potentials (see Bower & Beman [13]). We propose that in neural simulations the computationally-expensive model of biophysical phenomena can be replaced with a model based on a set of three shift register and that no essential output properties are lost because of such replacement.

The neuron properties we consider are frequency coding, a memory of a single input value, and a processing algorithm that facilitates a non-linear potential summation. Despite such a simplification, the proposed model demonstrates such phenomena as attenuation of receptors for external stimuli , delay and decay of postsynaptic potentials, modification of internal weights due to propagation of postsynaptic potentials through the dendrite, modification of properties of the analog memory for each input due to a pattern of LTP, output-spike generation when the sum of all inputs exceeds a threshold, and a refraction.

2. Firing Cell (FC)

The model of neuron we propose is called FC (firing cell) and occurs in three versions: excitatory, inhibitory and receptory (in this paper we discuss only the first one). FC consists of a dendrite, body and axon (Fig. 1). The dendrite is a string of compartments. Each compartment contains an input synapse. Each synapse is being checked and after a detection of an action potential the values of the table of a certain shift register are being changed according to the typical time course of EPSP or IPSP. Each of the registers is a string of data-boxes. The first data-box of one of the registers is reserved for the actual value of activation of the related compartment. Every 0,5 msec of the simulated time the actual values of all registers are checked and their weighted sums are compared with related thresholds. Generally, there is a positive correlation between the weight and a related synapse's proximity to the cell body.

The output takes at a given clock the value equal to 1, if and only if the accumulated postsynaptic potential at the level of the neuron's body got at least as high as the threshold that equals -50mV. The axon provides the output signal to the compartments of the dendrites of the destination FCs. The switching signal is being back-propagated to all dendrite compartments. The period between two state updates, i.e., between a given clock and the previous clock, is an equivalent of 0.5 msec of the simulated time. When an action-potential is generated, the registers are reset to the value of *resting potential* (using the switching signal) for and then the activity of all compartments is inhibited for 1.5 msec-period of refraction.The values of the resting potential and threshold as well as other initial parameters can be input independently for each neuron before each simulation session.

The minimal value of the single postsynaptic potential is calculated as dividing the difference between the threshold and the Kalium Equilibrium Potential -90mV by the number of inputs. For practical reasons, in first simulations we enhanced this value for EPSP by two. The object can then adjust all values proportionally to a given number of inputs.

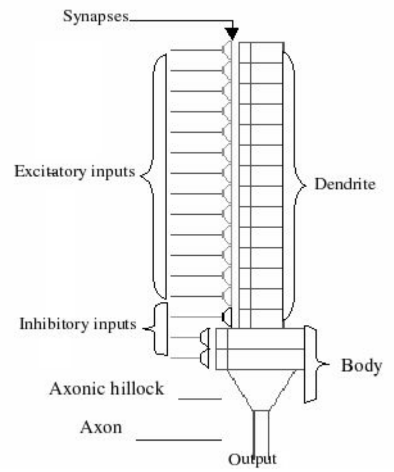

Fig. 1. Firing Cell (FC) in the configuration used in the experiments described in this paper.

We can consider the mentioned shift registers above as a very short-term local memory unit that remembers related events for up to 15 msec. The biological nervous system uses them to avoid the troublesome necessity of strict synchronization that takes pace in conventional computers. Yet we should also have a memory related to each input. The memory must work according to LTP rule. In each state-updating cycle the program calculates (based on actual values in the registers and appropriate weights) an accumulated local potential for postsynaptic region of each input synapse. If, after an action potential arrival at a particular input, the postsynaptic potential increase beyond the value of the local threshold (ca. -70mV), the second register (which simulates the rise of calcium ion content inside the cell) change and shift the contents of their data-boxes. Thus, the function operating on the registers substitute a time-consuming solving of differential equation related to the strength of synaptic potentiation versus calcium ion charge. The enhanced strength remains for a time calculated as power function of the charge.

If after some time an additional charge appears, the period of the calculated synaptic potentiation substantially increases. In the same pattern we can easily include for each input the third register, which can simulate the slower influence of neuromodulatory substances on theirs receptors; however, in our preliminary investigations we did not use them.

3. Experiment

We used the simulated FC as a model of a pyramidal hippocampal cell under conditions such as in the classical LTP experiment by Bliss and Lomo [14]. We configured the FC in such a way that it had 13 excitatory inputs and

3 inhibitory inputs. Two cases were tested. In the first case the assumed EPSP amplitude was 5mV (Fig. 2), in the second it was 7 mV.

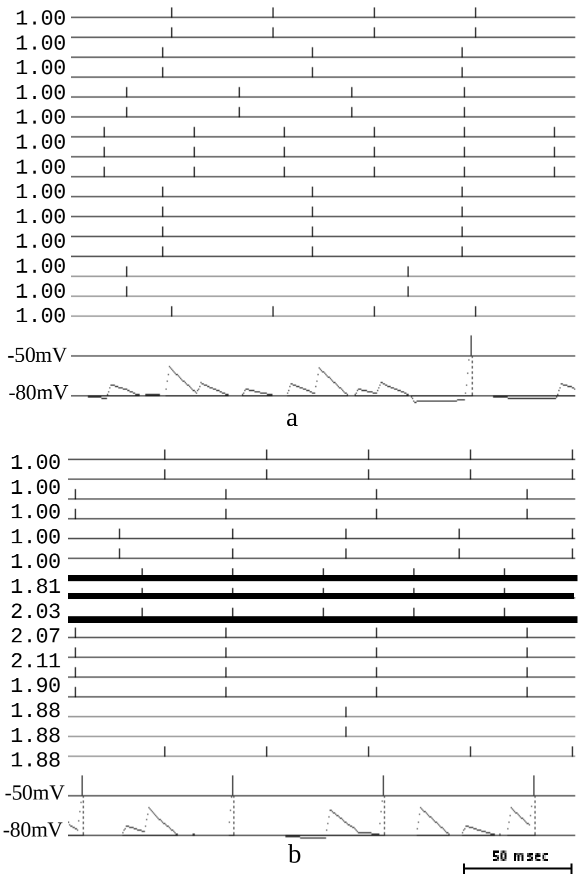

Fig 2. Behavior of an untrained FC (a) and trained FC (b) for EPSP 5mV. The peaks located on the input lines show history of action potential arrivals, while the vertical peaks above the threshold (-50mV) show action potential generation by FC. The zig-zag-shaped line between the threshold and resting potential (-80mV) is the plot of accumulated postsynaptic potential. The training of 400 msec at 100Hz was with action potential spike trains on the 7th, 8th and 9th input (b-thick lines). The frequency of action potentials and the state of the long term memory associated with the related input (real numbers on the left) increase after training (b). An animation of 2 sec of the firing cell's work is available at the web page of GABRI (http://www.gabri.pl)

In the first case each FC's synapse substituted ca. 1000 biological synapses, whereas in the second case each FC's synapse substituted ca. 1400 biological synapses. In both cases three of the excitatory inputs were subject to a stimulation that lasted for 400msec with spiketrains of the frequency 100Hz.

The results of the experiment confirmed the biological plausibility of FC as for information-processing-related mechanisms. In both tested cases the frequency of action-potential generation and the values of LTP increased after the training and in the case of EPSP amplitude 7mV the frequency were substantially higher both before and after the training.

For demonstration of regular, periodic or chaotic behavior of a spiking neuron we used the Poincare return maps. Our experiments showed differences between the neuron's behavior before, during, and after the training. (Fig. 3) We also noticed that change of initial values implicate change of FC's behavior. For detailed description we need further statistical calculations with numerous simulations at various initial values.

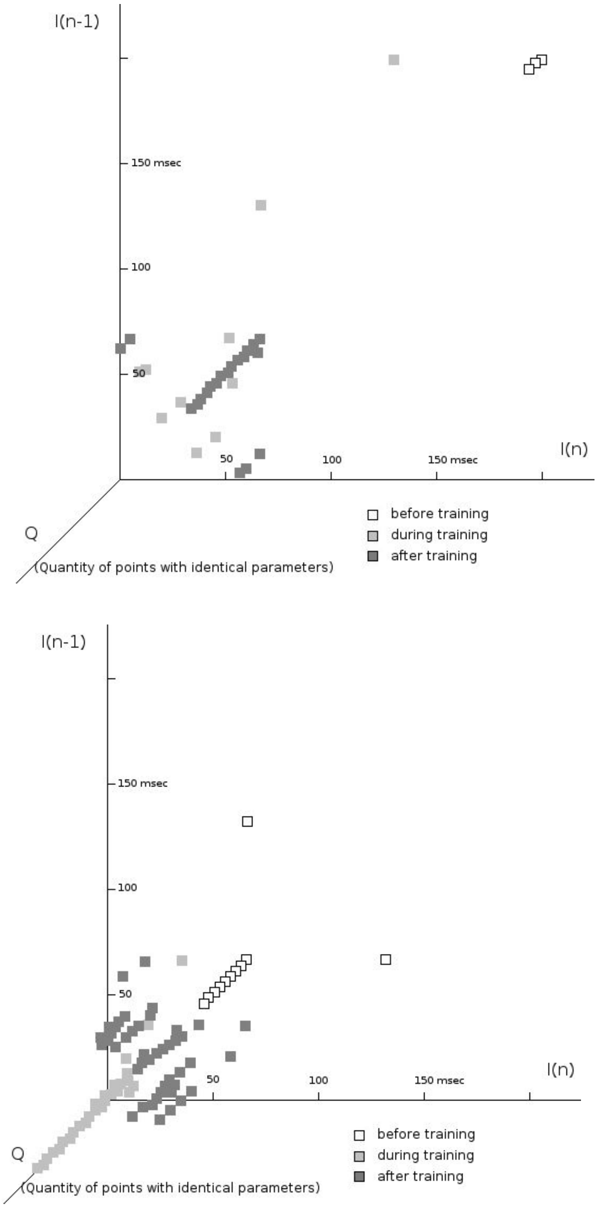

Fig 3. The Poincare return maps from total simulations time 2,5 sec. For EPSP 5mV (a) and 7mV (b). I(n) - interval between two subsequent spikes. Note the passages between various musters of spike trains.

4. Concluding Remarks

The way of information coding in the brain is still a mystery. Some neuroscientists suggest that encoding of information using firing rates is a very popular coding scheme used by cerebral cortex [15]. In the FC model this idea is followed thorough elaborating mainly the mechanisms that facilitate a frequency-based coding of information. To the best of our knowledge, no similar solutions have been published to date.

The realistic modeling requires a lot of computational power. Note that Amaral & Ishizuka [16] calculated 12,000 synapses on a single rat's hippocampal neuron.

The idea of representing near 1000 biological synapses by each of the FC's synapse is justified by the fact that during experiments in vivo a single electrode for technical reasons excites simultaneously multiple fibers. Hence, in information-processing oriented simulation there is no reason to calculate separately the states of thousands of synapses.

The set of functions employed in the FC model should be a subject to further simplification toward a future implementation in hardware, for which analog memories and field transistors (as processing devices) are being considered. The silicon neuron by Mahovald and Douglas [17] seems to well solve the problem of the generation of action potentials. A satisfactory model must properly react frequency and phase of action-potential spike-trains. Some reported solutions e.g. Elias & Northmore [18] seem to be a good step in this direction.

Acknowledgment: This research was supported by Gdansk Artificial Brain Research Initiative (GABRI). http://www.gabri.pl

References

[1] Atwood H. L. &. MacKay W. A. (1989) *Essentials of Neurophysiology*, Toronto: B.C. Decker Inc.

[2] Schmidt R. F. (1976) in R. F. Schmidt (Ed.) *Fundamentals of Neurophysiology*, New York, Heidelberg, Berlin: Springer-Verlag, pp. 64-92.

[3] Andersen P. (1990) Synaptic integration in hippocampal CA1 pyramids, In: J. Storm-Mathisen, J. Zimmer, & O. P. Ottersen (Eds.) *Progress in Brain Research 83*, Amsterdam-New York-Oxford: Elsevier, pp. 215-222.

[4] Muller D., Joly M. & Lynch G. (1988) Contributions of quisqualate and NMDA receptors to the induction and expression of LTP, *Science 242*, pp. 1694-1697.

[5] Grant S. G. N., O'Dell T. J., Karl K. A., et al. (1992) Impaired long-term potentiation, spatial learning, and hippocampal development in fyn mutant mice, *Science 258*, pp. 1903-1910.

[6] Bliss T. V. P. &. Collingridge G. L. (1993) Asynaptic model of memory: long-term potentiation in the hippocampus, *Nature 361*, pp. 31-39.

[7] Bekkers J. M. & Stevens Ch. F. (1990) Two different ways evolution makes neurons larger, In: J. Storm-Mathisen, J. Zimmer, & O. P. Ottersen (Eds.) *Progress in Brain Research 83*, Amsterdam-New York-Oxford: Elsevier, pp. 37-45.

[8] Ambros-Ingerson J., Granger R., & Lynch G. (1990) Simulation of paleocortex performs hierarchical clustering, *Science 247*, pp. 1344-1348.

[9] Ishikevich E. M. (2003) Simple model of spiking neurons, *IEEE Transactions on Neural Networks*, 14, pp. 1569-1572.

[10] Hines M. (1989) A program for simulation of nerve eqations with branching geometries, *International Journal of Biomedical Comput. 24*, pp. 55-68.

[11] Sikora M. A., Gottesman J., Miller R. F. (2005) "A computational model of the ribbon synapse", *Journal of Neuroscience Methods 145*, pp. 47-61.

[12] Traub R. D., Contreras D., Cunningham M. O., et al. (2005) "Single-Column Thalamocortical Network Model Exhibiting Gamma Oscillations, Sleep Spindles, and Epileptogenic Bursts", *Journal of Neurophysiology 93*, pp. 2194-2232.

[13] Bower J.M. & Beeman D. (2003) *The Book of GENSIS: Exploring Realistic Neural Models with the GEneral NEural SImulation System*, http://www.genesis-sim.org/ GENESIS/bog/bog.html

[14] Bliss T. V. P., & Lomo T. J. (1973) Long lasting potentiation of synaptic transmission in the dentate area of the anaestaetized rabbit following stimulation of the perforant path, *J. Physiol. (London) 232*, pp. 331-356.

[15] Rolls E. T. & Treves A. (1998) *Neural Networks and Brain Function*, Oxford: Oxford University Press.

[16] Amaral D. G. & Ishizuka N. (1990) Neurons, numbers and the hippocampal network, In: J. Storm-Mathisen, J. Zimmer & O. P. Ottersen (Eds.) *Progress in Brain Research 83*, Amsterdam–New York–Oxford: Elsevier, pp. 1-12.

[17] Mahovald M. & Douglas R. (1991) A silicon neuron, *Nature 354*, pp. 515-518.

[18] Elias J. G. & Northmore D. P. M. (1998) Building Silicon Nervous Systems with Dendritic Tree Neuromorphs, In: W. Maass & Ch. M. Bishop (Eds.), Pulsed Neural Networks, Cambridge, Mass.: A Bradford Books/The MIT Press, pp. 135-156.

The Eleventh International Symposium on Artificial Life and Robotics 2006 (AROB 11th'06),
B-con Plaza, Beppu, Oita, Japan, January 23-25, 2006

Land-cover/land-use mapping based on color feature extraction*

Tomasz Kubik† Witold Paluszyński†
Adam Iwaniak‡ Przemysław Tymków‡

† Institute of Computers, Control and Robotics, Wrocław University of Technology,
Janiszewskiego 11/17, Wrocław 50-372, Poland
E-mail: {Tomasz.Kubik|Witold.Paluszynski}@pwr.wroc.pl
‡ Department of Geodesy and Photogrammetry, Agricultural University of Wrocław
Norwida 25/27, Wrocław 50-372, Poland
E-mail: iwaniak@ar.wroc.pl, tymkow@kgf.ar.wroc.pl

Keywords: image segmentation, chromacity moments

Abstract

The article presents a method of automatic mapping of land-cover/land-use that can be used with aerial photographs or satellite images as sources of remotely sensed data. The method is based on image segmentation technique in which local color features are employed.

The color feature extraction is based on the concept of chromacities, as defined within the CIE XYZ color space, and chromacity moments, [1]. In this solution chromacities are characterized by two attributes: the chromacity diagram, and the chromacity distribution histogram. The nature of both attributes is captured by the set of moments forming the feature vector. This vector reflects color statistics of the region of interest.

The size of the region of interest is defined by the size of the custom window, which is moved across the image in order to calculate feature vectors at each window's position. The feature vectors obtained are used for classification. Classification of the feature vectors provides labels for the pixels defined by the window centers. The outcome is a segmented image.

The important issues in such segmentation are features and classifier choices. The article addresses this problem, showing the way of feature weighting and normalizing, and presents the classifier, which can be successfully applied in this case. The illustration of the segmentation proposed are results of the experiments conducted with aerial and satellite images.

1 Introduction

Current concerns about land-cover/land-use changes have lead to an increased demand for methods and techniques of automatic area estimates based on remotely sensed data. This subject has particular interest to government agencies responsible for economic or environmental policy at regional and up to global scales. The solutions, including per-parcel or per-field classification with further processing by the use of statistical classification filters, have been already published, [2, 3, 4].

The article presents a method of automatic mapping of land-cover/land-use that can be used with aerial photographs or satellite images as sources of remotely sensed data. The process of mapping is implemented as color feature based image segmentation.

The use of colors or multi-spectral information in image segmentation is usually done by setting ranges for them, and classifying individual pixels according to the pixel range membership. Better results can be achieved when the local statistics of analyzed image are taken under consideration. Such statistics is the base of methods using texture analysis, where the space relationship between pixels is concerned, [5]. In the solution proposed in this article the local statistics of colors, which does not take space dependency into account, are used instead. This statistic is provided in the form of chromacity moments, [1], which serve as features for classification ending up with image segmentation.

Originally, the segmentation based on chromacity moments was invented for the images taken as photographs in the RGB format. But there is no reasons against its use for the satellite image segmentation. It is enough to substitute RGB components with the values of different spectrum channels.

2 Methods

Let $I(i,j)$ for an image I denote the color of its pixel at position i, j, where $0 \leq i \leq L_x - 1$, and $0 \leq$

*This research was supported in part by the Committee for Scientific Research through grant 5T12E02924.

$j \leq L_y - 1$, and L_x, L_y correspond to the image width and the image height (in pixels).

2.1 RGB to CIE XYZ conversion

There are some slightly different formulas for RGB to CIE XYZ color space conversion. In the article it is assumed that this conversion is given by the equation:

$$\begin{bmatrix} X \\ Y \\ Z \end{bmatrix} = \begin{bmatrix} 0.607 & 0.174 & 0.200 \\ 0.299 & 0.587 & 0.114 \\ 0.000 & 0.066 & 1.111 \end{bmatrix} \begin{bmatrix} R \\ G \\ B \end{bmatrix} \tag{1}$$

2.2 Chromacity

The chromacities, x, y, z, apart from their physical interpretation, can be calculated as follows:

$$x = \frac{X}{L}, \; y = \frac{Y}{L}, \; z = \frac{Z}{L} \tag{2}$$

where $L = X + Y + Z$. It should be pointed out, that z value in the equation above is redundant. It can be calculated from x and y according to the rule: $z = 1 - x - y$. Moreover, the value of each of the three chromacities falls into the range $[0, 1]$, $(x, y, z \in [0, 1])$.

2.3 Chromacity distribution and chromacity trace

Chromacity distribution, $D(x, y)$, is given by:

$$D(x, y) = K, \tag{3}$$

where K is the number of pixels with chromacities equal to x and y. This can also be written as:

$$D(x, y) = \mathrm{card}\{(i, j) \mid I(i, j) \rightarrow (x, y)\} \tag{4}$$

Trace of the distribution, $T(x, y)$, is given by:

$$T(x, y) = \begin{cases} 1, & \text{if exist a pixel with chromacities } (x, y), \\ 0, & \text{otherwise.} \end{cases} \tag{5}$$

or:

$$T(x, y) = \begin{cases} 1, & \exists (i, j) : I(i, j) \rightarrow (x, y) \\ 0, & \neg\exists (i, j) : I(i, j) \rightarrow (x, y) \end{cases} \tag{6}$$

So $T(x, y)$ is in fact the projection of $D(x, y)$ onto the plane x, y.

The distribution D, and the trace of distribution T, need to be scaled and discretized in order to calculate the chromacity moments. Let $X_s, Y_s \in \aleph$ denote the scaling factors. Let $x_s = Int(X_s x)$, $y_s = Int(Y_s y)$ represent scaled values, where $x_s, y_s \in \aleph$, and Int is a function returning the integer part of its argument. Scaled and discrete chromacity distribution and its trace can now be expressed as follows:

$$D_s(x_s, y_s) = \mathrm{card}\{(i, j) | I(i, j) \underset{X_s, Y_s}{\rightarrow} (x_s, y_s)\} \tag{7}$$

$$T_s(x_s, y_s) = \begin{cases} 1, & \exists (i, j) : I(i, j) \underset{X_s, Y_s}{\rightarrow} (x_s, y_s) \\ 0, & \neg\exists (i, j) : I(i, j) \underset{X_s, Y_s}{\rightarrow} (x_s, y_s) \end{cases} \tag{8}$$

2.4 Chromacity moments

For the given scaled and discrete distribution with its trace, the chromacity moments can be calculated as follows:

$$M_D^{k,l}(x_s, y_s) = \sum_{x_s} \sum_{y_s} x_s^k y_s^l T_s(x_s, y_s) \tag{9}$$

$$M_T^{k,l}(x_s, y_s) = \sum_{x_s} \sum_{y_s} x_s^k y_s^l D_s(x_s, y_s) \tag{10}$$

where M_D is used to denote the chromacity distribution moments, and M_T is used to denote the moments of the trace of M_D.

2.5 Classifiers

The chromacity moments are the features that might be classified. The simple k-nearest neighbors method would be a good candidate for the classifier choice, but there is a problem with a distance measure. The problem is caused by the fact, that the values of the chromacity moments depend on the order of moments used. The chromacity moments of higher orders have values much higher comparing to the chromacity moments of lower orders. Therefore the classifiers utilizing a simple distance measure in the feature space are not appropriate. To use the Euclidian norm the chromacity moments have to be normalized, or weighted with appropriate weights.

The next candidate for the classifier choice could be a neural network based classifier (with a simple three-layer, feed-forward neural network architecture). This classifier works well, but the problem of normalization of the chromacity moments remains.

Both classifiers mentioned in this subsection were used in the experiments described hereafter preceded by a kind of feature normalization.

3 Experiments

The experiments were conducted as follows. At first a set of small reference images was prepared by an expert. These images were extracted from the original images representing areas with different land cover types. The extraction was done in such way, that each reference image contained only one kind of a separable land cover type (i.e. it was a representative of one class only). The reference images were processed then in order to create the training data. The processing was done by: moving a square window of a custom size across the image; and calculating chromacity moments at each window position.

The training data created contained a set of pairs: a vector consisting of the chromacity moments calculated (input) and a vector representing the land cover membership for each distinct class (output). The sizes of input and output vectors depend on the number of classes considered and the order of the chromacity moments used. Thanks to the knowledge of an expert, each output vector had 1 at the position corresponding to the class it should represent, and 0 elsewhere. The training data, prepared separately for satellite images and aerial photographs, were used to build two different classifiers. They were used later in the image segmentation.

The segmentation of aerial photographs and satellite images was done similarly as the training data creation. There was a moving window (of the same size as in the training phase) and the calculation of the chromacity moments. But this time the chromacity moments were further classified by the proper classifier built. This classification provided labels for the pixels defined by the current window position.

The size of the input vector used throughout the experiment was $18 = 2 * 3^2$ (for $k + l \leq 3$ there is 3^2 possible M_D moments, and the same number of M_T moments). The size of the output vector corresponded to the number of selected classes. The scaling factors X_s and Y_s were set to the value of 100. The size of the moving window was 20×20 pixels.

The satellite images used in the experiments were provided in the form of 4 spectra channels with 256 value levels, representing the same region covered by the different land cover types. Three of the channels were used as pseudo RGB components. The set of reference images used to build the classifier, the original image, and the segmentation results are shown in the Figure 2. The resolution of these images was 4 m.

The aerial photographs used in the experiments were provided in RGB format originally. The set of reference images used to build the classifier, the original image and the segmentation results are shown in the Figure 1. The resolution of these images was 0.5 m.

4 Conclusions

Calculation of chromacity moments makes no sense for the square windows smaller then 10 by 10. But the bigger this size is, the more extensive and expensive the computation becomes. Moreover, the values of the chromacity moments are getting higher and can result in overflow errors. Thus some kind of normalization is essential.

The normalization can be done through the division of each moment by the moment of 0 order. This is a good solution for the M_D moments ($M_D^{0,0}$ is always equal to $L_x \times L_y$, where L_x and L_y define the size of the moving window, and therefore can be omitted during classification). But it does not hold for T_D case ($T_D^{0,0}$ can vary and therefore might be crucial for the classification). Another way of normalization might be the division of each moment by the value $X_s^k \cdot Y_s^l$. This solution was successfully applied in the experiments performed.

References

[1] G. Paschos: Fast color texture recognition using chromaticity moments. *Pattern Recognition Letters*, 21:837–841, (2000).

[2] S. Berberoglu, C. Lloyd, P. Atkinson, and P. Curran: The integration of spectral and textural information using neural networks for land cover mapping in the Mediterranean. *Computers and Geosciences*, 26(4):385–396, (2000).

[3] X.-H. Liu, A. Skidmore, and H. Van Oosten: Integration of classification methods for improvement of land-cover map accuracy. *ISPRS Journal of Photogrammetry and Remote Sensing*, 56(4):257–268, (2002).

[4] Y. Venkatesh and S. Kumar Raja: On the classification of multispectral satellite images using the multilayer perceptron. *Pattern Recognition*, 36(9):2161–2175, (2003).

[5] M. Tuceryan and K. Anil: *The handbook of Pattern recognition and computer vision*, chapter 2.1 Texture Analysis, pp. 207–248 World Scientific Publishing Co., 2nd edition, (1998).

Figure 1: Reference images (top) and the test image with segmentation results (bottom) used in the experiment with aerial photographs

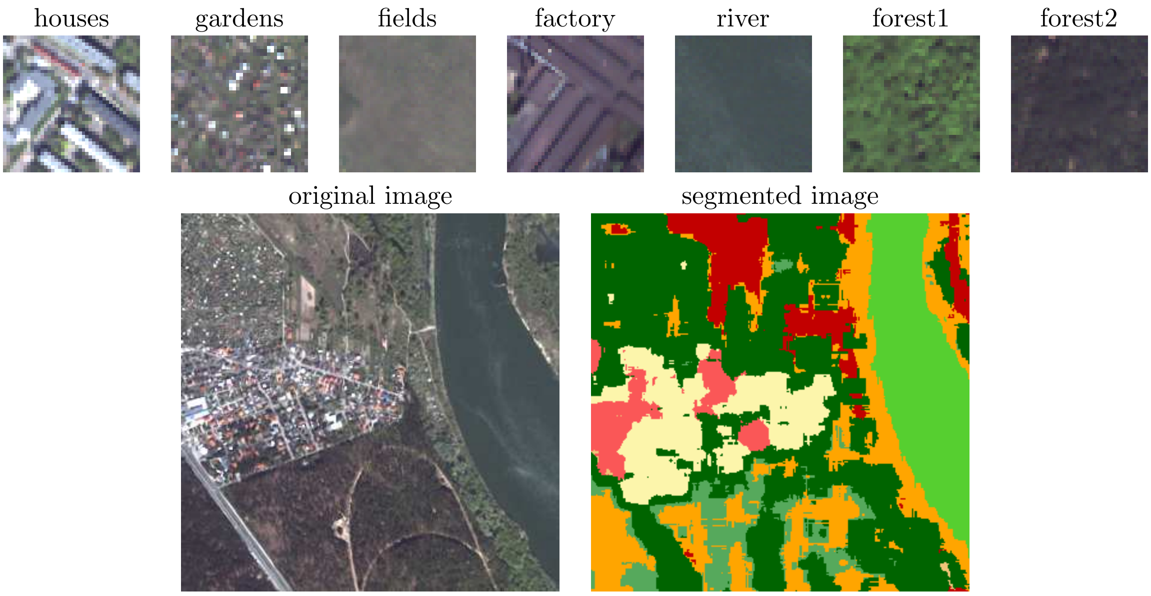

Figure 2: Reference images (top) and the test image with segmentation results (bottom) used in the experiment with satellite images

The Eleventh International Symposium on Artificial Life and Robotics 2006 (AROB 11th'06),
B-con Plaza, Beppu, Oita, Japan, January 23-25, 2006

A Functional Motif Scanning Algorithm for Invertebrate EST Analysis

Makoto Ohkubo and Futoshi Aranishi

Department of Biological and Environmental Sciences
Miyazaki University
Miyazaki 889-2192, Japan

ABSTRACT

Expressed Sequence Tag (EST) analysis is one of the functional genomics techniques and a mining method of physiological mechanisms by comprehensive analysis of the expressed genes. This technique is based on the systematical homology search of gene information on the international DNA databases. However, very little gene information of invertebrates has been accumulated on the present databases, and the molecular structures of their genes quite differ from those of vertebrate genes. A new algorithm for invertebrate EST analysis, termed fmEST algorithm, consisting of the systematical homology search and functional motif scanning has been developed. In this research, a total of 200 unidentified invertebrate ESTs including 100 arthropod ESTs and 100 mollusk ESTs were analyzed for the purpose to evaluate validity of the functional motif scanning for invertebrate EST analysis. A total of 18 and 21 ESTs were determined to contain the functional motif sequences for arthropod and mollusk, respectively. Their nucleotide lengths were distributed from 388 to 954 in arthropod and from 222 to 742 in mollusk. These ESTs were obviously identified as any functional genes, while they did not show significant homology to the gene information on the international DNA database by BLAST homology search. Results suggest that the functional motif scanning is a valuable approach enabling to break new grounds in invertebrate EST analysis.

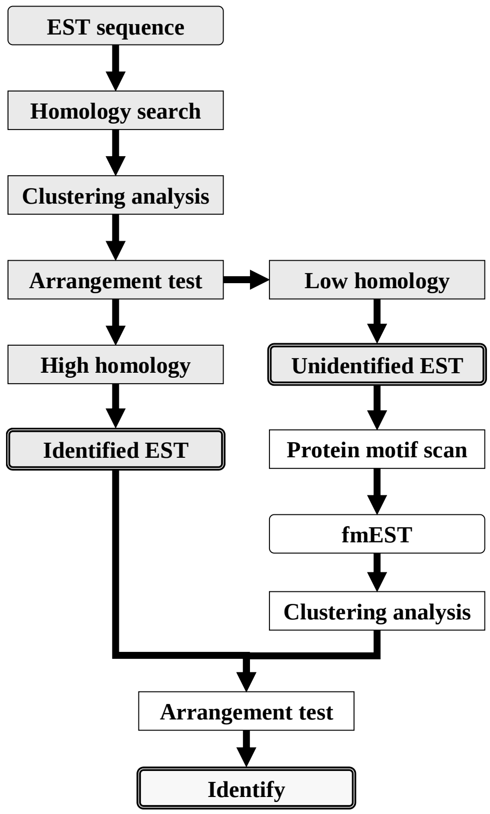

Figure 1. Scheme of fmEST algorithm. Gray boxes indicate the traditional procedure of EST analysis.

1 Introduction

Expressed Sequence Tag (EST) analysis is one of the functional genomics techniques and a mining method of physiological mechanisms by comprehensive analysis of the expressed genes. EST is the nucleotide sequence information of cDNA, a complementary single strand of DNA to mRNA, which is expressed in the sample tissue, cell and specimen.

The molecular biologists are used to identify EST clones as the functional gene homologues by comparing their nucleotide sequences with the gene information recorded in the international DNA databases. Based on these findings, the molecular biologists can survey the physiological mechanisms occurred in different levels of animal, tissue, organ, or cell [1].

An EST dataset for analyzing the expressed genes usually contains from 500 to 2000 EST clones. These large numbers of the gene information accumulated on the DNA databases are well applicable to broad scientific fields such as medical, pharmacology, microbiology, and phylogeny [2-5]. To date, functional genomic researches about invertebrate taxa have been increasingly required from physiological, ecological, and evolutional interesting [6-11]. The gene information on microorganisms and vertebrates, however, occupy the majority of the present databases [12]. In addition, the molecular structures of vertebrate genes quite differ from those of invertebrate genes. We have developed a new analytical algorithm for invertebrate EST analysis, termed as fmEST algorithm involving the traditional systematical homology search and a new “functional motif” scanning [12].

The functional motifs are functionally important secondary structures of proteins, such as receptor binding domains, immunological epitopes, and catalytic sites of enzymes. They are encoded by short nucleotide sequence (generally less than 20 nucleotides) and highly conserved during evolution. The functional motifs are a significant clue to annotate large EST dataset [13].

In this research, we analyzed the functional motif sequences from a total of 200 unidentified invertebrate ESTs including 100 arthropod ESTs and 100 mollusk ESTs, all of which showed no significant similarity to the known functional genes by the homology search, for the purpose of evaluating validity of the functional motif scanning for invertebrate EST analysis.

2 fmEST algorithm

The traditional systematic approach to EST analysis consists of BLAST homology search and subsequent CLUSTALW [14] clustering analysis of EST dataset to the gene information on the DNA databases. Several studies on invertebrate EST analysis have been reported that these traditional techniques enabled us to identify a limited part of EST dataset [6-11], because of less gene information of invertebrates than vertebrates on the DNA databases and divergent molecular structures between invertebrate and vertebrates genes. BLAST homology search therefore allows us to obtain a little information of the functional gene as a candidate for a certain EST clone having a short homologous nucleotide sequence.

The fmEST algorithm consists of two analysis steps, traditional systematical approach and functional motif scanning (Figure 1). Following BLAST homology search, the nucleotide sequence of the unidentified EST clones was deduced to amino acid sequence and then applied to the functional motif search programs; InterProScan (http://www.ebi.ac.uk/InterProScan/), PROSITE (http://www.expasy.org/prosite/), and Pfam (http://www.sanger.ac.uk/Software/Pfam/). Subsequently, its nucleotide sequence was applied to CLUSTALW clustering analysis as a seed sequence for the annotation of the contig containing the seed sequence.

For example, an unidentified EST clone (GenBank accession CI999386) was obtained from EST analysis of kuruma prawn *Marsupenaeus japonicus*. Although it did not show a significant match to the carboxypeptidase gene of sea hare *Aplysia californica* (GenBank accession U37755) by BLAST homology search (Score = 46.1, Expect value = 0.079), it was determined to contain the functional motifs of zinc carboxypeptidase (InterProScan accession IPR000834) by functional motif search. Two local short parts of the deduced amino acid sequences, PEFKYVANMHGNEV and LPSMNPDGW , which are the zinc-binding sites involved in the catalysis of carboxypeptidases, were well conserved in the prawn EST and sea hare enzyme gene by CLUSTALW analysis (Figure 2). These results enabled us to annotate the unidentified prawn EST as a gene encoding zinc carboxypeptidase.

3 EST dataset and analysis

A total of 200 unidentified invertebrate EST clones containing 100 arthropod ESTs (50 crustacean and 50 insect ESTs) and 100 mollusk ESTs (50 bivalve and 50 gastropod ESTs) were obtained from the GenBank under the accession numbers from CI999365 to CI999414 in kuruma prawn *M. japonicus*, DT777319 to DT777368 in flour beetle *Tribolium castaneum*, DR409845 to DR 409894 in akoya pearl oyster *Pinctada fucata*, and DT 725365 to DT725414 in snail *Biomphalaria glabrata*, respectively (Table 1).

Functional motif scanning was interactively carried out using InterProScan functional motif search program on the web (http://www.ebi.ac.uk/InterProScan/), which is operated by the European Bioinformatics Institute. The option of "translation table" was set to "Standard Code" for all ESTs. The option of the "minimum open reading frame size" was set to 20, 50, 100, and 150 for individual ESTs. The other parameters are set to default values.

```
Accession No.

U37755           ------MDTSKMLS--QCVLVFAAAVAIVSYQSIEASQDTEENGSKKTESTIFFHHTYEE
CI999386         MCVHSSADTMKYCWGHVGVLLLLLVASVCVQAASVAKPGTSGNGTPSKSEFVFKHHNNEE
                        ** *       **::  ..::    :  *. .*. **: .... :* **. **

U37755           MVSLMYEVNKACPEVTRIYNLSEPSVEKRNLTVLEITENPGVHVPGKPEFKYVANMHGNE
CI999386         LEQVLRETAEKCKDVTRLYALSEPSVRNVPLWVIEFSDNPGQHDLLEPEFKYVANMHGNE
                 : .:: *. : * :***:* ******.:  * *:*:::*** *   :*************

U37755           VVGKEMVLYFLVALCEEYKRGDKLANFIVSQTRVHVLPSMNPDGWQKAYKELQEKGEAGW
CI999386         VLGRELLLALAHYLCQGWKDGDEEIKKLIKSTRIHLLPSMNPDGWQLATDTGGKDYLR--
                 *:*:*::* :   **: :* **:  : ::..**:*:********** * .   :.
```

Figure 2. Arrangement of deduced amino acid sequences of unidentified EST and sea hare carboxypeptidase gene.

Table 1. Summary of EST datasets for functional motif search

Phylum	Class	Species	No. of clones	Av. nt length	Accession No.
Arthropoda	Crustacea	*Marsupenaeus japonicus*	50	480	CI999365 - CI999414
	Insecta	*Tribolium castaneum*	50	890	DT777319 - DT777368
Mollusca	Bivalvia	*Pinctada fucata*	50	350	DR409845 - DR409894
	Gastropoda	*Biomphalaria glabrata*	50	518	DT725365 - DT725414

4 Results and discussion

The lengths of the nucleotide sequences of ESTs obtained from various animals are generally distributed from 100 to 1000. Those of 200 EST dataset were distributed from 152 to 1025 in arthropod and from 147 to 743 in mollusk. The average nucleotide sequence length of 50 ESTs of flour beetle was estimated to be 890, which was higher than other species analyzed in this research (Table 1). Insect taxa are the most understood invertebrate class in recent molecular biology [15], and their EST clones with long nucleotide sequences could be easily prepared rather than other invertebrate taxa. In contrast, the average nucleotide sequence length of 50 ESTs of akoya pearl oyster was lower than the others. It is probably due to much less information on molecular biological techniques available for bivalves.

The lengths of the nucleotide sequences of 18 and 21 ESTs containing the functional motif were distributed from 388 to 954 in arthropod and 222 to 742 in mollusk, respectively (Figure 3). This result indicates that the functional motif sequences are difficult to be found in short ESTs less than approximately 200 nucleotides in length. Several studies on invertebrate EST analysis have reported that EST datasets generally contain from 500 to 2000 ESTs, and approximately 20 to 30 of these ESTs can be identified as any functional genes [6-11]. In this research, a total of 39 ESTs from 200 arthropod and mollusk ESTs were determined to contain the functional motif by functional motifs scanning (Figure 4). These findings suggest that at least additional 100 ESTs might be identifiable as any functional genes by the fmEST algorithm in conventional invertebrate EST analysis.

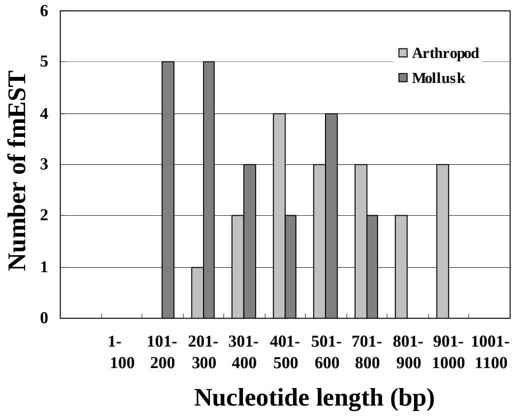

Figure 3. Distribution of nucleotide length of arthropod and mollusk ESTs containing functional motif.

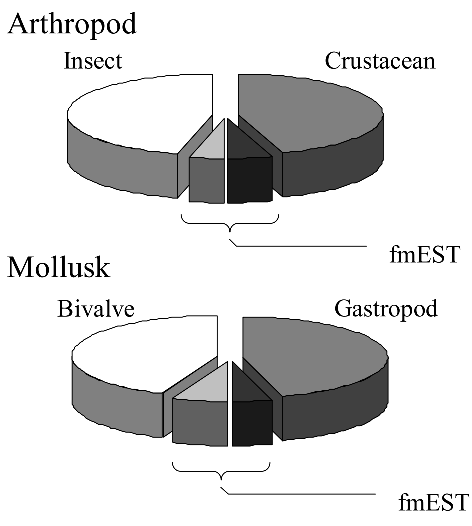

Figure 4. Proportion of ESTs containing functional motif in invertebrate EST datasets analyzed.

5 Conclusions

This research demonstrated that the functional motif search allowed us breaking new grounds in invertebrate EST analysis. However, the BLAST homology search program has no ability to refer to functional motifs, whereas it automatically deduces nucleotide sequences to amino acid sequences. In addition, the conventional automated EST annotation programs are not incorporated with the functional motif scanning program [16]. The molecular biologists thus require heavy labor for analysis of the functional motif sequences of large numbers of ESTs. A novel form of automated EST annotation system incorporated with fmEST algorithm is proposed to inspire molecular biology for a variety of invertebrate taxa, which are involved in human familiar sciences such as agriculture, fisheries, and ecology.

Acknowledgment

We thank Professor Ikuo Yoshihara, Department of Computer Science and Systems, Miyazaki University, for his helpful suggestions to the preparation of this article.

References

[1] Asamizu, E., and Nakamura, Y. 2004. System for expressed sequence tags (EST) analysis. *Tanpaku-shitsu Kakusan Koso*, 49 1847-1852.

[2] Angus, A.C., Ong, S.T., and Chew, F.T. 2004. Sequence tag catalogs of dust mite-expressed genomes: utility in allergen and acarologic studies. *Am. J. Pharmacogenomics*, 4 357-369.

[3] Samuels, A.K., Weisrock, D.W., Smith, J.J., France, K.J., Walker, J.A., Putta, S., and Voss, S.R. 2005. Transcriptional and phylogenetic analysis of five complete ambystomatid salamander mito-chondrial genomes. *Gene*, 349 43-53.

[4] Evans, D.L., Kaur, H., Leary, J. 3rd., Praveen, K., and Jaso-Friedmann, L. 2005. Molecular charac-terrization of a novel pattern recognition protein from nonspecific cytotoxic cells. *Dev. Comp. Immunol.*, 29 1049-1064.

[5] Faria-Campos, A.C., Cerqueira, G.C., Anacleto, C., de Carvalho, C.M., and Ortega, J.M. 2003. Mining microorganism EST databases in the quest for new proteins. *Genet. Mol. Res.*, 31 169-177.

[6] Gross, P.S., Bartlett, T.C., Browdy, C.L., Chapman, R.W., and Warr, G.W. 2001. Immune gene dis-covery by expressed sequence tag analysis of hemocytes and hepatopancreas in the Pacific White Shrimp, *Litopenaeus vannamei*, and the Atlantic White Shrimp, *L. setiferus*. *Dev. Comp. Immun.*, 25 565-577.

[7] Lehnert, S.A., Wilson, K.J., Byrne, K., and Moore, S.S. 1999. Tissue-specific expressed sequence tags from the black tiger shrimp *Penaeus monodon*. *Mar. Biotechnol.,* 1 465-476.

[8] Supungul, P., Klinbunga, S., Pichyangkura, R., Hirono, I., Aoki, T., and Tassanakajon, A. 2004. Antimicrobial peptides discovered in the black tiger shrimp *Penaeus monodon* using the EST approach. *Dis. Aquat. Organ.*, 61 123-135.

[9] Jenny, M.J., Ringwood, A.H., Lacy, E.R., Lewitus, A.J., Kempton, J.W., Gross, P.S., Warr, G.W., and Chapman, R.W. 2002. Potential indicators of stress response identified by expressed sequence tag analysis of hemocytes and embryos from the American oyster, *Crassostrea virginica*. *Mar. Biotechnol.*, 4 81-93.

[10] Lee, Y.H., Huang, G.M., Cameron, R.A., Graham, G., Davidson, E.H., Hood, L., and Britten, R.J. 1999. EST analysis of gene expression in early cleavage-stage sea urchin embryos. *Development*, 126 3857-3867.

[11] Ljunggren, E.L., Nilsson, D., and Mattsson, J.G. 2003. Expressed sequence tag analysis of *Sarcoptes scabiei*. *Parasitology*, 127 139-145.

[12] Ohkubo, M., and Aranishi, F. 2004. What does invertebrate EST analysis acquire from bioinfor-matics *Simulated Evolution and Learning* (Kim, J.-H., ed.) Genome Informatics pp. 1-5, KAIST, Daejeon, Korea.

[13] Whisstock, J.C., and Lesk, A.M. 2003. Prediction of protein function from protein sequence and structure. *Q. Rev. Biophys.*, 36 307-340.

[14] Thompson, J.D., Higgins, D.G., and Gibson, T,J. 1994. CLUSTAL W: improving the sensitivity of progressive multiple sequence alignment through sequence weighting, position-specific gap penalties and weight matrix choice. *Nucleic Acids Res.*, 22 4673-4680.

[15] Boutros, M., and Perrimon, N. 2000. Drosophila genome takes flight. *Nat. Cell Biol.*, 2 E53-E54.

[16] Hotz-Wagenblatt, A., Hankeln, T., Ernst, P., Glatting, K.H., Schmidt, E.R., and Suhai, S. 2003. EST Annotator: A tool for high throughput EST annotation. *Nucleic Acids Res.*, 31 3716-3719.

The Eleventh International Symposium on Artificial Life and Robotics 2006 (AROB 11th'06),
B-con Plaza, Beppu, Oita, Japan, January 23-25, 2006

Molecular Clocks in Aquatic Invertebrates

Futoshi Aranishi and Takane Okimoto

Department of Biological and Environmental Sciences
Miyazaki University
Miyazaki 889-2192, Japan

Genes to Clocks

The discovery of the molecular clock – a relatively constant rate of molecular evolution – provided an insight into the mechanisms of molecular evolution, and created one of the most useful tools in biology [1-3]. The unexpected constancy of rate was explained by assuming that most changes to genes are effectively neutral — that is, driven by drift not selection [4-7].

The molecular clock is a 'sloppy' clock. The neutral theory predicts several sources of variation in rate of molecular evolution that is influenced by mutation rate, drift pattern, and population size. Although the molecular clock allows time estimates of events in evolutionary history, which provides a method for testing a wide range of biological hypotheses from the origins of the animal kingdom, 1) stochastic fluctuations in substitution rate of genes over time in lineages make date estimates imprecise, and 2) variation in rate between lineages can cause substantial bias in date estimates. Attempts to use the molecular clock to date evolutionary divergences must account for these sources of imprecision and bias, and variation in rate must be expressed in confidence intervals around date estimates [8].

The molecular clock hypothesis is the basis of the modern molecular phylogenetic approach for dating and resolving evolutionary history. Such approach requires the comparison of orthologous genes. Orthologous and paralogous genes usually possess different evolutionary fates. In general, orthologs keep the same functions in species, but, particularly over a long time span, paralogs diverge functionally and may become pseudogenes or get lost [9].

The mitochondrial genome certainly represents a major model system in studies on evolutionary genomics in metazoan, because of its peculiar features, such as exclusive presence of orthologous genes, uniparental inheritance, lack of recombination, small size, and constant gene content. In 800 million years (My) of evolution, the gene content of metazoan mitochondrial genomes has remained practically frozen, but an array of evolutionary processes has taken place; variations in the genetic code and evolution of codon usage, arising of compositional asymmetry between the two strands, rearrangements of gene order, changes in base composition, and lineage-specific nucleotide substitution rates and evolutionary patterns [10].

Mitochondrial Clock is Precise or Imprecise?

The mitochondrial cytochrome c oxidase I subunit (COI) gene is suggested to have evolved neutrally, which means nucleotide alterations of this gene have occurred constantly. The COI therefore has been frequently used in resolving phylogenetic relationships and evolutionary history of various metazoan taxa. We first attempted to estimate its evolutionary constant for nucleotide alterations based on the genetic distances in the Kimura's two-parameter model [11].

Five anthropoid organisms belonging to the family Hominidae (phylum Vertebrata, class Mammalia, order Primates) were used, because they possessed relatively short evolutionary history, and numerous fossil records revealed their evolutionary nodes. These facts indicate that, if an appropriate orthologous gene is employed, the molecular clock calculated from the genetic distances among these organisms allows precise time estimates of evolutionary events, which well correspond to other non-molecular information including the fossil records.

The complete nucleotide sequences of the COI gene were obtained from the GenBank under the accession numbers of J01415 for human *Homo sapiens*, NC001646 for orangutan *Pongo pygmaeus*, NC001645 for gorilla *Gorilla gorilla*), NC001644 for bonobo *Pan paniscus*, and NC001643 for chimpanzee *Pan troglodytes*. Multiple sequence alignments were performed using the program CLUSTAL W ver. 1.7 [12], and genetic distances were calculated from multiple sequence substitutions by the two-parameter model [11]. Distance phylogram was constructed by the unweighted pair group method with arithmetic mean using the program MEGA ver. 2.1 [13].

Non-molecular information indicated that the node between orangutan and other four species was distributed around 8 My ago. In addition, the node between human and *Pan* taxa, chimpanzee and bonobo, was expected to be 4 to 6 My ago. Comparison of these findings with the distance phylogram of the COI gene, 0.01 distance (D) in the two-parameter model resulted in corresponding to 1.08 My (Figure 1). The D values from the nodes between two *Pan* species, human and the genus *Pan*, and Gorilla and the genera *Pan* and *Homo* to their present status were calculated to be 0.020 D (2.156 My), 0.046 D (4.998 My), and 0.055 D (5.929 My), respectively. All of these time estimates of evolutionary events correspond to non-molecular information, indicating that the molecular clock of the COI gene based on the genetic distances in the two-parameter model could be a precise evolutionary clock with the 0.01 D at 1.08 My.

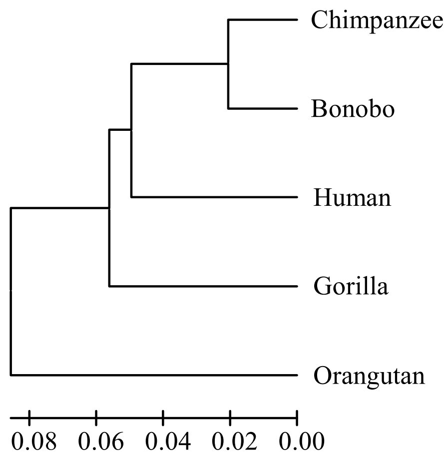

Figure 1. Distance phylogram of nucleotide sequences encoding the mitochondrial COI gene from 5 Hominidae species. Numbers of nucleotide alteration indicated by the scale are the Kimura's two-parameter distances.

Evolution of Oysters

Oysters are widely distributed throughout tropical and subtropical areas (Figure 2). They are benthic marine organisms inhabiting near-shore, shallow water, bay, and estuary locations [14]. The true oysters are more than 100 members of the family Ostreidae, and this includes edible oysters, which are mostly classified in the genera *Ostrea* or *Crassostrea* (Table 1).

Species belonging to the genus *Ostrea* generally live continually immersed in sea water and brood their fertilized eggs for various proportions of the period from fertilization to hatching. They can thrive in water with a not too thick concentration of phytoplankton. Otherwise, species belonging to the genus *Crassostrea* generally live in the intertidal zone and broadcast sperm and eggs into the sea. They thrive in water that is rich in phytoplankton. One of the most commercially important oysters world-wide is *Crassostrea gigas*, named as Japanese or Pacific oyster in English, and kaki or magaki in Japanese.

The classification of oysters is based on the form and structure of larval shell, mode of reproduction, life history, adult shell morphology, and foot shape, but their taxonomic positions have never been clearly established [15]. There is a hypothesis available for the evolution and classification of oysters; all species of the genus *Crassostrea* originated from a common fossil ancestor *C. gryphoides* and have remained unchanged for about 10 My [16].

On the basis of this hypothesis, the taxonomic positions of species of the genus *Crassostrea* could be established, if an approximate molecular clock enabled us to estimate times and orders of their classification events in evolutionary history. In the following part, we attempted to illustrate the phylogenetic relationships of species of the genus *Crassostrea* together with those of the genus *Ostrea* by means of the data set of nucleotide sequences encoding the mitochondrial COI gene (Table 1).

Mitochondrial Clock in Oysters

For a total of 13 Ostreidae species including 9 and 4 ones of the genera *Crassostrea* and *Ostrea*, respectively, nucleotide sequences encoding the mitochondrial COI gene were recorded in the GenBank (Table 1). As these sequences varied in the position and length, they were arranged to be 579 bp for the complete correspondences, and then subjected to multiple sequence alignments for calculation of the genetic distances in the two-parameter model as above. In order to date evolutionary events of oysters using the molecular clock of the COI gene along with their non-molecular information, it should be considered whether the fossil species of *C. gryphoides* was the common ancestor of either the genus *Crassostrea* or the family Ostreidae.

Table 1. List of mitochondrial COI nucleotide sequences of oysters analyzed in this study

Phylum	Class	Order	Family	Genus	Species	Common name	GenBank	Distribution
Mollusca	Bivalvia	Ostreoida	Ostreidae	*Crassostrea*	*gigas*	Japanese oyster	AF177226	1
					nippona	Iwagaki oyster	AF300616	1
					ariakensis	Suminoe oyster	AY632559	2
					sikamea	Kumamoto oyster	AY632568	2
					hongkongensis	Hongkong oyster	AY632557	3
					belcheri	Lugubrious oyster	AY038077	4
					iredelei	Philippine oyster	AY038078	5
					angulata	Portuguese oyster	AF152567	6
					virginica	Eastern oyster	AY905542	7
Mollusca	Bivalvia	Ostreoida	Ostreidae	*Ostrea*	*equestris*	Crested oyster	AY376609	8
					chilensis	Chilean oyster	AF112289	9
					aupouria		AY376630	10
					angasi	Australian oyster	AF540598	11

GenBank accession number.
Grobal distribution on Figure 1.

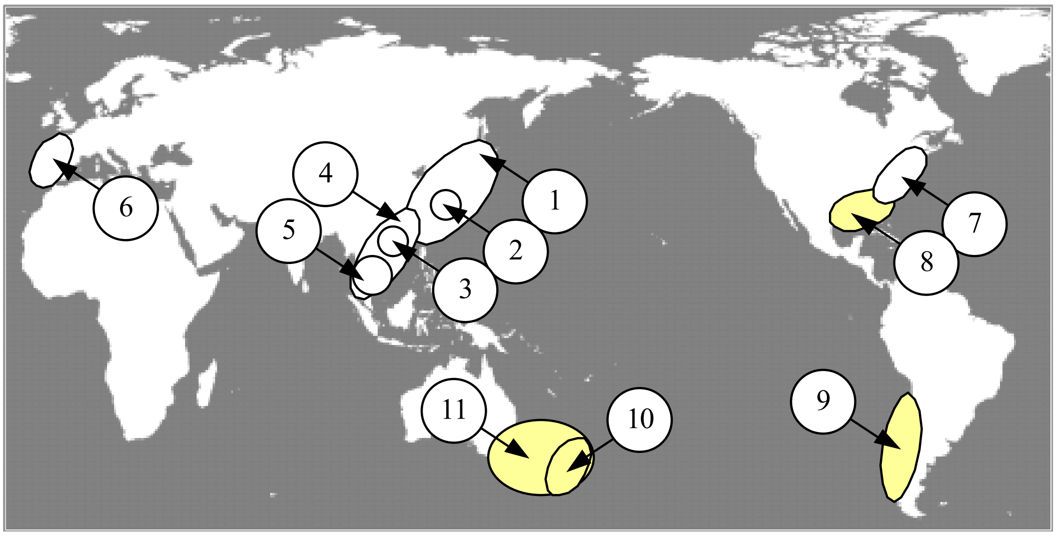

Figure 2. Global distribution of *Crassostrea* and *Ostrea* oysters.
1 – *C. gigas*, *C. nippona*; 2 – *C. ariakensis*, *C. sikamea*; 3 – *C. hongkongensis*; 4 – *C. belcheri*; 5 – *C. iredelei*; 6 – *C. angulata*; 7 – *C. virginica*; 8 – *O. equestris*; 9 – *O. chilensis*; 10 – *O. aupouria*; 11 – *O. angasi*

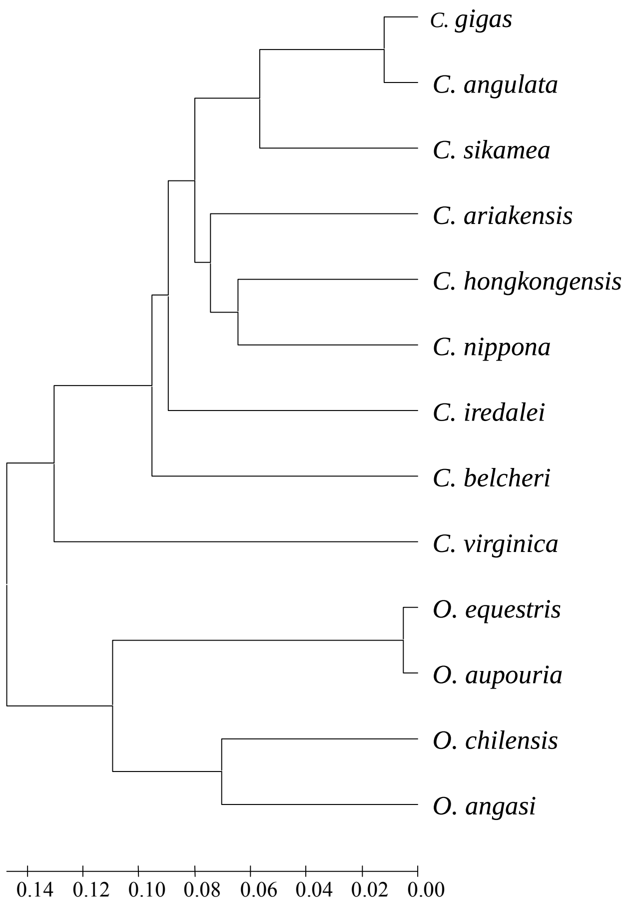

Figure 3. Distance phylogram of nucleotide sequences encoding the mitochondrial COI gene from 13 Ostreidae species listed in Table 1. Numbers of nucleotide alteration indicated by the scale are the Kimura's two-parameter distances.

The distance phylogram of the COI gene indicated that the D values of the nodes between the genera *Crassostrea* and *Ostrea*, and between *C. virginica* and other *Crassostrea* taxa to their present status were 0.142 D and 0.127 D, respectively (Figure 3). When the fossil *C. gryphoides* could be located at the respective nodes, 0.01 D in the two-parameter model resulted in corresponding to 0.71 My from 0.142 D and 0.79 My from 0.127 D. Both of these values were apparently lower than the 0.01 D at 1.08 My in case of the family Hominidae.

It is noteworthy that the distribution areas of two species, *C. virginica* and *C.angulata* are isolated far from other *Crassostrea* species, which are concentrated at the East Asia (Figure 2). The taxonomic status of *C. gigas* and *C. angulata* has been often questioned since no morphological or genetic differences had ever been observed between the two *Crassostrea* species. In addition, the recent molecular-based research using the COI and 16S ribosomal RNA (16S rRNA) genes as genetic makers concluded that *C. angulata* was certainly identical with *C. gigas* collected from Taiwan [17]. These facts indicate that only *C. virginica* is geographically (Figure 2) and genetically (Figure 3) isolated from other *Crassostrea* taxa.

We hypothesized that the fossil *C. gryphoides* may not be an ancestor of *C. virginica* but a common ancestor of other *Crassostrea* taxa. Based on this hypothesis, if the fossil species could be located on the node between *C. virginica* and others, its D value was determined to be 0.915 D. In addition, 0.01 D in the two-parameter model resulted in corresponding to 1.09 My. Interestingly, this value is well coincident with the 0.01 D at 1.08 My in case of the family Hominidae.

The mitochondrial COI gene is suggested to have evolved neutrally, particularly in vertebrate taxa, but it is not verified in invertebrate taxa because of much smaller numbers of its molecular phylogenetic and evolutionary studies on invertebrate taxa than vertebrate taxa. In this article, we introduced our preliminary study supporting that the COI gene could have altered at the constant rate from invertebrate though vertebrate taxa, if *C. virginica* and other *Crassostrea* taxa had evolved from different origins.

The complete mitochondrial nucleotide sequences were determined for only two *Crassostrea* species in the family Ostreidae. Those of *C. gigas* (NC001276) and *C. virginica* (NC007175) are, however, entirely divergent in length of nucleotide sequence, number and arrangement of genes, and structure of the control region. This fact is likely to support our assumption of different evolutionary histories between *C. virginica* and other *Crassostrea* taxa inhabiting in the East Asia.

Perspectives in Oyster Molecular Clock

Various deviations, which are caused by rate heterogenety between lineages from molecular clocks, have been observed for most genetic markers [18]. However, recent approach to molecular clock calculations provides the potential to obtain robust temporal reconstructions by assuming any number of local molecular clocks within a global phylogeny [19].

In addition to the COI gene, a data set of nucleotide sequences encoding the mitochondrial 16S rRNA is also available in the GenBank for 9 *Crassostrea* and 4 *Ostrea* species, the same taxa as we here analyzed using the COI gene. Our next investigation is to reconstruct molecular clock calculations based on two local clocks of the COI and 16S rRNA genes that are suggested to have evolved divergently.

References

[1] E. uckerkandl, and L. Pauling (1962) Molecular disease, evolution, and genic heterogeneity. "*Horizons in Biochemistry* (M. Kasha, and B. Pullman, eds.)". Academic Press, New York, pp. 97–166.

[2] E. uckerkandl, and L. Pauling (1965) Evolutionary divergence and convergence in proteins. "*Evolving Genes and Proteins* (V. Bryson, and H. J. Vogel, eds.)". Academic Press, New York, pp. 97–166.

[3] E. Margoliash (1963) Primary structure and evolution of cytochrome c. *Proc. Natl. Acad. Sci. USA.* 50:672–679.

[4] M. Kimura (1968) Evolutionary rate at the molecular level. *Nature* 217:624–626.

[5] M. Kimura (1969) The rate of molecular evolution considered from the standpoint of population genetics. *Proc. Natl. Acad. Sci. USA.* 63:1181–1188.

[6] M. Kimura (1983) "*The Neutral Theory of Molecular Evolution*". Cambridge University Press, Cambridge.

[7] M. Kimura, and T. Ohta (1971) Protein polymerphism as a phase of molecular evolution. *Nature* 229:467–469.

[8] F. J. Ayala (1999) Molecular clock mirages. *BioEssays* 21:71–75.

[9] C. Saccone, C. Caggese, A. M. D'Erchia, C. Lanave, M. Oliva, and G. Pesole (2003) Molecular clock and gene function. *J. Mol. Evol.* 57:277–285.

[10] C. Saccone, C. Gissi, A. Reyes, A. Larizza, E. Sbisa, and G. Pesole (2002) Mitochondrial DNA in metazoa: degree of freedom in a frozen event. *Gene* 286:3–12.

[11] M. Kimura (1980) A simple method for estimating evolutionary rates of base substitutions through comparative studies of nucleotide sequences. *J. Mol. Evol.* 16:111–120.

[12] J. D. Thompson, D. G. Higgins, and T. J. Gibson (1994) CLUSTAL W: improving the sensitivity of progressive multiple sequence alignment through sequence weighting, position-specific gap penaltyes and weight matrix choice. *Nucleic Acids Res.* 22:4673–4680.

[13] S. Kumar, K. Tamura, B. I. Jakobsen, and M. Nei (2001) MEGA2: Molecular Evolutionary Genetics Analysis software. *Bioinformatics* 17:1244–1245.

[14] D. Hedgecock (1995) The cupped oyster and the Pacific oyster. "*Conservation of Fish and Shellfish Resources: Managing Diversity* (J. Thorpe, G. Gall, J. Lannan, and C. Nash, eds.)". Academic Press, London, pp. 115–137.

[15] B. -H. Park, M. -S. Park, B. -Y. Kim, S. -B. Hur, and S. -J. Kim (1989) "*Culture of the Pacific Oyster (Crassostrea gigas) in the Republic of Korea*". FAO, Rome.

[16] H. B. Stenzel (1971) Oysters. "*Treatise on Invertebrate Paleontology* (K. C. Moore, ed.)". Geological Society of America and the University of Kansas, Boulder, pp. 953–1224.

[17] P. Boudry, S. Heurtebise, B. Collet, F. Cornette, and A. Gerard (1998) Differentiation between populations of the Portuguese oyster, *Crassostrea angulata* (Lamarck) and the Pacific oyster, *Crassostrea gigas* (Thunberg), revealed by mtDNA RFLP analysis. *J. Exp. Mar. Biol. Ecol.* 226:279–291.

[18] L. Bromham, A. Rambaut, and P. H. Harvey (1996) Determinants of rate variation in mammalian DNA sequence evolution. *J. Mol. Evol.* 43: 610–621.

[19] A. D. Yoder, and . Yang (2000) Estimation of primate speciation dates using local molecular clocks. *Mol. Biol. Evol.* 17:1081–1090.

The Eleventh International Symposium on Artificial Life and Robotics 2006 (AROB 11th'06),
B-con Plaza, Beppu, Oita, Japan, January 23-25, 2006

Self-Organizing Map of Species using Ribosomal Protein DNA Sequences

Yusuke HIGASHI
Graduate.School of Engineering,
Univ. of Miyazaki,
1-1, Gakuen-Kibanadai-Nishi,
Miyazaki,889-2192,Japan

Maki YOSHIHAMA
Frontier Science Research Center,
Univ. of Miyazaki,
5200, Kiyotake-Kihara,
Miyazaki,889-1692,Japan

Ikuo YOSHIHARA
Faculty of Engineering,
Univ. of Miyazaki,
1-1, Gakuen-Kibanadai-Nishi,
Miyazaki,889-2192,Japan

Kunihito YAMAMORI
Faculty of Engineering,
Univ. of Miyazaki,
1-1, Gakuen-Kibanadai-Nishi,
Miyazaki,889-2192,Japan

Naoya KENMOCHI
Frontier Science Research Center,
Univ. of Miyazaki,
5200, Kiyotake-Kihara,
Miyazaki,889-1692,Japan

Abstract

Eukaryotic gene has exon and intron. Exon is translated into protein, but intron is not. The intron has many unknown things one of which is so-called *intron evolution* or biological evolutional process. Comparing across species is a good way to make clear *intron evolution.* The *ribosomal protein gene* involved debris useful for clarifying *intron evolution.* We try to clarify *intron evolution* by analyzing base sequence of *ribosomal protein gene* using classification of species by self-organizing map (SOM). The input data is codon frequency that is appearance of frequency of three continuous bases. We prepare two kinds of data; one involves both intron and exon and the other does only intron. We experimented for to obtain maps of classified species.

1 Introduction

Eukaryotic gene has exon and intron. Exon is translated into protein, but intron does not directly contribute to protein synthesis. The intron has many unknown things one of which is so-called *intron evolution* or biological evolutional process. Comparing across species is an effective method to clarifying *intron evolution.*

We try to clarify *intron evolution* by comparing across species. Grantham clarified the feature of codon frequency in species gene by multiple classification analysis[1]. And, Abe classified species based on SOM using codon frequency, and demonstrate effectiveness for genome analysis[2][3][4]. Those researches focused on transcriptional region (exon and intron) , not applied to intron.

The *ribosomal protein gene* involves useful debris for clarifying *intron evolution*[5]. For example, all eukaryotic have it and the coding region (exon) is saved across species, etc. We analyze the *ribosomal protein gene* for clarifying *intron evolution.*

We clarify whether unique information of species is included in intron for to make clear *intron evolution.* First, we make map using base sequence of transcriptional region, and confirm that species are classified. Next, we apply to base sequence of intron region.

2 Self-Organizing Map

SOM is a kind of neural networks, and it is nonlinear projection form high-dimensional data to two-dimensional map[6][7]. It can see similarity of high-dimensional vector in two-dimensional map, and high-similarity of vectors is shown cluster in map. SOM is used by engineering, economic science and linguistics, etc that is field of analyzing large and complex data.

2.1 Algorithm

SOM has input layer and competitive layer, and those units are connected completely as shown in Figure1. The input vector of n piece is assumed to be $\mathbf{x}^{(n)}(= \;{}_1^{(n)}\;\;{}_2^{(n)}\;\;\;{}_k^{(n)})$, each nodes of competitive layer are shown by $i(=\;0\;1\quad I\quad 1)$ and $j(=\;0\;1\quad J\quad 1)$. The weight vector of each node of competitive layer is assumed to be $\mathbf{w}_{ij}(= w_{ij1}\; w_{ij2}\quad w_{ijk})$. Figure2 shows the learning process. In step1, the weight vectors on competitive layer are initialized randomly. In step2, the input vector is presented. In step3, the node on competitive layer with weight vector that is minimum Euclidian distance with input vector is searched. This node is called winner node. The Euclidian distance is defined as follows.

$$E = \sum_k (\;{}_k^{(n)}\quad w_k)^2 \tag{1}$$

In step4, the weight vector include in area of center on winner node are update conform presented input vector. The weight vector is updated as follow.

$$\mathbf{w}_{ij}^{(new)} = \mathbf{w}_{ij}^{(old)} + \;\;(\;)(\mathbf{x}^{(n)}\quad \mathbf{w}_{ij}^{(old)}) \tag{2}$$

$(=0\;1\quad T)$ represent iteration, $(\;)(0 < \;(\;) < 1)$ represent learning rate, and $(\;)$ represent area of the update. $(\;)$ and $(\;)$ is defined as follow.

$$(\;) = ma\quad 0\;01\quad {}_{init}(1\quad /T) \tag{3}$$

$$(\;) = ma\quad 0\quad {}_{init} \tag{4}$$

${}_{init}$ and ${}_{init}$ are each initial value.

3 Classification Experiments

3.1 Ribosomal Protein Gene

This study does classification species experiments. The used data is the *ribosomal protein gene*, because this gene has four effective features for intron analysis[5].

† All eukaryotic species has it.

† Number of intron region is more than other genes.

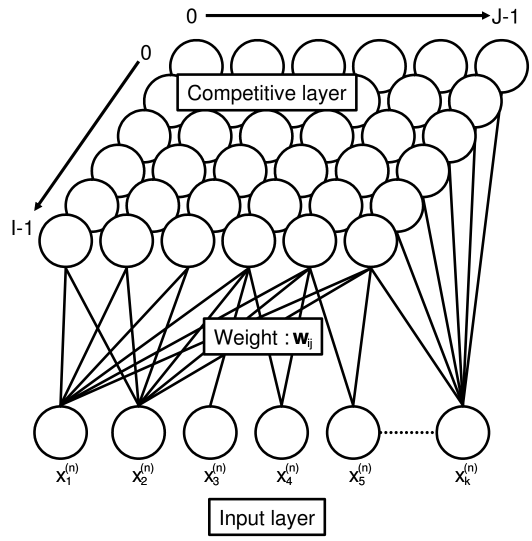

Figure 1: The structuer of SOM

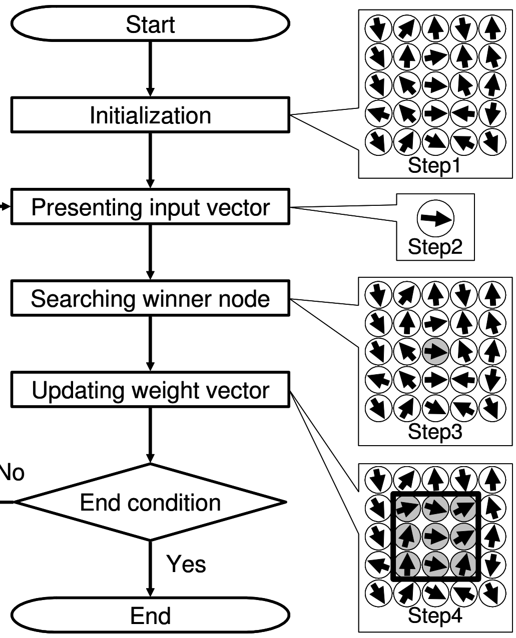

Figure 2: The learning process

† The coding region (exon) is saved across species.

† Number of intron in 1-kilo base is more than other genes.

In this paper, the input data to SOM is codon frequency that appearance of frequency of three continuous bases. We calculate codon frequency form base se-

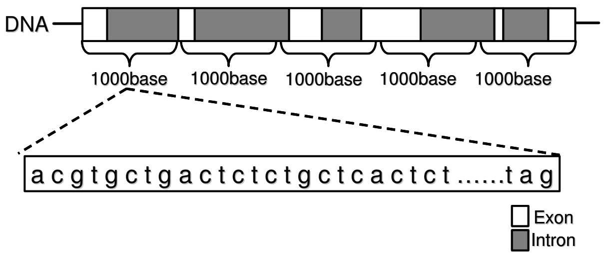

Figure 3: The codon frequency of transcriptional region

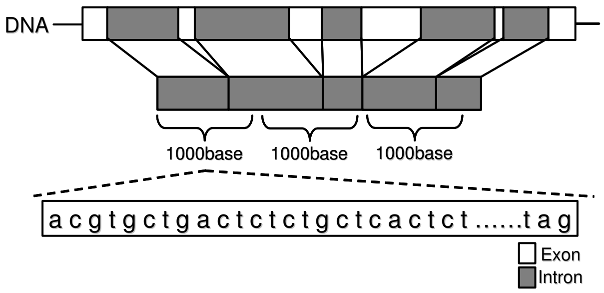

Figure 4: The codon frequency of intron region

quence of the *ribosomal protein gene* for experiments. Codon frequency of each species is made tow datasets by each methods.

Method 1: Codon frequency of transcriptional region
Base sequence of transcriptional region is cut out every 1-kilo base as shown in Figure3. In addition, codon frequency is calculated form 1-kilo base.

Method 2: Codon frequency of intron region
The intron regions are picked up from the transcriptional region and they join, and base sequence of joined intron region is cut out every 1-kilo base as shown in Figure4. In addition, codon frequency is calculated from 1-kilo base.

Here, the codon frequency is calculated by shifting every one base.

3.2 Experimental Conditions

The information of those dataset is as shown in Table1. The ID in Table1 is used to identify species on the map.

The parameters of SOM to each dataset are as shown in Table2.

Species	ID	Number of pattern Method 1	Method 2
Arabidopsis thaliana	A	273	119
Caenorhabditis elegans	B	66	21
Dictyostelium discoideum	C	61	22
Drosophila melanogaster	D	130	58
Homo sapiens	E	356	306
Plasmodium falciparum	F	73	24
Schizosaccharomyces pombe	G	80	10
Saccharomyces cerevisiae	H	102	36
Total		1141	596

Table 1: The dataset information

Parameter	Method 1	Method 2
Map size	34 34	25 25
$init$	0.5	0.5
$init$	17	14
Iteration	100 epochs	100 epochs

Table 2: The parameters of SOM

3.3 Experimental Results

Figure5 and Figure6 shows experimental results of each dataset. Figure5 is a map obtained in the dataset made from transcriptional region (method 1), and Figure6 is a map obtained in the dataset made from intron region (method 2). The displayed character on each map corresponds to species shown in Table1. The '-' expresses not plotting at all, and the '*' expresses plotting more than two species. Those results mean that species classifies it by seeing Figure5 and Figure6.

4 Discussion

Figure5 is making map using transcriptional region, and this map is classifies species. Therefore, transcriptional region include unique information of species. Next, Figure6 is experimental result of mapping using intron region. This map is classifies species just like analysis of transcriptional region.

In spite of what exon region translated protein, intron region do not directly contribute to protein synthesis. However, as the result, intron region have unique information of species.

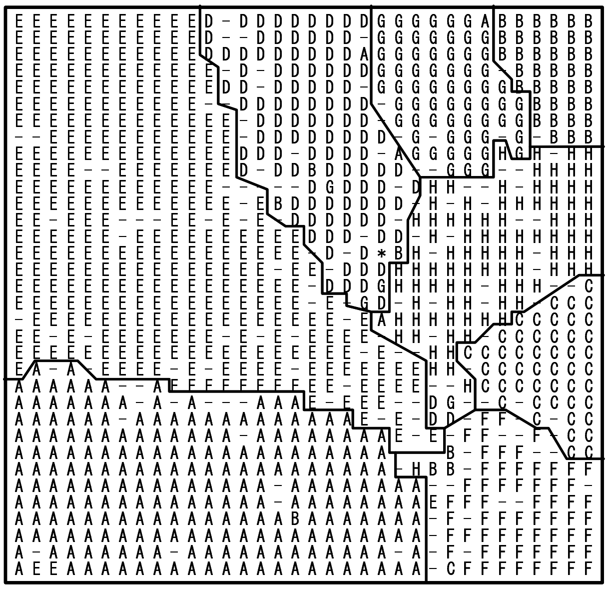

Figure 5: The result of method1

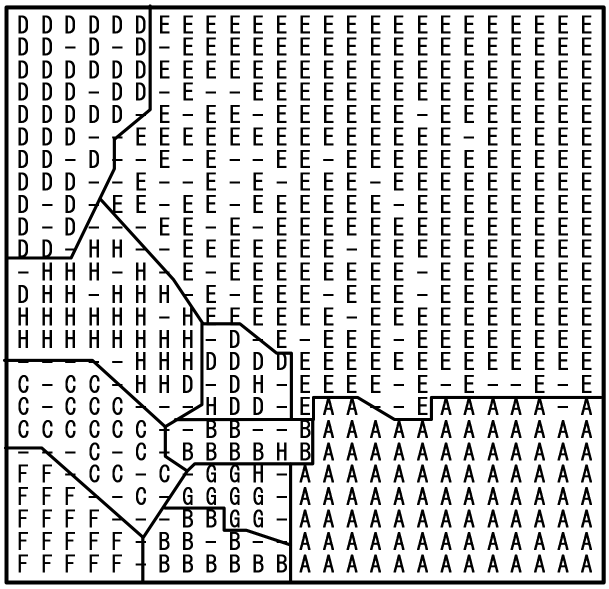

Figure 6: The result of method2

5 Conclusions

We tried to clarify *intron evolution* by analyzing sequence of the *ribosomal protein gene* using classification of species by SOM. The input data is codon frequency. Two datasets are prepared codon frequency of base sequence of transcriptional region (exon and intron) and base sequence of intron region. We obtained maps of classified species; one involves both intron and exon and the other does only intron. Experiment shows that base sequence of intron region has unique information of species.

The future works are to develop method of discovering for information of intron region based on obtained map, and to compare obtained map with evolutionary tree, etc.

Acknowledgements

This research is partly supported by MEXT grant (c) 17500146 in 2005

References

[1] R. Grantham, C. Gautier, M. Gouy, R. Mercier, A. Pave, Codon catalog usage and the genome hypothesis, Nucleic Acids Res, 8:r49-462

[2] T. Abe, S. Kanaya, M. Kinouchi, Y. Ichiba, T. Kozuki, and T. Ikemura, Informatics for unveiling Hidden genome signatures, Genome Research, 13:693-702, 2003

[3] T. Abe, S. Kanaya, M. Kinouchi, Y. Kudo, H. Mori, H. Matsuda, C.D. Carpio, T. Ikemura, and T. Ikemura, Gene classification method based on batch-learning SOM, Genome Informatics, 10:314-315, 1999

[4] S. Kanaya, M. Kinouchi, T. Abe, Y. Kudo, Y. Yamada, T. Nishi, H. Mori, and T. Ikemura, Analysis of codon usage diversity of bacterial genes with a self-organizing map: characterization of horizontally transferred genes with emphasis on E. coil 157 genome, Gene, 276:89-99, 2001

[5] A. Nakao, M. Yoshihama, and N. Kenmochi, RPG: Ribosomal Protein Gene database, Nucleic Acids Res, 32.D168-D170, 2004

[6] T. Kohonen, Self-organizing maps, Springer-verlag Tokyo, ISBN4-431-70700-x, 1996 (In Japanese)

[7] H. Tokutaka, S. Kishida, K. Fujimura, Application of self-organizing maps, Kaibundo Syuppan. Co, ISBN4-303-73230-3, 1999 (In Japanese)

The Eleventh International Symposium on Artificial Life and Robotics 2006 (AROB 11th'06),
B-con Plaza, Beppu, Oita, Japan, January 23-25, 2006

Non-transcriptional Region Analysis of Dictyostelium Discoideum using 1/f Noise

Masakazu SATO
Graduate School of Engineering,
University of Miyazaki
1-1,Gakuen-Kibanadai-Nishi,
Miyazaki, 889-2192,Japan

Ikuo YOSHIHARA
Faculty of Engineering,
University of Miyazaki
1-1,Gakuen-Kibanadai-Nishi,
Miyazaki, 889-2192, Japan

Kunihito YAMAMORI
Faculty of Engineering,
University of Miyazaki
1-1, Gakuen-Kibanadai-Nishi,
Miyazaki, 889-2192, Japan

Moritoshi YASUNAGA
Graduate School of Systems and Information,
Engineering, University of Tsukuba
1-1-1,Tennoudai,Tsukuba,
Ibaraki, 305-8573,Japan

Abstract

The eukaryotic genome has regions that do not contribute explicitly to synthesize protein. Those non-coding regions occupy most part of DNA base sequences of eukaryotic genome. To find embedded information in non-coding region is important to clarify evolution of species.

As a first step of research on non-coding region, we analyze non-transcriptional region which is also non-coding. We analyze DNA base sequences of *Dic os elium Discoideum* with $1/f$ noise in chaos theory. *Dic os elium Discoideum* is so-called model organism that has been investigated worldwide.

1 Introduction

The eukaryotic genome consists of two kinds of regions. One is coding region that operates to synthesize protein. The other is non-coding region that does not operate to synthesize protein. Most of DNA base sequences of eukaryotic genome are non-coding region. For instance, 95% or more of human genome is non-coding. To find embedded information in non-coding region is one of the most important tasks for clarifying evolution of species. We develop a method to find this information using 1/f noise in chaos theory.

Li and Kaneko [4] , and Voss [5] applied the 1/f-noise method in DNA base sequences. They suggest the power spectrum of DNA base sequences shows power-law scaling similar to the $1/f$ noise at low frequencies. The exponent of $1/f$ shows the gradient of the regression line of power spectrum. Takushi and Miyagi [1][2][3] showed that several fractal group-correlations exist in a partial sequence and total sequence of bacteriopahge ϕ-X174. The lengths of partial sequences are 64, 128, 256, and 512 etc., because they employed FFT with radix two. To avoid limitation of 2^n, we developed a FFT program with mixed radix (2, 3, 5) that enables to analysis various lengths of DNA base sequences.

As a first step of research on non-coding region, we analyze non-transcriptional region which is also non-coding. The process of synthesizing protein by transcription of a part of DNA is called gene expression (Figure 1). In non-transcriptional region, information to control the gene expression is included. We analyze non-transcriptional region of *Dic os elium Discoideum* using exponent of $1/f$. *Dic os elium Discoideum* is known as an important model organism [6][7], because it has the simple growth cycle.

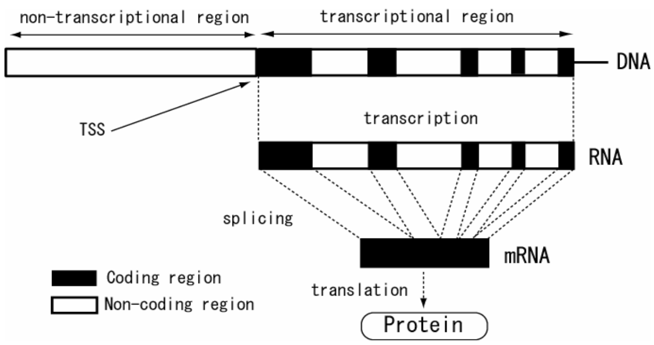

Figure 1: The Process of synthesizing Protein

2 Dictyostelium Discoideum

Dic os elium Discoideum is a kind of primitive eukaryote. Life cycle of *Dic os elium Discoideum* consists of four growth stages based on timing of gene expression (Figure2).

(1) Vegetative stage that lives independently with amoeboid and proliferates. (V stage)

(2) Aggregating stage that assembles in the center of the aggregate and forms pseudoplasmodium. (A stage)

(3) Slug stage that begins to move pseudoplasmodium. (S stage)

(4) Culminating stage that forms a fruiting body from pseudoplasmodium. (C stage)

And amoeba appears by germinating of spore of fruiting body.

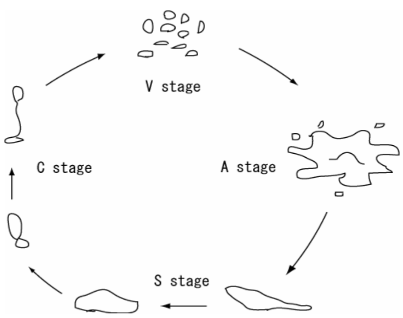

Figure 2: Life Cycle of *Dic os elium Discoideum*

3 1/f Noise

When gradient of graph obtained by the spectral analysis is -1, it is called the $1/f$ noise. The 1/f noise is observed in natural phenomena such as flame of candle, the breeze, and the classical music etc. It is said that the 1/f noise is related to a comfort sensation.

As for $1/f$ noise, if the gradient increases, an irregular transition decreases. On the other hand, if the gradient decreases, an irregular transition increases.

4 Calculation of of $1\ f$

The exponent of $1/f$ is calculated by the following procedure.

Step1 Numeric conversion of DNA base sequences

Step2 Calculation of power spectrum

Step3 Linear regression at low frequency by least-square method (Figure3)

Step4 Calculation of gradient ($-$) of regression line

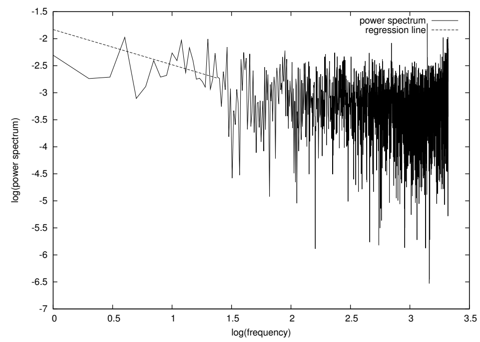

Figure 3: Power Spectrum and Regression Line

4.1 Numeric Conversion of DNA Base Sequences

DNA base sequences consist of four kinds of bases; A (Adenine), C (Cytosine), G (Guanine), and T (Thymine). It is necessary to convert each bases into the numerical value before Fourier transform. Each bases are converted into complex number, because the distance between four bases can arrange as evenly as possible (Figure4).

- A$\cdots(1+r_1)+(1+r_2)i$
- G$\cdots(-1+r_3)+(1+r_4)i$
- C$\cdots(1+r_5)+(-1+r_6)i$
- T$\cdots(-1+r_7)+(-1+r_8)i$

$r_n \in < -0\ 1\ \ 0\ 1 >$

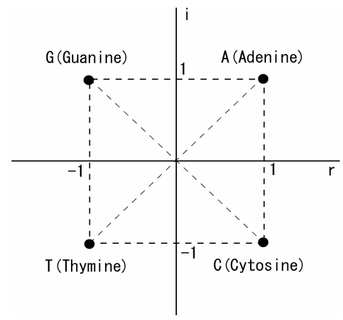

Figure 4: Numeric Conversion of DNA Base Sequences

4.2 Fourier Transform and Power Spectrum

The DFT (Discrete Fourier Transform) of discrete data $f_n(\quad = 0 \; 1 \; \cdots \quad -1)$ calculate by the following formula.

$$F_k = \sum_{n=0}^{N-1} f_n e^{\frac{-i2\pi kn}{N}} (k = 0 \; 1 \; \cdots \quad -1) \tag{1}$$

f_n :DNA base sequences expressed by numerical value

Next, the power spectrum is calculated by the following formula.

$$S_f = | F_k |^2 \tag{2}$$

FFT with mixed radix is employed to analyze various lengths of a partial sequence.

5 Experimental Data and Method

We used DNA base sequence of *Dic os elium Discoideum*. These data were created on experiments in Univ. of Tsukuba. Each data consists of non-transcriptional region (2000 bases) and transcriptional region (100 bases)(Figure 5). 2000 position is the transcriptional start sites (TSS).

- V stage ···141 data
- A stage ··· 92 data
- C stage ··· 58 data
- S stage ··· 63 data

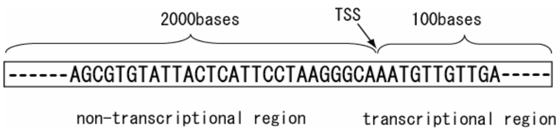

Figure 5: DATA of *Dic os elium Discoideum*

The length (L) of a partial sequence is decided , and the position of a partial sequence is moved one by one (Figure 6). The of $1/f$ of each a partial sequence is calculated. In the case DNA base sequence is M bases, a partial sequence is from $m - L + 1$ to m. $(m = L \; L + 1 \; \cdots \; M)$

6 Result and Discussion

Figure 7 shows the average of of partial sequence in non-transcriptional region, and Figure 8 shows the

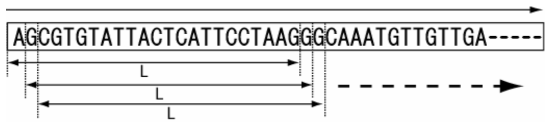

Figure 6: Movement of Position of a Partial Sequence

average of of partial sequence in transcriptional region. The of non-transcriptional region is larger than of transcriptional region. These results mean that DNA base sequences of non-transcriptional region is more regular than that of the transcriptional region. Average of converge from $L \approx 500$ in non-transcriptional region.

Figure 9 shows the transition of average of in each growth stage (V stage, A stage, C stage, S stage) at $L = 48$. In V stage and C stage, the average of increases in front of TSS. This increase might be an influence of the change in frequency of appearance of each bases in front of TSS as shown in Figure 10, Figure 11 . However, such an increase is not clearly observed in each result before the average is calculated.

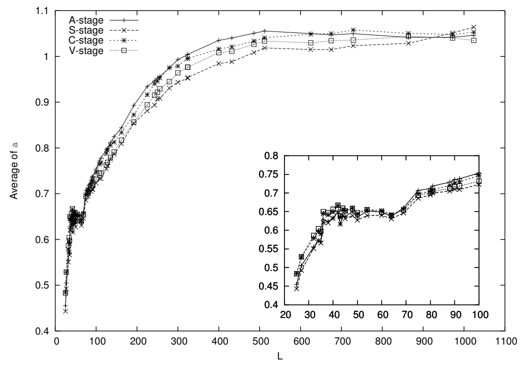

Figure 7: Avarage of in Non-transcribed Region

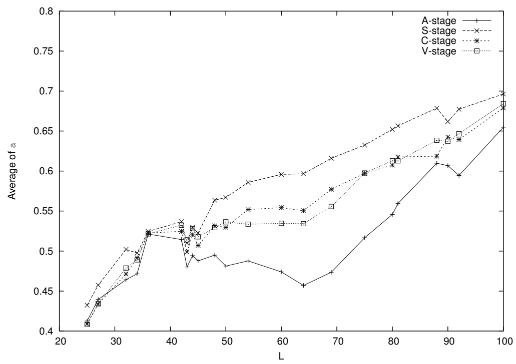

Figure 8: Average of in Transcribed Region

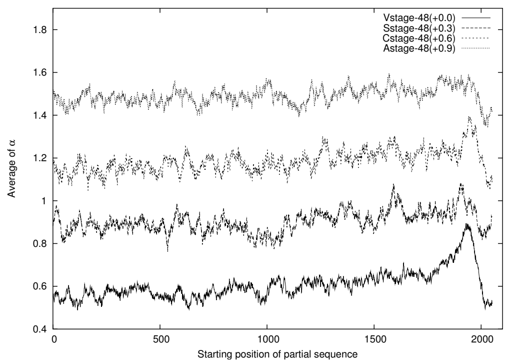

Figure 9: Transition of Average of in Each Growth Stage (L=48)

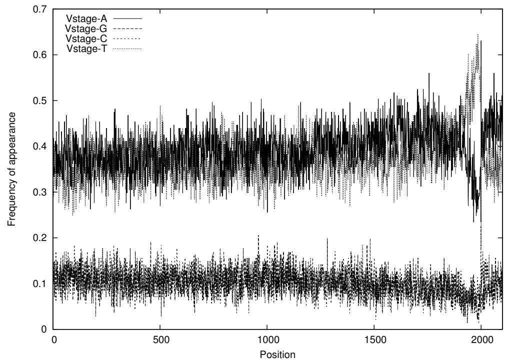

Figure 10: Frequency of Appearance of Each Bases in V Stage

7 Conclusion

We analyzed non-transcriptional region of DNA base sequence of *Dic os elium Discoideum* using exponent of $1/f$. The analyses showed that DNA sequences of non-transcriptional region are more regular than that of the transcriptional region. In addition, experiments showed that the average of increases in front of TSS in V stage and C stage. This paper mentions non-transcriptional region, but analysis of intron will be mentioned at the conference.

Future work is to apply our method to comparing DNA base sequences across species.

8 Acknowledgements

We are most grateful to Prof. Hideko URUSHIHARA at University of Tsukuba and also Prof. Naoya KENMOCHI and Dr. Maki YOSHIHAMA for providing us the information on DNA sequences.

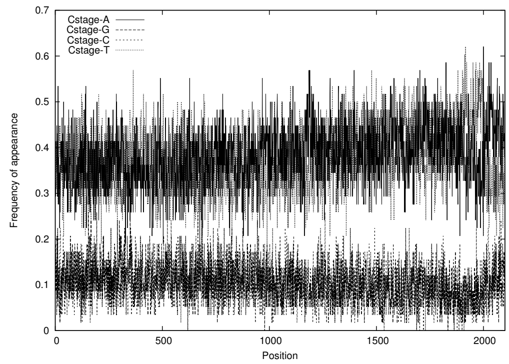

Figure 11: Frequency of Appearance of Each Bases in C Stage

This research is partly supported by MEXT grant (C) 17500146 in 2005

References

[1] E. Takushi and H. Miyagi, "Fractal Packing of the DNA Sequence of Bacteriophage ϕ-X174," *Bull.Fac.Sci.,Univ.Ryukyus* ,No. 70, pp.43-46,2000.(in Japanese)

[2] E. Takushi and H. Miyagi, "Fractal Packing of the DNA Sequence of Bacteriophage ϕ-X174 (II)," *Bull.Fac.Sci.,Univ.Ryukyus* ,No. 71, pp.21-23, 2001.

[3] E. Takushi and H. Miyagi, "Fractal Packing of the DNA Sequence of Bacteriophage ϕ-X174 (III)," *Bull.Fac.Sci.,Univ.Ryukyus* ,No. 72, pp.43-47,2001.

[4] W. Li and K. Kaneko, "DNA correlations," *Nature* ,Vol.360, pp.635-636,1992.

[5] R. F. Voss, "Evolution of Long-Range Fractal Correlations and 1/f Noise in DNA Base Sequences," *phys.Rev.Lett.,* , Vol.68 , pp.3805-3808, 1992.

[6] I. Yoshihara and T. Yamaguchi and K. Yamamori and M. Yasunaga, "Feature Ectraction of Cellular Slime Molds using 1/f fluctuation," *Memoirs of the Fac. of Engineering, Miyazaki Univ.,* Vol.32, pp.277-282, 2003.(in Japanese)

[7] T. Onitani and I. Yoshihara and K. Yamamori and M. Yasunaga, "Extraction of Feature Patterns Embedded in Non-Transcribed Region of Dictyostelium Discoideum," *SEAL04*, SWP-8, No. 123, 2004.

The Eleventh International Symposium on Artificial Life and Robotics 2006 (AROB 11th'06),
B-con Plaza, Beppu, Oita, Japan, January 23-25, 2006

A Bio-inspired Tracking-camera System

Kazuya Hayashi*, Noriyuki Aibe*, Yoshiki Yamaguchi*, Yorihisa Yamamoto†,
Moritoshi Yasunaga*, and Ikuo Yoshihara‡

*Systems & Information Engineering, University of Tsukuba,
1-1-1 Ten-ou-dai Tsukuba Ibaraki, 305-8573, Japan
hayashi@islab.cs.tsukuba.ac.jp

†Yamamoto System Design Inc.,
3481 Oozone Tsukuba Ibaraki, 300-3253, Japan

‡Faculty of Engineering, University of Miyazaki,
1-1 Gakuen Kibanadai Nishi Miyazaki Miyazaki, 889-2192, Japan

Abstract

We propose a bio-inspired reconfigurable tracking-camera system using FPGAs. In the system, a wide-lens camera captures an entire image while a zoom-lens camera tracks a target in the image magnifying it. In the current system, probabilistic neural network (PNN) and mosaic-processing are used for the image recognition and pre-processing, respectively. Thanks to the FPGA-based design, not only PNN and the mosaic-processing but other recognition and pre-processing algorithms can be implemented onto the system also to adapt the various images and targets.

1. Introduction

In order to prevent increasing number of crimes and accidents, novel approaches are required in the video-surveillance systems to achieve much higher precision in the image recognition than the conventional ones. Some new approaches, for example, using a CMOS camera-array[1] or multiple cameras[2] have been proposed already. In the above background, we propose an image recognition and tracking camera system that can give us high recognition-rate based on high resolution images of the targets.

The system has two features: The system is reconfigurable using FPGAs with which it can adapt to different algorithms for image recognition and its preprocessing. And the system is designed based on the eye-system in which we watch a target carefully while we see an entire image roughly. In order to mimic the eye-system, two cameras are used in our system: One wide-lens camera captures an entire image, while the other zoom-lens camera tracks a target with a servomotor magnifying it. Moreover, we use probabilistic neural network (PNN)[3] that is one of promising neural networks as a recognition algorithm in the recognition part. The system is thus designed totally based on the bio-inspired approach.

Thanks to the reconfigurability using FPGAs, not only the PNN and the mosaic-processing, but other algorithms can be implemented also in the system. Furthermore, in the system, parameter-tuning and servomotor-modeling, which are usually carried out offline using computer simulations, can be done online using FPGAs, i.e., different parameters and models can be implemented onto the FPGAs in the system and tested automatically and quickly, so that high-speed system-setting can be achieved.

2. Bio-inspired tracking-camera system

Figure 1 shows the system configuration. The system is mainly composed of three blocks: Camera-block, Video-image Recognition Block, and Servomotor Control Block. The camera-block consists of the above-mentioned two cameras(see Fig.2). The zoom-lens camera is controlled with two servomotors (MS1 and MS2) that move the camera perpendicularly and horizontally. An image from the wide-lens camera is input to the PNN processor[4][5] and the position of the target in x- and y-axis is detected in it. The position is then feed back to the position controller in the camera-block to train the zoom-camera on the target, and the zoom-camera outputs the magnified high-resolution image of the target. The magnified high-resolution image is sent to the PNN processor again and its information or property is retrieved in it.

The system can be applied, for example, to a face-recognition in the video-surveillance as follows. Faces in natural scenes are detected with the wide-lens camera and the PNN processor, and their positions are detected first. The zoom-camera is then trained on the faces and outputs the magnified face-images that are candidates. Those candidates are sent to the PNN and are finally recognized in the PNN compared with the face-images that are registered in advance. In the next section, we describe the PNN and the motor controller in details.

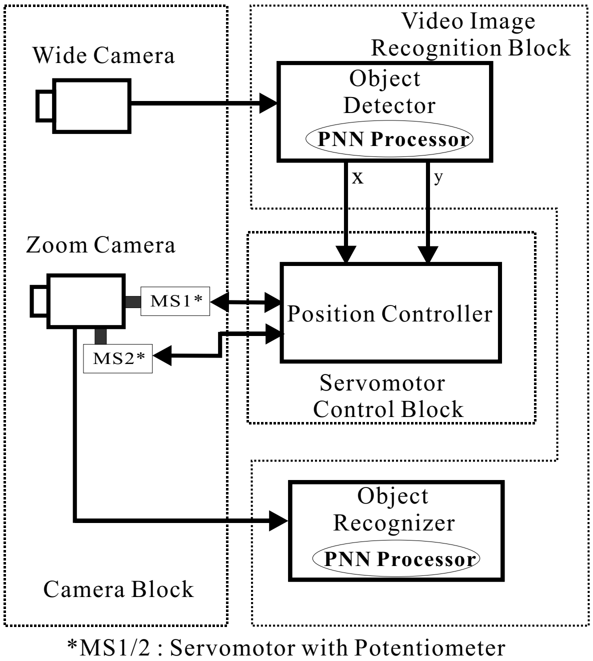

Figure 1. Outline of the BI-Camera System

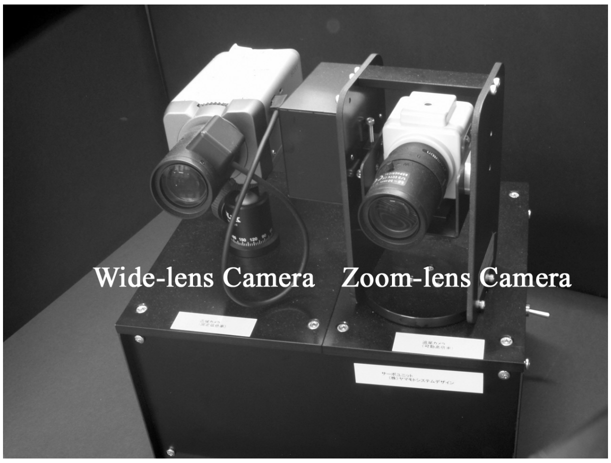

Figure 2. Photograph of the Camera Block

3. Video Image Recognition Block

Video Image Recognition Block mainly executes two processes. One process is to detect the position of the target based on the input image from the wide-lens camera. And the other process is to recognize the target based on the high resolution images from the zoom-lens camera. Figs. 3 and 4 show a photograph of the developed FPGA board and a detailed system configuration, respectively. As mentioned above, PNN is currently used for position-detection and recognition of the target. We have proposed a PNN processor[4] and its reconfigurable architecture using FPGAs[5] already. PNN is one of the statistical pattern recognition techniques, and is now applied to many real world applications. PNN consists of feed-forward three layers, that is, a kernel layer, a summation layer, and a decision layer. Each neuron (node) in the kernel layer calculates the kernel function $K\left(\mathbf{X}-\mathbf{S}_j^i\right)$, where $\mathbf{X}$ is the input pattern

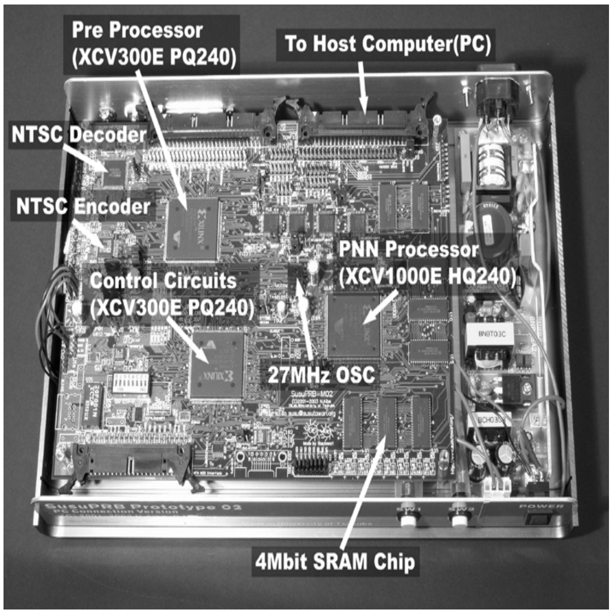

Figure 3. Photograph of Video Image Recognition and Servomotor Control Blocks

(unknown pattern) and $\mathbf{S}_j^i$ is the jth pattern in the category C_i. The superposition of the kernel functions that is calculated in the summation layer constructs the estimator of the probabilistic density function $p\left(\mathbf{X}|C_i\right)$ of the category C_i, that is,

$$p\left(\mathbf{X}|C_i\right)=\frac{1}{N_p}\sum_{j=1}^{N_p}K\left(\mathbf{X}-\mathbf{S}_j^i\right), \qquad (1)$$

where N_p is the number of sample patterns in each category. The neuron in the decision layer selects the highest $p\left(\mathbf{X}|C_i\right)$ and its category C_i is output as the answer (i.e., predicted category) to the input pattern (unknown pattern) $\mathbf{X}$.

The kernel function is the kernel in the PNN as it is named, and we adopted the uniform function

$$K\left(\mathbf{X}-\mathbf{S}_j^i\right)=\begin{cases}1: & \left|x_k-(s_j^i)_k\right|\le\frac{\sigma}{2}\\ 0: & \text{otherwise}\end{cases} \qquad (2)$$
$$(\text{for all } k, k=1,2,...,n)$$

because it is suitable for the digital hardware implementation. The smoothing parameter σ determines the width of the kernel function. Determining σ, which is just the learning in PNN, is much easier than other learning algorithms because it is the only one parameter in the network.

Fig. 5 shows a circuit block diagram of the PNN processor. An adder and a subtracter are for $\left(s_j^i\right)_1+\sigma/2$ and $\left(s_j^i\right)_1-\sigma/2$ in Eq. (2), respectively and they compose the kernel function. The condition $\left|x_k-\left(s_j^i\right)_k\right|\le\sigma/2$ in Eq. (2) is examined with two comparators sequentially in every component k. The counter increases by one if $\left|x_k-\left(s_j^i\right)_k\right|\le\sigma/2$ is satisfied for all components, while the calculation for Eq. (2) is canceled at the RS-FF once it is not satisfied. Finally, the number of kernels that include the input pattern, which is equal to Eq. (1), is set to the counter.

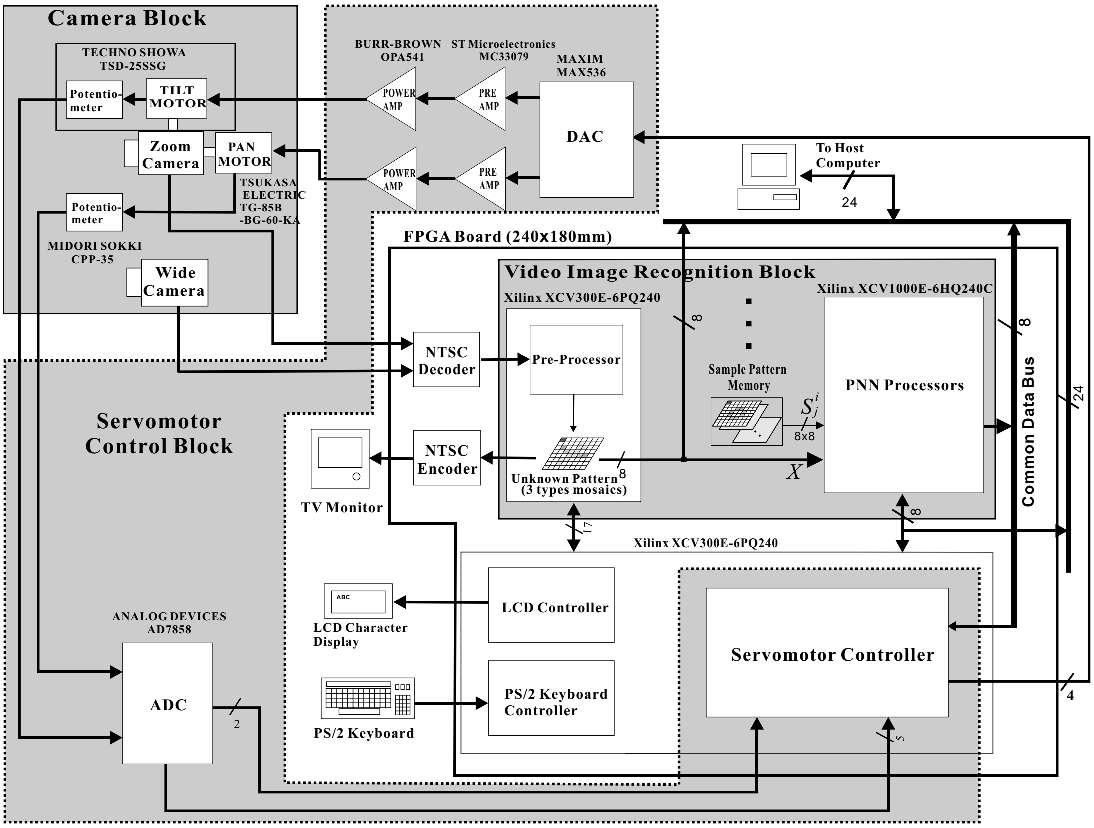

Figure 4. Configuration of the BI-Camera System

4 Servomotor control block

The servomotor control block controls the servomotors of the zoom-lens camera to track the target according to the detected position. The FPGAs in the block are used not only to control the servomotors but also to identify the servomotor feedback loop. In the case of system identification, a signal oscillator for a servomotor input and a data recorder for the servomotor output are implemented in the FPGA because of estimating parameters for the servomotor control for the high-precision tracking. The measured data are sent to a PC (host computer) and parameters are estimated. In this estimation, we used a model as shown in Fig.6.

From Fig.6, input-output relation is expressed as follows:

$$\theta = \frac{\beta}{s+\alpha} \cdot \frac{1}{s} V \qquad (3)$$

Where α is $\frac{K_T K_E}{RI}$ and β is $\frac{K_T}{RI}$. Using some mesured data to Eq.(3), we can determine optimum parameter of servomotor. After determining parameter of servomotor, reconfiguring FPGAs for control of servomotor, we can control servomotor using the same FPGAs. Using the same FPGAs, the system do not need external oscillator and et al., we can realize miniaturization of whole system scale.

Gain and phase properties, namely Bode plot, are shown as Fig.7 and Fig.8 respectively. As frequency turning up, the gain of servomotor as shown Fig.7 come down, and the response of servomotor as shown Fig.8 gradually delay. To research motor specification precisely such that, we could realize high accuracy performance for zoom-lens camera to track.

5 Conclusions

We proposed a bio-inspired reconfigurable tracking-camera system that is equipped with a wide-lens and a zoom-lens camera. The system is designed based on the eye and the brain system in the organism. We discussed the image recognition process, in which the probabilistic neural network (PNN) is used, and the motor control process in the system in detail. Thanks to the FPGA-based design, different algorithms for the recognition and other processes can be implemented in the system. And the motor identification process is also carried out using the FPGA without any simulations that are indispensable in the conventional motor control system. The system is now being developed and some fundamental evaluation results will be reported at the conference.

Acknowledgment

This research is supported in part by the 2005 Cooperation of Innovative Technology and Advanced Research in Evolutional Area and the 2005 grant of Japan Society for the Promotion Science(No.16360197)

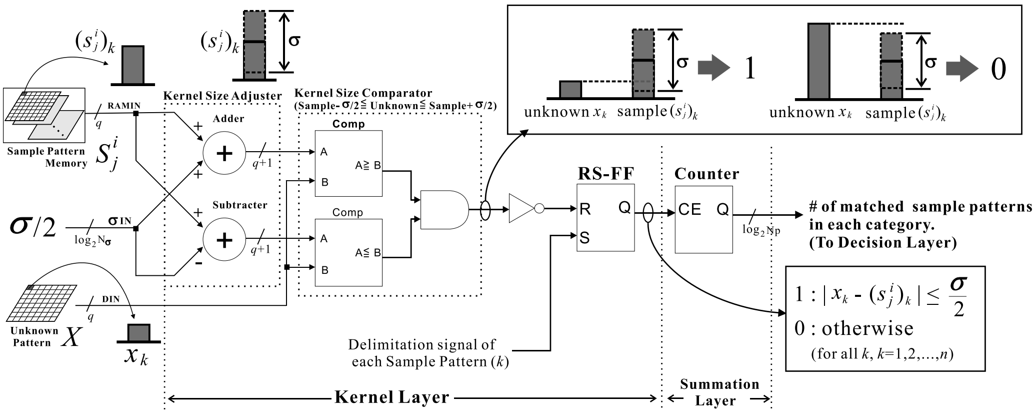

Figure 5. Configuration of one PNN Processor.

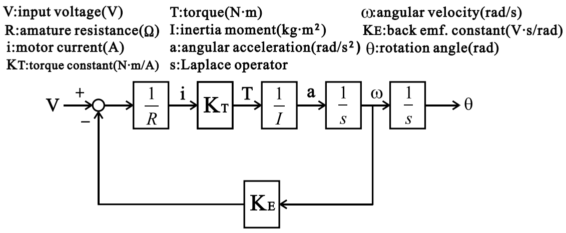

Figure 6. Block Diagram of a Servomotor with Descrete-Time Feedback

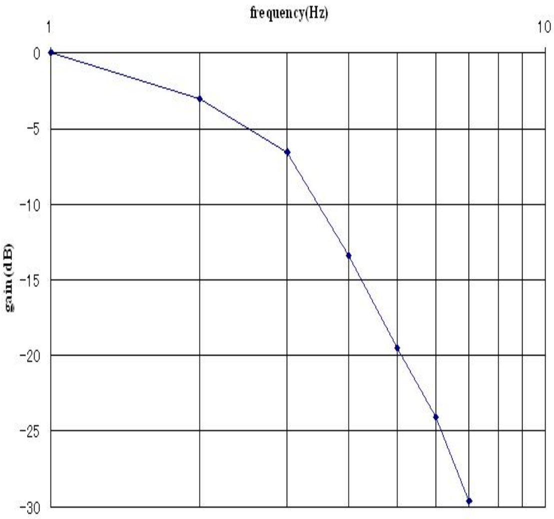

Figure 7. Magnitude (Bode Plot)

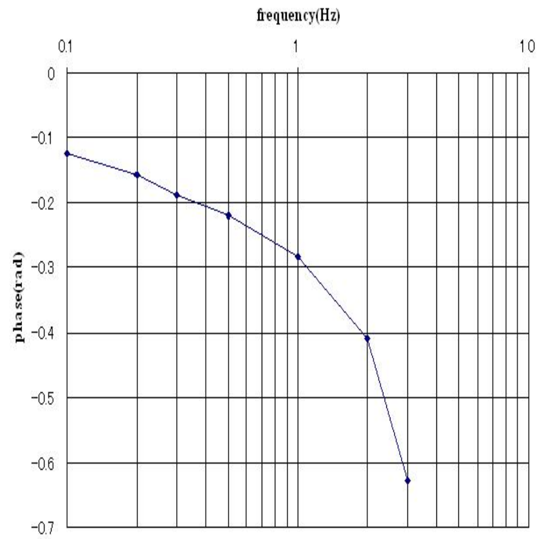

Figure 8. Phase (Bode Plot)

References

[1] Ryutaro Oi, Marcus Magnor, and Kiyoharu Aizawa, "A Solid-State, Simultaneous Wide Angle-Detailed View Surveillance Camera", *VMV2003, Munich, Germany, November 19-21, 2003*.

[2] Sohaib Khan, Omar Javed, Zeeshan Rasheed, and Mubarak Shah, "Human Tracking in Multiple Cameras", *The Eighth IEEE International Conference on Computer Vision, Vancouver, Canada, July 9-12, 2001*.

[3] D.F.Specht, "Probabilistic Neural Networks and the Polynomial Adeline as Complementary Techniques for Classification", *IEEE Trans. Neural Networks*,Vol.1, No.1, pp.111-110 1990.

[4] Noriyuki Aibe, Ryousuke Mizuno, Masanori Nakamura, Moritoshi Yasunaga, and Ikuo Yoshihara, "Performance Evaluation System for Probabilistic Neural Network Hardware", *The journal of Artificial Life and Robotics (Springer-Verlag)*, Vol.8, No.2, pp.208–213, 2004.

[5] Ryosuke Mizuno, Noriyuki Aibe, Moritoshi Yasunaga, and Ikuo Yoshihara, "Reconfigurable Architecture for Probabilistic Neural Network System", *IEEE International Conference on Field-Programmable Technology (ICFPT) 2003*, University of Tokyo, Tokyo, Japan, December 15-17 , pp.367-370, 2003.

[6] XILINX Inc. (2002, July). *Virtex–E 1.8V Field Programmable Gate Arrays Data Sheet (DS022-1 v2.3)*. [Online]. Available: http://www.xilinx.co.jp/bvdocs/publications/ds022.pdf

The Eleventh International Symposium on Artificial Life and Robotics 2006 (AROB 11th'06),
B-con Plaza, Beppu, Oita, Japan, January 23-25, 2006

A robot semantic recognition using support vector machine

Hung-Chuan, Lai, Chia-Te Chou, Shi-Jinn Horng

Dept. of Computer Sci.&Info.Eng., National Twaiwan University of Science and Technology; Taiwan Information security Center (TWISC)
D9115002@mail.ntust.edu.tw
#43,Sec.4,Keelung Rd.,Taipei,106,Taiwan,R.O.C

Gwo-Cheng Chao

Graduate Institute of Networking and Multimedia
National Taiwan Univ., Taipei, Taiwan

Abstract

Due to the development of the speech recognition which leads to various biometric applications, this field of research attracts a lot of attentions. In this paper, we use the Mel-Frequency Cepstrum Coefficients as the speaker's feature vectors and support vector machine as the training model, then the recognized speech is used to control the behavior of the robot.

The robot will be activated by the specified action which trained by speaker's speech, in other words, we need to know the content of the speech in advance, for example stand up, sit down, up, down, turn left, turn right and so on. In the experiment we should transform our speech from analog signal to digital data, we use Mel-Frequency Cepstrum Coefficients as our feature vectors, and use support vector machine as our training model. The speech is trained by a computer and then stored in the ROM of DM642 first, During testing, the test speech will go through the microphone of DM642 and A/D converter, and then the features vectors of it is extracted. Then we compare it to the speaker's model stored in the ROM, if it is successful, we will send the signal of the result to the control center of the robot by RS232 and the robot will perform the action. The better equal error rate of the voice, the less wrong action of the robot. In our experiment, the equal error rate is 0.5%, it is very effective.

1. Introduction

With the progress of the times, we have different robots help us to do many things in our daily life. Some robots help us with our housework, some robots are used to help the military, and some robots are used in the medicine [4]. They can not only save our energy, but to prevent people from some injury. In this thesis, we use speech technique to analyze speech data, so that the robots will be able to extract from a certain speaker's speech. Moreover, the robots will be capable of identifying the identity of the commander and understanding the command. By matching the sentence from the speaker and the action, the robot will follow the legal speaker's command.

We use the most popular learning machine—Support Vector Machine (SVM) to train a model. Due to the characteristics of SVM that it's easy to train and it can identify the speakers accurately and fast, we can take the speech features of a small group of people as the sample to process the training, and avoid the robots following other's commands. Furthermore, the robots will be able to understand legal commands and to work properly and efficiently.

2. Support Vector Machine

2.1 Optimal Separating Hyperplane

SVM is a method of machine learning, and is used in pattern classification and regression extensively. Because SVM can decrease training error (or called empirical risk) and testing error (or called risk) at the same time, SVM becomes the most popular algorithm in machine learning. SVM was built by Vapnik [6][7]. The simple binary classification problem is showed as follows: Given training set $S=\{(x_i,y_i)\}$, samples in the set are $x_i \in IR^d$, which belong to one of the two classes labeled as $y_i \in \{-1,+1\}$. The goal is to establish the equation of a hyperplane that divides S completely (no misclassification), this means that we can find some hyperplane so that all positive examples are on one side of the hyperplane, while all negative examples lie on the other side. This idea is illustrated at Fig.1. If we can obtain largest margin in separating two classes (see Fig. 1), then we can decrease the test errors (risks). Due to the reason there might be not only one hyperplane which can be used to separate two classes, with the idea of margin above, Vapnik and Chervonenkis describe an Optimal Hyperplane (OH), which means the optimal hyperplane can separate two classes and have the largest margin.

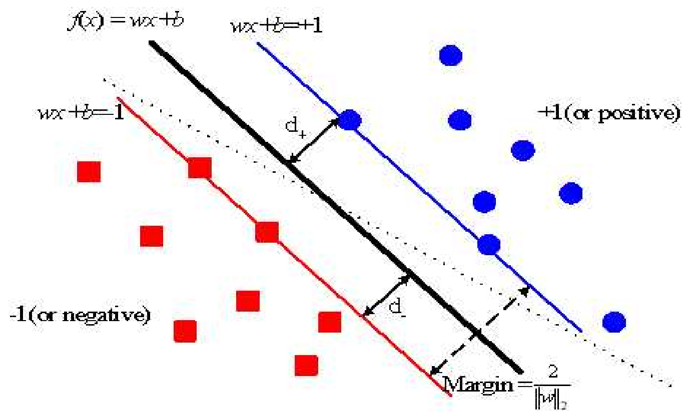

Fig. 1 Optimal hyperplane and margin

It can be probed that in this case the linear classifier that solve the problem is:

$$f(\mathbf{x}) = \mathrm{sgn}\{\sum_{i=1}^{l} \alpha_i y_i \mathbf{x}^T \mathbf{x}_i + b\} \qquad (1)$$

where is the solve of next equation

$$\text{Minimize} \qquad W(\mathbf{a}) = -\mathbf{a}^T\mathbf{l} + \frac{1}{2}\mathbf{a}^T\mathbf{Q}\mathbf{a} \qquad (2)$$

$$\text{Subject to} \qquad \mathbf{a}^T y = 0$$

$$0 \leqq \mathbf{a} \leqq \mathrm{Cl}$$

Where $(\mathbf{a})_i = \alpha_i$, $(\mathbf{l})_i = 1$, $(\mathbf{Q})_{ij} = y_i y_j \mathbf{x}_i{}^T \mathbf{x}_j$. It can be proved that there are only a few are not equal to 0, and the corresponding samples are support vectors. So the sum in Eq. (1) operates only on support vectors. B is the threshold value of classification, and can be calculated by and one of the support vectors.

2.2 Kernel Function

In real occasions, linear classifiers are not suitable, because these problems may have inherently nonlinear structures. An appealing property of SVMs is that they can be easily transformed into nonlinear learners by the kernel technique. This technique maps input data into a higher-dimensional space and constructs a separating hyperplane there. The higher dimensional space is called the feature space, as opposed to the input space to which input data belongs. In the dual problem, calculation of either the optimal function Eq. (2) or the classification function Eq. (1) involves only the inner product $(x_i \bullet y_i)$ of training samples. So only the inner production is needed for transformation to the high dimension space, which is implemented by the functions in the low dimension space, without knowing the form of transformation. In order not to directly calculate the inner product $(x_i \bullet y_i)$, we use the following connotative kernel function $k(x_i, y_i) = (x_i \bullet y_i)$ instead. By using kernel function to calculate data's inner product value in feature space, we do not have to project data into feature space. In this case, the corresponding classification function changes to

$$f(\mathbf{x}) = \mathrm{sgn}\{\sum_{i=1}^{l} \alpha_i y_i K(x \bullet x_i) + b\} \qquad (3)$$

This is the SVM.

To summarize up, the SVM first non-linearly transforms from low dimension space to a high dimension space by inner probuction, then finds the OH in this space.

Different kernel functions form different SVM algorithm. Here are three kind of kernel function that are often used:

- Polynomial: $K(xi, xj) = (\gamma x_i^T x_j + r)^d$, $\gamma > 0$.
- Radial basis function (RBF): $K(x_i, x_j) = \exp(-\gamma\|xi - x_j\|^2)$, $\gamma > 0$.
- Sigmoid: $K(xi, xj) = \tanh(\gamma x_i^T x_j + r)$ where γ, r, and d are kernel parameters.

Here, we use the RBF kernel function as our method.

3. System Design

Two important components contribute to this system. The first components is the speech based verification system and the second component send the signal to control the robot's behavior. These two components are described below.

3.1 Speech Utterance Verification System

The system includes three important stages: preprocess, feature extraction and pattern comparison. The preprocess stage aims to remove silent parts from the raw audio signal, as this part does not convey speaker dependent information. Then in order to deal with the channel distortion or convolution noise that is introduced by a microphone, the zero'th order cepstral coefficients are discarded and the remaining coefficients are appended with delta feature coefficients [5]. The cleaned audio signal is converted to 12^{th} order Mel-frequency cepstrum coefficients (MFCC) [3], complemented by their first and second derivatives, for a total of 36coeffiecients.

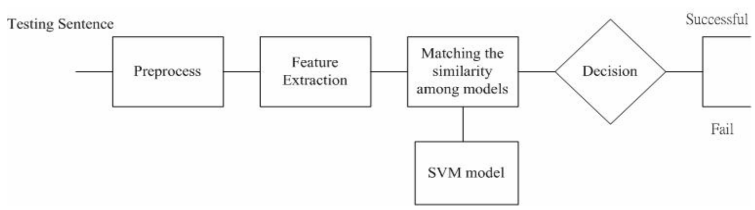

Fig. 2 the flow of the speaker identification

Mel-frequency cepstrum coefficients are defined according to the susceptibility of people's ears. Psychophysical studies have shown that human perception of the frequency contents of sounds for speech signals does not follow a linear scale. The Logarithmic waveform appears in order to catch the important features in voice syllables when the voice is in high frequency. If the voice expresses with Mel-frequency scale, it is a linear frequency space under 1000Hz, above 1000Hz it is a logarithmic space. Its analysis procedure is shown in Fig. 3, the operations of all parts are listed as follows.

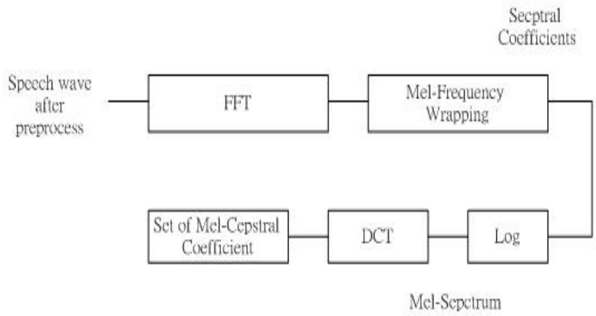

Fig. 3 MFCC feature parameters extraction procedure

Therefore we can use the following approximate formula to compute the mels for a given frequency f in Hz:

$$Mel(f)=2595*log10(1+f/700) \quad (4)$$

The last step is to transform Log Mel Spectrum into the time domain, which means we can receive mel-frequency cepstrum coefficients. After transforming the speech signal spectrum into cepstrum, it can describe the Local Spectral Properties of the frame completely.

Because of mel-frequency coefficients being a real number, so we use the Discrete Cosine Transform (DCT) to transform it into time domain. The formula is as follow:

$$C(k)=\sum_{m=1}^{M}\log\{|Y(m)|\}\cos\{k(m-\frac{1}{2})\frac{\pi}{M}\},\ k=1,2,\ldots 12 \quad (5)$$

We take 12 orders Mel-Frequency Cepstrum Coefficients as feature coefficients. Coefficient of the Zeroth Order is the average logarithm energy of frames. It carries less speech information which can be omitted [2].

3.2 System Hardware Architecture

The speech identification algorithm is preceded by TI-DM642 emulation board in our system, and we have already established various kinds of actions with corresponding sentence within the robot. After identifying the sentences, we will send the signal of the result to the control center of the robot by RS232 and the robot will perform the action. In this paper, we use this idea of hardware and software co-design to design this system, using DSP to execute FFT, triangle filter, and DCT program, and design SVM part into hardware.

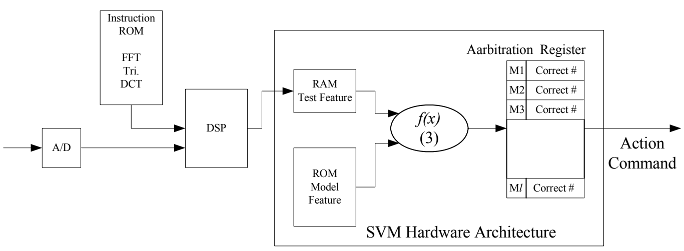

Fig.4 System Hardware Architecture

SVM hardware architecture is shown in Fig. 4. The speech models are trained first and then stored in the ROM. After converting the testing speech through A/D converter, FFT, triangle filter, and DCT, testing features would be generated and be stored in RAM. Next, SVM hardware substitute the testing features and the speech models which has been trained into $f(\mathbf{x}) = \mathrm{sgn}\{\sum_{i=1}^{l} \alpha_i y_i K(x \cdot x_i)+b\}$. Then, the result will be outputted into Arbitration Register. There are two columns in Arbitration Register. One is Mn(boolean) which represents if the testing speech and the original nth sentence are the same. Another is the correct number standing for a threshold value. We call it is a successful matching if Mn is not less than the number. If there's only one true value in Mn, the testing speech will be presumed as the original sentences. If there are more than one true value, the control unit will check the correct numbers and take the testing speech with the largest as the original sentences.

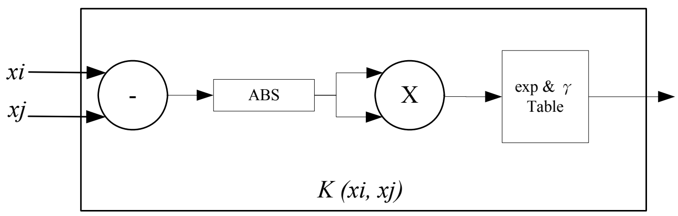

Fig.5 $K(x_i, x_j)$ Hardware Architecture

Fig.5 is the hardware architecture of $K(x_i, x_j) = \exp(-\gamma\|x_i - x_j\|^2)$,because of γ is a constant, we use the method of Table to design the hardware of exp and γ .

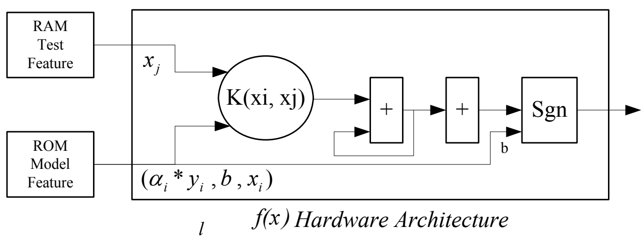

Fig. 6 $f(\mathbf{x}) = \mathrm{sgn}\{\sum_{i=1}^{l} \alpha_i y_i K(x \cdot x_i)+b\}$ Hardware Architecture

4. Result

In our system identification test, the correction rate of SVM is 99.67%. In speaker verification test, the performance was measured in terms of the Detection Error Tradeoff (DET) curve [1]. Fig.7 shows the results of speaker verification system based on SVM. The DET curve shows that the Equal Error Rate (EER) for SVM is 0.5%

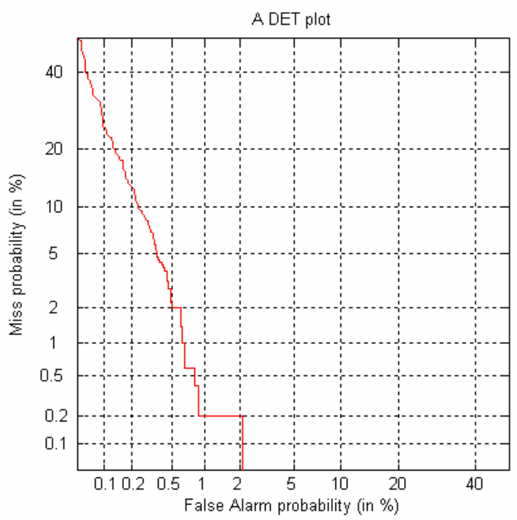

Fig. 7 DET curve of speaker verification

5. Conclusion

The advantage of our system is that our/the robot only follows the instructions from the correct user. Anyone who tries to command the robot should register first or the robot will reject his request. The disadvantage is that we need to connect a microphone to the robot. In the future, we can combine the image processing technology and it will help us do housework, like pick the newspapers up, sweep the floor and so on.

Reference

[1] Alvin M., George D., Terri K. etal (1997). The DET curve in assessment of detection task performance. Proceedings of Eurospeech, 1997pp. 1895-1898

[2] Douglas AR (1995), "Robust Text-Independent Speaker Identification Using Gaussian Mixture Speaker Models," IEEE Trans. on Speech and Audio Processing, Vol. 3, No. 1, Jan. 1995, pp.72-83.

[3] Molla KI, Hirose, K (2004), "On the effectiveness of MFCCs and their statistical distribution properties in speaker identification," Virtual Environments, Human-Computer Interfaces and Measurement Systems, 2004. (VECIMS). 2004 IEEE Symposium on 12-14 July 2004 pp.136-141

[4] Murphy RR, Riddle D, Rasmussen E (2004), "Robot and Human Interactive Communication," 2004. ROMAN 2004. 13th IEEE International Workshop on 20-22 Sept. 2004 pps.301-306

[5] Rabiner L, juang BH (1993), Fundamentals of speech recognition. United State: Prentice-Hall International, Inc

[6] Thomas E, Samuel K, Hong-Goo K etal (2005), "An information-theoretic perspective on feature selection in speaker recognition," Signal Processing Letters, IEEE Vol.12, Issue 7, July 2005 pp.500-503

[7] Vapnik, VN (1999), "An overview of statistical learning theory. Neural Networks," IEEE Transactions on Vol. 10, Issue 5, Sept. 1999 pp.988-999

The Eleventh International Symposium on Artificial Life and Robotics 2006 (AROB 11th'06),
B-con Plaza, Beppu, Oita, Japan, January 23-25, 2006

Flowering analysis based on image segmentation

Hiroko Kamikokuryo Masahiro Yokomichi
University of Miyazaki
1-1, GakuenKibanadaiNishi, Miyazaki, Japan
yokomich@cs.miyazaki-u.ac.jp

Abstract

The analysis of flowering situation by means of human being is very ambiguous because of individual variations. This paper proposes an approach for expressing the flowering situation numerically by means of image segmentation. It has been pointed out by several researchers that the segmentation of the region of petals from natural image is difficult. In this paper, we consider the case where the flower has tubular flowers. In such case, the tubular flowers must be surrounded by petals, so this rule can be used as a domain-specific knowledge. In this paper, it is shown that the task of extraction of the petals becomes easily by natural image experiments.

1 Introduction

At the present time, the flowering situation is analyzed by human being, which is not accurate because of individual variations. For example, in Japan, the situation that "cherry blossom are in full bloom" is defined as "80 percents of all flowers are in bloom (not necessary in full bloom).[1]" However, in practice, it is not easy for human beings to check this condition exactly. Therefore, certain computer vision-based approach is needed.

Recently, many authors have studied the image processing for flower images. In order to analyze the flowering situations from image, it is needed to extract the region of each flower correctly. In the case where natural images are used, the flowers are seen with various sizes and shapes. Furthermore, the background colors are not uniform. Thus, simple template matching cannot be applied. For this problem, several researchers have proposed the use of the domain-knowledge about the colors of each flower [2], [3] and [4]. Using the domain-knowledge, the regions of flowers can be extracted properly. However, each flower cannot be distinguished if several flowers are overlapping. In this case, the outline of the flower that hides another one has weak edge. Thus several flowers form single region so that we cannot estimate the position and the shape of each flower properly. We should note that, this case is also difficult one even if we use the pattern matching-based region extraction methods.

In this paper we restrict the species of the flowers to those having central tubular flower (CTF, for short). For such species, CTF's can be seen separately even if the petals are overlapping. Therefore, by extracting CTF at first, we can extract the region of each flower at least partially.
We describe the background removal, flower region segmentation, and an estimation of a position of an individual flower in Chapter 2, describe an individual flower and the total analysis method of a tree in Chapter 3, and describe an experiment method in Chapter 4.

2 Preprocessing

In this section, the elimination of the background, the extraction of the region of flowers, and the estimation of the position of each flower is explained.

2.1 Elimination of the background

In the natural images, the colors of flowers, leafs, and backgrounds are not unique. So the extraction of the domain of the flowers by certain threshold value is very difficult. However, it is known that the colors of flowers are limited to some colors. This can be used as the domain-specific knowledge [2] for the extraction of the domain of flowers. The colors of the flowers are limited to red, blue, yellow, white, orange, pink, and purple. On the other hand, there are few flowers whose colors are black, gray, brown, and green. Actually, on this earth, ratio of a color of a flower of the natural world, 33% are white, 28% are yellow, 20% are red, and purple plus blue is 17%. These other colors are 2%. On the flower image, black and gray pixel are region of almost shadow, and a brown pixel is region of such as a shadow, a branch, and soil. Therefore, without the loss of gene racy, we can consider these colors by an expert skill method as background colors.

According to this definition, we remove a background by color segmentation with threshold value (See Fig. 1).

Fig. 1 Example of background elimination (left: original image, right: processed image)

2.2 Searches for CTF

Even if we can eliminate the background regions by the method described above, we cannot distinguish each flower. This is because there may be some flowers that are hided by other ones. In such case, the contours of such flowers that are overlapped have weak edges, so the edge detection-based contour extraction methods do not work well.

In this paper, we restrict the class of the flowers such as *cosmos* and *sunflower* having CTF. For such flowers, even if the petals are overlapped, CTF's are not. Therefore, if we can extract CTF's from each flower region, we can estimate the position of each flower. Conversely, we can expect that any non-background regions that contain no CTF's are not the regions of flowers such as noise or other objects. The result of the searching CTF for the image shown in the previous section is depicted in Fig. 2.

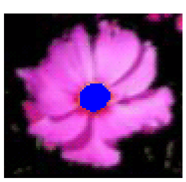

Fig. 2 Example of searched CTF

2.3 Flower region extraction

Because we were able to grasp an individual flower position, we extract an individual flower region. And we extract an contour with an contour extraction filter. But we cannot extract an contour of a flower piled up only by this processing, because petal is few changes of the density. Therefore we demand an approximate petal region and pull a boundary line.

2.3.1 Clustering in the color space

In order to eliminate the non-flower region, we use k-means clustering method on color space. In the following, we assume that the range of the rate of the radius of the CTF and that of the flower is already known, that is,

$$T_{\max} := \max\{R/r\}$$

$$T_{\min} := \min\{R/r\}$$

are known, where R denotes the radius of the flower and r denotes that of CTF. We note that this is not so unrealistic assumption if the spacies is already known. In this case, for each CTF, the region of its petal must be inside of the circle of radius $rT_{\max}$ whose center is that of the CTF. For all pixels in the circle, clustering is yielded in color space.

If we use the k-means clustering, the choice of the number of clusters is very important. The number of the clusters should be determined according to

- The number of the colors the flower has;
- How much does the color of flowers change when the flower is shadowed.

After clustering, pixels whose colors are far from the center of each cluster can be considered as the part of other objects.

Fig.3 Example of extracted flower region

Fig. 3 shows the result of the clustering of the colors in the non-background region for Fig. 2. We can see that the non-flower regions are removed properly.

2.3.2 Extraction of the contour

If each flower is seen separately, the region of it is a connected region with similar color which contains single corresponding central tubular flower. Thus it can be extracted by smoothing and edge detection. On the other hand, if overlap occurs, multiple CTF's are included in single region. Furthermore, the outline in the overlapping region has weak edge, thus extracting it is very difficult (See Fig. 4).

. In this paper, the main objective is to analyze the flowering situation rather than the extracting the shape of each flower completely. Thus It is sufficient if we can estimate R/r for each flower. Before explaining the estimation scheme, we assume that there are no central tubular flowers that are completely surrounded by other flowers. If this assumption is satisfied, for each central tubular flower, at least a part of the outlines is seen as edge whose distance to the central tubular flower ranges in $[rT_{\min} : rT_{\max}]$.

Fig. 4 Overlapping flowers (left: original image, right: extracted outlines)

Suppose that a CTF is located at (x_0, y_0) and its maximum radius is $r_0 > 0$. For each angle $0 \le \theta < 2\pi$, search the boundary of the corresponding region of petal on the line segment

$$x = x_0 + t\cos\theta$$
$$y = y_0 + t\sin\theta,\ r_0 T_{\min} \le t \le r_0 T_{\max}.$$

If there is a boundary pixel, then it is the boundary of the petal. On the other hand, the flower and some other flower overlap in this direction. About all directions which has

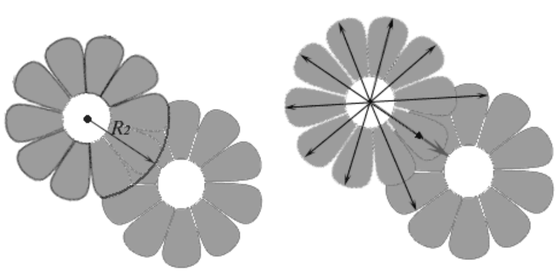

Fig. 5 Searching the outline of each flower in the overlapping case.

boundary, the mean value of R is computed and it is the estimate (See Fig. 5).

3. Flowering analysis

One simple approach to analyze the flowering situation from image is to analyze the area of the region of background (denoted as S_{bg}) and that of the flowers (denoted as S_{fl}). If the flowering progresses, the ratio S_{fl}/S_{bg} also increases. However, the correlation of these two values depends on each image, and when the flowering is near the full bloom, this ratio may saturates. Thus it may be difficult to analyze the flowering situation by this method.

On the other hand, if the flowering progresses, the value R/r also increases. Thus, we can analyze the flowering situation by analyzing the distribution of R/r for all flowers in the input image. The relationship between this ratio and the flowering situation does not depend on each image, thus we expect that we can estimate the flowering situation by this ratio precisely.

4. Experimental results

We prepared four natural images of cosmos (See Fig. 6). In Fig. 6a, single flower is seen and it is seen clearly. In Fig. 6b, single flower is seen too, but, not clearly. In Fig. 6c, we can see three flowers are seen and they overlap. In Fig. 6d, many flowers are seen and some of them are overlapping. In applying the k-means clustering method described in the section 2.3.1, the number of the clusters is set to 3. This is because we think that single flower is considered to be seen with three colors that are its original color, shadow and the color of the other flowers petal.

We show a result of search for CTF's and corresponding flower regions for Fig. 7. The percentage in the index of each image means how much flowers are detected correctly. Only circular template matching is incompetent as search for CTF's. In fact, ambiguous regions with orange color in Fig. 6b are detected. However, we were able to judge that they are not flower region because they have no CTF's.
When a flower crowds like Fig. 6d, extraction of CTF's is still difficult. In addition, it is inconvenient for a search when a stem and a leaf interrupted the flower. We observed that some flowers are detected smaller. This affects the precision of the extraction of flower region.

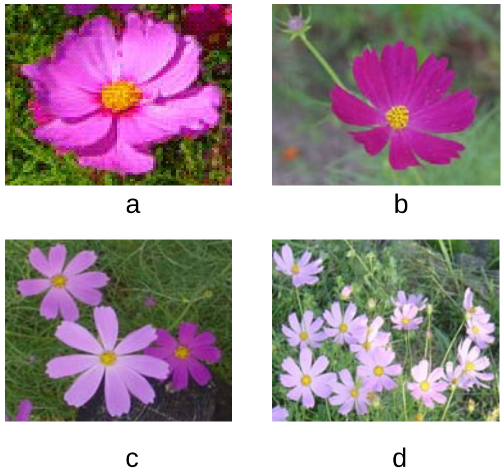

Fig. 6 Input images

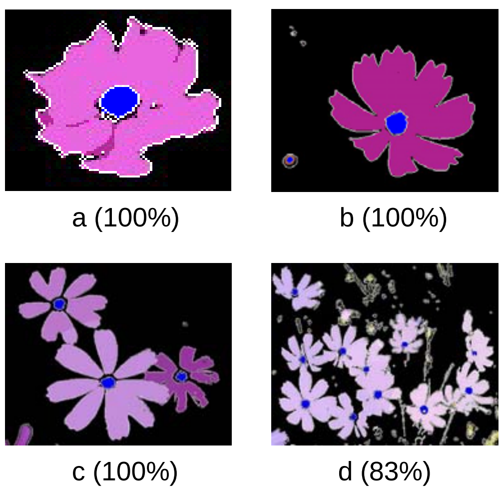

Fig. 7 Experiment result

5. Conclusion

In this paper, we showed a preprocessing method for flowering analysis when we use a natural flower image for flowers that have CTF. We were able to extract a flower region from an input image by an experiment. In addition, we were able to grasp a position of an individual flower. However, extraction of a bud is necessary if we consider it to be "flowering = a bud opens" as described in Chapter 1. We thought about only a species of flowers that have CTF. It is difficult to grasp a position of an non-outstanding tubular flower. However, we may do grasp of a position if we detect a bud from observation by an animation image. And, it is thought that analysis precision of flowering improves by using an animation.

References

[1] "Japan Meteorological Agency" http://www.jma.go.jp/jma/index.html

[2] Hong.A, Chen.G, "A flower image retrieval method based on ROI feature", J Zhejiang Univ SCI 2004 5 (7):764-772

[3] H.Takeichi, Y.Takeuchi, "Flower Information Retrieval Using Picture", IEICE Vol.102 No.707 PRMU2002-242, (2003-3, In Japanese)

[4] T.Saitoh, T.Kaneko, "Automatic Recognition of Wild Flowers", IEICE D-II Vol.J84 No.7 P1419-1429,(2001, In Japanese)

Recognition of Word Expressed by Sign Language Using Thermal Image Processing

Y.Yamagichi[1], Y.Yoshitomi[2] and H.Fushimi[3]

1:KKC Information System Corp.,369 Minamitsuji-cho Kamigyo-ku, Kyoto, 602-8466, JAPAN

2:Dept. of Environmental Information, Fac. of Human Environment, Kyoto Prefectural University,
1-5 Nakaragi-cho Shimogamo Sakyo-ku Kyoto 606-8522 JAPAN, E-mail:yoshitomi@kpu.ac.jp

3:NTT DATA SANYO System Corp,2-5-5 Keihanhondouri Moriguchi, Osaka, 570-8686, JAPAN

Abstract

A basic method for recognizing sign language has been developed with thermal image processing. In this method, the hand-traces of word expressed by Japanese sign language are inputted into computer as sequential coordinates with thermal image processing, then the word is recognized through finding out the most similar hand-traces in the database to that from the word. The 47 Japanese words expressed by sign language were recognized with 71% accuracy.

Keywords: Japanese sign language recognition, thermal image, image processing, hand tracing

1 Introduction

There have already been several researches on sign-language recognition. However, in these researches, some special apparatus such as data-glove has been used for inputting signal of sign language into a computer. For preparing system of sign-language recognition, hand tracing has been tackled with skin color detection on visible-ray image[1].

We have started a new approach for aiming sign-language recognition with skin region detection on infrared-ray image [2, 3, 4]. The principle of thermal image generation with infrared-ray comes from well-known law by Stefan and Boltzmann, which is expressed as $W = \epsilon \cdot \sigma \cdot T^4$, where W is radiant emittance (W/cm^2), ϵ is emissivity, σ is Stefan-Boltzmann constant, T is Temperature (K). For human skin, ϵ is estimated at 0.98 to 0.99 [5]. In this study, however, the approximate value of 1 is used as ϵ for human skin. The values of ϵ for almost all substances except human skin are lower than that for human skin[5]. Accordingly, human skin is easily extracted in the scene having its circumstances whose temperature are lower than that of human skin, when the range of skin temperature is selected for producing the thermal image, using the value of 1 for ϵ[6].

In our researches, hands have been detected as parts having human temperature. In this paper, our approach to on-line sign-language recognition with thermal image processing is open and then we discuss the performance of our method.

2 Hand tracing method

An example of input image is shown in Figure 1. The flowchart for tracing hand in performing sign language is shown in Figure 2. In this section, the detail procedure is explained.

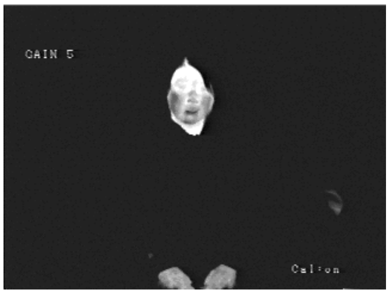

Figure 1: Input image.

2.1 Thermal image generation

Under the condition that emissivity is set as 1, thermal images extracting regions of human skin are produced by a thermal video system (Nikon LARD-3ASH) with infrared rays and these images are recorded on 8-mm-videotape. The detected temperature range is 302.3 to 306.7 K. Then, they are inputted into computer with an 8-mm-video camera(SONY Handycam CCD-TRV86 NTSC) and a video-signal input-board (SYBERTEK CT-3000A). The input-images in a computer have a spatial resolution of 320×240 pixels and a gray level of 256.

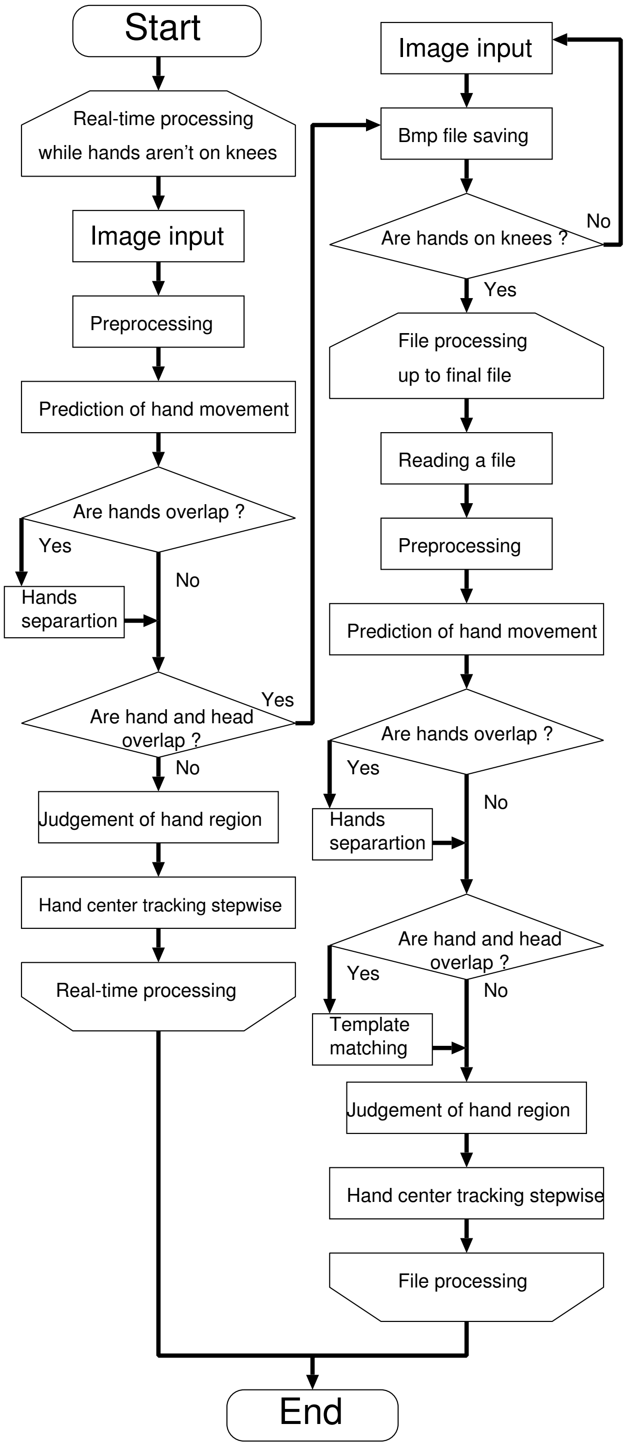

Figure 2: Flowchart for tracing hands in performing sign language.

2.2 Judgment of beginning and final frames

For finding out easily the beginning of sign language on a video film, a subject wearing a jacket with long sleeves sits on the seat and puts its left and right hands on its corresponding knees before and after performing sign language. After segmentation of input image, the area having the value of 1 on the specific region on subject's knee-parts is measured. Then, at the frame where the area firstly becomes less than the value of threshold, which has been experimentally decided beforehand, the forthcoming processing for tracing hands is started(Figure 3). After processing several frames, at the frame where the area on the specific region on subject's knee-parts becomes larger than the value of threshold, the processing for tracing hands is terminated.

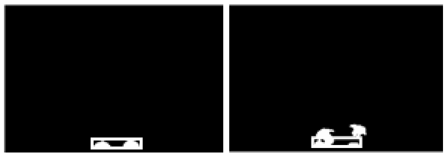

Figure 3: Recognition of start of sign language by measuring number of pixel. Left: more than threshold, Right: less than threshold (judged as start).

2.3 Preprocessing

After the judgment that the movement of hand for a sign language has started, the gray-level of meaningless parts that are characters and relatively hot regions on the subject's knees on which the hands stayed for a while is set as 0. Then, the averaging of gray level on local area is performed for erasing noise and the segmentation with a constant threshold is performed, followed by easements of small regions.

2.4 Prediction of hand movement

The coordinate of center of gravity for each hand at $t + \Delta t$ is predicted with Taylor series up to second order, where the first order differential coefficient of coordinate and the second one are approximately obtained in the usual way with the coordinates at $t-2\Delta t$, $t - \Delta t$ and t. However, this prediction cannot be used at the first and second frames from the beginning of sign language. Therefore, at these two frames, the region whose x coordinate of center of gravity is smaller between the regions having the second or third largest area on the segmented image at the frame is judged as a right hand-region. On the other hand, at these two frames, another region having the second or third largest area on the segmented image at $t+\Delta t$ is judged as a left hand-region.

2.5 Judgment of hand region

The rectangular partial-image circumscribing the left hand region at t is moved so that the coordinate of center of gravity for left hand region corresponds to the predicted one at $t+\Delta t$, and the moved rectangular partial-image is compared with the image at $t+\Delta t$. For the right hand region, the same procedure is performed. Then, the situation of hand region at $t+\Delta t$ is categorized into the following three cases; (a) the left and/or right hand-region overlaps face region, (b) the left and right hand-regions overlap each other, (c) the two hand-regions are isolated.

When the predicted left and/or right hand-region at $t+\Delta t$ overlaps face-region recognized as the largest region at $t+\Delta t$, the situation is judged as (a). If not (a), the next process is as follows. When the region whose coordinate of center of gravity is the nearest from that of the predicted left hand-region at $t+\Delta t$ is the same as that of the nearest from the predicted right hand-region, the situation is judged as (b). If neither (a) nor (b), the situation is judged as (c).

In the case of (a), the template matching mentioned later is performed. In the case of (b), the shrink of region mentioned later is performed.

In the case of (c), the region whose coordinate of center of gravity is the nearest from that of predicted left hand-region among some regions on the segmented image at $t+\Delta t$ is judged as the left hand-region at $t+\Delta t$. The right hand region at $t+\Delta t$ is also found out in the same manner as that for left hand-region.

In the case of (a) where the left and/or right hand-region overlaps face region, the hand region at $t+\Delta t$ is found out with the usual template matching. At first, the rectangular partial-image circumscribing left hand-region at t is set as the template. Then, the rectangle region circumscribing the left or right hand-region at t and the face region at $t+\Delta t$ is used as search area for template matching(Figure 4). In Figure 4, the smallest rectangle denotes a hand-region at t, while the second largest one denotes a face-region at $t+\Delta t$.

It takes much more time for tracing hands through a sign language with template matching, compared with that without template matching. Therefore, in the case of (a), it is difficult to perform an on-line processing to trace hands through a sign language. Accordingly, the frames after starting template matching are stored as BMP files, and the processing for tracing hands until the sign language is finished is performed just after storing the final frame of sign language.

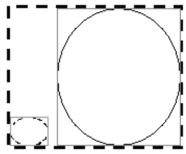

Figure 4: Region for template matching.

In the case of (b) where the left and right hand-regions overlap each other, the shrink on the segmented image is preformed until the region is divided into two regions (Figure 5). After dividing the region, the left and right hand-regions are judged in the same manner as case (c).

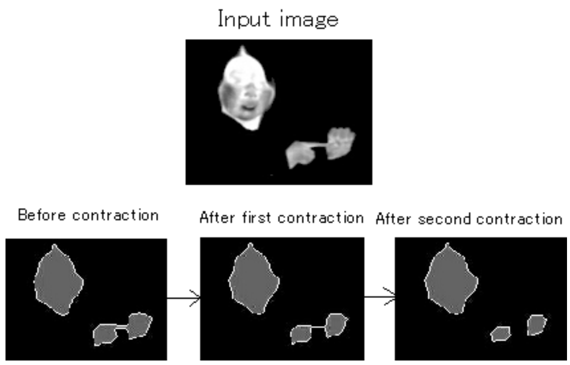

Figure 5: Separation of connected hand-regions by contraction.

3 Sign language word recognition

The training data that consists of successful hand tracing for each sign language are used for recognizing the testing sign language. The time for sign language used as training data is transformed to equal it to that of a testing sign language in calculating the sum of each difference between a coordinate of testing sign language and that of training data. In this process, the coordinate of training data at the transformed time is calculated with inside linear interpolation using two coordinates at the nearest and second nearest transformed time to the time of the testing sign language. The testing sign language is recognized as the sign language, which has the least sum of difference to coordinate of testing data among all training sign languages.

4 Experiments and discussions

In this experiment, a personal computer, DELL OPTIPLEX GX260 (CPU : Pentium 2.53GHz, main memory : 512 MB, OS : Windows XP) , was used. For programming, Microsoft Visual C++ 6.0 and WIN32 API were used.

At first, 71 sign languages were selected for preparing training data, according to the following necessary conditions; noun including neither meaningful movement on head nor that in the direction to listener or camera, big motion observed by listener or camera, no cross of hands, no need of initial pose.

These sign languages were three times stored on 8-mm video. The first series of theses sign languages were used for making training data that consisted of successful hand tracing for each sign language. The second and third sign-languages corresponding to the first ones whose hand tracings were successfully performed by our method were used for making testing data. The testing sign language was recognized with our method.

The speed of image input was 14 to 15 fps for on-line processing, and 25 to 27 fps in case of starting template matching and performing the forthcoming processing after inputting all input-frames of the sign language.

The hand-tracing of 47 sign-languages among the tried 71 ones was successful. For these 47 sign-languages, the time sequential data on traces of left and right hands were obtained and used as training data. For the second and third series of sign-languages, the 47 video-images of sign-languages, which had the same meanings as 47 ones of training data respectively, were used for evaluation of our method.

It took 58 to 64 msec per frame on the on-line processing of our method. To trace hands for the first series of sign-languages, input of image was three times started from the different time of the 8-mm video. It depends on the start-time of image input whether the hand-tracing was successfully performed. While the number of sign language was 44 in case that hand-tracing was successfully performed more than twice, that was 47 in case that more than once.

Under the criterion that the hand tracing was called as successful one when it was successfully performed more than twice, in the case of (a) where the left and/or right hand-region overlaps face region, the ratio of successful hand tracing was 23/47, in the case of (b) where the left and right hand-regions overlap each other, it was 3/20 and in all cases that was 44/71. In addition, it was 21/24 on the on-line processing and it was 23/47 with template matching. The main reasons of poor hand tracing were as follows; (1) overlap of both hands and head (30 %), (2) poor separation of both hands (26 %), (3) poor template matching for searching hand on the head region (22 %), (4) fast right-hand movement in the left direction just after starting the sign language (11 %), (5) others (11 %).

The raio of right recognition for sign language was 67/94 (71 %). It took 500 to 600 msec per one word to recognize sign language with data of hand-trace obtained by our method.

5 Conclusions

A basic method for recognizing sign language has been developed with thermal image processing. The Japanese words expressed by sign language were recognized with good accuracy. To shorten the time for hand-tracing and to overcome some factors causing poor hand-tracing are next targets.

References

[1] Imagawa K, Lu S, Igi S, Matsuo H (1998), Real-time tracking of human hands from a sign-language image sequence in consideration of disappearance by skin regions (in Japanese),*Trans. of IEICE*, Vol.J81-D-II(8), pp.1787-1795.

[2] Inada M, Yoshitomi Y, Tanaka S (2000), Analysis of finger characters in sign language using thermal image processing (in Japanese), *Proc. of 19th SICE Kyushu Branch Annual Conference*, pp.129-132.

[3] Yoshitomi Y, Nagayama S, Sugiyama M (2002), Sign language recognition using thermal image processing (in Japanese), *Information Technology Letters*, Vol.1, pp.191-192.

[4] Yoshitomi Y, Nagayama S, Sugiyama M (2002), Hand trajectory extraction and sign language recognition using thermal image processing (in Japanese), *Technical report of IEICE*, Vol.WIT2002-52, pp.21-26.

[5] Kuno H (1994), Sekigaisen Kougaku (in Japanese), IEICE, Tokyo.

[6] Yoshitomi Y, Kimura S, Hira E, Tomita S (1996), Facial expression recognition using Infrared rays image processing, *Proc. of the Annual Convention IPS Japan*, No.2, pp.339-340.

The Eleventh International Symposium on Artificial Life and Robotics 2006 (AROB 11th'06),
B-con Plaza, Beppu, Oita, Japan, January 23-25, 2006

Hierarchies Based on the Number of Counters or the Space Allowed by Four-Dimensional Multicounter Automata

Makoto SAITO[1], Makoto SAKAMOTO[1], Kouichi IIHOSHI[1], Takao ITO[1], Hiroshi FURUTANI[1], Michio KONO[1], and Katsushi INOUE[2]

[1] Dept. of Computer Science and Systems Engineering, University of Miyazaki, Miyazaki 889-2192, JAPAN
[2] Dept. of Computer Science and Systems Engineering, Yamaguchi University, Ube 755-8611, JAPAN

Abstract

Due to the advances in many application areas such as computer animation, motion image processing, virtual reality systems, robotics, and so forth, it has become increasingly apparent that the study of three-dimensional pattern processing along the time axis has been of crucial importance. Thus, we think that the research of four-dimensional automata as a computational model of three-dimensional pattern processing with the time axis has been meaningful, and we introduced four-dimensional multicounter (= k-counter) automata in [6]. This paper continues the investigation about this model, and shows the hierarchies based on the number of counters or the space allowed by four-dimensional multicounter automata.

Key Words **:** computational complexity, four-dimensional automaton, multicounter, nondeterminism.

1 Introduction and Preliminaries

Inoue et al. [4] introduced a two-dimensional multicounter automaton and investigated its basic properties. Szepietowski also investigated some of its properties [10]. A two-dimensional k-counter automaton M is a two-dimensional finite automaton [1] that has k counters. The action of M is similar to that of the one-dimensional off-line k-counter machine [3], except that the input head of M can move up, down, right, or left on a two-dimensional input tape. In [7], Sakamoto et al. introduced multicounter automata on three-dimensional input tapes.

By the way, during the past about forty years, several automata on two- or three-dimensional tapes have been proposed and many properties of them have been obtained [5,8]. On the other hand, recently, due to the advances in computer animation, motion image processing, and so on, the study of four-dimensional information processing has been of great importance. Thus, we think that the study of four-dimensional automata has been meaningful as the computational model of four-dimensional information processing [9].

In this paper, we introduce and investigate about eight-way four-dimensional multicounter automata as new four-dimensional computational models. An eight-way four-dimensional k-counter automaton (4-kCA), which consists of a finite control, k counters, a read-only four-dimensional input tape, k counter heads, and an input head which can move in eight directions — north, east, south, west, up, down, future or past. In general, when we must think about the algorithm of four-dimensional pattern processing by using the restricted computational resources, if the algorithm is fine in spite of its restricted computational resources, it will be valued highly. It is the same with automata theory. So we next introduce and investigate a seven-way four-dimensional k-counter automaton ($SV4$-kCA) which is a restricted type of 4-kCA. $SV4$-kCA is a 4-kCA whose input head can move in seven directions — north, east, south, west, up, down, or future. In this paper, we let each sidelength of each input tape of these automata be equivalent in order to increase the theoretical interest.

Let Σ be a finite set of symbols. *A four-dimensional tape* over Σ is a four-dimensional rectangular array of elements of Σ. The set of all the four-dimensional tapes over Σ is denoted by $\Sigma^{(4)}$.

Given a tape $x \in \Sigma^{(4)}$, for each $j(1 \leq j \leq 4)$, we let $l_j(x)$ be the length of x along the jth axis. The set of all $x \in \Sigma^{(4)}$ with $l_1(x) = m_1,\ l_2(x) = m_2,\ l_3(x) = m_3$, and $l_4(x) = m_4$ is denoted by $\Sigma^{(m_1,m_2,m_3,m_4)}$. When $1 \leq j_i \leq l_j(x)$ for each $j(1 \leq j \leq 4)$, let $x(i_1, i_2, i_3, i_4)$ denote the symbol in x with coordinates (i_1, i_2, i_3, i_4). Furthermore, we define

$$x[(i_1, i_2, i_3, i_4), (i'_1, i'_2, i'_3, i'_4)],$$

when $1 \leq i_j \leq i'_j \leq l_j(x)$ for each integer $j(1 \leq j \leq 4)$, as the four-dimensional tape y satisfying the following (i) and (ii) :

(i) for each $j(1 \leq j \leq 4)$, $l_j(y) = i'_j - i_j + 1$;

(ii) for each r_1, r_2, r_3, r_4 $(1 \leq r_1 \leq l_1(y), 1 \leq r_2 \leq l_2(y), 1 \leq r_3 \leq l_3(y), 1 \leq r_4 \leq l_4(y))$, $y(r_1, r_2, r_3, r_4) = x(r_1 + i_1 - 1, r_2 + i_2 - 1, r_3 + i_3 - 1, r_4 + i_4 - 1)$.

Four-dimensional tape is the sequence of three-dimensional rectangular arrays along the time axis. By $Cube_x(i)$ $(i \leq 1)$, we denote the ith three-dimensional rectangular array along the time axis in a tape $x \in \Sigma^{(4)}$ which each sidelength is equivalent.

We now introduce a seven- or eight-way four-dimensional multicounter automaton. An *eight-way*

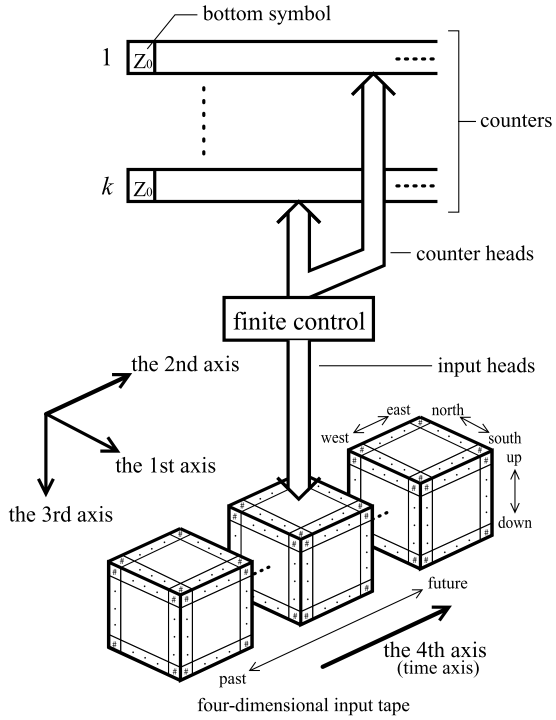

Fig. 1: Four-dimensional k-counter automaton.

four-dimensional k-counter automaton (4-kCA) M, $k \geq 1$, has a read-only four-dimensional input tape surrounded by *boundary symbols* $\sharp$'s and *k counters*. (Of course, M has a *finite control*, an *input head*, and *k counter heads*.) The action of M is similar to that of the two- or three-dimensional multicounter automaton [4, 7, 10], except that the input head of M can move in eight directions — east, west, south, north, up, down, future, or past. That is, when an input tape $x \in \Sigma^{(4)}$ (where Σ is the set of input symbols of M and the boundary symbols $\sharp$'s is not in Σ) is presented to M, M determines the next state of the finite control, the move direction (east, west, south, north, up, down, future, past, or no move) of the input head, and the move direction (right, left, or no move) of each counter head, depending on the present state of the finite control, the symbol read by the input head, and whether or not the contents of each counter is zero (i.e., whether or not each counter head is on the bottom symbol Z_0 of the counter). If the input head falls off the tape x with boundary symbols, M can make no further move. M starts in its initial state, with the input head on position (1,1,1,1) of the tape x, and with the contents of each counter zero (i.e., with each counter on the bottom symbol Z_0 of the counter). We say that M *accepts* the tape x if M eventually halts in a specified state (accepting state) on the bottom boundary symbol $\sharp$ of the input. We denote by $T(M)$ the set of all the four-dimensional tapes accepted by M. A *seven-way four-dimensional k-counter automaton* ($SV4$-kCA) is a 4-kCA whose input head can move in seven directions — east, west, south, north, up, down, or future (see Fig.1).

Let $L(m) : \mathbf{N} \mapsto \mathbf{N}$ (where $\mathbf{N}$ is the set of all the positive integers) be a function with one variable m. A 4-kCA ($SV4$-kCA) M is said to be $L(m)$ *counter-bounded* if for each $m \geq 1$ and each input tape x (accepted by M) with $l_1(x) = l_2(x) = l_3(x) = l_4(x) = m$, the length of each counter of M is bounded by $L(m)$. As usual, we define nondeterministic and deterministic 4-kCA's ($SV4$-kCA's). By $N4$-$kCA(L(m))$ (respectively, $D4$-$kCA(L(m))$, $NSV4$-$kCA(L(m))$, and $DSV4$-$kCA(L(m))$), we denote a nondeterministic 4-kCA (respectively, deterministic 4-kCA, nondeterministic $SV4$-kCA, and deterministic $SV4$-kCA) whose each sidelength of each input tape is equivalent and which is $L(m)$ counter-bounded. Let $\mathcal{L}[N4\text{-}kCA(L(m))] = \{T \mid T = T(M)$ *for some* $N4\text{-}kCA(L(m))$ $M\}$. $\mathcal{L}[N4\text{-}kCA(L(m))]$, $\mathcal{L}[NSV4\text{-}kCA(L(m))]$, and $\mathcal{L}[DSV4\text{-}kCA(L(m))]$ have similar meanings.

2 Hierarchies Based on the Number of Counters or the Space Allowed

This section investigates how the number of counters or the space allowed (of seven-way four-dimensional multicounter automata whose each sidelength of each input tape is equivalent) affects the accepting power.

To do this, we need to consider the following sets. For each $j \geq 1$, let $A(j)$ be the set of all the input tapes $x \in \{0,1\}^{(4)}$ such that :

(a) $l_1(x) = l_2(x) = l_3(x) = l_4(x) \geq j$.

(b) There are exactly j 1's in the first (1-2) plane of the first cube.

(c) All the (1-2) planes from the second to the last in the first cube contain only 0.

(d) All the cubes from the second to the last but one contain only 0.

(e) The last cube is equal to the first.

[Lemma 2.1] *For each $k \geq 2$ and $r \geq 1$, $A(j)$ can be accepted by a $DSV4$-$kCA(m^{2r})$ if $j \leq (k-1)r+1$.*

(Proof) We show how $A(j)$ can be accepted by a $DSV4$-$kCA(m^{2r})$ M if $j=(k-1)r+1$. The case when $j<(k-1)r+1$ can be proved similarly. Suppose that an input tape x with $l_1(x)=l_2(x)=l_3(x)=l_4(x)=m$ is presented to M. First M checks whether x satisfies conditions (a),(b), and (c) above (in the definition of $A(j)$). Let $d(i)$ denote the position of the i-th 1 in the first (1-2) plane of the first cube. Let $d(i)=(d_R(i), d_C(i))$, where $d_R(i)$ is the row number of the poisition of the i-th 1 of the first (1-2) plane of the first cube, and $d_C(i)$ is the column number. All $d(i)$'s, for $1 \leq i \leq j-1=(k-1)r$, are stored in $k-1$ counters in groups of r in each counter. The first r numbers from $d(1)$ to $d(r)$ are stored as

$$\sum_{i=1}^{r}\Big\{d_R(i)(m+1)^{2(r-i)}+d_C(i)(m+1)^{2(r-i)+1}\Big\}$$

in the first counter First M stores $d(1)$ on the first counter, and then, using the k-th counter. M stores $d_R(1)$ and going from one end of the first row to another, multiplies the first counter by $(m+1)$, then adds $d_C(i)$. Next, M multiplies the first counter by $(m+1)$, then adds $d(2)$, multiplies again, and so on. Similarly, for each l $(2 \leq l \leq k-1)$, the r numbers from $d((l-1)r+1)$ to $d(lr)$ are stored in the l-th counter. Then M stores on the k-th counter the position of the j-th 1 and checks whether all cubes from the second to the last but one contain only 0.

M assumes that the cube that contains the first 1 below the first cube is the last cube (M will reject the input if it finds another cube below). Next, M checks whether there are exactly j 1's in the first (1-2) plane of the last cube, and all the planes from the second to the last in the last cube contain only 0. After that, unloading the k-th counter M checks whether the last 1 in the first plane of the last cube stands on the $d(j)$ position and then, using the empty k-th counter, unloads one by one the numbers $d(i)$'s, $1 \leq i \leq j-1$, and checks whether there is 1 in the position $d(i)$ of the first plane. Unloading is done in the following way : If a number $2s(m+1)+d(i)$, with $d(i) \leq m$ is stored on a counter (say the g-th), where $d(i)=(m+1)+d_C(i)$, then M goes from the first cell of the first row to the symbol $\sharp$ standing on the other end, decreasing the g-th counter by 1, comes back to the beginning of the row, after each two steps, and after reaching $\sharp$ it adds 1 to the k-th counter, comes back to the beginning of the row, and repeats the process until the g-th counter is empty. At this moment M stands on the position $x(d_R(i), d_C(i))$ of the first plane and keeps s on the k-th counter. It is obvious that in this way all the numbers $d(i)$'s can be unloaded (in reverse order in which they were loaded) and the positions of all 1's in the first plane checked. $\Box$

[Lemma 2.2] *$A(j)$ cannot be accepted by any $NSV4$-$kCA(m^{2r})$ if $j > kr$.*

(Proof) Suppose that there is an $NSV4$-$kCA(m^{2r})$ M accepting $A(j)$ and $j > kr$. For each $m \geq j$, let

$$A(m,j)=\{x \in A(j) \mid l_1(x)=l_2(x)=l_3(x)=l_4(x)=m\}.$$

Any accepting computation of M reading any $x \in A(m,j)$ has to visit $x(1,1,1,2)$, $x(m,1,1,2)$, $x(1,m,1,2)$, and $x(1,1,m,2)$ in the second cube. Otherwise, if there is an $x \in A(m,j)$ accepted without visiting $x(1,1,1,2)$, then, putting $x(1,1,1,2)=1$, we obtain the tape that is not in $A(j)$ but is accepted by M. Let $conf(x)$ be the set of configurations of M while visiting $x(1,1,1,2)$ in the accepting computations on x. For any two different x, $y \in A(m,j)$, $conf(x) \cap conf(y) = \phi$. Otherwise, replacing the last cube in x by the last cube of y, we obtain the tape that is not in $A(j)$ but is accepted by M.

Clearly, $\quad |A(m,j)| = {}_m\mathrm{C}_j.$

Let $c(m)$ be the number of possible configurations of M while visiting $x(1,1,1,2)$. Then $c(m) \leq sm^{kr}$, where s is the number of states of the finite control. Since $j > kr$, there exists m such that $|A(m,j)| > c(m)$, and there must be two different x, $y \in A(m,j)$ such that $conf(x) \cap conf(y) \neq \phi$. This contradicts the above. $\Box$

We are now ready to prove the following theorems. First we show that for every $r \geq 1$ there exists an infinite hierarchy, with respect to the number of counters, of languages accepted by m^{2r} counter-bounded (deterministic or nondeterministic) seven-way four-dimensional k-counter automata.

[Theorem 2.1] *For each $r \geq 1$, $k \geq 1$, and $X \in \{D, N\}$, $\mathcal{L}[XSV4\text{-}kCA(m^{2r})] \subsetneq \mathcal{L}[XSV4\text{-}(k+1)CA(m^{2r})]$.*

(Proof) From Lemmas 2.1 and 2.2, it follows that for any $r \geq 1$, $k \geq 1$, and $X \in \{D, N\}$,

$$A(kr+1) \in \mathcal{L}[XSV4\text{-}(k+1)CA(m^{2r})]$$
$$\text{and } A(kr+1) \notin \mathcal{L}[XSV4\text{-}kCA(m^{2r})]. \quad \Box$$

Next, we show that for every $k \geq 2$ and $r < k$ there is an infinite hierarchy, with respect to the amount of space allowed, of the powers of nondeterministic seven-way four-dimensional k-counter automata.

[Theorem 2.2] *For each $k \geq 2$ and $r < k$, $\mathcal{L}[NSV4\text{-}kCA(m^{2r})] \subsetneq \mathcal{L}[NSV4\text{-}kCA(m^{2(r+1)})]$.*

(Proof) From Lemma 2.1, we have

$$A((r+1)(k-1)+1) \in \mathcal{L}[NSV4\text{-}kCA(m^{2(r+1)})].$$

On the other hand, if $r < k$, then $(r+1)(k-1)+1 > kr$, and thus, by Lemma 2.2, we have

$$A((r+1)(k-1)+1) \notin \mathcal{L}[NSV4\text{-}kCA(m^{2r})]. \quad \Box$$

We finally show that for each $k \geq 2$ and $r \geq 1$, $\mathcal{L}[DSV4\text{-}kCA(m^{2r})] \subsetneq \mathcal{L}[DSV4\text{-}kCA(m^{2(r+1)})]$. To do this, we consider the following sets. For each $j \geq 1$, let $B(j)$ be the set of all the input tapes $x \in \{0,1\}^{(4)}$ such that :

(a) $l_1(x)=l_2(x)=l_3(x)=l_4(x) \geq j$,

(b) there are exactly j 1's in the first (1-2) plane of the first cube,

(c) there is exactly one 1 in the (1-2) planes from the second to the last of the first cube (thus, there are exactly $j+1$ 1's on the first cube),

(d) all the cubes from the second to the last but one contain only 0, and

(e) the last cube is equal to the first cube.

[Theorem 2.3] *For each* $k \geq 2$ *and* $r \geq 1$, $\mathcal{L}[DSV4\text{-}kCA(m^{2r})] \subsetneq \mathcal{L}[DSV4\text{-}kCA(m^{2(r+1)})]$.

(Proof) For each $j \geq 1$, let $B(j)$ be the set described above. Let $j = (k-1)(r+1)$. By using the same ideas as in the proof of Lemmas 2.1 and 2.2, we can show that $B(j)$ is accepted by $DSV4\text{-}kCA(m^{2(r+1)})$, but not accepted by any $DSV4\text{-}kCA(m^{2r})$. □

[Theorem 2.4]
(1) $\mathcal{L}[DSV4\text{-}1CA(m^3)] \subsetneq \mathcal{L}[DSV4\text{-}1CA(m^4)]$,
(2) $\mathcal{L}[DSV4\text{-}1CA(m^2)] \subsetneq \mathcal{L}[DSV4\text{-}1CA(m^3)]$,
(3) $\mathcal{L}[DSV4\text{-}1CA(m)] \subsetneq \mathcal{L}[DSV4\text{-}1CA(m^2)]$, *and*
(4) $\mathcal{L}[DSV4\text{-}1CA(m^4)] = \mathcal{L}[DSV4\text{-}1CA(L(m))]$ *for any* $L(m) \geq m^4$.

(Proof) First, we prove (1). Let B_1 be the set of all the cubic tapes $x \in \{0,1,2\}^{(4)}$ such that
(1) $l_1(x)=l_2(x)=l_3(x)=l_4(x)\geq 4$,
(2) for one and only one i ($2\leq i\leq m-1$), the i-th cube contains only 2, where $m=l_1(x)=l_2(x)=l_3(x)=l_4(x)$,
(3) $x[(1,1,1,1),(m,m,m,i-1)]$ and $x[(1,1,1,i+1),(m,m,m,m)]$ each contain exactly one 1, and
(4) the Euclidean distance (from $x(1,1,1,1)$) to the position of 1 in $x[(1,1,1,1),(m,m,m,i-1)]$ is equal to the Euclidean distance from the position of $x(1,1,1,i+1)$ to the position of 1 in $x[(1,1,1,i+1),(m,m,m,m)]$.

It is an easy exercise to show that B_1 is accepted by a $DSV4\text{-}1CA(m^4)$. Thus, $B_1\in\mathcal{L}[DSV4\text{-}1CA(m^4)]$.

On the other hand, by using a technique of counting argment, we can show that $B_1 \notin \mathcal{L}[DSV4\text{-}1CA(m^3)]$.

Next, we prove (2). Let B_2 be the set of all the cubic tapes $x \in \{0,1,2\}^{(3)}$ such that
(1) $l_1(x) = l_2(x) = l_3(x) = l_4(x) \geq 3$,
(2) for one and only one i ($2\leq i\leq m-1$), the i-th cube contains only 2, where $m=l_1(x)=l_2(x)=l_3(x)=l_4(x)$,
(3) $x[(1,1,1,1),(m,m,m,i-1)]$ and $x[(1,1,1,i+1),(m,m,m,m)]$ each contain exactly one 1, and
(4) the Euclidean distance (from $x(1,1,1,1)$) to the position of 1 in $x[(1,1,1,1),(m,m,m,i-1)]$ is equal to the Euclidean distance from the position of $x(1,1,1,i+1)$ to the position of 1 in $x[(1,1,1,i+1),(m,m,m,m)]$.
It is easy to see that $B_2 \in \mathcal{L}[DSV4\text{-}1CA(m^3)]$. On the other hand, by using the same idea as in the proof of (1) above, we can easily show that $B_2(m) \notin \mathcal{L}[DSV4\text{-}1CA(m^2)]$. This completes the proof of (2).

Next, we prove (3). Let B_3 be the set of all the cubic tapes $x \in \{0,1\}^{(3)}$ such that
(1) $l_1(x) = l_2(x) = l_3(x) = l_4(x) \geq 3$,
(2) there is exactly one 1 in the first cube,
(3) all the cubes from the second to the last but one contain only 0, and
(4) the last cube is equal to the first.
It is easy to see that $B_3 \in \mathcal{L}[DSV4\text{-}1CA(m^2)]$. On the other hand, by using the same idea as in the proof of (1) above, we can easily show that $B_3(m) \notin \mathcal{L}[DSV4\text{-}1CA(m)]$. This completes the proof of (3).

(4) of the theorem is easily proved by using a standard technique of eliminating a loop. That is, if $DSV4\text{-}1CA$ M enters a loop while moving on a four-dimensional tape, at most $c\cdot|Q|\cdot(m+2)^4\cdot\lceil\log(|Q|\cdot(m+2)^4)\rceil$ cells, for some $c \in \mathbf{R}$, are sufficient for M to use the counter, where Q is a finite set of states, $|A|$ is the cardinality of a set A, and $\lceil x\rceil$ is the smallest integer greater than or equal to x. So M counts the number of move steps of M on the four-dimensional tape by using the counter, and find out, if the number of move steps is greater than $c\cdot|Q|\cdot(m+2)^3\cdot\lceil\log(|Q|\cdot(m+2)^3)\rceil$, that M will enter a loop. It will be obvious that $\mathcal{L}[DSV4\text{-}1CA^c(m^4)] = \mathcal{L}[DSV4\text{-}1CA(L(m))]$ for any $L(m) \geq m^4$. □

3 Conclusion

In this paper, we investigated the accepting powers of counter-bounded seven-way and eight-way four-dimensional multicounter automata. Then, we investigated a relationship between determinism and nondeterminism. In these subjects, we stated only for four-dimensional input tape which each sidelength is equivalent. It will be also interesting to investigate the accepting powers of 'alternating' four-dimensional multicounter automata (see [2] for the concept of 'alternation').

References

[1] M.Blum et al., *IEEE Symp. Switching & Automata Theory* : 155–160 (1967).

[2] A.K.Chandra et al., *J.ACM* 28(1) : 114–133 (1981).

[3] S.A.Greibach, *Theoret. Comput. Sci.* 1 : 269–288 (1976).

[4] K.Inoue et al., *Inform. Sci.* 19 : 1–20 (1979).

[5] K.Inoue et al., *Inform. Sci.* 55 : 99–121 (1991).

[6] M.Saito et al., *AROB2005* : CD-ROM (2005).

[7] M.Sakamoto et al., *IWPIPA1999* : 267–280 (1999).

[8] M.Sakamoto, *Ph.D. Thesis* (1999).

[9] M.Sakamoto et al., *WSEAS Trans. on Comput.* 5(3) : 1651–1656 (2004).

[10] A.Szepietowski, *Inform. Sci.* 55 : 35–47 (1991).

The Eleventh International Symposium on Artificial Life and Robotics 2006 (AROB 11th'06),
B-con Plaza, Beppu, Oita, Japan, January 23-25, 2006

Iterative use of a pair of the Self-organizing Maps looking at data in two different ways

Akira Date
Faculty of Engineering
University of Miyazaki
Miyazaki 889-2192
date@cs.miyazaki-u.ac.jp

Koji Kurata
Faculty of Engineering
University of the Ryukyus
Okinawa 903-0213
kurata@mibai.tec.u-ryukyu.ac.jp

Abstract

This paper describes a model neural network that can find a meaningful structure hidden in high-dimensional data. Suppose there are *n* input vectors, each of which is an *m*-dimensional vector and represents features; A set of inputs is represented as a matrix s_{ji} i 1 n j 1 m. Conventional Self-organizing Maps (SOM) use each $\boldsymbol{s}_i$ as input, and the method such as random-projection is used to convert a set of inputs into much-lower-dimensional vectors when each input is impracticably high-dimensional. We have developed a model which has two independent SOMs looking at data in two different ways, $\boldsymbol{s}_i$ and $\boldsymbol{s}_j$ In learning, each SOM influences the other in which, instead of random-projection, representation of the other SOM is used to reduce the dimensionality of data vectors. We demonstrate that the model is powerful enough to find a meaningful structure, and obtain an appropriate mapping in a much-lower dimensional space than the conventional method.

Keywords: self-organizing maps, dimensionality reduction

1 Introduction

The purpose of this paper is to describe the non-linear mapping algorithm whose purpose is to discover regularities in a high-dimensional environment. The presentation will be nontechnical and by example. Throughout this paper, we describe our method with its application to a data set (animal names and feature shown in Table 1), which is a famous one used for a demonstration of the Self-organizing Map (SOM [2]). By this, SOM and our method is compared with the same data set. The idea of our method is applied to any methods such as the Multidimensional Scaling (MDS) whose input data set is represented as a matrix.

2 Self-organizing Map

The mechanism to acquire the structure of the external world by self-organization is interesting in connection with the study of biological systems and the study of robots. Consider the situation in which a robot is moving around in a room. The input from a vision sensor, such as an image, is a function of the position and the direction of the robot. In order to acquire the position and direction of the robot from only the vision information, it is necessary to separate two kinds of information, i.e., the position in the room (2D information) and the direction (1D information), from the higher-dimensional information, i.e., the image.

The Self-Organizing Map of Kohonen can be used to summarize such high-dimensional information and to extract important variables. SOM consisting of a two dimensional (2D) array of units is often used; it is a mathematical model that describes the formation of the functional map in the visual cortex in the the brain in terms of a certain learning algorithm [1]. The point is to summarize the higher-dimensional data and to extract only the two most important variables. A 2D array is not essential: a 1D or 3D array can be used whenever necessary. Each unit retains an *n*-dimensional vector called the reference vector. Below, the reference vector of the *i*-th unit is written as $\boldsymbol{m}_i$. The dimension of $\boldsymbol{m}_i$ is the same as that of the input signal $\boldsymbol{x}$ given to the SOM. The learning algorithm is as follows.

(SOM1) Initial values of the reference vectors $\boldsymbol{m}_i$ i 1 n are randomly generated, in which *n* is the number of units in the SOM.

(SOM2) An input vector $\boldsymbol{x}$ is generated.

(SOM3) The unit which has the reference vector closest to the input (called the winner) is determined:

$$c \qquad \operatorname*{argmin}_{i} \; \boldsymbol{m}_i \quad \boldsymbol{x} \tag{1}$$

(SOM4) Learning of the reference vectors is performed by the following formulas:

$$\Delta\boldsymbol{m}_i \qquad \alpha h_{ci} \; \boldsymbol{x} \quad \boldsymbol{m}_i \tag{2}$$

$$h_{ci} \qquad \exp \; \frac{\boldsymbol{r}_c \quad \boldsymbol{r}_i \;\; ^2}{2\sigma^2} \tag{3}$$

Table 1: Animal names and their attributes

		dove	hen	duck	goose	hawk	eagle	fox	dog	wolf	cat	tiger	lion	horse	cow
	small	1	1	1	1	1	0	0	0	0	1	0	0	0	0
is	medium	0	0	0	0	0	1	1	1	1	0	0	0	0	0
	big	0	0	0	0	0	0	0	0	0	1	1	0	0	0
	2 legs	1	1	1	1	1	1	0	0	0	0	0	0	0	0
	4 legs	0	0	0	0	0	0	1	1	1	1	1	1	1	1
has	hooves	0	0	0	0	0	0	0	0	0	0	0	0	1	1
	mane	0	0	0	0	0	0	0	0	1	0	0	1	1	0
	hunt	0	0	0	0	1	1	1	0	1	1	1	1	0	0
likes	run	0	0	0	0	0	0	0	1	1	0	1	1	1	0
to	fly	1	0	0	1	1	1	0	0	0	0	0	0	0	0
	swim	0	0	1	1	0	0	0	0	0	0	0	0	0	0

Here, $\boldsymbol{r}_i$ is the position of the i-th unit in the array (neural field), and α is a positive constant representing the rate of learning.

(SOM5) The procedure goes back to (SOM2) and is repeated.

Learning occurs near the winner. It is called neighborhood learning, and h_{ci} is called the neighborhood function. The neighborhood function in the above formula is a Gaussian function, and the positive constant σ determines the spread of the neighborhood. The norm in Eq. (1) is the Euclidean distance in the input signal space, and the norm in Eq. (3) is the Euclidean distance in the unit array.

Let us consider a set of input data. Table 1 shows the animal names and their attributes, which is from Ritter and Kohonen (1989) [2] and modified slightly where there are 14 animals and 11 features. In this example, an input vector is $\boldsymbol{x}_i \; i \quad 1 \qquad 14$, each of which is 11-dimensional column vectors. We can look at this set of inputs as a matrix $\boldsymbol{S}$:

$$\begin{array}{c} \\ \boldsymbol{s}_1 \\ \boldsymbol{s}_2 \\ \vdots \\ \boldsymbol{s}_{11} \end{array} \begin{array}{c} \begin{array}{ccc} \boldsymbol{s}\ 1 & \boldsymbol{s}\ 2 & \qquad \boldsymbol{s}\ 14 \end{array} \\ \begin{pmatrix} s_{1\ 1} & s_{1\ 2} & \quad s_{1\ 14} \\ s_{2\ 1} & s_{2\ 2} & \quad s_{2\ 14} \\ & & \\ s_{11\ 1} & s_{11\ 2} & \quad s_{11\ 14} \end{pmatrix} \end{array} \tag{4}$$

3 Dimension reduction for SOM by random projection

In the given data (similarity or dissimilarity) matrix S, each object $\boldsymbol{x}_i$ is represented by $m \quad 11$ coordinates, $\boldsymbol{x}_i \quad \boldsymbol{s}\ _i \quad s_{1i}\ s_{2i} \qquad s_{mi}$. Dimension reduction on objects means representing objects by a smaller number of coordinates, say $a_{i1} \qquad a_{iR}$ with R smaller than m, which in some sense retain approximately the same information as the original coordinates. Similarly in the given data matrix S, each variable or feature $\boldsymbol{y}_j$ is represented by $n \quad 14$ coordinates $\boldsymbol{y}_j \quad \boldsymbol{s}_j \quad s_{j1} \qquad s_{jn}$. Dimension reduction on features means representing features by smaller number of coordinates, say, $b_{j1} \qquad b_{jR}$ with R smaller than n, which in some sense retain approximately the same information as the original coordinates.

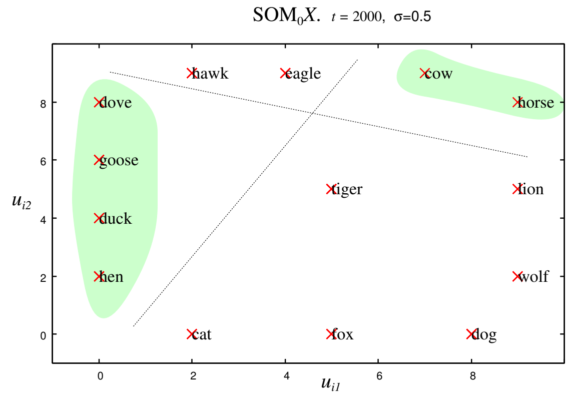

Figure 1: Self-organizing feature map obtained by single SOM after 2,000 learning trials. $\alpha \quad 0\ 1$, $\sigma\ t \quad \sigma_i\ \sigma_f/\sigma_i\ ^{t/t_{\max}}$ σ_i 4 $\sigma_f \quad 0\ 5$ $t_{\max} \quad 2000$. SOM of 10 10 was used.

As an example of dimension reduction, consider data of Ritter and Kohonen (1989) [2] on 14 animals $X_i \; i \quad 1 \qquad n \quad 14$ covering 3 size variables, 4 body variables, and 4 characteristic variables, for total of 11 variables Y_j. Thus these data may be regarded as 14 rows or points, each having 11 coordinates, that is 14 points in 11 dimensional space. Figure 1 represent the 2D configuration of animals which was obtained by 2D (10 10) SOM. Animals which share the similar characteristics are located in the nearest region. However, in the Fig. 1, the grass-eating animals and meat-eating animals are not separated correctly.

As mentioned in the appendix of the Ritter and Kohonen (1989)[2], if the dimensionality of features grows, the attribute vectors soon become impractically high-dimensional. It is difficult to study such a high-dimensional space array of data directly. The dimension of the input, therefore, should be reduced while preserving the metric relations among inputs. Ritter and Kohonen (1989)[2] also give a solution called *random-projection* method where each input $\boldsymbol{x}_i$ is represented as a weighted sum of vectors $\boldsymbol{r}_j \; j \quad 1\ 2 \qquad m \quad 11$

$$\tilde{\boldsymbol{x}}_i \qquad \sum_{j\ 1}^{m} s_{ji}\boldsymbol{r}_j \tag{5}$$

Note that if we take the following m-dimensional vectors:

$$\boldsymbol{r}_1 \quad \begin{pmatrix} 1 \\ 0 \\ \vdots \\ 0 \end{pmatrix} \quad \boldsymbol{r}_2 \quad \begin{pmatrix} 0 \\ 1 \\ \vdots \\ 0 \end{pmatrix} \quad \boldsymbol{r}_m \quad \begin{pmatrix} 0 \\ 0 \\ \vdots \\ 1 \end{pmatrix}$$

the projection produces the original data, $\tilde{\boldsymbol{x}}_i \approx \boldsymbol{x}_i$. In the random-projection method, we take $\boldsymbol{r}_j$ whose dimensionality is much smaller than that of $\boldsymbol{x}_i$ and each component of $\boldsymbol{r}_j$ is determined randomly, In this case, if the dimensionality of $\boldsymbol{r}_j$ is still large enough, the relation distortion in general will be small.

4 Iterative use of a pair of SOMs

In the random-projection method, a set of inputs is re-encoded in much smaller dimensional space. In the present paper, we look for a coding strategy other than the random-projection. In the random-projection method, independent random codes are assigned to features. For instance, features *small* and *2-legs* are highly correlated since only 2 of 14 features are different as shown in Table 1, but assigned codes independently and randomly. Here is our basic idea that this coding strategy must be improved so that we assign correlated code to the correlated features. To fix this idea, here we give an example.

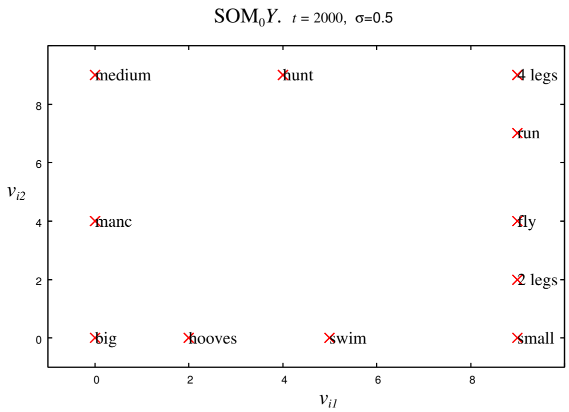

Figure 2: Self-organizing feature map obtained by single SOM after 2,000 learning trials. $\alpha = 0.1$, $\sigma(t) = \sigma_i(\sigma_f/\sigma_i)^{t/t_{\max}}$, $\sigma_i = 4$, $\sigma_f = 0.5$, $t_{\max} = 2000$. SOM of 10×10 was used.

A configuration obtained by 2D-SOM in Fig. 2 is a 2 dimensional representation of features for $\boldsymbol{y}_j = \boldsymbol{s}_j$ $(j = 1, \dots, m = 11)$ where inputs to the SOM were not column vectors of the matrix S but 14-dimensional raw vectors $\boldsymbol{s}_j$ $(j = 1, \dots, m)$. The representation shows low-dimensional base vectors $\boldsymbol{v}_j = (v_{j1}, v_{j2})$ of features where $\boldsymbol{v}_j$ $(j = 1, \dots, m)$ is the 2-dimensional coordinate which is the location of the winner unit of the trained SOM. Using this results, we can represent $\boldsymbol{x}_i$ in much lower-dimensional (2D) space

$$\tilde{\boldsymbol{x}}_i = \sum_{j=1}^{m} s_{ji}\boldsymbol{v}_j \tag{6}$$

Note that the random-projection method does not reflect dependencies among features but our method reflects the dependencies.

Since $\boldsymbol{v}_j = (v_{j1}, v_{j2})$ $(j = 1, \dots, m)$ is obtained by SOM which receives inputs of $\boldsymbol{y}_j = (s_{j1}, \dots, s_{jn})$. If n is large, the same problem occurs. We therefore consider to represent $\boldsymbol{y}$ in much-smaller dimensional space as

$$\tilde{\boldsymbol{y}}_j = \sum_{i=1}^{n} s_{ji}\boldsymbol{u}_i \tag{7}$$

where $\boldsymbol{u}_i$ $(i = 1, \dots, n)$ is considered to be the 2-dimensional coordinate which is the location of the winner unit of the SOM trained by a set of inputs $\tilde{\boldsymbol{x}}_i$ $(i = 1, \dots, n)$.

As described above, our model updates and refines $\tilde{\boldsymbol{x}}_i$ and $\tilde{\boldsymbol{y}}_j$ iteratively. In the remaining part of this article, we see whether this idea works.

The problem of determining the initial states of the model still remains. The simplest solution is this: we first use a conventional SOM to obtain the 2D configuration of animals $\boldsymbol{u}_i$ $(i = 1, \dots, 14)$. We call this SOM as SOM$_0$, and this obtained $\boldsymbol{u}_i$ as $\boldsymbol{u}_i(0)$ for convenience. When dimensionality of $\boldsymbol{x}_i$ is large, we can use $\boldsymbol{u}_i$ where each components are randomly generated. With this $\boldsymbol{u}_i(0)$, a set of input vectors to the SOM$_Y$, which is a new SOM, is generated as

$$\tilde{\boldsymbol{y}}_j = \frac{1}{k}\sum_{i=1}^{n} s_{ji}\boldsymbol{u}_i \tag{8}$$

where $k = \sum_{i=1}^{n} s_{ji}$. After trained this SOM$_Y$ with these inputs, we obtain the location of winner units $\boldsymbol{v}_j$ for each j. We call these $\boldsymbol{v}_j$'s as $\boldsymbol{v}_j(1)$ where 1 means at time 1. With these $\boldsymbol{v}_j$, a set of input vectors to the SOM$_X$, which is another new SOM, is generated as

$$\tilde{\boldsymbol{x}}_i = \frac{1}{k}\sum_{j=1}^{m} s_{ji}\boldsymbol{v}_j \tag{9}$$

where $k = \sum_{j=1}^{m} s_{ji}$. With this inputs, we train the SOM$_X$ and obtains the 2D configuration of animal names. The 2D coordinates thus obtained are called $\boldsymbol{u}_i(2)$ $(i = 1, \dots, 14)$. Similarly, we obtain $\boldsymbol{v}_j(3)$, $\boldsymbol{u}_i(4)$, $\boldsymbol{v}_j(5)$, $\boldsymbol{u}_i(6)$, $\boldsymbol{v}_j(7)$, $\boldsymbol{u}_i(8)$, $\dots$.

There are three 2D SOM's. SOM$_0$ receives high-dimensional inputs, $\boldsymbol{s}_i$ $(i = 1, \dots, n = 14)$. SOM$_X$ and SOM$_Y$ receive 2-dimensional inputs, $\boldsymbol{x}_i$ $(i = 1, \dots, n = 14)$, $\boldsymbol{y}_j$ $(j = 1, \dots, m = 11)$ respectively. In short, the learning procedure is as follows:

(P1) We train the SOM$_0$ and obtain $\boldsymbol{u}_i$.

(P2) We use $\tilde{\boldsymbol{y}}_j$ as inputs to the SOM$_Y$ where $\tilde{\boldsymbol{y}}_j$ is represented as a weighted sum of $\boldsymbol{u}_i$ i 1 n. We train the SOM$_Y$ and obtain $\boldsymbol{v}_j$.

(P3) We use $\tilde{\boldsymbol{x}}_i$ as inputs to the SOM$_X$ where $\tilde{\boldsymbol{x}}_i$ is represented as a weighted sum of $\boldsymbol{v}_j$ j 1 m. We train SOM$_X$ and obtain $\boldsymbol{u}_j$.

(P4) The procedure goes back to (P2) and is repeated.

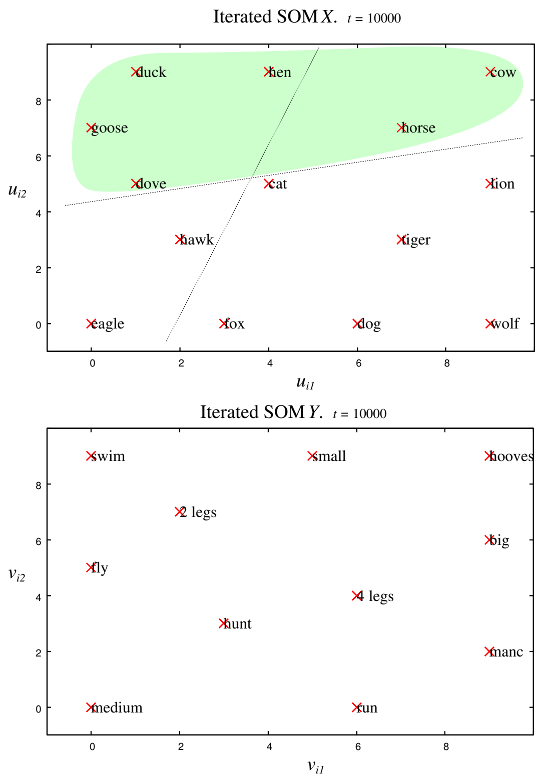

Figure 3: A pair of 2D SOM was used to obtain this map. We trained SOM$_Y$ 1000 times for each input (batch learning), then with that result, SOM$_X$ was trained 1000 times for each input (also batch learning). This figures show the result after this procedure repeated 10 times. Both SOM$_X$ and SOM$_Y$ consist of 10 10 units, and the learning coefficients we used were α 0 1, σ t σ_i σ_f/σ_i $^{t/t_{\max}}$ σ_i 4 σ_f 0 5 $t_{\max}$ 1000. Reference vectors are initialized in each repetition.

We have done the computer simulation of animal map formation by the present method (Fig. 3) and, for comparison, by the random-projection method [2] in which the dimension of a set of inputs were projected to the 2D and 5D (Fig.4) before applied to the SOM. We can see that the grass-eating animals and meat-eating animals are separated correctly in Fig.3 (our method) but not in Fig.4 (the random-projection method).

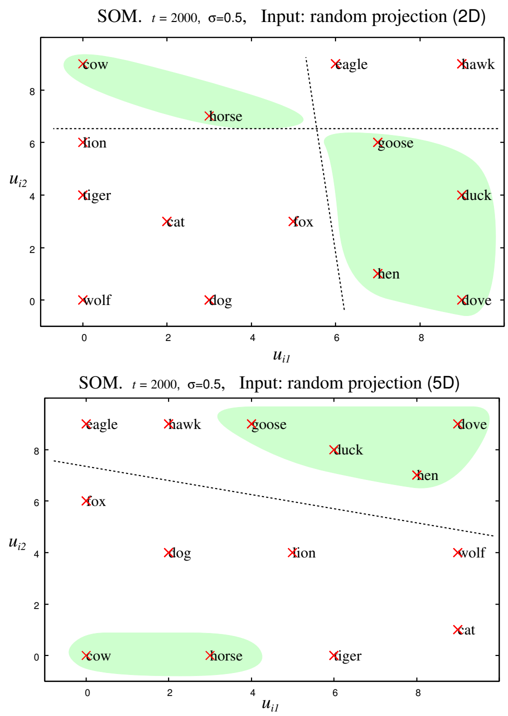

Figure 4: Comparison to the other methods. Dimensionality of a set of inputs were reduced by the random projection method[2] to 2D (upper) and 5D (lower panel) before applied to the SOM. The grass-eating animals and meat-eating animals are not separated correctly. Compare the results to those shown in Fig.3.

5 Summary

We have demonstrated a method which self-organizes a map by using a pair of SOMs to which the same set of input data was applied but in two different ways. Although we could not justified our method here, we have already confirmed that it works in the other problem. As we have mentioned before, our method can be applied to any method such as MDS where a set of inputs is represented as a matrix.

Acknowledgments

This works was partly supported by Grant-in-Aid (16700232) from the Japanese Ministry of Education, Culture, Sports, Science and Technology (MEXT).

References

[1] T. Kohonen, "Self-organized formation of topologically correct feature maps," *Biological Cybernetics*, vol. 43, pp. 59-69, 1982.

[2] H. Ritter and T. Kohonen, "Self-organizing semantic maps," *Biological Cybernetics*, vol. 61, pp. 241–254, 1989.

Orbit Control for the KEK 12GeV PS-MR by using NN algorithm

Hitaka Y*, Shirakata M**, Sato H**, Yokomichi M***, Kono M***

*Department of Control and Information System Engineering,
Kitakyushu National College of Technology, Japan
**Proton Synchrotron Accelerator Division, KEK, Japan
***Department of Computer Science and Systems Engineering, Miyazaki Univ., Japan

Abstract

At KEK 12GeV Main Ring (PS-MR), when the least square method is applied to correct whole beam orbit all at once, it remains unacceptable beam loss and it is necessary to adjust the local positions of the beam orbit by hands with the beam loss monitors until the beam loss is suppressed under an acceptable level. However, the corrected orbit by this way doesn't always satisfy the minimum-loss condition. In this paper, a new method is proposed. It focuses a fact that the beam loss distribution depends on the shape of the beam orbit, and formulates this relationship to a functional approximation by using a neural network algorithm, Then, solving an optimization problem for generated network system, data of the beam shape which is more suitable for the beam loss of the accelerator can be obtained. The description of the system construction and experimental results are presented.

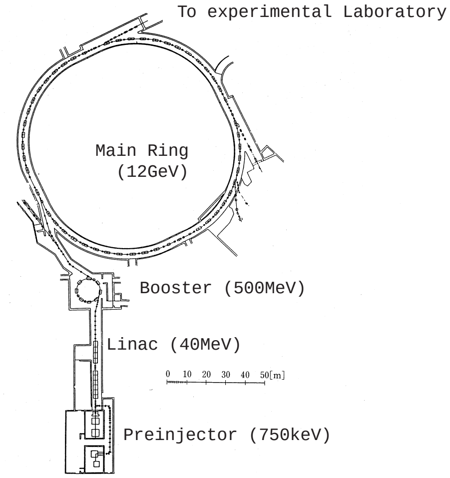

Figure 1: KEK 12GeV PS

1 Introduction

The accelerator is a device which accelerates electron, proton and many kinds of nucleus to provide high energy. The accelerated particles are called "beam" and it is accelerated close to the light and extracted to some kind of target. The accelerator can be used for physical experiments about atomic nucleus or elemental particles, medical purposes (ex. high-energy radiotherapy), structural analysis of the polymer macromolecule (Protein or DNA) and so on. In this paper, we consider an beam orbit control problem for an accelerator called "Proton Synchrotron (PS)" which is in High Energy Accelerator Research Organization, called KEK (Kou Enerugi kasokuki Kenkyuu kikou).

Figure 1 shows overall view of KEK 12 Giga electron Volt Proton Synchrotron (KEK 12GeV PS). As this figure indicates, this accelerator consists of four accelerators. These are called Preinjector, Liniac, Booster and main ring(MR), respectively. The beam is accelerated step by step from the preinjector to the main ring. At the main ring, the beam is accelerated with orbiting until the beam is given desired energy and extracted to any target. The main ring is designed for the orbiting beam to tracks the desired orbit. However, due to the measurement errors of the beam position, the setting errors of the internal device and the magnetic field error, the beam distorts and strays from the desired orbit and touches the wall of the beam pipes in the MR and losses. Thus, it is necessary to correct the beam orbit to decrease the beam loss until an acceptable level.

It is known that the least square method is effective to correct the orbit distortion which is caused by the magnetic field error[1]. Because this relationship can be described by the algebraic equations. This distortion is called COD (Closed Orbit Distortion). However, for the other disturbance, it is deficient to correct the COD (Closed Orbit Distortion) by using the least square method. Thus, it is necessary from the point of view of the beam loss monitors in order to minimize the beam loss.

At the PS-MR, the beam orbit is adjusted by the local bump method. The operators correct the beam orbit with the beam loss monitors until the beam loss is suppressed under an acceptable level. However, this strategy depends on the traditional history of the orbit tuning and operator's experience. Besides, the beam orbit tuned by this way doesn't always satisfy the minimum-loss condition for this accelerator.

Note a fact that the beam loss distribution depends on the shape of the beam orbit. If this relationship can be formulated in some way, it is expected that the minimum loss condition can be obtained by using some kind of the optimization methods. In this paper, a new strategy is proposed for the beam orbit tuning. It formulates the relationship between the control input of the beam steering magnets which decide the shape of the beam orbit and the values of the beam loss monitors by using the Neural Network algorithm. And then, for the trained network, adjusting the network inputs (inputs of the steering magnets) to reduce the network outputs (corresponding to the beam loss), we will obtain the steering input data which will minimize the beam loss of the accelerator. This method will be more efficient than the current orbit control method.

This paper is constructed by following sections. This section is introduction. Next section, the detail of new orbit control method proposed by us is described. Section 3, we represent about an experiment and a result for the proposed method. The Final section is Summary.

2 Construction a New Orbit Control System based NN Algorithm

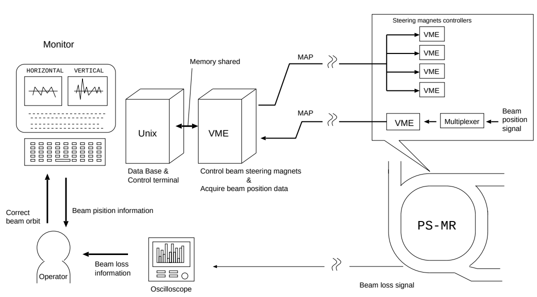

Figure 2: The beam orbit control system.

Figure 2 shows the structure of the beam orbit control system in KEK PS-MR. At PS-MR, there are 56 beam position monitors, 56 beam loss monitors, 28 beam steering magnets for the lateral direction and 28 beam steering mangets for the vertical direction. The measured data by those monitors are acquired to CCR (Central Control Room) and displayed on CRT monitors or some oscilloscopes. In current orbit correction, operators has corrected the beam orbit at each measured point of the beam position by using the local bump method until the beam loss is suppressed under an acceptable level. This method gives a local bump to the beam orbit at any measured point with corresponding three beam steering magnets. Above procedure takes so much time and the beam orbit tuned by this way doesn't always satisfy the minimum-loss condition for this accelerator.

For these problem, we propose a new orbit correction method by using NN algorithm. Giving some data set of the orbit shape and corresponding beam loss distribution, the NN can be identify both relationship. And then, for the trained network, we set a performance criterion for the output of the trained network and adjust the network input by some kind of optimization method to minimiize the performance criterion. Figure 3 is the idea of new orbit control method. Figure 3 denotes that the control input for

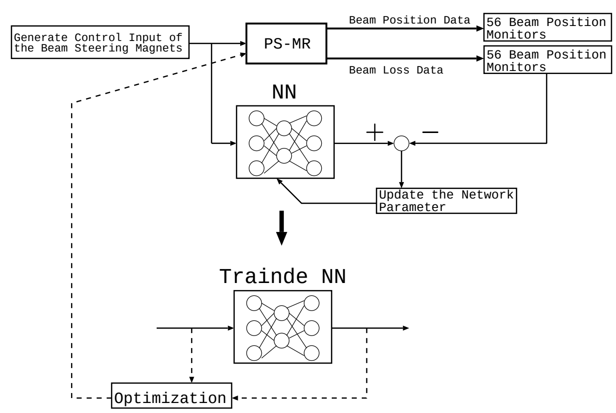

Figure 3: The idea of the Orbit Control baed on NN.

the beam steering magnets is used as the NN input for training and optimization. Because for the current data acquisition system in PS-MR, much time is necessary to acquire the beam position data. It is known that a steering input pattern specifies a shape of the beam orbit. Thus we use it as input for the NN.

2.1 NN Algorithm

There are various types of neural network algorithms. In this paper, the BackPropagation (BP) method [2] is used to formulate the relationship between the inputs of the beam steering magnets and the beam loss distribution. BP method has generated a lot of good results for many actual problems whose relationships between their inputs and outputs are nonlinear or high order correction.

2.2 The Technique of Optimization

Though the optimization problem about the inputs of the beam steering magnets realizes the minimum beam loss, it has many local minimum solutions. Avoiding these local minima and deriving a global optimal solution, we take the Simulated annealing (SA) which is one of the heuristic optimization methods. The detail of SA algorithm is described in [3].

3 Experiment and Result

In this section, an experiment and a result for our approach are described. For this experiment, a data logger system which logs the beam loss data from all loss monitors and a caluculator for the neural computing and the network optimization are installed. Figure 4 shows an updated orbit control system for this experiment. In this experiment, the network training

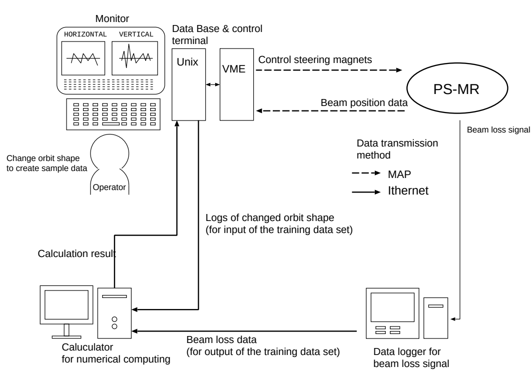

Figure 4: Correction chart of the system devices.

and optimization is operated off-line.

3.1 Data Acquisition

For KEK PS-MR, it is possible to correct the orbit shape for lateral direction and vertical direction. A precise orbit tuning is not necessary for lateral direction, because the dimensions of the beam pipes are landscape and there are enough clearance for the beam and the pipes wall for lateral direction. Thus, the NN is trained for a relationship between the contorl input for the beam steering magnets which decide the shape of the orbit for the vertical direction and corresponding beam loss data.

From 56 measured points of the beam position and beam loss (1-1F,1-1D,1-2F,...,4-7D; F means focusing, and D means defocusing), 9 steering magnets which give the bumps to the beam orbit for the vertical direction are chosen at the points of quarter range (2-1F !A2-7D) to acquire the NN training data. Because the capacity of the data transportation of the orbit control system is not satisfied to acquire the training data with sufficient quantities in the limited experiment time (about 1 hour). At this range, some training data set is acquired by deciding the shape of the beam orbit at random (maximum 4.0 mm from position zero, step 1.0 mm). The restriction of the maximum range 4.0 mm is to avoid huge beam loss and the radioactivation of the internal devices. At the experiment in June14, 2004, thirty sets of the training data could be obtained for 1 about hour.

3.2 Training

The NN for this experiment is constructed from 7 input units and 56 output units. The amount of middle layer units is decided 56. The NN training finished about 50 minutes, where, the error tolerance of the network outputs for training data was configured 0.002.

3.3 Optimization

For the optimization of the trained network, the best input pattern is searched by using normal random numbers (average 0, dispersion 0.2). The performance criterion for the evaluation of the solution was 1-norm of the network output vector.

Figure 5 and Figure 6 are the optimization results. Figure 5 indicates an ordinal (unadjusted) beam orbit and an optimal orbit which will minimize the beam loss. Left figure in Figure 6 indicates the beam loss for the ordinal orbit and right figure is the expectation of the beam loss corresponding to the optimal orbit.

Using the control input of the steering magnets derived by NN optimization, the beam orbit of PS-MR will be corrected to minimize the beam loss as the right figure in Figure 6.

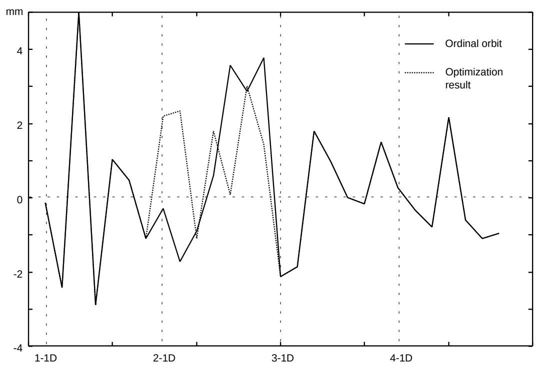

Figure 5: Expectation about the beam position.

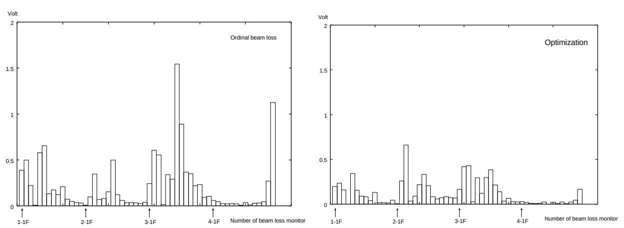

Figure 6: Expectation about the beam loss.

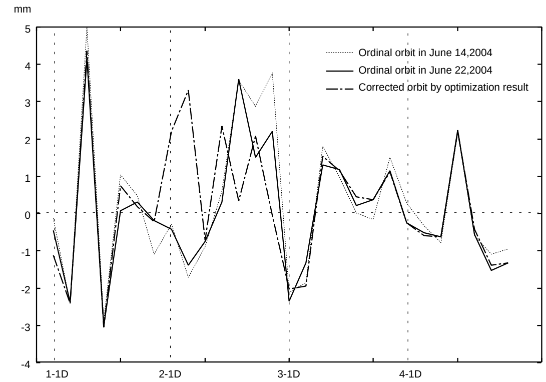

Figure 7: Experimental result about beam position.

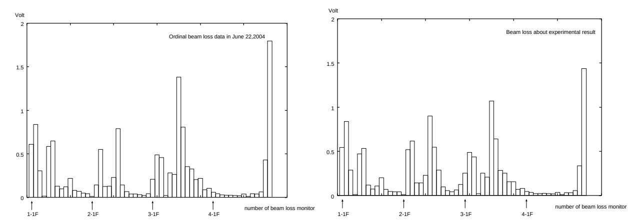

Figure 8: Experimental result about beam loss.

3.4 Result

Figure 7 and Figure 8 show actual results in June 21, 2004. Figure 7 indicates the ordinal orbit in June14, 2004, an ordinal orbit in June 22, 2004 and a corrected orbit by using above optimization result. Left figure in Figure 8 shows the beam loss for the ordinal orbit in June 22, 2004 and right figure corresponds to the corrected orbit. Figure 8 shows the total beam loss decrease slightly. However, expected result from optimization for the trained networkwas not obtained. For this result, two reasons are considered. First, we didn't have enough time to obtain appropriate amount of the training data. It is a solution that each devices of the orbit control system is update to enable more high-speed data acquisition. The second reason, as shown in Figure 4, the shape of the ordinal orbit is changed with the passage of time. For this problem, online training will be necessary to adapt the change of the accelerator's property.

4 Summary

The result of the experiment shows that the beam loss can be decreased slightly by using our method. When the beam orbit is corrected by the comparatable amounts of the control inputs which are decided at random, the beam loss must be unacceptable level, or the beam will be vanished in the accelerator. Thus, it is said that the relationship between the shape of the beam orbit and the beam loss can be formulated to a functional approximation by the NN algorithm.

Beam orbit tuning by hand is not effective that it needs quite a bit of time to reduce the beam loss under the acceptable level. Then, if the NN training with high-speed and high-precision can be achieved, our method will become an effective beam tuning method for many types of the accelerators.

References

[1] Kamei T, Kihara M (1993), The science of accelerator, Maruzen.

[2] Philip D. Wasserman (1993), ADVANCED METHODS IN NEURAL COMPUTING, Van Nostrand Reinhold.

[3] Colin R. Reeves (1993), Modern Heuristic Techniques for Combinational Problems, Blackwell Scientific Press.

Trajectory for Saving Energy of Direct-Drive Manipulator in Throwing Motion

Asaji SATO
Dept. of Mechanical Engineering,
Miyakonojo National college of Technology,
Miyakonojo, Japan. 885-8567

Osamu SATO, Nobuya TAKAHASHI and Michio KONO
Dep. of Computer Science and Systems Engineering,
Faculty of Engineering, University of Miyazaki,
Miyazaki, Japan. 889-2192

Abstract

In this paper, equations of motion of a closed-type manipulator, whose mechanism can easily be made lighter, are derived in consideration of characteristics of driving source. Considering the final condition about angular displacement and angular velocity in throwing motion, trajectories of velocity for saving energy are calculated by iterative dynamic programming. And, the dynamic characteristics of manipulator controlled based on the trajectory for saving energy are analyzed theoretically and investigated experimentally.

Keywords: Manipulator, Trajectory, Dynamic Programming, DC Motor, Minimum Energy, Throwing Motion

1 Introduction

For the purpose of enlarging the work space of the manipulator, it is necessary for studying the optimal control in throwing motion. In a previous report [1], a casting manipulator is introduced as a new type of manipulator, which includes flexible parts, such as a string, in its link mechanism. The merit of this type of manipulator is its large work space compared with its simple mechanism and its size.

But, direction angle about throwing is limited and the consideration of energy consumption of driving source is not enough.• Also, the throwing motion of 2-DOF robot was studied to reduce the target error, that is, the distance between the mark and the point at which the object hits the target [2]. But, the consideration about trajectory of saving energy is not enough.

In this paper, equations of motion of a closed-type manipulator, whose mechanism can easily be made lighter, are derived in consideration of characteristics of the DC servomotors, and a performance criterion for saving energy is defined in consideration of energy consumption of driving source. When the manipulator is operated in a vertical plane, the system is highly non-linear due to gravity and an analytical solution can not be found. Then, a numerical approach is necessary. Considering the final condition about angular displacement and angular velocity, trajectories of velocity for saving energy are calculated by iterative dynamic programming[3]. Initial searching region of dynamic programming is a shape which is surrounded by two sine-wave translated in parallel. This proposed searching region is used as an initial range of the iteration method, and the region is shifted along the axis of coordinate of angular displacement to minimize the energy consumption of the motor. The dynamic characteristics of manipulator controlled based on above mentioned trajectory are analyzed theoretically and investigated experimentally.

2 Modeling of manipulator

When the mechanism of the manipulator is open-loop, the consumed energy increases with the weight of a motor which is on the moving link. Then, we shall take a manipulator whose mechanism is closed-loop. And, the dynamic equations of the manipulator with two degrees of freedom as shown in Figure 1 which is able to move in a vertical plane are as follows.

$$\tau = H(\theta)\ddot{\theta} + C(\theta,\dot{\theta}) + G(\theta) \quad , \tag{1}$$

where

$\tau = [\tau_1, \tau_2]^T$: torque which acts on link 1 and link 2 ,

$\boldsymbol{\theta} = [\theta_1, \theta_2]^T$: angular displacement of link ,

$C(\boldsymbol{\theta},\dot{\boldsymbol{\theta}})$: torque about centrifugal force and Coriolis' force ,

$G(\boldsymbol{\theta})$: torque about gravity .

And the applied voltage of the servomotor is

$$e = b_1\dot{\theta} + b_2\ddot{\theta} + b_3\tau + b_3\tau_f\,\mathrm{sign}(\dot{\theta}\ ) \cdots\cdots (2)$$

where

$b_1 = k_v + (R_a/k_t)D_m$, $b_2 = (R_a/k_t)I_m$, $b_3 = R_a/k_t$,

i_a : electric current of the armature ,

R_a : resistance of armature ,

I_m : moment of inertia of armature,

D_m : coefficient of viscous damping.

Then, the electric current is $i_a = (e - k_v\dot{\theta})/R_a$. (3)

And, the consumed energy is $E = \int (e \cdot i_a)dt$. (4)

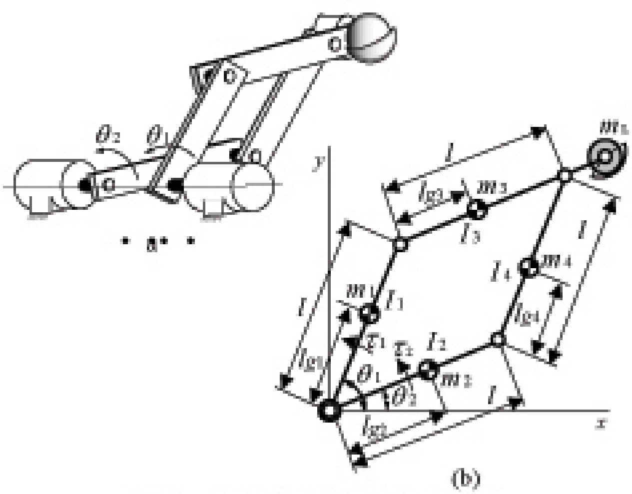

Fig.1 Mechanism of manipulator

3 Method for searching the trajectory

It is difficult to calculate the manipulated variables for the trajectory of the saving energy by the maximum principle [6], because the equations of motion about the system are highly nonlinear.

When the initial position is θ_{Ij} and the position of releasing is θ_{fj}, the initial trajectory for searching by iterative method is

$$\dot{\theta}_j = A_j t + B_j \sin\frac{\pi t}{T} + \dot{\theta}_{Ij} \quad , \tag{5}$$

$$\theta_j = \theta_{Ij} + \dot{\theta}_{Ij} t + \frac{1}{2} A_j t^2 + \frac{T B_j}{\pi}\left(1 - \cos\frac{\pi t}{T}\right) \quad ,(6)$$

where

$$A_j = \frac{\dot{\theta}_{fj} - \dot{\theta}_{Ij}}{T} \quad , \quad B_j = \frac{\pi}{2}\left(\frac{\Theta_j}{T} - \frac{\dot{\Theta}_j}{2}\right) \quad ,$$

$$\Theta_j = \theta_{fj} - \theta_{Ij} \quad , \quad \dot{\Theta}_j = \dot{\theta}_{fj} - \dot{\theta}_{Ij} \quad .$$

This proposed trajectory is used as a center line of initial searching region of the iterative dynamic programming [4], and the region is shifted along the axis of coordinate of angular displacement to minimize the energy consumption of the motor as follow, (as shown in Fig.2).

$$\theta_j = \theta_{Ij} + \dot{\theta}_{Ij} + \frac{1}{2} A_j t^2 + \frac{T B_j}{\pi}\left(1 - \cos\frac{\pi t}{T}\right) \pm \Delta\theta_{Ij}\frac{N-1}{2} \quad . (7)$$

The working time is divided into K elements, and the angular displacements are divided into N elements. In order to make the programming easy, we have calculated about the trajectory under the condition that the angular acceleration is constant in each section.

4 Simulations

4.1 Simulation for throwing motion

We shall take the parameters of the system as shown in Table 1. The simulations of the system are done as follows.

A response of the manipulator from initial position ($\theta_1 = -\pi/4$, $\theta_2 = -3\pi/4$) to the position of release ($\theta_1 = 3\pi/8$, $\theta_2 = \pi/8$) is shown in Fig.3, under the condition that the number for dividing is K=8,N=5, distance from origin to the point of arrival is x=-0.5 [m], release angle is $\phi = 3\pi/4$, and the working time is T=0.6 [s]. And, it is shown that the locus of every sampling time (0.002 [s]) is like a pendulum movement [5]. Angular velocity of the motors on the base are shown in Fig. 4. Because of the condition that the angular acceleration is constant in each section of searching, angular velocity changes in the line-shape.

Figure 5 shows the path for saving energy. The characteristics of proposed method is that some kinds of patterns are derived corresponding to the working time, T.

Figure 6 shows the relation between the consumed energy and the release point, under the condition that the distance from origin to the point of arrival is x=-2.0 [m], release angle is $\phi = 3\pi/4$, and the working time is T=0.6 [s]. It is clear that consumed energy is small at the position of release ($\theta_1 = 3\pi/8$, $\theta_2 = \pi/8$).

Table 1 Values of manipulator

Parameter	Value	Parameter	Value
l_j (j=1~4) (m)	0.080	k_{t1}, k_{t2} (Nm/A)	0.046
l_{gj}(j=1 4) (m)	0.044	k_{t3} (Nm/A)	0.010
I_1, I_2 (kgm^2)	1.73×10^{-5}	k_{v1}, k_{v2} (Vs/rad)	0.046
I_3, I_4 (kgm^2)	2.04×10^{-5}	k_{v3} (Vs/rad)	0.010
I_5 (kgm^2)	4.08×10^{-6}	R_{a1}, R_{a2} (Ω)	3.5
$m_1 m_2$ (kg)	0.0202	R_{a3} (Ω)	14.1
$m_3 m_4$ (kg)	0.0218	D_{mj} (j=1 3) (Nms/rad)	7.89×10^{-5}
I_{m1}, I_{m2} (kgm^2)	8.54×10^{-6}		
I_{m3} (kgm^2)	0.51×10^{-7}	τ_{fj} (j=1 3) (Nm)	0.0013

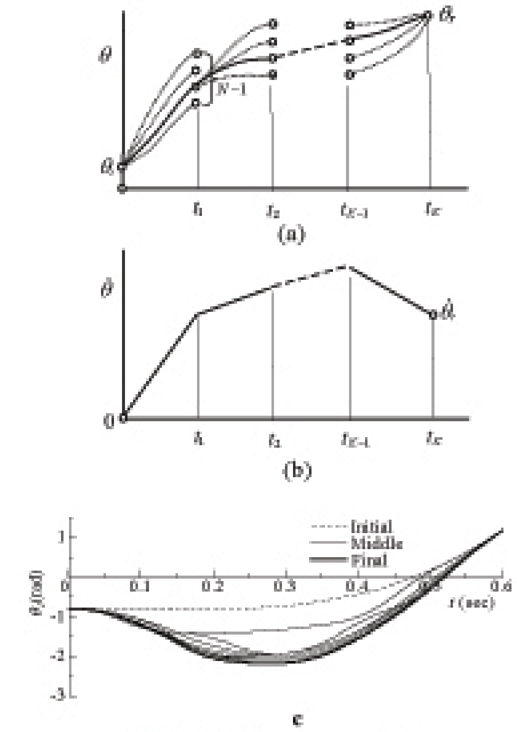

Fig.2 Trajectory for searching

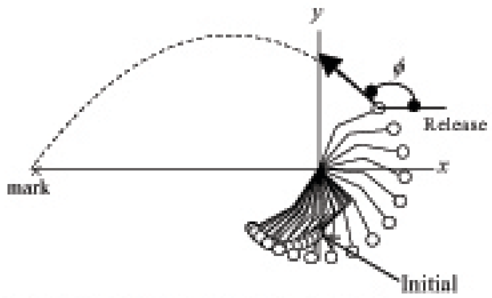

Fig. 3 Throwing motion of manipulator

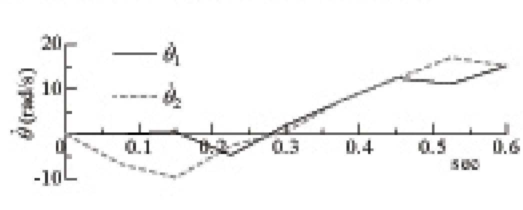

Fig.4 Angular velocity of motor

4.2 Simulation for holding the object

The case using the hand of tray type is as follows. Figure 7 shows the hand of the shape of sector (λ is angle in vertical plane). F is resultant force about gravity and inertia force , and the components of the force are Fx and Fy. In order to prevent the object falling from the tray, angle of the tray (θ_3) is controlled by the motor 3 on the link 3, as follows,

$$\theta_3 = \tan^{-1}\left(\frac{F_y}{F_x}\right) + \frac{\pi}{2} - \theta_2 \quad . \tag{8}$$

Figure 8(a), which looks like the stairs, shows the angular acceleration calculated from the angular velocity(as shown in Fig.4). And, response of resultant force which acts on the object is influenced by the angular acceleration, as shown in Fig.8(b). Then, the angle changes as the shape which looks like the stairs, as shown in Fig.8(c). In Fig.8(d), bold lines show the posture of the tray.

In order to make the response of angle about the tray smooth, we have substituted the angular displacements of the motors 1 and 2 by the function of time as follows,

$$\theta_j = \sum_{k=0}^{n} a_{jk} \cdot t^k \quad (j=1,2) \tag{9}.$$

where, a_{jk} is constant values which derived under the condition that consumed energy is nearly equal to the case of Fig.4.

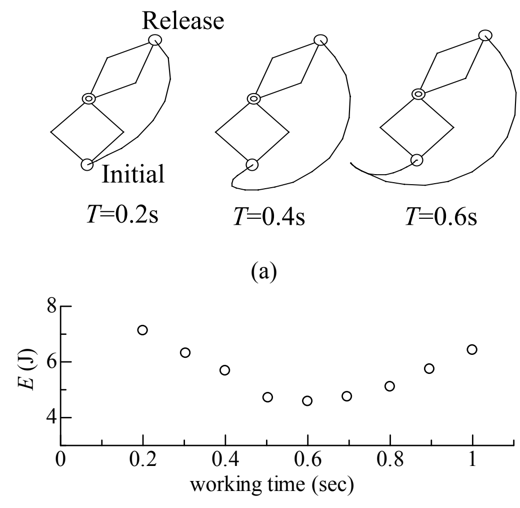

Fig.5 Relation between working time and consumed energy

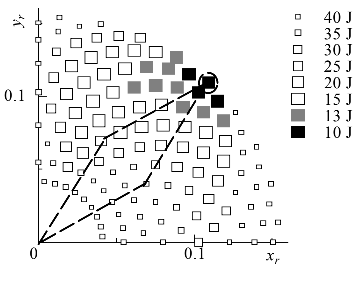

Fig. Relation between consumed energy and release point

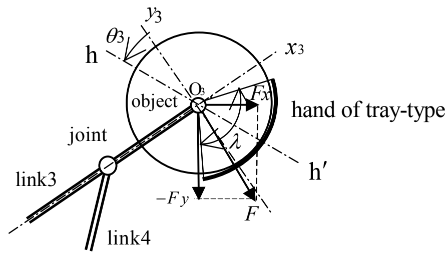

Fig. Inertia force about hand of tray-type

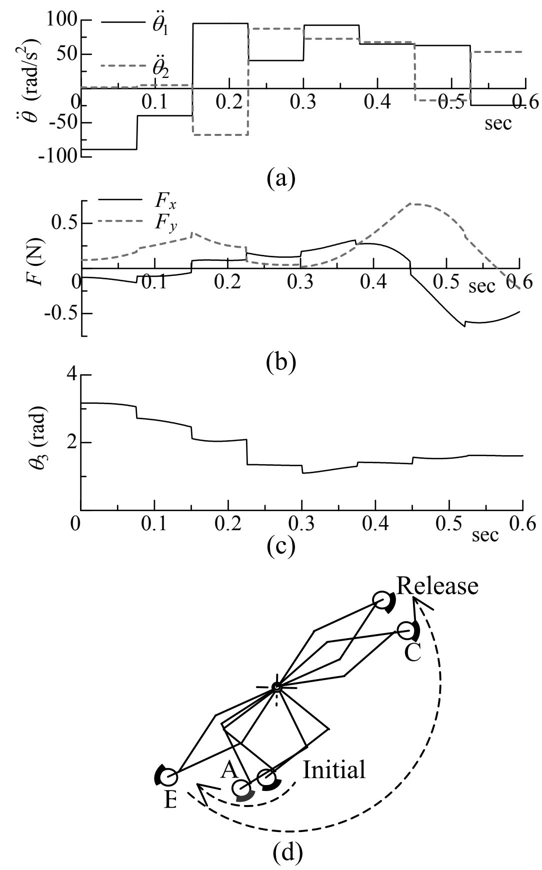

Fig.8 Response of manipulator

Figure 9 (a) shows the modified result which is derived using Eq.9 (solid line) and the same one as Fig.8 (a) (broken line). In Fig. 9 (b) and (c), angular displacement of motor 3 become smooth by using Eq.9, whereas the difference about angular velocity of motor 1 is small. Figure 10 shows the response of applied voltage of motor 3. The consumed energy of motor 3 becomes less than 1/4 by modification, and it is clear that proposed method is effective.

5 Experimental results

In this section, experimental results shown under the condition that the motion space of the manipulator is small. Figure 11 shows an experimental apparatus, which is two degree of freedom model with fixed tray for holding the object. The parameters of this system are the same as given in Table 1. The motors 1 and 2 (rated 24 V, 60 W) are on the frame. We shall measure the angular displacement of motors by rotary encoders. And, we shall measure the electric current as a potential difference of the resistor (rated 1.0 Ω, 10W).

Figure 12 shows the experimental response of the manipulator from initial position ($\theta_1 = \pi/4,\ \theta_2 = 0$) to the position of release($\theta_1 = 2\pi/3, \theta_2 = \pi/4$) , under the condition that the distance from origin to the point of arrival is x=−0.4 [m], release angle is $\phi = 3\pi/4$, and the working time is T=0.2 [s]. Sampling time of the control is 0.002 [s], and feedback gain for angular displacement is 50 [V/rad], feedback gain for angular velocity is 0.5 [Vs/rad]. Experimental result of angular velocity (solid line), which is calculated by angular displacement, agree with the theoretical result (broken line).

Figure 13 shows the consumed energy of the motors 1 and 2. The difference between the experimental result (solid line) and the theoretical result (broken line) are less than 6 . From these results, it is confirmed that modeling is effective.

Conclusions

The results obtained in this paper are summarized as follows.

(1) For throwing motion, it has been clarified that trajectory for saving energy calculated by proposed iteration method is effective.

(2) In order to hold the object, it is considered that proposed method to control the hand of tray type can be used.

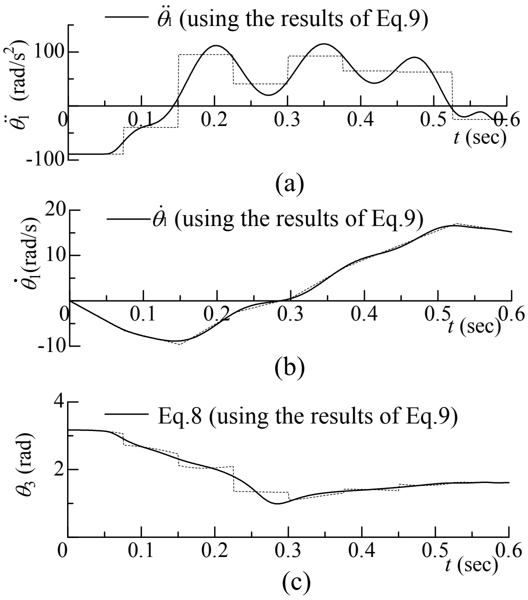

Fig.9 Response of manipulator (after modification)

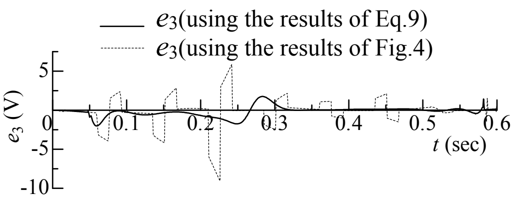

Fig.1 Voltage of motor 3

References

[1] H.Arisumi, K.Yokoi, T.Kotoku et al(2002), Casting Manipulation(Experiments of Swing and Gripper Throwing Control), International Journal of JSME, Vol. 45, No. 1C, pp. 267-274.

[2] N.Kato, and T.Nakamura (1997), Throwing Control for 2-DOF Robot(in Japanese), JSME, Vol. 63, No. 614C, pp.3571-3576.

[3] A.Sato, O.Sato, M.Kono et al(2003), Trajectory for Saving Energy of Direct-Drive Manipulator with Two Degree of Freedom in PTP Motion under Gravity (in Japanese), Journal of JSPE, Vol. 69, No. 9, pp.1281-1285.

[4] O.Sato , H.Shimojima, and H.Yoinara(1985), Minimum-energy Control of a Manipulator with Two-degree of Freedom, Bulletin of JSME, Vol. 29, No. 248, pp.573-579.

[5] T.Izumi(2000), Path Planning for Saving Energy of a Manipulator in PTP Motion(in Japanese), Journal of the Robotics Society of Japan, Vol. 18 , No.7, pp.972-978.

[6] Boltyanski,V.G(1967),(translated into Japanese by Sakamoto.M), Mathematical Method of optimal control (in Japanese), sougo-tosho.

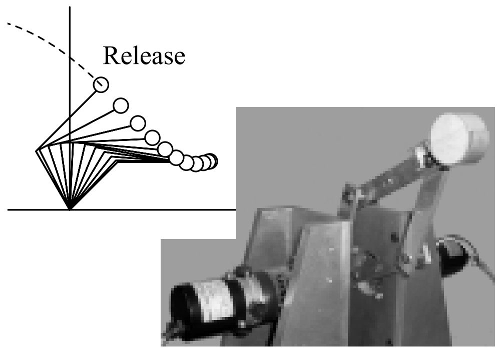

Fig. 11 Experimental apparatus

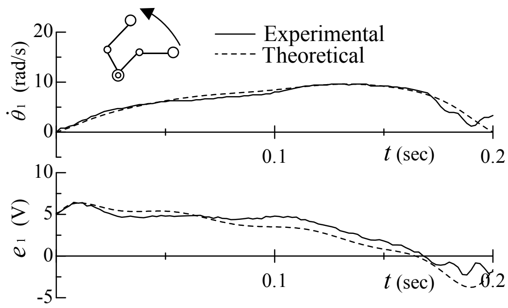

Fig.12 Experimental result

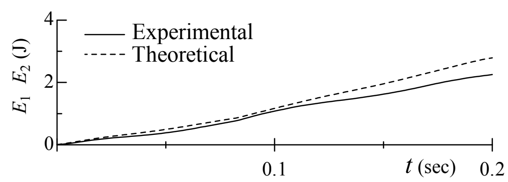

Fig.13 Experimental result (consumed energy)

Underwater Moving Object Tracking and Grasping with Telerobotic System

Ping Zhang, Etsuro Shimizu and Masanori Ito
Department of Marine Electronics and Mechanical Engineering
Tokyo University of Marine Science and Technology

Abstract

This paper introduces an underwater robot teleoperation system based on Internet and virtual reality model. The operator can control the action of the remote robot through the Internet and monitor the states of the robot displayed in a 3D-Graphics simulator. First, the technique and method implementing interactive robot 3D simulation based on the Java platform will be described. Since this real time teleoperation system is connected via a network communication, which is inevitably effected from the time delay. The system will be unstable due to the random time delays of the Internet. To overcome this problem, the research combines the event-triggered autonomous control and prediction method to achieve a moving target tracking and grasping teleoperating task. Another problem we have to face is losing track of the target. Because the teleoperation system uses visual feedback, cameras probably fail to collect image for a few samples when the target is out of view or be obstructed by the robot. This problem was solved with the help of our predictor. Experiments are conducted to examine the performance of the moving object tracking and grasping utilizing this teleoperation system and experimental results have verified the theoretical development and the validity of this proposal.

Keywords: 3D monitor, underwater manipulator teleoperation, moving target tracking

1. Introduction

There are some places which are not suitable for human presences, such as deep ocean, out space, nuclear site, etc. However, we still have to perform many tasks in these places such as maintenance and construction of oil drilling structures in deep sea, cleaning of sites with radioactive spill and disposal of radioactive material in nuclear sites, construction of structures like the Space Station and retrieval of satellites in outer space. Working in such places, not only need humans face life threatening in every moment, but also cost too much to equip the human in order to survive in these crucial environments. As a solution, in many cases, these tasks are performed with a robot instead of a human, and the robot will do works according to the commands sending by a human operator from some remote place [1,2,3]. Such remotely operated robots have been used in many remote working sites, for example, in deep ocean, a manipulator arm mounted on Kaiko, well known as deepest-dive ROV (Remote Operated Vehicle) of the world, can achieve tasks like collecting specimens and settling experimental equipments [4]. With the increase of ocean research, such as investigating a sunken ship, the seabed environment and resource, there will be more and more underwater robots be put into practical use.

Basing on this background, we developed the teleoperating system for an underwater manipulator, which can be equipped on an Autonomous Underwater Vehicle.

2.Teleoperation System Overview

The teleoperation system for the underwater arm robot consists of four hardware components: a robot control unit, a tele-operating console, an image-processing unit, and an underwater robot. The underwater robot has two arms with 7 links, built by Mitsubishi Heavy Industries Ltd Japan. The image-processing unit consists of two CCD cameras, a PC for processing images and another for transmitting position data to the operator. The tele-operating console consists of a monitor and the robot control GUI. In this system, a three dimensional model of the robot and its environment was created using Java 3 D. This allows the operator to command the robot from remote site and observe the state of the robot via such a real time updated GUI. Figure1 shows the hardware architecture of the teleoperation system.

Figure 1. Hardware Architecture of the system

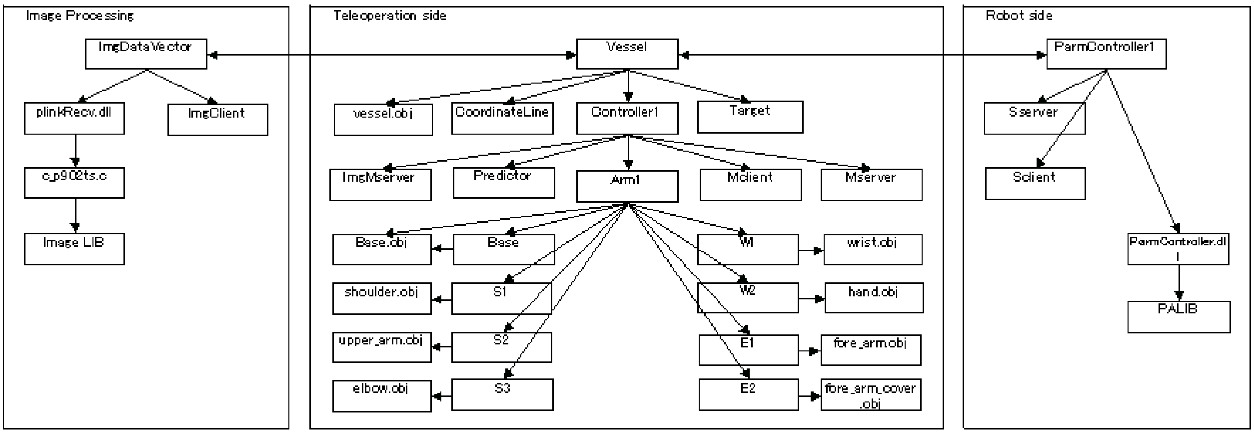

Figure 2　Software System Architecture

3. Programming Development

The project has developed a system, which use Java 2 to connect the operator site with robot site though network. The software architecture of whole system is shown in figure 2. It is composed of three main modules. The main module for the operator site is known as Vessel, which sets up the virtual model and calls Controller1 class. Controller1 class deals with robot unit and image-processing unit. Since the image processing and robot control algorithms are developed in C programming, a programming interface is necessary to make the Java methods to call the C functions. We created PlinkRecv.dll and ParmController.dll and then through the Java Native method to call them. The virtual model is coded by using Java 3D API. The graphic parts of robot and its environment are created by CAD and transferred to *.obj format. These object files can be loaded by Java programming and reunited into Java 3D coordinate to represent the virtual model. Figure3 is a screenshot of the 3D model.

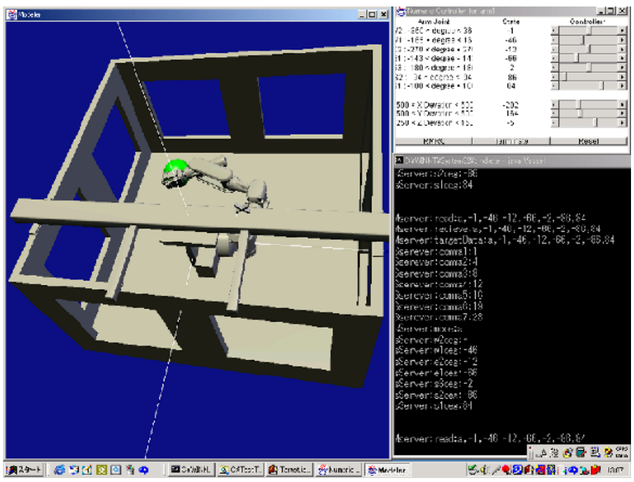

Figure3. Java 3D Model and Teleoperation Controller

4. Solution for time delay

Our real time teleoperation system utilizes a general network to transmit data. That will be inevitably affected from the time delay. Besides, considering that the teleoperation system uses visual feedback, cameras probably fail to collect image for a few samples when the target is out of view or be obstructed. As a solution for such these problems, the research combines the event-triggered autonomous control and optimum filter based prediction method to achieve a moving target tracking and grasping teleoperating task. The target positions are estimated through a varying gain Kalman Filter, which uses the past value of target trajectory to give a best predict about the target future position.

4.1 Kalman Filter Overview

According to R. E. Kalman's theory [5], a system model is required. Here we suppose the system is discrete linear, so the state equation can be presented as

$$X_{(k+1)} = AX_{(k)} + BU_{(k)} + W_{(k)} \quad \text{......................(4.1)}$$

The measurement output equation is

$$Z_{(k)} = CX_{(k)} + V_{(k)} \quad \text{....................................(4.2)}$$

In the above equations A, B, C are matrix; k is the time index; X is called the state of system; U is known input of the system; Z is the measurement value; w and v are system noise and measurement noise respectively. Each of these quantities is vectors and contains more than one element.

Although the vector X includes all of the information about the present state of the system, unfortunately it could not be measured directly. However we can use available measurement Z to estimate the true state X. Then, what criteria should our estimator satisfy? Two obvious requirements come to mind. First, we want the average value of our state estimate to be equal to the average value of the true state. Mathematically, we would say that the expected value of the estimate should be equal to the expected value of the state. Second, we want a state estimate that varies from the true state as little as possible. That is, not only do we want the average of the state estimate to be equal to the average of the true state, but we also want an estimator that results in the smallest possible variation of the state estimate. Mathematically, we would say that we want to find the estimator with the smallest possible error variance. It so happens that the Kalman filter is the estimator that satisfies these two criteria. But the Kalman filter solution does not apply unless we can satisfy certain assumptions about the noise that affects our system. Remember from our system model that *W* is the process noise and *V* is the measurement noise. We have to assume that the average value of *W* is zero and the average value of *V* is zero. We have to further assume that no correlation exists between *W* and V. That is, at any time *k*, W_k, and V_k are independent random variables. Then the noise covariance matrices S_w and S_z are defined as:

Process noise covariance

$$S_w = E\left[W_k W_k^{\ T}\right] \text{……………………………………}(4.3)$$

Measurement noise covariance

$$S_v = E\left[V_k V_k^{\ T}\right] \text{……………………………………..}(4.4)$$

where W^T and V^T indicate the transpose of the *W* and *V* random noise vectors, and E(•) means the expected value. Here we will not retrace the complete Kalman's derivation anymore.

The three final resulting equations are given as follows:

$$K_k = AP_k C^T\left[CP_k C^T + S_v\right]^{-1} \text{…………………..}(4.5)$$

$$\hat{X}_{k+1} = (A\hat{X}_k + BU_k) + K_k(Z_{k+1} - C\hat{X}_k) \text{ …….}(4.6)$$

$$P_{k+1} = AP_k A^T + S_w - AP_k C^T[CP_k C^T + S_v]^{-1} CP_k A^T \text{ ……………………………………………………..}(4.7)$$

In the above equations, a "-1"superscript indicates matrix inversion and a "T" superscript indicates matrix transposition. The *K* matrix is called the Kalman gain, and the *P* matrix is called the estimation error covariance. The state estimate $\hat{X}$ equation (4.6) consists of tow parts. The first term used to derive the state estimate at time *k* + 1 is just *A* times the state estimate at time *k*, plus *B* times the known input at time *k*. This would be the state estimate if we didn't have a measurement. The second term in the $\hat{X}$ equation is called the correction term and it represents the amount by which to correct the propagated state estimate due to our measurement. Inspection of the *K* equation (4.5) shows that if the measurement noise is large, S_v will be large, so *K* will be small and we won't give much credibility to the measurement *Z* when computing the next $\hat{X}$. On the other hand, if the measurement noise is small, S_v will be small, so *K* will be large and we will give a lot of credibility to the measurement when computing the next $\hat{X}$.

4.2 Application of Kalman Filter Predictor in Moving Target Tracking and Grasping

Now consider our moving target tracking system. We assumed the trajectory be liner and the object moving in a two-dimensional plane with constant velocity. Four signals are to be estimated: the position coordinates x_k , y_k and the velocity vector $\dot{x}_k$, $\dot{y}_k$. The state vector of the system, X_k , can be expressed as

$$X_k = \begin{bmatrix} x_k & \dot{x}_x & y_k & \dot{y}_k \end{bmatrix}^T \text{…………………….…….}(4.8)$$

Under the assumption that the target moves in constant velocity, the input acceleration is 0, and then the state equations of the signal model are:

$$x_{k+1} = x_k + T\dot{x}_k + w_{xk} \text{ ………………….……….}(4.9)$$

$$\dot{x}_{k+1} = \dot{x}_k \text{ ……………………………….……..}(4.10)$$

$$y_{k+1} = y_k + T\dot{y}_k + w_{yk} \text{ ………………….……..}(4.11)$$

$$\dot{y}_{k+1} = \dot{y}_k \text{ ……………………………….……..}(4.12)$$

Where T is the sampling interval. The noise term w_k accounts for deviation from the assumed constant velocity trajectory. We can rewrite the linear system equations in (4.1)(4.2) as following:

$$X_{k+1} = \begin{bmatrix} 1 & T & 0 & 0 \\ 0 & 1 & 0 & 0 \\ 0 & 0 & 1 & T \\ 0 & 0 & 0 & 1 \end{bmatrix} X_k + W_k \text{ …………..... …}(4.13)$$

$$Z_k = \begin{bmatrix} 1 & 0 & 0 & 0 \\ 0 & 0 & 1 & 0 \end{bmatrix} X_k + V_k \text{ ……..……}(4.14)$$

Here we suppose the process noise W_k =[w_{xk} 0 w_{yk} 0] ^{T} is a zero-mean, white, stationary random variable with variance σ_x^2, σ_y^2 respectively. The measurement noise V_k =[v_{xk} v_{yk}] also follows the same assumption given as variable with variance $\sigma_{xz}^2, \sigma_{yz}^2$. Hence the Process noise covariance can be simplified as

$$S_w = E\left[W_k W_k^{\ T}\right] = \begin{bmatrix} \sigma_x^2 & 0 & 0 & 0 \\ 0 & 0 & 0 & 0 \\ 0 & 0 & \sigma_y^2 & 0 \\ 0 & 0 & 0 & 0 \end{bmatrix} \text{………....}(4.15)$$

And the measurement noise covariance become

$$S_v = E\left[V_k V_k^{\,T}\right] = \begin{bmatrix} \sigma_{xz}^2 & 0 \\ 0 & \sigma_{yz}^2 \end{bmatrix} \quad \text{…………………(4.14)}$$

With the above signal model and measurement model, we can make the three general Kalman Filter equations (4.5)(4.6)(4.7) specialize to our practical system. The expression as follows:

$$K_{k+1} = \begin{bmatrix} 1 & T & 0 & 0 \\ 0 & 1 & 0 & 0 \\ 0 & 0 & 1 & T \\ 0 & 0 & 0 & 1 \end{bmatrix} P_k \begin{bmatrix} 1 & 0 & 0 & 0 \\ 0 & 0 & 1 & 0 \end{bmatrix}^T$$

$$\left[\begin{bmatrix} 1 & 0 & 0 & 0 \\ 0 & 0 & 1 & 0 \end{bmatrix} P_k \begin{bmatrix} 1 & 0 & 0 & 0 \\ 0 & 0 & 1 & 0 \end{bmatrix}^T + \begin{bmatrix} \sigma_{xz}^2 & 0 \\ 0 & \sigma_{yz}^2 \end{bmatrix} \right]^{-1}$$

…………..……….…………………..(4.15)

$$\hat{X}_{k+1} = \begin{bmatrix} 1 & T & 0 & 0 \\ 0 & 1 & 0 & 0 \\ 0 & 0 & 1 & T \\ 0 & 0 & 0 & 1 \end{bmatrix} \hat{X}_k + K_k \left[Z_k - \begin{bmatrix} 1 & 0 & 0 & 0 \\ 0 & 0 & 1 & 0 \end{bmatrix} \hat{X}_k \right]$$

…………………..……………...…(4.16)

$$P_{k+1} = \begin{bmatrix} 1 & T & 0 & 0 \\ 0 & 1 & 0 & 0 \\ 0 & 0 & 1 & T \\ 0 & 0 & 0 & 1 \end{bmatrix} P_k \begin{bmatrix} 1 & T & 0 & 0 \\ 0 & 1 & 0 & 0 \\ 0 & 0 & 1 & T \\ 0 & 0 & 0 & 1 \end{bmatrix}^T + \begin{bmatrix} \sigma_x^2 & 0 & 0 & 0 \\ 0 & 0 & 0 & 0 \\ 0 & 0 & \sigma_y^2 & 0 \\ 0 & 0 & 0 & 0 \end{bmatrix}$$

$$- \begin{bmatrix} 1 & T & 0 & 0 \\ 0 & 1 & 0 & 0 \\ 0 & 0 & 1 & T \\ 0 & 0 & 0 & 1 \end{bmatrix} P_k \begin{bmatrix} 1 & 0 & 0 & 0 \\ 0 & 0 & 1 & 0 \end{bmatrix}^T$$

$$\left[\begin{bmatrix} 1 & 0 & 0 & 0 \\ 0 & 0 & 1 & 0 \end{bmatrix} P_k \begin{bmatrix} 1 & 0 & 0 & 0 \\ 0 & 0 & 1 & 0 \end{bmatrix}^T + \begin{bmatrix} \sigma_{xz}^2 & 0 \\ 0 & \sigma_{yz}^2 \end{bmatrix} \right]^{-1}$$

$$\begin{bmatrix} 1 & 0 & 0 & 0 \\ 0 & 0 & 1 & 0 \end{bmatrix} P_k \begin{bmatrix} 1 & T & 0 & 0 \\ 0 & 1 & 0 & 0 \\ 0 & 0 & 1 & T \\ 0 & 0 & 0 & 1 \end{bmatrix} \quad \text{…………….(4.17)}$$

Now it remains only to specify the actual values taken by the two noises covariance S_w , S_v and to specify the values of the filter's initial state.

Suppose that the signal estimate at time interval k=2, $\hat{X}_2$, is computed from the first two measurements Z_1 and Z_2. The two components of signal X_2 can be estimated by

$$\hat{x}_2 = Z_{x2} \quad \text{……………………….……..…….. …(4.18)}$$

$$\hat{\dot{x}}_2 = (Z_{x2} - Z_{x1})/T \quad \text{………………………..…(4.19)}$$

$$\hat{y}_2 = Z_{y2} \quad \text{……………………………………….(4.20)}$$

$$\hat{\dot{y}}_2 = (Z_{y2} - Z_{y1})/T \quad \text{……………………...…..(4.21)}$$

The error on this estimate is calculated to be

$$X_2 - \hat{X}_2 = \begin{bmatrix} x_2 - Z_{x2} \\ \dot{x}_2 - (Z_{x2} - Z_{x1})/T \\ y_2 - Z_{y2} \\ \dot{y}_2 - (Z_{y2} - Z_{y1})/T \end{bmatrix} \quad \text{……..…..(4.22)}$$

Due to the velocity is constant, we have

$$\dot{x}_2 = \dot{x}_1 = [x_2 - x_1 - w_{x1}]/T \quad \text{………….……..(4.23)}$$

$$\dot{y}_2 = \dot{y}_1 = [y_2 - y_1 - w_{y1}]/T \quad \text{……………….(4.24)}$$

Considering the measurement noise the measurement should be

$$Z_{x2} = x_2 + v_{x2} \quad \text{……………….……………….(4.25)}$$

$$Z_{y2} = y_2 + v_{y2} \quad \text{………………..………………(4.26)}$$

So the equation 4.22 can be presented as

$$X_2 - \hat{X}_2 = \begin{bmatrix} -v_{x2} \\ [v_{x1} - v_{x2} - w_{x1}]/T \\ -v_{y2} \\ [v_{y2} - v_{y1} - w_{y1}]/T \end{bmatrix} \quad \text{…………(4.27)}$$

The covariance matrix of the estimate error P_2 can be gotten as

$$P_2 = E\left[\left[X_2 - \hat{X}_2\right]\left[X_2 - \hat{X}_2\right]^T\right]$$

$$= \begin{bmatrix} -v_{x2} \\ [v_{x1}-v_{x2}-w_{x1}]/T \\ -v_{y2} \\ [v_{y2}-v_{y1}-w_{y1}]/T \end{bmatrix} \begin{bmatrix} -v_{x2} \\ [v_{x1}-v_{x2}-w_{x1}]/T \\ -v_{y2} \\ [v_{y2}-v_{y1}-w_{y1}]/T \end{bmatrix}^T$$

$$= \begin{bmatrix} v_{x2}^2 & v_{x2}^2/T & 0 & 0 \\ v_{x2}^2/T & [v_{x1}^2+v_{x2}^2+w_{x1}^2]/T^2 & 0 & 0 \\ 0 & 0 & v_{y2}^2 & v_{v2}^2/T \\ 0 & 0 & v_{v2}^2/T & [v_{y1}^2+v_{y2}^2+w_{y1}^2]/T^2 \end{bmatrix}$$

$$= \begin{bmatrix} \sigma_{xz}^2 & \sigma_{xz}^2/T & 0 & 0 \\ \sigma_{xz}^2/T & [2\sigma_{xz}^2+\sigma_x^2]/T^2 & 0 & 0 \\ 0 & 0 & \sigma_{yz}^2 & \sigma_{vz}^2/T \\ 0 & 0 & \sigma_{vz}^2/T & [2\sigma_{yz}^2+\sigma_y^2]/T^2 \end{bmatrix} \quad ...(4.28)$$

The initial value P_3 can now be calculated using equation (4.17). The predicted signal $\hat{X}_3$ is obtained from equation (4.16)(4.18). Using equation (4.15), Kalman gain K_4 can be obtained. Repeating these procedures, the successive predictions are obtained.

5. Experiment Investigations and Result

To demonstrate the maximum permissibility of the teleoperating system, a time-limited task is chosen. A small ball is used as a target. For verifying the effectivity of the prediction system, we make the target move along X-axis with a constant velocity. So the Kalman Filter prediction system is simplified from 4 states to 2 states, they are position x_k and velocity $\dot{x}_k$. Before our Kalman Filter predictor can be implemented, specific values must be assigned to the noise variances σ_x^2, σ_{xz}^2. According to a series of tests in using different value of σ_x, σ_{xz}, finally we choose σ_x =0.2, σ_{xz} =10. The experiment result is showed in following Figure.

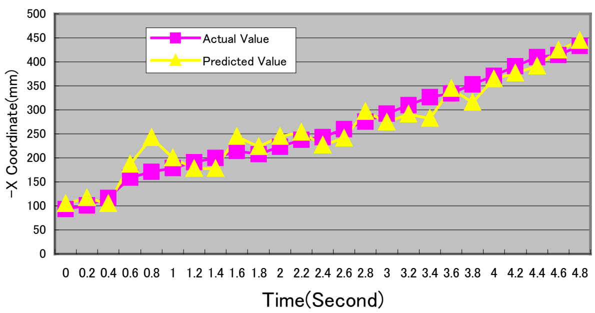

Figure 3. Target Position and Predicted Position

6. Conclusion

In this research, a virtual model based teleoperation system is developed. This experimental system includes a GUI in the operator side, which allows operator interact with remote robot by sending the control command through the virtual model input panel and view the robot state from the real time updated Java 3D model.

An on-line state estimate system is also explored. This paper presents a real time visual feedback tracking system to follow a moving target, predict its future position, and catch it. By using an optimum Kalman Filter based prediction algorithm, we successfully overcome the unavoidable time delay and achieve the task.

7. Reference

[1] Mitsuishi, T. Hori, and T. Nagao, "Predictive information display for telehanding/machining system". IEEE/RSJ/GI International Conference on Intelligent Robots and Systems 1994,pp.260-267.

[2] Tachi. S, "Real-time remote robotics- toward networked telexistence",IEEE Computer Graphics and Applications 1998,18(6),pp.6-9.

[3] M. Minsk, O. Y. Ming, O. Steele, F. P. Brooks, and M. Behensky, "Felling and Seeing: issues in force display". ACM SIGGRAPH Computer Graphics 1990,24(2), pp. 235-243.

[4] Kyo, M., E. Miyazaki, S. Tsukioka, H. Ochi, Y. Amitani, T. Tsuchiya, T. Aoki, and S. Takagawa. 1995. "The sea trial of "KAIKO", the full ocean depth research ROV ". OCEANS'95 3:1991-1996

[5] R. E. Kalman. "A New Approach to Linear Filtering and Prediction Problems". Transactions of the ASME-Journal of Basic Engineering, 1960, 82(Series D), pp.35-45.

The Eleventh International Symposium on Artificial Life and Robotics 2006 (AROB 11th'06),
B-con Plaza, Beppu, Oita, Japan, January 23-25, 2006

A designing method research of the control system for Autonomous Underwater Vehicle (AUV) using Linear Matrix Inequalities (LMIs)

Yohei Nasuno*, Etsuro Shimizu*, Masanori Ito*
Taro Aoki, Ikuo Yamamoto**, Satoshi Tsukioka**,**
Hiroshi Yoshida, Tadahiro Hyakudome**, Shojiro Ishibashi****

***Marine System Engineering, Tokyo Univ. of Marine Science & Technology, Tokyo, Japan**
****Japan Agency for Marine-Earth Science and Technology (JAMSTEC), Kanagawa, Japan**

Abstract

An Independent Administrative Corporation Japan Agency for Marine-Earth Science and Technology (JAMSTEC) is developing light-and-small Autonomous Underwater Vehicles (AUV)[1], named 'MR- 1' (Marine Robot Experimental 1), which can cruise, investigate and observe by itself without human's help. In this paper, we consider the motion control problem of 'MR- 1' and derive a controller. Since the dynamic property of 'MR- 1' is changed by the influence of the speed, the mathematical model of 'MR- 1' becomes the nonlinear model. In order to design a controller for 'MR- 1', we generally apply nonlinear control theories or linear control theories with some constant speed situation. If we design a controller by applying Linear uadratic (L) optimal control theory, the obtained controller only compensates the optimality at the designed speed situation, and does not compensate the stability at another speed situations. This paper proposes a controller design method using Linear Matrix Inequalities (LMIs)[2][3][4][9]. The algorithm to solve the LMI has a property that it can solve some number of LMIs simultaneously. By applying this property, it is considered that we can obtain the solution that satisfies the LMI condition under several speeds. And examples of numerical analysis using our designed controller are shown.

Keywords

Autonomous Underwater Vehicle (AUV), MR- 1 (Marine Robot Experimental 1), Linear Matrix Inequality (LMI), Linear uadratic (L) Optimal Control

1. Introduction

1.1 Background

Development of our science technology has been advanced drastically since industrial revolution. However, serious problems such as environmental destruction and energy problem are caused by the excess consumption of fossil fuel as typified by coal and coal oil. We have to accept this fact of the matter sincerely, and have to develop solutions. Especially, it is usually said that the sign of climate change is appeared prominently in ocean, so it is considered that we'll be able to get a solution by conducting oceanographic activities. However, the sea occupies about 70 percents of the surface of the earth, and it is the extreme environment that we can't step into easily. So it is difficult to investigate the ocean by human. And so development of marine robot, which can investigate, observe and operate for human, is urgent. If such kind of robots has been developed, we'll be able to avoid danger or advance working efficiency, and it is considered that we'll be able to contribute to the advancement of new science technology. Furthermore, in these years, the existence of 'Methane Hydrate', which exists under the bedrock of the ocean, attracts much public attention as a new clean alternative energy, which takes over from coal oil. If the investigation or dig of seabed resource can be realized by marine robots, it is considered that we'll be able to present one of the solution about environmental problem and energy problem. As above, the ocean has limitless possibilities, and the occasion of oceanographic investigation by marine robots is brought to international attention.

Unmanned Underwater Vehicles, which investigate, observe and operate of which take place of human that have ever developed, are classified two types. One is ROV (Remotely Operated Vehicle), and another is AUV (Autonomous

Underwater Vehicle). ROV has manipulators and it can operate undersea. And operator operates remotely by watching images of television camera. Typical examples of ROV are "KAIKO"[6] and "HYPER DOLPHINE"[7], which are developed at JAMSTEC. However, ROV has cables, so the moving area is limited. Therefore, in these days, AUV has been developing in order to observe more wide area. A typical example of AUV is "URASHIMA"[8], which is also developed at JAMSTEC. It can mission long-distance cruising and observation of seabed. However, in future, more efficient AUV, which operate autonomously replace ROV, is desired.

As above, marine robots are being shifted manned to unmanned and remotely operating type to autonomous type. Considering the case of developing seabed resource, we have to develop autonomous working robots. In order to realize it, JAMSTEC has been developing light-and-small AUV to explore and operate in the ocean. The AUV named MR- 1' can cruise, investigate and observe by itself without human's help. MR- 1' cruises autonomously, and in future, we load manipulators to MR- 1', and the goal is to make MR- 1' operate autonomously. So in this research, we focus autonomous cruising as the assumption that MR- 1' operates autonomously.

In order to operate MR- 1', five thrusters have to be controlled appropriately. However, two vertical thrusters are set up by inclining from the perpendicular, so if these vertical thrusters are rotated, MR- 1' not only moves the vertical direction but also moves the horizontal direction. In the case of considering the cruising MR- 1' with the constant altitude, both vertical and side thrusters have to be controlled appropriately. The present paper considers that MR- 1' is controlled to make it go straight on surge direction, and stop at the targeting point with the constant altitude. Furthermore, MR- 1' is a cruising AUV plus ROV, so it is necessary to design a controller, which adopt to cruising speed variations. In this research, we propose controller design method using Linear Matrix Inequality (LMI) in order to achieve this aim.

1.2 Autonomous Underwater Vehicle 'MR-X1'

MR- 1' is an AUV, which can observe and operate autonomously instead of human at the ocean that is an extensive, moreover an extreme environment. Appearance of MR- 1' is shown as Fig. 1. MR- 1' has some characters that it realizes light-and-small, and whole motions can control by using five thrusters. Principal specification is shown as follows.

Table 1• Principal specification of 'MR-X1'

Dimensions	2.5[m](total length) • • 0.8[m](width) • •1.2[m](height)
Weight	800[kg] (in the air)
Cruising Speed	2[kt]
Maximum Depth	4,200[m]
Power Source	Lithium Ion Battery
Cruising Mode	Acoustic communication, Optical communication, Autonomous
Actuators	Main thruster (400W) Two side thrusters (150W) Two vertical thrusters (150W)

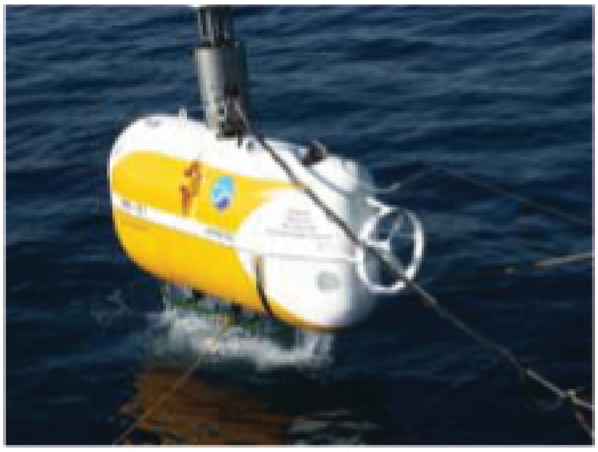

Fig.1• Autonomous Underwater Vehicle 'MR-X1'

2. Mathematical Model of 'MR-X1'

2.1 Coordinate Systems [5]

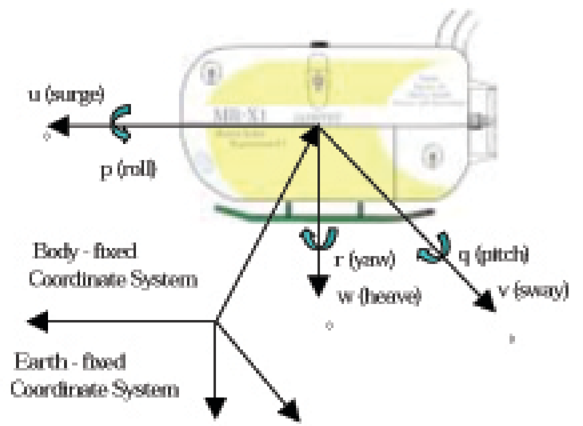

Fig.2 Coordinate system of MR- 1'

In this paper, we use two coordinate systems. One is the Earth-fixed coordinate system and the other is the Body-fixed coordinate system. Fig.2 shows the relation between each coordinate system. In general, linear and angular velocities are represented by using Body-fixed coordinate system, but the transformation to the Earth-fixed coordinate system is suitable to observe the motion of MR- 1'.

$$\dot{\eta} = J(\eta)\nu \qquad (2.1)$$

$\eta = [\ ,\ ,\vartheta,\ ,\phi,\varphi]^T$: Position and angle vector with the Earth-fixed coordinate system

$\nu = [u,\ ,\ ,\ ,p,r]^T$: Linear and angular velocity vector with the Body-fixed coordinate system

$\ ,\ ,\ $: Position ϕ,ϑ,φ : Attitude

$u,\ ,\ $: Linear velocity $p,\ ,r$: Angular velocity

$J(\eta)$: Velocity transformation matrix

2.2 Dynamics [5,9]

In this section, we derive mathematical model of MR- 1'. Following matrices are derived by numeric calculation or experiment. This model has been derived as faithful to MR- 1' as we could, but it isn't strictly. However, robust control theory has a property that even if the model is different or change from real character a little, the system will be able to adopt them. Therefore, it is considered that this theory can be covered these errors.

The motion of underwater vehicle is represented as the 6DOF nonlinear equation. In general, its motion can be treated as the motion of Rigid-body. We derived the nonlinear equation of MR- 1' following the method, which is suggested by Thor I. Fossen. The nonlinear equation is represented as follows.

$$M\dot{\nu} + C(\nu)\nu + \ (\nu)\nu + g(\eta) = \tau \qquad (2.2)$$

M : Inertial matrix

$C(\nu)$: Matrix of Coriolis and Centripetal

(ν) : Damping matrix

$g(\eta)$: Matrix of restoring forces and moments

τ : Thrusts

2.3 Parameter-dependent PD ineari ation

In this section, we treated the cruising speed for surge direction as a parameter, and under this condition, the mathematical model of MR- 1' is linearized. There are three reasons. First, in this research, we'd like to confirm that we'd be able to design a controller using LMI for the mathematical model of which includes non-linear components. However, both Linear uadratic (L) optimal control and LMI cannot solve non-linear model. So in order to design a controller using these design method, we have to linearize the mathematical model. Secondly, the aim of this research is long-distance cruising for surge direction. However, moving toward vertical and horizontal direction is not the aim but to keep the condition of origin vicinity. In short, the role of side and vertical thrusters is to reduce the deviation that occurs by moving toward surge direction. So we considered that it is sufficiently to be linearlized under first-order approximation. And the last reason is that if many parameters are existed, "Simultaneous LMIs that depends on parameters" can be high-dimensions, and it is difficult to solve. As above, we linearized the mathematical model of MR- 1' except the speed parameter of surge direction u'. Linearized model is represented as follows.

○Inertial matrix

$$M = \left[\begin{array}{ccc|ccc} m-\ _{11} & 0 & m & 0 & 0 & 0 \\ 0 & m-\ _{33} & -mx & 0 & 0 & 0 \\ m & -mx & I_{yy}-\ _{55} & 0 & 0 & 0 \\ \hline 0 & 0 & 0 & m-\ _{22} & -m & mx \\ 0 & 0 & 0 & -m & I_{xx}-\ _{44} & 0 \\ 0 & 0 & 0 & mx & 0 & I\ -\ _{66} \end{array}\right] \qquad (2.3)$$

○Matrix of coriolis and centripetal terms

$$C(u)_L = \left[\begin{array}{ccc|ccc} 0 & 0 & 0 & 0 & 0 & 0 \\ 0 & 0 & -(m-\ _{11})u & 0 & 0 & 0 \\ 0 & (m-\ _{11})u & 0 & 0 & 0 & 0 \\ \hline 0 & 0 & 0 & 0 & 0 & (m-\ _{11})u \\ 0 & 0 & 0 & 0 & 0 & 0 \\ 0 & 0 & 0 & -(m-\ _{11})u & 0 & 0 \end{array}\right] \qquad (2.4)$$

○Damping matrix

$$_L = -\left[\begin{array}{ccc|ccc} 0 & 0 & 0 & 0 & 0 & 0 \\ 0 & & & 0 & 0 & 0 \\ 0 & M & M & 0 & 0 & 0 \\ \hline 0 & 0 & 0 & & 0 & _r \\ 0 & 0 & 0 & & 0 & _r \\ 0 & 0 & 0 & N & 0 & N_r \end{array}\right] \qquad (2.5)$$

○Matrix of restoring forces and moments

$$g_L = \left[\begin{array}{ccc|ccc} 0 & 0 & 0 & 0 & 0 & 0 \\ 0 & 0 & 0 & 0 & 0 & 0 \\ 0 & 0 & (\ W-\ ) & 0 & 0 & 0 \\ \hline 0 & 0 & 0 & 0 & 0 & 0 \\ 0 & 0 & 0 & 0 & (\ W-\ ) & 0 \\ 0 & 0 & 0 & 0 & 0 & 0 \end{array}\right] \qquad (2.6)$$

○Matrix that transform thrusts into rotational speed

$$\tau_{R\ T} = \left[\begin{array}{ccccc} 1 & 0 & 0 & 0 & 0 \\ 0 & 0 & 0 & \cos\alpha & \cos\alpha \\ -|\ _{T\ M}| & 0 & 0 & |x_{TVL}|\cos\alpha & |x_{TVR}|\cos\alpha \\ \hline 0 & -1 & -1 & -\sin\alpha & \sin\alpha \\ 0 & -|x_{T\ F}| & |\ _{T\ R}| & -|\ _{TVL}|\sin\alpha - |y_{TVL}|\cos\alpha & |\ _{TVR}|\sin\alpha + |y_{TVR}|\cos\alpha \\ 0 & -|x_{T\ F}| & |x_{T\ R}| & |x_{TVL}|\sin\alpha & -|x_{TVR}|\sin\alpha \end{array}\right]$$

$$\bullet\begin{bmatrix} 9.3043 & 0 & 0 & 0 & 0 \\ 0 & 0.84628 & 0 & 0 & 0 \\ 0 & 0 & 0.98582 & 0 & 0 \\ 0 & 0 & 0 & 0.95576 & 0 \\ 0 & 0 & 0 & 0 & 0.96669 \end{bmatrix} \tag{2.7}$$

2.4 State Space Representation

State equation of MR- 1' is represented as follow.

$$\dot{x} = \quad (u)x + \quad \bar{\tau} \tag{2.8}$$

$$x = [\nu, \eta]^T = [u, \ , \ , \ , p, r, \ , \ , \vartheta, \ , \phi, \varphi]^T$$

$$\bar{\tau} = [n_{T\ M}, n_{T\ F}, n_{T\ R}, n_{TVL}, n_{TVR}]^T$$

$$= \begin{bmatrix} -M^{-1}(C(u)_L + \quad _L) & -M^{-1}g_L \\ J_L & 0_{6\times6} \end{bmatrix} \tag{2.9}$$

$$= \begin{bmatrix} M^{-1}\tau_{R\ T} \\ 0_{6\times6} \end{bmatrix} \tag{2.10}$$

3 Controller Design for PD ineari ed System

The aim of developing MR- 1' is to construct the AUV that it not only follows the given path but also stops at the objective point and keeps the point to investigate, observe and operate. In order to realize them, five thrusters, which equipped on MR- 1', have to be controlled to be appropriate rotational speeds. In order to check the dynamic characteristic of MR- 1', the main thruster was only rotated firstly. Since the displacement toward to the heave direction occurred, to keep constant altitude, two vertical thrusters have to be rotated. However, vertical thrusters set up by heaving the inclination from the perpendicular. If these thrusters are rotated, MR- 1' not only moves the vertical direction but also changes the horizontal direction. Therefore, in the case of cruising MR- 1' with the constant altitude, these five thrusters have to be controlled appropriately. The present paper considers the controller design problem for MR- 1' to make it go straight on surge direction, and stop at the objective point with the constant altitude. And we design a control system to adopt the variation of the speed for the surge direction.

PD linearized system is represented including only the speed parameter of surge direction u'. Thus, the condition, which depends on only u', is constructed. When we make controllable matrix using state equation (2.8) to (2.10), it becomes full rank. So it is obvious that this system is controllable. Therefore, we ll be able to solve Riccati equation or inequality, and derive positivistic symmetric definite.

3.1 Controller Design Strategy using Simultaneous Is that depends on parameters

In this section, the control system is designed to control MR- 1' moving toward the objective point and stopping at that point. If we treat this aim as regulator problem, we can design a control system that following the theory of origin convergence'. So we design a controller for MR- 1' that main thruster is used for only straight cruising and two side thrusters and two vertical thrusters are used for moving to make deviations zero from horizontal and vertical direction.

The control system is firstly designed using the L optimal control. Generally, in order to design the L optimal control system for linear systems, it is necessary to solve the Algebraic Riccati equation by using constant matrices A and B in the state equation. Since the Riccati equation is solved easily by using some computer software, the state feedback control system can be obtained easily. In order to apply the L control theory for MR- 1', we have to fix the cruising speed u. Therefore the optimality of the obtained control system is only compensated about the one speed. However, the obtained control system does not compensate the stability in other speed situations.

In order to solve this problem, we propose a new design method by using LMI, which correspond to the Riccati inequality. The algorithm to solve LMI has a property that can solve some number of LMIs simultaneously. By applying this property, it is considered that we can obtain the solution that satisfies the LMI condition under several speeds.

The LMI that corresponds to Riccati inequality in L optimal control on state equation is represented as (3.1).

$$\begin{bmatrix} (u_i) \quad + \quad (u_i)^T - \quad ^T & C^T \\ C & -I \end{bmatrix} < 0 \quad (i = 0, \ \cdot\ \cdot\ \cdot\ m)$$

$$> 0 \tag{3.1}$$

$$\bar{\tau} = - \quad x = - \quad ^T \quad ^{-1}x \tag{3.2}$$

Speed parameter u' is given appropriately. By solving "Simultaneous LMIs that depends on parameters", we can obtain one solution. The control input is represented as (3.2). The solution satisfies LMI conditions on all speed parameters. This means that the obtained control system compensates the stability for all speed situations, which substitute for parameters. For L optimal control systems, two types of controllers were designed. One is the optimal gain for the surge speed 0[m/s] (Case1), and another is for 0.3[m/s] (Case2). The speed of 0[m/s] corresponds to keeping the objective point. The speed 0.3[m/s] is the middle speed of MR- 1' since the maximum speed of MR- 1' is about 0.6[m/s]. On the other hand, for "Simultaneous LMIs that depends on parameters", we set the range of speed parameter between 0[m/s] and 0.7[m/s] (Case3). 0.7[m/s] is covered the maximum speed of MR- 1'.

3.2 umerical Examples

Table 2 Requirements of simulations

Simulation time	300[sec]
Initial position	[-100(m), 10(m), 10(m)]
Target point	[0(m), 0(m), 0(m)]

○Case 1

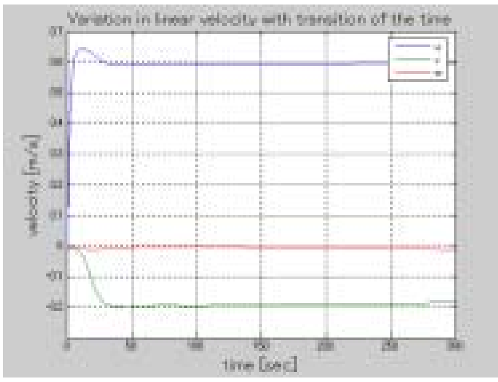

Fig.3 Variation in linear velocity with transition of the time

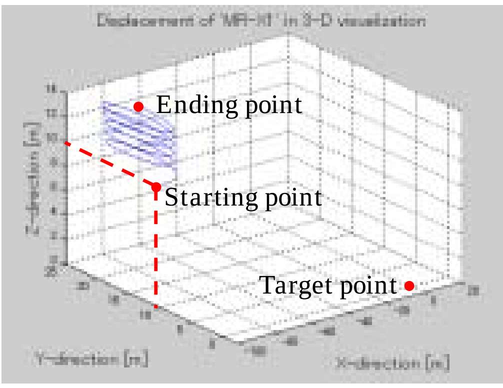

Fig.4 Displacement of MR- 1' in 3-D visualization

The movement from the initial position to the objective point occurs the velocity consequently, so the control system of 0[m/s] cannot compensate the stability at the speed occurring, and MR- 1' tends to diverge like Fig.3 and Fig.4.

○Case 2

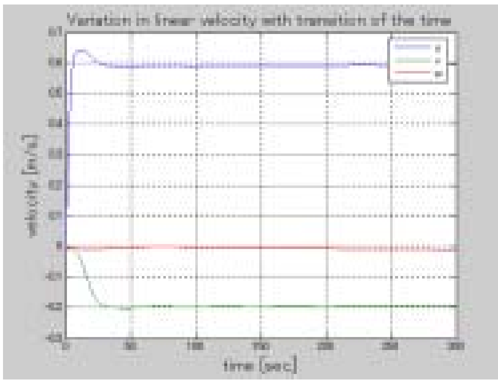

Fig.5 Variation in linear velocity with transition of the time

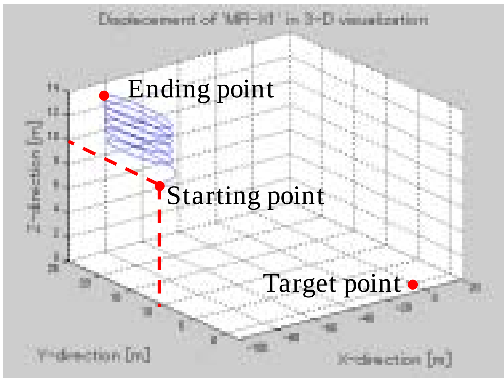

Fig.6 Displacement of MR- 1' in 3-D visualization

MR- 1' does not always cruise with the constant speed. Therefore, when speed changing occurs, the optimal gain will fluctuate in each case, and if we use the control system that derived under one fixed speed like this simulation, the obtained control system cannot compensate the stability at other speed situations, MR- 1' tends to diverge like Fig.5 and Fig.6.

〇Case 3

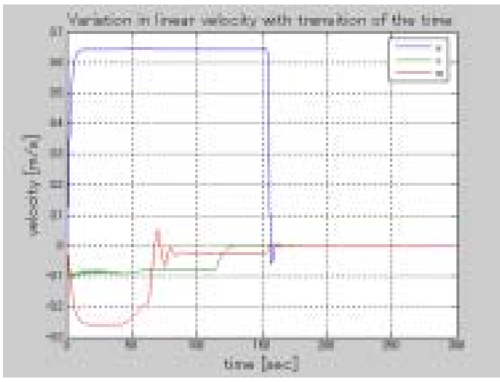

Fig.7 Variation in linear velocity with transition of the time

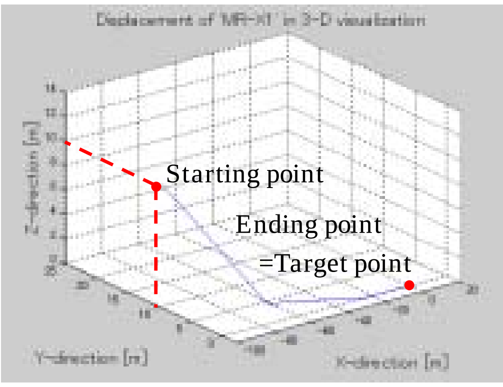

Fig.8 Displacement of MR- 1' in 3-D visualization

While MR- 1' cruises straight toward surge direction, initial deflections of Y-axis and -axis converge to the desired path on -axis. The speed of MR- 1' goes up to the maximum speed, and when MR- 1' comes close to the target point, the speed reduced and became 0[m/s] at the origin. Furthermore, this system can control MR- 1' even if the initial position has more distance from target point. So this new controller design method has effective property for designing controller of AUV.

4 Conclusions

In this paper, the mathematical model of Autonomous Underwater Vehicle named MR- 1', which is developing at JAMSTEC, was derived. And about the dynamic characteristic of MR- 1', which has nature of non-linear, we linearized the mathematical model in order to design a controller. And we set the aim on autonomous tracking given path and stopping at the objective point, and for this aim, we construct a control system, which was applied L optimal control system and new controller designing method "Simultaneous LMIs that depends on parameters". As the result, this new method made it possible to design a control system that corresponds to speed changing. This method has more effective performance than L optimal control system.

This research is the one that it proves the breadth of robustness in the case of using LMI method about AUV. This time, the aim was set as position control, and on that basis, the reality about this aim was suggested. Furthermore, we'll be able to confirmed sufficient controllability even if we linearized the model extremely, so it is considered that the system will be able to absorb little model error.

REFERA CES

[1] Hiroshi Yoshida: A Working AUV for Scientific Research, OCEAN '04 MTS／IEEE, TECHNO-OCEAN '04, Nov.9-12, 2004, Kobe, Japan

[2] P.Apkarian, G.Becker, P. Gahinet, H.Kajiwara: LMI Techniques in Control Engineering from Theory to Practice, IEEE CDC '96 Workshop, 1996

[3] Ikuo Yamamoto: Marine Control System, International Journal of Robust and Nonlinear Control, Vol.11, No.13, 2001

[4] Tetsuya Iwasaki: LMI and Control, Shokodo, 1997

[5] Thor I.Fossen: Guidance and Control of Ocean Vehicles, 1994

[6] Okutani, T. and N. Iwasaki (2003) Noteworthy abyssal mollusks (excluding vesicomyid bivalves) collected from the Nankai Trough off Shikoku by the ROV *ai o* of the Japan Marine Science Technology Center. Venus

[7] Yuichi Nishimura: The 2002-2003 seismic activity at Suiyo Seamount, Izu-Ogasawara (Bonin) Arc, as revealed by OBS observations

[8] Taro Aoki, Toshiaki Nakamura, Satoshi Tsukioka, Takashi Murashima, Hiroshi Ochi, Hidehiko Nakajo, Tadahiko Ida, Tadahiro Hyakudome: THE DEVELOPMENT OF THE AUV -URASHIMA-, OCEANS 2000 MTS／IEEE, 2000

[9] Yohei Nasuno, Etsuro Shimizu, Taro Aoki, Ikuo Yamamoto, Tadahiro Hyakudome, Satoshi Tsukioka, Hiroshi Yoshida, Shojiro Ishibashi, Masanori Ito: The design method of the control system for Autonomous Underwater Vehicle (AUV) using Linear Matrix Inequality (LMI), International Conference on Control, Automation, and Systems (ICCAS 2005), June 2-5, 2005, KINTE , Gyeonggi-Do, KOREA

The Eleventh International Symposium on Artificial Life and Robotics 2006 (AROB 11th'06),
B-con Plaza, Beppu, Oita, Japan, January 23-25, 2006

Three-Dimensional Synchronized Alternating Turing Machines

Takao ITO[1], Makoto SAKAMOTO[1], Makoto SAITO[1], Kouichi IIHOSHI[1], Hiroshi FURUTANI[1], Michio KONO[1], and Katsushi INOUE[2]

[1] Dept. of Computer Science and Systems Engineering, University of Miyazaki, Miyazaki 889-2192, JAPAN
[2] Dept. of Computer Science and Systems Engineering, Yamaguchi University, Ube 755-8611, JAPAN

Abstract

This paper introduces a three-dimensional synchronized alternating Turing machine (3-$SATM$), and investigates fundamental properties of 3-$SATM'$s whose input tapes are restricted to cubic ones. The main topics of this paper are: (1) a relationship between the accepting powers of 3-$SATM'$s and three-dimensional alternating Turing machines with small space bounds, (2) a relationship between the accepting powers of five-way and six-way 3-$SATM'$s, (3) a relationship between the accepting powers of 3-$SATM'$s and three-dimensional nondeterministic Turing machines.

Key Words: three-dimensional Turing machine, alternation, synchronization

1 Introduction and preliminaries

Synchronized alternating Turing machines were introduced in [2] to study the effect of allowing processes of an alternating Turing machine to communicate via synchronization. Informally, a synchronized alternating machine is an alternating machine with a special subset of internal states called synchronizing states. Each of these synchronizing states is associated with a synchronizing symbol. If, during the course of computation, some process enters a synchronizing state, then it has to wait until all other processes enter either an accepting state or a synchronizing state with the same synchronizing symbol. When this happens, all processes are allows to continue their computation; otherwise, the machine is said to have a deadlock. A computation is successful if no deadlocks occur and all processes terminate in accepting states. It turns out that synchronization significantly increases the computaional power of alternating Turing machines.

On the other hand, recently, due to the advances in many application areas such as computer vision, robotics, and so forth, it has become increasingly apparent that the study of three-dimensional pattern processing has been of crucial importance. Thus, the research of three-dimensional automata as a computational model of three-dimensional pattern processing has also been meaningful. From this viewpoint, we introduced three-dimensional alternating Turing machine [5].

In this paper, we continue the investigations about three-dimensional alternating Turing machines, introduce a three-dimensional synchronized alternating Turing machine (3-$SATM$), and investigate fundamental properties of 3-$SATM'$s whose input tapes are restricted to cubic ones.

Let Σ be a finite set of symbols. A *three-dimensional input tape* over Σ is a three-dimensional rectangular array of elements of Σ. The set of all the three-dimensional input tapes over Σ is denoted by $\Sigma^{(3)}$. Given an input tape $x \in \Sigma^{(3)}$, for each j $(1 \leq j \leq 3)$, we let $l_j(x)$ be the length of x along the jth axis. The set of all $x \in \Sigma^{(3)}$ with $l_1(x) = m_1$,$l_2(x) = m_2$ and $l_3(x)$=m_3 is denoted by $\Sigma^{(m_1,m_2,m_3)}$. If $1 \leq i_j \leq l_j(x)$ for each j $(1 \leq j \leq 3)$, let $x(i_1, i_2, i_3)$ denote the symbol in x with coordinates (i_1, i_2, i_3). Furthermore, we define $x[(i_1, i_2, i_3),(i'_1, i'_2, i'_3)]$, when $1 \leq i_j \leq i'_j \leq l_j(x)$ for each integer j $(1 \leq j \leq 3)$, as the three-dimensional input tape y satisfying the following;

(1) for each j $(1 \leq j \leq 3)$, $l_j(y) = i'_j - i_j + 1$;

(2) for each r_1, r_2, r_3 $(1 \leq r_1 \leq l_1(y)$, $1 \leq r_2 \leq l_2(y)$, $1 \leq r_3 \leq l_3(y))$, y $(r_1, r_2, r_3) = x$ $(r_1 + i_1 - 1$, $r_2 + i_2 - 1$, $r_3 + i_3 - 1)$. (We call $x[(i_1, i_2, i_3),(i'_1, i'_2, i'_3)]$ the $[(i_1, i_2, i_3),(i'_1,i'_2, i'_3)]$ *segment* of x.)

We now introduce a three-dimensional synchronized alternating Turing machine. A three-dimensional synchronized alternating Turing machine (denoted by 3-$SATM$) is a 10-tuple M = $(Q, q_0, U, E, S, F, \Sigma, \Pi, \Gamma, \delta)$, where

(1) $Q = U \cup E \cup S$ is a finite set of *states*,

(2) $q_0 \in Q$ is the *initial state*,

(3) U is the set of *universal states*,

(4) E is the set of *existential states*,

(5) $S \subseteq \{(q, s) : q \in U \cup E, s \in \Pi\}$ is the set of *synchronizing states* (*s-states*),

(6) $F \subseteq Q$ is the set of *accepting states*,

(7) Σ is a finite *input alphabet* ($\# \notin \Sigma$ is the *boundary symbol*),

(8) Π is a finite *alphabet of synchronizing symbols*,

(9) Γ is a finite *storage tape alphabet* containing the special *blank symbol* B,

(10) $\delta \subseteq (Q \times (\Sigma \cup \{\#\}) \times \Gamma) \times (Q \times (\Gamma - \{B\}) \times \{$*east,west,south,north,top,down,no move*$\} \times \{$*left,right,no move*$\})$ is the *next move relation.*

As shown in Fig.1, M has a read-only cubic input tape with boundary symbols #'s ($\# \notin \Sigma$) and one semi-infinite storage tape, initially filled with the blank symbols. M begins in state q_0. A *position* is assigned to each cell of the input tape and the storage tape, as shown in Fig.1. A *step* of M consists of reading one symbol from each tape, writing a symbol on the storage tape, moving the input and storage tape heads in specified directions, and entering a new state, according to the next move relation δ. When a process P enters a synchronizing state, it stops and waits until all the parallel processes either enter the states with the same synchronizing element or stop in accepting states.

An *instantaneous description* (ID) of a 3-$SATM$ $M = (Q, q_0, U, E, S, F, \Sigma, \Pi, \Gamma, \delta)$ is a pair of an element of $\Sigma^{(3)}$ and an element of

$$C_M = (N \cup \{0\}^3) \times S_M, S_M = Q \times (\Gamma - \{B\})^* \times \mathbf{N},$$

where $\mathbf{N}$ denotes the set of all positive integers. The first component of an $ID\ I = (x, ((i_1, i_2, i_3), (q, \alpha, k)))$ represents the input to M, and the first component (i_1, i_2, i_3) of the second component of I represents the input head position ($0 \leq i_1 \leq l_1(x)+1, 0 \leq i_2 \leq l_2(x)+1, 0 \leq i_3 \leq l_3(x)+1$), and the second component (q, α, k) of the second component of I represents the state of the finite control, nonblank contents of the storage tape, and the storage head position ($1 \leq k \leq |\alpha|+1$). An element of C_M is called a *configuration* of M, and an element of S_M is called a *storage state* of M.

An ID is *universal* (*existential*, *synchronizing*, *accepting*) depending on the type of the state of the finite control. The *initial ID* of M on input x is $I_M(x) = (x, ((1,1,1), (q_0, \epsilon, 1)))$, where ϵ is the null word.

Suppose I_1 and I_2 are two ID's of M and I_2 follows from I_1 in one step according to the next move relation δ. Then we write $I_1 \vdash_M I_2$ and say that I_2 is a *successor* of I_1. The reflexive and transive closure of $\vdash_M$ is denoted by $\vdash_M^*$.

A sequence of ID's of M, $I_0, I_1, \cdots, I_m (m \geq 0)$, is called a *sequential computation* of M if $I_0 \vdash_M I_1 \vdash_M \cdots \vdash_M I_M$. If $I_0 = I_M(x)$ for some x, we call this sequence a computation path of M on x.

The *full computation tree* of M on an input tape x is a (possibly infinite) labeled tree $\vdash_x^M$ such that

(1) each node v is labeled by some $ID\ I_v$ of M,

(2) the root is labeled by $I_M(x)$,

(3) v_2 is a direct descendant of v_1 iff $I_{v_1} \vdash_M I_{v_2}$.

(Each branch of $\vdash_x^M$ is called a *process*.)

The *synchronizing sequence* (*s-sequence*) of a node v in a full computation tree T with root v_0 is the sequence of synchronizing symbols occuring in labels of the nodes on the path from v_0 to v. Two s-sequences are *compatible* if one is a prefix of the other. If s_1 and s_2 are two compatible s-sequences, and s_2 is longer than s_1, then we use $s_2 - s_1$ to denote their difference.

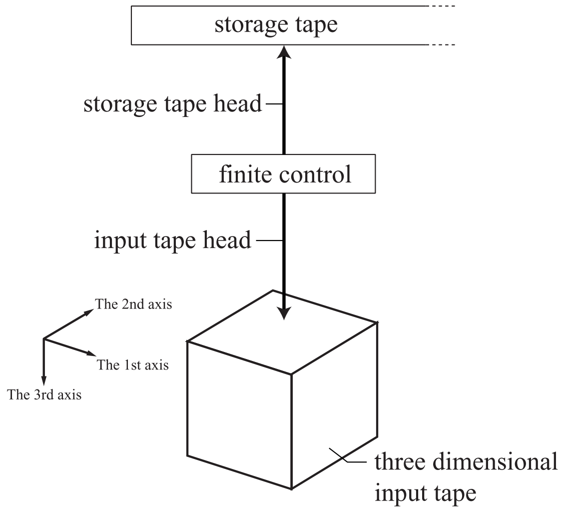

Fig. 1: Three-dimensional synchronized alternating Turing machine.

A *computation tree* of M on an input x is a (possibly infinite) subtree T' of the full computation tree T_x^M satisfying the following conditions:

(1) if u is an internal (non-leaf) node of the tree T', I_u is universal and $\{I \mid I_u \vdash_M I\} = \{I_1, \cdots, I_m\}$, then u has exactly m children $v_1, \cdots, v_m$, such that $I_{v_i} = I_i, 1 \leq i \leq m$,

(2) if u is an internal node of the tree and I_u is existential, then u has exactly one chiled v such that $I_u \vdash I_v$,

(3) For arbitrary nodes u and v of T', the *s-sequences* of u and v are compatible.

If M on input x has no computation trees, then any subtree of T_x^M that satisfies the first two conditions above must have two processes with incompatible s-sequences. In this case, we say M *deadlocks* on x. The two processes with incompatible s-sequences are called *deadlock processes* and the nonmatching s-states causing the deadlock are called *deadlock states*.

The longest synchronizing sequence of a node in the computation tree T is called the *synchronizing sequence of the computation tree* T.

An *accepting computation tree* of M on an input x is a finite computation tree of M on x such that each leaf node is labeled by an accepting ID. We say that M accepts x if there is an accepting computation tree of M on x. Let $T(M) = \{x \in \Sigma^{(3)} \mid M\ accepts\ x\}$.

We next introduce a five-way three-dimensional synchronized alternating Turing machine which can be considered as a synchronized version of five-way three-dimensional alternating Turing machine [5].

A *five-way three-dimensional synchronized alternating Turing machine* (denoted by $FV3$-$SATM$) is a 3-$SATM$ $M = (Q, q_0, U, E, S, F, \Sigma, \Pi, \Gamma, \delta)$, such that

$\delta \subseteq (Q \times (\Sigma \cup \{\#\}) \times \Gamma) \times (Q \times \Gamma - \{B\}) \times$ {*east, west, south, north, down, no move*} $\times$ {*left,right, no move*}).

That is, a $FV3$-$SATM$ is a 3-SAT M whose input head can move east, west, south, north, or down, but not up.

Let $L(m) : \mathbf{N} \rightarrow \mathbf{N}$ be a function with one variable m. With each 3-$SATM$ (or $FV3$-$SATM$) M we assosiate a *space complexity function* SPACE which takes ID's to natural numbers. That is, for each ID $I = (x, ((i_1, i_2, i_3), (q, \alpha, k)))$, let SPACE($I$) be the length of α. We say that M is "$L(m)$ *space-bounded*" if for all m and for all x with $l_1(x) = l_2(x) = l_3(x) = m$, if x is accepted by M, then there is an accepting omputation tree of M on input x such that for each node π of the tree, SPACE $(I(\pi)) \leq L(m)$. By "3-$SATM(L(m))$" ("$FV3$-$SATM(L(m))$") we denote an $L(m)$ space-bounded 3-$SATM$ ($FV3$-$SATM$) whose input tapes are restricted to cubic ones.

Three-dimensional alternating Turing machines (3-ATM's and five-way three-dimensional alternating Turing machines ($FV3$-$ATM's$) in [4] are 3-$SATM'$s and $FV3$-$SATM'$s, respectively, which have no synchronizing states. We use 3-$SUTM$ ($FV3$-$SUTM$, 3-UTM, $FV3$-UTM) to denote a 3-$SATM$ ($FV3$-$SATM$, 3-ATM, $FV3$-ATM) which has no existential states. By 3-$ATM(L(m))$ ($FV3$-$ATM(L(m))$, 3-$SUTM(L(m))$, $FV3$-$SUTM(L(m))$, 3-$UTM(L(m))$, $FV3$-$UTM(L(m))$), we denote an $L(m)$ space-bounded 3-ATM ($FV3$-ATM, 3-$SUTM$, $FV3$-$SUTM$, 3-UTM, $FV3$-UTM).

A *three-dimensional deterministic Turing machine* (3-DTM) (*five-way three-dimensional deterministic Turing machine* ($FV3$-DTM)) is a 3-ATM ($FV3$-ATM) whose ID's each have at most one successor, and a *three-dimensional nondeterministic Turing machine* (3-NTM) (*five-way three-dimensional nondeterministic Turing machine* ($FV3$-NTM)) is a 3-ATM which has no universal states. We denote an $L(m)$ space-bounded 3-DTM(3-NTM, $FV3$-DTM, $FV3$-NTM) by 3-$DTM(L(m))$ (3-$NTM(L(m))$, $FV3$-$DTM(L(m))$, $FV3$-$NTM(L(m))$). We use 3-$SAFA$ ($FV3$-$SAFA$, 3-AFA, $FV3$-AFA, 3-NFA, $FV3$-NFA, 3-DFA,$FV3$-DFA) to denote a *three-dimensional synchronized alternating finite automaton* (*five-way three-dimensional synchronized alternating finite automaton*, *three-dimensional alternating finite automaton*, *five-way three-dimensional alternaing finite automaton*, *three-dimensional nondeterministic finite automaton, five-way three-dimensional nondeterministic finite automaton, three-dimensional determinnistic finite automaton, five-way three-dimensional deterministic finite automaton*). That is, a 3-$SAFA$ ($FV3$-$SAFA$, 3-AFA, $FV3$-AFA, 3-NFA, $FV3$-NFA, 3-DFA, $FV3$-DFA) is a 3-SATM ($FV3$-$SATM$, 3-ATM, $FV3$-ATM, 3-NTM, $FV3$-NTM, 3-DTM, $FV3$-DTM) which doesn't have storage tape. Similarly, we use 3-$SUFA$ ($FV3$-$SUFA$, 3-UFA, $FV3$-UFA) to denote a 3-$SUTM$ ($FV3$-$SUTM$, 3-UTM, $FV3$-UTM) which doesn't have the storage tape. Furthermore, for any integer $k \geq 1$, 3-$SATM(L(m))[k]$ is used to denote a 3-$SATM(L(m))$ such that any computation tree of M on any input x has at most k leaves. $FV3$-$SATM(L(m))[k]$, 3-$SUTM(L(m))[k]$, $\cdots$, 3-$SAFA(L(m))[k]$, etc. have the similar meaning. For any integer k ≥ 1, 3-NFA(*k-heads*) (3-DFA(*k-heads*)) is used to denote a 3-NFA (3-DFA) which has k input heads. For any machine class C, let

$$\mathcal{L}\ [\mathrm{C}] = \{\ T \mid T = T(M) \text{ for some } M \text{ in } C\ \}$$

Thus, for example, $\mathcal{L}$[3-$SATM(L(m))$] denotes the class of sets accepted by 3-$SATM(L(m))'$s.

2 Synchronization versus non-synchronization

This section investigates a relationship between the accepting powers of 3-ATM's and 3-$SATM'$s.

Lemma 3.1. Let $T_1 = \{x \in \{0,1\}^{2m \times 2m \times 2m} \mid m \geq 1$ & $x[(1,1,1),(2m,2m,m)] = x[(1,1,m+1),(2m,2m,2m)]\}$. *Then,*

(1) $T_1 \in \mathcal{L}[FV3\text{-}SUFA[2]]$, *and*

(2) $T_1 \notin \mathcal{L}[3\text{-}ATM(L(m))]$ *for any* $L : \mathbf{N} \rightarrow \mathbf{N}$ *such that* $L(m) = o(\log m)$.

Proof: (1) We can construct an $FV3$-$SUFA[2]$ M accepting T_1 as follows: Given x with $l_1(x) = l_2(x) = l_3(x) = 2m$ $(m \geq 1)$, starting on position (1,1,1) of x, M first splits universally into two processes p_1 and p_2. Process p_2 moves its head to $(1,1,m+1)$ and then synchronizes with process p_1 to compare $x(i_1,i_2,i_3)$ and $x(i_1,i_2,i_3{+}m)$ for each i_1, i_2, i_3 $(1 \leq i_1 \leq 2m, 1 \leq i_2 \leq 2m, 1 \leq i_3 \leq m)$. M accepts x iff $x(i_1,i_2,i_3) = x(i_1,i_2,i_3+m)$ for each i_1, i_2, i_3 $(1 \leq i_1 \leq 2m, 1 \leq i_2 \leq 2m, 1 \leq i_3 \leq m)$.

(2) This proof is the same as that of Theorem 1 in [4].

From this lemma, we have

Theorem 2.1. *For any function* $L(m) = o(\log m)$,
(1) $\mathcal{L}[FV3\text{-}UTM(L(m))] \subsetneq \mathcal{L}[FV3\text{-}SUTM(L(m))]$,
(2) $\mathcal{L}[FV3\text{-}ATM(L(m))] \subsetneq \mathcal{L}[FV3\text{-}SATM(L(m))]$,
(3) $\mathcal{L}[3\text{-}UTM(L(m))] \subsetneq \mathcal{L}[3\text{-}SUTM(L(m))]$, *and*
(4) $\mathcal{L}[3\text{-}ATM(L(m))] \subsetneq \mathcal{L}[3\text{-}SATM(L(m))]$

Corollary 2.1.
(1) $\mathcal{L}[FV3\text{-}UFA] \subsetneq \mathcal{L}[FV3\text{-}SUFA]$,
(2) $\mathcal{L}[FV3\text{-}AFA] \subsetneq \mathcal{L}[FV3\text{-}SAFA]$,
(3) $\mathcal{L}[3\text{-}UFA] \subsetneq \mathcal{L}[3\text{-}SUFA]$, *and*
(4) $\mathcal{L}[3\text{-}AFA] \subsetneq \mathcal{L}[3\text{-}SAFA]$

Theorem 2.2. *For any function* $L(m) \geq \log m$,
$\mathcal{L}[3\text{-}SUTM(L(m))] = \mathcal{L}[3\text{-}UTM(L(m))]$.

Proof: Given a 3-$SUTM(L(m))$ M where $L(m) \geq \log m$, we construct a 3-$UTM(L(m))$ M' to accept the same set as follows. On input x of side-length $m \geq 1$,

M' simulates each process of M with a process of its own. When some process p of M enters an s-state, the corresponding process p' of M' spawns off a process c whose worktape contains the s-symbol associated with the s-state and the number of s-states p has entered so far. Since each process makes at most $d^{L(m)}$ moves (d is a constant), and $L(m) \geq \log m$, there is enough space to store them. Process c restars the computation of M on x and verifies that the corresponding s-symbols in other processes match with the one stored on its worktape. If a discrepancy occurs, M' rejects. It is easy to see that M and M' accept the same set.

By using a technique similar to that in the proof of Theorem 2.2, we have

Theorem 2.3. *For any function* $L(m) \geq \log m$,
$\mathcal{L}[FV3\text{-}SUTM(L(m))] = \mathcal{L}[FV3\text{-}UTM(L(m))]$.

3 Five-way versus six-way

This section investigates a relationship between the accepting powers of five-way and six-way synchronized machines.

It is shown in [3] that three-way two-dimensional synchronized alternating Turing machine are equivalent to two-dimensional synchronized alternating Turing machines. By using the same idea as in the proof of this fact, we can easily show that the following theorem holds.

Theorem 3.1. *For any function* $L : \mathbf{N} \to \mathbf{N}$,

$$\mathcal{L}[FV3\text{-}SATM(L(m))] = \mathcal{L}[3\text{-}SATM(L(m))].$$

Below,we investigate a difference betwecn the accepting powers of space-bounded $3\text{-}SUTM'$s and $FV3\text{-}SUTM'$s.

Lemma 3.1. *Let* $T_2 = \{x \in \{0,1\}^{m\times m\times m} \mid m \geq 2,\ \&\ x[(1,1,1),(m,m,1)] \neq x[(1,1,2),(m,m,2)]\ \&\ x[(1,1,3),(m,m,3)] \in \{0\}^{(3)}\}$. *Then,*

(1) $T_2 \in \mathcal{L}[3\text{-}DFA] (= \mathcal{L}[3\text{-}SUTM(0)[1]])$, *and*

(2) $T_2 \notin \mathcal{L}[FV3\text{-}SUTM(L(m))]$ *for any* $L : \mathbf{N} \to \mathbf{N}$ *such that* $L(m) = o(m^2)$.

Proof: (1) We can construct a $3\text{-}DFA\ M$ accepting T_2 as follows: Given x with $l_1(x) = l_2(x) = l_3(x) = m$ $(m \geq 2)$, starting on position (1,1,1) of x, M first checks that $x[(1,1,3),(m,m,3)] \in \{0\}^{(3)}$. Then, M repeats the following process from $j = 1$ to m; M records the input symbol $x[(1,1,1),(m,m,1)]$ in the finite control and checks that two symbols $x[(1,1,1),(m,m,1)] \neq x[(1,1,2),(m,m,2)]$. If so, M enters an accepting state. It is clear that $T(M) = T_2$.

(2) Suppose that there exists a $FV3\text{-}SUTM(L(m))$ M accepting T_2, where $L(m) = o(m)$. By using the technique of counting argument[3,4], we can get the desired result. □

Lemma 3.2. *Let* $T_3 = \{x \in \{0,1\}^{2m\times 2m\times 2m} \mid m \geq 1\ \&\ x[(1,1,1),(2m,2m,m)] \neq x[(1,1,m+1),(2m,2m,2m)]\}$. *Then,*

(1) $T_3 \in \mathcal{L}[3\text{-}DTM(\log m)]$ $(= \mathcal{L}[3\text{-}SUTM(\log m)[1]])$, *and*

(2) $T_3 \notin \mathcal{L}[FV3\text{-}SUTM(L(m))]$ *for any* $L : \mathbf{N} \to \mathbf{N}$ such that $L(m) = o(m^3)$.

Proof: (1) We can construct a $3\text{-}DTM(\log m)$ M accepting T_3 as follows: Given x with $l_1(x) = l_2(x) = l_3(x) = 2m$ $(m \geq 1)$, starting on position (1,1,1) of x for all i_1,i_2,i_3 $(1 \leq i_1 \leq 2m,\ 1 \leq i_2 \leq 2m,\ 1 \leq i_3 \leq m)$, M repeats the following process; M records the input symbol x (i_1,i_2,i_3) in the finite control and checks that two symbols $x(i_1, i_2.i_3) \neq x(i_1, i_2, i_3 + m)$. (This can be easily done by using $\log m$ cells of the storage tape.) If so, M and enters an accepting state. It is clear that $T(M) = T_3$.

(2) The idea is almost the same as in the proof of Lemma 3.1 (2). □

From Lemmas 3.1 and 3.2 we can get the following theorem.

Theorem 3.2. *Let* $L : \mathbf{N} \to \mathbf{N}$ *be a function such that* (i) $L(m) = o(m^2)$, *or* (ii) $L(m) \geq \log m$ and $L(m) = o(m^3)$. *Then,*

$$\mathcal{L}[FV3\text{-}SUTM(L(m))] \subsetneq \mathcal{L}[3\text{-}SUTM(L(m))].$$

Corollary 3.1. $\mathcal{L}[FV3\text{-}SUFA] \subsetneq \mathcal{L}[3\text{-}SUFA]$.

lt is easy to show that the following theorem holds.

Theorem 3.3. *For any function* $L(m) \geq m^3$,

$$\mathcal{L}[FV3\text{-}SUTM(L(m))] = \mathcal{L}[3\text{-}SUTM(L(m))].$$

4 Nondeterminism versus synchronized alternation

This section investigates a relationship between the accepting powers of three-dimensional synchronized alternating machines and three-dimensional nondeterministic machines.

Let f : $\mathbf{N} \to \mathbf{N}$ be a function. The function f is said to be *three-dimensionally fully space constructible* if there is a $3\text{-}DTM$ which for any input tape x with $l_1(x) = l_2(x) = l_3(x) = m$ $(m \geq 1)$ makes use of exactly $f(n)$ cells of the storage tape and halts.

Theorem 4.1. *For any function* $L(m) \geq \log m$,

$$\mathcal{L}[3\text{-}SATM(L(m))] = U_{c\geq 0}\mathcal{L}[3\text{-}NTM(m^3 c^{L(m)})].$$

Proof: We first show that $\mathcal{L}[3\text{-}SATM(L(m))] \subseteq U_{c>0}\mathcal{L}[3\text{-}NTM(m^3 c^{L(m)})]$. Given a $3\text{-}SATM(L(m))$ M, we can construct a $3\text{-}NTM(m^3 c^{L(m)})$ M' to simulate M by doing a breadth-first-like traversal of the computation tree of M on input x of side-length m. Each process of M is simulated until it enters an s-state; M' will compare the corresponding s-states to make sure that no deadlock occurs before continuing the simulation. Since there are at most $m^3 d^{L(m)}$ distinct configurations of M on an input x of side-length m, M' needs at most $m^3 e^{L(m)}$ space, for some constants d and e, at any time to maintain the current

ID's of all processes of M on x. Then on any input x of side-length m, M uses at most $L(m)$ space iff M' uses at most $m^3e^{L(m)}$ space.

On the other hand, by using same idea described in Lemma 3.4 in [1], we can show that $\bigcup_{c\geq 0}\mathcal{L}[3\text{-}NTM(m^3c^{L(m)})] \subseteq \mathcal{L}[3\text{-}SATM(L(m))]$. □

Theorem 4.2. *For any integer $k \geq 1$,*

(1) $\mathcal{L}[3\text{-}SAFA[k]] = \mathcal{L}[3\text{-}NFA(k\text{-}heads)]$, and

(2) $\mathcal{L}[FV3\text{-}SAFA[k]] = \mathcal{L}[3\text{-}NFA(k\text{-}heads)]$

Proof: We only prove (1). Given a 3-NFA(k-heads) M where $k \geq 1$, we can construct a 3-$SAFA[k]$ M'. Let $H_1, H_2, \cdots, H_k$ denote the input heads of M. These heads are simulated by a single input head of 3-$SAFA[k]$ M' in the following way. The computation of M' branches from the initial configuration in a universal manner into k processes. Note that, the initial configuration is the only universal configuration which occurs in the computation. The states of M' (in all processes of M') store the simulated state of M. If the stored state is an accepting (rejecting) state, then the state of M is also an accepting (rejecting) one. In the ith process, for any i $(1 \leq i \leq k)$, the input head of M' is at the same position as H_i.

One step of M is simulated by two steps of M'. Besides the state of M the symbols scanned by all heads of M have to be known to M'. Every process in the computation of M' has only a part of the necessary information. The processes can share this information via the synchronization. The synchronizing element consists of k components and represents the symbols scanned by the input heads of M. The ith process, for $1 \leq i \leq k$, sets the ith component according to the symbol scanned by the input head of M'. The other components are set nondeterministically. The synchronization is successful only in the case when every process has correctly guessed the remaining components.

The next synchronization is necessary because of nondeterminism. One configuration of M has several potential successors. All of the processes of M' must agree on the next step of M (they must simulate the same successor of the currently simulated configuration). The synchronizing element represents the new state of M and the actions of the heads of M. The successful synchronization means that all processes choose the same element of the next move relation of M. After that, M' moves its heads and enters a new state in accordance with the synchronizing element (i.e., in the ith process (for $1 \leq i \leq k$), M' moves by its input head like M by H_i). It will be obvious that M' can simulate M.

Conversely, given a 3-$SAFA[k]$ M, we can construct a 3-NFA(k-heads) M' such that $T(M) = T(M')$. The proof is omitted here. □

We next investigate a relationship betwen the accepting powers of five-way nondeterministic machines and five-way synchronized machines with only universal states.

Theorem 4.3.

(1) $\mathcal{L}[FV3\text{-}SUFA[2]] - \mathcal{L}[FV3\text{-}NTM(o(m^3)] \neq \phi$,

(2) $\mathcal{L}[FV3\text{-}NFA] - \mathcal{L}[FV3\text{-}SUTM(o(m^2))] \neq \phi$, *and*

(3) $\mathcal{L}[FV3\text{-}NTM(\log m)] - \mathcal{L}[FV3\text{-}SUTM(o(m^3)] \neq \phi$.

Proof: (1) Let T_1 be the set described in Lemma 2.1. By using the technique of counting argument, we can show that $T_1 \notin \mathcal{L}[FV3\text{-}NTM(o(m^3))]$. (1) follows from this fact and Lemma 2.1 (1).

(2) Let T_2 be the set of described in Lemma 3.1. It is easy to see that $T_2 \in \mathcal{L}[FV3\text{-}NFA]$. (2) follows from this fact and Lemma 3.1 (2).

(3) Let T_3 be the set of described in Lemma 3.2. It is easy to see that $T_3 \in \mathcal{L}[FV3\text{-}NTM(\log m)]$. (3) follows from this fact and Lemma 3.2 (2). □

Corollary 4.1. *For any function $L(m) = o(m^3)$, $\mathcal{L}[FV3\text{-}SUTM(L(m))]$ and $\mathcal{L}[FV3\text{-}NTM(L(m))]$ are incomparable.*

5 Conclusions

In this section, we conclude this paper by giving two open problems.

(1) For any function $L(m) \geq \log m$, $\mathcal{L}[3\text{-}ATM(L(m))] \subsetneq \mathcal{L}[3\text{-}SATM(L(m))]$? and $\mathcal{L}[FV3\text{-}ATM(L(m))] \subsetneq \mathcal{L}[FV3\text{-}SATM(L(m))]$?

(2) For any integer $k \geq 1$, $\mathcal{L}[3\text{-}SUFA[k]] \subsetneq \mathcal{L}[3\text{-}SUFA[k+1]]$? and $\mathcal{L}[FV3\text{-}SUFA[k]] \subsetneq \mathcal{L}[FV3\text{-}SUFA[k+1]]$?

References

[1] C.M. Ibara and N.Q. Trân, "On space-bounded synchronizing alternating Turing machines", Theoretical Computer Science 99, pp243-264,1992.

[2] J. Hromkovič, "How to organize the commmunication among parallel proceses in alternating computations", manuscript, 1986.

[3] J. Hromkovič, J. Karhumäki, B. Rován and A. Slobodová, "On the power of synchronization in parallel computations", Tech. Report, comenius Univ., Bratislava, Czechoslovakia, Dept. of Theoretical Cybernetics and Institute of Computer Science, 1989.

[4] M.Sakamoto, I. Sakuramoto, K. Inoue and I.Takanami, "A space lower-bound technique for two-dimensional alternating Turing machines", IEICE Trans. D-I, J74-DI(4), pp.311–314, 1991.

[5] M. Sakamoto, K.Inoue, and I.Takanami, "A note on three-dimensional alternating Turing machines with space smaller than $\log m$", Information Sciences 72, pp.225–249, 1993.

The Eleventh International Symposium on Artificial Life and Robotics 2006 (AROB 11th'06),
B-con Plaza, Beppu, Oita, Japan, January 23-25, 2006

Leaf-Size Bounded Computation for Four-Dimensional Alternating Turing Machines

Kouichi IIHOSHI[1], Makoto SAKAMOTO[1], Takao ITO[1], Makoto SAITO[1], Hiroshi FURUTANI[1], Michio KONO[1], and Katsushi INOUE[2],

[1]Dept. of Computer Science and Systems Engineering, Miyazaki University, Miyazaki 889-2192, JAPAN

[2]Dept. of Computer Science and Systems Engineering, Yamaguchi University, Ube 755-8611, JAPAN

Abstract

Recently, due to the advances in computer animation, motion image processing, and so on, it is very useful for analyzing computational complexity of multi-dimensional information processing to explicate the properties of four-dimensional automata. From this point of view, we first introduced four-dimensional alternating Turing machines 4-ATM's in [5]. In this paper, we continue the investigations about 4-ATM's, and maily investigate leaf-size bounded computation of 4-ATM's. Basically, the 'leaf-size' is the minimum number of leaves of some accepting computation trees of alternating Turing machines. Leaf-size, in a sense, reflects the minimum number of processors that run in parallel in accepting a given input.

KeyWords **:** alternation, configuration, four-dimensional input tape, space bound, Turing machine, leaf-size.

1 Introduction and Preliminaries

Blum et al. first proposed two-dimensional automata, and investigated their pattern recognition abilities in 1967 [1]. Since then, many researchers in this field have been investigating a lot of properties about automata on two- or three-dimensional tapes. In 1976, Chandra et al. introduced the concept of 'alternation' as a theoretical model of parallel computation [2]. After that, Inoue et al. introduced two-dimensional alternating Turing machines as a generalization of two-dimensional nondeterministic Turing machines and as a mechanism to model parallel computation [4]. Moreover, Sakamoto et al. presented three-dimensional alternating Turing machines in [6].

On the other hand, recently, due to the advances in many application areas such as computer animation, motion image processing, and so forth, it has become increasingly apparent that the study of four-dimensional pattern processing, i.e., three-dimensional automata with the time axis should be of crucial importance. Thus, we think that it is very useful for analyzing computation of four-dimensional pattern processing to explicate the properties of four-dimensional automata. From this viewpoint, we introduced some four-dimensional automata[5,8].

In this paper, we continue the investigations about four-dimensional alternating Turing machines[5], and mainly investigate fundamental properties of leaf-size bounded four-dimensional alternating Turing machines which each sidelength of each input tape is equivalent. Leaf-size bounded computation was introduced as a simple, natural new complexity measure for alternating Turing machines[4]. Basically, the 'leaf-size' (or 'blanching') is the minimum number of leaves of some accepting computation trees of processors that run in parallel in accepting a given input.

Let Σ be a finite set of symbols. A *four-dimensional input tape* over Σ is a four-dimensional rectangular array of elements of Σ. The set of all the four-dimensional input tapes over Σ is denoted by $\Sigma^{(4)}$. Given an input tape $x \in \Sigma^{(4)}$, for each $j (1 \leq j \leq 4)$, we let $l_j(x)$ be the length of x along the jth axis. The set of all $x \in \Sigma^{(4)}$ with $l_1(x) = m_1$, $l_2(x) = m_2$, $l_3(x) = m_3$, and $l_4(x) = m_4$ is denoted by $\Sigma^{(m_1,m_2,m_3,m_4)}$. If $1 \leq i_j \leq l_j(x)$ for each $j (1 \leq j \leq 4)$, let $x(i_1, i_2, i_3, i_4)$ denote the symbol in x with coordinates (i_1, i_2, i_3, i_4). Furthermore, we define $x\ [(i_1, i_2, i_3, i_4), (i'_1, i'_2, i'_3, i'_4)]$, when $1 \leq i_j \leq i'_j \leq l_j(x)$ for each integer $j (1 \leq j \leq 4)$, as the four-dimensional input tape y satisfying the following:

(i) for each $j (1 \leq j \leq 4)$, $l_j(y) = i'_j - i_j + 1$;

(ii) for each r_1, r_2, r_3, r_4 $(1 \leq r_1 \leq l_1(y), 1 \leq r_2 \leq l_2(y), 1 \leq r_3 \leq l_3(y), 1 \leq r_4 \leq l_4(y))$, $y(r_1, r_2, r_3, r_4) = x(r_1 + i_1 - 1, r_2 + i_2 - 1, r_3 + i_3 - 1, r_4 + i_4 - 1)$.

As usual, a four-dimensional input tape x over Σ is surrounded by the boundary symbols #'s ($\# \notin \Sigma$). Furthermore, four-dimensional tape is the sequence of three-dimensional rectangular arrays along the time axis. By $Cube_x(i)$ $(i \geq 1)$, we denote the ith three-dimensional rectanglar array along the time axis in $x \in \Sigma^{(4)}$ which each sidelength is equivalent.

We now recall the definition of a *four-dimensional alternating Turing machine* (4-ATM), which can be considered as an alternating version of a four-dimensional Turing machine (4-TM) [5].

4-ATM M is defined by the 7-tuple

$$M = (Q,\, q_0,\, U, F,\, \Sigma,\, \Gamma,\, \delta), \text{ where}$$

(1) Q is a finite set of *states*;
(2) $q_0 \in Q$ is the *initial state*;
(3) $U \subseteq Q$ is the set of *universal states*;
(4) $F \subseteq Q$ is the set of *accepting states*;
(5) Σ is a finite input alphabet ($\# \notin \Sigma$ is the *boundary symbol*);
(6) Γ is a finite *storage-tape alphabet* ($B \in \Gamma$ is the *blank symbol*), *and*
(7) $\delta \subseteq (Q \times (\Sigma \cup \{\#\}) \times \Gamma) \times (Q \times (\Gamma - \{B\}) \times$ {east, west, south, north, up, down, future, past, no move} $\times$ {right, left, no move}) is the *next-move relation.*

A state q in $Q - U$ is said to be *existential.* As shown in Fig. 1, the machine M has a read-only four-dimensional input tape with boundary symbols #'s and one semi-infinite storage tape, initially blank. Of course, M has a finite control, an input head, and a storage-tape head. A *position* is assigned to each cell of the read-only input tape and to each cell of the storage tape, as shown in Fig. 1. The *step* of M is similar to that of a two- or three-dimensional Turing machine, except that the input head of M can move in eight directions. We say that M *accepts* the tape x if it eventually enters an accepting state. Note that the machine cannot write the blank symbol. If the input head falls off the input tape, or if the storage head falls off the storage tape (by moving left), then the machine M can make no further move.

A *seven-way four-dimensional alternating Turing machine* (SV4-ATM) is a 4-ATM whose input head can move in seven directions – east, west, south, north, up, down, or future, and an alternating version of a seven-way four-dimensional Turing machine (SV4-TM).

Let $L(m)$: $\mathbf{N} \to \mathbf{R}$ be a function with one variable m, where $\mathbf{N}$ is the set of all positive integers and $\mathbf{R}$ is the set of all nonnegative real numbers. With each 4-ATM (or SV4-ATM) M we associate a space complexity function $SPACE$ that takes configurations to natural numbers. That is, for each configuration $c = (x, (i_1, i_2, i_3, i_4), (q, \alpha, j))$, let $SPACE(c) = |\alpha|$. M is said to be $L(m)$ *space-bounded* if for each $m \geq 1$ and for each x with $l_1(x) = l_2(x) = l_3(x) = l_4(x) = m$, if x is accepted by M, then there is an accepting computation tree of M on input x such that for each node v of the tree, $SPACE(L(v)) \leq \lceil L(m) \rceil^1$. We denote an $L(m)$ space-bounded 4-ATM (SV4-ATM) by 4-ATM ($L(m)$) [SV4-ATM ($L(m)$)].

[1] $\lceil r \rceil$ means the smallest integer greater than or equal to r.

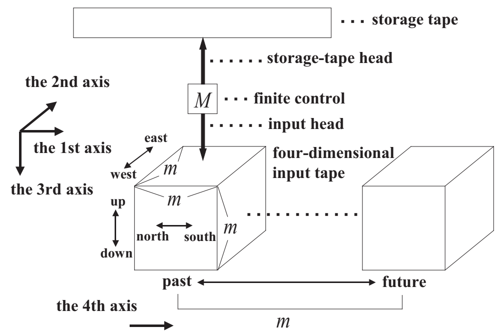

Fig. 1: Four-dimensional alternating Turing machine.

A 4-$ATM(0)$ [SV4-$ATM(0)$] is called a four-dimensional alternating finite automaton (seven-way four-dimensional alternating finite automaton), which can be considered as an alternating version of a four-dimensional finite automaton (4-FA) (seven-way four-dimensional finite automaton (SV4-FA)), and is denoted by 4-AFA (SV4-AFA).

In order to distinguish among determinism, nondeterminism, and alternation, we denote a deterministic 3-TM [nondeterministic four-dimensional Turing machine (4-TM), deterministic seven-way four-dimensional Turing machine (SV4-TM), nondeterministic SV4-TM, deterministic 4-TM ($L(m)$), nondeterministic 4-TM ($L(m)$), deterministic SV4-TM ($L(m)$), nondeterministic SV4-TM ($L(m)$), deterministic 4-FA, nondeterministic 4-FA, deterministic SV4-FA, nondeterministic SV4-FA] by 4-DTM [4-NTM, SV4-DTM, SV4-NTM, 4-DTM ($L(m)$), 4-NTM ($L(m)$), SV4-DTM ($L(m)$), SV4-NTM ($L(m)$), 4-DFA, 4-NFA, SV4-DFA, SV4-NFA].

Let M be an automaton on a three-dimensional tape. We denote by $T(M)$ the set of all three-dimensional tapes accepted by M. As usual, for each $X \in \{D,\, N,\, A\}$, we denote, for example, by £[3-XTM] the class of sets of all the four-dimensional tapes accepted by 4-XTM's. That is, £[4-XTM] = $\{T \mid T = T(M)$ for some 4-XTM $M\}$. £[SV4-XTM], £[4-XTM ($L(m)$)], £[SV4-XTM ($L(m)$)], £[4-XFA], and £[SV4-XFA] also have analogous meanings.

2 Results

Definition 2.1. Let $L(m)$: $\mathbf{N} \to \mathbf{R}$ be a function. For each tree t, let $LEAF(t)$ denote the leaf-size of

t (i.e., the number of leaves of t). We say that a 4-ATM M is $Z(m)$ *leaf-size bounded* if for all x with $l_1(x)$=$l_2(x)$=$l_3(x)$=m and for each computation tree t of M on x, $LEAF(t) \leq \lceil Z(m) \rceil$.

By 4-$ATM(L(m)$,$Z(m))$ (SV4-$ATM(L(m)$,$Z(m))$), we denote a $Z(m)$ leaf-size bounded 4-ATM ($L(m)$) (SV4-ATM ($L(m)$)). Especially, a 4-ATM (0, $Z(m)$) (SV4-ATM (0, $Z(m)$)) is denoted by 4-AFA ($Z(m)$) (SV4-AFA ($Z(m)$)). Define $\pounds$[4-ATM ($L(m)$, $Z(m)$)] = $\{T \mid T = T(m)$ for some 4-ATM ($L(m)$, $Z(m)$) $M\}$. $\pounds$[SV4-ATM ($L(m)$, $Z(m)$)] is defined similarly.

Definition 2.2. For any integer $k \geq 1$ and for any L: $\mathbf{N} \to \mathbf{R}$, let $\pounds^k$[SV4-NTM ($L(m)$)] = $\{A_1 \cap \cdots \cap A_k \mid$ each $A_i \in \pounds$[SV4-NTM ($L(m)$)]$\}$. $\pounds^k$[SV4-NFA], etc., are defined similarly.

It seems interesting to investigate the relationship between $\pounds$[SV4-$ATM(L(m)$,$k)$] and $\pounds^k$[SV4-NTM ($L(m)$)]. The main purpose of this section is to show that $\pounds^k$[SV4-NTM ($L(m)$)] $\subsetneq$ $\pounds$[SV4-$ATM(L(m)$,$k)$] for any integer $k \geq 2$ and any $L(m)$: $\mathbf{N} \to \mathbf{R}$ such that $L(m) = o(\log m)$.

From this result, we might say that for the space smaller than log$m$, a parallel machine with cooperative processors is more powerful than a mechanism with the same number of processors which run independently.

We first show that $\pounds^k$[SV4-NTM ($L(m)$)] $\subsetneq$ $\pounds^{k+1}$[SV4-NTM ($L(m)$)] for any $k \geq 1$ and any L such that $L(m) = o(\log m)$.

Lemma 2.1. *For any integer $k \geq 1$ and for any $L(m)$: $\mathbf{N} \to \mathbf{R}$, $\pounds$[SV4-$NTM(L(m))$] $\subseteq$ $\pounds$[SV4-$ATM(L(m)$,$k)$].*

Proof: For $k = 1$, the lemma is obvious. For any $k \geq 2$, let A in $\pounds^k$[SV4-NTM ($L(m)$)] be equal to $A_1 \cap \cdots \cap A_k$, where for each $i(1 \leq i \leq k)$, A_i is accepted by some SV4-$NTM(L(m))$ M_i. We consider an SV4-$ATM(L(m)$,$k)$ M' which acts as follows. Given an input x, M' first universally branches to directly simulate the actions of M_1,...,M_{k-1}, and M_k on x. M' enters an accepting state if and only if M_i, $1 \leq i \leq k$, enters an accepting state, It is obvious that $T(M') = A$. □

Lemma 2.2. *For any integer $k \geq 1$, let $T[k] = \{x \in \{0,1\}^{(4)} \mid \exists m \geq k[l_1(\mathrm{x}) = l_2(\mathrm{x}) = l_3(\mathrm{x}) = l_4(\mathrm{x}) = m]$ & (there exist exactly k 1's in $Cube_x(1)$) & $Cube_x(1) = Cube_x(2)\}$. Then,*

(1)$T[k] \in \pounds^k$[SV4-DFA], and

(2)$T[k+1] \notin \pounds^k$[SV4-$NTM(L(m))$] for any L: $\mathbf{N} \to \mathbf{R}$ such that $L(m) = o(\log m)$.

Proof: (1) For each $k \geq 1$ and each $r(1 \leq r \leq k)$, let $T_r[k] = \{x \in \{0,1\}^{(4)} \mid \exists m \geq k[l_1(\mathrm{x}) = l_2(\mathrm{x}) = l_3(\mathrm{x}) = l_4(\mathrm{x}) = m]$ & (there exist exactly k 1's both in $Cube_x(1)$ and in $Cube_x(2)$) & (the symbol (in $Cube_x(2)$) just below the r-th 1(counting from the first plane to the mth plane in a cube, from the first column to the mth column in a plane, and from the first row to the mth row in a column) in $Cube_x(1)$ is 1)$\}$. It is easily seen that for each $k \geq 1$ and for each $r(1 \leq r \leq k)$, $T_r[k] \in \pounds$[SV4-DFA]. From this and the fact that $T[k] = T_1[\mathrm{k}] \cap \cdots \cap T_k[\mathrm{k}]$, it follows that part (1) of the lemma holds.

(2) Suppose that there is an SV4-$ATM(L(m)$,$k)$ M (with $L(m) = o(\log m)$) accepting $T[k+1]$. By using the technique of counting argument [3], we can get the desired result. □

From Lemma 2.2, we can get

Theorem 2.1. *For any integer $k \geq 1$ and for any $L(m)$: $\mathbf{N} \to \mathbf{R}$ such that $L(m) = o(\log m)$,*
(1)$\pounds^k$[SV4-$DTM(L(m))$]$\subsetneq$$\pounds^{k+1}$[$SV$4-$DTM(L(m))$], and
(2)$\pounds^k$[SV4-$NTM(L(m))$]$\subsetneq$$\pounds^{k+1}$[$SV$4-$NTM(L(m))$].

Corollary 2.1. *For any integer $k \geq 1$,*
(1)$\pounds^k$[SV4-DFA]$\subsetneq$$\pounds^{k+1}$[$SV$4-$DFA$], and
(2)$\pounds^k$[SV4-NFA]$\subsetneq$$\pounds^{k+1}$[$SV$4-$NFA$].

As shown in the next theorem, if $L(m) \geq \log m$, then a situation which differs from Theorem 5.1 emerges. We first need the following lemma.

Lemma 2.3. *For each $X \in \{D,N\}$, $\pounds$[SV4-XTM ($L(m)$)] is closed under finite intersection for any that L such that $L(m) \geq \log m$ ($m \geq 1$).*

Proof : We only show that $\pounds$[SV4-DTM(log m)] is closed under intersection. Let M_1 and M_2 be any two SV4-DTM(log m)'s. We cosider the SV4-DTM(log m) M which acts as follows. M divides the storage tape into ten tracks, and uses tracks 1, 2, 3, 4 and 5 to simulate M_1, and tracks 6, 7, 8, 9 and 10 to simulate M_2. M first stores number 1 on track 4 and begins to simulate the action of M_1 in $Cube_x(1)$ of an input tape x (starting from x(1,1,1,1)), by using tracks 1,2 and 3. When M_1 leaves $Cube_x(1)$ of x from some position, M stores the number i_1, i_2, i_3 and 2 in a binary representation on tracks 1, 2, 3 and 4, respectively, and stores the position of the storage-tape head at that time on track 5. Then, M stores number 1 on track 9 and begins to simulate the action of M_2 in $Cube_x(1)$ of x (starting from x(1,1,1,1)), by using tracks 6, 7 and 8. When M_2 leaves $Cube_x(1)$ of x from some position, M stores the numbers i_1', i_2', i_3' and 2 in a binary representation on tracks 6, 7, 8 and 9, respectively, and stores the position of the storage-tape head at that time on track 10. M next begins to simulate the action of M_1 in $Cube_x(2)$ of x, by using the information stored on tracks 1,2,3,4 and 5. After that, M continues to simulate by turns the actions of M_1 and M_2 in each three-dimensional rectangular array of x by using the above techniques. Then M accepts x if and only if both M_1 and M_2 arrive at the bottom boundary symbol and accept x. It will be obvious that $T(M) = T(M_1) \cap T(M_2)$. By using the same ideas as those in the proof above, we can easily see that $\pounds[SV4\text{-}NTM(\log m)]$ is closed under intersection. $\square$

From Lemma 2.3, we can get

Theorem 2.2. *For any integer* $k \geq 1$ *and for function* $L(m) \geq \log m$ $(m \geq 1)$,
(1)$\pounds^k[SV4\text{-}DTM(L(m))] = \pounds^1[SV4\text{-}DTM(L(m))] = \pounds[SV4\text{-}DTM(L(m))]$, *and*
(2)$\pounds^k[SV4\text{-}NTM(L(m))] = \pounds^1[SV4\text{-}NTM(L(m))] = \pounds[SV4\text{-}NTM(L(m))]$.

We next derive the main theorem of this section. We need the following two lemmas.

Lemma 2.4. $\pounds[SV4\text{-}NTM(L(m))] \subseteq \bigcup_{c \geq 0} \pounds[SV4\text{-}DTM\ (m^3 L(m) c^{L(m)})]$ *for any function* $L(m)$: $\mathbf{N} \rightarrow \mathbf{R}$.
Proof: Let M be an $SV4\text{-}NTM(L(m))$, and s and r be the numbers of states (of the finite control) and storage tape symbols of M, respectively. We construct an $SV4\text{-}DTM(m^3 L(m) c^{L(m)})$ M' accepting the set $T(M)$, where c is a positive constant satisfying $m^3 L(m) c^{L(m)} > (m+2)^3 s L(m) c^{L(m)} (m \geq 1)$. Suppose that an input tape x with $l_1(x) = l_2(x) = l_3(x) = l_4(x) = m$ $(m \geq 1)$ is presented to M'. Let C be the set of possible storage states of M on x. Clearly, $\mid C \mid = sL(m)c^{L(m)}$. For each $i_4 (1 \leq i_4 \leq i_4(x)+1 = m+1)$, let $H(i_4)$ be a subset of $\{0,1,\ldots,m+1\} \times \{0,1,\ldots,m+1\} \times \{0,1,\ldots,m+1\} \times C$ defined as follows :

$H(1) = \{(1,1,1, p_0)\}$, where p_0 is the initial storage state of M (e.g., p_0 is the storage state component of the initial configuration of M on x).

$H(i_4)$, $i_4 \geq 2$, $= \{(i_1,i_2,i_3,p) \mid I_M(x) \vdash_M^* (x,((i_1,i_2,i_3,i_4\text{-}1),p')) \vdash_M (x,((i_1,i_2,i_3,i_4),p))$ for some $p' \in C$, i.e., there exists a computation path of M on x leading to the configuration $(x,((i_1,i_2,i_3,i_4),p))$ just after the input head of M has reached $Cube_x(i_4)$ of x $\}$.

M' simulates the action of M on x by successively generating $H(1),H(2),\ldots,H(i_4),\ldots$, on the storage tape, in such a way that for each $i_4 \geq 1$, M' replaces $H(i_4)$ with $H(i_4+1)$ on the storange tape. Note that, since, by assumption, $m^3 L(m) c^{L(m)} > (m+2)^3 s L(m) c^{L(m)} \geq \mid H(i_4) \mid$ for each $1 \leq i_4 \leq m+1$, M' can store each element of $H(i_4)$ on the storage tape. It will be easy to see that M' can generate $H(i_4+1)$ from $H(i_4)$ for each $1 \leq i_4 \leq m$.

M' enters an accepting state if and only if it finds out that for some $i_4 (1 \leq i_4 \leq m+1)$, $H(i_4)$ contains at least one element (i_1,i_2,i_3,p) such that $0 \leq i_1 \leq m+1$, $0 \leq i_2 \leq m+1$, $0 \leq i_3 \leq m+1$ and p is a storage state whose state-component is an accepting state of M. It will be obvious that $T(M') = T(M)$. $\square$

From Lemmas 2.1, 2.3 and 2.4, and by using the same idea as in the proof of Lemma 5.5 in [7], we get the following main theorem.

Thoerem 2.3. *For any integer* $k \geq 2$ *and for any* $L: \mathbf{N} \rightarrow \mathbf{R}$ *such that* $L(m) = o(\log m)$,

$$\pounds^k[SV4\text{-}NTM(L(m))] \subsetneq \pounds[SV4\text{-}ATM(L(m),k)].$$

Corollary 2.2. *For any integer* $k \geq 2$,

$$\pounds^k[SV4\text{-}NFA] \subsetneq \pounds[SV4\text{-}AFA(k)].$$

As shown in the following results, if $L(m) \geq \log m$, then a situation which differs from Theorem 2.3 emerges.

Theorem 2.4. *For any integer* $k \geq 1$ *and for any* $L: \mathbf{N} \rightarrow \mathbf{R}$ *such that* $L(m) \geq \log m$,

$$\pounds^k[SV4\text{-}NTM(L(m))] = \pounds[SV4\text{-}ATM(L(m),k)]$$

Corollary 2.3. *For any integer* $k \geq 1$,

$$\pounds^k[SV4\text{-}NFA] = \pounds[SV4\text{-}AFA(k)].$$

References

[1] M. Blum et al., *IEEE Symposium on Switching and Automata Theory* :155-160(1967).

[2] A. K. Chandra et al., *J. ACM* 28(1):114-133 (1981).

[3] J. E. Hopcroft et al., *Introduction to Automata Theory, Languages, and Computation*, Addison-Wesley, Reading, MA, (1979).

[4] K. Inoue et al., *Theoret. Comput. Sci.* 27:61-83 (1983).

[5] H. Okabe et al., *Proc. 7th Words Multiconf. on SCI* :241-246 (2003).

[6] M. Sakamoto et al., *Inform. Sci.* 72:225-249 (1993).

[7] M. Sakamoto, *Ph.D. Thesis* (1999).

[8] M. Sakamoto et al., *WSEAS Trans. on Computers*, Issue 5, Vol. 3 :1651-1656 (2004).

Existence and comparison for solutions in stochastic algebraic Riccati equation

N. Takahashi*, M. Nakai†, M. Ishitobi‡ and M. Kono*

*Univ. of Miyazaki, Faculty of Engineering, 1-1 Gakuenkibanadai Nishi, Miyazaki, 889-2192, JAPAN

†YASKAWA Electric Corp., 2-1 Kurosaki-Shiroishi, Yahatanishi-Ku, Kitakyushu, Fukuoka, 806-0004, JAPAN

‡Kumamoto Univ., Faculty of Engineering, 39-1, Kurokami 2-chome, Kumamoto, 860-8555, JAPAN

Abstract

The Riccati-like algebraic equation with the additional linear term appears in guaranteed cost control on the basis of the linear upper bound. It is called the stochastic algebraic Riccati equation and it plays the important role in designing a guaranteed cost controller. In this paper, we prove the existence of the maximal strong solution of stochastic algebraic Riccati equation under two assumptions i) the additional term is not too large ii) the system is stabilizable. Furthermore, we show the theorem on the comparison of the solution of two equations.

1 Introduction

Ran and Vreugdenhil considered the relation between the algebraic Riccati equation and the corresponding Riccati inequality, and they shown that the existence of the solution which satisfies the Riccati inequality guaranteed the existence of the maximal solution of the algebraic Riccati equation [2]. In addition, from this result, the theorem on the comparison of the solutions of two algebraic Riccati equations was given. In this paper, we extended these results to the case of algebraic Riccati equation with the additional term, which called a stochastic algebraic Riccati equation[1], which appears in the guaranteed cost control[3] and stochastic control with the state-dependency noise[4]. Furthermore, we prove the existence of the maximal solution of stochastic algebraic Riccati equation, and show the theorem on the comparison of the solutions of two equations.

2 Existence theorem

The stochastic algebraic Riccati equation (SARE) is defined as follows

$$A^*X + XA + XRX + Q + \Upsilon(X) = 0 \tag{1}$$

where Q, R are symmetric matrices, and $\Upsilon(\cdot)$ is positive linear map which maps a $n \times n$ symmetric matrix into itself. Function $\mathcal{Q}(X)$ is defined as

$$\mathcal{Q}(X) := A^*X + XA + XRX + Q + \Upsilon(X) \tag{2}$$

Definition 1 *A hermitian solution X_+ of (1) is called a maximal solution if $X_+ \geq X$ for all hermitian solution X of (1). The maximal solution is clearly unique.*

Following theorem is established.

Theorem 1 *Let $R = -BB^* \leq 0$ and there exists a hermitian matrix X which satisfies that $\mathcal{Q}(X) \geq 0$. If (A, R) is stabilizable and*

$$\inf_{\Psi} \| \int_0^{\infty} e^{(A+B\Psi)^T t} \Upsilon(I) e^{(A+B\Psi)t} dt \| < 1 \tag{3}$$

is satisfied, then there exists unique a maximal solution X_+ of the SARE (1). In addition, $X_+ \geq X$ holds for all X which satisfies $\mathcal{Q}(X) \geq 0$, and all eigenvalues of $A + RX_+$ are in the closed left half plane.

For the theorem 1, we introduce the following lemma.

Lemma 1 *Let X_i be a unique hermitian solution of*

$$A_i^* X_i + X_i A_i = -F_i^* F_i - Q - \Upsilon(K) \tag{4}$$

where $A_i = A + BF_i$. And we define $F_{i+1} = -B^* X_i$. For such X_i and F_i, we obtain following items:

(i) A_{i+1} is asymptotic stable, if $\mathcal{Q}(X) \geq 0, X_i - X \geq 0, K - X \geq 0$ and A_i is asymptotic stable.

(ii) Following equality is established

$$\begin{aligned}(X_i - X)A_i + A_i^*(X_i - X) \\ = -\hat{F}_i^* \hat{F}_i - \Upsilon(K - X) - \mathcal{Q}(X)\end{aligned} \tag{5}$$

where $\hat{F}_i = F_i + B^* X$.

(iii) Let X_{i+1} be the unique hermitian solution of

$$\begin{aligned} &A_{i+1}^* X_{i+1} + X_{i+1} A_{i+1} \\ &\quad = -F_{i+1}^* F_{i+1} - Q - \Upsilon(L) \end{aligned} \tag{6}$$

The following equality is established

$$\begin{aligned} &(X_i - X_{i+1})A_{i+1} + A_{i+1}^*(X_i - X_{i+1}) \\ &= -(F_{i+1} - F_i)^*(F_{i+1} - F_i) - \Upsilon(K - L) \end{aligned} \tag{7}$$

Next, we prove Theorem 1.

Proof Since $R \le 0$, it can be decomposed as $R = -BB^*$. According to the assumption of theorem 1, there exists F_0 that makes $A_0 = A + BF_0$ to be asymptotic stable and

$$\| \int_0^\infty e^{(A+BF_0)^T t} \Upsilon(I) e^{(A+BF_0)t} dt \| < 1 \tag{8}$$

Here, let us define X_0 as the hermitian solution of the following equation.

$$X_0 A_0 + A_0{}^* X_0 + F_0^* F_0 + Q + \Upsilon(X_0) = 0 \tag{9}$$

There exists unique hermitian solution of (9). From (ii) of lemma 1, if $i = 0$ and $K = X_0$, then we obtain

$$\begin{aligned} &(X_0 - X)A_0 + A_0^*(X_0 - X) + \Upsilon(X_0 - X) \\ &\quad = -\hat{F_0}^* \hat{F}_0 - \mathcal{Q}(X) \le 0 \end{aligned} \tag{10}$$

Since A_0 is asymptotic stable

$$X_0 \ge X \tag{11}$$

is established. Next, let us define a hermitian matrices sequence $\{X_j\}_{j=0}^\infty$ and corresponding matrix sequences $\{A_j\}_{j=0}^\infty, \{F_j\}_{j=0}^\infty$ as

$$\begin{aligned} &X_0 \ge X_1 \ge X_2 \ge \cdots \ge X, \quad X_j = X_j^* \\ &A_j = A + BF_j \quad \text{is asymptotic stable} \\ &F_j = -B^* X_{j-1} \\ &X_j A_j + A_j^* X_j = -F_j^* F_j - Q - \Upsilon(X_{j-1}) \end{aligned} \tag{12}$$

where $j = 1, 2, \cdots$.

(Proof in the First stage)

In this stage, firstly, we show that A_1 is the asymptotic stable. Secondly, we show $X_0 \ge X_1 \ge X$. In (i) of lemma 1, let $K = X_0$ and $i = 0$ then A_1 be asymptotic stable because $X_0 \ge X, \mathcal{Q}(X) \ge 0$ and A_0 be asymptotic stable. Let X_1 be a unique hermitian solution of the Lyapunov equation

$$X_1 A_1 + A_1{}^* X_1 + F_1^* F_1 + Q + \Upsilon(X_0) = 0 \tag{13}$$

In (ii) of lemma 1, if $i = 1, K = X_0$, then

$$\begin{aligned} &(X_1 - X)A_1 + A_1^*(X_1 - X) \\ &\quad = -\hat{F_1}^* \hat{F}_1 - \mathcal{Q}(X) - \Upsilon(X_0 - X) \le 0 \end{aligned} \tag{14}$$

In (iii) of lemma 1, if $i = 0, K = X_0, L = X_0$, then

$$\begin{aligned} &(X_0 - X_1)A_1 + A_1^*(X_0 - X_1) \\ &\quad = -(F_1 - F_0)^*(F_1 - F_0) - \Upsilon(X_0 - X_0) \le 0 \end{aligned}$$

Since A_1 is the asymptotic stable, and the following inequality is established

$$X_0 \ge X_1 \ge X \tag{15}$$

(Proof in the n stage)

In this stage, firstly, we show that A_n is asymptotic stable under the assumption that (12) are satisfied at $j = 1, 2, \ldots, n-1$. Secondly, we show $X_{n-1} \ge X_n \ge X$.

In (ii) of lemma 1, if $i = n-1, K = X_{n-2}$, then A_n is the asymptotic stable because $X_{n-2} \ge X, X_{n-1} \ge X, \mathcal{Q}(X) \ge 0$ and A_{n-1} is asymptotic stable. Let X_n be a unique hermitian solution of the following Lyapunov equation

$$X_n A_n + A_n{}^* X_n + F_n^* F_n + Q + \Upsilon(X_{n-1}) = 0 \tag{16}$$

In (ii) of lemma 1, if $i = n$, then we obtain

$$\begin{aligned} &(X_n - X)A_n + A_n^*(X_n - X) \\ &= -\hat{F_n}^* \hat{F}_n - \mathcal{Q}(X) - \Upsilon(X_{n-1} - X) \le 0 \end{aligned} \tag{17}$$

And in (iii) of lemma 1, if $i = n-1, K = X_{n-2}, L = X_{n-1}$, then

$$\begin{aligned} &(X_{n-1} - X_n)A_n + A_n^*(X_{n-1} - X_n) \\ &= -(F_n - F_{n-1})^*(F_n - F_{n-1}) - \Upsilon(X_{n-2} - X_{n-1}) \\ &\le 0 \end{aligned} \tag{18}$$

Since A_n is the asymptotic stability,

$$X_{n-1} \ge X_n \ge X \tag{19}$$

is established. By the inductive method, (12) is established at all j, because it is satisfied at $j = 1$.

Because the sequence $\{X_j\}_{j=0}^\infty$ is non-increase and $X_j \ge X$, then X_j is bounded below and there exists $X_f = \lim_{n\to\infty} X_n$ and following inequality is consistent

$$X_f \ge X \tag{20}$$

Here, $\mathcal{Q}(X_f) = 0$ is clearly established. Therefore, X_f is hermitian solution of the SARE (1).

Next, we show that X_f is a maximal solution of (1). Let M and N are defined as

$$M := \{X|X = X^*, \mathcal{Q}(X) \geq 0\}$$
$$N := \{X|X = X^*, \mathcal{Q}(X) = 0\}$$

Then, $N \subset M$. From the definition of X_f,

$$X_f \geq X \quad \text{for all} \quad X \in M$$

is established, and X_f is a maximal solution of the SARE (1), namely, $X_f = X_+$. According to the property of the maximal solution, X_f is unique.

Finally, we show the stability of the maximal solution. The eigenvalue of

$$A_f = A + BF_f = A - BB^* X_f = A + RX_f \qquad (21)$$

exists in the closed left half plane for $k \to \infty$, then A_n is the asymptotic stable.

□

Note 1 *The above-mentioned proof also gives the iteration for calculating the maximal solution. This procedure is shown as follows :*

(1) Find F_0 which satisfies $A_0 := A + BF_0$ to be asymptotic stable and

$$\|\int_0^\infty e^{(A+BF_0)^T t}\Upsilon(I)e^{(A+BF_0)t}dt\| < 1$$

(2) Solve $X_0A_0 + A_0^*X_0 + F_0^*F_0 + Q + \Upsilon(X_0) = 0$

(3) $F_{i+1} = -B^*X_i, A_{i+1} = A + BF_{i+1}$

(4) Solve $X_iA_i + A_i^*X_i + F_i^*F_i + Q + \Upsilon(X_{i-1}) = 0$

(5) If $\|X_i - X_{i-1}\| \leq \epsilon$(required accuracy), then finished, otherwise return to (3).

3 Comparison theorem

In this section, we introduce the following alternative SARE

$$\tilde{A}^*X + X\tilde{A} + X\tilde{R}X + \tilde{Q} + \tilde{\Upsilon}(X) = 0 \qquad (22)$$

Let $\tilde{X}_+$ be the maximal solution of (22), and $\tilde{\mathcal{Q}}(X)$ be the corresponding matrix function, and

$$T := \begin{bmatrix} Q & 0 \\ 0 & R \end{bmatrix}, \quad \tilde{T} := \begin{bmatrix} \tilde{Q} & 0 \\ 0 & \tilde{R} \end{bmatrix}$$

$$W := \begin{bmatrix} Q & A^* \\ A & R \end{bmatrix}, \quad \tilde{W} := \begin{bmatrix} \tilde{Q} & \tilde{A}^* \\ \tilde{A} & \tilde{R} \end{bmatrix}$$

Theorem 2 *If we assume that (A, R) and $(\tilde{A}, \tilde{R})$ are stabilizable, $R \leq 0, \tilde{R} \leq 0$ and*

$$\inf_\Psi \|\int_0^\infty e^{(A+B\Psi)^T t}\Upsilon(I)e^{(A+B\Psi)t}dt\| < 1$$

$$\inf_{\tilde{\Psi}} \|\int_0^\infty e^{(\tilde{A}+\tilde{B}\tilde{\Psi})^T t}\tilde{\Upsilon}(I)e^{(\tilde{A}+\tilde{B}\tilde{\Psi})t}dt\| < 1$$

Then the following items are satisfied:

(i) If $W \geq \tilde{W}$ and (22) has the hermitian solution X which satisfies $\Upsilon(X) \geq \tilde{\Upsilon}(X)$, then X_+ and $\tilde{X}_+$ exist. In addition, if $\Upsilon(\tilde{X}_+) \geq \tilde{\Upsilon}(\tilde{X}_+)$, then

$$X_+ \geq \tilde{X}_+ \qquad (23)$$

is established.

(ii) If $A = \tilde{A}, \Upsilon(\cdot) = \tilde{\Upsilon}(\cdot), T \geq \tilde{T}$ and (22) has the hermitian solution, then there exist X_+ and $\tilde{X}_+$, where $X_+ \geq \tilde{X}_+$.

(iii) If $Q \geq 0$, then there exists $X_+ \geq 0$.

Note 2 *Theorem 2 is the special case in a result of the literature [7].*

For the proof of theorem 2, we gave the following lemma.

Lemma 2 *If $A = \tilde{A}, \Upsilon(\cdot) = \tilde{\Upsilon}(\cdot)$, and X is hermitian solution of (22). Then the following equality is established.*

$$\mathcal{Q}(X) = \begin{bmatrix} I \\ X \end{bmatrix}^* \{T - \tilde{T}\} \begin{bmatrix} I \\ X \end{bmatrix} \qquad (24)$$

Proof
(i) Let X be a hermitian solution of (22) and it satisfies $\Upsilon(X) \geq \tilde{\Upsilon}(X)$. Then the following equality is established

$$\begin{bmatrix} I \\ X \end{bmatrix}^* \tilde{W} \begin{bmatrix} I \\ X \end{bmatrix} + \tilde{\Upsilon}(X) = 0 \qquad (25)$$

From the assumptions, we obtain $W \geq \tilde{W}$ and $\Upsilon(X) \geq \tilde{\Upsilon}(X)$, then the following equation is established

$$\mathcal{Q}(X) = \begin{bmatrix} I \\ X \end{bmatrix}^* \{W - \tilde{W}\} \begin{bmatrix} I \\ X \end{bmatrix} + \Upsilon(X) - \tilde{\Upsilon}(X) \geq 0 \qquad (26)$$

According to the theorem 1, there exist X_+ and $\tilde{X}_+$. In addition, if $\Upsilon(\tilde{X}_+) \geq \tilde{\Upsilon}(\tilde{X}_+)$, then $X_+ \geq \tilde{X}_+$ is established because $\mathcal{Q}(\tilde{X}_+) \geq 0$.

(ii) Let X be a hermitian solution of the (22). According to the lemma 2, since $A = \tilde{A}, \Upsilon(\cdot) = \tilde{\Upsilon}(\cdot)$ and $T \geq \tilde{T}$, then we obtain $\mathcal{Q}(X) \geq 0$. According to the theorem 1, there exist X_+ and $\tilde{X}_+$ which satisfies $X_+ \geq \tilde{X}_+$ because X is arbitrary.

(iii) From the assumption $Q \geq 0$, we obtain $\mathcal{Q}(0) = Q \geq 0$. X_+ exists, when theorem 1 is applied, and

$$X_+ \geq 0 \tag{27}$$

is established.

□

4 Numerical example

We consider the following SARE

$$\tilde{A}^* X + X\tilde{A} + X\tilde{R}X + \tilde{Q} + \tilde{A}_1^T X \tilde{A}_1 = 0 \tag{28}$$

where

$$\tilde{A} = \begin{bmatrix} 0 & 0 \\ 0 & -\sqrt{77} \end{bmatrix} \quad \tilde{R} = \begin{bmatrix} -7 & 0 \\ 0 & 0 \end{bmatrix}$$

$$\tilde{Q} = \begin{bmatrix} 11 & 0 \\ 0 & -1 \end{bmatrix} \quad \tilde{A}_1 = \begin{bmatrix} 0 & 0 \\ 0 & 1 \end{bmatrix}$$

From the theorem 1, (28) has a maximal solution and it is obtained by the procedure in the proof of the theorem 1 as

$$\tilde{X}_+ = \begin{bmatrix} 1.2536 & 0 \\ 0 & -0.0604 \end{bmatrix} \tag{29}$$

Next, we consider the alternative SARE as follows

$$A^* X + XA + XRX + Q + A_1^T X A_1 = 0 \tag{30}$$

where

$$A = \begin{bmatrix} 6 & 2 \\ 0 & -\sqrt{77} \end{bmatrix} \quad R = \begin{bmatrix} -1 & 0 \\ 0 & 0 \end{bmatrix}$$

$$Q = \begin{bmatrix} 20 & 4 \\ 4 & 1 \end{bmatrix} \quad A_1 = \begin{bmatrix} 0.2 & 0 \\ 0.1 & 0 \end{bmatrix}$$

It makes $W \geq \tilde{W}, A_1^T \tilde{X}_+ A_1 \geq \tilde{A}_1^T \tilde{X}_+ \tilde{A}_1$. Therefore, from (i) of theorem 2, there exists maximal solution $X_+ \geq \tilde{X}_+$ which is calculated as

$$X_+ = \begin{bmatrix} 13.5296 & 1.9049 \\ 1.9049 & 0.2844 \end{bmatrix} \tag{31}$$

Let $A = \tilde{A}, A_1 = \tilde{A}_1$ in the (30), then $T \geq \tilde{T}$. Therefore, from (ii) of theorem 2, there exists X_+ which satisfies $X_+ \geq \tilde{X}_+$. When maximal solution X_+ is calculated as

$$X_+ = \begin{bmatrix} 4.4721 & 0.3020 \\ 0.3020 & 0.0549 \end{bmatrix} \tag{32}$$

Here, we obtain $X_+ \geq \tilde{X}_+$ as a result of comparing $\tilde{X}_+$ with X_+. And, according to (iii) of the theorem 2, $X_+ \geq 0$ because $Q \geq 0$.

5 Conclusion

We obtain the maximal solution which makes the eigenvales of the nominal closed-loop system in the closed left half plain. In the guaranteed cost control, it is necessary to stabilize the system with uncertainty. So, it is necessary to show that our maximal solution can stabilize the uncertain system which Q is not positive semi-definite.

References

[1] W. M. Wonham, "On a matrix Riccati equation of stochastic control", *SIAM J. Control*, Vol. 6, No. 4, pp. 681-697, 1968.

[2] A. C. M. Ran, R. Vreugdenhil, "Existence and comparison theorem for algebraic Riccati equations for continuous- and discrete- time systems", *Linear Algebra and its Applications*, Vol. 99, pp. 63-83, 1988.

[3] N. Takahashi, M. Kono, K. Hiranuma, O. Sato, "Generalization of guaranteed cost control", *Transaction of Japan Society of Mechanical Engineers*, Vol. 66, No. 645, pp. 1531-1536, 2000.

[4] W. M. Wonham, "Optimal stationary control of a linear system with state-dependent noise", *SIAMJ. Control*, Vol. 5, No. 4, pp. 486-500, 1967.

[5] K. Zhou, J. C. Doyle, K. Glover, Robust and Optimal Control, *Prentice Hall*, 1996.

[6] Z. Gajic, M. Tahir, J. Qureshi, Lyapunov Matrix Equation in System stability, *Academic Press*, 1995.

[7] C. E. de Souza, M. D. Fragoso, "On the existence of maximal solution for generalized algebraic Riccati equations arising in stochastic control", *System & Control Letters*, Vol. 14, pp. 233-239, 1990.

[8] C. V. Hollot, B. R. Barmish, "Optimal quadratic stabilizability of uncertain linear systems", *Proc of the 18th Allerton Conf. on Communication, Contr. and Computing*, pp. 697-706, Univ. of Illinois, 1980.

[9] P. Dorato, C. Abdallah, V. Cirone, linear Quadratic Control an Introduction, *Prentice Hall*, 1995.

Authors' Index